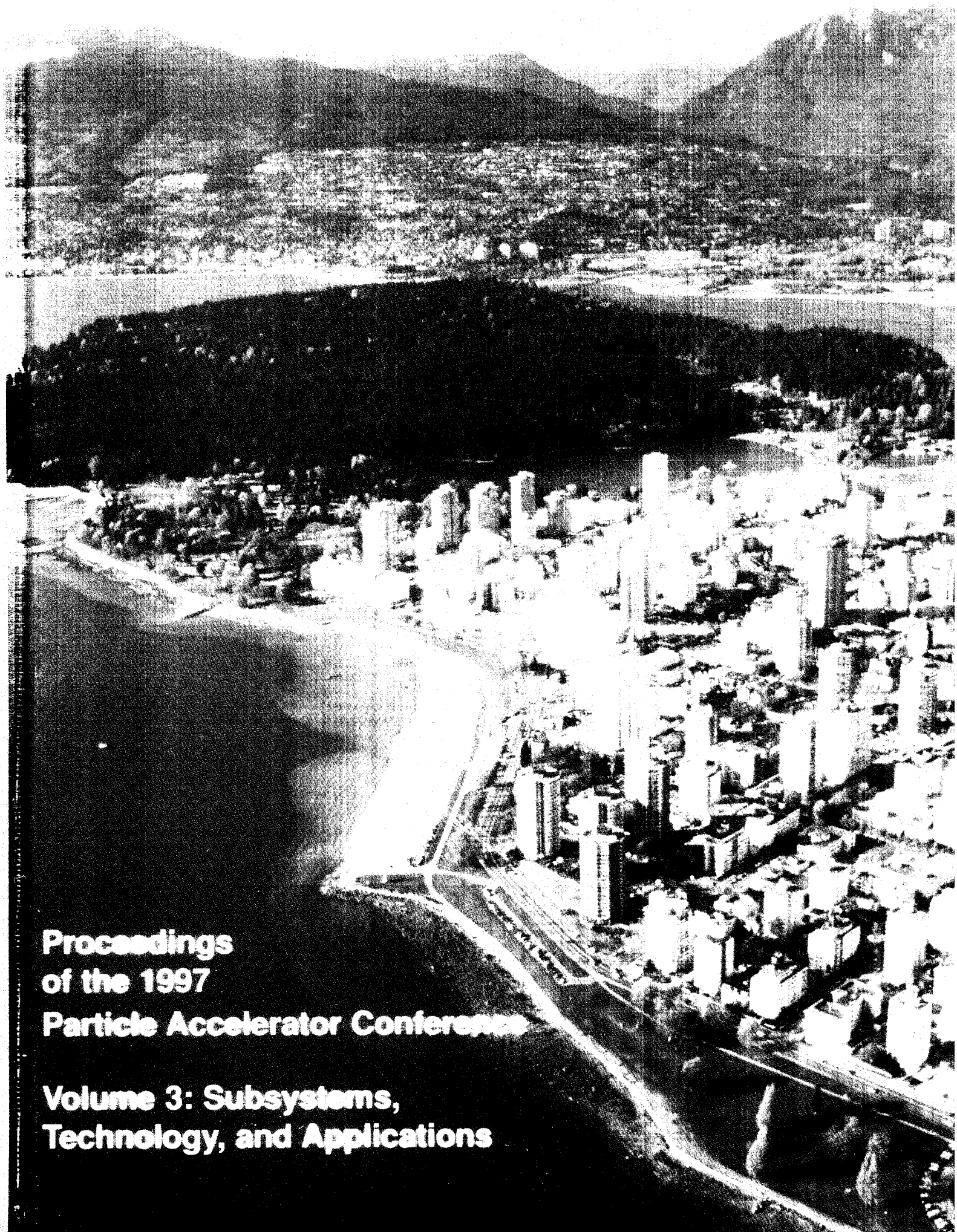


# Proceedings of the 1997 Particle Accelerator Conference

## Volume 3: Subsystems, Technology, and Applications



DISTRIBUTION STATEMENT A
Approved for Public Release
Distribution Unlimited

# Proceedings of the 1997 Particle Accelerator Conference

**Vancouver, B.C., Canada**
**12–16 May 1997**

19990526 077

**Editors**
**M. Comyn, M.K. Craddock, M. Reiser, J. Thomson**

## Volume 3 of 3
## Subsystems, Technology and Applications

*Organized by*
TRIUMF
University of Maryland

*Held under the joint auspices of*
Institute of Electrical and Electronics Engineers
(Nuclear and Plasma Sciences Society)
American Physical Society
(Division of Physics of Beams)

*Sponsored by*
US Department of Energy
National Science Foundation
Office of Naval Research

IEEE

The American Physical Society

DTIC QUALITY INSPECTED 4

## PROCEEDINGS OF THE 1997 PARTICLE ACCELERATOR CONFERENCE

Copyright and Reprint Permission: Abstracting is permitted with credit to the source. Libraries are permitted to photocopy beyond the limits of U.S. copyright law for private use of patrons those articles in this volume that carry a code at the bottom of the first page, provided the per-copy fee indicated in the code is paid through the Copyright Clearance Center, 222 Rosewood Drive, Danvers, MA 01923. For other copying, reprint, or republication permission, write to the IEEE Copyrights Manager, IEEE Operations Center, 445 Hoes Lane, Piscataway, NJ 08855-1331. All rights reserved.
Copyright © 1998 by The Institute of Electrical and Electronics Engineers, Inc.

| | |
|---|---|
| IEEE Catalog Number: | 97CH36167 (softbound)<br>97CB36167 (casebound) |
| Library of Congress Number: | 88-647453 |
| ISBN Softbound: | 0-7803-4376-X |
| ISBN Casebound: | 0-7803-4377-8 |
| ISBN Microfiche: | 0-7803-4378-6 |
| ISBN CD-ROM: | 0-7803-4379-4 |

Additional copies of this publication are available from

IEEE Operations Center
P. O. Box 1331
445 Hoes Lane
Piscataway, NJ 08855-1331
USA

| | |
|---|---|
| Phone: | 1-800-678-IEEE (1-800 678-4333)<br>1-732-981-0060<br>1-732-981-1393 |
| FAX: | 1-732-981-9667 (FAX) |
| Telex: | 833-233 |
| E-mail: | customer.service@ieee.org |

# OUTLINE OF CONTENTS

## VOLUME 1
## PLENARY AND SPECIAL SESSIONS; ACCELERATORS AND STORAGE RINGS


OPENING PLENARY SESSION ..... 1
SPECIAL SESSION ..... 16
FINAL PLENARY SESSION ..... 29
HIGH-ENERGY HADRON ACCELERATORS AND COLLIDERS ..... 47
*High-Energy Hadron Accelerators and Colliders* ..... 89
*Beam Injection, Extraction, Transport and Targetry W* ..... 156
*Beam Injection, Extraction, Transport and Targetry X* ..... 207
LEPTON ACCELERATORS AND COLLIDERS ..... 281
*Electron Storage Rings and Accelerators* ..... 324
*Circular Electron Colliders* ..... 363
*Muon Colliders* ..... 393
LINEAR COLLIDERS ..... 425
*Linear Collider Beam Dynamics* ..... 467
*Linear Collider Structure* ..... 518
*Linear Colliders (Other)* ..... 557
ADVANCED CONCEPTS ..... 611
*New Acceleration Techniques* ..... 633
LIGHT SOURCES AND FREE ELECTRON LASERS ..... 698
*Synchrotron Radiation Facilities* ..... 742
*Free Electron Lasers* ..... 871
LOW- AND MEDIUM-ENERGY ACCELERATORS AND RINGS ..... 915
*Proton Synchrotrons and Storage Rings* ..... 959
*Low- and Medium-Energy Circular Accelerators* ..... 1027
*RFQ Linacs* ..... 1078
*Proton and Ion Linacs* ..... 1111
*Electron Linacs* ..... 1197
*Electrostatic and Other Accelerators* ..... 1224
PULSED-POWER AND HIGH-INTENSITY BEAMS ..... 1230
*Pulsed Power Accelerators* ..... 1254
*Pulsed Power Technology* ..... 1269


## VOLUME 2
## BEAM DYNAMICS, INSTRUMENTATION AND CONTROLS


SINGLE-PARTICLE BEAM DYNAMICS AND OPTICS ..... 1331
*Lattice Design and Optics* ..... 1371
*Maps, Tracking and Dynamic Aperture* ..... 1418
*Error Effects, Experiments, Spin Dynamics* ..... 1460
*Other Single-Particle Beam Dynamics* ..... 1493
MULTIPARTICLE BEAM DYNAMICS I ..... 1532
*Instabilities and Cures (High Energy)* ..... 1575
*Wake Field* ..... 1658
*Impedance* ..... 1700

*Beam-Beam Interaction* ..... 1759
*Beam Cooling* ..... 1792
*Other Multiparticle Beam Dynamics* ..... 1810
MULTIPARTICLE BEAM DYNAMICS II ..... 1837
*High-Current Dynamics* ..... 1858
*Space Charge* ..... 1882
BEAM INSTRUMENTATION ..... 1971
*Short-Bunch Instrumentation* ..... 1996
*Instrumentation Electronics* ..... 2023
*Tune Measurement* ..... 2052
*Beam Position Monitors* ..... 2069
*Emittance and Profile Instrumentation* ..... 2149
*Other Beam Instrumentation* ..... 2207
INSTABILITIES AND FEEDBACK ..... 2276
*Feedback Systems (including Beam)* ..... 2290
CONTROLS AND COMPUTING ..... 2395
*Control Systems W* ..... 2437
*Control Systems X* ..... 2487
*Computer Codes W* ..... 2538
*Computer Codes X* ..... 2606

## VOLUME 3
## SUBSYSTEMS, TECHNOLOGY AND APPLICATIONS

SOURCES AND INJECTORS ..... 2657
*Particle Sources (including Polarized Sources)* ..... 2696
*RF Guns and Linac Injectors* ..... 2787
RADIOFREQUENCY SYSTEMS ..... 2879
*Room-Temperature RF* ..... 2920
*Superconducting RF* ..... 3072
*RF Sources/Systems* ..... 3111
*Related Hardware* ..... 3174
MAGNETS ..... 3201
*Room-Temperature Magnets* ..... 3227
*Superconducting Magnets* ..... 3338
*Power Supplies* ..... 3449
*Insertion Devices* ..... 3491
VACUUM, ALIGNMENT, RADIATION MONITORING AND OTHER TECHNOLOGY 3542
*Vacuum Technology* ..... 3580
*Alignment and Survey* ..... 3645
*Radiation Monitoring and Safety* ..... 3669
*Other Subsystems Technology and Components* ..... 3687
APPLICATIONS OF ACCELERATORS ..... 3770
*Medical Therapy* ..... 3813
*Medical Isotope Production* ..... 3834
*High-Power Accelerator Applications* ..... 3848
*Electron Beam Processing* ..... 3854
*Non-Destructive Evaluation and Other Applications* ..... 3866

# CONTENTS OF VOLUME 3

## SOURCES AND INJECTORS

**Chair:** G. Alton, *Oak Ridge National Laboratory*


**Sub-Picosecond High-Brightness Electron Injectors** *(Invited)* — *B.E. Carlsten* ..... no manuscript submitted
**Laser-Driven Plasma-Cathode Electron Injector** *(Invited)* — *Donald Umstadter, S.-Y. Chen, E. Dodd, J.K. Kim, A. Maksimchuk, R. Wagner* ..... 2657
**State of the Art of ECR Ion Sources** *(Invited)* — *Z.Q. Xie* ..... 2662
**Very-Low-Energy-Spread Ion Sources** *(Invited)* — *Y. Lee* ..... 2667
**Recent Progress of RIKEN 18 GHz ECRIS** — *T. Nakagawa, J. Ärje, Y. Miyazawa, M. Hemmi, T. Chiba, N. Inabe, M. Kase, T. Kageyama, O. Kamigaito, A. Goto, Y. Yano* ..... 2672
**Initial Test Results from a Multicusp Source for TRIUMF's Radioactive Beam Facility** — *T. Kuo, D. Yuan, K. Jayamanna, M. McDonald, R. Baartman, G. Mackenzie, P. Bricault, M. Dombsky, P. Schmor, G. Dutto, Y. Lee, K-N. Leung, D. Williams, R. Gough* ..... 2675
**Results from ZMEVVA: A New Source for Heavy-Ion Accelerators** — *B.M. Johnson, A. Hershcovitch, I.G. Brown, F. Liu, A. Anders* ..... 2678
**Intense, High Brightness $H^-$ Beams from Surface Plasma Sources** — *S.K. Guharay, M. Reiser* ..... 2681
**The Dependence of Longitudinal Emittance upon Surface Charge Density in a RF Photoinjector** — *D.H. Dowell, S. Joly, A. Loulergue* ..... 2684
**Emittance Studies of the BNL/SLAC/UCLA 1.6 Cell Photocathode RF Gun** — *D.T. Palmer, X.J. Wang, R.H. Miller, M. Babzien, I. Ben-Zvi, C. Pellegrini, J. Sheehan, J. Skaritka, H. Winick, M. Woodle, V. Yakimenko* . 2687
**Experimental Operation of a 17 GHz Photocathode RF Gun** — *S. Trotz, W. Brown, B. Danly, J.P. Hogge, K.E. Kreischer, M. Shapiro, R.J. Temkin* ..... 2690
**A High-DC-Voltage GaAs Photoemission Gun: Transverse Emittance and Momentum Spread Measurements** — *D. Engwall, C. Bohn, L. Cardman, B. Dunham, D. Kehne, R. Legg, H. Liu, M. Shinn, C. Sinclair* ..... 2693


### *Particle Sources (including Polarized Sources)*


**The Production and Transport of Radioactive $^{17}F$ at ATLAS for Research** — *B. Harss, J.C. Berger, F. Borasi, J. Greene, C.L. Jiang, J. Nolen, R.C. Pardo, M. Paul, K.E. Rehm, J.P. Schiffer, R.E. Segel, T.F. Wang* ..... 2696
**Beam Chopper for the Low-Energy Undulator Test Line (LEUTL) in the APS** — *Y.W. Kang, J. Wang, S. Milton, L. Teng, K. Thompson, J. Jones, D. Walters, J. Jagger* ..... 2699
**A New 14 GHz Electron-Cyclotron-Resonance Ion Source (ECRIS) for the Heavy Ion Accelerator Facility ATLAS** — *M. Schlapp, R.C. Vondrasek, J. Szczech, P.J. Billquist, Z.Q. Xie, R. Harkewicz, R.C. Pardo* ..... 2702
**Characterization and Recent Modification of a Compact 10 GHz ECRIS for Atomic Physics Experiments and Spectroscopic Investigations** — *M. Schlapp, R. Trassl, R.W. McCullough, J.B. Greenwood, E. Salzborn* .. 2705
**A Low Power Low Cost 2.45 GHz ECRIS for the Production of Multiply Charged Ions** — *M. Schlapp, R. Trassl, M. Liehr, E. Salzborn* ..... 2708
**Progress on an EBIS for RHIC** — *J. Alessi, E. Beebe, A. Hershcovitch, A. Kponou, R. Lockey, A. Pikin, K. Prelec, L. Snydstup, P. Stein* ..... 2711
**Improved Version of Surface Plasma Negative Ion Source** — *V.G. Dudnikov, W.L. Stirling, J.H. Whealton* ..... 2714
**Cadarache 1 MeV Negative Ion Accelerator Development for Application in Thermonuclear Fusion Research** — *A. Simonin, J. Bucalossi, C. Desgranges, M. Fumelli, P. Massmann, J. Pamela* ..... 2717
**First Beam of the CEA-Saclay CW High-Intensity Microwave Source** — *P-Y. Beauvais, P. Ausset, D. Bogard, O. Delferrière, J. Faure, R. Ferdinand, A. France, R. Gobin, P. Gros, J-M. Lagniel, P-A. Leroy* ..... 2720
**Space-Charge Neutralization Measurement of a 75-keV, 130-mA Hydrogen-Ion Beam** — *Robin Ferdinand, Joseph Sherman, Ralph R. Stevens Jr., Thomas Zaugg* ..... 2723
**Upgrade of the $H^-$-Injection System at the DESY Proton Linac III** — *C.-M. Kleffner, G. Jacobs, N. Holtkamp, M. Nagl, I. Peperkorn, J. Peters, A. Schempp, V. Paramonov* ..... 2726
**Trapped Ion Source** — *G. Brautti, A. Boggia, A. Raino, N. Ceci, V. Valentino, V. Variale* ..... 2729
**Beam Chopper for the 750 keV LEBT of MMF Linac** — *A.V. Novikov, P.N. Ostroumov* ..... 2732
**Test of Duoplasmatron with Cold Cathode for CW Operation** — *A. Kolomiets, B.K. Kondratiev, V.I. Turchin* ... 2735
**A Pulsed Ion Source for the IUCF Cooler Injector Synchroton** — *V.P. Derenchuk, R.R. Kupper, H.R. Petri, G.P.A. Berg, R.J. Brown, W.R. Fox, D.L. Friesel, W. Hunt, W.P. Jones, W.R. Lozowski* ..... 2737
**Mechanical Engineering of a 75-keV Proton Injector for the Low Energy Demonstration Accelerator** — *L.D. Hansborough, D.J. Hodgkins, E.A. Meyer, J.D. Schneider, J.D. Sherman, R.R. Stevens Jr., T.J. Zaugg* ..... 2740

**Performance of the LANSCE $H^-$ Source and Low Energy Beam Transport at Higher Peak Current** — *C. Pillai, R.R. Stevens, D.H. Fitzgerald, R.W. Garnett, W.B. Ingalls, F.E. Merrill, L.J. Rybarcyk, O.R. Sander* ... 2743
**Simulations of the LEDA LEBT $H^+$ Beam** — *H. Vernon Smith Jr., Joseph D. Sherman, Ralph R. Stevens Jr., Lloyd M. Young* ... 2746
**Simulations of the LEDA LEBT with $H^+$, $H_2^+$, and $e^-$ Particles** — *Lloyd M. Young* ... 2749
**Simulations of the LEDA RFQ 6.7 MeV Accelerator** — *Lloyd M. Young* ... 2752
**High Current Density Ion Sources for Heavy Ion Fusion Accelerators** — *J.W. Kwan, W.W. Chupp, S. Eylon* ... 2755
**$H^-$ Ion Source Development for the National Spallation Neutron Source** — *M.A. Leitner, R.A. Gough, K.N. Leung, M.L. Rickard, A.B. Wengrow, M.D. Williams, D.C. Wutte* ... 2758
**A Compact, RF-Driven, Pulsed Ion Source for Intense Neutron Generation** — *L.T. Perkins, C.M. Celata, K.N. Leung, D.S. Picard, R. Vilaithong, M.D. Williams* ... 2761
**Development of a High Duty Factor, Surface Conversion $H^-$ Ion Source for the LANSCE Facility** — *A.B. Wengrow, K.N. Leung, M.A. Leitner, M.D. Williams, D.C. Wutte, William B. Ingalls, Ralph R. Stevens Jr.* ... 2764
**Development of an RF Driven Plasma Cathode for Ion Sources** — *M.D. Williams, K.N. Leung, C.A. Matuk, S.B. Wilde, V.M. Benveniste, M.A. Graf, T.N. Horsky, K. Saadatmand* ... 2767
**A Multicusp Ion Source for Radioactive Ion Beams** — *D.C. Wutte, Y. Lee, M.A. Leitner, M.D. Williams, K.N. Leung, R.A. Gough, S.J. Freedman, Z.Q. Xie, C.M. Lyneis* ... 2770
**Ion Microwave Source for Linear Accelerator** — *A.V. Nesterovich, N.I. Abramenko, B. Bogdanovich* ... 2773
**Toward a Realistic and Tractable Model for Negative Ion Extraction from Volume Sources** — *J.H. Whealton, D.K. Olsen, R.J. Raridon* ... 2775
**60 keV Beam Transport Line and Switchyard for ISAC** — *R. Baartman, J. Welz* ... 2778
**OPPIS Development at TRIUMF** — *A. Zelenski, C.D.P. Levy, P.W. Schmor, W.T.H. van Oers, G.W. Wight, G. Dutto* ... 2781
**Reason for Free Electrons from the Surface of Ferroelectrics with a Metal Lattice Structure** — *H. Heydari, T. Tille* ... 2784

## *RF Guns and Linac Injectors*

**Effect of the Long Solenoid Tunnel on the Growth of Emittance in the PNC High Power Electron Linac** — *Masahiro Nomura, Hiroshi Takahashi* ... 2787
**Performance of Magnesium Cathode in the S-Band RF Gun** — *T. Srinivasan-Rao, I. Ben-Zvi, J. Smedley, X.J. Wang, M. Woodle, D.T. Palmer, R.H. Miller* ... 2790
**Longitudinal Emittance Compensation In a Photocathode RF Gun Injector** — *X.J. Wang, I. Ben-Zvi* ... 2793
**Beam Dynamics in RF-Gun Cavity with a Modified First Cell** — *V. Volkov, M. Karliner, V. Petrov, I. Sedlyarov, A. Tribendis, D. Janssen, P. vom Stein* ... 2796
**Single Bunch Injection System for an Electron Storage Ring Using an RF Photoinjector** — *P.G. O'Shea, J.A. Lancaster, J.M.J. Madey, R. Sachtschale, C.R. Jones* ... 2799
**A Plane-Wave-Transformer Photoelectron Linac** — *D. Yu, T. Lee, S. Rajagopalan, J. Chen, C. Pellegrini, J. Rosenzweig, X. Ding* ... 2802
**Proposed Intense Positron Source for TESLA Based on HERA-e** — *A.V. Kiselev, V.D. Shiltsev* ... 2805
**A Fully Demountable 550 kV Electron Gun for Low Emittance Beam Experiments with a 17 GHz Linac** — *J. Haimson, B. Mecklenburg, G. Stowell, E.L. Wright* ... 2808
**Commissioning of the IUCF 7 MeV $H^-$ Linac** — *D.L. Friesel, R.W. Hamm* ... 2811
**Performance of Electron Gun for SPring-8 Linac** — *T. Asaka, T. Hori, Y. Ito, T. Kobayashi, A. Kuba, A. Mizuno, H. Sakaki, S. Suzuki, T. Taniuchi, K. Yanagida, H. Yoshikawa, H. Yokomizo* ... 2814
**Thermionic RF Gun with High Duty Factor** — *Viktor Mitrochenko* ... 2817
**Obtaining the Linear Electron Beams by Using the Magnetron Injection Guns with Cold Secondary Emission Metallic Cathodes (Experiment)** — *Yu.D. Tur, A.N. Dovbnya, V.V. Mitrochenko, N.G. Reshetnyak, V.P. Romas'ko, V.V. Zakutin* ... 2820
**First Beam Tests of the TTF Injector** — *T. Garvey, M. Bernard, J.C. Bourdon, R. Chehab, M. Mencik, M. Omeich, J. Rodier, M. Taurigna-Quere, A. Variola, S. Chel, M. Desmon, J. Fusellier, F. Gougnaud, J.F. Gournay, M. Jablonka, J.M. Joly, M. Juillard, Y. Lussignol, A. Mosnier, B. Phung Ngoc, S. Buhler, T. Junquera* ... 2823
**Multi-Kiloampere Electron-Beam Generation from Bare Aluminum Photo-Cathodes Driven by an ArF Laser** — *Randolph L. Carlson, Rae N. Ridlon, Gerald J. Seitz, Thomas P. Hughes* ... 2826
**Development and Characterization of Diamond Film and Compound Metal Surface High Current Photocathodes** — *R.P. Shurter, D.C. Moir, D.J. Devlin, R.W. Springer, T.A. Archuleta* ... 2829
**High Voltage, High Current, Long Pulse Electron Beam Injector for DARHT** — *E. Henestroza, S. Yu, S. Eylon, B. Carlsten* ... 2832

**Focusing of Ribbon Beam in Undulator Linear Accelerator** — *E.S. Masunov, A.S. Roshal* ..... 2835
**The Development of a Superconducting RF Gun: Status of the Drossel Collaboration** — *D. Janssen, P. vom Stein, A. Bushuev, M. Karliner, S. Konstantinov, J. Kruchkov, V. Petrov, I. Sedlyarov, A. Tribendis, V. Volkov* ..... 2838
**Emittance Measurements for the SLAC Gun Test Facility** — *M. Hernandez, A. Fisher, D. Meyerhofer, R. Miller, D.T. Palmer, S. Park, D. Reis, J. Schmerge, J. Weaver, H. Wiedemann, H. Winick, D. Yeremian* ..... 2840
**Experimental Results of a Single Emittance Compensation Solenoidal Magnet** — *D.T. Palmer, X.J. Wang, I. Ben-Zvi, R.H. Miller, J. Skaritka* ..... 2843
**Beam Dynamics Enhancement Due to Accelerating Field Symmetrization in the BNL/SLAC/UCLA 1.6 Cell S-Band Photocathode RF Gun** — *D.T. Palmer, X.J. Wang, I. Ben-Zvi, R.H. Miller* ..... 2846
**Polarized Electron Sources for Future $e^+/e^-$ Linear Colliders** — *H. Tang, R.K. Alley, J.E. Clendenin, A.S. Fisher, T. Kotseroglou, R.H. Miller, G.A. Mulhollan, D.T. Palmer, A.D. Yeremian* ..... 2849
**NLCTA Injector Experimental Results** — *A.D. Yeremian, C. Adolphsen, R.H. Miller, C. Nantista, J. Wang* ..... 2852
**A Proposed Injector for the LCLS Linac** — *A.D. Yeremian, V.K. Bharadwaj, P. Emma, R.H. Miller, D.T. Palmer, M.D. Woodley* ..... 2855
**The Construction and Initial High Power Test Results of an X-Band RF Gun** — *C.H. Ho, W.K. Lau, T.T. Yang, S.S. Chang, J.Y. Hwang, Y.C. Liu, G.P. Le Sage, F.V. Hartemann, N.C. Luhmann Jr.* ..... 2858
**An Injection Modelocked Ti-Sapphire Laser for Synchronous Photoinjection** — *Curt Hovater, Matt Poelker* .. 2861
**Atomic Hydrogen Cleaning of Semiconductor Photocathodes** — *C.K. Sinclair, B.M. Poelker, J.S. Price* ..... 2864
**Laser System for the TTF Photoinjector at Fermilab** — *A.R. Fry, M.J. Fitch, A.C. Melissinos, N.P. Bigelow, B.D. Taylor, F.A. Nezrick* ..... 2867
**Cathodeless, High Brightness Electron Beam Production by Multiple Laser Beams in Plasmas** — *R.G. Hemker, K-C. Tzeng, W.B. Mori, C.E. Clayton, T. Katsouleas* ..... 2870
**Experimental Testing of the TTF RF Photoinjector** — *E. Colby, M. Conde, J. Rosenzweig, P. Colestock, H. Edwards, K. Koepke, F. Nezrick* ..... 2873
**Optimum Operation of Split RF Photo-Injectors** — *L. Serafini, J.B. Rosenzweig* ..... 2876

## RADIOFREQUENCY SYSTEMS

**Chair:** H. Mizuno, *KEK*

**Performance of the LEP2 SRF System** *(Invited)* — *D. Boussard* ..... 2879
**Overview of Advances in the Basic Understanding of Dark Current and Breakdown in RF Cavities** *(Invited)* — *Hasan Padamsee* ..... 2884
**Design of 250-MW CW RF System for APT** *(Invited)* — *D. Rees* ..... 2889
**Development of X-Band Klystron Technology at SLAC** *(Invited)* — *George Caryotakis* ..... 2894
**A New Generation of Gridded Tubes for Higher Power and Higher Frequencies** — *G. Clerc, J.-P. Ichac, C. Robert* ..... 2899
**Development of High-Power ARES Cavities** — *T. Kageyama, K. Akai, N. Akasaka, E. Ezura, H. Mizuno, F. Naito, H. Nakanishi, H. Sakai, Y. Takeuchi, Y. Yamazaki, T. Kobayashi* ..... 2902
**Progress in High Power Microwave Ferrite Circulators for Particle Accelerator Applications** — *E. Pivit, W. Arnold* ..... no manuscript submitted
**Design of Three Recirculating-Linac SRF Systems for a 4-TeV $\mu^+ - \mu^-$ Collider** — *Q.S. Shu, D. Neuffer, S. Simrock* ..... 2905
**Status and Developments of Superconducting Cavity for KEKB** — *Shinji Mitsunobu, K. Asano, T. Furuya, Y. Ishi, Y. Kijima, K. Sennyu, T. Tajima, T. Takahashi, S. Zhao* ..... 2908
**Design and Construction of a 500 kW CW, 400 MHz Klystron to be Used as RF Power Source for LHC/RF Component Tests** — *H. Frischholz, W.R. Fowkes, C. Pearson* ..... 2911
**Superconducting Cavities for the APT Accelerator** — *Frank L. Krawczyk, Robert C. Gentzlinger, Brian Haynes, Debbie I. Montoya, Brian Rusnak, Alan H. Shapiro* ..... 2914
**Test Results on the 9-Cell 1.3 GHz Superconducting RF Cavities for the TESLA Test Facility Linac** — *M. Pekeler* ..... 2917

### *Room-Temperature RF*

**ASTRID Electron Cavity Study** — *S.P. Møller, T. Korsbjerg, E.N. Zaplatine* ..... 2920
**Solving the Problem of Heating of RF Contacts in Cavity Tuners** — *Yu. Senichev, T. Korsbjerg, S.P. Møller, E. Zaplatine* ..... 2923

**A Divide-Down RF Source Generation System for the Advanced Photon Source** — *D. Horan, F. Lenkszus, R. Laird* ..... 2926
**Mechanical Design Upgrade of the APS Storage Ring RF Cavity Tuner** — *J. Jones, D. Bromberek, Y. Kang, R. Kustom, L. Morrison, R. Piech, E. Rotela, S. Sharma, I. Sheng* ..... 2929
**Coaxial Higher-Order Mode Damper Employing a High-Pass Filter** — *Y.W. Kang, X. Jiang* ..... 2932
**Reconfigurable High-Power RF System in the APS** — *Y.W. Kang, D. Horan* ..... 2935
**Upgraded Cavities for the Positron Accumulator Ring of the APS** — *Y.W. Kang, X. Jiang, D. Mangra, T.L. Smith* ..... 2938
**An Overview of the APS 352-MHz RF Systems** — *A. Nassiri, A. Cours, A. Grelick, D. Horan, Y.W. Kang, R.L. Kustom, T.L. Smith, J. Song* ..... 2941
**Higher-Order Modes of Storage Ring RF Cavities and Their Interaction with the Beam at the Advanced Photon Source (APS)** — *J.J. Song, K.C. Harkay, Y.W. Kang, R.L. Kustom, A. Nassiri* ..... 2944
**Modifying CERN SPS Cavities and Amplifiers for Use in RHIC** — *R. Connolly, J. Aspenleiter, S. Kwiatkowski* . 2947
**First Operation of the HAP/MOPA Traveling Wave Structure at Boeing FEL** — *A.M. Vetter, T.L. Buller, D.H. Dowell, P.E. Johnson* ..... 2950
**The PS 40 MHz Bunching Cavity** — *R. Garoby, E. Grier, E. Jensen, A. Mitra, R.L. Poirier* ..... 2953
**The Tuning of the Cavity Options for DIAMOND** — *C.L. Dawson, D.M. Dykes, P.A. McIntosh* ..... 2956
**Effective Compact Accelerating Structures for Heavy Ions** — *Valentin V. Paramonov* ..... 2959
**The Cut Disk Accelerating Structure for High Energy Linacs** — *Valentin V. Paramonov* ..... 2962
**The Design of High Reliable RF System for High Power Linacs** — *A.M. Kozodaev, A.A. Kolomiets, N.V. Lazarev, D.A. Liakin, V.K. Plotnikov, A.M. Raskopin, V.S. Skachkov* ..... 2965
**An RF System for a Compact Synchrotron** — *A. Pei, S. Anderson, D. Jenner, X. Kang, S.Y. Lee, D. McCammon* . 2968
**RF Stations of the SPring-8 Storage Ring** — *M. Hara, H. Ego, Y. Kawashima, Y. Ohashi, T. Ohshima, T. Takashima* ..... 2971
**Fundamental Mode Characteristics of ARES Cavity Under Beam Environment** — *N. Akasaka, K. Akai, E. Ezura, T. Kageyama, H. Mizuno, F. Naito, H. Nakanishi, H. Sakai, Y. Takeuchi, Y. Yamazaki, T. Kobayashi* ... 2974
**Coupling Cavity Damper for the ARES** — *F. Naito, K. Akai, N. Akasaka, E. Ezura, T. Kageyama, H. Mizuno, H. Nakanishi, Y. Takeuchi, Y. Yamazaki, T. Kobayashi* ..... 2977
**Construction of a 714-MHz RF System for the ATF Damping Ring** — *S. Sakanaka, K. Kubo, F. Hinode, H. Hayano, J. Urakawa* ..... 2980
**Development of a Broadband HOM Load for the 714-MHz HOM-Damped Cavity** — *S. Sakanaka, F. Hinode, K. Kubo, S. Tokumoto, K. Satoh, T. Miura, T. Naba* ..... 2983
**HOM Absorber for the ARES Cavity** — *Y. Takeuchi, K. Akai, N. Akasaka, E. Ezura, T. Kageyama, H. Mizuno, F. Naito, H. Nakanishi, H. Sakai, Y. Yamazaki, T. Kobayashi* ..... 2986
**Beam Test of an RF Damped Cavity at the Photon Factory Storage Ring** — *M. Izawa, S. Sakanaka, S. Tokumoto, T. Takahashi, T. Koseki, Y. Kamiya* ..... 2989
**Studies of Magnetic Cores for JHF Synchrotrons** — *M. Fujieda, Y. Mori, H. Nakayama, C. Ohmori, S. Sawada, Y. Tanabe, E. Ezura, A. Takagi, M. Toda, M. Yoshii, T. Tanabe, T. Uesugi* ..... 2992
**A Wideband RF Cavity for JHF Synchrotrons** — *C. Ohmori, M. Fujieda, S. Machida, Y. Mori, H. Nakayama, K. Saito, S. Sawada, Y. Tanabe, M. Yamamoto, E. Ezura, A. Takagi, M. Toda, M. Yoshii, T. Tanabe, T. Uesugi* ... 2995
**Plunger Frequency Control of a Side Coupled Accelerating Structure for the IFUSP Microtron** — *J. Takahashi, M.N. Martins, J.A. de Lima, A.A. Malafronte, L. Portante, M.T.F. da Cruz, P.R. Pascholati* ..... 2998
**Measurement and Identification of HOMs in RF Cavities** — *D.A. Goldberg, R.A. Rimmer* ..... 3001
**High-Power Testing of RF Cavities for the PEP-II B Factory** — *R.A. Rimmer, M. Allen, K. Fant, A. Hill, M. Hoyt, J. Judkins, M. Neubauer, H. Schwarz* ..... 3004
**Fabrication Processes for the PEP-II RF Cavities** — *R.M. Franks, R.A. Rimmer, H. Schwarz* ..... 3007
**Operation of the LNLS Storage Ring RF System** — *D. Wisnivesky, C. Pardine* ..... 3010
**On The Limitations of Accelerating Gradient in Linear Colliders Due to the Pulse Heating** — *O.A. Nezhevenko* ..... 3013
**Operational Characteristics of RF System Affecting PLS Beam Stability** — *M. Kwon, H.J. Park, I.H. Yu, J.Y. Huang, I.S. Ko* ..... 3015
**Design and Operation of PET Radio Frequency Quadrupoles** — *D. Sun, P. Young, A. Moretti, J. Dey* ..... 3018
**SLC Interferometer System and Phase Distribution Upgrades** — *R. Akre, F.J. Decker, R.K. Jobe, R. Koontz, M. Mitchell, R. Strozinsky* ..... 3021
**Calibration System for SLC 476 MHz to 2856 MHz Multipliers** — *R. Akre, G. Barillas, M. Mitchell* ..... 3024

**Low-Level RF Signal Processing for the Next Linear Collider Test Accelerator** — *S. Holmes, C. Ziomek, C. Adolphsen, R. Akre, S. Allison, S. Clark, T. Dean, R.W. Fuller, S. Gold, R.K. Jobe, R. Koontz, T.L. Lavine, C. Nantista, Z. Wilson, A. Young* ..... 3027
**Waveguide Stub-Line Tuning of RF Cavities with Heavy Beam Loading** — *P. Krejcik* ..... 3030
**HOM Power Generation and Propagation in the PEP-II B-Factory** — *Xintian E. Lin, C.-K. Ng, K. Ko* ..... 3033
**Experimental Study of Pulsed Heating of Electromagnetic Cavities** — *D.P. Pritzkau, A. Menegat, R.H. Siemann, T.G. Lee, D.U.L. Yu* ..... 3036
**Development of a Movable Plunger Tuner for the High-Power RF Cavity for the PEP-II B Factory** — *H.D. Schwarz, K. Fant, J.G. Judkins, M. Neubauer, R.A. Rimmer* ..... 3039
**RF System for the NLCTA** — *J.W. Wang, C. Adolphsen, R. Atkinson, W. Baumgartner, J. Eichner, R.W. Fuller, S.L. Gold, S.M. Hanna, S.G. Holmes, R.F. Koontz, T.L. Lavine, R.J. Loewen, R.H. Miller, C.D. Nantista, R. Pope, J. Rifkin, R.D. Ruth, S.G. Tantawi, A.E. Vlieks, P.B. Wilson, Z. Wilson, A. Yeremian* ..... 3042
**RF Breakdown Studies in X-Band Klystron Cavities** — *X. Xu, R.S. Callin, R. Fowkes, A. Menegat, G.P. Scheitrum, D.H. Whittum* ..... 3045
**Upgrade Issues of the TLS Storage Ring RF System** — *W.K. Lau, L.H. Chang, S.S. Chang, C.H. Ho, M.C. Lin, S.J. Lin, G.H. Luo, T.T. Yang, M.S. Yeh, Ch. Wang, C.C. Kuo* ..... 3048
**Design of a Third Harmonic Landau Cavity for the SRRC Storage Ring** — *Ch. Wang, L.H. Chang, T.T. Yang, R.H. Tzeng, M.C. Lin, W.K. Lau, C.C. Kuo* ..... 3051
**On the Mechanical Design of a 1.5 GHz Landau Cavity** — *T.T. Yang, M.C. Lin, Ch. Wang, L.H. Chang, S.S. Chang, W.K. Lau, C.C. Kuo* ..... 3054
**Sawtooth Wave Generation for Pre-Buncher Cavity in ISAC** — *K. Fong, M. Laverty, S. Fang, W. Uzat* ..... 3057
**Coarse and Fine Tuners for the CERN PS 40 MHz Bunching Cavity** — *A.K. Mitra, R.L. Poirier, E. Jensen* ..... 3060
**Measurements at TRIUMF on a 80 MHz Cavity Model for the CERN PS Upgrade for LHC** — *A.K. Mitra, R.L. Poirier, R. Losito* ..... 3063
**High Power Test of the Damped RF-Cavity** — *Tadashi Koseki, Masaaki Izawa, Kenji Shinoe, Shuichi Tokumoto, Yukihide Kamiya, Toshi Miura, Kiyokazu Satoh* ..... 3066
**HOM Characteristics of the ARES Cavity** — *T. Kobayashi, K. Akai, N. Akasaka, E. Ezura, T. Kageyama, H. Mizuno, F. Naito, H. Nakanishi, H. Sakai, Y. Takeuchi, Y. Yamazaki* ..... 3069

## *Superconducting RF*

**Niobium Quarter-Wave Cavity for the New Delhi Booster Linac** — *K.W. Shepard, A. Roy, P. Potukuchi* ..... 3072
**Development of Superconducting RF for CESR** — *S. Belomestnykh, P. Barnes, E. Chojnacki, R. Ehrlich, W. Hartung, T. Hays, R. Kaplan, J. Kirchgessner, E. Nordberg, H. Padamsee, P. Quigley, J. Reilly, D. Rubin, J. Sears* ..... 3075
**Superconducting RF System Options for DIAMOND** — *D.M. Dykes, P.A. McIntosh* ..... 3078
**Note on the SC Linear Collider TESLA Cavity Design** — *J. Sekutowicz, D. Proch, C. Tang* ..... 3081
**Mechanical Stabilisation of Superconducting Quarter Wave Resonators** — *A. Facco, V. Zviagintsev* ..... 3084
**Beam Test of a Superconducting Damped Cavity for KEKB** — *T. Furuya, K. Akai, K. Asano, E. Ezura, K. Hara, K. Hosoyama, A. Kabe, Y. Kojima, S. Mitsunobu, Y. Morita, H. Nakai, H. Nakanishi, T. Tajima, T. Takahashi, S. Yoshimoto, S.C. Zhao, Y. Ishi, Y. Kijima, T. Murai, K. Sennyu* ..... 3087
**Beam Test Results on HOM Absorber of Superconducting Cavity for KEKB** — *T. Tajima, K. Akai, K. Asano, T. Furuya, K. Hara, K. Hosoyama, A. Kabe, Y. Kojima, S. Mitsunobu, Y. Morita, T. Takahashi* ..... 3090
**Higher Order Mode Analysis of the APT Superconducting Cavities** — *Frank L. Krawczyk* ..... 3093
**In-Situ Proton Irradiation and Measurement of Superconducting RF Cavities Under Cryogenic Conditions** — *B. Rusnak, W.B. Haynes, K.C.D. Chan, R.B. Gentzlinger, R. Kidman, N.S.P. King, R.E. Lujan, M. Maloney, S. Ney, A.H. Shapiro, J. Ullmann, A. Hanson, H. Safa* ..... 3096
**Superconducting Cavities for the Reduced-Beta Section of a Proton Linac** — *C. Pasotti, P. Pittana, M. Svandrlik* ..... 3099
**New Window Design Options for CEBAF Energy Upgrade** — *L. Phillips, J. Mammosser, V. Nguyen* ..... 3102
**Improvement of the Operational Performance of SRF Cavities via In Situ Helium Processing and Waveguide Vacuum Processing** — *C. Reece, M. Drury, M.G. Rao, V. Nguyen-Tuong* ..... 3105
**Jefferson Lab IR FEL Cryomodule Modifications and Test Results** — *M. Wiseman, J. Benesch, M. Drury, J. Fisher, D. Machie, J. Mammosser, L. Phillips, J. Preble* ..... 3108

## *RF Sources/Systems*

**Phase Loop Bandwidth Measurements on the Advanced Photon Source 352-MHz RF Systems** — *D. Horan, A. Nassiri, C. Schwartz* ..... 3111
**7 GHz Pulsed Magnicon: Study and New Results** — *E.V. Kozyrev, I.G. Makarov, O.A. Nezhevenko, A.A. Nikiforov, G.N. Ostreiko, B.Z. Persov, G.V. Serdobintsev, S.V. Shchelkunoff, V.V. Tarnetsky, V.P. Yakovlev, I.A. Zapryagaev* . 3114
**High Efficiency TWT Amplifiers** — *S. Naqvi, G.S. Kerslick, J.A. Nation, Q. Wang* ..... 3117
**Microwave Cold Tests of Planar RF Cavities** — *J. Chen, T. Lee, D. Yu, A. Nassiri* ..... 3120
**The 101 MHz Amplifier System of the New CERN Lead Injector** — *G. Hutter, W. Hartmann, F. Klaus, H. Valter, W. Vinzenz, J. Broere, J. Evans, F. Nitsch, K. Bedermann, J. Braun, D. Vierlbeck, U. Hansen* ..... 3123
**Design of 135 MW X-Band Relativistic Klystron for Linear Collider** — *G.V. Dolbilov, I.N. Ivanov, N.I. Azorsky, V.S. Shvetsov, V.E. Balakin, P.V. Avrakhov, S.Yu. Kazakov, V.E. Teryaev, V.F. Vogel* ..... 3126
**Large-Signal Klystron Simulations Using KLSC** — *Bruce E. Carlsten, Patrick Ferguson* ..... 3129
**Rippled-Beam Free-Electron Laser** — *B.E. Carlsten* ..... 3132
**Annular-Beam, 17 GHz Free-Electron Maser Experiment** — *L.M. Earley, B.E. Carlsten, M.V. Fazio, C.M. Fortgang, P.C. Haddock, W.B. Haynes* ..... 3135
**The RF System for the National Spallation Neutron Source Linac** — *Paul Tallerico, James Billen, Andrew Jason, Michael Lynch, Thomas Wangler, Lloyd Young* ..... 3138
**Double-Sided Relativistic Magnetron** — *A.V. Agafonov, E.G. Krastelev* ..... 3141
**Circuit Aspects of the NRL/Industrial 94 GHz Gyroklystron Amplifier** — *D. Pershing, K. Nguyen, J. Petillo, J. Calame, B. Danly, B. Levush* ..... 3144
**Electron Beam Propagation with Premodulated Energy and Current** — *Han S. Uhm* ..... 3147
**Experimental Investigation of a W-Band Gyroklystron Amplifier** — *M. Blank, B.G. Danly, B. Levush, P.E. Latham* ..... 3150
**X-Band Magnicon Amplifier for the Next Linear Collider** — *Steven H. Gold, Arne W. Fliflet, Allen K. Kinkead, B. Hafizi, Oleg A. Nezhevenko, Viacheslav P. Yakovlev, Jay L. Hirshfield, Richard True, Robert J. Hansen* ..... 3153
**34-GHz Pulsed Magnicon for Linear Collider Application** — *O.A. Nezhevenko, V.P. Yakovlev, A.K. Ganguly, J.L. Hirshfield* ..... 3156
**High Power 35 GHz Gyroklystron Amplifiers** — *J.J. Choi, A.H. McCurdy, F. Wood, R.H. Kyser, J. Calame, B.G. Danly, B. Levush, R.K. Parker* ..... 3159
**Feasibility Study of a HOM IOT for TESLA** — *P. Schütt, T. Weiland, A. Gamp, Fuhai Lu* ..... 3162
**Operating Experience and Reliability Improvements on the 5 kW CW Klystron at Jefferson Lab** — *R. Nelson, S. Holben* ..... 3165
**Initial Operation of the Maryland Coaxial Gyroklystron Experiment** — *W. Lawson, M. Castle, J. Cheng, B. Hogan, G.P. Saraph, V.L. Granatstein, M. Reiser* ..... 3168
**High Power 20 GHz RF Source Based on Seventh Harmonic Co-Generation** — *Changbiao Wang, J.L. Hirshfield, A.K. Ganguly* ..... 3171

## *Related Hardware*

**High Peak Power Test of S-Band Waveguide Switches** — *A. Nassiri, A. Grelick, R.L. Kustom, M. White* ..... 3174
**Design of a High Average Power Waveguide Window** — *E. Chojnacki, T. Hays, J. Kirchgessner, H. Padamsee, M. Cole, T. Schultheiss* ..... 3177
**Electron Gun and Collector Design for 94-GHz Gyro-Amplifiers** — *K. Nguyen, B. Danly, B. Levush, M. Blank, R. True, K. Felch, P. Borchard* ..... 3180
**Experimental Evaluation of 350 MHz RF Accelerator Windows for the Low Energy Demonstration Accelerator** — *K. Cummings, D. Rees, W. Roybal, S. Lenci, S. Risbud, C. Shang, D. Wilcox* ..... 3183
**Electron Gun for a High-Power X-Band Magnicon Amplifier** — *V.P. Yakovlev, O.A. Nezhevenko, R.B. True* .... 3186
**An All-Metal High Power Circularly Polarized X-Band RF Load** — *W.R. Fowkes, E.N. Jongewaard, R.J. Loewen, S.G. Tantawi, A.E. Vlieks* ..... 3189
**The Next Linear Collider Test Accelerator's RF Pulse Compression and Transmission Systems** — *S.G. Tantawi, C. Adolphsen, S. Holmes, T. Lavine, R.J. Loewen, C. Nantista, C. Pearson, R. Pope, J. Rifkin, R.D. Ruth, A.E. Vlieks* ..... 3192
**Upgrade of the SLAC SLED-II Pulse Compression System Based on Recent High Power Tests** — *A.E. Vlieks, W.R. Fowkes, R.J. Loewen, S.G. Tantawi* ..... 3195
**Multipactor Discharge on a Dielectric** — *R.A. Kishek, Y.Y. Lau* ..... 3198

## MAGNETS

**Chair:** E. Willen, *Brookhaven National Laboratory*


**The Fermilab Permanent Magnet Antiproton Recycler Ring** *(Invited)* —
*G. William Foster* ..... no manuscript submitted

**Key Issues for the Use of High Temperature Superconductors for HEP Needs** *(Invited)* —
*David C. Larbalestier* ..... no manuscript submitted

**High Field NbSn Magnets for Accelerators** *(Invited)* — *H. ten Kate* ..... no manuscript submitted

**Overview of Hot Topics in Insertion Device Design** *(Invited)* — *Kem E. Robinson* ..... 3201

**Experiments and Cycling at the LHC Prototype Half-Cell** — *R. Saban, J. Casas-Cubillos, P. Collier, P. Cruikshank, K. Dahlerup-Petersen, B. Desforges, B. Hilbert, G. Krainz, F. Momal, A. Rijllart, F. Rodriguez-Mateos, R. Schmidt, L. Serio* ..... 3206

**Quench Performance and Field Quality Measurements of the First LHC Low-$\beta$ Quadrupole Model** — *R. Ostojic, G.A. Kirby, R. Schmidt, T.M. Taylor, S. Milward, J. Morris, S. Nobes, K. Smith, A. Street, M.C. Townsend, J. Treadgold, J. Wiatrzyk, S.A. Gourlay, J.B. Strait* ..... 3209

**Test Results for a High Field (13 T) $Nb_3Sn$ Dipole** — *A.D. McInturff, R. Benjegerdes, P. Bish, S. Caspi, K. Chow, D. Dell'Orco, D. Dietderich, C. Hannaford, W. Harnden, H. Higley, A. Lietzke, L. Morrison, M. Morrison, R. Scanlan, J. Smithwick, C. Taylor, J. van Oort* ..... 3212

**Low Field Magnets with High Temperature Superconductors for an Upgrade of CESR** — *G. Dugan, J. Rogers* 3215

**Vibrating Wire Field-Measuring Technique** — *Alexander Temnykh* ..... 3218

**The Advanced Light Source Elliptically Polarizing Undulator** — *S. Marks, C. Cortopassi, J. DeVries, E. Hoyer, R. Leinbach, Y. Minamihara, H. Padmore, P. Pipersky, D. Plate, R. Schlueter, A. Young* ..... 3221

**Magnetic Performance of Insertion Devices at the Advanced Photon Source** — *E.R. Moog, I. Vasserman, M. Borland, R. Dejus, P.K. Den Hartog, E. Gluskin, J. Maines, E. Trakhtenberg* ..... 3224


### *Room-Temperature Magnets*


**Temperature Compensation of NdFeB Permanent Magnets** — *S.H. Kim, C. Doose* ..... 3227

**The STAR Detector Magnet Subsystem** — *R.L. Brown, A. Etkin, K.J. Foley, W.J. Leonhardt, J.A. Mills, I. Polk, E.S. Rodger, J.A. Scheblein, R.D. Schlueter* ..... 3230

**Magnets for the National Spallation Neutron Source Accumulator Ring** — *J. Tuozzolo, J. Brodowski, G. Danby, J. Jackson, W. Meng* ..... 3233

**Permanent Magnet Quadrupoles for CESR Phase-III Upgrade** — *W. Lou, D. Hartill, D. Rice, D. Rubin, J. Welch* ..... 3236

**The Use of Correcting Coils in End Magnets of Accelerators** — *L.R.P. Kassab, P. Gouffon* ..... 3239

**Magnetic Field Measurements of the Main Injector Sextupole Magnets** — *C.M. Bhat, B.C. Brown, D.J. Harding, Si J. Fang, P.S. Martin, H.D. Glass, J.W. Sim, D.G.C. Walbridge* ..... 3242

**Design for Fermilab Main Injector Magnet Ramps which Account for Hysteresis** — *B.C. Brown, C.M. Bhat, D.J. Harding, P.S. Martin, G. Wu* ..... 3245

**Magnet Development for the BRF Positron Emission Tomography Accelerator** — *N. Chester, A. Makarov, P. Schlabach, I. Terechkine, D. Walbridge, T. Wokas, V. Yarba, D. Larson* ..... 3248

**Analysis and Measurements of Eddy Current Effects of a Beam Tube in a Pulsed Magnet** — *S. Fang, W. Chou* 3251

**Experience with the Procurement of Ferrite and Temperature Compensator for Permanent Magnets for Accelerators** — *William B. Fowler, Bruce Brown, James Volk* ..... 3254

**Permanent Dipole Magnets for the 8 GeV Transfer Line at FNAL** — *H.D. Glass, B.C. Brown, G.W. Foster, W.B. Fowler, J.E. Haggard, D.J. Harding, G.P. Jackson, M.P. May, T.H. Nicol, J.F. Ostiguy, P. Schlabach, G.A. Smith, J.T. Volk* ..... 3257

**Stability Tests of Permanent Magnets Built with Strontium Ferrite** — *H.D. Glass, B.C. Brown, G.W. Foster, W.B. Fowler, R. Gustafson, G.P. Jackson, J.-F. Ostiguy, J.T. Volk* ..... 3260

**Permanent Gradient Magnets for the 8 GeV Transfer Line at FNAL** — *H.D. Glass, K.J. Bertsche, B.C. Brown, G.W. Foster, W.B. Fowler, J.E. Haggard, D.J. Harding, G.P. Jackson, M.P. May, T.H. Nicol, J.F. Ostiguy, P. Schlabach, G.A. Smith, J.T. Volk* ..... 3263

**Automated Permanent Magnet Magnetization System for 8 GeV Transfer Line and Recycler Ring Production at Fermilab** — *Eric Haggard* ..... 3266

**Magnetic Field Strength and Shape Measurements of the Fermilab Main Injector Quadrupoles** — *D.J. Harding, B.C. Brown, J. DiMarco, H.D. Glass, T.K. Kroc, P.S. Martin, C.S. Mishra, D.G.C. Walbridge, E.G. Pewitt* ..... 3269

**Design and Magnetic Measurements of the Fermilab Main Injector Lambertson** — *D.E. Johnson, J.E. DiMarco, D.J. Harding, P.S. Martin, J.-F. Ostiguy, D.G.C. Walbridge, R. Baiod* ..... 3272
**Variations in the Steel Properties and the Excitation Characteristics of Fermilab Main Injector Dipoles** — *P.S. Martin, D.J. Harding, E.G. Pewitt, A.D. Russell* ..... 3275
**Modifications to the Excitation Characteristics of Fermilab Main Injector Dipoles by Machining** — *P.S. Martin, R. Baiod, D.J. Harding, J.F. Ostiguy, A.D. Russell* ..... 3278
**The Design and Construction of Permanent Magnet Lambertson for the Recycler Ring at Fermilab** — *M.P. May, G.W. Foster, G.P. Jackson, J.T. Volk* ..... 3280
**Design and Fabrication of Achromatic Bend for Medium Energy Electron Cooling at Fermilab** — *M.W. McGee, P.G. Hurh, K.J. Bertsche* ..... 3283
**Hybrid Permanent Quadrupoles for the 8 GeV Transfer Line at Fermilab** — *S.M. Pruss, B.C. Brown, G.W. Foster, H.D. Glass, D.J. Harding, G.P. Jackson, M.P. May, J.-F. Ostiguy, J.T. Volk* ..... 3286
**Selecting Magnet Laminations Recipes Using the Method of Simulated Annealing** — *A.D. Russell, R. Baiod, B.C. Brown, D.J. Harding, P.S. Martin* ..... 3288
**Air-Cooled Trim Dipoles for the Fermilab Main Injector** — *D.J. Harding, J.A. Carson, N.S. Chester, J.D. Garvey, G.E. Krafczyk, A. Makarov, I. Terechkine, V.A. Yarba* ..... 3291
**A Combined Function Magnet for a Compact Synchrotron** — *M. Tadokoro, J.I. Hirota, K. Hiramoto, M. Umezawa, S. Kakiuchi, Y. Iwashita, A. Noda, T. Shirai, M. Inoue* ..... 3294
**Field Measurements of PEP-II LER Dipoles and Quadrupoles at IHEP** — *R. Hou, F. Ren, Y. Hao, Y. Han, G. Ni, L. Li, J. Sun, L. Zheng, M. Wang, B. Yin, Q. Peng, G. Zhao, J. Zhang, Y. Li, W. Chen* ..... 3297
**The Fabrication of Quadrupole Magnets for PEP-II LER** — *Fuhe Huang, Yaolin Sun, Xiaoping Wang, Dunan Zhang, Bingsong Huang, Lan Dong* ..... 3300
**3D Design, Contruction, and Field Analysis of CIS Main Dipole Magnets** — *G.P.A. Berg, W. Fox, D.L. Friesel, T. Rinckel* ..... 3303
**Magnets and their Power Supplies of JHP 50-GeV Synchrotron** — *M. Muto, K. Niki, Y. Mori* ..... 3306
**Magnetic Design and Measurement of Nonlinear Multipole Magnets for the APT Beam Expander System** — *D. Barlow, R. Shafer, R. Martinez, P. Walstrom, S. Kahn, A. Jain, P. Wanderer* ..... 3309
**Optimization of the PEP-II Low Energy Ring Dipoles** — *P. Barale, N. Li, J. Osborn, J. Tanabe, R.B. Yourd, M.S. Zisman, Y. Sun, X. Xu* ..... 3312
**Harmonic Correction Rings for the PEP-II I.R. Quadrupole Magnets** — *D. Humphries, R. Schlueter* ..... 3315
**Performance of the PEP-II Low-Energy Ring Quadrupoles** — *N. Li, J. Osborn, J. Tanabe, D. Yee, R. Yourd, M. Zisman, Z. Cao, R. Hou, Y. Sun* ..... 3318
**Design of the PEP-II Interaction Region Septum Quadrupole** — *J. Osborn, J. Tanabe, D. Yee, F. Younger* ..... 3321
**Pulsed Septa for the LNLS Injector** — *A.R.D. Rodrigues, R.H.A. Farias, M.J. Ferreira, F.S. Rafael, G. Tosin* ..... 3324
**Eddy Current Effect of Very Long Time Constant of Block Magnets** — *M. Kumada, H. Ogawa, K. Sato, M. Kase, H. Okuno* ..... 3327
**Results from a Prototype Permanent Magnet Dipole-Quadrupole Hybrid for the PEP-II B-Factory** — *M. Sullivan, G. Bowden, S. Ecklund, D. Jensen, M. Nordby, A. Ringwall, Z. Wolf* ..... 3330
**Magnetic Measurements of the Prototype Dipole for the IR-FEL at the Thomas Jefferson National Accelerator Facility** — *J. Karn, G. Biallas, A. Guerra, L. Harwood* ..... 3333
**Magnets for the CERN PS Booster Transfer Line** — *George S. Clark, Alan J. Otter, Paul Reeve* ..... 3336

## *Superconducting Magnets*

**Removal of Axial Twist in RHIC Insertion Quadrupole Magnets** — *J. Cozzolino, M. Anerella, A. Jain, W. Louie, P. Muratore, P. Wanderer* ..... 3338
**Parameterization and Measurements of Helical Magnetic Fields** — *W. Fischer, M. Okamura* ..... 3341
**A Common Coil Design for High Field 2-in-1 Accelerator Magnets** — *Ramesh Gupta* ..... 3344
**Change in Field Harmonics after Quench and Thermal Cycles in Superconducting Magnets** — *R. Gupta, A. Jain, J. Muratore, P. Wanderer, E. Willen, C. Wyss* ..... 3347
**Magnetic Design of Superconducting Quadrupoles for a SC LINAC for APT** — *S. Kahn, P. Wanderer* ..... 3350
**Test Results from the Completed Production Run of Superconducting Corrector Magnets for RHIC** — *J. Muratore, A. Jain, G. Ganetis, A. Ghosh, A. Marone, A. Morgillo, W. Sampson, P. Thompson, P. Wanderer* ..... 3353
**RHIC D0 Insertion Dipole Design Iterations During Production** — *J. Schmalzle, M. Anerella, G. Ganetis, A. Ghosh, R. Gupta, A. Jain, S. Kahn, G. Morgan, J. Muratore, W. Sampson, P. Wanderer, E. Willen* ..... 3356
**Helical Dipole Magnets for Polarized Protons in RHIC** — *M. Syphers, E. Courant, W. Fischer, A. Luccio, F. Mariam, S. Peggs, F. Pilat, T. Roser, S. Tepikian, N. Tsoupas, E. Willen, T. Katayama, K. Hatanaka, T. Kawaguchi, M. Okamura, T. Tominaka, H. Wu, V. Ptitsin, Y. Shatunov* ..... 3359

**A Helical Magnet Design for RHIC** — *E. Willen, R. Gupta, A. Jain, E. Kelly, G. Morgan, J. Muratore, R. Thomas* 3362
**Dynamic Field Quality of LHC/Saclay Arc Quadrupole Magnet Prototype** — *A. Devred, J. Belorgey, J. Deregel, B. Gallet, P. Genevey, F. Kircher, J.M. Rifflet, J.C. Sellier, P. Védrine, J. Billan, T. Ogitsu* ..... 3365
**Mechanical Design and Layout of the LHC Standard Half-Cell** — *J.C. Brunet, P. Cruikshank, W. Erdt, M. Genet, V. Parma, A. Poncet, P. Rohmig, B. Skoczen, R. Van Weelderen, J. Vlogaert, U. Wagner, L.R. Williams* 3368
**State of the LHC Main Magnets** — *R. Perin, for the LHC Magnet Team* ..... 3371
**The Short Straight Sections for the LHC** — *T. Tortschanoff, V. Parma, P. Rohmig, M. Peyrot, J.M. Rifflet, P. Védrine, D. Vincent* ..... 3374
**Towards Series Measurements of the LHC Superconducting Dipole Magnets** — *L. Walckiers, Z. Ang, J. Billan, L. Bottura, A. Siemko, P. Sievers, R. Wolf* ..... 3377
**Forces on Interaction Region Quadrupoles and Dipoles Due to a Detector Solenoid Magnet** — *James J. Welch, Gerald F. Dugan* ..... 3380
**The Superconducting Interaction Region Magnet System for the CESR Phase III Upgrade** — *James J. Welch, Gerald F. Dugan, Emery Nordberg, David Rice* ..... 3383
**Configuration of the Proposed Diamond Superconducting Dipole Magnet** — *N. Marks, J.A. Clarke, E. Baynham, R. Coombs* ..... 3386
**Quench Protection of SC Quadrupole Magnets** — *S. Feher, R. Bossert, J. DiMarco, D. Mitchell, M.J. Lamm, P.J. Limon, P. Mazur, F. Nobrega, D. Orris, J.P. Ozelis, J.B. Strait, J.C. Tompkins, A.V. Zlobin, A.D. McInturff* ..... 3389
**Design and Operation of an Experimental "Double-C" Transmission Line Magnet** — *G.W. Foster, P.O. Mazur, T. Peterson, C.D. Sylvester, P. Schlabach* ..... 3392
**A New Facility to Test Superconducting Accelerator Magnets** — *M.J. Lamm, J. DiMarco, E. Desavouret, S. Feher, J.D. Garvey, C. Hess, P.J. Limon, J.M. Nogiec, D. Orris, J. Pachnik, T. Peterson, S. Sharonov, J.B. Strait, C. Sylvester, J. Sim, M. Tartaglia, J.C. Tompkins, A.V. Zlobin* ..... 3395
**Magnetic Design of a High Gradient Quadrupole for the LHC Low-$\beta$ Insertions** — *G. Sabbi, S.A. Gourlay, J. Kerby, M.J. Lamm, P.J. Limon, F. Nobrega, I. Novitski, J.B. Strait, A.V. Zlobin, S. Caspi, R. Scanlan, A. Ghosh, R. Gupta* ..... 3398
**A Mu Mu Collider Capture Solenoid System for Pions from a Tilted Target** — *M.A. Green, R.B. Palmer* ..... 3401
**Tutorial on Superconducting Accelerator Magnets** — *M.J. (Penny) Ball, Carl L. Goodzeit* ..... 3404
**Superconducting Solenoids for the Polarized Electron Spin Control System of the MIT-Bates South Hall Ring (SHR)** — *R. Averill, K. Dow, J. Dzengeleski, C. Sibley, Y. Shatunov, P. Vorobiev, P. Klimine, A. Smirnov* ..... 3407
**Measurement of Young's Modulus and Shim Calculation for LHC Prototype Dipole Magnets** — *F.G. Eysselein, W. Gärtner, J. Vlogaert, D. Perini* ..... 3410
**Progress in the Design, Manufacture and Testing of the KLOE Solenoid for the DA$\Phi$NE Ring at Frascati** — *D.E. Andrews, A.J. Broadbent, M. Greenslade, S.M. Harrison, D.M. Jenkins, J.S.H. Ross, K.D. Smith, A.J. Street, C. Timlin, J.M. Wiatrzyk, KLOE Collaboration, Spokesperson P. Franzini* ..... 3413
**Maxwellian Field Expansion of Helical Magnet** — *K. Hatanaka, T. Katayama, T. Tominaka* ..... 3416
**Design of the Sector Magnets for the RIKEN Superconducting Ring Cyclotron** — *T. Kawaguchi, T. Kubo, T. Mitsumoto, H. Okuno, T. Tominaka, J.W. Kim, S. Fujishima, K. Ikegami, N. Sakamoto, S. Yokouchi, T. Morikawa, Y. Tanaka, A. Goto, Y. Yano* ..... 3419
**Trim Coil System for the RIKEN Superconducting Ring Cyclotron** — *J.-W. Kim, A. Goto, T. Mitsumoto, T. Kubo, H. Okuno, T. Kawaguchi, T. Tominaka, S. Fujishima, K. Ikegami, N. Sakamoto, S. Yokouchi, T. Morikawa, Y. Yano* ..... 3422
**A Superconducting Solenoid for Heavy Ion Beam Focusing** — *J.W. Kim, T. Kubo, T. Kawaguchi, Y. Imai, T. Minato, K. Seo* ..... 3425
**Design of a Model Sector Magnet for the RIKEN Superconducting Ring Cyclotron** — *T. Kubo, T. Kawaguchi, T. Mitsumoto, T. Tominaka, S. Fujishima, J.-W. Kim, Y. Tanaka, K. Ikegami, N. Sakamoto, S. Yokouchi, T. Morikawa, A. Goto, Y. Yano* ..... 3428
**Three Dimensional Field Analysis of Helical Magnet for RHIC Siberian Snake** — *M. Okamura, T. Kawaguchi, T. Tominaka, T. Katayama* ..... 3431
**Multipole Expansion for a Single Helical Current Conductor** — *T. Tominaka, K. Hatanaka, T. Katayama* ..... 3434
**Analytical Field Calculation of Helical Dipole Magnets for RHIC Snake** — *T. Tominaka, M. Okamura, T. Katayama* ..... 3437
**Design Study of the Injection and Extraction Elements for the RIKEN Superconducting Ring Cyclotron** — *T. Tominaka, H. Okuno, S. Fujishima, T. Mitsumoto, T. Kubo, T. Kawaguchi, Y. Tanaka, J.-W. Kim, K. Ikegami, N. Sakamoto, S. Yokouchi, T. Morikawa, A. Goto, Y. Yano* ..... 3440
**Stress Management in High-Field Dipoles** — *N. Diaczenko, T. Elliott, A. Jaisle, D. Latypov, P. McIntyre, P. McJunkins, L. Richards, W. Shen, S. Soika, D. Wendt, R. Gaedke* ..... 3443

**Quench Simulation for 16 T Dipole Built at Texas A&M University** — *Damir Latypov, Peter McIntyre, Weijun Shen* ..... 3446

## *Power Supplies*

**Overview of the ATR Power Supplies** — *D. Bruno, A. Soukas, F. Toldo, B. Lambiase* ..... 3449
**Power Systems for the RHIC First Sextant Test** — *C. Schultheiss, D. Bruno, P.K. Feng, T. Haque, R.F. Lambaise* 3452
**The Power Supply Systems for Elliptical Multipole Wigglers** — *A.S. Medvedko, Yu.A. Evtushenko, B.A. Dovgenko, S.P. Petrov, V.F. Veremeenko, E.A. Medvedko, Om Vir Singh* ..... 3455
**Failure Statistics of DESY Power Supplies in 1996** — *Hans-Joerg Eckoldt* ..... 3458
**Four Quadrant DC to DC Switching Supply for the Fermilab Main Injector** — *L. Bartelson, G. Krafczyk, H. Pfeffer, D. Wolff* ..... 3461
**An Embedded Power Supply Controller** — *S. Sharonov, J.M. Nogiec* ..... 3464
**Magnet Power Supply System for KEK B-Factory** — *Tadashi Kubo, Masato Yoshida* ..... 3467
**Effect of Source Voltage Subharmonics on Rapid Cycling Synchrotron Power Supply** — *F.Q. Zhang, T. Adachi, K. Endo* ..... 3470
**Development of a High Speed Crowbar for LANSCE** — *C. Friedrichs, J. Lyles, J.M. Doub* ..... 3473
**Commissioning and First Year Operation of the LNLS Magnet Power Supplies** — *D. Wisnivesky, A.C. Lira, A.R. Silva, F.C. Arroyo, L.H. Oliveira* ..... 3476
**High Current Shunt Regulator for Quadrupole Magnets in PLS 2-GeV Storage Ring** — *S.H. Nam, J.H. Suh, K.M. Ha, J.Y. Huang, I.S. Ko* ..... 3479
**A Unique Power Supply for the PEP-II Klystron at SLAC** — *R.L. Cassel, M.N. Nguyen* ..... 3482
**PEP-II 16-Channel Corrector Controller Using BITBUS** — *R. Olsen* ..... 3485
**New Power Supply Control Interface and Energy Ramping in SRRC** — *C.S. Chen, Jenny Chen, J.S. Chen, C.J. Wang, K.B. Liu, C.Y. Liu, J.T. Sheu, K.T. Hsu* ..... 3488

## *Insertion Devices*

**An Electromagnetic Micro-Undulator** — *A. Nassiri, L.R. Turner* ..... 3491
**A Superconducting Wiggler Magnet for the NSLS X-Ray Ring** — *E.B. Blum, D.R. Lynch, P. Mortazavi, O.V. Singh, W. Thomlinson, M.H. Woodle, A.J. Broadbent, M.C. Coates, S.R. Milward, E.J.F. Moor, K.D. Smith* .3494
**Magnetic Measurements on an In-Vacuum Undulator for the NSLS X-Ray Ring** — *G. Rakowsky, J.J. Aspenleiter, W.S. Graves, L. Solomon, P.M. Stefan* ..... 3497
**Siberian Snakes for Electron Storage Rings** — *V. Ptitsin, Yu. Shatunov* ..... 3500
**The Magnetic Design of a High Field Permanent Magnet Multipole Wiggler for the SRS** — *J.A. Clarke* ..... 3503
**Recent Developments of Insertion Devices at ESRF** — *J. Chavanne, P. Elleaume, P. Van Vaerenbergh* ..... 3506
**Computing 3D Magnetic Fields from Insertion Devices** — *P. Elleaume, O. Chubar, J. Chavanne* ..... 3509
**Conceptual and Experimental Feasibility Study of a Superconductive Micro-Undulator** — *T. Hezel, R. Rossmanith, B. Krevet, H.O. Moser* ..... 3512
**Development of an In-Vacuum Minipole Undulator** — *Toshiya Tanabe, Hideo Kitamura, Peter Stefan* ..... 3515
**Novel Structure of Short-Period Twisted Undulator Spontaneous Emission Properties** — *A.V. Smirnov, A.S. Khlebnikov* ..... 3518
**Design of an Elliptical Undulator and X-Ray Beam Line at DSR of RIKEN RI Beam Factory Project** — *M. Wakasugi, T. Katayama* ..... 3521
**Operation of Insertion Devices in ELETTRA and Plans for Future Devices** — *R.P. Walker, B. Diviacco, D. Zangrando* ..... 3524
**Design of an Electromagnetic Elliptical Wiggler for ELETTRA** — *R.P. Walker, D. Bulfone, B. Diviacco, W. Jark, P. Michelini, L. Tosi, R. Visintini, G. Ingold, F. Schaefers, M. Scheer, G. Wuestefeld, M. Eriksson, S. Werin* ..... 3527
**Design Features of a Planar Hybrid/Permanent Magnet Strong-Focusing Undulator for Free Electron Laser (FEL) and Synchrotron Radiation (SR) Applications** — *Roman Tatchyn* ..... 3530
**Linear Beam Dynamics Effects of Three Dimensional Static Magnetic Fields of Insertion Devices at SRRC** — *Peace Chang, M.H. Wang, Chaoen Wang, C.C. Kuo, C.S. Hsue* ..... 3533
**Magnet Sorting Algorithms for a Prototype of the SRRC EPU** — *T.C. Fan, C.S. Hwang, C.H. Chang, Ch. Wang* 3536
**Insertion Devices Control Development at SRRC** — *K.T. Pan, Jenny Chen, J.S. Chen, C.J. Wang, C.S. Chen, K.H. Hu, Chaoen Wang, C.H. Chang, C.S. Hwang, T.C. Fan, K.T. Hsu* ..... 3539

# VACUUM, ALIGNMENT, RADIATION MONITORING AND OTHER TECHNOLOGY

**Chair:** W. Stoeffl, *Lawrence Livermore National Laboratory*


**The LHC Vacuum System** *(Invited)* — *O. Gröbner* ..... 3542
**Dust in Accelerator Vacuum Systems** *(Invited)* — *Darren R.C. Kelly* ..... 3547
**APS Storage Ring Vacuum System Performance** *(Invited)* — *J.R. Noonan, J. Gagliano, G.A. Groeppner, R.A. Rosenberg, D.R. Walters* ..... 3552
**Cryogenics for Particle Accelerators: Present State-of-the-Art and Future Trends** *(Invited)* — *Philippe Lebrun* ..... no manuscript submitted
**Advanced Photon Source Experience with Vacuum Chambers for Insertion Devices** — *P.K. Den Hartog, J. Grimmer, E. Trakhtenberg, G. Wiemerslage, S. Xu* ..... 3556
**Massive Titanium Sublimation Pumping in the CESR Interaction Region** — *N.B. Mistry, R. Kersevan, Yulin Li* 3559
**Interaction Region Vacuum System Design at the PEP-II B-Factory** — *L. Bertolini, O. Alford, P. Duffy, R. Holmes, L. Mullins, C. Ng, M. Sullivan* ..... 3562
**Survey of Electronic Safety Systems in Accelerator Applications** — *K. Mahoney* ..... 3565
**TiN Coating of the PEP-II Low-Energy Ring Aluminum Arc Vacuum Chambers** — *K. Kennedy, H. Harteneck, G. Millos, M. Benapfl, F. King, R. Kirby* ..... 3568
**Bremsstrahlung Measurements at the ESRF** — *P. Berkvens, P. Colomp* ..... 3571
**Design and Analysis of a Be Window for the APS Diagnostics Undulator Beam Line** — *I. Ching Sheng, B.X. Yang, S. Sharma* ..... 3574
**In Situ Measurement of Ceramic Vacuum Chamber Conductive Coating Quality** — *C. Doose, K. Harkay, S. Kim, S. Milton* ..... 3577


## *Vacuum Technology*


**An Ancillary Pumping System for the APS Vacuum System** — *D. Walters, J. Noonan, J. Gagliano, G. Harris, V. Svirtun* ..... 3580
**Stress Rupture Considerations in the Design of Large Aperture, Low Mass Composite Vacuum Windows** — *W.J. Leonhardt, J.R. Cullen, P.F. Gill* ..... 3583
**Mechanical Design Aspects of the LHC Beam Screen** — *P. Cruikshank, K. Artoos, F. Bertenelli, J.-C. Brunet, R. Calder, C. Campedel, I. Collins, J.-M. Dalin, B. Feral, O. Grobner, N. Kos, A. Mathewson, L. Nikitina, I. Nikitina, A. Poncet, C. Reymermier, G. Schneider, I. Sexton, S. Sgobba, R. Valbuena, R. Veness* ..... 3586
**Beam Induced Multipacting** — *O. Gröbner* ..... 3589
**Operation of CESR Distributed Ion Pumps at Reduced Voltage** — *Yulin Li, R. Kersevan, N.B. Mistry* ..... 3592
**A Titanium Sublimation Control System for the CESR Interaction Region** — *Yulin Li, Benjamin Manvell, William Lucas, Nariman Mistry* ..... 3595
**The Design, Construction and Testing of a Multipole Wiggler Magnet Titanium Vacuum Chamber for the SRS** — *N. Bliss, C.L. Dawson* ..... 3598
**FNAL Main Injector $\gamma_t$-Jump System Beamtube Design** — *J.R. Leibfritz* ..... 3601
**Comparison of the Quality of Two ECRIS Vacuum Stands** — *J. Pivarč, K.D. Tumanov, V.B. Kutner, A.I. Ivanenko, J. Pivarč jun.* ..... 3604
**Vacuum Beam Losses in the Axial Injection Systems of the FLNR Heavy Ion Cyclotrons** — *M.N. El-Shazly, M.V. Khabarov, A.I. Ivanenko, G.G. Gulbekian* ..... 3607
**Beam Loss Due to the Charge Exchange in the Residual Gas of the FLNR Heavy Ion Cyclotrons** — *G.G. Gulbekian, M.N. El-Shazly, A.V. Tikhomirov, B.N. Gikal* ..... 3610
**The Vacuum System of the Synchrotron Radiation Source ANKA** — *E. Huttel, D. Einfeld* ..... 3613
**Experience with the Ultra-High-Vacuum Protection System for the Synchrotron Radiation Beam Lines with High-Power Wigglers/Undulators at the Photon Factory** — *Noriichi Kanaya, Seiji Asaoka, Shogo Sakanaka, Hideki Maezawa* ..... 3616
**Status of the PEP-II Low-Energy Ring Vacuum System** — *D. Cheng, D. Hunt, H. Hsieh, J. Meneghetti, K. Kennedy, T. Stevens, G. Jones, T. Miller, D. Colomb, L. Bertolini, C. Belser, J. Kerns, E. Daly* ..... 3619
**Design of the Linear Non-Evaporable Getter Pump for the PEP-II B-Factory** — *L. Bertolini, D. Behne, J. Bowman, D. Hathaway, K. Kishiyama, M. Mugge, T. Swan* ..... 3622
**APT/LEDA RFQ Vacuum Pumping System** — *S. Shen, K. Kishiyama, J.M. Parker, N.G. Wilson, D. Schrage* ..... 3625
**LNLS Vacuum System Commissioning** — *M.J. Ferreira, R.O. Ferraz, F.A. Minuzzi, M.B. Silva* ..... 3628
**Internal Gas Targets in AmPS** — *A.P. Kaan, J.F.J. van den Brand, M. Doets, E. van Leeuwen, O. Postma* ..... 3630

**Operation Experiences for PLS Vacuum System** — *D. Park, Y.J. Han, C.K. Kim, S.M. Chung, I.S. Ko* ..... 3633
**Vacuum System Design Using Symbolic Numeric Processors** — *Wayne D. Cornelius* ..... 3636
**Final Design and Manufacturing of the PEP-II High Energy Ring Arc Bellows Module** — *Nadine R. Kurita, Artem Kulikov, Martin Nordby, John Corlett* ..... 3639
**Photon Stimulated Desorption Phenomena at the Taiwan Light Source Vacuum System** — *G.Y. Hsiung, Y.J. Hsu, J.R. Chen* ..... 3642

## *Alignment and Survey*

**Closed Orbit Feed-Back from Low-Beta Quadrupole Movements at LEP** — *F. Tecker, W. Coosemans, A. Marin, K. Rybaltchenko, J. Wenninger* ..... 3645
**Beam Position Monitor Offset Determination at LEP** — *F. Tecker, B. Dehning, P. Galbraith, K. Henrichsen, M. Placidi, R. Schmidt* ..... 3648
**Alignment of the High Beta Magnets in the RHIC Interaction Regions** — *D. Trbojevic, A. Jain, S. Tepikian, R. Grandinetti, G. Ganetis, J. Wei, F. Karl* ..... 3651
**The Superconducting Interaction Region Magnet Positioning System for the CESR Phase III Upgrade** — *James J. Welch, David L. Rubin, Alexander B. Temnykh* ..... 3654
**A Wire Position Monitor (WPM) System to Control the Cold Mass Movements Inside the TTF Cryomodule** — *D. Giove, A. Bosotti, C. Pagani, G. Varisco* ..... 3657
**Ground Motion Studies for Large Future Linear Colliders** — *Shigeru Takeda, Noboru Yamamoto, Katsunobu Oide* ..... 3660
**Precision Surveying and Smoothing Analysis for Pohang Light Source** — *K.W. Seo, A.H. Maeng, S.C. Lee, I.S. Ko* ..... 3663
**Survey and Alignment of SLAC's B-Factory** — *M. Pietryka, M.. Gaydosh* ..... 3666

## *Radiation Monitoring and Safety*

**Access Control and Interlock System at the Advanced Photon Source** — *J. Forrestal, R. Hogrefe, M. Knott, W. McDowell, D. Reigle, L. Solita, R. Koldenhoven, D. Haid* ..... 3669
**Radiation Levels Around the Fermilab Main Injector Extraction Septa** — *C.M. Bhat, N.V. Mokhov* ..... 3672
**Radiation Protection in the NLC Test Accelerator at SLAC** — *Theodore L. Lavine, Vaclav Vylet* ..... 3675
**Modular Reliability Modeling of the TJNAF Personnel Safety System** — *J. Cinnamon, K. Mahoney* ..... 3678
**Jefferson Lab Personnel Safety Fast Beam Kicker System** — *K. Mahoney, O. Garza, E. Stitts, H. Areti, M. O'Sullivan* ..... 3681
**Emerging Standards with Application to Accelerator Safety Systems** — *K.L. Mahoney, H.P. Robertson* ..... 3684

## *Other Subsystems Technology and Components*

**Design and Construction of a 1-MW, 352-MHz RF Test Load** — *D. Horan, Y. Kang* ..... 3687
**Design and Construction of the Advanced Photon Source 352-MHz RF System Switching Control** — *D. Horan, L. Solita, D. Reigle, N. Dimonte* ..... 3690
**Supports and Installation System of the RHIC Superconducting Magnets** — *Rudy Alforque, Jim Cammarata, Bill De Vito, Frank Karl, Tom Muller, Steve Kane, Gary McIntyre, Ray Savino, Jack Sondericker* ..... 3693
**Systems Layout of the Low-$\beta$ Insertions for the LHC Experiments** — *R. Ostojic, T.M. Taylor, S. Weisz* ..... 3696
**Higher Order Modes Power Loss in the Vertical Separators at CESR** — *S. Greenwald* ..... 3699
**Photocurrents in Electrostatic Separators at CESR** — *S. Greenwald* ..... 3702
**REC Quadrupole's Beam Pipe Temperature Control** — *Z. Greenwald, S. Greenwald, D.H. Rice* ..... 3705
**Improved Measurement of Electric Field Uniformity in Horizontal Electrostatic Separators** — *Alexander B. Temnykh, James J. Welch* ..... 3708
**Permanent Magnet Assembly Tooling for the 8 GeV Transfer Line and Recycler Ring at Fermilab** — *T.H. Nicol, A.B. Knauf* ..... 3710
**A Distributed Monitoring and Control System** — *J.M. Nogiec, E. Desavouret, D. Orris, J. Pachnik, S. Sharonov, J. Sim, J.C. Tompkins, K. Trombly-Freytag* ..... 3713
**Pulsed Magnetic Field Measurement Using a Ferrite Waveguide in a Phase Bridge Circuit** — *W. Pellico, P. Colestock* ..... 3716
**Longitudinal Impedance Measurements of an RK-TBA Induction Accelerating Gap** — *S. Eylon, E. Henestroza, J.-S. Kim, T.L. Houck, G.A. Westenskow, S.S. Yu* ..... 3719
**Stack Insulator Induction Accelerator Gaps** — *T.L. Houck, G.A. Westenskow, J.-S. Kim, S. Eylon, E. Henestroza, S.S. Yu, D. Vanecek* ..... 3722

**Resonant Ring For Testing of Accelerator RF Windows** — *E. Gerken, J.M. Gahl, D. Rees, W. Roybal, K. Cummings* ..... 3725
**Beam Expansion with Specified Final Distributions** — *Andrew J. Jason, Barbara Blind, Klaus Halbach* ..... 3728
**Development of a Fast Traveling-Wave Beam Chopper for National Spallation Neutron Source** — *Sergey S. Kurennoy, Andrew J. Jason, Frank L. Krawczyk, John Power* ..... 3731
**Design of Quasi-Travelling Wave Pinger Magnet for Beam Diagnostics on the Advanced Light Source** — *D.E. Anderson, G. Stover* ..... 3734
**TiN Coating of Accelerator Beamline Chambers** — *K.N. Leung, Y. Lee, A. Mashaw, D. Wutte, R.A. Gough* ..... 3737
**Ramping Efficiency Studies in the LNLS Synchrotron Light Source** — *R.H.A. Farias, L.C. Jahnel, Liu Lin, A.R.D. Rodrigues, P.F. Tavares* ..... 3740
**Power Factor Correction at MIT-Bates Linear Accelerator Center with Pulsed Loads of up to 180 MW Peak (2.7 MW Average)** — *R. Averill, K. Hatch, C. Sibley, R. Gross* ..... 3743
**Harmonic Resonance Analysis for PEP II Power Factor Correction Upgrades** — *C. Corvin* ..... 3746
**A Dynamic Local Bump System for Producing Synchrotron Radiation with an Alternate Elliptical Polarization** — *K.T. Hsu, C.H. Kuo, K.H. Hwu, K.K. Lin, C.S. Chen, J.S. Chen, J. Chen, C.T. Chen* ..... 3749
**A Method of Producing Surface Conduction on Ceramic Accelerator Components Using Metal Ion Implantation** — *F. Liu, I. Brown, L. Phillips, G. Biallas, T. Siggins* ..... 3752
**Interactive Troubleshooting Guide for Accelerators** — *R. Legg, B. Dunham, S. Higgins, R. Kazimi, D. Kehne, T. Oren* ..... 3755
**Runtime Accelerator Configuration Tools at Jefferson Laboratory** — *M.G. Tiefenback, L. Doolittle, J.F. Benesch* ..... 3758
**High Power Electron Beam Dumps at CEBAF** — *M. Wiseman, C.K. Sinclair, R. Whitney, M. Zarecky, R. Vetterlein* ..... 3761
**Diagnosis of Individual Cell Frequencies in a Coupled Cavity Chain Without Introducing Objects into the Cavity** — *Yi Ni, Liling Xiao, Dechun Tong, Bo Tian, Qingxiu Jin, Yuanzhong Huang* ..... 3764
**A New Measurement Method of the Delay Line Length in the X-Band Delay Line Distribution System (DLDS)** — *F. Tamura, H. Mizuno* ..... 3767

## APPLICATIONS OF ACCELERATORS

**Chair:** A. Lennox, *Fermi National Accelerator Laboratory*

**Review of Compact Commercial Accelerator Products and Applications** *(Invited)* — *Y. Jongen* ..... 3770
**A High Current Tandem Accelerator for Gamma-Resonance Contraband Detection** *(Invited)* — *B.F. Milton* ..... 3775
**The Accelerator Production of Tritium Project** *(Invited)* — *P.W. Lisowski* ..... 3780
**Commissioning of the 1 MW Spallation Neutron Source SINQ** — *G.S. Bauer, W.E. Fischer, U. Rohrer, U. Schryber* ..... 3785
**Synchrotrons and Beamlines for Proton Radiography** — *F. Neri, H.A. Thiessen, P.L. Walstrom* ..... 3788
**Clinical Requirements and Accelerator Concepts for BNCT** *(Invited)* — *B.A. Ludewigt* ..... 3791
**Market Driven Design of Accelerator Systems for Sterilization of Medical Products** *(Invited)* — *K. Whitham, T. Allen, H. Anamkath, F. Gower, R. Mendonsa, H. Schaffer, A. Zante* ..... 3796
**The GSI Cancer Therapy Project** — *H. Eickhoff, Th. Haberer, G. Kraft, U. Krause, K. Poppensieker, M. Richter, R. Steiner* ..... 3801
**A $^{3}He^{++}$ RFQ Accelerator for the Production of PET Isotopes** — *Ralph J. Pasquinelli* ..... 3804
**A New Intense Neutron Tool for Radiography and Detection of Water and Ground Contaminants** — *C.M. Celata, M. Amman, R. Donahue, K. Leung, P.N. Luke, L.T. Perkins, Peter T. Zawislanski, D. Hua* ..... 3807
**Electron-Linac-Based Radiation Facilities of the Ukrainian National Science Center "KIPT"** — *A.N. Dovbnya, M.I. Aizatsky, Ye.Z. Biller, V.N. Boriskin, V.A. Kushnir, V.V. Mitrochenko, V.A. Popenko, Yu.D. Tur, V.L. Uvarov, E.S. Zlunitsyn, A.I. Zykov* ..... 3810

### *Medical Therapy*

**A Compact Proton Synchrotron for Cancer Treatments** — *Kazuo Hiramoto, Masumi Umezawa, Kooji Matsuda, Masatsugu Nishi* ..... 3813
**Progress Report on the Construction of the Northeast Proton Therapy Center (NPTC) Equipment** — *Y. Jongen, M. Abs, J.-C. Amelia, W. Beeckman, W. Kleeven, M. Ladeuze, G. Lannoye, S. Laycock, D. Leyman, V. Poreye, D. Prieels, D. Vandeplassche, S. Zaremba, M. Heiberger, E. Hubbard, T. Hurn, L. Nissley, C. Silke, M. Tabor, Kiyotaka Ohtomo, Masami Sano, Takemi Satoh, Toshiki Tachikawa, Takeshi Takayama* ..... 3816

**Performance of Parallel Plate Ionization Chamber for Medical Irradiation** — *E. Urakabe, M. Inoue, Y. Iwashita, T. Shirai, T. Sugimura, A. Noda, M. Kanazawa, M. Torikoshi, K. Noda, S. Yamada, M. Tadokoro, M. Nishi, Y. Fujita* ..... 3819
**New Secondary Beam Course for Medical Use in HIMAC** — *S. Kouda, M. Torikoshi, M. Kanazawa, A. Kitagawa, T. Murakami, K. Noda, Y. Sato, E. Takada, J. Yoshizawa, Y. Futami, A. Higashi, T. Kanai, N. Matufuji, H. Tomura, S. Yamada, K. Kawachi, M. Suda, T. Tomitani, M. Kumada, H. Ogawa, Y. Ishikawa, H. Tsubuku, T. Kato* ..... 3822
**Design Study of a Linear Accelerator System for Neutron Capture Therapy** — *J.W. Kim, J.S. Chai* ..... 3825
**A Compact Proton Accelerator System for Cancer Therapy** — *A. Yamaguchi, K. Nakayama, T. Rizawa, S. Sukenobu, K. Satoh, Y. Morii, Y. Tanabe, Y. Chiba* ..... 3828
**Operation of the TRIUMF Proton Therapy Facility** — *E.W. Blackmore, B. Evans, M. Mouat, C. Duzenli, R. Ma, T. Pickles, K. Paton* ..... 3831

## *Medical Isotope Production*

**Initial Operation of CIAE Medically Used Cyclotron** — *Mingwu Fan, Tainjue Zhang, CYCIAE 30 Engineering Group* ..... 3834
**Charge Stripper and MEBT for the $^3$He RFQ Accelerator** — *F.M. Bieniosek, K. Anderson, R.J. Pasquinelli, M. Popovic, C.W. Schmidt, R. Weber, D.J. Larson, P. Young* ..... 3837
**Electron Accelerator's Production of Technetium-99m for Nuclear Medicine** — *V.L. Uvarov, N.P. Dikiy, A.N. Dovbnya, Ye.P. Medvedyeva, G.D. Pugachov, Yu.D. Tur* ..... 3840
**Encapsulated Target for Isotope Production Cyclotrons** — *Shervin Bakhtiari, William Z. Gelbart, Wendy Ho, Nigel R. Stevenson* ..... 3842
**High Current Encapsulated Target System for Radioisotopes Production** — *Wendy Ho, Shervin Bakhtiari, William Z. Gelbart, Nigel R. Stevenson* ..... 3845

## *High-Power Accelerator Applications*

**Program of Activities for the Linac-Driver of ITEP Subcritical Facility** — *A.M. Kozodaev, A.A. Drozdovsky, A.A. Kolomiets, V.V. Kurakin, R.P. Kuybeda, N.V. Lazarev, V.I. Pershin, V.K. Plotnikov, O.V. Shvedov, V.S. Skachkov, V.V. Vasiliev, R.M. Vengrov* ..... 3848
**Parameter and Cost Model for Spallation Neutron Source Studies** — *J.D. Galambos, D.K. Olsen* ..... 3851

## *Electron Beam Processing*

**Electron Beam Applications in Chemical Processing** — *G. Cojocaru, D. Martin, M. Dragusin, R. Moraru, M. Radoiu, C. Oproiu, S. Marghitu, I. Indreias, V. Bestea, R. Camariuc, A. Margaritescu* ..... 3854
**Realignment of a Diverging Electron Beam: A New Beam Delivery System for Rhodotrons** — *Y. Jongen, M. Abs, S. Zaremba, T. Delvigne, A. Herer* ..... 3857
**Electron Beam Scanning Systems** — *A.A. Zavadtsev* ..... 3860
**Cyclotron Autoresonance Accelerator for Electron Beam Dry Scrubbing of Flue Gases** — *J.L. Hirshfield, Changbiao Wang* ..... 3863

## *Non-Destructive Evaluation and Other Applications*

**Effective X-ray Bremsstrahlung Source (Is it Possible to Handle Quality of X-ray Bremsstrahlung?)** — *V.K. Grishin, B.S. Ishkhanov, S.P. Likhachev, D.A. Rodionov, V.I. Shvedunov* ..... 3866
**Small-Sized Electron Linear RF Accelerator with Beam Autoacceleration for Geology and Industry** — *B.Yu. Bogdanovich, V.I. Kaminsky, V.A. Senyukov, A.V. Nesterovich* ..... 3869
**A Small 1 MeV Electron Accelerator for Measuring Heavy Metal Concentrations in Smokestack Gases** — *A. Reppond, M. Ambrosia, B.C. Hansen, C.R. Meitzler, D.P. Redden, D.A. Swenson* ..... 3872

# LASER-DRIVEN PLASMA-CATHODE ELECTRON INJECTOR

D. Umstadter, S.-Y. Chen, E. Dodd, J.K. Kim, A. Maksimchuk and R. Wagner*
Center for Ultrafast Optical Science, University of Michigan, Ann Arbor, MI 48109

*Abstract*

We discuss the first experimental demonstration of electron acceleration by a laser wakefield over distances greater than a Rayleigh range (or the distance a laser normally propagates in vacuum). A self-modulated laser wakefield plasma wave is shown to have a field gradient that exceeds that of an RF linac by four orders of magnitude ($E \geq 200$ GV/m) and accelerates electrons with over 1-nC of charge per bunch in a beam with space-charge-limited emittance (1 mm-mrad). Above a laser power threshold, a plasma channel, created by the intense ultrashort laser pulse (I $\sim 4 \times 10^{18}$ W/cm$^2$, $\lambda = 1$ $\mu$m, $\tau$=400 fs), was found to increase the laser propagation distance, decrease the electron beam divergence, and increase the electron energy. The plasma wave, directly measured with coherent Thomson scattering is shown to damp—due to beam loading—in a duration of 1.5 ps or ~100 plasma periods We also discuss a new concept for controlled laser injection of electrons in order to create monoenergetic femtosecond electron bunches. As in the above experiments it uses the plasma itself as the cathode, but also an additional laser pulse as a trigger. By use of a 2-D particle-in-cell numerical code, it is shown that this technique will produce 1-femtosecond duration electron bunches with energy spread at the percent level.

## 1 INTRODUCTION

Due to recent advances in laser technology[1], it is now possible to generate the highest electromagnetic and electrostatic fields ever produced in the laboratory[2]. The interactions of these high-intensity and ultrashort-duration laser pulses with matter has come to be known as high-field science. In terms of basic research, these interactions permit for the first time the study of optics in relativistic plasmas. Technological applications include advanced fusion energy, x-ray lasers, and table-top ultrahigh-gradient electron accelerators. In the latter case, it may be possible to build an all-optical table-top injector, which produces GeV energy electron bunches with femtosecond pulse duration.

When an intense laser enters a region of gaseous-density atoms, the atomic electrons feel the enormous laser electromagnetic field, and begin to oscillate at the laser frequency ($\omega = 2\pi c/\lambda = ck$) . The oscillations can become so large that the electrons become stripped from the atoms, or ionized. At high laser intensity ($I$), the free electrons begin to move at close to the speed of light ($c$), and thus their mass $m_e$ changes significantly compared to their rest mass. This large electron oscillation energy corresponds to gigabar laser pressure, displacing the electrons from regions of high laser intensity. Due to their much greater inertia, the ions remain stationary, providing an electrostatic restoring force. These effects cause the plasma electrons to oscillate at the plasma frequency ($\omega_p$) after the laser pulse passes by them, creating alternating regions of net positive and negative charge, where $\omega_p = \sqrt{4\pi e^2 n_e/\gamma m_e}$, $n_e$ is the electron density, $e$ is the electron charge and $\gamma$ is the relativistic factor associated with the electron motion transverse to the laser propagation. $\gamma$ depends on the normalized vector potential, $a_o$, by $\gamma = \sqrt{1+a_o^2}$, where $a_o = \gamma v_{os}/c = eE/m_o\omega c = 8.5 \times 10^{-10}\lambda[\mu\text{m}]I^{1/2}[\text{W/cm}^2]$. The resulting electrostatic wakefield plasma wave propagates at a phase velocity nearly equal to the speed of light and thus can continuously accelerate hot electrons[3]. Up to now, most experiments have been done in the self-modulated laser wakefield regime[4, 5, 6], where the laser pulse duration is much longer than the plasma period, $\tau >> \tau_p = 2\pi/\omega_p$. In this regime, the forward Raman scattering instability can grow; where an electromagnetic wave ($\omega_o, \boldsymbol{k_o}$) decays into a plasma wave ($\omega_p, \boldsymbol{k_p}$) and electromagnetic side-bands ($\omega_o \pm \omega_p, \boldsymbol{k_o} \pm \boldsymbol{k_p}$).

## 2 RECENT RESULTS

A small number of relativistic hot electrons were observed in inertial-confinement-fusion experiments with long-pulse duration large-building size lasers and solid-density targets. However, it was shown only recently that electrons can be accelerated by a plasma wave driven by intense ultrashort-duration table-top laser pulses (I $\sim 4 \times 10^{18}$ W/cm$^2$, $\lambda = 1$ $\mu$m, $\tau \sim 0.5$ ps) and gaseous-density targets [7, 8]. Under similar conditions, electrons were even observed to have an energies up to 44 MeV, with an energy spread of 100%[9]. Recently, we have shown that the accelerated electron beam appeared to be naturally-collimated with a low-divergence angle (less than ten degrees), and had over 1-nC of charge per bunch[10].

In this experiment, we used a Ti:sapphire-Nd:glass laser system based on chirped-pulse-amplification that produces 3 J, 400 fs pulses at 1.053 $\mu$m. The 43 mm diameter beam was focused with an f/4 off-axis parabolic mirror to $r_o = 8.5$ $\mu$m (1/e$^2$), corresponding to vacuum intensities exceeding $4 \times 10^{18}$ W/cm$^2$. This pulse was focused onto a supersonic helium gas jet with a sharp gradient (250 $\mu$m) and a long flat-topped interaction region (75 $\mu$m). The

*We would like to thank M. Downer and P. LeBlanc for their collaboration on our Thomson scattering measurments. This work is sponsored by Department of Energy/Lawrence Livermore National Laboratory subcontract B307953 and the National Science Foundation Science and Technology Center contract PHY 8920108.

0-7803-4376-X/98/$10.00 © 1998 IEEE

maximum density varies linearly with backing pressure up to the maximum backing pressure of 1000 PSI, and an underdense plasma at $3.6 \times 10^{19}$ cm$^{-3}$ is formed by the foot of the laser pulse tunnel-ionizing the gas. This plasma density corresponds to a critical power of $P_c$ = 470 GW. A sharp gradient and long interaction region are found to be essential.

Moreover, as shown in Fig. 1, acceleration occured in this experiment[10] only when the laser power exceeded a certain critical value, $P_c$, the threshold for relativistic self-focusing. The total number of accelerated electrons

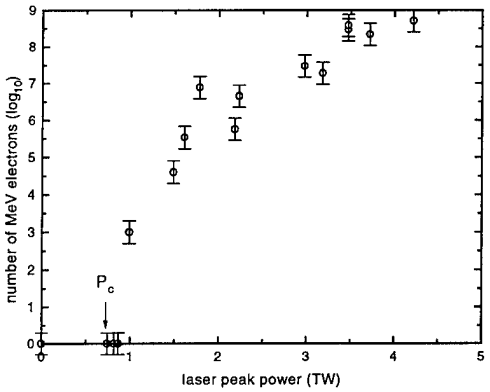



Figure 1: The number of relativistic electrons accelerated as a function of incident laser power focused in a gas of helium at atmospheric density.

(at all energies) was measured using either a Faraday cup or a plastic scintillator coupled to a photomultiplier tube, and the results were found to be consistent with each other. There is a sharp threshold for electron production at $\sim 1.5P_c$, and the total number of electrons increases exponentially and finally saturates beyond $4P_c$[10]. At $6P_c$, $6 \times 10^9$ accelerated electrons were measured coming out of the plasma in a beam. By using aluminum absorbers, we determined that 50% of the electrons detected have energy greater than 1 MeV (corresponding to 0.5 mJ of energy in the electron beam).

The electron energy spectrum (see Fig. 2) was measured using a 60° sector dipole magnet by imaging a LANEX scintillating screen with a CCD camera. The normalized distribution is found to have a functional form of $\exp(-\alpha\gamma)$ where $\alpha$ is a fitting parameter. In the low power case ($< 6P_c$, no channeling), the normalized distribution follows $\exp(-\gamma)$, and when the laser power increases ($> 6P_c$, with channeling), the electron energy distribution discretely jumps to follow exp(-0.67 $\gamma$). The abrupt change in the electron distribution also occurs if the laser power is held fixed and the density is increased, as it should given the critical power threshold dependence on density. Below 850 PSI ($3.1 \times 10^{19}$ cm$^{-3}$, no channeling), the electron distribution follows the same trend as the lower power distribution, and above 850 PSI (with channeling) it follows the higher power distribution. For the electron energy distribution greater than 3 MeV, a significantly less steep slope

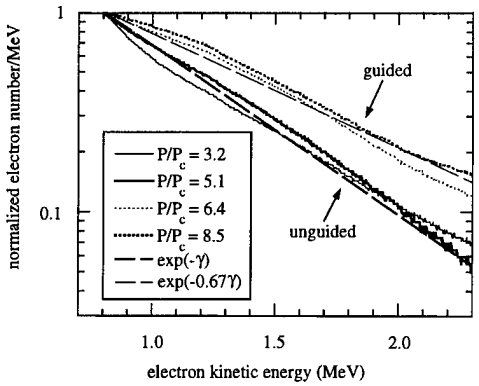



Figure 2: Normalized electron kinetic energy spectrum as a function of laser power at fixed electron density. The upper curves represent the spectra obtained when self-guiding was observed; the lower curves represent unguided spectra. The two exponential fits are also shown.

that extends to 20 MeV was measured using aluminum absorbers. Even though the plasma wave amplitude increases as the laser power increases, the distribution only dramatically changes when self-guiding occurs. This indicates that extension in the accelerating length is the primary factor in determining the fitting parameter $\alpha$.

Measurements of the satellites in the spectrum of the forward scattered light indicated that a self-modulated plasma wave occurred when the laser power exceeded $P_c/2$. Since then, two independent research groups have simultaneously reported direct measurements of the plasma wave amplitude with a Thomson-scattering probe pulse[11, 12]. The field gradient was reported[12] to exceed that of a radio-frequency (RF) linac by four orders of magnitude ($E \geq$ 200 GV/m). This acceleration gradient corresponds to an energy gain of 1 MeV in a distance of only 10 microns. The plasma wave was observed to exist for a duration of 1.5 ps or 100 plasma oscillations[12]. It was calculated that it damps only because all of the wave energy was converted to the accelerated electrons. Except for the large energy spread and low average power, these parameters compare favorably with medical linacs. In fact, the much smaller source size of a laser wakefield accelerator compared with that of a conventional linac, 10 microns compared with greater than 100 microns, may permit much greater spatial resolution for medical imaging.

This enormous field gradient would be of limited use if the length over which it could be used to accelerate electrons were just the natural diffraction length of the highly focused laser beam, which is much less than a millimeter. Fortunately, we recently demonstrated that electrons can be accelerated beyond this distance[13]. At high laser power, the index of refraction in a plasma varies with the radius. This is both because the laser intensity varies with radius and the plasma frequency depends on the relativistic mass factor $\gamma$. Above the above-mentioned critical laser power $P_c$, the plasma should act like a positive lens and focus the laser beam, a process called relativistic self-focusing. This

is similar to propagating a low power beam over an optical fiber optic cable, except in this case the intense laser makes its own fiber optic.

In order to diagnose the spatial extent of the plasma, a sidescattering imaging system with a spatial resolution of 15 $\mu$m was utilized. We were able to resolve the growth of the plasma channel as a function of both laser power and plasma density. Fig. 3 shows the sidescattered intensity distribution as a function of laser power, and the plasma channel clearly extends as the laser power increases. In

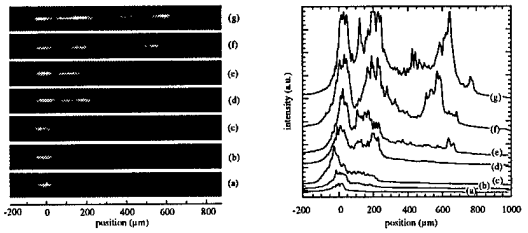



Figure 3: On-axis images (left) and corresponding lineouts (right) of sidescattered light at various laser powers and a fixed initial electron density of $3.6 \times 10^{19}$ cm$^{-3}$. The various images and lineouts represent laser powers of $P/P_c =$ (a) 1.6, (b) 2.6, (c) 3.9, (d) 5.5, (e) 7.2, (f) 8.4, and (g) 9.1. Note: the curves have been displaced vertically for ease of viewing.

the lower power cases ($< 2.6P_c$), the channel length is only $\sim$ 125 $\mu$m, which is smaller than the confocal parameter ($2Z_R$) of 430 $\mu$m. As the laser power increases for a fixed gas density, the channel length first jumps to 250 $\mu$m at $3.9P_c$ and then reaches 750 $\mu$m at $7.2P_c$. The maximum channel length was observed to be 850 $\mu$m at $9.1P_c$. Note this is limited by the interaction length of the gas jet. At $5.5P_c$, the sidescattered image formed has two distinct foci, and when the power exceeds $7.2P_c$, either multiple foci or a channel are observed, depending on shot-to-shot fluctuations and the gas jet position. A similar channel extension occurs if the gas density is varied at fixed laser power. For a 3.9 TW laser pulse, the channel extends to 250 $\mu$m at 400 PSI backing pressure ($1.4 \times 10^{19}$ cm$^{-3}$, $3.2P_c$) and 750 $\mu$m at 800 PSI ($2.9 \times 10^{19}$ cm$^{-3}$, $7.0P_c$). The consistent behaviour at specific values of $P_c$ for varying laser power or plasma density indicates that the channeling mechanism is relativistic self-focusing.

The sidescattered light was spectrally analyzed by an imaging spectrometer, and the bulk of the emission comes from incoherent Thomson scattering of the blue-shifted laser pulse. We were unable to obtain any information about the plasma density or temperature from this measurement. The divergence of the laser beam transmitted through the plasma was measured using a diffusing screen and a CCD camera with a 1.053 $\mu$m narrow bandpass filter. At all laser powers, the laser expands to twice the vacuum divergence, and we attribute this expansion to ionization defocusing. This is consistent with the strong blue-shifting we observe in the scattered spectra. Even though simulations indicate that the laser focuses to $\sim$2 $\mu$m[14], the complex dynamics that occur as the laser continually focuses and defocuses in the plasma make it impossible to determine the minimum self-focused beam width from the far field divergence angle.

A Maxwellian-like energy distribution has been observed in many previous experiments[15] and simulations[16], however no theoretical justification for it has been found to date. Because the energy distribution is exponential, a temperature in the longitudinal direction can be defined. The temperature of the low energy distribution changes from 500 keV (without guiding) to 750 keV (with guiding). In these plasmas, many different plasma waves can grow from various instabilities and local conditions. The interactions between these waves can lead to stochastic heating of the electron beam, so by extending the plasma length, the various waves will interact longer and heat the beam more. However, the dephasing length, $L_d = \lambda(\omega_o/\omega_p)^3$, which gives the maximum distance over which acceleration can occur (170 $\mu$m for our conditions), is significantly shorter than our accelerating length. From this expression, we would think that there would be no noticeable change in the electron spectrum when we extend the plasma length from 250 $\mu$m to 750 $\mu$m. Recent PIC simulations[16] indicate that this expression is too conservative for these highly nonlinear plasma interactions, and, in fact, the actual dephasing length may be many times longer. Consistent with our experimental results, these simulations indicate that the electron temperature, as well as the maximum energy, increase as the electrons propagate beyond the conventional dephasing length.

The relativistically self-guided channel was found to increase the laser propagation distance by a factor of four (limited thus far only by the length of gas), decrease the electron beam divergence by a factor of two (as shown in Fig. 4), and increase the electron energy. The electron beam

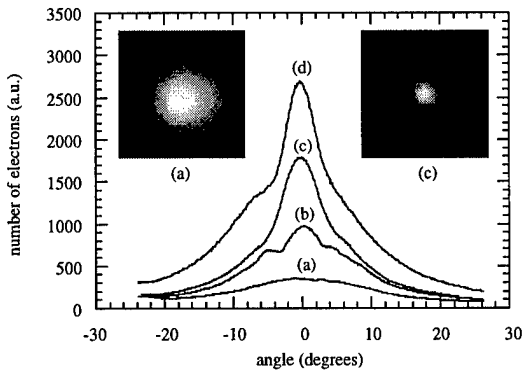



Figure 4: Electron beam divergence as a function of laser power. The various curves represent laser powers of $P/P_c =$ (a) 3.4, (b) 5.0, (c) 6.0, and (d) 7.5. The two insert figures show the complete beam images for curves (a) and (c).

profile was measured using a LANEX scintillating screen imaged by a CCD camera[10]. The LANEX is placed be-

hind an aluminum sheet which blocks the laser light, so only electrons greater than 100 keV can be imaged. Analysis of the electron spectrum indicates that the bulk of the electrons that create an image on the screen are in the 100 keV to 3 MeV range. We have found, using aluminum absorbers, that the electron divergence does not depend on electron energy in this range. At low power ($< 5P_c$), the electron beam has a Gaussian-like profile with a 10° radius at half-maximum (see Fig. 4). As the laser power increases and the plasma channel length increases to ~250 $\mu$m, a second peak seems to grow out of the low-power profile. Ultimately at the highest laser powers and longest channel lengths, the divergence decreases to 5°, and the profile becomes more Lorentzian-like. The electron beam divergence should decrease as the longitudinal energy of the electrons increases since space charge will be less and the relative transverse momentum decreases due to the longer accelerating length. However, there should be a minimum divergence due to the space charge effect after the electrons leave the plasma. This effect is significant since the electrons are in the few MeV range (small $\gamma$) and the peak current is high (large number of electrons in a short bunch). We have roughly estimated the space charge divergence to be 6° by assuming $10^9$ electrons at 1 MeV in a 1 ps bunch (note: $\theta_{hwhm} \propto \sqrt{N/\tau_e(\beta\gamma)^3}$, where $N$ is the number of electrons, $\tau_e$ is the electron bunch duration, and $\beta\gamma$ is the normalized momentum of the electrons)[17]. The electron beam emittance can be found from the measured divergence angle and the radius of the plasma channel, and in the best case (5° half-angle and 5 $\mu$m half-max radius), the calculated emittance ($\epsilon = r_o\theta_{hwhm}$) is 0.4 $\pi$-mm-mrad. To verify that the reduction in the beam emittance is due to the extension of the plasma channel, another gas jet with a narrower width was used and the same measurements repeated. In this case, the sidescattered images show that the channel length is limited to 360 $\mu$m and the electron beam divergence is fixed at 12° for all laser powers.

## 3 FUTURE DIRECTIONS

In several recent papers[18], we proposed an alternative accelerator concept, which we call the resonant laser-plasma accelerator (RLPA), having the following advantages: (i) by utilizing a train of laser pulses with independently adjustable pulse widths and interpulse spacings, which are varied in an optimized manner, resonance with both the changing plasma-wave period and phase resonance width can be maintained in the nonlinear regime, and the maximum plasma-wave amplitude is achieved; (ii) lower plasma densities can be used, thus avoiding electron-phase detuning; and (iii) lower peak laser intensities can be used, thus allowing for a reduction of laser-plasma instabilities. We numerically determined the characteristics of the plasma wave generated by a nonevolving, optimized laser pulse train in 1-D. In Fig. 5(a), we plot the wake field resulting from single pulse excitation (LWFA) including fast oscillations of the laser pulse.

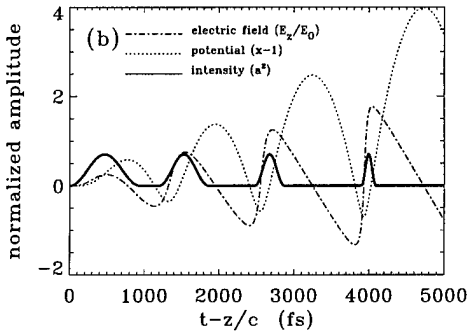



Figure 5: Numerical solutions for the RLPA with an optimized sine pulse train at $n_e = 10^{16}$ cm$^{-3}$ with $a_0 = 1.2$.

In the above experiments, the plasma itself acted as the cathode (the source of the electrons). Since the electrons were picked up by the wave and accelerated with random phases, their energy spread was large. This may be acceptable for medical radiological sources, where broadband bremstrahlung x-ray radiation is created anyway, by focusing the electron beam onto a metal target. However, in order to create monoenergetic femtosecond duration electron bunches, a new concept for laser injection of electrons was also developed theorectically (as shown in Fig. 6), again using the plasma itself as the cathode but with laser triggering[19]. Either transverse (as shown), collinear or

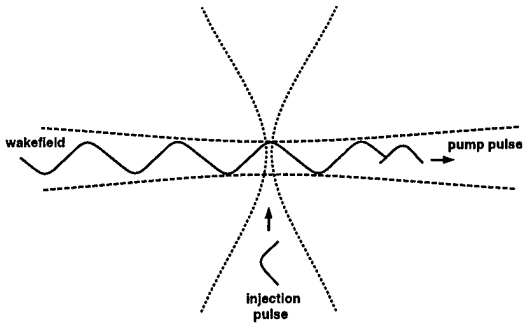



Figure 6: Schematic of the LILAC injector concept.

counter-propagating laser beams can be used for triggering. This is similar to giving several surfers identical pushes so that they all catch the same ocean wave in phase with one another. It was shown by use of a numerical code that with this method and by operating in the resonant wakefield regime ($\tau \sim \tau_p$), it should be possible to produce femtosecond electron bunches with energy spread at the percent level. We call the concept LILAC, which stands for Laser Injected Linear ACcelerator.

Normally, electrons oscillating in the plasma wave cannot be accelerated by the wake field since they are out of phase with it. Electrons that are not part of the plasma wave, however, can become trapped—i.e., continuously accelerated—by the plasma wave, provided that they are

moving in the correct phase at nearly the phase velocity of the wave [20]. Since this velocity is close to the speed of light, it is generally thought that the required pre-acceleration can only be accomplished with a conventional linac. However, the low-field gradient ($< 10$ MeV/m) [17], of a first-stage conventional linac prolongs the time during which beam emittance can grow before the beam becomes relativistic; after this point, self-generated magnetic fields can balance the effects of space charge. Even with state-of-the-art electron guns, the pulsewidth of the electron bunch can be considerably longer than the plasma wave period of a second-stage laser-plasma accelerator. It will thus fill multiple acceleration buckets uniformly in phase space, resulting in a large energy spread. Also, it is difficult to position and focus the electron-beam in the plasma channel with micron accuracy, and synchronize the electron beam with the plasma wave acceleration phase. We have shown theoretically that it can simply be done with an additional laser pulse[19]. The basic idea is that once a laser wake field is excited by the longitudinal ponderomotive force of one laser pulse (the pump pulse), the transverse ponderomotive force of a second, orthogonally directed laser pulse (the injection pulse) can then be used to locally alter the trajectories of some of the plasma wave electrons such that they become in phase with the wave's electric field and thus accelerated to the trapping velocity[19].

By permitting the use of laser wake fields in the injection stage, this concept not only dispenses with the need to merge two dissimilar technologies, as in proposed hybrid systems[21], it also significantly increases the capabilities and applications of plasma-based accelerators. It is easier to synchronize in phase and overlap in space the processes of electron injection and acceleration by employing the same basic mechanism for both. Improved electron beam emittance may result from the increased field gradient in the first acceleration stage, by minimizing the time during which electrons are non-relativistic and thus most susceptible to space charge effects. A device based on this concept can be used either as a stand-alone accelerator system or as an injector for either conventional or plasma-based high-energy accelerators. Both the energetic electrons and the high-energy photons into which they can be converted have numerous industrial, medical and scientific applications.

As an injector stage for linear electron colliders for nuclear and high-energy physics, this pulse length reduction may have several interesting consequences. In the case of an electron-electron linear collider, it would have a higher limit on attainable luminosity by permitting a shorter $\beta$ (in effect, the Rayleigh parameter of the magnetic optics) at the final focus/intersection point and it would also reduce beam-beam effects by reducing the time during which the beams overlap. There would also be a reduction in beam-beam Bremsstrahlung ("beamstrahlung") due to quantum mechanical effects. Such ultrashort-duration electron bunches may also become the basis for a new generation of table-top radiation sources. They may increase both the coherence and gain of synchrotrons, free-electron lasers, or Compton-scattering sources. Additionally, the ultrashort light-pulses that they may provide might be used to as "strobes" to probe temporal dynamics on the natural timescale of important ultrafast chemical, biological and physical processes.

## 4 REFERENCES


[1] P. Maine, D. Strickland, P. Bado, M. Pessot and G. Mourou, *IEEE J. Quantum Electron.* **QE-24**, 398 (1988).

[2] G. Mourou and D. Umstadter, *Phys. Fluids B* **4**, 2315 (1992).

[3] T. Tajima and J. M. Dawson, *Phys. Rev. Lett.* **43**, 267 (1979).

[4] N. E. Andreev, L. M. Gorbunov, V. I. Kirsanov, A. Pogosova and R. R. Ramazashvili, *Pis'ma Zh. Eksp. Teor. Fiz.*, **55** 551 (1992) [*JETP Lett.*, **55**, 571 (1992)].

[5] T. M. Antonsen, Jr., and P. Mora, *Phys. Rev. Lett.*, **69**, 2204 (1992).

[6] P. Sprangle, E. Esarey, J. Krall, and G. Joyce, *Phys. Rev. Lett.*, **69**, 2200 (1992).

[7] C. A. Coverdale, C. B. Darrow, C. D. Decker, W. B. Mori, K. -C. Tzeng, K. A. Marsh, C. E. Clayton, and C. Joshi, *Phys. Rev. Lett.* **74**, 4659, (1995).

[8] K. Nakajima, D. Fisher, T. Kawakubo, H. Nakanishi, A. Ogata, Y. Kato, Y. Kitagawa, R. Kodama, K. Mima, H. Shiraga, K. Suzuki, K. Yamakawa, T. Zhang, Y. Sakawa, T. Shoji, N. Yugami, M. Downer and T. Tajima, *Phys. Rev. Lett.* **74**, 4428, (1995).

[9] A. Modena, Z. Najmudin, A. E. Dangor, C. E. Clayton, K. A. Marsh, C. Joshi, V. Malka, C. B. Darrow, C. Danson, D. Neely and F. N. Walsh, *Letts. Nature* **377**, 606, (1995).

[10] D. Umstadter, S.-Y. Chen, A. Maksimchuk, G. Mourou, and R. Wagner, *Science* **273**, 472 (1996).

[11] A. Ting, K. Krushelnick, C. I. Moore, H. R. Burris, E. Esarey, J. Krall, and P. Sprangle, *Phys. Rev. Lett.* **77**, 5377 (1996).

[12] S. P. Le Blanc, M. C. Downer, R. Wagner, S.-Y. Chen, A. Maksimchuk, G. Mourou and D. Umstadter, *Phys. Rev. Lett.* **77**, 5381 (1996).

[13] R. Wagner, S.-Y. Chen, A. Maksimchuk and D. Umstadter, *Phys. Rev. Lett.* **78**, 3122 (1997).

[14] A. Chiron *et al.*, Phys. Plasmas **3**, 1373 (1996).

[15] C. Rousseaux, *et al.*, Phys. Fluids B, **4**, 2589 (1992).

[16] K.-C. Tzeng, *et al., Advanced Accelerator Concepts 1996*, to be published.

[17] S. Humphries Jr., *Principles of Charged Particle Accelerators* (Wiley, New York, 1986).

[18] D. Umstadter, E. Esarey, and J. Kim, Phys. Rev. Lett. **72**, 1224 (1994); D. Umstadter *et al.*, Phys. Rev. E **51**, 3484 (1995).

[19] D. Umstadter, J. K. Kim, and E. Dodd, *Phys. Rev. Lett.* **76**, 2073 (1996).

[20] E. Esarey and M. Pilloff, Phys. Plasmas **2** 1432 (1995).

[21] See *e.g., Advanced Accelerator Concepts, Fontana, WI, 1994*, Amer. Inst. of Conf. Proc. No. 335, P. Schoessow, ed., (AIP Press, New York, 1995) and references cited therein.

# STATE OF THE ART OF ECR ION SOURCES

Z. Q. Xie
Lawrence Berkeley National Laboratory
Berkeley, California, 94720

*Abstract*

Electron Cyclotron Resonance (ECR) ion source which produces highly-charged ions is used in heavy ion accelerators worldwide. Applications also found in atomic physics research and industry ion implantation. ECR ion source performance continues to improve, especially in the last few years with new techniques, such as multiple-frequency plasma heating and better methods to provide extra cold electrons, combined with higher magnetic mirror fields. So far more than 1 emA of multiply-charged ions such as $He^{2+}$ and $O^{6+}$, and 30 eμA of $Au^{32+}$, 1.1 eμA of $^{238}U^{48+}$, and epA currents of very high charge states such as $^{86}Kr^{35+}$ and $^{238}U^{60+}$ have been produced.

## 1 INTRODUCTION

Significant progress has been achieved since the first high charge state ECR ion source was developed more than two decades ago and it has become the choice of ion source for heavy ion accelerators worldwide [1,2]. Over the past years, ECR ion source development has evolved into two directions: production of higher charge states, more intense ion beams for accelerators; and compact ECR ion source with moderate performance for the production of radioactive ion beams and industry ion implantation. Figure 1 shows the present cw mode performance of high charge state ECR ion sources at various intensity levels as a function of atomic number [3,4].

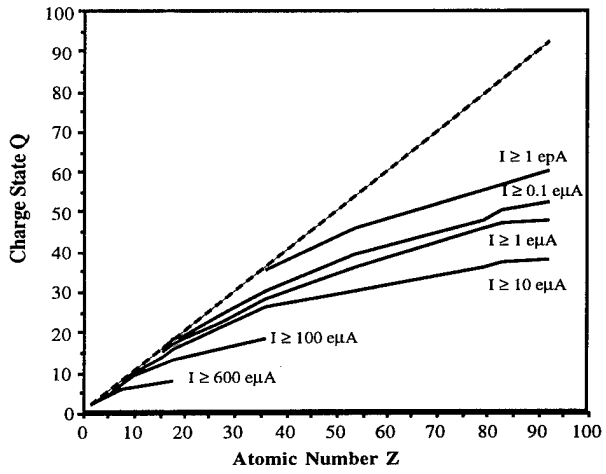



Figure: 1 Present ECR ion source performance at various intensity levels as a function of atomic number up to uranium.

ECR ion sources have been used to produce intense pulsed sulfur and lead ion beams for the heavy ion injector at CERN [5]. The present ECR ion source cw performance improved by pulsing (current ECR pulsed beam intensity is a factor of 2 to 3 or higher than its cw output [6]) or the next generation ECR ion sources with increased high charge state ion intensities could provide improved luminosity for the relativistic heavy ion colliders such as RHIC at Brookhaven National Lab.

This paper is not intended as a broad survey of ECR ion sources, instead it will review the progress made in the last few years that has significantly enhanced the performance of high charge state ECR ion sources.

## 2 ECR BASICS

In an ECR ion source microwave power is coupled by Electron Cyclotron Resonance Heating into a plasma confined in a minimum-B field magnetic bottle to produce ions. As the electrons spiral back and forth between the magnetic mirrors they are heated in a thin zone at an egg shaped ECR surface where the microwave frequency $\omega_f$ matches the electron cyclotron frequency $\omega_c$;

$$\omega_f = \omega_c = \frac{eB}{m_e}$$

where e, $m_e$ are the electron charge and mass, and B is the local magnetic field.

The primary source of cold electrons in an ECR ion source is the stepwise ionization of atoms and ions. Ions and electrons are kept in a dynamic equilibrium by ambipolar diffusion which maintains the neutrality of outgoing plasma. That is, the longer average electron confinement is the longer average ion confinement. There are two electron populations in a high charge state ECR ion source, cold and hot electrons due to the ECR heating [6]. The hot electrons have energies from about ten to a few hundred keV and confinement times in the range of milliseconds. The dominant electrons are the cold electrons which have energies up to a few hundred eV and confinement times in the range of hundred microseconds. These cold electrons are not magnetically confined and tend to escape more rapidly from the plasma than the ions because of their much higher mobility. The average electron confinement time $<\tau_e>$ in an ECR ion source can be expressed as;

$$<\tau_e> \approx (1 + \frac{n_{eh}}{n_{ec}})\tau_{ec}$$

where $n_{ec}$, and $n_{eh}$ are the cold and hot electron densities, and $\tau_{ec}$ is the cold electron average confinement time.

0-7803-4376-X/98/$10.00 © 1998 IEEE

This equation indicates that either a higher ratio of hot electrons to cold electrons or a longer cold electron confinement time $\tau_{ec}$ will increase the average electron confinement and thereby the average ion confinement time $\tau_i$. High hot electron density and long ion confinement are very essential to ECR ion sources for the production of high charge state ions, especially those ions with ionization potentials of tens of keV in which the ionization cross sections are very small. To produce the high charge state ions, ECR plasma always tends to run as high microwave power as possible if the plasma remains stable and low neutral pressure to reduce the charge exchange.

## 3 ECR ION SOURCE PROGRESS

The current methods to maximize the performance of high charge state ECR ion sources include multiple-frequency plasma heating, aluminum oxide surface coating to provide extra cold electrons into the plasma, and improved plasma confinement with higher magnetic mirror fields.

### *3.1 Multiple-frequency Plasma Heating*

The minimum-B field configuration in a high charge state ECR ion source can provide many closed and nested ECR heating surfaces, as graphically shown in Fig. 2, for incoming microwaves with various frequencies. Typically a single microwave frequency is used in an ECR ion source to produce only one egg-shaped ECR heating zone. The electrons are heated twice when they travel from one mirror point to the other. If two or more significantly different frequencies that match the minimum B-field are used, two or more well separate and nested ECR surfaces will exist in the ECR plasma. The lower frequency waves can propagate through the ECR plasma because a high charge state ECR ion source typically runs with an underdense plasma. With the multiple ECR surfaces, electrons can be heated four times or more for one pass from one end to the other and this will lead to a higher density of the hot electrons and enhanced production of high charge state ions.

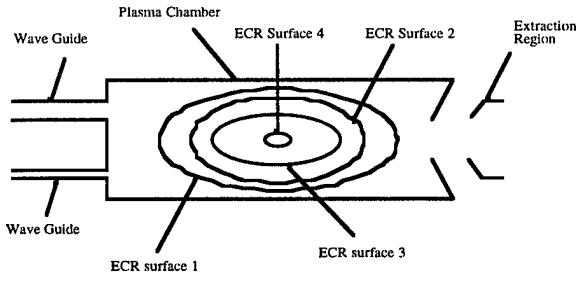



Figure: 2 Schematic view of the a few nested ECR surfaces in a high charge state ECR ion source.

Tests with two-frequency plasma heating on the LBNL AECR ion source [7] have shown that plasma was more quiescent than single-frequency heating [8]. The short-term and the long-term plasma stability were both improved and more total microwave power could be launched into the plasma. With the improved plasma stability, the source can run at lower neutral inputs which indicates a lower neutral pressure since the mechanical pumping are the same. The lower neutral pressure and higher microwave power result in higher hot electron density. Tests were done to compare two-frequency heating to single frequency heating with the same gas and vapor inputs and the same total microwave power. The two-frequency heating shifted the peak charge state of bismuth slightly and enhanced the high charge state ions by a factor of 2 for charge states 36+ to 40+ [8]. The intensity increase and slight peak charge state shift indicate the difference between single frequency and two-frequency heating. With 15% more microwave power than the case of single-frequency heating, the two-frequency heating shifted the peak charge state for uranium from 33+ to 36+ and increased the intensity by a factor of 2 to 4 for charge states from 35+ to 39+ and produced greater enhancements for the higher charge states as indicated by Curve 1 and Curve 2 in Fig. 3.

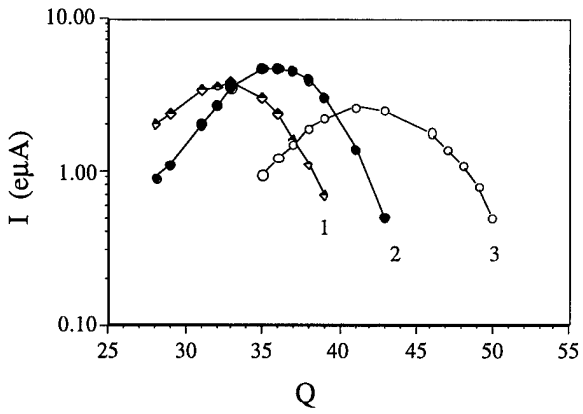



Figure: 3 Charge state distributions for uranium produced with the LBNL AECR and AECR-U ion source. Curve 1 indicates the case of single-frequency (14 GHz, at power of 1.54 kW) heating and Curve 2 is the case of two-frequency (14+10 GHz, at total power of 1.77 kW) heating. Curve 3 shows the higher charge state uranium ion beams produced with the AECR-U at higher microwave power (14+10 GHz, at total power of 2.1 kW).

### *3.2 Effects of the Extra Cold Electrons*

Besides the cold electrons from ionization process, ECR plasma needs additional cold electrons to enhance the production of high charge state ions. With these extra cold electrons, the high charge state ECR ion sources can run at lower neutral pressure and higher microwave power which are essential to the production of high charge state ions.

Various active methods, such as a microwave-driven first stage [9], an electron gun [10], a bias probe [11] and a plasma cathode [12], have been used to provide the extra cold electrons to ECR plasmas. The electrons injected by these active methods are mainly along the magnetic field lines. Except the bias probe, they are more complex and costly than plasma chamber surface coatings. In ECR ion sources the plasma chamber surface is parallel to the axis therefore a large portion of the secondary electrons emitted from the surface are perpendicular to the axis. Enhanced source performance by plasma chamber surface coatings with high yield of secondary electrons, such as $SiO_2$, $ThO_2$ and $Al_2O_3$, have been experimentally observed [13-15]. The improved source performance demonstrated that chamber surface coating is an excellent method to provide the additional electrons needed by an ECR plasma. Empirically speaking, a good surface coating for an ECR ion source should have:

1. High secondary electron emission.
2. Resistance to plasma etching.
3. Low material memory.

Although the secondary electron emission of $Al_2O_3$ ($\delta_{max} = 9$) is not the highest, it is very resistant to plasma etching and has relatively low material memory. Plasma potential measurements have shown that $Al_2O_3$ coating yields the lowest average plasma potential and it is almost independent of microwave power [16]. A lower plasma potential reduces the ion sputtering and improves plasma stability [17]. All of these desirable characteristics make $Al_2O_3$ the best surface coating for high charge state ECR ion sources. With an $Al_2O_3$ chamber surface coating, various ECR ion sources have shown that the ECR plasma can run at lower neutral pressure and substantially enhanced the production of highest charge state ions [3,4,18]. Listed in Table 1 are the performance of a few ECR ion sources with $Al_2O_3$ coating.

Table 1. Performance of a few ECR ion sources with aluminum oxide coating

| ION | LBNL AECR-U 14+10 GHz | Grenoble CAPRICE 14 GHz | RIKEN ECR-18 18 GHz |
|---|---|---|---|
| $O^{6+}$ | 570 | 760 | 500 |
| $O^{7+}$ | 306 | 100 | 130 |
| $Ar^{14+}$ | 77 | 15 | 25 |
| $Ar^{16+}$ | 21 | 1 | 5 |
| $Kr^{18+}$ | 100 | 55 | |
| $Kr^{25+}$ | 19.4 | 2 | |
| $Xe^{28+}$ | 21 | 10 | |
| $Xe^{31+}$ | 7 | | |
| $U^{36+}$ | 13.3 | 1.4 | |
| $U^{39+}$ | 9.3 | 0.17 | |
| $U^{48+}$ | 1.1 | | |

Currents are in eμA.

### *3.3 Higher Magnetic Mirror Fields*

Based on the so called "frequency scaling law" proposed in 1987 [13], a number of ECR ion sources were designed and built to operate at frequencies of 14, 18 and up to 30 GHz [19]. The designed magnetic fields of these sources were typically with maximum mirror ratios of 2 to 3. The significantly improved performance of these higher frequency ECR ion sources, as compared to the lower frequency sources with lower magnetic fields, indicates an increase in the $n_e\tau_i$.

Recent ECR ion source development demonstrated that the nominal magnetic mirror field with a maximum mirror ratio of 3 is not yet optimized for the current operating frequencies [20,21]. Significant improvement is still possible with higher magnetic mirror fields [22,23].

In an ECR ion source the plasma pressure $w_{pl}$ can be loosely related to the magnetic field as;

$$w_{pl} = K\,(n_{ec}T_{ec} + n_{eh}T_{eh}) \propto B^x \qquad (1 \le x \le 2)$$

where $K$ is the Boltzmann constant, $T_{ec}$ and $T_{eh}$ are the cold and hot electron temperatures, respectively. A higher magnetic mirror field will surely improve the plasma confinement. It can sustain a higher plasma pressure with either a higher total electron density or a higher density of the hot electrons when the source operates at lower neutral inputs. Naturally the higher magnetic mirror field should lead to an enhanced ECR ion source performance.

## 4 PERFORMANCE OF THE LBNL AECR-U ION SOURCE

Although its overall magnetic fields of the LBNL AECR were about 50% lower than other 14 GHz ECR ion sources, it had produced outstanding high charge state ion beams with the applications of two-frequency plasma heating and $Al_2O_3$ coating [8,16]. This ion source was recently upgraded (LBNL AECR-U) by increasing its magnetic fields. Shown in Fig. 4 is an elevation view of the AECR-U ion source. The maximum axial peak fields of AECR-U increased from 1.0 to 1.7 Tesla at the injection side and from 0.7 to 1.0 Tesla at the extraction region. With the center field remains at about 0.4 Tesla, the mirror ratios increased from 2.4 to 4.2 at the injection side and from 1.8 to 3.0 at the extraction region [3]. A new set of NdFeB permanent sextupole magnet raised the maximum radial field from 0.62 to 0.85 Tesla at the inner surface of the plasma chamber made from aluminum. After the magnetic field configuration was optimized to match the two-frequency plasma heating (14+10 GHz), the AECR-U demonstrated significantly enhanced performance compared to its predecessor. When tuned to produce the very high charge state ion beams or intense intermediate charge state ion beams, the source runs best at the maximum available microwave power of 2.1 kW from the 14 and 10 GHz klystrons (1.5 kW and 0.6 kW, respectively). The optimum operation neutral pressure is also lower. Table 2 lists the present performance of this

ion source for a few typical elements. So far, 30 eμA of $Au^{32+}$, 18.5 eμA of $Au^{35+}$ were produced. For heavy ions at intensity of about 1 eμA, the charge state shifted from 42+ to 48+ for uranium-238 (see Fig. 3). The production of about 1 eμA of the heaviest natural element with more than half its electrons removed represents a milestone in ECR ion source development. Besides the improvement on the heavy ions, an order of magnitude enhancement for fully stripped argon ions (I ≥ 60 enA) also has been achieved. Hydrogen-like krypton ions at intensity of about epA were first time produced from an ECR ion source. High charge state heavy ion beams of xenon-136 up to 46+ and uranium-238 up to 60+ were produced from the AECR-U source and were accelerated and extracted by the 88-Inch Cyclotron. $U^{60+}$ was accelerated to a record energy of 1.94 GeV at the cyclotron. The greatly improved performance of the AECR-U for the high charge state ions demonstrates the effect of higher magnetic mirror fields.

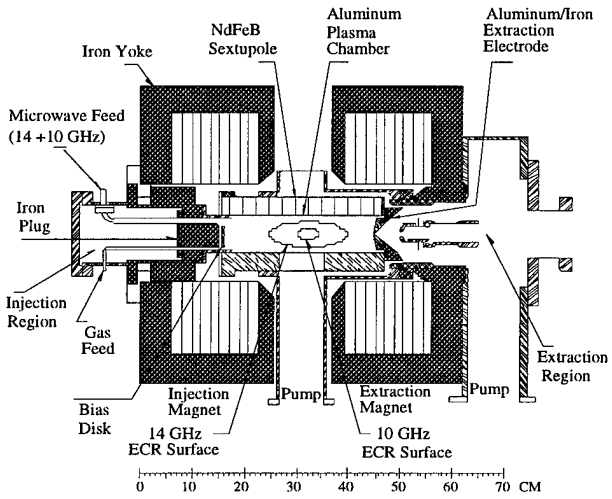



Figure: 4 An elevation view of the LBNL AECR-U ion source.

The AECR-U ion source and a similar version of this source under commissioning [24] at ANL are currently the only ECR ion sources that combine multiple-frequency plasma heating, aluminum oxide coating with a bias probe and higher magnetic mirror fields. The AECR-U has produced record intensities of high charge state ions. Unlike other high field ECR ion sources, the AECR-U has radial pumping through six radial slots, which also provide oven access. In the author's point of view this also contributes significantly to the source performance. The radial pumping results in better vacuum control inside the plasma chamber. A lower neutral density in a high charge state ECR ion source is critical for the production of high charge state ions as the charge exchange cross sections increase faster than the square of the charge state [25].

Table 2. Performance of the LBNL AECR-U ion source

| Q | O | Ar | Ca | Kr | Q | Xe | Au | Bi | U |
|---|---|---|---|---|---|---|---|---|---|
| 6+ | 570 | | | | 30+ | 10.2 | 35.5 | | |
| 7+ | 306 | | | | 31+ | 7 | 33.4 | 29.3 | 24.5 |
| 8+ | ~75 | | | | 32+ | 4.6 | 30 | 29.3 | 24 |
| 9+ | | | | | 33+ | 2.9 | * | 27 | 23 |
| 10+ | | | | | 34+ | * | 22.5 | 24.1 | 20 |
| 11+ | | 270 | 225 | | 35+ | 1.6 | 18.5 | * | 16 |
| 12+ | | 192 | 175 | | 36+ | 1 | 13.5 | 16 | 13.3 |
| 13+ | | 120 | 125 | | 37+ | 0.6 | * | 11.9 | 12.7 |
| 14+ | | 77 | 83 | | 38+ | 0.25 | 9.2 | 9.4 | 11.3 |
| 15+ | | * | * | | 39+ | | * | * | 9.3 |
| 16+ | | 21 | 25.6 | | 40+ | | 4.8 | 5.2 | * |
| 17+ | | 1.35 | * | 116 | 41+ | | 3.2 | 4.4 | 5 |
| 18+ | | 0.06 | 3.1 | 100 | 42+ | | * | * | 4 |
| 19+ | | | 0.25 | 79 | 43+ | | 2 | 3 | 3.1 |
| 20+ | | | | 63 | 44+ | | 1.5 | 2.2 | * |
| 21+ | | | | 50 | 45+ | | * | * | * |
| 22+ | | | | 40 | 46+ | | 1 | 1.2 | 1.8 |
| 23+ | | | | 29 | 47+ | | 0.5 | 0.9 | 1.4 |
| 24+ | | | | 22.6 | 48+ | | | 0.6 | 1.1 |
| 25+ | | | | 19.4 | 49+ | | | 0.25 | 0.8 |
| 26+ | | | | 18 | 50+ | | | 0.15 | 0.5 |
| 27+ | | | | * | 52+ | | | | 0.1 |
| 28+ | | | | 2.3 | 54+ | | | | 0.04 |
| 29+ | | | | 0.4 | 55+ | | | | 0.02 |

Note: Enriched isotopes of Kr and Xe were used.
Current are in eμA. *: Mixed ion species.

## 5 FUTURE ECR ION SOURCES

Recent ECR ion source development demonstrated the further enhanced performance on high charge state ions remains possible with higher magnetic mirror fields. However the maximum field strengths reached by conventional magnets of practical size and power consumption is about 2 Tesla while superconducting magnets can achieve higher magnetic mirror fields. Previous superconducting ECR ion sources built demonstrated the feasibility of higher mirror fields with superconducting magnets [19,26,27]. New superconducting ECR ion sources with magnetic fields up to 4 Tesla and maximum mirror of 10 are under construction and commissioning [28,29]. Shown in Table 3 are the design parameters for the new superconducting ECR ion sources, the Catania SERSE and the LBNL 3rd Generation ECR ion source. These higher magnetic mirror fields combines with multiple-frequency heating and better techniques to provide the extra cold electrons, should further greatly enhance the ECR ion source performance.

Table 3. Design parameters of the new superconducting ECR ion sources

| | LBNL 3rd ECR source | CATANIA SERSE |
|---|---|---|
| Mirror field on axis (T) | 4, 3 | 2.7, 1.5 |
| Central field (T) | 0 to 1.0 | 0.4 to 0.5 |
| Typical radial field on I.D. of plasma chamber (T) | 2.4 | 1.4 |
| Mirror-mirror spacing (cm) | 50 | 50 |
| I.D. of plasma chamber (cm) | 15 | 13 |
| Proposed operating frequency (GHz) | 10+14+18 or 6+10+14 ? | 14 to 30 or ? |

## 6 ACKNOWLEDGMENTS

The author would like to thank Dr. D. Hitz. Dr. T. Nakagawa for providing test results on the Grenoble 14 GHz CAPRICE and RIKEN ECR-18GHz ion source. Special thanks should be given to Dr. C.M. Lyneis for his help in clarifying many of the concepts presented here.

This work was supported by the Director, Office of Energy Research, Division of Nuclear Physics of the Office of High Energy and Nuclear Physics of the U.S. Department of Energy under Contract DE ACO3-76SF00098.

## REFERENCE

[1] R. Geller, IEEE Trans. Nucl. Sci. NS-**23**, 904 (1976).

[2] C. M. Lyneis, Proceedings of the 13th International Conference on Cyclotrons and their Applications, Vancouver, British Columbia, Canada, 1992, p. 301.

[3] Z. Q. Xie and C. M. Lyneis, Proceedings of the 13th International Workshop on ECR Ion Sources, College Station, Texas, Feb 1997, to be published.

[4] D. Hitz et al., Rev. Sci. Instrum. **67**, 883 (1996).

[5] M. P. Bougarel, C. E. Hill, H. Haseroth, K. Langbein and E. Take, Proceedings of the 12th International Workshop on ECR Ion Sources, RIKEN, Japan, 1995, p. 193.

[6] G. Melin and A. Girard, Chapter 2 in "Accelerator-based Atomic Physics techniques and Applications," edited by S. M. Shafroth and J. C. Austin, AIP Press, 1997.

[7] C.M. Lyneis, Z. Q. Xie, D.J. Clark, R.S. Lam and S.A. Lundgren, Proceedings of the 10th International Workshop on ECR Ion Sources, Oak Ridge, ORNL CONF-9011136, 1990, p. 47.

[8] Z. Q. Xie and C. M. Lyneis, Rev. Sci. Instrum. **66**, 4281 (1995).

[9] R. Geller, IEEE Trans. NS-26, No. **2**, 2120 (1979).

[10] Z. Q. Xie, C.M. Lyneis, R.S. Lam, and S.A. Lundgren, Rev. Sci. Instrum. **62**, 775 (1991).

[11] Melin, G., et al., Proceedings of the 10th International Workshop on ECR Ion Sources, Oak Ridge, ORNL CONF-9011136, 1990, p. 1.

[12] T. Nakagawa, T. Kageyama, Jpn. J. Appl. Phys. **30**, 1588 (1991).

[13] R. Geller et al, Proceedings of the International Conference on ECR Ion Sources and their applications, East Lansing, NSCL Report #MSUCP-47, 1987, p. 1.

[14] C.M. Lyneis, Proceedings of the International Conference on ECR Ion Sources and their applications, East Lansing, NSCL Report #MSUCP-47, 1987, p. 42.

[15] T. Nakagawa, Jpn. J. Appl. Phys. **30**, 930 (1991).

[16] Z. Q. Xie and C. M. Lyneis, Rev. Sci. Instrum. **65**, 2947 (1994).

[17] D. Meyer, D. O. Bolshukhin, I. P. Vinogradov and K. Wiesemann, Rev. Sci. Instrum. **67**, 883 (1996).

[18] T. Nakagawa, et al., Jpn. J. Appl. Phys. in press.

[19] T.A. Antaya, H. G. Blosser, J. M. Moskalik, J. A. Nolen and A. F. Zeller, Proceedings of the International Conference on ECR Ion Sources and their applications, East Lansing, NSCL Report #MSUCP-47, 1987, p. 312.

[20] B. Jacquot and R. Geller, Proceedings of the International Conference on ECR Ion Sources and their applications, East Lansing, NSCL Report #MSUCP-47, 1987, p. 254.

[21] T. A. Antaya and S. Gammino, Rev. Sci. Instrum. **65**, 1723 (1994).

[22] R. Leroy et al., Proceedings of the 12th International Workshop on ECR Ion Sources, RIKEN, Japan, April 1995, p. 57.

[23] D. P. May and G. J. Derrig, Proceedings of the 12th International Workshop on ECR Ion Sources, RIKEN, Japan, 1995, p. 170.

[24] M. Schlapp et al., in Proceedings of this conference.

[25] A. Müller and E. Salzborn, Phy. Letters **62A**, 391 (1977).

[26] Y. Jongen and G. Ryckewaert, Proceedings of the 5th International Workshop on ECR Ion Sources, Louvain-La-Neuve, Belgium, 1983, p. 93.

[27] H. Beuscher, Rev. Sci. Instrum. **61**, 262 (1990).

[28] G. Ciavola and S. Gammino, Proceedings of the 13th International Workshop on ECR Ion Sources, College Station, Texas, Feb 1997, to be published.

[29] C. M. Lyneis and Z. Q. Xie, Proceedings of the 12th International Workshop on ECR Ion Sources, RIKEN, Japan, 1995, p. 119.

# VERY-LOW-ENERGY-SPREAD ION SOURCES*

Y. Lee†
Lawrence Berkeley National Laboratory,
University of California, Berkeley, California 94720

*Abstract*

Axial ion energy spread of multicusp sources has been measured by three different techniques: an electrostatic energy analyzer for plasma ion measurement at the source exit; a magnetic deflection spectrometer; and a retarding-field energy analyzer for measurement of the accelerated beam. By introducing a magnetic filter inside the multicusp source chamber, it is shown that the energy spread of positive hydrogen ions can be reduced to approximately 1eV. The energy-spread values for $H^-$ ions are lower. New ion source configurations are now being investigated to further reduce the ion energy spread to below 1 eV and maximize source performance reliability and lifetime.

## 1 INTRODUCTION

The multicusp source has been the ion source of choice for many applications due to its capability to produce large volumes of uniform, quiescent and high-density plasmas with high electrical and gas efficiencies. Recently, new applications have found use for multicusp ion sources because of their capability to generate ion beams with low axial energy spread. Some of these applications are ion projection lithography where low axial or longitudinal energy spread (< 3eV) is required to minimize the chromatic aberrations of the projected pattern [1]. In radioactive ion beam projects for nuclear physics experiments, an ion source with axial energy spread of less than 1 eV is needed to perform isobaric separation with a magnetic deflection spectrometer [2]. In low energy ion beam deposition processes, very low energy spread is required in order to separate and focus the ions properly [3]. In neutron time-of-flight experiments, a low energy-spread beam is needed to obtain a well defined short pulse [4].

This article reviews different techniques for measuring the axial ion energy spread of the multicusp ion source. It is demonstrated that the presence of a permanent-magnet filter can reduce the ion energy spread from 6 eV to approximately 1 eV for moderate discharge power. The energy spread of the $H^-$ ions is generally lower than the source reliability and lifetime, various ion source configurations (such as the RF-driven and the co-axial type multicusp source) are being investigated. Preliminary results are presented in this article.

## 2 EXPERIMENTAL ASSEMBLY

### *6.1 Ion Source Arrangement*

The ion source tested have a multicusp generator arrangement: the external surface of the source chamber is surrounded by columns of samarium-cobalt permanent magnets with alternating polarity. These magnets generate longitudinal line-cusp magnetic fields that can confine the primary ionizing electrons efficiently. One end of the chamber is terminated by an end flange which is covered with rows of permanent magnets. The open end of the chamber is where the energy analysis takes place. As shown in Fig. 1, a magnetic filter system can be installed in the source chamber which provides a limited region of transverse magnetic field and divides the chamber into two regions: (1) the discharge or source chamber, where the plasma is formed and contains the energetic ionizing electrons and (2) the extraction chamber, where a plasma with colder electrons is found.

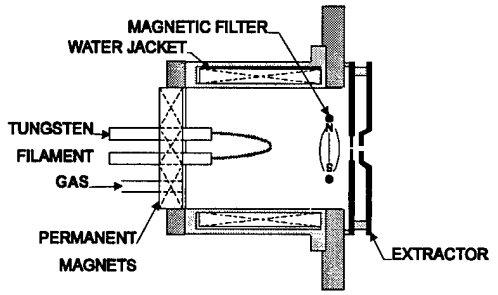



Figure. 1 Schematic of a multicusp ion source when is operated with a filament cathode.

Two different types of multicusp source configurations have been tested: dc filament-discharge ion source, rf-

* This work was supported by the Advanced Lithography Group (ALG) under CRADA BG-94-212(00) with the Lawrence Berkeley National Laboratory and the Division of Nuclear Physics, Office of Energy Research, U.S. Department of Energy under Contract No. DE-AC03-76SF00098.
† Also with the Nuclear Engineering Department, University of California Berkeley, California, USA.

0-7803-4376-X/98/$10.00 © 1998 IEEE

driven source. In the filament discharge, a steady-state plasma is produced by primary electrons emitted from a tungsten filament. The source is normally operated with a discharge voltage of 70 V and a discharge current between 2 - 10 A. In the rf-driven source, the tungsten filament of the filament discharge source is replaced by an rf-antenna operating at a frequency of 13.56 MHz. The antenna is fabricated with copper tubing and is coated with a thin layer of porcelain which enhances the discharge efficiency and prolongs the source lifetime.

*2.2 Axial Energy Spread Measurement Methods.*

A gridded retarding field energy analyzer has been used to study the longitudinal energy spread of the positive ion species at the plasma or first electrode [5]. The ion source and the energy analyzer assembly is illustrated in Fig.2. The energy analyzer contains a fine-meshed grid which is biased negatively for electron suppression and a collector for energy distribution measurement. The energy analyzer is connected to a computerized data acquisition system, cosisting of a computer and two multimeters.

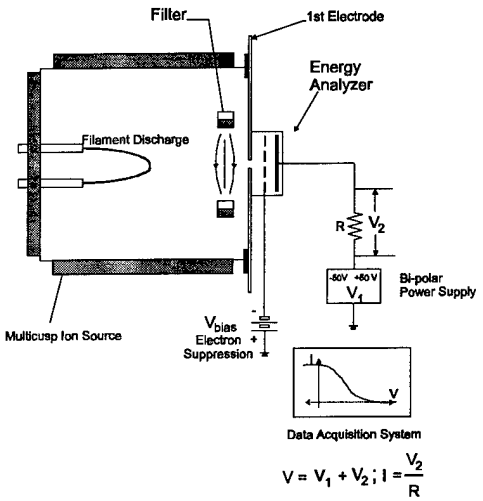



Figure. 2 Schematic of the ion source with the removable filter and the retarding field energy analyzer at the source aperture assembly.

This technique does not require an acceleration system and it measures the true ion energy spread of the source. In this arrangement, the collected ion current as a function of bias voltage is first measured. The I-V characteristic is then differentiated to determine the energy spread ($\Delta E$) which is defined as the full width at half maximum (FWHM) of the differentiated curve.

A three-electrode extractionn system with a 0.6 mm diameter aperture has been used for beam formation. In normal operation, the ion source and the first electrode are electrically biased at 7 kV, and the second electrode at -1 kV with respect to the ground potential. The last or third electrode is connected to ground. In this configuration, the second electrode operates as a suppresser to prevent backstreaming electrons from accelerating back to the ion source.

The retarding-field energy analyzer is used to measure the axial energy spread of the accelerated beam. Fig. 3 shows the experimental setup which includes the ion source, the extraction system and the retarding field energy analyzer. The expanding beam is collimated well enough that the ion trajectories are almost parallel by the time they reach the collector plate of the enrgy analyzer. The collector plate, where the energy analysis takes place, is electrically connected to the ion source. A small battery or variable power supply is used to adjust the collector plate potential to $\pm$ 90 V with respect to the source. The acfcelerated beam is slowed down by the time it reaches the collector plate in order to avoid high energy beam heating on metal.

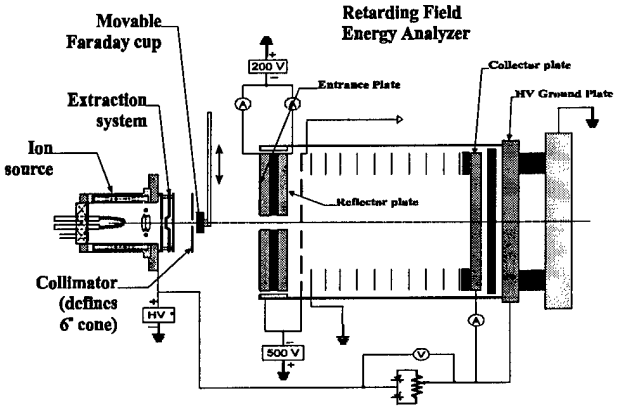



Figure. 3 Schematic of the retarding field energy analyzer system for accelerated beam energy spread measurements.

The magnetic energy analyzer is used to measure energy spread of various positive ion species and $H^-$ ions in the accelerated beam. A schematic of the source with the magnetic energy analyzer is shown in Fig. 4. The enrgy spread can be inferred from the output spectrum of the ion species. Each peak in the distribution has a finite width due to the axial energy spread of individual species [6].

The magnetic field B applied to deflect a singly charged ion of mass M and energy E to a gyroradius R is given by

$$B(\text{Gauss}) = 144\,[\mu E(\text{eV})]^{1/2}/R(\text{cm})$$

where $\mu = M/M_p$ and $M_p$ is the proton mass. As shown in the schematic of Fig. 5, the energy of the individual ion peaks is the same and the distance along the x-axis (the B-field) is proportional to $(ME)^{1/2}$. The center of the individual ion peak is the average energy of the extracted ion beam species. $\Delta E$ is the difference between $E_2$ and $E_1$. The energy spread also includes the

instrumental contribution to the width which provides the upper limit of the energy spread.

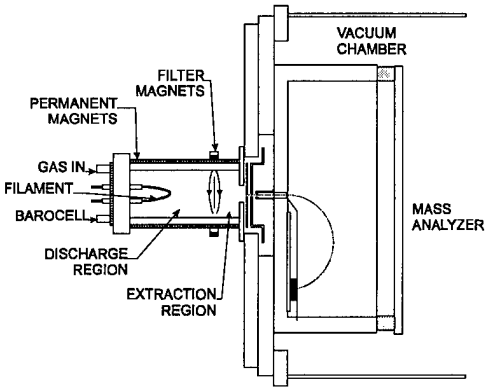



Figure. 4 Schematic drawing of a filament operated multicusp ion source mounted in a vacuum chamber. A magnetic analyzer is used for analyzing the collimated and accelerated beam.

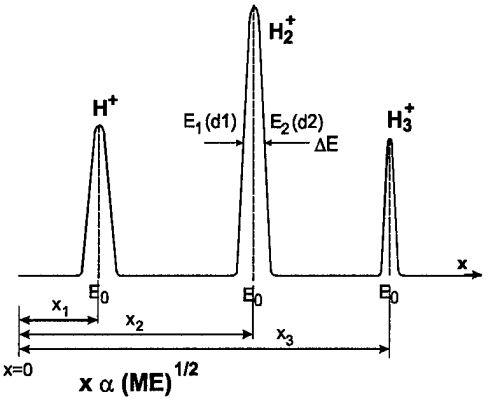
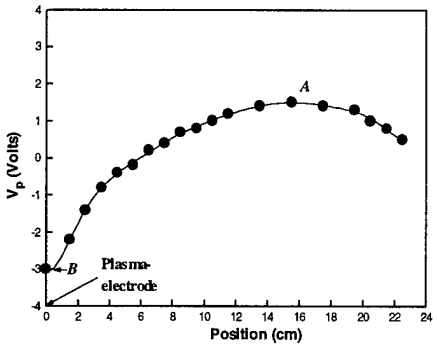



Figure. 5 The axial energy spread is found from the ion species traces. The energy of the individual ion peaks is the same and the distances are proportional to $(ME)^{1/2}$. The position of the individual ion peak center is the average energy of the extracted ion beam species.

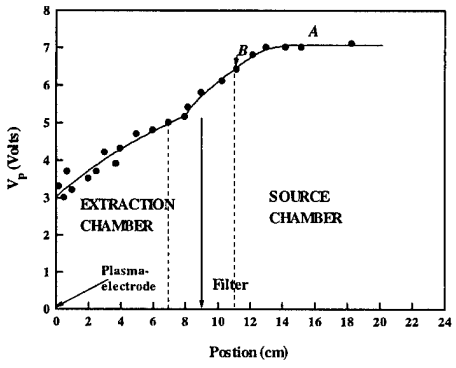
## 3 EXPERIMENTAL RESULTS

The results for the different analyzing methods are consistent. As expected, the axial energy spread of the ions is lower with the presence of filters than without [5]. When the source operates without a filter, the axial plasma potential decreases monotonically towards the plasma electrode, as shown in Fig. 6a. ***A*** and ***B*** are the maximum and minimum plasma potential values where ions can be formed. Ions formed at position ***A*** have more energy than ions formed in position ***B***, given by the difference in potential between the two points. Positive ions generated at high plasma potential ($V_p$) will reach the extractor as well as the ions created at lower potentials. Since the ions are generated at positions with different plasma potential, they will have a spread in axial energy when they arrive at the extraction aperture. Due to the presence of primary electrons everywhere in the source, ionization may take place in the plasma sheath of the extraction aperture [5].

The presence of the filter reduce the energy spread since it create a region with a relatively uniform $V_p$ profile in the discharge chamber region, as shown in Fig. 6b. Primary electrons are confined in the source chamber by the filter magnet fields as well as the multicusp field on the chamber walls. The potential gradient in the extraction region produces no effect on the energy spread. Since positive ions are produced within the source chamber region, they arrive at the plasma electrode with about the same energy due to the uniform $V_p$ distribution. However, there is still a small potential gradient, given by the potential difference between point ***A*** and ***B*** (approximately 1 V), between the center and the filter region that causes a small spread.




a)



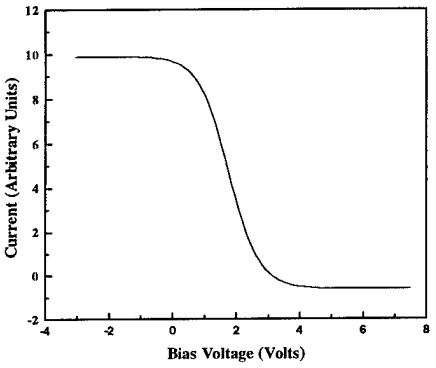

b)

Figure. 6 (a) Axial plasma potential profile inside the source in the absence of a magnetic filter. (b) Axial plasma potential profile inside the source in the presence of a filter.

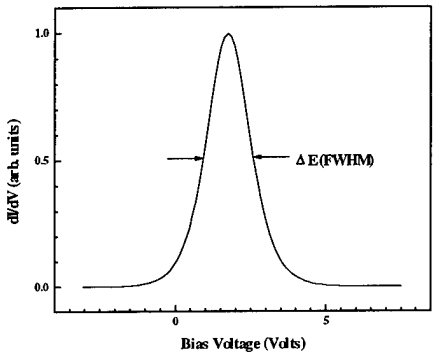
### *3.1 Energy spread analysis at the source exit*

The axial energy spread at the source exit of filament driven ion sources without the magnetic filter ranges from 3 to 7 eV under different conditions of discharge current, and pressure. A typical I-V characteristic curve and its corresponding differentiated curve are shown in Fig. 7a and 7b. The data in Fig. 8 show that ΔE

decreases with increasing pressure when the plasma electrode is connected to the anode. At high source operating pressures, ionization takes place close to the filament cathode. Primary electrons do not reach the extraction region where $V_p$ is decreasing rapidly. Secondary emission electrons originating from the plasma electrode will not have enough energy to ionize the neutral particles (similar to the effect of a filter) [5]. The energy spread of the source without filter increases with the increase of discharge current due to the increase of the plasma potential, as shown in Fig. 9. Such effects are absent in the case with filter because the relatively uniform plasma potential distribution remains in the discharge chamber.




a)




b)

Figure. 7 (a) The I-V characteristics of the energy analyzer for the filament discharge source. (b) The I-V curve of Fig. 5a is differentiated to obtain the axial energy spread.

*3.2 Retarding field enerergy analyzer measurements for accelerated beams.*

After accelerating the beam to 7 keV, the axial energy spread of the filament-driven source without filter is on the order of 5 eV due to the larger plasma potential variation inside the source where ions are formed. In the presence of the magnetic filter, ΔE is found to be 3.3 eV at a discharge current of 9 A. At a discharge current of 1 A, the axial energy spread is 1.2 eV.

The axial energy spread of the accelerated beam of the rf-driven multicusp ion source was measured with the rf power supply operated at ground potential. Voltage isolation is obtained by using a transformer with sufficient insulation in the matching circuit. Initial measurements of the axial ion energy spread for accelerated beam from the rf source were greater than 100 eV, very large compared to the measured values of 2 to 3 eV for filament discharge cases. This measured energy spread is comparable to the value that have been reported by Zackhary [7] and Olthoff et al [8].

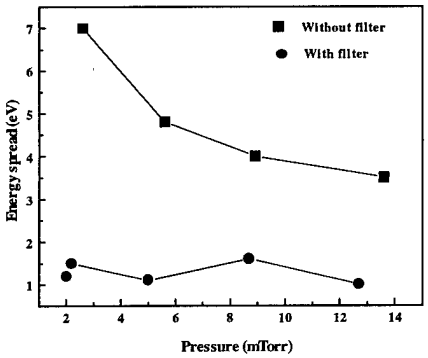



Figure. 8 Pressure vs. energy spread for a 10 cm diameter source with and without a magnetic filter.

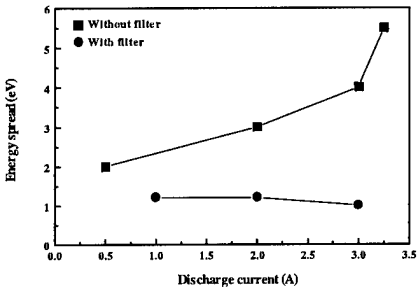



Figure. 9 Discharge current vs. energy spread for a 10 cm diameter source with and without a filter.

The large axial energy spread of the rf source may have been due to the rf voltage coupling to the extraction voltage, thus resulting in a modulation of the beam energy. The rf modulation has been eliminated through the following steps. Problems associated with ground loops between the measurement devices and the data acquisition circuits have been minimized with the use of fiber optics for electrical isolation and with longitudinal chokes (neutralizing transformers). Longitudinal chokes are used to eliminate longitudinal currents within the ground loop, while having an insignificant effect on the signal current [9].

The axial energy spread is reduced when the rf power supply is installed at the high voltage platform, so that it is operated at the same potential as the ion source. The leads between the matching network and the induction coil are shielded to reduce the energy spread. Operating the rf power supply at the extraction potential enables complete shielding of the leads between the matching network and the induction coil. A voltage isolator between the matching network and the source is no longer required. Furthermore a set of capacitors that function as a low-pass filter can eliminate the modulation of the dc acceleration voltage with rf-interference. With all these modifications, the axial energy spread was reduced to 3.6 eV at 1 kW, which is approximately the same value as the filament discharge case.

*3.3 Magnetic energy analyzer.*

The ion species distribution for energy spread analyses is obtained by the use of the magnetic deflection mass spectrometer. In the distribution, each peak has a finite width due to the axial energy spread of individual species. The axial energy spread is defined in this case as the full width at half maximum (FWHM) of the peak signals. The advantage of using this method is that the energy spread of each species of hydrogen can be evaluated. The energy spread of $H^+$ ions has been found to be 2.3 eV, $H_2^+$ 2 eV and $H_3^+$ 1.7 eV.

This technique can be used to measure the axial energy spread for $H^-$ ion as well. It has been found to be 1 eV, half of that of the positive ions. $H^-$ ions are formed in the extraction region. Since the plasma potential gradient in this region is small, the $H^-$ ion energy spread is expected to be lower than that of the positive ions [10].

## 4 ADVANCED ION SOURCE CONCEPTS

Ion source operation with a tungsten filament results in an erosion of the material that could contaminate the source and limit the lifetime. The RF-driven discharge is cleaner, and it does not have the lifetime limitation seen in the filament discharge. In the RF-driven source, an induction coil or antenna is used for the discharge. The antenna can be made of different materials: copper, aluminum, porcelain or glass coated copper, etc.. The porcelain coated antenna can better withstand the ion bombardment from the plasma and electrical as well as thermal damages than other known types of antennas. Furthermore, the coated antenna is more energy efficient since it eliminates the short-circuit between the plasma and the bare coil. With the increasing RF power requirements and different plasma conditions, the porcelain coated antenna sometimes fails to perform satisfactorily. A new antenna using quartz has been designed that will provide a longer lifetime and cleaner operation of the source.

In general, it has been demonstrated that the filament-discharge, rf-driven sources have relatively low axial energy spread on the order of 1.7 to 3.6 eV with the use of the magnetic filter that levels the plasma potential distribution in the discharge region. These axial energy spread values are acceptable for some applications but even smaller values are needed for other experiments. A new ion source design (co-axial source) that could deliver an energy spread of less than 1 eV is being constructed and tested at LBNL. Results of its development will be reported in a near future.

## 5 ACKNOWLEDGEMENT

The author would like to thank Dr. Ka-Ngo Leung, the Ion Beam Technology Program at LBNL, and members of the ALG for fruitful suggestions. This work was supported by the Advanced Lithography Group (ALG) under CRADA BG-94-212(00) with the Lawrence Berkeley National Laboratory and the Division of Nuclear Physics, Office of Energy Research, U.S. Department of Energy under Contract No. DE-AC03-76SF00098.

## REFERENCES

[1] W. Finkelstein and A. Mondelli, Semiconductor Int. 6 (1995), 107.

[2] G. H. Mackenzie, M. Dombsky, W.R. Rawnsley, G. Stanford and Y. Yin, Proc. 14th Int. Conf. On Cyclotron and its Applications, 1995, Cape Town, South Africa.

[3] Y. Ueda, T. Yoshikawa, Y. Ito, M. Nishikawa and S. Goto, Proc. 6th Int. Conf. On Ion Sources, 1995, Whistler, B.C., Canada.

[4] T. Vilaithong, S. Singkarat, W. Pairsuwan, J.F. Kral, D. Boonyawan, D. Suwannakachorn, S. Konklong, P. Kanjanarat and G. G. Hoyes, Proc. Int. Conf. At the Forschungszentrum Julich, 13-17 May 1991.

[5] Y. Lee, L. T. Perkins, R.A. Gough, M. Hoffmann, W. B. Kunkel, K. N. Leung, M. Sarstedt, J. Vujic, M. Weber, and M.D. Williams, Nucl. Instr. And Meth. In Phys. Res. A 374 (1996), 1.

[6] Y. Lee, R.A. Gough, W. B. Kunkel, K. N. Leung, L. T. Perkins, D. S. Pickard, L. Sun, J. Vujic, M.D. Williams, and D. Wutte, Nucl. Instr. And Meth. In Phys. Res. B 119 (1996), 543.

[7] S. G. Zakhary, Rev. Sci. Instrum. 66, 5419 (1995).

[8] J. K. Olthoff. R. J. Van Brunt, and S. B. Radoanov, Rev. Sci. Instrum. 67, 473 (1995).

[9] Y. Lee, R. A. Gough, W. B. Kunkel, K. N. Leung, L. T. Perkins, D. S. Pickard, L. Sun, J. Vujic, M. D. Williams, and D. Wutte, Rev. Sci. Instrum. 68 (3), March 1997, 1.

[10] K.N. Leung, P. Herz, W.B. Kunkel, Y.Lee, L. Perkins, D. S. Pickard, M.Sarstedt, M. Weber, and M. D. Williams, J. Vac. Sci. Technol. B 13(1995) 2600.

# RECENT PROGRESS OF RIKEN 18 GHz ECRIS

T. NAKAGAWA[a], J. ÄRJE[a,b], Y. MIYAZAWA[a], M. HEMMI[a], T. CHIBA[a],
N. INABE[a], M. KASE[a], T. KAGEYAMA[a], O. KAMIGAITO[a], A. GOTO[a], and Y. YANO[a]
[a] The Institute of Physical and Chemical Research (RIKEN) Hirosawa 2-1, Wako, Saitama 351-01, Japan
[b] Accelerator Laboratory, University of Jyväskylä, PB 35, FIN-40351 Jyväskylä, Finland

*Abstract*

We successfully produced intense beams of highly charged ions from various kind of gaseous elements, organic metallic compounds (by MIVOC method), and solid materials from RIKEN 18 GHz ECRIS. (e. g. 160eμA of $Ar^{11+}$, 5eμA of $Ar^{16+}$, 80 eμA of $Fe^{13+}$ ). The ion confinement time of highly charged ions was also determined under the pulsed mode operation.

## 1. INTRODUCTION

The intense beams of medium mass heavy ions, mainly metallic ions, has become one of the major requests of users in RIKEN Accelerator Research Facility. For satisfying such requests, a new ECRIS is demanded as an external ion source of the RILAC(Riken heavy Ion Linear ACcelerator)-Ring cyclotron accelerator complex[1]. This ECRIS is also required for the Radioactive Ion Beam Factory (RIBF) project, in which it is aimed to supply the various unstable nuclei beams to the experiments in various fields.[2] According to the scaling low proposed by R. Geller, the beam intensity increases with the micro wave frequency and magnetic field strength of ECRIS.[3] Therefore, we have chosen the micro wave frequency of 18 GHz for the new RIKEN ECRIS In this paper, we present the description of the 18 GHz ECRIS and its performance in producing multi-charged heavy ions

## 2. DESCRIPTION OF RIKEN 18 GHz ECRIS

The detailed design of the ECRIS was described in ref. 4. A single 18 GHz-1.5 kW klystron supplies RF power to the source. The axial confinement of plasma is obtained by two solenoid coils which provide magnetic mirror field. The source is completely enclosed by an iron yoke in order to reduce the current of the solenoid coils. The maximum electrical power consumption is 140 kW. The mirror ratio is about 3.0 ($B_{max}$ ~ 1.4 T, $B_{min}$ ~ 0.47 T). To confine the plasma radially, we use a hexapole magnet which consists of 36 segments, made of Nd-Fe-B permanent magnets. The field strength at the surface of the magnets is about 1.4 T.

## 3 PERFORMANCE FOR GASEOUS ELEMENTS

It was observed that the intensities of highly charged ions were dramatically enhanced by coating the surface of the plasma chamber with aluminum oxide or using an aluminum plasma chamber[5-7]. It is due to the increase of the electron number emitted secondary by the electron impact. In stead of using these methods, we use an aluminum tube to cover the inner wall of plasma chamber. It is much easier than to construct a whole plasma chamber with aluminum. Figure 1 shows the obtained beam intensities of O, Ar and Kr ions. The extraction voltage was 10 kV. Open and closed circles show the beam intensities with using a tantalum tube and an aluminum tube, respectively.

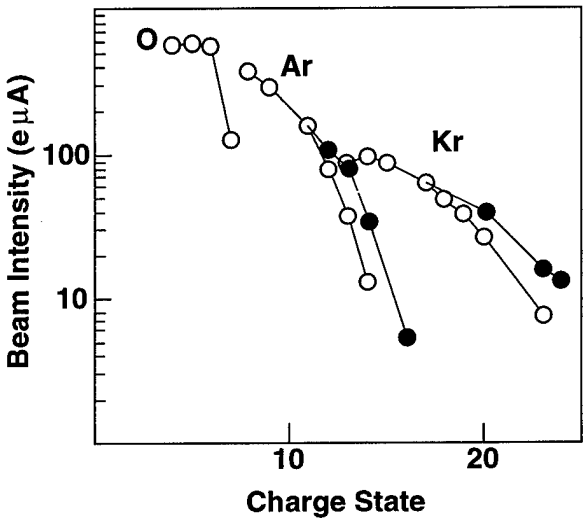



Fig. 1 Charge State distribution of Ar and Kr ions. Open and closed circles represent the results obtained using the Ta and Al tube, respectively

## 4. METALLIC IONS

*4.1. MIVOC method*

A MIVOC-method at an ECR ion source enables production of highly charged metal ion beams at room temperature conditions. In the MIVOC vapors of volatile compounds having metal atoms in their molecular structure are used to release metallic elements.[8-10] In the present experiments the MIVOC chamber was connected to the RIKEN 18 GHz ECRIS. The chamber( ~300 $cm^3$ in volume) was attached to the gas feed tube via a rough, large conductance regulation valve to control flow rate of the compound vapor. In order to minimize contamination,

0-7803-4376-X/98/$10.00 © 1998 IEEE

the plasma chamber wall was covered with a thin aluminum tube (thickness 1 mm) which could be easily replaced if necessary. Furthermore, the aluminum surface emits several secondary electrons per electron impact, which helps to increase plasma density.

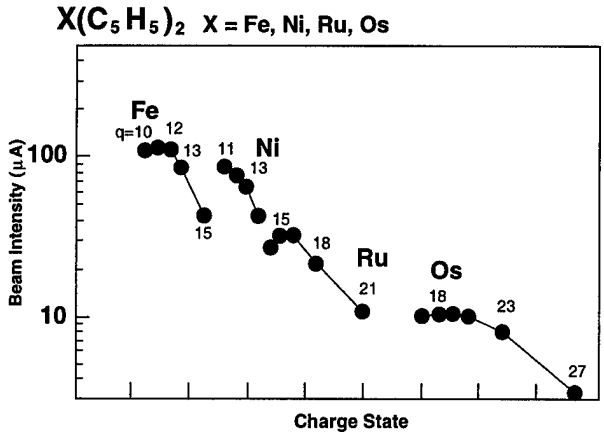



Fig. 2. Charge distribution of Fe, Ni, Ru and Os

Figure 2 shows the beam intensities of the highly charged Fe, Ni and Ru and Os ions. The ion beams were produced at room temperature from compounds of $Fe(C_5H_5)_2$, $Ni(C_5H_5)_2$, $Ru(C_5H_5)_2$, and $Os(C_5H_5)_2$. The extraction voltage was 10 kV. Typical gas pressure in the plasma chamber was $2\times10^{-6}$ mbar and in the extraction stage $7\times10^{-7}$ mbar. To produce these ions, we only need RF power of 150~500 w

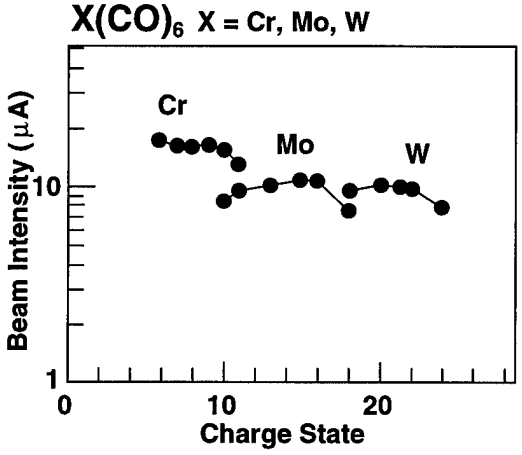



Fig. 3 Charge state distribution of Cr, Mo, W

The Cr, Mo, and W ion beams were produced from their hexacarbonyl compounds: $Cr(CO)_6$, $Mo(CO)_6$, and $W(CO)_6$. A typical operation pressure was ~$3\times10^{-6}$ mbar. Fig. 3 shows the beam intensity as a function of charge state of Cr, Mo, and W ions. The maximum beam intensities were around 10 μA. The beam intensities of the highly charged ions produced from these compounds are remarkably smaller than those from the metalocenes. In the case of the hexacarbonyls, the metal ions are bound with six CO molecules. To produce Cr, Mo and W ions, all the bounds have to be cut by electron impacts. As a result, the number of metallic ions may be insufficient to produce intense beams of highly charged ions.

*4-2 Ta ions*

In order to produce highly charged Ta ions, we insert a Ta-rod (the diameter is 2 mm) to the plasma directly. Figure 4 shows the best results of Ta ions at the extraction voltage of 14 kV.

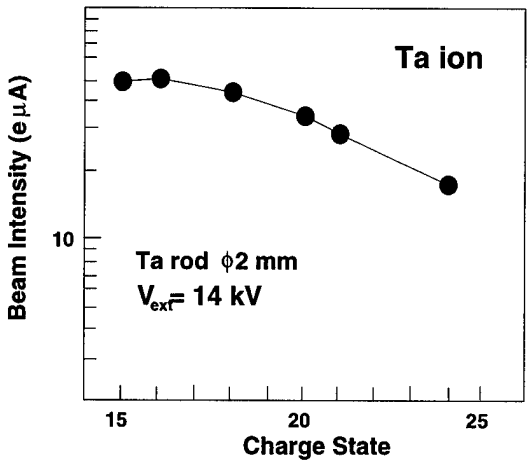



Fig. 4 Charge state distribution of Ta ions

## 5. Determination of Ion Confinement Time

To produce highly charged ions in a ECRIS, good ionization and confinement are necessary. To determine $t_{ic}$ (ion confinement time) and $t_{ion}$ ( ionization time), it is crucial to measure the ion production rate as a function of time. The afterglow current is a good tool for observing the condition of a plasma directly.[11] The duration of existence of a plasma can be controlled using pulsed mode operation. Figure 5 shows the $I_{afterglow}$ obtained for $Ar^{11+}$ ions as a function of the RF duration ($\Delta t$). We define the saturation time ($t_{saturation}$) as the point of the intersection of the curves obtained, as shown in Fig. 5. The RF power was varied between 200 and 800 W.

Figure 6 shows $t_{saturation}$ as a function of the RF power. In this figure, we classify two regions, Region I and Region II,. In Region II, $t_{ion}$ is shorter than $t_{ic}$. Usually $t_{saturation}$ is strongly dependent on $t_{ion}$ , which is proportional to $1/n_e$. The density and temperature of electrons in the ECRIS increase with increasing the RF power.[9] Then $t_{saturation}$ decreases as RF power increases. In Region I, however, $t_{ic}$ is shorter than $t_{ion}$.

In this case, $t_{saturation}$ is determined by $t_{ic}$. The staying time of the ions is too short to achieve equilibration. $t_{saturation}$ is influenced only slightly by the density and temperature of electrons in this case.

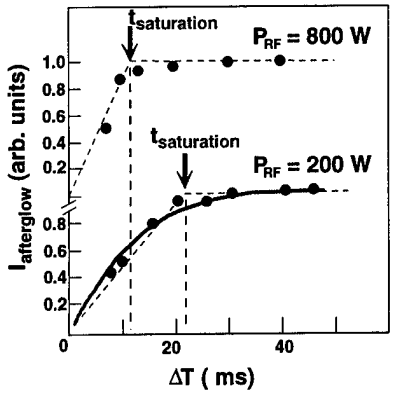



Fig. 5. The measured $I_{afterglow}$ as a function of the RF pulse duration ($\Delta t$).

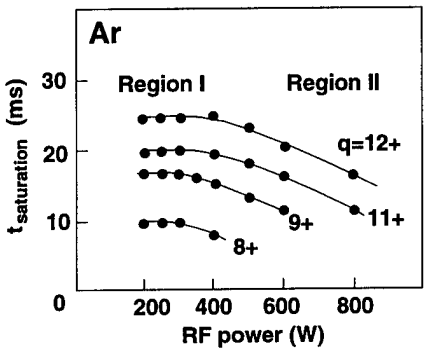



Fig. 6 The obtained $t_{saturation}$ as a function of RF power for argon ion charge state from 8+ to 12+

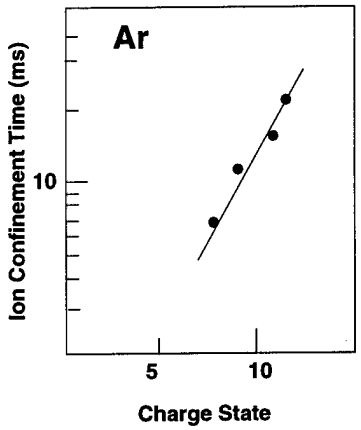



Fig. 7. The obtained ion confinement time as a function of the charge state of argon ion

When we assume $t_{ic} \ll t_{ion}$, the rate equation [12]can be written as

$$dn_i/dt \approx -(1/t_{ic})n_i \quad (1)$$

where $n_i$ is defined as the density of i-th charge state ions. When this equation integrated from t = 0 to t, then

$$n_i = n_{i\infty}( 1- \exp(-t/t_{ic}) ) \quad (2)$$

Using eq. (2), we fitted $I_{afterglow}$ for the lowest RF power in Region I to determine $t_{ic}$. Figure 7 shows the obtained $t_{ic}$ as a function of the charge state of Ar ions. $t_{ic}$ increases exponentially as a function of the charge state of the ions. Figure 8 shows the ion confinement time of highly charged Ar ions as a function of current to solenoid coils.

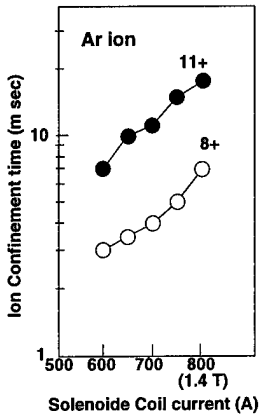



Fig.8 Ion confinement time as a function of current of solenoid coils

## 6. CONCLUSION

We have tested the RIKEN 18 GHz ECRIS to extract various ions. We successfully obtained the intense beams of highly charged ions from various kind of gaseous elements, organic metallic compounds (by MIVOC method), and solid materials. The ion confinement time of highly charged ions was also determined under the pulsed mode operation.

### References


[1] Y. Yano, Proceedings of 13th International Conference of Cyclotron and Their Applications (World Scientific Publishing, Singapore, 1993) p102.

[2] Y. Yano et al, in this proceedings.

[3] R. Geller, Annu. Rev. Nucl. Sci., 40(1990)15 and references therein.

[4] T. Nakagawa et al., Proc. of the 5th European Particle Accelerator Conference (IOP,Bristol, 1996)p1478

[5] T. Nakagawa , J.J.A.P. 30(1991)L930

[6] Z.Q. Xie and C. M. Lyneis. Rev. Sci. Instrum. 65(1994)29

[7] D. Hitz et.al, Poc. 12th Int. Workshop on ECR Ion Sources (Univ. Tokyo, Tokyo, 1995)p.126

[8] T. Nakagawa et al., submitted to Nucl. Instrum. and Methods A.

[9] Kiovista et al., Nucl. Instrum.Methods.B94(1994)291

[10]H. Waldmann and B. Martin Nucl. Instrum. Methods B98(1995)532

[11]R. Geller. Electron cyclotron resonance ion sources and ECR plasma (IOP, Bristol, 1996)p256 and references therein

[12]R. Geller. Electron cyclotron resonance ion sources a nd ECR plasma (IOP, Bristol, 1996)p266 and references therein

# INITIAL TEST RESULTS FROM A MULTICUSP SOURCE FOR TRIUMF'S RADIOACTIVE BEAM FACILITY

T. Kuo, D. Yuan, K. Jayamanna, M. McDonald, R. Baartman, G. Mackenzie, P. Bricault
M. Dombsky, P. Schmor, G. Dutto, -TRIUMF and
Y. Lee, K-N Leung, D. Williams, R. Gough –LBNL

*Abstract*

A multicusp source for positive ion beams has been designed and constructed in collaboration with the Ion Beam Technology Department of LBNL for the TRIUMF ISAC project. This type of source has demonstrated a high yield of singly charged ions, a low energy spread and a good emittance and is compact and simple. Several stages of tests and measurements using non-radioactive beams to characterize the source performance are being carried out both at LBNL and at TRIUMF prior to the final phase of radioactive target-source system tests. Results of these non-radioactive tests and certain problems encountered are reported and discussed in this paper.

## 1 INTRODUCTION

Radioactive ion species required for TRIUMF ISAC research project [1] will be mainly up to mass 30. In order to obtain a highest RIB to primary beam efficiency, ion sources which is efficient in producing singly charged ions are under study. The criteria for RIB ion sources are more restrictive than those for non-radioactive sources. In addition to having to have a high efficiency, good emittance and small energy spread, a particular source under consideration must be very simple, highly resistant to radiation damage and must have a fast transient time for isotope release. Since surface chemistry is extremely sensitive and critical between the radioactive isotopes and the material along their path to ionization/extraction, the RIB target-sources are nuclear chemistry and high temperature effect dominated.

At TRIUMF, surface ionization source [2] for alkaline species has been in use successfully for TISOL programs and it will be the first source to be used for ISAC. For gaseous and non-alkaline metallic species production we are exploring other source options such as compact microwave source and compact multicusp source.

## 2 TRIUMF-LBNL MULTICUSP SOURCE

Multicusp volume source [3] has demonstrated a high yield of single charged ions, a good emittance and a low energy spread. It was of great interest in 1994 to examine that whether such source can be a candidate for the ISAC project. Since then a source of this type has been designed and constructed in collaboration with the Ion Beam Technology Department of LBNL. The magnetic structure of this source is modeled after the LBNL's RF powered cusp source[4], using 10 rows of cusp lines on the cylinder, 10 radial lines in the front plate and 4 lines in the back plate for complete magnetic enclosure. All magnet bars are directly water cooled. The plasma chamber is 20 cm in length and 20 cm in diameter. A 48mm circular opening centered in the front plate allows the penetration of the plasma and extraction electrodes to the front surface of the plasma. The plasma electrode is not cooled and allowed to go up to near 2000°C. The plasma and extraction apertures are 3mm in diameter and a tungsten filament 18cm long, 2.4mm in diameter powered by 200 amperes is used. A 2000°C tantalum liner is designed for on-line use but not installed for non-radioactive beam tests. Typical arc power used ranges from a few ten of watts to 1.5kW. There is no threshold for plasma ignition, a mW (100V,10$\mu$A) will begin to show beam of interest. Several stages of tests and measurements using non-radioactive beams to characterize the source performance have been carried out both at LBNL and at TRIUMF.

## 3 FIRST TEST AT LBNL

In August 1995 the cusp source was shipped to LBNL for the first phase of test during which some subsets of source property such as ion species population, beam intensity, gas efficiency were measured. The source was first mounted on a teststand where a small mass energy-analyser was immediately after a single stage extraction at 600 volts. Argon and nitrogen were the gas samples been tested for species distribution. $Ar^{1+}/Ar^{2+}$ and $N_2^{1+}/N^{1+}$ ratios as a function of source pressure, gas flow, arc voltage and current were scanned through. About 200 scans were taken and some sample results are shown in Fig. 1(a) and 1(b).

As can be seen from Fig.1(a), the ratios of $Ar^{1+}/Ar^{2+}$ are mainly determined by arc voltage. For example, at $3.7\text{x}10^{-3}$ torr source pressure the ratio is about 40-50 to 1 at 50 volts then falls rapidly to 15 to 1 at 150 volts. Variation of arc current from 5A to 15A will not change the ratio appreciably but change the extracted beam intensity. For the case of nitrogen ions, however, the $N_2^{1+}/N^{2+}$ is in the factor of 1000 to 1 at 1A and 50 to 1 at 5A, rather insensitive to arc voltage at about $5\text{x}10^{-4}$sccs gas flow. Similarly, the $N_2^{1+}/N^{1+}$ ratios as seen from Fig.1(b), are more arc current dependent than voltage dependent. At 50 volts and low gas flow ($5\text{x}10^{-4}$ sccs), the ratio varied from 20 at 0.5A to 0.6 at 13.5A. These ratios do not change appreciably up to 150 volts.

0-7803-4376-X/98/$10.00 © 1998 IEEE

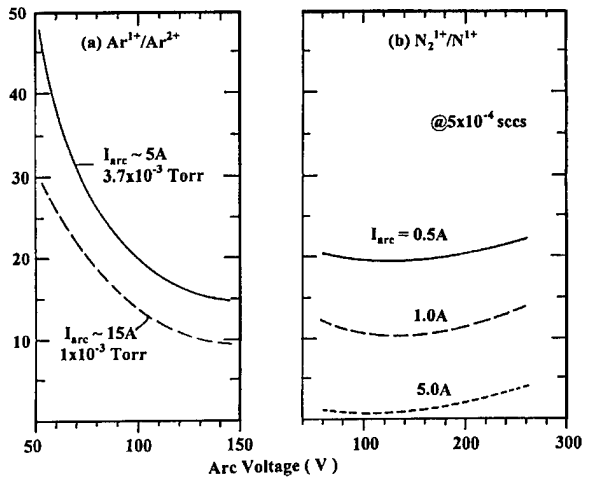



Fig. 1. Argon and nitrogen gaseous species as a function of arc voltage and current

The beam currents of argon and nitrogen ions were measured on another teststand which is equipped with a faraday cup and secondary electrons recapture mechanism. current intensity as a function of extraction voltage (Child-Longmuir curve) at 5 different arc currents were measured. With a gas flow of $6.6x10^{-4}$ sccs and an arc power of 150V/5A, we obtained 0.3 mA Ar beam at 1.3 kV, 0.8mA at 2 kV and 1.0 mA at 3.8 kV. Likewise, with $2.6x10^{-3}$ sccs nitrogen flow and an arc of 100V/4A, the total nitrogen beam ($N_2^{1+}$+$N^{1+}$) were 0.35, 0.95 and 1.2mA respectively. Below 1.5 kV the beam extracted is insensitive to arc power and gas flow variation.

## 4 TESTS AT ISAC TESTSTAND

A non-radioactive source/matching section/separator teststand for ISAC has been constructed for source study and optics verification. It is also used as a testbed for the new EPICS control system as well as various diagnostics devices. The cusp source was used to provide easy beams for the initial commissioning. Due to some instrumentation difficulties and uncertainty in measuring the beam emittance for the cusp source at the early stage of commissioning, a prototype ISAC surface ionization source [5] was later used for the optics verification for the matching section and the separator. Very good agreement has been obtained between the computed and measured emittance ellipses based on a given set of optics tune.

### *4.1 Cusp Source Emittance*

An Allison type scanner was constructed for heavy ion emittance measurement. However, the position of the scanner had to be located about 1.5 meter from the point of extraction. The divergence resolution of the device was found to be 3 mrad. These two limitations made it necessary to use a focused beam with a divergence less than +/- 8mrad for measurement. A focused beam gave an emittance of ~7.5 π-mm-mrad while an unfocused beam always showed a value larger than 10 π-mm-mrad. This discrepancy made it difficult to determine the waist size and the actual emittance value. In addition, the signal to noise ratio was poor for low current scanning. As a result, a systematic emittance data set as functions of energy, arc power, ion species and optics tunes has not yet been obtained.

### *4.2 Extraction*

The initial extraction system designed for the cusp source used a three electrode arrangement. The extractor was designed to be set at 4 kV negative to the plasma electrode while the third put at ground potential. When this extraction system was tested at the teststand with 30 keV beam energy, we were forced to use about 1.3 kV extraction to achieve the best beam transmission. This resulted in low current intensity and loss of benefit from higher arc power and gas flow. The "system gas efficiency" appeared to be very low. A new five-electrode system including an einzel lens has been designed using IGUN simulation code and was tested briefly at LBNL with a 15 keV nitrogen beam. A gain of 4 in beam intensity was obtained with the einzel lens on than without for a +/- 5 mrad divergence drift, mainly due to a higher extraction voltage permitted to be set by the einzel lens. The cusp source and the five-electrode extraction system will be reinstalled to the ISAC teststand for beam current, emittance and gas efficiency test up to 60 kV.

### *4.3 Source Gas Efficiency*

The source gas efficiency was obtained with a single extraction gap using extraction voltage above saturation and a Faraday cup immediately after the extractor electrode. This set up disregards any optics requirement. Since the dominating ion species is singly charged, the gas efficiency is approximately represented by the ratio of the extracted beam currents to a calculated currents as if all the inflow gas were singly ionized. For the source under test we observed that the efficiency increases as arc power increases and as gas flow decreases. The dependence on gas flow at 500 watts arc power is shown in Fig. 2. The ionization of Ar is quite efficient, up to 80% at a small flow ($0.4x10^{-3}$ sccs) but falls to 25% at a higher flow ($3x10^{-3}$ sccs). For $N_2$ gas the overall nitrogen beam has a less gradient dependence on gas flow, from 20% at $0.3x10^{-3}$ sccs to 15% at $2.2x10^{-3}$ sccs.

### *4.4 System Gas Efficiency*

The system gas efficiency was obtained from the beam current achievable after the image slit (2 mm in width) of the separator. The optics quality of the extraction system becomes very critical. Results from the initial commissioning of the teststand showed that only 5% of the source efficiency can be translated to the system efficiency for both $Ar^{1+}$ and $N_2^{1+}$ at 28 keV beam energy. The

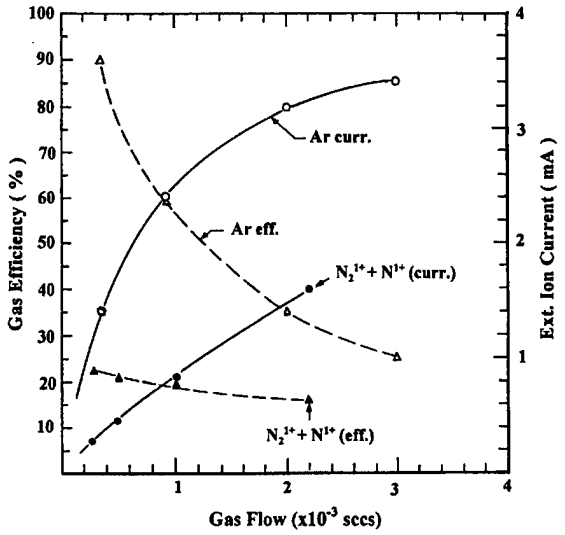



Fig. 2. Source gas efficiency as a fuction of flow at 0.5 kW.

system efficiency dependence on gas flow was very similar to that of the source efficiency except for a scaling factor of 1/20. A 0.8 mm image slit will drop the system efficiency further to about 3% of the source efficiency. In other words, only 0.6% system efficiency for $N_2^{1+}$ at the best.

A Neon leak gas of $2x10^{-6}$ sccs was sent to the source with $N_2$ or He as support gas. A total of 120 nA of $Ne^{1+}$ was recorded after the 2 mm image slit (1.3% system eff.) when a minimal $N_2$ support gas ($1x10^{-4}$ sccs) was used. As the $N_2$ support gas was increased the $Ne^{1+}$ beam current fell off very rapidly, to 0.05% when $N_2$ gas flow reached $2.2x10^{-3}$ sccs. The use of He as support gas improves the $Ne^{1+}$ efficiency to 1.5% and the falloff was not as steep.

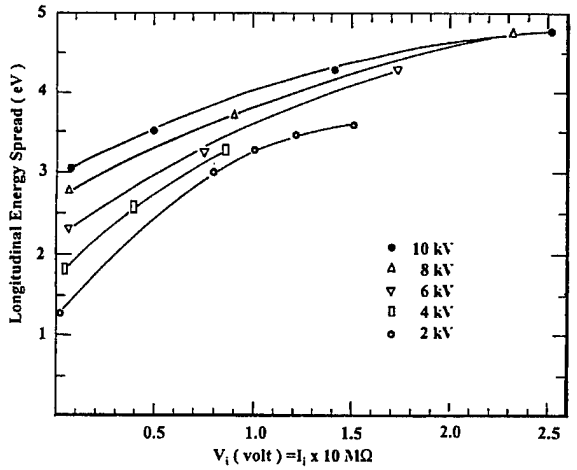



Fig. 3. Energy spread as a function of beam energy and $I_i$.

## 5 ENERGY SPREAD MEASUREMENT

The longitudinal energy spreads of the cusp source were measured at LBNL in April, 1997 using an axial retarding field energy analyzer designed by IMS [6] and optimized by LBNL. The details of the instrument and method of measurement is presented in the invited talk given by Y. Lee [7,8] at this conference. A very low energy spread of 1.25 eV was obtained with a 2 keV Argon beam.

The ion current $I_i$ through the 3 mm entrance aperture of the analyzer was used as an independent parameter. We observed a strong dependence of measured energy spread on the ion beam current $I_i$ while the beam energy is fixed. As shown in Fig. 3, Beams at 2, 4, 6, 8 and 10 KeV are plotted as a function of $I_i$. There is a common trend that energy spread increases as $I_i$ increases rather independent of beam species, arc power and beam optics. This ion current dependence is tentatively attributed to the severe space charge effect as the beam energy approach to zero. On the other hand, energy dependence trend might come from a deeper field penetration to the plasma and from the gas ionization effect inside the analyzer. It should be pointed out that measurements were made without an internal filter near the extraction. Adding a weak dipole field (~10 gauss) did not seem to have an observable effect.

## 6 SUMMARY

The TRIUMF/LBNL cusp source under test indeed shows its merit in generating copious singly charged gaseous ions. The *source gas efficiency* for argon beam can be up to 80% while the *system gas efficiency* is not yet optimized due to some deficiency in the extractor design. Initial emittance scan shows a figure less than 10 π-mm-mrad using a focused beam tune. At 2 keV beam energy the longitudinal energy spread can be as low as 1.25 eV. Further tests will be conducted using a new extraction system to search for a better system gas efficiency. Correspondingly a systematic emittance measurement through various arc conditions will be carried out.

## REFERENCES


[1] P. Schmor, et al.' Status of the TRIUMF ISAC Facility for Accelerating Radioactive Beam', these Proceedings.
[2] M. Dombsky, Triumf internal note.
[3] K. N. Leung, Rev. Sci. Instrum., Vol.65, No.4, (1994).
[4] M. D. Williams, et al.,Rev. Sci. Instrum. 67(3),(1996).
[5] M. Dombsky, et al., NIM B 126(1997)50-54.
[6] Ion Microfabrication System, Vienna, Austra.
[7] Y. Lee, et al., Rev. Sci. Instrum. 68(3), (1997).
[8] Y. Lee, 'Very Low Energy Spread Ion Source', these Proceedings.

# RESULTS FROM ZMEVVA: A NEW SOURCE FOR HEAVY-ION ACCELERATORS

B.M. Johnson, A. Hershcovitch, Brookhaven National Laboratory, Upton, NY 11973-5000 USA
I.G. Brown, F. Liu, A. Anders, Lawrence Berkeley National Laboratory, Berkeley, CA 94720 USA

*Abstract*

We are developing a new approach for heavy ion beam injection (e.g., into the Relativistic Heavy Ion Collider [RHIC] at BNL). While conventional Metal Vapor Vacuum Arc (MEVVA) ion sources (I.G. Brown, Rev. Sci. Instrum. 65, 3061 (1994).) can produce up to hundreds of milliamps or more of several-times-ionized metal ions (e.g., $U^{3+}$), the recent results from Batalin et al. (V.A. Batalin et al. ITEP, Moscow, Reprints 18-93 (1993), 33-94 (1994); Proc. EPAC 1994, p. 1453.) indicate that the addition of an energetic electron beam (EMEVVA) may lead to considerably higher charge states (e.g., $U^{17+}$). An alternative way to produce the electron beam is ZMEVVA, in which a z-discharge plasma is used to enhance multiple ionization. As the vacuum arc plasma plume expands into a magnetized drift region, a z-discharge is triggered in the drifting metal plasma. The ions are then extracted and analyzed using a time-of-flight system. We report recent results using applied discharge voltages from 1 to 2 kV.

## 1 INTRODUCTION

The Relativistic Heavy Ion Collider (RHIC) [1], now under construction at BNL, is expected to become operational early in calendar year 1999. Initially, the RHIC physics program will concentrate on Au+Au collisions with 100 GeV in each beam. However, there is physics justification for eventually colliding uranium beams in RHIC. The tandem preinjector is quite adequate and reliable for the Au+Au collision program, but the tandems are not expected to produce sufficient beam currents for uranium ions. Encouraging recent results lead us to believe that a viable preinjector for RHIC can be developed using EMEVVA and/or ZMEVVA, which are enhanced versions of the well-known Metal Vapor Vacuum Arc ion source [2].

### *1.1 Uranium Beams in RHIC?*

The first physics program at RHIC will study Au+Au collisions with 100 GeV in each beam, which is predicted to produce sufficiently high energy densities and temperatures to explore a new state of matter: the quark-gluon plasma (QGP). Characterizing the physics of the QGP will be a formidable experimental challenge, because theoretical guidance is qualitative at best. Planned comparisons of experimental results for Au+Au collisions with those obtained for p+p, p+A, and A+A collisions for lower mass species will help, but it could be very important to study a heavier collision system, such as U+U.

The mass of uranium is 20% higher than gold (238/197 = 1.21), but it is estimated [3] that the energy density in U+U collisions at RHIC will be 1.8 times higher than for Au+Au. This nearly factor of two enhancement occurs because the U nucleus is deformed (cigar shaped), while the Au nucleus is spherical. The randomly tumbling U nuclei will sometimes collide end to end producing the much higher energy densities and a 20% increase in the initial temperature. In addition, for central U+U collisions the range of transverse energies and particle multiplicities (due to the variation from end-to-end to side-to-side interactions) will be much larger than for central collisions of spherical nuclei, like Au.

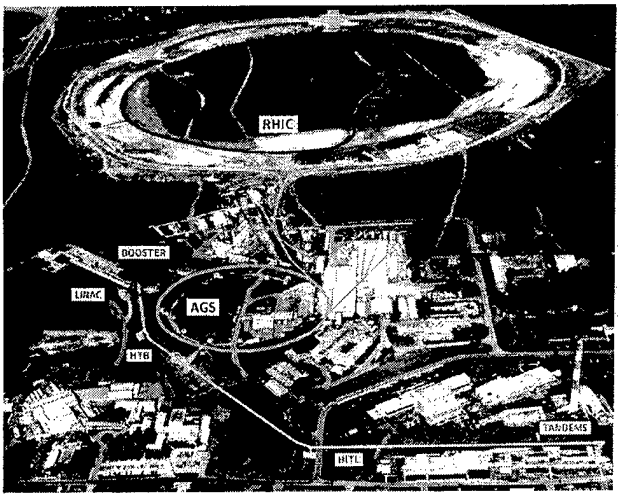



Figure: 1 The RHIC accelerator complex at BNL. The tandem Van de Graaff facility (lower right) is the initial RHIC preinjector for Au ion beams.

### *1.2 Long-term options for a RHIC preinjector.*

In 1986 a BNL committee [4] explored various options for a RHIC preinjector, including approaches based on the BNL tandem Van de Graaff versus an advanced heavy ion source like a laser source, an electron-cyclotron resonance (ECR), or an electron-beam ion source (EBIS). As illustrated in Fig. 1, the committee recommended that the tandem Van de Graaff should be the initial heavy-ion preinjector for RHIC. For the long term RHIC program (up to 25 years) the recommendation was to develop an EBIS-based preinjector. However, it was recognized that state of the art EBIS sources produced roughly two orders of magnitude less ion current than would be needed for RHIC. The 1986 committee concluded that low charge-state heavy-ion sources, like the Penning ionization gauge (PIG), Metal Vapor Vacuum Arc (MEVVA), and various sputter sources did not warrant serious consideration as a

0-7803-4376-X/98/$10.00 © 1998 IEEE

basis for a preinjector (other than their potential for providing primary ions to an advanced source).

Since 1986 a number of significant new developments have occurred, which strongly suggest that MEVVA-based approaches [5] could be viable for a future RHIC preinjector. Among these are the success of the Positive Ion Injector (PII) low β LINAC for ATLAS [6], great improvements in MEVVA sources [7], and encouraging results from an electron-beam injected EMEVVA ion source [8]. The latter was reported to generate large currents (several mA) of heavy metallic ions (e.g., $U^{17+}$).

## 2 THE MEVVA ION SOURCE

The MEVVA is a prolific generator of highly ionized metal plasma, from which metallic ions are extracted. A generic MEVVA consists of a series of electrodes (usually concentric) that are separated by ceramic insulators. The usual configuration is a solid electrode of the desired metal, followed by a trigger electrode, an anode, a suppressor, and a three-grid extractor. Triggering of the vacuum arc is accomplished by applying a short high voltage pulse between the trigger electrode and the cathode across an insulating surface. Discharge occurs due to formation of cathode spots, which are micron-sized spots on the cathode surface characterized by extremely high current densities. Cathode material is vaporized and ionized, producing a plasma plume. A good general reference on the MEVVA is the review by Ian Brown [2]. Recent improvements are described in [7].

## 3 THE FIRST EMEVVA (BATALIN, *et al.*)

The principle of EMEVVA is the same as for ECR or EBIS, namely stepwise ionization, in which an energetic electron "beam" successively removes bound electrons to reach the desired stage of ionization. To achieve very high ion charge states two things are needed: (1) high $j\tau$, which is the product of electron current density and electron-ion interaction time, and (2) high **E**, which is the effective electron "beam" energy. Donets [9] is credited with illustrating that the maximum charge state achievable for any element can be predicted on a plot of $j\tau$ versus **E**.

The first step toward EMEVVA was the addition of an 0.7 meter long magnetized drift channel between a MEVVA anode and extractor, into which the plasma plume expands. Recent results include 200 mA of extracted uranium ion current (40% of which was $U^{4+}$) with a drift channel [8] and 32 mA of $U^{4+}$ for a magnetized MEVVA without a drift channel [10].

For the first EMEVVA [8] an electron gun was added behind the hollow cathode. Impressive results were reported for copper ion production, in which a substantial component of the extracted beam was identified as being between $Cu^{13+}$ and $Cu^{21+}$! Experiments with uranium ions [8] yielded a 5 mA component of relatively high charge state uranium ions, 60% of which was identified [11] to be $U^{17+}$.

## 4 THE FIRST ZMEVVA (BNL/LBNL)

The encouraging initial EMEVVA results prompted us to pursue further approaches to enhance MEVVA. First we noticed that the EMEVVA electron beam, which was injected through the cathode, was co-propagating with the drifting ions. Therefore, the poloidal field of the high-current electron beam would produce a radially defocusing force on the ions. Batalin et al. have agreed to attempt to reverse the electron beam direction in their EMEVVA to see if performance can be improved. In the meantime, we decided to pursue a complimentary approach, ZMEVVA, in which a magnetized z-discharge would produce counter-propagating energetic electrons.

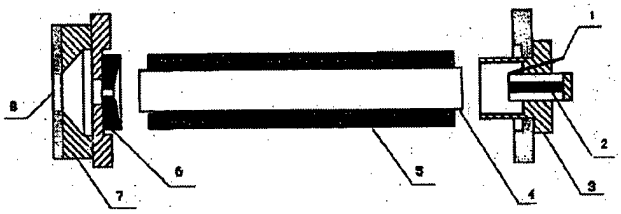



Figure: 2 Schematic layout of our initial ZMEVVA. The labeled elements are: (1) Trigger, (2) Cathode, (3) Anode, (4) Glass tube, (5) Coil, (6) Reflector, (7) Expander, and (8) Extraction grids.

Figure 2 illustrates our initial ZMEVVA setup. At the right is a conventional MEVVA plasma gun. While a 100 μsec pulse is applied to the coil (5), the trigger electrode is fired to produce a vacuum arc plasma plume (about 50 μsec long), which moves to the left into a magnetized drift region. Then, with external applied voltages of between 1 and 2 kV, a z-discharge is triggered in the drifting metal plasma. The voltage polarity is arranged so that the z-discharge forms an energetic "electron beam" moving from left to right. The hot electrons then counter-propagate with the drifting ions to hopefully maximize the effective $j\tau$. Highly charged ions are then extracted to the left and analyzed using a time-of-flight system (see Fig. 3).

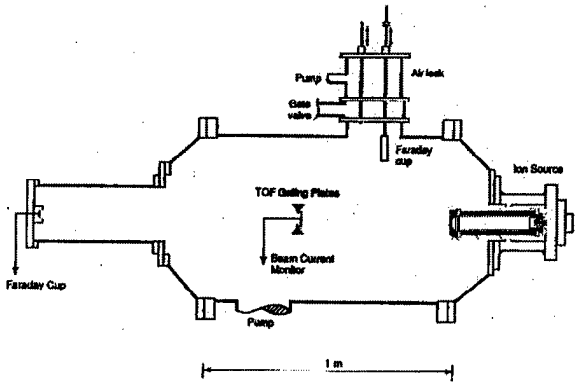



Figure: 3 Illustration of the 20-cm long ZMEVVA positioned in the MEVVA vacuum chamber at LBNL.

If we establish our goal as producing 1 mA or more of $U^{20+}$ ion current, then based on the considerations described above in Section 3, we need a $j\tau$ of about 1.2 Coulomb/cm2 and an **E** of 1 keV. We believed that using existing equipment at LBNL we could achieve these operating parameters with an electron current of 40 kA, a $\tau$ of 8 μsec, and applied z-discharge voltages of between 1 and 2 kV. Batalin [8] used a 70-cm long drift region. For direct comparison and to explore the effect of varying $\tau$, we constructed both a 70-cm long (see Figure 4) and a 20-cm long ZMEVVA.

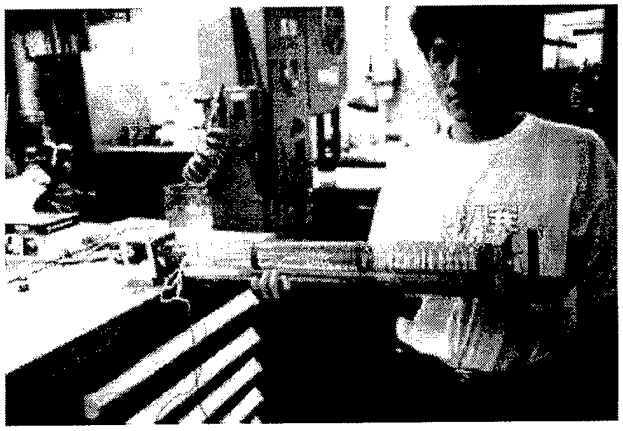


Figure: 4 Fenghua Liu holding the 70 cm long ZMEVVA during assembly and coil winding.

## 5 INITIAL ZMEVVA RESULTS

After only three week-long runs over the past few months we have produced encouraging, but also somewhat disappointing initial results. Our first good news was that comparison of titanium results with the 70-cm and 20-cm versions were consistent with our expectations that increased $\tau$ produced an enhanced yield of higher charge states. However, for gold ions we were disappointed to initially observe little yield above $Au^{3+}$. For data taken with no z-discharge we observed yields of about 20% $Au^{3+}$, 60% $Au^{2+}$, and 20% $Au^{1+}$. Then for data taken with applied z-discharge voltages of 1.0, 1.25, 1.5, and 2.0 kV we observed the yield of $Au^{3+}$ grow to nearly 100%, but there was no indication of $Au^{4+}$ or higher charge states.

Since the total Au ion yield was substantial, we assumed that the $j\tau$ was reasonable, so we suspected that somehow the effective **E** was far lower than the external voltage applied to produce the z-discharge. Consulting the Donets [9] plot we estimated that if the upper ionization limit was $Au^{3+}$, then the effective **E** was only 30 eV out of our applied voltage of as much as 2 kV. Upon further investigation we discovered that the capacitor bank had a measured inductance of about 2 μH, which corresponded to an impedance of 1.4 Ω when the full circuit fired. Furthermore, the length and thinness of wires from power supply to coil resulted in a total circuit impedance of about 2 Ω. Meanwhile, the resistivity of the plasma itself was estimated to be only 0.4 Ω or less. In other words, the applied external voltage was dropped almost entirely across the circuit with very little voltage drop across the plasma itself.

To test this assumption we moved the power supply closer to the ZMEVVA and made other changes to reduce the circuit impedance. With these changes we then observed significant yields up to $Au^{6+}$, which implies an **E** of 100 eV, or an effective voltage drop across the plasma of 100 V. With this improved circuitry we also experimented with our own version of EMEVVA and achieved comparable results. We conclude then that to achieve our objective of $U^{20+}$, we must build a much lower impedance z-discharge circuit, starting with a much lower inductance capacitor bank. Another problem we must address is time jitter in the z-discharge firing circuit which causes significant variations in the time-of-flight spectra.

## 6 CONCLUSION

There is good physics justification for eventually colliding uranium beams in RHIC, but the tandems will not be an adequate preinjector. The encouraging initial results reported here and previously [6-8] suggest that an enhanced MEVVA ion source could form the basis for a viable preinjector [5] to meet the long-term needs of the RHIC physics program. Further development of the ZMEVVA and EMEVVA concepts are needed (and are currently underway) to (1) reduce circuitry impedance to increase the effective electron energy **E** from the current estimate of ~100 eV to over 1 keV, and (2) to improve timing reliability and source stability.

## 7 ACKNOWLEDGEMENTS

Work supported by the U.S. Department of Energy under Contract Nos. DE-AC02-76CH00016 (BNL) and DE-AC03-76SF00098 (LBNL).

## REFERENCES

[1] Current information on the RHIC project, including the accelerator complex, the BRAHMS, PHENIX, PHOBOS, and STAR detectors, and the planned physics programs, is available at http://www.rhic.bnl.gov. (see also other contributions to these proceedings).

[2] I.G. Brown, Rev. Sci. Instrum. 65, 3061 (1994).

[3] P. Braun-Munzinger, private communication, 1992.

[4] BNL Memorandum to D. L. Lowenstein and A. Z. Schwarzchild from C. Chasman, A. Hershcovitch, Y. Y. Lee, K. Prelec, and H. Wegner dated December 15, 1986 (unpublished).

[5] A. Hershcovitch and B. Johnson, RHIC Detector Note 17 and AGS/AD/Tech. Note No. 416.

[6] R.C. Pardo, et al., Proc. 1993 Part. Accel. Conf., IEEE 93CH3279-7 (1993) 1694.

[7] I.G. Brown, P. Spadtke, H. Emig, D.M. Ruck, B.H. Wolf, NIM A295, 12 (1990).

[8] V. A. Batalin, Y.N. Volkov, T. V. Kulevoy, and S. V. Petrenko, ITEP, Moscow, Reprints 18-93 (1993) and 33-94 (1994); and in the Proceedings of EPAC 1994 p. 1453.

[9] E.D. Donets, Proceedings, Fifth All-Union Conference on Charged-Particle Accelerators, Vol. 1, Nuaka, Moscow, 1977, p. 346.

[10] P. Spadtke, H. Emig, B.H. Wolf, and E. Oks, GSI Sci. Report 1994 p. 227, GSI report 95-1; and E. Oks, et al. Appl. Phys. Lett. (in press).

[11] V. A. Batalin, private communication.

# INTENSE, HIGH BRIGHTNESS $H^-$ BEAMS FROM SURFACE PLASMA SOURCES

S. K. Guharay and M. Reiser
Institute for Plasma Research, University of Maryland, College Park, MD 20742

*Abstract*

High-current $H^-$ beams from a reliable surface plasma source are of great interests for spallation neutron sources and hadron colliders. At Maryland, $H^-$ beams have been studied using a magnetron and a Penning-type surface plasma source. Stable operating conditions with negligible beam noise have been achieved in both cases. The beam characteristics are much improved in the Penning geometry; the beam brightness is about an order of magnitude higher. An emission current density of ~ $1A/cm^2$ with normalized beam brightness of $\gtrsim 10^{12} A/(m\text{-}rad)^2$ has been achieved. The minimum energy spread $\Delta E$ (FWHM) is measured $\lesssim 2.5eV$. The actual $\Delta E$ is possibly much smaller since this value is close to the resolution of the energy analyzer. The results are sensitive to the beam noise, and the gas pulse is the key control parameter here. Long, stable operations with very limited source maintenance have been noted. So far, an emission aperture of diameter = 0.6mm is used when the $H^-$ beam current is $\gtrsim$ 2mA at 10kV. The beam current can be scaled to $\gtrsim$30mA for an emission aperture of diameter ~ 2.4mm. The critical issues for noiseless, high-brightness $H^-$ beams, the source performance, and the scaling of beam parameters are discussed.

## 1 INTRODUCTION

High-brightness ion beams are at the frontiers of many current research areas in basic and applied science including high energy accelerators, microelectronics, ion beam microscopy, and materials science. Many common physics and technology issues have been studied in the ion source development for these diverse applications. The present state-of-the art has been described in several articles [1-6], which clearly indicate the rapid pace of development in the field. Several national laboratories in the US including Los Alamos National Laboratory [7], Lawrence Berkeley National Laboratory [8], Oak Ridge National Laboratory [1,9], Fermi National Accelerator Laboratory [10] and Brookhaven National Laboratory [2], have been engaged over the years in advancing the frontier of ion source technology. However, this particular arena of research and development has been gaining renewed interests with the growing demands in the context of many new challenging programs, and therefore, new ideas and approaches are being attempted. One of the important major projects of current times is the Spallation Neutron Source program, where the critical needs of an ion source are highly emphasized. The executive summary of the workshop on spallation neutron sources indicates that the present state-of-the art of high-brightness ion sources falls short of the requirements for the program [11]. Depending on the power level of the facilities, being in the range of 1-5MW, the source peak current requirements vary from 40mA to about 150mA, and the duty factor is in the range of 1% to about 10%. The normalized emittance (90%) for typical beam current of 100mA needs to be $\lesssim$ 1mm-mrad (the factor of $\pi$ is excluded here), and the lifetime of the source should be ~ 1000 hours. It is highlighted in the workshop summary that $H^-$ beams from a surface plasma source (SPS), such as a Penning or a semiplanatron source, will be a good candidate for the pulsed spallation source scenarios currently under investigation.

At Maryland, efforts are made to develop high-quality surface plasma sources which have merits to satisfy the needs of both advanced accelerator applications and microfabrication. Experiments are being conducted with a Penning and a magnetron type SPS source, and the results are presented here. Note that the Penning source at Maryland has been operated so far using small extraction aperture with diameter = 0.6 mm, while beam characteristics have been studied for two sets of extraction apertures, one with a diameter of 2.5 mm and the other with a diameter of 0.5 mm, in the case of the magnetron source. These experimental results provide a good database for the performance characteristics of two SPS sources.

## 2 PENNING SOURCE AND $H^-$ BEAM MEASUREMENTS

The geometrical characteristics of a Penning-type ion source, developed in Maryland in collaboration with the Budker Institute of Nuclear Physics, have been described elsewhere [12-13]. This source has been running reliably for more than eight hundred hours over the past one year with limited maintenance. The source runs in a pulsed mode with the maximum pulse length of 1ms and repetition rate of 10Hz. The electronics of the ion source system, especially the power supplies, have good regulation, i.e., about 1V over 10kV. In typical operations, the discharge current is in the range of about 30-50A and the discharge voltage is about 200-250V. Forced air cooling is being used to control thermal load on the gas injection valve and on the cathode body. An improved cooling system will allow to increase the duty factor and eventually to run the source in cw mode.

Gas pressure plays a key role in determining the emission

0-7803-4376-X/98/$10.00 © 1998 IEEE

current density and the noise level of the beam. $H^-$ emission current density of more than $1A/cm^2$ has been achieved in an almost noiseless condition. A typical $H^-$ pulse is shown in Fig.1. Note that the noise on the beam pulse is close to its baseline value. Here, the $H^-$ emission current density

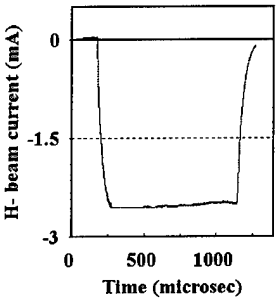



Fig. 1 Typical $H^-$ beam pulse from Penning SPS source with extraction aperture diameter $d_s$= 0.6mm.

is close to $1A/cm^2$. Figure 2 shows the dependence of $^-H$ current on extraction voltage for several values of discharge current over the range of 30-80A. These data represent the parameter space for the operation of the Penning SPS source.

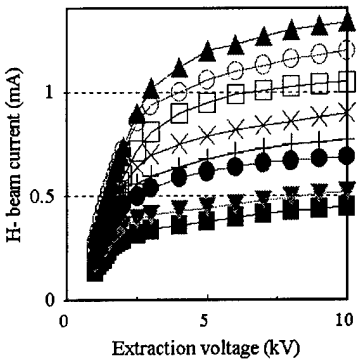



Fig. 2 $H^-$ beam current versus extraction voltage for discharge currents = 30A (■), 35A (▼), 40A (●), 45A (+), 50A (X), 60A (□), 70A (○), 80A (▲). These results correspond to the Penning SPS source with $d_s$= 0.6mm.

The beam brightness is a figure of merit of an ion source. The normalized beam brightness $B_n$ can be determined [14] from current density j and perpendicular temperature $T_\perp$ following the relation $B_n = mc^2j/(2\pi T_\perp)$. $T_\perp$ is obtained from emittance measurements. The emittance of the $H^-$ beam is measured using a pepper-pot system [15]. $T_\perp$ at the emission surface is estimated to be about 0.6eV for the situation in Fig.1, and the corresponding normalized brightness is about $2x10^{12}$ A/(m-rad)$^2$. These results represent the overall nature of the beam; the core beam is expected to exhibit much improved characteristics.

A retarding potential analyzer has been used to measure the energy spread [16]. The minimum energy spread of $\lesssim$ 2.5eV has been measured for angular beam intensity $I_\Omega$ of about 40mA/sr. This value of the energy spread is close to the resolution limit of the analyzer. Note that the beam intensity is about three orders of magnitude higher than liquid metal ion sources [17] or gas-field ionization sources [18]. The energy spread is observed to increase with noise level on the $H^-$ beam.

## 3 MAGNETRON SOURCE RESULTS

A magnetron-type negative ion source is operated in pulsed mode. The nominal pulse width is 50μs, and the duty factor is usually $1.5x10^{-4}$. We keep the anode body of the ion source at 165C, cesium (Cs) boiler temperature at 160C, Cs valve temperature at 270C and Cs line temperature at 300C. The discharge current is around 20-40A, the discharge voltage is about 180V, and the extraction voltage is varied over 0-30kV. Experiments have been conducted for different sizes of the extraction aperture -- diameter = 0.5mm and 2.5mm.

Figure 3 shows a typical $H^-$ beam pulse for extraction aperture of diameter = 2.5mm. The $H^-$ current is about 19mA for average $H_2$ gas pressure in the chamber =1.8-2.2x10$^{-5}$Torr,

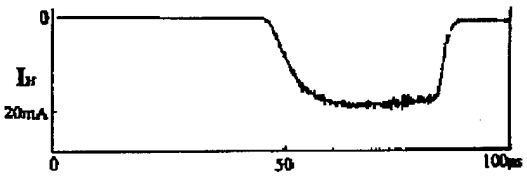



Fig. 3 Typical $H^-$ beam pulse for magnetron SPS source. Diameter of the extraction aperture $d_s$= 2.5 mm.

discharge current = 18A and extraction voltage = 30kV. This corresponds to an $H^-$ emission current density of $0.4A/cm^2$. Figure 4 shows typical beam pulse results for diameter of the extraction aperture = 0.5mm. The $H^-$ current is about 1.4mA, when the average $H_2$ gas pressure in the chamber = 1.0-1.5x10$^{-5}$Torr, discharge current = 25A, and extraction voltage = 20kV. This gives an $H^-$ emission current density of about $0.7A/cm^2$. The peak-to-peak noise level is about 0.15mA, which is about 5% of the total $H^-$ current. Higher beam current is obtained when the ion source runs at lower gas pressure. For an average pressure in the chamber at 0.8-1.2x10$^{-5}$Torr, the $H^-$ current is about 2.3mA, when the discharge current = 30A and extraction voltage = 26kV. This

yields an $H^-$ emission current density of about 1.15A/cm$^2$. The beam noise is less than 5% in this case.

The normalized emittance (90%) of the beam is measured in the small aperture case, and it is about 0.17mm-mrad. This yields a beam brightness (normalized) of about 8x10$^9$A/(m-rad)$^2$.

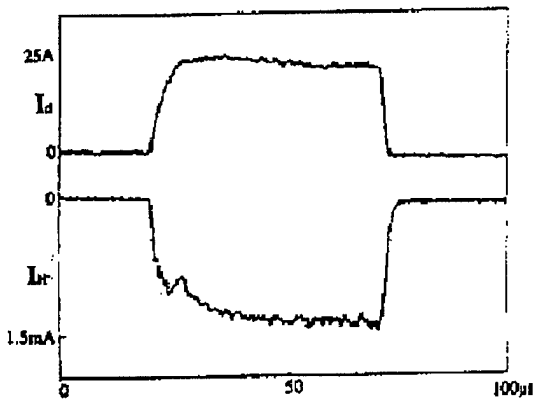



Fig. 4 Discharge current $I_d$ and $H^-$ beam current $I_{H^-}$ versus time for the magnetron SPS source. A smaller extraction aperture with diameter $d_s$= 0.5 mm is used here.

## 4 SCALING AND DISCUSSIONS

The results observed in the space-charge limited mode of operation of the two surface-plasma sources show the following behavior: (i) The $H^-$ beam current, $I_{H^-}$, increases almost proportionately with discharge current, $I_d$. (ii) $I_{H^-}$ increases with the aperture area and the extraction voltage. This trend of results suggests that the aperture of the Penning source can be increased from the current value of 0.6mm to about 2.4mm and that the source parameters can be appropriately scaled toward the requirements of a prototype high-current (~ 40mA), high duty factor (~ 10%) $H^-$ source suitable for pulsed spallation neutron source applications. It will be important to further extend our studies to critically examine the magnetron and Penning sources in higher duty-factor operations and test long-time reliability of the source and reproducibility of the beam characteristics. The excellent quality of $H^-$ beams with emission current density of ~1A/cm$^2$ and the minimum energy spread of about $\lesssim$ 2.5eV from the Penning surface plasma source may open up avenues for many novel applications.

## 5 ACKNOWLEDGMENTS

Special thanks are due to V. Dudnikov and G. Derevyankin of the Budker Institute of Nuclear Physics, Novosibirsk for their collaboration during the Penning source development. Also, the authors thank C.-H. Chen, W. Wang, V. Yun and E. Sokolovsky for their valuable help.

## 6 REFERENCES

[1] G. D. Alton, Rev. Sci. Instrum. **65**, 1141 (1994).
[2] J. Alessi, "$H^-$ ion sources", in High-brightness Beams for Advanced Accelerator Applications, AIP Conf. Proc. No. 253 (ed. W. W. Destler and S. K. Guharay, American Institute of Physics, New York, 1992), p. 193.
[3] W. Ensinger, Rev. Sci. Instrum. **63**, 5217 (1992).
[4] J. Melngailis, J. Vac. Sci. Technol. B **5**, 469 (1987).
[5] J. Orloff, Rev. Sci. Instrum. **64**, 1105 (1993).
[6] "The Physics and Technology of Ion Sources," ed. Ian G. Brown (Wiley, New York, 1989).
[7] H. V. Smith et al., Rev. Sci. Instrum. **65**, 1176 (1994).
[8] K. N. Leung and K. W. Ehlers, Rev. Sci. Instrum. **53**, 30 (1982); K. N. Leung et al., J. Vac. Sci. Technol. B **13**, 2600 (1995).
[9] W. K. Dagenhart et al., AIP Conf. Proc. No. 158 (American Institute of Physics, New York, 1987), p. 366.
[10] C. W. Schmidt, Proc. LINAC Conf., 1990, p. 259.
[11] Proc. Workshop on Ion Source Issues Relevant to a Pulsed Spallation Neutron Source, ed. L Schroeder, K. -N. Leung, Lawrence Berkeley Lab., Oct. 24-26, 1994, Report LBL-36347.
[12] V. Dudnikov, G. Derevyankin, D. Kovalevsky, V. Savkin, E. Sokolovsky and S. K. Guharay, Rev. Sci. Instrum. **67**, 1614 (1996).
[13] S. K. Guharay, et al., J. Vac. Sci. & Technol. B **14**, 3907 (1996).
[14] M. Reiser, Theory and Design of Charged Particle Beams (Wiley, New York, 1994).
[15] S. K. Guharay et al., Rev. Sci. Instrum. **67**, 2534 (1996).
[16] S. K. Guharay, et al., Microelectronic Engineering **35**, 435 (1997).
[17] A. E. Bell, K. Rao, G. A. Schwind, L. W. Swanson, J. Vac. Sci. & Technol. B **6**, 927 (1988).
[18] Th. Maisch, Ch. Wilbertz, Th. Miller, S. Kalbitzer, Nucl. Instrum. & Meth. in Phys. Res. B**80/81**, 1288 (1993).

# THE DEPENDENCE OF LONGITUDINAL EMITTANCE UPON SURFACE CHARGE DENSITY IN A RF PHOTOINJECTOR

D. H. Dowell, S. Joly and A. Loulergue
Commissariat a l'Energie Atomique, Bruyeres-le-Chatel, France

*Abstract*

This paper describes the analysis of experimental energy spectra and pulse shapes to determine the electron distribution in longitudinal phase space produced by a RF photocathode gun for microbunch charges below space charge limited emission. It is found that the longitudinal phase space distribution cannot be represented by a simple ellipse, and requires the use of an ad hoc model in which the usual beam ellipse is distorted to fit the data and extract the emittance. The physical origins of these distortions are space charge forces at the cathode, wakefields and curvature due to the RF waveform. These effects increase the emittance by introducing correlations in the distribution, which in some situations can be corrected. In the absence of these correlations, the area of the undistorted ellipse gives the uncorrelated emittance of the photocathode gun. In this work, the uncorrelated longitudinal emittance is found to scale linearly with the surface charge density up to the space charge limit. In this experiment the increase in emittance is principally due to growth in energy spread instead of pulse length elongation. The implications these results have upon the limits of pulse compression at high charge are discussed.

## 1 INTRODUCTION

This paper summarizes a portion of the experimental results described in a series of papers on the longitudinal emittance from RF photocathode guns[1-4]. This work explores the high charge regime of RF guns, and attempts to document the dependence of the longitudinal emittance and its distortion upon space charge forces at the photocathode. The data show that not only is the phase space distribution distorted but is also observed to breakup longitudinally. The current paper describes the dependence of the longitudinal emittance upon surface charge density at the photocathode below space charge limited emission.

Due to the complex features of the longitudinal phase space, we have sought to develop a model-dependent analysis for fitting the data and extracting the phase space parameters. This model is used to fit both the single microbunch data and the multi-bunch case. Only the single microbunch analysis is described here. Tomographic techniques can also be used to obtain model-independent phase space distributions[5].

The paper begins by reviewing the experimental technique, followed by a description of the data analysis. The results section summarizes the emittance and phase space parameters as a function of surface charge density. Only the analysis for data below space charge limited emission are presented in this paper. (The space charge limit occurs when the planar-diode space charge field exceeds the RF field at the photocathode surface.) The paper ends by estimating the limits of microbunch compression due to the longitudinal emittance.

## 2 THE EXPERIMENTAL TECHNIQUE

The details of the experimental configuration are described elsewhere[1,6] and therefore are only briefly given here. The ELSA (Etude d'un LaSer Accordable) free electron laser (fel) facility in Bruyeres-le-Chatel, France consists of a 144 MHz, one cell RF photocathode gun followed by three additional 433 MHz accelerator sections. The beam energy after the gun is 1.8 MeV and the final energy is 17.5 MeV. Following the accelerator is a three dipole, non-isochronous 180 degree bend (called the demi-tour) which in the fel experiments is used to compress the microbunch before injecting it into the wiggler. The beam energy spectrum is obtained at the center dipole of the demi-tour where the beam is dispersed, and the pulse shape is measured with a streak camera after the bend. Optical transition radiation view screens are used to image the beam.

The experiment consists of measurements of the beam energy spectra and pulse shapes at the full beam energy of 17.5 MeV for microbunch charges of 0.5, 1.0 and 2.0 nC over a range of the main, 433 MHz accelerator RF phases in order to deduce the electron distribution in longitudinal phase space at the exit of the RF gun.

## 3 THE DATA ANALYSIS

The data is analyzed by assuming the electron distribution in longitudinal phase space lies within an ellipse whose is distorted by quadratic and cubic terms[2,4],

$$\Delta E = \pm\sqrt{\left(\frac{\tau_{12}}{\tau_{11}}\Delta t\right)^2 - \frac{\tau_{22}\Delta t^2 - \frac{\varepsilon_l^2}{\pi}}{\tau_{11}}} + \frac{\tau_{12}}{\tau_{11}}\Delta t + a\Delta t^2 + b\Delta t^3 \qquad [1]$$

Here $\Delta t$ and $\Delta E$ are the phase space variables of the time and energy difference with respect to the reference particle. The quantities, $\tau_{11}$, $\tau_{12}$ and $\tau_{22}$, are the elements of the longitudinal beam matrix and are related to the longitudinal emittance, $\varepsilon_l$, by

$$\pi\varepsilon_l = \pi\sqrt{\det\tau} = \pi\sqrt{\tau_{11}\tau_{22} - \tau_{12}^2} \qquad [2]$$

The longitudinal phase space distribution is nearly identical to the transverse beam matrix[7], except for the quadratic and cubic distortions whose strengths are given by the coeficients, a and b. The effect these terms have upon the phase space ellipse is shown in Figure 1.

0-7803-4376-X/98/$10.00 © 1998 IEEE

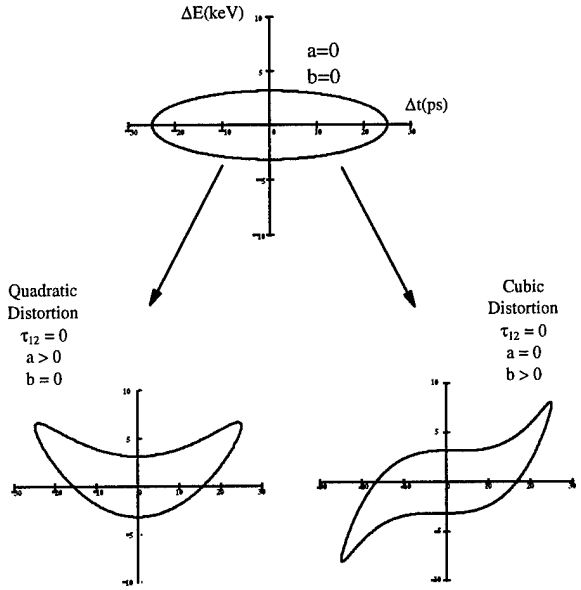



Figure 1. Distortions of the longitudinal phase space ellipse.

The analysis assumes the electron distribution is established inside the RF gun, after which it obeys simple transformation relations. The transformation of each macroparticle's energy and time coordinate, relative to the central ray, from the exit of the 144 MHz RF gun $(\Delta t_0,\Delta E_0)$, to the entrance of the demi-tour, $(\Delta t_1,\Delta E_1)$, (see References 1,4) is given by

$$\Delta E_1 = \Delta E_0 + E_{433}(\cos(\phi_{433} + 2\pi f_{433}\Delta t_0) - \cos(\phi_{433}))$$

$$\Delta t_1 = \Delta t_0$$

$E_{433}$ is the maximum energy gain a macroparticle can achieve when on the crest of the rf wave form, $\phi_{433}$ is the phase of the central ray relative to the rf crest and $f_{433}$ is the RF frequency. These relations assume the beam is relativistic, and no velocity bunching or debunching is possible. This is valid since the electrons are relativistic after leaving the injector cavity. Similarly the transport around the demi-tour is given in terms of its non-isochronicity, $\delta$,

$$\Delta E_2 = \Delta E_1, \quad \Delta t_2 = \Delta t_1 + \delta \Delta E_1$$

These simple relations are used to propagate the phase space distribution from the exit of the RF gun through the 433 MHz accelerator and around the demi-tour. The interior of the distorted ellipse is first uniformly populated with a gaussian electron distribution of typically 1000 to 3000 macroparticles. The macroparticles are then individually transformed through the accelerator and the bend to obtain the distributions at the locations measurements are made. Projections of the transformed phase space distribution are performed to obtain the computed energy spectra and pulse shapes for comparison with the data. The initial phase space parameters are then varied to best fit the observed energy spectra and pulse shapes for each micropulse charge.

## 4 RESULTS OF THE ANALYSIS

Typical fits to the data are shown in Figure 2. The data is for a microbunch charge of 1.0 nC and the 433 MHz RF phase adjusted for minimum energy spread. The corresponding phase space distributions are given in Figure 3. The phase space labeled 'After Bend' is the final distribution at 17.5 MeV whose projections are plotted with the data in Figure 2. The upper distribution, labeled 'Exit of Gun', is the deduced 1.8 MeV microbunch phase space at the RF gun exit. Comparing Figure 3 with Figure 1 shows the dominant distortion is cubic with a zero quadratic term. Similar distributions are obtained for the data analyses at 0.5 and 2.0 nC.

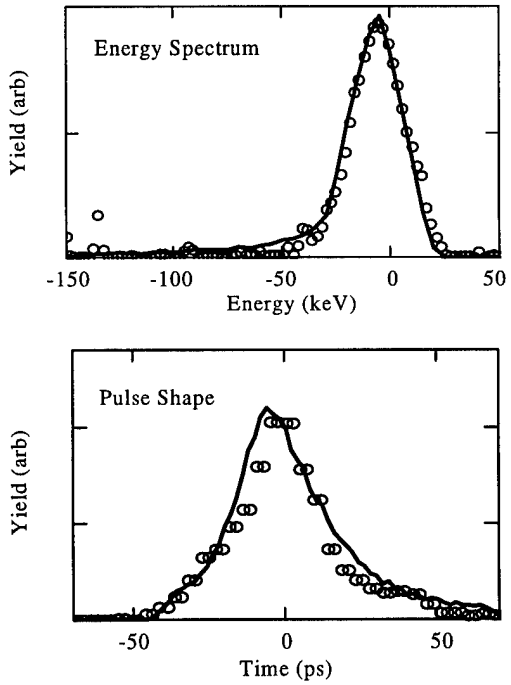



Figure 2. Fits of the 17.5 MeV energy spectrum (in the middle of the demi-tour) and pulse shape (after the demi-tour) for a microbunch charge of 1 nC. The rf is adjusted for minimum energy spread. The data is plotted as circles and the solid curves are the projections of the phase space distribution shown as 'After Bend' in Figure 3.

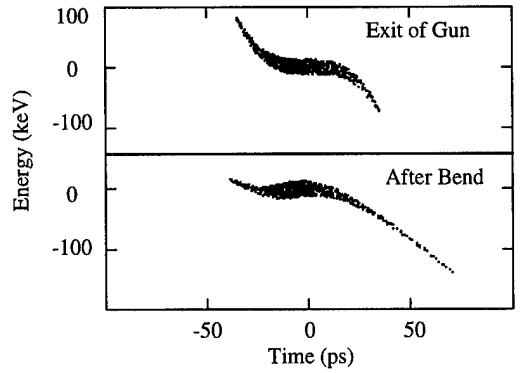



Figure 3. Longitudinal phase space distributions obtained from fitting the data in Figure2.

Ignoring the distortion terms and applying Equation 2 allows us to obtain the experimental, uncorrelated longitudinal emittance as a function of the surface charge density. Since the space charge electric field scales linearly with the surface charge density, this is used as the independent variable in the following figures. Figure 4 shows that the emittance varies linearly with the surface charge density.

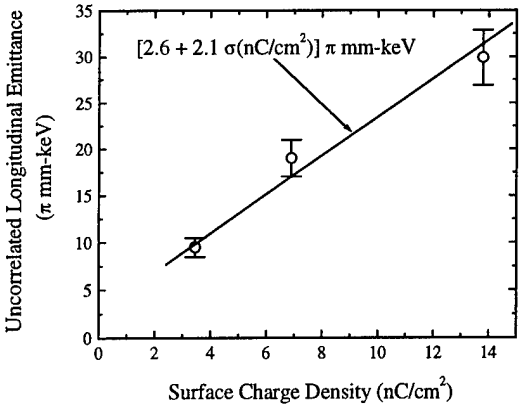



Figure 4. The uncorrelated, rms longitudinal emittance as a function of the surface charge density.

The analysis also shows the growth in longitudinal emittance results primarily from an increase in the uncorrelated energy spread, as shown in Figure 5, with negligible pulse length elongation. This occurs because, as the starting point for all the measurements, the launch phase of the electron microbunch from the photocathode is adjusted in concert with the 433 MHz RF phase for a

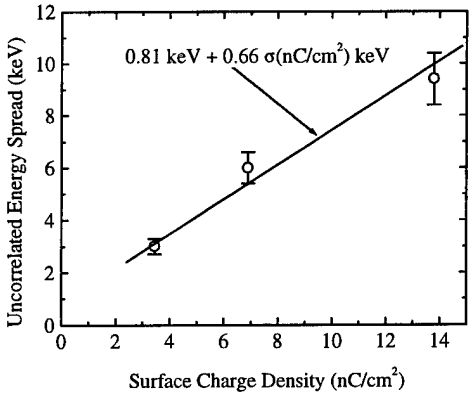



Figure 5. The uncorrelated, rms energy spread vs the surface charge density at the exit of the RF gun.

beam with minimum energy spread. This tuning algorithm tends to minimize any space charge driven pulse elongation by ballistically bunching the microbunch in the RF gun. Therefore we deduce a nearly constant width (11ps, rms) electron pulse at 0.5, 1.0 and 2.0 nC per microbunch. This is approximately the same length as that of the drive laser micropulse.

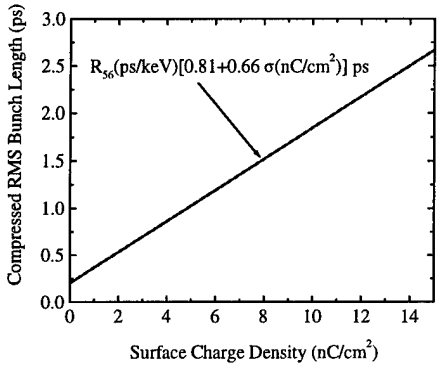



Figure 6. The compressed microbunch length acheived using the longitudinal data shown in Figures 4 and 5. The compressor $R_{56}$ is 0.25 ps/keV.

Given these results for the longitudinal emittance it is straightforward to estimate the compressed microbunch length in a magnetic buncher. As an example, consider the demi-tour used in this experiment which has a rather aggressive non-isochronicity of 0.25 ps/keV. In this case, one finds the minimum microbunch lengths shown in Figure 6. These results include only the uncorrelated emttance, and in general any correlations will increase this microbunch length.

## 5 CONCLUSIONS

Space charge limited emission for this RF gun occurs near a surface charge density of 20 nC/cm$^2$ at an electric field of 22 MV/m. One could expect that doubling the applied RF field from 25 to 50 MV/m would reduce the slope of the emittance growth from 2.1 to 1 $\pi$ mm-keV, as should be the case for higher gradient guns.

## REFERENCES


1. S. Joly et al., "Brightness Measurements of the ELSA Electron Beam", Proceedings of the 1994 Linear Accelerator Conference, Tsukaba, Japan.
2. D.H. Dowell et al., "The Space Charge Limits of Longitudinal Emittance in RF Photoinjectors", Proceedings of the Advanced Accelerator Workshop, Oct. 12-18, 1996, Lake Tahoe, CA.
3. D.H. Dowell et al., "Longitudinal Phase Space Experiments on the ELSA Photoinjector", NIM A375(1996)104.
4. D.H. Dowell et al., "Observation of Space Charge Driven Instabilities in a RF Photoinjector", submitted to Plasma Physics.
5. C.B. McKee et al., "Phase Space Tomography of Relativistic Electron Beams", NIM A358(1995)264.
6. R. Dei-Cas et al., NIM A296(1990)209, and J. Auturier et al., NIM A304(1991)305.
7. D.C. Carey, K.L Brown and F. Rothacker, SLAC-R-95-462.

# EMITTANCE STUDIES OF THE BNL/SLAC/UCLA 1.6 CELL PHOTOCATHODE RF GUN*

D.T. Palmer*, X.J. Wang†, R.H. Miller* M. Babzien†, I. Ben-Zvi†, C. Pellegrini**, J. Sheehan†, J. Skaritka†, H. Winick*, M. Woodle†, V. Yakimenko†

*Stanford Linear Accelerator Center, Stanford University, Stanford, CA 94309

†Brookhaven National Laboratory, Accelerator Test Facility, Upton, NY 11973

**University of California Los Angeles, Department of Physics, Los Angeles, CA 90095

*Abstract*

The symmetrized 1.6 cell S-band photocathode gun developed by the BNL/SLAC/UCLA collaboration is in operation at the Brookhaven Accelerator Test Facility(ATF). A novel emittance compensation solenoid magnet has also been designed, built and is in operation at the ATF. These two subsystems form an emittance compensated photoinjector used for beam dynamics, advanced acceleration and free electron laser experiments at the ATF. The highest acceleration field achieved on the copper cathode is 150 $\frac{\mathrm{MV}}{\mathrm{m}}$, and the guns normal operating field is 130 $\frac{\mathrm{MV}}{\mathrm{m}}$. The maximum rf pulse length is 3 $\mu$s. The transverse emittance of the photoelectron beam were measured for various injection parameters. The 1 nC emittance results are presented along with electron bunch length measurements that indicated that at above the 400 pC, space charge bunch lengthening is occurring. The thermal emittance, $\epsilon_o$, of the copper cathode has been measured.

## 1 INTRODUCTION

The BNL/SLAC/UCLA S-band emittance compensated[1] photoinjector has been installed at the Brookhaven Accelerator Test Facility(ATF) as the electron source for beam dynamics studies, laser acceleration and free electron laser experiments. The 1.6 cell rf gun is powered by a single XK-5 klystron, and is equipped with a single emittance compensation solenoidal magnet. There is a short drift space between the photoinjector and the input to the first of two SLAC three meter travelling wave accelerating sections. This low energy drift space contains a copper mirror that can be used in either transition radiation studies or laser alignment. There is also a beam profile monitor/Faraday plate located 66.4 cm from the cathode plane. The photoinjector beam line layout is presented in Fig. 1.

The high energy beam transport system consists of nine quadrupole magnets, an energy spectrometer, an energy selection slit and a high-energy Faraday cup. Diagnostics located in the high energy transport consist of beam profile monitors and strip lines. The strip lines are used for an on line laser/rf phase stability monitor.

The drive laser is a Nd:YAG master oscillator/power amplifier system. A diode pumped oscillator mode locked at 81.6 MHz produces 21 psec FWHM pulses at 100 mW of average power. Gated pulses seed two flash lamp pumped multi-pass amplifiers and are subsequently frequency quadrupled. This nonlinear process leads to a factor of two reduction in the laser pulse length. The 266 nm beam is transported to the rf gun area via a 20 meter long evacuated pipe. A spherical lens and a pair of Littrow prisms are used to compensate for the anamorphic magnification introduced by the 72° incidence on the cathode. The time slew across the cathode caused by this oblique incidence is also corrected by using a diffraction grating. The spot size of the laser beam on the cathode is 2 mm diameter edge to edge.

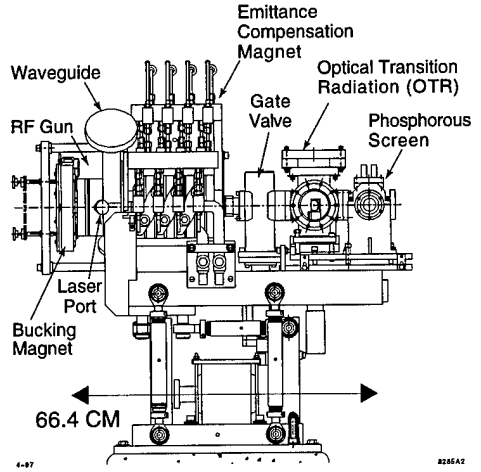



Figure 1: The BNL/UCLA/UCLA 1.6 cell S-band photoinjector

## 2 EMITTANCE STUDIES

The normalized transverse rms emittance, $\epsilon_{n,rms}$, was measured using the two screen method. The measured $\epsilon_{n,rms}$ values that are reported are greater than or equal to the real beam emittance. Table 1 list the relevant beam parameters used during these beam dynamics studies.

| | |
|---|---|
| Laser Spot Size | 1 mm radius hard edge |
| Cathode Field | 130 $\frac{\mathrm{MV}}{\mathrm{m}}$ |
| rf Gun Beam Energy | 5.75 MeV |
| Final Beam Energy | 40 MeV |
| Cathode Magnetic Field | $\leq$ 5 G |

Table 1: Beam Study Parameters

*WORK SUPPORTED BY THE DEPARTMENT OF ENERGY, CONTRACTS DE-AC03-76SF00515, DE-AC02-76CH00016 AND DE-FG03-92ER40793

0-7803-4376-X/98/$10.00 © 1998 IEEE

### 2.1 *Low Charge*

PARMELA[2] was used to simulate the emittance compensation process and the subsequent acceleration to 40 MeV. A correlation of the minimum spot size with an emittance minimum was noted during these simulations. This was experimentally verified during the commissioning of the 1.6 cell rf gun, using the beam profile monitor located at the output of the second linac section, as can be seen in Fig. 2. The result in Fig. 2 is for a total bunch charge of 0.329 $\pm$ 0.012 nC, an electron bunch length of $\tau_{95\%}$ = 10.9 psec with an $\epsilon_{n,rms}$ = 1.17 $\pm$ 0.16 $\pi$ mm mrad.

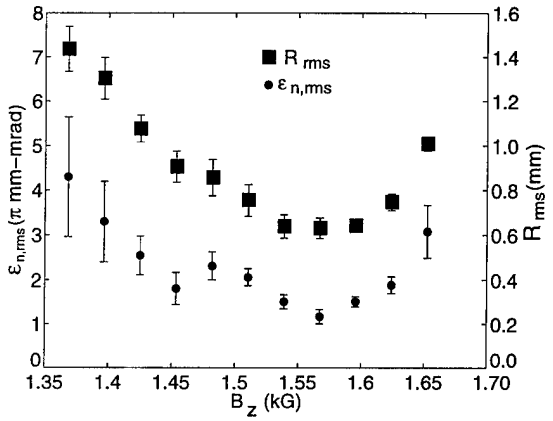



Figure 2: $\epsilon_{n,rms}$ and $R_{rms}$ versus $B_{z,max}$

The dependence of transverse emittance on the bunch charge under two different experimental conditions are presented in Fig. 3. The linear dependent emittance versus charge was conducted under constant solenoidal magnet field that was optimized for a total charge of 390 pC and only the laser energy on the cathode was varied. For the quadratic dependent emittance versus charge, as the laser energy was varied the beam was optimized using the solenoidal magnet and steering magnets to produce the smallest symmetric beam profile at the first high energy profile screen. Note that even under these diverse experimental condition the measured emittance are consistent with the data in Fig. 2.

We have noted that at Q=0 for the linear dependence emittance versus charge there is a residual emittance term of 0.8 $\pi$ mm-mrad. This term is due to $\epsilon_o$, $\epsilon_{rf}$ and $\epsilon_{mag}$. The magnetic term can be neglected since the initial cathode spot size and the small magnetic field at the cathode will contribute only 0.03 $\pi$ mm mrad [3]. The rf contribution should be small, since there is no transverse space charge forces to cause beam size expansions in the rf gun. The beam, in this limiting charge case, will only sample a small portions of the rf fields which decrease the rf contribution by $\sigma_x^2$ [4]. The beams intrinsic thermal emittance including the Schottky correction is given in Equation 1. A theoretical estimate of the thermal emittance at 130 $\frac{MV}{m}$ for a copper cathode was found to be 0.5 $\pi$ mm-mrad.

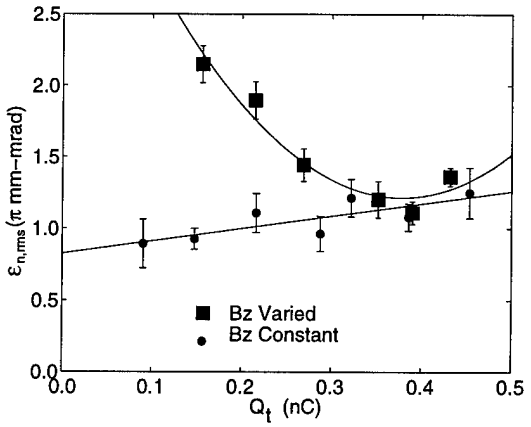



Figure 3: $\epsilon_{n,rms}$ versus $Q_t$

$$\epsilon_o \leq 0.8\,\pi \text{ mm mrad} \quad (1)$$

Due to laser power limitation, rf gun bunch compression and the Schottky effect it was not possible to keep the total charge constant for different laser injection phases. Therefore in Fig. 4 the plot of $\epsilon_{n,rms}$ as a function of laser injection phase is not for a constant charge but for a decreasing charge from a maximum of 400 pC to a minimum of 178 pC.

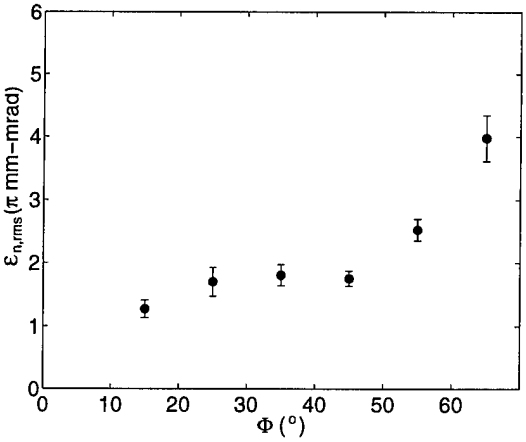



Figure 4: $\epsilon_{n,rms}$ versus $\phi$

### 2.2 *1 nC Emittance Studies*

For X-ray free electron laser application such as the Linear Coherent Light Source(LCLS)[5] the relevant photoinjector parameters are 1 nC, $\tau_{95\%}$ = 10 psec and 1.00 $\pi$ mm mrad normalized rms emittance. The measured and LCLS values are presented in Table 2.

| Parameter | LCLS | Experimental Results |
|---|---|---|
| $Q_T$ | 1 nC | 1.020 $\pm$ 0.059 nC |
| $\tau_{95\%}$ | 10 psec | 14.7 psec |
| $\epsilon_{n,rms}$ | 1.00 $\pi$ mm mrad | 4.74 $\pm$ 0.24 $\pi$ mm mrad |

Table 2: 1 nC emittance results

Simulation results using PARMELA with a longitudinal flat top electron pulse of $\tau_{95\%}$ = 10 psec, full width tenth maximum (FWTM), indicate that a $\epsilon_{n,rms} \leq 1\ \pi$ mm mrad is attainable[6]. The results of our experimental studies present two challenges. First is the increased $\tau_{95\%}$ and second is the larger than expected $\epsilon_{n,rms}$. These are not unrelated since the emittance contribution due to rf scales as $\sigma_z^2$. Therefore an important issue is to find the mechanism causing the electron bunch length to increase. Two possible mechanisms were studied; laser pulse bunch lengthening due to laser power saturation in a doubling crystal, or space charge bunch lengthening. Experimental studies of the correlation of the laser power and $\tau_{95\%}$ were undertaken. Figure 5 shows the results of these studies. While keeping the total electron bunch charge constant at 360 pC, the laser intensity in the green($\lambda$ = 532 nm) was increased. The results is that $\tau_{95\%}$ = 10.9 psec. Keeping the laser intensity in the green constant and varying the uv on the cathode to increase the electron bunch charge from 400 pC to 1 nC results in an increase in the $\tau_{95\%}$ from 10.9 psec to 14.7 psec(Fig. 5). This clearly shows that the 1 nC electron bunch length is not due to the laser pulse length but due to some beam dynamics issue, almost surely longitudinal space charge forces.

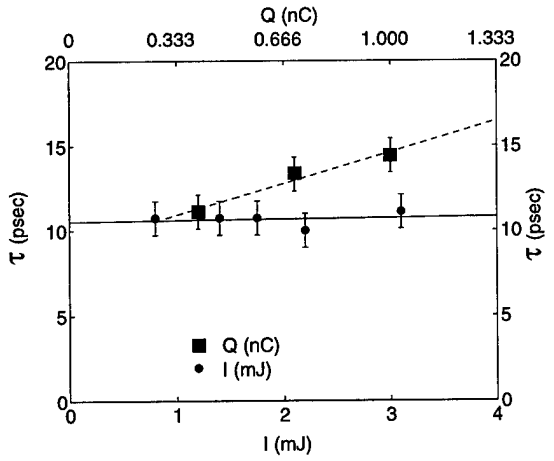



Figure 5: $\tau_{95\%}$ versus $I_{green}$ with $Q_t$ constant. $\tau_{95\%}$ versus $Q_t$ with $I_{green}$ constant.

PARMELA simulation do not show the space charge bunch lengthening seen in these experiments and this simulation error is being investigated. This debunching effect due to space charge forces can be corrected by decreasing the laser pulse length and using the debunching effect to lengthen the $\tau_{95\%}$ to the required 10 psec. This technique has the drawback the longitudinal phase mixing of the electron pulse could possible occur thereby degrading the emittance compensation process. A second possibility is to increase the laser spot size. But this would increase the emittance due to the rf emittance contribution, the remnant magnetic field at the cathode and also increase the intrinsic thermal emittance. Using a longitudinally flat top laser pulse would seem to be the best solution since the magnetic and thermal emittance would not increase and the longitudinal space charge forces would be decreased in the central portion of the bunch.

Due to the non-uniformity of the transverse laser pulse and transverse variation of the cathode quantum efficiency, the electron bunch transverse charge density $\rho(x, y)$ is not uniform. Laser assisted explosive electron emission(LAEEE)[7] has been used to smooth out this effect. The measured improvement in $\epsilon_{n,rms}$ due to LAEEE are presented in Table 3. Qualitative data for QE(x, y) of the copper cathode is not available, but for the magnesium cathode LASEEE improved the QE(x, y) by a factor of two, from an order of magnitude variation across the cathode spot to a 50% after LASEEE.

| Before Laser Cleaning | |
|---|---|
| $Q_t$ | 918 ± 77.5 pC |
| $\epsilon_{n,rms}$ | 5.18 ± 0.25 $\pi$ mm mrad |
| After Laser Cleaning | |
| $Q_t$ | 1020 ± 58.7 pC |
| $\epsilon_{n,rms}$ | 4.74 ± 0.24 $\pi$ mm mrad |

Table 3: High charge emittance study results before and after LAEEE

## 3 CONCLUSION

We have presented the results of emittance studies of the BNL/SLAC/UCLA 1.6 cell S-band emittance compensated photoinjector. Emittance as a function of laser injection phase, charge and peak magnetic field have been presented in the low charge regime. Emittance results for the 1 nC regime are presented before and after laser assisted explosive electron emission cleaning. Longitudinal bunch lengthening has been observed in the 1 nC studies and proposed solutions have been presented to counteract this effect. We have measured an upper limit to the beams intrinsic thermal emittance and found it to be $\epsilon_o \leq 0.8\ \pi$ mm mrad.

## 4 ACKNOWLEDGMENT

The authors would like to thank the technical staff at BNL, SLAC and UCLA for all their dedicated work on this project.

## 5 REFERENCES

[1] B. E. Carlsten, *NIM*, **A285**, 313 (1989)

[2] L. M. Young, private communications

[3] D. T. Palmer *et al.*, Proc. 1997 Part. Accel. Conf. (1997)

[4] K. J. Kim, *NIM*, **A275**, 201 (1989)

[5] H. Winick, *Electron Spectrosc. Relat. Phenom.*, **75**, 1-8 (1995)

[6] D. T. Palmer *et al.*, Proc. 1995 Part. Accel. Conf. (1995) p. 2432

[7] X. J. Wang *et al.*, J. Appl. Phys. 72(3), 888-894

# EXPERIMENTAL OPERATION OF A 17 GHz PHOTOCATHODE RF GUN

S. Trotz,W. Brown, B. Danly, J.P. Hogge, K.E. Kreischer, M. Shapiro, R.J. Temkin
Plasma Science and Fusion Center, M.I.T., Cambridge, MA 02139 USA,

*Abstract*

Initial operation of a 17 GHz RF photocathode electron gun has been achieved at MIT. This is the first photocathode electron gun to operate at a frequency above 2.856 GHz. Such electron guns have the potential for achieving record high values of electron beam quality. The 1.5 cell, π–mode, copper cavity was tested with 5-10 MW, 100 ns, 17.145 GHz pulses from a klystron amplifier built by Haimson Research Corp. Conditioning resulted in a maximum surface field of 250 MV/m. Dark current of 0.5 mA was observed at 175 MV/m, consistent with Fowler-Nordheim field emission theory if a field enhancement factor of about 100 is assumed. Electron bunches were generated by a regenerative laser amplifier that produces 20-40 μJ UV pulses. Faraday cup measurements indicated 0.12 nC bunches were produced with a kinetic energy of about 1 MeV. This corresponds to a peak current of about 120 A, and a density at the cathode of 8.8 kA/cm$^2$. Phase scans of laser induced emission reveal an overall phase stability of better than ±20°, corresponding to ±3 ps synchronization of the laser pulses to the microwave field.

## 1 INTRODUCTION

The goal of the 17 GHz photocathode experiment is to construct an ultra high-brightness source of electrons which can be used for free electron lasers or future linear colliders. The photocathode RF gun is a novel electron beam source intended to meet the requirements set by future high-energy linear colliders and next generation free electron lasers. A coupled pair of pillbox $TM_{010}$-like resonators is excited by sidewall coupled microwaves at 17 GHz. The axisymmetric copper cavity is shown in Figure 1. Note that the axial length of the structure is determined by the microwave wavelength. A picosecond ultraviolet laser pulse illuminates the back wall of the structure at the axis of symmetry. Electrons are released by the photoelectric effect and are accelerated by the axial electric field.

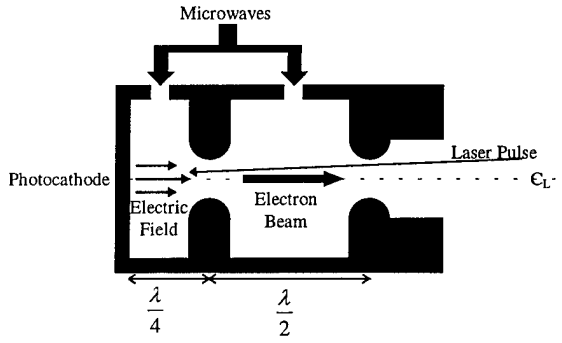



Figure 1: Schematic of the RF gun cavity

The M.I.T. experiment operates at a frequency of 17 GHz. Previous photocathode RF gun experiments have operated at 3 GHz or below. From an analysis of the Vlasov-Maxwell equations governing the dynamics of the electron beam production in the photocathode RF gun, scalings of the quality of the beam which can be produced in an RF gun with frequency have been derived [1]. According to these scaling laws, the brightness of the beam, a figure of merit for the beam quality, varies as the square of the RF gun frequency.

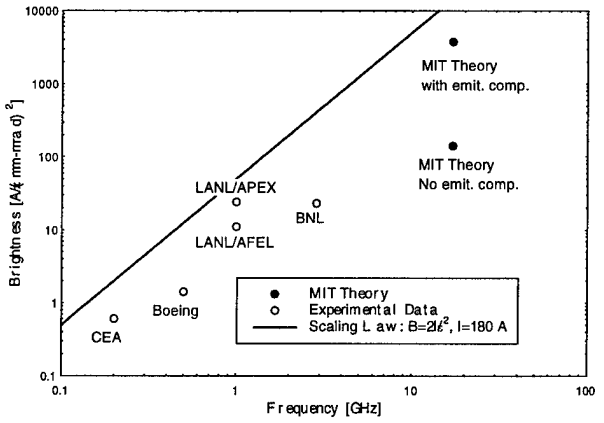



Figure 2: Scaling of brightness with frequency

Figure 2 illustrates experimental values of beam brightness for several frequencies. Theoretical values are given for the M.I.T. experiment for two cases. The lower value, corresponding to the present experimental setup, assumes no emittance compensation. The higher value assumes the use of a solenoidal field to achieve the maximum brightness possible. For our experiment, an axial field of 10 kG would be required.

## 2 DESIGN OF EXPERIMENT

The major system components of the MIT experiment are shown in Figure 3. The RF gun cavity is located in a large vacuum vessel shown at the bottom of the diagram.
The RF gun cavity is a traditional B.N.L.-style sidewall coupled 1.5 cell structure. The RF gun is composed of

0-7803-4376-X/98/$10.00 © 1998 IEEE

three pieces of OFHC copper which are clamped together and attached as a single piece to the WR-62 coupling waveguide. The RF gun has been studied theoretically by analyzing the eigenmodes of the accelerating structure in the absence of coupling holes and the excitation of the modes through the coupling to the waveguide. The coupling holes were modeled by choosing the magnetic polarizabilities of the holes empirically to match cold test data with theory. The polarizabilities were substantially smaller than the values predicted using Bethe's expressions for the polarizability of an elliptical aperture in an infinitely thin wall. However, the observed values were consistent with the finite thickness of the walls in which the RF gun coupling holes are located.

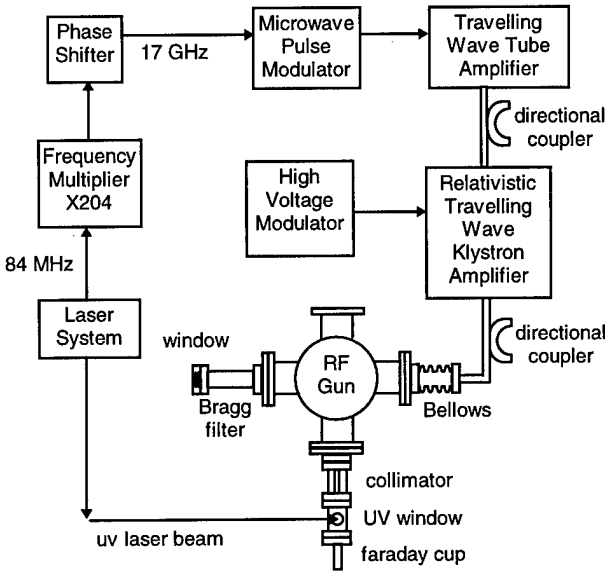



Figure 3: Major experimental components

The RF gun requires a 50 ns, 7.2 MW pulse of 17 GHz microwaves to achieve the design gradient of 250 MV/m fields at the cathode. The experiment utilizes a 17 GHz relativistic klystron amplifier constructed by Haimson Research Corporation. The klystron is driven by a 580 kV, 1 μs flattop modulator pulse. A Thomson CSF gun produces a 100 A pulse. The beam is space-charge limited and the gun perveance is 0.27 μperv. The amplifier chain includes a TWTA to provide about 10 W to the klystron. The klystron gain is approximately 60 dB. Dark current of 0.5 mA was observed when 3.5 MW of microwave power was coupled into the cavity. This corresponds to a peak electric field of 175 MV/m, and is consistent with Fowler-Nordheim field emission theory if a field enhancement factor of about 100 is assumed.

The klystron amplifier has been found to generate power in other spurious modes when connected to a mismatched load. Microwaves associated with these modes are slightly higher in frequency than the operating frequency of the klystron. To eliminate these modes, which reduce the stability and gain of the amplifier, a Bragg filter was designed and installed on the RF gun coupling waveguide. The Bragg filter structure is shown in Figure 4. This filter is reflective for frequencies between 16.7 and 17.2 GHz, and transmits for higher frequencies. The use of the Bragg filter allowed cavity coupling at 17.15 GHz, while minimizing impedance mismatches at higher frequencies that would cause the spurious oscillations to occur. Up to 8 MW of klystron power was coupled into the cavity, with amplitude stability of ±5%. Phase stability was also measured using a phase discriminator. This stability was found to be 8° from shot-to-shot, and less than 4° during a single shot.

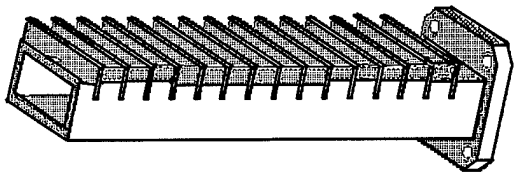


Figure 4: Bragg filter

The laser beam for the RF gun photocathode is generated by a Ti:Sapphire laser system, which produces 1.9 ps, 1.9 mJ, 2 mm diameter pulses at 800 nm. The pulse duration of 2 ps at 800 nm was verified using a single-shot autocorrelator. Pulse-to-pulse laser energy fluctuations are approximately ±10% at 800 nm. These pulses are frequency tripled to 20-40 μJ of UV, and then focused on the back wall of the copper cavity. The ultraviolet spot size is approximately 0.7 mm in diameter and 1 ps in duration estimated from the infrared pulse measurements using nonlinear optical theory. Measurement of the frequency sidebands using a spectrum analyzer [2] indicated a laser phase jitter of less than 5 ps, or 30 degrees.

The timing scheme used in the M.I.T. RF gun experiment is slightly different from that of other photocathode experiments. A photo-diode samples the light pulses bouncing back and forth in the optical cavity of the Ti:Sapphire laser oscillator. The IR pulses of this oscillator are used as input to a regenerative amplifier. The frequency of these pulses is 84 MHz and is dictated only by the length of the cavity. No external oscillator is used. The signal from this photodiode is used as input to a frequency multiplier box, which filters and amplifies the signal. The output signal is about 17 GHz and is phaselocked to the laser system. This milliwatt level signal is used as input to the microwave amplifier chain which drives the RF gun experiment (see Figure 3).

## 3 RESULTS

Initial operation of the RF-gun was achieved in December, 1996. Current associated with photo-emission was observed with a Faraday cup located about 20 cm from the cavity. A typical set of experimental traces is shown in Figure 5. Extremely narrow, 2 ns FWHM negative Faraday cup signals are observed following the positive photo-diode signal by about 6 ns. This delay is consistent with the physical locations of the two diagnostics and cable signal delay. The integrated Faraday cup signal indicates 0.12 nC of charge for an electric field strength of 130 MV/m at the cathode at the time of injection. This value is inferred from the forward and reflected power at the rf cavity. Assuming a 1 ps pulse, this corresponds to a peak current of about 120 A, and a density at the cathode of 8.8 kA/cm$^2$.

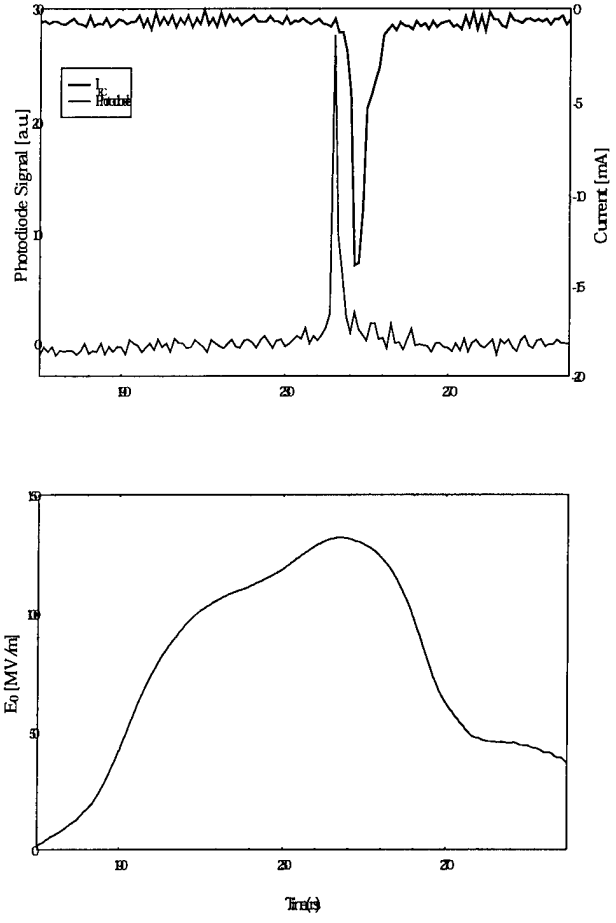



Figure 5: Experimental observation of emission

In order to verify that the laser pulses are injected at a nearly fixed phase relative to the 17 GHz microwaves, scans were performed using a variable phase shifter at the input to the relativistic klystron. Twenty shots were observed at each phase shifter setting and the percentage of shots exhibiting a Faraday cup signal was recorded. The percentages are graphed as a function of phase in Figure 6. The rising edge of the curve at about 180° is consistent with Schottky field enhancement causing an increase in photoemission. The falling edge at 300° is consistent with cathode back-bombardment due to electrons being reflected by the cavity electric field. The width of the 100% emission indicates a phase stability of better than ±20°. This corresponds to synchronization of the laser pulses to the microwave field with an error of approximately ±3 ps.

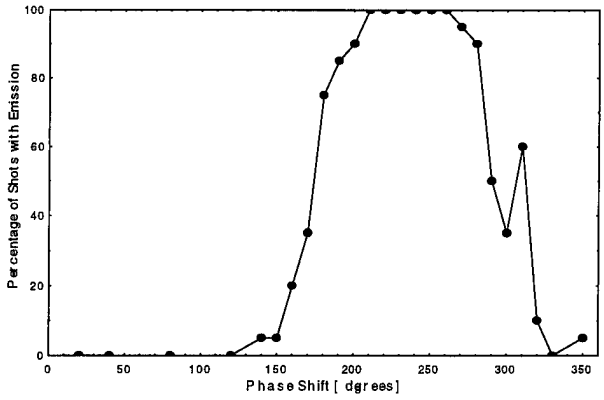



Figure 6: Dependence of emission on phase

Although the beam energy has not yet been directly measured, two factors suggest it is at least 1 MeV at the highest cavity RF fields. In earlier measurements of dark current, the transmission of electrons through metal sheets was measured These experiments indicated energies between 1.7 and 2.5 MeV. Secondly, assuming an initial beam size at the gun exit of 0.7 mm, then the space-charge divergence of the beam would be too large, and the beam would not reach the Faraday cup, unless its kinetic energy was >1 MeV.

## 4 FUTURE PLANS

The next step in the 17 GHz RF gun experiment is the characterization of the electron beam quality. A Browne-Buechner magnetic energy spectrometer is being installed at this time. This will provide information about the average energy and energy spread of the electron beam. The emittance of the electron bunch will be measured initially using magnetic steering coils and narrow collimators. Emittance compensation will be added later to increase the beam's brightness.

## REFERENCES


[1] Leon C.-L. Lin, S.C. Chen, and J.S. Wurtele, "On the frequency scaling of electron guns," AIP Conf. Proceedings Vol. 335, pg. 704 (1994).

[2] D. von de Linde, "Characterization of the noise in continuously operating mode-locked lasers," Appl. Phys. B, pg. 201 (1986).

# A HIGH-DC-VOLTAGE GaAs PHOTOEMISSION GUN: TRANSVERSE EMITTANCE AND MOMENTUM SPREAD MEASUREMENTS

D. Engwall, C. Bohn, L. Cardman, B. Dunham, D. Kehne, R. Legg, H. Liu,
M. Shinn, and C. Sinclair
Thomas Jefferson National Accelerator Facility
12000 Jefferson Avenue, Newport News, VA 23606

*Abstract*

We have built a high-DC-voltage photoemission gun and a diagnostic beamline permitting us to measure rms transverse emittance ($\tilde{\varepsilon}_x$) and rms momentum spread ($\delta$) of short-duration electron pulses produced by illuminating the cathode with light from a mode-locked, frequency-doubled Nd:YLF laser. The electron gun is a GaAs photocathode source designed to operate at 500 kV. We have measured $\tilde{\varepsilon}_x$ and $\delta$ for conditions ranging from emittance-dominated to space-charge-dominated. We report these measurements as functions of microbunch charge for different beam radii, pulse lengths, and voltages/field gradients at the cathode, and compare them with PARMELA calculations.

## 1 INTRODUCTION

We have designed a 500 kV GaAs photoemission gun with the intent of exploring the limits of high-DC-voltage photocathode sources. The aim is to demonstrate that such a gun can work reliably, to investigate experimentally the transverse and longitudinal properties of the beams produced, and to compare the measurements with PARMELA predictions to ascertain the validity of the code in the charge and energy regime explored. The highly uniform cathode field, the ability to decouple beam energy from accelerating gradient, and the ability to control both radial and temporal beam profiles (including beam length) through the drive laser makes this gun a platform uniquely suited to support our studies. Once characterized, the gun will serve as the electron source for the FEL currently under construction at Jefferson Lab[1].

We have built the gun, measured $\tilde{\varepsilon}_x$ and $\delta$ at 250 and 300 kV (after processing to 300 and 335 kV, respectively), and analyzed the data to compare with those values predicted by PARMELA. The reduced voltage was necessary due to ceramic punch-throughs that occured at 400 kV. The punch-throughs, believed due to a combination of field emission (from the cathode support tube) and an improper choice of ceramic material, were easily sealed, but reopened at voltages of 300–350 kV.

New ceramics[2] and a new cathode support tube recently allowed the gun to process to 400 kV and run at 350 kV. In the remainder of this paper we describe the experiment, simulations, and results of our measurements.

## 2 THE EXPERIMENT

### 2.1 *Experimental Apparatus*

The apparatus used in this experiment consists of the electron gun and diagnostic beamline. The layout of the gun and beamline is shown in Fig. 1.

The electron gun operates in a horizontal position. Its high voltage terminal is isolated by two ceramics stacked in series. The GaAs cathode wafer resides just inside the flattened end of a ball-shaped cathode which is supported from the high voltage terminal by a tube. The gun has planar anode-cathode geometry so that the field on the surface of the GaAs wafer at 500 kV is 10 MV/m, uniform to 1% over a 1 cm diameter. Optional inclusion of a spacer nipple at the base of the ceramic stack reduces the cathode field to 6.0 MV/m at 500 kV. A large-bore, water-cooled solenoid and RF-shielded gate valve immediately follow the gun vacuum chamber.

The beamline extends about 2 m beyond the valve. Immediately after the valve is the light box, a device that directs incident laser light onto the photocathode and outcouples light reflected from the wafer into a beam dump. The beam diagnostics reside in three vacuum crosses. A six-way cross houses a beam viewer and a scanning, $\sim$50 $\mu$m wide vertical slit that renders transmitted beamlets emittance dominated. A 45° dipole magnet follows the slit cross. After the magnet, the straight and branched sections of the beamline contain a five-way cross holding a beam viewer and wire scanner, and terminate in an isolated Faraday cup. The dipole horizontally images the slit onto wire scanner 2, yielding a spectrometer with 22.5 cm of dispersion. Current readouts for the Faraday cups and wire scanners are provided by Keithley 485 picoammeters.

The beam is centered through the solenoid and beamline and the average charge per pulse is determined from the current intercepted in the straight-ahead Faraday cup. For the emittance measurement, we use a variant of the two-slit method[3, 4]. We scan the slit horizontally (in the $x$ direction) across the beam, stopping at $\sim$13 locations, and record the current profile of each transmitted beamlet with wire scanner 1. After background subtraction, these current profiles are used in conjunction with the slit locations to calculate $\tilde{\varepsilon}_x$ using $\tilde{\varepsilon}_x \equiv \sqrt{\langle x_0^2\rangle \langle x_0'^2\rangle - \langle x_0 x_0'\rangle^2}$; where $x_0$ and $x_0'$ are, respectively, the beam's horizontal coordinate and angle of divergence at the slit, and $\langle\rangle$ signifies a current-weighted average. The rms normalized emittance is obtained in the ordinary manner: $\tilde{\varepsilon}_{x,n} = \beta\gamma\tilde{\varepsilon}_x$, with $\beta$

0-7803-4376-X/98/$10.00 © 1998 IEEE

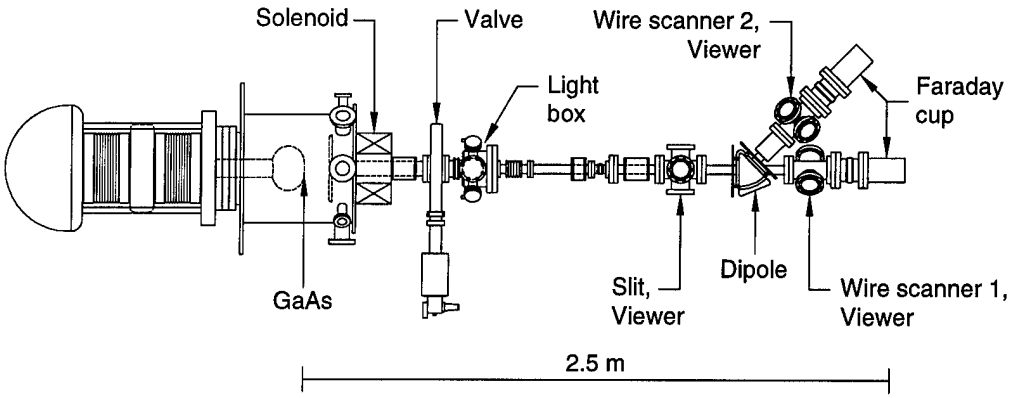



Figure 1: An overhead view of the gun (6 MV/m configuration) and the diagnostic beamline.

and $\gamma$ the usual relativistic factors. For the momentum-spread measurement, we energize the dipole, place the slit in the center of the beam, and record the transmitted beamlet's current profile with wire scanner 2. After background subtraction, the profile is used to calculate $\delta$ using $\delta \equiv \sqrt{\langle x_2^2 \rangle}/\mathcal{D}$; where $x_2$ is the beam's horizontal coordinate at wire scanner 2, $\mathcal{D}$ is the spectrometer's dispersion, and we exploit the slit narrowness and the point-to-point focusing of the spectrometer.

### 2.2 *Experimental Conditions*

We measure $\tilde{\varepsilon}_x$ and $\delta$ as functions of microbunch charge ($q$) for different combinations of beam radius, pulse length, and voltages (field gradients) at the cathode. We run the gun at 250 and 300 kV, with 3.0 and 3.6 MV/m cathode field strengths. The laser emits pulses with assumed-Gaussian temporal profiles of rms width $\sigma_t$. By changing the modelocker operating temperature or detuning the laser-cavity length, we obtain two stable pulse widths: $\sigma_t \approx$ 20 and 25 ps. We change the electron beam radius ($R$) by imaging three different diameter laser apertures onto the cathode, repeatably obtaining beam radii of 0.61, 1.06, and 1.95 mm. Due to the limited amount of experimental time (<100 hours) and the length of time (~1 hour) required to complete a measurement at a single charge, we used PARMELA to generate the solenoidal field values ($B$) for our experiment.

## 3 THE SIMULATIONS

We have simulated the experimental conditions as closely as possible using the standard Jefferson Lab version of PARMELA[6] with a slightly modified particle generation scheme. In our version, macroparticles are tracked using the McDonald point-to-point space charge algorithm[7] and the Liu variable-particle-size factor[6]. The modifications cause macroparticles to be emitted in an arbitrary, user-defined radial profile with a Maxwellian velocity distribution.

The electron bunches are simulated from the cathode to the slit using the same $B$ values as the experiment. Limiting the maximum particle size factor to 10[8] prevents over-shielding of the macroparticles. Use of POISSON-generated electric and magnetic field profiles for the gun and solenoid assures the proper treatment of aberrations in these elements. The radial and longitudinal profiles of the macroparticle distribution are identical to those of the laser beam at the photcathode except that the longitudinal profile is truncated at $\pm 3\sigma_t$. Finally, the macroparticles are emitted with a thermal energy of $\frac{1}{2}k_BT = 0.18$ eV. This value equates the simulated and measured values of $\tilde{\varepsilon}_x$ in the low-charge (emittance-dominated) regime for $R$=1.95 mm, and compares favorably to Dunham's value of 0.153±0.010 eV[5].

## 4 RESULTS

In this section we present some of the results of our measurements. We estimate the statistical error in $\tilde{\varepsilon}_x$ ($\delta$) to be ±5% (±1.5%). We determine the statistical error by comparing repeated measurements at selected charges throughout the measurement range. We calculate an upper bound of ±10% and ±6% for the non-recoverable systematic error in the $\tilde{\varepsilon}_x$ and $\delta$ measurements, respectively. The bound includes contributions from baseline subtraction, finite sampling effects, determination of slit/wire positions and separations, and determination of the spectrometer dispersion. PARMELA simulations of the measurement method indicate an upper bound of -15% for the recoverable systematic error in both measurements. Recoverable systematic errors arise from finite slit and wire widths, and "bent" wires. During vacuum bakeout, the wires in our scanners relaxed, resulting in a ~ 6° inclination of the wire with respect to the slit. These errors are deemed recoverable because future analysis will correct for them.

Figure 2 shows data taken for $R$=1.06 mm: at 250 kV with $\sigma_t$ =19 ps and $\sigma_t$ = 25 ps; and at 300 kV with $\sigma_t$ = 20 ps. Other data looks quite similar.

In terms of determining $\tilde{\varepsilon}_x$, PARMELA agrees quite well with experiment at the lowest charges, underestimates the value by ~25% at higher charges, overestimates the value by ~50% at even higher charges, and agrees quite well again with experiment at the highest charges. We believe the shape of the experimental curves, as well as the agree-

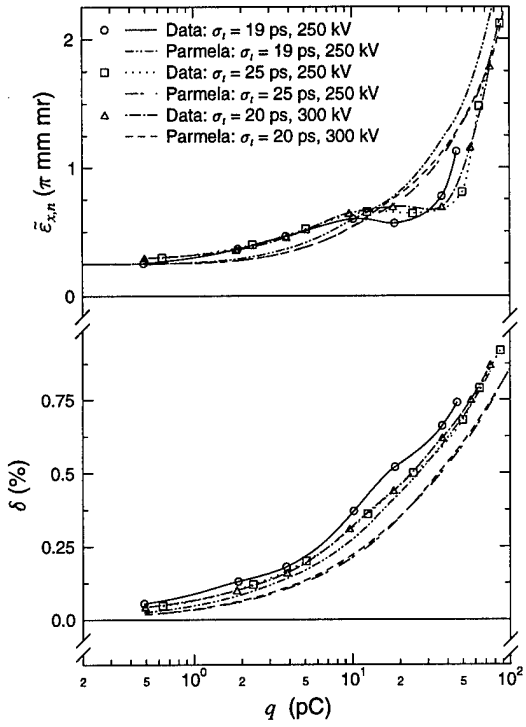



Figure 2: Results for measurements with $R$=1.06 mm showing the effects of pulse length and accelerating potential (cathode field) variation.

ment between the data and PARMELA simulations, to be the result of differing levels of solenoidal compensation for different $q$. To support our contention, we introduce Fig. 3, which shows $\tilde{\varepsilon}_x$ as a function of $B$ for $R$=0.61 mm, $\sigma_t$ = 20 ps, $q$ = 18.7 pC, and a beam energy of 250 kV.

From inspection of the experimental curve in Fig. 3, we see that if $B$ is too large for the beam space charge, solenoidal compensation is negligible and the experimental values exceed the simulation values. As $B$ drops and becomes better matched to the beam space charge, increased solenoidal compensation causes the experimental value to dip below the simulation values and flatten. As $B$ decreases further, it is too small for the beam space charge; solenoidal compensation dissipates and the experimental value rises towards the simulation curve again.

The behaviour just described qualitatively matches that of the experimental $\tilde{\varepsilon}_x$ curves in Fig. 2, implying that the Parmela-generated solenoid values used in the experiment are too large for the beam space charge at low $q$, nearly matched to the beam space charge at intermediate $q$, and too small for the beam space charge at high $q$. The differing levels of solenoidal compensation induced by these effects cause the the experimental $\tilde{\varepsilon}_x$ values to exceed the simulation values at low $q$ (once space charge effects become non-negligible), to level off and dip below the simulation values at intermediate $q$, and to rebound towards the simulation value at high $q$. Given the obvious insensitivity to solenoidal compensation that PARMELA shows in Fig. 3, such errors in $B$ are not surprising.

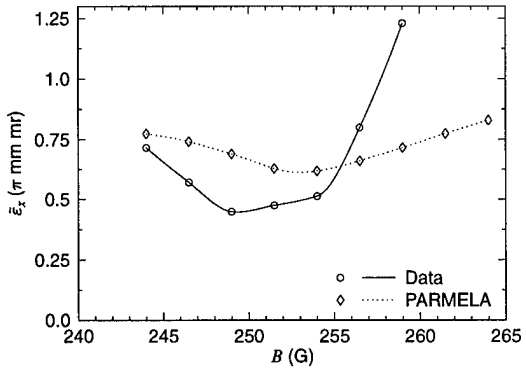



Figure 3: Results for measurements with $R$ = 0.61 mm, $\sigma_t$ = 20 ps, and $q$ = 18.7 pC, showing the dependence of $\tilde{\varepsilon}_x$ on $B$.

In terms of predicting $\delta$, PARMELA underestimates the value by 50–60% at lower charges, improving to underestimate the value by ~10% at higher charges.

## 5 CONCLUSIONS

In this charge and energy regime, PARMELA is able to predict $\tilde{\varepsilon}_x$ and $\delta$ to within 50%. The code displays a marked insensitivity to solenoidal compensation effects, possibly accounting for much of the discrepancy in predicting $\tilde{\varepsilon}_x$. Further research is necessary to determine the cause of this insensitivity.

## 6 ACKNOWLEDGEMENTS

Work supported by USDOE under contract DE–AC05–84–ER40150 and by USNSF under contract PHY–89–21146. We thank Richard Hill, Timothy Siggins, and Dawn Venhaus for their help.

## 7 REFERENCES

[1] C.L. Bohn, *"Recirculating Accelerator Driver for a High-Power Free-Electron Laser: A Design Overview"*, these Proceedings.

[2] F. Liu, *et al.*, *"A Method of Producing Surface Conduction on Ceramic Accelerator Components Using Metal Ion Implantation"*, these Proceedings.

[3] C. LeJeune and J. Aubert, in *Applied Charged Particle Optics*, A. Septier, Ed., Advances in Electronics and Electron Physics, Supp. **13A**, 159–259 (1980).

[4] B. Dunham, *et al.*, *"An Emittance Measurement System for a Wide Range of Bunch Charges"*, these Proceedings.

[5] B.M. Dunham, Ph.D. thesis, University of Illinois at Urbana-Champaign (1993).

[6] H. Liu, *et al.*, Nucl. Instr. and Meth., **A358** 475 (1995).

[7] K.T. McDonald, IEEE Trans. on Electron Devices, **35** 2052 (1988).

[8] H. Liu, CEBAF Technical Note 94–040 (1994).

# THE PRODUCTION AND TRANSPORT OF RADIOACTIVE $^{17}$F AT ATLAS FOR RESEARCH

B. Harss, J. C. Berger, F. Borasi, J. Greene, C. L. Jiang, J. Nolen, R.C. Pardo, M.Paul[†], K.E. Rehm, J. P. Schiffer, R. E. Segel[††], T. F. Wang[†††]
Argonne National Laboratory, Argonne, IL, USA 60439
[†]Hebrew University, Jerusalem, Israel 91904
[††] Northwestern University, Evanston, Illinois USA
[†††] Lawrence Livermore National Laboratory, Livermore, California USA

*Abstract*

A secondary beam of radioactive $^{17}$F was produced at the ATLAS accelerator and delivered to an experimental target station with an intensity of as much as $5 \cdot 10^5$ ions/s for use in the research program. Beams of $^{17}$F were produced via the p($^{17}$O,$^{17}$F)n or d($^{16}$O,$^{17}$F)n reactions by bombarding a gas-filled cell with up to 300 pnA beams of $^{17}$O or $^{16}$O from the ATLAS superconducting linac. The gas target, with HAVAR windows, was maintained at pressures as high as 500 Torr. The beam quality was dominated by small-angle scattering in the gas cell windows, by the reaction kinematics and beamline acceptance. Detailed beam parameters are presented. Plans for relocation of the target to allow improved capture efficiency and acceleration or de-acceleration of the secondary beam will also be discussed.

## 1 INTRODUCTION

Interest in the use of radioactive beams for research in nuclear physics and astrophysics has become intense in recent years and several accelerator laboratories around the world have begun to develop techniques to produce radioactive beams with useful intensities and controllable beam properties. At ATLAS[1] techniques have been developed to produce a beam of $^{17}$F($T_{½}$ = 65s) in-flight using inverse reactions, i.e. bombarding light targets with heavier projectiles. The goal of the effort is to produce a beam of $^{17}$F in sufficient quantity, purity and quality to allow the determination of cross-sections relevant to astrophysical environments as well as for the investigation of other nuclear reactions.

## 2 EXPERIMENTAL CONFIGURATION

For our first measurement with an $^{17}$F beam, the inverse reaction p($^{17}$F,$^{14}$O)α was chosen for study. To study this reaction at the $E_{cm}$ = 3.43 MeV, resonance an energy for $^{17}$F of 62 MeV is required.

A gas target cell of hydrogen or deuterium was bombarded with a primary $^{17}$O or $^{16}$O beam and partially transformed into a $^{17}$F beam. A bending magnet following the production target filters out most of the $^{17}$O isobar nuclei. Finally the $^{17}$F beam was delivered over a distance of 12 m to a secondary $CH_2$ target. Since p($^{17}$F,$^{14}$O)α is forward peaked in the laboratory system, a coincidence requirement between $^{14}$O particles detected in the ATLAS spectrograph and α-particles measured with a silicon detector was used to separate the particles of interest from the background reactions.

The physical layout showing the relationship of the $^{17}$F production target, the connecting beamline to the secondary target and the ATLAS spectrograph is shown in Fig. 1.

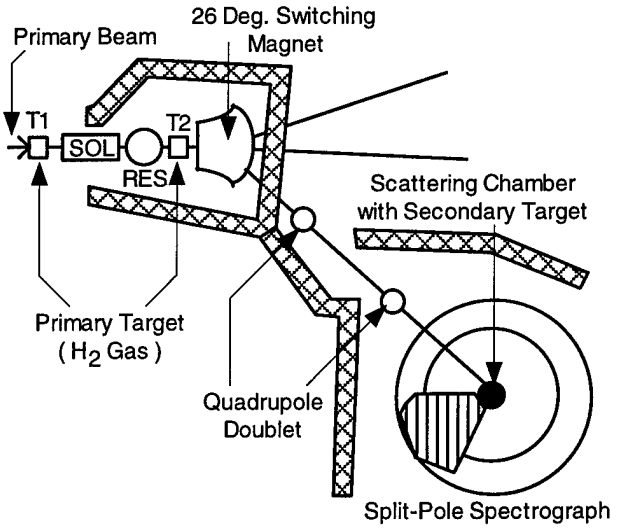



Fig. 1. Floor plan of the ATLAS radioactive beam region. The future (T1) and present (T2) positions of the primary gas target are shown as are the beam transport elements to the secondary target at the spectrograph. The relative positions of the super-conducting solenoid (SOL) and resonator (RES) which will be installed are also indicated.

### *2.1 Design of the $^{17}$F Production Target*

Our goal was to deliver at least $10^5$ $^{17}$F ions per second onto the secondary reaction target. For a $^{17}$F production cross-section [4] as low as 10 mb and a 1% transport efficiency, the production target must be capable of sustaining an $^{17}$O beam current of one pμA and have an effective thickness of 250 μg/cm$^2$.

0-7803-4376-X/98/$10.00 © 1998 IEEE

Experience indicates that foil ($CH_2$) targets, even in rapid rotation, cannot take the high beam current necessary. Therefore, a gas target with an effective length of 7.5cm and thin HAVAR [5,6] windows was chosen (see Fig. 2). To keep the temperature of both the windows and the hydrogen gas low, the chamber has double walls to accommodate a constantly flowing cooling liquid in the outer cylinder. Four support pipes supply cooling fluid and $H_2$ gas.

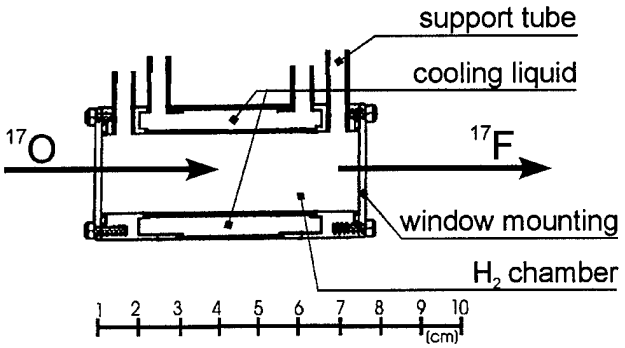



Fig. 2. A simplified cross-section of the cylindrical gas target used. The diameter of the windows is 1.27cm

The selection of window material and thickness was made as a compromise between the maximum sustainable gas pressure and the deleterious effect of thick windows on angular and energy straggling. The effect on the energy spread is negligible, since usually the reaction kinematics dominates this even near the reaction threshold. On the other hand, the contribution of the small-angle scattering to the beam divergence can dominate the transverse beam emittance. The required energy on the secondary target led to reaction energies between 73 to 77 MeV (threshold at 63.8 MeV) resulting in an maximum divergence of ±1.5° from kinematics (average of about ±1°). This relatively small cone is due to the negative Q-value of p($^{17}O$, $^{17}F$)n. A reaction with a positive Q-value would result in a much larger angular spread.

For two 1.9 mg/cm$^2$ HAVAR windows, the small angle scattering is also of the order of ±1°, which made this type of window a good choice. Glued in a mounting ring with an inner diameter of 1.27 cm, they withstood a 250 pnA beam of 83 MeV $^{17}O$ at $H_2$ pressures up to of 500 Torr. A higher pressure was not tested.

The divergence and energy width of the $^{17}F$ is estimated to be ±1.6° and ±4 MeV from the combined contribution of all effects. Calculations of the beam optics and examination of the windows after the run suggest a beam spot radius of 2 mm on the entrance windows. This makes a spot with a 3 mm radius on the exit windows. From this, we estimate the un-normalized emittance of the secondary $^{17}F$ to be 84 π·mm·mrad.

*2.2 Transport of the $^{17}F$ beam to the secondary target*

The program TRANSPORT [7] was used to calculate the beam optics for $^{17}F$ and predict the transport efficiency. For such a large emittance beam, a transmission of 3.5% is predicted, assuming a uniform density profile. It is also estimated that 50% [8] of the $^{17}F$ beam is in the $9^+$ charge state, resulting in another attenuation factor of 2. The calculated beam envelope is shown in Fig. 3 and compared to the limiting mechanical aperture in the system.

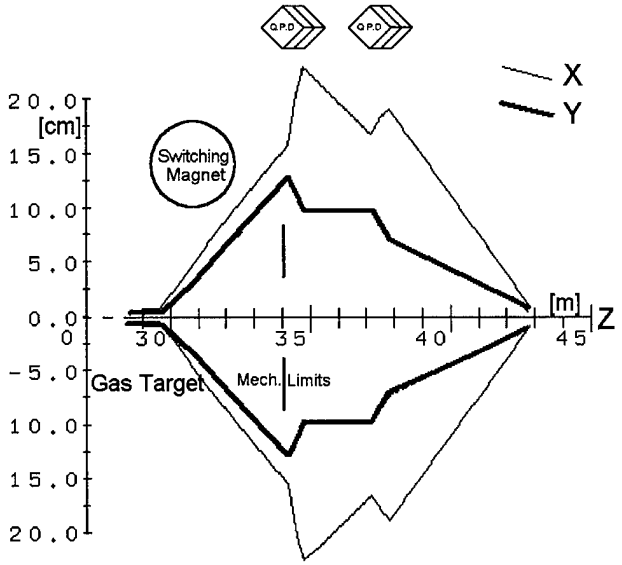



Fig. 3. The calculated envelope of the produced $^{17}F$ beam from the production target, located at 30m, to the reaction target, located at 43m. The quadrupole doublets are in a YX-YX-configuration.

Both energy and angular distributions of the $^{17}F$ beam are strongly affected by the reaction kinematics. Therefore, a correlation between energy and angle of a particle is to be expected. These correlations are not included in the TRANSPORT studies and place some uncertainty on the predicted transmission. However, this simple model leads to an expected overall efficiency of 1 to 2%.

## 3 PARAMETERS AND RESULTS

With a primary beam of 250 pnA $^{17}O$, a cross section of 50 mb, and a gas pressure of 500 Torr, one expects a $^{17}F$ production rate of ~$2\cdot10^7$ per second. At the spectrograph, a $^{17}F$ current of $1\cdot10^5$ per second was observed. The upper limit of the vertical spot size on the secondary target is calculated to be 1cm. The y-magnification of the spectrograph is three, and so the detector [9] in the spectrograph focal plane is unable to intercept all beam particles. We estimate a detection efficiency of only 50% due to this effect, resulting in a transport efficiency of 1%, in reasonable agreement with the estimate in the previous section.

The ratio of $^{17}F$ particles to other nuclei detected in the focal plane of the spectrograph in the experiment was better than 10:1, in a measurement taken at 0° and therefore with a much weaker primary $^{17}O$ beam of only 175ppA on the gas target (See Fig. 4). The contaminating $^{17}O$ peaks are due to the energy-distribution tail of particles scattered into the bending magnet's momentum acceptance.

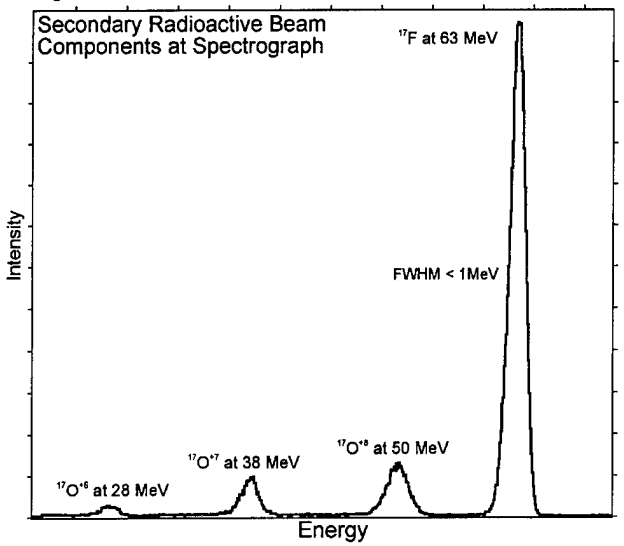



Fig. 4. The energy spectrum of the secondary beam in the ATLAS spectrograph at 0°.

The goal of the experiment was to detect $^{14}O$ nuclei from $^{17}F(p,\alpha)^{14}O$ in inverse kinematics. To provide discrimination between $^{14}O$ nuclei and background, the $\alpha$ particle was detected in coincidence in a silicon detector. While the spectrograph covered the angular range of 2° to 8° on the right side of the beam, the alpha detector measured $\alpha$-particles on the left side between 6° and 20°. In the coincidence spectrum, the $^{14}O$ particles are the most prominent group (see Fig. 5). The $^{17}F$ and $^{17}O$ particles scattered in the spectrograph are in random coincidence with uncorrelated particles in the silicon detector.

By slightly changing the field of the 26° switching magnet, a certain energy control of the secondary beam was available without retuning the accelerator. Due to the large energy spread in the $^{17}F$ particles, the current of the secondary beam did not change more than 50% when swept over a 2 MeV energy region. In an independent test run, the production of $^{17}F$ was measured over an energy range from 85 to 112 MeV. The yield of $^{17}F$ changed less than 10% over this range.

## 4 IMPROVEMENTS IN PROGRESS

The production technique used in these experiments suffers from the large transverse emittance produced by angular straggling and the reaction kinematics as well as the large energy spread created from the reaction. These effects and the acceptance of our beamline limits the transport efficiency to target to approximately 1%.

The transport efficiency can be increased significantly by a modification of the beam optical elements in the vicinity of the primary gas target to significantly improve the transverse capture efficiency and reduce the energy spread of the secondary beam. We have begun a modification of our production region which moves the primary production target to a new location indicated in figure 1. A superconducting solenoid will follow the production target in close proximity (about 50 cm) to capture more of the rapidly diverging beam. The beam divergence will be reduced and the maximum secondary beam size limited to a radius of less than 2 cm.

The solenoid is then followed by a superconducting resonator, approximately 1.5 meters from the target. The resonator provides approximately 1 MV of accelerating potential and will be used in a 'debunching' mode which will decrease the energy spread of the secondary beam from ~±4 MeV to ~±0.75 MeV. Energy variability of about ±4 MeV will also be possible using the resonator.

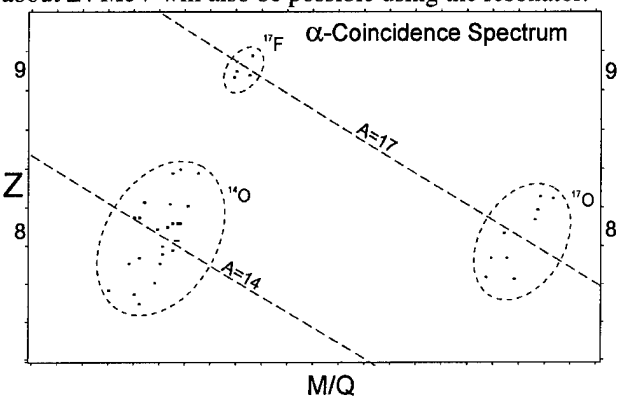



Fig. 5. The spectrum of nuclei in the spectrograph in coincidence with $\alpha$-particles in the silicon detector. The values of Z and M/Q have been linearized.

With these changes we expect the transport efficiency to increase by approximately a factor of 10. Therefore beam intensities greater than $10^6$ ion/s should be available by October, 1997.

## 5 ACKNOWLEDGMENTS

This work was supported by the US D.O.E., Nuclear Science Division, under contract No. W-31-109-ENG-38.

## REFERENCES

[1] L.M. Bollinger, et al., Nucl. Inst. and Meth. A328, (1993) 211.
[2] R.Coszach, et al., Phys. Lett. B353, (1995) 184.
[3] A.D.Roberts, et al., Nucl. Inst. and Meth., B103 (1995) 523.
[4] J.K.Blair, Phys. Rev. C8, (1), (1973) 120.
[5] L.S. Skaggs, et al., Proc. of the World Conf. of the Internatzional Nucl. Target Development Society, Boston, MA, USA (1979) 249.
[6] J.D. Carlson, Nucl. Inst. and Meth. 113 (1973) 541.
[7] K.L. Brown, Advances Particle Phys. 1, (1967) 71.
[8] K.Shima, et al., Atomic Data and Nuc. Data Tables, 34 (3) (1986) 358.
[9] K. E. Rehm, F. L. H. Wolfs, Nucl. Inst. and Meth., A273 (1988) 262.

# BEAM CHOPPER FOR THE LOW-ENERGY UNDULATOR TEST LINE (LEUTL) IN THE APS

Y. Kang, J. Wang, S. Milton, L. Teng, K. Thompson, J. Jones, D. Walters, and J. Jagger
Advanced Photon Source, Argonne National Laboratory
9700 South Cass Avenue, Argonne, Illinois 60439 USA

*Abstract*

The low-energy undulator test line (LEUTL) is being built and will be tested with a short beam pulse from an rf gun in the Advanced Photon Source (APS) at the Argonne National Laboratory. In the LEUTL a beam chopper is used after the rf gun to deflect the unwanted beam to a beam dump. The beam chopper consists of a permanent magnet and an electric deflector that can compensate for the magnetic deflection. A 30-kV pulsed power supply is used for the electric deflector. The chopper subsystem was assembled and tested for beamline installation. The electrical and beam properties of the chopper assembly are presented.

## 1 INTRODUCTION

A 2.856-GHz thermionic rf gun is used for the electron beam generation in the LEUTL [1]. The rf gun is capable of generating 1 A of beam during approximately 2 μs at a repetition rate of 10 Hz. Such a beam, accelerated to the energies envisioned for the LEUTL (650 MeV), would easily violate the radiation safety envelope of the APS linac vault. The beam chopper was conceived and designed to provide a fail-safe means of chopping the total quantity of generated beam down to a level which can safely be transported within the linac vault at the peak energies attainable. For control of electron beam bunches in the LEUTL, a beam chopper has been designed.

The beam chopper is placed between the rf gun and the alpha magnet injector to the linac and easily deflects the 3 MeV beam. The chopper consists of an electrostatic deflector located within a crossed permanent magnetic field. The electrostatic plates are spaced 10 mm apart and connected to a high voltage switched power supply through coaxial cables. Both plates are raised to 30 kV by the high voltage power supply. The plates are then switched sequentially to ground through a single switch and delay line. The rise and fall times are less than 50 ns. The electron beam can pass and travel to the linac only during the transient switching time determined by the delay lines, otherwise it is directed to a beam dump.

## 2 DESIGN AND CONSTRUCTION

The magnetic deflector is made of a permanent magnet for full-time deflection while the electrostatic deflector is designed to deflect the beam to the original beam axis. The high voltage for the electrostatic deflection is from the pulsed power supply. Figure 1 shows the chopper assembly between two quadrupole magnets in the beamline. The chopper dipole magnet is outside the electrostatic deflector chamber.

The high voltage operation requires special attention to insulation for reliability and safety. Also the high voltage short pulse operation requires good electromagnetic shielding for noise suppression. For this purpose, but not shown in the figure, an aluminum shroud will also be installed around the chopper assembly. A water-cooled copper beam dump with a vertical slot for beam passage is placed in the downstream 2.75" Conflat flange. The design specifications of the chopper system components are shown in Table 1.

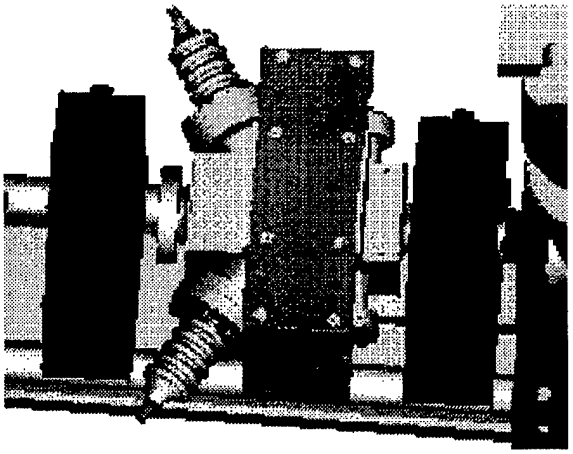


Figure 1: Chopper assembly.

Numerical simulations were made to see the approximate field distribution and rf resonance response of the structure. Calculations using the MAFIAcomputer code showed that resonances above ~2.5 GHz are severely damped within the electric kicker chamber. This is due to the loss on the stainless steel wall and the lossy ceramic dielectric of the high voltage feedthroughs and standoffs. The electric field distribution in the chamber was simulated using the Hewlett Packard High Frequency Structure Simulator (HFSS) computer code to see the electric field uniformity. The result showed that the electric field on the beam axis between the parallel electrodes is essentially flat except the fringing fields at both ends.

Table 1: Chopper Specification

| | |
|---|---|
| Beam energy | 3 MeV |
| Deflector plate length | 10 cm |
| Deflection at exit of plates | 3.57 mm |
| Deflection angle | 0.0714 rad |
| Integrated magnetic field | 82.7 G-m |

0-7803-4376-X/98/$10.00 © 1998 IEEE

*2.1 Deflector Magnet*

Since the required field strength is low, the dipole magnet has been designed to use a permanent magnet material of ceramic 8 [2]. The magnet structure has a 6.1-cm vertical gap, 10-cm-wide iron pole pieces, and 7.94-cm core length. Figure 2 shows the magnetic flux plot from OPERA-2d [3] for one quarter of the magnet in the transverse plane with respect to the beam axis. At most, a pair of 5-mm-thick slices of permanent magnet material are required between the pole tip and yoke at each pole. The magnet material is strontium oxide-ferrite ceramic from Hitachi. The effective length of the magnet is 10 cm and compensates the electrostatic deflector. However, the field along the beam axis is not uniform since the length is so short compared to the magnet gap. A pair of permanent magnet blocks is placed between the yoke and each pole piece. Each block measures 1 cm × 0.5 cm × 7.94 cm. The field along the beam axis is shown in Figure 3. The peak field is about 91 G. For accuracy of the field, the ceramic magnet is magnetized after machining and the field strength is optimized by placing magnetic steel shims into the air gaps adjacent to the permanent magnet blocks.

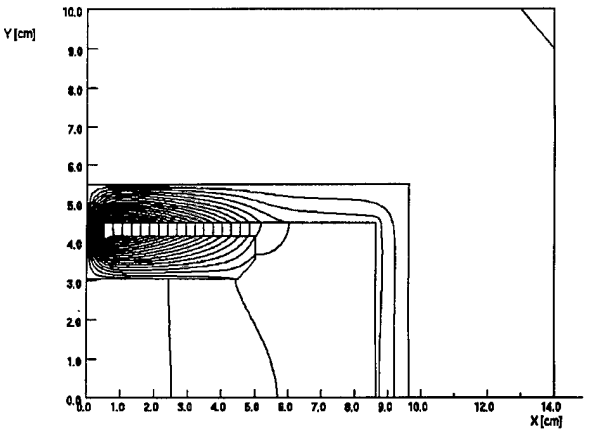



Figure 2: Magnetic flux of the deflector magnet.

*2.2 Electrostatic Deflector*

The mechanical design of the LEUTL electrostatic deflector is a compact functional design that will support a 30-kV potential between precisely aligned electrodes while being ultra-high-vacuum compatible. To minimize welding in the construction of the component that is enclosed within the permanent magnet field, the unit body is machined from one piece of 316L stainless steel. The tubing welded to the body is also 316L stainless steel in order to reduce magnetism of essential weld joints. The lectrodes are also of one piece 316L stainless steel construction. The electrical design of the kicker requires that the electrodes are supported by insulated standoffs and aligned to within 0.1 mm. This is achieved by mounting the electrodes on pairs of 35 kV vacuum-rated ceramic standoffs. The standoffs are stock alumina ceramic cylinders that are tapped at both ends to facilitate attachment.

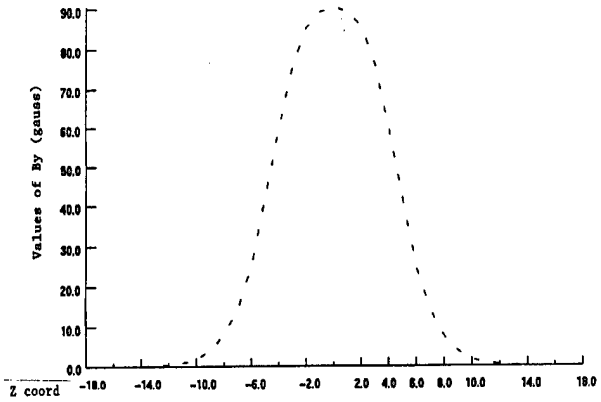



Figure 3: Magnetic field intensity in longitudinal direction.

The tapped holes are also employed to allow the horizontal positioning of the electrodes. The standoffs are tightly attached to threaded studs on the electrodes and then freely attached to studded flanges on ports on the body. The ports are sealed with rotatable Conflat flange joints. Rotating the joints before final sealing allows the positioning of the electrodes. The adjustable joints are preloaded with compression springs to maintain the position of the electrodes. The port positions are accurately machined to locate the electrodes longitudinally and vertically. Electrode alignment is measured on an electronic coordinate measuring machine. After electrode alignment, 35 kV vacuum-rated power feedthroughs are mechanically attached to the electrodes with silver-plated set screws. The kicker design maintains a modular assembly in which the feedthroughs, electrodes, and standoffs can be easily replaced.

Figure 4 shows the electric kicker chamber design. A water-cooled beam dump is integrated to the vacuum flange in the left-hand side. The electrodes are slightly shifted in order to eliminate beam scraping with magnet only deflection. For reliable high voltage operation, all body and electrode surfaces exposed to high voltage are rounded and electropolished to remove burrs and surface contaminants. An extra port with a 53.8-mm flange is provided for possible higher-order mode damping.

*2.3 Pulsed Power Supply*

The power supply for the electrostatic chopper consists of a high voltage unit, a thyratron switch, and a delay line. A picture of the circuit is shown in Figure 5.

The high voltage unit is an EMI 500A, which is a 30-kV constant-current-charging supply by Electronic Measurements, Inc. This supply outputs a constant current so the voltage on the delay line, like a capacitor for DC, rises linearly. When the voltage reaches the setpoint, the supply automatically switches to the voltage regulating mode to maintain a constant output voltage. The high voltage supply can be controlled by a charging command to minimize the time when the system carries high voltage, to reduce the stress on the insulation material.

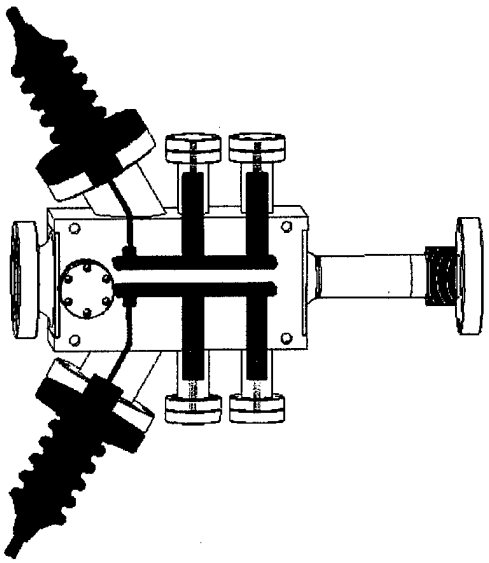


Figure 4: Electric kicker chamber design.

The thyratron is an EEV CX1 154C. It is a single-gap tube rated at 35 kV. Its grid 1 is driven with a current pulse of 23 A, and grid 2 is driven with a voltage pulse of 800 V plus a negative bias of 150 V. To reduce the stray inductance which will slow down the speed of the pulse and cause difficulty for impedance matching, the thyratron housing is carefully designed as a coaxial structure. The terminating resistors for the coax cables are also integrated as part of the thyratron structure. The measured turn-on time (the voltage goes from 100% to 0) is less than 20 ns.

The delay line is made of high voltage coaxial cable 2124 manufactured by Dielectric Sciences, Inc. The cable has a characteristic impedance of 61 Ω. The length of the short cable is about 1.8 m and is the minimum necessary to make the connection between the thyratron and one electrode. At the other electrode side, a capacitor-resistor string is connected to the short cable. The purpose of the string is to eliminate the overshoot caused by the imperfection in the impedance match at the thyratron. The side effect of the string is that the rise time of the pulse is slowed down to 50 ns instead of the 20 ns thyratron turn-on time. The propagation speed of the delay line is 6.6 ns/m. This means the required length of the delay line is 22.9 m.

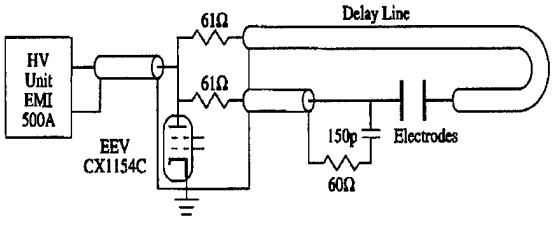



Figure 5: Pulsed power supply circuit schematic diagram.

Figure 6 shows a measured voltage waveform across a mock-up deflector. At the time this paper was written, the delay line was 30.5 m long. Therefore, the pulse width is 200 ns.

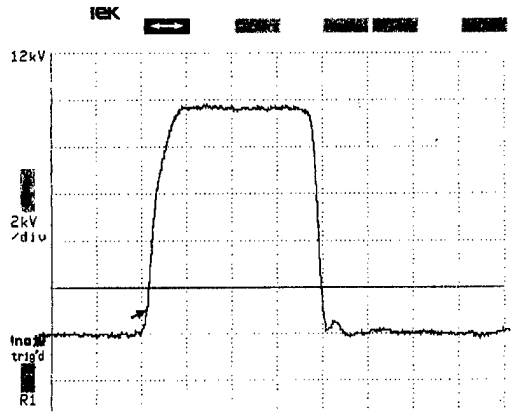



Figure 6: Outputs from high voltage pulsed power supply. 50 ns/div.

## 3 DISCUSSION

The complete beam chopper system has been fabricated for the design described earlier in this paper. The electrostatic kicker structure is driven by a switched high voltage pulsed power supply through a delay line. The power supply has been made and tested for 10-kV operation with a good pulse waveform. With proper adjustment of the capacitance parallel to the load, the pulse risetime slightly degraded but the overshoot has been reduced. The kicker system will be assembled and tested completely before installation in the beamline.

## 4 ACKNOWLEDGMENT

We would like to thank Kerry Potter for his contribution to this project in the mechanical design process for design, detailing, and integration of the chopper into the beamline. This work was supported by the U.S. Department of Energy, Office of Basic Energy Sciences, under Contract No. W-31-109-ENG-38.

## 5 REFERENCES

[1] S. V. Milton et al., "The Advanced Photon Source Low-Energy Undulator Test Line," these proceedings.

[2] Specified by the Magnetic Material Producers Association Standard Specification for Permanent Magnet Materials-0100 (-90).

[3] Code OPERA-2d (formerly PE2D) is available from Vector Fields, Inc., Aurora, Illinois.

# A NEW 14 GHZ ELECTRON-CYCLOTRON-RESONANCE ION SOURCE (ECRIS) FOR THE HEAVY ION ACCELERATOR FACILITY ATLAS

M. Schlapp[1], R.C. Vondrasek[1], J. Szczech[1], P.J. Billquist[1], Z.Q. Xie[2], R. Harkewicz[3] and R.C. Pardo[1]

[1]Argonne National Laboratory, Argonne, IL 60439

[2]Lawrence Berkeley National Laboratory, Berkeley, CA 94720

[3]National Superconducting Cyclotron Laboratory, East Lansing, MI 48824

*Abstract*

A new 14 GHz ECRIS has been designed and built over the last two years. The source design incorporates the latest results from ECR developments to produce intense beams of highly charged ions. An improved magnetic electron confinement is achieved from a large mirror ratio and strong hexapole field. The aluminum plasma chamber and extraction electrode as well as a biased disk on axis at the microwave injection side donate additional electrons to the plasma, making use of the large secondary electron yield from aluminum oxide. The source will be capable of ECR plasma heating using two different frequencies simultaneously to increase the electron energy gain. To be able to deliver usable intensities of the heaviest ion beams the design will also allow axial access for metal evaporation ovens and solid material. The main design goal is to produce several eμA of at least $^{238}U^{34+}$ in order to accelerate the beam to coulomb-barrier energies without further stripping. First charge state distributions for $^{16}O$ and $^{40}Ar$ have been measured.

## 1 INTRODUCTION

This new ECR ion source has been constructed as part of an improved high-charge state injector for the heavy ion accelerator facility ATLAS, providing the Positive Ion Injector (PII) section with a second, independent ECRIS. A layout of the ion source, beam line and associated components mounted on a high voltage platform, designed for 275 kV operation is given elsewhere [1]. The design goal of producing usable beam intensities of heavy elements such as uranium, lead or gold in charge states sufficiently high so that acceleration to the coulomb barrier is possible without foil stripping will increase the beam intensity available for experiments by at least an order of magnitude. In addition to that the beam quality should be significantly improved over beams requiring stripping for acceleration.

## 2 SOURCE DESIGN

### *1.1 Mechanical Design*

The mechanical design of this single stage ECRIS is shown in Fig. 1. It shows the complete ion source assembly including solenoid coils and iron yoke together with a cross sectional view of the microwave injection tank with microwave inputs for two frequencies and a detail of the extraction system assembly. For the production of metallic ions the source allows the installation of high temperature ovens and sample insertion for sputtering. A Glazer lens is used as a beam focusing element between the ECRIS and a 90° double focusing analyzing magnet. All intensities are measured in a Faraday cup directly behind a set of 2-jaw slits at the exit focal point of the dipole magnet.

### *1.2. Magnetic System*

The magnetic system for confining the hot plasma electrons takes into account the latest understanding that a high axial mirror ratio as well as a strong radial field inside the plasma chamber are extremely important parameters for improving the performance of high charge state ECRIS. The axial magnetic field is produced by two solenoids each consisting of 9 double layer pancake coils with 16 turns per layer and a surrounding iron yoke and plugs. The power supplies are capable of providing up to 750 A to each pancake. Fig. 2 shows the calculated (POISSON-code [2]) axial magnetic field distribution on axis for different iron yoke configurations. For the dashed line an additional iron plug between injection tank and plasma chamber and an extraction electrode partly made out of iron has been added. The iron plugs allow a very similar axial field distribution at 78% of the power level required without the plugs. This power saving is important on a high voltage platform when the available power is limited. In addition part of the iron between the coils has been removed. The hexapole magnet mounted into the aluminum plasma chamber consists of 6 double trapezoidal NdFeB magnets and produces a maximum radial field of 1.0 T inside the plasma chamber. This open permanent magnet structure also allows for radial pumping.

### *1.2. Double frequency heating*

The ion source features the possibility of heating the plasma with two different frequencies simultaneously (see cross sectional view of the injection tank in Fig. 1) to enhance the density of hot electrons in the plasma and

0-7803-4376-X/98/$10.00 © 1998 IEEE

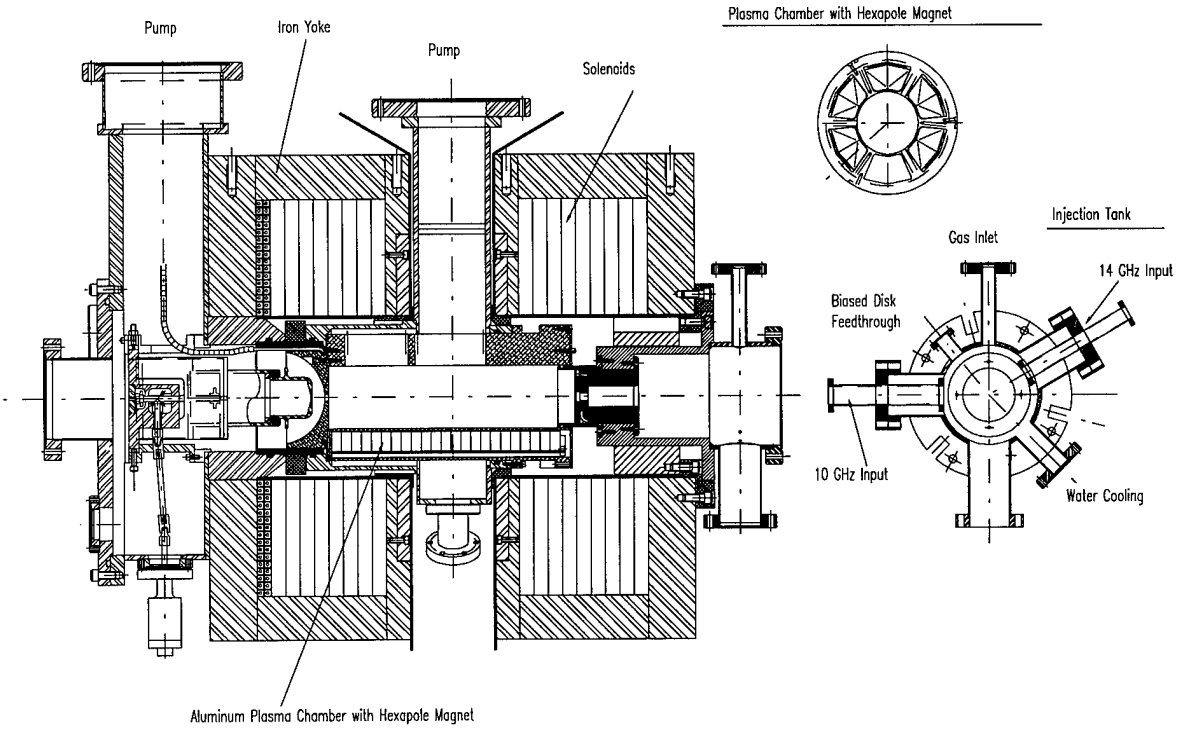



Fig. 1: Schematic overview of the mechanical set up of the 14 GHz ECR II.

improve the production of high charge states. The idea is to create two well separated ECR zones were the electrons can gain energy [3]. In addition to the confined electrons traveling between the axial magnetic mirrors and passing through the 14 GHz resonance zone, there will be electrons only heated at the 10 GHz resonance zone, located much closer to the minimum of the magnetic mirror. The electron density enhanced by this additional heating may increase the negative potential well assumed to be responsible for the confinement of the ions and therefore the production of high charge states.

Previous reports on the effect of double frequency heating by the group at LBL [3] and the Grenoble group [4] showed significantly different results. The Berkeley group used two significantly different frequencies 10.3 GHz and 14 GHz, creating well separated resonance zones. They reported a shift of the peak in the charge state distribution towards higher charge states, higher intensities for the same charge state and an increase in total RF power applied to the plasma. The French group using a fixed frequency at 10 GHz and a second frequency tunable between 9.6 GHz and 11 GHz could not find any improvement over single frequency operation.

We have obtained a transmitter which allows us to tune the second frequency over a wide range in the X-band between 8.75 GHz and 10.85 GHz using a magnetron tube. We will study the two frequency heating in order to provide some further understanding of the effect.

*1.3. Extraction system*

The Accel-Decel puller electrode assembly (shown in detail in Fig. 1) is movable along the beam axis allowing adjustment of the extraction system for operation with different ion species. The Accel- or screening electrode is introduced into the main extraction gap and biased to a sufficiently low potential (up to -4 kV) so as to create a negative potential well and form an electron trap to reduce the space charge influence of the ion beam [5].

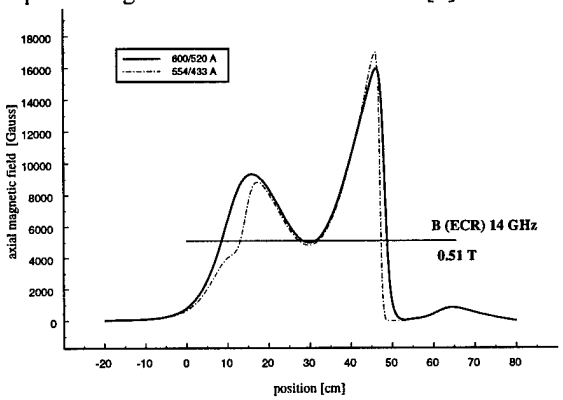



Fig. 2: Axial field distribution with different iron yoke configurations

## 3 FIRST RESULTS

For test runs so far we used $^{16}O$ and $^{40}Ar$ as operating gases. The ion source operated in a single frequency mode (14.25 GHz) with up to 850 watts of microwave power delivered to the plasma. In Fig. 3 and 4 spectra for $^{16}O$ and $^{40}Ar$ (at 15 kV and 12.5 kV extraction voltage, respectively) are shown. Using the magnetic field configuration show in fig. 2 as a solid line, the best observed $^{4+}Ar^{12+}$ current was 21eμA. The biased disk was optimized between -550 V and -650 V. For the $O^{7+}$ current we obtained a enhancement of a factor of two with respect to source operation without the biased disk. One can still

observe relatively large carbon peaks (32 eμA of $C^{4+}$), which limits the output of high charge states. Tests of the source performance for heavy elements, i.e. $^{238}U$ are expected in late Spring 1997 after all features of the ion source stated in the abstract have been implemented.

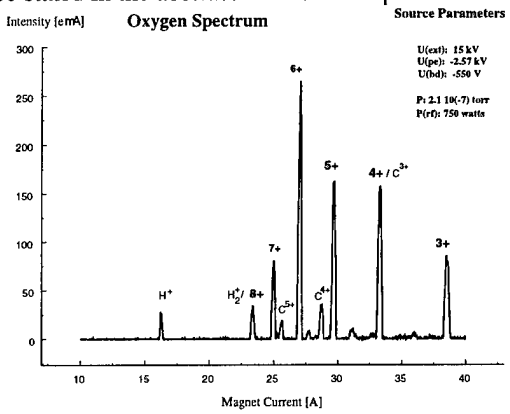



Fig. 3: $^{16}O$ spectrum optimized on 7+, extracted at 15 kV. Oxygen peaks are identified by their charge state only. The best observed $O^{7+}$ current was 78 eμA.

## 4 ACKNOWLEDGMENTS

This work was supported by US D.O.E. Nuclear Physics Division under contract W-31-109-ENG-38.

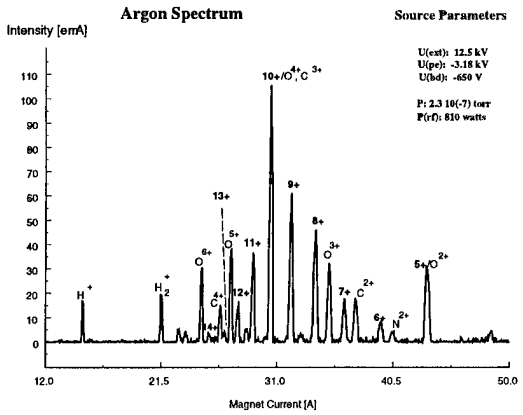



Fig. 4: $^{40}Ar$ spectrum optimized on charge state 12. Argon peaks are identified by charge state only.

## REFERENCES

[1] M. Schlapp et al., 13th International Workshop on ECR Ion Sources, College Station/Texas (1997), in course of publication [2] A.M. Winslow, J. Comp. Phys. **2** (1957) 149

[2] Z.Q. Xie and C.M. Lyneis, 12th Intern. Workshop on ECR Ion Sources, Riken, Japan (1995) 24

[3] R. Geller et al., International Conference on ECR Ion Sources and their Applications, East Lansing, NSCL Report #MSUCP-47 (1987) 1

[4] I.G. Brown, *The Physics and Technology of Ion Sources*, Wiley, N.Y. (1989) 53

# CHARACTERIZATION AND RECENT MODIFICATION OF A COMPACT 10 GHZ ECRIS FOR ATOMIC PHYSICS EXPERIMENTS AND SPECTROSCOPIC INVESTIGATIONS

M. Schlapp[1] , R. Trassl[2] , R. W. McCullough[3] , J.B Greenwood[3] and E. Salzborn[2]
[1] Argonne National Laboratory, Argonne, IL 60439
[2] Inst. fuer Kernphysik, Strahlenzentrum, JLU Giessen, Germany
[3] Department of Pure and Applied Physics, QUB, Belfast, UK

*Abstract*

A compact 10 ECR ion source (200 mm long, 170 mm diameter) has been developed and tested. The complete magnetic structure made from permanent magnet material is comprised of four ring magnets producing an asymmetric axial magnetic field and a hexapole magnet with a maximum radial field of 0.94 T inside the plasma chamber. The coupling of the microwave to the plasma shows efficient ECR plasma heating at microwave power levels around 10 watts. Charge state distributions for various elements with intensities up to 320 eμA and their dependence on operation parameters will be presented as well as VUV spectra in the wavelength region down to 15 nm.

## 1 INTRODUCTION

There is a growing interest in the use of compact ECR ion sources with medium performances. In special environments, like small accelerators (Van-de-Graaff, Microtron), high voltage terminals or on line radioactive beam production systems with restricted space and low electrical power availability, this represents the only possibility to accelerate multiply charged ions. Recent advances in permanent magnet technology allow the design of compact all-permanent ECR ion sources operating at high frequencies. For use in an ion-ion experiment, employing the crossed beams technique [1] a first version of a compact 10 GHz ECRIS was built [2]. A detailed description of the ion source is given elsewhere [3,4]. Furthermore the ionization and recombination processes occurring in an ECR plasma produce photons which are the basis for well established spectroscopic diagnostics [5]. These photons can be used for atomic structure studies and spectroscopic application, e.g. spectrometer wavelength scale calibration. Of special interest is the spectral range of the extreme ultraviolet (EUV) below 20 nm, where existing PIG sources produce spectral lines with low intensities and short operations times, due to the lifetime of their cathodes. ECR ion sources on the contrary show excellent long term stability and reproducibility because of only two operating parameters, gas pressure and microwave power [6].

## 2 MODIFICATIONS

### *2.1 Source Description*

A cross section of the source is shown in Fig.1. Due to the poor extraction efficiency in previous runs a new insulation flange with a larger opening and a tapered puller electrode assembly has been built. All intensities shown below are obtained using this set up [7].

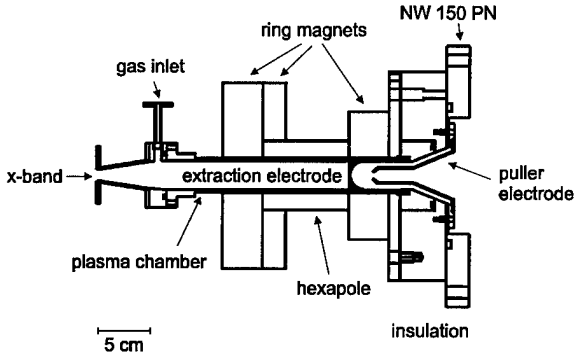



Fig. 1: Schematic view of the 10 GHz ECRIS

### *2.2 Magnetic Field*

The axial magnetic confinement of the hot plasma electrons has been improved by using larger magnet rings at the microwave injection side. The axial mirror ratio $B_{max}/B_{min}$ has been enhanced to 2.5 with a field maximum of 0.8 T and 0.5 T, respectively. The Halbach-type 24-segment hexapole magnet [8] (75mm long) gives a radial magnetic field of 0.94 T at the inner wall of the plasma chamber.

### *2.3 Frequency Dependence*

The dependence of extracted intensities and charge states distributions on the applied microwave frequency has been investigated after installing the new magnetic system. The magnetron based microwave generator is tunable in the range of 8.75 to 10.5 GHz with a maximum output power of 275 watts c/w. Fig. 2 shows the change in the extracted $Ar^{2+}$ ion current at different microwave frequencies together with the axial magnetic field distribution for this experiment. It can be clearly seen that the best result is obtained when the frequency is set to a value where the minimum of the magnetic field is close to the resonance magnetic field strength. This result could be varified by

0-7803-4376-X/98/$10.00 © 1998 IEEE

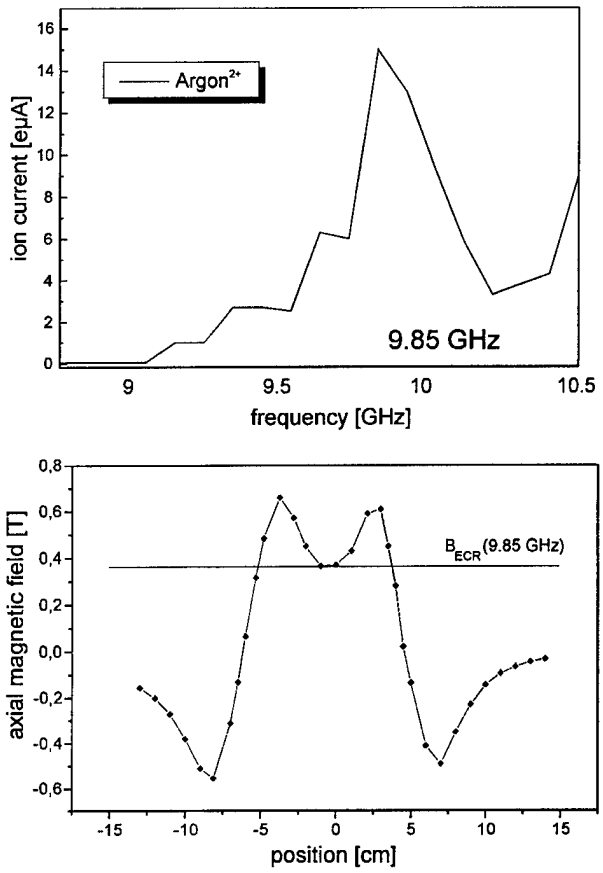



Fig. 2: Frequency dependence of the extracted Ar 2+ beam intensity with cossesponding axial magnetic field using another permanent magnet configuration with a mirror ratios of 2.5 and 1.6, respectively. The best results were obtained at a frequency of 8.85 GHz, for which the resonance field was close to the minimum of the magnetic mirror.

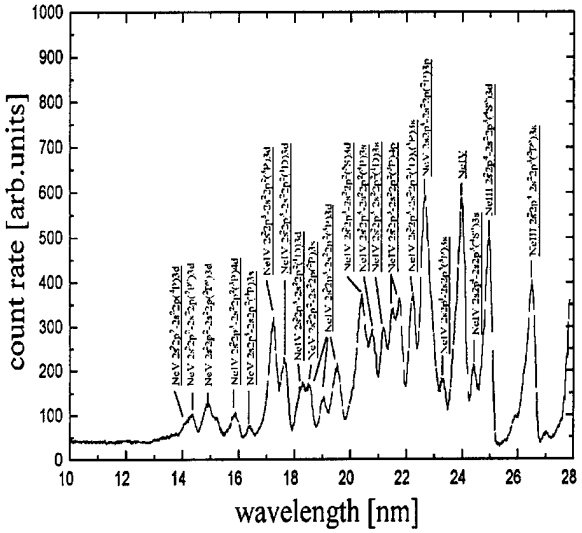



Fig. 3: Detailed line spectrum obtained from a Ne plasma using a 32cm grazing incidence spectrometer

*2.4 VUV Spectroscopy*

Measurements regarding the photon yield from an ECR plasma were performed by using a 32cm grazing incidence spectrometer with a grating of 550 g/mm with maximum efficiency at 15 nm. The resolution of the spectrometer was 0.4 nm at a dispersion of 2 nm/mm using an entrance slit of 100 μm. Fig. 3 shows a spectrum of a Neon plasma in the spectral range between 10 and 28 nm, where mainly Ne IV and Ne V transitions could be identified. The stability of the plasma was measured by monitoring a single Ne II transition line, $2s^2\ 2p^5$ -$2s2p^6$ ($^2P$- $^2S$), at 44.7 nm over a period of 8 hours. Using this transition line we also found an excellent reproducibility after extinguishing and reigniting the plasma by turning the microwave power off and on. Spectroscopy at higher resolution using a 5m grazing incidence spectrometer has been performed recently and showed intense lines down to 12 nm obtained from a Ne plasma. No detailed results can be presented at this time.

*2.5 Beam Intensities*

The maximum beam intensities obtained from the compact ECR ion source are shown in Fig. 4. All beam currents were optimized on the respective charge state and measured in a Faraday cup after a 90° analyzing magnet, at 9 kV extraction voltage using a 5 mm diameter extraction aperture. Recent experiments using calibrated leaks of Ne and $CHF_3$ for studies of the ionization efficiency have shown a poor transmission of the beam line used for these measurements. The ionization efficiency is an important factor in determining the usability for on line production systems in radioactive beam facilities.

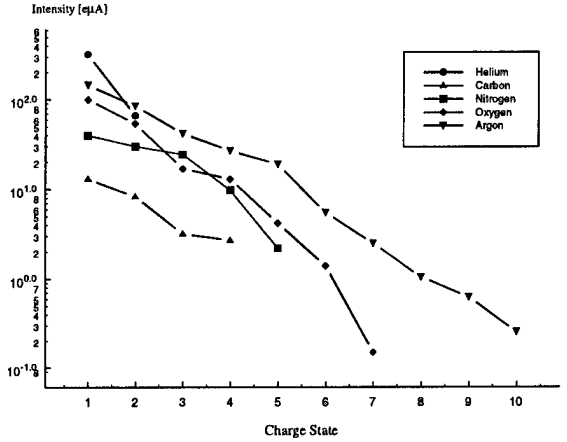



Fig. 4: Beam intensities for various gases at an extraction voltage of 9 kV.

## 3 OUTLOOK

Work is in progress to improve the residual gas pressure and the ion optical system which should result in higher charge states as well as in higher intensities. Recent measurements using calibrated leaks to determine the ionization efficiency have shown a preliminary value of approximately 30% for Neon. Identical measurements at

both ECR ion sources at Argonne National Laboratory, a 2 stage 10 GHz ECRIS and a newly constructed single stage 14 GHz ECRIS [9] will allow to compare the effieciency of a compact source to high performance ECRIS.

## 4 ACKNOWLEDGMENTS

This work was supported by US D.O.E. Nuclear Physics Division under contract W-31-109-ENG-38. The authors gratefully acknowledge the support of the Queen's University in Belfast, the British Council and the German DAAD.

## REFERENCES

[1] K. Rinn, F. Melchert, E. Salzborn., J. Phys. B. **19** (1986) 3717

[2] M. Schlapp, R. Trassl, E. Salzborn, R.W. McCullough, T.K. McLaughlin, H.B. Gilbody, Nucl. Instrum. Meth. **B98** (1995) 525

[3] M.Schlapp, et al., 12th Intern. Workshop on ECR Ion Sources, RIKEN/Japan (1995) 71

[4] R. Trassl, P. Hathiramani, F. Broetz, J.B. Greenwood, R.W. McCullough, M. Schlapp, E. Salzborn, Physica Scripta (1997) (in print)

[5] W. Pöffel, K.H. Schartner, G. Mank, E. Salzborn, Rev. Sci. Instrum. **61** (1990) 613

[6] B. Lommel, K.H. Schartner, M. Schlapp, R. Trassl, E. Salzborn, 5th EPS Conf. on Atomic and Molecular Physics, Edingburgh/UK (1995) 601

[7] M. Schlapp, R. Trassl, R.W. McCullough, J.B. Greenwood, E. Salzborn, CAARI 96, Denton/Texas, USA (1996) (in print)

[8] K. Halbach, Nucl. Instrum. Meth., **169** (1980) 1

[9] M. Schlapp, R.C. Vondrasek, J. Szczech, P.J. Billquist, Z.Q. Xie, C.M. Luneis, R. Harkewicz, R.C. Pardo, 13th Intern. Workshop on ECRIS, College Station, Texas, USA, (1997) (in print)

# A LOW POWER LOW COST 2.45 GHZ ECRIS FOR THE PRODUCTION OF MULTIPLY CHARGED IONS

M. Schlapp[1] , R. Trassl[2] , M. Liehr[3] and E. Salzborn[2]
[1] Argonne National Laboratory, Argonne, IL 60439
[2] Institut fuer Kernphysik, Strahlenzentrum, JLU Giessen, Germany
[3] Leybold-Heraeus, Hanau, Germany

*Abstract*

A low cost, low power ECR ion source designed for the use on a high voltage platform with limited electrical power available, has been developed. To reduce the power consumption of the source the radial and axial magnetic confinement are produced entirely by permanent magnets. An axial magnetic mirror ratio of 2.7 is obtained by a configuration of two times four block magnets. A radial magnetic field of 0.5 T inside the plasma chamber of 60 mm inner diameter is produced by a hexapole magnet. Microwave power up to 300 watts c/w can be applied to the plasma by using different slow-wave structures which allow the use of a plasma chamber much smaller in diameter than required by the wavelength of the used frequency of 2.45 GHz. The ion source can be operated in different modes either for producing multiply charged ions with intensities up to several hundred e•A or for the production of high intensity beams of singly charged ions, i.e. 6.5 mA of $He^+$ . Applications for the ion source are in crossed beams experiments and as injectors for small accelerators as well as for spectroscopic investigations in the VUV wavelength region.

## 1 SOURCE DESCRIPTION

The main features of the described 2.45 GHz ECR ion source as shown in Fig. 1 are low set up costs, low electrical power consumption due to the use of permanent magnets to produce the minimum-B-structure and two different operation modes for the production of multiply charged ions or the production of high intensities of singly charged ions. A detailed description of the ion source with different microwave injection lines is given elsewhere [1,2]. The figure shows the mechanical set up of the ion source including parts of the microwave system: the combined high-voltage/vacuum window and the transition from rectangular waveguide to coaxial line.

### *1.1 Magnetic System*

The magnetic system is made from high remanence (1.12 T), high coercivity (1920 kA/m) NdFeB permanent magnet material. It consists of two radially magnetized rings (each consists of 6 block magnets) producing an axial magnetic field of 2.14 kG at the maximum with a mirror ratio of 2.85. The hexapole magnet for the radial component is made from the same block magnets and induces a maximum radial magnetic field of 5 kG inside the plasma chamber of 60 mm inner diameter.

### *1.2 Microwave System*

An inexpensive magnetron amplifier based microwave system operating at 2.45 GHz was chosen. The magnetron amplifier, which is pretty similar to the ones in microwave ovens, can produce up to 300 watts of microwave power in c/w-mode and is connected to a waveguide system [2]. The high voltage vacuum transition uses PTFE as the insulating material. Calculating the attenuation in a circular waveguide for 2.45 GHz the smallest plasma cavity would be 9.5 cm in inner diameter, allowing both basic modes ($TE_{11}$ and $TM_{01}$ ) to penetrate the plasma chamber with an attenuation of less than 0.1 dB/m [3,4]. To reduce the physical size of the ion source different slow wave structures have been used to launch the microwave into the plasma. A detailed description of a Lisitano-Coil used as an antenna in a previous version has been given earlier [1,5]. In this paper the use of a helical antenna will be described. As shown in fig. 1 the antenna results from the inner conductor of a coaxial line. The characteristics of radiation of a helical antenna is given by the ratio of circumference of one turn to the free space wavelength ($l/\lambda_0$ ) and by the distance between two turns (the angle between the turns and the axial direction has to be 12 to 14 degrees). The circumference of one turn has to be close to the free space wavelength (123 mm). In case of a diameter of the antenna between $D=0.75*\lambda_0/\pi$ and $D=1.35*\lambda_0/\pi$, the helical structure operates in a mode T1 with negligible attenuation. Using these parameters, circular polarized waves are radiated in an axial direction. The directivity of the antenna increases with the number of turn as does the degree of polarization. The angle at Half Power Beam Width is given by $\Theta = 105/n$, with n representing the number of turns [6,7]. For this application seven turns with an outer diameter of 41 mm, using a 3 mm diameter wire have been chosen. That allows to use a plasma chamber much smaller in diameter with respect to the smallest circular waveguide.

## 2 EXPERIMENTAL RESULTS

### *2.1 Production of Multiply Charged Ions*

The ion source has been operated using the helical antenna for the production of multiply charged ions. Fig. 2 shows a mass analyzed spectrum for Argon at an extraction voltage of 12.5 kV. The intensities were measure in a 20 mm diameter Faraday cup at

0-7803-4376-X/98 /$10.00 © 1998 IEEE

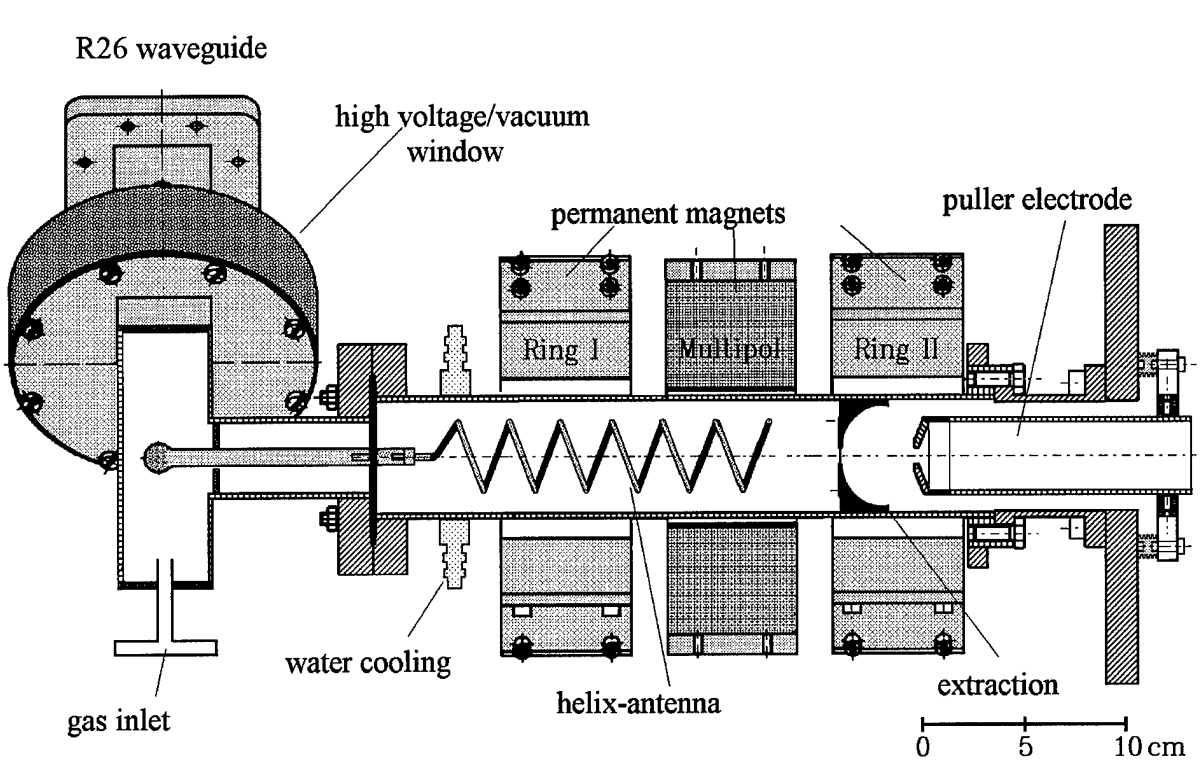



Fig. 1: Mechanical set up of the 2.45 GHz ECRIS

approximately 1.5 m from the extraction aperture after a $45^0$ analyzing magnet. The source parameters were 240 watts of microwave power at a gas pressure of $3.6*10^{-6}$ mbar, measured in a vacuum chamber outside the puller electrode. Maximum obtained beam currents for other gases are shown in Table 1 at comparable source parameters.

| Charge State | $^{14}N$ | $^{16}O$ | $^{20}Ne$ | $^{40}Ar$ |
|---|---|---|---|---|
| 1 | 210 | 150 | 133 | 68.2 |
| 2 | 11.5 | 14.2 | 98 | 58.8 |
| 3 | 0.16 | 0.27 | 8 | 11.5 |
| 4 | 0.01 | 0.017 | .11 | 1.2 |
| 5 | / | / | 0.028 | 0.2 |

Table 1: Beam currents for different charge states and gases in eμA

*2.2 High Intensities of Singly Charged Ions*

In a second mode of operation we studied the production of high intensities of singly charged ions, namely $He^+$. Using a modified axial magnetic confinement with maxima at 1.75 kG and a mirror ratio of 2.15. The magnetic field maxima could be varied on-line by changing the radii of the axial rings and have been optimized to the above value. With this set up, a $He^+$ beam of 6.5 mA at an extraction voltage of 20 kV could be obtained. The microwave power applied was 225 watts. Gas pressure during the run was $2.1*10^{-5}$ mbar in a vacuum chamber outside the puller electrode and $3*10^{-2}$ mbar at the gas inlet of the ion source. All vacuum readings are corrected for Helium. The beam was measured in a 20 mm diameter Faraday cup, 1.5 m from the extraction aperture of 10 mm diameter. An Einzel lens (46 mm diameter) mounted directly behind the puller electrode was used as a beam focusing element. The diameter of the ion beam ($U_{ext}$ =20kV, $U_{EL}$ =17kV) was measured to be 3.2 mm at a 90% emmittance of 76 •• mm mrad. The emittance was measured employing the slit-wire technique [8].

## 3 DISCUSSION AND OUTLOOK

The production of highly charged ions in an ECR plasma shows possible spectroscopic applications, especially in the vacuum-ultraviolet (VUV) region of the spectral range [9]. To enhance the performance for the production of multiply charged ions a new magnetic structure has been designed, producing higher mirror ratios.

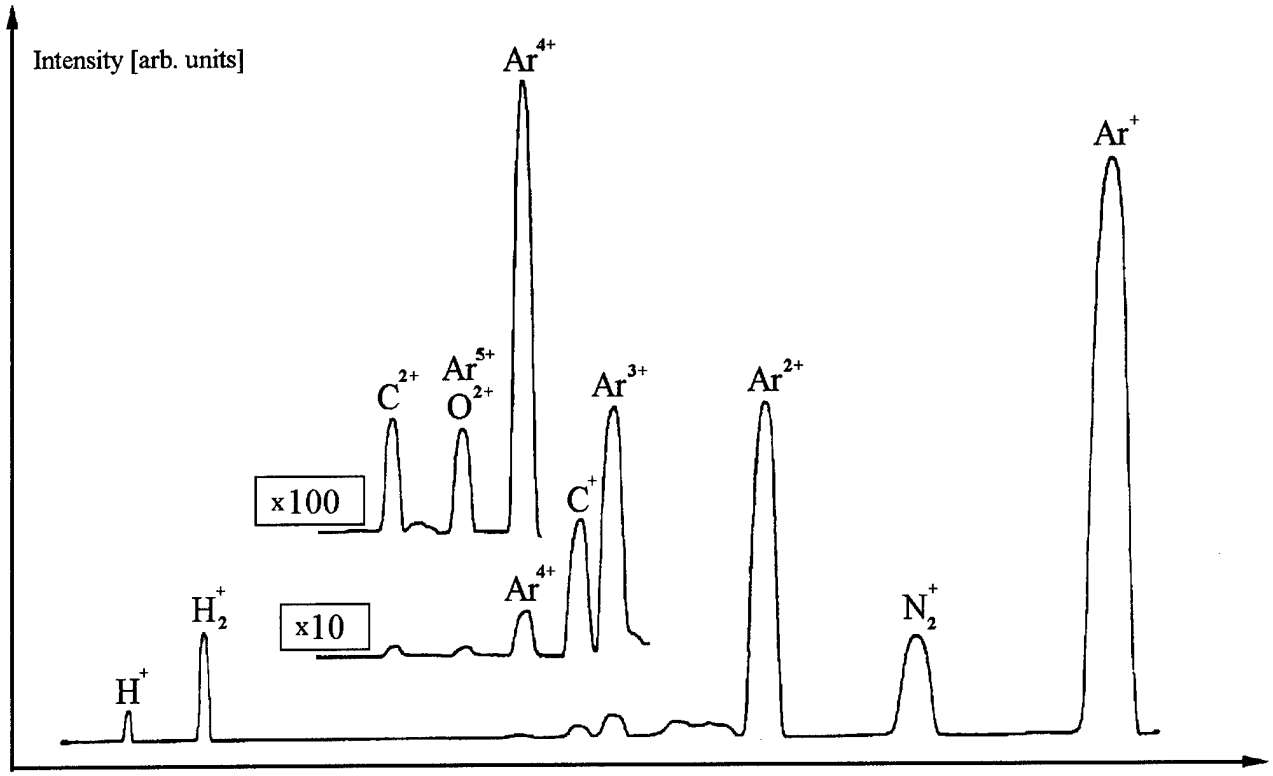



Fig. 2: Mass analyzed 40 Ar spectrum obtained at 12.5 kV extraction voltage.

## 11 ACKNOWLEDGMENTS

This work was supported by US D.O.E. Nuclear Physics Division under contract W-31-109-ENG-38.

## REFERENCES

[1] M. Liehr, R. Trassl, M. Schlapp, E. Salzborn, Rev. Sci. Instrum. **63** (4) (1992) 2541

[2] M. Schlapp et al., 5th Intern. CASOSALP, Meudon, France (1995) 182

[3] G.L. Ragan, Microwave Transmission Circuits, McGraw-Hill (1948)

[4] T.S. Laverghetta, Microwave Measurements and Techniques, Artech (1974)

[5] G. Lisitano, 9th Intern. Symposium on Plasma Chemistry, Pugnochiuso, Italy (1989)

[6] GJ.D. Kraus, Antennas, McGraw-Hill (1988) 271

[7] H. Meinke, F.W. Gundlach, Taschenbuch der Hochfrequenztechnik, Springer Verlag Berlin (1986)

[8] W. Krauss-Vogt, Ph.D. Thesis, Jülich (1985) Jül-2043

[9] M. Schlapp et al., 12th Intern. Workshop on ECRIS, RIKEN, Japan (1995) 71

# PROGRESS ON AN EBIS FOR RHIC*

J. Alessi, E. Beebe, A. Hershcovitch, A. Kponou, R. Lockey, A. Pikin, K. Prelec, L. Snydstrup, P. Stein, AGS Department, Brookhaven National Laboratory, Upton, NY 11973, USA

*Abstract*

Work is continuing on the development of an Electron Beam Ion Source (EBIS) which could be used as part of a new heavy ion injector for RHIC. On a test EBIS, we have operated with an electron beam current of up to 1.14A, and have extracted ions such as $Tl^{41+}$, $Xe^{26+}$, $Ar^{14+}$, $N^{7+}$, and $Na^{7+}$. Recent experimental results are reported. In addition, we discuss plans for a new electron beam test stand that is now being built. This will allow operation with electron currents of 10 A, as well as testing of a warm-bore superconducting magnet system, methods for fast extraction of ions, and possible off-axis collection of the electron beam.

## 1 INTRODUCTION

Present performance of the BNL tandem Van de Graaff accelerator should be adequate to fulfill RHIC requirements. Disadvantages of this approach are limitation of the ion species to those that can be produced as a negative ion, an 840 m long transport line from the tandem to the Booster, and a fairly large staff required to operate and maintain the accelerator. In looking at alternatives to the tandem as a RHIC injector, it becomes clear that a major consideration is the choice of ion source. Low charge state heavy ion sources exist which could fulfill the RHIC requirements, but the accelerators in such a scheme are large and costly. Although higher charge state ion sources produce fewer extracted particles, we feel that it is appropriate to put some effort now into the development of a source which produces sufficient intensity of intermediate charge state heavy ions, in order to greatly simplify the initial acceleration stages. Starting with higher charge state heavy ions, the accelerator can become quite compact. For example, an ion source producing $U^{45+}$ could be followed by a 3 m RFQ and a ~4m superconducting linac, both available technologies. This would give a Booster injection energy at least equal to the present tandem injection energy of 1.1 MeV/amu.

Several candidate ion sources have been considered, and while no source can presently produce sufficient quantities of intermediate charge states, we feel that the EBIS source shows the greatest promise of fulfilling our needs. The Electron Cyclotron Resonance (ECR) source, while very widely used and clearly the best choice for steady state applications, seems more difficult to scale up in current. For our pulsed operation the EBIS has the very nice feature of providing essentially a fixed charge per pulse, almost independent of pulse width, allowing extraction of very high currents (mA's) in very short pulses (10 μS). This is a big advantage in that it would allow single turn injection into the Booster - a large simplification that will improve injection efficiency and reduce the emittance of the beam in Booster. Other features of the EBIS are the fact that high charge state ions can be produced of any species that can be injected either as a gas or a low charge state ion, and the extracted charge state can be selected, optimized to the application.

In order to meet the requirement of $10^9$ ions/bunch in RHIC, an EBIS with parameters as shown in Table I is required. These parameters are based on present performance of other EBIS sources (neutralization efficiency, charge state distribution), and conservative estimates for accelerator efficiencies. While the electron current is an order of magnitude higher than present EBIS sources, it is not high compared to currents achieved in devices such as travelling wave tubes. Due to the low duty-factor required for RHIC injection, we also have the advantage of being able to pulse the electron beam, which can lead to an order of magnitude reduction in electron beam power.

**Table I**
**Tentative parameters for EBIS meeting RHIC requirements**

| | |
|---|---|
| Electron beam | 10 A, 20 kV |
| Trap length | 1.5 m |
| Trap capacity | $1.1 \times 10^{12}$ charges |
| Yield, positive charges | $5.3 \times 10^{11}$ |
| Yield, $Au^{35+}$ | $3 \times 10^9$ ions/pulse |

## 2 EBIS SOURCE R&D PROGRAM

We were fortunate to have received on long term loan from Sandia National Laboratory major parts of a near state-of-the-art EBIS. Additional necessary components (stand, electron gun, two sources for ion injection, time-of-flight spectrometer, control system) were fabricated, and the source is operational at BNL. We have operated with gas injection and external ion injection, and produced nitrogen (peaked at $N^{7+}$), argon (peaked at $Ar^{14+}$), sodium (peaked at $Na^{7+}$), thallium (peaked at $Tl^{41+}$), and xenon (peaked at $Xe^{26+}$).

Some of the specific goals for fiscal year 1997 on this EBIS are to use a 3mm diameter $LaB_6$ cathode to produce a 1A electron beam, and to obtain ion yields of at least 50% of the theoretical trap capacity (full neutralization of the electron beam space charge) at up to a 1A electron beam. Other goals are to study ion injection with heavy ions including uranium, and to develop and improve the control system. To date, we have met or made significant progress towards all these goals.

The projected design parameters of a RHIC EBIS injector are based on the possibility of compensating the

* Work supported under the auspices of the U.S. Department of Energy

0-7803-4376-X/98 /$10.00 © 1998 IEEE

electron beam with ion charge to 50% neutralization and also producing a narrow charge state distribution with at least 20% of the charge in the desired charge state. In past runs it has been demonstrated that the EBIS is capable of producing the charge states of interest in narrow charge state distributions [1]. The main challenge is to maintain neutralizations of 50% or greater while raising the electron beam current to sufficient levels, in our case 10A. In recent runs we have produced neutralizations above 50% for electron beams up to 0.5A. This was demonstrated for various ions including residual helium, and nitrogen and xenon injected via a neutral gas injection system, as shown in Fig. 1. The focus of these particular experiments was to demonstrate high electron neutralization, and in general the confinement times were short and the charge states were low. We are now studying the loss of ion charge with increasing confinement time. For some of the nitrogen trials the source operated very ideally, and both high charge state and high neutralization (above 50%) were achieved. A xenon charge state spectrum centered about 26+ and with neutralization at 41% is shown in Fig. 2.

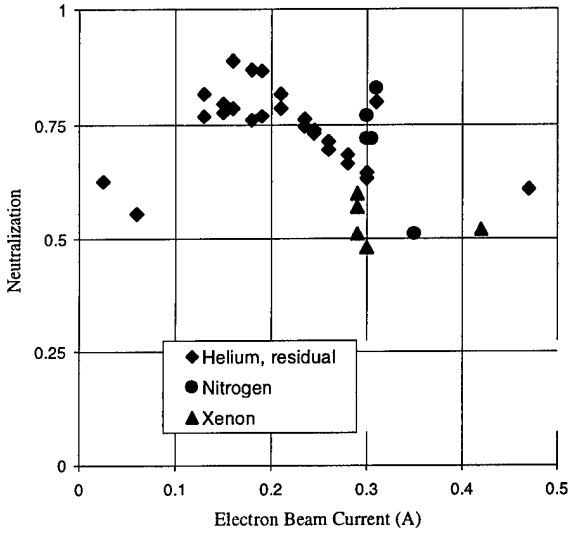



**Figure 1 Neutralization vs. electron beam current, taken under various conditions.**

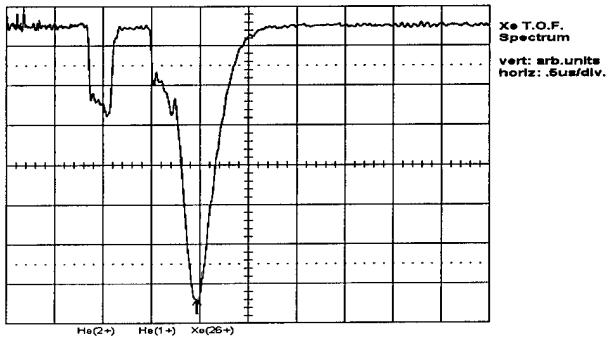



**Figure 2 Xenon time-of-flight spectrum, with a peak at 26+.**

Adjustable transverse magnetic fields (~10 Gauss) in the gun and collector regions of the unshielded main solenoid were installed [2]. In addition we developed the capability to produce pulsed electron beams, allowing us to operate at very low duty factors. These modifications were significant in reducing average electron beam loss during the optimization process so that we were able to increase the propagated electron beam to 1.14 A. Two rf pickups have been introduced within the ion trap region. Only limited observations have been made using a simple wide-band coaxial probe with a straight wire pickup, and the second, a quadrupolar pickup configured adjacent drift tubes, split along the beam direction, has not yet been monitored.

The gas injection system has been modified to allow the efficient introduction of gases such as xenon, which are condensable at temperatures higher than previously allowed by the system. Briefly, a gas cell was created over a 20 cm region and was isolated from the 4K surrounding structure. The cell can be heated to greater than 100 K using metal film resistors, and the temperature is monitored using Lakeshore TG-120 diodes. The use of a relatively long, low-pressure gas cell instead of a radial gas jet seems to provide superior gas injection at lower feed rates. This is important for avoiding long term contamination of the EBIS and subsequent degradation of performance.

Progress has been made both in control and monitoring, which has resulted in greatly improved operation of the EBIS. An EBIS voltage and timing controller has been developed to apply the time dependent potential distribution to the ion trap. The controller also coordinates the application of all time dependent voltages and timing references associated with the ion source, with a time resolution of 1 μs. The controller is operated through a graphical interface built using Labview and Labwindows programs.

During the balance of the year we will work on obtaining 50% neutralization for electron beams up to 1A. We are making preparations for injecting uranium from an external source (perhaps MEVVA). One of the main goals of this EBIS is to produce $U^{45+}$ with a 1A electron beam and neutralization of 50%.

## 3 ELECTRON BEAM TEST STAND

The existing BNL EBIS has some disadvantages for R&D work, since its vacuum chamber includes the cold-bore of the superconducting solenoid, making turnaround times on modifications slow. The magnet also has an unusually high helium consumption, which, for practical reasons, limits the frequency of runs. Therefore, we are now in the process of building an Electron Beam Test Stand (EBTS). While the primary function of this test stand is the study of higher current electron beams, it is intended to be a versatile device to develop technologies that are relevant for a high intensity EBIS and to study the physics of ion confinement in a trap. The EBTS will have all the main attributes of EBIS: superconducting solenoid, electron gun, drift tube structure, electron collector, vacuum system, ion injection system, appropriate control and instrumentation. Thus, it can be considered a short prototype of an EBIS for RHIC. The test stand will be designed with a warm bore superconducting solenoid,

with bakeable inner structure. We expect improved high-current performance with this type structure, and this will allow us to test the design with respect to vacuum technology. The concept of a warm EBIS has important advantages over a cold bore. The drift tubes do not condense gases and thus do not have a "memory effect", and all operations requiring exposure of EBIS to atmosphere can be done without warming up and cooling down the superconducting solenoid.

For electron beam focusing and confinement in the region of the ion trap, we have on order an unshielded superconducting solenoid with maximum magnetic field 5T and warm bore. The requirement to modify the axial distribution of magnetic field for various types of electron guns determined our choice of an unshielded solenoid. The longitudinal axis of the solenoid will be oriented horizontally. The length of the solenoid coil will be 1 m and the inner diameter of the warm bore will be 155 mm. The period between refilling of the cryostat with liquid helium will be not less than 30 days in the persistent mode.

The drift tube structure will be mounted in a vacuum tube inside the warm bore of the superconducting solenoid. It will be at room temperature, and its design will employ UHV technology. In the drift tube region, we will be able to test various schemes for fast extraction of ions, in order to determine the optimum method. We will also test the use of "lossy" ceramics to suppress oscillations in the drift tube structure. (Any sort of excitation of the electron beam is highly undesirable because it can cause heating of ions in the trap). The system of drift tubes should allow us to have as low as possible radial potential and as low as possible ion losses during confinement in the trap. These requirements are contradictory, and the optimum ratio of drift tube diameter to diameter of electron beam is to be found experimentally. The initial inner diameter of the drift tubes is planned to be 32 mm, and the electron beam diameter $\approx$2 mm.

Several alternative cathode types, and various electron gun launching conditions will be tested, eventually operating with a 10 A electron beam through the solenoid and drift tube structure. A collaboration has been set up with the group of G. Kuznetsov at Novosibirsk for the design and construction of a 10 A gun, using a partially immersed $LaB_6$ cathode.

The energy of the electron beam in the ion trap region should be as low as possible for increased trap capacity, and will be limited by stability of the electron beam and formation of a virtual cathode. For electron current $I_{el}$=10 A and energy of the electron beam in the ion trap $E_{el}$=20 keV (microperveance of ion beam $P_{\mu}$=3.5) the total charge of the electron beam in the volume of the ion trap with length $L_{trap}$=0.6 m will be $Q_{el}=4.5\cdot10^{11}$ el.ch. If $\phi_{drift\ tube}/\phi_{beam}$=16, the total radial potential well inside the drift tube will be $\Delta U_{rad}$=7.1 kV. This is a substantial fraction of the electron energy. Tests will be made of ways to minimize the energy of the electron beam while maintaining stability, such as increasing the current of the electron beam during ion injection, so the electron space charge is considerably compensated, or injecting ions into an initially high energy electron beam with subsequent deceleration.

The construction of the electron collector must be such that the temperature of the inner wall is well below the melting point of copper under a wide range of operating conditions, and the outgassing of the electron collector must be low. The total inner area of the electron collector is ~1000 $cm^2$. For a power of 50 kW the calculated temperature difference between the cooling water and the wall of electron collector is ~30$^0$C. The electron collector has bucking and transverse magnet correcting coils, a heater, and a thermocouple mounted in a separate chamber above the water-cooled shield. This assembly is installed inside an iron magnet shield and mounted on a high voltage (40 kV) insulator such that only the entrance aperture in the electron collector connects the inner volume of the electron collector to the central part of EBTS. The construction of the electron collector and materials used for its manufacture allow baking to 450$^{\circ}$C. We are also considering tests of an electron collector which is off-axis, so the electron beam can be dumped far from the trap region, eliminating reflected and backscattered particles, and collector gas load, from the trap region.

A primary consideration in EBTS construction is the vacuum system. The pressure of residual gas in the ion trap region must be $P\leq1\cdot10^{-10}$ Torr with an electron beam of 10 A passing through it. This is a challenging requirement, considering the expected power dissipation in the electron collector is up to 50 kW. There have, however, been encouraging results from Saclay on vacuum technology of a warm EBIS [3]. To satisfy the high vacuum requirements, it is planned to do a preliminary high temperature vacuum firing of almost all components of the central drift tube region before installation, and to bake this part of the EBTS to 300$^{\circ}$C after each exposure to atmosphere. The electron collector will be baked to 450$^{\circ}$C after each exposure to atmosphere. The vacuum conductance will be restricted between the central part, containing the ion trap, and heavy outgassing regions such as the electron collector and the electron gun, while at the same time providing high pumping speed for these systems with separate vacuum pumps. The central part of the EBTS will be pumped by the combination of cryopump, titanium sublimation pump, and turbopump. This combination, with a total pumping speed $F\geq2000$ l/sec for $H_2$ (the main expected component of residual gas), is capable of providing the required pressure $P=1x10^{-10}$ Torr if the total gas load does not exceed $Q\leq2x10^{-7}$ Torr·l/sec.

## 4 ACKNOWLEDGEMENTS

We thank D.Boeje, W.Hensel, R.Jackson, D. McCafferty, and W. Tramm for their valuable role in this project.

## REFERENCES

[1] E. Beebe, et.al., Rev. Sci. Instrum. 67, (1996), 878.
[2] Ross Marrs, private communication, Sept., 1995.
[3] R. Gobin, et.al., Rev. Sci. Instrum. 67, (1996), 1168.

# IMPROVED VERSION OF SURFACE PLASMA NEGATIVE ION SOURCE

V. G. Dudnikov*, W. L. Stirling, and J. H. Whealton
Oak Ridge National Laboratory, Oak Ridge, TN 37831-8088, USA

*Abstract*

The best features of two independently developed surface-plasma negative ion sources with separated function (independently controlled plasma generation and negative ion emission), have been combined in an optimized configuration; as a result, we propose to add a new mode of operation that will allow a 50-fold reduction in the negative ion temperature. The process of cesium injection developed for the semiplanotron negative ion source at the Budker Institute of Nuclear Physics (BINP), Novosibirsk [1-6], along with the hot cathode, first anode configuration and neutral gas injection of the ion source development at Oak Ridge National Laboratory (ORNL) [7-8], combines the best features of both for the continuous wave (CW) high-density, low-pressure generation of negative ions. Converter-generated cw negative ion densities of 750 mA/cm$^2$ are expected from the existing data base. These ions are generated with a temperature of about 7 eV; focusing these ions by a factor of 5 increases the current density to 3500 mA/cm$^2$ (with some mutual neutralization loss included). The ion temperature becomes 50 eV; however, according to Louville's theorem, the brightness of the beam remains at a value of 100 mA/cm$^2$ eV (Volume ion sources with a cw current per channel of 100 mA, have a brightness one-third this value.) The configuration of the source geometry and atomic gas control is optimized for maximum charge exchange reduction of the ion temperature by a factor of 50. The configuration involves appropriate shaping of the converter, anode slot, and hot cathode use of a supersonic gas jet of H0, and pumping the jet into the source. Increasing the beam brightness to 1000 mA/cm$^2$ eV corrects for a factor of four loss in recovery of charge-exchanged ions. The concept proposed here results in a net cw brightness increase of 10, which is about 30-times greater than that otherwise available.

## 1 INTRODUCTION

Many modifications of surface-plasma sources (SPS), with cesium catalysis of negative ion generation, have been constructed, tested, and optimized for various applications since 1971. [1-8]

* On leave from Budker Institure of Nuclear Physics, 630090 Novosibirsk, Russia

## 2 APPROACHES TO THE IDEAL SURFACE PLASMA SOURCE-A MODIFIED SITEX CONFIGURATION

Understanding the main processes and problems of negative-ion formation in surface plasma sources with cesium catalysis allows us to start the development of an ideal SPS. An ideal SPS with cesium catalysis would have a highly ionized plasma with very low gas density. The plasma must be dense enough to supply the required high positive ion current density on the converter-emitter surface, but thin enough for transparent transport of negative ions into the accelerator. An independently biased converter-emitter must be used for additional optimization of negative ion generation in the surface-plasma interaction. The careful optimized distribution of catalyst (cesium) on the emission surface must be developed. The emission surface must have a special curvature for a good focusing of negative ions moving across the magnetic field lines to the emission hole of the extraction system. In this variant of SPS, it is possible to have negative ion beam production with high emission current density and high gas efficiency, but the transverse temperature of the ions emitted from the surface is quite high, and this reduces the brightness of the negative ion beam. For additional improvement of the beam brightness, it is necessary to cool the very dense negative ion flux.

The basic operating principles and the construction features of the modified SITEX SPS are shown in the figures.

In using the Penning plasma discharge, it is helpful to have the plasma column with a high ion density near the emitter surface and in a thin plasma sheet to minimize the negative-ion destruction. This is very important for high current density negative ion production. The negative ions focused toward the emission slit can be extracted by the extraction system formed in the beam and accelerated for future applications. This configuration of plasma generator and surface-plasma emitter is helpful in combining the high-current density from the emitter with the large surface of the emitter (R ~ 1 cm) for convenient dc operation. We can separately optimize plasma generation and the conditions for the surface plasma production of negative ions. However, the energy spread of negative ions emitted from the emitter surface is quite high-as is the momentum spread.

0-7803-4376-X/98/$10.00 © 1998 IEEE

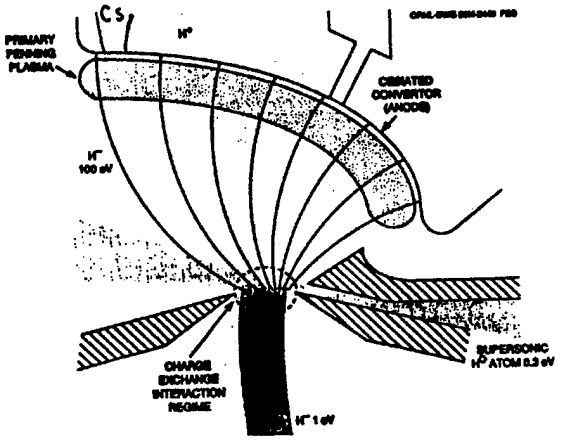



Fig. 1 Elevated view of hydrogen negative ion source showing connector, cesium feed, Penning discharge region, supersonic atomic jet, accelerator, primary, and negative ions formed at the connector and secondary charge exchange negative ions.

The negative ion flux can be cooled by conversion into cold-negative ions in a resonance charge exchange process with cold atoms. The cross section of resonance charge exchange for H- with an energy of 0.1 keV is $5\times10^{-15}$ cm$^2$ and for effective cooling of $H^-$ flux in volume on a mm scale near the emission slit, it is necessary to have an $H^0$ density of > $2\times10^{-15}$ cm$^2$. A high-gas density throughout the 1-cm gaps between the emitter surface and the emission slit can destroy the negative ions.

Charge exchange note: A major development in this concept is the utilization of charge exchange "temperature reduction" of the negative hydrogen ions. This process relies on the cross section of charge exchange. A convenient and much referred to source on charge exchange is the "Red Book" which has posted editions in 1977 (Ref. 9) and 1990 (Ref 10). The experimental work quoted for energies below 1kV is from Hummer et. al., (Ref. 11). However, the 1977 edition erred in the scaling of the Hummer (Ref. 10) measurements. For the energies of 100 V that are of interest here, the error is a factor of 8 too small ($1.5\times10^{-15}$ vs. the real values of $1.0\times10^{-14}$). In the 1990 edition, the error was corrected without comment. This inconsistency was discovered by accident by one of the authors. From 1977 to 1990, this error could have inhibited negative ion source development.

A practical solution to this problem is to use the supersonic atom flow with high-local density of $H^0$ near the emission slit and to decrease gas density in all other volumes of its discharge chambers. A possible configuration of this high density atomic flux generator is shown in Fig. 2.

It is convenient to use the RF dissociator and a flat nozzle located near the emission slit. The expanded atomic flux must be pumped at high speed. For testing, it is convenient to use the pulse regime of dissociator operation.

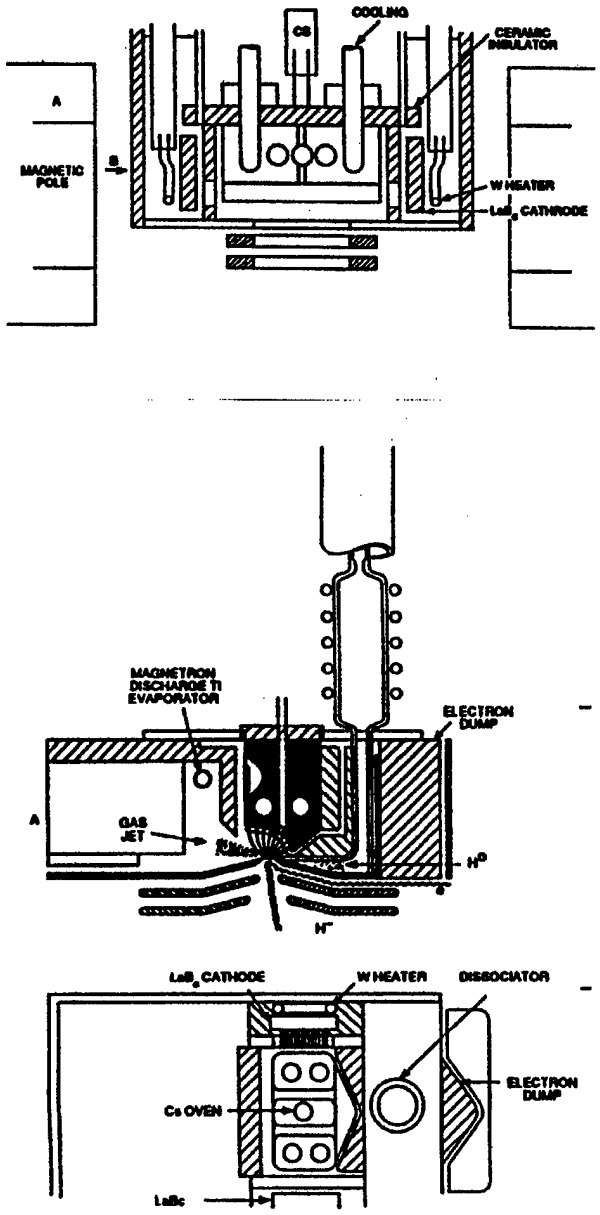



Fig. 2 Basic operating principles and the construction features of the modified SITEX SPS.

## 3 SUMMARY AND CONCLUSIONS

We have combined the best features of two independently developed and independently controlled surface-production negative-ion sources and added a new mode of operation that causes a 50-fold reduction in the negative ion temperature. The features of cesium injection, magnetron operation of the ion source development at INP, Novosibirsk, with the features of hot-cathode and first-anode configuration and neutral gas injection of the ion source development at ORNL, combine the best features of both; namely, the cw high density low-pressure generation of negative ions. Converter generated cw negative ion densities of 750 mA/cm$^2$ are expected from the extant mutual data base. These ions are

generated with a temperature of about 7 eV; focusing these ions by a factor of 5 increases the current density to 3500 mA/cm$^2$ (some mutual neutralization loss). The ion temperature becomes 50 eV; however, due to Louville's theorem, the brightness of the beam remains at a constant value of 100 mA/cm$^2$ eV. (Volume ion sources with a cw current per channel in excess of 100mA have a brightness one-third this value.) The configuration of the source geometry and atomic gas control is optimized for maximum charge exchange reduction of the ion temperature by a factor of 50. The configuration involves appropriate shaping of the converter/anode slot and hot cathode, use of a supersonic gas jet of $H^0$ , pumping the jet in the source, and increasing the beam brightness to 1000 mA/cm$^2$ eV (correcting a factor of four loss in recovery of charge exchanged ions). Thus, the concept proposed here achieves a net cw brightness increase of 10, which is about 30-times greater than otherwise available.

## REFERENCES


[1] V. G. Dudnikov, p. 2660 in Rev. Sci. Instrum. 63(4), 1992.

[2] G. Dudnikov, SU Author Certificate, CIH013/04, Application No. 411542, March 10, 1972, Bulletin No. 2, 1974; V. G. Dudnikov, "Production and Neutralization of Hydrogen Negative Ion and Beams," BNL 51034, p. 137 in Second Internat. Sympos., 1980.

[3] Yu. I. Belchenko, G. I. Dimov, and V. G. Dudnikov, p.113 in Nucl. Fusion, 14, 1974.

[4] Yu. I. Belchenko and V. G. Dudnikov, p.479 in Jour. Phys. Colloq., C-7 40, 1979, preprint IYAF 78-95; Yu. I. Belchenko et al., p.1847 in Revue Phys. Appl., 23, 1988.

[5] A. Bashekev and V. G. Dudnikov, p. 329 in AIP Conf. Proc., 210, 1989.

[6] Yu. I. Belchenko, G. I. Dimov, and V. G. Dudnikov, BNL 50727, p. 79 in Proceedings of the Symposium for Production and Neutralization of Hydrogen Negative Ion and Beam, 1977.

[7] Requirements Workshop, Gaithersburg, Maryland, Conf-771281, 1977.

[8] K. Dagenhart et al., BNL 51304, p. 217 in Proc. of the Second International Symposium on the Production and Neutralization of Negative Hydrogen Ions and Beams, 1980.

[9] F. Barnett et al., Atomic Data for Controlled Fusion Research, ORNL-5206.

[10] F. Barnett, Collisions of H1H2, He and $L_i$ Atoms and Ions with Atoms and Molecules, ORNL-6086 1990.

[11] G. Hummer et al., p. 668 in Phys. Rev. 119, 1960.

[12] On leave from Budker Institure of Nuclear Physics, Novosibirsk, Russia.

# CADARACHE 1MeV NEGATIVE ION ACCELERATOR DEVELOPMENT FOR APPLICATION IN THERMONUCLEAR FUSION RESEARCH

A. Simonin, J. Bucalossi, C. Desgranges, M. Fumelli, P. Massmann, J. Pamela
Association EURATOM-CEA
Departement de Recherches sur la Fusion Contrôlée
Commissariat à l'Energie Atomique - Cadarache
13108 Saint-Paul-lez-Durance FRANCE.

*Abstract*

Additional plasma heating in the new generation of large magnetic fusion devices like ITER requires deuterium atom beams of about 1MeV at a total neutral power of >50MW based on negative ions. At Cadarache, ITER relevant research is performed regarding the development of a 1MeV high beam current density (10-20mA/cm$^2$) electrostatic accelerator (SINGAP). The SINGAP experiment consists of the acceleration to 1MeV of a substantial $D^-$ current (100mA) in a simplified accelerating electrode structure. This is composed of only two acceleration stages: a pre-acceleration to 60keV in a multi-aperture structure for ion extraction and electron suppression, and a post-acceleration stage to 1MeV. The particular feature of the SINGAP accelerator is that the post-accelerator by means of an electrostatic lens merges the 60keV beamlets into a single beam and accelerates the merged beam to 1MeV in a single gap. Subjects of the study are the voltage holding at 1MV with large electrode areas (about 60m$^2$) and insulators in vacuum in the presence of an intense ion beam and radiation. The first experimental results of SINGAP are very encouraging. Up to now, $H^-$ beams of 40mA have been accelerated to 915keV.

## I INTRODUCTION

The objective of Fusion research is to produce plasma conditions under which thermonuclear power is produced. In magnetic confinement systems such as the Tokamak, this requires the plasma to be heated to an ion temperature of the order of >10keV. One method currently used for plasma heating is the injection of beam of energetic atoms, which transfer their energy by collisions to the plasma particles. The new generation of large magnetic fusion devices requires deuterium atom beams with energies in the range 0.5-1MeV and power of tens of MW; ITER for instance requires steady state 50MW $D^0$ beams at 1MeV energy [1]. These high energy neutral beams are created by charge exchange of 1MeV negative ions with deuterium molecules in a gas cell (called the neutralizer). High quality beam optics with low divergence (< 5mrad) are required, because the accelerator has to be installed about 25m from the Tokamak.

The research in the field of Neutral Beam Injection (NBI) focuses on the development of large area high current density negative ion sources, and the development of DC electrostatic high power high energy accelerators.

In this paper, we present a 1MeV 100kW electrostatic accelerator (SINGAP) which has been in operation since September 1995. The objective of the SINGAP accelerator is to demonstrate for the ITER NBI system design the acceleration of a substantial $D^-$ current (100mA) in a simplified scaleable accelerator concept. The SINGAP is a long pulse (several seconds) electrostatic accelerator composed of two acceleration stages: a pre-acceleration stage up to 60keV in multi-hole structure for ion extraction and electron suppression, and a post-acceleration stage to 1MeV. The particular feature of the SINGAP accelerator, is that the post-accelerator merges by means of an electrostatic lens the 60keV beamlets in a single beam, thus accelerating the whole beam to 1MeV in a single gap. After a brief description of a standard NBI system, we present in the second part of this paper the SINGAP concept and the very encouraging experimental results obtained up to now.

## II NEUTRAL BEAM INJECTOR BASED ON NEGATIVE IONS

Electrostatic acceleration has up to now demonstrated its reliability and efficiency in the 20-160keV DC NBI systems based on positive ions (at JET for instance: 14keV, and 25MW of $D^0$ [2]).

But for higher energy, their neutralization efficiency in a gas target drastically decreases, in constrast to Negative Ions (about 60% at 1MeV).

NI are formed in a cesiated cold plasma (a few eV), which is confined in a multi-cusp ion source. The ions are then extracted from the plasma and accelerated in independent channels (several tens or hundreds), to form so called beamlets. The geometry of one beamlet, shaping and gap distances, is designed by 2D and 3D space charge simulation codes [3]. The accelerator is composed of copper plates (grids) in which matrices of cylindrical apertures are drilled. The first grid separates the source plasma from the accelerating column, and is at source potential. The second grid (extraction grid) has two functions: 1) to extract negative ions following the Child-Langmuir law [4] : $I_{D^-} \propto V^{3/2}$ in the range 5-10keV; 2) to stop the plasma electrons extracted simultaneously with the negative ions (typically from 1 to 5 electrons per ion), in order to prevent them from being further accelerated.

0-7803-4376-X/98/$10.00 © 1998 IEEE

The electron suppression efficiency must be as high as possible (near 100%) [4]; this is realized by deflecting the electrons out of the beamlet by permanent magnets inserted in the grid. The extraction grid design is determined by a 3D electron trajectory code which takes into account the secondary emission and backscattered electrons. The third and following grids are the accelerating grids which give the relevant energy to the ions. After acceleration, the beam passes through the neutralizer gas cell. After the neutralization, a last device (Residual Ion Dump: RID) is necessary to deflect out from the neutral beam the residual positive and negative particles (for ITER: about 20% for each species). The total NBI system efficiency is in the order of 25% at JET (140keV and positive ions), and estimated at about 35% at 1MeV.

## III 1MeV ACCELERATOR FOR ITER

Two different designs are proposed for ITER:

*1. Multi-grids concept:*

A Multi-Aperture MUlti-Grid (MAMUG) system is proposed by JAERI (Japan) [5]; it is composed of 5 large post accelerating grids (area about $1m^2$, and 200kV per grid) where 1300 beamlets (30mA of $D^-$ per beamlet) are accelerated independently to 1MeV.

*2. SINGAP concept:*

In this case, 1300 negative ions beamlets are in a first step pre-accelerated at 60keV with a multi-aperture grid system, and then merged by means of positive electrostatic lenses into 25 beams and accelerated up to 1MeV in a single gap [6]. This concept allows a consistent simplification of the system, it provides also a high neutral gas pumping speed necessary to reduce beam losses (stripping), with subsequent reduction of the costs.

## IV THE SINGAP EXPERIMENT

The experiment has several purposes: firstly, to study the high voltage problems: HV holding under vacuum in the presence of an intense ion beam and radiation plus the development of critical 1MV devices (large insulators, bushing, etc.); secondly, to demonstrate the feasibility of the SINGAP concept for high current beams (up to 40A of $D^-$ with high current densities about 20-30mA/$cm^2$) in the 1MeV range.

Figure 1 shows a schematic of the experiment: the pre-acceleration stage with the ion source on the left, where negative ions are produced and pre-accelerated in 12 beamlets up to 60keV. Then, an electrostatic lens merges these beamlets into a single beam which is accelerated in a single gap (see figure 2) toward the high voltage electrode (anode). This electrode is suspended in vacuum by a 1MV feed-through insulator (bushing). The ion beam is finally dumped onto an inertial monodirectional graphite (CFC) target closing the exit of the anode. An infrared camera located outside the tank monitors the rear face of this target, and records in real time the temperature profile from which the beam power density can be derived.

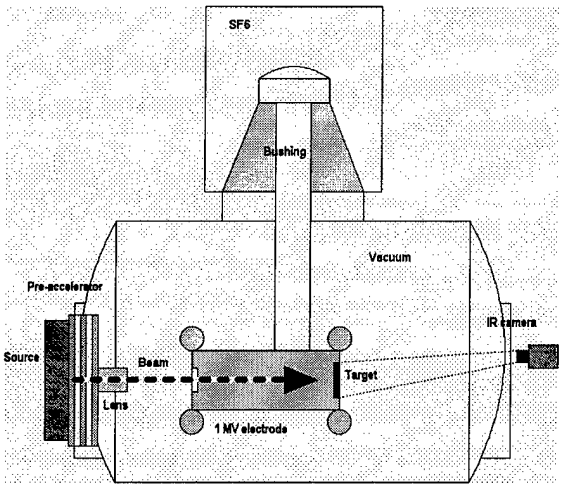



Figure 1. The Cadarache "SINGAP" experiment

The bushing is an important device; it has to sustain 4 bars of $SF_6$ externally (transmission line from the power supply) and the internal vacuum; it is located about 3m away from the accelerator and beam, minimizes the radiation and particle bombardment rates.

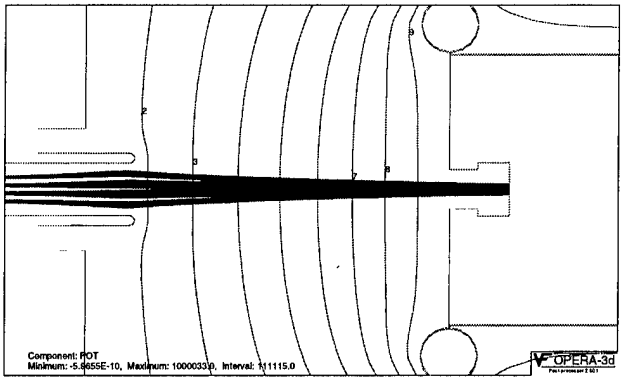



Figure 2: A 3d simulation of SINGAP post-acceleration (electrostatic lens on the left, anode on the right)

## V MAIN EXPERIMENTAL RESULTS OF SINGAP

*A. High Voltage conditioning:*

Dark current: One characteristic of this experiment is the large electrode dimensions (about $60m^2$ cathode, and $5m^2$ anode); these dimensions are comparable to those required for ITER injectors. The application of voltage on the anode gives rise to a "field emission-like" electron current (dark current), associated with outgassing and intense luminescence at the most stressed electrode surfaces [7]. For a given state of conditioning, the dependence of the dark current on the applied voltage has the same functional behavior as the Fowler-Nordheim field emission law but the emission level is larger by orders of

magnitude; the average applied electric field being 2MV/m.

(1) $I = AV^2\exp(-B/V)$

It was also observed that the coefficients A and B in (1) are strongly dependent on the pressure in the tank, and on the total voltage on-time whose effects are to reduce the dark current level. The 1MV was consequently achieved at a helium pressure of $10^{-4}$ mbar in the tank. After about 2000s of voltage on-time, the 700kV is reached with a pressure of $10^{-8}$ mbar, and a dark current level of 100mA (maximum current of power supply). We notice that during high voltage conditioning, very few breakdowns occur.

Electrostatic stored energy: Due to the large electrode dimensions, the stored electrostatic energy is about 300 Joules. This energy released during breakdowns has not induced apparent damage on the electrode metallic surfaces. However, in a series of experiment, a degradation in the high voltage holding occurred at 900kV. Important damage (perforations) was observed on the two upper insulator rings (glass epoxy). This seems to have two reasons: 1) a non-uniform distribution of the potential between the different stages of the bushing insulators (despite a resistor divider of 100MΩ per ring) due to intermediate screens (now removed) which intercepted an important fraction of the dark current; 2) a faulty construction of the rings (voids in the epoxy insulator).

*B. Beam Acceleration:*

Figure 3 shows the beam profile (recorded by the infrared camera on the rear face of a CFC target) for four beam energies (from 400keV to 700keV), and profiles obtained in the same conditions by simulation. At low energy (400keV) the energy is matched to the current density ($4mA/cm^2$): the 12 beamlets are well focused by the lens (beam divergence less than 5mrad). At 700keV, the beam is "over-focused", and the beam is split into 12 discrete beamlets. We can find a good agreement between experimental profiles and simulation. Up to now, $H^-$ beams of 915keV 40mA have been achieved.

*C. Neutral beam analysis:*

A partial neutralization (5-10%) of the $D^-$ beam occurs in the anode due to the residual gas. A preliminary measurement of the divergence of these neutrals emerging through a slot in the target has been made by an array of secondary emission probes located 3m downstream from the anode. Divergences of the order of 0.34° (6 mrad) have been measured from beams of low energy: 500keV-45mA $D^-$ in accordance with the predictions.

*D. Next step:*

Having replaced the damaged insulators, we are now trying to achieve a $D^-$ beam of 1MeV 100mA. Neutralization of 1MeV beam and study of the neutral optics will also be undertaken to demonstrate that SINGAP is scaleable for higher current (several tens of amperes) for ITER. This experiment should take place before the end of this year.

## VI CONCLUSION

Up to now, despite some problems due to DC high voltage (dark current, damages of insulators), which should be resolved soon, this first step of experiment is very encouraging. Negative ion beams (40mA $H^-$) have been accelerated up to 915keV This experiment has up to now demonstrated that the SINGAP concept is a good candidate to meet the objectives for ITER NBI.

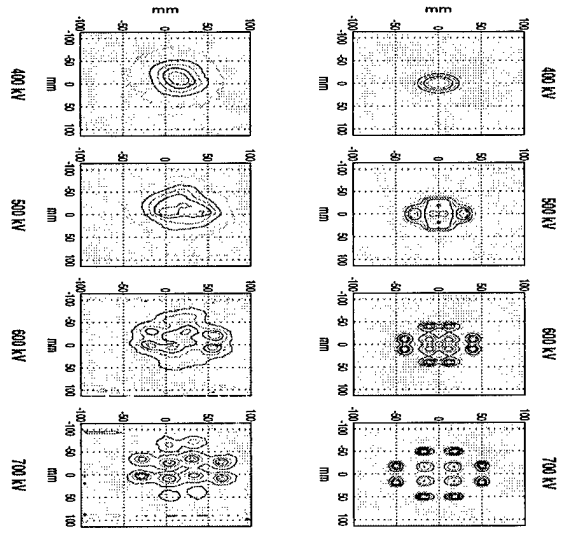



Figure 3: Beam profile (experiment and simulation) for different energies at the same D- current.

## ACKNOWLEDGMENTS

The authors wish to thank G. Delogu, S. Dutheil, P.Heister, P. Van Coillie and R. Yattou for their contribution to the experiment.

## REFERENCES

[1] ITER Joint Central Team : Design Description Document, Neutral Beam Injection, WBS 5.3.1995.

[2] Fumelli et al.;'Powerful 160keV neutral deuterium beam..'; 1266 Rev. Sci. Inst. 57(7), July 1986.

[3] Vector Fields Limited; 24 Bankside; Kidlington; Oxford OX5 1JE England

[4] Simonin, Negative Ion accelerator development at Cadarache, Rev. Sci. Inst., 67 (1996) 1092.

[5] Inoue et al.; 'Design study of Prototype Acceleration and MeV test facility'; JAERI-Tech 94-007, Aug 1994

[6] SINGAP" acceleration of high energy negative ion beams,

[7] *Massmann et al.*,16th IAEA Fusion Energy Conference, 7-11 October 1996, Montréal, Canada.

[8] J. Bucalossi et al; 'Results of the Cadarache 1MeV SINGAP experiment'; 19th Symposium on Fusion Technology, September 16-20, 1996, Lisboa, Portugal.

# FIRST BEAM OF THE CEA-SACLAY CW HIGH- INTENSITY MICROWAVE SOURCE.

P-Y. Beauvais, P. Ausset, D. Bogard, O. Delferrière, J. Faure, R. Ferdinand, A. France,
R. Gobin, P. Gros, J-M. Lagniel, P-A. Leroy
CEA-DSM-GECA and LNS (CEA-DSM & CNRS-IN2P3)
CEA-Saclay, LNS, 91191 Gif-sur-Yvette Cedex, France

*Abstract*

The High Intensity Light Ion Source SILHI is designed to be a prototype source for high power proton and deuteron accelerators. The aim is to achieve beam currents greater than 100 mA at 95 keV with rms normalized emittance lower than 0.2 π.mm.mrad. Installed at CEA Saclay, this ECR source delivered its first proton beam in July 1996. In February 1997, a 107 mA CW beam has been extracted through a 8 mm diameter extraction aperture ($J = 213$ mA/cm$^2$). A microwave power of 900 W at 2.45 GHz was needed. Diagnostic hardware, first beam measurements and last results are presented.

## 1 INTRODUCTION

A wide range of activities is presently being undertaken at the CEA in the field of high power proton or deuteron linear accelerators. We are now studying the CW IPHI demonstration project [1]. This accelerator will consist of the ECR source presented in this paper, an RFQ and a DTL up to 10 or 11 MeV. The main applications of this kind of accelerators are the production of high flux neutron beam for spallation reactions (TRISPAL, APT, ESS), the international IFMIF program and nuclear waste treatment.

In 1994, it was decided to develop a new ECR proton or deuteron source and a 3 m Low Energy Beam Transport (LEBT) to analyze the beam characteristics. We choose this source-type for simplicity and reliability reasons as demonstrated by Chalk River National Laboratory and Los Alamos National Laboratory. The requirements are: 100 mA proton or 140 mA deuteron in 90% of the total extracted beam, at 95 keV and 0.2 π.mm.mrad rms normalized emittance.

The source, installed on a 100 kV high voltage platform, delivered its first proton beam in July 1996: 46 mA at 70 keV extracted through a 10 mm diameter extraction aperture. In November, a 54 mA beam at 95 keV through a 6 mm diameter extraction aperture ($J = 191$ mA/cm$^2$) and in February 1997, a 107 mA at 97 keV through a 8 mm diameter extraction aperture ($J = 213$ mA/cm$^2$) have been extracted.

In this paper, we describe the different diagnostics installed on the LEBT [2], and present the beam analysis.

## 2 THE SILHI SOURCE AT CEA-SACLAY

To design the High Intensity Light Ion Source (SILHI) and the LEBT (Fig 1), we took the experiences of other teams into account [3], [4], [5]. The plasma chamber is cylindrical, with a 90 mm diameter and a 100 mm length. Both ends of the plasma chamber are lined with 2 mm thick boron nitride discs. The RF signal is produced by a 1.2 kW magnetron source at 2.45 GHz and is fed to the source via standard rectangular waveguides with a four stub automatic tuning unit. A three section ridged waveguide transition is placed between the plasma chamber and the cooled bend to enhance the axial RF field. The RF window is located behind the water cooled bend in order to be protected from backstreamed electrons. The magnetic field is produced by four coils tuned and positioned independently.

All these components are placed on the 100 kV high voltage platform with the ancillary equipments. The power supplies are controlled by a computer through optical fibers.

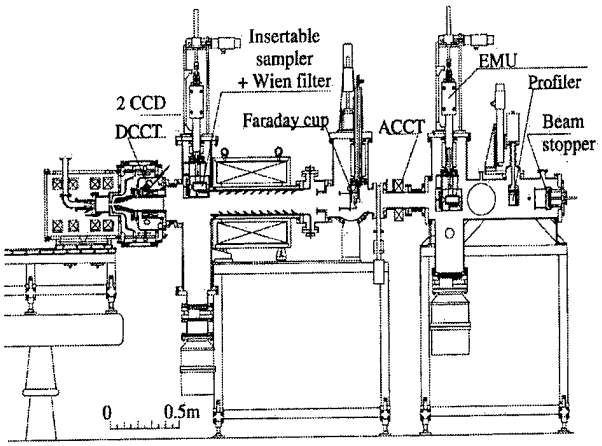



fig. 1: Source and LEBT assembly

The source is connected to the LEBT via a 300 mm long High Voltage (HV) column. The total extraction system includes five electrodes. An adjustable intermediate electrode is located in the acceleration gap to minimize the distortions in the phase-space distribution [6] and allow a beam focusing.

Along the LEBT, several diagnostics are placed in order to analyze the extracted beam [2]. Two CCD cameras allow x and y profile measurements at the end of the HV column. A Bergoz DCCT is located very close to the extraction system. An ACCT is inserted around the chamber for noise measurements. Two water cooled beam stopper are designed to stop the 10 kW total beam

0-7803-4376-X/98/$10.00 © 1998 IEEE

power (0.8 kW/cm$^2$). Thermocouples measure the two grounded electrodes temperature increases, and a residual gas analyzer is placed at the accelerator column exit.
The 2200 Gauss, 500 mm long solenoid, centered 1.1 m from the plasma electrode aperture, focuses the proton beam on the Emittance Measurement Unit (EMU) installed 1.2 m farther downstream.
The EMU is composed of a water cooled copper beam stop, with a 0.2 mm diameter aperture tantalum sampler placed at the center and a 64 wire profile monitor 0.5 m downstream. The unit is moved across the beam by two stepping motors. In order to measure the emittance of only the proton beam, a Wien filter is inserted close to the sampler. This species-separator combines a 2000 Gauss permanent magnetic field and a 1 MV/m adjustable electric field. Its total horizontal acceptance is +/- 5 mrad.

## 3 RESULTS:

The first plasma was produced in July 1996. Two weeks later a 46 mA total proton beam current at 70 keV was extracted through a 10 mm diameter extraction aperture. Beam losses destroyed the 1 mm thick stainless steel intermediate electrode as shown by thermal simulations. New drawing of the five-electrodes extraction system has been made using Axcel [7] and Opera 2D codes [8].

### *3.1 New extraction system.*

To increase the electrode power dissipation, we chose more appropriate material and we slightly modified the shape of the electrodes. For the same beam extraction conditions, the maximum calculated electric field at the electrode surfaces decreased from 82 kV/m for the earlier design to 58 kV/m for the new one. The intermediate electrode and the first grounded electrode are now made in two parts (Fig. 2). For each one, the part close to the beam is made of tantalum and the other part is made of cooper. The intermediate electrode has been thickened from 1 to 2 mm and the first grounded electrode thickness was increased from 1 to 4 mm. The thickness of the copper electron trap electrode has also been reduced from 12 mm to 4 mm.

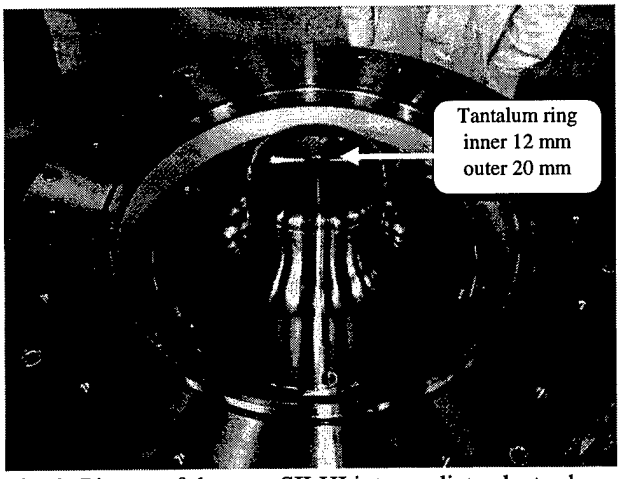


Fig. 2: Picture of the new SILHI intermediate electrode.

The aperture diameter is chosen to be 8 mm for the plasma electrode and 12 mm for the last four electrodes.
The intermediate electrode voltage can now be set from 0 to 65 kV (relative to the ground potential) to optimize the beam extraction.
With the new extraction system, the conditioning is easier; only few sparkdowns have been observed at the pressure limit, for a 100 kV source potential. Compared to the former extraction system, and for the same plasma conditions, the extracted beam is more stable. Sparkdowns due to beam rarely occur. A continuous 8 hours run has been achieved with a 80 mA total extracted beam. The resulting availability was found to be 96 %.
The AC toroid showed a beam noise about ± 2%.

### *3.2 Plasma tuning.*

For the following experiments, we installed a 8 mm diameter aperture plasma electrode. The other four extraction electrodes were set at 12 mm diameter aperture. The diameter aperture of the boron nitride disc close to the plasma electrode was 11 mm.
A complete mapping of the total extracted beam current as a function of the magnetic field inside the plasma chamber has been done. Two set of current coils gave a maximum extracted beam [2]. Computations indicate that these magnetic field values (875 Gauss) overlap with the ECR zone located at both plasma chamber extremities.

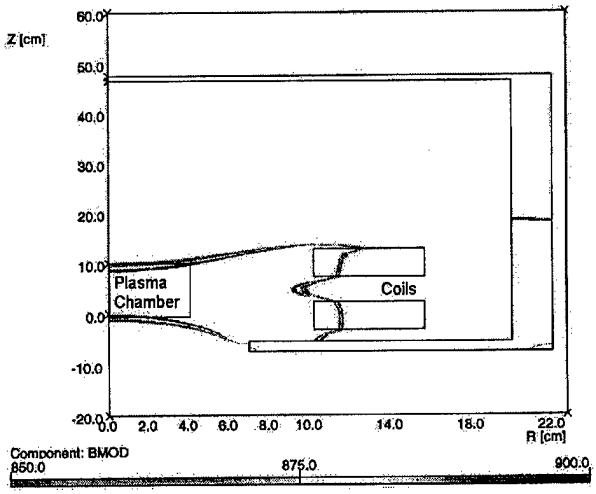


Fig. 3: Magnetic field calculation for the maximum extracted beam. Two ECR areas are located at both plasma chamber extremities.

We then decided to set two ECR zones located at both plasma chamber extremities simultaneously (Fig 3). For this requirement, we used only two coils with adequate current intensity. The total extracted beam current increased significantly up to 107 mA (J = 213 mA/cm$^2$) at 97 keV in February 1997.

*3.3 Species fractions.*

The species fraction is analyzed 2.3 m from the plasma electrode, through the sampler and the Wien filter. The particles are detected at the beam stopper 75 cm downstream. During measurements, the LEBT solenoid is turned off and the Wien filter electric field increases from 0 to 6 kV.

Preliminary results indicated a poor fractions : 67 % $H^+$, 23 % $H_2^+$ and 10 % $H_3^+$.

With the new electrode design, the diameter aperture in the boron nitride disc close to the extraction was changed to 8 mm, exactly the same as the plasma electrode aperture. Measurements have been done as a function of RF power, hydrogen gas flow, and sampler position within the beam diameter (± 2 cm with a 5 mm step). The species fraction were found to be 75% to 88% for $H^+$, 20% to 9% for $H_2^+$ and 5% to 3% for $H_3^+$ (Fig. 4).

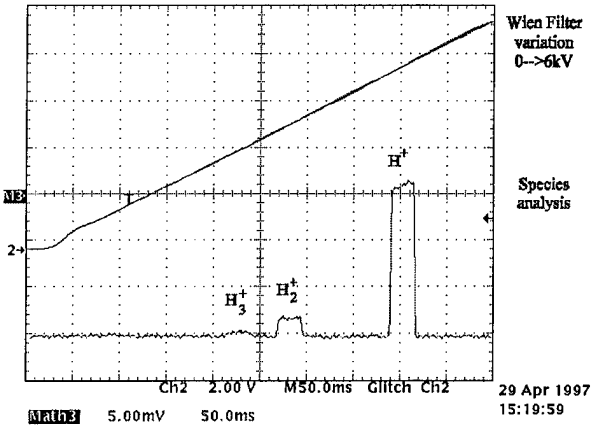



Fig. 4: Species fraction analysis

*3.4 Emittance measurements.*

The influence of the intermediate electrode potential has been checked on the proton beam emittance at 57 mA and 78 keV. The beam was focused with a cross-over point 50 cm upstream from the sampler. The rms normalized emittance decreased from 0.26 π.mm.mrad to 0.11 π.mm.mrad as the intermediate electrode voltage rose from 32 kV to 49 kV. This result is in good agreement with previous calculation. Typical emittance value for a 80 mA total beam current is 0.17 π.mm.mrad (fig. 5).

## 4 REMARKS.

The new extraction system enhanced greatly the general working of this source. The proton fraction and the extracted beam seems to be slightly better, perhaps due to the new boron nitride diameter aperture. The temperature increase of the grounded electrodes are less important. The reliability of the whole device has been greatly improved with the new connection of the intermediate electrode power supply. The beam extraction tuning is now easier.

One of the next steps will be to install an automatic fault recovery system.

The source instabilities did not allow us to make emittance measurements with a total extracted current higher than 100 mA. Our next goal is to enhance the reliability of the source.

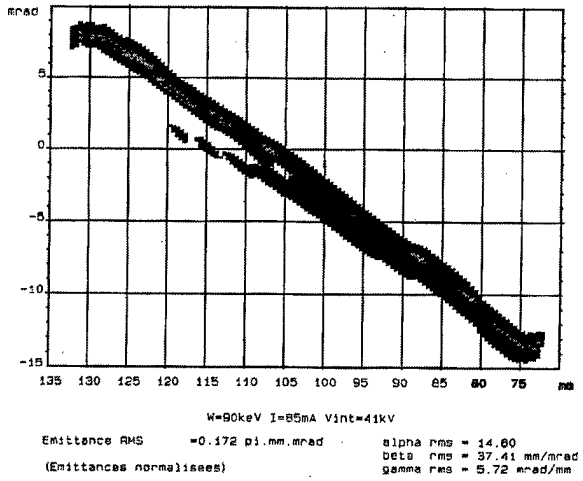



Fig. 5: Proton beam emittance measurement with 80 mA


## ACKNOWLEDGMENTS:

The authors would like to thank the other team members for their contributions to this work especially G. Charreau, O. Dalifard, F. Harrault, J.L. Jannin, F. Launay, D. Libault, J-P. Penicaud, V. Voisin, and also J. Sherman and S. Nath from LANL for their help.


## REFERENCES


[1] J-M. Lagniel et al., "IPHI, the Saclay High-Intensity Proton Injector project.", this conference 5W.04

[2] P-Y Beauvais et al., "The Saclay high-current proton and deuteron ECR source", LINAC Conference 1996, Geneva, Switzerland.

[3] T. Taylor and J. Mouris, "An advanced high-current low-emittance dc microwave proton source" , N.I.M., A336 (1993) 1-5.

[4] J. D. Sherman et al., "Microwave proton source development for a high-current linac injector", International Conference on Ion Sources 1995, Wistler, Canada.

[5] J. D. Sherman et al., "Development of a 110 mA, 75 keV proton injector for high-current, CW linacs", LINAC Conference 1996, Geneva, Switzerland.

[6] A. France et al., "High-current proton and deuteron ECR source developments at CEA", EPAC 1996, Barcelona, Spain.

[7] P. Spädtke, "Axcel-V 3.42", INP, D-65205 Wiesbaden, Germany.

[8] Opera 2D, © Vector Fields Limited, Oxford, England.

# SPACE-CHARGE NEUTRALIZATION MEASUREMENT OF A 75-keV, 130-mA HYDROGEN-ION BEAM

Robin Ferdinand CEA-Saclay, DSM-GECA, LNS, 91191 GIF-sur-Yvette France, and
Joseph Sherman, Ralph R. Stevens, Jr., and Thomas Zaugg, Los Alamos National Laboratory, Los Alamos, NM87545 USA

*Abstract*

A 75-keV, 130-mA dc mode proton injector is being developed at Los Alamos. The two-solenoid focusing system used in this injector relies on effective beam space-charge (s.c.) neutralization by beam ionization of the residual gas. The degree of s.c. neutralization is determined by measurement of the energy distribution of slow ions created in the beam region. A non-interceptive gridded-energy analyzer is used for the slow ion-energy measurement. Application and development of this diagnostic to a positive hydrogen-ion beam is presented. One feature of the ion-energy distribution measurement is a double-humped distribution. The higher energy component contains less than 20% of the total ion current. Measurements are reported which help validate the axisymmetric model used here to derive the degree of beam s.c. neutralization, f. Fairly weak dependencies of f on beam current and background gas densities are found, and f is typically found to vary between f = 95 - 99% depending on the presence of the "high-energy" tail on the slow ion distribution. This degree of beam s.c. neutralization assures good transport of the hydrogen positive ion beam to the next accelerator.

## 1 INTRODUCTION

Low-energy (50 - 75 keV) beam transport (LEBT) of high-current (50 - 130 mA) positive-ion beams in background gas pressures of order $10^{-5}$ Torr are predicted to have their s.c. largely neutralized by electrons accumulated in a beam plasma [1]. The degree of s.c. neutralization f is an important parameter in beam transport calculations. One technique [2,3] developed for the experimental investigation of f for positive ion beams is the measurement of the slow ion energy distribution. In a one-dimensional axisymmetric model of the beam-plasma interaction, where plasma ions are born cold (25 meV), measurement of the ion-energy distribution can be interpreted in terms of the residual beam space potential, $\Delta\phi$. This method has the advantage of not intercepting the primary ion beam.

A four-grid energy analyzer (FGA) has now been applied to the measurement of dc positive hydrogen-ion beams in a magnetic solenoid focusing channel. This diagnostic has previously been used for determinations of f in low energy (35 keV) $H^-$ ion beam in a solenoidal LEBT [4], and high-energy (870 keV) proton transport [5] in a quadrupole focusing channel. Design considerations for the FGA used in these measurements are given in ref. [6].

## 2 EXPERIMENTAL METHOD

The FGA diagnostic is mounted in the injector prototype for the low-energy demonstration accelerator (LEDA) project at Los Alamos [7]. Hydrogen-ion beams at 75-keV energy and 50-130 mA beam currents are used in these measurements. A microwave proton source originally developed at Chalk River Laboratories [8] has been extended to meet LEDA requirements. A line drawing of the injector is shown in ref. [9]. The hydrogen-ion beams are produced with 600 - 800 W of microwave power, which typically yield a 85 - 90% proton beam fraction. The $H_2^+$ ion comprises the remaining beam fraction. The FGA is located at an axial distance z = 44 cm from the ion source extraction electrode. For all measurements discussed here the LEBT solenoids are off. The magnetic field at the FGA location is 10 gauss. The FGA is heated to 300°C to maintain reproducible energy distribution measurements [3,6].

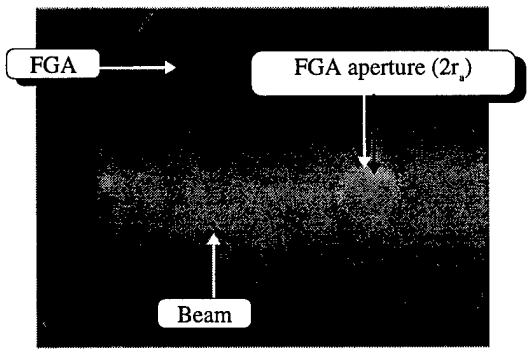



Fig. 1. An image of the hydrogen-ion beam passing the FGA.

The FGA is mounted opposite a video diagnostic port, and a video image of the beam propagating by the FGA is shown in Fig. 1. The light is generated by a 100-mA, 75-keV beam interacting with the background gas at a pressure of $1.9\times10^{-5}$ Torr. The FGA aperture diameter ($2r_a$) is 8 mm. The residual gas in the low-energy beam transport (LEBT) is $H_2$.

Before beam measurements were made, the FGA was calibrated in an auxiliary test stand by a low energy electron beam obtained from a tungsten wire heated to thermal electron emission temperature. The tungsten filament heating current is pulsed off, and the wire biased from voltages ranging from 2 to 40 V. The emitted electrons current are recorded in the FGA's Faraday cup ($I_{FGA}$). Figure 2 shows $I_{FGA}$ plotted vs. grid 3 voltage (dotted line) for a 2 eV electron beam. Voltage

0-7803-4376-X/98/$10.00 © 1998 IEEE

biases on grid 2, grid 4 and the Faraday cup are set in order to transmit the electrons with energy greater than the absolute value of grid 3 voltage ($V_3$). The equation $I_{FGA}(V_3) = \int_{|eV_3|}^{\infty} f(E)dE$ relates the energy distribution $f(E)$ to $I_{FGA}$ and $V_3$ by $f(E) = dI_{FGA}/d(eV_3)$. The $f(E)$ from the electron gun measurement is shown as the solid curve in Fig. 2. The distribution peak occurs at $V_3 = -2$ V with an estimated error of $\pm 0.1$ V, and with a full-width half-maximum energy spread of 0.67 eV. These data show the absolute energy calibration is sufficient (< 1 eV), and the energy resolution (<1 eV) is similarly acceptable for the expected range of ion energies (0 - 10 eV) to be measured from the beam plasma [1]. The analyzer temperature is maintained at 325 °C during these calibration measurements.

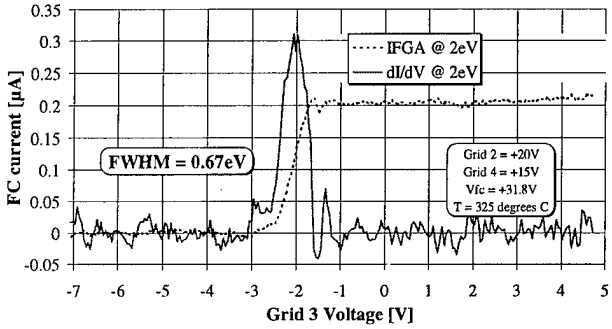



Fig. 2. Electron gun calibration of the FGA.

The data acquisition program was made using Labview v4, with around 250 points on grid 3 voltages, each point averaged at least 700 times. Data acquisition takes 10 to 30 s, so data described here is an average over possible fast beam fluctuations.

## 3 BEAM PLASMA MEASUREMENTS

A measured ion spectrum from a 120 mA beam at 75 keV energy is shown in Fig. 3. The LEBT pressure during this measurement is $1.9\times10^{-5}$ Torr or a background $H_2$ gas density of $1.4\times10^{12}$ (cm)$^{-3}$. The main section of the figure shows $I_{FGA}$ measured as a function of $V_3$ (dashed line). Its saturation value of 0.14 μA is found for $V_3 < +1$ V, and then it decreases to 0 in the $V_3 = 1$ to 12 V range. The derivative of this curve is the ion distribution function $f_i(E)$ (solid curve). A deviation from the higher FGA current characteristic decrease is noted at $V_3 = 3 - 4$ V where the $I_{FGA} = 0.02$ μA. This current and its derivative are shown as an insert to Fig. 3. This accounts for about 10% of the saturated $I_{FGA}$ at this pressure, but this component may increase to order 20% at higher LEBT pressures.

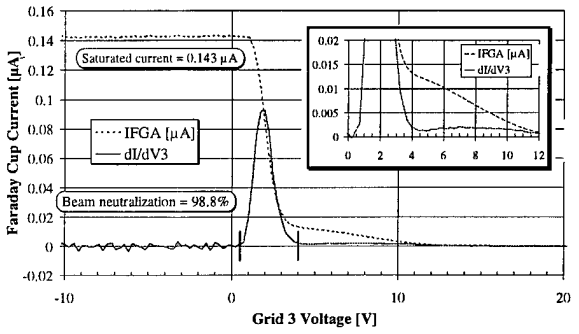



Figure 3. The FGA Faraday cup current and its derivative with respect to grid 3 voltage are plotted vs. $V_3$.

The width of the ion energy distribution ($\Delta\phi$) is taken to be the width of $f_i(E)$ at the distribution base. The degree of beam space-charge neutralization is given by $f = 1 - \Delta\phi/\Delta\phi_u$ where $\Delta\phi_u$ is the potential drop across a uniform unneutralized beam $\Delta\phi_u = i_b R/\beta$ where $i_b$ is the beam current (A), $R = 30\ \Omega$, and $\beta$ is the beam velocity. The unneutralized beam potential is about 285 V at $i_b = 0.12$ A for 75 keV beam. The increased width of the ion distribution $\Delta\phi$ then decreases f.

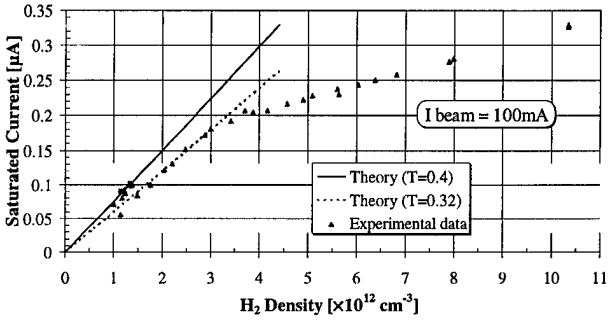



Fig. 4. Comparison of the measured and calculated FGA saturated currents.

The saturated FGA current $(I_{FGA})_s$ may be related to the FGA solid angle, beam current, neutral gas density ($n_g$), and positive ion production cross section ($\sigma_i$) by applying the 1-D continuity equation [6]. The equation is $(I_{FGA})_s = (r_a)^2 T i_b (\Sigma n_g \sigma_i)/2d$ where $r_a$ is the FGA entrance aperture radius of 0.4 cm, T is the FGA grid material transparency (40%), $\sigma_i = 2.9\times10^{-16}$ cm$^2$, and d the distance of the FGA entrance aperture from the beam centerline (10.5 cm). Figure 4 shows the measured and calculated $(I_{FGA})_s$ vs. the LEBT gas density. Here an auxiliary gas feed was attached to the LEBT box, and hydrogen gas was introduced to study the effect of larger LEBT pressures on f. The solid line shows the prediction while the discrete points show the measurement. Two calculations are shown for T = 0.4 and T = 0.32. There is good agreement considering the possible systematic measurement errors.

Figure 5(a) shows f vs. $n_g$, taking $\Delta\phi$ from the low ion energy distribution (cf. Fig. 3). Little variation in f is observed with increasing $n_g$. If $\Delta\phi$ were taken from the full ion distribution width, f is again independent of $n_g$, but it's value reduced to 95%. Figure 5(b) shows f vs. total beam current for 75 keV beam energy with $n_g = 1.2\times10^{12}$ cm$^{-3}$. It increases slowly from 96 to 99% with increasing beam current.

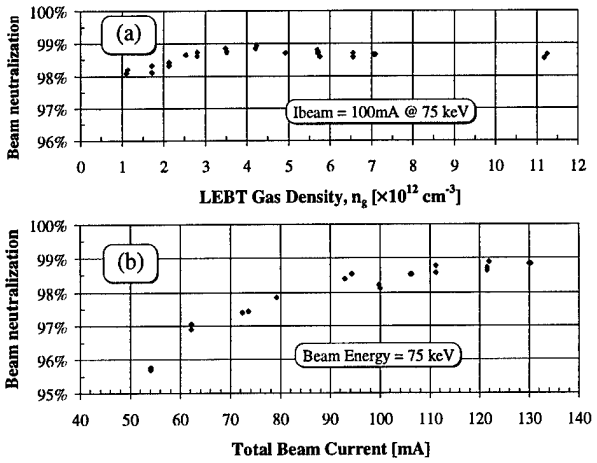



Figure 5. Plot of f vs. (a) the $H_2$ gas density in beam transport, and (b) total beam current.

## 4 DISCUSSION

Using a gridded-energy analyzer technique we have found residual beam potentials in the 0 -4 V range, or 0 - 10 V range for 75 keV hydrogen-ion beams with up to 130 mA current. The two potential ranges depend on whether a lower-intensity (< 20% of the FGA saturated current) but higher energy distribution is included in the analysis (Fig. 3). This leads to f ranging from 99 to 95%. The range of measured residual beam potentials (3 - 10 V) for an equilibrium beam agrees with that calculated by Soloshenko [1]. TRACE beam envelope calculations [10, 11] for the proposed LEDA LEBT for LEDA RFQ matching show that this range of beam s.c. neutralization may be successfully matched. Further, higher-order beam transport calculations show that this range of beam space-charge neutralization may be transported to the RFQ without large beam emittance growth [11].

We do not have a clear physical understanding of the measured two-energy ion distribution. It is unlikely an instrumental effect. However, since the higher energy portion of the distribution becomes more dominant at the higher gas pressures, we propose that the detected higher-energy ions come from a process other than lower energy ions being accelerated out of the beam channel by the residual beam s.c. potential. At higher gas densities the beam plasma would become more dense, and this may lead to excited $H_2$ molecules which decay to charged particles with ≈10 eV [12]. This interpretation is supported by the observation that the measured electron temperature increases from 1 to 3 eV as the LEBT gas density increases.

Earlier high-energy (870 keV) proton beam neutralization measurements [5] invoked halo $H_2^+$ and $H_3^+$ beam contributions to the measured ion energy distribution to explain multiple low energy distributions. However, the present distribution occurs at higher energy than the main distribution, and it seems unlikely the 10 - 15 % $H_2^+$ beam component can account for the ion distribution at $V_3 > 4$ V observed here.

Another possibility is the beam is rapidly oscillating between two s. c. neutralization states by collective oscillations in the ion-beam plasma [1]. This experiment would record the time-average of such a collective oscillation. This could possibly lead to emittance growth, but cannot be very large, as the rms beam emittance at the end of the beam transport has been determined to be 0.20 π mm-mrad [9].

## 5 ACKNOWLEDGMENTS

We acknowledge the support of Dave Hodgkins for technical help, and Eric Pitcher for discussions on some of the results. We acknowledge the support of the US DOE and the French DSM-GECA organizations.

## REFERENCES

[1] I. A. Soloshenko, "Physics of Ion Beam Plasma and Problems of Intensive Ion Beam Transportation", Rev. Sci. Instrum. 67(4), (April, 1996), 1646.

[2] P. Kreisler, H. Baumann, and K. Bethge, "Measurements of Space Charge Compensation of Ion Beams", Vacuum 34(1-2), (1984), 215.

[3] R. Dolling, J. Pozimski, P. Gross, J. Klabunde, and P. Spadtke, "Investigation of Space-Charge Compensation with Residual-Gas-Ion Energy Analyzer", Proceedings of the XVIII International Linear Accelerator Conference, CERN Report 96-07, (August, 1996), 83.

[4] Joseph Sherman, Eric Pitcher, Ralph Stevens, and Paul Allison, "H⁻ Beam Neutralization Measurements in a Solenoidal Beam Transport System", Proceedings of the Sixth International Symposium on the Production and Neutralization of Negative Ions and Beams, AIP Conference Proceedings No. 287, (November, 1992), 686.

[5] Joseph Sherman, M. Olivo, and E. Mariani, "H⁺ Beam Neutralization Measurements at 870 keV Beam Energy", Rev. Sci. Instrum. 63(4), (April, 1992), 2776.

[6] Joseph Sherman, Eric Pitcher, and Paul Allison, "H⁻ Beam Neutralization Measurements with a Gridded-Energy Analyzer, a Non-Interceptive Beam Diagnostic", Proceedings of the 1988 International Linear Accelerator Conference, CEBAF Report 89-001, (October, 1988), 155.

[7] J. David Schneider, "APT Accelerator Technology", Proceedings of the XVIII International Linear Accelerator Conference, CERN Report 96-07, (August, 1996), 22.

[8] Terence Taylor and Jozef Mouris, "An Advanced High-Current, Low-Emittance dc Microwave Proton Source", Nucl. Instrum. And Methods in Phys. Res. A336, (1993), 1.

[9] J. D. Sherman, et al, "Development of a 110-mA, 75-keV Proton Injector for High-Current, CW Linacs" Proceedings of the XVIII International Linear Accelerator Conference, CERN Report 96-07, (August, 1996), 701.

[10] K.R. Crandall, and D. P. Rusthoi, "Documentation for TRACE : and Interactive Beam Transport Code" Los Alamos National Lab. Internal Report, LA-10235-MS (Jan. 1985).

[11] H. V. Smith, "Low-Energy Beam Transport Calculations for the LEDA Injector", PAC97, these proceedings.

[12] A. Crowe and J. W. McConkey "Experimental Evidence for New Dissociation Channels in Electron-Impact Ionization of $H_2$." Phys. Rev. Letters 31 (July 1973) 192.

# UPGRADE OF THE H⁻-INJECTION SYSTEM AT THE DESY PROTON LINAC III

C.-M. Kleffner, G. Jacobs, N. Holtkamp, M. Nagl, I. Peperkorn, J. Peters
Deutsches Elektronen Synchrotron DESY, Germany,
A. Schempp, IAP, Universität Frankfurt, Germany
and V. Paramonov, INR Moscow, Russia

*Abstract*

In the near future the injection system of the proton linac at DESY will be upgraded. Two different types of H⁻-sources are operated at DESY. The new rf-driven volume source is free of cesium. On a long-term basis this source is planned to replace the present operating magnetron source.

For reasons of reliability of the proton linac and for further developments of ion sources a parallel operation of two sources should be possible at the Alvarez linac. Each source has a separate RFQ to accelerate the ions to an energy of 750 keV. A new transport line with one dipole, 8 quadrupoles and one intermediate buncher was designed to match the beam between both RFQs and the Alvarez linac.

The codes COPPOC and TRANSPORT were used to determine the length of the transport line and the parameters of the dipole and the buncher. Because of the high current of 20 mA and above the estimation of the space charge forces is of special interest. The macro-particle-code PARMTRA takes into account the particle-to-particle electric forces among all particles. The properties of the beam line have been studied in connection with the effects on the final beam quality after acceleration with the 50 MeV Alvarez linac.

## 1 INTRODUCTION

At present the H⁻-ion accelerator facility LINAC III at DESY consists of a magnetron ion source followed by a RFQ (Radio-Frequency-Quadrupole)-accelerator in front of a 50 MeV Alvarez linac [1].

The H⁻-injection system upgrade program which is under development at present will enable parallel operation of two ion sources at the Alvarez linac. The proposed MEBT (Medium Energy Beam Transfer) between the two RFQs and the Alvarez linac has a twofold goal: i) it is designed to match the beam of both ion sources to the acceptance of the Alvarez linac. ii) the mechanical construction of the upgrade will facilitate further developments of ion sources and tests at the Alvarez linac.

Concerning the reliability of the H⁻-injector for HERA operation in the near future, it is essential that the time necessary to switch from the new volume source to the magnetron ion source will become as short as possible. The MEBT between the two ion sources and RFQs and the Alvarez was therefore designed to operate in two modes without the need of altering the mechanical structure.

The new volume source will be installed on the axis of the Alvarez linac, whereas the beam coming from the magnetron source will be bent by a 60°-magnet to this axis. A rebuncher is needed for the longitudinal dynamics in the MEBT.

The optical design of the MEBT is important insofar as the beam quality in the low energy part determines the characteristic of the beam in the high energy part of the linac.

## 2 DESIGN OF THE MEBT

The design procedure for determing the parameters of the MEBT is as follows:

The space charge force at the high current of 20 mA at the energy of 750 keV finally limit the overall length of the MEBT due to the strong debunching of the ion beam.

As part of the design calculations for the new MEBT a number of options were investigated. Various combinations of one or two dipole magnets with 30°, 45° or 60° and different edge angles were tested in simulations. It was found that the effect of the dispersion generated by a 60° sector magnet on the beam quality can be minimized. A MEBT with only one short dipole gives the possibility to reduce the distance between both RFQs and the rebuncher to less than 60 cm.

The number of quadrupoles was kept small to save space. Since there is no space to install steering magnets the quadrupoles can be displaced transversally in order to align the beam in horizontal and vertical direction.

Eight quadrupoles – 6 for each transport line – arranged in doublets are used to focus the beam transversally. The parameters of the rebuncher cavity have been estimated by calculating the phase and energy spread at its position and the optimized drift length from rebuncher to the first Alvarez tank. A sketch of the layout of the MEBT is shown in figure 1.

## 3 PARAMETERS OF THE MEBT COMPONENTS

### *3.1 Magnets*

For the beam focusing only one standard Alvarez type of quadrupole is employed. Steering angles of up to 10 mrad will be realized by transverse displacements of the quadrupoles of up to 1 mm. The 60°-bending magnet is a pulsed sector dipole magnet. The manufacturing of the magnets was given to industry. All magnets will be powered with the same type of DESY-developed pulsed power

0-7803-4376-X/98/$10.00 © 1998 IEEE

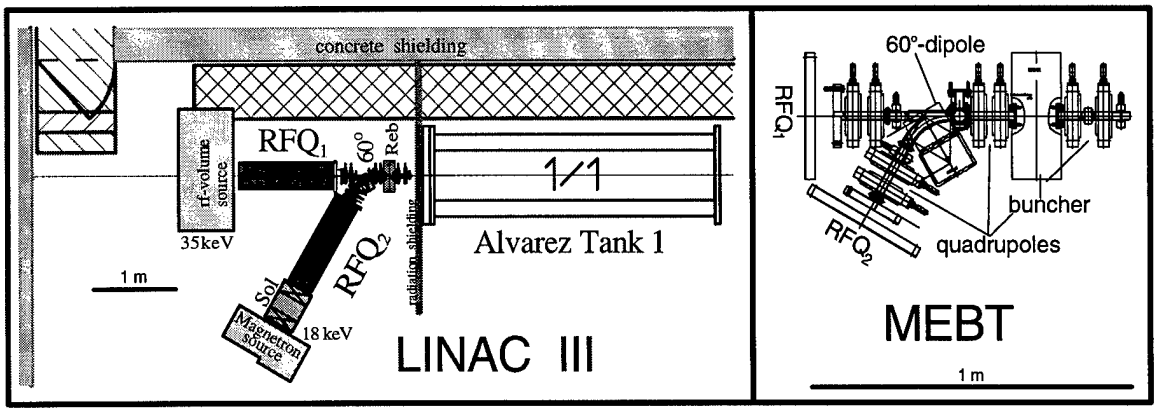



Figure 1: Layout of the MEBT.

supplies. Due to the small duty factor of the proton linac of 1:4000 at a repetition rate of 0.25 Hz air-cooling is sufficient.

### 3.2 *RFQ accelerator*

The new RFQ accelerator is based on the design of the operating 4-ROD RFQ [2] at LINAC III and was delivered by the IAP Frankfurt. The design input energy has been increased from 18 keV to 35 keV in order to permit the operation of the volume source with higher extraction voltage.

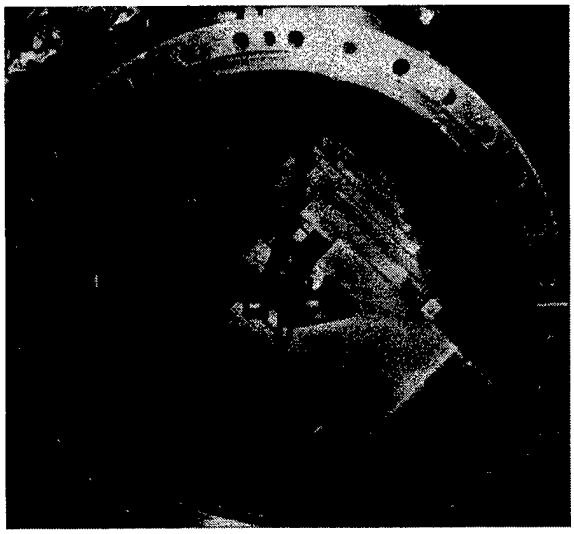


Figure 2: View of the RFQ accelerator.

Figure 2 shows the low energy part of the RFQ. Both RFQs will be powered by the same rf-amplifier.

### 3.3 *Rebuncher cavity*

A new rebuncher cavity is under construction at the IAP Frankfurt. It is a two gap spiral loaded resonator operating at 202 MHz. The design values are as follows:

A rf-amplifier for the rebuncher cavity is under construction at DESY.

| | |
|---|---|
| $f_0$ | 202 MHz |
| $U_{\text{eff}}$ | 58 kV |
| $U_{\text{gap}}$ | 45 kV |
| $P$ | 5 kW |
| length | 12 cm |

Table 1: Main parameters of the rebuncher cavity for the MEBT.

### 3.4 *The Ion Sources*

Currently a 18 keV magnetron source is operating as the $H^-$-ion source for LINAC III. To reduce the work functions for the electrons the magnetron source must be operated with cesium. The rf-driven volume source [3] at DESY makes a cesium-free operation possible with high currents and smaller emittances compared to the magnetron source.

### 3.5 *Beam diagnostic*

The measurement of the beam parameters will be performed by DESY standard devices. At the exit of the RFQs and in front of the Alvarez tank the current will be measured by commercially available current transformers. Screen monitors at two different places in the MEBT will be used to optimize the beam alignment and the focusing strengths of the quadrupoles. The bunch length at the entrance of the Alvarez tank will be derived from signals of a capacitive pick-up and of the new BSM monitors inside the Alvarez linac [4]. As an alternative an additional BSM [5] can be installed between MEBT and the Alvarez linac.

## 4 BEAM DYNAMICS CALCULATIONS

The beam optic was developed using the codes COPPOC [6] and PARMTRA [7]. The first order code COPPOC was used because of its powerful optimizer and the intuitive interface. PARMTRA is a particle tracking code for ions that takes into account the space charge forces and the rf-defocusing in the rebuncher cavity.

The transversal and longitudinal envelopes in the MEBT are shown in figure 3 to figure 5. The parameters of the $H^-$-beam behind the RFQs differ according to the different

electrode design. Following parameters have been assumed in the calculation:

| | MEBT 1: rf-source & $RFQ_1$ $\rightarrow$ Alvarez | MEBT 2: magnetron source & $RFQ_2$ $\rightarrow$ Alvarez |
|---|---|---|
| $\epsilon_{x,y}$ | 36 $\pi$ mm mrad | 36 $\pi$ mm mrad |
| $\Delta\phi$ | $\pm$ 19° | $\pm$ 29° |
| $\Delta W$ | $\pm$ 10 keV | $\pm$ 14 keV |

Table 2: Beam properties (at 750 keV) at the exit of the RFQ.

The quadrupole strengths and the gap voltage of the buncher were optimized with the code PARMTRA. The equivalent defocusing force of the rebuncher amounts to 40% of that of the following quadrupole magnet. Thus, it cannot be neglected in finding the matching parameters of the beam line.

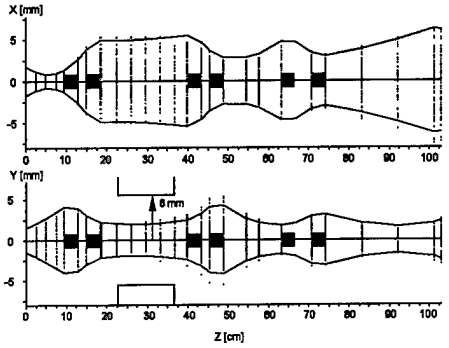



Figure 3: Transversal beam envelopes ($2\sigma$) for the MEBT 1 transport line with 20 mA.

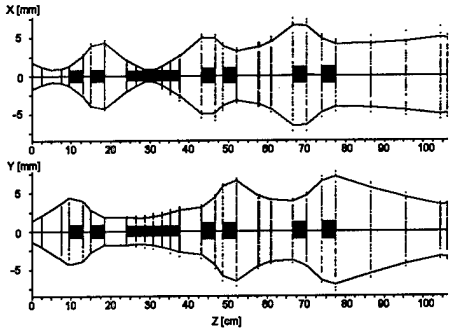



Figure 4: Transversal beam envelopes ($2\sigma$) for the MEBT 2 transport line with 20 mA.

There is some enlargement in the emittances (table 3). The rf-defocusing inside the buncher causes a transverse emittance growth due to the nonlinear forces. The dispersion induced by the bending magnet cannot be fully compensated but was minimized due to the small horizontal $\beta$-function inside the dipole magnet.

The calculated beam properties with currents of up to 30 mA are suitable for further acceleration with the Alvarez. Compared to the present situation the beam matching to the Alvarez linac can be improved and compensates

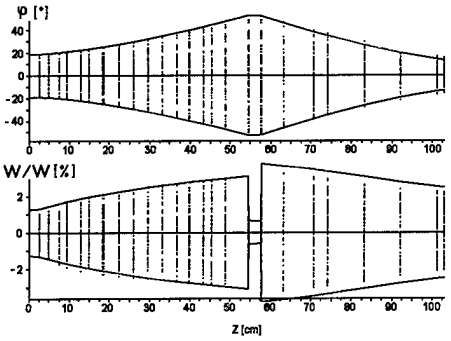



Figure 5: Longitudinal beam envelopes ($2\sigma$) for the MEBT 1 transport line with 20 mA.

| $I$/[mA] | $\epsilon_x/\epsilon_{x,0}$ | $\epsilon_y/\epsilon_{y,0}$ | $\epsilon_z/\epsilon_{z,0}$ |
|---|---|---|---|
| 0 | 1.1 | 1.0 | 1.0 |
| 10 | 1.3 | 1.2 | 1.1 |
| 20 | 1.4 | 1.3 | 1.2 |
| 25 | 1.6 | 1.4 | 1.2 |
| 30 | 1.7 | 1.6 | 1.3 |

Table 3: Emittance growth factors at different currents in the MEBT 2 transport line.

the influence of emittance growth within the MEBT on the final beam quality. Tracking calculations of the Alvarez linac with and without the MEBT are still in progress and show that a reduction of the emittance at the high energy end should be possible with the usage of the MEBT.

## 5 SCHEDULE

The modifications of the accelerator system are planned to be made during the HERA shutdown in winter 1997/98. First tests are scheduled for March 1998.

## 6 ACKNOWLEDGMENTS

The authors are grateful to the technical groups at DESY for their support.

## 7 REFERENCES

[1] LINAC III collaboration, Rev. Sci. Instruments **62** (4), April 1991.

[2] M. Ferch, Dissertation, IAP Frankfurt, 1984.

[3] J. Peters, **The status of DESY $H^-$ sources**, LINAC96, p199-201.

[4] A.V. Feschenko, A.V. Liiou, A.N. Mirzojan, A.A. Menshov, P.N. Ostroumov, N. Holtkamp, C.-M. Kleffner, M. Nagl, I. Peperkorn, **Bunch Shape Monitors for the DESY $H^-$-Linac**, this conference.

[5] A.V. Feschenko, private communication.

[6] **COPPOC**, I. Borchardt, U. Naujokat, H. Ruge, DESY 1985.

[7] **PARMTRA**, J. Struckmeier, GSI Darmstadt, Germany, private communication.

# TRAPPED ION SOURCE

G.Brautti, A. Boggia, A. Raino' Dipartimento di Fisica e INFN sez. di Bari
N. Ceci, V. Valentino, V. Variale INFN sez. di Bari

*Abstract*

In this paper it is shown the design and the mechanical construction of a Trapped Ion Source (TIS). TIS is a new type of source capable, in principle, of producing very highly charged ions and, at the same time, it is a radio frequency quadrupoles linear trap suitable to study the interaction of the trapped ions (or charged microparticles) with electrons, high energy particles or laser beams. In practice, it is a modified version of an Electron Beam Ion Trap (EBIT) recently developed in some laboratories mainly to study X and UV rays spectroscopy for "hydrogenic" and "helium-like" ions. Among the goal of TIS, other than the production of highly charged particle, it can be foreseen the production and trapping of radioactive isotopes, ion cooling, analysis of macromolecules and also "dust targets" for high energy accelerators.

## 1 INTRODUCTION

The ability to produce very highly charged ions in a small laboratory apparatus at a small fraction of the cost of producing them at a large accelerator represents a great opportunity. In fact new EBIT are being built in several laboratories around the world, and the initial operation of two of them has recently been reported [1].
Highly charged ions play important roles in hot plasmas physics, controlled fusion devices and x-ray lasers.
Production of a very highly charged ion is extremely difficult, requiring successive collisions having center-of-mass energies greater than the binding energies of the electrons to be removed. One can achieve such type of collisions either by directing a relativistic heavy ion beam from a large accelerator into a stationary foil target or by directing an electron beam a thousand folds less energetic into a stationary ion target. The latter method is used in an EBIT. Although the EBIT was initially developed for X-ray measurements of trapped ions, one can change its mode of operation to provide an efficient source of very slow, very highly charged ions.
In this paper we present the design and the construction of a Trapped Ion Source (TIS) that can be seen as a modified version of an EBIT and an EBIS. One can foresee that TIS could overcome some drawbacks of the EBIT and EBIS making it a more flexible device. In fact an EBIS presents the following problems:
In an EBIS (or EBIT) a continuous electron beam is used to produce and contain the ions. The highly charged ions can be obtained by electron bombardment ionization in two different ways:
i) single-step ionization
ii) multi-step ionization
i) in the single step-ionization the incident electrons must have an energy of at least the sum of all the ionization potentials of the removed electron;
ii) in the multi-step ionization, for the incident electrons, it is required only the energy of each electron removed from the atom or ion.
The multi-step ionization process is, greatly, the most probable way to obtain high charge state ions [2] but this process, of course, takes time. This time depends on the plasma density and on the ionization cross-section. It must be shorter than the ion life-time in the plasma if one wants obtain significant number of highly charged ions.
As an example, one can consider the effective cross sections for sequential ionization of a given element by electron impact, $\sigma_{k\to k+1}$, then the ionization time can be given by

$$\tau_i = \frac{1}{j}\sum_{k=1}^{Z-1}\frac{1}{\sigma_{k\to k+1}}$$

where j is the electron current density and Z is the ion charge state.
Applying this equation, to generate $N^{+7}$ with a current density of $1.8X10^{20}$ el/cm$^2$/s (30 Amp/cm$^2$) at an energy of 3 keV, an ionization time of 50 ms is obtained. Such a long ionization time, requires a residual gas pressure of $10^{-10}$ - $10^{-11}$ Torr (very high pressure) in the trap region. In fact only under these conditions the replacement of working gas ions by the residual gas can be practically excluded, and the ionization will be effective. In other word the potential well generated by the electron beam must not be leveled by the ions issued from the background gas. This problem imposes very high density electron beam to reduce the interaction time and the residual gas pressure constraint [2]. On the other hand the use of high density electron beam can induce plasma instabilities [3].
In fact the other problem related is the ion losses. Three possible ways for losing the highly charged ions are: a) transverse ejection (due to elastic collision with the continuous eb); b) electron recombination (that in this condition can be neglected [2]); c) plasma instabilities (that prevent the increase of eb density and of the ion trap length).
In TIS the utilization of a rf quadrupole field to contain the ions in a selective way allow to use a pulsed electron beam and in this way these kind of problems could be overcome (see below).
Applications that can be foreseen for TIS are in the following.
1) Development of cooling methods and eventually production of Wigner crystals. Most of the existing ion traps are of the static type. Cooling can be also applied in large storage rings, where ordered forms of relativistic ions

0-7803-4376-X/98/$10.00 © 1998 IEEE

can be obtained. TIS is designed mainly to allow cooling experiments on ion groups in slow controlled linear motion. The ions will be contained in a potential well nearly flat in the longitudinal direction, with potential barriers of a few keV at the extremities, while the rf quadrupole field produces a transverse harmonic potential. Several forms of filtering can select the trapped ion type, since by suitable bias TIS works as quadrupole mass spectrometer, or by pulsing some electrode it can work as a time of flight spectrometer in the longitudinal direction.
2) Dating with Long Lifetime Isotopes (LLI). The method of dating with isotopes of long lifetime (e.g. $C^{14}$) has been used for many years by measuring the residual radioactivity of the specimen to be dated. However the method is insensitive and time consuming, since only a very small fraction of the nuclei to be detected decay during the measurement. More recently the atoms to be detected were accelerated with tandem accelerators, fully stripped, and their charge verified by magnetic analysis and by nuclear detectors. The ability to highly strip and isotopic selection with different methods allows to TIS a similar performance using much less expensive apparatus.
3) Use as a target for high energy ion or particle beams. TIS can suspend powder particles or macromolecules that can be exposed to a high energy ion beam. The molecular recoil can be detected, allowing the measurement of very low energy loss and momentum transfer.

## 2 ION SOURCE DESIGN

In fig.1 is shown the operation scheme of the device. In that figure one can see the electron gun that generates the electron beam needed to ionize the atoms. Since an electron gun designed and built for another experiment is intended to use for TIS experiment a couple of iris are been used to match the electron beam emittance to the acceptance of the TIS transport channel.

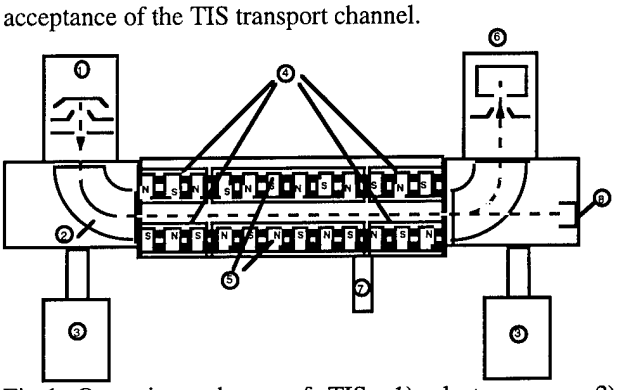


Fig.1 Operation scheme of TIS: 1) electron gun, 2) bending magnet, 3) vacuum pump, 4) static potential electrodes $U_0$ for longitudinal ion trapping, 5) rf quadrupole electrodes with inside the focusing magnetic quadrupoles, 6) electron collector, 7) gas-inlet, 8) ion collector.

The transport channel that drives the beam until to the electron collector and the electron beam envelope is shown in fig.2. The main new feature of TIS, with respect to an EBIT (or EBIS), is the adding of radial ion confinement of the rf quadrupoles to the potential well of the eb space charge when it is on. When the eb is off (the eb will be pulsed) only the desired ions will remain trapped.

*2.1 Ion confinement*

The ion containment in the transverse direction can be obtained by a rf quadrupole field or by the same electron beam needed to produce ions (like in a EBIS or EBIT). In the longitudinal direction the containment is obtained by two repelling electrodes placed at the edges of the quadrupole electrodes. These electrodes can be pulsed to pull-out the trapped ions for external use (e.g. acceleration).
In TIS The rf radial ion confinement is obtained by applying a time varying potential to the rf cylinder shaped electrodes. This results in a harmonic pseudo-potential well of the form [4]:

$$\Phi_p = \frac{qV_0^2}{4m\varpi_{rf}R^4}r^2 = \frac{m}{2q}\Omega^2 r^2 \quad \text{with } \Omega = \frac{qV_0}{\sqrt{2}m\omega_{rf}R^2}$$

where R is the radial position of the cylinder shaped electrodes (fig.1), and $V_0$ is the voltage amplitude applied. $\Omega$ is, of course, the oscillation frequency in the radial direction of the trapped ions. The condition to be satisfied for the formation of a pseudo-potential well is: $\Omega << \omega_{rf}$.
In fig.2 are shown the depths of the pseudo-potential well, at 1 cm from the axis, for different ion mass and different $\omega_{rf}$ values. In those figures the pseudo-potential well has been put to zero when the previous condition on the "secular" frequency $\Omega$ was not satisfied.

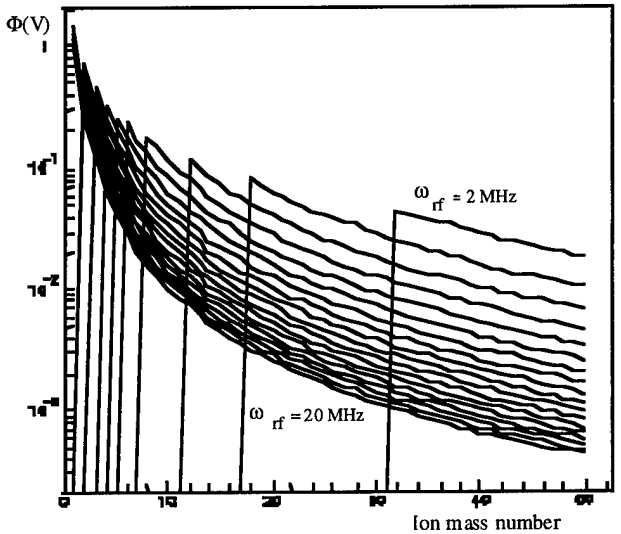



Fig.2 Potential well depth *vs* ion mass numbers at 1 cm from the axis for different rf frequency.

As mentioned before in the EBITs the ions are contained transversally from the eb space charge and longitudinally from the potential set by the electrodes on the edges. In this situation residual gas ions can be trapped together with the wanted ions. In this way all these ions can easily fill the pseudo-potential well and then reduce the ion containment capability.
In order to avoid this drawback a pulsed electron beam will be used in such a way that the transversal ion containment

is maintained only by the rf quadrupoles. In this way by adding to the rf field a continuous quadrupole field it is possible to select the ion type to be contained in the pseudo-potential well (as is done in a common mass spectrometers). In meanwhile, the slow electrons generated form successive ionization's are swept away because the rf period is much less than the electron transit time of the quadrupole field. For this reason multipacting phenomena should be avoided.

In this condition the stable (trapped) ion trajectories , in both planes, are given by the Mathieu equation solutions). From these solutions , one can see that, once fixed the rf and the continuous quadrupole potential, the stability region for the ion trajectories depends only on the charge to ion mass ratio [5].

As an example, one can take an ion mass number A= 40, it has a charge to mass ratio (for one charge) $e/m_A$ = $2.4X10^6$, fixing $\omega_{rf}$=6 Mhz , $V_0$=100 V and U=7 V, the stability region obtained for $e/m_a$ is in the range $2.4X\ 10^6$-$5.4X\ 10^7$ , then, this ion can be ionized for 20 times ($e/m_A=4.8X10^7$) and remain in the stability region.

For the confinement along the longitudinal axis a static voltage $U_0$ is applied to the electrodes placed at the edges of the quadrupole electrodes in the longitudinal direction (see fig.1). It can be seen that the radial potential well is slightly weakened by the axis potential $U_0$ [4]. In its normal operation, an electron beam pulse is injected transversally in the trap and then bent in the axial direction. Transversally, in the center of the trap, gas, vapor or powder jet can be injected by a valve, then it is ionized and confined by the rf quadrupole field.

The ion extraction will be done by changing the axial static voltage U0 (on the left of the trap) to a negative value to eject the ions towards a Faraday cup placed on the axis to collect the ions (about -100 V).

The rf quadrupoles electrodes have a cylinder shape that approximates near the symmetry axis the pure quadrupole field generated by hyperbolic shape electrodes. An optimization of this approximation, given for a particular ratio between the distance from the axis and the cylinder radius, is shown in fig.4, where a value of $A_4/A_6$ = 2.7x $10^4$ has been found for the ratio of the Fourier quadrupole coefficient with the sextupole coefficient. The other multipole fields Fourier coefficients are practically negligible.

*2.2 The electron beam transport channel*

The electron beam will be generated by an electron gun with a Pierce design originally built for an electron cooler and then modified for our needs. To get a pulsed electron beam the first electrode will be connected to a Bloomlein type pulser. The density electron current obtained in the simulations is about 80 $mA/cm^2$ with a perveance of 0.11 $\mu P$. The couple of iris have a radius of 2mm and are placed at a distance of 210 mm to give at gun exit an emittance of about 50 mm x mr. To make the operation more easy, the gun cathode is set at high voltage and the transport channel at ground.

From the exit of the gun the electron beam will be transported till the collector trough two 90° electron bending magnets (BM) and a new kind of magnetic quadrupoles (see below) inserted inside the rf quadrupole electrodes. The eb envelope in the horizontal and vertical plane along a 1 m long transport channel is shown in the computer simulations of fig.3. The BM curvature radii are 95 mm, The Quadrupole gradient values are symmetric with respect the center of the transport channel.

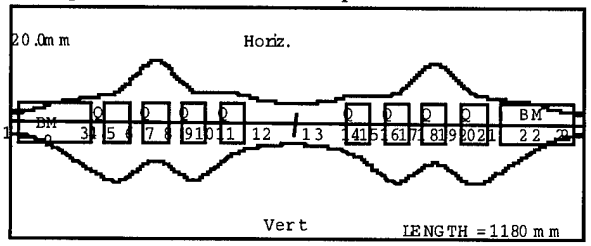



Fig.3 Beam envelope transportation along the trap, from the entrance of the first bending magnet to the entrance of the electron collector. The central region is the trapping region.

A mechanical design of the new type of magnetic quadrupoles that we think to utilize for the eb focusing is also shown in fig.1. This quadrupoles will be built by turning four iron bars, alternating a section of larger to one of smaller diameter. Around the smaller ones are wound the excitation coils with alternating polarity from coil to coil.

After the second bending magnet the eb will be decelerated and then recovered by a collector placed at a voltage about 1kV less than the high voltage of the gun cathode to recover all the electrons.

## 3 CONCLUSION

The mechanical design and the computer simulations of the device has been concluded. The vacuum chamber, the electron gun, the electron collector and the cylinder shaped electrodes for the rf quadrupole field are already available.

The construction and the test of the new type focusing quadrupoles for the eb are under way.

In the first phase of the experiment pick-up electrodes will be used as sensors for the electromagnetic signals given by trapped ions and in a second phase they will be used to apply a stochasting cooling to the trapped ions.

## REFERENCES

[1] R.E. Marrs, P. Beiersdorfer, D. Schneider, Phisics Today, October (1994) 27

[2] J. Arianer and C. Goldstein, IEEE Trans. on Nucl. Sci., NS 23 (1976)

[3] M.A. Levine et al., Phys. Scri., T22 (1988) 157.

[4] M. G. Raizen et al., Journal of Mod. Optics, **39** (1992) 233.

[5] W. Paul, "Electromagnetic Traps for Charged and Neutral Particles", Proceedings of the international School "Enrico Fermi", Course CXVIII, ed. by E. Arimondo, W. D. Phillips and F. Strumia.

# BEAM CHOPPER FOR 750 KEV LEBT OF MMF LINAC

A.V.Novikov and P.N.Ostroumov

Institute for Nuclear Research of the Russian Academy of Sciences
60-th October Anniversary prospect 7a, Moscow 117312, Russia

*Abstract*

A travelling wave beam chopper for the 750 keV $H^+$, $H^-$ ions of INR Linac is described. The chopper consists of a helix and a ground plate. The latter serves as a beam absorber which allows operation with a deflecting voltage below 4.5 kV. The chopper aperture can be varied from 2 to 6 cm, the plate length is 80 cm. The ion beam with unnormalized emittance ~8 π·cm·mrad is deflected and absorbed at the water-cooled ground plate. Available chopped beam pulse edges are less than 20 ns. A special shape of ground plate is used in order to depress the secondary electron emission arising from proton beam deflection. The deflecting plate structure and electronic circuits are presented, and theoretical and experimental results are discussed.

## 750 KEV $H^+$, $H^-$ TRANSPORT LINE OF MMF LINAC

The neutron experiments at the Moscow Meson Factory (MMF) and the MMF proton storage ring operation need a device for a creation of beam time structure. Travelling-wave chopper for 750 keV $H^+$, $H^-$ ions in the MMF transport line has been developed and installed on the LEBT. The MMF chopper consists of a helix and a ground plate. The use of the ground plate permits ion beam absorption directly inside the chopper [1,2]. Therefore no additional beamstop is needed. In addition the chopper has only one electronic modulator. The chopper deflects 750 keV ion beam with the emittance ≤8 π·cm·mrad with pulse rise and fall times less than 20 ns. The chopper consist of 80 cm plates and occupies 90 cm along the beam line.

The chopper is located downstream of the high voltage column in the first part of the beam transport line to protect a transport line equipment and especially diagnostic equipment that makes direct contact with the beam, from damage during accelerator commissioning. The charged particle current in the first part of the MMF is a train of pulses ~100 μs long repeated at 50 Hz containing 200 mA. This corresponds to 1.5 kW as several macroimpulses are deflected into the absorber. The injected beam unnormalized emittance is 8-10 π cm mrad, its transverse diameter is about 5 cm and this complicates considerably the situation with the beam deflection and particularly with fast chopping over the beam current macroimpulse. All of these have demanded a creation of a special device for a macroimpulse deflection, an absorption and a fast chopping.

To measure the beam microstructure a special wideband Wall Current Monitor (WCM) has been designed and installed downstream of the $45^0$ bending magnet. Bending magnet operates like a particle separator so undesirable ions flowing from the injector are reduced.

## DEFLECTING PLATES

Chopper deflecting plates are placed into a vacuum chamber. There is a possibility of changing a distance between upper spiral plate and lower ground one. The deflecting structure scheme is shown in Fig.1.

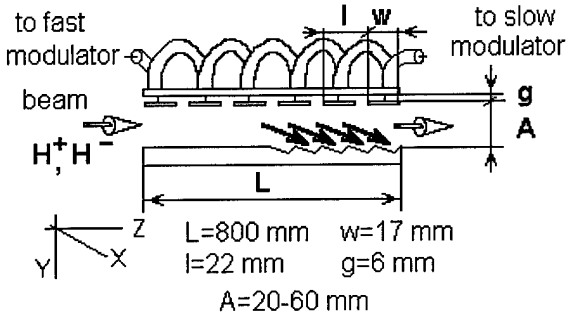



Figure 1 Scheme of deflecting plates structure

The aperture (A) can be changed from 20 to 60 mm without vacuum violation by a manual actuator during chopper commissioning to achieve optimum conditions of the beam deflection. The upper plate represents a train of spiral-like connected strip and coaxial lines with a 75 Ω wave resistance hence the wave propagation along beam line equals a beam velocity v= βc, where β= 0.04 (750 keV beam), c is the speed of light in vacuum. This field moving together with the particles deflects them to the lower ground plate. The deflected particles are absorbed at the ground plate.

0-7803-4376-X/98/$10.00 © 1998 IEEE

The lower plate is made from metal and water-cooling is provided for heat irradiation. The special lugs are made to decrease deflected beam angle of incidence and to prevent secondary electron emission from the surface. For small angles of incidence (θ) an amount of a secondary electron production is proportional to $1/\cos^4(\theta)$ [3]. A deflecting field for positive particles also is an accelerating field for electrons. So all secondary emissioned electrons get to the upper plate. This can change the deflecting field and even damage a deflecting voltage power source. We found there is no influence of secondary electrons on this chopper operation with relatively high beam power: beam energy is 750 keV, beam current is 200 mA with 100 μs pulse length at 50 Hz. Using absorber plate allows to have small aperture of the chopper and only a 4.5 kV modulator. Also this minimises the electronic equipment considerably.

The electric field distribution inside deflecting plates in a quasi static approximation can be obtained by means of a Fourier analysis:

$$E_y(r,t)=\sum_m A_m(\omega_m)\sum_n K_n(r)\cdot\cos(\omega_m t+\varphi_m+\varphi_n), \quad (1)$$

where $A_m(\omega_m)$, $\varphi_m$ are amplitude, phase of a frequency domain $\omega_m$ in Fourier-series expansion, $K_n(r)$ and $\varphi_m$ are the influence coefficient and phase from the n-th strip to the point with a radius-vector r(x,y,z). For $K_n(r)$ with x= 0 (for simplicity) one can obtaine the following expression (see Fig.1):

$$K_n(r)=\frac{\sigma}{2\pi\varepsilon_0}\sum_{i,j=0,1}\left\{(-1)^i\operatorname{arctg}\frac{(z-nl+(-1)^i w/2)l}{2(2jA-(-1)^j y-g)R_{ij}}\right\}, \quad (2)$$

where $R_{ij}=\sqrt{(z-nl+(-1)^i\,w/2)^2+(2jA-(-1)^j y-g)^2+(l/2)^2}$,

where σ is the surface charge density of n-th plate, $\varepsilon_0$ is a permittivity of vacuum. (2) shows the influence superposition of the n-th strip and its reflections from metallic surfaces. σ can be expressed from a deflecting voltage U according with [4]:

$$\sigma=\varepsilon_0 w_{eff} U/wg,\ w_{eff}=w\left[1+1{,}735(w/g)^{-0{,}836}\right], \quad (3)$$

Summing (2) for different strips n one can get a static deflecting electric field distribution. The corresponding distributions along with Z and X axes are shown in Fig.2, U/A represents an electric field of a flat condensor with the same aperture.

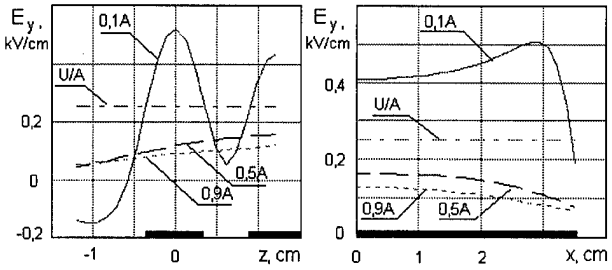



Figure 2 Electric field distribution along with Z and X axes for different value of Y over an aperture

Using a Fourier-series expansion of an input signal, one can calculate dynamic characteristics of the deflecting field at any point between the deflecting plates with help of above expressions. Corresponding calculations for MMF transport beam line show that for deflecting structure parameters in Fig.1 and aperture A=4 cm, the deflecting electric field intensity rise and fall times can not be more than 10 ns. However the beam rise and fall times can be much smaller that the rate of icrease of the deflecting voltage. This is one of principal advantages of the described deflecting structure.

## ELECTRONIC CIRCUITS

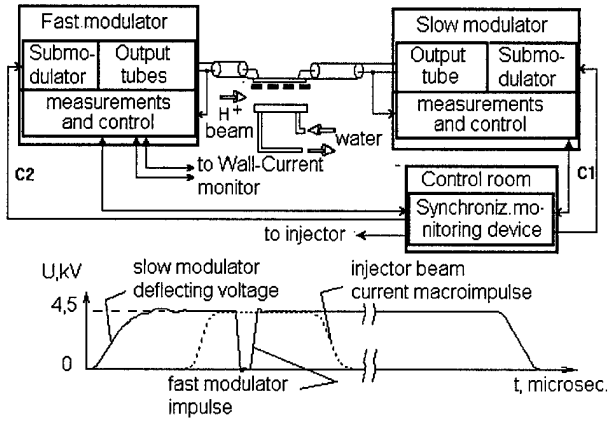



Figure 3 Electronic circuits block diagram

The electronic circuits block scheme is shown in Fig.3. Since only one plate has a special spiral structure and the other one always has a ground potential, only one modulator is needed for time microstructure creation. It is the fast modulator shown in Fig.3 used for this purpose. The slow modulator serves for a beam macroimpulse deflection to implement an emergency fast beam stop and control the average beam intensity by means of deflection of a part of beam macroimpulses. These functions could be realised with help of the fast modulator but it is difficult to overlap a duration time range from few nanoseconds to few hundred microseconds. The fast modulator overlaps a range from few nanoseconds to 5

microseconds with 10 ns rise and fall times. The slow one operates with 400 μs duration, 20 μs edges and up to 5 kV impulses, usually 4- 4,5 kV is used.

If a positive (for $H^+$) or negative (for $H^-$) voltage is applied to the upper plate charged particles are deflected and absorbed at the lower ground plate. A beam goes through the deflecting structure without an absorption if no voltage is applied. It is necessary to mention that a special two level fast protection system (deflecting voltage and syncronization shifting) was designed and realised on a base of the beam control device (see Fig.3) which monitors and synchronises the operation of the injector and two chopper modulators.

The slow modulator serves for the fast modulator like an anode voltage power supply, so the upper plate is on the anode circuit of the fast modulator output tubes. The GI-30 (impulse generator) tubes are used. They do not need a water cooling, are compact enough (about 10 cm) and each of them provides an impulse current more than 10 A with a 5-10 ns pulse edges. Four tubes in parallel connection are used at the output circuit of the fast modulator. To compensate a rest voltage of an open tube a 500 V negative bias power source is applied to a tube cathode.

A matching circuit on a slow modulator cable terminal has been included in order to prevent reflected wave propagation and slow modulator signal oscillations. The corresponding circuits are shown in Fig.4.

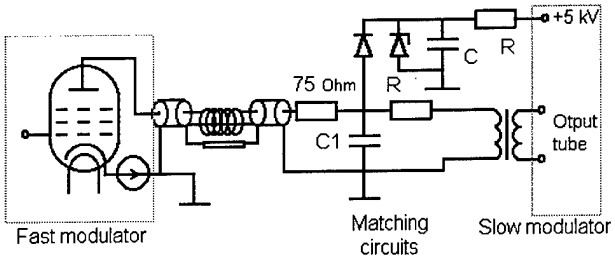



Figure 4 Matching circuits

The capacity C1 value matches the pulse duration from the fast modulator. This value has been chosen to overlap the fast modulator possibility (up to 5 μs). No matching circuits are need at the fast modulator cable terminal, so as it is not important for slow waves with 20 μs pulse edges and moreover it would double the power dissipation.

A specially designed detector with a wide frequency range from 20 kHz to 1 GHz to measure the continuous 750 keV proton beam impulses with a time duration up to 5.0 μs and pulse edges about 20 ns is used. The wall-current monitor (WCM) was created for these measurements. A shape of the chopped beam current impulse is shown in Fig.5.

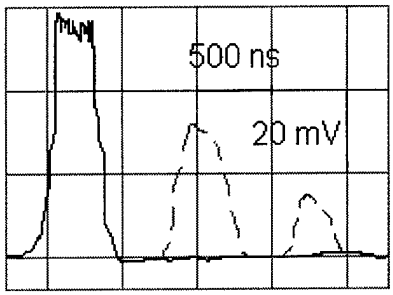



Figure 5 Wall-current Monitor signal from $H^+$ beam

The dash line represents the shape of tail beam current impulses which would occur together with a single impulse (solid line) due to a reflected waves if no matching circuit were used. However the WCM does not measure the absolute beam current amplitude of the chopped beam because of its frequency dependence. This estimation can be made with help of neutron beam loss monitors or by means of a Faraday cup signal integration. One can estimate a correlation between full and chopped beam current amplitudes from knowing the shape and an amplitude of a full beam current macroimpulse also a shape of a chopped one (from WCM) and analysing the values of loss monitors or a Faraday cup in both cases. The analysis shows that the chopped beam current amplitude is at least 95% of a full one.

## CONCLUSION

The chopper operates at the proton beam transport line. A number of physics experiments with impulse neutron sources have been done successfully at the MMF. The design of such device for the $H^-$ beam transport line is under progress.

## ACKNOWLEDGEMENTS

Authors gratefully acknowledge support and interest to this work from Prof. S.K.Esin and Prof. Yu.Ya.Stavisskii (INR, Russia). We are grateful to Y.Yin (TRIUMF, Canada) for co-operation during wall-current monitor design.

*References*

[1]. Novikov A.V. et al, XIV Accel.Conf., Protvino, v.1, 1994 (in Russian).
[2]. Lunsford J.S. et al, IEEE Trans on Nucl. Science, 1983.
[3]. Bronstein I.M. et al, Secondary electron emission, Moscow, Science, 1969 (in Russian).
[4]. Handbook of SHF stripline devices calculation and design, Moscow, Radio i Sviaz, 1982 (in Russian).

# TEST OF DUOPLASMATRON WITH COLD CATHODE FOR CW OPERATION

A. Kolomiets, B.K. Kondratiev, V.I. Turchin
Institute for Theoretical and Experimental Physics, Moscow, Russia

*Abstract*

Pulse duoplasmatron with cold cathode used at preinjectors of ITEP proton linacs has been tested for generation of dc proton beam. The operation of duoplasmatron was studied experimentally with low currents of discharge. The test bench experiments allowed to modify construction of pulsed ion source for stable dc operation with high life time. The ion source generated dc beam of protons with current ≈12 mA at 30 kV.

## 1 INTRODUCTION

Main type of the ion source (IS), using at ITEP's ion linacs, is the duoplasmatron with a cold cathode. Originally this IS was developed for I-2 linac - the ITEP proton synchrotron injector [1]. This IS showed high reliability and easy maintenance during many years. It provided operation of I-2 linac with high beam quality on its output. The amplitude of the accelerated pulse protons current from the source achieved 1 A with normalized emittance - 0.4 - 0.8 cm·.mrad. The same source has been used at "Istra" linac and also provided excellent quality of the pulse beam. A version of the IS with a cold cathode was used in ITEP also for production of both light and heavy ion beams with low charge state. The life time of the duoplasmatron with a cold cathode in pulse operation is determined by life time of pulse shatter installed on ion source outlet for decreasing of gas flow in the preinjector vacuum chamber and practically does not depend on cathode time operation [1].

The investigation of possibility of use the duoplasmatron with a cold cathode for direct proton beam production in framework of ITEP's feasibility study of high power linac for waste transmutation (ISTC project N 17) was carried out. Choice of duoplasmatron as a source for direct current beam production is caused by the following reasons: it has very simple and cheep construction; it is well studied ion source which capable to provide pulse intense proton beam with high brightness; it does not require the complicated and expensive power supply.

## 2 EXPERIMENTS DESCRIPTION

The results of study of cold cathode IS operation in pulse mode and beam parameters are given in [2]. In order to investigates operation in dc special test bench has been built. Its scheme is shown in Fig. 1. It consists of vacuum chamber (1), pumping by two turbomolecular pumps with total pumping speed 1000 l/s, The operation pressure in the chamber was about $10^{-4}$ Tore.

The chamber was provided by three-electrodes ion - optics system (3) made from stainless steel with 20 mm aperture. The optics was designed for 30 kV extracting voltage. The electrodes of ion-optics can change their position respectively to ion source.

Current collector (2) was used for beam current measurements. It represents copper cylinder with inner diameter 90 mm and 30 mm depth. It is placed at 350 mm distance from ion source. The ion source installed on insulator flange (4).

In contrast to its pulsed prototype the experimental ion source has a additional cooling system for the cathode, intermediate electrode and anode. The two cylinders or multicylinders cold cathodes were installed in it. The cathodes were manufactured from molybdenum instead copper as it took place in IS I-2.

The construction of the duoplasmatron is schematically shown in Fig. 1. It consists of the copper anode (6); with outlet (7) with aperture 0.8 mm. The intermediate electrode (8) is connected to power source (11) placed at the high voltage platform (13). The power supply (12) provides discharge current in the range from $10^{-3}$ to 5 A. The solenoid (9) creates the magnet field in the gap between the anode - intermediate electrode. The hollow metal cold cathode (10) with gas channel is installed into the intermediate electrode. Different construction of cold cathodes could be installed in this source. The cathode voltage is fed by power source (12) placed at the high voltage platform, which potential is equal to the accelerating voltage. The voltage is supplied from the industrial high-voltage power source. The voltage can be changed from 0 to 50 kV.

The designs of the cathodes used in tests are shown in Fig. 2 and Fig. 3. The cathode shown in Fig. 2 consists of two coaxial hollow cylinders, placed at a common base. In contrast to cathode in Fig. 2 the cathode shown in Fig. 3 consists on 7 or 13 thin-walled hollow cylinders placed circularly with respect to the axis, which wall thickness and depth of hollow were determined by condition to get maximum hollow cathode effect [3, 4]. During experiments the cathode material was varied. There were used copper or molybdenum as material for cathode. The hydrogen gas was supplied to ion source.

Thermal and radioactive loads on cathodes materials during experiments were investigated. The stability of different electric discharges was tested in dependance on cathode materials and design at direct current. Efficiency of ion generation in aria of emission was evaluated. The

0-7803-4376-X/98/$10.00 © 1998 IEEE

peculiarities of the ion source with cold cathode operation under steady electric arc were studied. The experiments showed that under gas pressure 1.5-2.0 Tore the arc is ignited and is stable. Maximum extraction of ions was provided. at negative voltage 280-300 V on intermediate electrode (8) (Fig. 1).

Current of discharge was varied in our experiment in the range 5.0 - 30.0 mA. The current value was controlled by power supply unit (12) Fig. 1. In this case maximum current of extracted ion beam depended to a certain extent on material and construction of the cathode. The maximum ion beam current has been achieved with cathode shown in Fig. 3. This cathode consists of 13 copper cylinders. The maximum value of the proton current was 0.3 mA at extracted voltage 25 kV. The initial voltage applied to discharge gap was 2.0 - 2.2 kV. No erosion of the cathode or ion source electrodes after 30 hours of operation was observed.

Ion beam current has practically no dependence of cathode construction at discharge current 0.4 - 0.5 A. The ignition of the discharge occurred at initial voltage 2.4 - 2.5 kV. The steady value of discharge voltage was 500 - 700 V. This type of discharge can be considered as smolder one[4]. Under above mentioned conditions the life time of copper cathodes did not exceed 10 - 12 hours. They had remarkable destroying of the construction after this period. The cathodes made from molybdenum had no destroying after operation during the same period. The ion current 9.0 - 10.0 mA has been obtained in test experiments using molybdenum cold cathode. The construction of the cathode is shown in Fig. 2.

The installation in ion source of molybdenum cold cathode with construction shown in Fig. 2 allowed to achieve proton beam current of 12 mA at 30 kV extracting voltage. The total electrical power consumption of the ion source was about 500 W. The discharge current was very stable during all period of operation. The instability of the current value was ·≤5%. The pressure in the vacuum chamber of test bench was $10^{-5}$ Torr.

## 4 CONCLUSION

The carried out experiments shows that duoplasmatron with cold cathode can be used for generation of intense proton beam at CW operation. The developed design of the source produced in experiments proton beam with current about 10 mA during period several tenth of hours without any damages of the source parts. Power consumption did not exceed 500 W.

The results of experimental study of cold cathode duoplasmatron on CW operation allow to conclude that this type of duoplasmatron is suitable for using in CW high power linac. The advantages of this ion source are very simple and cheep mechanical design as well as power supply, stability of proton beam parameters and long life time. The main drawback of the ion source is high pressure of gas in discharge chamber and, therefore, high load on vacuum system of the preinjector.

## REFERENCES


[1] V.A.Batalin, A.A. Kolomiets, B.K. Kondratiev, R.P. Kuibida, "Duoplasmatron with cold cathode", "Pribory i Technika Experimenta", N 2, 1975, p.21.

[2] B.K.Kondratiev, V.I.Turchin. "Proton source for linacs", Pre-print ITEP 51-9, 1992.

[3] "Cold cathodes", Ed. M. Elinson, Sov. Radio, Moscow, 1974.

[4] V.L.Granovsky . "Electric current in gas", "Nauka", Moscow, 1971.

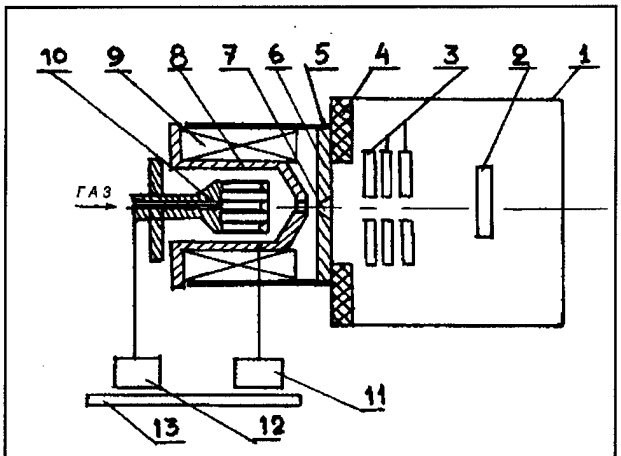




Fig.1. Sceme of IS with cold cathode and test bench

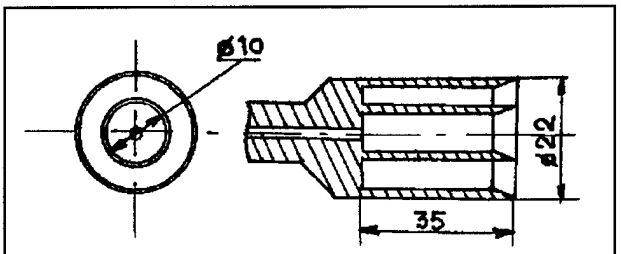



Fig. 2. Coaxial cathode

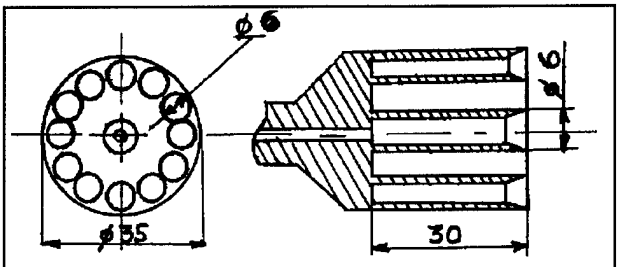



Fig.3.Multicylinder cathode

# A PULSED ION SOURCE FOR THE IUCF COOLER INJECTOR SYNCHROTRON

V.P. Derenchuk, R.R. Kupper, H.R. Petri, G.P.A. Berg, R.J. Brown, W.R. Fox, D.L. Friesel, W. Hunt, W.P. Jones, W.R. Lozowski, Indiana University Cyclotron Facility, Bloomington, IN 47408

*Abstract*

A pulsed source of $H^-$ ions has been constructed with minimal cost and is currently being used for commissioning of the Indiana University Cyclotron Facility (IUCF) Cooler Injector Synchrotron[1]. A commercially available duoplasmatron, previously used with the IUCF cyclotrons, was modified for pulsed operation and has produced 25 keV $H^-$ ion beams of up to 1 mA in an emittance of less than 0.38 $\pi$-mm-mrad normalized (80%) and can operate up to 10 Hz with 50 $\mu$s to 4 ms pulse length. A simple and economical pulsed high-power MOSFET circuit is used to drive the arc and the gas valve. The beam transport line to the 7 MeV RFQ-DTL[2][3], features an Einzel lens doublet immediately upstream to match the beam from the source. The design, development and performance of the ion source and beam transport line is presented.

## 1 INTRODUCTION

The IUCF 'Cooler Injector Synchrotron' (CIS), a 200 MeV fast cycling synchrotron (up to 5 Hz), is being commissioned at IUCF and will be used to inject beam into the IUCF Cooler ring[3]. In order to save on cost, it was decided to commission the system using an existing DC $H^-$ duoplasmatron ion source, modify it for pulsed operation and to design and build in-house a 25 keV beam transport and diagnostics line. The RFQ was defined as having an acceptance of $\approx$1.0 $\pi$-mm-mrad (normalized to $\beta^*\gamma$) with Twiss parameters of $\alpha$ = 0.87, $\beta$ = 0.0137 mm/mrad, and $\gamma$ = 128.2 mrad/mm. Beam pulses of 300 $\mu$A, into the RFQ acceptance, for 300 $\mu$s duration at 1 Hz to 5 Hz repetition rates were required.

The duoplasmatron was modified to operate in a pulsed mode by increasing the diameter of the anode aperture and adding a pulsed gas valve. Pulsed power for the arc and gas valve is supplied by a simple and economical MOSFET based circuit with a fast rise time and the capability to easily adjust the pulse length and power level.

An Einzel lens doublet was designed to match the duoplasmatron beam to the acceptance of the RFQ. Ray tracing calculations were performed to test the design and subsequent emittance measurements verified the calculations. The emittance scanner is a moving slit and harp assembly that scans across the beam. Figure 1 shows the layout of the ion source and low energy beam transport line.

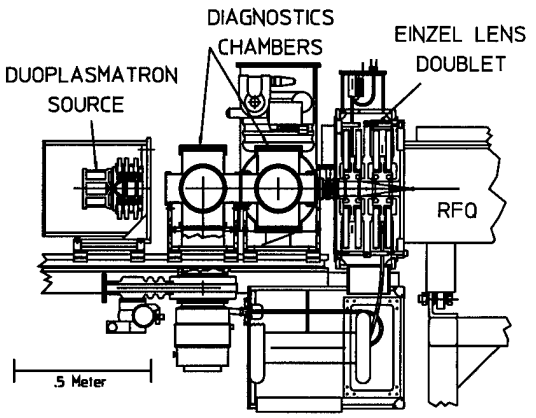



Figure 1: Pulsed $H^-$ ion source and low energy beam transport line layout showing the Einzel lens matching doublet.

## 2 HARDWARE

### 2.1 *Pulsed $H^-$ Ion Source*

One of the first reliable techniques of producing a pulsed low-emittance milliampere beam of $H^-$ ions was by pulsing a negative hydrogen ion duoplasmatron[4]. In order to save cost and development time associated with starting up a source with technology new to IUCF, it was decided to modify one of the two negative ion duoplasmatrons previously used in DC mode.

The conventional General Ionex Duoplasmatron[6] was set up to operate in the pulsed $H^-$ mode. Little modification to the source was necessary other than the use of an extraction aperture of 1.25 mm to increase the extracted beam intensity and allow for faster gas pumping from the large source volume. Originally, the duoplasmatron was designed to run at a maximum of 2.0 A of DC arc current. Due to the low duty factor, operation of the arc with a peak current of 40 A or greater is possible. During the CIS commissioning phase, the source is operated at 5 Hz and with a peak arc current of $\geq$35 A.

An automobile fuel injector gas pulser was first used to pulse hydrogen gas into the source. The fuel injector was very inexpensive but proved to be too variable from pulse to pulse. These valves also tended to leak slightly when closed which increased the average gas load. The fuel injector was later replaced with a General Valve Corporation 'Series 9 High Speed Solenoid Valve'[5] fitted with an optional 3 $\Omega$ solenoid. Using this valve and a MOSFET drive circuit, a gas valve repetition rate of over 100 Hz was demonstrated with pulse-to-pulse throughput variations no larger than 5% and a FWHM less than 160 $\mu$s. For oper-

0-7803-4376-X/98/$10.00 © 1998 IEEE

ation with the small aperture and large volume of the duoplasmatron, pulsed gas operation could benefit the beam intensity only up to a maximum repetition rate of 5 Hz.

### 2.2 *Pulsed Power Circuit*

A fast (few $\mu$s rise and fall time) MOSFET circuit was developed to supply the pulsed power needed for the gas valve drive coil and the arc current. Although the two loads are significantly different in character, the gas valve has a large inductance and the arc has an initially high impedance which drops to nearly the ballast resistance after the arc strikes. In both cases it is desirable to stabilize and control the current and easily adjust the pulse length. Both circuits, mounted in a 25 kVdc platform, provide excellent stability, reliability and immunity from source spark downs.

The driver circuit for the MOSFET receives its on or off signal from a low cost plastic fiber optic line. The driver itself limits the maximum on time and the maximum duty cycle to prevent damaging the power MOSFET as the peak power for valve operation exceeds 250 W. For the maximum arc current of 50 A and 300 V the peak power of the arc circuit is 15 kW. The arc drive circuit and the MOSFET switch are enclosed in a Faraday shield with full protection on the two external wire connections.

Power for driving the valve is derived from a small 75 Vdc regulated power supply. In this case, the MOSFET switch has active current limiting at 4 A. When the drive is removed, the inductive kickback is clamped by a 150 V power zener.

Power for the arc circuit (Figure 2) is derived from a voltage doubler with 120 VAC input and an 1800 $\mu$F storage capacitor on the output, resulting in about 300 Vdc, unregulated. The switch is in series with a current limiting ballast resistor and a 100 $\mu$H bifilar wound air-core inductor.

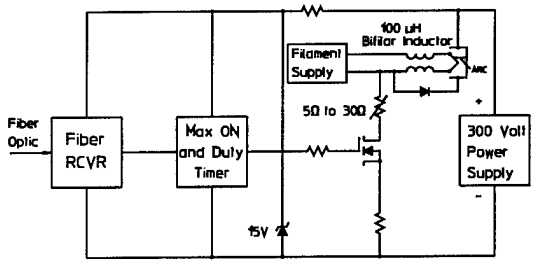



Figure 2: Circuit diagram of an inexpensive and compact pulsed power source for the duoplasmatron arc. The peak current and pulse length is easily adjustable.

### 2.3 *Emittance Scanner*

The emittance measuring system[7] consists of a 48 wire harp of 0.5 mm wire spacing 113 mm downstream of a 0.5 mm slit. The system is PC controlled and moves the slit and harp together in step sizes of 0.25 mm or 0.5 mm. Since the beam is pulsed it is necessary to collect data for a full scan over many beam bursts. For example, in taking 0.25 mm steps across a 3 mm wide beam a completed emittance scan will contain at least 12 beam profiles, each from a separate beam pulse. The pulse-to-pulse reproducibility is usually excellent but there is also a provision to signal average several beam pulses for each scanner position. The PC moves the slit and collects and stores the data from which ray angles as a function of position in the beam are then calculated off line.

### 2.4 *Beam Transport Design*

The beam transport line consists of an Einzel lens whose first ground electrode is also the extraction electrode of the ion source. An Einzel lens matching doublet is mounted physically onto the RFQ entrance flange, about 110 cm downstream from the ion source. Horizontal and vertical magnetic steering elements and a diagnostics chamber occupy the intermediate section of the beam line. The diagnostics chamber contains a biased Faraday cup, a BeO scintillator, a single dimension 48 wire harp and has provision for mounting the emittance scanner.

The emittance from the duoplasmatron was predicted using a charged particle optics design program, EMP/TRAK[8]. This prediction was used as input for the design of the matching doublet. Several Einzel lens designs, including a triplet, were considered. The matching turned out to be easy enough that it was possible to reduce the number of lenses to two in the final design. The requirement of a strongly convergent beam at the entrance of the RFQ was satisfied with voltages of 20 kV and 60 kV on the upstream and downstream lenses respectively. The lenses were finally designed to operate at up to 40 kV and 100 kV if necessary. Beam properties before and after the matching doublet were measured using a biased Faraday cup and the emittance scanner.

## 3 SOURCE OPERATION

### 3.1 *Source Optimization*

To optimize the peak beam intensity, it was found that the timing and width of the arc voltage and gas valve drive pulse were effective parameters. A timing program allowed one to vary pulse frequency, gas valve delay, gas valve duration arc delay and arc duration. Pulse rate, gas valve duration and arc duration were found to be the parameters that had the greatest effect on beam intensity. Output current was optimized at various pulse rates and combinations of gas valve and arc duration and delay. Other parameters varied were; the position of the intermediate electrode with respect to the extraction aperture, pinch magnet current, and the arc current.

The highest peak beam intensities occurred at 1 Hz or less for a gas valve drive pulse duration of 238 $\mu$s and an arc duration of over 3.0 ms, see Figure 3 for example. This optimal condition can produce a beam intensity of over 1.0 mA. This behavior is partly due to the ability of the pumping system to efficiently clear out the gas in the ex-

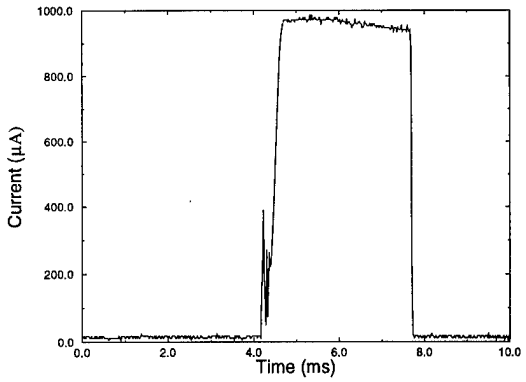



Figure 3: Beam pulse measured on a Faraday cup with ion source conditions typical for 1 mA operation.

traction region of the source before admitting a new pulse, decreasing stripping losses.

| Rep Rate (Hz) | 1 | 5 | 10 |
|---|---|---|---|
| Pulse Length (ms) | 3.5 | 1.0 | 1.0 |
| Peak Beam ($\mu$A) | 950 | 620 | 350 |
| Arc Current (A) | 40 | 40 | 40 |
| Average Pressure ($10^{-5}$mbar) | 4.7 | 6.7 | 6.7 |

In order to produce noise free, stable beam from pulse to pulse, it was necessary to start the arc in advance of the pressure maximum of the gas pulse. When the arc was struck in this starved mode, the source was less apt to spark and the beam flat top was free of 10 kHz to 60 kHz noise. Later runs were made with much shorter arc durations, on the order of 300 $\mu$s at 5 Hz and 10 Hz rates and 620 $\mu$A and 350 $\mu$A beam intensities respectively. Table I above includes some typical operating values after the addition of a second 500 l/s turbo molecular pump. Emittance measurements were taken with the single pump source configuration.

### *3.2 Emittance Measurements*

The goal of the emittance measurements was to ensure that the RFQ matching lenses were capable of providing beam within the RFQ acceptance for varying source conditions. In particular, the lenses were varied through the predicted values for best matching to the acceptance. A 'best fit' ellipse was calculated for each set of data and the 80% contour used to display the emittance envelopes.

Figure 4 shows a series of three data sets, C 106 to C 108, which refer to measurements in the horizontal plane where the lenses were adjusted through the calculated matching value. The measured beam fits well within the acceptance limits. The normalized vertical emittance was measured to be 0.38 $\pi$-mm-mrad and the horizontal emittance 0.21 $\pi$-mm-mrad.

The error in these measurements is due to a quantization error that arises from the fixed linear and angular steps in the emittance data. Also, the resolution is dependent on the slit width and the distance between the slit and the harp.

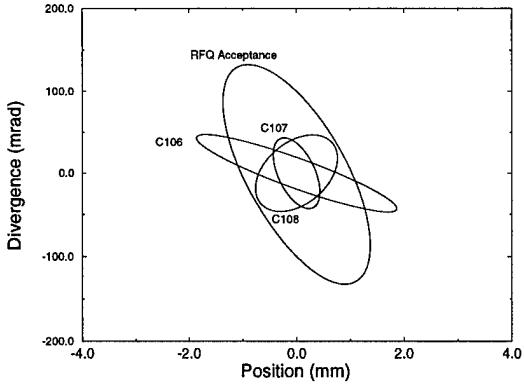



Figure 4: Emittance envelopes of the beam drifted from the emittance scanner back to the RFQ entrance for three settings of the matching lenses.

Using the mathematical formalism developed by Ludwig et. al.[9], it can be calculated that these measurements overestimate of the emittance area by about 25%. The plots are not corrected for this error.

Transmission measurements during initial operating tests of the RFQ-DTL have confirmed the expected matching[3].

## 4 ACKNOWLEDGMENTS

This research was supported by the Indiana University and NSF Grant PHY-93-147-83. It was also supported by many excellent technical and scientific staff not listed as authors on this paper. Without their help, this work could not be done.

## 5 REFERENCES

[1] D.L.Friesel and S.Y.Lee, 'Status of the IUCF Cooler Injector Synchrotron' this conference, 8B 5.

[2] 7 MeV RFQ-DTL was purchased from AccSys Technology, Inc., 1177 Quarry Lane, Pleasanton, CA 94566.

[3] D.L. Friesel, R.W. Hamm, 'Commissioning of the IUCF 7 MeV $H^-$ LINAC' this conference, 3W 31.

[4] M.A. Abroyan, G.A. Nalivaiko and S.G. Tsepkin, 'Pulsed Source of Negative Hydrogen Ions', Soviet Physics-Technical Physics Journal, **17**(4), 690, October 1972.

[5] General Valve Corp., 19 Gloria Lane, P.O. Box 1333, Fairfield, NJ 07004.

[6] Peabody Scientific, P.O. Box 2009, Peabody, Massachusetts, 01960.

[7] M. Ball, V. Derenchuk, B.J. Hamilton, 'Beam Diagnostics in the Indiana University Cooler Injector Synchrotron', AIP Conf. Proc. **390**, 544.

[8] EMP 3.0 and TRAK 2.0, Field Precision, P.O. Box 13595, Albuquerque, NM 87192.

[9] T. Ludwig, K. Volk, W. Barth and H. Klein, 'Quantization Error of Slit-Grid Emittance Measurement Devices', Rev. of Sci. Inst. **65**(4), 1462, April 1994.

# MECHANICAL ENGINEERING OF A 75-keV PROTON INJECTOR[‡] FOR THE LOW ENERGY DEMONSTRATION ACCELERATOR

L. D. Hansborough, D. J. Hodgkins, E. A. Meyer, J. D. Schneider, J. D. Sherman,
R. R. Stevens, Jr., and T. J. Zaugg, LANSCE Division, Los Alamos National Laboratory
Los Alamos, New Mexico 87544.

*Abstract*

A dc injector capable of 75-keV, 110-mA proton beam operation is under development for the Low Energy Demonstration Accelerator (LEDA) project at Los Alamos. The injector uses a dc microwave proton source which has demonstrated 98% beam availability while operating at design parameters. A high-voltage isolation transformer is avoided by locating all ion source power supplies and controls at ground potential. The low-energy beam transport system (LEBT) uses two solenoid focusing and two steering magnets for beam matching and centroid control at the RFQ matchpoint. This paper will discuss proton source microwave window design, $H_2$ gas flow control, vacuum considerations, LEBT design, and an iris for beam current control.

## 1 INTRODUCTION

At Los Alamos, the cw LEDA radio frequency quadrupole (RFQ) accelerator[1] has been designed to produce a 100-mA, 6.7 MeV beam from a 75-keV, 110-mA dc proton injector beam. Design of the LEDA proton injector originated at Los Alamos in late 1993 when a prototype injector was designed and subsequently fabricated. This injector comprises a dc proton source and a dual solenoid low-energy beam transport (LEBT) system which has been extensively tested and found to deliver LEDA RFQ quality beams[2]. A LEBT, suitable for flexible beam matching to the LEDA RFQ, will first be tested with a 1.25 MeV cw RFQ brought from Chalk River Laboratories (CRL)[3]. In following sections, we present the mechanical design features of the proton source and accelerating column, injector reliability development, discussion of a 2.5-m-long LEBT for initial operation of the LEDA RFQ, and a final 2.8-m-long LEDA LEBT which incorporates beam duty factor control.

## 2 PROTON SOURCE AND ACCEL COLUMN

The microwave proton source, originally developed at CRL[4] for the 50-keV Chalk River Injector Test Stand (CRITS), has been further developed to operate at higher beam energy, current, and microwave power. Figure 1 illustrates the configuration of the ion source, new high voltage (HV) column, solenoid magnet insulator, and

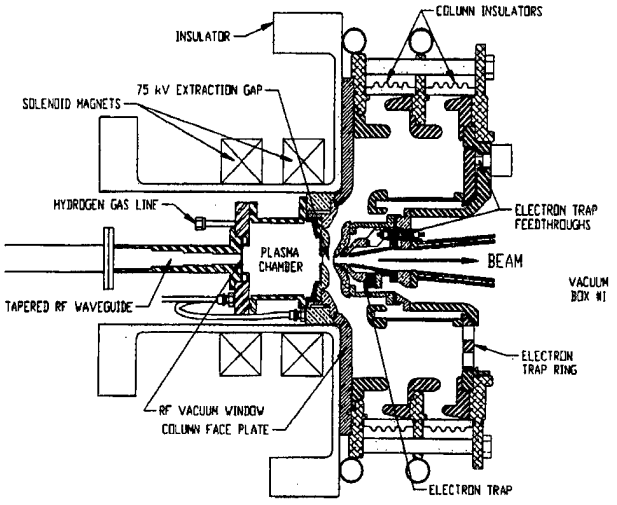



Figure 1. LEDA proton source and HV column.

extraction geometry. Figure 2 shows an exploded view of the microwave vacuum window assembly. All source electronics operate at ground potential, and beam extraction is across a single 75 kV gap. Extraction geometry is based on the Fusion Materials Irradiation Test (FMIT)[5] accelerator extractor. The extractor electron trap at -1.5 kV prevents backstreaming electrons from reaching the source. A ground potential electrode then terminates electric fields thus establishing beam space- charge neutralization.

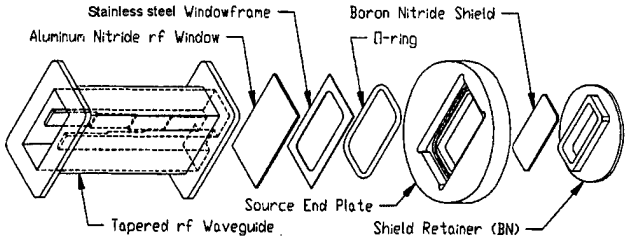



Figure 2. LEDA proton source microwave window.

Figure 3 shows the gas flow control system with a mass flow controller at ground potential. A variable leak valve keeps the pressure in the tube near atmospheric to

[‡] Work supported by the US DOE, Defense Programs.

0-7803-4376-X/98/$10.00 © 1998 IEEE

prevent arcdowns through the tube. System response is a function of gas flow rate, pressure, and volume between the flow controller and variable leak valve. Use of a

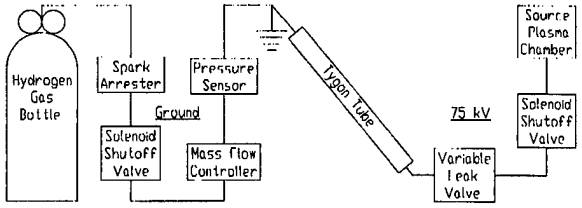



Figure 3. Gas flow control for the LEDA ion source.

pressure sensor having an internal volume of only 0.1 $cm^3$ enabled a minimum 3 $cm^3$ test system volume. For a step change between 0.095 and 0.101 T-l/s, the test system achieved an average time constant of 17.5s. The more complex gas system in use on the LEDA ion source has an approximate 6 $cm^3$ volume, but normally operates at 0.05 T-l/s resulting in approximately the same time response as the test system.

The HV column insulators are 95% alumina, and are vacuum sealed by o-rings under compression by 12 cryogenic grade G-10 rods. Internal vacuum-ceramic-metal electron emitting "triple points" are shielded by stainless steel inserts. Average beam power density in the nominal 4 cm diameter beam is 775 watts/$cm^2$; cooling protects internal vacuum system components from heating by spilled beam. A 100 mA proton beam current causes a 0.01 T-l/s gas load at a beam stop, and the hydrogen gas flow may be up to 0.09 T-l/s during source start up. Vacuum pumping of the HV column region is through a circular electron trap plate into diagnostics/vacuum box #1 equipped with a 2500 l/s turbomolecular pump.

## 3 INJECTOR RELIABILITY DEVELOPMENT

Two failure mechanisms of microwave window have been observed: (1) failure of the o-ring seal after less than 40 hours of operation, and (2) thermal fracture of the aluminum nitride (AlN) window. Failure mode (1) may arise from microwave and/or ion source-plasma induced heating of the o-ring. A solution was found by adding a 0.8mm thick stainless steel frame glued to the AlN window. Use of a pressure jig ensures an intimate Torr Seal bond between the stainless and AlN. Tight assembly tolerances then result in a metal to metal seal surrounding the o-ring (cf Fig. 2). The microwave window is now capable of indefinite operation at greater than 1 kW microwave power.

Rf window failure mode (2) is a product of operation at higher beam energies. Proton source rf efficiency is highest with a single AlN microwave window; however, back streaming electrons focused by the solenoidal field impact on a small point (approximately 1mm diameter) in the center of the window. Stress in the pinhole from electron impingement after an arc down can result in fracture of the AlN. A 1.3 mm thick pane of boron nitride (BN) shields the AlN window and does not measurably reduce the rf efficiency. The pinhole erosion rate is a function of mA-hours, and the 1.3 mm thick shield is expected to have a 400 hour lifetime under operating conditions. Tests are underway to further this lifetime by increasing the BN thickness, and investigating the use of Shapal SH-15 AlN (with excellent strength in compression and over three times the thermal conductivity of BN).

Initial operation of the new HV column was compromised by an unacceptable arcdown rate. External arcing problems were eliminated by modifications to the solenoid magnet insulator, a new solenoid magnet stand, addition of corona rings, a revised G-10 compression rod design, and careful routing of the water resistor lines. Internal arcing was eliminated by moving the extractor electron trap voltage feedthrough to a position within the extractor assembly. However, this relocation caused a glow discharge to occur near the extraction gap which unacceptably hindered injector operation.

Elimination of the glow discharge was successively accomplished by (1) reducing the magnetic field across the extraction gap by installation of an iron HV column face plate, (2) shielding the "triple points" from beam-produced x-rays, (3) improving the vacuum in the extraction gap by a new electron trap ring which increased the vacuum conductance by a measured factor of 3.2 (vs. a calculated factor of 4.1), and (4) modifying electron trajectories toward the extraction gap by an electron trap shield around the extractor.

During injector testing, an oil contamination incident occurred. Because of a control system problem, the roughing line valve to vacuum box #1 began to repeatedly cycle and introduced a large amount of rough pump oil into the vacuum box. Residual gas analysis indicated that conventional cleaning techniques did not remove all the oil contaminant, and a complete disassembly of the vacuum box would be necessary unless another decontamination method were found. After operation of the source with an oxygen beam (less than 6 hours total run time), residual gas analysis showed the oil was reduced. An oil-free scroll roughing pump has been installed to ensure the injector remains oil free.

## 4 INJECTOR LEBT

For initial operation of the LEDA RFQ, a 2.5-m-long LEBT is being assembled. This LEBT will be tested with the 1.25 MeV cw CRITS RFQ and includes the present injector vacuum box #1, twin LEBT solenoid magnets, vacuum box #2 which contains a copper-swirl-tube plunging beam stop, and a small diagnostics box at the RFQ entrance. This LEBT will be fitted with a variable iris (Figure 4) for beam current control. Eight internally-cooled, flat copper plates form the iris. As the drive ring is rotated, a camming action causes the iris

aperture to vary. The flat plate design and copper construction limits the power absorption capability of the iris, but we estimate the life of the iris as adequate for tests with the CRITS RFQ and initial operation of the LEDA RFQ.

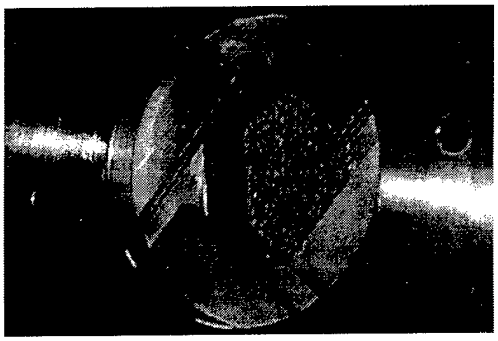


Figure 4. Beam iris developed for the LEDA LEBT.

Figure 5 shows a final 2.8-m-long LEDA LEBT[6]. A pulsed beam is required for LEDA RFQ commissioning tests, and two techniques for doing this are being investigated. This LEBT incorporates a kicker magnet to provide the capability to produce a pulsed beam. Vacuum box #2 provides the required drift length for the angled beam to hit the retracted beam stop. The plunging beam stop and beam iris are projected to have inclined faces of molybdenum and be capable of long operational life. Vacuum box #3 will be a mounted on the LEDA RFQ, and accommodates beam diagnostics, beam shields, an isolation valve to the RFQ, and a 1100 l/s turbomolecular pump.

## 5 CONCLUSIONS

Integrating the mechanical design features outlined above enabled a 168 hour endurance run (total run time excluding delays from electronic problems). This injector test met the LEDA beam availability requirement, and demonstrated a robust design. Table 1 shows the injector is capable of producing a proton beam of requisite quality for the LEDA RFQ. The first 2.5-m-long LEDA LEBT will be tested in mid-1997 and be ready for operation with the LEDA RFQ in early 1998.

Table 1. Summary of LEDA injector requirements and present status.

| Parameter | Required | Status |
|---|---|---|
| Energy (keV) | 75 | 75 |
| Current (mA) | 110 | 117 |
| Duty factor (dc) | 100 | 100 |
| Duty factor (pulsed) (%) | 1 (10Hz, 1 ms) | To be tested |
| Reliability (%) | 98 | 96 - 98 |
| Lifetime (hr) | >168 | 168 |
| LEBT exit emittance ($\pi$mm-mrad) | 0.20 | 0.20 |
| $H_2$ gas flow (T-l/s) | .04 -.10 | .05-.09 |

## REFERENCES


[1] L. M. Young, "An 8-Meter-Long Coupled Cavity RFQ Linac," Proc. of the 1994 International Linac Conference, Tsukuba, Japan, 178(1994)

[2] J. D. Sherman, G. O. Bolme, L. D. Hansborough, D. J. Hodgkins, M. E. Light, E. A. Meyer, J. D. Schneider, H. V. Smith, Jr., M. W. Stettler, R. R. Stevens Jr., M. E. Thuot, T. J. Zaugg, and R. Ferdinand, "Development of a 110-mA, 75-keV Proton Injector for High-Current, CW Linacs." Proc. of the 1996 International Linac Conf, CERN 96-07, Geneva, Switzerland, 701(1996).

[3] J. David Schneider, et.al. "Installation of a CW Radiofrequency Quadrupole Accelerator at Los Alamos National Laboratory." Proc. of the 1994 International Linac Conference, Tsukuba, Japan, 149(1994)

[4] Terence Taylor and Jozef F. Mouris. "An Advanced High-Current, Low-Emittance dc Microwave Proton Source." Nucl. Instrum. and Methods in Physics Res. A 336,1(1993).

[5] J. D. Schneider and D. D. Armstrong, "Electrode Shaping for Ion and Electron Extractors", IEEE Trans. On Nuclear Science, Vol. NS-30 (4), 2844(1983).

[6] H. Vernon Smith, Jr., J. D. Sherman, R. R. Stevens Jr. and L. M. Young. "Simulations of the LEDA LEBT $H^+$ Beam", these Conference Proceedings.

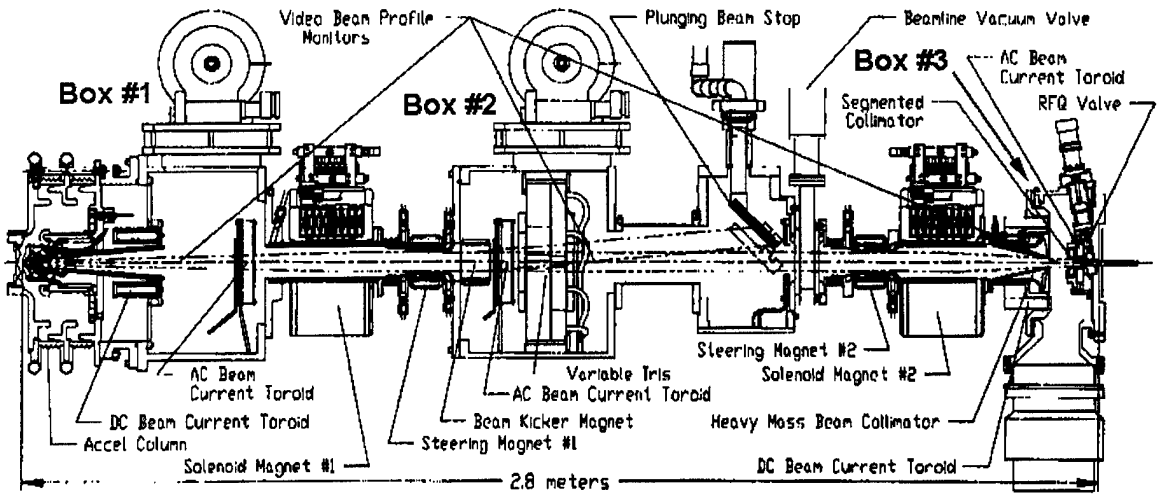




Figure 5. 2.8 m long LEDA LEBT.

# PERFORMANCE OF THE LANSCE H⁻ SOURCE AND LOW ENERGY BEAM TRANSPORT AT HIGHER PEAK CURRENT

C. Pillai, R. R. Stevens, D. H. Fitzgerald, R. W. Garnett, W. B. Ingalls, F. E. Merrill, L. J. Rybarcyk, and O. R. Sander, LANSCE Division, Los Alamos National Laboratory, Los Alamos, NM 87545.

*Abstract*

The Los Alamos Neutron Science Center (LANSCE) 800 MeV accelerator facility uses a multicusp-field, surface production ion source to produce H⁻ beam for delivery to the Proton Storage Ring (PSR) and to the Weapon Neutron Research (WNR) areas. The average current delivered to the short-pulse spallation target is nominally 70 μA. One goal of the present PSR upgrade project is to increase the average beam current to 200 μA. This will be accomplished by a combination of increased repetition rate (from 20 Hz to 30 Hz), upgraded PSR bunchers, and a brighter H⁻ ion source that is being designed to produce higher peak current with lower beam emittance. The present ion source and LEBT system were studied to investigate beam quality and performance at higher peak currents. Beam parameters from the ion source and in the LEBT at higher currents are comapred to those for standard operating conditions.

## 1 INTRODUCTION

An H⁻ ion beam is produced using a cesiated, multicusp, surface-production source[1]. This source uses a large area converter electrode biased at ~250 V to attract H⁺ ions in a plasma produced by filament arcing. Cesium is used to enhance electron emission from the converter by lowering its work-function. About 1-2% of the H⁺ ions are converted into H⁻ ions by electron attachment and are repelled back by the converter. The ion beam produced on the surface of the converter electrode has sufficiently large emittance to completely fill the phase space region defined by the extraction aperture. Thus, theoretically, the beam emittance is determined by the source geometry. However, several other factors can cause emittance growth[2]. At the exit of the source, the cusped magnetic field focuses the beam. A dipole field at the extraction region suppresses secondary electrons from the converter. The source typically operates at a duty factor of 9.6% (120 Hz, 800 μsec long pulse) delivering a peak current of about 14 mA at 750 keV. Each beam macropulse is chopped to create a sequence of 360 ns long pulses, each with a 110 ns "extraction notch" for injection into the PSR.

The 750 keV beam is produced in a two-stage acceleration system. In the first stage, beam from the source, which is housed in the dome of a 670 kV Cockcroft-Walton accelerator, is increased to 80 keV. Following the source, the transport consists of an 80 kV column, focusing solenoid, a deflector called the dome-level deflector, an emittance measuring station, a 4.5° bending magnet to remove electrons from the beam, a second solenoid magnet, steering magnets, and current monitors as shown in Figure 1. The total length of this section is 3.3 m. The 670 kV Cockcroft-Walton accelerates the beam to an energy of 750 keV for injection into the drift tube linac. The 750 keV LEBT is shown in Figure 2 and consists of quadrupole magnets, a slow-wave chopper to produce the desired micropulse pattern for PSR and WNR, RF bunchers, emittance measuring stations, apertures, and steering magnets. An electrostatic deflector (ground-level deflector) is used to inhibit beam delivery to the linac when warranted.

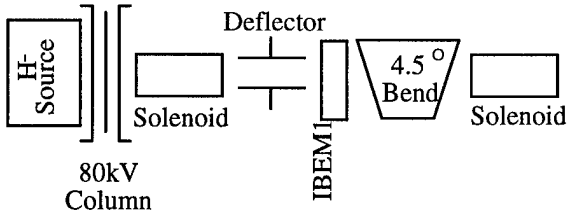



Figure 1: Schematic of the H⁻ source, 80 kV colum and LEBT

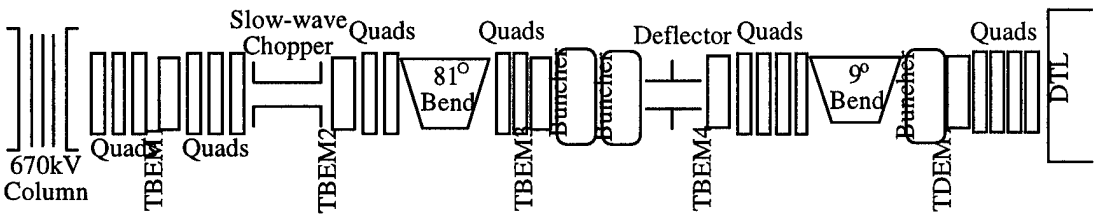



Figure 2: Schematic of the 670 kV column and 750 keV LEBT

0-7803-4376-X/98/$10.00 © 1998 IEEE

## 2 EXPERIMENT

The beam measurements were made in two stages. First, the beam emittance and transmission were measured in each LEBT under normal operating conditions. The beam emittance was first measured in the middle of the 80 keV LEBT (IBEM1). To determine the time it takes for the beam to stabilize, the emittances were measured at different times during the beam pulse. The 80 keV beam was drifted to the location downstream of the 670 kV column (TBEM1) to determine the emittance growth, if any, of the 80 keV beam in this section of the transport.

The 670 kV column was then energized to accelerate the beam from 80 to 750 keV. The beam emittance was measured at five locations in the 750 keV LEBT: 1) TBEM1, 2) TBEM2 (downstream of the slow-wave chopper), 3) TBEM3 (downstream of the first RF buncher), 4) TBEM4 (downstream of the ground-level deflector) , and 5) TDEM1 (just before the entrance to the drift tube linac). The beam transmission was also measured along the 750 keV LEBT.

Second, the ion source current was increased to 20 mA by increasing the filament currents and then adjusting the hydrogen gas flow and Cs temperature to attain equilibrium operating conditions at the normal converter voltage of 250 volts. Measurements of the beam emittance and transmission were repeated in both the 80 keV and 750 keV LEBT under these new conditions. Results of these emittance measurements, along with the program TRACE, were used to tune the channel for maximum transmission and the desired Twiss parameters at the entrance to the 201.25 MHz drift tube linac.

Finally, attempts were made to increase the peak current of the ion source above 20 mA by increasing filament currents and then adjusting the gas flow and Cs temperature. Maintaining a stable beam above 20 mA was not feasible for the present source.

## 3 RESULTS

Figures 3 and 4 show the results of the emittance measurements under both normal and high-current operating conditions. The "source emittance" shown in these figures is a calculated geometric admittance and is used to estimate the emittance at the source exit. It can be seen that for the 15 mA peak beam the emittance, as measured at IBEM1, is a factor of 1.6 larger than the "source emittance". For the 20 mA peak beam, it is a factor of 2.1 larger. Thus, the total emittance for the 20 mA peak beam is about 31% larger than that of the 15 mA peak beam as measured at IBEM1. Larger total emittance observed for the 20 mA peak beam is due in part to the larger tails in the beam as shown in Figure 5.

Emittance of the 80 keV beam measured at TBEM1 (670 column off) showed no significant increase compared to that measured at IBEM1. This indicates that the 80 kV LEBT after IBEM1 does not introduce any noticeable emittance growth to the 80 keV beam. A comparison of the emittance measured at TBEM1 for the 750 keV beam with that measured at IBEM1 for the 80 keV beam indicates that the effect of the 670 kV column on the emittance of the beam is minimal.

The results of the emittance measurements at different times during the beam pulse revealed that source stabilization occurs about 175 μsec after turn-on for the 15 mA peak beam and after about 200 μsec for the 20 mA peak beam. This means that higher peak beams may take longer time to stabilize.

The results of the emittance measurements at the other five locations in the 750 keV LEBT are also shown in Figures 3 and 4. An 18±5% emittance growth was observed between TBEM1 and TDEM1 for both beam currents, indicating no dependence on beam currents up to 20 mA. No significant degradation in the transmission was observed for a well-tuned 20 mA beam in the LEBT.

The majority of beam losses (~1 mA) occur at limiting apertures used to remove beam tails. By using the measured emittances as input to TRACE calculations, beam sizes were calculated at different locations in the LEBT. These calculations show that the beam sizes at a few locations in the LEBT are nearly equal to the beam pipe diameter indicating a potential limitation to operating the present ion source at higher currents.

Lifetime of the source filaments is estimated by measuring the variations in the resistance of the filaments. Using this technique, the lifetime of the present source when operated at 20 mA peak current was estimated to be about a week compared to more than 3 weeks when the source is operated at 15 mA peak current.

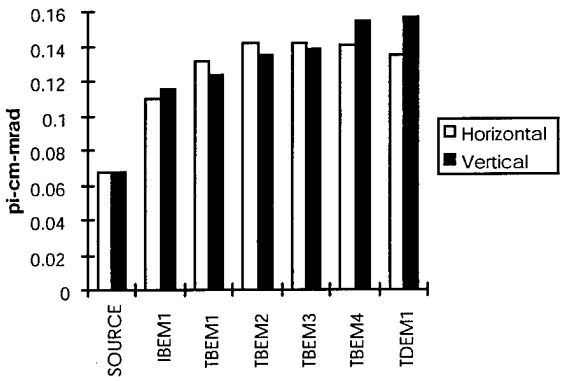



Figure 3: Total normalized emittance for 15 mA beam in LEBT.

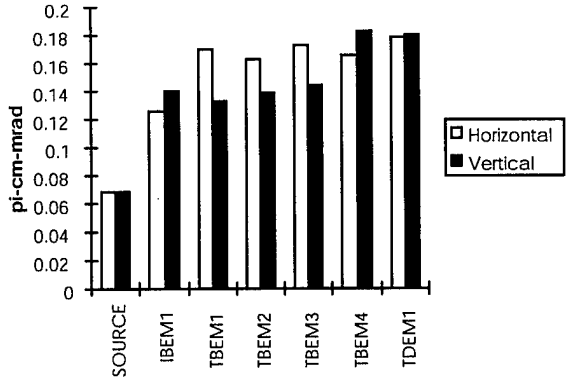



Figure 4: Total normalized emittance for 20 mA beam in LEBT.

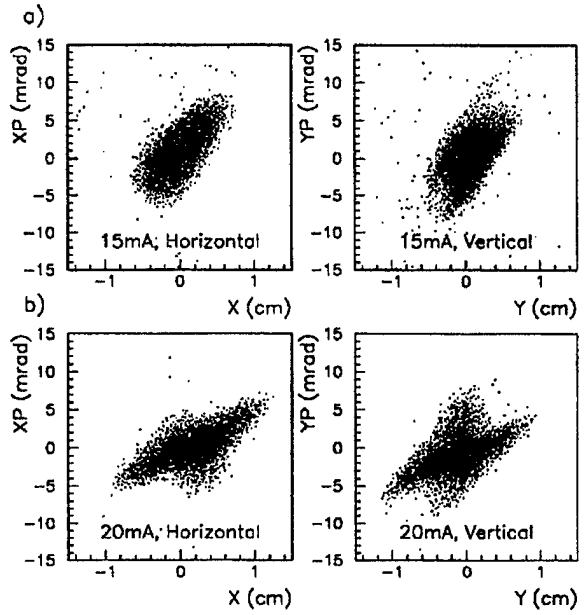



Figure 5: Measured phase-space distributions at TDEM1 for (a) 15 mA peak current beam and (b) for 20 mA current peak beam.

## 4 CONCLUSIONS

1. Measurements of emittances at IBEM1, TBEM1 (with 670 kV column on and off) and other locations in the LEBT indicate that the majority of the observed emittance growth appears to occur in the 80 kV column. The present design of the 80 kV column which was chosen to reduce arcdowns may be a source of the observed emittance growth[3].

2. Emittance growth in the 750 keV LEBT is not very significant.

3. The ability to transport higher than 20 mA peak beam from the present source may be constrained by beam size and matching requirements to the drift tube linac.

## REFERENCES

[1] R. L. York and R. R. Stevens, Jr., "A cusped field H⁻ ion source for LAMPF" IEEE Transactions on Nuclear Science, Vol. NS-30, No. 4, August 1983.

[2] R. R. Stevens, "High-Current Negative-Ion Beam Transport", Production and neutralization of negative ions and beams, AIP conference proceedings, p. 646, No. 287, 1992.

[3] R. R. Stevens, Jr. "H⁻ Injector Upgrade for LANSCE- Beam Extraction and Low Energy Beam Transport", LANSCE internal report, 1997.

# SIMULATIONS OF THE LEDA LEBT $H^+$ BEAM†

H. Vernon Smith, Jr., Joseph D. Sherman, Ralph R. Stevens, Jr., and Lloyd M. Young
Los Alamos National Laboratory, Los Alamos, NM 87545

*Abstract*

The computer codes TRACE and SCHAR model the Low-Energy Demonstration Accelerator (LEDA) Low-Energy Beam Transport (LEBT) for 75-keV, 110-mA, dc $H^+$ beams. Solenoid-lens location studies verify that the proposed LEBT design gives a near-optimum match to the LEDA RFQ. The desired RFQ transmission (≥ 90%) and output emittance (≤ 0.22 π mm mrad, transverse) are obtained when PARMTEQM transports the file for the SCHAR-generated optimum beam through the RFQ.

## 1 INTRODUCTION

The LEDA microwave-driven source $H^+$ beam (75 keV, 130 mA, 85% $H^+$ fraction) is matched to the LEDA RFQ [1] using the two-solenoid, gas-neutralized LEBT [2] described in Ref. [3]. Two steering-magnet pairs provide the desired beam position and angle at the RFQ match point. Beam neutralization of 95-99% occurs in the LEBT residual hydrogen gas [4]. We model the emittance growth in the LEDA LEBT design (Fig. 1) using TRACE [5] and SCHAR [6]. The RFQ output beam is calculated by transporting the SCHAR-generated beam through the RFQ with PARMTEQM [7].

## 2 INPUT PARAMETERS

The LEBT input $H^+$ beam parameters are determined from measurements on the prototype LEDA injector, shown in Fig. 1 of Ref. [8]. TRACE drifts the beam (Fig. 4 of Ref. [8]) back along that 2.1-m long LEBT, from the emittance-measuring unit (EMU) to the 8.6-mm-diam ion source emitter. At the EMU this beam has total current = 130 mA, proton fraction = 87.7% ($H^+$ current = 114 mA), rms normalized emittance $\varepsilon_N$ = 0.207 π mm mrad, and $\alpha$ = -2.087 and $\beta$ = 16.908 mm/mrad at 10% threshold.

TRACE gives an $H^+$ beam size at the ion source emitter $\leq R_{emit}$ (= 4.3 mm) for unneutralized currents ($I_{eff}$) between 0.6 and 4.0 mA. The beam is converging for 0.6 mA; for 4.0 mA, it is diverging. The diverging beam is used because it is the "worst case." Unlike TRACE, SCHAR is a "6rms" code, so a value of $I_{eff}$ that gives a beam size of 4.3 mm/$(1.5)^{1/2}$ = 3.51 mm is chosen for the SCHAR calculations. The TRACE calculation for $I_{eff}$ = 3.5 mA, with $\alpha$ = -0.620, $\beta$ = 0.19 mm/mrad, and $\varepsilon_N$ = 0.207 π mm mrad, matches this value closely (3.52 mm).

† Work supported by the US DOE, Defense Programs.

* $v_o = [2E/m_pc^2]^{1/2}c$, $r_{12} = -\alpha/[1+\alpha^2]^{1/2}$, $x_{max} = [\beta\varepsilon(6rms)]^{1/2}$, $v_{x\,max} = [\gamma\varepsilon(6rms)]^{1/2}v_o$

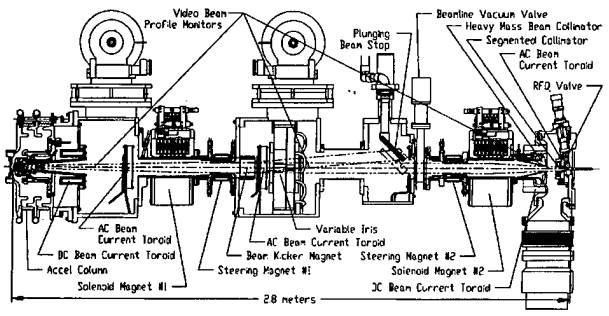



Fig. 1. The LEDA baseline LEBT design.

Using those TRACE parameters, SCHAR* predicts $\varepsilon_N$ = 0.243 π mm mrad at the EMU, about 17% higher than the measured value. The input parameters are scaled using $\alpha_{new} = \alpha_{old}[\varepsilon_{old}/\varepsilon_{new}]$ and $\beta_{new} = \beta_{old}[\varepsilon_{old}/\varepsilon_{new}]$, keeping the phase-space ellipse orientation and $x_{max}$ the same but adjusting the phase-space area up or down depending on $[\varepsilon_{old}/\varepsilon_{new}]$. SCHAR gives the measured $\varepsilon_N$ to within 0.01% after two iterations. The resulting SCHAR-predicted input beam (Table 1) has $\varepsilon_N$ = 0.175 π mm mrad. Using SCHAR to transport the beam parameters in Table 1 through the 2.1-m LEBT also gives the approximate measured phase-space shape at 10% contour (Fig. 5 of Ref. 8). The LEDA LEBT TRACE and SCHAR simulations described below use the input $H^+$ beam parameters given in Table 1.

## 3 LEDA LEBT TRACE SIMULATIONS

The $H^+$ beam matching parameters for the RFQ are $\alpha$ = 1.909 and $\beta$ = 0.1175 mm/mrad for an RFQ input $H^+$ beam current = 110 mA and $\varepsilon_N$ = 0.20 π mm mrad. The TRACE-calculated tuning curves for the baseline LEBT design are shown in Fig. 2. These tuning curves are generated by fixing the magnetic field of solenoid #1 ($B_{sol\#1}$) and varying the magnetic field of solenoid #2 ($B_{sol\#2}$). The matched $\alpha$ and $\beta$ values result for $B_{sol\#1}$ = 2700 G and $B_{sol\#2}$ = 3667 G. The 21.59-cm-long, 10-cm-i.d. solenoid lenses provide dc fields ≤5000 G, so the LEBT design shown in Fig. 1 has the tuning capability to match the $H^+$ beam from the source into the RFQ.

Table 1. TRACE and SCHAR parameters that reproduce the previously-measured phase-space distribution [8].

| TRACE ($I_{eff}$ = 4.0 mA) | SCHAR ($I_{eff}$ = 3.5 mA) |
|---|---|
| E = 75 keV | $v_o = 3.79 \times 10^6$ m/s |
| $\alpha$ = -0.873 | $r_{12}$ = 0.585 |
| $\beta$ = 0.26 mm/mrad | $x_{max} = 4.32 \times 10^{-3}$ m |
| $\varepsilon_N$ = 0.207 π mm mrad | $v_{x\,max} = 9.14 \times 10^4$ m/s |

0-7803-4376-X/98/$10.00 © 1998 IEEE

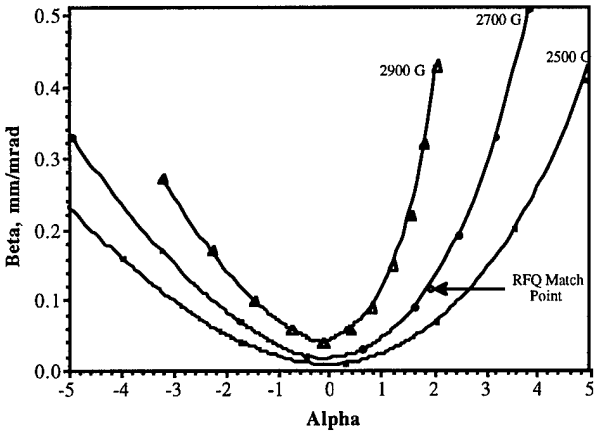



Fig. 2. The TRACE-calculated tuning curves for the baseline LEBT design. The RFQ match point is indicated.

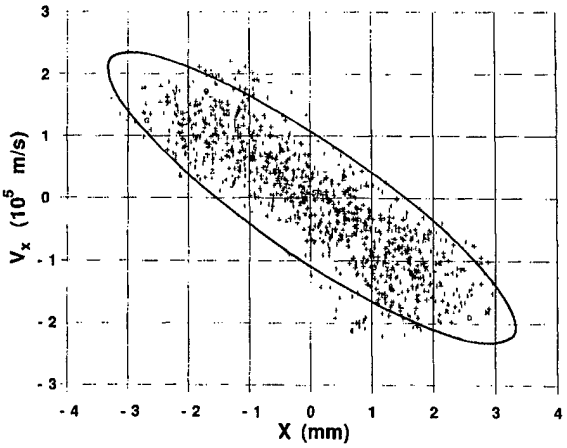



Fig. 3. SCHAR-calculated phase space (crosses) at the RFQ match point for the baseline LEBT design (Case No. 1). The curve is the RFQ acceptance ellipse for a 110-mA, 0.20-π mm mrad beam.

## 4 LEDA LEBT SCHAR SIMULATIONS

The LEBT (Fig. 1) is simulated with the non-linear space-charge computer code SCHAR. These simulations use a 4-volume distribution and the line mode with 999 lines. Case No. 1 in Table 2 has the LEBT dimensions used for the SCHAR model of the baseline design. The distance between the center lines of the two solenoids is 151.72 cm for all simulations in this paper. The beam neutralization is assumed to be 2.7% ($I_{eff}$ = 3.5 mA), about mid-way in the 1-5% range measured [4] on the prototype LEDA injector.

The TRACE-derived solenoid settings, $B_{sol\#1}$ = 2700 G and $B_{sol\#2}$ = 3667 G, are used as starting values. SCHAR predicts that the best match to the RFQ (Fig. 3) is obtained for $B_{sol\#1}$ = 2500 G and $B_{sol\#2}$ = 3500 G. The predicted $\varepsilon_N$ at the RFQ match point is 0.228 π mm mrad. SCHAR predicts that most of the 30% emittance growth is due to spherical aberrations in solenoid #1 (12%) and solenoid #2 (14%). The non-linear, space-charge-induced emittance growth is low (4%). The SCHAR output file is used to generate a 5,000 particle input beam for the PARMTEQM computer code to estimate the RFQ transmission and output $\varepsilon_N$. The result is transmission = 93.0% and output $\varepsilon_N$ = 0.214 π mm mrad (Fig. 4). This is the baseline case against which the rest of the SCHAR modeling is compared.

Next the distance between the source and solenoid #1 center line and/or the distance between solenoid #2 center line and the RFQ match point (z) are varied. The SCHAR beams are then rematched and used as input for the PARMTEQM code to predict the RFQ transmission and $\varepsilon_N$. The results of these simulations are given in Table 2 and are discussed below. When the source-Solenoid #1 distance is reduced by 30 cm (Case 2), the SCHAR-predicted RFQ input $\varepsilon_N$ drops by only 3.5%, the PARMTEQM-predicted RFQ output $\varepsilon_N$ drops by only 3.7%, and the RFQ transmission is almost unchanged. When both the source-Solenoid #1 and Solenoid #2-RFQ

Table 2. Results of the LEBT and RFQ simulations with SCHAR and PARMTEQM, respectively. The LEBT dimensions are in columns 2 and 3, the SCHAR-calculated $\varepsilon_N$ at the RFQ match point in column 4, the input $\varepsilon_N$ for the PARMTEQM RFQ simulations in column 5, and the PARMTEQM-calculated RFQ transmission and output $\varepsilon_N$ in columns 6 and 7.

| Case No. | Extrac-tor to Sol#1, cm | Sol#2 to RFQ Match Point, cm | SCHAR RFQ $\varepsilon_{in}$, π mm mrad | PARM-TEQM RFQ $\varepsilon_{in}$, π mm mrad | PARM-TEQM RFQ $\varepsilon_{out}$, π mm mrad | RFQ trans-mission % |
|---|---|---|---|---|---|---|
| 1 | 87.58 | 40.70 | 0.228 | 0.226 | 0.214 | 93.0 |
| 2 | 57.58 | 40.70 | 0.220 | 0.218 | 0.206 | 92.7 |
| 3 | 87.58 | 25.70 | 0.204 | 0.202 | 0.200 | 93.4 |
| 4 | 57.58 | 25.70 | 0.189 | 0.188 | 0.196 | 92.7 |
| 5 | 87.58 | 45.70 | 0.246 | 0.244 | 0.225 | 91.9 |
| 6 | 87.58 | 50.70 | 0.383 | 0.382 | 0.251 | 79.2 |
| 7 | 87.58 | 55.70 | 0.456 | 0.467 | 0.274 | 77.2 |

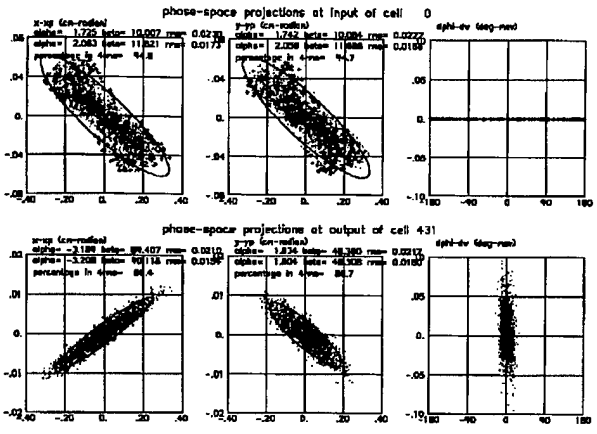



Fig. 4. PARMTEQM-calculated RFQ input (top) and output (bottom) phase space for the baseline LEBT design.

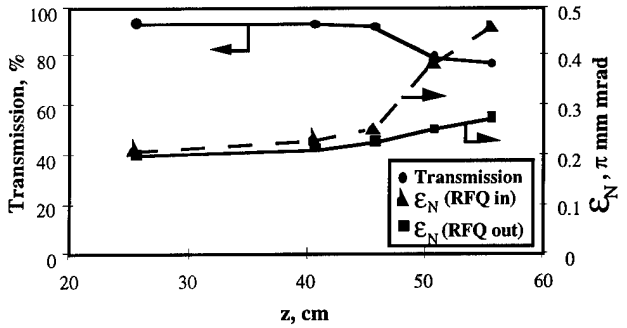



Fig. 5. PARMTEQM-calculated RFQ transmission (circles) and output $\varepsilon_N$ (squares), and SCHAR-calculated RFQ input emittance (triangles) as a function of the distance between Solenoid #2 and the RFQ match point.

distances are shortened by 30 cm and 15 cm, respectively (Case 4), the SCHAR-predicted RFQ input $\varepsilon_N$ drops by 17% and the PARMTEQM-predicted RFQ output $\varepsilon_N$ drops by 8.4%, but the RFQ transmission is almost the same. The codes predict that reducing the source-Solenoid 1 distance by as much as 30 cm gives no significant gain.

When the Solenoid 2 center line-RFQ distance (z) is shortened by 15 cm (Case 3), compared with Case 1 the SCHAR-predicted RFQ input $\varepsilon_N$ drops by 11% and the PARMTEQM-predicted RFQ output $\varepsilon_N$ drops by 6.5%, but the predicted RFQ transmission is higher by 0.4%. This small difference in output RFQ $\varepsilon_N$ would not significantly effect the rest of the LEDA accelerator.

Increasing z would allow adding more beam diagnostics and/or beamline components in front of the RFQ. In Cases 5-7 (Table 2) z increases from 40.7 to 55.7 cm in 5-cm steps. For the baseline case (z = 40.7 cm), the beam size in solenoid #2 is small enough that spherical aberrations are low (Fig. 3). When z increases to 45.7 cm (Case 5), the LEDA RFQ transmission lowers slightly (from 93.0% to 91.9%) and the RFQ output $\varepsilon_N$ rises slightly (from 0.214 to 0.225 π mm mrad). Increasing z to 50.7 and 55.7 cm increases the beam size in solenoid #2 enough that spherical aberrations dominate $\varepsilon_N$ at the RFQ match point (Fig. 5), causing unacceptable RFQ transmission (Cases 6 and 7). Increasing z from 40.7 cm to 45.7 cm is acceptable, if there is a good reason to do so.

## 5 TRACE STEERING SIMULATIONS

The LEDA injector will provide a range of beam centroid motion at the RFQ match point. Error studies show that if the input phase space distributions are centered on the RFQ axis to within ±0.2 mm in position and ±10 mrad in angle, the transmission degrades by <1%. The solenoid lenses will be aligned to meet these tolerances, but there will be inevitable misalignments between the ion source, column and RFQ that can produce centroid errors in excess of these tolerances. The LEBT steering system will permit rapid, on-line correction of these errors.

Independent control of X and Y motions is desirable

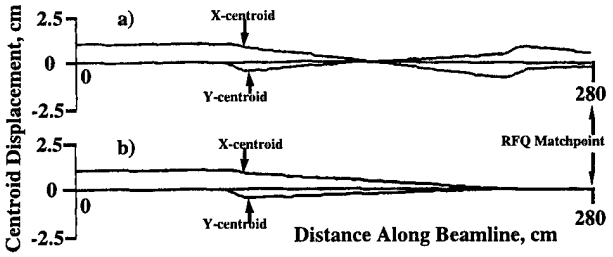



Fig. 6. a) Beam centroid motion for an initial 1 cm offset. b) Beam centroid motion after steering.

to match the symmetry of the RFQ. We place two steering pairs in the LEBT between the solenoid lenses (Fig. 1) and provide a computer algorithm to decouple the desired steering motion in the X and Y planes from the rotation effects produced by the solenoid lenses [9]. It is desirable to align the optical elements in the beam line so that changes in the focusing strength of the solenoids do not result in the introduction of steering errors. This makes the matching and steering control independent and greatly facilitates tuning this beam line.

We use TRACE to model the effects of misalignment errors in this beam line and to determine the required steering corrections. The two steering pairs can correct a 1 cm horizontal offset in the alignment of the ion source to the LEBT as shown in Fig. 6.

## 6 SUMMARY

For the LEDA RFQ operating at 110 mA, high beam transmission is more important than low beam emittance within the range of RFQ output emittances reported here. Because the PARMTEQM-predicted RFQ transmission is about as high (or higher) for the baseline LEBT design as for any of the other geometries studied, we conclude that the LEDA baseline LEBT design is near optimum. Also, TRACE predicts that the steering proposed for the LEDA LEBT will allow correct spatial and angular positioning of the $H^+$ beam for injection into the RFQ.

## REFERENCES


[1] L.M. Young, "An 8-m-Long Coupled-Cavity RFQ Linac," Proc. 1994 Int. LINAC Conf. (Aug., 1994, Tsukuba, Japan), 178.

[2] R. R. Stevens, Jr., "High-Current Negative-Ion Beam Transport," AIP Conf. Proc. No. 287 (1994) 646.

[3] L. D. Hansborough *et al.*, "Mechanical Engineering of a 75-keV Proton Injector for LEDA," this conf.

[4] R. Ferdinand, *et al.*, "Space-Charge Neutralization Measurement of a 75-keV, 130-mA Hydrogen-Ion Beam," this conf.

[5] K. R. Crandall "TRACE: An Interactive Beam-Transport Program," Los Alamos Scientific Laboratory report LA-5332 (October, 1973).

[6] R. J. Hayden and M. J. Jakobson, "The Space-Charge Computer Program SCHAR," IEEE Trans. Nucl. Sci. **NS-30** (1983) 2540.

[7] K. R. Crandall *et al.*, "RFQ Design Codes," Los Alamos National Laboratory report LA-UR-96-1836 (February 12, 1997 revision).

[8] J. D. Sherman *et al.*, "Development of a 110-mA, 75-keV Proton Injector for High-Current, CW Linacs," Proc. XVIII Int. Linac Conf. (Geneva, 26-30 Aug. 1996), pp. 701-3.

[9] S. K. Brown and W. H. Atkins, "Beam Steering in the Ground Test Accelerator Low Energy Beam Transport," Los Alamos National Laboratory report LA-UR-93-358 (1993).

# SIMULATIONS OF THE LEDA LEBT WITH $H^+$, $H_2^+$, AND $E^-$ PARTICLES*

Lloyd M. Young
Los Alamos National Laboratory, MS H817, Los Alamos, NM 87545, USA

*Abstract*

The low-energy-beam transport (LEBT) system for the Low-Energy Demonstration Accelerator (LEDA) transports the beam from the ion-source plasma surface to the LEDA RFQ entrance. The code PARMELA performed these simulations of the beam transport through the LEBT. This code can simultaneously transport three particle types of different charge-to-mass ratio. Electrostatic fields, magnetic fields, and space charge influence the beam particles in this simulation. The electrostatic fields exist in the ion-source extractor. The magnetic field exists in the ion source and in the solenoid lenses. The $e^-$ particles, introduced into the beam of $H^+$ and $H_2^+$, simulate the space charge neutralization by the residual gas in the LEBT. The $H^+$ and $H_2^+$ ions leaving the source emerge from a longitudinal magnetic field, which causes the beam to rotate.

## INTRODUCTION

Ions of $H^+$ and $H_2^+$ originate on a curved plasma surface, which intersects the beam axis at z = 0. The ions accelerate through the electrostatic fields of the ion source's accelerating column[1]. Then the beam goes through the LEBT, which has two magnetic solenoid lenses, and arrives at the input of the RFQ[2].

Two other papers[3,4] at this conference describe details of the LEBT for LEDA. Extensive modifications of the computer code PARMELA[5] added the ability to track multiple particle types. This paper discusses simulations of the LEBT that exploited this new multiple-particle feature. PARMELA can now track simultaneously three different particle species, each one with a different charge-to-mass ratio. The code can create new particles in the beam ($e^-$, for example) at the location of another particle ($H^+$, for example). One of the input parameters in the code is the probability for creating a new particle. This feature simulates space-charge neutralization of the $H^+$ and $H_2^+$ beam by electrons. The physical process is ionization of the residual gas in the beam line. The residual gas is mostly hydrogen. The ionization process strips an electron from the hydrogen molecule producing an $H_2^+$ ion and an electron. The space-charge potential well traps the $e^-$ and expels the $H_2^+$ ion. The simulation ignores the $H_2^+$ ions created in this manner to speed the calculation. Note the distinction between these $H_2^+$ ions created by ionization of the residual gas and those that emerge from the source. The code does not ignore the $H_2^+$ ions emerging from the ion source.

## PARMELA

First, PARMELA simulated the emittance measuring unit(EMU)[6] to validate the techniques used in the code. PARMELA uses time as the independent variable in the beam-dynamics simulations. Even though the beam has no bunch structure, PARMELA measures the time steps in degrees of the 350-MHz RFQ frequency. The goal of the simulation is to construct the input phase-space distribution of $H^+$ particles at the RFQ entrance. Because the PARMELA simulation starts with no beam at all, we must inject a long enough stream of $H^+$ and $H_2^+$ ions to reach a steady-state condition. One problem is that the $H_2^+$ ions move slower than the $H^+$ ions. To reduce the number of time steps in the calculation, PARMELA advances time faster for the $H_2^+$ ions so they keep up with the faster $H^+$ ions. With this adjustment, the beam arriving at the end of the LEBT after 20 350-MHz RF periods has achieved a steady state. The simulation continues through 40 RF periods, and the code builds a phase-space distribution from periods 20 to 30.

The program POISSON[7] calculated the electrostatic field of the ion-source accelerating column, the magnetic field from the Helmholtz coils surrounding the source, and the magnetic field of the solenoid lenses in the LEBT. PARMELA reads these fields and uses them in the beam-dynamics calculation. For the magnet calculations, measured values of the coil currents fix the magnetic-field strengths. For the electrostatic calculation, the only unknown is the radius of curvature $r_p$ of the plasma boundary in the ion-source-extraction aperture. With different values of $r_p$, PARMELA followed the beam to the EMU at z = 213.5 cm. A video camera at z = 43 cm measures the beam profile. The value $r_p$ = 4.9 cm reproduces the beam diameter measured by the beam profile monitor.

The amount of beam neutralization also affects the beam size. We varied the beam neutralization by changing the probability of introducing electrons. At every time step for each $H^+$ particle, PARMELA creates electrons at random according to this probability. The electron has the coordinates of the $H^+$ particle, but zero kinetic energy. For too large a probability, too many electrons are added to the beam, causing the space-charge potential well to disappear. Without the potential well, the $e^-$ particles leave the beam radially.

Modeling the space-charge neutralization by injecting electrons works well until the beam approaches the solenoid lens. Here, the lens strongly focuses the $e^-$ beam. After a long enough time (>400 RF periods), the electrons would eventually reach equilibrium. However, this calculation would take at least 10 times more particles and about 10 times more time steps. Such a calculation would require >900 hours on today's fastest PC. To reduce computation time, we switch to a different model of the space-charge neutralization for particles beyond z = 40 cm. After this point, we drop electrons from the calculation and assign only 4% of the normal charge to the $H^+$ or $H_2^+$ ions in the space-charge calculation. The value

*Work supported by the US Department of Energy.

0-7803-4376-X/98/$10.00 © 1998 IEEE

of 4% is consistent with a measurement (95-99%) of the space-charge neutralization[8]. The 4% value comes from comparing the simulated distribution (Figure 1) at the EMU position with the measured distribution (Figure 2).

Figure 3 shows the beam and the accelerating column. The electron suppressor at −1.2 kV prevents electrons from flowing from the neutralized beam to the ion source. This figure shows that the beam is neutralized by electrons beyond about 3.3 cm from the source. Electrons created closer to the source than this accelerate toward the source.

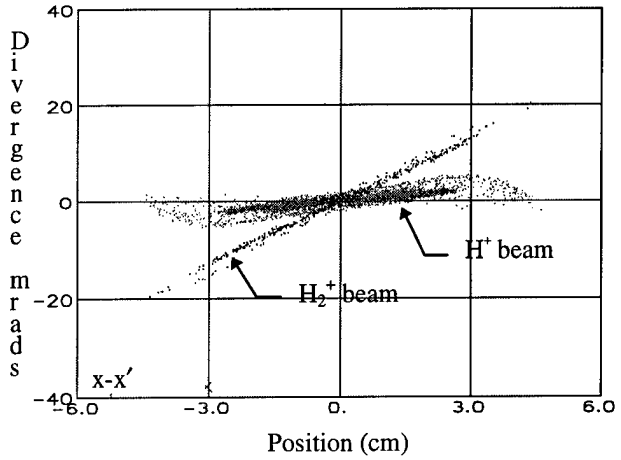



Figure 1. Simulated distribution of $H^+$ and $H_2^+$ at the position of the EMU. The solenoid lenses do not focus the $H_2^+$ beam as strongly as the $H^+$ beam, so the $H_2^+$ beam diverges more than the $H^+$ beam. This beam contains 118 mA of $H^+$ and 12 mA of $H_2^+$. The rms emittance of the simulated $H^+$ beam is 0.028 cm-mrad. (If viewing in color, $H^+$ ions are green and $H_2^+$ ions are red.)

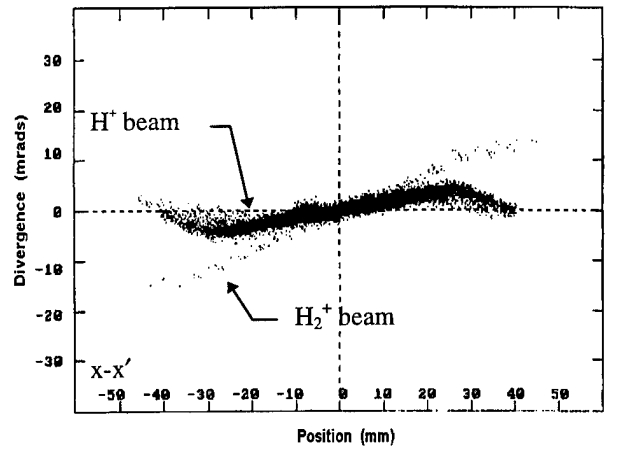



Figure 2. The measured beam distribution from the EMU. The rms emittance of this $H^+$ beam is 0.0207 cm-mrad.

Figure 4 shows equipotentials calculated by POISSON for the ion-source accelerating column. A comparison of electron locations in Figure 3 with the −954-Volt equipotential in Figure 4 shows that the electrons remain to the right of this equipotential.

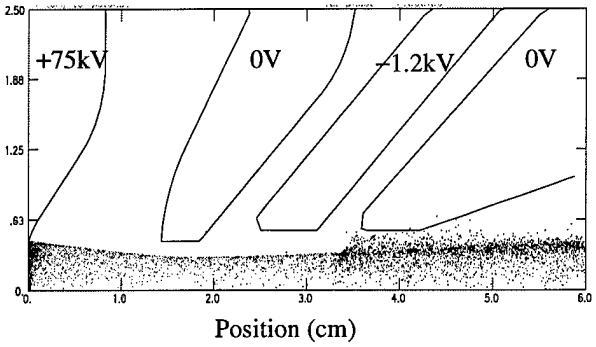



Figure 3. The ion-source accelerator column showing the simulated beam of $H^+$, $H_2^+$, and $e^-$ particles. The −1.2-kV electrode suppresses the electron current flowing toward the ion source at 75kV. The dark black points are electrons. (If viewing in color, $H^+$ ions are green and $H_2^+$ ions are red.)

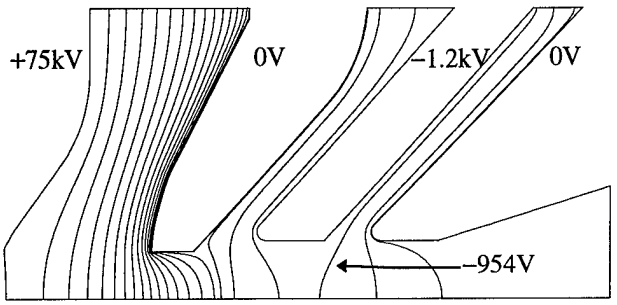



Figure 4. Equipotentials from the POISSON solution of the ion-source accelerating column. The equipotential spacing is dense near 0 Volts and sparse near 75 kV.

The best fit between the simulated beam size in Figure 5 and the measured beam size in Figure 6 occurred with a convex plasma surface with $r_p$ = 4.9 cm at the ion-source extractor. The measured beam size depends on the ion-source parameters. The emittance scan data was taken Feb. 9, 1996 and the profile scan in Figure 6 was taken on Jan. 23, 1996. A simultaneous set of EMU data and profile data is not available.

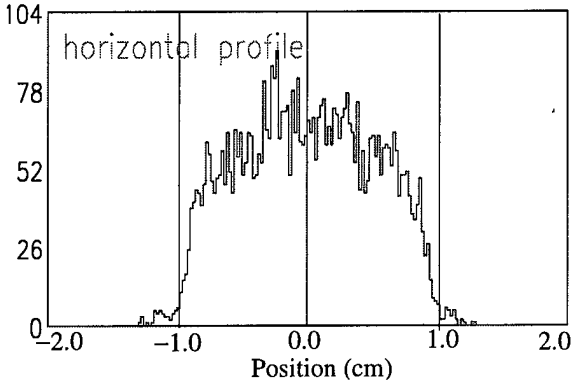



Figure 5. Simulated horizontal profile at 42.3 cm from ion source.

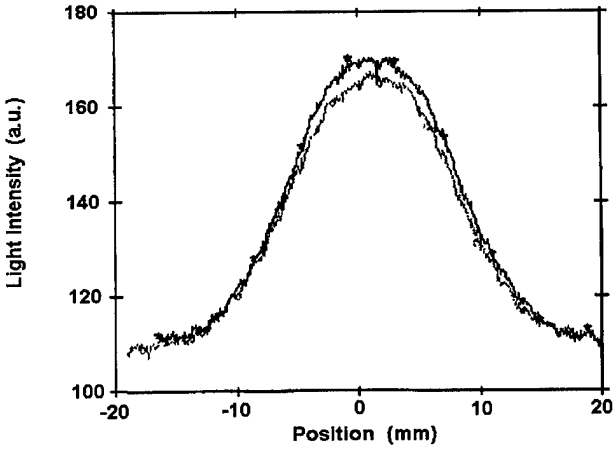



Figure 6. Representative profile from the video monitor at z = 43 cm. This profile was taken about 2 weeks earlier than the emittance scan shown in Figure 2.

The beam leaving the central part of the convex plasma diverges as shown in Figure 7. The outer part of the beam is focused strongly by the accelerating-column electrostatic fields. Because the plasma is in a strong longitudinal magnetic field (746 gauss), the beam begins to rotate as it leaves the magnetic field. Ions moving toward the axis in Figure 7 revolve around the axis, leaving a hole in the beam density near the axis beyond z = 15 cm. This hole persists throughout the EMU simulation.

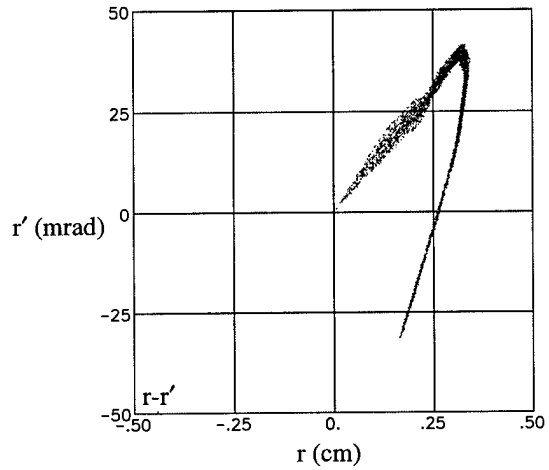



Figure 7. Plot of r versus r′ at 3.5 cm from ion-source extractor (near the point where the beam becomes neutralized). The convex plasma surface causes the center part of the beam to diverge. The shape of the electrodes focus the outer portion of the beam.

## THE LEDA LEBT SIMULATION

PARMELA simulated the LEDA LEBT using the radius of the plasma surface determined from the simulation of the EMU. The space-charge neutralization factor of 4% used in the simulation of the EMU is also used in the simulation of the LEDA LEBT.

Initial simulations of the LEBT resulted in unsatisfactory input beam distributions to the LEDA RFQ. The transmission through the RFQ was less than the required 90%. Transmission is defined as the percentage of input beam that is accelerated through the RFQ. The radial aperture of the LEBT beam line through the last solenoid is 5 cm. Aberrations in the solenoid lenses focused the beam particles beyond 2.5 cm from the axis more strongly than the particles closer in. These beam particles at large radius are lost in the RFQ, spoiling the transmission. Installing 2.5-cm-radius apertures between the LEBT solenoid lenses removed particles from the beam that would later be lost in the RFQ. The RFQ transmission improved to 95%. Beam lost in the RFQ becomes $H_2$ gas. The RFQ vacuum system can pump the equivalent of 10 mA of $H^+$ and still maintain an adequate vacuum. In the LEBT, which is easier to pump, good vacuum is not as critical as it is in the RFQ. Therefore, using the apertures in the LEBT is desirable.

## CONCLUSIONS

PARMELA simulations of the LEBT beam line showed that aberrations in the solenoid lenses reduced the RFQ transmission to unacceptable levels. One way to solve this problem is to install apertures in the LEBT. A better solution (not proven at present) might be to use solenoid lenses with less aberrations.

## ACKNOWLEGEMENTS

I thank Joseph Sherman and Thomas Zaugg for Figures 2 and 5 that show typical data obtained from measurements on the beam from the LEDA ion source. I also thank Vernon Smith and Joseph Sherman for discussions on the properties of ion-source beams.

## REFERENCES

[1] J. D. Sherman et al., "Development of a 110-mA, 75-keV Proton Injector for High-Current, CW Linacs," Proceedings XVIII Int. Linac Conference, p.701-3 (Geneva, 26-30 Aug. 1996).

[2] L. M. Young, "An 8-Meter-Long Coupled Cavity RFQ Linac," Proceedings of the 1994 Intl. Linac Conference, Tsukuba, Japan, p. 178 (1994).

[3] L. Hansborough, "Mech. Eng. of a Proton Injector for LEDA," this conference.

[4] H. V. Smith, Jr., J. D. Sherman, R. R. Stevens, Jr., and L. M. Young, "Simulations of the LEDA LEBT $H^+$ Beam," this conference.

[5] L. M. Young and J. H. Billen, "PARMELA," Los Alamos National Laboratory report LA-UR-96-1835 (revision March 14, 1997).

[6] R. R. Stevens, Jr., P. Schafstall, J. D. Schneider, J. D. Sherman, T. Zaugg, and T. Taylor, "DC Proton Beam Measurements in a Single-Solenoid Low-Energy Beam Transport System," Proc. of the 17th International Linac Conf., Tsukuba, Japan, p. 549 (1994).

[7] J. H. Billen and L. M. Young, "POISSON SUPERFISH," Los Alamos National Laboratory report LA-UR-96-1834 (revision April 22, 1997).

[8] R. Ferdinand, J. D. Sherman, R. R. Stevens, Jr., and T. Zaugg, "Space-Charge Neutralization Measurement of a 75-keV, 130-mA Hydrogen-Ion Beam," this conference

# SIMULATIONS OF THE LEDA RFQ 6.7-MEV ACCELERATOR *

Lloyd M. Young
Los Alamos National Laboratory, MS H817, Los Alamos, NM 87545, USA

*Abstract*

The codes PARMTEQM and RFQTRAK simulate the beam transport through the radio-frequency-quadrupole (RFQ) accelerator for the low-energy-demonstration accelerator (LEDA). They predict 95% transmission for a matched 110-mA proton beam with a normalized-rms emittance of 0.02 mm mrad. RFQTRAK simulates the effects of arbitrary vane-tip misalignments. This RFQ includes some new features in its design. It consists of four resonantly coupled 2-m-long segments that make up its 8-m length. It has higher vane-gap voltages at the high-energy end than the low-energy end. The entrance end of the RFQ has lower transverse focusing strength to facilitate beam matching. The exit of the RFQ has a transition cell and a radial-matching section. The exit radial-matching section matches the beam into the following accelerator.

## INTRODUCTION

LEDA requires 100 mA of beam from the 350-MHz RFQ. The energy needs to be as high as possible for injection into the coupled-cavity drift-tube linac (CCDTL). Therefore, the LEDA RFQ is an 8-m-long RFQ that accelerates the proton beam to 6.7 MeV. A recent experiment with the LEDA RFQ low-power model[1] demonstrates resonantly coupling four 2-m-long segments to form an 8-m-long RFQ. The LEDA RFQ will use this configuration.

Conventional RFQ designs with a small entrance aperture require a very strongly focused beam at the entrance aperture for proper matching to the RFQ. In LEDA the final lens in the low-energy-beam transport (LEBT) is far enough from the input of the RFQ to require a large aperture and weak focusing at the beginning of the RFQ. Low vane modulation at the RFQ entrance allows weaker focusing, but still has a large transverse current limit. The combination of a large-aperture radial matching section and weak focusing makes matching the beam into the RFQ easy. As shown in Fig. 1, the transverse focusing strength smoothly increases in the first 32 cm of the RFQ. At about 130 cm, the vane gap voltage starts ramping up, the aperture starts increasing, and the focusing starts decreasing. The combination of these parameters reduces the beam loss at the end of the gentle buncher, which is the usual choke point where significant beam loss occurs.

The increase in gap voltage increases the accelerating gradient in the high-energy portion of the RFQ and shortens the length. The transverse focusing at the end of the RFQ matches the transverse focusing of the CCDTL, which makes the transition independent of the beam current.

*Work supported by the US Department of Energy.

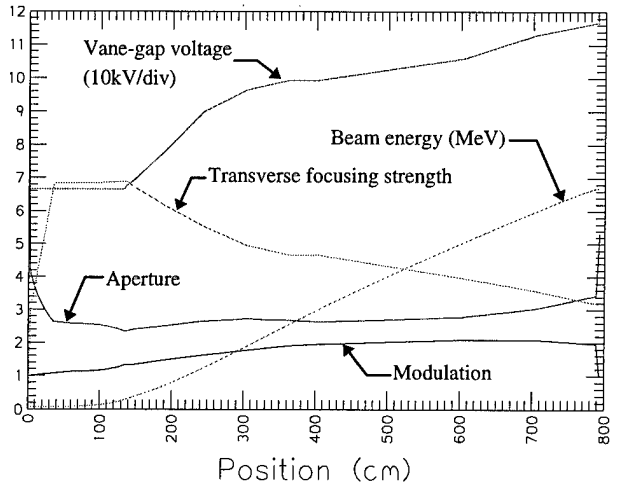



Figure 1. Shows some important parameters versus position in the RFQ.

## PROGRAM RFQTRAK

RFQTRAK [2] tracks the particles through the RFQ using time as the independent variable. Particles enter a cell pair with known phase, position, and divergence angle. For each time step, RFQTRAK advances all the particles and calculates the space-charge-potential distribution. Tracking through the cell pair takes 3 RF cycles. The first cycle, which does not include space-charge fields provides the leading pulse. The third cycle provides a trailing pulse for the correct calculation of the space-charge fields. At start of the second cycle, RFQTRAK initiates the space-charge calculation. The code discards particles whose velocity falls below half the cell's synchronous velocity. Particles from the second cycle that actually exit the cell pair, provide the starting coordinates for all three cycles in the next cell pair.

RFQTRAK constructs a finite-element model of the potential distribution inside an RFQ accelerator cell. The mesh generator includes details of the topology of an RFQ cell. Mesh elements are three-dimensional bricks with 20 nodes. This number of nodes allows a quadratic variation of the potential in each dimension. The program RFQCOEF [3] calculates the first 8 multipole components of the potential in one quadrant of a single cell or optionally in all 4 quadrants of the cell. PARMTEQM [4] uses the same 8 multipole components. The 4-quadrant calculation also includes the dipole and sextupole terms.

RFQTRAK employs another finite-element mesh similar to the one used for the potential distribution to calculate the effects of space charge during the beam dynamics simulation. In this calculation, the image charge effect is naturally included by the boundary conditions. In this paper, the term space-charge effect includes the image charge effect. The finite-element model spans a pair of cells of total length $\beta\lambda$, where $\beta\lambda$ is the distance traveled

0-7803-4376-X/98/$10.00 © 1998 IEEE

by a particle of velocity βc in one RF period. For solving Poisson's equation: $\nabla^2\Phi = -4\pi\cdot\rho$, the right-hand terms come from the beam charge distribution. The vane potentials are assigned to be zero as a boundary condition. The code maps the potential on nodes of the entrance plane to the corresponding nodes on the exit plane. A direct (Gauss Elimination) method solves for the potentials. An advantage of this method is that the solution matrix can be reused several times, with only an update of the right-hand side as the charge distribution changes. Then only a back substitution is required to solve for the fields. Space-charge fields are obtained from the potentials by differentiation of the element-shape functions.

## THE SIMULATIONS

RFQTRAK simulated the LEDA RFQ with errors in the vane-tip locations and vane-tip potentials. Table 1 lists a set of randomly generated errors used in these simulations. Figure 2 shows the result of the RFQTRAK simulation with these errors. Notice that the transverse beam size shrinks in the first part of the RFQ where the focusing increases. The code RFQPROC, which is part of the PARMTEQM suite of codes, plotted all the beam distribution figures.

Table 1. Voltage and position errors for RFQ vane tips.

| Vane | Voltage error (%) | Error in Vane-tip radial position (mm) | Error in vane-tip azimuthal position (mm) |
|---|---|---|---|
| 1 | -2.124 | -0.0046 | +0.0231 |
| 2 | -0.159 | -0.0066 | -0.022 |
| 3 | +3.033 | +0.0017 | +0.0030 |
| 4 | -0.751 | -0.0414 | +0.040 |

Figure 3 shows the phase-space projections at the input of the RFQ and at the output of cell 142. The bold-black points in the input-phase-space projections are particles that were lost before reaching cell 143. At this point in the calculation, the lost particles are the outer most particles injected into the RFQ. The input beam for this simulation came from a simulation of the LEBT beam line[5]. The butterfly shape of the transverse phase-space distributions results from the large variation of the RF phase when the particles reach the cell 142-exit plane. The particles' transverse velocity at the cell exit plane depends on the RF phase.

The ellipses in these plots correspond to the rms Twiss parameters of the beam. The area is 4 times the rms emittance. The separatrix, shown in the lower right of Figure 3, defines the stable region of the phase-energy plane.

Figure 4 shows the phase space plots from the RFQTRAK simulation at cell 430, the last regular cell of the RFQ. The butterfly shape visible in the cell-142 transverse phase planes does not appear at cell 430 because the phase spread is small. Compare the RFQTRAK simulation with Figure 5, which shows the same phase-space plots from the PARMTEQM simulation. Tables 2 and 3 list the rms-beam properties of the two simulations.

The LEDA RFQ has a transition cell and a radial matching section[6]. The exit radial-matching section matches the beam into the following accelerator. PARMTEQM can simulate the transition cell and exit radial matching section, but RFQTRAK cannot. Cell 430 is the last cell where a comparison between the two codes is possible. A modification of RFQTRAK will add this capability in the near future.

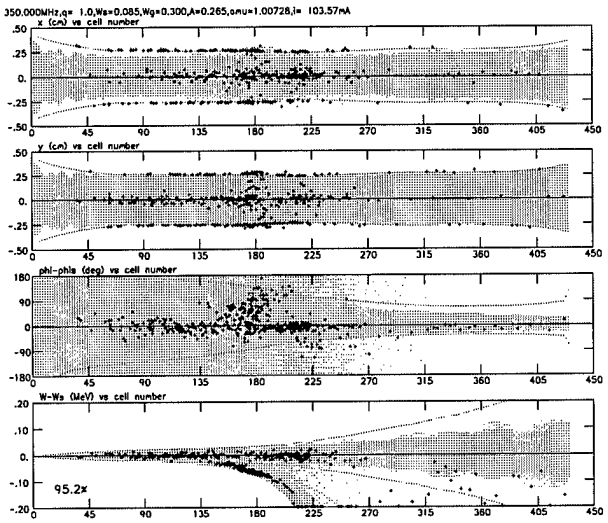



Figure 2. RFQTRAK simulated the LEDA RFQ using 100,000 macro particles. From top to bottom are: x, y, phase, and energy coordinates versus cell number. Bold-black points indicate lost particles. Only 10% of the lost particles are shown for clarity. The percentage transmission is 95.2%.

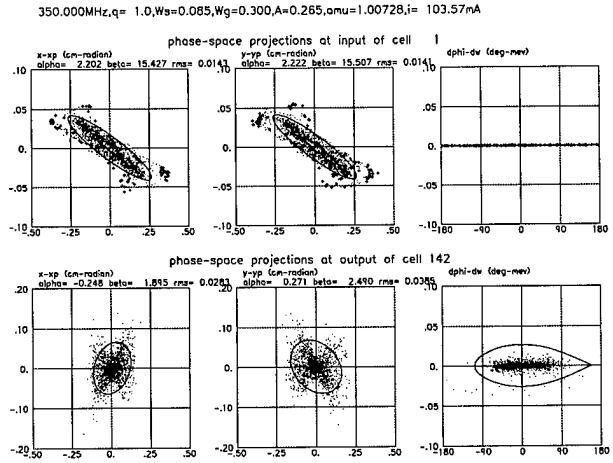



Figure 3. RFQTRAK simulation showing phase-space plots of the input beam and the beam at cell 142. Only 2% of the particles are plotted. The bold-black points in the input phase space show 10% of the particles in the input beam that have been lost up to and including cell 142. The phase-space plots from left to right are: x-x′, y-y′, and phase-energy, where x′=dx/dz and y′=dy/dz.

## PARMTEQM

PARMTEQM, which uses the z position as the independent variable and a cylindrically symmetric space-

charge calculation, cannot handle the type of errors listed in Table 1. However, PARMTEQM needs less computer resources and runs several times faster than RFQTRAK. For these reasons, we used PARMTEQM to design the LEDA RFQ. We used the PARMTEQM beam distributions to match the beam into the CCDTL. The validity of the PARMTEQM simulations can be accessed by comparing the beam distributions from PARMTEQM to the distributions from the fully 3D simulation performed in RFQTRAK.

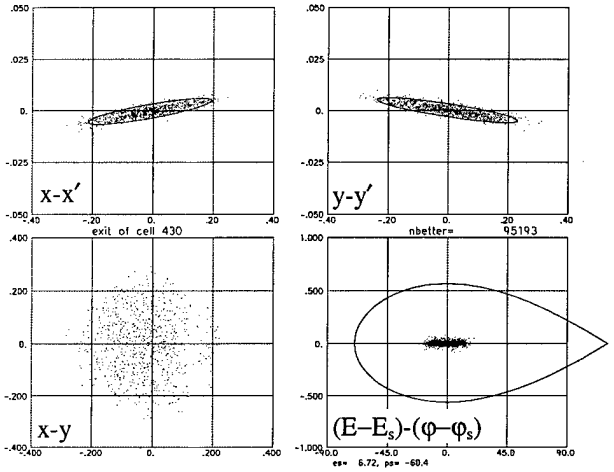



Figure 4 Phase-space projections near the end of the RFQ. Only 2% of the particles are plotted. RFQPROC calculates the Twiss parameters, α and β, and the rms emittance ε from the 95,193 macro particles remaining in the beam. It then draws the ellipses using 4×ε for the area. Table 2 lists these Twiss parameters.

Table 2. RFQTRAK Twiss parameters at cell 430.

| | Twiss parameters | | |
|---|---|---|---|
| Parameter | x-x′ | y-y′ | (E–Es)-(φ–φs) |
| α | –1.525 | 1.509 | 0.065 |
| β | 59.02 | 73.48 | 424.4 |
| ε (cm-mrad) | 0.0211 | 0.0223 | 0.03407 |

Table 3. PARMTEQM Twiss parameters at cell 430.

| | Twiss parameters | | |
|---|---|---|---|
| Parameter | x-x′ | y-y′ | (E–Es)-(φ–φs) |
| α | -0.750 | 0.591 | -0.087 |
| β | 63.297 | 81.752 | 410.2 |
| ε (cm-mrad) | 0.0172 | 0.0181 | 0.0387 |

RFQTRAK calculated 95.2% transmission, which is nearly the same as 95.4% from PARMTEQM. The most significant difference between beam distributions calculated by the two codes is the difference in the emittance. In RFQTRAK the longitudinal emittance is smaller and the transverse emittance is larger. There is also a difference in the α's and β's. These differences are large enough that the match to the CCDTL should be checked. RFQTRAK requires the addition of the transition cell and exit radial-matching section before we can make this check. Then the PARMILA code can transport the RFQTRAK particle distribution through the CCDTL. The results of this simulation will provide the required check of the match to the CCDTL.

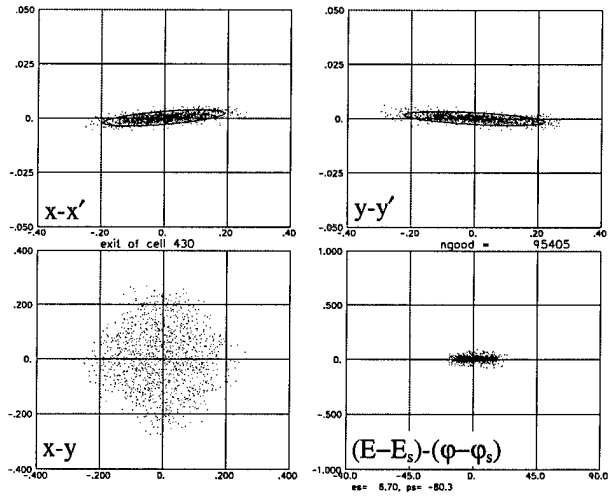



Figure 5. Phase-space projections near the end of the RFQ. Only 2% of the particles are plotted. PARMTEQM calculates the Twiss parameters, α and β, and the rms emittance ε from the 95,405 macro particles remaining in the beam. It then draw the ellipses using 4×ε for the area. Table 3 lists these Twiss parameters.

## CONCLUSIONS

RFQTRAK and PARMTEQM simulations are in substantial agreement. The transmission the two codes calculate, with the same input beam, is nearly identical. There are small differences in the emittance and Twiss parameters calculated by the two codes. RFQTRAK needs further development to add the transition cell and exit radial matching section. Then PARMILA could use RFQTRAK's output beam for the CCDTL simulation.

## REFERENCES


[1] L. M. Young, "An 8-meter-long coupled cavity RFQ Linac," Proc. 1994 Intl. LINAC Conf., p. 178 (Tsukuba, Japan, Aug. 21-26, 1994).

[2] N. J. Diserens, "Progress in the Development of a 3D finite Element Computer Program to Calculate Space and Image Charge Effects in RF Quadrupoles," IEEE Trans. Nucl. Sci., NS-32, (5), 2501 (1985).

[3] N. J. Diserens, "RFQCOEF a Package for Extracting the Harmonic Coefficients for the Potential Function in an RF Quadrupole," Proc. 1984 Linear Accel. Conf., Darmstadt, Germany, GSI-84-11, 324 (1984).

[4] K. R. Crandall et al., "RFQ Design Codes," Los Alamos National Laboratory report LA-UR-96-1836. (revision February 12, 1997)

[5] L. M. Young, "Simulations of the LEDA LEBT with $H^+$, $H_2^+$, and $e^-$ particles," this conference.

[6] K. R. Crandall, "Ending RFQ Vane tips with Quadrupole Symmetry," Proc. 1994 Intl. LINAC Conf., p. 227(Tsukuba, Japan, Aug. 21-26, 1994).

# HIGH CURRENT DENSITY ION SOURCES FOR HEAVY ION FUSION ACCELERATORS

J.W. Kwan, W.W. Chupp, Lawrence Berkeley National Laboratory, Berkeley, CA and
S. EYLON, FARTECH, Inc., San Diego, CA

*Abstract*

Testing of the alumino-silicate ion source and the contact ionizer at high current density was satisfactory. The dispensers embedded in the extraction electrode were capable of providing sufficient cesium vapor coverage to the ionizer thus shows a promising way of constructing an ionizer for long term heavy ion fusion applications.

## 1 INTRODUCTION

A heavy ion fusion (HIF) driver requires ion sources that can deliver intense heavy ion beams with low emittance. The choice of ion species depends on the range of penetration into the fusion target at the accelerator beam voltage. Typical ions of interest are those of Bi, Pb, Hg, Cs, Xe, Rb, K, Ar, and Ne. Some lighter ions like K, Ar and Ne are included because at the early stages of driver development, they provide the opportunity to do experiments at driver scale ion velocities on a less than full length accelerator facility.

Naturally, not all the ion species of interest can be produced effectively from a single type of ion source. For example, a gas source is suitable for generating Hg, Xe, Ar and Ne ions whereas a metal vapor vacuum arc (MEVVA) source would be more appropriate for ions such as Gd and Bi. In fact the MEVVA source has an additional advantage of generating ions with high charge states, thus reduces the required accelerator beam voltage. Both the gas source and the MEVVA source still need further development in order to meet the driver requirements. So far, the surface ionization sources have been used in most HIF driver designs. The surface ionization type of ion source can efficiently produce singly charged alkali ions such as $Cs^+$ and $K^+$. The major advantages of this type of ion source are the absence of gas flow, excellent beam current control and low emittance (due to low ion temperature and a solid emitter boundary). The main concerns here are the source life time, the alkaline vapor delivery system, and the deposition of alkaline vapor onto beam line components.

A typical heavy ion fusion (HIF) driver can have of the order of 100 ESQ injectors at the front-end of an induction linear accelerator [1]. Based on beam transport considerations, a 2-MeV injector should provide a beam with a line charge density of approximately $0.25 \times 10^{-6}$ C/m. The actual beam current will depend on the ion velocity (or equivalently the square root of the charge/mass ratio). For a potassium ion beam, the corresponding beam current is 0.8 A per ion source. For HIF driver applications, the required pulse length is about $20 \times 10^{-6}$ s with a rise time preferably not more than $1 \times 10^{-6}$ s and a repetition rate of 10 Hz.

Previously, an alumino-silicate ion source has been developed for the ILSE project [2]. The ion source has a diameter of 17 cm, thus the potassium current density is approximately 3.5 mA/cm$^2$. Although this ion source has met the original specifications for the ILSE project, the latest conceptual designs for the next HIF research facility calls for an injector with an ion source that has a current density $\geq$15 mA/cm$^2$ of $K^+$ (a factor of 4 increase from the previous case). The major reason for choosing a high current density, compact size injector is to reduce the overall cost of a fusion driver.

In this paper, we present experimental results on testing the ion sources to meet the new specifications. Both the alumino-silicate type and the alkaline vapor contact ionizer have been tested. The results suggest that both types of ion sources will meet the current density requirement and eventually the selection will depend on further experiments relating to the life-time and reliability of the ion sources.

## 2 EXPERIMENTAL SETUP

### *2.1 The Ion Extractor and Diagnostics*

A schematic diagram of the ion source and the extraction electrodes is shown in Fig. 1. The ion source has a 2-cm diameter concave emission surface (10-cm radius of curvature). The structure, which includes the cylindrical sidewall and the threaded center post, is made of porous tungsten. Heating of the ion source is provided by a molybdenum filament surrounded with ceramic shields. It takes approximately 100 watts to heat the ion source to the operating temperature of about 1000°C. The 3-electrode extractor was designed to extract ion beams uniformly at space-charge-limited flow from the emitter. High voltage is obtained from a pulse forming network feeding into a bi-polar step-up transformer. Typical pulse length is about $1.5 \times 10^{-6}$ s. The Pierce electrode, which has the same potential as the ion source, receives the positive high voltage output while the last electrode receives the negative high voltage output and the middle electrode is at ground potential. This arrangement allows us to provide the maximum electric field gradient for ion extraction. Although the ions are decelerated in the region between the last electrode and the diagnostic equipment, the beam diameter is kept small enough to avoid collision into the last electrode and to produce a spot size smaller than the opening of the Faraday cup. There is a another advantage of applying negative high voltage to the last electrode because it suppresses electrons from either back streaming into the ion source as well as assists the Faraday cup in capturing its own secondary electrons.

0-7803-4376-X/98/$10.00 © 1998 IEEE

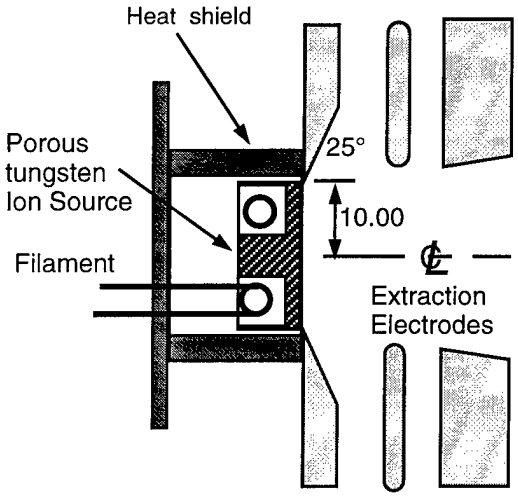



Figure: 1 Schematic diagram of the ion source and extraction electrodes.

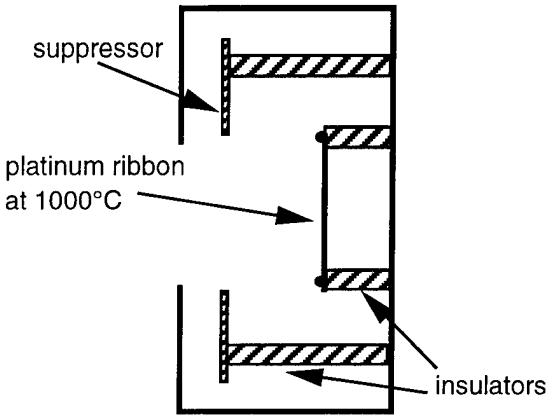



Figure: 2 Schematic diagram of the neutral detector

The ion beam current density profile was measured by moving a 2-mm diameter pinhole across the Faraday cup entrance. A pair of permanent magnets was mounted behind the pinhole to produce a transverse magnetic field for stopping secondary electrons that were generated at the pinhole from entering the Faraday cup. The pinhole plate and the Faraday cup aperture are located at 1 cm and 3 cm downstream of the last electrode respectively.

A platinum-ribbon contact ionization detector was used to measure the alkaline neutrals flowing out of the ion source, see Fig. 2. Platinum has a high work function which offers excellent ionization efficiency. In steady state, the amount of adsorbed alkaline atoms on the hot platinum surface (approx. 1 $cm^2$) will reach equilibrium in such a way that the flux of incoming alkaline atoms equals to the ion current emitted by the surface. Here, we assume that the ionization probability is near 100%. The emission is measured by monitoring the drain current on the 2 kV bias power supply (after subtracting the leakage background current). Good agreement was obtained by calibrating our measurement against the flow rate specified by the manufacturer of an alkaline vapor dispenser.

*2.2 Two Types of Surface Ion Sources*

For the alumino-silicate ion sources, a thin layer (approx. 0.3 mm) of alumino-silicate was melted on top of the porous tungsten curved surface. Some recently developed techniques have improved the coating quality to reliably achieve surface uniformity. In testing the contact ionizer scheme, the bare porous tungsten surface was loaded with a fraction of a monolayer of cesium (or potassium) by either doping the source with a solution of alkaline carbonates or by using alkaline dispensers.

For the contact ionizers, six 12 mm long commercially available dispensers (by SAES GETTERS) are embedded around the center opening in the middle electrode, so that the dispensers output release slits are facing the source emitter surface. Fig. 3 shows the dispenser layout schematics. Since this electrode is facing an hot ion source, there is indirect heating from radiation. Additional electrical heating of the dispensers can be done to control the vapor release. In order to avoid overheating, the middle electrode is cooled by a waterline at the edge.

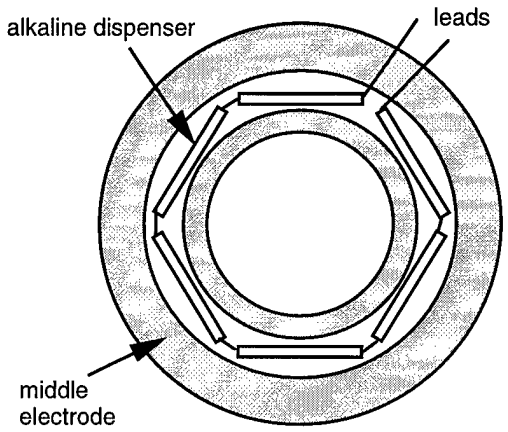



Figure: 3 Front fed vapor source dispenser layout.

## 3 EXPERIMENTAL RESULTS

The beam current extracted from the ion source depended on the ion source temperature and the applied extraction voltage. The I-V characteristics are shown in Fig. 4 (the extraction voltage is defined as the total potential difference between the positive Pierce electrode and the negative last electrode). In the space-charge-limited flow regime, the beam current increased according to the "$V^{3/2}$ law". This relationship sustained until the ion source reached the emission limit mode. The emission limit increased with the ion source temperature. At 44.5 kV and at an ion source temperature of 1050°C, we have obtained 43.2 mA of $K^+$ ions. This corresponded to an average current density of 13.75 $mA/cm^2$.

As shown in Fig. 5, the current density profile of the ion beam was uniform to within ±5%. There was a data uncertainty of a few percent due to signal noise and digitization.

Also shown in Fig. 4 and 5 are the performance of an ionizer doped with potassium carbonate. As the source

was heated to operating temperature, the carbonate decomposed and subsequently reached an equilibrium coverage of potassium atoms adsorbed to the emitter surface. This is an easy way of "delivering" alkaline atoms to an ionizer. The doped source usually lasted only for a few days of operation before completely depleting the alkaline storage, thus it is mainly used for calibration purposes and is not considered a long term solution for HIF applications.

A long life ionizer must have some way of continuously feeding the alkaline vapor, either from the front side or via diffusion through the porous tungsten from the back side. In our experiment, we have tested the effectiveness of delivering cesium vapor from dispensers embedded inside the extraction electrode. It was found that the radiation from the ion source produced sufficient heat to the dispenser, without requiring any additional electric heating, to release Cs vapor. During initial operation, there was enough cesium coverage to produce a beam current density as high as 15.4 mA/cm$^2$ (space-charge equivalent to 29.4 mA/cm$^2$ of $K^+$). The I-V characteristics are shown in Fig. 6. As time went on, additional electric current could be used to drive the remaining cesium content out of the dispenser.

In measuring the alkaline neutrals at 15 cm downstream of the extractor, we compared the signals for 2 detector positions, at beamline center and away from center without line of sight. The background pressure was about $5\times10^{-7}$ Torr. The cesium neutral flow rate arriving at the platinum foil was determined to be $7.5\times10^{11}$ /cm$^2$/s while the ion source was kept at 1100°C. This corresponds to an atomic emission rate of $1.7\times10^{14}$ /cm$^2$/s (0.14 mg/cm$^2$/hr) from the ion source.

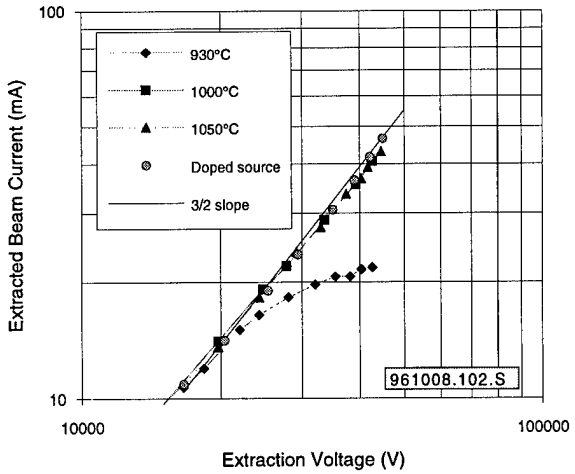



Figure: 4 I-V characteristics for the alumino-silicate $K^+$ ion source and the doped source.

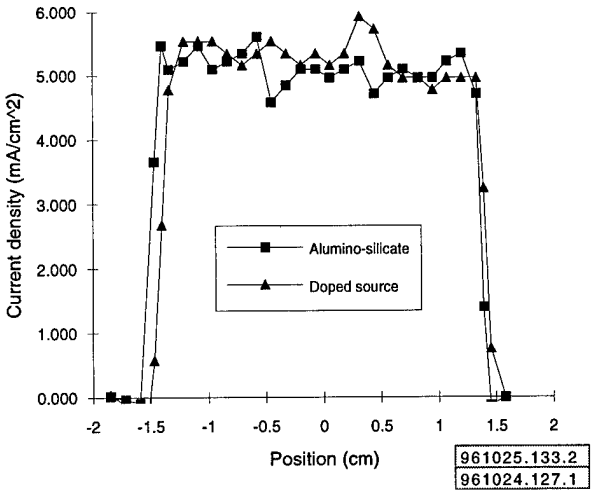



Figure: 5 Beam profiles for the alumino-silicate ion source and the doped source.

## 4 DISCUSSION

We have shown that both types of ion sources can produce the required current density. The current denstiy uniformity is good. The method of using alkaline dispensers embedded inside the extraction electrode was proven to be adequate for even the highest current density cesium beam that we have achieved. Further investigation of this concept can lead to the successful development of a long life front-fed contact ionizer.

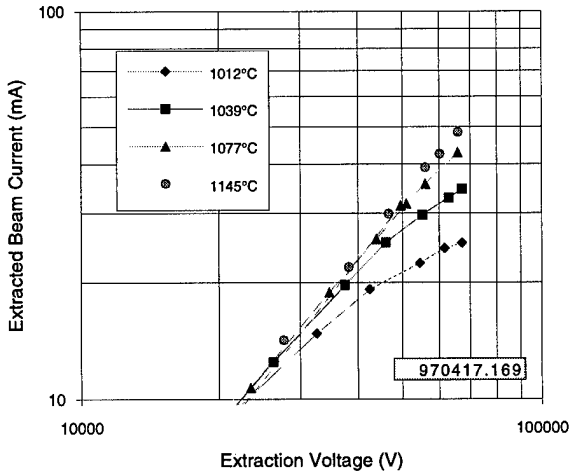



Figure: 6 I-V characteristics for the cesium vapor ionizer.

## 5 ACKNOWLEDGEMENTS

The authors wish to thank C.F. Chan for consultation in beam optics, and R. Hipple and his staff for technical supports. This work is supported by the Office of Fusion Energy, US DOE under contract No. DE-AC03-76SF00098.

## REFERENCES

[1] R.O. Bangerter, Proc. of Inter. Symp. on Heavy Ion Inertial Fusion, Frascati, Italy, May 25-28, 1993, Nuovo Cimento 1445 (1993).

[2] S. Eylon, E. Henestroza, W.W. Chupp, and S. Yu, Proc. of Inter. Symp. on Heavy Ion Inertial Fusion, Frascati, Italy, May 25-28, 1993, Nuovo Cimento 1509 (1993).

# H⁻ ION SOURCE DEVELOPMENT FOR THE NATIONAL SPALLATION NEUTRON SOURCE*

M.A. Leitner, R.A. Gough, K.N. Leung, M.L. Rickard, A.B. Wengrow, M.D. Williams, D.C. Wutte
Ernest Orlando Berkeley National Laboratory, University of California at Berkeley
Berkeley, California 94720

*Abstract*

The ion source for the 1 MW National Spallation Neutron Source (NSNS) is required to provide 35 mA of H⁻ beam current (1 ms pulses at 60 Hz) at 65 keV with a normalized rms emittance of less than 0.2 pi mm mrad. The same ion source should be able to produce 70 mA of H⁻ at 6% duty factor when the NSNS is upgraded to 2 MW of power. For this application, a radio-frequency driven, magnetically filtered multicusp source is now being developed at LBNL. In preliminary experiments with an existing ion source developed for the Superconducting Super Collider, 15 mA of H⁻ ions were extracted at an accelerated voltage of 10 kV and an RF output power of 20 kW without cesium. The design of a new source equipped with a cesium dispenser collar, a fast ion beam pre-chopper (rise times < 100 ns) and a strong permanent-magnet insert for electron deflection will be presented.

## 1 INTRODUCTION

Volume produced, low temperature (< 2 eV) H⁻ ions can be directly extracted from a multicusp, rf-driven, plasma source to form a high-brightness beam as required for the National Spallation Neutron Source (NSNS). To verify that the performance objectives of the ion source, as mentioned in the abstract, can be achieved at the relatively high duty factor of 6%, we performed some initial experiments with an existing source, which was originally developed at LBNL for the SSC [1]. A schematic of such a multicusp, rf-driven (1.8 MHz), H⁻ ion source is shown in Fig. 1. A detailed design of this source has already been described elsewhere [2,4].

## 2 EXPERIMENTS

### *2.1. Total Current*

All of our experiments were limited to an rf input power of 23 kW and an extraction voltage of 5 kV. The extraction hole was 6 mm diam., and there was no cesium added to the ion source. Fig. 2 shows, that under these conditions we could extract up to 15 mA of H⁻. The H⁻ current increases linearly with rf power, as seen in previous experiments [3]. This shows that an ion source operated for NSNS needs at least 50 kW of rf input-power without cesium added.

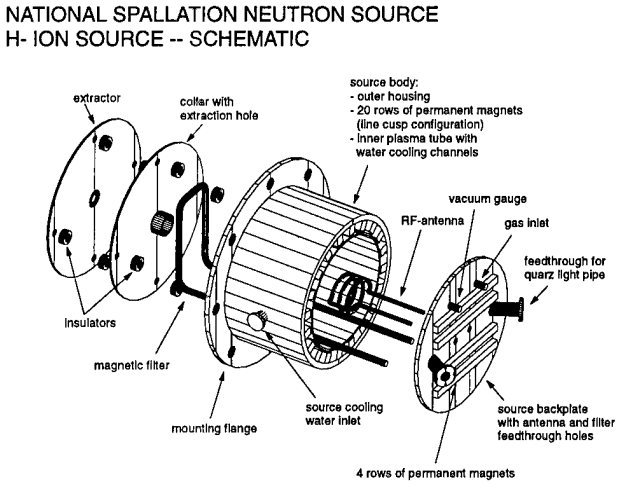



Figure: 1 Rf-driven, multicusp volume H⁻ ion source.

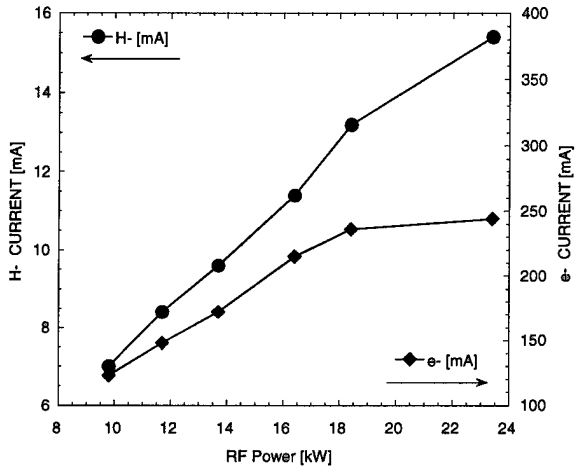



Figure: 2 Extracted H⁻ current vs. rf power at 6% duty factor.

* This research is sponsored by the Lockheed Martin Energy Research Corporation under the U.S. Department of Energy, Contract No. DE-AC05-96OR22464, through the Lawrence Berkeley National Laboratory under Contract No. DE-AC03-76SF00098.
† Also with the Institut für Allgemeine Physik, Technical University Vienna

0-7803-4376-X/98/$10.00 © 1998 IEEE

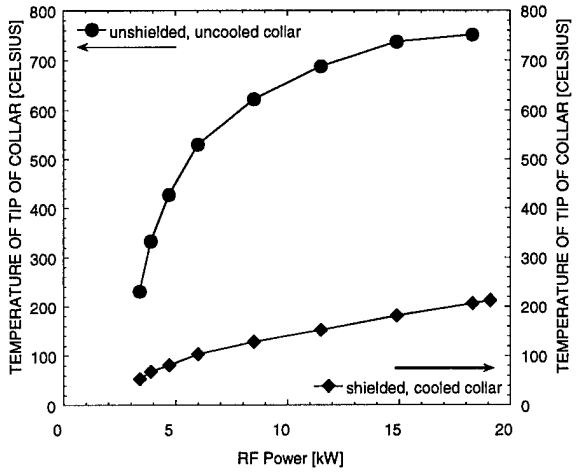



Figure: 3 Collar temperature vs. rf power for different collar geometries as explained in the text.

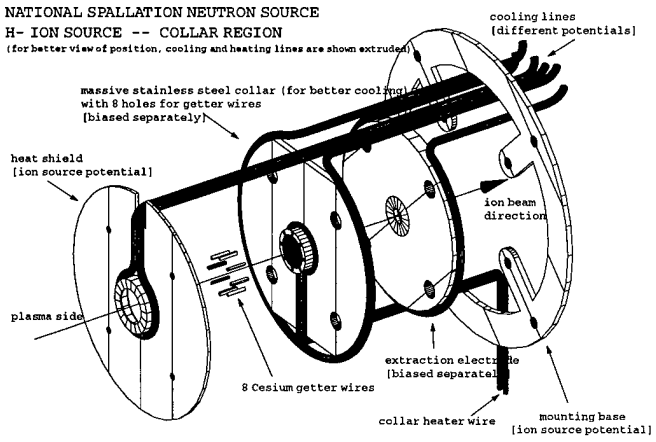



Figure: 4 Expanded view of the new collar design for the NSNS R&D ion source.

*2.2 Collar Geometry*

By installing a collar electrode around the extraction aperture, the extracted electron current can be reduced by a factor of two without significant change in the $H^-$ output current [3]. In such an arrangement a small cylinder (~1 cm diam., 9 mm long) is mounted on the plasma electrode, facing the plasma side. A basic collar configuration is shown in Fig. 1.

It has been demonstrated that the $H^-$ output current can be enhanced by introducing only a trace amount of cesium into the collar region [4]. This can be achieved by placing tiny cesium getter wires in vertical cuts around the collar. It has been shown, that cesiation of the collar region is critical to temperature [5], with an optimum at ~200°C. Therefore we investigated the variation of the collar temperature at various conditions (Fig. 3). At 6% duty factor and 20 kW pulsed rf-power an uncooled and unshielded collar reaches temperatures above 700°C. A slightly modified, better-cooled collar stayed at considerably lower temperatures.

In order to meet the NSNS ion source requirements of 50 kW pulsed rf-power, an enhanced collar design was necessary to control the collar temperature. Fig. 4 shows the new collar region design: Eight cesium getter wires slide into the massive stainless steel collar, which is directly water-cooled by a tube, mounted on the outer perimeter of the collar aperture. For further temperature control a heater wire is attached to the collar. A heat shield was placed in front of the collar. The collar was isolated from the extraction electrode, to allow independent biasing of both electrodes in respect to the ion source potential. This feature is necessary for fast ion beam chopping.

*2.3 Magnetic Extraction Insert*

Unavoidably with volume ion sources, a high-current electron beam (hundreds of mA) is extracted together with the $H^-$ ions. It has been shown previously that a

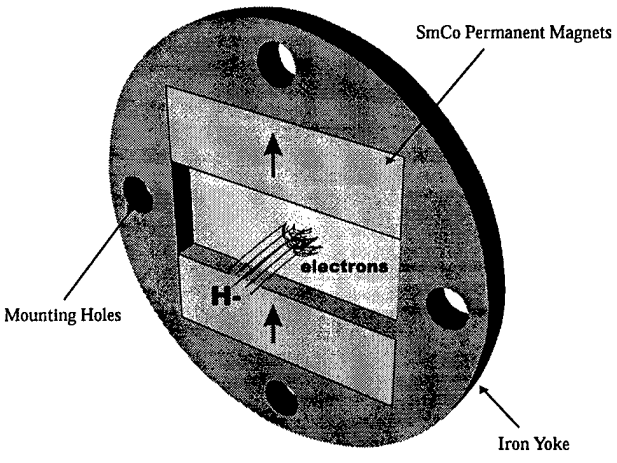



Figure: 5 The new electron deflection scheme at the first electrode (TOSCA 3D simulation).

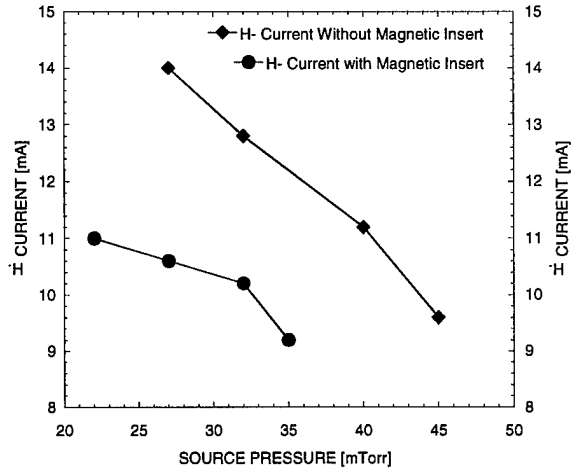



Figure: 6 $H^-$ current vs. source pressure, with and without magnetic deflection insert.

transverse magnetic field at the extraction hole can deflect nearly all the electrons out of the $H^-$ ion beam [6]. The electrons are then dumped at the second electrode at the extraction energy. For NSNS at 6% duty factor and a proposed 85 kV potential drop at the extraction gap, this would result in a very high power loading on the second electrode. For this reason, we are developing a new scheme for electron dumping.

Computational results in Fig. 5 show the effect on the extracted electrons from a pair of permanent magnets located inside the first electrode. Due to the high magnetic field (>1000 G), the electrons gyrate back to the extraction electrode. The collection of the electrons at source potential results in no power loss due to the extracted electrons.

We could show experimentally that with the magnetic insert installed, all of the electrons could return to the source, resulting in no current lost to the second electrode. Nevertheless a strong magnetic insert results in increased $H^-$ beam deflection. Traces at the Faraday cup showed that we were not collecting the whole $H^-$ beam. Therefore measured $H^-$ currents are less with the strong magnet insert installed, as shown in Fig. 6. Further computational and experimental investigation is needed to ensure that the $H^-$ ions are focused properly for further beam transport. We have started 3 dimensional simulations with TOSCA 3D (magnet code) and ARGUS (space charge ion beams), but results are still preliminary.

*2.4 Beam Chopping*

The NSNS requires 300-ns gaps in the beam to eliminate activation of the extraction septum in the accumulated ring during the turn-on time of the extraction kicker. At LBNL we have tested beam chopping at the multicusp ion source by connecting a dc power supply with a fast electronic switch between the plasma electrode and the source chamber wall. If a positive voltage (~100 V) pulse is suddenly applied to the plasma electrode, the $H^-$ current can be extinguished [7]. We developed a voltage modulator with rise/fall times of less than 100 ns. Experiments with the chopper installed at the ion source are planned. For more control over the pulse shape of the chopped ion beam, both, the collar and the extraction electrode, can be biased independently in the new ion source design

## 3 CONCLUSION

We have performed first experiments with an existing $H^-$ volume ion source to define the design requirements of an R&D ion source for NSNS. This led to an enhanced ion source design with an improved collar region, a magnetic deflection scheme for complete electron removal and a fast ion beam chopper. A design drawing is shown in Fig. 7. The new source also features a longer plasma chamber, a movable antenna and a movable magnetic filter, which is inserted from the backflange - therefore eliminating the need for an additional filter flange. The purpose of this ion source is to find the optimum operational conditions for the NSNS. Construction of the ion source is already completed and first experiments will follow. Results of the new ion source testing will be reported in the near future.

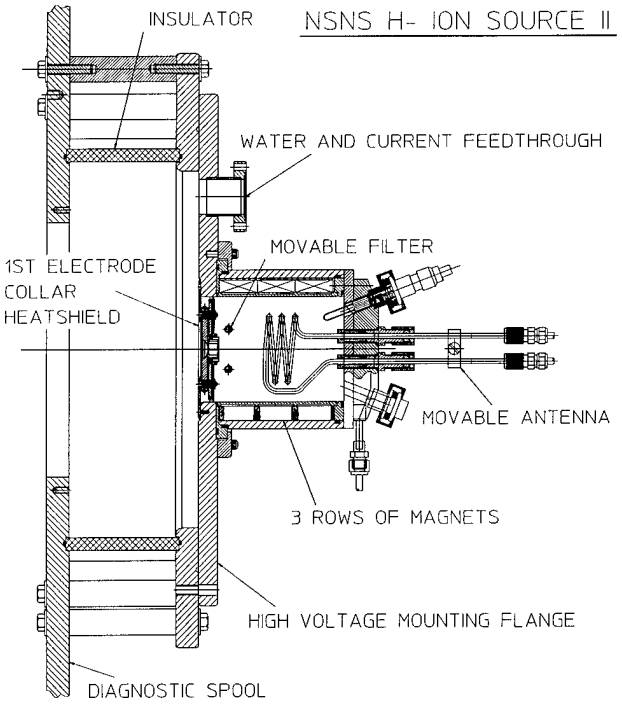



Figure: 7 The new NSNS R&D $H^-$ ion source design. The extraction region is shown in more detail in Fig. 4.

## 4 ACKNOWLEDGEMENTS

Daniela Wutte gratefully acknowledges the support by the Schrödinger Fellowship granted by the Fonds zur Förderung der wissenschaftlichen Forschung in Österreich under contract number J01220-PHY.

## REFERENCES

[1] K.N. Leung, G.J. DeVries, W.F. DiVergilio, R.W. Hamm, C.A. Hauck, W.B. Kunkel, D.S. McDonald, M.D. Williams, Rev.Sci.Instrum. **62**, 100 (1991)

[2] K. Saadatmand, J. Hebert, N. Okay, Rev.Sci.Instrum. **62**, 1173 (1994)

[3] K.N. Leung, C.A. Hauck, W.B. Kunkel, S.R. Walther, Rev.Sci.Instrum. **61**, 1110 (1990)

[4] K. Saadatmand, G. Arbique, J. Hebert, R. Valicenti, K.N. Leung, Rev.Sci.Instrum. **66**, 3438 (1995)

[5] Y. Okumura et al, Proc. of the 5th International Symposium. on the Production and Neutralization of Negative Ions and Beams, Brookhaven, p169 (1990)

[6] Luke T. Perkins, P.R. Herz, K.N. Leung, D.S. Pickard, Rev.Sci.Instrum. **67**, 3497 (1996)

[7] K.N. Leung, C.F.A. van Os, W.B. Kunkel, Appl.Phys.Lett. **58**, 1467 (1991)

# A COMPACT, RF-DRIVEN, PULSED ION SOURCE FOR INTENSE NEUTRON GENERATION*

L. T. Perkins, C. M. Celata, K. N. Leung, D. S. Pickard, R. Vilaithong, and M. D. Williams
Lawrence Berkeley National Laboratory, Berkeley, CA 94720 USA

*Abstract*

Lawrence Berkeley National Laboratory is currently developing a compact, sealed-accelerator-tube neutron generator for activation analysis applications. This portable generator is projected to produce a neutron flux in the range of $10^9$ to $10^{10}$ D-T neutrons per second. A 2 MHz radio-frequency (rf)-driven ion sources, designed to fit within a ~ 5 cm diameter borehole, is used. Typical operating parameters include repetition rates up to 100 pps, with pulse widths between 10 and 80 μs and source pressures as low as 4 mTorr. In this configuration, peak extractable hydrogen current exceeding 35 mA from a 2 mm diameter aperture, together with $H_1^+$ yields over 94% have been achieved. The required rf impedance matching network has been successfully miniaturized to ~ 5 cm diameter and tested. Given the low duty cycle operation, the ion source and matching do not require any cooling.

## 1 INTRODUCTION

The Ion Beam Technology Program of Lawrence Berkeley National Laboratory (LBNL) is currently developing a compact, rf-driven, pulsed ion source for neutron generation. The motivation for this work is to integrated this neutron generator into an activation analysis instrument for the detection of subsurface pollutants. The details of this application are discussed in another paper in these proceedings (C.M. Celata et al.). LBNL's rf-driven ion sources have found numerous applications ranging from neutral beam injection systems for fusion reactors to particle accelerators, proton therapy machines, and ion implantation systems [1]. Such sources are simple to operate, have long lifetimes, high gas efficiencies and provide high density plasmas with high monatomic species yields. These characteristics make the rf-driven ion source a viable candidate for the next generation of compact, high output, sealed neutron generators. An attempt has been made to miniaturize the rf-driven ion source [2,3] and the necessary impedance matching network to fit in a ~ 5 cm borehole with the goal of producing $10^9$ to $10^{10}$ D-T neutrons per second, when coupled to a 100 kV accelerator. Typical operating parameters are: repetition rates of up to 100 pps with pulse widths between 10 and 80 μs, and source pressures as low as 4 mTorr, which is essential for reducing both charge exchange and high-voltage break-down in the accelerator column. Presently, the repetition rate is limited only by the available rf power supply. The choice of the pulse width stems from the characteristic time (neutron inelastic scattering time) for the activation analysis application. In this configuration, peak hydrogen current densities exceeding 1180 mA/cm$^2$ with $H_1^+$ ion species yields over 94% have been extracted from a 2-mm-diameter exit aperture. Though all testing was done with hydrogen to minimize radioactive hazards, a similar ion source performance is expected with deuterium.

## 2 EXPERIMENTAL SETUP

The schematic diagram of the ion source is shown in Fig. 1. Three components can be identified as follows. The first is the rf power source which consists of a main 70 kW (pulse), broad band, rf power amplifier driven at 2 MHz by a signal generator. A pulse generator gates the amplifier so as to generate plasma pulses with durations of up to 80 μs and repetition rates up to 100 Hz.

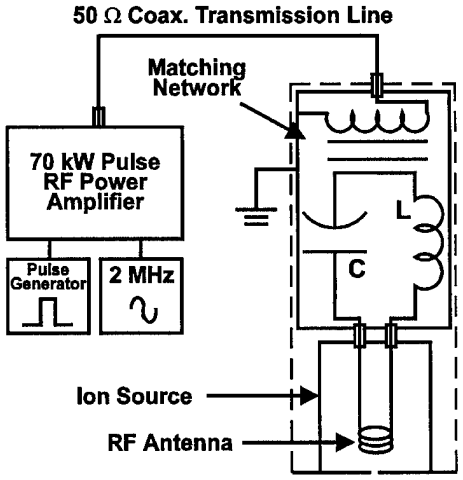



Figure: 1 Schematic of the rf-driven ion source setup.

The next element in the circuit is the impedance matching network. It comprises a 10:1 step-down transformer and an LC tank circuit. The purpose of this network is to match the nominal 50 Ω output impedance of the rf amplifier to the typical low impedance (~ 1 Ω) of the plasma-antenna load.

* This work is supported by the U.S. Department of Energy under Contract No. DE-AC03-76SF00098

0-7803-4376-X/98/$10.00 © 1998 IEEE

Lastly, to deliver rf energy to the plasma, a coupler in the form of a multi-turn induction coil is used. This 3½-turn rf induction coil is fabricated from a solid 1.6 mm diameter copper or stainless-steel wire. This wire is coated with a thin layer of porcelain for electrical insulation from the conducting plasma.

The antenna is immersed in a 2.5 cm I.D., 8 cm long copper cylinder. The source is closed-off at one end with a back flange carrying the necessary feedthroughs for the antenna, a gas inlet and a capacitance manometer to monitor source pressure. The extraction system, which closes off the other end of the ion source chamber, contains 2 electrodes with 2 mm diameter apertures. The first electrode and source body are connected to a 0-25 kV, high voltage extraction power supply, while the second electrode is tied to ground. The two electrodes are separated by a gap of ~2 mm. As dictated by the application, no water cooling is employed, which is possible given the low duty cycle operation (< 0.1%) limited by the available rf power amplifier.

Two kinds of beam diagnostics are used to characterize the ion source performance. The first is a Faraday cup to measure the total beam current. The current density is obtained by dividing the extracted current by the aperture area. The second is a magnetic mass spectrometer with which the hydrogen ion species distribution can be determined.

Since the beam is pulsed, a sample-and-hold circuit is used to measure the cup current of the mass spectrometer. To properly suppress any secondary emission electrons, the Faraday cups of both diagnostics are made of graphite and have a pair of permanent magnets embedded at the cup entrance.

## 3 EXPERIMENTAL RESULTS

### *3.1 Current Density Measurements*

Because of the difficulty in designing an optimized diode extraction system that can accommodate the broad range of plasma densities for this testing, there were conditions when a fraction of the beam sprayed onto the second electrode. Though this second electrode current to ground can be readily measured, it is difficult to quantify its origin given the variation of the secondary emission coefficient with beam energy and species distribution. As a result, the second electrode current was not measured, making the Faraday cup current a lower bound estimate of the ion source output.

The current density measurements were carried out with the antenna coils centered within the source chamber as well as moved forward, with the tip of the induction coil 0.7 cm from the first electrode aperture. The rf pulse width was adjusted so that the extracted current pulse length was on the order of ~ 10 μs.

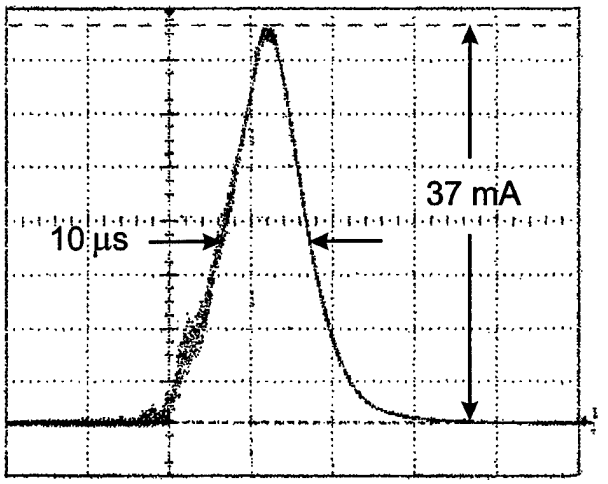



Figure: 2 Typical extracted current pulse shape from a 2 mm diameter aperture, corresponding to 1180 mA/cm$^2$ (at 6.2 mTorr and 52 kW pulse rf input power)

Figure 2 shows the characteristic shape of such short pulses. The beam current pulse taken at the forward antenna position shows a peak value of 37 mA at 6.2 mTorr source pressure and 52 kW pulse rf input power. Figures 3 shows the extractable peak current density versus rf input power for three different source pressures. The current density is seen to increase with increasing rf input power. This data was taken with the antenna centered within the source chamber. The extractable current was observed to increase ~ 30-50% when the antenna was moved forward.

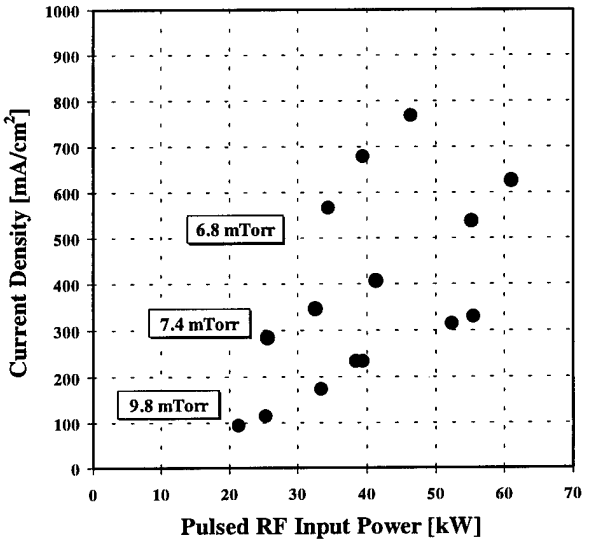



Figure: 3 Peak extractable current density at three different source pressures versus pulse rf input power. Note: 100 mA/cm$^2$ corresponds to a beam of 3.1 mA from the 2 mm diameter aperture.

### 3.2 *Hydrogen Ion Species Measurements*

With the rf antenna located at the center of the source, the proton output was found to be in the 60-70% range, regardless of power and pressure. As the antenna was moved forward, the $H_1^+$ ion fraction increased to the 80-94% range. Figure 4 shows a characteristic mass spectrum with ~ 94% $H_1^+$ ion yield taken at 60 kW rf input power and 6 mTorr of source pressure. Figure 5 shows the hydrogen ion species distribution versus rf power for source pressures ranging from 6 to 9 mTorr. The proton yield is seen to increase with increasing power but is somewhat insensitive to pressure in this range.

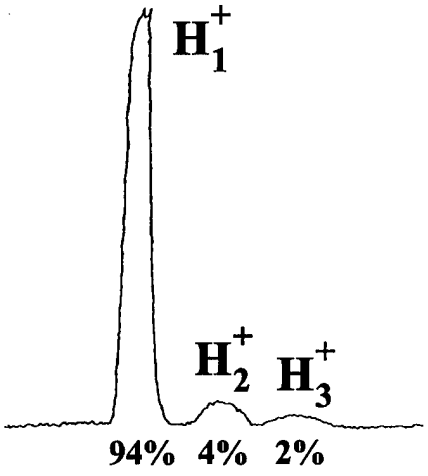



Figure: 4 Hydrogen mass spectrum taken at 5.6 mTorr and 56 kW pulse rf input power, with the antenna moved forward, near the exit aperture.

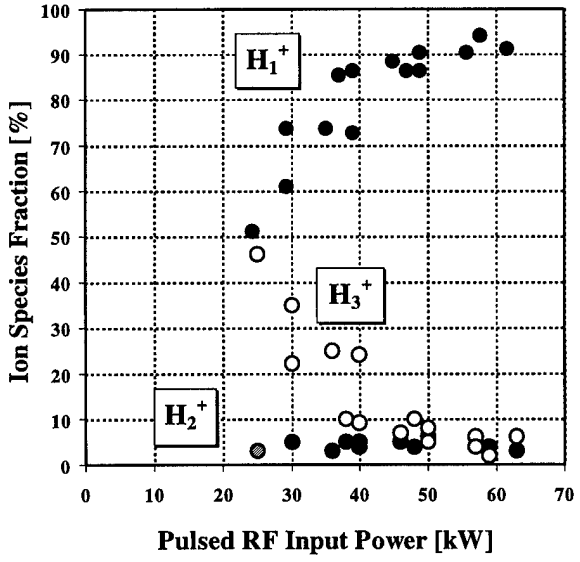



Figure: 5 Hydrogen ion species distribution versus pulse rf input power for pressures in the 6 to 9 mTorr range, with the antenna moved near the exit aperture

## 4 RF IMPEDANCE MATCHING NETWORK

For the above measurements, a larger sized matching network was employed. A miniature size matching network was also constructed to fit into a ~ 5 cm diameter borehole. Given the large current on the secondary side of the transformer (up to 300 A at full power (< ~400 $W_{avg.}$)), care was taken in the selection of capacitors with low dissipation factors and temperature coefficients. Furthermore, improved electrical wiring (e.g., stranded) and contacts (e.g., silver plated) played a significant role in reducing reduce resistive losses in the secondary circuit. Under full power testing (> 50 kW) and without any active cooling, the drift in the matching network resonant frequency due heating of the capacitors was on the order of 10 kHz/hr at 0.1% duty cycle. Further design improvements are being implemented to improve the matching network performance at higher duty factors.

## 5 DISCUSSION

Further experimental details on the development of this compact neutron generator can be found in Ref. [4]. Included in this reference is a detailed estimate of neutron yield assuming a 50%-50% D-T discharge, 100 kV accelerator voltage, and taking into account losses in the accelerator (due to charge exchange). The result of this calculation shows a neutron output of $10^9$ n/s with 60 μA of average beam current and 80% monatomic species fraction. With an available duty factor of 0.1% at 100 Hz, this average current corresponds to 60 mA/pulse. The ion source output is expected to be sufficient to achieve at least $10^9$ D-T neutrons per second with a larger 3 mm beam aperture accelerator design. Without cooling considerations, a neutron yields in excess of $10^{10}$ n/s can be expected with a further increase in beam aperture and/or increase in the repetition rate of the rf amplifier.

## 6 ACKNOWLEDGEMENTS

We would like to thank, G. J. DeVries, R. Keller, W. B. Kunkel, M. Rickard, and S. Wilde for their technical assistance. This work is supported by the U.S. Department of Energy under Contract No. DE-AC03-76SF00098.

## REFERENCES

[1] Leung, K. N., *Rev. Sci. Instrum.*, **67**, 1302, 1996.
[2] Perkins, L. T., Herz, P. R, Leung, K. N, and Pickard, D. S., *Rev. Sci. Instrum.*, **65**, 1186, 1994.
[3] Perkins, L. T., DeVries, G. J., Herz, P. R., Kunkel, W. B., Leung, K. N., Pickard, D. S., Wengrow, A., and Williams, M. D., *Rev. Sci. Instrum.*, **67**, 1057, 1996.
[4] L. T. Perkins et al., Proceedings of the 14th ICAARI, Denton, TX, Nov. 6-9, 1996

# DEVELOPMENT OF A HIGH DUTY FACTOR, SURFACE CONVERSION H⁻ ION SOURCE FOR THE LANSCE FACILITY*

A. B. Wengrow, K. N. Leung, M. A. Leitner, M. D. Williams, and D. C. Wutte†
Lawrence Berkeley National Laboratory, Berkeley CA 94720

William B. Ingalls, and Ralph R. Stevens Jr.
Los Alamos National Laboratory, Los Alamos NM 87545

*Abstract*

The next generation spallation neutron sources, such as the upgrade to the Los Alamos Neutron Science Center (LANSCE) will require high intensity negative hydrogen ($H^-$) beams. The new LANSCE source in particular will need to generate 40 mA of $H^-$ beam current at a duty factor of 12% (1 ms pulse at 120 Hz). One option that we are currently studying concerns altering the existing LANSCE source to utilize an RF induction plasma discharge. However, before proceeding with any changes a full understanding and optimization of our current prototype ion source was required. This surface conversion source, similar to the present LANSCE source, will be used as a benchmark against which to measure future modifications, as well as to provide direction for those modifications. Results to date along with future plans will be presented.

## 1 INTRODUCTION

The upgrade of the Los Alamos Neutron Science Center (LANSCE) to 160 kW of beam power to the spallation target will require a corresponding improvement of its $H^-$ ion source. Specifically the new LANSCE ion source will need to more than double its intensity from 16 to 40 mA. In addition, source emittance, reliability, and availability will need to be improved. All of which must be achieved while operating under the facility's prescribed 12% duty factor. While there are many options that may lead to the achievement of these goals, a thorough study of the original R & D prototype source developed at Lawrence Berkeley National Laboratory (LBNL) was necessary. The LBNL source is slightly different in size and configuration from the current LANSCE surface conversion source. Therefore a series of experiments was initiated first to optimize the LBNL source to reproduce the results of the LANSCE source, and second to set a standard to evaluate future modifications. This work furnished a better understanding of how the operating conditions of the source affect $H^-$ production, in addition to providing direction for future source hardware modifications.

## 2 EXPERIMENTAL SET-UP

The typical multicusp $H^-$ surface conversion source is primarily composed of a plasma chamber and a negatively biased converter electrode [1]. The ions present in the hydrogen plasma ($H^+$, $H_2^+$, $H_3^+$) are accelerated towards the converter surface. $H^-$ can then be formed either through a *back scattering* process [2], or a *sputtering* process [3] when the ions collide with the converter surface. The converter is either composed of, or coated with a low work-function metal such as barium or cesium which greatly enhances the $H^-$ yield [4].

The LBNL source is composed of a stainless steel multicusp plasma chamber 20 cm in diameter and 23 cm in height. A picture of the source and its interior can be seen in Fig. 1. The molybdenum converter has a cross-sectional diameter of 3.8 cm with a spherical face

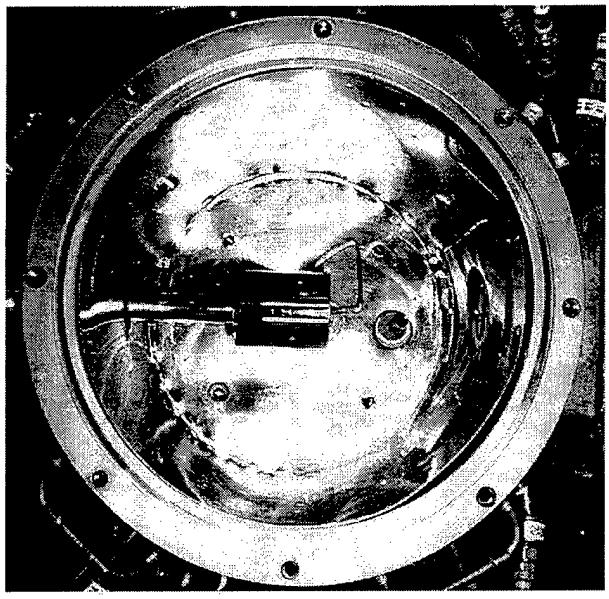


Fig. 1. Close-up of LBNL surface conversion source interior (top down view).

* This work was supported by Los Alamos National Laboratory in association with Lawrence Berkeley National Laboratory and the Division of Nuclear Physics, U.S. Depaertment of Energy under contract No. DE-AC03-76F00098
† Also with the Institut für Allgemeine Physik, Technical University Vienna

0-7803-4376-X/98/$10.00 © 1998 IEEE

cut to a 12.7 cm radius of curvature. The converter is typically operated at a DC bias of -250 V. To coat the converter, cesium vapor is injected into the source through a nozzle connected to an oven mounted on the lower end-flange. The cesium neutrals will condense on the water-cooled converter (or any other cool surface), and if ionized they will simply be accelerated towards the converter surface. The plasma is generated by two 1.5 mm diameter tungsten filaments mounted through the top and bottom end-flanges. The plasma is pulsed by switching the filaments' arc voltage with a 1 ms pulse at 120 Hz to produce the necessary 12% duty factor. Arc power delivered to the plasma is controlled by maintaining a constant arc voltage (~ 60 V) while adjusting the filament heater current.

The exit region of the source contains a plasma aperture plate, a beam aperture cone, and a Faraday cup. All three of which are isolated from the source, and from each other. A schematic of the source and its exit section is shown in Fig. 2. The isolation of the plate and cone allows for more complete beam diagnostics than with the Faraday cup alone. The aperture cone has the same dimensions as the LANSCE source, and the same distance to the converter. The major difference between the LBNL source and the current LANSCE source is the magnetic cusp field which crosses the LBNL source's exit aperture. While this does prevent electrons from leaving the source along with the $H^-$ ions, it also perturbs the $H^-$ ion trajectories, making accurate beam measurements difficult.

## 3 RESULTS AND DISCUSSION

In the process of reproducing the $H^-$ yield of the existing LANSCE source it became evident that a good deal of interdependency existed between the parameters of operation (duty factor, gas pressure, arc power, etc.). Two parameters of interest, namely filament cathode location and the quantity of cesium, were found to greatly influence high $H^-$ yield.

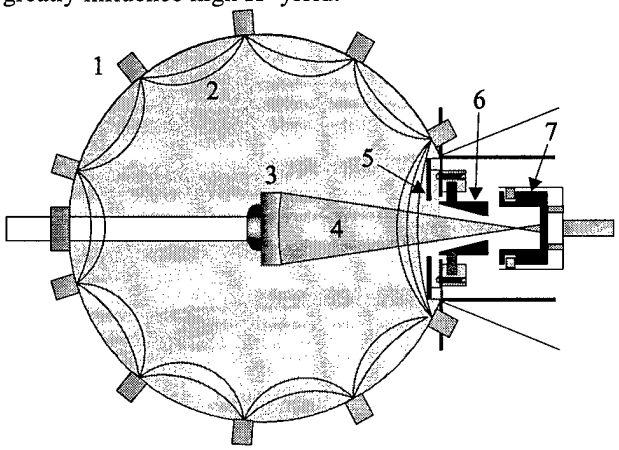



Fig. 2. Schematic of source interior (1. Cusp Magnet, 2. Cusp Field, 3. Converter, 4. $H^-$ Beam, 5. Aperture Plate, 6. Aperture Cone, 7. Faraday Cup).

### *3.1 Cesium Factors*

The amount of cesium in the source and more importantly the amount condensed on the converter surface is a significant factor affecting $H^-$ yield [5]. If there is not enough cesium, the $H^-$ output is low. As the cesium oven temperature is increased, more cesium vapor enters the source, and $H^-$ current increases. However, if cesium injection continues beyond a certain level the $H^-$ yield begins to drop, eventually going to zero as is shown in Fig. 3. In fact, the amount of cesium must be tailored to the very operating conditions of the source. For example, duty factor, arc power, and converter bias all effect what the optimal cesium oven temperature will be.

Along with $H^-$ yield considerations the time required for the source to reach its optimal yield is strongly influenced by the cesium level. The source conditioning time is affected by the time it takes for the cesium to come to an equilibrium within the source. Source conditioning is a lengthy process by which the source is operated until optimal beam is achieved (the current LANSCE source is conditioned for more than 12 hours). In order to reduce the source conditioning time, and to better control the cesium dosage, a molybdenum liner was added to the interior walls of the source. The liner keeps the walls at a high temperature, thus preventing cesium condensation while still maintaining a good electrical contact for the plasma anode. By keeping the interior surfaces of the source warm enough to prevent condensation (except the converter), cesium usage efficiency increases, enabling less cesium to provide the same converter coverage, as well as providing that coverage more quickly. After the addition of the liner, conditioning time for the LBNL source was nearly cut in half without any observable decrease in source performance.

### *3.2 Cathode Position*

High $H^-$ yield was also found to depend on the location of the filament cathode relative to the converter

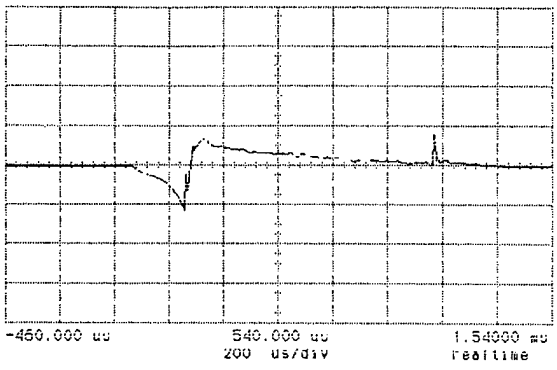



Fig. 3. $H^-$ beam current on Faraday cup with complete over-cesiation, (1 mA per division) 10 mA present before occurrence of over-cesiation.

and to that of the nearest end-flange. Initially, long filaments were positioned away from the cusp field of the end-flanges, and the cathode was in a nearly field-free region with a clear line of sight to the converter face. It was thought that creating the plasma near the converter face and in a field free region, would lead to high $H^-$ yield. This was not the case. The longer filaments consistently performed poorly, yielding no more than 12 mA of total $H^-$ beam current. These filaments were then replaced with a shorter set that were closer to the end-flange with their cathodes roughly parallel to that of the converter surface. With this filament configuration the $H^-$ yield on the Faraday cup was 20 mA, and a total beam current (aperture cone current plus Faraday cup current) of 33 mA was observed.

Due to the geometry of the source it was difficult to separate filament location (with respect to the converter) with that of magnetic filtering effects associated with the cathode in the cusp field [6]. To deal with this problem and to determine the source of the increase in yield, two 10 cm long plasma chamber extensions were added to the source. The extension chambers allow one to change the filament location easily, and the increased space permitted a movable magnetic filter to be added (see Fig. 5). With the extension chambers in place (without filter) and the two filament cathodes in field-free regions, total beam current was increased to 43 mA. It was also observed that with no filter in place as the arc power was increased $H^-$ current approached an asymptotic value.

## 4 CONCLUSION AND FUTURE PLANS

Future experiments will involve a set of a movable magnetic filters to use in association with the plasma chamber extensions. Previous experiments using a similar source with a barium converter showed that this separation of the plasma chamber into a high electron temperature region and a low electron temperature region dramatically increased $H^-$ production at higher arc powers [7]. This greatly extended the linear response of the $H^-$ current as a function of arc power unlike the diminishing return problem that was evident without the magnetic filter.

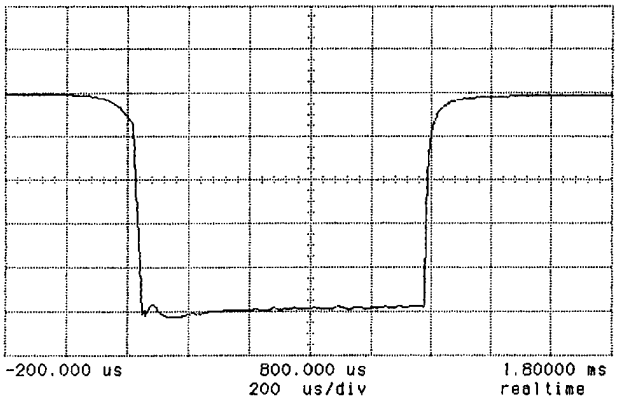


Fig. 4. 20 mA of $H^-$ beam current on the Faraday cup.

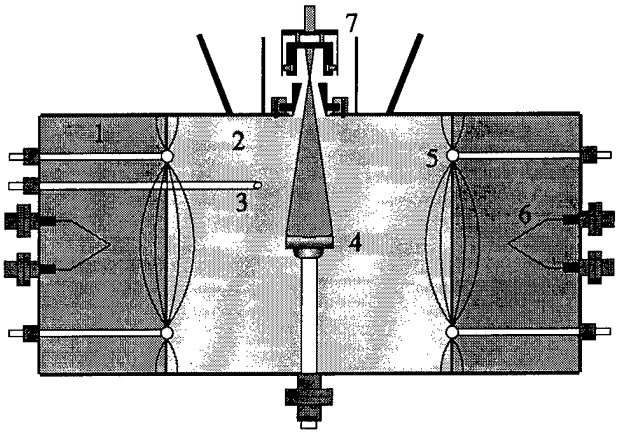


Fig. 5. Source schematic with chamber extensions and magnetic filter (1. High $T_e$ Region with Filter, 2. Low $T_e$ region with Filter, 3. Cesium Nozzle, 4. Converter, 5. Magnetic Filter, 6. Filament, 7. Faraday Cup).

Once these experiments have been completed we will be able to turn our attention to RF induction plasma generation. While it is quite possibly that the new LANSCE source's beam requirements could be met using filament discharge, filament lifetime and reliability are still a concern which RF discharge could easily mitigate. With the increased cesium efficiency of the molybdenum liner and the increased durability of an RF antenna over filaments, source lifetime and reliability should be greatly enhanced along with that of beam current.

## 5 ACKNOWLEDGEMENTS

We would like to take this opportunity to thank T. McVeigh, L. Mills, M. Rickard, and S. Wilde for their technical assistance.

## REFERENCES

[1] K. W. Ehlers and K. N. Leung, *Rev. Sci. Instrum.*, vol. 51, pp. 721-727, 1980.
[2] J. R. Hiskes, A. Karo, and M. Gardner, *J. Appl. Phys.*, vol. 47, pp. 3888-96, 1976.
[3] M. Siedl and A. N. Paragellis, *Bull. Am. Phys. Soc.*, vol. 23, p. 804, 1978.
[4] C. F. A. van Os, K. N. Leung, and W. B. Kunkel, *J. Appl. Phys.*, vol. 69, pp. 3485-3493, 1991.
[5] ibid.
[6] K. W. Ehlers and K. N. Leung, *Rev. Sci. Instrum.*, vol. 54, pp. 1296-1299, 1983
[7] C. F. A. van Os, K. N. Leung, and W. B. Kunkel, *Appl. Phys. Lett.*, vol. 57, pp. 861-863, 1990

# DEVELOPMENT OF AN RF DRIVEN PLASMA CATHODE FOR ION SOURCES*

M. D. Williams, K. N. Leung, C. A. Matuk, and S. B. Wilde
Lawrence Berkeley National Laboratory, University of California, Berkeley, CA 94720

V. M. Benveniste, M. A. Graf, T. N. Horsky, and K. Saadatmand
Eaton Corporation, Semiconductor Equipment Operations, Beverly, Massachusetts 01915

*Abstract*

Conventional tungsten cathode driven plasma sources are limited in the ability to provide large discharge currents and high discharge voltages for CW discharge plasmas. An RF driven plasma cathode based on the multicusp ion source technology has been developed at LBNL. It is shown that large electron currents at high discharge voltage can be achieved for CW discharge operation while maintaining very long cathode lifetime.

## 1 INTRODUCTION

Multiple-charge-state ions are of current interest for several applications, such as MeV ion implantation, nuclear physics experiments, and radioactive beam accelerators.[1] Many of these applications require DC or 100 % duty factor operation. Production of multiple charge state ions requires high energy primary electrons. It has been demonstrated that modest charge state ions can be produced in a conventional tungsten filament driven multicusp ion source, however, cathode lifetime is limited.[2] As the discharge voltage is increased, the plasma density increases causing increased ion bombardment of the filament. At some point the ion bombardment dominates the heating of the filament and temperature runaway will occur. This can result in either exceeding the current limit of the discharge power supply causing the discharge voltage to drop or the filament to burn out. Results have been reported for a programmed filament ion source which produced a high voltage pseudo-CW discharge with good percentages of multiply-charged ions while improving cathode lifetime.[3] The ion source presented here is based on RF driven multicusp ion source technology.

## 2 EXPERIMENTAL SETUP

An RF driven multicusp plasma cathode was utilized for these tests. It was coupled to a multicusp plasma chamber by a two grid extraction system.

A schematic representation of the ion source configuration is shown in Figure 1. The cathode chamber is 10 cm diameter by 13 cm long. Plasma confinement in the cathode chamber is maintained by 20 line cusp magnets on the side cylindrical wall and 4 line cusps placed on parallel chords on the back flange. The front

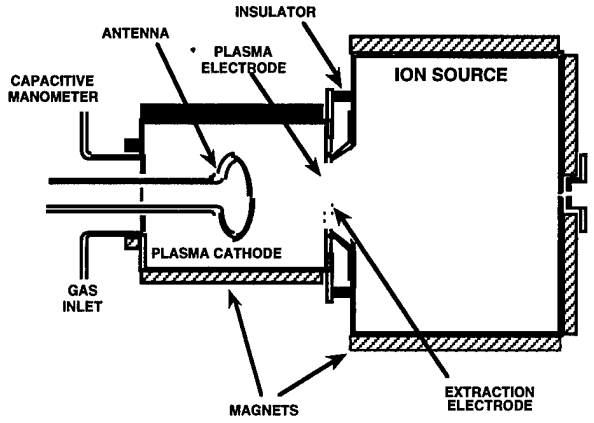



Figure 1: Schematic of the plasma cathode/ion source arrangement.

wall contains the plasma electrode which is a molybdenum disk with two hundred 2 mm diameter holes. They are arranged to provide 50 % transparency over an area approximately 4 cm in diameter. The electron extraction electrode has a similar pattern and is spaced 2 mm from the plasma electrode. The source chamber is 20 cm in diameter, 15 cm long. Magnetic cusp confinement is present on the side and front walls. The cylindrical wall has ten columns of samarium-cobalt magnets installed longitudinally on the external surface. The front wall, the extraction end, has ten magnets placed radially with an iron ring located at the hub to close the magnetic field lines at the center. This arrangement provides a 3 cm diameter field free region around the 2 millimeter diameter extraction aperture. Access ports are provided between the side wall magnets for viewing windows, gas feeds or diagnostics. A simple two-electrode system was used to extract ions from the source chamber.

Figure 2 shows a schematic of the experimental set-up. The plasma cathode was driven by a 13.56 MHz RF generator. The generator was coupled through a matching network to a single loop antenna mounted within the cathode. The network includes an adjustable turn-ratio transformer to match the 50 Ω output impedance of the RF generator to the single loop antenna. It also provides high voltage isolation between the generator and the ion source.

Cathode and source chamber pressures were measured with capacitive manometers. The operating gases were

0-7803-4376-X/98/$10.00 © 1998 IEEE

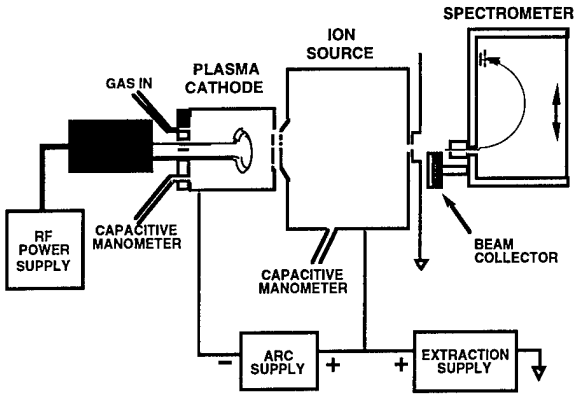



Figure 2: Experimental setup.

introduced into the plasma cathode chamber. Analysis of the extracted beam was performed with a 180° mass analyzer. The analyzer magnet was energized by a programmable power supply. The magnet current and Faraday cup signals were used to drive the input channels of an X-Y recorder. Total extracted current could be measured with a separate Faraday cup mounted on the front of the spectrometer. In this arrangement one could either measure the ion species distribution or the total beam current.

## 3. EXPERIMENTAL RESULTS

The primary goal of these tests was to demonstrate that the RF driven multicusp plasma cathode could provide large currents of primary electrons at various energies. All reported data was obtained with argon as the operating gas. The gas was introduced to the plasma cathode and allowed to flow through the electron extraction electrodes to the ion source chamber. Measurements showed that the plasma cathode pressure was less than 5 % higher than the ion source chamber. Quoted pressures are for the plasma cathode chamber.

The plasma cathode was driven by a 13.56 MHz RF generator capable of delivering 2500 watts. The electron extraction power supply could supply 16 amps up to 600 volts. It was found that the extraction power supply current limit was typically attained at an RF power less than 1600 watts. Figure 3 is a plot of extracted electron current as a function of RF power at several plasma cathode pressures. The extraction voltage was 100 volts. It can be seen that the extracted electron current is a strong function of RF power. The dependence of extracted electron current on pressure is modest. It was difficult to maintain a cathode discharge below 400 watts of RF power.

Figure 4 shows the relationship between extraction voltage and extracted current at a fixed plasma cathode power for two cathode pressures. The cathode RF power was 1000 watts. It can be seen that at the lower voltages the extracted current is a weak function of extraction

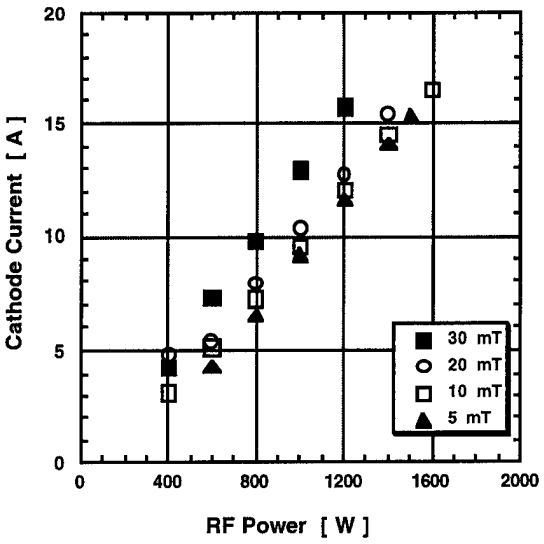



Figure 3: Extracted electron current as a function of plasma cathode pressure.

voltage. There were some problems with breakdown at the higher voltages and the data may be effected by the breakdowns.

The principal purpose for these tests was to enhance the production of multiply-charged ions. It can be seen in Figure 5 that the production of doubly charged argon was enhanced as the discharge voltage was increased. Discharge current was held constant at 6 amps and the cathode pressure at 30 mT. CW discharge operation was maintained for several hours. There were voltage breakdowns in the extraction electrodes for discharge voltages above 200 volts.

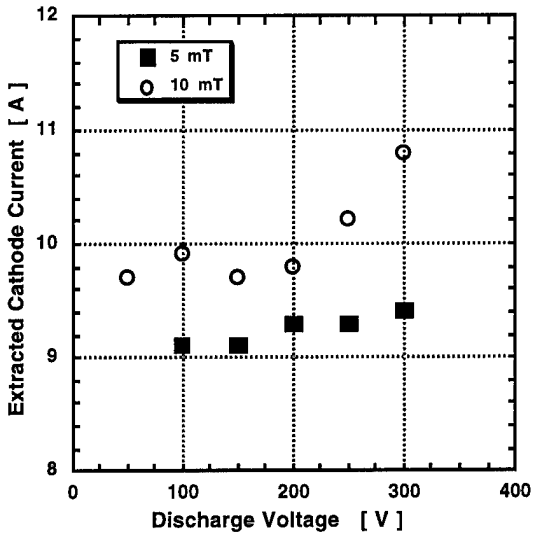



Figure 4: Extracted cathode current as a function of extraction voltage.

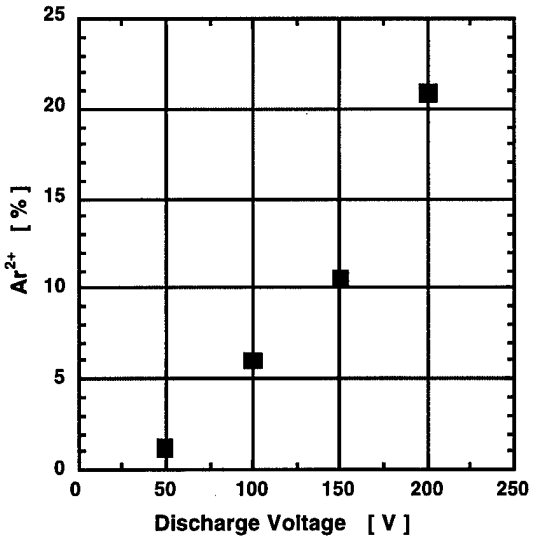



Figure 5: $Ar^{2+}$ as a function of discharge voltage.

## 4 CONCLUSIONS

These preliminary studies have indicated that a plasma cathode based on RF driven multicusp technology can supply significant DC electron currents at high voltages. It is shown that production of multiply-charged ions can be enhanced with the higher discharge voltages and currents while maintaining cathode lifetime. The primary problem encountered was deformation of extraction electrodes due to heating from the plasma and intercepted extracted electrons. This contributed to breakdown problems at higher extraction voltages. New extraction electrodes have been fabricated and the cathode is being modified. The new electrode design will allow for free expansion of the grid structure which should eliminate grid deformation. This should allow for more stable operation with less breakdowns. Tests will continue with the goal of expanding this technology to more applications.

## 5 ACKNOWLEDGMENTS

We would like to thank T. A. Mc Veigh, M. L. Rickard and L. W. Mills for their technical assistance. This research is supported by Eaton Corporation and the U.S. Dept. of Energy under Contract No.DE-AC03-76SF00098.

## REFERENCES

[1] K. N. Leung and R. Keller, Rev. Sci. Instrum. 61,333 (1990)

[2] M. Monroy, Private communication.

[3] M. D. Williams, G. J. deVries, R. A. Gough, K. N. Leung, and M. Monroy, Rev. Sci. Instrum. 67,(3) March 1996

# A MULTICUSP ION SOURCE FOR RADIOACTIVE ION BEAMS *

D. C.Wutte†, Y. Lee, M. A. Leitner, M. D. Williams, K.N. Leung, R. A. Gough
S. J. Freedman, Z. Q. Xie, C. M. Lyneis
Lawrence Berkeley National Laboratory, University of California, Berkeley, California 94720

*Abstract*

In order to produce a radioactive ion beam of $^{14}O^{+}$, a 10 cm-diameter, 13.56 MHz radio frequency (rf) driven multicusp ion source is now being developed at Lawrence Berkeley National Laboratory. In this paper we describe the ion source performance with respect to its capability as an ion source for radioactive ion beam (RIB) production. using Ar, Xe and a 90% Ar / 10% CO gas mixture. In addition ion optic simulations for the radioactive beam line leading to the design of the ion beam extraction/transport system for the actual experimental setup will be discussed.

## 1 INTRODUCTION

At LBNL we are presently testing a 10 cm diameter multicusp ion source for the production of radioactive $^{14}O^{+}$ ions [1]. It will be used as part of an integrated target/ion source system now under development for a radioactive ion beam experiment at the 88" Cyclotron in LBNL. $^{14}O$ will be produced in the form of CO via the $^{12}C(^{3}He^{+},n)^{14}O$ reaction using a 45 MeV/n $^{3}He$ beam from the LBNL 88" cyclotron. Neutral radioactive CO will be transferred via a gas tube into the multicusp source, ionized, accelerated, implanted into a carbon target and analyzed in a beta spectrometer within the 70 sec lifetime of $^{14}O^{+}$. Since the amount of radioactive CO produced will be very small, the ion source discharge will mainly be argon. In order to design a dedicated extraction and ion beam transport system for the RIB experiment the ion source performance was characterized for Ar and 10% CO in Ar gas mixture for generating the discharge.

## 2 EXPERIMENTAL SETUP

### *2.1 Ion Source Design*

A schematic view of the multicusp ion source setup and with the accelerator column is shown in Fig. 1. The source chamber is a copper cylinder (10 cm diameter by 9 cm long). The magnetic confinement is achieved with a "closed" cusp configuration. 14 columns of samarium-cobalt magnets form a longitudinal line cusp configuration for the plasma confinement. The magnetic field reaches a maximum of 1.5 kG at the plasma chamber wall. There is a nearly field-free region in the center of the source of approximately 3 cm diameter. This region determines the maximum extraction area, where the plasma density is homogeneous. An additional 14 magnets are mounted radially in the extraction flange. These magnets are imbedded in soft iron in order to keep the extraction area field free. The front magnets together with four rows of magnets mounted on the back flange establish the closed cusp configuration.

Six layers of molybdenum sheets line the inner chamber wall as well as the front and the back plate. This liner provides a hot plasma chamber surface to minimize the gas hold up time and to increase the dissociation rate of molecular gas.

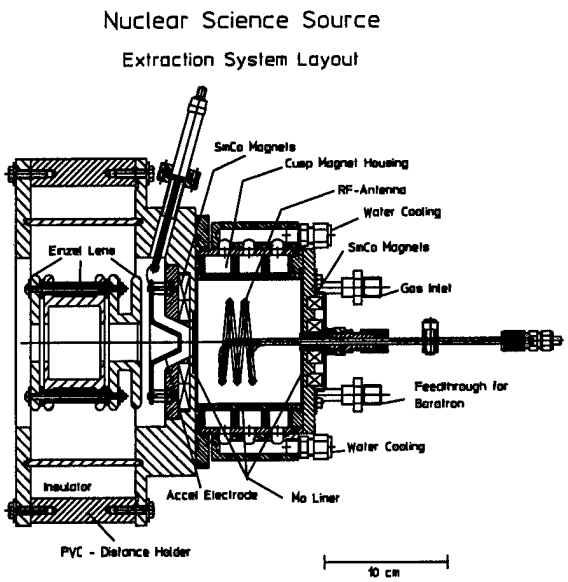



Figure: 1 Design layout of the rf driven multicusp ion source and the accelerator column.

* This work was supported by the Director, Office of Energy Research, Office of High Energy Physics and Nuclear Physics Division of the U.S. Department of Energy under contract No. DE-AC03-76SFF00098

† also with the Institut fur Allgemeine Physik of the Technical University Vienna

0-7803-4376-X/98/$10.00 © 1998 IEEE

*2.2 RF System*

Rf power up to 3 kW at a fixed frequency of 13.56 MHz is inductively coupled into the plasma via a water-cooled, porcelain-coated antenna in the shape of a 2.5 turn induction coil. To ensure maximum rf power transfer, an impedance matching network is used to match with 0° phase the nominal 50 Ω output impedance of the rf amplifier to the plasma-antenna load. (typically a few ohms). In this setup a 4:1 turn-ratio isolation transformer was used to accomplish the impedance matching which also permits isolation of the ion source at high voltage up to 30kV from the instrumentation ground. Additionally, an inductor in series with a variable capacitor forms the secondary circuit accomplishing the fine tuning of the matching network.

For high power operation and with the molybdenum liner installed, the lifetime of the porcelain-antenna is limited. Therefore experimental investigations, where the porcelain-coated copper antenna is replaced by a glass antenna, are in progress. Preliminary results indicate an improved lifetime with the new glass antenna arrangement.

*2.3 Ion Source Test Stand*

A dedicated new ion source test stand is currently under construction to examine the transport system. The ion source test stand consists of the following components: a multicusp ion source, an accelerator column, a diagnostic spool with a Wien (ExB) filter and a Faraday cup for analyzing the ion beam species and currents. The diagnostic spool provides a drift length of 1 m between the Wien filter and the Faraday cup. The Wien filter has a homogenous field of 0.4 T over its length of 30 cm and in a gap of 1 cm by 1 cm. The extraction system incorporates an electrostatic lens, that allows one to focus the ion beam through the homogenous region of the Wien filter gap (see section 4). With this new test stand, measurements are planned for the efficiency of the transport and mass separation system as well as the gas hold up time for oxygen in the source.

## 3 ION SOURCE PERFORMANCE

The ion source performance has been reported in detail elsewhere [1]. In this paper we only summarize the ion source characteristics with respect to its capability as a prospective ion source for the production of radioactive ion beam. The ion source shows promising features: a gas efficiency of up to 60% for argon and up to 80% for xenon has been obtained, a relatively low axial energy spread of 2 to 3 eV for the filament driven source and 4 to 7 eV were observed for the case of the rf driven source. The molybdenum liner provides a hot plasma chamber surface where temperatures up to 1100°C can be achieved [1].

A two-grid extraction system was used to determine the total extracted current and current densities for an argon discharge with plasma conditions similar for the planned $^{14}O^+$ experiment. The current densities for these operating conditions vary from 30 to 60 mA/ cm$^2$. These values correspond to a total extracted current of 1 to 2 mA out of our 2 mm extraction hole and determine the range of current the ion beam transport system has to handle.

In order to explore the ion source performance at operation conditions similar to the planned experiment a 90% Ar with 10% $^{12}C^{16}O$ gas mixture was used for the discharge. Ion species measurements were conducted by

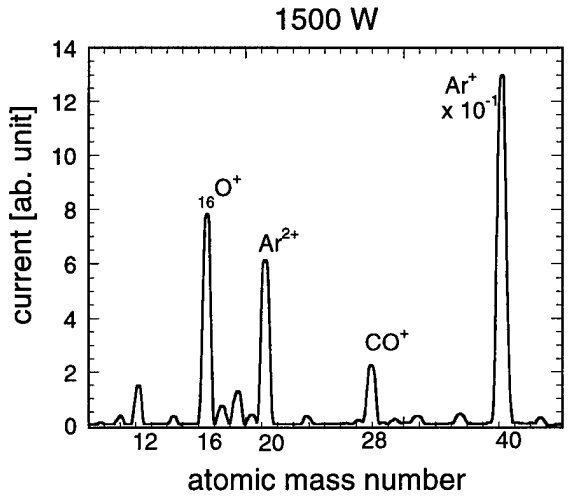



Fig. 2 Ion species distribution for a Ar/CO discharge at 1500 W rf input power. The $Ar^+$ current was reduced by a factor of 10 to fit it on the graph.

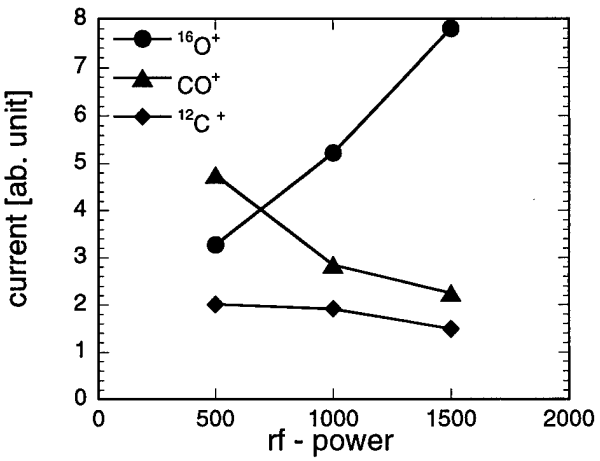



Fig. 3 Relative current change for $O^+$, $C^+$, $CO^+$ versus rf input power for a fixed discharge pressure of 1.1 mTorr.

using a 90° spectrometer magnet.

It has been shown that CO can be efficiently dissociated in the ion source at rf input power levels above 1500 W. Fig. 2 shows a typical ion species spectrum with 1500 W discharge power for the Ar/CO gas mixture. Fig. 3 shows

the relative current change for $O^+$, $C^+$, $CO^+$. The discharge pressure was maintained at 1.1 mTorr to achieve the maximum gas efficiency.

## 4 DESIGN OF THE EXTRACTION SYSTEM

### *4.1 Layout of the electrostatic LEBT*

The ion source insulation allows a maximum extraction voltage of 30 kV. An all electrostatic LEBT design was chosen, because the construction is compact and cost effective. The system consists of three electrodes (accel-decel type), followed by an einzel lens that focuses the beam through the Wien filter. This arrangement will keep the beam envelope from expanding in the mass separator due to space charge. The LEBT has a total length of 15 cm and is incorporated in the ion source insulator (Fig.1). The design of the extraction system was optimized by using the 2D ion optics code IGUN [2]. Fig. 4 shows the layout for the extraction system in the IGUN simulation. For the actual design the extraction and the einzel lens were simulated in different runs with higher resolution (see Section 4.2).

### *4.2 Plasma Extraction Region*

A careful study of the plasma region is essential for the design of the extraction system, since the plasma surface provides the starting condition for all the following lenses. In order to achieve an accurate plasma simulation the region has to be resolved in a much higher resolution grid.

To adjust the electric field at the plasma/extraction boundary, the accel electrode potential can be varied up to -5 kV. This electrode allows an optimal match of the different plasma conditions to the focusing lens. The measured current densities of 30 to 60 mA/ $cm^2$ require an minimum electric field strength of 3 kV/mm for the low and 4 kV/mm for the high densities in the first gap to transport the beam into the Faraday Cup. These experimental values were used as a guidance for the design of the first gap.

Beside the geometry, IGUN requires the input of the plasma electron temperature in order to self consistently compute the plasma potential. The electron temperature also determines the plasma densities required to extract a given ion current. In our simulation we measured the total extracted ion currents used in the calculation. In order to get an estimate for the plasma potential, we used the axial energy spread distribution of the extracted ion beam from the rf driven multicusp ion source and we compared these values with the ones IGUN calculated. It was found, that setting the electron temperature in IGUN to 1-2 eV leads to plasma parameters, which are in good agreement with measured values for multicusp ion sources [3].

## 5 ACKNOWLEDGEMENTS

Daniela Wutte gratefully acknowledges the support by the Schrödinger Fellowship granted by the Fonds zur Förderung der wissenschaftlichen Forschung in Österreich under contract number J01220-PHY.

## REFERENCES

1] 'Development of an rf driven multicusp ion source for radioactive ion beams', D Wutte, R. Gough, Y. Lee, M. Leitner, K. N. Leung, C, Lyneis, D.S. Pickard, M. D. Williams, Z. Q. Xie, submitted to Nuc. Instrum. Meth. in Phys. Res. B

[2] 'IGUN- A program for the simulation of positive ion extraction including magnetic fields' R. Becker, W. B. Hermannsfeldt, Rev. Sci. Instrum. 63, 2756 (1991)

[3] Y. Lee, L.T. Perkins, R. Gough, M. Hoffmann, K. N. Leung, M. Sarstedt, M. Weber, M. D. Williams, Nuc. Instrum. Meth. in Phys. Res. A 374 (1996) 1-6

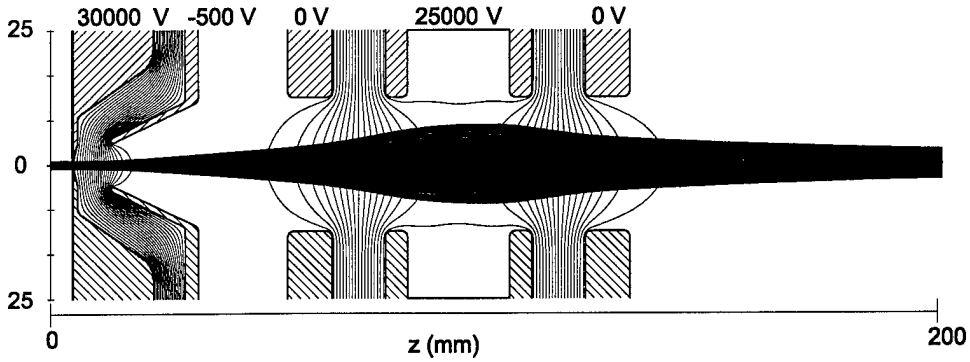



Fig. 4 Typical IGUN simulation run for an Argon beam showing an overview of the extraction system including the einzel lens. The dimensions are shown in mm.

# ION MICROWAVE SOURCE FOR LINEAR ACCELERATOR

A.Nesterovich, N.Abramenko, B.Bogdanovich, Moscow Physics Engineering Institute,
115 409 Kashirskoe shosse, 31, Moscow, Russia

In the report microwave source with improved characteristics for linear accelerator is described. It is known, that ion microwave sources [1-3] have several advantages in comparison with other types of sources, working in continuous mode. It, the first of all, large full operation time, absence of incandesces elements with short life time, high stability of the characteristics.

From sources, creating beams of circle cross section, one of the most suitable is the source with RF power coaxial feeder and constant magnet [3]. The source provides beam of hydrogen ions with current up to 3 mA. Extraction aperture has diameter 2 mm in this source. Power feeding is small enough and not larger than 30 W. This source satisfies to the requirements to linear accelerator injector, however, it is desirable to receive a greater current of beam.

As a result of the analysis of the technical decisions, contained in known designs, following conclusions about ion source construction were made:

- RF power feeding to discharge chamber should be coaxial for reception of the beam minimum sizes,
- Expediently to make closed magnetic circuit, taking place through discharge chamber and ion extraction system,
- It is necessary to supply transverse components of electrical RF field in the discharge region, belonging close to extract aperture.

Except listed features of designing the new approach to the problem decision of the feeding waveguide and plasma accommodation was applied, which permits to receive the steady accommodation and to concentrate plasma in the ions' extraction area. In known ion microwave sources [1-3] for the plasma and RF- feeding waveguides accommodation the matching units are applied. For example, it can be transformer installed in the waveguuide near ion source input. Waveguide segment between transformer and source entrance is a resonator. As the plasma can widely change its impedance, it is difficult to choose suitable matching transformer, that satisfies resonance condition. The new approach consists in the compensation of plasma reactance inside breakdown region. This reactance is responsible for dismatching of feeding waveguide.

The ion source scheme, realizing given approach, is submitted on fig.1. The discharge region 1 is between two electrodes, one of which is central conductor of coaxial line 2, and other - central conductor of coaxial loop 3 with short connected piston, the electrical length of which can be selected during source setup. Loop entrance impedance is chosen in such way to compensate reactance of plasma pole between electrodes. Ion source magnetic system consists from two solenoids 4, magnetic screen 5 and extracting electrode 6 fabricated from magnetic soft material. It creates longitudinal magnetic field 0.1 T in the RF discharge region. Magnetic flux goes through the discharge region. The elements of the magnetic circuit are shown on fig.1. RF power is fed to discharge area from magnetron generator 7 through the coaxial quarter wave transformer 8, thus the electrical component vector of RF field between electrodes is directed perpendicularly to vector of the constant magnetic field. The ion source contains gas injection system 9 also.

The active impedance of plasma pole should be accommodated with feeder by means of one or several quarters of wave transformers. At magnetic field absence, as show valuations, the active impedance of plasma is very small. At availability of external magnetic field more intensive absorption of RF power by plasma at resonance occurs, consequence that is higher active impedance.

The volt - ampere characteristics' measurement of ion source was executed after beam extraction system geometry choice. In proposed system the ions' extraction was made from plasma border, located in plane of emission hole. Beam formation was executed by Pierce geometry. It was found the geometry, appropriate to the largest current $I_i$, flowing from the hole in extracting electrode, and minimum current on extracting electrode $I_{ee}$ at extraction chosen working voltage U. On fig.2 the $I_i$ and $I_{ee}$ dependencies on U for chosen geometry, which is represented on the same drawing, are submitted. For given geometry the current on extracting electrode becomes rather small at voltage more than 12 kV. The further growth of extraction voltage does not lead to essential growth of beam current $I_i$, since current increase at $U < 12$ kV occurs only because of current redistribution between these two components. Extracting current remains constant.

Volt-ampere characteristics were measured at magnetron power 200 - 300 W and gas consumption 15 - 20 $cm^3$ per hour. Ions beam maximum current in separate modes of operation reaches 10 mA, that corresponds to reasonably high current density 250 - 300 $mA/cm^2$.

The degree of the plasma accommodation with RF feeder was determined with the help of measuring line, installed between magnetron and ion source, with the help of which VSWR dependence from short circuit loop length was measured. The results of measurements are submitted on fig. 4. It is visible that there is region, where the steady break down takes place. VSWR acquires essentially large significance (at least more than

0-7803-4376-X/98/$10.00 © 1998 IEEE

6). From the other hand, there is region, where discharge is unstable. Minimum achieved VSWR, as it is visible from fig. 3, makes 1.6, that corresponds to power 95 % absorbing in plasma.

The plasma concentration and electronic temperature were measured by cold probe method. Probe characteristics were removed on known techniques, after processing of which plasma concentration and electronic temperature were received. Its values were $10^{12}$ $cm^{-3}$ and 12 eV accordingly.

The gas profitability was evaluated from the gas consumption, made by 15 - 20 $cm^3$ per hour, and ion current. At 100 % ionization to get beam current 1 ìÀ it is necessary to consume about 1 $cm^3$ of gas per hour, located at atmospheric pressure. Thus, in the source best mode of operations with beam current 10 mA the gas profitability makes about 50 %.

Conducted experimental researches have confirmed expected main laws of given source and showed it's good characteristics. In particular, source surpasses known analogues on gas profitability, absorption factor of RF power, current density.

## REFERENCES


[1] Sakudo N., Tokiguchi K., Koike H., Kanomata I.-Rev.Sci.Inctrum., 54, 1983, No 6, pp.681-684

[2] Sakudo N.-Nucl. Instr. and Meth. in Phys. Res., B21, 1987, pp. 168-177

[3] Ishikawa J., Takeiri T., Takagi T.-Rev.Sci.Inctrum., 55, 1984, No 4, pp. 449-456

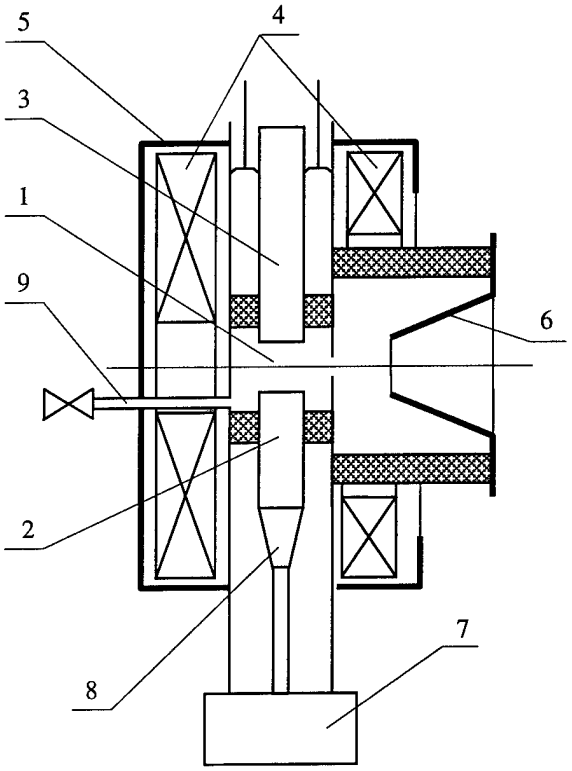




Fig.1. Ion source scheme.

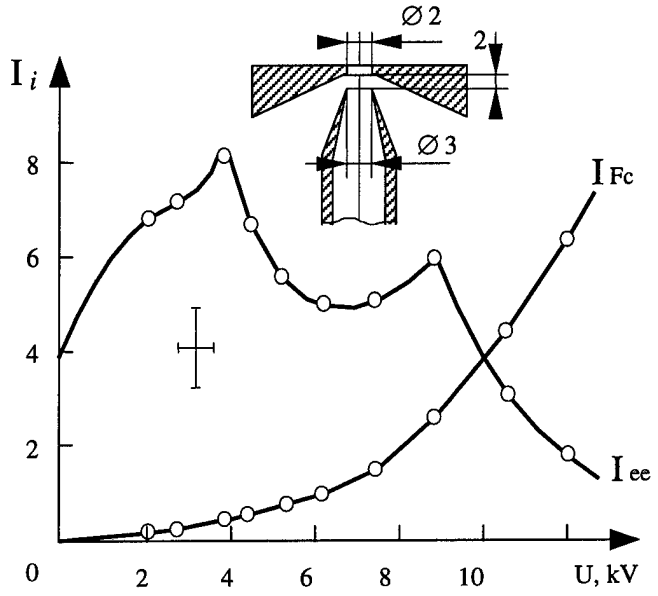



Fig.2. Ion and extracting electrode current dependence on operating voltage.

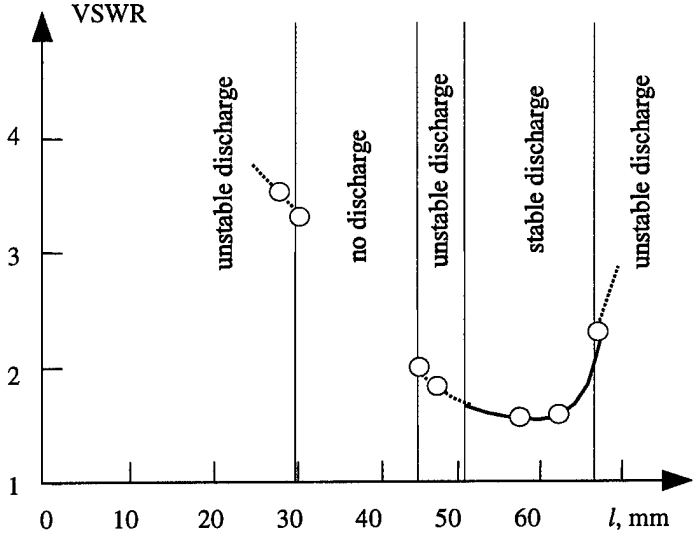



Fig.3. VSWR dependence on short circuit loop length.

# TOWARD A REALISTIC AND TRACTABLE MODEL FOR NEGATIVE ION EXTRACTION FROM VOLUME SOURCES

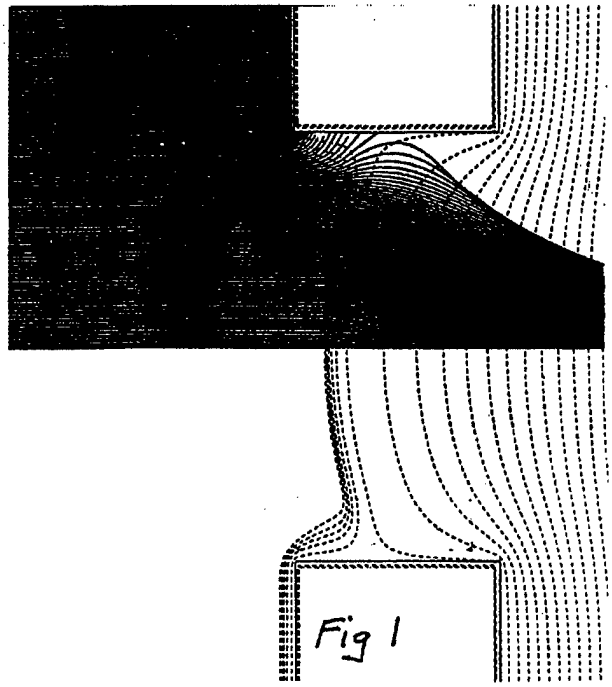
J.H. Whealton, D.K. Olsen, and R.J. Raridon
Oak Ridge National Laboratry, Oak Ridge, Tennessee

*Abstract*

The physics of negative ion formation is fundamentally different than that for positive ion formation. For example, with negatively biased plasma electrodes, relative to the plasma, it can be shown that the Bohm sheath stability criteria is not generally satisfied and that, in addition, the potential structure near the extraction region is a saddle point. Traditional modeling of volume negative ion sources treats them in a manner similar to positive ions with a monatomic downhill run of the negative ions from source plasma to extraction and acceleration. This method (for positive ions) consists of finding self consistent solutions to a multidimensional Poisson Equation, with the plasma electrons represented as a Boltzmann Distribution, and ions as a Vlasov Equation simulated by a suitably large number of trajectories with space charge embeddings. Ideally for negative ions, one would like to model the positive and negative ions and the electrons everywhere in a Vlasov description. However, so far this is an untractable formulation since a stable convergence scheme has yet to be developed of this extremely nonlinear problem. The tractability of an alternate formulation that will be explored consists of: (1) a Vlasov treatment for the positive ions in the conventional manner, (2) a Boltzmann treatment for the electrons on the plasma side on the extraction sheath, (3) a Vlasov formulation of negative ions formed in the plasma volume, and (4) a Vlasov treatment of electrons. A self-consistent treatment of the above scheme will produce the entire potential structure in the presheath and extraction region. The Boltzmann electron component is expected to be a key ingredient in establishing a convergent scheme while at the same time modeling much of the salient and nontrivial features of the negative ion extraction from volume sources with a negatively biased plasma electrode.

## 1 POSITIVE IONS

Extraction modeling for positive ion sources has been shown to be a very effective tool for predicting and optimizing the performance of position ion sources [1]. This success has obtained even though the models used are very nonlinear and several dimensional [2]. One of the reasons for this success is that the physical formulation is apparently rather accurate; it consists of a self-consistent solution of a Poisson Equation with source terms for the plasma ions obtained directly through a solution of the kinetic ion-Vlasov Equation and the plasma electrons represented by a Boltzmann equilibrium distribution. Boundary conditions consist typically of a quasineutral plasma with a negatively biased plasma electrode (to electrostatically contain the plasma electrons). This plasma electrode has a hole in it that reveals applied ion extraction and acceleration fields, as shown in Fig. 1.



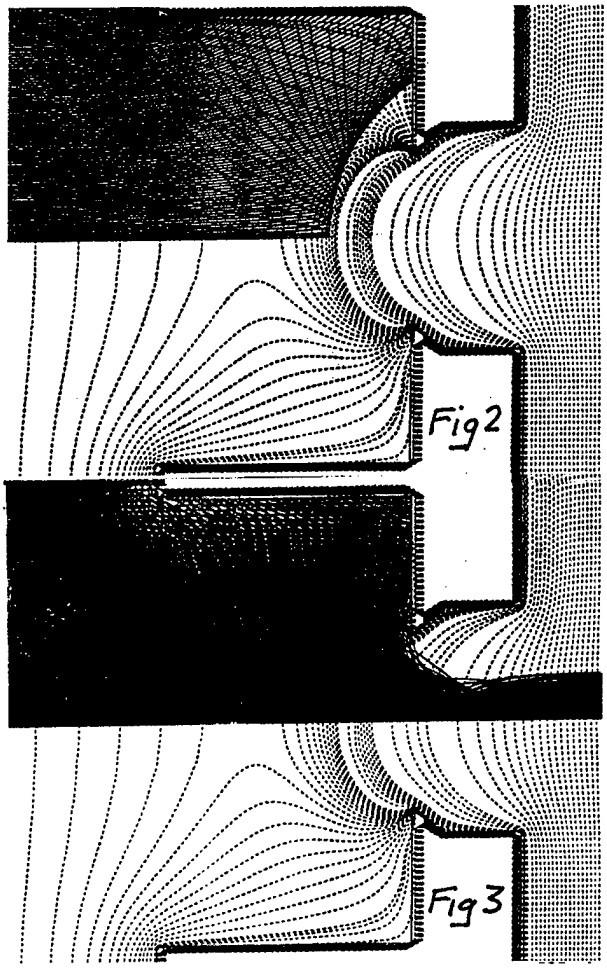

With this formulation and suitable boundary conditions, a self-consistent Debye-length scale sheath results for the transition between the neutralized plasma and the non-neutralized ion beam. The geometric configuration of this sheath has a large effect on the ion optics and RMS beam emittance (see Fig. 1). That there is apparent agreement between experiment and modeling results [1] suggests that this nonlinear sheath is correctly arrived at.

## 2 NEGATIVE IONS

For negative ion extraction, the usual ploy is to assume perfect symmetry using the same model with the fields reversed [3]. There were some hints that this perfectly symmetric model was not capable of predicting negative ion extraction optics or optimum presence correctly. A single heuristic alteration to the basic positive ion model showed some prospects of correlating with experimental data [4].

However, the actual asymmetries which exist between positive ion extraction and negative ion extraction suggest that a more serious treatment is called for to obtain a reliable tool for predicting and optimizing the beam formation process. The first, and most obvious asymmetry, is that the charge compensation in the negative ion source plasma is obtained by the space charge of the positive ions instead of the equilibrium electrons, as is the case for positive ion sources. However, these positive ions are far from equilibrium — in fact, a collisionless one shot pass at the extraction sheath and subsequent reflection appears to be a more accurate picture.

0-7803-4376-X/98/$10.00 © 1998 IEEE




A second, and most considered asymmetry [3], is the extraction of electrons along with the negative ions. In the presence of magnetic fields, these electrons can have a significantly different beam distribution than the ions which must be accounted for to predict power loading on electrode surfaces. Of perhaps equal importance is the fact that the electrons affect the sheath geometry and, thus affect the ion motion. In the presence of magnetic fields, the electrons, due to their E × B drifts, produce an oblique sheath that cause nonlinear space charge effects to occur throughout the extracted beam, even if the ions were generated uniformly [3].

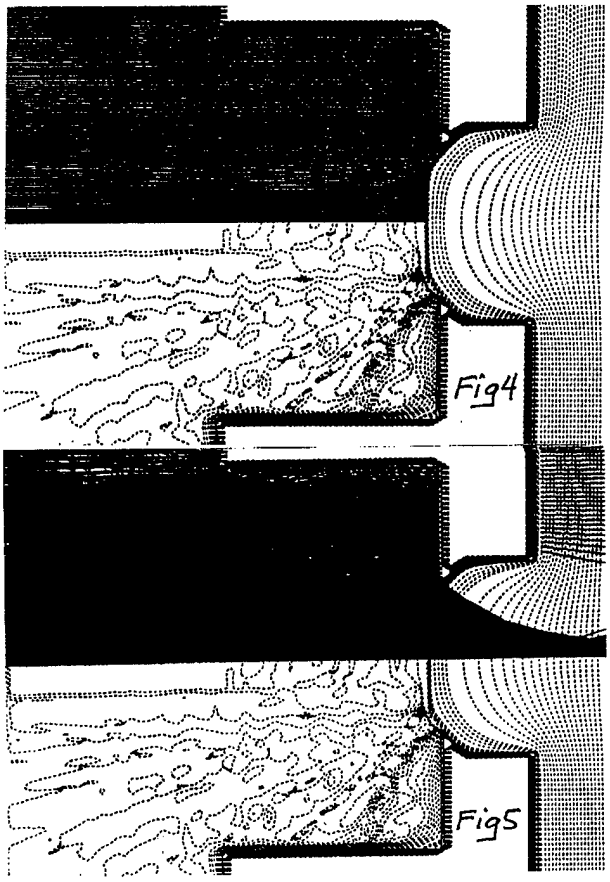
A third asymmetry, that may be no less important but which appears to be totally ignored up to this point, is that the plasma electrode is not biased in a symmetric way with respect to the plasma potential. For positive ion sources, the plasma electrode is biased negative relative to the plasma potential in order to electrostatically contain the highly mobile plasma electrons. The symmetric situation would be that the plasma electrode is biased positive relative to the plasma for negative ion sources. However, the reason for biasing the plasma electrode negative is unchanged for negative ion sources since confinement of the plasma electrons is still a priority. The consequence of this in the pre-extraction region is significant: a monatomic downhill run of positive ions from the center of the source plasma to the accelerated beam occurs for both positive and negative ion sources. There is therefore a saddle point in the pre-extraction region for volume negative ion sources with negative ions that might be created near the center of the plasma being repelled by the plasma electrode. Only those negative ions created near the extraction region, on the down stream side of the electrostatic potential ridge passing through the saddle point are attracted to the extraction region.

## 3 A MULTIPLE VLASOV NEGATIVE ION MODEL

For application requiring minimum negative ion emittance or halo, such as those in colliding beam high energy physics or spallation neutron sources, attention to detail in the extraction of negative ions could be important. Therefore, a more comprehensive multi-Vlasov model is proposed. In addition to considering just positive ions kinetically and Boltzmann electrons (or for the symmetric model — negative ions kinetically and Boltzmann positive ions), we will also consider volume produced negative ions in a kinetic (Vlasov) description.

Results of this model for low densities are shown in Figs. 2-3. As example, Fig. 2 illustrates the positive ion trajectories from the center of the source plasma being reflected by the extraction sheath. It also illustrates the saddle point in the potential. Figure 3 illustrates the volume produced negative ions, some of which are extracted and the rest of which go back into the ion source plasma. At higher plasma densities, we see the compression of the saddle point region toward the extraction sheath as shown in Figs. 4 and 5.

Three features of this physical circumstance tends to produce ion time scale instabilities in the extraction presheath. First, the Bohm sheath criteria is not generally satisfied, as evidenced by the presence of ion acoustic frequency arc noise [5]. Second, the presence of additional negative space charge, due to the presence of volume produced negative ions, could add to the extent the Bohm sheath criteria is violated. Third, reflected positive ions from the sheath could produce a two stream instability with the outgoing stream of positive ions. Figure 4 shows a hint of these two stream instabilities, although a resolution of these and other ion acoustic instabilities has only been done for positive ion extraction [5]. The present study only involves steady state considerations. Figure 5 shows the trajectories of volume produced negative ions.




The opportunities afforded by exploitation of this model appear to be significant since not only can beam emittance be minimized, but the extractable current itself.

## REFERENCES

[1] J.H. Whealton, *Jour. Appl. Phys.*, 2811, **53**, 1982; J.W. Wooten, et al., *Jour. Appl. Phys.*, **52**, 6418, 1981; J. Kim et al., *Jour. Appl. Phys.*, **49**, 517, 1978; L.R. Grisham et al., *Rev. Sci. Instrum.*, **48**, 1037, 1977;

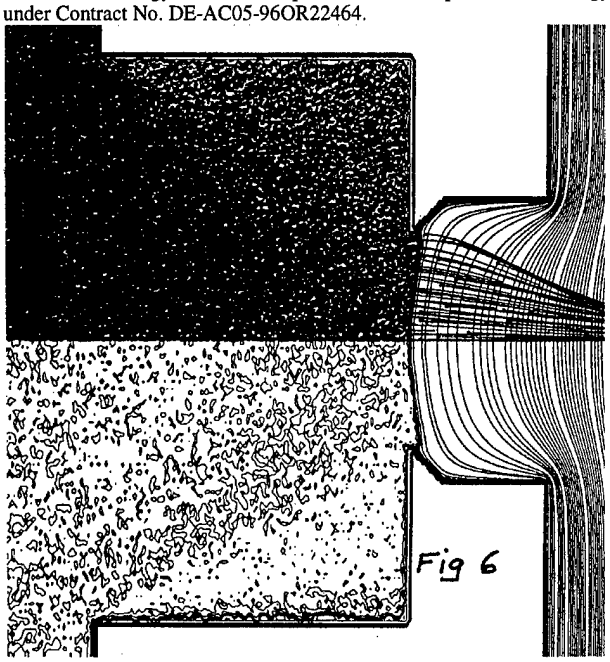
[2] J.H. Whealton, R.W. McGaffey, and P.S. Meszaros, *Jour. Comput. Phys.*, **63**, 20, 1986;

[3] J.H. Whealton et al., *Rev. Sci. Instrum.*, **61**(1), 436, 1990;

[4] J.H. Whealton et al., *Revue Phys. Appl.*, **24**, 945, 1989;

[5] J.H. Whealton et al., *Physical Review A*, **45**(4), 4036, 1992; P.M. Ryan et al., p. 1134 in *Bull. APS*, **27**, 1982.

Research sponsored by the Laboratory Directed Research and Development Program of Oak Ridge National Laboratory, managed by Lockheed Martin Energy Research Corp. for the U.S. Department of Energy under Contract No. DE-AC05-96OR22464.



# 60 keV BEAM TRANSPORT LINE AND SWITCH-YARD FOR ISAC

R. Baartman and J. Welz
TRIUMF, 4004 Wesbrook Mall, Vancouver, B.C., Canada V6T 2A3

*Abstract*

The ISAC project under construction at TRIUMF[1] is to consist of radioactive ion sources, a high resolution mass separator, a low-energy (60 keV) experimental area, RFQ and DTL linacs to reach 1.5 MeV per atomic mass unit (amu), and a high-energy experimental area. Additionally, there will be a stable off-line source primarily for commissioning the linacs but also for use by the low-energy experimental program. The transport line which connects these elements therefore includes a switch which allows either the radioactive beam to supply the low energy area simultaneously with the off-line source supplying the RFQ, or the radioactive beam supplying beam to the RFQ simultaneously with the off-line source supplying beam to the low-energy experiments. The maximum ion source voltage is 60 kV. The RFQ accepts particles with 2 keV per amu, so masses less than 30 must have lower energy and masses larger than 30 can only be accelerated if they are multiply-charged. All optics is electrostatic; the bends have spherical electrodes. Alignment tolerances are given. Aberrations are kept sufficiently small that the maximum beam emittance of 50 $\pi$mm-mrad is transported with negligible distortion. Of particular interest are the achromatic bend sections, the sawtooth buncher insertion, and the matching section to the RFQ.

## 1 BEAM PROPERTIES

For acceleration in the RFQ, particles must have a velocity corresponding to 2 keV per amu. The lightest mass considered will be 6 amu; therefore the smallest momentum is $B\rho = 386$ gauss-m.

After considering variously reported emittances for radioactive ion sources, we have chosen 50 $\pi$mm-mrad as the upper limit nominal emittance. This means we desire to be able to transport this emittance easily with negligible degradation. In practical terms, this means that the acceptance of the transport system should be at least 200 $\pi$mm-mrad.

In some cases, the beam after the separator may have a much smaller emittance in the bend plane than in the non-bend plane. Somewhat arbitrarily, we impose the condition that for an emittance ratio of 25, the smaller emittance be allowed to increase by no more than 20%.

The intensity of the radioactive beam is not envisaged to exceed 1 $\mu$A, so space charge is not important.

## 2 OPTICS ELEMENTS

All optics will be electrostatic. This is cheaper than magnetic, but also simpler to tune since the settings depend only upon beam energy, and not on mass. One can go from one mass to another by simply changing the separator dipole, without retuning the quadrupoles and electrostatic bends in LEBT. The voltages are not high, since the highest beam energy is only 60 keV.

At TRIUMF, we have been using electrostatic optics since 1974 in our 20 m long, 300 keV, $H^-$ injection line for the cyclotron (ISIS)[2].

The ISAC LEBT quadrupoles will be similar to the ISIS quads, with a bore radius of 25 mm. Typical lengths will be 50 mm as opposed to the ISIS standard length of 100 mm. For the typical focal length $f = 0.3$ m, the required electrode voltage is 2.5 kV at the maximum beam energy of 60 keV. The electrodes are cylindrical in section, with radius 1.145 times the bore radius. They are cut from an aluminum extrusion: the ends are not shaped in any special way[3], but slightly rounded to remove the sharp edge.

The bends are similar to the ISIS bends with an aperture of 38 mm, except that the radius is 254 mm instead of 381 mm, and the shape is spherical instead of cylindrical. Spherical electrodes give equal focusing in the bend and non-bend directions. The electrode potentials are $\pm 9$ kV at the full energy of 60 keV. The outer electrode can swing open on a pivot to allow switching between straight-through (bend off) and 45° bend. See Fig. 1. Special care is taken in alignment: the tolerance on positioning the electrodes is $\pm 0.4$ mm and on the roll angle is $\pm 1.4$ mrad.

A first order transport code was used for designing the optics. However, 3rd order aberrations were calculated for individual quads using the formula[3] $\frac{\Delta f_x}{f} = \frac{1}{fL}\left(\frac{7}{6}x^2 - \frac{1}{2}y^2\right)$ for $x$, and similarly for $y$. Fractional increases in emittance for individual quads were added in quadrature as well as the emittance increase incurred from an inexact match. This was minimized using a simulated annealing optimization engine. Optimization parameters were quadrupole strengths and positions: the optimization algorithm works efficiently for any number of optimization parameters.

`GIOS` was used in a final check of the transport from buncher to RFQ. It confirmed that an emittance of 200 $\pi$mm-mrad was transported with only slight distortion.

## 3 OPTICS MODULES

Besides special sections for matching from the separator, from the Off-Line Ion Source, and to the RFQ, there are only 3 different modules; the periodic cell, 90° bend, and an insertion for creating small waists e.g. for the buncher.

The backbone of the transport is FODO periodic with a phase advance of 90° degrees per cell. Each cell is

0-7803-4376-X/98/$10.00 © 1998 IEEE

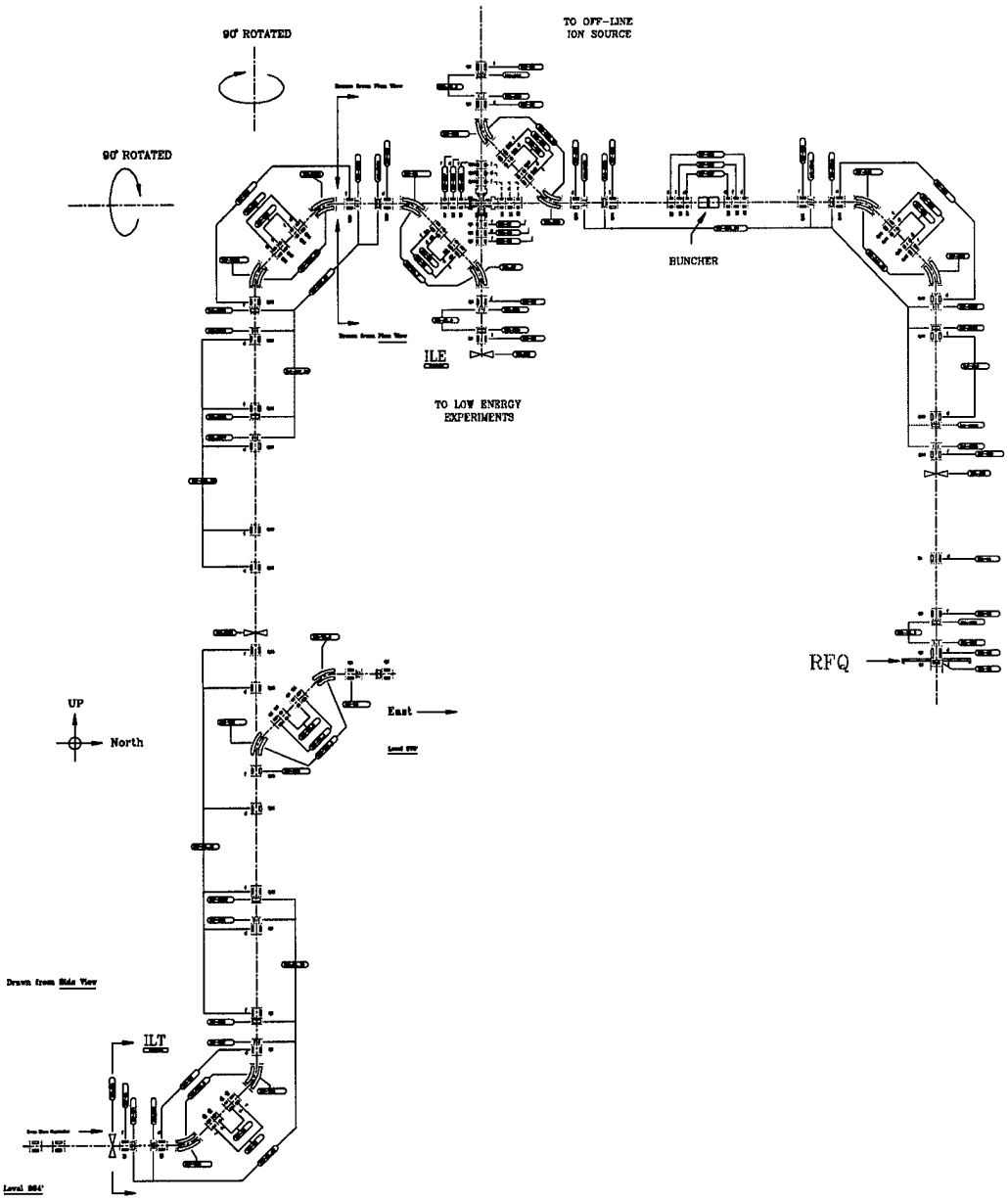



Figure 1: Layout of LEBT

$L_c = 1$ metre in length, and the quads are arranged in doublets, 0.31 m between quad centres. The quadrupoles themselves are only 5 cm in length. (See, for example, Fig. 2, which shows a periodic section cell on either side of a bend section.) These parameters are of course a compromise between good optical properties and minimum cost.

The main optical condition was that the beam not be easily perturbed by outside influence. A fairly good approximation for motion in the periodic section under the influence of a stray magnetic field is $x'' + k^2 x = 1/\rho$, where $k$ is the focusing strength ($= \pi/2/L_c$ for 90° per cell) and $\rho$ is the radius of curvature in the stray field. This shows that the average beam deflection is $\Delta x = (k^2\rho)^{-1}$, and we wish this to be small compared with the quadrupole aperture. Stray field from the earth and the TRIUMF cyclotron combined is approximately 1 gauss. This yields $\Delta x = 1$ mm for the 6 amu case, which is tolerably small compared with the quadrupole aperture radius of 25 mm. Since $\Delta x \propto L_c^2$, it would be 4 mm for a 2 m cell length, and this would have required magnetic shielding.

Monte Carlo calculations were made for periodic section quads with random roll angles. It was found that to meet the above condition for maintaining emittances of non-round beams, the rms roll angle be no more than 5 mrad.

The bend module (Fig. 2) consists of two 45° bends with a symmetric triplet between. The triplet is tuned to make the module achromatic. Since it is symmetric as well, this also zeroes the transfer matrix elements $M_{51}$ and $M_{52}$. This is essential for the bend module between the buncher and the RFQ.

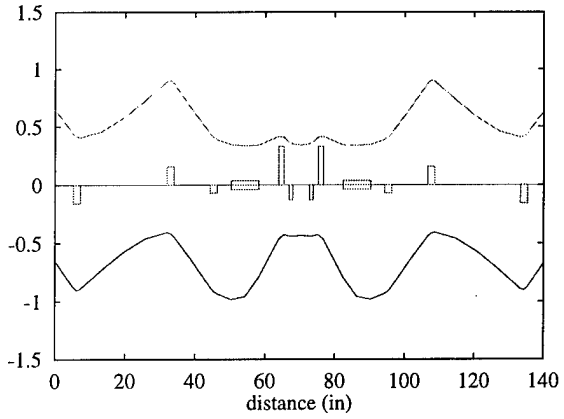



Figure 2: Beam envelopes in cm for $\epsilon = 50\,\pi\mu$m through the bend section, showing periodic sections on either side. The upper trace is for the bend plane, and the lower trace is the non-bend-plane envelope. The step-shaped traces are the focusing strength $k$; $k_x$ plotted positive and $k_y$ plotted negative. (The traces for $k_x$ and $k_y$ coincide in quads since $k_x = -k_y$, but not in spherical bends where $k_x = k_y$.)

Note that the 45° bend element can be installed in any long drift of the periodic section. Only the quadrupole nearest the bend needs to changed from its periodic setting. This is to be used in the Low Energy Experimental Area to allow switching into an experiment at any periodic cell.

The buncher insertion uses a triplet on either side to create the waist. The optics is sufficiently flexible that waist radii from 2 mm to 5 mm are possible.

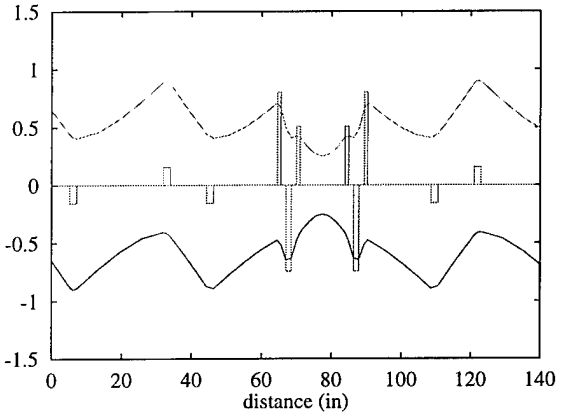



Figure 3: Beam envelopes for matching the periodic section to a narrow waist at the buncher. The tune shown is for a 2.5 mm waist.

Matching to the RFQ is achieved with 5 quadrupoles, the last one being half of normal size (radius = 12.5 mm, length = 25 mm, see Fig. 4). This is because the beam required by the RFQ is highly convergent (28 mrad), and a short final quad avoids the beam being overly large in the second-to-last quad in the direction of defocusing in the final quad. The matching section and the shapes of the electrodes at the RFQ entrance were optimized together[4]. Laplace's equation was solved for a given electrode shape, particles were tracked to find the acceptance ellipses, an optimal matching section was designed as described above by minimizing the 3rd order quad aberrations; then a new RFQ configurationwas calculated again and the procedure repeated. In this way, a design was found in which the emittance increase for 200 $\pi$mm-mrad was only 10%.

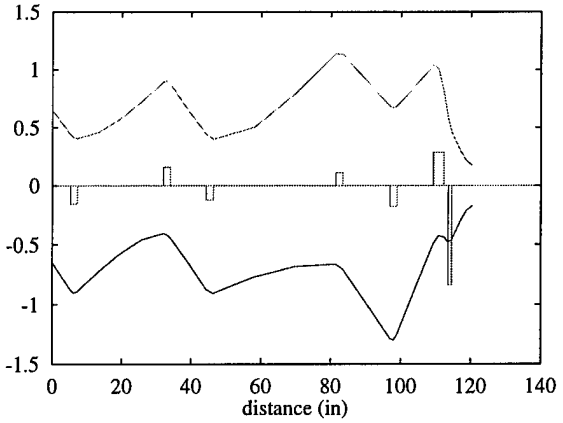



Figure 4: Beam envelopes matching the periodic section to the RFQ.

## 4 LAYOUT

The layout is shown in Fig. 1. The beam arrives from the separator at the lower left of the figure, traveling North. It is bent vertically, and here there is a 90° rotation of the coordinate system in the figure, so that when it is again bent onto the horizontal plane, it is traveling West. There are two locations where the beam can be bent onto the horizontal plane: on the top (ground) floor, and on a mezzanine between the separator pit and the ground floor. There is another coordinate transformation so that from the point on the figure where the beam is again bent to the horizontal plane, it is in Plan View. The beam can either cross over the beam from the Off-line Ion Source (OLIS), towards the RFQ, or it can be bent toward the North, to the Low Energy Experimental Area. If the radioactive ion beam is supplying the LE area, the OLIS can be used by the RFQ, and if the radioactive beam is supplying the RFQ, the OLIS can be used for the Low Energy experiments.

## 5 REFERENCES

[1] P.W. Schmor, et al. *Status of the TRIUMF ISAC Facility for Accelerating Radioactive Beams* These proceedings (8B.12).

[2] See, for example, P. Schmor, R. Baartman, et al., *Progress Towards Higher Intensities and Improved Beam Stability at TRIUMF* Proc. PAC IEEE Trans. **NS-30** (1983) 2092.

[3] R. Baartman, *Intrinsic Third Order Aberrations in Electrostatic and Magnetic Quadrupoles* These proceedings (4V.23).

[4] S. Koscielniak, et al. *Beam Dynamics Studies on the ISAC RFQ at TRIUMF* These proceedings (2W.28).

# OPPIS DEVELOPMENT AT TRIUMF

A.N.Zelenski, INR Moscow/ TRIUMF, Vancouver, B.C., Canada
C.D.P.Levy, P.W.Schmor, W.T.H.van Oers, G.W.Wight and G.Dutto , TRIUMF,
4004 Wesbrook Mall, Vancouver, B.C., Canada V6T 2A3

*Abstract*

The TRIUMF OPPIS (Optically Pumped Polarized Ion Source) provides the precision quality beam for the experiment on parity-nonconservation in proton- proton scattering at 230 MeV beam energy. The results of recent developments and studies for the minimization of contributions to the experiment systematic error due to the beam energy and position modulations correlated with spin- reversal are presented.

Studies of high current production have also been done in collaboration with INR, Moscow and BINP, Novosibirsk. The feasibility of a 10 mA polarized $H^-$ ion current was demonstrated. The pulsed OPPIS application for the future RHIC and HERA polarization facilities are discussed. The polarization technique of the radioactive nuclide beam is proposed for beta-NMR condensed matter studies with a new ISAC facility at TRIUMF.

## 1 INTRODUCTION

Collider experiments with polarized proton beams, approved at RHIC /1/ and under consideration at HERA /2/, will provide fundamental tests of QCD and the electroweak interaction. Polarized beams should allow better identification of new objects produced in proton-proton collisions and expand the limits of searches for possible manifestations of New Physics beyond the Standard Model. Such experiments will require the maximum available luminosity, and therefore polarization must be obtained as an extra beam quality without sacrificing intensity. Typical currents for unpolarized $H^-$ ion injectors are in the 20-50 mA range. With a lower current polarized source the use of multiturn charge- exchange injection into a booster ring will partially compensate the loss, but only a 20-30 mA source will completely solve the problem. A 1.64 mA dc polarized $H^-$ ion current was obtained at the TRIUMF OPPIS, with a promise of further increases to the 2-3 mA range /3/. The ECR-type primary proton source used at the TRIUMF OPPIS has a comparatively low emission current density and high beam divergence, which limits further current increase and gives rise to inefficient use of the cw laser power for optical pumping. In pulsed operation, suitable for high energy accelerators, the ECR source shortcomings have been avoided by using an INR-type OPPIS with a high-brightness proton source situated outside the magnetic field /4/. Studies performed in collaboration with INR, Moscow and BINP, Novosibirsk have demonstrated the feasibility of producing 10 mA polarized $H^-$ ion currents using this scheme. Proposals on pulsed OPPIS developments for future polarization facilies at RHIC and HERA are considered below.

The TRIUMF OPPIS provides a precision quality beam for studies of parity- nonconservation in proton-proton scattering at 230 MeV /5/. It operates very reliably and delivers beam for about 40% of the cyclotron operational time.

Beta-NMR studies of surfaces with polarized radioactive nuclide beams are proposed for the new ISAC (Isotope Separator and Accelerator) facilities at TRIUMF /6/. The application of the optical pumping polarization technique for radioactive nuclides is described for lithium-8 and neon-23 beams.

## 2 POLARIZED BEAM FOR PARITY-NONCONSERVATION STUDIES

At present the TRIUMF OPPIS is heavily used for the E497 "parity" experiment. The goal of this experiment is the measurement of the parity- violating analyzing power $A_z$ for the scattering of a longitudinally polarized 230 MeV proton beam in a hydrogen target to an accuracy of $\pm 10^{-8}$. This imposes very severe constraints on the polarized beam quality. From the very beginning, OPPIS development at TRIUMF has been pushed by this very demanding experiment. The initial expectation that spin-reversal-correlated modulations of the beam parameters should be smaller in the OPPIS than in the ABS have been demonstrated experimentally, although it took some time to understand its origins, develop the apparatus and find the optimal set of source parameters. At present, the helicity-correlated current modulations are below the $10^{-5}$ level and energy modulation can be reduced below 0.010 eV /7/. The correlated beam position modulations are less than 20 nm. The optimum beam current required at the target for the parity experiment is 0.20 uA, but to achieve very small helicity correlated modulations, most of the beam intensity must be sacrificed for beam quality. Therefore, high brightness source performance is required, and the ongoing high current OPPIS development at TRIUMF is of benefit to the parity experiment. At present, polarized beam quality meets the experimental requirements. The extension of the parity experiment to 450 MeV has been proposed /8/.

## 3 PROPOSAL FOR A POLARIZED 800 GEV PROTON BEAM AT THE HERA COLLIDER

Studies of the hadron spin-structure functions in collisions of polarized electrons with polarized helium-3 , hydrogen and deuterium internal targets are in progress at DESY (HERMES experiment). The proposal to significantly expand the kinematic range of these studies and measure the gluon contribution to the proton spin in collisions of an 800

0-7803-4376-X/98/$10.00 © 1998 IEEE

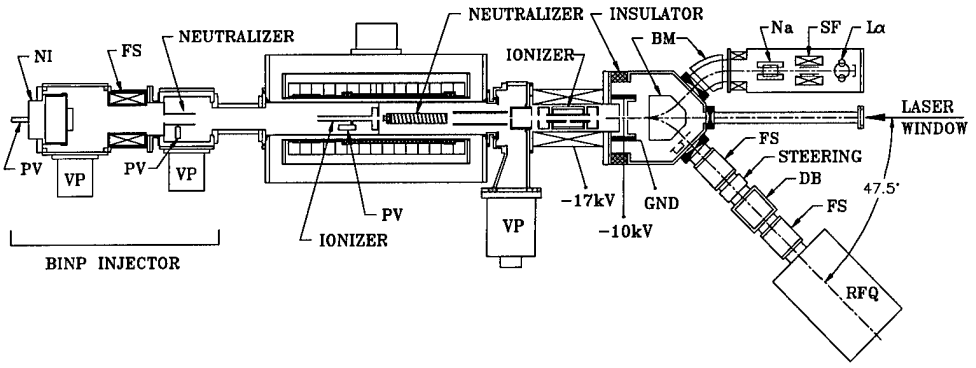



Figure 1: Pulsed Polarized $H^-$ Ion Injector Layout. BM - Bending Magnet; DB - Diagnostics Box; FS - Focussing Solenoid; La - Lyman-Alpha Detector; Na - Sodium Cell; NI - Neutral Injector Plasmatron; PV - Pulsed Valve; RFQ - Radio Frequency Quadrupole; SF - Spin Filter; VP - Vacuum Pump.

GeV polarized proton beam with a 30 GeV polarized electron beam was recently examined /2/. TRIUMF is a part of the SPIN Collaboration, which is working on a proposal for polarized proton acceleration in HERA to 800 GeV and experiments with the polarized beams.

The TRIUMF task is development of the high intensity polarized $H^-$ ion source. A polarized $H^-$ ion current of 10-20 mA is required to provide sufficient luminosity of the polarized beam for the above experiments. At present, the design luminosity has not yet been obtained, even with an unpolarized 50 mA injector.

The feasibility of 10 mA polarized $H^-$ ion current production in the INR- type pulsed OPPIS was demonstrated in experiments with the atomic H injector at BINP, Novosibirsk and experiments at TRIUMF on optical pumping of high density Rb vapor in the presence of a high-intensity proton beam /9/. The 20-30 mA current may be feasible in the "combined" polarization scheme, where space-charge compensation is easier to achieve /10/. The development of a pulsed OPPIS is in progress at TRIUMF. The atomic H injector is being constructed and tested on a test bench. A 16 mA pulsed $H^-$ ion current of a 6 keV beam energy was obtained at the test-bench for the geometry which closely reproduce the pulsed OPPIS layout. After optimization it will be installed at the TRIUMF OPPIS setup , as shown in Fig.1. The optical pumping of the high-density, large diameter Rb vapor cell will be produced by a pulsed Ti:sapphire laser. Nearly 100% Rb polarization has already been obtained in an experiment with a pulsed laser under development. The $H^-$ nuclear polarization will be measured and optimized using the powerful OPPIS diagnostic tools.

The high-current low energy polarized $H^-$ ion beam must be accelerated immediately after the ionizer to 20-50 keV to prevent increase of the beam divergence due to space-charge effects. This can be done by biasing of the whole source to a potential of 20-50 kV. After acceleration in a two gap system, which will also provide the required focusing, the beam will be deflected by a bending magnet through 46.7 degrees to preserve longitudinal polarization. Alternatively, a 15 degree bend plus a solenoidal rotator can be used to align spin vertically. The beam will then be injected into an RFQ accelerator.

## 4 OPPIS INJECTOR FOR RHIC

The polarization facilities at RHIC will provide 70% polarized proton- proton collisions at the energy up to sqrt(S) = 500 GeV and luminosity of $2x10^{32}/cm^2s$ /1/. The polarized injector must produce in excess of 0.5 mA $H^-$ ion current during the 300 us pulse, within a normalized emittance of less than 2 pi mm mrad. This is an ideal application for the TRIUMF-type OPPIS, where the 1.64 mA current was obtained in the dc mode. The required pulsed operation will greatly simplify and reduce the cost of the laser system, while providing the best source performance due to a surfeit of optical pumping laser power. The possibility of the KEK OPPIS upgrade for RHIC in a collaboration between BNL, KEK and TRIUMF is under consideration.

## 5 POLARIZED RADIOACTIVE BEAMS FOR MATERIAL STUDIES AT ISAC

Implantation of several beta-radioactive beams in a material surface (high-temperature superconductors, and semiconductors are of the greatest interest) and observation of the spin-precession due to the local magnetic field can be a useful tool for surface studies, similar to the MuSR technique for bulk materials /11/. The polarization precession can be detected by measuring the asymmetry of beta-decay. For example, a $^8Li^+$ ion beam intensity in excess of $10^8$/s will be available from the TRIUMF ISAC facility for a 10 uA proton beam at the target. The polarization will be produced by direct optical pumping of $^8Li$ atoms in the setup shown in Fig.2. The 20 keV $Li^+$ beam will be neutralized in a sodium vapor cell and then optically pumped by a collinear 669 nm wavelength dye laser beam ($2S_{\frac{1}{2}}$ to $2P_{\frac{1}{2}}$ transition). The optical pumping region must be shielded

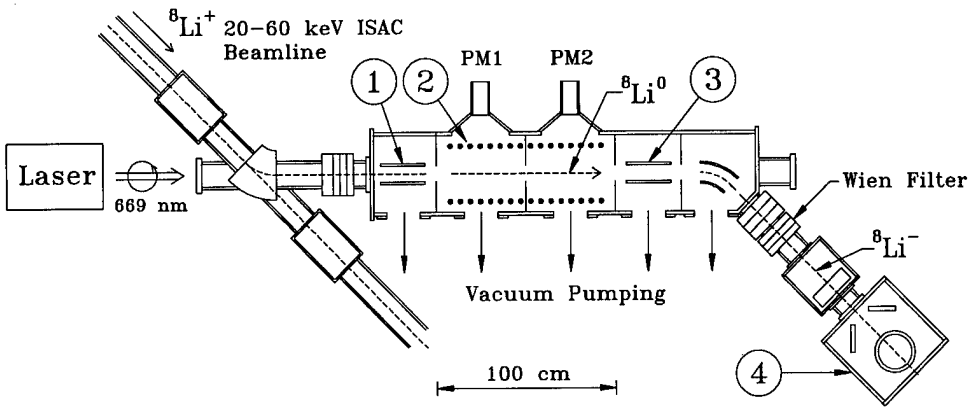



Figure 2: $^8$Li Polarization Layout. (1) Alkali Vapour Neutralizer Cell; (2) Optical Pumping Region; PM - Photomultipliers; (3) Gaseous Ionizer Cell; (4) Analyzing Chamber.

from external magnetic fields and a homogeneous longitudinal field of 10-20 G will be provided. The laser power density required for pumping both F=3/2, 5/2 states is about 0.5 W/cm$^2$ for a multimode laser with a bandwidth of about 500 MHz, the latter determined by hyperfine splitting of 382 MHz in the $2S_{\frac{1}{2}}$ state and 44 MHz in the $2P_{\frac{1}{2}}$ state. After polarization, the Li beam is ionized to $Li^-$ in a second alkali cell with an efficiency of about 10%, or to $Li^+$ in a gaseous argon cell with about 30% efficiency. The ion beam is bent and transported to the sample. The bending prevents direct deposition of sodium vapor on the sample surface and provides a convenient entrance for the laser beam. The ion beam can be easily transported a few meters, thus simplifying the obtaining of an UHV in the analyzing chamber. It is estimated that about 10% of the primary beam can be optically pumped to 70-80% polarization. Another choice of probe is a Ne-17 beam, which can be polarized by selective excitation of hyperfine substates in the metastable Ne* ($^3P_2$) state. In the sodium neutralization cell about 10-20% of the initial 20 keV $Ne^+$ beam is produced in this metastable state ,which is easy for optical pumping using $^3P_2$ — $^3D_3$ transition and 640 nm laser. Selective ionization of the metastable atoms in a second charge-exchange cell will produce a high of about 50% nuclear polarization of the $Ne^+$ ion beam for implantation.

## 6 CONCLUSIONS

The powerful techniques of optical pumping and polarization transfer collisions are very successfully implemented in the high current OPPIS, which meets the demands of the new generation of high-energy accelerators and colliders. The OPPIS also provides the high quality beam for precision experiments at TRIUMF. We believe that development of new polarization facilities at RHIC and HERA will benefit from OPPIS technology and will, in turn, boost the further development of polarized sources.

## 7 ACKNOWLEDGEMENTS

We would like to thank J.Alessi, D.Barber, V.Davydenko, R.Kiefl, A.Krisch, Y.Mori, S.Page, T.Roser and T.Sakae for useful discussions. We acknowledge SPIN Collaboration and INR-Moscow support of this work.

## 8 REFERENCES

[1] G.Bunce et al., Particle world, v.3, (1992), 1-12.

[2] "Prospects of the spin physics at HERA", DESY-Zeuten, DESY Report 95-200, (1995).

[3] A.N.Zelenski et al., Proc. of the 1995 IEEE PAC, Dallas, (1995), 864.

[4] A.N.Zelenski et al., Nucl. Instr. Meth., A245, (1986), 223-229.

[5] J.Birchall et al., AIP Conf. Proc. 339, (1995), 136.

[6] "A proposal for an intense radioactive beam facility", TRIUMF, TRI-95-1, (1995).

[7] A.N.Zelenski et al., to be published in the Proc. of 12th Int. Symposium on High Energy Spin Physics, Amsterdam, (1996).

[8] TRIUMF-research proposal E-761, spokesperson J.Birchall.

[9] A.N.Zelenski et al., Rev. Sci. Instr. v.67, (1996), 1359.

[10] A.N.Zelenski et al., Proc. 1995 Int Workshop on polarized beams and targets, Cologne 1995, World Scientific, ed. H.Paetz gen.Schieck,(1996),111.

[11] A.N.Zelenski et al., to be published in the Proc. of 12th Int. Symposium on High Energy Spin Physics, Amsterdam, (1996).

[12] R.Kiefl, TRIUMF letter of intent.

# REASON FOR FREE ELECTRONS FROM THE SURFACE OF FERROELECTRICS WITH A METAL LATTICE STRUCTURE

H. Heydari[1], T. Tille[1,2]
[1]Institute of Theoretical Electrical Engineering, Technical University of Berlin, Germany
[2]Institute of Technical Electronics, Technical University of Munich, Germany

*Abstract*

This work is an analytical description of a phenomenon known as electron emission from ferroelectrics. The production of free electrons from the surface of ferroelectrics with a metal lattice structure will be explained. An analytical field calculation shows that with a given structure the apparent surface charges of the ferroelectrics produce an electric field, which causes an electron emission from the metal lattice because of the tunnel effect. The emission process is described on the basis of the Fowler-Nordheim formula. After the polarization change of the ferroelectrics, free electrons are produced as a result of the Coulomb interaction. In theory this work analyzes the question of producing high density electron currents by means of ferroelectric materials. The calculated values are compared to empirically found data.

## 1 INTRODUCTION

First it should be stated that the experimental investigation of ferroelectrics in terms of electron emission is not new. After a fast pole-changing (≈ a few nano seconds) of the spontaneous polarisation $P_S$ (Fig. 1) an intensive electron beam could be measured in a period of time ≈50 ns. About the causes (production of many free electrons) the above mentioned authors offered approaches yet no thorough descriptions of the phenomenon.

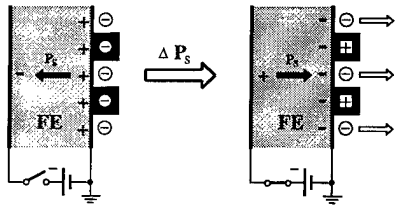



Figure: 1 Sketch of the pole change with subsequent emission of electrons from the surface

Next section it is assumed that the production of free electrons can be described as follows: It is shown that there is an equality of the measured emitted free charge carriers in the electron beam because of the Coulomb-repulsion (between the apparent surface charge density, the polarization of the ferroelectrics which was changed shortly beforehand, and the free charge carriers which tunnelled out of the metal for saturating the apparent surface charge density) and the apparent surface charges which in total of their charges correspond to the amount of charges tunneling out of the metal.

Hence, the interpretation of the cause of this phenomenon as described in this paper is contradictory to the approaches regarding the numerous free charge carriers in the electron beam to originate from an emission process out of the ferroelectrics. This phenomenon was observed by means of the test configuration below (Fig. 2).

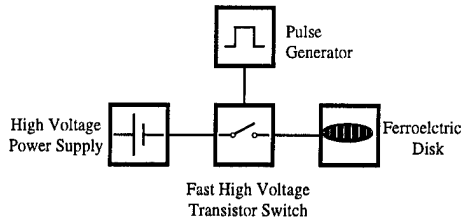



Figure: 2 Configuration used for electron production

The test configuration mainly consists of a pre-poled ferroelectric disk (Fig. 3), e.g. PLZT: 2/95/5, the backside completely coated with metal (gold) and the front side covered with a metal lattice layer (gold: line structure ≈200 µm).

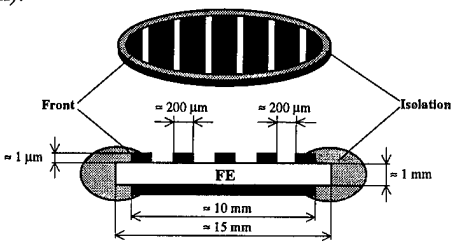



Figure: 3 Design of the FE-sample

Thus the disk acts as a capacitor. When applying a higher negative pulsed voltage (several kV) to the backside the shortly intensive (≈10 to 30 µC) electron beam (Fig. 5) was registred with a Faraday cup.
Considering a small latice hole to be a cylindrical bore hole (Fig. 3) in the metal of one of the capacitor plates (front), the electric field strength within the bore hole can be calculated for the time being for an uncompensated apparent surface charge density of the ferroelectric which in that place is uncovered and pre-poled.
On the basis of field emission, the density of the tunnel current coming out of the metal can be calculated using the Fowler-Nordheim formula. The differential equation for the compensation charges tunneling out (corresponds to the free charge carriers of the later on - after the change of polarization - emitted electron beam) can be integrated exactly and allows to state a relation between the apparent surface charge load, the period of half-life and the initial tunnel current density [1].

0-7803-4376-X/98/$10.00 © 1998 IEEE

## 2 DETERMINATION OF THE POTENTIAL AND OF THE ELECTRIC FIELD STRENGTH

We consider two capacitor plates with the distance $l$ between which there is a ferroelectric with the potential $U_0$. One of the capacitor plates has several cylindrical bore holes at regular distances which are relatively long as compared to the diameter of the bore hole; in other words: one single lattice segment is approximated by a cylindrical bore hole. We want to determine the electric field in the capacitor near a representative bore hole and in the bore hole itself (Fig. 4). The geometrical, electric influence of the other bore holes on the representatively selected one shall be neglected.

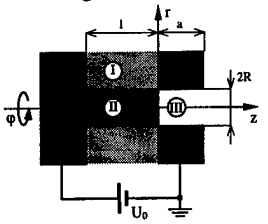



Figure: 4 Geometrical arrangement for the calculation of the electric field

After introducing cylindrical coordinates ($z$, $r$, $\varphi$ ) the potential function $v(r, z)$, which is to be determined and which is independent of $\varphi$ both within the capacitor and in the bore hole itself in the general case, can be written as an infinite series over Bessel $J_0$ or Neumann functions $N_0$, respectively:

$$V(r,z)=(A+B\cdot z)\cdot(C+D\cdot\ln(r))+\sum_{n}^{\infty}\left\{E_n\cdot J_0\left(\frac{J_{0_n}}{R}\cdot r\right)+F_n\cdot N_0\left(\frac{J_{0_n}}{R}\cdot r\right)\right\}\cdot \left\{G_n\cdot\exp\left(-\frac{J_{0_n}}{R}\cdot z\right)+H_n\cdot\exp\left(\frac{J_{0_n}}{R}\cdot z\right)\right\} \quad (1)$$

where $J_{ON}$ are the (tabulated) zeros of the Bessel function, and $R$ is the Radius of the bore hole.

The integration constants $A$, $B$, $C$, $D$, $E_n$, $F_n$, $G_n$, $H_n$ have to be found through boundary and transition conditions. In order to describe the ferroelectric adequately in the parts I and II, the relation

$$\vec{D}=\varepsilon_0\cdot\vec{E}+\vec{P}=\varepsilon\cdot\vec{E}+\vec{P}_s \quad (2)$$

between the dielectric displacement $D$, the electric field strength $E$ and the spontaneous polarization $P_S$ is valid. Hence we assume that the absolute dielectric constant $\varepsilon$ as well as the spontaneous polarization are constant.

After a few elementary transformations and taking transition conditions into account we come to the following formula for the potential in part III [2]:

$$V_{III}(r,z)=-2\cdot R\cdot\left(P_s+\frac{U_0}{l}\cdot\varepsilon\right)\cdot\sum_{n=1}^{\infty}\frac{J_0\left(\frac{J_{0_n}}{R}\cdot r\right)\cdot\exp\left(-\frac{J_{0_n}}{R}\cdot z\right)}{J_{0_n}^2\cdot J_0(J_{0_n})\cdot\left(\varepsilon_0+\frac{\varepsilon}{\tanh(J_{0_n}\cdot l/R)}\right)} \quad (3)$$

hence using

$$E_{III_r}(r=R,z>0)=-\left.\frac{\partial V_{III}(r,z)}{\partial r}\right|_{(r=R,z>0)} \quad (4)$$

for the $r$-component of the electric field strenght $E_{IIIr}$ inside the cylindrical bore hole we receive

$$E_{III_r}(r=R,z>0)=2\cdot\left(P_s+\frac{U_0}{l}\cdot\varepsilon\right)\sum_{n=1}^{\infty}\frac{\exp\left(-\frac{J_{0_n}}{R}\cdot z\right)}{J_{0_n}\cdot\left(\varepsilon_0+\frac{\varepsilon}{\tanh(J_{0_n}\cdot l/R)}\right)} \quad (5)$$

In the case of

$$P_S\approx 10^4\cdot\varepsilon_0\cdot\frac{U_0}{l}\approx\frac{30\mu C}{cm^2}$$

the electric field strength amounts to approximately $2\cdot10^8$V/cm. Using formula (5) we can find the electric field strength on the inner metal edge which on the basis of tunnel effect enables the metal electrons to overcome the work function.

## 3 CURRENT DENSITY AS A RESULT OF THE TUNNEL EFFECT

In quantum mechanics, the calculation of the permeability factor $D$ is well known, and for the movement of an electron with the energy $W$ through a potential energy barrier $U=U(x)$ is given by

$$D\approx\exp\left(-\frac{2}{\hbar}\cdot\int_{x_1}^{x_2}\sqrt{2\cdot m_e\cdot(U(x)-W)}\,dx\right) \quad (6)$$

In our situation, the barrier $U=U(x)$ is determined by the Fermi energy $W_F$ and the work function on the one hand, and by the applied electric field $E$ on the other hand.

$$U(x)=-E_{III_r}\cdot x\cdot e_0+W_0 \quad (7)$$

Inserting $U(x)$ into the fundamental formula (6) of quantum mechanics for the tunnel effect, and after simple integration we finally arrive at

$$D=\exp\left(-\frac{2}{3\cdot\hbar\cdot m_e\cdot E_{III_r}}\cdot\sqrt{(2\cdot m_e\cdot(W_0-W))^3}\right) \quad (8)$$

The electric field strength found in the above paragraph and for the work function $W_0$ the permeability factor e.g. for copper amounts to $4{,}2\cdot10^{-8}$. Here the potential barrier is approximately as wide as four times the Bohr radius. When applying an electric field strength to a metal some electrons tunnel according to the permeability formula (6) from the metal into the vacuum so as to compensate the positive unfree apparent charge of the high spontaneous polarization in terms of absolute value. In order to estimate how fast the compensation effect goes it is necessary for the time being to determine the current density $J_T$ of the electrons tunneling out. It is known that the current density results from the Fermi distribution of the electrons in metal and from the permeability formula (6), giving the Fowler-Nordheim formula.

$$J_T=\frac{e^3\cdot E_{III_r}}{h\cdot8\pi\cdot(W_0-W_F)}\cdot\exp\left(-\frac{2\cdot\sqrt{(2\cdot m_e\cdot(W_0-W_F))^3}}{3\cdot\hbar\cdot m_e\cdot e\cdot E_{III_r}}\right) \quad (9)$$

Writing the electric field strength $E_{IIIr}$ in V/m, the work function $W_A$ in eV and the tunnel current density $J$ in A/m$^2$ the Fowler-Nordheim formula in dimensionless quantities to be measured reads:

$$J_T=1{,}54\cdot10^{-6}\cdot\frac{E_{III_r}^2}{W_A}\cdot\exp\left(-6{,}826\cdot10^9\cdot\frac{\sqrt{W_A^3}}{E_{III_r}}\right)\text{ in }\left[\frac{A}{m^2}\right] \quad (10)$$

Again inserting in (10) the electric field strength of our example and the work function $W_A$ of copper for the tunnel current density amounts to approximately 1200 A/cm$^2$ and is the higher the shorter the period is. Moreover, we note that a slight increase in the electric field strength immediately results in a considerably higher tunnel current density and hence, as will be explained in the following paragraph, there is just a faster

compensation of the apperent surface charges by the electrons tunneling out of the metal.

## 4 SATURATION OF THE FERROELECTRIC SURFACE IN TERMS OF TIME

The relations (5) and (9) allow us to write a differential equation for the still uncompensated apparent surface current density $\eta_s(t)$

$$\eta_s(t) = \eta_s - \frac{Q(t)}{\pi \cdot R^2} \tag{11}$$

where $P_S = \eta_s(t=0) = \eta_s$ and $Q(t)$ is the charge which tunneled out of the metal by the time $t$:

$$J_T(t) \cdot a \cdot 2\pi \cdot R = \frac{dQ}{dt} = a \cdot 2\pi \cdot R \cdot \frac{6{,}2 \cdot 10^{-6}}{11{,}1} \cdot \sqrt{\frac{7{,}1}{4}} \cdot \left(\varepsilon \cdot \frac{U_0}{l} + \eta_s(t)\right)^2 \cdot \sigma^2 \cdot \exp\left(-\frac{6{,}8 \cdot 10^9 \cdot \sqrt{4^3}}{\left(\varepsilon_0 \cdot \frac{U_0}{l} + \eta_s - \frac{Q(t)}{\pi \cdot R^2}\right) \cdot \sigma}\right) \tag{12}$$

Here $a$ means the depth of the bore hole, and $\sigma$ is a shortcut for the following:

$$\sigma = -2 \cdot \sum_{n=1}^{\infty} \frac{\exp\left(-\frac{J_{0_n}}{R} \cdot z\right)}{J_{0_n} \cdot \left(\varepsilon_0 + \frac{\varepsilon}{\tanh(J_{0_n} \cdot l / R)}\right)} \tag{13}$$

After introducing further suitable shortcuts

$$\Psi = \left(\varepsilon \cdot \frac{U_0}{l} + \eta_s\right) \cdot \pi \cdot R^2, \quad \Omega = \frac{M}{\pi^2 \cdot R^4} \cdot \frac{6{,}2 \cdot 10^{-6}}{11{,}1} \cdot \sqrt{\frac{7{,}1}{4}} \cdot \sigma$$

$$\Phi = \frac{6{,}8 \cdot 10^9 \cdot \sqrt{4^3} \cdot \pi \cdot R^2}{\sigma} \tag{14}$$

our differential equation can be transformed as follows

$$\frac{dQ}{dt} = \Omega \cdot (\Psi - Q)^2 \cdot \exp\left(-\frac{\Phi}{\Psi - Q}\right) \tag{15}$$

It can be solved by separation of the variables, and using the initial condition $Q(t=0)=0$ (by the time t=0 there has been no tunnel charge emission) we get

$$Q(t) = \Psi - \frac{\Psi}{\ln\left(\Phi \cdot \Omega \cdot t + \exp\left(\frac{\Phi}{\Psi}\right)\right)} \tag{16}$$

We note that $Q(t = \infty) = \Psi$. As the standard for the time behaviour of the compensation we use half-life $\tau$ :

$$\tau = \frac{1}{\Phi \cdot \Omega} \cdot \exp\left(\frac{\Phi}{\Psi}\right) \cdot \left(\exp\left(\frac{\Phi}{\Psi}\right) - 1\right) \tag{17}$$

Inserting the values of our example in (17) results in $\tau = 4\ 10^{-4} ns$, i.d. in a very short period of time a considerable part of the apparent surface charge density will be saturated by the electrons tunneling out of the metal. Finally, since we arrive at

$$\exp\left(\frac{\Phi}{\Psi}\right) \approx 15 >> 1 \tag{18}$$

in our example an approximated formula for $\tau$ is:

$$\tau = \frac{1}{\Phi \cdot \Omega} \cdot \exp\left(\frac{\Phi}{\Psi} \cdot 2\right) \tag{19}$$

Moreover, (12) in combination with (16) at $t=0$ provides the tunnel current density. Since $\Phi$ and $\Omega$ are independent of the apparent surface charge density $\eta_s$ we get a relation which combines $\eta_s$ with $\tau$ and $J_T(t=0)$:

$$\eta_s \cdot \pi \cdot R^2 = \sqrt{\tau} \cdot J_T(t=0) \cdot M \cdot \sqrt{\frac{\Phi}{\Omega}} \tag{20}$$

Formula (20) shows the relations between relevant quantities in the compensation process as a result of the tunnel effect. After fast pole change ($P_S \rightarrow -P_S$) the compensation charges are suddenly confronted with apparent surface charge densities with the same sign and are hence repelled. A corresponding pulse of current $I_M(t)$ if integrated over time is then exactly

$$\eta_S \cdot \pi \cdot R^2 = \int_{t=0}^{\infty} I_M(t)\, dt = \bar{I}_M \cdot t_M \tag{21}$$

the previous compensation charge. Thus, we showed in this paper that compensation charges can appear mainly as a result of the tunnel effect from the metal of the capacitor charge. We get

$$\bar{I}_M \approx \frac{1{,}8}{5} A$$

which corresponds with the data measured [3].

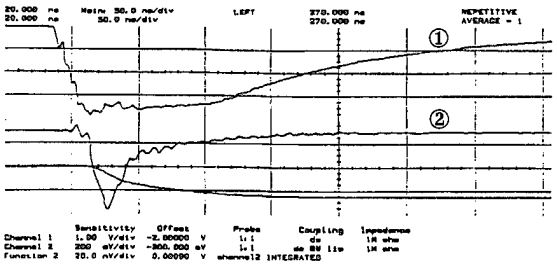



Figure: 5 The sample response ② to a negative pulse applied to the backside ①

## 5 CONCLUSION

The results of this paper allow to conclude that the problem of the place where the compensation charges for the saturation of high apparent surface charge densities in ferroelectric materials come from has a relative simple solution. The physical explanation is that the apparent surface charges of the ferroelectric create very strong electric fields within the lattice holes, with the lattice having a potential of $V=0$. These fields cause the emission of electrons from the metal lattice (quantum mechanic tunnel effect). These electrons create the compensation charges, so that after the pole change of the ferroelectric ($V=-U_0$) they can be registered [4] as free charge carriers in the electron beam (as a result of the Coulomb force between the apparent charges and the compensation electrons).

## REFERENCES


[1] H. Heydari: "Analytical description of a phenomenon known as electron emission from ferroelectrics", TET-Note 91/006, Technical University of Berlin, 1991.

[2] T. Tille: "Pollutant free emission of exhaust fumes based on a pulsed ferroelectric high current electron source", Diploma thesis, Technical University of Berlin, April 1995.

[3] H. Gundel, H. Heydari, D. Suchland, K. Schmidt, H. Henke: "Profile Measurements on a Pulsed Ferroelectric Electron Beam", EPAC'92, pp. 1023-1025, Berlin, March 1992.

[4] D. Suchland, F. Heinrich, H. Heydari: "Temperature dependence of electron emission from PLZT by laser induced switching", TET-Note 91/007, Technical University of Berlin, 1991.

# EFFECT OF THE LONG SOLENOID TUNNEL ON THE GROWTH OF EMITTANCE IN THE PNC HIGH POWER ELECTRON LINAC

MASAHIRO NOMURA, HIROSHI TAKAHASHI*,
Power Reactor and Nuclear Fuel Development corporation, Japan
* Brookhaven National Laboratory , Upton, NY

*Abstract*

We developed a new, three-dimensional simulation code ETRA3D to calculate beam dynamics in the injector of PNC s high-power, high-duty electron linac. In ETRA3D, beam dynamics are calculated by Hamiltonian equations and the space-charge force is calculated by the potentials produced by other electrons. The Hamiltonian is calculated at each time step and the length of the time step is varied by a change in the Hamiltonian to reduce the error of transition and the calculation time.

The precision of ETRA3D was checked by comparing it with the envelop equation. The agreement between them was good. We demonstrated the capabilities of ETRA3D by an example in which the electron beam is not launched along the axis of the series of the solenoid coils. Under this condition, two-dimensional codes can not calculate the beam dynamics.

## 1 INTRODUCTION

The Power Reactor and Nuclear Fuel Development Corporation (PNC) is developing a high-power, high-duty electron linac for various applications including the transmutation of fission products, a Free Electron Laser, and as a positron source [1,4]. The injector for this linac consists of an electron gun, two magnetic lenses, an RF chopper, chopper slits, a pre-buncher and a buncher. Its main specifications are listed below;

| | |
|---|---|
| Electron Gun High Voltage | 200 kV(DC), |
| Beam Current | 300 mA, |
| Pulse Length | 4 m sec, |
| Pulse Repetition | 50 Hz, |
| Duty Factor | 20 %, |
| RF Frequency | 1249.135 MHz. |

Table 1. Main specifications of the injector

There is 2.3 m concrete radiation shield between the electron gun room and the accelerator room. The electron beam must pass through this region without significant growth in emittance, as far as possible. In the low-energy-region, a space-charge force is the predominant factor causing growth in emittance. To reduce such growth, there is a series of solenoid coils, covered from the exit of the electron gun to the first accelerator guide, except between the RF chopper and chopper slits. The shape and strength of the magnetic field produced by the solenoid coils is arranged by estimating the space-charge effect properly. We developed a new, three-dimensional simulation code ETRA3D for the PNC injector which is designed to account for the space-charge force accurately.

## 2. SIMULATION CODE ETRA3D

In ETRA3D, the positions and momentums of each electron are calculated at each time step according to Hamiltonian equations.[5]

$$H = \sum_{i}^{N} \sqrt{(p_i - eA_i)^2 c^2 + (m_e c^2)^2} + e\sum_{i}^{N} \frac{\phi_i}{2}, \tag{1}$$

$$\dot{x}_i = \frac{(p_{x_i} - eA_{x_i})c^2}{\sqrt{(p_i - eA_i)^2 c^2 + (mc^2)^2}}, \tag{2}$$

$$\dot{p}_{x_i} = \frac{qc^2 \sum_{j}^{x_i, y_i, z_i} (p_j - eA_j)\frac{\partial A_j}{\partial x_i}}{\sqrt{(p_i - eA_i)^2 c^2 + (mc^2)^2}} - e\frac{\partial \phi_i}{\partial x_i}. \tag{3}$$

Actually, the positions and momentums of each electron are calculated from eq.(2) and (3) by the Runge-kutta method.

When calculating the space charge force, ETRA3D does not use mesh which is used in PARMELA. When the beam dynamics are calculated by PARMELA, a suitable mesh size and number of the mesh intervals must be chosen because the results are depend on them. In ETRA3D , the space-charge force is calculated by the potentials produced by other electrons, so that the space charge effects are accurately included in ETRA3D. However, if there is an increase in the number of electrons, a longer calculation time is needed. To reduce calculation time, ETRA3D restricts the range where the particles produce the potentials.

In ETRA3D, beam dynamics are calculated at each time step according to the Hamiltonian equations; the transition matrixes are not used. If the time step is large, calculation time will be reduced, but then errors will be introduced. It is difficult to find a suitable length of the time step because it strongly depends on several conditions, namely, the beam current, electron energy, beam radius and the number of the electrons used for the calculations. In ETRA3D, the length of the time step is varied automatically to reduce a change in Hamiltonian if the external fields do not depend on the time. When they do not depend on the time, the Hamiltonian must be conserved. The main purpose of ETRA3D is to calculate the beam dynamics in the injector of PNC s high-power, high-duty electron linac, especially the electron gun to

0-7803-4376-X/98 /$10.00 © 1998 IEEE

RF chopper. These parts do not include the RF fields; therefor, we can use this method. It can reduce the errors arising from the time step and save calculation time.

## 3 EXAMPLES AND DISCUSSIONS

*3.1 Envelop equation.*

The usual way to check the precision of a numerical procedure is to evaluate a variant for which a solution is known. We chose the case of beam dynamics in free space. The envelop of a round beam under the influence of the space charge can be calculated numerically by the envelop equation[6].

$$\frac{d^2R}{ds^2} + KR - \frac{\varepsilon^2}{R^3} = \frac{\xi}{2R}, \qquad (4)$$

where R is the beam radius, and K, ε, and ξ are the focusing strengths, emittance, and space-charge parameter, respectively. The space charge parameter, ξ , is given by:

$$\xi = \frac{4Q^2 r_0 \lambda}{\beta^2 \gamma^2}, \qquad (5)$$

where the beam particles have a charge Qe, λ is a uniform longitudinal particle-density, and $r_0$ is a classical radius of the electrons. We calculated the beam envelops using the envelop equation and ETRA3D under the following conditions:

| | |
|---|---|
| Beam current $I_e$ | 0.3A DC, |
| Electron energy $E_e$ | 200 keV, |
| Beam radius $r_b$ | 0.002 m, |
| Emittance ε | 0 π mm mrad. |

Table 2. The conditions for calculating the beam envelop

The results from the envelop equation and ETRA3D are shown in figs.1 and 2, respectively: the correspondence between them is close.

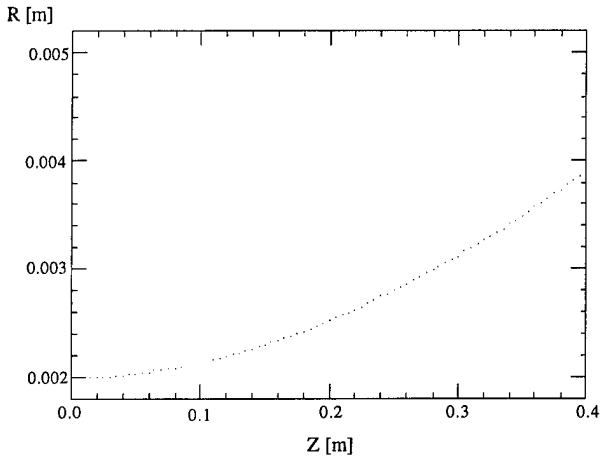



Figure 1 The result of envelop equation

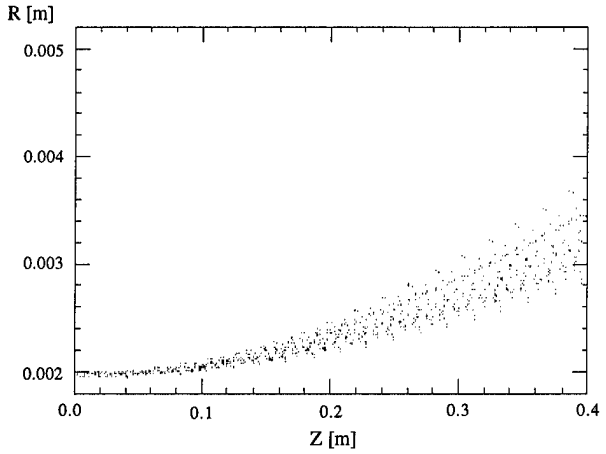



Figure 2 The result of ETRA3D

*3.2 beam dynamics in the series of the solenoid coils.*

To demonstrate the capabilities of our code, we choose the case in which the electron beam is not launched along the axis of the solenoid coils because of alignment errors between the electron gun and solenoid coils. We assumed that the cylindrically symmetric electron beams from the electron gun are at an angle to the axis of the solenoid coils.

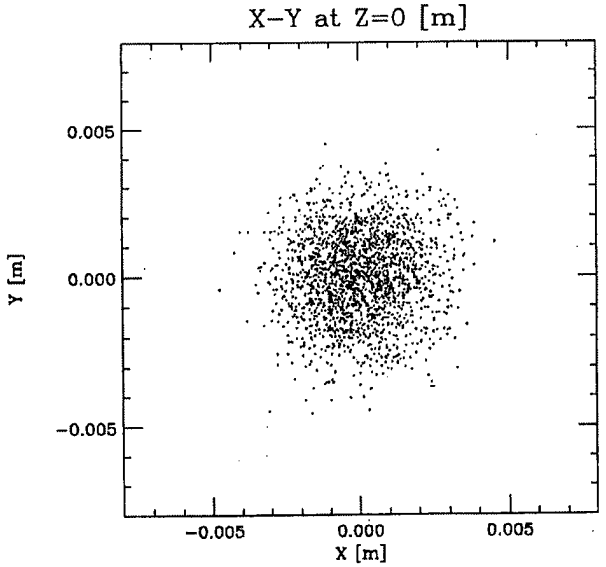



Figure 3. The beam distribution.

The beam current $I_e$ and the electron energy $E_e$ are same as in the example of the envelop calculations. The beam distribution at z=0 is shown in fig.3. The distributions of the beams are cylindrically symmetries and their centers coincides with the axis of the solenoid coils at z=0. But they are set at an angle to the axis of solenoid coils by adding 3 mm mrad to all $\theta_x$ and $\theta_y$. Figs.4 and 5, respectively, shown the magnetic field produced by the solenoid coils and the beam trajectories.

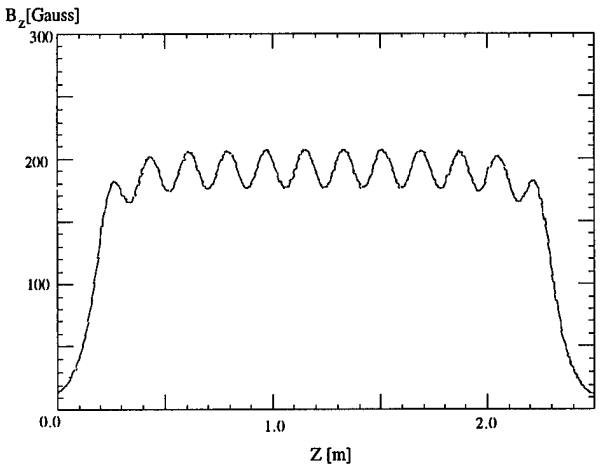



Figure 4. The magnetic field.

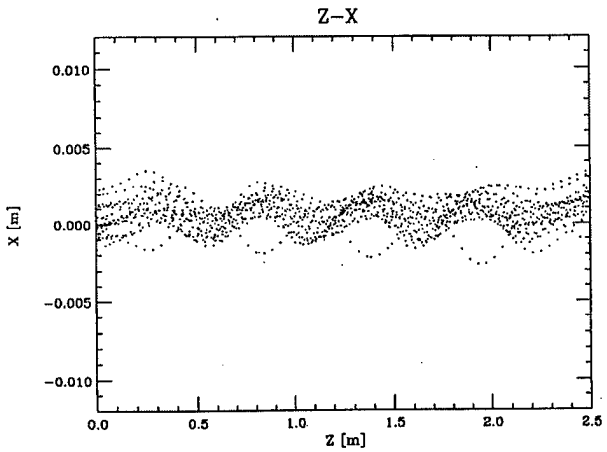



Figure 5. The beam trajectories.

In fig.5, the whole beams spiral along the axis of the solenoid coils.

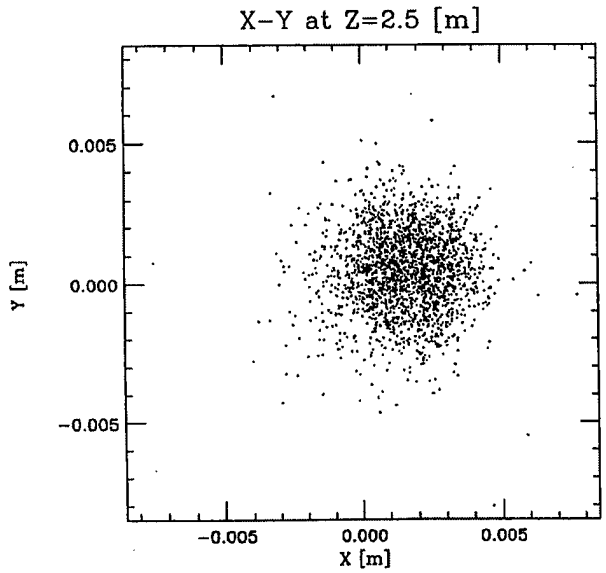



Figure 6. The beam distribution

The beam distribution at z = 2.5 m is shown in fig.6. It is clear from fig.6 that the centers of the beams do not coincide with the center of the solenoid coils, and the distributions of the beams has lost their cylindrical symmetry. If the centers of the beams do not coincide but the distributions still keep their shape, it is not difficult to launch the beam along the beam transport system. But if the shape of the distributions change, they can not be restored to the original shape. This simple example demonstrates that two-dimensional codes can not calculate beam dynamics when the electron beam is not launched along the axis of a perfectly aligned beam transport system.

## 4 ACKNOWLEDGeMENT

The authors are grateful Dr. An Yu for valuable discussions and Dr. Woodhead for editorial work. This work was performed under the auspices of the U.S. Department of Energy under Contract No. DE-AC02-76CH00016, and the Power Reactor and Nuclear Fuel Development Corporation.

## 5 REFERENCES

[1] S.Toyama et. al., Transmutation of Long-lived Fission Product ($^{137}C_s$, $^{90}S_r$) by Reactor-Accelerator System, Proc. International Symposium on Advanced Nuclear Energy Research 1990.

[2] M.Nomura et. al., Status of High Power CW Linac at PNC, Proc. EPAC London, 1994.

[3] Y.Yamazaki et. al., The electron gun for the PNC high power CW linac, Proc. LINAC 94 Japan, 1994.

[4] Y.L.Wang et. al., A novel chopper system for high power CW linac, Proc. LINAC 94 Japan, 1994.

[5] Herbert Goldstein, Classical Mechanics, Addison-Wesley, 1950.

[6] Chao, A.W., Physics of Collective Beam Instabilities in High energy Accelerators, Wiley & Sons, New York, 1993.

# PERFORMANCE OF MAGNESIUM CATHODE IN THE S-BAND RF GUN

T. Srinivasan-Rao, I. Ben-Zvi, J. Smedley, X. J. Wang, M. Woodle
Brookhaven National Laboratory, Upton, NY 11973, and
D. T. Palmer, R. H. Miller, SLAC, Stanford University, Stanford, CA, 94305

*Abstract*

In this paper, we present the preliminary results of the performance of magnesium cathode in a high frequency RF gun. The quantum efficiency of Mg showed a dramatic improvement upon laser cleaning, increasing from $10^{-5}$ to $4x10^{-4}$ after two hours of cleaning, and to $2x10^{-3}$ after systematic cleaning. The cleaning procedure for this increase is described in detail. Charge measured as a function of the laser injection phase relative to the RF phase indicates that the temporal variation of the field on the cathode both due to the RF and the shielding effect of the emitted electrons play a critical role in the emission and extraction of electrons. A model that includes this variation is numerically fitted to the measured charge and the results are presented. The unexpected outcome of the fit was the low field enhancement factor (0.1) predicted by the model for the photoemission. The physical origin of this is still under investigation.

## 1 INTRODUCTION

In the past decade, there has been considerable research[1] in identifying a photocathode material that would be both rugged and efficient at the same time. Progress in cesiated materials has resulted [2,3] in quantum efficiencies of a few percent and life times of a few weeks. Metal photocathodes with 0.5% quantum efficiency and infinite life times have been identified[4]. For the first time, such a high quantum efficiency metal has been processed and studied systematically in a RF gun under high fields, and the results are presented in this paper.

## 2 EXPERIMENTAL ARRANGEMENT

The RF gun used in these experiments is the injector[5] of the Brookhaven Accelerator Test facility (ATF). It is a 1.6 cell, S-band, copper gun with a removable back plate, the center of which acts as the photocathode. The cathode can be illuminated by the ATF photocathode laser system delivering up to 100 μJ of laser energy at 4.66 eV photon energy on the cathode at 72° incident angle. The spatial ellipticity and temporal tilt caused by this oblique incidence were compensated by a pair of prisms and gratings. The spot size of the laser beam on the cathode can be changed by changing the telescoping lenses and imaging apertures in the beam. The laser energy irradiating the gun was measured simultaneously by a calibrated pick-off for laser energies > 10 μJ. For lower energies, an energy meter was inserted in the main beam and the laser energy was measured directly.

A 2-cm diameter, 99.8 % pure, magnesium disc was press fitted in to an indent in the center of the copper back plate of the gun and secured with a bolt in the back. The surface was then machined carefully to be in level with the Cu plate. The center of the plate was then polished with 600 grit soft polishing paper, followed by diamond polishing compound (Beuhler Metadi) of 9, 6, and 1 μm grain size. The plate was then rinsed with hexane and cleaned in an ultrasonic hexane bath for 20 minutes. It was then immediately transported to a vacuum oven where it was backed for 48 hours at 150°C. The plate was then subjected to vacuum-bake-pressurize cycle to ensure good electrical contact at the Cu-Mg interfaces. The back plate was then mounted on to the gun and the system was baked for a week at 200°C before applying the RF. Both the photocurrent and the dark current from the cathode were measured by the Faraday cup immediately after the gun.

## 3 MEASUREMENTS AND DISCUSSION

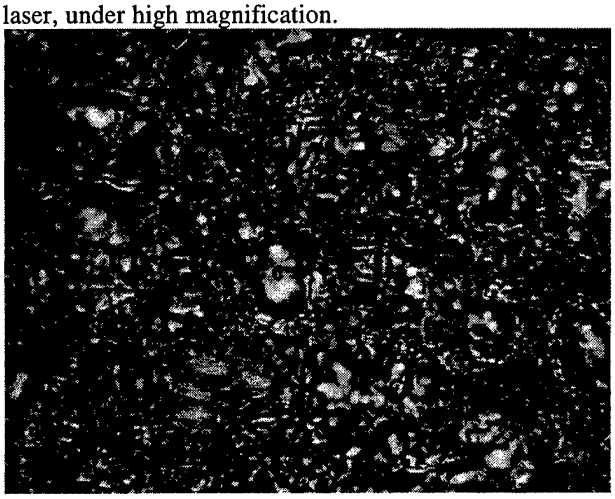
### *3.1 Cleaning Procedure*

After conditioning the gun, the quantum efficiency was measured by measuring the emitted charge and the laser energy simultaneously. The cathode was then cleaned with 160 $\mu J/mm^2$ energy without the RF. The QE was measured at different locations on the cathode after irradiation and was found to vary from $9x10^{-5}$ to $6.6x10^{-4}$. The cathode was then slowly scanned with the laser, maintaining a RF field of 67 MV/m on the cathode. At each scan site, the laser energy was adjusted till there was explosive emission from the cathode for at least 3 consecutive shots. After this scan, the QE increased to $2x10^{-3}$ and the variation in QE decreased dramatically to a factor of two. Fig. 1 is a photograph of the magnesium surface when it was removed from the gun. It can be seen from the picture that the surface has been modified during cleaning, but the depth of damage is < 12 μm as measured with a depth gauge. This cathode was in use for more than 3 months, and no irreversible decay in the QE was measured. Breakdowns and arcing in the RF gun tend to reduce the QE. However, the high QE could be restored by repeating the slow scan cleaning procedure. Measurement of charge as a function of the laser energy indicates that for charges <1nC, the collected charge

0-7803-4376-X/98 /$10.00 © 1998 IEEE

varies linearly with the laser energy for both cases, implying a one photon process for the photoemission.

Fig. 1: Mg cathode surface after being irradiated by the laser, under high magnification.



*3.2 Dependence of measured charge on the injection phase of the laser*

The instantaneous photoelectric current density can be expressed [6] as:

$$\frac{d\sigma}{dt} = AI(t)\left(h\upsilon - \phi + \alpha\sqrt{\beta E(t)}\right)^2 \quad [1]$$

Here I(t) is the intensity distribution of the laser, $\beta E(t)$ is the surface field at the cathode for a field enhancement of $\beta$. A is a material dependent constant, $h\upsilon-\phi$ is the difference between the photon energy and the work function and $\alpha=3.786\times10^{-5}$ in MKS units. Eq. 1 is integrated over the laser distribution to obtain the total charge density of a bunch injected at a given phase. The field dependent term in Eq. 1 represents the Schottky reduction of the work function [7]. For sufficiently low charge,

$$E(t) = E_0 \sin(\theta + \Delta\theta(t)),$$

the RF field at the cathode, where $\theta$ is the injection phase of the laser with respect to the RF, and $\Delta\theta$ is the variation of the RF phase during the laser pulse duration. For higher charges, the surface field should also include the space charge of the preceding electrons,

$$E(t) = E_0 \sin(\theta + \Delta\theta(t)) - \frac{1}{\varepsilon_0}\int_{-\tau}^{t} \frac{d\sigma}{dt'}dt'.$$

$\tau$ is the start time of the laser, and $\varepsilon_0$ is the dielectric constant of vacuum

Experimentally, for a constant laser energy and RF field, the injection phase of the laser was varied and the charge at the Faraday cup was measured at each of the phase. The measurements were repeated for different laser energies and RF fields. Each of these data sets was numerically fitted to Eq. 1. Since only the relative phase between the laser and the RF is known, the zero offset for the RF phase was an initial input parameter. The temporal profile of the laser was also an initial input parameter. $A^{1/2}(h\nu-\phi)$ and $(A\beta)^{1/2}$ were used as fitting parameters. It is useful to note that the data can be broken into sections, each section depending primarily on one of the above parameters. The fit at low injection phases depends strongly on the zero offset. The slope in this region is determined by the laser width. The phase at which the Schottky effect becomes significant is determined by the parameter $A^{1/2}(h\nu-\phi)$. Beyond this phase, the slope depends only on $(A\beta)^{1/2}$. The cut off at the high injection phase is due to the electron transport in the gun and is determined by the acceptance energy of the gun and the Faraday cup. The slope of the falling edge is again an indication of the laser width. A Lorentzian temporal profile with a FWHM of 14 ps was used as the laser profile for the low charge data. For high charge, a charge dependent asymmetry was added to the trailing edge of the pulse to account for the change in electron bunch length due to space charge effects. The energy cut off for the low charge data was a $\gamma$ of 4.5, while for the high charge, higher cut off energies were assumed. Table 1 lists the best fitting parameters for 7 different data sets. Two data sets, one with low charge at 120 MV/m and a laser energy of 1.98 $\mu$J, and another with high charge at 120 MV/m and a laser energy of 10.8 $\mu$J along with their best fits are shown in Fig. 2a and 2b respectively.

Table 1: Best Fitting Results ($\phi$=3.66 eV has been assumed) SL: symmetric Lorentzian, ASL: asymmetric Lorentzian, Half Width at Half Maximum of leading edge =7 ps.

| $E_0$ MV/m | Laser Energy $\mu$J | Laser Profile | Zero field QE ($10^{-5}$) | $\beta$ |
|---|---|---|---|---|
| 120 | 1.98 | SL | 6.0 | .05 |
| 116 | 1.98 | SL | 6.1 | .09 |
| 112 | 1.98 | SL | 6.5 | .09 |
| 105 | 1.98 | SL | 6.5 | .1 |
| 120 | 3.24 | SL | 5.6 | .11 |
| 120 | 8.14 | ASL | 6.6 | .11 |
| 120 | 10.8 | ASL | 6.1 | .1 |

As can be seen both from the Table and the Figures, the simple model predicts the emission and transport of electrons fairly accurately. The best fitting QE at zero field is 6 x $10^{-5}$, well within our experimental measurements. The fit, however, predicts a $\beta$ value that is significantly less than 1, in contrast to our expectation of the field enhancement factor. Fig. 3 is a plot of the least square deviation vs.$\beta$ for a laser energy of 1.98 $\mu$J, FWHM of 14 ps and $E_0$ of 120 MV/m. The data deviates significantly from the prediction of the model even for $\beta$ = 1. The physical origin of this low $\beta$ is still under investigation.

Fig. 2a: Charge vs. RF phase, data at 120 MV/m field, 1.98 μJ laser energy.

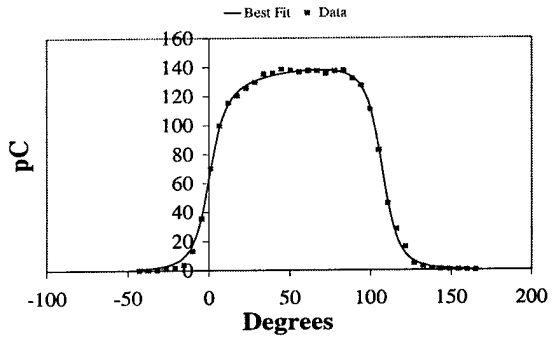



Fig. 2b: Charge vs. RF phase, data at 120 MV/m field, 10.8 μJ laser energy.

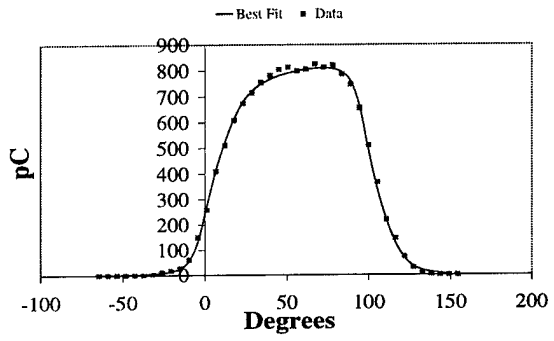
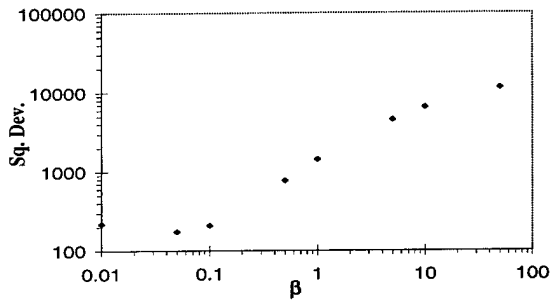



Fig. 3: Square deviation vs. β, with 120 MV/m field and 1.98 μJ laser energy.




## 4 FUTURE PLANS

At present, Eq. 1 describes only the emission process at the cathode in the presence of the time dependent RF and space charge fields. The energy and temporal distribution of the electrons in the vicinity of the cathode in the presence of space charge, as well as the energy dependent focusing property of the solenoid are not included in the model. A more accurate model with these effects will be developed and tested against measurements. Understanding the physical origin of the low β will also be the focus of our future investigations.

## 5 ACKNOWLEDGMENTS

The authors would like to acknowledge the technical help of all the ATF staff and John Schill. This work was performed under the auspices of the U. S. Department of Energy under contract number DE-AC02-76CH00016.

## REFERENCES

[1] C. Travier, `An introduction to Photoinjector Design', Nucl .Instr. and Meth. in Phys. Res. A340, (1994) 26-39.

[2] E. Chevallay, J. Durand, S. Hutchins, G. Suberluq, M. Wurgel,'Photocathodes Tested in the dc Gun of the CERN Photoemission Laboratory', Nucl. Instr. and Meth. in Phys. Res. A340, (1994), 146-156.

[3] P.Michelato et al. 'Charecterization of CsTe Photoemissive Film: Formation, Spectral Responses and Pollution' Proc. of FEL 1996, Aug.26-31,1996 Rome, Italy

[4] T. Srinivasan-Rao, J. Fischer, T. Tsang, 'Photoemission Studies on Metals Using Picosecond Ultraviolet Laser pulses" J. Appl. Phys (1991), 3291-3296.

[5] D. T. Palmer et al. "Commisioning Results of the Next Generation Photoinjector' presented at the 7th Advanced Accelerator Concepts Workshop, Lake Tahoe, CA Oct 13-18, 1996

[6] M. Cardona and L. Ley, in Photoemission in Solids I, edited by M. Cardona and L. Ley (Springer-Verlag, NY, 1978), p 23.

[7] M. Cardona and L. Ley, in Photoemission in Solids I, edited by M. Cardona and L. Ley (Springer-Verlag, NY, 1978), p 22.

# LONGITUDINAL EMITTANCE COMPENSATION IN A PHOTOCATHODE RF GUN INJECTOR

X.J. Wang and I. Ben-Zvi, BrookhaveAccelerator Test Facility, BNL, Upton, NY 11973

*Abstract*

Electron beam bunch compression directly from photocathode RF gun injector was experimentally observed at the Brookhaven Accelerator Test Facility (ATF). The analysis is presented in this report shows that, the configuration of transverse space-charge emittance compensation photoinjecotor can also be operated in bunch length compression mode for modest amount charge (<1.0 nC), i.e., longitudinal emittance compensation. For a constant laser energy, the electron beam bunch length almost linearly decrease with the RF gun phase, and the compression ratio as large as factor of 30 was experimentally observed for a 40 pC charge. We also discuss the effect of electron beam bunching inside the RF gun on the transverse emittance, and compared with experimental results.

## 1 INTRODUCTION

In the past few years, there is tremoundous interest in ualtra -short electron beam production for high energy linear collider, free electron laser , laser accelerators and many other applications[1-4]. Sub-picosecond electron beam can be generated either using the femntosecond laser or magnetic bunch compression, but they are either limited by the total charge or the emittance growth. In this report, we further elucidate a technique using 10 picosecond laser driven photocathode RF gun injector for subpicosecond electron beam generation.

The electron beam micro-bunching in the photocathode RF gun injector was experimental observed at the Brookhaven Accelerator Test Facility (ATF) [5]. The ATF photocathode RF gun injector was designed for transverse space-charge emittance compensation[8]. It consists of a 1.6 cell RF gun mounted on the emittance compensation solenoid magnet, followed by a drift distance and two sections of SLAC type traveling wave linac. The photocathode RF gun injector is driven by a 10 ± 2 ps (FWHM) frequency quadrupoled Nd: Yag laser system. We will show in the following sections, that the photocathode RF gun injector designed for the space-charge emittance compensation can be very efficient operated as buncher for sub-picosecond electron beam generation. We will present latest experimetal results, and discuss the effect of electron beam bunching inside the RF gun on the transverse emittance, and compared with experimental results.

## 2 LONGITUDINAL EMITTANCE COMPENSATION

Fig. 1 is the schematic of the layout of space-charge emittance compensation photocathode RF gun injector. Though several authors [1,6,7,9] studied electron beam bunching process inside the RF gun, the roles of the solenoid magnet, drift distance and linac were not discussed. When the space-charge emittance compensation photocathode RF gun injector operated in the small launch phases, the electron beam bunch length can be significantly shorter than the driving laser pulse length (for modest amount charge). The electron beam bunch lenghth compression process can be divided into four stages:

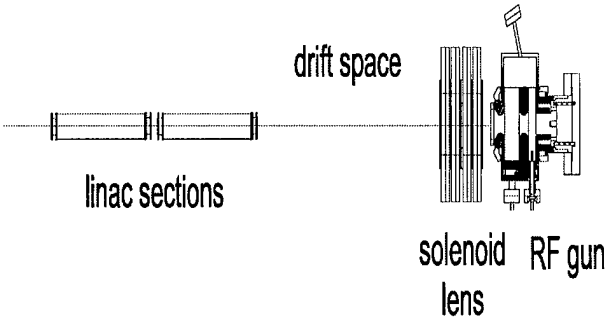



Fig.1 Schematic layout of emittance compensation injector.

*Initial launching and expansion*: For a $\tau$ ps long laser pulse, the initial electron beam pulse length is much shorter than $\tau$ ps for the initial $\tau$ ps time interval because the electrons come out photocathode are nonrelativistic. For example, for a peak field of 100 MV/m on the cathode, the electron beam bunch length after initial laser pulse during tion is about one sixth of the laser pulse length.

After the inital stage, the electron beam will expand because the head of the bunch moving faster than the tail becaused it gains more energy. This process usually last several laser pulse duration.

*RF compression inside the RF gun cavity*: For electron beam launches in small RF phase, the tail of the beam gains energy *faster* than the head. There are several paper discuss the bunch lenght compression inside the RF gun[1,6,7,9] cuased by the RF force. For normalize field $\alpha = eE/mc^2$ k rnage between 1 and 4, reference 9 gives a analytical expression for ratio of electron beam bunch length change $\Delta l$ to the laser pulse lenghth $l_{laser}$

0-7803-4376-X/98/$10.00 © 1998 IEEE

$$\frac{\Delta l}{l_{laser}} = \frac{1}{\sqrt{\alpha^{*2}(1+\cos(\phi_0))^2+1}} \cdot \frac{2\alpha(1-\sin(\phi_0))\cos(\phi_0)}{1+2\phi_0/\pi} \quad (1)$$

where $\alpha^*$ is so called modified normalized field, $\phi_0$ is the electron beam launch phase, $\alpha^*$ can be writtern as,

$$\alpha^* = \frac{\alpha + \frac{\alpha^2}{6}\sqrt{\sin(\phi_0)}}{1+\frac{\sqrt{\sin(\phi_0)}}{6}} \quad (2)$$

Fig.2 shows that the bunch lenght of the electron beam is almost linearly decrease with the electron beam launch phase[6]. The relative energy spread of the beam also almost linearly increase with the decreasing phasing after the launching phase below the phase $\phi_0$ which corresponding to the electron beam exit phase $\pi/2$.

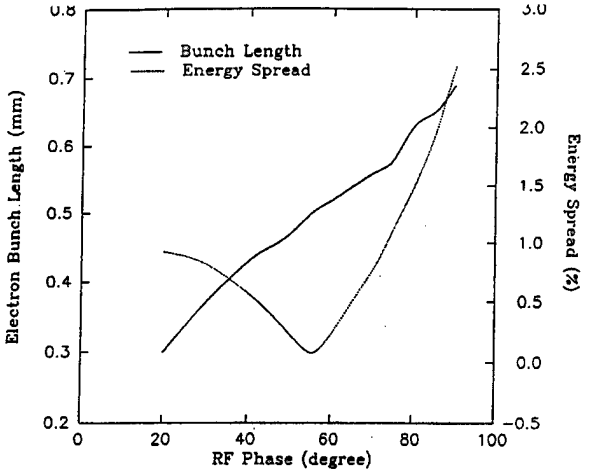



Fig.2 Electron beam bunch lenghth and energy spread as function of the launching phase for a 2.5 ps laser pulse.

*Drift space bunch compression*: Solenoid magnet plays an important role in transverse phase realignment in space charge emittance compensation photocathode RF gun injector, and hence achieaving the emittance compensation. If the injector to be operated as a bunch compressor, solenoid magnet is critical in preserving and further compress the electron beam to achieave sub-picosecon bunch length. The electron beam bunch lenght change in the drift space can be express as,

$$\Delta l = \int \frac{1}{2}(x'^2+y'^2) + (L-L_0)(1-\frac{\delta}{\gamma^2}) - L\frac{\delta}{\gamma^2}_0 \quad (3)$$

The first term represent bunch lengthening. For a 1 mm, radius laser spot, the beam divergence x' at gun exit is about 10 mrad. After one meter drift distance (roughly the drift distance between the gun and linac), bunch lengthed about 0.3 ps due to the beam divergence. The focusing of the solenoid magnet reduce the beam diverence about a factor of 3 to 5, this reduce the bunch lengthening caused by the beam divergence to less than 30 fs. The second term of Eq. 3 is negligible. For a 10 ps laser pulse, the energy spread of the electron beam is about 5 percent when beam was launched in the small phase, this will leads to about 1.5 ps bunch lenght reduction in the drift space. For a 10 ps laser pulse, electron bunch length can be easily reduce by factor of 3 to 4 inside the gun (if psace charge effect is small), so the bunch lenght of the e-beam at gun exit is about 3 to 2 ps, and after further bunch compression in the drift distance, sub-picosecond electron beam can be generated with modest charge. Our experiment confirmed above analysis [5]. We have experimentally measured 370 fs (FW) electron beam with 40 pC charge.

*Longitudinal emittance compensation through linac*: The linac plays very similar role for longitudinal emittance compensation as for transverse space-charge emittance compensation. It reduces space charge effects and preserve the electron beam bunch lenghth. As electron beam is accelerated through linac, followings are realized,

1. Further bunch length reduction on the order of 5 to 10% caused by the early injection due to the relative low energy from the RF gun ($\gamma < 10$).
2. Space charge reduction as $1/\gamma^2$.
3. Energy spread will be reduction as $1/\gamma$, and the final energy spread will be determined by the bunch lenghth($\Delta l^2/8$) and the wake field.

Summarize 1 to 3, after linac acceleration, the short bunch lenghth was preserved, and achieve smaller energy spread (assume will be dominated by the bunch effect), hence longitudinal emittance compensation.

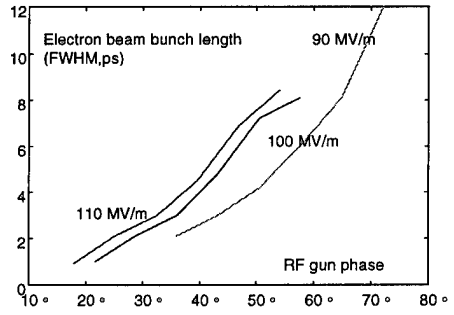



Fig. 3 Electron beam bunch length as function of the RF gun phase for 3 electric fields.

The electron beam bunch lenghth was measured for three electric fields at different RF phases (Fig.3). It confirmed basic features predicted in out discussion. One interesting feature should be pointed out that,the

experiments was carried out for a constant laser energy, and it seems no space-effect was observed as bunch was compressed. This can be explained by the Schottky effect.

## 3 DISCUSSION

Just as any bunch compressor, there are many debunching effects in a photocathode RF gun injector. Directly borrow from the analysis from reference 1, the bunchlenghthening caused by the beam emittance inside the RF gun can be reduced much less than 100 fs. Space charge effect will limit the photocathode RF gun injector operating as a bunch compressor in modest charge (<1.0 nC). We have observed recently significant bunch comrpression for a charge of 0.7 nC for a peak current of 160 A (Fig.4).

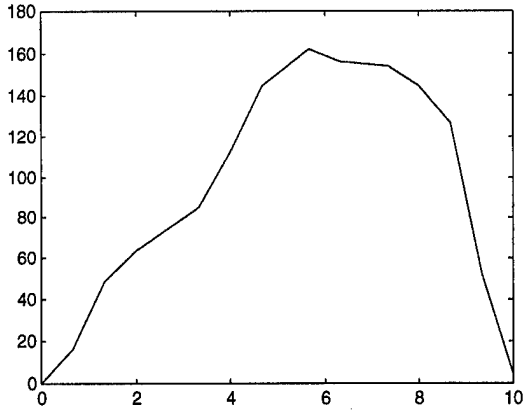



Fig.4 Electron beam charge distribution for 0.7 nC charge, bunch compression is about a facot of 2.5 comparing the laser pulse.

Since the most applications require not only short bunch, but also the high-brightness. The emittance of the compressed beam as the function of the RF gun phase were measured for two RF injectos [5,11]. The result is reproduced in Fig. 5 [11]. One of the most interesting feature is the nonlinear emittance decrease with the RF gun phase. The measurements were performed with a constant laser energy, so the charge in the beam decrease almost linearly with the RF gun phase due to Schottky effect. To the first order, the space charge effect remains roughly constant. Eletron beam produced by the RF gun acquires most its transverse momentum, hence its RF emittance at the exit of the RF gun [10]. As electron beam bunch lenghth was compressed inside the gun, the quadratic dependency of the RF emittance on the bunch length qualitatively agrees with the measurement. Calculated RF emittance [12] using our beam parameters is about one order magnitude smaller than the measured value. This means meausred emittance was dominated by the space charge effect, which we pointed out earlier should remain roughly constant. The physics lies in the correlation between the RF emittance and space induced emittance [12]. It is well known that space charge emittance growth will be minimized for smaller beam in the transport line. Silimar argument applied for space charge emittance growth inside the RF gun.

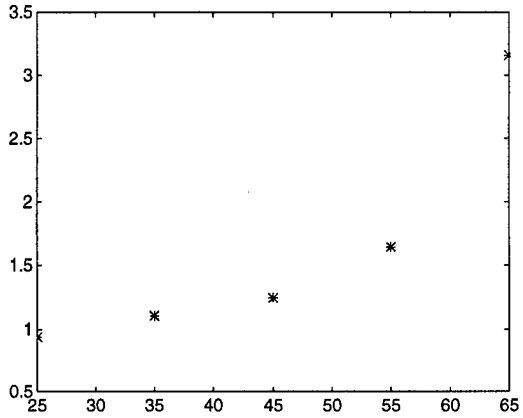



Fig.5 Normalize RMS emittance as function of the the RF gun phase for a constant laser energy.

## 4 ACKNOWLEDGEMENT

Authors gratefully acknowledge discussion with D.T. Palmer, the technical support form Mr. W. Cahill, R. Harington and M. Montemgo made the work present here possible. This work is supported by the U.S. D.O.E. contract No. DE-AC02-76CH00016.

## REFERENCES

[1] L. Serafini, R. Zhang and C. Pellegrini, Nucl. Instr. and Meth. A387 (1997) 305 - 314.
[2] P. Kung, H. Lihn and H. Wiedemann, Phys. Rev. Lett. 73, 967 (1994).
[3] B.E. Carsten and S.J. Russell, Phys. Rev. E. 53, R2072 (1996).
[4] J.B. Rosenzweig, N. Barov and E. Colby, IEEE Trans. on Plasma Sci. Vol.24, No.2, 400 (1996).
[5] X.J. Wang, X. Qiu and I. Ben-Zvi, Phys. Rev.E. 54, R3121 (1996)
[6] X.J. Wang, UCLA P.h.D thesis (1992).
[7] L. Serafini, IEEE Trans. on Plasma Sci. Vol.24, No.2, 421 (1996).
[8] B.E. Carlsten, Nucl. Inst. and Meth. A 285 (1989) 313.
[9] B.E. Carslten, D.C. Nguyen and R. L. Sheffeld, LA-UR-96-424 (1996).
[10] K.J. Kim, Nucl. Inst. and Meth. A 275 (1989) 201.
[11] D.T. Palmer, X.J. Wang et al, to be published in the Proc. of the 7th Advanced Accelerator Concepts Workshop, BNL-63808 (1996).
[12] C. Travier, Nucl. Inst. and Meth. A 340 (1994) 26.

# BEAM DYNAMICS IN RF-GUN CAVITY WITH A MODIFIED FIRST CELL

V.Volkov, M.Karliner, V.Petrov, I.Sedlyarov, A.Tribendis
Budker Institute of Nuclear Physics, Novosibirsk, Russia and
D.Janssen, P. vom Stein, Research Center Rossendorf, Dresden, Germany

*Abstract*

The results of beam dynamics simulation with bunch charges up to a few tens pC in superconducting linear accelerator for ELBE project [1] are presented. The accelerator consists of 3+1/2 TESLA cells RF-Gun and two 9-cell TESLA cavities. It is shown that the change of a flat back wall of the half-cell with cathode in its center by a conical back wall results in reduction of transversal bunch sizes and also of its emittance at the accelerator exit by a factor of 20.

## 1 INTRODUCTION

In the RF-gun a superconducting accelerating cavity with the laser driven photocathode on the back wall of the cavity first cell is used. The projects of similar superconducting RF-guns were discussed elsewhere [2,3,4,5,6] but only a "pure" half cell with the flat back wall was used as the cavity first cell.

The goal of this paper is to find out an influence of the shape of the first cell on the beam dynamics in RF-gun cavity and to study the possibility to achieve extremely low full beam emittance.

The shape changed as following: a) from flat back wall of the half first cell to the conical one; b) modifying the full length of the first cell with respect to generally adopted $\lambda/4$.

For this purpose, the beam dynamics in the 3+1/2 RF-Gun cavity with gradually modifying first cell and in the accelerator consisting of an RF-gun and two standard 9-cell TESLA cavities at the frequency of 1300 MHz was simulated.

## 2 CALCULATION TECHNIQUE

All the calculations have been carried out with the use of the program **TRAJECT** [7]. The program calculates the beam dynamics only for a small charge at which the effects of the beam spatial charge are negligible. A high calculation speed of the program gives a possibility to sort out by iteration cycle an optimal regime of beam injection and cavity excitation. The calculation results agree with PARMELA's calculation if the bunch charge is no more then few tens of pC [1]. RF fields in the cavities are calculated with the use of program **SLANS** [8].

The rms length of the beam is given to be 10 ps.

In the transverse direction the current density is distributed by the rectangular law. If the current transverse distribution Gaussian, the beam emittance would be 4 times higher than that in this case [2].

The photocathode radius **ro** is given to be 1.5 mm.

The normalized transverse beam emittance **εn** is calculated by the known formulas [9].

The dynamics simulations were executed for the field gradient of **Eacc = 15 MV/m** - as an attainable in reality in supercondacting accelerating cavities at 1300 MHz.

5 versions of the first cell have been taken fo calculations: 0°, 10°, 15° back wall and 10° back wall with $\lambda/4\pm10$ mm length of first cell.

In the paper the calculations results for two versions of accelerators are given: for the gun with a flat back wall in the first cell and with a 10° conical wall (Figure). Here the injection phase $\phi$ of bunch from the cathode is equal to the optimal one which results in minimum of a beam energy spread at the RF-Gun exit. The phases of excitation of first and second TESLA cavities are being optimal too.

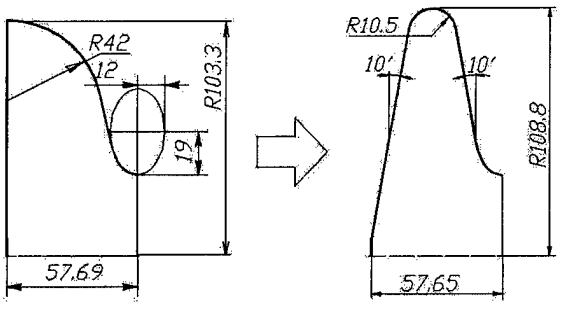



Figure 1. Accelerator RF-gun first cells.

## 3 RF-GUN CALCULATION RESULTS

The calculation results of a beam dynamics show that the presence of the conical back wall in the first cell causes an explicit **focusing effect** such that the beam radius

0-7803-4376-X/98 /$10.00 © 1998 IEEE

decreases in average along the whole cavity and if the conical angle is more than 15 degrees, the beam of the RF-gun output is focused.

The peak field in the first modified cell is located at the surface near the hole and it is approximately the same as the peak field in the other cavity cells.

There are two **optimal** injection phases which appear when the gradient field in the cavity is more than some **threshold gradient.** The beam has a minimum transversal emittance for one optimal phase and has a minimum longitudinal emittance for another one. Its values differ 2 times approximately. The difference between these phases increases with the first cell length as it changes from generally adopted $\lambda/4$. So we always can find proper cell length which provide the coincidence of both minima simultaneously at only one optimal phase. It is assumed that the minimum of the beam energy spread coincides with minimum of a longitudinal emittance. We have found that the optimal first cell length is less than $\lambda/4$ by 2÷4 %.

The optimum injection phases increase monotonously with the growth of the field gradient at the cathode and so we can determine a value of threshold gradient as the field gradient at the cathode when the beam has a zero optimal phase. It's values are **9.9÷19.0 MV/m** for all 5 RF-gun variants. Table 1 shows other results.

**Table 1.** RF-gun calculation results.

| Ec | εn | σW | Δφ | φ |
|---|---|---|---|---|
| Ethresh | .007÷.02 | .015÷.03 | - | - |
| 20 | .07÷.27 | .07÷.36 | 5÷100 | 22÷54 |
| 40 | .44÷.56 | .25÷.45 | 2÷43 | 49÷69 |

**Ec** -Peak field at the cathode, **MV/m.**
**εn** -Normalized transverse emittance of a beam, **π mm mrad.**
**σW** -Rms energy spread of the beam particles., **%.**
**Δφ** -Differences between optimal phases which leads to a minimum transversal emittance in one case and to a minimum longitudinal emittance in another case, **%.**
**φ** -Optimum phase of beam emission, **degrees.**

## 4 ACCELERATOR CALCULATION RESULTS

The beam transverse emittance is decreased significantly at the accelerator exit if a conical back wall is used (Figure 2 and Table 2). This effect occurs due to the focusing influence of the first cell. In the first cell the beam is not relativistic and following acceleration 'freezes' the influence of the geometry of the first cell.

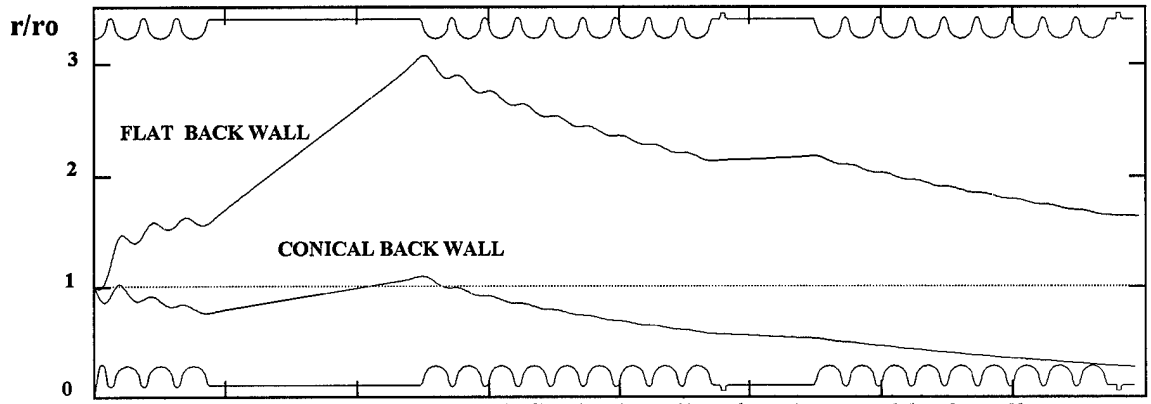



**Figure 2.** Beam radius in the accelerator: with flat back wall and with conical back wall.

**Table 2.1**. Beam parameters in the accelerator having RF-gun with first cell's flat back wall.

| Ec (E) MV/m | φ (φrf) degree | εn mm mrad | σW×2 % | W MeV | σL×2 ps | r/ro | Focus m | |
|---|---|---|---|---|---|---|---|---|
| 30 | 49.00 | .488 | .659 | 6.548 | 16.63 | 1.772 | -0.90 | RF-gun |
| (30) | (-66.42) | 7.133 | 0.648 | 21.48 | 16.62 | 2.138 | -24.3 | 1 cavity |
| (30) | (-70.02) | **10.81** | 0.643 | 36.43 | 16.62 | **1.630** | 20.76 | 2 cavity |

**Table2.2**. Beam parameters in the accelerator where RF-gun has first cell's conic back wall of 10°

| | | | | | | | | |
|---|---|---|---|---|---|---|---|---|
| 19.6 | 34.6 | 0.206 | 0.440 | 6.061 | 13.38 | 0.800 | -1.90 | RF-gun |
| (30) | (-67.12) | 0.478 | 0.420 | 21.00 | 13.33 | 0.552 | 4.500 | 1 cavity |
| (30) | (-71.62) | **0.605** | 0.417 | 35.96 | 13.33 | **0.264** | 2.030 | 2 cavity |

**Ec** -Peak field at the cathode. **E** -peak field at the cavity axis, E=2×Eacc. **φ** -Phase of beam emission. **φrf** -RF exciting phases in TESLA cavities. **εn** -Normalized transverse emittance. **σW** -Rms energy spread. **W** -Beam energy. **σL** -rms length. **r/ro** -Beam radius/photocathode radius, **ro = 1.5 mm.** **Focus** - Average distance from the structure beam tube end to the point where all beam electron trajectories are converged.

Also there are two optimal phases of excitation for the first TESLA cavity which result in a minimum of the beam transversal emittance in one case and a minimum of longitudinal emittance in another. In order to close these phases it is necessary to decrease the injection phase in RF-Gun down to 29° from 34°. I.e. the injection phase for the accelerator has to be less than the one for an isolated RF-Gun by 15%. The best beam parameters for phases optimized in this way are shown in Table 2.3.

**Table 2.3**. The best beam parameters in accelerator having the 10°conical first cell in RF-gun for optimized injection ($\phi$) and excitation phases ($\phi$rf1, $\phi$rf2)

| $\phi$ deg. | $\phi$rf1 deg. | $\phi$rf2 deg. | $\varepsilon$n mm mrad | $\sigma$W % |
|---|---|---|---|---|
| 29 | -61.5 | -67 | 0.211*) | 0.168 |

The emittance and other beam parameters, except $\sigma$W, are weakly dependent of exciting phase of the second TESLA cavity. Figure 3 depicts the dependence of the particle energy distribution in the beam on their position in a beam and on the misalignment by ±20° of exciting phase $\phi$rf2 from its optimal value in the second TESLA cavity.

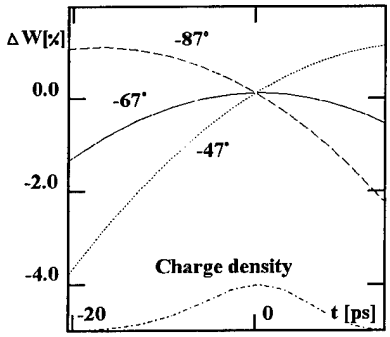



**Figure 3.** Beam energy distribution at the accelerator exit

**Table 3**. Beam parameters at the accelerator exit as a functions of RF excitation phase $\phi$rf2.

| $\varphi$rf2 degrees | $\varepsilon$n mm mrad | $\sigma$W×2 % | W MV |
|---|---|---|---|
| -87.0 | 0.22 | -1.311 | 35.12 |
| -67.0 | 0.211 | 0.336 | 35.96 |
| -47.0 | 0.191 | 1.527 | 35.07 |

## 5 CONCLUSION

The use of a conical shape of the back wall of the first cell in a 3+1/2 cavity for an RF-gun leads to focusing of the beam if the conical angle is more than 15°.

The application of such an RF-gun with the first cell's conical back wall in an accelerator consisting of a couple of TESLA cavities complementary leads to a decrease of beam transversal emittance down to 0.21*) $\pi$ mm mrad and energy spread ($\sigma$W) down to 0.17 %.

A beam will have an extremely low emittance, if the field gradient in the cavity is more than some threshold gradient by 10÷19 MV/m.

There exists an optimal length of the RF-gun first cell which is less than $\lambda/4$ by 2÷4 %.

There exists an optimal accelerator injection phase which is less than the one for an isolated RF-gun by 10÷20 %. In both this cases the beam have a minimum of transversal and longitudinal emittance simultaneously.

The calculations were carried out for beam charge up to few tens of pC but focusing effect of conical back wall is also very actual for greater charge as it is shown by PARMELA calculations in [1].

## 6 REFERENCES


[1] P.vom Stein et al., *The DROSSEL Project for the Development of a Supercondacting RF-Gun* (Presented here).

[2] K.J.Kim, Nucl. Instr. and Meth. A275 (1989) 201.

[3] J.Edighhoffer et al., Nucl. Instr. and Meth. A358 (1995) 18-19

[4] C.Pagani et al., Nucl. Instr. and Meth. A340 (1994) 17-25.

[5] L.Serafini/ Nucl.Instr.and Meth.in Phys.Res. A 340 (1994) 209-213

[6] A. Michalke. Ph.D. Thesis. Wuppertal University, rep.WUB-DIS 92-5.

[7] V.N.Volkov, BINP, Novosibirsk, RUSSIA. e-mail: VNVOLKOV@inp.nsk.su, tel.: +7-3832-35-91-06

[8] D.G.Myakishev,V.P.Yakovlev, *An Interactive Code SuperLANS for Evaluation of RF-Cavities and Acceleration structures*, Proc.of the 1991 Particle Accelerator conference, Vol.5, p.3002-3004

[9] P.M.Lapostolle, IEEE Trans. Nucl. Sci. NS-18 (1971) 1101


*) We should note for Gaussian transverse charge distribution of the beam it's emittance mast be large by 4 times, i.e. 0.84 $\pi$ mm mrad [2].

# SINGLE BUNCH INJECTION SYSTEM FOR AN ELECTRON STORAGE RING USING AN RF PHOTOINJECTOR *

P.G. O'Shea, J.A. Lancaster, J.M.J. Madey, R. Sachtschale,
Department of Physics, Duke University, Durham NC 27708 and
C.R. Jones,
Department of Physics, North Carolina Central University, Durham NC 27709

*Abstract*
RF photoinjectors have gained acceptance as the source of choice for high-brightness electron accelerators, but have been quite expensive to build and difficult to operate. In this paper we describe the successful operation of an inexpensive, simple and reliable rf photoinjector suitable for single bunch injection into storage rings.

## 1. INTRODUCTION

For optimum storage ring FEL and Compton backscatter performance on the Duke Storage Ring, we require that the electrons be injected to specified ring rf buckets and no others at up to 1nC per bunch [1].

The Duke Ring operates with a bucket spacing of 5.5 ns. For clean injection, i.e. no spill-over into adjacent buckets, we require a system which has the following features:

- Delivery of beam only during injection with seamless and rapid switching between injection and non-injection mode
- The sum of the full pulse width of the injected beam plus any timing jitter be less than 5 ns
- Capable of being upgraded to 1 nC per pulse.
- Use the existing thermionic rf gun system
- Be easy to operate, reliable and inexpensive

Traditionally such requirements are met by using pulsed electromagnetic kickers [2]. A conventional rf photoinjector with a picosecond mode-locked and frequency multiplied drive-laser [3] could not satisfy the last of the requirements and therefore is unacceptable. Nothing precludes the use an inexpensive, longer-pulse laser in conjunction with a buncher and momentum selector [4]. A 337-nm, TEA nitrogen laser appears to be a suitable candidate. The Duke rf gun [5] previously had a conventional drive laser [6], and so has a port suitable for drive-laser injection, and a $LaB_6$ cathode of know quantum efficiency. Nitrogen lasers are commercially available for approximately $7000 which can produce 100-μJ of 337-nm light in sub-ns long pulses with sub-ns timing jitter [7].

This system differs from conventional rf photoinjectors a number of ways. Because the drive-laser pulse (600 ps FWHM) is longer than the linac rf period (350 ps for a 2.856 GHz system), there is no pre-bunching of the beam by the laser. Therefore a buncher/momentum filter α-magnet is required after the gun. In this way the system acts like a thermionic rf gun system with enhanced electron emission from the cathode. The system produces a 1-ns macro-bunch of three linac microbunches. The system operates in a single macro-bunch per rf macropulse mode. Unlike conventional drive lasers, no up-conversion of the photon energy is required, because the fundamental emission is at 377 nm.

## 2. DRIVE LASER

The nitrogen laser is a self contained system which is straightforward to operate. Details of the laser specifications are given in Table 1.

| Model | Laser Photonics LN203C |
|---|---|
| Spectral output (nm) | 337.1 |
| Spectral Bandwidth (nm) | 0.1 |
| Pulse width (ps, FWHM) | 600 |
| Energy per pulse (μJ) | 100 |
| Amplitude stability (%) | 1 |
| Peak Power (kW) | 167 |
| Rep. Rate (max) (Hz) | 50 |
| Command timing jitter (ns) | <1 |
| Beam dimensions at laser (mm) | 5 x 3 |
| Beam divergence (mrad) | 6 x 2 |
| Nitrogen flow rate (STD l/s) | 0.016 |
| Laser Dimensions (cm) | 71 X 21 x 13 |

**Table1**: Drive-laser specification

Apart from AC power, safety interlocks and standard TTL trigger, only a source of dry nitrogen is required. The boil-off from a 500-litre liquid nitrogen Dewar is sufficient for several weeks of laser operation .

* Work supporeted by AFOSR contract F49620-93-1-0590,
ONR Contract N00014-94-1-0818
and USASDC Contract DASG-60-84-C-0028.

0-7803-4376-X/98/$10.00 © 1998 IEEE

## 3. SYSTEM CONFIGURATION

The laser was installed within 1 m of the gun so that optical transport would be as simple as possible. The optical transport consisted of a pair of alignment apertures, a 30 cm focal length lens, and two turning flats. The laser beam was focused on the 2-mm diameter single crystal $LaB_6$ cathode at an incident angle of 45°.

All the lenses and the vacuum window are uncoated glass, and the mirrors are front surface aluminum. Measurements of the electron beam current were made using a fast wall current monitor at the end of the linac at an energy of 270 MeV. The linac is a standard SLAC type traveling-wave linac [8]

## 4. SYSTEM PERFORMANCE

A summary of the system performance is given in Table 2 . A typical macro-bunch profile is shown in fig.1. The resolution of the signal analyzer was not sufficient to resolve the individual linac micropulses.

| | |
|---|---|
| RF Macropulse length (μs) | 2 |
| Nominal injection energy (MeV) | 270 |
| E-beam macropulse length (ns FWHM) | 1 |
| Energy spread (macropulse)(%) | 0.2 |
| Energy jitter (%) | < 0.1% |
| Ratio of charge desired ring bucket to neighboring buckets | <0.001 |
| Macropulse rep. rate (Hz) | 2 |

**Table 2.** Performance of single bunch injection system

The $LaB_6$ cathode can be operated in a pure thermionic mode, a laser switched photoemission mode, or in a combined mode. A single laser pulse produced a macro-bunch of three linac micropulses. We operated with one macro-bunch in each 2-μs rf macropulse. The macro-bunch pulse duration was short enough that beam loading was not an issue. Therefore, the accelerator was tuned using the thermionic emission set at a very low level. In the photoemission mode, the temperature of the cathode was heated to approximately 1250 K, just below the threshold for significant thermionic emission.

Fig. 2 shows the charge per bunch emitted vs. cathode temperature in both the thermionic mode and the photoelectric mode. The cathode temperature was measured using a hot-wire optical pyrometer [9]. The temperature readings are corrected for the emissivity of $LaB_6$. With the cathode temperature at the threshold of thermionic emission, the charge per pulse was 0.09 nC. The pulse FWHM was < 1ns. The overall timing jitter of the electron beam relative to the ring rf timing was approximately 2 ns. Therefore the combined pulse length and timing jitter of the injected electron pulse had a full range of 3.5 ns, meeting the specification of < 5 ns combined pulse length and jitter, and resulting in reliable single-pulse injection and stacking.

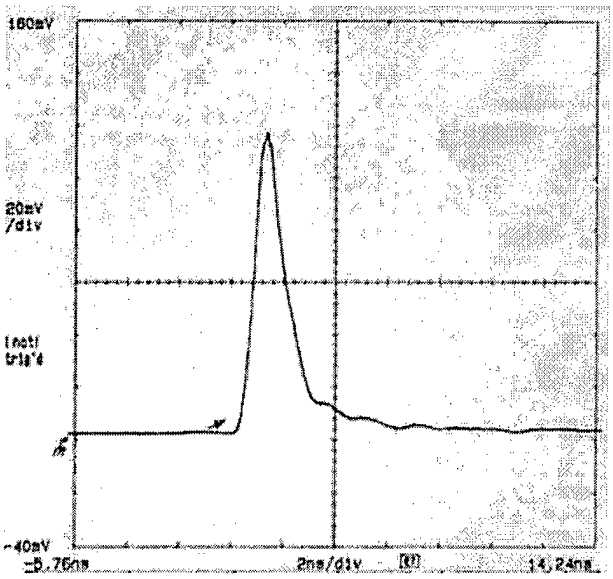



**Fig. 1.** Electron beam pulse profile as measured on the fast wall current monitor. The measured FWHM is 1 ns.

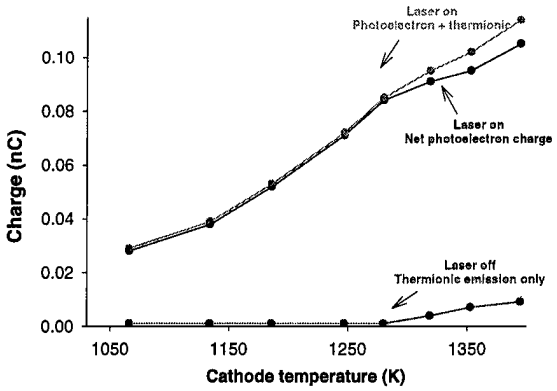



**Fig. 2** Charge per bunch versus cathode temperature

## 5. ESTIMATE OF $LaB_6$ CATHODE QUANTUM EFFICIENCY

As is evident from fig. 2, we observe as others have [10,11], that the photoemission from the cathode is a function of the applied cathode heater power. When the heater power is lowered the electron current dropped at a rate much slower than the rate of drop of the cathode temperature. On removal of power from the cathode heater, the initial rate of drop in temperature is approxi-

mately 250 K/s. The characteristic time for the drop in emitted current is on the order of 10 minutes. We conclude from this that at lower temperatures the cathode was subject to significant contamination because of poor vacuum. The gun is operated at a pressure in the low $10^{-8}$ torr range. At this pressure, a monolayer will form on the surface in a few minutes (if a sticking factor of unity is assumed).

We did not attempt to measure the quantum efficiency of the cathode directly. We have estimated quantum efficiency of the $LaB_6$ cathode by using the measured photoelectron current transported to the end of the linac and the known transport efficiency of the linac in the standard thermionic cathode mode. The quantum efficiency (QE) of the $LaB_6$ cathode is estimated using the following equation:

$$QE = \frac{C_m}{\eta_p \eta_G \eta_\alpha N_p e}$$

where $C_m$ is the measured charge per pulse at the end of the linac; $\eta_p$ is the efficiency of photon transport from the laser to the cathode; $\eta_G$ is the gun efficiency (i.e. fraction of the time that the drive laser can produce electrons which are accelerated out of the gun) [11]; $\eta_\alpha$ is the efficiency of transport of electrons through the $\alpha$-magnet to the end of the accelerator; and $N_p$ is the number of photons per pulse striking the cathode; and e is the electronic charge. We estimate $\eta_p \approx 0.3$; $\eta_G \approx 0.25$ , $\eta_\alpha \approx 0.25$, $N_p = 1.7 \times 10^{14}$.

Fig. 3 shows the inferred quantum efficiency versus cathode temperature. The data for the quantum efficiency represent the stable, equilibrium values at a given cathode temperature. Asakawa et al [12] have reported $LaB_6$ quantum efficiency data measured at 355 nm from 300-1273 K. For comparison, these data are shown in fig. 3 in the temperature region where they overlap with our data.

## 6. CONCLUSION

We have demonstrated that a TEA nitrogen laser can provide a simple and reliable method of generating electron pulses for a single bunch injection system. Further plans for improvement of the system include the replacement of the existing optics with UV-grade anti-reflection coated elements, and the procurement of a laser with greater pulse energy, with the goal of achieving 1 nC per macro-bunch.

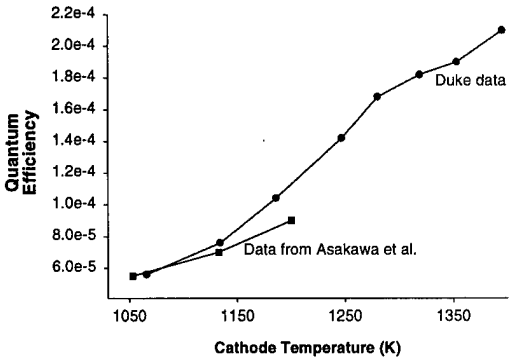



**Fig. 3** Inferred quantum efficiency for the $LaB_6$ cathode versus cathode temperature. Duke data at 337 nm, Asakawa data at 355 nm

## 7. ACKNOWLEDGEMENTS

We would like to thank V. Litvinenko and I. Pinayev for assistance with this work.

## 8. REFERENCES

1. V.N Litvinenko, et al. *Unique features of the OK-4/Duke storage ring XUV FEL and monochromatic gamma-ray source,* these proceedings
2. Yokoyama, etal., Nuclr. Instr. and Meth. A 341, 367 (1994)
3. P.G. O'Shea, *Nuclr. Inst.s and Meth A*, **358**, 36, (1995).
4. C.B. McKee and B. Hooper, Duke FEL memorandum "Long Pulse photocathode", unpublished (1993)
5. G.A. Westerskow and J.M.J. Madey, Laser and Particle Beams, vol. 2, part 2, 223 (1984)
6. M. Curtin et al. Nuclr. Instr. and Meth. A296, 127 (1990)}.
7. Laser Photonics, Inc, 12351 Research Parkway, Orlando FL 32626
8. P.G. O'Shea et al., Proceedings of the 1995 Particle Accelerator Conference, 1090 (1996)
9. Microtherm model, manufactured by Pyrometer Instrument Company, 234 Industrial Parkway, Northvale NJ 07647
10. D. J. Banford, M. H. Bakshi, and D. A.G. Deacon, Nuclr. Instr. and Meth. A318, 377 (1992).
11. C.B. McKee, Ph.D Dissertation, Duke University, unpublished (1994)
12. M. Asakawa et al., Nuclr. Instr. and Meth. A331, 302 (1993)}.

# A PLANE-WAVE-TRANSFORMER PHOTOELECTRON LINAC

D. Yu, T. Lee, S. Rajagopalan, J. Chen
DULY Research Inc., Rancho Palos Verdes, CA 90275
C. Pellegrini, J. Rosenzweig, X. Ding
University of California, Los Angeles, CA 90024

*Abstract*

We develop a novel photoelectron linear accelerator using a plane wave transformer (PWT) design [1]. In this design the input RF power is coupled to the accelerating cavities via a large concentric manifold cavity. The scheme makes possible very strong coupling between the accelerating cells, and relaxes manufacturing tolerances. The compact photoelectron linac integrates a photocathode directly into a PWT linac structure, and eliminates the drift space between a photoinjector and the linac which would otherwise lengthen the electron bunches. Using an emittance compensation scheme [2], the PWT photoelectron linac produces a high-brightness beam. We have demonstrated by simulations the feasibility of a 20-MeV PWT photoelectron linac design with a set of eleven iris-loaded disks suspended and cooled by four water tubes inside a large cylindrical tank.

## INTRODUCTION

In this Small Business Innovation Research (SBIR) project DULY Research Inc. teams up with University of California at Los Angeles (UCLA) to develop a novel photoelectron linear accelerator using a plane wave transformer (PWT) design [3]. The goal is to accelerate a short pulse (~5 ps), low emittance (~1 mm-mrad), high charge (~1 nC) electron beam in a compact (~30 MV/m), inexpensive linear accelerator. This kind of compact linac will have broad commercial and research applications [4].

The conventional RF electron linac design, typified by that of the Stanford Linear Accelerator Center (SLAC) and by commercial medical linacs, consists of iris-coupled disks separated by metal cup spacers and enclosed in a cylindrical tube to form a set of accelerating cavities. The RF input power is fed into an accelerating section by means of waveguide(s) coupled to a single input cavity. Once inside the slow-wave linac structure, the electron beam is accelerated by RF fields traveling in phase with the bunched beam. In general, the manufacturing tolerances of the accelerator components are extremely tight, and consequently the cost of machining and brazing is high, because the precise dimensions determine the phase and cavity properties essential for proper RF acceleration. It would be desirable to find methods to relax manufacturing tolerances and reduce cost for linac structures, especially for repetitive production of accelerating sections as in a linear collider, or for mass production of commercial linacs.

A novel plane-wave-transformer (PWT) accelerating structure which is recently under development at the University of California at Los Angeles (UCLA) [1] has the potential of making such improvements. The PWT linac structure is a multi-cell, standing-wave system operating in the $\pi$-mode. A schematic of our 20 MeV PWT linac is shown in Fig. 1. The structure consists of an assembly of iris-coupled disks suspended along the axis of a large cylindrical tank. In this design of the PWT linac, the disks are connected longitudinally by cooling tubes which are supported at the end plates of the tank. The input RF power is fed into the cylindrical tank outside the disk/iris assembly and propagates predominantly in a TEM-like mode in the coaxial manifold, which resembles a plane wave propagating in free space. This TEM-like accelerating mode transfers external RF power into a TM-like accelerating mode between the irises. As there are no walls separating the disk assembly and the manifold tank, all individual cells are strongly coupled to the manifold and to each other. The unique and simple design of the PWT linac structure allows tolerant dimensions (about 100 μm for an S-band structure), and is easy and inexpensive to build. The PWT is also easy to operate due to its large vacuum conductance.

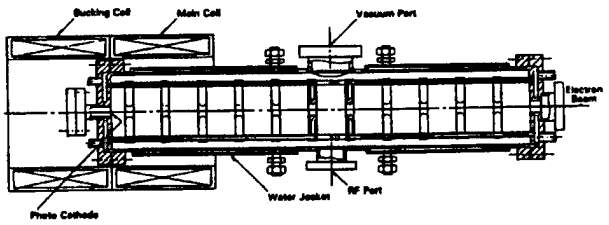



Figure 1. Schematic of a 20-MeV PWT photoinjector linac

## TECHNICAL APPROACH

The previous UCLA photoinjector is based on a well-tested Brookhaven National Laboratory design [5] currently adopted by many laboratories over the world. It consists of a 1 + ½ cell RF cavity operating at S-band, with the cathode placed at the center of the end wall of the first half-cell. The photoinjector is currently driven by a mode-locked YAG laser which uses chirped pulse amplification and compression to obtain 7.5-ps (FWHM) pulses containing up to 300 μJ per pulse of UV light (262 nm).

In this DULY/UCLA project, the photoinjector is modified and integrated into a PWT electron accelerator in which the RF cavities are open to a large cylindrical tank, and the fields therein are strongly coupled between cells. This is an integrated structure with a total of eleven (11) full cells and one (1) half cell, including the photoinjector and the linac structure. The accelerating structure consists of a row of equidistant, circular washers which are aligned along the axis of a large cylindrical tank (Fig. 1). These copper disk washers are fixed in position by

0-7803-4376-X/98/$10.00 © 1998 IEEE

means of four metal tubes parallel to the tank axis. The metal tubes are also water conduits for cooling the disks. Because the disks are separated from the cylindrical tank, they act as a center conductor to support a TEM-like mode in the coaxial manifold, which is excited by high power RF coupled through an input slot on the tank wall. The strong coupling between the TEM wave in the manifold and a TM-like mode along the beam axis provides a $\pi$-mode longitudinal accelerating field profile, through the irises, by which electrons are accelerated. These features of the PWT linac provide advantages of high shunt impedance and strong coupling between individual cells, thus relaxing manufacturing tolerances and reducing manufacturing costs.

The design objective is optimization of a photoelectron accelerator design and performance of parametric studies of beam dynamics for a 20-MeV PWT photoinjector linac, to be built and tested in the following experiment. Specific technical objectives include: (1) accelerator design, (2) beam dynamics study; (3) solenoid magnet design, with results presented in the following sections.

## CALCULATION OF ELECTROMAGNETIC FIELDS AND RF PROPERTY

The RF structure of the PWT linac has been specified in a two-stage design process: initial optimization of the field profile for acceleration using 2-D electromagnetic field solver, SUPERFISH, followed by a 3-D analysis using the code MAFIA. In the first stage, we make a first specification of a baseline geometry and the nominally axisymmetric fields in the beam channel. This specification is subject to the following constraints:

- maximizing shunt impedance
- minimizing higher spatial harmonic content
- cell number and gradient appropriate to deliver 20 MeV beam
- good coupling and mode separation
- relatively low $Q_0$ to allow for structure filling in < 6 μs
- minimizing outer diameter to allow compact focusing solenoid

The SUPERFISH results have been used to deduce the spatial harmonic content of the accelerating field. It is important that the higher spatial harmonic content be minimized in an RF photoinjector, so that the beam would not suffer nonlinear RF-derived emittance growth. The amplitudes of the high spatial harmonics have been well minimized given our desire for high shunt impedance.

While the shunt impedance in the PWT is mainly derived from the properties of the iris geometry, the cell-to-cell coupling, and therefore the mode separation is a function of the distance from the inner radius of the outer wall to the outside of the disks. In the SUPERFISH calculations, we have chosen the wall radius to be 5.5 cm, and the disk radius to be 4.07 cm. For these parameters, the coupling is quite large — the width of the lowest passband is over 795 MHz. The mode separation between the $\pi$ and the $11\pi/12$ is 13 MHz, which is many times the width of the modes due to the finite $Q_0$. This mode separation compares favorably with the 0-$\pi$ mode separation in the current UCLA 1.5-cell, 2856 MHz gun (< 2 MHz), and is larger than the mode separation of the next generation 1.625 cell guns being developed by a BNL/SLAC/UCLA collaboration.

We have studied several configurations of the support rod structure using MAFIA: a no-rod, a two-rod, and a four-rod PWT structure, each supporting 11 metal disks (1.2065 cm thick) with 1.5875-cm irises, inside a cylindrical tank with a radius of 5.5 cm. The dimensions of each structure are chosen to allow a $TM_{01n}$ accelerating $\pi$-mode at a frequency of 2856 MHz. The structure is tuned by adjusting the position of the support rods and the disk radius. Arrow plots of the electric field for the 4-rod PWT structure accelerating mode as simulated by MAFIA are shown in Fig. 2. The shunt impedances and $Q_0$-values for these cases are shown in Table 1. The ratio of $R/Q_0$ is seen to be roughly constant (even increasing slightly with the introduction of rods), while the $Q_0$ degrades with the introduction of extra rods. The zero-rod structure represents both an ideal baseline, and a representation of a DULY innovation in RF structure design. The two-rod case, while offering a high $Q$ and shunt impedance, is problematic from two points of view: the field perturbation, which is at lowest order quadrupole, and the mechanical integrity of the structure. Because of these considerations, we have decided to pursue our program of building a PWT prototype using the four-rod design, and at the same time continue R&D on a highly promising no-rod design.

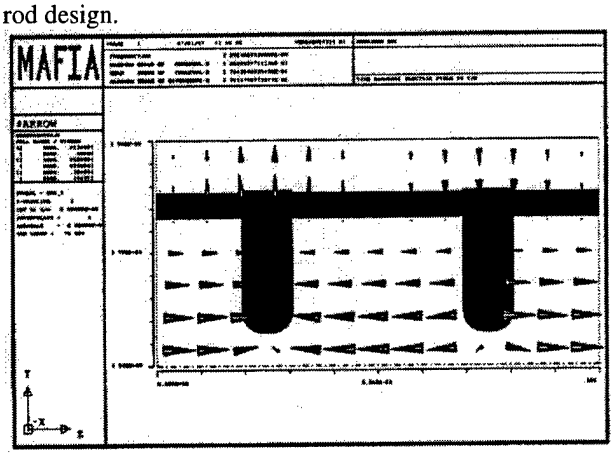


Figure 2. The electric field in the 4-rod PWT structure

Table 1. RF Characteristics of PWT Designs (for 4-rod, 2-rod and no-rode cases, from the MAFIA simulations)

| | $Q_0$ | $R$(MΩ/m) | $R/Q_0$ (Ω/m) |
|---|---|---|---|
| 4-rods | 24,560 | 121.3 | 4939 |
| 2-rods | 28,316 | 128.8 | 4547 |
| No rods | 32,572 | 141.7 | 4350 |

## THERMAL AND MECHANICAL ANALYSIS

The high frequency RF power used to accelerate the electron beam also produces heating on the surfaces of the metallic structure. A design of the PWT structure uses four stainless steel tubes to provide mechanical support of eleven suspended disks, and to carry cooling water to the disks for heat removal. To control the temperature, an annular channel carrying flowing water (~10 liters/min

at the reservoir) at a constant temperature (~65°F) is cutaway around the interior of each disk to carry heat away from the metal. Water from an external constant-temperature bath flows into one reservoir, passes into the disks via two of the four water tubes, returns to another reservoir through the remaining two tubes, back to the bath to form a closed loop. We have performed a thermal analysis of a typical PWT disk subject to pulsed RF heating and continuous water cooling, using a PC version of a general finite-element thermal/structure code, COSMOS/M. The temperature result is sensitive to the value of the convective film coefficient, which is dependent on the flow, and can vary between 1-10°C because of the uncertainty in the film coefficient. A higher flow rate (> 15 liters/min at the reservoir) and a larger hydraulic diameter will ensure better turbulent flow and heat transfer. The temperature variation between different disks can be tightly controlled by adjusting the size of the flow orifice connecting to the cooling channel. Such cell-to-cell tuning is probably not necessary because of the strong coupling between individual cells in the PWT linac.

## BEAM DYNAMICS CALCULATIONS

The design of beam optics in an RF photoinjector linac is intimately related to the RF design of the structure, as well as to the design of the focusing solenoid, in sometimes subtle ways. We made use of an emittance compensation technique to achieve low beam emittance and high beam brightness.

The analytical theory developed by SR [2] also allows the beam parameters which give emittance compensation to be specified. It requires that, in order to prevent the beam from expanding unnecessarily in the initial few cells, the peak in the solenoid focusing field of the solenoid be placed as close to the cathode as possible. This has been done for our preliminary design, as discussed further below. Another condition is that the parameter $a = eE_0/k_{RF}m_ec^2$ be limited to the order of unity, thus setting the peak field (on the order of 60 MV/m), the accelerating gradient (on the order of 30 MV/m), and the nominal launch phase (32 degrees, where 90 is taken by convention to be the RF crest). This condition can be explained as follows: for higher gradients, the invariant envelope is smaller, and thus the launched beam must be radially smaller in order to be matched to the invariant envelope well beyond the solenoid. In that case, the beam is too dense (the beam plasma frequency is high) and expands excessively in the first half-cell, thus denying the possibility of invariant envelope matching. Therefore, in order to minimize the emittance, we have chosen a moderate accelerating gradient of 33 MV/m.

## PRELIMINARY DESIGN OF THE SOLENOID MAGNET

To implement emittance compensation, the transverse beam profile should be immediately under control by the external focusing field after the electrons are emitted from the cathode. This can be accomplished by a focusing solenoid with a very fast-rising longitudinal field profile which increases linearly in the first half-cell and is maximum and close to constant in the first full cell. In our preliminary design, the focusing solenoid is integrated in a single yoke assembly with its mirror image bucking solenoid. The mirror symmetric bucking coil is run in series with the focusing coil. Each coil has 144 water-cooled, ¼-inch square, copper windings, and runs at approximately 140 A to obtain the design field values. The inner radius of the coil and the yoke is 6.5 cm, which provides a one-centimeter clearance between the inner radius of the RF tank and the solenoid assembly; the outer radius is 15 cm. This design is similar to that used in several UCLA projects, but here with even more modest field and current values. We are working on a new compact solenoid design in which the large mirror bucking coil is replaced by a very small one located behind the cathode.

## COLD TEST OF A PWT LINAC WITH A PHOTOCATHODE

In order to demonstrate the feasibility of integrating a photocathode into a PWT linac structure without significantly perturbing its RF properties, we have outfitted an existing PWT linac structure at UCLA with a cathode plug (and associated spring-contact RF joint), and performed cold microwave measurements on the combined structure. This structure consists of seven (7) full cells and two (2) half cells with eight nearly identical disks, held together by four rods. It has fewer cells and a larger tank than the PWT structure we propose to build in the next step, but otherwise has many similar features.

## CONCLUSIONS

Our work has successfully demonstrated the feasibility of an integrated PWT photoelectron linac system design. The system concepts and detailed dimensions of a prototype 20-MeV PWT photoelectron linac using a 4-rod design have been specified. We have used computer simulations and emittance compensation techniques to optimize the system performance. Limited cold tests have been performed to support the viability of integrating a photocathode and a PWT linac into a combined system. Based on these results, we can now move into the next step of the construction and test of a compact, high brightness, PWT photoelectron linac prototype system.

## REFERENCES

Work supported by DOE SBIR Grant No. DE-FG03-96ER82156.

[1] R. Zhang, et. al., Proc. of the 1995 Particle Accelerator Conf., 1102 (1995).

[2] L. Serafini and J. Rosenzweig, "Envelope Analysis of Intense Relativistic Quasi-Laminar Beams in RF Photoinjectors: A Theory of Emittance Compensation," to be published in Phys. Rev. E.

[3] V.B. Andreev, Soviet Physics – Technical Physics, 13, 1070 (1969).

[4] W.B. Herrmannsfeldt, A.M. Sessler and J.R. Alonso, Proc. of Workshop on Applications of Accelerators, LBL-35023, SLAC-430 (1994).

[5] K.T. McDonald, "Design of the Laser-Driven RF Electron Gun for the BNL Accelerator Test Facility," IEEE Trans. On Electron Devices, 35, 2052 (1988).

# PROPOSED INTENSE POSITRON SOURCE FOR TESLA BASED ON HERA-e *

A.V. Kiselev, Budker INP, 630090, Novosibirsk, Russia,
and V.D. Shiltsev, FNAL†, M.S.221, P.O.Box 500, Batavia, IL 60174

*Abstract*

In this article we perform a general study of possible positron source for linear collider TESLA based on the HERA electron ring. 30 GeV electrons passing 10T wiggler can produce intense synchrotron radiation with characteristic energy of photons of about 6 MeV. High energy photons are converted to few-MeV positrons in a suitable target. The ability of such a source to fit for the TESLA requirements is discussed.

## 1 INTRODUCTION

Linear collider TESLA [1] intends to operate with some 1100 bunches in electron and positron beam each populated with about $3.7 \cdot 10^{10}$ particles. Thus, the linac cycle of 5Hz yields the production requirement of $2 \cdot 10^{14}$ particles per second. While one expects no severe problems with the electron production, several types of the positron source options are now under consideration (see e.g. [2, 3]) which have to fit in requirements of the TESLA linac and damping ring [4]. In particular, one scheme assumes conversion of electrons from a powerful electron linac into positrons in a target [5], and the second concept is based on target conversion of high-energy gamma quanta produced by a high-energy electron beam in short-period helical undulator [6]. Several more sophisticated positron production schemes were discussed at *Sources'94* Workshop [7].

This paper presents a brief consideration of another possible positron production option with use of existing high current HERA electron storage ring - see general layout in Fig.1. 30 GeV electrons pass some 10T magnetic wiggler (presumably, superconducting) and produce powerful synchrotron radiation (SR) with the characteristic energy of photons of about 6 MeV. These photons are converted into positrons in a target and captured by special optics for further acceleration and injection into the TESLA damping ring.

As the mean electron current in the storage ring is much higher than in electron linacs to be used for positron production, then the ring-based scheme may have an advantage in obtaining the required positron production rate.

## 2 STORAGE RING-BASED POSITRON SOURCE

The idea of positron production with use of SR from a storage ring is not new. For example, ring-based sources

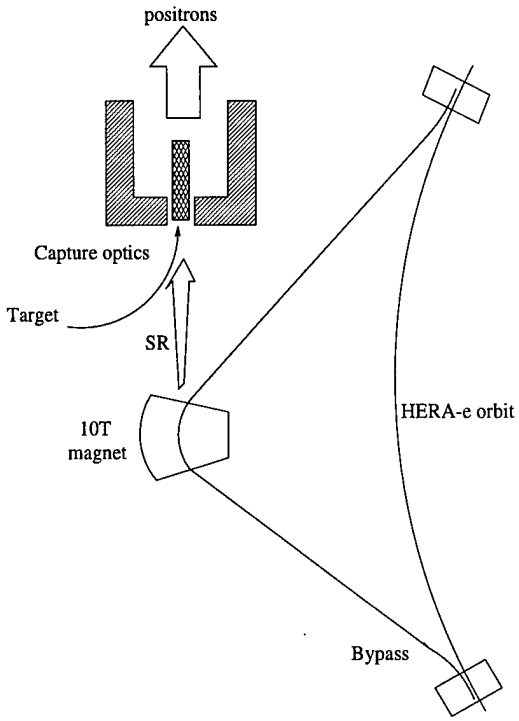



Figure 1: General layout of the proposed $e^+$ source.

of slow positrons for technological applications were proposed in Refs.[8, 9]. Few MeV positrons are much more suitable for the Linear Collider sources. Below we discuss several aspects of production of such particles.

### 2.1 *SR from Superconducting Wiggler*

Let us estimate the rate of photon production in a wiggler with a high magnetic field. We assume the undulator parameter of the device $K = \theta_{max}\gamma$ to be much bigger than 1, therefore, the known formula of the photon flux density can be applied [10, 11]:

$$\frac{dN_\gamma}{dt\,d\theta}\,[\frac{photons}{s\,mrad}] \approx 3.96 \cdot 10^{16}\,E[GeV]\,I[A]\,S(\varepsilon/\varepsilon_c)\frac{\Delta\varepsilon}{\varepsilon}, \quad (1)$$

where $I$ is the electron beam current, $\varepsilon$ is the photon energy, $S(\varepsilon/\varepsilon_c)$ is the spectral function [11] defined as

$$S(x) = \frac{9\sqrt{3}x}{8\pi}\int_x^\infty K_{5/3}(y)dy, \quad \int_0^\infty S(x)dx = 1. \quad (2)$$

The characteristic photon energy is

$$\varepsilon_c = 2.218[keV]\,\frac{E^3[GeV]}{R[m]}, \quad (3)$$

the curvature radius $R$ of electron trajectory in magnetic field $B$ is equal to

* work is supported in part by DESY, Hamburg

† Operated by Universities Research Association, Inc., under contract with the U.S. Department of Energy

0-7803-4376-X/98/$10.00 © 1998 IEEE

$$R[m] = \frac{3.33E[GeV]}{B[T]}. \quad (4)$$

For $B = 10$T and energy of HERA-e $E = 30$ GeV, the radius is equal to $R = 10$m and characteristic photon energy $\varepsilon_c = 6$ MeV that is much bigger than the $e^-e^+$ pair production threshold $\varepsilon_{th} = 2m_0c^2 \approx 1.022\,MeV$, or $x_{th} = (\varepsilon_{th}/\varepsilon_c) \approx 0.16$.

The integral of $\int_{x_{th}}^{\infty} S(\varepsilon/\varepsilon_c) \simeq 1$, thus, for the storage ring with $I = 50$ mA the total flux of photons which can produce electron-positron pairs is equal to

$$\frac{dN_\gamma}{dt\,d\theta}\,[\frac{photons}{s \cdot mrad}] \approx 6 \cdot 10^{16}. \quad (5)$$

The corresponding power of the SR is about 57 $kW/mrad$. If we assume the that the total electron current of 50 mA is distributed uniformly between 10 bunches, then each bunch produces some $1.3 \cdot 10^{11}\ \gamma/mrad$ per single passage through the magnet with the HERA revolution frequency of 47 kHz.

### 2.2 *Positron Production*

The process of positron production and interaction with the target material involves several physical phenomena (pair creation, ionization losses, scattering, etc.). Some analytical estimations of the conversion efficiency can be found elsewhere (see, e.g [8, 2, 9] and references there). Our further consideration is based on computer simulations [12].

All the results below are obtained for tungsten target (3.5 mm radiation length) under the following parameters: the distance from the 8T magnet to the target is 10 m, the width of the target is $w$ =10 mm (therefore, horizontal angular size of the target is $\theta = 1\,mrad$), its height is 0.3mm, the thickness of the target is 10 mm. In a good accordance with Eq.(1), the code estimates the photon flux on the target of $5 \cdot 10^{16}$ photons per second in the photon energy range from 1.022 MeV to 20 MeV. The conversion efficiency is found to be of the order of $N_{e^+}/N_\gamma \simeq 0.11$. For SR from 10T magnet this value arises up to $\simeq$0.13.

Fig.2 and Fig.3 present kinetic energy and angular distribution of the positrons, correspondingly. One can see that the mean particles energy is about 2 MeV while the FWHM of the energy distribution is some 3 MeV. Positrons leave the target in orthogonal plane to the orbit of HERA-e with broad spread of angles $\simeq \pi/2$ rad.

### 2.3 *Capture Efficiency and Injection Scheme*

The efficiency of the capture optics and acceptance of further acceleration are key issues for the source. Major problems to solve are to capture as many particles as possible and, at the same time, to avoid unacceptable pulse lengthening (initially the rms length of the HERA-e bunch is about 1 cm) when the pulse can not be accelerated as a whole. For the considered source, a two stage system could be proposed which consists of initial part with low frequency RF (e.g., 500 MHz) acceleration up to 20-30 MeV with large transverse and longitudinal acceptance, weak

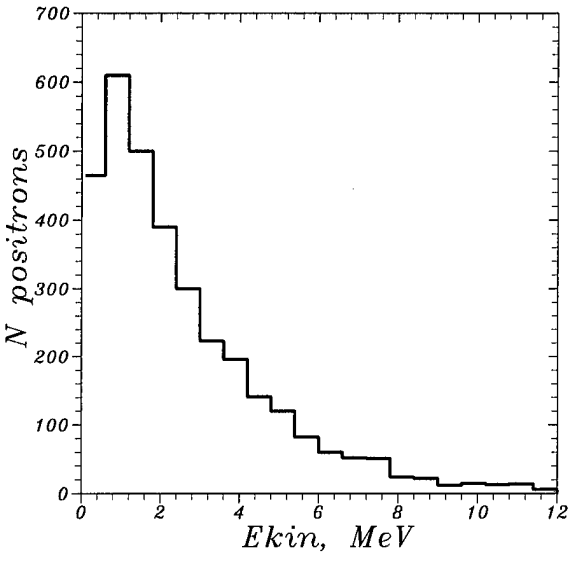



Figure 2: Kinetic energy distribution for positrons emitted from tungsten target 0.3×10×10 mm under impact of SR photons from HERA-e 8T wiggler.

longitudinal magnetic field in the section, as high as possible pulsed magnetic field at the target position and/or other measure to focus positrons leaving the target. Then the bunch has to be compressed in $\alpha$-magnet or other magnetic structure for further acceleration to some 3 GeV in the high gradient S-band accelerating structure.

We will characterize the capture efficiency by a factor of $\eta = N^{e^+}_{accelerated}/N^{e^+}_{produced}$. Assuming the angular width of the target equal to $\theta$, each of 10 HERA-e bunches passing the wiggler with $N_P$ periods gives outcome of:

$$N_{e^+} = 1.3 \cdot 10^{11} \cdot 0.13 \cdot \eta \cdot N_P \cdot \theta = 1.7 \cdot 10^{10} \cdot \eta N_P \theta. \quad (6)$$

The TESLA damping ring requires bunch population of $3.7 \cdot 10^{10}$ which can be obtained with multi- or single-turn injection. At present time, the multiturn injection into the ring does not look very attractive because due to limited linac shot cycle of 200 ms the damping time have to be reduced down to some 5–10 ms (compare with the design value of 37 ms [4]) that needs several times longer damping wiggler and more powerful RF system.

Thus, the better choice is single-turn bunch-by-bunch injection. Comparison of the design bunch population with (6) yields the requirement:

$$\eta \cdot N_P \cdot \theta \approx 2.2. \quad (7)$$

Taking as an optimistic estimate the value $\eta = 0.25$, we get for the single pole wiggler $\theta \approx 8.7$ mrad. As an example, the target could be 2 cm wide and set at the distance of 2.3 m from the wiggler. Corresponding wiggler pole length has to be more than $\theta R = 8.7$ cm. The total radiated SR power is equal to 0.5 MW which requires rotating or liquid target as it is assumed in other $e^+$ sources for LC [2].

If (7) is satisfied, then filling of the TESLA DR with use of 10 bunches in HERA-e will take 110 revolutions, or

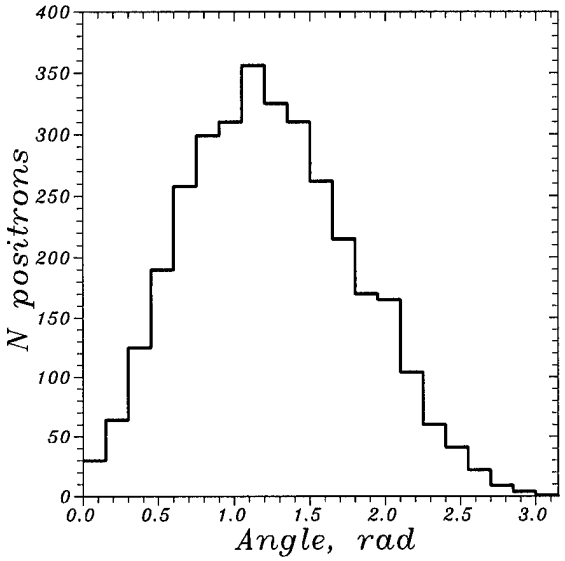



Figure 3: Distribution over $\Theta$ for positrons from 1-20 MeV SR photons, tungsten target size 0.3 × 10 × 10 mm, all positrons are emitted from target.

about 2.3 ms. It is much less than 200 ms of the TESLA linac repetition time and allows to use the bypass with the wiggler in the pulsed regime while all other time the HERA-e ring can work for high energy physics experiments.

### *2.4 Effects on the Electron Beam*

The vertical tune shift and distortion of the amplitude function due to installation of the wiggler are estimated to be $\Delta\nu_y \simeq 0.001$ and $(\Delta\beta_y)/\beta_y \leq 1$ % that could be compensated by tuning the strength of nearby quadrupoles.

While some 10 MeV energy loss of 30-GeV electrons in the 9-cm long 10T wiggler is much less than the total losses of 70 MeV/turn in HERA-e, than the effects on the electrons' damping times, energy spread and emittances does not look drastic, although not negligible. Certainly, these effects are weak if the bypass will operates in the pulsed mode.

Other important issues such as changes of dynamic aperture due to the wiggler installation and the electron beam stability in the presence of the SR absorbers, collimators and other discontinuities of vacuum chamber have to be checked numerically as soon as more detailed design of the source will appear.

## 3 DISCUSSION AND CONCLUSIONS

The proposed scheme of positron production – through conversion of energetic photons of synchrotron radiation from 30 GeV electrons of HERA in the target material – looks very promising and fits into the TESLA requirements, although further detailed studies of the positron production efficiency, the target, the capture optics and acceleration systems optimization are necessary. The efficiency of the positron capture looks the most important parameter to investigate.

An obvious disadvantage of the source is that it needs operation of the HERA-electron ring (although with a small duty factor).

As the 5 mA single bunch current looks to be an upper limit for HERA-e [13], we would note a possibility of further increase of positron production with use of several-poles wiggler or a wiggler with higher field. An experience with construction and exploitation of "state-of-the-art" high field magnets (see e.g. [14]) has shown a good field quality in them.

We would like also note that with the use of elliptical wiggler the proposed scheme allows to obtain polarized photons and therefore, polarized positrons. This topic needs further thorough numerical studies.

Authors are thankful to P.Ivanov, G.Kulipanov, E.Saldin, R.Brinkmann, K.Flöttmann, N.Holtkamp, J.Rossbach, G.-A.Voss, N.Walker, H.Weise for useful discussions and valuable suggestions.

## 4 REFERENCES

[1] R. Brinkmann, *Proc. of IEEE PAC'95*, Dallas (1995), see also DESY Internal Report M-95-08 (1995), pp.57-59.

[2] K. Flöttmann, DESY 93-161 (1993).

[3] J. Rossbach, *NIM*, A309 (1991), p.25.

[4] V. Shiltsev, TESLA Print 96-02, DESY (1995).

[5] F.Bulos, *et. al*, SLAC-PUB-3635 (1985).

[6] V.E. Balakin and A.A. Mikhailichenko, Preprint INP 79-85, Novosibirsk (1979); see also in *Proc. of XII Int. Conf. on High Energy Accelerators*, Fermilab (1983), p.127.

[7] R. Wanzberg, ed., *Proc. of Int. Workshop on $e^+e^-$ Sources and Preaccelerators for Linear Colliders*, Schwerin, Germany (1994).

[8] V.N. Belyaev et. al, Preprint MEPhI 026-92, Moscow, (1992).

[9] A. Ando et. al, paper submitted to *NIM A*, (1995).

[10] S. Krinsky, M.L. Perelman and R.E. Watson, in *Handbook on Synchrotron Radiation*, Vol.I, Horth Holland Publ.(1983).

[11] H.Wiedemann, *Particle Accelerator Physics II*, Springer-Verlag, Berlin-Heidelberg (1995).

[12] A.V. Kiselev, $e^+$ production simulation code (Novosibirsk).

[13] R. Brinkmann, private communication.

[14] A. Grudiev,*et. al, NIM A359* (1995), p.101.

# A FULLY DEMOUNTABLE 550 kV ELECTRON GUN FOR LOW EMITTANCE BEAM EXPERIMENTS WITH A 17 GHz LINAC*

J. Haimson, B. Mecklenburg, G. Stowell and E. L. Wright
Haimson Research Corporation, Santa Clara, CA 95054-3104 USA

*Abstract*

The design details and fabrication features of a 550 kV electron source for operation with a 17 GHz chopper-prebuncher linac injector are described, and initial test results using the M.I.T. Plasma Fusion Center HV pulse modulator are presented. The electron gun was designed to satisfy the stringent injection specifications required for the linac to demonstrate a 20 MeV beam with a bunch current of 100 A and a normalized emittance of 5 mm-mradian. Fine mesh simulations of the electron gun optics revealed that, to minimize geometric contributions to the source emittance, a very tight tolerance (±25 μm) was required for the edge spacing between the cathode and focus electrode. Means of accurately locating the gun electrodes are discussed; and the vacuum demountable features that enable convenient field replacement of the anode, focus electrode and cathode/heater are described.

## 1 INTRODUCTION

The 17 GHz linac system [1] comprises a chopper-prebuncher injector and a 94 cavity, 2π/3 mode, quasi-constant gradient structure having an RF filling time of 58ns. The injection system is designed to operate with a 550 kV, 1 A, low emittance electron source to produce fully gated bunches of < 20° at injection into the linac with a bunch current of 6 A and a pulse current of 280mA. The accelerator structure is designed to provide subsequent bunch compression to 1° and a steady-state beam loaded energy of 20 MeV. A new style, racetrack shaped, dual feed input coupler has been developed [2] and incorporated into the linac structure to avoid beam emittance contributions due to field asymmetry.

## 2 DEMOUNTABLE GUN ASSEMBLY

Based on a ceramic to copper, dry hydrogen furnace brazing technique (previously established during the development of a family of low beam emittance, 250 to 550 kV dc electron guns [3]), a thick wall, large diameter, tapered ceramic shell terminated with brazed copper/stainless steel subassemblies was the design of choice for this pulsed HV application. This concept enabled standard vacuum flanges to be attached to the ceramic insulator (13-1/4″ ϕ at the HV end and 16-1/2″ ϕ at the ground end) and provided a variety of electron gun assembly options. For example, in the Figure 1 layout of the demountable assembly, the low emittance gun configuration for the 17 GHz linac is shown as (A) below the centerline; and means for retrofitting a higher perveance, larger diameter cathode and focus electrode assembly is shown as (B) above the centerline.

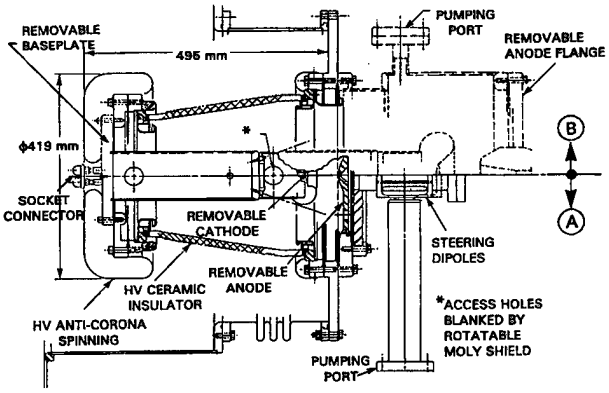



Figure 1: Demountable Electron Gun Concept Showing Alternate Retrofit Configurations (A) for the 17 GHz Linac Low Emittance Injector and (B) for High Power Microwave Tube Research.

The POISSON code equipotential plots and electric field gradients for the 17 GHz linac electron gun (mounted in the HV modulator oil tank) are shown in Figure 2. At a pulse voltage of 550 kV, the maximum gradients on the surface of the focus electrode and anode are 195 and 151 kV/cm, respectively. Iterative design adjustments of the HV seal braze joints and shields were performed in order to achieve the indicated low gradients (20 and 11 kV/cm) at the critical ceramic/metal interfaces, so that the possibility of achieving satisfactory HV operation, without baking-out the system and without TiN coating of the ceramic, could be investigated.

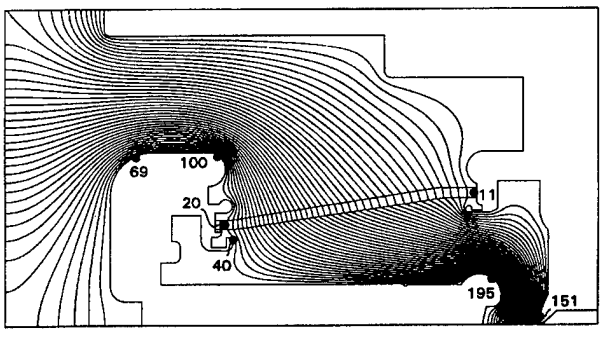



Figure 2: 550 kV Electron Gun Assembly POISSON Equipotential Plots and Electric Field Gradients (kV/cm).

*Work performed under the auspices of the U.S. Department of Energy SBIR Grant No. DE-FG03-94ER81774.

0-7803-4376-X/98/$10.00 © 1998 IEEE

## 3 EMITTANCE SENSITIVITY

Fine mesh simulations were performed with EGUN to study the effects of small changes in gun geometry, and in particular, the sensitivity of beam emittance to the radial clearance and axial separation between the cathode and focus electrode edges. The dashed curves in Figure 3 show the sensitive dependence of emittance on this axial distance for two slightly different focus electrode designs, without the cathode temperature related transverse velocity contributions of the emitted electrons being taken into account. The Figure 3 solid curve shows the results of EGUN simulations that take into account thermal effects associated with a 1350°K, 2.5 mm radius cathode. This data indicated that, with a carefully constructed system, a 1 A beam having a normalized emittance of between $2\pi$ and $3\pi$ mm-mradian should be attainable.

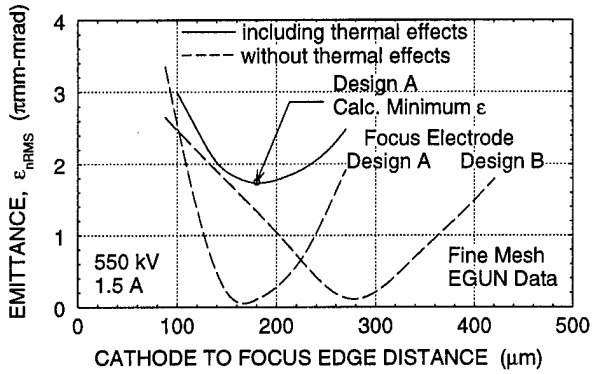



Figure 3: Normalized Emittance Dependence on Distance Between the Cathode and Focus Electrode Edges.

## 4 FABRICATION FEATURES

To accurately determine the small but critical movement of components caused by the cathode/heater dissipation (including radiation and reflection effects), prior to final machining of the focus electrode, the electron gun was fully assembled, fitted with an array of ceramic insulated thermocouples (refer to Figure 4), and operated in high vacuum with the cathode heater at full power. This temperature survey also enabled the thermal dynamics of the system to be evaluated, in particular, the delay in reaching equilibrium due to the high thermal isolation of the rigid stainless steel cantilevered support. For example, the Figure 5 curves reveal that a cathode preheating period of between 6 and 8 hours is required before achieving the steady-state condition. Reduction of the temperature survey data enabled the room temperature dimensions of the focus electrode to be accurately established, the contour machining finalized and the gun assembly completed. Views of the HV ceramic assembly and internal components of the gun are shown in Figure 6. Self centering and sealing of the ceramic and copper components during the brazing process was accomplished, without the need for peripheral grinding of the large ceramic, by using novel graphite fixtures; and the copper sealing technique ensured the complete absence of magnetic materials (e.g., Kovar or other Ni-Fe alloys).

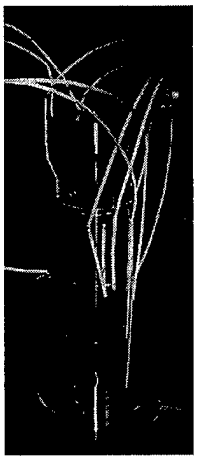


Figure 4: Focus Electrode, Cathode/Heater and Support Subassembly Fitted with Ceramic Insulated Thermocouples.

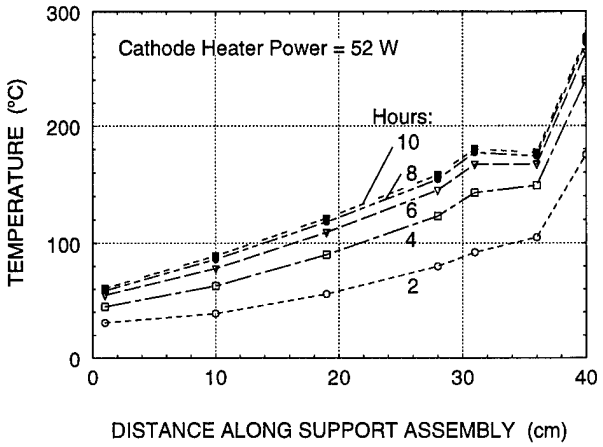



Figure 5: Cantilever Support Temperature-Time Curves.

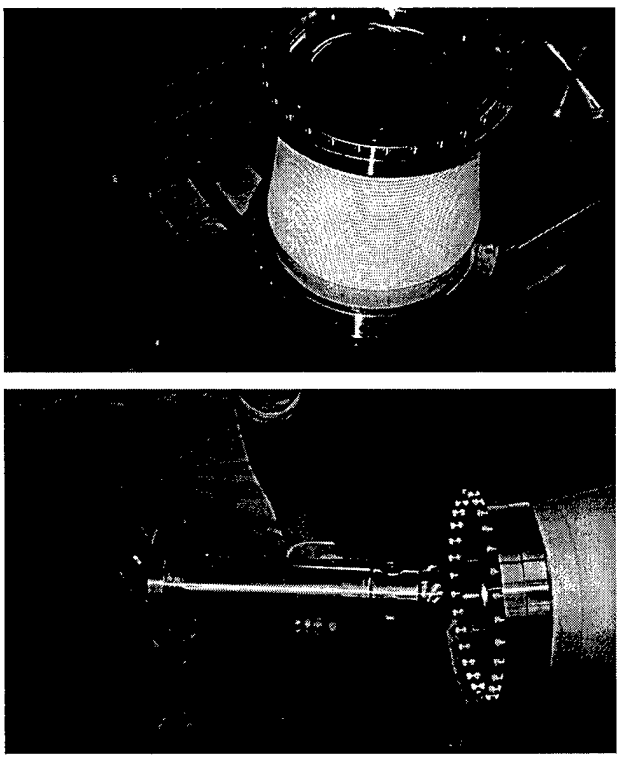


Figure 6: Upper View - HV Ceramic Insulator; Lower View - Installing the Focus Electrode and Cathode/Heater Subassembly.

Following prior design practice [3], the cathode/heater assembly was mounted directly to the focus electrode, and piloted to an accuracy of 25 μm to maintain a radial clearance of 380 μm. A built-in adjustment system enabled the large diameter focus electrode to be centered and spaced with respect to the anode to a tolerance of 25μm, and then locked in position using an alignment fixture as shown in Figure 7. This technique enabled errors due to small misalignments, and cumulative buildup of fabrication tolerances, to be corrected with a single final adjustment.

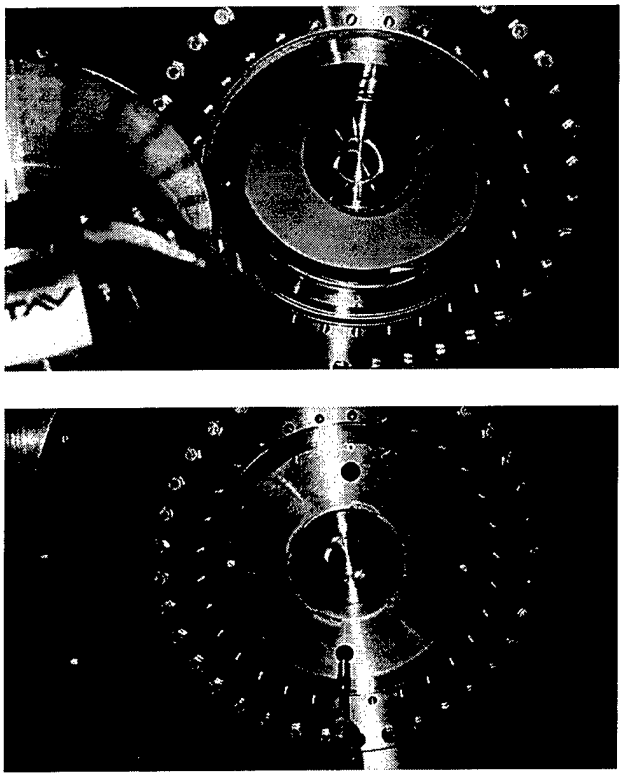


Figure 7: Upper View - Gun Assembly with Anode Removed; Lower View - Final Positioning of the Focus Electrode Using the Alignment Fixture.

## 5 PRELIMINARY TEST RESULTS AND FUTURE PLANS

The 550 kV electron gun assembly was integrated into the HV modulator, used at MIT [4] for operating the high power TW relativistic klystron for the 17 GHz linac, by attaching an external gun chamber to the side of the modulator tank (refer Figures 1 and 2). Prior to completing the HV processing of the gun, a preliminary simple beam emittance test was performed at 440 kV with a cathode emission current of 1 A. Using a low aberration thin lens, the beam waist from the gun was re-imaged at a 0.8 mm radius collimator, then after drifting 37.5 cm to the location of a 3.4 mm radius collimator, the transmitted beam was collected in a evacuated Faraday cup. Pulse waveforms of the electron gun voltage and the current transmitted through both collimators into the Faraday cup are shown in Figure 8. These preliminary tests were

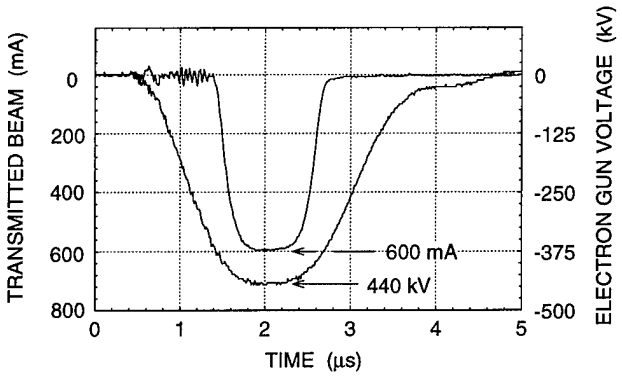



Figure 8: Electron Beam Transmitted into Faraday Cup through 0.8 mm and 3.4 mm Radii Collimators Separated by 375 mm ($\beta\gamma\epsilon = 2.8\ \pi$ mm-mradian).

performed with a space charge limited cathode but without attaining thermal equilibrium of the gun structure (the preheat period was only 2 hours - refer Figure 5). For the given geometric conditions, the results indicate that an rms emittance of approximately $1.8\pi$ mm-mradian was achieved at an energy of 440 kV with a transmitted beam of 600 mA and a pulse width of 600 ns.

At this writing, the electron gun has been successfully hi-potted to 550 kV, and is to be processed and beam characterized to a higher level prior to installation of the 17 GHz linear accelerator and spectrometer, and the chopper/prebuncher injector, scheduled for later this year.

## 6 ACKNOWLEDGEMENTS

We gratefully acknowledge the graphite fixture design contributions by Mat Hengel; and we are indebted to the staff of the MIT Plasma Fusion Center for their dedicated efforts in the HV processing and beam testing of this prototype demountable 550 kV electron gun system.

## 7 REFERENCES

[1] J. Haimson and B. Mecklenburg, "HV Injection Phase Orbit Characteristics for Sub-Picosecond Bunch Operation with a High Gradient 17 GHz Linac," in *Proc. IEEE PAC 1995*, 95CH35843, vol. 2, 1995, pp. 755–757.

[2] J. Haimson, B. Mecklenburg and E. L. Wright, "A Racetrack Geometry to Avoid Undesirable Azimuthal Variations of the Electric Field Gradient in High Power Coupling Cavities for TW Structures," in *Advanced Accelerator Concepts, AIP Conference Proceedings, 398,* New York: AIP Press, 1997, pp. 898–911.

[3] J. Haimson, "Recent Advances in High Voltage Electron Beam Injectors," *IEEE Trans. Nucl. Sci.* NS-22 No.3, pp.1354–1357, June 1975.

[4] W. J. Mulligan, S.C. Chen, G. Bekefi, B.G. Danly and R.J. Temkin, "A High Voltage Modulator for High-Power RF Source Research," *IEEE Trans. Electron Dev.*, 38, pp. 817–821, April 1991.

# COMMISSIONING OF THE IUCF 7 MeV H$^-$ LINAC

D.L. Friesel, Indiana University Cyclotron Facility, Lane, Bloomington, IN 47408,
and R.W. Hamm, AccSys Technology Inc, Pleasanton, CA 94566

*Abstract*

Construction of a 2.24 T-m, rapid-cycling booster synchrotron (CIS) to inject polarized ions (p, d) into the Indiana Cooler [1] is nearing completion at IUCF. Designed to provide $2.5 \times 10^{10}$ particles per pulse for Cooler injection, the booster is also well suited for use as a source of 60–220 MeV protons for medical therapy. An AccSys Technology Model PL-7 Linac consisting of a 3 MeV RFQ coupled to a 4 MeV DTL is used to pre-accelerate H$^-$ ions to 7 MeV for strip injection into CIS. Two 350 kW, 425 MHZ rf amplifiers power the Linac, which accelerates variable pulse width H$^-$ beams with duty factors up to 0.2%. The Linac accepts up to 1.0 $\pi$ mm mrad (norm), 25 keV H$^-$ beams and accelerates them to 7 MeV with 1% energy spread and no emittance growth. Following delivery to IUCF in December, 1996, beam commissioning began in January, 1997. The measured Linac beam performance characteristics from this work are presented.

## 1 INTRODUCTION

The low intensity of even the most advanced polarized ion sources ($\sim$ 1 mA) requires the use of H$^-$ strip injection and accumulation to reach the intensity goal for **CIS** [2]. Intensity gain calculations for H$^-$ ions on thin Carbon foils ($\leq$2–8 $\mu$gm/cm$^2$) as a function of energy indicate that greater than 3 MeV was needed to insure $\geq 10^{10}$ protons per pulse from CIS for Cooler injection [3]. Hence, an AccSys Technology, Inc [4] 7 MeV H$^-$ Linac consisting of a 3 MeV RFQ coupled directly to a 4 MeV DTL was selected as an H$^-$ pre-injector. IUCF and AccSys entered into an "Industrial Partnership" agreement in June, 1995, whereby AccSys designed and built the Linac accelerating structures and power amplifiers and IUCF supplied the H$^-$ source and LEBT, RFQ vacuum tank, all major commercial equipment (power supplies, pumps, etc) and manpower support. Specifications for the Model PL-7 Linac are listed in **Table I** and a layout of the H$^-$ source, LEBT, Linac and7 MeV injection beam line is shown in Fig. 1. The fully assembled Linac (serial No. 001) was delivered to IUCF on December 13, 1996 and installed between the waiting 25 keV H$^-$source and 7 MeV injection beam line. Beam commissioning began on January 12, 1997 and concluded with the injection and accumulation of both 3 and 7 MeV protons in the **CIS** ring this April.

## 2 LINAC DESCRIPTION

The 4 RFQ vanes are fabricated from copper plated, precision contoured aluminum extrusions with continuous water cooling paths near the vane tips. The stainless vacuum vessel has a removable lid so that the patented self aligning $q/A = 1$ vanes can be replaced with $q/A = 1/2$ vanes for the later development of deuteron beams in CIS. A full scale, low rf power aluminum model of the DTL tank and drift tubes was used to measure frequency response and finalize the mechanical dimensions of the resonator tank and endplates. Each of the 22 water cooled, Cu plated stainless drift electrode assemblies house permanent magnet quadrupoles for transverse focussing. The RFQ and DTL were fabricated separately and assembled on a common rigid support structure with no matching beam line between them. Matching the 3 MeV RFQ exit beam to the DTL acceptance is done in the last few cells of the RFQ. A closed loop water/glycol cooling system regulates both resonator temperatures to $\pm 1^\circ$ C.

The 350 kW rf amplifiers (1 each for the RFQ and DTL) are upgraded versions of an AccSys Technology three stage amplifier based on the EIMAC YU-176 planar triode tube. The final 12 tube amplifier is designed for quick tube replacement and to operate with several failed tubes if necessary. RF power is delivered to the cavities via 3-1/8 inch semi-rigid coaxial cables and side mounted cavity drive loops. The DTL tank is fitted with a slug tuner which has a $\pm$100 kHz tuning range. These amplifiers define the duty factor limit for the Linac.

Each amplifier is equipped with an enhanced Instrument Monitor and Control Unit (IMCU) which communicates with the CIS VISTA controls system [5] via a MIL-STD-1553B bus interface. The IMCUs contain hardware interlocks and electronic monitoring and controls for all Linac functions, including the vacuum systems. In **CIS**, software programs were developed to control, monitor and record amplifier tube operating parameters and spark information, and to automatically recover from VSWR and tube spark-down faults. The information provided by the IMCU's and the effective architecture of the amplifier cabinets greatly simplified trouble shooting during initial commissioning of the Linac.

## 3 LINAC PERFORMANCE

The 25 keV unpolarized H$^-$ source and LEBT was designed to match the input beam requirements specified by AccSys for the RFQ. Built at IUCF, it routinely delivers 0.4 mA peak intensity, 0.6 $\pi$ $\mu$m (norm), 25 keV H$^-$ beams at $\leq$5 Hz with 125 mrad symmetric convergence and 2.5 mm diameter to the RFQ entrance [6]. The source, RFQ and DTL triggers and pulse widths are independently adjustable via the CIS timing system. An example of the rel-

0-7803-4376-X/98/$10.00 © 1998 IEEE

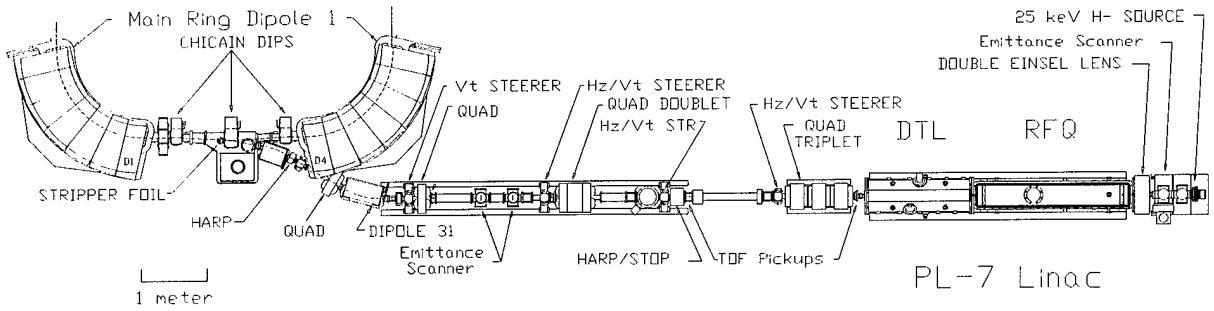



Figure 1: The CIS keV $H^-$ Source, 7 MeV PL-7 Linac and injection beam line through the CIS ring injection straight section.

ative timing sequence used for these devices is shown in Fig. 2.

Table I: PL-7 Linac Performance Specifications

| | |
|---|---|
| I. Linac (RFQ and DTL) | |
| Operating Frequency | 425 MHZ |
| Duty Factor | $\leq$0.2% |
| Design Repetition Rate (variable) | 1–5 Hz |
| rf Pulse Width (variable) | 35–300$\mu$s |
| Overall Linac Length | 3.979 m |
| Operating Vacuum (oil Free) | 0.08 $\mu$Torr |
| Min. Guaranteed $H^-$ Beam Transmission | $\leq$80% |
| Design Intensity Range | .1–1.0 mA |
| II. RFQ Properties | |
| Input Energy ($H^-$) | 25 keV |
| Acceptance (norm.) | 1.0 $\pi$ |
| Vane average Bore Radius | 2.48 mm |
| Inter-vane Voltage | 71 kV |
| Maximum rf Power | 0.3 MW |
| Cavity Q | 7350 |
| Output Energy | 3.0 MeV |
| III. DTL Properties | |
| Input Energy ($H^-$) | 3 MeV |
| DTL Cavity Q | 48000 |
| Maximum rf Power | 0.3 MW |
| Output Energy ($H^-$) | 7.0 MeV |
| Nominal Energy Spread ( T) | $\pm$70 keV |
| Output Emittance (norm.) | 1.0$\pi$ |

The DTL cavity field duration is longer than the RFQ field because 3 MeV $H^-$ beam passes unattenuated through the unpowered DTL cavity, resulting in both 3 and 7 MeV $H^-$ beam from the Linac entering the injection beam line. The source pulse, however, must also begin after the DTL cavity has reached full field. Injection of $H^-$ beam prior to the DTL cavity field reaching full potential clamps the field to zero volts, presumably due to multipactoring. (Initial application of full power to the RF accelerating structures required less than 1 hour of conditioning) De-tuning the source beam and extended DTL operation at full field to condition against multipactoring have not stopped this effect, which was not observed with positively charged proton beams at AccSys. While surprising, this is not a liability for our application because the Linac duty factor is larger than required for CIS injection.

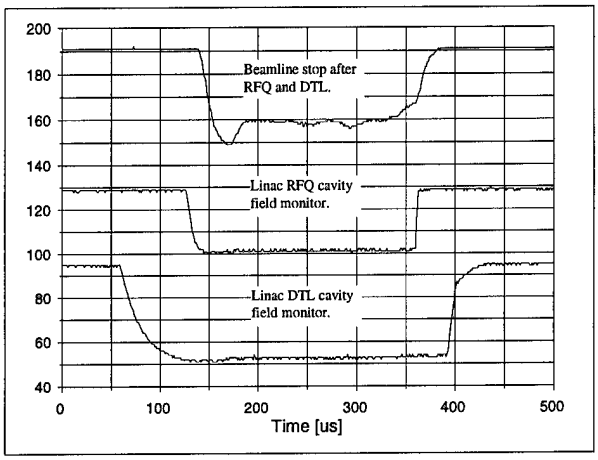



Figure 2: Source, RFQ, and DTL Pulse Sequence

### *3.1 RFQ and DTL Cavity Threshold Voltage Measurements*

The required **CIS** injected beam properties are achieved from the Linac only when operated at the design (threshold) cavity field with all 7 amplifier feedback loops (frequency, phase, and cavity field) closed and operating properly. The PL-7 threshold voltages were measured open-loop at AccSys with protons and again with all 7 amplifier loops closed at IUCF with $H^-$ ions using the diagnostics in the CIS injection beam line shown in Fig. 1. Beam transmission through the Linac increases with RFQ cavity field until the threshold pickup voltage of $V_o$ = 4.35 V is reached for both measurements, as shown in Fig. 3, and requires 295 kW of rf power, slightly higher than the predicted 284 kW. The DTL $V_o$ was determined by measuring the $H^-$ beam energy as a function of the its cavity field as determined by the beam position on a multi-wire HARP at the exit of a 31° bending magnet and the output of a beam TOF energy measurement system. These only measured energy changes, and could not be used to precisely determine beam energy. The data for several measurements are shown in Fig. 4. The DTL Vo of 3.57 V is obtained at an amplifier output power

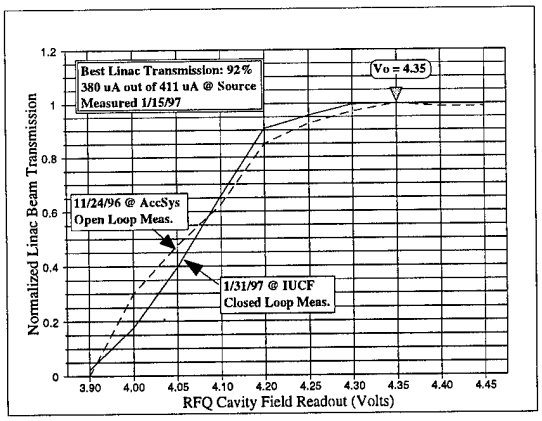



Figure 3: RFQ Threshold Measurement

of 300 kW, also higher than predicted. The beam energy at these threshold values was later determined to be 6.987 MeV by measuring the orbit period of circulating beam in the ring.

### 3.2 *Linac Transmission and Accelerated Beam Properties*

Beam property measurements were made at both 7 and 3 MeV by running with both RFQ and DTL cavity fields set to their $V_o$ and by turning the DTL cavity field off and scaling the beam line accordingly. Beam transmission from the source to a compensated beam stop located 2.5 m from the Linac exit range from as high as 90% to as low as 75% from run to run. Typically, 320 $\mu$A of the 400 $\mu$A available at the source are recorded on this stop. The beam profile measured on a multi- wire HARP in front of this stop is a 6 mm (FWHM) waiste as predicted for the calculated currents in the quad triplet at the Linac exit, verifying that the optical properties of the accelerated beam their are as predicted by AccSys. Beam transmission from this stop to the stripper foil in the CIS injection region is typically 80%, again with all beam line focussing elements operating within 5% of the values calculated using the AccSys beam focussing predictions. Similar transmission is achieved for 3 MeV $H^-$ with beam line quads operating within 10% of the values scaled from 7 MeV.

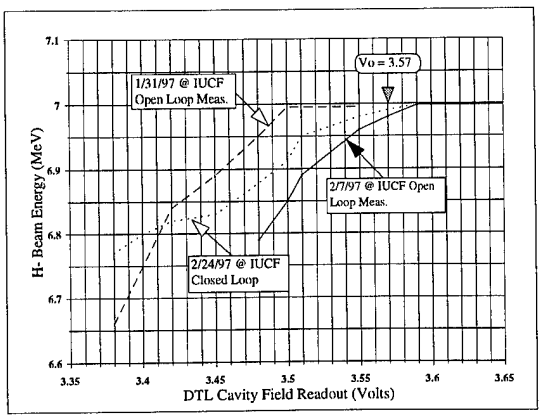



Figure 4: DTL Threshold Measurement

Both the 3 and 7 MeV $H^-$ beams have been injected and accumulated in the CIS ring [7]. Over 250 uA (peak) of protons of the 400 uA $H^-$ available at the source are strip injected into the CIS ring, as measured on a compensated stop between ring main dipole magnets 1 and 2. The beam profile on the foil is a 6 mm dia double waste. Alignment of the source, Linac and injection beam line is excellent, as beam steering requirements are minimal. The 7 MeV $H^-$ horizontal beam emittance was measured on several occasions to be $\leq 1.0\ \pi$ mm mrad (norm.), also as predicted.

### 3.3 *Amplifier Feedback Loop and Beam Stability*

The Linac amplifier feedback loops required continued development at IUCF to get the optimum 7 MeV $H^-$ beam properties desired for CIS injection. Primarily, the specified beam energy, energy spread and emittance are required to maintain stable strip injection into the ring. The measured stability of the feedback loops for both amplifiers are $\pm 2°$ phase and $\pm 0.5\%$ amplitude. The stability of the RFQ-DTL relative phase loop, also important to maintain energy stability, is about $\pm 2°$, as determined by the beam energy stability using the beam line TOF system. These closed loop operating parameters provide reproducible and stable beam injection into the CIS ring [2]. A beam energy spread measurement has not been made, but is likely near the specified $\pm 1\%$ based on initial ring strip injection performance studies. Occasional departures from the RFQ/DTL relative phase stability are observed during operations, which significantly reduces injection efficiency. Development work is continuing to improve the long term performance of the feedback loops and the Linac beam stability.

## 4 ACKNOWLEDGMENTS

The present performance of the PL-7 Linac is the result of the support provided by AccSys Technology, Inc and the dedicated and competent efforts of the IUCF technical and professional staff. Their efforts contributed significantly to the timely commissioning of the ring injection system this April. Supported by Indiana University and National Science Foundation Grants NSF PHY 93-147-83 & 23-423-10.

## 5 REFERENCES

[1] R.E Pollock, IEEE 89CH2699-0, 17 (1989).

[2] D.L. Friesel and S.Y. Lee, IEEE 95CH35843, 336 (1995).

[3] K. Hedblom, IEEE 95CH35843, 1861 (1995).

[4] AccSys Technology, Inc, 1177 Quarry Lane, Pleasanton, CA 94566

[5] J. Callahan *et al*, "A High Reliability Accelerator Control System", this publication.

[6] V. Derenchuk *et al*, "Pulsed Ion Sources for the IUCF Cooler and Injector Synchrotron", this publication.

[7] D.L. Friesel *et al*, " Status of the IUCF Cooler Injector Synchrotron ", this publication.

# PERFORMANCE OF ELECTRON GUN FOR SPRING-8 LINAC

T. Asaka, T. Hori, Y. Ito, T. Kobayashi, A. Kuba, A. Mizuno, H. Sakaki,
S. Suzuki, T. Taniuchi, K. Yanagida, H. Yoshikawa and H. Yokomizo
SPring-8, Kamigori, Ako-gun, Hyogo, 678-12 Japan.

*Abstract*

A thermionic gun of the injector linac for SPring-8 is required to generate different beam pulse width, 1nsec, 10-40nsec, 1μsec. Three types of grid pulsers were prepared to generate different beam pulse width. The gun uses cathode-grid assembly (EIMAC Y796) and operates up to 200kV anode voltage. In order to research characteristics of the electron gun, emission current from gun were measured by the wall current monitor. In this paper, the pulser system and characteristics of the emission current in region from 30mA to 19A are described.

## 1 INTRODUCTION

SPring-8 is one of the largest ultrahigh brilliance X-ray synchrotron radiation facilities under construction at harima science garden city in Hyogo prefecture. The facility consists of a 1GeV S-band injector linac, an 8GeV booster synchrotron ring and an 8GeV storage ring. The 1GeV linac is not only a injector linac of an 8GeV booster synchrotron but also injector linac of a 1GeV NEW SUBARU ring (VUV-soft X-ray ring, under construction) and to utilize for some experiments like to a slow positron facility and the parametric X-ray source[1]. The injector linac composes of a 250MeV high current linac, an electron / positron converter, a 900MeV main linac and a beam transport line. This linac is able to produce various kind of the beam pulse width from 1nsec to 1μsec, which are requested by the storage ring operation mode; multi bunch operation and a single bunch operation. In addition, the peak current from injector linac is defined by two modes; one is a high current mode (>15A) for positron production, and the other is relatively low current mode for electron use. The beam current is controlled with varying the emission current from a gun, and also by physically defining the beam size using an iris that is placed just behind the gun. The basic requirements for SPring-8 gun are summarized in table 1.

| | Pulse width | Electron |
|---|---|---|
| Single bunch mode | 1nsec | 300mA |
| Short pulse mode | 10-40nsec | 300mA |
| Long pulse mode | 1μsec | 100mA |

Table 1 Beam parameters of the gun

A beam commissioning of the injector linac has been started from August 1996 after sufficient rf processing, and the commissioning of the booster synchrotron has been started from December 1996. In especially, a peak electron beam current of 50mA with beam pulse width of 40nsec is required from the first beam condition for the commissioning of booster synchrotron. However, the range of 50mA for the beam current is too low to control with varying a grid potential of Y796 owing to strain of the waveform of emission current that is observed by the wall current monitor[2]. In order to generate the low beam current with rectangular waveform, the gun was operated with controlling of both heater power and grid voltage. The optimum parameters of the gun system is obtained from the measurement results of emission current dependence on anode voltage, heater power and grid voltage under consideration for shaping waveform of emission current.

## 2 GUN DESIGN AND PULSER SYSTEM

The thermionic gun is the EIMAC Y796 cathode grid assembly, which has a circular cathode area of $2cm^2$ equivalent to 8mm in radius. The gun is pulsed at 60Hz with a rectangular waveform variable from 1nsec to 1μsec in pulse width.

E-GUN was used to design the thermionic gun focus, anode electrode shape and the gap between cathode and anode, and to simulate the beam parameters in the gun region. The optimum of gun geometry was determined by obtained minimum emittance at the gun exit (150mm from cathode plane). The anode cathode gap distance is 30mm and the perveance is 0.20μperv. A space charge limited flow at 200kV is 18.2A. The anode voltage of 200kV has been chosen as high as possible in order to reduce the space charge force at high current beam generation. The normalized emittance at the gun exit is 15.3πmm.mrad and the beam radius is 8.1mm.

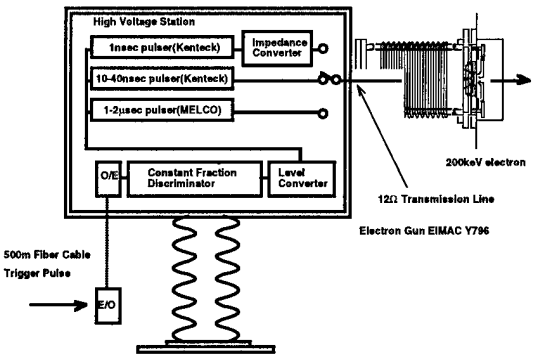



Fig.1 Schematic of the gun system

A schematic drawing of the gun system is shown in Fig.1. Three types of grid pulsers are prepared to generate different beam pulse width. A long pulse of more than

0-7803-4376-X/98 /$10.00 © 1998 IEEE

1μsec is generated by a constant voltage pulse generator (MELCO), and a short pulse of 10-40nsec is generated by nano second pulser (Kentech Instruments Ltd.), and a single pulse of 1nsec is generated by a high voltage modular pulse source (Kentech Instruments Ltd.). These pulsers are installed in a high voltage station, and are connected by two types of the transmission lines which are made of 1068mm long axial rigid tubes with 12Ω impedance. One is used for generating short pulse and long pulse, and other is used for generating single bunch, it is composed of impedance converter and short stab[3].

Since the timing jitter of trigger signal of less than 30psec (FWHM) is required to inject the 2nsec rf bucket of the 508.58MHz booster synchrotron and the 508.58MHz storage ring in single bunch beam operation, the gun trigger system and transfer line used the passive circuit, the fast rf amplifier, the optical fiber cable and the E/O, O/E transmitter and receiver which have low jitter and low temperature dependence[4].

## 3 EMISSION CURRENT MEASUREMENT

The first beam tests selected short pulse mode using the nano second pulser. The beam pulse width is determined by the delay cable length between ON trigger output and OFF trigger input at this pulser. In order to make impedance matching at the driving cathode impedance (12Ω), the output channel of pulser are prepared four connectors (BNC type, 50Ω for one channel). Fig.2 shows the observed the waveform of pulser output for 10nsec mode and 40nsec mode, respectively.

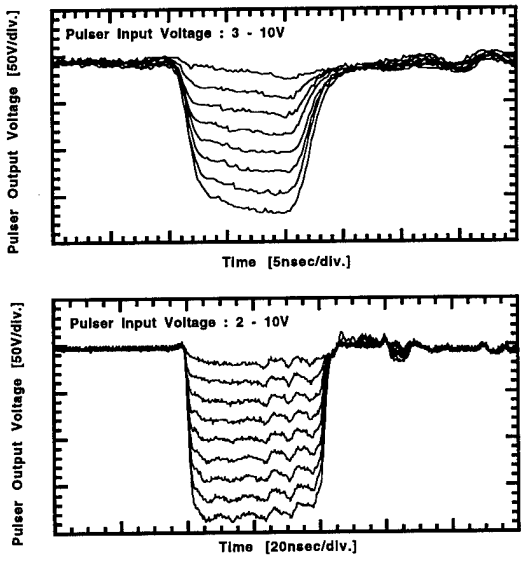



Fig.2 The waveform of nano second pulser output

The emission current from the gun was observed by the wall current monitor which was calibrated by means of a tapered coaxial test stand. The monitor is placed at the beam pipe prolongs for about 45cm after the cathode. The helmholtz coil is positioned right next to the gun. An adjustment of the beam size was performed by using the helmholtz coil and the fluorescent screen monitor.

The waveform of the emission current at 10nsec pulse width is shown in Fig.3. The gun parameters are follows: iris none, heater voltage of 6.7V (heater power of 40W), anode voltage of 180kV and grid net drive voltage of 110V. And the pressure level of the gun is kept in the range of $10^{-8}$Torr. For the results of the first gun test without using the iris, the behavior of emission current as a function of the grid pulser voltage for different values of the heater power, the anode voltage and the bias voltage are shown in Fig.4, 5, 6. The perveance from Fig.5 is 0.35μperv which is higher than design value.

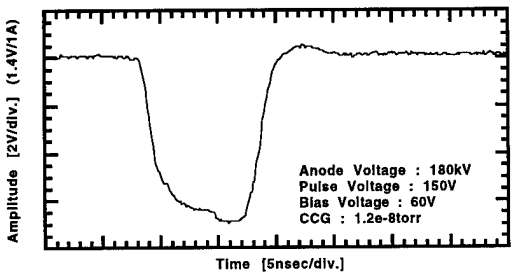



Fig.3 The emission current at 10nsec pulse width

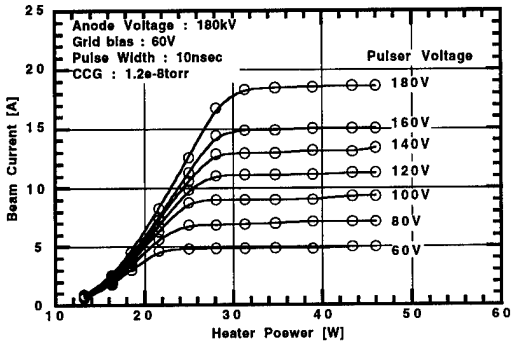



Fig.4 Emission current characteristics versus heater power

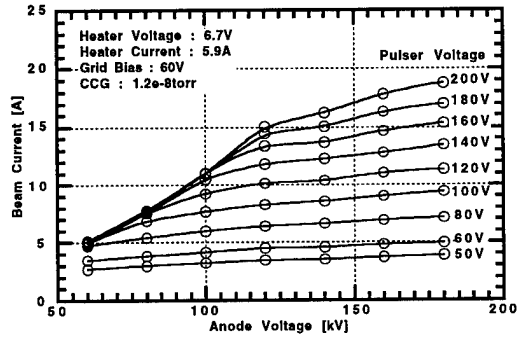



Fig.5 Emission current characteristics versus anode voltage

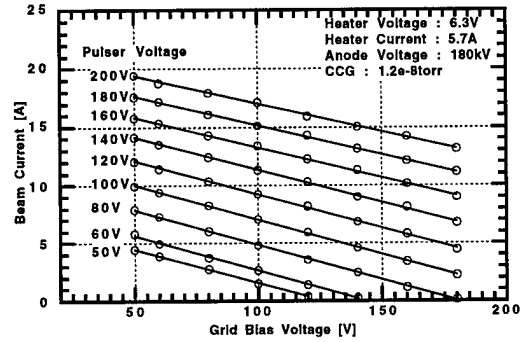



Fig.6 Emission current characteristics versus grid voltage

The emission current from the gun is reduced with the two types of iris. The reduction ratio are measured 7% of $\phi$1.2mm iris and 26% of $\phi$2.6mm one, respectively. These values were independent of the operating heater voltage in region from 3.5 to 6.5V.

In order to investigate the relations of the emission current and the waveform, the beam pulse width and the flatness of pulse height for different values of the emission current is measured by the wall current monitor. The gun parameters are follows: operation mode of 40nsec beam, iris of $\phi$1.2mm and anode voltage of 180kV. Fig.7 shows the example of pulse width (FWHM) which depends on the grid bias voltage with the heater voltage of 4.0V (heater power 15W). In this figure, it is shown that the beam pulse width reduce with increasing grid bias voltage with regard to the pulser voltage below 90V. Fig.8 shows the flatness of waveform as a function of the heater power for different values of the emission current on condition that the pulse width (FWHM) is region from 35 to 43nsec. In case of the commissioning of the booster synchrotron, the optimum value (flatness <3%, peak current 50mA) is determined 3.6V in heater voltage from the results of Fig.8. In addition, Fig.9 shows the heater voltage versus flatness for different value of pulse and bias voltage under the above condition. The deterioration of flatness with net voltage below -50V depends on the flatness of pulser output in Fig.2 The state of flat-top for the pulser output is independent of the different pulse height.

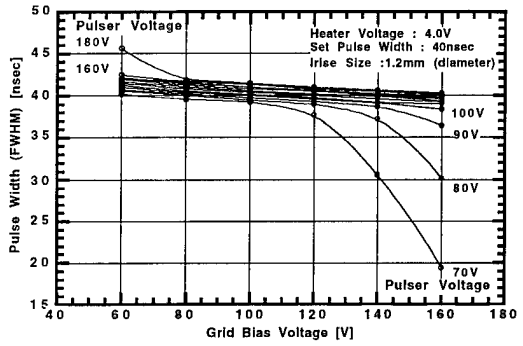



Fig.7 Pulse width characteristics versus grid voltage

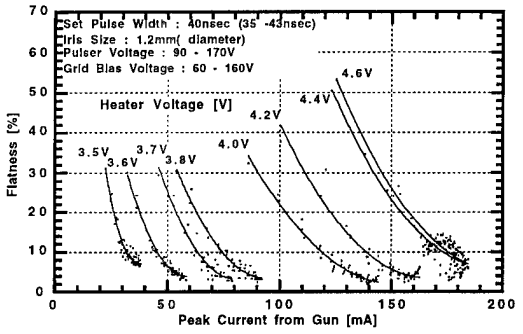



Fig.8: Dependence on the pulse flatness

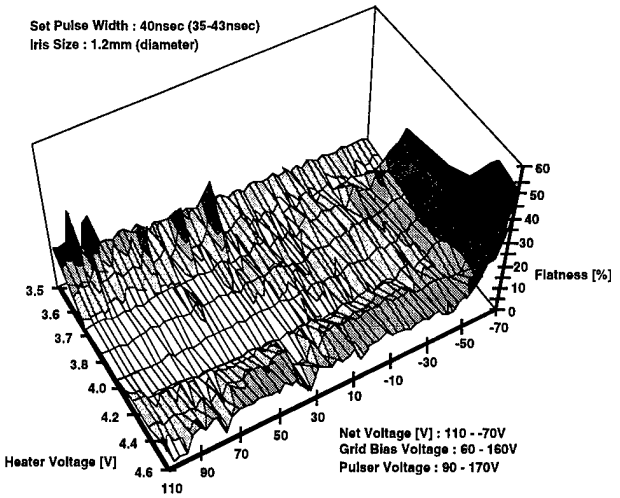



Fig.9: The heater voltage versus flatness for different value of pulser and bias voltage

## 4 CONCLUSION

We have generated the emission current in region from 30mA to 19A with the fast rise and fall time using nano second pulser. In order to produce rectangular waveform at the low current beam generation (flatness <3%, peak current 50mA), it is performed by control both of an iris and the heater power, simultaneously. In especially, the deteriorating flatness with the low bias and pulser voltage is caused by waveform of the nano second pulser output. Further experiments will be continue to examine the stability for the long term of operation on the gun.

## 5 ACKNOWLEDGEMENTS

We also thank to H. Akimoto, T. Onishi, S. Nagasawa, M. Yamazaki, K. Harumoto, T. Hasegawa, N. Hirota, T. Iida, K. Makino, K. Nakashima, S. Nakajima, H. Ohkubo, S. Suwa, A. Tuboi, T. Watanabe and M. Yoshioka of SPring-8 service corporation for the beam operation, the data taking, cooperation and support.

## 6 REFERENCES

[1] S. Suzuki, et al., "Update Plan of Spring-8 Linac", Proc. of the 18th International Linac Conference (Geneva), Aug. 1996

[2] K. Yanagida, "Wall Current Monitor for SPring-8 Linac", JAERI-M 94-078.

[3] H. Yoshikawa, et al., "High Current 1ns Pulse Electron Gun", Proc. of the 17th International Linac Conference (Tsukuba), Aug. 1994

[4] H. Suzuki, et al., "Characteristics of RF Reference and Timing Signal Distribution for SPring-8", Proc. of the 9th Symposium on Accelerator Science and Technology (Tsukuba), 1993

# THERMIONIC RF GUN WITH HIGH DUTY FACTOR

V.V. Mitrochenko, NSC KIPT, 1, Academicheskaya Str., Kharkov, 310108 Ukraine

*Abstract*

Back bombarding limits wide usage of thermionic RF guns. The article presents one of the possible field distribution on-axis of a RF gun, which allows to reduce back bombarding power of a cathode. Simulation predicts 20 kW of pulsed back bombarding power on the $LaB_6$ cathode under 0.51 A of output current and 0.908 MeV of maximum energy of electrons. Average current can be increased until average power of back bombarding reaches the initial filament power of a cathode. Therefore it is expected to reach at least 0.5 mA of average output current. Energy spectrum and bunch phase length are suitable to inject the beam directly into the accelerator structure with the phase velocity equal to the velocity of light. Ramp of the cathode temperature during RF pulse and long time stability of output current are discussed.

## 1 INTRODUCTION

It is well known, that beside providing high quality beams RF guns allow to simplify the injector part of resonant linacs. This fact caused our interest to use RF gun as injector of linacs for a wide application. In particular, it would allow to eliminate such a complicated and unreliable device as a high voltage power suppler of a DC gun. However, such linacs operate with a high duty factor. In this case an application of RF guns is limited due to the following reasons:

i) for the photo-emission RF guns: huge cost of a laser system and short life time of the efficient photo-cathodes.

ii) for the thermionic RF guns: the back bombarding effect as well as wide energy and phase spectra.

The work was aimed at a search of such an on-axis electric field distribution that would allow to reduce back bombarding power and would provide suitable energy and phase spectra of electrons to inject the beam directly into the acceleration structure with the phase velocity vp equal to the velocity of light.

## 2 RF GUN WITH LOW BACK BOMBARDING POWER

Back electrons increase cathode temperature of thermionic RF gun. To compensate this increase it is necessary to reduce filament power of the cathode. It is obvious that it can be done until average power of the back bombarding exceed the initial filament power. The pulse power of back bombarding electrons is about 100 kW for single cell RF gun [1] and about 50 kW for double-cell RF gun [2]. Filament power of the latter one is about 12 - 15 W (pressed oxide Ba-Ni cathode). Filament power for a RF gun that is similar to the gun described in [1] is about 30 W [3] ($LaB_6$ cathode). It is clear, that these guns can not operate with a high duty factor, for example, of 0.1%.

On the basis of the RF gun design experience it is possible to formulate some criteria of a field distribution search. The electric field that accelerates electrons about 1 MeV per cell is rather high for space charge that is characteristic for thermionic RF guns, so to reach the beam energy about 1 MeV it is necessary to use several cells. The length of the first cell should be chosen in such a way that it would be possible to deliver a substantial part of electrons emitted from the cathode to the entrance of the second cell. The second cell is not to make a considerable acceleration of the electrons. The fundamental acceleration should be made at the next cells. In such a way it is possible to reduce back bombarding and to provide suitable bunching to inject the beam directly into the acceleration structure.

Simulation of the RF gun was made on basis of SUPERFISH [4], PARMELA [5] and the simple edint codes. The edint code allows to simulate two-dimensional electron motion in RF guns taking into account influence of the Schottky effect on the cathode emission. It was used to calculate the back bombarding power of a ring cathode. To simulate a thermionic RF gun with PARMELA the imput0 was used. The diout file was prepared by addition code which changed "superparticle" charge according to the Schottky effect.

The design of the RF gun which consists of three accelerating cells was chosen on the basis of the mentioned criteria. On-axis field distribution is shown in Fig. 1. Fields in the adjacent acceleration cells have opposite phases, that is $\pi$-mode. Electrons were emitted

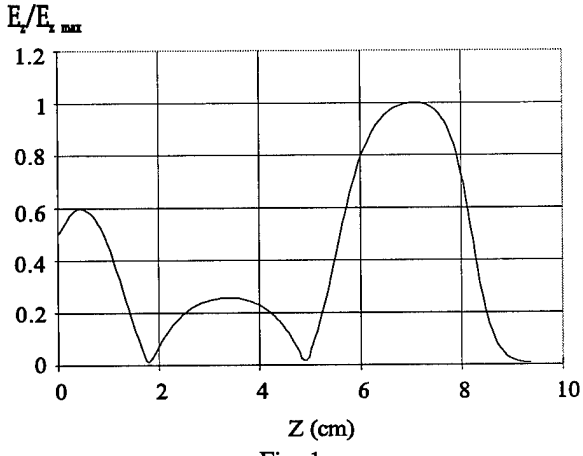



Fig. 1

0-7803-4376-X/98/$10.00 © 1998 IEEE

by $LaB_6$ cathode with diameter 5 mm. Simulation results of electron motion for maximum value of on-axis field $E_{z\,max}$ = 30 MV/m are the following. Maximum energy of electrons $W_{max}$ at the gun exit is 908 keV while their average energy $W_{av}$ is 760 keV. The RF gun exit is reached by 51% of particles emitted from the cathode. 70% of particles at the RF gun exit are within the phase interval $\Delta\varphi$ = 43° and have the fractional energy spread $\Delta W/W_{av}$ = 35%. The root mean square normalized emittance $\varepsilon_{n\,rms}$ is 21 mm·mrad. The pulse power of back bombarding electrons $P_{back}$ is 20 kW for 0.51 A of the output current. The back bombarding electrons have average energy $\overline{W}_{back}$ =49 keV. Fig. 2 shows phase and energy spectra of output beam while Fig. 3 shows phase-energy and $x - x'$ distributions of the particles. It follows from above mentioned data and figures that output beam is bunched enough, so it can be injected directly into the acceleration structure with $v_p$=$c$.

ring $LaB_6$ cathode with an outside diameter of 5 mm and an inner diameter of 2 mm showed that cathode back bombarding power was 13 kW. The part of back bombarding electrons which passes through the inner hole of the cathode can be dissipated inside the cathode housing unit. Of course, the ring cathode increases the beam emittance in 1.5 times, but it is still less than the emittance of a great number of convenient injectors. A ring cathode allows to obtain the necessary output current for operating with a high duty factor by changing the inner diameter.

It is necessary to note that increasing the average temperature of the cathode is not the only harmful factor. A ramp of the cathode temperature that occurs during RF pulse can also cause some troubles. To estimate the temperature ramp with good accuracy it is necessary to take into account energy and spatial spreads of back bombarding electrons as well as spread of heat. For rough estimation of the temperature ramp very

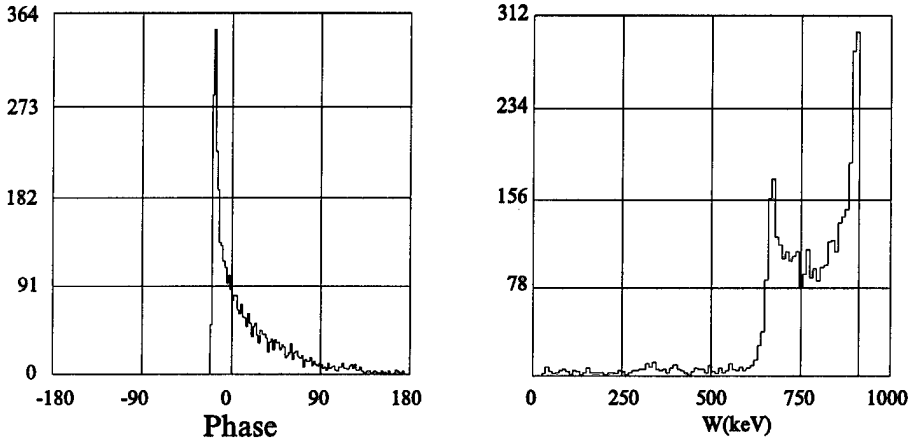



Fig. 2

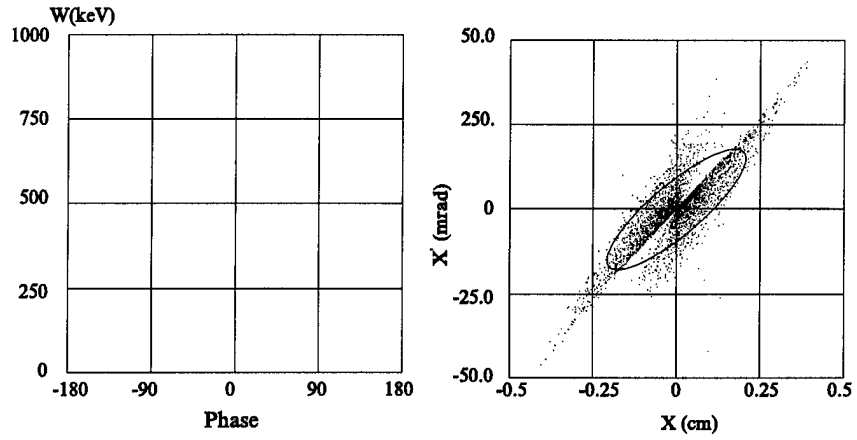



Fig. 3

For duty factor of 0.1% (300 pps and pulse duration $\tau_p$ = 3,3 μs) average power of the back bombarding takes a considerable part of filament power. There is an experience of RF gun operation with increased pulse repetition rate under switching off filament power [3,6], but in both cases the steady state cathode emission was too high. It is necessary to use a ring cathode to eliminate this effect. The simulation performed for the simple approaches were used. Let's assume that all back electrons have the same energy which is equal to $\overline{W}_{back}$ and they are uniform distributed on the cathode surface. Let's also assume that power of back electrons dissipates within the slice of the cathode the depth $l$ of which is equal to the extrapolated penetration length of electrons with energy $\overline{W}_{back}$, spread of the heat is

neglected. In this case the ramp of the temperature $\Delta T$ is equal:

$$\Delta T = \frac{P_{back}\tau_p}{c_p S\, l\rho},$$

were $c_p$ -- thermal capacity, $S$ -- square, $\rho$ - density of the cathode.

For the solid and the ring cathodes the temperature ramps are 44°K and 34°K, respectively. These ramps increase emission of the cathodes to the end of RF pulse on 70% and 40%, respectively. The temperature ramps are overestimated in this approximation because for the pulse duration the heat spreads on the length that is comparable with a penetration length of electrons.

The main question is how to provide long time stability of the output current when back bombarding power takes a considerable part of filament power. It can be done by using negative feedback on cathode temperature and making RF gun slightly undercoupled with a waveguide for operation current. For undercoupled cavity system a change of the cathode emission causes the opposite change of accelerating field and, consequently, a change of back bombarding power is less than that for the overcoupled cavity system. So it can stop runaway of cathode temperature. Of course, long time stability is an enough complicate question and ultimate answer can give experimental test of the real RF gun.

## 3 CONCLUSIONS

The on-axis field distribution in a thermionic RF gun has been found that allows to reduce considerably the back bombarding power and providing suitable bunching to inject the beam directly into the acceleration structure. It is expected to reach at least 0.5 mA of average current at the gun exit. Long time stability needs further experimental study.

## 4 ACKNOWLEDGEMENTS

The author wishes to thank Prof. M.I. Ayzatsky and Dr. V.A. Kushnir for useful discussions. The author also acknowledges with grace the support that had been rendered to him during the simulations by the AOT-1 group of LANL USA.

## REFERENCES

[1] C.B. McKee and John M.J. Madey, "Optimization of a thermionic microwave gun", Nuclear Instruments and Methods in Phys. Research A304 (1991) p. 386--391.

[2] V.A. Kushnir, V.V. Mitrochenko, "Simulation of beam performances of the two-cell RF gun", Proc. of the fifth European Particle Accelerator Conference, Sitges (Barcelona), 10 to 14 June 1996, Editorial board S. Myers, A. Pacheco et. al., vol. 2, pp. 1414-1416.

[3] V.A. Kushnir, V.V. Mitrochenko, Wang-Gang, "Reducing the back bombarding effect in a thermionic RF-gun", Proc. of the 14 Conference on charge Particle Accelerators, Protvino, Russia, 1994 v.3, p. 97-102.

[4] J.H. Billen, L.M. Young, Proceedings of the 1993 Particle Accelerator Conference, Vol.2. of 5. 790 -- 792 (1993).

[5] K.R.Crandal, L. Young, LANL report, LAUR-90-1766 (1990), 57

[6] J.N. Weaver, R.D. Genin, P. Golceff et. al., "Experience with a Radio frequency Gun on the SSRL injector linac", Proceedings of the 1993 Particle Accelerator Conference, p. 3018 -- 3020 (1993).

# OBTAINING THE LINEAR ELECTRON BEAMS BY USING THE MAGNETRON INJECTION GUNS WITH COLD SECONDARY EMISSION METALLIC CATHODES (EXPERIMENT)

Yu.D. Tur, A.N. Dovbnya, V.V. Mitrochenko, N.G. Reshetnyak, V.P. Romas'ko, V.V. Zakutin
NSC KIPT, 1, Academicheskaya Str., Kharkov, 310108 Ukraine

*Abstract*

The problem of extending the life-time, of increasing the pulse and average power of many RF-sources is closely related to the design of their electron guns. As it is known, the magnetron injecting guns with secondary emission metallic cathodes (SEMIG) are specified by the high current emission density and long life-time. The main goal of these investigations is to determine the advantages and limitations of using SEMIGs as the electron source in high-power RF devices and accelerator injector systems. At this stage we have studied some questions concerning the operational beam stability, voltage and current increasing. The experiments have been performed by using the experimental setup to investigate SEMIG linear electron beam parameters from single and multiple beams gun assemblies with the anode voltage up to 100 kV, pulse duration up to 10 μs, repetition rate 50 Hz and 0.1-0.2 T magnetic field strength. Pulse-to-pulse long-term stability of the annular electron beams (internal diameter nearly equal to the cathode diameter, wide of ring 1-2 mm (wavelength of cyclotron oscillations)) with beam density up to 70 A/cm$^2$ have been achieved. It is shown, that the cathode diameter extension provides a proportionate increasing of the beam current, and in the case of multiple beam gun assemblies we have separate identical electron beams with the similar parameters of single-beam gun.

## 1 INTRODUCTION

A task of creating the long lived, high-energy electron sources is one of the main problems in the acceleration engineering. As it was shown earlier [1,2] the so-called secondary-emission magnetron guns (SEMIG) with cold metal cathodes are specified by a high beam density, high lifetime and instantaneous operation readiness. On our opinion the guns of such a type are highly promising for the use in RF-sources and accelerators, in particular, in multybeam and cluster klystrons [3,4] as well as in high-current injector systems, for example, in the installation such as RK TBA [5] and CESTA TEST FACILITY [6].

The present paper continues the experimental study of characteristics of such guns. We studied the current-voltage and spatial characteristics, conditions of beam generation and stability. The amplitude modulation of the emission current in the variable electric fields was investigated. Presented are the results of studies concerning the multybeams systems and considering the possibility to increase the output current amplitudes by changing the geometrical dimensions of guns.

## 2 DESCRIPTION OF FACILITIES

Constructionaly SEMIG represents a coaxial structure with a copper inner rod being the cathode and a more extended external cylinder placing the role of the anode placed in the solenoid providing the longitudinal magnetic field. Experimental studies have been carried on the test setup comprising:

i) the high-voltage pulse modulator of a linear type capable to change the pulse shape (duration 2-10 μs, repetition rate 10-50 Hz, pulse voltage 20-100 kV);

ii) the focusing solenoid providing the magnetic field strength up to 0.25 T with a inhomogeneity in the longitudinal direction no more than 8%;

iii) the vacuum system which gives a vacuum not worse than $10^{-7}$ Torr;

iv) the indication system i.e. the pick-up of pulse current and voltage of modulator, the Faraday cup with the calorimetric measurer of the beam power located at a distance of 70 mm from the anode section; photometry system for control of the transversal characteristics of the linear electron flow.

We have carried out the study of beam characteristics for separate SEMIG's with cathode diameters in the range from 5 to 40 mm, anode diameters from 14 to 80 mm, electrode length from 40 to 100 mm. The measurement were performed for parameters of the multybeam system consisting of six SEMIG disposed is a circle of a radius 60 mm, every of them have had a cathode diameter 5 mm, an anode diameter 26 mm.

## 3 EXPERIMENTAL RESULTS

The characteristic oscillograms of the voltage pulse on the cathode and beam current on the Faraday cup are given in Fig. 1. As in the case when the outer generator is used, the beginning of the secondary-emission process, and respectively, of SEMIG operation as a source of the linear electron flow, coincides with the fall time of the burst on the high-voltage pulse. The minimum rate for voltage decrease of the plan pulse part up to 100 kV is 20 kV/μs. The increase of a steepness up to 50 kV/μs does not change the amplitudes of the resulting current, and the change of a burst time in a wide range ( from 0.1

0-7803-4376-X/98/$10.00 © 1998 IEEE

to 10 μs) has no effect on the beam characteristics. A comparison of the total current in the system with the current amplitude on the Faraday cup shows that in all the cases these values are dose.

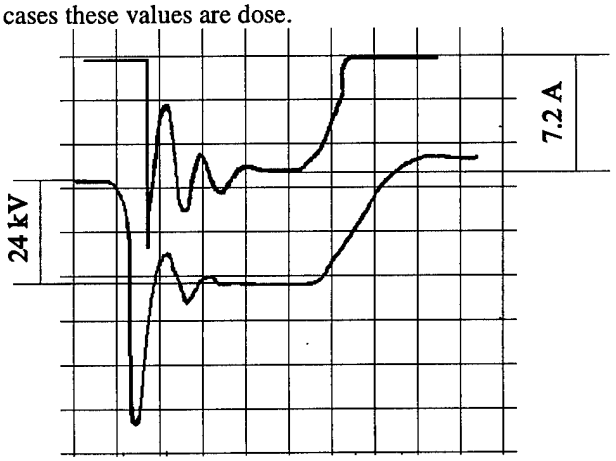



Fig. 1 - The characteristic oscillograms of the voltage pulse on the cathode and beam current on the Faraday cup

In Fig.2 presented is also the typical characteristics of the beam current as a function of the magnetic field amplitude for a constant anode voltage.

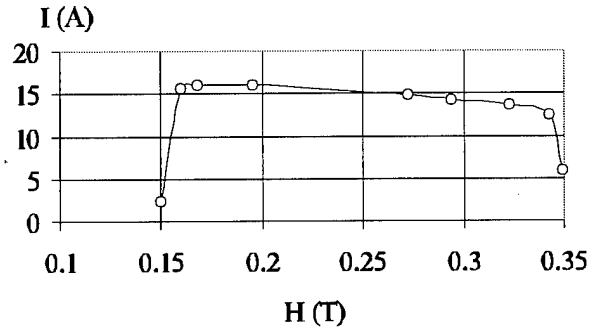



Fig. 2 - Beam current vs. magnetic field

A clearly defined existence of the beam generation stable one can be explained using the model proposed in [7]. If the magnetic field strengths are less than the critical one, the Larmour radius is so large that the quantity of primary particle collisions with the surface can not to furnish a sufficient quantity of secondary electrons for balance maintenance. On the other hand already at high magnetic field the Larmour radius as so small that the energy gained by the electron when colliding with the surface is loss than that of the threshold one for the secondary-emission process be existent. The constant value of the beam current amplitude is determined by the limiting regime by the space charge. The current voltage characteristic of SEMIG's conforms so the low "3/2" (see Fig.3)

The investigation of the gun operation stability dependency on the interpulse stability of the anode voltage has shown that in the constant magnetic field the beam formation retains in the range of amplitude application ±5% of the nominal value.

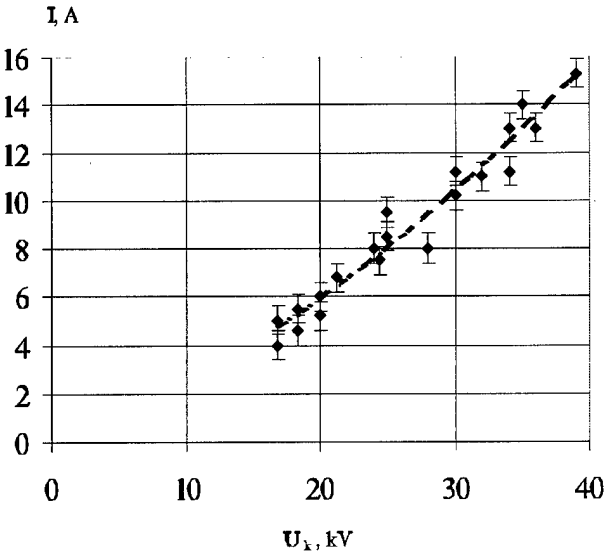



Fig. 3 - The beam current vs. anode voltage

The intrapulse voltage instability can also lead to the break-down of secondary-emission processes (see the oscillogram in Fig. 4) due to the incident electron energy decrease below the critical value of moment of the field strength increase in time.

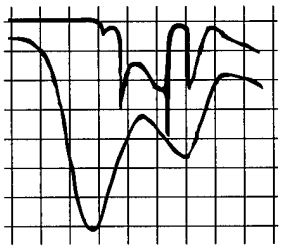


Fig. 4 - The beam current (an upper curve) and the cathode voltage (a lower curve), horizontal scale - 0.5 μs/div

The use of this effect in our experiments allowed us to attain the full amplitude modulation of the emission current at frequencies up to 1 MHz (see Fig. 5).

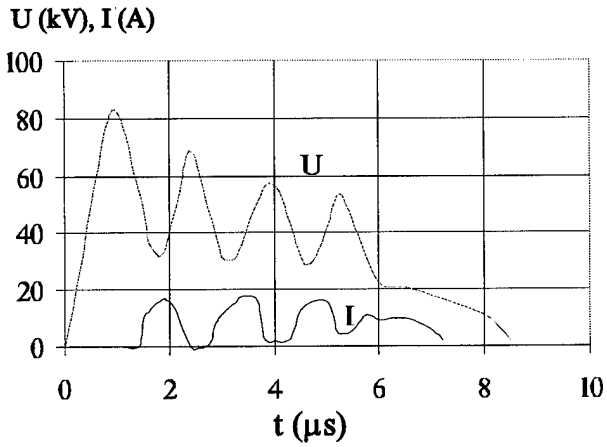



Fig. 5 - The anode voltage (U) and cathode current (I)

Also studied were the characteristics of electron flows from SEMIG's with different electrode diameters. In particular, Fig. 6 represents the beam current change as a function of the cathode diameter increase.

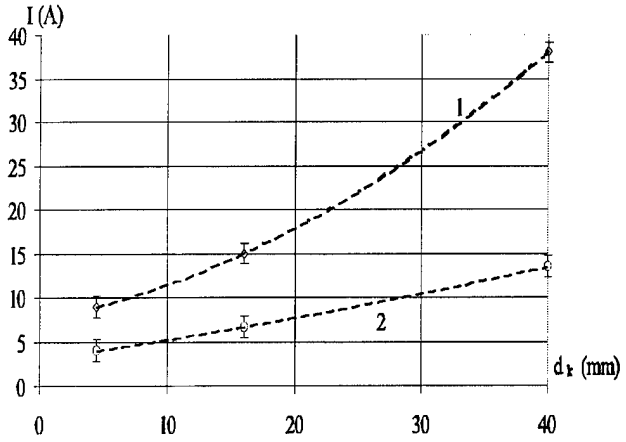



Fig. 6 - The beam current vs. the cathode diameter

The measurements were performed at voltages 24 kV for the interelectrode space in coaxial guns 5 and 20 mm (the curves 1 and 2, respectively). The analysis of these characteristics enables one to confirm that when the values of longitudinal and transverse components of electric field do not change the output current increases proportionally to the area of the cathode emitting surface.

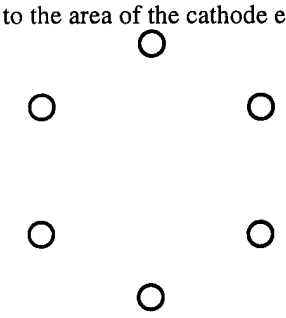


Fig. 7 - The photograph of the transversal profiles of beams

The investigations of the ensemble consisting of a number of SEMIG's located in the field of a common solenoid and energized from the one and the same high-voltage source have shown that in this case we possess a complex of independent flows with a similar parameters.

Fig 7 illustrates the photograph of the transversal profiles of identical beams with the current 15 A each and the energy 40 keV obtained in the ensemble of 6 SEMIG's located in the circle of the diameter 60 mm (cathode diameter 5 mm, anode diameter 26 mm). The recalculation shows that the beam density in such annular beams is equal to 70 A/cm$^2$.

## CONCLUSIONS

The experimental research evidences that SEMIG's offer a means of obtaining the stable linear electron beams of a high intensity and can be used as electron sources for accelerators and RF-facilities. It is clear that the carrying out of further researches is necessary for a successive study of gun characteristics as well as peculiarities of such electron beams RF modulation. Namely these problems lay in the base of our program of researches.

## REFERENCES


[1] F.Skrowron: The Continuous-Cathode (Emitting-Sole) Crossed-Field Amplifier - Proc. of the IEEE, v.61 (1973), No 3, pp. 330-356

[2] A.N.Dovbnya et al.: Secondary Emission Magnetron Injection Gun as High Current Durable Electron Source - Proc. of 1994 Pulsed RF Source for Linear Colliders Workshop (RF'94), October 1994, Montauk, Long Island, New York., AIP Conference proceeding 337 1995, p.350-359

[3] R.B.Palmer et al.: An Immersed Field Cluster Klystron - Particle Accelerators, v.30 (1990), pp. 197-209.

[4] R.B.Palmer et al.: Status of the BNI - MIT-SLAC Cluster Klystron Project - Proc. of 1994 Pulsed RF Source for Linear Colliders Workshop (RF'94), October 1994, Montauk, Long Island, New York., AIP Conference proceeding 337 1995, p. 12

[5] G.A.Westenskow et al.: Relativistic Klistron Two-Beam Accelerator - IEEE Transaction on Plasma Science, Special Issue on High Power Microwave Generation, 22 (5), pp. 750-755, (Oct. 1994).

[6] I.Wilson for the CLIC Study Group: CLIC Test Beam Facilities-Status and Results - Proc. of the XVIII Jnt. Linear Accel. Conference, Geneva, 1996, v.1, pp.552-557.

[7] Yu.D.Tur et al.: Obtaining the Linear Electron Beams by the Magnetron Injection Guns Secondary Emission Metallic Cathode (Theory) - This Conference.

# FIRST BEAM TESTS OF THE TTF INJECTOR

T. Garvey, M. Bernard, J.C. Bourdon, R. Chehab, M. Mencik, M. Omeich, J. Rodier,
M. Taurigna-Quere and A. Variola.
Laboratoire de l'Accélérateur Linéaire, IN2P3 - CNRS, Orsay, France.

S. Chel, M. Desmon, J. Fusellier, F. Gougnaud, J.F. Gournay, M. Jablonka, J.M. Joly,
M. Juillard, Y. Lussignol, A. Mosnier and B. Phung Ngoc.
CEA, DSM/DAPNIA, Saclay, France.

S. Buhler and T. Junquera.
Institut de Physique Nucléaire, IN2P3-CNRS, Orsay, France.

*Abstract*

Following tests of the various sub-assemblies at Saclay and Orsay, installation of the entire TESLA Test Facility Injector was completed in Hall 3 at DESY in December 1996. The first phase of operation employs a 250 kV thermionic electron source providing an 800 μs train of bunches, each containing 37 pC, and followed by a 216.7 MHz pre-bunching cavity. Subsequent bunching and acceleration is achieved using a standard 1.3 GHz superconducting 9 cell TESLA cavity operated in pulsed mode (10 Hz). Prior to injection in the main linac, the beam parameters are verified using a spectrometer consisting of a dipole magnet and SEM profile monitor. Once the beam is adjusted it is transported to the linac using an optical matching system employing two triplets. We present results of the first beam tests of the completed injector which took place early in 1997.

## 1 INTRODUCTION

The TESLA Test Facility (TTF) is a high duty cycle superconducting (SC) electron linac and its associated infrastructure. The L-band (1.3 GHz) linac will be used as a test bed to validate the principle of a SC $e^+e^-$ linear collider (TESLA). TTF is currently under construction by an international collaboration at the DESY laboratory (Hamburg). Within the collaboration the three French laboratories named above have undertaken the task of constructing a pulsed SC injector for the linac. Descriptions of the linac and its injector can be found elsewhere [1,2] and here we will restrict ourselves to a report of the first beam tests with the complete injector which took place in January/February of this year. Tight scheduling of the installation of the first linac cryomodule meant that only four weeks of operation were available for these tests.

## 2 THE CAPTURE CAVITY

The capture cavity is a standard 9 cell TESLA cavity fabricated by CERCA. Its cryostat (CRYOCAP) was built and tested by the IPN-Orsay. Cryogenic tests and tests of the analogue feedback loops were performed at Orsay and Saclay. The feedback system is described in a companion paper [3]. It allows the cavity to operate with an amplitude stability better than 0.1% and a phase stability of less than 1 degree. Although the cavity has operated at 18 MV/m without field emission (FE) in a horizontal cryostat, we restricted our tests to 14 MV/m. This was due to the FE now seen at the latter gradient which results in a reduction of the Q factor to $5x10^8$ and a high X-ray level around the cryostat. No high power RF processing was applied following the installation. During operation at 14.8 MV/m we measured a dark current level of 300 nA on a Faraday cup ($\phi$ = 25 mm) placed 1.15 m upstream of the first cavity iris.

## 3 BEAM ACCELERATION TESTS

The "pre-injector" consists of a 250 keV electron source, a 216.7 MHz sub-harmonic buncher (SHB) and four solenoidal focusing elements. Tests of the pre-injector have been reported previously [4]. The SC 'capture cavity' is used to provide further longitudinal bunching and to accelerate the beam to the desired energy (typically 8 to 12 MeV). Tuning of the injector is achieved by varying the amplitudes and phases of the SHB and capture cavity. The criteria for correct tuning during these tests has been the achievement of a minimum in the beam energy spread while ensuring maximum current transmission along the injector. The energy spread is measured using a spectrometer arm consisting of a magnetic dipole and an SEM-grid to measure the horizontally dispersed beam profile [5]. The current is measured with the use of toroidal current monitors. Four such monitors are mounted on the injector. Toroids #1 and #2 are at the entrance and exit respectively of CRYOCAP, #3 is on the spectrometer arm (upstream of the SEM-grid) and #4 is at the end of the injector.

### 3.1 *Beam transmission measurements*

The required current for TTF is 8 mA during an 800 μs macropulse at 10 Hz repetition rate. As the average beam power in the TTF linac is high, a differential protection system, based on the toroidal current monitors, is used to protect the machine against beam losses [6]. This system cuts off the gun if an integrated charge loss of 80 nC is detected between successive toroids during the macropulse. This corresponds to an average current loss of 0.1 mA during an 800 μs pulse (or 1.25% of the 8 mA beam). The same system is employed on the injector and

0-7803-4376-X/98/$10.00 © 1998 IEEE

thus setting up the injector requires careful adjustment of the RF cavities and magnetic elements. Consequently, the injector is tuned using a "short pulse mode" of 30 μs duration. For the commissioning tests the loss threshold for the long pulse or "un-restricted mode" was increased to 200 nC between toroids #2 and #3.

With the beam well centred at the entrance to CRYOCAP one quickly obtains 100% transmission of 8 mA through the capture cavity and upto the end of the injector. The beam energy is measured using the spectrometer while the cavity gradient can be estimated from the incident power. The ratio of the energy gain to field gradient is consistent with calculations [7]. Typically we obtain 11 MeV for 12.5 MV/m. Figure 1 shows signals from the first three toroid monitors superimposed. The SHB uses a feedback loop to correct the phase and amplitude changes induced by beam loading. Left uncorrected, an 8 mA beam would induce a phase shift of 18° of the 216.7 MHz. In practice, the feedback system is capable of compensating for the beam loading with the exception of the first 8 μs during which a residual phase shift of < 5° is present. This effect explains the difference in current level between the first two toroids and the dispersed beam on toroid #3 during the pulse rise time (Fig. 1, left). This can be cancelled by applying a "phase-jump" to the cavity with a sense opposed to that induced by the beam (Fig. 1, right).

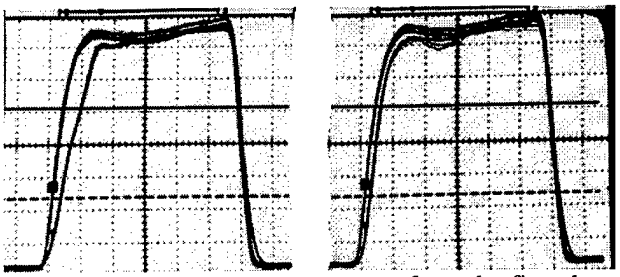


Figure 1. 7 mA, 30 μs current trace from the first three toroids; (left) without phase jump, (right) with phase jump (see text for details).

### 3.2 *Energy spread measurements*

The spectrometer dipole produces a dispersion of 16 mm/% of energy spread at the location of the SEM-grid. The grid contains tungsten wires of 20 μm diameter spaced at 2 mm intervals and is intended for use with the full pulse width. The first tests with 8 mA of accelerated beam showed that the transmission to the beam analysis line was only 90%, insufficient for switching to the long pulse mode. In view of the limited time available for injector tests, rather than investigating this loss in detail, we reduced the current to 6 mA for which the transmission to the analysis line was 97%, just enough to operate in long pulse mode and thus to investigate the distribution in energy. Figure 2 shows the output of the grid for an 11 MeV beam. The RMS energy spread is 68 keV. Several measurements made for different current levels (from 2 to 6 mA) show that the fractional RMS energy spread is always inferior to 0.8% when the injector is properly adjusted.

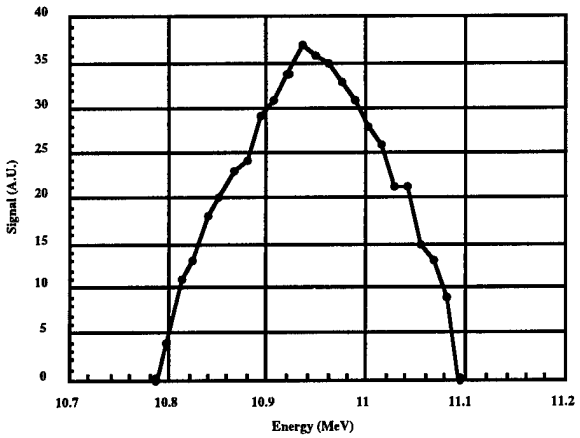



Figure 2. Beam energy distribution obtained on the SEM-grid.

## 4 EMITTANCE MEASUREMENTS

The transverse emittance has been obtained from measurements of the transverse beam profile using optical transition radiation (OTR). An aluminium foil of 20 μm thickness is employed as the radiator. Light from the OTR foil is focused onto a gated, intensified CCD camera using a telescope composed of two achromatic lenses with a magnification of 0.5. Data acquisition is obtained by means of a CPU operating in a VxWorks environment. A frame grabber and the camera record signals with an 8 bit resolution. The camera is synchronised to the master oscillator of the injector and the gain and shutter time are contolled by a serial port of the CPU. Acquisition, image processing and statistical analysis are performed using an "in-house" computer program so allowing on-line calculation of the emittance. Fig. 3 shows a typical example of an acquired profile. Emittance measurements are taken with a macropulse of 30 μs width to avoid damage to the aluminium foil.

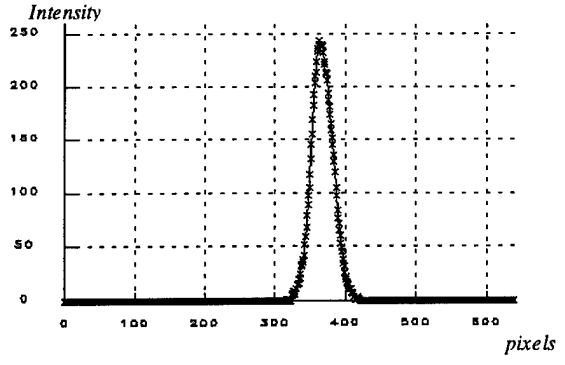



Figure 3. Horizontal profile of the beam from the OTR image. The scale is 37 μm/pixel.

To obtain the Twiss parameters of the beam we have used the method of "three gradients". The focusing of the beam is varied by means of a magnetic triplet placed

upstream of the OTR foil and the beam profile recorded for each setting. To improve the reliability of the fit between the beam radii and the triplet strengths, ten images are recorded for each of eleven different settings of the triplet. Statistical analysis of the image sets allows the beam radii and the related standard errors to be calculated. The radii are calculated for 50% and 90% intensity contours as well as for the FWHM. These calculations are performed both for the integrated profiles and for the horizontal and vertical profiles through the centre of charge of the beam. All these data are then fitted using an "in-house" chi-square minimisation routine. At our energy and with our experimental layout the approximation of a thin lens for the triplet is not valid. Consequently, we use the real transport matrix values. As well as the emittance, we also calculate the error to the fit, the covariance matrix, the beam matrix coefficients and the chi-square value as a measure of the statistical degree of confidence of the measurement [8].

Emittance measurements have been performed for various beam energies and linac optics. At 10.6 MeV, and with correct setting of the injector optics, the 90% contours give normalised emittances of $\varepsilon_x$ = 16.5 mm-mrad and $\varepsilon_y$ = 18 mm-mrad for the horizontal and vertical planes respectively. During the triplet scan, the beam centroid was seen to displace in the verical direction and so the larger emittance values in the this plane may be due to an imperfect vertical alignement of the beam in the triplet. The corresponding figures for the 50% contour are 2.4 mm-mrad and 2.8 mm-mrad. Similar values were obtained for a beam energy of 8.7 MeV. In varying the trigger time and acquisition period of the camera, time resolved measurements of the emittance were also obtained by recording profiles for 1 μs slices within the macro-pulse. These data show slightly smaller values for the "slice" emittance during the pulse rise-time with stable values found during the flat-top.

## 5 CONTROLS

The control system for the injector has been described elsewhere [9]. The system is based on EPICS with VME crates for equipment interface and SUN workstations as operator consoles. During the entire commisioning period the controls have been very reliable. Extensive use has been made of the EPICS task to 'save' and 'restore' machine parameters. The operator can create special "parameter' pages which can be assigned to eight encoder 'knobs' allowing analog control of eight parameters and making visible useful information. Binary control, such as the insertion of diagnostics or ON/OFF control of power supplies, is also permitted with these pages.

## 6 CONCLUSIONS

We have presented results of the first operation of a high field gradient (> 10 MeV/m), pulsed mode, superconducting linac. These tests show that the linac performs as foreseen and that certain specified beam parameters have been met (table 1). The emittance values are consistent with measurements made on the gun and pre-injector [4,10]. Injector tests will resume in May of this year and the transmission of 8 mA onto the spectrometer arm will be investigated further. In addition, the measurement of the micropulse length will be performed by streak camera analysis of the OTR.

Table 1. Comparison of achieved and specified parameters.

| | Specified | Achieved |
|---|---|---|
| Energy | > 8 MeV | 8 - 13.5 MeV |
| Current | 8 mA | 8 mA |
| Pulse width | 800 μs | 800 μs |
| RMS energy spread | < 100 keV | ~ 70 keV* |
| RMS emittance | < 5 mm-mrad | < 4 mm-mrad |

(* at 6 mA)

## 7 ACKNOWLEDGEMENTS

We are indebted to the technicians from Saclay and Orsay for their efficient installation of the injector on the DESY site. The participation of K. Honkavaara (SEFT, Helsinki) in the tests is gratefully acknowledged. We are pleased to acknowledge the enthusiastic participation of DESY personnel during the commisioning period of the injector, especially to B. Aune, A. Gamp, K. Rehlich, T. Schilcher and H. Weise. The injector uses a timing system that was built by M. Shea and M. Kucera of Fermilab.

## REFERENCES

[1] The TESLA Collaboration, "TESLA Test Facility Linac - Design Report", (Ed. D.A. Edwards), DESY print TESLA 95-01.

[2] R. Chehab et al., "Progress in the Study and Construction of the TESLA Test Facility Injector", Proc. of the 1995 Particle Accelerator Conference, pp 998-1000, (Dallas), 1995.

[3] A. Mosnier et al., " RF Control System for the SC cavity of the TESLA Test facility", these proceedings.

[4] J. Fusellier et al., " First Tests of the 250 keV Electron Source and Beamline for the TESLA Test Facility Injector", Proc. of the 1996 European Particle Accelerator Conference (Sitges), pp 1541-43.

[5] M.Bernard et al., "Secondary Emission Grids for Low Energy and High Energy Electron Beams", Proc. of the 1996 European Particle Accelerator Conference (Sitges), pp 1690-02.

[6] J. Fusellier and J.M. Joly, "Beam Intensity Monitoring and Machine Protection by Toroidal Transformers on the TESLA Test Facility", Proc. of the 1996 European Particle Accelerator Conference (Sitges), pp 1591-93.

[7] M. Ferrario et al., "Multi-bunch energy spread induced by beam loading in a standing wave structure", Particle Accelerators, Vol 52, pp1-30, 1996.

[8] A. Variola, Ph.D. thesis in preparation.

[9] F. Gougnaud et al., "The TESLA Test Facility Controls" presented at the International Conference on Accelerator and Large Experimental Physics Control Systems (Chicago), 1995.

[10] T. Garvey et al., "Simulations and Measurements of the TTF phase I injector gun", Proc. of the 1995 Particle Accelerator Conference, pp 935-37.

# MULTI-KILOAMPERE, ELECTRON-BEAM GENERATION FROM BARE ALUMINUM PHOTO-CATHODES DRIVEN BY AN ArF LASER

Randolph L. Carlson, Rae N. Ridlon, and Gerald J. Seitz
Los Alamos National Laboratory, Los Alamos, New Mexico, 87545, USA
Thomas P. Hughes
Mission Research Corporation, Albuquerque, NM 87106

*Abstract*

An electron-beam-pumped laser operating at ArF (193 nm) producing up to 5.0 joules in a 150-ns pulse has been used to illuminate micro-machined aluminum cathodes. The cathode was pulsed from 2.25- up to 2.95-MV across a 20-cm-AK gap producing fields up to 145 kV/cm using REX (a 4-MeV, 5-kA, 100-ns pulsed diode). Extracted current versus laser power gives a quantum efficiency increasing with power density from 0.07 to 0.11 percent. The present work is significant in that the cathode operates in the presence of out-gassing materials with a background vacuum pressure in the mid $10^{-6}$ torr region and 100-ns-long electron beams of up to 3 kA have been produced. Both emission limited (current follows laser pulse) and space-charge-limited (current follows pulsed power) regimes have been studied up to ~ 50 A/cm$^2$ by varying the cathode diameter. The beam temperature has been measured to be < 5 eV and directly compared in the same experimental setup to velvet based cathodes that measure ~ 100 eV.

## 1 INTRODUCTION

This work is a continuation of experiments reported in [1] with higher laser power illumination of the diamond turned (~ 0.5 μm finish), 6061-T6, aluminum alloy cathodes. In addition, the measurement of the effective electron beam temperature of the cathode source has been made.

The primary advantage of a cathode utilizing the photo-electric effect from bare metals as compared to the more conventional photo-alkali or thermionic sources is the ability to have the cathode function in a modest vacuum environment (~ $10^{-6}$ torr). The disadvantage is that high laser energies (~ joules) are required to drive multi-kA beams over 100-ns-long time periods as required of our present application [2,3]. Other researchers have investigated means of increasing the quantum efficiency by heating [4] or preferentially grooving [5] aluminum cathodes to increase the probability that an electron escapes the metal surface. The quantum efficiency, QE, is defined in this paper as: QE = (I/P)(eV/photon) where I is the emitted beam current, P is the laser power incident on the cathode, and the energy/photon is 6.42 eV. Small-scale, short-pulse, ArF studies are ongoing to address the relative QE's of other candidate metals and films, their preparation, and the effects of temperature, vacuum, and mono-layer contaminants [6].

## 2 EXPERIMENTAL TEST SETUP

Figure 1 shows the REX Facility [7] comprising an E-beam diode, excimer laser with beam paths, and diagnostics. The laser beam was directed by a turning mirror, focused toward a second turning mirror, through a window, and onto the cathode for beam temperature measurements. An elliptical aperture (2:1 aspect ratio) was used at the entrance window to make the beam circular on the cathode. To measure QE's at normal incidence, an alternate beam path utilized a turning mirror and lens combination that directed the laser beam through the entrance window of the test section that contained the E-beam mask and scintillator hardware.

The energy and spatial profile of the laser beam were recorded at the cathode conjugates by an Energy Monitor (Pyrex based, Scientech Inc., 10-cm absorbing calorimeter) and a Profile Monitor (Star Tech Instruments Inc., BIP-3100/Z6/F100, 10-cm, UV to CCD converter). The laser light was monitored by vacuum photo-diodes (see Fig. 1) at the source (SAM PD) and cathode (REX PD). Beam current was monitored 5 cm after the anode aperture and 125 cm from the cathode at the test section entrance with beam size controlled by the anode extraction magnet. The AK gap voltage was monitored by an array of four, integrated E-Dots flush-mounted on the anode face and were cross-calibrated by an energy spectrometer. Beam temperature diagnostics included a 3.2-mm-thick brass E-beam mask (located 160 cm from the cathode) containing an array of fifteen 1-mm-diam holes spaced on 10-mm centers except for a 2-mm-diam reference hole 2 cm on either side of center. Electrons transmitted through the array of holes drifted either 30, 50, or 85 cm to a strip of 0.5-mm-thick Bicron 422 scintillator. The resulting light was recorded on Kodak T-MAX 400 film by a Thompson-CSF, TSN-506-N streak camera located within a shielded screen room. The image was analyzed by techniques developed in [8,9] and yields both space and time resolved beam temperature of the cathode source.

## 3 QUANTUM EFFICIENCY

Figure 2 shows the voltage/current (VI) characteristics of a 6.35-cm-diam velvet cathode with the calculated [10] space-charge-limited (SCL) current plotted in Fig. 3. At 2.25 MV the calculation over-predicts the current by 10%: 1.360- versus 1.215-kA measured. The plot is very useful in estimating the effective beam diameter on the photo-cathode.

0-7803-4376-X/98/$10.00 © 1998 IEEE

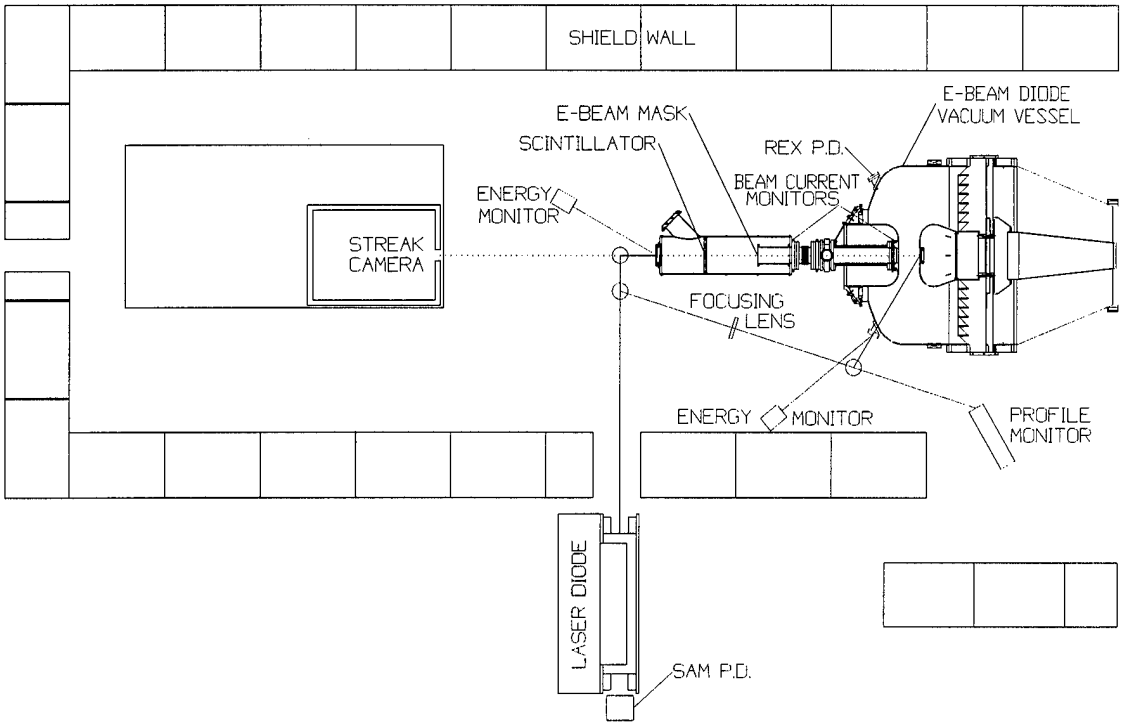



Figure 1. Layout of REX electron-beam facility with electron-beam-pumped excimer laser diode.

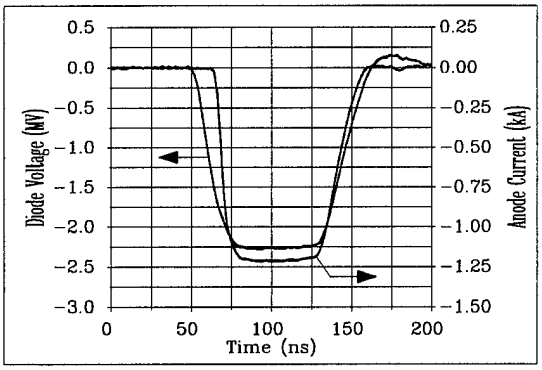



Figure 2. VI characteristics of 6.35-cm-diam velvet cathode at 2.28 MV, AK gap is 20 cm; note delay of diode turn-on.

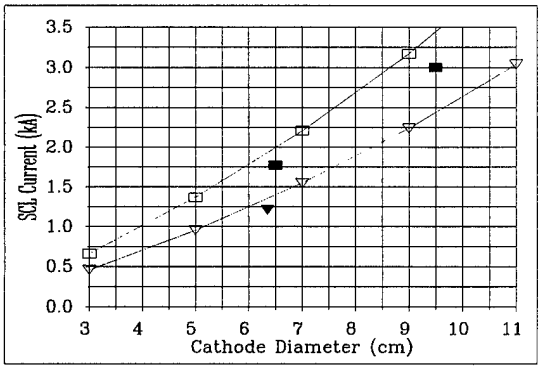



Figure 3. Calculated SCL current at 2.25- (▽) and 2.90-MV (□), AK gap is 20 cm, velvet (▼) and photo (■) SCL data.

For beam temperature and low laser power normal incidence experiments, the laser was focused to a $1/e^2$ diameter of 6 .0 cm as measured by the Profile Monitor. The larger (~ 9.5 cm) laser beam could only be estimated by imaging the visible light emission at the cathode. ArF propagation losses experienced in our previous work [1] were greatly reduced by moving the laser close to REX. As the laser power was increased from a few- to 30-MW, the current for each beam size approached the SCL current region (current follows voltage) as indicated by the current plateaus in Fig. 4. The QE is bounded by a value of 0.07% at the lower power densities and by 0.11% at much higher power densities which is consistent with our previous work [1]. The SCL currents for this data are 1.77- and 3-kA. The anode current, diode voltage, and REX PD for the larger-beam case are shown in Fig. 5. At 28 MW the laser power is ~ 50% greater than that needed for SCL conditions. At 8.6 MW the current of 1.47 kA is emission limited (current follows laser). Other measurements at lower currents from 100- to 1200-A and laser powers from 1- to 10-MW in a 6.0 cm-diam beam gave QE's of 0.07- and 0.078-% for incident angles of normal and 60 degrees, respectively.

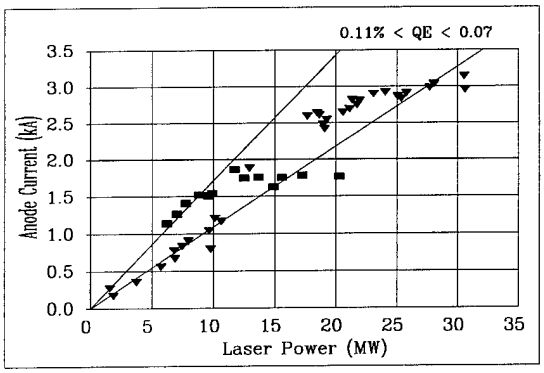



Figure 4. Anode current vs laser power at 2.95 MV, AK gap is 20 cm, 6.0- (■) and 9.5-cm-diam (▼) laser beams.

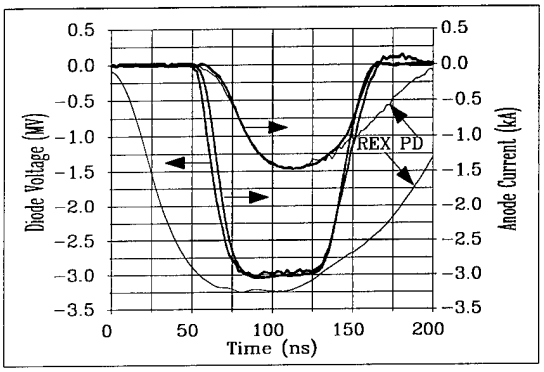



Figure 5. VI of photo-cathode at 8.6- and 28-MW.

## 4 BEAM TEMPERATURE

The effective beam temperature, $T_{eff}$, is defined as: $T_{eff} = 0.511 \times 10^6 \times (\beta\gamma\theta_{rms})^2 eV$, where $\theta_{rms}$ is the rms angle of the distribution of the electrons on the scintillator due to the transverse momentum of the electrons created at the cathode and the self space charge of the beamlet as it drifts from the E-beam mask hole. $\theta_{rms}$ must be modified by Rm/Rc which is the ratio of the electron beam at the mask to the cathode. The scintillator was placed 30- and 50-cm from the E-beam mask for the velvet and 50- and 85-cm for the photo-cathode data. The resultant T-MAX film image was scanned by a Perkin-Elmer micro-densitometer with 10- and 20-μm-square apertures for the photo-cathode and velvet data, respectively. The center three beamlets were each time averaged over a 10-ns window, the data corrected for the film density versus exposure curve, and gaussians fit to each distribution. The resultant rms radii of the gaussians were used to calculate $\theta_{rms}$ knowing the drift distance and Rm/Rc. The data were also corrected for the finite hole size in the mask; this effect is ~ 20% for a 5 eV beam drifting 85 cm with Rm/Rc ~ 1. $T_{eff}$ averaged over the center three beamlets for the photo-cathode

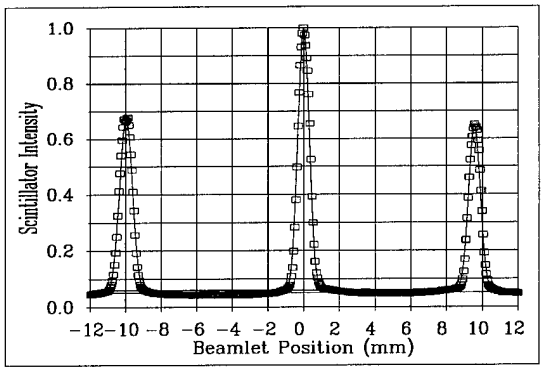



Figure 6. Gaussian fits of photo-cathode beamlet data (□) (averaged over 10 ns) at 510 A and 2.28 MV, drift is 85 cm.

data of Fig. 6 is 4 eV which is at the limit of the present technique. The velvet data at 1.2 kA gave 90- and 85-eV at 30- and 50-cm, respectively. The value of $T_{eff}$ remained constant spatially and temporally across the flat-top portion of the beam.

In summary, multi-kA (~ 3 kA), 100-ns-long beams can be produced with an ArF laser at a QE ~ 0.1% on bare aluminum. The beam temperature of the photo-cathode was measured to be < 5 eV for currents ~ 500 A at 2.28 MeV.

## 5 ACKNOWLEDGMENTS

This work was supported under the auspices of the U.S. Department of Energy.

## 6 REFERENCES

[1] R.L. Carlson, et al: BEAMS'96, *Proc. 11th International Conference on High Power Particle Beams*, pp. 188-191.
[2] M. Burns, et al: LINAC'96, *Proc. 18th International LINAC Conference.*
[3] T.P. Hughes, D.C. Moir, and P.W. Allison: *Proc. 1995 IEEE Particle Accelerator Conference*, pp. 1207-1209.
[4] R.P. Shurter, et al: BEAMS'96, *Proc. 11th International Conference on High Power Particle Beams*, pp. 993-998.
[5] T. Tanabe, Y. Kawamura, D. Li, and K. Toyoda: Rev.Sci.Instrum. **66** (2), (1995), pp. 1010-1014.
[6] R.P. Shurter, et al: paper at this conference.
[7] R.L. Carlson, T.J. Kauppila, and R.N. Ridlon: *Proc. 1991 IEEE Pulsed Power Conference*, pp. 82-85.
[8] T.P. Hughes, R.L. Carlson, and D.C. Moir: J.Appl.Phys. **68** (6), (1990), pp. 2562-2571.
[9] T.J. Kauppila, R.L. Carlson, et al: *Proc. 1991 IEEE Particle Accelerator Conference, pp. 2107-2109.*
[10] PBGUNS Code developed by J. Boers: *Proc. 1993 IEEE Particle Accelerator Conference, pp. 327-332.*

# DEVELOPMENT AND CHARACTERIZATION OF DIAMOND FILM AND COMPOUND METAL SURFACE HIGH CURRENT PHOTOCATHODES

R.P. Shurter and D.C. Moir
Dynamic Experimentation Division
D.J. Devlin, R.W. Springer & T.A. Archuleta
Materials Science and Technology Division
Los Alamos National Laboratory, Los Alamos, NM 87545

*Abstract*

High current photocathodes operating in vacuum environments as high as 8xE-5 torr are being developed at Los Alamos for use in a new generation of linear induction accelerators. We report quantum efficiencies in wide bandgap semiconductors, pure metals and compound metal surfaces photocathode materials illuminated by ultraviolet laser radiation.

## INTRODUCTION

The first axis of the DARHT (Dual Axis Radiographic HydroTest) accelerator [1] is a 20 MeV, 4 kA electron beam linear induction accelerator (LIA) producing a single 60 ns pulse. At the final focus magnet of the accelerator the beam is focused to a 1.2 mm spot on a high Z target producing intense bursts of bremsstrahlung radiation with a flux of 1000 R at 1 meter from the target.

The ability to focus the high current electron beam to the 1 mm spot is dependent on the on beam energy dispersion, centroid motion and emittance. The beam emittance is determined by the injector source temperature.

The cathode presently used in the DARHT injector is a velvet field emission cathode producing an electron beam with a temperature above 100 eV. Experiments at the DARHT Integrated Test Stand (ITS) now demonstrate that with the velvet cathode injector and the initial 5.75 MeV acceleration a beam emittance of 0.15 $\pi$ cm-rad results in a focused spot radius of $\cong$ 0.5mm. This emittance measurement meets the baseline physics design criteria but does not provide
a sufficient margin of safety should unforeseen conditions in the full system lead to emittance growth, increased energy spread or centroid motion.

The DARHT accelerator system architecture includes the use of plastic insulators in the accelerator and in the 4 MeV injector. The use of plastic dielectric materials along with the extensive use of elastomer vacuum seals results in the need to operate the electron beam vacuum diode at total pressures of 1E-6 torr.

Traditionally used low temperature, high current electron beam sources, such as thermionic and multi-alkali metal cathodes will not operate in the present DARHT vacuum environment.

The development of a photocathode operating at modest vacuum pressures has been identified as the best technology to gain the needed reduction in beam temperature for the DARHT 1st axis. A factor of 10 reduction in beam temperature would reduce the emittance contribution to the spot size by 1.8.

Investigations into the development of photocathodes for the DARHT moderate vacuum environment has been broken into two areas. The best understood approach, with the simplest emission mechanisms is the use of low work function bare metals [2,3]. This approach is reasonably straight forward but requires high ultraviolet laser fluences due to low quantum efficiencies of metals even at the highest photon energy laser wavelength available for practical application (ArF, 193nm) [4]. The second, and higher risk approach is to develop new high quantum efficiency photocathodes based on the emerging technology in wide bandgap semiconductors, particularly diamond films.

The photoelectric [5] processes differ considerably between metals and wide bandgap semiconductors such as diamond. In metals the photoelectron created within the solid has an energy above the other electrons at thermal equilibrium and are commonly referred to as hot electrons. The photoelectron is likely to be scattered elastically and inelastically by other electrons because of the abundance of free electrons in a metal and thus approach thermal equilibrium within a short distance. The scattering processes limit the emission to an escape depth of only a few atomic layers. The emission process in metals can be enhanced by increasing the surface temperature of the metal thereby statistically increasing the number of electrons above thermal equilibrium at the surface/vacuum interface.

In a semiconductor, photoemission takes place when a photon is absorbed and converted into a free electron with sufficient energy to cross the bandgap from the valance to the conduction band, in diamond this energy is ~5.47eV. The electron must now overcome the electron affinity of the material to escape into the vacuum level. This process is accomplished by downward band-bending through boron doping of the bulk material and hydrogen surface termination to move the vacuum energy level below the conduction band allowing the electron to fall into the vacuum level thus resulting in a surface with a negative electron affinity (NEA) [6].

Diamond films exhibit unique physical properties, such as thermal conductivity 3 times that of Cu and can withstand over 1 joule/cm2 of 193nm laser radiation.

0-7803-4376-X/98/$10.00 © 1998 IEEE

## EXPERIMENT

To facilitate rapid evaluation of various photoemissive materials we have assembled the PhotoCathode Test Stand (PCTS).

The PCTS has the ability to illuminate small scale samples with an ArF laser producing 193 nm (6.4 eV) laser radiation, normal to the cathode emitter surface. A d.c. voltage of 40kV is applied to the cathode. The anode/cathode gap spacing is nominally 6.7mm. The 6.0-mm-diameter laser radiation incident on the cathode surface is regulated in intensity by using a series of quartz attenuator plates at the inlet aperture to the vacuum diode. The laser fluence on the cathode can be varied over one order of magnitude allowing for photoelectron extraction at very low emission limited currents to past the space charge limit. The extracted electron current generated by the pulsed laser radiation is collected in a tubular charge collector ballasted close to ground by a radial resistor between the collector tube and the grounded anode support tube. This charge collector also contains a defining aperture to size the diameter of the laser beam and the exposed ends of three optical fibers to sample the laser fluence on a shot to shot basis. The fibers are coupled to a 193-nm-line-filtered Hamamatsu photodiode that is calibrated by substituting a pyroelectric calorimeter in place of the photocathode test sample. The photocathode test samples are heated to 125 deg C by means of intense incandescent light introduced into the vacuum through a Pyrex light pipe. The radiant heat is incident on the back surface of the photocathode substrate. The planar diode is configured with an easily removable standard cathode holder. The anode is a flat fine wire mesh >93% transparent tungsten screen. The vacuum chamber is pumped with a 1500 L/s cryo pump and a residual gas analyzer is used to monitor the constituent background gas species.

Recent test data has been acquired on 8 different sample types listed in Table I. Since aluminum has been tested in larger scale systems and has been investigated more extensively in recent years, it was chosen as the baseline standard for purposes of comparison to other materials. Aluminum has a work function of 4.2 eV and a melting point of 660C. Samples were prepared by micro-machining (diamond turning) a 6061 alloy and then applying a 2000 angstrom layer of pure Al by physical vapor deposition (PVD). Data were taken at two temperatures, ambient and ~125C [7,8]. Another aluminum sample was prepared in the same manner with the exception that the surface was glass bead blasted, creating a fine pitted surface structure prior to the PVD process. This process has the effect of increasing the surface area exposed to the laser radiation and may enhance multi-photon effects.

The two other metal samples are compound metal surfaces made of samarium and aluminum created with a flow through ion system in conjunction with metal vapor condensation. Samples were created with varying ratios of Sm/Al. Samarium was chosen as an alloying material due to the low work function (3.2 eV), is nearly a total absorber at the ArF 193nm wavelength and has a melting point 400C higher than Al.

The three semiconductor samples are two polycrystalline, boron doped diamond films (bandgap=5.47 eV) and a single crystal-silicon-carbide-wafer doped with aluminum (bandgap=3.03 eV).

One boron doped polycrystalline diamond sample was grown on a molybdenum substrate using a microwave assisted chemical vapor deposition process. The other boron doped polycrystalline diamond sample was grown on P type silicon using a hot filament vapor deposition technique.

## RESULTS

The summary table below is based on data sets with a minimum of 100 pulses for each sample measured at 10 different laser energies ranging over an order of magnitude. The average quantum efficiency is obtained by fitting a line to peak current density as a function of peak laser power for data which is emission limited. The slope of the line multiplied by the 6.4eV photon energy yields the quantum efficiency (Q.E.). Figure 1 is a overlay of the data and linear fits for two samples with the highest quantum efficiencies.

| Sample type | Sample temperature (degree C) | Ave. Quantum efficiency (electrons/photon-%) |
|---|---|---|
| Pure Al | 25 | 0.061 |
| Pure Al | 125 | 0.076 |
| Bead blasted Al | 125 | 0.049 |
| Al/10%Sm | 125 | 0.029 |
| Al/50%Sm | 125 | 0.027 |
| SiC (single crystal) | 80 | 0.013 |
| Diamond/Mo (polycrystal) | 125 | 0.028 |
| Diamond/ P type Si (polycrystalline) | 125 | 0.325 |

Table 1

If polycrystalline diamond mounted on p-type silicon were used as a photocathode to produce a 3kA-60ns-electron beam with a 76.2mm cathode, the necessary laser energy on the photocathode would be 0.36 J. For a similar aluminum cathode the necessary laser energy would be 1.5 J.

Workers have reported quantum efficiencies above 1% for boron doped polycrystalline diamond on Si [8] and 4% for natural type IIb single crystal diamond [9].

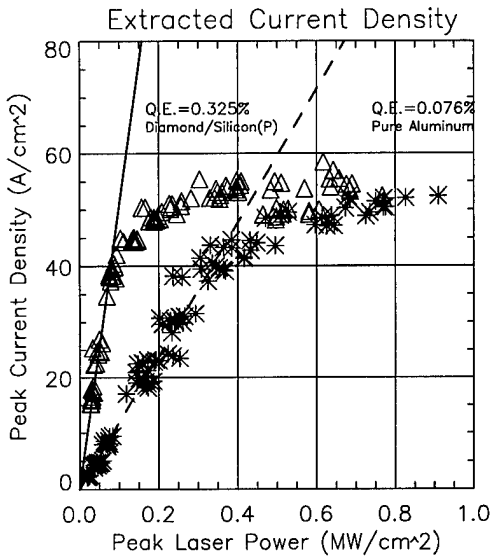



Figure 1 Peak current vs peak laser energy for two samples.

## CONCLUSIONS

The photoyield of the polycrystalline diamond film grown on P type silicon is significantly higher than the other candidate materials tested.

The high photoyield of polycrystalline diamond, scaled to the DARHT size cathode will produce 3 kA beam with a laser fluence of 0.36 joules in a 60 ns pulse. This low fluence will allow the use of ultra-high reliability, commercially available excimer lasers which will have a significant impact on the total system reliability.

Large area growth of polycrystalline diamond films has been demonstrated and are presently available from private industry.

Follow on experiments will focus on photoemission from polycrystalline diamond as a function of temperature, illumination uniformity and the diamond/substrate contact potential.

Other issues to be investigated will include high current electron emission stability and emission effects related to constituent vacuum background gasses.

## ACKNOWLEDGMENTS

The authors gratefully acknowledge the insightful advice and support of Jon Twichell and our other colleagues at MIT / Lincoln Laboratory, without whose help this work would have not been possible.

We thank the members of the DARHT mechanical fabrication team, under the leadership of Louis Montoya for their advice on hardware issues and the fabrication of apparatus often with unreasonably short lead-times.

Thanks also to Gary Green for procurement support and advice on materials issues. And finally a special thanks to Steve Eversole for the diagnostic and data acquisition support without which we would have spent much longer hours in the lab.

## REFERENCES

[1] M Burns et al, "Status of the Dual-Axis Radiographic Hydrodynamics Test Facility" Proc. XVIII Int'l LINAC conf., Aug. 26-30, 1996

[2] R.J Adler et al "Improved Electron Emission by use of a Cloth Fiber Cathode" Rev. of Sci. Instrum. 56 (5), May 1985

[3] S. W. Downey, L.A. Builta and D.C.Moir "Simple Laser Driven, Metal-Photocathode Electron Source" Appl. Phys Lett. 49 (15), 13 Oct, 1986

[4] R. L Carlson et al, "Multi-Kiloampere Electron Beam Generation using Metal Photo Cathodes Driven by ArF and KrF lasers". Proc. 11th Int'l Conf. on High Power Particle Beams. June 10-14, 1996

[5] A. Einstein, Ann. Physik, 17, 132 (1905)

[6] J. van der Weide et al, Phys Rev. B (50),8 pp5803, aug, 1994

[7] R. H. Fowler "The analysis of photoelectric sensitivity curves for clean metals at various temperatures" Phys. rev.,vol 38, pp45-56, 1973

[8] R.P. Shurter D.C.Moir and David J. Devlin, "Characterization of Diamond Film and Bare Metal Photocathodes as a Function of Temperature and Surface Preparation" 11th Int'l conf. on High Power Particle Beams. June 10-14, 1996

[9] J. Twichell, MIT, Lincoln Laboratory, private communication

[10] F.J. Himpsel et al , "Quantum photoyield of diamond (111)-a stable negative-affinity emitter" Phys. rev. B (20),2 pp624 July 1979

# HIGH VOLTAGE, HIGH CURRENT, LONG PULSE ELECTRON BEAM INJECTOR FOR DARHT

E. Henestroza, S. Yu, S. Eylon
Lawrence Berkeley National Laboratory, Berkeley, CA 94720 USA,
B. Carlsten
Los Alamos National Laboratory, Los Alamos, NM 87545 USA

*Abstract*

An injector design for the long pulse option for the second axis of the Dual-Axis Radiographic Hydrotest Facility (DARHT) has been studied. This design is based on the LBNL Heavy Ion Fusion Injector technology. The proposed injector consists of a single gap diode extracting electrons from a thermionic source and powered through a high voltage ceramic insulator column by a Marx generator. The key issues in the design are the control of beam quality to meet the DARHT 2nd axis final focus requirements, to minimize high-voltage breakdown risks, and to fit the injector structure within the available space. We will present the injector conceptual design as well as beam dynamics simulations in the diode and in the injector-main-accelerator interface.

## 1 INTRODUCTION

A high voltage (2 to 4 MV), high current (4 kA), long pulse (2 μs flat-top) electron beam injector for a linear induction accelerator for flash-radiography applications has been under study at LBNL. Based on LBNL Heavy Ion Fusion Injector technology [1] and beam dynamics simulations we have studied an injector that will mantain the beam quality, minimize high voltage breakdown problems, and have the required reliability. Figure 1 shows the main components of a 3 MV electrostatic injector.

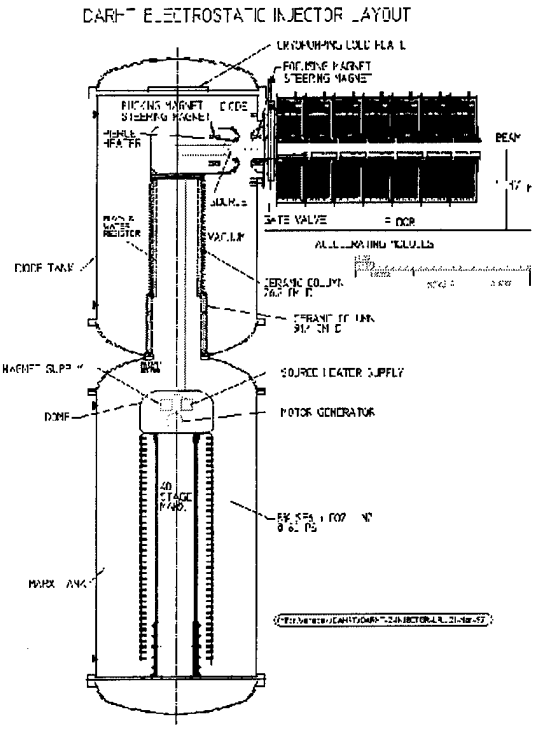



Figure: 1 Main components of a 3 MV electrostatic injector.

## 2 HIF 2 MV INJECTOR

A driver-scale injector for the Heavy Ion Fusion Accelerator program has been in operation at LBNL for several years. Figure 2 shows a schematic of the 2 MV Injector that has exceeded the design goals of high voltage (> 2 MV), high current ( > 0.8 A of potassium ions) and low normalized edge emittance ( < 1 π mm-mr). The injector consists of a 750 keV pre-injector diode followed by an electrostatic quadrupole accelerator (ESQ) which provides strong (alternating gradient) focusing for the space-charge dominated beam and simultaneously accelerates the ions to 2 MeV. The injector is powered by a 2 MV Marx generator which consists of 38 trays with parallel LC and RC networks to produce a 4 μs flat-top pulse to accommodate the entire ion beam plus the transit time across the injector. Pulse lengths of about 1.5 μs and energy flatness of around ±0.15% have been achieved.

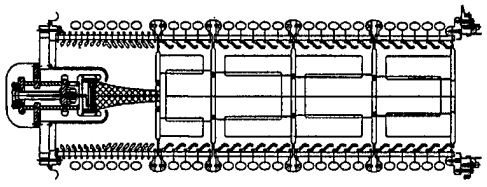


Figure: 2 Schematic of the 2 MV HIF Injector.

The main design effort for the HIF Injector was concentrated on minimizing breakdown risks; the design was based on breakdown data from previous (ions and electron) injectors as well as breakdown tests performed on several of its components. Other important features of the 2 MV HIF Injector are reproducibility and energy flatness. These fatures make this injector a highly reliable machine.

The 3 MV long pulse electron beam injector design is based on the HIF 2 MV Injector operating experience regarding breakdown issues, reproducibility and energy flatness.

0-7803-4376-X/98/$10.00 © 1998 IEEE

## 3 MARX GENERATOR AND INSULATING COLUMN

The 3 MV pulse generator design is based on the LBNL HIF 2.3 MV MARX. It consists of 55 identical pulse forming network stages connected in series to generate the output pulse and is connected to the insulating column through a dome. The MARX and the inside of the insulating column are contained in pressurized $SF_6$. The 100 inches insulating column consists of 50 ceramic brazed rings with an ID of 30 inches and an OD of 32 inches. The outside of the column is in vaccuum and is protected from stray electrons and heat by copper shields. The field stress along the column is less than 50 kV/cm in vaccuum and less than 200 kV/cm in $SF_6$. MOV's and water resistors are used to by-pass excess MARX energy during a breakdown. A hydraulic motor generator placed inside the dome provides, at the pulse 3 MV level, the heating power for the source (around 4 kW) and current for the focusing magnet.

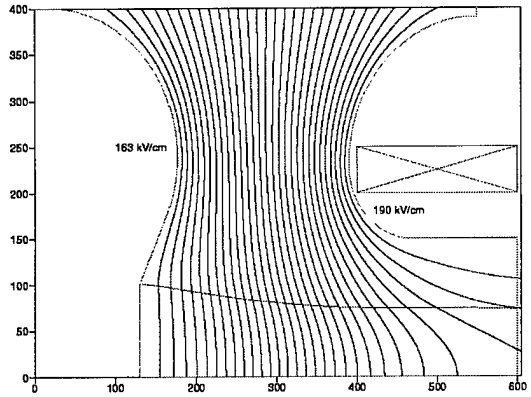



Figure: 3 Electron beam envelope and field equipotential lines as calculated by EGUN.

## 4 THE 3 MV ELECTRON DIODE

The electron beam is generated in a 3 MV diode. It consists of a thermionic source surrounded by a Pierce electrode and focused by a solenoid located at the anode entrance. A bucking coil is located close to the source to zero the axial magnetic field in order to minimize the initial canonical angular momentum of the beam; outside the magnetic field this canonical angular momentum would be transformed into beam emittance.

The beam dynamics inside the diode has been studied using the electron trajectory computer code EGUN [2]. Figure 3 shows the electron beam envelope and field equipotential lines as calculated by EGUN for the 3 MV case.

In order to have a reliable machine the diode design has to minimize breakdown risks. This requirement translates into a design with maximum current extraction for a given maximum field stress. From final focus requirements at the end of the machine, the beam quality has to be controlled and the normalized emittance be maintained under 1000 $\pi$ mm-mr.

For a given field stress limit, maximum current extraction is obtained from cathodes surrounded by a flat shroud as compared to diodes incorporating Pierce electrodes. On the other hand, the beam quality is better controlled by a Pierce electrode; flat shrouds produce hollow beams whose normalized emittance grow as being transported and accelerated along the induction linac. A compromise between the two conflicting requirements is to design the diode with a Pierce electrode assuming the maximum voltage holding capability that can be obtained using special surface handling procedures; this peak field is around 165 kV/cm on the cathode side of the diode and above 200 kV/cm on the anode side. For this design the emittance at the end of the diode is under 1000 $\pi$ mm-mr as calculated by EGUN.

## 5 BEAM DYNAMICS ALONG THE LINAC

A two-dimensional particle-in-cell (PIC) slice (x-y) code [3] has been used to study the transverse beam dynamics of the electron beam generated at the injector as it is transported and accelerated along the induction linac.

The main linac consists of 87 induction cells each providing 200 kV of acceleration. Each cell contains a solenoid used to focus the electron beam. Figure 4 shows electron trajectories for an EGUN simulation of the diode and the first 7 induction cells; the beam quality is preserved. In Figure 5 it is shown the beam envelope and the normalized beam emittance along the induction linac for a complete transverse dynamics run using SLICE, which takes into account all the external fields as well as the space charge. No emittance growth is predicted.

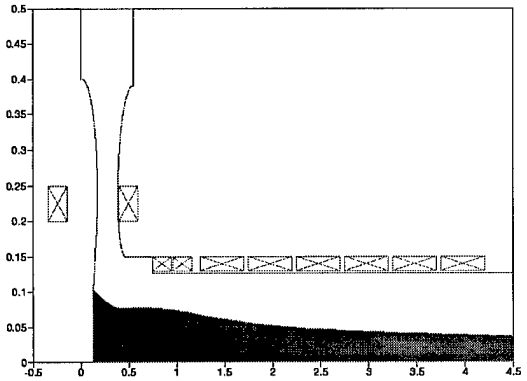


Figure: 4 EGUN simulation of the electron beam from source to the end of the first acceleration section (7 cells).

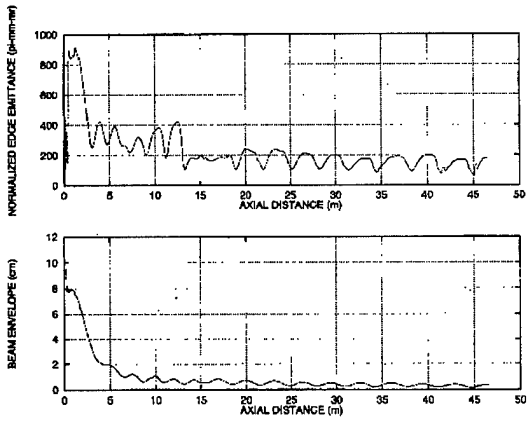



Figure: 5 Particle in cell calculation of the transverse beam dynamics along the induction linac.

## 6 ACKNOWLEDGEMENTS

This work was performed under the auspices of the U.S. Department of Energy under contract AC03-76SF00098. We thank Glen Westenskow for advice and David Vanecek for technical support during the design period.

## REFERENCES

[1] E Henestroza, "Injectors for Heavy Ion Fusion", invited talk, 11th International Workshop on Laser Interaction and Related Plasma Phenomena, Monterey, CA, October 25-29, 1993. AIP Conference Proceedings 318, Ed. G.H. Miley, pp 577-582.

[2] W.B. Herrmannsfeldt, "EGUN- An electron optics and gun design program," SLAC-Report-331, 1988.

[3] B. Carlsten, "The PIC-xy 2-D SLICE code", private communication.

# FOCUSING OF RIBBON BEAM IN UNDULATOR LINEAR ACCELERATOR*

E.S. Masunov, A.S. Roshal, Moscow Engineering Physics Institute, Moscow 115409,Russia

*Abstract*

The possible versions of undulator linear accelerator (UNDULAC-E) using a ribbon beam is discussed. The electrodes shape for 2D transverse focusing of the ribbon beam is suggested. The influence of space charge on the beam focusing for narrow accelerating channel is investigated. Simulation results of beam dynamics and detailed study of the focusing and acceleration fields for the intensive beam are given.

## 1 INTRODUCTION

Early in the paper [1] it was suggested to use the compact high-frequency linear accelerators for ITER's neutral injection system ( NIS ), where the fast neutral deuterium atoms with energy 1.3 MeV for heating and maintenance of stationary current in tokamak's plasma are used. Among all types of the high intensity RF accelerators undulator linear accelerator of a ribbon $D^-$ beams are suitable for NIS. The using of the ribbon beams in ITER's injector has the following features: i) high value of beam current for large width of the beam, ii) large surface for effective beam neutralization, iii) suitable combination of high current ion sources and large slot for ion extraction.

In high intensity RFQ accelerators the ribbon beam can not be accelerated because of limitations of the focusing channel aperture. In this paper the linear accelerator with the plane electrostatic undulator (UNDULAC-E) are used. The accelerating force is produced by a combination of the RF field and the plane undulator field. In UNDULAC-E the ribbon beam has small thickness and large width. A few aspects of the ribbon beam focusing in undulator linear accelerator are discussed below.

## 2 CHOOSING OF FIELDS AND TRANSVERSE BEAM FOCUSING ANALYSIS

The ion beam dynamics in UNDULAC with the plane electrostatic undulator, where the electrical fields were functions only from one transverse coordinate, was in detail studied in paper [2]. It was shown that in this case the focusing force is normal to the plane surface of the ribbon beam and conserves it's thickness. However it is important to ensure the beam focusing in another transverse direction - along the ribbon width. In this paper for 2D transverse focusing it was suggested to change the form of electrodes in order to create a nonuniform distribution of undulator field along the ribbon width.

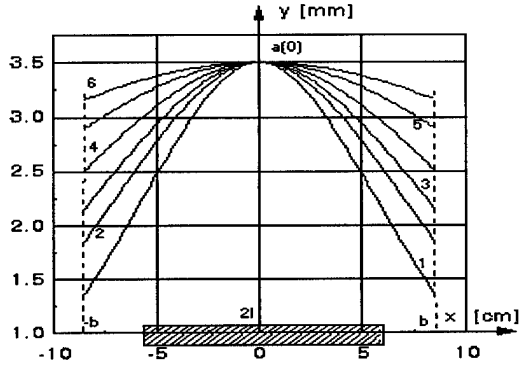



Figure 1.The shapes of the channel upper electrodes for different beam energies W: 1-50 keV, 2-100 keV, 3-150 keV, 4-250 keV, 5-500 keV, 6-1MeV ($k_y/k_x$=23, $\omega$=1.256*$10^9$ 1/s).

Let us choose the Cartesian coordinate system so that x axis is along width of a ribbon (Fig.1). The beam is accelerated along the longitudinal axis z. We consider the simplest case, when the form of electrodes is convex (transverse field Ey increases from a center). The required field distribution is created by system of the electrodes, mounted in a resonator and dc-isolated between each other. A periodic undulator field is generated by electrostatic potential differences, imprinted across the adjacent pairs of electrodes. Simultaneously RF-potentials $-\pm U_v \sin\omega t$ are applied to the electrodes of the upper and bottom row respectively. So the same electrodes are used to generate both the fields. The electrostatic field, created by the periodical system, can be represented as the sums of space harmonics

$$U_o = -\sum_{n=1}^{\infty} \Phi_{o,n} \cosh(nk_x x)\sinh(nk_y y)\cos(nk_z z) \quad (1)$$

where $k_x$,$k_y$ are the transverse wave numbers, $k_z=\frac{2\pi}{D}$ is the longitudinal wave number, D is a period of the undulator, $k_x^2+k_y^2=k_z^2$. The RF field can be expressed by the series, similar to (1) except that now the summation is carried out on even harmonics, including n=0:

* The work was supported by RFFI, grant #95-02-05886

0-7803-4376-X/98/$10.00 © 1998 IEEE

$$U_v = -(\Phi_{v,0} + \sum_{n=1}^{\infty} \Phi_{v,2n}(x,y)\cos(2nk_z z))\sin\omega t \quad (2)$$

Calculating all three components of undulator and RF fields and substituting them in the motion equation of particle after averaging over rapid oscillations, as it had been done in [2], we can obtain the equation describing the slow evolution of radius-vector $\vec{r}$ in smooth approximation.

$$\frac{d^2\hat{\vec{R}}}{d\tau^2} = -\frac{1}{4}\nabla_{\hat{R}} U_{eff} \quad (3)$$

Here $\hat{\vec{R}} = \frac{2\pi\vec{r}}{\lambda}$, $\tau=\omega t$, $U_{eff}$ is the effective potential function depending on harmonics amplitudes of the undulator and the RF fields, as well as on slow phase $\psi = 2\pi\int\frac{dz}{D} - \omega t$ of a combinational wave field. The fundamental space harmonics amplitudes $E_{0,1}$, $E_{v,0}$ are responsible for the mechanism of ion acceleration and focusing.

Taking into account only the main space harmonics of the undulator and RF fields, the expression for $U_{eff}$ can be written in the form

$$U_{eff} = \frac{1}{4}\{a_{0x}{}^2\cosh(2k_x x)\sinh^2(k_y y) + a_{0y}{}^2\cosh^2(k_x x) * \\ *\cosh(2k_y y) - 2a_{v,0}a_{0,y}\cosh(k_x x)\cosh(k_y y)\sin\varphi\} \quad (4)$$

Here $\vec{a}_0 = \frac{e\vec{E}_{0,1}\lambda}{2\pi mc^2}$, $a_{v,0} = \frac{eE_{v,0}\lambda}{2\pi mc^2}$ are the dimensionless amplitudes of the first undulator field harmonic $E_{0,1}$ and the zero Rf field harmonic $E_{v,0}$

Substituting ( 4 ) in equation ( 3 ) we obtain the system of three equations for x, y and z. The analysis of this system for paraxial particles ( $k_x x<<1$, $k_y y<<1$ ) shows, that simultaneous focusing along x and y directions is possible if

$$a_{0y} > a_{v,0}\sin\varphi \quad (5)$$

Oscillation frequency $\Omega_x$ will always smaller than oscillation frequency $\Omega_y$:

$$\Omega_y{}^2 = c^2 k_y{}^2\left(\frac{a_{0x}{}^2 + a_{0y}{}^2}{2}\right) + \frac{k_y{}^2}{k_x{}^2}\Omega_x{}^2 \quad (6)$$

The main factor limiting the beam intensity in the ion accelerator is space-charge forces. In order to take into account Coulomb defocusing of particles, it is necessary to add the space-charge field of the beam in the right part of the equation ( 3 ).

## 3 COMPUTER SIMULATION OF SPACE CHARGE FIELDS AND BEAM DYNAMICS

To simplify estimation of the space charge fields we assumed that the cross-section of focusing channel is a rectangle, having ideally conducting walls, with a width 2b and a thickness 2a. The symmetrically disposed in this channel ribbon beam has a width of 2l and a thickness of 2t (fig.2). The computer simulation show that the installing of side walls at x=±b slightly influences simulation results if the ratio l/t>>1 and the ribbon width l< b.

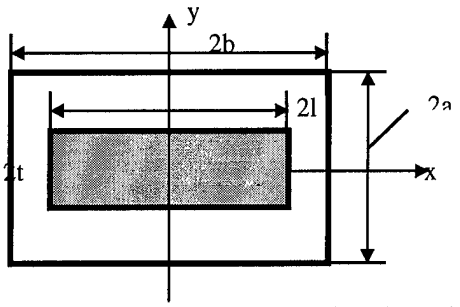



Figure 2.The cross-section of the focusing channel.

Let us designate $E_l$ , $E_t$ the maximum values of x- and y- components of the space charge field $E_q$ accordingly. The frequencies of transverse oscillations $\Omega_x$, $\Omega_y$ are chosen to take values of $El$, $E_t$ and the ratio $k_y/k_x$ into consideration. In our case $E_l$ and $E_t$ can be written as

$$E_{l,t} = \frac{\Lambda}{\varepsilon_0\pi(l+t)}\Gamma_{l,t} \quad (7)$$

Where $\Lambda$ is a linear space charge density, $\Gamma_{l,t}$ is the beam form factor which depends from the electrostatic shielding. If space charge shielding is neglected then $\Gamma_{l,t}$= 1 for any beams having circular (l=t) or elliptic ( l > t ) cross sections. But if the beam cross section is a rectangular $\Gamma_l \neq \Gamma_t$ ($E_l/E_t$=1 for l=t and then $E_l/E_t$ increase from 1 to 2 for l>>t).

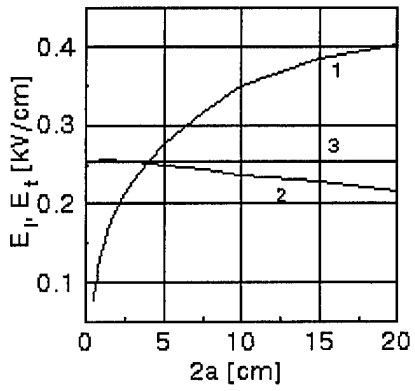



Figure 3. The dependencies of $E_l$ and $E_t$ on the channel thickness 2a.

Electrostatic shielding of the space charge field in the channel varies significantly. The ratio $\Gamma_l/\Gamma_t$ found above for free space and the amplitude $E_l$ can be decreased for narrow channel. The fig.3 shows the dependencies of $E_l$ (curve 1) and $E_t$ (curve 2) versus the

channel thickness 2a. The other parameters are constant: 2l= 11.5 cm, 2t= 0.5 cm, 2b=17 cm, I=0.2 A. The most interesting here is the curve 1, which demonstrates that the narrowing of the channel from 20 cm to 0.51 cm causes strong electrostatic shielding and the space charge field $E_t$ decreases in some times. The $E_t$ component varies under these conditions slightly (curve 2). The theoretical value of Et for an infinitely wide beam having the same values t and beam current density j is shown in fig.3 (straight line 3). Consequently it is possible to reduce significantly the space charge fields $E_t$ using beams with large magnitude of l/t. However this approach is limited by the condition of focusing in the x-direction. Indeed as it follows from formula (4) the transverse focusing can be realized if the ratio $k_y/k_x \approx l/t$. In real systems (fig.1) the electrode shape is not a straight line but it is determined by the equation

$$\cosh(k_x x)\sinh(k_y y) = \sinh(k_y a(0)) \quad , \qquad (8)$$

where the wave numbers $k_x$ and $k_y$ and the synchronous particle velocity $v_s$ are connected by the equation

$$k_x^2 + k_y^2 = \frac{\omega^2}{v_s^2(z)} \, . \qquad (9)$$

The channel thickness 2a(x) is described by the curve

$$2a(x) = \frac{2}{k_y}\sinh^{-1}\left(\frac{\sinh(k_y a(0))}{\cosh(k_x x)}\right) \qquad (10)$$

and decreases from 2a(0) to 2a(l). The minimum size a(l) must be more then the beam thickness t. This condition and also $E_{y\,max}$ are limited the ribbon width 2l.

The 2D particle simulation of self-consisting beam dynamics in the UNDULAC-E confirms the preliminary estimations obtained. The ion beam is represented by particles ('superparticles'). The dispersion of ion axial velocities were neglected, and all velocities were assumed to be equal to the one of the synchronous particle. The acceleration and focusing fields were calculated by the derivation of the effective potential $U_{eff}$ . the equation of axial motion of synchronous particle was solved numerically using the Runge- Kutta method of 4th order. For the space-charge field calculations 2D regular mesh was put on the cross-section of the channel.

The space charge density in the mesh nodes is calculated by the ordinary area-weighting (PIC) method. It is accounted in this calculation that the ion concentration in a z-plane is proportional to the factor $v_s(z)/v_s(0)$, where $v_s(0)$ is the injection velocity of ions. The space charge potential $U_q$ on the mesh was obtained from solution of the Poisson's equation using sequential over-relaxation (SOR). The space charge field $E_q$ was obtained by numerical derivation of the calculated potential. To solve the ordinary differential equations of ions transverse motion we used well-known "leap-frog" numerical method.

Consider $D^-$ ions dynamics in UNDULAC having L=2.5 m, wave length of the RF field $\lambda$=1.5 m, maximum amplitudes of RF-field $E_{v\,max}$=150 kV/cm; wave numbers $k_x$=14.2 1/m, $k_y$=332 1/m; the transverse sizes of the channel a=3.5 mm, b=8.5 cm; input sizes of the beam t=2.5 mm, l=5.75 cm; input energy of ions $W_i$=150 keV and input angular dispersion of ion transverse velocities 0.001. In this UNDULAC the ion current 0.6 A is accelerated without losses acquiring output energy 1.07 MeV. However, neglecting the shielding of the space charge fields in the same UNDULAC would result in channel 0.36 A and even 0.2 A current loss of about 6%. The beam current may be increased even more by using wider ribbons. So if in the same UNDULAC the channel has a=4 mm, b=11 cm and the beam has t=2 mm, l=10cm then the current of 1A is accelerated without loss.

More accurate estimations of UNDULAC's possibilities may be obtained in the future by 3D simulation.

## 4 CONCLUSION

The ribbon beam concept was used to increase the beam current in the undulator linear accelerator. The electrodes shape for 2D transverse focusing of the ribbon beam is found. It was shown that the electrostatic shielding of the space charge field reduces Coulomb defocusing of the particles in the narrow accelerating channel. The results of the numeral simulation of intense $D^-$ beam dynamics confirm the possibility to receive the beam current of about 1 A in the UNDULAC-E.

## REFERENCES


[1] ` E.S. Masunov, V.D. Danilov, A.A. Panasencov," Conception of multichannel RF accelerator for $D^-$ ions ITER injector", Proc. XIV Particle Accelerator Conference, Protvino 1994, vol.1, p.53

[2] E.S. Masunov, A.P. Novicov "Application of electrostatic undulators for acceleration of intense ion beams", Proc. 1991 Particle Accelerator Conference, San-Francisco, vol.5, p.3177 (1991) f

# THE DEVELOPMENT OF A SUPERCONDUCTING RF GUN: STATUS OF THE DROSSEL COLLABORATION

D.Janssen, P.vom Stein *, Forschungszentrum Rossendorf, Dresden, Germany
A.Bushuev, M.Karliner, S.Konstantinov, J.Kruchkov, V.Petrov, I.Sedlyarov,
A.Tribendis, V.Volkov, Budker Institute of Nuclear Physics, Novosibirsk, Russia

*Abstract*

In the beginning of 1996 the Drossel collaboration was established between the FZR and the BINP Novosibirsk for the development of a new electron injector. The injector combines the principle of a photocathode rf gun [1] with the use of superconducting (sc) accelerating cavities. The objective of this development is a sc rf gun, which delivers a bunched electron beam in continuous wave (cw) mode. The beam parameters should fulfill the requirements of the ELBE project [2, 3], a superconducting accelerator currently under construction at Forschungszentrum Rossendorf. The applications of this accelerator are an infrared FEL user facility and nuclear physics, radiation physics experiments, which demand a high flexibility for the beam parameters of the injector.

## 1 DESIGN OF THE SUPERCONDUCTING RF GUN

First a new design was developed to insert a high quantum efficiency photocathode ($Cs_3Sb$, $Cs_2Te$) into the sc cavity. According to the results of an experiment at the University of Wuppertal [4], the heat load of the photolayer, caused by dielectric rf losses, is a severe problem. Therefore the photocathode is hold into a cooling insert with an independent liquid nitrogen circuit (fig.1. The heat load will be transported out of the cryostat without causing additional liquid helium losses. This insert has also the function of a multistaged rf filter to solve the problem of a parasitic rf coupling by the cathode stem to the sc cavity. A dc bias voltage supplied to the cathode stem avoids electron multipacting in the coaxial line between cathode stem and sc cavity.

## 2 BEAM DYNAMICS SIMULATIONS

In parallel the cavity shape of the rf gun was optimized. The conical back wall of the first half cell focusses the beam at low energy and compensates beam blow up due to space charge effects. Beam dynamics simulations (PARMELA [6]) show a transverse emittance of 6.1 mm mrad for 200 pC bunch charge and a gradient of 20 MV/m at the cathode. The full cell cavities of the rf gun have the TESLA geometry [5] to simplify production by using existing sc cavity technology. The low gradient allows both single bunch and cw mode of operation without exceeding present field limits for sc cavities.

To generate an electron beam with low energy spread for the nuclear physics experiments, the injection angle $\phi$ is set to $5^o$. This effects a bunch compression of the electron pulse by a factor of four. The resulting short bunch length of less than 1.5 ps diminishes the energy spread increasing influence of the rf field in the main accelerator. In the FEL mode $\phi$ is $34.6^o$ with slightly higher electrical peak field. The higher momentarilly cathode field $E_{peak} * \sin(\phi)$ allows the extraction of bunch charges up to 500 pC from the cathode, which is necessary to achieve high peak currents for FEL operation. The beam parameters are summarized in table 1.

## 3 OUTLOOK

First tests with a 1.3 GHz half cell to prove the feasibility of our design concepts are scheduled for the middle of 1997. The test cavity is currently into production at the workshops of BINP. First design considerations and price estimations for the laser system were done by the Max Born Institute, Berlin. For the design of the cryogenic system we are in contact with the TU Dresden and VIK Dubna.

## 4 REFERENCES

[1] C.Travier, Nucl.Instr.& Meth. A304(1991) 285-296

[2] F.Gabriel ed., FZR Internal Design Report, Dresden (1995)

[3] D. Janssen, P.vom Stein, Nucl.Instr.& Meth. A380(1996) 497-504

[4] A. Michalke et al.,Proc. of the 3rd EPAC, Berlin (1992)

[5] D. Edwards ed., TESLA Design Report, DESY, Hamburg (1995)

[6] J.Billen, L.Young, Proc. of the 1993 PAC, Vol.2 790-792

* Corresponding author, email: steinp@fz-rossendorf.de

0-7803-4376-X/98/$10.00 © 1998 IEEE

| | Nuclear physics mode | FEL mode |
|---|---|---|
| **Beam parameters** | | |
| $E_{cath}$ | 14.5 MV/m | 19.6 MV/m |
| Bunch charge | 1 pC | 200 pC |
| Energy | 4.2 MeV | 5.7 MeV |
| Energy spread (rms) | $1 * 10^{-4}$ | $3 * 10^{-3}$ |
| trans. emitt. (rms) | 0.18 mm mrad | 5.3 mm mrad |
| long. emitt. (rms) | 0.040 deg keV | 6.1 deg keV |
| **Laser parameters** | | |
| Injection angle $\phi$ | 5.0 deg | 34.6 deg |
| Pulse length (FWHM) | 5 ps | 10 ps |
| Spot size | 3 mm | 3mm |

Table 1: Beam parameters of the prototype gun

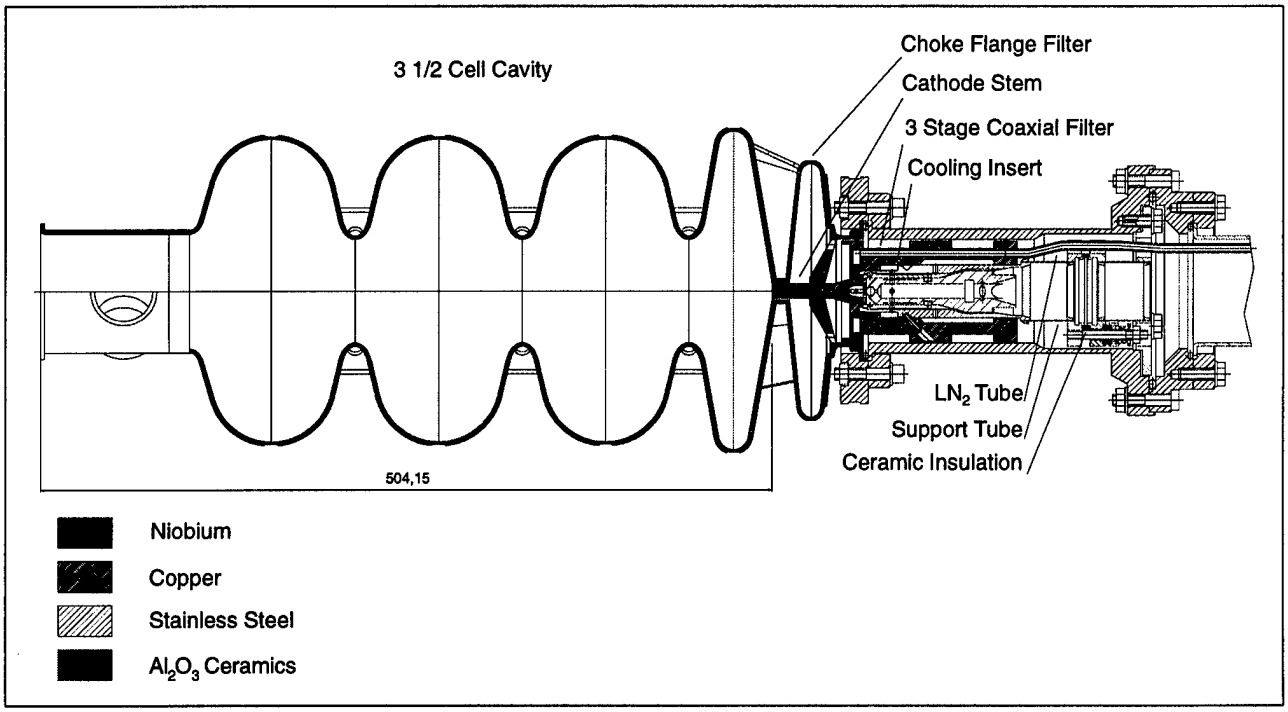



Figure 1: Draft of the prototype rf gun

# EMITTANCE MEASUREMENTS FOR THE SLAC GUN TEST FACILITY

M. Hernandez, A. Fisher, D. Meyerhofer[a], R. Miller, D.T. Palmer, S. Park, D. Reis[a],
J. Schmerge, J. Weaver, H. Wiedemann, H. Winick, D. Yeremian
Stanford Linear Accelerator Center, PO Box 4349, MS 69, Stanford, CA 94309
[a]University of Rochester, Department of Physics and Astronomy, Rochester, NY 14627

*Abstract*

The requirement of a high brightness electron source for the proposed Linac Coherent Light Source (LCLS) project at SLAC[1] has led to the development of the Gun Test Facility (GTF). The facility consists of a photocathode RF gun, emittance compensation solenoid, a single 3-meter SLAC S-band linac section, a single XK-5 klystron, low and high energy diagnostic sections and a cathode drive laser. In this paper, the specifications of the desired electron beam will be discussed along with results of PARMELA simulations to determine the optimum laser pulse shape for minimum beam emittance. The diagnostics of the GTF will be discussed and measurements will be presented which were made at the SUNSHINE Facility at Stanford to develop the instrumentation to be used at the Gun Test Facility once it is operational. Future beam diagnostics will also be discussed.

## 1 INTRODUCTION

### *1.1 Facility*

The goal of the GTF is to produce single bunches with 1 nC of charge, 10 ps(FWHM) bunch length, and a normalized emittance of 1πmm-mr. The first photocathode RF gun to be characterized was developed by a collaboration of SLAC, BNL and UCLA[2]. The laser driven copper cathode 1.6 cell RF gun is operated in π–mode at S-band with multi-pole mode suppression achieved through cavity symmeterization. In order to obtain the smallest possible emittance the beam must be quickly accelerated in the gun to reduce space charge induced emittance growth. The desired gradient in the gun is 140 MV/m which will require 12-14 MW of rf power. Immediately following the gun is an emittance compensation solenoid which enables the correction of linear space charge emittance growth. After the solenoid there are two pop-in phosphor screens for examining the beam and a toroid for current measurements. The beam is then accelerated by a single 3-meter SLAC S-band linac section for which initially 6 MW of rf power will be available, enough to accelerate the beam to 27 MeV. Future RF upgrades this summer will allow the use of a single XK-5 klystron for the linac with approximately 16 MW of RF power which should enable energies of 45-50 MeV with the single linac section. After acceleration the emittance will be measured with the standard quadrupole scan technique utilizing a phosphor screen and a wire scanner. The three screen method will also be employed. The bunch length will be determined through the use of linac phasing and possibly a streak camera. Another toroid enables measurement of the beam current. The beam is then passed through a $60^0$ bend magnet for energy analysis using a screen and finally the beam will be dumped into a Faraday Cup.

### *1.2 Gun Drive Laser*

The laser system [3] consists of an Nd:YLF oscillator and a Nd:glass amplifier which will enable generation of near Gaussians 1 ps long laser pulses. A Nd:glass oscillator will be installed which will allow pulses down to 200 fs FWHM. Temporal pulse shaping may be done in either the time domain by stacking gaussian beamlets or frequency domain through the use of amplitude or phase masks. The system is capable of producing 200 μJ of UV (263 nm) on the cathode at normal incidence. This is sufficient to produce 1 nC of charge assuming a quantum efficiency of $2\ 10^{-5}$. Ports on the half cell of the gun will enable the laser to also strike the cathode at grazing incidence.

## 2 EMITTANCE COMPENSATION

The emittance compensation scheme utilizes a linear lens to remove the projected emittance growth caused by linear space charge forces [4]. Consider a section of beam line which consists of a drift, a linear lens and another drift. For a slug beam, a right circular cylinder with uniform charge density, the phase space distribution of the beam can be described by a rectangle. If the beam is allowed to drift and only linear space charge effects are considered, the phase space plot of the beam becomes a rotated fan shaped distribution with increased area. The increased area indicates an increase in the projected emittance of the beam. This is due to differing rates of expansion for the electrons in various locations in the beam. Particles which are in the middle of the beam longitudinally and on the radial outer edge of the slug experience the maximum radial space charge force while those on the radial outer edges of the beam which are at the maximum longitudinal positions experience less radial space charge force. This differing force leads to a variation in the radial velocity for electrons in the beam. If the drifting beam passes through a linear lens the phase space distribution undergoes a clockwise shear due to the lens. After the lens the beam drifts and space charge forces cause differing rates of expansion for different parts of the beam which leads to a collapse of

0-7803-4376-X/98/$10.00 © 1998 IEEE

the fan shaped distribution and so a reduction of the projected phase space area of the beam.

## 3 SIMULATIONS

The GTF beam has been simulated using PARMELA with the details of the gun, solenoid and linac provided by D. T. Palmer [2]. A field map from SUPERFISH is used for the gun and a POISSON field map is utilized for the emittance compensation solenoid. The field in the gun was set at 140 MV/m and the linac was run at 7-10 MV/m. The 1 nC electron beam is simulated using 10,000 macroparticles with space charge effects included. The laser spot on the cathode is $\sigma_r$=.09 cm with a maximum radial extent of $r_{max}$=2.0 cm and a pulse duration of 10 ps. Simulations for the ATF at BNL [2], which uses two linac sections indicate that a transverse Gaussian with a temporal flat top bunch should produce a normalized emittance of 1 πmm-mr RMS. Whereas simulations with a bunch which is Gaussian both transversely and temporally produces a normalized emittance of 2.5 πmm-mr RMS. Recent measurements of 5 πmm-mr RMS at BNL have been achieved [5]. Simulations of the GTF have been done with bunches which are flat top temporally and Gaussian transversely and Kapchinsky-Vladimirsky (KV) distributions, which are uniform in space with a parabolic line charge density. The transverse Gaussians were also clipped. Since the emittance compensation solenoid is capable of removing the emittance growth from linear space charge forces, the more uniform the bunch transversely the smaller the RMS emittance of the bunch. This has been observed in the simulations. From a nonlinear field energy consideration, the optimum electron distribution is a uniform distribution, such as the KV, since it leads to the least emittance growth from the thermalization of the field energy, as described in [6]. Time dependent RF also contributes to emittance growth and can be reduced by shortening the bunch. The 10 ps bunch length was chosen from requirements of the bunch compression of the LCLS. For the GTF system simulations with the KV distribution has produced .90 πmm-mr, a Gaussian clipped at $\pm\ \sigma_r$ gave .96 πmm-mr, and the flat topped Gaussian have produced 1.12 πmm-mr normalized RMS emittances. The clipped Gaussian is more uniform than the full Gaussian and was used since it will be the most convenient to produce initially.

| Transverse | KV | Clipped Gaussian | Gaussian |
|---|---|---|---|
| Longitudinal | KV | Flat Top | Flat Top |
| $\varepsilon_{normalized}$[π mm mr] | 0.9 | 0.96 | 1.12 |
| $\sigma_z$ [pS FWHM] | 11 | 10 | 10 |
| $B_{Solenoid}$[kG] | 2.75 | 2.82 | 2.79 |
| $E_{Linac}$[MV/m] | 7 | 7 | 10 |
| Energy[MeV] | 27.7 | 27.7 | 31.3 |

Figure 1: Parameters for PARMELA simulations of the GTF.

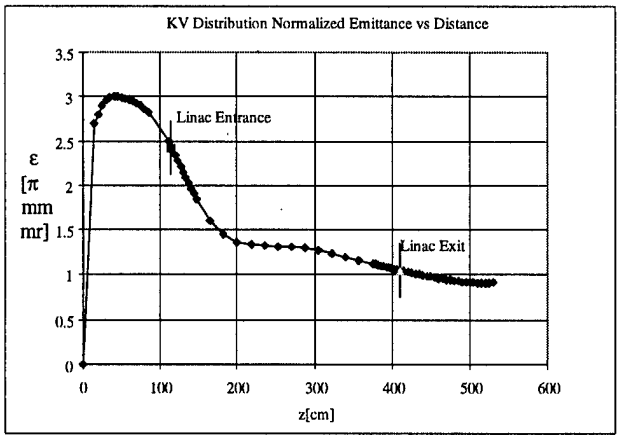



Figure 2: Plot of normalized emittance vs. distance along the GTF for the KV distribution from PARMELA.

## 4 MEASUREMENTS

Since the GTF is under construction, the SUNSHINE facility at Stanford campus was utilized to test the instrumentation for emittance measurements. SUNSHINE [7] consists of a 1.5 cell S-band RF gun with a thermionic cathode, an alpha magnet for bunch compression and one SLAC type linac section for acceleration. Existing instrumentation includes toroids and Faraday Cups for current measurements, phosphor screens for profile measurements, and bend magnets for energy measurements. Normal operation of the machine produces a 1.5 μs macropulse with about 200 pC of charge per microbunch, the alpha magnet allows bunch compression down to 100 fs rms after acceleration. Instead of accelerating the beam it can be directed straight through the Alpha magnet after degaussing to a low energy beam line (2-3 MeV.) This portion of the beam line was used to test emittance instrumentation. After the beam exits the gun it is focused by four quadrupole magnets. A dipole is then used in conjunction with a set of slits to set the energy spread of the beam. Measurements were done at $\pm$ .1, .2, .3 .4 percent energy spread. This enabled minimization of chromatic effects in the final doublet used to perform the quad scan. Ideally, a double bend achromat would have been used to minimize the horizontal dispersion of the beam, however existing instrumentation did not allow this. The beam profile was observed with a screen made from SLAC chromate. Finally, the beam was dumped into a Faraday Cup to determine the current. The image of the beam was captured using a Pulnix CCD camera and DataTranslation 8-bit frame grabber synchronized to the beam. A neutral density filter and a remotely controllable iris were used to control saturation of the camera. The

beam was focused to the smallest possible spot and the iris and frame grabber ADC were adjusted to keep the maximum pixel value less than 255. The quadrupole was then re-standardized and the current was raised incrementally and images of the beam were captured. The data was analyzed off line by least squares fitting of the widths of the beam profiles with the values for the beamline parameters. The widths of the beam profiles were obtained by fitting to a Gaussian distribution from which the sigma of the profile was obtained. The fits were quite good as expected since the beam is generated by a thermionic cathode. The resolution of the system was determined to be 50 μm/pixel and 60 μm/pixel horizontally and vertically respectively. The resolution of the system is ultimately limited to the response and granularity of the screen. The resolution of this type of screen is approximately 50 μm/pixel [8]. The camera was placed as close as possible to the screen, this gives higher resolution but radiation effects must be considered. The resolution given above was for a setup in which a 45 degree mirror was used to reflect the image of the beam to the camera which was located behind 2-4 inches of lead to provide shielding from the source point. The wire scanner has the potential for 10 μm resolution. However the lower beam current densities (about 10 pC per macropulse depending on the slit settings), for the energy filtered beam only allowed integrated measurements over the macropulse. This served to debug electronics and motion control of the system. Also a high impedance amplifier was shown to improve signal levels. Future plans are to move the wire scanner to the high energy part of the beam line where higher current densities are available. The 1 nC beam of the GTF is expected to produce sufficiently high current densities for the wire scanner.

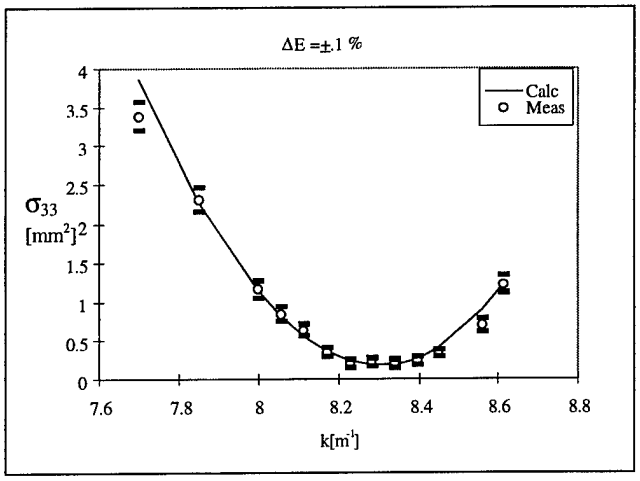



Figure 3: Plot of measured and calculated $\sigma_{33}$ versus quadrupole strength for the SUNSHINE facility. Where $\sigma_{33}$ is the square of the vertical beam size.

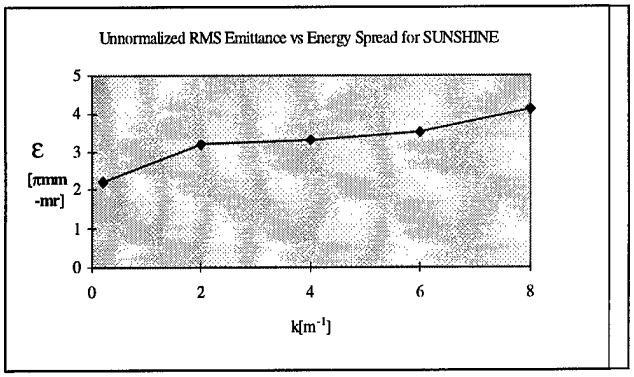



Figure 4: Plot of unnormalized RMS emittance vs. energy spread for SUNSHINE. The energy of the beam was 3.1[MeV] for all measurements.

## 5 FUTURE INSTRUMENTATION

As is evident in the simulations of the GTF, the emittance of the beam will increase due to space charge effects if it is allowed to drift after acceleration. In order to eliminate these effects on the measurements, single shot emittance measurements using TR will be investigated. If OTR intensities are insufficient, Coherent TR will be used since it will have greater intensity. Either masks and a room temperature pyroelectronic bolometer or movable bolometers would be used to determine the divergence of the TR. Low energy emittance measurements will be made with a pepper pot or slits. Also a low energy beam line is being considered. This would require the temporary removal of the linac so that a double bend achromat could be installed.

## 6 ACKNOWLEDGEMENTS

The authors would like to acknowledge the entire SSRL staff ant the collaborators at ANL, BNL, UCLA, and the University of Rochester for the support. This work supported under the Department of Energy contract DE-AC03-76SF00515.

## REFERENCES

[1] R. Tatchyn et al, Nucl. Instr. and Meth., A 375, p. 274, 1996

[2] D.T. Palmer et al, Proc. of SPIE, vol. 252, p. 514, 1995

[3] J. Schmerge et al, Proc. of SPIE, vol. 2988, 1997.

[4] B.E. Carlsten: 'New photoelectric injector design for the Los Alamos National Laboratory XUV FEL accelerator,' Nucl. Instrum Methods Phys. Res., vol. A285, p. 313, 1989.

[5] D.T. Palmer et al, Proc. of SPIE, vol. 2988, 1997.

[6] 'Theory And Design Of Charged Particle Beams', by M. Reiser, John Wiley & Sons, 1994.

[7] P. Kung, HC Lihn, D. Bocek, and H. Wiedemann, Phys. Rev. Lett. **73**, 967 (1994).

[8] S. Yencho and D.R. Walz: 'A High-Resolution Phosphor Screen Beam Profile Monitor,' IEEE Trans., 32:2009-2011, 1985.

# EXPERIMENTAL RESULTS OF A SINGLE EMITTANCE COMPENSATION SOLENOIDAL MAGNET*

D. T. Palmer*, X. J. Wang†, I. Ben-Zvi†, R. H. Miller*, J. Skaritka†
*Stanford Linear Accelerator Center, Stanford University, Stanford, CA 94309
†Brookhaven National Laboratory, Accelerator Test Facility, Upton, NY 11973

*Abstract*

A new iron dominated single emittance compensation solenoidal magnet was designed to be integrated with the BNL/SLAC/UCLA 1.6 cell S-Band Photocathode rf Gun. This emittance compensated photoinjector is now in operation at the Brookhaven Accelerator Test Facility. It has produced a 0.329 $\pm$ 0.012 pC, $\tau_{95\%}$ = 10.9 psec electron bunches with a normalized rms transverse emittance of $\epsilon_{n,rms} = 1.17 \pm 0.16\,\pi$ mm mrad. POISSON field maps were used with PARMELA to optimize the emittance compensation solenoidal magnet design. Magnetic field measurements show that at the cathode plane $B_z \leq 10$ G for a peak magnetic field of $B_{z,max} = 3$ kG. Which is in agreement with POISSON simulation. A single emittance compensation solenoidal magnet will produces a initial angular momentum of the electron bunch that manifests itself in a initial magnetic emittance term that cannot be eliminated. This magnetic emittance $\epsilon_{n,rms}^{mag}$ scales as $0.010 \frac{\pi \text{ mm mrad}}{\text{G}}$ at the cathode, which is in agreement with PARMELA simulations. Experimental beam dynamics results are presented that shows relative angular rotation and spot size as a function of cathode magnetic field. These results are compared to theory.

## 1 INTRODUCTION

The BNL/SLAC/UCLA S-band emittance compensated [1] photoinjector has been installed at the Brookhaven Accelerator Test Facility(ATF) as the electron source for beam dynamics studies, laser acceleration and free electron laser experiments. The 1.6 cell rf gun is powered by a single XK-5 klystron, and is equipped with a single emittance compensation solenoidal magnet. We have experimentally investigated the physical consequence of this single solenoidal magnet design as they relate to emittance growth. The simulation results, mechanical design, theory and experimental beam dynamics results of the single emittance compensation solenoidal magnet are presented.

## 2 SIMULATIONS

POISSON [2] field maps were generated for a number of different emittance compensation magnet designs. PARMELA [3] was then used to evaluate these designs as a function of the minimum emittance attainable using the ATF beamline as a model. These field maps were developed using a Dirichlet boundary condition at the cathode plane. Due to mechanical constraints of the BNL/SLAC/UCLA 1.6 cell S-band rf gun [4], the compensation magnet could not be positioned in the optimal emittance compensation position but at the location shown in figure 1 which gives a 15 % higher emittance than the optimum.

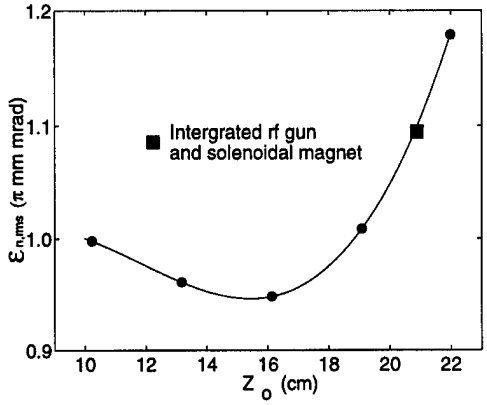



Figure 1: PARMELA simulations of the normalized rms emittance versus emittance compensation magnet position

## 3 SOLENOIDAL MAGNET DESIGN

The solenoidal magnet is constructed out of eight double layer hollow core copper conductor pancakes. The flux return was manufactured out of 1006 steel, as are the seven dipole field flux aligners [5]. These dipole field flux aligner are used to eliminate any dipole fields that arise from the current pancake asymmetries and misalignments during assembly. Penetrations thru the flux return were designed to have four fold symmetry. The external current conductors are fed to alternate sides of the solenoid to eliminate a dipole contribution due to the individual pancake conductor crossovers. A schematic drawing of the solenoidal magnet is show in figure 2.

In the previous ATF emittance compensation magnet design the solenoidal magnet was an air core magnet. We have extended this initial design that included dipole field straighteners to incorporate an iron flux return that eliminates the need of a congruent magnet symmetrically located upstream of the cathode to buck the cathode magnetic field to zero. The use of the magnetic flux return has decreased the cathode magnetic field to $B_z \leq 10$ G for a peak magnetic field of $B_{z,max} = 3$ kG as seen in figure 3.

* Work supported by the Department of Energy, contracts DE-AC03-76SF00515 and DE-AC02-76CH00016

0-7803-4376-X/98/$10.00 © 1998 IEEE

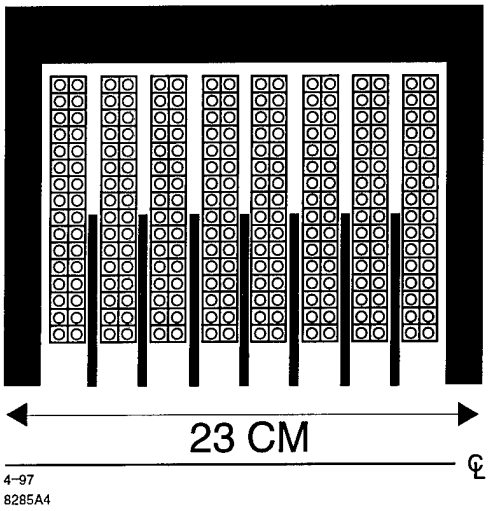



Figure 2: Compensation Magnet Design

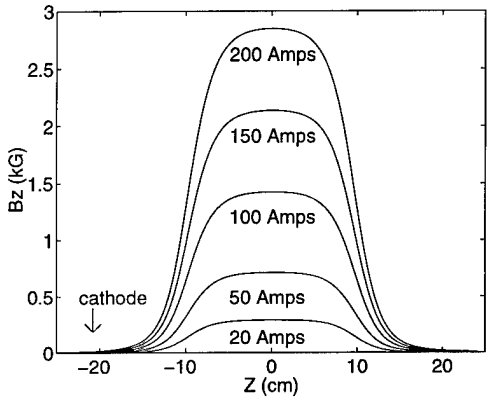



Figure 3: Magnetic Field Measurements

A bucking magnet is located at the upstream end of the gun. It is only used for beam dynamics studies. A $\cos(\theta)$ deflection magnet is located in the emittance compensation magnet bore. This deflection magnet is used for energy measurements of the electron bunch energy at the exit of the gun.

## 4 THEORY

In this section we will delineate the effect of the finite cathode magnetic field due to the bucking magnet. There are three effects that will studied first the relative angular rotation due to the cathode magnetic field, spot size and finally the normalized rms emittance due to this magnetic field. From Busch's theorem [6] we know that

$$\dot{\theta} = \frac{e}{2\gamma m_o}(B_{z_o} - B_z) \tag{1}$$

where $B_{z_o}$ and $r_o$ is the cathode magnetic field and laser spot size. Integrating equation 1 we find that the angular rotation as a function of cathode magnetic field varies linearly with the cathode magnetic field.

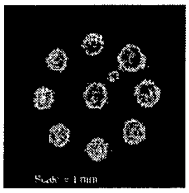


Figure 4: 8 fold symmetric beamlets

$$\delta\theta = \int \frac{e}{2\beta\gamma m_o c} dz\, B_{z_o} \tag{2}$$

Busch's theorem can also be used to study the effect of cathode magnetic field on spot size. Starting with the definition of $x'_{rms}$.

$$x'_{rms} = \frac{p_{x,rms}}{p_z} = \frac{v_{x,rms}}{\beta c} = \frac{e r_o |B_{z_o}|}{4\beta\gamma m_o c} \tag{3}$$

Which follows from the definition of rms velocities we know that

$$v_{x,rms} = \sqrt{\frac{\int\int r^2\dot{\theta}^2 \cos^2(\theta) r dr d\theta}{\int\int r dr d\theta}} \tag{4}$$

Therefore, the rms spot size increases as $|B_{z_o}|$

$$x_{rms} = \int x'_{rms} dz = \int \frac{e r_o}{4\beta\gamma m_o c} dz\, |B_{z_o}| \tag{5}$$

The magnetic emittance scales as $\epsilon_{n,rms} \propto r_o^2 |B_{z_o}|$ given in equation 6 where we assume that the $< xx' >= 0$.

$$\epsilon_{n,rms} = \beta\gamma\sqrt{< x'^2 >< x^2 >} = \frac{e r_o^2 |B_{z_o}|}{8 m_o c} \tag{6}$$

## 5 EXPERIMENTAL RESULTS

Due to the small but finite field at the rf gun cathode the electron bunch are produced with a finite angular momentum. We have measured the relative angular rotation due to this finite field. In this experiment a 8-fold symmetric mask [7] [8] was inserted into the the laser beam thereby producing the laser profile on the cathode shown in figure 4.

The smallest beamlet located at 45° is used to break the symmetry. In this way we were able to measure the betatron rotation of the beam thru the solenoidal magnet which was found to be approximately 90°. The 8-fold beamlet relative angular rotation was measured as a function of bucking magnet field for point to point imaging of the 8-fold beamlets from the cathode to a beam profile monitor located 66.4 cm from the cathode. Figure 5 represents the relative angular rotation of the 8-fold symmetric beamlets due to the cathode magnetic field and has a linear dependence predicated in equation 2.

The rms spot size as a function of cathode magnet field was measured at both low and high energy. The functional dependence of the high energy spot size data in figure 7

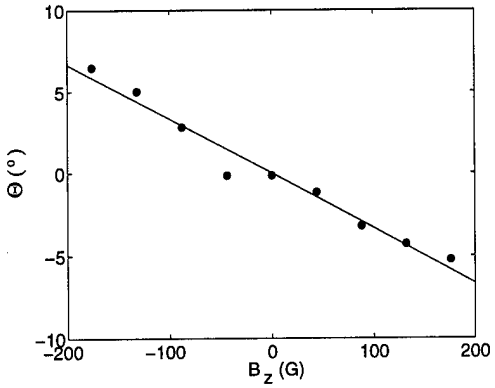



Figure 5: $\Phi_{rel}(z = 0)$ versus $B_z(z = 0)$

| | |
|---|---|
| Experimental Result | 0.010 $\frac{\pi \text{ mm-mrad}}{\text{G}}$ |
| PARMELA | 0.006 $\frac{\pi \text{ mm-mrad}}{\text{G}}$ |
| THEORY | 0.007 $\frac{\pi \text{ mm-mrad}}{\text{G}}$ |

Table 1: Comparison of experimental results, simulation and theory for the emittance growth due to the cathode magnetic field

has been fit to equation 5 with a minimum spot size occurring with a cathode magnetic field of -5 G. The cathode field with the bucking magnet off is +4 G. The low energy spot size data in figure 6 is not fitted to equation 5 since the beam is space charge dominated in the low energy regime. Fitting this data with two linear functions has the minimum spot size occurring at the -3.6 G. Which is consistent with the high energy minimum spot size bucking field. This data indicates that the cathode field can not be zeroed better than the mechanical construction and alignment of the photoinjector itself.

Due to experimental instabilities it was not possible to measure the emittance growth due to the induced cathode magnetic field. From the spot size variation at high energy due to the induced cathode magnetic field and the correlation between spot size and measured $\epsilon_{n,rms}$ [9], the emittance growth as a function of cathode magnetic field can be estimated. In table 1 the correlated experimental results of $\epsilon_{n,rms}$ growth as a function of induced cathode magnetic field is presented along with PARMELA simulation and theoretical [10] predications.

## 6 CONCLUSION

We have present the design and experimental results of a single emittance solenoidal magnet. Relative angular rotation, low and high energy rms spot size have been presented as a function of cathode magnet field. Mechanical constraints limit the compensation magnet to a position that is not optimal for the emittance compensation process. Redesigning the waveguide feed into the full cell would correct this limitation in the injector design.

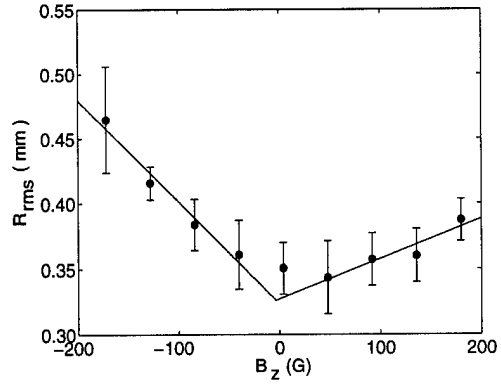



Figure 6: Low energy $R_{rms}$ versus $B_z(z = 0)$

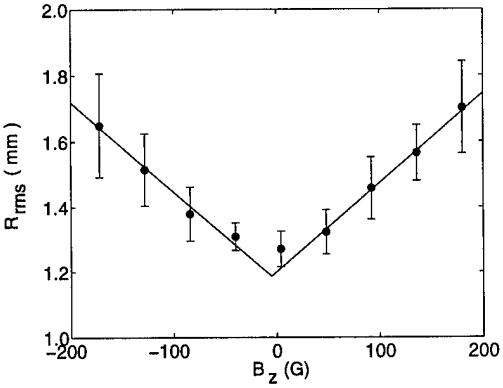



Figure 7: High energy $R_{rms}$ versus $B_z(z = 0)$

## 7 ACKNOWLEDGEMENT

The authors would like to thank the technical staff at UCLA, SLAC and BNL for all their dedicated work on this project. We would also like to thank Dr. K. Halbach for his technical assistance in the design of the single emittance compensation solenoidal magnet and Dr. V. Yakimenko for conducting the magnetic field measurements on the solenoidal magnet.

## 8 REFERENCES

[1] B. E. Carlsten, *NIM*, **A285**, 313 (1989)

[2] K. Halbach and R. F. Holsinger, *Particle Accelerators*, **7**, 213 (1976)

[3] L. M. Young, private communications

[4] D. T. Palmer *et al.*, Proc. 1995 Part. Accel. Conf. (1995) p. 982

[5] K. Halbach, LBL 4270

[6] H. Busch, *Z. Phys.*, **81**, 974 (1926)

[7] Z. Li, Ph.D. Thesis

[8] D. W. Feldman *et al.*, IEEE J. Quantum Electronic, **27**, 12, 2636-2643 (1991)

[9] D. T. Palmer *et al.*, Proc. 1997 Part. Accel. Conf., 2C.10

[10] K. Flotmann, private communications

# BEAM DYNAMICS ENHANCEMENT DUE TO ACCELERATING FIELD SYMMETRIZATION IN THE BNL/SLAC/UCLA 1.6 CELL S-BAND PHOTOCATHODE RF GUN*

D. T. Palmer*, X. J. Wang†, I. Ben-Zvi†, R. H. Miller*
*Stanford Linear Accelerator Center, Stanford University, Stanford, CA 94309
†Brookhaven National Laboratory, Accelerator Test Facility, Upton, NY 11973

*Abstract*

A 1.6 cell photocathode S-Band gun developed by the BNL/SLAC/UCLA collaboration is now in operation at the Brookhaven Accelerator Test Facility (ATF). One of the main features of this RF gun is the symmetrization of the RF coupling iris with a identical vacuum pumping port located in the full cell. The effects of the asymmetry caused by the RF coupling iris were experimentally investigated by positioning a metallic plunger at the back wall of the vacuum port iris. The higher order modes produced were studied using electron beamlets with 8-fold symmetry. The 8-fold beamlets were produced by masking the laser beam. These experimental results indicate that the integrated electrical center and the geometrical center of the gun are within 175 $\mu$m. Which is within the laser alignment tolerance of 250 $\mu$m.

## 1 INTRODUCTION

The BNL/SLAC/UCLA S-band emittance compensated [1] photoinjector has been installed at the Brookhaven Accelerator Test Facility(ATF) as the electron source for beam dynamics studies, laser acceleration and free electron laser experiments. The 1.6 cell rf gun is powered by a single XK-5 klystron, and is equipped with a single emittance compensation solenoidal magnet. There is a short drift space between the photoinjector and the input to the first of two SLAC three meter travelling wave accelerating sections. This low energy drift space contains a copper mirror that can be used in either transition radiation studies or laser alignment. There is also a beam profile monitor/Faraday plate located 66.4 cm from the cathode plane. The photoinjector beam line layout is presented in figure 1.

The drive laser is a Nd:YAG master oscillator/power amplifier system. A diode pumper oscillator mode locked at 81.6 MHz produces 21 psec FWHM pulses at 100 mW of average power. Gated pulses seed two flash lamp pumped multi-pass amplifiers and are subsequently frequency quadrupled. This nonlinear process leads to a factor of two reduction in the laser pulse length. The 266 nm beam is transported to the RF gun area via a 20 meter long evacuated pipe. A spherical lens and a pair of Littrow prisms are used to compensate for the anamorphic magnification introduced by the 72° incidence on the cathode. The time slew across the cathode caused by this oblique incidence is also corrected by using a diffraction gradient.

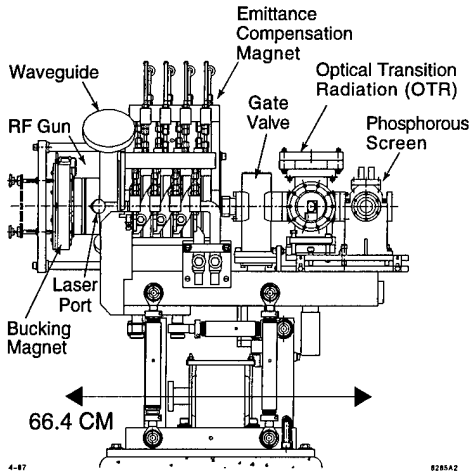



Figure 1: The BNL/UCLA/UCLA 1.6 cell S-band photoinjector

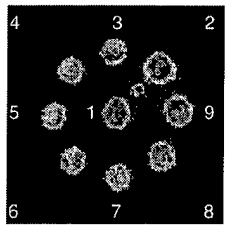



Figure 2: Beamlet profile on cathode, the distance from beamlet 1 to beamlets 2-9 is 1mm

To probe the electromagnetic fields of the 1.6 cell gun an 8-fold symmetric aperture [2] [3] was introduced into the laser beam line. This 8-fold aperture produces a laser image on the cathode seen in figure 2 with the radius of 1 mm from the center beamlet to the outer ring of beamlets. This produces an electron beam with 8-fold symmetry. This aperture was rotated to align the symmetry breaking beamlet to be collinear with the waveguide feed into the gun.

## 2 EXPERIMENTAL SETUP

The rf guns half cell is fully symmetrized by two laser ports which are located rotated 45° from the tuner/waveguide coordinate system in the fully cell. These two laser ports al-

* Work supported by the Department of Energy, contracts DE-AC03-76SF00515 and DE-AC02-76CH00016

0-7803-4376-X/98/$10.00 © 1998 IEEE

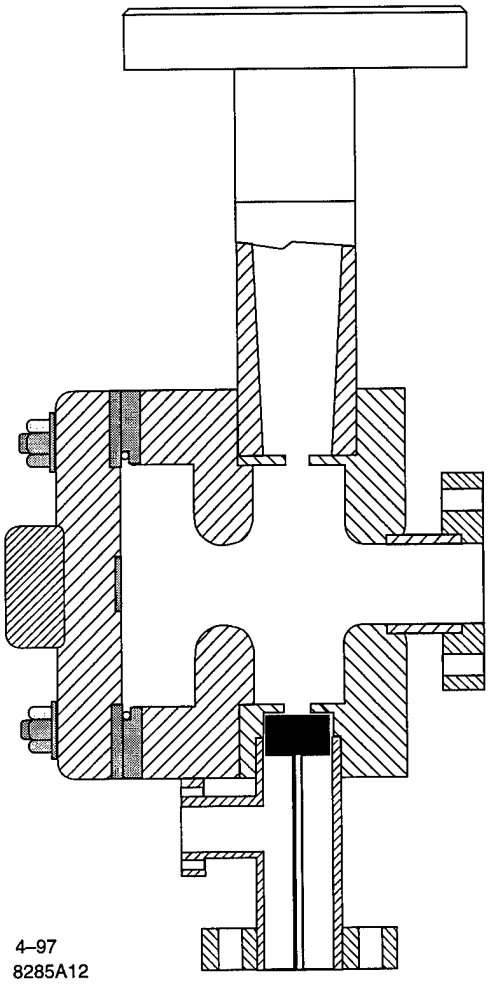



Figure 3: rf gun in the unsymmetrized case

low for uv light to illuminate the cathode at a grazing incidence angle of 72° from beam line and also prevents multiple scattering of the uv in the half cell of the gun. Since the half cell is full symmetrized the integrated asymmetry of the rf gun is only due the full cell.

In these experiments an stepping motor controlled UHV linear motion feed-thru drawing a shorting plunger with a total travel of 10 cm was used to symmetrize or unsymmetrize the full cell of the rf gun. The shaft of the linear motion feed-thru was connected to a OFHC copper shorting plug that had no direct rf current path between it and the vacuum pipe wall.

In the symmetrized case, the shorting plunger is 10 cm from the vacuum port iris and the rf coupled into the vacuum port decays exponential. There is a rf power monitoring loop located in the vacuum pipe which is -70 db down from the input power.

The unsymmetrized case is shown in figure 3 with the shorting plunger at the maximum travel of the linear motion feed-thru. This positions the plunger to within 1.25 mm from the back wall of the full cell to vacuum port coupling slot which is 2.25 mm thick. Therefore we were not able to fully unsymmetrize the full cell the rf gun. The vacuum coupling slot is never eliminated and allows for some degree of symmetrization, even in the symmetrized mode of operation.

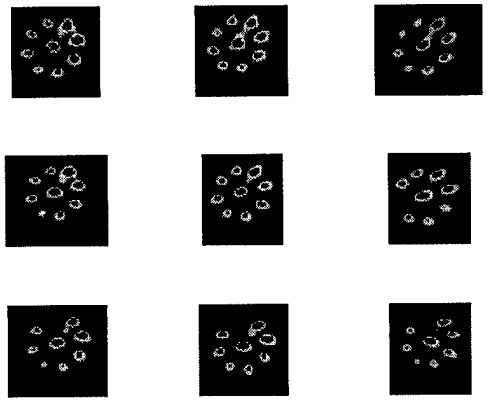


Figure 4: Beamlets profile with rf gun symmetrized

Another problem, in the unsymmetrized mode of operation, is that the vacuum tube and shorting plunger form a TEM coaxial transmission line and power is coupled from the full cell into the vacuum tube. In this case, the rf power monitoring loop is -20 db down from the input power. Combining the TEM coaxial transmission line problem along with our inability to fully unsymmetrize the full cell, a direct comparison of low power rf tests [4] and high power test is not possible.

## 3 HIGH POWER BEAM STUDIES

Phase variations in the rf gun, due to rf breakdown in the TEM coaxial conductor, prevented measurement of emittance growth due to gun asymmetrization from being conducted.

In the either mode of operation, the 8-fold beamlets were point to point focused, using the single emittance compensation magnet [5], to a beam-profile monitor screen located 66.4 cm from the cathode plane. The center beamlet profile in figures 4 and 5 represent the beamlet profiles in the symmetric and asymmetric mode of operation respectively, with the central beamlet on the geometric center of the rf gun. Mechanical alignment and dark current studies indicate that the geometrical and integrated electrical centers of the rf gun are with in 50$\mu$m of each other in the symmetrized mode. Steering the laser beam $\pm$ 1 mm on the x and y axis we are able to probe the electromagnetic field in the 1.6 cell rf gun out to a radius of approximately 2.4 mm and produce the eight additional images in both figures 4 and 5. It should be noted that the betatron rotation of the solenoidal magnet has been removed numerical from these images so that a direct comparison of the individual beamlet position and distortion can be directly compared to the full cells cavity penetrations.

In the analysis of the center 8-fold beamlets in figures 4 and 5 for the symmetrized and unsymmetrized mode of operation we have seem no centroid deflection for the outer

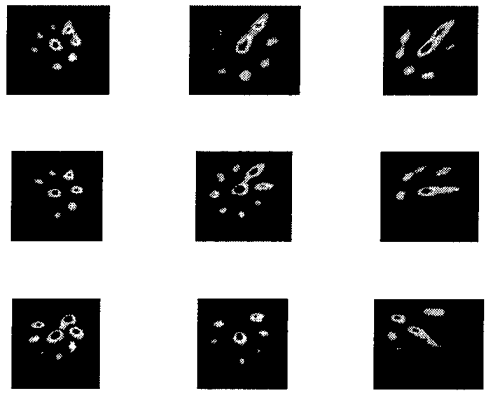


Figure 5: Beamlets profile with the rf gun unsymmetrized

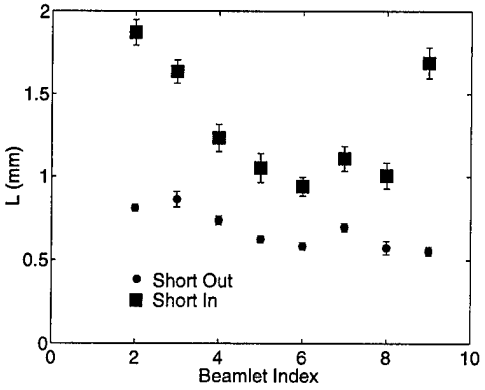



Figure 7: Individual beamlet radial extent

ring of beamlets with respect to the on axis beamlet, as is expected since the $TM_{110}$ magnetic field is uniform in the beam region of the cavity. This effect is seem in figure 6. The difference in total deflection between the different modes of operation is due to the peak rf field that the rf gun could hold off was lower in the unsymmetrized cases, since the vacuum/plunger TEM coaxial conductor would breakdown at the higher rf fields used in the symmetrized mode of operation. The normalized deflection in both modes are approximately the same.

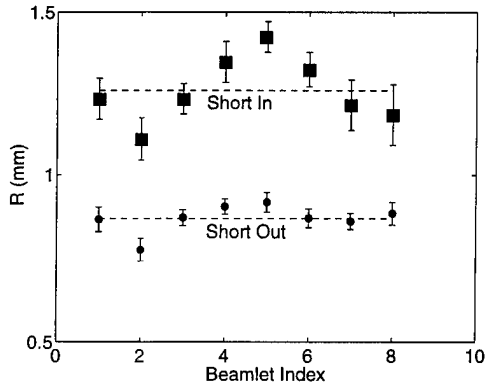



Figure 6: Beamlet centroid position from center beamlet

The effect of the symmetrized versus unsymmetrized mode of operation can be seem in figure 7. This figure represents the individual beamlets Full Width Tenth Maximum(FWTM) profiles. The data that represents the unsymmetrized mode of operation has a dominate dipole mode contribution as would be expected. In the symmetrized case the dipole contribution is minimized with the dominate mode being the quadrupole contribution, as would be expected from theory. Analyses is ongoing to fully understand this effect.

Multi-pole field effects were also studied by decreasing the laser spot size to 400 $\mu$m and setting the laser injection phase to the Schottky peak. This injection phase causes an effective electron bunch-lengthening and a noticeable energy-spread tail was observed. By adjusting the laser spot position we were able to eliminate this energy spread tail. This alignment minimizes the integrated higher-order-mode contribution to the beam distortion. Analysis indicates that the symmetrized BNL/SLAC/UCLA 1.6 cell photocathode rf gun's electrical and geometric center are within 170 $\mu$m of each other, which is within the laser spot alignment error. Compared to similar experimental results of the 1.5 cell BNL gun [6] whose electrical and geometric centers differ by 1.0 mm, the 1.6 cell gun has fulfilled the symmetrization criteria.

## 4 CONCLUSION

We have presented experimental data that indicates the dipole contributions has been significant reduced by symmetrizing the BNL/SLAC/UCLA 1.6 cell rf gun. Centroid deflection data is consistent with a uniform, magnetic field that is present with a $TM_{110}$ contribution to the $\pi$ accelerating mode. Beamlet energy spread profiles indicate the presence of a dominant dipole mode when in the unsymmetrized mode of operation and in the symmetrized mode the dominant mode is the quadrupole mode.

## 5 ACKNOWLEDGMENT

The authors would like to thank the technical staff at BNL, SLAC and at UCLA for all their dedicated work on this project.

## 6 REFERENCES

[1] B. E. Carlsten, *NIM*, **A285**, 313 (1989)

[2] D. W. Feldman *et al.*, IEEE J. Quantum Electronic, **27**, 12, 2636-2643 (1991)

[3] Z. Li, Ph.D. Thesis

[4] D. T. Palmer *et al.*, Proc. 1995 Part. Accel. Conf. (1995) p. 982

[5] D. T. Palmer *et al.*, Proc. 1997 Part. Accel. Conf., 2W.10

[6] X. J. Wang *et al.*, Proc. 1995 Part. Accel. Conf. (1995) p. 890

# POLARIZED ELECTRON SOURCES FOR FUTURE $e^+/e^-$ LINEAR COLLIDERS*

H. Tang, R.K. Alley, J.E. Clendenin, A.S. Fisher, T. Kotseroglou,
R.H. Miller, G.A. Mulhollan, D.T. Palmer and A.D. Yeremian
Stanford Linear Accelerator Center, Stanford University, Stanford, CA 94309

*Abstract*

Polarized electron beams will play a crucial role in maximizing the physics potential for future $e^+/e^-$ linear colliders. We will review the SLC polarized electron source (PES), present a design for a conventional PES for the Next Linear Collider (NLC), and discuss the physics issues of a polarized RF gun.

## 1 INTRODUCTION

Since 1992 the SLC has been operated exclusively with a polarized electron beam. Despite that the $Z^0$ boson production rate at SLC is nearly two orders of magnitude lower than at LEP, the use of a highly polarized electron beam with a beam polarization approaching 80% has vastly improved the physics luminosity of SLC and rendered it very competitive against LEP in the measurements of important Standard Model parameters such as the weak mixing angle $\theta_W$ [1]. For a future $e^+/e^-$ linear collider such as NLC, polarized electron beams will again play a powerful role in its physics programs. The benefits of using a highly polarized electron beam range from simply enhancing the luminosity to effectively extending its physics reach by suppressing backgrounds that would otherwise completely overwhelm the signal that one wishes to measure. Therefore, the development of a high performance PES is of crucial importance to future $e^+/e^-$ linear collider projects.

The successful operation of the SLC PES [2] has established the basic principles for the design, construction, and operation of accelerator-use polarized electron sources. In this paper, we will briefly describe the SLC PES, review its performance parameters and some of the fundamental properties of polarized electron photocathodes. We will then describe a conventional NLC PES design that is based on a DC high voltage photocathode gun similar to the one used in the SLC PES. In particular, we will discuss the necessary improvements in the photocathode design for the realization of an NLC PES. Finally, we will evaluate the feasibility of a polarized electron RF gun for the NLC from the standpoint of photocathode physics considerations.

## 2 THE SLC PES

At the heart of the SLC PES is a DC high voltage gun that utilizes a thin, $p$-type doped, strained GaAs semiconductor photocathode. The lattice distortion in the cathode induced by the strain removes a degeneracy between the heavy-hole and light-hole valence bands, making it possible for the generation of >50% polarized electrons from GaAs. The surface of the photocathode is treated with Cs and F to lower its workfuction to a so-called negative electron affinity (NEA) state, which enables the cathode to attain a high quantum efficiency and permits the use of photons with just enough energy to excite electrons from the valence band into the conduction band for yielding the highest possible electron beam polarization. The electron gun provides an ultrahigh vacuum environment suitable for prolonged operation of an NEA cathode and a sufficiently high extraction electric field at the cathode surface for the production of a high intensity electron beam. A Ti:sapphire laser system using frequency-doubled Nd:YAG for pumping generates two 2-ns laser pulses which are used to produce electron pulses from the gun, one for the collision beam and the other for the positron target drive beam. A bunching system consisting of two 178.5 MHz subharmonic bunchers (SHB) and one S-band buncher bunches the electron pulses into 20° of 2856 MHz S-band main linac RF. Table 1 lists the important operating parameters of the SLC PES.

An important discovery made during the course of PES R&D at SLAC was the cathode charge limit (CL) phenomenon [3,4]. In short, the CL effect states that, owing to the nature of an NEA semiconductor photocathode, its quantum efficiency (QE) in response to a laser pulse is increasingly suppressed with increasing laser pulse energy and the maximum integrated charge extractable during the pulse is limited to a value determined by the intrinsic properties of the cathode and the extracting field at the surface. The mechanism that appears responsible for the CL effect is the surface photovoltaic effect [5]. In the SLC PES, the maximum CL for a 2-ns pulse from an optimally prepared cathode is about $18\times10^{10}$ electrons, which is a factor of 2.6 higher than the PES's typical operating charge production level.

Some of the fundamental characteristics of the CL effect are summarized as follows. (i) Given an NEA photocathode with fixed operating conditions, the CL in general scales with its linear QE. (ii) The relaxation time for an NEA photocathode to recover from its suppressed QE state caused by the illumination of an intense laser pulse critically depends on the cathode's doping concentration — the relaxation time for the typical doping concentration of $5\times10^{18}$ $cm^{-3}$ used for the SLC PES is on the order of 100 ns whereas for a $2\times10^{19}$ $cm^{-3}$ doping it decreases to about 10 ns. (iii) For long pulse operations, i.e., with the pulse length longer than the cathode's relaxation time, the CL effect manifests itself as a limit in the maximum steady-state emission current from the cathode, and this maximum current is inversely proportional to the CL relaxation time. It is characteristic (iii) that bears the most significant implication for the

* Work supported by the U.S. Department of Energy under contract DE-AC03-76SF00515.

0-7803-4376-X/98/$10.00 © 1998 IEEE

development of a PES for a future $e^+/e^-$ linear collider such as NLC which requires a long (>100 ns) beam pulse.

**Table 1**: Operating Parameters of the SLC PES and Design Parameters of the NLC PES

| Parameters | SLC | NLC-II |
|---|---|---|
| Gun vacuum (Torr) | $<10^{-11}$ | $<10^{-11}$ |
| Cathode bias (kV) | −120 | −120 |
| Dark current (nA) | <25 | <25 |
| Extraction field (MV/m) | 1.8 | 2.0 |
| Photocathode area ($cm^2$) | 3.1 | 3.1 |
| Space charge limit (A) | 15.5 | 13 |
| No. bunches per pulse | 2 | 90 |
| Bunch spacing at gun (ns) | 62 | 1.4 |
| Bunch FWHM at gun (ns) | 2 | 0.7 |
| Bunch charge ($10^{10}$ $e^-$) | 7 | 2.8 |
| Peak current (A) | 5.6 | 6.4 |
| Average pulse current (A) | 0.4 | 3.2 |
| Beam polarization | ~80% | ~80% |
| Laser oscillator | Ti:sapphire | |
| Pulse energy (μJ) | 100 | 90×20 |
| Repetition rate (Hz) | 120 | 120 |
| No. of SHB's | 2 | 2 |
| SHB frequency (MHz) | 178.5 | 714 |
| rms $\gamma\varepsilon$ at 80 MeV (mm-mrad) | ~100 | 46 |

## 3 DESIGN OF THE NLC PES

In contrast to SLC which operates in a single bunch mode, the NLC is designed to collide 90 bunches of closely spaced $e^+$ and $e^-$ beams per pulse [6]. While the required single-bunch charge for the NLC is less than that of an SLC bunch, the integrated charge per beam pulse is more than an order of magnitude greater. Using the SLC PES as a design basis, we have completed a design of a conventional PES for the NLC [6]. The design includes a slightly modified SLC-type DC high voltage gun with a thin, improved strained layer GaAs cathode, a more complicated Ti:sapphire laser system with an additional stage for power amplification to produce the required high-power long pulse trains, and a subharmonic bunching system consisting of two 714 MHz SHBs and an S-band buncher. The design parameters for NLC-II, namely the 1.0 TeV center-of-mass energy machine, are summarized in Table 1, along side those of the SLC PES.

The single most challenging issue for materializing such a PES design lies with the photocathode technology. For this reason, we shall not concern ourselves with other issues, such as the laser system or the bunching system, for which there are no significant technological obstacles to overcome. The present generation of SLC strained GaAs cathodes have a CL or QE relaxation time of on the order 100 ns and a maximum steady-state emission current of about 0.7 A, which is only about 20% of the design value of the average pulse beam current for the NLC PES. To overcome this deficiency, improved photocathode charge performance is the key.

Cathode CL studies on a variety of photocathodes have shown that a 100 nm $2\times10^{19}$ $cm^{-3}$ doped strained GaAs photocathode, which differs from a standard SLC PES photocathode only in doping concentration (i.e., four times higher) appears capable of producing the required steady-state emission current for the NLC PES [6,7]. However, due to the increased doping density, the cathode's polarization performance is degraded significantly to the 60 – 65% range. To meet both the polarization and charge specifications of the NLC PES, the so-called graded doping scheme will be essential. By selectively doping a thin (~10 nm) surface layer of a 100 nm properly strained GaAs photocathode to a high concentration, e.g., $2\times10^{19}$ $cm^{-3}$, while leaving the remainder of the cathode (~90 nm) at low doping, e.g., $1\times10^{18}$ $cm^{-3}$ would be a good choice, high polarization and high charge production that meet the NLC requirements should be simultaneously achievable.

The charge performance of a GaAs photocathode may be further improved if the atomic cleanliness of the cathode surface can be preserved prior to an NEA activation. A thick As cap layer on the order of a few microns thick grown on top of the cathode at the end of growth by the manufacturer should accomplish this purpose adequately. As a result, a two-fold increase in the cathode's QE should be possible following an NEA activation, which should lead to a proportional increase in the charge production capability for the cathode. In addition, future R&D efforts will likely lead to further advancement in both photocathode and gun technologies. It is safe to conclude that our conventional NLC PES design is sound. If the bunch spacing is doubled, a major design change now under serious consideration, then, the required average pulse current will be halved, rendering our design even more feasible.

## 4 POLARIZED RF GUN CONSIDERATIONS

Because of the low beam emittance that an RF gun promises and a simplified injector design, i.e., without the need for a bunching system, a polarized RF gun utilizing an NEA GaAs photocathode is a very compelling idea. However, major technological breakthroughs are required towards the realization of a polarized RF gun, the most outstanding being attaining a $<10^{-11}$ Torr vacuum in an RF gun under operation so that an NEA cathode may have a reasonable lifetime. Technological difficulties aside, the physics of photoemission from NEA cathodes will play a deciding role as to whether the idea of an S-band polarized electron RF gun is a viable one in the first place. In the following we will address the main physics issues related to this question and show that there are no apparent fundamental problems with the RF gun idea.

An S-band RF gun is required to produce a beam with a bunch length less than ~20 ps, thus placing an upper limit on the cathode response time at about 10 ps. For an NEA photocathode, the photoemission response time is determined by the minority carrier (i.e., excited electron) diffusion coefficient and the thickness of the active layer, which is taken to be 100 nm as appropriate for an

optimally performing strained GaAs cathode. Assuming a bulk doping density of $1\times10^{18}$ cm$^{-3}$ for a graded doping GaAs cathode, the diffusion coefficient at room temperature is approximately 75 cm$^2$/s [8]. Then, on the average it will take about 1.3 ps for an excited electron to diffuse through the 100 nm thick active layer along the normal direction. Of course, most electrons will diffuse along off-normal directions and will take longer times to reach the surface (perhaps 2 ps on the average). More importantly, once an electron reaches the cathode surface it has a rather small probability (as small as a few percent as one study suggested [9]) of escaping at once. It will likely be reflected back into the cathode interior, bounce back and forth via interactions with the lattice and the backside surface, and need multiple emission attempts before finally escaping [10]. Taking all factors into account, we may place an estimated upper limit of 10 ps on the response time for our proposed GaAs cathode.

Recent measurements by Hartmann et al. using a 150 nm, $5\times10^{18}$ cm$^{-3}$ doping, strained $GaAs_{0.95}P_{0.05}$ cathode yielded a response time of 10 ps [11]. We note that the QE of this cathode was about ten times below the operating level required for NLC PES applications. A higher QE will lead to a slower response time. On the other hand, the thickness of the cathode we propose to use is 100 nm instead of 150 nm, and the response time scales quadratically with thickness. In addition, at a doping level of $1\times10^{18}$ cm$^{-3}$ the response time should be a factor of 2 faster due to an increased diffusion coefficient. Thus, the estimated $\leq$10 ps response time for our proposed cathode seems quite reasonable.

The other issue is whether an NEA cathode can produce the required single-bunch charge in an RF gun. The bunch charge requirement at the RF gun is $2.2\times10^{10}$ electrons (or 3.6 nC), which is taken to be 80% of the design value of the proposed conventional NLC PES as allowance for beam loss in the bunching process is no longer needed. Though this requirement is less than that in the conventional design, the charge must be extracted from the cathode within a much smaller area, e.g., ~2 mm (rms) radius, in order to generate a beam with a normalized rms emittance close to the desired mm-mrad level. This area is an order of magnitude smaller than the corresponding value chosen for the conventional design. Thus, the CL per unit area in the RF gun needs to be an order of magnitude higher than in an SLC-type gun.

Before proceeding to address this important question, it is advatangeous to clarify a few other issues which otherwise might complicate our discussion. (i) With an extraction electric field of >100 MV/m in an RF gun, which is nearly two orders of magnitude higher than that in an SLC-type gun, the space charge limit should not be a problem. Indeed, experiments with an S-band RF gun have demonstrated an order of magnitude higher charge production than required for the NLC for an emission area of 5 mm (rms) radius [12]. (ii) The CL on a much shorter time scale, i.e., 20 ps, should not be grossly different from the CL on a time scale of 2 ns, as in the case of SLC. The only reason that the CL should depend on the pulse length at all is because it has been defined, with a good reason, as the maximum extracted charge instead of the saturated charge when the laser pulse energy approaches "infinity". To first order, the saturated charge should not depend on the pulse length and is therefore a purely intrinsic parameter of the cathode itself. The CL as defined is attained in a transient state while the cathode is undergoing through a change from the initial low-intensity linear response state to the saturated (or constant yield) state and does indeed depend on the pulse length, albeit weakly. Based on the available 2-ns CL data, a good estimate on the CL for a 20 ps pulse would be about half the CL for a 2 ns pulse. (iii) Multiple bunch charge production should be much less of a problem for a cathode operated in an RF gun than in an SLC-type gun in the conventional design so long as single bunch charge production is adequate.

With everything else kept the same, the CL has been shown to scale almost linearly with the extraction field within a range from 0.15 to 1.8 MV/m [4]. If this scaling law remains valid up to the 100 MV/m field range typical for an S-band RF gun, then, the CL for a similar NEA cathode with a CL of $18\times10^{10}$ electrons in an SLC gun will be about $45\times10^{10}$ electrons in an RF gun with a pulse length of 20 ps and an emission area of 2 mm (rms) radius. This value is more than an order of magnitude greater than the single-bunch charge specification for the RF gun design, suggesting that the CL will not be a problem. While this conclusion is very encouraging, the linear scaling with extraction field is most questionable as this behavior is not satisfactorily understood. It is quite possible that the field dependence of the CL may deviate significantly from linear in an extended field range. If any deviation occurs, the dependence can only become weaker, which would make our estimate too optimistic, but unlikely off by an order of magnitue. Thus, it is fair to state that the above conclusion appears well justified.

## 4 REFERENCES


[1] See, for example, The LEP collaborations ALEPH, DELPHI, L3, OPAL; the LEP Electroweak Working Group; the SLD Heavy Flavour Group; "A Combination of Preliminary Electroweak Measurements and Constraints on the Standard Model", CERN-PPE/96-183 (1996).

[2] R. Alley, *et al.*, Nucl. Instrum. & Meth. A**365**, 1, (1995).

[3] M. Woods, *et al.*, J. Appl. Phys. 73, 8531 (1993).

[4] H. Tang, *et al.*, Proc. of *the Workshop on Photocathodes for Pol. Electrn Sources for Accel.*, Stanford, CA, p.344. (1993); H. Tang, *et al.*, Proc. of *the 4th Europ. Part. Accel. Conf.*, London, England, p. 46 (1994).

[5] A. Herrera-Gomez, *et al.*, J. App. Phys. **79**, 7318 (1996).

[6] The NLC Design Group, *Zeroth-Order Design Report for the Next Linear Collider*, Chapters 1 and 2, SLAC Report 474, (1996).

[7] H. Tang, *et al.*, Proc. of *the 11th Intern. Symp. on High Energy Spin Phys.*, Bloomington, IN, 641 (1995).

[8] S.M. Sze, *Physics of Semiconductor Devices*, 2nd Edition (John Wiley & Sons, NY,1981), pp. 29-30.

[9] A.S. Terekhov, private communication.

[10] In fact, a significant fraction of the excited electrons will fail to escape due to limited escape probability.

[11] P. Hartmann, *et al.*, "Picosecond polarized electron bunches from a strained layer GaAsP photocathode", to be published.

[12] R. Bossart, *et al.*, "A 3 GHz photoelectron gun for high beam intensity", CLIC Note No. 292, 1995.

# NLCTA INJECTOR EXPERIMENTAL RESULTS*

A. D. Yeremian, C. Adolphsen, R. H. Miller, C. D. Nantista, J. W. Wang
*Stanford Linear Accelerator Center*
*Stanford, California 94309*

*Abstract*

The purpose of the Next Linear Collider Test Accelerator (NLCTA) at SLAC is to integrate the new technologies of X-band accelerator structures and RF systems for the Next Linear Collider (NLC), demonstrate multibunch beam-loading energy compensation and suppression of higher-order deflecting modes, measure the transverse components of the accelerating field, and measure the dark current generated by RF field emission in the accelerator [1]. For beam loading R&D, an average current of about 1 A in a 120 ns long bunch train is required. The initial commissioning of the NLCTA injector, as well as the rest of the accelerator have been progressing very well. The initial beam parameters are very close to the requirement and we expect that injector will meet the specified requirements by the end of this summer.

## 1 INTRODUCTION

Much of the NLC related R&D for X-band accelerator systems can be accomplished with a simple bunch train, with bunches one X-band period apart. Thus a simple injector with only X-band components was chosen for the first phase of NLCTA. The possibility of upgrading the injector to produce the actual NLC bunch train format was taken into consideration during the design of the simple injector. For example enough space was left in the tunnel for additional beamline; magnet power supplies that would need to run at higher current for the upgrade were installed for the first phase. The fundamental frequency of the NLCTA as well as the NLC accelerator is 11.424 GHz.

The NLCTA injector consists of a thermionic gun, two X-band standing wave prebunchers, and two X-band traveling wave accelerators, and diagnostics as shown in figure 1. The phase velocities of the first three cavities of the first accelerator are tapered from 0.6c to 0.9c to accommodate the less than c speed of the electrons entering the accelerator. After the first few cavities the electrons reach the speed of light. Following the injector is a chicane which is currently set up to be isochronous. The profile monitor in the high dispersion region of the chicane is used to measure the beam energy spread from the injector. Current, beam position, profile, bunch length, energy, energy spread, and emittance monitors throughout the injector allow for tuning and measurement of the necessary electron beam parameters.

The injector was constructed based on simulation results using PARMELA and SUPERFISH [2]. The Injector has been producing 0.5 A, 120 ns long, 55 MeV electron bunch trains routinely during the initial commissioning of NLCTA. Very recently we have turned the current up to 1 A, but this report primarily addresses the injector commissioning at 0.5 A current.

## 2 BEAMLINE SETUP

The electrons are produced from a DC HV thermionic gun with a grided 2 $cm^2$ cathode, operated at 10 Hz. Flat top electron pulses of up to 2 A, 20 to 130 ns variable length, with a 5 ns rise and fall time electron pulses are generated from the gun by pulsing the grid. For a typical operations we have been generating 0.5 A, 120 ns pulses at the gun. This pulse is bunched and chopped into bunches in every X-band period by the first prebuncher. The bunching is further enhanced by the second prebuncher and the first 0.9 m buncher/accelerator section. The second 0.9 m section is used to further accelerate the beam.

One RF station, consisting of a single, 11.424 GHz, klystron and a SLED II [3] system powers both prebunchers and the two 0.9 m accelerator sections. Independent phase and amplitude control is available for each of the RF components in the injector [4]. According to simulation predictions a gap voltage of 8 and 30 KV is required in the first and second X-band prebunchers respectively for optimum bunching. The gradient in the two 0.9 m traveling wave sections should be about 50 MeV/m including the beam loading compensation. Beam loading compensation is accomplished by introducing a ramp in the leading 50 ns of the RF pulse until the beam loading reaches a steady state [5]. The plan is to condition the injector system to operate with 90 MW, 225 ns, RF power available to each of the 0.9 m accelerating sections. Currently for steady operating conditions we run with 155 MW, 225 ns RF power out of the SLED system. After accounting for losses in the rectangular wave guide and coupling of RF into the prebuncher systems, we currently have 65 MW available for the injector accelerating sections for routine operation. We have been able to achieve the 90 MW requirement during processing and expect to be able to run routinely at 90 MW soon.

The magic-T type phase-shifter/attenuator for the prebunchers [4] currently do not operate in an orthogonal fashion, because the prebunchers are overcoupled and are not matched to their respective magic-T. This makes it very difficult to tune the bunching parameters of the beam. Each prebuncher will be isolated from the Magic-T so that the phase and amplitude can be changed in an orthogonal fashion. We expect this to be very helpful in the proper setup of the injector bunching parameters.

The transverse beam profile is managed with axial magnetic field from solenoids covering the injector from the gun to the end of the second accelerator section. A bucking coil is used to zero the field at the cathode. The experimental settings for the solenoids are as required by

* Work supported by Department of Energy contract DE-AC03-76SF00515

0-7803-4376-X/98/$10.00 © 1998 IEEE

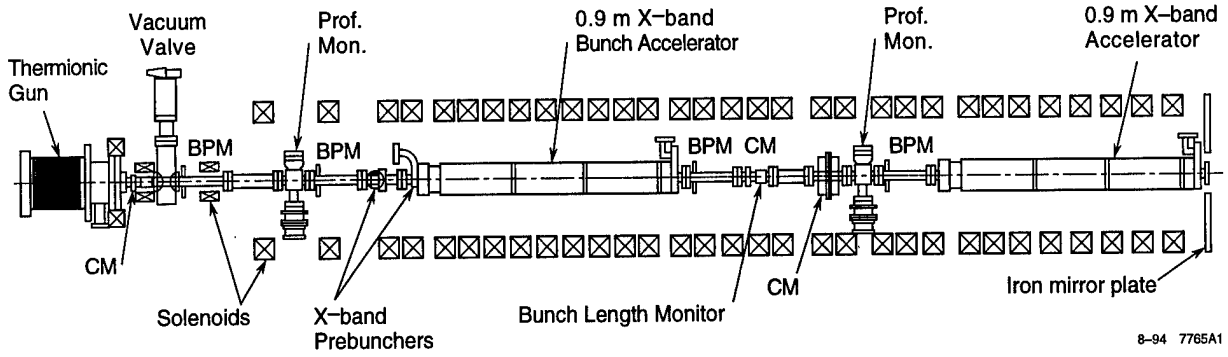



Figure 1. The NLCTA injector layout

simulations and the beam is to be optimized at these settings.

The current from the gun is measured and set using a gap current monitor [6], while the current out of the injector and after the chicane is measured with toroids [7]. The energy and energy spread of the beam are measured with the profile monitor in the high dispersion region of the chicane and the emittance of the beam is measured using quad scans and a screen upstream and downstream of the chicane [8]. Bunch to bunch energy and energy spread variations are measured at the end of the machine close to the final dump using a pulsed bend magnet with a ramped current to sweep the bunch train vertically for the duration of the pulse, while a DC bend magnet bends the bunches in the horizontal plane allowing the measurement of the energy spread, from the head to the tail of the train [5]. A bunch length monitor [4,9] after the first accelerator section is used to set the power and phase of the two prebunchers with respect to the first accelerator section for optimum bunching. The bunch length is not measured directly but is inferred from the minimum energy spread achievable as seen on the dispersion screen in the chicane and at the end of the linac.

## 3 EXPERIMENTAL RESULTS

Table 1. shows the achieved beam parameters, thus far, compared to the NLCTA requirements and expectations from simulation. While we have recently accelerated 1 A current from the gun, the data presented here is for 0.5 A, the current used for most of the initial running of NLCTA. Figure 2 shows the signal from the gap current monitor at the gun and the two toroids at the end of the injector and at the end of the chicane respectively. The slope on the top of the current pulses is a monitoring effect [7]. The actual current pulse shape is a flat top. The transmission from the gun to the entrance of the chicane is about 85% and the gun to the end of the chicane transmission is 75%.

**Table 1.** Initial NLCTA injector performance compared to requirements and simulated expectations.

| | Needed | Simulated | Experiment so far |
|---|---|---|---|
| Gun Current (A) | 1 | 1 | 0.5 |
| Gun pulse length (ns) | 120 | - | 120 |
| Transmission gun to end of injector. (%) | - | 84 | 85 |
| Power in accelerator sections (MW ) | 90 | 90 | 65 |
| Energy at chicane with 65 MW in ea. acc. sec. (MeV) | | 70 | 55 |
| Energy spread at the chicane FWHM (%) | < 0.5 | 0.3 | 0.6 to 1 |
| Emittance out of injector rms ( $10^{-5}$ m- rad) | <5 | 1 | 5 to 8 |

Figure 3 shows the energy spread for the entire 120 ns long macro pulse at the dispersion screen in the chicane. The FWHM energy spread is 0.6 to 1%, twice as high as the requirement. Inproved bunching energy spread is expected after the full commissioning of the injector.

With 65 MW available for each of the injector accelerating sections the expected electron beam energy at the end of the injector is 70 MeV for 0.5 A beam, however, we measure 55 MeV. At the end of the first accelerator section the beam is ahead of the crest by about 40 degrees, thus resulting in lower energy and larger energy spread than we expected. To minimize the energy spread at the end of the injector we phase the beam behind the RF wave crest in the second accelerator. This results

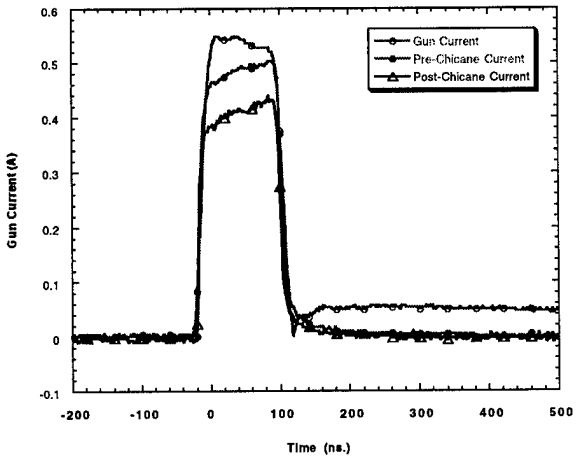



**Figure 2.** Electron beam current transmission from the gun to the exit of the chicane. The slope at the top of the current pulse is actually a monitoring effect.

in further reduction of energy out of the injector than expected from simulation. It is presently not clear why the beam is 30 degrees more ahead of the RF wave crest than expected from simulations. This problem can be studied more carefully this summer once the injector is operating at the design RF power level.

The measured normalized rms emittance before and after the chicane is 5 to 8 x $10^{-5}$ m-rad. This emittance is good enough for beam loading compensation R&D at the NLCTA however we expect it will improve by about a factor of two after the full commissioning of the injector.

## 4 SUMMARY

The initial commissioning results from the NLCTA injector show that NLCTA will meet the NLC R&D requirements it was designed for. The electron beam is very close to meeting the initial design goals, and with further RF processing and commissioning scheduled for this summer we expect to achieve these goals.

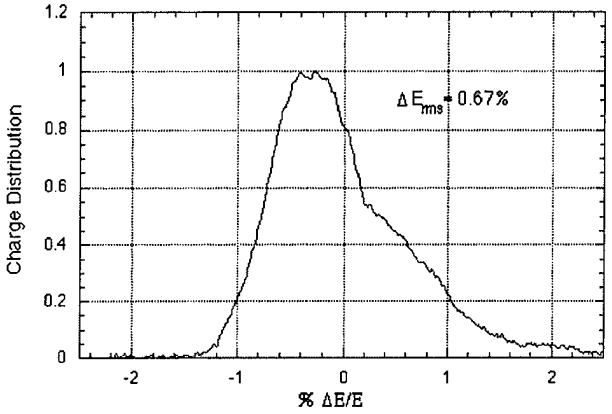



**Figure 3.** Energy spread as measured on the high-dispersion screen in the chicane for a 120 ns, 0.5 A beam from the gun.

## 5 ACKNOWLEDGEMENTS

We are grateful to the Mechanical Engineering, Microwave, Controls, Power Conversion, Fabrication and Operation groups for their diligence and persistent attention to detail that has contributed to the successful operation of the NLCTA injector.

## 6 REFERENCES

[1]. R. Ruth et. al., " Test Accelerator for the Next Linear Collider", SLAC PUB - 6293, 1993.

[2]. A. D. Yeremian et. al., Next Linear Collider Test Accelerator Injector Design and Status", Proceedings of LINAC 94, Tsukuba Japan, August 1994, p 89.

[3]. S. G. Tantawi, et. al., "The NLCTA Pulse Compression and Transportation system", proceedings of EPAC 96, Barcellona Spain, 1996.

[4]. J. W. Wang, et. al., "RF System for the NLCTA", these proceedings.

[5]. C. Adolphsen, et. al., "Beam loading Compensation in the NLCTA", these proceedings.

[6]. R. F. Koontz and R. H. Miller, "Nanosecond Electron Beam Generation and Instrumentation at SLAC", IEEE proceedings on Nuclear Science, Vol 22 no. 3, June 1975, p1350.

[7]. C. D. Nantista, et. al., "Beam Current Monitors in the NLCTA", These proceedings.

[8]. C. D. Nantista, et. al., "Beam Profile Monitors in the NLCTA", These proceedings.

[9] R. H. Miller, "Proposed Bunch Monitor", SLAC TN-63-65, August, 1963

# A PROPOSED INJECTOR FOR THE LCLS LINAC*

A. D. Yeremian, V. K. Bharadwaj, P. Emma, R. H. Miller,
D. T. Palmer, M. D. Woodley
*Stanford Linear Accelerator Center*
*Stanford, California 94309*

*Abstract*

The Linac Coherent Light Source (LCLS) will use the last portion of the SLAC accelerator as a driver for a short wavelength FEL. The injector must produce 1-nC, 3-ps rms electron bunches at a repetition rate of up to 120 Hz with a normalized rms emittance of about 1 mm-mrad. The injector design takes advantage of the photocathode rf gun technology developed since its conception in the mid 1980's [1], in particular the S-band rf gun developed by the SLAC/BNL/UCLA collaboration [2], and emittance compensation techniques developed in the last decade [3,4]. The injector beamline has been designed using the SUPERFISH, POISSON, PARMELA, and TRANSPORT codes in a consistent way to simulate the beam from the gun up to the entrance of the main accelerator linac where the beam energy is 150 MeV. PARMELA simulations indicate that at 150 MeV, space charge effects are negligible.

## 1 BEAMLINE

The injector beamline for LCLS consists of a 1.6 cell S-band photocathode rf gun, 4 SLAC type 3 m S-band constant gradient traveling wave accelerator sections, emittance compensation solenoids at the gun (after accelerator section 2 and after accelerator section 3), a 14° achromatic, isochronous translation bend system (dog-leg) into the main linac, and instrumentation for beam diagnostics as shown in Fig. 1.

The rf distribution system is also shown in Fig. 1. Two un-SLEDed 5045 klystrons will be used: one to power the gun and the first two accelerator sections and the other for the last two accelerator sections. High power rf attenuators and phase shifters will allow independent control of the rf power, phase and amplitude for the gun and each of the first two accelerating sections.

Many diagnostics have been designed into the injector to characterize the beam and to aid in tuning the injector. In the drift section from the gun to the first accelerator there will be a beam position monitor (BPM) a current monitor, and a profile screen/Faraday cup pop-in device. A mask in the laser beam into the photocathode can be used to produce beamlets in various patterns to study emittance trends from the gun, or just as a tuning aid to optimize the steering. After each accelerator section there is a BPM, a current monitor, and a screen. After the second accelerator section there is a bunch length monitor which is an x-band cavity outside the beamline near a ceramic gap in the beamline [5]. While this monitor will not characterize the longitudinal bunch profile, it will be a useful tuning aid to minimize the bunch length.

A full transverse emittance diagnostic section is included prior to the dog-leg which consists of four wire-scanners [6] separated by 45° of $x$ and $y$ betatron phase advance. The matched input beam produces an $x$ and $y$ rms beam size of 67 $\mu$m at each wire. A fifth wire scanner in the dog-leg allows the energy spread measurement. Emittance and energy scrapers are also planned in this region.

## 2 SIMULATION

Emittance growth and compensation in the LCLS injector from the gun to the end of the fourth accelerator section has been thoroughly studied using PARMELA simulations. The electric field map of the rf gun was obtained with SUPERFISH and directly used in PARMELA. SUPERFISH was used to simulate the fields in the traveling wave accelerator sections and space harmonics were calculated for use in PARMELA. The rf fields were assumed to be cylindrically symmetric. Much care has been taken to symmetrize the dominant dipole rf fields in the gun [2] thus assuming cylindrical symmetry in the rf fields is not unreasonable.

A magnetic field map for the solenoid magnets at the gun was produced using POISSON and passed to PARMELA. Single coils were used to represent magnetic fields from solenoids between accelerator sections.

Space charge effects were included assuming cylindrical symmetry. For these simulations, the thermal emittance at the cathode and the emittance growth due to multipole electric fields were ignored. The magnetic and electric fields in the gun and the accelerator region were optimized to minimize the emittance at 150 MeV at which point the normalized emittance is virtually constant.

The peak electric field in the gun is 150 MV/m at the cathode and the laser is injected at 23 degrees ahead of the rf crest. In the first and second accelerator sections the centroid of the beam is about 5 degrees ahead of the crest and the gradient is 7 MV/m. This introduces about a 1.5% energy spread for the full beam at the exit of the second accelerator but helps slightly in emittance compensation. This energy spread is removed by the third accelerator section by phasing the rf such that the beam arrives

* Work supported by Department of Energy contract DE-AC03-76SF00515

0-7803-4376-X/98/$10.00 © 1998 IEEE

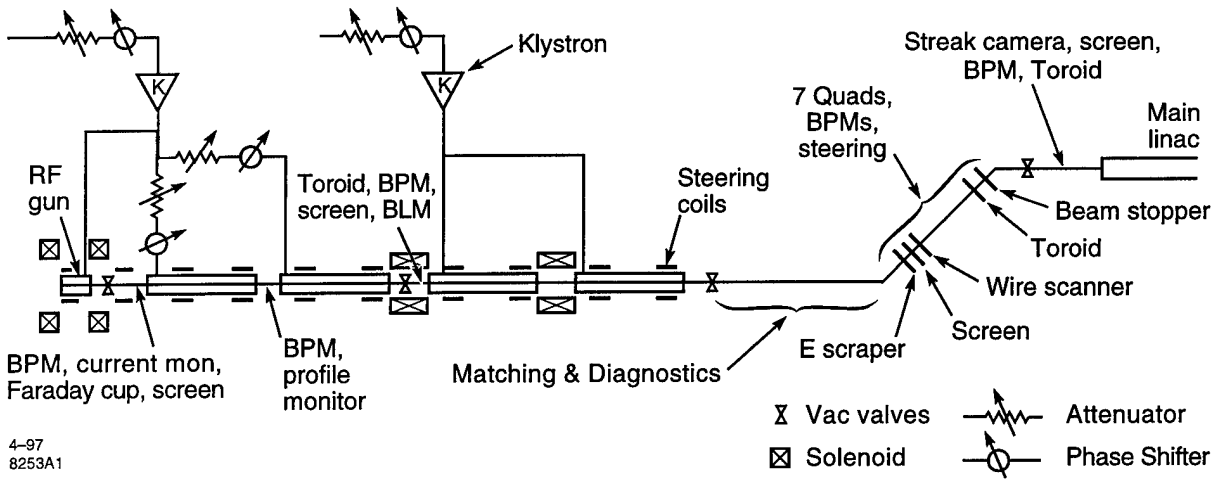



**Figure 1.** Beamline layout from rf gun to injection into the SLAC main linac. The 'matching & diagnostics' section includes matching quadrupoles, 4 wire scanners for transverse diagnostics, 4 phase space scrapers, a toroid, BPMs and a streak camera station for bunch length measurements. The two dog-leg inflector bends follow the diagnostic section.

slightly behind the crest. The gradient of the third and fourth accelerator sections is 17 MV/m.

The magnetic field at the gun is generated by two solenoids placed symmetrically up and downstream of the cathode such that the axial magnetic field at the cathode is zero. The field then rises sharply after the cathode to about 3 kG with an effective length of about 20 cm. The axial magnetic field between accelerator sections is slightly greater than 3 kG with an effective length of 70 cm. Fig. 2 shows the axial magnetic fields along the length of the beamline where $s = 0$ is the cathode location.

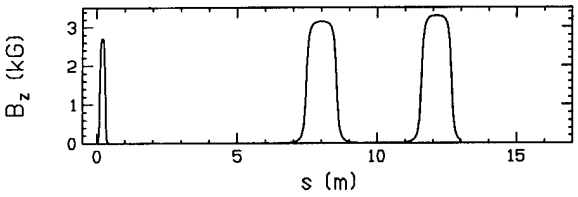



**Figure 2.** Solenoidal magnetic field along the beamline from the cathode ($s = 0$) to the 150 MeV point.

At the cathode, the edge beam radius is about 0.9 mm dictated by emittance compensation—a balance between space charge, magnetic field, and electric field effects. At the entrance of accelerator-section-3, however, radial rf fields have a more dominant effect on emittance growth than space charge since the beam energy is nearly 50 MeV In addition, the accelerating gradient in section-3 is more than twice that of sections 1 and 2. Thus the beam radius is drastically reduced at the entrance of the third accelerator section to reduce the emittance growth due to radial electric field effects.

The transverse distribution at the cathode is assumed to be uniform, but the temporal shape is assumed to be a truncated Gaussian achieved by using a Gaussian pulse with an rms of 4.4 ps which is then truncated at $\pm 2\sigma$. The overall rms length is then 3.8 ps. In fact, a uniform temporal distribution is more desirable for optimal emittance compensation, however a truncated Gaussian results in a bunch-compression system which is much less sensitive to injection timing jitter [7].

It should be noted here that simulations indicate a 40% shorter beam at 150 MeV than at the cathode due to bunching because the laser is fired 23 degrees ahead of the rf. However there is experimental indication of bunch lengthening in the 1.6 cell S-band rf gun at these current densities which is not manifested in PARMELA simulations [8]. Thus the expected bunch length at 150 MeV may be longer than indicated in simulation by possibly 30-40%. Fig. 3 shows the temporal and energy distributions and phase space as well as an $x$-$y$ particle scatter plot of the simulated bunch at 150 MeV.

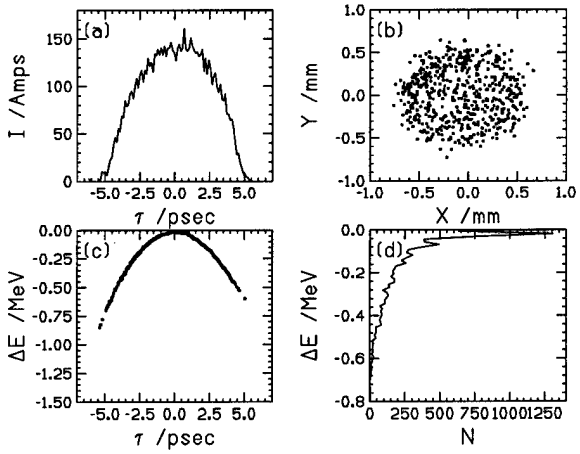



**Figure 3.** Temporal distribution (a), $x$-$y$ space (b), longitudinal phase space (c), and energy distribution (d) at 150 MeV for Table 1 parameters.

Fig. 4 is a plot of the horizontal normalized emittance ($\beta\gamma\varepsilon_x$, where $\beta \equiv v/c$) along $s$ for an optimized parameter set of the injector beamline shown in Fig. 1. Bunch parameters at the end of the fourth accelerator section are

given in Table 1. The core emittance (excluding a 7.7% halo) at 150 MeV is 1.08 mm-mrad for the truncated Gaussian temporal bunch shape.

If a uniform distribution with rise and fall of less than 1 ps is used at the gun, the emittance at 150 MeV is 0.95 mm-mrad (excluding a 3% halo). We have also simulated the 1 nC, uniform transverse and Gaussian temporal bunch truncated at $\pm 4\sigma$ (i.e. nearly a full Gaussian pulse). In this case the core emittance at 150 MeV is 1.07 mm-mrad with the exclusion of 8.1% halo.

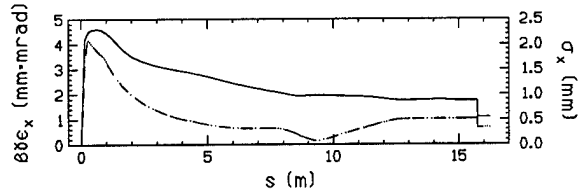



**Figure 4.** Normalized emittance (solid) and rms beam size (dash) along the beamline from cathode ($s$ = 0) to 150 MeV. The step at $s$ ~ 16 m is a 7.7% halo cut (in simulation only).

**Table 1.** Simulated electron beam parameters at 150 MeV.

| | | |
|---|---|---|
| Longitudinal distribution | — | Gaussian |
| Transverse distribution | — | uniform |
| Bunch charge | nC | 1.0 |
| Halo population | % | 7.7 |
| rms pulse length | psec (mm) | 2.3 (0.69) |
| Energy | MeV | 150.5 |
| rms relative energy spread | % | 0.13 |
| Norm. rms core emittance | mm-mrad | 1.08 |

## 3 DOG-LEG INFLECTOR

The function of the dog-leg inflector is to transport the 150 MeV electron beam from the new injector linac into the existing SLAC linac. It is possible to design the dog-leg as a first bunch compression stage, but this necessitates a large incoming correlated energy spread of 1-2% and the chromaticity of the quadrupole magnets within the dog-leg—required for linear achromaticity—generate large second order dispersion which requires sextupole compensation. Due to this, and also the need to tune the momentum compaction of the compressor (not natural in a dog-leg), the dog-leg is designed as a simple transport line, not a compressor.

The design requirements of the line are: 1) should provide a horizontal beamline inflection of ~1 meter over a few meters distance, 2) should not alter the bunch length (isochronous), and 3) should introduce no significant transverse emittance dilution. The inflection may also be made in the vertical plane or a rolled plane. However, there is no strong motivation to do so. A simple system which satisfies these conditions is composed of two dipole magnets of opposite strength separated by a **+I** optical transformer (seven quadrupoles) to produce a linear achromat. The dipoles are rectangular bends.

The beamline is 4 meters long with two 14°, 20-cm long bends providing the ~1 meter inflection. This produces a momentum compaction, $R_{56}$, of 4 mm. An extreme electron which is off energy by 1% will move axially by 40 $\mu$m which is small compared to the ~1 mm bunch length. The effect of the second order momentum compaction, $T_{566}$, is even less. Note, the incoming rms energy spread from the injector is 0.13%. The system is therefore, for all practical purposes, isochronous with no significant chromatic emittance dilution.

## 4 SUMMARY

The injector design for the LCLS takes advantage of the present development of photocathode rf gun technology to produce 150 MeV, 1 nC, 3 ps rms electron bunches with a normalized rms emittance of 1.1 mm-mrad. The necessary beamline and rf systems have been defined to produce such beams and the design includes sufficient diagnostic components to aide in the production and characterization of the electron bunches.

## 5 ACKNOWLEDGMENTS

We are grateful to Dr. Luca Serafini of INFN-Milan in Italy and Dr. James Rosenzweig of UCLA for many helpful discussions on the production and maintenance of the high brightness beams from rf photocathode guns.

## 6 REFERENCES

[1]. J. S. Fraser, et. al., "Photocathodes in Accelerator Applications", Proceedings of the IEEE Particle Accelerator Conference, Wash. DC, 1987, p 1705.

[2]. D. T. Palmer, et. al., "Microwave Measurements of the BNL/SLAC/UCLA 1.6 Cell Photocathode RF Gun", Proceedings of the 1995 IEEE Particle Accelerator Conference, Dallas, 1995, p982.

[3]. B. E. Carlsten, "New Photoelectric Injector Design for the LANL XUV FEL Accelerator", NIM, A285, 1989, p313.

[4]. L. Serafini and J. B. Rosenzweig, "Envelope Analysis of Intense Relativistic Quasi-Laminar Beams in RF Photoinjectors: A Theory of Emittance Compensation", to be published in Phys. Rev. E.

[5]. R. H. Miller, "Proposed Bunch Monitor", SLAC TN-63-65, August 1963.

[6]. M. C. Ross, et. al., "Wire Scanners for Beam Size and Emittance Measurements at the SLC", Proceedings of the IEEE Particle Accelerator Conference, San Francisco, 1991, p 1201.

[7]. V. K. Bharadwaj, et. al., "Linac Design for the LCLS Project at SLAC", these proceedings.

[8]. D. T. Palmer, et. al., "Emittance Studies of the BNL,/SLAC/UCLA 1.6 cell Photoacthode rf gun", these proceedings.

# THE CONSTRUCTION AND INITIAL HIGH POWER TEST OF AN X-BAND RF GUN

C.H. Ho, W.K. Lau, T.T. Yang, S.S. Chang, J.Y. Hwang, Y.C. Liu
Synchrotron Radiation Research Center, Hsinchu, Taiwan
G.P. Le Sage, F.V. Hartemann, and N.C. Luhmann, Jr.
University of California at Davis, Department of Applied Science, Davis, CA, USA

*Abstract*

The collaboration between the UC Davis Department of Applied Science (DAS), and the Synchrotron Radiation Research Center (SRRC) has reached high power test stage. An X-Band (8.5 GHz) high power rf cavity and a pair of solenoids were constructed at SRRC and installed at UC Davis at LLNL. The initial high power test results are presented.

## 1 INTRODUCTION

The requirements of high brightness and high intensity for relativistic electron beams for Free Electron Laser (FEL) and laser scattering and acceleration experiments have made the photoinjector an attractive source.

A collaborative research effort for the rapid development of the X-Band photoinjector system has been formed between UC Davis DAS, and SRRC. The high power, ultra-high vacuum, brazed structure was constructed at SRRC. The gun was installed and characterized at LLNL by the UC Davis DAS personnel and the SRRC staff.

## 2 DESIGN AND CONSTRUCTION

Extensive simulation runs using the codes SUPERFISH and PARMELA predict an energy of 4.3 MeV with a peak gradient of 150 MV/m, corresponding to a drive power of 9 MW [1]. With a microbunch charge of 0.1 nC, the predicted transverse, rms, invariant emittance is less than 1 p mm-mrad at the gun exit. The energy spread for this case is 0.31 %. A prototype X-Band rf accelerator cavity has been fabricated at SRRC, and has been characterized and optimized at UC Davis DAS [2].

The 3-D drawing of the high power cavity constructed is shown in Fig. 1.

A 22.5 cm long, 200 turn, 3.400 kG solenoid is installed at the exit of the rf gun for focusing the diverging beam. An identical bucking solenoid is located at an equal distance behind the cathode plane, providing zero field on the cathode surface where the electron beam is photoemitted.

The measured field profile at the maximum drive current of 256 amps is found to be in excellent agreement with the simulation.

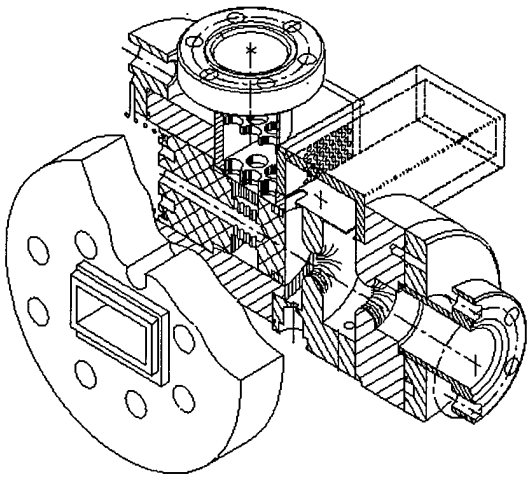


Figure 1: High power cavity 3-D drawing.

The first brazed RF accelerator cavity that was produced had a few problems. The brazing joints between the various cavity components failed between the water cooling channel and the inner surface of the RF cavity. All cavity leaks were sealed with vacuum epoxy. External cooling was applied in the form of heat sink and copper tubing wound around the body of the accelerator cavity.

## 3 HIGH POWER TEST RESULTS

Final cold test adjustments of the high power cavity were performed to achieve critical coupling, regardless of field balance. As verified by measurements with the Klystron presented later in this section, the cavity resonances were separated by a few MHz. Fortunately, critical coupling of the Klystron signal corresponded to half cell coupling. Critical coupling allowed the accelerator to be safely used as a resonant load for the Klystron despite this non-optimized condition. In addition, since the half cell was energized, high energy photoelectron production is still possible. Acceleration of field emission electrons is presented later in this section.

0-7803-4376-X/98/$10.00 © 1998 IEEE

| Day | Peak Input Power [kW] | Repetition Rate [Hz] | Conditioning Time [Hours] |
|---|---|---|---|
| 1 | 17 | 2 | 2 |
| 2 | 78.5 | 5 | 4 |
| 3 | 188 | 30 | 4 |
| 4 | 480 | 30 | 4 |
| 5 | 1500 | 20 | 4 |
| 7 | 1910 | 20 | 4 |

Table 1: Initial RF Conditioning Summary

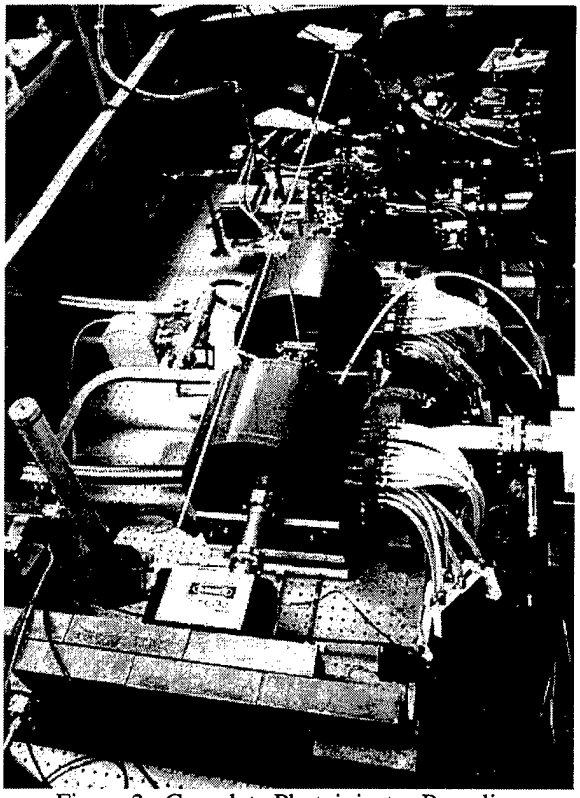


Figure 2: Complete Photoinjector Beamline

The RF cavity was baked at 125 °C for four hours prior to final installation in the RF system. The experimental apparatus is shown in Fig. 35. The base pressure obtained after the bake was in the range of $10^{-9}$ Torr. The waveguide feed and RF cavity vacion pumps were in the low $10^{-9}$ Torr range when high power RF operation was initiated. An attenuator between the TWTA and Klystron reduced the RF power production of the Klystron in the early stages of RF conditioning. The modulator was operated up to a 30 Hz repetition rate, which greatly reduced the conditioning time required to reach the MW level of drive in the RF cavity. The initial progress of the RF conditioning is summarized in Table 1. Figure 2 shows the whole experimental setup.

For the initial measurements of the dark current signal from the RF gun, a Faraday cup consisting of a ceramic DC break and a blank conflat flange was attached directly to the output of the accelerator. Resistors were attached across the ceramic break to provide a return path for the electron dark current. A matched load of 50 W was constructed using 20 1 kW Carbon resistors in parallel. This arrangement minimizes inductance and allows measurement of short time scale events. Very large electron current signals were measured when arcing occurred inside the RF cavity. These corresponded to electrons drawn from a plasma in the gun. Vacuum levels as measured by Vacion pumps near the accelerator cavity reached the $10^{-7}$ Torr range following especially large RF breakdown events.

The peak charging voltage seen by the capacitance of the scope and coaxial cable gives the total charge collected during each RF pulse. Assuming that the RF pulse length remains constant, the collected charge corresponds to the current level during the RF pulse. The electric field scaling inside the RF cavity is found directly by taking the square root of the drive power. These power levels can be scaled to the expected gradient on the photocathode surface given the simulated correspondence between the cathode gradient and drive power (Fig. 3).

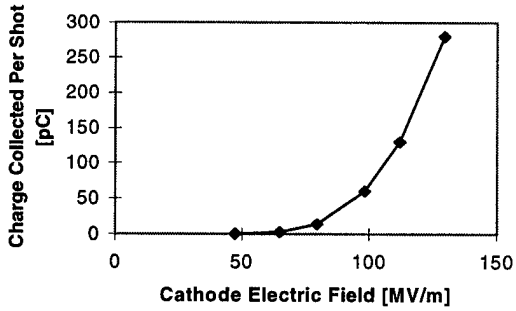



Figure 3: Dark Current Charge Collection

Given the form of the dark current, a plot of $\ln\left(Q/E^2\right)$ versus $1/E$ indicates field emission scaling, as shown in Fig. 4. The electric field in this case is determined using the square root of the drive power multiplied by a factor that gives the cathode field for a balanced p-mode. The points fall along a fairly straight line, indicating field emission current, as opposed to emission due to other mechanisms. The linear fit of the data points, and an extrapolation to the expected dark current level corresponding to an acceleration gradient that produces 4.3 MeV electrons is displayed as the top point on the trace. The expected integrated charge at that gradient is ~ 1.6 nC, corresponding to an average current of 0.8 mA, compared to 1 kA of peak current for photoemitted electron bunches with 1 nC of charge emitted in 1 ps.

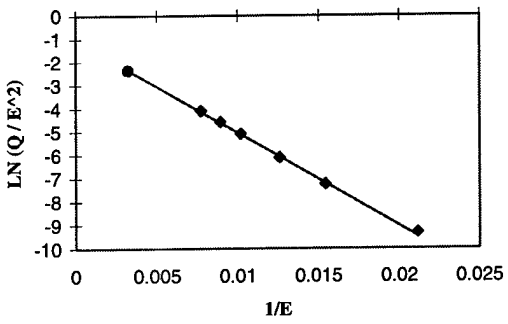



Figure 4: RF Cavity Fowler-Nordheim Field Emission Curve

The horizontal and vertical steering of the crossed dipole electromagnets were used on separate occasions to characterize the energy of the dark current beam. Since the profile did not distort significantly with steering, one can assume that the dark current spot on the phosphor screen was fairly monochromatic, as indicated by the Fowler-Nordheim field emission dependence. Electrons with energy significantly lower than the phosphor spot were likely overfocused by the solenoids and spilled on the walls of the laser feedthrough or gate valve. This may explain why the beam which did propagate the entire 35.85 in from the photocathode plane to the phosphor screen appeared to have a relatively small energy spread. The result of the first dipole scan of electron energy is shown in Fig. 5. The linear fit of the deflection versus drive current indicates electron energy of 321 keV, gained by the electrons in the first cell (5.42 mm).

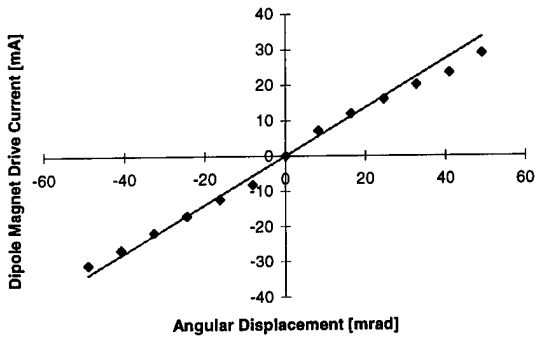



Figure 5: First Energy Scan: 0.321 MeV Electrons

## 4 SUMMARY

The cavity was conditioned to the multi MW level, with peak surface fields in excess of 150 MV/m. Field emission or "dark" current measurements were performed, and matched to theoretical expectations. Electron energy was also measured. Phase noise and jitter characteristics were measured for the TWTA, Klystron, and resonant accelerator cavity. Phase stabilization measurements were conducted with the high power cavity at the multi MW, >150 MV/m level.

Despite the limitations of the first attempt for the high power cavity and the absence of a functioning pump laser, valuable data and experience were obtainable with the parts that were available. Input power levels in excess of 2 MW were applied to the resonant cavity. Processing of the accelerator from the 200 kW level to the 2 MW level was achieved in less than 1 week. Accelerating gradients (at the photocathode) in excess of 170 MV/m were verified. A beam generated by field emission was transported through the beamline and diagnostics. Beamline focusing and steering elements were utilized, and the field emission electron energy was determined.

With a second attempt at a balanced, leak-free cavity and a stable laser system proceeding, the data presented in this section represents the complete operation of the high power RF system, and the complete characterization of the resonant accelerator cavity.

## 5 ACKNOWLEDGMENTS

We would like to thank Dr. G. Westenskow (LLNL) and Dr. Y.J. Chen (LLNL) for many useful discussions and suggestions. We also would like to thank Dr. Roger Miller (SLAC) and Dr. Dian Yeremian (SLAC) for useful insight directly prior to cavity machining. This work is supported in part by the National Science Council (Taiwan), as well as by MURI (USA) under contract F49620-95-1-0253, by ATRI (USA) under contract F30602-94-2-0001, and by DoE (USA) under contract DE-FG03-95ER54295.

## 6 REFERENCES

[1] G.P. Le Sage, et al., "A Ghz Repetition Rate X-Band Photoinjector", in AIP Proc. for the 7 th Workshop on Advanced Accelerator Concepts(Oct. 12-18, 1996, Lake Tahoe, California, USA).

[2] C.H. Ho, et al., "The Design and Fabrication of an X-Band RF Gun", in AIP Proc. for the 7 th Workshop on Advanced Accelerator Concepts(Oct. 12-18, 1996, Lake Tahoe, California, USA).

# AN INJECTION MODELOCKED TI-SAPPHIRE LASER FOR SYNCHRONOUS PHOTOINJECTION

Curt Hovater and Matt Poelker
Thomas Jefferson National Accelerator Facility
12000 Jefferson Ave., Newport News, VA 23606

*Abstract*

The CEBAF 4 GeV accelerator has recently begun delivering spin-polarized electrons for nuclear physics experiments. Spin-polarized electrons are emitted from a GaAs photocathode that is illuminated with pulsed laser light from a diode laser system synchronized to the injector chopping frequency (499 MHz) [1]. The present diode laser system is compact, reliable and relatively maintenance-free; however, output power is limited to less than 500 mW. In an effort to obtain higher average power and thereby prolong the effective operating lifetime of the source, we have constructed an injection modelocked Ti-sapphire laser with picosecond pulsewidths and gigahertz repetition rates. Modelocked operation is obtained through gain modulation within the Ti-sapphire crystal as a result of injection seeding with a gain-switched diode laser. Unlike conventional modelocked lasers, the pulse repetition rate of this laser can be discretely varied by setting the seed laser repetition rate equal to multiples of the Ti-sapphire laser cavity fundamental frequency. We observe pulse repetition rates from 223 MHz (fundamental) to 1560 MHz (seventh harmonic) with average output power of 700 mW for all repetition rates. Pulsewidths ranged from 21 to 39 ps (FWHM) under various pump laser conditions.

## 1 INTRODUCTION

Historically, successful operation of spin-polarized electron sources has been subject to maintaining a long photocathode lifetime. Photoelectron yield (i.e., quantum efficiency) diminishes with time for a number of reasons [2]; eventually the photocathode must be reactivated or replaced. Such procedures are labor and time intensive and reduce polarized-electron beam availability. For this reason, there is great interest within the accelerator community to develop methods for enhancing the effective operating lifetime of the source. Although laser issues do nothing to address the causes for quantum efficiency degradation, a high power laser source allows gun operation for a longer period of time before the photocathode must be reactivated or replaced.

A new approach to synchronous photoinjection is to use a modelocked Ti-sapphire laser [3]. Modelocked Ti-sapphire lasers are high power, tunable light sources with pulse repetition rates typically less than 100 MHz. Basu et al., used a gain switched diode laser to injection seed a Ti-sapphire laser pumped with a Q-switched doubled Nd:YAG laser [4]. They obtained 19.4 ps (FWHM) pulses at a rate of 200 MHz within the Q-switched macropulse. In a similar manner, we report using a gain-switched diode laser to modelock a slightly modified, commercial standing-wave Ti-sapphire laser. In contrast to work reported in Ref. 4, the pulse repetition rate of the modelocked Ti-sapphire laser was varied by setting the diode seed laser repetition rate equal to different multiples of the Ti-sapphire laser cavity fundamental frequency. Pulse repetition rates from 223 MHz to 1.56 GHz were observed with 700 mW average output power for all repetition rates. In this manner, GHz repetition rates are obtained with manageable cavity length (70 to 30 cm) and no intracavity modelocking elements are necessary. The gain switched diode laser serves as a simple, stable master oscillator; it is a trivial matter to obtain gain-switched pulse repetition rates to 4 GHz [5] suggesting that operation at even higher repetition rates may be achieved with this method.

## 2 EXPERIMENT

### *2.1 Injection Modelocked Ti-Sapphire Laser*

Experiments were performed with a modified Spectra Physics Ti-sapphire laser Model 3900 (Fig. 1). The flat high-reflector (HR) mirror supplied with the laser was replaced with a 2% transmissive "input" coupler. The input coupler serves as an input port for the seed laser beam. Both the output and input coupler mirrors were wedged at 2 degrees to avoid etalon effects that might cause undesirable optical feedback. The Ti-sapphire crystal (20 mm x 5 mm dia.) was mounted on a water-cooled copper heat sink. The pump laser was focused into the crystal with a 15 cm radius of curvature mirror and approximately 80% of the pump laser light was absorbed. The free running Ti-sapphire laser operated at ~ 852 nm. When pumped with 6 W of green light from a multiline argon laser, the Ti-sapphire laser emitted 700 mW through output coupler mirror (5% transmissive) and 300 mW through the input coupler. The cavity length was 67 cm as determined by observing the beat signal between different longitudinal modes of the laser using a fast photodiode (Optoelectronic Model PD-15) and an RF spectrum analyzer.

The seed laser (SDL 5410-G1) was gain switched the usual way [5]. The laser was biased near threshold and an RF signal (~ 1 W) of the appropriate frequency was added using a bias-tee network. It was important to

0-7803-4376-X/98 /$10.00 © 1998 IEEE

operate the diode laser within a narrow range of DC bias current. Beyond this range, pulsewidths broadened and/or secondary pulses were observed with the fast photodiode and sampling oscilloscope (Tektronix Model 11801B with SD-32 sampling head). The average output power from the gain-switched diode laser was approximately 5 mW although there was some variation associated with pulse repetition rate. The wavelength of the diode laser output was ~ 859 nm, roughly 7 nm different from the free-running Ti-sapphire laser wavelength. The gain-switched diode laser output was passed through an optical isolator (approx. 40 dB isolation) and then directed into the Ti-sapphire laser cavity through the 2% transmissive input coupler.

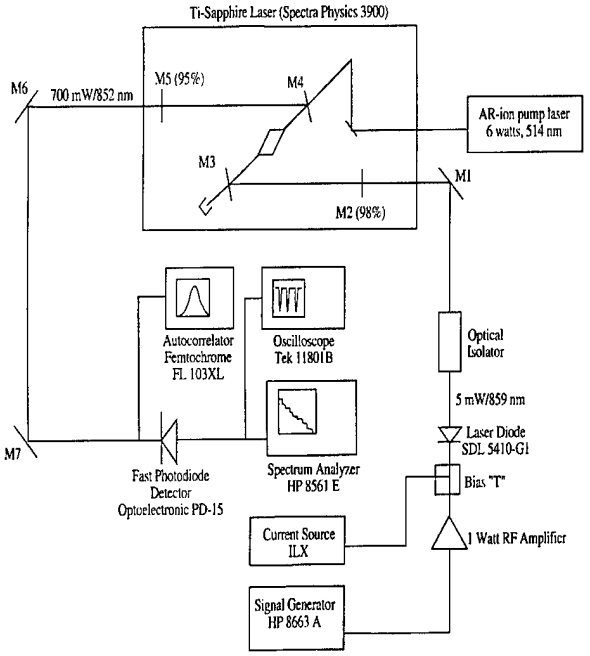



Figure 1. Schematic of the injection modelocked Ti-sapphire laser.

The Ti-sapphire laser output went from DC to pulsed modelocked when the seed laser was aligned to ensure proper spatial modematching between the two lasers and the pulse repetition rate of the seed laser was set to within 10 kHz of the Ti-sapphire laser cavity fundamental frequency (or harmonic). We believe that modelocking occurs as a result of gain modulation caused by the presence of the seed laser beam within the Ti-sapphire laser crystal. The pulsed seed laser extracts gain from the Ti-sapphire laser crystal, which effectively serves to provide period loss in a manner similar to an acoustooptic modulator within a conventional modelocked laser. It was a relatively simple matter to obtain pulse repetition rates equal to harmonics of the Ti-sapphire laser cavity fundamental frequency; only the frequency of the RF signal applied to the diode laser was changed (Fig. 2). We observed pulse repetition rates up to 1.56 GHz, the seventh harmonic of the Ti-sapphire laser cavity fundamental frequency. The modelocked average output power remained nearly the same compared with DC operation; maximum average power through the output coupler was 700 mW with 6 W pump power. The wavelength of the modelocked Ti-sapphire laser output was ~ 854 nm, which was 2 nm different from the free-running operation and 5 nm different from the seed laser wavelength. Unfortunately, the laser in its present state suffers from severe pulse-to-pulse amplitude noise. There were brief periods of amplitude-stable pulsed operation. Typically, however, slight adjustments to the seed laser alignment were necessary and/or the seed laser pulse repetition rate needed to be adjusted by several kHz to reestablish amplitude-stable pulsed output.

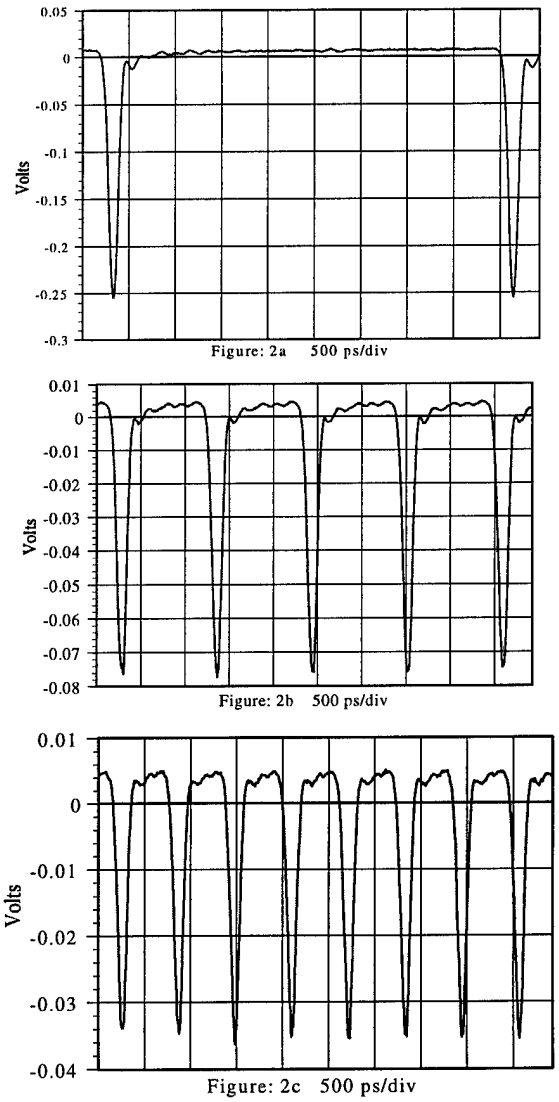



Figure 2. Oscilloscope traces showing the fast photodiode signals for three different pulse repetition rates: a. 223 MHz, b. 892 MHz, and c. 1.56 GHz.

### *2.1. Pulsewidth Measurement*

Autocorrelator measurements were performed to ascertain gain-switched diode seed laser and modelocked

Ti-sapphire laser pulsewidths. The autocorrelator (Femtochrome Model FR-103XL) relies on non-colinear, background-free second harmonic generation within an $LiIO_3$ crystal. The seed laser pulsewidth was ~ 47 ps (FWHM), a value consistent with gain-switched operation of common diode lasers. Modelocked Ti-sapphire laser pulsewidths ranged from 21 to 39 ps (FWHM); pulsewidth increased with higher pump laser power.

*2.2. Phase Noise Measurement*

Phase noise measurements were performed to quantify pulse timing jitter of the gain-switched diode laser master oscillator and modelocked Ti-sapphire slave laser. These measurements were performed with an HP 8563B spectrum analyzer and vendor-supplied software. Integrated RMS phase noise (10 Hz to 1 MHz) was measured at the fifteenth harmonic of the fundamental frequency. Measurements indicate that phase noise on the seed laser pulsed output is slightly less than 0.1 degree, a value comparable to the phase noise of the synthesized source used to excite gain-switched operation. A phase noise plot of the modelocked Ti-sapphire laser output is shown in figure 3.

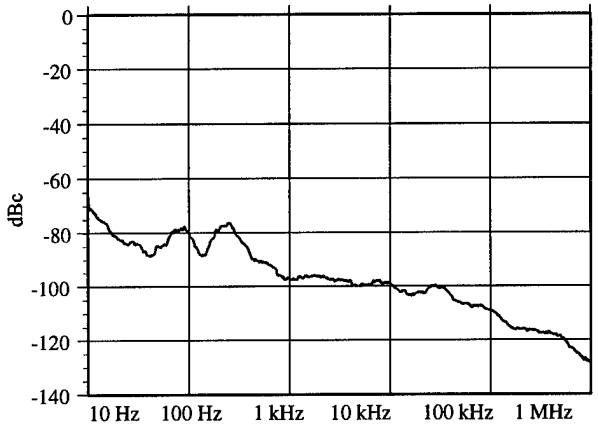



Figure 3. Phase noise measurement of the Ti-sapphire laser at 223 MHz measured at the 15th harmonic.

The integrated RMS phase noise is 0.2 degrees, a value two times that of the gain switched diode laser output. Phase noise of 0.2 degrees corresponds to timing jitter of 2.5 ps. This value compares favorably with the Jefferson Lab IRFEL modelocked Nd:YLF drive laser and is adequate for most photoinjector applications [6].

## 3 SUMMARY

Although pulse-to-pulse amplitude fluctuations prevent the laser in its present state from being used for photoinjection, it has a number of appealing features that warrant further research. The laser emits GHz pulse repetition rates that meet Jefferson Lab requirements and average output power is higher than can be obtained from the diode laser system presently used. Modelocked Ti-sapphire laser pulsewidths range from 21 to 39 ps (FWHM) and will provide manageable electron beam at Jefferson Lab that is not dominated by severe space charge effects. The modelocked Ti-sapphire laser has low timing jitter as a result of injection seeding using a simple, stable gain switched diode laser. We are presently designing a Ti-sapphire laser that incorporates active cavity length control in an effort to minimize amplitude noise on the Ti-sapphire laser output. The new laser will also use an intracavity Faraday rotator to force unidirectional, traveling wave oscillation in an effort to reduce amplitude noise associated with spatial hole burning within the Ti-sapphire crystal. In addition, unidirectional traveling wave oscillation will provide for more efficient output coupling. The present laser design has an output coupler and an input coupler. Although it was not discussed in detail, there is significant pulsed output that is wasted through the input coupler (~ 40%). The new ring cavity, design has one mirror that serves as both the output and input coupler. All of the pulsed output is usable because the seed and Ti-sapphire laser beams are not colinear when oscillation within the Ti-sapphire laser is forced to be unidirectional. In conclusion, the results presented here provide "proof of principle" that injection modelocking using a gain switched diode laser is a promising method to obtain high power, pulsed laser light with GHz pulse repetition rates.

## 4 ACKNOWLEDGEMENTS

Authors would like to thank Chris Cuevas who assisted in the data acquisition. This work was supported by the U.S. Department of Energy under contract number DE-AC05-84ER40150.

## REFERENCES

[1] M. Poelker, Appl. Phys. Lett ., **67**, 2762 (1995).
[2] K. Aulenbacher, Proc. of the Workshop on Photocathodes for Polarized Electron Sources for Accelerators, edited by M. Chatwell et al., SLAC Report 432 rev. p. 1, 1993.
[3] J. Hoffmann, P. Hartmann and C. Zimmermann, accepted for publication Nucl. Instrum. Meth. A.
[4] S. Basu, P. May, and J. M. Halbout, Opt. Lett., **14**, 1272 (1989).
[5] P.T. Ho, in *Picosecond Optoelectronic Devices*, edited by C. H. Lee (Academic, New York, 1984).
[6] M. Shinn and S. Benson, Proc. IEEE PAC, 1052 (1995).

# ATOMIC HYDROGEN CLEANING OF SEMICONDUCTOR PHOTOCATHODES

C. K. Sinclair, B. M. Poelker, and J. S. Price, Thomas Jefferson National Accelerator Facility, 12000 Jefferson Avenue, Newport News, VA 23606

*Abstract*

Negative Electron Affinity (NEA) semiconductor photocathodes are widely used for the production of polarized electron beams, and are also useful for the production of high brightness electron beams which can be modulated at very high frequencies. Preparation of an atomically clean semiconductor surface is an essential step in the fabrication of a NEA photocathode. This cleaning step is difficult for certain semiconductors, such as the very thin materials which produce the highest beam polarization, and those which have tightly bound oxides and carbides. Using a small RF dissociation atomic hydrogen source, we have reproducibly cleaned GaAs wafers which have been only degreased prior to installation in vacuum. We have consistently prepared very high quantum efficiency photocathodes following atomic hydrogen cleaning. Details of our apparatus and most recent results are presented.

## 1 INTRODUCTION

NEA photocathodes have two broad areas of application as electron sources for accelerators. They are at the heart of essentially all polarized electron sources in use at the present, and they provide a high quantum efficiency photocathode for the generation of high brightness beams which may be modulated at very high frequencies [1]. These cathodes are formed on atomically clean surfaces of direct bandgap semiconductors by the addition of cesium and an oxidant, typically oxygen or nitrogen trifluoride. The preparation of an atomically clean surface on the semiconductor is an essential step in this process, and the quantum yield of the resulting photocathode depends strongly on the quality of the result achieved in the cleaning step [2]. Most cleaning techniques used to date have employed some type of wet chemical processing prior to the introduction of the semiconductor material into the gun vacuum system, followed by heating the cathode to high temperatures in the gun after a suitable ultrahigh vacuum environment has been established. More recently, with the use of epitaxially grown semiconductors, it has been possible in some cases to grow a protective cap layer on the semiconductor surface which can later be removed by heating in vacuum.

Each of the above cleaning methods has its drawbacks. Wet chemical processes typically remove a significant amount of material - more than is present in the case of the thin layers which produce the highest beam polarization, for example. Heating in vacuum cannot remove certain oxides and carbides from many semiconductors. Heating in vacuum may also crack residual gases and thereby create contamination on the semiconductor surface. Heating may damage some of the specialized semiconductor structures developed to provide either high polarization or high quantum yield. Finally, growth of protective cap layers has a record of mixed success to date, and cannot be done with all methods of epitaxial growth.

It is highly desirable to have a cleaning process which can be employed in ultrahigh vacuum; which will remove all oxides, carbides, and other contamination without removing a significant amount of the base semiconductor material; and which will minimize the maximum temperature and the temperature-time product of any heating cycles involved. Cleaning by exposure to atomic hydrogen meets all of these criteria.

It is well established that the exposure of many III-V, II-VI, and elemental semiconductors to atomic hydrogen, typically at modestly elevated temperatures, produces a semiconductor surface entirely free of contamination [3]. In particular, atomic hydrogen exposure is capable of removing such difficult contaminants as oxygen on silicon, and carbon on GaAs. This cleaning process, possibly followed by a heating cycle, leaves surfaces which show sharp LEED patterns, indicating good stoichiometry and surface order. The process is readily adaptable to *in situ* use in ultrahigh vacuum.

## 2 CLEANING PROCEDURE DEVELOPMENT

Our initial experiments were done by placing the sample to be cleaned in DC hydrogen glow discharges in various geometries. These experiments demonstrated clear evidence for surface cleaning in some cases, both by Auger measurements on the cleaned surface, and by the photoresponse of the cleaned surface to cesium. However, we also saw evidence of transport of contamination from the chamber walls to the semiconductor surface. In addition, it was difficult to imagine adapting this scheme for use in an ultrahigh vacuum electron gun. Accordingly, we decided to develop an RF dissociation atomic hydrogen source.

Our atomic hydrogen source is a modification of one developed for use in a polarized atomic hydrogen target [4]. It employs a helical resonator surrounding a 2.5 cm diameter Pyrex tube containing the hydrogen. Ultrapure hydrogen is admitted to this chamber through an ultrahigh vacuum leak valve. Atomic hydrogen exits the discharge

0-7803-4376-X/98/$10.00 © 1998 IEEE

region through a small aperture (typically 1 mm or smaller), and is conducted to the sample to be cleaned by an aluminum tube. Aluminum is chosen as it has a low atomic hydrogen recombination coefficient. The resonator is made of stainless steel, as it is within the region subject to ultrahigh vacuum bakeout. The source is mounted on a multiport stainless steel vacuum chamber which contains the sample, ultrahigh vacuum pumping, and apparatus to permit the illumination and fabrication of a NEA photocathode on the clean sample. The sample itself is mounted on a stalk which may be heated, and which is identical to those used in our photoemission electron guns. The complete apparatus, including the atomic hydrogen source, is bakeable to 250 C, and is shown schematically in Figure 1.

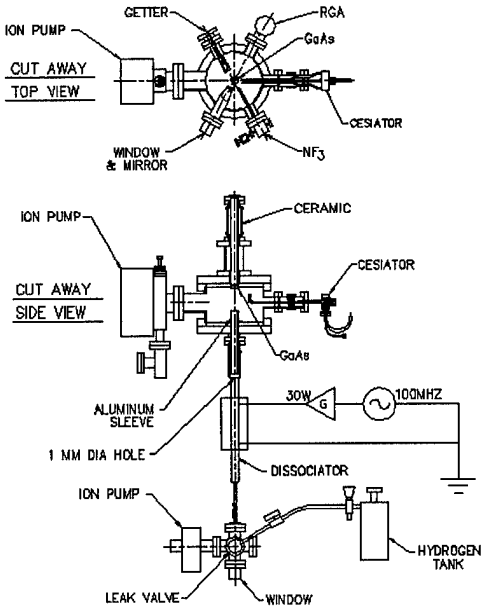



Figure 1. Schematic view of the experimental apparatus.

Following an initial vacuum bakeout, the chamber pressure typically fell below $10^{-8}$ mbar within a few hours after careful dry nitrogen backfilling and the introduction of a new sample. At these low pressures, it is feasible to conduct atomic hydrogen cleaning and cesium photoresponse measurements without the need for a time consuming bakeout. This allowed us to make a large number of photoresponse measurements relatively easily, to establish suitable parameters for the atomic hydrogen cleaning process. We determined the proper RF frequency, power and hydrogen pressure to achieve a high degree of hydrogen dissociation and a good atomic hydrogen flux on the sample, as well as the cleaning time and sample temperature which resulted in the best photoresponse to cesium. While hydrogen dissociation occurs over a broad range of hydrogen pressure and RF frequency, it is necessary to consider recombination as well as dissociation to obtain the optimum cleaning conditions. With our resonator, we typically operate with 40 W of RF power at 90-110 MHz, and a hydrogen pressure of 24-30 mbar. We estimate the atomic hydrogen flux at the sample is of order $10^{16}/cm^2/sec$.

Much hydrogen, both molecular and atomic, enters the vacuum chamber during the cleaning, requiring a high hydrogen pumping speed. In the test chamber, this was provided by a 30 l/s DI pump and a 220 l/s non-evaporable getter. The non-evaporable getter pumps hydrogen reversibly, and can be used for a large number of cleaning cycles. Under our conditions, the pressure in the main chamber during the cleaning cycle is below $10^{-5}$ mbar. Once the cleaning cycle is complete and the hydrogen flow stopped, the chamber pressure rapidly recovers to the ultrahigh vacuum range.

## 3 RESULTS

Once we established a reasonable set of parameters for the atomic hydrogen cleaning process in the unbaked chamber, we installed a wafer of relatively low dopant density (*ca* 2-3 x $10^{18}/cm^3$ Zn) bulk GaAs which had been only degreased. The entire apparatus was vacuum baked at 250 C for about 30 hours, and reached a base pressure below $10^{-10}$ mbar following cooldown. Atomic hydrogen cleaning of the sample was done at a sample temperature of ~ 300 C for 45 minutes. Following the cleaning cycle, the sample was heated to ~ 450 C to remove bound and sorbed hydrogen [3]. After cooling to room temperature, the sample was activated to NEA by the application of cesium and either nitrogen trifluoride or nitrous oxide.

A typical measurement of quantum efficiency as a function of wavelength is shown in figure 2. These results have been repeated in this apparatus on several similar GaAs samples. It is interesting to note that these very good quantum yields are obtained on samples with low dopant density. It is believed that higher dopant density is detrimental to producing the highest beam polarizations, but necessary for obtaining the highest quantum yields. It will be interesting to explore this tradeoff using the atomic hydrogen cleaning process.

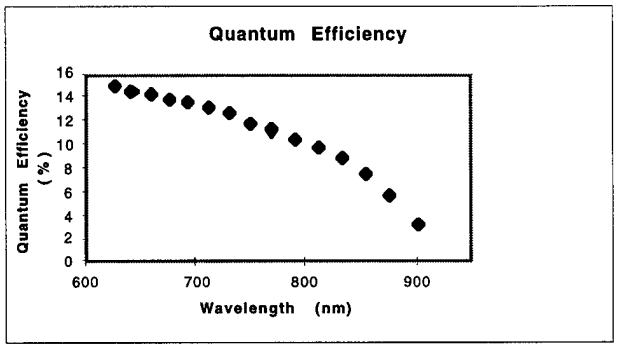



Figure 2. Quantum Efficiency versus wavelength for an NEA GaAs photocathode prepared after atomic hydrogen cleaning.

Following the excellent results above, we transferred this process to the polarized source group of the MAMI accelerator at Mainz. This group has obtained similarly good quantum efficiency on bulk GaAs, and has activated samples of thin strained GaAs with good results as well. The Mainz group has measured the beam polarization from atomic hydrogen cleaned bulk GaAs and found it to be normal [5].

Okada and Harris [3] have pointed out that the atomic hydrogen cleaning process leaves a fully passivated GaAs surface. It should thus be possible to transfer an atomic hydrogen cleaned GaAs sample through air without detrimental effects. Accordingly, we constructed a small "roll-around" atomic hydrogen cleaning station. Using this, we cleaned GaAs wafers, and, after venting the cleaning station to dry nitrogen, transported the cleaned wafers through room air and installed them in our photoemission guns. We have successfully prepared high quantum yield cathodes on wafers transported through air after atomic hydrogen cleaning.

We plan to incorporate the atomic hydrogen cleaning process directly into our photoemission guns. To do this, we have constructed a modified version of the atomic hydrogen source. In this design, the volume containing the hydrogen glow extends into the primary vacuum chamber of the electron gun. The atomic hydrogen exits through a small aperture directly below the cathode wafer. The RF resonator is outside the vacuum chamber. We have demonstrated that the glow in this arrangement extends fully into the vacuum, even though the RF excitation is entirely outside the vacuum. This source is mounted on a bellows, allowing us to position the exit aperture under the cathode for cleaning, and to remove it for electron beam operation. Tests will be conducted in a complete photoemission electron gun shortly.

## 4 ACKNOWLEDGMENTS

This work began in collaboration with Bruce Dunham at the University of Illinois. Khaled El-Amrawi and Dr. Hani Elsayed-Ali, of Old Dominion University, participated in some of the early measurements. Prof. Roy Holt of the University of Illinois provided support for the Pyrex glassblowing. This work was supported by the U.S. DOE under contract number DE-AC05-84ER40150.

## REFERENCES

[1] D. Engwall *et al.*, "*A High-DC-Voltage GaAs Photoemission Gun: Transverse Emittance and Momentum Spread Measurements*", these proceedings.

[2] J. J. Uebbing, J. Appl. Phys. **41**, 802 (1970); J. S. Escher in *Semiconductors and Semimetals*, v. 15, Academic Press, N.Y., 1981, p. 195.

[3] There is a very extensive literature on this topic, primarily directed to device applications. Recent examples include: Y. Luo *et al.*, Appl. Phys. Lett. **67**, 55 (1995); Y. Okada and J. S. Harris, J. Vac. Sci. Technol. **B14**, 1725 (1996); Z. Yu *et al.*, Appl. Phys. Lett. **69**, 82 (1996).

[4] M. Poelker *et al.*, Nucl. Instr. Meth. **A364**, 58 (1995).

[5] Peter Hartmann, Johannes Gutenberg Universität, Mainz, private communication.

# LASER SYSTEM FOR THE TTF PHOTOINJECTOR AT FERMILAB

A. R. Fry, M. J. Fitch, A. C. Melissinos, N. P. Bigelow, B. D. Taylor,
University of Rochester, Rochester, NY 14627
F. A. Nezrick, Fermi National Accelerator Laboratory, Batavia, IL 60510

*Abstract*

We have developed a solid-state laser system to meet the requirements of the TESLA Test Facility (TTF) photoinjector, currently under development at Fermilab. The laser produces a 1 MHz train of up to 800 equal-amplitude pulses with up to 1 mJ per pulse (0.8 J per macropulse) at $\lambda = 1054$ nm. The laser pulse train is produced by a phase-stabilized, mode-locked, Nd:YLF oscillator and a fast selection Pockels cell. The pulses are amplified in an Nd:glass amplifier chain consisting of a multipass rod amplifier and a 5-pass zig-zag slab amplifier. The laser system employs chirped pulse amplification (CPA) to produce 10 ps pulses. After fourth harmonic generation of the laser to $\lambda = 263$ nm, 10 nC electron bunches can be extracted from a $Cs_2Te$ photocathode in the RF gun.

## 1 TTF PHOTONINJECTOR DEVELOPMENT

A collaboration has been formed between FNAL, DESY, UCLA, INFN Milano, and the University of Rochester to develop a state-of-the-art photoinjector with a novel bunch structure for the Tesla Test Facility (TTF). The injector will consist of an RF gun[1] (UCLA, FNAL) with a high-quantum efficiency photocathode[2] (INFN Milano) driven by an advanced laser system[3] (Rochester), and a superconducting linear accelerator cavity (DESY).

The FNAL/TTF RF photoinjector is designed to match the requirements of the TTF accelerator[4], namely high bunch charge (8 nC), low emittance (< 20 mm-mr) and high duty cycle (1%). The TTF pulse train consists of 800 bunches of 8 nC, spaced 1 $\mu$s apart, with a 10 Hz rep rate. The beam optics are optimized for an overall injector consisting of the electron gun followed by one linac capture section and a dipole chicane for magnetic bunch compression[1].

## 2 LASER PERFORMANCE REQUIREMENTS

The production of high charge, high brightness electron beams place increasingly challenging demands on the drive lasers used with RF photoinjectors[5]. The design of a laser suited to the requirements of the TTF photoinjector is largely determined by the unique temporal beam structure and high laser pulse energy required to produced high-charge electron bunches.

The macropulse structure of the laser pulse train must produce the required 800 bunch electron pulse train. The width of each laser pulse must be small compared with the RF period, but not so small that longitudinal space charge effects become unmanageable in the electron bunch; the nominal design pulse length is 10 ps. The laser must be phase locked to the accelerator RF with minimum (< 1 ps) timing jitter.

Each laser pulse must have enough energy to emit the required bunch charge (10 nC) from the photocathode. UV photons are required for high quantum efficiency, so harmonic generation is used. Assuming a 1% efficient photocathode, 5 $\mu$J/pulse is required to produce 10 nC/bunch. At least 10 times this much energy per pulse must be available at the fundamental (infrared) laser wavelength.

The need for constant beam loading in the superconducting capture cavity requires high bunch charge stability. Each laser pulse in the pulse train must have the same energy as the others; our goal for the pulse train "flatness" is $\leq$5% deviation from the average energy in a 100 $\mu$s time scale. Similarly the energy per laser pulse should not vary significantly from shot to shot; this presents a considerable challenge for a pulsed laser system.

## 3 LASER SYSTEM

### *3.1 Overview*

A block diagram of the laser system is shown in Figure 1. A mode-locked Nd:YLF oscillator produces a low energy, continuous pulse train at 81.25 MHz. Pulses from the oscillator are stretched and chirped in a 2 km fiber. After the fiber, a train of 800 pulses is selected at 1 MHz from the oscillator pulse train by a high speed, low voltage, lithium tantalate (LTA) Pockels cell (Conoptics Inc., model 360-80 modulator). The narrow (18 ns) gate of the Pockels cell provides $\geq$ 50:1 discrimination of adjacent pulses.

Each of the 800 pulses are injected into a multipass amplifier which contains a flashlamp-pumped, $1/4 \times 6$ inch Nd:glass rod amplifier and a fast KD*P Q-switching Pockels cell (Conoptics Inc., model 350-105). Each pulse is trapped in the cavity by the Pockels cell and makes 20 passes through the cavity, amplifying up to 2 $\mu$J before it is ejected by the Pockels cell. A Faraday isolator separates the input and output pulses. Another flashlamp pumped, Nd:glass rod amplifier is used in a two-pass configuration to provide an additional gain of 5. The high energy amplification in the system is provided by a flashlamp-pumped, zig-zag, slab amplifier. The pulse train makes five passes in the slab to achieve a gain of up to 1000. The energy in each pulse after the slab amplifier is expected to be 1 mJ, which corresponds to 800 mJ in the macro pulse and 0.8 W average power at a 1 Hz repetition rate.

Following the slab amplifier, the beam is spatially filtered and then compressed in time using a pair of parallel diffraction gratings. The pulse length is adjustable from 3–

0-7803-4376-X/98/$10.00 © 1998 IEEE

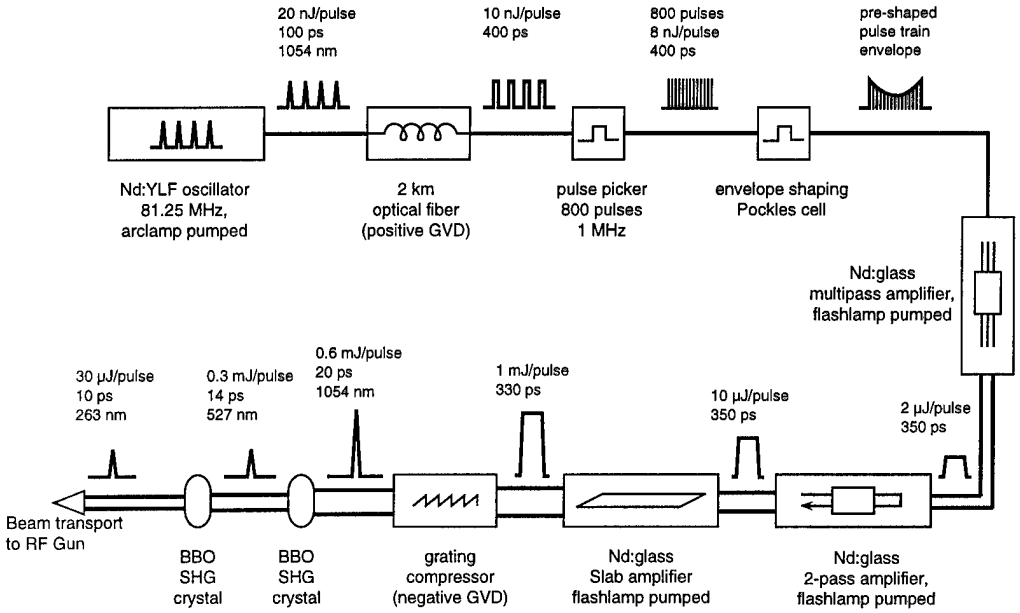



Figure 1: Block diagram of the FNAL/TTF photoinjector laser system.

30 ps. The pulses are frequency doubled and quadrupled in a pair of BBO crystals. The UV pulse train is expanded and transported 15 m in vacuum to a final set of imaging optics which relay the beam to the photocathode.

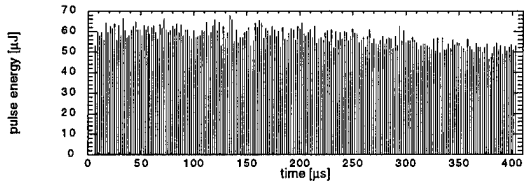



Figure 2: 200 pulses at 0.5 MHz spacing extracted from the multipass amplifier after 24 passes. The total pulse train energy is 11.5 mJ.

### *3.2 Laser Performance*

#### 3.2.1 Timing

The oscillator is mode-locked by an acoustooptic modulator which is phase-locked to the same master oscillator that produces the 1.3 GHz RF for the photoinjector. To reduce the timing fluctuations in the oscillator relative to the phase of the photoinjector RF, an electronic feedback loop is used to shift the phase of the mode-locker RF relative to the 81.25 MHz reference signal. We use a commercial phase-lock loop timing stabilizer (Lightwave Model 1000) designed specifically to stabilize the timing of mode-locked, solid-state lasers. A detailed description of the operation of the Lightwave stabilizer can be found in Ref. [6].

The oscillator timing jitter is measured by monitoring the laser output with a photodiode and a spectrum analyzer and measuring the relative powers of a high order (5–100) laser harmonic and its phase-noise sidebands; in the 81.25 MHz oscillator we measure a timing jitter of $\lesssim$2 ps RMS.

#### 3.2.2 Amplification

The multipass and 2-pass amplifiers were built and tested at FNAL during 1996–97. A train of 200 pulses at 0.5 MHz from the multipass is shown in Figure 2. The the glass and the mounting/cooling frame for the slab amplifier have been fabricated and assembled, and the 20 kJ, 1 Hz power supply for the four slab flashlamps is nearly complete. We expect to commission and test the slab amplifier during the summer of 1997.

The primary challenge in the laser system is in producing uniform amplification for all pulses in the 800 $\mu$s pulse train. The gain of each amplifier can vary substantially during the macropulse depending on the pump rate and the rate at which stored energy is extracted by amplifier action and spontaneous emission. An analysis of the time-dependent gain of the amplifier chain during the macropulse is given in Ref. [3].

In order to provide a flat-top macropulse laser energy profile, each of the laser amplifiers is driven by a custom designed power supply which provides nearly constant current discharge to the flashlamps for $\geq$800 $\mu$s.

An additional correction to the flatness of the macropulse envelope is made by pre-shaping the profile of the injected micropulses by means of an amplitude modulating Pockels cell. Preliminary results using a static correction pulse train shape have significantly improved the flatness of a train of 600 pulses (Figure 3). Preshaping the input pulse changes the gain loading of the amplifiers, so the input shape must be iteratively corrected to produce a flat output. We are currently working on an adaptive feedback system to monitor the the pulse train shape over several shots and produce a best-average-correction shape.

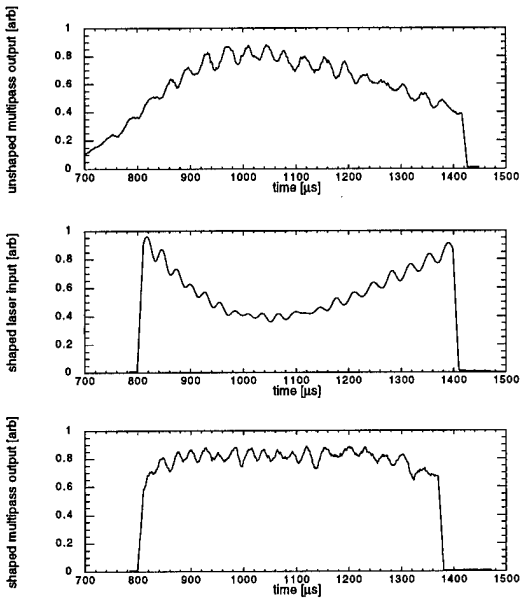



Figure 3: Amplified pulse train envelope with no preshaping (top), shaped input pulse train envelope (middle), and the resulting, amplified pulse train envelope (bottom).

Because the amplifiers are not run to saturation, the amplitude of the output is sensitive to small changes in the gain on a shot-to-shot basis. Consequently it is preferable to run with high gain and fewer passes in the multipass amplifier to reduce amplitude fluctuations. The peak flashlamp power required to achieve the necessary gain in the multipass amplifier limits the rep rate to $\leq$1 Hz.

Currently, the standard deviation of shot-to-shot pulse train energy is >40% of the average. We are working to improve the shot-to-shot variation by improving the optical alignment, designing resonator cavities for the oscillator and the multipass amplifier with increased mechanical stability, and adding feedback systems to the flashlamp power supplies.

### 3.2.3 Pulse Compression

Short, high energy pulses are produced using the technique of chirped pulse amplification (CPA)[7]. In CPA, pulses from the oscillator are stretched in time and swept in frequency ("chirped") by propagation through an optical fiber. The long, chirped pulse is amplified at low peak intensity through the amplifier train. After amplification the chirp is reversed by the the negative group veleocity dispersion of a pair of parallel diffraction gratings to produce a 3–30 ps pulse.

Each stage of frequency doubling reduces the FWHM of a gaussian pulse by a factor of $\sqrt{2}$, so the IR pulse should be ~20 ps to produce a 10 ps UV pulse. The Nd:glass amplifiers in the laser system have a broad enough gain bandwidth to produce sub-picosecond pulses, so it is relatively easy to produce the 10 ps pulses required for the photoinjector.

The grating compressor is set for a particular frequency chirp, and variations in the pulse width or the bandwidth of the laser pulses will affect the compressed pulse width. We do not yet have an instrument to measure the pulse width on a single shot basis (such as a streak camera or single-shot autocorrelator), but the width can be measured over several shots with a scanning autocorrelator. On a shot-by-shot basis we infer the amplified width by compressing the oscillator output in a second pair of compression gratings and measuring the compressed pulse width in a rotating-mirror autocorrelator.

### 3.2.4 Harmonic Generation

The pulse train undergoes second harmonic generation (SHG) in a 5×5×10 mm BBO crystal and 4th harmonic generation (4HG) to the UV in a second 5×5×10 mm BBO crystal. The conversion efficiency is a non-linear function of the intensity of the laser. With 200 $\mu$J/ IR pulses we have measured SHG efficiency as high as 50% and 4HG efficiency as high as 10%. With the higher pulse energy available with the slab amplifier, we expect even higher overall conversion efficiency.

## 4 CONCLUSIONS

The laser system is currently capable of producing up to 800 1 MHz-spaced pulses amplified to 10 $\mu$J/pulse with limited pulse-train flatness. The CPA technique enables us to produce IR pulses from 3–30 ps. Even at 20% of the design energy, the 4HG efficiency is 10%. With the addition of the slab amplifier and the preshaping system, we will be able to produce a considerably flattened pulse train with 1 mJ/pulse. Commissioning of these systems is expected in the summer of 1997.

DC illumination tests of the $Cs_2Te$ photocathode show that the quantum efficiency is >10%[2]. Even if the QE degrades by a factor of 10 when exposed to the RF of the photoinjector, the laser system will still be able to deliver enough UV energy per pulse to extract 10 nC/bunch. First tests of the photocathode in the photoinjector will begin in spring 1997 using the laser to produce a reduced (200 pulse) pulse train.

## 5 REFERENCES

[1] E. Colby, *et al.*, these proceedings.

[2] P. Michelato, *et al.*, these proceedings.

[3] A. R. Fry PhD thesis, University of Rochester, 1996.

[4] TTF conceptual design report. Technical Report TESLA 95-01, DESY, March 1995.

[5] T. Srinivasan-Rao, editor. *Lasers for RF Guns*, number BNL-52435, Anaheim, CA, May 14–15 1994.

[6] M. J. W. Rodwell, D. M. Bloom, and K. J. Weingarten. *IEEE Journal of Quantum Electronics*, 25(4):817, 1989.

[7] P. Maine, D. Strickland, P. Bado, M. Pessot, and G. Mourou. *IEEE Journal of Quantum Electronics*, 24(2):398, 1988.

# CATHODELESS, HIGH BRIGHTNESS ELECTRON BEAM PRODUCTION BY MULTIPLE LASER BEAMS IN PLASMAS

R.G. Hemker, K.-C. Tzeng, W.B. Mori, C.E. Clayton, UCLA, and T. Katsouleas, USC

*Abstract*

The use of two crossed laser pulses in a plasma for the cathodeless production of high current low emittance electron beams [1] is examined with fully relativistic 2-1/2D Particle-in-Cell (PIC) simulations. Estimates for the number of injected particles, their energy spread, and their emittance are given as functions of the amplitude and timing of the injection pulse relative to the drive pulse of the LWFA. The physical mechanism of the trapping of particles is examined based on single particle phase space trajectories in the self-consistent PIC simulations.

## 1 INTRODUCTION

Recently D. Umstadter et al.[1] proposed the use of two orthogonal laser pulses in a plasma to trap and accelerate an ultra-short bunch of electrons. As envisioned the first (or drive) pulse creates a plasma wave which is below its self-trapping or wavebreaking threshold. The transverse ponderomotive force of the second (or injection) pulse gives electrons an extra kick forward in the wake direction, enabling them to be trapped and accelerated in the wake of the drive pulse (fig. 1). Such a cathodeless injector is of interest for a wide variety of applications including as an injector for future linear accelerator technologies with short wavelength accelerating structures. The scheme also naturally overcomes problems of synchronizing the injector with a plasma based accelerator.

In this article, we present results from a detailed two-dimensional (2D) PIC simulation analysis of this concept. We find that our results clearly support the feasibility of such a cathodeless injection scheme, but that the physical mechanism for the trapping is different from the one originally suggested at least for the parameter regime studied in this paper. We will show that the number of particles, emittance , and energy spread can all depend sensitively on the laser parameters and the injection phase. These results place constraints on the allowable shot to shot jitter of the injection laser. Last, based on the new insight into the trapping mechanism, we put forth additional geometries, e.g., co- and counter-propagating pulses, as well as related injection

## 1 SIMULATION RESULTS

The simulations are conducted with the single node version of the fully relativistic 2-1/2D PIC code Pegasus[2]. This code implements a moving simulation box that can follow the laser pulse for extended periods of time. Pegasus uses the charge conserving algorithm algorithm in ISIS and solves locally for E and B fields. Fig. 1 shows the basic set up of the simulations.

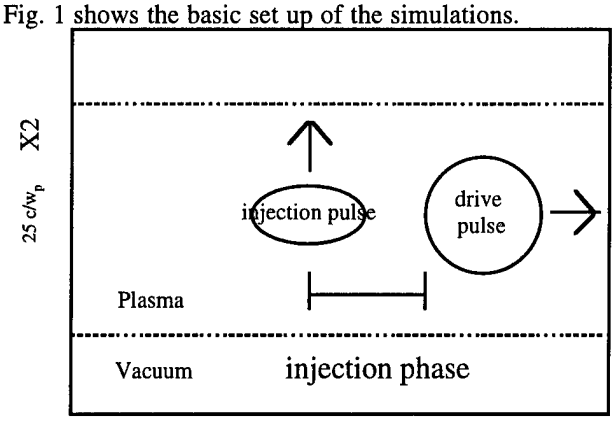



Fig. 1. Geometry of the cathodeless injector concept. The injection phase of the injection pulse is defined by the distance between the trailing edge of the drive pulse and the center of the injection pulse when it crosses the drive pulse.

In each of the simulations a drive pulse starts to move in the $x_1$ direction and at a later time an injection pulse is launched from a vacuum region at the side of the box propagating in the $x_2$ direction as illustrated in fig. 1. The following parameters are valid for most of the simulations evaluated below and should be assumed for all of the results presented if not stated differently. The frequency ratio $\omega_0/\omega_p$ between the laser frequency and the plasma frequency is 5 for both; thus the simulations have fewer laser cycles than is typical in experiments. Both pulses have their polarization in the plane of the simulation. For the drive pulse the normalized vector potential is $a = eA_y/mc^2 = 1.00$. For the injection pulse the normalized vector potential is $b = eA_x/mc^2 = 2.0$ unless stated otherwise. The transverse profile is given by a gaussian. Both the drive and the injection pulse have a spot size of $3c/\omega_p$. The pulse length, full width from zero to zero, is $2\pi c/\omega_p$ for the drive pulse and $\pi c/\omega_p$ for the injection pulse. We define the injection phase $\psi$ to be the distance between the back of the drive pulse and the center of the injection pulse as it crosses the axis (fig. 1).

The engineering results of the simulations are summarized in fig. 2. In order to convert the simulation results to physical units, we assume a plasma density of $10^{16}cm^{-3}$. Note that the number of electrons as well as the

0-7803-4376-X/98/$10.00 © 1998 IEEE

normalized emittance both scale with $n^{-1/2}$[3]. All quantities including the energy spread are calculated after the final timestep of the calculation. The energy of the trapped particles is around 10 MeV at that time (compared to a theoretical maximum value of about 25MeV for these simulations).

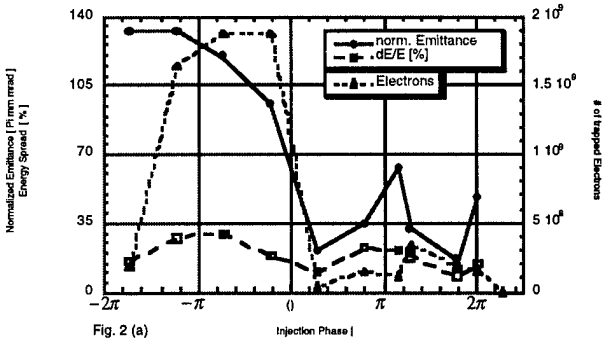



Fig. 2. (a) The number of trapped electrons, the normalized emittance, and the energy spread of the trapped particles as a function of the injection phase. The injection amplitude b is 2.0.

In fig. 2a we plot the number of trapped electrons, the normalized emittance, and the energy spread as a function of the injection phase for a fixed value of the injection amplitude. That value is b = 2.0. Note that negative values for $\psi$ mean that the center of the injection pulse crosses before the end of the drive pulse. The most notable feature of fig. 2a is the great variation of the three beam quantities as a function of $\psi$ and especially the strong difference in the number of particles and their emittance between positive and negative injection phases. The direct overlap of the injection pulse with the drive pulse (i.e. negative injection phase) clearly yields the largest number of trapped particles. The maximum number of trapped electrons corresponds to 1.9 x $10^9$ at a plasma density of $10^{16}$cm$^{-3}$ (or to 6 x $10^7$ at a density of $10^{19}$cm$^{-3}$). The number decreases by an order of magnitude for positive injection phases. The emittance on the other hand is smallest for the positive injection phases, corresponding to the smallest normalized value of $16\pi$ mm mrad in a $10^{16}$ cm$^{-3}$ density plasma (or $0.5\pi$ mm mrad at $10^{19}$ cm$^{-3}$). It increases by a factor of five for negative injection phases. We believe that the relatively larger emittance and number of particles at negative $\psi$ are both due to stochastic motion of the plasma in the overlapping laser fields. The energy spread of the accelerated bunch does not vary as significantly as the particle number and emittance ; it is between 8% and 22% at a beam energy of 10 MeV and would be expected to scale as $1/\gamma$ if the simulations with larger dephasing energies were done. There is an interesting periodicity to the curves in fig. 2a. The energy spread, and to some extend the number of particles, oscillate with a period of roughly $2\pi$, suggesting that they follow the periodicity of the accelerating plasma wave field. The emittance oscillates with a period of $\pi$ which follows the periodicity of the magnitude of the focusing field of the accelerating wake.

Although the simulations with b = 2.0 produce similar numbers of particles at $\psi = 1.3\pi$ or $1.8\pi$, as can be seen from fig. 2a, for b =1.8 the number of particles changes from several $10^8$ at $\psi = 1.3\pi$ (see fig. 2b) to nearly zero at $\psi = 1.8\pi$ (data not shown in figures). The results of the simulations are therefore sensitive to these parameters and the curve found in fig. 2a for the injection phase dependence at injection amplitudes of 2.0 is not readily applicable to other values of this parameter.

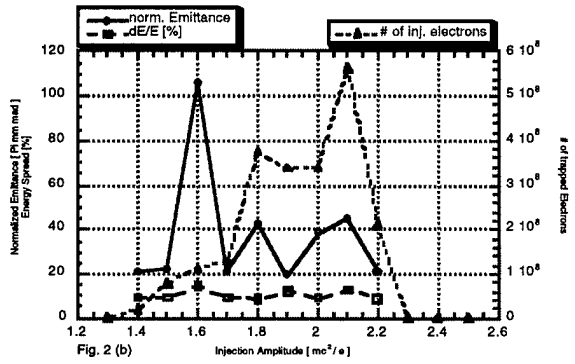



Fig. 2. (b) The number of trapped electrons, the normalized emittance, and the energy spread of the trapped particles as a function of the injection amplitude. The injection phase $\psi$ is $1.3\pi$.

In fig. 2b we plot the same quantities as in fig. 2a but as a function of the injection amplitude for a fixed value of the injection phase $\psi$. The value of $\psi = 1.3\pi$ is chosen for the simulations of fig. 2b since it seems to be close to an optimal injection phase judging from the data of fig. 2a. As a function of the injection amplitude the normalized emittance and the energy spread do not seem to show any systematic behavior on the scale that is resolved by our simulations. The values of the energy spread vary between 8 % and 15 %, while most of the values for the emittance are between 20 $\pi$ mm mrad and 50 $\pi$ mm mrad. In one case the emittance goes up to 106 $\pi$ mm mrad. This means that the beam quality is quite sensitive to variations in the injection amplitude. The number of trapped electrons on the other hand shows a systematic behavior. As should be expected the number of trapped particles first rises with increasing injection amplitude and then falls off. We explain this decrease with the increase in transverse momentum ($p_2$) that is transferred to the particles by the injection pulse. At a certain value this transverse momentum becomes large enough to prevent the trapping of the particles.

The above results indicate that the properties of the electron bunches obtained in the simulation is promising. We give here the values for the simulation at $\psi = 1.8\pi$ with an injection amplitude of a = 2.0 interpreted at a density of $n = 10^{16}cm^{-3}$. The average current of a bunch is 170 A. The normalized brightness is $6.8 \times 10^{10}$ A/m$^2$. The beam is not space charge dominated [4]. It is an approximately matched beam and its emittance is about 10% of the acceptance of the plasma wave[3]. The beam density is $3x10^{14}cm^{-3}$, 3% of plasma density. Note that the beam brightness and density increase linearly with the plasma density.

To gain a deeper understanding of the process we follow the momentum of a single, typical, trapped particle as function of time in the 2D simulation. We consider a particle for the case of $\psi = 1.3\pi$ and b = 1.8. The data are shown in fig. 3. The initial momentum is zero since the simulation uses cold plasma.

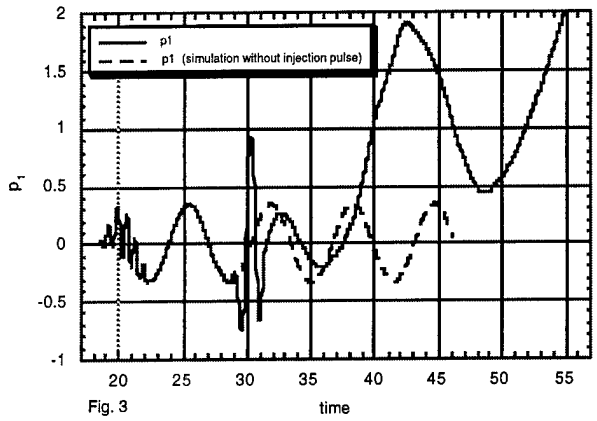



Fig. 3. $p_1$ of a test particle as a function of time. The two curves are the results from simulations with (solid) and without (dashed) an injection pulse. $\psi = 1.3\pi$ and b = 1.8 for the simulation with an injection pulse.

The solid curve in fig. 3 shows the longitudinal momentum of the particle; the dotted curve shows $p_1$ for the same particle in a simulation were the injection pulse is not launched but that is otherwise identical. As expected, this particle simply oscillates in the wake of the drive pulse. In the full simulation we can see that the injection pulse has completely passed by the test particle at about the time t=31.7. Although the injection pulse has an impact on the particle, the really large changes occur later at a time when the injection pulse has already left the area of the test particle. This means that the particle gets the actual momentum needed for getting trapped not from any effect directly related to the laser pulses (since those have already left the area of the particle), but by effects related to the interaction of the two plasma wake fields created by these pulses. Note that the trapped particle goes through one full oscillation (accelerating, decelerating, and accelerating again) before it is trapped. This feature that the particles get accelerated above the trapping threshold in a multi-step process (acceleration-deceleration-acceleration) caused by the interaction of the wake fields is not unique to this particular simulation. Other simulations with different values for $\psi$ and b show the same process.

## 1 CONCLUSIONS

In this paper, we have found that the beam brightness and quality found in our simulations compares reasonably with that of electron bunches produced by other technologies. The mechanism for the trapping of particles is not the transverse ponderomotive force of the injection pulse, rather it comes from the interaction of the particles with the two plasma wakes. It should be noted however that this does not rule out the possibility that a different choice of parameters for the injection pulse might result in trapping due to a direct kick by the transverse ponderomotive force. The results of our research open up a number of possibilities for future investigations.

Two important goals of future research would be to find an analytical model of the process that is able to predict the results seen in the simulations and to use 3D PIC simulations. This will facilitate optimizing parameters and determining what are the fundamental limits on beams produced by this scheme. Secondly additional geometries need to be investigated , such as co- and counter-propagating drive and injection lasers. The crucial idea here is that the Rayleigh length of the injection pulse is much shorter than the Rayleigh length of the drive pulse. This means that the injection pulse will interact significantly with the plasma only for a short distance. Our preliminary results show that the combined plasma wakes have an amplitude that is temporarily large enough to cause local wavebreaking. The fact that the plasma wave is responsible for the trapping of particles in our simulations suggests also to investigate other ways to excite this plasma wave that causes this trapping. If a method could be used that builds up the plasma wave gradually over time like a PBWA[5], then less powerful lasers would be required.

This work was supported by DOE Grant No. DE-FG03-92ER40727 and LLNL.

## REFERENCES

[1] 'D. Umstadter, J.K. Kim, and E. Dodd, Phys. Rev. Lett. **76**, 2073 (1996).
[2] K.-C. Tzeng, W.B. Mori, Phys. Rev Lett. **76**, 3332 (1996).
[3] R.G. Hemker, K.-C. Tzeng, W.B. Mori, C.E. Clayton, T. Katsouleas , submitted to Phys. Rev. E.
[4] J.D. Lawson, The Physics of Charged Particle Beams, 2nd Ed. (Oxford Univ. Press, New York, 1988).
[5] IEEE Trans. Plasma Sci., vol. **24**, no. 2.

# EXPERIMENTAL TESTING OF THE TTF RF PHOTOINJECTOR

E. Colby, M. Conde, J. Rosenzweig, University of California, Los Angeles
P. Colestock, H. Edwards, K. Koepke, F. Nezrick, Fermi National Accelerator Laboratory*

*Abstract*

Results from the experimental testing of the prototype TESLA Test Facility (TTF) RF photoinjector are summarized. Preliminary measurements of the performance of the injector indicate that, with refinement, the design values for the transverse emittances ($20 \times 20\pi$ mm-mr) are not unrealistic, with uncompressed transverse emittances of $40\pi$ mm-mr having been obtained under somewhat less ideal circumstances than those simulated. Preliminary pulse length measurements with and without the pulse compressor suggest pulse compression, but further study is required.

## 1 INTRODUCTION

The TTF linac is a 0.5 GeV super-conducting L-band accelerator designed to test engineering issues associated with constructing and maintaining a super-conducting linear collider. Two injectors have been designed and built for beam tests of the linac[1], the first a low bunch charge (37 pC) thermionic injector producing 8 mA average current to test the RF feedback, beam line and control systems, the second a high bunch charge (8 nC) RF photoinjector also producing 8 mA, but in 1 kA peak current bunches to probe wakefield losses at cryogenic temperatures.

A prototype injector was built, similar in all respects to the planned TTF Injector except duty cycle, to test the single-bunch beam dynamics issues associated with producing reasonable quality high charge bunches with short pulse lengths (1 mm)[2]. Testing of the prototype injector occurred in two phases. The 1.625 cell RF gun was tested initially alone, with a short beamline with charge, profile, emittance and energy diagnostics. Studies of the gun under variations of the launch phase, bunch charge, and solenoid field were made to test the PARMELA model used to design the injector.

Once tests of the gun alone were completed, the 9-cell booster linac and pulse compressor were added. Charge, profile, emittance, energy and bunch length diagnostics were installed along the beamline to permit testing of critical issues such as "freezing" of the transverse emittance at the space charge correlation corrected value, emittance preservation, and pulse compression.

## 2 RF TESTS OF GUN AND LINAC

Cold-test measurements of the gun have been presented elsewhere[3]. RF conditioning proceeded with the the $4\mu$s long RF pulses from the AWA RF system, with sample traces shown in figure 1 below. It is clear from the loop signals that the gun cavity is still filling when the RF pulse ends, with the result that the Ø-mode of the cavity may well still be weakly excited when beam is launched, giving a field imbalance.

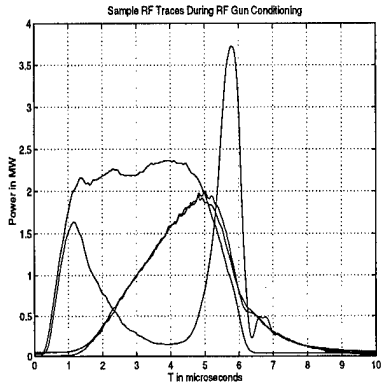



Figure 1: RF Forward, reverse and loop traces from gun during conditioning.

The booster linac was fabricated from a cold test model of the TTF super-conducting 9-cell cavity, made from copper rather than niobium. Cooling tubes were bonded to the cavities with thermally conductive epoxy, a high power input coupler was designed and mounted to the central ($5^th$) cell, as opposed to the beam-tube coupling used in the super-conducting case. A clamping assembly was added to tune subgroups of the cells to achieve field balance. The opening in the central cell for power coupling drastically changed the field balance qualities of the structure, requiring significant retuning. The final field profile, coupler mounted and properly coupled, is shown in figure 2 below.

The linac was conditioned to 10 MW (giving an estimated field of 15 MV/m) with $4\mu$s pulses, again only very incompletely filling before the end of the RF pulse. The field imbalance present during the fill (and hence during beam) may well be the reason the beam energy was lower than expected (17 MeV measured, versus 19 MeV computed).

## 3 GUN BEAM TESTS

Gun beam tests were devoted to understanding the various technical issues associated with commissioning an injector. Specifically, the alignment of the solenoids and the transverse effects of launch phase, gradient and solenoid focussing field. Measurements of the horizontal emittance as a function of solenoid strength are shown in figure 3 be-

* Operated by the Universities Research Association, Inc., under contract for the U. S. Department of Energy

0-7803-4376-X/98/$10.00 © 1998 IEEE

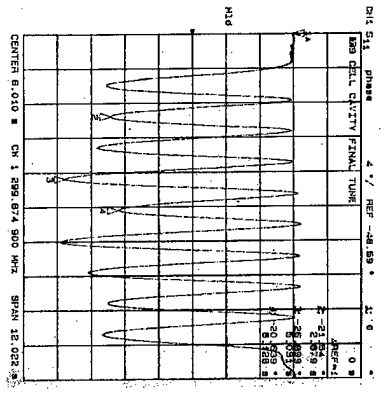


Figure 2: Final field balance condition of 9-cell booster linac cavity.

low. Poor laser spatial characteristics and wide laser amplitude variations made measurements prone to substantial fluctuation. Attempts to gate data to a limited charge range around the target value of 8 (or 10) nC using charge data from a gun-mounted integrating current transformer helped, but could not eliminate the spatial profile problems.

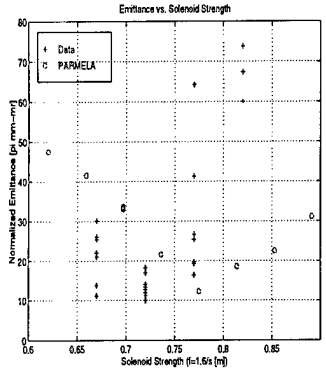



Figure 3: Measured and calculated transverse emittances measured at 3.5 MeV

It is suspected that the narrow acceptance of the $10\mu$m wide slits used in this emittance measurement scraped off the most divergent particles, resulting in potentially large underestimates of the emittance. Emittance slits were widened to $35\mu$m on these grounds.

Gun shunt impedance is estimated from beam energy measurements to be 19 M$\Omega$/m, as compared with the Superfish calculated value of 24.6 M$\Omega$/m, a discrepancy arising from two factors: first, the calculated shunt impedance assumes $\beta = 1$ throughout, whereas the electrons slip nearly $\lambda/8$ against the RF wave as they accelerate, and second, imperfections in the cavity itself.

## 4 INJECTOR BEAM TESTS

The bunch energy spectrum was measured for a variety of gun and linac phasing conditions to establish correct phases for optimal energy operation and the correct offset phase for pulse compression to occur. Measured energy profile for the beam is shown in figure 4 for the case of maximum energy (beam uncompressed). Comparison of the calculated (1.5%) and measured (1.5%) energy spreads shows good agreement.

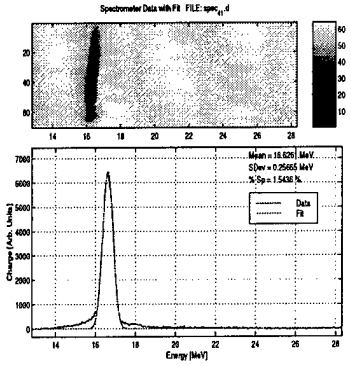



Figure 4: Energy spectrum of uncompressed 8 nC bunch at end of injector.

Transverse emittance was measured after the booster linac (before the pulse compressor) for several launch phases and several solenoid settings, with the results shown in figures 5 and 6. Again, wide fluctuations in initial beam parameters induced by laser fluctuations contributes to the substantial error bars on the measurement.

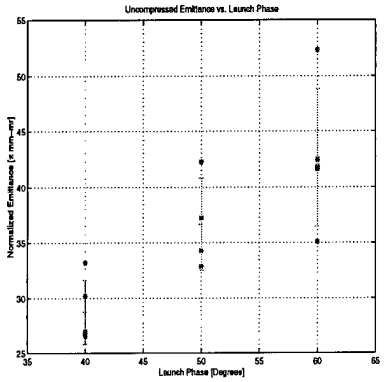



Figure 5: Emittance measured for several launch phases.

The spatial uniformity of charge emission from the cathode was measured and discovered to be rather sharply peaked toward the center of the cathode. Rough patches were observed on the cathode surface suggesting arc damage, and occurring in a concentration close to center of the cathode, which prompted a careful polishing of the surface with $0.3\mu$m alumina to obtain a smooth but optically poorly reflective surface for emission. Re-measure of the quantum efficiency after the polishing showed improved uniformity, and absence of the central peak.

A novel Čerenkov emitter was tried and found to produce excellent light output. A 3mm thick block of Aerojel,

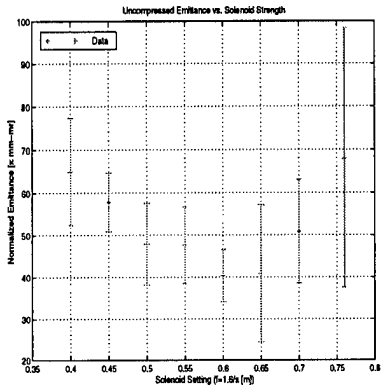



Figure 6: Emittance measured for several solenoid field focal lengths.

mounted in a special pressure cell to prevent damage from the vacuum, was installed after the pulse compressor to permit measurement of compressed and uncompressed bunch lengths. Light from the radiator was transported some 15 meters to a Hamamatsu streak camera with a nominal resolution of 1 ps. Preliminary analysis of the data indicate pulse lengths on the order of 2 mm at best, with some evidence of pulse compression observed, but detailed analysis of the data remains.

## 5 HIGH POWER TESTING AT FERMILAB

Following decommissioning at Argonne, the injector was partially reassembled at Fermilab to enable continued testing until the high duty cycle gun is fabricated. Ultrahigh vacuum tests and long-pulse tests have been completed, with the gun attaining a resting vacuum in the upper $10^{-10}$ Torr range, and a running vacuum in the mid $10^{-9}$ Torr range with $50\mu s$ pulses of 3.5 MW at 5 Hz. Gun Conditioning to RF pulse lengths as long as $400\mu s$ at full power has been completed. Dark current is estimated to be $\sim 4-6$ mA, with the specific source of the dark current still under investigation.

## 6 DESIGN IMPLICATIONS

Several design concerns have been addressed with the high power, extended RF pulse operation for the Argonne gun, namely, the proof that water-turbulence induced wall vibrations within the RF cavity produce no measurable cavity phase shifts, and that excellent running vacuum, of particular interest for operation with exotic photocathode materials such as $Cs_2Te$, is attainable without modification of the gun. The suspected large dark current, however, may point to the need to redesign the cathode electrical contact altogether, with a resonant RF trap replacing the choke spring currently in use.

Wakefield effects have recently been calculated using a modified version of PARMELA, with the results indicating that further advance of the phase of the linac is needed to overcome the short-range wakefield, which tends to cancel the phase-energy correlation needed for pulse compression, with the gun and linac irises contributing the largest wakefield kicks of all the beamline components. A collimator, planned in the initial design, has been found in simulations to effectively double the entire longitudinal wake in the injector, prompting its removal.

## 7 FUTURE EXPERIMENTS

Re-commissioning of the old injector for continued testing at Fermilab will continue until the high duty factor gun is complete. Laser facilities[4] will be completed early this summer. Testing of the full injector under both single pulse and full macropulse conditions will be top priority through early 1998, with the commissioning of the high duty cycle RF photoinjector DESY occurring shortly thereafter. A second, similar photoinjector, being fabricated in parallel with the first, will allow an advanced accelerator research and development program to continue after injector II ships to DESY. Thomson-scattering based picosecond x-ray source and plasma acceleration experiments will begin preparations for planned beam experiments to begin in earnest by late 1997 in the AØ building at Fermilab.

## 8 ACKNOWLEDGEMENTS

The authors wish to gratefully acknowledge the members of the Argonne Wakefield Accelerator group, and in particular Jim Simpson and Wei Gai, for their hosting of this prototype experiment at the AWA facility.

## 9 REFERENCES

[1] TESLA Test Facility Linac - Design Report, D. A. Edwards, Ed., TESLA-95-01, (1995).

[2] E. Colby, F. Ostiguy, and J. Rosenzweig, Fermilab TM-1900, (1994).

[3] E. Colby, *et al*, IEEE Part. Accel. Conf., 1995, p. 967-9.

[4] A. Fry, *et al*, in these proceedings.

# OPTIMUM OPERATION OF SPLIT RF PHOTOINJECTORS

L. Serafini[$], J.B. Rosenzweig,
*Department of Physics and Astronomy, UCLA, Los Angeles, CA 90095*

*Abstract*

We describe how to achieve minimum transverse emittance in RF photoinjectors by applying theoretical predictions from a fully analytical model of beam dynamics in a split injector. This device consists of a short two cell (full+partial) RF gun followed by a drift and a booster RF linac. Matching the beam in the booster to the invariant envelope, an equilibrium mode of laminar beam flow, is shown to be the basis of emittance correction. Analytical predictions are compared to numerical simulations, finding excellent agreement. We also show how a further improvement of the beam quality can be obtained by matching the beam out of the booster into a Brillouin flow with proper control of the envelope oscillations. If these are actually coherent plasma oscillations in the laminar regime, then the normalized rms transverse emittance can be even further reduced.

## I. THE INVARIANT ENVELOPE EQUILIBRIUM OF RELATIVISTIC LAMINAR BEAMS

The beam dynamics in RF photoinjectors is mainly characterized by an rms beam envelope behavior which is almost insensitive to the initial temperature emittance $\varepsilon_{nth}$ - this is set up by the photoemission processes at the photo-cathode surface - but is mostly affected by the equilibrium set up by the space charge outward pressure on the beam and the counteracting combined focusing effects of the ponderomotive RF focusing, the external solenoid and the adiabatic damping caused by strong acceleration in the device.

The resulting equilibrium represents a laminar beam flow described by an exact analytical solution of the rms envelope equation $\sigma'' + \sigma'\frac{\gamma'}{\gamma} + K_r\sigma - \frac{\kappa_s(\zeta)}{\sigma\gamma^3} - \frac{\varepsilon_{nth}^2}{\sigma^3\gamma^2} = 0$ which has been recently derived - under the laminarity approximation $\varepsilon_{nth} \equiv 0$ - and called invariant envelope[1]:

$$\hat{\sigma} = \frac{2}{\gamma'}\sqrt{\langle I\rangle / \left[2I_0\gamma\left(1+4\Omega^2\right)\right]} \qquad (1)$$

where $\gamma'$ is the accelerating gradient ($\gamma = \gamma_i + \gamma' z$), $\langle I\rangle$ is the rms beam current ($I_0 = 17$ kA for electrons), and $\Omega$ is the dimensionless focusing frequency. This is related to the average focusing gradient $K_r$ by $K_r = \left(\Omega\gamma'/\gamma\right)^2$, implying a second order focusing channel made up by the combination of solenoid focusing and ponderomotive RF focusing, and is given by $\Omega^2 = \eta/8 + b^2$, where $b = cB_0/E_0$ is the ratio between solenoid field and peak RF field, and $\eta$ depends on the space harmonics of the RF field - it is close to 1 for standing wave structures in use for photoinjectors, while is almost vanishing in case of travelling wave structures[2].

The reason for the term invariant envelope (IE) is that this particular beam mode performs correction of the emittance growth[3] caused by linear space charge correlations. These are related to the dependence of space charge field on the longitudinal coordinate - the slice position $\zeta$ - in the electron bunch, as shown by the beam perveance term $\kappa_s(\zeta) = Ig(\zeta)/2I_0$ in the envelope equation - here $I$ is the peak current in the bunch and $g(\zeta)$ is a geometrical factor describing the field distribution, which for a Gaussian bunch in the central region ($|\zeta| \le \sigma_z$) is well described by $g(\zeta) = e^{-\zeta^2/2\sigma_z^2}\left\{1 + A_r^2\left[\left(1-\zeta^2/\sigma_z^2\right)\left(1/2 + \ln A_r\right) - 1\right]\right\}$, while for a uniform bunch of length $L$ is $g_{un}(\zeta) = 1 - 2A_r^2\left[1 + 12\left(\zeta/L\right)^2 + 80\left(\zeta/L\right)^4\right]$. ($A_r \equiv \sigma/\gamma\sigma_z$ is the bunch aspect ratio in its rest reference frame - for the uniform $A_r \equiv R/L\gamma$).

The emittance correction process is effective as long as the beam is in the laminar regime, so that it behaves like a cold plasma undergoing surface plasma oscillations. The validity of the laminarity assumption holds whenever the dimensionless parameter $\rho = \left[\langle I\rangle g(\zeta)/\gamma\varepsilon_{nth}I_0\gamma'\sqrt{1+4\Omega^2}\right]^2$ is much larger than 1, which is usually the case even up to 40 MeV for a typical photoinjector beam[4]. In this regime, since the incoherent betatron motion associated to the temperature emittance is negligible (by definition of laminarity), the emittance blow-up turns out to be a reversible effect which can be corrected by a proper control of the plasma oscillations.

## II. OPTIMUM RF GUN OPERATION

The optimum operation of a split photoinjector is achieved when the RF gun setting is such as to match the beam onto the IE at injection into the booster linac. This requires not only that the beam rms size $\sigma$ at the booster entrance should be as specified by Eq.1, but also that the beam must go through a waist with $\sigma' = 0$ at the same location, because the entrance focusing kick imposed by the conservation of canonical momentum when the particles enter the RF field is exactly equal to the negative beam divergence of the IE, which is $\hat{\sigma}' = -\gamma'\hat{\sigma}/2\gamma$ .

[$] Perm. address: INFN , Via Celoria 16, 20133 Milano, Italy

Work supported by US DOE grants DE-FG03-90ER40796 and DE-FG03-92ER40693, and Sloan Foundation grant BR-3225

0-7803-4376-X/98/$10.00 © 1998 IEEE

In order to find the optimum setting for the six free parameters specifying the RF gun working condition, namely the bunch charge $Q$, the laser cathode spot size $\sigma_r$ and length $\sigma_z$, the cathode peak field $E_0$, the solenoid field amplitude $B_0$ and the accelerating phase $\varphi$, we have to trace back the beam through the drift down to the gun exit by means of the rms envelope equation for laminar beams in drifts, which reads

$$\nu'' - 1/\nu = 0 \qquad (2)$$

where $\nu \equiv \sigma/P$ and $P = I/2I_0\gamma_c^3$ is the beam perveance ($\gamma_c$ is the beam energy at the gun exit, typically $\gamma_c \geq 6$). The general solution of Eq.2 is $\int_1^{\nu/\nu_c} dx/\sqrt{\nu_c'^2 + 2\ln x} = \Delta z/\nu_c$, which allows to express the beam spot $\nu_w$ at the waist and its position $\Delta z_w$ as functions of rms size $\nu_c$ and divergence $\nu_c'$ at the gun exit:

$$\Delta z_w = \nu_c f(\nu_c') \;;\; \nu_w = \nu_c e^{-\nu_c'^2/2} \qquad (3)$$

where the function $f(\nu_c') \equiv \int_{e^{-\nu_c'^2/2}}^{1} dx/\sqrt{\nu_c'^2 + 2\ln x}$ can be very well approximated in the range $|\nu_c'| \leq 6$ by the simple expression : $g(\nu_c') = 1.09\nu_c'/1.69 + \nu_c'^2 + 0.423\nu_c' e^{-0.296\nu_c'^2}$. Since Eqs.3 are valid for any laminar space charge dominated beam they actually represent the generalization of a previous result derived by Reiser[5].

In order to finally link the beam conditions at the waist, which must be matched to the IE, with the beam conditions at the cathode we have to perform two transformations:

1) from the 6D physical parameter space ( $Q$, $\sigma_r$, $\sigma_z$, $E_0$, $B_0$ and $\varphi$ ) to a 4D parameter space described by $A \equiv \gamma A_r$, $\alpha \equiv eE_0/2m\omega_{RF}c$, $b$ and the Cauchy current $\Lambda \equiv I/\gamma'^2\sigma_r^2$.

2) from the physical beam rms size $\sigma_c$ at the gun exit, as given in Ref.6, to the dimensionless $\tau_c \equiv \sigma_c\gamma'\sqrt{\gamma_c/\kappa_s(\zeta)}$.

As a final result of imposing two conditions (beam size and divergence) on the set of four free parameters, we may specify what are the optimum values for $\Lambda$ and $b$ in order to achieve emittance correction, once the aspect ratio $A$ and the dimensionless field amplitude $\alpha$ are fixed. We find

$$\Lambda^{opt}\ [kA] = 57.3 - 12.4\alpha + 2.63\alpha^2 + 26.2A - 1.78\alpha A + 1.86A^2 \qquad (4)$$

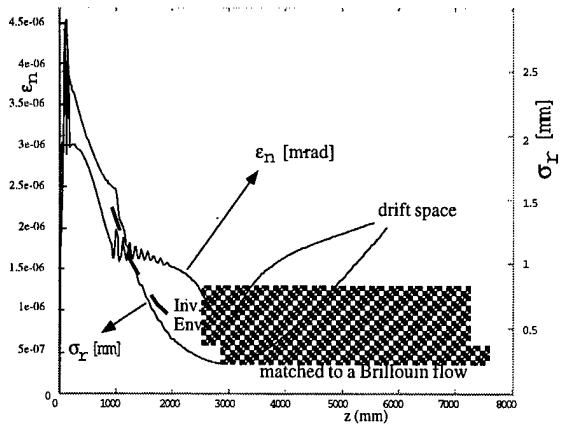



Figure 1: Beam envelope $\sigma$ and associated normalized rms transverse emittance $\varepsilon_n$ in a typical L-band split Photoinjector, showing control of the emittance oscillations by matching to a Brillouin flow

for the Cauchy current, while for the solenoid field amplitude $b^{opt} = 1.49 + 1.67/\sqrt{\alpha} - 2.07/\alpha^{1/4}$.

We test these analytical predictions versus a CIC simulation performed with ITACA[7] of a typical L-band split photoinjector (1+1/2 cell) whose booster linac is a 9-cell superconducting TESLA cavity placed 1 m far from the photo-cathode plane and operated at 25 MV/m peak accelerating field. Choosing $\alpha = 1.8$ and $A = 1/2$ we have $E_0 = 50$ MV/m (at 1.3 GHz, $\gamma' = 49$ m$^{-1}$) and we find $\Lambda^{opt} = 56$ kA from Eq.4. From the definition of $\Lambda$ and the peak current in a gaussian bunch $I = Qc/\sqrt{2\pi}\sigma_z$ we find the cathode spot size as a function of $\Lambda$, $Q$, $A$ and $\gamma'$, *i.e.* $\sigma_r = \sqrt[3]{QcA/\sqrt{2\pi}\Lambda\gamma'^2}$.

Choosing for the bunch charge $Q = 1$ nC, we find for the cathode spot size $\sigma_r = 0.76$ mm, so the laser pulse length should be (from $A = 1/2$) $\sigma_z = 1.5$ mm. The predicted optimum value for the solenoid field amplitude is, from $b^{opt} = 0.94$, $B_0 = 1.6$ kG.

The simulation result is presented in Fig.1, where the norm. rms emittance, $\varepsilon_n \equiv \gamma\sqrt{< r^2 >< r'^2 > - < rr' >^2}/2$, and the envelope are plotted: the actual laser intensity distribution has been taken uniform in time and radius with rms sizes equal to the ones listed above.

As clearly visible, the beam follows closely the IE along the booster, achieving an effective emittance damping down to 0.8 mm·mrad at the minimum ($z = 3$ m), with an emittance behavior reproducing quite well the prediction from the model based on weak stable oscillations around the IE: this gives $\varepsilon_n \cong \sqrt{\frac{\langle I \rangle}{3I_0\gamma}}\left|\left(\delta\sigma_i + 2\delta\sigma_i'\frac{\gamma_c}{\gamma'}\right)\cos(\psi) + \left(\delta\sigma_i'\frac{\gamma_c}{\gamma'} - \delta\sigma_i\right)\sqrt{2}\sin(\psi)\right|$ where $\delta\sigma_i$ and $\delta\sigma_i'$ are the rms mismatches w.r.t. the IE at injection into the booster and $\psi = \ln(\gamma/\gamma_c)/2$ is the

phase advance. The emittance is therefore expected to be damped as $1/\sqrt{\gamma}$, on average over a plasma wavelength $\lambda_p = \sqrt{8/3}\,\pi\gamma/\gamma'$, with anharmonic oscillations whose periodicity is two times shorter than the period of the perturbations about the IE.

## III. EMITTANCE CONTROL IN LAMINAR BEAMS

The property of the IE to make the beam exit the booster as a parallel beam ($\sigma' = 0$) makes possible to match the IE to a Brillouin flow in order to avoid a further emittance growth, as shown in Fig.1, after the laminar waist where the minimum emittance occurs. Since the equilibrium rms beam size $\sigma_{eq}$ in a Brillouin flow has the same scaling *vs* the current of the IE, $\sigma_{eq} = \sqrt{I/2I_0\gamma_f^3 K_r}$ ($\gamma_f$ being the exit energy), a uniform focusing channel of gradient $K_r = \left(\sqrt{3/8}\,\gamma'/\gamma_f\right)^2$ can perform such a matching. In Fig.1 a solenoid of field amplitude $B_0 = \sqrt{3/2}mc\gamma'/e$ has been used to keep the beam close to a Brillouin flow equilibrium: the weak envelope oscillations are clearly associated with emittance oscillations of twice the frequency. This somewhat unusual behavior of emittance scaling with the rms size is typical of a beam in the laminar space charge dominated regime: indeed, this 65 A beam, accelerated up to 19.8 MeV, still retains a large value for the parameter $\rho$, namely $\rho = 80$.

This implies that the emittance can be even further reduced: indeed, the particle distribution plotted in Fig.2a (configuration space) and 2b (trace space), shows that the bunch tail and head behave like bifurcated parts, *i.e.* independent beams which have been overfocused since they were subject to a local space charge field weaker than in the bunch core (see previous expression for $g(\zeta)$). These bifurcated tails usually go through a crossover thus producing a halo in trace space (see Fig.2b) which clearly contaminates the emittance correction process. By filtering the bifurcated tails only 10% of the bunch charge is lost but the emittance is reduced down to 0.5 mm·mrad.

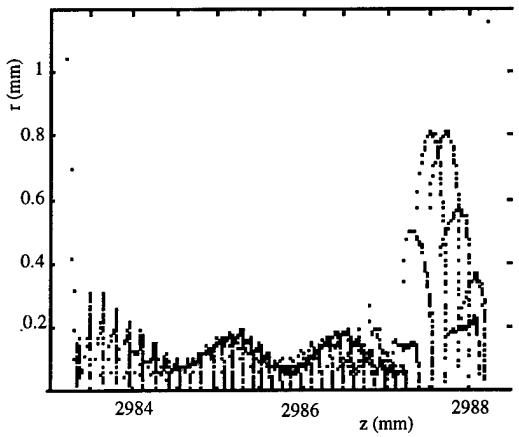



Figure 2a: Particle distribution in the configuration space (r,z) at the location of minimum emittance

We found that these bifurcated tails can be locally corrected by properly adjusting the matching from the IE to Brillouin flow into the solenoid field. With respect to the setting shown in Fig.1, we moved the solenoid further ahead and increased the solenoid field up to 1.9 kG. This makes the beam perform more gentle envelope oscillations: during the first one the bifurcated tails are overlapped in phase space to the beam core, producing a local minimum in the normalized rms emittance (calculated over all the particles) at an unprecedented ultra-low value of 0.3 mm·mrad .

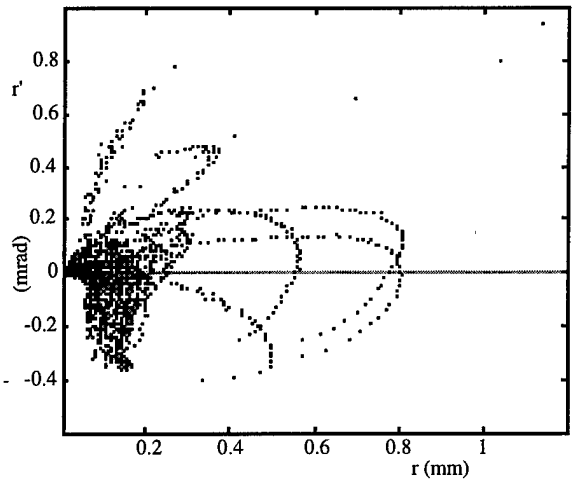



Figure 2b: Particle distribution in transverse trace space (r,r') at the location of minimum emittance

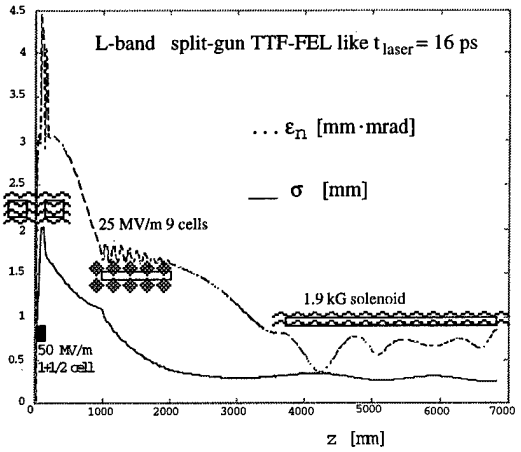



Figure 3: Envelope and emittance behavior of a beam matched from the IE to Brillouin flow with local correction of bifurcated tails

## IV. REFERENCES


[1] L.Serafini, J.B.Rosenzweig, *Envelope Analysis of Intense Relativistic Quasi-Laminar Beams in RF Photoinjectors*, to appear in *Phys.Rev.E* , June 1997

[2] J.B.Rosenzweig, L.Serafini, *Phys. Rev. E* **49** (1994) 1599

[3] K.J. Kim, NIM A **275** (1989) 201

[4] L.Serafini, *Overview on Production and Dynamics of High Brightness Beams*, Proc. of ICFA workshop on Nonlinear and Coll. Phen. in Beam Phys., Arcidosso, Italy, September 1996

[5] M.Reiser, *Theory and Design of Charged Particle Beams*, (John Wiley & Sons, New York, 1994), p.201

[6] L. Serafini, *Particle Accelerators* **49** (1995) 253

[7] L.Serafini and C.Pagani, Proc. 1st EPAC, Rome, June 1988, Ed. World Scientific, p.866

# PERFORMANCE OF THE LEP2 SRF SYSTEM

D. Boussard, CERN, Switzerland

*Abstract*

In 1996, LEP2 operated at an energy of up to 86 GeV per beam using, in addition to the conventional RF system, 176 newly installed superconducting (SC) cavities, which together provide up to 2 GV per turn at 352 MHz. Almost all SC cavities are of the niobium film on copper type; they ran at an average operating gradient of 6 MV/m with a total beam current of up to 5.5 mA. The behaviour of SC cavities and couplers has been very satisfactory: only two cavities out of 176 were field limited; they have however been recovered *in situ* since. Small modifications in the liquid helium distribution reduced to a large extent turbulent phenomena and the associated microphonic effects. However the intrinsic electroacoustic instabilities (ponderomotive oscillations) remain the major concern for the operation of the RF system at high intensity. Their effect on the beam is minimized using RF feedback (on the vector sum of individual cavity signals); this also suppresses the intensity limitations due to beam loading instabilities. Installation, commissioning and operation of a huge new RF power plant (24 MW installed RF power) went as expected, despite a few weak points which are now being fixed.

## 1 INTRODUCTION

LEP, the largest particle accelerator in the world, is an electron-positron collider which started operation in 1989 at a collision energy of 45 GeV (the $Z_0$ energy) with a room-temperature RF system operationally capable of delivering up to 340 MV at 352 MHz.

The so-called LEP2 programme started in 1991 was aimed at increasing LEP energy and reaching at least the energy of W pair production. It is essentially based on the superconducting (SC) cavity technology developed at CERN since 1979.

The basic choices for the LEP SC cavities were made early in the project: 352 MHz frequency (for compatibility reasons and to minimize the critical transverse impedance of LEP), four-cell structure with couplers on the beam tubes, 4.5 K operating temperature, modular cryostat with easy access to the cavities and ancillary equipment, thermal and magnetostrictive tuners inside the cryostat. It was also decided that industrial firms would produce the SC cavity modules. The major difference, when compared to other large SC cavity projects (notably CEBAF) is that the cavities would be specified and accepted by CERN according to their RF performance (RF quality factor at the design accelerating field), as measured by CERN.

After an intense period of development it was decided that the LEP2 programme would be based on the niobium copper (Nb/Cu) technology. The inherent advantages of Nb/Cu cavities – much better thermal stability against quenching, savings on Nb material, insensitivity to small magnetic fields, higher quality factor – turned out to be very welcome in the course of the project.

## 2 SC CAVITY PERFORMANCE

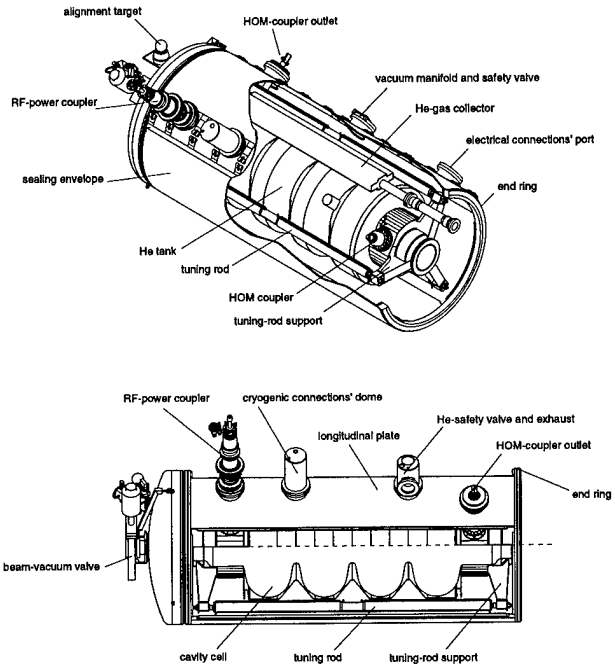



Fig. 1 The LEP2 SC cavity

Fig. 1 shows the four cell LEP2 cavity in its cryostat. The cavity itself surrounded by its helium tank and its three tuner bars is suspended inside the cryostat. The length of the tuner bars is controlled by their thermal expansion and by the magnetostrictive effect. The cryostat, with its three wide-barrel staves provides easy access to the cavity as neither a magnetic shield nor an intermediate thermal shield is necessary. Thermal insulation is achieved with superinsulation mattresses only. Four cavities are assembled together in a common cryostat to form a cryomodule 12.5 m long, including the end elements [1] [2].

Table 1 shows the major parameters of the LEP2 cavities, the most critical being the quality factor $Q_0$ at the operating field (6 MV/m). This is the parameter which is measured during the acceptance tests made at CERN of all cavities and modules produced by industry. Fig. 2 shows typical Q(E) curves of cavities fabricated by three different firms following the technique developed at CERN by which a copper cavity is coated inside with a thin niobium film (average thickness 1.5 μm) using a magnetron discharge. This measurement is no longer possible when the RF couplers are installed; however the

0-7803-4376-X/98/$10.00 © 1998 IEEE

cryogenic losses of a cryomodule can be estimated directly from the cryoplant parameters. The results are coherent with previous RF measurements showing that there is no significant degradation of the cavity performance after mounting of RF couplers, transport and installation in the tunnel.

| | | |
|---|---|---|
| Frequency | | 352.209 MHz |
| Operating field | | 6MV/m |
| Operating voltage | | 10.2 MV |
| Number of cells | | 4 |
| Effective length (four cells) | | 1.702 m |
| Modular length (between cryostat flanges) | | 2.553 m |
| Diameter: | equator | 755 mm |
| | iris | 241 mm |
| Relative pass band $2(f_p-f_0)/(f_p+f_0)$ | | 1.76% |
| $E_{pk}/E_{acc}$ | | 2.3 |
| $B_{pk}/E_{acc}$ | | 3.9mT/(MV/m) |
| R/Q ($R=V^2/2P$) | | 232½ |
| Field flatness toleranceE/<E> | | ±5% |
| Tuning sensitivity | | +40 kHz/mm |
| He pressure sensitivity | | <10 Hz/mbar |
| Tuning range: | slow | 50 kHz |
| | fast | 1.6 kHz |
| $Q_0$ at operating field (4.5K) | | $>3.2 \times 10^9$ |
| $Q_0$ at low field (4.5K) | | $>6.4 \times 10^9$ |
| RF losses at 6 MV/m and 4.5K/cavity | | <70W |
| Cryogenic standby losses per complete module | | <90W |
| $Q_{ext}$ of RF coupler (nominal) | | $2 \times 10^6$ |
| Loss factor for a complete module (four cavities and two end tapers) at $\sigma_z$ =10 mm: | | |
| | longitudinal | 5V/pC |
| | transverse | 8V/pC.m |

Table 1 LEP2 cavity parameters

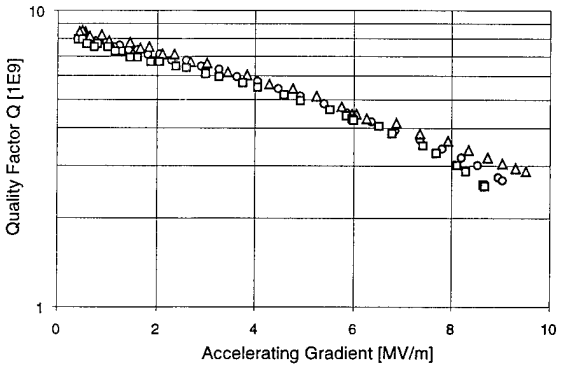



Fig. 2 Best Q vs E curves from three manufacturers

To reach the specified performance helium processing is often used during acceptance tests (without RF couplers). It has also been applied successfully on a defective cavity in the tunnel, equipped with RF couplers. However, possible discharges, or even arcing in the coupler, are potential risks of this technique. Pulsed power processing (pulses a few ms long, peak fields up to about 8 MV/m) is used more commonly both in the power test bench and in the tunnel to reach maximum cavity performance.

A vacuum accident occurred during the last LEP shutdown, where a complete warm module was rapidly vented with filtered nitrogen. Due to a very tight installation and testing schedule it was not possible to recheck the cavities until now. We are eagerly waiting for the new measurements of cavity performance to see whether this module can be recovered *in situ* or must be taken out of the tunnel for repair. Some years ago, a similar accident happened in the SPS: a cold cavity was slowly vented with unfiltered air; nevertheless, the cavity could still be operated afterwards.

Fig. 3 shows typical radiation levels measured at the end of several modules 15 cm off axis. The sharp increase with accelerating field indicates a strong field emission. The measured spectrum of the field-emitted electrons extends up to the maximum accelerating voltage of the module (40 MeV) and in some cases leads to activation of elements.

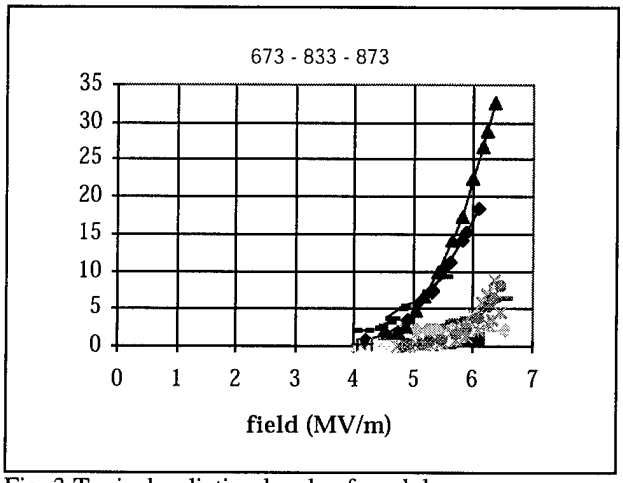



Fig. 3 Typical radiation levels of modules

In the early phases of the project, the main cavity coupler was a very serious cause of concern. Recurrent multipacting discharges plagued the operation of the couplers when installed on the cavities. This is attributed to the strongly enhanced secondary electron emission coefficient of a cold surface if it becomes covered with adsorbed gases. Such a situation occurs on the cold part of the outer conductor of the coaxial coupler (Fig. 4). The problem is cured by baking the window (the source of gas molecules) *in situ* before cooling the outer conductor of the coaxial line (cooled last) and by applying DC bias (+ 2.5 kV) on the inner conductor, which completely prevents multipacting during operation [3].

LEP couplers, including their variable version have been extensively tested on a dedicated cold cavity, simulating the real operating conditions. An RF power of 300 kW has been transferred through the cavity during

long periods, limited only by the load on the output coupler. Short pulses of 500 kW, 1.5 ms duration have also been transmitted through the test cavity, in pure travelling-wave mode.

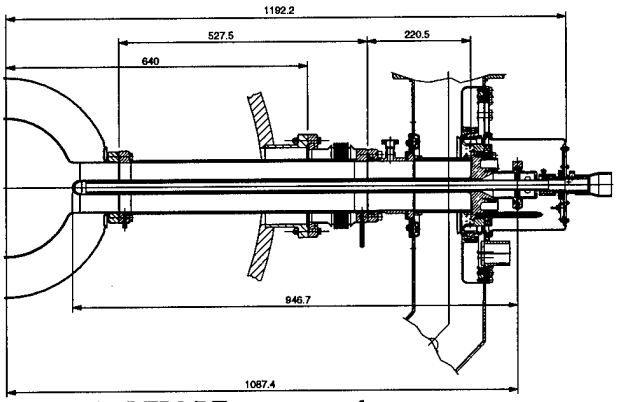


Fig. 4 The LEP2 RF power coupler

The production of cavities and modules by industry is by now almost complete. Table II shows the past and future steps in the installation programme [4].

| | June 96 | Oct. 96 | May 97 | May 98 |
|---|---|---|---|---|
| # Cu cav | 120 | 120 | 84 | 48 |
| MV Cu | 300 | 300 | 215 | 130 |
| # Nb cav | 4 | 12 | 16 | 16 |
| MV Nb | 34 | 102 | 136 | 136 |
| # Nb/Cu cav | 140 | 160 | 224 | 256 |
| MV Nb/Cu | 1434 | 1638 | 2294 | 2621 |
| Σ MV max | 1768 | 2040 | 2645 | 2887 |
| Σ $MV_{op}$ | 1600 | 1873 | 2478 | 2720 |
| E (GeV) | 80.5 | 86 | 92 | 96 |

Table 2 Number of cavities in LEP and available voltage

## 3 MICROPHONICS

Superconducting cavities, with their narrow bandwidth (±90 Hz for LEP2 cavities) are usually prone to microphonic effects. Indeed RF field fluctuations are normally observed on LEP2 cavities at frequencies corresponding to the first mechanical resonances (longitudinal) of the cavity, around 100 Hz. Transverse resonances, occurring at lower frequencies do not seem to be harmful.

A source of mechanical vibration external to the cavity itself was identified and subsequently cured on most modules. It was due to thermoacoustic oscillations occurring in the outlet gas helium connection to the transfer lines, which showed a reduced cross-section to the warming helium gas flow. The solution was to damp this oscillation with a thin kapton® film wrapped around the inner tube.

The other observed effect is intrinsic to the cavity itself and turned out to be more difficult to eliminate. It is a ponderomotive closed loop instability occurring when the cavity resonant frequency is shifted by the tuning system, to keep the load to the RF generator real, in the presence of beam loading [5]. In such a situation, any resonant frequency disturbance results in a disturbance on the field, which itself perturbs the cavity frequency due to radiation "pressure" on the walls. This results in a potentially unstable closed loop. The observed instabilities occur at the first longitudinal resonances of the cavity (~ 100 Hz) unfortunately very close to the -3dB points (± 90 Hz) of the cavity bandwidth. They are strongly dependent on the cavity fields and on beam current (via the cavity detuning), and at present are a major limitation for LEP2.

A study has been launched to actively damp the mechanical resonances of the cavity, acting on the fast magnetostrictive tuner. The difficulty here is to damp simultaneously two very close resonances (separated by about 5 to 10 Hz) with a robust enough system. The problem, in principle disappears if one keeps the cavity exactly on tune with the RF frequency, irrespective of beam loading. The additional RF power consumption in this case is perfectly acceptable (4.25 kW per cavity at 90 GeV and 10 mA for the LEP2 parameters). However the RF field in the coupler increases significantly, but as explained before, a large safety margin is available in the couplers and this should not be a problem.

Actually, by injecting a phase offset in the tuner phase detector, one can suppress the instability for a given voltage and current. However the cavity phasing errors, the dispersion in coupling factors and cavity fields makes it rather dificult to program the tuner offsets especially during ramping energy and field. In particular, a common offset cannot be simply applied to all eight cavities driven by the same klystron. Despite its limitations and difficulties, this is the technique presently used to avoid ponderomotive instabilities as much as possible.

Another method is being actively tested where a cavity is excited mechanically, via the fast tuner, at a single frequency (at present 40 Hz). The 40 Hz cavity voltage modulation detected by a synchronous demodulator provides an error signal when the cavity is out of tune. This signal can replace the usual phase detector signal (phase between cavity field and klystron drive) to close the tuning servo loop. Such a system (already tested without beam) is independent of beam current and insensitive to phasing errors; it keeps the cavity always on tune. The cavities would be modulated by pairs, with opposite phases, to cancel out the residual phase modulation at 40 Hz (further reduced by the "vector sum feedback").

## 4 HIGHER ORDER MODES

Each LEP2 cavity is equipped with two higher order mode (HOM) couplers. They are of the "hook" type where a series notch filter at the RF frequency is established with the inductance of the "hook" and its capacitance to the wall of the cavity port [6]. The connecting RF line between the cold coupler and the cryostat wall is a 25 Ω "rigid" coaxial line made of two thin stainless steel, copper plated tubes. Finger contacts

at either end of the line allow some mechanical displacements during cool down.

It has been demonstrated experimentally that more than 850 W can be transmitted through the HOM coupler and its line at 630 MHz (frequency of the dominant longitudinal HOM of the LEP2 cavity). This figure is beyond what is expected in LEP2 operation. However, it has been observed that many HOM loads failed during operation, due to transients. They are now being replaced by long, lossy RF cables.

Initial measurements of power deposited by single bunches in the HOM coupler loads have confirmed the expected value of the loss factor of the cavities (0.44 V/pC at $\sigma_z$ = 16 mm, excluding the fundamental).

Above 2.2 GHz (cut-off frequency of the 10 cm diameter beam tube) HOM power may propagate outside the SC cavity module. Using calorimetric measurements on RF ferrite absorbers installed in the LEP vacuum chamber (one close to an SC module, one far away), the first experimental evidence of HOM power radiated outside the SC modules was obtained.

During the last run of 1996, it was observed that the cryogenic consumption of the modules was increasing with higher beam current and shorter bunches, leading to the suspicion of HOM trapped inside the 4-cavity structure. A concomitant increase of the temperature of the cold intercavity bellows (copper plated stainless steel, diameter 20 cm) has also been observed and supports this hypothesis. An energy dependence of the power deposited in standard warm bellows outside the modules has also been noted, without any convincing explanation for the moment. Synchrotron radiation, as well as the radiation coming out of the modules as a result of field emission, has been considered, but obviously more measurements are needed to analyse these effects.

## 5 RF POWER SYSTEM

The LEP RF system is based on high power klystrons (1.3 MW), each feeding 8 SC cavities via a circulator and a series of symmetrical magic tee splitting stages [7]. The circulator is terminated on its third port by a 300 kW water load; each magic tee is terminated by a 100 kW load. To improve crosstalk between adjacent cavities, better matching of the 100 kW loads is required. The solution which is being implemented now is to dope the cooling water of the load with sodium nitrite ($NaNO_2$).

The 24 klystrons of the SC units have so far accumulated between 1000 and 9000 operating hours, with an average of 3500 hours. The average lifetime of these high power klystrons is expected to be 18000 hours (DESY statistics); in the LEP copper RF system nine tubes reached more than 28000 hours. We therefore do not expect klystron problems in the near future.

The reflected wave peak power from a SC cavity when the RF source is abruptly switched off amounts to four times the zero beam current forward power (1 MW in the LEP2 case). It was found that these high power bursts (duration in the ms range) can induce arcs in the line and RF transformer connecting the 300 kW load to the circulator. The arcs eventually propagated to the circulator itself; two of them had to be changed. The solution is to replace the coaxial elbows and wave guide transformer between circulator and 300 kW load by waveguide components and to improve the klystron reflected power interlock. In addition, fast detuning of unused cavities is implemented to avoid strong beam induced power reaching the circulator.

## 6 CONTROLS AND OPERATION

In addition to the classical regulation circuits, notably the slow amplitude loop acting via the DC current and hence the RF gain, the LEP2 klystrons are now equipped with an RF "vector sum" feedback loop (Fig. 5). The total RF voltage seen by the beam when crossing the eight cavities driven by a common klystron is reconstructed from the fieldprobe signals of each cavity. Great care must be applied to the calibration of the probes and cable connections (in amplitude and phase) to ensure that the overall vector sum signal is a faithful representation of the RF voltage experienced by the beam. The "vector sum" signal is maintained equal to the demanded RF voltage by the action of the RF feedback loop.

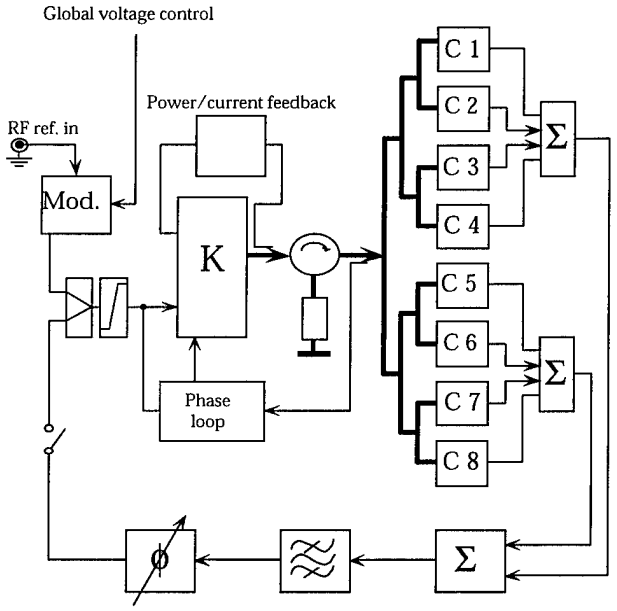



Fig. 5 Simplified block diagram of the vector-sum feedback

The open loop gain of the vector sum feedback RF loop has been adjusted to 26 dB for a klystron current of 10 A but it varies linearly with the klystron current. It is actually limited by the precision with which the vector sum can be constructed.

The loop gain is sufficient to reduce the equivalent impedance of the SC cavities so that cavity coupling via the beam becomes negligible and the operating conditions of the RF system remain far from the Robinson threshold. The phase deviations of the cavities (either from residual microphonics or from various phase settings of the servo tuners) are corrected by the vector sum RF feedback, as well as the cavity overvoltage when the beam is suddenly lost.

The minimum attainable RF voltage, at the injection energy of 22 GeV is limited by the tuning loops of the cavities. These loops are sensitive to spurious signals from RF ripple, crosstalk between cavities, finite directivity of the directional couplers and to imperfect phasing of the cavities. The associated problems have been largely alleviated by running at a higher voltage (450 MV, $Q_s$=0.14) at injection, with all cavities turned on.

With the experience gained in running the RF system in 1996 it is now possible to envisage automation of certain procedures. Application software to perform automated checks of cavity tuning and unit phase could be provided, as could an automated procedure for optimising the tuner setpoints to suppress ponderomotive oscillations. The major candidate for automation from the operational point of view is, however, the automatic switch-on of tripped units.

In 1996 it was standard procedure to stop the ramp a few GeV below physics energy. The RF voltage was then ramped to its operational maximum, any tripped RF units restarted and any ponderomotive oscillations controlled by means of tuner adjustments. Only when the RF system was stable was the machine ramped to physics energy.

There is a significant spread in the voltages produced by the eight cavities driven by a common klystron. This indeed limits the maximum voltage available and is due to differences in cavity coupling factors ($Q_{ext}$) and possible asymmetries in the waveguide and magic tees distribution. A very simple $\lambda/4$ transformer can be inserted in the waveguide to compensate for large variations of $Q_{ext}$ (this has been successfully tested, even with beam). With high beam loading (especially at injection) additional cavity voltage dispersion results from differences in waveguide electrical length or longitudinal position of the cavities inside the cryostat. To correct all these effects will require tedious adjustments, which were not really possible during the last busy years.

## 7 CONCLUSION

The largest superconducting RF system in the world is now in operation. The energy of LEP has been pushed from 45 GeV up to 86 GeV and physics above the W pair production threshold has started. The SC cavities and couplers behaved in the machine as expected; no degradation of performance was recorded. Final adjustments of the RF system will be a tedious, but straightforward task, and it seems that the control of ponderomotive instabilities is within reach. Finally the overall performance of the RF system might be limited by the capacity of the cryoplants. Upgrading of the installed cooling capacity, which was anyhow planned for LHC, might therefore be implemented earlier than foreseen (hopefully in 1999) to the benefit of LEP2.

## 8 ACKNOWLEDGEMENTS

Finally, it is a pleasure to associate to this presentation all the team who engineered, constructed and put into operation the LEP2 RF system and whose competence, dedication and long-lasting enthusiasm were essential to its success.

## 9 REFERENCES

[1] 'The LEP design report', vol. III, LEP2, C. Wyss, editor, CERN AC/96-01, LEP2

[2] D. Boussard: 'Operational experience with the LEP2, S.C. cavity system', Proc. 5th EPAC, Sitges (Barcelona, Spain), p. 187

[3] H. P. Kindermann: 'Status of RF power coupler for superconducting cavities at CERN', ibid. p. 2091

[4] E. Chiaveri: 'Large scale industrial production of superconducting cavities', ibid. p. 200

[5] D. Boussard, P. Brown, J. Tückmantel: 'Electroacoustic oscillations in the LEP S.C. cavities', ibid. p. 2097

[6] E. Haebel: 'Couplers for cavities'. Proc. CAS, Hamburg 1995, S. Turner, editor, CERN 96-03 (1996), p. 231

[7] H. Frischholz: 'The LEP2 RF power generation system'. Proc. IEEE PAC, Washington 1993, p. 1247 and CERN SL/93-20

# OVERVIEW OF ADVANCES IN THE BASIC UNDERSTANDING OF DARK CURRENT AND BREAKDOWN IN RF CAVITIES

Hasan Padamsee[†], Cornell University, Nuclear Studies,
Newman Lab, Ithaca, NY 14853-5001

*Abstract*

In the last decade there have been substantial advances in understanding the nature of field emission through DC high voltage studies that locate emission sites, followed by electron microscopy studies to examine the sites. Emission sites have also been located in superconducting RF (SRF) cavities by temperature mapping. The sites found were also examined in an electron microscope after dissecting the cavities. In many RF tests, the emission current from individual sites was tracked with increasing field until a voltage breakdown occurred. The breakdown event was generally followed by decreased field emission. The RF test was stopped, the cavity dissected and the breakdown site analyzed by microscopy. Scanning electron microscopy, energy dispersive x-ray analysis, and Auger studies were used to obtain topographical and elemental information about the emission and breakdown sites. Although these studies were primarily motivated by the desire to reduce field emission in superconducting niobium cavities, the lessons learnt, and the models that have emerged, apply to all field emitting surfaces.

## 1 INTRODUCTION

The superconducting approach to the next linear collider aims for surface fields $E_{pk}$ >50 MV/m in ten thousand cavities. At these electric fields, an important limitation to the performance of superconducting cavities arises from the emission of electrons from high electric field regions. Power is absorbed by the electrons and deposited as heat when electrons impact the cavity walls. If the emission grows intense, it can even initiate thermal breakdown of superconductivity. In the normal conducting, high frequency approach to linear colliders the goal is to operate ten thousand copper structures at $E_{pk}$ between 100–200 MV/m with klystrons that will supply 50–100 MW of power. Field emission (dark current) is a major concern for the accelerating structures as well as for the output cavities of klystrons, which must operate at comparably high electric fields. Field emission electrons can be captured and accelerated along the structure. A high dark current in the structure may cause transverse wakefields, and spoil the emittance of the beam. It can present problems to various diagnostic equipment in the accelerator.

One of the consequences of high field emission is electrical breakdown, or sparking. Voltage breakdown is found to be beneficial to rf cavities. In a process referred to as conditioning, after several breakdown events, the dark current decreases, and the field in a structure can be raised. However, excessive breakdown events can physically damage a klystron output cavity, changing its resonant frequency and destroying the klystron. There is a need to understand how field emission leads to breakdown and processing, so that the important parameters for conditioning can be identified, for e.g., power level, field level, pulse length.

To address these issues, there have been extensive studies about the nature of field emission sites and the development of voltage breakdown. Based on the results from DC and RF studies, as well as from extensive DC breakdown studies in the literature, models have emerged that elucidate the nature of field emission as well as the nature of breakdown. These studies have stimulated the invention of techniques to avoid emission sites and to destroy them.

## 2 DC STUDIES OF EMISSION SITES

Using needle-shaped tungsten electrodes, $cm^2$ surface area samples were scanned for emission sites. Niobium, copper and gold cathodes were studied at Geneva[1], Saclay[2] and Wuppertal[3]. The number of sites observed increased rapidly with increasing field. Artificial emission sites were also introduced and studied.

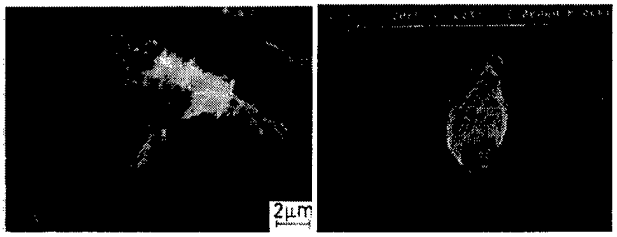



Figure 1. Microparticle field emitters. Foreign elements found were (left, scale bar = 2 μm) C (right, scale bar = 5 μm) Si and O (Geneva and Saclay)

Once individual sites were identified, they were examined by surface analytical instruments. In general no whiskers were found. However, if the surface was scratched, the projections at the edge of the scratch were strong field emitters. But scratches are rare on well prepared surfaces. Instead, the predominant emitters found were "metallic" microparticle contaminants. Fig. 1 shows electron microsocpe pictures of field emission sites found

[†] Supported by the National Science Foundation.

0-7803-4376-X/98/$10.00 © 1998 IEEE

in DC studies at Geneva and Saclay. The foreign elements found in these emitters are listed in the captions. After extensive studies, the following list of elements have been found in particulate emitters: Ag, Al, C, Ca, Cl, Cr, Cu, Cs, F, Fe, K, Mg, Mn, Na, Ni, O, S, Si, Ti, W, and Zn.

## 3 EMISSION SITES IN CAVITIES

Individual field emission sites were located in single cell niobium superconducting cavities by temperature mapping. The heat deposited by the impacting electrons is detected by an array of thermometers placed on the outer wall of the cavity. The heating profile can be unfolded with the help of the calculated electron trajectories to yield the FN properties and the location of the emitting site to within a few mm. Occasionally it was even possible to detect the RF heating due to the emission site.

By many tests on several cavities at CERN[4] and Cornell[5], the density of emission sites found in RF cavities is compared in Fig. 2 with the density of sites observed in DC studies. Note that the Geneva DC samples were exposed to ordinary room air and show a larger density of sites as compared to the Wuppertal samples which were prepared in a class 100 clean room. For emitters found in SRF cavities, the Fowler Nordheim (FN) $\beta$ values were between 100–700, and the emissive area values were between $10^{-9}$ to $10^{-19}$ $m^2$, in rough agreement with the range of FN emitter properties found in DC studies.

Some of the emission sites found in the SRF cavities were subsequently examined in an electron microscope after dissecting the cavities. Fig. 3 shows two such emitting areas; one site consists of stainless steel particles[6], and the other site is an indium particle[7]. Note that there are small regions where the particles are melted. It is likely that the melting occurred due to the joule heating from the high field emission current density which, according to the measured $\beta$ values was estimated to be $10^{11}$ to $10^{12}$ $A/m^2$.

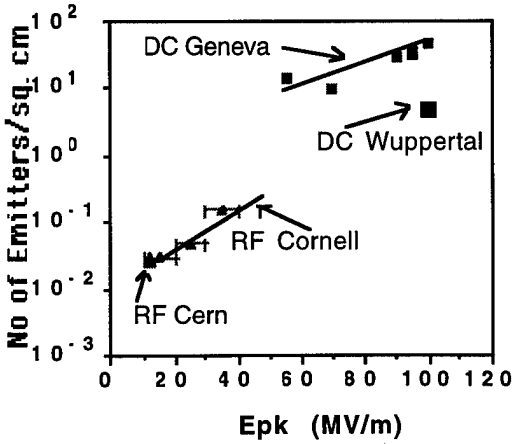



Figure 2. Density of field emission sites in DC and RF studies

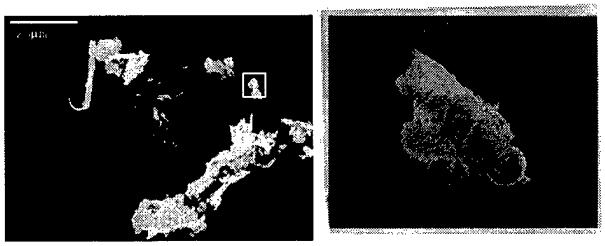


Figure 3. SEM micrograph of (left, scale bar = 20 mm) stainless steel particles found to be emitting and (right, scale bar = 5 mm) an indium metal flake field emitter. Small melted regions can be recognized by their spherical shape.

So far, the range of FN properties, the typical morphology and the elemental composition of emitters in RF and DC studies are very similar. To test the exact same emitter under RF and DC conditions, iron particles were placed on a cathode and studied in a DC field emission microscope at Saclay[9]. Subsequently, the cathode (and the particles) were transferred into a copper RF cavity. In both DC and RF fields, the FN properties were found to be nearly the same.

The only known difference between DC and RF field emission is the behavior of insulating particles. At Geneva[1], insulating particles, identified by their tendency to charge up during SEM examination, were found not to emit. In artificial contaminant studies at Saclay[9], insulating particles, such as $A_2O_3$ and $SiO_2$, when placed on a niobium or gold surface, did not emit in a DC field, but were found to emit when placed in a copper RF cavity. One possible explanation for the difference is that the theramally isolated and insulating particles heat up to high temperatures in RF fields, and become more conducting, due to excitation of electrons across the insulating band gap. Thus even insulating particles could behave "metallic" in RF fields.

It is often found that emission switches on at a certain field level, and remains on when the field is lowered. Recent thermometry studies[10] with a niobium cavity showed that the switch-on is associated with the arrival of a particle, detected by the increased RF heating at the emission site. DC studies have also shown that particles in high electric field regions can tear away from the surface, thereby producing a mechanism for emitter switch-off[9].

## 4 NATURE OF FIELD EMITTERS

A remarkable finding from DC studies is that only 5–10% of the total number of foreign particles are emitters. What makes a micron-size particle into a field emitter?

As already mentioned, if it is insulating it is not an emitter in a DC field. Another important distinguishing aspect between emitting and non-emitting particles is the jagged structure of emitting particles. In DC field emission studies conducted at Saclay[11] with artificially introduced particles, it was found that smooth, spherical iron or nickel particles do not emit, but jagged particles

emit strongly. In a simple geometrical interpretation, the particle as a whole enhances the field and smaller protrusions on the particle further enhance the field, so that the combined enhancement is sufficient to explain large $\beta$ values.

This simple geometric explanation can only be part of the story, however. Not all irregular shape artificially introduced "metallic" particles of $MoS_2$ were found to emit[1]. Results from DC field emission studies at Wuppertal[3] suggest that the interface between the particle and the substrate plays an important role. As shown in Fig. 5, heating a Nb surface and its emitting particles to 1400 C renders the surface emission free. Many emitting particles disappear with the heat treatment, but not all. One may argue that at 1400 C the jagged residual particles became smooth. However, as Fig. 5 also shows, re-heating a 1400 C heat-treated, emission-free Nb surface to 200 C converts residual non-emitting particles into emitters. It is unlikely that heating to 200 C will make a smooth particle into a jagged one. One possibility is that the interface between the particle and the underlying surface plays an important role, and is responsible for the changes in emission with heat treatment.

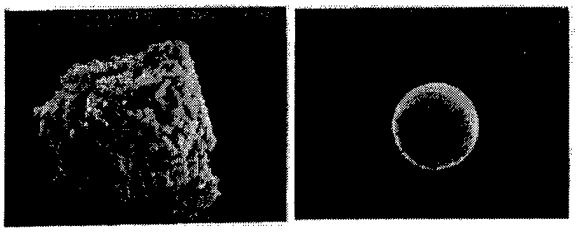


Figure 4. SEM micrographs of nickel, (left) the jagged particle is emitting (right) the smooth particle is non-emitting up to 100 MV/m (Saclay)

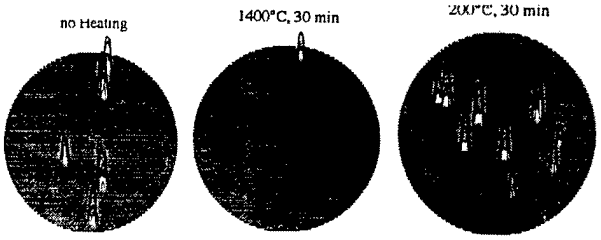



Figure 5. DC field emission show peak areas of high emission. (left) Without heat treatment. (middle) An emission-free niobium surface obtained by heating to 1400°C. (right) Reheating a 1400°C treated field emission-free surface to 200°C creates new emitters. (Wuppertal).

Based on studies of emitted electron energy spectra, the Aston group[12] has proposed a Metal-Insulator-Metal model which involves an insulating interface between the emitter and the base metal. In the presence of a local field enhancement due to the metal particle, electrons tunnel into the insulator from the metal substrate. Here they acquire kinetic energy from the penetrating electric field and are "heated". The electron population at high energy is similar to that of a metal surface at a high temperature. Those electrons with enough energy to pass over the surface potential barrier are emitted into the vacuum as in a standard thermionic emission process. The detail nature of the insulating interface determines the surface potential barrier and therefore the magnitude of the emission current. Emitter switch-on mechanisms are also proposed based on the formation of conducting channels in the insulating interface.

Another important factor that plays a role in whether a particle is a field emitter or not is the influence of condensed gas. There is substantial evidence to show that condensed gas can start field emission[13]. The emission landscape observed by temperature maps was found to change on warming a cavity to room temperature and re-cooling. New emission sites were activated when He and $O_2$ were admitted into a cold cavity. These sites became dormant when the cavity was warmed up to room temperature. Re-admission of gas was found to activate the exact same sites. A theoretical model of resonant tunelling due to adsorbed atom states was proposed a long time ago[14]. Adsorption of hydrocarbons, on the other hand, was found to decrease emission, by raising the work function[15].

## 5 VOLTAGE BREAKDOWN

In many instances, during tests[7,10] on 1-cell 1.5 GHz and 3 GHz niobium cavities, increasing field emission current from individual sites was tracked with increasing field using temperature maps, until a processing event occurred. This event was recognized by decreased emission. After the event, the RF test was stopped, the cavity dissected and the breakdown site analyzed by electron microscopy. Sites such as those shown in Figs. 6 were found at the processed emitter locations. They have a starburst shape with molten, crater-like core regions. In most cases the craters were molten niobium. Micron size molten particulate debris near the molten craters were analyzed by EDX to reveal contaminants, such as copper, indium, iron and titanium. Thin layers of foreign metals coating the craters were analyzed by the more surface sensitive Auger method to reveal foreign elements[16].

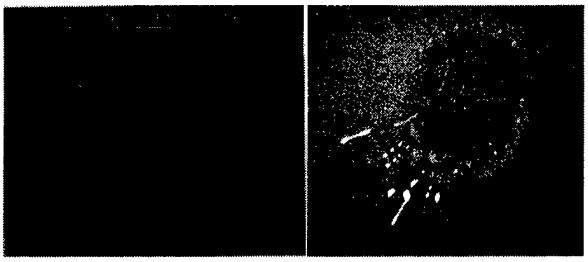


Figure 6. SEM pictures of a processed site found at the (left) Low magnification shows a starburst believed to be caused by a plasma. (right) High magnification SEM picture shows a central crater region within the starbursts, e.g. molten indium particles in a splash pattern.

After analysis of nearly 100 processed sites, the list of foreign elements found near exploded emitter craters is C, Ca, Cr, Cu, F, Fe, In, Mn, Ni, O, Si, Ti. This list has a substantial overlap with the list from DC studies.

Studies of cathode spots from DC arcs[17] reveal many similarities to the results discussed here. Photographs show 100 μm luminous spots (plasma), and post-mortem pictures show molten crater areas. As in the cavities, individual craters found have a characteristic size on the order of microns. But the starburst features found in Nb cavities were never reported in DC studies. Pursuing these close similarities, experiments were carried out to look for the starbursts by initiating a spark with high DC voltage across a small gap between two Nb electrodes in UHV[18]. The Nb surface was prepared by the same treatment as cavity surfaces. SEM studies of the Nb cathode in the sparked area showed a starburst with molten cores. (Fig. 7), similar to those found in Nb cavities. It is therefore plausible to conclude that starbursts found in RF cavities also take place during a spark or discharge.

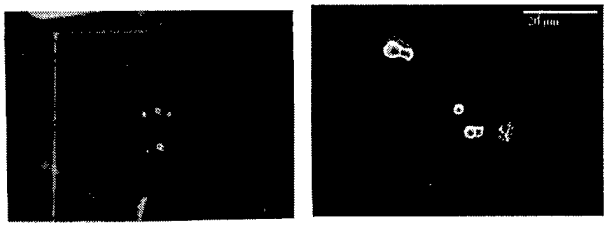


Figure 7 (left) SEM micrograph of a starburst and central molten crater found on a Nb surface at the location of a DC spark at 100 MV/m. (right) Large molten iron drops found at the periphery of a starburst show high temperatures reached inside a starburst region.

Further surface studies of starburst regions reveal much about the activities within the plasma. Auger studies[16] have shown that the surface within the dark starburst region is cleaner, i.e an absence of foreign elements. Occasionally (Fig. 7) large molten particles are found at the outer periphery of a starbusts, suggesting that the temperature of the starburst region exceeds 1000 C.

Extensive tests have been carried out at SLAC [19] on 3 GHz and 11.4 GHz copper cavities using high power (50–100 MW) pulsed RF (μsec). Surface fields between 200–600 MV/m were reached after many hours of spark conditioning which reduced the dark current by orders of magnitude. During the sparks the emitted current increased by a factor of 20–30 and the vacuum degraded from $10^{-8}$ to $10^{-7}$ torr. The pressure bursts suggest gas evolution during sparks. Subsequent visual inspection of high field regions show numerous crater areas, with many overlapping craters. After processing to very high fields the entire iris is pock marked by overlapping craters. It would be interesting to conduct Auger studies of craters in copper cavities to reveal the foreign elements responsible.

That the presence of gas is important to initiate a breakdown event was confirmed by a He processing experiment on a Nb cavity[6]. Temperature maps showed that at the maximum field level and available RF power a field emission site did not yield to RF processing. However, when He gas was admitted, the site processed immediately. After dissection, SEM pictures at the site showed the explosive event of Fig. 8.

Recent DC high voltage studies show gas desorption plays an important role in the onset of voltage breakdown[15].

## 6 A MODEL FOR BREAKDOWN AND PROCESSING

We have seen in Fig. 3 that field emission is accompanied by partial melting of the site even before the site is processed and, from the He processing event, that the presence of gas is important for the breakdown event. The gas for the discharge could come from the metal vapors issuing from the molten regions, or from the evolution of surface-adsorbed gases. Additional heating due to ion bombardment may be responsible for further melting and gas evolution. The field emitted electrons ionize the gas forming a plasma. The activity in the plasma region leaves a clean starburst as a physical trace on the Nb surface or appears as a luminous spot reported in DC studies.

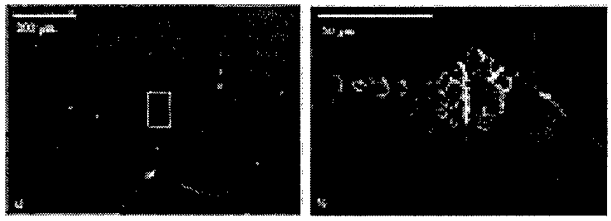


Figure 8. (Left, scale = 200 μm) SEM picture of the helium-processed site showing (a) a starburst and (right, scale = 50 μm) molten craters in an expanded view. Note that (right) is rotated by about 60 degrees relative to (left).

Recently, MASK simulations[10] have been carried out to study how the field emission current ionizes gases present in the vicinity of the emitter. These studies show that, since the ions move slowly relative to the electrons, a significant number of ions accumulate near the emitter, and lead to a substantial electric field enhancement. The ion enhanced fields can become very large. For example, if the peak RF applied field is 30 MV/m at an emitter with $\beta = 250$ and area of $3 \times 10^{-14}$ m$^2$, the ion enhanced field is 100 MV/m at 1 μm from the original emission site, 200 MV/m at 0.5 μm and higher still closer to the emitter. When the field emission current starts to increase unstably, the simulation is stopped. We deduce that a discharge follows when the large number of ions produced nearby the site cause an instability in the field emission current. At the core of the spark the avalanche heating must be sufficiently intense to cause the melting and

explosive cratering found. Unlike the original particle, which has jagged features, the crater and other melted particles do not emit because they are smooth particles. Foreign elements from the original emission site are left behind after the explosion as debris, or as a thin film over the melted region. Both types of debris have been identified. The enhanced fields from the slowly spreading ion cloud may also initiate multiple arcs between the ion cloud and the surface, resulting in multiple craters from an individual emission site. It is plausible that the ion enhanced fields stimulate emission from regions of the surface that have lower $\beta$ values.

According to the MASK simulation, the number of ions produced and the associated field enhancement depends on the total current from the emitter. Previous estimates based on processed emitter data[7] have also indicated that it is necessary for the total current to approach a threshold level ($\approx$ mA) in order for an emitter to process.

## 7 IMPLICATIONS & CONCLUSIONS

The DC and RF studies show that most emitters are micron-size contaminants that come from surface preparation, cavity assembly procedures and the vacuum apparatus. To minimize such contaminants it is important to assemble cavities in class 100, dust free clean rooms. However, even though clean room assembly is necessary, it is not enough to give field emission free cavities for $E_{pk}$ > 20 MV/m. Additional cleaning measures, or emitter destruction measures, are needed. High pressure (80–100 bar) water rinsing of the cavity surface has been found to provide field-emission-free surfaces to $E_{pk}$ = 60 MV/m in superconducting cavities[20].

We have seen that individual emitters can be exploded during breakdown event. The model of breakdown suggests ways to improve processing of emission sites. For a site with a particular value of $\beta$ and $A_e$, the field must be increased to reach a $\beta E$ value corresponding to an emission current density of > $10^{11}$ A/m$^2$ to approach heating and melting at the site so that a sufficient gas density is created. But to process a site the total current must be increased to a threshold value approaching $\approx$ mA. To reach the necessary field level, high RF power is required. Short pulses are sufficient, because the emitter explosion takes place very fast ( < $\mu$sec) when the conditions are ripe. MASK simulations and DC field emission studies using very short pulses show that spark formation times are between nsec to $\mu$sec[21].

From systematic pulsed power conditioning experiments carried out[7,22] with 1-cell, 2-cell and 9-cell niobium cavities at 1.3 and 3 Ghz using pulsed power levels between 50 kW and 1 MW, and pulse length between 5 $\mu$sec and 0.5 msec, we find that the most important parameter for successful processing is the value of the surface field reached. To obtain *field emission free* behavior at a certain operating field level, experiments show that it is necessary to condition cavities to approximately twice the operating field. Conditioning for longer times at the same field level, or with longer pulses at the same field level did not help to reduce the dark current or to reach higher fields.

## REFERENCES


[1] Ph. Niedermann, PhD Thesis No. 2197, Univ. of Geneva (1986).

[2] C. Chianelli, Proc. of the 5th Workshop on RF Superconductivity, DESY, ed. D Proch, p. 700, DESY-M-92-01 (1991).

[3] N. Pupeter et al, Proc. of the 7th Workshop on RF Superconductivity, ed., B. Bonin CEA/Saclay 96 080/1, p. 67 (1995) & E. Mahner, Proc. of the 6th Workshop on RF Superconductivity, CEBAF, Ed. R. M. Sundelin, p. 252 (1994).

[4] W. Weingarten, Proc. of the 2nd Workshop on RF Superconductivity, CERN, ed. H. Lengeler, CERN , p. 551 (1984).

[5] H. Padamsee, Proc. of the 4th Workshop on RF Superconductivity, KEK, ed. Y. Kojima, Rep. 89-21, p. 207(1990).

[6] J. Knobloch et al, Proc. of the 1995 Part. Acc. Conf., Dallas, p. 1623 (1995).

[7] J. Graber, Nucl. Inst. and Meth. in Phys. Res. A 350, p. 572 & p. 582 (1994).

[8] B. Bonin et al, Proc. of the 6th Workshop on RF Superconductivity, CEBAF ed. R. Sundelin, p. 1033 (1993).

[9] J.Tan Proc. of the 7th Workshop on RF Superconductivity, ed., B. Bonin CEA/Saclay 96 080/1, p. 105 (1995).

[10] J. Knobloch, PhD Thesis, Cornell University.

[11] M. Jimenez et al, J. Phys.D, Appl. Phys. 27, 1038 (1994).

[12] N.S. Xu, High Voltage Vacuum Insulation, Ed. R.V. Latham, Academic Press, p. 115 (1995).

[13] Q.S.Shu et al, IEEE Trans. Mag-25, 1868 (1989).

[14] C.B. Duke and M.E. Alferieff, J. Chem. Phys. 46, 923 (1967).

[15] W.T. Diamond, Chalk River Internal Report Nos. TASCC-P-97-4&5.

[16] T. Hays in refs [8] p. 750 (1994).

[17] Pulsed Electrical Discharge in Vacuum, G.A. Mesyats and D.I. Proskurovsky, Springer Verlag (1988).

[18] D. Moffat et al. Part. Accel. 40, 85 (1992).

[19] J.W. Wang and G.A. Loew, Proc of the 1989 Particle Acc. Conf. IEEE Catalog No. 89CH2669-0, 1137 (1989).

[20] P. Kneisel and B. Lewis, in refs [9] p.311 (1995).

[21] G. A. Mesyats, IEEE Trans. Electrical Insulation, EI-18,(3). 218 (1983). & B. Juttner, IEEE Trans. Plasma Science, PS-15(5),474 (1987).

[22] C Crawford et al, Particle Acc. 49, 1 (1995).

# DESIGN OF 250-MW CW RF SYSTEM FOR APT*

D. Rees, Los Alamos National Laboratory, PO Box 1663, Los Alamos, NM 87545

*Abstract*

The design for the RF systems for the APT (Accelerator Production of Tritium) proton linac will be presented. The linac produces a continuous beam power of 130 MW at 1300 MeV with the installed capability to produce up to a 170 MW beam at 1700 MeV. The linac is comprised of a 350 MHz RFQ to 7 MeV followed in sequence by a 700 MHz coupled-cavity drift tube linac, coupled-cavity linac, and superconducting (SC) linac to 1700 MeV. At the 1700 MeV, 100 mA level the linac requires 213 MW of continuous-wave (CW) RF power. This power will be supplied by klystrons with a nominal output power of 1.0 MW. 237 klystrons are required with all but three of these klystrons operating at 700 MHz. The klystron count includes redundancy provisions that will be described which allow the RF systems to meet an operational availability in excess of 95 percent. The approach to achieve this redundancy will be presented for both the normal conducting (NC) and SC accelerators. Because of the large amount of CW RF power required for the APT linac, efficiency is very important to minimize operating cost. Operation and the RF system design, including in-progress advanced technology developments which improve efficiency, will be discussed. RF system performance will also be predicted. Because of the simultaneous pressures to increase RF system reliability, reduce tunnel envelope, and minimize RF system cost, the design of the RF vacuum windows has become an important issue. The power from a klystron will be divided into four equal parts to minimize the stress on the RF vacuum windows. Even with this reduction, the RF power level at the window is at the upper boundary of the power levels employed at other CW accelerator facilities. The design of a 350 MHz, coaxial vacuum window will be presented as well as test results and high power conditioning profiles. The transmission of 950 kW, CW, power through this window has been demonstrated with only minimal high power conditioning.

## 1 ACCELERATOR DESIGN

The APT Linac design is based on copper, water-cooled, NC, accelerating cavities that accelerate the beam to an energy of 217 MeV and inject it into SC accelerating cavities. Final output energy can be varied from 1300 MeV to 1700 MeV. This hybrid Linac architecture is illustrated in Figure 1. During operation, a 75-keV injector housing a microwave-driven ion source generates a continuous proton beam at 110 mA nominal current. From this input, a 350-MHz, 8-m radio-frequency quadrupole (RFQ) produces a CW 100-mA beam at 6.7 MeV. The RFQ output beam is matched into a 700-MHz coupled-cavity drift-tube-Linac (CCDTL) that accelerates it to 100 MeV. Acceleration to an energy of 217 MeV takes place in a coupled cavity Linac (CCL) that uses 700-MHz side-coupled cavities.

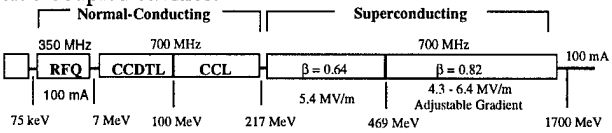



Figure 1. APT Accelerator Schematic.

The SC Linac is composed of cryomodules that contain 5-cell 700-MHz accelerating cavities. There are two kinds of cryomodules, each designed for efficient acceleration in a different proton energy range. Cavities in the medium-energy section, from 217 MeV to 469 MeV, are optimized at $\beta = 0.64$, and in the high-energy section at $\beta = 0.82$.

The RF system requirements by section are presented below in Table 1. The justification for the generator selection and power capacity is presented in subsequent sections. The table serves to illustrate the scope of the APT RF system. 237 1-MW capacity klystrons are required for the desired level of Tritium production.

| Structure | Freq. (MHz) | No. of RF Systems | Total RF Required | Klystron Size |
|---|---|---|---|---|
| RFQ | 350 | 3 | 2.3 MW | 1.2 MW |
| CCDTL | 700 | 21 | 16.6 MW | 1 MW |
| CCL | 700 | 27 | 19.7 MW | 1 MW |
| SC ß=0.64 | 700 | 30 | 29.1 MW | 1 MW |
| SC ß=0.82 | 700 | 156 | 151 MW | 1 MW |
| Totals | | 237 | 219 MW | |

Table 1. RF system requirements by accelerating structure.

## 2 RF SYSTEM DESIGN

The magnitude of the RF system requirements result in the RF system being the one of the predominant cost factors for the APT facility. The RF system DC-to-RF conversion efficiency has a primary influence on the operating costs for the APT facility. The size of the APT RF system makes component failures a statistical certainty. The RF system must be designed to minimize the number of single point of failure components to

*Work supported by the Department of Energy, contract W-7405-ENG-3

0-7803-4376-X/98 /$10.00 © 1998 IEEE

insure high availability. An additional requirement imposed by the end user of the facility is that the RF system be based on existing, proven technology or low risk extensions of existing technology.

### *2.1 RF System Cost and Generator Size*

The RF generator size has the single biggest influence on the RF system cost. The RF system cost increases by a factor equal to approximately the square root of the ratio of a 1 MW generator divided by the power capacity of the reduced generator size. This relationship was generated from point designs of RF system architectures based around different generator sizes spanning 125 kW to 1 MW. The scaling relationship is qualitatively justified by considering how the costs of various RF system components scale with generator size. High voltage power supplies, power conditioning, crowbars, resonance control and RF window costs are weak functions of generator size. Waveguide, water load, fast RF controls, RF reference, computer interface, circulator, safety interlocks, klystron support electronics, and RF generator costs are strong functions of RF generator size.

Based on this data, previous experience at CERN and KEK, and conversations with klystron vendors, 1.2 MW was selected as the generator size for the 350 MHz klystrons and 1.0 MW was selected as the generator size for the 700 MHz klystrons. Based experience at other CW accelerator facilities, klystrons with modulating anodes have been selected as the baseline approach. The operating parameters of these 350 MHz and 700 MHz klystrons are similar. Both klystrons have a saturated efficiency of 65 %, a maximum beam voltage of 95 kV, a gain of 40 dB, a modulating anode, and can take the full beam power in the collector and operate into a 1.2:1 VSWR at any phase. The 350 MHz tube has a maximum output power capacity of 1.2 MW and 1 dB bandwidth of .1 MHz while the 700 MHz klystron has a maximum power capacity of 1.0 MW and a 1 dB bandwidth of 1.4 MHz.

These klystrons have one additional requirement that differs from the historical requirement for this class of CW klystrons. The APT klystron collectors are required to dissipate the full klystron beam power for a duration in excess of one hour. This requirement is driven by the demand load that the APT RF system places on the local utility. The APT RF system AC demand is in excess of 10% of the generating capacity of the local utility. At this fraction of the total system-wide AC demand, the turn-on and turn-off transients and resulting imbalance of supply and demand are not manageable without expensive infrastructure changes and energy storage additions to the local grid. The response rate of the local grid would also significantly impact recovery times from short duration faults (faults lasting 30 minutes or less). Consequently, if the full RF power is not required from the klystrons for intervals of up to one hour, the excess energy will be dissipated in the klystron collector. The 350 MHz klystron design has demonstrated during acceptance tests the ability of the collector to take the full beam power for more than two hours. Two of the 350 MHz klystrons have been tested and both have achieved all performance requirements. Two 700 MHz klystrons, one each from two vendors, are scheduled for test in June and July of 1997. The 350 MHz klystrons are being supplied by English Electric Valve (EEV) and the 700 MHz klystrons are being supplied by EEV and Communication and Power Industries (CPI, formerly Varian Associates).

### *2.2 Conversion Efficiency*

The required DC-to-RF conversion efficiency of the APT klystrons is 65%. This efficiency has been demonstrated in acceptance test for the 350 MHz klystron and has been predicted by large signal analysis for the 700 MHz klystron. However, klystron physics dictate that the high efficiency is only realized at the saturated output-power level. At any level below saturation, the efficiency is decreased proportionally to the reduced output power. In accelerator service, we must provide high bandwidth control of the accelerating-cavity-field amplitude and phase by modulation of the RF drive to the klystron. This forces us to operate below the saturated output level to allow margin for control. Control system modeling based on the expected cavity field perturbations indicates a 10% margin should be sufficient to provide this control. This results in a nominal operational efficiency of 58.5% for the klystrons.

The high voltage DC power supply is required to provide an AC-to-DC conversion efficiency of 95 %. The design goal for the APT power supply is 97 %.

The other source of inefficiency in the RF system is the insertion and return loss from the RF waveguide and waveguide components, including the RF window and coupler. The allocation for this loss is 7.5%. Combining these efficiency allocations the conversion efficiency of AC power from the grid to RF power to the beam and cavity is 51.4 %. This efficiency is also slightly reduced by the AC power required for the klystron support electronics.

### *2.3 Availability*

The RF system is required to meet an 11 month availability of 95 %. Because of the size of the RF system and the number of RF systems required, it is impossible to achieve the availability requirement without installed redundancy. We have chosen to implement redundancy at the RF system level rather than designing redundancy into the RF component level to minimize cost. The NC and SC sections of the accelerator utilize different approaches to provide the redundancy. In the SC, higher-energy portion of the Linac, it is possible to detune cavities, disable the associated RF system, and coast the beam through the detuned cavity. Five percent spare

cavities and RF stations are installed on the SC Linac. If a single cavity or a klystron that powers several cavities fails, the beam phase beyond the failure point will be different than what would have been otherwise provided and, unless corrected, would generally result in poor acceleration efficiency and poor longitudinal focusing in the cavities downstream of the failure. Such an uncorrected situation could also ultimately lead to radial loss of beam. However, rephasing the linac beyond the point of failure is a simple operation where the RF phase in the SC cavities is shifted by calculable amounts, setting the new injection phases to the correct values.

For NC accelerating structure the RF system is arranged into what we refer to as supermodules. The supermodule concept uses the accelerating cavity as the power combiner where, if n klystrons are required to meet the RF requirements of the accelerating cavity, then n+1 klystrons are connected to the cavity, providing a readily available spare. During normal operation, the n+1 klystrons are operated at an output power reduced by the fraction of n/(n+1). This operating scenario is recommended by tube vendors to increase the operational life of the klystrons. If a failure disables one of the n+1 klystrons or associated klystron electronics, then the failed RF station is removed from the accelerating structure by a waveguide switch positioned to show the accelerating cavity an effective short circuit at the coupling point. The output power of the remaining klystrons is increased, and the supermodule still meets all operational requirements.

The supermodule RF architecture is illustrated in Figure 2. The figure shows a supermodule where seven klystrons are connected to a CCDTL accelerating structure while only six of the klystrons are needed to meet the operational requirements. The klystrons are protected from high VSWR with Y-junction circulators. The power from each klystron is split before being delivered to the accelerating structure to minimize RF window stress and a waveguide switch is provided to take any of the seven RF systems off line in the event of a failure in one of the stations. The low level RF controls are not shown in the figure.

There are two primary cost increases associated with the improved reliability of the supermodule concept. The most obvious increase is capital costs of the spare RF stations. There is also an impact on operating cost. When n+1 klystrons are operated at an output power reduced by the fraction of n/(n+1) an operational efficiency penalty must be paid.

The supermodule size is limited to a maximum of 200 accelerating cells to maintain stability within the levels required by the beam dynamics. Since the "real estate" gradient is fixed, where the cell sizes vary with energy, the number of klystrons per supermodule can vary with beam energy. There is also a practical upper limit on the supermodule size dictated by differential thermal expansion and alignment issues. Therefore some variation in the number of klystrons per supermodule exists depending on energy. The range spans four to seven klystrons per supermodule.

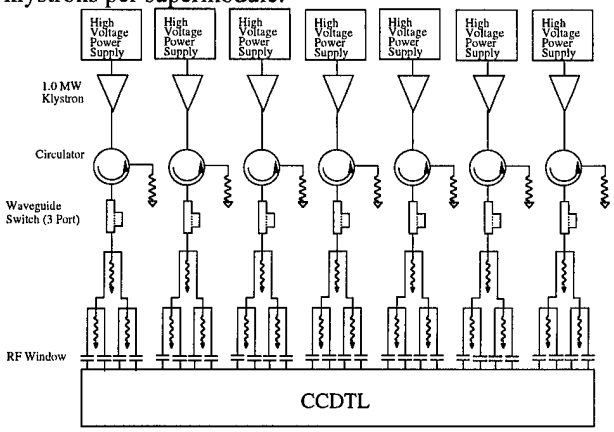


Figure 2. RF Supermodule

The RF windows pose a challenging reliability problem. In order to maximize window reliability a nominal power level of 210 kW has been selected for the CCDTL, CCL, and the high beta SC cavities, 140 kW for the medium beta SC cavities, and 250 kW for the RFQ. These power levels are marginally higher than the experience base at other high average power accelerators world wide. To complicate matters, APT requires over 1000 RF couplers. Even if the coupler windows have a very long life, the large number of windows results in a failure rate that is unacceptably high. To address this potential source of unavailability, we are implementing dual windows on the SC couplers that will allow the accelerator to continue to operate in the event of a window failure. With the dual SC windows the APT RF system can meet the 95 % availability requirement.

## 3 ADVANCED DEVELOPMENT

Although one of the APT RF system design requirements is that the RF technology be based on existing technology it is easy to justify advanced development activities which increase efficiency (reduce operating costs), decrease initial constructions costs, or insure high availability. Three such developments are discussed below.

### *3.1 Advanced RF Generator Development*

Since the RF power required for APT is large and the AC power required from the grid to produce the RF power is the single largest component of the APT AC power demand, even small improvements in efficiency can have a significant effect on the operating cost for the APT accelerator. A reasonable estimate based on the operational availability and the cost of electricity suggests that the operating costs reduce by approximately $1 million per year for each percentage point increase in RF generator DC-to-RF operating efficiency.

Efficiency improvements can be realized in two ways: (1) by increasing saturated generator efficiency, and (2) by changing the saturation to eliminate the efficiency penalty

that must be paid with klystron technology to exercise accelerator field control. The inductive output tube (IOT) family of generators has demonstrated a soft saturation characteristic with a relatively constant efficiency over the upper 20% of output power. Demonstrated saturated efficiencies are on the order of 70 - 75%. Unfortunately, the current state of art in CW IOT generators is 250 kW at 267 MHz. This device also has a very low perveance and correspondingly high beam voltage, a poor reliability record, and low gain. Los Alamos is funding CPI to develop a high order mode (HOM) IOT. The HOM-IOT is shown in Figure 3.

The HOM-IOT is an annular beam device. The annular beam is formed by a number of segmented cathodes. The portions of the segmented cathode structure which do not contain active material allows for the inclusion of radial fins to support the interior structures of the device and to break up the propagation of any coaxial mode along the device longitudinal axis. The annular beam allows for a very low per unit perveance while achieving a very high device perveance and low operating voltage (-45 kV). The predicted gain of the device is moderately higher than the gain achieved in conventional IOTs (24 dB vs. 21 dB) and the predicted efficiency is comparable to the demonstrated efficiency in previous IOTs (73%).

The operating parameters of the IOT as compared to the 700 MHz klystron under development for APT are shown in Table 2. From the table it is observed that the saturated and operational efficiency as well as the reduced beam voltage are the primary advantages while the reduced gain is the primary disadvantage. However, because of the substantial amount of RF power required for APT, the operational savings resulting from the improved efficiency dominate the economic tradeoff between a klystron and HOM-IOT with a high-power driver. The savings and reliability improvements from a lower voltage power supply are also substantial.

*3.2 Stacked Inverter Power Supply*

The baseline design for the APT accelerator is one, SCR regulated, 12 pulse power supply with crowbar per klystron. Operating several klystrons from a single supply has been considered and rejected because of the impact on operational flexibility and reliability. This baseline technology is currently under test at Maxwell Laboratories. An alternate technology is also under development at Continental Electronics. This technology utilizes series connected solid state modules which are switched on to provide the high voltage DC. The switching is accomplished with Insulated Gate Bipolar Transistors (IGBT). A low pass filter follows the series connected modules which remove the switching signals and allows the DC to pass to the RF amplifier. A schematic of the IGBT supply is shown in Figure 4. The topology in the figure results in a 24 pulse supply with

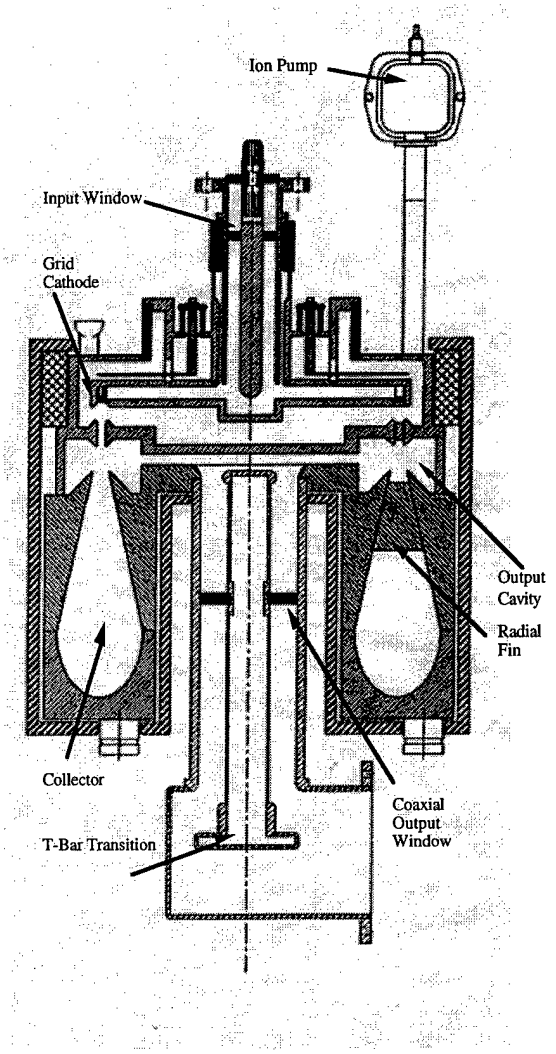



Figure 3. Cross-sectional view of HOM-IOT.

| | Klystron | IOT |
|---|---|---|
| Efficiency at Saturation | > 65 % | > 73 % |
| Efficiency at 90 % of Saturation | > 58.5 % | > 73 % |
| Beam Voltage | 95 kV | 45 kV |
| Beam Current | 17 A | 31 A |
| Gain | 40 dB | 24 dB |
| Filament Power | < 900 W | < 4000 W |
| Magnet Power | < 14.4 kW | < 10 kW |
| Collector | Full Beam Power | 40 % Full Beam Power |
| VSWR At Any Phase | 1.2:1 | 1.2:1 |

Table 2. Comparison of 700 MHz HOM-IOT and klystron requirements.

minimal stored energy in the output low pass filter. This combined with the IGBT switching speed allows for the elimination of the crowbar while limiting energy delivered to a klystron arc to an acceptable value.

The solid state module control circuitry allows for additional modules to be included in the design, and failed

modules can be switched off line. This feature provides for graceful degradation of the power supply. In addition, since most modules are either fully utilized or off for any voltage setting, the efficiency of the supply is very high (97 %) over a variable voltage range. Table 5 compares the baseline 12 pulse SCR power supply with the IGBT regulated power supply. Requirements not listed in the table are comparable for both power supply approaches. . Details of the solid state module design can be found in Reference [1].

### *3.3 RF Vacuum Windows*

The APT design is based around splitting the power from individual klystron 4 or 6 ways resulting in a required window power capacity spanning 140 to 250 kW. Since this power capacity is in excess of the conventional experience base at other CW accelerators of comparable frequency and extensive effort is under way to insure window reliability and design robustness. Our baseline approach is to utilize coaxial windows as illustrated in Figure 5. The window in Figure 5 has been tested to 950 kW CW on a test stand with two windows in a back to back configuration separated by a vacuum region. Only 20 hours of conditioning were required to achieve this 950 kW of transmission. The details of this testing are described in Reference [2].

## 4 CONCLUSIONS

An RF system design for the APT accelerator has been presented. The design basis was described. All major components of the baseline design are currently in test or have completed acceptance testing and the prototype RF system for APT will be operational at Los Alamos at the end of fiscal year 1997. Advanced developments for RF generators and power supplies were presented and discussed. These components will be considered for inclusion in the baseline once they demonstrate their capabilities and undergo long term testing on the Low Energy Demonstration Accelerator at Los Alamos.

## 5 ACKNOWLEDGMENTS

The author would like to acknowledge the contributions of the entire APT High Power RF System Team which includes: Joeseph Bradley, Karen Cummings, Michael Lynch, William Roybal, and Paul Tallerico.

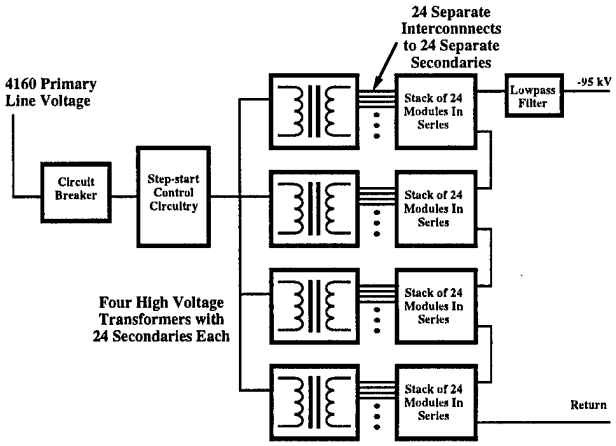



Figure 4. Solid state power supply topology.

| | SCR Regulated Power Supply | IGBT Regulated Power Supply |
|---|---|---|
| Efficiency | 97 % | 95 % |
| Power Factor | .99 | .93 |
| Crowbar Required | Yes | No |
| Footprint | Small | Large |
| HV Insulation | Mostly Oil | Mostly Air |
| Normalized Cost | 1.0 | .5 |

Table 4. Comparison of SCR regulated power supply and IGBT regulated power supply

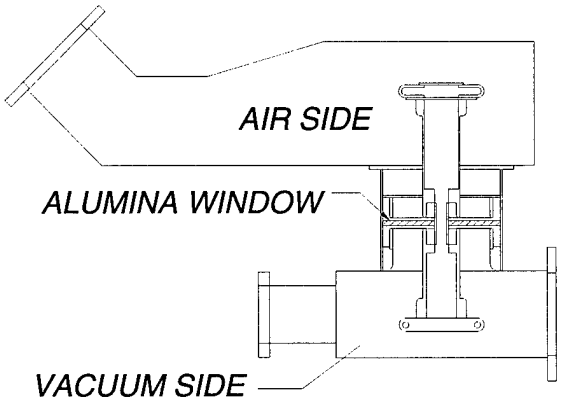



Figure 5. 350 MHz RF coaxial window.

## REFERENCES

[1] J. Bradley et al, 'An Overview of the Low Energy Demonstration Accelerator (LEDA) Project RF Systems,' these proceedings.

[2] K. Cummings et al, 'Experimental Evaluation of 350 MHz RF Accelerator Windows for the Low Energy Demonstration Accelerator,' these proceedings.

# DEVELOPMENT OF X-BAND KLYSTRON TECHNOLOGY AT SLAC

George Caryotakis, Stanford Linear Accelerator Center
P.O. Box 4349 Stanford, CA 94309

*Abstract* *

The SLAC design for a 1-TeV collider (NLC) requires klystrons with a performance which is well beyond the state-of-the-art for microwave tubes in the United States or abroad.

The electrical specifications for the NLC klystrons are not fully established, but they are approximately as follows:

| | |
|---|---|
| Frequency: | 11.4 GHz |
| Peak Power: | 75 MW |
| Pulse Length: | 1.5 μs |
| Repetition Rate: | 180 Hz |
| Gain: | 50 dB |
| Efficiency: | |
| (including beam focusing) | 50% |

SLAC is in the seventh year of a program to develop these klystrons. The choice of X-band as the operating frequency, along with the sheer size of the NLC, have resulted in some new, most demanding standards for the klystrons which may power this future machine. These are related to the overall efficiency required, to the high rf gradients that must be supported at the output circuit without vacuum breakdown, and to the manufacturing cost of the 5,000-10,000 klystrons needed for the collider.

## 1. THE EARLY PROGRAM

It is generally accepted that the manufacturing cost of two identical klystrons is higher than that of a single klystron at twice the power, provided that production yield is not compromised by the increased power. We have opted for the highest power output consistent with a reasonable life cycle cost for the tube. In the beginning of the development program this was 100 MW per klystron.

Several experimental klystrons were designed, constructed and tested in the early 90's to meet that objective. The results were disappointing, for two reasons: In order to use existing modulators, which were limited to about 450 kV, a relatively high beam current was chosen (Perveance of 1.8 x $10^{-6}$)[1]. This resulted in poor beam optics and some beam interception; the high perveance also limited klystron efficiency.

The very first klystron in the XC series, (XC1), which was built with a conventional single-gap output cavity, produced 70 MW. However, this was only for pulses below 50 ns. At longer pulses, rf breakdown drastically limited peak power, with the result that, at the required 1.5 μs pulse length, this tube could produce only 20 MW. In further tests, it was found that the output cavity resonance was higher than the design frequency, because the cavity gap had been eroded by repeated discharges. After that, all subsequent XC klystrons were built with extended interaction cavities of one type or another, but the design eventually converged to a multi-gap, disc-loaded output cavity, operating in either a standing or a traveling-wave mode. These were the output circuits used for the 50-MW XL series klystrons.

## 2. THE XL SERIES OF 50-MW KLYSTRONS

It was decided to target the next series of tubes to 50 MW and to lower the perveance to 1.2x$10^{-6}$. The reduced perveance resulted in stable and more efficient XL-series klystrons. Five such tubes were built and tested. All produced the desired 50 MW at 1.5 μs, within the 440 kV beam voltage.

XL-1 and XL-2, employed standing-wave output circuits. XL-3 was a 4-gap traveling-wave output klystron and exhibited improved efficiency over the previous two tubes, although its output was conditionally stable, i.e. it was necessary to adjust the beam-confining magnetic field to eliminate parasitic oscillations. The next klystron, XL-4, built with the same output circuit, but with added loss, was stable and operated faultlessly up to 75 MW, where its efficiency was close to 50%. The design for these solenoid-focused tubes was frozen at that point. The next klystron, XL4-2, is identical to XL-4 and has been tested with identical results.

The cavity arrangement used and the test results at the 75 MW level are shown in Figs 1 and 2.

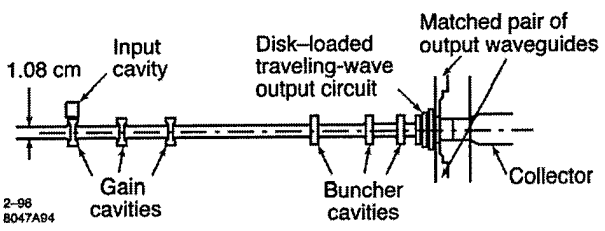



Figure 1

A total of six conventional cavities are employed. The first three "gain cavities" are of the reentrant type in order

* Supported by Department of Energy contract DE-AC03-765SF00515

[1] Beam perveance is defined as Current/(Voltage)$^{3/2}$

0-7803-4376-X/98/$10.00 © 1998 IEEE

to enhance R/Q and are stagger-tuned to obtain the bandwidth necessary for the pulse compressors used in the NLC, which require rapid 180° phase switching in the klystrons. The next three cavities are "pill-boxes" and are tuned well above the operating frequency to bunch the beam, while dividing the voltage among them to avoid rf breakdown. The output circuit is a 4-section, disk-loaded structure coupled symmetrically to two output waveguides, which are subsequently re-combined in a single guide leading to a mode transducer.

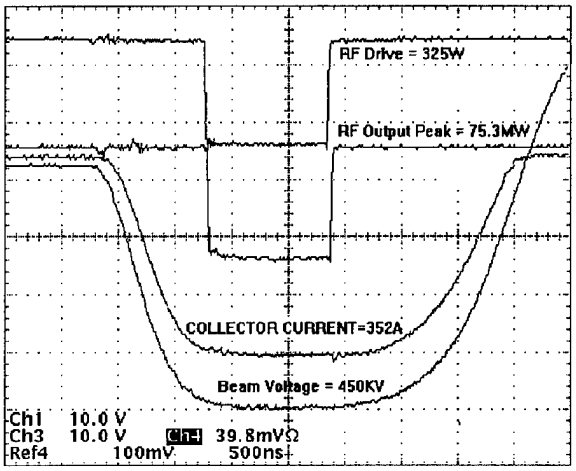



Figure 2

The output circuit deserves particular mention. As indicated above, the XL1 and XL2 output circuits were designed as standing-wave cavities. (Fig 3) They were 3-section, disc-loaded circuits operating in the $\pi$ mode. The objective was to develop an rf voltage comparable to beam voltage across the three gaps, in phase with the beam. Thus the beam voltage and the cavity dimensions chosen for the $\pi$ mode to be at 11.4 GHz determined the spacing of the disks. The field strengths across the three gaps were made more or less equal, with adjustments made for end effects and for the two coupling irises. In the $\pi$-mode, the overall R/Q of this extended cavity was about 50 and the coupling coefficient about 0.8, these being conventional klystron definitions. The $Q_{ext}$ was 60 and was chosen to produce a total voltage across the entire cavity approximately equal to the beam voltage. The goal was a lower maximum surface gradient in the cavity, compared to the gradient of a single-gap cavity at the same total decelerating voltage. The method succeeded, by a factor of approximately 2. A larger number of sections would have further reduced the surface gradient, but would have introduced the possibility of a monotron oscillation at the 0-mode. This actually occurred in the case of one of the XC klystrons, where a four-section output was employed.

The foregoing is a description of ordinary klystron design. Although it resulted in two successful tubes, this method treats the output circuit as a single cavity. It does not take into account the fact that the beam slows down as it interacts with each gap; nor that the rf current flowing into each section increases at each step, since it is made up of current flow from previous sections and current coupled from the beam. Thus, two available degrees of freedom in the design are not utilized, if the klystron approach is taken. A design method based on traveling-wave tube theory can be more effective, and leads to both velocity and impedance tapering along the disk-loaded circuit. This is the method used in the XL3 and XL4 klystrons, where the output circuit operates near the $\pi/2$ mode and has a total of four sections. Oscillations in the 0-mode are avoided because the coupling to the output waveguide is much tighter in the traveling-wave circuit, thanks to impedance tapering. Nevertheless, XL3 exhibited some higher frequency instabilities, which were traced to the last two drift tunnels. In XL4 these were made of stainless, rather than copper, and the tube was unconditionally stable.

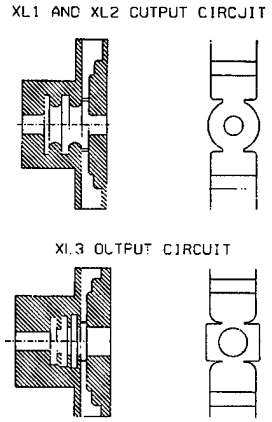



Figure 3

The original XL4 has accumulated 500 or more hours of operation at rated pulse energy and at a repetition rate of 60 Hz. As indicated above it has been operated at 75 MW and it is believed to be capable of even higher peak power. XL4-2 was tested up to 90 MW, at 100 ns pulse length. Two design changes since the XC series contributed significantly to the reliability of the tube. The first was the use of a $TE_{01}$ window, rather than the traditional $TE_{11}$ design, in which rf current crosses the interface between the window and its copper casing. This required the use of a "flower-petal" mode converter within the klystron vacuum. The second change was to attach an ion pump directly to the electron gun, although this required floating it at beam voltage. The improved pumping speed shortened tube processing considerably. Window and gun ceramic failures at test were very frequent in the XC program. There were none in the five XL klystrons tested.

Although the XL4 is not expected to be the rf source for the NLC, four more XL4's are currently being produced at SLAC for use in the NLC Test Accelerator and for experiments at KEK. A power-voltage plot of the first two XL4's is shown in Fig 4. Working drawings are

available to potential industrial manufacturers of NLC klystrons, to prepare them for an eventual procurement of final prototypes.

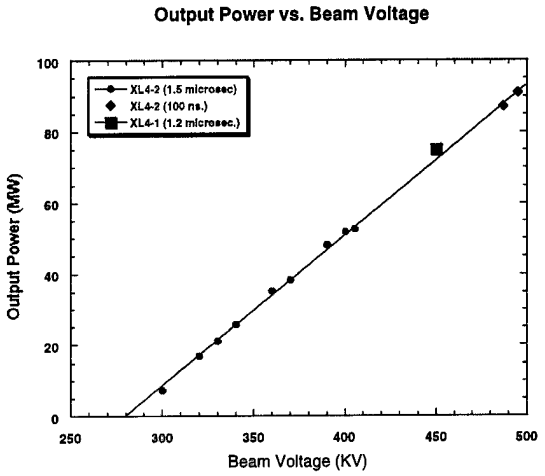



Figure 4

## 3. PPM KLYSTRONS

The NLC source cannot be a solenoid-focused klystron. The solenoid power is of the order of 20 kW, which is higher than the average power of the klystron and hence results in an unacceptable overall efficiency. Superconducting solenoids have always been a fallback option, but they present a considerable complication to the design of a machine with several thousand such devices. Periodic permanent magnet focusing (PPM) was more attractive, but although very common with traveling-wave tubes, relatively untried with klystrons. It was decided to further drop the klystron perveance for the PPM version. A new gun was designed with a microperveance of 0.6. It was felt that, although this would require a higher beam voltage, and a new modulator, it would probably also result in improved efficiency, and hence not quite as high a voltage. This indeed turned out to be the case.

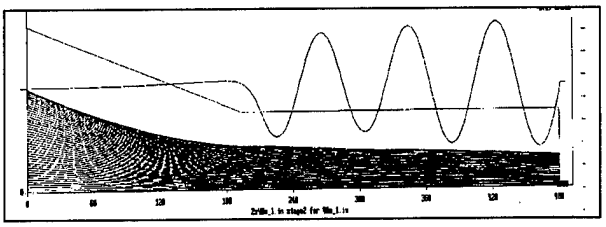


Figure 5

The parameters of these X-band klystrons are very favorable to PPM focusing. The high voltage and low perveance resulted in a long space charge wavelength, and the small cavities allow short magnetic periods. The key to PPM focusing is a high ratio of beam plasma wavelength to magnetic period. There is a stop band in beam transmission at low voltages and the edge of the stop band is a function of this ratio. In helix TWT's a typical $\lambda_p/L$ ratio is 2.5. In the NLC klystron it was possible to attain twice that ratio.

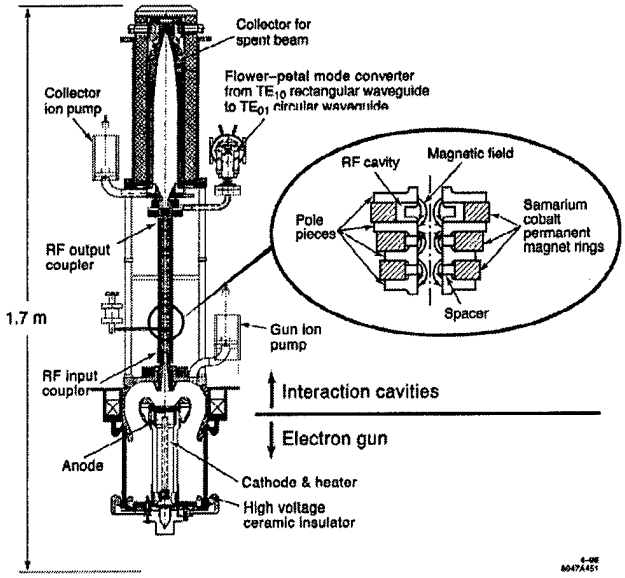



Figure 6

The result was that the stop band was pushed down to a very low voltage. Fig 5 shows that that there is not even a slight ripple in the beam as a result of the periodic focusing. A low beam interception during the rise and fall of the beam pulse (as well as during the pulse) is essential to these klystrons, which carry an extremely high power density in the beam.

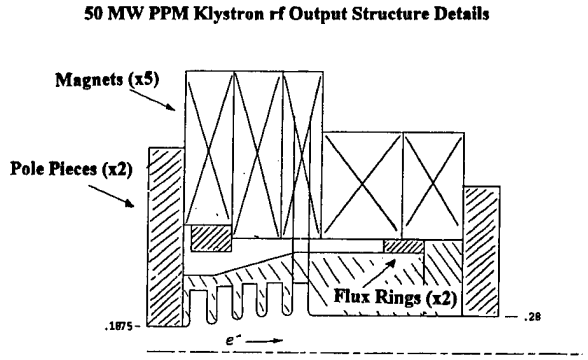



Figure 7

A beam tester was first built to confirm simulations on gun optics and PPM focusing. The magnet material used was Samarium Cobalt with a peak field about 3000 Gauss. There were 20 magnetic periods, approximately the number the klystron would require, and the device was operated up to 550 kV. Beam transmission was found to be excellent (of the order of

99.9%). Furthermore, it was better than 99% down to 100 kV, which was what was hoped for.

An experimental klystron followed. It employed the same type and number of cavities as the XL4 but, because of the higher voltage and lower current, the output was a 5-section traveling-wave circuit. The gain and bunching cavities were nested between pole pieces (Fig 6) and larger magnets were used to provide a straight field at the output circuit. (Fig 7) Output power was taken in two waveguides and two $TE_{01}$ windows. A number of small, low-power solenoids were used in the vicinity of the gun to control beam entrance conditions, but turned out to be unnecessary. Beam transmission was again excellent.

Stanford Linear Accelerator Center

**50-MW X-Band PPM Klystron Simulation and Test Results**

| Item | Experiment | Simulation | Unit |
|---|---|---|---|
| Peak RF Power Output | 56 | 59 | MW |
| Peak Beam Power | 93 | 91 | MW |
| RF Efficiency | 60 | 65 | % |
| Gun Perveance | 0.66 | 0.60 | μK |
| Beam Voltage | 459 | 465 | kV |
| Beam Current | 205 | 190 | A |
| Intercepted Beam Power @Rated RF Output | 1 | 0.0 | % |

Figure 8

Test results compared to simulations are shown in Fig 8. Power output up to 60 MW was measured, at an efficiency of 60 per cent. Beam transmission at full power was lower (96%) but, apparently, the interception was of slow electrons, because there was no appreciable temperature increase at the output circuit at full saturation. The CONDOR simulation is shown in Fig 9 and a picture of the tube is Fig 10.

**CONDOR Simulation at 465 kV and 57.8 MW**

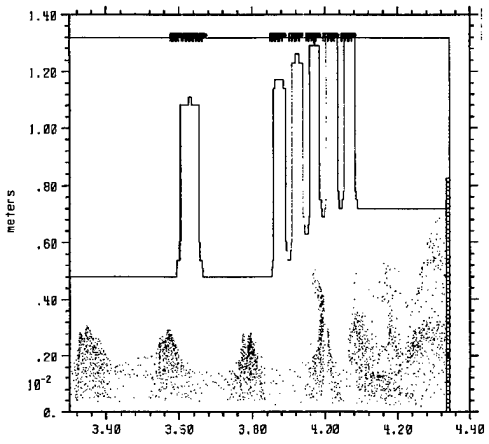



Figure 9

Current plans for the NLC call for 75-MW sources, with 1.1 μs pulses. A new PPM klystron has been designed, this time at a microperveance of 0.75. It is expected to reach test in September. It will be very similar to the experimental PPM klystron, but it will employ larger, stainless, drift tunnels. It is expected that this will be the prototypical electrical design for the NLC.

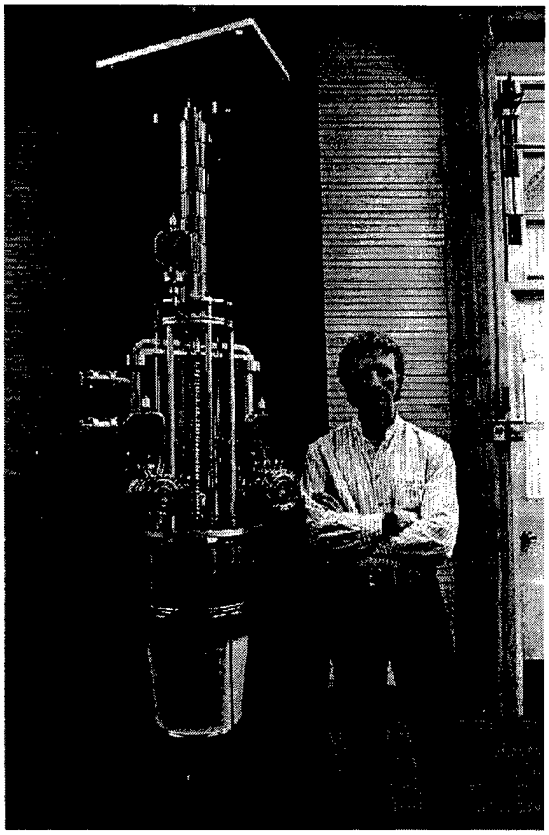


Figure 10

## 4. COST ISSUES

Obviously, life cycle cost is a major consideration in designing these klystrons. It is a function of the acquisition cost, tube efficiency, and useful life of the klystrons. Acquisition cost has particular importance because of the number of klystrons in the collider and their impact on the total cost of the machine. There has never been comparable klystron procurement in the history of the microwave tube industry. Not only are the quantities very large, but the specifications will be much more difficult than those for any klystron now commercially available. For this reason, SLAC has initiated a separate program to design for manufacture the PPM 75-MW klystron now under development. The plan is to run the two programs in parallel, eventually producing several prototypes, which can be demonstrated to meet the final specifications for NLC klystrons. The cost in quantity of these prototypes will be estimated by using outside parts quotes and by amortizing the cost of the necessary production equipment and tooling over the quantity of tubes produced. The cost target for the 75-MW PPM klystrons is of the order of $30,000 each, in quantity 5000 and in 1997 dollars. The current scenario, if the NLC is funded, calls for supplying

industry with working drawings of the prototype klystron and inviting competitive bids. It is likely that at least two contract awards will be made to produce the initial complement of tubes, which will be near 5000 pieces.

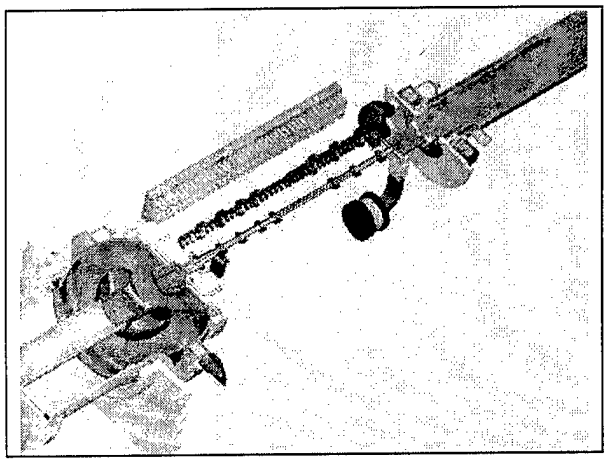


Figure 11

A preliminary sketch of the proposed design for manufacturing is shown in Fig 11. It features a drastic reduction in the number of vacuum joints, by leaving the magnetic pole pieces and their spacers outside the vacuum. The output circuit will probably be assembled by diffusion bonding the diamond tool-machined copper parts, following the method now used in the fabrication of the NLCTA accelerator sections. Other tube subassemblies will be aggressively simplified. A great deal of emphasis is being placed in cost-reducing the gun, and the cathode in particular. In a separate program, partially funded by the Air Force Office of Scientific Research, we are investigating producing oxide cathodes by plasma deposition.

In calculating the cost of the equipment necessary to produce the NLC klystrons, an important issue is the time necessary to pump and test a klystron, since that will determine the number of pump and test stations that must be purchased by the manufacturer. It will be assumed that potential manufacturers do not currently possess manifolded exhaust equipment, capable of processing 4-5 klystrons at a time, nor arrays of 500 kV automated modulators. This processing time is intimately associated with the gases, primarily hydrogen, that are evolved in bakeout or in tube test. SLAC is conducting experiments to establish processes, which either avoid hydrogen brazing of parts, or outgas them, without tying up expensive equipment.

Another issue, and one that affects all rf components of the collider, is vacuum breakdown in the presence of high rf gradients in the klystron, or in waveguides, pulse compressors and the accelerator sections themselves. Rf processing time, for klystrons or rf components, can be a critical cost factor. The problem is being aggressively investigated at SLAC, along two fronts: Dark current emission from test surfaces is being studied in a resonant ring, with an embedded X-band cavity; X-ray imaging techniques will be used to determine emission sites, which can be subsequently studied with an Atomic Force Microscope. An electron microscope is also used to examine surfaces subjected to the treatment necessary for making rf parts in order to determine how these treatments must be modified to reduce or eliminate emission sites.

The X-band klystron program at SLAC is now in its eighth year and is probably the most comprehensive project ever undertaken to develop a microwave tube. It is not completed as yet, but when it is, it should serve not only as the foundation for the industrial production of the NLC klystrons, but also as a valuable milestone in the state-of-the-art of all high-power microwave tubes.

## ACKNOWLEDGMENT

This program is obviously a team effort. Credit must go to the Tube Development Group under Robert Phillips, with Daryl Sprehn responsible for the PPM klystron design; the Klystron Manufacturing Group under Chris Pearson (who built a dozen or more experimental tubes with 100% yield); the RF Component Group, under Arnold Vlieks; The Electronic Engineering Department, under Ron Koontz; and the supporting personnel of the SLAC Klystron/Microwave Department.

# A NEW GENERATION OF GRIDDED TUBES FOR HIGHER POWER AND HIGHER FREQUENCIES

G. Clerc - JP Ichac - C. Robert
Thomson Tubes Electroniques,
18, avenue du Maréchal Juin, 92366 Meudon-La-Foret (France)

## 1 INTRODUCTION

Until recently, triodes and conventional tetrodes have satisfied most of the requirements in accelerators applications. The present and future physicists specifications in this field, calling for increased duty factor, peak power, pulse length and reliability, reach or exceed the possibilities of such components. Power grid tubes technology must evolve to answer these demands.

## 2 LIMITATIONS

### *2.1 Triodes*

Triodes can reach very high peak power (3 to 5 MW). But for these ratings, the control grid current is very high and the dissipating power capability of the grid only authorizes very short pulse duration (≈ 1 ms) and very low duty factor (≈ 1/100).

Operational examples :

| | | | | | |
|---|---|---|---|---|---|
| TH 116: | 2.2 | MW | 3/100 | 700 ms | 200 MHz |
| 7835: | 4 | MW | 6/100 | 2000 ms | 250 MHz |

### *2.2 Tetrodes*

Tetrodes do not have the problem of excessive control grid current. Because of the positive screen grid voltage, high output power can be reached with a very low control grid current. With the other advantage of good efficiency, tetrodes have been developed for high average or cw power.

Operational examples:

*TH 526 / TH 525*
VSWR _ 1.5 / 2 MW / 30s / 12.5% duty factor up to 80MHz
VSWR _ 1.1 / 1.5 MW CW up to 60 MHz
*TH 781*
VSWR _ 1.1 / 200 kW / 200 MHz / CW
VSWR _ 1.1 / 300 kW / 110 MHz / CW
VSWR _ 1.1 / 400 kW / 200 MHz /1.4 ms / 120 Hz
*TH 681*
VSWR _ 1.1 / 130 kW / 200 MHz / CW
VSWR _ 1.1 / 200 kW / 110 MHz / CW

The TH 525 / TH 526 are operational in accelerators and fusion applications. The TH 681 and TH 781 are in use in industrial accelerators or for cavities testing.

#### *2.2.1 Limitations with the conventional tetrodes*

Tetrode in an amplifier is a part of the one quarter or three quarters wavelength resonant circuit. Also its geometrical dimensions act on and dictate the RF voltages and currents (left hand side of fig. 2). The power delivered by tetrodes is the product of the plate RF voltage by the fundamental anodic current. As explained below, the RF voltage is necessarily limited to 30 kV maximum; therefore, reaching high performances requires a large cathode area. This increase of the cathode area can be achieved in two ways:

Cathode diameter

Cathode diameter increase has two effects on the electrical parameters:

- a lowering of the TE11 resonance mode frequency. If this frequency is too close to the nominal frequency or to the first harmonic, it will be difficult, if not impossible, to damp parasitic oscillations.
- an increase of the tube end stray capacitance.

Cathode height

The rule of experience adopted by the tubes' manufacturers is: never exceed 1/16 of wavelength for the height of the cathode at the highest operation frequency when the tube works at high duty cycle. For example, at 80 MHz the maximum height would be 234 mm.

This rule has to be interpreted and is dictated by the RF losses generated on the tube electrodes, in particular on the screen grid mesh.

In the output circuit, in the space between screen-grid and anode, RF voltages and currents can be represented by these two equations:

$$V(x) = Vmax \cdot \cos \beta x = \sqrt{Pout \cdot RL} \cdot \cos \beta x$$

$$I(x) = J \frac{Vmax}{Zc} \sin \beta x \qquad with: \beta = \frac{2\pi}{\lambda}$$

X = distance from the top of the tube
RL = load impedance applied on the tube
Vmax = voltage on the axis (at x = 0)
Zc = characteristic impedance of the anode-screen grid space.

In the last cm of the screen-grid mesh, if R is the resistance of the screen-grid taking into consideration the skin effect, the RF losses P will be:

$$P = R \cdot \left(\frac{Vmax}{Zc} \sin \beta l\right)^2 \qquad \text{If } l = \lambda/16, \quad \beta l = 22.5°$$

*Example:* Vmax = 20 kV
Zc = 8 Ω
R = 1 mΩ
P(at x = λ/16) = 915 W
P(at x = λ/32) = 238 W (see fig. 1)

0-7803-4376-X/98/$10.00 © 1998 IEEE

Losses being proportional to the maximum anode voltage, this voltage must be relatively low, depending on the frequency, and in all cases not higher than 30 kV.

These V(x) and I(x) equations clearly show that the distribution of voltage and current along the screen-grid to anode space is not uniform. Consequently, the power distribution is also not uniform, and power is higher at the top than at the bottom. We can see also that the power capability of the tube is depending on the frequency of operation. After analysis of these physical realities, THOMSON TUBES ELECTRONIQUES has developed the Diacrode to overcome the conventional tetrode limits.

The Diacrode design combines in a tetrode the capabilities and advantages of an up-to-date technology with the concept which had been implemented by RCA long time ago in their very high peak power double ended triodes.

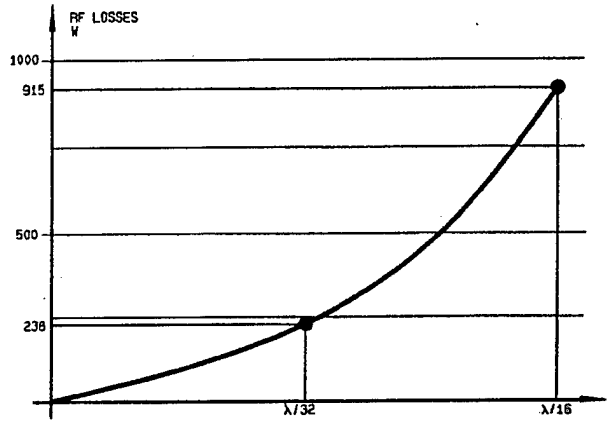



**Fig. 1** RF losses versus screen grid length

## 3 THE DIACRODE

As discussed above, the tetrode main limitation is the length of the active part of the tube relative to the wavelength.

### *3.1 Diacrode or double ended tetrode*

The losses variations are proportional to the square of the cathode height. So, the idea is to obtain the same equivalent height for the cathode by putting in parallel two half tetrodes. In this case, the connections are double and with a proper output circuit this device can be tuned in a half wavelength with the maximum anode voltage placed in the middle of the active part (fig. 2). With this conception, the voltage variation along the active part of the tube and the losses are minimized. So, with this kind of tube, the maximum acceptable length for the cathode is not l/16 but l/8 and the power can be double, provided that the operating point is carefully chosen.

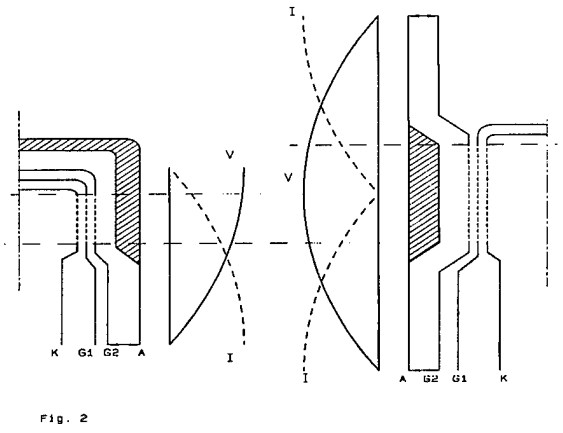



**Fig. 2** Tetrode to diacrode evolution

### *3.2 Results*

This principle has already been applied by THOMSON TUBES ELECTRONIQUES.

In UHF TV (470-860 MHz) the most powerful tetrode was the TH 563 which can deliver 30 kW in combined amplification of vision and sound.

The diacrode TH 680 with its double height cathode compared with the TH 563 can deliver 60 kW in combined amplification of vision and sound. A prototype of the diacrode TH 628 is now in testing phase. The measured results are compared below with those obtained with the tetrode TH 526 currently used in accelerators and in fusion Tokamaks.

TETRODE TH 526 / DIACRODE TH 628
- RESULTS AT 200 MHZ -

| | | PULSED OPERATION | |
|---|---|---|---|
| | | **TH 526** | **TH 628** |
| Pulse duration | (ms) | 1.2 | 2.5 |
| Peak output power | (kW) | 1600 | 3000 |
| Average output power | (kW) | 240 | 600 |
| Anode voltage | (kV) | 24 | 26 |
| Screen-grid voltage | (kV) | 1.5 | 1.6 |
| Control grid voltage | (kV) | - 0.315 | - 0.550 |
| Anode current | (A) | 124 | 164 |
| Screen-grid current | (A) | 3.6 | 5.1 |
| Control grid current | (A) | 4.5 | 3.6 |
| Peak input power | (kW) | 64.9 | 122.5 |
| Gain | (dB) | 13.9 | 13.9 |

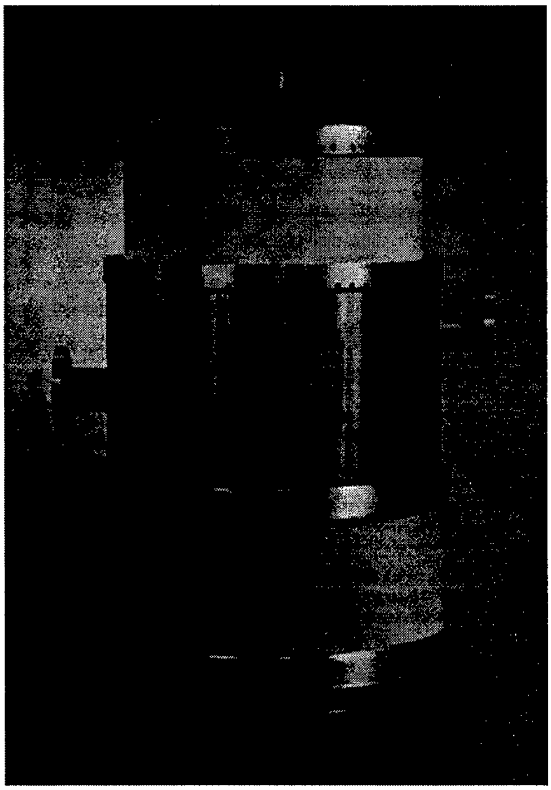
TETRODE TH 526 / DIACRODE TH 628
- RESULTS AT 200 MHZ -

| | | CW OPERATION | |
|---|---|---|---|
| | | **TH 526** | **TH 628** |
| Output power | (kW) | 300 | 1000 |
| Anode voltage | (kV) | 11.5 | 16 |
| Screen-grid voltage | (kV) | 1.5 | 1.6 |
| Control grid voltage | (kV) | - 0.315 | - 0.300 |
| Anode current | (A) | 75 | 96 |
| Screen-grid current | (A) | 0.8 | 2.97 |
| Control grid current | (A) | 0.85 | 1.96 |
| Input power | (kW) | 21 | 32 |
| Gain | (dB) | **11.5** | **15** |

## 4 CONCLUSION

Power grid tubes need a large cathode area to cope with the limitation brought by the maximum allowed anode voltage. Cathode diameter increase is limited by the TE11 parasitic oscillation frequency. Cathode length increase is limited by a poor utilization of this cathode, and by the excessive RF losses on the screen-grid (in its lower part mainly), resulting in unacceptable high temperatures inside the tube. This problem shows that the tetrode has some limitations which can not be overcome with the conventional tetrode design. These limitations can be circumvented by the use of the diacrode concept. THOMSON TUBES ELECTRONIQUES has demonstrated the validity of the Diacrode principle and design first with its TH 680 UHF TV Diacrode now in operational service in a number of commercial TV transmitters. In another frequency and power range, tests have been effected with the TH 628 on our own high power test facility in THONON. The results which were expected have been measured and are now a fact. At 200 MHz, the targets of 1 MW CW and 3 MW pulsed with high duty cycle have been achieved. The knowledge acquired by TTE with its family of Diacrodes allows to go further. Then, the next step for TTE is to develop a new diacrode for fusion application. The performance target of 3 MW CW on VSWR £ 1.1 at 70 MHz can be considered as a realistic goal.

DIACRODE TH 628



# DEVELOPMENT OF HIGH-POWER ARES CAVITIES

T. Kageyama, K. Akai, N. Akasaka, E. Ezura, H. Mizuno, F. Naito,
H. Nakanishi, H. Sakai, Y. Takeuchi, Y. Yamazaki
KEK, High Energy Accelerator Research Organization, 1-1 Oho, Tsukuba, 305 JAPAN
T. Kobayashi
Institute of Applied Physics, Tsukuba Univ., 1-1 Ten-nodai, Tsukuba, 305 JAPAN

*Abstract*

The ARES (Accelerator Resonantly coupled with Energy Storage) structure is a three-cavity system operated in the $\pi/2$ mode, where a HOM-damped accelerating cavity is coupled with an energy storage cavity via a coupling cavity equipped with a coaxial antenna damper to reduce the impedances of the parasitic 0 and $\pi$ modes. Two high-power prototypes with different HOM-damping schemes have been developed, where one is with a quadrupole counter-mixing (QCM) choke structure and the other with grooved beam pipe one. Both prototypes have been tested with an electron beam of about 500 mA in the TRISTAN accumulation ring (AR). This paper reports their RF structures together with some results of the high-power and high-current beam tests.

## 1 INTRODUCTION

The operation of conventional copper cavities under heavy beam loading in KEKB will give rise to a serious instability problem. That is the longitudinal coupled bunch instability driven by the accelerating mode itself. The resonant frequency of the accelerating mode should be detuned from the RF frequency toward the lower side so as to compensate for the reactive component of the cavity voltage induced by the beam. In KEKB, the required detuning frequency will exceed the revolution frequency, leading to the large excitation of a coupled-bunch synchrotron oscillation.

An RF structure named ARES [1] has been developed as a countermeasure against the above problem. In the ARES scheme, an accelerating cavity and an energy storage cavity operated in a high-Q mode ($TE_{013}$) are resonantly coupled via a coupling cavity. The storage cavity is employed to reduce the required detuning frequency, which is inversely proportional to the ratio of the electromagnetic stored energy with respect to the reactive part of the beam-field interaction energy. Needless to say, the accelerating cavity itself must be a HOM-damped cavity in order to reduce the HOM impedances also driving coupled-bunch instabilities.

The ARES structure operated in the $\pi/2$ mode employing a coupling cavity has several advantages listed in Ref. [2] over a non-ARES one, where the accelerating and the storage cavities are directly coupled and operated in the $\pi$ (or 0) mode. In addition, the coupling cavity functions as a kind of filter for some HOM's to isolate the accelerating cavity from the storage cavity.

## 2 HIGH-POWER PROTOTYPES

Two high-power ARES cavities with different HOM-damping schemes have been developed and constructed. The first one constructed in 1995 was named ARES95, and the second one ARES96.

### *2.1 ARES95*

The RF design and characteristics of ARES95 were reported in the previous conference in Europe [2]. The accelerating cavity of ARES95 employs a HOM-damping scheme named Quadrupole Counter Mixing (QCM) choke structure [3]. The HOM characteristics of ARES95 are reported in Ref. [4].

### *2.2 ARES96*

In parallel with the construction of ARES95, another prototype has been developed taking into account the cavity structure symmetry, the HOM-damping performance, and the total cost including HOM loads.

Figure 1 shows a schematic drawing of ARES96. Figure 2 is a photograph of ARES96 installed in the TRISTAN AR tunnel. The accelerating cavity has four rectangular waveguides brazed to the upper and lower sides in order to damp monopole and dipole (V) HOM's, where the capital V means deflecting the beam in the vertical direction. The waveguide width was chosen 240 mm, which gives a cutoff frequency of 625 MHz for the dominant $TE_{10}$ wave. As the HOM load, two bullet-shape SiC ceramic absorbers are inserted at the end of each waveguide. The absorber dimensions are 55 mm in diameter and 400 mm in length including a tapered section. Both beam pipes with an inner diameter of 150 mm are grooved at the upper and lower sides as shown in Fig. 1 in order to damp dipole (H) HOM's deflecting the beam in the horizontal direction. The structure of grooved beam pipe [5] is effective to damp dipole HOM's in a cavity by selectively lowering the cutoff frequency of the $TE_{11}$ wave for a circular beam pipe. The groove dimensions for ARES96 are 30 mm in width and 85~95 mm in depth, which lowers the $TE_{11}$ cutoff frequency below 650 MHz. Eight SiC ceramic tiles are arranged in a line in each groove to absorb the HOM power. Details of the HOM loads for ARES96 are reported in Ref. [6].

The coupling cavity structure is almost the same as that of ARES95. A coaxial antenna coupler [7] is installed into the central port of the coupling cavity. To

0-7803-4376-X/98/$10.00 © 1998 IEEE

terminate the coupler, a water-cooled dummy load capable of 40 kW of RF power (CW) was used in the high-power and beam tests. Figure 3 shows the $\pi/2$ accelerating mode and the damped 0 and $\pi$ modes measured for ARES96 with $Q_c \approx 55$, where $Q_c$ is the loaded Q value of the coupling cavity and adjustable from 30 to 100 by changing the antenna insertion. A slight asymmetry of the 0 and $\pi$ modes with respect to the $\pi/2$ mode came from a tuning error, where the coupling cavity frequency was lower than that of the accelerating mode by about 300 kHz. The fixed tuner for the coupling cavity should have been inserted a little more.

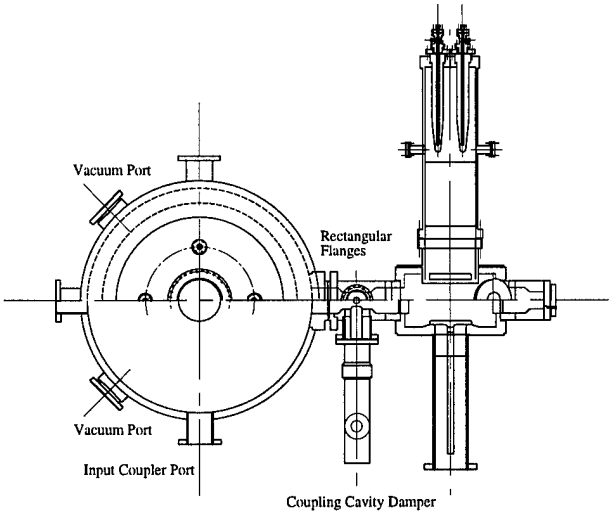
The storage cavity is also almost the same as that of ARES95, which is a large cylindrical cavity (1070 mm in diameter and 1190 mm in axial length) operated in the $TE_{013}$ mode. The cavity is a steel structure whose inner surfaces are copper-plated. The storage and coupling cavities are mechanically connected with rectangular flanges, and vacuum seal is obtained by TIG-welding thin flange sleeves.

## 3 HIGH-POWER TESTS

Fundamental RF parameters for ARES95 and ARES96 are listed in Table 1. The first high-power test of ARES95 was carried out at an RF test hall in July 1996. After the test was completed, ARES95 was installed in the TRISTAN AR tunnel. On the other hand, ARES96 was directly installed in the tunnel, and the high-power test was started there about two weeks before the beam experiment scheduled in October 1996..

In high-power testing, the cavity was fully equipped with an input coupler [8], a coupling cavity damper, tuners, and HOM loads. ARES95 was tested up to the design RF power of 160 kW, which generates a cavity voltage of 0.5 MV. The cavity was stably operated for a long time at that power level. However, a slow vacuum pressure rise probably due to local heating was observed beyond ~180 kW. On the other hand, ARES96 was tested up to 240 kW without any problem.

In high-power operation at 150 kW, the RF power leakage to the coupling cavity damper was measured



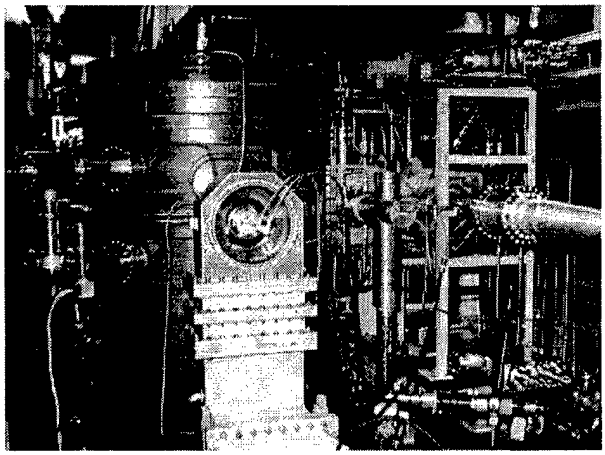



Figure 2: ARES96 installed in TRISTAN AR

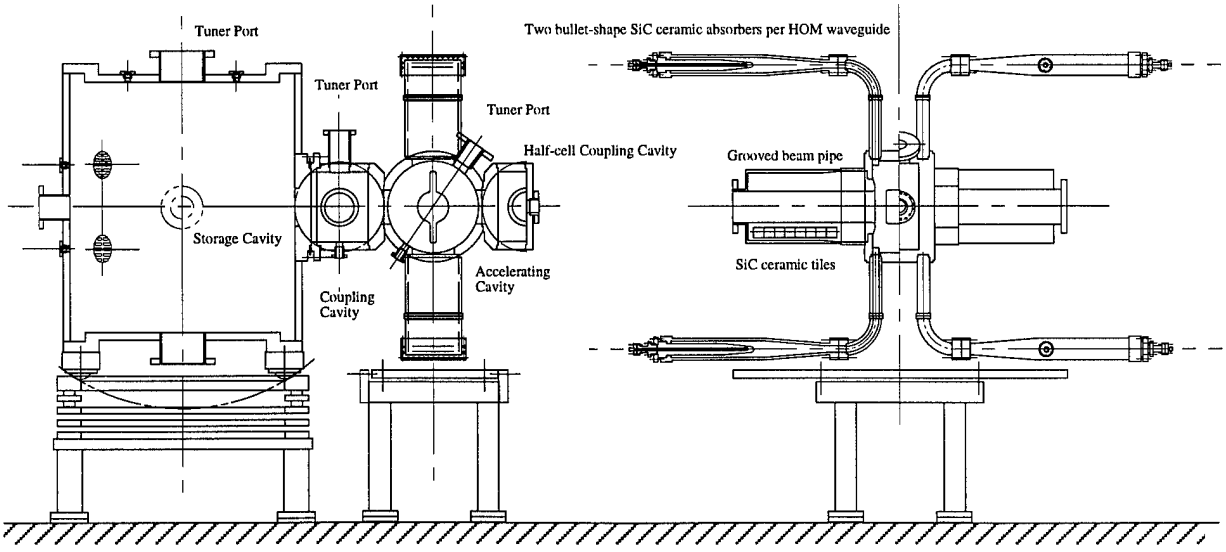



Figure 1: A schematic drawing of ARES96

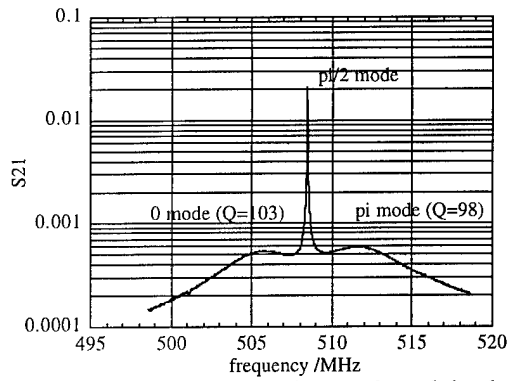



Figure 3: The $\pi/2$ accelerating mode and the damped 0 and $\pi$ modes of ARES96 when $Q_c \approx 55$.

Table 1: Fundamental RF parameters

| | ARES95 | ARES96 |
|---|---|---|
| $U_a/U_s$ | 1 / 8.9 | 1 / 8.3 |
| $Rsh/Q$ ($\Omega$) | 14.8 | 16.3 |
| $Q$ | $1.12\times10^5$ | $1.17\times10^5$ |

~180 W, while a coupled resonator model predicts 150 W. This power leakage is resulting from the energy flow from the storage cavity to the accelerating cavity.

## 4 BEAM EXPERIMENTS

Beam experiments were carried out for both of ARES95 and ARES96 in TRISTAN AR. The major items were:

- To check out whether the ARES scheme functions as expected.
- To check out the performances of devices such as the tuners, the input coupler, the coupling cavity damper, and the HOM loads.
- To survey HOM spectra excited by the beam for various conditions changing the tuner insertion and the beam position with respect to the cavity axis.

Some results of the beam experiments are reported elsewhere [4], [9].

Figure 4 shows a HOM spectrum of ARES96 observed with a probe antenna at the endplate of the accelerating cavity when a single bunch of 100 mA was circulating. A simulation with the MAFIA-T3 code (a time-domain simulation code for three-dimensional structures) reproduced the observed spectrum shape well, including several sharp peaks in Fig. 4. According to further simulation, it was found that the longitudinal impedances of the two modes at 807 MHz and 1389 MHz, indicated by C1 and C2 in Fig. 4, are critical and may possibly exceed the design threshold for the KEKB low-energy ring (LER). The modes C1 and C2 are trapped in the coupling cavity and have almost no fields in the accelerating cavity. The mode C1 has a $TM_{110}$-like field pattern in the coupling cavity and the mode C2 has a $TE_{111}$-like pattern. These dipole modes in the coupling cavity can be damped by attaching a rectangular waveguide at the opposite side of the circular port for the coupling cavity damper. At present we are planning to

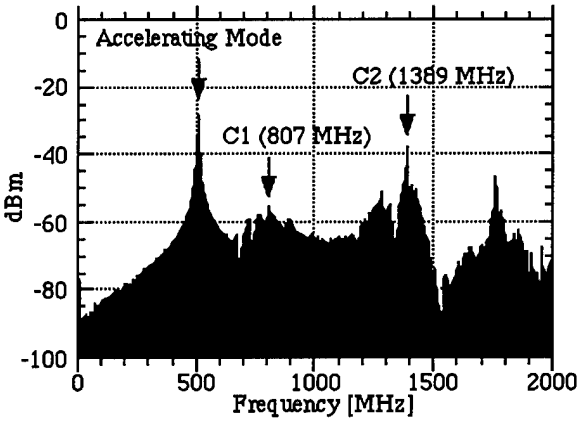



Figure 4: HOM spectrum of ARES96

make a rectangular spare port (240 mm by 28 mm) for the coupling cavity in order to damp the modes C1 and C2 if necessary.

Similar sharp peaks were also observed for ARES95 [4]. One of them is a $TM_{110}$-like trapped mode in the coupling cavity and has almost the same frequency as the C1 mode of ARES96. That is because the coupling cavity structures of ARES95 and ARES96 are almost the same.

## 4 SUMMARY

Two high-power prototypes ARES95 and ARES96 with different HOM-damping schemes have been constructed and demonstrated in high-power and high-current beam experiments. Final design of the production cavity based on ARES96 is being in progress.

## REFERENCES

[1] Y. Yamazaki and T. Kageyama, Part. Accel.**44** 107 (1994)

[2] T. Kageyama et al., "The ARES Cavity for the KEK B-Factory", Proc. of EPAC96, p2008.

[3] N. Akasaka et al., "Quadrupole Counter Mixing Choke Structure for the KEKB ARES Cavity", Proc. of EPAC96, p1997.

[4] T. Kobayashi et al., "HOM Characteristics of the ARES Cavity", in this conference.

[5] T. Kageyama, "Grooved Beam Pipe for Damping Dipole Modes in RF Cavities", Proc. of the 8th Symposium on Accelerator Science and Technology, p116, 1991

[6] Y. Takeuchi et al., "HOM Absorber for the ARES Cavity", in this conference.

[7] F. Naito et al., "Coupling Cavity Damper for the ARES Cavity", in this conference.

[8] F. Naito et al., "The input coupler for the ARES cavity", Proc. of EPAC96, p2014.

[9] N. Akasaka et al., "Fundamental Mode Characteristics of ARES Cavity under Beam Environment", in this conference.

# DESIGN OF THREE RECIRCULATING-LINAC SRF SYSTEMS FOR A 4-TeV $\mu^+$-$\mu^-$ COLLIDER

Q. S. Shu, Thomas Jefferson National Accelerator Facility / Northrop Grumman Co. Newport News, VA 23606 USA, D. Neuffer, Fermilab, Batavia, IL 60510 USA
S. Simrock, DESY, Hamburg, D-22603 Germany

*Abstract*

In a conceptual design of the accelerating systems for a 4-TeV $\mu^+$-$\mu^-$ collider, three recirculating superconducting linacs (with energies reaching 70 GeV (with 350 MHz SRF), 250 GeV (800 MHz) and 2000 GeV (1300 GHz), respectively) are used. We briefly describe design concepts for the acceleration features, superconducting RF cavities, input couplers, RF control and the RF power systems.

## 1 INTRODUCTION

Muon colliders can provide strong potential advantages in high-energy physics, but also present serious technical challenges, as described in the Snowmass feasibility study [1]. In this paper, we explore the superconducting RF (SRF) components of a possible $\mu$-acceleration system. The central difficulty in the $\mu^+$-$\mu^-$ collider is the muon's decay, with a lifetime of $2.2\times10^{-6}\gamma_\mu$ s (where $\gamma_\mu = E_\mu/m_\mu c^2$) that implies a requirement for very rapid increases in muon energies.

In an accelerator the decay and acceleration rates can be combined to obtain an expression for beam survival:

$$N_{final} = N_{initial}\left[\frac{E_{initial}}{E_{final}}\right]^{\frac{m_m c^2}{L_m (dE/ds)}},$$

where N, and E are the number and energy of muons before and after acceleration, $L_\mu$ = 660 m is the $\mu$ decay length, and dE/ds is the acceleration gradient (including all lengths). Small decay loss requires $dE/ds >> m_\mu c^2/L_\mu$ = 0.16 MeV/m, which is relatively large, but can be reached in multipass systems with moderately high gradient.

In the feasibility study, an acceleration scenario is presented which consists of an ~1 GeV linac injecting into a sequence of four recirculating linacs (RLAs), each of which increases beam energy by ~ an order of magnitude, and which accelerates beam up to 2 TeV for injection into a collider ring. Figure 1 shows a conceptual overview of a 4-RLA system.

The basic accelerating unit in this scenario is the RLA, which consists of two linacs with return arcs in a racetrack configuration. The beams are accelerated and returned for several passes in the same linacs, but with separate return arcs (9–16 turns).

For high luminosity, the $\mu^+$-$\mu^-$ collider will require a large charge per bunch of $\sim2\times10^{12}$ in a 3 mm bunch, so short-range wake-field effects and higher-order mode (HOM) loads will be enlarged. Also the $\mu$-beam will decay throughout the system, producing electrons with a mean energy of 1/3 $E_\mu$. The mean e-beam energy deposition is a constant: $dE/ds = m_\mu c^2/(3L_\mu)$ per $\mu$ (0.053 MeV/m/$\mu$). Beam can be accelerated from 1 GeV to 2 TeV with <20% decay loss and <10% longitudinal phase-space dilution. [2]

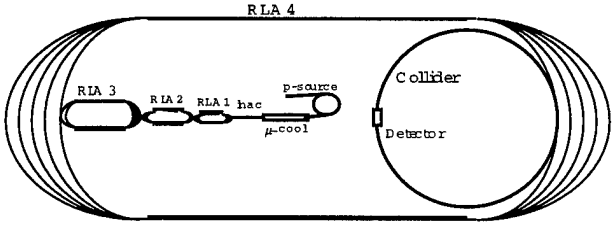



Figure 1. Overview of a $\mu^+$-$\mu^-$ collider system.

There are many possible variations in RLA scenarios. The present case is simply an initial example, from which more detailed specifications of rf and transport systems may be developed, with eventual reoptimization.

## 2 SRF ACCELERATION SYSTEMS

### *2.1 Basic Design Considerations*

The RLA permits economic multipass acceleration, but the separate transport for each turn with cost and complexity considerations limits the number of turns to ~10–20 per RLA, which is very compatible with the $\mu$ lifetime constraint. Counterrotating $\mu^+$ and $\mu^-$ bunches can be accelerated in the same RLAs. In the baseline

Table 1. Parameters of a 4-RLA $\mu$-accelerating system.

| | RLA 1 | RLA 2 | RLA 3 | RLA 4 |
|---|---|---|---|---|
| Beam energy (GeV) | 1→9.6 | 9.6→70 | 70→250 | 250→2000 |
| RF frequency (MHz) | 100 | 350 | 800 | 1300 |
| N turns | 9 | 11 | 12 | 16 |
| $V_{rf}$/turn (GV) | 1.0 | 6 | 16 | 11.2 |
| $L_{turn}(2L_{linac}+2\pi R)$ (km) | 0.26 | 0.95 | 2.32 | 12.6 |
| Beam Survival | 91% | 94.8% | 97.6% | 96.4% |
| $\sigma_{z,beam}$ (cm) | 8.3→4.8 | 1.3 | 0.6 | 0.3 |
| Temp. K | | 4.2 | 2 | 2 |

0-7803-4376-X/98/$10.00 © 1998 IEEE

scenario, the RF frequency increases from RLA to RLA as the beam increases in energy, and the bunch length is correspondingly shortened to match final collider requirements. Table 1 displays system parameters. In this scenario, RF systems at 100, 350, 800 and 1300 MHz are needed. While Cu cavities are suitable for the ~100 MHz RLA, the higher-energy RLAs require a relatively long multipass pulse and high efficiency. The relatively large apertures of SRF cavities can contain the large-emittance μ-beams (with decay products) and reduce the wake-fields. Significant difficulties in the adaptation of SRF technology to $\mu^+$-$\mu^-$ acceleration exist. High-power HOM loads will be needed and the beam transport and SRF cavities must accommodate any spillage from μ-decay.

If the total RF voltage and beam current are fixed, the total investment costs depend on three items: 1. total length L of the cavities and cryostat-'linear cost', 2. total RF power to be transferred to the beam, and 3. total RF power dissipated in the SRF cavities: 'cryogenic cost'. Also, we must take into account the five-year operational cost of RF generator power and cryogenic power.

For a CW machine the cost minimum is located where the first item is equal to the third, but not the maximum attainable gradient. However, the use of pulsed RF can reduce the 'cryogenic cost' and allow for us to choose higher $E_{acc}$. The remaining issues for a 'pulsed' muon collider are: (1) should we cut the Linac length while keeping the same number of beam transport components in the arcs, or vice versa? And (2) what is the highest Eacc which we expect will be used in a pulsed operation in the future?

### 2.2 *1300 MHz (RLA4) SRF*

In RLA4, the muon energy increases from 250 GeV to 2000 GeV. As a baseline design 25 MV/m ($Q_0$=5 x $10^9$) and 16 turns are chosen that need about 112 GV of cavities at 2 K, or 4.5 km active linac. Encouraged by the pulsed test results of the TESLA cavities, it is possible to use a higher $E_{acc}$. If 35 MV/m becomes realistic, the linac could be reduced to 3.2 km. The HOM load requirements for the 1300 MHz SRF can be estimated using the formula:

$$P_{HOM} = k_{HOM} Q^2 f_{rf}$$

With $k_{HOM} \approx 4$ V/pC/m for μ-TESLA cavities, Q is the charge per bunch (3 x $10^{-7}$ C) and $f_{rf}$ is the frequency of bunch passages through the cavity (15×4×16 =960). For 16 passes, 4 bunches, 15 Hz cycles, we obtain ~300 W/m. This compares with the TESLA 1995 design HOM load of ~4.6W/m. Therefore a substantially different HOM coupling system should be developed, with ~99% of the energy coupled out at higher temperatures. One alternative will be to enlarge the aperture of the cavity from existing 70 mm to 102 mm. That will help the HOM mode damping (reduce the $k_{HOM}$ by 50%). This change, of course, will cost the ratio of $E_{pk}/E_{acc}$ (17%) and R/Q (-33%). Figure 2 shows a modified arrangement of the TESLA type cryomodule [3].

### 2.3 *800 MHz (RLS3) & 350 MHz (RLA2) SRF*

Because of larger apertures and longer bunches, $k_{HOM}$ is expected to decrease as ~ $1/\lambda_{RF}^3$ so HOM loads at 800 MHz and 350 MHz should be much less (~60 W/m and 2 W/m in this scenario). Decay losses at this intensity are ~16 W/m; we require that the cryogenic system tolerate ~10% of this at 2 K (1.6 W/m); the remainder would be absorbed at higher temperature.

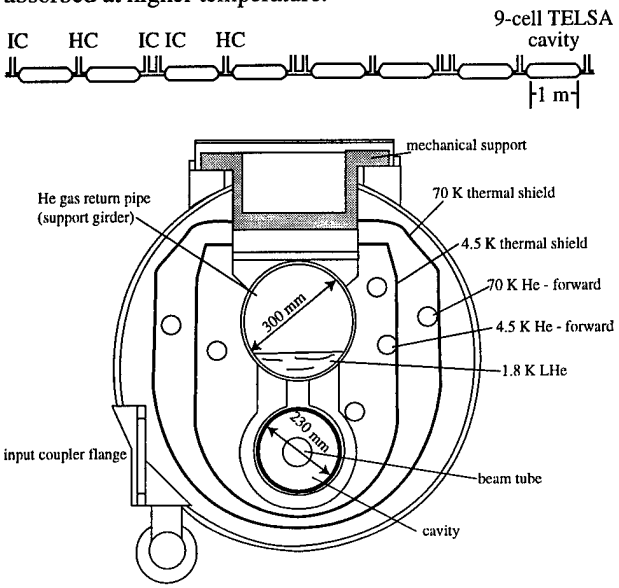



Figure 2. A cryomodule based on the TESLA cavities; input couplers - IC and HOM couplers - HC.

The 800 MHz RLA3 requires 16 GV of SRF or 1.07 km of linac at 15 MV/m ($Q_0$=5 x $10^9$) and 2 K. These are modeled on the LANL PILAC SRF test module which obtained 15 MV/m in a pulsed mode.

The 350 MHz RLA2 requires 6 GV of SRF cavities, or 600 m at 10 MV/m. Our model for the 350 MHz RF system is the CERN cavity, which obtains 6 MV/m in Cw mode at 4 K [4]. An experiment was proposed for a CERN 350 MHz SRF cavity (Figure 3) to be operated in pulsed mode to determine its gradient limit (which will develop guidelines for the RLA2 SRF design). Preliminary tests of the pulsed behavior of a 350 MHz superconducting LEP cavity were conducted at CERN. The maximum peak RF power reached was 507 kW for a 1 ms pulse. At that incident power a maximum field of 7.9 MV/m could be reached without field degradation [5].

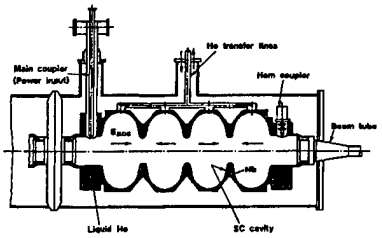


Figure 3. Cross-section of a CERN 350 MHz SRF cavity

### 2.4 *Input Couplers Design Concepts*

RF input couplers and HOM couplers are very important components in the acceleration systems. Our strategy is to apply the experience obtained in development at the leading labs to the concept design shown in Fig. 4. The design features are (1) co-axial structure with two warm windows to isolate the cavity vacuum, (2) use of DC bias of the center conductor and proper dimensions of the co-axial structure to suppress multipacting, and (3) baking the assembly with ceramic windows.

## 3 RF CONTROLS & RF SYSTEMS

Important constraints on the RF system derive from the large charge per bunch. The voltage droop from a bunch passage could be as large as ~10%, and that droop must be recovered before the next bunch passage. However uneven spacing of multiple bunches should be avoided, since the following bunch would not receive the same energy. Other problems may occur from uneven beam loading due to simultaneous acceleration of counterrotating $\mu^+$ and $\mu^-$ bunches, but this effect should average to zero. Other effects that must be considered are effects of momentum fluctuations on arrival time in each pass, bunch charge fluctuations from pulse to pulse, differential fluctuations for $\mu^+$ and $\mu^-$ bunches, microphonic effects, and control of multiple cavities by single klystrons.

### 3.1 *RF System Design*

The RF system (Figure 4) for the three multiturn RLAs must provide RF power for acceleration of the $\mu$- and $\mu$+ bunch and maintain constant energy at the output of each RLA from pulse to pulse. During the multiturn acceleration, a cavity voltage droop is acceptable but must well defined and controlled. Due to the large stored energy in the cavities it is possible to reduce the power requirements in all RLAs to 200 kW/m. A digital feedback system will sample the cavity field every bunch revolution period and provide (time-varying) gradient and phase control for consecutive bunch acceleration cycles. Differential bunch charge fluctuations are not controlled excessive power requirements. A worst case scenario of ±10% bunch charge fluctuation will result in only ±0.27% energy gain fluctuation in RLA2.

### 3.2 *RF Power Requirements*

The RF power requirement is dominated by the power needed for the acceleration of the beam. Additional power is required for RF control. The control power needed depends on the magnitude of perturbations to be controlled.

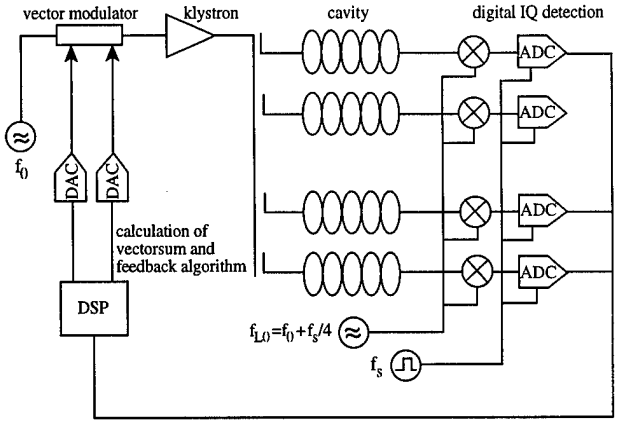



Figure 4. RF system Design.

A voltage droop during consecutive intra-pulse acceleration cycles of the $\mu$- and $\mu^+$ bunch is permissible but must be reproducible from pulse to pulse. In the recirculating linacs RLA2 and RLA3 a considerable voltage droop of 8.6% and 11.9 % respectively is tolerated to reduce the power required for acceleration. S energy in the cavities is used for acceleration. In RLA4 the average current is sufficiently low (due to the large circumference of the accelerator) that a constant gradient can be maintained with moderate power. Table 2 presents some of the RF parameters.

Table 2. RF System and RF Power

| | RLA2 | RLA3 | RLA4 |
|---|---|---|---|
| RF pulse length, μs | 35 | 84.2 | 672 |
| Loaded Q to min. P | $1 \times 10^6$ | $1 \times 10^6$ | $1 \times 10^6$ |
| $\Delta E_{acc} / E_{acc}$ | 0.018 | 0.027 | 0.033 |
| Average I, mA | 100 | 45.6 | 7.6 |
| Available RF Power, kW/m | 200 | 200 | 200 |
| Voltage drop | 0.086 | 0.12 | 0.00 |
| RF on - cryogenic loss, W/m | 119 | 71 | 78 |
| Ave. wall power for RF, kW/m | 5.2 | 2.6 | 5.25 |

## 4 ACKNOWLEDGMENTS

This work was supported by the U.S. DOE under contract number DE-AC05-84ER40150.

## REFERENCES

[1] $\mu^+\mu^-$ Collider - A Feasibility Study, BNL-52503, Fermi-Lab-Conf.-96-092, LBNL-38946, presented at the Snowmass workshop (1996)..

[2] D. Neuffer, to be published in NIM A (1996).

[3] Q-S. Shu for the TESLA Collaboration, in Advances in Cryogenic Engineering, P. Kittel, edited Vol. 41A, p. 827 (1996).

[4] G. Geschonke to be published in Proc. of CEC/ICMC-97, Portland, Ore., July, 1997.

[5] Private Communications with I. Campisi of CERN, 1997.

[6] S. N. Simrock, et. al, EPAC-96, Barcelona, Spain, (1996).

# STATUS AND DEVELOPMENT OF SUPERCONDUCTING CAVITY FOR KEKB

S.Mitsunobu,K.Asano,T.Furuya,Y.Ishi*,Y.Kijima*,K.Sennyu**,T.Tajima,T.Takahashi and S.Zhao***,KEK High Energy Accelerator Research Organization,1-1 Oho Tsukuba Ibaraki Japan
* Mitsubishi Electric Co.,Ltd.
** Mitsubishi Heavy Industries,Ltd.
***IHEP Beijing

*Abstract*

After successful test of 500 mA (Max 573 mA) electron beam at TRISTAN Accumulation ring (AR) using a prototype superconducting cavity, more than 4 superconducting cavities will be installed in high energy ring (HER) of KEK B-factory. The initial 4 superconducting cavities are almost same as the prototype one. The tests and results of the critical components of superconducting cavity system is described.

## 1 INTRODUCTION

The development of Superconducting cavity for KEK B-factory (KEKB) has started since 1991[1] on the basis of the experiences in the construction and 7 years operation of the 32 TRISTAN Superconducting cavities.
A single cell cavity with a cylindrical large beam pipe was designed to propagate HOMs toward the beam axis and damp them by ferrite absorbers bonded on inner surface of beam pipes[2].The absorber was made by HIP(Hot Isostatic Press) method and tested upto 15 kW RF power. For the feasibility study of the superconducting cavity for KEKB, a prototype module was constructed. This module was installed in AR and tested[3]. Fig 1 shows the prototype module installed in AR. Detailed discussion for high current beam test is presented on the other paper[4] in this conference

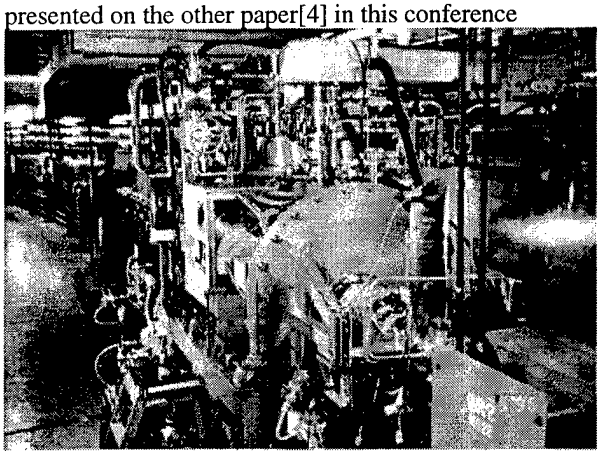


Fig.1 Prototype module for KEKB.

## 2 CAVITY

A single cell cavity was chosen to reduce the number of HOMs and to minimize the coupler power less than 500 kW. The diameter of aperture of 220 mm was chosen to provide the desired coupling of the lowest monopole modes of TM-011 and TM-020. A large cylindrical beam pipe(LBP) of 300mm diameter was connected on one side to obtain a sufficient coupling of the lowest dipole modes of TE-111 and TM-110. The same cavity shape is used for the AR prototype cavity and the HER superconducting cavity. The cavity parameters of the accelerating mode are summarized in Table 1.

Table 1: Cavity parameters of a HER Superconducting cavity.

| | | |
|---|---|---|
| Frequency | 508.8 | MHz |
| Gap length | 243 | mm |
| Dia.of aperture | 220 | mm |
| R/Q | 93 | Ohm |
| Loss factor | 0.074 | V/pC |
| Geometrical factor | 251 | Ohm |
| Esp/Eacc | 1.84 | |
| Hsp/Eacc | 40.3 | Gauss/(MV/m) |

The prototype cavity was formed by spinning method of 2.5 mm thick Nb sheet of RRR 200. The surface treatment process using electropolishing is almost same as TRISTAN cavities. For high current application like as B factory, more stable surface is desired,so hydropreoxide rinsing was replace by ozonized ultrapure water rinsing(OUR)[5]. The OUR treatment removes completely the carbon contamination on electropolished Nb surface. The tested 508 MHz Nb cavities for KEKB showed high $Q_0$ values and the maximum accelerating field of 14.4 MV/m was obtained at 4.2K. Air exposures up to 4 days at 1 atm did not show degradations of cavity performances. The prototype cavity was rinsed by OUR and exposed to air for 2 days during full assembling in to the cryostat. In fully assembled cavity performance test,we call horizontal test, the field was improved by CW processing to 8 MV/m but standstill like a TRISTAN cavity. The pulse aging, in which the pulse power of 5% duty was added to the CW power[3] of just below the quench level, broke the deadlock and improved the field to 11.4 MV/m. In the high current beam test in AR, cavity

0-7803-4376-X/98/$10.00 © 1998 IEEE

performance was recovered by pulse aging from some degradation of field due to a large amount of condensed gas. The cavity performance was completely recovered by warming up to room temperature. One critical problem was frequent trips due to discharges in the superconducting cavity and the input coupler region. From the experience of TRISTAN operation, the trips were caursed by condensed gas on cold surface. In the first and second beam test at AR, the prototype cavity could not be operate stably due to frequent trips by arcing discharge interlock of the coupler. At that time vacuum condition was bad and a large amount gas condensed from both sides of the cavity. Before the third test (Oct.-Dec. 1996) the vacuum pump system of the beam ducts on both sides of the cavity were improved and the beam ducts were rinsed with OUR to reduce out gas rate. These were very effective to reduce the trip rate and the stable cavity operation continued for two weeks. The maximum beam current of 573 mA, which exceeded the world record of 220 mA set by a CESR superconducting cavity tested in CESR at Cornell university in 1994[6], was stored at 1.2 MV. A high current of 350 mA was also stored at 2.5 MV(10 MV/m) ,which is higher than the design voltage of 1.6 MV. The current limitations were not by cavity performances, but by the other things such as heating of ring components. For the beam ducts around the superconducting cavity of HER, we will use improved pump system like as improved AR one.

Additional loss of the cavity related to the beam current was observed[3]. In the third beam test, more detailed measurements of additional loss were done. The additional loss has seams like linear dependence on beam current. So higher current of two times more will not be too much additional loss in HER. The reason of additional loss is not clear now. We observed low energy (few electron volts) electrons at both side of the cavity using pick up probes of HOM power at taper transition beam ducts. The low energy electron current of up-stream side (LBP side) showed nonlinear dependence on the beam current and about one tenth intensity of the down stream one. The low energy electron current of down stream side(SBP side) depend on the beam current linearly. The direct synchrotron light could not hit the pick up probes and the cavity, and the electron produced by direct synchrotron light was swept out by magnet, but scattered photons might hit both, and have linear dependence on beam current. The vacuum pressure of the cavity dependent on beam current nonlinearly. So up stream side might be shade of scatted photon and only collect ionized electron. These electrons may increase electron loading in superconducting cavity and this type electron loading is one of the candidate reason for the additional loss.

## 3 HOM DAMPER

The loss parameter of the prototype module is 2.9V/pC for the designed bunch length of 4 mm. The main part of the loss comes from the tapers between the cell and beam ducts. Therefore, the loss parameters can be reduced to 1.6 V/pC in HER of KEKB by using the beam ducts of larger diameter and longer tapers. The expected power dumped to the HOM load for HER is 5 kW per module. The HOM dampers were made by IB-004 ferrite using HIP method. The power test of the damper were made using coaxial line with 508 MHz klystron. The maximum power of 11.7 kW and 14.8 kW were given to the 220 mm diameter and the 300 mm diameter damper. In the high current beam test in AR, the maximum HOM power of 4.2 kW was absorbed by the HOM dampers without any damage.

## 4 INPUT COUPLER

The input coupler for KEKB superconducting cavity has almost same design as that used for TRISTAN superconducting cavities. The gap of 3 mm of choke structure was changed to 4 mm to reduce the field strength at ceramic disk. Three monitoring ports were set near the ceramic window to monitor vacuum pressure, electron and discharge light(arc sensor) for protection and diagnosis. The couplers tested up to 800 kW[7] by the traveling wave and 300 kW totally reflected standing wave, changing phase up to half wave (in short time 500 kW which equivalently corresponding 2 MW traveling wave). In the second beam test, frequent discharge around the coupler occurred and temperature changed by cool gas flow rate affect to this trip rate. So condensed gas affected the surface condition and multipacting of the coupler occurred. Before the third test we prepared a biased type doorknob transition which can supply a bias voltage to the inner conductor of the coaxial input coupler. The biased type doorknob transition was tested at the test bench up to 300 kW standing wave changing phase of half wave length and traveling wave. Fig 2 shows the biased type doorknob transition for KEKB superconducting cavity.

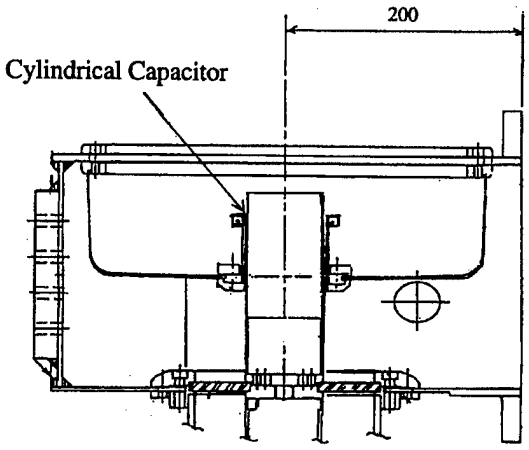



Fig.2 Biased type doorknob transition for KEKB.

Between the inner conductor and the doorknob, a capacitance of 1520 pF was inserted. The insulating

material was two layer of polyimide(like as Kapton) films of 0.125 mm thick each.
At the test bench ,the bias voltage of +/- 2000 volts range was tested. The bias voltage of around -700 V is most stable.(Fig.3)

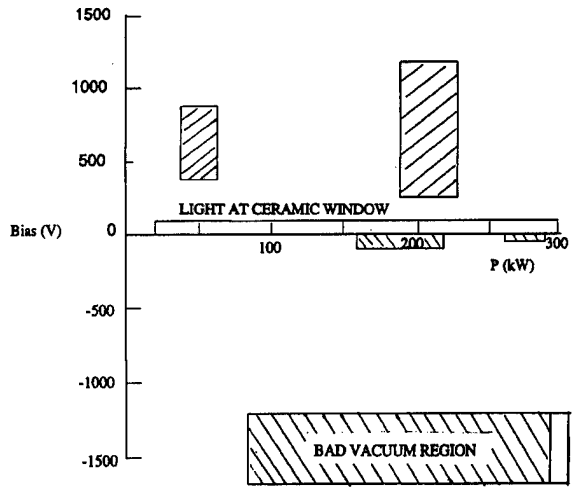



Fig. 3 Mapping of bias voltage for input coupler.

At third beam test the effect of the bias voltage was tested in short time of 2 hours to apply -700 V after frequent trip. After this test the cavity warmed up to room temperature for out gasing,and cool down again. The cavity was operated stably with and without the bias voltage in good vacuum condition for two weeks.

## 5 SUMMARY

Development of the critical components required for KEKB have been continued. The test results of the critical components of superconducting cavity for KEKB are summarized in Table 2.

Table 2: Design and test results of the critical components of superconducting cavity for KEKB.

| | design | Bench test | Beam test |
|---|---|---|---|
| Cavity Max Vc | 1.6 MV | 3.3 MV | 2.5 MV (2.9MV) |
| Coupler | 500 kW | 800 kW (300 kW) | 160 kW (280 kW) |
| HOM load | 5 kW | 15 kW | 4.2 kW |

We reached the design requirement but should continue detailed test for critical components.
The improvement of the vacuum pumps and the surface treatment of vacuum ducts nearest to the superconducting cavity is essential for stable operation of superconducting cavity. For HER we will add NEG pumps on usual ion pumps and the OUR rinse will be used to clean up vacuum ducts.

To apply bias voltage for the inner conductor of input coupler is effective to reduce multipacting and to improve the aging process precisely. The biased type doorknob transition will be used for HER modules.
The construction of 4 superconducting cavities for HER have been started and they will be installed in next year.

## 6 ACKNOWLEDGEMENTS

The authors would like to thank Prof. S.Kurokawa,Prof. E.Ezura and Prof. Emeritus Y.Kojima for their continuous encouragement and discussion.

## REFERENCES

[1] S.Mitsunobu, et al.,Proc.5th SC-RF Workshop, DESY,1991
[2] T.Takahashi, et al.,Proc.9th Symposium on Accelerator Scie. and Tech.,Tukuba,Japan,p327,1993
[3] T.Furuya,et al.,Proc. 5th European Particle Accelerator Conference,Sitges,Spain,June 10-14,1996.
[4] T.Furuya,et al., This conference
[5] K.Asano,et al.,Proc. 7th SC-RF Workshop,CEA-Saclay,France,
[6] H.Padamsee,et al.,Proc.of the 1995 Part. Accel. Conf., Vol 3,P 1515.
[7] S.Mitunobu,et al.,Proc. 7th SC-RF Workshop CEA-Saclay,France,P.735,1995

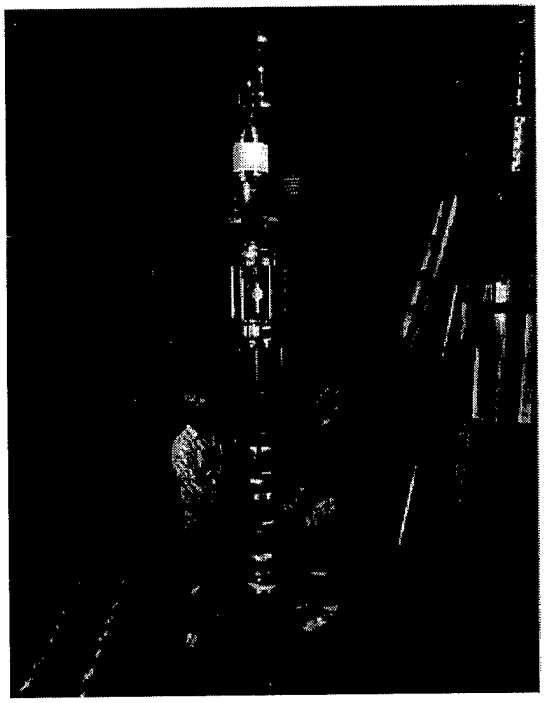
# DESIGN AND CONSTRUCTION OF A 500 KW CW, 400 MHZ KLYSTRON TO BE USED AS RF POWER SOURCE FOR LHC/RF COMPONENT TESTS

H. Frischholz, CERN, Geneva, W.R. Fowkes and C. Pearson, SLAC, Stanford

*Abstract*

A 500 kW cw klystron operating at 400 MHz was developed and constructed jointly by CERN and SLAC for use as a high-power source at CERN for testing LHC/RF components such as circulators, RF absorbers and superconducting cavities with their input couplers. The design is a modification of the 353 MHz SLAC PEP-I klystron. More than 80% of the original PEP-I tube parts could thus be incorporated in the LHC test klystron which resulted in lower engineering costs as well as reduced development and construction time. The physical length between cathode plane and upper pole plate was kept unchanged so that a PEP-I tube focusing solenoid, available at CERN, could be re-used. With the aid of the klystron simulation codes JPNDISK and CONDOR, the design of the LHC tube was accomplished, which resulted in a tube with noticeably higher efficiency than its predecessor, the PEP-I klystron. The integrated cavities were redesigned using SUPERFISH and the output coupling circuit, which also required redesigning, was done with the aid of MAFIA. Details of the tube development and test results are presented.

Figure I: 500 kW, 400 MHz LHC Klystron



## 1 INTRODUCTION

SLAC already constructed a 500 kW cw klystron for CERN in 1980. At that time this was a PEP-I tube with an operating frequency of 353.2 MHz, which at CERN was tuned to 352.2 MHz, the LEP/RF frequency. This klystron served for many years as RF power source, required for the conditioning of LEP RF cavities.

Since a similar RF power source would be required in 1997 for the testing of LHC/RF equipment, such as cavities, windows, couplers, circulators and absorbers, it was proposed by the first author, while on sabbatical leave at SLAC, to redesign the PEP-I klystron so that it could be operated at 400.8 MHz, the LHC/RF frequency. The redesigned PEP-I klystron, in the following referred to as LHC tube, was manufactured by SLAC and shipped to CERN in 1996. More than 80% of the original PEP-I tube parts could be incorporated, among them major components such as the collector with its water jacket, the electron gun assembly, parts of the five stainless steel RF cavities, and the coax-to-waveguide output transition with the cylindrical ceramic window. The first two components could be used without any modifications whereas the two latter ones had to be matched to the higher operating frequency. The re-use of auxiliary equipment of the PEP-I tube, still available at CERN, such as cathode oil tank with HV plug, beam focusing solenoid and main support girder, resulted in lower engineering costs too.

Prior to shipment the LHC tube was high-power tested at SLAC. The test results were in good agreement with those obtained at CERN, where the high-power test was repeated. As predicted by computer simulations the DC-to-RF conversion efficiency of the LHC tube, an important parameter for high power sources, was measured and found to be noticeably higher than that of its predecessor.

## II DESIGN

As mentioned above, the PEP-I electron gun assembly and collector have been incorporated in the LHC tube without any modifications. The cathode is of the dispenser type which is less susceptible to poisoning by metal vapours and gases than an oxide one.

With a cooling water flow $\geq$ 400 l/min the collector can dissipate up to 770 kW. This corresponds to the DC input power required when the tube is operated at rated RF output (500 kW cw). Consequently there is no need to switch the HV off or to reduce it in case of an RF drive trip.

0-7803-4376-X/98/$10.00 © 1998 IEEE

The output transition, consisting of a 56 Ω coaxial line, a cylindrical ceramic window, and a reduced-height WR 2100 waveguide, followed by a full-height one, had to be matched to the higher operating frequency. After having repositioned an existing inductive post in the full-height waveguide section and properly terminated both line ends, the input reflection (S11) of the assembly was measured to be -44 dB (VSWR = 1.01) at 400.8 MHz.

Since the operating frequency of the LHC tube is only 13.5% higher than that of its predecessor, the drift tube diameter of 7 cm could be maintained as well. At nominal operating voltage ($V_b$ =63 kV) and a focusing field of B = 210 Gauss, which is 2.7 times the Brillouin induction, the beam diameter is 4.5 cm, yielding a fill factor of 0.64 for both tubes. The normalized drift tube radii, the product of radial phase propagation constants,$\gamma$, and drift tube radius, of the PEP-I and LHC tube, are 0.5 and 0.57 radians respectively. Both values in combination with the given fill factor result in a high coupling coefficient between beam and cavity fields, a prerequisite for a good tube efficiency.

The unusually short drift tube between anode housing and input cavity of the PEP-1 tube was replaced by a longer one in order to reduce the risk of RF leakage from the first cavity into the cathode region. A 34 mm longer input drift section, already incorporated for the same reason in the B-Factory prototype klystron [1], was chosen. In order to preserve, however, the above-mentioned interchangeability of the beam-focusing solenoid both tubes must exhibit the same physical length between cathode plane and upper pole plate. Therefore the section between input and output cavity gap, constituting the RF interaction space, had to be made shorter in the LHC tube.

With the aid of the one-dimensional klystron simulation code JPNDISK and the two-dimensional CONDOR code the lengths of the drift sections between the five cavities and the cavity frequencies, required for optimum efficiency, were determined. The geometries of the cavities, which are all of the re-entrant type, were established by using SUPERFISH. It appeared that all but one of the cavity shells could be re-used without modifications; only the gap widths had to be widened by shortening one of the two drift tubes inside each cavity. In the penultimate cavity, however, the original gap was relatively wide and its width could not be further increased without sacrificing tube performance. Keeping the diameter of this cavity unchanged but reducing its length by 65.3 mm resulted in the desired gap transit angle of 0.78 radians.

For optimum efficiency all fundamental cavities have been tuned to frequencies which are higher than the tube operating frequency. The 2nd harmonic cavity, (cavity#3),however, had to be tuned 0.5% below the second harmonic of the operating frequency in order to achieve maximum tube efficiency. JPNDISK predicted that the efficiency would drop from 70 to 45% when the resonant frequency of this cavity is increased by less than 1% above its optimum value. Computer simulations also indicate that the 2nd harmonic cavity, when correctly tuned, contributes approximately 3% to the tube efficiency.

The output cavity resonant frequency and external Q could not be directly determined using SUPERFISH. The resonant frequency is due to the presence of the PEP-I output coupling loop typically about 2.5% lower than that of an uncoupled cavity. This was taken into consideration when the output cavity frequency of the LHC tube was calculated. SUPERFISH calculations indicated that the gap width had to be increased by 16 mm. Unfortunately, when the PEP-I loop configuration was kept unchanged, the measured $Q_{ext}$ was then 123, much higher than the desired optimum of 83. At an external Q of 123 CONDOR simulations predicted an abundance of returning electrons from the output gap, a high electron interception by the output drift tube and an 11% decrease of tube efficiency.

It was decided that the so-called Kroll-Yu method [2] would be used to determine the required changes in the output loop configuration in order to achieve the desired external Q and resonant frequency. For this methode,the cavity with its coaxial output is shorted and modeled on MAFIA. The resonant frequencies of the cavity are calculated for several positions of the short. From these results the external Q and resonant frequency of the cavity, when terminated by a matched load, can be determined.

The Kroll-Yu methode predicted an external Q of 83 when the portion of the loop which is parallel to the tube axis is moved by 10 mm towards this axis. The output cavity was then built as modeled giving a measured $Q_{ext}$ of 85, and the desired resonant frequency was obtained with a small change in the upper nose length.

Table I: Main Design Parameters

| | |
|---|---|
| Operating Frequency, $f_0$ | 400.8 MHz |
| Beam Voltage, $V_b$ | 63 kV |
| Beam Current, $I_b$ | 11.8 A |
| Beam Perveance, $\mu p$ | 0.75 $\mu A/V^{3/2}$ |
| RF Output Power, $P_{out}$ | 506 kW cw |
| Efficiency at rated Output Power, $\eta$ | 0.68 |
| Saturation Gain, g | 42 dB |
| RF Drive Power, $P_{in}$ | 20 W |
| Focusing Magnetic Field, B | 210 Gauss |
| Reduced Plasma Wavelength, $\lambda_q$ | 4.69 m |
| Number of Cavities (incl. 2nd Harm.) | 5 |
| RF Interaction Length | 1.962 m |
| Normalized Drift Tube Radius, $\gamma a$ | 0.57 radians |
| Normalized Beam Radius, $\gamma b$ | 0.37 radians |
| Beam Fill Factor, b/a | 0.64 |

All design parameters, which are a compromise between using as many original tube parts as possible and yielding optimum tube performance, are listed in tables I

and II. When inserting these parameters the efficiency calculated by means of the JPNDISK code is 70% and by using CONDOR 61%. Both values are 1.13 times higher than the corresponding ones for the PEP-I tube. Consequently there was good reason to assume that an LHC tube efficiency of approximately 68% could be achieved, since that of the PEP-I tubes was 60% in average.

Table II: Interaction Space Parameters

| Cavity No. | Frequency (MHz) | R/Q (Ω) | $Q_{ext}$ | Gap Transit Angles (Radians) | Drift Lengths (m; $\lambda_q$ angle) |
|---|---|---|---|---|---|
| 1 | 401.1 | 91 | 1000 | 0.47 | |
| | | | | | 0.442; 34° |
| 2 | 402.4 | 103 | ∞ | 1.14 | |
| | | | | | 0.142; 11° |
| 3 | 797.5 | 84 | ∞ | 1.27(@$2f_0$) | |
| | | | | | 0.870; 67° |
| 4 | 407.9 | 100 | ∞ | 0.78 | |
| | | | | | 0.508; 39° |
| 5 | 401.5 | 94 | 83 | 0.78 | |

## III KLYSTRON MANUFACTURING

The LHC klystron incorporated many of the manufacturing practices used at SLAC in the manufacture of high peak power pulsed klystrons. The incorporation of some of these more stringent techniques has had a clear benefit on the tube performance.

The SLAC klystron manufacturing philosophy is to obtain as high a vacuum as is economically achievable. Therefore, tube materials are carefully selected and tested, a high degree of cleanliness is maintained throughout the manufacturing process and the entire gun assembly is pre-processed at temperatures up to 1100°C by vacuum induction heating the assembly while simultaneously applying power to the cathode. This outgassing process takes approximately one week and removes the bulk of the gas load from the dispenser cathode assembly. The final processing of the assembled tube is at 550°C on a double vacuum bake station. A consequence of the relatively high bake temperature, combined with the ultra-high vacuum, is that high vapour pressure elements may coat surfaces in the tube. For this reason, silver, which is known to have a detrimental effect on cathode emission, and other high vapour pressure elements have been eliminated from materials used in the construction of klystrons at SLAC. Assembly brazing is therfore conducted in clean dry hydrogen furnaces by using only copper gold brazing alloys.

Another feature is the application of anti-multipactor coatings on suspected surfaces inside the klystrons. In the case of the LHC tube a titanium nitride coating was applied by evaporation technique to the output window and electron gun ceramic. In addition, titanium coatings were applied to the input cavity with coupling loop, cavity 2, the output cavity and output coax areas.

## IV TEST RESULTS

The LHC tube was first high power tested at SLAC in June 1996. In less than three days of HV and RF conditioning an output power of 503 kW was achieved at an operating voltage of 65.5 kV and a beam current of 11.9 A.

From these values result a beam perveance and tube efficiency of 0.71 $\mu A/V^{3/2}$ and 64.5% respectively. As both parameters were 5% below their design values a higher operating voltage than the design one was required at saturated output power. A tube gain of 42 dB was measured, which corresponds to the value predicted by the simulation codes.

When the high-power tests were repeated at CERN a slightly higher efficiency, $\eta = 65\%$, was achieved by optimizing the focus coil currents. After about 100 hours of operation the beam perveance also increased slightly to 0.72 $\mu A/V^{3/2}$ so that an output power of 504 kW was attained at $U_b = 65$ kV. The -1 dB output bandwidth was measured to be 650 kHz with the -1 dB frequency points situated at 250 kHz below and 400 kHz above the operating frequency.

During high power tests at SLAC and at CERN no signs of instability were observed in the output signal. Possible causes of instabilities are returning electrons, which usually manifest in an amplitude modulation (side bands) of the output signal, and multipacting which results most likely in an unstable output amplitude.

The absence of multipacting and the short time required for the high-power conditioning are very probably to be attributed to the stringent manufacturing techniques which were applied.

## V ACKNOWLEDGEMENT

The authors wish to thank D. Boussard, SL/RF group leader at CERN and G. Caryotakis, head of the SLAC Klystron Department for their continuous support and encouragement in the realization of this project. We also wish to thank all members of the SLAC Klystron Department who contributed to making the LHC tube project a successful achievement. Particular thanks go to E.L. Wright who performed the MAFIA simulations of the output cavity with its loop and H.V. Taylor who dressed the tube and installed it on the test stand.

Special gratitude is expressed by the first author to T.G. Lee for familiarizing him with the simulation codes required for designing the tube, and to all members of the Klystron Department who made his stay at SLAC a pleasant experience.

## REFERENCES

[1] W.R. Fowkes, G. Caryotakis, T. G. Lee, C. Pearson, and E.L. Wright, Proc. 1993 IEEE Part.Accel.Conf. Vol.2, pp. 1259-1261.

[2] N.M. Kroll and D.U.L. Yu, Particle Accelerators, 1990, Vol 34, p. 231.

# SUPERCONDUCTING CAVITIES FOR THE APT ACCELERATOR

Frank L. Krawczyk, Robert C. Gentzlinger, Brian Haynes,
Debbie I. Montoya, Brian Rusnak, Alan H. Shapiro,
LANL, LANSCE-1, MS H817, Los Alamos, NM 87545, USA

*Abstract*

The design of an Accelerator Production of Tritium (APT) facility being investigated at Los Alamos includes a linear accelerator using superconducting rf-cavities for the acceleration of a high-current cw proton beam. For electron accelerators with particles moving at the speed of light ($\beta \approx 1.0$), resonators with a rounded shape, consisting of ellipsoidal and cylindrical sections, are well established. They are referred to as "elliptical" cavities. For the APT-design, this shape has been adapted for much slower proton beams with $\beta$ ranging from 0.60 to 0.94. This is a new energy range, in which resonators of an elliptical type have never been used before. Simulations with the well-proven electromagnetic modeling tools MAFIA and SUPERFISH were performed. The structures have been optimized for their rf and mechanical properties as well as for beam dynamics requirements. The TRAK_RF simulation code is used to investigate potential multipacting in these structures. All the simulations will be put to a final test in experiments performed on single cell cavities that have started in our structures laboratory.

## 1 THE CAVITY SHAPE

Superconducting 5-cell cavities at a $\pi$-mode frequency of 700 MHz will be used for the major part of the APT facility. Due to the large velocity acceptance of these cavities only structures for two values of $\beta$ (0.64 and 0.82) are needed [1]. For each value of $\beta$ two different cross-sections have been determined, one for the mid-cells and one for the end-cells, where compensation for field penetration into the attached beam-pipe is required. The choice of cavity shape made use of previous design experience at other labs, including Cornell, KEK and DESY [2]. Figure 1 shows the shape description for the chosen geometries. The shape of both the medium-$\beta$ (0.64) and the high-$\beta$ (0.82) cavities uses elliptically shaped noses, straight side walls and a circular dome. The upright nose ellipses have an aspect ratio of 2:1.

In a first step the shapes of the resonators were determined to minimize electric and magnetic peak surface fields as far as possible. The resulting cavity shapes turned out to lack sufficient mechanical stability. The medium-$\beta$ structure needed stiffener support to sustain the vacuum load without yielding the material. Encouraged by recent cavity tests at JAERI for a $\beta = 0.5$ superconducting cavity at 500 MHz[3], we revisited the proposed cavity shapes and came up with an improved design that had less steep straight walls while maintaining good performance in terms of rf properties. Table 1 gives the relevant geometric parameters for all 4 shapes. The design procedure used fixed beam-pipe apertures based on beam-dynamics requirements, and fixed straight wall slopes (5 and 7 degrees in the first design and 10 degrees for both $\beta$ values in the final design). The elliptical noses were varied to find shapes with good peak-fields. The equator radius has been used to tune the cavities to the proper frequency. All other parameters fell into place automatically, assuming smooth transitions between the different parts of the cavity shapes.

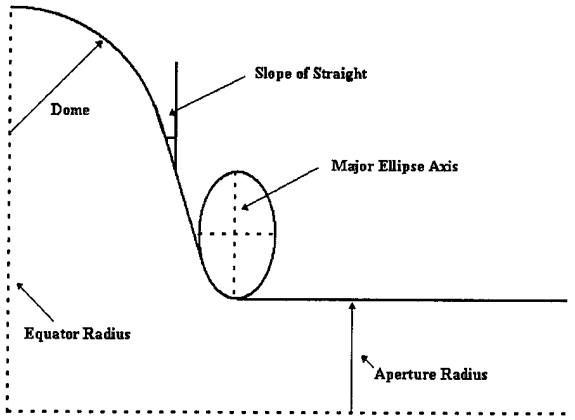



Figure 1: The describing parameters for the elliptical cavity shapes

| $\beta$ cell-type | 0.64 mid | 0.64 end | 0.82 mid | 0.82 end |
|---|---|---|---|---|
| aperture[cm] | 6.5 | 6.5 | 8.0 | 8.0 |
| equator[cm] | 19.95 | 19.95 | 20.1 | 2 0.1 |
| major axis[cm] | 10.00 | 12.00 | 14.00 | 17.80 |
| slope[degree] | 10.00 | 10.00 | 10.00 | 10.00 |
| dome[cm] | 3.233 | 2.811 | 4.969 | 4.167 |
| cell-length[cm] | 13.71 | 13.71 | 17.56 | 17.56 |

The end-cell geometries use inner half-cells identical to the mid-cells. The outer half-cell uses an equator radius and a cell length identical to the mid-cells, and the elliptical nose and the circular dome radii have been used to retune the cell to the desired 700 MHz.

The simulations have been done on single cavity cells, using $\pi$-mode boundary conditions at iris positions where neighboring cells exist. This was sufficient and more efficient in optimizing the cells for the accelerating mode. An investigation of the higher order mode (HOM) spectrum has been done for the full 5-cell geometry. These results will be reported in a separate contribution [4].

0-7803-4376-X/98/$10.00 © 1998 IEEE

## 2 PERFORMANCE DATA

The electromagnetic design of the cavity-cells has been done with MAFIA [5] and SUPERFISH [6]. From the electromagnetic fields, a set of secondary quantities has been derived that describe the rf performance of these structures and their interaction with the beam. Table 2 gives the numbers for the most important quantities in a comparison of the mid-cells of the original design with the new shapes with larger side-wall slope.

| $\beta$ | 0.64 new | 0.64 old | 0.82 new | 0.82 old |
|---|---|---|---|---|
| $Q_0$ [$10^{10}$] | 1.02 | 1.08 | 1.34 | 1.35 |
| Geometry Factor | 162 | 177 | 213 | 215 |
| $ZT^2/Q$ [$\Omega/m$] | 246 | 256 | 297 | 299 |
| $E_{pk}/E_a$ | 2.94 | 2.96 | 2.48 | 2.50 |
| $H_{pk}/E_a$[G/5MV/m] | 355 | 340 | 305 | 303 |
| $P_{cav}$ [W] | 8.13 | 7.32 | 9.25 | 9.16 |

The unloaded $Q_0$ assumes a surface resistance ($R_s$) of 15.9 $n\Omega$, $ZT^2/Q$ is the ratio of effective shunt-impedance and $Q_0$, $E_{pk}/E_a$ and $H_{pk}/E_a$ give the ratio of peak surface-fields over accelerating gradient ($E_a$=$E_0T$). $P_{cav}$ is the power dissipated into the cavity by the accelerating mode. These power value reflect the dissipated power to achieve the average accelerating gradient (5.16 MV/m at $\beta$=0.64 and 5.92 MV/m at $\beta$=0.82) for the TM010 $\pi$-mode. The transit time factor (T) for a particle with the design-$\beta$ is 0.78 for all mid-cells.

In terms of the rf-parameters there is only a small difference in performance between both designs. The major driver for switching to the new shapes is the potential gain in structural stability. The increase of power deposited into the medium-$\beta$ cavities by 10 % does not have a significant effect, since most of the accelerator consists of high-$\beta$ structures. The results for the end-cells are very similar, the only major difference being the transit time factors that are only 0.59 for the end-cells. This drop is partially compensated by a increase in $E_0$, so that $E_0T$ is only about 10 % smaller than for the mid-cells.

## 3 STRUCTURAL ANALYSIS

Some preliminary structural analysis has been done on 2D models of the cavity shapes [7]. The shapes with the 10 degree slopes in the side-walls seem to be structurally more stable. Both shapes can withstand the vacuum loads without stiffening. The other consideration in applying stiffeners has to do with raising the resonant frequencies of the cavity mechanical modes to decrease the microphonic detuning sensitivity in operation. These studies are continuing. Even if these studies indicate that stiffeners are needed, they can probably be less complex than the conical stiffeners used for our first single-cell test cavity with the original steeper-sloped side-walls.

The choice for a 10-degree slope came from the preliminary 2D structural analysis. The medium-$\beta$ cavity showed a clear minimum in von-Mises stresses for a shape with a straight wall slope around 10 degrees (with and without constrained iris). For the high-$\beta$ cavity this minimum was not so clear, in fact even larger inclinations showed the sames stresses as the 10 degree slope did. But, for these larger inclinations the rf performance deteriorated strongly. The peak surface magnetic fields also increased, so did the frequency sensitivity with radius variations.

## 4 MULTIPACTING

Another concern is the potential for multipacting in these elliptical structures. So far experimental results for cavities with $\beta \approx 0.85$ at Cornell and SACLAY[8], as well as the above mentioned result from JAERI, indicate that there should be no principal problem for such geometries. A final resolution of the multipacting aspect will come from the laboratory tests on single-cell structures that is presently under way in Los Alamos. To support the experimental work, there is a numerical study under way at the University of New Mexico [9]. The TRAK_RF code is being used to investigate the single-cell geometries of both cavity shapes for multipacting susceptibility. First simulations indicate possible multipacting for values of $E_a$ between 2.8 and 4.5 MV/m.

## 5 SINGLE CELL CAVITY TEST

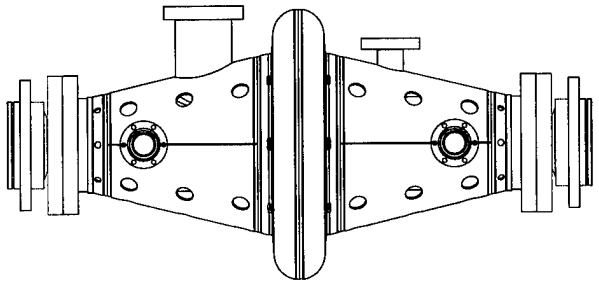


Figure 2: The tested $\beta$=0.64 single-cell cavity with stiffener

In the LANL superconducting structures laboratory we have completed assembly of the equipment for a vertical test of superconducting cavities at 700 MHz under moderate rf power without beam. We are presently testing a single cell cavity at $\beta = 0.64$ with the end-cell shape of the original choice of geometry. This is seen as a meaningful test of the operability of cavities as proposed for the APT facility, since it will provide data on the presence of multipacting in the medium-$\beta$ structures and it will also provide some field performance data. The end-cell geometry of a multi-cell cavity is more critical in determining performance. This is due to a) the wider elliptical nose that brings the opposing cavity walls closer together than in the mid-cells, and b) the steeper sloped side-walls result in opposing walls that are closer to parallel walls, which increases the potential for two-point multipacting. The cavity uses niobium with a RRR=250 and material of a thickness of 1/8". These spec-

ifications are identical to the ones for the planned accelerator facility.

## 6 ACKNOWLEDGEMENTS

This work is supported by the US Department of Energy.

## 7 REFERENCES

[1] G. Lawrence, T. Wangler, "Integrated Normal-conducting/Superconducting High Power Proton Linac for APT", these proceedings

[2] D. Proch, (Ed.), "Proceedings of the 5th Workshop on RF Superconductivity", August 19-23, 1991, DESY M-92-01

[3] Nobuo Ouchi, JAERI, private communication

[4] Frank L. Krawczyk, "Higher Order Mode Analysis of the APT Superconducting Cavities", these proceedings

[5] M. Bartsch et al. "Solution of Maxwell's Equations", Computer Physics Comm. **72**, 22-39 (1992)

[6] J. H. Billen and L. M. Young, "POISSON/SUPERFISH on PC Compatibles," Proceedings of the 1993 Particle Accelerator Conference, Vol. 2, p. 790.

[7] Dale Schrage, LANL, LANSCE-1, private communication

[8] Henry Safa, SACLAY and Hassam Padamsee, Cornell, private communication

[9] Stan Humphries, Daniel Rees, "TRAK_RF - Electromagnetic Field and Charged Particle Simulations in RF Devices", these proceedings

# TEST RESULTS ON THE 9-CELL 1.3 GHZ SUPERCONDUCTING RF CAVITIES FOR THE TESLA TEST FACILITY LINAC

M. Pekeler*, DESY, Notkestr. 85, 22603 Hamburg, Germany

*Abstract*

The design goal for the TESLA Test Facility Linac is an accelerating gradient of 15 MV/m at a quality factor of $Q = 3 \cdot 10^9$. In the linac the cavities are operated in pulsed mode (constant gradient for 800 $\mu$s with 10 Hz repetition rate). The majority of the first 17 industrially produced cavities exceeded the specification. Several cavities reached 25 MV/m at $Q > 1 \cdot 10^{10}$. Due to cleaning by high pressure water rinsing most of the cavities showed no field emission loading; the major limitation was thermal instability. In cavities with poorer performance, two types of field limitations were identified by temperature mapping and further surface analysis: tantalum impurity in the bulk niobium and defects in the equator welds. Eight cavities, equipped with main power coupler, HOM couplers and tuning system have been successfully tested in a horizontal cryostat in pulsed mode. Also here the majority of the cavities exceeded the design goal and gradients up to 25 MV/m could be achieved.

## 1 INTRODUCTION

TESLA (TeV Superconducting Linear Accelerator) is one of the proposed future TeV scale $e^+e^-$ linear colliders. It differs from other projects in its choice of superconducting accelerating structures and of low frequency (1.3 GHz).

In order to prove the technical basis of TESLA the TESLA Test Facility (TTF) is under construction at DESY within the framework of an international collaboration. The aim is to show that accelerating gradients above 15 MV/m at quality factors above $3 \cdot 10^9$ are reproducibly achieved and can be maintained after assembly to the linac together with the necessary auxiliary system [1].

All together seventeen 9-cell cavities manufactured by three different companies have been tested in a vertical cryostat so far. In addition eight cavities were fully equipped with all components in a horizontal cryostat and tested. A summary and comparison of the vertical and horizontal tests are given in this paper.

The first cryomodule of the TTF Linac containing eight superconducting 9-cell cavities has been assembled. First acceleration of the beam by this module is expected in June 97 [2].

## 2 CAVITY TEST PROCEDURE

After delivery from industry, the cavities receive the following treatment and test procedures:

- Visual inspection and dimensional check;
- Removal of the inner damage layer by 80 $\mu$m buffered chemical polishing (BCP). This is done by a closed loop etching facility with active cooling in order to avoid heating of the acid to temperatures above 12°C.
- Removal of 10 $\mu$m from the outer surface by BCP;
- Heat treatment with titanium getter at 1400°C for 4 hours in order to raise the residual rest resistivity ratio (RRR) of the cavities from 300 to 500;
- 80 $\mu$m BCP from the inside in order to remove titanium from the superconducting surface. 30 $\mu$m BCP from outside in order to improve the Kapitza conductance.
- Field profile measurement and tuning to correct frequency;
- Final inner BCP of 20 $\mu$m;
- High pressure (100 bar) water rinsing (HPR) [3], drying in air in a class 10 clean room;
- Assembly, additional HPR, drying by pumping;
- Acceptance test in a vertical cryostat including the possibility to apply high power processing (HPP) [4];
- Field profile check;
- Welding of the He-vessel made out of titanium;
- Inner BCP 20 $\mu$m, HPR, drying in a class 10 clean room;
- Assembly of high power and HOM-couplers;
- HPR and drying by pumping;
- Assembly of the tuning mechanism and magnetic shielding;
- Test in a horizontal cryostat including high power coupler processing;
- Assembly of eight cavities in a cryomodule;

## 3 VERTICAL TESTS

Seventeen 9-cell cavities produced by three European companies have been tested so far in a vertical cryostat. The average gradient was 17.2 MV/m at $Q$ values above $3 \cdot 10^9$. The main limitation of the cavities was thermal instability. Field emission could be strongly suppressed by means of careful high pressure water rinsing.

Seven cavities showed gradients above 20 MV/m. Their $Q(E)$-behaviour is shown in figure 1. Two cavities reached 25 MV/m at $Q > 10^{10}$ without any field emission loading.

In the linac the cavities are operated in the $\pi$-mode with equal gradients in all cells. By excitation of the other coupled modes a non-uniform field distribution can be achieved which allows to determine the high field performance of individual cells. In five cavities of lower gradients a single cell was identified to be responsible for the

* for the TESLA Collaboration

0-7803-4376-X/98/$10.00 © 1998 IEEE

limitation while the other cells could be excited to much higher fields.

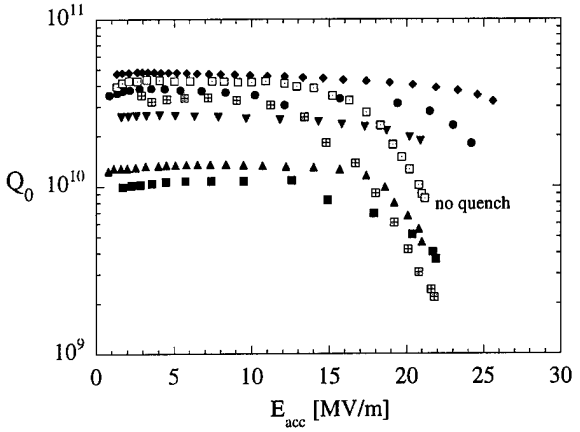



Figure 1: $Q(E)$-behaviour of TESLA 9-cell cavities which reached more than 20 MV/m. One cavity was limited by the available incident power, all others showed a thermal breakdown, some under field emission loading.

### *3.1 Defects in the bulk niobium*

Three niobium cavities from one manufacturer, produced from the same ingot, showed quenches at gradients from 8 to 14 MV/m. They also exhibited a so called "$Q$-switch", which is a sudden drop in quality factor with increasing incident power (see figure 2). Localized areas with excessive heating were found by temperature mapping. In one cavity the defective cell was cut out and investigated with X ray fluorescence spectroscopy. A tantalum grain close to the RF surface was found. A sensitive eddy current scanning system, developed at the Bundesanstalt für Materialforschung, Berlin, was able to detect the inclusion. In the future this type of material defects will be excluded by eddy current scan of the niobium sheets. 5 % of recently produced niobium sheets had to be rejected.

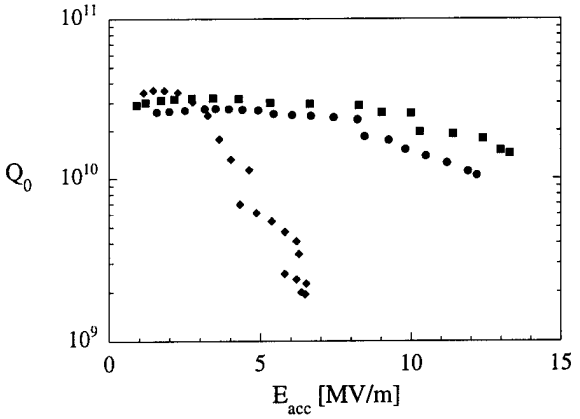



Figure 2: $Q(E)$-behaviour of 9-cell cavities which showed a "$Q$-switch". All cavities were produced by one manufacturer from the same ingot material. The $Q$-switches and quenches are probably caused by foreign material inclusions.

### *3.2 Defects in the equator welds*

All cavities produced by another manufacturer exhibited a thermal breakdown in the 11 to 15 MV/m regime combined with a so called "$Q$-slope", a continuous reduction of the quality factor from approximately $3 \cdot 10^{10}$ at low gradient to about $1 \cdot 10^{10}$ near the quench field (figure 3). No field emission was observed.

Three of the cavities were investigated with temperature mapping. Several locations with field-dependent surface resistance were found in the equator welds which caused the $Q$-slope and also the quench. An analysis showed that the welding procedures at this company were not adequate for gradients in the 20-25 MV/m regime.

A cavity with improved welding technique has recently been fabricated by this company. The preliminary test result is shown in figure 4. A remarkable improvement is observed. The maximum gradient of 22 MV/m is not limited by quench but by the available incident power. There is no $Q$-slope visible up to gradients of 16 MV/m, however field emission sets in at 16 MV/m. This cavity will be high pressure water rinsed soon and retested again.

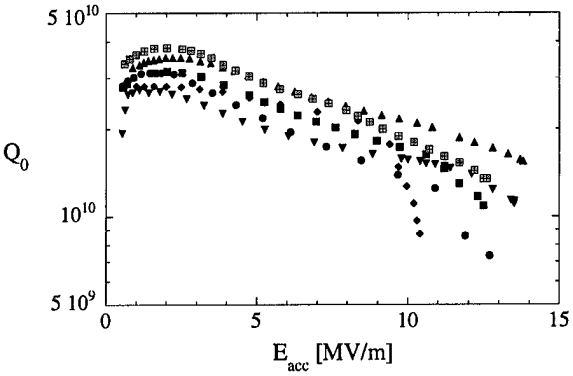



Figure 3: Cavities showing a "$Q$-slope" and quench in the 11-15 MV/m regime. There was no field emission present. All cavities were produced by the same manufacturer.

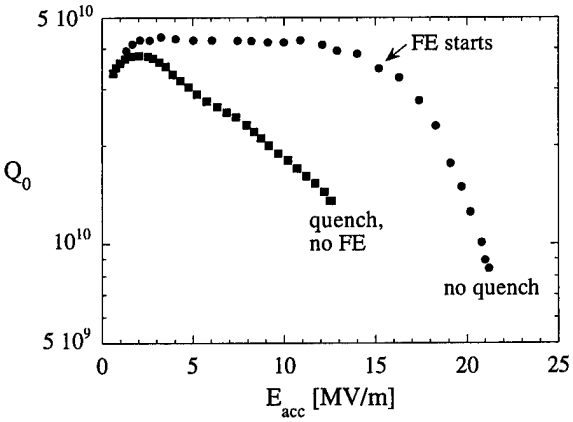



Figure 4: $Q(E)$-behaviour of a cavity produced with new welding technique. The cavity showed field emission above 16 MV/m. For comparison one of the previous cavities (figure 3) is shown.

### 3.3 *Test in pulsed mode*

A number of cavities were tested in the vertical cryostat also in the pulsed mode as foreseen in the linac operation. For this purpose the cavity was equipped with a high power coupler tunable from $Q_{ext} = 10^{10}$ (needed in cw operation) to $3{\cdot}10^6$ (needed in pulsed operation). In pulsed mode the gradient is kept constant for 800 $\mu$s at a 10 Hz repetition rate. The gradients achieved in the pulsed mode are always higher than in cw operation (figure 5).

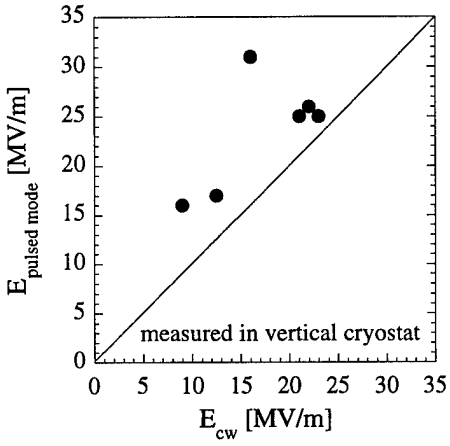



Figure 5: Comparison of cw and pulsed operation of cavities tested in the vertical cryostat.

## 4 HORIZONTAL TESTS

Eight cavities equipped with all auxiliary components (helium-vessel, high power coupler, HOM-couplers, tuning mechanism and magnetic shielding) were tested in a horizontal cryostat. Because of the low $Q_{ext}$ of the high power input coupler only measurements in the pulse mode were possible.

The cavities reached an average gradient of 17.5 MV/m at $Q > 3{\cdot}10^9$ (see figure 6) compared to an average gradient of 18.6 MV/m at $Q > 3{\cdot}10^9$ in cw mode in the vertical test stand. In contrast to the vertical tests, field emission has been observed more frequently. The reason is probably particle contamination due to the more complicated assembly and to the processing of the main power coupler. The higher field emission loading is responsible for the slight degradation in performance.

Cavities showing strong field emission can be further improved by applying high power processing (HPP) [4]. For this purpose, short pulses of high instantaneous power ($\approx$ 400 $\mu$s, up to 1 MW) are applied to destroy field emitters. The power coupler has to be carefully processed up to 1 MW, which may take several days. Due to a tight timeschedule HPP was not applied during the horizontal test. It still can be done after the installation of the cavities in the first cryomodule and in the linac.

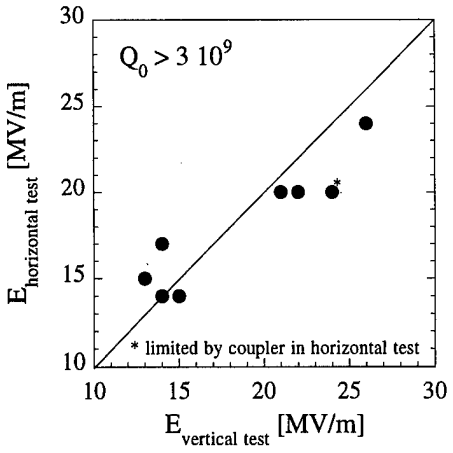



Figure 6: Comparison of the performance of cavities tested in the vertical cryostat in cw mode and in the horizontal test cryostat in the pulsed mode.

## 5 CONCLUSION

Most of the first TESLA 9-cell cavities for the TTF Linac exceeded the specifications of 15 MV/m at $Q = 3 \cdot 10^9$. Seven cavities reached gradients above 20 MV/m, two reached 25 MV/m with $Q > 10^{10}$.

In cavities with poorer performance, two types of limitations were found: tantalum inclusion in the bulk niobium, and imperfect equator welds.

Cures have been found for both types of imperfections. Using a dedicated eddy current scanning system defective niobium sheets will be rejected from the next cavity production. The second limitation has been overcome with a new welding technique. The first cavity built with this new welding procedure showed no quench at 22 MV/m. With better material control and better welding technique, gradients higher than 20 MV/m are expected to be routinely possible now.

In the horizontal tests, a slight reduction in gradient caused by higher field emission loading compared to the vertical test is. Work is in progress to improve the cleaning and mounting procedures prior to the horizontal test.

## 6 REFERENCES


[1] D.A. Edwards: 'TESLA TEST FACILITY LINAC - Design Report', TESLA 95-01, 1995.

[2] B. Aune: 'Results from the DESY TESLA Test Facility', this conference.

[3] P. Kneisel, B. Lewis, Part. Acc. **53**, 1996 Ph. Bernard et al., Proc. Eur. Part. Acc. Conf., Berlin, 1992

[4] J. Graber, PhD thesis, Cornell University, 1993 C. Crawford et al.: 'High gradients in linear collider superconducting accelerator cavities by high pulsed power to suppress field emission', Part. Acc. **49**, pp. 1-13, 1995

# ASTRID ELECTRON CAVITY STUDY

S.P. Møller and T. Korsbjerg
Aarhus University, Aarhus, Denmark,
E.N. Zaplatine,* DESY, Hamburg, Germany

*Abstract*

An accelerating cavity of ASTRID (Aarhus Univ.). Electron Storage Ring[1] was studied. The cavity was simulated with two 3D numerical codes MAFIA[2] and GdfidL[3]. The HOM influence on the cavity components was investigated.

## 1 INTRODUCTION

Some parameters of ASTRID Electron Storage Ring related to RF system are presented in Table 1. The accelerating cavity is a capacitively loaded coaxial TEM cavity (Fig. 1).

Table 1: Some ASTRID Electron Synchrotron Parameters.

| | | |
|---|---|---|
| Energy | 100–600 | MeV |
| Circumference | 40 | m |
| Revolution Frequency | 7.4948 | MHz |
| RF Frequency | 104.927 | MHz |
| Designed Acc. Voltage | 50 | kV |

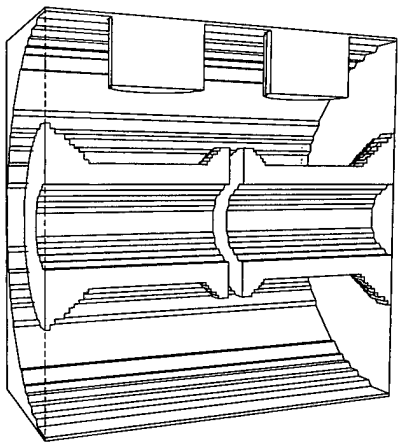


Figure 1: Cavity Geometry.

An electrical field is concentrated in the accelerating gap and a magnetic field is circulating around beam pipes in the same direction for the whole cavity length. Two plungers, placed symmetricaly to the midplane, are used for a magnetic tuning to compensate a beam loading during a beam injection.

RF-spring contacts are used electrical isolation of the plunger housing from the cavity[4].

* Guest Scientist from JINR, Dubna, Russia

## 2 3D CAVITY SIMULATION

To simulate this cavity with the plunger structure two 3D MAFIA and GdfidL codes were used. On Fig. 1 a half part of the cavity geometry is shown as it was generated by MAFIA mesh generator. The results of 3D MAFIA simulation for two plunger positions are given in Table 2. The plunger position is measured from the cavity tank circumference. The modes 1 and 3 are essentially the fundamental and its second harmonic. The modes 2 and 4 are the first and second harmonics of the transverse mode.

Table 2: 3D Cavity Simulation.

| | xplunger = 0.0 mm | | |
|---|---|---|---|
| mode | $f_0$/MHz | Q | $R_{sh}$/Ohm |
| 1 | 102.5032654 | 20414 | 1763470 |
| 2 | 509.9479675 | 18997 | 0 |
| 3 | 546.9269409 | 40925 | 64615 |
| 4 | 632.9127808 | 28986 | 0 |
| 5 | 689.9231567 | 54431 | 0 |
| 6 | 727.2523804 | 37248 | 7845 |
| | xplunger = 98.0 mm | | |
| 1 | 103.4529190 | 19197 | 1637202 |
| 2 | 437.5782166 | 24244 | 10936 |
| 3 | 526.5858154 | 22095 | 14694 |
| 4 | 584.1299438 | 25730 | 14325 |
| 5 | 658.9996948 | 38795 | 1145 |
| 6 | 703.0874023 | 32683 | 3833 |

### 2.1 *Shunted Inductive Loop*

The plunger of the ASTRID electron cavity is moved in its full length (90–100 mm) during injection and acceleration of the beam. A plunger insertion changes field distribution causing the HOM's B-field to circulate around it. It means that one of the possible solution to damp HOMs can be a shunted inductive loop (Fig. 2), installed close to the plunger body. The square of such loop should be parallel to the fundamental mode magnetic field and it will be perpendicular to HOM's magnetic fields. The result of such loop use is shown on Fig. 3. The shunting simulation can be done by an electrical conductivity change of a small part of the loop where it connects with the ground. Since we don't know the conductivity value to shunt resistance relationship the simulation has been done for a series of the conductivity values.

0-7803-4376-X/98/$10.00 © 1998 IEEE

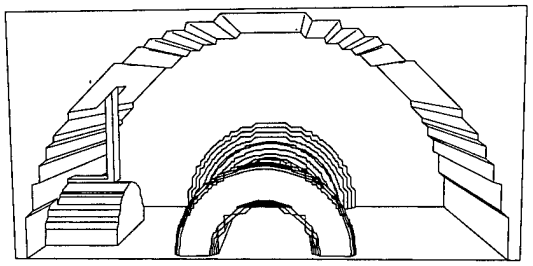


Figure 2: Cavity with Inductive Loop.

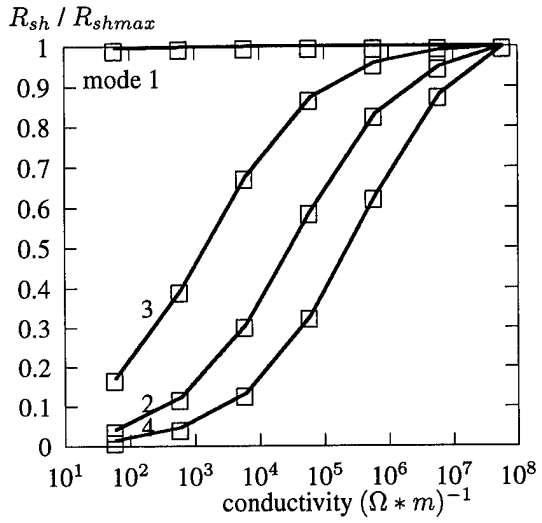



Figure 3: Cavity Shunt Impedance with Shunted Loop.

### 2.2 *Shunted Capacitive Load*

The only disadvantage of the proposed above inductive shunted loop is that in order to install it in the working cavity some additional holes should be made in the cavity walls. To avoid that we looked into the possibility of using already exsisting holes. There are some vacant holes in the cavity end flange. These holes can be used for the installation of a capacitive load (Fig. 4) which in the simulation represents a rod with 20 x 10 mm$^2$ cross section.

The results of the cavity simulation with capacitive load are shown in Fig. 5. To provide an experimental test a 10 mm diameter rod connected to a water cooled 50 Ohm load was installed. Experimental results are summarized in Table 3.

### 2.3 *Z – Plungers*

Considering the field distributions in the cavity, a plunger position in the end flange (Fig. 6) is preferable. Firstly, because the magnetic field strength is highest close to this wall and second, the magnetic field of the cavity transversal mode is parallel to the plunger which will not result in the current induction flowing along the plunger.

Simulating with such z-plungers, keeping volumes unchanged and comparing to an x-plunger simulation, gives

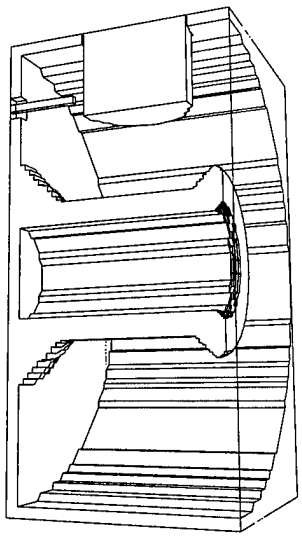


Figure 4: Cavity with Capacitive Load.

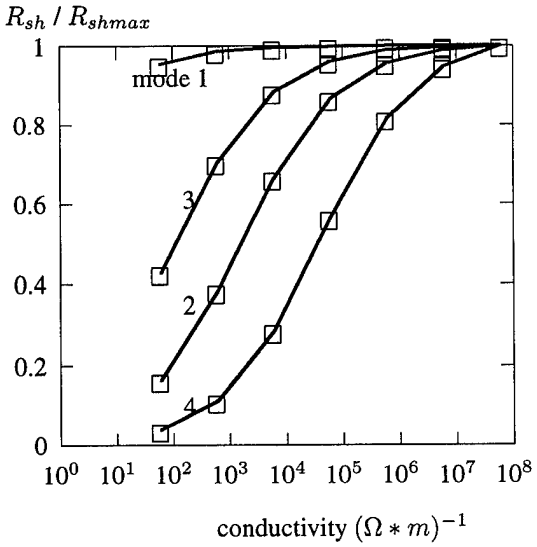



Figure 5: Cavity Shunt Resistance with Capacitive Load.

the results shown in Figs. 7–8. As expected, the frequency change is much bigger now and if one stays with such structure, the different working plunger position also results in a shunt resistance gain.

## 3 CONCLUSIONS

- The best solution for the higher order mode damping in this cavity is the shunted inductive loop.
- The capacitive shunted load can be very practical option for the HOM damping in this cavity in the situation, when no big mechanical modifications in the cavity can be done.
- Z-Plunger(s) are stronger in terms of the cavity frequency change and preferable compared to x-plungers. But the HOM damping system should be considered in this case, too.

Table 3: HOM Damping Results.

| mode | $f_0$/MHz | Q | $Q_l$ |
|---|---|---|---|
| | MHz | | |
| 1 | 105.027 | 6327 | 6484 |
| 2 | 443.696 | 3872 | — |
| 2-3 | 486.483 | 1986 | 231 |
| 3 | 527.075 | 6230 | 663 |
| 4 | 583.088 | 329 | 125 |
| 5 | 654.985 | 4043 | 602 |

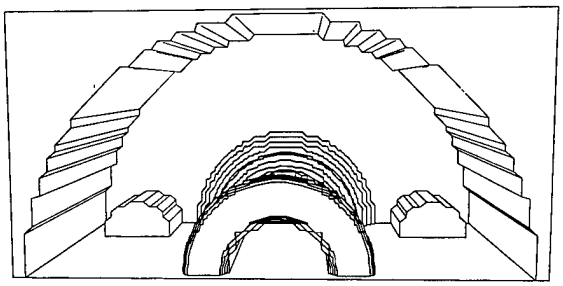


Figure 6: Cavity with Z-Plungers.

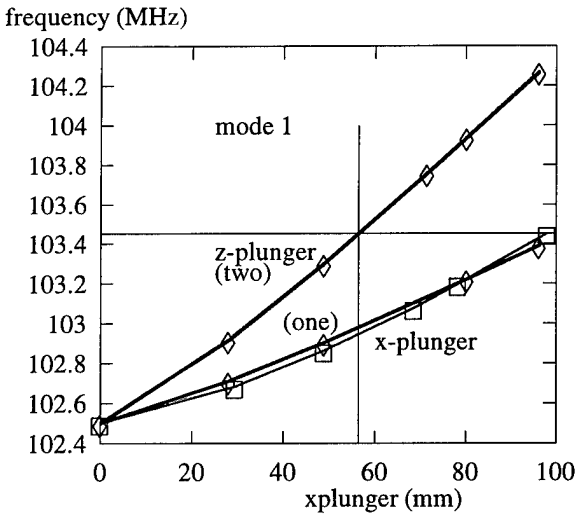



Figure 7: Cavity Fundamental Mode Frequency with Z-Plungers.

## 4 ACKNOWLEDGEMENTS

The authors are very grateful to Prof. E. Uggerhoj for a permanent interest and support of this work.

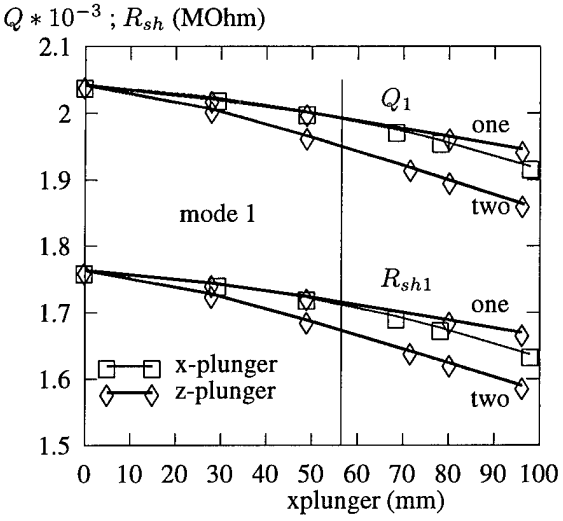



Figure 8: Cavity Parameters with Z-Plungers.

## 5 REFERENCES

[1] S.P. Møller, "ASTRID – a storage ring for ions and electrons", Conference Record of the 1991 IEEE PAC, San Francisco.

[2] T. Weiland, "Solving Maxwell's Equations in 3D and 2D by means of MAFIA", Proc. of Conf. on Computer Codes And The Linear Accelerator Community, LA-11857-C (1990).

[3] W. Bruns, "GdfidL: A Finite Difference Program With Reduced Memory and CPU Usage", this congerence.

[4] Yu Senichev, T. Korsbjerg, S.P. Møller, E. Zaplatine "Solving the Problem of Heating of RF Contacts in Cavity Tuners", this conference.

# SOLVING THE PROBLEM OF HEATING OF RF CONTACTS IN CAVITY TUNERS

Yu. Senichev*, T. Korsbjerg, S. P. Møller, Aarhus University, Aarhus, Denmark,
E. N. Zaplatine† , DESY, Hamburg, Germany

*Abstract*

The accelerating cavity of the ASTRID Electron Synchrotron was studied. The cavity is a capacity loaded TEM cavity resonating at 104.95 MHz. Two plungers driven in parallel keep the cavity in tune, yielding a tuning range of about 0.8 MHz to compensate the beam loading. The RF spring contact liners placed on the entrance of the plunger housing are used to isolate the plunger housing from the RF field. The surface current flowing through the contacts limits the power in the cavity to less than 5 kW due to heating. We analyse the electrodynamics of the tuner and investigate two options of a new tuner geometry, one with contacts and one without contacts. The new design should remove the power limitation due to contact problems.

## 1 INTRODUCTION

There are many methods of RF cavity frequency adjustment. For accelerating cycles with a low repetition frequency a mechanical plunger moved in a housing is used to tune the cavity resonant frequency. Independent of method, the frequency is changed due to a redistribution of the electrical or magnetic component of the electromagnetic field. The frequency variation is proportional to the integral field perturbation. The behaviour of the fundamental and the HOM modes in the ASTRID cavity with the plunger position has been investigated[1]. The necessary frequency change is set by the reactive beam loading. Conventionally the magnetic component is perturbed, since the electrical component is responsible for the acceleration. It is done by inserting the plunger in the maximum magnetic field. However, the maximum magnetic component coincides with the maximum surface current, which causes a heating of the surface proportionally to $H^2$. The electromagnetic field can penetrate inside the housing of the plunger and excite its eigenmodes. It causes heating of the bellow as well. To prevent the penetration of the electromagnetic field into the housing, sliding electrical contacts are used. This shielding of the housing helps to avoid heating of inside elements, but a problem of heating of contacts themselves arises. The transient resistance between the sliding contacts and the plunger surface is determined by the contact pressure, the cleanliness of the surfaces and the spotty wear. Moreover, the damage of the plunger surface by the sliding contacts looks as scratches perpendicular to the current direction on the plunger surface, leading to amplification of the heating effect. All these circumstances make the work with such plungers unreliable and restrict the power delivered to the cavity to a level less than around 5 kW. To find a solution to this problem we investigated the electrodynamics of the tuner.

* on leave from Institute for Nuclear Research, Moscow

† guest scientist from JINR, Dubna, Russia

## 2 ELECTRODYNAMICS OF TUNER

### 2.1 *Antenna effect*

We observed experimentally that the maximum heating of the cavity takes place around each tuner housing entrance with two maxima located with 180° symmetry relative to the entrance and lying on the line joining the entrances. We have investigated the electrodynamics of the cavity together with the plunger and can explain the nature of this phenomena by two effects. The first one is due to the antenna effect. Figure 1 schematically shows the current construction of the cavity with plunger removed from the housing and the magnetic component distribution simulated by MAFIA. In the current construction the contacts are installed on the entrance to the housing. The original (without plunger) magnetic component distribution of the cavity TEM mode is inversely proportional to the radius $H \propto 1/r$ and it is disturbed by the plunger. The plunger is a good conductor and plays the role of an antenna with the length $l_{ant}$ inserted in the cavity. It generates a mixing mode, which converts the cavity TEM mode into the coaxial TE11 "plunger-housing" mode. The mixing mode is distributed along the plunger without the $1/r$ damping and therefore the magnetic field is amplified on the surface of the cavity near the entrance with the factor $\propto \frac{R_{cav}}{R_{cav}-l_{ant}}$. Hence the heating power grows by the square of this value. Due to this effect the power dissipated on the surface around the tuner housing entrance is higher in comparison with other places and in our case this factor is about 1.5.

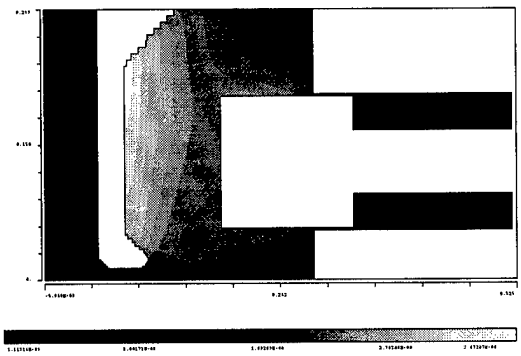


Figure 1: The magnetic field distribution in the cavity with the plunger.

0-7803-4376-X/98/$10.00 © 1998 IEEE

### 2.2 *TE11 coaxial "plunger-housing" mode*

Obviously, if we place the contacts just at the entrance of the housing, we get the high current flowing through the contacts. So, we have to move the contacts deeper into the housing and the depth depends on how far the electromagnetic field penetrates. To answer this question we should know what modes are excited in the housing. Let us consider the electrodynamics of the system "cavity-plunger-housing". Since the slot between the plunger and the housing could be considered as the coupling element between two resonant volumes, the cavity itself and the housing, the intensity of the mode excited in the housing is proportional to the integral:

$$A_s \propto \frac{1}{\frac{\delta\omega}{\omega_s} Q_s} \int_{slot} (\omega_s \dot{E}_c \dot{E}_s^h - \omega_c \dot{H}_c \dot{H}_s^h) dv \ , \qquad (1)$$

where $\dot{E}_s^h$,$\dot{H}_s^h$ are the eigenmode components of the housing, $\dot{E}_c$,$\dot{H}_c$ are the fundamental mode components of the cavity, $Q_s$ is the quality factor of $S$ -th mode, $\delta\omega = \omega_s - \omega_c$ and $\omega_s$, $\omega_c$ are the eigen frequencies of of $S$ -th mode and the cavity fundamental mode correspondingly. From the distribution of the cavity fundamental mode (in this case TEM mode) we can conclude that the coaxial mode TE11 with one variation along azimuth can be excited in the housing. The TE11 cut off frequency $f_{cut}$ is determined by the inside radius of the housing $r_h$ and the outside radius of the plunger $r_p$

$$\frac{\pi^2 f^2}{c^2}(r_h + r_p)^2 \approx \left[1 + \frac{1}{3}\left(\frac{r_h - r_p}{r_h + r_p}\right)^2\right] \ . \qquad (2)$$

For our case the cut off frequency equals 640 MHz. Thus, TE11 is beyond cut off frequency mode. But it penetrates into the housing with a length proportional to the damping decrement equal to $\tau = 7 \div 8$ cm. Figure 2 shows the distribution of the magnetic component inside the housing and around the plunger moved into the cavity. In this figure the vertical Z direction shows the value of the magnetic field in the XY plane passing through the centre of the cavity and the housing.

The exponential decay and the decrement value corroborate that this mode is exactly the TE11 mode. If we want the flowing current through contacts reduced by a factor of $k_1$=10, the contacts have to be moved into the housing by $l = 2.3\tau$. Taking into account the antenna effect $k_2$=1.5 and the reflection of the power from the contacts $k_3$=2, the depth has to be $l = 3.4\tau$. Since the stroke of the plunger is 10 cm, the plunger housing height has to be about 35 cm.

### 2.3 *TEM coaxial "plunger-housing" mode*

If the cavity TEM mode has a different value of the magnetic component at opposite points relative to the entrance of the housing, the TEM coaxial "plunger-housing" mode can be excited as well. Owing to the big capacity between

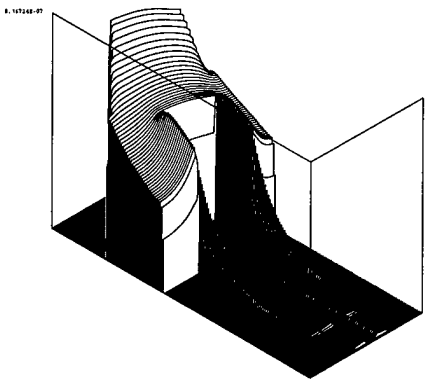


Figure 2: Magnetic field inside cavity and housing.

the drift tube of the cavity and the plunger itself, the resonant frequency of this mode can cross the working frequency of the cavity. The 3D MAFIA code simulation confirms this assumption. Figure 3 shows the distribution of the TEM coaxial "plunger-housing" mode magnetic component. The electrical component has a small value, because the capacity is located outside the housing. Since the TE11 mode damps very fast, the residual field inside the housing is determined by the TEM coaxial "plunger-housing" mode. The change of magnetic component symmetry corroborates that. To remove this mode from the working region we have to change the induction, which is proportional to the inside volume of the housing. Due to a necessity to damp TE11 we are restricted to decrease the housing size and we can only decrease the resonant frequency of the plunger mode. We have developed two options of new tuner design with and without contacts.

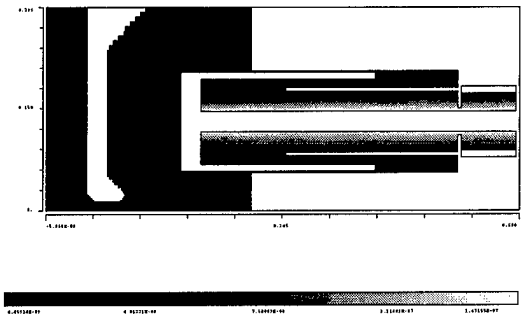


Figure 3: The TEM coaxial "plunger-housing".

## 3 TWO OPTIONS OF NEW TUNER DESIGN

### *3.1 With contacts*

To increase the inside volume of the housing we use the idea of an enclosed coaxial. Figure 4 shows a quarter of the cavity geometry generated by MAFIA mesh generator. The plunger is made like an empty cup and the additional built-in cup is inserted into the plunger and is mounted on the upper flange of the housing. The contacts are installed on the second cup and they slide on the inside surface of the plunger. This construction decreases the plunger mode frequency and removes the contacts from the maximum magnetic field. Unfortunately, the latter has little effect due to the small housing size to resonant wave length ratio.

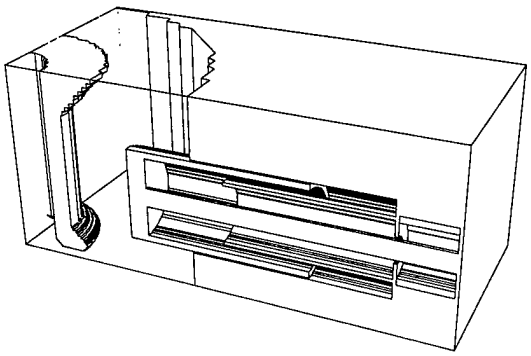


Figure 4: The tuner geometry.

### *3.2 Without contacts*

In the first option the contacts play the role of bellow shielding. The bellow can be heated only by the TEM plunger mode if the TE11 mode is damped. But if we do not use contacts at all, the entrance inside the housing for electromagnetic field will be open, the induction will grow significantly and the plunger mode frequency will go down by a factor of two. The heating of the bellow has to decrease inversely proportional to the detuning. So, the second option is characterised by the absence of contacts. Actually, in this design we do not need the additional built-in cup from a electrodynamics point of view, but it increases the vacuum resistance between the bellow surface and the accelerating gap in the cavity. Figure 5 shows the drawing of the tuner port, which could be used in two options with and without contacts. To improve the cooling conditions of the bellow we moved it out from the housing. In both cases we cool the housing externally at the entrance as well as the plunger itself.

## 4 CONCLUSIONS

We have investigated the main reasons for RF contact heating:

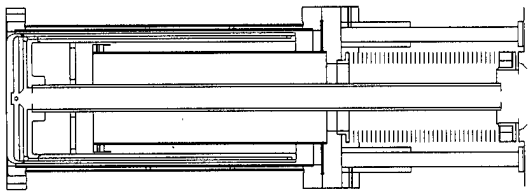


Figure 5: The tuner design.

- The antenna effect amplifies the magnetic field near the entrance inside the housing.
- The beyond cut off coaxial mode TE11 penetrates inside the gap "housing-plunger".
- The TEM "plunger-housing" mode due to the significant capacity between the plunger and the drift tube of the cavity has a resonant frequency in the working region of the fundamental mode.

We have developed two options of a tuner design with and without contacts and both meet the required conditions for the tuner. Experimental verification will be made in 1997.

## 5 ACKNOWLEDGEMENTS

The authors are very grateful to E. Uggerhoj for great interest in this work, to M. Isawa from KEK for helpful discussions at the initial stage of our work, to K. Iversen for many interesting technical solutions and to D.Z. Lassen for the good drawings.

## 6 REFERENCES

[1] S.P. Møller, T. Korsbjerg, and E. Zaplatine, "Astrid Electron cavity study", this proceeding.

# A DIVIDE-DOWN RF SOURCE GENERATION SYSTEM FOR THE ADVANCED PHOTON SOURCE

D. Horan, F. Lenkszus, R. Laird
Advanced Photon Source, Argonne National Laboratory
9700 South Cass Avenue, Argonne, Illinois 60439 USA

*Abstract*

A divide-down rf source system has been designed and built at Argonne National Laboratory to provide harmonically-related and phase-locked rf source signals between the APS 352-MHz storage ring and booster synchrotron rf systems and the 9.77-MHz and 117-MHz positron accumulator ring rf systems. The design provides rapid switching capability back to individual rf synthesizers for each one. The system also contains a digital bucket phase shifter for injection bucket selection. Input 352-MHz rf from a master synthesizer is supplied to a VXI-based ECL divider board which produces 117-MHz and 9.77-MHz square-wave outputs. These outputs are passed through low-pass filters to produce pure signals at the required fundamental frequencies. These signals, plus signals at the same frequencies from independent synthesizers, are fed to an interface chassis where source selection is made via local/remote control of coaxial relays. This chassis also produces buffered outputs at each frequency for monitoring and synchronization of ancillary equipment.

## 1 RF SOURCE SIGNAL REQUIREMENTS

The APS positron accumulator ring (PAR) uses two rf systems, operating at 9.77 MHz and 117.30 MHz ($12^{th}$ harmonic). These frequencies must be phase-locked to themselves and to the booster-synchrotron frequency of 351.930 MHz. For proper injection, maximum allowable jitter between the source frequencies is approximately 70 ps p-p [1]. In the PAR low-level rf systems, the phase of both the 9.77-MHz and 117.30-MHz signals is shifted to enable bucket-selection in the booster synchrotron during the injection cycle. This phase shifting is achieved by using separate calibrated analog phase shifters in the low-level rf signal paths or by shifting the phase of the rf source driving each PAR rf system. These source signals can be generated either by separate rf synthesizers or by a divide-down rf source generator board which divides the 351.93-MHz booster synchrotron source frequency into the two PAR frequencies and provides digitally-clocked phase shifting of the PAR frequencies. The separate rf synthesizers are supplied an external 10-MHz timebase signal distributed from a multiple-output master 10-MHz oven source. PAR rf source selection between the independent synthesizers and the divide-down generator board is provided by an interface chassis which uses coaxial relays for rf switching and also contains filtering and buffering for the divide-down generator outputs.

## 2 DIVIDER BOARD DESIGN

The divide-down rf source generator is a VXI-based ECL digital divider board (see Figure 1) which divides a 351.93-MHz sinewave input signal into 117.30-MHz and 9.77-MHz signals that are phase locked to each other and to the 351.93-MHz source. The board provides both CW and phase-shifted outputs at each PAR frequency and enables remote programming and control of the phase shift commands for storage ring bunch fill pattern control via the APS EPICS control system.

A block diagram of the divide-down rf source generator board is shown in Figure 2. The 351.93-MHz input signal is transformer-coupled to an ECL zero-crossing detector where it is converted to a 351.93-MHz square-wave. This signal is fanned-out and used as a timing clock to synchronize the digital phase shifters for each frequency and is also applied to the input of a programmable binary counter that performs a divide-by-three function and produces a 117.30-MHz square-wave signal. This 117.30-MHz square wave is fed to the input of another programmable binary counter to divide the signal by 12 and produce the 9.77-MHz square-wave output. The 9.77-MHz and 117.30-MHz outputs of the dividers are fanned out to feed CW signals to the front panel connectors and to drive the input of a digital phase shifter for each frequency.

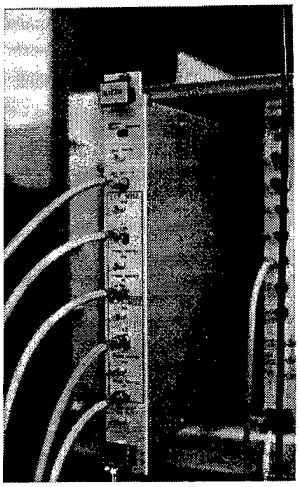


Figure 1: Digital rf source generator VXI module.

The digital bucket phase shifters consist of independent clocked programmable shift registers that execute preprogrammed output phase shifts upon receipt of a "load phase" command. Using separate command steps, the phase-shift specification (bucket selection) is pre-loaded into the programming registers of the phase shifters, and then the phase shift is executed at the appropriate time during injection. The 117.30-MHz and 9.77-MHz phase shifters are capable of 3 and 36 possible output phase selections, respectively. At the present time during accelerator operation, only 12 selections are used.

0-7803-4376-X/98/$10.00 © 1998 IEEE

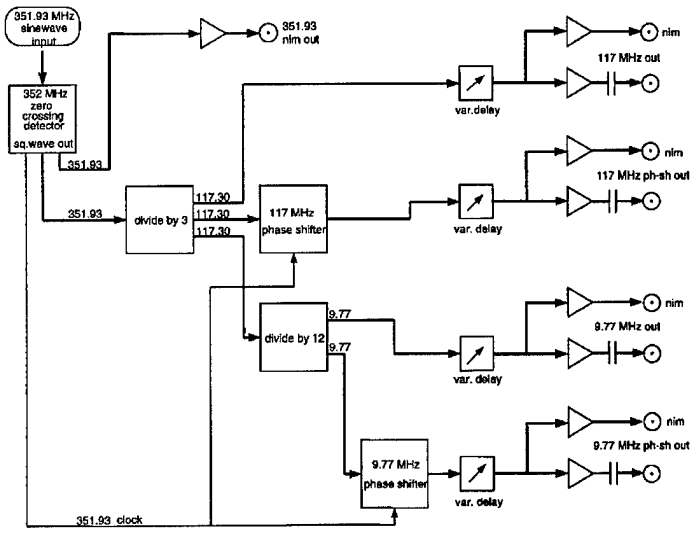



Figure 2: Digital rf source generator board diagram.

The CW and phase-shifted square-wave outputs at 9.77 MHz and 117.30 MHz are passed through programmable delay generators to provide in-phase signals at the board output connectors. The output signals are fed to the front panel connectors through buffers which provide NIM and AC-coupled 50-ohm outputs at each frequency. Circuit board foil layouts use a combination of stripline and microstrip construction techniques to correct for propagation delays which would introduce timing errors.

## 3 SYSTEM INTEGRATION

The divider board outputs are interfaced to the existing PAR low-level rf systems by a chassis which provides essential filtering, amplification, and switching (see Figure 3). This enables operation of the PAR rf systems using either the divide-down source generator or individual rf synthesizers as the rf source signals and either the analog or digital bucket phase shifters.

The 9.77-MHz and 117.30-MHz square-wave rf source outputs of the divider board are low-pass filtered immediately upon entry to the interface chassis, using filters which have a minimum -60 dB rejection from 19.54 MHz and 234.4 MHz to 352 MHz, respectively, to resolve the fundamental component of each signal. At both PAR frequencies a coaxial relay switches either the CW output, if the downstream analog bucket phase shifter is to be used, or the phase-shifted divide-down rf source output to the input of the PAR low-level rf system through a leveling amplifier to insure constant rf drive amplitude. Again, at both PAR frequencies, another coaxial relay allows a stand-alone rf synthesizer to supply rf drive to the low-level rf system. Cable lengths are adjusted and attenuators provided to minimize the phase shift between source and phase shifter selections. Buffer amplifier/splitter networks are provided to supply multiple isolated rf outputs at each PAR frequency for timing and test purposes. Remote control and status readback of the interface chassis is provided.

## 4 PERFORMANCE MEASUREMENTS

The theoretical performance of the divide-down rf source in terms of relative phase jitter between the output signals and the 351.93-MHz input was expected to be on the order of 20 ps p-p. Such levels of phase jitter are below the capability of available measurement equipment

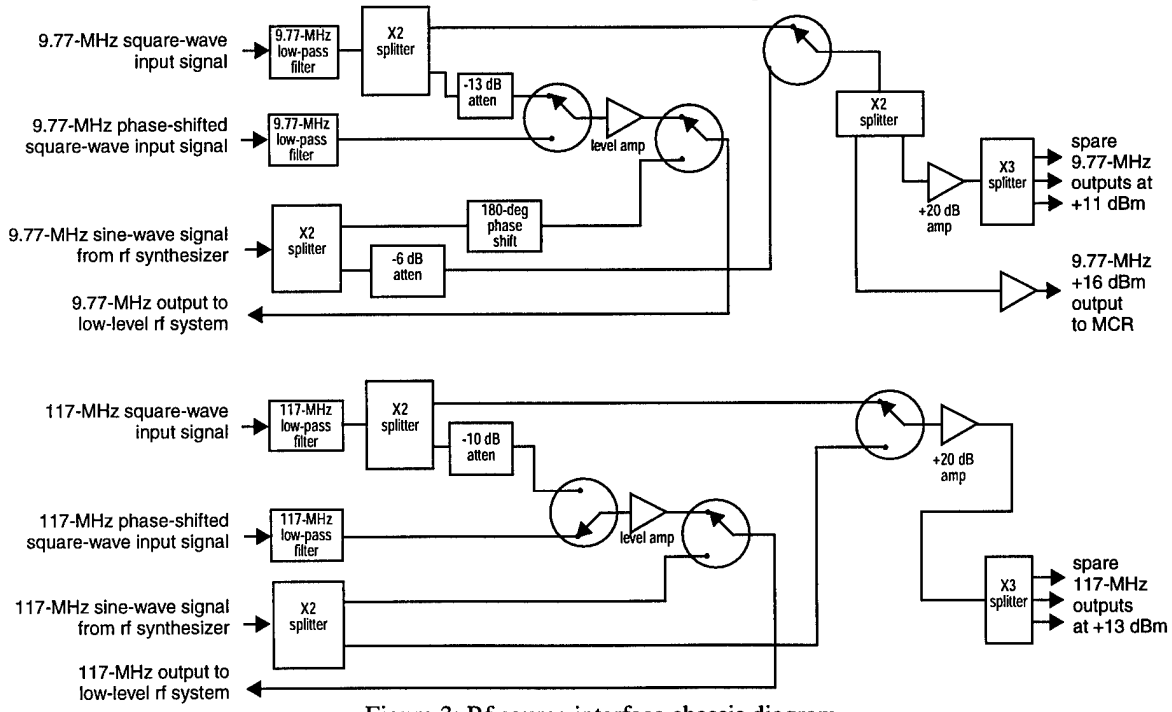
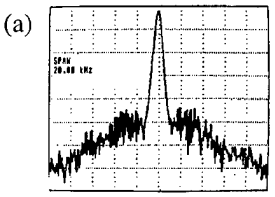


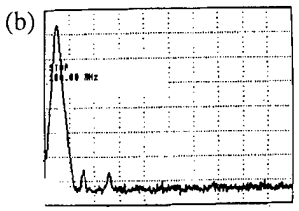

Figure 3: Rf source interface chassis diagram.

and are well under the accelerator specification. The divide-down source system was initially tested on the PAR rf systems under beam conditions in the summer of 1996. Accelerator operation during that test showed no degradation in accelerator performance using the divide-down rf source. Measurement on the filtered rf output signals of the divide-down source system indicates the frequency division process contributes nothing significant to the overall phase noise level of the system (see Figures 4(a) and (b)). The estimated phase noise specification for ideal ECL dividers is approximately -148 dBC/Hz [2]. This is well below other unavoidable sources of phase noise in the rf systems, such as the 800-foot cable run and 20-dB trunk amplifier necessary to supply the booster synchrotron 351.93-MHz source signal to the input of the divide-down board at an adequate level (see Figure 4(c)). As can be seen in Figure 4(a) and (b), low-pass filtering of the 9.77-MHz and 117.30-MHz divide-down board square-wave outputs proved adequate to attenuate harmonic components of the signals to acceptable levels.

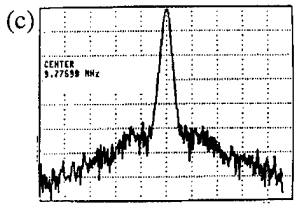
Using the digital bucket phase shifter for storage ring fill pattern control has resulted in more uniform bunch-to-bunch charge in the stored beam. Figures 5(a) and (b) show the bunch charge uniformity measurements made on



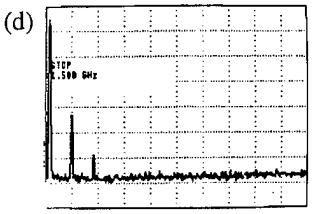

CENTER FREQ = 351.93
SPAN = 20 KHZ



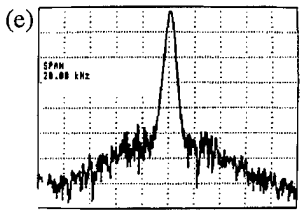

FREQ SWEEP
5 MHZ TO 100 MHZ




CENTER FREQ = 9.77 MHZ
SPAN = 20 KHZ




FREQ SWEEP
100 MHZ TO 1 GHZ




CENTER FREQ = 117 MHZ
SPAN = 20 KHZ

Figure 4: (a) 351-MHz source, (b) and (c) 9.77-MHz filtered divide-down rf source signal, (d) and (e) 117-MHz filtered divide-down rf source signal.

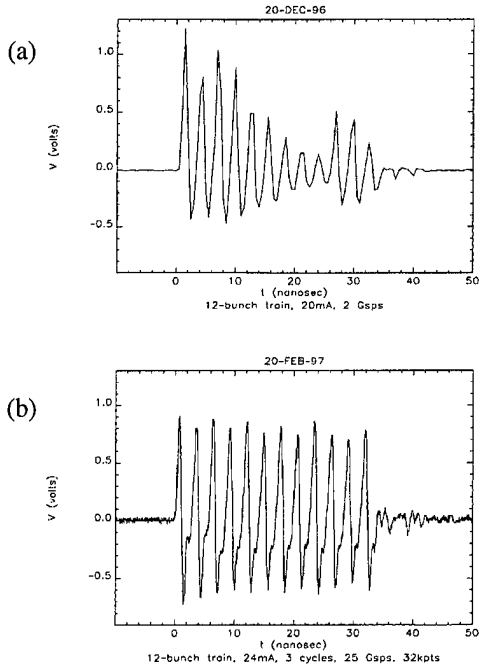



Figure 5: Storage ring bunch charge uniformity (a) analog bucket phase shifter, and (b) digital bucket phase shifter.

storage ring beam, using identical fill patterns. Figure 5(a) represents two separate storage ring fills where separate rf synthesizers were used for the PAR rf source signals, and downstream analog phase shifters were used for bucket selection during injection. Figure 5(b) is the same measurement on stored beam, using the same fill pattern, after using the divide-down rf source system and digital bucket phase shifters for bucket selection.

## 5 CONCLUSION

The PAR divide-down rf source system has logged approximately 1500 hours of on-line accelerator use and has contributed to improvements in injection efficiency and bunch fill pattern repeatability. It also improves the long-term stability between the APS injector and storage ring, reducing overall fill time. Future improvements to this system include efforts to further reduce phase noise in the 352-MHz divider input signal.

## 6 ACKNOWLEDGMENTS

I would like to recognize APS RF Group technicians Ernie Cherbak and Gian Trento for their efforts in construction and installation of the divide-down rf source hardware. This work was supported by the U.S. Department of Energy, Office of Basic Energy Sciences, under Contract No. W-31-109-ENG-38.

## 7 REFERENCES

[1] Steve Milton, private communication.
[2] U. L. Rhode, Digital PLL Frequency Synthesizers – Theory and Design, Prentice-Hall, pp. 85-88, 1983.

# MECHANICAL DESIGN UPGRADE OF THE APS STORAGE RING RF CAVITY TUNER

J. Jones, D. Bromberek, Y. Kang, R. Kustom, L. Morrison, R. Piech, E. Rotela,
S. Sharma, I.C. Sheng.
Advanced Photon Source, Argonne National Laboratory
9700 South Cass Avenue, Argonne, Illinois 60439 USA

*Abstract*

The Advanced Photon Source (APS) storage ring (SR) rf system employs four banks of four spherical, single-cell resonant cavities. Each cavity is tuned by varying the cavity volume through insertion/retraction of a copper piston located at the circumference of the cavity and oriented perpendicular to the accelerator beam. During the commissioning of the APS SR, the tuners and cavity tuner ports were prone to extensive arcing and overheating. The existing tuners were modified to eliminate the problems, and two new, redesigned tuners were installed. In both cases marked improvements were obtained in the tuner mechanical performance. As measured by tuner piston and flange surface temperatures, tuner heating has been reduced by a factor of five in the new version. Redesign considerations discussed include tuner piston-to-housing alignment, tuner piston and housing materials and cooling configurations, and tuner piston sliding electrical contacts. The tuner redesign is also distinguished by a modular, more maintainable assembly.

## 1 INTRODUCTION

The APS SR rf cavity tuners have been redesigned to improve mechanical and vacuum performance while maintaining consistent rf performance. The tuner consists of a moveable piston that is inserted/retracted into the 352-MHz spherical cavity, thus changing the volume and the frequency of the resonant cavity. The approximate size of the components are as follows: the rf cavity radius is 13 inches, the tuner piston radius is 2.75 inches, and the overall length of the tuner is 25 inches. The piston, housing, electrical contacts, bellows, and drive have all been redesigned. The piston diameter and motorized drive performance have been maintained to allow consistent rf feedback and controls. Diagnostic thermocouples have been added to the tuner piston within the vacuum housing and to the exterior of the piston housing mounting flange to monitor tuner temperatures for interlock and performance logging purposes. Figure 1 is a section drawing of the tuner assembly highlighting major design features. The tuner piston is shown in the approximate cavity-tuned position.

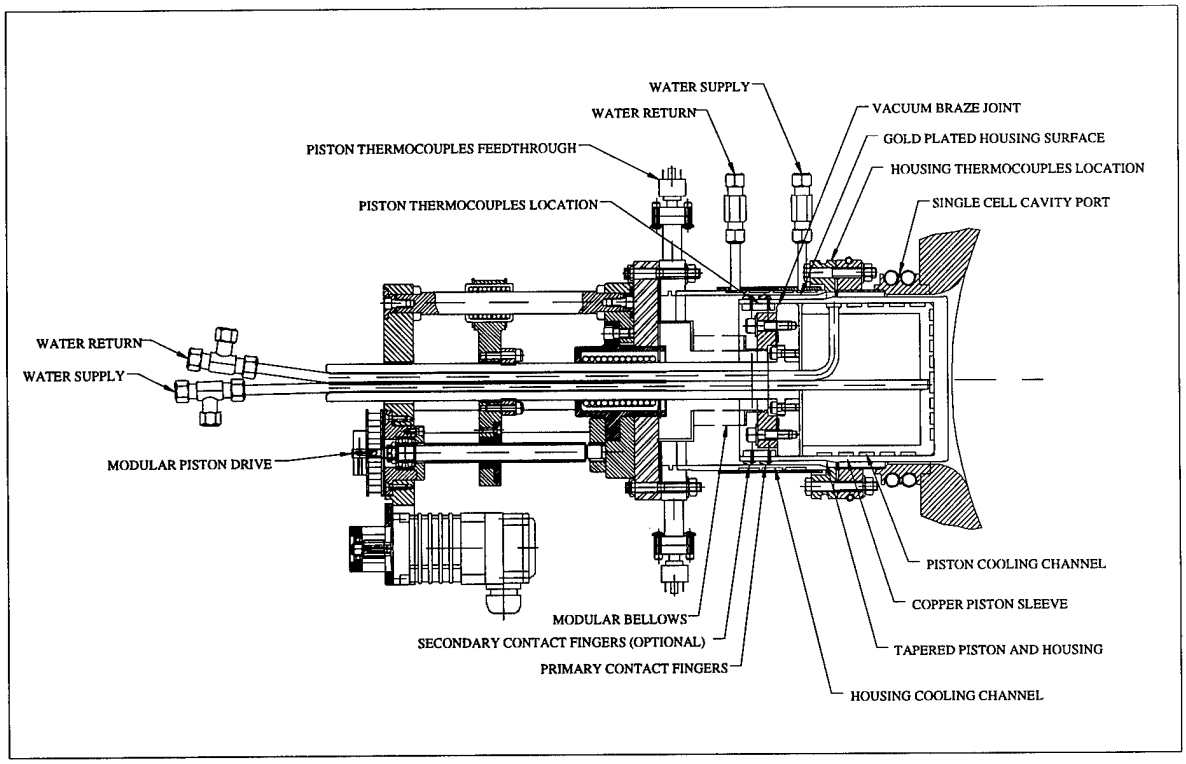



Figure 1: APS storage ring rf cavity tuner.

0-7803-4376-X/98/$10.00 © 1998 IEEE

## 2 TUNER DESIGN DISCUSSION

### *2.1 Tuner Piston*

The tuner piston consists of a one-piece, oxygen-free, high-conductivity (OFHC) copper cylinder hollowed out to include water cooling channels. The water channel is a spiral at the base of the piston and a helix on the circumferential surface of the piston. The water flow inlet is at the center of the base of the piston; from there the water flows outward to the circumference of the piston and then upward toward the sliding electrical contacts. The coverage area of the water channels has been increased toward the electrical contacts to more effectively cool the piston and sliding contacts as described in section 2.3. The interior of the piston also includes the vacuum-to-air joint that consists of a standard Conflat-type flange joint (a policy of no vacuum-to-water joints has been maintained throughout the tuner assembly). One flange is brazed to the inner diameter of the piston, while the second flange is welded to a modular welded bellows. The piston itself is modular as the piston can be removed solely by unfastening the Conflat flange joint. In the current design only the copper sheath portion of the piston is exposed to cavity rf energy. All braze joints and stainless steel vacuum hardware is enclosed and protected. The piston is electrically shorted to the stainless steel vacuum housing via sliding electrical contacts. The contacts are attached to the piston with silver-plated stainless steel pan head screws. The screws are fastened to a tapped retaining ring inserted into the piston body. The retaining ring interlocks with the piston vacuum flange and additionally functions as a redundant attachment of the piston to the flange. All braze joints are made using a copper-gold braze material. Finally, the cylindrical copper surface of the piston sheath is coated with titanium by a vacuum vapor deposition process to reduce secondary emission of electrons and potentially eliminate the problem of multipactor.

### *2.2 Piston Housing*

The piston housing functions as the tuner vacuum enclosure, the tuner-to-cavity mount, and the piston drive support. The housing is constructed as a 304 stainless steel tube within a tube welded to Conflat flanges at either end. The interior tube is machined with a helical cooling channel groove that is enclosed by the outer tube. The flange surfaces are carefully maintained perpendicular to the housing bore as critical piston-to-housing alignment and ultimately piston-to-cavity alignment is set by these flange positions. The interior of the housing is exposed to cavity rf fields and currents and is the running surface of the sliding electrical contacts. To optimize the performance of this surface both surface finish and surface composition have been considered. The surface should be as fine as possible and free of all circumferential cracks and protuberances. As such, the surfaces are mechanically polished to an 8-microinch finish and then electropolished to remove any remaining surface burrs and contaminants. The surface is then gold plated 0.0002-0.0005 inch thick to reduce electrical resistance and sliding contact friction.

### *2.3 Sliding Electrical Contacts*

The sliding electrical contacts are attached to the upper portion of the piston outer diameter. The fingers electrically short the piston to the piston housing and protect the bellows from the cavity rf energy. The contacts are fabricated from 98% Cu-2% Be alloy spring finger stock [1]. The material is silver-plated 0.0002-0.0005 inch thick to reduce both surface and contact resistivities. Also, an additional 0.003 inch of silver is plated onto the sliding surface for contact lubrication. A primary goal of the improved cooling of the piston and housing is to reduce the operation temperature of the sliding contact fingers. Cooler finger temperature is expected to prolong the lifetime of the fingers by slowing elevated temperature annealing and thermal set. Reduced spring force will increase electrical contact resistance and finger heating. The linear stroke of the piston has been extended to allow inspection and replacement of the finger components without additional disassembly of the tuner. The design incorporates the location for an optional second set of contact fingers, but operational tests with only the primary set of fingers indicate that this redundancy is not necessary.

### *2.4 Modular Bellows*

The linear motion of the tuner piston is accommodated by a welded bellows assembly. The bellows is modular, terminating to Conflat flanges by interior weld joints. A modular bellows was developed to both facilitate bellows replacement and avoid final assembly welding processes in the tuner assembly. Previous experience has shown that welding of the bellows assembly to the tuner piston shaft results in distortion of the shaft and a corresponding loss of control of the piston orientation and alignment. The bellows is cooled by circulating air over the surface of the bellows.

### *2.5 Tuner Drive*

The tuner drive is a modular linear motion system that is capable of delivering three inches of travel. The drive is compactly nested within and attached to the bellows upper flange. All drive components are accurately machined to eliminate angular misalignment of the piston. The tuner piston is supported by a stainless steel shaft bolted directly to the piston vacuum flange. To ensure piston alignment, the final machining of the piston is performed relative to the attached, pin-located shaft. In the final assembly the piston is aligned to the housing bore such that the piston axis is colinear to the housing bore axis to within 0.010 in. The alignment is verified by employing a coordinate measuring machine. Drive motion is powered by a stepper motor turning a pulley, timing belt, pulley, and lead screw system.

### 2.6 *Tuner Piston Mechanical Analysis*

Cooling and stress analyses of the piston, electrical contact, and housing systems have been performed using the ANSYS finite element modeling system. The piston and housing water systems have been designed to accommodate the 150 psi cooling water system. Thermal analyses of the electrical contact fingers have demonstrated that with the one-piece, copper piston sheath construction the fingers operate at a temperature of 77°C; the temperature rise is 50 percent of that of the original tuners.

### 2.7 *Tuner Rf Analysis*

Computer analysis of the electromagnetic properties of the rf cavity and tuner piston was performed to estimate electrical power dissipation for cooling system design. Analysis is based on the tuner piston-to-cavity port radial gap being set at 2 mm. The gap size was developed to support the piston-to-cavity port potential while minimizing finger contact heating. In the case of the piston aligned concentric to the cavity port, the power dissipated on the piston and housing surfaces is approximately 2 kW for a cavity input power of 100 kW. In the case of the piston misaligned to the housing and cavity port, the power dissipated in the tuner surfaces can increase to approximately 4 kW for a similar 100 kW of cavity input power; the power dissipated in the spring fingers also increases with the misalignment of the tuner piston. This result neglects the contribution of dissipated power due to arcing between the piston and the housing and/or cavity port. In fact, analysis shows that the maximum electrical field strength surpasses 1 MV/m when the piston is completely offset in the cavity port and arcing is a distinct possibility.

### 2.8 *Tuner Diagnostics*

The tuners were instrumented with K-type thermocouples attached to the piston inside the vacuum enclosure and attached to the housing flange circumference. In vacuum thermocouple wire is insulated with binderless fiberglass braid sleeving. The piston thermocouples are screw clamped to the interior of the piston opposite the sliding contact fingers. Exterior thermocouples are clamped to the tuner mounting flange. The redesigned tuner operating temperatures have consistently proven to be significantly lower than any of the original tuners that were modified to include thermocouple instrumentation. Typical temperature rises of 5°C on piston temperatures and 15°C on housing flange temperatures are, respectively, 20% and 50% of the temperature rises for properly functioning, original tuners. Two thermocouples are also installed on the air side of the bellows to indirectly monitor the performance and condition of the sliding electrical contact finger.

## 3 CONCLUSIONS

As discussed, significant improvements have been made to the SR rf cavity tuners. The one-piece piston sheath design, improved piston cooling, and piston alignment have reduced tuner operating temperatures by a factor of five. Additionally the maintainability was improved with the increased accessibility of the system.

## 4 ACKNOWLEDGMENTS

The authors would like to thank Cathy Eyberger for her assistance in editing this paper. Also, we would like to thank Payman Mortazavi (BNL) and Heinz Schwarz (SLAC) for their assistance in the development of the tuner design. Additionally, we would like to thank the brazing department at SLAC for design consultation and fabrication of the improved tuners. Lastly, we would like to acknowledge the support of the ANL central shops and inspection department and the APS vacuum group for their efforts in the fabrication and test of the new tuners. This work was supported by the U.S. Department of Energy, Office of Basic Energy Sciences, under Contract No. W-31-109-ENG-38.

## 5 REFERENCE

[1] Instrument Specialties, Co., Inc., Delaware Water Gap, PA 18327-0136.

# COAXIAL HIGHER-ORDER MODE DAMPER EMPLOYING A HIGH-PASS FILTER

Y. W. Kang and X. Jiang
Advanced Photon Source, Argonne National Laboratory
9700 South Cass Avenue, Argonne, Illinois 60439 USA

*Abstract*

Two different types of coaxial higher-order mode (HOM) dampers have been investigated for the Advanced Photon Source (APS) storage ring cavities: e-probe dampers and h-loop dampers. Realization of the h-loop dampers has been difficult because the loop antenna couples not only to the HOMs but also to the accelerating mode and results in loss of Q at the fundamental frequency. Previously, a first-order fundamental rejection filter was tested with unsatisfactory rejection characteristics. This problem can be overcome by using a higher-order high-pass filter between the loop and the matched load. Prototype dampers have been fabricated and tested in a storage ring single-cell cavity and the damping characteristic was analyzed.

## 1 INTRODUCTION

The single-cell cavities being used in the APS storage ring are optimized spherical type cavities whose fundamental accelerating mode frequency is 352 MHz. Each cavity frequency is adjusted with a mechanical plunger tuner. The cavities are manufactured to have a slight elongation with an increment in the lengths for a staggered frequency characteristic at the HOMs. The effect of the staggering cavity HOM frequencies was studied and the instability growth rates and the deQing requirement on higher-order modes of the APS storage ring were reported [1, 2].

For the APS storage ring cavities, dampers with E-probe and H-loop couplers have been developed to damp HOMs in 352-MHz single-cell cavities for the storage ring of the APS. The H-loop dampers employ high-pass filters for fundamental frequency rejection. The fundamental frequency rejection filter has a very steep rejection response and minimum deQing at the fundamental frequency. A similar H-loop coupled coaxial damper with a higher-order high-pass filter has been used for 433-MHz cavities of an accelerator for free-electron laser application [3].

For HOM dampers, broadband damping and less fundamental mode damping are important. In the waveguide dampers, the fundamental frequency rejection is achieved by the cutoff characteristic of the waveguide. For coaxial HOM dampers, a proper fundamental frequency rejection scheme must be implemented. E-probe dampers can be used in the cavity equatorial plane without the rejection filter, since the radial component of the $TM_{01}$-like electric field is zero in the midplane. Since the H-loop dampers are used in the equatorial plane of the cavity, the loop plane must be perpendicular to the fundamental mode H-field to couple with the many transverse magnetic HOMs, and a fundamental frequency rejection filter is needed. Previously, H-loop dampers with a half-wavelength short stub in parallel or a quarter-wavelength short stub in series have been tested [4]. The rejection characteristics of the single stub designs were poor and also rejected some HOM frequencies around the even and odd multiples of fundamental frequency. Since the poor rejection characteristic increased the fundamental mode power loss, a damper with a better rejection filter has been investigated.

## 2 LOOP COUPLED DAMPER

Figure 1 shows the loop coupling coaxial damper assembly. The H-loops are used in the cavity midplane. The loop plane is perpendicular to the $TM_{01}$ mode H-field. Two dampers are used to damp the dipole modes. Both the size of the loop and the location in the cavity determine the coupling to specific mode fields and thus the damping ratio.

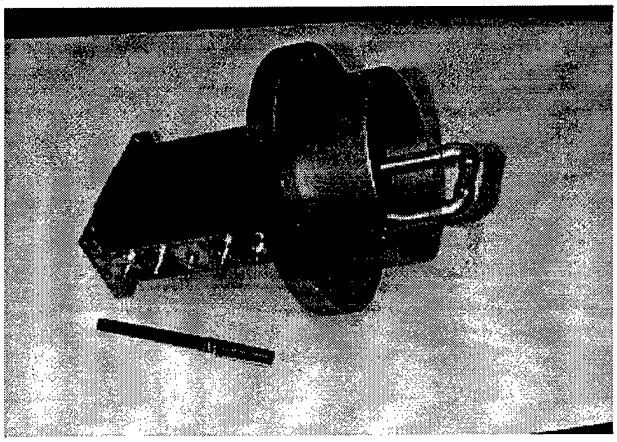


Figure 1: H-loop type coaxial damper with high-pass filter.

### *2.1 Coupling Loop*

Two H-loop type dampers are used on the 6" ports in the cavity midplane with an angular separation of 90°. The loop plane in this position strongly couples to the $TM_{01}$ mode field. Therefore, the measured input impedance of the coupling loop shows low impedance values for overcoupling. The coupling loop is made of 0.5"-diameter copper tube.

Figure 2 shows the measured input impedance of the damper coupling loop of various sizes. The low impedance of the loop at a resonant frequency shows that the mode of the frequency can be damped by the resistive termination whose resistance value is greater than the input resistance. The different coupling gives varied damping at other mode frequencies. Greater loop sizes have lower loop input

0-7803-4376-X/98 /$10.00 © 1998 IEEE

resistance and provide greater damping due to greater over-coupling in general. However, the damping of the higher frequency HOMs are sensitive to the loop sizes, since the loop inductance may approach or exceed the quarter wavelength at these frequencies. For the higher frequency HOMs, the high loop input impedance may result in under-coupling which gives poor damping. For the low loop impedance, the fundamental frequency rejection filter needs to have low input resistance in order to have smaller fundamental frequency damping. From the measurement, it can be seen that 50-Ω load resistance is adequate for damping the HOMs.

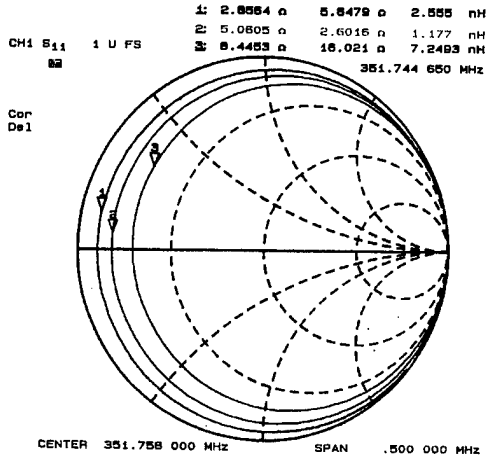



Figure 2: Input impedance of the coupling loop of various sizes: (1) 5 inch$^2$, (2) 3.7 inch$^2$, (3) 2.4 inch$^2$.

### 2.2 *High-Pass Filter*

A fundamental frequency rejection is necessary to minimize the loss of the accelerating field using a band-stop or a high-pass filter. For the APS, an H-loop damper design employing a high-pass filter has been investigated to obtain a good fundamental frequency rejection. For the rejection at 352 MHz in a compact package, a 9-th order coaxial Chebyshev-type filter was chosen [5]. The filter has a 0.5-dB pass-band ripple and 70 dB rejection at 350 MHz, and a corner frequency of 480 MHz. Figure 3 shows the measured frequency characteristics of the high-pass filter. This frequency response is very close to the predicted response from calculation. The construction of the filter is shown in Figure 4. All coaxial transmission line sections have a 1" outer diameter and a 50-Ω characteristic impedance. The crossed tuning stubs support the center conductor of the filter which consists of four capacitors and five copper pieces. The capacitors are made with kapton dielectric and copper sheets around the dielectric. Sliding shorts are used on the stubs to adjust the stub inductances for the desired frequency response. The input and output impedances are chosen to be 50 Ω for simplified measurement and near optimum Q-factor of the transmission lines. The circuit component values of the filter elements are shown in Table 1.

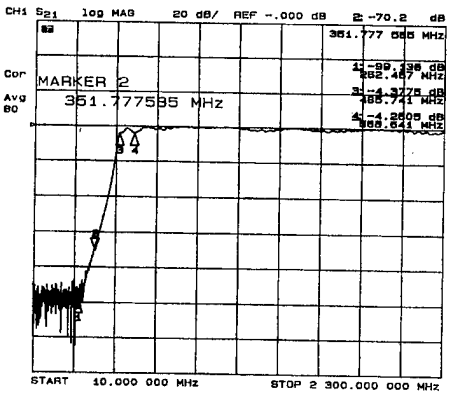



Figure 3: Measured frequency response of the filter.

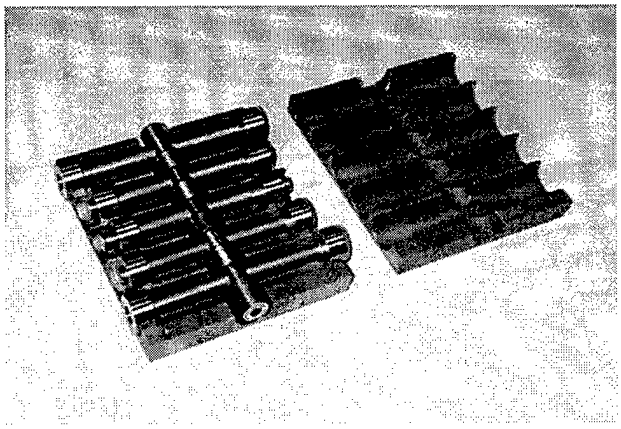


Figure 4: Coaxial high-pass filter structure.

### 2.3 *Rf Absorber*

For the dampers, matched load terminations are used. The load must be able to dissipate a certain amount of power with good vacuum properties if no vacuum barrier is used. Water cooling is needed for the high-power couplers and the load. Since reliable water cooling with metal tubing always forms a short circuit for the rf signal, a lossy dielectric-type load is desirable unless a noninterfering water passage is provided. Therefore, in an E-probe damper with water cooling through the center conductor of the coaxial structures, an aluminum nitride (AlN) ceramic absorber was used. However, in the H-loop damper design, the center conductors of the coaxial stubs can provide water passage, and so compact broadband, high power resistor-type rf loads can be used. This type of load is made of a carbon resistor on a beryllium oxide (BeO) ceramic substrate. The mechanical and electrical properties of this termination are shown in Table 1. The measured frequency characteristic of the coaxial termination is shown in Figure 5.

Table 1: Termination Specification

| | |
|---|---|
| Impedance | 50 Ω nominal |
| Power handling capability | 250 W CW, 1000W peak |
| Thermal resistance | 0.3° C/W |

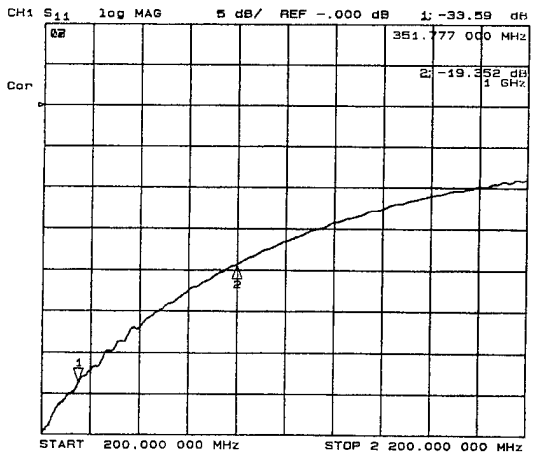



Figure 5: Frequency response of the 50-Ω resistive termination.

## 3 MEASUREMENT

Each cavity will have two E-probe dampers and two H-loop dampers when the dampers are ready. In the present measurements, only two H-loop dampers with 9-th order Chebyshev high-pass filters have been used. The measured deQing ratios are shown in Table 2. The coupling loops have an area of 3.7 $in^2$. The listed modes are the most dangerous HOMs in the single-cell cavity being used in the APS and can cause beam instability. Q-factors are measured using a vector network analyzer and compared with the computed results. In mode designation, 0 and 1 denote the monopole modes and the dipole modes, respectively. M and E denote the boundary conditions with magnetic and electric walls in the cavity equatorial plane, respectively. The result shows that most dipole modes are damped effectively; the fundamental mode is damped little while the first dipole mode is damped significantly. Note that some monopole modes can also be damped with the H-loop dampers since the loop is offset from the cavity midplane.

Table 2: Measured Q-factors for the Higher-Order Modes with Two Dampers with High-Pass Filters

| Mode | Frequency (MHz) | Unloaded Q | Damped Q |
|---|---|---|---|
| 0-E-1 | 351.7 | 48,000 | 44,270 |
| 0-M-1 | 535.7 | 43,610 | 306 |
| 0-E-1 | 582.3 | 60,200 | 302 |
| 0-E-2 | 742.6 | 57,760 | 455 |
| 1-M-2 | 758.4 | 44,370 | 757 |
| 0-E-3 | 916.6 | 82,920 | 688 |
| 1-E-3 | 952.1 | 46,470 | 1,113 |
| 1-M-4 | 1014.8 | 31,800 | 8,022 |
| 1-E-5 | 1147.2 | 42,710 | 5,262 |
| 0-E-6 | 1511.5 | 89,690 | 1,566 |

## 4 DISCUSSION

For the coaxial HOM dampers, it was desired to have lower deQing at the fundamental frequency while having higher damping at other harmful HOMs. The fundamental mode deQing is due to the finite Q of the input coupler and the high-pass filter at the frequency. Although the rejection ratio of the filter alone is measured to be ~70 dB which provides almost no power transmission, fundamental deQing still exists. Since the filter characteristic is measured for a 50-Ω system, the low resistance of the loop cannot have a high rejection ratio. The intrinsic resistance of the copper parts in the loop and the filter input contribute to a loss that is not negligible. The next step is brazing an annular alumina ceramic window between the coupling loop and the filter input in order to eliminate the exposure of the filter circuit to the vacuum. High power testing of the dampers will be performed with the ceramic window.

The measurements show that the coaxial dampers can provide good performance for the cavities without provision for special waveguide-type damper ports. The measured fundamental frequency deQing factor is about 9% with two dampers. This is a great improvement from previous studies and may be one of the lowest values with the HOM damping. The dampers are compact and will dissipate low power at the fundamental frequency. Compared with the deQing requirement of the HOMs in the APS storage ring, the results of measurements show that many HOMs can be damped successfully with the coaxial dampers. This result is promising for use of the design in the storage ring of the APS.

## 5 ACKNOWLEDGMENT

The authors thank Arther Vetter of Boeing Defense and Space Group for helpful information on the damper with high-pass filter. The authors also thank W. Yoder and D. Bromberek for their effort in prototype fabrication and measurement of the dampers. This work was supported by the U.S. Department of Energy, Office of Basic Energy Sciences, under Contract No. W-31-109-ENG-38.

## 6 REFERENCES

[1] L. Emery, "Coupled-Bunch Instabilities in the APS Ring," Proc. of the 1991 Particle Accelerator Conference, pp. 1713-1715, 1991.

[2] L. Emery, "Required Cavity HOM deQing Calculated from Probability Estimates of Coupled Bunch Instabilities in the APS Ring," Proc. of the 1993 Particle Accelerator Conference, pp. 3360-3362, 1993.

[3] A. M. Vetter, T. L. Buller, and T. D. Hayward, D. R. Smith, and V. S. Starkovich, "APLE Accelerator Prototype Cavity Fabrication and Low Power Tests," Proc. of the 1993 Particle Accelerator Conference, pp. 1075-1077, 1993.

[4] P. J. Matthews, Y. W. Kang, and R. L. Kustom, "Storage Ring Cavity Higher-Order Mode Dampers for the Advanced Photon Source," Proc. of the 1995 Particle Accelerator Conference, pp. 1684-1886, 1995.

[5] G. Mathei, L. Young, and E. M. T. Jones, *Microwave Filters, Impedance- Matching, Networks, and Coupling Structures*, Artech House, 1980.

# RECONFIGURABLE HIGH-POWER RF SYSTEM IN THE APS

Y. W. Kang and D. Horan
Advanced Photon Source, Argonne National Laboratory
9700 South Cass Avenue, Argonne, Illinois 60439 USA

*Abstract*

The 352-MHz high-power system for the Advanced Photon Source (APS) storage ring and booster synchrotron has been configured to allow two to four klystrons to power the storage ring and one klystron to power the booster. A quadrature hybrid combines two klystron outputs with two 45° phase shifters at each output of the hybrid for proper phasing at the storage ring cavities for the selected mode. The phase shifters in the hybrid outputs and three waveguide switches are used to choose an operation mode in any one of twelve possible configurations using three to five klystrons to power the storage ring and booster. The system can be configured to use one klystron as the power source of a test station.

## 1 INTRODUCTION

For reliable and continuous operation of the booster synchrotron and the storage ring of the APS, a reconfigurable high-power rf system is needed. The goal is to have a system that is operational even with one or two klystrons turned off for maintenance or other tasks such as high-power conditioning or testing of other rf components.The APS high-power rf system consists of five rf stations: one for the booster and the other four for the storage ring. Each rf station consists of one 1.0-MW klystron and a 95-kV, 20A DC power supply. The storage ring has four rf sectors and each sector has four uniformly spaced single-cell cavities. All sixteen cavities in the storage ring need to be powered for reliable beam quality. Therefore, a way of combining two or more klystron outputs and splitting the combined rf power to the sixteen cavities has been implemented.

The design of the waveguide switching system for rf power distribution in the APS is shown in Figure 1. The 90° quadrature hybrids and 45° phase shifters in the WR2300 waveguide are used as the elements for combining and splitting the power. Other hybrids, such as 180° or magic tee types, have been used [1], but the availability of the hardware and lower phase shifting requirements made the present design attractive.

The switching system is equipped with an equipment safety interlock system through an rf power monitoring system. The system is controlled by a programmable logic controller (PLC) unit independent from the main computer control system of the accelerators. The waveguide circuit has been completely installed and has powered the booster and storage ring systems successfully.

## 2 OPERATION

In Figure 1, klystron outputs of the RF1 and RF4 stations are combined through a hybrid and feed cavities in sectors 38 and 40. Klystron outputs of RF2 and RF3 are combined through a hybrid and feed cavities in sectors 36 and 37. The hybrid output feeds a sector with four single-cell cavities. The system includes all five klystrons (RF1-RF5) for the booster and storage ring of the APS. For the storage ring, one or more klystrons may be turned off, but not the two for one hybrid. For the booster, RF3 can be used when RF5 is not available. RF1 may be switched to the test station; RF4 alone feeds sectors 38 and 40. Each klystron output is connected to the hybrid through a 1MW, three-port ferrite circulator that is used as an isolator with a water load in the isolation port. Basic operation and construction of the waveguide system design are discussed below.

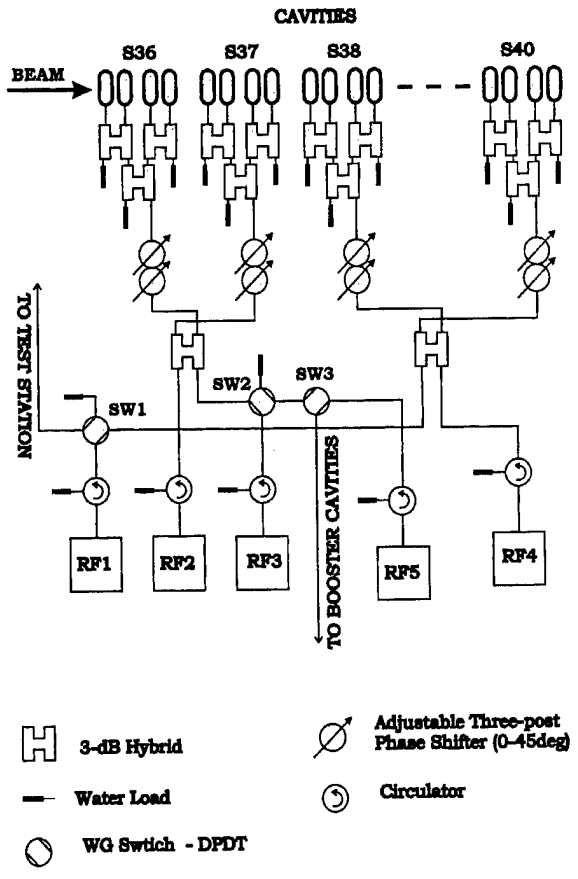



Figure 1: Reconfigurable waveguide switching system.

Figure 2 shows a part of Figure 1 where a 90° quadrature hybrid combines two inputs from two klystrons through circulators and splits into two outputs with two adjustable output phase shifters. For convenience, one phase shifter is shown in each output arm in Figure 2 instead of two as in Figure 1.

0-7803-4376-X/98/$10.00 © 1998 IEEE

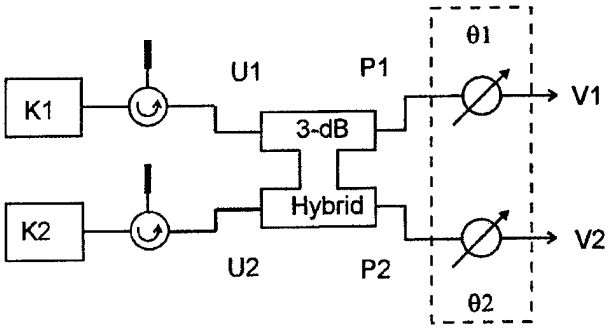



Figure 2: Two klystron-two sector feeding through a hybrid.

With two input port voltages of the quadrature hybrid $U_1 = \sqrt{2}ae^{j\omega t}$ and $U_2 = \sqrt{2}be^{j\omega t}$, the combined hybrid output rf voltages through the phase shifters are superpositions of split outputs from each input and can be expressed as

$$V_1 = \left(ae^{j\omega t} + be^{j\omega t}e^{-j\frac{\pi}{2}}\right)e^{-j\theta_1}$$

$$= ce^{j(\omega t-\phi_1-\theta_1)} \quad (1)$$

$$V_2 = \left(ae^{j\omega t}e^{-j\frac{\pi}{2}} + be^{j\omega t}\right)e^{-j\theta_2}$$

$$= ce^{j(\omega t-\phi_2-\theta_2)} \quad (2)$$

where $c = (a^2+b^2)^{1/2}$, and the phases $\phi_1 = \text{atan}(b/a)$ and $\phi_2 = \text{atan}(a/b)$. For identical output phases, the phase difference between the two phase shifters is expressed as

$$\Delta\phi = \phi_1 - \phi_2 = \theta_2 - \theta_1 \quad (3)$$

$$\Delta\phi = \text{atan}(r) - \text{atan}\left(\frac{1}{r}\right) \quad (4)$$

where the power ratio r = b/a. The differential phase with respect to the input power imbalance is

$$\frac{d(\Delta\phi)}{dr} = \frac{2}{(1+r^2)} \quad (5)$$

where $\Delta\phi$ is shown with respect to the amplitude ratio r in Figure 3. Note that the abscissa is in logarithmic scale. Using Eq. (5), phase fluctuation between sectors is found as ~0.6°/1% amplitude difference between the two klystrons when $a \approx b$.

In Figure 2, three configurations are possible; these cases can be compared in terms of the phase requirement at the hybrid outputs. The three cases are 1) both K1 and K2 are turned on, 2) only K1 is turned on, and 3) only K2 is turned on.

For delivery of rf power with specified phase relations at the cavities, the phase shifters must be adjusted properly. The phase shift requirements for the three different cases described above are as follows:

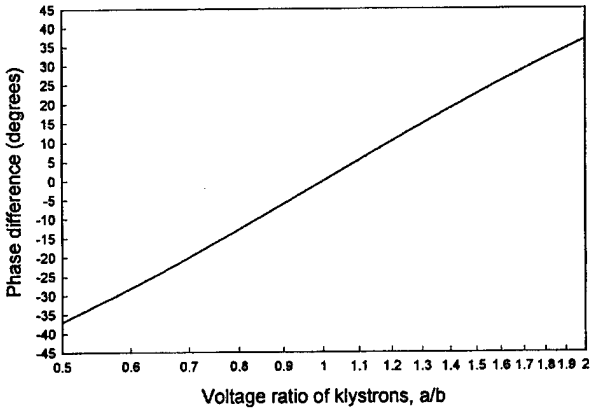



Figure 3: Phase difference between two outputs vs. the input power imbalance.

1. If a = b,

$$V_1 = \sqrt{2}ae^{j\left(\omega t-\frac{\pi}{4}-\theta_1\right)}, \quad V_2 = \sqrt{2}ae^{j\left(\omega t-\frac{\pi}{4}-\theta_2\right)}$$

$$\theta_1 = \theta_2 = 45°$$

2. If b = 0,

$$V_1 = ae^{j(\omega t-\theta_1)}, \quad V_2 = ae^{j\left(\omega t-\frac{\pi}{2}-\theta_2\right)}$$

$$\theta_1 = 90°, \ \theta_2 = 0°$$

3. If a = 0,

$$V_1 = be^{j\left(\omega t-\frac{\pi}{2}-\theta_1\right)}, \quad V_2 = be^{j(\omega t-\theta_2)}$$

$$\theta_1 = 0°, \ \theta_2 = 90°$$

Note that, if all cavities are matched, there is no reflected power. If any backward traveling wave exists due to cavity mismatch or coupled cavity higher-order modes, it can be absorbed by the loads on the isolation ports of circulators.

## 3 CONFIGURATION

Table 1 shows the possible configurations for the switching system. A minimum of two klystrons are used for supplying the needed rf power to the storage ring cavities. However, for two-klystron operation, each hybrid must be powered by one klystron to feed all sixteen cavities. The system is reconfigurable to one of the twelve modes by moving a key in a bank of keyswitches, which provides a mode change signal to the PLC. All waveguide switches, phase shifters, power monitors, and safety interlocks are switched to position with a movement of the key.

### *3.1 Waveguide Switch*

The waveguide switches are a motor-driven vane type with spring contacts between the vane and the waveguide

wall and limit-switches. These waveguide switches do not contribute to any phase shifting but direct the rf power to other systems. The equipment safety interlock system assures that no hot switching is made while rf power is present in the waveguides. Directional couplers are placed on each arm of the switches to detect any rf signal above a threshold.

Table 1: RF System Operation Switching Modes

| RF System Status | | | | |
|---|---|---|---|---|
| Mode | System Energized | | | Down |
| | Storage Ring | Booster | Test Station | |
| 1 | RF1, RF2, RF3, RF4 | RF5 | | |
| 2 | RF2, RF3, RF4 | RF5 | RF1 | RF1 |
| 3 | RF1, RF3, RF4 | RF5 | | RF2 |
| 4 | RF1, RF2, RF4 | RF5 | | RF3 |
| 5 | RF1, RF2, RF3 | RF5 | | RF4 |
| 6 | RF1, RF2, RF4 | RF3 | | RF5 |
| 7 | RF2, RF4 | RF3 | RF1 | RF1, RF5 |
| 8 | RF1, RF2 | RF3 | | RF4, RF5 |
| 9 | RF1, RF2 | RF5 | | RF3, RF4 |
| 10 | RF3, RF4 | RF5 | RF1 | RF2, RF1 |
| 11 | RF2, RF4 | RF5 | RF1 | RF3, RF1 |
| 12 | RF1, RF3 | RF5 | | RF2, RF4 |

*3.2 Phase Shifter*

The three cases for phasing shown in section 2 above can be achieved by using adjustable phase shifters. For the waveguide switching system, motorized three-post phase shifters have been used to properly phase the cavities in the four rf sectors. The three-post phase shifters are not expensive and are readily available from several vendors. However, since the adjustable phase range of a single phase shifter is about 50°, two phase shifters must be connected in series to form a 90° phase shifter at each output of the hybrids. A total of eight 45° three-post waveguide phase shifters are used in the system. Micro-limit switches are preset for a 0°-45° shifting range. Again, the control interlock system assures no hot shifting is made while the rf power is present.

## 4 DISCUSSION

So far, the system has run in a few different two-klystron modes without problem. The klystron powers are ~600 kW for a 100-mA beam current. With two klystrons in a hybrid, for the modes with three or four klystrons, the hybrid outputs need to be controlled to have a certain phase stability that can directly affect cavity rf phases and, therefore, the beam. The klystrons are being equipped with AC-coupled feedback loops for uniform power outputs to minimize the effect of amplitude-phase conversion and offset phase control to maintain proper inter-station phase when operating klystrons in parallel. This rf control is somewhat similar to the system implemented for the LEP system [2]. A test station is needed for various reasons and rf station RF1 can be used for this purpose. Other arrangements can be used for the phase shifting with fixed phase shifters. In this approach, each hybrid needs four fixed-length waveguide sections—two 0° and two 45°—and three double-pole waveguide switches. This method costs more since the waveguide switches are more expensive than the waveguide phase shifters.

## 5 CONCLUSION

The system has been completely tested for mode selection and interlocks and has been running in a few different modes without problem. The need for feedback control in the hybrid inputs raises the question of the system's stability and reliability. Since the rf signal input phases through the driver amplifiers to the klystrons can be tightly controlled, it is anticipated that the system can be made stable and reliable. Reliability of the high-power system has been improving steadily in the APS. Additionally, the maintainability has improved with the increased accessibility and flexibility of the system. Installation and testing of the klystron feedback control for the configurations with three or more klystrons remains to be done.

## 6 ACKNOWLEDGMENT

The authors would like thank Gian Trento, Mike Phelan, and William Yoder for their assistance in planning, installing, and testing the switching system. This work was supported by the U.S. Department of Energy, Office of Basic Energy Sciences, under Contract No. W-31-109-ENG-38.

## 7 REFERENCES

[1] H. Frischholz, "The LEP Main Ring High Power RF System," Proc. of the 1989 PAC Conference, pp. 1131-1133, 1989.

[2] J.-C. Juillard and E. Peschardt, "Phase and Voltage Control in the LEP Radio-Frequency System," Proc. of the 1989 PAC Conference, pp. 1639-1641, 1989.

# UPGRADED CAVITIES FOR THE POSITRON ACCUMULATOR RING OF THE APS

Y. W. Kang, X. Jiang, D. Mangra, and T. Smith
Advanced Photon Source, Argonne National Laboratory
9700 South Cass Avenue, Argonne, Illinois 60439 USA

*Abstract*

Upgraded versions of cavities for the APS positron accumulator ring (PAR) have been built and are being tested. Two cavities are in the PAR: a fundamental 9.8-MHz cavity and a twelfth harmonic 117.3-MHz cavity. Both cavities have been manufactured for higher voltage operation with improved Q-factors, reliability, and tuning capability. Both cavities employ current-controlled ferrite tuners for control of the resonant frequency. The harmonic cavity can be operated in either a pulsed mode or a CW mode. The rf properties of the cavities are presented.

## 1 INTRODUCTION

The APS PAR rf system employs two frequencies at 9.8 MHz and 117.3 MHz for the fundamental and the twelfth harmonic subsystems, respectively. Each subsystem has an rf cavity for the frequency. The cavities now used in the system were made as prototypes and were installed for initial commissioning of the APS. They have been working all right for positron accumulation and bunch compression so far. However, for higher reliability and performance of the PAR, new cavities are needed. Problems observed in the fundamental frequency cavity so far are narrow frequency tuning range, lower gap voltage limit, and rf heating at the joint of the ceramic flange and the cavity center conductor that effect degradation of the cavity Q-factor. Since the cavity volume outside the beampipe is exposed to the room air in each cavity, some corrosion due to the water in the air has been considered responsible. The harmonic cavity was made with stainless steel for lower Q-factor, but it has shown an even lower Q-factor than originally planned. The harmonic system also needed an option for CW operation mode. Therefore, a set of new cavities has been made and tested for the PAR. These new upgraded cavities were designed to provide improved performance in the electronic tuning range, immunity to corrosion, and higher voltage capability. For the fundamental frequency cavity, the design goal was a 40-kV accelerating gap voltage, a Q-factor of 6000, and an R/Q of 74 Ω for the accelerating mode. For the harmonic cavity, the goal was a 30-kV gap voltage, an R/Q of 41 Ω, and a Q-factor of 3000. The rf characteristics of both cavities were calculated using the URMEL-T computer codes.

## 2 CAVITY DESIGNS

The 9.8-MHz fundamental frequency coaxial cavity with capacitive loading plunger is shown in Figure 1. The fundamental cavity is a plunger-loaded reentrant coaxial structure [1] that can provide a low operating frequency in a specified volume with a moderately high Q-factor without using any dielectric or magnetic material inside. The end of the inner conductor near the ceramic window is a piston-shaped loading structure which consists of a circular disk and a cylinder. Designing low-frequency tuned rf accelerating cavities for high-power operation with a cavity length much less than a quarter wavelength needs extra capacitive loading. The center conductor contributes mainly as the inductor and the gap between the outer and inner cylinders form a capacitor.

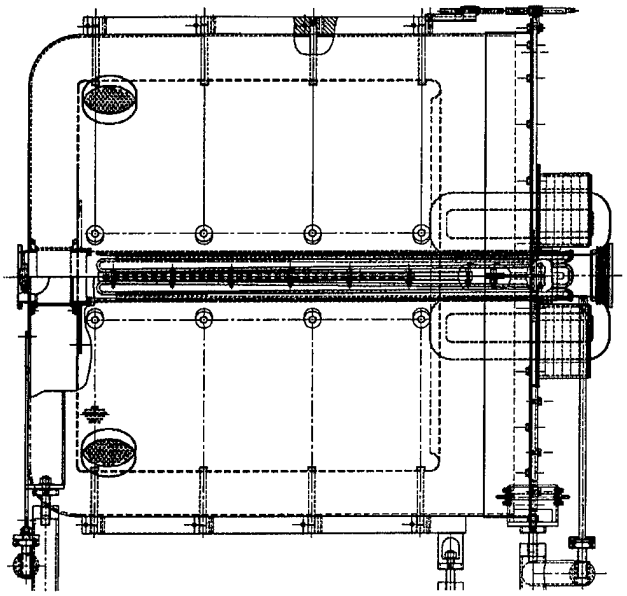


Figure 1: Fundamental cavity structure.

### *2.1 Fundamental Frequency Cavity*

The cavity has a length of 1.6 m, a radius of 0.72 m, and an accelerating gap length of 13.0 cm. The voltage across the loading capacitor was found to be greater than 90% of the gap voltage across the ceramic window [1]. The inner cylinder is supported with rexolite dielectric posts. The input coupler is placed in the back plate where the tuners are located. The input impedance of the coupler is matched for 50 ohms with a smaller loop area. Therefore, the coupler is moved closer to the center conductor where the magnetic field strength is greatest. The measured frequency and Q of the cavity are shown in section 4 below.

The inner coaxial structure has a minimum of 12.5 cm of separation between conductors for reliable high voltage operation. The center conductor is made around the beam

0-7803-4376-X/98/$10.00 © 1998 IEEE

pipe where the vacuum is maintained. Outside, an air blower fills the center conductor with air for additional cooling of the cylindrical shells. The center conductor is made of silver-plated copper with copper tubing underneath for water cooling.

### 2.2 *Harmonic Frequency Cavity*

The harmonic frequency cavity is a reentrant type coaxial cavity as shown in Figure 2. The cavity is made of aluminum with a ceramic window at the center of the cavity inner conductor. During initial operation of the harmonic system, the automatic gain control loop developed oscillation problems that were caused by a multipactoring effect at the inner surface of the ceramic window. The ceramic window has been titanium coated from the inside surface that is in vacuum during operation. The cavity length is 60 cm, the outer conductor diameter is 1 m, and the inner conductor diameter is 30 cm.

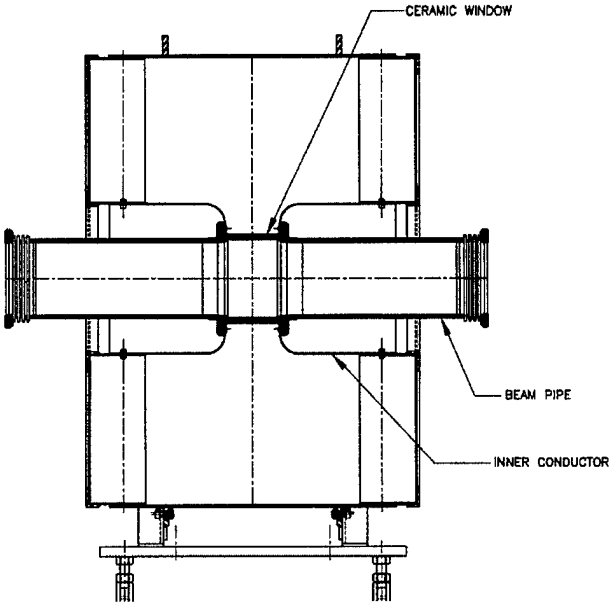



Figure 2: Harmonic cavity structure.

## 3 FERRITE TUNERS

For both cavities, ferrite tuners are used for electronic tuning of the cavity resonant frequencies. Copper housings are used with toroidal ferrite cores. The windings are placed inside the coupling loop that provides complete shielding and also penetrates the cavity. For all tuners, 250°C-rated high temperature wires were used. For CW operation in either system, the temperature in the tuners was measured at less than 55°C. These cavity tuners are needed for compensation of the resonant frequency drift of the cavity due to temperature change. The ferrite materials used for the tuners are shown in Table 1.

Table 1: Ferrite Materials Specifications

| | Toshiba M4C21A | Stackpole C/14 |
|---|---|---|
| O. D. (inches) | 8.0 | 8.0 |
| I. D. (inches) | 5.0 | 5.0 |
| Height (inches) | 1.0 | 1.0 |
| Initial permeability | 42 | 12.5 |
| Magnetic loss tangent | 0.0085 | |
| Curie temperature (°C) | 340 | 510 |
| Saturation magnetization (gauss) | | 2100 |
| Dielectric constant | 13.0 @40MHz | 10.5 |
| Dielectric loss tangent | 0.0003 @40MHz | |

### 3.1 *Fundamental Cavity*

Figure 3 shows the fundamental frequency cavity tuner. The coupling loop of the tuner needs to be placed near the cavity center conductor to permit greater coupling with the magnetic field with a minimum loop area. Therefore, the tuners are positioned in the back plate. Four tuners were needed to obtain the required frequency tuning range of 50 kHz. The control winding must be isolated from the rf field for better rf properties. The windings are put inside the coupling loop so that the winding can do its job without interfering with the rf field. Since the Toshiba material has low loss up to ~50 MHz with a greater initial permeability, this material is used in the fundamental frequency tuners. Six toroids are stacked together in each tuner.

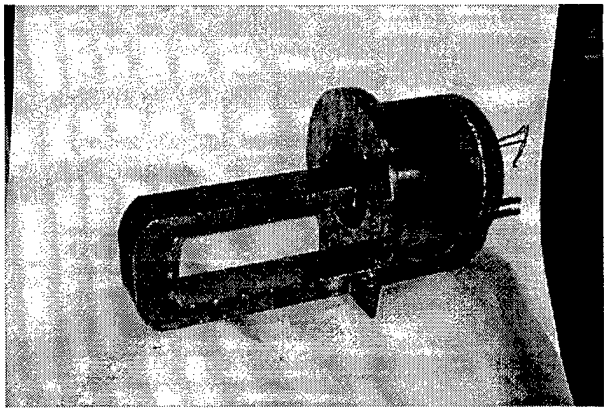


Figure 3: Ferrite tuner for the 9.77-MHz fundamental frequency cavity.

### 3.2 *Harmonic Cavity*

Two different ferrite tuners have been tested for pulse mode and CW mode. For pulse mode operation, cavity deQing is desired for improved beam stability during accumulation with the fundamental cavity. A detuned and

damped cavity characteristic is obtained by a tuner using Toshiba material that is lossy for the frequency. However, for CW mode the cavity does not need to be damped but must be tunable with a stable, high Q-factor. For this purpose two separate tuners were built; and one tuner is used for each mode of operation. Two Stackpole toroids that have lower loss at higher frequency were used in the CW mode tuner. They can be mechanically switched for the two operation modes. Construction of the tuners is similar to the fundamental cavity tuners.

## 4 MEASUREMENT

Figure 4 shows the measured frequencies and Q-factors of the fundamental cavity. The fundamental cavity showed virtually no change in the Q-factor with a changing tuner control current. The measured frequencies agreed well with the simulation. The frequency tuning range of ~50 kHz is sufficient for tuning the cavity from frequency drift caused by any change in the operating conditions. For the required accelerating voltage of 40 kV, the input power is estimated to be about 4 kW.

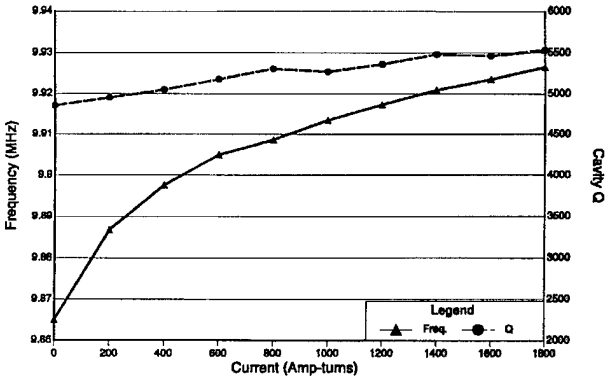



Figure 4: Fundamental cavity Q and frequency tuning characteristic vs. tuner control current.

Figure 5 shows the harmonic cavity Q and frequency tuning characteristic vs. tuner control current for pulse mode operation. Figure 6 shows the harmonic cavity Q and frequency tuning vs. the tuner control current for CW mode operation.

The harmonic cavity Q-factor is deQed and the frequency is detuned for pulse mode operation. The Q is about 20% of the maximum value and the detuning is about -150 kHz at zero current. The ferrite material is lossy in the operating frequency range, and the varying magnetization changes the permeability of the material and thus the resonant frequency. The increased magnetization decreases the magnetic loss and the permeability in the ferrite; the frequency increases as the Q increases. The peak tuner current will be varied to stabilize the frequency. The CW mode tuner has low loss and the change in Q of the cavity is much less than the change with the pulse mode tuner.

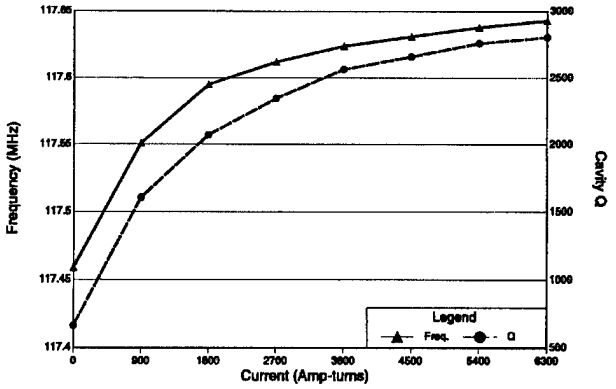



Figure 5: Harmonic cavity Q and frequency vs. tuner control current for pulse mode operation.

## 5 CONCLUSION

The loaded gap cavity is considered to be a good choice for the low frequency application. Comparing the simulation result with measurements for the above two cavities, it was found that they agree well. The ferrite tuners perform well and satisfy the system requirement. The upgraded cavities have improved rf characteristics and can be used in the system.

## 6 ACKNOWLEDGMENTS

The authors thank John Reid of Fermi National Laboratory for loaning the ferrite toroids for the tuner development. We also thank Bill Yoder, Tim Jonasson, and Ralph Bechtold for measurement and fabrication of the cavities and tuner housing, and completion of the tuner windings. This work was supported by the U.S. Department of Energy, Office of Basic Energy Sciences, under Contract No. W-31-109-ENG-38.

## 7 REFERENCES

[1] Y. Kang et al, "RF Cavities for the Positron Accumulator Ring (PAR) of the Advanced Photon Source (APS)," Proc. of the 1995 Particle Accelerator Conference, pp. 1693-1695, 1996.

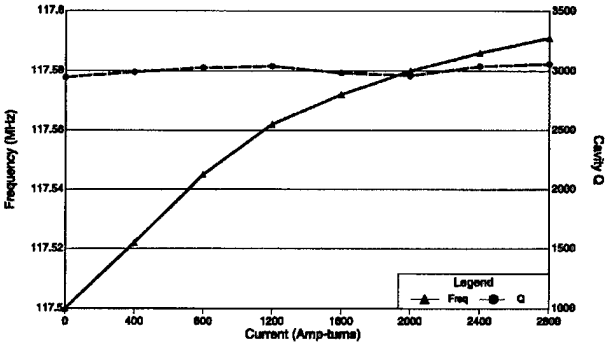



Figure 6: Harmonic cavity Q and frequency vs. tuner control current for CW mode operation.

# AN OVERVIEW OF THE APS 352-MHZ RF SYSTEMS

A. Nassiri, A. Cours, A. Grelick, D. Horan, Y.W. Kang, R.L. Kustom, T. L. Smith, and J. Song
Advanced Photon Source, Argonne National Laboratory
9700 South Cass Avenue, Argonne, Illinois 60439 USA

*Abstract*

The Advanced Photon Source (APS) is a 7-GeV full energy positron storage ring for generating synchrotron radiation with an injector. The booster synchrotron rf system consists of a single 1-MW klystron which drives four five-cell cavities at 352 MHz. The storage ring cavities consist of four groups of four single cells powered by two 1-MW klystrons for 100-mA operation. An overview of the operation of the APS 352-MHz rf systems is presented.

## 1 INTRODUCTION

The Advanced Photon Source (APS) at Argonne National Laboratory is a national user facility for synchrotron x-ray research constructed by the U. S. Department of Energy. It is a third-generation synchrotron radiation source specifically designed to accommodate insertion devices and operates beamlines from bending magnet radiation sources. The storage ring is designed to operate at 7 GeV with a full energy positron injector. The injector booster synchrotron consists of a single 1-MW klystron which drives four five-cell cavities at 352 MHz. These cavities are identical to those used in the ESRF and LEP storage rings [1].

The rf transmitters in the storage ring are nearly identical to those of the booster synchrotron. The storage ring cavities consist of four groups of four single cells, powered by two 1-MW klystrons for 100-mA operation. Two additional 1-MW transmitters are added to the existing system to support the ultimate design goal of 300 mA at 7 GeV. At least three transmitters are needed for 300-mA operation, affording one hot spare for 300-mA operation.

For reliable and continuous operation of the booster synchrotron and the storage ring rf systems, the five rf transmitters can be reconfigured to afford redundancy in operation using high-power WR-2300 waveguide switches [2]. An overview of the APS 352-MHz rf systems are presented.

## 2 BOOSTER SYNCHROTRON

### *2.1 Overview*

Four LEP-type five cell cavities are powered by a single 1-MW klystron (Thomson 2089). The power is split by waveguide hybrids with terminations on the fourth port going into the 250-kW water-cooled resistive loads. The cavities are grouped in two pairs, each pair located symmetrically on opposite sides of the booster synchrotron ring. Since the klystron for the booster is located near one pair of the cavities (on the extraction side of the synchrotron ring), a motorized waveguide phase shifter is used in the 150-meter waveguide run to the cavities on the injection side of the synchrotron ring. This phase shifter is used to compensate for any temperature-related changes in the length of the waveguide. The shunt impedance of each cavity is 55.3 MΩ with peak fundamental mode cavity dissipation of 475 kW.

Injection rf voltage is about 100 kV, enough to capture the 450-MeV positron beam. Energy gain per turn is 16 keV. At the extraction energy of 7 GeV, the synchrotron radiation is 6.38 MeV/turn and the rf voltage per turn is 10.4 MV, requiring about 480 kW power from the klystron.

### *2.2 Low-Level Rf*

The low-level system generates the rf signal to drive a klystron amplifier. The synchrotron signal generator is phase locked to the storage ring master oscillator. The storage ring rf signal is transmitted to the synchrotron signal generator over phase stabilized cable [3].

#### 2.2.1 Tuners

The second and fourth cells of each of the booster 5-cell cavities have piston-type tuners. The cavity tuner port has an 11.5-cm diameter and a 6.0-cm travel. This results in a frequency tuning range of 500 kHz to compensate for beam loading and temperature effects. By adjusting these two plungers both cavity tuning and amplitude balance in the cells are maintained. A feedback system monitors the phase difference in the cavity and adjusts the tuners in tandem to keep the cavity at the resonant frequency with $\pm 0.1°$ under rf heating. Also, the field amplitude in each of the two cells are detected and the tuners are adjusted deferentially to balance the cell voltage to within $\pm$ 1 dB.

#### 2.2.2 Timing and Phasing

The cavities are not a multiple wavelength apart; therefore, the waveguide feed between each pair of cavities is adjusted to 144 degrees so the beam sees the correct accelerating voltage. The sum signal is phased by the opposite amount to ensure proper combining. The cavities on the symmetrically opposite sides of the synchrotron are adjusted to a multiple of an rf wavelength by the motorized waveguide phase shifter so that proper accelerating phase is maintained in all four cavities.

### *2.3 Beam Loading*

The booster synchrotron accelerates a single bunch (natural bunch length at 7 GeV is 76 ps) of 4.7 mA (average beam current). The beam-induced voltage in each cell is 47 kV or 940 kV induced in all four 5-cell cavities. At injection, the synchrotron radiation loss is small, and for an energy gain per turn of 16 keV, the synchronous phase angle is 9.2 degrees. For a 100-kV ring voltage, the detun-

0-7803-4376-X/98/$10.00 © 1998 IEEE

ing angle is 83 degrees. In this case the cavity voltage can be increased to several hundred kilovolts to make the detuning and the beam injection tuning transient smaller. As the beam energy increases, radiation losses increase to 6.38 MeV/turn at 7 GeV and the rf voltage increases to 10.4 MV with a synchronous phase angle of 37.5 degrees.

A set of measurements were made to characterize the effects of beam loading and other rf-related longitudinal beam instability in the booster synchrotron. The first measurement was made of the booster synchrotron tune as a function of time (using an HP vector signal analyzer to monitor the signal from a pickup electrode). A spectrograph of this measurement is shown in Figure 1.

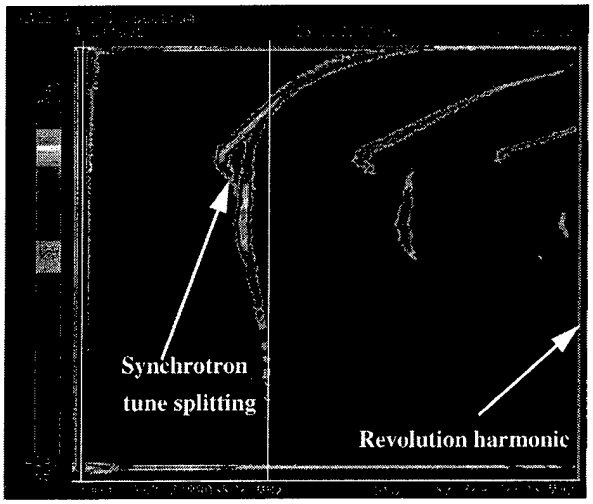



Figure 1: Spectrograph of the booster synchrotron tune vs. time (energy) for a full ramp. The duration of the spectrograph extends over the entire 223 ms of the ramp from 400 MeV to 7 GeV.

The splitting of the synchrotron tune line partly up the ramp is an indication of beam loading. A streak camera was also used to study the longitudinal bunch distribution as a function of time during the booster ramp cycle. An image of the longitudinal bunch distribution is shown in Figure 2. The time scale is 100 ms horizontal and 1.5 ns in the vertical directions. This clearly shows the beam blow up (splitting of the bunch) during a beam loading episode. This happened approximately at the same time as observed on the splitting of the tune line in Figure 1.

The effect of beam loading was compensated by detuning all four cavities to about 20% of reflected power. Figure 3 shows the streak camera image of the longitudinal bunch distribution where the initial beam loading in the cavities is compensated.

## 3 STORAGE RING RF

### *3.1 Overview*

In the current 100-mA (positron beam) operation of the APS storage ring, two 1-MW klystrons (Thomson 2089) are used to provide rf power to sixteen cavities.

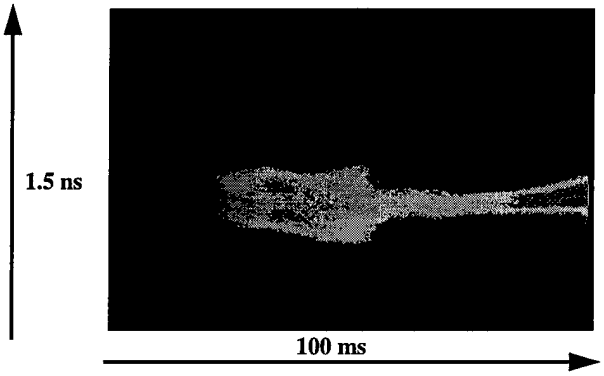



Figure 2: Longitudinal bunch distribution vs. time in the booster during a beam loading episode.

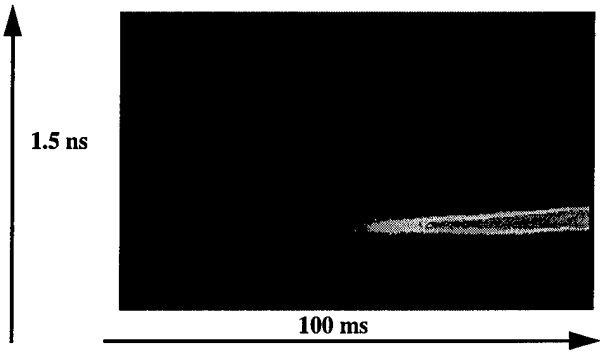



Figure 3: Longitudinal bunch distribution vs. time (initial beam loading is compensated).

Each klystron is powered and controlled by a 95-kV, 20-A DC power supply. These power supplies provide a high level of protection for the klystrons by using a combination of fast and slow interlock circuits and a very fast crowbar switch. Each power supply has a remote interface over an IEEE 488 bus to a remote computer control.

The sixteen cavities are divided into a group of four, with one group of cavities per rf sector. The cavities in each rf sector are uniformly spaced.

### *3.2 Low-Level Rf*

The low-level rf system for the storage ring klystron consists of two phase loops, one nested within the other; an AGC loop to provide constant rf drive to the klystron; slow and fast interlock systems which disable rf drive in the event of a fault; and a 200-watt amplifier to drive the klystron. The internal phase loop removes phase jitter in the klystron output caused by high-voltage power supply (HVPS) ripple, and the second phase loop removes any residual phase jitter caused by the power supply and any phase distortion caused by other sources including beam-cavity interaction. The interlock system removes rf drive at the milliwatt level in the event of a fault occurrence such as incorrect cavity temperature or water flow, vacuum in the cavities, resistive water load temperature and flow, or arcs in the waveguide, particularly at the klystron and cavity windows. The cavity low-level rf system consists of a

phase loop around each cavity, maintaining proper phase between the forward power and field probe output. Phase errors are fed to the input of a stepping motor controller that moves a piston tuner to keep the cavity at resonance. Envelope detectors are used throughout the system to measure rf power and to determine gap voltage.

### *3.3 Rf controllaw*

To maintain the rf gap voltage in the cavities, a software feedback program for collecting and processing data is interfaced to hardware through EPICS [4]. The rf controllaw is an application of **sddscontrollaw** [5] which performs simple feedback on process variables (PVs). Basically, a set of readback process variables is regulated to a set of control process variables to maintain rf gap voltage. In the present rf configuration each klystron powers a set of eight cavities in two separate rf sectors of the storage ring. There is one **sddscontrollaw** for each klystron. The output quantities are the probe power readbacks from the eight cavities. The control quantity for each **sddscontrollaw** process is the klystron mod anode voltage. Since there are eight output PVs and one control PV for each **sddscontrollaw** process, the gain matrix is a $1 \times 8$ matrix. The readback PVs are the cavity probe power measurements. The sum of the probe powers is kept constant. The individual probe power values are not mathematically constrained to be held constant; they may change individually due to sudden detuning of cavities or unequal coupling constants. The cavities probe powers are sampled as fast as possible. This allows faster response to beam loading transients when a beam dump occurs. The hardware interface to EPICS limits the probe powers reading to a 2-Hz rate.

### *3.4 Reconfigurable High-Power Rf*

To improve system reliability and availability, the APS 352-MHz rf systems have been configured to allow two to four klystrons to power the storage ring and one klystron to power or allow operation of the booster with one of the storage ring klystrons using high-power WR-2300 waveguide switches. A quadrature hybrid combines two klystron outputs with two 45° phase shifters at each output of the hybrid. Phase shifters in the hybrid outputs and three waveguide switches are used to choose any one of the twelve possible configurations.This system has been tested for mode selection and interlocks [2].

### *3.5 Higher-Order Modes (HOMs)*

Longitudinal coupled-bunch (CB) instability was observed in the APS storage ring. This instability was found to depend on the bunch fill pattern as well as on the beam intensity. The beam spectrum exhibited a coupled-bunch signature for different symmetric bunch fill patterns with a nominal beam current of 100 mA. The beam fluctuations exhibited two periodicities, which were found to be correlated with the rf cavity temperatures. This intensity-dependent collective effect is driven by long-range wakefields such as those produced in the excitation by the beam of high-Q HOMs in the rf accelerating cavities. To suppress the CB instability, the cavity water supply temperatures were increased to shift HOMs out of resonance with the beam [6].

Measurements of the beam-excited rf cavity HOM spectra for different bunch patterns in the storage ring suggest that the 1210-MHz mode is involved in the observed CB instability. Spectra were measured using E-type probes in the rf cavities [7]. To damp the HOMs in the storage ring rf cavities, coaxial higher-order-mode dampers with high-pass filters are being designed and tested. These are E-type and H-type probe dampers with minimal deQing at the fundamental frequency [8].

### *3.6 Beam Loading*

Computer simulation of the storage ring rf system for the nominal 100 mA operation (assuming a total gap voltage of 8 MV) with optimal detuned cavities (i.e., zero loading angle) shows that the Robinson stability criterion is satisfied. The Robinson stability criterion is met for the ultimate goal of 300 mA operation, with a total ring voltage of 12 MV and a cavity detuning angle of -42 degrees [9]. For the APS storage ring cavity this amounts to a -17 kHz detuning from the no-beam resonance condition to the fully loaded condition for the 300-mA beam operation.

## 4 ACKNOWLEDGMENTS

We would like to thank K. C. Harkay, A. Lumpkin, and B. Yang for valuable discussions and assistance with the beam loading measurements of the booster synchrotron rf cavities; L. Emery for implementing the controllaw software for the storage ring rf system; and J. N. Galayda for his support. This work is supported by the U. S. Department of Energy, Office of Basic Sciences, under Contract No. W-31-109-ENG-38.

## 5 REFERENCES

[1] J. Stepp, J. Bridges, "General Overview of the APS Low-Level RF Control System," Proc. of the 1993 Particle Accelerator Conference, p. 1157 (1993).

[2] Y. W. Kang et al.,"Reconfigurable High-Power RF System in the APS," these proceedings.

[3] D. Horan et al., "A Divide-Down RF Source Generation System for the Advanced Photon Source RF Systems," these proceedings.

[4] L. R. Dalesio et al., "EPICS Architecture," Proc. of ICALEPCS '91, Tsukuba-Ibaraki, Japan, KEK Proce. 92-15, 278-282, (1992).

[5] L. Emery, "Commissioning Software Tools at the Advanced Photon Source," Proc. of the 1995 Particle Accelerator Conference, p. 2238 (1996).

[6] K. C. Harkay et al., "Compensation of Longitudinal Coupled-Bunch Instability in the Advanced Photon Source Storage Ring," these proceedings.

[7] J. Song et al., "Higher-Order Modes of the Storage Ring RF Cavities," these proceedings.

[8] Y. W. Kang et al., "Coaxial Higher-Order Mode Damper Employing a High-Pass Filter," these proceedings.

[9] C. Schwartz et al., "Simulation of the APS Storage-Ring RF Accelerating System," these proceedings.

# HIGHER-ORDER MODES OF STORAGE RING RF CAVITIES AND THEIR INTERACTION WITH THE BEAM AT THE ADVANCED PHOTON SOURCE (APS)

J.J. Song, K.C. Harkay, Y.W. Kang, R.L. Kustom, and A. Nassiri
Argonne National Laboratory, Argonne, IL 60439, USA

*Abstract*

The higher-order modes (HOMs) of APS storage ring (SR) rf cavities and waveguides were measured under various operating conditions. The HOMs of the 352-MHz rf cavity can be one of the major contributors to the coupled bunch (CB) instability. The distribution of HOMs under various conditions of beam current, cavity temperature, cavity tuning, single-bunch and multi-bunch operation, and fill patterns, are presented. The HOMs' shunt impedance of the loaded cavities were also measured. The effect of stagger tuning of the 16 cavities and their waveguide system is compared, and the HOM dampers are examined.

## 1 INTRODUCTION

To provide stable and useful x-rays from insertion devices such as undulators and wigglers from the APS, the main storage ring (SR) has to supply a positron beam of 100 mA with a lifetime of at least 10 hours at the nominal operation. Some CB-related APS SR parameters are found in Table 1.

Table 1: Some CB-related APS/SR Parameters

| | |
|---|---|
| Beam Energy | 7 GeV |
| Maximum Beam Current | 300 mA |
| Revolution Frequency | 271.55 kHz |
| Harmonic Number | 1296 |
| RF Frequency | 351.927 MHz |
| Synchrotron Frequency | 1.8 kHz |
| Longitudinal Damping Rate | 213 $sec^{-1}$ |
| Transverse Damping Rate | 106 $sec^{-1}$ |
| Cavity Coupling Factor for nominal current (100mA) | 2.5 |
| Cavity Tuning Range | 3 MHz |
| Cavity Water Temperature | 75 to 95 ° F |

In previous work, calculations were performed to determine the deQing requirements of cavity HOMs to ensure that the growth rates for CB instabilities do not exceed the synchrotron radiation damping rate [1]. The results for the monopole modes are summarized in Table 2, where the fundamental mode is included for comparison. HOM dampers were designed, and bench measurements of their effectiveness were reported [2]. The HOM dampers are tested and will be installed in the SR in the near future [3].

Experimental observations show that for specific bunch fill patterns, a longitudinal CB instability is encountered for beam currents around 100 mA [4]. The instability could be suppressed by changing the temperature of the rf cavities. Detailed measurements were performed on the rf cavities in situ in order to characterize the influence of temperature and tuner position on the HOMs. The beam-HOM interaction was also studied in order to identify the driving impedance for the instability.

Table 2: Required Q for Frequency-Staggered Cavity HOMs (only monopole modes are shown)

| Monopole HOMs (MHz) | $Q_o$ (1000) | $R_s$ (MΩ) | DeQing Factor $Q_o/Q$ | Calculated Staggering (kHz/mm) |
|---|---|---|---|---|
| 352 | 49 | 5.60 | * | 5.1 |
| 538 | 41 | 1.67 | 64 | 210. |
| 922 | 107 | 0.62 | 16 | 330. |
| 939 | 42 | 0.23 | 6.4 | 330. |
| 1172 | 44 | 0.18 | 6.4 | 390. |
| 1210 | 94 | 0.49 | 16 | 600. |
| 1509 | 88 | 0.40 | 16 | 810. |

## 2 HOM MEASUREMENTS

### *2.1 Measurement Setup*

The rf system consists of four power supplies, four klystrons, and four rf cavity sectors (S36, S37, S38, and S40). Each cavity sector has four single-cell cavities, each of which is connected to a WR2300 waveguide by an H-loop type of input coupler. Measurements were made on the cavities and waveguides in sectors 38 and 40. There are various types of field probes: H-loop for the low-level rf feedback, E/H-type HOM probes, E-detector probe for the electron-emission current, and the directional coupler in the waveguide.

### *2.2 HOMs vs. Cavity Length--Staggering Effect*

The frequency, Q-values, and amplitudes of HOMs were measured for a total of ten cavities (eight from S38 and S40, and two spare cavities). Sample results for both unloaded and loaded cavities are shown in Table 3. These are also compared with the URMEL calculations. Most of the HOMs do not appear to couple to the waveguide through the input coupler, except two monopoles at 922 and 1210 MHz and one dipole at 1145 MHz. Due to the asymmetry of the cavity, one of the degenerate dipole modes was significantly deQed. When the frequencies of a typical HOM for eight cavities are plotted, one can see a staggering effect, as shown in Fig. 1 for the 0-M-1 mode at 536 MHz. The frequency linearly decreases with the cavity center

0-7803-4376-X/98 /$10.00 © 1998 IEEE

length. There are some HOMs, however, for which the field configuration/strength is not simply correlated to the cavity center length.

Table 3: Comparison of HOMs in Three Cases: URMEL Calculation, Unloaded Cavity, and Loaded Cavity

| Mode | URMEL Calculation | | Spare(#4) 201.88 mm | | S38 C3(#5) 202.18 mm | |
|---|---|---|---|---|---|---|
| | f(MHz) | $Q_o$ | f(MHz) | $Q_o$ | f(MHz) | $Q_L$ |
| 0-E-0 | 353.6 | 49000 | 351.93 | 47500 | 351.93 | 25900 |
| 0-M-1 | 536.7 | 41000 | 539.23 | 37700 | 539.19 | 34600 |
| 1-E-1 | 588.7 | 68000 | 582.09 | 55500 | 582.45 | 58500 |
| | | | 584.64 | 48200 | 584.24 | 51000 |
| 0-E-2 | 744.9 | 43000 | 735.26 | 22500 | 735.26 | 22200 |
| 1-M-2 | 761.1 | 53000 | 756.83 | 8700 | 756.49 | 6800 |
| | | | 761.67 | too small | | too small |
| 0-E-3 | 922.5 | 10700 | 914.92 | 51600 | 915.76 | 21700 |
| 0-M-2 | 939.0 | 42000 | 933.06 | 1200 | 931.29 | 600 |
| 1-E-3 | 962.0 | 54000 | 955.71 | 34000 | 955.21 | 8600 |
| | | | 957.73 | 8600 | 957.01 | 16200 |
| 1-M-4 | 1017 | 41000 | 1020.5 | 20000 | 1020.74 | 40300 |
| | | | 1020.90 | 17000 | 1021.31 | 10800 |
| 1-E-5 | 1145.1 | 92000 | 1143.65 | 84000 | 1142.42 | 35900 |
| | | | 1144.79 | 61800 | 1143.16 | too small |
| 0-E-4 | 1173.2 | 44000 | 1166.82 | 61000 | 1166.76 | 57200 |
| 0-M-3 | 1210.8 | 94000 | 1205.86 | 31900 | 1207.14 | 26200 |
| 1-E-6 | 1219.2 | 41000 | 1231.07 | 19000 | 1230.40 | 31100 |
| | | | 1231.30 | 28500 | 1231.00 | 41300 |
| 0-E-6 | 1509.1 | 88000 | 1508.73 | 58800 | 1503.76 | N/A |

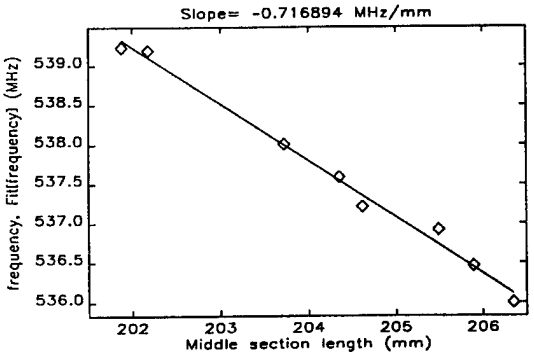



Figure 1: Cavity staggering effect at 536 MHz.

### 2.3 *HOMs vs. Cavity Temperature*

The S38 cavity water temperature was changed from 95° F to 73° F in 3-degree increments by mixing the cavity return water with the chilled water. The frequencies of the HOMs shift due to the change of the cavity's volume. The cavity body temperatures follow the water temperature change, which includes fluctuation of the order of +/- 1 C. The bunch current is constant at 0.8 mA. Figure 2 shows the beam-excited HOM amplitudes as a function of cavity temperature. The amplitude changes in most of the HOMs due to temperature variation appear to be significant, except at 744 and 1509 MHz.

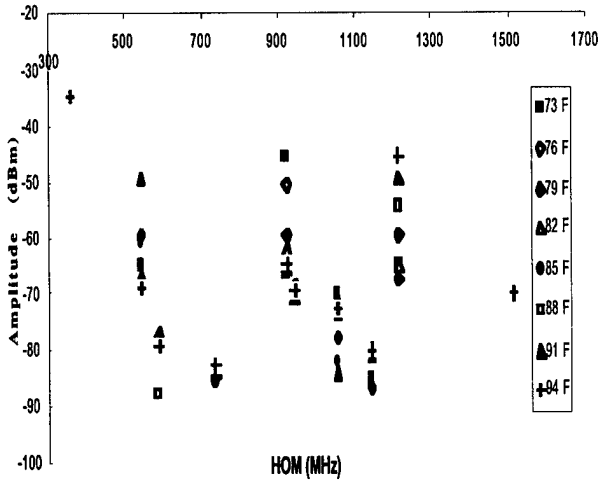



Figure 2: Amplitude variation of the HOMs vs. S40 #2 cavity temperature.

### 2.4 *HOMs vs. Cavity Detuning*

At a low bunch current (1 mA) the excitation of HOMs was measured while S38 cavities 1 and 2 were detuned, one at a time, by changing the tuner setpoint. There is a cavity temperature change associated with the cavity detuning, probably because the reflected power increases and less power is getting into the cavity. This may make the HOM amplitude results more difficult to interpret. These setpoint changes are rather large, resulting in phase shifts greater than 45° in the fundamental mode relative to the source frequency, and do not represent normal cavity operating points. Later, the threshold detuning on all the rf-sector cavities to sustain stability was carried out with a beam current of 100 mA. The beam spectrum center at an rf harmonic for the unstable case is shown in Fig. 3.

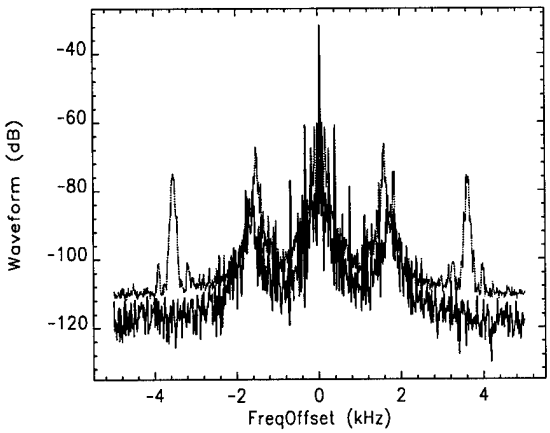



Figure 3: Beam spectrum from S35 BPM, while detuning the cavity; the solid line is the stable and the dotted line is the unstable beam.

In this figure the beam spectrum from a dispersion BPM for an unstable beam is plotted with a spectrum for

a stable beam. The synchrotron frequency is about 1.7 kHz. Both dipole and quadruple synchrotron sidebands appear in the unstable beam.

## 3 DISCUSSION

When the beam is unstable, it oscillates longitudinally at the synchrotron frequency, which modulates specific revolution harmonics in the spectrum corresponding to the specific CB mode. The resonant frequency of the driving HOM determines which CB mode is observed. For each unstable fill pattern, the same CB mode was observed in the beam, implying that the same HOM is responsible. Each particular bunch fill pattern has a characteristic set of revolution frequencies which are then detected by the cavity probes. Of interest are those frequencies which show an increased cavity response when the beam becomes unstable.

Presented first are measurements at a resolution bandwidth of 300 kHz to show a large frequency span. Figure 4 shows the spectrum in one cavity for four groups of 12 bunches when the beam is stable. In this case, the 12 bunches are in a train of adjacent rf buckets, and the four groups are placed symmetrically around the ring. Figure 5 shows the cavity spectrum with the same bunch pattern, when the beam is unstable. The HOM near 1210 MHz shows an increase.

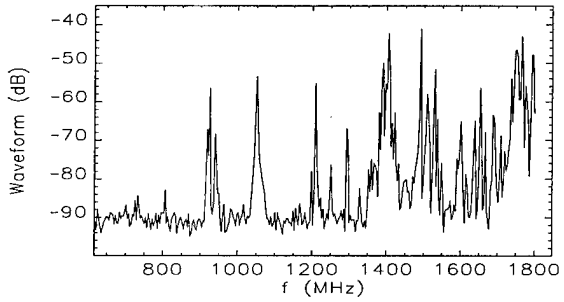



Figure 4: RF cavity HOM spectrum for stable beam.

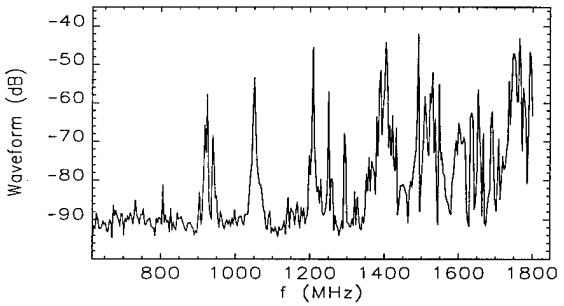



Figure 5: RF cavity HOM spectrum for unstable beam.

A narrowband measurement in Fig. 6 shows that the excitation occurs mainly in the upper synchrotron sideband. The two traces in the figure compare the cases for the unstable and stable beam, respectively. The single-sided response is as one would expect for a CB instability. Based on the measurement of the beam-induced power, one can calculate the shunt impedance of the cavity HOMs, which is summarized in Table 4. The equation used to calculated the shunt impedance is

$$P_{HOM} = P_c + P_{rad} = 2\langle I_b \rangle^2 (R/Q_o)Q_L,$$

where $P_{HOM}$ is the HOM power induced by the beam, $P_c$ is the HOM power lost to the cavity wall, which the field probe sees, $P_{rad}$ is the HOM power radiated to the waveguide, $I_b$ is the average beam current, R is the shunt impedance, $Q_o$ is the unloaded Q, and $Q_L$ is the loaded Q. There are some discrepancies between the measurement and the calculation, but they are of the same order of the magnitude. More analysis is required to understand the differences.

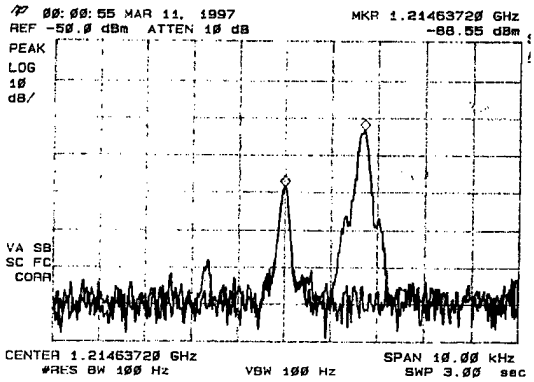



Figure 6: RF cavity signal centered on a revolution harmonic at 1214.64 MHz.

Table 4: Shunt Impedance of the S38 C3 HOMs

| Freq (MHz) | Power (W) | $Q_o$ | $Q_L$ | Coupling Factor | Shunt Imp(MΩ) |
|---|---|---|---|---|---|
| 351.75 | 24400 | 47500 | 18700 | 1.54 | 5.60 |
| 536.00 | 85.63 | 37700 | 34600 | 0.10 | 0.21 |
| 733.13 | 0.39 | 22500 | 22200 | 0.02 | 0.01 |
| 912.28 | 0.26 | 51600 | 21700 | 0.38 | 0.01 |
| 939.00 | 7.54 | 1200 | 600 | 1.00 | 0.33 |
| 1173.20 | 0.30 | 44000 | 35900 | 0.23 | 0.02 |
| 1210.80 | 7.16 | 31900 | 26200 | 0.22 | 0.62 |
| 1505.93 | 4.71 | 58800 | 3300 | 16.8 | 0.82 |

## 4 ACKNOWLEDGMENTS

The authors would like to thank K. Kim and W. Dower for their assistance. This work was supported by the U.S. Department of Energy, Office of Basic Energy Sciences, under Contract No W-31-109-ENG-38.

## REFERENCES

[1] Emery, Proc. of the 1993 Particle Accelerator Conference, 549 (1993).
[2] J.J. Song et al., Proc. of the 1993 Particle Accelerator Conference, 1057 (1993).
[3] Y.W. Kang, "Coaxial Higher-Order Mode Damper Employing a High-Pass Filter," in these proceedings.
[4] K. Harkay et al., "Compensation of Long. Coupled-Bunch Instab. in the Adv. Photon Source," in these proceedings.

# MODIFYING CERN SPS CAVITIES AND AMPLIFIERS FOR USE IN RHIC

R. Connolly, J. Aspenleiter, S. Kwiatkowski
Brookhaven National Lab, Upton, New York 11973

*Abstract*

A system of ten rf cavities operating at 197 MHz will provide longitudinal focusing during beam storage in the Relativistic Heavy Ion Collider (RHIC). The cavities and tetrode amplifiers are from CERN where they had been used in the Super Proton Synchrotron to accelerate leptons for injection into LEP. The amplifier-cavity system had an impedance pole about 3 MHz below cavity resonance which was a possible source of oscillation with rf feedback. This was not a problem at CERN because the cavities were operated without feedback. The impedance pole was moved lower in frequency by extending the length of the drive line. When this was done it was no longer possible to tune the amplifier to give a good match to the drive loop resulting in about 50% anode efficiency. In the class of operation we are using, an efficiency of 65%-70% is expected. A good match was achieved by increasing the loop coupling from 16Ω to 19Ω.

## 1 INTRODUCTION

The Relativistic Heavy Ion Collider (RHIC) at Brookhaven National Lab will accelerate and store beams ranging from protons to gold nuclei [1]. One system of four rf cavities operating at 28 MHz [2] accelerates the beam from injection energy to storage energy, and a system of ten cavities operating at 197 MHz provides longitudinal focusing during storage. The storage system cavities and tetrode amplifiers are from the Super Proton Synchrotron at CERN where they accelerated leptons for injection into LEP [3].

The amplifier-cavity system has an impedance pole about 3 MHz below cavity resonance which is a possible source of oscillation with rf feedback. At CERN the cavities were operated without feedback and care was taken to avoid external feedback, so the impedance pole was not a problem [4].

Experiments were conducted at RHIC to move this pole away from cavity resonance. We found that the pole could be moved lower in frequency by increasing the length of the final drive line. Evidently the drive line had been made quite short because of space limitations in the SPS tunnel. When the longer drive line was installed it was no longer possible to tune the amplifier to give the required impedance transformation, limiting the amplifier to about 50% anode efficiency. The efficiency was increased to about 70% by increasing the loop coupling from 16Ω to 19Ω. This paper describes these experiments and the performance results.

## 2 IMPEDANCE POLE

Figure 1 shows the 16Ω drive line with the base of the amplifier clamped to the flanges on the top of the coaxial elbow and the drive loop installed in the cavity. The line has forward- and reverse-power directional couplers and the cavity has small pickup loops. Two $S_{21}$ network analyzer traces, fig. 2, were made by driving the amplifier with the analyzer.

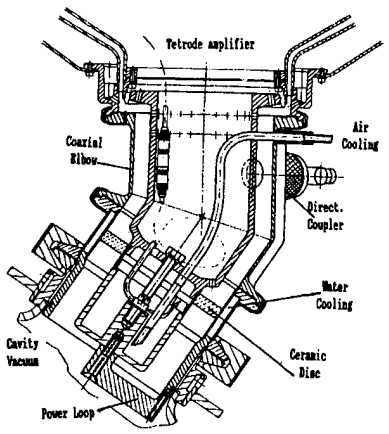



Figure 1. The transmission line connecting the amplifier to the cavity. This figure is copied from reference 3.

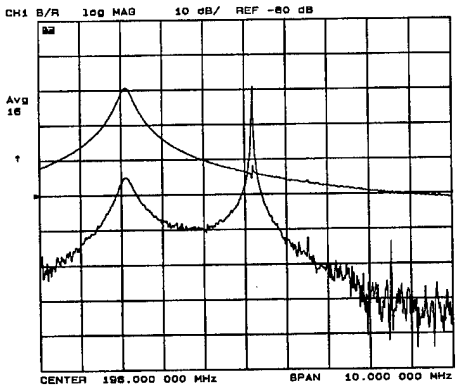



Figure 2. Network analyzer traces showing the impedance pole and cavity resonance. Top trace is the signal from the forward-power coupler in the drive line, and the bottom trace is from a loop inside the cavity. The cavity was tuned to 196 MHz when these measurements were made.

0-7803-4376-X/98/$10.00 © 1998 IEEE

The top trace is the signal from the forward-power coupler in the drive line and the bottom trace is the signal from one pickup loop. In the cavity, the power received at the pole frequency is only 25 dB lower than at cavity resonance. With rf feedback this resonance can be the same or larger than the cavity resonance.

The first experiment was to separate the amplifier from the drive line flange and to short the inner and outer conductors at the amplifier base with copper tape. A network analyzer and broad-band amplifier were used to drive the amplifier and the signal was picked up on a diagnostic probe at the base of the amplifier. The result, fig. 3, shows that the amplifier transforms an electrical short at its output to impedance poles which are symmetrical about 197 MHz. Since the drive loop is a short circuit off resonance this shows that the pole does not result from the impedance transformation in the amplifier.

Next an adapter was placed on the drive line flange and an $S_{11}$ measurement was made of the impedance presented to the amplifier. The network analyzer measurement showed the electrical length of the transmission line to be about 3/8 $\lambda$ giving an off-resonance impedance which is capacitive. By adding a phase offset equivalent to 19.4 cm of transmission line at 197 MHz the transformed impedance presents an impedance zero off resonance.

Reference 4 describes the impedance transformation within the amplifier as being approximately a $\lambda/4$, $3\Omega$ transmission line in series with a $\lambda/4$, $18.5\Omega$ line. PSPICE was used to calculate the impedance of a short circuit transformed through a 3/8 $\lambda$ section of $16\Omega$ line in series with the two $\lambda/4$ lines of the amplifier. This calculation gives poles at 197 and 232 MHz and both move lower in frequencies when the $16\Omega$ line is lengthened. When the line is $\lambda/2$ long the upper and lower poles are symmetric around 197 MHz.

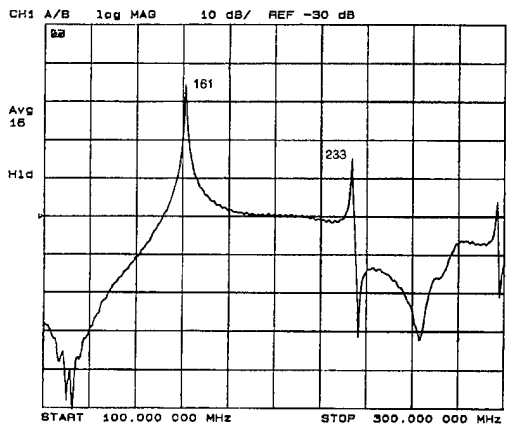



Figure 3. Anode impedance as a function of frequency with an electrical short across the output of the amplifier.

The drive-loop transmission line was lengthened by adding a 17.1cm insert in the coaxial elbow section. This insert initially was made 19.4 cm but measurements made before the pieces were welded indicated it was too long. With the longer line installed the impedance poles were 12 MHz below and 18 MHz above resonance. The initial length of 19.4 cm would have placed them symmetrically about the resonance.

## 3 AMPLIFIER EFFICIENCY

After the drive line was extended it was no longer possible to get the required power from the tetrode without exceeding the tube specification for power dissipation on the screen. A storage cavity has a shunt impedance of 8.5 $M\Omega$ and requires about 60 kW of rf power to produce 1 MV in the gap. To deliver 60 kW without drawing excessive screen current requires the loop impedance be transformed to an anode impedance of about $625\Omega$. This transformation is accomplished by two sections of transmission line in the amplifier base which approximate $\lambda/4$ transformers of $3\Omega$ and $18.5\Omega$ connected in series.

The tetrode amplifier that drives the cavity is operated in class AB with the grid biased at -200 V, the screen at 900V and the anode at 10kV. At full power the conduction angle is 190° and the tetrode should give ~70% efficiency. We measured 54% efficiency (see table) on a test stand consisting of a $50\Omega$ water-cooled load transformed to $16\Omega$ by a $\lambda/4$ transformer of $Z_t$=28.3$\Omega$. To increase the efficiency it was necessary to measure the loop-anode impedance transformation from the operating parameters of the tube.

For small anode rf voltages the electron current in a tube varies with grid voltage approximately as,

$$I(t) \propto (V_{g0} + V_{g1} \cos \omega t)^{1.5} \qquad (1)$$

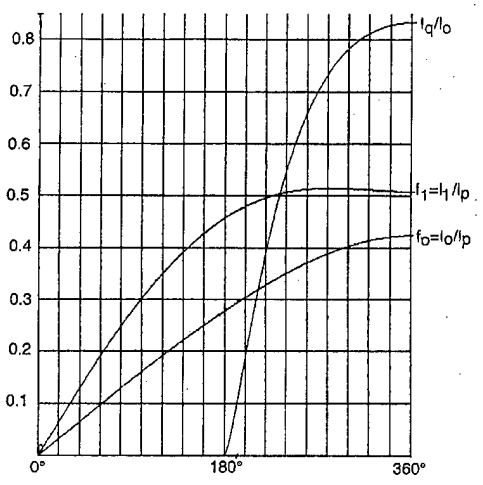



Figure 4. Tube current form factors calculated by W. Pirkl. Bottom axis is conduction angle of tube. All measurements were made with an angle of 190°-200°.

where $V_{g0}$ is the grid bias voltage and $V_{g1}$ is the grid drive amplitude. This expression can be used to calculate the Fourier components of the current [5]. The dc and rf fundamental components are,

$$I_0 = \frac{1}{T}\int_0^T I(t)dt = I_P f_0 \qquad (2)$$
$$I_1 = \frac{2}{T}\int_0^T I(t)\cos(\omega t)dt = I_P f_1$$

where $I_p$ is the peak current during the rf cycle. These form factors, $f_0$ and $f_1$, are plotted in fig. 4 together with a curve of quiescent current divided by anode current, $I_q/I_0$. We measured the ratio $I_q/I_0$ and read the conduction angle from the graph. The ratio $f_1/f_0$ could then be determined from the graph and the rf current, $I_1$, calculated as the anode current times this ratio. The tube power and anode current were measured and the impedance calculated from $P=I_1^2R/2$.

A series of measurements was made on the test stand in which output power was measured as both the frequency and the amplifier tuning position were varied. The tube socket can be raised and lowered for tuning and it was not known whether this changed only the frequency or both the frequency and transformed impedance. Figure 5 shows the family of curves generated. For all of these measurements the anode current was 3.1A and the quiescent current was 0.6A giving a ratio of $f_1/f_0$ equal to 1.52. All of the tuning curves peak at 6.1 kW showing the tuning changes only the frequency of the impedance transformation. A power of 6.1 kW with an rf current of 4.7 A gives an impedance of 550Ω. The same analysis on other data sets gave values in the range of 515Ω-550Ω. From these measurements we concluded that the amplifier transforms 16Ω to about 525Ω.

The test stand presents an impedance to the amplifier equal to $(Z_t)^2/50$. The impedance of a coaxial line increases as the diameter of the center conductor decreases so we were able to increase the impedance presented to the amplifier in 1Ω steps by machining down the inner conductor of the λ/4 transformer. The measured efficiency peaked at 20Ω, however the screen current started to get very high. We chose a loop impedance of 19Ω.

## 4 CONCLUSION

The loop was rotated to give 19Ω coupling and the drive-line extension was installed. The cavity was then conditioned to a peak gap voltage of 1.0 MV at which time the measurements in the third column of the table were made. These two modifications have increased the amplifier efficiency from about 50% to about 70% and have moved the impedance pole 12 MHz away from the cavity resonance.

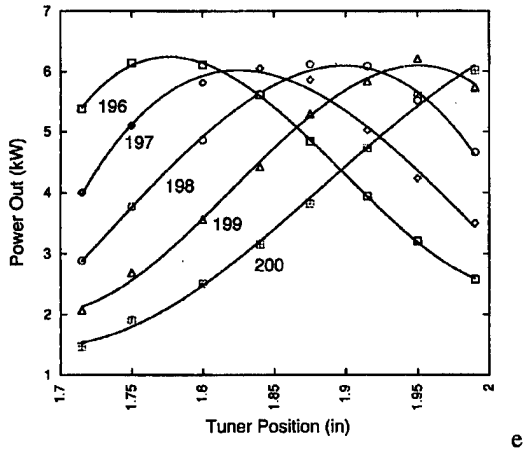



Figure 5. Measured power as a function of tuner position for five frequencies. Tuner changes the frequency of maximum anode impedance but not the magnitude.

Comparison of amplifier parameters reported by CERN [4], those measured at BNL on 16Ω load, and those measured on cavity after modifications. The final efficiency of 73% is from a single measurement and is probably a little too high.

| | CERN | 16Ω load | Final |
|---|---|---|---|
| Anode voltage | 10 kV | 10 kV | 9.8 kV |
| Anode quiescent current | 0.5 A | 0.5 A | 0.5 A |
| Anode current | 9.4A | 9.95 A | 7.77 A |
| Screen grid voltage | 900 V | 900 V | 900 V |
| Screen grid current | 320 mA | 405 mA | 150 mA |
| Control grid voltage | -200 V | -200 V | -200 V |
| RF output power | 62 kW | 53 kW | 57 kW |
| RF drive power | 1.8 kW | 1.75 kW | 1.44 kW |
| Gain | 15.4 dB | 14.8 dB | 16.0 dB |
| Anode efficiency | 64% | 54% | 73% |

## 5 ACKNOWLEDGEMENT

The authors benefited from discussions with Ralph Sanders, Mike Brennan, and Alessandro Ratti. Mike Witte operated the test stand for much of this work. This work was performed under the auspice of the U.S. Department of Energy.

## 6 REFERENCES

1. "RHIC Design Manual", (Brookhaven National Laboratory, Upton, NY 1996)
2. J. Rose, et.al., "The RHIC 28 MHz RF System," these proceedings.
3. P.E. Faugeras, et.al., "The New RF System for Lepton Acceleration in the CERN SPS," Proc. 1987 IEEE PAC Conference, p. 1719.
4. W. Herdrich and H.P. Kindermann, "RF Power Amplifier for the CERN SPS Operating as LEP Injector," Proc. 1985 IEEE PAC Conference, p.2794.
5. W. Pirkl, private communication

# FIRST OPERATION OF THE HAP/MOPA TRAVELING WAVE STRUCTURE AT BOEING FEL*

A.M. Vetter, T.L. Buller, D.H. Dowell, and P.E. Johnson, Boeing D&SG
P.O. Box 3999 M/S 2T-50, Seattle, WA 98124-2499 USA

*Abstract*

The first of six 1.3-GHz, 18-cell, constant impedance, traveling wave linac structures has been placed under RF power and used to accelerate an electron beam. The design of the structures and low power measurements of insertion loss and group delay are described. The observed voltage gain under high power is compared with predictions based on low power measurements and URMEL calculations for the accelerator mode in a single cell.

## 1 INTRODUCTION

A set of six 1.3-GHz traveling wave linac structures was partially fabricated in the late 1980's for an FEL accelerator project (known as HAP/MOPA) which was terminated before completion. These structures were left in varying stages of completion, only one being fully ready for operation. Under current plans to complete a kilowatt-capable, visible FEL [1] at the Boeing FEL facility in Seattle, fabrication and tuning of these linac structures have been completed, and installation in the beam line is in progress. The sections, of which the first has been operated with electron beam under high RF power, will produce roughly 80% of the energy gain required for FEL operation in the visible spectrum.

## 2 STRUCTURE DESIGN

The linac structures, shown in Fig. 1, are of the traveling wave type, operating in the $3\pi/4$ mode at a frequency of 1.3 GHz. The design is adapted from an earlier series of traveling wave linac sections built and operated for the Visible Oscillator FEL [2].

### *2.1 Design objectives*

Designed specifically for FEL applications which demand very low beam emittance with high peak current, these sections feature beam apertures which are very large (approximately 5 cm) for a structure operating at this

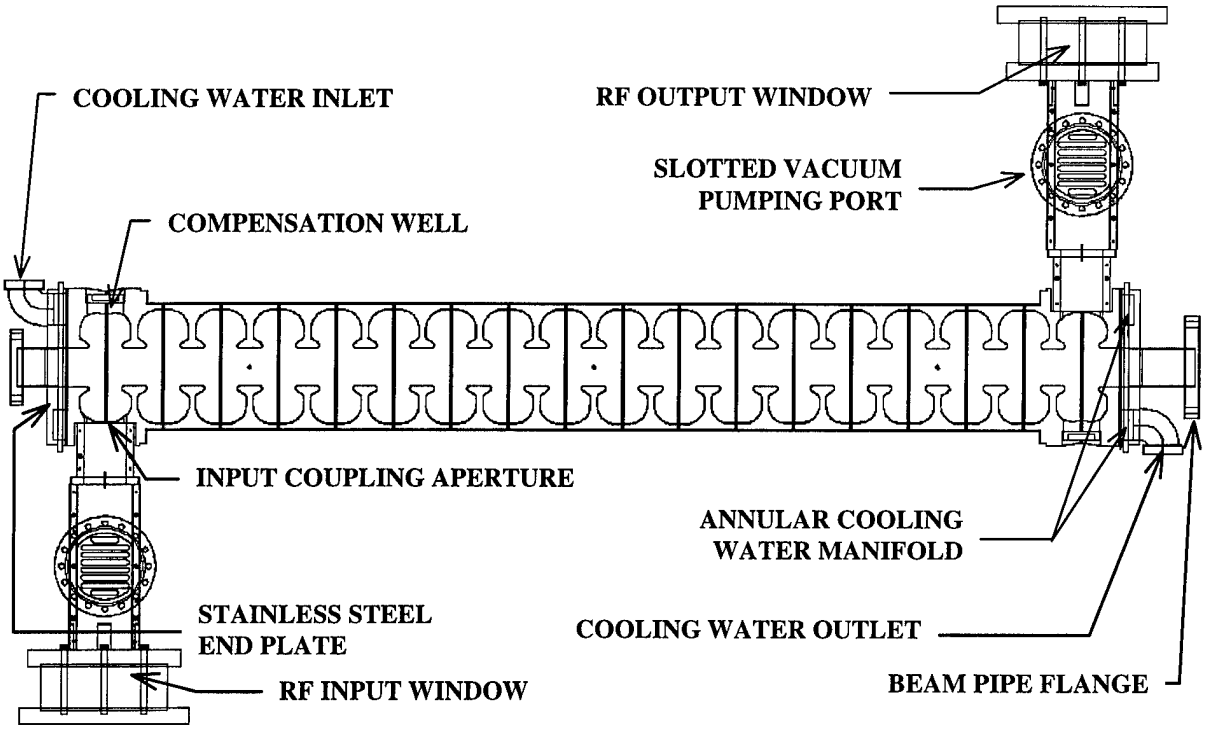



Figure 1. 18-cell constant impedance traveling wave linac section, shown without cooling water jacket.

*Work supported by USA/SSDC under Contract DASG60-90-C-0106.

frequency in order to minimize emittance growth due to transverse wake fields. If the cells were of the conventional disk loaded geometry, such large apertures would produce excessive cell-to-cell coupling, so that the group velocity would be far too high to achieve reasonable gradients with the 10 MW of RF input power available. By introducing a modest nose cone around the aperture, the intercell coupling is brought down to the desired level while improving the *R/Q* ratio for the cell. Further improvement in shunt impedance is obtained by rounding the outside contour of the cell. Finally, the shift in operating mode from the typical disk loaded structure phase advance of $2\pi/3$ to $3\pi/4$ provides a little more space into which to fit the noses and allows for a slight reduction in number of irises, which also improves the wake field performance of the section.

The present structures, whose principal parameters appear in Table 1, retain the cell geometry and operating mode of the earlier structures. They differ from the earlier structures in being much shorter (18 cells *vs.* 35) and in being of constant impedance instead of constant gradient. They also feature extended coupler boxes with slotted pumping ports. These changes allowed for substantial reduction in fabrication costs, and are expected to yield improvements in operating vacuum and effort required to condition to high field, and in the sensitivity of the beam energy gained in the structure to fluctuations in cooling water temperature. There will be a slight penalty in the theoretical efficiency of the structure, but this will be offset by improvement in thermal sensitivity.

| PARAMETER | | VALUE |
|---|---|---|
| Operating frequency | $f_o$ | 1.3 GHz |
| Number of cells | $N$ | 18 |
| Electrical length | $L$ | 1.56 m |
| Cell-to-cell phase shift | | 3/4 π |
| Normalized phase velocity | $v_p/c$ | 1.0 |
| Normalized group velocity | $v_g/c$ | .35 % |
| Fill time | $\tau$ | 1.5 μs |
| Field attenuation parameter | $\alpha$ | .192 neper/m |
| Insertion loss (no beam) | | 2.6 dB |
| Shunt impedance/unit length | $V_a^2/P_c$ | 33 MΩ/m |
| Wave impedance | $V_a^2/P_i$ | 22.4 MΩ |
| Beam impedance | $-dV_a/dI_b$ | 7.2 MΩ |
| Physical length | | 1.76 m |
| Beam aperture (end-to-end) | | 5.56 cm |

Table 1. HAP/MOPA traveling wave linac section parameters.

*2.2 Mechanical design*

The present structures retain the fabrication approach, cooling and RF coupling concepts, RF window types, and numerous mechanical design features of the earlier structures. The interior cells are formed by brazing together stacks of solid OFHC Cu parts, each of which has the last half of one cell and the first half of the next cut into its top and bottom sides, respectively. All cooling occurs at the cylindrical outer surface of the cells, where de-ionized cooling water flows longitudinally along the structure in the ~ ¼ inch gap between the copper exterior cell surface and the stainless steel water jacket (not shown in Fig. 1) A fiberglass insulating jacket, also not shown in Fig. 1, covers the water jacket, providing thermal isolation between the structure and its cooling system (which is required to maintain the structure at 45 C, even when operating at negligible average power) and the surrounding air.

The outer walls of the end cells are made thick enough (~ 1 inch) to allow for longitudinal holes to carry cooling water from the annular manifold cut into the stainless steel end plate brazed to the end wall, across the end cell, to the end of the water jacket which falls over the iris joining the end cell to its neighbor. Cooling water connections are made to stainless steel elbows welded into holes in the stainless end plates which lead to the annular manifolds cut into the back sides of the end plates.

Conflat end flanges are welded onto stainless steel tubes brazed into the end walls of the structure. Conflat flanges are also brazed over the slotted pumping ports on the input and output coupler waveguide boxes to allow the attachment of cryopumps. Pumping speed through the coupling apertures will be greater than through the beam pipes, and moving the pumps to the couplers reduces congestion around the beam diagnostic boxes which attach to the ends of the linac sections.

## 3 LOW POWER ELECTRICAL MEASUREMENTS

At the operating frequency, the measured phase length of the 18-cell structure varies with frequency at the rate of 525°/MHz, implying a normalized group velocity

$$\frac{v_g}{c} = \frac{\phi}{f}\frac{1}{d\phi/df} = .00356 ,$$

where $\phi = 3\pi/4$ is the phase advance per cell at the operating frequency. This is consistent with results of the cavity code URMEL [3], from which a normalized group velocity of .00351 is deduced based on the difference between the $TM_{010}$ mode frequencies for electric and magnetic boundary conditions imposed in the center of the iris between cells (these boundary conditions correspond to the conditions in an infinite structure operating in the "zero" and π modes, respectively).

The structure insertion loss at the operating frequency has been measured at 2.6 dB, or 0.144 dB/cell. This is related to the cell quality factor $Q_o$ through the relation

$$\frac{\Delta P_f}{P_f} = -\frac{\phi}{Q_o\,(v_g/c)} ,$$

where $P_f$ is the RF power flowing through the cell. The corresponding $Q_o$ is 19630, which is also consistent with the URMEL result (19990).

## 4 PERFORMANCE PREDICTIONS

A simple spread sheet calculation shows that the load line equation for the structure is

$$V_a(I_b) = \sqrt{R_s P_i} - R_b I_b ,$$

where $R_s$ = 22.4 MΩ and $R_b$ = 7.2 MΩ (based on URMEL result $R/Q$ = 71.75 Ω for a single cell) and where $P_i$ is the input RF power and $I_b$ is the beam current.

## 5 HIGH POWER OPERATION

The first of the traveling wave linac sections was installed in the beam line following the 433.3 MHz standing wave structures (Fig. 2). During the first day of operation, the structure was conditioned to accept 4 MW with a 30 μs RF pulse length at a repetition rate of 1 Hz. A few days later, the structure accepted 8 MW for a 100 μs pulse duration, still at 1 Hz prf, with a return loss slightly in excess of 20 dB. This being judged sufficient for the subsequent beam tests, further conditioning to higher power was deferred.

For acceleration tests in early May, 1996, the beam was produced by illuminating a $K_2CsSb$ photocathode situated in the first cell of the 433.3 MHz accelerator with a mode-locked, frequency-doubled Nd:YLF laser running at a frequency of 108.3 MHz, with average beam current on the order of 10 mA. The beam energy at the entrance to the traveling wave linac structure was 20.7 MeV. With an RF input power of 6.3 MW to the traveling wave structure, the beam energy increased to 32.4 MeV, for an accelerating voltage of 11.7 MV in the traveling wave structure. Both the RF power measurement and the energy gain have an estimated experimental error of at least ±5%. For 6.3 MW input power and .01 A beam current, the load line equation above predicts an accelerating voltage of 11.8 MV, well within the experimental error.

## 6 ACKNOWLEDGMENTS

The authors gratefully acknowledge the contributions of Tom Hayward, Christy Lancaster, Loren Milliman, Kelly Murphy, and Doug Smith in preparing and operating the linac section and accelerator for the high power beam measurements. The cell shape of the traveling wave structure is due to the late William J. Gallagher.

## REFERENCES

[1] J.L. Adamski, et al., "A Kilowatt Class Visible Free Electron Laser Facility," Proc. 1995 Particle Accelerator Conference, p. 251.

[2] J.L. Adamski, et al., "The Boeing 120 MeV RF Linac for FEL Research," IEEE Trans. Nucl. Sci., **NS-32,** No. 5, Oct., 1995, p. 3397.

[3] T. Weiland, DESY **83**-005, 1983 and DESY M-82-24 (1982) and Nucl. Instr. and Meth., **216** (1983) p. 329.

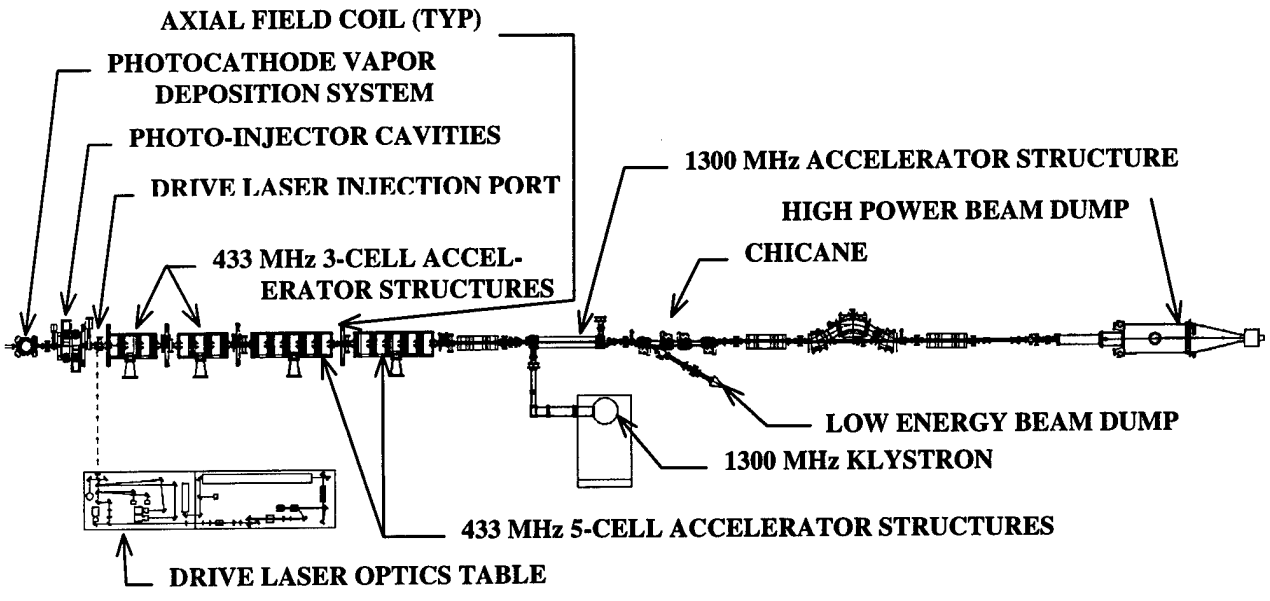



Figure 2. Beamline layout for first high power operation of HAP/MOPA linac section.

# THE PS 40 MHZ BUNCHING CAVITY

R. Garoby, D. Grier, E. Jensen, CERN, 1211 Geneva 23, Switzerland;
A. Mitra, R. L. Poirier, TRIUMF 4004 Wesbrook Mall, Vancouver, B.C., Canada V6T 2A3

*Abstract*

A 40 MHz cavity has been designed and built at CERN as part of the preparation of the PS as injector for LHC. The cavity will provide the necessary bunch spacing of 25 ns prior to injection into SPS and subsequently LHC. The mechanical design of the copper coated steel cavity was dominated by space constraints in the PS tunnel and by vacuum requirements. The salient design features described are i) tight, multipactor-free, capacitive coupling from the power amplifier, ii) fast RF feedback, iii) inductively coupled tuners, iv) an efficient, pneumatically operated gap short-circuit. The operation cycle consists of an adiabatic capture up to 100 kV gap voltage, a non-adiabatic jump to 300 kV, and subsequent bunch rotation. The multipactor voltage level at the gap lies below the operating voltage range and is easily passed through. A fast RF feedback system with a total group delay of 220 ns copes with heavy beam loading ($10^{11}$ protons/bunch) and prevents unwanted interaction with other beams in the PS. The cavity has recently been installed, the nominal gap voltage of 300 kV has been attained, and bunch lengths below 8 ns have been achieved in first tests at nominal intensity. Experimental results are reported.

## 1 INTRODUCTION

For the LHC era, the PS will have to provide a new type of beam [1] compatible with SPS injection, and in particular to cope with a fast growing microwave instability at the SPS injection front porch. The 3.8 ns length bunches, spaced at 25 ns, will have an intensity of up to 1.7 $10^{11}$ particles per bunch and a longitudinal emittance of 0.35 *e*Vs (corresponding to $\Delta p/p = 2.5\ 10^{-3}$). This bunch structure will be impressed on the beam in the PS at the end of the acceleration cycle, at 26.4 GeV/*c* momentum, by a new RF system consisting of one cavity producing a gap voltage of 300 kV at 40 MHz as described in this paper and a set of two 80 MHz cavities (under construction) with nominal gap voltage of 300 kV each. The design was strongly influenced by the severe space restrictions in the PS and the requirement not to deteriorate the performance of other beams.

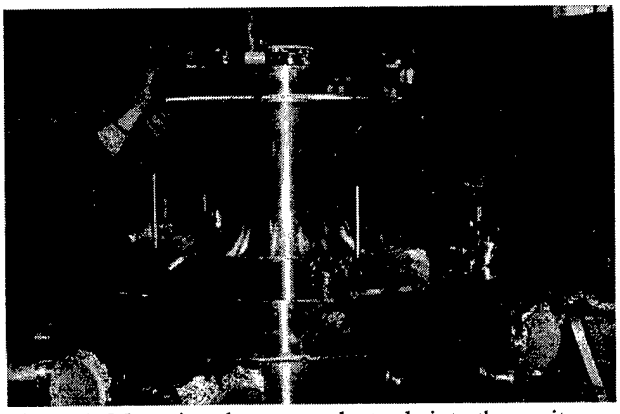


Figure 1: Mounting the center electrode into the cavity.

### *1.1 Operation Cycle*

After acceleration on harmonic $h$=16, the beam is adiabatically debunched. The bunching process at 40.055 MHz starts with a quasi-adiabatic compression from 4 to 100 kV, followed by a non-adiabatic (20 μs) rise to 300 kV. After 180 μs (the synchrotron period is •1 ms), when the bunch is tilted in phase space, the 80 MHz cavities with 600 kV will be switched on. This further increases the bucket height, bunch rotation continues and the final 3.8 ns, 0.35 *e*Vs will be attained 110 μs later.

## 2 CAVITY DESIGN

### *2.1 Choice of parameters*

In order to fit into a short section (1 m) of the PS the cavity has strong capacitive loading. As a compromise between power requirements and sensitivity to beam loading a moderate *R/Q* of 33 Ω was chosen, which, with an unloaded *Q* of 12000 (measured), corresponds to the equivalent circuit parameters of Fig. 2. Approximately 100 kW are needed to produce a gap voltage of 300 kV, with 5.4 J stored in the cavity. The instantaneous power required to fill the cavity to 300 kV during 25 μs is 300 kW.

### *2.2 Cavity behavior under beam loading*

A reactive beam current $I_B$ is equivalent to a detuning of the cavity by $\frac{\Delta\omega}{\omega} = \frac{1}{2}\frac{R}{Q}\frac{|I_B|}{V}$, which cannot be corrected during the very fast non-adiabatic gap-voltage variations. In our case, $V$ changes rapidly by a factor 3 during 20 μs while $I_B$ is virtually constant, leading to a rapidly varying and strongly reactive load on the power amplifier (PA). Fig. 2 b) and c) illustrate, in the complex plane, the conditions before ($I_{G1}$) and after ($I_{G2}$) this voltage step respectively. In order to minimize the maximum PA anode current, the cavity has to be pre-tuned such that $|I_{G1}|=|I_{G2}|$. The detuning angle is kept within acceptable limits by the moderate *R/Q*.

0-7803-4376-X/98/$10.00 © 1998 IEEE

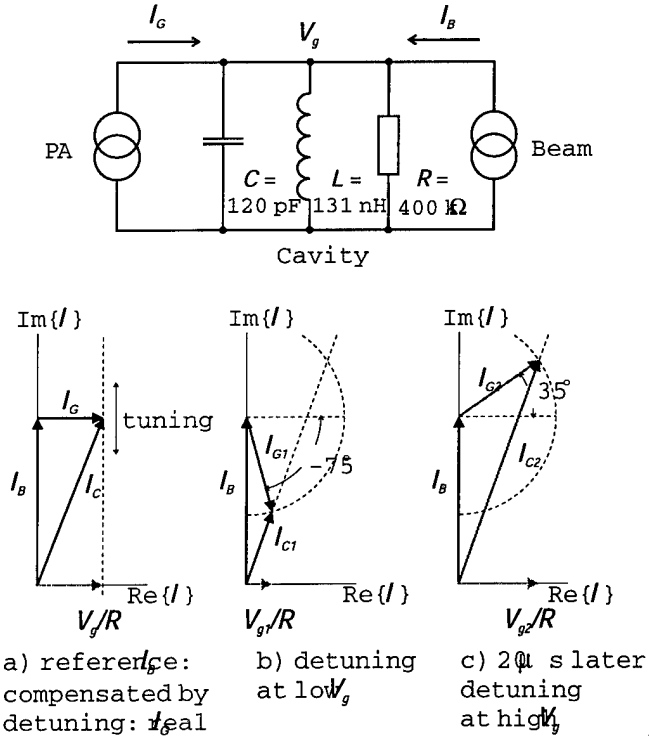



Figure 2: Varying tuning angle with non-adiabatic variation of the gap voltage.

### *2.3 Higher order mode damping*

The strong capacitive loading (low $R/Q$) results in a cavity in which the main electric and magnetic field energies are stored at different locations in the cavity. As a result, the first higher order mode (HOM) appears more than 2 octaves above the fundamental which alleviates the problem of HOM damping. The higher order mode dampers are described elsewhere [2].

### *2.4 Coarse and servo tuners*

Although the cavity is designed to operate at a fixed frequency, it is nevertheless equipped with 2 types of tuners. These tuners are described in detail in [3].

### *2.5 Mechanical and vacuum aspects*

For mechanical stability and for good magnetic and vacuum characteristics, the cavity is manufactured from forged 316LN steel with an internal 40 μm copper plating (4 skin-depths). The accelerating gap of 50 mm is located close to the upstream end, which allows enough space for an efficient, pneumatically operated gap short-circuit.

Four ion pumps of 400 l/s each and three sublimation pumps bring the vacuum to a level of below $10^{-9}$ mbar. The cavity is equipped with heating jackets for in-situ bake-out at 120 °C.

## 3 GAP SHORT-CIRCUIT

During normal operation, the cavity impedance seen by the beam is kept low by means of the fast RF feedback. The gap is otherwise closed by the pneumatically operated short-circuit (S-C).

The S-C consists of a tube which moves like a piston across the gap (stroke 78 mm). The tube has the diameter of the vacuum chamber and is constrained by a cylindrical ball guide. RF contacts assure well defined current paths and two bellows assure vacuum tightness. The gap is opened or closed in 0.6 s by two pneumatic arms, and end-switches serve as indicators and interlocks. The S-C system has proven reliable.

## 4 AMPLIFIER AND CAPACITIVE COUPLING

The choice of power amplifier design was influenced by two major constraints :

1. The need for a fast RF feedback loop with about 40 dB loop gain.
2. A reactive amplifier load with a varying impedance and phase angle due to strong beam loading .

In a feedback loop such as shown in Fig. 3, a safe working value for the group delay $T_g$ round the loop is approximately given by $T_g = 0.7 \cdot Q/(A\omega_0)$, which yields, for a loaded $Q$ of 10000, about 280 ns. With the high gain 40 kW RF driver amplifier chain occupying 160 ns, the power amplifier could have been conveniently sited beside the PS ring at about 10 m distance and coupled to the cavity with 50 Ω cables. This solution was abandoned because of the difficulty of maintaining loop stability in the presence of intrinsic strong resonances in the plane of the anode at a few MHz from $f_0$.

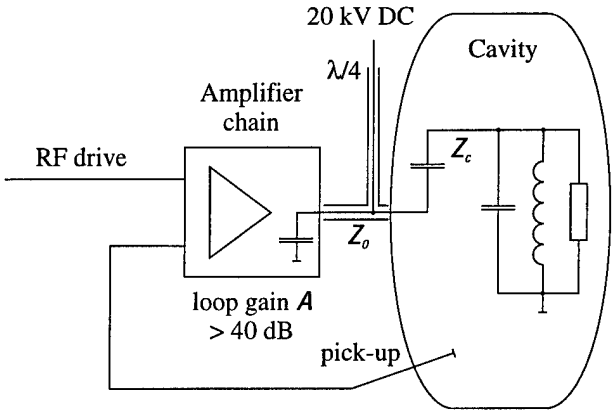



Figure 3: Simplified block diagram of the amplifier/cavity feed-back system.

With the power amplifier coupled to the cavity via a line of appropriate length (≈λ/10) and $Z_0$, the resonances close to $f_0$ are avoided. Care must be taken in the choice of the coupling impedance $Z_c$ and of $Z_0$ under these conditions, such that the transformation, at the anode, of the off-resonance impedance of the cavity in series with $Z_c$ does not cause unacceptable distortion of the anode to gap step-up ratio when operating with beam loading.

Since the form of the cavity gave a strong electric field in the vicinity of a convenient coupling port, capacitive coupling was adopted. The 18 kV peak RF envelope at the anode reduces to a low value at the

coupling window where the anode 20 kV DC (via a λ/4-line) and cooling water enter. The tube is a Thompson type TH 681 and delivers up to 400 kVA to the cavity during operation.

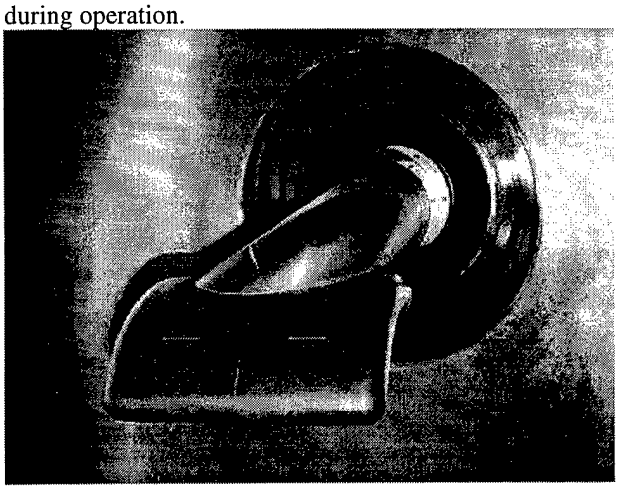


Figure 4: The capacitive power coupler mounted inside the cavity. The form is adapted to the electrode, which is not mounted.

The presence of the DC anode voltage on the coupler inside the cavity suppresses multipactor (MP) at the coupler window [4]. The value of $Z_c$, which determines the anode/gap step-up ratio, is adjustable by rotation of the coupler around the axis of the window.

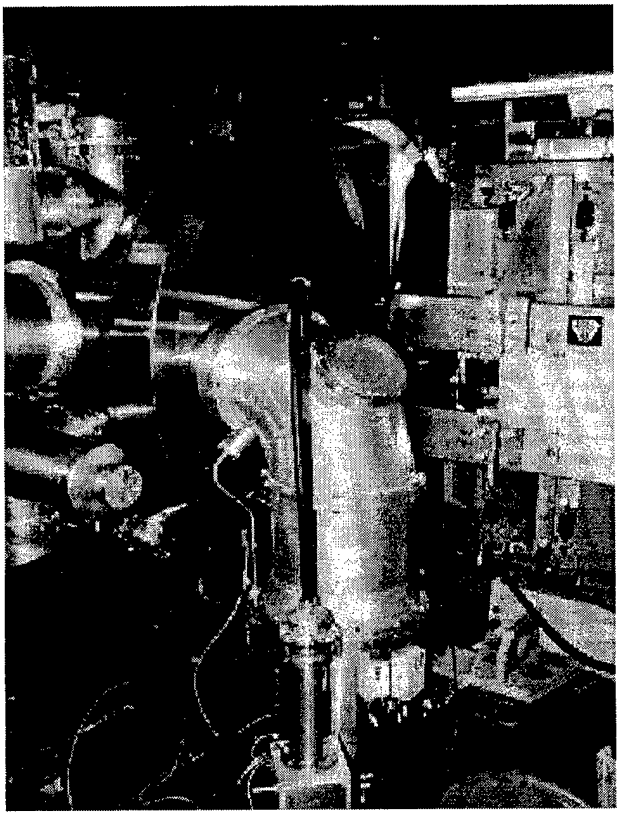


Figure 5: The cavity installed in the PS tunnel. The 400 kW final amplifier and the λ/4-line for the HV supply are visible in the foreground.

## 5 EXPERIMENTAL RESULTS

The cavity was first installed and commissioned in the PS tunnel in October 1996. The required gap voltage range, rise time and stability were readily obtained. A loop gain of 43 dB was measured yielding an effective cavity $Q$ of 72.

A MP level at about 500 V gap voltage was identified as 2-point MP in the gap, but could easily be passed through without conditioning. Above a lower limit of 1 kV no other MP levels were observed. The fringe field of the nearby main magnets (cf. Fig. 5) increases this lower limit to about 4 kV.

It was observed that for beams of low intensity, the MP alone limits the induced gap voltage. For higher intensities this voltage breaks through the MP, but is suppressed by the RF feedback.

With the appropriate RF programme, the PS beam was successfully rebunched on $h$=84 with bunch lengths of ≈10 ns. Rotation of a single bunch [from $h$=20] is shown in Fig. 6.

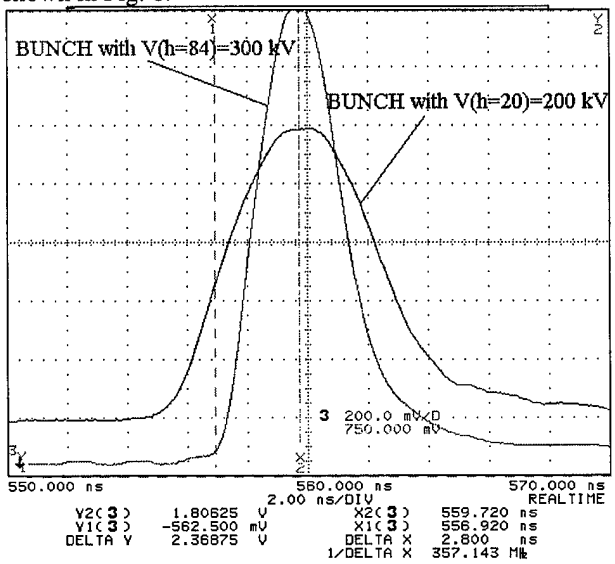



Figure 6: Single bunch rotation: bunch length ≈ 5 ns

## 6 ACKNOWLEDGEMENTS

We are indebted to many colleagues both at CERN and TRIUMF, in particular R. Hohbach, H.-P. Kindermann, F. Pedersen and W. Pirkl for many helpful discussions.

## 7 REFERENCES

[1] F. Blas and 23 co-authors: 'Conversion of the PS Complex as LHC Proton Pre-Injector'; this conference, 9W.11.

[2] E. Jensen, R. Hohbach, A. Mitra, R. L. Poirier: 'Higher Order Mode Damping of the CERN PS 40 MHz Cavity'; EPAC 96, Sitges, Spain, WEP093L.

[3] A. K. Mitra, R. L. Poirier, E. Jensen: 'Coarse and Fine Tuners for the CERN PS 40 MHz Bunching Cavity'; this conference, 8P.37.

[4] J. Tückmantel: 'Multipacting Calculations for a Power DC-biased 75 Ω Coupler'; CERN LEP2 Note 94-26.

# THE TUNING OF THE CAVITY OPTIONS FOR DIAMOND

C.L. Dawson, D.M. Dykes and P.A. McIntosh
CLRC Daresbury Laboratory, Warrington, WA4 4AD, UK.

*Abstract*

The RF group is considering both normally conducting [1] and super-conducting [2] cavity systems for DIAMOND. This paper will discuss using temperature and longitudinal deformation as methods of tuning for a normally conducting cavity. The longitudinal deformation of a super-conducting cavity is also discussed with its added technical difficulties of nanometer resolution and its cryogenic environment. Finite Element Analysis and URMEL-T [3] software has been used extensively to predict cavity geometry changes and the associated frequency shift.

## 1 INTRODUCTION

The current method of RF cavity frequency tuning on the SRS uses a non-contacting plunger. Recent experience at Daresbury has shown that normal plunger movement over a stored beam decay causes beam movement of >20μm horizontally and >10μm vertically. This movement is accommodated by the SRS, due to its relatively large source size, but must be avoided in DIAMOND.

Superconducting and warm systems are currently being considered, as a result tuning techniques for both systems are being assessed.

## 2 NORMAL CONDUCTING RF

At present, the normal conducting RF system for DIAMOND has been based on a frequency of 500MHz. The storage ring RF system will consist of six 250 kW klystrons feeding six normal conducting cavities.

### *2.1 The RF Cavity*

Following investigation and optimisation of the three most common geometry configurations (nose-cone, pill-box and bell-shaped) an optimised nose-cone cavity was selected for DIAMOND [4], shown in figure 1. The investigation of a tuning mechanism for a normal conducting system has been based on this geometry.

### *2.2 Finite Element Analysis (FEA)*

FEA of the DIAMOND Cavity was performed using the Ansys™ Version 5.1 [5] Code. Cavity modelling is required to predict the dimensional changes that occur when the cavity temperature is changed, the force required to axially deform the cavity and to determine the stresses in the cavity, due to tuning techniques.

A 2-D axisymmetric model was constructed using Plane 55 thermal elements, which were switched to Plane 42 structural elements for structural analyses. The cavity will be manufactured and installed at room temperature, therefore a reference temperature of 20°C has been assumed for thermal strain calculations. The distribution of the RF power fluxes was calculated using URMEL-T and applied to the model. Each cavity will be required to dissipate 105 kW of RF power.

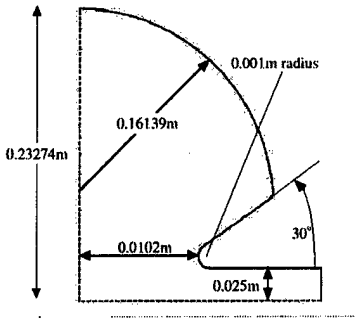



Figure 1. DIAMOND Cavity

### *2.3 Tuning using Cooling Water Temperature Variation*

Operating the cavity at different temperatures changes the fundamental frequency of the cavity and the frequency of High Order Modes (HOM's). The temperature of the cavity can be changed by altering the temperature of its coolant. This technique has been used at many laboratories, including the SRS [6] and ELETTRA, to fight multi-bunch instabilities [7].

To confirm that the relationship between cavity geometry and temperature is linear, three analyses have been carried out. Analyses were carried out for bulk temperatures of 40°C, 50°C and 70°C. A convection boundary condition was added to the model to simulate the water flow around the cavity with a film coefficient of $0.02W/mm^2/°C$. A typical temperature contour result is shown in figure 2.

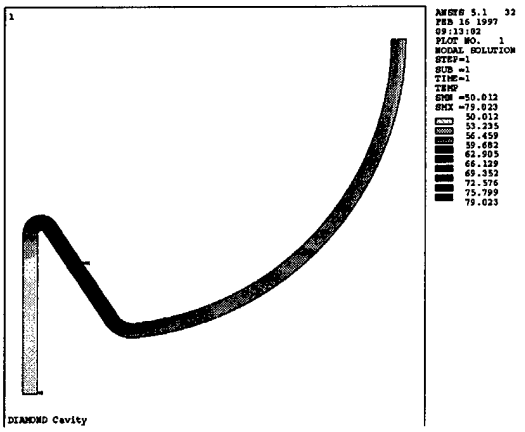



Figure 2. Temperature Contour Plot

0-7803-4376-X/98/$10.00 © 1998 IEEE

The area of maximum temperature rise is indicated on the diagram. In all three analyses the minimum cavity body temperature is the same as the temperature of the coolant and the maximum temperature is equal to the coolant temperature +29°C. This large deviation between the minimum and maximum temperatures can be reduced by careful design of the cooling channels.

Structural analyses were then carried out on each model to determine the cavity dimensional changes.

| Water Temp | Max Cavity Temp | Movement per nose-cone into the cavity |
|---|---|---|
| 40°C | 69.023°C | 41.7μm |
| 50°C | 79.023°C | 69.9μm |
| 70°C | 99.023°C | 99.5μm |

It is clear that this is a linear relationship, for each 1°C change in cavity temperature there is 1.92μm nose cone movement. Figure 3 shows typical cavity deformation.

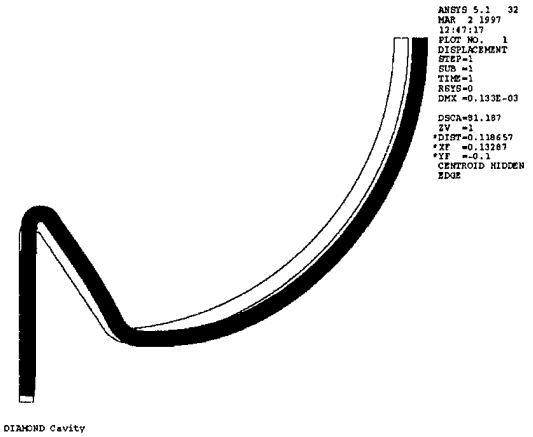



Figure 3. Deformed Cavity Shape

### *2.4 URMEL-T Results*

This information was inputted into URMEL-T. Due to the geometry of the nose-cone cavity, the most significant frequency shift is due to the movement of the nose-cones along the axis of the cavity. For 1°C rise in temperature the fundamental frequency shift of the cavity is 6.824kHz. Using similar techniques to those used at other 3rd generation sources, cavity temperature can be controlled to ±0.1°C, giving a frequency resolution in the region of 682Hz.

### *2.5 Tuning by Longitudinally Squeezing the Cavity*

If cavity temperature is used to prevent HOM instabilities, the fundamental frequency will also shift in addition to the troublesome HOM frequency. Therefore, a second tuning system is necessary to return the cavity to its fundamental frequency. The technique of squeezing the cavity on axis is being investigated. To prevent any waveguide sealing problems due to the squeezing of the cavity it is essential that the cavity is designed with all ports on the cavity centre-line. From URMEL-T calculations, a 1μm movement of the nose-cones corresponds to a frequency shift of 3.554kHz. The frequency range should be in the order of 200kHz. A closed loop controls system with a frequency resolution of 500Hz or better is required.

It is desirable to restrict the cavity movement so that it remains within the elastic region of the material to prevent any work-hardening of the cavity, ultimately leading to fatigue failure. This is achievable in the DIAMOND nose-cone cavity, as frequency shifts are relatively large for small nose-cone movements, but this produces a challenging mechanical resolution for the mechanism. A mechanical resolution of 0.14μm is required for a 500Hz frequency resolution. If the option to select a 100Hz frequency resolution is added, the mechanical resolution would need to be in the order of 28nm.

Using the 2-D model, it is anticipated that the force required to deform the cavity ±40μm on axis will be in the region of 2kN. The equivalent maximum stress in the cavity is 48.1MN/m$^2$, just below the 0.1% Proof Stress of Oxygen Free High Conductivity (OFHC) Copper, which is given in most texts to be 49-78MN/m$^2$. This will give a frequency range of 284.32kHz.

Two methods of squeezing the cavity are currently being investigated, a hydraulic system and a left/right handed leadscrew system.

Hydraulic drives can produce large forces for the size of actuator and have an excellent power to weight ratio. Actuators are available with a 100μm range and a resolution of up to 1nm. However, the unit required to generate the hydraulic pressure is large and expensive. It is also difficult to prevent the vibration from the equipment being transmitted through the hydraulic fluid to the cavity [8].

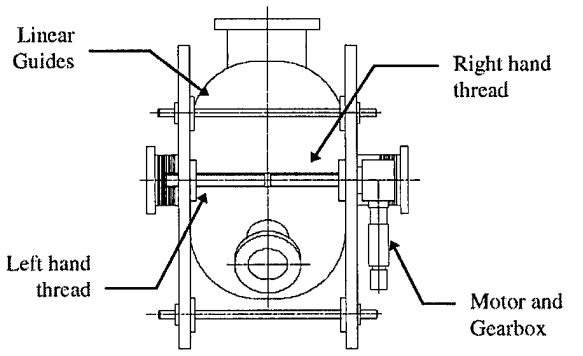



Figure 4. Leadscrew System

The left/right handed leadscrew, as shown in figure 4, is a relatively low cost solution, but there are some disadvantages. The use of a leadscrew of any description means that the system will display backlash and thermal properties are poor. Most of these problems can be overcome by careful design and choice of leadscrew. A ball screw has very low backlash and high accuracy, but due to its low friction motor brakes would need to be fitted to prevent the cavity reactive force winding the ballscrew

back. However, by deforming the cavity using frequency feedback, the accuracy of the leadscrew is less important and a conventional leadscrew could be used and the need for motor brakes eliminated. Thermal problems are not anticipated due to the environmental control of the DIAMOND tunnel. The main disadvantage with this system is the very high gear ratio required to obtain the specified resolution.

## 3 SUPERCONDUCTING RF

If superconducting technology is used, it is likely that DIAMOND will move to a 350MHz system, to take advantage of the development work of other sources in this area. Work has recently started on the super-conducting system and the development of the tuning system is much less advanced. This section will describe some preliminary thoughts on the subject.

### *3.1 Additional Problems Associated with Tuning Superconducting Cavities.*

There are more problems to be overcome when designing a tuning mechanism for a superconducting cavity. The cavity is housed in a helium cryostat and all components should be accessible for maintenance. Any mechanism used to modify the cavity geometry must make the transition from atmospheric to cryogenic temperatures. The geometry deformations required for tuning are in the nanometer region and speed of response is critical as the system must be capable of combating the frequency shifts and oscillations which can occur, due to changes in pressure in the cryostat.

### *3.2 Methods of Super-conducting Cavity Tuning*

Two methods of tuning are usually required, a coarse tuner with a range in the order of 500kHz and a fine tuner working over approximately 10kHz. There are several actuators available which are capable of nanometer resolution, three of the most common are discussed [9] here.

Piezoelectric materials experience a dimensional change on application of an electrical potential. Devices based on these materials are commercially available, with a range/resolution ratio of 10,000:1 and are capable of high response speeds. However, they are prone to hysteresis and creep, which limit the achievable accuracy. Actuators are available with a traverse of up to 100mm in step sizes of 2nm or less. However, in devices of this length, stiffness and response speed are compromised.

Electrostrictive devices are very similar to the piezoelectric actuator. However they exhibit reduced hysteresis and have a low thermal expansion coefficient making them ideal for high accuracy applications. Simpler electrical drives may make them cheaper than the equivalent piezoelectric system. The main disadvantage is they are distinctly non-linear, but this is readily overcome with modern computer controls. In many cases the range is compromised to remain in a relatively linear portion of the working range. Hysteresis increases rapidly when operated below 273K, making any benefit over piezoelectric materials negligible.

Magnetostrictive devices are again very similar to piezoelectric actuators, but the strain is caused by the presence of a uniform magnetic field. The displacement per unit field is a linear relationship. They are ideal for heavy duty actuators working in the 100μm range. However, they are subject to hysteresis and creep.

## 4 FUTURE WORK

Work is progressing steadily on both systems, but there is a significant amount of work to do before comprehensive design schemes are available. The majority of the work on the warm system has been based upon the results taken from a 2-D axisymmetric model. The results must be confirmed on a complete 3-D cavity. Preliminary calculation work is to be started on the super-conducting cavity.

## 5 ACKNOWLEDGMENTS

The authors wish to thank all those who contributed to this paper. Particularly, M.J.Collier for his contributions to the design and A.R.Goulden for his advice on the cooling of RF cavities.

## REFERENCES

[1] D.M.Dykes, 'The DIAMOND RF System', EPAC'96 Proceedings, p1943.

[2] D.M.Dykes, 'A Super-conducting RF System for DIAMOND', these Proceedings.

[3] U.Lauströer, URMEL+URMEL-T User Guide, DESY M-87-03, 1988.

[4] P.A.McIntosh, 'Comparison of RF Cavity Designs for 3rd Generation Light Sources', EPAC'96 Proceedings, p1955.

[5] Ansys Users Manual Rev.5, Swanson Analysis Systems Inc., DN-R300:50, February 1994.

[6] P.A.McIntosh et al., 'Temperature dependant High Order Modes (HOM) in the SRS Cavities', EPAC'96 Proceedings, p1961.

[7] A.Fabris et al., 'Characterisation of the Low Level System of the ELETTRA RF Plants', EPAC'96 Proceedings, p1917.

[8] S.T. Smith and D.G. Chetwynd, 'Foundation of Ultra Precision Mechanism Design', Gordon and Breach Science Publishers, 1992.

[9] 'Proceedings of the 4th Workshop on RF Superconductivity. Vol.1.', 14-18 August 1989, KEK, Japan.

# EFFECTIVE COMPACT ACCELERATING STRUCTURES FOR HEAVY IONS

Valentin V. Paramonov
Institute for Nuclear Research of the RAS, 117312, Moscow, Russia

*Abstract*

The well known interdigital IH structure is now widely used for acceleration of heavy ions in low $\beta$ range. Using the main idea of the IH cavities - transformation of the transverse rf voltage into longitudinal accelerating one, but differing in realization of this principle, several rf structures are considered.

In comparison with the IH cavities, the proposed versions originally have practically uniform field distribution along beam axis and no problems with end walls. With the small outer tank diameter, the effective shunt impedance is high enough. The design of the structures and preliminary results of optimization are presented.

## 1 INTRODUCTION

For acceleration of charged particles in low velocity range ($\beta \leq 0.1$) it is usually to apply InterDigital structures (ID). Let remember the main idea of the ID. There should be two conductors (electrodes) parallel to the beam axis. If one will supply rf voltage to these conductors, then rf electric field will be generated between electrodes, perpendicularly to the beam axis and no acceleration is possible. But, if drift tubes trough short stems will be connected to these conductors in turn, then rf voltage will be between drift tubes, generating longitudinal accelerating field. So, drift tubes convert 'perpendicular' rf field into 'longitudinal' one.

Let remember the idea of another classical device - Radio Frequency Quadrupol (RFQ). There should be four conductors (electrodes) parallel to the beam axis. To provide quadrupol electric field distribution, one needs to supply rf voltage with opposite signs to neighboring conductors.

In the complete device there should be not only conductors, but also the resonant system to provide rf voltage between conductors. RFQ and ID structures differ in the utilization of the rf voltage, but may be very similar in resonant system to provide it. At least, if there is the solution for RFQ cavity, one can easy adapt it to ID structure.

Below options of cavities, known before for RFQ, are considered for ID applications.

## 2 DIFFERENT RESONANT SYSTEMS

This section comprises brief review of existing resonant systems, suitable for ID and RFQ structures, together with proposals given. The resonant systems both with distributed electrodynamic parameters and with lumped ones may be used both for RFQ and ID realizations.

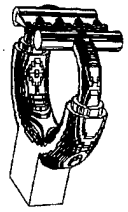


Figure 1: The Split Ring Interdigital Structure. The outer cylindrical wall is not shown.

## 3 H-TYPE CAVITIES

H-type cavities are now well known both for RFQ and for ID (IH structure). The example of application practically the same (in design) cavity both for IH and for RFQ is given in [1].

H-cavity is the system with distributed parameters. Instead of the electric field is strongly concentrated between conductors, the magnetic field is distributed more or less uniform in the remaining cavity volume. The original mode has longitudinal magnetic field and can not exist without variation along the cavity length (if one use simple end plates). To equalize field distribution, one should provide undercuts in vanes and girders near end plates. With modern software the problem of design for end regions simplifies [2], but some times configuration of girders remains complicated.

Another problems is also associated with end plates. For short cavities, when the cavity length is comparable with the cavity diameter, additional rf losses in end plates, where magnetic flux turns, lead to the reduction in shunt impedance.

Nevertheless, IH structure is good investigated, developed, there are solutions for problems and question is only price of solutions.

## 4 SPLIT RING RESONANT SYSTEM

Let consider resonant systems, which are more close to quaterwave oscillators. Both in RFQ and in ID conductors provide the capacitive part and one needs only add inductive part to complete the resonant circuit. Different solutions for inductive part are possible.

0-7803-4376-X/98/$10.00 © 1998 IEEE

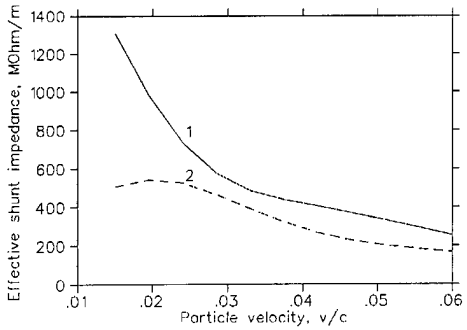



Figure 2: $Z_e^r$ of the SRIS. 1 - for $\beta \leq 0.03$, $2a = 1.0cm, \beta \leq 0.05$, $2a = 1.4cm, \beta \leq 0.06$, $2a = 1.6cm$; 2 - for $2a = 1.4cm$, $2r_t = 3.0cm$, $2r_c = 3.0cm$

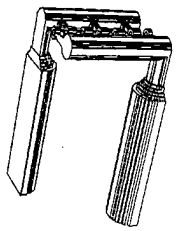


Figure 3: The Post Interdigital Structure. The outer cylindrical wall is not shown.

The Split Ring RFQ cavity is now under development in TRIUMF [3]. We propose the Split Ring Interdigital Structure (SRIS), Fig. 1.

Let define regular effective shunt impedance of the structure $Z_e^r$ as the effective shunt impedance of uniform periodical structure, consisting from similar modules. The length of the module $L_m$ is the subject for choice and depends on tolerable tilt in difference of rf potential between electrodes. The potential difference between conductors is larger and the end of the module then in the middle, where conductors are connected to the ring. This tilt depends on $L_m$ and capacitive loading due to drift tubes. The capacitive loading due to drift tubes depends on number of drift tubes per unit length and dimensions of drift tubes. The results of numerical simulations with MAFIA shows, that for $L_m \approx 0.06\lambda$, where $\lambda$ is the operating wavelength, this tilt is less than 2% for $0.015 \leq \beta \leq 0.06$ and any reasonable tube dimensions. With increasing $L_m$ the tilt rise very fast, especially for higher $\beta$ (to $5\% \div 15\%$ for $L_m \approx 0.12\lambda$), providing upper limit for $L_m$.

The SRIS has high effective shunt impedance. The dependencies of $Z_e^r$ vs $\beta$ are shown in Fig. 2. All results of numerical simulation are given ( if it is not defined specially) for operating frequency $f_0 = 105MHz, L_m = 0.06\lambda$, drift tube diameter $2r_t = 2a + 1.0cm$, where $2a$ is aperture diameter and conductors diameter $2r_c = 3.8cm$.

The SRIS cavity diameter $2R_c$ slightly rise from $2R_c = 52cm$, $\beta = 0.015$ to $2R_c = 62cm$, $\beta = 0.06$.

## 5 POST RESONANT SYSTEM

The Post RFQ cavity was realized [4] in Variable Energy RFQ option. With movable plate one can change effective length of the posts, changing the resonant frequency and, as the result, changing designed $\beta$ for the cavity.

The Post Interdigital Structure (PIS), Fig. 3, also permits such option with the same question in rf contact between the plate and the posts. At the Fig. 3 one half of the structure period (from the middle of one post to the middle of next) is shown.

In comparison with SRIS, PIS has smaller cavity diameter ($2R_c = 40cm, \beta = 0.02$). Effective shunt impedance remains high ($Z_e^r = 687M\Omega/m$, $\beta = 0.02$, $2r_a = 1.0cm$).

## 6 SPIRAL RESONANT SYSTEM

The spiral cavities for RFQ applications are considered in [5]. Following to our approach, the Spiral Interdigital Structure (SIS) may be developed. One can imagine transformation of all posts in PIS (Fig. 3) into spirals, resulting in spiral-type resonant system. This structure has smallest cavity diameter in comparison with SRIS and PIS. For operating frequency $f_0 = 105MHz$ the cavity is diameter very small, providing difficulties with placement of conductors and drift tubes. For this structure frequency range $20 \div 60MHz$ is more comfortable. In comparison with resonant systems "one turn of the spiral to one drift tube" [6], SIS has essentially higher shunt impedance, because one spiral serves for several drift tubes and total rf losses are associated mainly with rf losses in spirals.

## 7 DISCUSSION

All stuctures considered above have very high $Z_e^r$. To get it, one should minimize capacitive load. In all calculations simple cylindrical drift tubes were considered with gap ration $\alpha = 0.5$. In reality, the shape of the drift tube should be chosen as the compromise to minimize maximum electric field on the surface $E_s$, to minimize capacitance (taking into account the stem for support) and to have large transit time factor $T$. Diameter of conductors should be as small as possible but providing possibility for cooling chanel inside. Distribution of rf losses at elements differs no so strong for different structures. For $L_m = 0.06\lambda$ rf losses at drift tubes (including short stems) are $\approx (5\% \div 8\%)$, at conductors - $\approx (20\% \div 28\%)$, at the cylindrical wall - $\approx (14\% \div 20\%)$. Main part of rf losses takes place at the ring (SRIS), post (PIS) or spiral (SIS).

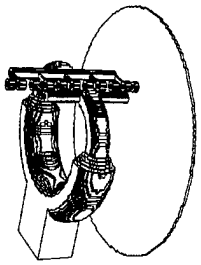


Figure 4: The SRIS short cavity. The outer cylindrical wall and front end one are not shown.

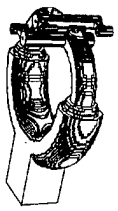


Figure 5: The SRIS module for long cavities.

It is not necessary to have complicated shape (with two radii) for ring or post. These elements with smooth shape provide practically the same value of $Z_e^r$.

All structures considered have their own particularities. The Split Ring Structure has very high shunt impedance. Because there no rf current along the supporting leg (Fig. 1), there are no rigid requirements for rf contact between the leg and outer cavity wall. It simplifies procedure of the structure adjustment.
By using Post Structure, variable energy structure may be developed.
The Spiral Structure may be used for low frequency range. For all structures electric field is concentrated between drift tubes and magnetic field is concentrated near inductive elements. This case end walls of the cavity do not disturb parameters of the structure.
Both short and long cavities may be with using SRIS. The example of short nine gap (8 total gaps and 2 reduced gaps near end walls) cavity with one ring is shown in Fig. 4, $L_m = 0.1\lambda, \beta = 0.02, 2a = 1.0cm, 2r_c = 2.0cm, Z_e = 756M\Omega/m$. This case reduction in $Z_e^r$ is associated mainly not with end walls, but with nonsymmetry. One conductor carries 5 drift tubes and another only 4. It provides nonsymmetry in the distribution of magnetic field and additional rf currents along the leg. The symmetrical ten gaps cavity has higher shunt impedance.

Long cavity may have several modula (Fig. 5). Each module should be designed for his own average $\beta$, because with increasing of $\beta$ capacitive load decreases and outer radius of the ring increases. Differing from RFQ cavity, it looks not reasonable to connect modula directly trough conductors. The coupling with longitudinal electric field is sufficient. Each module should be equipped with own tuner. With appropriate tuning of own frequency for each module (keeping the frequency of the cavity at the designed value), one can adjust increased rf voltage at modula with higher average $\beta$. Because average (along structure period) electric field is inverse proportional to the period length (to $\beta$), increased voltage at modula with higher $\beta$ leads to constant average electric field along the cavity.

## 8 CONCLUSION

In this paper, developing idea of interdigital line, several accelerating structures are considered. All this structures have high effective shunt impedance and small transverse dimensions. For every structure there is RFQ analog. It allows to provide 'uniform' accelerating system by using RFQ initially and ID as extension with the same type of the resonant system. Such approach allows to use similar scientific, technical and technological solutions both for RFQ and for ID part, leading to reduction in total costs for development and production of the system.

## 9 ACKNOWLEDGMENTS

The author thanks V.G. Andreev and Yu.V. Bylinsky for fruitful discussions, and DESY for providing good conditions for this work.

## 10 REFERENCES

[1] U. Ratzinger, The New Prestripper Linac for High Current Heavy Ion Beam, Proc. of the 1996 Linac Conf., v.2, p. 288, 1996

[2] B. Krietenstein et al. Numerical Simulation of IH Accelerators with MAFIA and rf Model Measurements, Proc. of the 1996 Linac Conf., v.1, p. 243, 1996

[3] R.L. Poirier, et al. The RFQ Prototype for the Radioactive Ion Beam Facility. Proc. of the 1996 Linac Conf., v.1, p. 405, 1996

[4] A. Schempp, RFQ Ion Accelerator with Variable Energy, NIM B40/41, p. 937, 1989

[5] U. Besser, A. Schempp et al. Experiments with Heavy-Ion Beams and RF-Tests with the 27 MHZ High Current Spyral-RFQ Prototype. Proc. of the 1996 Linac Conf., v.1, p. 56, 1996

[6] C.M. Kleffner et al. Progress of the Heidelberg High Current Injector. Proc. of the 1995 PAC, v.2, p. 1131, 1995

# THE CUT DISK ACCELERATING STRUCTURE FOR HIGH ENERGY LINACS

Valentin V. Paramonov
Institute for Nuclear Research of the RAS, 117312, Moscow, Russia

*Abstract*

New accelerating structure for particles velocities $0.4 \leq \beta_p \leq 1.0$ is proposed. The Cut Disk Structure (CDS) is the compensated one, has coupling coefficient to 30% without distortions in the dispersion curve and 3D calculated effective shunt impedance not less than for another Coupled Cells Structures (CCS). There are no parasitic modes in the operating passband. The outer diameter is small enough ($\approx 0.6\lambda$). Accelerating cells in CDS are open for effective cooling. The design of the structure provides simple manufacturing and tuning procedures.
The philosophy of the structure, design, criteria of optimization and results are presented.

## 1 INTRODUCTION

Several compensated accelerating structures are now widely used for acceleration of charged particles for relative velocities $\beta_p > 0.4$. 'Compensated' are named the structures in which at operating frequency coincide frequencies of two modes with differing parity of field distribution (accelerating and coupling modes). Examples of compensated structures are well known Side-Coupled Structure (SCS) [1], On-axis Coupled Structure (OCS) [2], Annular-Coupled Structure (ACS) [3], Disk And Washer structure (DAW) [3], and so on. These structures combine high efficiency with high stability of the accelerating field distribution to deviations in cells parameters and beam loading. The value of the coupling coefficient $k_c$ defines this stability.
Comparison and present state of art in the structures development are given in [4]. The structures, mentioned above, may be distinguished into two groups - structures with coupling slots - $k_c \approx 3\% \div 5\%$ (SCS, ACS, OCS) and $k_c \approx 40\%$ (DAW). In this paper new structure (CDS) [5], which combines the features of CCS with high coupling of DAW, is described.

## 2 THEORETICAL BASIS

From electrodinamic consideration of compensated structures follows [6], that group velocity $\beta_g$ (or coupling coefficient $k_c = \frac{4\beta_g}{\pi\beta_p}$) are:

$$\frac{\beta_g}{\beta_p} = \mid \frac{\pi \int_V (\epsilon_0 \vec{E}_a \vec{E}_c - \mu_0 \vec{H}_a \vec{H}_c) dv}{\sqrt{2 W_a W_c}} \mid,$$

$$W_{a,c} = \frac{\mu_0}{2} \int_V \mid \vec{H}_{a,c} \mid^2 dv, \qquad (1)$$

where $V$ - the volume of one half of the structure period, $\vec{E}_a, \vec{H}_a, \vec{E}_c, \vec{H}_c$ - distributions of electric and magnetic field of the accelerating mode and coupling one. Taking into account $TM_{011}$-like field distributions and different parities, one can show $\epsilon_0 \mid \int_V (\vec{E}_a \vec{E}_c) dv \mid \ll \mu_0 \mid \int_V (\vec{H}_a \vec{H}_c) dv \mid$.
For structures with coupling slots, considering the slot as the part of transmission line, one can derive [7] estimation for $k_c$:

$$k_c \sim \frac{l_s^3 \Delta H_{as} H_{cs}}{t \sqrt{W_a W_c}}, \qquad (2)$$

where $\Delta$ and $l_s$ - are the width and the length of coupling slot, $t$ - is the thickens of the web between cells, $H_{as}, H_{cs}$ - magnetic fields of accelerating mode and coupling one at the slot.
For CCS there are no big reserve in $k_c$ increasing due to $l_s$ increasing, because all time it assists with reduction in effective shunt impedance $Z_e$. The coupling slots provide perturbation for rf current distribution in accelerating cell. The maximum value of rf current density $j_{max}$ takes place at the ends of slots, the minimum one $j_{min}$ - in the middle. Strong dependence of $k_c$ and rf current redistribution from the $l_s$ increasing takes place due to resonant-like character of coupling with slots.

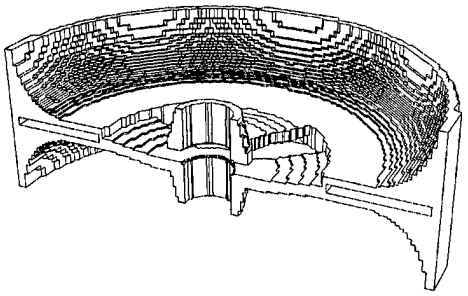


Figure 1: One half of the Cut Disk Accelerating Structure (CDS) period, two windows option.

Our investigations show [5] that SCS and ACS are limited in $k_c$ increasing due to the design particularities. Better result ($k_c \approx 12\% \div 15\%$, [8]) is for OCS with reduced thickens of the web between cells and optimization of coupling cells.
Anyhow, if the structure has clearly distinguished cells, overlapping of $\vec{H}_a, \vec{H}_c$ will be in restricted region near the slots and $k_c$ will be not big (1). For big coupling overlapping of $\vec{H}_a, \vec{H}_c$ should be in total volume of the structure (like DAW).

0-7803-4376-X/98/$10.00 © 1998 IEEE

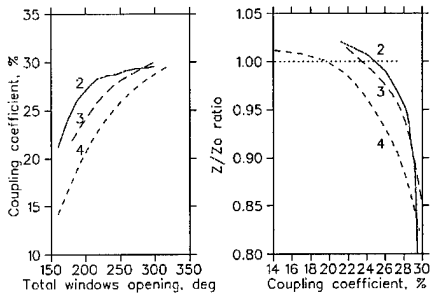



Figure 2: The coupling coefficient vrs total opening and reduction in $Z_e$ for 2, 3 and 4 - windows options.

## 3 THE STRUCTURE FORMATION

Let suppose one has the set of half of drift tubes, placed in couples along the axis of the cylinder. The distance between couples is $l_a$ (accelerating gap in future), between half tubes in the couple - $l_c$ (coupling gap), $l_c \ll l_a$. There are also the disks in the middle of coupling gap perpendicularly to the axis and in radial direction from the radius of tubes $r_t$ to the radius of the cylinder $R_c$. Suppose, we excite $TM_{011}$-like coupling mode, which must satisfy to 'magnetic' boundary conditions in the middles of accelerating gaps. Electric field of such mode will be strongly concentrated in the coupling gap, because $l_c \ll l_a$, but magnetic one will be distributed outside tubes. The disks do not perturb these fields distributions. Then, we will Cut the Disks along radius from $r_t$ to $r_c, r_t < r_c < R_c$ in $m$ petals, ($m = 4, 6, 8...$), and connect in turn petals to half of drift tubes. First petal connects to left half-tube, second to right one, third to left and so on. If at an angular position given at left side from coupling gap the petal is connected to left half-tube, at right side there is no connection, there is the window from coupling gap to right accelerating cell. Such alternating connection of petals to left and to right is essential to have big coupling. Finally, we decrease the thickness of petals (approximately to one half from the disk width) from the side of coupling gap.

After this transformation of the disks we do not disturb strongly fields distributions of coupling mode, but the half of drift tubes are attached to the cylindrical wall and cells of the CDS structure (Fig. 1) are formed as follows:

- accelerating cells of usual $\Omega$-shape with distributed electric and magnetic fields;
- coupling cells, with electric field concentrated in the short space between half tubes, but **main part of magnetic field is distributed in the volume of accelerating cell.**

For CDS radius of the windows is the radius of coupling cell. Extension of coupling cell beyond windows is not nessary and may be only from technological or decorative purposes. The description of the CDS formation has only one purpose - to show this structure realizes another idea than OCS with coupling slots. The main principle and the difference of the CDS from structures with slots is **non-resonant character of coupling.** Instead of CDS is very

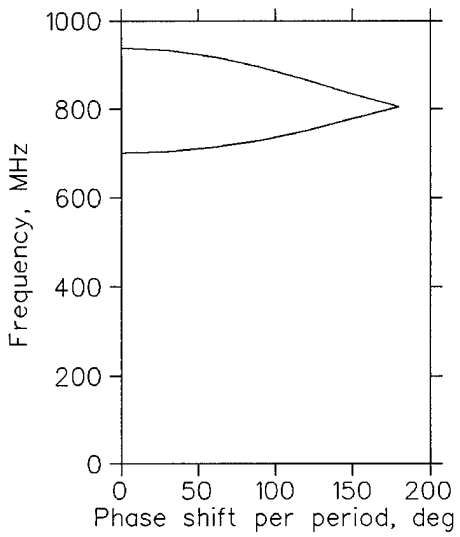



Figure 3: The operating part of the Brillouin diagram for CDS. $\beta_p = 0.6, f_0 = 805MHz$.

similar to OCS outwardly (and formally speaking, CDS is the structure with On-axis Coupling, but with another realization of coupling), some time conclusions, based on experience with coupling slots, are not correct for CDS.

## 4 THE CDS PROPERTIES

Below are results of 3D numerical simulations (using MAFIA) of CDS parameters.

Main particularity of the CDS is big $k_c$, because overlapping of magnetic fields $\vec{H}_a$ and $\vec{H}_c$ takes place in main part of accelerating cell and in the region (near drift tube), where $\mid \vec{H}_a \mid$ and $\mid \vec{H}_c \mid$ have maximal values. The plots of dependencies $k_c(\Phi_w)$ are shown in Fig. 2(a) for two - (Fig. 1) three - and four windows options. The total opening $\Phi_w$ means the sum of opening of all windows at one side of the disk. One can see from Fig. 2(a), that dependence $k_c(\Phi_w)$ do not satisfies to relation (2) and saturation take place. There are no, also, strong dependence of $k_c$ from the petal thickness.

To tune coupling mode to operating frequency, one should match the window opening $\phi$ and cut radius $r_c$. Critical point in the choice of dimensions for coupling gap is the value of maximum electric field of coupling mode at the surface of the structure $E_{csm}$, which is related to $W_c$. One should control $E_{csm}$ (by the choice of $l_c$ and $r_t$) to avoid:

- sparking in coupling cells during transient;
- sparking in coupling cells in steady state regime;
- multipactoring in coupling cells in steady state regime;

Relations between requirements depend on regime of the accelerator and for different regimes one of these requirements widd come in front.

The shunt impedance $Z_e$ decreases with increasing of $\Phi_w$ (Fig. 2b). For small $\phi$ values $Z_e > Z_0$, where $Z_0$ is

effective shunt impedance of solid accelerating cell without any windows, because we remove a part of metal surface in the region of strong magnetic field $\vec{H}_a$. With $\Phi_w$) increasing total angle opening of petals $\Phi_p$ appropriately decreases and the density of rf currents along petals rises, leading to $Z_e$ reduction. For the accelerating mode magnetic field turns around petal. From this reason we consider preferable two windows option with $\Phi_w \approx (200^0 \div 220^0)$. It provides very good coupling ($k_c \approx 26\%$) and $Z_e \approx Z_0$. This particularity of the CDS provides higher $Z_e$ in comparison with another structures. Really, the accelerating cell has the same shape as for another structures. It is known, that $Z_e$ of the CCS decreases with increasing of the web thickness between accelerating cells, but this decreasing is smooth and with reasonably thick web we have reduction in $Z_e$ not more than $5\% \div 10\%$. This reduction is the price for thick web, but **there is no reduction in $Z_e$ due to coupling slots** and finally 3D calculated $Z_e$ for CDS with $k_c \approx 25\%$ is at $5\% \div 15\%$ higher than for SCS with $k_c \approx 5\%$. The thick web allows to place cooling chanel (Fig.1, Fig. 4) not so far from drift tubes, providing (together with thick petals) good conditions for the structure cooling.

Mutual orientation of windows at opposite sides of accelerating cell is important not for $k_c$ value, but for perturbation of axial symmetry of accelerating field. Like slots, windows provide quadruple ($m = 4$), sextuple ($m = 6$) and so on, components in accelerating field. Because all CCS have $\pi$-type operating mode, perturbations from windows (slots) at opposite sides add if windows are rotated at the angle $2\pi/m$ and subtract if windows are placed face to face.

As one can see (Fig. 1, Fig. 4), the design of the structure is very simple. Instead of high precision of mashinering must be done for windows and petals (to reduce frequency spread for coupling mode), it is no problem for modern Numerically Controlled equipment. To reduce $E_{csm}$ all sharp edges at petals, windows and coupling gap should be rounded.

The structure is open from cylindrical wall for vacuum and cooling equipment. The outer diameter (for accelerating cell) $2R_c \approx 0.6\lambda$ and the structure has the smallest transverse dimensions in comparison with another CCS. This case we can consider 'low frequency' applications for CDS, because even for $f_0 \approx 400MHz$ dimensions remain technologically reasonable ($2R_c \approx 45cm$).

For $\Phi_w \approx 210^0 \Phi_w > \Phi_p$ and one can look through the structure (it provides some improvement in the vacuum conductivity of the CDS). Nevertheless, CDS has 'ideal' spectral properties. The passbands of the Brillouin diagram for operating mode (calculated in 3D approximation by using MAFIA with Floquet boundary conditions) are shown in Fig. 3. Fitting with the standart five parameters lumped circuit model shows neighbor coupling coefficients $k_1$ and $k_2$ being practically zero. Nearest high order modes $TM_{11n}$-type are placed at frequencies $\approx 1.5 f_0$.

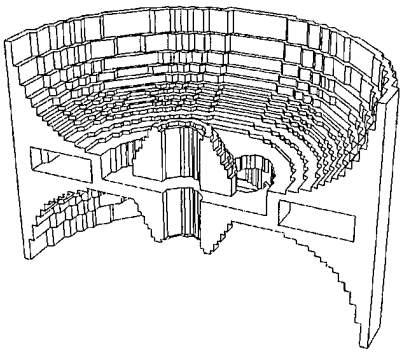


Figure 4: The CDS for electron linac with heavy heat loading. $\beta_p = 1.0, f_0 = 2450MHz, k_c = 25\%, Z_e = 89M\Omega/m$.

## 5 CONCLUSION

New accelerating structure for high energy linacs is described. Differing from known CCS, CDS realize idea of nonrezonant coupling. As the result, CDS combines:
high coupling ($k_c \approx 25\%$);
high effective shunt impedance;
simple, mechanically strong design;
small transverse dimensions.
With the combinations of these parameters, CDS looks as very attractive candidate for proton and electron linacs both for fundamental investigations and for industrial applications.
Theoretical study of the structure continues and experimental investigations are now under way.

## 6 ACKNOWLEDGMENTS

The author thanks V.G. Andreev, S.K. Esin, L.V. Kravchuk for fruitful discussions, and DESY for providing good conditions for this work.

## 7 REFERENCES

[1] E.A.Knapp, B.C.Knapp, J.M.Potter, Rev. Sci. Instr., v. 39, p. 979, 1968

[2] T.Nishikawa, S.Giordano, D.Carter, Rev. Sci. Instr., v. 37, p. 652, 1966

[3] V.G. Andreev et al. Proc. of the 1972 Proton Linac Conf. p. 114, 1972

[4] Y. Yamazaki. Proc. of the 1972 Linac Conf. p. 580, 1992

[5] V.V.Paramonov. Proc. of 15-th Part. Accel. Conf., Protvino, v.3, p. 76, 1997, (in Russian)

[6] I.V. Gonin, V.V. Paramonov, Proc. of 10-th Part. Accel. Conf., Dubna, v.l, p. 182, 1985, (in Russian)

[7] N.P. Sobenin, B.V. Zverev, Characteristics of accel. cavities, Energoatom, Moscow, 1993.

[8] L.V. Kravchuk, V.V. Paramonov, Proc. of the 1996 Linac Conf. v. 2, p. 490, 1996

# THE DESIGN OF HIGH RELIABLE RF SYSTEM FOR HIGH POWER LINACS *

A.M.Kozodaev, A.A.Kolomiets, N.V.Lazarev, D.A.Liakin,
V.K.Plotnikov, A.M. Raskopin, V.S.Skachkov
Institute for Theoretical and Experimental Physics (ITEP), 117259, Moscow, Russia

*Abstract*

Possibility of substantial reliability growth of high intensity linear ion accelerators, for solving of a number of nuclear power engineering problems is considered. A way of uninterrupted maintenance accelerating RF field in a Main Part of such Accelerators - MPA, where particles receive the main part of energy is suggested. If each section of MPA contains 1-3 accelerating gaps and is excited from separate RF channel, the failure of one or even several channels will not destroy the resonant acceleration. Besides of that it is easy to compensate the acceleration shortage (on time of channel repair) by small automatic increase of accelerating field strength in the rest operating sections. The great quantity of sections from a disadvantage is transformed into advantage because failure-free MPA operation can be maintained. In the report quantitative estimations for the method suggested and its comparison with variants of RF channel reserve are presented.

## 1. INTRODUCTION

A high power ion linear accelerator for a nuclear power engineering at a beam current in a range from 10 up to 100 mA and more should have an increased reliability, that is mainly determined by its MPA RF system reliability [1], where particles acquire about 90 % of whole energy. In the offered projects of high-power accelerators the MPA consist of several thousands separate single-gap resonant cells, which are assembled in multigap resonator - section on RF field and channels of RF supply [2-5].

The rise of a reliability is promoted by use of high-performance components, reduced regime of operation, regularity of preventive maintenance, forecasting. However the key approach to solution of the problem is a reserve. We shall estimate its efficiency on an example of the MPA linac, offered by ITEP [5].

Several parameters of the MPA and of its RF system [5] are presented below.

| | |
|---|---|
| Particle energy at the MPA entrance and exit | 100 MeV - 1 GeV |
| Beam current | 100 mA |
| Cell number (n) | 2300 |
| Energy gain on one cell ($\Delta W_{1C}$) | 390 keV |
| Cell efficiency | 0.72 |
| RF feeders efficiency | 0.9 |
| Channel RF power reserve for control | 15 % |
| RF power for one cell | 70 kW |
| Total RF power of all output stages | 160 MW |

* Work supported by the ISTC

## 2. RF SYSTEM WITHOUT RESERVE CHANNELS

At a steady state of long operation in absence of a reserve (Fig.1.1) relative idle time of the whole system-$T_D$ and the average time of its operation to a refusal - $T_C$ is:

$$T_D = t_R/(T_C + t_R); \qquad T_C = t_F/N;$$

where:

$t_R$ - average restoring time of a single RF channel serviceability;

$t_F$ - average operating time of single channel to a refusal;

N - the number of working RF channels (each channel contains the whole equipment, ensuring exciting of RF power, including the rectifier as well as control, interlock and signalling systems) [6].

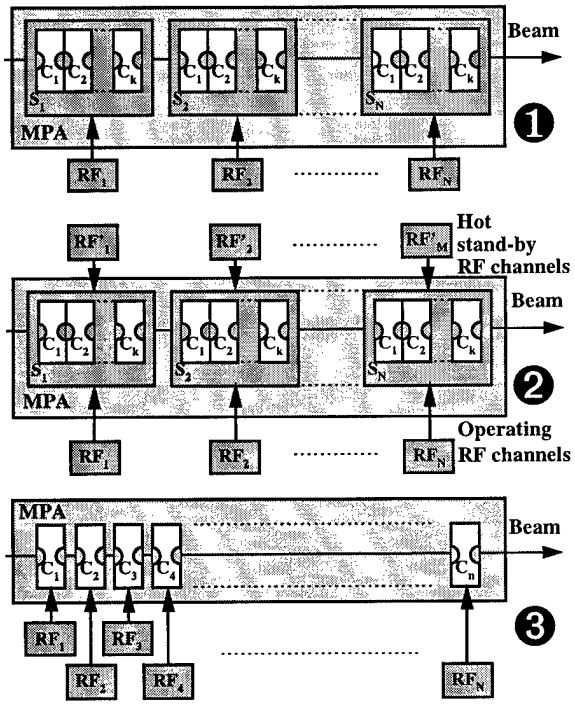



Figure 1. The scheme of MPA RF power supply: 1 - without a reserve, 2 - at hot reservation, 3 - at individual excitation of cells. C - cell, S - section.

0-7803-4376-X/98/$10.00 © 1998 IEEE

Let us $P_{1max}$ = 1 MW and $t_F$ = 1000 hours being the maximum technically available RF power of the single channel and time of its operation to a refusal, respec-tively. By such channel it is possible to excite section, containing k = 14 cells. In the other limiting case, when each cell is energized individually (k = 1), channels on power of 70 kW are required, for which we specify $t_F$ = 2000 hours. We evaluate restoring time $t_R$ by the value of 2 hours for channels of any power. Then depending on cell number k per each section the parameters N, $P_1$ and $T_D$ will have values, shown on Fig.2. It is naturally that the use of RF channels with limiting power ($P_1$ = 1 MW, k = 14), when the idle times are minimum: $T_D$ = 25 %, $T_C \approx$ 6 hours, is preferable.

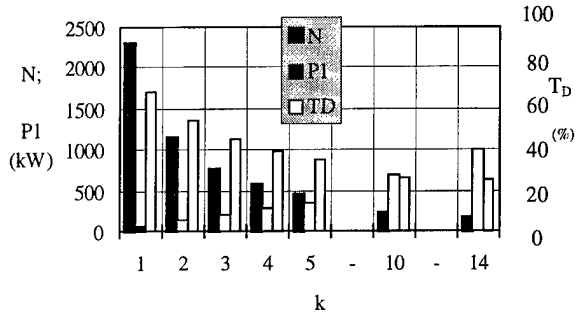



Figure 2. The value N, $P_1$ and $T_D$ dependence on k, when no reserve channels.

However the result is not satisfactory and the necessity of redundancy is well known. Rather small number of reserve channels (with respect to their total number) improves significantly the situation, but turns out the severe problem of RF power fast switching.

## 3. "HOT" RF CHANNEL RESERVATION

Tending to full elimination of RF system refusals, we consider the "hot" reservation variant (Fig.1.2), when two channels is simultaneously connected to one section and each of channels having hot filaments is capable to produce full power (redundancy 100 %). In case of working channel failure the ready reserve channel takes immediately a load per self. Leaving in the side all technical complexities of similar switching of power we shall consider such approach being allowable and acceptable. Setting the switching time onto a reserve channel is equal to zero, the relative value of idle times for the whole system will be determined by probable deficit of a reserve [6] and is estimated as follows:

$$T_D \approx N(N/M+1)(t_R/t_F)^2 = 2N(t_R/t_F)^2;$$

where M - reserve channel number
(in considered case M = N).

The softer mode is possible at simultaneous operation on each section both working and reserve channels when each of them returns only half power and is ready to return full power at a refusal of the adjacent channel.

The designed values of $T_D$ in these variants are close and are represented on Fig.3. The "Hot" 100 % reservation of RF channels reduces extremely relative value of idle times of the whole system to $T_D < 0.5$ %, but does not eliminate idle time completely, requires double store installed RF power, double number of channels, operation expenses and power, consumed by filament supply chains.

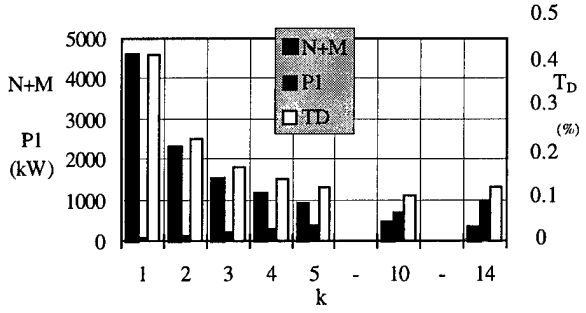



Figure 3. (N+M), $P_1$, $T_D$ dependence on k at "hot" reservation of channels.

## 4. USE OF REDUNDANT POSSIBILITIES OF AN ACCELERATING CHANNEL

Qualitatively new approach to the problem of a MPA reliability is opened, if we shall proceed from the support of RF channels serviceability to organization of accelerating process itself. In the case the reliability is determined by redundant possibilities of the whole accelerating channel.

Such approach will be realized, if separate RF channel feeds each cell (Fig.1.3) or section, consisting of a few cells, considering the chain like a unified circuit. When a RF channel failure has occurred all units of the given circuit, cell included, become disable but appropriate automatic increase of accelerating RF field strength or its phase adjustment in several circuits followed by the failed one fill the shortage of energy. After repair the failed channel is put into operation again, and strength or phase of accelerating field in all cells returns in the normal state.

One can estimate efficiency of an offered way. During serviceability restoring of the first RF channel failed $t_R$ yet N' channels leave out of operation:

$$N' = t_R / T_C = t_R \cdot N / t_F .$$

Thus, during time $t_R$ in common N'+1 channels will be under repair. At keeping of the time allotted to the channel restoring the average frequency of repaired channels placing in service will be equal to average frequency of the RF system refusals occurred.
Consequently,

$$\Delta N = 1 + t_R \cdot N / t_F$$

channels or

$$\Delta n = \Delta N \cdot k$$

accelerating gaps will be continuously out of operation, in average, and the relative value of an additional energy gain

$$w = \Delta N / (N - \Delta N)$$

should be provided by gaps staying in operation.

Because the most relative energy gain per one section $\Delta W_{1S}/W$ takes place in the beginning of MPA, where the least value W= 100 MeV is, just here the section refusal can cause the greatest response in the beam longitudinal motion. Therefore, especially precise operation of the compensation shortage energy system is required. In this place the particle momentum spread is estimated by the value of $\Delta p/p$ = (1-1.2) % or absolute energy spread makes $\Delta W$ = (2-2.4) MeV.

The section refusal will effect on the beam dynamics to a lesser extent, and requirement to the electronic system of amplitude and phase tuning will be softer, at the condition

$$\Delta W_{1S} << \Delta W, \quad \text{that is} \quad \Delta W_{1C} \cdot k << \Delta W.$$

Variants with k =1-3 cells per section can satisfy this condition, though our example [5], in which $\Delta W_{1S} = \Delta W_{1C}$ = 390 keV, is oriented on k = 1 cavity. The failure-free (on RF field) acceleration regime of MPA operation [5] is presented in Table 1.

Table 1. MPA parameters for failure-free ($T_D$= 0) acceleration, suggested here.

| | | |
|---|---|---|
| Cell number per section | k | 1 |
| Section number | S | 2300 |
| RF channel number | N | 2300 |
| Power per one RF channel | P (kW) | 70 |
| Average time between consequent refusals of channels | T (h) | 0.87 |
| Number of channels repaired continuously N | | 3 - 4 |
| Energy increasing required for compensation | w (%) | 0.18 |

Taking into account sluggishness of cavities and feedback channels, the time required for adjustment of field parameters in working sections can be estimated by the value of 30-50 μs. During this time particle energy at the section entrance followed by the failed one will be 0.4 % less than nominal, and momentum - 0.2 %. That is why at a separatrix width of ± 1.2 % there is no any substantial difficulties. Simultaneous failure of two adjacent channels can take place extremely seldom (once per many years at continuous operation) and is not disastrous (during 30-50 μs the particle momentum will be shifted on 1/3 of a separatrix width).

If a particle is given an energy shortage, for example, in the first 100 cells after failed, the field strength in them should be increased by 1% of nominal. At so small increase there is no necessity to make special reserves in electric strength of cells and RF power generators, and can be covered by usual technological tolerances. Therefore the function of a field parameter adjustment can be assigned to the standard control system, which should be intended for fast amplitude and phase adjustment in wide range, under the influence of the beam current instability as well as of a channel parameter or power supply line changes.

## 5. CONCLUSIONS

1. If the RF channel reservation gives only reduction, though rather significant, of idle time of a high current accelerator, use of the whole accelerating MPA channel possibility allows to achieve failure-free its operation.
2. Integrating on 1-3 cell in section powered from one RF channel, it is possible to compensate failure of several channels by small increase of regime strength in the rest channels during all the time for channels under repair restoring.
3. Regime strength changes required are not out of usual technological tolerances (<1%) and add increase of RF channel power is not necessary.
4. In the ITEP scheme MPA proposal there is no accelerator shut-down when small number of accelerating cells fail. Cell refusal is compensated by the rest working cells and repair can be set aside for a long time to the schedule shut-down.
5. Note that cavities failed are excited by the beam resulting particle energy losses. However tested solution of fast electronic cavity tuning change [7] can be useful to displace cavity own resonant frequency out of the probable band of such excitement for all repair time.
6. Detailed analysis of cell and section technique (as well as RF channel scheme, probable solutions of self-balancing system and RF equipment choice and common economics factors) influence upon beam dynamics should be fulfilled to chose the final solution on failure-free MPA RF power supply scheme for considered high current accelerator.

## REFERENCES


[1] P.J.Tallerico, M.T.Lynch, G.Lawrence. "Reliability and Availability Consideration in the RF Systems of ATW-Class Accelerators". *Proc. of the Intern.Conf. on Acceler.-Driven Transmut. Technolog. and Applications*, Las Vegas, 1994, p. 580.

[2] G.Lawrence. "Los Alamos High-Power Proton Linac Designs", ibid., p.177.

[3] T.Takizuka et al. "JAERI R&D on Accelerator-Based Transmutation under OMEGA Program", ibid., p.64.

[4] V.G.Andreev et al. "High-Beta Linac Accelerating Structure". *Proc. of the PAC'1993*, p.980.

[5] V.A.Andreev et al. "A New Approach for High Power Ion Linac Design". *Second Intern. Conf. on Accelerator-Driven Transmut. Technologies and Applications,* 3-7 June 1996, Kalmar, Sweden.

[6] V.S.Volkov et al. "A Problem of the RF Reliability at Mezon Factory". *Proc. of the Third All-Union Conf. on Acceler. of the Charge Particles*, V.1. M., "Nauka", 1973, p. 269.

[7] A.Facco et al. "Experience with the Low-β rezonators at LNL". *Heavy Ion Acceler. Technology Conf.*, Canberra, 17-23 Sept. 1995.

# AN RF SYSTEM FOR A COMPACT SYNCHROTRON*

A. Pei, S. Anderson, D. Jenner, X. Kang, S.Y. Lee and D. McCammon
Indiana University Cyclotron Facility
2401 Milo B. Sampson Lane, Bloomington, IN 47405

*Abstract*

A 17.4 m circumference 200 MeV proton synchrotron, the Cooler Injector Synchrotron (CIS), is being commissioned at the Indiana University Cyclotron Facility. The compact synchrotron will be used as the injector for the electron-cooled IUCF Cooler Synchrotron. The RF system design uses digital signal processing (DSP) to directly modulate a digital rf synthesizer for beam feedback control. A wide band tunable rf cavity uses non-uniform ferrite biasing to achieve a 10:1 frequency coverage with good VSWR performance and low power requirement.

## 1 INTRODUCTION

The rf system[1] for the compact synchrotron[2] is designed to capture a 7 MeV proton beam from a two-stage linear accelerator consisting of an RFQ and a DTL or a 3 MeV proton beam directly from the RFQ. The beam from the linac injector has 425 MHz bunch structures which will coalesce into a near DC beam during the $H^-$ strip multi-turn injection. The ring rf system needs to adiabatically rebunch the beam into an $h = 1$ bucket and accelerate the beam to the desired extraction energy. The rf system supports a synchrotron cycle rate up to 5 Hz. Once the beam is bunched, the phase and radial loop beam feedback is used to suppress longitudinal phase space oscillations and to automatically center the beam orbit. For extraction, the rf system synchronizes and phase-locks the beam between the two synchrotrons to make bucket-to-bucket injection into the electron-cooled IUCF Cooler Synchrotron.

## 2 LOW LEVEL SYSTEM DESIGN

The low-level system design combines a digital signal processor with a direct digital rf synthesizer (DDS) for frequency ramp and beam feedback control. This results in a compact module that has powerful signal processing and interfacing capabilities. The DDS also has good frequency stability over the entire range of operating frequencies, making fixed intermediate frequency (IF) circuits and mixers unnecessary for the rf signal source. A block diagram of the beam control unit is shown in Figure 1.

The single-chip DDS synthesizer Analog Devices AD7008 was chosen for its good spectrum purity and high integration. A numerically controlled oscillator (NCO), a 10-bit high speed DAC, and phase and amplitude modulators have all been integrated in a single 44-pin PLCC. Our evaluation showed that the single chip integration technology achieved comparable specifications as separate NCO and DAC products.

A Motorola MC56002 digital signal processor (DSP) is used to perform the DSP functions. A variety of interface ports and interrupt capabilities of the DSP chip are also used for communication with the control computer, interfacing with the timing system, frequency ramp generation, and digital control of the rf synthesizer.

The built-in asynchronous serial port of the MC56002 down-loads commands and data directly from the control computer. The synchronization of command execution is accomplished via a hardware interrupt pin on MC56002. When a command that needs synchronization with the rest of the system, such as "start ramp" or "close loop", is received by the DSP, it is not immediately executed. Rather, the DSP waits for an appropriate interrupt signal provided by the timing system to start execution. Non-latency-critical commands (such as an operator manual change of rf frequency) are executed immediately upon reception by the DSP.

The analog interface of the beam-control module to the rf and beam parameters is via a 4-channel multiplexed 10-bit ADC. Important parameters such as the beam phase error, radial error, $\dot{B}$, etc. are processed by the DSP to generate feedback corrections to the frequency ramp-vectors. The beam feedback control is a digital implementation of "DC coupled VCO phase loop with radial correction."[3] The combined control loop transfer functions are designed to achieve a beam response of:

$$\frac{\phi_b}{\phi_r} = \frac{1}{1+\tau s} \tag{1}$$

where $\phi_b$ is the beam phase, $\phi_r$ the rf phase, and $\tau$ a time constant determined by the gain ratio between the phase and radial loops. It is desirable to set $\tau$ such that it is much greater than the synchrotron period. Rf and dipole magnet transients are thus filtered by the low-pass transfer function and the beam moves adiabatically in the phase space[3].

The entire control and signal processing software is stored in a 32 kB flash EEPROM that can be updated in-circuit quickly. The rf synthesizer, DSP and the multiplexed ADC are all housed in a single NIM module, making maintenance and repair relatively simple.

During the ramp, the rf synthesizer is guided by the frequency versus time ramp-vectors defined by the operator. Because of the fast computation speed of the DSP, it is possible to perform "real time" function synthesis, i.e., the actual frequency values are computed in real-time by the DSP during the ramp by an interpolation algorithm instead

* Work supported in part by NSF Grant No. PHY-92-21402, PHY-93-14783 and PHY-23-42310.

0-7803-4376-X/98/$10.00 © 1998 IEEE

of being looked up from a memory based table. Only the end points of the ramp-vectors are down-loaded and stored in the DSP memory. The total length of frequency samples is thus essentially not limited by the DSP memory. With beam feedback, the interpolated frequency value is digitally corrected by the beam feedback loop using digitally processed beam radial and phase errors.

The binary input format of AD7008 DDS is preferred because it is native to the calculations of the DSP. However, a binary synthesizer requires a special binary clock to keep the output frequency increments in integers. For AD7008, the synthesizer output frequency is determined by:

$$f = \frac{\Delta\phi \times f_{clk}}{2^{32}} \text{ (Hz)} \qquad (2)$$

where $f$ is the synthesizer output frequency, $\Delta\phi$ an integer determining the synthesizer phase advance in a reference clock period, and $f_{clk}$ the reference clock frequency in Hz.

A voltage controlled crystal oscillator (VCXO) is used to generate a $2^{25}$ Hz clock that is locked to the 10 MHz laboratory time base. The phase locked loop uses a second binary DDS as a fractional frequency scaler.

Extraction for CIS is designed with a period of constant "flat top" dipole field at 1 Hz operation mode. Bucket-to-bucket synchronization between the two synchrotrons is accomplished by replacing the beam radial feedback loop with an rf phase locked loop between the two rf systems. At higher operation rates without a field "flat top" period, phase matching can be achieved by precise frequency control of the DDS just before extraction, steering the injector synchrotron rf phase toward that of the Cooler. To sequentially inject the Cooler Synchrotron rf buckets which operate at a harmonic five times the rf frequency of the CIS fundamental harmonic, a modulo-5 digital circuit is used to divide the Cooler rf reference to the same frequency as the CIS rf. For each extraction, the digital logic momentarily switches to modulo-6 and switches back to modulo-5, delaying exactly one Cooler rf bucket.

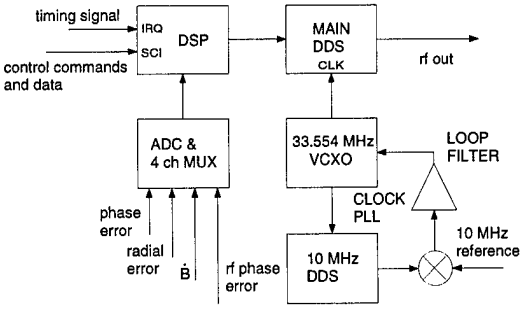



Figure 1: CIS rf source and beam control unit block diagram.

## 3 HIGH LEVEL ELECTRONICS AND RF CAVITY

A tuned ferrite cavity design is chosen for a higher gap impedance and smaller power requirement. An ENI A300 broadband amplifier can drive the cavity up to 500 V, which is more than enough to develop a required 0.015 eVs fundamental harmonic stationary or accelerating rf bucket.

The tuned cavity uses an external quadrupole biasing magnet design which places a magnet and the bias windings outside the coaxial rf resonant structure. This avoids potential rf resonances and arcing of the biasing structure, especially when there are many turns of bias windings[4]. With 40 to 50 turns on each quadrupole magnet tip coil, a compact power supply rated at 20 A can be used to achieve sufficient ampere-turns for ferrite ring biasing[5].

A common problem with driving a tuned ferrite cavity with a solid state amplifier is that it is difficult to achieve a low VSWR over a wide range of frequencies as the ferrite loss is heavily frequency dependent. In the design of this cavity, the rf $\mu$ of the ferrite rings enclosed by the driving loop is independently adjustable, varying the transformation ratio between the gap shunt impedance and the loop input impedance. This non-uniform biasing approach achieves good impedance matching of the driving loop throughout the operating band and makes the reflected rf drive power insignificant[6].

Figure 2 is a mechanical illustration of the construction of the cavity. The quarter-wave-length coaxial rf cavity consists of a perforated inner conductor, an outer conductor made of copper strips, and loading variable vacuum capacitors. 10 Phillips 8C12 ferrite rings are stacked axially with spacings. Cooling air enters the cavity between the outer conductor copper strips, flows through the surface of the ferrite rings, and exits the cavity through the holes on the inner conductor. The biasing quadrupole magnet uses 1 mm steel laminations and forms part of the rf shielding of the cavity. The laminations facing the two ferrite rings enclosed by the the driving loop are separated from the rest of the magnet by an aluminum spacer and its coils are also separate. The rf shield consisting of the magnet and aluminum lids is pressurized by a fan for air-cooling.

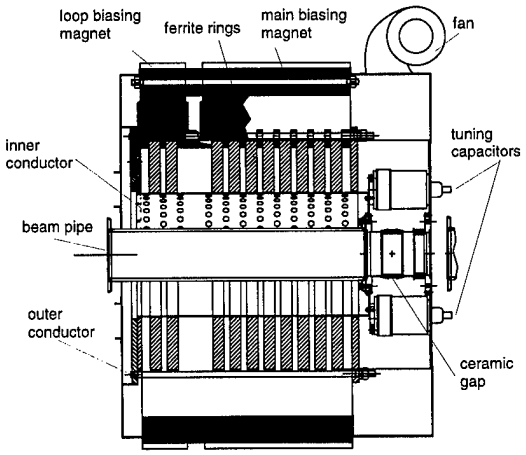



Figure 2: Rf cavity for CIS.

Figure 3 is a bias current versus frequency plot for the main and the driving loop biasing magnets for minimum

reflection ( less than 5% of driver power is reflected in most frequencies ). As the driving loop magnet current is almost always less than that of the main magnet, the two magnets can be connected in series using a single bias supply and power MOSFETs can be programmed to shunt a part of the current from the driving loop magnet to achieve good VSWR.

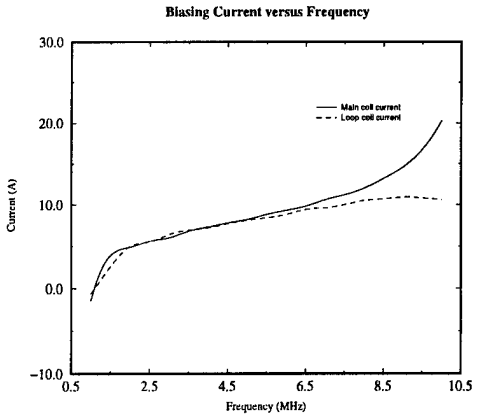



Figure 3: Biasing current versus frequency for optimum VSWR.

Figure 4 shows the shunt gap resistance of the cavity. The data were taken with 150 W of rf driving power. The loading capacitor was set at 570 pF to cover a frequency band of 1-10 MHz from zero to full bias.

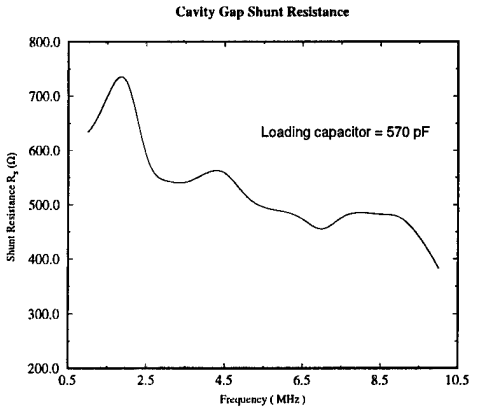



Figure 4: Measured cavity shunt resistance with 150 W driving power.

## 4 CONCLUSION

Most of the hardware for the rf system has been built and bench-tested. At the time of writing, the IUCF CIS ring has achieved bunched circulating beam with the rf cavity installed.

## 5 ACKNOWLEDGEMENTS

The rf cavity design benefited greatly from the calculations and measurements made by Dr. R.E.Pollock in the design of the IUCF Cooler MPI Cavity. We also would like to thank Dr. G.Berg for his tutoring and help in the 3-D analysis of the quadrupole magnet design. The significant effort made by Dr. D.Friesel and Dr. W.Fox in the mechanical design and lamination manufacturing is gratefully acknowledged. This work was made possible by the dedicated effort from all the IUCF staff involved, especially that from the mechanical design and machining staff.

## 6 REFERENCES

[1] A.Pei *et al.*, "The Indiana University Cooler Injector Synchrotron RF System", Proc. PAC95, 1705-1707.

[2] D.L.Friesel and S.Y.Lee, "Status of the IUCF Cooler Injector Synchrotron Construction Project", Proceedings of this conference.

[3] D.Boussard, CERN 92-03, (June 1992), 474-500.

[4] S.Papureanu, MPI internal publications, MPI, 1989.

[5] R.E.Pollock, "IUCF Cooler Design Notes", IUCF, 1990.

[6] A.Pei *et al.*, "The Indiana University Cooler Injection Synchrotron Rf Cavity", Proc. PAC95, 1708-1710.

# RF STATIONS OF THE SPRING-8 STORAGE RING

M. Hara, H. Ego, Y. Kawashima, Y. Ohashi, T. Ohshima and T. Takashima
SPring-8, Kamigori, Ako-gun, Hyogo 678-12, Japan

*Abstract*

Construction of three RF stations in the SPring-8 storage ring was completed. Twenty-four single-cell cavities were installed in the storage ring. Three klystrons and their power equipments were also installed. Low power control system such as tuner control, feedback control for phase lock loop and cavity voltage control was assembled and operated. High power test up to 800 kW was carried out in each RF station and verified to satisfy the designed specification.

## 1 INTRODUCTION

Low power and high power tests for twenty-four bell-shaped single cell cavities and input couplers were carried out at a test stand from January and completed in the end of September, 1996. There are three RF stations in the storage ring, named B, C, D stations. Installation of cavities, couplers, waveguides, vacuum components etc. was started in parallel with high power test from April in D-station and completed in November '96 in C-station.

A klystron and its power equipment were installed in each RF station. Various kind of tests, in particular, interlock test for protection of a klystron were carefully done. After installation of waveguides, low power control system was assembled by using NIM modules. Then phase difference between each cavity was measured and adjusted with phase shifters of the waveguides. A measurement of attenuation of co-axial cables from pick-up ports on cavities and from directional couplers was done using a network analyzer.

To check total system under high power operation, a program for computer control was prepared based on a prototype program which had been developed to test a cavity [1]. A final version in beam operation was developed through high power test. The high power test was started from July and completed in December. During high power test, water temperature of cavity inlet was stable within ±0.15°C in the range of zero to 800 kW. Beam was injected into the storage ring in March, 1997. Three RF stations are being operated stably. Here, processes and results mentioned above are reported.

## 2 INSTALLATION OF CAVITIES

Figure 1 shows the cavity assembly in one of the stations. The assembly consists of the cavities, the vacuum equipments, waveguides, input couplers and frequency tuners and so on. The cavities are connected to each other with special vacuum vessels; three vacuum manifolds and four bellows made of stainless steel. Two cavities at both sides of one vacuum vessel are connected smoothly by the slit copper pipe fixed in the vessel so as

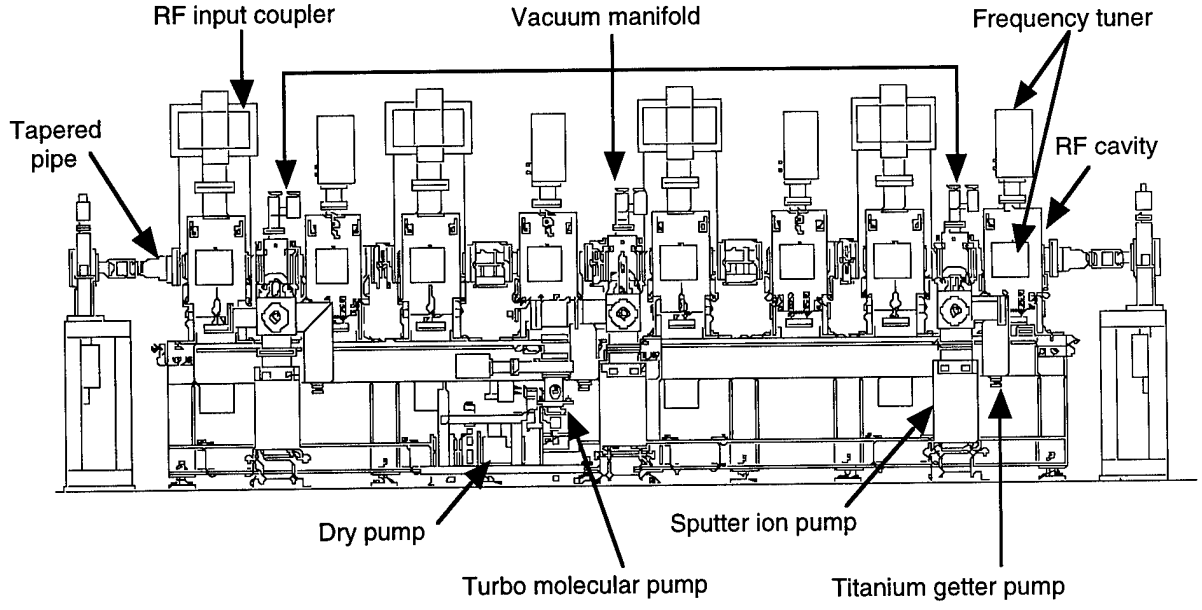



Fig. 1 Cavity assembly of the SPring-8 storage ring.

0-7803-4376-X/98/$10.00 © 1998 IEEE

to reduce the parasitic impedance. Rings made of beryllium-copper alloy or silver with a diameter of 100 mm are used as an RF contact between a cavity and a vacuum vessel. The cavities at both ends of the assembly are connected to the vacuum chambers which are mounted in the quadrupole magnets with tapered ducts made of stainless steel and transforming the shape of cut-view with a diameter of 100 mm to the elliptical one with a semi-major radius of 50 mm and a semi-minor radius of 20 mm. The cavities are evacuated through beam ports with a diameter of 100 mm connected to the manifolds. Cold cathode gauges, main vacuum pumps, sputter ion pumps ( pumping speed of 400 litters per second for $N_2$ gas ) and titanium getter pumps ( pumping speed of 800 litters per second for $N_2$ gas ), are attached to the ports of each manifold. A thermocouple gauge, an extractor ion gauge, a mass-spectrometer and a roughly pumping system are connected to the manifold in the center position of the assembly. The roughly pumping system consists of a turbo molecular pump ( pumping speed of 285 litters per second for $N_2$ gas ) and a dry pump ( pumping speed of 450 litters per second for $N_2$ gas ).

After the success of a helium-leak test, the assembly was evacuated to less than $1\times10^{-5}$ Pa by the roughly pumping system and was baked at 150 °C for more than 100 hours. After completion of baking, we started to operate the main pumps. The attained value of pressure in the assembly was about $1\times10^{-7}$ Pa. The mass-spectrometer showed that there was only $H_2$ gas in the assembly after baking.

## 3 LOW POWER CONTROL

Reference RF signal of 508.58 MHz is distributed to three RF stations located at the storage ring and the synchrotron ring through optical fiber cables. The phase of a reference line is kept constant with the accuracy of ±0.1° when phase lock loop ( PLL ) is on. Even if PLL is off, the phase difference is ±1°. This error is mainly due to temperature dependence of electric circuits and due not to the optical fiber cable [2].

Low power RF system in an RF station consists of (a) an automatic level control (ALC) and phase lock loop (PLL) of RF power, (b) a cavity tuning, (c) an anode modulation, (d) an interlock, and (e) various monitorings. Low power RF control diagram is shown in Fig. 2. A part (a) has a function to level klystron-out power and cavity voltage, and to lock klystron-out and cavity phase, respectively. A part (b) is to keep cavity resonating at 508.58 MHz with slight detuning offset by using a movable tuner. A part (c) makes klystron power handling stable compared with cathode modulation (independent anode power supply is installed in two RF stations out of three). A part (d) is for protecting equipments from break down, beam abort, and radiation safety. A part (e) is to check running condition and to respond to system failure.

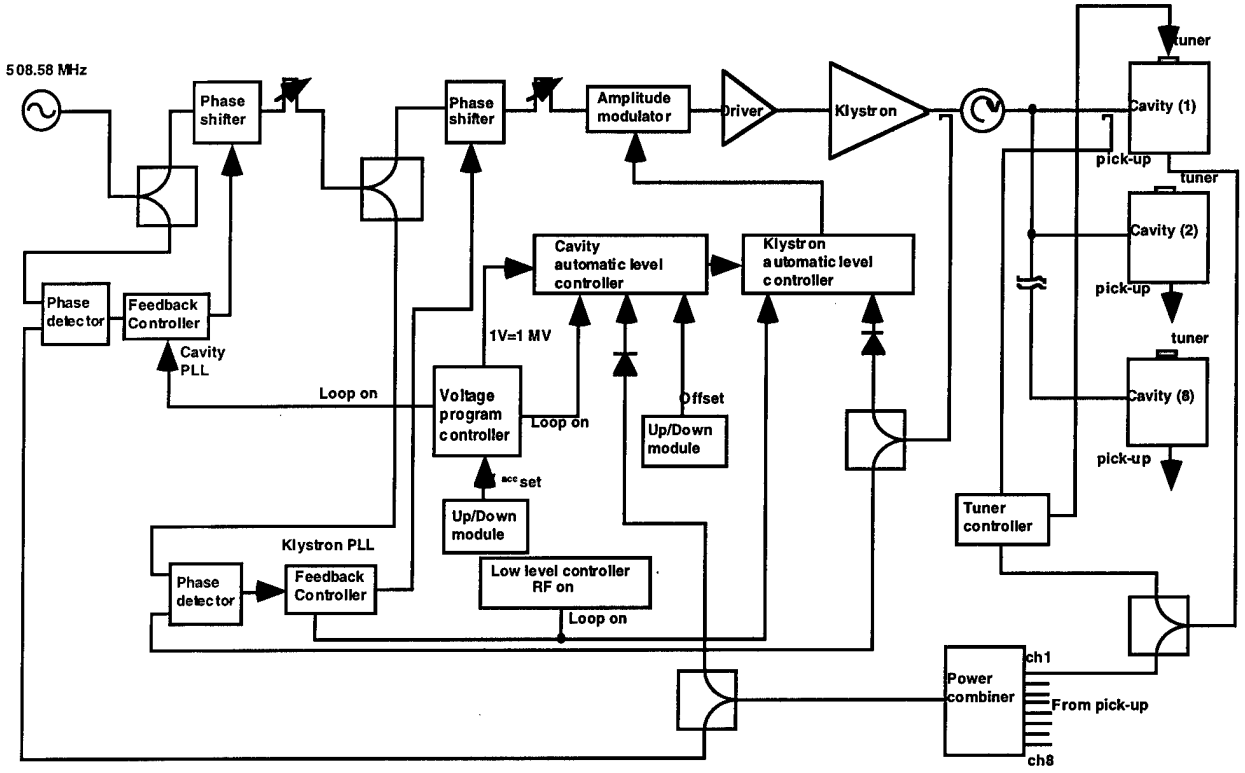



Fig. 2 Block diagram of low power system.

## 4 COMPUTER CONTROL OF RF SYSTEM

We developed a control program for cavity conditioning based on a personal computer system [1]. Based on this experience, a computer control program has been developed for the operation of RF system of the storage ring under the frame of the SPring-8 control system.

An operator uses a graphical user interface (GUI) to control RF system. A command is sent to a message server (MS) from GUI, then is sent to an access server (AS), and finally is reached to an equipment manager (EM) working on a VME. There the command is interpreted and is executed to control RF equipments through VME I/O modules. Control commands are sent in a text format. For example, to turn on the RF switch in B-station, a command of "put/sr_rf_rfsw_b/on" is sent to EM, then a digital pulse signal is sent to turn on the RF switch. As another example, to get the vacuum pressure in C-station, the command of "get/sr_rf_ccg_1_c/pressure" is sent to the EM, then an analog data of a cold cathode gauge is taken from an analog input board. The voltage is converted to the vacuum pressure using a conversion coefficient and the result is sent back to the GUI program.

The RF control system consists of three kind of panels; a main panel, a control panel for klystron power equipments and a low level control panel for each RF station. Functions on a main panel are to set following data; total acceleration voltage, a phase of each RF station, frequency of a master synthesizer, present values of the acceleration voltage, phase and vacuum pressure in cavities of each RF station. The control panel for klystron power equipments is used to start up, to shut down and to monitor power supplies. The main roll of the low level control panel is to change the acceleration voltage and station phase. These values are stored in the parameter database written on the main panel. They are manually input on a low level control panel, too. Another roll of the panel is monitoring the status of each klystron and cavities such as sensing an occasional arcs in wageguides, reflection power from the cavities and vacuum pressure. These control panels are working well now. Updating of the program is continued.

## 5 HIGH POWER TEST AS A TOTAL SYSTEM

We conditioned the assembly in high and continuous wave RF power operation. RF power up to 90 kW was successfully put into each cavity with the power control system aided by a computer mentioned in section 4. Figure 3 shows the time chart of the output power from a klystron and the pressure in the assembly. The left vertical axis shows the RF power from the klystron. About 89 % of the power is consumed in the eight cavities. The rest of the power is reflected from the cavities because coupling coefficient between a cavity and an input coupler is 2.0. The right vertical axis shows the pressure in the manifold between the first cavity and the second cavity at the right-hand side shown in Fig. 1. In the beginning of feeding RF power into the cavities, the vacuum pressure increased over $1\times10^{-5}$ Pa at small RF power by the outgas from the inner surface of the cavities exposed to the excited electric field. The outgas was gradually reduced by the continuous exposure of the surface to the electric field. Finally the value of pressure reached to about $5\times10^{-7}$ Pa while the RF input power of 90 kW was put into all cavities. The value of pressure without feeding RF power was also improved to about $6\times10^{-8}$ Pa. Now, three RF stations are stably operated.

## 6 REFERENCES


[1] T. Ohshima et al., Proc. of the 5th European Particle Accelerator Conf., SITGES (Barcelona), 2047 (1996).

[2] H. Suzuki et al., 9th Symp. on Accel. and tech., 252 (1993)

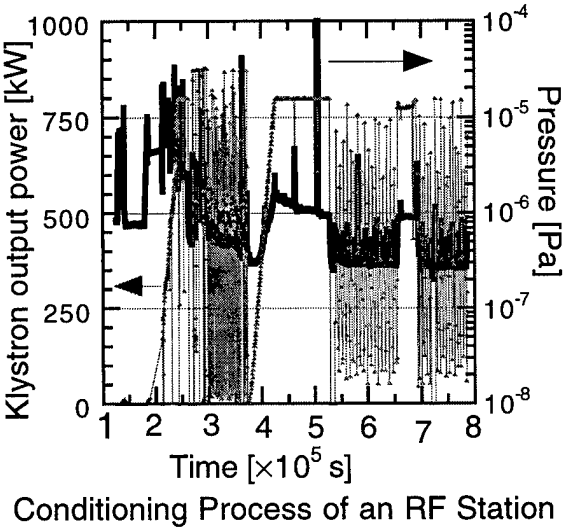




Fig. 3 Result of the conditioning by feeding the RF power into the cavities. The thin dotted line shows the output power from a klystron. The thick solid line shows the pressure in the manifold at the right-hand side in Fig. 1.

# FUNDAMENTAL MODE CHARACTERISTICS OF ARES CAVITY UNDER BEAM ENVIRONMENT

N. Akasaka, K. Akai, E. Ezura, T. Kageyama, H. Mizuno, F. Naito, H. Nakanishi, H. Sakai, Y. Takeuchi, Y. Yamazaki,
High Energy Accelerator Research Organization (KEK), 1-1 Oho, Tsukuba, Ibaraki, 305 Japan, and
T. Kobayashi, Institute of Applied Physics, Tsukuba Univ., 1-1 Ten-nodai, Tsukuba, 305 Japan

*Abstract*

Two types of ARES cavities were tested in the TRISTAN accumulation ring in KEK. In this paper, results relating to the fundamental mode in the accelerating cavity are reported. The status of the cavity, including the detuning frequency under beam loading and the output power from the coupling cavity damper, was measured at different beam current and with various bunch patterns. Its behavior agrees well with the calculation based on a coupled resonator model.

## 1 INTRODUCTION

The ARES cavity was developed to suppress multi-bunch instabilities induced by both fundamental and higher order modes (HOM) in KEKB [1]. It consists of three cavities: accelerating (a-), coupling (c-) and storage (s-) cavity. As a consequence of their coupling, the accelerating $\pi/2$-mode and parasitic 0- and $\pi$-modes are formed. The characteristics of ARES is:

1. The a-cavity is a damped cavity. The instability due to HOMs in the a-cavity is suppressed.
2. The $R/Q$ of the accelerating mode is about 10 times lower than that of the a-cavity alone so that the resonant frequency of the accelerating mode do not cross integral multiples of the revolution frequency during the current build-up.

Table1 Parameters of the accelerating mode of ARESs.

| | ARES95 | ARES96 | |
|---|---|---|---|
| Shunt Impedance $R_{sh}$ | 1.66 | 1.91 | MΩ |
| $Q_0$ | $1.12\times10^5$ | $1.17\times10^5$ | |
| $R_{sh}/Q_0$ | 14.8 | 16.3 | Ω |

Table2 Machine parameters of AR high current experiment.

| | | |
|---|---|---|
| Beam Energy | 2.5 | GeV |
| Radiation Loss | 0.15 | MeV/Turn |
| Momentum Compaction | 0.0129 | |
| Long. Damping Time | 21.6 | ms |
| Trans. Damping Time | 43.1 | ms |
| RF Frequency | 508.58 | MHz |
| Harmonic Number | 640 | |

Two types of ARES cavity have been fabricated and tested under high RF power. They adopt different scheme of HOM damping for their a-cavity. The chokemode cavity [2] is used for the first ARES cavity (ARES95) [3]. The second ARES cavity (ARES96) is equipped with four rectangular waveguides and grooved beam pipes [4]. The parameters of their accelerating mode are listed in Table1.

These two ARES cavities were installed in the TRISTAN Accumulation Ring (AR) for preliminary testing under the electron beam current up to 570 mA. Main parameters of AR is listed in Table2. Principal aims of the test are:

1. Confirm its basic function and performance.
2. Study effects of HOMs on the beam.
3. Establish the cavity control method.

In this paper, the result of the first and third subjects above are reported. Effects of HOMs is reported elsewhere[5].

## 2 OPERATING ENVIRONMENT

### *2.1 Power Feed*

The two ARES cavities were installed at one straight section in the TRISTAN AR ring. At another straight section, a superconducting cavity (SCC) and a choke mode cavity (CMC) were also installed. Only one ARES cavity was operated at a time while the other is detuned in order not to affect the beam stability.

The input RF power is fed to the s-cavity through the input coupler with a disk-type ceramic window [6]. The cooling water flow is 400l/sec for each ARES cavity.

### *2.2 Tuning of the A- and S-Cavities*

The frequencies of the a- and s-cavities were controlled automatically with movable tuners independently [7]. The tuner for s-cavity controlled the relative phase between the input RF field and the field inside s-cavity so that the input impedance be purely resistive as usual. On the other hand, the frequency of the a-cavity is controlled so that the phase between the a- and c-cavity is $\pi/2$. The field in the c-cavity is excited as a consequence of energy flow from the s-cavity to the a-cavity.

0-7803-4376-X/98/$10.00 © 1998 IEEE

## 3 RESULTS

Mostly the study was concentrated on ARES96, which has been adopted as the normal conducting cavity for KEKB. It was operated for about 20 days while ARES95 was about 2 days. The following results are about ARES96 except 3.4.

### *3.1 Heavy Beam Loading*

The maximum current while the cavity is operating is 500mA. No anomalous behavior was observed.

In the case of KEKB LER, the ratio of the power consumed by the beam to that by the cavity wall will be

$$\frac{P_b}{P_c} = \frac{200\,\mathrm{kW}}{150\,\mathrm{kW}} = 1.33.$$

In order to simulate the operation under a large beam loading, $P_c$ is lowered to 85kW ($V_c$=0.4MV) and the relative phase between ARES and CMC was shifted to increase $P_b$ in ARES. At the beam current of 300mA, the ratio was

$$\frac{P_b}{P_c} = \frac{75\,\mathrm{kW}}{85\,\mathrm{kW}} = 0.9,$$

and there was no anomalous behavior in the cavity control.

### *3.2 Frequency Detuning*

The frequency detuning due to beam loading is expressed as

$$\Delta f = -\frac{f_{rf}}{2}\left(\frac{R_{sh}}{Q}\right)\frac{I_b}{V_c}\sin\phi, \qquad (1)$$

where $R_{sh}$ and $Q$ are the shunt impedance and $Q$ value of the mode, and $f_{rf}$, $I_b$, $V_c$ and $\phi$ are the RF frequency, beam current, cavity voltage and synchronous phase, respectively. In the scheme of ARES, the amount of frequency shift of the a-cavity is the same as in the case without the c- and s-cavities. However, the resonant frequency of the accelerating $\pi/2$-mode changes by

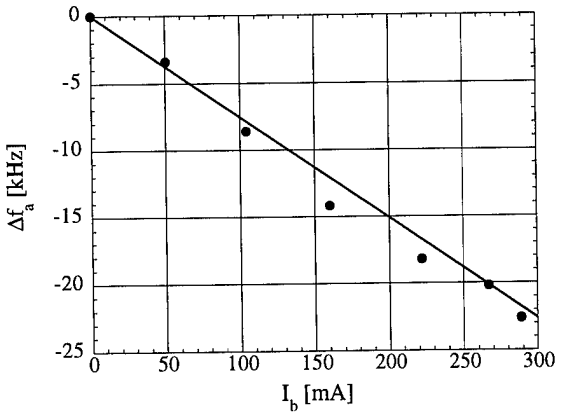



Fig.1 Frequency detuning of the a-cavity as a function of the beam current. The dots are measured value and the straight line is the expected value.

$$\Delta f_{\pi/2} = \frac{U_a \Delta f_a + U_s \Delta f_s}{U_a + U_s},$$

where $\Delta f_n$ and $U_n$ are the frequency shift and stored energy of the $n$-cavity. The detuning of the $\pi/2$-mode is $\Delta f_a/10$ since $\Delta f_s$ is zero and $U_a$:$U_s$=1:9. Thus in KEKB LER, the largest detuning frequency will be about 30kHz, which is well below the revolution frequency of 99kHz.

The frequency detuning of the accelerating mode under beam loading could not be measured directly. It was estimated from the tuner positions of the a- and s-cavities. The frequency shift of the a-cavity is plotted as a function of the beam current in Fig.1. The total $V_c$ was 1MV, which was the sum of 0.5MV of ARES96 and 0.5MV of CMC. The straight line in the figure is calculated from Eq.(1) with the a-cavity parameters $R_{sh}$=4.8MΩ and $Q_0$=3($10^4$. The measurement agrees well with the calculation. On the other hand, the frequency of the s-cavity changed only slightly when the beam current changes. There was no frequency shift observed beyond random fluctuation when the beam current was kept constant.

The above measurement of the tuner positions indicates that the frequency detuning of the accelerating $\pi/2$-mode is in good agreement with the theory.

### *3.3 Power Output from the C-Cavity Damper*

A coaxial waveguide is attached at the center of the c-cavity to damp the parasitic 0- and π-modes. A water load is connected on the other end of the waveguide with a ceramic window [8] between them. Only a small output power (measured 180W and expected 150W at $V_c$=0.5MV) flows out through the waveguide with no beam current. The output was observed with a peak power analyzer (HP8991A).

#### 3.3.1 Single Bunch

Figure2(a) shows the output waveform with a current of 100mA single bunch. The distance between the two large peaks is the revolution time of 1.26μs. The time difference between a large peak and the following small peak is about 150ns, which corresponds to the beat frequency of the 0- and π-modes separated by 6.6MHz. The computer simulation based on a coupled resonator model [7] is shown in Fig.2(b), which reproduces the measured waveform pretty well. Although their absolute value cannot be compared precisely due to possible errors in the calibration of the measurement system, their difference is within a factor of 2.

#### 3.3.2 Multiple Bunches

*With equally spaced 64 bunches, there was no prominent feature* except small noises as expected.

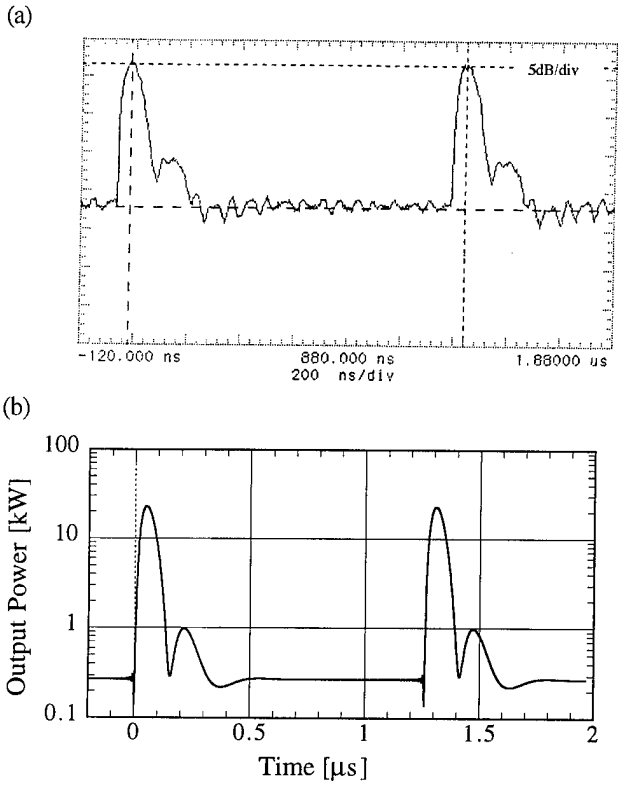



Fig.2 Output of the c-cavity with a current of 100mA single bunch. (a) is the measurement and (b) is the simulation.

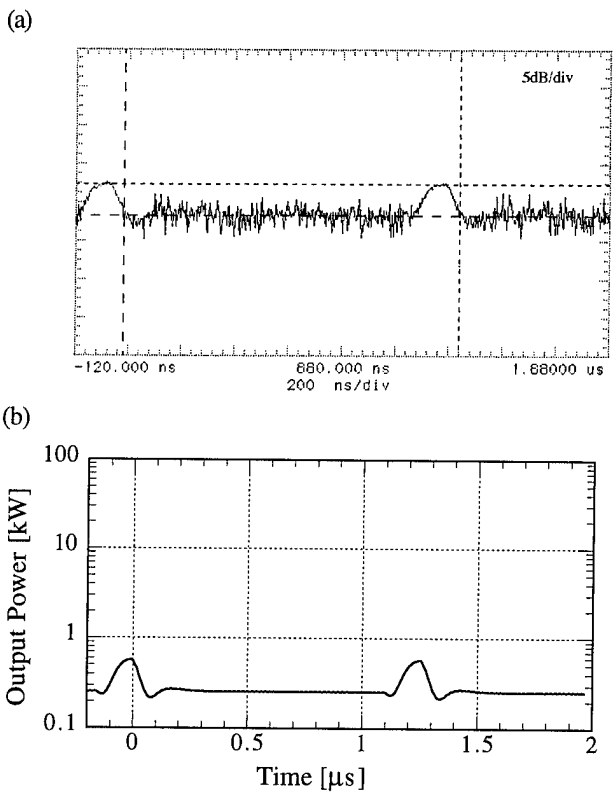



Fig.3 Output of the c-cavity when consecutive 56 buckets are filled out of equally spaced 64 buckets. The current was 164mA. (a) is the measurement and (b) is the simulation.

3.3.3 Multiple Bunches with a Gap

When 8 consecutive bunches were removed from the equally spaced 64 bunches, a small hill emerges at the missing bunches (Fig.3(a)). Similar situation is expected in KEKB in order to avoid the instability due to ion trapping. The measured waveform is reproduced well by computer simulation as in the single bunch case.

*3.4 Cavity Start-up with a Circulating Current*

In KEKB, accelerating cavity may have to start up with its full circulating current. This is because the refilling of the beam would take much time.

ARES95 was used for the start-up test. SCC provided the accelerating voltage while the input RF power was not fed into ARES95. Below 300mA, ARES95 started up without losing the beam. In some cases above 300mA, the beam was lost during the cavity startup. The beam loss occurred when the feedback changed from controlling the klystron output to controlling the cavity field. Although the effect of the start-up is smaller in KEKB because of the larger number of operating cavities, more sophisticated means of smooth feedback changing or a direct RF feedback system will be desirable.

*3.5 Absorbed Power into the HOM dampers*

There are several HOM dampers of SiC in ARES [9]. The maximum total power absorbed in one ARES was about 7kW. This value is not enough as a high power test for KEKB. They will be tested using a klystron up to higher power level.

## 4 SUMMARY

Two ARES cavities were tested under beam environment in TRISTAN AR. Their behavior agreed well with the prediction based on a coupled resonator model.

## REFERENCES

[1] Y. Yamazaki and T. Kageyama, Part, Accel. 44, 107 (1994).
[2] T. Shintake, The Choke Mode Cavity, Jpn. J. Appl. Phys. Lett. 31, L1567 (1992).
[3] The ARES Cavity for the KEK B-Factory, T. Kageyama et al., Proc. of EPAC96, p2008.
[4] Development of high-power ARES cavities, T. Kageyama et al., in this conference.
[5] HOM Characteristics of the ARES Cavity, T. Kobayashi et al., in this conference.
[6] The Input Coupler for the KEKB ARES Cavity, F. Naito et al., Proc. of EPAC96, p2014.
[7] Tuning Control and Transient Response of the ARES for KEKB, K. Akai et al., Proc. of EPAC96, p1994.
[8] Coupling cavity damper for the ARES cavity, F. Naito et al., in this conference.
[9] HOM absorber for the ARES cavity, Y. Takeuchi et al., in this conference.

# COUPLING CAVITY DAMPER FOR THE ARES

F. Naito, K. Akai, N. Akasaka, E. Ezura, T. Kageyama, H. Mizuno,
H. Nakanishi, Y. Takeuchi, Y. Yamazaki
KEK, High Energy Accelerator Research Organization, 1-1 Oho, Tsukuba, 305 Japan
T. Kobayashi
Institute of Applied Physics, Tsukuba Univ., 1-1 Ten-nodai, Tsukuba, 305 Japan

*Abstract*

The coaxial (WX120D) antenna damper has been developed for damping the parasitic 0 and π modes of the KEKB ARES cavity. It is installed in the coupling cavity of the ARES. The damper consists of a disk-type coaxial ceramic window and a cross stub angle. The damper has a broadband rf property in order to absorb the rf power of the parasitic modes. The cross angle is utilized for supplying the cooling water to the antenna. The damper was designed by using a computer simulation code without a cold model test. Finally the properties of the damper has been confirmed by the high-power and the beam test for the ARES cavity.

## 1 INTRODUCTION

Accelerator Resonantly coupled with Energy Storage (ARES) has been developed for the KEK B-factory [1,2]. The ARES is an effective countermeasure against the coupled-bunch instability due to the accelerating mode in KEK B-factory. It is composed of three cavities: an accelerating cavity, an energy storage cavity and a coupling cavity. Thus ARES has three modes: the 0, π/2 and π modes. The resonant frequencies of them are about 505, 509 and 513 MHz respectively. The operation mode is the π/2 mode. The parasitic π and 0 modes must be damped, because they contribute to the longitudinal coupled bunch instability. For damping them, an antenna damper has been installed in the coupling cavity in which both π and 0 modes have an rf-field but the π/2 mode has no field. The ARES with the coupling cavity damper is shown in Fig.1 [3].

Our practical targets for the damper are as follows:

(1) The damper reduces the loaded Q values of the π and 0 modes.

(2) The damper can handle the average rf power of a few kW [4].

The following rf property is required to achieve the targets described above;

(3) the VSWR of each components of the damper is less than about 1.2 in the frequency range from 500 to 520 MHz.

The damper which fills our requirements is shown in Fig. 2. The dimensions of the damper is shown in Fig. 3. The damper is comprised of an antenna, an rf window and a cross stub angle. The rf properties of every components of the damper were calculated by using a computer simulation code (HFSS) [5]. The details of the design are reported in the following section.

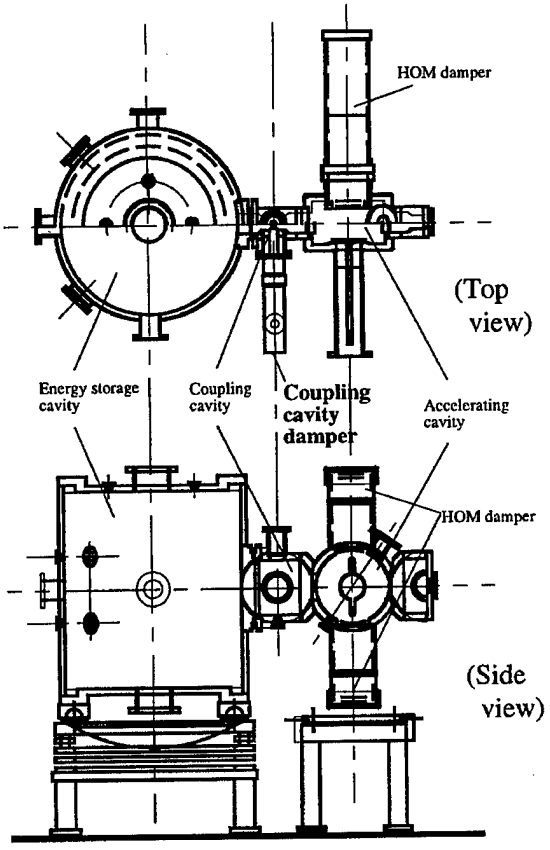



Figure 1: Schematic view of the ARES [3]



Figure 2: Photograph of the high-power model of the coupling cavity damper [2]

0-7803-4376-X/98/$10.00 © 1998 IEEE

## 2 RF WINDOW

The coaxial ceramic (95 % pure Alumina) disk is used for the rf window in the damper. The outer and the inner diameter of the window are 140 mm and 40 mm respectively. The thickness of the window is 8 mm. The surface of the vacuum side of the window has 10 nm thin TiN coating in order to reduce the electron emission coefficient of the ceramic surface. The impedance is matched by using an under- and an over-cut structure of the coaxial waveguide around the window. The under- and the over-cut window structure is also used in the input coupler of the ARES [6]. The values of $S_{11}$ calculated for the window by HFSS are plotted in Fig. 4. The $S_{11}$ values are small enough around the operation frequency.

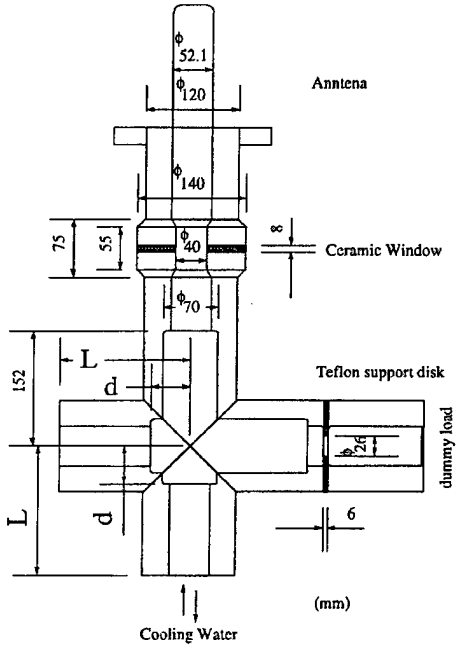



Figure 3: Schematic view of the coupling cavity damper

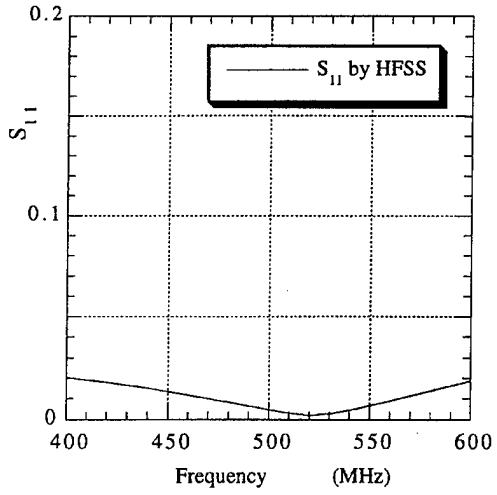



Figure 4: Calculated $S_{11}$ for the ceramic window

## 3 CROSS STUB ANGLE

The damper is terminated by a coaxial dummy load in order to absorb the rf-power of the parasitic modes. Unfortunately we can not supply the cooling water to the antenna through the dummy load, because the water cooling system of the dummy load is closed itself. Thus we make use of a stub angle as a line of the cooling water of the antenna. Since the rf band width of the damper is chiefly limited by that of the stub, it is very important to find the broadband stub angle structure.

The structure we finally chose is the cross stub angle shown in Fig. 3. The diameter of the inside cylinder of the coaxial waveguide near the angle is enlarged in order to get the desired broadband rf property [7]. The calculated results of $S_{11}$ for the cross angle are shown in Fig. 5 with two parameters L and d which are seen in Fig. 3. The values of L and d in the original design are 175 mm and 35 mm respectively. The original value of d was increased by 15 mm to 50 mm during the production of the damper in order to solve an assembling problem. By the change of the dimension, the frequency of the $S_{11}$ minimum point was shifted. It is shown by the dot line in Fig. 5. However the VSWR is still small enough in the desired frequency range. Thus the cross angle with these dimensions was used for the first high-power and the beam test.

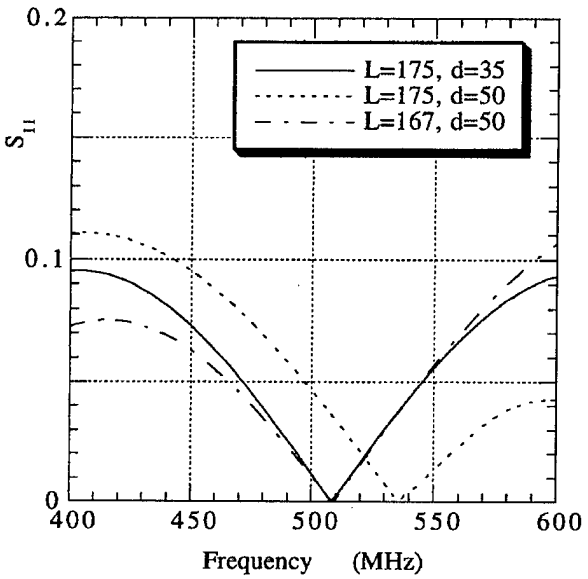



Figure 5: Calculated $S_{11}$ parameter for the cross-stub L and d are shown in figure 3.

Figure 5 shows one more line (d=167 mm, l=50 mm) which has the almost same frequency dependence as that of the originally designed cross angle. We are going to use these values for the next coupling cavity damper of the ARES.

Figure 6 shows the $S_{11}$ values for the damper includes the rf window and the cross stub angle with a Teflon bead support. It shows that the VSWR of the damper is small enough in the very wide frequency range.

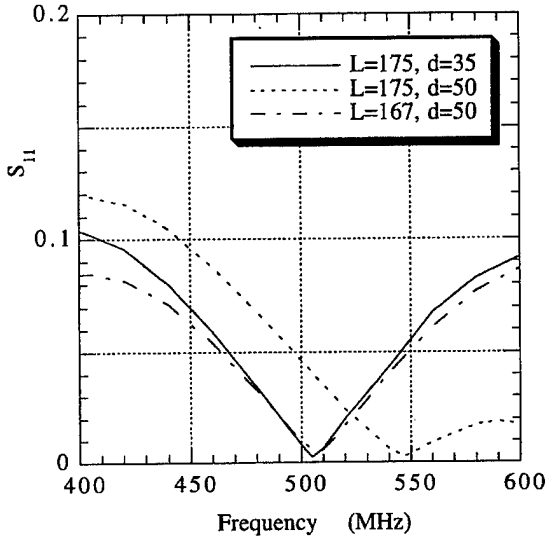



Figure 6: Calculated $S_{11}$ for the damper includes the ceramic window and the cross stub angle with the Teflon bead support.

## 4 ANTENNA

The external Q value ($Q_C$) of the antenna to the coupling cavity has been estimated by the phase shift of the reflected RF wave from the coupling cavity. The phase shift values were calculated by HFSS as a function of the rf frequency. (The calculation method is described in the references [8,9].) The calculated $Q_C$ is about 56 on the condition that the insertion length of the antenna into coupling cavity is 10 mm from the wall of the coupling cavity.

The equivalent circuit analysis shows that the loaded Q value ($Q_L$) of the $\pi$ and 0 modes are approximately two times of the $Q_C$ [1]. Thus the expected $Q_L$ is about 112 for the $\pi$ and the 0 modes.

If the $Q_L$ values are too large to suppress the contribution from the parasitic modes to the longitudinal coupled instability, we can easily increase the insertion length more in order to reduce the $Q_L$ values of $\pi$ and 0 modes.

## 5 EXPERIMENTAL RESULTS

The $\pi/2$ mode and damped $\pi$ and 0 modes of ARES are shown in Fig. 7 which was measured for the high-power ARES cavity with the coupling cavity damper [2]. The measured $Q_L$ values of the $\pi$ and the 0 modes are about 100. The measured $Q_L$ values are consistent with the calculated values described in the previous section.

During the high-current beam experiment by the accumulator ring (AR) in TRISTAN, the measured power flow from the damper was about 1 kW for the 100 mA single-bunch beam. Although it is very preliminary result, it does not contradict with the estimation [3,10].

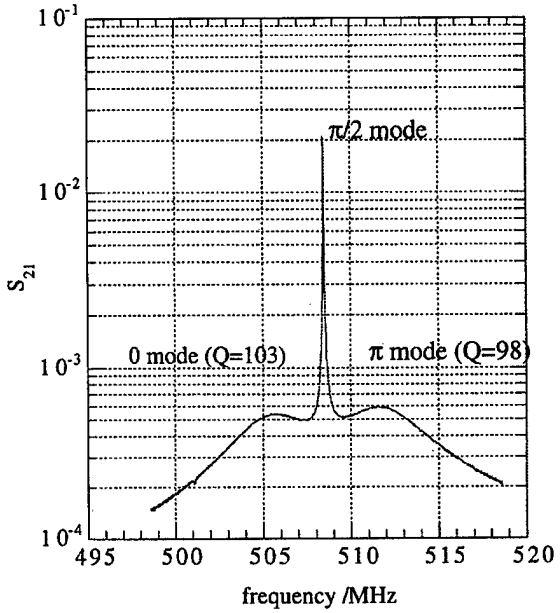



Figure 7: The $\pi/2$ mode and the damped 0 and $\pi$ modes measured for the high-power ARES cavity [2].

## 6 CONCLUSION

The coaxial (WX120D) antenna damper with the ceramic window and the cross stub angle has been developed in order to damp the parasitic 0 and $\pi$ modes of the KEKB ARES cavity. The damper was installed in the coupling cavity of the high-power ARES cavity and it has been tested by the high-current beam experiment in the AR of the TRISTAN. Measured properties for the damper are consistent with the estimated values.

## REFERENCES

[1] Y. Yamazaki and T. Kageyama, Part. Accel., 44, p107 (1994)
[2] T. Kageyama, et al, Proc. 5th European Part. Accel. Conf., p2008 (1996)
[3] T. Kageyama, et al, "Development of high-power ARES cavities", in this conference.
[4] K. Akai, et al, Proc. 5th European Part. Accel. Conf., p1994 (1996)
[5] HP Part No. 85180A, Hewlet Packard Corp.
[6] F. Naito, et al, Proc. 5th European Part. Accel. Conf., p2014 (1996)
[7] G. L. Ragan "Microwave Transmission Circuit", McGraw-Hill, New-York, p170 (1948)
[8] J.C. Slater "Microwave Electronics", D.Van Nortrand, Princeton, p84 (1950)
[9] T. Kageyama, KEK Report 89-4, 1989.
[10] N. Akasaka, et al, "Fundamental mode characteristics of ARES cavity under beam environment", in this conference.

# CONSTRUCTION OF A 714-MHz RF SYSTEM FOR THE ATF DAMPING RING

S. Sakanaka, K. Kubo, F. Hinode, H. Hayano, J. Urakawa
High Energy Accelerator Research Organization (KEK), Oho, Tsukuba-shi, Ibaraki-ken, 305 Japan
M.G. Minty, Stanford Linear Accelerator Center, Stanford, CA94309, USA

*Abstract*

A 714-MHz RF system for the Accelerator Test Facility (ATF) damping ring has been constructed and commissioned. The RF system comprises two higher-order-mode (HOM) damped cavities, a 50-kW klystron, a WR-1150 waveguide network and low-level RF electronics. By using HOM-damped cavities, longitudinal and transverse coupled-bunch instabilities can be avoided even at a maximum beam current of 600mA. A low-level control scheme, which can manage heavy transient beam loading, was designed, and a subset of the system was implemented. We report in this paper the construction and commissioning of this RF system.

## 1 INTRODUCTION

The KEK-ATF is a dedicated test facility for accelerator study concerning future $e^+e^-$ linear colliders [1]. It comprises a 1.54-GeV electron damping ring and a full-energy injector linac. Design parameters of the damping ring are given in Table 1. Beams consisting of 10-60 bunch bunch-trains are injected. During the short store time (~200 msec), the beam emittance will be radiation damped to about 1 nm·rad. It will be most challenging to obtain the very-low emittance beams with sufficient stability under high-intensity and multibunch conditions.

The RF system of the ATF damping ring (DR) is required to provide a sufficient cavity voltage to obtain a short bunch length (less than 5 mm) and to compensate for synchrotron radiation losses (155 keV/turn). At the same time, it must lower the higher-order-mode impedance of the accelerating cavities in order to avoid coupled-bunch instabilities. In addition, transient beam-loading effects at injection should be well regulated by the low-level system.

A 714-MHz RF system, which will meet these requirements, was designed [2] using 714-MHz HOM-damped cavities, which were developed at KEK. The original RF system was designed to use four cavities driven by a 250-kW klystron. We have so far constructed a subset of the system which used two cavities driven by a 50-kW klystron, due to limited funds. The ATF DR started commissioning using this RF system. With this system our temporary goal is to circulate a 100 mA beam with a total gap voltage of 0.5 MV. In the future, the RF system will be extended to the full system, which will allow us to attain the design beam current of 600 mA.

Table 1. Design parameters of the ATF damping ring.

| | |
|---|---|
| Beam energy: 1.54 GeV | Circumference: 138.6 m |
| RF frequency: 714 MHz | RF voltage: 1 (0.5)† MV |
| Number of bunch trains: 5 - 2 | Bunches/train: 10 - 60 |
| Particles/bunch: 1-3 $\times 10^{10}$ | |
| Horizontal beam emittance: 1.4 nm·rad | |
| Vertical beam emittance: 0.01 nm·rad | |
| Maximum beam current: 600 (100)† mA | |

† Parameters in parentheses indicate temporary target.

## 2 HOM-DAMPED CAVITY

Each cavity has four waveguide ports to extract HOM power, and additional HOM absorbers in the beam pipe. This scheme significantly reduces the longitudinal and transverse HOM impedances [3]. Cavity fabrication techniques were established through the construction of a prototype cavity [4]. This cavity was successfully tested under a dissipated power of up to 50 kW which is about three times higher than required.

With the same design, two cavities were manufactured by Toshiba corporation in fiscal year 1995. The Q-value of the cavities obtained was about 23,000, and the coupling coefficient was set to 2.3. Each cavity was conditioned on a test bench up to an input power of 44 kW for about 50 hours. The base pressures before and after the conditioning were about $1\times10^{-7}$ and $2\times10^{-8}$ Torr, respectively. These cavities were then installed in the

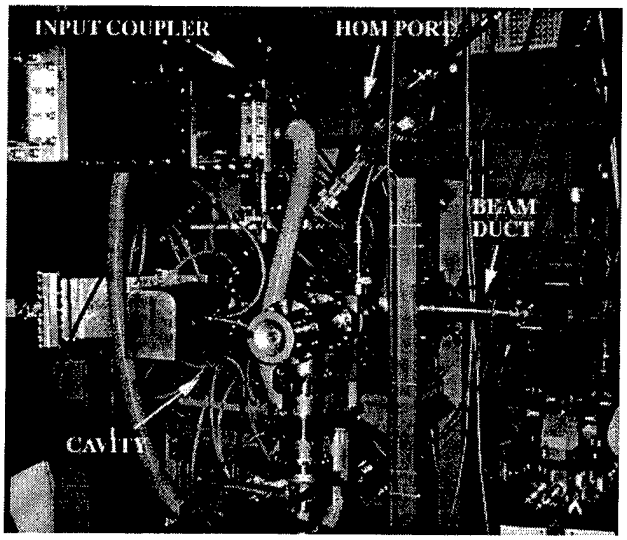



Fig. 1. The 714 MHz HOM-damped cavity installed in the ATF damping ring.

0-7803-4376-X/98/$10.00 © 1998 IEEE

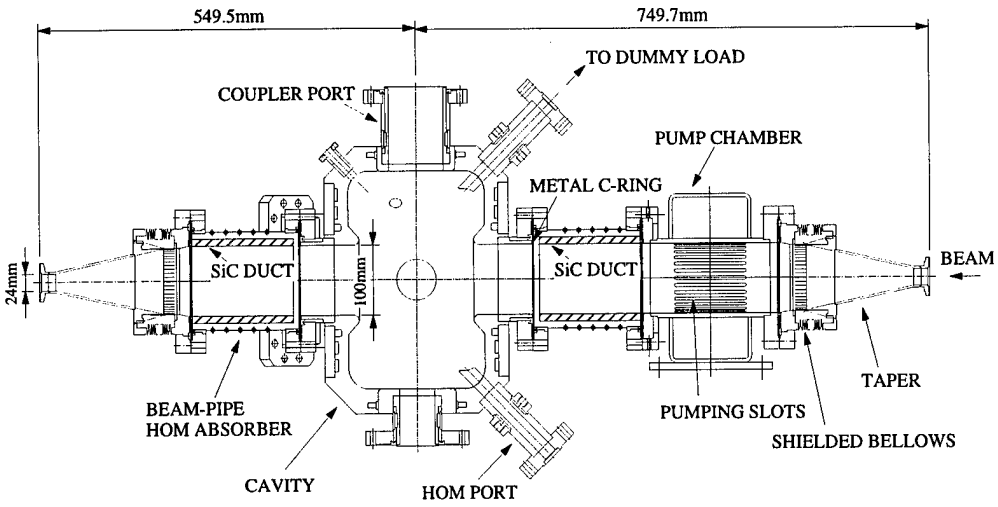



Fig. 2. Cross section of one cavity unit.

damping ring during October to December, 1996. They were further conditioned in the ring, which resulted in the base pressure of $1\times10^{-8}$ Torr before the commissioning. Figure 1 shows the cavity as installed.

Figure 2 shows a layout of one cavity unit. Two beam-pipe HOM absorbers were installed next to the cavity. Each cavity was evacuated by a turbo-molecular pump (300 l/s) and a sputter ion pump (200 l/s) which were connected to the rectangular pump chamber. Inside the pump chamber, a smooth passage for wall currents was provided using an inner duct of 6 mm thickness with thirty pumping azimuthal slots ($105\times5$ mm$^2$). Effective cavity pumping speeds were approximately 50 l/s (turbo pump) and 80 l/s (ion pump). The vacuum duct in the RF section was connected to the ring through taper-bellows assemblies. Each bellows was screened from the beam by beryllium-copper fingers, which are very similar in design as those used at the KEKB [5]. In order to arrange a smooth inner wall, a metal C-ring was installed between the conflat flanges used on the beamline.

## 3 HOM ABSORBERS

For the beam-pipe HOM absorbers, we adopted a shrink-fit technique, as was reported in ref. [6], with a small modification on its design. We first prepared a copper-duct assembly (a copper duct with both cooling-water pipe and stainless-steel collars brazed), and a duct of silicon-carbide (SiC) used for the microwave absorber. While heating the copper-duct to ~200°C in an inert-gas atmosphere, the SiC duct was inserted into the copper duct. After they were cooled to room temperature, the SiC was tightly fit in the copper duct (shrink-fit). Finally, vacuum flanges were TIG welded to the collars. In this way, five absorbers were manufactured, four of which were installed in the ring.

As the absorbing material, we investigated a special SiC material which has a conductivity of about 100 Siemens/m (about 20 times larger than the popular SiC material) in the frequency range of about 2-10 GHz. As reported in ref. [6], we first succeeded to produce a suitable SiC material by increasing the carbon amount contained in the SiC, but we could not obtain reproducible products at the second manufacturing attempt. We then tried another SiC material containing about 700 ppm of aluminum (higher than the regular product) after consulting with Toshiba Ceramics corporation. Through trial productions, we obtained reproducible SiC samples which have an effective conductivity of ~110 S/m at 3 GHz and of 57-68 S/m at 5-7 GHz. We therefore decided to use this type of SiC material. The effective conductivity of the four SiC absorbers, installed in the ring, were 65-90 S/m (at 3 GHz).

We have also developed waveguide HOM loads for termination of the HOM ports. The development of the load is described in an accompanying paper [7]. The cavities were initially commissioned without attaching any loads due to some delay in fabrication. At present, nine HOM loads have been completed, and eight of them will be installed during summer shutdown in 1997.

## 4 RF POWER SOURCE

A block diagram of the RF system is shown in Fig. 3. A commercial TV klystron, YK1265 from Phillips, was used as a power source. It can deliver the maximum RF power of 50 kW in CW mode. A power supply for the klystron was purchased from NEC corp. The power from the klystron is delivered to the cavities through a WR-1150 waveguide network. A newly developed 100-kW circulator was used to isolate the klystron from the cavities. The performance of the circulator include an input VSWR of less than 1.2, an insertion loss of less than 0.2 dB and an isolation of larger than 20 dB in the frequency range of 714±2 MHz. Waveguide components, such as E- and H- corner bends and a coaxial-waveguide transformer, were newly designed using a computer code HFSS [8].

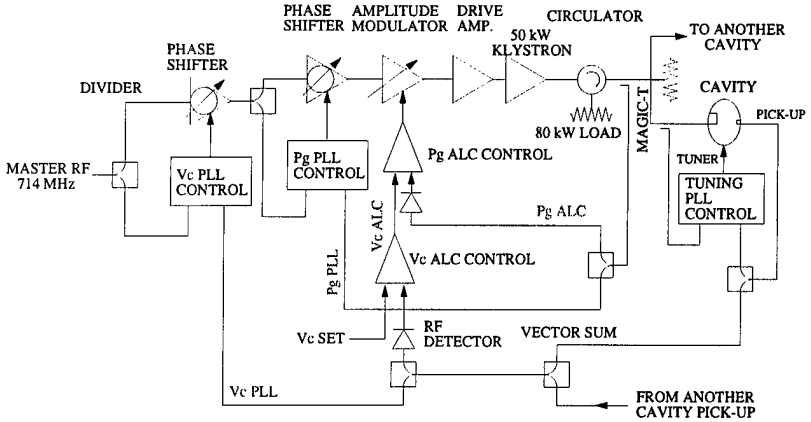



Fig. 3. Block diagram of the damping ring RF system.

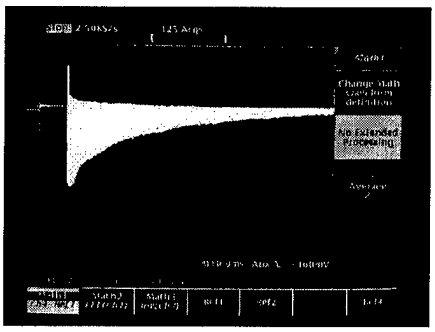


Fig. 4. Signal of the wall current monitor showing first stored beam in the ATF DR. Abscissa: time (100 msec full scale), ordinate: voltage (200 mV full scale).

## 5 LOW-LEVEL RF SYSTEM

The low-level RF system is required to minimize both steady-state and transient beam loading effects in accelerating cavities. In particular, a sudden change in the beam current at injection, which amounts to 120 mA per train, should be managed. Based on numerical simulations, we designed a low-level control scheme [9] that fulfills these requirements. Both cavity pre-detuning and phase jump at injection will be used. Direct feedback will be used to avoid the beam loading limit for experiments requiring high beam currents and low cavity voltages.

At present, the control scheme for the heavy transient beam loading has not been implemented, however will be installed in the near future. The current system is similar to that of TRISTAN [10], and many electronics modules for the TRISTAN were adapted. Some narrow-band modules, such as the phase shifter and the RF modulator, were newly developed.

In the main RF line (see Fig. 3), there are four feedback loops, referred as Vc PLL, Vc ALC, Pg PLL and Pg ALC. The first two loops regulate the phase and amplitude of the total accelerating voltage which is monitored by a vector sum of signals from the cavity pick-up probes. The other two are auxiliary loops to suppress both phase and amplitude fluctuations of the klystron output. Tuning of each cavity is controlled by another phase-lock loop.

## 6 COMMISSIONING

The ATF damping ring started commissioning on January 22, 1997, with a single-bunch beam of about 1 GeV. On January 30, the beam was successfully circulated in the ring for over 500 turns with RF turned off. Then, we applied an RF voltage of 180 kV, and succeeded to store the beam on January 31. Figure 4 shows the signal from the wall current monitor, which shows the first stored beam in the damping ring. Commissioning and tuning operations are currently underway. Multibunch operations will be started in autumn of 1997.

## 7 CONCLUSIONS

The damping ring RF system was designed and constructed. The damping ring started commissioning using this RF system, and we obtained the first stored beam in January, 1997. Tuning operations of the ring are underway to obtain the full specification of the beam parameters. The present RF system is a subset of the full RF system, which allows for a straight extension of the system in future.

## 8 ACKNOWLEDGMENTS

We wish to thank Profs. K. Takata and Y. Yamazaki for their encouragement and valuable advice, and S. Tokumoto and Y. Funahashi for useful discussions on mechanical designs. We also acknowledge much help and support given by the ATF collaboration team and by E-CUBE corporation during the construction of the RF system.

## REFERENCES

[1] "ATF Design and Study Report", KEK Internal 95-4.
[2] S. Sakanaka et al., Proceedings of the 1995 Particle Accelerator Conference, p. 1791.
[3] S. Sakanaka et al., Proceedings of the 1993 Particle Accelerator Conference, p. 1027 ; S. Sakanaka et al., Proceedings of the 1994 International Linac Conference, p. 281.
[4] S. Sakanaka et al., Proceedings of the 1995 Particle Accelerator Conference, p. 1788 ; S. Sakanaka et al., Proceedings of the Fifth European Particle Accelerator Conference, p. 2017.
[5] Y. Suetsugu, KEK Proceedings 96-6, p. 189.
[6] F. Hinode et al., Proceedings of the 1995 Particle Accelerator Conference , p. 1756.
[7] S. Sakanaka et al., in these proceedings.
[8] "HP85180A High-Frequency Structure Simulator", Hewlett-Packard Company.
[9] M.G. Minty et al., in these proceedings.
[10] M. Ono et al., KEK Internal 87-6, 1987.

# DEVELOPMENT OF A BROADBAND HOM LOAD FOR THE 714-MHz HOM-DAMPED CAVITY

S. Sakanaka, F. Hinode, K. Kubo, S. Tokumoto
High Energy Accelerator Research Organization (KEK), Oho, Tsukuba-shi, Ibaraki-ken, 305 Japan
K. Satoh, T. Miura, T. Naba
Toshiba Corporation, 2-4 Suehiro-cho, Tsurumi-ku, Yokohama, 230 Japan

*Abstract*

A 714-MHz higher-order-mode (HOM) damped cavity was developed at KEK, and two cavities of this design are under operation in the Accelerator Test Facility (ATF) damping ring. Each cavity is equipped with four waveguide ports to extract HOM power. In order to achieve the very low HOM impedance required for the damping ring, each waveguide port should be terminated by a broadband, low-reflection load. We have developed a broadband HOM load for this purpose. We describe the design, construction and RF characteristics of the HOM load.

## 1 INTRODUCTION

For RF acceleration in the ATF damping ring [1], a 714-MHz HOM-damped cavity has been developed at KEK. After a successful test of the prototype cavity under high-power operation, two cavities were manufactured and installed [2] in the damping ring. Each cavity is equipped with four rectangular waveguide ports to damp higher-order-modes [3]. In order to attain the very-low HOM impedance, that is required for the damping ring, each HOM port should be terminated by a broadband, low-reflection load. Incoming power to the load is excited by an interaction between the beam and the cavity HOM impedance. The spectrum of the HOM power will spread over a wide frequency range of about 1-10 GHz, which comes from the short bunch length (5 mm) and narrow beam pipe (24 mm in diameter) of the ring. The total power to the load will be less than 500 W, which was estimated using a parasitic-mode loss parameter of 1.0 V/pC/cavity.

As the starting point, a preceding design of the HOM load [4] for the PEP-II cavity was very helpful. We have also decided to install a microwave absorber inside the vacuum, since this can eliminate a potential source of reflection due to the vacuum window. To operate the cavity under a ultra-high vacuum, the load should have a low outgassing rate, and should be bakable up to a temperature of about 150°C.

## 2 DESIGN AND FABRICATION

The waveguide HOM load is required to have a low-reflection rate over a very-wide frequency range of 1-10 GHz. We set a practical design goal to achieve an input VSWR of less than 1.5 over a frequency range from 0.95 to 4 GHz. The specification of the HOM load is summarized in Table 1. For the microwave absorber, we have chosen silicon-carbide (SiC), which is a lossy dielectric material, because of its high loss-tangent, high thermal conductivity (170 W/m/K) and low outgassing rate.

Table 1. Specifications of the broadband HOM load.

| | |
|---|---|
| Working frequency: | 0.95 - 4 (0.95 - 10)† GHz |
| Waveguide dimensions: | 170×20 mm² (corner:R5 mm) |
| Cutoff frequency: 887.3 MHz | Input VSWR: < 1.5 |
| Maximum input power: 500 W | († Final target) |

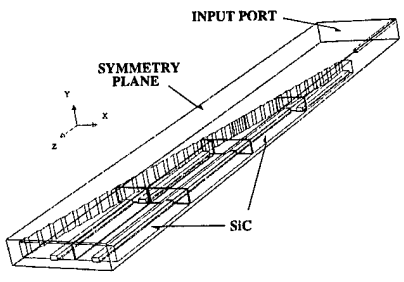



Fig. 1. A simulation model of the HOM load. Only one half of the structure was modeled.

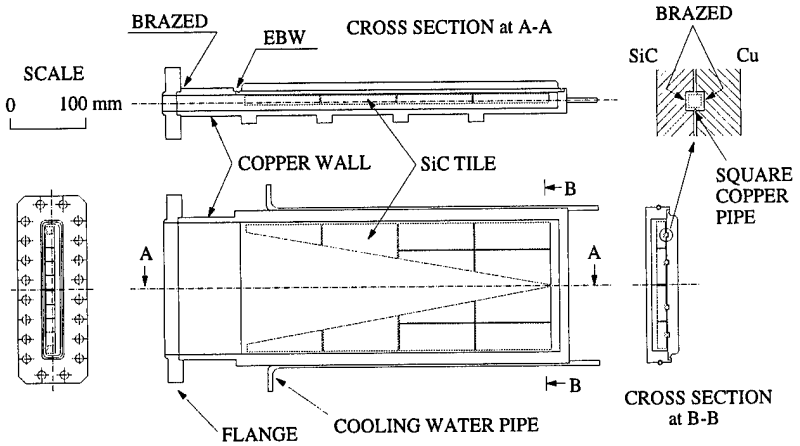



Fig. 2. Design of the HOM load.

0-7803-4376-X/98/$10.00 © 1998 IEEE

The basic design was made using computer codes. We mainly used the MAFIA code [5], and sometimes verified the result using the HFSS code [6]. An example of the simulation model is shown in Fig. 1. In parallel with the simulations, we carried out R&D on brazing SiC tiles to a copper plate (used for the wall). The R&D results were then fed back to the basic design.

Figure 2 shows our final design. Several SiC tiles, separated by a gap of ~1.5 mm, were arranged to form two taper wedges. The SiC tiles were brazed on a wider side of the waveguide wall; cooling-water pipes were arranged at the side wall. The dimensions of each SiC taper are 400 mm in length, 12 mm in thickness and 10-81 mm in width. The thickness of the taper was optimized to obtain as low a reflection as possible for a given taper length.

During brazing the SiC tiles to the copper wall, a large thermal-stress arises due to the considerable difference in the thermal-expansion coefficient between them. In order to effectively ease this stress, we adopted a square copper-pipe (6mm×6mm, 1-mm thick) as a strain buffer (see Fig. 2). Although this causes a certain reduction in the thermal conductance, this is quite acceptable (see Section 5). An active joining material (Ag-Cu-Ti-In alloy) was used for the brazing. The optimum brazing conditions, such as a temperature and forced pressure, were established through R&D.

A prototype HOM load was manufactured by the following process. The main body of the load was first machined from an OFHC copper plate; then, a stainless-steel vacuum flange and cooling-water pipes were brazed. Each SiC taper was sintered by two pieces, 200-mm long each. These tapers were cut to several pieces, and a groove for the brazing was cut in each tile. After the SiC tiles were brazed on a copper-plate, this plate assembly was electron-beam welded to the main body, like a lid. To relax thermal stress due to the welding, we arranged a lip structure along the welding line.

## 3 DIELECTRIC CONSTANT OF THE SIC

In order to obtain low-reflection characteristics in the mass-production stage, it is very important to reproduce the dielectric constant of the SiC, which was obtained previously. We used an SiC product, named CERASIC-B, from Toshiba Ceramics corporation. In collaboration with industry, we produced SiC samples, and measured their complex dielectric constant using an HP85070A dielectric probe and an HP8510C network analyzer. After carrying out production several times, we have almost established reproducibility. The SiC tiles used for the load were then manufactured.

Figure 3 shows the measured dielectric constant of the SiC tiles which were used for the prototype load. At this time, we obtained an unforeseen result: two kinds of SiC tiles were produced in the same batch. About half of the tiles (referred as type A) had a permittivity close to that of the previous samples; the other half (type B) had a quite

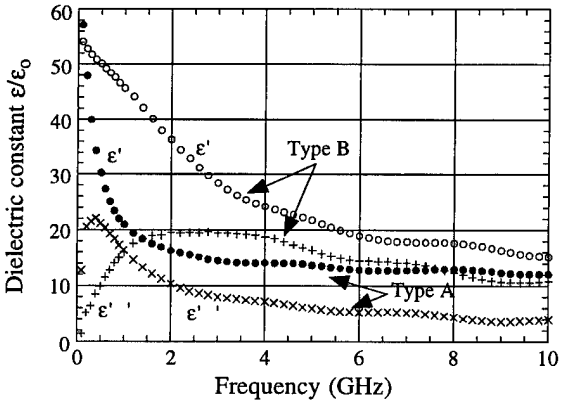



Fig. 3. Measured dielectric constant of SiC tiles used for the prototype load. The real and imaginary parts of the dielectric constant are shown for two different types of SiC tiles produced (for type A (regular) and type B (irregular)).

larger permittivity. It was found out that a large number of tiles had become warped due to a manufacturing error; these tiles had to be sintered once more to correct the warp. It was guessed that the irregular type-B dielectric property would be caused by this second sintering.

Fortunately, most of the irregular tiles were those used for the latter half of the taper. It was shown from a simulation that the reflection rate would be well within our specifications if we use irregular tiles only at the latter half of the taper. Therefore, we decided to use them for the prototype load as well as for mass-production.

## 4 RF CHARACTERISTICS

After successful fabrication, the reflection coefficient of the prototype HOM load was measured using an HP8510C network analyzer. We prepared four pairs of coaxial-waveguide transformers which, in combination, covered the frequency range of 0.95-4 GHz. In the measurement setup, the network analyzer was connected to a regular coaxial-waveguide transformer, and then transformed to the flat waveguide using a taper. Figure 4 shows the prototype HOM load being measured. Before the measurement in each frequency band, we carried out a full two-port TRL (Thru/Reflect/Line) calibration at the output ports of the tapers. The calibration was verified using an offset short and a sliding load.

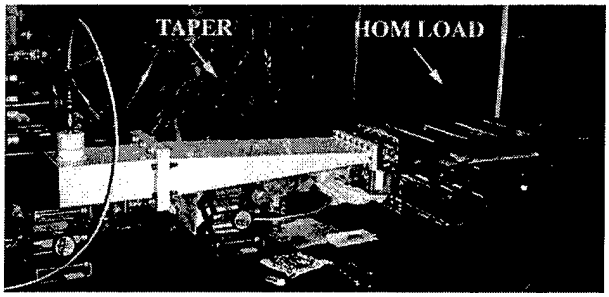



Fig. 4. Broadband HOM load under measurement.

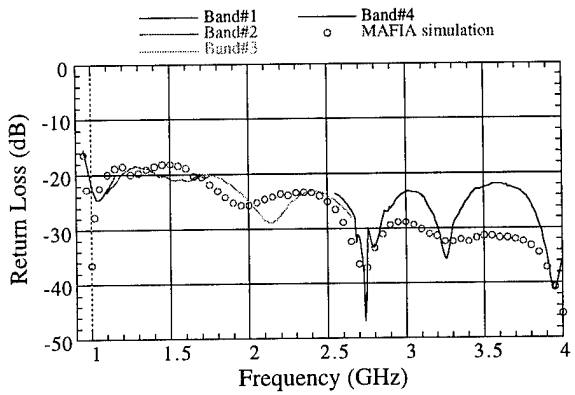



Fig. 5. Measured return loss of the prototype HOM load. The open circles indicate the MAFIA simulation results.

Figure 5 shows the results of the measurement and a simulation. The obtained return loss was less than -18 dB in the frequency range 1-4 GHz, which corresponds to a VSWR of less than 1.3. Even at the lowest frequency of 0.95 GHz, only 1.07-times the cutoff frequency, we obtained a return loss of -15.5 dB (VSWR: 1.4), which was sufficiently small.

The simulation result, indicated by open circles, was obtained from seven MAFIA runs. Each run covered a frequency span of about 0.5 GHz; we used the measured permittivity of the SiC at the center frequency of the span. There was a fairly good agreement between the measured and simulation results.

For the measurement in the frequency range 2.55-4 GHz, we used an $S_{11}$ 1-port calibration rather than the TRL calibration, by using a flash and offset shorts as well as a sliding load. In this case, we obtained a better (but not sufficiently good) result when the calibration was verified using another offset short. This certain difficulty in the calibration would come from a possible mode conversion between the $TE_{10}$ and $TE_{30}$ modes, since the cutoff frequency (2.66 GHz) of $TE_{30}$ mode lies in this range.

## 5 THERMAL ANALYSIS

Figure 6 shows a time-averaged power-loss distribution in the SiC tiles calculated with the MAFIA code. A monochromatic input wave of 1 GHz, with a total power of 500 W per load, was assumed in this simulation, although an actual incoming wave would have a broadband spectrum. It can be seen that there are

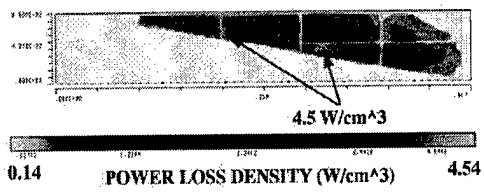



Fig. 6. Power-loss density in the SiC absorber on the median (half of the thickness) plane.

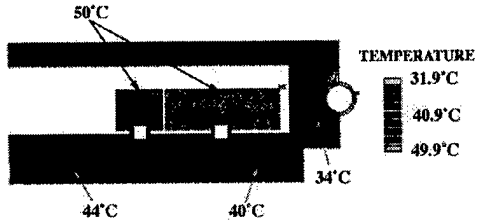



Fig. 7. Temperature distribution on a plane cut at ~230 mm away from the tip of the taper, which was calculated using the ANSYS [7] code. We assumed a film coefficient of 1.4 W/cm$^2$/K and a bulk temperature of 30°C for the cooling water.

two locations (about 110 and 230 mm apart from the tip of the taper) where the power-loss density obtains a maximum of about 4.5 W/cm$^3$.

Figure 7 shows the result of a thermal analysis at the location where the maximum power is deposited. We assumed a longitudinally-uniform model and a rough power distribution. The maximum temperature in the SiC was expected to be about 50°C, or even lower, by considering that the power density at other longitudinal location was smaller. The strain-buffer pipe caused the temperature difference of about 4°C between the opposite sides, which is quite acceptable.

## 6 CONCLUSIONS

A broadband HOM load was designed based on computer simulations and R&D on fabrication techniques. A prototype load was then fabricated and measured under low power. It was shown that the load had excellent low-reflection characteristics. The VSWR of the load was less than 1.3 in the frequency range of 1 - 4 GHz.

With the same design, we have completed eight additional HOM loads. These loads will be installed in the damping ring during the summer shutdown of 1997.

## 7 ACKNOWLEDGMENTS

We would like to thank Yasunao Takeuchi for valuable discussions and offering useful data of SiC properties, and H. Matsumoto for valuable advice. We also acknowledge the great effort to reproduce the SiC properties made by S. Fukuoka and other members of Toshiba Ceramics corporation, as well as valuable advice given by Y. Sakai.

## REFERENCES

[1] "ATF Design and Study Report", KEK Internal 95-4.
[2] S. Sakanaka et al., in these proceedings.
[3] S. Sakanaka et al., Proceedings of the 1993 Particle Accelerator Conference, p. 1027.
[4] R. Pendleton et al., Proceedings of the 1995 Particle Accelerator Conference, p. 1800 ; R. Pendleton et al., Proceedings of the Fourth European Particle Accelerator Conference, p. 2013.
[5] CST GmbH, Computer Simulation Technology.
[6] Hewlett-Packard Company.
[7] Swanson Analysis Systems, Inc.

# HOM ABSORBER FOR THE ARES CAVITY

Y. Takeuchi, K. Akai, N. Akasaka, E. Ezura, T. Kageyama, H. Mizuno,
F. Naito, H. Nakanishi, H. Sakai, Y. Yamazaki
KEK, High Energy Accelerator Research Organization, 1-1 Oho, Tsukuba, 305 Japan
T. Kobayashi
Institute of Applied Physics, Tsukuba Univ., 1-1 Ten-nodai, Tsukuba, 305 Japan

*Abstract*

Two types of sintered SiC (silicon carbide) ceramics has been developed and applied as the HOM absorbers for the second prototype ARES cavity (ARES96). One is bullet-shape SiC ceramics and the other is a tile one. The prototype cavity equipped with these absorbers was successfully tested with an electron beam in the TRISTAN accumulation ring. High power tests of these absorbers were carried out using an L-band RF power source. The HOM absorber designs and the results of the tests are discussed.

## 1 INTRODUCTION

A second prototype of ARES cavity (ARES96) for KEKB was built[1]. Figure 1 shows a schematic drawing of the accelerator cavity of ARES96. The accelerator cavity has four rectangular waveguides, in each of which two bullet-shape SiC ceramics are inserted at the end as the HOM absorbers. Two grooved beam pipes with 32 SiC tiles are connected to the accelerator cavity to absorb dipole modes of the HOMs.

The HOM power (at frequencies above 0.7 GHz) to be handled will be on the order of ~10 kW per cavity, corresponding to ~1.25 kW per bullet-shape absorber.

On the other hand, the design value of the maximum RF power (at frequencies above 0.7 GHz) absorbed by the SiC tiles in the grooved beam pipes is about 400 W per cavity, corresponding to ~100 W per eight tiles in the groove.

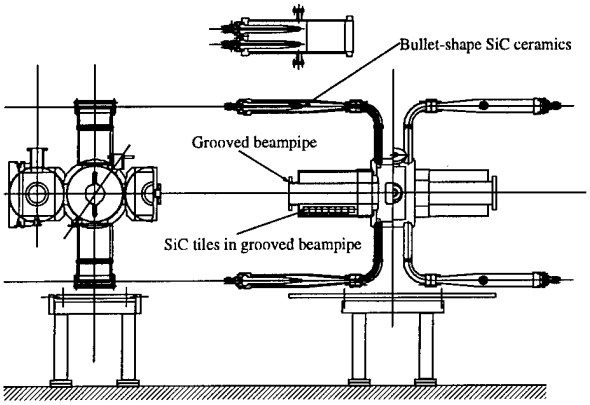



Figure 1: A schematic drawing of the accelerator cavity of ARES96.

ARES96 which equipped with these absorbers was successfully tested with an electron beam (~500 mA) in the TRISTAN accumulation ring. The maximum HOM powers absorbed by the waveguide HOM loads and the SiC tiles in the grooved beam pipe were 0.8 kW and 120 W. These values were not enough as high power tests for KEKB. Therefore high power tests were carried out using an L-band RF power source to verify the performance as the HOM loads.

## 2 BULLET-SHAPE SiC ABSORBER

### *2.1 Design*

The first prototype of the ARES cavity (ARES95) adoped sixteen bullet-shape SiC absorbers (diamiter 40 mm, effective length 400 mm)[2]. Using the results[3][4], a new bullet-shape SiC absorber was designed for ARES96. The absober dimensions are 55 mm in diameter, and 400mm in total effective length including a 150mm nosecone section. The SiC absorber has a cooling water channel which is bored inside and led near the nosecone tip. The distance between the nosecone tip and the water channel is 30 mm.

Figure 2 shows the dielectlic constant $\varepsilon'_r$ and loss tangent of the SiC ceramics, measured using a dielectric probe kit (HP85070B). Figure 3 shows the frequency response of the reflection ($S_{11}$) from the HOM waveguide including the E-bend and taper waveguide, which was simulated with hfss[5]. The $TE_{10}$ mode in the waveguide was assumed in this simulation. The absorption under

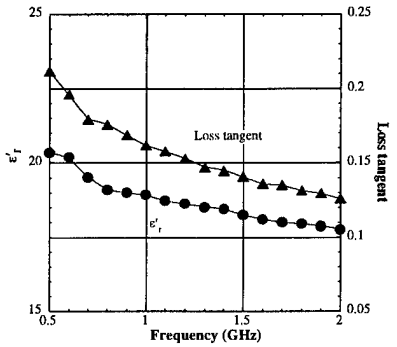



Figure 2: The dielectric constant and loss tangent of the SiC ceramics are plotted as a function of frequency.

0-7803-4376-X/98/$10.00 © 1998 IEEE

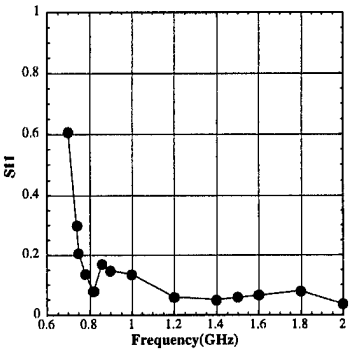



Figure 3: The frequency response of the reflection ($S_{11}$) from the HOM waveguide including the E-bend and taper waveguide.

1GHz was improved by adopting thicker SiC than that of ARES95. The RF characteristics of this type absober were precisely analized [4].

### *2.1 High power test*

Figure 4 shows a layout of the high power test. The SiC absorber was inserted from the end of an L-band rectangular waveguide (WR650). The standing-wave ratio VSWR was measured ~1.14. The high power test was carried out using a CW klystron ($f$ = 1296 MHz) up to a power of ~3.3 kW. Temperature at the position $P$ of the SiC absorber was monitored using a infrared thermometer. The SiC absorber functioned normally without any vacuum, thermal, or discharge trouble up to 3.3 kW of RF power. Figure 5 shows the temperature rise at the position $P$ and the vacuum pressure corresponding to the RF power loss in SiC. After this test, we also measured temperatures at the position $A$~$G$ in figure 4 using thermosensitive labels, which indicate the maximum temperature by changing their colors. The maximum temperature rise is about 33~38 deg. at the position $C$ when the RF power loss was 1.25 kW.

This SiC absorber satisfies our specification enough and would handle much higher power than 3.3 kW.

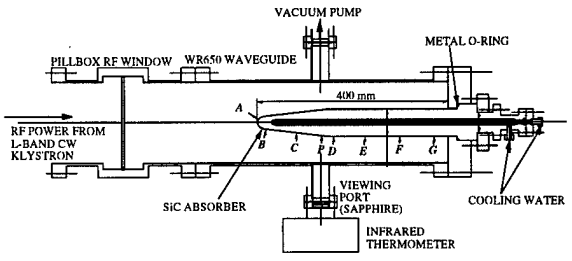



Figure 4: A layout of the high power test.

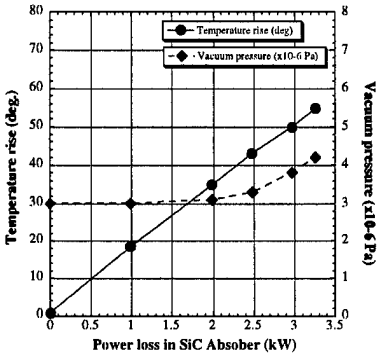



Figure 5: The temperature rise at the position P and the vacuum pressuer corresponding to the RF power loss in SiC.

## 3 SiC ABSOBERS IN THE GROOVED BEAM PIPES

### *3.1 Design*

Two grooved beam pipes with 32 (8x4) SiC tiles were connected to the accelerator cavity of ARES96 to absorb dipole modes of the HOMs. Two tiles (48 x 48 x 10 mm$^3$) and 6 tiles (48 x 48 x 20 mm$^3$) were fastened with stainless steel bolts (M6, tightening torque 150 kgf·cm) on the stainless steel plate in the groove. And the plate was cooled by water. Gold foil (0.05 mm thickness) was sandwiched between the SiC tiles and the stainless steel plate to make a better thermal contact.

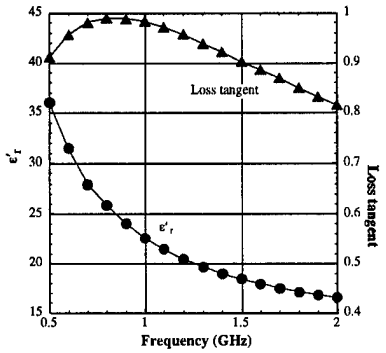



Figure 6: The frequency response of the dielectlic constant $\varepsilon'_r$ and loss tangent of the SiC ceramic tile.

Figure 6 shows the frequency response of the dielectlic constant $\varepsilon'_r$ and loss tangent of the SiC ceramics. We adopted a SiC ceramics which has relatively large dielectric constant and loss tangent at the frequencies under 1 GHz in order to design a compact load. Figure 7 shows the frequency response of the reflection ($S_{11}$) from the grooved beam pipe with the SiC tiles, which was simulated with hfss. The $TE_{11}$ mode in the beampipe was assumed in this simulation.

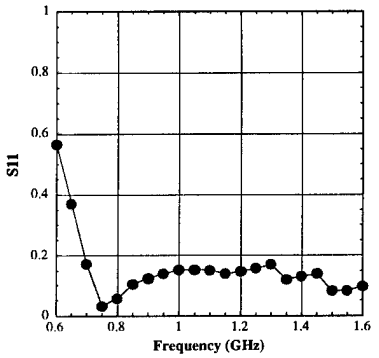



Figure 7: The frequency response of the reflection ($S_{11}$) from the grooved beam pipe with the SiC tiles.

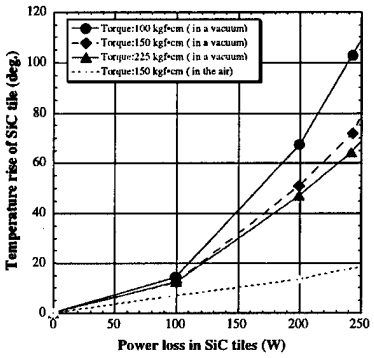



Figure 9: The temerature rise of the #4 SiC tile with different tightening torques in a vaccum. The open circles shows the teperature rise of the #4 SiC tile in the air.

### *3.2 High power test*

Eight SiC tiles with gold foil fastened on the cooling plate with bolts (M8) were tested using the same test waveguide set shown in figure 4. Figure 8 shows a schematic drawing of the test sample. The SiC tiles on the cooling plate was put in the waveguide from the end plate. The temperature of the #4 SiC tile was monitored by the infrared themometer. And the temperature of each SiC tile was measured by using termosensitive labels.

Figure 9 shows the temerature rise of the #4 SiC tile with different tightening torques. The open circles in figure 9 show the teperature rise of the SiC tile in the air. The temperature rise of the tile in the air increase linearly with the power loss. On the other hand, the temperature rise in a vacuum does not. It was considered that the thermal coductivitiy under vacuum between the SiC tile and the cooling plate depend on the temperature rise. The tensile stress in the bolt decreases as the temperatures of the SiC tile and bolt increase, because the coefficient of thermal expansion of the SiC ceramics ($4.5x10^{-6}$ /K) is smaller than that of the stainless steel ($17x10^{-6}$ /K). The tension in a stainless steel bolt (M8, degreased) is about 500 kgf at a tightening truque of 150 kgf·cm. If we assume that the temperatures of the SiC tile and the bolt tightened with the toruqe of 150 kgf·cm are equarl, then the tension in the bolt becomes 0 when temperature rise is about 55 deg.. Therefore we have to pay attention to the temperature rise of the SiC tiles and the tension in the bolts. We are planning to test using coned disk springs to keep the tension in the bolt. Titanium bolts, which has the smaller coefficient of thermal expansion than stainless steel, will be tested.

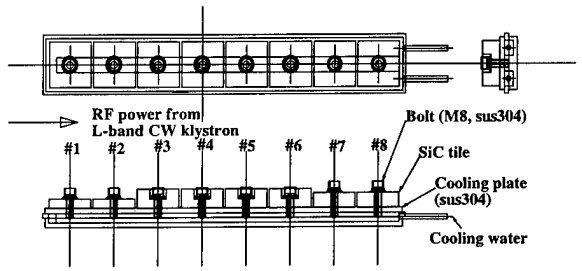



Figure 8: The schematic drawing of the test sample.

The maximum temperature rise in the SiC tiles (tightening torque 225 kgf·cm) was measured about 20~25 deg. on the #3 SiC tile when the RF power loss was 100 W. Since the temperature rise is small enough at 100 W of RF power, we will apply this simple cooling scheme of fastening SiC tiles with bolts to the ARES cavity for KEKB.

## 4 CONCLUSION

Two types of sintered SiC ceramics has been developed and applied as the HOM absorbers for the second prototype ARES cavity (ARES96). One is bullet-shape SiC ceramics and the other is a tile one. ARES96 was successfully tested with an electron beam (~500 mA) in the TRISTAN accumulation ring. Furthermore, high power tests of these absorbers were carried out using an L-band RF power source. These HOM absorbers were demonstrated to be capable of the RF power specifications. Based on these studies, designing the HOM absorbers for the production cavity is in progress.

## REFERENCES

[1] T. Kageyama et al., "Dvelopment of high-power ARES Cavities", in this conference.
[2] T. Kageyama et al., "The ARES Cavity for the KEK B-Factory", Proc. of EPAC96, p2008.
[3] Y. Takeuchi et al., "HOM Absorber for the KEKB Normal Conducting Cavity", 1995 Particle Acc. Conf., KEK Preprint 95-69 (1995).
[4] Y. Takeuchi et al., "The SiC Absorber for the KEKB ARES Cavity", Proc. of EPAC96, p2020.
[5] HP Part No. 85180A, Hewlet Packard Corp.

# BEAM TEST OF AN RF DAMPED CAVITY AT THE PHOTON FACTORY STORAGE RING

M. Izawa, S. Sakanaka, S. Tokumoto and T. Takahashi , Photon Factory, KEK, Tsukuba-shi, IBARAKI, 305, Japan and
T. Koseki, Y. Kamiya, Institute for Solid State Physics, The University of Tokyu, Minato-ku, Tokyo, Japan

*Abstract*

We have developed a new 500 MHz damped cavity[1~6], the feature of which is that the beam ducts with large diameter are attached to the cavity and that a part of the beam ducts is made of SiC[7,8]. The higher-order-modes (HOM's), which propagate out from the cavity through the beam duct, are damped by the SiC parts. The low power measurement using a cold model and the high power test[9] using a prototype model had been already done. In the autumn of 1996, two damped cavities were installed in the PF ring and operated in the scheduled user run for about two months. The operation of these new cavities was quite successful. On the last day of the scheduled user run before long shut down, we tried very high current beam and succeeded to store the current of 773 mA, the new record in the PF ring.

## 1 INTRODUCTION

The Photon Factory storage ring is a 2.5 GeV electron / positron ring dedicated for synchrotron radiation experiments. The ring is now being remodeled to provide a lower emittance beam. The reconstruction started in the beginning of this year (1997). The new damped cavity was designed for this new high brilliant configuration ring. Ahead of remodeling of the ring, two of four cavities working in the PF ring were replaced by new damped cavities. These new damped cavities together with two old ones were operated in the last scheduled user run.

The high current storage was also tried on the last day of the scheduled user run before the start of reconstruction of the ring.

Figure 1 shows a schematic view of the damped cavity. The cavity has a beam ducts with somewhat large diameter. HOM's whose frequencies are above the cutoff frequency of the duct propagate out to the beam duct and are absorbed by SiC. HOM's below the cutoff frequency of the beam duct still remain in the cavity, however, these can be detuned not to introduce the coupled-bunch instability by the frequency shift method using two fixed tuner[10].

Unloaded Q of the accelerating mode was 39500 with two fixed tuners, a movable tuner and an input coupler attached. The shunt impedance of the accelerating mode is estimated to be 6.9 MΩ. The SiC is a kind of sintered SiC and has the dimension of the inner diameter of 140 mm, the outer diameter of 160 mm and of the length of 150 mm. The resistivity of the SiC was about 50 Ωcm in the frequency range of 1~5 GHz. The SiC is fixed inside of the copper duct by shrink fit. The copper duct has a water-cooling channel on the outer surface. The SiC has good thermal conductivity, therefore, the rise of temperature of the SiC duct is negligible in the usual operation of the PF ring.

The conditioning of the cavity was carried out in both CW and pulse mode. The power of up to 90 kW(CW) and 120 kW(pulse) was input to the cavity during the conditioning.

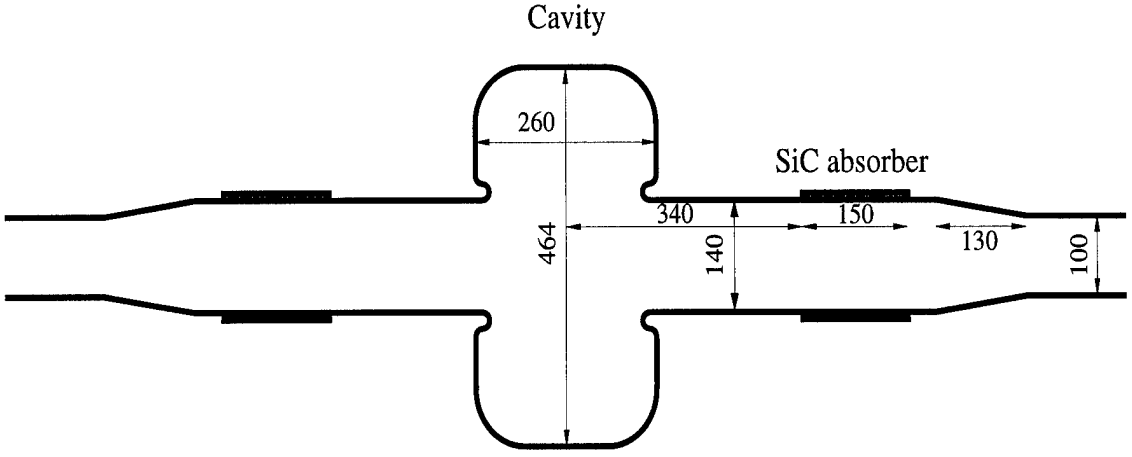



Figure: 1 Schematic view of the damped cavity

0-7803-4376-X/98/$10.00 © 1998 IEEE

## 2 INSTALLATION

Figure 2 shows two damped cavities installed in the ring. The input coupler is attached to the upper part of the cavity. The movable tuner is set in the side port of the cavity. Two fixed tuners are set in the bottom and the other side port. In the figure, a part of wave guide is removed. Between two cavities, an evacuation chamber is placed which has two 400 l/s ion sputter pumps, two Titanium sublimension pumps, a vacuum gauge and a quadruple residual gas analyzer. The base pressure was in the range of $10^{-10}$ Torr after baking.

## 3 BEAM TEST

Figure 3 shows the vacuum pressure together with the output power of the klystron. Data were taken when the beam was at first stored. Each cavity has one klystron as a power source. Therefore the output power in the figure shows the generator power for each cavity. The stored current is also printed in the figure. The range of vacuum pressure is $10^{-8}$ Torr before the elapsed time of about 5 hours and $10^{-7}$ Torr after that time. As seen in the figure, the vacuum pressure became higher and higher with the increase of the stored current, however, gradually lowered. Apart from such slow change of the vacuum pressure, there exist burst outgassing. The worst one among such burst outgassing took place at the elapsed time of about 3.5 hours, however, the peak pressure did not exceeded the range of $10^{-7}$ Torr. About 10 hours after the first beam injection, the stored current of more than 400 mA was attained without any serious rf and vacuum problem.

The conditioning using beam continued for 4 days with the maximum stored current of 500 mA. After the conditioning, the base pressure decreased to the range of $10^{-9}$ ~$10^{-10}$ Torr at the stored current of 350 mA. No burst

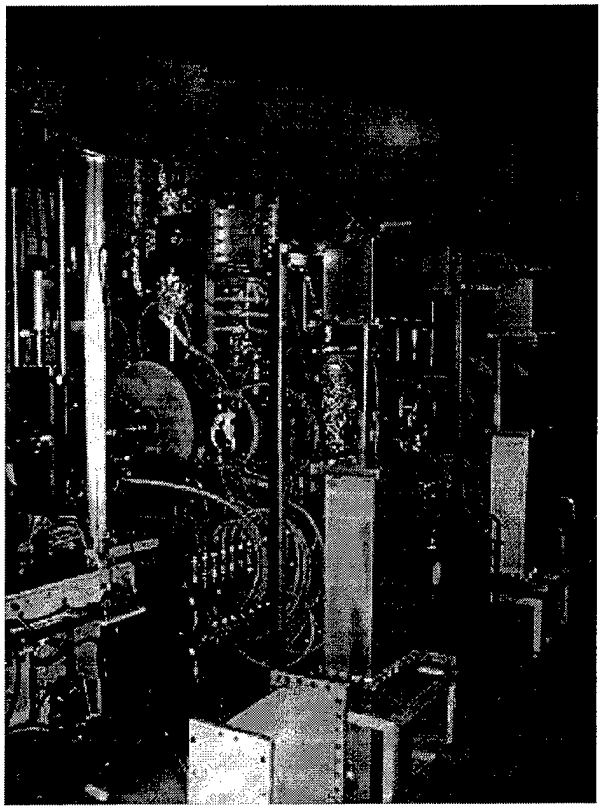


Figure: 2 The damped cavities installed in the ring

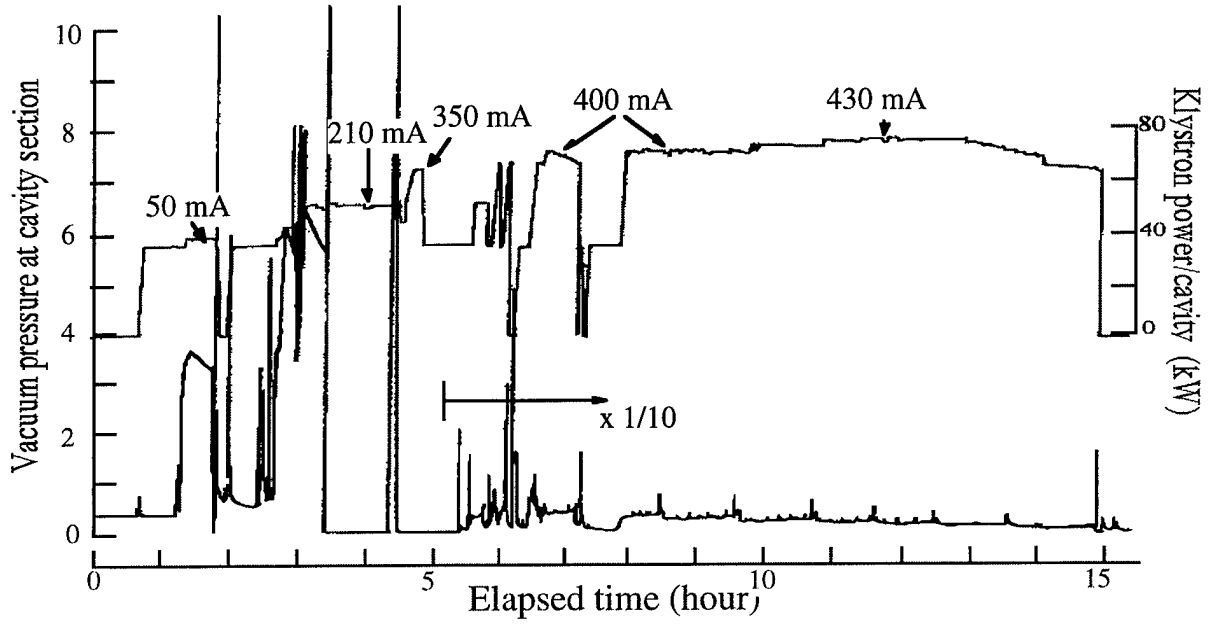



Figure: 3 Change of the vacuum pressure at first storage

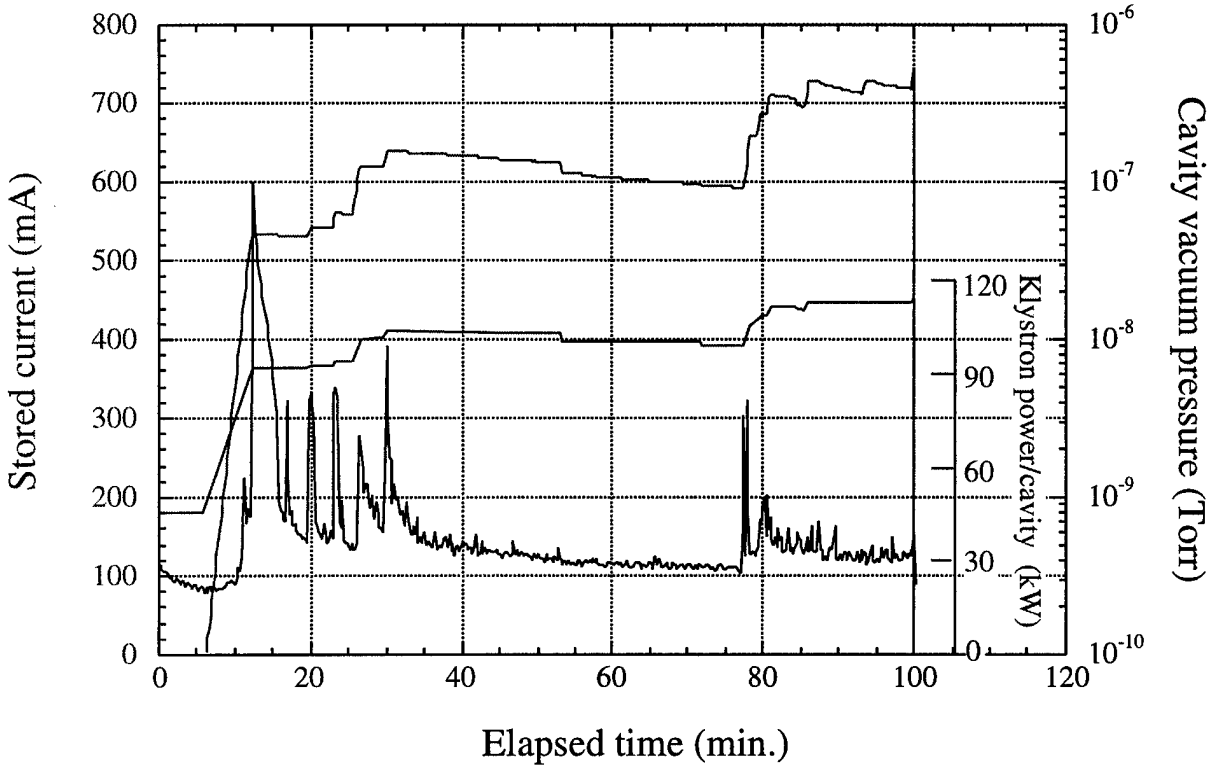



Figure:4 Change of vacuum pressure at high store current.

outgassing was observed in the usual operation after the conditioning.

The detuning of HOM's was quite successful. We could not find out any transverse coupled bunch instability. The longitudinal coupled bunch instability was still observed. However, it is considered to be due to old type cavities since the frequency of the beam spectrum was different from the resonance frequency of HOM's in the new cavities.

## 4 HIGH CURRENT BEAM TEST

In the end of the scheduled user run in 1996, we tried to store the electron beam as much as possible. The record of the stored current in the PF ring was around 500 mA. Figure 4 shows the new record was achieved. As mentioned in section 1, CW conditioning was made below the power of 90 kW. The vacuum pressure began to rise when the cavity input power exceeded 90 kW. Although the rise of the pressure was not so large, the data in figure 4 suggest the outgassing come from the input coupler. Though the beam was down at 743 mA in the figure, the maximum stored current was 773 mA, the new record in the PF ring. The transverse coupled bunch instability was not observed up to the maximum current. The longitudinal instability was clearly seen on the spectrum analyzer, however, it was not so harmful since the injection rate did not decreased drastically. We could not find out any difficulties to operate the ring at such high current except for the lifetime of the beam, which would be overcome by conditioning using beam to get the low vacuum pressure around the ring.

## REFERENCES


[1] T. Koseki, M. Izawa and Y. Kamiya, Proceedings of the 1993 Paticle Accelerator Conference, 2 (1993)p930.

[2] T. Koseki, Y. Kamiya and M. Izawa, Proceedings of the 9th Symposium on Accelerator Science and Technology, (1993) p246.

[3] T. Koseki, Y. Kamiya and M. Izawa, Proceedings of the 4th European Particle Accelerator Conference,3 (1994) p2152.

[4] T. Koseki, Y. Kamiya and M. Izawa, Rev. Sci. Instrum, 66 (1995) p1926

[5] T. Koseki, M. Izawa and Y. Kamiya, 1995 Particle Accelerator Conference and International Conference on High-Energy Accelerators, Dallas, TX, May 1-5, 1995,p1794.

[6] T. Koseki , K. Shinoe, Y.Kamiya, M. Izawa, S. Tokumoto, T. Miura, and K. Sato, Proceedings of the 5th European Particle Accelerator , Sitges, Barcelona 10-14 June 1996

[7] M. Izawa, T. Koseki, Y. Kamiya and T. Toyomasu, Rev. Sci. Instrum, 66(1995)p1910

[8] M. Izawa, T. Koseki , Y.Kamiya, S. Tokumoto, T. Tajima, N. Taniyama and M. Kudo, Proceedings of the 5th European Particle Accelerator , Sitges, Barcelona 10-14 June 1996.

[9] T. Koseki, et al, somewhere in this proceedings.

[10] M. Izawa, H. Kobayakawa, S. Sakanaka and S. Tokumoto, KEK Internal 88-7, 1988

# STUDIES OF MAGNETIC CORES FOR JHF SYNCHROTRONS

M.Fujieda*, Y.Mori, H.Nakayama, C.Ohmori, S.Sawada, and Y.Tanabe†,
KEK-Tanashi, 3-2-1 Midori-cho, Tanashi 188, JAPAN
E.Ezura, A.Takagi, M.Toda and M.Yoshii, KEK, 1-1 Oho, Tsukuba 305, JAPAN
T.Tanabe and T.Uesugi, CNS, University of Tokyo, 3-2-1 Midori-cho, Tanashi 188, JAPAN

*Abstract*

Magnetic cores suited for the RF cavities of JHF (Japanese Hadron Facility) synchrotrons have been studied. The shunt impedance of the cavity is required about 2kΩ/m because of the high acceleration voltage of more than 10kV/m. The permeability of the core should meet with the RF frequencies of the 3GeV booster and the 50GeV ring. Characteristics of several ferrites and a Fe-based soft magnetic alloy composed of amorphous and ultra-fine grain structure have been measured with a test bench. The shunt impedance of the soft magnetic core named "FINEMET" is high enough. It is stable when input RF power is increased, while those of samples of ferrites drop rapidly. The permeability of "FINEMET" strongly depends on the bias current. Because of its low Q value, the bias current is not necessary for its new material. "FINEMET" is considered as one of the most probable candidate for JHF synchrotrons.

## 1 INTRODUCTION

The main parameters of the two synchrotrons for the JHF (Japanese Hadron Facility) are given in Table 1.

Table 1 : Main parameters

| | 3GeV booster | 50GeV ring |
|---|---|---|
| average beam current | 200$\mu$A | 9.6$\mu$A |
| average circulating current | 7A | 7A |
| repetition rate | 25 or 50Hz | 0.3Hz |
| accelerating voltage | 420kV | 270kV |
| RF frequency | 2~3.4MHz | 3.4~3.5MHz |

Because of the space limit for the RF apparatus, we need the voltage of more than 10kV/m. For stable acceleration under high beam current, the shunt impedance seen by beam of more than 1kΩ/m is necessary. Taking into account the RF amplifier, we need more than 2kΩ/m for the real shunt impedance of the cavity. If about 20 cores can be loaded in one meter, we require maximum accelerating voltage more than 500V and shunt impedance more than 100Ω per one core consequently.

In order to shift RF frequency tuned to momentum of proton, bias current is supplied. The permeability of core has to vary according to bias current quickly.
Consequently the required characteristics of a core are shown as follows:

- shunt impedance ~ 100Ω
- quick response for bias current

The measurements for searching cores satisfying above requirements was performed. This paper presents the results of their RF characteristics for 4 ferrites and one soft magnetic core, particularly about their permeability and shunt impedance.

## 2 MEASUREMENT APPARATUS

### 2.1 *Components of the test bench*

The measurements every one core were done with the test bench. The cross section of the test bench is shown in Figure 1.
The inner diameter of cavity was 732mm and its height was 255mm. The magnetic core was put on between two cooling plates. It was held by a stainless steel plate and adhered to the cooling plates. The RF power was supplied through the RF feeder and flowed to the earth through the variable vacuum capacitors and inside of the cavity. The bias current up to 1000A was able to be supplied.

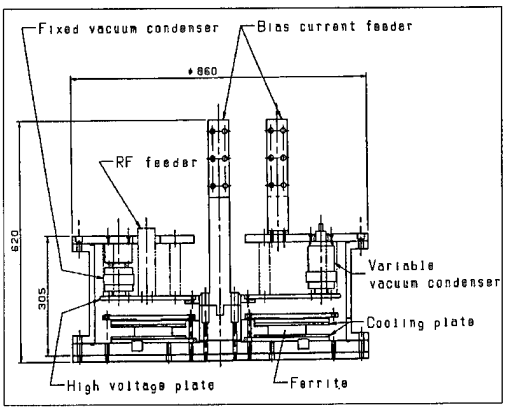



Figure 1: Cross section of the test bench.

*also : Nuclear Science Research Facility,Institute for Chemical Research, Kyoto University, Gokanosho, Uji, Kyoto 611, JAPAN
†also : TOSHIBA Co.

0-7803-4376-X/98/$10.00 © 1998 IEEE

### 2.2 *Equivalent circuit*

Figure 2 shows the equivalent circuit including the RF amplifier and the bias current supply. The output impedance of the RF amplifier was 50Ω. But the shunt impedance of the cavity was not usually 50Ω. So the impedance matching circuit was incorporated between cavity and power supply.

The waveforms of the voltage and current detected by a probe and a current transformer were monitored by an oscilloscope. Then their maximum value $V_{max}$, $I_{max}$ and phase difference were measured and the impedance was calculated. The inductance was obtained from the resonant frequency and the value of the variable capacitors. The complex permeability and quality factor of the core were evaluated from the impedance and inductance.

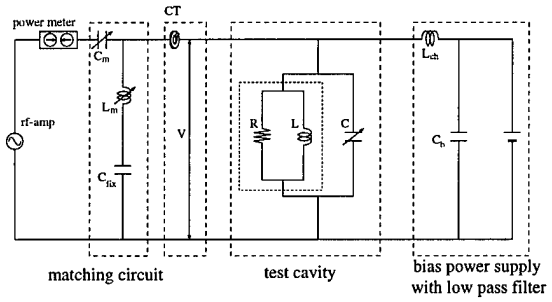



Figure 2: Equivalent circuit of the test bench.

## 3 MEASUREMENTS

### 3.1 *Magnetic cores*

We show the list of cores selected in Table 2.

Table 2 : List of cores

| Name | I.D.[mm] | O.D.[mm] | $\mu_p^{'}$ at 3MHz |
|---|---|---|---|
| N5C | 260.0 | 635.0 | 225 |
| FT3M | 320.0 | 579.0 | 2821 |
| 4M2-302 | 200.0 | 500.0 | 39.5 |
| 4M2-303 | 250.0 | 500.0 | 58.1 |
| SY2 | 299.8 | 500.1 | 181 |

I.D. and O.D. mean inner and outer diameter, respectively. The real permeability $\mu_p^{'}$ at 3MHz is shown in the third column of Table 2. All the cores have one inch thickness. The cores except FT3M are Ni-Zn ferrites. N5C and SY2 have lower Q value and 4M2-302 and 4M2-303 have higher one than usual ferrites. FT3M is one of the soft magnetic cores named "FINEMET". This is a Fe-based soft magnetic alloy composed of amorphous and ultra-fine grain. This complex permeability is about $(\mu_p^{'}, \mu_p^{''}) = (1000, 1000)$ around 4MHz and the Curie temperature is $570°C$.

### 3.2 *permeability*

The bias current dependence of the permeability and shunt impedance were measured. We fixed RF frequency at 3.0MHz and changed dc bias current from 0A to 1000A. With changing the value of variable capacitors, the resonant condition was achieved. Figure 3 shows the bias current dependence of SY2 and FT3M. In the 3GeV booster, the RF frequency has to vary from 2MHz to 3.4MHz. The permeability of All the samples varied enough within bias current of 1000A FT3M was more sensitive for bias current than SY2. We do not have to supply bias current because the Q value of FT3M is so low that FT3M keeps high impedance over the wide frequency range.

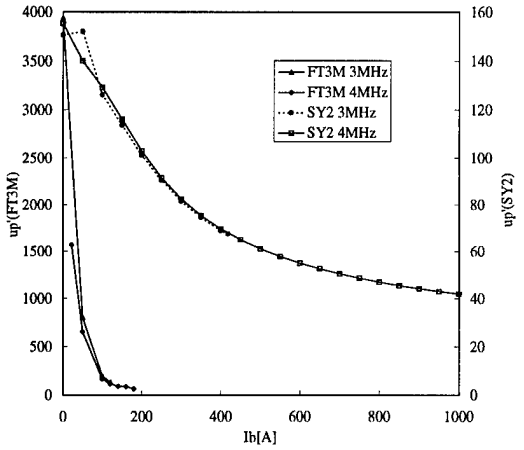



Figure 3: Bias current dependence of SY2 and FT3M.

### 3.3 *Shunt impedance*

Shunt impedance is given from the following formula.

$$R_p = \mu_0\, t\, ln(\frac{O.D.}{I.D.}) \times \mu_p^{'} Qf$$

In this paper, $\mu_p^{'} Qf$ which is independent of size of core shows shunt impedance. $B_{RF}$ stands for RF flux density and it is written as : $B_{RF} = \frac{V_{RF}}{\omega S}$. $V_{RF}$ and S mean input RF voltage and cut surface area, respectively. If the accelerating voltage of 500V per one core is replaced with $B_{RF}$, it becomes about 80~100 gauss at 2MHz. The increment of accelerating voltage as 2 times in the future is considered. Therefore the range of $B_{RF}$ applied for a core becomes about from 80 to 200 gauss. The shunt impedance and the Q value of ferrite are decreasing as the input RF power is increased. The temperature rise of core causes this and leads to reduce its shunt impedance. We have to apply more RF power to keep a constant voltage consequently. The core is desired to maintain a regular impedance for RF flux density. Figure 4 shows the change in shunt impedance for

increase of RF flux density with dc bias current at 2MHz. The data of 4M2 was measured at 2.7MHz.

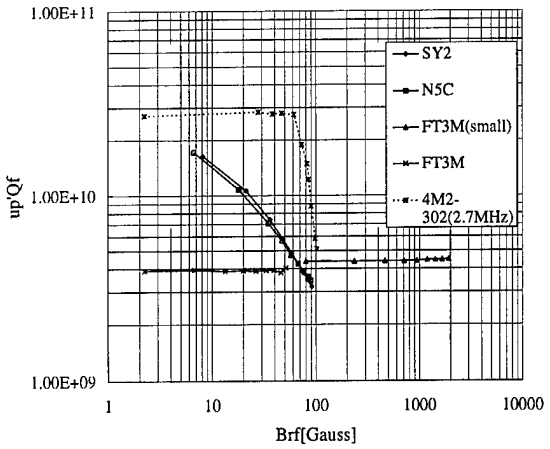



Figure 4: Change in shunt impedance for RF flux density.

Here the inner and outer diameter of FT3M(small) were 32mm and 70mm, respectively. 4M2 had the highest shunt impedance. However it caused High Loss Effect(HLE) beyond about 60 gauss. Its shunt impedance was decreased suddenly, while FT3M kept stable impedance for $B_{RF}$. The ferrites except 4M2 had much higher impedance than FT3M up to about 70 gauss. But FT3M showed higher impedance in the practical range of $B_{RF}$.

In a proton synchrotron, RF frequency must be tuned as the revolution frequency of protons. Bias current is varied as rapid as the repetition rate of accelerator in order to shift RF frequency. The fast repetition occurs that the RF characteristics of magnetic cores become worse. So the test with varying ac bias frequency was performed. The result at the RF frequency of 2MHz and bias frequency of 50Hz are shown in Figure 5. All ferrites had less shunt impedance than the results at the constant bias current.

### *3.4 Others*

Temperature rise of FT3M was measured. Surface temperatures of FT3M were monitored with thermocouples. The temperature reached $140°C$ after 8 hours with RF power of 500W. FT3M did not show any variation of the characteristics.

FT3M has much higher Curie temperature than ferrites, as $570°C$. The cooling system of cores will be easy accordingly.

The RF cavity with "FINEMET" core will have low Q value. If the Q value of RF cavity is enough low to make beam instability dumped quickly, instabilities do not matter for high intensity proton synchrotrons.

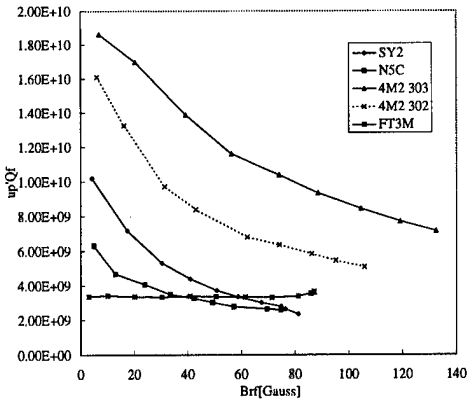



Figure 5: Shunt impedance for RF flux density with ac bias frequency of 50Hz.

## 4 CONCLUSION AND PERSPECTIVE

We studied characteristics of magnetic cores for JHF. The frequency and bias current dependences were measured. FT3M satisfies our required terms for both synchrotrons. The shunt impedance of FT3M is independent of RF flux density and very stable. It is not necessary for FT3M to be supplied bias current, for the Q value of FT3M is low enough. 4M2 seems to be suitable to 3GeV booster, but it cannot be used for 50GeV ring because of HLE.

Taking account of present results, we have developed a test RF cavity with FT3M cores. FT3M has very low Q value. The beam instability may be reduced by inserting FT3M to a RF cavity accordingly. But it is unknown how the beam loading is in case that the Q value is less than 1.0. The power test, temperature test and impedance measurement have been done for this cavity. The beam loading will be studied with electron gun and this cavity.

## 5 REFERENCES

[1] Y.Mori et al., INS Report, JHP-30 July(1996) (in Japanese).

[2] T.Uesugi et al., INS Report, JHP-31 January(1997) (in Japanese).

[3] K.Saito et al., Beam Science and Technology, published by Nuclear Science Research Facility, Inst. for Chem. Res., Kyoto Univ. 2(1997) pp.15-19.

# A WIDEBAND RF CAVITY FOR JHF SYNCHROTRONS

C. Ohmori, M. Fujieda[1], S. Machida, Y. Mori, H. Nakayama, K. Saito[2], S. Sawada, Y. Tanabe[3], M. Yamamoto[4], KEK-Tanashi, 3-2-1 Midori-cho, Tanashi, Tokyo 188, Japan
E. Ezura, A. Takagi, M. Toda, M. Yoshii KEK 1-1 Oho, Tsukuba, Ibaraki 305, Japan
T. Tanabe and T. Uesugi, University of Tokyo, 3-2-1 Midori-cho, Tanashi, Tokyo 188, Japan

*Abstract*

Thirty kilo watt "wide band" cavity has been developed for a test cavity of Japanese Hadron Facility(JHF). A new material, "FINEMET" which has very broad band impedance for the RF frequency, high permeability and large shunt impedance is used for the magnetic core of the cavity. Acceleration voltage of 10.4 kV which is larger than the designed value has been obtained. The characteristics of the core are also suitable to generate isolated RF pulses for the barrier bucket. The results for the barrier bucket are described.

## 1 INTRODUCTION

Accelerator complex of JHF[1, 2, 3] consists of 200 MeV linac, 3 GeV booster and 50 GeV main ring. The accelerators will be constructed at the north end of the KEK site. The booster is a rapid cycling proton synchrotron with a repetition rate of 25Hz. The required voltage for the acceleration is 420 kV and the frequency range is 2 to 3.4 MHz[4]. The voltage and frequency range for the main ring are 270 kV and 3.4 to 3.5 MHz, respectively. The expected beam intensity in the booster is $5x10^{13}$ppp (protons per pulse). The designed beam intensity in the main ring is $2x10^{14}$ppp. Circulating currents of both synchrotrons are about 7 A. Because of the very high beam currents, the cure of the space charge effects[5], the beam loading effects and some instabilities is essential. One of the most significant instabilities is the coupled bunch instability[6] because the harmonic numbers are 4 for the booster and 17 for the main ring. In order to cure these problems, a wide band radio frequency (RF) cavity is considered. It is expected that the wakefield which causes the coupled bunch instability is damped very quickly because of the low Q value.

### 1.1 *Requirements*

The requirements for the JHF cavity are following:

- Because of the limited space for the accelerating cavity, the RF voltage of more than 10 kV/m is necessary for the main ring. And about 13 kV/m is required for the booster.
- In order to satisfy the stability condition for the beam loading, the impedance seen by the beam should be about 1 kΩ/m.
- As the growth rate of the coupled bunch instability is very fast for the high-Q parasitic resonance, there should not be any high Q parasitic one.

### *1.2 Characteristics of FINEMET*

The wide band cavity , in which the ring cores of a new material are loaded, has been developed in order to prove these advantages of the wide band cavity. The material, "FT3M(FINEMET)", is made with the thin tape of the Fe-based alloy which consists of amorphous and crystal with the size of nano-meter. The tape is coated with silica for insulation. It has a very high permeability and a low Q factor. Typical parameters of the core are tabulated in Table 1. Characteristics of the core have been measured by another ferrite test cavity[7,8] which has been developed for the measurements of magnetic cores in order to find the most suitable magnetic material for the RF cavities of the JHF synchrotrons. The amorphous cores have been measured. However, the FT3M core was the most suitable material for the wide band cavity at this moment. Other characteristics of the core are summarized as following:

- Shunt impedance is independent of the RF voltage.
- Characteristics of the core are stable for high temperature more than 150 °C because of very high Curie temperature (about 600 °C).
- It is technically possible to make a large core because it is not necessary to press the core with a heavy weight.

Table 1. Parameters of the core

| | |
|---|---|
| Diameters | 67 cm(O.D), 30cm(I.D) |
| Thickness | 2.5 cm |
| Permeability@3.4MHz | 1550 |
| Q@3.4MHz | 0.63 |
| R@3.4MHz | 83Ohm |

### *1.2 The aims of the test cavity*

The aim of the 30 kW test cavity is to prove the following:

- The required accelerating voltage of 10 kV/m can be obtained.
- The isolated pulse for the barrier bucket can be generated.

[1] Also Institute for Chemical Research, Kyoto University.
[2] Also Hitachi Co. Ltd.
[3] Also Toshiba Co. Ltd.
[4] Also Research Center for Nuclear Physics, Osaka University.

0-7803-4376-X/98 /$10.00 © 1998 IEEE

- The frequency of the parasitic resonance is very high and/or the quality factor is low enough to avoid the dangerous growths of the instabilities.
- The beam loading and transient beam loading effects are controllable.

## 2 RF CAVITY

Figure 1 shows the test cavity and the 30 kW RF amplifier. Behind the cavity, there is a high voltage station and a power supply for an electron gun which will be used for the experiments on the beam loading effects. A tetrode, 4CM30,000A is employed to drive. The cavity has two acceleration gaps which are connected by bus bars. Figure 2 shows the schematic diagram of the cavity and amplifier. The RF excitation is provided inductively through a loop around 6 cores in the cavity without any direct DC connection to the cavity. The two turn loop between the plate of the tube and the plate power supply was employed to increase the impedance which the amplifier sees.

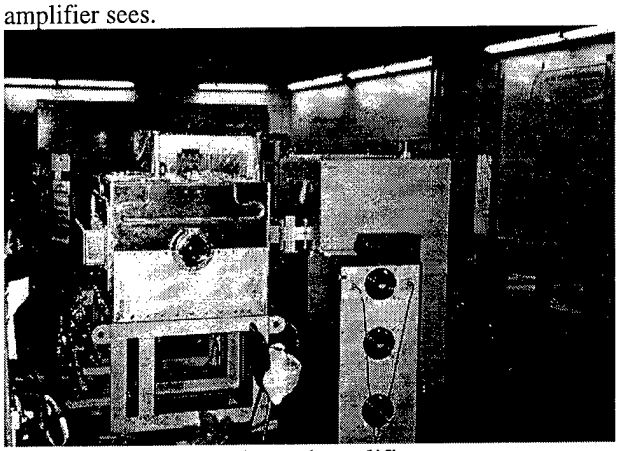


Figure: 1 The test cavity and amplifier.

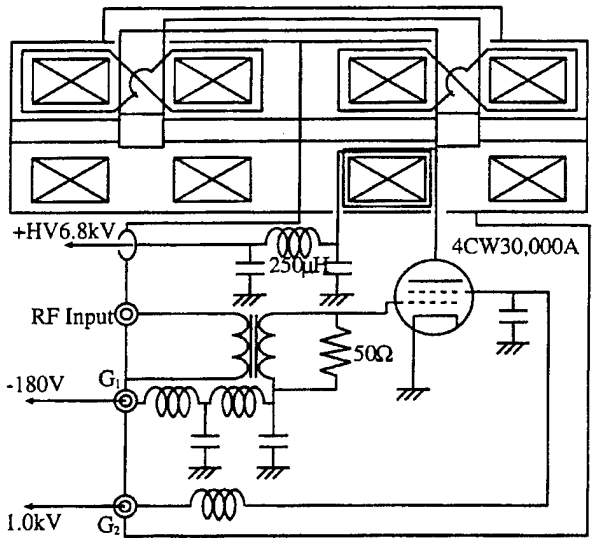



Figure: 2 The schematic diagram of the cavity and amplifier

## 3 IMPEDANCE MEASUREMENTS

The impedance of the cavity was measured by a network analyzer. No dangerous parasitic resonance which may excite the coupled bunch instability has not been observed up to 30 MHz by the measurement at the acceleration gap. Figure 3 shows the impedance curve obtained. The peak impedance is consistent with the measurement for each core by the ferrite test cavity. Each cell of the cavity has 12 cores and the total impedance of the cores is about 900 Ω at the resonant frequency. As the each cell is connected as a parallel circuit, the peak impedance becomes about 450 Ω.

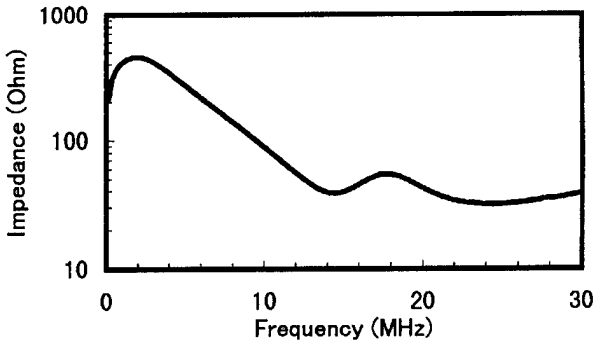



Figure: 3 The impedance of the cavity.

## 4 RF VOLTAGE

The RF voltage of the cavity was measured by the high voltage probe of 1000:1. The driving RF current wass also observed by a current transformer(CT). Figure 4 shows the typical RF voltage when the amplifier was operated in class AB operation. Because of the class AB, the distortion of the RF voltage by the higher harmonics was small. However, it became larger in the class B operation. The modification of the amplifier to the push-pull one by two tetrodes is being planed. Figure 5 shows the gap voltage respect to the observed RF current where Ip means the direct current from the plate power supply. The maximum voltage obtained in the safe operation condition was 10.4 kV per cavity and it is larger than required voltage for the main ring. The tetrode was driven by the class B operation. The impedance of the cavity calculated by this figure was 450 Ω and it was consistent with the impedance measured by the network analyzer. The maximum voltage obtained was limited by the available power of the amplifier and the plate voltage. It is expected that higher power amplifier can excite higher voltage because the impedance of the cavity is constant.

In order to obtain the higher voltage, the development of a new material has been started. The measurement for a small core of the material, FT3L, shows that it has higher Q-value and larger impedance than FT3M. The perpendicular magnetic field more than 3 kG is required during the heat treatment to make the core. We are designing the special high temperature oven and large aperture magnet.

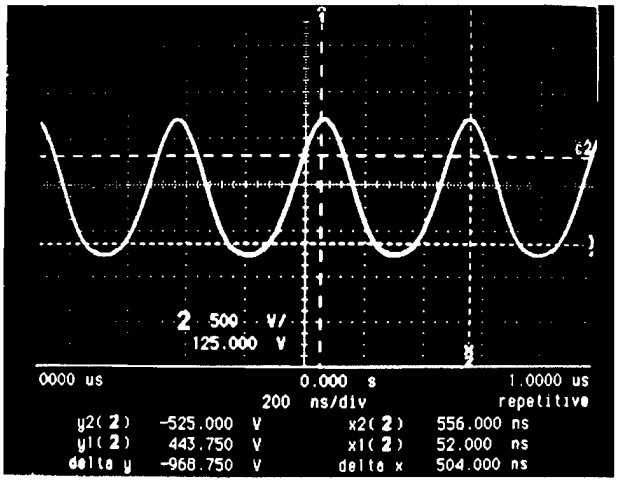



Figure 4: The typical RF voltage signal in the class AB operation.

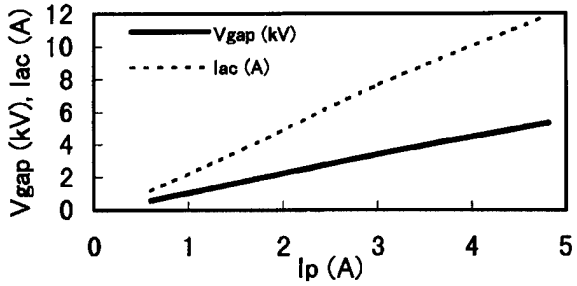



Figure: 5 The gap voltage (solid line) and RF current observed by the CT (dashed line) respect to the plate current.

The frequency sweep was performed with no bias condition. As shown in Fig. 3, the impedance was almost constant for the frequency range of 2 to 3.4 MHz. Although there is no tuning system, the RF voltage was very stable for the frequency sweep from 2 to 3.4 MHz as shown in Fig. 6.

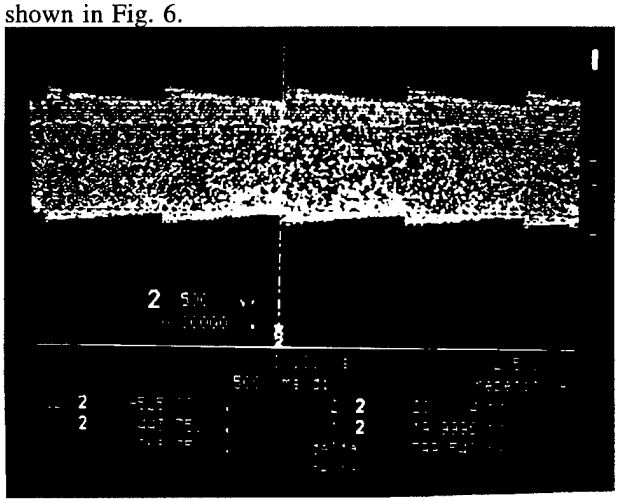


Figure 6: The RF voltage for the frequency sweep of the range of 2 to 3.4 MHz. The repetition rate is 1 Hz.

## 5 BARRIER BUCKET

Another advantage of the wide band cavity is that it is suitable for the barrier bucket. The brier bucket requires an isolated pulse. Figure 7 shows the typical RF voltage obtained in the class AB operation. The gap voltage was twice of the voltage measured. The maximum gap voltage of about 11.3 kV was obtained by the class B operation of the tube, increment of the plate voltage and modification of the cavity into one gap structure by removing the bus bars which is connecting with another cell. By this modification, the cavity impedance became twice and was suitable for the high voltage operation. However, the distortion of the voltage is not negligible as the operation of the tube was class B. This distortion will be cured by the modification of the amplifier into a push-pull amplifier by two tetrode tubes.

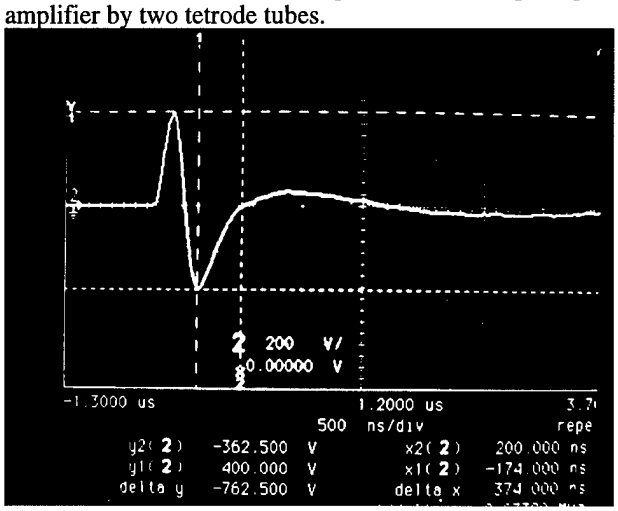



Figure 7: The typical barrier bucket voltage signal in the class AB operation.

## CONCLUSIONS

The test cavity using a new material has been developed. The voltage more than the designed value has been obtained. In order to achieve the higher voltage, a new material is being developed. The impedance measurement shows that the cavity has no dangerous parasitic resonance. An isolated pulse for the barrier bucket was generated and the maximum voltage of 11.3 kV was obtained. However, the distortion of RF voltage was not small because of the class B operation of the single tube. It is expected that the distortion will be improved by the planned modification of the amplifier to a push-pull amplifier.

## REFERENCES

[1] Y. Mori et al.: `The Japanese Hadron Facility`, contribution to this conference.
[2] Y. Mori et al.,: Proc. of 10th Symp. On Acc. Sci. and Tech. , Tokai 1995.
[3] S. Machida et al., Proc. of 5th EPAC, Sitges 1996.
[4] C. Oomori et al., Proc. of 10th Symp. On Acc. Sci. and Tech., Tokai 1995.
[5] S. Machida et al.: 'High Beam Current Handling and its Cures in the JHP Synchrotrons`, contribution to this conference.
[6] T. Uesugi et al.: `Longitudinal Coupled Bunch Instability in the JHP 50GeVMain Ring`, contribution to this conference.
[7] M. Fujieda et al.: `Studies of Magnetic Cores for JHF Synchrotrons`, contribution to this conference.
[8] T. Uesugi et.al., JHP-31, in Japanese.

# PLUNGER FREQUENCY CONTROL OF THE SIDE COUPLED ACCELERATING STRUCTURE FOR THE IFUSP MICROTRON

J. Takahashi, M.N. Martins, J.A. de Lima, A.A. Malafronte, L. Portante, M.T.F. da Cruz, P.R. Pascholati
Laboratório do Acelerador Linear, Instituto de Física da Universidade de São Paulo
Caixa Postal 66318, 05315-970, São Paulo, SP, Brazil

*Abstract*

A $\beta = 1$ accelerating structure for the IFUSP Microtron has been built. The 17-cavity structure and the tuning plungers placed at both ends of the structure are described. Details from some of the processes, like machining and pre-tuning of the cavities, brazing of the pieces and the final tuning of the whole structure are given. The final results obtained for the structure are presented and the dynamic tuning system based on moving plungers described.

## 1 INTRODUCTION

The Instituto de Física da Universidade de São Paulo (IFUSP) is building a 31 MeV cw racetrack mictrotron (RTM). This is a two-stage microtron that includes a 1.93 MeV injector linac feeding a five-turn microtron booster (RTM-1). After 28 turns, the main microtron (RTM-2) delivers a 31 MeV continuous electron beam. The injector linac consists of a 0.97 m long capture section and a 1.35 m long pre-accelerator. The whole accelerator uses only 38 kW of RF power, provided by a single 50 kW cw klystron, operating at 2.450 MHz. The 100 keV injection beam line, the end magnets for the microtron booster and the $\beta = 1$ accelerating section for the main microtron have been assembled. The fabrication of the other 3 RF sections is under way.

## 2 THE $\beta$=1 IFUSP STRUCTURE

The 1.04 m long $\beta = 1$ structure for the main microtron is composed of 17 accelerating cells (AC) and 16 coupling cells (CC) brazed together as showed in Fig. 1. The

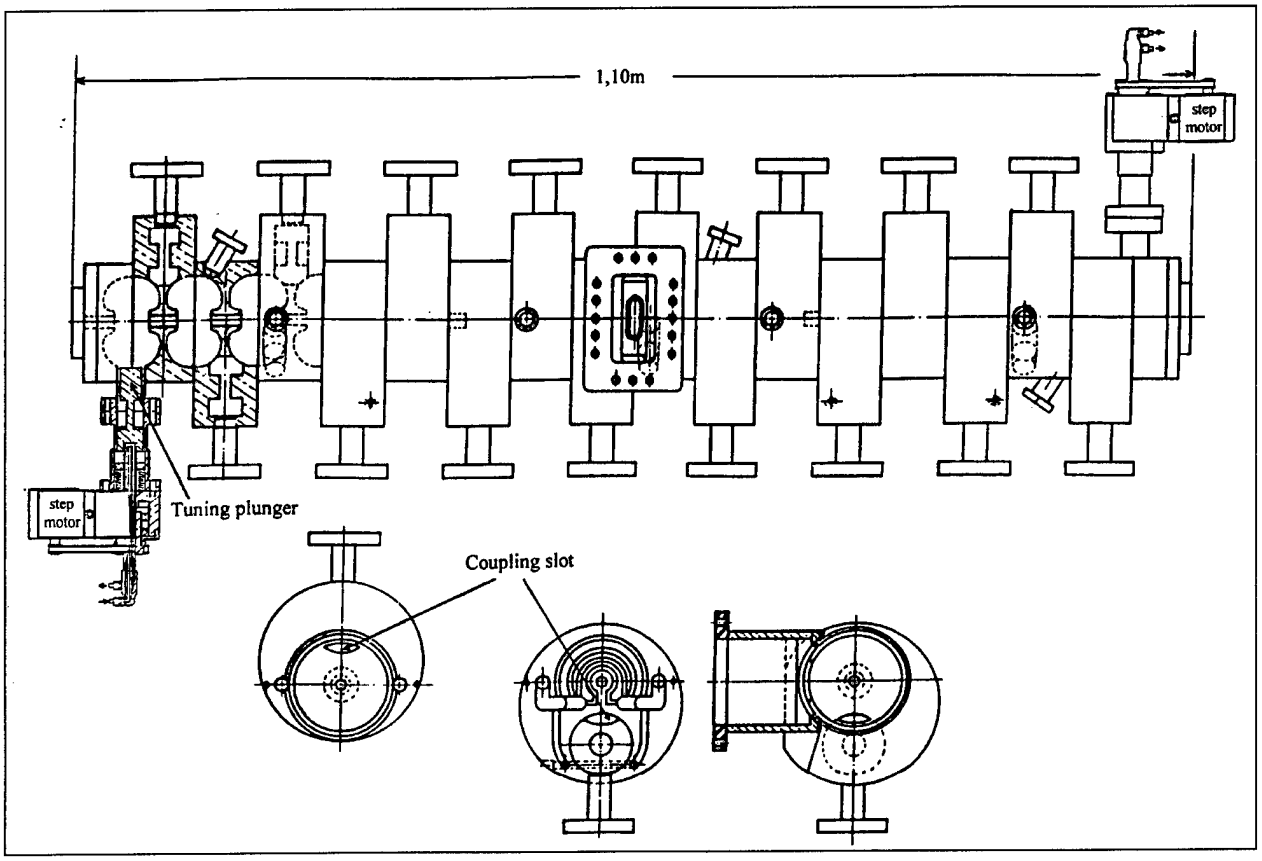



Figure 1: Schematic drawing of the $\beta$=1 structure

0-7803-4376-X/98/$10.00 © 1998 IEEE

engineering project is a side coupled design (SCS) developed at Los Alamos National Laboratory [1]. We chose the side coupled design because the vacuum properties are better and the power flow droop is lower than those of the coaxially coupled design, and it presents a shunt impedance better than 81 MΩ/m with a coupling factor between 3 to 5 %.

Two tuning plungers located at both end cells of the accelerating section compensate automatically for the resonance frequency variations caused by eventual changes in the structure temperature. The tuning plunger design (see Fig. 2) is based on the one used in the Mainz Microtron [2]. The plunger is moved whenever a phase difference between the RF input and one of the structure cavities is detected. The position of the plungers was chosen by practical considerations (see Fig. 1). Each section carries three 50 dB diagnostic probes, two with the same phase difference relative to the RF input.

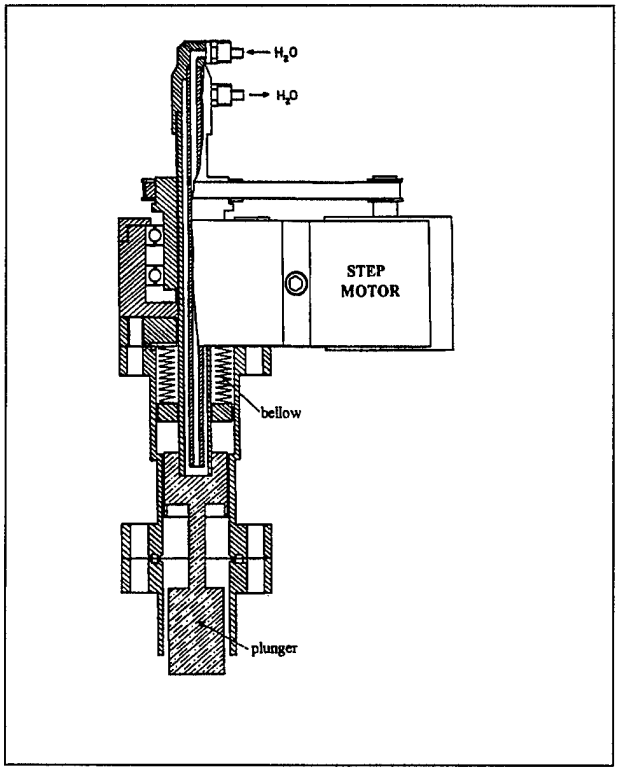



Figure 2: Schematic drawing of the plunger

## 3 FABRICATION

### *3.1 Machining*

The segments were rough machined to 0.2 mm, annealed under vacuum for 4 hours at 600°C and then fine machined for their final dimensions, except for the lengths of the nose cone of the accelerating cavity and the cylindrical nozzle of the coupling cavity, that were kept longer by 1 mm and 0.5 mm, respectively. Then, instead of trying to determine the nose cone length with the required mechanical accuracy for the tuning, the nose cone was machined to its final dimension by measuring the resonance frequency of the cavity with it still fastened to the lathe. During this procedure the temperature of the cavity was kept constant. An analogous procedure was adopted for the coupling cavities. The quality factor, Q, of the accelerating cavities was rather sensitive to the finishing of the surface. The finishing was performed with a diamond tool with a 0.5 mm radius semicircle profile. A surface roughness of 0.3 μm (RMS) was measured.

The final step before brazing was the machining and tuning of the cavity with the wave guide coupling, to be placed in the midst of the structure. The dimensions of the opening slot (8.8×33.4 $mm^2$) were determined empirically to give a slightly overcritical coupling. The SWR is 1.18 without beam loading and 1.05 with a beam loading of 10% (corresponding to a 50 μA current).

### *3.2 Brazing*

Due to the complex shape of the side coupled structure, the brazing of its several components could not be done in a single step. The number of steps was reduced to three by the use of special supports and dynamic guides developed in order to allow the brazing of pieces in both horizontal and vertical positions s imultaneously.

The following brazing alloys were used: for copper/copper-joints the eutectic Ag/Cu (Cusil, 780°C), for stainless steel/copper-joints Ag/Cu/Pd (Palcusil 10, 832-853°C), and for the wave guide and the wave guide coupling cavity joints, Ag/Cu/Pd (Palcusil 15, 853-900°C). All brazings were done in a vacuum furnace (made in the lab) with molybdenum heating elements and, therefore, a highly oxygen free vacuum (~$5\times10^{-6}$ torr at 850°C). Thus, nickel plating of the stainless steel pieces was not necessary. Due to the extreme care taken to machine and braze the cavities and to the excellent characteristics of the vacuum furnace, no vacuum leaks were detected in any of the 64 junctions of the structure.

### *3.3 Final Tuning*

During the brazing procedure, small changes in the geometry of the cavities may happen, due to the thickness of the filling alloy. They affect the frequency of the cavities, thus changing the resonance frequency of the structure. Four methods were developed in order to allow changing the frequency either up or down on both accelerating and coupling cavities [3]. Those methods allow corrections of ± 2 MHz in the frequencies. Every cavity was tuned to within ± 10 kHz of the nominal frequency. Fig. 3 shows the accelerating field distribution after the tuning, measured by the bead pull method.

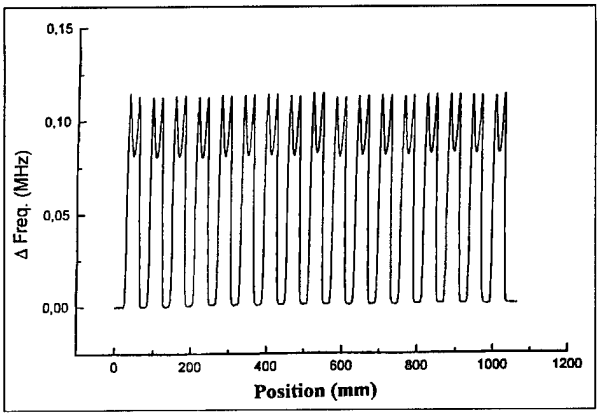



Figure 3: Accelerating field distribution

## 4 RESULTS

After the brazing and the final tuning of the structure, its parameters were measured in order to have an accurate description of its performance. Table 1 shows the parameters that were directly measured, while Table 2 presents the parameters that were derived from those measured.

TABLE 1. Parameters of the structure (measured)

| Parameter | Value |
|---|---|
| Resonance frequency | 2,450,000(5) kHz |
| Ratio $Z_{ef}/Q_0$ | 5,580(36) Ω/m |
| Quality factor | 16,000 |
| SWR (standing wave ratio) | <1.18 |
| SWR with a 10% beam loading | <1.05 |

TABLE 2. Parameters of the structure (derived)

| Parameter | Value |
|---|---|
| Frequency of accelerating cavity | 2,458.31 MHz |
| Frequency of coupling cavity | 2,444.67 MHz |
| Nearest neighbor coupling constant, k | 3.2% |
| Direct coupling between accelerating cells, $k_a$ | -0.68% |
| Direct coupling between coupling cells, $k_c$ | 0.46% |
| Stop band width | 510 kHz |

## 5 DYNAMIC TUNING

The accelerating field amplitude is controlled by the RF power injected in the structure and also by the resonance frequency of the structure. There are two ways to control the resonance frequency: controlling the temperature of the structure or de-tuning the frequency of some of the cavities. The second method can be achieved by the use of moving plungers that change the geometry, and thus de-tune the frequency, of the two extreme accelerating cavities. A de-tuning of the two end cavities by 425 kHz produces a change of 50 kHz in the resonance frequency of the structure. Frequency changes of that order can be made very fast through the plungers and are very slow through the temperature. The accelerating field distribution was measured along the structure for several positions of the plungers. We noticed that changes of up to 80 kHz (~2°C) in the structure frequency can be made without any noticeable change in the structure parameters. We developed an automatic system, using a Double Balanced Mixer to probe the structure frequency, to control the step motor that move the plungers. With this system we managed to keep the frequency tuned and the accelerating field stable within 0.15%, with the temperature of the structure kept within ± 2°C.

## 6 CONCLUSION

The accelerating structure built at IFUSP has been tested, showing excellent parameters. The effective shunt impedance is 10% higher than expected, which is very promising, since this will allow us to operate the RTM using ~9% less RF power than initially planned.
The dynamic tuning system that uses moving plungers in the extreme cavities, developed at IFUSP, proved to be very efficient and fast in keeping the structure tuned, even when submitted to conditions worse than the expected to occur during normal operation.
The machining and brazing of the pieces that compose the structure, which were done at the lab, proved to be of excellent quality, since the structure performance was higher than the expectations.

## 7 ACKNOWLEDGEMENTS

The authors would like to thank the support of the IEAv-CTA that was very important during our work. We thank Dr. L.M. Young for his teaching about the details of the SCS structure and Prof. H. Herminghaus, who gave us the design of the tuning plungers. This work had financial support from FAPESP, FINEP, CNPq and BID.

## REFERENCES

[1] L.M. Young and J.M. Potter, "CW side coupled linac for the Los Alamos-NBS racetrack microtron", Los Alamos National Laboratory Report, LA-9324-C, 1982.
[2] H. Euteneur and H. Schöller, "Experience in fabrication and testing the RF sections of the Mainz Microtron", Proceedings of the 1986 Linac Conference, SLAC-303, pp.508,1986.
[3] G.R. Swain, "Cavity tuning for the LAMPF 805 MHz Linac", Los Alamos National Laboratory Report, LA-5216, 1973.

# MEASUREMENT AND IDENTIFICATION OF HOM'S IN RF CAVITIES

D.A. Goldberg and R. A. Rimmer, LBNL, 1 Cyclotron Road, Berkeley, CA 94720, USA

*Abstract*

One of the major sources of beam impedance in accelerators is the higher-order modes (HOM's) of the RF cavities. We report here on a number of techniques for the identification of HOM's and measurement of their properties. Central to these techniques is the application of symmetry principles and the effects of symmetry-breaking perturbations (including mode-mixing) to the "standard" techniques of spectrum measurements and bead pulls. A fuller report is being prepared for publication[1].

## INTRODUCTION

In the course of a recent study, involving the RF cavities for the PEP-II B-factory,[2] we have developed a number of techniques for the identification and measurement of HOM's. In the belief that others working on similar problems might benefit from our experience, we offer the present summary of those techniques.

Throughout the discussion it will be assumed that the cavity can be approximately characterized by some symmetry for which a classifiable set of excitation modes exist (e.g., multipoles, for a figure of revolution). We further assume a one-to-one correspondence between these idealized modes and the modes of the actual cavity, although we will point out instances where this latter assumption may break down.

To illustrate for the non-specialist the complexity of the problem, we present in Fig. 1 a portion of the spectrum of the prototype PEP-II cavity. The dashed curve shows the spectrum obtained when the asymmetries in the cavity are "removed" by masking the various apertures to make it into a figure of revolution; the solid curve shows the spectrum for the cavity with all symmetry-breaking apertures open, but with the HOM-damping loads absent.

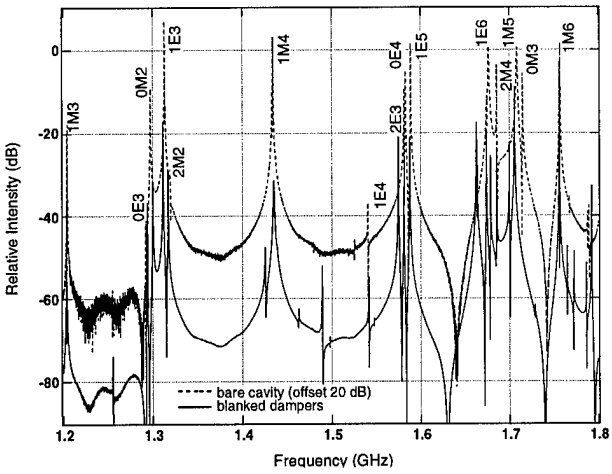



FIG. 1. Partial spectra of the "bare" cavity (offset by 20 dB for clarity) and the cavity with all symmetry-breaking ports open. The bare-cavity peaks are labelled with the mode designation obtained from the modelling code URMEL (see text).

*This work was supported by the U.S. Department of Energy under contracts DE-AC03-76SF00098 (LBNL), DE-AC03-76SF00515 (SLAC)

## FUNDAMENTALS

### *Tools and Methods*

*Experimental Tools:* The techniques described here involve transmission ($S_{21}$) measurement of the frequency spectra of the cavity: A signal is injected by an antenna at one end of the cavity and detected by an antenna at the other. Since only TM modes are of interest, our antennas take the form of electric probes which are oriented parallel to the longitudinal axis of the cavity at the inner radius of the beam tube aperture (see Fig. 2). Their mounting structure permits both longitudinal and angular positioning of the probes.

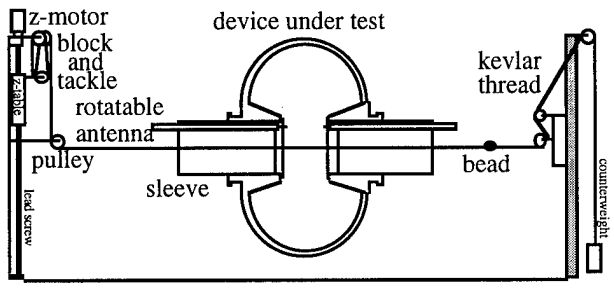



FIG. 2. The prototype PEP-II RF cavity mounted in the bead puller (see text); the "bead" used in the work described here is actually in the shape of a needle. The $S_{21}$ measurements are made by connecting the ports of a network analyzer to the two rotatable antennas.

We also make measurements of the *shift* of the spectrum resulting from the introduction of a perturbing object, a technique known generically as a "bead pull".[2] The method makes use of the fact that the introduction of a perturbing object produces a frequency shift which is proportional to the square of the local electric and magnetic fields at the location of the object (the

0-7803-4376-X/98/$10.00 © 1998 IEEE

"bead").[3] For TM fields, a needle probe oriented parallel to the longitudinal axis responds almost exclusively to the longitudinal electric field. Measuring the frequency shift as a function of the axial position of the needle permits one to map the axial distribution of the longitudinal electric field and, in turn, to calculate longitudinal beam impedance (see Ref. 3). A series of longitudinal bead pulls with the bead offset at different transverse positions (a "transverse scan") permits calculation of transverse impedance. Independent control of the $x$- and $y$- transverse positions permits moving the bead along a circular path in the transverse plane, enabling measurement of the angular variation of the longitudinal field ("angular scan").

Analytical Tools: The principal tool is a 2-D simulation code, such as URMEL [4],which provides a catalogue of the modes of an idealized (symmetrical) model of the cavity, and identifies the modes by their multipolarity and longitudinal parity (see below) . While a 3-D numerical field solver can, in principle, predict frequencies exactly, it does not provide such identification, and in practice is generally limited by computer memory size as to the accuracy and/or the number of the modes it can calculate.

Also useful is an impedance-calculating routine which can obtain the multipolarity of a given mode from transverse-scan data. Finally, we utilize a curve-fitting routine, which helps determine (relative) longitudinal parity, and measure Q-values for highly damped modes (needed for impedance determination), and can also determine the mixture of multipoles from angular scans.

*Symmetry Considerations*

Longitudinal Parity- For a cavity which exhibits reflection symmetry about the longitudinal midplane, the modes can be classified according to whether the longitudinal electric field is symmetric or anti-symmetric about the symmetry plane. In URMEL parlance, such modes are classified as E and M modes respectively, referring to whether the boundary conditions at the longitudinal midplane are "electric" (the electric field is normal to the midplane) or "magnetic" (the magnetic field is normal to the midplane). Since for E modes $E_z(-z) = E_z(z)$, the E fields of these modes are said to be of even parity, and those of the M modes, odd. Using the same convention, for any $TM_{mnq}$ mode, the parity is even for even $q$; odd, for odd $q$.

Transverse Parity - For a cavity with rotational symmetry or with a plane of transverse reflection symmetry, modes can be classified according to their transverse reflection symmetry. Modes other than monopoles occur in pairs, e.g., for a cavity with (a possibly broken) rotational symmetry, these are in pairs of $2n$ poles. For odd $n$ (e.g., dipoles), one member will exhibit odd parity with respect to reflection in the symmetry plane and even parity with respect to the orthogonal plane, and the other member the opposite parities; for even $n$, the one member will exhibit both parities to be even, and the other, both odd (e.g., the normal and skew quadrupole pair, respectively).

*Mode Mixing and Mode Anchoring*

Attempts at mode identification applying the above principles in an overly simplistic way can be confounded by the phenomenon of mode mixing.[5] The presence of perturbing objects can couple not only modes which were degenerate in the absence of the perturbation, but even modes which were not.

The most obvious adverse consequence of mode mixing is simply that one fails to account for it and assumes that the modes of the unperturbed, symmetric cavity retain their identities in the presence of perturbations such as dampers, couplers, etc., and overlooks the the fact that if, for example, a nearby monopole and dipole mix, to assess their effect on the beam, one must take into account the monopole impedance of both the resulting modes, *as well as* the dipole impedance of both. A more subtle problem occurs when one attempts to identify the modes of the unperturbed cavity by measuring the spectrum with the insertions removed and the ports covered over. In that highly symmetric configuration, the measuring probes themselves become the symmetry-defining objects. Hence if one wishes to use a probe-positioning technique to identify the modes, it is generally necessary to deliberately include some symmetry-breaking perturbation in order to "anchor" the modes so that their orientation is unaffected by the probe postions.

## EXPERIMENTAL TECHNIQUES

*Probe Positioning*

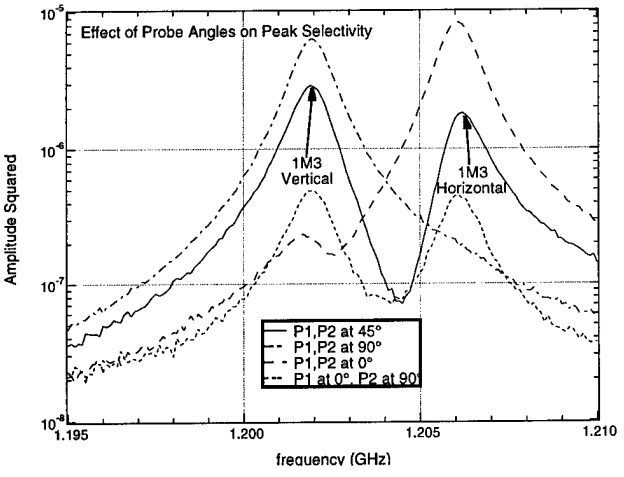



FIG. 3. Effect of probe angle on relative amplitudes of members of the 1M3 dipole pair.

For multipoles whose components are suitably anchored, selective suppression of the components can be achieved as the probe angles are varied relative to the anchoring axes, and multipole identification can be made based on periodicity of suppression. This is illustrated in Fig. 3. for the case of the 1M3 dipole pair. Note that with probes at a relative angle of 90° (it would be 45° for quadrupoles, etc.), and one of them aligned with the anchoring axis, probe 2 is insensitive to the dipole component excited by probe 1.

*(Longitudinal) Parity Signature*

One can identify the (relative) longitudinal parities of adjacent modes according to whether the region between them is characterized by a notch in the amplitude and a discontinuity of $\pi$ in the phase (like parity) or their absence (opposite parity). The case of modes of like parity is illustrated in Fig. 4. Note that the more well-separated the peaks are (relative to their respective Q-values) the more closely their interfering amplitudes approach a relative phase of $\pi$, and hence the more nearly complete the cancellation (the deeper the notch). The smooth transition between peaks of opposite parity can be seen in Fig 1, in the region between the 1M4 and 1E4 peaks.

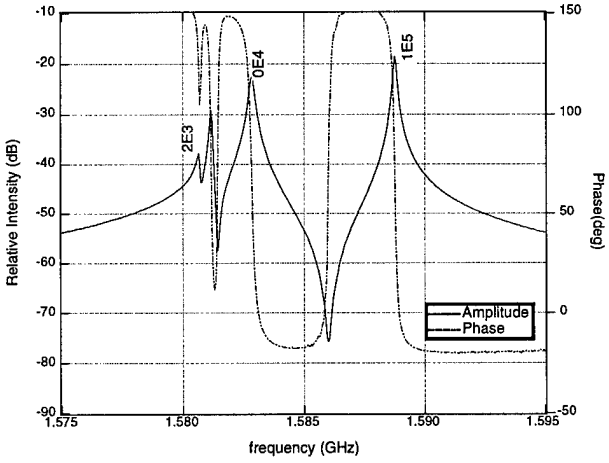



FIG. 4. Characteristic notches between adjacent peaks of like longitudinal parity, accompanied by an abrupt phase jump of $\approx\pi$.

*Bead Pulls*

Longitudinal scans, primarily intended for measuring longitudinal shunt impedance, can assist in mode identification by enabling one to compare the longitudinal field distribution with URMEL predictions. Transverse scans (for unmixed, or non-overlapping modes) permit quantitative determination of multipolarity and transverse impedance by plotting the longitudinal shunt impedance *vs* transverse displacement. Angular scans principally aid in determining the multipole mixture for cases of overlapping modes or mode mixing. This is shown in Fig.5 for the case of the 1E6 dipole, which, in the presence of damping, experiences overlap with the nearby 2M4 quadrupole and 0M3 monopole. A similar scan taken 10 cm downstream of the midplane shows a reversal of the dipole phase relative to that of the monopole and quadrupole, consistent with the latter two having longitudinal parity opposite that of the 1M3.

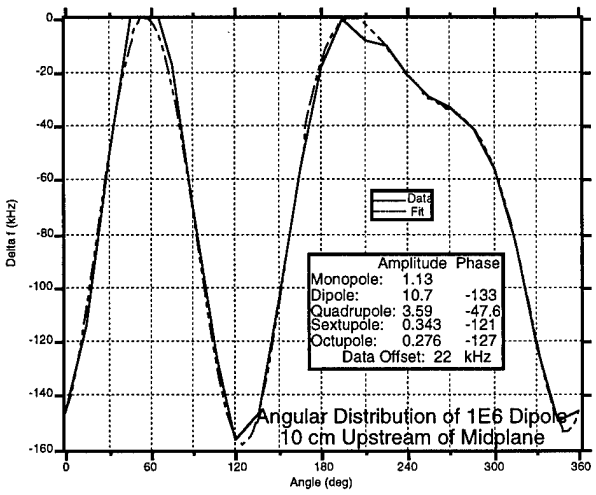



FIG. 5. Angular scan of the 1E6 dipole in the presence of damping.

## CONCLUSION

A fairly complete characterization of an RF cavity is possible with a few basic tools and concepts including movable antennas, bead pulls on and off axis, signatures arising from mode parity and angular distribution, in addition to a catalog of the unperturbed modes of the system.

## ACKNOWLEDGEMENTS

The authors would like to than Michael Irwin for his assistance in taking many of the data illustrated in this report.

## REFERENCES

1. "Techniques for Identifying and Measuring Higher Order Modes in RF Cavities," D.A. Goldberg and R.A. Rimmer (to be published); also LBNL-40290.
2. "Updated Impedance Estimate of the PEP-II RF Cavity", R.A. Rimmer et.al., Proc EPAC 96, Sitges, Barcelona, 10-14 June, 1996 (PEP-II AP Note 96.06, LBNL 38929, SLAC PUB 7211), and references therein.
3. D. A. Goldberg and R. A. Rimmer, "Automated Bead-Positioning System for Measuring Impedances RF Cavity Modes," in Proc. 1991 IEEE Particle Accelerator Conf., pp. 871-873, and references therein.
4. T. Weiland, "On the Computation of Resonant Modes in Cylindrically Symmetric Structures, Nucl. Inst. Meth. 216 (1983), p. 329.
5. D. A. Goldberg, " Understanding the Mixing of Higher-Order Modes of Multiply Resonant Systems, LBNL CBP Tech Note-119 (unpublished).

# HIGH-POWER TESTING OF RF CAVITIES FOR THE PEP-II B FACTORY*

R. A. Rimmer, LBNL, 1 Cyclotron Road, Berkeley, CA 94720, USA

M. A. Allen, K. Fant, A. Hill, M. Hoyt, J. Judkins, M. Neubauer, H. D. Schwarz, SLAC, Stanford University, Stanford, CA 94309 USA

*Abstract*

We describe the process of conditioning and high-power testing of RF cavities for PEP-II. Procedures for vacuum assembly, bakeout and automated processing are described. Interlocks and safety precautions for protection of equipment and personnel are discussed and performance data of tested cavity assemblies are reported. Performance of ancillary components such as windows, couplers and tuners is also discussed. Comments are included on handling, alignment, installation and commissioning issues where appropriate.

## 1 INTRODUCTION

The RF system for the PEP-II asymmetric B factory [1] uses 26 copper accelerating cavities to replenish the energy lost by the beams as they circulate in the high- and low-energy storage rings. The high-energy ring (HER), requires 20 cavities powered by five 1.2 MW klystrons. The low-energy ring (LER), which requires less voltage but more beam current, uses 6 cavities and 3 klystrons. Each cavity is installed on a raft along with all of the ancillary components, window, coupler, tuner, HOM loads, etc., and each completed assembly is individually power tested and conditioned in a dedicated test stand before installation in the tunnel. This reveals any possible faults before installation and greatly simplifies station commissioning in the rings because the pre-conditioned cavities can be brought back up to operating power in a short time.

## 2 CAVITY PREPARATION

Each cavity is cleaned for UHV operation, including a final mild chromic acid etch, and delivered to the assembly clean room filled with dry nitrogen to minimize reoxidization of the surface. Care is taken in the cleaning process to remove any particulates, high-points and evaporated coating from the final e-beam welding processes, which take place inside the cavity.

Vacuum assembly takes place in a class 100 clean room with a constant nitrogen purge through the chamber and care is taken to minimize the ingress of dust or contaminants. All openings are flanged off or covered with clean aluminum foil unless otherwise required for assembly. The HOM loads, tuners, coupler, window, ion pump, vacuum gauge, pick-up loop and view-port flanges are all fitted at this stage, see figure 1, and the assembly is leak-checked with helium before moving to the bake-out oven.

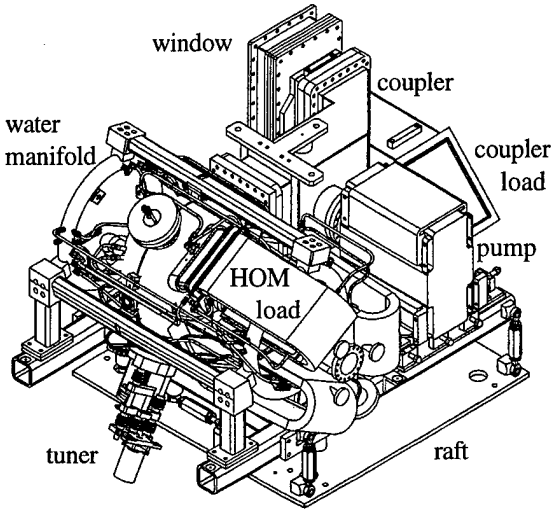



Figure 1. HER cavity raft assembly.

The completed raft assembly is installed in a panel oven with radiant heater elements that are shielded to prevent direct illumination of the cavity. The hot air is circulated with a fan to minimize temperature gradients within the cavity assembly and reduce the chance of vacuum leaks due to differential expansion of flanges. The oven follows a programmed ramp up to 155°C at 5°C/hour or slower if the vacuum pressure exceeds $2\times10^{-6}$ Torr, see figure 2.

The temperature is held until the pressure stabilizes at less than $5\times10^{-7}$ Torr and then ramps down at 5°C/hour. The base pressure at room temperature after bakeout is usually less than $5\times10^{-9}$ Torr. The window and coupler flanges are retorqued after baking.

## 3 RF CONDITIONING

The baked cavity assembly is then made ready for high-power testing by fitting the water pipes, thermocouples and tuner actuator. The raft is installed in the test bunker and hooked up to the deionized water supply, which is stabilized at 35°C. The bunker is a concrete vault with a lead lined door and safety interlocks, including a search sequence, to prevent possible exposure

*This work was supported by the U.S. Department of Energy under contracts DE-AC03-76SF00098 (LBNL), DE-AC03-76SF00515 (SLAC)

0-7803-4376-X/98/$10.00 © 1998 IEEE

of personnel to radiation during processing (the cavity produces low-levels of X-rays during processing and significant radiation from dark current at high fields). The power source for RF processing is a 500 kW PEP-I type klystron, rebuilt and retuned to operate at 476 MHz, and protected by a circulator. Processing of the cavities is controlled by a Macintosh™ computer running Labview™ software. Fast interlocks for vacuum pressure, klystron reflected power and arc detectors (window and cavity) are hard-wired into the test stand "crowbar" circuit, along with those interlocks required to protect the klystron and the Personnel Protection System (PPS) interlocks from the bunker.

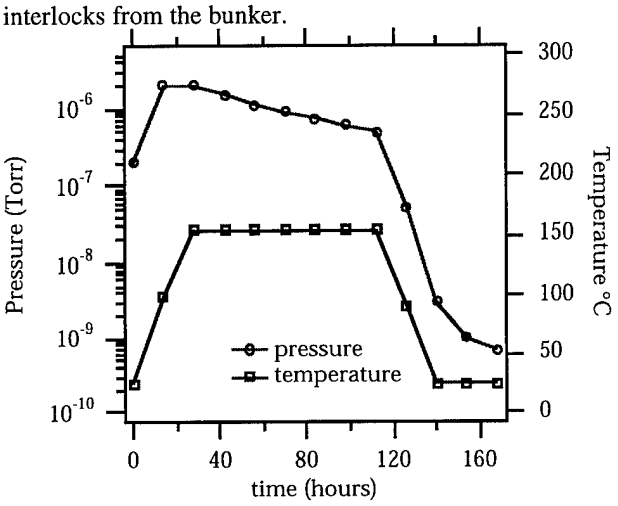



Figure 2. Typical cavity bakeout profile.

The computer can control the RF drive level to the klystron and monitors the cavity vacuum, cell voltage, forward and reflected power, window and body temperatures and turns off the drive if they go outside of acceptable ranges. It also registers which interlock signal triggered first in the event of a station trip. The interlock status can be reset from the computer but this is not done automatically for safety reasons. The RF source is a signal generator that can be operated in continuous wave (CW) or frequency modulated (FM) modes. The test stand can be operated manually from the computer interface or the cavities can be processed automatically by the control program. The computer interface can be monitored or controlled remotely (with password protection).

The initial conditioning of the cavity is done with FM sweeping about the cavity resonant frequency. This allows controlled outgassing of the cavity and processing through various multipactor levels with less risk of breakdown than in CW operation. FM sweeping achieves similar results to amplitude modulation (AM) with low duty factor, but is easier on the klystron since it produces a constant output. The power reflected from the cavity off resonance ends up in the circulator water load. Most FM processing is done with a 320 kHz frequency deviation at a 1 kHz sweep rate, although a 640 kHz deviation, 400 Hz rate is sometimes used to scrub out residual gas (this covers a wider range of voltages and moves slightly more slowly through resonance giving a longer pulse length). The vacuum interlock is set to trip the station off at $5 \times 10^{-7}$ Torr to prevent operation at high power with bad vacuum, which may be hazardous to the window. The automated processing algorithm slowly ramps up the drive power while keeping the vacuum pressure below a pre-set threshold, usually on the low $10^{-8}$ Torr scale. The gas is typically evolved in small bursts and by using a suitably slow ramp rate these can usually be kept below the trip level. If the vacuum goes above the user set-point the drive level ramps down and the vacuum quickly recovers. Once the pressure is good again the upward ramp resumes. Occasionally a larger gas burst or other fault will trip off the station and this must be manually reset by the operator.

Once the cavity has been conditioned through the low-voltage regime, where a lot of multipactor-induced outgassing occurs, the amplitude will usually increase more quickly until the maximum cell voltage required is attained. This is generally set a little higher than the desired CW operating voltage. This maximum FM amplitude is maintained until the vacuum pressure drops to a suitably low level, usually on the mid $10^{-9}$ Torr range. The base pressure without power at this stage is usually on the low $10^{-9}$ Torr scale.

Once FM processing is complete the source is switched to CW at 476 MHz and the auto processing loop ramps up as before. The vacuum threshold is usually set lower in this case (e.g.: $1 \times 10^{-8}$ Torr), because of the increased power available in case of breakdown. A tuner feedback loop keeps the cavity on resonance.

During CW processing at high power there is occasional arcing in the cavity or the coupler which is picked up by photo-diode detectors which trip the RF power off within 15 μs to prevent damage. Occasional arcing appears to be a normal part of high-power conditioning as small surface imperfections or dust particles are burned off and the frequency of arcs should decrease with processing. Persistent arcs in the cavity may indicate a more serious problem and repeated arcs or glowing at the window may indicate a defective or contaminated window coating.

A TV camera is used in the bunker to observe the movable tuner through a small viewport in the cavity. Occasionally some glowing in the tuner gap, outgassing with tuner movement or small incandescent sites on the wall of the cavity are observed during processing [2]. These generally diminish or disappear with time and do not appear to limit cavity performance.

Once full operating power has been achieved this level is held constant while the vacuum improves. Occasional arcs or gas bursts may trip off the station but the cavity can usually be brought back to full power very quickly, and the frequency of such trips generally decreases with running time. The cavities are processed in

the test stand until they can run for at least 24 hours without tripping. Reliability is expected to continue to improve with operation in the accelerator. Figure 3 shows the conditioning history for a typical HER cavity. Because of time lost to trips etc., the conditioning process usually takes about a week.

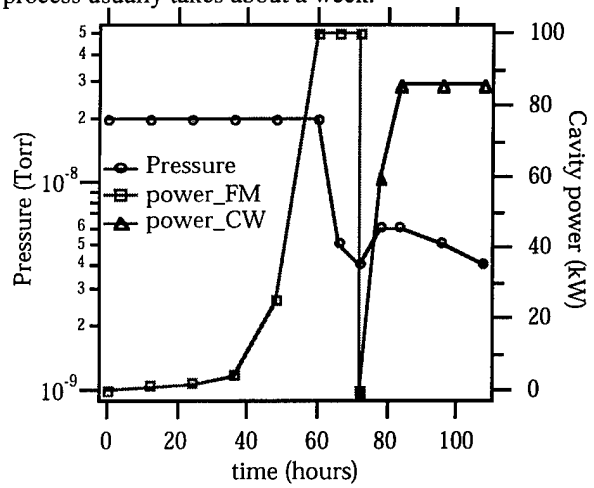



Figure 3. Typical HER cavity processing history

## 4 CAVITY PERFORMANCE

All of the 12 cavities tested so far have been successfully processed to the HER commissioning voltage of 800 kV (about 86 kW wall dissipation), or above in a reasonable time. About 700 kV per cavity will be required for normal HER operation. Some cavities have been processed up to LER voltage (850 kV, 103 kW), which takes a little longer but otherwise appears to be straightforward. The cavities were designed for a maximum of 1 MV at 150 kW dissipation.

The windows have all performed well, with temperature rises in the ceramic of 17 to 24 °C at HER power levels. One cavity assembly exhibited some air-side window arcing, possibly due to charging of the ceramic, but this conditioned away with further FM processing. All of the tuners have behaved well at full operating power with no sparking at the spring-finger contacts.

## 5 TUNNEL INSTALLATION

The tested RF cavity raft assemblies are delivered to the tunnel under vacuum, installed in the straight-sections, connected to the waveguides and the water supply and aligned using a six-strut support system. The cells are continuously purged with dry nitrogen while the connections are made to the neighboring vacuum chambers.

The cavity pick-up loops are connected to the low-level RF electronics upstairs via calibrated low-loss cables and the length of each arm of the waveguide network is adjusted to achieve the correct phases at the cavities.

## 6 STATION COMMISSIONING

Once the PPS interlocks for the tunnel are made up the RF cavities can be energized. The high-voltage power supplies are previously tested up to full power with the klystron output going into water loads. Once the stations are connected to the cavities a processing algorithm similar to that used in the test bunker is used to bring them back up to operating power levels. So far the first two HER stations (8 cavities) have been successfully commissioned. In the normal case of a controlled vent for installation this happens quickly, however if the cavities are accidentally exposed to tunnel air then several days of re-processing are required. The cavities appear to recover completely from such exposure although the long term effects, if any, on the cavity or window performance are not yet known.

## 7 CONCLUSIONS

The processes for cavity cleaning, bakeout and automated conditioning have been shown to be effective in achieving operational levels of performance in a reasonable time. Testing, installation and commissioning of high-energy ring cavities is proceeding smoothly and production of the remaining HER and LER raft assemblies is expected to continue in this vein. Careful bakeout following a prescribed temperature profile and with a sustained hold at greater than 150°C has proven valuable in speeding conditioning time compared to previous unbaked examples [3], especially with regards to window performance. Processing with FM sweeping to peak voltages above those required for operation allows for the controlled evolution of gas with minimal breakdown and safe window operation and permits rapid processing in CW mode with good vacuum.

## 8 ACKNOWLEDGMENTS

The authors wish to acknowledge the contribution of Lawrence Livermore National Lab. to the high quality fabrication and careful preparation of the cavities [4], and to thank the many technicians and support staff who have assisted in the cavity assembly and processing.

## REFERENCES

[1] "PEP-II, An Asymmetric B Factory", Conceptual Design Report, June 1993, LBL-PUB-5379, SLAC-418, CALT-68-1869, UCRL-ID-114055, UC-IIRPA-93-01.

[2] H. D. Schwarz et. al., "Development of a Movable Plunger Tuner for the High-Power RF Cavity for the PEP-II B Factory", these proceedings.

[3] R. A. Rimmer et. al., "High-Power Testing of the First PEP-II RF Cavity", Proc. EPAC 96, June 10-14, 1996, Sitges, Barcelona, Spain, LBNL 38147, SLAC-PUB-7210.

[4] R. M. Franks et. al., "Fabrication Processes for the PEP-II RF Cavities", these proceedings.

# FABRICATION PROCESSES FOR THE PEP-II RF CAVITIES*

R.M. Franks, LLNL, PO Box 808 Livermore, CA 94551, USA
R.A. Rimmer, LBNL, 1 Cyclotron Road, Berkeley, CA 94720, USA
H. Schwarz, SLAC, 2575 Sand Hill Road, Menlo Park, CA 94025, USA

*Abstract*

This paper presents the major steps used in the fabrication of the 26 RF Cavities required for the PEP-II B-factory. Several unique applications of conventional processes have been developed and successfully implemented: electron beam welding (EBW), with minimal porosity, of .75 inch (19 mm) copper cross-sections; extensive 5-axis milling of water channels; electroplating of .37 inch (10 mm) thick OFE copper; tuning of the cavity by profiling beam noses prior to final joining with the cavity body; and machining of the cavity interior, are described here.

## 1 INTRODUCTION

"Rarely [have we] faced so complex a manufacturing task as the cavities" [1]. To present all of the interactions, dependencies, and processes among the different disciplines and organizations involved in the 1700 labor hour effort to produce a single RF Cavity is difficult. This paper is therefore divided into major subsets of the process.

## 2 CAVITY BODY FABRICATION

### *2.1 Fabricating Copper Bowls*

The fabrication process begins with a class 2 [2] OFHC copper plate of 1.5 inch (38 mm) thickness and 39 inch (1 m) diameter. The thickness is reduced to 1.25 inch (32 mm) by diamond fly-cutting an equal amount of stock from each side. This removes any subsurface contaminants that may have been imbedded during the rolling process at the mill. Relief of skin stresses is an additional benefit of this procedure.

The desired shape is obtained by forcing the stock plate through a 21.75 inch (552 mm) diameter ring with a mandrel. This operation is performed at room temperature. The mandrel's shape is a slightly undersized version of the cavity's inner contour.

### *2.2 Equatorial Electron Beam Weld Preparation*

A numerically controlled lathe is used to machine the inner contour of the bowls, leaving .08 inch (2 mm) stock material for removal after subsequent processing. We allowed .02 inch (.5 mm) on the face of the bowls to compensate for shrinkage during the welding together of the two halves. The outer contour is machined to final size at this point. Datum features, used until late in the fabrication process, are cut into the bowl halves at this time

### *2.3 Electron Beam Welding the Equatorial Joint*

For the prototype cavity we developed EBW parameters that would bury the root porosity in a 0.5" (12.5 mm) thick sacrificial backing-bar located on the exit side of the weld joint. The backing-bar was removed during a subsequent machining operation. For the production cavities we adapted the "over penetration" technique used for the equatorial ports, thus eliminating the backing bar. We effectively mitigated problems with porosity in the weld taper-off by centering a port penetration over the taper off area. Distortion due to welding proves to be negligible; therefore, we are not forced to reestablish datum surfaces following this welding operation.

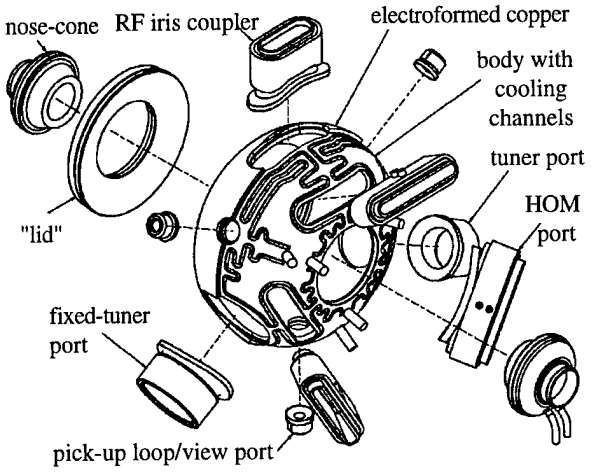



Figure 1: An exploded view of a PEP-II RF cavity, body cooling channels on one half (exposed), equatorial and HOM port inserts, nose-cones and "lid" section.

### *2.4 5-Axis Milling of Water Channels*

The cavity body contains six discrete cooling circuits totaling approximately 780 inches (20 m) in combined length, figure 1. The intricate geometry was electronically transferred from the designer's computer to the manufacturer's programming system. The water channels were cut into an epoxy model, then inspected to verify the accuracy of the machine tool program before proceeding on the copper cavity body. A reference hole is

* This work was supported by the US Department of Energy under contracts W-7405-ENG-48 (LLNL) DE-AC03-76SF00098 (LBNL), DE-AC03-76SF00515 (SLAC)

0-7803-4376-X/98/$10.00 © 1998 IEEE

incorporated to establish a clocking orientation for the water channel and port penetration.

*2.5 Electroplating of OFE Copper*

A machinable wax is placed into the water channels. This serves as a space holder during the electroplating operation that generates the covering for the channels. Silver powder is burnished into the wax to provide a conducting surface. The activation procedure removes excess silver and any other residues from the copper body to ensure proper adhesion between the plating and the cavity body.
The cavity is rotated at 5 RPM while fully submerged in an acid sulfate chemistry. An intermediate machining of the outer contour is required prior to achieving the final plating thickness of .4 inch (10 mm).

*2.6 Water Channel I/O Location and Port Penetrations*

Referencing the clocking hole allows us to locate the inlet and outlet points of each cooling channel after they have been covered by the electroplating. We place a pipe threaded hole at each end of the cooling channels to ensure a positive joint during the dewaxing procedure. These holes are reworked in a future operation to accept welded fittings.
We cut the port penetrations into the body leaving them .08 inch (2 mm) undersize to avoid damaging the final penetrations during dewaxing. The precise location of the port penetrations ensures the proper relationship between cooling water and port bodies. This is crucial due to the high body temperature predicted by computer models during the design phase [3].

*2.7 De-Waxing of Water Channels*

The cavity body is heated to approximately 100 °C with a hot air gun to soften the wax. The viscous wax is forced from the water channels with 90 psi (620 kPa) of air pressure. Once an air passage is established teflon hoses are attached and perchloroethylene is pumped through the cooling channels for 30 minutes to remove the remaining wax. A final rinse with clean solvent is done to ensure the wax is cleared from the water channels. A 15 minute hydrostatic test at 300 psi (2 MPa) is performed to ensure the integrity of the bond between the electroplated copper and the parent material.

*2.8 Finishing of Port Penetrations*

The nine port penetrations are finished to a tolerance of .002 inch (.05 mm) to help ensure successful EBW of ports to the cavity body. The electroplated copper is relieved from the weld joint area so that the EB weld is only in the parent metal, thus avoiding potential water to vacuum leak paths.
The cavity body is degreased, deoxidized, and etched in a chromic acid bright dip, removing approximately .0002 inch (.005 mm) to provide a clean part for EBW. The cavity is then wrapped in lint free paper and aluminum foil for shipping to the welding vendor.

## 3 PORT AND LID FABRICATION

The 11 ports welded to the cavity consist of five styles -- Iris, Tuner, Observation, HOM, and Beam nose -- performing different functions, yet all using similar fabrication techniques.

*3.1 Fabrication of Ports*

The ports are fabricated as piece parts; the copper components are assembled by hydrogen furnace brazing with a 35Au65Cu alloy. The features that mate with the cavity body are then machined to final specification. The beam nose ports retain .4 inch (10 mm) stock material in length during this fabrication stage, allowing for the tuning process.
The HOM port fabrication process incorporates the stainless steel vacuum flange blank during brazing. The vacuum and RF sealing surfaces of the flange are machined after this brazing to avoid the distortion due to welding processes typically used for this type of component. The features that mate with the cavity are then finalized.

*3.2 Lid Fabrication*

The cavity lid is fabricated from a 16 inch (406 mm) diameter by 2 inch (50 mm) thick plate of OFHC copper. The lids are processed similarly to the cavity bodies, namely, water channel formation by plating, and EBW joining of a port. The lid/beam nose sub assembly is machined after welding to generate precise locating features that mate with the cavity body. The beam nose is machined to its final length prior to being joined to the cavity body.

## 4 ELECTRON BEAM WELD ASSEMBLY OF CAVITY AND PORTS [4]

The cavity body and nine ports are joined with EBW technology. We developed several different techniques to ensure we met the vacuum, structural, and electrical criteria for the PEP-II RF Cavity. At this stage the mounting pads are also EB welded to the cavity body.

*4.1 Two Stage Welding of HOM Ports*

Three HOM ports are welded into the cavity body from the inside using a 75% penetration structural weld followed by a cosmetic wash-weld. The wash-weld uses a very diffuse beam that gently "stirs" the weld pool, resulting in a smooth, uniform surface. No porosity is visible in the weld taper-off area after finish machining.

*4.2 Over Penetration Welding of Equatorial Ports*

We theorized that the root porosity could be "blown through" the weld joint from the outside when attaching the six equatorial ports. This process requires the beam to over penetrate the joint, necessitating a beam stop. We anticipated small porosities in the weld taper-off area when we machine the surface final RF; therefore, the

taper-off area is positioned so EB wash welding is possible for repairs.

## 5 FINAL MACHINING OF THE CAVITY

### *5.1 Datum Transfer*

We transfer the original datum to surfaces on the mounting pads using a horizontal spindle CNC milling machine. This transfer is required since the original datum must now be removed. This operation enables us to mount the cavity in a fixture that will be used for all subsequent operations, thus ensuring the proper relationship among the final features. Mounting holes and fiducial locations are precisely located for attaching and aligning the cavity in its raft assembly.

### *5.2 Final Machining of RF Surface*

The openings for the lid sub assembly and its opposing beam nose are machined on a CNC vertical turning lathe. This joint is for EBW; therefore, tolerances of .002 inch (.05 mm) are held.

The final machining of the RF surface is also performed at this step. Using the lid opening for access, the tungsten carbide tool shaves away the .08 inch (2 mm) stock that was left in the initial processing of the bowls. The final RF surface is a 40 μinch (1 μm) Ra finish and is within .005 inch (.012 mm) of the nominal profile.

This operation reveals any pits we will see in the weld taper-off area of the equatorial port welds. These voids are sealed with EBW, leaving smooth repaired spots which are preferable to the pits.

### *5.3 Electron Beam Welding of Lid to Cavity Body*

The lid subassembly is EB welded to the cavity body in a two stage process. The initial weld, a 75% penetration structural and vacuum weld is made from the outside of the cavity. This is followed by a cosmetic wash weld on the inside surface. The smooth undulations of the internal weld bead do not significantly affect the operation of the cavity. The internal welds do however result in the deposition of a copper foil on the RF surface which must be removed during the cleaning procedure.

### *5.4 TIG Brazing of Water fittings*

Stainless steel water fittings are attached to the electroplated copper of the cavity using a conventional TIG torch and 72Ag28Cu braze alloy. Weld prep grooves are needed to thermally isolate the weld area, as the heat otherwise dissipates throughout the cavity too rapidly.

## 6 TUNING AND FINAL FABRICATION PROCESSES

### *6.1 Tuning*

A beam nose, precut to leave .1 inch (2.5 mm), is temporarily installed into the cavity. The frequency is measured and a determination made as to how much material to remove from the beam nose in order to attain the target frequency. After this material is removed the beam nose is cleaned and reinstalled for verification prior to final EB welding.

### *6.2 Electron Beam Welding of Nose*

The beam nose is EB welded to the cavity body in a fashion similar to the lid/cavity EBW. As with the lid weld, the minor undulations of the internal weld bead do not significantly affect the operation of the cavity. Final frequency and vacuum integrity verifications are made.

### *6.3 Cleaning*

The finished cavity is cleaned according to an approved process. An alkaline cleaner is used to remove extraneous dirt followed by a deoxidizer to remove the surface oxidation. The copper residue from the EB welding is removed using 600 grit aluminum oxide paper followed by a white abrasive pad. We repeat this process until a visual inspection of the cavity shows that the foil is removed. A chromic acid bright dip bath is used to remove approximately .0002 inch (.005 mm) of copper and any embedded abrasive material. This leaves the RF surface with a 24 μinch (.6 μm) Ra or better finish.

The cavity is rinsed in deionized water and then blown dry with bottled nitrogen, then all openings are covered with foil for transporting to the assembly area. A nitrogen purge is maintained while the flanges are blanked off and a nitrogen atmosphere of 2 psig (14 kPa) is left in the cavity to prevent reoxidation of the inner surfaces. The cavity is then mounted in its installation raft and cooling lines attached prior to shipment [5].

## 7 ACKNOWLEDGMENTS

The authors thank the many machinists and technicians for their personal commitment and technical excellence in producing the PEP-II RF Cavities.

## REFERENCES

[1] A. Heller, "The B-Factory and the Big Bang," Science and Technology Review, UCRL-52000-97-1/2 pp. 4-13.

[2] "Standard Specification for Oxygen Free Copper in Wrought Forms for Electron Devices", ASTM designation F68-82.

[3] R.A. Rimmer et. al "High Power RF Cavity R&D for the PEP-II B Factory," Proc. EPAC 94, June 27-July 1 1994, London, LBL-34960, PEP-II EE note 3-94.

[4] R.M. Franks, et. al. "Electron Beam Welding of Thick Cross-Section Copper with Minimal Porosity," Proc. 1997 AWS Convention, Los Angeles, American Welding Society, Miami, Florida, 1997, pp. 184-85, UCRL-JC-125896 Ext Abs

[5] R.A. Rimmer, et. al., "Development of a High-Power RF Cavity for the PEP-II B Factory" Proc. PAC95, Dallas, Texas, May 1-5 1995.

# OPERATION OF THE LNLS STORAGE RING RF SYSTEM

D. Wisnivesky° and C. Pardine
Laboratório Nacional de Luz Síncrotron - LNLS/CNPq
Cx Postal 6192, 13083-970 Campinas SP Brazil
°also IFGW/ UNICAMP

*Abstract*

The LNLS storage ring RF system operates at 476 MHz and delivers up to 60 kW CW into a single RF cavity. Injection and accumulation in the storage ring are done at low energy after which the beam energy is ramped up to 1.37 GeV. Correspondingly the RF power changes from a very low initial value up to a high power determined by the amount of stored current. Several temperature and mechanical tuning control systems operate during ramping and steady state to keep the cavity tuned and away from instabilities. In this paper we discuss the results and experience obtained after more than one year of operation of the system.

## 1 INTRODUCTION

The light source of the Laboratório Nacional de Luz Síncrotron (LNLS) Campinas, SP Brazil has been in operation for over one year. It includes an electron linear accelerator (linac), a transport line and a booster-storage ring [1].

The storage ring has a single cell, 476 MHz RF cavity. The adjustable cavity coupling has been set at ß= 1.35. The RF transmitter uses a Philips YK 2065 klystron which can deliver 60 kW CW power into the cavity. The main RF parameters of the LNLS storage ring are listed in table 1

| | |
|---|---|
| Frequency: | 476.076 MHz |
| Cavity: Single cell bell shaped built by Sincrotrone Trieste. | |
| Effective shunt impedance: | 3.4 MΩ ($P=V^2/2R$) |
| Unloaded Q: | 41.000 |
| Coupling: | ß=1.35 |
| RF power: | 60 kW CW |
| Effective cavity voltage: | 480 kV |
| Revolution frequency: | 3.216 MHz |
| Harmonic number: | 148 |

Table 1 Storage ring RF parameters

Temperature of the cavity walls is controlled by water flowing through 14 parallel circuits. The water temperature is controlled by a combination of a 17 kW heater, located together with the cavity in the secondary circuit of a heat exchanger. The heat exchanger primary flow is adjusted with a controlled 3-way valve. The maximum flow in the primary is 300 l/min. and the temperature is 32 ± 0.1 °C. The water system has been designed in order to permit the cavity temperature to be adjusted between 45 and 60 °C with a thermal load of 35 kW. According to calculations, this temperature range is available for operation free of HOM instabilities, with beam currents up to 200 mA. Figure 1 shows the cavity mounted in straight section 5 of the storage ring. On the top to the left is the coaxial feed through with the adjustable coupling loop. The mechanical plunger can be seen on the right hand side of the picture and, next to it, part of the motor-driven mechanism that produces the tuning of the cavity frequency by means of longitudinal deformations of the cavity. The plunger, together with the longitudinal deformation of the cavity permits a 500 kHz tune range. Also visible are the input and output water pipes, part of the temperature control system and cooling system of the cavity. The beam entrance port is on the lower part of the picture.

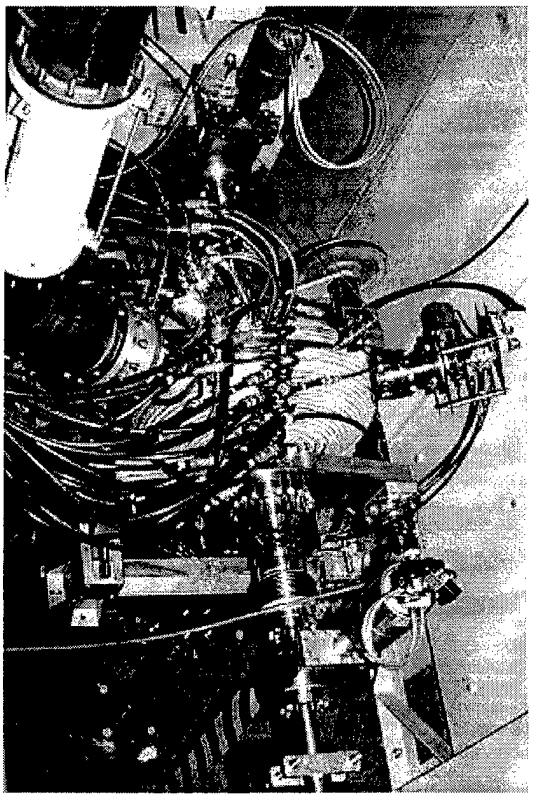


Figure 1: the cavity mounted on the storage ring

0-7803-4376-X/98/$10.00 © 1998 IEEE

The different parts that comprise the RF system have been described elsewhere [2]. In this paper, we will discuss the operation of the system, in particular those aspects related to low energy accumulation in the storage ring followed by energy ramping.

## 2 OPERATION

The RF system can be controlled and supervised from the control room during normal operations and for test purposes, from a local computer next to the transmitter area. This allows to turn on and off the different sub-systems including the high voltage power supply, adjust gap voltage and cavity to transmitter frequency difference (detune angle) and provides on-line information on interlocks and status, including cavity temperature, pressure and RF power values at 6 different locations along the transmission line: power input and output in the klystron, incident and reflected power in the circulator, incident and reflected power in the cavity and cavity gap voltage. Figure 2 shows the transmitter in the center of the ring. To the left is the rack with the low power RF electronics, tuning drivers, interlocks and computer interface systems. The cabinet on the right encloses the high-power klystron and auxiliary systems.

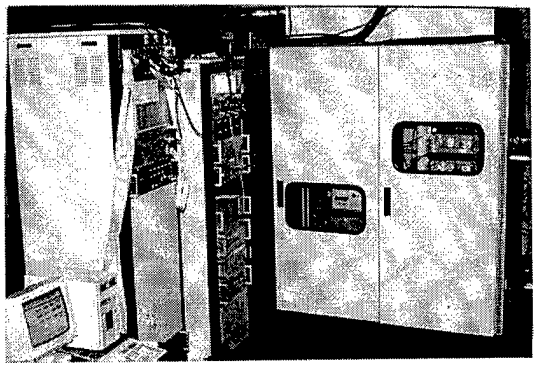


Figure 2: the RF panel.

The energy of the stored electron current in the LNLS storage ring varies from 120 MeV at injection up to 1.37 GeV. The operating conditions of the cavity and cooling system are very different along this large energy range. During accumulation at low energy, synchrotron radiation is negligible, beam current is rapidly varying and the beam is subjected to large synchrotron and betatron oscillations. The RF cavity parameters during accumulation are determined empirically, so as to maximize the accumulation rate. Typically, the power in the cavity is about 400 W and the effective gap voltage is 55 kV. Very little power is dissipated in the cavity walls during this phase. Thus, in order to keep the wall temperature at the set value, the temperature stabilizing system must supply 17 kW of heat to the water that flows around the cavity. Injection from the linac proceeds at about 8-10 mA per pulse until the equilibrium current is achieved. These relativily large pulses detune the cavity and drive the cavity towards the generator frequency. To avoid Robinson's instability, the cavity is detuned by several kHz during accumulation. At low energy, the cavity pressure stays in the upper $10^{-10}$ mbar range.

Once the low energy equilibrium current is attained, the storage ring magnets and RF power are ramped. The speed at which the gap voltage can increase is determined by 2 factors: the mechanical tuning mechanisms (axial mechanical deformation of the cavity and mechanical plunger) and the cooling capacity of the water system. Several options have been tested for the RF control method during ramping in order to rapidly increase the gap voltage, reduce the cavity temperature variations and limit the cavity detuning. Figure 3 shows the evolution of the gap voltage after a sudden variation in the voltage reference with the gap voltage feedback loop turned off.

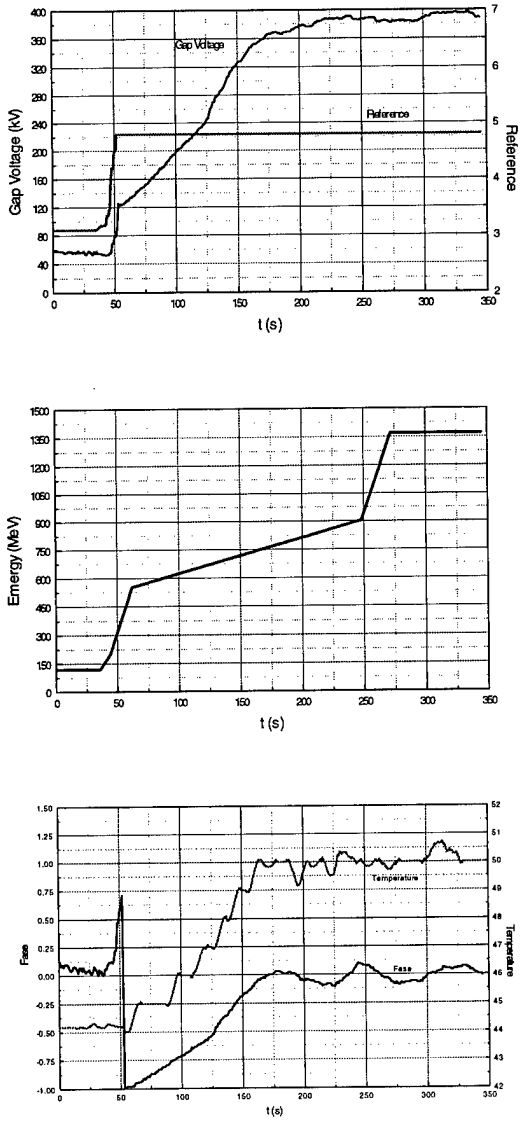



Figure 3: cavity parameter changes without feedback loop.

As can be seen, the cavity response is slow, about 2 minutes and lags behind the applied reference. In this case, a gap voltage of 200 kV is attained when the beam energy is in the 620 MeV range. The gap voltage is maximum when the energy reaches 1.1 GeV, wich is when synchrotron radiation becomes significant.

A different ramping set up is shown in figure 4. In this case, the gap control loop is on. The gap voltage reference is varied in smaller steps along the ramp and the gap voltage tracks the reference closely. Inspite of the advantage of ramping with closed loop control of the gap voltage, it is observed that low energy accumulation is more efficient when the gap voltage feedback loop is off.

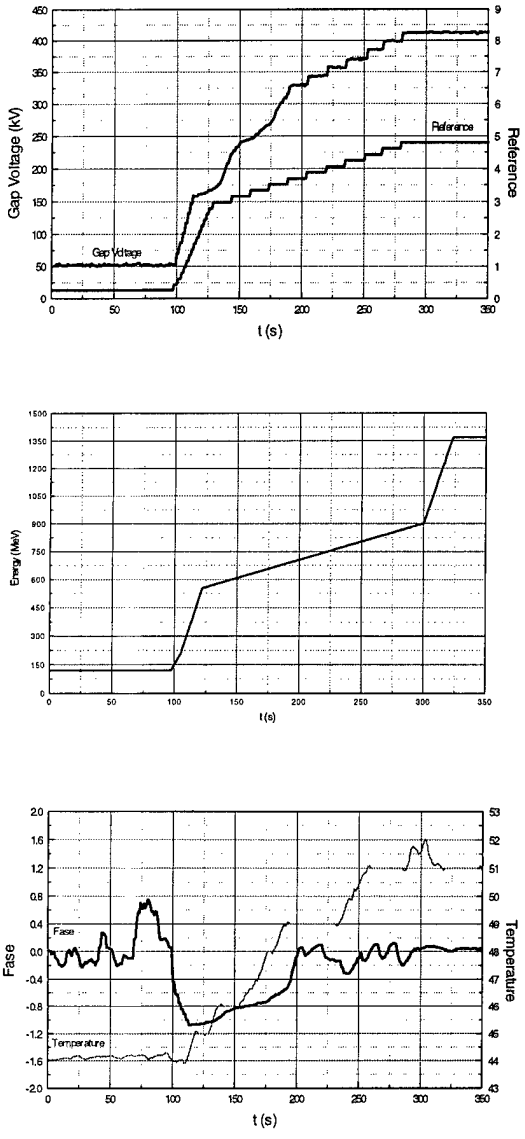



Figure 4: cavity parameter changes with feedback loop on.

At 1.37 GeV synchrotron radiation in the bending magnets amounts to 11 kW for every 100 mA. The high energy gap voltage is set at 450 kV. With this value, the beam life time is limited at present by the vacuum chamber pressure. With 50 mA of stored current, the cavity pressure stays in the high $10^{-9}$ level. Also at high energy, the detuning of the cavity is reduced from a large value, needed during accumulation down to 2 kHz, so that the reflected power stays low.

## 3 CONCLUSIONS

The LNLS storage ring RF system has been in operation for over 1 year. We have learned the operating conditions for the different beam situations: low energy injection and accumulation, RF ramping and steady final energy operation. The system has proven flexible, reliable and adequate for the machine.

## REFERENCES


[1] A. R. Rodrigues et al. ìLNLS Commissioning and Operationî. In these proceedings.

[2] D. Wisnivesky et al. ìThe LNLS RF Systemî. Proceedings of the 5th European Particle Accelerator Conference EPAC 96, p. 2038, 1996.

# ON THE LIMITATIONS OF ACCELERATING GRADIENT IN LINEAR COLLIDERS DUE TO THE PULSE HEATING

O.A.Nezhevenko*, Omega-P, Inc., 202008 Yale Station, New Haven, CT 06520

*Abstract*

In this work, we consider the limitation of the maximal accelerating gradient in linear colliders due to the pulse heating by the RF magnetic field at the cavity walls. Heating of the thin surface layer creates pulse mechanical stresses which may cause destruction of the inner surface of the cavities within a limited period of time. Because of this limitation the accelerating gradient can't exceed 300 MV/m even for frequences over 40 GHz, despite the fact that other factors allow to reach substantially higher gradients.

## 1. INTRODUCTION

In the longer-range future electron-positron linear colliders with 5-15 TeV center of mass energy will be in growing demand for high energy physics studies. A high accelerating gradient will be required to maintain a reasonable overall length of this collider.

The accelerating gradient is strongly correlated with the operating frequency - the energy stored per meter of accelerating structure varies approximately as $(G_0\lambda)^2$, where $G_0$ is the unloaded gradient and $\lambda$ is the RF wavelength. Hence, it is possible to design high energy colliders keeping the length and AC power within a reasonable bounds by operating at higher frequences [1].

Several factors must be taken into account in scaling a linear collider to higher frequences. Basic factors are a breakdown threshold, "dark current" capture threshold and problems caused by pulse heating by the magnetic fields at the accelerating cell walls. As for the breakdown and "dark current" capture thresholds, these factors make it possible to increase the gradient up to 250 MV/m for a frequency 34.3 GHz or up to 500-600 MV/m for a 91.4 GHz frequency [1]. At the same time a strong magnetic field on the cell walls causes the temperature increase by 110-510 $^0$C in a pulse. Pulse heating of the thin surface layer creates pulse mechanical stresses which may result in destruction of the inner surface of the accelerating cavities within a limited period of time.

It will be shown below that the life time of the accelerating structure i.e. the number of pulses the structure can sustain without surface destruction appears acceptable only if the pulse heating does not exceed ~150 $^0$C.

## 2. PULSE HEATING AND MECHANICAL STRESSES

A high frequency magnetic field on the cavity walls causes pulse heating. The temperature rise at the end of a pulse of duration $\tau_p$ is [1]

$$\Delta T = \frac{R_s}{K}\left(\frac{D\tau_p}{\pi}\right)^{1/2}\left(\frac{G_0}{Z_H}\right)^2. \qquad (1)$$

Here $R_s$ is the surface resistance, K is the thermal conductivity and D is the thermal diffusivity, given by $D=K/C_s\rho$, where $C_s$ is the specific heat, $\rho$ is the density (D=1.15 cm /sec and K=3.95 W/cm/ $^0$C for copper). $Z_H$ is an impedance defined as $Z_H = G_0/H_s$, where $H_s$ is the peak surface magnetic field. Formula (1) is derived on the assumptions that $R_s$, D, $C_s$ and $\rho$ do not change with temperature and the depth of thermal diffusion is far bigger than skin depth. The latter is valid for the range of parameters which is of interest (f= 11.4-91.4 GHz, $\tau_p$=12-250 ns) where the skin depth is 0.2-0.6 μm and thermal diffusion depth is 3.5 - 17 μm.

Mechanical stresses appears in the thin (3 - 17 μm) surface layer of metal due to the pulse heating. When the rise in temperature is above a "safe" value ($\Delta T_s$), the mechanical stress grows large enough to create microscopic damages in the metal. The damage accumulates with each suceeding pulse and the cavity surface is destroyed after the certain number of pulses (n). It is possible to define $\Delta T_s$ and n from the theory developed in the 70's by researches in the USSR to investigate the distruction of collectors and other parts of the microwave tubes resulting from the pulse heating by an electron beam [2-4].

In practice, the destruction of the metal surface occures when the mechanical stress exceeds its elastic limit. From this, the approximate value of the "safe" temperature rise can be written as [2]

$$\Delta T_s = \frac{2\sigma}{\alpha E}, \qquad (2)$$

where $\sigma$ is an elastic limit, $\alpha$ is coefficient of linear expansion and E is Young's modulus. For copper $\alpha=16.5\cdot10^{-6}/^0$C, $\sigma$= $1.2\cdot10^4$ N/cm$^2$ , E=$1.31\cdot10^7$ N/cm$^2$ and a "safe" pulse heating is only $T_s$ ~110 $^0$C !

Once the pulse heating exceeds this limit, plastic deformation occurs in the metal, which leads to accumulation of defects causing destruction of the heated surface after n pulses [3,4], given approximately by [2]

* Permanent address: Budker INP, 630090 Novosibirsk, Russia

0-7803-4376-X/98/$10.00 © 1998 IEEE

TABLE 1

| Frequency (GHz) | $G_0 \sim \omega^{5/6}$ (MV/m) | $\tau_p \sim \omega^{-1.5}$ (ns) | $\Delta T \sim \omega^{1.42}$ ($^0$C) | $T_0$ = 27 $^0$C n and life | | $T_0$ = 77 $^0$C n and life | |
|---|---|---|---|---|---|---|---|
| 11.424 | 100 | 250 | 23 | | | | |
| 22.848 | 180 | 90 | 61 | | | | |
| 34.272 | 250 | 50 | 112 | | | | |
| 45.696 | 320 | 30 | 165 | $3.6 \cdot 10^{10}$ | 14 years | $2.5 \cdot 10^{9}$ | 1 year |
| 57.120 | 380 | 22 | 225 | $1.5 \cdot 10^{9}$ | 3500 hours | $1.8 \cdot 10^{8}$ | 420 hours |
| 68.544 | 440 | 17 | 290 | $1 \cdot 10^{8}$ | 230 hours | $1.8 \cdot 10^{7}$ | 42 hours |
| 79.968 | 500 | 14 | 370 | $9.8 \cdot 10^{6}$ | 23 hours | $2.6 \cdot 10^{6}$ | 6 hours |
| 91.392 | 560 | 11 | 440 | $1.4 \cdot 10^{6}$ | 3 hours | $4.7 \cdot 10^{5}$ | 1 hour |
| 102.816 | 620 | 9 | 520 | $2.6 \cdot 10^{5}$ | 36 min | $1 \cdot 10^{5}$ | 14 min |
| 114.240 | 680 | 8 | 600 | $6 \cdot 10^{4}$ | 8 min | $3 \cdot 10^{4}$ | 4 min |

$$n \sim \frac{U - 50T_0}{16.7U} \cdot \exp\left(\frac{U}{6(T_0 + \Delta T)}\right), \qquad (3)$$

where U is heat of evaporation of the material (76320 cal/mole for copper), $T_0$ is the temperature before the pulse start ($^0$K).

## 3. RESULTS

The calculations made are for NLC - like TW accelerating structure with $Z_H = G_0/H_s$=307 Ohms [1] for frequences from 11.424 GHz (NLC) to 114.24 GHz (10xNLC). The increase in surface resistance due to the temperature rise and the accumulation of microdamages [5] was not taken into account.

To consider the influence of temperature before the pulse start, the exact value of which depends upon the design, the calculations were made for two values of $T_0$ - 300 $^0$K (27 $^0$C) and 350 $^0$K (77 $^0$C). Keeping in mind that the life time of the collider must be about 20 years at a repetition rate of 120 pulse/sec and for 6000 hours of operation per year, the requirement is that the accelerating structure should at least stand the number of pulses n $\sim 5 \cdot 10^{10}$ without destruction.

The results of the calculations are shown in TABLE 1.

One can see from the Table that the temperature rise at the end of the pulse should not exceed, say, $\Delta T \sim 150$ $^0$C, than $G_0 \sim 300$ MV/m at a frequency of 40 GHz. It can be shown that for fixed $\Delta T$, the gradient will increase with frequency as $G_0 \sim \omega^{1/8}$. $G_0$ can not exceed 330 MV/m at 91.4 GHz. It is obvious, that pulse heating limits the maximum value of RF fields in the cavities of microwave sources at a level lower than that in accelerating structures, because the pulse duration in the former is 4-16 fold as long.

## 4. CONCLUSION

The surface destruction of accelerating cells due to the pulse heating limits the gradient to about 300 MV/m and, consequently, decreases the attractiveness of linear colliders with a frequency substantially higher than 34.3 GHz.

More accurate experimental measurements of the maximal acceptable pulse heating for different materials may possibly be made at the NLC frequency (11.4 GHz) where the 50 MW klystrons with a pulse of 1.5 μs are available.

## 5. ACKNOWLEDGMENTS

This work is supported by the Department of Energy, Division of High Energy Physics. The author also would like to thank Dr. B. Persov for helpful discussion and Dr. A. Ganguly for careful reading the manuscript.

## 6. REFERENCES

[1] P.B.Wilson, "RF Power Sources for 5-TeV - 15-TeV Linear Colliders",SLAC-PUB-7256 (1996), 12pp.

[2] V.F.Kovalenko, "Termophysical Processes and Electrovacuum Devices", Moscow, SOVETSKOE RADIO (1975), pp. 160-193.

[3] V.A.Khmara, "The Theory of Metal Destruction at a Pulse Electron Bombardment", ELECTRONNAJA TECHNICA, SERIES 1 (1970), v.12, pp. 71-77.

[4] V.A.Khmara, "To the Question of Material Longevity of High Power Pulsed Electron Devices", ELECTRONNAJA TECHNICA, SERIES 1 (1971), v.1, pp. 77-82.

[5] M.G.Losinsky, in the book "Material Strength Under Cyclic Stresses", Moscow, NAUKA (1967), pp. 44-54.

# OPERATIONAL CHARACTERISTICS OF RF SYSTEM AFFECTING PLS BEAM STABILITY

M. Kwon, H. J. Park, I. H. Yu, J. Y. Huang, and I. S. Ko
Pohang Accelerator Laboratory, POSTECH, Pohang 790-784 Korea

*Abstract*

The fourth RF station was installed to the Pohang Light Source (PLS), whereas its station consists of a 60 kW klystron amplifier and a nose cone type cavity connected by a coaxial transmission line. Total 240 kW RF power is available for storing electrons up to 400-mA at 2-GeV and 200-mA at 2.5-GeV of beam energy. During the normal operation, some dangerous higher order modes (HOMs) induced by cavities have been identified. Making an effort to suppress instabilities caused by HOMs has been started by enhancing the capability of cavity cooling temperature control and adding the transverse and longitudinal feedback systems. Besides these efforts, characterizations of the beam loss transient due to RF have been underway. A modulation experiment of the accelerating voltage is also planned using the fourth cavity. We present performance test results with newly installed low level system.

## 1 INTRODUCTION

The PLS is a third generation storage ring which has twelve-period TBA lattice with 5 meter long straight sections. The nominal operation beam current during the user shift is 120 - 150 mA with over twelve hours of lifetime. Currently six beamlines (VUV, X-ray scattering, NIM, EXAFS, Lithography, and Microprobe) are operational and two more beamlines are under construction. The first undulator, U7, is ready for installation this summer and the dedicated beamline by the end of next year. A typical operation parameters of PLS RF system are shown in Table 1. The RF system consists of four cavities independently powered by four TV-klystrons. The fourth station was added last summer. The accelerating voltage is maintained at 0.4 MV/cavity and the required RF power is 20 kW each[1].

Table 1: Parameters of the PLS RF System

| | |
|---|---|
| Beam Energy | 2.0 GeV |
| Number of Station | 4 |
| Momentum Compaction Factor | 0.00181 |
| RF Frequency | 500.082 MHz |
| Revolution Frequency | 1.068 MHz |
| Harmonic Number | 468 |
| Accelerating Voltage | 1.6 MV |
| Synchrotron Frequency | 11.5 kHz |
| Tune(n_x/ n_y /n_z) | 14.28/8.18/0.013 |

## 2 PERFORMANCE WITH FOUR SYSTEMS

During the summer shut down period in 1996, the fourth RF station was added to the PLS storage ring. The total available RF power increases to 240 kW and total accelerating voltage becomes 1.6 MV, which increases the RF bucket height to 2.2%. For 2 GeV operation, 400 mA of beam current can be stored with enough margin, while it would be around 200 mA at 2.5 GeV. The maximum current achieved so far is 375 mA at 2 GeV, and 100 mA at 2.5 GeV. Fig. 1 shows the operation window of the PLS RF system in terms of the stored beam current for different beam energies and accelerating voltages. The newly installed cavity is located at the

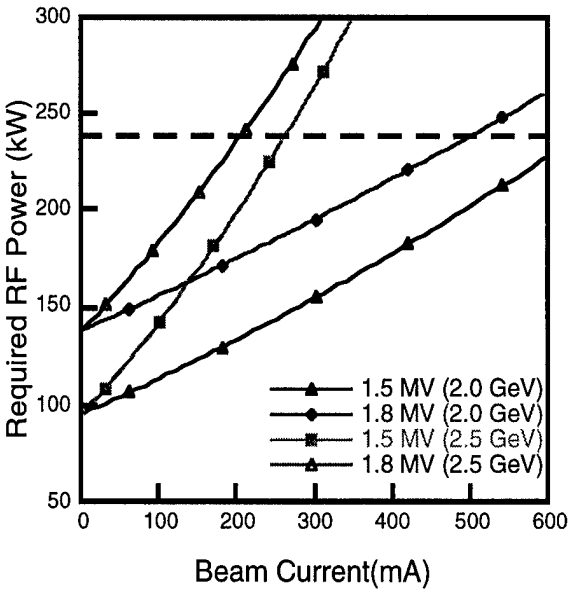



Figure 1: PLS operation window as a function of the beam energy and the current.

upstream in the RF straight section, 43 cm away from the next one. A refurbished version of the low level system was also installed. In the new system, various new and enhanced features are included. For higher reliability and stable operation, filter stages are added and dynamic ranges of the RF detection circuits are extended. For better isolation from outer noise, housings for RF parts are separated and multi-shot circuit is added to the trip signal processor. Also system installation and wiring are simplified to ease the mainte-

0-7803-4376-X/98/$10.00 © 1998 IEEE

nance, test and measurements.

During the normal beam operation of the ring, beam losses with unknown causes occurred and RF system trips were accompanied in most time. To monitor these transients, a relatively fast data acquisition system was installed to monitor RF parameters with pre-triggering. RF system trip signal triggers the acquisition system with preset pre-triggering time. It is observed that most of the beam loss with unknown causes force the RF system to be tripped by high reflection power or high vacuum pressure. However, what causes to increase the reflect power or the vacuum pressure is still not clear. Sometimes beam is lost owing to the instabilities. In Fig. 2, a periodic oscillation of the reflected power signal is observed just before the beam loss. The frequency of the periodic oscillation happens to be similar to the one of the low frequency oscillation[2].

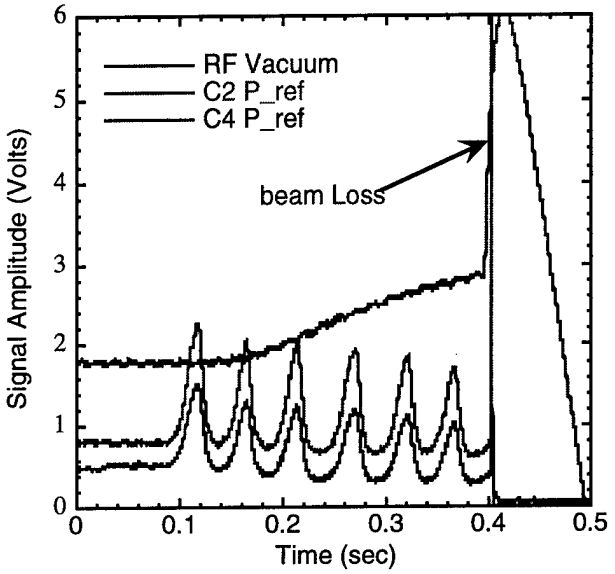



Figure 2: Behaviors of the vacuum pressure and RF reflected power signals at a beam loss transient.

## 3 EFFECTS ON THE BEAM STABILITY

With three cavities, at the level of beam current of 120 mA, collective effects can predominantly limit the maximum stored beam current in the storage ring for the user opeartions. The HOMs in the cavity #2 was found to be the major source to invoke the collective instabilities.

For studying longitudinal instabilities, mode identification experiments have been performed[2]. Using the normal mode method with a uniform fill pattern, HOMs invoking coupled bunch instabilities can be identified. Using the sum signal from the four BPM buttons, the beam current spectrum has frequency components at multiples of the bunch frequency and the oscillations of individual unstable modes appear as sidebands about the bunch harmonics. The oscillation amplitude of unstable modes can be determined from the ratio of the sideband to the carrier. By changing fill pattern, since HOMs appeared at different aliased frequencies, the reliability of a specific mode identification increases. The most dangerous two modes were found to be 758 MHz, and 1,707 MHz HOMs, identified by comparing with the calculation.

To check the stability of the photon beam, a photodiode is placed at the focal point of the VUV beamline, measuring the oscillation frequency of the photon beam. At certain condition, the time signal shows a discrete frequency component, which is turned out to be the synchrotron oscillation frequency. By changing conditions such as cavity temperature, this apparent oscillation has disappeared. A sampling data from the stripline signal shows that the phase between bunches are oscillating(phase jittering).

The limit was relieved somehow as the cooling path of the cavity #2 was modified. With a narrow controllable range (~4°) of the cavity temeperature control system, the maximum quiescently stored current is extended to 180 mA. Adding one more station, however, a severe dipole mode was observed at 62 mA, which is not possible to remove by the present cavity temperature control system. Fig. 3 shows the beam shape just before and after the threshold current.

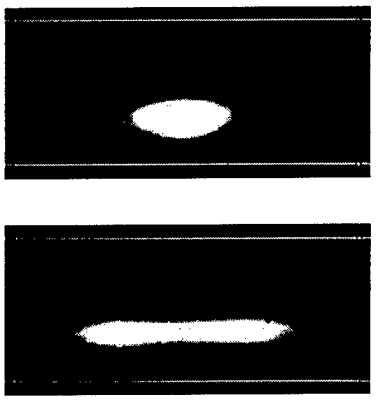


Figure 3 : The electron beam cross section monitored from the diagnostic beam line before (top) and after (bottom) when the stored beam passes the threshold current for the cavity 1.

In Fig. 4, it is illustrated how the cavity temperature sensitively affects the beam qualities. A small variation of the cavity temperature forces to change the lifetime when it is set near a 'critical' temperature. As the temperature decreases below this 'critical' value, a dipole longitudinal mode is invoked, forcing the beam unstable to reduce the lifetime. The stored beam current was above the threshold. When the beam current is above the threshold for a transverse mode, however, the lifetime increases as the temperature passes the 'critical' range invoking the instability. This reverse phenomenon occurs owing to the emittance growth, which

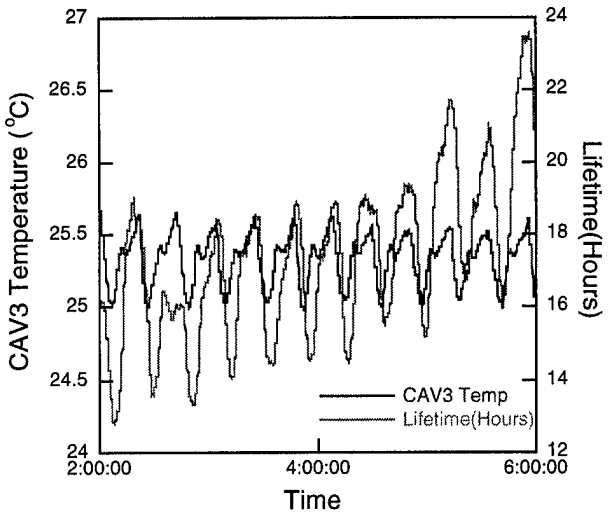



Figure 4: The correlation of the stored beam lifetime with the variation of the cavity cooling temperature in the PLS storage ring

increases the damping time.

## 4 EFFORTS TO PROVIDE HIGH CURRENT QUIESCENT PHOTON BEAM

In the previous section, it is shown that the cavity temperature affects the beam stability sensitively, and the present temperature control system has very limited capability, not suitable for wide varieties of temperature setting. Now a plan for upgrading the cavity temperature control system is underway, in which a wide range of temperature variation (30 °) and precise regulation (0.2°) will be achieved. When this will be finished, it is expected to lower the impedances of the HOMs substantially, which will also save the power requirement of the longitudinal feedback system to be mentioned below.

The gap voltage modulation technique was also performed using the cavity 1. Without modulation, as mentioned before, above 62 mA the beam size increased with a strong dipole instability mode. This limit was extended to 90 mA when a modulation was given to the input RF signal of cavity 1. The modulation frequency was varied and it was observed that a best result was obtained with harmonics of the synchrotron oscillation frequency. The modulation amplitude of the RF level was kept less than 10% of the total input power.

The most important effort of all should be the development of the longitudinal and transverse feedback systems. The transverse feedback system is installed and being tested[3]. A PEP-II-type longitudinal feedback system was being ordered and a kicker for this is under development. All these systems should be working by the middle of the year 1998.

A new disk type input coupler is developed which inherently has better damping capability of HOMs than the present tube-type one. Upon using this coupler with proper HOM absorbing technique, it will also help lessen the harmful effects of HOMs.

## 5 SUMMARY

Longitudinal and transverse coupled bunch instabilities were observed and some strong modes were identified by the normal mode method. Though cavity temperature change is effective to some extent to suppress these modes, with the present narrow range system it is difficult to remove all the dangerous HOMs. A plan for upgrade is underway.

The fourth RF station was added to the PLS RF system. It will improve the power requirement for high current operation. However, to utilize its full function, the cavity temperature control system should be improved. In the mean time, the cavity 1 is used as a modulating Landau cavity.

Unknown beam loss transient was closely monitored by fast sampling, which provides informations how RF parameters are altering during the transient and clues what causes the beam loss.

## 6 ACKNOWLEDGMENT

This work has been supported by the Korean Ministry of the Science and Technology (MOST) and the Pohang Iron and Steel Company (POSCO).

## 7 REFERENCES

1.M. Kwon, I. H. Yu, H. J. Park, D. H. Han, M. Yoon, and Y. S. Kim, Proc. of 1995 Particle Accelerator Conference, 1812 (1995).

2.M. Kwon, J. Y. Huang, H. J. Park, M. K. Park, I. H. Yu, and M. Yoon, Proc. of 1996 European Particle Accelerator Conference, 1096 (1996).

3.J. Y. Huang, M. K. Park, D. T. Kim, and I. S. Ko, In these proceedings.

# DESIGN AND OPERATION OF PET RADIO FREQUENCY QUADRUPOLES

D. Sun, P. Young, Science Applications International Corporation
A. Moretti, J. Dey, Fermi National Accelerator Laboratory

*Abstract*

The PET isotope production accelerator built by a collaboration of BRF, FNAL, SAIC, and UW consists of four RFQ's to accelerate $^3He^{2+}$ ions to 10.5 MeV for production of radioactive $^{18}F$, $^{11}C$, $^{15}O$ and $^{13}N$ isotopes. The design, tuning, and operational results are presented.

## 1 STATUS OF PET RFQ'S

The PET (Positron Emission Tomography) accelerator has been built to accelerate $^3He^{2+}$ ions for production of radioactive $^{18}F$, $^{11}C11$, $^{15}O$ and $^{13}N$ isotopes. The accelerator consists of an ion source, four RFQ's, a charge stripper, and beam transport system (Figure 1) [1]. The ion source generates 20 keV $^3He^+$ ions. The $^3He^+$ ions are accelerated to 1 MeV through the first RFQ (pre-stripper RFQ) operating at 212.5 MHz. After exiting the first RFQ, $^3He^+$ ions are stripped off the second electrons by a charge stripper. Then $^3He^{2+}$ ions go through the MEBT transport system (consisting of two 270 degree bending magnets and five quadrupole magnets) to enter a three RFQ string (post-stripper RFQ's) operating at 425 MHz. $^3He^{2+}$ ions are accelerated from 1 MeV to 10.54 MeV by these RFQ's (5.05 MeV at the end of RFQ A, 8.025 MeV at the end of RFQ B and 10.54 MeV at the end of RFQ C.)

This accelerator was originally designed and built by SAIC to accelerate $^3He^{2+}$ to 8 MeV using three RFQ's (one pre-stripper and two post-stripper RFQ's) The accelerator was operated by SAIC and delivered 2.5 mA $^3He^{2+}$ current at 1% duty factor before the project stopped in 1992 [2].

In 1995, the project was re-started. The designed final energy has been increased to 10.5 MeV. At higher energy, the beam loss is less when $^3He^{2+}$ ions passing through a thin foil window in the target area and the yield of isotope production is higher. A new post-stripper RFQ (RFQ C) has been added to the previous RFQ's to accelerate $^3He^{2+}$ from 8 MeV to 10.5 MeV. Water leaks caused by corrosion in cooling channels of vanes were found in all previous RFQ's. Therefore vanes of the two existing post-stripper RFQ's have been replaced with new ones and have been re-tuned. The whole pre-stripper RFQ will be replaced later with a new one. All cooling channels are now coated with a thin layer of Teflon to prevent corrosion.

## 2 DESIGN PARAMETERS

The design of pre-stripper RFQ has been reported before [3]. It is a segmented four vane structure with a rectangular "window" cut out in the middle of each vane. This structure reduces the dimensional requirement of resonant frequency of quadrupole mode and move it to below both dipole modes. Recent simulation showed that transmission of this RFQ is ~60-65% for input current of 20-25 mA. So the contour of new vanes of pre-stripper RFQ has been modified to improve the transmission to 80-85%. The three post-stripper RFQ's are all traditional four vane RFQ's (not segmented) and have acceleration section only. The transverse curvature of vane tip is constant. There is no rf tuner in the cavity since the designed tuning method dose not require any extra tuner. Computer codes MAFIA and SUPERFISH are used to calculate the theoretical Q, power and other rf properties. The basic parameters are listed in Table 1. Since RFQ B and C are similar to A, only parameters of pre-stripper RFQ and post-stripper RFQ A are listed in Table 1.

**Table 1. Design Parameters of PET RFQ's**

| | pre-stripper | post-stripper A |
|---|---|---|
| Particle | $^3He^+$ | $^3He^{++}$ |
| $f_0$ (MHz) | 212.5 | 425 |
| Aperture (cm) | 0.25 | 0.18 |
| Modulation | 1.78 | 2.1 |
| Input energy (MeV) | 0.02 | 1.0 |
| Output Energy (MeV) | 1.0 | 5.05 |
| Voltage (kV) | 57.0 | 58.4 |
| Max. Field (MV/m) | 32.2 | 39.9 |
| $Q_0$ (MAFIA) | 7600 | 9500 |
| Power (kW) | 59.0 | 63.0 |
| Pulse Width (μs) | 70 | 70 |
| Rep. Rate (Hz) | 360 | 360 |
| Inject Current (mA) | 25 | 28 |
| Transmission | 80% | 90% |
| Length (cm) | 103.9 | 137.1 |

0-7803-4376-X/98/$10.00 © 1998 IEEE

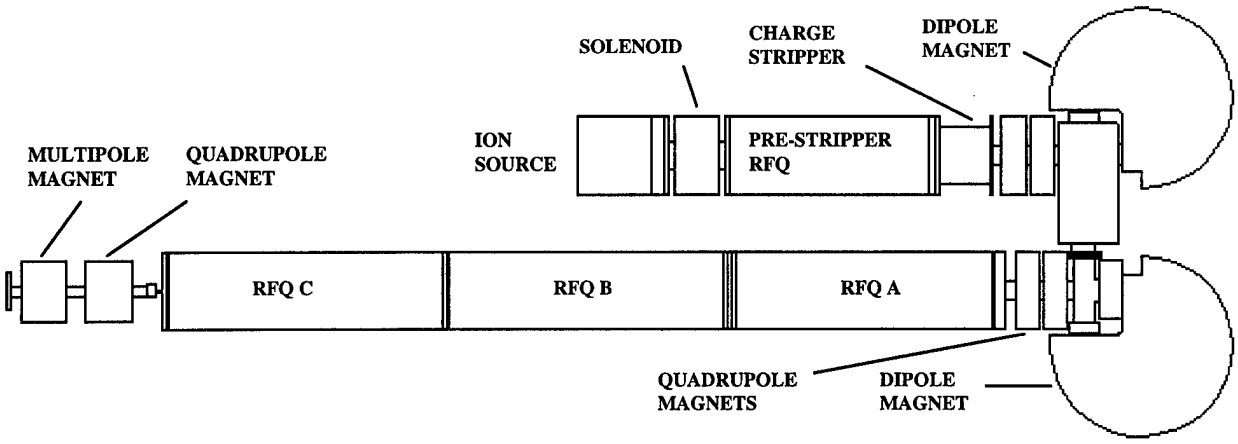



**Figure 1 PET ACCELERATOR**

## 3. SIMULATION RESULTS

Simulation of particle transport through pre-stripper RFQ and three post-stripper RFQ's are performed using PARMTEQ. The results are listed in Table 2 and 3. Two versions of PARMTEQ were used: SAIC version (denoted as SAIC in Table 2 and 3) and the version used in ANL (originally written at Chalk River Laboratory ) which has the option to use 2 or 8 potential terms (denoted as ANL (2-term) or ANL (8-term) in Table 2 and 3.)

Shown in Table 2 is the simulation results of particles through pre-stripper RFQ which is performed separately from other three post-stripper RFQ's.

Transport of particles through the string of three post-stripper RFQ's is simulated from entrance of RFQ A to the end of RFQ C (end to end simulation.) There is a plate with aperture of 0.635 cm between each RFQ, so the RFQ's are not coupled. This plate and the space between the end of vanes and this plate create a gap of 1.16 cm long between each RFQ. In end to end simulation, a drift space of 2.16 cm between each RFQ was used which represents the above mentioned 1.16 cm gap as well as other end effect of each RFQ. Simulation results show that beam loss in RFQ B and C is mainly due to this 2.16 cm drift space between each RFQ since beam becomes mismatched to next RFQ after such a drift space. Shown in Figure 2 is the total transmission at the end of RFQ C versus length of drift spaces between each two RFQ's. One can see the beam loss in RFQ B and C is small if there is no drift space in between.

Although the design for post-stripper RFQ's is based on the transverse emittance of 0.0019 $\pi$ cm-rad, simulations are also done with various transverse emittance, currents and number of particles. Shown in Figure 3 is the total transmission at the end of RFQ C versus various transverse emittance.

**Table 2. Simulation Result of Transmission of 212.5 MHz RFQ** (input current 25 mA, transverse emittance: 0.016 (x), 0.016 (y) $\pi$ cm-rad )

| | existing pre-striper rfq | modified pre-stripper rfq |
|---|---|---|
| SAIC | 0.59 | 0.80 |
| ANL (2-term) | 0.66 | 0.87 |
| ANL (8-term) | 0.32 | 0.65 |

**Table 3. Simulation Results of Total Transmission of RFQ A, B and C** (input current 28 mA, emittance: 0.0019 (x), 0.0019 (y), 0.0091 (z) $\pi$cm-rad and 65° phase spread)

| | End of A | End of B | End of C |
|---|---|---|---|
| SAIC | 0.865 | 0.655 | 0.600 |
| ANL (2-term) | 0.990 | 0.518 | 0.333 |
| ANL (8-term) | 0.960 | 0.545 | 0.485 |

## 4. EXPERIMENTAL DATA AND OPERATIONAL RESULTS

### *4.1 Tuning*

All RFQ's were tuned by mechanically adjusting each vane using equally spaced screws. For three recent-tuned post-stripper RFQ's, the final field balance is tuned to a

level that the average dipole components is less than 2% for RFQ A and B, and less than 1% for RFQ C. Resonant frequency of these RFQ's are tuned to ~425.3 MHz at room temperature. The operating frequency of 425 MHz is achieved by controlling the differential temperature between vanes and cavity.

The unloaded Q's of RFQ's are: 6100 (pre-stripper RFQ), 7667 (RFQ A), 8900 (RFQ B), and 8900 (RFQ C) while the unloaded Q's given by MAFIA code is 7300 (pre-stripper RFQ) and 9500 (post-stripper RFQ's).

There are 12 rf pickup loops in each of post-stripper RFQ's. In each quadrant there are three of them: one is at middle of the RFQ, other two are at ~15 cm from each end of the RFQ. They can be used to monitor the field unbalance which may occur during operation or other problems such as electrical breakdown. So far we have used these probes to check if the field balance changed after the vane is heated and the frequency is adjusted to 425.0 MHz. No significant change of field balance has been observed.

*4.2 Operational Results*

There are four RF power amplifier systems, one for each RFQ. Each amplifier system consists of a solid state amplifier with maximum power of 850 W, a Burle 7651 tube amplifier with maximum power of 4 kW and a Burle 4616 tube amplifier with maximum power of 200 kW.

The pre-stripper RFQ has been operated for a long time (even with small leaks in water cooling channels of vanes.) This RFQ was run (without beam) up to power level of 135 kW without sparking problem. Higher power levels are possible but were not tried, since 135 kW is already more than needed. This RFQ is normally operated at 100-110 kW level with beam load of 20-24 kW. The threshold of power level to accelerate beam is about 80 kW. The emittance at entrance of this RFQ is 0.024 - 0.03 $\pi$ cm-rad which is larger than the value used to guide the design. So far output current of 16 mA has been measured while the current out of ion-source is 24 mA. This result is in agreement with recent results of PARMTEQ simulation.

RFQ A, B and C are still being commissioned. Output current of 12 mA at the end of RFQ A and 6 mA at end of RFQ C have been measured while the input current at the entrance of RFQ A is about 20 mA (measured at the exit of MEBT system.). This result is close to the transmission predicted by PARMTEQ simulation for a beam with emittance of 0.0030 $\pi$ cm-rad. The measured emittance of input beam at entrance of RFQ A is indeed 0.0030-0.0040 $\pi$ cm-rad which is larger than the value (0.0019 $\pi$ cm-rad) used to guide the design. To get the above mentioned output current, RFQ A is operated at power level of 100-110 kW while RFQ B and C are operated at power level of 80-90 kW. These power levels are also in agreement with results of PARMTEQ and MAFIA simulation.

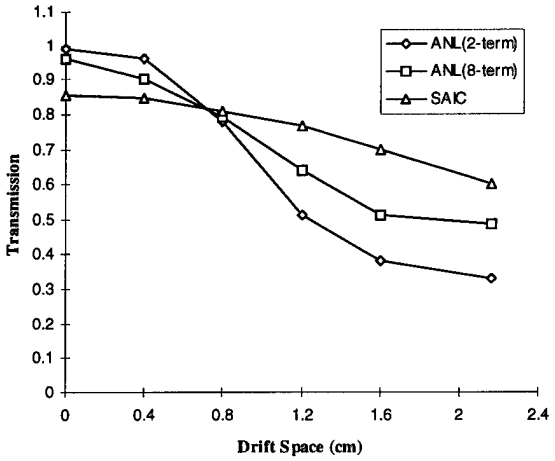
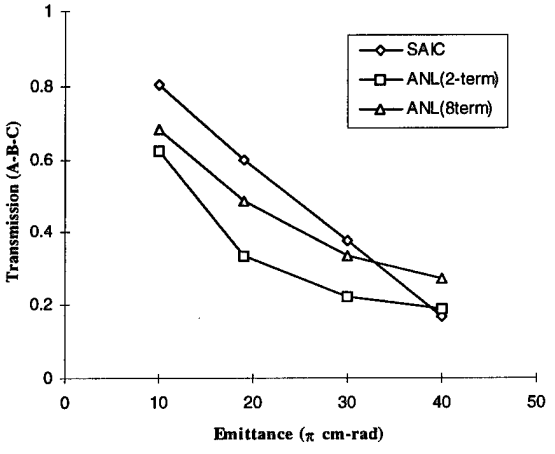



**Figure 2. Transmission (A-B-C) vs. Drift Space**




**Figuer 3. Transmission (A-B-C) vs. Emittance**

## ACKNOWLEDGMENTS

The authors are grateful to the effort and contribution of all people in current collaboration as well as previous collaboration team. Special thanks go to Gerald McMichael at ANL for his constructive comments and assistance to run ANL/Chalk River Lab version of PARMTEQ.

## REFERENCES

1. R. J. Pasquinelli, this conference, 9B.9
2. W. D. Cornelius *et al.*, 1992 Linear Accelerator Conference Proceedings, p. 139.
3. W. D. Cornelius and P. E. Young, Nuclear Instruments and Methods in Physics Research, B79 (1993) p. 933.

# SLC INTERFEROMETER SYSTEM AND PHASE DISTRIBUTION UPGRADES

R. Akre, F.J. Decker, R.K. Jobe, R. Koontz, M. Mitchell, R. Strozinsky
Stanford Linear Accelerator Center†, Stanford University, Stanford, CA 94305,USA

*Abstract*

Many of the components used in the Stanford Linear Collider (SLC) phasing system date back 30 years to the construction of SLAC. At the start of SLC the phase reference system was upgraded with many of the original components remaining. The R.F. drive system phase stability requirements became tighter with operation and optimization of the SLC. This paper describes analysis done on the R.F. drive system and interferometer system during the 1996 run and down time, modifications to the systems during the 1996-97 down time, and the improvements in stability from the modifications.

## 1 INTRODUCTION

The sun coming up in the morning on a beautiful sunny day for someone in Stanford, California is not such a nice experience if one is an operator of the Stanford Linear Collider (SLC) trying to maintain luminosity. The improvements on the SLC the past decade have decreased the emittance of the beam to a point where the existing phase variations in the RF, due to diurnal temperature changes, significantly effect luminosity. The effects are greatest at sunrise when the temperature gradient with respect to time is the largest.

During the 1996-97 down time the front end phase distribution system was reconfigured. The phase critical path was moved from the low level RF system before the high powered amplifier which drives the Main Drive Line (MDL) to the front of the MDL. The phase distribution system is described in reference [1]. Time Delay Reflectometry (TDR) measurements on the MDL showed problem areas which were rebuilt.

## 2 FRONT END PHASING CHANGES

The front end phase distribution of the SLC has been upgraded to move temperature sensitive devices out of the phase critical path. The phase critical path begins where the RF reference signal is first split to feed more than one device of which relative phase is critical. Figure 1 shows that the point at which the phase from the master oscillator splits to feed different areas was in the distribution chassis. RF outputs of this chassis feed Sector 0 and 1, CID and Damping Rings, and the Linac. The items of interest to remove from the phase critical path were the Master Amplifiers and Switch, the Fiducial Generator, and about 60 feet of cable. The Master Amplifiers are used to increase the RF power level to 30 watts. The Fiducial Generator puts a 120 watt 1/2 cycle timing pulse on the RF before it is sent into the MDL for distribution of RF, timing and phase information in the linac.

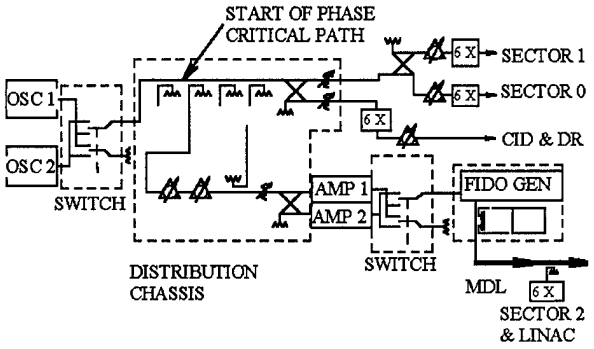



Figure: 1 SLC Old Front End Phase Distribution

### *2.1 Motivation for Changes*

Operators constantly adjust phase to maintain luminosity during times of large outside temperature changes. The most common adjustments are the injection phase from the damping rings to the linac and injection phase of positrons entering sector 1.

In order to verify that the suspected area of RF phase shifts was the section from the distribution chassis to the MDL, an 80k BTU heater was placed in the sector 0 alcove where these electronics and cables are located. The heater was turned on at 04:20AM on June 20, 1996 to simulate the sun coming up. The temperature in the rear of the RF components rack rose from 65°F to 87°F at 06:00AM at which time the heater was turned off. Figure 2 is a plot of the phase difference between sector 2 in the linac and sector 1 from 18-June-1996 at 01:20 to 20-June-1996 at 07:20.

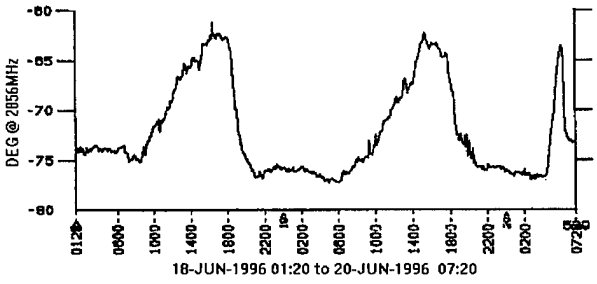



Figure: 2 Sector 1 to Sector 2 Phase Variations

† Work Supported by the Department of Energy, Contract DE-AC03-76F00515

The sharp rise and fall at the end of the graph is the heater turning on and then off. Normal diurnal phase variations are about 15° @ 2856 MHz with outside temperature changes of 30° F. With the injection phase tolerance into the linac being much less than 1° @ 2856 MHz, the phase variations observed in the RF would cause difficulty in maintaining luminosity.

*2.2 Changes to the SLC Front End Phase Distribution*

The phase distribution system was changed to the configuration shown in figure 3.

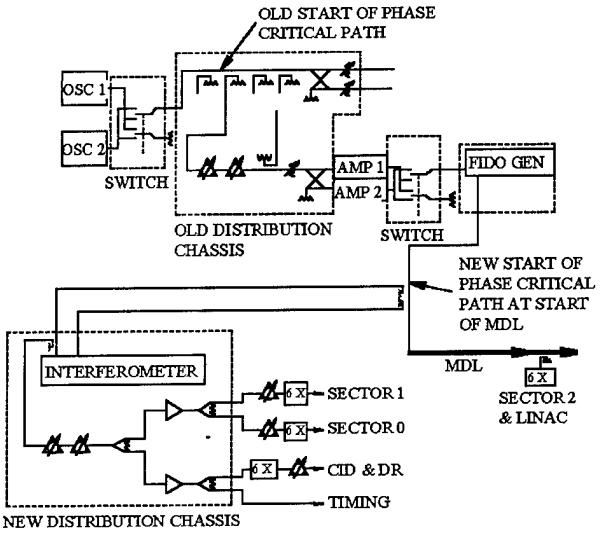



Figure 3. SLC Front End RF Distribution

The phase critical path now starts after the old distribution chassis, the power amplifiers, the power amplifier switch, the fiducial generator and many connectors and cables. The phase critical path now starts at the front of the MDL where the distribution chassis is a 6 foot Heliax cable away. The distribution chassis contains on a single FR4 circuit board the phase sensitive interferometer components and amplifier, two wide band tuning diode phase shifters, splitters and amplifiers. N-type connectors mount to an aluminum housing which supports the board. The aluminum housing is then mounted on a water temperature stabilized plate. A 5.25-19 inch rack mount chassis, 8 inches deep, houses the unit, figure 4.

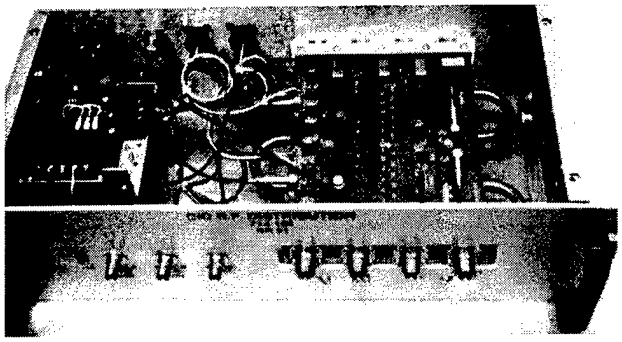


Figure 4. RF Distribution Chassis

*2.3 Diode Delay Line Phase Shifters*

In order to make the changes to the front end phasing it was necessary to develop a wide band phase shifter which would be able to shift the phase of the 476MHz by 60° which shifts the 2856MHz by 360°. The phase shifter would need to change and stabilize phase between pulses, at 120 rep rate, within 8mS. The phase shifter must also be able to transmit the timing pulse which contains components much higher in frequency. A series of tuning diodes was connected to a microstrip structure in a three layer FR4 board. Figure 5 is a scope image of the timing pulse into and out of the phase shifter. The pulse out has been scaled to the same height as the pulse in, to better see any distortion. Loss through the phase shifter is 6dB.

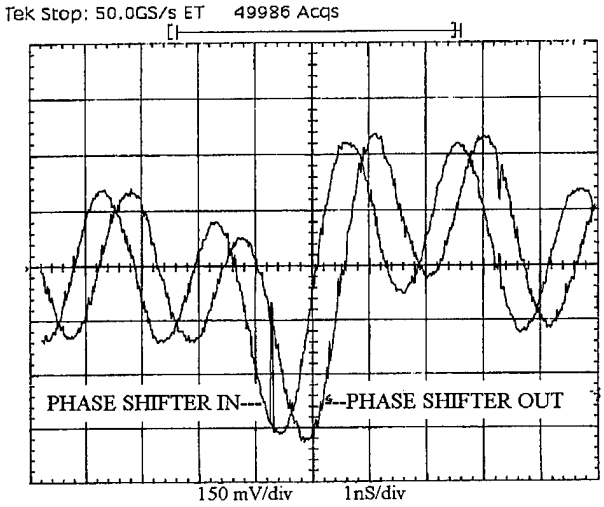



Figure 5. Fiducial Pulse Through the Phase Shifter.

*2.4 Phase Variations After Changes*

The variation in phase as seen by the sector 2 to sector 1 phase monitor has significantly decreased since the upgrade. Diurnal variations which would cause 15° phase variation at 2856MHz now only cause 3° phase variation.

## 3 INTERFEROMETER UPGRADES

The interferometer system is used to measure the electrical length of the MDL. Variations in the electrical length of the MDL to each sector from sector 2 are calculated assuming that the variation is distributed uniformly. The calculated phase variation is then used to correct the phase of the sector.

*3.1 Interferometer System*

The interferometer system, figure 6, uses a dual directional coupler at the front of the MDL to measure RF into and out of the MDL. At sector 30, about 9700 ft later, the RF is coupled off, phase modulated by 180° at 750Hz, run through a nulling phase shifter, amplified and sent back through the MDL to the front. A vector

sum of the modulated 750Hz signal from sector 30 and the forward RF into the MDL is run through a 750Hz bandpass filter and feedback amplifiers. The output is used to adjust the nulling phase shifter in sector 30. The variation in MDL phase is measured by 1/2 the amount the nulling phase shifter must move to adjust for the electrical length of the RF path up and back the MDL.

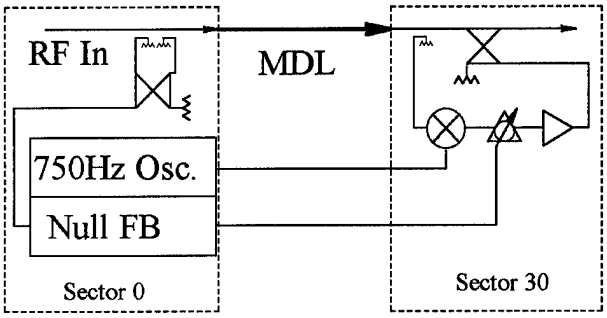



Figure 6 Interferometer System

Matches throughout the system are critical if phase errors are to be kept to levels of 1° 2856MHz or 0.17° 476MHz. The amount of power required to change the phase of an RF signal by 0.17° is -50dB relative to the RF signal, if the phase is off by 90°. A fixed reflection would just add an offset and not effect the relative phase measurement, but in a system which is changing up to 4° diurnally a reflection of -14dB could cause a phase change of 0.17°, which would be 1° of the frequency multiplied by 6.

To reduce some errors in the interferometer system, the MDL input dual coupler and phase sensitive electronics were moved from the sector 0 alcove, about 50 feet of Heliax away to the input of the MDL. The phase sensitive electronics were made part of the temperature stable CID RF Distribution chassis.

*3.2 Main Drive Line Maintenance*

The MDL is almost about the same as it was 30 years ago as described in reference [2]. Figure 7 shows a TDR measurement from sector 30 to sector 21. The TDR was done using an HP 215A pulse generator with a 60nS wide, 10 volt, 0.5nS rise and fall time pulse. The scope used to collect the data was a Tektronix 544A, 1GS/Sec, 500MHz, 64kB buffer. The expansion joints and couplers stand out in the measurement. The center conductor of the expansion joints at sector 24 and sector 22 appear at 4.2μS and 5.5μS respectively.

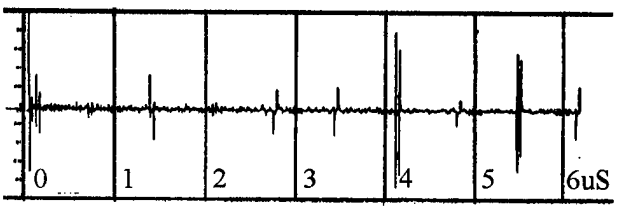



Figure 7. TDR from Sector 30 to Sector 21.

These expansion joints when examined were found to have a reversed center conductor. The outer diameter of the center conductor is matched to the inner diameter of the outer conductor to maintain a 50 ohm line. Figure 8 shows the construction of the expansion joint. The joints exhibited reflection of -11dB when tested on the bench. With the expansion joints expanding and contracting about 1 cm diurnally, the phase of the reflection could change by 10°. This could cause a 4° phase change at 2856MHz. Expansion joints in sectors 2 to 9, 17, 21, 22, and 24 were rebuilt during the down time.

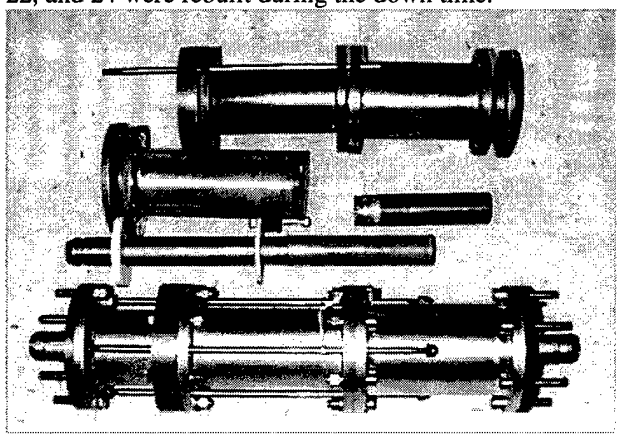


Figure 8. SLC MDL Expansion Joint.

## 4 PROSPECTS

Beam based phase measurements showed signs of phase variation in the phase reference system, reference [3]. With refinement of beam based phase measurements, locations of phase instabilities may become more apparent. The work done so far should increase stability and will be most noticed with the startup of SLC in June of 1997. We expect to see significant improvements in the positron injection phase stability.

## 5 ACKNOWLEDGMENTS

We would like to thank M. Breidenbach, T. Markiewicz D. McCormick, and the AMRF group for there assistance in diagnosing and correcting problems with the MDL and interferometer systems. We would also like to thank M. Ross for his assistance and support in making these projects possible.

## REFERENCES

[1] R. K. Jobe, H. D. Schwarz, "RF Phase Distribution Systems at the SLC" April 1989, SLAC-PUB-4893

[2] 'The Stanford Two Mile Accelerator' R. B. Neal, published by W. A. Benjamin, Inc., New York 1968

[3] F.-J. Decker, R.W. Assmann, M.G. Minty, N.Phinney, W.L. Spence (SLAC), "Beam-Based Analysis of Day-Night Performance Variations at the SLC Linac" Presented at PAC 1997

# CALIBRATION SYSTEM FOR SLC 476MHZ TO 2856MHZ MULTIPLIERS

R. Akre, G. Barillas, M. Mitchell
Stanford Linear Accelerator Center[†],Stanford University, Stanford, CA 94309 USA

*Abstract*

The two mile long Main Drive Line (MDL) distributes 476MHz at each of the 31 sectors along its length. Each of the 31 sectors has a six times multiplier which drives the 2856MHz phase reference system for that sector. This system is used to set and maintain phase of the accelerator structures over time. During previous runs significant down time resulted from sector phasing which was required after multiplier replacement. A system was designed to calibrate the phase of the 476MHz input to the phase of the 2856MHz output of the multiplier units. This enabled multipliers to be replaced without rephasing sectors.

## 1 INTRODUCTION

The phase distribution system of the 2 mile long Stanford Linear Accelerator consist of a Main Drive Line (MDL) which distributes 476MHz to each of 31 subbooster stations, reference [1]. At each subbooster station there is a 19 inch rack mount chassis which takes the 476MHz from the MDL multiplies it by 6 to 2856MHz. The chassis is referred to as the SubBooster Drive Unit (SBDU). The 2856MHz in the SBDU is amplified and split to drive the Phase Reference Line (PRL) and the subbooster klystron. Electronics for control of the phase and amplitude of the subbooster klystron are also in this chassis. The SBDU is temperature controlled by a water regulated mounting plate.

The phase of each of the klystrons in a sector is set based on the phase of the PRL. During the 1994 to 1995 Stanford Linear Collider (SLC) run several SBDU were replaced for various modes of failure. The replacement of the unit takes about 1 hour but setting the phase of the 8 klystron sector had taken significantly more time. This recovery time was a significant portion of RF related down time. It was desired by the Accelerator Operations Department that the units all have the same phase length for the phase reference system output. This would allow the unit to be replaced without having to rephase a sector. Since the unit multiplies the RF from 476MHz to 2856MHz the calibration could not be easily done with standard test equipment.

## 2 CALIBRATION SYSTEM

In order to calibrate the phase of the SBDU's a calibration unit was built figure 1. With this unit all SBDU were calibrated to the same phase length from the -0.2dbm of 476 MHz in to the 1.3W of 2856MHz out to drive the Phase Reference Line (PRL).

The SubBooster Drive Calibration Unit (SBDCU) consist of a 3 dB hybrid to split the 476MHz input power. One side of the hybrid output goes to the DUT and the other side goes to a six times multiplier. The output of the multiplier, 2856MHz, is passed through a phase trimmer, used for calibration of the unit, an isolator, and then into the LO port of a mixer used as a phase monitor. The PRL output of the DUT goes to into 20 dB coupler with a termination. The -20dB coupled out is further attenuated, passed through a phase trimmer and isolator, and into the RF port of the phase monitor mixer. The output of the phase monitor mixer is on a front panel BNC for viewing with a DVM. All internal phase critical units are mounted to a temperature stabilized plate. The controller with temperature readout is on the front panel.

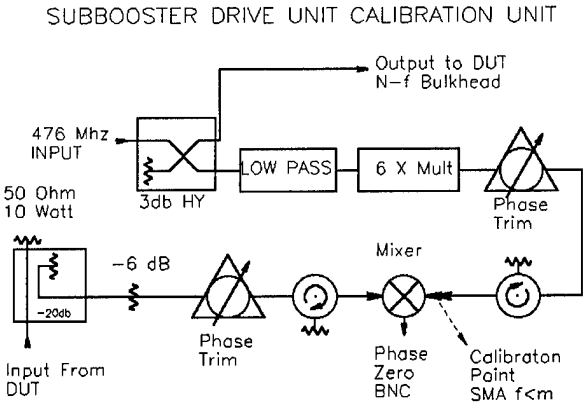



Figure: 1 SubBooster Drive Unit Calibration Unit

### *2.1 Calibration of the Calibration Unit*

Since the SBDU were calibrated against the SBDCU, the SBDCU needed to be calibrated. Calibration of the unit was done in two steps.

Step 1 calibrates the phase of the 476 MHz on the output port to the DUT, to the phase of the 2856 MHz on the SMA male connector to the mixer. The calibration uses a HP54120A 20Ghz sampling scope, a phase

[†]Work Supported by the Department of Energy
Contract DE-AC03-76SF00515

0-7803-4376-X/98/$10.00 © 1998 IEEE

shifter, a 476 MHz phase stable source, a 476 MHz 10dB directional coupler, power meter, the calibration adapter (N-male to SMA-male) and RF test cables. The only above item which directly effects calibration is the calibration adapter. The same adapter is used for all calibrations of this unit and is stored inside the SBDCU. The channels of the scope are first cross calibrated using the phase shifter to make sure the phase delay from the input of the cables to the scope screen is the same for channel 1 and 2. Since the phase through a step recovery diode multiplier is power dependent all measurements must be done at the operational power levels. The positive going zero crossings of the 476MHz from the DUT output port to the 2856MHz mixer input is lined up to within 1picosecond using the phase trimmer.

Step 2 of the calibration consists of zeroing the mixer when the phase at the Input from DUT port is equal to the phase at the input to the mixer on the 6 x multiplier output side. Equipment used is a network analyzer, 10 dB directional coupler, 33dB - 2W amp with isolator at output, 30dB directional coupler with 10 watt load at output used as high powered 30dB attenuator, power meter, phase shifter, calibration adapter (N-male to SMA-female), DVM, and test cables. The calibration adapter used effects calibration. The adapter used is stored inside the SBDCU. The power from the analyzer is split and one side amplified. The two cables, one with 1.3 Watts and the other with 3mW, are adjusted to the same phase length and then used to zero the mixer, see figure 2.

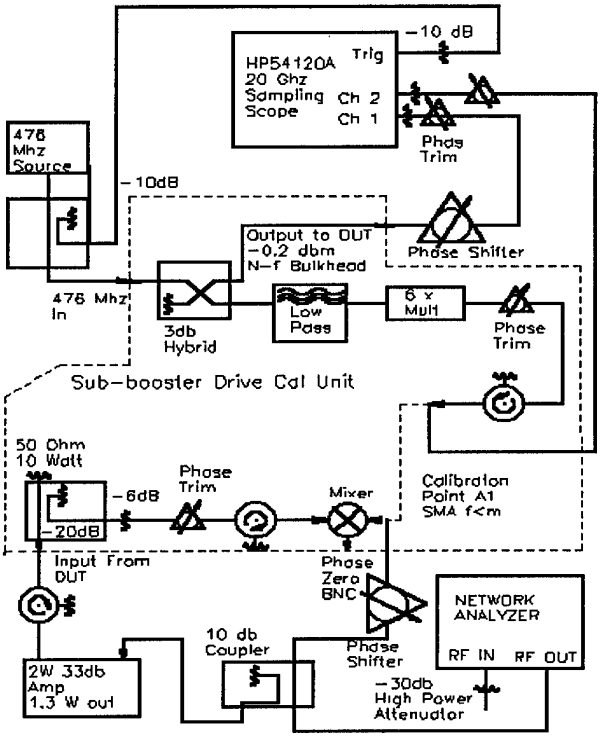



Figure 2 SubBooster Drive Calibration Unit Cal.

*2.2 SBDU Calibration*

The calibration setup requires a 476 MHz phase stable source, a phase shifter, a network analyzer, power meter, the SubBooster Drive Calibration Unit (SBDCU), three N type test cables and a temperature stabilized water system. Temperature stability is reached in the SBDCU about an hour after turn on. The SBDU is turned on with water temperature stabilized flow for 1/2 hour before measurement.

The phase length of the external phase shifter with a cable on each end is matched to the third cable on a network analyzer. The phase shifter and cable assembly connects the SBDCU output to the SBDU 476MHz input, figure 3. The remaining cable connects the 2856MHz 1.3Watt PRL output of the SBDU to the input of the SBDCU. A phase trimmer installed in the SBDU is then adjusted to zero the mixer, aligning the phase.

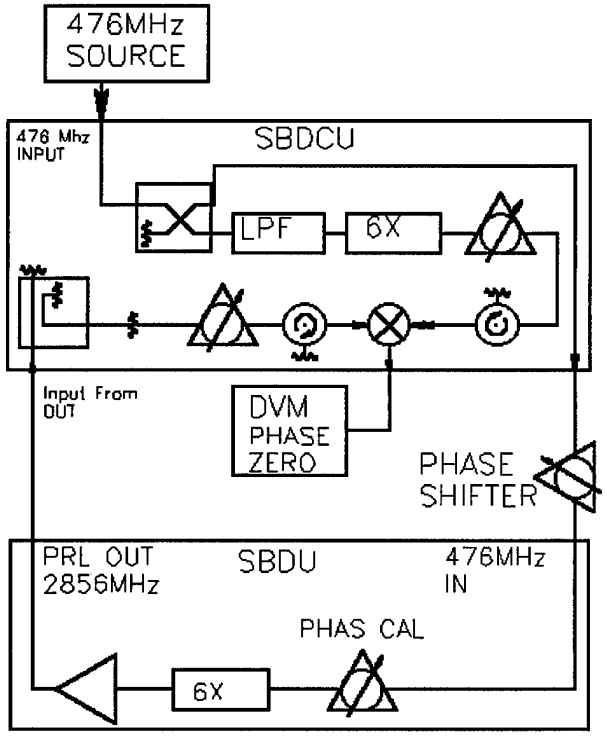



Figure 3 Calibration of Subbooster Drive Unit

## 3 CALIBRATION PERFORMANCE

Since the upgrade several units have been replaced with no time lost due to rephasing sectors. Figure 4 is a graph of a phase monitor of which the SBDU in sector 19 is in its phase loop. On the 23 of September, 1995, the SBDU was replaced. The spike in the plot is due to RF being removed during replacement. After replacement the phase returned to within 1° @ 2856MHz.

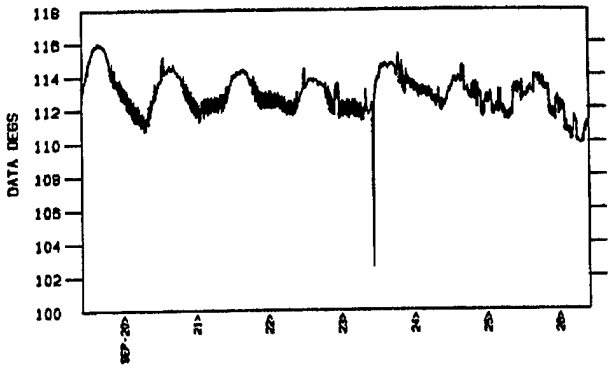


Figure 4 Phase of Sector 19 PRL

*3.1 SBDU Calibration Data*

During calibration of the SBDU, data was taken on the effects of temperature and amplitude on phase length. A summary of the results are given in Table 1. Phase is measured in °S which is degrees at 2856MHz.

| | °S/dB | °S/°C |
|---|---|---|
| MIN | -9.98 | -2.71 |
| MAX | 4.71 | 4.17 |
| AVG | -2.39 | -2.71 |
| STD | 2.92 | 4.17 |

Table 1. SBDU Phase Characteristic

The temperature of the SBDUs are held to within ±1°C and in most cases is within ±0.5°C. The 476MHz drive amplitude varies diurnally with temperature of the Main Drive Line. At Sector 30 where the variations are the greatest the power levels stay within ±0.5dB.

## 4 COMMENTS

The calibration of the SBDUs will save many hours of beam time in phasing of sectors. The data collected on the SBDUs will also help in understanding diurnal variations in the linac.

## 5 ACKNOWLEDGMENTS

We would like to thank K. Jobe, R. Koontz, M. Ross, and H. Schwarz for the fruitful discussions and support of this project.

## REFERENCES

[1] `RF Phase Distribution Systems at the SLC', R.K. Jobe and H. D. Schwarz, Stanford Linear Accelerator Center, Stanford University, Stanford, CA 94309, USA. SLAC-PUB-4893 April 1989

# LOW-LEVEL RF SIGNAL PROCESSING FOR THE NEXT LINEAR COLLIDER TEST ACCELERATOR

S. Holmes, C. Ziomek, C. Adolphsen, R. Akre, S. Allison, S. Clark, T. Dean, R. W. Fuller, S. Gold, R.K. Jobe, R. Koontz, T.L. Lavine, C. Nantista, Z. Wilson, A. Young,
Stanford Linear Accelerator Center, CA 94309

*Abstract*

In the X-band accelerator system for the Next Linear Collider Test Accelerator (NLCTA), the Low Level RF (LLRF) drive system must be very phase stable, but concurrently, be very phase agile. Phase agility is needed to make the Stanford Linear Energy Doubler (SLED) power multiplier systems work and to shape the RF waveforms to compensate beam loading in the accelerator sections. Similarly, precision fast phase and amplitude monitors are required to view, track, and feed back on RF signals at various locations throughout the system. The LLRF is composed of several subsystems: the RF Reference System generates and distributes a reference 11.424GHz signal to all of the RF stations, the Signal Processing Chassis creates the RF waveforms with the appropriate phase modulation, and the Phase Detector Assembly measures the amplitude and phase of monitored RF signals. The LLRF is run via VXI instrumentation. These instruments are controlled using HP VEE graphical programming software. Programs have been developed to shape the RF waveform, calibrate the phase modulators and demodulators, and display the measured waveforms. This paper describes these and other components of the LLRF system.

## 1 INTRODUCTION

The Next Linear Collider Test Accelerator (NLCTA) is an experimental high-gradient X-band linac at SLAC designed to integrate the technologies of X-band accelerators, klystrons, and RF pulse compression systems. The NLCTA will serve as a test bed as the design of the Next Linear Collider (NLC) evolves. The Low-Level RF (LLRF) Signal Processing System was designed to produce and monitor the highly phase agile RF drive to achieve the small (≅ .1%) bunch-to-bunch energy spread required for the NLC [1].

## 2 11.424GHZ RF REFERENCE SYSTEM

A single RF Drive System supplies RF to all of the NLCTA high-power RF stations [2]. This RF drive system is derived from a 476MHz drive-line signal. The 476MHz CW signal is processed through a train of preamps, level-set attenuators, and mixers to produce signals at 2856-MHz and 11.424GHz, in the power range of 10 to 20dBm. The 2856MHz signal is used for phase-reference purposes. The 11.424GHz signal is transmitted to each Signal Processing Chassis where it is phase modulated, and to each Phase Detector Assembly where it is a reference signal that is used to precisely measure the amplitude and phase of several RF monitoring points in the RF system. After further amplification, the modulated 11.424GHz signal is transmitted to the klystrons.

## 3 SIGNAL PROCESSING CHASSIS

RF phase and amplitude are coded as two orthogonal components: I (in phase) and Q (in quadrature), where phase is arctan(Q/I) and amplitude is $(I^2 + Q^2)^{1/2}$. A signal processing chassis for each NLCTA RF Station contains the low-level microwave electronics needed to create an RF output with arbitrary phase modulation. An I/Q modulator in the signal processing chassis up-converts baseband I and Q signals into an appropriately phase modulated, 10mW RF signal for driving the TWT that drives a 50MW klystron at X-band. Because the klystron is operated in saturation, the I/Q modulator is used as a fast phase shifter only, with its RF output kept at a constant power level [3]. Figure 1 shows the HP VEE graphical interface used to calibrate the phase modulators.

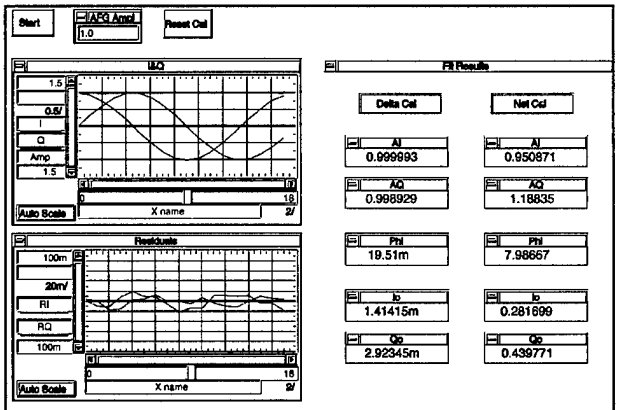



Figure 1. Phase Modulator Calibration Software

Calibrations are done to characterize the I/Q modulator accurately at a single RF output level. On-line calibrations (using a designated detector in the Phase Detector Chassis) must be done everyday to correct for changes in the modulator characteristics.

0-7803-4376-X/98/$10.00 © 1998 IEEE

*3.1 Phase Profiles*

Two programmable Arbitrary Function Generators (AFG's) produce the I and Q waveforms that are used by the Signal Processing Chassis to modulate the phase of the RF that drives a saturated TWT (and klystron) [4]. The phase modulation is eventually converted, by a high-power pulse compression system (SLED-II, described by Tantawi et al., in these proceedings [5]) to amplitude modulation which compensates for transient beam loading in the accelerator (see Adolphsen et al., in these proceedings [6]). Figure 2 shows an example of a phase profile and the predicted RF amplitude waveform that results after high-power RF pulse compression.

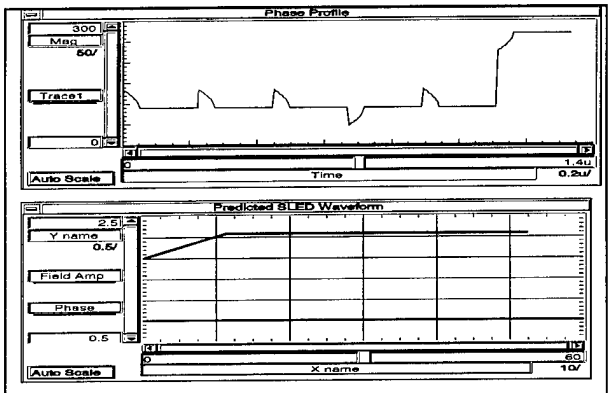



Figure 2. Example of a Phase Profile produced with the AFG's and the SLED Waveform it is predicted to generate.

*3.2 Station Phase*

Real-time adjustments of the station phase is provided to compensate for phase drifts and drifts caused by thermal expansion. In order to accomplish this, the station phase adjustment has been divided into two hardware devices: a fixed phase setpoint incorporated in the AFG waveform and an analog phase shifter that allows +/-180 degrees of phase adjustments to be performed in real time. The fixed phase setpoint incorporated into the AFG is accomplished through software during initial turn-on and remains fixed thereafter. Real-time adjustments of +/-180 degrees around the station phase setpoints are accomplished with an analog phase shifter that is driven by a VXI module. This analog phase shifter allows an operator to adjust a knob and see phase changes occur in real-time.

## 4 PHASE DETECTOR ASSEMBLY

There is one Phase Detector Assembly per NLCTA RF Station, consisting of eight I/Q demodulators. These I/Q demodulators are used to downconvert RF signals for precision amplitude and phase measurements. The RF signals that are measured are from various monitor points in the RF system. (E.g., Vector Modulator Output, TWT Output, Klystron Output, Accelerator Input). The pairs of downconverted I/Q signals from one Phase Detector Chassis Assembly are multiplexed into two digitizer channels and simultaneously sampled at 1GHz.

*4.1 Software Calibrations*

The Calibrations of both the Modulator and Demodulators are done through HP VEE software. The software operations performed upon the I/Q data include data correction, data conversion, and data display. Figure 3 shows the software algorithm for the I/Q demodulator. The data correction step consists of four multiply and two add operations. The six constants used in this correction (II, QI, IQ, QQ, Ioffset, and Qoffset) are determined by a calibration algorithm that is described below. The data conversion step performs the non-linear operations that convert I/Q to amplitude/phase. The algorithm in Figure 3 is performed upon each measured I and Q in the data sample.

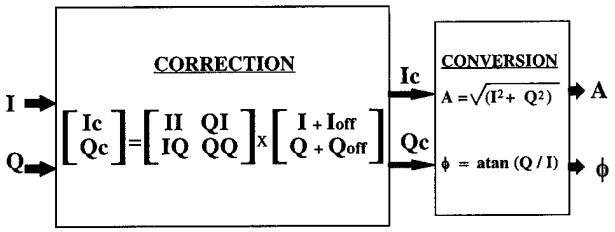



Figure 3. Software algorithm for the I/Q Demodulators

To measure the six calibration constants of a demodulator an 11.414-GHz source switched into the RF input of the demodulator. The calibration signal is offset by 10-MHz from the RF center frequency, resulting in 10-MHz sinusoids on the output I and Q signals from the I/Q demodulator. The calibration signal is digitized over three complete cycles of the 10 MHz sinusoids. This data is then analyzed to find the six constants in Figure 3 that make Ic and Qc orthoginal sinusoids of equal amplitude and zero offset.

## 5 VXI INSTRUMENTATION

Each NLCTA RF Station consists of a VXI Crate containing one GPIB controlled command module, two analog multiplexers (MUX's), one Digitizing Ocilloscope, and two Arbitrary Function Generator's (AFG's). An additional VXI Crate, which is used for other purposes, contains a HPUX processor that is used to control the RF VXI Crates via GPIB and HP's VEE graphical interface software. The AFG's are programmed to output user-defined arbitrary waveforms which go into the Signal Processing Chassis Phase Modulator. The I (in-phase) and Q (quadrature) waveforms from the Phase Detector

Assembly are multiplexed using the MUX's. Figure 4 is display of the amplitude and phase for one of the demodulator channels. These waveforms were acquired with the digitizing scope.

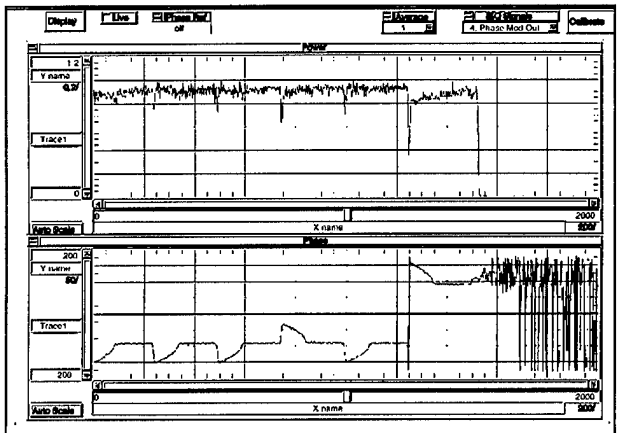


Figure 4. Output display of one I/Q Phase Demodulator

### *5.1 Timing*

There is one Camac Simple Timing Buffer (STB) card per RF station that provides the NIM-level triggers used for synchronization of the LLRF system [7]. The VXI scope trigger starts the digitizer data acquisition cycle at the normal machine repetition rate. The Calibration trigger enables the on-line calibration of the I/Q demodulators by switching on a calibration source. The ARB Trigger initiates the AFG's waveform outputs. The LLRF Trigger is used by the RF Trigger Chassis to create the RF Gate pulse. This RF Gate is used by the RF Signal Processing Chassis to pulse modulate the LLRF output.

## 6 CONCLUSIONS

The design of the LLRF Signal Processing system for the Next Linear Collider will be based heavily on experience gained from existing systems developed for the NLCTA. The experimental program of the LLRF system for NLCTA has been successful in acheiving the ability to make RF phase and amplitude measurements with time resolutions comparable to the NLC bunch spacing (1.4ns). Upon completion of the NLCTA the design of the NLC will progress with a better understanding of X-band LLRF Signal Processing systems.

## REFERENCES


[1] Physics and Technology of the Next Linear Collider: A Report Submitted to Snowmass '96. BNL 52-502, Fermilab-Pub-96/112, LBNL-Pub-5425, SLAC Report 485, UCRL-ID-124160

[2] NLC Test Accelerator Conceptual Design Report Stanford Linear Accelerator Center, Stanford, California, August 1993. SLAC-Report-411

[3] C. Ziomek "Low-Level RF Signal Processing Software", Stanford Linear Accelerator Center, March, 1996. NLCTA-Note-56.

[4] T. Lavine, "Preliminary Functional Specification for Klystron Phase Modulation Control," Stanford Linear Accelerator Center, July, 1994. NLCTA-Note-26.

[5] S. Tantawi et al., "The Next Linear Collider Test Accelerator's RF Pulse Compression and Transmission," these proceedings.

[6] C. Adolphsen et al., "Beam Loading Compensation in the NLCTA," these proceedings.

[7] S. Allison, S. Clark, T. Dean, C. Adolphsen, T. Lavine, C. Ziomek, "NLCTA RF High Level Controls Software", Stanford Linear Accelerator Center, October, 1996. NLCTA-Note-50.1.

# WAVEGUIDE STUB-LINE TUNING OF RF CAVITIES WITH HEAVY BEAM LOADING*

P. Krejcik,

Stanford Linear Accelerator Center, Stanford University, Stanford, CA 94309 USA

*Abstract*

A method is proposed for using adjustable, waveguide stub-line tuners to match the load impedance of the cavity plus beam to the power source, without the need to detune the cavity. Adjustable stub-line tuners are shown to be able to completely match the resistive and reactive parts of the load impedance to a generator under all conditions of beam loading, ensuring optimum power transfer between generator and cavity. This technique may have advantages in high-current storage rings such as the SLC damping rings and the new PEP II storage rings. The coupled-bunch instability driven by the fundamental mode of the cavity is re-appraised in this coupling scheme in which the cavity is no longer detuned. The consequences of this matching scheme are also considered for the beam loading stability limit.

## 1 INTRODUCTION

The beam in an RF cavity is seen by the generator (klystron) as a complex load impedance. The reactive component of this beam load impedance is determined by the synchronous phase angle, $\phi_s$, of the beam and consequently held fixed by other parameters of the accelerator. In high-current storage rings it is necessary to fully match this complex load to the generator to ensure efficient transfer of power.

In a typical storage ring cavity this is done in two steps by matching the real, or resistive, part with the coupling ratio at the cavity port and secondly detuning the cavity to match the imaginary, or real, part of the load. The resistive component of the match is not typically adjustable and is fixed by the geometry of the cavity coupler. In such cases the matching is only optimized for one design beam intensity. The reactive matching through cavity detuning can be achieved with a mechanical tuner and adjusted according to the average beam current.

The impedance seen by the generator determines the power transfer efficiency to the beam, but the impedance seen by the beam determines the stability of the beam. In high-current, multiple bunch "factory" machines the cost and feasibility of feedback systems to damp these instabilities must be weighed against the cost of the installed RF power. Coupled bunch instabilities are driven by the asymmetric impedance at the betatron sideband frequencies which is a direct consequence of detuning the cavity[1]. The beam loading stability threshold is also lowered as the cavity is detuned to obtain efficient matching.

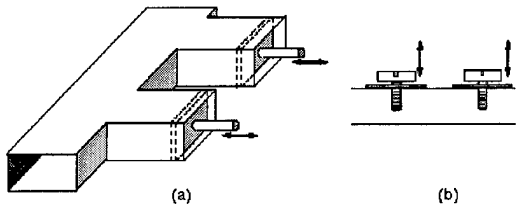



Figure 1: a. Adjustable stub lines perpendicular to the waveguide between the cavity and klystron, b. an equivalent alternative using adjustable posts in the waveguide.

As the cavity impedance angle is increased with the beam intensity the generator component, $V_G$, of the cavity voltage becomes increasingly out of phase with the total cavity voltage, $V_C$, until the Robinson limit is reached where $V_G$ is 180° out of phase to the beam current, $I_B$, and no longitudinal focusing remains[2,3].

The load matching discussed in this paper utilizes adjustable stub lines placed in the waveguide between the cavity and the klystron. Rather than adjusting the cavity parameters to match the generator, the stub lines add an extra degree of freedom to transform an unmatched load to its source. Once the new matching conditions have been established with the stub lines the impedance, seen by the beam, of the cavity plus the generator is analyzed and the conditions for beam stability described.

The stub line matching of the load impedance to its power source does appear to have the advantage of providing all of the adjustment outside of the cavity vacuum. Furthermore, the matching for both the resistive and reactive components can be adjusted for any beam intensity. In the conventional coupling scheme only the reactive matching is adjustable. The capability to vary the resistive component of the match becomes more critical for machines where the synchronous phase is large.

## 2 THE BEAM AND CAVITY LOAD

The equivalent circuit model of the cavity resonator coupled by a transmission line to a generator such as a klystron, shown in figure 2, has been described in detail by Wilson [4]. In this model the fundamental mode of the

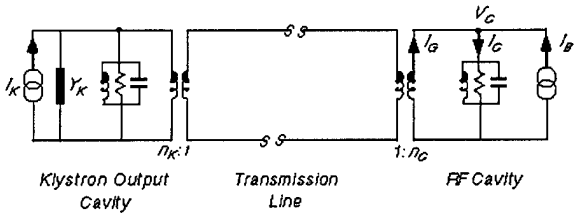



Figure 2: Equivalent circuit model of klystron, transmission line and cavity (after Wilson [4]).

* Work supported by Department of Energy Contract DE-AC03-76SF00515.

cavity is represented by a parallel RLC circuit [5]. The beam current $I_B = 2I_0 e^{-j(\omega t+\phi_B)}$, where $\phi_B = \frac{3\pi}{2} - \phi_S$, can be represented as a load admittance, $Y_B$, with real and imaginary components

$$\mathrm{Re}(Y_B) = \mathrm{Re}\left(\frac{I_B}{V_C}\right) = -\left|\frac{I_B}{V_C}\right| \sin\phi_S$$
$$\mathrm{Im}(Y_B) = \mathrm{Im}\left(\frac{I_B}{V_C}\right) = \left|\frac{I_B}{V_C}\right| \cos\phi_S \quad (1)$$

The total current in the cavity, $I_C$, is the vector sum of the generator and beam currents, $\hat{I}_C = \hat{I}_G + \hat{I}_B$. The combined impedance contributions from the beam and the cavity gives a total real and imaginary admittance of

$$\mathrm{Re}(Y_G) = \mathrm{Re}\left(\frac{I_G}{V_C}\right) = \frac{1}{R_{sh}}\left(1 + \left|\frac{I_B}{V_C}\right| R_{sh} \sin\phi_S\right)$$
$$\mathrm{Im}(Y_G) = \mathrm{Im}\left(\frac{I_G}{V_C}\right) = -\frac{1}{R_L}\tan\phi_Z + \left|\frac{I_B}{V_C}\right| \cos\phi_S \quad (2)$$

Matching of the load to the generator for optimum power transfer is done in two independent steps. To match the real part of the impedance requires finding $\beta_C$ such that the admittance in equation (2), when transformed to the generator side of the transformer, becomes equal to the characteristic line admittance. This gives

$$\beta_C = 1 + \left|\frac{I_B}{V_C}\right| R_{sh} \sin\phi_S \quad (3)$$

In order to match the imaginary part of the impedance we find that the beam has introduced a reactive term that in present designs is compensated by reactive tuning of the cavity [6, 7]. The cavity has a non-zero imaginary admittance when tuned away from its resonant frequency,

$$Y_c(\omega) \approx \frac{1}{R_{sh}}(1 - j\tan\phi_Z) \quad (4)$$

where $$\tan\phi_Z \equiv -Q_o \frac{\omega^2 - \omega_o^2}{\omega\omega_O} \approx -2Q_o \frac{\Delta\omega}{\omega_o} \quad (5)$$

The condition for making the total imaginary component of the impedance, as given in equation (2), zero is

$$\tan\phi_Z = \left|\frac{I_B}{V_C}\right| R_L \cos\phi_S \quad (6)$$

## 3 TRANSMISSION LINE MATCHING

When a mismatch occurs because the load impedance is not equal to the characteristic impedance of the transmission line, some of the wave is reflected. The reflection coefficient is defined as the ratio of the amplitudes of the forward and backward wave,

$$\Gamma = \frac{V_{L^-}}{V_{L^+}} = \frac{Z_L - R_0}{Z_L + R_0} = \frac{\bar{Z}_L - 1}{\bar{Z}_L + 1} \le 1 \quad (7)$$

where $\bar{Z}_L = \frac{Z_L}{Z_0}$, is the normalized load impedance. Superposition of the forward and reflected waves leads to a standing wave pattern. A quantity that can actually be measured is the voltage standing wave ratio (VSWR), $S$, that is related to the reflection coefficient by

$$S = \frac{|V_{\max}|}{|V_{\min}|} = \frac{1+|\Gamma|}{1-|\Gamma|} \quad (8)$$

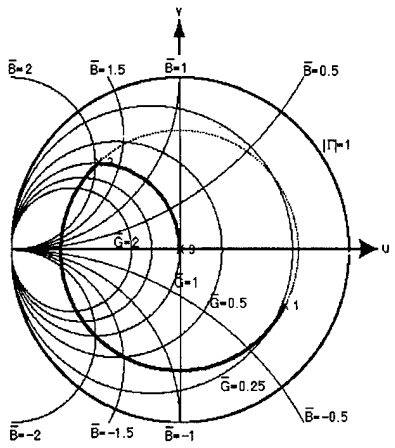



Figure 3: Smith chart representation of the reflection coefficient from a load with mismatched admittance at point 1. A length of waveguide, $d$, transforms it on a circle to point 2 where a stub of length $d_1$ transforms it along a line of constant conductance to a match at 3.

The impedance properties of a transmission line can also be represented graphically on a Smith chart. At the load, the reflection coefficient will be designated $\Gamma_L$, so that at a distance $l$ from the load

$$\Gamma(l) = |\Gamma_L| e^{-2j\beta l}, \quad \beta = \frac{2\pi}{\lambda} \quad (9)$$

Equation (7) may now be rearranged to give the normalized *input* admittance, located at a distance $l$ from the load,

$$\bar{Y}_I = \frac{1}{\bar{Z}_I} = \frac{1-\Gamma(l)}{1+\Gamma(l)} = \bar{G} + j\bar{B} \quad (10)$$

where $\bar{G}$ is the normalized input conductance and $\bar{B}$ is the normalized input susceptance. The load admittance as defined by equation (2) can be represented as a point on the Smith chart in figure 3, for a given waveguide impedance $Z_o$.

Moving away from the load a distance $l$ toward the generator is equivalent to a clockwise rotation of a point on the chart through an angle $2\beta l$ at a constant radius, allowing the transformed resistance and reactance of the load to simply read off the graph. Adding a length, $d$, of shorted line which is terminated in zero resistance has the effect of adding an admittance

$$\bar{Y}_S = \frac{Y_S}{G_0} = 0 + \frac{j}{\tan\beta d} \quad (11)$$

which is equivalent to moving along a circular contour of constant conductance on the Smith chart. In the next section we will use this graphical technique to illustrate the use of stub lines for matching a complex load impedance, like a beam loaded cavity, to a generator. Note that a matched load impedance is equivalent to a normalized

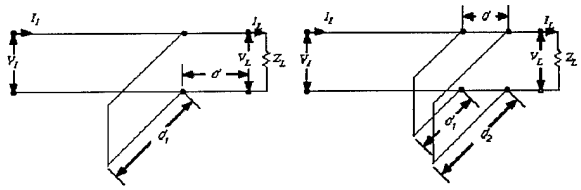


Figure 4: Single (left) and double stub matching(right).

resistance of 1 and zero reactance, corresponding to a point at the origin of the Smith chart.

*3.1 Single stub matching*

The principle of matching with a single stub lies in choosing the length, $d_1$, of the stub and its distance, $d$, from the load such that the reflected wave from the stub just cancels the reflected wave from the load, as shown in figure 4a. The procedure for choosing $d$ and $d_1$ was shown graphically in figure 3. Alternatively, if the VSWR from the load is measured before the addition of the stub line the values for $d$ and $d_1$ can be determined from $S$,

$$\cot \beta d_1 = \pm \frac{S-1}{\sqrt{S}}, \quad \tan \beta d_m = \pm \sqrt{S} \tag{12}$$

where $d_m$ is now the distance of the stub line measured toward the generator from the position of the voltage maximum. The positive square root sign is used for $0<d_m<\lambda/4$ and is negative for $\lambda/4< d_m<\lambda/2$.

*3.1 Double stub matching*

It is usually not possible to vary the distance of the stub line from the load to compensate for load impedance changes. This difficulty can be overcome by using two adjustable stub lines of length $d_1$ and $d_2$ as the two variables, at an arbitrary distance from the load but separated by a distance $d \neq \lambda/2$ from each other, as shown in figure 4b. The distance of the first stub from the load is completely arbitrary as the transformed load impedance at that location is now taken as the new load impedance to be matched.

The matching procedure is shown graphically in figure 5, where point 1 represents the normalized load admittance at the junction of the stub $d_2$. The stub line of length $d_2$ adds susceptance only, so the locus moves to point 2 along a contour of constant $\bar{G} = \bar{G}_L$. The length of transmission line $d$ between the two stubs transforms point 2 through an angle $2\beta d$ where it intercepts the circle $\bar{G} = 1$ at point 3. The stub line $d_1$ adds susceptance to move the point along the contour $\bar{G} = 1$ until it meets the origin at point 4.

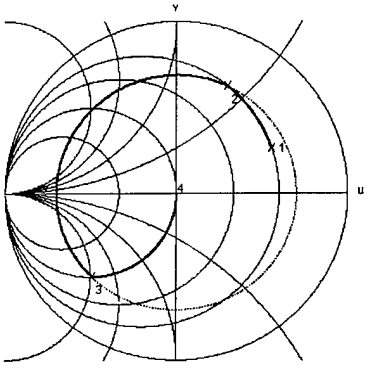


Figure 5: Smith chart representation of double stub matching.

As with the single stub, the matching conditions can be expressed in terms of the measured VSWR, so that in the example for $d=\lambda/4$:

$$\cot \beta d_1 = \pm \sqrt{S-1}, \quad \cot \beta d_2 = \pm \frac{\sqrt{S-1}}{S} \tag{13}$$

If the range of load impedances to be matched is unusually large, or if it is physically difficult to make $d$ small enough to accommodate the range of impedances, then a third adjustable stub can be added. Adding a third degree of freedom in a triple stub matching arrangement is sufficient to ensure all load conditions can be matched.

## 4 BEAM STABILITY

At first sight it might appear that not detuning the cavity would be advantageous for the driving terms of the coupled bunch instability. However, the beam sees both the cavity and generator impedance in parallel and the generator now appears as a reactive impedance when transformed through the stub line. In fact, the beam must see exactly the same reactive impedance component as the conventionally detuned cavity. The main advantage remains the practical aspect of placing the moveable tuning element outside of the vacuum system in the waveguide.

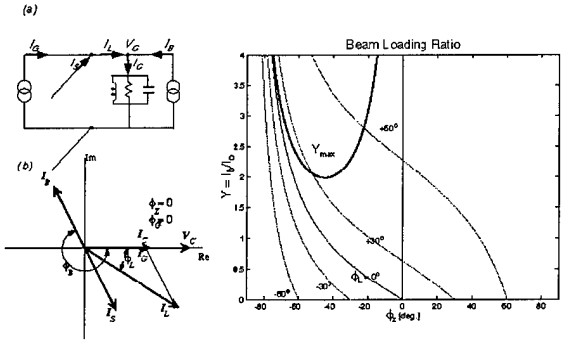



Figure 6: Equivalent circuit (a) with stub line matching and the phasors (b) including the stub line current. Beam loading limit (right) as a function of impedance angle and loading angle.

Similarly, the Robinson beam loading limit, according to

$$Y_{\max} = \frac{2\sin\phi_B}{\sin 2\phi_Z}, \quad \tan\phi_L = \frac{-\tan\phi_Z + Y\cos\phi_B}{1 - Y\sin\phi_B} \tag{14}$$

appears to increase when $\phi_z$=0, as in fig. 6. However, stability is now lost when $V_L$ is 180° out of phase with $I_B$, even though $V_G$ is in phase with $V_C$, so the beam loading limit is the same as for conventional matching.

## 6 REFERENCES


[1] F. Pedersen, "RF Cavity Feedback", Proceedings of B Factories, SLAC-400, pp. 192-207.

[2] K. W. Robinson, CEA Report CEAL-1010, 1964.

[3] F. Pedersen, IEEE Trans. on Nucl. Sci. Vol NS-32, 1985 pp. 2138-40.

[4] P. B. Wilson, AIP Conf. Proc. 87, p.450-563; SLAC-PUB-2884 1982.

[5] R. E. Collin, "Foundations of Microwave Engineering", 2nd ed. 1992, McGraw Hill

[6] A. Gamp, Proc. 1991 CERN Accel. School, CERN 92-03, p. 396-415.

[7] E. Raka, AIP Conf. Proc. 184, p.288-342

# HOM POWER PROPAGATION AND ATTENUATION IN PEP-II B-FACTORY *

Xintian E. Lin, C.-K. Ng and K. Ko
Stanford Linear Accelerator Center, Stanford University, Stanford, CA 94309

*Abstract*

Most of the higher-order-mode (HOM) power that propagates in the PEP-II rings is generated in the RF cavities but its content in terms of TE and TM components has not been accurately determined. For purpose of shielding beamline components such as bellows and BPMs from TE power penetration and determining the heating on the cavity HOM absorber, this HOM power content and its distribution profile around the rings are needed. This paper calculates the TE and TM contributions of the RF cavities to the circulating HOM power and their transmission properties at another cavity downstream. By considering both the generation in, and scattering by the cavities, as well as the attenuation along the vacuum chamber, a complete distribution profile for the TE and TM HOM power can be obtained.

## 1 HOM POWER GENERATION IN PEP-II

The PEP-II B-factory is a high current machine that generates enormous amount of RF energy in the vacuum chamber. The total HOM power for all beamline elements is estimated to be $P_0 = 200$ Kilowatts[1]. Assuming that the HOM power is uniformly generated around a storage ring and the attenuation length $l$ is constant for all the propagating modes of the vacuum chamber, the HOM power $P$ at any location of the ring is given by the equilibrium condition

$$dP/dz + P_0/L = -P/l + P_0/L = 0, \qquad (1)$$

where $L$, the PEP-II ring circumference, is 2200 m. The straight sections of the PEP-II rings consist of stainless steel pipes with a diameter of 9.525 cm. The attenuation length of the $TM_{01}$ mode in these pipes is about 60 m at 5 GHz, the roll-off frequency of the PEP-II nominal 1 cm bunch. Thus the resulting HOM power at any ring location is roughly given by

$$P = \frac{l}{L} P_0 = 5.5 \text{ KW}. \qquad (2)$$

## 2 MULTIPLE REFLECTIONS

The above calculation assumes no reflections by beamline elements. On the contrary, multiple reflections may happen even in a two-element network. To illustrate the significance of multiple reflections, we study the cascade of two simple 2-port elements as shown in Fig. 1. Here, S represents the scattering matrix of the two identical elements,

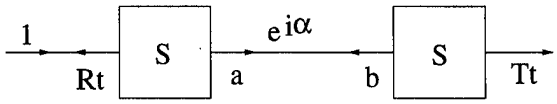



Figure 1: Cascade two 2-port elements with one unit of power incident from left.

and $e^{i\alpha}$ indicates the propagation through the beampipe between the two elements. The amplitudes of the right-going and left-going waves between the two elements are represented by $a$ and $b$, respectively. We parameterize the S-matrix in the form of

$$S = \begin{bmatrix} r & i\sqrt{1-r^2} \\ i\sqrt{1-r^2} & r \end{bmatrix}, \qquad (3)$$

where $r$ represents the reflection coefficient. The particular form is chosen to satisfy symmetry and unitarity. With one unit of power incident from the left, the total transmission $T_t$ is obtained by summing over all the reflections as follows:

$$T_t = Te^{i\alpha}T(1 + re^{i\alpha}re^{i\alpha}(1 + re^{i\alpha}re^{i\alpha}(1 + ...))), \qquad (4)$$

where $T = S_{12} = i\sqrt{1-r^2}$. The first term is the direct transmission, and the second term has two extra reflections on the network interfaces and two extra phase propagations. Summing the geometric series, we obtain

$$T_t = -(1-r^2)\frac{e^{i\alpha}}{1 - r^2 e^{2i\alpha}}. \qquad (5)$$

Following the same procedure, we also have

$$R_t = r\frac{1 - e^{2i\alpha}}{1 - r^2 e^{2i\alpha}} \qquad (6)$$

$$a = \frac{i\sqrt{1-r^2}}{1 - r^2 e^{2i\alpha}} \qquad (7)$$

$$b = re^{i\alpha}a. \qquad (8)$$

In Fig. 2, the transmission coefficient and amplitudes $a$ and $b$ are plotted as a function of the phase $\alpha$. One prominent consequence of multiple reflections is the power enhancement with respect to the input power at certain $\alpha$. It can be seen that resonant transmissions are evident at $\alpha = 0^o, 180^o, 360^o$. At resonance, due to coherent addition, the amplitudes $a$ and $b$ can be substantially higher than the input amplitude. For example, for $r = 0.8$, as much as $a^2 + b^2 = 4.56$ times of the input power flows in the beampipe between the elements at resonance.

* Work supported by U.S. Department of Energy, contract DE-AC03-76SF00515

0-7803-4376-X/98/$10.00 © 1998 IEEE

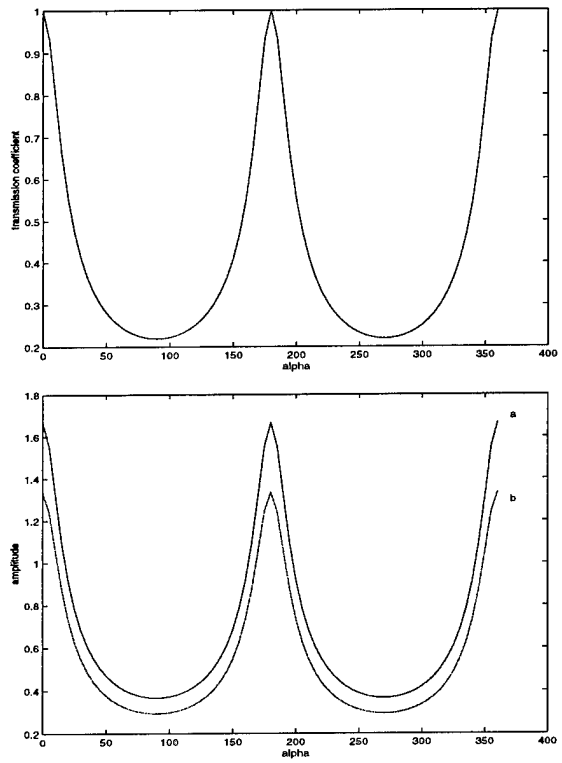



Figure 2: Amplitude $T_t$ (upper figure), $a$ and $b$ (lower figure) as a function of $\alpha$. The $r$ is 0.8.

## 3 APPLICATIONS TO PEP-II

Several factors need to be considered in applying the simple two 2-port elements model to the PEP-II rings. First, the power generation in a PEP-II ring is not uniform. The layout of the PEP-II rings is illustrated in Fig. 3. There are 6 straight and 6 bending regions numbered according to the clock face. The HOM power is mainly generated by the RF cavities which are located in some of the straight sections. For the High Energy Ring (HER), the RF cavities are located in Region 8 and Region 12. Currently 8 cavities have been installed in Region 12 as shown in Fig. 4.

Second, the model described above is for simple two-port elements with only one propagating mode. The RF cavity has 6 external ports, namely, the upstream and downstream beampipes, three HOM damping waveguides and an iris coupler. At a moderately small frequency of 2.856 GHz compared with the beam roll-off frequency, all the ports have more than one propagating modes. Thus a multi-mode S-matrix for a multi-port network needs to be calculated.

Third, the stainless steel beampipe connecting the cavities is lossy. Therefore, the phase delay $\alpha$ also has an imaginary part to account for the attenuation.

Last, the beam excites a broad frequency spectrum. For a 1 cm beam, the frequency spectrum extends to about 10 GHz. Thus, HOM power can propagate in the frequency range between the beampipe cutoff of 1.85 GHz to 10 GHz. However, the periodic nature of the bunch train in PEP-II

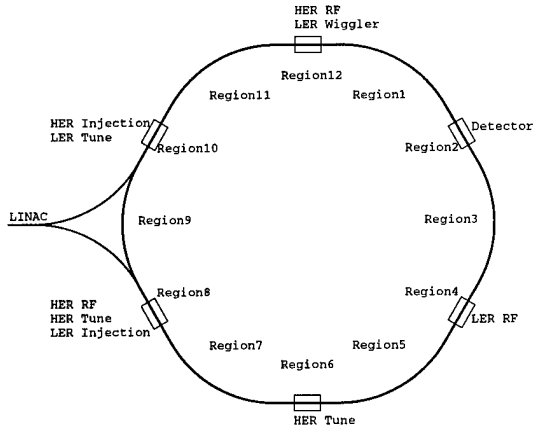



Figure 3: PEP-II ring layout.

suppresses all frequency contents except multiples of 238 MHz[1]. Therefore, about $\frac{10-1.85}{0.238} = 34$ beam harmonics in the frequency spectrum need to be considered

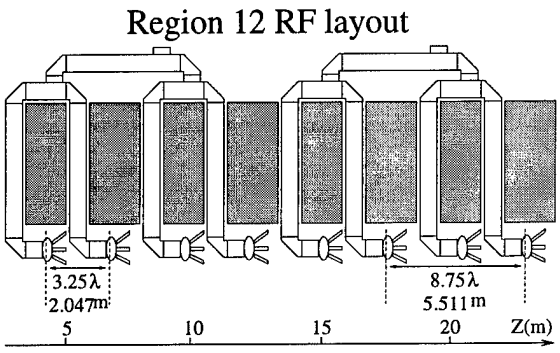



Figure 4: RF Cavity layout in Region 12.

## 4 HOM POWER DISTRIBUTION IN PEP-II

In this paper, we present the multiple reflection calculation at Region 12 only. Eight cavities and the stainless steel beampipes in between them are taken into account. Taking advantage of symmetry, we modeled half of the cavity (Fig. 5) by MAFIA. There are 2 beampipe ports (one is invisible in Fig. 5), 2 HOM ports and a coupler port on the top. MAFIA time domain simulations are used to calculate the S-parameters and the HOM power generated by a Gaussian charged beam. A couple of assumptions were made in the analysis. First, the HOM power generated by the cavity is assumed to propagate equally in the upstream and downstream beampipes in the form of $TM_{01}$ mode. This is justified as the asymmetry of the cavity only generates a relatively small portion of TE power. Second, for sim-

[1]The 5% ion clearance gap is ignored here for simplicity. Because its contribution to the current at other frequency is less than 5%, the power induced by such current is negligible

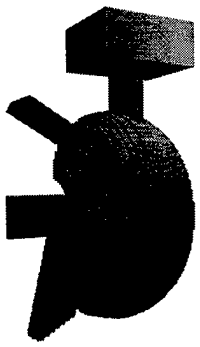


Figure 5: MAFIA model of RF cavity.

plicity, the S-parameter calculations are carried out for the $TE_{11}$ and $TM_{01}$ modes of the beampipe at 2856 MHz by allocating all the HOM power to this frequency.

The equilibrium distribution of the HOM power propagating in the beampipes is plotted in Fig. 6 as a function of longitudinal location in Region 12. Each discontinuity

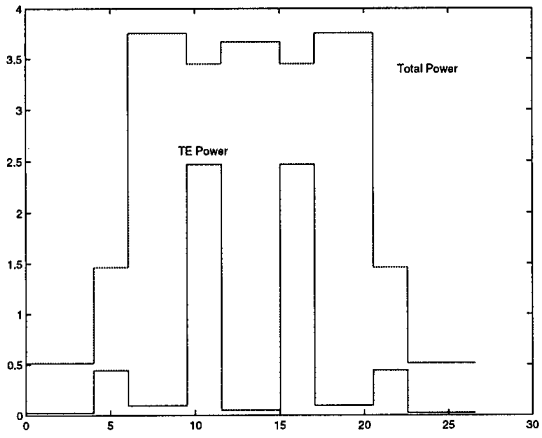



Figure 6: HOM power propagating in the beam pipe, normalized to one cavity HOM output(4 KW)

of the curve represents the location of a cavity. Generally, $TM_{01}$ mode dominates in the beampipe. But in particular locations, for instance, between cavities 3 and 4, 5 and 6, $TE_{11}$ power is high ($\sim$ 10 KW).

HOM power, in particular TE power, can penetrate through openings in beamline components. It was estimated that 0.01% of the TE power can penetrate through the bellow shield fingers[2]. This means that about 1 W is deposited in a bellows in the proximity of a cavity and this is small compared with 100 W design spec. For the BPM at the downstream of a cavity, about 0.12% for $TE_{11}$ mode and 0.05% for $TM_{01}$ mode couple to the buttons. The total power into the cable is therefore 14 watts maximum, which is well under 100 W designed for the BPM electronics.

We also obtained the HOM power going to the cavity load (Fig. 7). Without the coupler port, the three

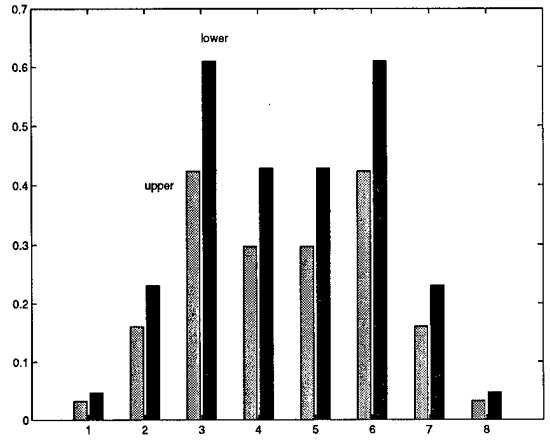



Figure 7: Power going into upper and lower HOM ports of each cavity, normalized to one cavity HOM output(4 KW)

HOM ports are symmetrically placed around the beam pipe. Therefore, with the beam on axis, each port will receive equal amount of HOM power. Since we only modeled half of the upper port, ideally, there are half as much power going into upper port as that going into lower port. But the coupler port breaks the symmetry, and Fig. 7 shows that the ratio of power going into half of the upper port and that into the lower port is 0.69:1 instead of 0.5:1. The total heating of upper port is still less than the designed 10 KW cooling capacity.

## 5 CONCLUSION

Multiple scattering of HOM by the beam line elements can substantially increase the local power density. Furthermore, TM to TE conversion is enhanced at particular locations, resulting in as much as 10 KW of TE power. The bellow heating and HOM power penetration through BPM cable turn out to be acceptable due to very small absorption coefficients.

This method can be scaled to the whole ring easily if S-matrix of other beam line elements are available. The resulting HOM profile is extremely useful in engineering design.

## 6 REFERENCES

[1] 'Impedance Study for the PEP-II B-factory', by S. Heifets et al. SLAC-AP-99. March 1995.

[2] 'Absorption of RF Power in the HER PEP-II Bellows' By G.V. Stupakov, S.A. Heifets. SLAC-PEP-II-AP-NOTE-96-12, May 1996.

# EXPERIMENTAL STUDY OF PULSED HEATING OF ELECTROMAGNETIC CAVITIES

D.P. Pritzkau, A. Menegat, and R.H. Siemann
Stanford Linear Accelerator Center, Stanford University, California 94309[†]
and T.G. Lee and D.U.L. Yu
DULY Research Inc., Rancho Palos Verdes, CA 90275[††]

*Abstract*

An experiment to study the effects of pulsed heating in electromagnetic cavities will be performed. Pulsed heating is believed to be the limiting mechanism of high acceleration gradients at short wavelengths. A cylindrical cavity operated in the $TE_{011}$ mode at a frequency of 11.424 GHz will be used. A klystron will be used to supply a peak input power of 20 MW with a pulse length of 1.5 μs. The temperature response of the cavity will be measured by a second waveguide designed to excite a $TE_{012}$ mode in the cavity with a low-power CW signal at a frequency of 17.8 GHz. The relevant theory of pulsed heating will be discussed and the results from cold-testing the structure will be presented.

## 1 INTRODUCTION

Pulsed heating will place a limit on the surface magnetic field in electromagnetic cavities due to thermal stress and through it a constraint on the maximum acceleration gradient possible for future linear colliders. A similar limitation has been encountered in optics for short pulse $CO_2$ lasers[1], and based on these results we expect the essential problem to be the low yield strength of materials such as fully annealed OFE copper. Different materials such as glidcop® with much higher yield strengths must be investigated. The purpose of the proposed experiment is to test several different materials under high power RF. The first set of experiments will test OFE copper.

## 2 BACKGROUND

Pulsed heating arises from the instantaneous local power dissipation at the surface of the metal due to the surface magnetic field and the surface resistance of the material. Ignoring radiation effects, the heat deposited at the surface of the metal must flow into the material inducing stress in the lateral dimensions through thermal expansion. Heat flow is governed by the heat diffusion equation knowing the metal's specific heat and thermal conductivity. It is found that the maximum temperature rise occurs at the surface of the metal.

The temperature rise scales as

$$\Delta T \propto \sqrt{\frac{fT_p}{\sigma c_\varepsilon k}}$$

where f is the RF frequency, $T_p$ is the RF pulse length, $\sigma$ is the electrical conductivity, $c_\varepsilon$ is the specific heat at constant strain and k is the thermal conductivity.

Based on the considerations of thermal stress due to pulsed heating, the threshold for plastic deformation is[1]

$$\Delta T_y = \frac{(1-\nu)Y}{\alpha E}$$

where ν is Poisson's ratio, Y is the yield strength, α is the coefficient of linear expansion, and E is Young's modulus. Surface roughening and fatigue cracks are expected to appear for temperature rises of $\Delta T > 2\Delta T_y$[1]. For fully annealed OFE copper this temperature rise corresponds to 40 °K and for glidcop 240 °K. However, there have been reports of substantially higher temperature rises in RF cavities[2] which suggest that this surface damage does not affect RF performance.

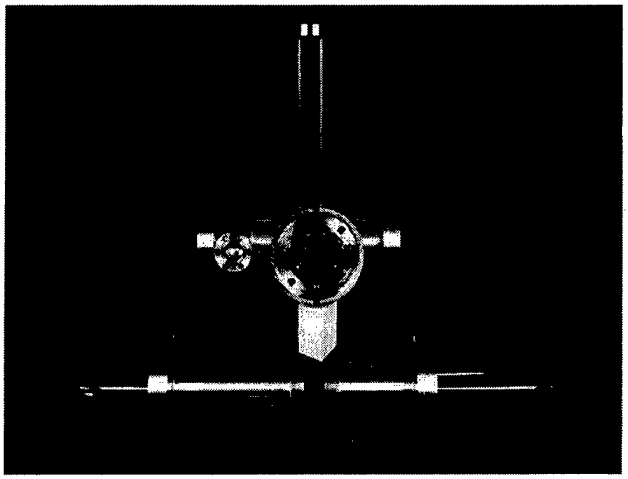


Fig. 1: Picture of test cavity with the endcaps outside. The actual length of the cavity is pictured. The water tubes can be seen at the end of the cylinders.

## 3 EXPERIMENTAL SETUP

The experiment will consist of two cylindrical cavities connected to a 50 MW X-band klystron through an asymmetric magic tee. The cavities will be operated under high power in the $TE_{011}$ mode at 11.424 GHz. Each

[†] Work supported by Department of Energy contract DE-AC03-76SF00515
[††] Work supported in part by U.S. DOE SBIR grant number DE-FG03-96ER82213

0-7803-4376-X/98/$10.00 © 1998 IEEE

cavity has a radius of 2.21 cm and an axial length of 1.9 cm. These dimensions were chosen to maximize the heating at the endcaps while keeping the heating along the cylindrical wall as small as possible. The endcaps are designed to be removable so that different materials may be used in future experiments. This design also allows the use of optical and electron microscopes to examine the surface. An annular gap of 1.0 mm exists between the endcaps and the cylindrical wall to remove the degeneracy of the $TM_{111}$ mode and to facilitate vacuum pumping. One such cavity is shown in Fig. 1.

The copper endcaps are brazed onto long cylinders because the width of the WR-90 coupling waveguide is longer than the axial length of the cavity. Since the endcaps will receive the most heating, the cylinders were made hollow to allow water-cooling.

In this particular experiment the local temperature rise will be inferred by measuring the change in the wall Q of the cavity as well as the change in its resonant frequency during the length of a pulse. A second port designed to perform this measurement will excite a steady-state $TE_{012}$ mode in the cavity at 17.8 GHz. The waveguide at the second port near the cavity has a width of a WR-42 waveguide and a height of a WR-62 waveguide. At this point the waveguide is cutoff from 11.4 GHz and no power will propagate from the $TE_{011}$ mode. The waveguide is tapered to a full WR-62 after a length of 10 cm in which 11.4 GHz is attenuated by 150 dB. The taper is required to allow the use of available vacuum windows for WR-62 at 17.8 GHz. A schematic of the diagnostic setup is shown in Fig. 2. In the future a more direct way of measuring the local temperature rise along the surface of the endcaps will be devised.

A third cavity will function as a control that will not receive high power. After a high power run is performed with the other two cavities, the endcaps will be removed and tested in the third cavity. This test will isolate the RF properties of the endcaps.

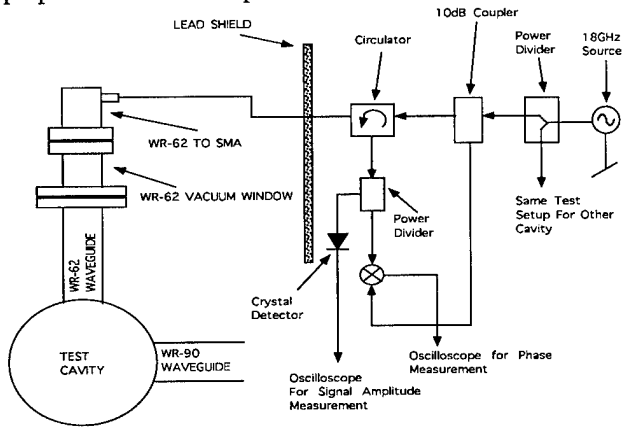



Fig. 2: Diagram of diagnostic setup

## 4 THEORY

A realistic assessment of pulsed temperature rise requires the temperature dependence of the specific heat, thermal conductivity and surface resistance of the material. For pure copper, this data can be found in references[3],[4]. Hence, an integral equation for the local temperature rise at the surface is developed

$$\Delta T(\vec{x},t)=\frac{1}{2\sqrt{\pi\rho}}\int_0^t \frac{dt'}{\sqrt{t-t'}}\frac{R_s(\Delta T)\left|H_{\parallel}(\vec{x},t',\Delta T)\right|^2}{\sqrt{c_\varepsilon(\Delta T)k(\Delta T)}}$$

where $\vec{x}$ is the position along the surface of the cavity, $\rho$ is the density and $R_s$ is the surface resistance. The specific heat at constant strain is approximated as the specific heat at constant volume. The surface magnetic field is found from a differential equation that governs a cavity-waveguide coupled system. The result for the temperature distribution along the surface of the cavity at the end of a pulse is given in Fig. 3. The maximum temperature rise in the cavity is predicted to be approximately 350°K. The time evolution of the maximum temperature rise over the course of a pulse is shown in Fig. 4.

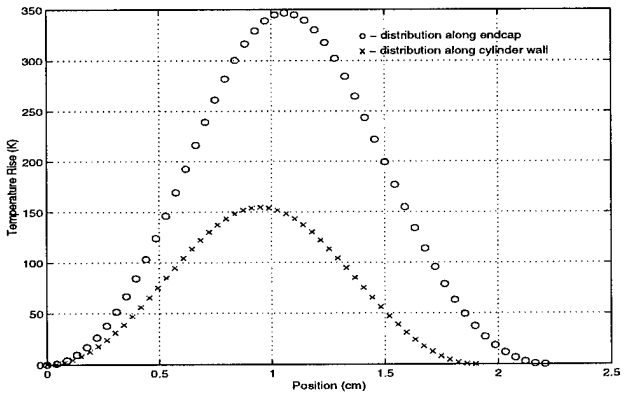



Fig. 3: Instantaneous temperature along the surface of the cavity after a 1.5 μs, 20 MW pulse

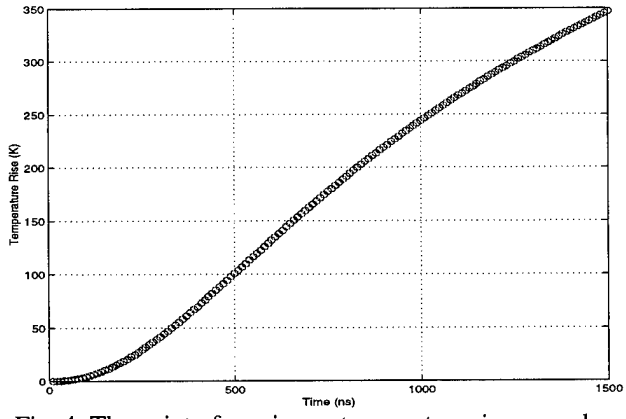



Fig. 4: The point of maximum temperature rise on endcap over the course of a pulse for 20 MW incident power

Since the surface resistance changes with temperature, the wall Q of the cavity will also be temperature dependent. A measurement of the wall Q will provide information on the global temperature rise in the cavity. The global temperature rise is just the weighted average of the local temperature changes over

the surface of the cavity. The temperature rise at a local point will be inferred by comparison with theory.

It is necessary to measure the Q as a function of time during a high-power pulse. The measurement becomes complicated if it is conducted on the same high power line at the fundamental mode frequency. For this reason a steady-state $TE_{012}$ mode will be driven by a CW low-power source. Refer to Fig. 2. The coupling of this measurement port will change as the wall Q of the cavity changes. The amplitude and phase of the reflected power will be measured. Initially the port will be matched to the cavity and there will be no reflected power. A phase shift will occur due to the change in resonant frequency of the cavity during a pulse. Fig. 5 shows the expected amount of reflected power over time and Fig. 6 shows the expected phase shift over time. There are plans to calibrate this measurement.

The equation for the temperature rise in the cavity is based on a one-dimensional analysis. This equation does not account for structure in the lateral dimensions. This equation also does not take into account the effect of acoustic waves. Acoustic waves set up in the metal by pulsed heating can lead to damage even at low temperature rises[5]. More study of this part of the phenomenon of pulsed heating needs to be done.

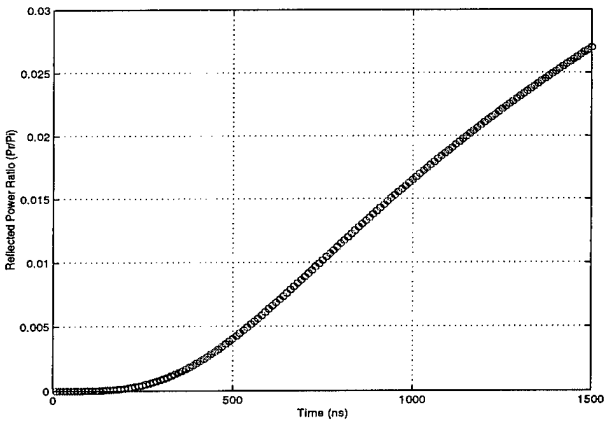



Fig. 5: Reflected power for $TE_{012}$ mode over the course of a pulse

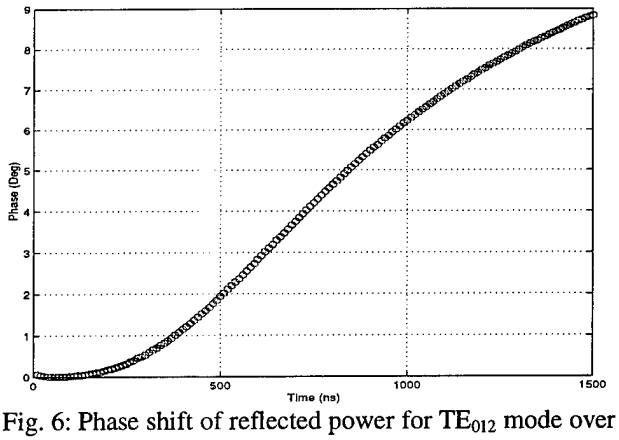



Fig. 6: Phase shift of reflected power for $TE_{012}$ mode over the course of a pulse

## 5 RESULTS OF COLD-TEST

The cavities were designed with an axial length shorter than necessary so that they may be tuned by machining the endcaps. The sensitivity of the $TE_{011}$ mode for these cavities is 7 MHz for every 25 μm that is machined off an endcap. The bandwidth of these cavities is approximately 1 MHz, so the final tuning procedure will involve varying how much the copper gaskets in the vacuum flanges will be crushed. Vacuum loading and water pressure from cooling must also be taken into account and is found to increase the frequency of the $TE_{011}$ mode by approximately 10 MHz.

The coupling of the WR-90 waveguide to the $TE_{011}$ mode is close to the design value of $\beta$=1.2 chosen to optimize the heating in the cavity. While determining the coupling to the $TE_{012}$ mode, it was discovered that a coaxial mode was set up in the long gaps between the cylinders and the cavity inner surface. This coaxial mode caused a low-Q mode to overlap the high-Q $TE_{012}$ mode. This problem has been solved using finger stock on the long cylinder to short out the coaxial mode. Since the $TE_{012}$ mode is operated under low power, a slide-screw tuner will be used to match the WR-42/WR-62 waveguide to the cavity.

## 6 STATUS AND FUTURE PLANS

The cold-test measurements on the structures are almost complete. We expect to run at high power within a month.

## 7 ACKNOWLDGEMENTS

The authors wish to acknowledge Prof. S. Schultz of UCSD for his idea of using a second mode to measure the change in the Q of the cavity. The authors also wish to thank G. Bowden, K. Ko, N.M. Kroll, and C.K. Ng for many helpful discussions.

## REFERENCES

[1] H.M. Musal, Jr., Laser Induced Damage in Optical Materials 1979, Nat. Bur. Standards Spec. Pub 568, 159, 1980.

[2] J. Wang and T. Chen, private communication

[3] Furukawa et al., American Institute of Physics Handbook, 3rd ed., "Heat Capacities", 1972

[4] D.R. Lide, editor, Handbook of Chemistry and Physics, 77th ed., 1996-1997

[5] Dieter Walz, private communication

# DEVELOPMENT OF A MOVABLE PLUNGER TUNER FOR THE HIGH-POWER RF CAVITY FOR THE PEP-II B FACTORY*

H. D. Schwarz, K. Fant, J. G. Judkins, M. Neubauer, SLAC, Stanford, CA 94309;
R. A. Rimmer, LBNL, Berkeley, CA 94720

*Abstract*

A 10 cm diameter by 5 cm travel plunger tuner was developed for the PEP-II RF copper cavity system. The single cell cavity including the tuner is designed to operate up to 150 kW of dissipated RF power. Spring finger contacts to protect the bellows from RF power are specially placed 8.5 cm away from the inside wall of the cavity to avoid fundamental and higher order mode resonances. The spring fingers are made of dispersion-strengthened copper to accommodate relatively high heating. The design, alignment, testing and performance of the tuner is described.

## INTRODUCTION

The PEP-II B-Factory uses 26 copper cavities which are designed to dissipate 150 kW of RF power at 476 MHz to produce a gap voltage of 1 MV each [1]. Beam currents of up to 3 A are anticipated causing excitation of higher order mode resonances.

A movable frequency tuner was developed for these cavities (Fig. 2) in form of a 9.2 cm diameter copper plunger which is used to compensate for temperature related frequency changes and beam caused reactive detuning. The total tuning range is mostly determined by the detuning of ± 340 kHz required to park pairs of cavities, when they are not energized. To cover these requirements a total tuner range of 1 MHz was specified which can be realized by a tuner movement from 2 cm outside the cavity wall to 3 cm penetration into the cavity (see Fig. 6).

The tuner uses bellows as a vacuum barrier to translate the tuner movement into the vacuum envelop and spring fingers are used to prevent fundamental and higher order mode RF currents from reaching the bellows.

Tests of the tuner assembly were performed in cavities operating at power levels below the design level of 150 kW because presently planned cavity operating levels for the PEP-II rings are lower.

## TUNER DESIGN

The plunger design was optimized using a surface mesh model of the cavity and tuner created in the mechanical stress analysis code ANSYS [2]. This model was the basis for calculating the RF power dissipation using a Boundary-Integral Method Code developed at Chalk River Labs in Canada [3]. Once the power dissipation was established the ANSYS code could then predict temperature rise and stress and allow optimization of the plunger shape and cooling.

The corner of the tuner plunger penetrating into the cavity is radiused to 1/2 inch to minimize current concentration (Fig. 2). The power dissipated in the tuner plunger for operation at 150 kW dissipation in the cavity was calculated to be 5.1 kW at full insertion into the cavity and 2.5 kW at the nominal insertion point. Average surface power dissipation on the flat part of the plunger at full insertion is 28 W/cm$^2$ with a peak of 36 W/cm$^2$ at the radius.

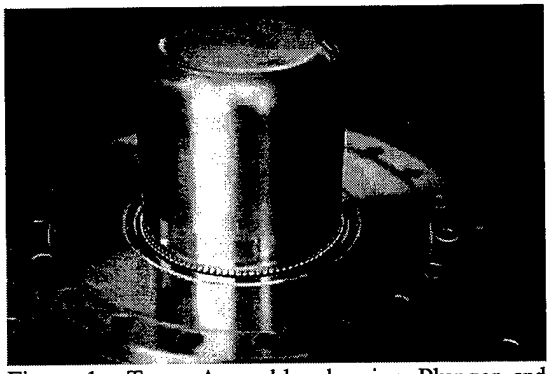


Figure 1: Tuner Assembly showing Plunger and Mounting Flange with Spring Fingers.

The gap between the tuner plunger and the tuner port was originally planned to be 1 mm to stay below multipactor threshold but was increased to 4 mm when it was found that alignment and arcing in the gap were a problem. Surface currents in the gap did not change significantly for the different gap widths as calculated by MAFIA [4] simulations.

The placement of the fingers is determined by two conflicting requirements:

1) The fingers should be placed far away from the high field area of the cavity to reduce fundamental mode currents and power dissipation. With only rapidly decaying evanescent waveguide modes launched into the gap between the tuner plunger and the tuner port of the cavity, placement of the spring fingers in the gap about 10 cm away from the cavity wall would make the dissipated power manageable.

2) The fingers should be placed in the tuner gap close to the cavity wall to avoid 1/4 or 3/4 wavelength resonances in the gap at the fundamental cavity resonance and higher order modes which can be excited by the multibunch beam. The lowest two longitudinal cavity modes at 750 MHz and at 1300 MHz are of particular concern since they are likely to be excited by the multi-bunch beam even though they are damped to a Q of 70 or 500 respectively by the higher-order-mode loading of the cavity. An optimum position for the fingers was determined to be 8.5 cm back from the cavity wall, placing the 1/4 wavelength resonance of the gap between these two higher order modes. The 1/4 wavelength resonance in the tuner gap was simulated with MAFIA to move with tuner position between 780 MHz and 1100 MHz.

0-7803-4376-X/98/$10.00 © 1998 IEEE

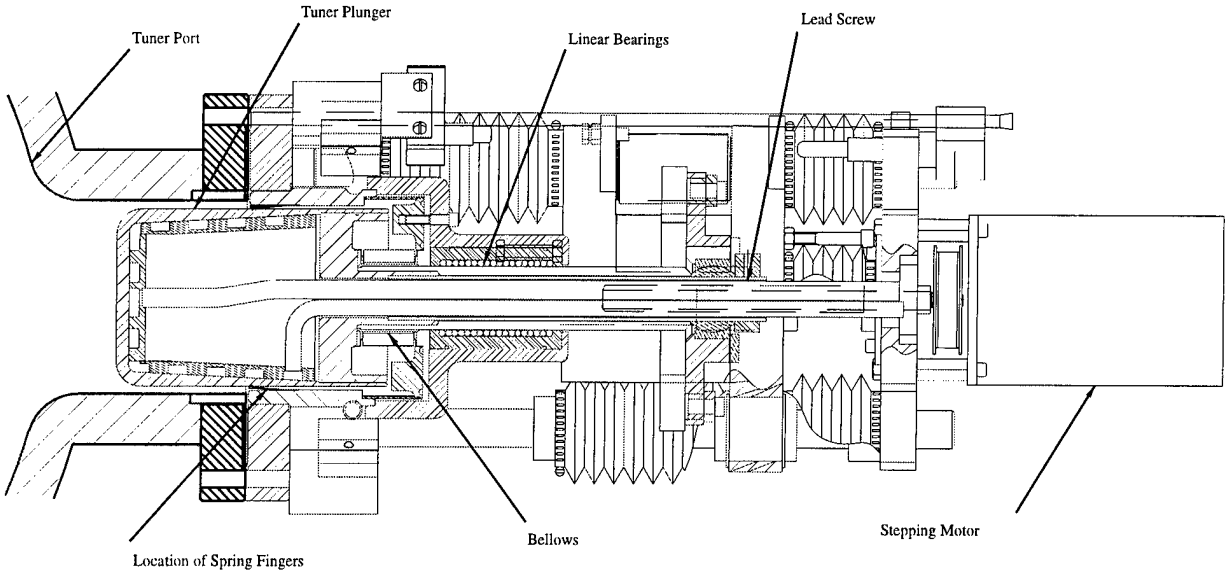



Figure 2. Tuner Cross-Section with Stepping Motor Drive.

The 8.5 cm finger location was adopted with the fingers fixed to the tuner port flange (Fig. 4.). The fundamental mode wall currents in this finger position were calculated to 26.5 A/cm peak and the related power dissipation is 2 W/cm$^2$ for the tuner at a nominal position of 10 mm insertion and 150 kW power loss in the cavity.

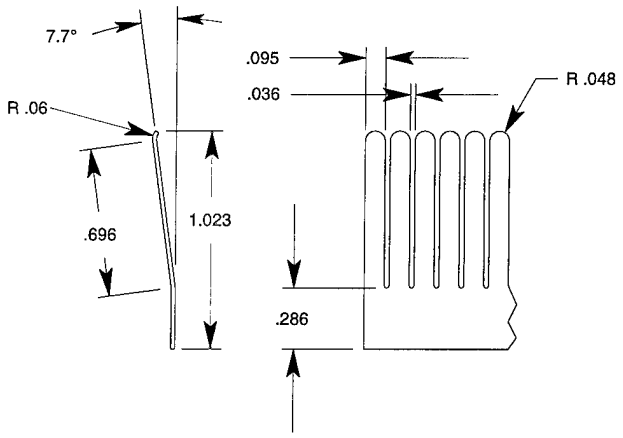



Figure 3. Spring finger Dimensions in Inches.

This relatively high power dissipation led to the design of spring fingers made of dispersion-strengthened copper or GlidCop® [5] after tests with beryllium copper alloy fingers had failed. The advantage of the GlidCop is its high thermal conductivity similar to that of copper compared to beryllium-copper alloys with 25% the conductivity of copper. The stress relaxation temperature for GlidCop is 350 °C compared to 150 °C for commercial beryllium copper alloy spring fingers.

## SPRING FINGER DESIGN

GlidCop spring fingers were designed using the grade AL-25 (0.46% $Al_2O_3$). Since no fingers of this material were available commercially the fingers were fabricated by a photo-etching process and then bent to the right shape (Fig. 3). The GlidCop fingers are electron beam welded (Fig. 4) into the tuner flange which is used to mount the tuner onto the tuner port of the cavity.

Dissipation of the calculated RF power of 2 W/cm$^2$ would cause the tip of the fingers to experience a temperature rise of 40°C. Additional heating comes from the electrical resistance at the contact point which is not well known. To facilitate a good contact under ultra-high vacuum condition it was decided to silver plate the finger tips (0.0004 inch Ag) and plate the polished sliding surface on the tuner plunger with rhodium (0.0002 inch Rh). In order to assure good alignment and uniform contact pressure of 113 grams per finger it was necessary to use a linear bearing at the shaft of the tuner.

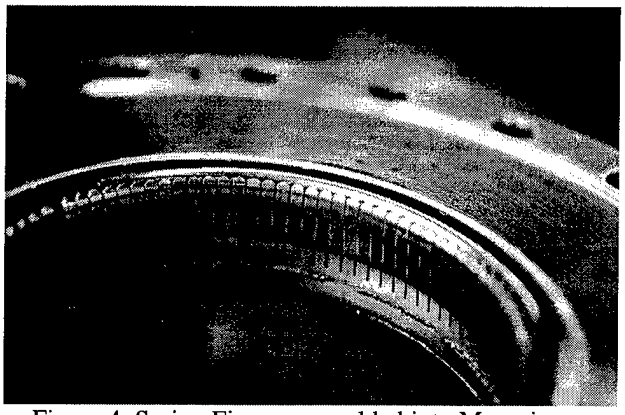


Figure 4. Spring Fingers as welded into Mounting

## TUNER TEST RESULTS

The spring fingers were tested for mechanical life in a test fixture which in a vacuum of $4x10^{-7}$ Torr moves a flat sample of the fingers with the nominal contact pressure over a rhodium-plated plate. The test ran for 90,000 cycles with a stroke of 4 mm simulating the tuner movement associated with a beam fill one an hour over

the period of 10 years. At the end of the test most of the silver plating on the finger contact area was transferred to the rhodium-plated surface, a result of normal contact wear (Fig. 5). Some small pieces of silver were actually broken off at later tests seen as glowing spots in the cavity. Overall the test shows that the fingers sliding on the hard rhodium surface can withstand the rigors of 24 cycles a day for a 10 year total life of the tuners.

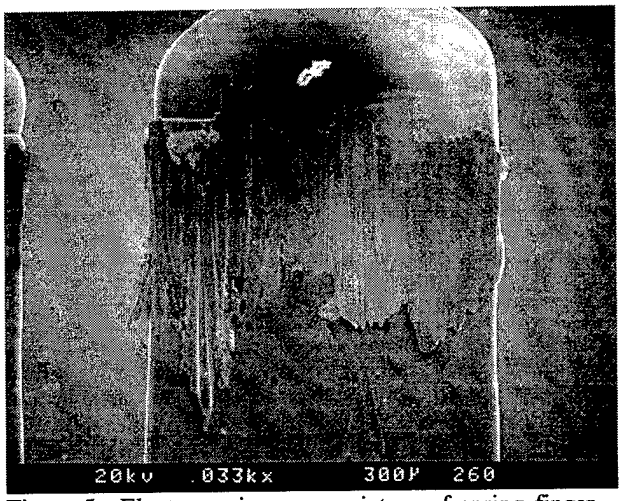



Figure 5. Electron microscope picture of spring finger contact area showing wear after 90,000 cycles on silver plating and silver chips.

The spring fingers were also tested as part of a prototype tuner in the RF environment of the prototype cavity and were operated at 120 kW cavity wall power, 20% above the highest power needed for the low energy ring. The source frequency was swept and a tuner feedback loop kept the cavity in tune forcing the tuner to follow the swept frequency. This test assembly operated successfully for 17,000 cycles over a stroke of 9 mm. Again the test showed that some small amount of silver had transferred from the fingers to the rhodium plated surface of the tuning plunger and some silver chips had separated. Although the test had to be terminated for reasons not related to the tuner it appears there was considerable life left on the spring finger contacts.

Tuners have since been installed and operated in 12 production cavities. Each cavity is processed in a test stand [6] up to the operating level of the high energy ring (85 kW wall dissipation) and several cavities have been processed higher to the low energy ring level (103 kW wall dissipation). The cavities are first processed in a pulse mode by sweeping the frequency of the source with a fixed tuner position and then reprocessed CW keeping the vacuum in the $10^{-8}$ Torr range. A video camera is trained on the tuner through a window on the opposite wall of the cavity. No arcing was observed but at 1 kW power level occasionally some glow from multipactor is seen. Another observable phenomenon is the bright glow of some silver chip removed from the spring fingers being heated up by the RF power. No deleterious effect of this glow was ever noticed. The measured power dissipation in the tuner plunger is 1.85 kW at nominal position and a cavity power of 85 kW. This indicates a 30% higher loss compared to the calculated plunger loss of 2,5 kW at nominal position and 150 kW wall dissipation. This increase in loss is partially attributed to the higher resistivity of the rhodium plating on the skirt of the copper plunger. The tuning curve for the tuner showing its range of 1.2 MHz is shown in figure 6.

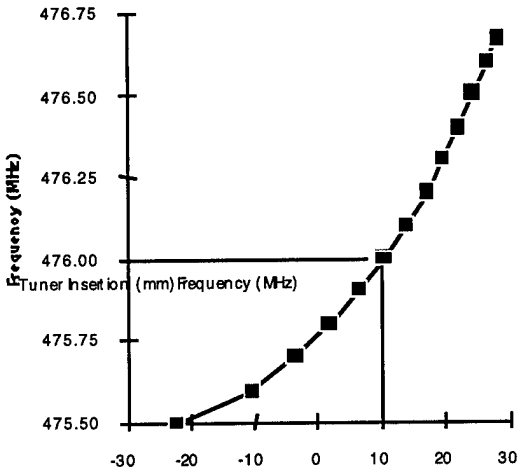



Figure 6. Cavity frequency versus tuner insertion.

## CONCLUSION

A tuner plunger was developed which incorporates a rugged finger contact design capable of operating in the ultra high vacuum and high power environment of the PEP-II RF cavities. Many years of operation with tuner movements several times a day are predicted by the tests.

## ACKNOWLEDGMENTS

The authors wish to thank John Hodgson for running the stress simulations, Joe Saba for the initial tuner design, Nadine Kurita for the design of the GlidCop fingers and Doug Berger, LLNL for developing the electron-beam welding of the spring fingers.

## REFERENCES

[1] "Development of a High-Power RF Cavity for the PEP-II B Factory", R. A. Rimmer et al, PAC95 proceedings, pp 1729

[2] ANSYS F.E. software from Swanson Analysis Systems Inc., P.O. Box 65, Houston, PA 15342.

[3] "Cavity RF Mode Analysis Using a Boundary-Integral Method", M.S. de Jong, PAC93 proceedings, pp 835.

[4] MAFIA design code, available in US from AET Associates, Inc., 20370 Town Center Lane, Suite 260, Cupertino, CA 95014, tel: (408) 996-1760, fax: (408) 996-1962.

[5] GlidCop is a dispersion-strengthened copper alloy made by SCM Metal Products, Inc., Research Triangle Park, North Carolina, USA.

[6] "High-power Testing of RF Cavities for the PEP-II B-Factory", R. A. Rimmer et al, these proceedings.

# RF SYSTEMS FOR THE NLCTA*

J. W. Wang, C. Adolphsen, R. Atkinson, W. Baumgartner, J. Eichner, R. W. Fuller, S. L. Gold, S. M. Hanna, S. G. Holmes, R. F. Koontz, T. L. Lavine, R. J. Loewen, R. H. Miller, C. D. Nantista, R. Pope, J. Rifkin, R. D. Ruth, S. G. Tantawi, A. E. Vlieks, P. B. Wilson, Z. Wilson, A. Yeremian
Stanford Linear Accelerator Center, Stanford University, Stanford, CA 94309

*Abstract*

This paper describes an X-Band RF system for the Next Linear Collider Test Accelerator.[1] The RF system consists of a 90 MeV injector and a 540 MeV linac. The main components of the injector are two low-Q single-cavity prebunchers and two 0.9-m-long detuned accelerator sections. The linac system consists of six 1.8-m-long detuned and damped detuned accelerator sections powered in pairs. The rf power generation, compression, delivery, distribution and measurement systems consist of klystrons, SLED-II energy compression systems, rectangular waveguides, magic-T's, and directional couplers. The phase and amplitude for each prebuncher is adjusted via a magic-T type phase shifter/attenuator. Correct phasing between the two 0.9 m accelerator sections is obtained by properly aligning the sections and adjusting two squeeze type phase shifters. Bunch phase and bunch length can be monitored with special microwave cavities and measurement systems. The design, fabrication, microwave measurement, calibration, and operation of the sub-systems and their components are briefly presented.

## 1 INTRODUCTION

There are four RF stations in the first stage of the NLCTA project. One station is dedicated to the injector. Each of three stations feeds a pair of 1.8 m accelerator sections. This paper will focus mainly on the injector RF system since it is more complex than other three, using both general and special microwave components. The injector RF system is comprised of the following components:

- An RF pulse compression system.
- Two X-Band prebunchers for velocity modulation.
- A 0.9 m detuned accelerator section with capture cavities in its front end.
- A 0.9 m detuned accelerator section.
- Two magic-T type phase shifter/attenuators for RF feeds of the prebunchers.
- Two squeeze type phase shifters for RF feed of the second 0.9 m accelerator section.
- A bunch length monitor for injector tuning.
- A beam phase monitor for beam phase analysis.

Fig. 1 shows schematically the RF system for the injector. An XL-4 75 MW X-Band klystron is used as a single source to power the system. All components are monitored or controlled in a nearby control room. The system has been successfully operating since the summer of 1996.

## 2 RF PULSE COMPRESSION SYSTEM

The RF source for each RF system is a 75 MW klystron. Each klystron feeds a SLED-II RF pulse compression system,[2] which compresses the 50 MW, 1.5 $\mu$s klystron pulse by a factor of six in time and multiplies the peak power by factor of four. The 200 MW output of the SLED-II pulse compressor is transmitted in low-loss oversized circular waveguides, which enter a shielded accelerator vault. structures. The overall efficiency of the operating RF systems exceeded our expectation.

## 3 ACCELERATOR STRUCTURES

In order to achieve the desired luminosity and suppress the long range transverse wakefields for multi-bunches, we have developed several types accelerator structures.[3] The two 0.9 m injector structures were constructed by using even number cells (for 1st section) and odd number cells (for 2nd section) of the 1.8 m detuned structure. The first three cavities of the first section have an RF phase velocity of 0.6c, 0.7c and 0.9c respectively. This design preserves the detuning characteristics for HOM (High Order Modes) and has a flat accelerating field distribution along the axis while beam loading is present. Two all-metal RF loads, capable of handling 100 MW RF power are connected to each accelerator output coupler.[4]

## 4 PREBUNCHERS AND BEAM PHASE MONITOR

The two standing wave single-cavity type prebunchers require 0.25 KW and 4 KW respectively, for optimum bunching. The second prebuncher is driven by the output from a 25 db coupler in the WR 90 feed line to the first 0.9 m section. The first prebuncher is driven by the output of the 10 db coupler in the WR 90 feed line of the second prebuncher. In order to reduce the transient beam loading effect on bunching, both prebunchers were designed to be over-coupled with a coupling coefficient $\beta$ $\sim$100 and time constant $\sim$1.1 ns. Each prebuncher cavity consists of a copper body with two nose-pieces and a WR 90 feed (see Fig 2). The drift distance between the second prebuncher and the bunching section in the front of the first 0.9 m section is 5.9 cm. This minimizes the debunching due to space charge effects. This small distance required the second prebuncher to be an integrated part of the second 0.9 m ac-

* Work supported by the Department of Energy, contract DE-AC03-76SF00515

0-7803-4376-X/98/$10.00 © 1998 IEEE

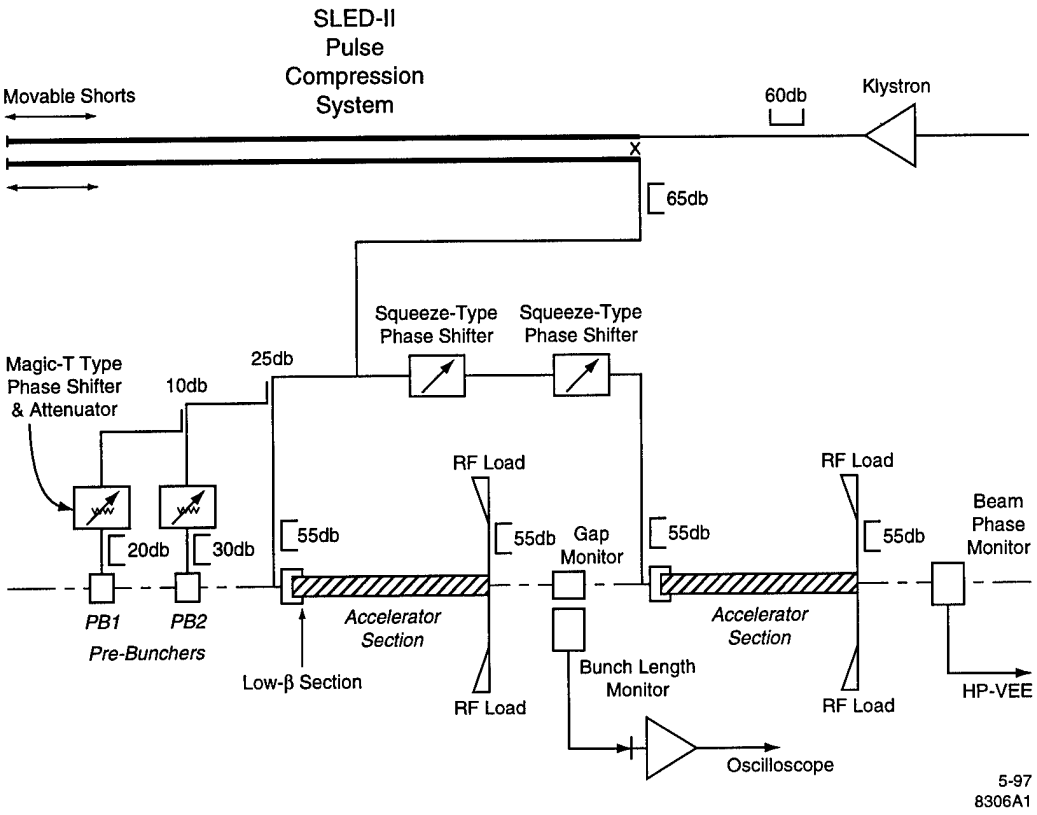



Figure 1: NLCTA Injector RF System Layout.

celerator section. The beam phase monitor uses the same design as the first prebuncher assembly. The beam excited signal is sent to an HP VEE (Virtual Engineering Environment) system for data analysis.

## 5 MAGIC-T TYPE PHASE SHIFTER/ATTENUATOR

Electrons from a 150 KeV thermionic-cathode gun are velocity modulated in each prebuncher. These are followed by drift sections in which the bunching occurs. In order to obtain the best bunching, both the RF phase and amplitude of each prebuncher need to be accurately and independently adjusted. To accomplish this we have inserted a magic-T type phase shifter/attenuator in each RF feed. As shown in Fig 3, this device has non-contacting movable shorts on two collinear arms which are driven by mover mechanisms. The two remaining arms are input and output ports. Keeping the RF amplitude of the output port constant, the RF phase can be changed by moving both shorts equal distances either toward or away from the junction. Keeping the RF phase of the output port constant, the RF amplitude can be changed by moving the shorts equal distances, but opposite in direction relative to the junction. Microwave measurements show the orthogonality of the RF phase and amplitude adjustments. The top plot of Fig 3 shows that the RF phase can be changed 360° without changing the amplitude by more than 0.05 db. The bottom plot of Fig 3 shows that the RF amplitude can be changed by -40 db without changing the phase by more than 5°. Precision linear actuators are attached to the movable shorts, and LVDT's (Linear-Variable Differential Transformer) give signals for RF phase and amplitude calibration.

## 6 SQUEEZE TYPE PHASE SHIFTER

Two squeeze type phase shifters[5] allow us to optimize the beam RF phase for the second 0.9 m accelerator section in order to obtain the minimum energy spread within the individual bunches. They have 18 in. long slots centered in the broad wall of copper WR 90 waveguide, with vacuum pumping on both sides of each slot. The slotted vacuum chambers are designed so that they are anti-resonant to unwanted RF coupled through the slots. The slot width is adjusted using a stepper motor driven differential screw system, and its position is monitored with an LVDT. The slot width is adjustable from 0.030 in to 0.090 in. and results in a phase change over a range of $\pm 30°$.

## 7 BUNCH LENGTH MONITOR

The principle of non-intercepting RF bunch length measurement was proposed and experimentally tested at SLAC.[6],[7] As shown in Fig. 1, a bunch length monitor cavity is installed adjacent to the beam line between the two injector sections. The fields radiated from the beam traversing a ceramic gap enter the bunch length monitor

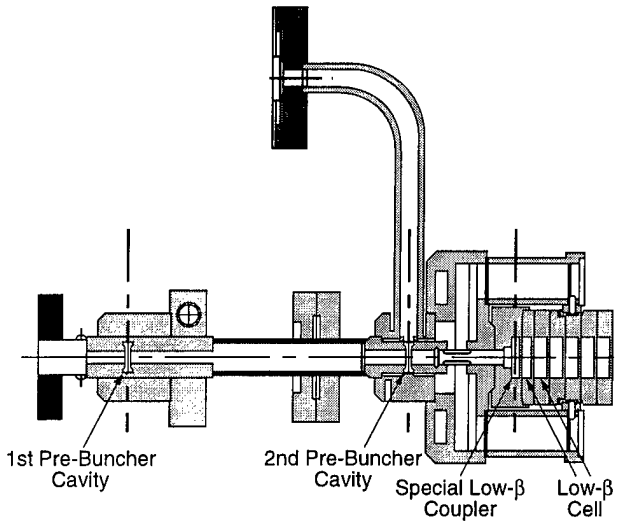



Figure 2: Prebunchers and Front End of 1st 0.9 m Accelerator Section.

cavity and excite a resonant mode. The radiated power is proportional to $exp(-\omega^2{\sigma_z}^2/c^2)$, where $\sigma_z$ is the standard deviation for a Gaussian bunch. Fig. 4 shows the theoretical beam power spectra for three different bunch lengths with $\sigma_z$ equal to 0.5 mm, 1.0 mm, and 1.5 mm respectively. For the first stage of the NLCTA project, the injector delivers a 140 ns pulsed beam, consisting of bunch trains of 1600 micro-bunches. They are 0.4 mm (RMS) in length and 88 ps apart. A $TM_{020}$ mode cylindrical copper cavity was designed to resonate at 34.272 GHz, the 3rd harmonic of the micro-bunch frequency. The cavity signal is transmitted through WR 22 rectangular waveguide to a crystal detector and an amplifier. In the NLCTA control room a 600 mV signal was observed for 0.5 A accelerating currents. The bunch length monitor has been a powerful tool for injector tuning.

## 8 REFERENCES


[1] R. D. Ruth *et al.*, Results from the SLAC NLC Test Accelerator, This Conference.

[2] S. G. Tantawi *et al.*, The Next Linear Collider Test Accelerator's RF Pulse Compression and Transmission, This Conference.

[3] K. Thompson *et al.*, Design and Simulation of Accelerating Structures for Future Linear Colliders, SLAC-PUB-6032, Particle Accelerator, November 1993.

[4] W. R. Fowkes *et al.*, An all-metal High Power Circularly Polarized 100 MW RF Load. This Conference.

[5] W. R. Fowkes *et al.* Component Development for X-Band Above 100 MW, SLAC-PUB-5544, PAC91, San Francisco, May 1991.

[6] R. Miller, SLAC-TN-63-65, August 1963.

[7] E. Babenko *et al.*, Length Monitor for 1 mm SLC Bunches, SLAC-PUB-6203, PAC93, Washington, D.C., May 1993.

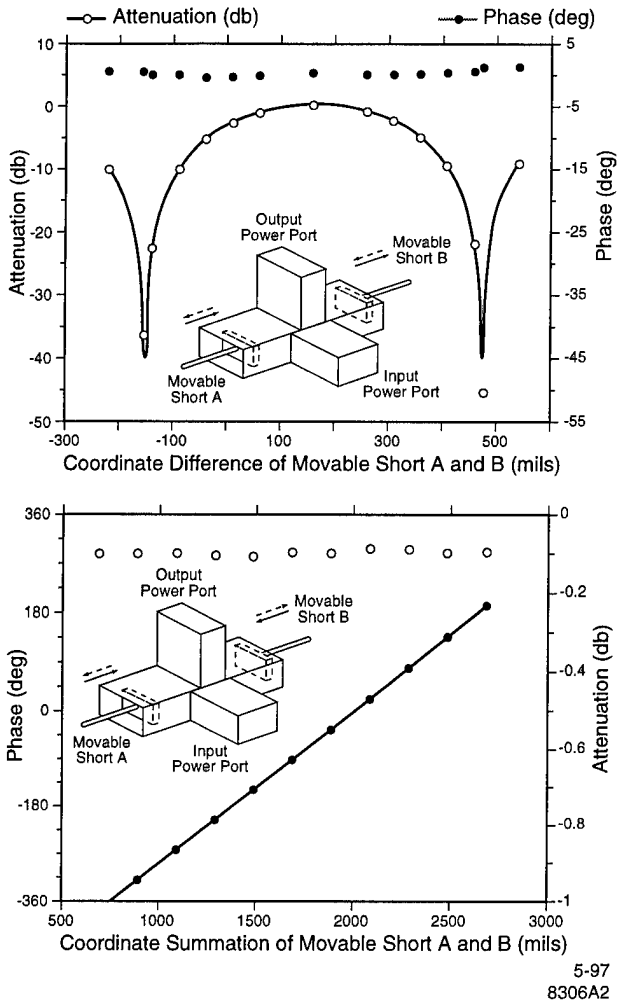




Figure 3: Calibration curves for Magic-T Type Phase Shifter and Attenuator.

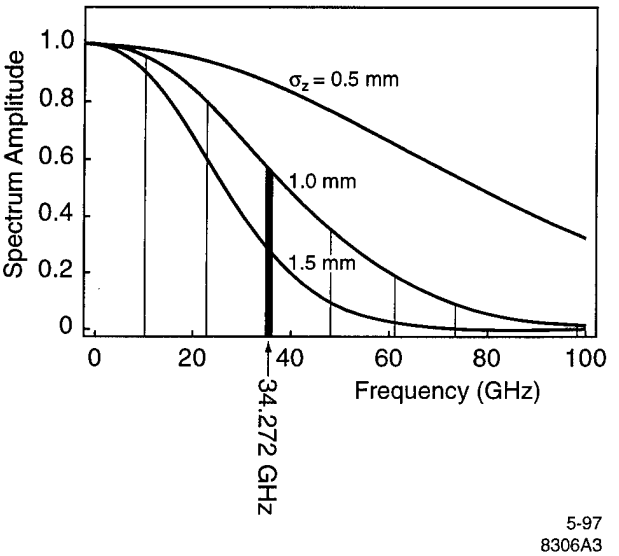



Figure 4: Theoretical Beam Power Spectra for Three Different Bunch Distributions.

# RF BREAKDOWN STUDIES IN X-BAND KLYSTRON CAVITIES

X. Xu, R. S. Callin, W. R. Fowkes, A. Menegat, G. P. Scheitrum, D. H. Whittum
Stanford Linear Accelerator Center, Stanford University, Stanford, CA 94309, U.S.A.

*Abstract*

RF breakdown studies are presently being carried out at SLAC with klystron cavities in a traveling wave resonator (TWR). Different kinds of fabrication methods and several kinds of semiconducting and insulating coatings have been applied to X-Band $TM_{010}$ cavities. RF breakdown thresholds up to 250 MV/m have been obtained. Dark current levels were found to be depressed in TiN-coated and single-point diamond turned cavities. A new $TM_{020}$ cavity with demountable electrodes has been designed and will be used to test a variety of materials, coatings, and processes. Recent tests of klystron output windows at 119 MW are also presented in this paper.

## 1 INTRODUCTION

RF breakdown is a critical issue in the development of high power microwave sources and next generation linear accelerators since it limits the output power of the microwave sources and the accelerating gradient of the linacs. The motivation of the RF breakdown study is to determine the maximum electrical field gradient that can be used safely in klystrons and next generation accelerator structures, find better materials and surface treatments that can raise the field limit, reduce the dark current, and to contribute to the basic understanding of the RF breakdown phenomenon.

The development of high power microwave sources to the performance levels required by future linear colliders has been limited by RF breakdown in the output resonator. Raising the breakdown threshold could increase the peak output power capability of the X-band klystrons for the next linear collider. Lowering the field emission for a given electric field would improve klystron and linac performance. Furthermore, the next generation of linear colliders will have to reach the TeV energy range, and the accelerating gradient will be one of the crucial parameters affecting their design, construction and cost. For a specified total energy, the gradient sets the accelerator length, and once the RF structure, frequency and pulse repetition rate are selected, it also determines the peak and average power consumption. Recent overall parameter studies for a 1 TeV linear collider indicate that accelerating gradients approching 100 MV/m are desirable.

Considerable research has been done on RF breakdown phenomenon in vacuum structures[1,2,3]. However, no coherent picture of the mechanism of the RF breakdown has been obtained due to the large number of variables and the range of parameters involved. Consequently, more systematic work is needed to gain further understanding into the underlying physics, to determine if the required output power is obtainable in the X-band klystron and the acceleration gradient is achievable in long and complicated structures. We also wish to verify that the dark currents which can absorb RF energy, cause parasitic wakefields and spurious x-rays along the RF structures are tolerable.

## 2 EXPERIMENTAL SETUP

The experiments are carried out by putting a field enhancing cavity into a traveling wave resonant ring (TWR) as shown in Fig.1. The power source is an X-band klystron (XC-2) with a frequency of 11.426 GHz, peak output power of 30 MW and pulse width of 1.5 μs. The power multiplication in the resonant ring is obtained by wrapping a WR-90 waveguide around into a ring configuration and recombining it with a 10 dB bridge coupler. A precision variable phase shifter and 6-element tuner, both designed to withstand extremely high RF electric fields, are put into the ring in order to achieve the resonant condition and also to tune out the small residual reflections. All RF conducting surfaces are OFC copper or copper plated stainless steel. No organic vacuum seal is used. A stored RF traveling wave that is 10 times greater in power than the input can be obtained [4].

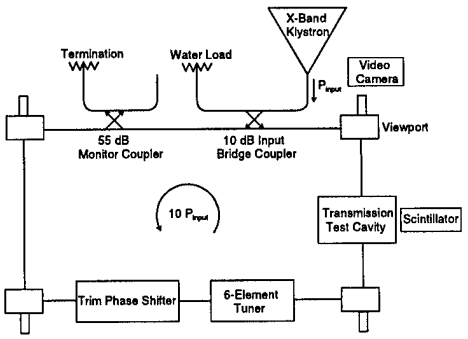



Fig. 1. Experimental setup

The parameters of the TWR are shown in Table 1. The test cavity is a symmetrical transmission type with reentrant noses, and is coupled to two waveguides through a pair of inductive irises (Fig.2). The cavity is designed by SUPERFISH and is capable of producing an electric field surface gradient as high as 600 MV/m. The maximum surface electrical field gradient is given by

$$E_s = 42.5\sqrt{P_{Ring}} \qquad (1)$$

where $E_s$ is in MV/m and $P_{Ring}$ is in MW.

0-7803-4376-X/98/$10.00 © 1998 IEEE

Table 1. TWR Parameters

| | |
|---|---|
| Highest TWR Power | 300 MW, 800 nsec, 60 pps |
| Maximum Available Source Power | 30 MW |
| Resonant Loop Length | 340 cm |
| Number of Guide Wavelengths | 106 @ 11.424 GHz |
| Input Bridge Coupler Ratio | 10.1 dB |
| Separation Between Resonance | 71.5 MHz |
| High Power Gain | 10.6 dB |
| One-Way Loss in Loop | 0.354 dB |
| Variable Phase Shifter Range | ±30° (±6 MHz) |
| 6-Element Tuner Range | ≤ 0.10 @ any frequency |
| Loaded Q | 5500 |
| RF Voltage Time Constant | 153 nsec |
| Input Coupling Coefficient | 1.23 |

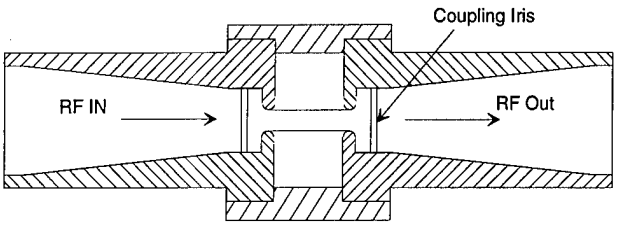



Fig. 2. $TM_{010}$ RF breakdown test cavity geometry with field enhancing noses.

## 3 RESULTS OF $TM_{010}$ CAVITY TEST

Five $TM_{010}$ cavities have been tested in the traveling wave resonant ring, each with a different combination of surface polish, coating. As shown in Fig. 1, a scintillator and photomultiplier were mounted beside the test cavity to measure the x-ray level from the cavity to characterize the breakdown process. A video camera was used to monitor sparks in the test cavity during RF processing. The tests were performed starting from low RF power for about 80 hours for each cavity. The onset of breakdown was pushed up to 250 MV/m in a 12 μinch surface finish cavity with TiN(100Å) coating and a single-point diamond turned cavity with less than 1 μinch surface finish, as shown in Table 2. Although the two uncoated cavities were fabricated by different methods with different surface finish, the breakdown threshold of these two cavities was the same, 210 MV/m. A 1 μinch surface finish with TiN(600Å) coated cavity was also processed to 210 MV/m but the breakdown threshold of the cavity was not reached due to a vacuum leak from the top of this cavity. The amplitude of field emission currents from the tested cavity surface as a function of peak surface electrical field is shown in Fig. 3 taking the observed scintillator voltage $V_{scint}$ an indicator of the field emission current. The lowest dark current was obtained with the single-point diamond turned cavity. The TiN coating was very helpful for depressing the field emission.

Table 2. Test results of $TM_{010}$ cavities

| Fabrication Method | Surface Finish (•inch) | Coating | RF Breakdown Threshold |
|---|---|---|---|
| Mechanical Polish | 12 | None | 210 (MV/m) |
| Mechanical Polish | 12 | TiN(100Å) | 250 (MV/m) |
| Diamond Polish | 1 | None | 210 (MV/m) |
| Diamond Polish | 1 | TiN(600Å) | 220 (MV/m) |
| Single-Point Diamond Turning | <1 | None | 250 (MV/m) |

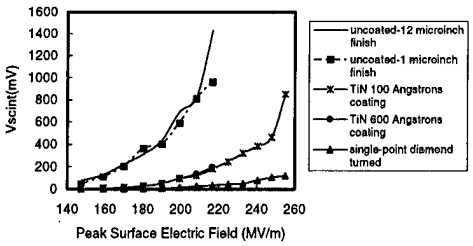



Fig. 3. Scintillator voltage as a function of peak electric field in the test cavities.

## 4 $TM_{020}$ CAVITY DESIGN

It was quite difficult to make various coatings on the noses of the $TM_{010}$ cavities because of the very small gap between the nose tips. The $TM_{010}$ cavities must be cut apart in order to make surface analysis. Furthermore, the irises are very close to the reentrant noses of the $TM_{010}$ cavities and perturb the electrical field distribution in the cavities. This may cause the local surface electrical field gradient in the cavity to be much higher than that calculated from Eq. (1).

A $TM_{020}$ cavity with replaceable cavity noses has been designed, and a sketch of the cavity is shown in Fig. 4. The irises are far from the nose tips. The high field surfaces on the two cavity noses can be coated more easily, and some coating techniques such as sputtering, ion bombardment can be used. This demountable device not only simplies the surface analysis of the nose surfaces before and after the high power RF test, but also makes it possible to evaluate surface damage nondestructively.

A large number of different materials, coatings and surface finishes will be performed on the $TM_{020}$ cavity noses. The materials that will be tested are Glidcop, copper-zirconium, HIP (hot isostatic pressed) copper, single crystal copper, tungsten, stainless steel and Monel. There is some evidence that surface roughness, surface contamination and surface treatment are directly related to the RF breakdown. It is also shown in our experiments that better surface finish can decrease the field emission current. Consequently, wire electrodischarge machining, precision diamond grinding, single-point diamond turning

and elastic emission machining together with surface treatments such as electropolish and high pressure water rinse will be applied to the cavity noses to get a very clean surface with a surface finish up to 2 nm.

In order to get real-time x-ray image from the cavity noses using a CCD camera, a tungsten pinhole (0.005") with a beryllium window is designed in the cavity. A germanium gamma-ray detector will be used to measure the spectrum of x-rays, and an optical port in the cavity back wall will be used to measure infrared output from the field emission sites on the electrode surfaces.

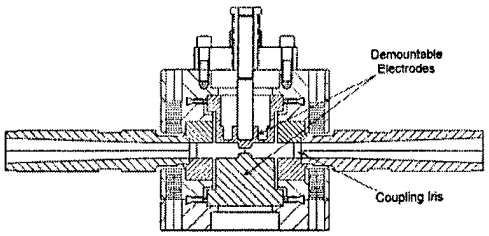



Fig. 4. $TM_{020}$ RF breakdown test cavity assembly

## 5 X-BAND KLYSTRON OUTPUT WINDOW TEST

Another very important component in a high power klystron is its output window. Because very high RF powers must be transmitted through the output window, there are several different types of breakdown phenomena of concern, e.g. multipactor and puncture. Many studies and tests have been performed to investigate the breakdown mechanism and to find a window design with a high probability of long life [5]. The X-band ceramic output window is shown in Fig.5. The window is 0.086" thick, and the window material is 99.7% alumina (NTK-HA-997) with TiN(10Å) coating in order to avoid the buildup of surface charge and to reduce secondary electron emission.

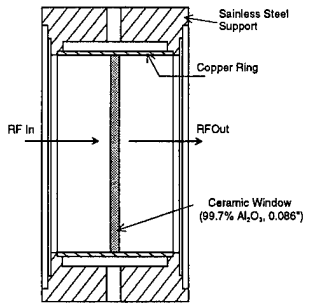



Fig. 5. Output ceramic window.

The window was tested in the traveling wave resonant ring at a frequency of 11.425 GHz with a pulse width of 1.5 μs and pulse repetition rate of 60 pps. The RF power was coupled in and out of the window through two $TE_{10}/TE_{01}$ flower petal mode transducers[6]. The window was processed carefully for more than 150 hours, the highest stable operating power obtained to date was 119 MW. X-ray levels from the window were very low implying that there was no breakdown at the window. This result was limited by the performance of our Test Stand not by the window itself. The window has been taken off and checked, no obvious damage has been found.

## 6 SUMMARY

Different kinds of fabrication methods and several kinds of semiconducting and insulating coatings have been applied to the X-band $TM_{010}$ cavities. RF breakdown thresholds up to 250 MV/m (pulse width: 1.5 μs, pulse repetition: 60pps) have been obtained. Dark current levels from the TiN-coated and single-point diamond turned cavities are far less than those from traditionally machined cavities. A new $TM_{020}$ cavity with demountable electrodes will be used to test a variety of materials, coatings and processes. The real-time x-rays output from the electrodes will be detected to get more information about the RF breakdown phenomenon. The spectrum of x-rays will be measured to calibrate the surface electrical field gradient in the $TM_{020}$ cavity, and the temperature of the electrodes will be measured to clarify the relationship between the field emission and the surface temperature. The peak power of 119 MW (pulse width: 1.5 μs, pulse repetition: 60 pps) through the X-band klystron output window has been obtained, and the tests suggest that higher output power is possible.

## 7 ACKNOWLEDGMENT

The authors would like to thank R. Siemann and J. W. Wang for their helpful discussions.

This work is supported by the Department of Defense, contract F49620-95-1-0253, and the Department of Energy, contract DE-AC03-76SF00515.

## 8 REFERENCES

[1] G. A. Loew, J. W. Wang, 'RF Breakdown Studies in Room Temperature Electron Linac Structures', SLAC- PUB-4647, May 1988.

[2] E. Tanabe, J. W . Wang, G. A. Loew, 'Voltage Breakdown at X-Band and C-Band Frequencies', Proc. 1986 Linear Accelerator Conference.

[3] W. Peter, 'Vacuum Breakdown and Surface Coating of RF Cavities', J. Appl. Phys. **56**, 1546 (1984).

[4] W. R. Fowkes, R. S. Callin, M. Studzinski, 'Component Development for X-Band Above 100 MW', SLAC-PUB-5544, May 1991.

[5] A. E. Vlieks, et al., 'Breakdown Phenomena in High Power Klystrons', SLAC-PUB-4546, March 1988.

[6] S. Tantawi, K. Ko and N. Kroll, 'Numerical Design and Analysis of a Compact $TE_{10}$ to $TE_{01}$ Mode Transducer', SLAC-PUB-6085, April 1993.

# UPGRADE ISSUES OF THE TLS STORAGE RING RF SYSTEM

W.K. Lau, L.H. Chang, S.S. Chang, C.H. Ho, M.C. Lin, S.J. Lin, G.H. Luo, T.T. Yang, M.S. Yeh, Ch. Wang, C.C. Kuo, Synchrotron Radiation Research Center, No. 1, R & D Road VI, Hsinchu, Taiwan, Republic of China

*Abstract*

To achieve the goals in the TLS storage ring performance upgrade plan, the necessity of adding the third rf station to the storage ring for radiation loss compensation at 1.5 GeV/350 mA operation and lifetime improvement are analyzed. We estimated the rf power required to compensate the radiation losses by bending magnets and various insertion devices. Effects of the proposed passive Landau cavity on power consumption is also studied.

## 1 INTRODUCTION

TLS has been operating smoothly for years. Efforts have been made by SRRC staff to ramp the beam energy up to 1.5 GeV with improved beam stability at 240 mA. The W20 wiggler has also been operating routinely during during user shifts. In the near future, undulators such as U5, U9 and EPU will be installed and serve for the users. Superconducting wiggler has been proposed to push the spectrum up to X-ray regime. In order to achieve the goal of operating the storage ring at 1.5 GeV/350 mA, the necessity of adding the third 60 kW, 500 MHz rf station to the storage ring for radiation loss compensation as well as Toushcek lifetime elongation has been thoroughly discussed and studied in the light source division. In this report, we summarize the findings of our studied and hopefully would help decision making on whether the third rf station should be built in the following years.

Assuming the superconducting wiggler will be installed, the rf power required to compensate the radiation losses of electron beam due to bending magnets and various insertion devices are estimated. To ensure the stability of rf system operation under beam loading, the stored beam current cannot exceed certain limit for a given acceleration voltage. The maximum stored beam currents at different gap voltages for an rf system with two and three cavities are also estimated. The increase of lifetime by increasing rf gap voltage was experimentally tested in the multibunch mode up to 950 kV. From this simple experiment, we can have a picture of how lifetime improves by pursuing higher gap voltages. On the other hand, the passive Landau cavity project has been proposed also to improve beam Touschek lifetime. Extra power consumed by the Landau cavity should also be taken into account.

Addition of the third cavity will complicate the impedance (especially the narrow band impedance) of the storage ring. Coupled-bunch instabilities excited in the stored beam may spoil the emittance. The degradation effects due to coupled-bunch instabilities are difficult to predict and are not considered here due to the fact that consistent ongoing plans have already existed to cure these instabilities. These plans include rf cavities operated with two tuners [1], transverse and longitudinal dampers [2] and addition a third harmonics passive Landau cavity in the storage ring [3]. A Landau cavity will simultaneously increase beam lifetime if the mcahine is Tousheck effect dominated.

## 2 POWER CONSUMPTION AND BEAM CURRENT LIMITATION

The energy loss of the electron beam due to synchrotron radiation is compensated by the electromagnetic wave energy supplied by the rf system. It is essential to have enough power from the rf system to compensate this loss. Since the energy loss of an electron for each turn due to radiation from dipole magnets is proportional to the fourth power of electron energy, it has a 80 % increase of energy loss as electron energy increases from 1.3 to 1.5 GeV. On the other hand, we are targeting a stored beam current of more than 350 mA at 1.5 GeV in the future operation. Hence, the expected radiation power loss by the electron beam is at least 3 times more than the original value at 1.3 GeV. However, for a more precise estimation, one should consider also the radiation losses by insertion devices, the cavity parasitic mode dissipation and the transmission circuit loss.The results of these estimations are organized in Table 1.

In Table 1, the operation mode #1 indicated that the rf power required per station is 38 kW. This value is in good agreement with our operation experiences in spite of the fact that some of the insertion devices do not exist at this time. The required rf power per station in operation mode #2 is only 9% smaller. From power consumption point of view, very little benefit is gained from adding the third rf station and operating the ring at 1.3 GeV/200 mA. However, in the 1.5 GeV/350 mA operation modes, rf power required per station will be reduced by 17% for the three stations case (mode #4) in comparison with to the two stations case (mode #3). One may notice also that the power delivered to the cavity by each station in mode # 3 is very close to the station power limit that is 60 kW. Although we may still have a chance to achieve 350 mA, each rf station has to be operated at its full power. In mode #3, the rf power lost

0-7803-4376-X/98/$10.00 © 1998 IEEE

to beam is close to the rf power dissipated on the cavities. According to the beam loading theory, the beam will be unstable longitudinally or even lost. Hence, mode #3 represents a marginal operation condition. The machine will become touchy as the current approaches this limiting current which is 350 mA. Although operation at 1.5 GeV with beam current close to or beyond 350 mA is still possible by means of cavity detuning for Robinson damping or direct rf feedback, however, the available rf power from the rf system becomes another limiting factor. For operation beyond 350 mA at 1.5 GeV, the third rf station is absolutely necessary. Even in the three rf stations case (mode #4), the operational beam current is only ~20 % lower than the theoretical limit. This implies beam loading of rf system is still heavy. Further increase of gap voltage, detuning cavities for Robinson damping or rf feedback should be employed to stabilize the beam. And extra rf power is essential to implement any one of these schemes.

| Operation Modes | #1 | #2 | #3 | #4 |
|---|---|---|---|---|
| Beam Energy (GeV) | 1.3 | | 1.5 | |
| Beam Current (mA) | 200 | | 350 | |
| Total Gap Voltage (kV) | 800 | 1200 | 800 | 1200 |
| Number of Cavities | 2 | 3 | 2 | 3 |
| Radiation Loss per Electron per Turn (keV): | | | | |
| dipoles | 72.28 | | 128.12 | |
| W20(1.8T) | 73.15 | | 129.18 | |
| U5 | 74.39 | | 130.51 | |
| U9(1.25T, 4.5m) | 75.09 | | 131.11 | |
| EPU(0.67T, 4.0m) | 76.93 | | 132.57 | |
| SW(6.0T, 0.2m) | 77.70 | | 133.25 | |
| Total | 100.54 | | 165.74 | |
| Power Dissipation per Station (kW): | | | | |
| Fundamental Mode | 26.7 | | 26.7 | |
| Parasitic Modes | 27.053 | | 0.162 | |
| Citcuit Loss (minimum) | 28.5 | | 1.5 | |
| Total | 28.25 | | 28.36 | |
| Total RF Power Required (kW) | 76.62 | 104.8 | 114.7 | 143.1 |
| RF Power Required per Station (kW) | 38.31 | 34.96 | 57.37 | 47.70 |

Table 1. Estimations of Power Required from the RF System Under Various Operation Modes

It is important to note that rf power will be consumed by the passive Landau cavity to build up the necessary gap voltage at the third rf frequency harmonics. The effect will be discussed separately in section 4.

## 3 POSSIBILITY OF TOUSCHEK LIFETIME ELONGATION BY INCREASING GAP VOLTAGE

In order to find out whether one could expect an increase in beam lifetime by using a third rf system to increase the gap voltage $V_g$ [9]. Assuming that the total beam lifetime is dominated by the Touschek effect [10] which is given by

$$\tau_T^{-1} = ( r_e^2 cN/8\pi\gamma^5\sigma'_x\sigma_l\sigma_x\sigma_z ) \{F(\delta)/\delta\} \quad (3)$$

where $\sigma_{x'}$ is the rms of the beam divergence, $\delta$ is defined as

$$\delta = \{(\Delta p/p)/\gamma\,\sigma_{x'}\}^2 \quad (4)$$

where $\Delta p/p$ is the momentum acceptance of the machine. The function $F(\delta)$ is given by

$$F(\delta) \approx -\ln(\gamma_e\delta) - 3/2 \quad (5)$$

for $\delta <$ or $\approx 10^{-2}$ and $\gamma_e \approx 1.78$ is the Euler's constant.

From the above equations, we can calculate Touschek lifetime at different gap voltages (Figure 1). Figure 1 shows a linear dependence between Touschek lifetime and total gap voltage. One might expect an increase of beam lifetime as gap voltage increases.

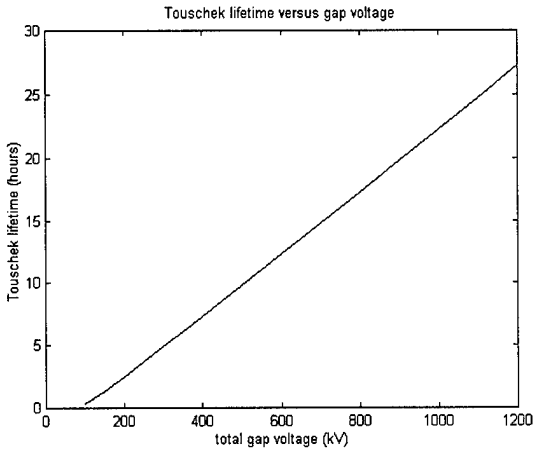



Figure 1. Calculated Touschek Lifetime vs. Gap Voltage

To check this expectation, a measurement of the lifetime was done under machine conditions typical for user operation, with wiggler gap opened, making sure that the average ring vacuum and the beam current did not vary by more than 10 %. As shown in Figure 2, the lifetime increases with gap voltage up to voltages of about 800 kV and then saturates. This means that at higher cavity voltages the lifetime is dominated by other effects than energy acceptance limited Touschek scattering. At low gap voltage, the lifetime drops dramatically because the stored beam current exceeded

the beam loading current limits. These measurements were repeated, with wiggler gap closed and transverse feedback turned on, at 1.5 GeV/190 mA. The result shows the same trend.

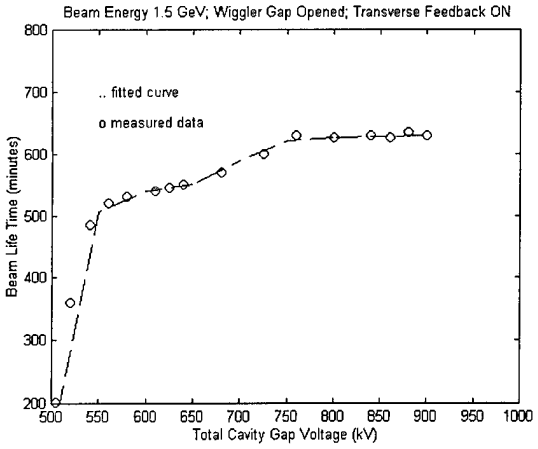



Figure 2. Lifetime vs. Gap Voltage ( Wiggler Gap Opened)

## 4 EFFECTS OF THE PASSIVE LANDAU CAVITY

Theoretically, passive Landau cavity has no effect on bunch length at low beam current since the induced voltage across the cavity gap approaches to zero and therefore no power will be dissipated on the cavity. The gap voltage induced by the beam across the Landau cavity will depends on the tuning angle at higher beam current. The effects of the passive Landau cavity on bunch length and Touschek lifetime will therefore depend on the cavity tuning angle.

| Beam Energy (GeV) | 1.5 | |
|---|---|---|
| Total Gap Voltage (kV) | 800 | 1200 |
| Number of Cavities | 2 | 3 |
| Available RF Power per Station (kW) | 60 | 60 |
| Total Available RF Power (kW) | 120 | 180 |
| Total Radiation Loss per Electron for Each Turn (keV) | 165.74 | |
| Maximum Power Loss on Passive Landau Cavity (kW) | 20 | |
| Power Dissipation per Station (kW): | | |
| Fundamental Modes | 26.7 | |
| Circuit Loss | 1.5 | |
| Total | 28.2 | |
| Maximum Beam Current (mA) | 260 | 450 |

Table 2. Maximum Beam Current of TLS Storage Ring with Power Loss on Landau Cavity Included.

In analysis of power consumption, we assume the Landau cavity has a rated power of 20 kW. This loss has to be compensated by the 500 MHz rf system. Adding this power consumption to operation mode #3 of Table 1, there will be an extra power required for each station by 17.4% (i.e., 67.37 kW). This value already exceeded the norminal available power for each rf station. For operation mode #4, we need 14 % more rf power with Landau cavity than the case without. Since we have three cavities, the required rf power per station is about 51 kW that is within our capability. In Table 2, we set the available power for each station at 60 kW to deduce the maximum stored currents in the cases with two cavities and three cavities (assume the gap voltages for each cavity are set at 400 kV) at 1.5 GeV. Since the HOM parasitic loss per cavity depends on beam current and is small in comparison with other kinds of power losses, we ignored here for simplicity. The last row of the Table shows the maximum stored beam current in the two cavities case is only 260 mA. In the three cavities case is 450 mA.

## 5 SUMMARY

According to the above analysis, we summarize our findings for 1.5 GeV operation as follows. Based on theoretical calculations, one might expect a linear increase of Touschek lifetime at higher gap voltages. From the experiments we described in section 3 and assuming that the essence of these observations can be confirmed by further experiments, however, it is likely that a third 500 MHz rf system will not help to improve the beam lifetime for the machine status. The mechanism(s) that limits beam lifetime at higher gap voltage is still unclear and further study is needed. Without Landau cavity, the maximum beam current the storage ring can stored for an rf system with two rf stations is limited to 350 mA at 800 kV. By increasing the total gap voltage with three rf stations to 1200 kV, the storage ring has a beam current limit of about 480 mA. In operation with the passive Landau cavity, two rf stations have a current limit of 260 mA at 800 kV. The three station case has a current limit of 450 mA at 1200 kV gap voltage.

## REFERENCES

[1] Ch. Wang,"Stabilization of the Spectral Intensity Fluctuations with the High Order Mode Frequency Tuners",these proceedings.
[2] W.K. Lau,"Development of a Longitudinal Damper for the TLS Storage Ring",these proceedings.
[3] L.H. Chang,"Effects of Landau Cavity on the Electron Beam",these proceedings.

# DESIGN OF A THIRD HARMONIC LANDAU CAVITY FOR THE SRRC STORAGE RING

Ch. Wang, L.H. Chang, T.T.Yang, R.H. Tzeng, M.C. Lin, W.K. Lau, C.C. Kuo
Synchrotron Radiation Research Center, Hsinchu 300, Taiwan

*Abstract*

We present here our design of the SRRC third-harmonic Landau cavity to be operated on the first stage in a passive mode for bunch lengthening so as to increase the Touschek life-time. Its implementation will also be helpful for suppression of the longitudinal coupled-bunch instabilities observed in the storage ring of SRRC. The cavity profile was optimized with the 2D code URMEL with the following criteria: (1) maximization of the shunt impedance; (2)minimization of the maximal power flow density on the cavity surface; (3) feasibility of the mechanical constructions. A prototype is now under construction.

## 1 INTRODUCTION

The storage ring of SRRC, as one of the third generation synchrotron light sources, has routinely operated at 1.3-1.5 GeV since 1993. The beam current lifetime is about 5 hours at 200 mA when the 1.8 Tesla wiggler and the transverse feedback system are on. Such short beam life-time is mainly limited by the Touschek scattering[1]. This limitation can be released by the implementation of a Landau cavity[2], cooperated with the 500 MHz storage ring main RF cavities, to provide a flat profile of the accelerating gap voltage. It can lengthen the bunch and therefore increase the Touschek life-time. Moreover, the Landau damping can be enhanced with Landau cavity. This will be helpful for the suppression of the longitudinal coupled-bunch instabilities observed in the storage ring of SRRC. Here, we present our design of the SRRC third harmonic Landau cavity. A prototype is being constructed.

## 2 DESIGN CONSIDERATIONS

The SRRC Landau cavity will be operated in the third harmonic after we considered among the following factors: the percentage of bunch lengthening[3], the feasibility of cooling capability[4], the constraint on the cavity length (for available length of 260 mm), and the availability of the RF source for active operation in the future. The cavity profile was optimized with the 2D code URMEL[5] by the maximization of the shunt impedance $R_s$ as well as by the minimization of the maximal power flow density $p_{max}$ on the cavity surface subject to the feasibility of the mechanical constructions. We used the definition of shunt impedance $R_s = V_c^2/2P_c$. Here $P_c$ is the power dissipated on the cavity surface; $V_c$ is the effective voltage seen by the electron beam as it travels through the cavity gap, i.e., the gap voltage. The power flow density $p_{sur}$, in terms of Watt/m$^2$, is given by $p_{sur} = \frac{1}{2} R_{sur} H_{tan}^2$, where $R_{sur}$ is the surface resistivity expressed as $R_{sur} = \sqrt{\omega\mu/2\sigma}$ and is 0.0101$\Omega$ for the oxygen-free copper (OFC) at 1498.98 MHz at 27°C.

**2.1 Maximization of the shunt impedance:** The optimization of the cavity profiles began from a pill-box cavity with a beam pipe radius of 40 mm. The SRRC standard aluminum vacuum chamber has an elliptical cross-section with a horizontal full axis of 2x40 mm as well as vertical full axis of 2x19 mm. The shunt-impedance $R_s$ is inverse proportional to the radius of the cavity beam pipe. Moreover, the larger the beam pipe radius, the longer the copper beam pipe is to be required to minimize the reduction of cavity shunt impedance due to field penetration in the aluminum vacuum chamber. A neck with 60 mm diameter for the Landau cavity was then selected in order to compromise between the acceptance reduction and the shunt impedance increment.

A taper of 65 mm was selected for smooth transition of the beam pipe cross-section from a circular one (the neck) with radius of 30 mm to the SRRC standard elliptical vacuum chamber. Such taper has a slope similar to that of the wiggler chamber, and its contribution to the broad-band impedance can be ignored, based on our wiggler experience. With such design, not only the constraint of the available cavity length is fulfilled, but also the fundamental mode of the Landau cavity is fully concentrated in the available longitudinal length of 260 mm.

For simplicity, we assumed that the cavity has a round beam pipe with diameter varied from 60 mm to 80 mm in our 2D modeling. Two optimized cavity profiles are finally available: bell-shape one with and without nose-cone, as shown in Fig. 1 and 2.

The fundamental frequency of the Landau cavity was adjusted to be closed to three times of the storage ring accelerating frequency, i.e., 499.660-499.666 MHz, by slight variation of the cavity height. The profile of the cavity shape with nose-cone shows a decrease of the resonance frequency of the $TM_{010}$-like fundamental modes. An increment of the shunt impedance of 15% is achieved for the cavity with nose-cone. A simple bell-shape cavity was selected for our application because technicalwise it is more or less easier to construct.

As mentioned above, the cavity taper sections have a full 3D structure, as shown in Fig. 3, which was modeled by the 3D code SOPRANO/OPERA[6]. Because the cavity higher order modes are beyond the cut-off frequency of

0-7803-4376-X/98/$10.00 © 1998 IEEE

Table 1: Calculated results for the proposed cavities with and without nose-cone. The maximal surface power flow density $p_{sur,max}$ and total dissipated power $P_c$ are at the gap voltage of 250 kV. 3D results for the cavity without nose cone calculated by the code SOPRANO are shows a good agreement with the 2D URMEL results. The simplification of the elliptical taper section (3D-e) by a circular taper section (3D-c) seems to be reasonable.

| nose cone | freq [MHz] | Rs [MΩ] | $p_{sur,max}$ [w/cm$^2$] | $P_c$ [kW] |
|---|---|---|---|---|
| with | 1499.88 | 1.62 | 41.50 | 19.32 |
| without | 1499.78 | 1.41 | 36.15 | 22.22 |
| (3D-c) | 1504.76 | 1.37 | 37.95 | 22.81 |
| (3D-e) | 1504.01 | 1.38 | 37.45 | 22.58 |

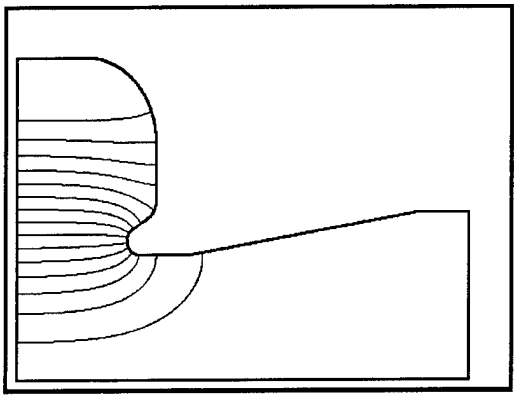


Figure 1: The optimized profile of a 1.5 GHz Landau cavity (with nose-cone). The field pattern of the $TM_{010}$-like mode is calculated by the 2D code URMEL.

the SRRC standard vacuum chamber, it HOM effects on the beam dynamics may be neglected. In Table 1, the calculated results for the proposed cavities are listed.

**2.2 Mechanical tuners:** The tuning range should be large enough to compensate the following factors: the frequency shift due to the modeling uncertainty, mechanical tolerance, cavity temperature variation, structure deformation from the vacuum pressure, 3D structure beam pipe, coupling network, pick-up probes, etc. On the other hand, the tuning resolution should be fine enough for the selection of the optimal cavity tuning angle so as to optimize the bunch lengthening percentage. Therefore, two cylindrical mechanical tuners will be implemented, as shown in Fig. 3. For simplicity of numerical modeling, only one tuner was modeled. One of the tuners will be driven by the microstepping motor, and the other is adjusted manually. The motorized tuner will have a small diameter such that the tuning resolution can be improved in a range of 2x500 kHz.

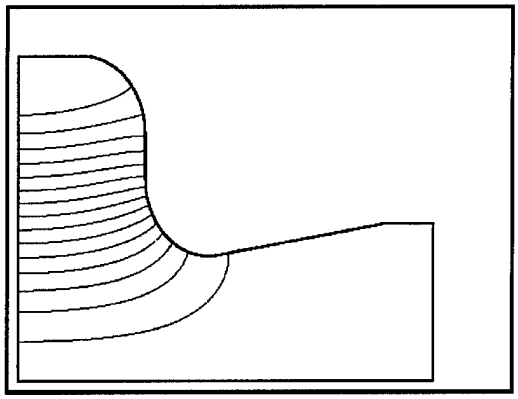


Figure 2: The optimized profile of a 1.5 GHz Landau cavity (without nose cone). The field pattern of the $TM_{010}$-like mode calculated by the 2D code URMEL is given.

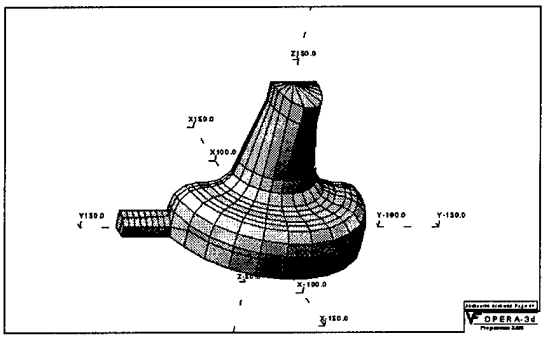



Figure 3: A 3D schematic drawing for the 1.5 GHz Landau cavity

The other tuner will have a larger diameter to guarantee a reasonable tuning range for different modes of operation.

The 2D code URMEL was first applied for a rough estimation of the required tuner diameters, in which the cylindrical tuner was assumed in the simulation with a ring disk of same volume. However, the 3D code predicts that as the tuner pulls out from the cavity surface, its effects on the frequency shift decay quickly. The modeling uncertainty will be compared with the measured data later, and the tuner final dimensions will be directly determined by the cold test of the prototype for the practical reasons. It is expected to be no fatal consequence by simplifying the tuner circuit without chock structure. Nevertheless, a careful numerical study will be performed in next step.

**2.3 Thermal loading:** Setting the Landau cavity gap voltage at 250 kV, the corresponding maximal power flow densities on the thermal spot are 41.50 and 36.15 W/cm$^2$ for the copper cavity with and without nose-cone, respectively. Such thermal spot is compatible for the RF

cavities for the B-Factory with a maximum power flow density of 33 W/cm$^2$ and with 150 kW dissipation power load[8]. For such a thermal loading, the mechanical design as well as construction for the cavity cooling channels is obviously quite challenging. A numerical connection between the code URMEL and the finite element code ANSYS[7] has been established to verify the feasibility of the mechanical design[4].

**2.4 Multipactoring:** In addition to the built-in temperature sensors, ion gauges will be mounted on the cavity beam pipes to serve as interlock units to avoid any unexpected break-down or damage of the Landau cavity. The ion gauge is one of the most sensitive detectors to reflect any abnormal operation conditions of the cavity. Such a interlock signal will electronically directly connect to the low-level systems of the main RF systems for the storage ring.

However, an unfavorable situation might be involved due to multipactoring which resulting in a higher vacuum pressure. Basically, the multipactoring may be finally depressed by long-term RF power conditioning. However, the SRRC third harmonic Landau cavity will be first operated in a passive mode. An off-line RF conditioning will be impossible. It will be inconvenient, if there is any multipactoring in between the operating gap voltage range of the Landau cavity up to 250 kV[3]. To be more conservative, a coating of about 100 Angstroms titanium on the cavity inner surface will be applied to decrease the coefficient of secondary electron emission. Besides, it will also decrease the shunt impedance. About 16% of extra reduction on the shunt impedance (1.2 M$\Omega$) was assumed for estimation on the bunch length performance. A setup and procedure for the titanium coating, similar to the one developed by Wisconsin Synchrotron Laboratory, will be adopted[9]. A numerical simulation by using the code TW-TRAJ[10] to predict the possibility of multipactoring is in progress.

**2.5 Coupling network:** There are some intrinsic disadvantages, if the Landau cavity is operated in the passive mode[11]. Therefore, the Landau cavity will be operated in an active mode in the next step. To avoid long term interference to the machine normal operation, the cavity is designed to be suitable for the operation of both modes. A coupling port will be reserved and terminated by a flange during the period of passive operation. A hole coupler will be selected for the sake of mechanical simplicity. The final size of the coupling hole will be determined experimentally.

**2.6 External circuit:** Suitable klystrons are available for active operation of the Landau cavity. Either of the Varian tube VKL-7811W with transmitter of VKL-7811W or Thomson tube TH2466 with transmitter of H20424 provides a 1.5 GHz, 5 kW, CW RF source with bandwidth of few MHz. Moreover, the Varian tube VKL-7811ST with transmitter VKL-7811ST, original designed for operation at the central frequency of 1.3 GHz, is possible to be modified for the operation at the central frequency of 1.5 GHz with 10 kW, CW output. The RF power will be transported by wave-guide WR650.

## 3 DISCUSSION

The construction of a prototype third harmonic Landau cavity is in progress at SRRC. Its photograph can be found elsewhere[4]. The cold test measurements for the prototype will be started soon. The Landau cavity is planned to be installed in the summer next year.

**Acknowledge**: We have benefited the discussions with Å. Andersson, J. Byrd, M. Eriksson, B. Rimmer, and E. Weihreter. We appreciate R.A. Bousch, K. Kleman, Kroll, R. Parodi, J.M. Wang, and W.T. Weng, for kindly providing technical information and/or numerical codes. We thanks for their kind technical support on our project.

## 4 REFERENCES

[1] C.C. Kuo, et al., "Beam Lifetime Investigations at SRRC", 1996 EPAC conference proceedings.

[2] A. Hofmann and S. Meyers, "Beam Dynamics in a Double RF System", 11th Int. Conf. on High Energy Accelerators, 1980, Geneva, pg 610.

[3] L.H. Chang, et al., "Effects of the Landau Cavity on the Beam Dynamics", this conference.

[4] T.T. Yang, et al., "On the Mechanical Design of a 1.5 GHz Landau Cavity", this conference.

[5] URMEL is a 2D code of RF structure frequency domain solver, developed by T. Weiland.

[6] SOPRANO is a 3D commercial code of RF structure frequency domain solver in the numerical package of OPERA, a product of Vector Field Limited.

[7] ANSYS is a commercially available 3D finie element code suitable for simulation of thermal expansion, structure deformation, etc., a product of Swanson Analysis System, Inc..

[8] H.D. Schwarz, et al., "DEsign of a High-Power Test Model of the PEP-II RF Cavity", 1993 PAC conference proceedings.

[9] K. Kleman, private communication, 1996.

[10] TW-TRAJ is a 2D code suitable for simulation of cavity multipactoring, developed by R. Parodi and P. Fernandes, 1990.

[11] R. Biscardi, "Bunch Length Control in the NSLS VUV Ring", Nucl. Instrum. & Mech. A 366, pg. 26, 1995.

# ON THE MECHANICAL DESIGN OF A 1.5 GHz LANDAU CAVITY

T.T. Yang, M.C. Lin, Ch. Wang, L.H. Chang, S.S. Chang, W.K. Lau, C.C. Kuo
Synchrotron Radiation Research Center, Hsinchu 300, Taiwan

*Abstract*

A third harmonic Landau cavity with the fundamental mode of about 1.5 $GHz$ is under development at SRRC. The cavity consists of inner copper layer and outer stainless steel layer. The vacuum-brazing process is adopted for cavity construction. The maximal power flow density on the cavity surface will be about 52.19 $W/cm^2$, as the total thermal loading of 32 $kW$. To verify the cooling capacity, the finite element method is adopted to perform the thermal and stress analyses. Under 15 $m^3/hr$ water flow rate, the temperature rise on the cavity body will be less than 14 $^\circ C$. And the maximal equivalent stress on the copper layer of 29.75 $N/mm^2(MPa)$ is achieved, which is much less than the yielding stress of copper.

## 1 INTRODUCTION

A third harmonic Landau cavity with the fundamental mode of about 1.5 $GHz$ is under development at SRRC[1, 2]. The inner profile of the cavity is of bell-shape without nose cone. The cavity body is consisted of inner copper layer and outer stainless steel layer. During normal operation, the total thermal loading on the inner surface of the cavity will not exceed 32 $kW$, and the corresponding maximal surface power flow density is 52.19 $W/cm^2$[1]. Obviously, a suitable cooling system is necessary for such a high power loading. The cooling design is to make the the temperature rise so low that the thermal stress is lower than the materials' yielding stress.

The 3D finite element models have been established to estimate the temperature rise and the stress distribution on the Landau cavity, and then the improvements on the cavity stucture and cooling system were progressed[3]. The commercially available finite element codes ANSYS[4] and P3/PATRAN[5] were used in our calculations. A prototype cavity has been constructed based on these optimal results. The mechanical design and machining process of the 1.5 $GHz$ Landau cavity, and some analytical results are described in this article.

## 2 MECHANICAL DESIGN

The prototype Landau cavity at SRRC consists of two metallic layers. The inner layer will be fabricated from oxygen-free electrical (OFE) copper C10100, while the outer one is made of stainless steel. The mechanical drawing of the cavity body is shown in Fig. 1. The strength and stiffness of stainless steel are much better than those of OFE copper. Moreover, the coefficient of thermal expansion of stainless steel, $17 \times 10^{-6}/^\circ C$, is close to the one of copper, $16.6 \times 10^{-6}/^\circ C$. Therefore, the stainless steel is chosen as the material of the outer layer of the Landau cavity to protect the cavity and to increase its rigidity.

As shown in Fig. 1, most of the cooling channels are located at the inner copper layer for better cooling efficiency. For the same reason, some cooling channels are directly cut on the cavity body instead of buring the cooling pipes. On each curved part of the cavity, the cooling channels are distributed as seven rings. These ring-typed channels are connected in serial by additional shortcut channels to produce single-directional water flow. The water inlets and the corresponding outlets are expressed by arrows in Fig. 1. On the central cylindrical part of the cavity, the cooling channels, locating on the copper layer, are straight and parallel to the beam-flying direction (Z-axis). Total thirty-two straight cooling channels are equally distributed around the circumference. Moreover, there are some connecting shortcut channels on the stainless steel layer to make the cooling water flow serially along the straight cooling channels. These straight parallel cooling channels are divided into two groups, sixteen channels for each group with individual inlet and outlet, so that each group cools half of the central cavity body.

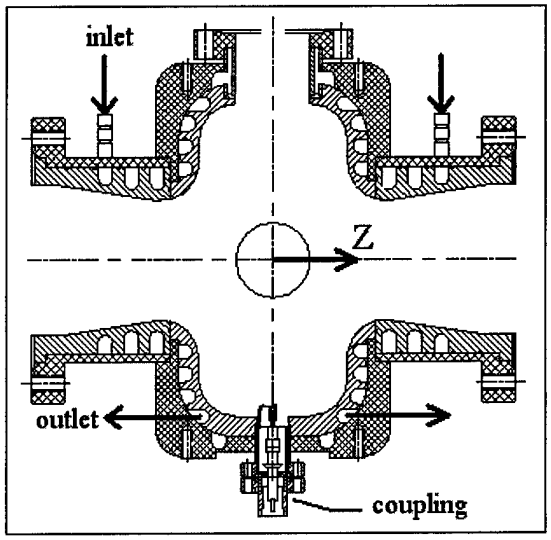



Figure 1: Cross section of the 1.5 $GHz$ Landau cavity in SRRC

0-7803-4376-X/98/$10.00 © 1998 IEEE

For easy machining, both the OFE copper and stainless steel layers will be fabricated in four sections: two end sections and two symmetric sections for the main body. These sections are lathed first to get the desired shape. The ring-typed cooling channels and welding slots are also machined by a lathe. The inner copper layer of the prototype of the Landau cavity after this manufacture process is shown in Fig. 2.

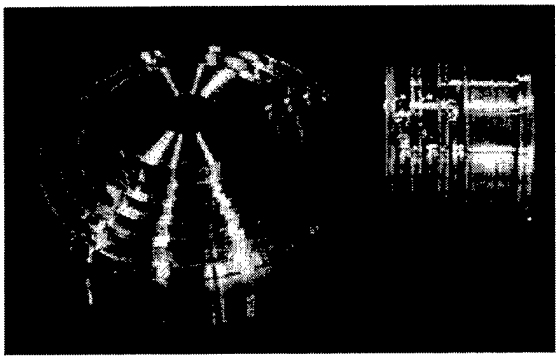


Figure 2: The OFE copper layer of the Landau cavity with the ring-typed cooling channels finished

Notice that the straight parallel cooling channels have not been made yet.

Secondly, every corresponding copper section and steel section are put into a vacuum-brazing machine to be precisely brazed together with the help of the Au-Cu solder under the temperature of about 1010 $^{\circ}C$. As the central copper and steel sections are brazed together, the straight parallel cooling channels will be made by a boring machine. Then, the vacuum-brazing operations are proceeded again and again to construct the whole cavity. Obviously, the vacuum-brazing process is quite a complex and time-consuming work.

To compensate the resonant frequency shift due to the mechanical tolerance, the modeling uncertainty, the operation requirement, the structure deformation from thermal expansion, etc., two mechanical plunger turners will be installed on the cavity. In addition, the RF-power will be inputted through a hole coupler as the cavity to be operated in the active mode in the future. The turners and the coupling network are all located at the middle plane of the cavity, as shown in Fig. 1. A boring machine is used to dig three holes on the brazed cavity body for the connecting rings of the turners and the coupling network. The outer stainless steel layer is now very useful to prevent the cavity from the damaged defromation during the digging process. However, the diameters of these three holes are larger than the distatnce between two straight parallel cooling channels, the cooling channels are discontinuous now. So the corresponding cooling channels are cut on the connecting rings for the turners and the coupling network to maintain the cooling water flow.

## 3 THERMAL LOADING AND COOLING

Under the estimation of 300 $kV$ gap voltage, the calculation on the power flow density distribution[1] shows that the total RF power dissipation on the inner surface of the Landau cavity is about 32 $kW$ with a maximal local power flow density of 52.19 $W/cm^2$. The power density distribution is applied to the finite element models as the applied surface heat flux. Because the applied thermal loading on a single element surface must be the same for the ANSYS thermal element "SOLID 90", the power flow density distribution is transferred to an equivalent heat flux.

The heat transfer between a moving fluid and a solid face can be simply expressed as:

$$q'' = h(T_s - T_m) \tag{1}$$

in which $q''$ is the heat flow per unit area, $h$ the surface heat transfer coefficient, and $T_s$ and $T_m$ the solid surface temperature and bulk fluid temperature, respectively. The formulas used in this work for heat transfer can be found elsewhere[6].

In the finite element anslysis, the surface heat transfer coefficient $h$ has to be assigned on the surfaces of the channels as boundary conditions. However, this coefficient depends on the cross-section of cooling channels which affects the mean fluid velocity $u_m$. For our cooling channel design, the cross-sections of the cooling channels are not identical, so a complete spreadsheet calculation for $h$ on every cooling channel is necessary. It is clear from Eq. (1) that, under the same heat flow density $q$ and bulk fluid temperature $T_m$, the larger the surface heat transfer coefficient $h$, the lower the solid surface temperature $T_s$ will be. Therefore, the larger $h$ means a better cooling efficiency.

As the mean fluid velocity $u_m$ increases, so does $h$. But it will also increase the pressure difference between the corresponding inlet and outlet of the cooling water. Restricted to the pumping capacity, the overall pressure difference is expected to be less than 5 $kgw/cm^2$ for every serial cooling channel group. The spreadsheet calculations show that the optimum water flow rates for the ring-typed cooling channels and the straight parallel ones are 3.5 $m^3/hr$ and 4.0 $m^3/hr$, respectively. The surface heat transfer coefficient $h$ will then distribute between 3.471 and 5.745 $W/cm^{2\circ}C$. The pressure differences for the ring-typed cooling channels and the straight parallel ones are 4.8 and 4.6 $kgw/cm^2$, respectively. Under the 32 $kW$ thermal loading and the 15 $m^3/hr$ cooling water flow rate, the water temperature rise of less than 1.9 $^{\circ}C$ is deduced for steady state.

## 4 FINITE ELEMENT ANALYSIS

In our numerical study, the thermal analysis is first performed to obtain the nodal temperature solution. Then the nodal temperatures are applied as body loads to a compatible structure model in the subsequent stress analysis. The compatible 20-node solid elements "SOLID90" and "SOLID95", provided by ANSYS, were adopted in the thermal and stress analyses, respectively. Both the elements have 3 nodes for single edge and are well suited to model curved boundaries.

Beause there are three holes on the middle circumference of the cavity for the turners and the coupling network, the cavity is asymmetric. The special conditions around these three holes were neglected, so the cavity was treated as a symmetric structure and only one sixteenth of the cavity body was modeled for the simplicity of the numerical modeling. There are 7344 elements and 37552 nodes for this model. The material constants adopted in analyses are listed in Table 1.

The analytical results show that the maximal temperature rise is 13.99 $°C$, which is located at the central cylindrical part of the cavity. In the subsequent stress analysis the nodal temperatures were applied as body loads, while the reference temperature was set to zero. The surface pressure of 1 $kgw/cm^2$ was applied on the outer surface of the cavity to simulate the vacuum effect, while a pressure of 5 $kgw/cm^2$ was applied on the surface of cooling channels to simulate the water pressure. The equivalent stress, $\sigma_e$, i.e., Von-Mises stress, was adopted to check the thermal stress. This equivalent stress is defined as:

$$\sigma_e = \frac{1}{\sqrt{2}}\sqrt{(\sigma_1-\sigma_2)^2+(\sigma_2-\sigma_3)^2+(\sigma_3-\sigma_1)^2} \quad (2)$$

Here $\sigma_1$, $\sigma_2$, and $\sigma_3$ are three principal stresses. The calculated equivalent stress is shown in Fig. 3. It can be seen that the maximal equivalent stress is 29.75 $MPa$, and the high stress region locates at the central cylindrical part of the cooper layer. Notice that the yielding stress for anneal copper is 55 $MPa$, i.e., the safety factor for stress is 1.85.

The temperature rise will also bulk up the cavity. This will change the resonant frequency of the cavity.

Table 1: Summary of the material constants used in the finite element analysis of the Landau cavitay.

| | Copper | Steel |
|---|---|---|
| Young's modulus ($kN/mm^2$) | 110 | 200 |
| Poisson's ratio | 0.33 | 0.3 |
| coefficient of thermal conductivity ($W/m°C$) | 401 | 14.9 |
| coefficient of thermal expansion ($\times 10^{-6}/°C$) | 16.6 | 17 |

According to the FEM results, the maximal expansion will happen at the central part due to the thermal effect. The maximal radial deflection is 5.7 $\mu m$. The elongation on the longitudinal direction is also in the same order as the radial deflection. The bellows in connection between the cavity and the vacuum chambers can take this longitudinal elongation. However, such effect is so small that the bulk can be easily compensated by movement of the turners installed on the cavity body.

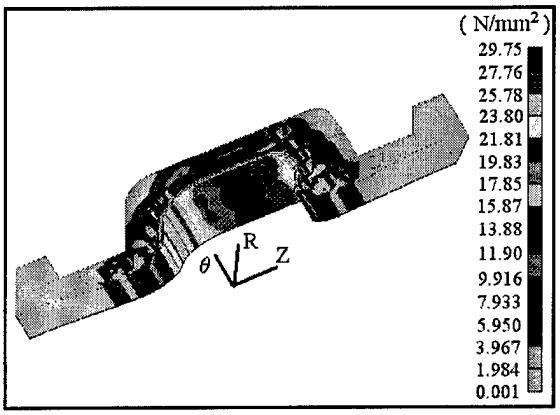



Figure 3: The equivalent stress of the cavity body under 32 $kW$ thermal loading.

## 5 CONCLUSION

The 3D finite element thermal and stress analysis is useful not only to improve the mechanical structure of the 1.5 $GHz$ Landau cavity, but also to verify the capability of the cooling channels. Both the water flow rate and the cooling channels were optimized to reduce the thermal effects. The manufacture of the cavity is very complicated, in particular in the complex vacuum-brazing process.

## 6 REFERENCES


[1] Ch. Wang, L.H. Chang, T.T. Yang, R.H. Tzeng, M.C. Lin, W.K. Lau and C.C. Kuo, "Design of a Third Harmonic Landau Cavity for the SRRC Storage Ring," this conference.

[2] L.H. Chang, Ch. Wang, W.K. Lau and C.C. Kuo, "Effects of the Landau Cavity on the Electron Beam," this conference.

[3] M.C. Lin, Ch. Wang, T.T. Yang and L.H. Chang, "On the Thermal and Stress Analysis of a 1.5 $GHz$ Landau Cavity," in progress.

[4] Program ANSYS, a product of Swanson Analysis System, Inc., is a commercially available 3D code by using finite element method.

[5] Program P3/PATRAN, a product of MacNeal-Schwendler Corporation (MSC), is a commercially available 3D code that can be used as pre-processor and post-processor for some other finite element codes.

[6] F. P. Incropera and D. P. DeWitt, "Fundamentals of Heat and Mass Transfer," 2nd Edition, John Wiley & Sons, Inc., 1985, Ch. 8, pp. 367-416.

# SAWTOOTH WAVE GENERATION FOR PRE-BUNCHER CAVITY IN ISAC

K. Fong, M. Laverty, S. Fang and W. Uzat
TRIUMF 4004 Wesbrook Mall, Vancouver, B.C., Canada V6T 2A3

*Abstract*

Two phase-locked loops operating with a reference frequency of 11.667 MHz are used to generate the Fourier components for a sawtooth waveform with a repetition frequency of 11.667 MHz. These frequencies are combined at signal level, amplified and used to power a set of parallel plates inside the pre-buncher cavity up to 600 $V_{p-p}$. The resultant sawtooth waveform is feedback regulated by I/Q regulation of its individual Fourier components.

## 1 INTRODUCTION

A pre-buncher cavity is used in the ISAC low energy beam transport line to increase the energy acceptance[1]. This cavity consists of a set of parallel plates that is driven by a 600 $V_{p-p}$ sawtooth waveform at 11.667 MHz. The sawtooth waveform is synthesized by summing the fundamental to 4th harmonics Fourier components. Two phase-locked loop frequency synthesizers are used to generate these frequency components. The In-phase and Quadrature phase of each frequency component are individually regulated by a digital signal processor to produce a stable sawtooth waveform at the cavity. These frequency components are summed together at signal level. The summed output is predistorted, compensating for the group dispersion and nonlinearity caused by the components downstream, to obtain a sawtooth waveform at the cavity. A single 125 W MOSFET rf power amplifier is used to raise the combined signal to 220 $V_{p-p}$ at 50 Ω. Coaxial cable transmits the rf power to the cavity. The rf is then stepped up to 600 $V_{p-p}$ at 450 Ω with a 1:9 balun mounted on the outside of the cavity. The unbalanced-to-balanced transformation also allows the rf power to be fed effectively into a set of parallel plates inside the cavity. The sawtooth voltage is feedback regulated. Pickup probes at each plate monitor the waveform at the cavity. A digital signal processor regulates the In-phase and Quadrature-phase components of each of the Fourier frequencies of the sawtooth waveform, which are obtained by a set of 4 bandpass filters.

Modular design is used in the hardware architecture. Circuits for different functions are housed in separated modules. All the signal level modules, including the waveform synthesizer, the feedback controller, safety interlocks and local supervisory controller, are housed in a VXI mainframe. The rf power amplifier, due to its different power requirements, is housed in another chassis with its own power supplies. The pre-buncher cavity with its impedance matching balun/transformer, is located in the beam line 10 m away.

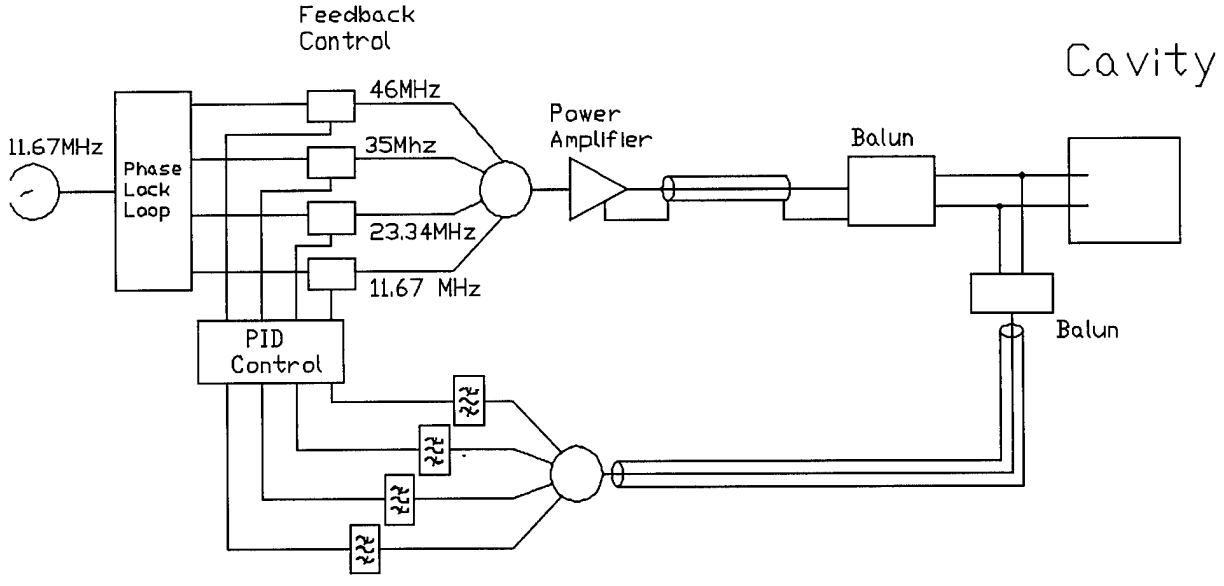



Figure 1. Block diagram of sawtooth wave generator

0-7803-4376-X/98/$10.00 © 1998 IEEE

## 2 WAVEFORM SYNTHESIZER

The waveform synthesizer occupies two VXI modules. One module houses two analogue phase-locked loops. With an input reference of 11.667 MHz, one loop produces the 2nd and the 4th harmonics frequencies of 23.334 MHz and 46.667 MHz, while the other loop produces the 3rd harmonic frequency of 35.000 MHz. Small scale integration and medium scale integration emitter-coupled logic circuits are used in the digital part of the loops. In particular, synchronous counters are used in frequency division to reduce phase jitter. The phase comparator is a type 4 Phase-Frequency detector[2]. First order loop filters are used for both loops, and the bandwidths of the filters are 2 kHz. The loop filter circuitry has a special feature which prevents large frequency excursions during locking and unlocking of the loop. Figure 1 shows a simplified schematic of one of the loop filters. An analogue-to-digital converter controlled by a microcontroller continuously duplicates the output of the loop filter at a digital-to-analogue converter. A pulse detector, not shown in the figure, detects the presence of the reference signal. A level detector monitors the pump-up/pump-down signal from the frequency-phase detector. When the reference input pulse detector cannot detect the presence of the reference signal, the voltage oscillator circuit is biased by the output of the digital-to-analogue converter, whose voltage is the last VCO control voltage before the reference is lost. Transition into this operating mode is glitchless

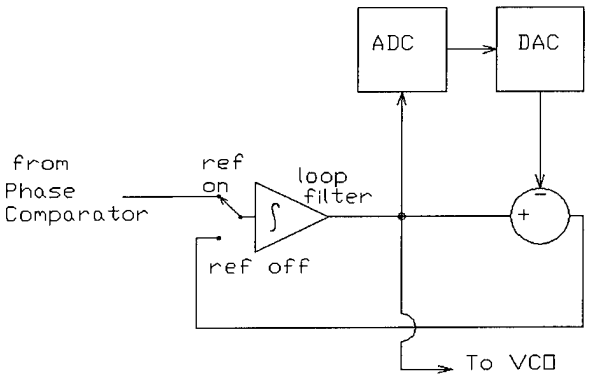



Figure 2. Phase-locked loop bumpless switching block diagram

since the output of the digital-to-analogue converter has been tracking the output of the loop filter. Furthermore, the loop filter capacitor remains in the circuit to achieve bumpless switching when switching back to the phase locked mode. Upon reacquisition of the reference, the reference frequency is usually far enough from the VCO frequency that the Phase-Frequency detector operates in the frequency mode. The microcontroller monitors the difference in frequency via a second detector. The VCO bias is stepped up or down by the microcontroller until the frequency error from the phase comparator is smaller than a prescribed value. The error voltage from the phase comparator again becomes input to the loop filter, and the output frequency is allowed to lock the reference. The output is cleaned up by a combination of a second order bandpass and a third order lowpass filters. Low power rf amplifier modules isolate the output from the phase locked loops and provide output levels of 6 dBm.

Another VXI module has four manually adjustable delay lines, operating on the four frequency components from the previous module, and combines them after the delay lines. Electronic modulators located in the In-phase and the Quadrature-phase path will fine tune the amplitude and phase of each frequency component to obtain the desired sawtooth wave shape. Figure 3 shows the frequency spectrum of the composed sawtooth waveform. It shows the individual frequency components and their relative magnitude. Figure 4 uses an expanded frequency scale and shows the spectral purity of the 3rd harmonics alone. The desired frequency component appears as a sharp peak at 35 MHz. The frequency stability of this peak is better than the resolution (10 Hz) of the spectrum analyzer used. Two broad noise bands at -60 dBc extending to 25 kHz on either side of the central peak are results of the phase detector and loop filter noises. Thermal noise is the main contributor to these noises. At frequency offsets beyond the unity gain bandwidth of the phase-locked loop the VCO noise shows the expected $1/f^2$ dependence.

## 2 POWER AMPLIFIER AND BALUN

Since the pre-buncher operates from 11.667 MHz to 46.667 MHz, wide band designs are necessary in the power amplifier and the cavity termination. The power amplifier is a 2 stage, transformer coupled wide band solid

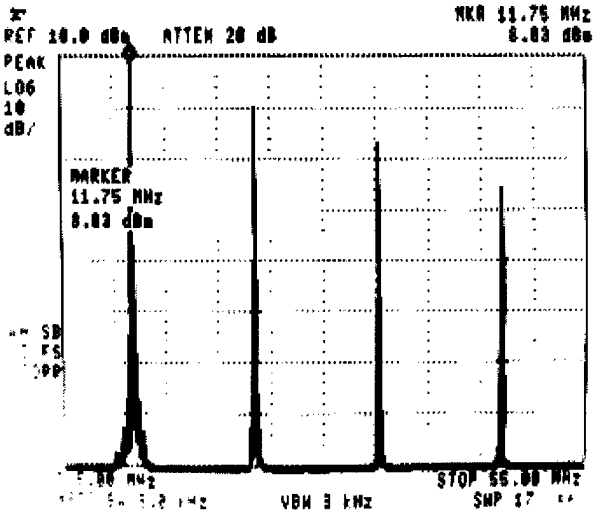



Figure 3. Frequency spectrum of sawtooth waveform

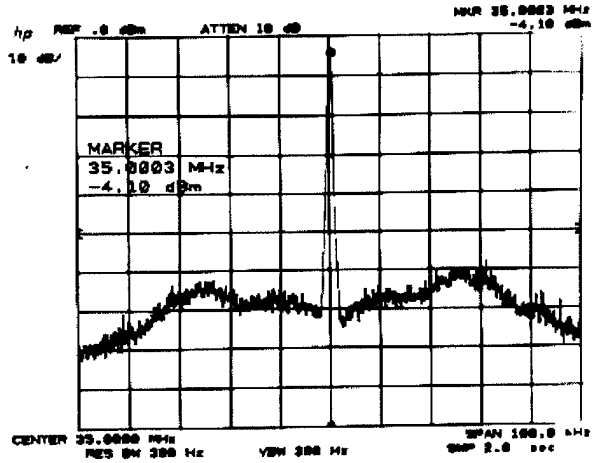



Figure 4. 3rd harmonic output from frequency synthesizer

state amplifier. Each stage consists of a pair of MOSFETs operating class AB in push-pull mode. Overall power gain from 10 MHz to 30 MHz is 38 dB, and the gain reduces at higher frequencies. Although the 3rd and the 4th harmonics lie outside this range, the power requirements for 3rd are 16 dB down from the fundamental, and 4th harmonic is 25 dB down. Their reduced power requirement is low enough such that this power amplifier can still have sufficient gain in order to produce a sawtooth waveform. Overall power output capability is 125 W. A temperature sensor and VSWR monitor protect the power transistors by removing the power supply in abnormal conditions. Since the cavity is located 10m from the amplifier, coaxial cable is used to transfer the power from the amplifier to the cavity. In order to develop 500 Vp-p at the cavity plates, a 1:9 impedance transformer/balun is used to step up the voltage and to provide unbalanced-to-balance transformation. The balun is constructed from three ferrite loaded $\lambda/4$ transmission lines. A 200W, 500 $\Omega$ resistor provides termination for the proper operation of the balun. The balun and the resistor are mounted on a large heat sink and cooled by forced air. The top trace of Figure 5 shows the resultant summed sawtooth waveform at the input of the power amplifier. The trace is a distorted sawtooth, but has been adjusted to give an undistorted sawtooth at the cavity plate. This signal level waveform has been predistorted to allow for the group dispersion characteristics of the balun and the cavity plates, as well as for the nonlinearity of the power amplifier. The bottom trace of Figure 5 shows the amplified voltage at one of the plates in the pre-buncher cavity, where the trace has good resemblance to a sawtooth waveform. The actual voltage across the two plates in the pre-buncher cavity would be twice the voltage as shown in the figure.

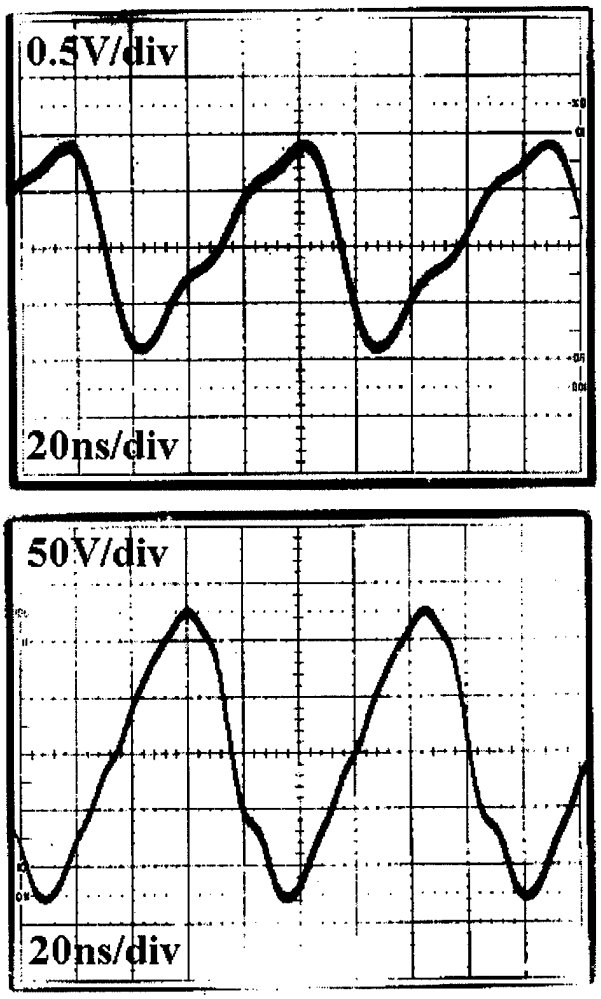



Figure 5. Top trace shows the predistorted waveform at the input of the power amplifier. Bottom trace shows the voltage at one of the plates in the pre-buncher cavity

## 3 CONCLUSION

There are numerous ways to generate a 400 $V_{p-p}$ sawtooth waveform. In order to achieve an undistorted sawtooth waveform at the cavity one has to pre-distort the waveform at the input of the power amplifier. For ease of tuning we have chosen to synthesize the sawtooth waveform from its Fourier components, and maintain control on the shape of the final waveform by adjustments of the amplitude and phase of the component frequencies.

## 4 ACKNOWLEDGMENTS

The authors wish to acknowledge the contribution of G. Dennison and R. Chow in the development and construction of this project.

## REFERENCES

[1] S. Koscielniak et al, 'Beam Dynamics Studies on the ISAC RFQ at TRIUMF', this proceedings.
[2] Best, R. E., 'Phase-locked Loops', published by McGraw-Hill, 1984.

# COARSE AND FINE TUNERS FOR THE CERN PS 40 MHZ BUNCHER CAVITY

A.K. Mitra, R.L. Poirier, TRIUMF 4004 Wesbrook Mall, Vancouver, B.C., Canada V6T 2A3 and
E. Jensen, CERN, 1211 Geneva 23, Switzerland

*Abstract*

A 40 MHz cavity has been constructed at CERN as part of the PS upgrade program for injection into LHC. To compensate for the variable capacitive power coupling and mechanical tolerance during fabrication, a coarse tuner has been envisaged to correct the resonant frequency of the PS 40 MHz cavity. This consists of a shorted loop inside the cavity and by rotating the loop, the magnetic coupling to the cavity can be varied and hence a coarse tuning is obtained. The coarse tuner can not be changed when the cavity is in vacuum. The fine tuner is to compensate for slow variation of resonant frequency of the cavity due to temperature and pressure variation. The tuner employs a variable capacitor as the tuning element. It is connected to a loop inside the cavity via a ceramic window and a rigid transmission line of suitable length. The desired tuning range of the coarse tuner is 1% and the fine tuner is 0.5 %. The coarse tuner has been designed and tested at TRIUMF on a full scale wooden model of the CERN cavity. The fine tuner was designed using PSPICE with the same loop as the coarse tuner. This tuner has been constructed at CERN and also installed in the cavity. Excellent agreement was found between the predicted and the measured tuning ranges of both the tuners on the 40 MHz CERN cavity.

## 1 INTRODUCTION

A 40 MHz cavity has been built at CERN for LHC injection. The cavity has been recently installed in the PS and a nominal gap voltage of 300 kV has been attained [1]. The cavity is equipped with inductively coupled tuners to provide coarse and fine tuning. A coarse tuner is required to compensate for the mechanical tolerance during fabrication and the capacitive loading of the power coupler. The fine tuner is in the form of a mechanical servo tuner for correcting the slow varying frequency change of the 40 MHz cavity due to temperature and pressure variation. The coarse tuner was designed at TRIUMF on a full scale copper lined wooden model of the CERN cavity [2]. The fine tuner was designed with PSPICE and built at CERN.

## 2 THEORY

The de-tuning of a resonant cavity with a coupled loop is outlined in the following section. In figure 1, the resonant cavity is represented in a series equivalent circuit, where $L_2$ and $C_2$ are the equivalent inductance and the capacitance of a resonant cavity and $r_2$ is the series equivalent resistance. If $L_1$ is the self inductance of the loop coupled to the cavity and $Z_l$ is a load terminating the loop, as shown in figure 1, then the impedance coupled to the cavity [3], is given by

$Z_c = (\omega M)^2 / (Z_l + j\omega L_1)$

where M = mutual inductance and is related to the coupling coefficient k by : $M = k\sqrt{(L_1 L_2)}$

The resonant frequency $\omega_c$ and quality factor $Q_c$ of the coupled circuit is given by

$\omega_c = 1/\sqrt{(L_{eff} C_2)}$ and $Q_c = \omega_c L_{eff} / r_2$

where $L_{eff} = L_2(1 - k^2/(1 + Z_l / j\omega L_1))$

This equation becomes the basis of the tuners discussed in this paper.

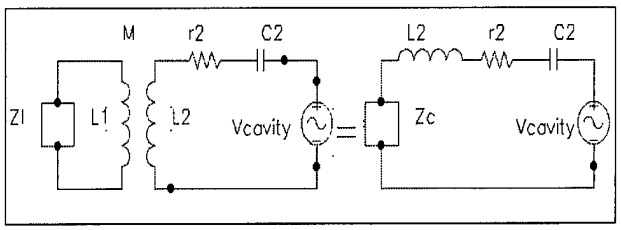



Figure 1: Equivalent circuit of cavity-loop coupled system.

case 1: when $Z_l = 0$ i.e. the loop $L_1$ is short circuited

$L_{eff} = L_2(1-k^2)$

case 2: when $Z_l = \infty$ i.e. the loop is open circuited

$L_{eff} = L_2$

If $\Delta f$ is the frequency shift from open loop to short-circuited loop

then $\Delta f / f = 1/2\ k^2$

It can be also shown that $\Delta Q/Q = k^2$

where $\Delta Q$ is the change in Q value from open loop to short-circuited loop

case 3: If $Z_l = -j\omega L_1$ (i.e. the loop is terminated with a capacitance whose value $C = 1/\omega^2 L_1$) then the cavity resonance is destroyed due to series resonance of C and L1. This case must be avoided for any tuner design. It is obvious that a short circuited loop increases the resonant frequency of the cavity and decreases Q of the cavity.

## 3 COARSE TUNER

A short circuited loop placed inside the magnetic field of 40 MHz cavity de-tunes the cavity resonant frequency.

0-7803-4376-X/98/$10.00 © 1998 IEEE

If the loop with an area A is located at a radius $r_o$ inside the cavity, the mutual inductance $M=\mu_0 A/(2\pi r_o)$
where $\mu_o=4\pi.10^{-7}$ henry/m
Hence $k=\mu_0 A/(2\pi r_o)/\sqrt{(L_1 L_2)}$
Since $\Delta f$ is proportional to $k^2$, for a given cavity and loop position, $\Delta f$ can be maximized by increasing the loop area or decreasing the self inductance. The position of the loop inside the CERN cavity was optimized with MAFIA.

Table 1: Measurements of $L_{self}$, $\Delta f$ and $\Delta Q$ for different types of loops.

| Type of loop | Loop Area $cm^2$ | Lself μH | Δ f kHz | ΔQ % |
|---|---|---|---|---|
| circular loop, 34cm ϕ 2.1 mm ϕ tube | 907 | 1.16 | 152 | 16.2 |
| circular loop, 34cm ϕ 6.35 mm ϕ tube | 907 | 0.870 | 194 | 8.5 |
| octagonal loop 30 cm mean ϕ 33 mm ϕ tube | 710 | 0.48 | 240 | 7.0 |
| rectangular loop, 25.4 mm width strip | 1100 | 0.79 | 285 | 10.5 |

Different loops were installed on the TRIUMF wooden model at the same position as mentioned above and self inductance, $\Delta f$ and $\Delta Q$ were measured. Table 1 shows the results of such measurements. The loop was shorted and rotated to produce variable coupling. The variation of cavity resonant frequency and Q with loop rotated through 90 degree is shown in figure 2. 90 degree represents maximum coupling and 0 degree represents minimum coupling of magnetic flux.

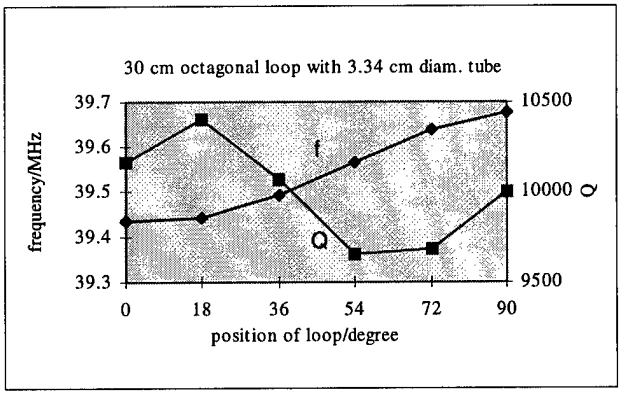



Figure 2: Variation of f and Q with coupling coefficient k

A circular loop was easier to construct than a rectangular loop and gave better mechanical stability. A circular loop of 30.5 cm diameter was constructed at CERN from a copper tube with an outer diameter 3.34 cm and was installed on the CERN cavity. It was estimated to have a self inductance of 0.44 μH and produce $\Delta f$ of 0.62 % and $\Delta Q$ of 11 % for the CERN cavity. Measurement showed that with minimum coupling, the resonant frequency and Q was 39.051 MHz and 19200 respectively. With maximum coupling of the loop, the resonant frequency of the cavity changed to 39.358 MHz and Q changed to 16300. Hence frequency de-tuning was 0.78 % with a loss of Q of 15 %. This showed an excellent agreement between the measured and the expected values of the de-tuning and Q .

## 4 SERVO TUNER

Instead of shorting the loop inside the cavity as in the case of the coarse tuner, if a variable reactance is connected to the loop, a fine tuner can be obtained. A transmission line with suitable length and a variable capacitor forms the reactance. Figure 3 shows such a scheme of a servo tuner which has been employed for the CERN 40 MHz cavity. The rigid transmission line is 650 mm long with a characteristic impedance of 120 Ω. The loop is the similar to the one used for the coarse tuner. The ceramic window uses an existing CERN window

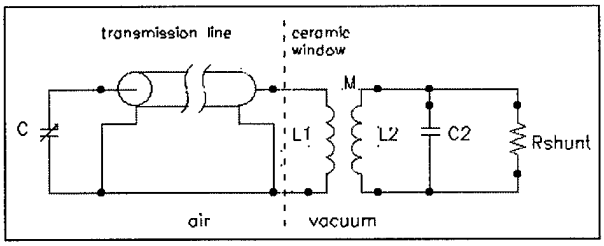



Figure 3 : Schematic of servo tuner.

which had to be modified to withstand high voltages. The variable capacitor is a COMET CV7W 300F/90 whose capacitance varies from 20 pF to 300 pF. PSPICE was used to evaluate the performance of this servo tuner [4]. Voltages at the ceramic window, and capacitor, and the associated circulating currents were calculated with a cavity gap voltage of 300 kV and is shown in figures 4 and 5. The cavity parameters are $L_2$=0.132 μH, $C_2$=121.3 pF, Rshunt=640 kΩ, Q=19400 and f=39.76 MHz. The frequency offset is 170 kHz when the capacitor is 300 pF and the tuning range is 160 kHz as the capacitor is varied from 300 pF to 20 pF. The maximum voltage across the capacitor is 55 kV. Since the voltage gradient on the air side of the window is > 30 kV/cm, the window and the rigid transmission line are pressurized to cope with the high electric gradient. The detail design and fabrication of the servo tuner was implemented at CERN on the basis of the design outlined in this section. Measurements on the servo tuner is shown in figure 6. The tuning range is large, and it has been limited by mechanical stops to use only the range where the Q is high and the window voltage is low.

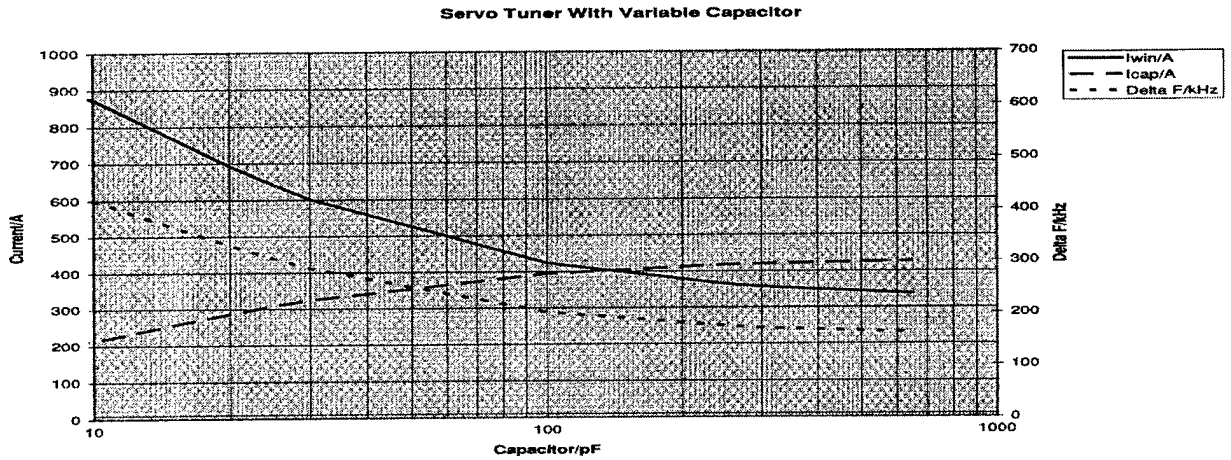



Figure 4: Current and Δf with capacitance variation

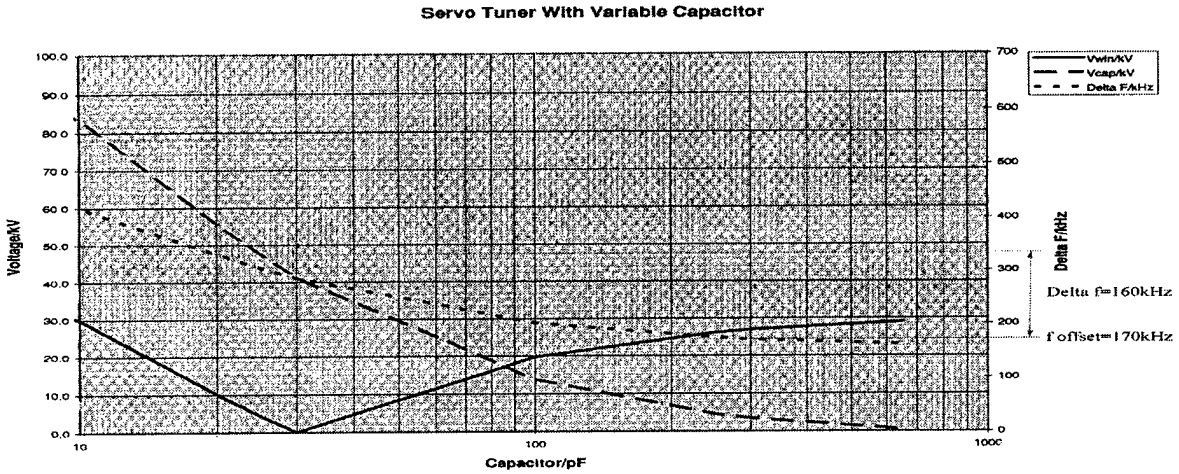



Figure5. Voltage and Δf with capacitance variation.

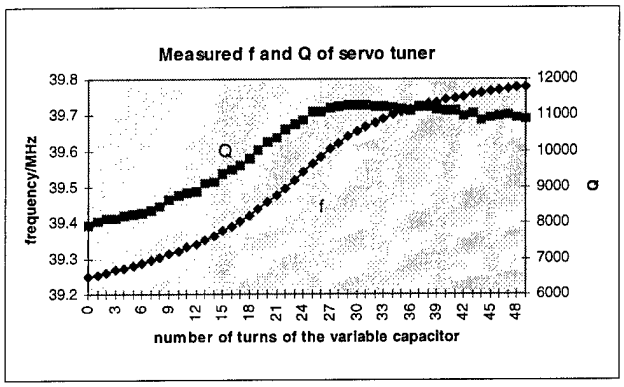



Figure 6. Resonant frequency and Q of the cavity with capacitance variation of the servo tuner.

## 5 ACKNOWLEDGMENTS

The authors would like to thank Ivan Enchevich, Peter Harmer, Mark. Lipnicki and Franco Cifarelli of TRIUMF and Marc Corcelle of CERN for various jobs associated with the tuners.

## REFERENCES

[1] E. Jensen, R. Garoby, E. Grier (CERN), A. K. Mitra, R.L. Poirier (TRIUMF), "The PS 40 MHz Bunching Cavity", these Proceedings.

[2] E. Jensen, R. Hohbach, A.K. Mitra, R.L. Poirier, "Higher order mode damping of the CERN PS 40 MHz cavity" , Proc. Of the 5th EPAC Conference, Sitges, 1996.

[3] R.M. Hutcheon, "Modeling Studies of PETRA II Cavity Frequency Tuner: A Comparison of Resonant/Non-Resonant Perpendicular Biased External Ferrite Loaded Tuning Lines", HERA-TM-23

[4] A. K. Mitra, " Servo Tuner for 40 MHz Cavity", PS/RF Note 96-20, 17 July 1996.

# MEASUREMENTS AT TRIUMF ON A 80 MHZ CAVITY MODEL FOR THE CERN PS UPGRADE FOR LHC

A.K. Mitra, R.L. Poirier, TRIUMF 4004 Wesbrook Mall, Vancouver, B.C., Canada V6T 2A3
R. Losito, *CERN.*, 1211 Geneva 23, Switzerland

*Abstract*

The RF system of the CERN PS is being upgraded to bunch a beam that can be captured by the SPS 200 MHz RF system for injection into LHC. Two identical 80 MHz cavities are part of this PS upgrade program. At CERN, the cavity has been designed using SUPERFISH and MAFIA concerning its shape, tuning devices and amplifier coupling loop. TRIUMF has built a simplified full-scale, copper-lined, wooden model, designed such that the field patterns of the fundamental accelerating mode and the longitudinal modes agree closely to CERN cavity ones. The aim of constructing the wooden model was primarily to check the design of the capacitive tuners, the power coupling loop and the HOM dampers for the longitudinal modes up to 1 GHz. The results of the measurements were used to define the parameters of the tuners and a reliable model to describe the interaction of the coupling loop with the fundamental mode of the final CERN cavity. Four quarter-wave antennae are adequate to damp the first fifteen longitudinal modes. In order not to decrease the shunt impedance of the fundamental mode by more than 5%, three-element filters have been used with the antenna which damps the longitudinal mode at 256 MHz, 336 MHz and 912 MHz.

## 1 INTRODUCTION

The upgrade program of the CERN PS for the injection to LHC foresees the installation of some new RF system in the PS ring. A 40 MHz cavity has already been installed [1] and provides a beam with the required bunch spacing of 25 ns with a bunch length of about 8 ns. To match the SPS RF bucket dimensions the length of the bunch must be reduced to less than 5 ns. To achieve this aim two identical 80 MHz cavities will be installed in the PS in 1998. The bunch length reduction will be obtained with a 90° rotation of the bunch in the phase space.

The cavity is water cooled since it is operated nearly at CW (70 % duty cycle) due to the lepton cycle of the PS. Also, a heavy transient beam loading will take place during the LHC cycle and its dynamics will be too fast to be compensated by fast feedback or de-tuning method. A strongly over-coupled amplifier-coupling loop system was designed with PSPICE to cope up with the beam loading and to provide a consistent voltage step-up ratio between the amplifier anode and the cavity gap in a wide band around the cavity resonance. The value of the self inductance of the coupling loop and the voltage step-up ratio between the loop and the cavity gap was difficult to be evaluated reliably from MAFIA and SUPERFISH calculations.

In the frame of the collaboration between CERN and TRIUMF for LHC, a full scale cold model of the 80 MHz cavity has been built at TRIUMF to verify the design of the coupling loop and to develop a set of Higher Order Modes (HOM) dampers based on the quarter wave antennae as already done for the PS 40 MHz cavity [2]. To prevent the antennae from damping the fundamental mode, a coaxial three-element filter was developed to maintain the Q-factor loss within 5 %.

Two capacitive tuners are also foreseen to compensate atmospheric variation and deformation due to heating of the cavity walls during the start-up. The achievable tuning range has been measured. Figure 1 shows the shape of the CERN cavity with coupling loop and capacitive tuner.

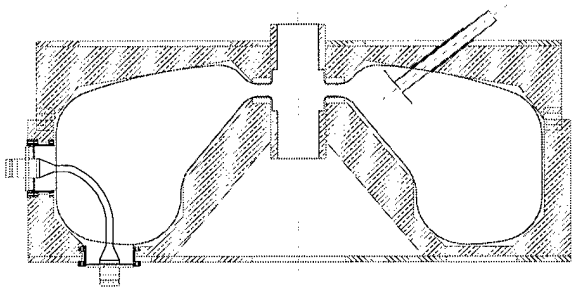


Figure 1. The CERN PS 80 MHz cavity shape (dashed line) and the TRIUMF wooden model with the coupling loop and the capacitive tuner.

## 2 AMPLIFIER COUPLING LOOP DESIGN AND MEASUREMENT RESULTS

Because of the proposed strongly over-coupled amplifier to deal with heavy transient beam loading, the amplifier coupling loop has to fulfill two requirements: voltage set-up ratio between the loop and the cavity gap close to ten, and a self inductance of the loop in the range of 130 - 160 nH. An approximate shape for the loop was found using MAFIA postprocessing capabilities, integrating the electric field along some different paths and relating the result to the integral on the cavity gap. The value for the self inductance was determined by measurements on different loops mounted on the TRIUMF model. The conclusion is that the cavity loop-system can be described by the circuit shown in figure 2, where the transmission line T2 represents the self inductance of the loop, and the Network Analyzer represents a current source shunted by a 50Ω load. The input impedance measurements on the TRIUMF wooden model is shown in figure 3. The error on the frequencies

0-7803-4376-X/98/$10.00 © 1998 IEEE

of the resonances between the PSPICE simulation of the circuit in figure 2 and the measurements is less than 0.2 %.

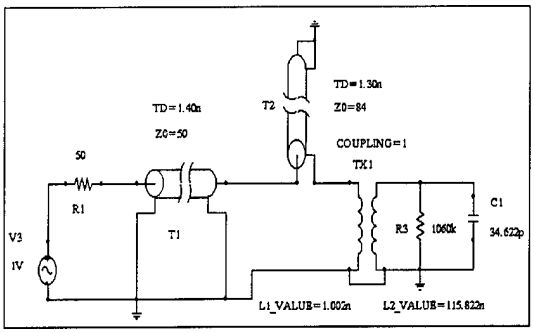



Figure 2. The equivalent circuit of the cavity-loop system

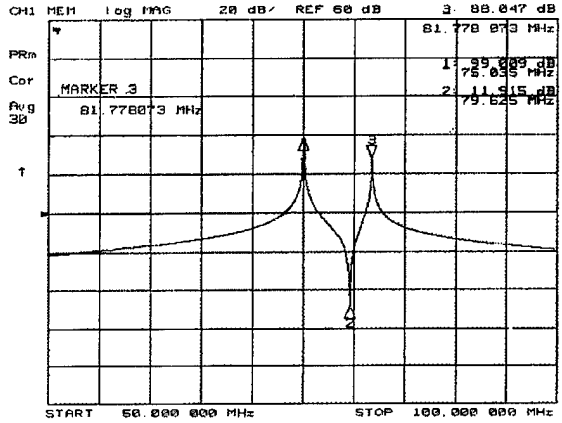



Figure 3. Input impedance measurement.

With the help of the measurements, an analogy between the loop and a strip line [3] was established which allows the dimensions of the loop to be determined. The difficulties in simulating such geometry with MAFIA or similar programs is thus bypassed.

## 3 CAPACITIVE TUNERS

Using MAFIA to design the capacitive tuners is also difficult to achieve because of the non symmetrical geometry and the dimensions of the tuners. The tuning range measured on the cold model was ±0.4 % for the 80 mm nominal stroke, which is about the half the value calculated by MAFIA. The error is essentially due to mesh problems.. It is interesting to note that the capacitive tuner stores essentially electrical energy. Thus, high voltage and low current associated with the tuners lead to two advantages : they are protected against multipactor problems and do not increase the ohmic losses.

## 4 HIGHER ORDER MODE DAMPERS

The wooden model built at TRIUMF was extensively used to design the higher-order-mode dampers for the longitudinal modes up to 1 GHz [4]. The physical location of the ports where dampers could be installed was predetermined from SUPERFISH and MAFIA calculations of the electric field configuration of the modes for the CERN 80 MHz cavity. Four loosely coupled capacitive probes (two at each side of the gap and 90 degree apart) at the gap in conjunction with in-phase combiners, provided a clear spectrum of the longitudinal modes and rejected most of the dipole modes. The Q of a particular mode was obtained by $S_{21}$ measurement on a Network Analyzer. Four $\lambda/4$ antennae were constructed from standard 3/8" O.D ( 10.0mm ) copper pipe and their position and length was optimized to provide the lowest Q for the modes under investigation. Although each antenna was optimized for a specific mode, it also damped other modes which had strong E-field in the close vicinity of the antenna. Table 1 shows the four antennae with their length and frequency of the principal mode being damped. All dampers were terminated with a 50 Ω load .

Table 1 : Antennae profile

| antenna number | length cm | reference mode MHz |
|---|---|---|
| #1 | 28.0 | 255 |
| #2 | 23.5 | 436 |
| #3 | 16.5 | 538 |
| #4 | 21.0 | 912 |

A 3-element high-pass filter was attached to antenna#1 because of substantial coupling to the fundamental mode at 79.64 MHz. The damping of the fifteen longitudinal modes up to 1 GHz by the four antenna is shown in figure 4. Antenna#2 required an angled flange to improve coupling to the fourth mode (436 MHz). Antenna#3 had improved coupling on the twelfth harmonic (910 MHz) by a 25 mm offset on the flange. It can be seen from figure 4 that the damping is very effective up to 800 MHz. Since, the field patterns of the fundamental accelerating mode and the longitudinal modes for both wooden model and CERN cavity were in close agreement, the loaded shunt impedance values for the CERN cavity could be scaled from the measurements. High-pass filters with an attenuation of >20 dB at 80 MHz will be used for antennae1,2 and 4 in order to keep loss of Q below 5% for the fundamental accelerating mode due to the antennae. All the four antennae will be water cooled since estimated maximum copper loss is 7 W (for a cavity gap voltage of 200 kV) for antenna#1 and consequently smaller for the other three.

## 5 TRANSMISSION LINE HIGH-PASS FILTER

The high-pass filter was designed with transmission line components instead of lumped capacitors or inductors. A prototype filter was successfully simulated on PSPICE and then constructed and tested by using the capacitive and the inductive characteristics of an open and shorted transmission line respectively [4].

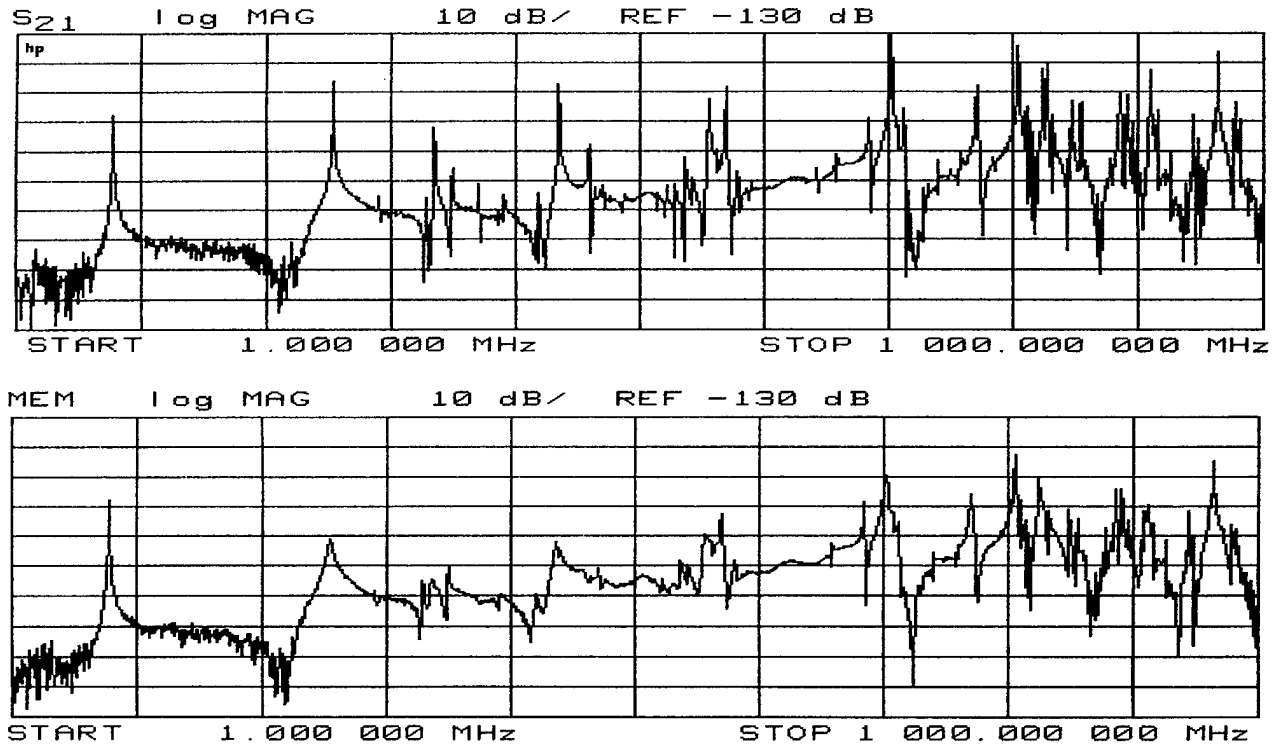



Figure 4. Frequency spectrum of the model cavity with (bottom trace) and without (top trace) HOM dampers

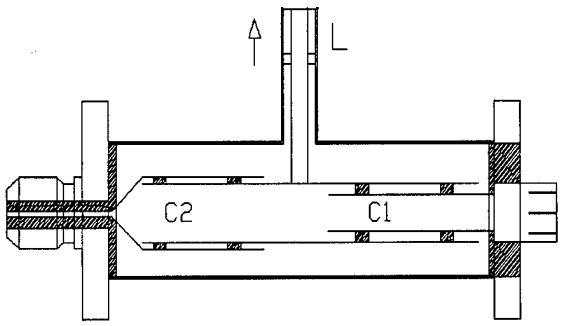



Figure 5. Transmission line design of filter

Figure 5 shows the prototype high-pass filter being built. The overall length of the filter is 30 cm and diameter is 8 cm. It is designed to withstand at least 7 kV at the input of the filter. The transmission line prototype provided an attenuation of 21 dB at 80 MHz . The insertion loss was more than 1.0 dB beyond 760 MHz. This was mainly due to poor rf connection of the input and the output flanges to the outer casing in the prototype.

## 6 CONCLUSION

The measurements done at TRIUMF on the wooden model has achieved the desired results. The capacitive tuner has been defined from model measurements. The voltage step up ratio of the coupling loop and the cavity gap, the shape and dimensions of the loop, and a PSPICE model was successfully developed to describe the cavity-loop system. The higher-order modes up to 810 MHz was effectively damped by the four $\lambda/4$ antennae. The desired value of loaded shunt impedance of 1 k$\Omega$ was achieved for most of the higher order modes. Also, the transmission line high-pass filter has been used for three antennae to reject the fundamental mode and thus maintained the Q loss below 5%.

## 7 ACKNOWLEDGMENTS

The authors would like to thank Peter Harmer for constructing the wooden model. Thanks are also due to Franco Cifarelli for producing fabrication drawings for the HOM damper and the filter . WE also wish to thank Spencer Rose for his contribution towards the damper and filter developments and Mark Lipnicki for his help in making measurements.

## REFERENCES

[1] E. Jensen, R. Garoby, D. Grier, A.K. Mitra, R.L. Poirier, "The PS 40 MHz bunching cavity", this conference, 2P 36.

[2, E. Jensen, R. Hohbach, A. K. Mitra , R.L. Poirier, "Higher Order Mode Damping of the CERN PS 40 MHz cavity", EPAC 96, Sitges, Spain, WEPO93L

[3] A. K. Mitra, R. Losito, "Measurements and simulation on the 80 MHz wooden model", PS/RF/Note 96-31.

[4] A. K. Mitra, S. Rose, "Higher-order-mode damping of the CERN 80 MHz cavity", TRIUMF Design Note TRI-DN-97-8.

# HIGH POWER TEST OF THE RF DAMPED CAVITY

Tadashi Koseki, Masaaki Izawa*, Kenji Shinoe, Syuichi Tokumoto*, Yukihide Kamiya ,
Toshi Miura** and Kiyokazu Satoh**

Synchrotron Radiation Laboratory, Institute for Solid State Physics (ISSP),
The University of Tokyo, Tanashi, Tokyo 188, Japan
* Photon Factory, High Energy Accelerator Research Organization (KEK),
Tsukuba, Ibaraki 305, Japan
** Toshiba Corporation, Tsurumi, Yokohama 230, Japan

*Abstract*

This paper describes the recent results of high power test of the damped cavity which has been developed at ISSP, the University of Tokyo and KEK-PF. We have fabricated four damped cavities to install at the Photon Factory (PF) storage ring with high brilliance configuration. High power conditioning of all four cavities has been carried out successfully. The temperature rise and thermal deformation of the cavity were understood by the thermal structure analysis.

## 1 INTRODUCTION

We have developed an RF cavity which has SiC beam ducts for damping the higher-order mode (HOM's) [1, 2]. Figure 1 shows the cross sectional view of the cavity. The cavity aims at being installed in two low emittance electron/positron storage rings. One is a third-generation VUV and SX synchrotron radiation source, the VSX storage ring, and the other is a high brilliance configuration of the Photon Factory storage ring at KEK.

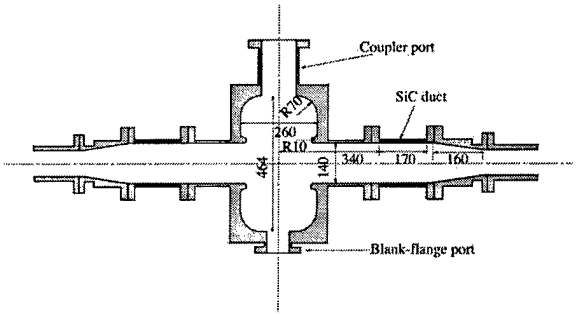



Figure 1: The cross sectional view of the damped cavity

The VSX storage ring is a future project of the University of Tokyo. The ring has a beam energy of 2.0 GeV, a circumference of about 400 m, an emittance less than 5 nm·rad, four 14-m long straight sections and twelve 7-m semi-long straight sections for extensive use of insertion devices [3,4]. Three RF cavities will be installed at one of the semi-long straight sections. The proposal for constructing the VSX facility was submitted to Japanese government in 1996, and the government decided to give a budget for preliminary study of the facility in the fiscal year 1997.

The reconstruction for the emittance upgrade of the PF storage ring is now in progress. The beam emittance will be reduced from 130 nm·rad to 27 nm·rad by doubling the number of the quadrupole magnets in the FODO cells [5]. All of existing four cavities will be replaced with the new damped cavities described here. The commissioning with high brilliance configuration of the PF ring will be started in October 1997.

## 2 DAMPED CAVITY

The design parameters of the damped cavity are summarized in Table 1. The nominal RF voltage of the cavity system is 1.7 MV for the PF ring and 1.5 MV for the VSX ring. The numbers of the cavities to be installed are four (PF) and three (VSX). For the VSX ring, the nominal RF voltage per cavity is 0.5 MV which requires the power of about 33 kW to be dissipated in the cavity. Therefore, the design of 150 kW wall loss has large safety margin and operational flexibility.

Table 1: Parameters of the cavity.

| | |
|---|---|
| RF frequency | 500.1 MHz |
| Shunt impedance | 7.68 MΩ |
| Unloaded Q | 44000 |
| RF voltage / cavity | 0.50 (VSX), 0.43 (PF) |
| Maximum wall loss | 150 kW |
| Coupling coefficient | 1.9 (VSX), 2.3 (PF) |
| Number of cavities | 3 (VSX), 4 (PF) |

The high power model of the cavity was fabricated in 1995. The high power test of the cavity was carried out successfully. The input power of 150 kW was achieved without any severe problem [6].

From 1996 to 1997, we have fabricated four cavities for the PF ring. The design of the cavities are same as the model fabricated in 1995. They were manufactured at Keihin Product Operations of Toshiba Corporation. The main parts of the cavities are made of class1-OFHC copper which has been treated with Hot Isostatic Press (HIP) before. After fabrications, the cavities were pre-

0-7803-4376-X/98/$10.00 © 1998 IEEE

baked at 150 °C for 24 hours at Keihin Product Operations.

## 3 HIGH POWER TEST

### *3.1 setup*

The high power conditioning has been performed on the high power test bench at the Photon Factory ( Fig. 2). An RF power was supplied by 500.1 MHz, 180 kW klystron (Toshiba E3774). A 250 kW circulator of Y-junction type was used to protect the klystron against the reflection wave from the cavity. Reflected power was dissipated in a 50 kW dummy load.

The cavity was cooled by water; the flow of cooling water was about 150 *l*/min and the inlet temperature was kept at 23±1°C. A 300 *l*/sec turbo molecular pump was attached to the cavity, and an ionization gauge and a quadrupole mass filter were placed between the beam port and the turbo pump.

The reflected power signal was used as an interlock trigger. A thermal detuning of the cavity was compensated by the tuning plunger. The conditioning data, input power, vacuum pressure and residual gas spectrum were recorded every 20 seconds by a personal computer. The temperature distribution of the outside wall of the cavity was monitored by eight thermocouples.

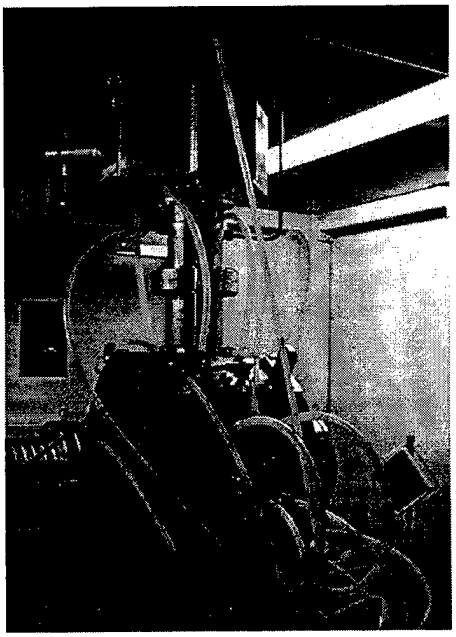


Figure 2: The cavity on the test bench.

### *3.2 High Power Conditioning*

We have carried out conditioning for all four cavities. In order to generate the nominal gap voltage of 0.43 MV/cavity, a dissipated power of about 24 kW is needed. On the other hand, if the PF ring is operated with three cavities, the required RF voltage and the dissipated power per cavity are 0.57 MV and 42 kW, respectively. In general, large safety margin for the RF system is necessary to secure a stable operation of the ring and to avoid a long shutdown caused by a trouble of RF power source. The goal of the conditioning was, then, set to achieve the input power of 80 kW, about two times higher than 42 kW.

Figure 3 shows a whole process of the conditioning for one cavity. In this case, the vacuum pressure of the cavity before applying RF power was less than $1\times10^{-7}$ Torr. The conditioning started with an input power of a few hundreds watt. The power level was slowly increased, so that the vacuum pressure was kept below $5\times10^{-6}$ Torr. The input power of 80 kW was attained after 4.2 hours without any severe trouble.

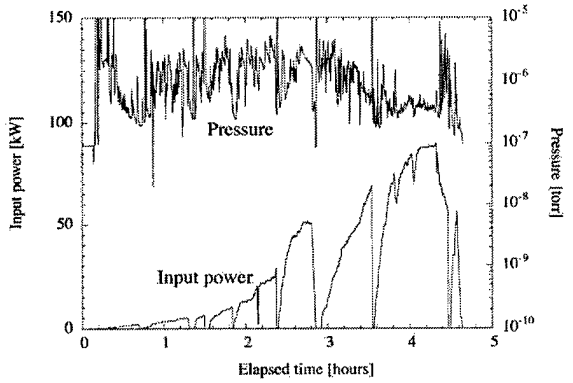



Figure 3: An example of cavity conditioning.

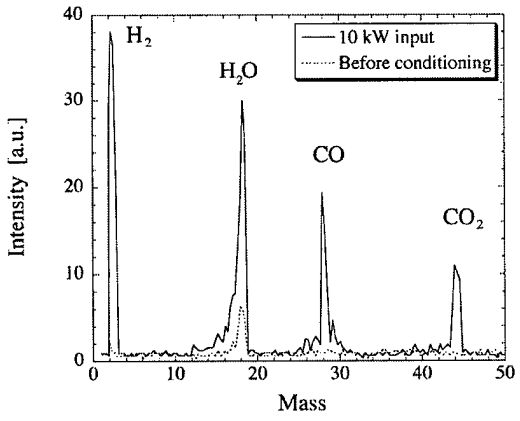



Figure 4: Residual gas spectrum.

The residual gas spectrum measured by the quadrupole mass filter is shown in Fig. 4. The dotted line and the solid line are the mass spectra before conditioning and during conditioning, respectively. The data of solid line was taken for an input power of 10 kW after about 1 hour conditioning. Before the conditioning, partial pressure of $H_2O$ was much higher than those of the other gases. On the other hand, during the conditioning, the main

components of outgas from cavity wall were not only $H_2O$ but also $H_2$ ,CO and $CO_2$. At the beginning, the levels of CO and $CO_2$ were higher than that of $H_2$. After the conditioning progressed, however, $H_2$ became most dominant among all components of outgases from cavity wall.

*3.3 Thermal analysis*

We carried out the thermal structure analysis of a two-dimensional cavity model using the ANSYS code. The analysis assumed the water flow of 140 *l*/min and the inlet water temperature 22 °C. For 80 kW total power dissipation, the peak power density around the nose cone is calculated to be 15 W/cm$^2$ by the SUPERFISH code. Figure 5 shows the temperature distribution calculated by ANSYS. The inner surface of the cavity becomes 37 - 50 °C and the edge of the nose cone has the maximum temperature. The calculated temperature of the outer wall is 27 - 34 °C, while the measured one is 33 - 37 °C.

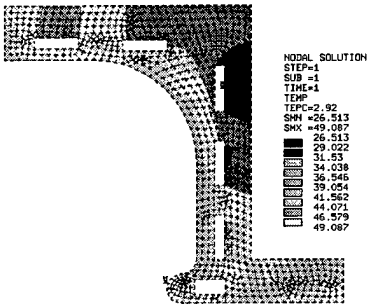



Figure 5: Temperature distribution of the cavity for 80 kW total power dissipation.

Thermal deformation of the cavity was also calculated by ANSYS. The thermal deformation for 80 kW total power dissipation is shown in Figure 6. From the result, the frequency shift caused by the thermal expansion is found to be -130 kHz for the fundamental mode.
In the high power conditioning, the frequency shift due to thermal expansion can be estimated by measuring the position movement of the tuning plunger. The frequency shift was about -150 kHz for input power of 80 kW.

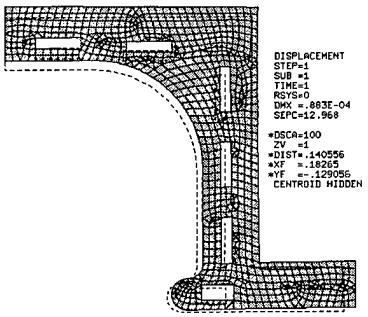



Figure 6: Thermal deformation of the cavity for 80 kW total power dissipation.

## 4 SUMMARY

We have fabricated four damped cavities for the PF ring with high brilliance configuration. High power conditioning of all four cavities has been already carried out. The temperature rise and thermal deformation were well understood by the thermal structure analysis with a two-dimensional model.
In 1996 summer, the two damped cavities were installed in the PF ring to replace two of four old cavities. The beam test of the new cavities was carried out successfully [7]. The remaining two cavities were then replaced by new ones in 1997 spring.

## 5 REFERENCES

[1] T. Koseki, M. Izawa and Y. Kamiya, Proc. 4th European Particle Accelerator Conference, London, 1994, p. 2152.
[2] T. Koseki, M. Izawa and Y. Kamiya, Rev. Sci. Instrum., 66 (1995) 1892.
[3] Y.Kamiya *et al.*, Proc. 4th European Particle Accelerator Conference, London, 1994, p. 639.
[4] H. Takaki *et al.*, "A Lattice for the Future Project of VUV and Soft X-ray High Brilliant Light Source" in these proceedings.
[5] M. Katoh and Y. Hori, Proc. 5th European Particle Accelerator Conference, Barcelona, 1996, p. 650.
[6] T. Koseki *et al.*, Proc. 5th European Particle Accelerator Conference, Barcelona, 1996, p. 1988.
[7] M. Izawa, "Beam Test of an RF Damped Cavity at the Photon Factory Storage Ring" in these proceedings.

# HOM CHARACTERISTICS OF THE ARES CAVITY

T.KOBAYASHI,
Institute of Applied Physics, Tsukuba University, 1-1 Ten-nodai, Ibaraki 305 JAPAN
K.AKAI, N.AKASAKA, E.EZURA, T.KAGEYAMA, H.MIZUNO, F.NAITO, H.NAKANISHI, H.SAKAI,
Y.TAKEUCHI, and Y,YAMAZAKI
KEK, High Energy Accelerator Research Organization, 1-1 Oho, Tsukuba, Ibaraki, 305 JAPAN

*Abstract*

The ARES (Accelerator Resonantly coupled with an Energy Storage) cavity, which consists of three cells, has been developed for the KEK B-Factory, and two types of the ARES cavity have been constructed for the beam test. Both the types were installed in the KEK TRISTAN Accumulation Ring and beam-tested. The accelerating cell of the ARES has a HOM-damped structure to lower the impedance of HOM's in order to store a high current beam. The spectra excited by the beam (single bunch, 100mA) were measured for both the cavities with scanning of the resonant frequency. Basically these results are consistent with those of calculations. The HOM's appear to be damped as expected. But the actual spectra for three cells are more complicated than only the accelerating cell. During this experiment, however, any beam instabilities due to the impedance of the cavities were not observed. This paper describes only the "ARES95"- one of the two types of the ARES.

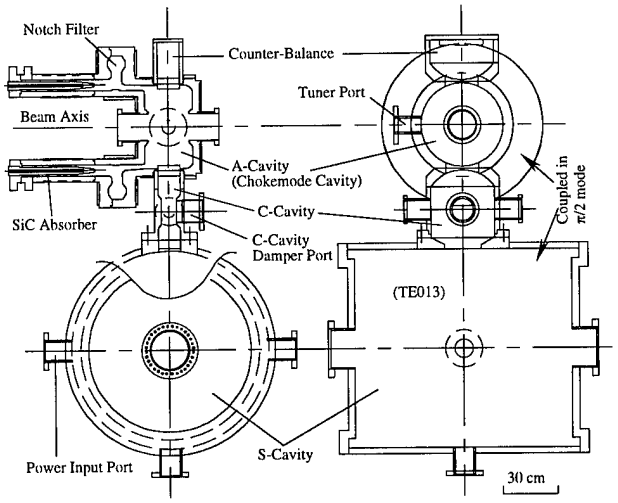



**Figure 1** : A schematic drawing of the "ARES95."

## 1 INTRODUCTION

A new system of a normal conducting RF cavity , called "ARES[1]", has been developed for KEKB accelerator which has to store high current beam. This cavity system(See Fig.1), which consists of three cells of an accelerating cavity(A-cavity), a coupling cavity(C-cavity) and a storage cavity(S-cavity), suppresses the coupled-bunch instability associated with the accelerating mode. The accelerating mode is operated in the $\pi/2$ mode of the three cells at 508MHz. The 0 and $\pi$ modes are damped with a "coupling cavity damper[2]" which has a choke filter to block the $\pi/2$ mode. For more details of the ARES system, refer to Ref.[1], and for more of the accelerating mode, refer to Ref.[3].

Last year, two types of the ARES, which are named "ARES95" and "ARES96[4]" respectively, have been designed and constructed. The difference between the two types is the structure to damp the HOM's of the accelerating cavity. For the "ARES95", the accelerating cavity is loaded with a coaxial waveguide, which is equipped with a notch filter of a radial-waveguide type(Fig.1). The filter reflects back the TEM wave coupled with the accelerating mode, the frequency of which is located at the first stop frequency of the filter. The RF waves passing through the filter are absorbed by sixteen bullet-shape sintered SiC absorbers inserted from the waveguide end[5]. Both the types were installed in the TRISTAN Accumulation Ring(AR) and beam-tested. This paper describes the HOM's of the "ARES95". For the details of the "ARES96", refer to Ref.[4].

## 2 HOM CHARACTERISTICS

The system of the A-cavity(without C,S-cavity) has been already beam-tested, and its HOM characteristics were reported in Ref.[6]. Basically the three-cell system, ARES95, has similar HOM characteristics as those of the A-Cavity, but it has more complicated HOM's with the S,C-cavity. Table 1 summarizes the HOM's, which has been observed only in the "ARES95." Figure 2 shows the HOM spectra which were measured at the AR beam-test. The longitudinal coupling impedance and the HOM spectrum calculated by using the electromagnetic field simulation code "MAFIA [7]", are shown in Figure 3 and 4 respectively. The low power measurement was performed for the distinguished peaks in the HOM spectra.

### *2.1 AR Beam Test*

The two types of the ARES, high-power tested and beam-tested were installed in the AR(See Table 2 for the machine parameters). These cavities were placed in the straight section, the beam-bore diameter of which is 150mm. Both ends of the straight section are tapered down to the standard vacuum chamber. The HOM's that propagate through the beam pipe are damped by the cylindrical SiC absorbers attached to the walls of the vacuum chamber of both sides of the cavity.

In the beam test, the HOM spectra which were excited by the beam(single bunch, 100mA) in the cavity were measured with scanning of the resonant frequency of the accelerating mode by moving the tuner of the S and A-cavity. The results superimposed for four tuner positions are shown in Figure 2. The accelerating mode resonant frequency at each tuner position is separated by

0-7803-4376-X/98/$10.00 © 1998 IEEE

300 kHz from the other. Among various peaks, two high peaks around 3.4GHz are distinguished. A mode at 807MHz has been only observed in the ARES ( not in the A-cavity only).

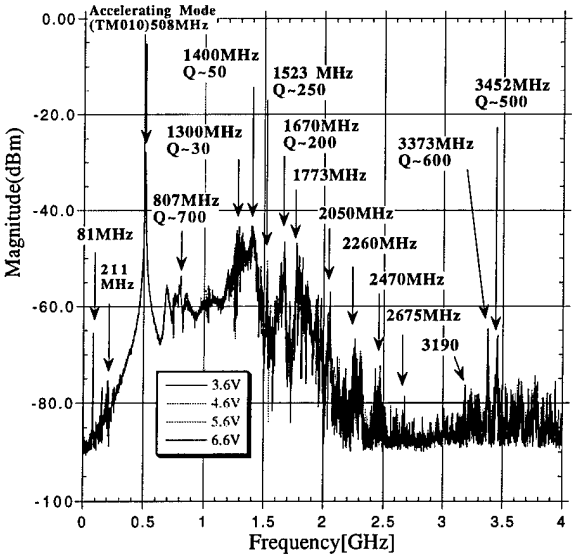



**Figure 2:** The HOM spectra excited by the beam (single bunch,100mA) in the "ARES95."

*2.2 Calculation*

The HOM properties were calculated by using the "MAFIA" 3D time domain solver (MAFIA-T3). Figure 3 shows the structure used for the calculation. This structure includes only the A and C-cavity(and the counter balance).

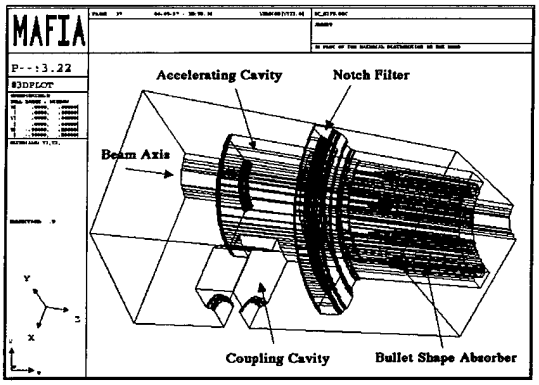



**Figure 3:**The structure of the "ARES95" used for the calculation of the wake potential.

Figure 4 shows the longitudinal coupling impedance obtained by the Fourier transformation of the wake potential which was calculated for the bunched beam passing through the cavity along the beam axis. The curve in Figure 4 represents the threshold impedance per cavity for the instability. The spectrum shown in Figure 5 is the Fourier transformation of the calculated time-dependent field at the position of the antenna used in the beam-test measurement. This spectrum corresponds to Figure 2. See Ref. [6] for the details of the calculations.

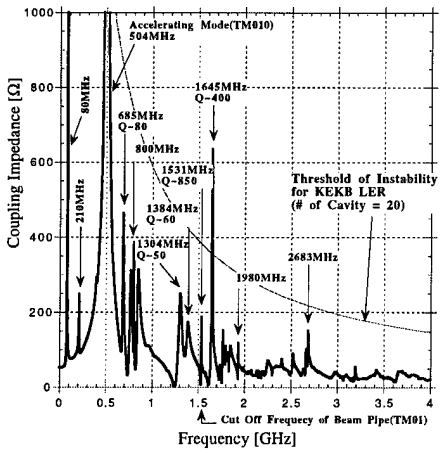



**Figure 4:** The longitudinal coupling impedance obtained by the Fourier transformation of the wake potential (0<s<132m) calculated by using the MAFIA-T3.

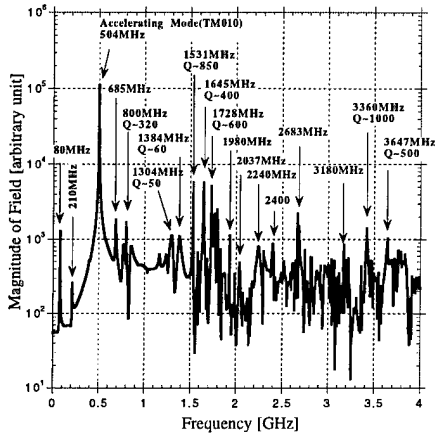



**Figure 5:** The HOM spectrum calculated by using MAFIA-T3.

*2.3 Low Power Measurement*

For the distinguished peaks obtained by the beam-test, the low power measurement was performed. The transmission spectrum was measured by using the network analyzer. The shunt impedance of the 807MHz could be measured with bead measurement method[8]. The results are also shown in Table 1.

## 3 RESULT AND DISCUSSION

During the beam test any beam instabilities due to the impedance of the cavity were not observed even in the case of the multi-bunch, 700mA beam. The summary of the HOM's which only appeared in the "ARES95" is shown in Table 2. For most of the modes, the Q-values obtained by the beam-test, by the calculation and by the low power measurement are largely different from each other. In the beam test the frequency resolution is limited by the revolution frequency of the beam, while in the calculation it is limited by the time duration of the wake potential calculation. Therefore, the results of the low power measurement are most reliable for high Q-value modes.

The peak at 807MHz was observed in both the spectra of the two types of the ARES - "ARES95" and "ARES96", although their A-cavities are different. This is a dipole mode of the C-cavity, being coupled with the counter balance in the $\pi/2$ mode. The magnetic filed pattern calculated by using the MAFIA eigen mode solver (MAFIA-E) is shown in Figure 6. It can not be damped by the "coupling cavity damper," which needs longitudinal electric field there. The coupling impedance of this mode was about 500Ω (=R/Q x Q / 2) as determined by the bead-pull measurement. However, this impedance is not dangerously high in comparison with the threshold in Figure 4. Since we could not exclude the possibility that the similar modes can have a higher impedance at higher frequencies, we are improving the "coupling cavity damper" in order to damp this kind of mode[4]. The improvement is also necessary in order to damp the two peaks at 1.3GHz and 1.4GHz, which are located at the second stop band of the choke filter of the "coupling cavity damper."

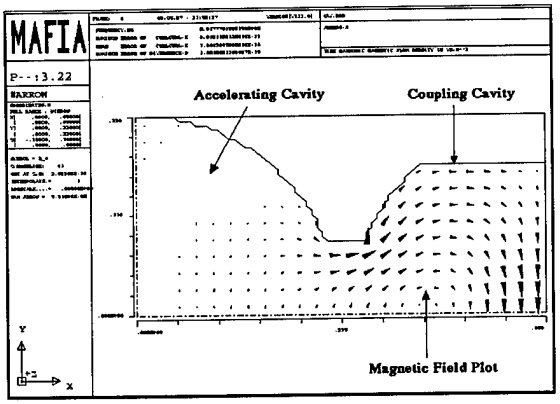



**Figure 6:** The magnetic field pattern of the mode at the 807MHz

Two more high peaks are seen in Figure 2 around 3.4GHz, where no high peak was found in the calculation without the S-cavity. Thus it is natural to assume that they are associated with the S-cavity. However, no distinguished peaks were observed in the low power measurement either.

The calculated impedance in Figure 4 has a higher peak than the threshold at 1.65GHz which corresponds to 1.67GHz in Figure 2. This mode is located at the second stop band of the notch filter of the A-cavity [6]. The calculation of the wake potential with the longer time duration makes this peak higher. This indicates that it has actually even higher Q-value or that the calculation is not accurate (already two times as high as measured), because it is located in the vicinity of the cut-off frequency of the beam pipe. So further investigation is needed.

The transverse impedance modes are not observed partly because they are hard to distinguish on account of the complication of the HOM spectrum of the three-cell system, and partly because the threshold impedance for the transverse instability of the AR is about ten times as large as that of the KEKB.

## 4 SUMMARY

During the beam-test any beam instabilities due to the impedance of the cavity were not observed. The HOM spectra excited by the beam were measured. Basically these results are consistent with those of calculations which exclude the Storage cavity. The HOM's appear to be damped as expected. Since we cannot exclude the possibility that the beam is strongly coupled with a special kind of C-cavity mode, it is preferable to further improve the "coupling cavity damper". The two high peaks around 3.4GHz and the peak at 1.67GHz require further investigation.

| Beam Test Spectrum | | Calculated(MAFIA) ( 3D TD , s < 132m) | | | Low Power Measurement (Bead Measurement) | | |
|---|---|---|---|---|---|---|---|
| Freq. [MHz] | $Q_L$ | Freq. [MHz] | Q | $R_{sh}/Q$ [Ω] | Freq. [MHz] | $Q_L$ | $R_{sh}/Q$ [Ω] |
| 807 | 700 | 800 | 320 | | 807 | 10000 | 0.1 |
| 1300 | 30 | 1304 | 50 | | 1300 | 50 | |
| 1400 | 50 | 1384 | 60 | | 1400 | 100 | |
| 1523 | 250 | 1531 | 850 | | ? | | |
| 1670 | 200 | 1645 | 400 | | 1670 | 200 | |
| 1773 | 450 | 1728 | 600 | | 1773 | 2500 | |
| 2050 | 500 | 2037 | 200 | | 2054 | 8700 | |
| 3373 | 600 | 3360 | 1000 | | ? | | |
| 3452 | 500 | ? | | | ? | | |

**Table 1 :** The summary of the HOM's peculiar to the "ARES95." For definition of the shunt impedance, see Ref.[8].

| | |
|---|---|
| RF Frequency | 508.5808 MHz |
| Harmonic Number (h) | 640 |
| Revolution Frequency | 794.6575 kHz |
| Beam Energy | 2.5 GeV |
| RF Voltage | 0.4~2.0MV |
| Momentum Compaction factor (a) | 0.01250 |
| Tune (H,V ) | 10.14, 10.25 |
| Synchrotron Tune | 0.017~0.032 |

**Table 2:** The machine parameters of the TRISTAN Accumulation Ring (AR)

## REFERENCES


[1] Y.Yamazaki,T.Kageyam, "A Three-Cavity System which Suppresses the Coupled-Bunch Instability Associated with the Accelerating Mode", Particle Accel., 1994, Vol. 44, pp.107-127

[2] F.Naito et al., "Coupling Cavity Damper for the ARES Cavity", in this conference (PAC97 ,1997)

[3] N.Akasaka et al., "Fundamental Mode Characteristics of ARES Cavity under Beam Environment", in this conference (PAC97 ,1997)

[4] T.Kageyama et al., "Development of High-Power ARES Cavity", in this conference (PAC97 ,1997)

[5] Y.Takeuchi et al., "HOM Absorber for the KEKB Normal Conducting Cavity", KEK Preprint 95-69, June 1995.

[6] T.Kobayashi et al., "HOM Characteristics of the Choke-Mode Cavity for the KEK B-Factory", EPAC96, 1996, pp2074-2076

[7] The MAFIA Collaboration, "Users Guide Ver. 3.20", CST, 1994

[8] Y.Yamazaki et al., "Measurement of The Longitudinal and Transverse Coupling Impedances of The Higher-Order Modes of The Re-Entrant Accelerating Cavity", KEK80-8,1980.

# NIOBIUM QUARTER-WAVE CAVITY FOR THE NEW DELHI BOOSTER LINAC

K. W. Shepard, Argonne National Laboratory, 9700 South Cass Avenue, Argonne, IL 60439 USA, and A. Roy, P. N. Potukuchi, Nuclear Science Centre, JNU New Campus, P. O. Box 10502, New Delhi 110067 INDIA

*Abstract*

This paper reports the completion of development of a 97 MHz niobium coaxial quarter-wave cavity to be used in a booster linac for the New Delhi 16UD pellatron electrostatic accelerator. A prototype cavity, which incorporates a niobium-bellows tuning device, has been completed and operated at 4.2 K at accelerating gradients above 4 MV/m for extended periods of time.

## 1 INTRODUCTION

Several recent heavy-ion booster linac projects employ superconducting quarter-wave coaxial-line (QWCL) resonant cavities [1 - 5]. The QWCL geometry is characterized by excellent mechanical stability and broad velocity acceptance. Also, QWCL resonators made with superconducting niobium have achieved high accelerating gradients [3]. The present project is aimed at developing a high-performance structure based on the QWCL geometry, with the design focussed on reducing construction costs and maximizing operational simplicity and stability. The superconducting accelerating structure discussed here is to be employed in a heavy-ion booster linac for the 16UD pelletron electrostatic accelerator at the Nuclear Science Center in New Delhi, India [6,7]..

### *1.1 Cavity Design*

Figure 1 shows the 100 MHz, two-gap resonant cavity which is optimized for particle velocity á = v/c = .08, but has a broad enough velocity acceptance that a single resonator geometry can be used for the entire booster linac, as presently envisioned [7].

The cavity is formed entirely of niobium, rather than bonded niobium-copper composite as is used in the ATLAS linac and several other accelerators. This choice was taken both because of the cost of forming and welding the composite material, and also because this cost is further increased by the relatively large number of two-gap cavities required.

The high-voltage end of the coaxial line consists of a relatively large diameter section which capacitively loads the quarter-wave line and shortens the cavity nearly 20 cm. By using a cylindrically symmetric drift tube, large capacitive loading can be obtained while keeping the peak surface electric field low. This both reduces the size of the resonant cavity and improves mechanical stability, which decreases rapidly with increasing length of the coaxial line. The niobium cavity is closely jacketed in an outer vacuum vessel of stainless steel, which contains the liquid helium required to cool the superconducting structure. This design permits an array of cavities to operate in a cryostat with the beam-line vacuum and cryogenic vacuum being one common system. Such an arrangement is almost universally used in superconducting heavy-ion linacs, because it facilitates the large number of connections to room temperature required to operate an array of short,

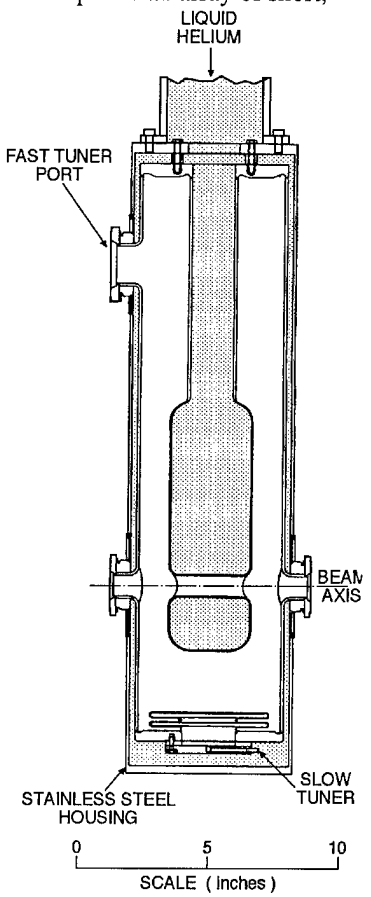



Figure: 1 Schematic figure showing the primary features of the 97 MHz, beta = 0.08 coaxial-line cavity.

0-7803-4376-X/98/$10.00 © 1998 IEEE

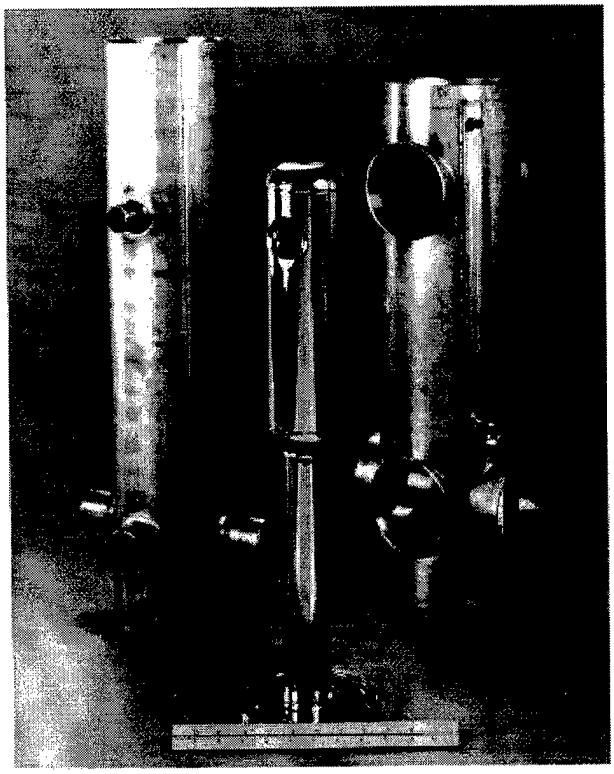


Figure 2: Major components of the niobium quarter-wave coaxial-line cavity prior to final weldment. Elements shown are the quarter-wave line and drift-tube, the 6.5 inch OD niobium outer housing and the 7.5 inch OD stainless-steel outer jacket

independently-phased resonant cavities. Where the outer jacket and niobium resonator join, i.e. at all beam ports and coupling ports, a flange made of explosively-bonded niobium and stainless steel is used to provide a welding transition between the two materials.

A pneumatic tuner, shown in Figure 3, is incorporated into the bottom end face of the resonant cavity and consists of a two-section niobium bellows. The end face moves about 2 mm with 1 atm of internal pressure, and provides a tuning range of approximately 70 KHz.

Resonator parameters (at an accelerating gradient of 1 MV/m) are:

| | |
|---|---|
| Resonant Frequency | 97.0 MHz |
| Synchronous Velocity | 0.08 c |
| Drift Tube Voltage | 85 KV |
| Energy content | .131 |
| Peak Magnetic Field | 100 G |
| Peak Electric Field | 3.6 MV/m |
| Geometric factor QRs | 17.3 |
| Active Length | 15.9 cm |

## 2 EXPERIMENTAL RESULTS

Extensive cold tests have been performed on a final prototype cavity, which performs as shown in Figure 4. The minimum performance goal of 3 MV/m with 4 watts of rf input at 4.2 K has been substantially exceeded.

Multipacting in the cylindrically symmetric structure, although more severe than in the niobium split-ring and interdigital cavities employed in the current ATLAS accelerator, does not present any novel problems. The multipacting behaviour has been very repeatable. On repeated and numerous cool-downs, the cavity has required rf conditioning, with typically 1 watt of rf input, for a period of 14 to 18 hours in order to completely eliminate multipacting barriers. Under similar conditions, the split-ring and interdigital superconducting cavities employed in the ATLAS accelerator typically require one to five hours of rf conditioning. Although multipacting in the present cylindrically symmetric geometry is appreciably more severe, as manifested by the increased conditioning time, the multipacting does not reappear as long as the cavity temperature is kept below 100 K.

The cavity has been continuously operated at an accelerating gradient of at least 4 MV/m for a period of more than one week and exhibited no appreciable recurrance of multipacting.

The slow tuner bellows assembly has been tested at low temperatures and performs satisfactorily, providing the expected range of motion and causing no observable performance degradation at high field levels. The thermal stability of the slow tuner is excellent, even though it is cooled only by conduction to the main resonator body.

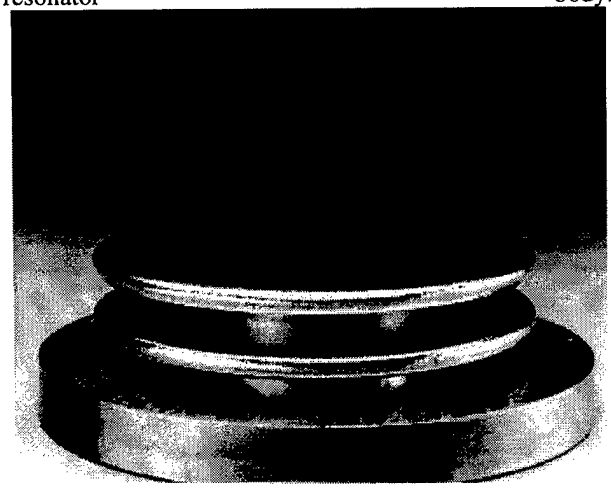


Figure 3: Niobium bellows tuner assembly. The tuner can be pressurized with helium gas and provides a two millimeter range of motion with 0 - 1 atmosphere internal pressure. A 70 kHz tuning range results.

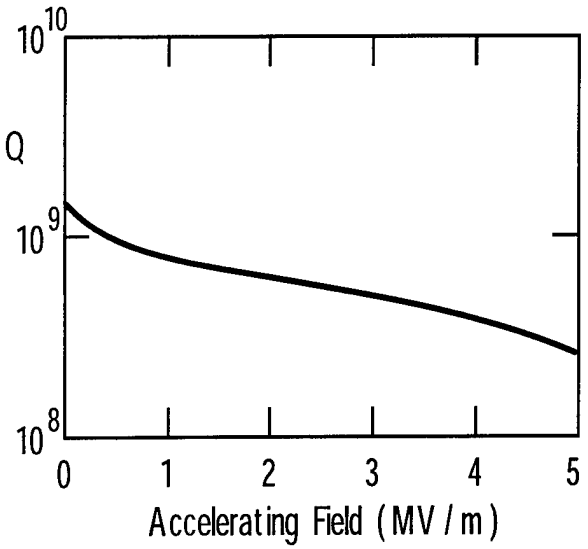



Figure 4: Resonator Q as a function of accelerating gradient at 4.2 k.

Rapidly filling the slow tuner with room temperature helium, a more severe test than would occur in normal operation, caused warming of the bellows above 9.1 K, the niobium transition temerature, for only a few seconds. Within 10-15 seconds the system entirely recovers.

## 3 CONCLUSIONS

The results described above conclude the development process for the New Delhi linac cavity. Production of an initial ten of an eventual thirty-two cavities has been initiated, with completion of the initial group expected within two years.

## 4 ACKNOWLEDGEMENTS

The authors gratefully acknowledge the assistance of John Brawley of the Jefferson National Accelerator Facility in performing a critical electron beam weld.

This work is being performed at Argonne National Laboratory, and is funded through the Nuclear Science Centre, New Delhi by the University Grants Commission ot the Government of India.

## REFERENCES

[1] I. Ben-Zvi and J. M. Brennan, Nucl. Instr. And Meth. 212, p73 (1983).

[2] D. W. Storm, et al., Proc of the 2nd Workshop on RF Superconductivity, Geneva, p. 173, (1984)

[3] K. W. Shepard, S. Takeuchi, and G. P. Zinkann, IEEE Trans. Magn. MAG-21, p146 (1985).

[4] S. Takeuchi, Proc. of the 5th Workshop on RF Superconductivity, DESY, p76 (1991).

[5] A. Facco, et al., Proc of the 5th Workshop on RF Superconductivity, DESY p58 (1991).

[6] K. W. Shepard and A. Roy, Proc. of the1992 Linear Accelerator Conference, August 24-28, 1992, Ottowa canada, p441 (1992).

[7] A. Roy,et al., Proc of the 7th Workshop on RF Superconductivity, Gif sur Yvette, France, p14 (1996).

# DEVELOPMENT OF SUPERCONDUCTING RF FOR CESR*

S. Belomestnykh†, P. Barnes, E. Chojnacki, R. Ehrlich, W. Hartung‡, T. Hays, R. Kaplan, J. Kirchgessner, E. Nordberg, H. Padamsee, S. Peck, P. Quigley, J. Reilly, D. Rubin, J. Sears
Laboratory of Nuclear Studies, Cornell University, Ithaca, NY 14853

*Abstract*

After the successful CESR beam test of August 1994 the continued development of a superconducting RF system for the CESR Luminosity Upgrade is in progress at the Laboratory of Nuclear Studies, Cornell University. The system description as well as recent results are presented.

## 1 INTRODUCTION

The Phase III of the CESR Luminosity Upgrade Plan [1] demands higher total beam current (up to 1 A in two beams) in order to achieve luminosity of $10^{33}$ $cm^{-2}sec^{-1}$. The present RF system, consisting of four 5-cell normal conducting copper cavities, can not cope with such a big current. In fact, one of the limiting factors for further increasing CESR luminosity is longitudinal multi-bunch instability due to the beam-cavity interaction [2,3].

Single-cell superconducting RF (SRF) cavities are called upon to overcome this limitation. There are two factors which achieve this goal: i) the use of superconducting cavities allows one to operate at higher gradient in each cell and therefore to use fewer accelerating cells; ii) the shape of the Cornell BB1 cell with attached beam tubes of a big diameter provides an opportunity to strongly damp higher-order modes (HOMs) and hence to decrease an impedance of the RF cavity. Thus, we have 1) lesser impedance per cell, and 2) fewer number of RF cells in the storage ring.

The detailed information about the cavity, the beam test of the cavity/cryostat module prototype, and the new RF system one can find elsewhere [4,5,6]. In this paper we describe the recent results in development of the system components.

## 2 SYSTEM AND COMPONENTS

The SRF system will consists of four single-cell niobium cavities [6]. Each cavity has its individual cryostat, input coupler and RF window, two ferrite HOM loads, taper transition(s) to the adjacent CESR beam tube, and some other beam-line components. New software is being developed to incorporate the SRF system into the CESR control system and to display the current status of the SRF system on the screen of X-terminal.

* Work supported by the National Science Foundation, with supplementary support under the U.S.-Japan Agreement

† On leave from Budker Institute of Nuclear Physics, 630090 Novosibirsk, Russia

‡ Presently at Fermilab, Batavia, IL 60510

### *2.1 BB1 500 MHz Superconducting Cavity*

Two cavities, BB1-1 and BB1-2, have been manufactured to date by Dornier and ACCEL correspondingly. Three more cavities are on order from ACCEL. The BB1-2 cavity has been tested in vertical cryostat up to design accelerating field of 6 MV/m. The preparation procedure now includes a new step: rinsing the cavity with high pressure water.

### *2.2 MARK II Cryostat*

This new cryostat [7] has been manufactured and tested with the full size copper cavity model at Meyer Tool and Mfg. Presently the cryostat (Figures 1 and 2) has been assembled with the BB1-2 cavity at Cornell and is being tested.



Figure: 1 MARK II cryostat: round beam tube end.

0-7803-4376-X/98/$10.00 © 1998 IEEE

*2.3 Refrigeration and Distribution*

We have ordered a dedicated refrigerator system for the CESR Phase III. The first 600 W unit has been installed and tested and another 600 W system is presently being installed in parallel for the CLEO solenoid and the superconducting quadrupoles to be added near the interaction point in Phase III. Details of the refrigerator system are reported elsewhere [6].

The 2000 liter storage dewar, refrigerator output lines, transfer lines, and satellite distribution valve box for the RF processing area were installed and tested. The main and two tunnel satellite distribution valve boxes are on order and will be installed this summer.

*2.4 RF Window*

We have previously reported the test of the new high power RF vacuum window manufactured by Thomson [8]. Since that time we received and tested two more windows from Thomson. The new windows have been tested up to 450 kW CW (limited by the available RF power) and 520 kW pulsed at 25% duty cycle. One of the windows is used on the MARK II/BB1-2 cryostat/cavity module.

A study has been performed in collaboration with Northrop Grumman Corp. to design a waveguide vacuum window capable of propagating more than 1 MW of average RF power. Results are presented in a separate paper [9].

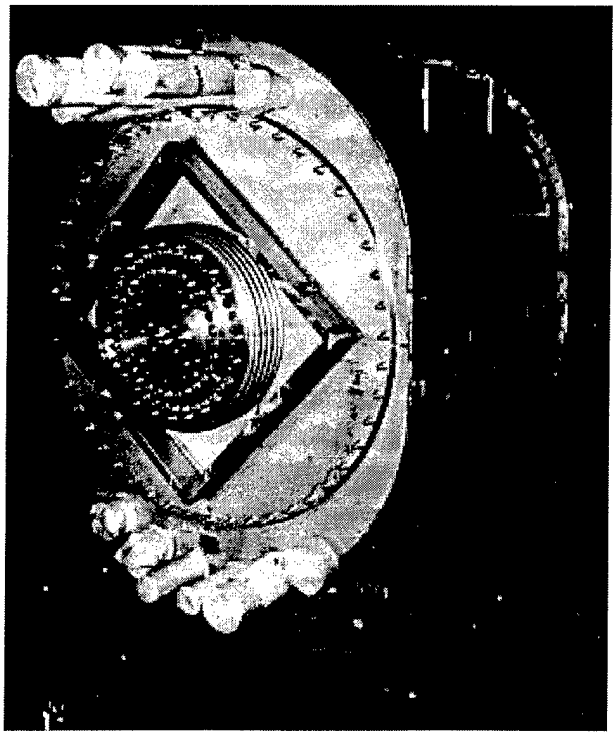


Figure: 2 MARK II cryostat: fluted beam tube end.

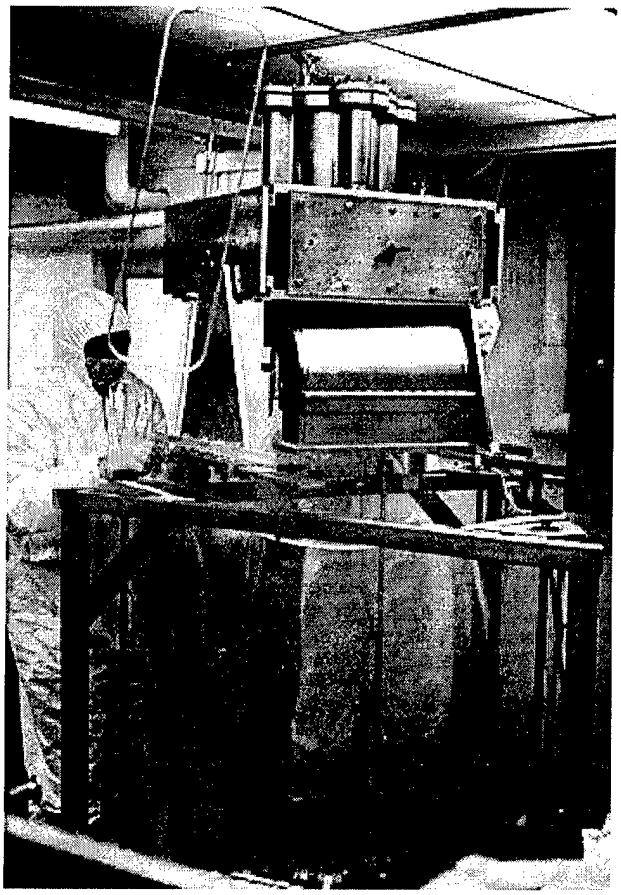


Figure: 3 BB1-2 cavity on high pressure water rinsing system.

*2.5 Other Components*

Following encouraging results from the TJNAF (formerly CEBAF) [10] and other labs, we developed a high pressure rinsing system as an additional step in cavity preparation. We designed our high pressure rinsing system basing on the TJNAF design. It provides 1000-1200 psi rinsing water. Qualifying tests with 1.5 and 1.3 GHz Nb cavities have been performed prior to the rinsing of the BB1-2 cavity (Figure 3).

The tuner mechanism has been changed due to the height restrictions in the tunnel. Essentially the same scheme [11] is used but with a folded, double lever arm to conserve space. The CESR III cavity/cryostat module exhibits a resonant frequency sensitivity to the helium vessel pressure of 325 kHz/Bar which is quite high value. A special pressure compensation scheme has been developed in order to decrease the sensitivity.

There will be only one cavity in the first installation so two taper transitions to the adjacent CESR beam pipes will be placed on the both sides of it. In the consequent installations, when cavities will be grouped in pairs, there will be no taper in between the cavities. The stainless steel tapers have water cooled copper synchrotron radiation absorbers welded to them.

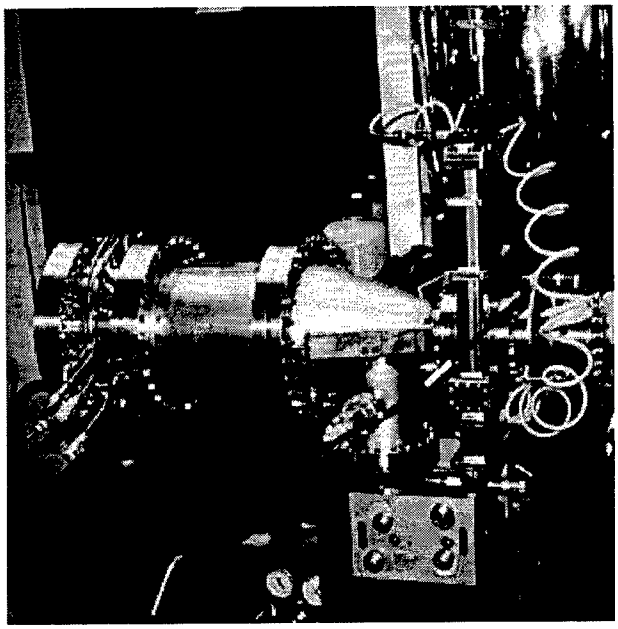


Figure: 4 Beam line assembly: HOM load, taper, gate valve and sliding joint.

## 3 INTERACTION WITH BEAM

At present the maximum beam current at CESR is limited by the multi-bunch beam instability [2]. Measurements [3] and calculations indicate that the higher-order modes (HOMs) in the present CESR 5-cell RF cavities are responsible for that.

In order to evaluate the threshold current of coupled-bunch instabilities due to the SRF cavities, the HOM spectrum of the SRF cavity assembly has been calculated [12] and a study of the stability of multi-bunch longitudinal oscillations in CESR has been started using the computer code MBI [13]. Preliminary results indicate that the threshold current of the instabilities is much higher than the CESR III goal.

## 4 SUMMARY

The first of the five cavity/cryostat systems has been assembled and is being tested now at Cornell. This module is scheduled for installation in CESR in July 1997 to replace one of the present 5-cell cavities.

All components for the rest four modules are on hands or order. We anticipate to have all components manufactured by late '97.

## REFERENCES


[1] D. Rubin, *Proc. of the 1995 Part. Accel. Conf.,* Vol. 1, pp. 481-485.
D. Rice, *Proc. of the 5th European Part. Accel. Conf.*, Vol. 1, pp. 17-21.

[2] M. Billing, this conference.

[3] A. Temnykh, et al., this conference

[4] H. Padamsee, et al., *Part. Accel.*, Vol. 40, pp. 17-41 (1992).

[5] H. Padamsee, et al., *Proc. of the 1995 Part. Accel. Conf.*, Vol. 3, pp. 1515-1517.

[6] S. Belomestnykh, et al., *Proc. of the 5th European Part. Accel. Conf.*, Vol. 3, pp. 2100-2103.

[7] J. Kirchgessner, et al., *Proc. of the 7th Workshop on RF Superconductivity*, Vol. 1, pp. 35-37.

[8] M. Pisharody, et al., *Proc. of the 1995 Part. Accel. Conf.*, Vol. 3, pp. 1720-1722.

[9] E. Chojnacki, et al., this conference

[10] P. Kneisel and B. Lewis, *Proc. of the 7th Workshop on RF Superconductivity*, Vol. 1, pp. 311-327.

[11] E. Nordberg, et al., *Proc. of the 1993 Part. Accel. Conf.*, Vol. 2, pp. 995-997.

[12] B. Vakoc, Cornell LNS Report SRF 950811-11 (1995).

[13] N. Mityanina, Cornell LNS Report SRF/D 970314-01 (1997).

# SUPERCONDUCTING RF SYSTEM OPTIONS FOR DIAMOND

D.M.Dykes and P.A.McIntosh, CLRC, Daresbury Laboratory, Warrington, WA4 4AD, UK.

*Abstract*

The proposed UK Light Source DIAMOND has an operating energy of 3 GeV, with a current of 300 mA. With the full complement of insertion devices the energy loss per turn is greater than 2.25 MeV, and the required RF energy acceptance is greater than 3 %, consequently an accelerating voltage of 5.1 MV is needed. Investigations using a warm cavity system for DIAMOND have been reported elsewhere [1], this paper discusses the advantages of using a superconducting RF system, and outlines a possible system arrangement that fulfils the requirements.

## 1 INTRODUCTION

During the feasibility study for the proposed UK Light Source DIAMOND, the reference RF system design was based on normal conducting (or warm) technology. This paper briefly reviews this reference design, and suggests possible alternatives using superconducting technology. Table 1 below summarises the basic DIAMOND parameters used to design this reference system.

| | | |
|---|---|---|
| Beam Energy | 3 | GeV |
| Beam Current | 300 | mA |
| Magnet Bending Radius | 7.128 | m |
| No Multipole Wiggler Magnets | 9 | |
| No of Superconducting Dipoles | 4 | |
| Momentum Compaction | 0.000849 | |
| RF Acceptance | 3 | % |
| Energy Loss per Turn | 2.25 | MeV |
| Overvoltage | 2.35 | |
| Beam Power | 653 | kW |
| Required Peak Voltage | 5.1 | MV |

Table 1. DIAMOND Parameters.

## 2 REFERENCE DESIGN

Assuming an effective shunt impedance of 4 MΩ per cavity, (taking into account the various losses due to beam ports, tuner port, coupling port and changes in the material conductance due to high power loading, etc.), six normal conducting cavities are used. As can be seen from figure 1 there are 3 cavities located in two straights, and there is one klystron feeding each cavity. An RF power of 540 kW is required to produce the accelerating voltage.

The reference 500 MHz cavity [2] has 109 higher order modes (HOM's) below the beam tube cut off, and with the full complement of insertion devices (increasing the radiation damping), 52 of these modes are potentially unstable.

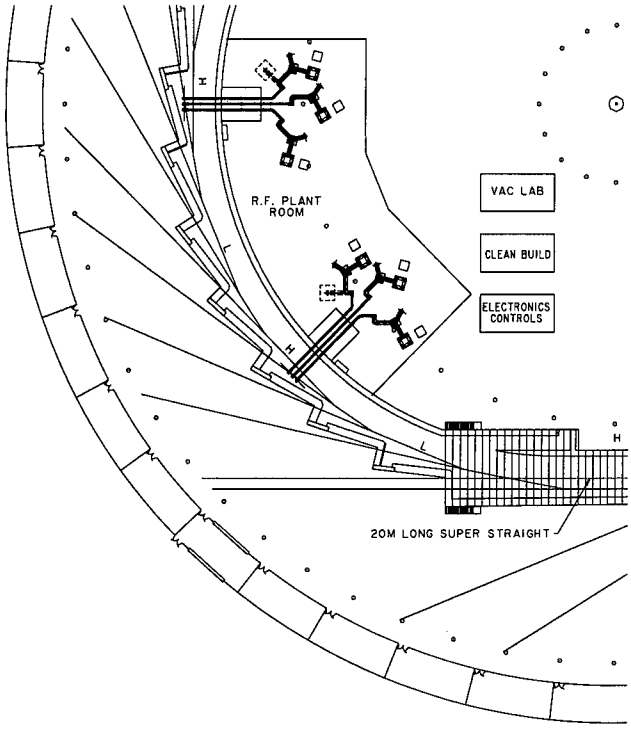



Figure 1. Layout of DIAMOND Storage Ring showing RF System Configuration.

HOM's can be eliminated or suppressed in a number of ways: during the design stage damping waveguides can be added to the cavity - this along with longitudinal and transverse beam feedback is being used at the SLAC B Factory [3]. At Elettra [4] the modes are avoided by the use of accurate temperature control of the cavity and fixed HOM phase shifters in the cavity – but this is only effective with a small number of modes and a large orbit frequency. Other methods would include harmonic separation of one or more cavities, using gapped beam to increase Landau damping or damping wigglers. The latter would of course increase the required RF power.

## 3 SUPERCONDUCTING RF SYSTEM

Until recently superconducting RF systems for light sources have rarely been considered. They were regarded as too complex and costly, however the use of a superconducting system gives the ability to damp all the monopole modes and the significant dipole modes. With the development of superconducting RF for other accelerators the capital costs for both warm and

0-7803-4376-X/98/$10.00 © 1998 IEEE

superconducting systems have become comparable. The performance already achieved at Cornell [5] is that required for DIAMOND. Recent CERN experience has shown that the fault time with superconducting systems is no greater than equivalent warm systems.

Using the same parameters as in table 1 above, but now assuming an effective shunt impedance of 4000 MΩ, only 3 superconducting cavities, with a much simpler geometry (with an R/Q of 40, say) are required. The number of possible HOM's is drastically reduced, and they can be damped, either with ferrite dampers in the beam tube [5] or with HOM couplers as at CERN. Table 2 compares the RF parameters for both options.

| | 'WARM' | 'COLD' |
|---|---|---|
| | | |
| Beam Power | 653 kW | 653 kW |
| Cavity Power | 541 kW | 86 W |
| No. Cavities | 6 | 3 |
| Window Power | 199 kW | 217 kW |
| No. Klystrons | 6 | 3 |
| Klystron Power | 250 kW | 250 kW |
| Total RF Power | 1314 kW | 718 kW |

Table 2. Comparison of RF Parameters for Warm and Cold Systems.

As can be seen the total RF power needed for the superconducting case is approximately half that required for the normal case. Also the number of RF systems is halved, however two straights of the ring are still required. Figure 2 is a representation of a possible 350 MHz superconducting cavity, based on the CERN design for LHC, and figure 3 shows the proposed DIAMOND layout.

There are , of course, disadvantages as well:

1. The enormous beam power compared to the cavity power results in the necessity to provide complex feedback systems to prevent system instability.
2. The development of superconducting RF systems for a relatively low number of cavities, particularly if the Laboratory has no relevant expertise, is expensive.
3. The recovery time from a cryogenic incident can be long.

## 4 HYBRID RF SYSTEM

A third option is to use a combination of normal conducting cavities to provide the beam power and accelerating voltage, then to use an idle superconducting system to provide the required overvoltage. Such a system was proposed by Marchand for the CERN/PSI B-factory project [6] and more recently to improve the energy acceptance in the SLS storage ring [7].

For DIAMOND the beam power and acceleration voltage could be supplied by 3 normal conducting cavities with a low number of HOM's, which could be controlled by temperature compensation, and then use two idle superconducting cavities to provide the potential well to give a longer beam lifetime and the associated energy acceptance.

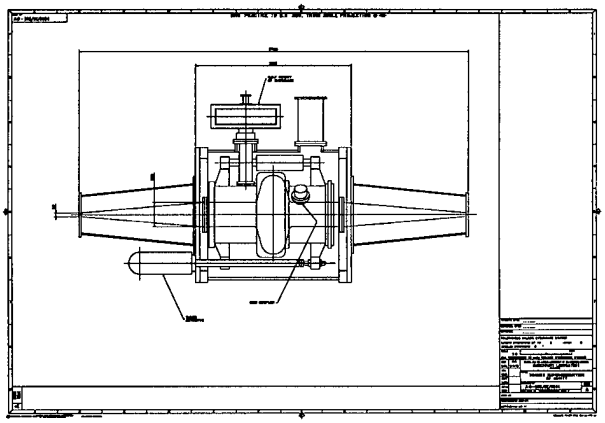


Figure 2. 350 MHz Superconducting Cavity in Cryostat

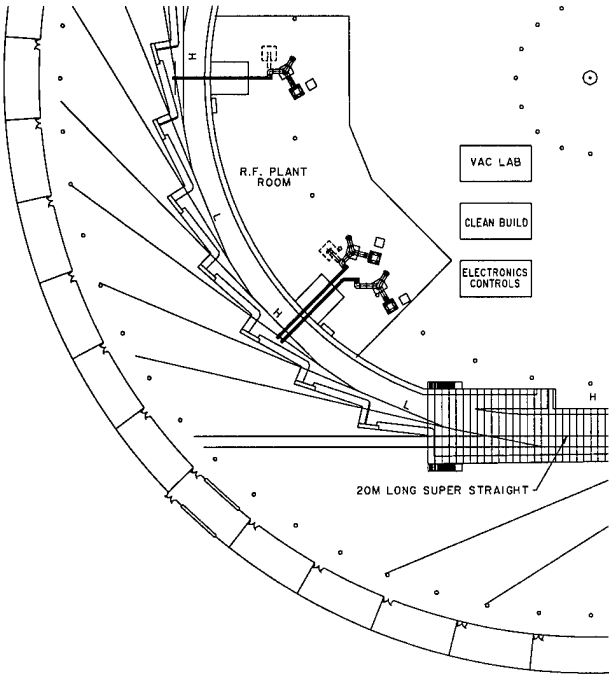



Figure 3. Layout of DIAMOND Storage Ring showing Superconducting Cavity Option.

As derived by Marchand [7] when a cavity is detuned far from resonance ($\delta f >> fr/Q$), the voltage induced by the beam passing through is given by:

$$V \sim Ib\,(R/Q)\,fr/\delta f$$

Where V is the induced voltage in the idle cavity
Ib is the beam current
fr is the RF frequency
$\delta f$ is detuned frequency
and Q is the cavity quality factor

As this formula shows, the induced RF voltage can be controlled by frequency tuning the cavity. For a superconducting cavity the Q is very high ($\sim 10^9$), and the R/Q is typically 40 Ω, so an induced voltage of 1.5 MV is easily achievable. The power lost by the beam as it passes through the cavity is less than 300 watts.

The RF parameters for a hybrid system for DIAMOND are given in table 3.

| | | |
|---|---|---|
| Beam Current | 300 | mA |
| Energy Loss per Turn | 2.25 | MeV |
| No 'Warm' Cavities | 3 | |
| No 'Cold' Cavities | 2 | |
| Peak Voltage | 5.35 | MV |
| Energy Acceptance | 3.2 | % |
| Beam Power | 654 | kW |
| 'Warm' Cavity Power | 230 | kW |
| 'Cold' Cavity Power | 570 | W |
| Total RF Power | 970 | kW |

Table 3. RF Parameters for DIAMOND Using a Hybrid RF System.

The hybrid system has the advantage of using normal conducting cavities, which have fewer HOM's than the case for the reference design, and then uses superconducting cavities with no external feed, where the HOM's will be suppressed using couplers in the beam pipe.

The superconducting cavity system will be relatively simple, as there is no external feed. The cavity will consist of the basic cavity, with a tuning system, in a cryostat: no input couplers.

## 5 SUMMARY

There are 3 possible options for the DIAMOND RF system:

1. Normal conducting cavities: would require 6 cavities each with 52 potentially dangerous HOM's. The total RF power required is 1314 kW.
2. Superconducting cavities: would require 3 cavities, modes could be damped using HOM couplers. Daresbury has no superconducting RF experience. The total RF power required is 718 kW.
3. Hybrid system: Requires 3 normal conducting cavities, with few HOM's and 2 superconducting cavities with no external feed. The total RF power required is 970 kW.

## REFERENCES


[1] 'The DIAMOND RF System', D.M.Dykes, EPAC'96 Proceedings, pp 1943-45, Sitges, 1996

[2] 'Comparison of RF Cavity Designs for 3rd Generation Light Sources', P.A.McIntosh, EPAC'96 Proceedings, pp 1955-57, Sitges 1996.

[3] Bunch-by-Bunch Longitudinal Feedback for PEP-II', G.Oxoby *et al*, EPAC'94 Proceedings, pp 1616-18, London 1994.

[4] 'Investigations of the Higher Order Modes in ELETTRA Cavities', M.Svandrlik *et al*, EPAC'94 Proceedings, pp 2134-36, London 1994.

[5] 'Current Status of the CESR-III RF System', H.Padamsee, Compte Rendu de la Reunion Radiofrequence, SOLEIL, CRR/A/95-13, 1995.

[6] Hybrid Normalconducting/Superconducting RF System for High Luminosity Circular e+ e- Colliders, P.Marchand, Particle Accelerators, Volume 36, Numbers1-3 (1991) p 205 – 222, March 1991.

[7] Use of an Idle Superconducting Cavity for Improving the Energy Acceptance in the SLS Storage Ring, P.Marchand, SLS Note 19/96, October 1996.

# NOTE ON THE SC LINEAR COLLIDER TESLA CAVITY DESIGN

J. Sekutowicz, D. Proch, C. Tang , DESY-MHF, 22603 Hamburg, FRG

*Abstract*

The experience we have gained over the last few years from experiments with superconducting cavities for the TESLA test facility, justifies a revision of the design proposed almost five years ago [1,2]. The proposed new design, presented here, takes the advantage of the high quality factor $Q_o > 10^{10}$ and low electron emission at the specified accelerating field of 25 MV/m, as demonstrated by some tested cavities. The main aim of the design is to simplify production and preparation of superconducting (sc) cavities and thus to reduce the cost of the linear collider. The new cavity shape has an enlarged iris diameter with the following advantages: significantly lower loss factors, a simplified and less expensive scheme for the HOM damping and the suitability of hydroforming and higher stability of the field profile.

## 1 INTRODUCTION

The quality factor, $Q_o$ , vs. $E_{acc}$ of two 1.3 GHz, 9-cell TESLA cavities is shown in Fig. 1. The $Q_o$ reaches a very high value ~ $5 \cdot 10^{10}$ at low field region and stays above $1.7 \cdot 10^{10}$ for one cavity and above $3 \cdot 10^{10}$ for the second one, for the accelerating field of $E_{acc}$=25 MV/m, the specified value for the sc linear collider [3]. The power dissipated in the cavity wall $P_{diss}$ , cooled by 2 K

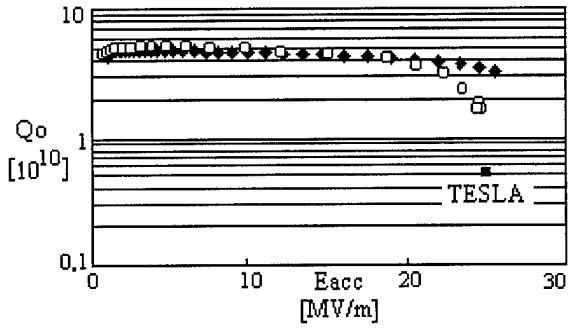



Fig. 1 $Q_o$ vs. $E_{acc}$ as measured in a vertical cryostat

LHe, is inverse proportional to $(R/Q) \cdot Q_o$ , where (R/Q) is the characteristic impedance of a cavity. For cavities with quality factors depicted in Fig. 1, the $P_{diss}$ at 25 MV/m is 3.4 and 6 times respectively, lower than for a cavity with the specified value of $Q_o = 5 \cdot 10^9$ [3]. The small slope of both curves demonstrates the important feature that cavities have low electron emission. It results from careful cleaning during the cavity preparation and the low field enhancement factor $E_{peak}/E_{acc}$. The shape of the TESLA structure, proposed almost five years ago, has been chosen to minimize: $E_{peak}/E_{acc}$ to keep electron emission loading low and $H_{peak}/E_{acc}$ to shift quench level towards higher $E_{acc}$ and to maximize (R/Q) to provide low cryogenic load. Final values of these parameters (see Table 1) have been achieved by means of a small iris diameter, but there are few negative consequences of the small aperture.

## 2 WEAK POINTS OF THE CURRENT DESIGN

The error of the field amplitude in an individual cell for the accelerating $\pi$ mode is proportional to $(N)^2/k$, where N is the number of cells in the structure and k is the coupling. Since the cell-to-cell coupling k is small, the profile of the accelerating field is sensitive to the frequency perturbation of an individual cell. Any mechanical, chemical or thermal preparation of TESLA structures causes a perturbation of the field configuration. Many TTF cavities from the first production had to be re-tuned several times to keep the field unflatness below the specified level of 5 %. Since tuning had to be performed outside the clean room, each re-tuning required that the cavity must be re-cleaned. This makes the preparation more expensive and more time-consuming to an unacceptable level for 20000 sc cavities. After the helium vessel is welded, no access to the cells is possible and therefore re-tuning, even when necessary, is impossible.
Field unflatness decreases the effective accelerating field. Since the energy of colliding beams has been fixed, a compensation must be made for the lower effective gradient, either with additional length of the collider or by an operation of some cavities at $E_{acc}$ above 25 MV/m. This requires only negligible additional RF power but the operation at a higher gradient may lead to an increased $\gamma$-radiation and a higher probability of quenches.
The second complication coming from the field unflatness is a difference in $Q_{ext}$. The acceleration process in the TESLA collider is performed during the transient. This requires all cavities to be at 25 MV/m at the same time, 533 μs after the RF pulse is switched on. As the cavity fill time depends on the loaded Q (in case of sc cavities mainly on $Q_{ext}$) differences in $Q_{ext}$ yield to differences in the accelerating gradient during acceleration. This means that the energy gain, in cavities with non nominal $Q_{ext}$, changes from the beginning to the end of the pulse. To avoid this source of energy spread two adjustable fundamental mode (fm) coupler designs, based on a coaxial line technique, have been proposed [4,5]. In both designs, the adjustment of $Q_{ext}$ is performed by a change of penetration of the inner conductor in the beam tube. The adjustment unfortunately makes the design more complicated and expensive. Additionally, a fast voltage control loop will be used to reduce the energy spread, but this will require more RF power.

0-7803-4376-X/98/$10.00 © 1998 IEEE

A third problem resulting from the field unflatness is an increase of characteristic impedance of other modes, belonging to the fm passband. If the cavity is well tuned, then the characteristic impedances of these modes are negligible. Perturbation of an individual cell causes that especially the impedance of the mode $8\pi/9$ increases. The damping of these parasitic modes is possible only by fm coupler. So, it is expected that the external Q's of these modes are in the range of the nominal value of $Q_{ext}$ of the fm. A typically observed field unflatness of 15 % increases (R/Q) of the $8\pi/9$ mode from almost 0 to 5 Ω. In this case the impedance of this mode is 15 MΩ, as high as the impedance of monopole modes from the $TM_{011}$ passband with the highest (R/Q) ≅150 Ω.

In the present design, neighboring cavities in a cryomodule are separated by a 3/2 λ long beam tube. Therefore the ratio of the active length to the total length of the TESLA structure is only 0.75. Thus one quarter of both linacs length, 7 km, is not used for the acceleration. The effective average accelerating field is then reduced from 25 MV/m to almost 19 MV/m. One can improve the fill factor by increasing the number of cells per cavity and by shortening the interconnections between the cavities. Since the field profile of the present TESLA structures is already sensitive to frequency errors, an increase of N is impossible, so only interconnections could be made shorter to improve the fill factor.

The cost of the electron beam welding is a significant part of the cavity fabrication cost. Eighteen half cells and two beam tubes per cavity must be specially prepared to provide nineteen high quality welds. Alternative fabrication methods are under consideration to lower the production costs. Two of them hydroforming [6] and spinning [7], show a strong potential. The hydroforming of Nb cavities needs still more R&D, but the experience with Cu cavities proofs that the required shape can be obtained with high precision and good reproducibility. The hydroforming process becomes simpler when the ratio of the maximum radius (equator ) to the minimum radius ( iris) of a cavity is 2 or less. In the current design this ratio is almost equal to 3. The shape of the cavity plays also an important role. Also here, the tests performed on copper cavities showed that any narrow or small curvature, especially in the iris region, makes hydroforming more complicated. Unfortunately this is the case for the current cavity design.

The very high intensity FEL (λ= 1 Å) is one of the proposed new applications of the 3 km part of the TESLA e-linac. This operation requires very short bunches with $\sigma_z$ = 25 μm, which can excite wake fields to the THz region. Since the longitudinal loss factor $k_{\|}$ and thus the energy loss scale approximately with $(\sigma_z)^{-1/2}$, the total energy deposited by single bunch will be big. This will influence the beam. Additionally, the high energy photons may brake Cooper pairs in the superconducting material and increase the wall losses of the fm. As a remedy, to keep the energy deposition low, one can decrease $k_{\|}$ by enlarging the iris opening.

## 3 NEW SHAPE

We expect that the improved cavity shape should :
-increase cell-to-cell coupling,
-simplify hydroforming or spinning of the structure,
-reduce the loss factor $k_{\|}$,
-simplify HOM mode damping,
- simplify the design of the fm coupler (not variable),
-increase the ratio of the active length to the total length.

Besides, the new design should keep, as much as possible, the advantages of the current shape. These advantages are parameters like: (R/Q), $E_{peak}/E_{acc}$ and $H_{peak}/E_{acc}$. Some of the disadvantages we have pointed out can be overcome with an increase of the iris diameter [2]. The proposed new shape (Fig. 2) has an iris aperture of 102 mm The iris is circularly formed with r = 17 mm. The parameters of the old and the new shape are listed in Table 1.

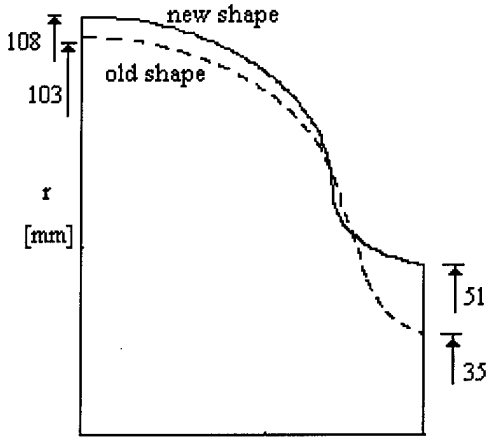



Figure 2 The new and the old shape of the inner cell (not in scale)

Table 1 Parameters of the old and the new cavity shape

| Parameter | Old | New | Change [%] |
|---|---|---|---|
| (R/Q) [Ω] | 1035 | 695 | - 33 |
| k [%] | 1.84 | 5.51 | 200 |
| $E_{peak}/E_{acc}$ | 2.0 | 2.34 | 17.0 |
| $H_{peak}/E_{acc}$ [Oe/(MV/m)] | 42.6 | 50.2 | 17.8 |
| $k_{\perp}$ (σ=1mm) [V/(pCm)] | 18 | 6.7 | - 63 |
| $k_{\|}$ (σ=1mm) [V/pC] | 8.7 | 5.5 | - 37 |
| iris diameter [mm] | 70 | 102 | 46 |
| iris shape<br>h./v. axis, radius [mm] | ellip.<br>12/19 | circle<br>17 | |
| $r_{equ}/r_{iris}$ inner /end cell | 3 / 2.7 | 2 / 1.9 | - 29 / -27 |

## 4 DISCUSSION

The cell-to-cell coupling increased by a factor of three as compared to the current design. This makes the structure less sensitive to any machining tolerances and provides room to increase the number of cells per cavity. The new geometry is more suitable for hydroforming or spinning. The ratio of the equator radius to the iris radius is near 2 for the inner cell and even below 2 for the end cell. The iris region is now wider and the wall can be made thicker in this region. Hereby stiffening rings, used in the current design to reduce the Lorentz force detuning, can be avoided [6].

The loss factors of the new geometry are significantly lower. The single passage deposited energy is reduced by 37 % for the monopole modes and by 63 % for the dipole modes. The decrease of the loss factors indicates a decrease of HOMs characteristic impedances, too. Therefore the energy deposited in the resonantly excited parasitic modes will be reduced. This gives more relaxed requirements for the damping of these modes.

The enlarged iris of the new end cell enables an increase in diameter of the beam tube. We have fixed this diameter to 0.11 m. It is the smallest size that allows propagation of all monopole modes in the tube. The first eight dipole modes stay under cutoff but their field in the beam tube seems to be high enough for damping to the BBU limit. Two HOM couplers shifted angularly by 90° and attached at every second beam tube may be used for the damping of parasitic modes excited in two neighboring cavities. This damping scheme requires only one HOM coupler per cavity. Due to the HOM propagation the distance between HOM coupler and end cells can be much larger than for the current design. Since the fundamental mode is under cutoff and the distance to end cells is large, a very little fm rejection, achievable without any additional filter, is needed to prevent output cables and feedthroughs from overheating. This simplifies the design of the HOM coupler.

As the field pattern is stable, variable couplers are not necessary. If operation of the collider should differ from the nominal one, $Q_{ext}$ can be changed by means of a 3-stub waveguide transformer installed in the input line of each cavity. The transformer also makes the RF distribution system more flexible for phase adjustment and gives more freedom in the length of intersections.

There are mainly two negative consequences of the larger iris aperture. As predicted, a larger aperture lowers (R/Q) of the fm. The reduction is compensated by a high $Q_o$ and finally the cryogenic loss is smaller. In order to keep cavities matched for the nominal operation: U=26 MV/cavity and the $I_b$=8 mA, $Q_{ext}$ should be increased by 33 %, and fill time will therefore be longer by 240 μs. When $Q_{ext}$ has still its previous nominal value, 2 % of the RF power will be reflected but fill time will be longer by 180 μs. This problem should be investigated in more detail. The ratios of $E_{peak}/E_{acc}$ and $H_{peak}/E_{acc}$ have increased by 17 %. This means more γ-radiation at the specified $E_{acc}$ and higher quench probability. Surface cleaning methods (BCP, high pressure water rinsing) and assembling methods are still in an optimization phase. Also inspection methods of the Nb material, which help to eliminate Nb sheets with defects leading to quenches, are under development. It is the hope that further progress in the fabrication, the assembly and the cleaning methods can compensate for the increase of these parameters.

## 5 CONCLUSION

Table 2 Summary of features of the new shape

| | |
|---|---|
| k , cell-to-cell coupling | + |
| $k_{\parallel}$ , longitudinal loss factor | + |
| $k_{\perp}$ , transversal loss factor | + |
| $r_{equ}/r_{iris}$ inner cell and end cell | + |
| fill factor of both linacs | + |
| simplified scheme for HOM damping | + |
| simplified fm coupler | + |
| (R/Q) fm characteristic impedance | - |
| $E_{peak}/E_{acc}$ , $H_{peak}/E_{acc}$ | - |

A summary of the positive and the negative features of the new cavity shape is given in Table 2. We plan to build copper models of the new structure to prove experimentally the stability of the accelerating field, the proposed scheme of the HOM damping and the coupling between structures for the fm and the HOMs. As a next step, Nb prototypes should be fabricated to investigate the hydroforming method, the Lorentz detuning and to check new limitations in the accelerating field.

## 6 ACKNOWLEDGMENTS

We would like to express our gratitude to the TESLA collaboration group for many helpful discussions.

## 7 REFERENCES

[1] E. Haebel, A. Mosnier, J.Sekutowicz, „Cavity Shape Optimization for Superconducting Linear Collider", Proc.of HEACC'92, Hamburg, 1992.

[2] E. Haebel, A. Mosnier, „Large or Small Iris Aperture in SC Multicell Cavities", Proc. of The 5th SRF Work.,Hamburg, 1991.

[3] D. A. Edwards, „TESLA TEST FACILITY LINAC-Design Report", TESLA Rep. 95-01.

[4] B. Dwersteg, „Mechanical Concept of TESLA Main Coupler Development at DESY",TESLA Rep 93-15

[5] M.Champion, „RF Input Coupler and Windows: Performances, Limitations and Recent Developments", Proc. of 7th Work. on S RF, Gif sur Yvette, 1995.

[6] H. Kaiser, DESY; private communication.

[7] V. Palmieri et al., „Recent Experience with the Spinning of 1.5 GHz Seamless Copper Monocells", Proc. of 7th Work. on SRF, Gif sur Yvette, 1995.

# MECHANICAL STABILISATION OF SUPERCONDUCTING QUARTER WAVE RESONATORS

A. Facco, INFN- Laboratori Nazionali di Legnaro, via Romea 4, 35020 Legnaro (Padova) Italy;
V. Zviagintsev, ITEP, B. Cheremushkinskaya 25, Moscow,117259, Russia.

*Abstract*

A device which is capable to reduce significantly the amplitude of mechanical vibrations in superconducting quarter wave resonators was designed, constructed and tested. This device can eliminate the necessity of fast tuners and related electronics in many superconducting cavities, resulting in a significant cost saving both in the construction and in the operation of superconducting low beta linacs.

## 1 INTRODUCTION

Mechanical stability is a very important requirement in superconducting cavities; their very small rf bandwidth, a consequence of their very high quality factor, makes very difficult to lock them to an external frequency, requiring a very accurate tuning. The resonator eigenfrequency can be modified by mechanical deformations, caused mainly by mechanical noise in the environment and by liquid helium pressure fluctuations. In some cases frequency shifts are caused also by radiation pressure [1]. Different resonators have different response to these external solicitations; while usually slow frequency changes can be compensated by slow mechanical tuning, fast vibrations, particularly when they act close to a mechanical eigenfrequency of a resonator, can cause very wide frequency changes, making the phase-lock to an external reference impossible. Overcoupling allow to increase the effective bandwidth; however, it requires an increase of the power flow through the rf lines and, consequently, larger rf power sources and more liquid helium consumption. This solution is often not sufficient and a fast tuning device, either an electronic or a mechanical one, is needed, at the price of a higher complexity of the system and of an increase in liquid helium dissipation [2].

## 2 THE LNL, LOW β CAVITIES APPROACH

The LNL low beta quarter wave resonators [3] are cylindrical coaxial cavities with very good rf performance; they have only one dangerous mechanical resonance at 42 Hz, related to the oscillation of the inner conductor with respect to the outer one. The mechanical quality factor $Q_M$ of this mode is about 2000 (decay time: ~8 s). The effect of this resonance can be observed by looking at the phase error signal when the resonator is phase-locked at 80 MHz: hitting cryostat can induce an oscillation which persists for many seconds. The high mechanical $Q_M$ prevents a fast setting up of the oscillation in the case of white noise; on the other hand, when a 42 Hz mechanical vibration is applied for a long enough time, the frequency error can reach such an amplitude that the phase-lock system capabilities are exceeded. In the ALPI linac cryostats this condition can appear, for a few minutes, almost everyday; this could make the operation of many resonators at the same time problematic. We have exploited a new approach to this problem: we have added to the resonator a mechanical dissipator, capable to absorb energy from the dangerous mechanical mode and, consequently, to reduce its amplitude. One problem in this approach is the difficulty of building a device with a linear, or at least smooth, response at liquid helium temperature; another problem is that new resonant modes could be easily introduced by adding to the resonator new parts. To be acceptable, the dissipator must fulfill also the following requirements: it must damp efficiently even very small oscillations, it must be simple and reliable, it must not affect the good rf performance of the resonator; moreover, it should be possible to add the dissipator to the existing resonators without modifying them.

## 3 DISSIPATOR DESIGN

The dissipator that we have developed consists of two main parts: an enforcing tube, welded to the stainless steel flange connected to the top of the resonator, protruding inside the inner conductor and terminated with a disk, and a load which is tightly connected to the inner conductor and oscillates together with it. Load and disk are in contact and any oscillation of the inner conductor make them slide with respect to each other (see figure n.1). The device can be mounted and dismounted without any difficulty.

*3.1 The enforcing tube.* The enforcing tube, a stainless steel cylinder, must be as rigid as possible and its lower resonance must be higher than 150 Hz which is believed to be a tolerable frequency ; its length and its outer diameter (48 mm) result from a compromise which guarantees a high enough resonant frequency and proper cooling of the inner conductor. Holes along the tube allow liquid and gas helium flow. The bottom disk can be made of different shapes and materials; after examining the the static and the dynamic friction coefficients for different coupling materials our choice was a flat, brass disk.

*3.2 The load.* The load is made of stainless steel parts; it is designed to sit automatically in the right position,

0-7803-4376-X/98 /$10.00 © 1998 IEEE

move together with the inner conductor and slide over the bottom disk. The lower surface of the load is of 40 mm radius spherical, convex shape. Three pins are pushed by the load onto the inner conductor in order to provide the contact. Due to the low temperature, it is impossible to use springs and any contact at a desired pressure must be provided by gravity.

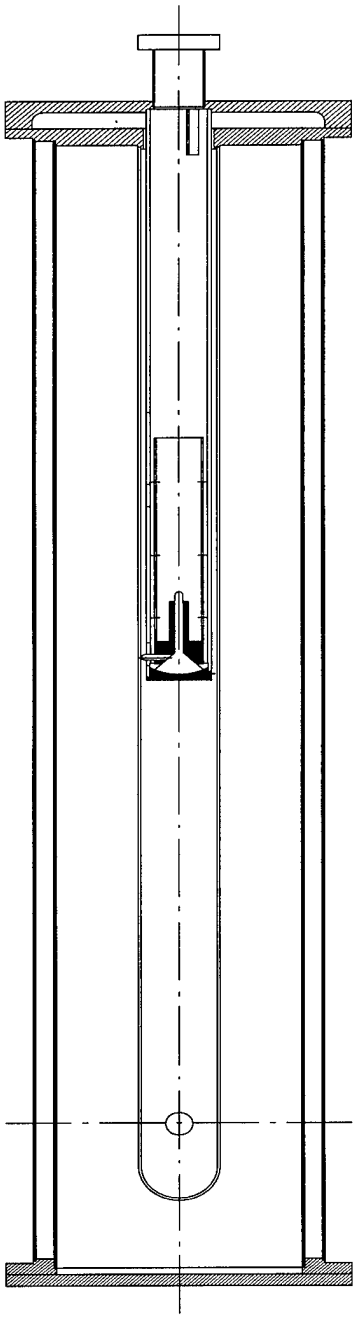


Fig. 1. Schematic of the mechanical damper inserted in a quarter wave resonator

*3.3 Theory.* A simple model allows us to calculate the main parameters of the device. We will assume that the inner conductor (of length $l_C$ and mass $M_C$ ) and the enforcing tube (of length $l_T$ and mass $M_T$ ) are connected to the same rigid plane (see fig. 1). The mechanical eigenfrequency of the inner conductor without dissipator is $\omega_C=\sqrt{(k_C/m_C)}$, where $k_C=(8/5)E_C I_C l_C/l_T^4$ , $E$ is the Young modulus of the material, $I$ is the geometrical moment of inertia of the tube and $m_C=(1/5)M_C(l_C/l_T)^4$ . The dissipator load of mass $m_D$ is located at the end of the enforcing tube and slides over the brass disk when the inner conductor oscillates. The load mass will change this frequency to $\omega_{CD}=\sqrt{(k_C/(m_C+m_D))}$. In a similar way we can calculate the enforcing tube eigenfrequency: $\omega_T=\sqrt{(k_T/m_T)}$ where $k_T=(8/5)\ E_T I_T/l_T^3$ and $m_T=(1/5)M_T$ . For very small oscillations the two tubes will move together, coupled by the static friction force between load and disk, at a frequency $\Omega_{CM}=\sqrt{\{(k_C+k_T)/(m_C+m_D+m_T)\}}$. If the oscillation amplitude at the top of the inner conductor , $x_0$, is sufficient to overcome the static coupling force, i.e. if

$$x_0=\{m_D g s/(\omega_T^2-\omega_C^2)\}\{(m_C+m_D+m_T)/[(m_C+m_D)m_T]\}(l_C/l_T)^2 ,$$

the two tubes will oscillate independently and the dissipator will slide on the brass disk; assuming a rigid enforcing tube the power dissipated will then be

$$P=\{(m_C+m_D)\omega_{CD}^3/(2Q_M)\}(l_T/l_C)^4 x_0^2+\{2\omega_{CD}m_D dg/\pi\}(l_T/l_C)^2 x_0$$

where g=9.8 $ms^{-2}$, $Q_M$ is the mechanical quality factor of the mode in absence of dissipator and s, d are the static and the dynamic friction coefficients between brass and stainless steel. For small oscillations the rf frequency error induced by this deformation is proportional to the displacement of the top of the inner conductor: $\delta f=\eta\ x_0$ . These formulas allow us to choose the main parameters of the device.

## 4 CONSTRUCTION AND MEASUREMENTS

We have built a few prototypes: the main differences were the length of the enforcing tubes (36 and 50 cm), the shape of the bottom disk (flat or spherical) and the disk material. For our particular case a flat disk is sufficient; however, a parabolic surface $y=\alpha x^2$ would introduce an additional term $P=\{8\omega_{CD}m_D dg\alpha/(3\pi)\}(l_T/l_C)^6 x_0^3$ in the power dissipation formula which would damp strongly at higher amplitudes. Measurements were done at room temperature to compare various prototypes; a test was done also at liquid helium temperature to verify that the device would not affect the resonator performance.

We have connected to the resonator a mechanical vibrator (Brüer & Kjaer mod. 4808) driven by a spectrum analyser HP 4195A which was reading at the same time the phase error signal, proportional to the frequency error for small oscillations, of the resonator locked to an external reference. We have calibrated our system in order to have a frequency error signal of 1 mV/Hz. We have verified the linearity between the applied vibration and the the frequency error up to about 200 Hz; then we have connected the dissipator and measured its effects. We have detected the peaks of the common mode oscillation resonance and explored their

evolution at different vibrator amplitudes. We have done our test sweeping the frequency of the vibrator and in steady state mode. The test in superconductive regime was done after mounting a 50 cm long enforcing tube with a spherical surface stainless steel disk.

## 5 EXPERIMENTAL RESULTS

The results of our test are summarised in fig.2, where the maximum frequency error versus the vibrator input power is plotted in three different cases: for the resonator without dissipator, for the short and for the long tube dissipator, respectively. In the absence of dissipator the frequency error at the mechanical resonance is proportional to the square root of the vibrator power, as expected: this means both that our vibrator is linear and that the frequency error is proportional to the amplitude of the inner conductor oscillation.

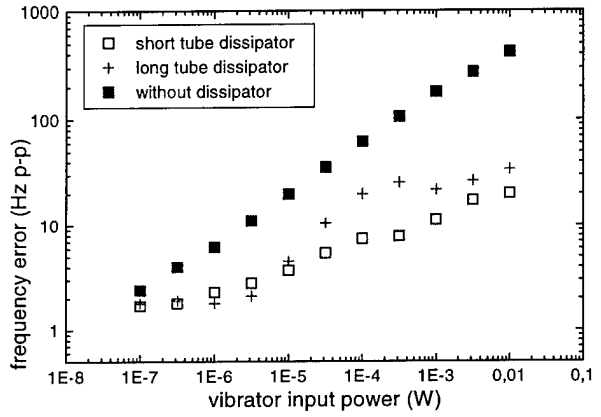



Fig. 2. Frequency error vs. vibrator input power.

The effects of dissipators are rather strong; the best results were obtained with a 36 cm long enforcing tube and a brass disk: this configuration starts working well even at very low level of external vibration and its response is very smooth. No new strong resonances were introduced, except for the expected common mode vibration at about 48 Hz, very weak in comparison with the original 42 Hz one. The attenuation of the frequency error is very significant and increasing with the external vibration amplitude; instead of being proportional to the frequency error amplitude, the power losses seem to increase with the fourth power of it. This means that other dissipation mechanisms are active in addition to the load sliding. At the maximum vibration level the frequency error, originally at 400 Hz, is being attenuated down to 20 Hz. We have mounted a dissipator with a spherical surface stainless steel disk and a 50 cm enforcing tube inside a low beta niobium resonator of the ALPI type. During this test we have verified that the good resonator performance were preserved by this addition and that the resonator could be locked to an external reference in the presence of vibratior noise. However, during the measurement we could not disconnect the dissipator for a comparative measurement. The common mode vibration was present but it seemed always to be well within the rf controller capabilities.

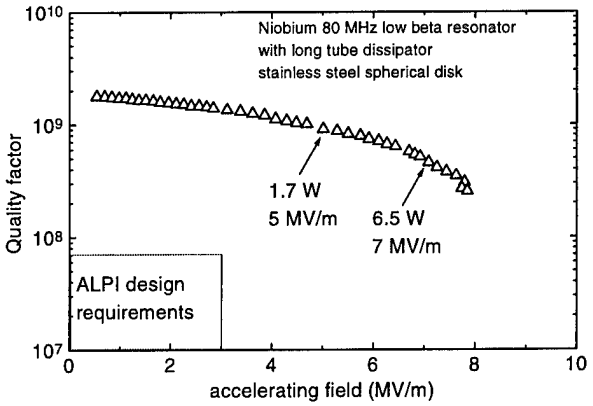



Fig. 3. Quality factor vs. accelerating field measured in the cavity equipped by a dissipator.

## 6 CONCLUSIONS

Mechanical dissipators appear to be an interesting alternative to electronic fast tuners in superconductive quarter wave resonators; they can attenuate the frequency error induced by environmental vibration by at least one order of magnitude and they seem not to present drawbacks. Their construction cost is very modest and they have no operation cost; it seems reasonable to install them even in resonators equipped with a fast tuner: the effective tuning range of the system would be increased significantly or, in alternative, the original fast tuner could be changed with a less demanding one. In our resonator, which is supposed to work with a 8 Hz bandwidth, the dissipator that we have tested is equivalent to a 100 Hz fast tuner. Particular attention must be paid to the design parameters in order to avoid the introduction of new mechanical resonances or setting up of high $Q_M$ common mode oscillations; other models using the same principles could be developed for superconducting resonators of different geometries. Further developments are foreseen in the next future at LNL to optimise the dissipator characteristics and to verify the behaviour at 4.2 K; we planned to equip all low beta cavities with these devices.

## 7 ACKNOWLEDGMENTS

We are grateful to L. Bertazzo and A. Dainese of the LNL mechanical workshop for their excellent work in developing the prototypes.

## REFERENCES

[1] H. Lengeler, "Superconductive cavities", Proc. of the CERN Accelerator School Superconductivity in Part. Acc., internal report CERN 89-04, edited by S. Turner, Geneva 1989, p.214.

[2] N. Added, B.E. Clifft and K.W. Shepard, Proc. Of the 16th Int. Linear Acc. Conf., 1992, Ottawa, Ontario.

[3] A. Facco and J.S. Sokolowski, Proc. of the 4th European Part. Acc. Conf., London 1994, World Scientific Publishing, p. 2054.

# BEAM TEST OF A SUPERCONDUCTING DAMPED CAVITY FOR KEKB

T. Furuya, K. Akai, K. Asano, E. Ezura, K. Hara, K. Hosoyama, A. Kabe, Y. Kojima,
S. Mitsunobu, Y. Morita, H. Nakai, H. Nakanishi, T. Tajima, T. Takahashi, S. Yoshimoto,
KEK, 1-1 Oho, Tsukuba, Ibaraki 305, Japan,
S. Zhao, IHEP, Beijing,
Y. Ishi, Y. Kijima, T. Murai , Mitsubishi Electric Co.,
and K. Sennyu, Mitsubishi Heavy Industries, Ltd.

*Abstract*

For the feasibility study of a superconducting damped cavity for KEK B-factory, a prototype module was constructed and tested in TRISTAN Accumulation Ring. This module accelerated the beam current of 500mA with the cavity voltage of 1 - 2MV, and 350mA with 2.5MV (10.3MV/m). These currents were limited by heating up of other ring components. The peak current of 573mA was achieved in 16 bunches with 1.2MV.

## 1 INTRODUCTION

Because of a heavy beam loading of KEKB, a new RF system which has sufficiently damped higher order modes(HOMs) is required to avoid beam instabilities. The desired RF voltages in a high luminosity operation are 5-10MV for the positron ring (LER) and 8-16MV for the electron ring(HER) under the beam currents of 2.6A and 1.1A, respectively. The maximum RF power transferred to the beam is estimated as 4MW in both rings[1]. For these requirements, the development on both superconducting (SC) and normal conducting damped cavities is in progress.

The SC damped cavity has a single cell structure with large-aperture beam pipes on both ends so that the HOMs can propagate out of the cavity and be damped by ferrite absorbers bonded on the inner surface of beam pipes[2]. Therefore, damping characteristics of the HOM dampers under high beam currents are the important factor as well as the cavity voltage and the input coupler power. A prototype cryomodule of the SC cavity was completed and cooled at a test stand in 1995. The field gradient of 11.4MV/m was obtained after several hours processing[3].

In 1996 the cavity was installed in the east RF section of TRISTAN Accumulation Ring(AR). The total beam injection extended for more than 1000hours and the SC cavity accelerated the beam for the half of the period. In this paper the summary of the test will be described.

## 2 CRYOMODULE

Before assembling the cavity was tested to 3.2MV (13MV/m) in a vertical cryostat. The gradient of 12MV/m in AR test is comparable but not continuously, because of a large amount of LHe consumption due to the cavity loss of more than 250W.

A coaxial antenna coupler was used as the input coupler. The length of the inner conductor was designed to obtain the coupling Q of 1 x $10^5$. The aging to 430kW had been given at a test stand.

Table: 1 Parameters of the module.

| | |
|---|---|
| R/Q of acc. mode | 93 ohm/cavity |
| module total length | 3158 mm |
| gap length | 243 mm |
| loaded Q | 8.9 x $10^4$ |
| tuner stroke (motor tuner) | 508.48 - 508.88 MHz |
| (piezo tuner) | 6.7 kHz |
| cryostat LHe volume | 290 liter |
| static loss | 30 Watts |
| HOM damper | ferrite(IB-004) size |
| for LBP | 4t x 300$\phi$ x 150mm |
| for SBP | 4t x 220$\phi$ x 120mm |
| max. acc. voltage | 2.9MV (12MV/m) |

A pair of ferrite dampers was fabricated by the HIPping method. The RF power tests of 12kW and 15kW were made to the 220$\phi$ damper(SBP) and the 300$\phi$ damper(LBP), respectively. Further, the 300$\phi$ damper was

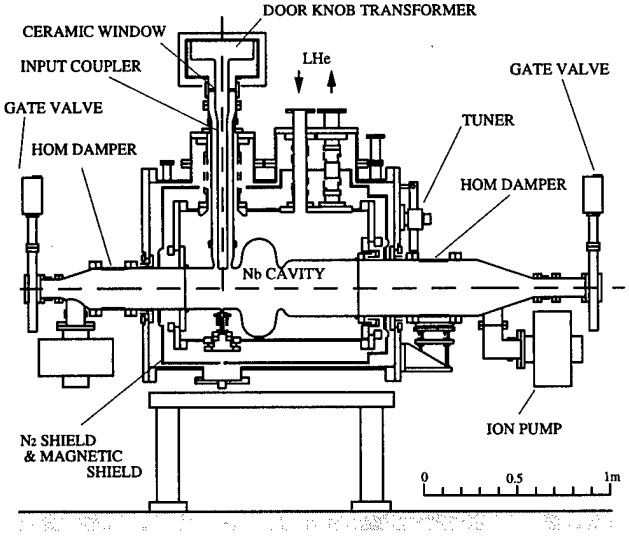



Figure 1: A sketch of the SC cavity module.

0-7803-4376-X/98/$10.00 © 1998 IEEE

Table 2. The outline of the AR Beam Test.

| | period | beam total | beam by SC | remarks |
|---|---|---|---|---|
| 1st stage | Mar.28 - Apr.2 | 80 hours | 30 hours | system tuning<br>single bunch study up to 110mA(σ=8-9cm) |
| 2nd stage | Jul.1 - Jul.22 | 340 hours | 200 hours | multi bunch study to 500mA in 16 bunches<br>acceleration to 3.5GeV<br>frequent RF trips due to coupler arc |
| 3rd stage | Oct.17 - Dec.2 | 600 hours | 290 hours | improvement of dust vacuum on both side<br>changing a door-knob transformer to a biased-type<br>Max. current of 573mA with Vc=1.2MV<br>500mA with 1- 2MV (4.1 - 8.2MV/m)<br>350mA with 2.5MV (10.3MV/m)<br>Max. HOM power absorbed by dampers was 4.2kW. |

exposed to the beam of TRISTAN Main Ring before assembling[4]. During the beam test in AR, absorbed HOM power was monitored by the temperature rise and the flow rate of cooling water for each damper. The cavity was equipped with an ion pump of 300 l/sec on each side and evacuated to 2 x $10^{-9}$Torr before cooling. Figure 1 is a sketch of the cryomodule and the parameters of the module are listed in Table 1.

## 3 RESULTS OF BEAM TEST

### *3.1 Summary of the Figures*

The outline of the beam test is in Table 2. The 1st stage was spent mainly for the system tuning and the HOM study using a single bunch beam. The maximum current of 110mA was limited not by the cavity performance but by heating of HOM dampers of the normal conducting APS cavities in the west RF section. These APS cavities were removed before the 2nd stage.

In the 2nd stage, a beam of 500mA in 16 bunches was stored. The beam intensity was determined by the rate of injection and the loss due to the residual gas in the ring. As the vacuum pressure improved, the beam current increased and reached to the limitation set by heating up of the ring components. The maximum RF power transferred to the beam was 160kW which was obtained by accelerating the beam of 280mA to 3.5GeV. In the 1st and 2nd stage, the cavity was suffered from frequent RF trips due to vacuum bursts and arcs near the RF window. To continue the test, warming up to 85K or frequent aging processes had to be given to the cavity and coupler. A large quantity of gas came out from the cavity by the warming up. This suggested that the coupler arc was caused by the condensed gas around the coupler.

Before the 3rd stage, the improvement of vacuum circumstances was made on both neighboring beam ducts by increasing the number of pumping units and replacing the ducts to new ones which were chemically polished and rinsed with ozonized ultra-pure water[5]. These efforts improved the vacuum pressure near the cavity by a factor of ten and eliminated the arc trips except for a few trips at the beginning of the 3rd stage. The door-knob transformer of the coupler was replaced to a new bias-type which could supply a DC voltage to the inner conductor, however, the effect of the bias voltage was not verified because of few arc trips. The figures obtained at the beam test are as follows;

- the maximum of 110mA in single bunch(1.4 x $10^{-7}$ C/bunch) and 573 mA in 16 bunches;
- accelerating voltage of 2.5MV for 350mA and 1- 2MV for 500mA;
- current limitation was set by other ring components;
- RF power transferred to the beam was 160kW;
- absorbed HOM power of 4.2kW.

### *3.2 Cavity Loss*

Cavity loss was estimated from a LHe consumption rate. The loss related to a beam intensity was observed as shown in Figure 2. Therefore, the cavity loss under various conditions were compared.

- beam acceleration (from 2.5GeV to 3.5GeV).
- change the bunch configuration (8,16,24 bunches).

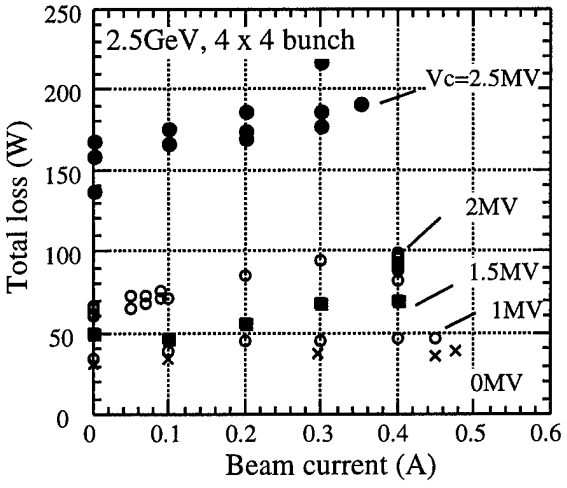



Figure 2: Additional loss related to beam currents.

- deflection of photo electrons by using small coils located on the beam ducts.
- supply a DC bias voltage to the input coupler.
- cavity detuning to change the input RF power.

These studies showed no difference of the additional loss. Though the mechanism of this loss is still not clear, it seems not to be a serious problem for 1.1A of HER. The Q-values in every steps are compared in Figure 3.

Loss factors measured in various bunch configurations are summarized in Figure 4. The results are agree with the calculated ones which contains the loss of ferrites as well as that of the cavity shape. The bunch length was obtained from the beam profiles measured by a streak camera.

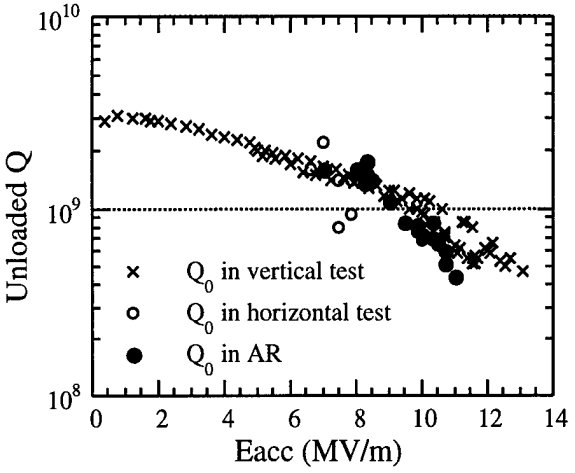



Figure 3: Summary of the $Q_0$ vs. Eacc.

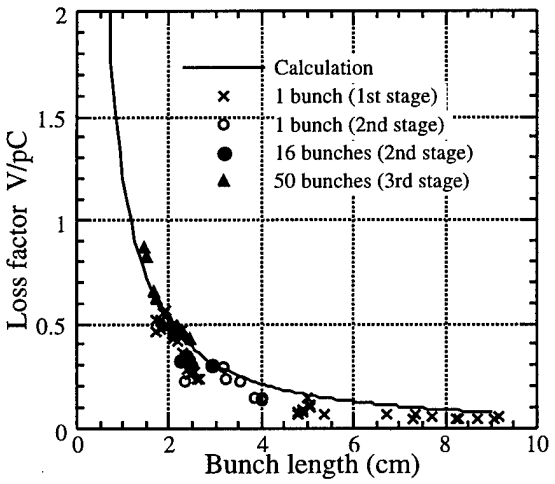



Figure 4: Loss factor vs. bunch length.

## 4 CONCLUSION

Stable operation of the cavity voltage up to 2MV with a 500mA beam and at 2.5MV with 350mA was obtained. The current limitation was not set by the SC cavity.

The HOM modes were damped sufficiently. No beam instability was induced by scanning the cavity frequency by 400kHz or deflecting the beam position by ±10mm in horizontal and ±4mm in vertical. The HOM power absorbed by a pair of dampers reached to 4.2kW. The surface temperature of the ferrite was estimated as 50°C for the tested water flow rate of 2 l/min. In the designed flow rate of 5 l/min, this temperature rise corresponds to that for the total absorbed power of 8kW. Because of a large aperture of vacuum ducts in KEKB, a loss factor of the HER cavity is smaller than that of this test module. The beam of 1.1A with the bunch length of 4mm will induce the HOMs of 5-6kW for each cryomodule in HER, which is within reach of the dampers . The details of the damper tests will be described in Reference[6].

The coupler power of 280kW and the beam transferred power of 160kW are almost half the powers required in HER. The most serious problem is the RF trip due to coupler arcing. The trip was suppressed drastically by the improvement of vacuum pressure around the SC cavity( 1 x $10^{-9}$ Torr). The bias-voltage of the coupler was tested with and without beams. The vacuum pressure at the ceramic window was measured as the cavity voltage, cavity tuning angle and the bias voltage. The best bias voltage of -500V was found, where the pressure was not influenced by other parameters. However, the effect did not confirmed because the trips have already been suppressed by the vacuum improvement. The tests on the coupler will be reported in Reference[7]

The results of the AR beam test verify the application of the SC cavities to high current accelerators. The Machine Advisory Committee of KEKB has recommended the use of SC cavities in HER. Four modules will be installed together with the normal conducting ARES cavities for the commissioning of 1998. The HER module has the same cavity shape except for the longer taper connections to the beam ducts for the reduction of the loss factor. The construction of the cavities is in progress.

## 5 ACKNOWLEDGMENTS

The authors would like to thank Prof. S.Kurokawa on his enthusiastic support for our program. They are deeply indebted to the vacuum group for their help to improve the vacuum circumstances beside the SC cavity.

## 6 REFERENCES

[1] `KEK B-Factory Design Report', KEK Report 95-7, August 1995, A.
[2] T.Furuya, et al., Proc.7th SC-RF Workshop, CEA-Saclay, France, 1995, p.729.
[3] T.Furuya, et al., Proc. 5th EPAC(EPAC'96), Sitges, Spain, 1996, p.2121.
[4] T.Tajima, et al., Proc. 5th EPAC(EPAC'96), Sitges, Spain, 1996, p.2127.
[5] K. Asano, KEK Preprint 93-216, March 1994,A.
[6] T.Tajima, et al. in this conference.
[7] S. Mitsunobu, et al. in this conference.

# BEAM TEST RESULTS ON HOM ABSORBER OF SUPERCONDUCTING CAVITY FOR KEKB

T.Tajima, K.Akai, K.Asano, T.Furuya, K.Hara, K.Hosoyama, A.Kabe, Y.Kojima, S.Mitsunobu, Y.Morita, T.Takahashi, KEK 1-1 Oho, Tsukuba, Ibaraki, 305, Japan, S.C.Zhao, IHEP, Beijing

*Abstract*

A series of beam tests using TRISTAN Accumulation Ring (AR) was dedicated to verify the feasibility of RF system and other components planned for KEKB, B Factory project at KEK. In this paper, we describe the results on Higher Order Mode (HOM) absorbers used for Superconducting Cavities (SCC). The absorber was manufactured by HIPping of ferrite powder onto copper tube. The SCC system was operated stably with HOM's being damped, and up to total of 4.2 kW was absorbed through the absorber without any problem.

## 1 INTRODUCTION

HOM absorbers made of ferrite have been developed for SCC's to be used for KEKB High Energy Ring (HER) [1,2]. To check the validity of our manufacturing technique using Hot Isostatic Press (HIP) of pre-sintered ferrite powder, a full-size absorber alone was beam tested in TRISTAN MR [3]. Finally, a SCC with two absorbers was beam tested three times in 1996 in TRISTAN Accumulation Ring (AR). This paper presents a summary of these tests mainly concerning HOM absorbers.

## 2 INSTRUMENTATION

Installation process of the absorbers and preparation for the tests will be described below in terms of hardware and software.

### *2.1 Hardware*

Figure 1 shows the full set up of the system with detailed dimensions of absorbers on each side. Hardware consists of a SCC, a cryostat, an input coupler, two HOM absorbers, two tapers with ducts and ports for gauges, two 270 L/s ion pumps and two gate valves.

#### 2.1.1 Assembly of absorbers

Absorbers were degreased and rinsed with ethanol using a closed system with ultrasonic agitation. Then they were assembled with tapers, bellows and gate valves. Before installing to SCC, up-stream and down-stream sets were connected together and baked at about 120 °C for a few days. Finally, after venting with filtered pure nitrogen gas, they were attached to SCC in a clean hut of class ~1000.

#### 2.1.2 Installation of sensors

Two cold cathode gauges were set on both up-stream and down-stream tapers. To analyze gas species, a Quadrupole mass analyzer was set on the duct attached to up-stream taper. 2 rows of 8 azimuthally distributed thermo-couples were taped on the outer surface of absorbers. Moreover, two sets of Pt thermometers were inserted in the inlet and outlet of the copper cooling pipes as well as a digital flow rate meter for precise calorimetric measurements of absorbed power. Also, 3 RF pick up antennas were set at 0, 45 and 90 degrees from top of each taper.

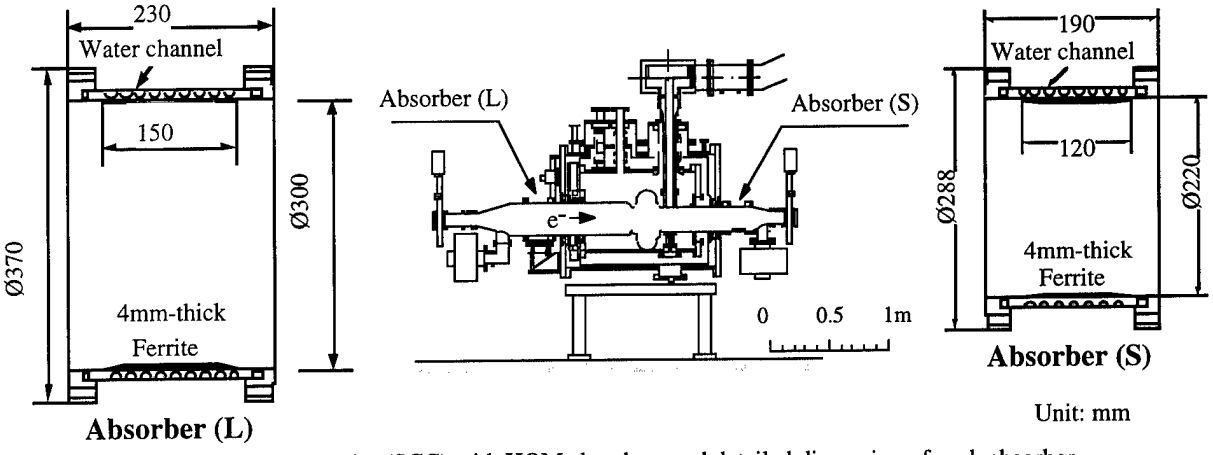



Figure: 1 Superconducting Cavity (SCC) with HOM absorbers and detailed dimension of each absorber.

0-7803-4376-X/98/$10.00 © 1998 IEEE

### 2.2 *Software*

Software consists of GP-IB based data acquisition system operated with a software named Labview. Total of about 130 data were taken and stored in a MO disk every 30 sec. These data were retrieved with another application software named Kaleida Graph for further analyses.

## 3 RESULTS

The beam tests ended with successful results after strengthening the pumping power of the neighboring ducts [4,5]. The pumping power and the amount of the gas entering the SCC are estimated to be 3 times stronger and 1/10, respectively [6]. This fact reconfirmed the importance of keeping the SCC clean against gases. The number of trips decreased drastically and stable operation was possible. Below are the summary of HOM absorbers.

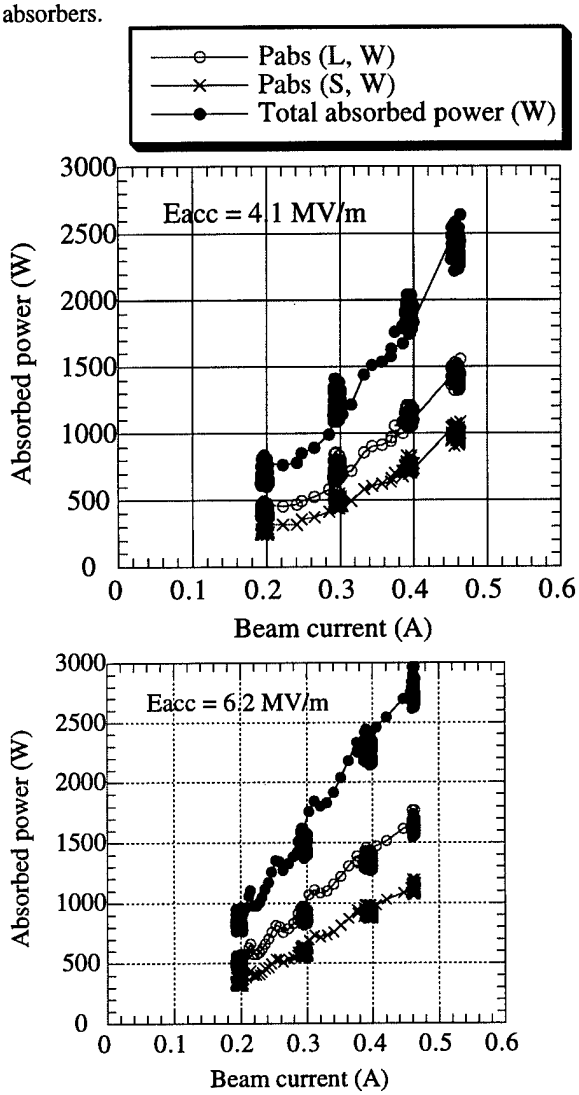



Figure: 2 Absorbed power as a function of beam current at different cavity accelerating fields. "L" and "S" denote Large and Small absorber, respectively.

### 3.1 *HOM Damping*

HOM's were searched with a spectrum analyzer. With our tuner, up to 400 kHz of fundamental mode could be searched and no significant increase of HOM were found, confirming the capability of damping.

### 3.2 *Power Handling*

The maximum power absorbed went up to 4.2 kW in total. Figure 2 shows a typical absorbed power as a function of beam current at Eacc = 4.1 and 6.2 MV/m. The cavity voltage can be obtained by multiplying the gap length of 0.243 m with Eacc. As one can see, the absorbed power did not increase quadratically because the bunch length got elongated with higher currents, resulting in the decrease of loss factor as shown below. The uncertainty of the absorbed power was mainly due to the fluctuation of inlet water temperature caused by regulated cooling system.

No symptom of degradation on the absorbers were observed during the tests.

### 3.3 *Loss Factor*

As mentioned above, bunch length changed with beam current and cavity voltage. Figure 3 shows the bunch length measured with a streak camera. As one can see, increasing cavity voltage could make the bunch length shorter, but not much. Also, the bunch length became

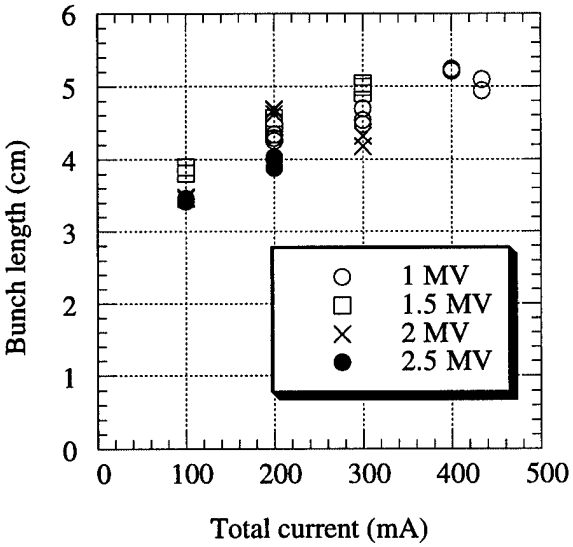



Figure: 3 Bunch length as a function of total current at various cavity voltages. 4x4 bunches. Data were taken with a streak camera.

longer with beam current.

To obtain the bunch lengths as short as possible with absorbed power large enough to measure loss factor precisely, we used 50 bunches with feedback on [7]. As shown in Fig. 4, we could get as short as 1.5 cm, which

is still far from KEKB design value, 0.4 cm, though. The calculation in Fig. 4 is the sum of ABCI calculations without absorbers and analytic calculations of absorber themselves. Neither entering nor outgoing power from SCC were considered. The measured data were close to the calculation at shorter bunches and lower at longer bunches as shown in Fig. 4.

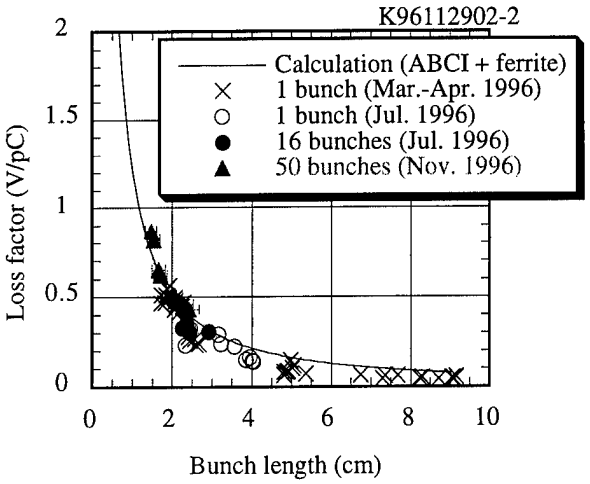



Figure: 4 Comparison of the measured loss factor with calculation.

*3.4 Outgas*

As mentioned earlier, drastic decrease of trip rate of SCC after strengthening the pumping power of the neighboring ducts made it clear that the entering gas from outside had caused most trips. Also, it suggests that, if the integration of outgas from absorbers at high losses exceeds a certain amount, it might cause trips in the future. The threshold roughly estimated from obtained data is about 1 Torr liter, though we could not reach this level at the last test in which the amount of gas from absorbers seems to have been comparable or larger than the gas entering from outside.

3.4.1 Gas species detected with a mass analyzer

As shown in Fig. 1, quadrupole mass analyzer was set on a duct at up-stream taper. The most gas detected was hydrogen. A summary of the analyses is as follows.

- For some reason, back ground level of mass analyzer increases with cavity fields higher than ~6 MV/m.
- The amount of hydrogen increases with beam currents.
- It also increases during aging of the input coupler.
- At 8.3 MV/m and 400 mA with SCC on, the amount of hydrogen is much higher (~x3<), compared to the operation (450-500 mA) with SCC off.
- Apart from hydrogen, the observed mass numbers during warm-up are 18, 16, 12, 28, although they were much less than hydrogen.

## 4 DISCUSSION

On the mass analyses, though the detected gas was chiefly hydrogen, we are not 100 % sure that the contamination or condensation on SCC that cause the trips can be attributed to hydrogen alone because the other gases condense on the surface of SCC more easily than hydrogen and they might not have been detected well with the mass analyzer.

On the loss factor, it seems to get higher than present prediction at 4 mm. It will be important to clarify the sources for additional losses and estimate the loss factor at KEKB HER more accurately.

## 5 CONCLUSION

Beam tests of SCC with HOM absorbers made of HIPped ferrite were performed using TRISTAN AR. The SCC was operated stably with HOM's being damped especially after the reduction of gas condensation on its surface.

The power absorbed through absorbers went up to 4.2 kW at maximum and 2 to 3 kW for more than 120 hours. No symptom of degradation was observed on the absorbers. Loss factor at 1.5 to 2.5 cm agreed well with calculation but was lower than calculation at longer bunches.

Since we did not face many trips at the last beam test in which we could estimate the amount of the condensed gas more accurately than the previous tests, we cannot conclude on the threshold level of the amount of condensed gases at which trips start occuring. However, from previous tests our rough estimate is about 1 Torr liter. To avoid this problem in the future, the outgas rate of absorbers should be reduced further along with the efforts to minimize the amount of gases that enter from outside.

## 6 ACKNOWLEDGEMENTS

We would like to thank M.Tobiyama for helping with the loss factor measurements. We also would like to thank Y.Funakoshi and operation group members for their enormous efforts to the success of the beam tests. Finally, continued encouragement of Professors E.Ezura, Y.Kimura, S.Kurokawa, Y.Yamazaki, K.Takata and Professor emeritus Y.Kojima is greatly appreciated.

## REFERENCES

[1] T. Tajima et al.: Proc. 1995 PAC, p. 1620.
[2] T. Tajima et al.: Proc. 1996 EPAC, p. 2127.
[3] T. Tajima et al.: KEK Report 96-7 (1996).
[4] S. Mitsunobu et al: in this conference.
[5] T. Furuya et al.: in this conference.
[6] Y. Suetsugu: private communication
[7] M. Tobiyama: private communication

# HIGHER ORDER MODE ANALYSIS OF THE APT SUPERCONDUCTING CAVITIES

Frank L. Krawczyk,
LANL, LANSCE-1, MS H817, Los Alamos, NM 87545, USA

*Abstract*

In another contribution to this conference [1] the design of superconducting cavities for low velocity proton beams will be reported. Besides an optimization of the rf properties of the accelerating $\pi$-mode, other modes, possibly excited by the traversing proton beam, need to be regarded. The full spectrum of modes in $\beta = 0.64$ and $\beta = 0.82$ 5- cell cavities, as proposed for the Accelerator Production of Tritium (APT) facility [4], has been calculated up to frequencies higher than 2.0 GHz. These have been evaluated for their potential to affect the beam. The presence of "trapped" modes has also been investigated. In addition to the specific mode spectrum, the total power deposited into the cavities by the beam has been determined from the induced wake-fields. Due to the operation with beams below the velocity of light, extreme care was required to prevent incorrect results by wave reflections from the boundaries of the calculation volume. The simulations indicate that a power deposition of up to 17 W per cavity can be expected in the worst case. This power might have to be removed by higher order mode couplers, which is a technically feasible task. Transporting this power out to a room temperature dump does not even noticeably increase the requirements to the cryogenic system. Also for the prevention of beam break-up effects and for suppression of resonant excitation of specific higher order modes (HOMs) it is of interest to investigate the removal of this HOM-power. Different approaches to implement this removal technically are entertained.

## 1 INTRODUCTION

The HOM spectrum, which includes modes with frequencies above and below the accelerating TM010 $\pi$-mode, has been calculated with the MAFIA rf-solver[3]. The simulations have been done for the monopole modes that can deposit energy into the cavity and can change the energy of the traversing bunches. Also the dipole modes that can cause beam deflection have been investigated. The simulations for both $\beta$s have been done in an axisymmetric 2d model of a full five-cell cavity.

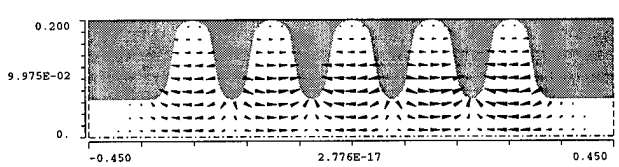



Figure 1: The $\beta$=0.64 five-cell cavity with the accelerating mode.

## 2 THE HIGHER ORDER MONOPOLE MODE SPECTRUM FOR THE $\beta = 0.64$ CAVITY

The monopole spectrum of the medium-$\beta$ cavity has been calculated up to a frequency of about 2.8 GHz. The two lowest mode bands (TM010 and TM020) and some of their properties are presented in the following Table:

| Mode Order | $\Delta\Phi$/cell | Frequency [MHz] | $k_{loss}$ [V/pC] | R/Q [$\Omega$] |
|---|---|---|---|---|
| TM010 | 0 | 681.59 | 0.0001 | 0.105 |
| TM010 | $2\pi/5$ | 686.54 | 0.0015 | 1.396 |
| TM010 | $3\pi/5$ | 692.64 | 0.0011 | 1.014 |
| TM010 | $4\pi/5$ | 697.56 | 0.0041 | 3.733 |
| TM010 | $\pi$ | 699.53 | 0.2033 | 185.00 |
| TM020 | 0 | 1396.82 | 0.0023 | 1.034 |
| TM020 | $2\pi/5$ | 1410.73 | 0.0045 | 2.049 |
| TM020 | $3\pi/5$ | 1432.74 | 0.0002 | 0.106 |
| TM020 | $4\pi/5$ | 1458.80 | 0.0059 | 2.595 |
| TM020 | $\pi$ | 1481.02 | 0.0004 | 0.172 |

The modes of the TM010 band are not equally spaced, this indicates that the coupling between cells is determined by next-neighbor and second-neighbor coupling. This behavior is due to the large pipe and iris size of 6.5 cm. All modes in the bands given in Table 1 are below the pipe cut-off and need to be considered for a potential deposit of power into the cavity, if excited by the traversing bunches. The potentially most dangerous mode is the TM020 "zero" mode. Its frequency is close to a multiple of the bunch repetition frequency of 350 MHz. We are looking into a slight modification of the end-cell geometry, to remove this multiplicity. All other monopole modes are above pipe cut-off. They can travel out of the cavities and pose a lower risk for dangerous bunch interaction or increasing the cryogenic load. Their only danger could be, if they are structure modes, whose significant field-amplitudes could be trapped in the inner cells of a cavity. The spectrum, up to the limit it was calculated, did not indicate any such modes. These results have been obtained using an average pipe-length between neighboring cavities. A detailed study using all distinct cavity distances present in the design, is under way to rule out any mode trapping for certain cavity arrangements. It should be mentioned that the loss-factors listed above are valid for particles at $\beta$=1.0. The loss-factors at the velocities seen in the actual accelerator are lower. See also the section on wake fields.

0-7803-4376-X/98/$10.00 © 1998 IEEE

## 3 THE HIGHER ORDER MONOPOLE MODE SPECTRUM FOR THE $\beta = 0.82$ CAVITY

The monopole spectrum of the high-$\beta$ cavity has been calculated up to a frequency of about 2.3 GHz. The two lowest mode bands (TM010 and TM020) and some of their properties are presented in the following Table:

| Mode Order | $\Delta\Phi$/cell | Frequency [MHz] | $k_{loss}$ [V/pC] | R/Q [$\Omega$] |
|---|---|---|---|---|
| TM010 | 0 | 674.20 | 0.0001 | 0.049 |
| TM010 | $2\pi/5$ | 681.16 | 0.0018 | 1.666 |
| TM010 | $3\pi/5$ | 689.94 | 0.0006 | 0.577 |
| TM010 | $4\pi/5$ | 697.19 | 0.0047 | 4.381 |
| TM010 | $\pi$ | 699.92 | 0.3161 | 287.38 |
| TM020 | 0 | 1357.69 | 0.0009 | 0.415 |
| TM020 | $2\pi/5$ | 1367.65 | 0.0100 | 4.671 |
| TM020 | $3\pi/5$ | 1384.50 | 0.0018 | 0.830 |
| TM020 | $4\pi/5$ | 1409.56 | 0.0227 | 10.252 |
| TM020 | $\pi$ | 1439.37 | 0.0016 | 0.727 |

Also for the high-$\beta$ cavity the cell-to-cell coupling is influenced by second neighbor coupling. The modes of the TM010 and the lowest four modes of the TM020 band are below the pipe cut-off. The TM020 $\pi$-mode and all other monopole modes are above cut-off. Up to approximately 2.3 GHz no mode has been found close to a multiple of the bunch repetition frequency of 350 MHz. So resonant excitation is not expected. A further investigation of the higher modes indicates a potentially trapped mode at 1.944 GHz. Also, a recalculation with explicit pipe length instead of the average pipe length needs to be done.

## 4 DIPOLE MODES FOR THE $\beta = 0.64$ AND $\beta = 0.82$ CAVITIES

Dipole modes in the cavities of the APT linac could cause deflections of the proton beams. Bob Gluckstern, in an analysis independent of the specific mode spectrum, looked at the most important issues for beam break-up (BBU) for the APT accelerator [2]. His findings indicate that BBU is not an issue for several reasons:

- Presence of substantial external transverse focusing (estimate based on [5]). BBU forces act like small perturbations on the coherent motion of the beam under the focusing forces.
- Fabrication variations in the APT cavities (approximately 400 are in the accelerator) result in a distribution of frequencies of the deflecting modes along the linac. This lowers the effective Q of these modes significantly (estimate based on [6]).

These estimates do not depend on a Q reduction by the presence of HOM couplers. Further investigations of these estimates using the explicit mode spectrum are under way.

The next two tables give the lowest dipole mode-bands and their R/Q values.

| $\beta = 0.64$ | Mode Order | $\Delta\Phi$/cell | Frequency [MHz] | R/Q [$\Omega$/m] |
|---|---|---|---|---|
| | TM110 | $\pi$ | 924.60 | 0.0003 |
| | TM110 | $4\pi/5$ | 929.66 | 0.017 |
| | TM110 | $3\pi/5$ | 938.45 | 0.003 |
| | TM110 | $2\pi/5$ | 950.87 | 0.090 |
| | TM110 | 0 | 963.42 | 0.018 |
| | TE111 | 0 | 1072.50 | 0.003 |
| | TE111 | $2\pi/5$ | 1124.77 | 0.058 |
| | TE111 | $3\pi/5$ | 1196.22 | 0.060 |
| | TE111 | $4\pi/5$ | 1277.79 | 0.727 |
| | TE111 | $\pi$ | 1359.41 | 0.861 |
| | TE111 | $6\pi/5$ | 1412.15 | 0.027 |

The TE111 modes above the $\pi$ mode are above cut-off. The higher part of the mode band is affected by the pipe between neighboring cavities. Thus there are more than 5 modes in this band. Only the lowest 6 modes are listed here. No mode is close to a multiple of 350 MHz.

| $\beta = 0.82$ | Mode Order | $\Delta\Phi$/cell | Frequency [MHz] | R/Q [$\Omega$/m] |
|---|---|---|---|---|
| | TE111 | 0 | 860.16 | 0.035 |
| | TE111 | $2\pi/5$ | 876.25 | 0.495 |
| | TE111 | $3\pi/5$ | 890.63 | 0.015 |
| | TE111 | $4\pi/5$ | 898.01 | 0.016 |
| | TE111 | $\pi$ | 939.59 | 0.145 |
| | TM111 | 0 | 976.07 | 0.069 |
| | TM111 | $2\pi/5$ | 1007.21 | 0.357 |
| | TM111 | $3\pi/5$ | 1054.47 | 0.804 |
| | TM111 | $4\pi/5$ | 1104.96 | 0.866 |
| | TM111 | $\pi$ | 1125.50 | 0.040 |
| | TM111 | $6\pi/5$ | 1192.00 | 0.001 |

The TM111 modes above the $3\pi/5$ mode are above cut-off. The higher part of the mode spectrum is determined by pipe and cavities. Thus there are more than 5 modes in this band. Only the lowest 6 modes are listed here. The $3\pi/5$-mode is close to a multiple of 350 MHz and needs a closer look, to evaluate its danger for BBU.

## 5 WAKE FIELD SIMULATIONS

Wake-field calculations give an estimate of the integrated power deposited into HOMs by bunches traversing a cavity. So far the power deposition into the monopole modes has been calculated with the MAFIA T2 solver. The difficulty in these simulations is the velocity of the bunches. The wake excitation is strongly $\beta$-dependent. Modern wake-simulation codes have formulations for open boundary conditions. These can simulate beam pipes that have no reflection for out-going waves. Unfortunately these formulations depend on moving charges with $\beta = 1.0$. For slower bunches closed boundary conditions have to be chosen. These result in reflection of the outgoing waves that move faster than the bunches. The reflections can act back on the bunch and change the wake potentials. Thus these simulations have to be set up carefully to minimize these

effects. I have used long beam-pipes that were tapered off at the ends. This increased the time needed for waves to travel between the boundaries. Also, their velocity is artificially reduced by enforcing multiple reflections between the pipe walls. All wake-functions have been inspected visually to rule out the possibility that the bunch saw the large excursions of the artificially added reflected waves.

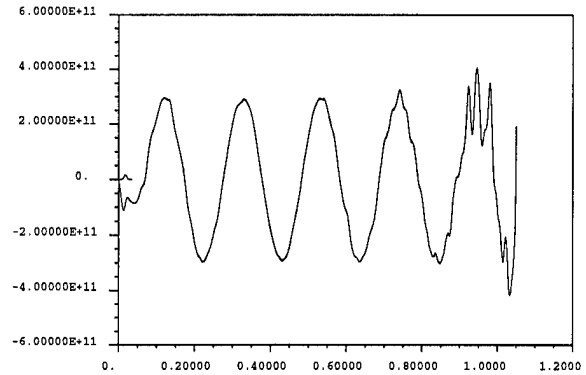



Figure 2: A typical wake function for a low-$\beta$ simulation. At the left end of the plot you see an overlap of the calculated wake and the charge distribution in a bunch, assumed to be Gaussian. The choice of calculation volume has to make sure that the large wake excursions due to the artificial reflections occur outside of the bunch-frame.

| $\beta$ | $k_{loss}$ [V/pC] | $\sigma_z$ [mm] | $P_{HOM}$ [W] |
|---|---|---|---|
| 0.64 | 0.204 | 3.5 | 5-6 |
| 0.82 | 0.584 | 4.0 | 7-17 |
| 1.00 | 9.0 | 1.0 | - |

Table 5 gives the loss factors for the design-$\beta$s of both the medium and high-$\beta$ sections. These have been calculated for bunch-lengths derived from the beam-dynamics simulations for the linac. The simulations have been done for the full range of $\beta$s the bunches have in each of the linac sections. From these ranges the actual HOM power for a 5-cell-cavity has been derived. The power data assume:

- a 100 mA beam with a bunch repetition rate of 350 MHz,
- all excited power would go into the structure.

The latter assumption is an overestimate. A major part of the HOM spectrum goes into modes above pipe cut-off. These modes can leave the structure without adding to the cryogenic load of the cavity. Their power could be removed in a warm part of a beam-pipe. Also most modes are not at multiples of the bunch repetition frequency. Their HOM power is out of phase with the traversing bunches and some of the power could on average go back into succeeding bunches of the beam. We are working on a less conservative estimate of HOM power to be removed. It should also be mentioned that the wake simulations have been done for a single-cell cavity. The 5-cell cavity value has been assumed to be five times this value. The validity of this approach has been tested for a $\beta$ = 1.0 beam. For comparison also some numbers for an electron linac have been added to the table to demonstrate the strong variation with $\beta$ and bunch-length, that both work in advantage of the proton linac.

## 6 HIGHER ORDER MODE COUPLERS

HOM power needs to be considered for two different reasons. First, the power deposited into the cavities can add significantly to the cryogenic load of the system. The worst case estimate done in the previous section indicates that the HOM power can be of the same order as the rf-losses from the accelerating mode itself. Second, HOM modes can have an adverse effect on the beam-dynamics if single modes act on the bunch to cause deflection or emittance growth. Since the APT facility needs to run very reliable for a long time without a long start-up time, it was decided to add HOM coupling as a safety measure. There are two venues investigated right now. The first is to add dedicated HOM couplers at both ends of each cavity. For this approach we look at loop-coupler geometries. These coaxial type couplers have a broad band capability to remove unwanted modes without affecting the accelerating mode strongly. A second path is to investigate the main-coupler potential to remove HOM power. In particular, all $TM_{0nk}$-type modes will couple strongly to this coupler. If all modes that need to be considered show a sufficiently strong coupling to this coupler, and if we find a setup that allows to remove this power before it would reach the coupler window, we will try to avoid additional dedicated HOM couplers.

## 7 ACKNOWLEDGEMENTS

This work is supported by the US Department of Energy. I want to thank Bob Gluckstern for his estimate of the BBU potential.

## 8 REFERENCES

[1] F. Krawczyk et al., "Superconducting Cavities for the APT Accelerator", these proceedings,

[2] Bob Gluckstern, University of Maryland, private communication

[3] M. Bartsch et al. "Solution of Maxwell's Equations", Computer Physics Comm. **72**, 22-39 (1992)

[4] G. Lawrence, T. Wangler, "Integrated Normal-conducting/Superconducting High Power Proton Linac for APT", these proceedings

[5] Gluckstern, Cooper, Neri, "Cumulative Beam Breakup With Randomly Fluctuating Parameters", Particle Accelerators **23**, 37 (1988)

[6] Gluckstern, Cooper, Neri, "Cumulative Beam Breakup in RF Linacs", Particle Accelerators **16**, 125 (1985)

# IN-SITU PROTON IRRADIATION AND MEASUREMENT OF SUPERCONDUCTING RF CAVITIES UNDER CRYOGENIC CONDITIONS

B. Rusnak, W. B. Haynes, K.C.D. Chan, R. B. Gentzlinger, R. Kidman, N.S.P. King, R. E. Lujan, M. Maloney, S. Ney, A.H. Shapiro, J. Ullmann, Los Alamos National Laboratory, Los Alamos, NM 87545, A. Hanson, Brookhaven National Laboratory, H. Safa, CEA Saclay

*Abstract*

The Accelerator Production of Tritium (APT) Project is investigating using a superconducting linac for the high-energy portion of the accelerator. As this accelerator would be used to accelerate a high-current (100-mA) CW proton beam up to 1700 MeV, it is important to determine the effects of stray-beam impingement on the superconducting properties of 700-MHz niobium cavities. To accomplish this, two 3000-MHz elliptical niobium cavities were placed in a cryostat, cooled to nominally 2 K in sub-atmospheric liquid helium, and irradiated with 798-MeV protons at up to 490-nA average current. The elliptically shaped beam passed through the equatorial regions of both cavities in order to maximize sensitivity to any changes in the superconducting surface resistance. Over the course of the experiment, $6x10^{16}$ protons were passed through the cavities. After irradiation, the cavities were warmed to 250 K, then recooled to investigate the effects of a room-temperature annealing cycle on the superconducting properties of the irradiated cavities. A detailed description of the experiment and the results shall be presented. These results are important to employing superconducting RF technology to future high-intensity proton accelerators for use in research and transmutation technologies.

## 1 INTRODUCTION

A significant driver for the APT conceptual design is the minimization of beam loss through the accelerator, which would allow hands-on maintenance. Extensive steering error and beam halo studies have been used to keep stray beam to a maximum of 0.2 nA/m in the overall design. However, even at this low level, the question remained as what effect this amount of lost beam might have on the superconducting properties of a niobium accelerator cavity.

In a previously published paper [1], an experiment was done where a superconducting cavity was irradiated and measured under cryogenic conditions. The results of the experiment indicated a deleterious effect on the cavity $Q_0$ at a proton fluence comparable to the 0.2 nA/m figure calculated for APT. While the experiment was done over 25 years ago and many things in superconducting cavity technology have changed since these early days, the reported change in the $Q_0$ was enough to motivate further investigation.

Work supported by the US Department of Energy

## 2 EXPERIMENTAL APPROACH

The intent of the experiment was to evaluate, in a timely manner, if there was an observable effect on the superconducting properties of a niobium cavity that was exposed to a relatively large fluence of high energy protons. Given the constraints on beam availability, cost, and schedule, the experiment was designed to look for an overall effect, instead of trying to closely emulate the actual "spilled beam" configuration a real accelerating cavity may see. This was seen as a way of bounding the problem.

The approach was to measure the cavity $Q_0$ as a function of fluence. Changes in the $Q_0$ would indicate a change in the surface resistance ($R_s$). To see subtle changes in the $Q_0$, the cavities were operated between 1.8 and 2.2 K.

To increase sensitivity further, the cavities were irradiated on their equators with an elliptical beam profile of 1x3 cm to achieve the largest practical radiation-affected zone relative to the active cavity area. Irradiating the cavities while immersed in liquid helium was done to mimic the actual environment of the cavities in a working accelerator. This also allowed us to evaluate what effect room-temperature annealing had on the superconducting electrical properties due to healing radiation damage, in the event changes were observed.
To do this, the assembly was warmed to 250 K, then recooled to 2 K and measured before the cavities were physically moved, in order to minimize possible contamination. A schematic layout of the configuration is shown in Figure 1.

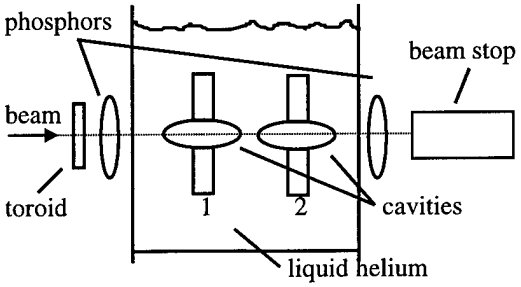



Figure 1. Schematic of the experimental set up, showing the beam going through a current toroid, the phosphors, the cryostat, the two 3 GHz cavities, and stopping in the beam stop.

0-7803-4376-X/98/$10.00 © 1998 IEEE

## 3 BEAM DELIVERY

The cavity and cryostat assembly was irradiated using the LANSCE accelerator in an area called the Blue Room. The Blue Room is a shielded area that can be configured for direct access to 798-MeV protons with average currents up to 500 nA.

Since a major goal of the experiment was to measure the cavity properties as a function of proton fluence, accurate beam measurements were important. Beam current was directly measured using a beamline toroid upstream of the Blue Room. The measurement was corroborated using an additional toroid before the cryostat.

Phosphors were used primarily for profiling the beam going into and coming out of the cryostat. They also served to give another corroboration of the overall beam current profile by looking at the digitized light intensity from the phosphors.

Finally, induced-activity dosimetry was done on the cavities and confirmed the cavities did indeed have the beam delivered on the equator.

During the actual measurement, the beam was run for prescribed amounts of time at increasing average current levels. RF measurements of the cavities were done both while the beam was on and when it was off between irradiations. There was no observed difference in the measured values between beam on and beam off, indicating beam-induced secondaries were not a problem. The cumulative profile of the fluence achieved is shown in Figure 2.

Achieving a fluence of $5 \times 10^{15}$ p/cm$^2$, which corresponds to a beam loss of 0.2 nA/m, was the minimum goal. In the actual experiment, we achieved fluences in excess of $1.5 \times 10^{16}$ p/cm$^2$, which was a factor of 3 greater than the expected worst-case lifetime beam-loss fluence for APT.

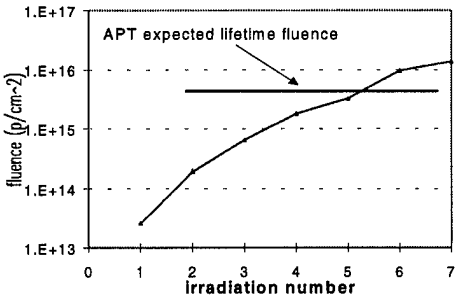



Figure 2. Plot showing proton fluence as a function of time in arbitrary units. The horizontal line shows the expected 40 year lifetime fluence for APT.

## 4 LOW-POWER MEASUREMENTS

Irradiating two cavities was done primarily for redundancy, in the event one leaked. However, since neither cavity leaked, having two cavities allowed running one at low power until the end of the experiment. This was desirable as it was a way to eliminate the changes in the $Q_0$ that could occur due to RF conditioning at higher fields.

The first cavity in the beam was run only at low power levels, less than 50 mW, throughout the run. With $E_0T$ field levels in the cavity held consistently around 4-5 MV/m, conditioning-related changes in $Q_0$ were kept to a minimum. Only after the low power data was obtained was the power level in this cavity increased to determine its field performance at full fluence. Low power points from the second cavity were also examined for corroborative purposes. The low power data for both cavities is shown in Figure 3. Within experimental accuracy, there was no observable change in the $Q_0$ with increased fluence.

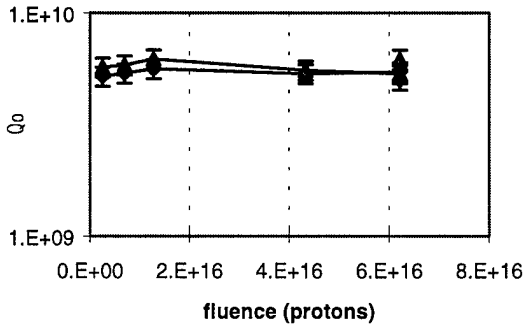



Figure 3. Plot showing the low-power unloaded $Q_0$ of both cavities as a function of proton fluence. Data normalized to 2.0 K.

## 5 HIGH-POWER MEASUREMENTS

The second cavity in the beam path was swept in power after each incremental increase in the fluence. The intent was to look for degradation in performance as a function of increased radiation damage. As shown in Figure 4, a variation in the $Q_0$ as a function of power was observed for increasing fluence that is attributed primarily to uncertainties in the temperature normalization and errors in the measurement of the $Q_0$.

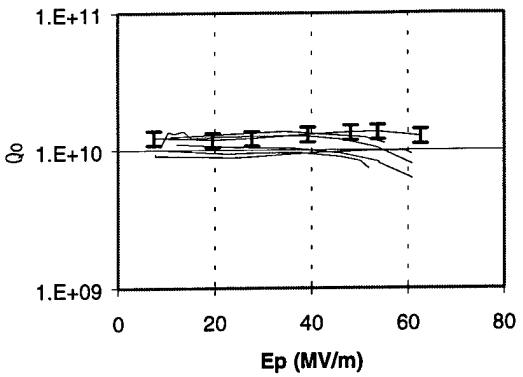



Figure 4. Variation of the $Q_0$ related to the peak surface electric field. The different curves represent different fluence levels. The downward trend did not consistently correlate with increased fluence. Data normalized to 1.8 K.

For the quench field level, a mild downward trend of approximately 15 % was observed in the second cavity up to a fluence of $4.3 \times 10^{16}$ protons, as shown in Figure 5. Above this level, mechanical problems necessitated running the cavity at a higher temperature (2.0-2.2 K), and the resultant larger temperature normalization as well as changes in the niobium thermal conductivity are seen as contributing to the observed recovery in the quench field level to pre-irradiation levels.

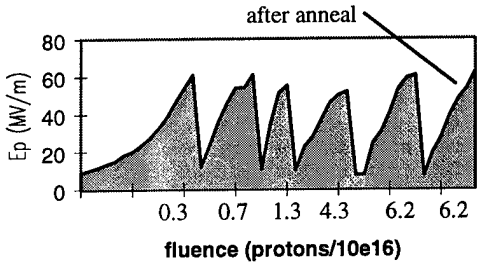



Figure 5. Peak electric fields obtained in multiple power sweeps as a function of fluence.

In general, no significant degradation in $Q_0$ was observed with increased radiation damage, and a mild downward trend in the quench field was observed. As the field levels for the APT cavities are conservative, i.e., not near the quench limit, this magnitude of change in quench field is not a concern.

## 6 CONCLUSION

The objective of this experiment was to evaluate the effect proton irradiation had on the superconducting properties of cryogenic niobium cavities. To a fluence level of $6.2 \times 10^{16}$ protons ($1.6 \times 10^{16}$ p/cm$^2$) at 798 MeV, there was no significant degradation observed in the $Q_0$. After the 250 K anneal, changes of less than 13% in the low-power cavity $Q_0$ were observed.

A downward trend of approximately 15% in the cavity quench field was also observed, but for the modest gradients needed for APT, this is not a concern.

## 7 ACKNOWLEDGMENTS

The authors would like to express their gratitude to Frank Krawczyk, George Morgan, Brock Roberts, Bob Hammock, Ernie Newman, and Marv Barney for their help with the experiment fabrication, set up, and operation.

## REFERENCES

[1] H.J. Halama, "Effects of Radiation on Surface Resistance of Superconducting Niobium Cavity", Appl. Phys. Let., v. 19, no. 4, Aug. 15, 1971.

# SUPERCONDUCTING CAVITIES FOR THE REDUCED-BETA SECTION OF A PROTON LINAC

C. Pasotti, P. Pittana and M. Svandrlik,
Sincrotrone Trieste, S. S. 14 per Basovizza, km 163.5, 34012 Trieste, Italy

*Abstract*

A proton linear accelerator with energies beyond 1.0 GeV has been proposed in [1] where the LEP2 superconducting ( SC ) cavities are to be used after decommissioning of LEP, in the high energy part of the linac. Energies ranging from 100 MeV to 1.0 GeV will be covered by superconducting cavities designed to accelerate protons with reduced value of beta. The basic idea is to keep the shape of the spherical LEP cavities for $\beta = 1.0$ and to adjust their length, for $\beta < 1.0$ in order to get an optimal acceleration for low energy protons. Three different values of $\beta$ allow to cover the required range with a reasonable acceleration efficiency. The design of superconducting cavities for $\beta = 0.50$, 0.625 and 0.80 is presented here. In particular the choice of an elliptic iris profile is discussed.

## 1 CAVITY DESIGN

All the LEP2 radiofrequency equipment, such as the RF plants and HOM couplers could be used in a lower energy range, i.e. 100 MeV up to 1 GeV, if new SC accelerating cavities with the same resonant frequency of 352 MHz can accelerate the beam with an acceptable efficiency. Three reduced-$\beta$ SC cavities have to be designed with axial length $L_{cell}=\beta\lambda/2$.

A simple linear scaling [2] of the already existing LEP2 cavity [3] has shown a remarkable deterioration of the cavity electromagnetic (EM) parameters with respect to the LEP2 due to the smaller volume and the electric field density decrease along the cavity axis. For the cavity with $\beta = 0.5$ the ratio between the peak surface electric field and the accelerating electric field $E_{sp}/E_a$ is doubled with respect to LEP2. This ratio is one of the most important parameter for the SC Nb/Cu cavity since it is related to the field emission limitation and to the maximum gradient that the cavity can substain. An improvement of the cavity shape is then required.

The cavity profile should be optimized according to fixed design constraints coming from the SC design technique and the manifacturing experience. The door-bell geometry of the LEP2 cavities should be maintained to minimize the multipacting risk. In order to utilize the CERN equipment the external cavity diameter should be close to that of LEP2 cavities. Flat cell side walls should be avoided for mechanical stability reasons, their inclination should be $\geq 8°$- $10°$.The cell to cell coupling factor K should be kept sufficiently high to achieve acceptable field flatness, so the iris beam tube radius can not be decreased too much. The Higher Order Modes should not be trapped in the cavity, and this also limits the size of the beam tube radius.

All the simulations have been performed with the computer code OSCAR2D [4] and the EM cavity parameters have been calculated for normal conducting copper at room temperature.

### *1.1 The reduced-beta cell with an Elliptic Iris Shape*

The design of the lowest $\beta = 0.5$ cavity is the more troublesome to perform. This cavity is the smallest one with an axial length half of the LEP2 cavity.

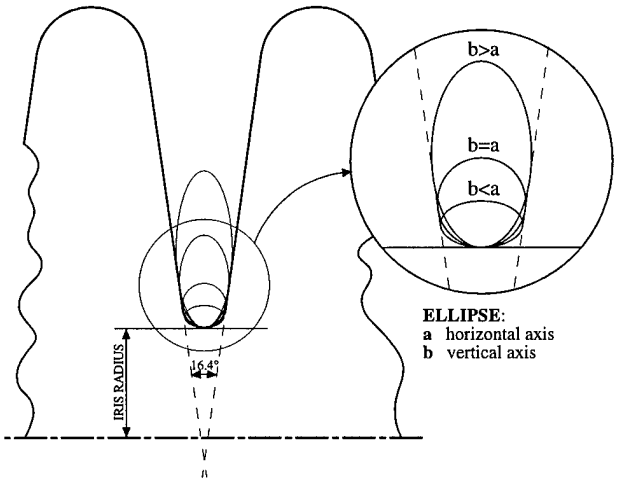



Figure 1: Sketch showing the elliptical iris shape. When the eccentricity is changed, the tangency condition to the side wall should be matched. The inclination of the side walls is kept constant.

A cavity with circular iris shape tailored for particles with $\beta = 0.48$ has been presented in [5] and [6]. Starting from these shapes and taking into account the design specifications, the optimization of two cavity size parameters, the beam tube radius and the iris shape have been done to improve the EM cavity parameters. This optimization should take into account that these two parameters are strongly correlated. In fact, once the cavity side wall inclination has been fixed, the decreasing of the iris beam tube radius leads to the decreasing of the circular iris radius tangent to the side wall, as shown in figure 1. The basic idea is to replace the circular iris radius with an elliptic shape and to investigate the behavior of main EM cavity parameters

0-7803-4376-X/98/$10.00 © 1998 IEEE

as a function of the elliptic sizes. It should be noted that the design guidelines do not allow to modify other cavity dimensions. In addition, when the beam iris radius is changed some adjustments of the cell diameter are required to tune the resonant frequency.

The variation of the $E_{sp}$ as a function of the ellipse eccentricity b/a is shown in figure 2 for different beam tube radii.

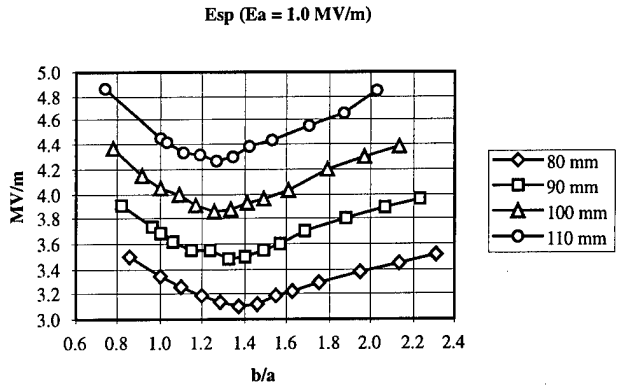



Figure 2: The $E_{sp}$ as a function of b/a.

The results show that the minimum values occur far from the circular profile. Lessening the beam tube radius the $E_{sp}$ becomes smaller.

The $E_{sp}$ value as a function of the ellipse's vertical axis b is skctched in figure 3 for different beam tube radii.

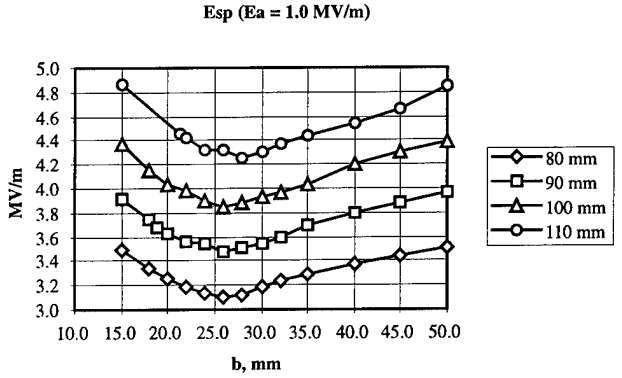



Figure 3: The $E_{sp}$ as a function of b.

The requested reduction of the $E_{sp}$ with respect to the circular iris profile ranges from -4.6% ( r = 100 mm) to -7.2% ( r = 80 mm). The other EM cavity parameters are not influenced by this elliptic profile. The elliptical shape of the iris seems to be a good alternative that matches the SC design specifications.

*1.2 The EA-1 cell design for* $\beta = 0.5$

The present choice of $\beta = 0.5$ for the first accelerating structure allows a more comfortable design, since the cavity axial length is increased. All the previous results on the elliptical iris profile still hold. Due to the increased sizes, another cavity shape parameter can be further optimized, the hat radius R. Preliminary studies suggest to keep $R \geq 50$ mm. Once the elliptical iris profile is optimized the $E_{sp}$ value for both hat radius R = 55 mm and R = 50 mm does not change. But a big difference is found in the shunt impedance value, which is 30 % greater for R = 55 mm. The choice of which profile is better depends on the possibility to use the existing CERN manifacturing tools or on the possibility to save the 30% of the refrigerator power. Figure 4 shows one of the optimized profile and table 1 the $TM_{010}$ $\pi$-mode for both the shapes.

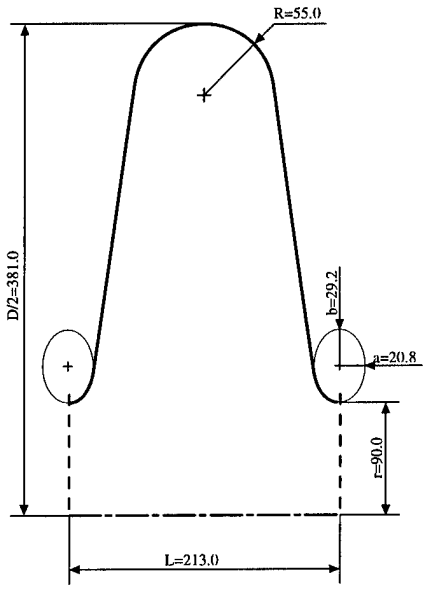



Figure 4: The EA-1 cell final shape.

| | R=55mm | R=50mm | LEP2 |
|---|---|---|---|
| Fr, MHz | 352.2 | 352.2 | 352.0 |
| K, % | 1.55 | 1.92 | 1.76 |
| $E_{sp}/E_a$ | 3.29 | 3.33 | 2.35 |
| $H_{sp}/E_a$ Gauss/MV/m | 62.4 | 71.2 | 39.1 |
| Z, MΩ | 0.47 | 0.37 | 3.51 |
| Q | 29400 | 27800 | 57600 |

Table 1: Parameters of the $TM_{010}$ $\pi$-mode for both the two EA-1 cells and the LEP2 cell, as a reference values.

*1.3 The EA2 cell design for* $\beta = 0.625$

The increase of the axial cell length also enlarge the hat radius.

It has been shown that the $E_{sp}$ does not change once the elliptical profile has been chosen. This result allows to start the design with a cell shape that matches the requested specifications and then to optimize the elliptical iris profile.

To keep the K value greater than 1.5%, the hat radius for the EA-2 cell should be greater than 70 mm. Better values of the peak surface magnetic field and shunt impedance are found for R = 80 mm and beam tube

radius r = 100 mm. Starting with these dimensions the elliptic iris shape is optimized. The minimum value of $E_{sp}$ is reached for an ellipsis axis b = 48 mm and b/a=1.59. Table 2 shows the cavity EM parameters.

*1.4 The EA3 cell design for* $\beta = 0.80$

This is the last and less difficult cavity to design, since, due to its axial length, the hat radius R ranges from 51.0 mm to 65.0 mm.

Trying to increase the shunt impedance with a larger value of R and smaller value of r leads to an increase of the peak surface electric field. A good compromise is reached with R = 120 mm and r = 110 mm. The miminum value of $E_{sp}$ is found as before, for an elliptic axis b = 58 - 60 mm and an eccentricity b/a=1.6.

| | EA-2 | EA-3 | LEP2 |
|---|---|---|---|
| Fr MHz | 352.2 | 352.2 | 352.0 |
| K % | 1.57 | 1.58 | 1.76 |
| $E_{sp}/E_a$ | 2.65 | 2.27 | 2.35 |
| $H_{sp}/E_a$ Gauss/MV/m | 54.1 | 45.2 | 39.1 |
| Z, MΩ | 0.94 | 1.95 | 3.51 |
| Q | 36900 | 47000 | 57600 |

Table 2: EA-2 and EA-3 optimized cavity parameters.

## 2 MULTICELL DESIGN

The full cavity is made up of four cell structure. This number seems to be a good compromise between a cavity with a larger number of cells, which has more fabrication drawbacks and a smaller acceptance range in β, and a cavity with fewer cells, which has lower accelerating voltage for similar costs.

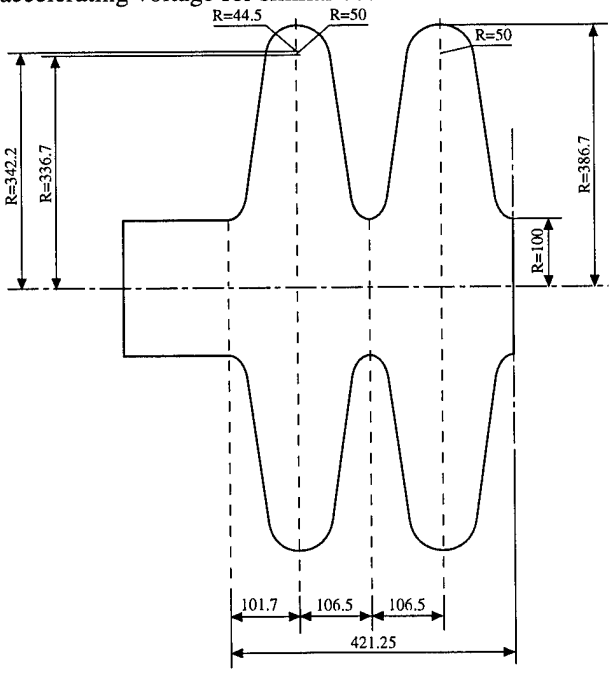



Figure 5: Half of theEA-1 cavity.

In all cavities the external cell has been adjusted to get an acceptable field flatness for the operating $TM_{010}$ π-mode. To compensate this mode the cell hat radius of the external half-cell has been changed. The side wall inclination and the length of the axes of the ellipse have been kept constant by adjusting correspondingly the axial length of the external half-cell. In this way the peak electric field behaviour in the external cell iris region is similar to the one found for the single cell. The beam tube radius has been left untouched as well. Figure 5 shows the final result for the EA-1 cavity. Similar considerations hold for the EA-2 and EA-3 multicell design.

The acceleration efficiency η of each cavity for all proton energies in consideration has been evaluated. Due to the tail behavior of the end cell electric field the η reaches the peak value for a particle speed that is slightly higher than the $\beta = \beta_0$ value.

| Cavity | EA-1 | EA-2 | EA-3 |
|---|---|---|---|
| Input Energy, MeV | 100 | 209 | 411 |
| η at Input Energy | 0.64 | 0.86 | 0.83 |
| Output Energy, MeV | 209 | 411 | 997 |
| η at Output Energy | 1.09 | 1.04 | 1.03 |
| Number of cavity | 32 | 36 | 80 |

Table 3: Energy range, efficiency and number of cavities of the Linac sections. The η normalization has been done for $\beta = \beta_0$.

## 3 ACKNOWLEDGEMENTS

The authors are pleased to acknowledge D. Boussard, E. Chiaveri and J. Tückmantel of CERN-SL, Geneva, and R. Parodi of INFN, Genoa, for their helpful discussions.

## 4 REFERENCES

[1] C. Rubbia and J.A. Rubio, "A Tentative Programme Towards a Full Scale Energy Amplifier", CERN/LHC/96-11 (EET), 15th July 1996.

[2] C. Pasotti, P. Pittana, M. Svandrlik, "LEP SC Cavities for Particles with β<1", Sincrotrone Trieste internal note August 1996, unpublished.

[3] E. Haebel, P. Marchand and J. Tückmantel, "An Improved Superconducting Cavity Design for LEP", CERN/EF/RF 84-2, 2nd April 1984.

[4] P. Fernandes and R. Parodi, "LALAGE-A Computer Program to Calculate the TM01 modes of Cylindrically Symmetrical Multicell Resonant Structures", *Particle Accelerators*, 1982, Vol. 12 pp. 131-137.

[5] J. Tückmantel, "Superconducting Cavities for Reduced β", CERN-SL-Note 96-64 RF, 1996 Geneva.

[6] C. Pasotti, P. Pittana and M. Svandrlik, "LEP SC cavities modified for Particles with β<1", minutes of the Meeting on EA-Accelerator held at CERN, Geneva, on the 23rd September 1996.

# NEW WINDOW DESIGN OPTIONS FOR CEBAF ENERGY UPGRADE

L. Phillips, J. Mammosser, and V. Nguyen, Thomas Jefferson National Accelerator Facility,
12000 Jefferson Avenue, Newport News, VA 23606 USA

*Abstract*

As the Jefferson Laboratory upgrades the existing CEBAF electron accelerator to operate at higher energies, the fundamental power coupler windows will be required to operate with lower RF dissipation and increased immunity to radiation from cavity field emission. New designs and modifications to existing designs which can achieve these goals are described.

## 1 INTRODUCTION

The Continuous Electron Beam Accelerator Facility (CEBAF) located at Thomas Jefferson National Accelerator Facility, in Newport News, Virginia is fully operational. The accelerator consists of 165 hermetically sealed cavity pairs, each providing 5 MeV energy gain per pass for the machine. RF power from a 5 KW klystron, coupled through two RF windows, drives each cavity independently to accelerating gradients in excess of 5 MV/m. One of these windows is made of ceramic and, attached to the cavity, operates at 2 K (fig 1). The history and performance of this cold window, a discussion of needs for new designs for the machine energy upgrade and the concepts being developed at Jefferson Lab will be discussed.

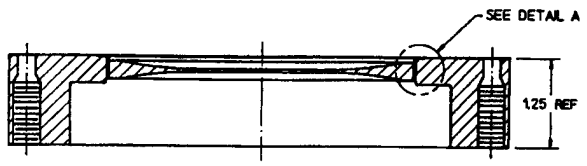



Figure 1

## 2 ORIGINAL DESIGN

The original input coupler for the CEBAF accelerator includes two windows in series (Fig. 2). This design attempts to minimize the contamination of the cavity pairs by hermetically sealing the cavity pair early in the assembly process. A ceramic window, indium seals and gate valves at the ends of the pair provide the hermiticity. The design requirements for the cold window were: low voltage standing wave ratio (VSWR) at the fundamental frequency, propagation of the certain higher order modes (HOM) which are not adequately damped by the HOM absorbers, and a cryogenically compatible metal-ceramic design with low particulate generation. The window design (Fig. 1) consists of a thin ceramic with small compensating irises to minimize VSWR both at the fundamental and HOM frequencies. The resulting VSWR is 1.1 at 1500 MHz and 1.3 at 1800 MHz.

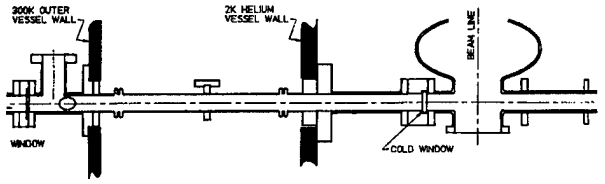



Figure 2

## 3 PERFORMANCE OF CEBAF WINDOW

The most serious performance limitation experienced with the CEBAF cold window is its contribution to machine interlock trips [1,2,3]. The fundamental power coupler, consisting of a cold window separated from a warm window by an evacuated waveguide, is protected by two primary interlocks. One interlock is a photomultiplier tube viewing the waveguide region between windows that shuts off RF klystron power if light appears. A second interlock shuts off RF power if the pressure in the waveguide rises above 1 x $10^{-7}$ Torr. These interlocks protect both windows from damage due to sustained RF discharge. There are two types of coupler related interlock trips which are not distinguishable in operation as to cause.

A pressure burst in the waveguide vacuum space can occur from an RF transient or phase glitch which rapidly alters the thermal profile of the waveguide releasing hydrogen, for example, from the cold end of the waveguide where the thermal time constant is short. Such transients are known to occur when RF power is switched off to an entire cryomodule at once, tripping all cavities in the cryomodule. A pressure burst can cause a gas discharge producing both a light trip and a vacuum trip.

Surface flashover on the window will also produce a light trip and initiates gas desorption, producing a vacuum trip as well. This leaves some ambiguity with respect to the cause of a trip.

Cavities tripping at regular intervals however indicate that perhaps 90% of the coupler-related interlock trips in CEBAF are due to surface flashover on the ceramic [2] resulting from a charging process.

A number of studies have shown that the ceramic window becomes charged from electronic activity in the RF cavity in the presence of field emission. Ultimately, the surface charge builds to some threshold and is relieved by surface flashover. The RF fields alone at the window are not sufficient to induce surface flashover in the absence of surface charge. This charging effect followed by a discharge leads to a periodicity in the interlock trips for a given cavity operated with field emission at a fixed gradient. The period is observed to decrease with increasing RF power dissipated in field emission in a test

0-7803-4376-X/98/$10.00 © 1998 IEEE

cavity, consistent with a model of surface charging and breakdown threshold.

For these reasons it is necessary to eliminate surface charging of the RF windows in order to take advantage of higher gradients with reduced interlock trip rate. Some smaller percentage of trips could be eliminated by improving the waveguide vacuum stability.

A second performance issue with the cold ceramic window is heat load and economics. The ceramic window loss at 5 MV/m is about 0.5 watts but at 10 MV/m it would be 2.0 watts. At 2 K this represents an objectionably high power cost.

Sources of loss for this window were examined through a series of waveguide resonator tests. A window model with various interchangeable parts was tested at 2 K by measuring the $Q$ of the resonator under differing test conditions. Different ceramic materials were compared as well as ceramic metallization and position of the window in the resonator standing wave pattern.

In general, very-high-purity ceramics such as sapphire and pure polycrystalline aluminas have lower loss than glass-bearing ceramics. Ceramic metallization was the dominant source of heat, and total loss was highest when the window was placed in an electric field maximum.

### *3.1 Punctures*

Very small window punctures are also related to the presence of field emission in the cavity. These are very small leaks, invisible to the naked eye and induced by window charging/discharging [1]. Several such leaks are know to exist in the accelerator. Their impact on machine operation is difficult to assess since the primary purpose of the cold window is to reduce particulate contamination of the cavity during initial assembly and installation in the cryomodule. Once a vacuum is maintained on both sides of the window it continues to serve this function even with a puncture. The major risk might be the possibility of shedding small particulates of ceramic from the puncturing process which could end up in the cavity.

## 4 LIMITATIONS OF CEBAF WINDOW FOR ENERGY UPGRADE

The current machine energy upgrade plan requires each cavity to operate at an accelerating gradient around 10 MV/m at $Q$-value of $5X10^9$. With 60% of the cavities limited by field emission in vertical test at gradients of 7-8 MV/m, the cavities for upgrade will most likely need to operate with some field emission, and this could produce an objectionable machine trip rate if modifications are not implemented. In order to reduce this trip rate, the window ceramic will have to be shielded from electron spray and radiation. Currently 153 cavities in the accelerator are gradient-limited by arcing [5]. At present, care has been taken in understanding each cavity trip limitation, and gradient settings are administratively controlled to minimize the impact on machine performance.

A second performance issue with the ceramic window is one of economics. The ceramic window adds to the power dissipated in the 2K bath during operation and any reduction of this power could be a cost savings. The loss generated by the ceramic window has two components, the metallization of the ceramic which is the dominant loss and dielectric loss of the ceramic. Design for higher-energy operation must address this heat load.

Cold window punctures are a product of field emission in the cavity. There are certain cavities which have repeatedly punctured replacement windows. Figure 3 shows cavity IA174 RF performance in a vertical test that resulted in a punctured window. This was typical of the type of performance that resulted in a ceramic puncture, with heavy field emission at low accelerating gradient. In this particular case, the puncture was located in the radius where the ceramic is ground from 6mm to 1mm and 4.3 cm from the end. Punctures typically were located at this ground radius. The circumstances producing punctures are now sufficiently understood that we can expect this problem to disappear when surface charging of the window ceramic is eliminated.

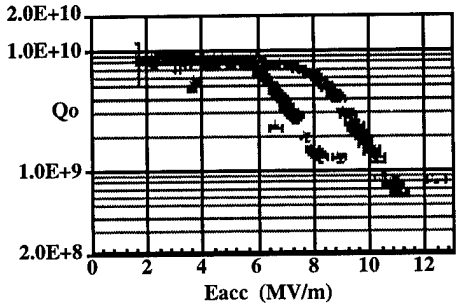



Figure 3 IA174 vertical test data that resulted in a ceramic puncture.

## 5 DESIGN MODIFICATIONS FOR THE ENERGY UPGRADE

### *5.1 2K Heat Load*

RF loss occurs primarily in the ceramic braze metallization, and its reduction could be accomplished several ways.

One is to reduce the total area of metallized ceramic exposed to RF current. Test windows have been constructed with braze areas reduced to one half of the original production value without sacrificing seal integrity. Using this technique window loss, as measured in a waveguide resonator, has been reduced to less than half the production value.

Another opportunity presently being explored is to shield the seal area, where possible, from RF currents. This is not as easy to do for current crossing the seal as for current in the direction of the seal. An ideal location

for this is at the iris protruding from the short wall of the waveguide. RF current is concentrated on the iris, running along the iris at the midplane of the guide. Extending the metallization into the heavy niobium portion of the iris transfers this current to the niobium and away from the braze metallization. MAFIA studies and infrared thermal imaging have shown that most of the loss occurs at the iris.

### *5.2 Interlock Trips*

Currently, interlock trips are not expected to be a serious limitation to the operation of CEBAF at energies up to 5 GeV [4]. In going to significantly higher energies, interlock trips would be the chief constraint on the energy reach of the machine using the current coupler configuration. The simplest approach is to remove the window from a position of exposure to the electron and x-ray flux from the cavity. Consequently, prototypes were built incorporating the window into the end of a waveguide extension which joins the cavity to the wall of the 2 K cryostat vessel. This extension moves the window about 15 cm from its original position at the cavity FPC waveguide flange. It can still view the cavity, but the solid angle is reduced. Extended windows of this style were installed on four cavities in the accelerator but interlock trips were reduced not eliminated [6].

Another extension window design, the "dogleg coupler", shields the ceramic from direct view of the cavity using an opaque undulation of the waveguide. Direct electron paths are eliminated and the undulation is deep enough to allow external lead shielding interrupting direct x-ray paths as well. The VSWR of the undulation is 1.06 at 1.5 GHz and 1.013 at 2 GHz.

A prototype of this design was tested in a vertical dewar with interlock circuitry attached and the window electrically isolated such that window charging could be monitored with an electrometer. The cavity was first tested with a production window in the normal machine configuration but also electrically isolated. This window produced 7 interlock trips in 5 hours of operation with 11 watts of RF power dissipated in field emission. Window current varies from 1 to 20 nanoamperes.

A dogleg coupler was installed on the same cavity and run for 10 hours with no interlock trips. Window current was approximately 3 x $10^{-11}$ amperes with 17 watts of RF power in field emission. Further tests are planned (Figure 4).

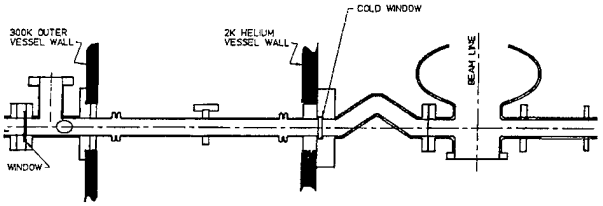



Figure 4 Dogleg Fundamental Power Coupler

The remaining issue of waveguide vacuum stability can be eliminated by using a waveguide choke joint. One side of the choke joint would be superconducting and the other side at the heat shield gas temperature. A bellows spanning the choke joint would experience a continuous thermal transition but no RF current. The thermal profile would be constant in this arrangement for all portions of the coupler below the radiation shield intercept at 50 K.

In addition to improved pressure stability in the waveguide vacuum space, a choke joint provides the additional benefit of eliminating both RF and conduction heat loads from the waveguide into the 2 K bath. The design issues which must be satisfied are: 1.) adequate damping of higher order modes which are only damped through the input coupler, 2.) absence of multipacting within the choke joint, and 3.) no significant energy density within the bellows. This option is currently being explored.

## 6 CONCLUSION

Interlock trips, 2 K heat load, and punctures are currently limiting features of the CEBAF cold RF window design. These limitations do not significantly limit machine performance up to 5 GeV. In order to reach higher energies for the CEBAF upgrade, new window designs are required. Several modifications to the window design have been identified to accomplish this. No interlock trips have been observed in preliminary tests of a dogleg coupler design. Lower loss design options are being studied and some significant heat load reduction has been achieved.

## 7 ACKNOWLEDGMENTS

The authors would like to thank for valuable contributions: C. Reece of Jefferson Lab, E. Chojnacki of Cornell, T. Schultheis and M. Coleman of Grumman and S. Spata of Jefferson Lab.
This work was supported by the U.S. DOE under contract number DE-AC05-84ER40150.

## REFERENCES

[1] Larry Phillips, Current Status of Our Understanding of Electronic Phenomena at the Cold Window. CEBAF Tech Note TN#93-084

[2] V. Nguyen-Tuong, N. Luo, L. Phillips, C. Reece, Electronic Activity at the CEBAF Cold RF Window Induced by Cavity Operation.

[3] L. Phillips, C. Reece, T. Powers, V. Nguyen-Tuong, Some Operational Characteristics of CEBAF RF Windows at 2K, Proceedings of the 1993 Particle Accelerator.

[4] Charles Reece, Private Communications.

[5] C. E. Reece, M. Drury, M. G. Rao, V. Nguyen, Improvement of the Operational Performance of SRF cavities via in situ Helium Processing and Waveguide Processing these proceedings.

[6] J. Benesch, Private Communcations

# IMPROVEMENT OF THE OPERATIONAL PERFORMANCE OF SRF CAVITIES VIA *IN SITU* HELIUM PROCESSING AND WAVEGUIDE VACUUM PROCESSING

C. E. Reece, M. Drury, M. G. Rao, and V. Nguyen-Tuong
Thomas Jefferson National Accelerator Facility
12000 Jefferson Avenue, Newport News, VA, 23602 USA

*Abstract*

The useful performance range of the superconducting rf (SRF) cavities in the CEBAF accelerator at Jefferson Lab is frequently limited by electron field emission and derived phenomena. Improvements are required to support future operation of the accelerator at higher than 5 GeV. Twelve operational cryomodules have been successfully processed to higher useful operating gradients via rf-helium processing. Progress against field emission was evidenced by improved high-field $Q$, reduced x-ray production and greatly reduced incidence of arcing at the cold ceramic window. There was no difficulty reestablishing beamline vacuum following the processing. Cavities previously limited to 4–6 MV/m are now operating stably at 6–9 MV/m. By applying a pulsed-rf processing technique, we have also improved the pressure stability of the thermal transition region of the input waveguide for several cavities. [1]

## 1 INTRODUCTION

The CEBAF accelerator at Jefferson Lab was designed and constructed to provide 200 μA, 4 GeV CW electron beams for physics research. Some portions of the acceleration system significantly exceeded the specifications and provide a good basis for extending the energy reach of the machine.[2] In addition, we have begun exploring means of obtaining incremental performance gains via *in situ* processing techniques. We intend to exhaust the opportunities for such gains as a first step toward significant upgrades of the machine into the 6–8 GeV region.

The 330 SRF cavities in CEBAF are individually powered by 5 kW klystrons. The principal limitation of the installed cavities is electron field emission and associated phenomena, such as x-ray production, charging and arcing at the cold ceramic rf window, and anomalous 2 K heat load. In addition, some cavities are constrained by the stability of the vacuum in the region between the 2 K and 300 K rf windows. Present capabilities project to possible operation of CEBAF at 5.5 GeV.

### *1.1 Motivation*

Based on progress to date, it appears a reasonable goal to make 6.0 GeV operation possible using existing cryomodules by gaining the additional 10% through *in situ* processing. If achieved, this would be the most economical route to 6.0 GeV.

As CEBAF has entered the mode of sustained beam delivery for physics experiments, opportunities for *in situ* processing are infrequent. Thus, we pursue effective methods which minimize the preclusion of beam operations and dove-tail with regular machine maintenance.

### *1.2 Background*

Helium processing of SRF cavities has been an established technique for many years, even though the exact mechanism by which it effects change remains unclear.[3] It is used to reduce electron field emission in a cavity. Helium is admitted inside the cavity to a pressure just below that suitable for rf discharge, and the cavity is operated at high stored energy with active field emission. Typically, a gradual weakening of the field emission is observed, although processing by events have been reported. It has been variously suggested that the FE current locally ionizes the helium gas, forming a local plasma which heats and melts the emission source, provides microscopically directed helium ion bombardment of the source, or enhances the local field to the point of drawing out current densities sufficient to explode the emitter.[4]

### *1.3 Cavity limitations*

The CEBAF cavities, though performing substantially better than initial specifications, are predominately limited in performance by field emission. Arcs at the cold ceramic rf window are strongly correlated with field emission in the associated cavity. Though some uncertainty remains, the arcs are understood as the discharge of charge accumulated on the ceramic due to either a shower of secondary electrons produced by impingement of primary FE electrons on the waveguide/beampipe region and/or photoelectric charging by low-energy x-rays.[5] The extremely high bulk resistivity of the 2 K ceramic produces long relaxation times, with the result that different cavities can be made to arc with periods that range from a few minutes to several hours, depending upon at what operating gradient they are set. Of the 330 SRF cavities, 153 are now limited in usable gradient by this arcing phenomenon.

## 2 METHODS

### *2.1 Instrumentation*

To accomplish the processing in the CEBAF tunnel, helium gas was supplied to a cryomodule through a port in a beamline ion pump. The attached manifold provided a turbomolecular pump and an RGA. A fixed volume of ~0.5 L was precharged with high-purity helium and connected to the manifold through a 0.2 micron particle filter and a remotely

0-7803-4376-X/98/$10.00 © 1998 IEEE

controlled needle valve. The quantity of helium admitted was measured by the reduction of pressure in the reservoir volume (typically ~ 5 standard torr-liters).

Ten cryomodules were processed in pairs supplied with helium from the warm girder between them. The beamline gate valves bracketing the cryomodule(s) to be processed were closed for the duration of the activity.

Rf drive for the klystron was provided by a VCO phase-locked-loop (PLL) rather than the standard CEBAF fixed-frequency rf controller. Standard system interlocks, except for beamline vacuum, were required to provide a permissive to the VCO system output.

### *2.2 Radiation measurements*

The best indicator of progress against field emission is an increased $Q_0$ at high gradient. Unfortunately, measurements of $Q_0$ on the cavities in CEBAF implies time-consuming calorimetric methods incompatible with beam operations. With very limited amount of time available for processing activities, we chose to use the x-radiation produced by a cavity as its signature of field emission.

Six Geiger-Müller tubes were placed around the cryomodule under test, one between each pair of rf warm windows and one on the beamline at each end of the module. The response of the G-M tubes was measured for each cavity, both before and after processing.

For the first cryomodule processed, we took the time to measure $Q_0$ before and after processing. These data correlated well with the radiation measurements.

### *2.3 RF controls for processing*

In the interest of enabling parallel processing, we attempted to develop a scheme for He processing using the standard rf control system. This proved unsuccessful. The CEBAF SRF cavity geometry is such that there exist, somewhere in the structure, conditions suitable for a multipacting (MP) barrier at a stored energy corresponding to $E_{acc}$ ~0.7 MV/m.

Although this barrier was occasionally observed in vertical testing during construction, it always processed away and has presented no operational problems. With the introduction of helium into the cavities, however, the situation changed. With only a few exceptions, the barrier was always present and when present, never processed. The helium effectively amplified the secondary electron yield, producing a hard barrier. The multi-bandwidth reactive tuning produced by the multipacting process made fixed-frequency operation impossible.

Although the MP barrier was encountered while using the VCO systems, we developed a technique which routinely bypassed the barrier so that helium-rf processing could proceed at high gradients. Noting that the MP always shifted the frequency higher, we found that if one detuned the VCO high, and slowly approached the upper limit of the capture range of the PLL, one could immediately bypass the MP barrier. The need to use a VCO PLL has thus far limited us to processing only two cavities at a time.

### *2.4 Thermal cycle*

A critical part of applying *in situ* helium processing is fully removing the supplied helium from the beamline to support beam operations. For this purpose, we have found that a warmup to 20 K is quite adequate for removal of the helium. Limiting the warmup to this range allows us to avoid mechanical stresses and also minimize the total time required.

Following the completion of the helium processing, the inlet JT valve of each cryomodule was closed and 140–250 W supplied through resistive heaters. The valve to the low pressure (40 mbar) return header remained fully open. This heat reduced the 2 K liquid helium level to ~5% in 6–10 hours. The balance of the helium was boiled off with 60 W and the helium vessel and cavities warmed to ~20 K, as measured by diode thermometers mounted on the cavity assemblies.

During this warmup the turbopump was allowed to pump on the beamline to remove the helium, and also whatever hydrogen was liberated. After a dwell time of approximately 1 hour at 20 K, with beamline pressure now in the $10^{-8}$ torr range, refill of the module began. Typically, a module refilled in 6–10 hours, at which time it was ready for rf testing. In one case, the cavities were tuned up and immediately applied to beam operations, with post-processing characterization deferred for several days.

## 3 GAS DYNAMICS

We established the target He pressure to be $4\times10^{-4}$ torr as measured by an RGA at ambient temperature. Equilibration times for 2 K helium at these pressures was observed to be at least several hours. Operation of the rf during the addition of the helium seemed to speed gas migration to the far end of the cryomodule.

Each of the 90 cavities processed was operated at elevated field levels for 20–60 minutes. Frequently, the applied rf power was limited by instabilities in the vacuum between the cold and warm rf windows. After the 20 K warmup, we noticed improved stability of this vacuum, which prompts us to plan future helium processing efforts to include both a before and after cryocycle.

There were no difficulties reestablishing beamline vacuum due to residual helium. In a few instances, there was a slow recovery of the hydrogen partial pressure in the $10^{-9}$ torr range that caused some concern. A similar response was observed following a thermal excursion of the 50 K heat shield circuit of the accelerator, suggesting that the phenomenon was due to redistribution of adsorbed hydrogen in the thermal transition regions.

## 4 RESULTS

To date, we have applied helium-rf processing at 2 K to 90 cavities in 12 of the 41 installed CEBAF cryomodules. We have also applied pulsed-rf processing to condition the input waveguide region in 10 cryomodules.

### *4.1 Reduced radiation production*

Progress against field emission was observed by the reduction of x-radiation produced by the field-emitted electrons. Figure 1 illustrates this shift as measured by the G-M tubes outside the cryomodule.

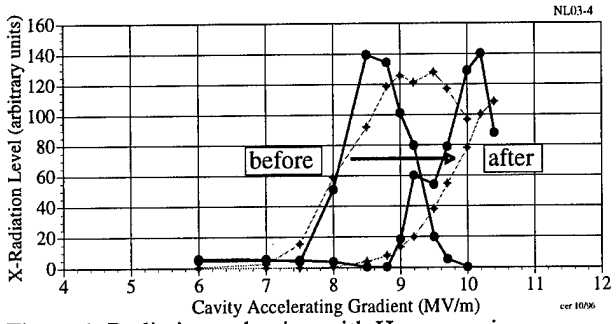



Figure 1. Radiation reduction with He processing.

### *4.2 Reduced arcing and higher gradients*

Many of the cavities subjected to helium processing were previously limited by arcing at the cold window. Following processing, the cavities could be operated stably at higher gradients. Figure 2 shows the distribution of maximum gradients for the processed cavities according to their performance-limiting constraint.

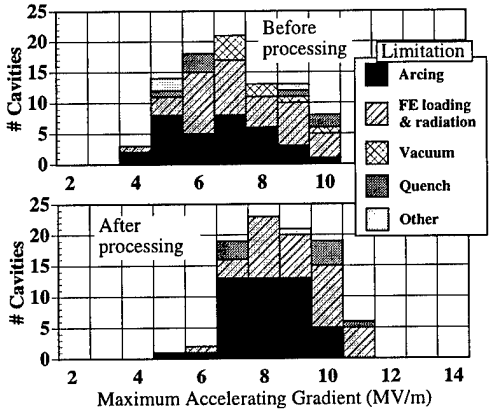



Figure 2. Cavity improvements with helium processing.

During the last year, we have recalibrated the cavity accelerating gradients based on actual beam acceleration. Following this, the helium processing effort also permitted us to reestablish the operational limits for some cavities.

### *4.3* Q *improvements*

Careful measurements were made of the unloaded $Q$-factor for cavities in the first cryomodule processed. All FE-limited cavities showed improvement.

| Cavity # in NL03 | $E_{acc}$ (MV/m) | $Q_0$ ($\times 10^9$) | |
|---|---|---|---|
| | | Before | After |
| 2 | 7.7 | 1.5 | 3.3 |
| 4 | 8.7 | 2.5 | 4.1 |
| 6 | 6.8 | 2.1 | >5.3 |
| 8 | 8.8 | 2.85 | 4.7 |

### *4.4 Waveguide vacuum processing*

The waveguide vacuum in 10 cryomodules was conditioned by applying low duty cycle rf pulses to each cavity, first detuned, and then tuned. The forward power was gradually increased to 4–5 kW, subject to maintaining the waveguide vacuum better than $1\times10^{-7}$ torr. The process requires ~4 hours. In many cases, the vacuum stability improved markedly. This stability reduces a complication that arises when a cavity is slightly mistuned. The relative merits of this compared with a thermal cycle to 20 K or higher remain an open question.

## 5 SUMMARY AND PROSPECTS

Helium processing and requalification of cavities have increased the installed CEBAF voltage by 63 MV, corresponding to an added 315 MeV for 5-pass beam. This improvement made possible the 1.12 GeV single-pass test run completed in April 1997. At this rate we project an additional 135 MV gain from processing the balance of the machine, which could be adequate for extending the energy reach of CEBAF to 6 GeV. Figure 3 presents the present voltage capacities of the CEBAF cryomodules.

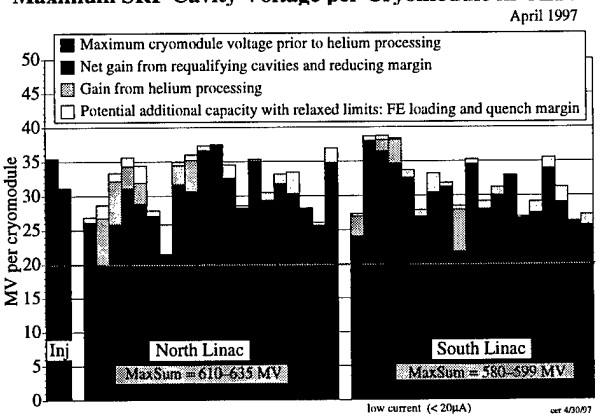



Figure 3. Maximum cryomodule voltages in CEBAF

## 6 ACKNOWLEDGMENTS

During processing, we received valuable assistance from L. Phillips, T. Powers, J. Mammosser, J. Brawley, K. Ryan, A. Lapolla, L. Harwood, G. Marble, F. Humphrey Jr., J. Heckman, K. Macha, J. Preble, and R. Bennett.

## 7 REFERENCES

[1] Work supported by the U.S. Department of Energy, contract DE-AC05-84ER40150.

[2] 'Operation of CEBAF with Heavy Beam Loading', A. Hutton, these proceedings.

[3] 'Evidence for surface-state-enhanced field emission in rf superconducting cavities', H. A. Schwettman, J. P. Turneaure, and R. F. Waites, J. Appl. Phys., **45**, (1974) 914.

[4] 'Microscopic Investigation of Field Emitters Located by Thermometry in 1.5 GHz Superconducting Niobium Cavities', J. Knobloch and H. Padamsee, Particle Accelerators, **53**, (1996) 53.

[5] 'Electronic Activity at CEBAF Cold RF Window Induced by Cavity Operation', V. Nguyen-Tuong, N. Luo, L. Phillips, C. Reece, EPAC 94 Proceedings, Volume 3, pp. 2200–2202.

# JEFFERSON LAB IR FEL CRYOMODULE MODIFICATIONS AND TEST RESULTS

M. Wiseman, J. Benesch, M. Drury, J. Fisher, D. Machie, J. Mammosser, L. Phillips, and J. Preble, Thomas Jefferson National Accelerator Facility, 12000 Jefferson Avenue, Newport News, Virginia 23606 U.S.A.

*Abstract*

The Infrared Free Electron Laser being constructed at the Thomas Jefferson National Accelerator Facility will require a 42 MeV, 5 mA electron accelerator. The accelerator design requires a 10 MeV injector and a two pass 32 MeV linac, one pass for acceleration and one pass for energy recovery. In order to minimize the cost of the linac, standard CEBAF 1497 MHz Superconducting Radio Frequency cavities and cryomodules are being used with minimal changes. Two SRF cavities, housed in a quarter cryomodule, operate at a nominal 10 MV/m to provide the injector energy. The linac is composed of one cryomodule, housing eight SRF cavities operating at an average gradient of 8 MV/m. The modifications to the cryomodule are being made to handle the higher beam current, to improve RF control, and to increase machine reliability. The modifications to the higher order mode (HOM) loads, cavity tuners, cavity beam line, warm and cold RF windows, and cryogenic shield are described. Test results from the injector quarter cryomodule are also presented.

## 1 INTRODUCTION

The Infrared Free Electron Laser currently being constructed at the Thomas Jefferson National Accelerator Facility (Jefferson Lab) is to serve as a research tool for both the DOD and industry [1]. This facility will deliver up to 1 kW of 1 to 3 micron IR light to one of six user laboratories. A photocathode electron gun produces a 500 keV, 5 mA beam which is boosted to 10 MeV by a Continuous Electron Beam Accelerator Facility style quarter cryomodule containing two 1497 MHz Superconducting Radio Frequency cavities before injection into the main accelerator ring. The accelerator linac boosts the electron energy to 42 MeV via a cryomodule containing eight SRF cavities. The beam then passes through the IR wiggler magnet which generates the IR light. The electron beam is then recirculated back through the cryomodule, where the electron energy is recovered before being dumped at 10 MeV. The photocathode electron gun and the quarter cryomodule for the injector have already been built and are currently being tested at Jefferson Lab.

The higher beam current, 5 mA vs. CEBAF's 200 μA, required that certain modifications be done to the standard CEBAF cryomodule. The design changes for the cryomodule are compatible with the requirements for a possible upgrade of the 42 MeV IR FEL accelerator to a 200 MeV UV FEL accelerator. Other changes have also been incorporated to improve machine reliability and operability.

## 2 SRF REQUIREMENTS AND TEST RESULTS

The FEL requirements for the SRF cavities are given in Table 1. The energy requirements chosen were based on the average CEBAF cavity results and RF control requirements for the FEL. Changes have been made to several of the cavity peripherals with no changes to the CEBAF 1497 MHz SRF cavities themselves. New higher order mode assemblies have been developed to route the HOM energy to the cryomodule's 50 K thermal shield.

TABLE 1. IR FEL SRF Cavity Requirements.

| | Injector Quarter Cryomodule | linac Cryomodule |
|---|---|---|
| Avg. Gradient (MV/m) | 10 | 8 |
| $Q_0$ at Avg. Gradient | $3 \times 10^9$ | $3 \times 10^9$ |
| $Q_{ext}$ (+/- 20%) | $1.3 \times 10^{11}$ | $5.2 \times 10^{11}$ |
| $Q_{fpc}$ | $1.3$ to $4.4 \times 10^6$ | $3.3$ to $6.6 \times 10^6$ |
| HOM Power/Load | 3.8 W | 7.5 W |
| RF Power/Cavity | 30 kW | 2.5 kW |

The cavities chosen for the injector quarter cryomodule have undergone extensive testing and special processing including heat treatment before being selected for use in the FEL [2]. The cavity pair has been tested four times, twice in the vertical test area and twice since being assembled into the quarter cryomodule. Cavity IA 362 exceeds the design requirements while cavity IA 328 is limited by $Q_0$ degradation to 9 MV/m. The required injection energy of 10 MeV can be met by running the cavities at 11 and 9 MV/m respectively.

## 3 HOM LOADS, HEAT SINKS, AND THERMAL SHIELD

The design changes for the HOM loads, heat sinks and thermal shields meet the requirements of a possible upgrade to a 200 MeV UV FEL accelerator. For the UV linac, the higher order mode power per load is presently 15 W, or 240 W per cryomodule. Design changes were made to the HOM assemblies and cryostat in order to heat sink this power to the 50 K thermal shield where it is more efficiently dissipated (FIGURE 1). Each heat sink and the thermal shield was designed to dissipate 30 W of power per load.

Each HOM load assembly now consists of a ceramic load, a copper base and heat sink rod, and a stainless steel flange with a pant leg thermal stand off to limit the total static and dynamic heat load to 2 K to less than 1 W. For

0-7803-4376-X/98/$10.00 © 1998 IEEE

the quarter cryomodule, ceramic loads [3] were used and brazed to the copper base. This assembly required expensive machining of the copper base and proved difficult to produce a reliable ceramic to copper braze joint. In addition, the glassy carbon ceramic originally used in CEBAF because of its 2 K RF absorption characteristics, is difficult to produce to the required specifications. For these reasons, the design for the cryomodule has been changed. The ceramic load for the cryomodule will be a silicon carbide ceramic which has adequate RF absorption for the FEL at temperatures above 40 K. The ceramic to copper base has also been changed to a bolted joint with an indium gasket. This design has proven to be more reliable and much more cost effective to produce (FIGURE 2).

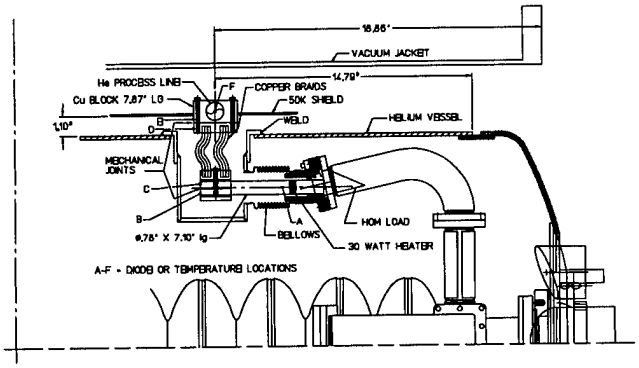



FIGURE 1. FEL cryomodule cross section showing modifications and test instrumentation.

The rest of the heat sink design consists of a copper braid assembly which is bolted to both the HOM assembly heat sink rod and to the 50 K thermal shield. Copper braids were used to provide flexibility in the design to allow for assembly, mechanical tuning of the SRF cavities, cooldown mechanical contractions, and to mitigate microphonic coupling to the cavities from the thermal shield. The 50 K thermal shield was also modified in order to route the helium process lines as close to the HOM loads as possible and to provide adequate thermal area for convective cooling of the localized HOM heat loads. The process line was also enlarged to accommodate higher helium flow rates and to reduce flow induced vibration effects.

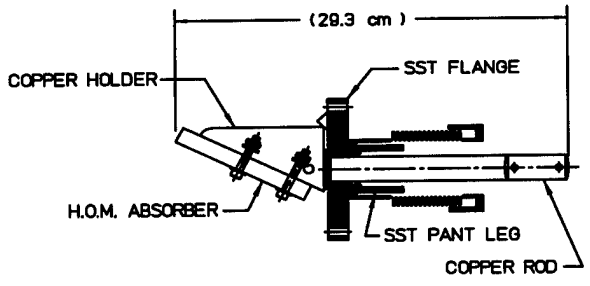



FIGURE 2. FEL HOM load and heat sink design.

Provisions for testing the heat sink design were made in the quarter cryomodule before beginning cyromodule production. Thirty watt strip heaters were mounted on the copper heat sink rods near the HOM loads and diodes were mounted along the heat sinks as shown in FIGURE 1. Test results during the quarter commissioning showed good agreement with the design values. The heat strap connection from the HOM loads to the shield for the production cryomodule has been modified slightly to make assembly of the cryomodules easier with only a small reduction in thermal performance. Microphonic effects on the SRF cavities from the heat sink design and increased shield flow were also tested with no measurable effects.

## 4 MAGNETOSTRICTIVE TUNER

The FEL will use energy recovery to reduce the RF power needed, thereby improving the overall efficiency of the machine, and to reduce the beam power deposited in the dumps. To ease the demands on the RF controls, a magnetostrictive tuner has been added to the existing CEBAF mechanical tuner. The magnetostrictive tuner is designed to deliver +/- 250 Hz of mechanical tuning on a 1 second time frame and will be used during machine operations. The CEBAF mechanical tuner delivers +/- 200 kHz of tuning, but is slow and is only used during machine setup. The magnetostrictive tuner is a 200 alloy nickel tube surrounded by a 2.5 kgauss superconducting solenoid. An iron sheath is used to concentrate the magnetic fields. Two layers of Mu metal provide magnetic shielding for the cavities prior to cooldown and one layer of Nb is used to provide shielding at 2 K during operation. The design and early test results are better described elsewhere [4].

## 5 QUARTER CRYOMODULE WARM RF WINDOWS AND VACUUM RF WAVEGUIDE

In the injector quarter cryomodule, 30 kW of RF power is used to accelerate the 5 mA beam in each cavity. This is ten times the power used in the CEBAF and FEL linacs. In order to handle this power, the polyethylene window used in the linacs has been replaced with a ceramic window and additional heat intercepts have been added to the vacuum RF waveguide to prevent thermal runaway and improve vacuum stability in the waveguide. The warm ceramic window is the same ceramic and essentially the same design used for the cold RF windows in CEBAF. The window is vacuum brazed into a 0.25 cm thick nickel eyelet and then electron beam welded into a stainless steel flange. The flange is copper plated to reduce RF heating around the window. A Helicoflex seal is used to complete the vacuum/RF seal with the existing waveguide. The windows will be qualified with 50 kW of RF power prior to use on the quarter cryomodule.

The thermal effects of the additional RF power in the CEBAF RF waveguide were studied using a finite difference program [5]. These results indicated a possible

thermal runaway condition in the existing CEBAF waveguide. Two additional thermal intercepts were added and their location optimized to minimize the static and dynamic heat loads to both the thermal shield and the 2 K bath (FIGURE 3). Additionally, active cooling will be used at the room temperature end of the waveguide to both stabilize the waveguide, and to prevent undue heating of the warm RF window.

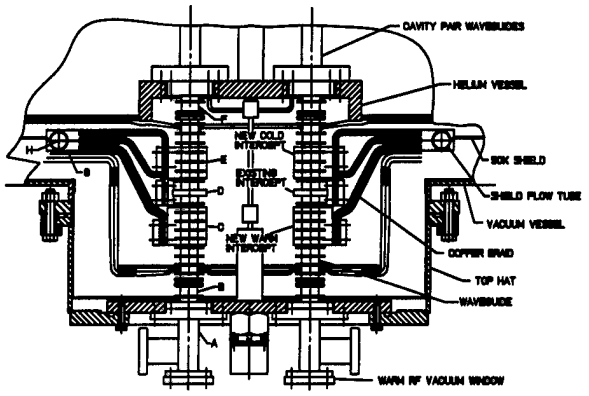



FIGURE 3. FEL quarter cryomodule showing waveguide modifications.

The FEL quarter cryomodule has recently undergone two different cold tests. The static thermal profile in the waveguide agrees quite nicely with the predicted results. The warm window and waveguide have been tested off resonance for extended periods with up to 15 kW of forward power and for short periods with up to 19 kW of RF power. The thermal profiles in the waveguide are in general agreement with those predicted (FIGURE 4) with no thermal runaway. There has been some difficulty in producing reliable warm ceramic windows. Several different materials and assembly techniques have been tried. Several failures have occurred during testing and more work is required before a window is available that will be considered ready for machine operation.

## 6 CRYOMODULE BEAM LINE

The FEL's 5 mA beam and recirculation for energy recovery require two changes in the cryomodule stainless and Nb beam line. First, in order to reduce the beam impedance effects and RF induced heating to 2 K, RF shielding has been employed on all cold stainless steel bellows in both the quarter and full cryomodule. RF shielding was also employed on the 2.8 cm gate valves on the quarter cryomodule and on the beam line pump drops for the linac cryomodule. The second change was made in order to increase beam transmission through the cryomodule during energy recovery. The Nb spool pieces between the cavities were increased from 3.5 cm to 4.8 cm. The spool piece diameter was not increased further due to RF crosstalk concerns between the cavities. The stainless steel beam pipe into and out of the cryomodules were similarly increased. An economical 5 cm RF shielded gate valve was not readily available to replace the eight gate valves inside the cryomodule, so the three sections of stainless steel beam pipe between the cavity pairs were increased to 7 cm ID and unshielded gate valves were used.

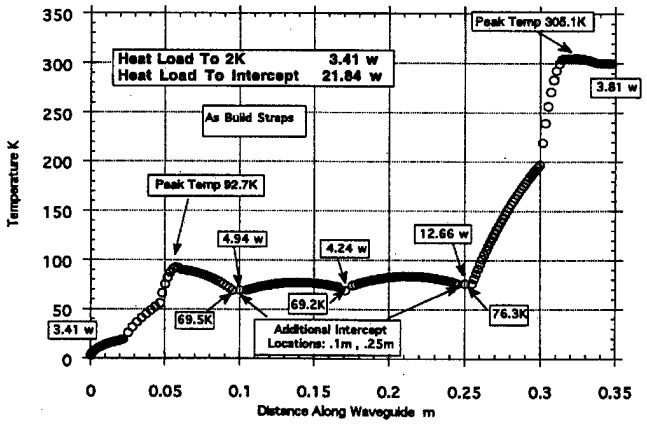



FIGURE 4. Predicted temperature profile in the vacuum waveguide.

## 7 SUMMARY

The prototypical quarter cryomodule has been built for the FEL injector with a cavity pair meeting the design goal for gradient and $Q_o$. The majority of changes in the CEBAF cryomodules necessitated for the Jefferson Lab FEL project have been incorporated into, and tested in a quarter cryomodule. The remaining changes are presently being assembled into the first linac cryomodule, which is scheduled for completion this summer. The changes tested so far in the quarter cryomodule have mostly met their design goals, and a few minor changes are being incorporated in the cryomodule as a result of lessons learned. Testing and development of reliable warm RF windows is ongoing.

## 8 ACKNOWLEDGMENTS

This work was supported by the U.S. DOE under contract number DE-AC05-84ER40150.

## REFERENCES

[1] Benson, S., "Overview of the Jefferson Lab IR FEL Program", JLAB-TN# 96-064.

[2] Kneisel, P., "Qualification of "Spare" Cavities for FEL Use", JLAB-TN-97-003.

[3] Campisi, I. et al., "Higher-Order -mode Damping and Microwave Absorption at 2K", CEBAF-PR-92-010, March 1992,.

[4] Benesch, J. F., and Wiseman, M., "Tests of a Prototype Magnetostrictive Tuner for Superconducting Cavities" to be published in *IEEE Transactions in Applied Supreconductivity*, 1997, as part of Proceedings.

[5] Wiseman, M., Machie, D., and Schultheiss, T. (Northrop/Grumman), "RF Vacuum Waveguide Design for the Injector Test Stand", CEBAF-TN#-95-054.

# PHASE LOOP BANDWIDTH MEASUREMENTS ON THE ADVANCED PHOTON SOURCE 352-MHZ RF SYSTEMS

D. Horan, A. Nassiri, C. Schwartz
Advanced Photon Source, Argonne National Laboratory
9700 South Cass Avenue, Argonne, Illinois 60439 USA

*Abstract*

Phase loop bandwidth tests were performed on the Advanced Photon Source storage ring 352-MHz rf systems. These measurements were made using the HP3563A Control Systems Analyzer, with the rf systems running at 30 kilowatts into each of the storage ring cavities, without stored beam. An electronic phase shifter was used to inject approximately 14 degrees of stimulated phase shift into the low-level rf system, which produced measurable response voltage in the feedback loops without upsetting normal rf system operation. With the PID (proportional-integral-differential) amplifier settings at the values used during accelerator operation, the measurement data revealed that the 3-dB response for the cavity sum and klystron power-phase loops is approximately 7 kHz and 45 kHz, respectively, with the cavities the primary bandwidth-limiting factor in the cavity-sum loop. Data were taken at various PID settings until the loops became unstable. Crosstalk between the two phase loops was measured.

## 1 RF SYSTEM OVERVIEW

The Advanced Photon Source has four identical 1-megawatt klystron rf systems dedicated to supplying power to 16 storage-ring single-cell cavities, arranged four cavities to a sector. The present operational mode uses two klystrons, each supplying power to eight cavities (two sectors, four cavities per sector) through a series of 3-dB hybrids to divide the klystron rf output by eight.

A single-line schematic of an APS rf system is shown in Figure 1. Two phase control loops, one nested within the other, are used to stabilize the phase of the rf voltage in the cavities. The power-phase loop closes around he klystron, 100-watt driver amplifier, and klystron driver AGC loop. This loop removes phase noise caused by the ripple on the DC output of the klystron high-voltage power supply (HVPS) and changes in rf modulator output due to the AGC loop action. The cavity-sum phase loop closes around the entire rf station and maintains phase stability between the input rf source signal and the cavity sum signal, which is composed of the vector sum of the field probe outputs of all eight cavities (two sectors combined) fed by the klystron. This loop removes remaining HVPS ripple-induced phase shift in the klystron output and any phase noise generated in the cavity. Measurements have shown that the combined performance of the two phase control loops reduces the phase jitter in the cavity rf signal to less than 1 degree peak-to-peak.

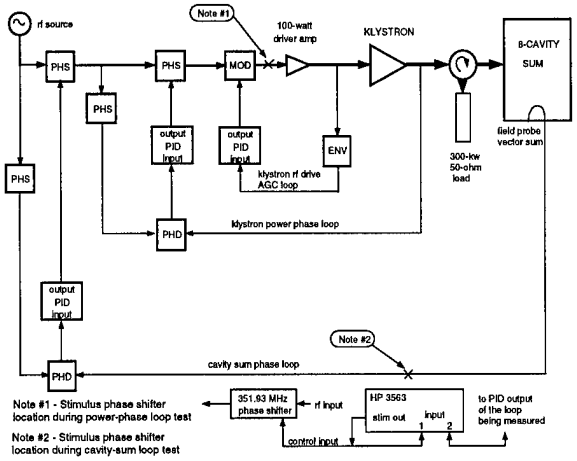



Figure 1: The rf system layout and closed-loop response measurement setup.

Each of the storage ring cavities is tuned by a motor-driven piston tuner that is controlled by a phase loop around the cavity, comparing the phase of cavity forward power to the phase of the cavity field probe output signal. The phase error signal is amplified and conditioned by a PID controller that supplies an input signal to the tuner drive stepping motor, moving the tuner piston in the direction of cavity resonance. The low-level rf system utilized for cavity tuning is physically located a distance from the klystron low-level rf system and operates totally independent of the klystron system.

The low-level rf hardware is packaged in VXI modules which house analog rf modules digitally interfaced to the APS EPICS (Experimental Physics and Industrial Control System) [1] system for remote control and monitor functions. The 100-watt klystron driver amplifier is located in the same equipment rack as the klystron low-level rf VXI crate, all of which is located approximately 30 feet from the klystron.

## 2 MEASUREMENT SETUP

Initial closed-loop phase loop response measurements were performed on the RF#1 and RF#2 stations in the fall of 1996, and the test results showed little difference in performance between them. Similar testing at the RF#4 station indicated performance very close to the other stations. Since it was the most mature system of the three at that time, RF#4 was selected as the subject of extensive response tests. Two basic types of measurements were made: real-time, closed-loop response with the stimulus

0-7803-4376-X/98/$10.00 © 1998 IEEE

injected in the rf domain and open-loop characteristics with the loops closed using a summing junction for injection of the stimulus signal into the PID controller output. During both measurements, the rf system under test was operating at approximately 30-kilowatts per cavity, with the klystron operating at 85 kV and 10.0 amps of beam current. No stored beam was present in the machine.

Closed-loop measurements of the phase loop frequency response were made on our RF#4 station using a direct method of phase noise injection using an electronic rf phase shifter, an even wavelength long, inserted into the rf system at points within each phase loop (see Figure 1). These measurements were made at different PID gain settings to determine the maximum loop gain allowable for stable rf system operation. The stimulus rf phase shifter was driven with a swept-frequency sinusoidal AC control signal, a 1-volt peak AC component superimposed on a +1-volt offset, to produce rf phase stimulation within the loop. The +1-volt offset was necessary for this test, as the phase shifter response becomes very nonlinear with a negative-going control voltage. The phase shifter has a frequency response of +/-1.6 dB from 100 Hz to 100 kHz. This control voltage produced approximately 14 degrees peak-to-peak of rf phase shift at 351.93 MHz. The output amplitude of the PID amplifier in each phase loop was then measured to determine the loop response and the amount of crosstalk between the loops. The HP3563 Control Systems Analyzer was used to generate the stimulus signal that drove the rf phase shifter and also to measure the PID output signal amplitude relative to the stimulus signal.

Making true open-loop measurements of these phase loops is impossible. The DC gain of the PID amplifier is immense, and breaking the loop causes the PID output to saturate at one of its output limits. Measurements of open-loop characteristics with the loop closed were made by using a unity-gain summing junction for injection of the stimulus signal into the PID amplifier output, while measuring the output amplitude of the PID amplifier at a point before the summing junction [2]. This measurement setup is detailed in the partial system schematic shown in Figure 2. These measurements were made using two different methods, swept Fourier transform (SFT) and fast Fourier transform (FFT). In the SFT tests, the stimulus signal consisted of a 500-mV peak sine-wave slowly swept in frequency from 100 Hz to 100 kHz. In the FFT tests, the stimulus signal was a 500-mV peak broadband noise source. Both stimulus signals were generated by the control system analyzer. The PID amplifier gains were set to unity (P=1, I=1, D=1) for these tests.

## 3 LOOP RESPONSE DATA

The closed-loop response tests were performed with the PID amplifier AC gains set at the normal values for accelerator operation (see Figures 3(a) and (b)). The power-phase loop was tested with the PID gain set to 4, and exhibits a response that is essentially flat within 3 dB to approximately 10 kHz. It has an apparent gain margin of 16 dB. The cavity-sum phase loop was tested with the PID P-gain set to 1.56; it has flat response to 3 kHz and is down 20 dB at 10kHz, with an apparent gain margin of over 28 dB. The more narrow response of the cavity sum loop is due to the effect of the 7-kHz bandwidth of the storage ring cavities on the field probe signals.

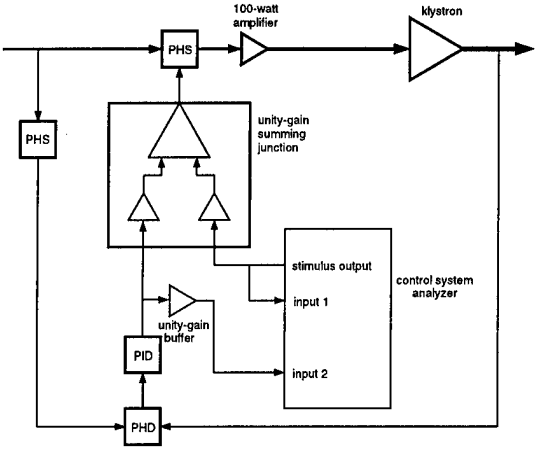



Figure 2: Setup for measuring open-loop characteristics.

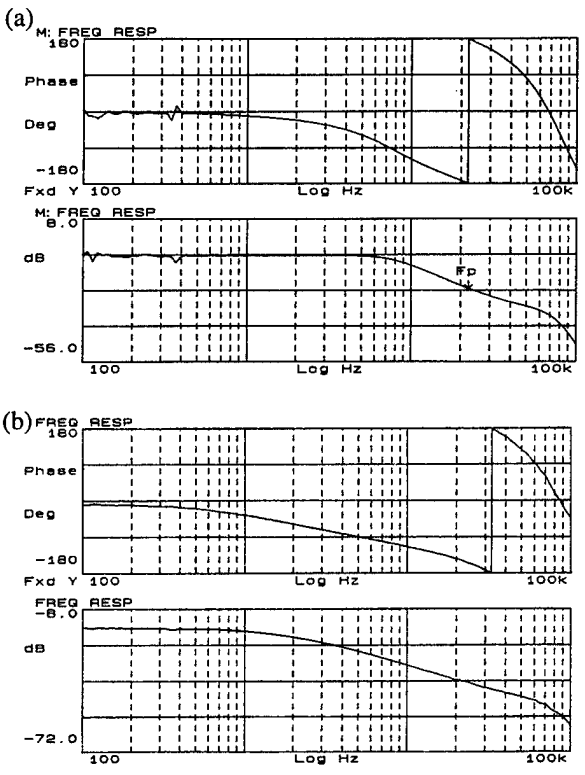



Figure 3: (a) Power-phase closed-loop response test—PID GAIN = 4; (b) cavity-sum phase closed-loop response test —PID GAIN = 1.56.

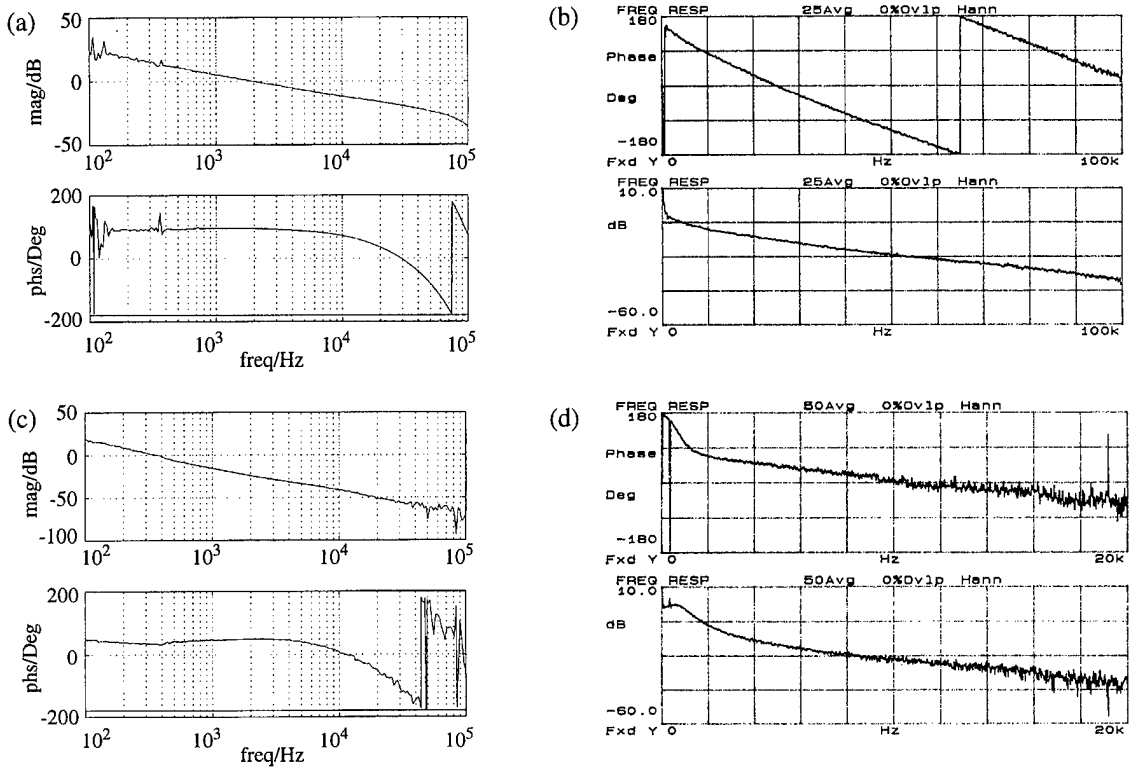



Figure 4: (a) Power-phase loop open-loop characteristics using SFT method; (b) power-phase loop open-loop characteristics using FFT method; (c) cavity-sum phase loop open-loop characteristics using SFT method; (d) cavity-sum phase loop open-loop characteristics using FFT method.

The open-loop characteristic data are shown in Figures 4(a) through (d). These measurements were made with the PID amplifier AC gains set to unity in both loops. The SFT tests on the power-phase loop indicate gain and phase margins of approximately 25 dB and 270 degrees, respectively. The conclusions are closely matched by data obtained using the FFT method. The SFT tests on the cavity-sum loop indicate gain and phase margins of approximately 75 dB and 270 degrees, respectively, again with the cavity bandwidth increasing the gain margin significantly. The FFT tests on the cavity-sum loop were performed from DC to 20 kHz only, as the signal level back from the cavities at test frequencies greater than 20 kHz was very low. Test results here indicate that in the operating bandwidth of the field probe signal, there is no evidence of 180-degree phase shift to invite instability. The fluctuations in all of the data at 60, 120, and 360 Hz are due to the loops actively working to reduce phase shift caused by power supply ripple on the klystron cathode voltage, resulting in distortions in the data at these frequencies.

Power-phase to cavity-sum crosstalk was measured at -26 dB between 100 Hz and 1 kHz, rising to -16 dB at 5 kHz and falling to -42 dB at 100 kHz. Cavity-sum to power-phase crosstalk was found to be between -50 dB and -60 dB down from 100 Hz to 100 kHz. There measurements were made at the RF#1 station, with the PID AC gains set at the normal operating values mentioned.

## 4 CONCLUSION

These response measurements show that rf system operation with phase loop PID amplifier P-gains of 1.56 and 4 provides adequate performance with comfortable gain and phase margins at a storage ring current of 100 mA. Crosstalk between the loops is within acceptable limits and does not contribute to performance degradation.

## 5 ACKNOWLEDGMENTS

I would like to acknowledge the efforts of Mike Phelan and Bill Yoder in constructing the summing junction amplifier used for these tests, as well as Don Voss and Ernie Cherbak for their assistance during the tests. This work was supported by the U.S. Department of Energy, Office of Basic Energy Sciences, under Contract No. W-31-109-ENG-38.

## 6 REFERENCES

[1] L.R. Dalesio, M.R. Kaimer, A. J. Kozubai, "EPICS Architecture," Proc. of ICALEPCS '91, Tsukuba-Shi, Ibaraki, Japan, KEK Proceedings 92-15, pp. 278-282, December 1992..

[2] "Control System Measurement Fundamentals Using Dynamic Signal Analyzers," Hewlett-Packard Application Note 243-6.

# 7GHz PULSED MAGNICON: STUDY AND NEW RESULTS

E.V. Kozyrev, I.G. Makarov, O.A. Nezhevenko, A.A. Nikiforov, G.N. Ostreiko, B.Z. Persov,
G.V. Serdobintsev, S.V. Shchelkunoff, V.V. Tarnetsky, V.P. Yakovlev, I.A. Zapryagaev,
Budker Institute of Nuclear Physics, Novosibirsk, Russia

*Abstract*

The report presents new experimental results obtained on 7 GHz pusled magnicon amplifier. In 1996, the following parameters were achieved: maximum output power of 46 MW, efficiency of 49%. We relate the further magnicon parameters improving with elimination of electromagnetic fields disturbing in the output cavity induced by the large coupling holes with the loads.

## 1 INTRODUCTION

7 GHz pulsed magnicon has been designed at INP as an alternative microwave power source for linear colliders. This device is the result of extended work on a new class of high power microwave sources development for accelerator application [1, 2, 3]. This class of microwave sources has been developed at Institute (INP) since 1967. The main difference of these devices from others is the method of beam modulation which is provided by the relativistic electron beam circular deflection. This paper presents the new experimental results and the study of the magnicon operation features.

## 2 THE MAGNICON DESIGN

A diagram of the experimental magnicon system is shown in Fig.1. The magnicon consists of: an electron source (diode gun), RF and magnetic systems, and collector. RF system cosists of the deflection system for beam modulation and output cavity for conversion of the beam energy into the RF oscillations. The tube is an amplifier operating in frequency-doubling mode. So in all deflection cavities the circular-polarized $TM_{110}$ mode is excited at the frequency of 3.5 GHz. In the output cavity the modulated beam excites the $TM_{210}$ mode with the frequency of 7 GHz. The angular frequency of this mode is equal to the drive signal frequency. All the cavities are located inside the solenoid producing a longitudinal magnetic field with the required field distribution.

This tube design is the result of numerical simulations and experimental study of the various versions of the device (see [4, 5]). Beam dynamics simulation and magnicon components optimization (the electron gun, RF cavities, magnetic system) were carried out with the special computer codes SAM and SuperLANS [6, 7]. Also the computer codes were used for simulation of steady-state and time-dependent magnicon operating conditions [8].

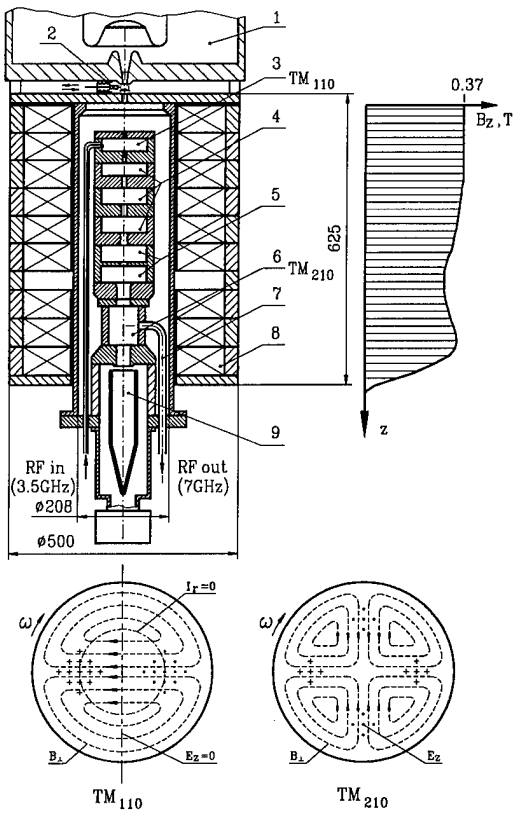



Figure 1: Sketch of the magnicon: 1 – electron source; 2 – vacuum valve; 3 – drive cavity; 4 – gain cavities; 5 – penultimate cavity; 6 – output cavity; 7 – waveguide (*2); 8 – solenoid; 9 – collector

## 3 THE MAGNICON STUDY AND THE ACHIEVED PARAMETERS

The previous experiments with the device have shown that its parameters are limited mostly by the deficient matching the electron source optics with the magnicon magnetic system as well as RF field distorsion in the output cavity [4].

The deficient matching between the gun optics and magnetic system led to strong electron beam transverse size scalloping. In 1996, the electron gun was improved in order to eliminate this problem. Experiments proved that pulsing decreased, and the maximum beam diameter within the operating range of the accompanying magnetic field has decreased from 4 mm to less than 3 mm.

By the time of the new gun testing it was also found that during the device conditioning self-excitation in the output cavity arose and after a time disappeared at various

0-7803-4376-X/98/$10.00 © 1998 IEEE

frequencies [5]. Note, that the self-excitation frequencies were not the drive signal harmonics. One of possible reasons for them could be the bad vacuum.

The magnicon RF system consists of separated copper parts connected with one another by indium seals. This design allows to change the RF systems part operatively but does not allow to bake-out cavities up to high temperatures. This leads to long condition times for the cavities. In the decribed experiments the RF cavities were previously heated and then the whole magnicon quick-assembling were carried out. Moreover, the waveguide sections forming a single vacuum chamber with the output cavity and loads (there are no ceramic windows) were provided by the additional pumping system. Further experiments shown that these provisions have reduced the device conditioning time and eliminated the self-excitation. Present-time magnicon parameters are listed in the table below, which also contains the calculated values.

| Magnicon parameters | achieved | design |
|---|---|---|
| Operating frequency, GHz | 7.002 | 7.000 |
| Drive frequency, GHz | 3.501 | 3.500 |
| Output power, MW | 46 | 55 |
| Gain, dB | 62 | 55 |
| Efficiency, % | 49 | 56 |
| Pulse duration, μs | 1.0 | 1.3 |
| Beam voltage, kV | 405 | 420 |
| Beam current, A | 230 | 240 |
| Repetition rate, pps | 3 | 5 |

The oscillograms presented in Fig.2 are: beam voltage (U), signal from the drive cavity (DC), signal from the first gain cavity (GC), signal from the penultimate cavity (PC), and output signal (OUTC). The output peak power calibration was carried out by the calorimetric measurements of the average RF power.

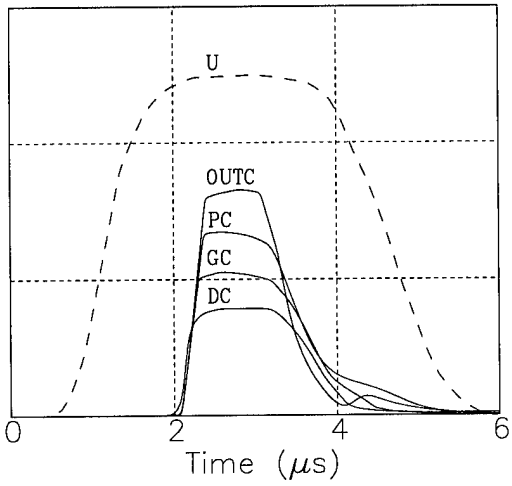



Figure 2: The oscillograms.

Figure 3 represents the measured dependencies of the efficiency versus: a) the drive signal; b) the drive frequency; c) the accompanying magnetic field; d) the electron beam power (2 – calculated curve).

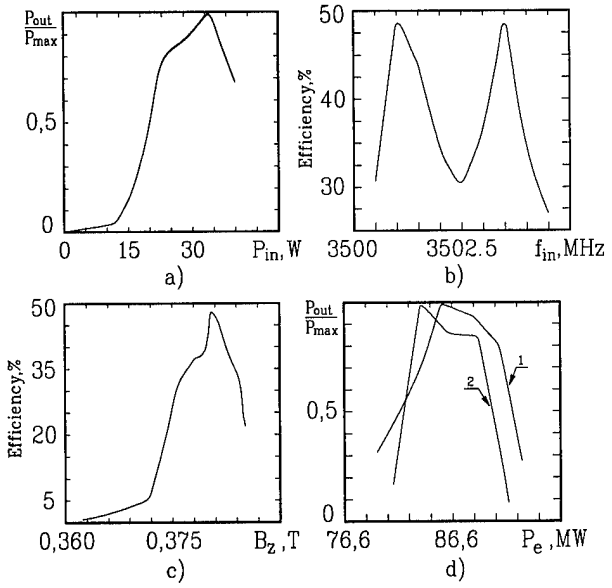



Figure 3: Experimental curves.

Strong output power dependence on the beam power and thus on the beam voltage (diode gun) explaines the decreasing of the output signal pulse duration. Numerical simulations show that for a given voltage pulse profile at the electron gun the ouput signal duration cannot exceed 1.3 μs at half-power level.

By this means the measured tube efficiency comprises 89% from the predicted value that results mainly from longitudinal and azimuthal inhomogeneity of the RF fields in the output cavity because of presence of the coupling windows with waveguides [9]. An azimuthal non-uniformity leads to a difference between the loaded Q-factors for orthogonal $TM_{210}$ modes, superposition of which defines the RF fields distribution in the output cavity.

The calculated curve of efficiency versus the output cavity loaded Q-factor is shown on Fig.4. Numerical simulations show that the difference between Q-factors also leads to the output signal duration decreasing.

To compensate the azimuthal disturbance in that experiment the output cavity with two protrusions was used (see Fig.5a). However, 2D-simulations shown that this is not enough. The problem, can be solved by increasing the number of protrusions as shown in Fig.5b. But 2D-simulation and model tests show that this action leads to a major distorsion of the RF fields longitudinal distribution (Fig.6b). The distorsion decreases the efficiency of the given magnicon design considerably. To eliminate this effect the compensating local increasings of the output cavity diameter were made near the upper and lower cavity faces (Fig.6c). These local increasings are azimuthal homogeneous and do not give rise to an azimuthal non-uniformity.

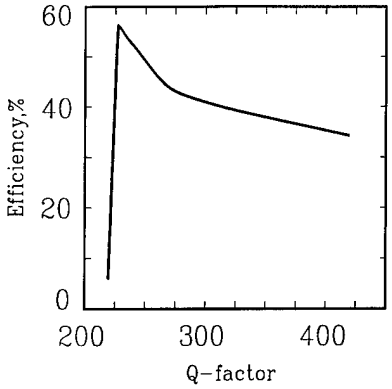



Figure 4: Efficiency versus loaded Q-factor.

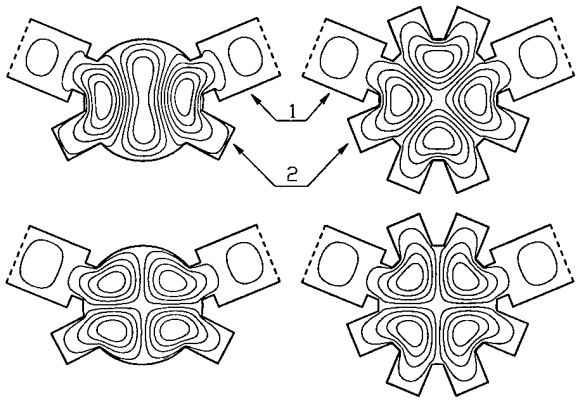



Figure 5: Output cavity design.

## 4 SUMMARY

In the course of 7 GHz frequency-doubling magnicon amplifier investigation the peak power of 46 MW and efficiency of 49% has been achived. The measured parameters are 89% of the calculated values. This allows to consider the magnicon as an attractive candidate for linear colider applications. The improved version of the output cavity has been produced and installed into the magnicon. The tube is under putting into operation now and we hope to obtain the design parameters in the nearest future.

## 5 REFERENCES

[1] G.I. Budker et al., "The Gyrocon – an Efficient Relativistic High-Power VHF Generator," Particle Accelerators vol. 10, 1979, pp. 41–59.

[2] M.M. Karliner et al., "The Magnicon – an Advanced Version of the Gyrocon," NIM-A, vol. A 269, No. 3, 1988, pp. 459–473.

[3] O.A. Nezhevenko, "Gyrocons and Magnicons: Microwave Generators with Circular Deflection of the Electron Beam," in IEEE Trans. of Plasma Science vol. 22, No. 5, October 1994, pp. 756–772.

[4] E.V. Kozyrev et al., "The Latest Experience with 7 GHz Pulsed Magnicon Amplifier," in Proc. RF96 Conf. (to be published).

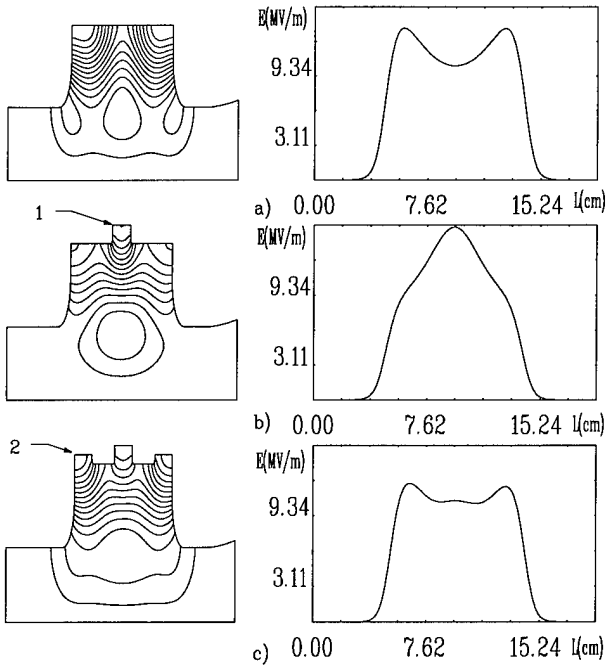



Figure 6: Field maps and longitudinal electric field distributions in the output cavity: a) without holes; b) with coupling windows and protrusions (1); c) with the additional local increasings of the cavity diameter near the faces (2).

[5] E.V. Kozyrev et al., "Performance of the High Power 7 GHz Magnicon Amplifier," Particle Accelerators vol. 55, 1996, pp. 55–64.

[6] B. Fomel, M. Tiunov and V. Yakovlev, "Computer-Aided Electron Gun Design," in Proc. XIII Int. Conf. on High-Energy Acc., vol. 1, 1987, pp. 353–355.

[7] D. Myakishev and V. Yakovlev, "The New Possibilities of SuperLANS Code," in Proc. Part. Acc. Conf., Dallas, 1995.

[8] V. Yakovlev et al., "Numerical Simulation of Magnicon Amplifier," in Proc. Part. Acc. Conf., Dallas, 1995.

[9] E.V. Kozyrev et al., "Investigation of 7 GHz High Power Pulsed Magnicon Amplifier", in Proc. 7th Adv. Acc. Concepts Workshop, Lake Tahoe, California, October 12-18, 1996, (to be published).

# HIGH EFFICIENCY TWT AMPLIFIERS *

S. Naqvi, G. S. Kerslick, J. A. Nation, Q. Wang
School of Electrical Engineering & Laboratory of Plasma Studies
Cornell University, Ithaca NY 14853, USA

*Abstract*

We report on a research program to increase the efficiency of relativistic traveling wave amplifiers to $> 50\%$. The two stage amplifier consists of a bunching periodic structure with phase velocity significantly higher than the beam velocity and a decelerating section with phase velocity significantly lower than the beam velocity. The position of the decelerating stage with respect to the bunching stage is chosen such that the narrowest bunches are sustained in the decelerating field for the longest possible time before significant debunching occurs. Two schemes are under investigation. In the first scheme, a resistive sever is placed between the two stages to suppress temporal phenomena. In the second scheme, the bunching and deceleration stages merge into each other by a gradual change in the iris radius over a wavelength. An absorbing section in this case is placed before the start of the bunching stage. Coaxial extraction geometry [1] is used in both schemes. Efficiencies obtained from MAGIC simulations are comparable to those obtained in high efficiency klystrons [2] (50-60%) but carry the important advantage of broad-bandwidth, low sensitivity on dimensions, low surface fields, and simplicity of design.

## 1 INTRODUCTION

The TWT is a potentially viable ultra-high power microwave source for various applications if the beam-to-electromagnetic energy conversion efficiency can be raised to over 50%. Specific advantages offered by the TWT, over other sources, include low surface electric fields, broad bandwidth, and low sensitivity to dimensions and beam quality. In this paper, we present a simple design of a high efficiency TWT based on a traveling wave bunching section merging into a traveling wave deceleration section.

The efficiency of a TWT is limited by inefficiencies in the bunching process, spatial and momentum spread of the bunches, and the entry of the bunches into the accelerating phase of the RF field. The usual technique suggested for increasing the efficiency involves tapering of the wave phase velocity so that the decelerated bunches remain within the decelerating phase of the wave.

The electric field in the amplifier arises from the quasi-static fields of bunches and the radiation field from decelerated electrons. The spatial position of bunches with respect to the wave can be changed by changing the local phase velocity in the slow-wave structure. This fact will be used in the design described here. However, the forces due to the collective effect of space charge strongly determine the spatial spreading of the bunch. Hence both the position and size of the bunch with respect to the radiation wave need to be considered for designing an efficient amplifier. Single particle or rigid bunch models which are often used the design of high efficiency devices, frequently neglect the effects of the quasi-static bunch forces on the electron dynamics. These fields are frequently comparable to the radiation fields in TWT's operating at a few 100 kV and few 100 A's, In order to design a high efficiency and high power TWT, it is necessary to use a fully non-linear and self-consistent analysis. This is best achieved by the use of PIC codes.

## 2 CONCEPTUAL ILLUSTRATION

In a traveling wave tube the electron beam bunches gradually accumulate in the decelerating phase as a result of interaction with the co-propagating structure wave. Uniform structure TWTs are usually operated such that the beam velocity is equal to or greater than the cold phase velocity in the supporting slow-wave structure. Typical efficiencies for synchronous structures are about 25%, which can be increased to 30-35% by use of a structure with a lower phase velocity. We propose to use a structure with phase velocity *faster* than that of the beam electrons to produce efficient bunching followed by a lower phase velocity region to extract bunch energy into RF field.

To illustrate the effect of different phase velocities on bunching and the self-consistent generation of rf power from bunch deceleration, we consider three PIC simulations performed with MAGIC code. For ease of presentation, we use a dielectric slow-wave structure. A uniform circular waveguide of radius 15.5 mm lined with a dielectric of radius 6 mm, and operated at 9 GHz. The system ends with a non-reflecting termination. A 700 kV, 500 A, 3 mm radius pencil beam is chosen for all simulations. In Fig.1 a,b and c, the axial electric field and the instantaneous beam current are shown, from simulations corresponding to cold wave phase velocities of $1.01c$, $0.90c$ and $0.82c$ respectively. ($\epsilon_r$ of the dielectric = 1.8, 2.1, and 2.4 respectively). Consider Fig.1a, corresponding to the 'fast wave' case. Even though the radiation wave grows at phase velocity $< c$, the the bunches lag the wave more than in the other two cases. This causes reduction in growth rate and a slow spatial rise in current. However, the peak current in the fast-wave case exceeds the peak current achieved in the synchronous and slow-wave cases. Because $E_z$ for a given rf current is the least in this case, the bunch energy spread as well as its average energy drop (and hence rf power) is

* Work supported by U.S. D.O.E. & AFOSR MURI Program

0-7803-4376-X/98 /$10.00 © 1998 IEEE

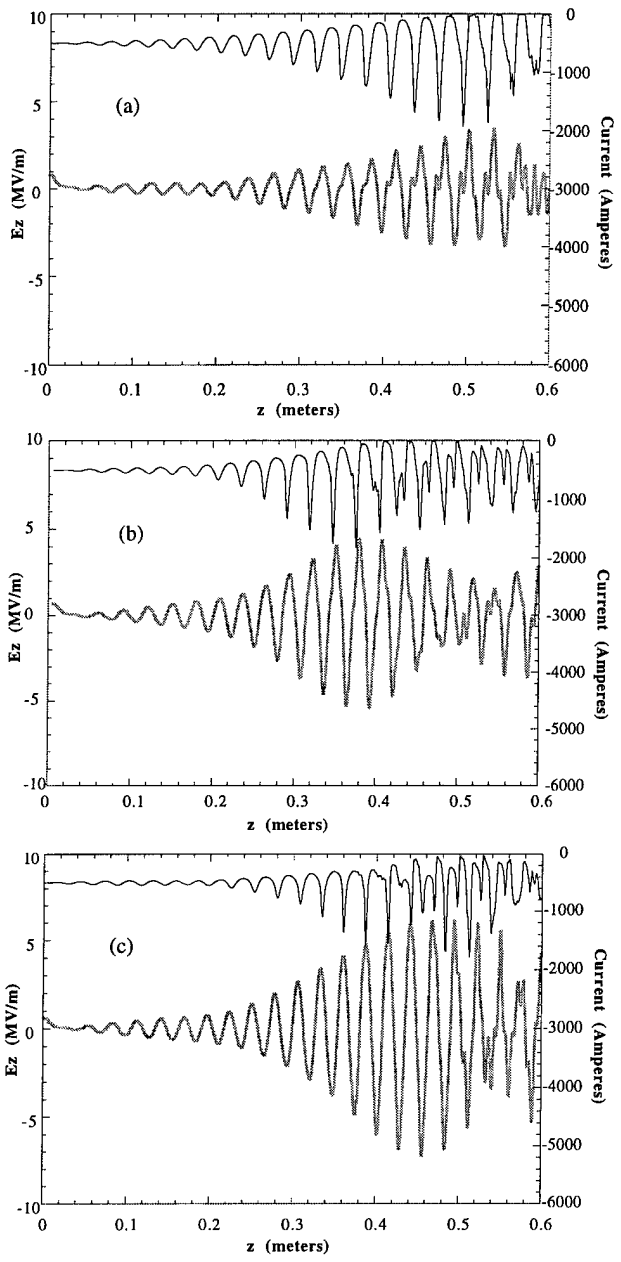



Figure 1: Current (top curve) and $E_z$ (bottom curve) profiles for cases with cold phase velocities (a) $v_p = 1.01c$ (b) $v_p = 0.9c$, and (c) $v_p = 0.82c$, indicating highest bunching level and lowest $E_z$ for the 'fast-wave' case.

also the lowest for the fast-wave case. These conditions are desirable for a good buncher, but not for extraction of bunch energy into the electromagnetic field. As expected, the initial growth rate is highest for the synchronous case (Fig. 1b) and the saturation power is highest for the lowest phase velocity case (Fig. 1c). The latter result follows since the bunches are taken to lower velocities before they enter the accelerating phase of the wave.

We conclude that the amplifier in Fig. 1a is an efficient beam buncher and the amplifier in Fig. 1c is an efficient decelerator (hence rf converter). A combination of the two may be expected to result in a high efficiency amplifier. To make use of the bunching in Fig. 1a, a change in phase velocity in the slow-wave structure is needed close to the point where the bunches are beginning to enter the accelerating phase ($z \sim 42$ cm). At this point we use a 4 cm long transition to a region with $v_{ph} = 0.82c$. This transition and its corresponding effect on the amplifier dynamics is illustrated in Fig. 2. The narrow bunch from around $z \sim 40$ cm slips back into the center of the decelerating field within the transition region and rapidly loses energy to the electromagnetic field. This yields over 50% efficiency. Note that when the bunch has spread to a width that is comparable to a half-wavelength, then no real advantage is gained by further lowering the phase velocity since part of the bunch has inevitably entered the accelerating phase. Power should therefore be extracted close to the E-field maximum in Fig.2.

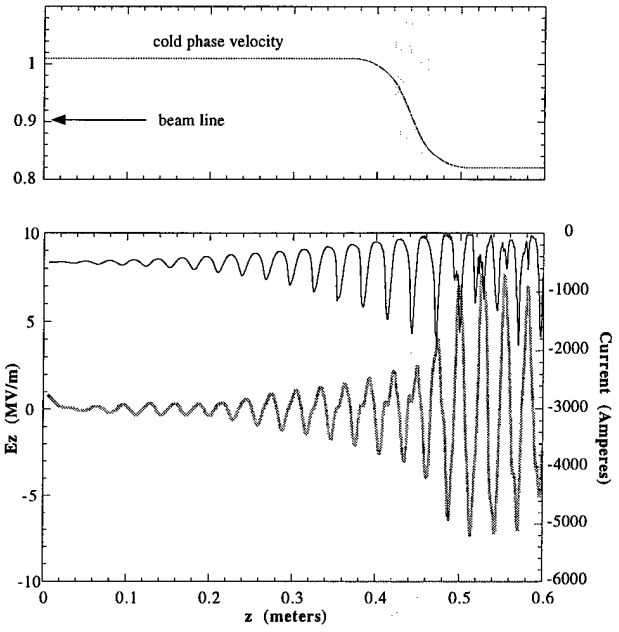



Figure 2: (c) Phase velocity = $0.90c$ for $z < 42cm$ and 0.82 for $z > 46cm$

## 3 EXPERIMENTAL IMPLEMENTATION I

The two-phase velocity concept is implemented with an iris-loaded waveguide periodic structure. The change in cold phase velocity from 1.2 $c$ to 0.75 $c$ is produced by changing the iris aperture while keeping the outer wall radius constant (Fig.3 top). The tapering at the ends is done to reduce reflections. An coaxial inner conductor placed in the output tapered section is used to shield the particles from the wave close to the power maximum, so that no reacceleration occurs and hence the peak power is extracted. The coaxial extraction scheme, described previously [1], provides a broad-band, low-reflection coupling of peak rf power into a TEM coaxial mode. A SiC absorber is also placed at the input end of the amplifier to further absorb any residual reflections from the output of the system. At present, a short traveling wave section is used to provide a few percent initial modulation to the system. A MAGIC simulation with this structure demonstrates 200 MW power at 9 GHz into the coaxial guide, when a 700 kV, 500 A beam is launched into the system. This corresponds to 57% efficiency. The amplifier described has been fabricated and tests are presently in progress to check the validity of the design.

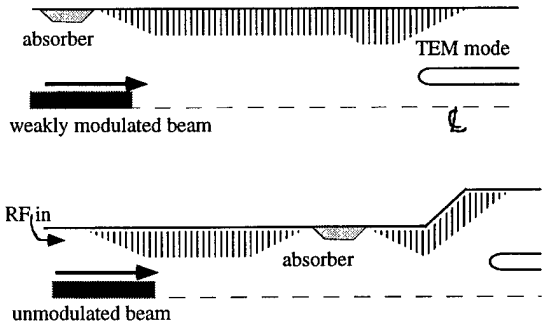



Figure 3: Experimental Implementation I (top) and II (bottom)

## 4 EXPERIMENTAL IMPLEMENTATION II

Fig.3 (bottom) shows a variation of the above idea. In this case, a SiC sever is placed between the TWT bunching and deceleration sections. The rf power obtained in the first stage is dumped into the absorber while the bunched beam traverses the sever and excites the required electromagnetic mode in the 2nd stage. The radiation field reconstructs from zero such that the bunches automatically lie in the decelerating phase of the electric field. This results in rapid growth of the rf field. The size of the first stage and the length of the sever are optimized via simulation to minimize the phase angle spread of the bunches entering the 2nd stage. The extraction section in this case is also enlarged to reduce the risk of rf breakdown. This also provides greater flexibility in the choice of radius and position of the inner conductor. Fig. 4 shows initial experimental measurements of the output power from the device. The

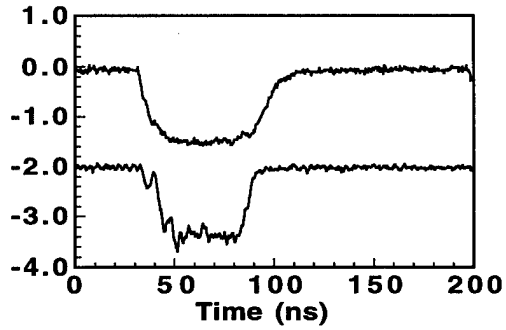



Figure 4: (Top) Beam current (Bottom) Output RF

upper part of the figure shows the beam current and the lower part the output rf envelope detected by an $E_r$ probe, mounted in the side wall of the coaxial output section. The power level at the end of the first stage is a few MW with a single frequency output. The pulse is phase stable to $\pm 3.5^o$, which lies within error range of the diagnostic. At present the peak output power is found to be 45 MW for beam input of 800 kV at 300 A. Simulation done with 1000 kV, 500 A beams indicates an rf conversion efficiency of 50% with output power of 250 MW. Experiments are underway to change the modulator output voltage and current closer to the intended design.

## 5 CONCLUSION

We have proposed TWT configurations based on a two section slow-wave structure, such that the first section optimally bunches the beam, while the second section efficiently decelerates the bunches. The bunching and deceleration aspects of the problem are therefore treated on equal footing in order to maximize efficiency. MAGIC simulations indicate that 50-60% beam-to-electromagnetic efficiency can be achieved in both experimental designs described. Because of the pure traveling-wave nature of the interaction, the designs are not sensitive to input frequency or system dimensions. For example, a few centimeters change in the transition point of the structure only alters the efficiency by a few percent. Also a wide range of phase velocities can be chosen for the design of the two sections. The simplicity of the design, combined with all the desirable properties of the traveling wave interaction could could make this scheme a viable and efficient ultra high power microwave source in X-band. Design studies have also indicated that similar designs at 35 GHz are experimentally feasible and should yield efficiencies of $\geq 40\%$.

## 6 REFERENCES

[1] S. Naqvi, G. S. Kerslick, J. A. Nation, and L. Schächter, *Appl. Phys. Lett*, **69**, 1550 (1996).

[2] G. Caryotakis, *IEEE Trans. Plasma Sci.* , **22**, 683 (1994).

# MICROWAVE COLD TESTS OF PLANAR RF CAVITIES*

J. Chen, T. Lee, D. Yu
DULY Research Inc., Rancho Palos Verdes, CA 90275
A. Nassiri
Argonne National Laboratory

*Abstract*

The RF cavities for a sheet-beam klystron [1] are designed for a strip electron beam interacting with the electromagnetic fields. The axial electric field for these cavities is constant over the width of the beam. The cavity design can be adapted as a basic cell structure for high-frequency, traveling-wave, planar accelerators. We report here rf measurement results on the field uniformity, isolation between cavities and other pertinent characteristics of the cavities at a scaled frequency of 11.4 GHz. Comparisons are made with MAFIA simulations.

## INTRODUCTION

Recent interest in planar rf cavities has stemmed from two developments. First, it has been found that a sheet electron beam with a large aspect ratio can be used in a high power klystron to avoid many of the shortcomings of a conventional round beam klystron. A sheet beam klystron with a low perveance per square is capable of high rf conversion efficiency. Yu *et al* [1] have designed a 200-MW X band sheet beam klystron with an efficiency of over 65%, using a flat beam of dimensions 0.5 cm × 16 cm, at a beam current of 770 A and a beam voltage of 400 kV. The sheet beam klystron is particularly suited to operate at high frequencies (up to 100 GHz), because its output power scales linearly with wavelength, rather than quadratically as in the case of a round beam klystron. The sheet beam klystron cavities have a planar, barbell-like geometry providing a flat axial field in the region through which the beam traverses [2]. A schematic of a barbell cavity is shown in Figure 1.

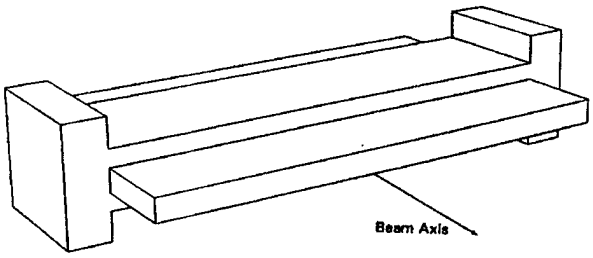



Figure 1 Schematic of a Planar Barbell Cavity

Another recent development for which planar cavities would be useful is high-frequency rf accelerators [3]. High gradient acceleration requires operation at high frequencies. At high frequencies (e.g. > 50 GHz), it is almost certain that the tolerance requirements of a cylindrical, disk-loaded structure of a conventional design cannot be met by traditional manufacturing techniques, i.e. precision machining and brazing. Modern microfabrication techniques [4] such as LIGA or wire EDM, on the other hand, are particularly suitable for planar structures. A planar traveling wave accelerating structure may consist of a series of barbell-like planar cavities, or variants thereof, connected by short rectangular beam pipes [5] as shown below.

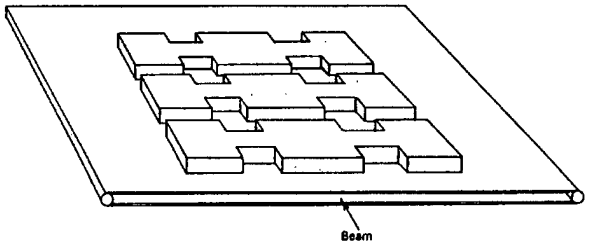



Figure 2 Schematic of a Planar Tugboat Traveling-Wave Structure (3 cells illustrated)

Planar accelerators and sheet beam klystrons using flat field cavities can in principle be mass produced with new microfabrication techniques.

## DESIGN AND FABRICATION OF THE BARBELL CAVITY

Traditional cylindrical pillbox rf cavities have axial electric fields quite uniform near the axis in both magnitude and phase, at any given instant of time, along the transverse dimensions. This important feature has been exploited in many klystron and accelerator applications in which the electromagnetic field in the cavity interacts with a bunched beam of finite size. The accelerating fields should be constant in the region traversed by the beam as it goes through betatron motion in an external axial magnetic field.

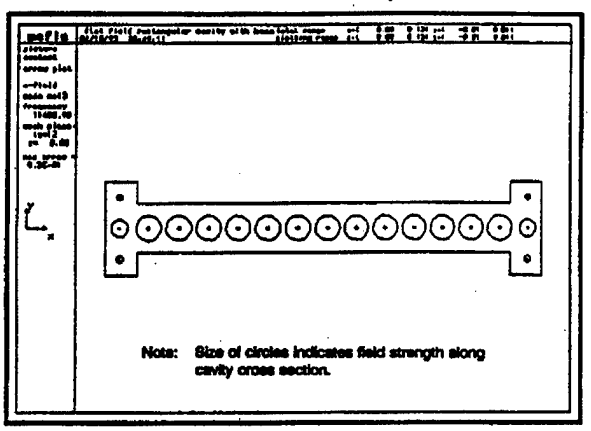
The axial electric field ($E_z$) in a rectangular cavity of width $L$ and height $H$ assumes a profile of $\sin(m\pi x/L)\sin(n\pi y/H)$, where $m$ and $n$ = 1,2,3... Thus, rectangular cavities (including the so-called muffin tin [5]), unlike their cylindrical counterparts, have a sine-like accelerating field along the transverse direction of the cavity. For the lowest order mode, the field exhibits a maximum at the center and vanishes at the walls.

The barbell cavity features a constant axial electric field along the transverse direction near the beam axis. Flat field is important for acceleration of a flat beam, either in a klystron or in an accelerator. Even if a round beam is used in a planar structure, the field should be flat at least within the betatron radius. The design principle of a planar barbell cavity is that the resonant frequency of the central section of the cavity is at or near cutoff for rf

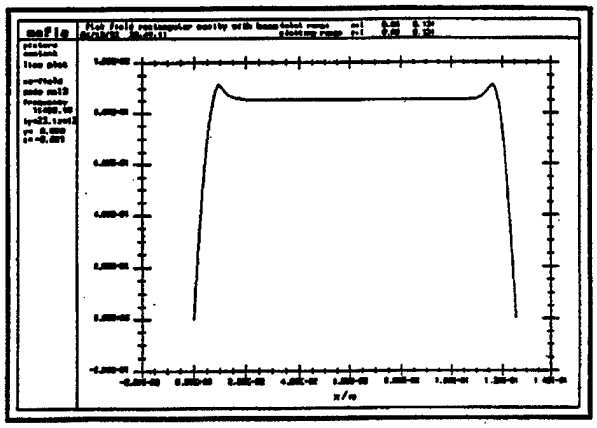
* Work supported by DOE SBIR Grant No. DE-FG03-96-ER82213.

0-7803-4376-X/98 /$10.00 © 1998 IEEE

propagation in the transverse direction, while the two ends of the cavity are below cutoff, thus producing a flat electric field in the central region of the cavity. Figure 3 shows a MAFIA axial field plot of the fundamental TM mode of our first X band barbell cavity.




(a)



(b)

Figure 3 MAFIA Axial Electric Field Plots of a Barbell Cavity. a. Arrow plot b. Line plot

The flat surfaces defining the boundaries of the barbell cavity, or variants thereof such as the "Tugboat" and "H-block" cavities [6], can be etched using deep x-ray lithography techniques. Alternately, they can be cut with wire EDM techniques, and different layers of the structure can be bonded together using diffusion bonding techniques. These manufacturing techniques are particularly useful at high frequencies, at which the structures become increasingly miniaturized. At frequencies below 30 GHz, these structures can still be made with conventional machining and brazing techniques.

As a first experiment to demonstrate the rf properties of the planar flat-field structure and to verify the MAFIA simulations, we designed a barbell cavity at 11.4 GHz. The properties of the cavity are calculated with MAFIA. The electric field for the fundamental TM mode, shown in Figure 3, is constant over a wide aperture of 8.8 cm. The calculated Q of this mode is 6800. The frequencies of the higher order TM modes are listed in Table 1.

Table 1 Resonant Frequencies (MHz) of TM Modes of an X-Band Barbell Cavity

| MAFIA | Measured |
|---|---|
| 11420 | 11498 |
| 11491 | 11547 |
| 11695 | 11734 |
| 12026 | 12060 |
| 12474 | 12508 |
| 13026 | 13038 |
| 13669 | 13747 |

If two barbell cavities are connected by a rectangular beam pipe, it is possible to couple the fundamental TM mode of two adjacent cavities through a propagating TE mode in the beam pipe connecting them, provided there is any asymmetry due to fabrication imperfection, or if the beam is off axis.

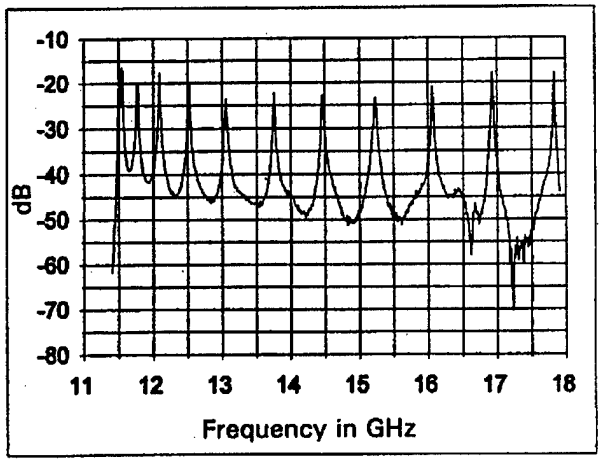



Figure 4 TM Modes frequency Spectrum of a Barbell Cavity as Measured with a HP8510C Network Analyzer

## COLD TEST RESULTS

A structure consisting of two identical barbell cavities connected by a short beam pipe was fabricated by ANL using design drawings provided by DULY Research. We performed cold tests for these cavities on a HP8510C Network Analyzer. Test data were displayed and stored on a PC using LABVIEW4. To measure the frequencies of the cavity, a small current loop was inserted through a hole on the cavity end wall to excite the magnetic fields of the cavity modes. Depending on the orientation of the current loop with respect to the beam axis, TM or TE modes of the cavity would be excited. After properly calibrating the network analyzer for the frequency range of interest, we measured in a straightforward way the frequencies of the modes excited by the current loop. The measured and calculated resonant frequencies of the first few TM modes of the barbell cavity are shown in Table 1 and Figure 4. The Q of each mode was measured directly from the half width of the resonance. To measure the transmission through the beam pipe, a small current loop is inserted through a hole in a first cavity, and another loop is inserted through a small hole on the side wall of a second cavity, connected to the first by a beam pipe. The cold measurements confirmed the modal frequencies pre-

dicted by MAFIA, and the large coupling between the TM modes of the cavities.

In a cavity with a wide transverse dimension, spurious higher order TM modes may exist. However, if there is sufficient frequency separation between the fundamental and higher order modes, and if the Q values of the modes are high, then the existence of the higher order TM modes need not adversely affect the beam acceleration which occurs in the narrowband fundamental TM mode.

The cavities fabricated by ANL unfortunately were welded rather than brazed as specified in the drawings. The measured Q for the fundamental TM mode was 1100, compared with a calculated Q of about 6800. Because of the lower Qs resulting from fabrication imperfection, the separation between the fundamental mode and the first higher order TM mode was not as clean as it could be. Consequently, measurement of the electric field of the fundamental mode alone was difficult. A bead pull measurement confirmed that there was considerable mixing between the first two TM modes.

In order to improve the results, we have designed another cavity by shortening the transverse dimension by one-third, thus increasing the frequency separation between the fundamental and the first higher order TM modes from 60 MHz to 170 MHz. The calculated frequencies for the TM and TE modes of the shortened cavity are shown in Table 2. The new cavity has now been fabricated in a precision machine shop at Los Angeles and is being brazed together for final test. We expect that the larger modal separation, combined with higher Q values, should enable measurements to confirm the flat field predicted by MAFIA.

Table 2 TE and TM Modes of a Shortened Barbell Cavity

| TM modes | TE modes |
|---|---|
| 11439.3 | 5992.38 |
| 11608.5 | 7100.01 |
| 12058.7 | 8197.42 |
| 12733.8 | 8629.78 |
| 13713.1 | 9053.06 |
| 14829.8 | 10388.2 |
| 16077.0 | 11859.9 |
| 17407.8 | 11859.9 |
| 17844.9 | 12264.0 |

We thank A. Menegat (SLAC) and J. Rosenzweig (UCLA) for helpful discussions.

## REFERENCES

[1] D. Yu, J. Kim, P. Wilson, "Design of a High Power Sheet Beam Klystron", AIP Conference Proceedings 279, Advanced Accelerator Concepts Workshop, Port Jefferson, Long Island, NY, June 14-20, 1992. pp. 85-102.

[2] D. Yu, P. Wilson, "Sheet Beam Klystron Cavities", Proceedings of the 1993 Particle Accelerator Conference, Washington D.C., pp. 2681-2683, May, 1993.

[3] D. Yu *et al*, "Design and Microfabrication of Planar Accelerating Structures", Proc. of the 6th Adv. Accelerator Concepts Workshop, Lake Geneva, Wisconsin, June 12-18, 1994.

[4] P. Chou *et al*, "The Fabrication of Millimeter-Wavelength Accelerating Structures", SLAC-PUB-7339, November, 1996, presented at the 7th Workshop of Advanced Accelerator Concepts, Lake Tahoe, California, October 12-18, 1996.

[5] H. Henke, "Planar Structures for Electron Acceleration"; Proc. of 1995 Particle Accelerator Conf., p. 1750, Dallas, Texas, May 1995; D. Yu and H. Henke, patent pending.

[6] DULY SBIR Phase I Final Report, DE-FG03-96-ER82213, May, 1997.

# THE 101 MHZ AMPLIFIER SYSTEM OF THE NEW CERN LEAD INJECTOR

G.Hutter, W.Hartmann, F.Klaus, H.Valter, W.Vinzenz, GSI Planckstraße 1, D64291 Darmstadt and
J.Broere, J.Evans, F.Nitsch, CERN and
K.Berdermann, J.Braun, D.Vierlbeck, BERTRONIX Electronic GmbH, München and
U.Hansen, Dressler Hochfrequenztechnik GmbH, Stolberg

*Abstract*

The 101 MHz rf amplifiers for a RFQ, an IH-structure and two bunchers for the CERN Lead Injector were provided by GSI Darmstadt. The accelerating structures required amplifiers up to 400 kW while the bunchers needed about 2 kW, both with a pulse length of 1 ms at a repetition rate of 10 Hz. The special properties of the amplifiers, technical difficulties and their cure in respect of rf-circuits, output coupling, parasitic oscillations of the final stage and fulfillment of the new CE-Standards are reported. A second part of the report describes the low level rf-circuits which were built by CERN.

## 1 INTRODUCTION

The CERN LINAC 3 (Pb-Linac) consists of a RFQ, an IH-structure and two bunchers at 101,28 MHz and two IH -structures at 202,56 MHz [1].
The three IH-structures and the rf power for all 101 MHz cavities were supplied by GSI Darmstadt.
The 2.5 kW transistor amplifiers for buncher and debuncher were specified at GSI and developed and delivered by Dressler as reported earlier[2].

This paper mainly describes the special features of the two 101 MHz / 400 kW amplifiers, and the low level rf-system. The amplifiers were specified in detail by GSI and CERN and ordered from BERTRONIX, Munich, while the work on the low level rf was done by the CERN PS RF-staff. Fig. 1 shows a picture of one of the 400 kW amplifiers installed at CERN while table 1 gives data at full power operation at BERTRONIX.



fig.1 One of the 400 kW amplifiers installed at CERN

| CERN 400 KW 101.28 MHz | DRIVER STAGE | FINAL STAGE |
|---|---|---|
| Ufil / V | 8.7 | 14.2 |
| Ifil / A | 107 | 172 |
| Ug1 / V | 130 | 200 |
| Ig1 / mA | 5 | 1600 |
| Ua / kV | 9 | 18 |
| Ia / A | 3.6 | 38 |
| Ug2 / V | 900 | 1150 |
| Ig2 / mA | 70 | 1200 |
| Pforw / kW | 19 | 400 |
| Prefl / kW | 0.4 | 3.5 |

table 1 Data for maximum output power

## 2 AMPLIFIER DESIGN

The 400 kW amplifiers consist of three rf-stages.
The predriver, a 400 W transistor amplifier, uses the Valvo transistors BLF278. It was built by Dressler[2] and adapted to the system by BERTRONIX.
The 20 kW driver is a new development of BERTRONIX. It is equipped with the new long-life Siemens tetrode RS2068CL. This tube has been developed for 20 kW FM-transmitters and is operated cathode driven with a kapton capacitor between g1 and g2. The output circuit is a coaxial λ/4 resonator with a disk kapton dc-blocking capacitor around the anode. One characteristic of the amplifier design is that the coaxial resonators anode-g2 and g1-cathode are going straight down from the tube connector-rings, thus guaranteeing optimum access to the tube. The input-coupling and the input λ/4 resonance can be adjusted as well as the output resonator's frequency and the mixed galvanic/inductive output-coupling by motordriven plungers with a digital position-readout.
The final 400 kW amplifier uses the same design except the g1-g2 circuit, built here by a short-circuited λ/2 coax. The schematic design of this stage is shown in fig.2. The chosen Siemens tetrode RS2054SK is a very slim tube with long internal supports to its active system. Consequently, this results in a high inductance in the screengrid area of the output-resonator which made it nearly impossible to bring its resonance frequency to the required 101 MHz in a λ/4 resonator.

0-7803-4376-X/98 /$10.00 © 1998 IEEE

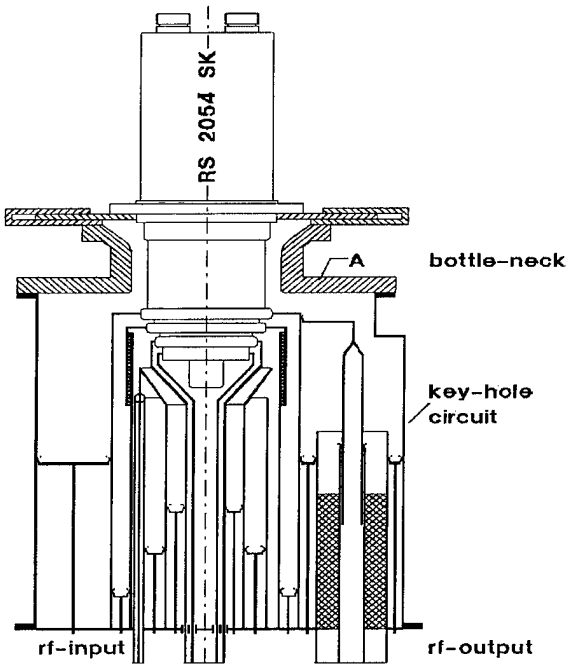



fig.2 Principal drawing of the final amplifier

The λ/4 resonance of the anode-screengrid area of the tube itself, measured with a tin foil short-circuiting closely the anode-screengrid ceramic was already 135 MHz. So an extremely small space was left for sufficient output coupling and for the needed 20 kV bypass capacitor in the external part of the anode resonator at 101 MHz. For the shortest cylindrical coaxial circuit, a SuperCompact[R] simulation, made by GSI, gave a maximum frequency of 92 MHz. To reach the proper frequency with the required low loaded Q-factor of the anode circuit, three sophisticated measures had to be introduced to the amplifier design:
First, the output coupling was arranged partly penetrating the outer cylindrical wall of the anode circuit, which by that led to the shape given in fig.3.

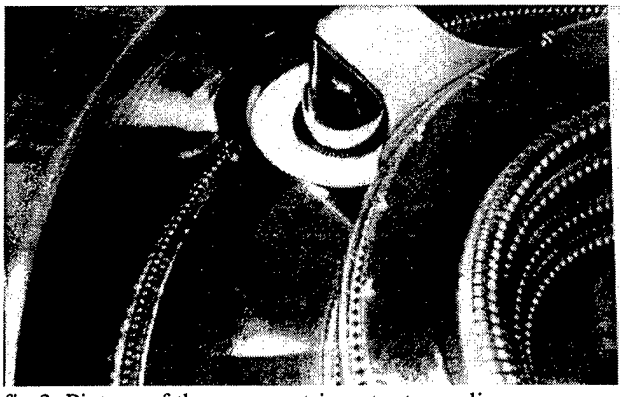


fig.3 Picture of the asymmetric output coupling

This so called key-hole circuit gives a characteristic impedance as low as possible with nevertheless good voltage capability and effective coupling. Its disadvantage is the complicated and expensive production of the resonator-shape and the movable short-circuit-plane.
Second, another low impedance part was introduced into the anode circuit to increase the resonance frequency. This so called „bottle-neck" is shown as part A in fig.2.. A SuperCompact[R] simulation of the anode resonator with this device gave the required frequency and agreed well with a model made out of aluminum-sheet-covered polyfoam. The λ/4 resonance of the circuit simulation and the model-measurement was within 1%, while the calculated 3/4 λ resonance of about 570 MHz was measured to be 590 MHz. The separation of the 3/4 λ resonance from the third harmonic promised the low harmonic spectrum later reached in operation.
The third measure was a transformation of the 50 Ω load of the cavity (or a dummy load) to about 25 Ω at the output-coupling-loop by adjusting the location of a polyethylene filled part of the output coaxline.

## 3 POWER-SUPPLIES

All the controllable output power supplies for the two tetrodes , filament, g1, anode and g2 were built using primary variable-ratio transformers. Apart from the high-current filament transformers and the anode power-part, all other supplies were housed in modular plug-in units.
The g1 voltages of driver and final stage are switched between two sources from a C working point to A/A-B during the rf-pulse by a high voltage power-mosfet transistor, while another one acts as an electronic load for the g1-current.
The crowbar system of the anode supplies is a modified fail-save GSI development which fires the ignitron at a preset anode-current without any electronic-circuit[3].

## 4 CONTROL AND MEASUREMENT EQUIPMENT

A programmable SIMATIC (SPS 105U) controls all the necessary command, status and interlock signals with 320 possible inputs and outputs. It stores all errors and also acts as an interface to the CERN remote-control.
A local alphanumeric read-out (COROS), connected to the SIMATIC, gives the present status and the last error-codes and can be used for statistic records.
The main-software for the SIMATIC was written by GSI while the COROS program was provided by BERTRONIX.
The transmission of more than 20 analogue signals is made via optical-fiber, digitized with a sampling rate of 250 kHz, to a separate plug-in, where video signals of all pulsed currents and rf-powers are provided.
This plug-in also limits all directly measured and derived values to their allowed levels, partly by analog feedback to the amplitude-regulator, partly by a reduction of the pulse-length and with the help of the SIMATIC.

## 5 PARASITIC MODES AND EMC

One main problem was to get rid of a parasitic mode at 1050 MHz, which the RS2054SK produced in the final stage's geometry. It was probably the „bottle-neck", facing closely the anode-screengrid-ceramic which prohibited sufficient radiation out of the tube at this frequency. By this the Q-value of an internal circumference resonance increased, producing self oscillations at higher anode dc-currents, especially, when the tube was pulsed to the A-working point without rf-drive. About twenty different measures were tried to damp these oscillations. Resonant loaded loops were integrated in the anode circuit, the „bottle-neck" was partly filled with ferrites, using the design of an earlier GSI-patent (fig.4), ferrites were located between g1 and g2 and polyethylene rings with different ferrite mixtures were mounted between anode-ceramic and the „bottle-neck" at different distances. One of the last measures produced the highest damping and together with a timed dc-gridpulse in relation to the rf-drive, trouble-free operation was obtained.

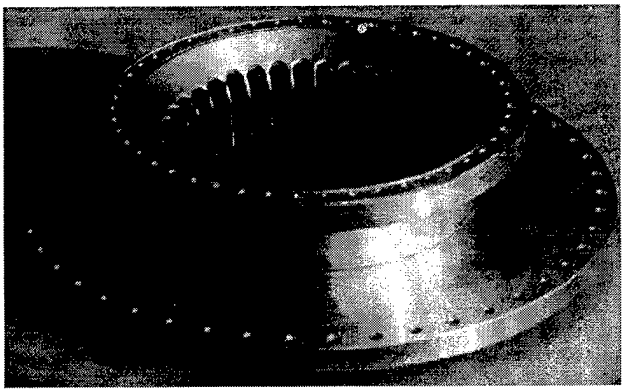


fig.4 Ferrite loaded „bottle-neck"

As these procedures were very time consuming, the rf-radiation of the amplifier in respect of the new EMC-standards was measured in parallel. The limits of the allowed radiation levels were reduced by about 20 dB during the project lifetime. Standard EMC-racks were no longer sufficient. Many parts had to be connected by additionally welding and sealing. Also the anode-voltage filter of the final stage had to be redesigned to meet the new requirements besides several smaller improvements. The final result regarding EMC was that measurements, done by an external „competent body" could not identify the radiation of the amplifier at 10 meter distance from the building at a total distance of about 16 meters.

## 6 TEMPORARY LOAN AMPLIFIERS BY GSI

All the described additional necessary work led to a significant delivery delay. To avoid an unacceptable delay to the beginning of the operation of the otherwise completed LINAC 3, GSI provided temporarily two amplifier-chains from 108.4 MHz UNILAC single-gap-cavities, modified to 101.28 MHz. Along with modified driver- and final-anode-power supplies these units were sent to CERN within about three months. They were assembled by CERN and GSI personnel and operated satisfactorily until the last BERTRONIX amplifier was installed and all spare units of the new amplifiers were tested successfully.

## 7 LOW LEVEL RF AND CONTROL CIRCUITS

The low level rf was based on the existing system of the CERN LINAC 2, modified for 101 MHz (fig. 5).
The fundamental frequency of 101.28 MHz is distributed by equal length, minimum phase drift coaxial cable to the low level equipment of each rf chain. The return tank signal is carried by the same type and length of cable to keep temperature dependence as low as possible (calculated phase drift for the linac length has been estimated as $< 0.1°$ per °C). The very stringent 0.3° phase-stability specification imposed by the use of the IH structures required the development of a new high- resolution electronic phase shifter in the reference line of each rf chain. The final design is adjustable in 0.1° steps and has an overall stability of $< 0.3°$.

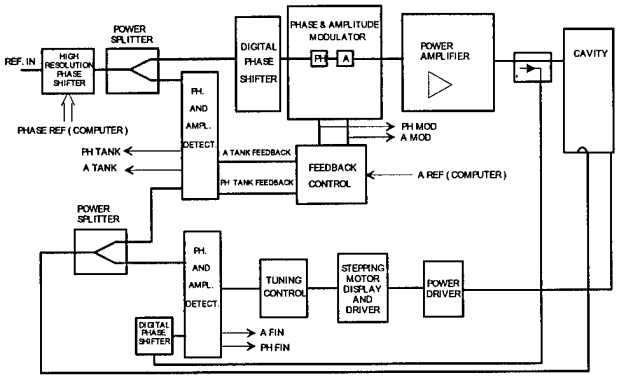



fig 5. RF control layout

Each amplifier chain is remotely controlled by means of a local G64 rf chassis linked to a VME Device Stub Controller. This chassis contains analogue and digital interface cards and also some local intelligence. Its main functions are to supply and acquire the cavity reference voltage, its reference phase and to interface to the SIMATIC SPS 105U. Additional sampled analogue signals allow the rf performance of each amplifier stage to be monitored. This immediately highlights any performance degradation due to failing tubes etc..

## REFERENCES


[1] H.D.Haseroth, Pb Injector at CERN, LINAC96 pp. 283-287
[2] G.Hutter et.al., A New Generation of Solid State Amplifiers for Accelerators, EPAC 94 pp.1909-1911
[3] G.Hutter et.al. New Power Amplifiers for 200 kW at 27 MHz, EPAC 92, pp.1203-1205

# DESIGN OF 135 MW X-BAND RELATIVISTIC KLYSTRON FOR LINEAR COLLIDER

G.V. Dolbilov, I.N. Ivanov, N.I. Azorsky, V.S. Shvetsov
Joint Institute for Nuclear Research, 141980 Dubna, Moscow Region, Russia
V.E. Balakin, P.V. Avrakhov, S.Yu. Kazakov, V.E. Teryaev V.F. Vogel
Branch of Budker Institute of Nuclear Physics, 142284 Protvino, Moscow Region, Russia

*Abstract*

It has been reported at EPAC-96 Conference on successful experimental results on achievement of 100 MW output rf power in a wide aperture, 15 mm, high gain, 80 dB, 14 GHz VLEPP klystron with distributed suppression of parasitic oscillations [1]. This report presents design of an electrodynamic structure of the X-band klystron for linear collider with a higher efficiency up to 54 % to be achieved at the same parameters of the electron beam ($U = 1$ MeV, $I = 250$ A, emittance $0.05\pi$ cm·rad). Design rf output power of the klystron is equal to 135 MW.

## 1 INTRODUCTION

The cost of RF power system will constitute significant fraction of the total cost of future linear collider. Appropriate design of the klystron can reduce this cost. The focusing system of the klystron should be based on permanent magnets to reduce operational cost. The power gain of the klystron should be high enough to provide an opportunity of using cheap semiconductor devices as master amplifiers. The requirements to the quality of the driving electron beam should also be reduced in order to simplify the design of the gun and the modulator.

## 2 PARAMETERS OF THE KLYSTRON

A prototype of a high efficiency and low cost X-band klystron is developed by the collaboration of the BINP (Protvino) and JINR (Dubna). Parameters of the klystron are presented in Table 1. Frequency and amplitude characteristics of the klystron are presented in Figs. 1 and 2. Design output rf power is equal to 135 MW. High gain of the klystron, 83 dB at saturation, will allow to use low powerful, 0.6 W, semiconductor master amplifier. The klystron has large aperture of drift tubes, 15 mm ($a/\lambda = 0.7$) which will allow to use relatively low quality driving electron beam from a gridded electron gun.

Focusing system of the klystron is designed on the base of permanent magnets. Output rf system of the klystron is designed to obtain maximal efficiency at reduced value of maximal surface electric field.

Table 1: Parameters of 135 MW VLEPP klystron

| | |
|---|---|
| General parameters | |
| Beam voltage | 1 MeV |
| Beam current | 250 A |
| RF frequency | 14.0 GHz |
| Power gain | 83 dB |
| RF peak output power | 135 MW |
| Efficiency | 54 % |
| Focusing system | |
| Type of magnets | Permanent |
| Max. magnetic field | 0.4 T |
| rms magnetic field | 0.28 T |
| Period | 64 mm |
| Number of periods | 14.5 |
| Acceptance | $0.1\pi$ cm·rad |
| Buncher | |
| Drift tube diameter | 15 mm |
| Length of drift section | 52 mm |
| Number of drift sections | 10 |
| Length of cavity | 12 mm |
| Number of cavities | 11 |
| Mode of operation | $\pi$ |
| Q-factor of loaded cavity | 830 |
| Max. surface field strength | 300 kV/cm |
| Output structure | |
| Design | expanded conic |
| Mode of operation | $\pi/2$ |
| Number of cells | 22 |
| Length | 110 mm |
| Aperture | 15 mm to 20 mm |
| Max. surface field strength | 700 kV/cm |
| # of power outputs | 2 |

## 3 BUNCHER

### 3.1 *The choice of the aperture*

An increase of the drift tube diameter simplifies the problem of beam transport. On the other hand, a risk of self-excitation of the system is increased. From this point of view, several cases can be identified.

1. The diameter is smaller than the cut-off value for the modes with frequencies less than the double operating frequency. This diameter is a standard choice. At the frequency of 14 GHz the diameter should be less than 6.28 mm.

2. The diameter is less than the cut-off value for the operating frequency. At the frequency of 14 GHz the diameter should be less than 12.56 mm. The diameter of the klystron under development at BINP is equal to

0-7803-4376-X/98 /$10.00 © 1998IEEE

11 mm [2, 4]. In this device the self-excitation occurs at frequencies higher than 16 GHz when the beam current is higher than 100 A.

3. The diameter is larger than the cut-off value for TE-modes (overmoded channel) and less than the cut-off value for TM-modes. At the frequency of 14 GHz the drift tube diameter should be in the range from 12.56 mm to 16.4 mm. The klystron described in this paper belongs to this range.

Positive feedback for $TE_{11}$ leads to the self-excitation of parasitic oscillations near the operating frequency when the drift tube diameter is larger than the critical value for TE-modes. Another mechanism of self-excitation is connected with the synchronous interaction between the electron beam and $TE_{11}$ mode field (beam velocity is approximately equal to a phase velocity of a wave). At the frequencies higher than the critical value for TM-modes there is a risk to get an additional excitation due to these modes.

### *3.2 The choice of the cavity parameters*

The choice of the cavity parameters has been defined by the following suggestions:

1. At a low beam microperveance of 0.25, the Q-factor of loaded cavity is still high, Q = 830. To provide amplification bandwidth up to 40 MHz, it is necessary to have several intentionally detuned cavities.

2. A low beam perveance, a large diameter of the channel and large transit time factor reduce amplification in the cavity. Due to these reasons the number of the buncher cavities should be larger than six.

3. To maintain optimized beam bunching at the beam voltage of 1000 kV, the bunching field should be distributed over several cavities. The requirement to keep the field strength on the cavity surface below 300 kV/cm threshold requires to have at least 3 output cavities.

4. An optimal length of the klystron is about 100 cm. On the other hand numerical simulations shows that an increase of the klystron length from 70 cm to 100 cm leads to the efficiency increase less than 5 %.

Due to these reasons the bunching unit length in our klystron is equal to 70 cm and the number of the cavities is equal to 11.

To improve the bunching characteristics of the klystron the cavities of the wide aperture buncher are designed as two-gap $\pi$-mode cavities which provide better transit time factor.

One more detrimental factor of the larger diameter of the drift tube is the dependence of the bunching properties of the cavity on the radius of the electron beam. This circumstance might have a strong effect in the case of a nonrelativistic beam. In our case, however, the dependence on the radius is reduces significantly because of using relativistic beam [6].

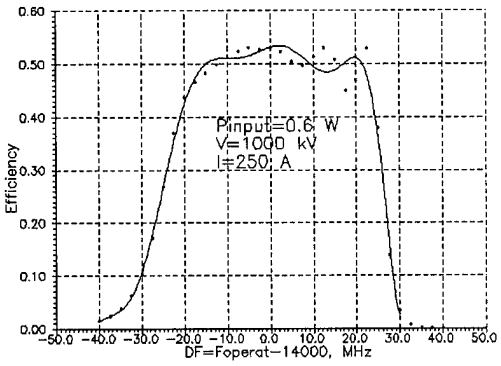



Figure 1: Frequency characteristic of the klystron.

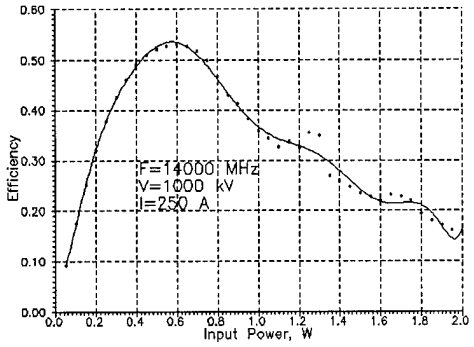



Figure 2: Amplitude characteristic of the klystron.

## 4 FOCUSING SYSTEM

Focusing system of the klystron is designed on the base of permanent magnets. The magnetic field has been calculated with two-dimensional codes and measured afterwards in a real device. The electron beam transport through such a system has been optimized using numerical simulations taking into account angular spread of the electron velocities and the space charge fields. The results of these simulations are presented in Fig. 3.

## 5 OUTPUT STRUCTURE

The design of the output system has changed with respect to previous one [3]. At present it is manufactured in a form of a segment of expanding conic diaphragm waveguide with the mode of oscillations close to $\pi/2$. The aperture of the output structure is increased from 15 mm at the entrance up to 20 mm at the exit. Such a design correspond to higher impedance and higher efficiency, up to 54 % (previous design provided efficiency of 44 % [3]).

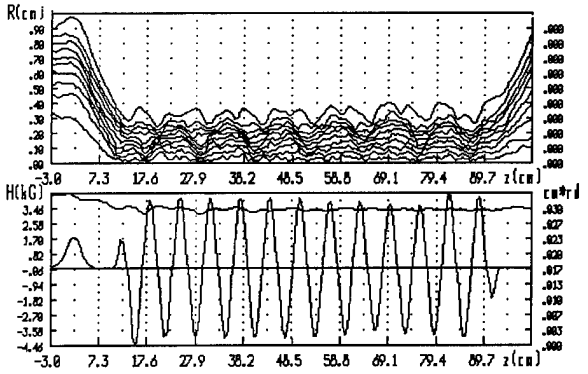


Figure 3: Magnetic field of the klystron and numerical simulations of the electron beam transport.

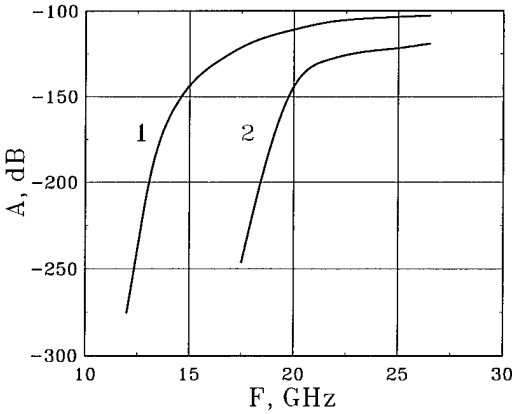



Figure 4: Integral frequency characteristic of the distributed suppression filter composed of ten RF absorbing drift tubes (1 – $H_{11}$-mode and 2 – $E_{01}$-mode).

Symmetrical design of two rf power outputs improves conversion efficiency of operating TM-mode of the output structure into TE-mode of the output waveguide. To prevent penetration of the rf field to the electron beam collector, the transit section between the power output and the collector is installed. It has appearance of a segment of an irregular diaphragm waveguide with the suppression band of the filter at the frequency of 14 GHz (plug-type filter).

To increase the reliability of the klystron, the elements of the output structure where the electric field strength exceeds 300 kV/cm are manufactured of stainless steel. The surfaces of the stainless steel insertions are strengthened mechanically and shined. We suppose that such a technology will provide a safe margin of operation up to maximal electrical field strength on the surface of 700 kV/cm.

## 6 SUPPRESSION OF PARASITIC OSCILLATIONS

To suppress parasitic oscillations we use the technique of RF absorbing insertions installed inside the drift tubes [4, 7]. We have studied several methods to obtain absorbing materials. Investigations have shown that glass-carbon and "SiC" materials are more suitable for this applications.

Such a distributed suppression filter provides significant attenuation of the parasitic modes and does not perturb the klystron operating mode (see Fig.4). Operating experience has shown that materials do not affect vacuum conditions and are stable to the heat and radiation load. Investigations of the beam dynamics have not shown any evidence of resistive instabilities of the beam [8].

## 7 REFERENCES


[1] G.V. Dolbilov et al.,"Experimental Study of 100 MW Wide-Aperture X-band Klystron with RF Absorbing Drift Tubes", Proc. EPAC-96, Sitges (Barselona), 10-14 June,1996, Vol. 3, p. 2143.

[2] L.N,Arapov et al., "14 GHz VLEPP Klystron", Proc. EPAC-92, vol.1, p.330, (1992) Berlin

[3] L.N.Arapov et al., "High Power Source for VLEPP", Proc. of the 1994 International Linac Conf., vol.2, p.643, (1994), Tsukuba, Japan

[4] N.I.Azorsky et al., "Study of the 14 GHz Relativistic Klystron for VLEPP". Proc. of the 1994 International Linac Conf., vol.2, p.421 (1994), Tsukuba, Japan.

[5] G.V. Dolbilov et al. "Development of Linear Induction Accelerators at JINR". Proc. of the 1994 International Linac Conf., vol.1, p.363(1994), Tsukuba, Japan.

[6] V.A.Vagin, V.I.Kotov, I.I.Semenyushkin Uspekhi Fizicheskih Nauk, v.82, vyp.4, str.707, 1964

[7] G.V.Dolbilov et al., AIP Conference Proceedings 337 (Proc. of the International Workshop on Pulsed RF Sources for Linear Colliders, Montauk, NY, October 1994),p. 122

[8] G.V.Dolbilov et al., "A concept of wide aperture klystron with absorbing drift tubes for a linear collider", Nuclear Instruments and Methods in Physics Research A 383 (1996), p. 318

# LARGE-SIGNAL KLYSTRON SIMULATIONS USING KLSC

Bruce E. Carlsten, Los Alamos National Laboratory, Los Alamos, NM 87545 USA and
Patrick Ferguson, MDS Company, Oakland, CA 94611 USA

*Abstract*

We describe large-signal klystron simulations using the particle-in-cell code KLSC. This code uses the induced-current model to describe the steady-state cavity modulations and resulting rf fields, and advances the space-charge fields through Maxwell's equations. In this paper, an eight-cavity, high-power S-band klystron simulation is used to highlight various aspects of this simulation technique. In particular, there are specific issues associated with modeling the input cavity, the gain circuit, and the large-signal circuit (including the output cavities), that have to be treated carefully.

## 1 INTRODUCTION

We have recently developed a new large-signal klystron simulation code, KLSC. KLSC is a particle-in-cell code, and represents a significant advance over previously available simulation tools [1,2], which tended to use point-by-point space-charge forces, and were thus limited to less than a hundred simulation particles. In addition to the limitation on the number of particles, these codes also assumed that the space-charge fields could be solved electrostatically in some beam frame of reference, which is certainly not true when the beam is in the output cavity and there is a large energy spread. KLSC uses a uniform, rectangular mesh to calculate the space-charge fields, and advances the fields according to the Maxwell curl equations [3]. Particles travel along this mesh, being pushed by the Lorentz force equation. A charge-conserving algorithm is used to evolve the space-charge fields, where the current is determined from the particles' motion on the mesh. The cavity rf fields are superimposed on this mesh (the field distribution is provided by the code SUPERFISH), and superposition of both the space-charge and rf fields is used to determine the particle motion. This separation of the rf and space-charge fields is allowable; the only approximation that arises is that the boundary condition on the space-charge mesh does not include the cavity gaps and shapes around the cavity noses. The particle motion is used to calculate the driven modulation of the rf cavities. An iteration scheme is then used to converge on an rf field amplitude that leads to a self-consistent particle motion.

There are three separate regimes of large-signal klystron simulation, each with distinct simulation issues. These are the input cavity, the gain circuit (the cavities providing the gain from the small-signal amplitude in the input cavity to the large-signal amplitude in the penultimate and output cavities), and the large-signal circuit (the penultimate and output cavities).

TABLE 1: Operating Parameters

| | |
|---|---|
| Operating frequency | 3 GHz |
| Beam current | 796 A |
| Beam voltage | 720 kV |
| Input power | 3.5 watt |
| Output power | 310 MW |
| Efficiency | 54% |

The difficulties in the input cavity and the gain circuit are due to numerical stability of the iteration procedure. The iteration scheme is more straightforward for the large-signal circuit, and the issue here is the self-consistent simulation of multiple coupled output cavities.

In the next section, we will describe the induced current model used as a basis for the self-consistent calculation of the rf cavity field amplitudes, and the iteration schemes available for determining the self-consistent parameters. Following that, we will use a simulation of a high-power, S-band klystron, designed by MDS Company, to describe features of the simulation technique. First, we will present the model describing the input cavity's interaction with both the external drive and the electron beam, including the required input power as a function of input cavity loaded and unloaded Q and resonant frequency. Then, we will describe the calculation of the gain circuit, comparing the cavity modulation to that predicted by using the beam impedance in parallel to the cavity impedance. Finally, we will demonstrate the code's ability to handle multiple penultimate and output cavities, with three penultimate and two coupled output cavities. The nominal beam and cavity parameters are shown in Tables 1 and 2.

TABLE 2: Cavity Parameters

| Cavity | Resonant Frequency | Shunt Impedance | R/Q | Voltage |
|---|---|---|---|---|
| 1 | 3015 MHz | 351 kΩ | 124 Ω | 709.3 V |
| 2 | 2991 | 351 | 117 | 18.4 kV |
| 3 | 3009 | 351 | 115 | 195 |
| 4 | 3330 | 432 | 144 | 182 |
| 5 | 3350 | 435 | 145 | 265 |
| 6 | 3420 | 450 | 150 | 310 |
| 7 | | | | 894 |
| 8 | | | | 1211 |

0-7803-4376-X/98/$10.00 © 1998 IEEE

The first cavity is the input cavity. Cavities two and three are for gain and constitute the gain circuit. Cavities four through six are penultimate cavities, and, along with cavities seven and eight (the output cavities), make up the output circuit. Cavities seven and eight are coupled, with impedances $Z_{77}$ = (14.1+$j$569) Ω, $Z_{78} = Z_{87}$ = (175-$j$5.3) Ω, and $Z_{88}$ = (2315-$j$67.2) Ω.

## 2 CAVITY/BEAM-INTERACTION MODEL

In Fig. 1 we see the circuit model for a cavity. The cavity impedance, $Z_{cav}$, is given in terms of the cavity shunt impedance $R$, the cavity resonant frequency $f_0$, the operating frequency $f$, and the cavity $R/Q$ factor by

$$\frac{1}{Z_{cav}} = \frac{1}{R} + j\left(\frac{f}{f_0} - \frac{f_0}{f}\right)\frac{1}{R/Q} \quad .$$

There can also be some coupling to an external drive, which is not shown. The gap voltage is given by

$$V_{gap} = Z_{cav} i_1 \quad ,$$

where $i_1$ is the current in the cavity circuit due to the beam, usually known as the fundamental component of the beam induced current. The instantaneous induced current $i_{ind}(t)$ is given by Ramo's theorem [4],

$$i_{ind}(t) = \frac{\int_V \vec{J}(t)\cdot\vec{E}(t)\,dV}{V_{gap}(t)} \quad ,$$

where the space-charge current is given by $\vec{J}$, the electric field $\vec{E}$ is only from the cavity rf fields, and the integral is taken over the entire cavity volume $V$. The fundamental component of the induced current is defined by the expansion

$$i_{ind}(t) = i_0 + i_1\cos(\omega t + \phi_1) + i_2\cos(2\omega t + \phi_2) + \ldots$$

This set of equations (along with the Lorentz force equation for the particle motion due to the rf cavity fields) fully represent the self-consistent solution to the cavity excitation. The iteration scheme in KLSC is based on guessing a cavity voltage, pushing the electrons for an rf period, evaluating the fundamental component of the induced current, and re-evaluating the cavity voltage. If the re-evaluated cavity voltage is sufficiently close to the guess, the solution is considered to be self-consistent. If not, this procedure is iterated, typically using a weighted average of the newly calculated cavity voltage and the original guess as the guess for the next iteration, until a self-consistent solution is reached. The weighting factor is called the relaxation factor.

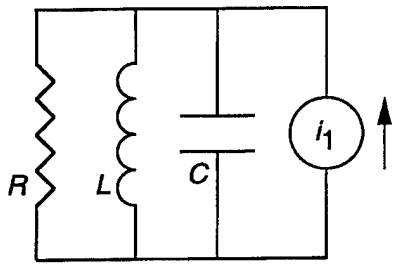



Figure 1. Beam/cavity interaction circuit

## 3 INPUT CAVITY

For the input cavity, we wish to calculate the input power drive required to establish a certain field amplitude. We could use the iterative procedure outlined above to find the effect of the induced current in the input cavity, but it does not typically converge (because the induced current counters nearly all of the input drive and thus small errors in the cavity voltage guess will lead to very large fluctuations in the re-evaluated cavity voltage). However, the procedure to find a self-consistent solution is straightforward for this cavity. The effect of the induced current is to establish an effective beam impedance, $Z_{beam}$, which acts in parallel with the cavity impedance. This beam impedance can be found by numerically calculating the induced current for a given cavity modulation - the induced current only depends on the cavity modulation and not on the cavity impedance itself. The beam impedance is then given by the cavity voltage divided by the fundamental component of the induced current [5]. The power required from the generator is

$$P_{in} = \frac{1}{8}|1+\beta|^2 \frac{|V_{gap}|^2}{|Z_{cav}||\beta|}\left|1 - \frac{Z_{cav}}{(1+\beta)Z_{beam}}\right|^2 \quad ,$$

where the cavity-input waveguide coupling is given by $\beta = Z_0 Z_{cav}/(2\pi f)^2 M^2$, and where $Z_0$ is the input waveguide characteristic impedance and $M$ is the mutual inductance between the waveguide and the cavity. The cavity Q loaded by the input waveguide is given in terms by the coupling and the unloaded cavity Q, $Q_0$, by $Q_l = Q_0 \frac{1}{1+\mathrm{Re}(\beta)}$. If the cavity is matched (no reflected power), the power from the generator is given by

$$P_{in} = \frac{1}{2}|V_{gap}|^2\left|\frac{Z_{cav} - Z_{beam}}{Z_{cav}Z_{beam}}\right| \quad .$$

The input is matched if the cavity detuning is

$$\frac{f_0 - f}{f} = -\frac{R/Q}{2}\mathrm{Im}(1/Z_{beam})$$

and the externally loaded cavity Q is

$$Q_l = Q_0 \frac{1}{1 + \mathrm{Re}\left(\frac{Z_{beam} - Z_{cav}}{Z_{beam}}\right)} \quad .$$

## 4 GAIN CIRCUIT

The relaxation iteration scheme outlined in Section 2 also does not work well for the high gain cavities, for the same reason as for the input cavity. However, we cannot now simply use the beam impedance in parallel with the cavity impedance to find the cavity modulation - the cavity modulation directly affects the current modulation driving the cavity. For this case, the particles' motion must be simulated through the cavity and the induced current calculated. Instead of using relaxation to determine a new guess for the cavity voltage, the derivatives of the voltage equal to the induced current times the cavity impedance with respect to both the real and imaginary part of the guess voltage is found, and a new voltage is predicted. This two-dimensional Newton-Raphson approach is needed because the function defined by the induced current times the cavity impedance is not analytic.

The resulting self-consistent cavity voltage is somewhat different than would be found by simply assuming that the cavity and beam impedances were driven by the input current modulation. For the second cavity in this example, the self-consistent voltage is 18.35 kV, with a phase of 2.73 radians. Using the simple beam impedance approximation (and the induced current in the second cavity due only to the fields in the first cavity), one would have guessed that the cavity voltage should be 22.6 kV, with a phase of 2.96 radians. The error in the magnitude is from correlations between the induced current arising from the two cavities, and the error in phase is from the fact that there is no external drive power and the power in the cavity must come from the beam itself.

## 5 OUTPUT CIRCUIT

The output circuit, defined by the penultimate and output cavities, is comparatively simple to simulate. The relaxation iteration scheme works well for these cavities (the induced current is not drastically modified by the fields within the cavities themselves).

In Fig. 2, we plot the axial electric field at the center of the beam as a function of time at an axial location roughly between the output cavities. We see the axial field has reached steady-state after about 40 rf cycles, and that the higher harmonic fields are slipping in phase relative to the fundamental, due to the relatively large beam pipe. In Fig. 3, we plot the instantaneous current as a function of time at the same axial location. The beam is clearly well-bunched (the induced current in the output cavities is about 80% of the average beam current). The gentle exponential rise of the current is also evident at the beginning of the plot. In Fig. 4, we plot the particles' $\gamma\beta_z$ as a function of axial position, at the end of the simulation. For this simulation, the first output cavity is centered at 1.1 m and the second at 1.14 m. The bunching and energy extraction is clear in this plot.

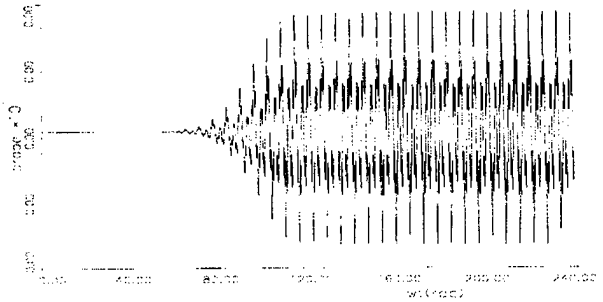


Figure 2. Axial electric field versus time in the output circuit.

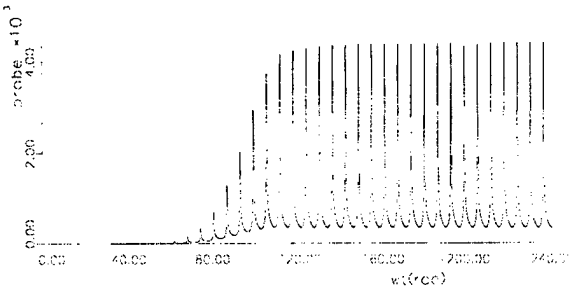


Figure 3. Current modulation versus time in the output circuit.

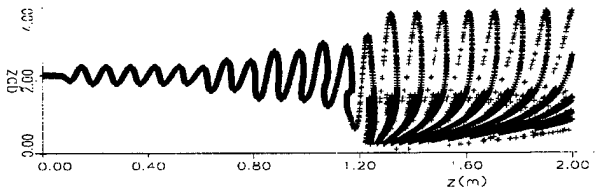



Figure 4. Particle $\gamma\beta_z$ versus axial position at the end of the simulation.

## REFERENCES


[1] H. Yonezawa and Y. Okazaki, "A one-dimensional disk model simulation for klystron design," SLAC technical note SLAC-TN-84-5 (1984).

[2] B. E. Carlsten, "A self-consisten numerical analysis of klystrons using large-signal beam-wave interaction simulations," PhD Thesis, Stanford University, Stanford (1985).

[3] C. K. Birdsall and A. B. Langdon, Plasma physics via computer simulations, McGraw-Hill Book Company, New York (1985).

[4] J. W. Gewartowski and H. A. Watson, Principles of electron tubes, Van Nostrand, New York (1965).

[5] B. E. Carlsten and P. Ferguson, "Numerical determination of the matching conditions and drive characteristics for a klystron input cavity with beam," *IEEE Trans. Elec. Dev.*, **44**, 894 (1997).

# RIPPLED-BEAM FREE-ELECTRON LASER

B. E. Carlsten, Los Alamos National Laboratory, Los Alamos, NM 87545 USA

*Abstract*

We describe a new microwave generation mechanism involving a scalloping annular electron beam. The beam interacts with the axial electric field of a $TM_{0n}$ mode in a smooth circular waveguide through the axial free-electron laser interaction, in which the beam ripple period is synchronous with the phase slippage of the rf mode relative to the electron beam. Due to nonlinearities in the orbit equation, the interaction can be made autoresonant, where the phase and amplitude of the gain is independent of the beam energy.

## 1 INTRODUCTION

In this paper, we will introduce a new amplifier interaction mechanism between an annular electron beam and a fast-wave rf mode in a smooth waveguide, in which the electron beam is radially rippled to establish synchronism. There is a uniform, axial magnetic field, and the beam ripple is caused by injecting the beam either displaced from its equilibrium position or with some initial radial velocity. The rf mode profile is unperturbed in the interaction region, leading to a smooth transition between the input signal and the growing mode and also between the growing mode and the output signal. The beam interacts with the axial electric field of a mode with a phase velocity greater than the speed of light and is bunched axially, and thus this interaction is in the class of the axial free-electron laser. We demonstrate this interaction in Fig. 1, where a $TM_{02}$ mode is used and the beam oscillates about the radius where there is a null in the axial electric field. Assume that the axial electric field opposes the electronic motion at position A, where the electron is at a radius greater than the null of the axial field. As the electron travels to the right, the rf phase slips by because the phase velocity is greater than the speed of light. At position B, the electron is now at a radius less than the null of the axial field. If exactly one-half of an rf wavelength has slipped by the electron, the axial field at this location will also oppose the electronic motion, and a synchronous interaction between the electron and the rf will be established. The single-particle synchronism equation,

$$\frac{\omega}{c\beta_z} = \frac{\omega}{v_p} + \frac{2\pi}{\lambda_r} \quad , \qquad (1)$$

is exactly the same as for all FEL interactions (where $\omega$ is the radian mode frequency, $c$ is the speed of light, $\beta_z$ is the electron's axial velocity normalized to the speed of light, $v_p$ is the phase velocity of the rf mode, and $\lambda_r$ is the period between ripples). The resonant axial electric field seen by an electron at an arbitrary phase is given by

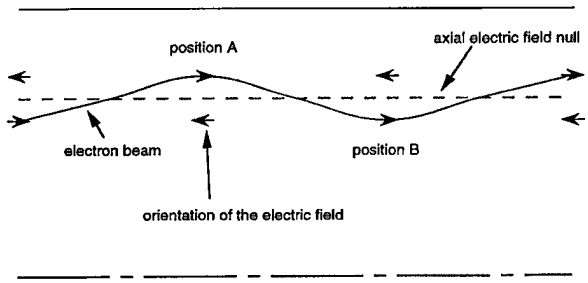



Figure 1. Rippled beam interaction, showing single electron synchronism.

$$E_z = Ak_c\kappa J_1(k_c r_o)\cos(k_r z)\cos(k_r z + \phi) \quad , \qquad (2)$$

where the mode has a maximum on-axis axial field strength of $A$, $k_c$ is the mode's radial wavenumber, $\kappa$ is the maximum ripple amplitude, $r_o$ is the equilibrium annulus radius, $k_r$ is the ripple wavenumber ($k_r = 2\pi / \lambda_r$), and $\phi$ is the relative phase between the rf and the electron. For an intense electron beam, Eqn. (1) is somewhat modified by the effects of the axial space-charge forces between particles; we will derive the more general dispersion relation in Section 3, which we will then use to numerically calculate the growth rate of the mode in Section 4. Note that this interaction vanishes on axis, and is only suitable for an annular electron beam. This interaction shares some features with the cyclotron autoresonance maser (CARM) interaction [1]. In particular, we will see that due to the inherent nonlinearities in the orbit equation, the rippled beam interaction can stay in resonance as either the axial magnetic field or the beam energy is changed, demonstrating autoresonance characteristics.

## 2 ORBIT EQUATIONS

The radial equation of motion of the center of an annular beam in a uniform axial magnetic field is

$$m\frac{d}{dt}\gamma\dot{r} = e\frac{E_r}{\gamma^{*2}} - ev_\theta B + \gamma m\frac{v_\theta^2}{r} \quad , \qquad (3)$$

where a dot refers to a time derivative, $\gamma$ is the relativistic mass factor, $m$ and $e$ are the electronic mass and charge, respectively, $E_r$ is the radial space-charge force at that point, $\gamma^*$ is the effective relativistic mass factor from the beam's axial velocity only

0-7803-4376-X/98 /$10.00 © 1998 IEEE

$\left(\gamma^* = \left(1-\beta_z^2\right)^{-1/2}\right)$, $v_\theta$ is the azimuthal velocity of the center of the annulus, $B$ is the total axial magnetic field. We assume that the radius of the annulus center is very close to an equilibrium radius $r_o$, and can be written as $r = r_o + \delta r$.

After reducing Eqn. (3) [2], the equation for the equilibrium radius becomes

$$r_o^2 = \frac{b + \sqrt{b^2 + 4\hat{r}^4}}{2} \quad , \tag{4}$$

where $I_A = 4\pi\varepsilon mc^3/e$, $\hat{r}$ is the injection radius, and $b = \left(\gamma cm/eB\right)^2 4I/I_A\gamma\gamma^{*2}\beta_z$. The radial displacement from the equilibrium orbit is then to lowest order

$$\delta r = \kappa e^{j\left(\frac{eB\sqrt{\left(r_o^4+\hat{r}^4\right)/2}}{\gamma m r_o^2}\right)t + j\phi} \tag{5}$$

where $\kappa$ is the maximum orbit displacement and $\phi$ is the phase of the oscillation. The ripple period is given by $\lambda_r = 2\pi c\beta_z\gamma m r_o^2 / eB\sqrt{\left(r_o^4+\hat{r}^4\right)/2}$. The average axial velocity is

$$\beta_z^2 = 1 - \frac{1}{\gamma^2} - \overline{\beta}_r^2 - \overline{\beta}_\theta^2 \tag{6}$$

where the rms azimuthal velocity is

$$\overline{\beta}_\theta = \frac{eB}{cm\gamma}\kappa\left(\frac{1}{2} + \cos^2(\phi)\right)^{1/2} \quad , \tag{7}$$

and the rms radial velocity is

$$\overline{\beta}_r = \frac{eB}{cm\gamma}\kappa\frac{1}{\sqrt{2}} \quad . \tag{8}$$

## 3 SINGLE MODE DISPERSION RELATION

We can use standard techniques to derive the single mode dispersion relation [2,3,4], which becomes

$$\left(\left(\beta_e + j\Gamma\right)^2 + \left(\Gamma^2 + k^2\right)\hat{\beta}_q^2\right)\left(\left(\Gamma - jk_r\right)^2 + \beta_1^2\right) + 2\beta_1^4 C^3 \frac{\left(k^2+\Gamma^2\right)}{k_c^2} = 0 \quad , \tag{9}$$

where $C$ is Pierce's gain parameter, defined by $C^3 = K\beta_e/2R_o\beta_1$, $\Gamma$ is the exponential growth rate of the mode (all rf terms vary as $e^{-\Gamma z}$), $\beta_e = \omega/c\beta_z$, $k = \omega/c$, $\beta_1 = \omega/v_p$, $k_c$ is the mode's cutoff wavenumber, $R_o = 2\gamma^3 m(c\beta_z)^2/eI$, $K$ is the peak magnitude of the synchronous electric field (Eqn. (2)) squared divided by the product of four times the power in the waveguide times $\beta_1^2$, and $\hat{\beta}_q^2$ is the square of the reduced plasma wavenumber, given by

$$\hat{\beta}_q^2 = 2\chi_o \frac{I}{I_A\gamma^3\beta_z^3}\ln\frac{r_w}{r_o} \quad , \tag{10}$$

where $r_w$ is the wall radius, $\chi_o$ is the geometrical factor $I_o(hr_o)\left(K_o(hr_o)I_o(hr_w) - K_o(hr_w)I_o(hr_o)\right)/I_o(hr_w)\ln\frac{r_w}{r_o}$ and $h^2 = (j\Gamma)^2 - k^2$.

## 4 NUMERICAL EXAMPLES

In this section, we present some examples in which we numerically solve Eqn. (9) along with the orbit equations. For our nominal case, we will assume a 4.5-kA, 650-keV electron beam with an annulus radius of 2.9 cm in a waveguide with radius 3.37 cm. A 17-GHz rf signal in the $TM_{02}$ mode will have a cutoff wavenumber of $k_c = 163.8\ \mathrm{m}^{-1}$ in this waveguide, with an axial wavenumber of $\beta_1 = 316.4\ \mathrm{m}^{-1}$. We will additionally assume that there is an inner conductor in the waveguide, located at the radius of the first axial electric field null of the $TM_{02}$ mode (at 1.47 cm), which will not affect the mode pattern, but will reduce the power required for a given field strength. For a $TM_{02}$ mode with on-axis amplitude $A$, the power required in the mode is $P_{req} = A^2 6.43\left(10^{-7}\right)$ watts. The space charge term used in the dispersion relation is $\hat{\beta}_q^2 = 0.00358/\beta_z^3$.

Our nominal case will be a 10% ripple with a period of 5.19 cm (an axial field of 0.40 T). This ripple period and ripple amplitude leads to a gain of about 26 dB per meter of interaction. We plot the normalized electronic admittance $\left(2\beta_1^4 C^3/\left(\left(\beta_e + j\Gamma\right)^2 + \left(\Gamma^2 + k^2\right)\hat{\beta}_q^2\right)\right)$ in Fig. 2, along with the normalized circuit admittance $\left(-\left(\left(\Gamma - jk_r\right)^2 + \beta_1^2\right)k_c^2/\left(k^2+\Gamma^2\right)\right)$, as a function of $j\Gamma$ (the dashed line is the circuit admittance and the solid line is the electronic admittance). The dispersion relation is satisfied where these two curves meet, in which case $\Gamma$ is purely imaginary (there is no gain). Since the dispersion relation is quartic, there will always be four roots, and in order to have gain, there must be only two intersections between these two curves (as in Fig. 2). In order to have a root with gain, as the circuit admittance crosses the $j\Gamma$ axis, it must pass through the left gap where the electronic admittance separates due to the slow space-charge wave [3]. With small ripple amplitudes, we can change the detuning by varying the axial magnetic field; by increasing the magnetic field, the ripple period

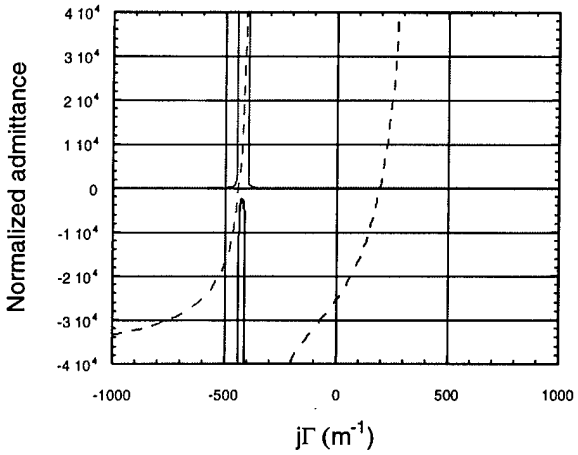



Figure 2. Normalized electronic admittance (solid line) and normalized circuit admittance (dashed line) as a function of $j\Gamma$.

decreases, and the ripple wavenumber $k_r$ increases, making the detuning more negative and shifting the circuit admittance curve more to the left. As the magnetic field is increased, the average axial velocity also drops, making both $\beta_e$ and $\hat{\beta}_q$ larger, and moving the slow space-charge wave gap in the electronic admittance also to the left. For large ripple amplitudes, the movement in the electronic admittance is larger than the movement in the circuit admittance, and for sufficiently large amplitudes, the slow space-charge wave gap is always further to the left than the lowest zero-crossing of the circuit admittance, and there is no resonance. Because the amount of space-charge determines the separation between the slow and fast space-charge wave gaps, this effect increases as the beam current is increased.

There is a peculiar regime in between these extremes where the movements are matched, and there is resonance for a very large range of axial magnetic fields and resulting ripple periods, and where a beam will stay in resonance as it loses energy to the rf field.

In Fig. 3, we plot the gain per meter of interaction length as a function of the applied axial magnetic field, for a 10% ripple amplitude. There are two regions of gain - one with a field ranging from 0.38-0.42 T, and a second, more narrow region at a field of about 1.05 T. Resonance is established in the first region with a fairly high $\beta_z$, where the axial field effectively only modifies the ripple period. Resonance is established in the second region with a relatively low $\beta_z$ (< 0.5), where the increasing axial field mostly increases the space-charge wavenumber $\hat{\beta}_q^2$.

At 22 kA (Fig. 4), the zero-crossing of the electronic admittance and the gap in the electronic admittance due to the slow space-charge wave are cotangent at a magnetic field of about 0.7 T. This is the condition of auto-stable resonance, and the first derivative of the phase and of the amplitude of the gain with respect to energy vanish here.

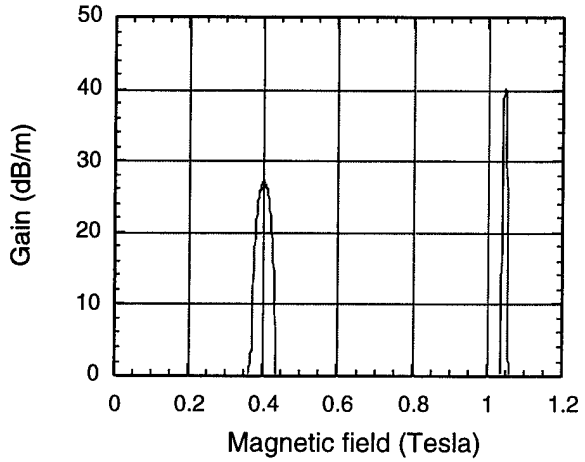



Figure 3. Gain of nominal case as a function of axial magnetic field, 10% beam ripple.

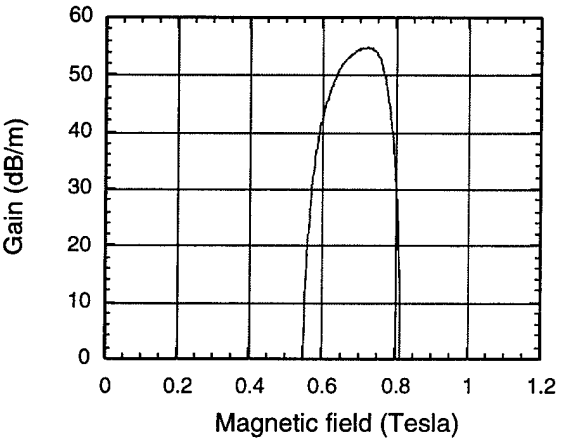



Figure 4. Gain curve for 22 kA (auto-stable resonance condition is at about 0.7 T).

## 5 ACKNOWLEDGEMENTS

This work was supported by funds from the Laboratory-Directed Research and Development program at Los Alamos National Laboratory, operated by the University of California for the US Department of Energy.

## REFERENCES

[1] I. E. Botvinnik, V. L. Bratman, A. B. Volkov, G. G. Denisov, B. D. Kol'chugin, and M. M. Ofitserov, "Cyclotron-autoresonance maser with a wavelength of 2.4 mm," *Sov. Tech. Phys. Lett.*, **8**, p. 596 (1982).

[2] B. E. Carlsten, "Rippled beam free-electron laser amplifier using the axial free-electron laser interaction," *J. Appl. Phys.*, May (1997).

[3] M. Chodorow and C. Susskind, Fundamentals of microwave electronics, McGraw-Hill, New York (1950).

[4] Y. Y. Lau, "Some design considerations on using modulated intense annular electron beams for particle acceleration," *J. Appl. Phys.*, **62**, p. 351 (1987).

# ANNULAR-BEAM, 17GHz FREE-ELECTRON MASER EXPERIMENT

L. M. Earley, B. E. Carlsten, M. V. Fazio, C. M. Fortgang, P. C. Haddock, W. B. Haynes
Los Alamos National Laboratory, Los Alamos, N.M. 87545

*Abstract*

Experiments have been conducted on a 15-17 GHz free electron maser (FEM) for producing a 500 MW output pulse with a phase stability appropriate for linear collider applications. The electron beam source is a 1 μs, 800 kV, 5 kA, 6-cm-dia annular electron beam machine called BANSHEE. The beam interactes with the $TM_{02}$ and $TM_{03}$ mode Raman FEM amplifier in a corrugated cylindrical waveguide where the beam runs close to the interaction device walls to reduce the power density in the fields. This greatly reduces the kinetic energy loss caused by the beam potential depression associated with the space charge which is a significant advantage in comparison with conventional solid beam microwave tubes at the same beam current. The experiment operates in a single shot mode with a large number of diagnostics to measure power, frequency and energy.

## 1 INTRODUCTION

Future linear colliders require microwave power sources in the 10-30 GHz frequency range with output powers of at least several hundred megawatts. The klystron has historically been the source of choice for accelerator applications. For output power levels above several hundred megawatts, new approaches are needed for microwave power generation. One example is a microwave tube based on a large diameter annular electron beam instead of the small diameter solid beam used in a klystron [1]. More power can be transported in an annular beam because the space charge limiting current in an annular beam is higher than in a solid beam of the same voltage and current. Free-electron lasers and FEMs have demonstrated high peak power and extraction efficiencies. An FEL or FEM offers the possibility of a way to avoid this fundamental power density limitation by operating in a higher-order mode in a large microwave structure. In 1992, Conde and Bekefi tested an FEM that produced 61 MW at 33 GHz at 27% efficiency [2]. This tube was driven by a 750 kV, 300 A, 30 ns, solid electron beam. FEM phase stability has been examined in detail by Carlsten [3] for an axial interaction FEM with an annular beam operating in the exponential growth regime. Fazio presented a background description of the development of the Los Alamos FEM [4].

## 2 EXPERIMENTAL SETUP

The FEM experimental configuration is shown in Fig. 1. The FEM is run on the BANSHEE pulsed power electron beam machine which produces the 500-800 kV annular electron beam with a stainless steel field-emission cathode. The beam has a nominal 2.8 cm radius with a thickness of 4 mm. The beam drift pipe has a 3.6 cm mean radius. The input microwave pulse to this amplifier is supplied by a surplus military magnetron. The input pulse is adjustable from 0.3 to 3 μs at a peak power of 100 kW. The magnetron frequency can be varied from 15.5 to 17.5 GHz. The magnetron output is coupled from WR-62 rectangular waveguide through a six-way power divider and fed symmetrically into the circular waveguide. This waveguide feed was designed to reduce the number of higher order modes which could couple into the FEM circular waveguide input section. The input section is followed by the rippled wall structure with 15 ripple periods. The ripple wavelength is 3.5 cm with a 7% ripple modulation. After the ripple wall structure is a section of cylindrical waveguide which acts as the beam dump. A pulsed solenoidal magnet operating at 0.5 T is used to confine the beam from the cathode to 10 cm beyond the end of the rippled structure. The electrons spread after the end of the solenoid and are absorbed on the waveguide walls over an area large enough to avoid damage. A permanent magnet dipole is located another 10 cm downstream to prevent any electrons from reaching the diagnostics. Two types of diagnostics are located in the circular waveguide after the beam dump section. The directional couplers are used to measure the pulse shape, power and frequency while a calorimeter acts as a waveguide load and energy measuring device.

## 3 DIAGNOSTICS DESCRIPTION

Diagnostics were developed for this experiment to operate in circular waveguide with a diameter of 7.2 cm for frequencies between 12 and 18 GHz. The energy of each FEM pulse was measured using a five channel circular waveguide calorimeter. Similar calorimeters have been developed [5,6] for previous intense pulse microwave sources. A cross sectional view of the calorimeter is shown in Fig. 2. A novel multi-layer absorber for the calorimeter was developed using Contex textile sheets from Milliken [7]. An optimized multi-layer absorber has an $S_{11}$ of -20 dB when measured with an HP8510 network analyzer. The Contex sheets are

0-7803-4376-X/98 /$10.00 © 1998 IEEE

available in a large range of resitivities from a few Ω/□ to hundreds of kΩ/□.

The multi-layer absorber was an excellent match over a broad frequency range since most of the modes of interest had characteristic impedance greater than 300 Ω which varied slowly with frequency since most modes were far from cutoff. The first several sheets are high resistivity to reduce reflections. The resistivity is then lowered for each sheet. Table 1 shows the resistivities for the sheets in the final design of the calorimeter.

| Absorber number | Resistivity |
|---|---|
| 1,2 | 28 kΩ/□ |
| 3,4 | 16 kΩ/□ |
| 5,6 | 8.5 kΩ/□ |
| 7-10 | 500Ω/□ |
| 11,12 | 70Ω/□ |

Table 1. Calorimeter load absorbing sheet resistivities in order from the input of the device.

The calorimeter contains a sealed air cell with one Lucite window for the vacuum on the input side and another window seal for the air on the back side. A Setra model 239 pressure gauge measures the rise in cell pressure due to the increase in temperature of the absorbing sheets. The sensitivity of the pressure calorimeter was 70 mV/J for a volume of 200 $cm^3$.

Most of the energy that is deposited on the absorbing sheets is located near the thermistors for the $TM_{02}$ and $TM_{03}$ modes. More than 50% of the energy is absorbed by the last two sheets. The last sheet is thermally isolated from the rest by a foam insulator. Thermistors are placed on the last sheet only. Four thermistors located every 90° around the azimuth of the absorbing sheet, measure the temperature rise of the microwave absorber. The final design of the absorbing load used twelve sheets. The thermistors are connected to a bridge circuit which provides an output voltage proportional to the microwave energy of the FEM. The four channel thermistor calorimeter had a sensitivity of 20 mV/J.

The pulse characteristics of the FEM were measured using three circular waveguide loop directional couplers [8]. Each loop directional coupler was optimized for a particular mode either $TM_{01}$, $TM_{02}$ or $TM_{03}$. The measured signals from each of the loop couplers were divided into several paths. One path was sent to a crystal detector, another path went through a bandpass filter to a crystal detector and the third path went to a heterodyne frequency measuring circuit. In this way signals from different modes and frequencies could be measured separately.

The beam current was measured at the diode and at three locations along the beam path using Rogowski coils. The magnetron output signal was measured prior to the six way divider input section. Three B-dots measure microwave signals in the circular waveguide before and after the rippled wall section.

All circular waveguide diagnostics were tested and calibrated using a gated 100 W traveling wave tube (TWT). A circular waveguide test bed was constructed for these calibrations. Various modes could be launched in the test bed to measure the diagnostics response. All modes were verified using the liquid crystal sheets. Power coupled from the TWT into the circular waveguide was monitored with conventional microwave directional couplers.

## 4 EXPERIMENTAL RESULTS

The FEM experiment has been operated in the beam OFF condition to determine a baseline for the diagnostics. Both the calorimeter and loop coupler measure the coupled power from the magnetron into the circular waveguide. The coupled power varies with frequency and mode. The six way coupler can excite both $TM_{02}$ and $TM_{03}$ modes from 15.5 to 17.5 GHz. Power coupled into the FEM structure varied with frequency from 2 to 25 kW. The drive mode was measured by removing the calorimeter and allowing energy to radiate out the open waveguide. Liquid crystal sheets with thick film carbon absorbers attached, monitor the radiated mode pattern in the waveguide. In this way we were able to photograph the mode pattern at a given frequency and measure the signal from the loop coupler to determine power. The mode pattern on the liquid crystal sheet displayed the $J_1$ Bessel function for a given TM mode. The response of the carbon absorber on the liquid crystal sheet was power density, which corresponds to $E^2$. Then, by installing the calorimeter we could measure the pulse energy of the magnetron for approximately 100 pulses and determine the peak power. Thus, we were very confident of our mode and power level of the drive signal to the FEM.

Initial results from this FEM experiment indicate that the amplified signal is concealed by oscillations

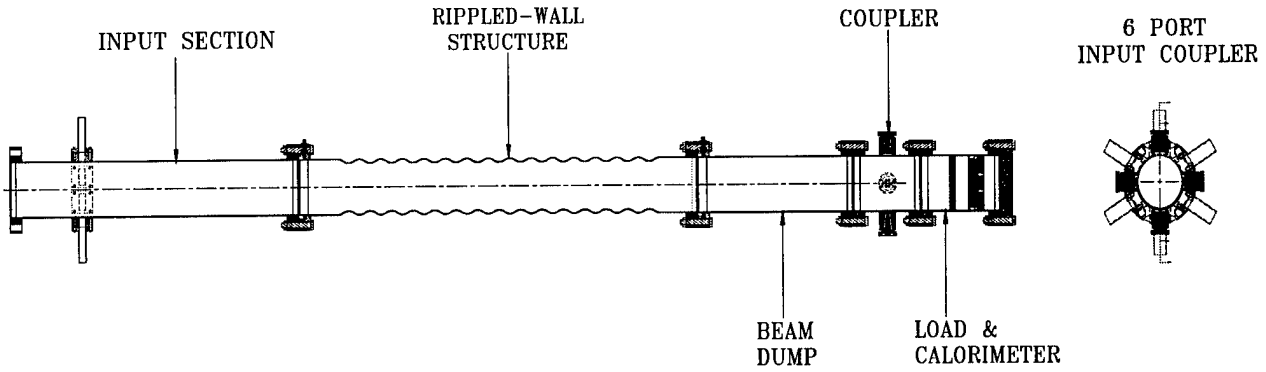



Figure 1. Cross sectional view of the FEM experimental configuration.

with a larger generated power. Measurements show oscillations at 11.2 and 16.4 GHz at power level of a few megawatts. Our amplifier would need a minimum of 20 dB of gain for the output signal to equal the oscillator peak power. We are currently working to increase the coupled power from our magnetron which would increase the amplifier drive.

The signals from the calorimeter five channels agree within 20%. The measured pulse energies were less than 1 J and the resolution for the calorimeter was approximately 50 mJ.

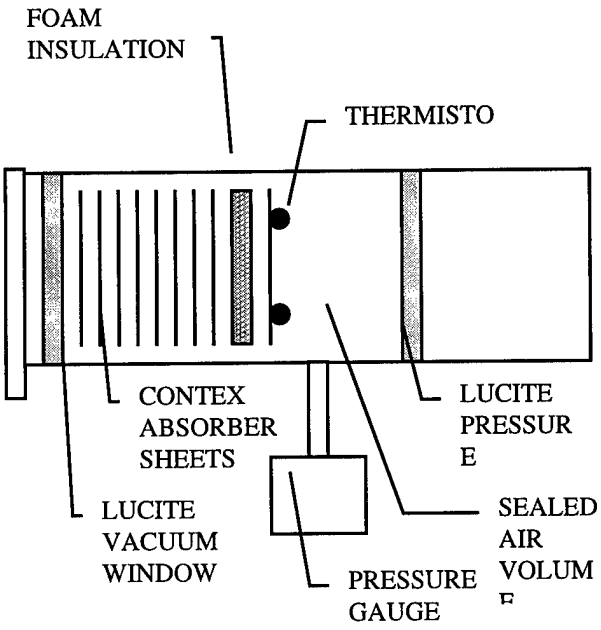



Figure 2. Cross sectional view of circular waveguide calorimeter.

## 5 CONCLUSION

The initial FEM experiments have been completed. The measurements from the diagnostics are excellent. We have not been able to measure the amplification process due to unwanted oscillations.

Our plans include reducing the beam current below 1 kA and increasing our coupled drive power to 40 kW. The unwanted oscillations should be reduced to the point that amplification can be measured. In addition we will explore both $TM_{02}$ and $TM_{03}$ modes to determine mode growth rates. Once we clearly measure amplification in the desired mode, we will explore parameters to optimize the FEM interaction.

## REFERENCES

[1] P. Wilson, "RF Sources for 5-15 TeV Linear Colliders," presented at 3rd ICFA Workshop on Pulsed RF Sources for Linear Colliders (RF96), April 8-12, 1996, Hyama, Japan.

[2] M. E. Conde and G. Bekefi, "Amplification and superradiant emission from a 33.3 Ghz free electron laser with a reversed guide magnetic field," *IEEE Trans. Plasma Sci.*, **20**, 240 (1992).

[3] B. E. Carlsten, "Enhanced phase stability for a raman free electron laser amplifier in the exponential growth regime," *Physics of Plasmas*, **2**, 10, p.3880 (Oct. 95).

[4] M. V. Fazio et. al., "The Development of an Annular-Beam High power Free-Electron Maser for Future Linear Colliders," Proc. XVIII International Linear Accelerator Conference, pp. 228-230, August 1996.

[5] L. M. Earley et. al., "Comprehensive approach for diagnosing intense single-pulse microwave sources," Rev. Sci. Instrum. 57 (9), pp. 2283-93, Sept. 1986.

[6] C. B. Wharton, L. M. Earley, and W. P. Ballard, "Calorimetric measurements of single-pulse high-power microwaves in oversized waveguides," Rev. Sci. Instrum. 57 (5), pp. 855-8, May 1986.

[7] H. H. Kuhn, "Characterization and Application of Polypyrrole-Coated Textiles," *Intrinsically Conducting Polymers: An Emerging Technology*, Kluwer Academic Publishers, pp. 25-34, 1993.

[8] L. M. Earley, W. P. Ballard and C. B. Wharton, "New Directional Couplers for Multimode Circular Waveguides Applied to Intense Pulsed Microwave Systems," *IEEE Trans. on Nuclear Science*, Vol. NS-32, No. 5, pp. 2921-3, October 1985.

# THE RF SYSTEM FOR THE NATIONAL SPALLATION NEUTRON SOURCE LINAC[1]

Paul Tallerico, James Billen, Andrew Jason, Michael Lynch,
Thomas Wangler, Lloyd Young, Los Alamos National Laboratory, P.O. Box 1663, MS H-817, Los Alamos, NM 87545

*Abstract*

The National Spallation Neutron Source (NSNS) system has been proposed to dramatically improve the neutron capabilities for science applications in the US. The NSNS is a fast pulse neutron source that would consist of a 1000 MeV H- linac, an accumulator ring, a neutron target, and an experimental area. Although the NSNS is to be built at Oak Ridge, the design responsibility is delegated to five US national laboratories, and the Los Alamos National Laboratory is responsible for the linac portion of this machine, from the output of the radio frequency quadrupole (RFQ) accelerator, to the entrance to the accumulator ring. In the baseline design, a total of fifty-nine klystrons are used to provide the rf power for a 1-MW average power beam in the accumulator ring, and a 1.04 ms pulse length, 6.24% duty factor beam in the linac. The frequencies chosen are 402.5 MHz for the RFQ and drift tube linac (DTL) portions of the machine, and 805 MHz for the coupled-cavity DTL (CCDTL) and coupled cavity (CCL) portions of the linac. The baseline 805 MHz klystron is capable of 2.5-MW peak power into a flat load, and it contains a modulating anode. The backup 805 MHz klystron is cathode pulsed, and has a 5-MW peak output power. The modulators for these two klystrons are vastly different. The challenges and compromises for the two klystrons and their associated modulators and RF systems are discussed. The baseline design RF system is presented in detail.

## INTRODUCTION

The klystron is used in most high-power high-energy proton accelerators, and so it was the logical choice as the RF generator for the NSNS project, which requires over 104 MW of peak power for 1.04 ms H⁻ pulses at a beam duty factor of 6.24%. We must add at least 70 μs to fill the standing-wave accelerator structures and to lock the control loops for the fields in the accelerator. Thus the rf power is applied for about 1.1 ms, and the rf duty factor is 6.6%.

A schematic drawing of the 1-MW accelerator[1] is shown in Fig. 1, along with a schematic of the 4-MW upgrade.

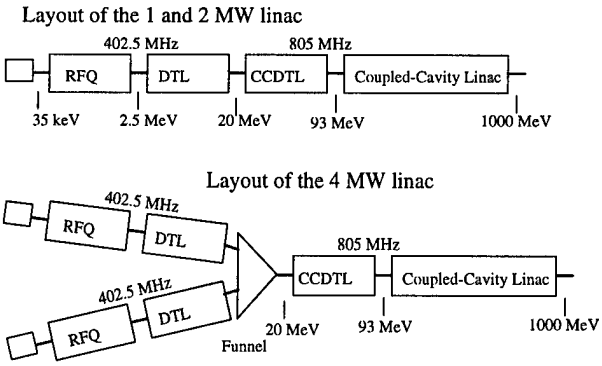



Figure 1. Layout of the accelerator structures for the 1-, 2-, and 4-MW NSNS linacs.

The power applied to the klystron has 100 μs rise and fall times. Thus, the pulse of power through the klystron will be about 1.25 ms long, and the klystrons will have a 7.5% video duty factor. This accelerator is to be comprised of an RFQ and DTL, operating at a low frequency, and then a CCDTL and CCL at an integer multiple of the base frequency. NSNS is to be upgradeable, to both 2 MW and 4 MW of beam power, with a funnel and two parallel 402.5-MHz front ends for the final upgrade to 4 MW. The frequencies chosen are 402.5 MHz for the RFQ and DTL portions of the accelerator, up to 20 MeV. From 20 to 93 MeV, the accelerator is a CCDTL, and from 93 to 1000 MeV, the linac is a CCL. Both the CCDTL and CCL operate at 805 MHz. The amplifier size was chosen as 2.5 MW, the maximum power for a long-pulse klystron with a modulation anode[2], to minimize the cost and maximize the reliability of the rf system. Two klystrons will be placed in each modulator, and Fig. 2 is a schematic diagram of a dual-klystron-modulator rf system at 805 MHz. The schematic diagram for the 402.5-MHz system is identical, except that only two modulators and four klystrons are used for the 1-and 2-MW linacs.

[1] This research is sponsored by the Division of Materials Sciences, DOE, under contract DE-AC05-OR22464 with Lockheed Martin Energy Research Corp.

0-7803-4376-X/98/$10.00 © 1998 IEEE

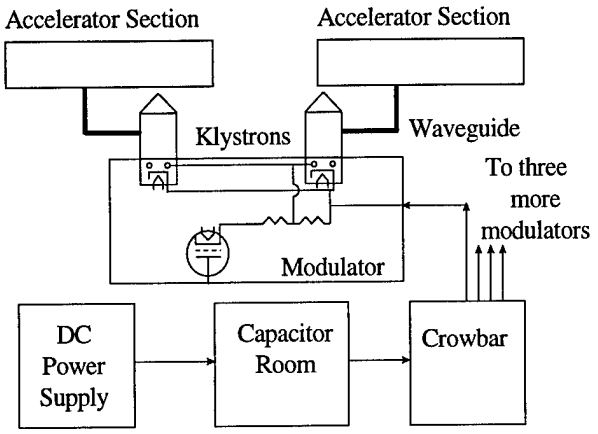



Figure 2. Schematic of the RF system with the dual-klystron modulator.

Although Fig. 2 is just a schematic, notice that only one switch tube is used. This reduces the capital cost, and increases the reliability of the modulator, at the expense of a somewhat longer fall time of the cathode current pulse, and therefore yields a slightly higher operating cost.

## TECHNOLOGY CHOICES

We have chosen the high main frequency of 805 MHz for this project to keep the sizes of the accelerator structures as small as possible, consistent with enough stored energy in the RF structure. The large cw linacs being proposed for tritium production use 700 MHz for their high frequency[3], and the Japanese waste-transmutation prototype accelerator is proposing[4] 600 MHz for the high frequency part of that accelerator. Both machines are proton linacs. Klystron vendors indicated that many technical solutions are possible for the NSNS project, including the conventional klystron, the multiple beam klystron (MBK), and higher-order mode inductive output tube (HOM-IOT). Only the conventional klystron has been used in accelerator work to date, so it was chosen as the baseline RF amplifier. Even with the conventional klystron, the vendors were not in agreement about the most economical and maintainable solution for this project. The frequencies of the linac were chosen at 402.5 and 805 MHz, although it is expected that the minimum cost is almost independent of frequency over a wide range[5]. The frequency of 805 MHz has been used for several pulsed proton linacs, which have used very long-lived klystrons. The LANSCE klystrons, at 1 ms, 120 Hz, and 1.25 MW have a life of over 80,000 hours, and the FermiLab 100-μs, 10-Hz, 12-MW klystrons also appear to have an excellent life of over 30,000 hours. For klystrons with a modulating anode, the opinion is that a 2.5-MW output power should result in a good rf system design. The cathode pulsed klystron, without a modulation anode, could be made to much higher power, and 5 MW was chosen as a reasonable limit for this project[2]. Higher peak powers at this pulse length may be possible, but the klystron would require development, and this means risk to the program. With the lower power klystron, it is entirely feasible to put two klystrons into one modulator, but it is much more difficult to do this with the 5-MW cathode-pulsed klystron. A schematic diagram of a dual 2.5-MW klystron rf system was shown in Fig. 2, and the corresponding diagram for a single 5-MW klystron is shown in Fig. 3. Both systems can drive the same two accelerator modules. The main switching element in the 5-MW modulator is a solid state assembly made of a series connection of insulated-gate bipolar transistors (IGBT), and only the crowbar is a classic electron tube.

Another advantage of the configuration shown in Fig. 3 is that all the electronics, except the pulse transformer and klystron socket, are in air-insulated enclosures, so the amount of insulating oil is greatly reduced compared to the circuit in Fig. 2. This has fire safety, cost, and maintenance advantages. The capacitor bank in Fig. 3 stores only about 25% of the energy per peak MW of output power, compared to the energy stored per MW in the Fig. 2 circuit. The lower stored energy would cause much more distortion in the output pulse of the modulator, but the bouncer circuit, which contains another capacitor and inductor, is triggered so that its voltage changes during the pulse, to compensate for the capacitor drop.

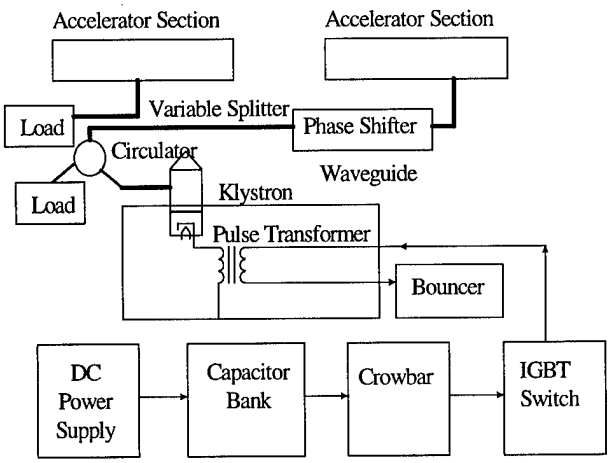



Figure 3. The solid-state modulator with a 5-MW klystron and waveguide splitter system.

The 5-MW-klystron system has the potential to reduce costs, since the 5-MW klystron is much less expensive than two 2.5-MW klystrons. However, the 2.5-MW klystron would operate at a much lower beam voltage of about 110 kV for a 60% efficiency. This klystron voltage is in the optimum range for a modulation anode floating deck modulator. The 5-MW klystron would operate at 155 kV for the same perveance and efficiency, and this voltage makes it very difficult to make a floating-deck modulator. The fields inside the electron guns for the two

klystrons are also different, with the higher fields in the higher power klystron. The higher-power klystron therefore requires a series-type or transformer-type modulator, in which the switch transmits the entire pulse power. In the floating-deck modulator (in Fig. 2), the switch only has to transmit a fraction of the pulse power, since only the capacity of the modulation anode is being charged and discharged. With the 5-MW klystron, the reflected power levels are at a damaging level due to the higher forward power, so the system requires a circulator. The single klystron would drive two accelerator modules, and we feel that since the beam loading will be different in each module, we will also require a high-power variable-ratio power splitter and phase shifter with the 5-MW klystron. With this type of modulator, a single power supply is used for each klystron, and this raises the capital costs.

A cost study has given the preliminary results that a 10% savings in the rf system are possible with the 5- MW klystron, but the modulator is so large that it must be repaired in situ, which reduces the availability of the rf system.

## SYSTEM DETAILS

The baseline system has fifty-six 2.5-MW peak, 805-MHz klystrons and three active plus one spare 1.25-MW peak, 402.5-MHz klystrons for the 1-MW beam. The system is easily upgradeable by adding more modulators and power supplies for both 2- and 4-MW beams. In the latter case, there are six 402-5 MHz and eighty-four 805-MHz klystrons required. The pulsed power system is a major cost of a pulsed rf system, so two klystrons are placed in each modulator. Thus, the baseline 1-MW system has two 402.5-MHz modulators and twenty-eight 805-MHz modulators. All the klystrons have modulation anodes, and the modulators are the floating deck type, in which only the potential of the modulation anode varies to pulse the rf system. Figure 2 shows a schematic diagram of this type of modulator, with the two klystrons installed. This modulator is small and simple, but heavy and oil-filled. Whenever the klystrons or modulator needs repair, the entire unit is removed by fork lift and replaced. The repair is then done off line. The power supplies for the klystrons also can be expensive, and to minimize this cost, eight klystrons are to be driven by a single power supply, capacitor bank, and crowbar for the 805-MHz rf system, and a single supply, crowbar, and capacitor bank is to be used for the 402.5- MHz system. The 805-MHz klystrons will have a saturated efficiency of 60%, and operate at 110 kV.

Since the system is pulsed, the control margin allowance is 20% of the rf power, so each klystron will deliver a maximum of 2.0 MW to the accelerator module. Methods of using adaptive feed forward techniques to reduce this margin are being studied.

## FUTURE WORK

The baseline rf system and the system with the 5-MW klystrons will both be designed in more detail so that more accurate cost and reliability data can be assembled. Early next year, the 805-MHz development effort will begin on the baseline 2.5-MW klystrons and their modulators. A development contract for an advanced rf generator (such as the multiple-beam klystron) will be placed.

## REFERENCES


[1] A. Jason, T. Bhatia, J. Billen, D. Schrage, S. Kurennoy, F. Krawczyk, M.Lynch, S. Nath, R. Shafer, H. Takeda, P. Tallerico, T. Wangler, R. Wood, L., P. Grand, R. Mckenzie-Wilson, "A High Intensity Linac for the National Spallation Neutron Source", These Proceedings.

[2] G.Faillon and C. Bearzatto, "Very long pulse high power klystrons for FEL and their generating conditions", International Journal of Electronics, vol. 65, pp. 579-588, March 1988.

[3] G.P. Lawrence, "Transmutation and Energy Production with High Power Accelerators", Proceedings of the 1995 Particle Accelerator Conference, pp. 35-39, Dallas, 1995.

[4] H. Mizumoto, et al., "High Intensity Proton Accelerator Nuclear Waste Transmutation", Proceedings of the 1992 Linear Accelerator Conference, Ottawa, pp. 749-751,1992.

[5] G.P. Lawrence, "Los Alamos High-Power Proton Linac Designs", International Conference of Accelerator-Driven Transmutation Technologies and Applications, Las Vegas, Nevada, pp. 177-186, 1994.

# DOUBLE-SIDED RELATIVISTIC MAGNETRON

A. V. Agafonov and E. G. Krastelev
P. N. Lebedev Physical Institute, Leninsky Prosp. 53, Moscow 117924, Russia

*Abstract*

A new scheme of a symmetrically powered relativistic magnetron and several methods of localized electron flow forming in an interaction region are proposed to increase the efficiency of relativistic magnetrons (RM).

As was reported for many experiments, the efficiency of RM is about 10 — 30% and considerably lower than that of $\geq$ 70% for the classic magnetrons. A very important reason is the effect of nonsymmetric feeding of power from one side of a magnetron, which is typical for experiments. One-sided powering leads to the axial drift of electrons, to the transformation of transverse velocities of electrons to a longitudinal one and to the generation of a parasitic electron beam which does not take part in energy exchange between electrons and waves at all.

A special driver was designed for double-sided powering of RM. The proposed system is compact, rigid and capable of reliable operation at high repetition rates, which is advantageous for many applications.

Several smooth-bore magnetrons were tested by means of computer simulations using PIC code KARAT. The results showed a difference between the dynamics of electron flow for one- and two-sided power feeding of the structure under test. It was shown that all electrons emitted from the cathode are captured inside the interaction region under the condition of proper choice of the electrostatic and/or external magnetic field distributions. This situation is practically impossible for a one-sided magnetron.

Design of a driver and computer simulation results are presented.

## 1 INTRODUCTION

The high efficiency of "ordinary" classic magnetrons has been achieved as a result of intense experimental and theoretical investigations [1]. Relativistic magnetrons, in spite of a 20-year history of development, are in an "initial" stage. The main purpose of experimental investigations was the demonstration of achievement of extremely high RF-power [2], [3]. Note that most results were obtained using high-current accelerators in existence as drivers, but not specialized drivers.

Actually RM generators were adapted for use with those drivers and looked like an additional part to alien drivers. However, achieved levels of pulsed power exceeding several GW are attractive, though the efficiency of RM is low as compared with low voltage classic magnetrons.

It appears that one way of increasing the efficiency of RM is symmetric powering of RM that suppresses parasitic beam current in the longitudinal direction, i.e., the construction of a specialized driver for this purpose.

## 2 COMPUTER SIMULATION

The main idea of symmetric powering is rather clear and will not be discussed here. Calculations of beam dynamics inside a simple model of a smooth-bore RM were carried out with 2.5-D electromagnetic PIC-code KARAT [4]. In Fig. 1 configurations of electron flows inside a coaxial

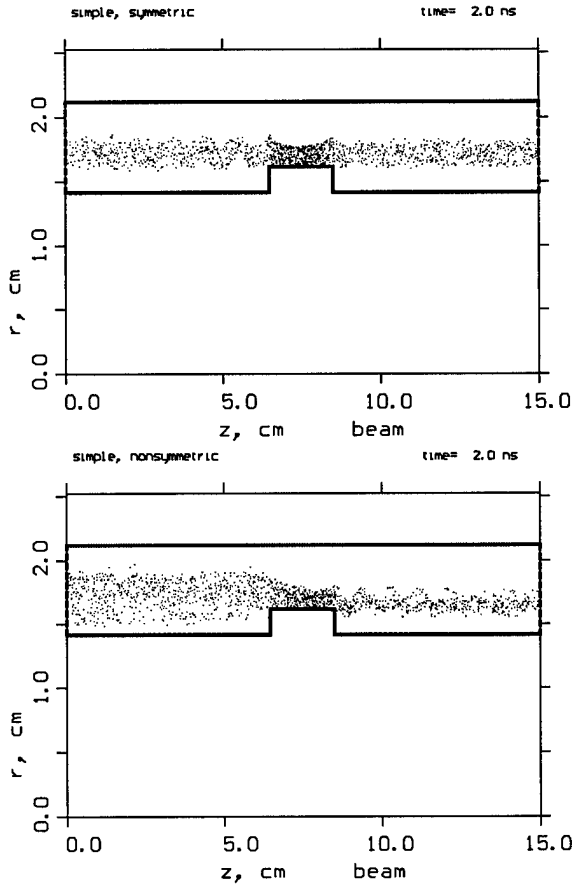



Figure 1: Configurations of electron flows for double-sided (above) and one-sided powering (below).

diode with an insertion are presented under conditions of symmetric and nonsymmetric powering. In the latter case a TEM-wave is launched through the left side of the diode. The diode is embedded in a longitudinal magnetic field of 8 kGs. A maximum voltage of 500 kV and maximum emission current of 10 kA were taken in the calculations.

Fig. 2 illustrates two possible methods of localizing electron flow within the interaction region: use of symmetric

0-7803-4376-X/98/$10.00 © 1998 IEEE

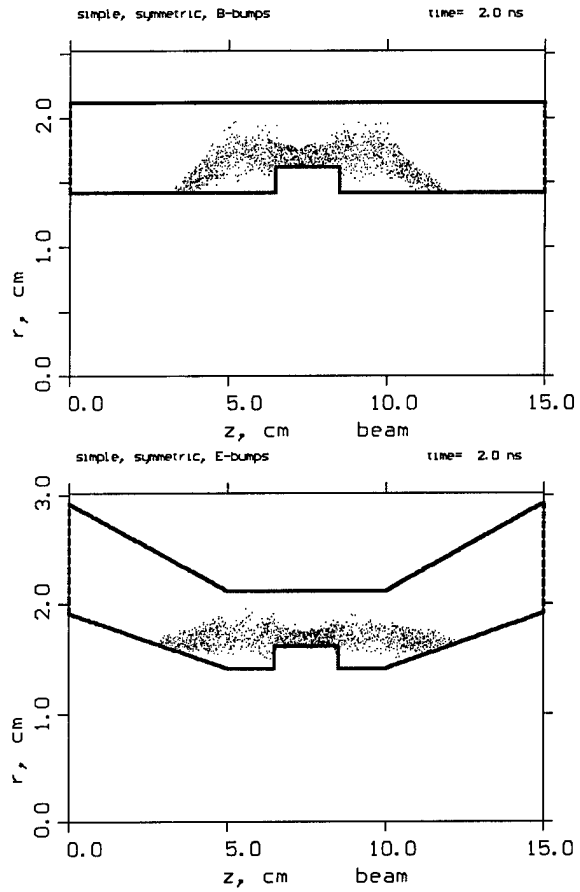



Figure 2: Configurations of electron flows for double-sided powering with magnetic bumps (above) and electrostatic bumps (below).

magnetic bumps or electrostatic mirrors on both sides of the diode, under condition of symmetric powering. In the latter case electrostatic mirrors are formed by curved coaxial electrodes embedded in a longitudinal magnetic field.

Variation of magnetic field distribution and/or form of electrodes permit to form a desirable geometry of electron flow. Comparison of characteristics of flows inside diodes with magnetic and electrostatic bumps shows that the scheme with electrostatic bumps is preferable for RM.

## 3 DRIVER

From our point of view a symmetric induction driver correspondes to a certain extent the idea of two-sided powering of RM. Fig. 3 shows the scheme of such a driver integrated with a magnetron. The driver consists of two identical sections of LIA (areas 1 and 2 in Fig.3) placed symmetrically relative to the magnetron (area 3) and connected with a magnetron by a common central electrode — the voltage adder. Both ends of the central electrode join to flanges which are at ground potential. The central part of the electrode performs as the RM cathode. Merits of the driver are the merits of LIA with a voltage adder. Such a

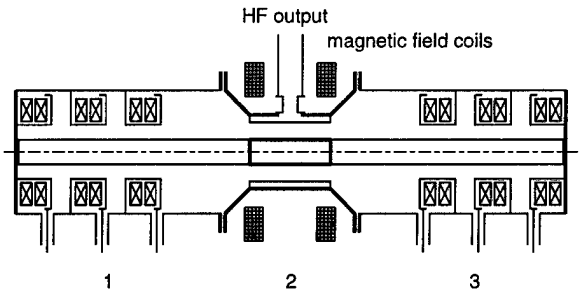



Figure 3: Schematic of a driver with a magnetron.

scheme are broadly used in modern high-current accelerators (HERMES-III, COBRA etc.).

RF-power is led out through slots in resonators of the magnetron to radial waveguides followed by short matching sections — transformers of impedance. This scheme has been successfully used in experiments with pulsed high power RM [2], [3].

## 4 MELF PROJECT

To realize the idea of two-sided powering of RM we have developed a project of an multipurpose experimental laboratory facility (MELF) with the following parameters:

- maximum voltage of 250 kV on a load of 25 — 50 Ohm;
- pulse duration of 80 ns;
- 5 induction cells per section;
- maximum voltage of 50 kV for exciting induction cell.

### *4.1 Sections of LIA*

Fig. 4 shows the design of a LIA section. The section con-

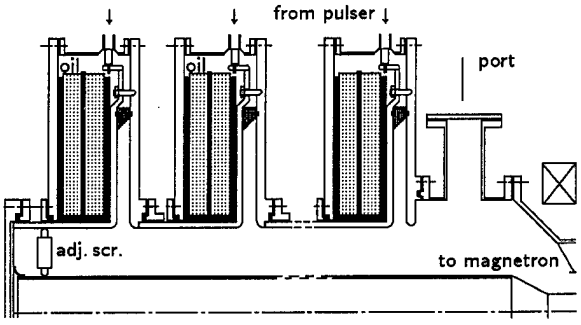



Figure 4: Section of LIA.

sists of 5 inductions cells, a short transition section to a magnetron region and a mechanism for fastening and aligning the voltage adder.

Each inductor cell contains two high quality magnetic cores made of metglass with a polymer interlayer insulation of 12-cm inner diameter, 22-cm external diameter and

2-cm thickness. With the project parameters given above maximum alteration of magnetic induction is as little as 2.4 T.

Cores and high voltage inputs are embedded in transformer oil. All metallic parts of the inductor cell are made of aluminium. Parts of the transition section to the magnetron region are made of stainless steel to reduce distortion of pulsed magnetic field.

### *4.2 High voltage generator*

As the first step we plan to modify one of the existing modulators at the base of a water-insulated, coaxial pulse-forming line with a gas switch.

We have developed and later we are going to construct a new compact high voltage generator with a repetition rate of several Hz. The key elements of the generator are fast capacitors with internal circuits forming quasirectangular pulses of ns-duration. We have chosen the following parameters of industrially produced capacitor-shaper:

- 80-kV charge voltage;
- 1.7-Ohm impedance;
- 80-ns duration of output pulse;
- 28-nF overall capacitance.

Fig. 5 shows the scheme of the generator. This approach

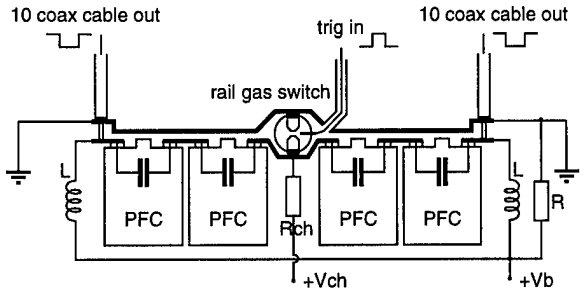



Figure 5: Scheme of high voltage generator.

simplifies the construction of generator and decreases its dimensions. Successful operation of a compact 400-kV generator was reported in [5].

Work supported in part by RFFI under grant 96-02-19215a.

## 5 REFERENCES

[1] Okress E. (ed.). Crossed-field microwave devices. Academic Press. N.Y., 1961.

[2] J.Benford, H.Sze, D.Bromley, B.Harteneck. Progress on relativistic magnetron. Proc. of the 6th Intern. Conf. on High-Power Particle Beams, Japan, 1986, v. 2, 577–580.

[3] J.Benford, H.Sze, W.Woo, R.R.Smith, B.Harteneck. Phase locking of relativistic magnetrons. Proc. of the 7th Intern. Conf. on High-Power Particle Beams, Germany, 1988, v. 2, 1359–1364.

[4] P.V. Kotetashwily, P.V. Rybak, V.P. Tarakanov. KARAT — a Means for a Computer Experiment in Electrodynamics, Institute of General Physics, Moscow, Russia, Preprint no. 44, 1991.

[5] V.V. Bulan, E.V. Grabovsky, A.N. Gribov, V.G. Lujnov. The nanosecond generator RG-1 with near-rectangular pulse. Proc. of the 11-th Intern. Conf. on High Power Particle Beams, Czech Republic, 1996, v. 2, 942–945.

# CIRCUIT ASPECTS OF THE NRL/INDUSTRIAL 94 GHz GYROKLYSTRON AMPLIFIER

D. Pershing
Mission Research Corporation, Newington, VA 22122
K. Nguyen
KN Research, Silver Spring, MD 20906
J. Petillo
Science Applications International Corporation, Burlington, MA 01803
J. Calame
Omega-P, Inc., New Haven, CT 06520
B. Danly, and B. Levush
Naval Research Laboratory, Washington, DC 20375

*Abstract*

A wide bandwidth, high average power W-band gyroklystron amplifier is currently under cooperative development by NRL, Litton Electron Devices, and Communication and Power Industries. The amplifier circuit is comprised of 4 stagger-tuned cavities operating in the fundamental $TE_{011}$ circular cavity mode. The input coupler is the first cavity of the circuit and must exhibit reasonable coupling strength between the $TE_{10}$ mode in rectangular waveguide and the desired $TE_{011}$ circular cavity mode over a better than 600 MHz bandwidth centered at 93.4 GHz, with high $TE_{01}$ mode purity. A single WR-8 rectangular waveguide drives a combined coaxial/cylindrical cavity system. The coaxial cavity resonating in the $TE_{411}$ mode is tightly coupled to the cylindrical cavity, excited to resonate in the $TE_{011}$ mode. The rf magnetic field couples the cavities through 4 azimuthally spaced apertures.

## 1 INTRODUCTION

Single aperture excitation of the $TE_{01}$ mode with high mode purity is difficult in a low Q cylindrical cavity. The logical step of splitting the excitation into several azimuthally separated apertures introduces a 'plumbing' complexity to precisely split the source power with the appropriate amplitude and phase. However, the amplitude and phase splitting can be accomplished via an intermediate coaxial cavity [1,2]. In the design discussed below, this coaxial cavity resonates in the $TE_{411}$ mode, and is tightly magnetically coupled to the cylindrical cavity via 4 rectangular apertures, equally spaced azimuthally. The coupling apertures are oriented 45° with respect to the single WR-8 rectangular drive waveguide. A schematic of the field solution region for the coupler is shown in Fig. 1, including the gun taper and a dielectric ring isolating Cavity 1 (the input coupler) and Cavity 2.

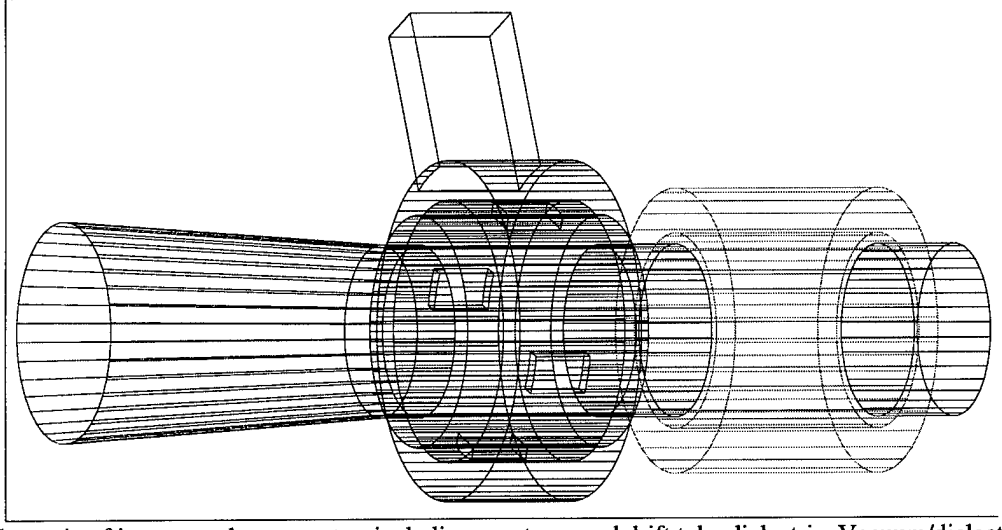


Figure 1: Schematic of input coupler geometry, including gun taper and drift tube dielectric. Vacuum/dielectric regions are shown.

Generally, a reduced geometry utilizing symmetry considerations, without taper and drift tube dielectric was modeled (see Fig. 2). Modeling tools include HFSS (High Frequency Structures Simulator) from HP [3] and ARGUS from SAIC [4]. HFSS is a finite element code that computes field distributions and S-parameters for passive 3D structures at a driven frequency. Material properties can be included. ARGUS is a 3D, volumetric simulation model for systems involving electric and magnetic fields and charged particles, including the capability to embed materials in the simulation region, with either time- or frequency-domain operation.

The cylindrical cavity radius and length are approximately set by gyroklystron performance

0-7803-4376-X/98 /$10.00 © 1998 IEEE

calculations that determine the resonant frequency and Q of all cavities. Additionally, the wall thickness between the cylindrical and coaxial cavities is fixed at 10 mils for mechanical strength. This sets the inner radius of the coaxial cavity. For the initial simulation, the remaining coaxial cavity dimensions are chosen so that the unperturbed resonant frequency is the desired resonant frequency. The aperture width and height, coax cavity length and outer radius are adjusted to achieve the desired (cold) frequency and $Q_{ext}$, 93.4 GHz and 150, respectively, with better than 90% $TE_{01}$ mode purity. Large apertures are used in this design for tight coupling between the cylindrical and coaxial cavities. They are rectangular for simulation and fabrication convenience.

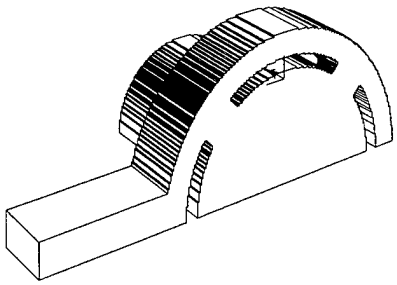


Figure 2: Input coupler simulation geometry for one quarter of the cavity.

## 2 SIMULATION METHODOLOGY

Both HFSS and ARGUS were used with various methods of solution to model many issues concerning the input coupler, including resonant frequencies, modes, Q's, resistive loading, mode purity, parameterization, and manufacturing tolerance. In particular, ARGUS and HFSS were used to model the Q and resonant frequency for the operating mode of the input coupler, as a means of benchmarking code performance for the coupler simulations. Excellent agreement was achieved between the two codes, where accuracy exceeding 0.1% was predicted.

Several techniques were employed with HFSS to determine the resonant frequency and Q of the $TE_{01}$ mode in the cylindrical cavity. As a first approximation, the stored electric field energy (proportional to $|\mathbf{E}|^2$) was integrated over the cavity and drift tube volumes when driven through the drive port at several frequencies. Frequency and Q, are determined from the peak and 'half-energy' points. A second method 'de-embeds' $S_{11}$ at the drive port to find the 'detuned short' position. The resonant frequency and Q are calculated from the phase of the reflection coefficient. HFSS has also been used to model a 'transmission' measurement by launching the $TE_{01}$ mode in the cylindrical cavity by evanescent coupling through the drift tube and 'receiving' at the rectangular port.

Resonant frequencies and Q's in ARGUS are determined from a variation of the 'detuned short' method due to Kroll and Yu [5,6]. Also, both HFSS and ARGUS were used to estimate the mode purity of the $TE_{011}$ circular cavity mode [7].

## 3 SIMULATION RESULTS

Performance of the input coupler is found using both HFSS and ARGUS to be quite sensitive to dimensions. The sensitivity of $f$ and Q to slot dimensions and cylindrical cavity radius is shown in Figs. 3 & 4, respectively. Note that a 0.0006 cm change in radius shifts the resonant frequency by ~200 MHz. It is important that the slot angular orientation be within ~1° of 45° with respect to the input waveguide. A 1° slot rotation increases $f$ by ~ 20 MHz and reduces Q by 3%. A 5° slot rotation increases $f$ by ~ 36 MHz and reduces Q by 30%. A frequency and Q within +/- 100 MHz and +/- 50, respectively, of the design values are acceptable from overall circuit performance considerations.

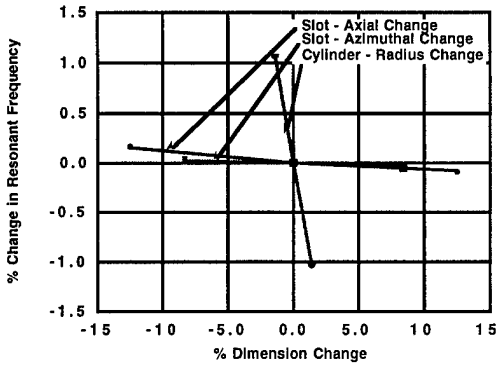



Figure 3: Resonant frequency change vs. dimensional change for a) slot axial size, b) slot azimuthal size, and c) cylinder radius.

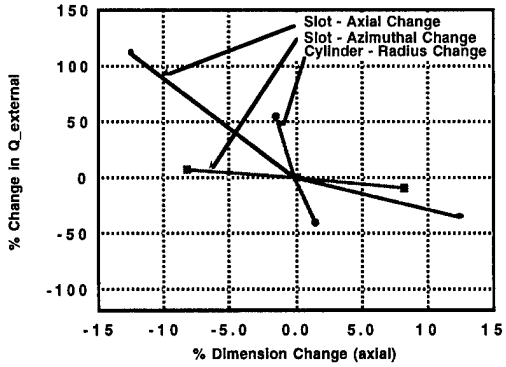



Figure 4: $Q_{ext}$ change vs. dimensional change for a) slot axial size, b) slot azimuthal size, and c) cylinder radius.

For the final design, the best compromise between coupling strength and bandwidth was achieved by 'stagger tuning' the cylindrical and coaxial cavities. The resonant frequency of the coaxial cavity was sufficiently higher than the cylindrical cavity that only ~ 10% of the combined stored energy is in the coaxial cavity over the nominal operating frequency range. For the final cavity dimensions, including stagger tuning, HFSS and ARGUS are in close agreement, as shown in Table 1.

| Simulation | Resonant frequency | Q |
|---|---|---|
| **HFSS** (base case) | 93.468 GHz | 149 |
| **HFSS** (w/taper, dielectric) | 93.467 GHz | 136 |
| **ARGUS** (base case) | 93.477 GHz | 157 |

Table 1. Resonant frequency and $Q_{ext}$ simulation results.

The calculated $TE_{01}$ mode purity is shown from both codes to be greater than 96% over a 600 MHz bandwidth. A color intensity plot of |**E**| through axial and transverse planes is shown in Fig. 5. The ohmic Q for the coupler is about 715, using 7.6e5 S/m for the conductivity of stainless steel in W-band. This conductivity is based on cold tests of simple cavities.

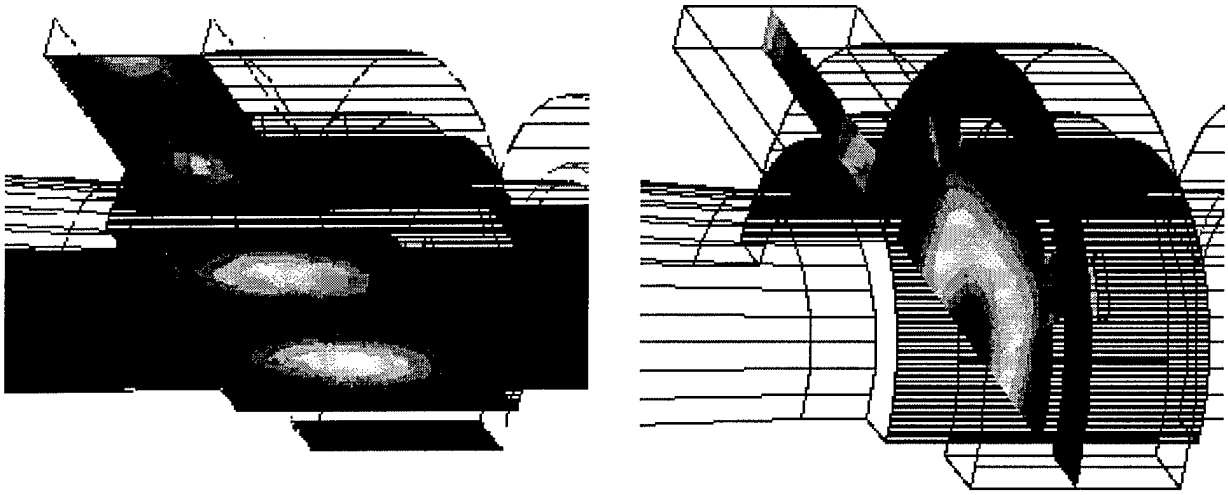


Figure 5. Intensity plot of |**E**| for transverse and axial cutplanes at 93.1 GHz.

## 4 COLD TEST RESULTS - SUMMARY

A prototype input coupler was constructed for testing. For the dimensions of this coupler, the calculated $f$ and $Q_{ext}$ are approximately 93.14 GHz and 110 GHz, respectively, without wall resistivity. Based on other simulations with resistivity included, we expect $f$ and $Q_{ext}$ to be 93.1 GHz and 95, respectively. Note that not all dimensions were available for simulation purposes, so that there is some uncertainty in these values.

The resonant frequency measured with a HP 8510C network analyzer, is 92.98 GHz in transmission mode and 92.96 GHz in reflection mode, in good agreement with predictions, although the test set-up is less than ideal. Power is injected into the drive port and a fraction of the power radiated from the drift tube is sampled with a WR8 waveguide for transmission mode measurements. $Q_{total}$ measured in transmission mode is 117, which implies $Q_{ext} \sim 140$ if $Q_{ohm}$ is 715. More accurate comparisons between simulation and measurement will be made following modifications in the measurement hardware.

## REFERENCES


[1] G. S. Park, C. M. Armstrong, R. H. Kyser, J. L. Hirshfield, and R. K. Parker, Int. J. Electronics **78**, 983 (1995).

[2] J. J. Choi, A. K. Ganguly, M. Blank, F. Calise, B. G. Danly, R. H. Kyser, B. Levush, P. Latham, A. H. McCurdy, G. S. Park, and R. K. Parker, Conference Proceedings, 21st International Conference on Infrared and Millimeter Waves, AM15 (1996).

[3] High Frequency Structures Simulator, Part No. HP 85180A.

[4] A. Mankofsky, Linear Accelerator and Beam Optics Codes, C.R. Eminheizer, ed., A.I.P. Conf. Proc. No. 177 (American Institute of Physics, New York, 1988), p. 137ff.

[5] N. M Kroll and D. U. L. Yu, Particle Accelerators **34**, 231 (1990).

[6] J. Petillo, W. Kreuger, A. Mondelli, and J. Potter, Proceedings of the 1993 Particle Accelerator Conference, **2**, 1004 (1993).

[7] A. K. Ganguly, private communication.

# ELECTRON BEAM PROPAGATION WITH PREMODULATED ENERGY AND CURRENT

Han S. Uhm, Naval Surface Warfare Center, West Bethesda, MD 20817-5700

*Abstract**

This paper considers an electron beam whose energy and current are simultaneously premodulated at the injection point of a drift tube. A theoretical model is developed for the subsequent current and energy modulations which propagate downstream. A closed integrodifferential equation for the normalized beam current is obtained in terms of time and propagation distance. To make the nonlinear current modulation analytically tractable, a small signal theory is introduced into the modulation calculation. The current modulation in the linear regime is a linear combination of the forward and backward waves of the initial current and energy modulations. The downstream energy modulation is also expressed by a linear combination of the forward and backward waves of the initial current and energy modulations. It is shown that the initial energy modulation is a very effective means for downstream current modulation. Numerical data even for a large initial current and energy modulations agree reasonably well with analytical results predicted by the linear theory.

## I INTRODUCTION

Prebunched charged particle beams have been investigated for various applications, including accelerator physics[1-7] and high-power traveling wave tubes (TWT).[8,9] Prebunched beams may make possible compact traveling wave tubes, eliminating the amplification regions. The recent experiment[8,9] on micro-field-emission gates indicates a strong possibility of the prebunched beams in near future. Unlike klystron amplifiers,[10-14] initiated by energy modulation at the input cavity, the prebunched TWT is operated by a premodulated electron beam, where the initial current modulation is a driving factor. A large initial current-modulation may considerably reduce size of the amplification region in TWT. In this context, a nonlinear theory of a prebunched electron beam propagating through a drift tube has been reported in a previous paper.[15] When the prebunched electron beam enters the drift tube, the initial electron current of the beam is modulated according to a prescribed current profile $f(\omega t_0)$, where $\omega$ is the bunching frequency of the beam and $t_0$ is the entering time of each beam slice. In addition to initial current modulation, we may also modulate the beam energy at the beginning. In reality, energy of the beam electrons[13] in the klystron amplifiers is modulated at the injection point by the input cavity without the current modulation. It is useful to investigate the influence of the initial energy modulation on the prebunched beam current during propagation. This article develops a theoretical model describing the current and energy modulations of an electron beam propagating downstream, when the beam's energy and current are simultaneously premodulated at the injection point.

## II PROPAGATION THEORY OF AN ELECTRON BEAM

A premodulated electron beam enters a drift tube at $z = 0$. The electron beam is radially confined by a strong magnetic field. For simplicity in the subsequent analysis, we assume that the electron beam current at $z = 0$ is premodulated according to a periodic function $f(\theta)$. Here, the normalized time$\theta = \omega t_0$ represents the time $t_0$ at which the beam segment labeled by $t_0$ enters the drift tube and the parameter $\omega$ is the modulation frequency. The function $f(\theta)$ can be an arbitrary function that represents the initial current modulation. For example, the function $f(\theta) = 1 - h\cos(\theta)$ shows a sinusoidal current modulation with the strength of h. Electron beam energy is also premodulated according to

$$\gamma_0(\theta) = \gamma_b + g(\theta), \tag{1}$$

where $\gamma_0$ and $\gamma_b$ are the relativistic mass factor at $z = 0$ and its average value over one period of the energy modulation function $g(\theta)$. The propagation distance z is related to the present time t and the injection time $t_0$ by making use of the velocity definition $dz/dt = \beta c$. Defining $\theta = \omega t_0$ and $\varphi = \omega t$, we obtain

$$\varphi - \theta = \int_0^\zeta \frac{d\zeta'}{\beta} = \int_0^\zeta d\zeta' \frac{\gamma}{\sqrt{\gamma^2 - 1}}, \tag{2}$$

where $\zeta$ is the normalized propagation distance defined by $\zeta = \omega z/c$ and $\gamma(\zeta,\theta) = (1 - \beta^2)^{-1/2}$ is the instantaneous relativistic mass factor of the beam segment labeled by $\theta$. The present time $\varphi$ is uniquely described by the injection time $\theta$ and propagation distance $\zeta$.

The self-electric field E, which exerts in the beam segment $\theta$ is calculated to be[13]

$$E(\zeta,\theta) = 2G(R_b)\frac{\omega}{\beta^2\gamma^2 c^2}\left(\frac{\partial I}{\partial \varphi}\right)_z, \tag{3}$$

where the geometrical factor G is determined in terms of system configuration. For convenience in the subsequent analysis, we define the normalized current $F(\zeta,\theta)$ by

* This work was supported by IR Fund at NSWC

U.S. Government work not protected by U.S. copyright

$$F(\zeta,\theta)=\frac{I(\zeta,\theta)}{I_b}, \tag{4}$$

where $I_b$ is the average beam current in one period of the current modulation at the injection point and the normalized distance $\zeta$ is defined by $\zeta = \omega z/c$. Velocity modulation of the beam segment labeled by $\theta$ is obtained from

$$mc^2\frac{d}{dz}\gamma = eE(z,\theta), \tag{5}$$

with the initial condition $\gamma = \gamma_0(\theta)$ at the entrance point $z = 0$ of the beam segment $\theta$. Substituting Eq. (3) into Eq. (5), we obtain

$$\frac{d}{d\zeta}\left(\frac{\gamma^3}{3} - \gamma\right) = \kappa\left[\frac{\partial}{\partial\varphi}F(\zeta,\theta)\right]_\zeta, \tag{6}$$

where the self-potential depression $\kappa$ is defined by[16] $\kappa = 2I_bG/I_A$ and $I_A = 17$ kA is the Alfven current. Carrying out the integration of Eq. (6) and making use of the initial condition, we obtain

$$\frac{\gamma^3}{3} - \gamma = \frac{\gamma_0^3(\theta)}{3} - \gamma_0(\theta) + \kappa\int_0^\zeta d\zeta'\left(\frac{\partial F}{\partial\varphi}\right)_{\zeta'}, \tag{7}$$

where the initial beam energy $\gamma_0(\theta)$ is determined from Eq. (1). Once the current modulation F is known, the energy modulation $\gamma(\zeta,\theta)$ is also known from Eq. (7). Differentiating Eq. (7) with respect to $\theta$, we obtain

$$\frac{d\gamma}{d\theta} = \frac{\gamma_0^2 - 1}{\gamma^2 - 1}\frac{dg}{d\theta} + \frac{\kappa}{\gamma^2 - 1}\int_0^\zeta d\zeta'\left(\frac{\partial^2 F}{\partial\theta\,\partial\varphi}\right)_{\zeta'}, \tag{8}$$

where $g(\theta)$ is the energy modulation function defined in Eq. (1).

It is useful in subsequent analysis to obtain

$$\frac{\partial\varphi}{\partial\theta} = 1 - \int_0^\zeta \frac{d\zeta'}{(\gamma^2 - 1)^{3/2}}\left(\frac{\partial\gamma}{\partial\theta}\right)_{\zeta'}, \tag{9}$$

from Eq. (2). Substituting Eq. (8) into Eq. (9) gives

$$\left(\frac{\partial\varphi}{\partial\theta}\right)_\zeta = 1 - (\gamma_0^2 - 1)\frac{dg}{d\theta}\int_0^\zeta \frac{d\zeta'}{(\gamma^2 - 1)^{5/2}} - \kappa\int_0^\zeta \frac{d\zeta'}{(\gamma^2 - 1)^{5/2}}\int_0^{\zeta'} d\zeta''\left(\frac{\partial^2 F}{\partial\theta\,\partial\varphi}\right)_{\zeta''}. \tag{10}$$

Note that the derivative $\partial\varphi/\partial\theta$ in Eq. (10) is uniquely described by the history of the current modulation F until the present time in which the beam segment labeled by $\theta$ arrives at the distance z.

The beam segment $t_0$ passes the injection point at time $t = t_0$. When this segment arrives at z in time t, it is stretched by a factor of $dt/dt_0$. Thus, the beam current of the segment $t_0$ at z is proportional to $(d\theta/d\varphi)f(\theta)$. In this regard, the normalized current ratio $F(\zeta,\theta)$ in Eq. (4) is expressed as

$$F(\zeta,\theta) = \frac{N(\zeta)\,f(\theta)}{\left|d\varphi/d\theta\right|}, \tag{11}$$

where the normalization constant $N(\zeta)$. After carrying out a straightforward calculation, we obtain the nonlinear integrodifferential equation

$$\frac{N(\zeta)}{F(\zeta,\theta)}f(\theta) = 1 - (\gamma_0^2 - 1)\frac{dg}{d\theta}\int_0^\zeta \frac{d\zeta'}{(\gamma^2 - 1)^{5/2}} - \frac{\kappa}{2}\int_0^\zeta \frac{d\zeta'}{(\gamma^2 - 1)^{5/2}}\int_0^{\zeta'} \frac{d\zeta''}{N(\zeta'')}\frac{\partial}{\partial\theta}\left[\frac{1}{f(\theta)}\left(\frac{\partial F^2}{\partial\theta}\right)\right]_{\zeta''}, \tag{12}$$

where use has been made of the relation $\partial\theta/\partial\varphi = F/Nf(\theta)$. The term that is proportional to $dg/d\theta$ in Eq. (12) originates from the initial energy modulation at the injection. The initial condition of the integrodifferential equation (12) is $F(0,\theta) = f(\theta)$. Equations (7) and (12) are two principal results in this article, and can be used to find the nonlinear current evolution as the premodulated beam propagates downstream. The numerical calculation of Eq. (12) is not so simple. The main difficulty in numerical calculation of Eq. (12) is the double integration of $\zeta$ in the right-hand side, which requires a long computer time.

## III SMALL SIGNAL THEORY

In order to find a scaling law, we linearize Eq. (12), assuming a small level of modulation. Therefore, the initial and later current modulations are expressed as

$$f(\theta) = 1 + \delta f(\theta), \qquad F(\zeta,\theta) = 1 + \delta F(\zeta,\theta), \tag{13}$$

where the amplitudes of $\delta f$ and $\delta F$ are much less than unity. We also assume that the initial energy modulation $g(\theta)$ is much less than the mean value $\gamma_b$ of the relativistic mass factor. A previous study[13] indicates that results from the small signal theory in the subsequent analysis agree remarkably well with results from numerical solution of Eq. (13), even when the modulation amplitude is close to unity. The function $\delta f(\theta)$ in Eq. (13) is a periodic function with a periodicity of $2\pi$. The initial current $f(\theta)$ and energy $g(\theta)$ profiles must satisfy the normalization condition that the average values of the functions $\delta f(\theta)$ and $g(\theta)$ must be zero over one period. Substituting Eq. (13) into Eq. (12) and linearizing, we find

$$\delta F(\zeta,\theta) = \delta f(\theta) + \xi\frac{d}{d\theta}g(\theta) + \eta^2\int_0^\zeta dy\int_0^y dx\left[\frac{\partial^2}{\partial\theta^2}\delta F(x,\theta)\right]_x, \tag{14}$$

where the frequency $\eta$ of the amplitude oscillation is defined by

$$\eta^2 = \frac{\kappa}{(\gamma_b^2 - 1)^{5/2}}, \quad \xi = \frac{\zeta}{(\gamma_b^2 - 1)^{3/2}}, \tag{15}$$

and the normalization constant $N(\zeta)$ in Eq. (12) has been approximated by $N(\zeta) = 1$ for small oscillations.

Differentiating both sides of Eq. (14) by $\zeta$, we obtain

$$\frac{\partial^2}{\partial \zeta^2} \delta F(\zeta,\theta) = \eta^2 \frac{\partial^2}{\partial \theta^2} \delta F(\zeta,\theta), \tag{16}$$

which is a typical equation for wave propagation. The physically acceptable solution to Eq. (16) is

$$\delta F(\zeta,\theta) = A(\theta + \eta\zeta) + B(\theta - \eta\zeta), \tag{17}$$

where the functions A and B must satisfy the boundary conditions

$$A(\theta) + B(\theta) = \delta f(\theta) \tag{18}$$

and

$$\left(\frac{\partial A}{\partial \theta}\right)_{\zeta=0} - \left(\frac{\partial B}{\partial \theta}\right)_{\zeta=0} = \frac{1}{\eta}\left(\frac{dg}{d\theta}\right)\left(\frac{d\xi}{d\zeta}\right) \tag{19}$$

at the injection point $\zeta = 0$. Equation (19) is equivalently expressed as

$$A(\theta) - B(\theta) = \frac{g(\theta)}{\sqrt{\kappa}\,(\gamma_b^2 - 1)^{1/4}}, \tag{20}$$

where the definitions in Eq. (15) have been used. The functions $A(\theta)$ and $B(\theta)$ are determined to be

$$A(\theta) = \frac{1}{2}\left[\delta f(\theta) + \frac{g(\theta)}{\sqrt{\kappa}\,(\gamma_b^2 - 1)^{1/4}}\right],$$
$$B(\theta) = \frac{1}{2}\left[\delta f(\theta) - \frac{g(\theta)}{\sqrt{\kappa}\,(\gamma_b^2 - 1)^{1/4}}\right], \tag{21}$$

from Eqs. (18) and (20). The solution in Eq. (17) is therefore given by

$$\delta F(\zeta,\theta) = \frac{1}{2}[\delta f(\theta + \eta\zeta) + \delta f(\theta - \eta\zeta)] + \frac{1}{2\sqrt{\kappa}\,(\gamma_b^2 - 1)^{1/4}}[g(\theta + \eta\zeta) - g(\theta - \eta\zeta)], \tag{22}$$

which is expressed by a combination of the initial energy and current modulations. We thus conclude that the downstream current modulation is described by a linear combination of the initial energy and current modulations. Substituting Eq. (22) into Eq. (7) and carrying out the linearization, we obtain the downstream energy modulation

$$\gamma(\zeta,\theta) = \gamma_b + \frac{1}{2}[g(\theta - \eta\zeta) + g(\theta + \eta\zeta)] + \frac{\sqrt{\kappa}\,(\gamma_b^2 - 1)^{1/4}}{2}[\delta f(\theta + \eta\zeta) - \delta f(\theta - \eta\zeta)].$$

The current modulation $F(\zeta,\theta)$ in the linear regime is a linear combination [Eq. (22)] of the forward and backward waves of the initial current and energy modulations (f and g). Properties of the current and energy modulations were numerically investigated from the integrodifferential equation (12) for a broad range of system parameters. Magnitudes of the energy and current modulations were determined in terms of the modulation frequency, initial energy $g(\theta)$ and current $f(\theta)$ profiles, geometrical configuration, beam intensity and initial kinetic energy of the beam. Numerical data from Eq. (12), even for large initial current and energy modulations, agree reasonably well with analytical results predicted by the linear theory.

## REFERENCES


[1] C. A. Kapetanakos, and P. Sprangle, Phys. Today, **38**(2), 58 (1985).

[2] P. Chen, J. M. Dawson, R. W. Huff, and T. Katsouleas, Phys. Rev. Lett. **54**, 693 (1985).

[3] J. B. Rosenzweig, Phys. Rev. A **40**, 5249 (1989).

[4] J. B. Rosenzweig, and P. Chen, Phys. Rev. D **39**, 2039 (1989).

[5] M. Rosing, E. Chojnaki, W. Gai, C. Ho, R. Konecny, S. Mtingwa, J. Norem, P. Schoessow, and J. Simpson, *Proceedings of the 1991 IEEE Particle Accelerator Conference,* San Francisco, CA (Institute of Electrical and Electronic Engineers, New York, 1991), Vol I, p. 555.

[6] E. Chojnaki, W. Gai, P. Schoessow, and J. Simpson, in Ref. 5, Vol. IV, p. 2557.

[7] H. S. Uhm, Phys. Fluids B **5**, 972 (1993).

[8] M. A. Kodis, N. R. Vanderplaats, and E. G. Zaidman, *Technical Digest of the International Electron Devices Meeting 1990,* San Francisco, CA (Institute of Electrical and Electronic Engineers, New York, 1990), Vol I, p. 893.

[9] M. A. Kodis, H. P. Freund, N. R. Vanderplaats, and E. G. Zaidman, *Technical Digest of the International Electron Devices Meeting 1991,* Washington, D. C. (Institute of Electrical and Electronic Engineers, New York, 1991), Vol I, p. 589.

[10] M. Friedman, J. Krall, Y. Y. Lau, and V. Serlin, J. Appl. Phys. **64**, 3353 (1988).

[11] M. Friedman, V. Serlin, A. Drobot, and A. Mondelli, IEEE Trans. Plasma Sci. **PS-14**, 201 (1986).

[12] M. Friedman, J. Krall, Y. Y. Lau, and V. Serlin, IEEE Trans. Plasma Sci. **PS-18**, 553 (1990)

[13] H. S. Uhm Phys. Fluids B **5**, 190 (1993).

[14] H. S. Uhm, G. S. Park, and C. M. Armstrong, Phys. Fluids B **5**, 1349 (1993).

[15] H. S. Uhm, Phys. Plasmas **3**, 168 (1996).

[16] H. S. Uhm, Phys. Fluids B **5**, 1919 (1993) and the references therein.

# EXPERIMENTAL INVESTIGATION OF A W-BAND GYROKLYSTRON AMPLIFIER

M. Blank, B.G. Danly, B. Levush, Naval Research Laboratory, Washington, D.C. 20375 and
P.E. Latham, Omega P, Inc., New Haven, CT 06520

*Abstract*

A four cavity W-band gyroklystron amplifier experiment is currently underway at the Naval Research Laboratory. The gyroklystron has produced 67 kW peak output power and 28% efficiency in the $TE_{011}$ mode with a 55 kV, 4.3 A annular electron beam. The full width half maximum (FWHM) bandwidth is greater than 460 MHz. Small signal and saturated gains of 36 dB and 29 dB, respectively, have been observed. The amplifier is zero drive stable and the limiting oscillation is the $TE_{011}$ operating mode in the output cavity. Experimental results are in good agreement with theoretical predictions.

## 1 INTRODUCTION

The continuing need for high power sources of millimeter wave radiation for such varied applications as high resolution radars, linear accelerators, and communications, has led to extensive research on gyroklystron amplifiers. Much like a conventional klystron, the gyroklystron consists of several resonant cavities separated by drift sections cut-off to the operating mode. As evidenced in numerous experiments, the interaction of the beam with the trapped mode in the cavity, based on the electron cyclotron maser instability, can reliably and efficiently generate high power, moderate bandwidth electromagnetic radiation at microwave and millimeter wave frequencies. For example, a three cavity C-band gyroklystron amplifier produced 54 kW peak output power and 30% efficiency in the $TE_{101}$ at 4.5 GHz [1]. The saturated gain was 30 dB and the FWHM bandwidth was 0.4%. A three cavity X-band gyroklystron achieved 16 kW peak output power 45% efficiency with a 1% bandwidth [2]. Fundamental and second harmonic two cavity gyroklystron amplifiers at 9.87 GHz and 19.7 GHz, designed as drivers for linear colliders, achieved peak output powers of 20 MW and 30 MW, respectively, with efficiencies near 30% [3,4]. A two cavity Ka-band gyroklystron, developed for radar applications, produced 750 kW at 35 GHz in the $TE_{021}$ mode at 24 % efficiency [5]. In W-band, a pulsed four cavity gyroklystron amplifier achieved 65 kW peak output power at 26% efficiency with 300 MHz bandwidth [6]. A continuous wave version of the device demonstrated 2.5 kW average output power. The goal of the present work is to enhance the bandwidth of the W-band gyroklystron amplifier while maintaining high efficiency, peak output power, and gain.

## 2 THEORY AND DESIGN

This paper presents an experimental study of a four cavity W-band gyroklystron amplifier operating in the $TE_{011}$ mode near the fundamental cyclotron frequency. The circuit consists of a drive cavity, two idler cavities, and an output cavity. The circuit was designed with a time-dependent version of the non-linear code MAGYKL [7]. The wave equation solved in MAGYKL is given by

$$\frac{da}{dt} + \left(\frac{1}{2} + i\Delta_{\omega}\right)a = -\frac{QI_b}{2\omega W_{EM}} \int d\xi \frac{c}{\omega} \left\langle \frac{v_{perp} \cdot E_c e^{-i\omega t}}{v_z} \right\rangle$$

where $a$ is the complex amplitude of the fields, $\Delta_{\omega}=Q\{\mathrm{Re}\{\omega_c\}-\omega\}/\omega$ is the normalized frequency shift, $Q$ is the quality factor of the cavity, $\omega$ is the drive frequency, $\omega_c$ is the cold resonant frequency, $I_b$ is the beam current, $W_{EM}$ is the stored energy, $c$ is the speed of light, $v_{perp}$ and $v_z$ are the perpendicular and axial electron velocities, $\boldsymbol{E}_c$ is ite cold cavity electric field, and $t$ is the normalized time $\omega/Q$.

In the formulation, the cavities are modeled by a series of straight uniform sections with abrupt discontinuities at the boundaries. The fields in each section, expanded as a radial series of TE, TM, and TEM modes, are determined through a scattering matrix solution [8]. Theoretical studies have shown that it is necessary to include many modes in the field description to correctly predict the resonant frequency of the cavity. In order to accurately predict the bandwidth of the amplifier, the formulation detailed in reference [7] was modified to include a frequency dependent drive power, as dictated by the resonant frequency and Q of in input cavity. The theoretical model was used to design the interaction circuit and determine the parameters of each cavity, which are summarized in Table 1.

| | Design | | | Cold Test | |
|---|---|---|---|---|---|
| | L (cm) | $f_0$ (GHz) | Q | $f_0$ (GHz) | Q |
| cavity 1 | 0.43 | 93.00 | 125 | - | - |
| cavity 2 | 0.50 | 93.52 | 175 | 93.56 | 130 |
| cavity 3 | 0.50 | 92.89 | 175 | 93.02 | 128 |
| cavity 4 | 0.80 | 93.18 | 300 | 93.21 | 299 |

Table 1 Summary of cavity parameters.

0-7803-4376-X/98 /$10.00 © 1998 IEEE

The drive power is coupled into the circuit through a coaxial cavity [9]. A single cylindrical waveguide excites the $TE_{411}$ mode of the outer cavity. Power is then coupled from the $TE_{411}$ mode in the outer cavity to the $TE_{011}$ mode in the inner cavity through four slots positioned symmetrically around the azimuth of the cavity. The coaxial cavity was analyzed with the High Frequency Structure Simulator (HFSS) and found to have a resonant frequency of 93.0 GHz and a diffractive Q of 150. HFSS simulations also show that 75% of the energy is stored in the $TE_{411}$ mode and 25% is stored in the $TE_{011}$ inner cavity mode. Thus, 6 dB of drive power arriving at the input cavity is stored in the outer cavity and is not available for interaction.

Because the second and third cavities are terminated by drift sections that are cut-off for the $TE_{011}$ mode at 93 GHz, the diffractive Q's are quite large. The design Q's of 175 are achieved through dielectric loading of the cavities. The output cavity consists of a 0.8 cm straight section, followed by an iris which is cutoff to the $TE_{011}$ mode at 93 GHz, and a 5 degree linear uptaper to the collector radius. The wave is coupled out diffractively and there is no ceramic loading the output cavity. The first and second cut-off drift lengths are loaded only by the dielectrics on the upstream walls of the idler cavities, and the drift length separating the penultimate cavity and output cavity is unloaded.

## 3 EXPERIMENTAL RESULTS

The circuit was built and cold tested on a vector network analyzer. The cavities were excited and sampled through two 0.075 cm diameter holes positioned 180 degrees apart in the side wall. The transmission spectra for the idler and output cavities are shown in Fig. 1 and the measured resonant frequencies and Q's are summarized in Table 1.

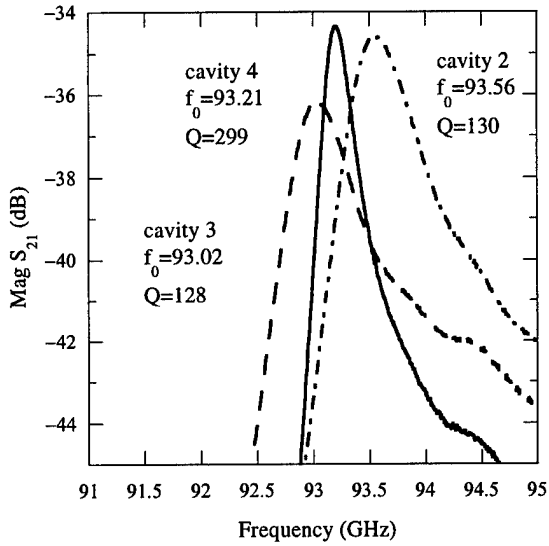



Figure 1 Cold test transmission spectra for cavity 2 (dashed-dot line), cavity 3 (dashed line) and cavity 4 (solid line).

Upon completion of the cold test, the circuit was installed in the test stand. Figure 2 shows a schematic of the gyroklystron amplifier experiment. A 4 A, 55 kV annular electron beam is produced by a double anode magnetron injection gun. The magnetic field at the cathode, which is nominally 1.5 kG, can be varied to control the beam velocity ratio, $\alpha$. The beam is adiabatically compressed as it enters the region of high magnetic field generated by the 4 T superconducting magnet. The four cavities of the gyroklystron circuit are positioned in a region of constant magnetic field. The output cavity tapers up to the collector, which is followed by a quartz vacuum window. A conically shaped, water backed teflon load is positioned on the atmosphere side of the vacuum window. The temperature rise of the water is used to measure the average rf power. The frequency of the input and output rf signals are measured with a spectrum analyzer. The drive power is supplied by a 1 kW peak power EIO, which is mechanically tunable from approximately 92.5 GHz to 95.5 GHz. The EIO provides pulses up to 2 microseconds in duration with a duty cycle up to 1%. The beam and EIO are typically pulsed at 250 Hz for an rf duty cycle of 0.05%.

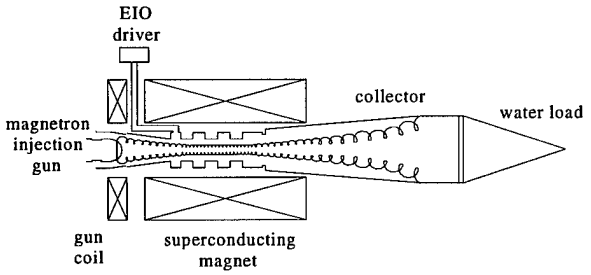



Figure 2 Schematic of the experimental test stand.

Figure 3 shows the measured and predicted output power and efficiency as a function of frequency for the amplified $TE_{011}$ mode. A peak saturated output power of 67 kW, corresponding to 28% efficiency, was achieved with a 55 kV, 4.3 A electron beam. The FWHM bandwidth is greater than 460 MHz. The input power, measured at the output of the EIO, was 87 W, which gives 29 dB saturated gain. For the theory curve in Fig. 3, the experimentally determined values of cold resonant frequencies and Q's for the idler and output cavities were used. The HFSS predictions of the drive cavity resonant frequency and Q were assumed. The experimental values of beam voltage, beam current, and magnetic field in the

interaction circuit were used. The beam α was taken to be 1.5, and the perpendicular velocity spread was assumed to be 9%, values that were obtained through a combination of modeling and empirical determination. As shown in Fig. 3, the theoretical predictions are in good agreement with experimental data.

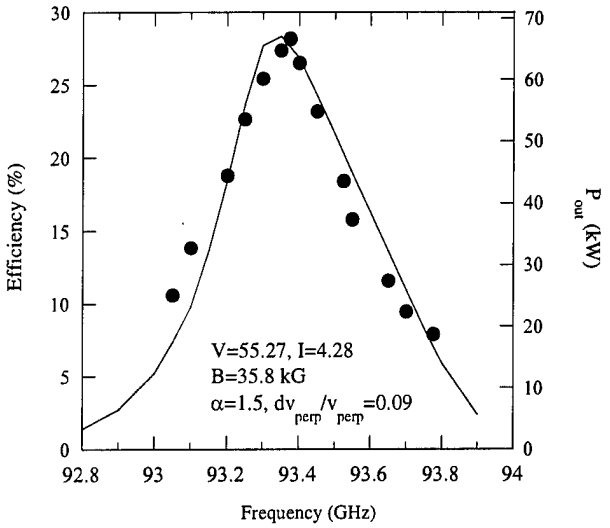



Figure 3 Measured values (filled circles) and theoretical predictions (solid curve) of peak output power and efficiency.

The limiting oscillation in the circuit was found to be the $TE_{011}$ operating mode in the output cavity. The start oscillation current was measured and the results are shown in Fig. 4.

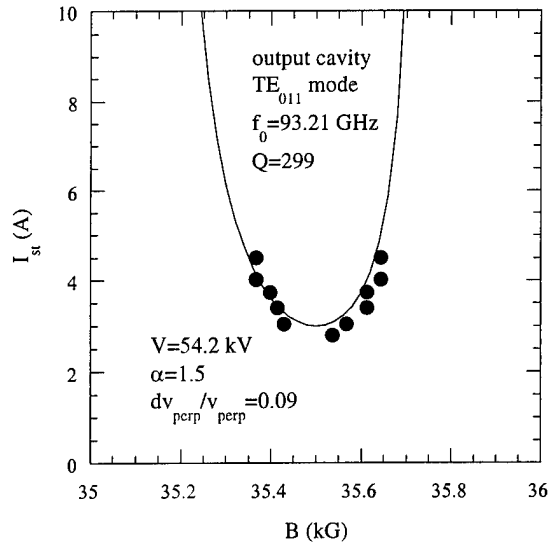



Figure 4 Measured values (filled circles) and theoretical prediction (solid curve) for start oscillation current of the $TE_{011}$ mode in the output cavity.

The measured data points, indicated by the filled circles, are compared with the theoretical start current,
shown with the solid line. In the theory, the measured values of beam current, cold resonant frequency, and cold cavity Q were used. The beam α was taken to be 1.5, and the perpendicular velocity spread was assumed to be 9%. As shown in Fig. 4, the experimental data and theoretical predictions are in good agreement.

## 4 SUMMARY

In summary, a four cavity W-band gyroklystron amplifier circuit was designed, built, and tested. Peak output powers of 67 kW, corresponding to 28% efficiency, were achieved in the $TE_{011}$ mode with a 55 kV, 4.3 A electron beam. The FWHM bandwidth is greater than 460 MHz. The small signal and saturated gains are 36 dB and 29 dB, respectively. The circuit is zero drive stable and the limiting oscillation is the $TE_{011}$ operating mode in the output cavity. The experimental data is in good agreement with predictions of theory using calculated values of beam velocity ratio and velocity spread. Future experiments will focus on increasing bandwidth through more aggressive stagger tuning and reduced output cavity Q.

## 5 ACKNOWLEGEMENTS

The authors would like to thank M. Barsanti, F. Robertson, B. Sobocinski, and M. Ngo for their technical assistance. This work was supported by the Office of Naval Research. The computational work was supported in part by a grant of HPC time from the DoD HPC Center NAVO.

## REFERENCES

[1] W.M Bollen, A.H. McCurdy, B. Arfin, R.K. Parker, A.K. Ganguly, IEEE Trans. Plasma Sci. **13,** 417 (1985).
[2] E.V. Zasypkin, M.A. Moiseev, E.V. Sokolov, V.K. Yulpatov, Int. J. Electron. **78**, 423 (1995).
[3] W.G. Lawson et al., Phys. Rev. Lett. **67**, 520 (1991).
[4] H.W. Matthews et al., IEEE Trans. Plasma Sci. **22**, 825 (1994).
[5] E.V. Zasypkin, M.A. Moiseev, I.G. Gachev, I. I. Antakov, IEEE Trans. Plasma Sci. **24**, 666 (1995).
[6] I.I. Antakov, E.V. Zasypkin, E.V. Sokolov, Conf. Digest of the Eighteenth Intl. Conf. On Infrared and Millimeter Waves, Proc. SPIE **2104**, 166 (1993).
[7] P.E. Latham, W. Lawson, V. Irwin, IEEE Trans. Plasma Sci **22,** 804 (1994).
[8] J.M. Neilson, P.E. Latham, M. Caplan, W. Lawson, IEEE Trans. Microwave Theory Tech. **37**, 1165 (1989).
[9] G.S. Park, C.M. Armstrong, R.H. Kyser, J.L. Hirshfield, R.K. Parker, Int. J. Electronics **78**, 983 (1995).

# X-BAND MAGNICON AMPLIFIER FOR THE NEXT LINEAR COLLIDER

Steven H. Gold and Arne W. Fliflet
Beam Physics Branch, Plasma Physics Division,
Naval Research Laboratory, Washington, DC 20375–5346

Allen K. Kinkead
Sachs/Freeman Associates, Inc., Landover, MD 20785

B. Hafizi
Icarus Research, Inc., P.O. Box 30780, Bethesda, MD 20824–0780

Oleg A. Nezhevenko,† Viacheslav P. Yakovlev,†
and Jay L. Hirshfield
Omega-P, Inc., 202008 Yale Station, New Haven, CT 06520
†Permanent Address: Budker Institute of Nuclear Physics, Novosibirsk, Russia 630090

Richard True and Robert J. Hansen
Litton Systems, Inc., Electron Devices Division, San Carlos, CA 94070

*Abstract*

The magnicon is a scanning-beam microwave amplifier that is being developed as a high power, highly efficient microwave source for use in powering the next generation of high gradient electron linear accelerators. In this paper, we present a progress report on a new thermionic magnicon experiment designed to produce more than 50 MW at 11.4 GHz, using a 210 A, 500 kV beam from an ultrahigh convergence thermionic electron gun driven by a rep-rated modulator. This new design has a predicted efficiency in excess of 60%.

## 1 INTRODUCTION

The magnicon [1] is a scanning-beam microwave amplifier tube that is under development as a radio-frequency (RF) source to power future high gradient electron accelerators such as the proposed TeV Next Linear Collider (NLC). The magnicon uses rotating TM modes to spin up a pencil electron beam to high transverse momentum in a series of deflection cavities, the first externally driven, and then a synchronously rotating RF mode of the output cavity is used to extract the transverse momentum as microwave power at the drive frequency or one of its harmonics.

The Naval Research Laboratory (NRL) has been investigating magnicon physics for the past five years with the goal of building a high power 11.4 GHz magnicon tube. We published a design study for a 50 MW, 50% efficient frequency-doubling 11.4 GHz magnicon employing a 500 kV, ~170 A, 2-mm-diam. electron beam from an advanced thermionic electron gun [2], and then designed and built an initial magnicon experiment using a cold-cathode diode on the NRL Long Pulse Accelerator Facility. However, the experiment employed a 5.5-mm-diam. beam, for which the predicted efficiency falls to ~20%. The experiment demonstrated high power operation (14 MW ±3 dB) at ~10% efficiency in the synchronous magnicon mode at 11.120 GHz, but a plasma loading problem restricted operation to parameters for which the final deflection cavity (the penultimate cavity) was unstable. Nevertheless, good agreement was found with predictions of a simulation based on the actual experimental parameters [3,4].

The Budker Institute of Nuclear Physics (INP) is carrying out thermionic magnicon experiments at 7 GHz [5]. They recently reported 46 MW at 49% efficiency in a 1 μsec pulse. Some members of the INP magnicon team are collaborators in the present work.

In this paper, we present a progress report on a new thermionic magnicon amplifier (see Fig. 1) that is under construction at NRL in collaboration with Omega-P, Inc. The design has been optimized for the parameters of a new ultrahigh convergence 500 kV, 210 A thermionic electron gun, and incorporates improvements that should raise the efficiency while reducing the possibility of RF breakdown. The predicted efficiency is greater than 60%.

The essential components of a high power thermionic magnicon experiment are a high power mod-

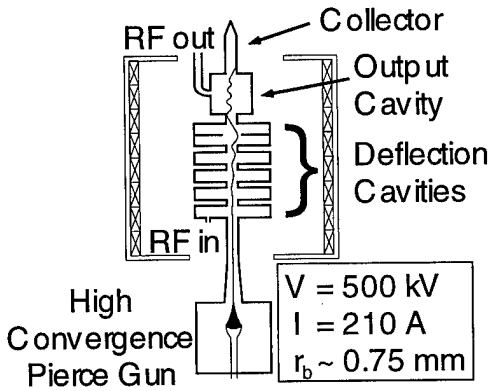



Figure 1: Schematic of the high efficiency thermionic magnicon amplifier.

0-7803-4376-X/98 /$10.00 © 1998 IEEE

ulator, an ultrahigh convergence electron gun, a matched magnet system, and a set of cavities designed for high vacuum, high temperature bakeout, and high efficiency operation. In the next sections, we discuss the design of a novel high convergence electron gun to produce a 500 kV, 210 A, <2-mm-diam. beam, and the redesign of the magnicon circuit to optimize the efficiency, to lower the peak surface RF fields, and to side-couple the microwave power from the output cavity into X-band waveguide.

## 2 THE ELECTRON GUN

The point design for the 11.424 GHz magnicon amplifier uses a 500 kV, 210 A, 1.5-mm-diam. electron beam, with a 1.5 μsec pulse width and a 10 Hz repetition rate. It should be noted that the Brillouin diameter is ~1.3 mm at 6.5 kG. The electron gun is a novel high convergence relativistic Pierce gun using a dispenser cathode. The gun design and beam matching into the magnetic field were carried out using the codes DEMEOS [6], SAM [7], and SUPERSAM [8]. Beam compression in the gun must be high in order to limit the field gradient at the focus electrode and to limit cathode loading. A 7.5-cm-diam., 30°-half-angle cathode was used, implying an overall compression ratio of 2500:1 and a mean cathode loading of 4.5 A/cm$^2$. The gun design is shown in Fig. 2, and its properties are summarized in Table I. A key feature of the gun is an electrically isolated focus electrode next to the cathode. This electrode is biased negatively by a few hundred volts with respect to the cathode in order to control the beam edge discharge angle and to eliminate emission from the outer cathode cylinder, both of which can give rise to unwanted halo electrons. This gun is being built by Litton Systems, Inc., with delivery expected in July of this year, and a matching magnet has been built by the INP.

## 3 THE MAGNICON CIRCUIT

The new magnicon circuit consists of a drive cavity, three gain cavities, a penultimate cavity, and an output cavity, as illustrated in Fig. 1. The drive and gain cavities are similar to those in the previous NRL design [2].

TABLE I. Electron gun design parameters

| | |
|---|---|
| Current | 210 A |
| Voltage | 500 kV |
| Microperveance | 0.59 |
| Cathode radius | 3.77 cm |
| Beam radius | 0.75 mm |
| Compression ratio | 2500:1 |
| Current density | 12 kA/cm$^2$ |
| Maximum field on focusing electrodes | 186 kV/cm |
| Mean cathode loading | 4.5 A/cm$^2$ |
| Pulse duration | 1.5 μsec |

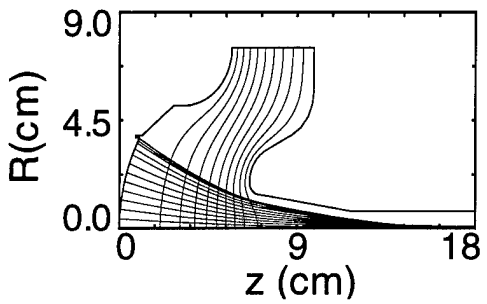



Figure 2: Design for the 500 kV, 210A magnicon electron gun, showing electrode geometry, selected electron trajectories and equipotentials.

In the following subsections, we discuss the redesign of the penultimate and output cavities, and the simulation of the entire magnicon circuit.

### *3.1 The penultimate cavity*

The penultimate cavity is an iris-coupled $TM_{110}$ π-mode two-section cavity that carries out the final stage of beam spin up. As a result, it contains very high RF fields, creating the danger of RF breakdown. The objective of the new design was to optimize the beam spin-up, while minimizing the surface RF fields. The redesign involved adjusting the beam pipe diameter, rounding of the beam tunnel and the iris, and reducing the length of the first cavity section. For the new penultimate cavity, the combination of reduced field enhancements, and of more effective beam spin-up due to shortening the first cavity section, reduced the maximum surface electric field from 670 kV/cm in the original design to 572 kV/cm, comparable to values employed in high power X-band klystrons at SLAC. The maximum electric field on the iris aperture is 472 kV/cm.

### *3.2 The output cavity*

In order to improve the efficiency and lower the rf fields, the output cavity was also redesigned, reducing the beam tunnel diameter, increasing the rounding of the beam tunnel apertures, and shortening the cavity from 5 cm to 4 cm. This is discussed in greater detail in Ref. 9. As a result, the maximum surface rf field in the output cavity was reduced from 830 kV/cm to 520 kV/cm. The second goal is to redesign the cavity for side coupling rather than end coupling, in order to extract the output power directly into X-band waveguide, rather than through a circular pipe that must also serve as the beam collector. The INP 7 GHz magnicon employs two rectangular waveguides separated by 135° to couple out both non-rotating components, and uses additional wall perturbations to restore the quadrupole symmetry [5]. This is the approach that we have adopted.

Figure 3 shows a cross section of the new magnicon circuit, and shows the ten magnet coils and a portion of

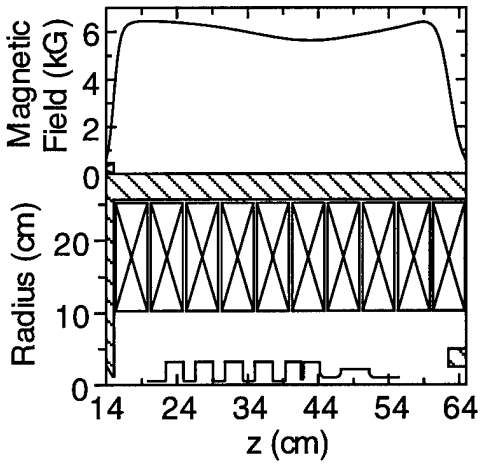



Figure 3: Cross-section of the magnicon circuit, showing the axial magnetic field.

the iron yoke and pole pieces. The new circuit consists of a drive cavity, three simple gain cavities, and a redesigned penultimate cavity, all operating in the $TM_{110}$ mode at 5.712 GHz, followed by a new output cavity operating in the $TM_{210}$ mode at 11.424 GHz. The addition of a gain cavity has increased the gain to 58 dB, reducing the drive power for a 66 MW device to approximately 100 W at 5.712 GHz. This gain is consistent with values used at SLAC in the design of X-band klystrons for the NLC. Figure 3 also shows the calculated on-axis magnetic field. The magnetic field is decreased in the vicinity of the penultimate and output cavities by lowering the current through the sixth coil, in order to stabilize the penultimate cavity against oscillation and to increase the output efficiency.

### *3.3 The complete circuit*

Figure 4 shows a simulation of the complete magnicon circuit for a 1.5-mm-diam. electron beam, showing the trajectories and the spatial evolution of the electron energy through the asymptotic rf fields from a complete time-dependent simulation. The transverse dimension is stretched in order to show details of the orbits. The beam scalloping that is evident results from simulating a zero canonical momentum beam without space charge. Notice that energy spreads and large energy excursions occur in the region of the penultimate cavity, but that the energy loss in the output cavity is remarkably uniform. The result is 66 MW at 63% efficiency. The magnicon design parameters are shown in Table II. Our simulations show a loss in efficiency of only a few percent at beam diameters up to 2.5 mm.

TABLE II. Thermionic magnicon design parameters

| | |
|---|---|
| Frequency | 11.424 GHz |
| Power | 66 MW |
| Efficiency | 63% |
| Pulse width | 1.5 μsec |
| Repetition rate | 10 Hz |
| Drive frequency | 5.712 GHz |
| Drive power | 100 W |
| Gain | 58 dB |

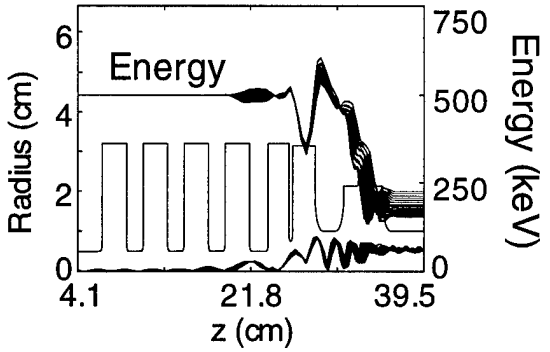



Figure 4: Steady-state simulation of the thermionic magnicon design for a 1.5-mm-diam. beam.

## 4 SUMMARY

We have designed an electron gun and circuit for a high gain, high efficiency 11.424 GHz frequency-doubling magnicon amplifier. The beam parameters are 500 kV, 210 A, and 1.5-mm beam diameter. The electron gun will be driven by a 1.5 μsec, 10 Hz modulator. The predicted power is 66 MW at 63% efficiency. The maximum surface electric field is approximately 570 kV/cm, a value that is consistent with 1.5 μsec pulse widths. This design is the basis of a new thermionic magnicon experiment, which we plan to assemble and test in 1997.

## 5 ACKNOWLEDGMENTS

This work was supported by the U.S. Department of Energy (DoE) and the Office of Naval Research under Interagency Agreement DE-AI02-94ER40861. A portion of this work was also supported by a DoE Small Business Innovation Research (SBIR) grant to Omega-P, Inc. and carried out under a Cooperative Research and Development Agreement (CRADA) between NRL and Omega-P.

## 6 REFERENCES

[1] O.A. Nezhevenko, *IEEE Trans. Plasma Sci.* **22**, 765 (1994).
[2] O.A. Nezhevenko *et al.*, *IEEE Trans. Plasma Sci.* **22**, 785 (1994).
[3] S.H. Gold *et al.*, *IEEE Trans. Plasma Sci.* **24**, 947 (1996).
[4] S.H. Gold *et al.*, *Phys. Plasmas*, May 1997, in press.
[5] E.V. Kozyrev *et al.*, paper in this proceedings.
[6] R. True, in *Handbook of Microwave Technology*, ed. K. Ishii (Academic, New York, 1995), Vol. I, p. 497.
[7] D.G. Myakishev and V.P. Yakovlev, Int. J. Mod. Phys. A **2** (Proc. supp.), 915 (1993).
[8] M.A. Tiunov *et al.*, in *Proc. 13th Int. Conf. on High Energy Accelerators* [NAUKA (Siberian Branch), 1987], Vol. 1, p. 353.
[9] S.H. Gold *et al.*, *NRL Memo Report 7857* (1996).

# 34-GHz PULSED MAGNICON FOR LINEAR COLLIDER APPLICATION

O. A. Nezhevenko*, V. P. Yakovlev*, A. K. Ganguly and J. L. Hirshfield
Omega-P Inc., 202008 Yale Station, New Haven, CT 06520

*Abstract*

The feasibility of a third harmonic magnicon amplifier at 34.272 GHz as a RF source for future multi-TeV $e^+$-$e^-$ linear collider is examined. A third harmonic operation of the magnicon is necessary to stay within the constraints imposed by cathode loading, breakdown field and pulse heating of the conductive walls. A low emittance 500 keV, 200A pencil electron beam interacts with the cylindrical $TM_{110}$ mode in the deflection system and the cylindrical $TM_{310}$ mode in the output cavity. The drive signal is at 11.424 GHz. Preliminary calculations show an efficiency of about 42% with output power in excess of 42 MW. The surface RF field in the cavities is in the range of 700 - 900 kV/cm which is below the breakdown level at 34 GHz for 1 μs pulse length. The maximal cathode loading does not exceed 15 A/cm$^2$.

## 1 INTRODUCTION

Recently there is a great deal of interest in developing electron-positron multi-TeV colliders. The next linear colliders (NLC) have been designed in the 0.5 Tev - 1.0 TeV center of mass energy (c.m.) range[1]. The RF operating frequencies for these accelerators range from 1.3 GHz to 30 GHz and the beam-loaded accelerating gradients range from 25 MV/m to 90 MV/m. Considerations are being given to future linear colliders in the 5 - 15 TeV c.m. energy range[2]. High accelerating gradients will be required to keep a reasonable over-all length for these high energy colliders. As a result, the accelerating structure will require high peak power per unit length and a high peak power per RF source. The accelerating gradient is strongly correlated to the operating frequency. At a constant stored energy per unit length in the accelerating structures, the gradient increases linearly with frequency. Hence, it is possible to design high energy colliders keeping the active length and ac power within reasonable limits ($L_A$ ~ 30 km and $P_{ac}$ ~ 200 - 300 MW) by operating at higher frequencies. The scaling relations for the variation of RF power with frequency and gradient has been investigated by Wilson[2] and design parameters are provided in the 1 - 15 TeV c.m. energy range. The parameters for 5 TeV linear colliders are: f = 34.272 GHz (12 times SLC frequency of 2.856 GHZ and 3 times NLC frequency of 11.424 GHz), $L_A$ = 30 km, $P_{ac}$ = 300 MW, peakpower per meter, $P_m$ = 825 MW/m, unloaded accelerating gradient, $E_0$ = 250 MV/m and pulse length at the structure, $T_p$ = 50 ns. A repetition rate of 120 Hz is assumed in the designs. The accelerating gradient is limited by the breakdown threshold, dark current capture threshold and the rise in temperature due to pulse heating of the walls. The high peak power at the accelerating structure may be obtained by pulse compression techniques. New pulse compressors, e.g. [3], are being developed to have a compression ratio of 32 with an efficiency of 78% and a power gain of about 25. Thus, for an output pulse length of 50 ns, the RF source pulse length is 1.6μs. If two 0.6m structures[2] are fed from each compression unit, the required RF power is ( 825 MW/m x 1.2)/25 = 39.6 MW/source. A magnicon amplifier[4] will be a suitable RF source to meet these requirements.

In scaling magnicon amplifiers to higher frequencies (consequently, smaller physical dimensions), a few design problems will arise at high power due to the limitations imposed by cathode loading, breakdown field and pulse heating of the cavity walls. The concept of a third harmonic magnicon amplifier is introduced to overcome these problems. It is possible to design electron gun and microwave circuits satisfying the restrictions on current density, electric field and cooling. Fundamental or second harmonic operation of the output cavity is not possible at the frequency and power of interest. At the fundamental frequency, the Larmor diameter will be large and the beam tunnel will not be cut-off to the operating mode of the output cavity. For the second harmonic, the RF fields will exceed the breakdown limit in the penultimate cavity. Of course, it is possible to use harmonics higher than third, but the efficiency will be lower at higher harmonics.

## 2 THIRD HARMONIC MAGNICON

The magnicon amplifier at 34.272 GHz will operate with a 500 kV, 200 A electron beam to produce about 40 MW output power with 1.5 μs pulse duration. The drive frequency is 11.424 GHz in the $TM_{110}$ mode and the output cavity will operate in the $TM_{310}$ mode at the third harmonic of the drive frequency. A schematic of the magnetic and RF systems are shown in Fig. 1. For efficient interaction in the output cavity, the beam diameter should be less than 1 mm, i.e., one-eight of the radiation wavelength. Hence, the electron gun is to be designed to produce a 200A beam with a diameter of 0.8 mm at the entrance to the drive cavity. Since the

* Permanent address: Budker INP, Novosibirsk 630090, Russia

0-7803-4376-X/98 /$10.00 © 1998 IEEE

maximum cathode loading is 15 A/cm$^2$, a cathode diameter of 4.4 cm is chosen. Therefore, a beam area compression ratio of 3000:1 will be required. The total compression will be achieved through a 630:1 electrostatic compression and a 4.8:1 magnetic compression. An electrostatic compression of 630 is necessary to obtain a maximum dc electric field on the electrostatic focusing electrode of about 265 kV/cm which is acceptable[5] at 1.5 μs pulse duration. The gun layout is shown in Fig. 2. The shape of the electrodes are optimized to produce the required perveance, beam compression and the electric field strength. This design is based on an electron gun [6] already in operation at INP with an area compression ratio of 2400:1.

Careful design of the output and penultimate cavities are necessary to minimize the RF field without sacrificing the efficiency. Due to perturbations of the beam opening, the oscillations in the output cavity are

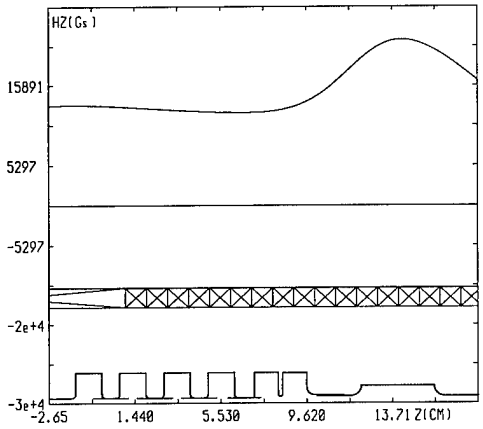



Fig.1 Magnetic field profile in Gauss vs coordinate in cm (top); and layout of coils, cavities (bottom) for 34.272 GHz magnicon.

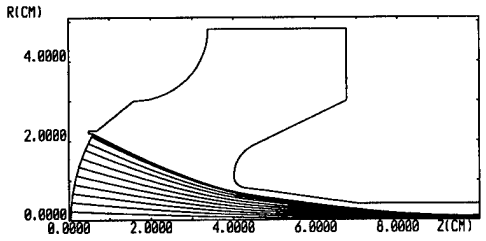



Fig. 2. The electron gun layout and the electron trajectories

not pure $TM_{310}$ mode but has some admixture of the $TE_{312}$ mode which depend on the length of the cavity and the shape of the beam tunnel opening. The maximum value of E at the cavity surface as a function of the cavity length is shown in Fig. 3 for different beam openings. The surface electric field is an oscillatory function of the cavity length. The output cavity length and the radius of the beam opening are chosen to produce a maximum electric field of about 860 kV/cm in the output cavity. The penultimate cavity is formed as a double-gap structure where the maximum electric field is 730 kV/cm.

The deflection system consisting of a drive cavity, three passive cavities and a penultimate cavity is placed

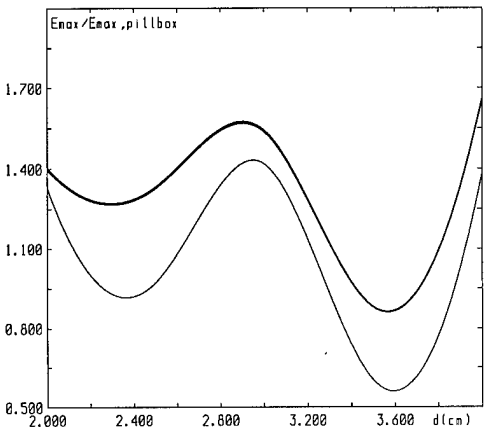



Fig.3. Dependence of surface electric field on cavity length. Beam opening radius of curvature r = 5.0 mm (upper curve) and r =3.0 mm (lower curve).

inside a superconducting solenoid providing a magnetic field of 13 kG (i.e.,$\Omega/\omega \approx 1.45$). The relativistic cyclotron frequency is denoted by W. All cavities of the deflection system are 1.3 cm long with a diameter of 3.2 cm. The penultimate cavity is made up of two such cavities. The diameter of all deflection cavity apertures is 0.5 cm except the output aperture of the penultimate cavity which has a diameter of 0.7 cm to match the aperture of the output cavity. The electrons exiting the penultimate cavity have a deflection angle of about 39 degrees. The deflection angle is further increased to about 50 degrees as the electrons pass through an uptapered magnetic field in the drift region between the penultimate and the output cavities. The output cavity (length = 3.5 cm, diameter = 1.75 cm) is placed inside the second part of the superconducting solenoid giving a magnetic field of 22 kG (i.e.,$\Omega_2/3\omega \approx 0.9$). Efficient interaction occurs when the cyclotron frequency is close the operating frequency. The applied magnetic fields in the deflection system and the output cavity are different, but there is no field reversal. The axial magnetic field profile is also shown in Fig. 1

The simulation results for the beam propagation during deflection and deceleration shown in Fig. 4 are based on the numerical code developed at INP, Novosibirisk. The physical and numerical models in the code are described in ref. [7]. The physical model considers finite transverse beam size, spatial distribution of dc magnetic fields, and actual rf fields of the cavities. The numerical model is based on macro particle method. The space charge effects and the finite beam emittance are neglected in the numerical code. The evolution of the

electron trajectories and the rf fields are done self-consistently. Both steady state and time dependent simulations were done. Steady state calculations are used

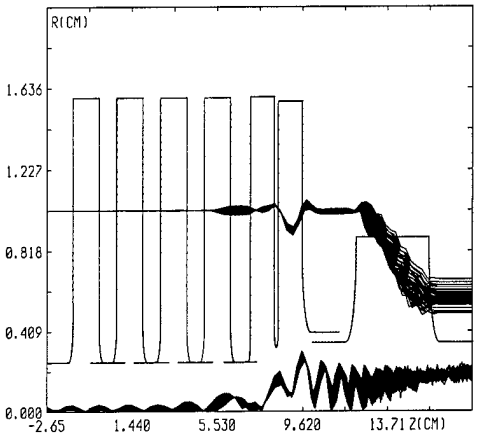



Fig. 4. Simulation results for 34.272 GHz magnicon. Shown is an outline of the RF cavities, energy and radial coordinates of beam electrons as functions of coordinate along the axis.

for magnicon optimization and stability analysis. The time dependent code is applied for investigation of transient processes. The results of the preliminary optimization are given in table I. The results in the table are obtained with an electron beam 0.8 mm in diameter and a cathode loading of 15 A/cm$^2$. The efficiency of a magnicon amplifier decreases with increase in the beam diameter. The calculated efficiency of the 3rd harmonic amplifier drops to 34% as the beam diameter is increased to 1.2 mm. The cathode loading for this beam is 6.7 A/cm$^2$ assuming the same beam area compression of 3000:1. The magnicon amplifier can be operated with a cathode loading lower than 10 A/cm$^2$ with only a moderate decrease in efficiency.

## III CONCLUSIONS

Design parameters have been obtained for a 34.272 GHz third harmonic magnicon amplifier for powering a 5 TeV c.m. energy electron-positron linear collider. The calculated efficiency is 42% with a peak power of 42 MW in a pulse of 1.5 μs duration. The drive frequency is 11.424 GHz and the gain is 51 dB. The design takes into consideration the limitations imposed by cathode loading, breakdown field and pulse heating of the conductive walls. The cavities have been carefully designed to avoid self excitation and spurious harmonics generation.

**Table I**

| | | |
|---|---|---|
| Operating frequency | 34.272 | Ghz |
| Output power | 42.0 | MW |
| Pulse duration | 1.5 | μs |
| Repetition rate | 10.0 | Hz |
| RF energy | 60.0 | J/pulse |
| Efficiency | 42.0 | % |
| Drive frequency | 11.424 | Ghz |
| Drive power | 300.0 | W |
| Gain | 51 | dB |
| Output cavity $E_{max}$ | 860 | kV/cm |
| Output cavity $E_{max}/H_{max}$ | 240 | Ohm |
| Temperature rise (Output cavity) | $120^0$ | C |
| Penultimate cavity $E_{max}$ | 730 | kV/cm |
| Penultimate cavity $E_{max}/H_{max}$ | 250 | Ohm |
| Temperature rise (Penultimate cavity) | $45^0$ | C |
| Beam voltage | 500.0 | kV |
| Beam current | 200.0 | A |
| Microperveance | 0.56 | |
| Beam diameter | 0.8 | mm |
| Cathode diameter | 4.4 | cm |
| Total Area compression | 3000 | |
| Electrostatic compression | 630 | |
| Maximum cathode loading | 15 | A/sq.cm |
| $E_{max}$ (focusing electrode) | 265 | kV/cm |
| Beam emittance (thermal) | π | mrad-cm |
| Beam emittance (geometric) | 0.15π | mrad-cm |

This research was supported by the Department of Energy, Division of High Energy Physics.

## REFERENCES

[1] P. B. Wilson, SLAC-Pub-7263, 1, 1996.

[2] P. B. Wilson, SLAC-Pub-7256, 1, 1996.

[3] M. I. Petelin, et al., Proc. 7th workshop on Advanced Accelerator Concepts, Lake Tahoe, 1996.

[4] O. A. Nezhevenko, IEEE Trans. Plasma Sci., vol. 22, 756, 1994.

[5] M. Cattelino and G. Miram, Tri-Service Cathode Life Test Facility Annual Report, Dec 1995.

[6] Y. V. Baryshev et al., Nuclear Instruments & Methods in Physics, vol. A 340, 241, 1994.

[7] V. Yakovlev, et al. , Proc. 1995 Particle Accelerator Conf., vol. 52, 1569, 1995.

# HIGH POWER 35GHz GYROKLYSTRON AMPLIFIERS

J. J. Choi, A. H. McCurdy§, F. Wood&, R. H. Kyser&, J. Calame, B. G. Danly, B. Levush, and R. K. Parker
Naval Research Laboratory, Code 6840, Washington, DC 20375
§USC, Los Angeles, CA 90089
&DynCorp, Rockville, MD 20850

*Abstract*

High power coherent radiation sources at 35GHz are attractive for high gradient, compact particle accelerators and next generation high resolution millimeter wave radar/communications. A multi-cavity gyroklystron amplifier is considered a promising candidate for high power millimeter wave generation. Experiments on two-cavity and three-cavity gyroklystron amplifiers are underway to demonstrate 140kW, 35GHz coherent radiation amplification. Initial experiments show an efficiency of 32%, a bandwidth of 0.4%, and a saturated gain of 22dB which corresponds to peak power of 130kW. Experimental results are moderately in agreement with large signal simulations. Calculations also show that a stagger tuned three cavity circuit increases the bandwidth to more than 0.7%.

## 1. TWO-CAVITY GYROKLYSTRON AMPLIFIER

### *1.1 Design and Experimental Arrangement*

35GHz gyroklystron amplifier experiments are currently underway to demonstrate peak radiation power of 140kW and bandwidth > 0.5%. An experimental layout is depicted in Figure 1. A high power electron beam is produced from magnetron-injection-gun (CPI) which is optimally designed for $TE_{01}$ cylindrical cavity mode coupling at fundamental beam cyclotron mode. The gyrating electron beam is adiabatically compressed through a high magnetic field of 13.2kG which is powered by a 14 coil superconducting magnet. An electron trajectory code, EGUN predicts an axial velocity spread of 10% at 60kV, 6.72A, and $\alpha$=1.5. A capacitive probe is placed directly before the input cavity to measure the beam velocity ratio.

The two-cavity gyroklystron amplifier is designed using large signal non-linear time-dependent gyroklystron codes [1] Cavity dimensions of input and output cavities and drift tube length are optimized for maximum efficiency at a beam axial velocity spread of 15%. For the two-cavity circuit, the resonant frequency of the input cavity is same as that of the output cavity. An operating cavity mode ($TE_{011}$) is chosen which has low ohmic power dissipation at high average power operation. All the tube components are relevant to 10% duty operation.

An input drive signal for beam modulation is injected through a coaxial coupler [2]. The TE01 mode purity is more than 99% in the central cavity. The coaxial input coupler is also attractive because of a single port excitation through a rectangular $TE_{10}$ mode. By the use of a 3-D finite element code, HFSS [3], the coaxial input coupler is designed and fabricated. Cold-test shows Q of 188 and resonant frequency of 34.89GHz.

The output cavity, as shown in Figure 1, has a small radial step to control cavity external Q and is followed by a non-linear uptaper section which guides the amplified $TE_{01}$ mode to 1.5" diameter circular waveguide with minimum mode conversion. The output cavity length (2.75$\lambda$) is optimized for maximum efficiency and gain while ensuring that the cavity is not self-oscillating. The non-linear uptaper has a Dolph-Chevychev profile [4] which has a minimum mode conversion to other $TE_{0n}$ modes. Calculation predicts less than -30dB mode conversion into a $TE_{02}$ mode.

A $TE_{01}$ output vacuum window is designed using HFSS. An 1.5" diameter, half-wavelength thick BeO window which is brazed directly into the conflat flange shows a good rf match better than -25dB over 3.7% bandwidth (34.3-35.6GHz). The measured data is in good agreement with the HFSS prediction. The input waveguide vacuum window is a pillbox window which is that used in CPI coupled cavity tubes.

Lossy ceramic rings (80% BeO, 20% SiC) with different radii are inserted in the drift tube between the input cavity and the output cavity in order to avoid oscillations. CASCADE code [1] predicts high attenuation (<-20dB) of $TE_{11}$ mode in the drift tube filled with the lossy ceramic rings. In addition, a beam tunnel between the input cavity and electron gun is filled with lossy ceramics. Ceramic thickness varies along the beam tunnel so that all the TE modes crossing a beam cyclotron line have a maximum attenuation. The clearance between the gyrating beam and the drift tube is designed at 30mils, which permits high average power operation of the amplifier. A water-cooled beam collector (1.5" diameter and 15" long) is made of copper for good heat conduction. With a careful magnetic field tapering, an average power density of the electron beam dissipated on the collector is estimated less than 0.5kW/cm$^2$ at 10% duty operation.

A high average power calorimeter is designed and fabricated to measure the gyroklystron output power. In order to have a good rf match, teflon with a 20 degree cone angle is chosen. Cold-test shows rf match better than -20dB over the entire operating frequency range. Two different power calibrations are performed; DC heater power and RF power driven by a conventional TWT and a high power EIO. The power calculations obtained from

0-7803-4376-X/98 /$10.00 © 1998 IEEE

the temperature difference between inlet and outlet thermistors submerged in octanol agree within ± 5% for both calibration methods.

A simple thin circular hole on the waveguide is used to sample rf signal for frequency measurement and monitoring rf pulse shapes.

*1.2 Experiment Results*

Typical experimental beam parameters are V=60kV, I=6.72A, $\alpha$=1.5, and B=13.2kG. Maximum power is obtained with -0.7% downtaper of the magnetic field in the output cavity region. Figure 2 shows a drive curve, efficiency as a function of input drive power at 34.942GHz. This result is compared with non-linear code simulations for various beam axial velocities. The maximum efficiency is measured at 32±2%, corresponding to amplified radiation power of 130kW. This is the highest power at 35GHz ever reported in US power tube amplifiers.

Instantaneous bandwidth is measured and compared with theory as shown in Figure 3. Although the peak efficiency is lower than the predicted value, the measured bandwidth of 0.4% agrees very well with simulations. The discrepancy between the experiments and theory is maybe due to the lack of self-consistent calculation of output cavity field when beam is present and improper modeling of a beam velocity distribution function. The present code assumes a flat-top velocity distribution. The beam loaded frequency upshift is also observed as shown in Figure 3. There is a 70MHz upshift (0.2%) with respect to the cold resonance frequency, which is in good agreement with code prediction.

Rf oscillations in the output cavity are observed when beam current exceeds a threshold current. Figure 4 shows start oscillation current as a function of magnetic field. Measured oscillation frequency is near 34.93GHz which indicates that the oscillation originates from a $TE_{011}$ cavity mode. Maximum efficiency is achieved just below the starting oscillation point which is in the region of negative beam loading in the cavity. It is also plotted with calculated starting oscillation curves for various beam $\alpha$ and spreads. From this comparison, beam $\alpha$ is estimated to be 1.5, which is consistent with the value obtained from EGUN code simulation.

MAGIC [5] is used to examine transient behavior of the two-cavity gyroklystron. As shown in Figure 5, when the phase of input drive frequency instantaneously changes by $\pi$, a 13nsec delay is observed in the output cavity. Further investigation will be performed with experiments.

## 2. THREE-CAVITY GYROKLYSTRON AMPLIFIER

In order to enhance gain and bandwidth, a stagger tuned three-cavity gyroklystron is designed using the non-linear codes and the stability code. The best design parameters are 30% efficiency, 35dB saturated gain and 0.7% bandwidth at $\Delta v_z/v_z$=15%, Q(1)=130, Q(2)=150, and Q(3)=175. The bandwidth increases nearly by a factor of 2 compared with that of the two-cavity gyroklystron. Further increase of gain and bandwidth is possible by adding more buncher cavities at the expense of lower efficiency.

## 3. ACKNOWLEDGMENTS

The work is supported by the Office of Naval Research. The authors would like to acknowledge technical and engineering support from G. Longrie, B. Myers, L. Malsawma, F. Robertson, and B. Sobocinski.

## REFERENCES

[1] P. Latham, W. Lawson, and V. Irwin, IEEE Trans. Plasma Sc. 22, p. 804, 1994.

[2] A. H. McCurdy, J. J. Choi, and W. Manheimer, Int. Conf. Plasma Sci., 1997

[3] HP High Frequency Structure Simulator, Version 4.01, Hewlett Packard Co. and Ansoft Co.

[4] W. G. Lawson, IEEE TRans. MTT, 38(11), pp.1617-1622, 1990.

[5] B. Goplen, L. Ludeking, D. Smithe, and G. Warren,, MAGIC User's Manual (MRC), Newington, VA, 1993.

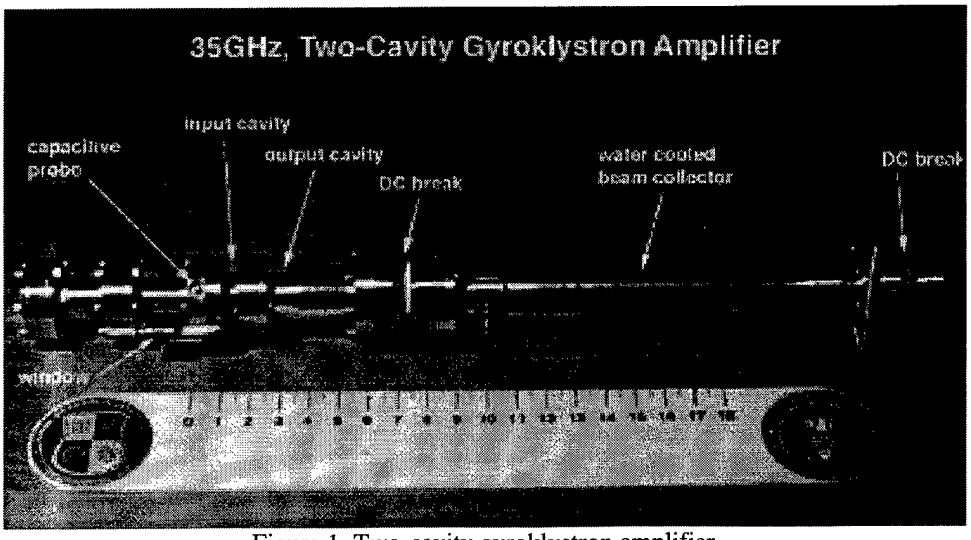



Figure 1. Two-cavity gyroklystron amplifier

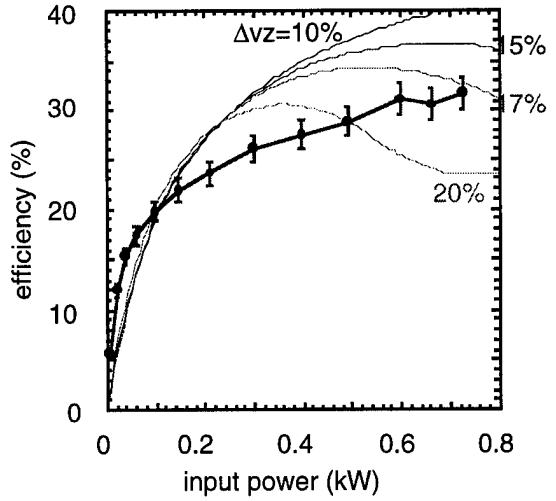



Figure 2. Experimental results on the drive curve. Simulation curves are Δvz=10%, 15%, 17%, and 20%.

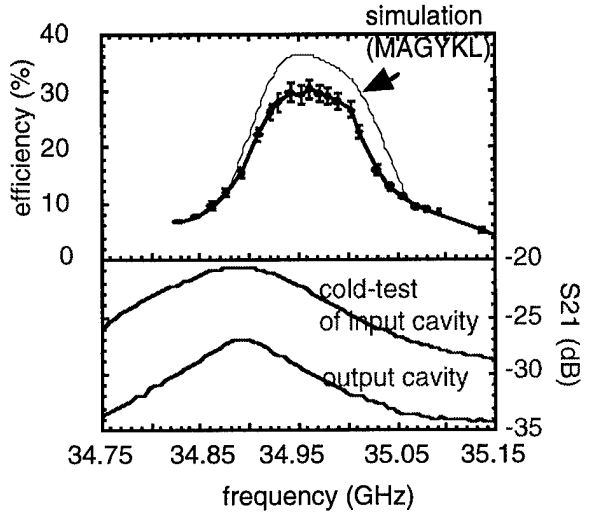



Figure 3. Large signal bandwidth

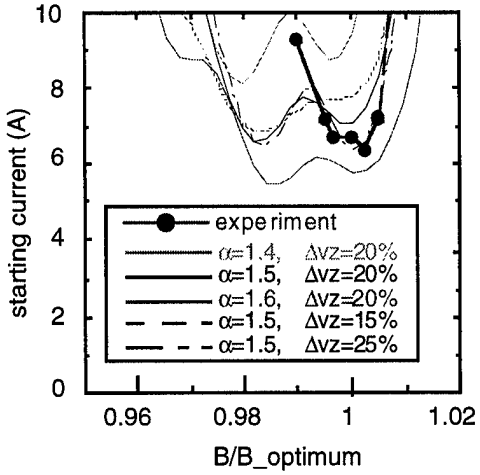



Figure 4. Start oscillation curve as a function of magnetic field detuning.

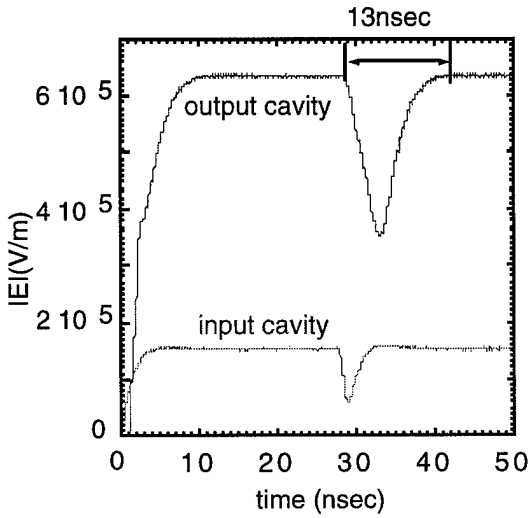



Figure 5. MAGIC simulations on the transient behavior of two-cavity gyroklystron. A phase shift by $\pi$ in the input drive signal is switched on at 28nsec.

# FEASIBILITY STUDY OF A HOM IOT FOR TESLA

P.Schütt, T. Weiland,
Technische Hochschule Darmstadt, FB 18, Schlossgartenstraße 8, D-64289 Darmstadt, Germany,
A. Gamp, Lu-Fuhai, DESY, Notkestraße 85, D-22603 Hamburg, Germany

*Abstract*

For the TESLA linear collider 1.3 GHz RF sources with 10 MW peak power and about 70% efficiency are needed. As an alternative to the development of a Multibeam-Klystron, we investigate the feasibility of an IOT (Inductive Output Tube). This is a very compact RF source: The time structure of the beam is produced by a gated emission cathode and the output cavity is directly adjacent to the anode. Unlike IOTs, conventional klystrons lose some of their design efficiency when they are operated below saturation, because only the RF component of the beam is reduced and not the DC beam current. In contrast to this the cathode current of an IOT is controlled by the drive power. In order to keep the gun voltage low, we plan to investigate a device with a hollow beam where the output cavity is excited in a higher order mode (HOM), as was recently suggested by CPI[1].

Computer simulations are carried out with the CAD-system MAFIA. First, an existing Klystrode$^{TM}$ IOT built by CPI is analysed. Simulation results will be shown and compared to experimental data. Based upon this experience, a design strategy is discussed for the HOM IOT.

## 1 INTRODUCTION

The "TeV Superconducting Linear Accelerator" (TESLA) requires 1.3 ms long RF pulses at the operating frequency 1.3 GHz. The state of the art of klystrons for such long pulses is represented by the TH 2104 Diode-Klystron built by Thomson which can deliver up to 5 MW RF pulses of 2 ms length at a rep. rate of 10 Hz. The efficiency is 45 %, the gun voltage 130 kV.

In view of the estimated 30 MW average RF power consumption of the linear collider efficiency is a major issue. A contract with industry has been signed for the development of an 1.3 GHz 10 MW multibeam klystron with 1.7 ms pulse length and an efficiency of more than 70 %. But even if this challenging goal is reached, the efficiency will be decreased in practical use, since for the operation of the linac, a variation of the output power of at least 10 % must be possible. But reducing the RF drive power has no influence on the average dc electron beam current and hence more energy is wasted in the collector.

In the medium power UHF regime, a new design of RF sources has been successfull which overcomes this drawback. The goal of our investigations is to analyse whether this IOT concept can be applied to the high power L-Band requirements of TESLA.

### *1.1 The IOT (Inductive Output Tube)*

IOT's have been used successfully for more than 10 years for TV service at operating frequencies in the UHF regime [2]. The operating principle is briefly described in this section (see Figure 1). The basic components are:

- a gated-emission gun
- a resonator (output cavity)
- and a collector for the spent beam

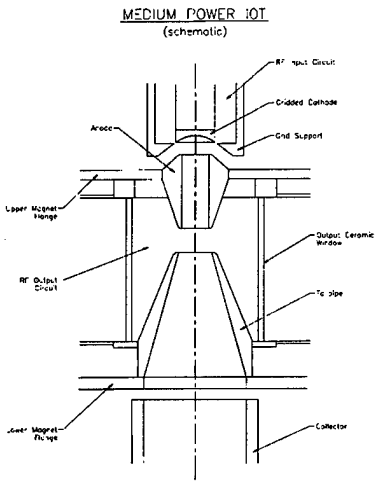



Figure 1: Schematic view of a medium power IOT.

The gun consists of a spherical cathode and a closely spaced spherical grid. The grid support together with the cathode forms a resonant coaxial input cavity which can be used to generate RF voltage at the operating frequency between grid and cathode. A DC bias voltage on the grid shuts off the electrons between bunches and controls the bunch length. The bunched electrons are then accelerated in the anode potential. As they traverse the output resonator gap, they excite the resonator RF and lose energy. The spent beam then enters the collector where the remaining kinetic energy is converted to thermal energy in the collector walls.

Thus, the main advantages as compared to a klystron are

- The beam current is a function of the RF drive. Therefore only as much beam current is produced as is needed to reach the desired output power.
- Since the beam is already bunched at the cathode, the overall design can be very compact.
- Magnetic field requirements are lower, since the beam only travels a short distance.

A disadvantage of the IOT is the relatively low gain of less than 30 dB.

0-7803-4376-X/98/$10.00 © 1998 IEEE

### 1.2 *The HOM IOT*

The IOT concept cannot simply be upgraded to TESLA requirements by adjusting the frequency and increasing beam current and gun voltage. Limiting factors are

- breakdown of the gun voltage
- space charge density
- emission density at the cathode
- power density in the output cavity
- thermal stress in the collector

Thus we investigate an IOT with a hollow beam that does not excite the fundamental but a higher order mode (HOM) in the output cavity[3, 1].

### 1.3 *Design Tools*

Existing design tools including fast-running, one-dimensional optimizing codes, cannot simply be employed to study the HOM IOT. Although they are well tested for existing IOTs, they are based on approximations which are valid only near the beam axis for solid beams.

We plan to use the MAFIA[4, 5] package for our analysis. This package offers modules for the RF investigation of the resonant cavities as well as PIC modules for the self-consistent calculation of the electron motion. It has been used successfully for klystron design[6] before.

## 2 SIMULATION

In a first step, we used MAFIA to analyse an existing medium power Klystrode$^{TM}$ IOT. The working frequency for the analysis was chosen to be 700 MHz, the design output power is 60 kW.

### 2.1 *Parameters and Assumptions*

The whole device is rotationally symmetric and can be simulated in $rz$-Geometry. In practice, the RF power is extracted through a cavity coupling loop. In order to maintain the rotational symmetry, this was replaced by a layer of lossy material at the outer boundary of the cavity. The geometry of the cavity and material constants of this artificial load were chosen such that the impedance $R$ and the quality factor $Q$ correspond to experimental data: $R$=12.8 k$\Omega$, $R/Q$=95.4$\Omega$, $Q$=134.

For the HOM IOT, the output cavity will be designed using 3D resonator codes which include waveguide boundaries to simulate the RF extraction. 2D resonator as well as time domain codes will be used to investigate the input circuit and determine the bunch shape.

For the analysis of the existing IOT, we assumed that the gridded gun workes perfectly and yields a bunched electron beam with the time structure shown in figure 2. The gun voltage was 32 kV and the corresponding electrostatic field was also calculated in MAFIA. Whereas for a beam current of 1 A no magnetic field is necessary to focus the beam, for higher currents we assumed a solenoid field of 250 Gauss between the flanges and less than 15 Gauss at the cathode surface.

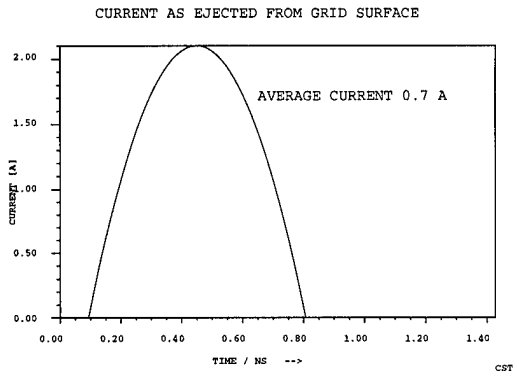



Figure 2: Time structure of the current. This pattern repeats every 1.43 ns.

### 2.2 *Typical Results*

Some simulation results are shown in figures 3 and 4.

Due to the high quality factor $Q$=134 of the output cavity the time to reach the steady state of the excitated mode amounts to a few hundred RF-periods. It is not possible to simulate the complete build-up process until the system reaches steady state, because it would take too much CPU-time and noise would increase to intolarable values. The port approximation[7] cannot be used for the HOM case. Therefore we calculate the mode pattern and preload the cavity with the excited mode. A good guess for the amplitude and phase can be drawn from a simulation of the first 20 RF-periods of the build-up process.

In steady state, the RF output power is replaced by the beam in every period. The rest energy of the beam is dissipated in the collector walls a few periods later. Thus, steady state can be identified through the fact, that the average beam energy loss is equal to the RF power loss in the artificial load. The efficiency is determined in different ways which agree only in steady state (see table 1).

| Initial RF power | Efficiency calculated from RF cavity field | dissipated power |
|---|---|---|
| 32.5 kW | 51.4 % | 55.6 % |
| 40.0 kW | 57.3 % | 57.9 % |
| 42.0 kW | 57.3 % | 56.4 % |

Table 1: Identification of steady state. Average beam current 2 A, bunch length 180°. The efficiency in steady state is 57.3 %.

For three different cases, we compared our results for the efficiency with the results of a simple one-dimensional program which usually yields good results for medium power IOT's but cannot be extended for the calculation of the HOM IOT (see table 2).

Both calculations show that the efficiency $\eta$ increases for higher output power even for gap voltages well above the

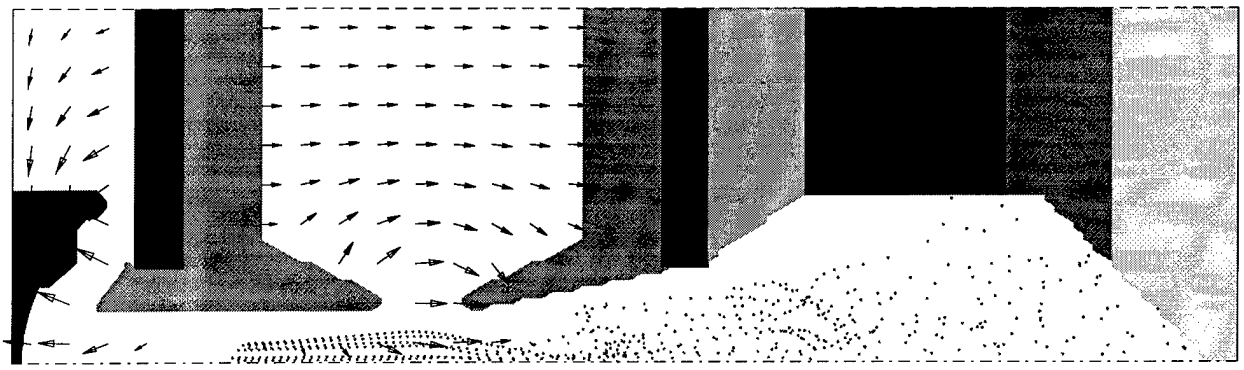


Figure 3: Typical simulation output. Electrons move from left to right. They are emitted from the surface of the grid and accelerated in a static electric field. Passing the output cavity, electron bunches excite an RF field. The spent beam is dumped into the collector.

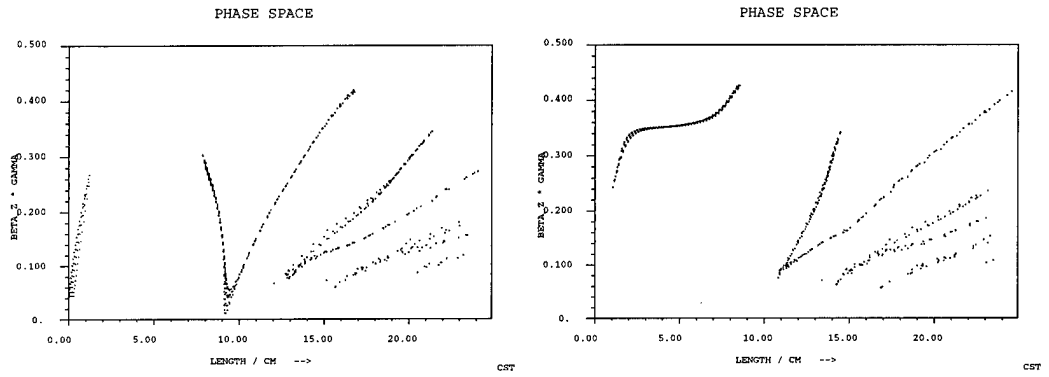



Figure 4: The momentum $\beta_z * \gamma$ is plotted against the longitudinal position for $t = t_0$, and $t = t_0 + T/2$ . The average beam current is $I_{ave}$ =2.93 A, the gap voltage is $V_{gap}$ =40.8 kV.

| | Reference results | | | MAFIA results | | |
|---|---|---|---|---|---|---|
| $I_{ave}$ [A] | 2.93 | 2.03 | 1.10 | 2.93 | 2.03 | 1.10 |
| $I_{max}$ [A] | 11.36 | 7.89 | 4.32 | 8.79 | 6.09 | 3.30 |
| $P_{out}$ [kW] | 61.0 | 29.7 | 8.7 | 65.0 | 36.7 | 11.1 |
| $\eta$ [%] | 64.9 | 45.7 | 24.8 | 69.3 | 56.5 | 31.5 |
| $\hat{V}_{gap}$ [kV] | 37.0 | 25.6 | 13.9 | 40.8 | 30.7 | 16.9 |

Table 2: Comparison of Results to a Reference Calculation

gun voltage $V_{gun}$ =32 kV. Figure 4 shows that even for this case no particles move back to the gun region.

MAFIA yields higher absolute values for the efficiency because of the higher harmonic content of the simplified bunch shape used (see figure 2). We expect lower values for $\eta$ when the realistic bunch shape is considered.

## 3 ACKNOWLEDGEMENTS

We gratefully acknowledge fruitful discussions of our results with Heinz Bohlen (CPI) who provided us with technical data of the medium power IOT and the reference calculation.

## 4 REFERENCES

[1] E.Lien, H.Bohlen, US Patent Application Serial No. 08/413,034

[2] D.H. Preist, M.B. Shrader, *The Klystrode$^{TM}$ — An unusual transmitting tube with potential for UHF-TV* Proc. IEEE 70 (1982)

[3] H. Bohlen, F. Friedlander, E. Lien *HOM-Klystrons, a possible "low-voltage" solution for high-power pulse applications* contrib. RF 96, Shonan Village, Japan, April 1996

[4] T. Weiland, *On the Numerical Solution of Maxwell's Equations and Applications in the Field of Accelerator Physics*, Particle Accelerators, 1984, Vol. 15, S. 245-292

[5] The MAFIA collaboration, *User's Guide MAFIA Version 4.00*, CST GmbH, Lauteschlägerstr. 8, D-64289 Darmstadt, Germany

[6] U. Becker, M. Dohlus, S. Lütgert, D. Sprehn, T. Weiland *Comparison of CONDOR, FCI, and MAFIA Calculations for a 150 MW S-Band Klystron with Measurements*, Proc. of the PAC'95, Dallas, Vol. 4, p. 2190-2192

[7] U. Becker, M. Dohlus, T. Weiland *Three Dimensional Klystron Simulation*, Particle Accelerators, 1995, Vol. 51, pp. 135-154

# OPERATING EXPERIENCE AND RELIABILITY IMPROVEMENTS ON THE 5 KW CW KLYSTRON AT JEFFERSON LAB

R. Nelson, S. Holben, Thomas Jefferson National Accelerator Facility, 12000 Jefferson Avenue, Newport News VA USA 23606

*Abstract*

With substantial operating hours on the RF system, considerable information on reliability of the 5 kW CW klystrons has been obtained. High early failure rates led to examination of the operating conditions and failure modes. Internal ceramic contamination caused premature failure of gun potting material and ultimate tube demise through arcing or ceramic fracture. A planned course of repotting and reconditioning of approximately 300 klystrons, plus careful attention to operating conditions and periodic analysis of operational data, has substantially reduced the failure rate. It is anticipated that implementation of planned supplemental monitoring systems for the klystrons will allow most catastrophic failures to be avoided. By predicting end of life, tubes can be changed out before they fail, thus minimizing unplanned downtime. Initial tests have also been conducted on this same klystron operated at higher voltages with resultant higher output power. The outcome of these tests will provide information to be considered for future upgrades to the accelerator.

## 1 BACKGROUND

### *1.1 Number & Type*

An original purchase of 350 klystrons was made over a three year period.

| | | |
|---|---|---|
| Beam voltage | 11.6 | kV |
| Beam current | 1.3 | Amps |
| $P_{out}$ | 5 | kW |
| $P_{in}$ | 2 | watts (max) |
| Frequency | 1497 | MHz |
| Bandwidth | 6 | MHz |
| Heater voltage | 7.3 | Volts dc |
| Heater current | 4.3 | Amps (typ.) |
| Magnetics | PM | |
| Cooling | water (LCW) | 35° C |

Table 1 - Varian VKL8711W Parameters [1]

The contract was awarded to a single vendor, Varian Associates (now Communications & Power Industries - CPI).

## 2 KLYSTRON FAILURES

### *2.1 Failure Rates*

As could be expected, klystrons failed. To date, some 83 have died. As tubes failed, the few spares originally purchased dwindled and additional tubes were purchased to supplement the 350 originals. Concurrent with the purchase of spares, a vendor was also selected to repair and rebuild the failed klystrons. Both contracts were the result of a competitive bid process. New tubes would be supplied by Litton Electron Devices, while a startup company, Pendulum Electromagnetics (PendEl) in Raleigh NC, would handle all the repairs and rebuilding.

The spec requested tubes with at least 20-25k hours life. Overall, even with a high number of early failures, the MTBF was around 22k hours by 1994. Currently, the hours/failures ratio shows about 90K hours of filament operation and 67k hours of HV operation average. None of the failures so far has been from normal wear out, that is, cathode depletion. Instead, catastrophic failures have ranged from open heaters to external arcing.

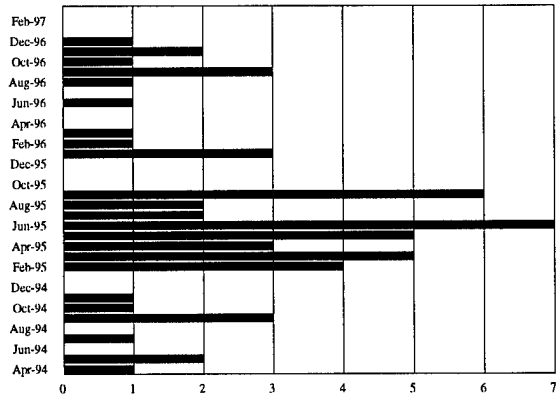



Figure 1 - Klystron Failures by Month

The high voltage power supplies each feed eight klystrons and did not arrive with a crowbar. A crowbar was later added but is not used because of nuisance trips and other issues. Though the power supply turned off when a tube arced, operators usually made several attempts to restart the zone before technicians were called. By that time, if the tube had arced, there was a

0-7803-4376-X/98 /$10.00 © 1998 IEEE

substantial track across the ceramic and the tube would be dead.

Partly because full RF power wouldn't be required for awhile, and partly to try and reduce the rising rate of failures, the klystron's operating voltage was lowered. This seemed to give some relief for a time, but failures continued.

### 2.2 *Failure Modes*

The largest number of failures were the result of *external* arcs across the ceramic of the gun assembly. The gun assembly is potted with a silicone RTV to prevent problems with dust and humidity. In many cases, the RTV closest to the gun reverted to either a thick soup of silicone oil and solids or a dry and crumbling material. While the RTV was rated at 250 °C [2] and measured surface temperatures according to data provided were well below that point, silicone supplier GE Silicone felt the material was being exposed to temperatures too high.



Figure 2 - Gun assembly showing degraded potting

Besides obvious interruptions to machine operation, most of the failures also made repairs more difficult since tubes typically went to air with resultant internal contamination from silicone oil being sucked in. If catastrophic failures couldn't be prevented completely, it seemed prudent to try and remove suspect tubes from service before they took the machine down.

### 2.3 *Locating the Bad Actors*

We felt that the decay of the RTV was contributing to the arcing across the ceramic so methods of determining the condition of the potting were examined.

The RTV should have a good bond to the ceramic and metal and be free from voids, so all potting was checked for voids using ultrasound measuring techniques. When a tube failed, the test results of the ultrasound were checked. There didn't seem to be any obvious correlation between the test results and tube failure.

A second *tactile* test was also used, wherein the potting was squeezed and twisted lightly to determine whether it was still solid and well attached. This picked up on some bad RTV but once again didn't reliably allow us to spot potential candidates for failure.

### 2.4 *Repotting*

Recognizing that we couldn't consistently spot bad potting or predict failures, a decision was made to repot all the tubes in the machine. This time the RTV was Stycast 5952 from Emerson & Cuming., a product with higher thermal conductivity [3] and one that didn't require stage curing.

Tubes were swapped out with spares and those tubes were then repotted. The old RTV had to be removed first. In many cases it turned out to be still perfectly intact, in which case it was difficult to remove. The material was cut, pried , scraped, and wiped off, and then abrasive blasted with aluminum oxide and liquid washed to insure clean surfaces. New leads were attached and a primer coat was applied to help the RTV bond. A three piece clamshell mold was placed over the gun assembly, the RTV mixed, de-aired, poured, and cured with the aid of a heat tape wrapped around the mold. After the mold was removed the leads were cut and terminated and the tube put on the test stand for a full battery of tests. The results of these tests have been put in a database to allow comparison, both among the group, and against itself in the future if it is retested.

### 2.5 *A Different Failure*

Failures continued among tubes with original potting, and eventually, one of the repotted tubes failed. The gun ceramic fractured and took the tube up to air. This time the potting closest to the ceramic appeared dry, gritty and hard. A potting sample submitted to Emerson & Cuming came back with a suggestion that the apparent reason for failure was high temperature. So we looked for other heat sources.

Hipotting the tubes had shown that some tubes had a voltage at which the tube didn't break down completely, but where leakage current started to climb rapidly. These breakpoints, or knees, were determined to be related to field emission. Internal ceramic contamination caused a different, more linear resistance. Again, hipotting didn't reliably predict life or death for all tubes, but it was a good indicator for certain problems. Also, hipotting was done on a cold tube and couldn't be continuously monitored.

## 3 HEAT SOURCES

### 3.1 *Mod Anode Intercept*

Measuring operating temperatures on a potted and operating gun was difficult because of the high voltage on the gun. Thermocouples placed in the potting had measured temperatures with only heater power applied, and those temperatures were satisfactory. We presently monitored and could log, cathode and body currents, but

not mod anode current. As a test, a metering panel was assembled on a clear acrylic panel and mounted in spare rack space on the HPA. As predicted, we found that a few tubes had higher than normal mod anode current.

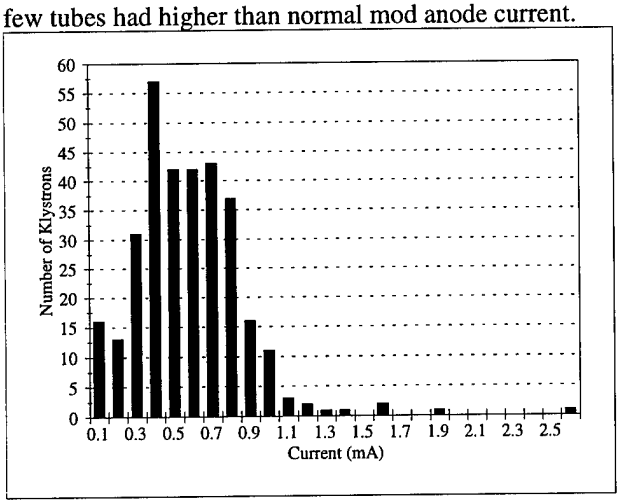



Figure 3 - Mod Anode Current Distribution

Original specs required mod anode intercept to be < 1% of beam current, which equated to <13 mA. Assuming that most of the current intercepted by the modulating anode was dissipated by the metal and ceramic through the potting material, we simulated additional heat on our thermocouple equipped tube by increasing heater power. The temperature reached 250 °C with another 30 watts input. So while 12 mA of intercept would fall within the specs, it would also generate 139 watts of heat. The gun would fracture well before that point. In fact, at least three tubes have suffered that fate, so it's convincing that excessive mod anode current was probably a major contributor to potting failures.

### *3.2 Controlling Mod Anode Current*

We had lowered the cathode voltage but kept the heater setting at the nameplate value. Running a curve of cathode emission vs. filament voltage, we found that most tubes would operate satisfactorily with about 75% of the rated voltage. Running cathodes hot had resulted in excessive barium boil off and internal contamination. Since resetting individual filament voltages based on emission curves, the failure rate has dropped noticeably.

Even though heater power was lowered, those tubes with high mod anode current and a sharp breakdown knee still had problems. We found that the knee could, in most cases, be raised beyond our operating voltage and the tube recovered. Reconditioning was accomplished either with multiple hits from a capacitor discharge setup or by slowly raising cathode voltage while insuring mod anode current didn't exceed about 2.5 mA.

Because mod anode current was found to be a critical measure of the tube's health and an indicator of impending failure, permanent monitoring has been installed on all klystron positions. This parameter is now remotely monitored, and can be logged or trip the power supply if a preset threshold is exceeded.

## 4 MORE RF POWER

### *4.1 The Future*

While present RF capacity may accommodate a machine upgrade to 6 GeV, more power will be required to reach 8 GeV. A Free Electron Laser project (FEL) presently in the construction phase also requires higher RF power for its superconducting cavities.

### *4.2 Options*

Three options for generating more RF power include replacing the present klystrons and their power supplies, replacing the current klystron with a higher efficiency unit and possibly retaining the existing power supplies, and operating the present klystrons at higher voltage by replacing the present power supplies. The latter will be used to meet short term FEL requirements.

### *4.3 5 kW Klystrons Running at 8 kW*

Increasing the cathode voltage to 14 kV scales the output power to 8 kW. DC input power rises a similar percentage so cooling is increased to maintain tube temperatures at approximately the same point.

Some of our present tubes have been run at various voltages from the nominal 11.6 kV up to 14 kV. The original Varian tube had a robust collector. With increased cooling it has easily accommodated the 60% additional beam power. The primary concerns dealt with body and mod anode currents. Body current can be tweaked if necessary by placement of magnetic shunts inside the bowl magnets.

Tubes from all three sources, Varian, Litton and PendEl have been run at 14 kV and delivered 8 kW. It should be noted, though, that some will require conditioning to run reliably at 14 kV. Some, with excessive leakage due to barium deposits on the ceramic, may not be suitable for 8 kW service at all.

## 5 ACKNOWLEDGMENTS

This work was supported by the U.S. DOE under contract number DE-AC05-84ER40150.

## REFERENCES

[1] CEBAF Specification EE0043
[2] `GE Silicone RTV-31 Data Sheet', GE Silicones
[3] `Technical Data Sheet, Stycast 5952', document number 2M793C-J107, Emerson & Cuming

# INITIAL OPERATION OF THE MARYLAND COAXIAL GYROKLYSTRON EXPERIMENT

W. Lawson, M. Castle, J. Cheng, B. Hogan, G. P. Saraph, V. L. Granatstein, and M. Reiser,
Electrical Engineering Department and Institute for Plasma Research University of Maryland
College Park, MD 20742 USA.

*Abstract*

We describe results from the initial operation of our coaxial gyroklystron experiment, which is being evaluated as a potential driver for future linear colliders. The interaction is designed to occur between a 500 kV, 500 - 700 A beam and a series of coaxial $TE_{0n1}$ microwave cavities. Output powers in excess of 100 MW at 8.568 GHz are expected with an efficiency of about 40% [1]. We detail performance of our single anode magnetron injection gun in addition to the stability and amplification properties of our preliminary microwave circuit. We also discuss our designs of near-term future tubes which are expected to have comparable performance at 17.136 GHz.

## 1 INTRODUCTION

At the University of Maryland, we have been running a comprehensive program to study the suitability of gyroklystrons as drivers for linear collider applications [1]. We have previously reported a variety of experimental results, all of which were achieved on a test bed which produced a small-orbit beam with a nominal voltage and current of 450 kV and 200 A, respectively. Published accounts of our effort include an amplified power level of 27 MW at 32% efficiency in a three-cavity first harmonic gyroklystron near 10 GHz [2] and 32 MW at 29% efficiency in a two-cavity second harmonic gyroklystron near 20 GHz [3].

In this paper we present the design details of two coaxial gyroklystron tubes which are predicted to produce at least 100 MW of output power with an efficiency of nearly 40%. These tubes utilize a fundamental mode $TE_{011}$ input cavity which is driven by a 150 kW magnetron at 8.568 GHz. The first tube also has an 8.568 GHz $TE_{011}$ output cavity, whereas the second tube has 17.136 GHz $TE_{021}$ buncher and output cavities. We present details of all system aspects, including the test bed modifications required to produce the enhanced beam characteristics, simulated beam properties, and simulated circuit interactions. Cold and hot test results of the first experimental tube are discussed before the project status and a description of our future plans are summarized.

## 2 TEST BED MODIFICATIONS

We have just completed an upgrade of our facility which should enable us to produce amplified microwave powers in excess of 100 MW (see Fig. 1). Our modulator voltage and current have been increased to 500 kV and 800 A, respectively. We have designed, installed, and completed acceptance testing of a single-anode Magnetron Injection Gun (MIG) which is capable of producing a 480 - 720 A rotating electron beam at the nominal beam voltage with an axial velocity spread less than 7%. The simulated space-charge-limited perveance of 5.5 μP was in good agreement with the measured result. The maximum current produced in the acceptance test was limited by our modulator (due to an applied voltage which was lower than the nominal operating voltage) to 670 A.

The original water-cooled magnets have been used, but a larger power supply for the gun coil was required because of a decrease in the magnetic compression. We reduced our drive frequency from 10 GHz to exactly three times the current SLAC frequency, so a new coaxial magnetron and a modified input waveguide were required. The output waveguide (uptapers, beam dump,

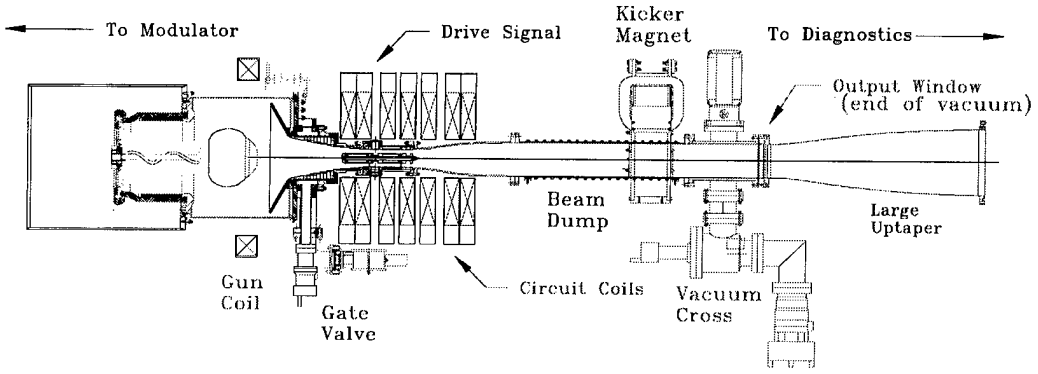



Fig. 1. The gyroklystron test bed.

0-7803-4376-X/98/$10.00 © 1998 IEEE

window, kicker magnet, pumping cross) was totally rebuilt to accommodate the expected larger peak powers. The anechoic chamber was modified to accommodate the new output waveguide and the directional coupler diagnostic was completely redesigned.

## 3 THEORETICAL CIRCUIT PERFORMANCE

A detailed design analysis has been carried out on a number of coaxial, two- and three-cavity gyroklystron systems with the aid of our partially self-consistent nonlinear code. The input cavity in all tubes is in resonance with the signal frequency at 8.568 GHz and the output cavity is resonant with either the first (8.568 GHz) or the second harmonic (17.136 GHz) frequency. In a three-cavity system, an additional buncher cavity is introduced which is resonant at either the first or second harmonic frequency. In the following sections, we describe only the first harmonic tube which has been hot-tested and the second harmonic tube which is scheduled to undergo hot testing in the near future.

### *3.1 Two-Cavity First Harmonic Tube*

The first harmonic tube consists of an input cavity and an output cavity separated by a drift section. The input cavity is defined by a decrease in the inner conductor radius only and the quality factor is brought down to Q ≈ 70 by loading the cavity with a thin ring of carbonized aluminum-silicate placed at one end of the cavity. The inner radius is 1.05 cm and the length is 2.29 cm. Power is injected through two radial coupling ports which are separated by 180° and excited in phase. Our start-oscillation code predicts that the input cavity is completely stable up to a current of 800 A.

The drift section has inner and outer radii of 1.825 cm and 3.325 cm, respectively. The inner conductor is required so that the drift tube is cutoff to the operating mode. The regions adjacent to each cavity are made of copper, but lossy ceramics line the majority of the drift tube to eliminate spurious modes. The total length of the drift region is 9.1 cm. Lossy ceramics are also used in the downtaper between the gun and the input cavity.

The output cavity is defined by changes in both radii and has a length of 1.70 cm. Power is extracted axially into the output waveguide via a coupling aperture. The aperture has the same radii as the drift tube and has a length of 0.9 cm. The diffractive quality factor is about 122. The start-oscillation code also predicts the output cavity to be stable at the nominal current, which is given in the middle column of Table 1 along with the other operating parameters. The efficiency is nearly 40% and the output power is about 95 MW. The dependence of tube efficiency on axial velocity spread is plotted in Fig. 2 with the solid line. The simulated velocity spread of the electron gun is 6.4 % at the nominal current. The curve shows a slow but steady decrease in efficiency with increasing spread and indicates that an efficiency of 37% is still possible if the spread is as high as 10%. A simplified schematic of the tube dimensions along with the optimal axial magnetic field profile is indicated in Fig. 3.

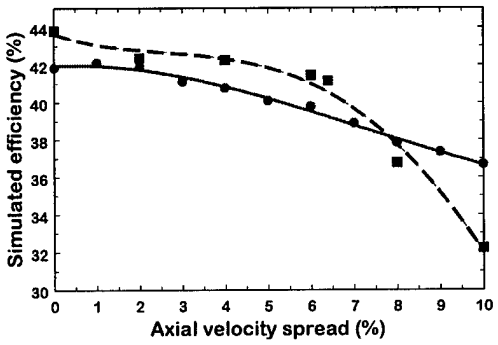



Fig. 2. Efficiency of the first (solid line) and second harmonic (dashed line) tubes vs. velocity spread.

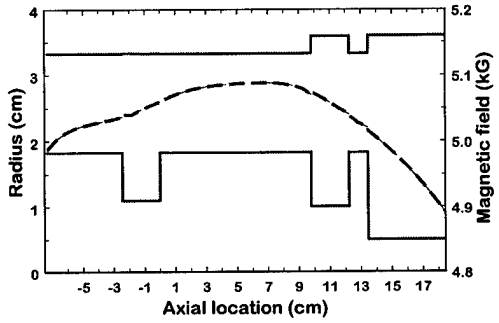



Fig. 3. The first-harmonic two-cavity tube and the optimal magnetic field profile.

### *3.2 Three-Cavity Second Harmonic Tube*

The second harmonic design which we intend to test is a three-cavity system. The buncher cavity operates at the second harmonic and is formed with non-adiabatic radial wall transitions. Mode conversion from the $TE_{02}$ mode to the $TE_{01}$ is estimated to be about -40 dB. Dielectric loading of the cavity is used in order to obtain a Q of 389 and is achieved by reducing the thickness of the copper sections that separate the cavity from the drift tube dielectrics. The linear start oscillation code indicates that the buncher cavity is stable to beam currents below about 1000 A at the design value of the magnetic field ($B_0$ = 4.81 kG). The output cavity is also designed with non-adiabatic radial wall transitions. The scattering matrix code estimates the purity of the $TE_{02}$ operation in the output cavity to be 97%. The ratio of the power flowing

into the drift tube to the power flowing into the output waveguide is better than -24 dB. Furthermore, the lossy dielectric loading in the drift tube, which will have a minimum effect on the Q-value of the operating mode, will suppress the excitation of the spurious modes and reduce the cross-talk.

**TABLE 1.** Comparison of the 1st and 2nd harmonic designs.

| Parameters | 1st harmonic | 2nd harmonic |
|---|---|---|
| Voltage | 500 kV | 500 kV |
| Current | 480 A | 770 A |
| Velocity ratio | 1.508 | 1.508 |
| Input Cavity Q | 50 | 50 |
| Buncher Cavity Q | - | 389 |
| Output Cavity Q | 122 | 320 |
| Gain | 21 dB | 49 dB |
| Efficiency | 39.4% | 41.1 % |
| Output Power | 94.6 MW | 158.2 MW |

The simulated results at the nominal operating point are indicated in the final column of Table 1. The optimal current according to the simulations is 770 A and the estimated peak output power is over 150 MW. The corresponding gain and efficiency are 49 dB and 41%, respectively. The dependence of efficiency on velocity spread is shown as the dashed line in Fig. 2. Note that the efficiency begins to drop off fairly rapidly for spreads above 7%. However, these simulations are not re-optimized with respect to magnetic field profile, etc., at each point, and additional investigations indicate that higher efficiencies can be achieved if the velocity spread is higher than expected.

## 4 COLD AND HOT TEST RESULTS

The construction, cold testing, and hot testing of the first experimental tube has been completed. Cold-testing yielded the final dimensions of the input cavity required to achieve the frequency of 8.568 GHz and a quality factor of 70. They are quite near the theoretical estimates given in the previous section. Cold-test drift tube attenuation measurements have indicated adequate isolation. The results for the output cavity were also quite close to the predicted values.

The performance of the microwave amplification experiment was limited by an input power coupling problem that developed after the tube was installed on the test bed. The net result was that we were only able to inject about 5 kW of power into the input cavity. The two cavity system had a predicted gain slightly above 20 dB, so the tube was severly gain limited. The best amplification results yielded a peak power of about 600 kW with a pulse width of over 1.5 μs at a beam voltage of 270 kV and a current of 290 A. The performance at this reduced operating point was consistant with our simulations. While some instabilities were observed in the output waveguide, performance of the tube at these beam parameters was not limited by spurious modes.

## 5 PROJECT STATUS AND FUTURE PLANS

We have nearly completed a rebuild of the first harmonic tube which incorporates two major changes. First we have added a third port on the vacuum jacket at the input cavity so that we can use transmission measurements to characterize the input cavity parameters in situ. Second have have lenghtened the overall system in order to add a buncher cavity so that the tube should not be gain limited. The buncher cavity is nearly identical in shape to the drive cavity and has the same resonant frequency and Q. We expect this tube to go on-line early in June 1997.

We continue to work on improving our simulation capabilities. Time-dependent capability has been added to our nonlinear (single-mode) code by researchers from the Naval Research Laboratory and initial results have confirmed the steady-state code predictions. We hope in the future to add multi-mode capability to our time dependent code.

We are also looking at advanced cavity concepts for future tubes. For the input cavity, we are using the High Frequency Structure Simulator code HFSS to simulate a single waveguide injection scheme which couples to the input cavity via an outer coaxial cavity. Furthermore, we are investigating an output cavity which couples through the inner radial wall to a circular waveguide, thereby decoupling the microwaves and the beam beyond the output cavity and enabling the use of additional tube stabilization schemes. Preliminary HFSS simulations of this output cavity scheme have been successful. Both concepts promise to improve performance of the gyroklystron tubes beyond the current predictions.

Finally, we are beginning to look at the application of gyroklystron circuits to Ka-band and beyond.

## 6 ACKNOWLEDGEMENTS

This work was supported by the Department of Energy.

## REFERENCES

[1] Granatstein, V. L. and W. Lawson, "Gyro-Amplifiers as Candidate RF Drivers for TeV Linear Colliders," *IEEE Trans. Plasma Sci.* **24**, 648 - 665 (1996).

[2] Tantawi, S., W. Main, P. E. Latham, G. Nusinovich, W. Lawson, C. D. Striffler, and V. L. Granatstein, "High Power X-Band Amplification from an Overmoded Three-Cavity Gyroklystron with a Tunable Penultimate Cavity," *IEEE Trans. Plasma Sci.* **20,** 205 - 215 (1992).

[3] Matthews, H. W., W. Lawson, J. P. Calame, M. K. E. Flaherty, B. Hogan, J. Cheng, and P. E. Latham, "Experimental Studies of Stability and Amplification in a Two-Cavity Second Harmonic Gyroklystron," *IEEE Trans. Plasma Sci.* **22,** 825 - 833 (1994).

# HIGH POWER 20 GHz RF SOURCE BASED ON SEVENTH HARMONIC CO-GENERATION*

Changbiao Wang[1], J. L. Hirshfield[1,2], and A. K. Ganguly[2]
[1]Physics Department, Yale University, New Haven, Connecticut 06520-1820
[2]Omega-P, Inc., 202008 Yale Station, New Haven, Connecticut 06520

*Abstract*

The $TE_{72}$ mode in cylindrical waveguide has its group velocity nearly equal to that of the $TE_{11}$ mode when the operating frequency of the former is seven times of that of the latter. Thus the two modes have almost the same resonant magnetic field, and coherent radiation can be generated at the 7th harmonic when the fundamental energizes a gyrating electron beam by the cyclotron autoresonance interaction. It is shown analytically that the electron's gyration radius, normalized to waveguide radius, must be less than 0.5431 in the cyclotron autoresonance interaction. This analytical prediction is well confirmed by computer simulations. For a 300 kV, 30 A warm beam driven by 20 MW rf power at 2.856 GHz, simulations indicate that 7th harmonic power of up to 16 MW at 20 GHz can be obtained.

## 1 INTRODUCTION

Gyroharmonic conversion as a process for efficient production of high-power radiation has been investigated and analyzed in a number of prior publications [1-4]. Gyroharmonic conversion is a frequency-multipler concept, for which two approaches have been proposed. In the first [1,2], low frequency rf drive power is used to accelerate an electron beam using the $TE_{11}$ mode by CARA (cyclotron autoresonance acceleration) [5-8], and the beam is then allowed to selectively emit coherent radiation at a harmonic of the drive frequency in a converter section. To cause the accelerated beam from CARA to fulfill both synchronous and grazing conditions in the converter, a drift region is inserted [6], and the harmonic index is specified by proper choice of converter circuit parameters. The second approach to gyroharmonic conversion is co-generation [4], where the lowest mode with almost the same required resonant magnetic field as that of $TE_{11}$ at the drive frequency is the $TE_{72}$ at the 7th harmonic, and transfer of drive power and generation of harmonic power occur in the self-same structure. The harmonic index is selected by the interaction mechanism, instead of only by circuit parameters. Because no drift region is needed in co-generation, strong rf trapping is always present and preserves good gyrophase coherence among the beam particles, resulting in better beam quality and higher interaction efficiency.

* The work was supported by the U. S. Department of Energy, Division of High Energy Physics.

## 2 PRINCIPLES OF CO-GENERATION AND MAXIMUM GYRATION RADIUS

Co-generation can be understood by examining the cyclotron autoresonance condition that maintains electron synchronism with rf electric fields. The resonance condition for $TE_{sl}$ mode at the $s$th harmonic is

$$s\omega = s\Omega_0/\gamma + ck_{z,sl}\beta_z \quad \text{or} \quad \Omega_0 = \omega\gamma\left(1-n_{sl}\beta_z\right), \qquad (1)$$

where $\omega$ is the drive frequency, $c$ is the light speed in free space, $\gamma$ and $\beta_z$ are the electron's relativistic energy factor and normalized axial velocity, the refractive index or normalized group velocity for $TE_{sl}$ mode is $n_{sl} = k_{z,sl}c/\omega$ with $k_{z,sl}$ the axial wave number, and the rest gyration frequency is $\Omega_0 = eB_0/m_0$ with $e$ the electron's charge, $m_0$ the electron's rest mass, and $B_0$ the axial magnetic field. For a waveguide radius of 3.3 cm and fundamental operation at 2.856 GHz, the refractive index $n_{11}$ is 0.3605 and $n_{72}$ is 0.3521, these differ by only 2.3%. From Eq. (1) we find the resonance magnetic fields for $TE_{11}$ and $TE_{72}$ modes are nearly identical, with difference of less than 1.3% for $\beta_z = 0.99$, 0.5% for $\beta_z = 0.5$, and 0.3% for $\beta_z = 0.3$. Calculations indicates that $TE_{13,3}$, $TE_{24,5}$, and $TE_{30,6}$ are also of near-degenerate [4].

When an electron beam is pumped by drive power in the $TE_{11}$ mode, all electrons rapidly get phase-trapped and accelerated synchronously. At the same time, the beam begins to emit coherent radiation preferably into $TE_{72}$ mode, although $TE_{13,3}$, $TE_{24,5}$, and $TE_{30,6}$ modes also have nearly equal resonant magnetic fields. This is because the larger the azimuthal mode index, the more the electric field distribution is concentrated in the region close to the waveguide wall. Radiation into higher modes decreases with increase in mode index. Moreover, higher harmonics are more sensitive to beam phase spread.

A larger gyration radius is preferred for interaction with high harmonics, since high-order mode field distributions are closer to the waveguide wall. However, the gyration radius is constrained by the synchronous condition Eq. (1), resulting in

$$\frac{r_L}{R_w} \le \frac{\beta}{j'_{11}}\left[\frac{1-n_{11}^2}{1-\left(n_{11}\beta\right)^2}\right]^{1/2} < 0.5431, \qquad (2)$$

where $r_L$ is the gyration radius, $R_w$ is the waveguide radius, $j'_{11} = 1.841184$ is the first root of the derivative of Bessel function $J_1(\chi)$, and $\beta = (1-1/\gamma^2)^{-1/2}$ is the

0-7803-4376-X/98 /$10.00 © 1998 IEEE

normalized total electron's velocity. Eq. (2), which is in good agreement with computer simulation, states that the normalized gyration radius must be less than 0.5431 regardless of the beam's energy and waveguide radius in CARA.

## 3 RESULTS OF SIMULATION

Simulation results are presented here for co-generation with parameters given in Table I. For all examples, a single-energy injected electron beam with a guiding center spread of 10% and an rms axial velocity spread of 0.02% is assumed. This velocity spread value is scaled from that for the Litton $K = 1\times10^{-6}\,\mathrm{A-V^{-3/2}}$ 100 kV gun now in operation in the Yale/Omega-P 4th harmonic converter experiment. 512 computational particles are taken, with 8 values of velocity spread, 8 values of phase spread, and 8 values of guiding center spread.

TABLE I: Parameters in simulation of co-generation.

| | |
|---|---|
| Injection gun voltage | 300 kV |
| Injector gun perveance | $0.18\times10^{-6}\,\mathrm{A-V^{-3/2}}$ |
| Beam current | 30 A |
| rms axial velocity spread | 0.02% |
| Beam guiding center spread | 10% |
| Waveguide radius | 3.3 cm |
| Refractive index ( $TE_{11}$ mode) | 0.3605 |
| Refractive index ( $TE_{72}$ mode) | 0.3522 |
| rf drive frequency | 2.856 GHz |
| rf drive power | 20 MW |
| Output frequency | 19.992 GHz |
| Guide magnetic field | < 2.4 kG |

To measure performance of co-generation, one can define a direct efficiency, given by

$$\eta_{\mathrm{direct}} = \frac{P_{72}(\mathrm{out})}{P_{11}(\mathrm{in}) + P_{72}(\mathrm{in}) + P_{\mathrm{beam}}(\mathrm{in})}, \qquad (3)$$

where $P_{sl}(\mathrm{in})$ is the $TE_{sl}$ mode input power, $P_{\mathrm{beam}}(\mathrm{in})$ is the input beam power, and $P_{72}(\mathrm{out})$ is the $TE_{72}$ output power. Fig. 1 shows the results for a co-generator with an optimized detuning of $\Delta = -0.02$. Detuning, defined as $\Delta \equiv \Omega_0/\left(\omega < \gamma >< \beta_z >\right) + n_{11} - 1/< \beta_z >$, measures how much the magnetic field profile deviates from exact resonanance; introduction of detuning reduces impairment of beam quality caused by initial velocity spread. In this case, at $z = 83.8$ cm, output power at the 7th harmonic is seen to be 5.52 MW, at the fundamental to be 10.45 MW, and at the 13th harmonic to be 0.04 MW. Possible competing modes $TE_{13,3}$, $TE_{62}$ and $TE_{82}$ are seen to have only a minuscule influence on 7th harmonic co-generation. The direct efficiency is 5.52/(20+9) = 19.03%. The failure of normalized average gyration radius $< r_L/R_w >$ to fall below 0.3 indicates that particles have lost good phase synchronism with the $TE_{11}$ mode, and thus can not give up more than a limited amount of transverse momentum.

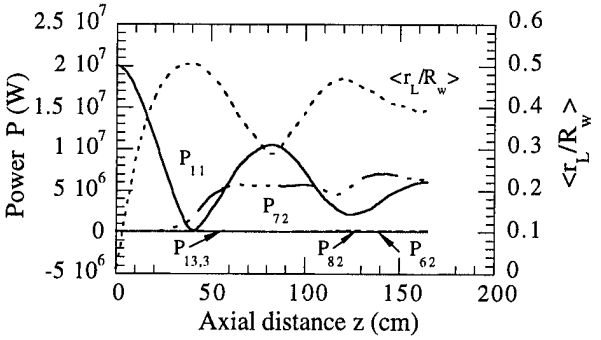



Figure 1: Dependence of rf power $P$ and normalized gyration radius $< r_L/R_w >$ on axial distance $z$. $TE_{11}$ and $TE_{72}$ modes always coexist and a detuned resonant magnetic field profile is used. Peak value of 7th harmonic power at 20 GHz is 5.52 MW at $z = 83.8$ cm.

To increase efficiency, one can kill the $TE_{11}$ mode after drive power is depleted, using a selective absorber. It is found that use of a segmented straight-line magnetic profile beyond the power-depleted point can also increase 7th harmonic power. As shown in Fig. 2, 7th harmonic output is seen to rise to 10.20 MW at $z = 99$ cm, and the direct efficiency is increased to 35.17%. Comparing Fig. 2 with Fig. 1, we find that mode suppression and adjustment of magnetic profile has considerably improved direct efficiency, but the circuit becomes longer and somewhat more complicated.

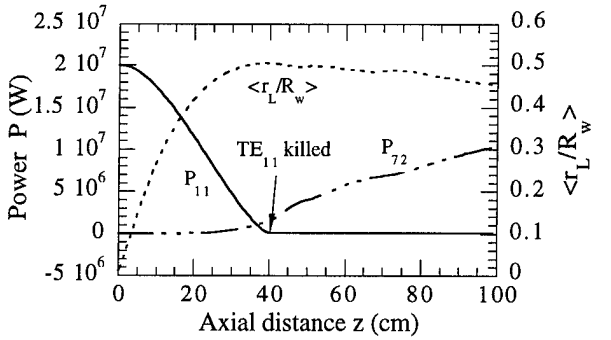



Figure 2: Dependence of rf power $P$ and normalized gyration radius $< r_L/R_w >$ on axial distance $z$. $TE_{11}$ mode is killed and segmented straight-line magnetic field profile is employed after $TE_{11}$ mode is depleted. 7th harmonic 20 GHz power is 10.20 MW at $z = 99$ cm.

It is found by simulations that injection of a portion of 7th harmonic power with proper phase can effectively reduce gyrophase spread. Fig. 3 shows results with a 7th harmonic injection power of 2.0 MW, but with other parameters the same as in Fig. 1. Now it is seen that the 7th harmonic output at $z = 86.5$ cm is 12.11 MW, indicating a net gain of 10.11 MW, as compared with 5.52 MW output without injection. Fundamental power at $z = 86.5$ cm is 9.27 MW. The significant increase in 7th harmonic output results from much better particle trapping when injection is employed. Now the direct efficiency is 12.11/(9+2+20) = 39.06%.

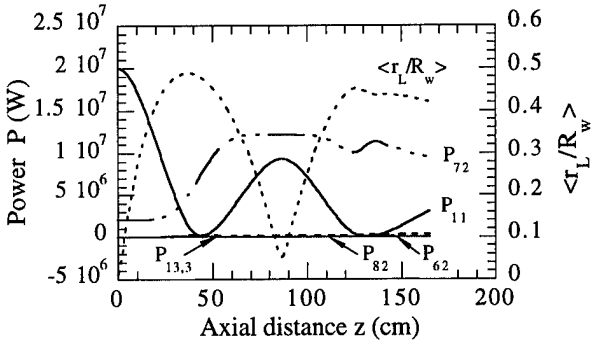



Figure 3: Dependence of rf power $P$ and normalized gyration radius $< r_L/R_w >$ on axial distance $z$. An injection power of 2.0 MW at 20 GHz is used, with other parameters the same as in Fig. 1. 7th harmonic power at 20 GHz is 12.11 MW at $z = 86.5$ cm.

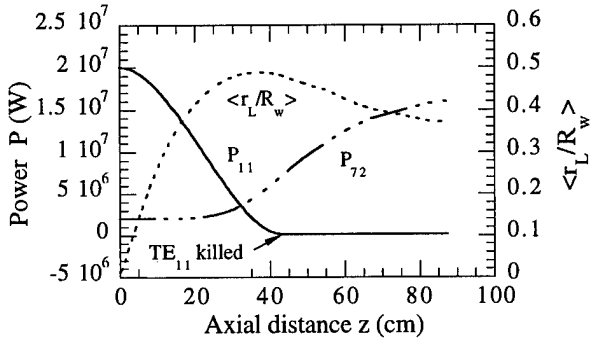



Figure 4: Dependence of rf power $P$ and normalized gyration radius $< r_L/R_w >$ on axial distance $z$. An injection power of 2.0 MW at 20 GHz is used, with other parameters the same as in Fig. 2. 7th harmonic power at 20 GHz is 15.96 MW at $z = 87.5$ cm.

Harmonic injection also benefits co-generation for the Fig. 2 case where $TE_{11}$ mode is killed beyond its power-depleted point. Fig. 4 shows results with a 7th harmonic injection power of 2.0 MW, but with other parameters the same as in Fig. 2. It is seen that 7th harmonic power grows to 15.96 MW at $z = 87.5$ cm, corresponding to a direct efficiency of 51.48%.

In a configuration requiring a large number of sources, such as a high energy electron-positron collider, one could interconnect neighboring sources in tandem, so that any 2.856 GHz output of one source would partially feed the next source; in that case the "makeup" power required for each source (except for the first one) would be reduced. In this case, one can define the output efficiency of a single co-generator in the tandem sequence as

$$\eta_{\text{output}} = \frac{P_{72}(\text{out})}{P_{11}(\text{makeup}) + P_{72}(\text{in}) + P_{\text{beam}}(\text{in})}. \quad (4)$$

A higher efficiency can be achieved through recovery of spent beam energy if a depressed collector is employed [9]. Inclusion of beam energy recovery leads to a definition of an enhanced efficiency, defined as

$$\eta_{\text{enhanced}} = \frac{P_{72}(\text{out}) + \eta_{\text{rec}} P_{\text{beam}}(\text{out})}{P_{11}(\text{makeup}) + P_{72}(\text{in}) + P_{\text{beam}}(\text{in})}, \quad (5)$$

where $\eta_{\text{rec}}$ is the efficiency for recovery of spent beam power, and $P_{\text{beam}}(\text{out})$ is the beam power at the end of the co-generator. For an ideal collector, the recovery efficiency is given by $\eta_{\text{rec}} = (\gamma_{\min} - 1)/(< \gamma > -1)$, where $\gamma_{\min}$ is the minimum relativistic energy factor in the spent beam. Table II shows comparison for the four configurations of co-generation discussed above. Effects of power injection on co-generation can be found by comparing the Fig. 1 and Fig. 2 cases with the Fig. 3 and Fig. 4 cases respectively; effects of beam energy recovery on co-generation can be found by comparing the output efficiency $\eta_{\text{output}}$ with the enhanced efficiency $\eta_{\text{enhanced}}$.

TABLE II: Comparison for four configurations of 7th harmonic co-generation at 20 GHz.

| | $P_{72}$-out (MW) | $\eta_{\text{direct}}$ (%) | $\eta_{\text{output}}$ (%) | $\eta_{\text{rec}}$ (%) | $\eta_{\text{enhanced}}$ (%) |
|---|---|---|---|---|---|
| Fig. 1 | 5.52 | 19.03 | 29.75 | 69.1 | 77.6 |
| Fig. 2 | 10.20 | 35.17 | 35.17 | 78.6 | 85.4 |
| Fig. 3 | 12.11 | 39.06 | 55.73 | 94.4 | 96.5 |
| Fig. 4 | 15.96 | 51.48 | 51.48 | 90.2 | 94.4 |

## 4 CONCLUSIONS

Co-generation is a novel means for efficient gyro-harmonic conversion. By injection of harmonic power to improve particle trapping and recovery of spent beam energy to enhance efficiency, simulations have shown that an overall 7th harmonic efficiency of over 90% can be achieved for a 16 MW 20 GHz co-generators with a 300 kV, 30 A electron beam pumped by 20 MW power at 2.856 GHz.

## 5 REFERENCES


[1] A. K. Ganguly and J. L. Hirshfield, Phys. Rev. E **47**, 4364 (1993).

[2] J. L. Hirshfield, A. K. Ganguly, and C. Wang, in *Pulsed RF Sources for Linear Colliders*, edited by R. C. Fernow, AIP Conf. Proc. No. 337, (AIP, New York, 1995), p. 200.

[3] J. L. Hirshfield, C. Wang, and A. K. Ganguly, IEEE Trans. Plasma Sci. **24**, 825 (1996).

[4] C. Wang and J. L. Hirshfield, and A. K. Ganguly, Phys. Rev. Lett. **77**, 3819.

[5] B. Hafizi, P. Sprangle, and J. L. Hirshfield, Phys. Rev. E **50**, 3077 (1994).

[6] C. Wang and J. L. Hirshfield, Phys. Rev. E **51**, 2456 (1995).

[7] M. A. LaPointe, R. B. Yoder, C. Wang, A. K. Ganguly, and J. L. Hirshfield, Phys. Rev. Lett. **76**, 2718 (1996).

[8] Hirshfield, M. A. LaPointe, A. K. Ganguly, R. B. Yoder, and C. Wang, Phys. Plasmas **3**, 2163 (1996).

[9] K. Sakamoto, M. Tsuneoka, A. Kasugai, T. Imai, T. Kariya, K. Hayashi, and Y. Mitsunaka, Phys. Rev. Lett. **73**, 3532 (1994).

# HIGH PEAK POWER TEST OF S-BAND WAVEGUIDE SWITCHES

A. Nassiri, A. Grelick, R. L. Kustom, and M. White
Advanced Photon Source, Argonne National Laboratory
9700 South Cass Avenue, Argonne, Illinois 60439 USA

*Abstract*

The injector and source of particles for the Advanced Photon Source (APS) is a 2856-MHz S-band electron-positron linear accelerator (linac) which produces electrons with energies up to 650 MeV or positrons with energies up to 450 MeV. To improve the linac rf system availability, an additional modulator-klystron subsystem is being constructed to provide a switchable hot spare unit for each of the five existing S-band transmitters. The switching of the transmitters will require the use of SF6-pressurized waveguide switches at a peak operating power of 35 MW. A test stand was set up at the Stanford Linear Accelerator Center (SLAC) Klystron-Microwave laboratory to conduct tests characterizing the power handling capability of these waveguide switches. Test results are presented.

## 1 INTRODUCTION

The APS linac structures are powered by five 35-MW klystrons, two for the electron linac and three for the positron linac. The upstream accelerating structure in each linac is directly powered by a klystron, while the remaining 12 structures are powered in groups of four by a klystron and a SLED [1].

To improve the overall availability of the linac rf system to deliver beam to the APS storage ring, a sixth rf station comprised of a modulator and a klystron has been added to the five existing rf transmitters. This system is currently under construction and high-voltage power supply testing [2]. Once on-line, this rf station will serve as a hot spare unit for any of the five on-line S-band transmitters through a suitable and reliable SF6-pressurized waveguide switching system.

Currently, rf waveguide switches in pressurized systems are used in routine operation of S-band linacs at other accelerator facilities. For example, the 295-MeV S-band injector linac for the Duke University storage ring uses aluminum WR-284 waveguide pressurized with 26 PSIG of sulfur hexafluoride (SF6) throughout the entire system. Commercially available waveguide switches have been incorporated into the pressurized waveguide system to provide rf power switching capability. This pressurized waveguide switching system has been operating reliably at a peak rf power of less than 30 MW, an rf macropulse length of 2 μs, and a repetition rate of 2 Hz without significant arcing or rf breakdown. The pressurized SF6 in this system circulates through a dryer to remove moisture and other contaminants [3].

The pressurized waveguide switches to be used in conjunction with the APS linac hot spare transmitter must be capable of handling a peak rf power of 35 MW at a maximum repetition rate of 60 Hz and an rf pulse width of 5 μs. No S-band pressurized waveguide switches are currently being operated at this power level. To investigate the operational reliability of these pressurized switches under high peak rf power, an experimental rf setup was assembled at the SLAC Klystron and Microwave Test Laboratory as described below.

## 2 EXPERIMENTAL SET-UP

Two types of commercially available waveguide switches were tested. In the first setup, two WR-284 switches (from two different vendors) were configured as shown schematically in Figure 1. The layout is comprised of a bi-directional coupler downstream of the klystron output to monitor forward and reflected power, and two rf windows (before the switch and upstream of the water load) to separate the pressurized section of the waveguide from the vacuum side. In the second setup, the WR-284 switch was replaced by a WR-340 switch. There were matching tapered transitions between the two waveguide sizes, and WR-340 windows were used instead of WR-284 windows.

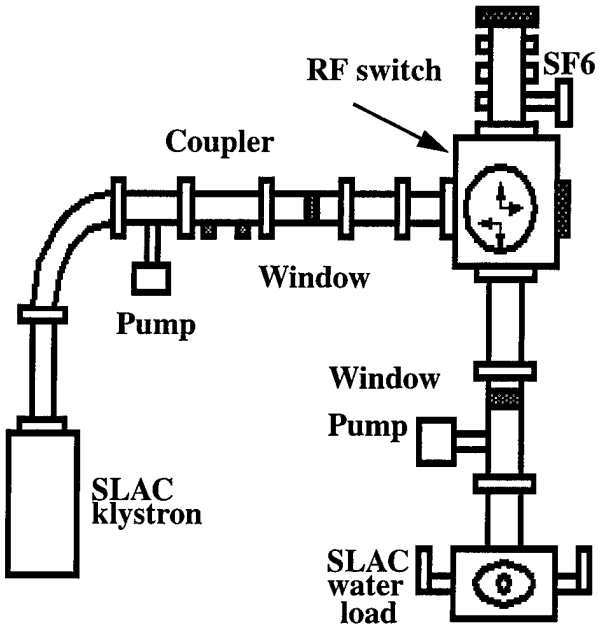



Figure 1: Schematic layout of the rf pressurized waveguide switch test.

Rf power for the test setup was provided by a SLAC type 5045 klystron operating at 2856 MHz with a nominal beam voltage of 350 kV and 393 A of beam current. The

0-7803-4376-X/98/$10.00 © 1998 IEEE

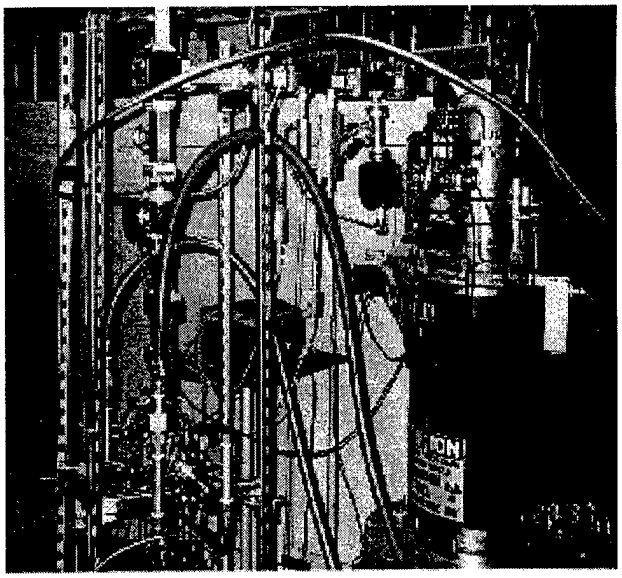


Figure 2: Waveguide switch test set-up.

peak rf power was 40 MW, with a 3.5 μs rf pulse width and a 60-Hz repetition rate. A photograph of the test set-up is shown in Figure 2. Vendor 1's WR-284 waveguide switch is pictured in Figure 3 and Vendor 2's WR-340 waveguide switch is pictured in Figure 4.

For each test set-up, the appropriate waveguide-switch section was pressurized with SF6, and the rf power was gradually increased until an arc or other operational problem occurred. The klystron forward and reflected power were monitored at the bi-directional coupler at the output port of the klystron using a peak power analyzer. Forward rf power through the switch was calculated from water load calorimetric measurements.

## 3 TEST RESULTS

### *3.1 The WR-340 Switch*

With the waveguide-switch section pressurized to 30 PSIG, rf power from the klystron was gradually increased. Arcing occurred at about 5 MW peak rf power. The rf power could not be increased due to persistent arcing and eventual SF6 breakdown. After purging and refilling with fresh SF6, rf power was again applied and the power level was gradually increased to 10 MW. Within a short time, arcing occurred in the straight waveguide section approximately six inches upstream of the switch. A few more attempts were made, but the rf power could not be increased above 10 MW due to continuous waveguide arcing and rf trips on klystron reflected power.

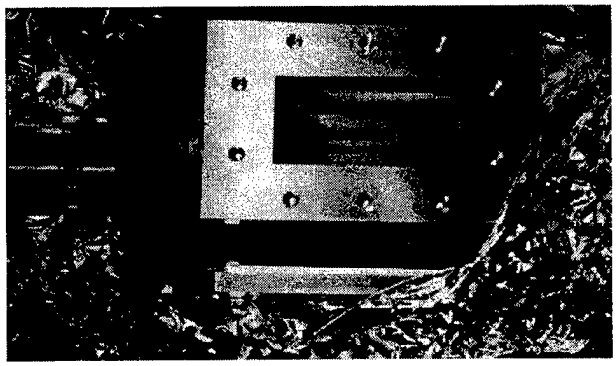


Figure 3: Vendor 2's WR-340 waveguide switch.

### *3.2 WR-284 Switches*

The rotatable blades in both of the WR-284 switches became permanently stuck in position after a short period of operation at 30-MW peak power.

The WR-284 switch from vendor 1 was tested first, and was initially pressurized to 30 PSIG with SF6. With an rf pulse width of 3.5 μs and a 60-Hz repetition rate, the rf peak power was gradually increased to 40 MW. At 25 MW, some arcs occurred inside the pressurized waveguide upstream of the input port of the switch. It was necessary to purge the contaminated SF6 and refill, and we then reached 40 MW peak power at 30 PSIG of SF6 with no arcs. The rf match between the switch and the waveguide was quite poor. The measured return loss was 17 dB, and the klystron experienced a few reflected power trips as a result of the poor match.

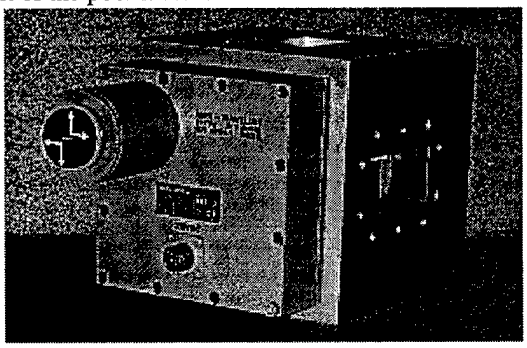


Figure 4: Vendor 1's WR-284 waveguide switch.

Next, vendor 2's WR-284 switch was installed into the test setup and the waveguide was again pressurized to 30 PSIG with SF6. Rf power was applied and increased to 30 MW. Aside from occasional vacuum bursts, there was no sign of arcing in the pressurized section. The rf power was kept at 30 MW for one hour and was then increased to 40 MW in 1-MW steps. The setup also ran well at 40 MW with no rf breakdown. The rf match for vendor 2's WR-284 waveguide switch was significantly better than for vendor 1's WR-284 switch in the same setup. The measured return loss for vendor 2's switch was 22 dB. Figure 5 shows a typical oscilloscope waveform indicating, with different vertical scales, the signals for forward and reflected rf power.

## 4 NETWORK ANALYZER CHECKS

To determine possible causes of the failure of the WR-340 switch, various configurations of the switch with and without the tapered transitions were bench tested using a network analyzer, as shown in Figure 6. Return losses were checked in an attempt to explain the observed breakdown at relatively low peak power (~5 MW). The low peak

power breakdown could have been caused by standing waves in the WR-340 waveguide system. All bench measurements indicated that the transitions had the smallest return losses of any components, but losses were at least 22 dB for all transitions.

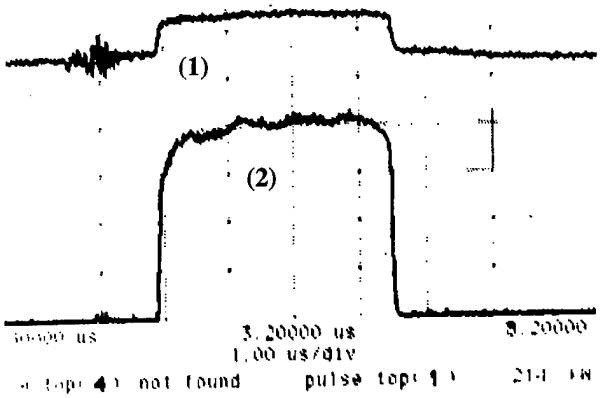



Figure 5: Oscilloscope waveforms showing: (1) forward power, (2) reflected power with a pulse width of 3.3 μs. Vertical scales are different in (1) and (2).

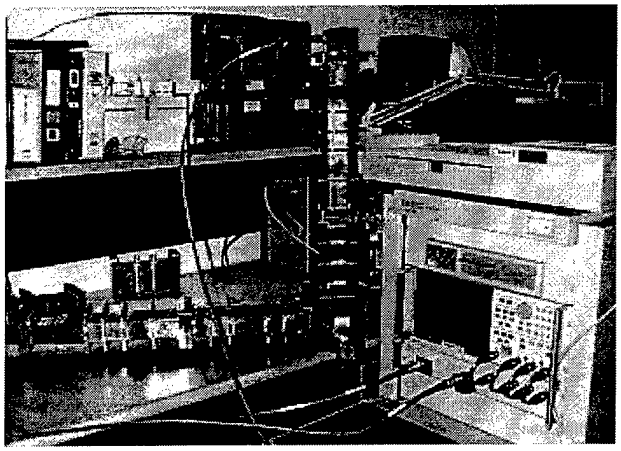


Figure 6: Network analyzer measurements of the WR-340 switch and tapered transitions.

## 5 DISCUSSION

One goal of these measurements was to find the dependence of peak rf power on SF6 pressure in the waveguide switches at peak power levels of 35 MW. The measurements were not possible for the WR-340 switch due to breakdown problems, however some data were obtained for the WR-284 switches. In all cases, the rf pulse width was 3.5 μs, and the repetition rate was 60 Hz. At a given SF6 pressure, the klystron output power was increased until an arc occurred, at which time the SF6 pressure was increased. The procedure was repeated until a maximum peak power of 40 MW was achieved. Although both WR-284 switches were tested to a peak power of 40 MW, there were rf breakdowns that required purging and refilling the SF6. Both WR-284 switches malfunctioned mechanically above 30 MW, causing the rotating mechanism inside the switch to get stuck. The rf match of vendor 2's switch was about 5dB better than that of vendor 1's switch in this setup. Visual inspection of both WR-284 switches after the high power tests showed evidence of arcing inside the switch.

## 6 CONCLUSIONS

There were indications from these tests that 35 PSIG may be a desirable operating pressure for the high-power SF6 waveguide components. There was a an observable inflection point at 35 PSIG, corresponding to the end of the linear relationship between pressure and breakdown power.

Commercially available WR-284 waveguide switches are not likely to operate reliably under the APS conditions of 35-MW peak power, 5-μs pulse width, and 60-Hz repetition rate without modification or development. Peak and average power levels, and number of joules per pulse are greater than is the case for other pressurized waveguide switches currently in operation at other facilities.

The WR-340 results cannot be understood without further high power tests. Scaling suggests that this waveguide should be able to handle the 35-MW peak power without arcing when pressurized with SF6. Low power inspection and post-testing did not reveal any reason for the failure at low rf peak power.

## 7 ACKNOWLEDGMENTS

The authors wish to thank G. Caryotakis and R. Koontz of SLAC for providing access to their laboratory to do these tests, and R. Goldsberry and G. Sandoval, also from SLAC, for their help in operating the test set-up.

We also thank J. Hoyt and M. Phelan of APS for mechanical assistance, G. Mavrogenes for technical advice, and J. Galayda for support. This work was supported by the U. S. Department of Energy, Office of Basic Sciences, under Contract No. W-31-109-ENG-38.

## 8 REFERENCES

[1] M. White et al.,"Construction, Commissioning, and Operation of the Advanced Photon Source (APS) Linear Accelerator" Proc. of the XVIII International Linac Conference, Geneva, Switzerland, 26-30 August 1996, pp. 315-319.

[2] R. Fuja et al., "Constant-Current Charging Supplies for the Advanced Photon Source (APS) Linear Accelerator Modulators," these proceedings.

[3] P. Wang, N. Hower, P. O'Shea, "RF Phasing of the Duke Linac," Proc. of the 1995 Particle Accelerator Conference, Dallas, Texas, May 1995, pp. 932-934 (1996).

# DESIGN OF A HIGH AVERAGE POWER WAVEGUIDE WINDOW

E. Chojnacki, T. Hays, J. Kirchgessner, H. Padamsee, CORNELL UNIVERSITY, Ithaca, NY and
M. Cole and T. Schultheiss, NORTHROP GRUMMAN CORP, Bethpage, NY

*Abstract*

A study has been performed to design a waveguide vacuum window capable of propagating >1 MW average power operating at 500 MHz. This would extend current technology by about a factor of 2 in average power for stand-alone windows, made possible by advances in available ceramic size and quality. The work to be presented comprises of RF design and corresponding thermo-mechanical analysis.

## 1 INTRODUCTION

A facet common to many current and proposed accelerator projects is extremely high luminosity, demanding ever increasing beam current, one consequence of which is the need to transfer high average power to the beam. One component in the chain of power transfer is an RF vacuum window.

For frequencies around 500 MHz, at least two rectangular waveguide window designs have been successfully tested at 500 kWCW. One is manufactured by Thomson Tubes for the CESR III upgrade [1] and the other is an in-house design for the PEP-II B Factory [2]. Cornell's testing of the Thomson window indicates that it has the potential to operate at the 1 MWCW level from a thermal point of view if the Titanium anti-multipactor coating on the ceramic is sufficiently thin. But this comes at the expense of lengthy RF conditioning and greater potential of troublesome operation when attached to an accelerator cavity. A coaxial window designed by KEK for their B Factory has been tested at 850 kWCW [3], which certainly exceeds expectations for a coaxial geometry.

Factors that limit RF window performance are: 1) heating of the vacuum barrier (ceramic), 2) multipactor discharge, and 3) violent arcing. High average-power windows are most susceptible to the first two items. Multipactor discharge is a precarious phenomenon, and in the end usually addressed by applying a sufficiently thick anti-multipactor coating, such as Titanium or Titanium Nitride, to trouble spots. This coating, though, is RF lossy and contributes to the other problem encountered in high average-power windows, heating of the ceramic.

In addition to surface heating by the anti-multipactor coating, bulk heating of the ceramic occurs due to its non-zero dielectric loss tangent. Typically, the perimeter of the ceramic disk is held at a fixed temperature by a cooling water interface, and the thermal gradient of the disk interior induces mechanical stress which will cause fracture of the ceramic at sufficiently high gradient.

It is mainly the problem of heating of the ceramic and induced mechanical stress which will be addressed in this paper. In Section 2 is the RF design of two types of windows, in Section 3 thermo-mechanical analyses corresponding to the RF designs, and in Section 4 comparison of designs.

## 2 RF DESIGN

A survey was taken among ceramic manufacturers to determine what sizes, shapes, and materials are readily available with low dielectric loss tangent ($\delta \sim 10^{-4}$). Besides the well-known Alumina, plates of low-loss Beryllia may be available in sizes up to 18" x 9" x 1/2" [4]. Beryllia is an attractive choice since it has a high thermal conductivity, resulting in lower thermal gradients, although the material has a lower tensile strength than Alumina. Thus, the two ceramics considered here are Alumina and Beryllia.

The 3D computer code MAFIA with its *s*-parameter macro was used for RF designs. A satisfactory degree of confidence exists in MAFIA's accuracy given comparisons of computations to measurements performed on Cornell's Thomson window. Ultimate fine tuning of a prototype, though, will always be in order.

Two different waveguide window geometries were considered. The first type utilizes posts in the waveguide to compensate the mismatch of the ceramic vacuum barrier and the second is a self-matched design.

### *2.1 Tuning-Post Matching*

The geometry of a quarter section of a tuning-post matched window is shown in Fig. 1. For such a window, MAFIA is first used to generate curves of scattering parameters (mainly $s11$) of only the symmetric pair of tuning posts in waveguide, where the RF reference plane is at the center of the posts. Sample curves are shown in Fig. 2. Next, MAFIA is used to determine the scattering parameters of only the ceramic disk embedded in the metal frame in waveguide, again with the RF reference plane at the center of the ceramic. Then a curve as in Fig. 2 is used to determine displacement of the posts from $x$=0 to match the *amplitude* of $s11$ for the ceramic. Given the phase of $s11$ for this post displacement, the posts are then translated toward the RF generator from the center of the ceramic to a plane where the *phase* of the ceramic's transformed $s11$ is the negative of the post's $s11$ phase. With this positioning, the impedances of the ceramic and tuning-post obstacles are complex conjugate at the post's reference plane and the assembly is RF matched. The physical distance translated toward the generator is simply the fraction of a guide half-wavelength represented by the phase difference in $s11$ of the individual obstacles,

$$L = \frac{\Delta\phi}{360} \cdot \frac{\lambda_g}{2} \quad . \qquad (1)$$

0-7803-4376-X/98/$10.00 © 1998 IEEE

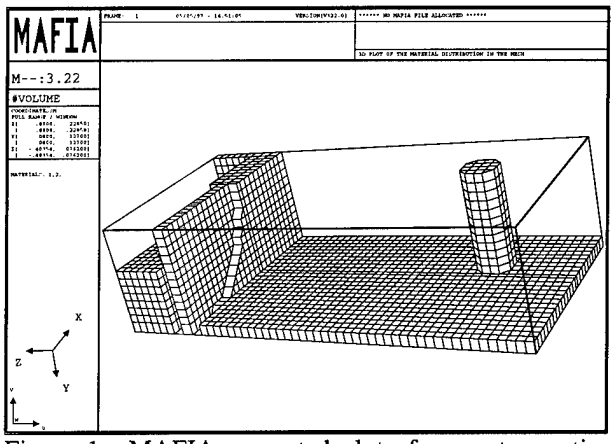



Figure 1. MAFIA-generated plot of a quarter section of a tuning-post matched window, utilizing symmetries to reduce computation volume. The reduction in waveguide height and width after the ceramic is peculiar to a Cornell application.

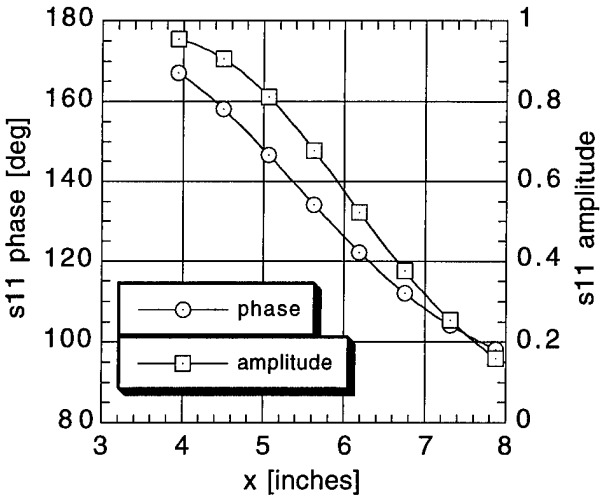



Figure 2. Computed phase and amplitude of $s11$ at 500 MHz for a pair of 1.5" diameter posts symmetrically located about the $x$=0 plane in WR1800 waveguide.

In the long run, this matching technique saves much effort over the trial-and-error method of tuning-post placement.

In this design, the tuning posts reside in what will be the air side of the vacuum barrier. This is so that the standing wave set up between the posts and the ceramic will not exist in the vacuum region where multipactor and general arcing are most susceptible.

### *2.2 Self Matching*

The geometry of a quarter section of a self-matched window is shown in Fig. 3. Matching such a window is a straightforward trial-and-error process where the width of the iris (and consequently ceramic) is adjusted until RF reflection is minimized. In performing this adjustment, the enhanced capacitance of the obstacle due to the dielectric is balanced by the enhanced inductance due to the iris, providing a wave impedance $\sqrt{L/C}$ equal to that of the surrounding waveguide. Fine tuning can also be performed by adjusting the ceramic thickness and iris thickness.

### *2.3 Design Subtleties*

It is worth mentioning a couple of design features adhered to in consideration of sound practice for both window types discussed above.

First, at the ceramic-metal-vacuum boundary (so-called triple point), no corners, not even rounded, were allowed on the metal, only on the ceramic. A metallic corner abutting a dielectric is the focus of electric field enhancement exceeding that of a metal corner alone.

Second, the shape of the perimeter of the ceramic plate was kept circular or elliptical, no "flats". This is to facilitate brazing of the ceramic into a metal sleeve, allowing the sleeve to maintain close contact with the ceramic during brazing, similar to the fit of hoops on a wine barrel. The perimeter of the ceramic and sleeve could also be tapered longitudinally to mimic a press fit.

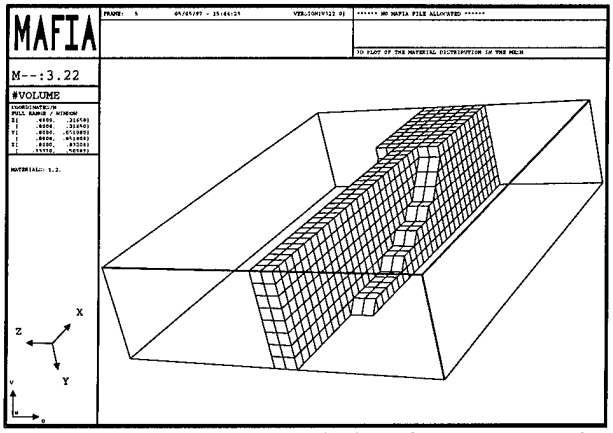



Figure 3. MAFIA-generated plot of a quarter section of a self-matched window.

## 3 THERMO-MECHANICAL ANALYSIS

Once the RF design is settled, a perturbation calculation can be performed in MAFIA to give the power density dissipated in each mesh cell of the ceramic due to a non-zero loss tangent. This data table can then be manipulated and read into the 3D thermo-mechanical computer code ANSYS. ANSYS is then used to compute the thermal profile of the ceramic and the resultant stresses, where in this study the perimeter of the ceramic is held at a fixed temperature and a 15 psi pressure differential exists across the ceramic.

The location and magnitude of peak stress within the ceramic is closely coupled to how the component is mechanically constrained. For this study, the perimeter of the ceramic was taken to be attached at the center of a 1/8" thick copper sleeve about twice as long as the ceramic. The very ends of the copper sleeve were then taken to be immobile. This is close to what is intended in the final mechanical design

Table 1. Results of ANSYS thermo-mechanical analysis for 1 MWCW propagating at 500 MHz and $\delta = 3\times10^{-4}$.

| Ceramic | Waveguide Configuration | Ceramic Perimeter | Ceramic Thickness | ΔT [°C] Center to Perimeter | Max Principal Stress % of Tensile Strength |
|---|---|---|---|---|---|
| Beryllia | self-matched red hgt | elliptical | uniform | 4.2 | 2.8 |
| Beryllia | posts, full hgt - red hgt | circular | uniform | 5.3 | 6.8 |
| Beryllia | self-matched red hgt | elliptical | tapered | 2.8 | 8.6 |
| Beryllia | posts, full hgt - red hgt | circular | tapered | 4.8 | 12.7 |
| Beryllia | self-matched full hgt | elliptical | uniform | 5.8 | 14.1 |
| Alumina | self-matched red hgt | elliptical | tapered | 51.4 | 14.7 |
| Alumina | posts, full hgt - red hgt | circular | tapered | 105.0 | 32.1 |
| Alumina | posts, full hgt - red hgt | circular | uniform | 130.0 | 58.1 |
| Alumina | self-matched red hgt | elliptical | uniform | 111.0 | 60.8 |

where the copper sleeve is part of a cooling water circuit.

It is a matter of interesting discussion as to which type of stress in which ceramic fracture scenario is most important to consider. But to have a common parameter by which different window designs can be compared, the maximum principal stress was chosen as the parameter to be minimized. And as a conservative limit, during window operation this stress should not be allowed to exceed 25% of the ceramic's tensile stress.

An interesting feature explored in this study was to taper the thickness of the ceramic, making it thin at the center and thick at the perimeter. If the cooling circuit is at the ceramic perimeter (fixed temperature), tapering the thickness will result in a lower thermal gradient than uniform thickness. This is since at any radius, the tapered ceramic will have a larger area through which to conduct heat from a smaller bulk-heated volume than if the thickness were uniform.

Table 1 lists the results of ANSYS computations for several window configurations to be discussed next.

## 4 COMPARISON OF DESIGNS

The results shown in Table 1 are for 1 MWCW propagating at 500 MHz. The effective loss tangent of all ceramics is taken to be $3\times10^{-4}$. Alumina's actual loss tangent tends to be much smaller, but experience with four Thomson windows at Cornell indicates that the contribution of the anti-multipactor coating can be random and significant, and in the end a coating resulting in $\delta \sim 3\times10^{-4}$ is just about right. It is hoped that industry can fabricate large plates of Beryllia that do not exceed this loss tangent.

From Table 1 it is seen that tapering the ceramic thickness does indeed result in a lower operating temperature. However, for Beryllia, the lower temperature did not translate into lower peak stress since the tapered thickness also altered mechanical loading. For Alumina, the reduction in stress from tapering the ceramic is large enough in only one case to justify the added complexity and cost of ceramic fabrication: the self-matched ellipse in reduced-height waveguide. (The case of a self-matched Alumina ellipse in full-height waveguide had such high temperature and stress, it was dropped early in the study).

The design in Table 1 that shows the greatest promise is the first listed, a self-matched Beryllia ellipse of uniform thickness in reduced-height waveguide. This is the window shown in Fig. 3. This design's peak stress being only 2.8% of Beryllia's tensile strength leaves great margin for error in many fabrication parameters. The only concern is the enhanced electric field in reduced-height waveguide making this design more susceptible to multipactoring. Many MAFIA runs were performed for this window design to map dimensional and material property sensitivity, the result of which showed no drastic dependence within expected tolerances. It is hoped that a prototype of this design will be built and tested.

As fallback positions, the cases of a tuning-post matched Beryllia disk of uniform thickness and a self-matched Beryllia ellipse of uniform thickness in full-height waveguide are quite promising. And finally, the first Alumina case listed in Table 1, a self-matched ellipse of tapered thickness in reduced-height waveguide, may still be considered if Beryllia doesn't prove out in loss tangent or ease of brazing. This is similar to the window shown in Fig. 3.

## REFERENCES


[1] M. Pisharody, *et. al.*, "High Power Window Tests on a 500 MHz Planar Waveguide Window for the CESR Upgrade", *Proc. 1995 Part. Accel. Conf.* (Dallas, TX, 1995), p. 1720.

[2] M. Neubauer, *et. al.*, "High-Power RF Window and Coupler Development for the PEP-II B Factory", *Proc. 1995 Part. Accel. Conf.* (Dallas, TX, 1995), p. 1803.

[3] S. Mitsunobu, *et. al.*, "High-Power Test of the Input Coupler for KEKB SC Cavity", *Proc. 7th Workshop on RF Superconductivity* (Gif sur Yvette, France, 1995), p. 735.

[4] Communications with Brush Wellman Engineered Materials, (520) 746-0699, Tucson, AZ.

# ELECTRON GUN AND COLLECTOR DESIGN FOR 94-GHZ GYRO-AMPLIFIERS

K. Nguyen*, B. Danly, B. Levush, and M. Blank
Naval Research Laboratory, Washington D.C. 20375
R. True
Litton Electron Devices, San Carlos, CA 94070
K. Felch and P. Borchard
Communications & Power Industries, Palo Alto, CA 94304

*Abstract*

This paper presents the electrical design of the magnetron injection gun and collector for high average power $TE_{01}$ gyro-amplifiers. Both the gun and collector are currently under construction.

## 1 INTRODUCTION

The development of high-average power w-band gyro-amplifiers is currently being pursued by the Naval Research Laboratory, together with Litton Electron Devices and Communication & Power Industries as industrial partners. In addition to interaction circuit design aspects [1], key issues include the design of a high-quality electron gun and a collector capable of high average power operation. The gun and collector electrical designs were performed with the EGUN code [2], and were independently confirmed with the deformable-mesh gun code, DEMEOS [3]. Excellent agreement between the two codes has been realized.

The magnetron injection gun (MIG) design employs an optimized double-anode geometry and a radical cathode angle of $50^0$ to achieve superior beam optics that are relatively insensitive to electrode misalignments and field errors. Perp. velocity spread of 1.6% at a velocity ratio of 1.52 is obtained for a 6 A, 65 kV beam. The design objective of the collector, which also serves as the output waveguide, is to minimize the required collector length while avoiding hot spots on the collector surface. Average power density of < 350 W/cm$^2$ on a 1.28" diameter collector is achieved for 59 kW average beam power.

## 2 94-GHZ MAGNETRON INJECTION GUN DESIGN

Efficient operation of gyro-devices depends critically on the quality of the electron beam. Consequently, for the current design, special emphasis has been placed not only in obtaining the best point design which exceeds all the requirements of the interaction circuit, but also in identifying and evaluating all factors which may contribute to the beam velocity spreads. Such factors include cathode surface roughness, electrode misalignments, and fabrication tolerances.

Specifically, the MIG design is subjected to the following RF circuit requirements:

| | |
|---|---|
| Beam Current | 5 - 7 Amperes |
| Beam Voltage | 65 - 70 kV |
| Velocity Ratio | 1.3 - 1.8 |
| Perp. Vel. spread | 2.5% |
| Max.Beam Radius | 1.25 mm |
| Guiding Radius | 0.8 - 1.1 mm |
| Oper. Magn. Field | 36 - 38 kG |

In addition, practical considerations dictate the need to maintain cathode loading, $J_{cat}$, below 8 A/cm$^2$ for reasonable cathode lifetime, peak electric field, $E_{max}$, well below 100 kV/cm to avoid arcing, and gun magnetic compression ratio, $B_f/B_o$, at or below 25 to minimize electron reflection and beam alignment problems. Moreover, since the gun will be operating at high-repetion rate, the modulating voltage required for beam pulsing must be minimized to avoid stressing the voltage modulator. It is due in part to this last requirement that the present gun design employs the double-anode geometry. The other key advantage of this geometry is the ability to adjust the beam perpendicular to axial velocity ratio, $\alpha$, independent of the magnetic field profile.

Shown in Figure 1 is the MIG geometry and beam trajectory. It is essentially comprised of three regions: the cathode–mod-anode region, the mod-anode–anode region, and the beam tunnel or adiabatic compression region (partly shown). In performing the design, care has been taken to ensure to the largest extent possible that each region will perform mainly one key function. Such modular approach allows a much more rapid convergence

* KN Research, Silver Spring, MD 20906

0-7803-4376-X/98/$10.00 © 1998 IEEE

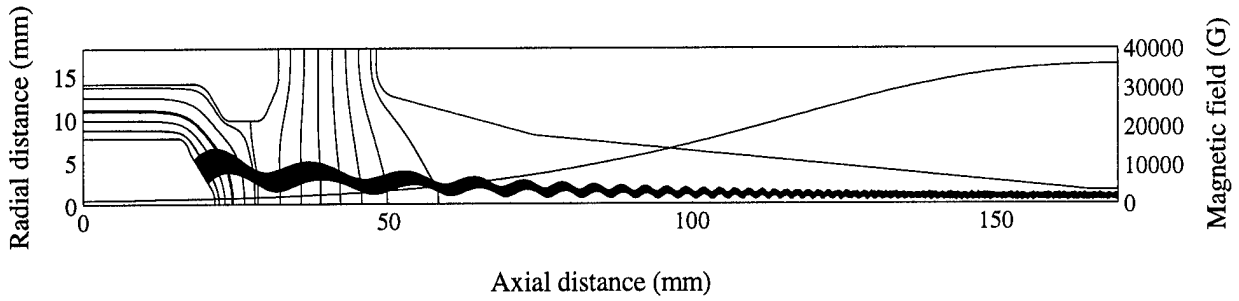



Figure 1: Geometry and beam trajectory of the 94 GHz magnetron injection gun point design

to the final design. Consequently, in the design, the initial beam perpendicular velocity is controlled mainly by the geometry and voltage of the cathode–mod-anode region, the mod-anode–anode region provides mainly axial acceleration to bring the beam up to full potential, and the beam is adiabatically compressed in the beam tunnel region to the final beam velocity ratio. An additional advantage of the modular approach is the ability to locally pinpoint and control beam velocity spread. For instance, the transverse beam spread can be minimized by shaping the cathode and mod-anode geometries.

Key elements of the design include a cathode well-recessed under the mod-anode shroud, a relatively large cathode angle of $50^0$, and relatively parallel potential contours in the mod-anode–anode region. We shall discuss these key elements in turns.

The recessed cathode is critical for three reasons. First, by recessing the cathode deep inside the mod-cathode shroud, we essentially shield the cathode from the high anode potential (~65 kV relative to cathode). This design choice reduces the maximum electric field on the cathode tip to less than 67 kV/cm (This value has also been independently confirmed with ANSYS [4] ), well below the dc breakdown threshold. Second, it allows for the relatively independent control of the beam initial transverse velocity ($\mathbf{E}_c/\mathbf{B}_c$) with just the voltage and geometry of the cathode - mod-anode region. Finally, it minimizes the leakage electric field (i.e., when $V_{mod\text{-}anode} = V_{cathode}$) on the thermionic emitting strip from the anode voltage. This reduces the required negative mod-anode voltage swing relative to the cathode for complete beam shutoff (i.e., less stress on the modulator). For this design, this is -1.7 kV.

The relatively large cathode angle of $50^0$ is a consequence of trading off between various conflicting requirements. Chief among these is the need to maintain the overall coherency of the cyclotron phase for all beam electrons at least until the electric field is primarily axial. This is important because to the lowest order unless all beam electrons picks up the same amount of transverse energy, in their cycloidal motion through the region of substantial radial electric field, serious beam spread will result. For this design, because of the small mean radius of the emitter strip, the relatively high beam current, and cathode loading considerations, the emitter strip width is a substantial fraction of the cyclotron period; thus, the need for large cathode angle to compensate.

In the relatively long region between the mod-anode and anode, it is critical that the electric field is primarily axial. Even though, in principle, for a fixed set of operating parameters, one can shape the potential contours in this region to greatly correct for any initial beam spread. However, due to the fact that the beam can perform more than two cycloidal orbits in this region, any deviation from the operating parameters will also greatly degrade the beam quality; hence, reducing flexibility. Consequently, it is more advantageous to ensure that mainly axial acceleration is performed in this region, consistent with the modular design methodology.

The optimized point design parameters are shown in the table below. Agreement between EGUN and DEMEOS is excellent in terms of beam velocity ratio, velocity spreads, position, and size.

| | |
|---|---|
| Anode Voltage | 65 kV |
| Mod-anode Voltage | 17 kV |
| Beam Current | 6.0 A |
| Velocity Ratio | 1.5 |
| Perp. Velocity Sprd. | 1.6% |
| Max. Beam Radius | 1.25 mm |
| Beam Guiding Center | 0.82 mm |
| Circuit Magnetic Fld. | 36 kG |
| Mag. Comp. Ratio | 25 |
| Cathode Loading | 6.76 A/cm$^2$ |

Additionally, simulations have been performed to explore the gun performance under various operating parameter ranges, i.e., mod-anode voltage, beam current, and beam voltage. This study indicates that the perpendicular velocity spread does not exceed 2% within the operating range required by the interacting circuit, and that the design is indeed optimized. This is exemplified by Figure

2 which shows the beam velocity and perpendicular velocity spread as a function of mod-anode voltage.

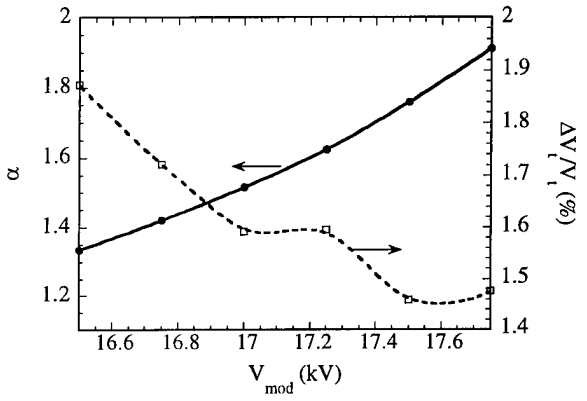



Figure 2: Beam velocity ratio and perp. velocity spread versus mod-anode voltage.

Of the 1.6% final perpendicular velocity spread in the point design, 0.6% of which is a direct result of electron phase-mixing in the present of the beam space-charge in the adiabatic compression region. This is independently confirmed with the Univ. Of Maryland code MAGUN [5].

We have also investigated the impact of cathode surface roughness on beam spread [6-7]. Our results indicate an additional 0.7% beam transverse velocity spread can be expected from bumps of 1 microns in height and width.

In addition, an exhaustive study of the resulting beam quality sensitivity with respect to misalignments, fabrication tolerances, and geometric deviations from the design has been performed. Within the fabrication tolerance and alignment specifications, the study indicates that the beam perp. velocity spread does not exceed 2%.

## 3 COLLECTOR DESIGN

The design requirements for the collector of the 94-GHz gyroklystron call for: no voltage depression, the ability to handle up to 91 kW average beam power (7A, 65kV, 20% duty), collector loading below 750 Watts/cm$^2$ desirable (1.0 kW/cm$^2$ is hard limit), collector compatible with RF output requirements, and no sweeping of collector magnetic field. Numerous collector sizes and magnetic profiles were evaluated for various beam parameters from the MIG design. The final collector design employed a 1.28" diameter pipe with 4 collector magnet coils. The resulting peak loading of 600 W/cm$^2$ for a 7A, 65kV beam at 20% duty is well within the cooling limit.

Shown in Figure 3 are the EGUN beam trajectory plot in the collector for a 6 A, 65 kV beam from the MIG point design. Good agreement between EGUN and DEMEOS has also been obtained as illustrated by Figure 4. A sensitivity study of the collector power loading with respect to the magnetic field profile has also been performed. It indicates that the peak power loading (but not necessarily the profile) on the collector remains relatively constant if the current in each of the four collector coils can be maintained within +/-5% of the design value.

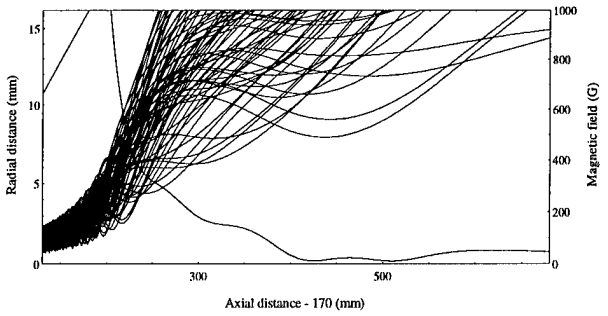



Figure 3: Beam trajajectory in the 1.28" collector

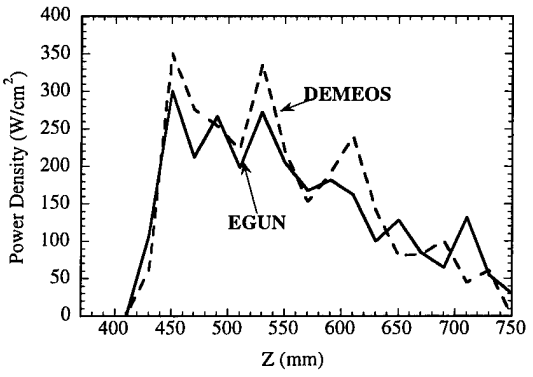



Figure 3: Comparison of average power loading on collector wall between EGUN and DEMEOS.

## 4 ACKNOWLEDGEMENTS

This work is supported by Office of Naval Research, Defense Advanced Research Projects Agency, and in part by grants of HPC time from the Department of Defense HPC centers, NAVO and CEWES.

## REFERENCES

[1] D. Pershing, K. Nguyen, J. Petillo, J. Calame, B. Danly and B. Levush, in these proceedings.
[2] W.B. Herrmannsfeldt, AIP Conf. Proc. 177, pp. 45-58, 1988.
[3] R. True, IEDM Tech. Digest, pp. 257-260, 1975
[4] ANSYS/Emag, Ansys Inc..
[5] T. Antonsen Jr., et al., Conf. Dig. of 20th Int. Conf. On Infrared & mm waves, p126 (1995).
[6] S. E. Tsimring, Izv. Radiofiz. **15**, 1247 (1972).
[7] Y.Y. Lau, J. Appl. Phys. **61**, 36 (1987).

# EXPERIMENTAL EVALUATION OF 350 MHz RF ACCELERATOR WINDOWS FOR THE LOW ENERGY DEMONSTRATION ACCELERATOR*

K. Cummings, D. Rees, W. Roybal, Los Alamos National Laboratory, Los Alamos, NM 87545 and
S. Lenci, Communications and Power Industries, Inc, Palo Alto, CA 94303 and
S. Risbud, University of California, Davis, CA 95616 and
C. Shang, Lawrence Livermore National Laboratory, Livermore, CA 94551 and
D. Wilcox, EEV, Ltd. Chelmsford, England

*Abstract*

Radio frequency (RF) windows are historically a point where failure occurs in input power couplers for accelerators. To obtain a reliable, high-power, 350 MHz RF window for the Low Energy Demonstration Accelerator (LEDA) project of the Accelerator Production of Tritium program, RF window prototypes from different vendors were tested. Experiments were performed to evaluate the RF windows by the vendors to select a window for the LEDA project. The Communications and Power Industies, Inc. (CPI) windows were conditioned to 445 kW in roughly 15 hours. At 445 kW a window failed, and the cause of the failure will be presented. The EEV windows were conditioned to 944 kW in 26 hours and then tested at 944 kW for 4 hours with no indication of problems.

## 1 INRODUCTION

For the LEDA project, the radio frequency quadrupole (RFQ) requires 2.1 MW of RF power. This power is supplied by three 1.2 MW continuous wave (CW) klystrons in a redundant configuration. The power from each klystron is divided into four equal parts to minimize the window stress. Under typical operating conditions, each window is designed to transmit up to 300 kW of CW RF power. The goals of these experiments are to select a reliable window, to determine what diagnostic equipment is needed to ensure window reliability, to develop a conditioning routine, and to increase the durability of RF windows by better understanding the failure mechanism of windows.

## 2 EXPERIMENTAL APPARATUS AND PROCEDURE

### *2.1 Window Geometry*

The RF window prototypes from CPI and EEV are both coaxial windows and are illustrated in Fig. 1 and Fig. 2, respectively. The cross section of the EEV window is shown in Fig. 3. Both windows used half-height WR 2300 waveguide and AL995 alumina ceramic. For both prototypes the waveguide transition on the vacuum side was copper plated stainless steel waveguide, and on the air side it was aluminum.

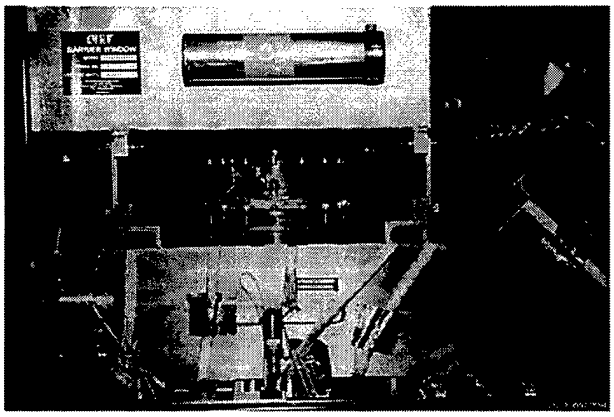


Figure: 1 CPI RF Window

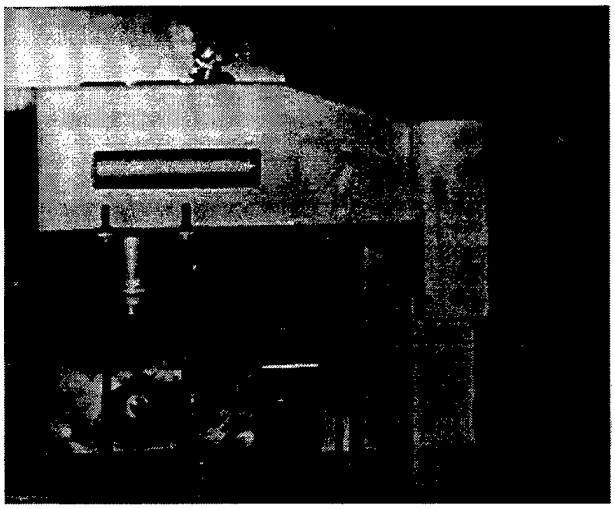


Figure: 2 EEV RF Window

### *2.2 Test Stand Description*

An experimental test stand was designed and built to test the windows to 1.0 MW of CW RF power. The test stand includes diagnostic equipment to test, condition, and

*Work supported by U.S. Department of Energy.

0-7803-4376-X/98/$10.00 © 1998 IEEE

evaluate the RF window prototypes. The power was transmitted from the klystron through a circulator to the experimental test section, and finally into a water load where it was absorbed. The experimental test section includes an RF window, vacuum waveguide, and a second RF window in a back-to-back configuration. Thus, the vacuum section was bounded by the two windows. Each window has a four-inch pump port and the vacuum waveguide between the windows included an eleven-inch pump port. The vacuum was obtained by using three CT-8 Cryo-pumps. STABIL-ION gages, calibrated to a 2% accuracy, were used to monitor the vacuum pressure. Saito, et. al. have found that for the dominant method of coaxial window failure is thermal fracture[1], therefore, infrared imaging of the ceramics windows was used as a diagnostic tool. PRISM DS infrared imaging cameras by Flir Systems (320 x 244 pixels) were used to monitor the temperature of the ceramic during conditioning and testing. The infrared cameras were connected to a VCR to record video footage. Images could also be stored on a PC card which could be downloaded for further data analysis. On the CPI windows, a special port was dedicated for infrared imaging. NaCl windows, which have a high transmission in the IR range, were used for thermal imaging. These windows could be interchanged with a Lexan lens. On the EEV windows, a port with a sapphire lens was used which could mount either an arc detector or be used for infrared imaging. Both window prototypes had arc detectors which were interlocked to the RF drive power. Dual directional couplers were used to measure the forward and reflected power both before and after the test section. Resistive Thermal Devices (RTD) were attached

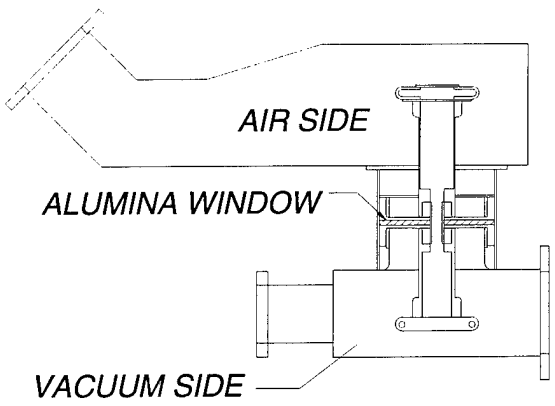



Figure: 3 Sketch of the EEV window

to the outside surface of the coaxial window near the alumina ceramic to measure the surface temperature. Both windows were air and water cooled. The air and water supply and return temperatures and flow rates were also monitored. An X-ray detector was used to detect X-rays near the vacuum section as a multipactor diagnostic. A LabVIEW program recorded the forward and reflected power on the three directional couplers, the coaxial surface temperatures near the ceramic, the air and water supply and return temperatures, and the vacuum pressure. The arc detector and vacuum pressure were interlocked to the RF power, and the interlock set points could be varied.

### *2.3 Test Parameters*

Half-height WR 2300 waveguide was used to join the RF window prototypes to the test stand and to the vacuum section between them. For the rest of the test stand, full-height WR 2300 waveguide was used. The power was generated by a Thomson klystron capable of producing 1.3 MW CW RF power at 351.93 MHz; however, the power was limited to the 1.0 MW because of the power limitation of the water load.

## 3 EXPERIMENTAL RESULTS

### *3.1 CPI RF Window Test Results*

A low temperature bakeout was performed for 8 hours at roughly 130 °C on the CPI windows. Before conditioning began, the air flow was measured as 85 cfm through one window and 95 cfm through the second window. The water flow rate was set to 3 gpm. The CPI window was conditioned with pulsed RF power. The RF "Tickle" method of processing (a short pulse on top of a pulse), was used[2]. However, the benefit was not quantifiable. The approach was to start with a short pulse width and then increase the pulse width with time. During conditioning the vacuum pressure was allowed to rise to a maximum of 5E-8 Torr while maintaining the RF power level. Once the vacuum pressure decreased to approximately 2E-8 Torr, the RF power was increased. The windows were conditioned for approximately 15 hours to 445 kW CW power before failure. On one CPI window, excessive heating was observed using the IR camera in the center conductor region. It was first attributed to multipactor; however, we later learned this to be incorrect and now believe that the failure mechanism described below led to a source of molten copper being available which was deposited onto the window ceramic by a subsequent arc. After the arc occurred, no significant CW power could be transmitted through the window because of excess heating in the window; nevertheless, the window did maintain the vacuum seal. The testing was discontinued and the window was shipped to CPI for analysis. The analysis showed that a bolted connection close to the ceramic window was made from a inappropriately soft material. Due to thermal cycling a gap opened in the connection, resulting in a plasma and an arc. This led to localized ceramic melting and the deposition of evaporated materials on the ceramic surface. CPI decided to do some minor modifications to the design of the window, and both windows were rebuilt. The

redesigned windows have not yet undergone high-power testing.

*3.2 EEV RF Window Test Results*

The air flow rates were measured as 80 cfm and 100 cfm through the two windows. The water flow rate was set to 4.5 gpm on each window. No bakeout was conducted on the EEV window, and it was conditioned using only CW power. The EEV window was conditioned to 950 kW in approximately 26 hours, as illustrated in Fig. 4. At low power levels, the arc detectors would occasionally trip and a corresponding increase in gas pressure was observed. These trips were suspected as being caused by a fluorescence due to multipactor, which was not seen at higher power levels. Saito, et. al. have observed a fluorescence with a monochrometer on a test window and correlated it with multipacting associated with the impurities in alumina ceramic [3]. The vacuum pressure interlock was set to 5E-7 Torr. Slight increases in the gas pressure over 5E-7 Torr lead to a "run away" in the pressure, thus the gas pressure was carefully controlled by reducing the RF power when necessary. The high-power acceptance test for the EEV windows consisted of running the EEV windows at approximately 950 kW for 4 hours. During this time, there were no indications of any problems. The EEV window had both air and vacuum region arc detector viewports. After the high-power acceptance tests, the air

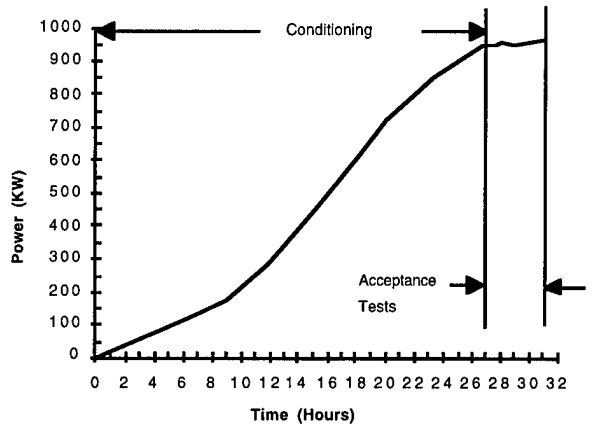



Figure: 4 EEV Forward Power vs Time

side arc detector was replaced by an IR camera. The IR imaging on the EEV window showed no indications of any problems or hot spots during operation. Another test conducted on the EEV windows was to use the windows in a degraded vacuum environment. Two of the three Cryo pumps were shut off, and the vacuum pressure was increased to 3.9E-6 Torr. There were no indications of any problems after running one hour at full power. The EEV windows were also tested using a reduced air flow rate of 25 cfm as opposed to the 80 cfm to 100 cfm used during the conditioning and acceptance tests. At full power, there was no noticeable increase in the water cooling temperature, but the vacuum pressure did increase by half an order of magnitude. The temperature of the ceramic increased by approximately 10 °C; nevertheless, the temperature gradient across the window remained small.

## 4 DISCUSSION

Monitoring the power during the pulsed conditioning method was more difficult than the CW conditioning method. Since there was no quantifiable benefit observed for pulsed conditioning, future windows will be conditioned CW. The IR camera is an invaluable diagnostic tool to observe the temperature profile on the ceramic window, especially during conditioning, to detect any indications of failure. For example, the IR camera showed an elevated temperature on the CPI window before the failure. The benefit of the X-ray detector as a diagnostic was not evident, as during the entire conditioning and test procedure, no X-rays were detected.

## 5 CONCLUSIONS

Los Alamos National Laboratory has ordered an additional 15 windows from EEV for the RFQ on LEDA. There seems to be no indication of any problems with the EEV windows. We realize that testing the windows into a matched load is not the same environment as passing RF power through the windows into an accelerator cavity with beam. Our future tests include testing the EEV windows passing power into RF cavities, as well as retesting the modified CPI windows, and finally testing the EEV windows to destruction by increasing the voltage standing wave ratio (VSWR).

## 6 ACKNOWLEDGEMENTS

The authors thank Doug Horan and Bob Kustom at Argonne National Laboratory. Also the authors acknowledge the people from LANL that helped with the experimental set up, especially Rafael Cordova, Stephen Ruggles, John Gahl, Roy Przeklasa, Michael Collins, Don Clark, J.D. Smith, and Bruce Lanier.

## REFERENCES

[1] Y. Saito, N. Matuda, S. Anami, `Breakdown of Alumina RF Windows', Rev. Sci. Instrum., Vol. 60, No. 7, July 1989.

[2] M. Pisharody, P. Barnes, E. Chojnacki, R. Durand, T. Hayes, R. Kaplan, J. Kirchgessner, J. Reilly, H. Padamsee, J. Sears, 'High Power Window Tests on a 500 MHz Planar Waveguide Window for the CESR Upgrade', 1995 Particle Accelerator Conference, Dallas, Tx.

[3] Y. Saito, N. Matuda, S. Anami, A. Kinbara, G. Horikoshi, J. Tanaka, `Breakdown of Alumina RF Windows', IEEE Trans. on Elect. Insul. , Vol. 24, No. 6, Dec 1989.

# ELECTRON GUN FOR A HIGH-POWER X-BAND MAGNICON AMPLIFIER

V.P. Yakovlev* , O.A. Nezhevenko* , Omega-P, Inc, 202008 Yale Station, New Haven, CT 06520
and R.B. True, Litton Systems, Inc., San Carlos, CA 94087

*Abstract*

This paper presents a high-power, high brightness gun design for an 11.4 GHz magnicon amplifier. Results of gun geometry optimization, and gun matching to the magnetic system, are described. A method to eliminate beam halo, decrease beam emittance, and reduce the effect of gun tolerances, is proposed.

## I. INTRODUCTION.

The magnicon is a new RF source with circular beam deflection invented in the 1980's at Budker INP [1,2]. An 11.4 GHz magnicon [3] is being developed jointly by Omega-P, NRL, and Litton as a potential very high efficiency RF source for future supercolliders. The magnicon under development is a second-harmonic amplifier designed to provide 60 MW 1.5 μsec pulses at a repetition rate of 10 pps. This paper describes a 500 kV, 210 amp (0.59 microperv) gun and beam focusing system design for this RF source.

According to [1] and investigations reported in [4], the focused beam diameter in a magnicon magnetic system must be small in order to achieve high efficiency. Small beam diameter requires that the gun be carefully matched to the main magnetic field. In the magnicon under development, the main field of 6.5 kG is capable of focusing an idealized beam of about 1.3 mm (the Brillouin diameter). We have achieved a diameter close to the Brillouin limit (1.5 mm) which is quite acceptable for achievement of the magnicon perfomance goals stated above.

A 7.5 cm diameter, 30 degree half-angle cathode is used in this gun. The peak current density in this case is less than 5 A/cm$^2$ which is consistent with very long dispenser cathode life. The beam area compression ratio is 2500:1.

A unique feature of the gun is use of an electrically isolated focus electrode biased negative with respect to cathode [5]. This serves to reduce or eliminate beam halo, decrease beam emittance, helps to overcome the effect of gun tolerances, and, thus, helps in the achievement of high beam compression and intensity.

Our level of confidence is high in achieving all of the goals reported herein in view of the fact that a 100 MW gun with high beam compression has been built for the Novosibirsk 7 GHz magnicon and is working successfully. This gun has a measured beam compression ratio of 2300:1 at a microperveance level of 0.83 [6]. The present gun design is based partly on this experience.

## II. GENERAL

The gun layout is presented in Fig. 1. In the design, the shape of the electrodes was optimized to achieve the required perveance, beam compression, and acceptable electrostatic field gradient levels.

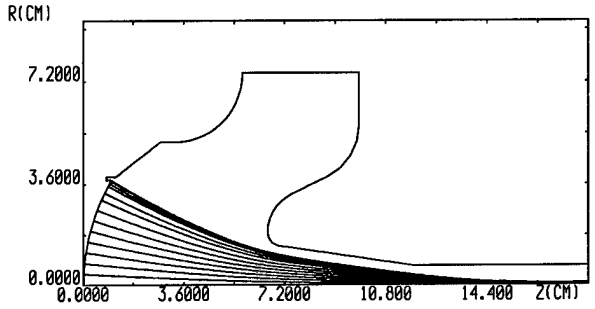



Fig. 1. The gun layout and electron trajectories

1. The initial design was developed using DEMEOS [5] (a finite element method (FEM) code utilizing six linear triangle elements [7]). The final design optimization was carried out using SUPERSAM (a FEM code which uses second-order quadrangle elements [8]). Both codes use a relativistic beam model and agreement of the results is excellent. To simulate gun matching to the magnicon magnetic system taking into account thermal emittance, PIC code BEAM [6] was used. Beam dynamics were simulated in a realistic magnetic field obtained from the SAM code [9].

2. The following physical factors may increase the equilibrium beam diameter in the magnetic system:

-residual cathode magnetic field;

-geometrical aberration;

-thermal emittance.

The equilibrium beam radius $r_0$ in the uniform magnetic field may be estimated by the formula [6], which may be obtained from Vladimirsky-Kapchinsky equation:

$$r_0 = (r_b^2/2 + (r_b^4/4 + r_h^4 + r_m^4)^{1/2})^{1/2} \qquad (1)$$

where $r_b$ is Brillouin radius, $r_h$ is "thermal" equilibrium radius (i.e., the beam radius of a beam emitted from a

* Permanent address: Budker INP, Novosibirsk 630090, Russia

0-7803-4376-X/98 /$10.00 © 1998 IEEE

perfectly shielded cathode without taking into account space charge), and $r_m$ is "magnetic" equilibrium radius (i.e.,the minimal equilibrium radius of a beam with zero emittance without taking into account the space charge). According (1), to get a beam diameter of 15% greater than Brillouin, it is necessary to have a residual cathode magnetic field not greater than 1.2 G, and a total effective transverse emittance not greater than $2.5\pi$ mrad-cm. Effective emittance is determined by thermal emittance and geometrical aberrations. The gun geometry is chosen to compensate the anode aberration by the "near-cathode" one [6].

3. The aberration caused by the gap between the focus electrode and the cathode is compensated in general by applying a negative potential of few hundred volts (with respect to cathode) to the focusing electrode. This potential not only improves the beam optics near the cathode edge, it also eliminates emission from the side of the cathode which is often the major ultimate origin of beam halo. The beam thermal emittance is about $1.6\pi$ mrad-cm which does not significantly influence the beam diameter in the magnetic system.

4. The following method is used to match the gun to the magnicon magnetic system. First, the input pole piece of the magnetic system is placed in the plane of the beam minimum without any magnetic field. Next, the gun optics are chosen such a way that the minimal value of beam radius $r_{min}$ is located on the magnetic force line, which coincides in the magnetic system with the equilibrium beam envelope having radius of $r_0$, i.e., $r_{min}=r_0\sqrt{2}$. Finally, the radius of the hole in the input pole piece is chosen to match the magnetic force lines and beam trajectories before the magnetic system entrance [6]. Calculations show that it is possible to achieve good matching this way.

5. The electric field gradient off the main focus electrode must be low enough to avoid high voltage breakdown in the gun. Empirical relationships and data on high voltage breakdown are given in [7,10]. Based upon these works, the tolerable gradient level for reliable operation even at 2 μsec is approximately 200 kV/cm. In the magnicon gun the shape of the focus electrode is optimized such that the peak negative surface gradient is 186 kV/cm, which should be quite safe.

## III. THE RESULTS OF SIMULATIONS

1. The optimized gun geometry with electron trajectories is presented in Fig. 1. Calculated beam effective emittance (caused by geometrical aberrations only) is less than $0.5\pi$ mrad-cm. The beam minimum radius without magnetic field is 0.92mm. Inhomogeneity of emission is not greater than 1.3:1 excluding the cathode edge. 2. Fig.2 shows equipotentials and trajectories for the case of optimal negative voltage on the focus electrode (-400V with respect to the cathode). The equipotential lines are almost parallel to the cathode surface in the gap between the cathode and focus electrode. We made more detailed investigations of the electron flow near the cathode edge. Its real shape was simulated by a round edge of 50μm radius.

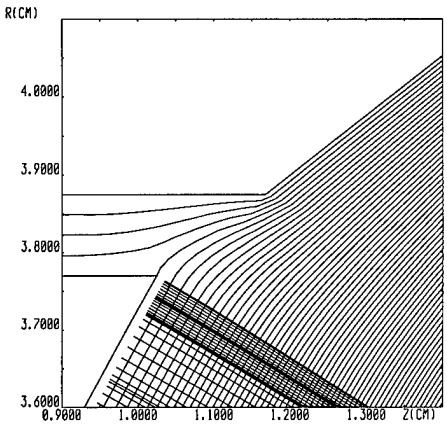



Fig. 2. Equipotentials and trajectories near a gap between the cathode and the focus electrode.

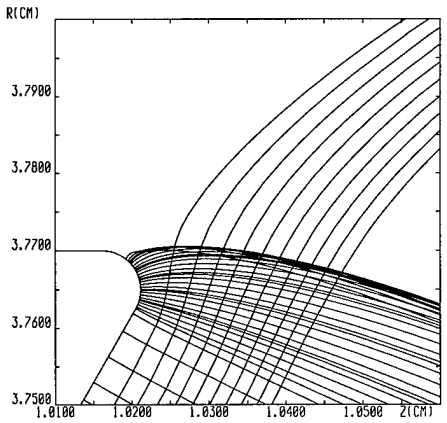



Fig. 3. Some equipotentials and trajectories near the cathode edge.

The size of area with distorted optics is about the round radius, i.e., 50μm (see Fig.3). The total current emitted from the edge is about 1 A. It gives a very small contribution to the beam emittance compared to another sources.

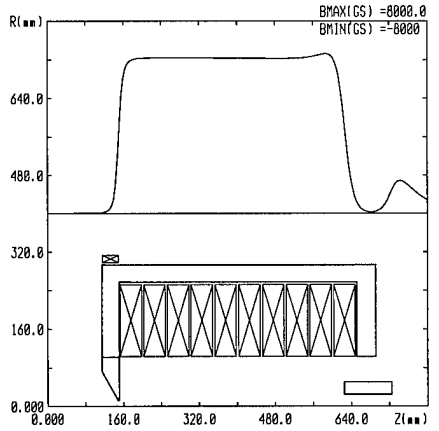



Fig. 4. Magnetic system layout.

3. The magnetic focusing system layout and axial magnetic field distribution are shown in Fig.4, and Fig.5 presents optimized beam envelopes in this magnetic system containing different fractions of the total current. The thermal emittance was not taken into account. The amplitude of beam scalloping is not greater than 5%. Thermal spread of velocities gives the halo which contains 3% of the beam current. 97% of the beam current lies within a radius of 0.75 mm. This gives a beam current density of 12 kA/cm$^2$, a pulse power density of 6 GW/cm$^2$ and an energy density of 9 kJ/cm$^2$ for a pulse duration of 1.5 μsec.

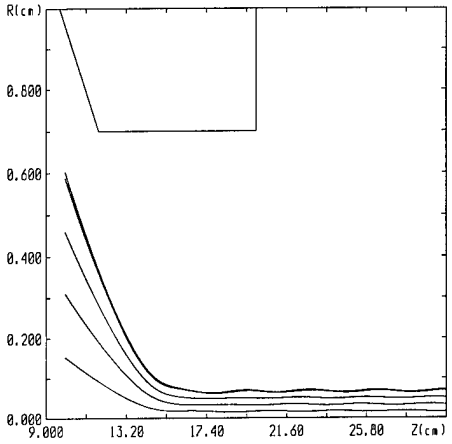



Fig. 5. The beam envelopes containing 6%, 25%, 56%, 95%, 100% of total current, respectively.

4. As was mentioned above, the electrically isolated focus electrode provides the ability to compensate for positional differences between the cathode and focus electrode via adjustment of the focus electrode voltage. This reduces the tolerance which must be held between the cathode and focus electrode. Figure 6 shows plots of maximal beam radius in the magnetic system versus cathode position for zero voltage, and optimal negative voltage applied to the focus electrode. These data indicate that spacing differences of ±0.2 mm are quite acceptable for the optimal negative voltage case.

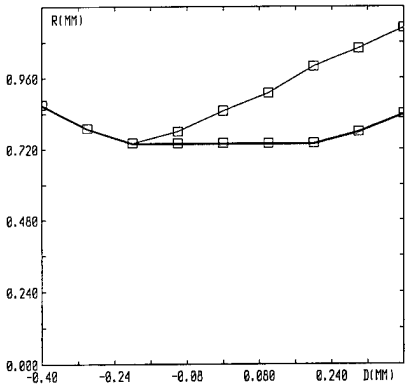



Fig. 6 The beam radius in the magnetic system versus the cathode position for optimal negative voltage (lower curve) and with zero voltage (upper curve).

## IV. SUMMARY

The gun design parameters are:

| | |
|---|---|
| Beam current, A | 210 |
| Beam voltage, kV | 500 |
| Microperveance | 0.59 |
| Pulse duration, μsec | 1.5 |
| Repetition rate, pps | 10 |
| Cathode radius, mm | 37.5 |
| Beam radius in magnetic system, mm | 0.75 |
| Beam compression | 2500:1 |
| Maximal electric field on the focus electrode, kV/cm | 186 |
| Maximal electric field on the anode, kV/cm | 265 |
| Beam transverse emittance, mrad-cm | 1.6π |
| Beam current density, kA/cm$^2$ | 12.0 |
| Beam power density, GW/cm$^2$ | 6.0 |
| Beam energy density, kJ/cm$^2$ | 9.0 |

## V. ACKNOWLEDGMENTS

Work supported by US DoE SBIR contract DEFG002-95-ER-82045. The authors would like to thank I.A. Zapryagaev for help in calculation of the gun matching with the magnetic system and D.G. Myakishev for SUPERSAM code improvements to simulate emission from the cathode edge.

## VI. REFERENCES.

[1] O.A.Nezhevenko, "Gyrocons and Magnicons: Microwave Generators with Circular Deflection of the Electron Beam," IEEE Trans. on Plasma Sci., v.22, pp. 756-772, Oct. 1994.

[2] M.M. Karliner, E.V. Kozyrev, I.G. Makarov, O.A. Nezhevenko, G.N. Ostreiko, B.Z. Persov and G.V. Serdobintsev, "The Magnicon - An Advanced Version of the Gyrocon," Nucl.Instr. Methods Phys. Res., vol. A269, pp. 459-473,1988.

[3] S.H. Gold, A.W. Fliflet, B. Hafizi, O.A. Nezhevenko, V.P. Yakovlev, J.L. Hirshfield, A.K. Kinkead, R.B. True, R.J. Hansen, "The X-Band Thermionic Magnicon Amplifier Experiment," these Proceedings.

[4] E.V. Kozyrev, I.G. Makarov, O.A. Nezhevenko, B.Z. Persov, G.V. Serdobintsev, S.V. Shchelkunoff, V.V. Tarnetsky, V.P. Yakovlev and I.A. Zapryagaev, "Perfomance of the High Power 7 GHz Magnicon Amplifier," Particle accelerators, v.52, 1996, pp.55-64.

[5] R.B. True and G.R. Good, "Design of a Very High Convergence 500 Kilovolt Gun for the NRL X-Band Magnicon," IEEE Microwave Power Tube Conference, Monterey, CA, May 1996.

[6] Y.V. Baryshev, I.V. Kazarezov, E.V. Kozyrev, G.I. Kuznetsov, I.G.Makarov, O.A. Nezhevenko, B.Z.Persov, M.A.Tiunov, V.P.Yakovlev and I.A.Zapryagaev, "A 100 MW electron source with extremely high beam area compression," Nucl. Instr. Methods Phys. Res., vol.A340, pp. 241-258,1994.

[7] R.B.True, "Electron Beam Formation, Focusing and Collection in Microwave Tubes," Handbook of Microwave Tech., K.Ishii (Ed.), Academic Press, San Diego, CA, v.1. Chap. 14, pp. 497-567, 1995.

[8] D.G.Myakishev, V.P.Yakovlev, "Code SUPERSAM for Calculation of Electron Guns with High Beam Area Convergence," XV-th International Conference on High Energy Accelerators, 1992, Hamburg. Int. J. Mod. Phys. A (proc. Suppl.) 2B (1993), v.2, pp.915-917.

[9] M.A.Tiunov, B.M.Fomel and V.P.Yakovlev, "Computer -Aided Electron Gun Design," Proc. 13th Int. Conf. High Energy Accelerators, Novosibirsk,v.1, p. 353 (1987).

[10] A.J. Durand and A.M. Schroff, "High Voltage Breakdown in the Electron Gun of Linear Microwave Tubes," High Voltage Vacuum Insulation, R.V.Latham (Ed.), Academic Press, London, Chap. 11, pp. 403-431.

# AN ALL-METAL HIGH POWER CIRCULARLY POLARIZED X-BAND RF LOAD*

W. R. Fowkes, E. N. Jongewaard, R. J. Loewen, S. G.Tantawi and A. E. Vlieks
Stanford Linear Accelerator Center, Stanford University, Stanford CA 94309 USA

*Abstract*

A compact rf load has been designed using a cascaded array of lossy radial rf chokes to dissipate 100 MW peak and 8 kW average power uniformly along the length of the load. Operation in the circularly polarized $TE_{11}$ mode assures uniform dissipation azimuthally as well.

## INTRODUCTION

The usual high power termination used for klystron testing at SLAC is the so-called SLAC "grapefruit load" because of its compact size and shape. Both X and S band versions have been designed [1]. These designs consist basically of a circular quarter wave ceramic window separating a water chamber from the waveguide vacuum. A circular to rectangular transition and an inductive post provide a sufficiently broadband match. The X band design uses a circular taper as well.

The accelerator community has always steered clear of any components where there is even the remotest possibility of water entering the accelerator vacuum due to the failure of a non-metal seal such as the ceramic window in the grapefruit load. All-metal loads with lossy conducting surfaces such as Kanthal have been used in both the long taper and disk loaded waveguide form. Kanthal coated surfaces are usually rough and can absorb large amounts of gas and water vapor when exposed to air resulting in prolonged outgassing and lengthy rf conditioning. Field emmission and multipactor can impede operation. Loads using lossy ceramic tiles have been used successfully at some laboratories but they also have outgassing problems and there are difficulties bonding the ceramics to a metal substrate, usually copper, for thermal conductivity reasons.

Tapered X-band loads made from type 430 magnetic stainless steel have been used at SLAC with limited success because of the inherent low pumping speed of the small cross-section taper and the ever-present liklihood of multipactor in a tapered structure.

## ALL-METAL RADIAL CHOKE LOAD

*Design*

The theoretical design of the load described in this paper appears in an earlier paper [2]. It was designed with the following requirements in mind:

1. All-metal, ultra-clean, high vacuum
2. Uniform power dissipation both axially and azimuthally.
3. Resistant to RF breakdown and multipactor
4. Good heat transfer to water cooling passages.
5. No weld or braze joints separating water cooling passages and the internal vacuum.

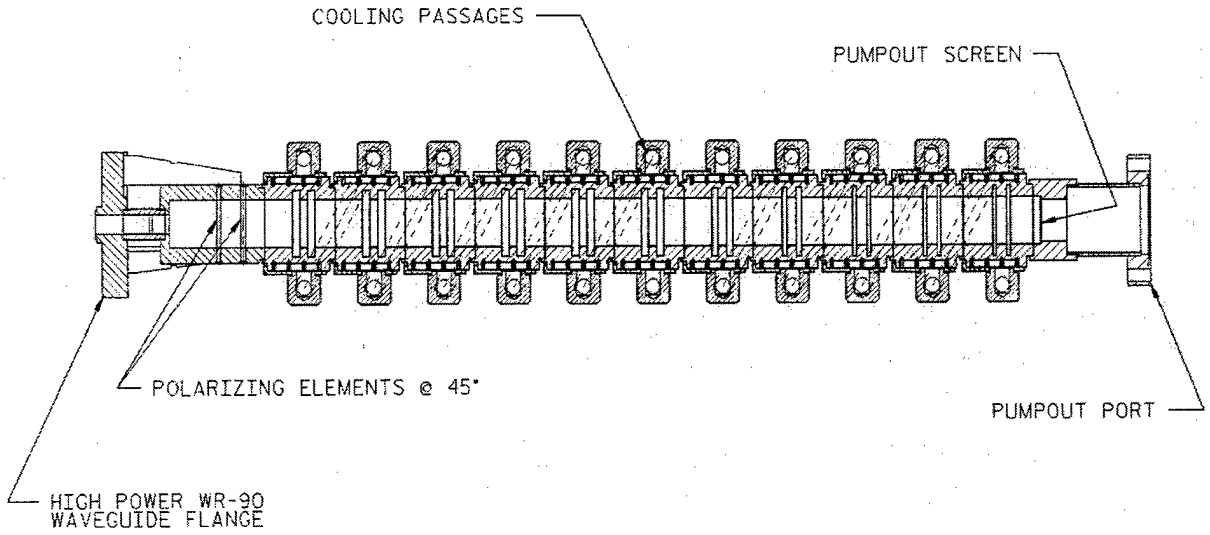



**Fig. 1.** 11 cell Radial Choke load operating in circularly polarized TE11 mode at 11.424 Ghz

* Work supported by Department of Energy contract DE-AC03-76SF00515

0-7803-4376-X/98/$10.00 © 1998 IEEE

The first version of this type of load consisted of five lossy modules, each absorbing 20% of the input power thereby requiring the attenuation in each successive module to increase in the direction of power flow. The rf fields and the heat load per module is this design turned out to be excessive for most of the needed applications.

An improved version is being built that will handle twice the power of the unit described above. It contains 11 cells with approximately 10% of the input power being dissipated in each of the first 9 cells and the remainder in the final 2 cells at the design frequency. The two way attenualtion is about 32 dB.

The load operates in a circularly polarized $TE_{11}$ mode in 25.4 mm diameter magnetic stainless steel waveguide. The circular polarization offers two advantages over the normal $TE_{11}$ mode operation. First, the power dissipation is approximately uniform azimuthally. Second, the peak rf electric field is lower by the square root of 2. The polarizer, to be described later, is at the front end of the load following a rectangular to circular waveguide transition.

Each module or cell consists of a pair of self-matching radial chokes made from type 430 magnetic stainless steel. The radial extent and axial length of the choke slots determine the loss. The spacing between choke slots is critical for a good match. All of these dimensions are dependent upon frequency. The design of the choke slots was done using MLEGO which was developed at SLAC for accurately computing the scattering coefficients of circularly symmetric elements in circular waveguide. The details of the choke pair design is described in reference [2]. To discourage breakdown, the edges of the choke slots are radiused, the effect of which cannot be modeled accurately using MLEGO and had to be determined experimentally. The effect of the radius is to raise the frequency at which the maximum loss occurs. A cutaway view of one of the choke-pair cells is shown in figure 4.

*Cooling Design*

The load material, 430 stainless steel was chosen for its high RF loss characteristics at x-band. Unfortunately this material also exhibits poor thermal conductivity, limiting the average power handling capability of loads fabricated from this material. To allow operation at reasonable average power levels, cooling channels are placed as close as possible to the lossy surfaces of the load to minimize the conductive path through the stainless steel load material. These cooling channels are formed by circumferential grooves machined into the outer diameter of each load subassembly and an outer sleeve brazed over the load subassembly. This construction method provides cooling close to the load choke surfaces while eliminating any potential leak paths from water to vacuum joints. With this design we see a maximum temperature in the inner web between chokes of approximately 150 °C at an average power of 600 W per choke pair (6 kW total load power). The peak surface temperature at the end of an RF pulse may reach 500°C or more depending on the peak RF power and pulse length.

*Circular Polarizer*

The polarizer section consists of a pair of inductive posts, each having a normalized susceptance of -j2.0, and are spaced 3/8 $\lambda_g$ apart. The 2.3 mm diameter posts are oriented at an angle of 45° with respect to incident rf electric polarization in the $TE_{11}$ mode. This incident wave can be considered as the superposition of two orthogonal, in-phase, $TE_{11}$ waves, one of which is normal to the posts and is relatively unaffected by their presence. The other component undergoes a phase shift that differs by 90° from its partner. The two components, orthogonal to one another and 90° apart in time, recombine as a circularly polarized wave emerging from the post pair region. The result is a rotating vector at any cross section beyond the polarizing section.

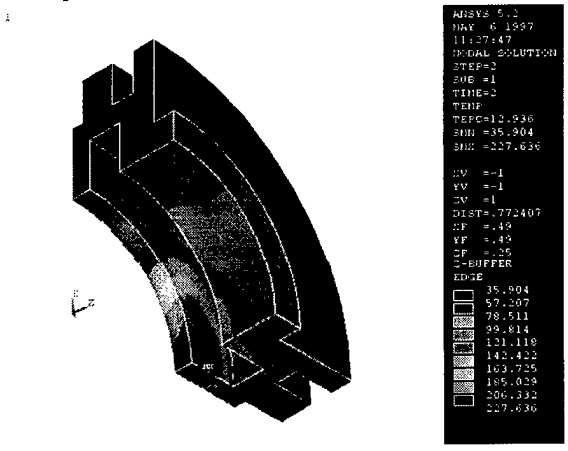



**Fig 3a**. Plot of surface temperature of load choke **without** circular polarization. The temperature at the "hot spot" reaches 227 °C with 600 watts dissipated in each cell.

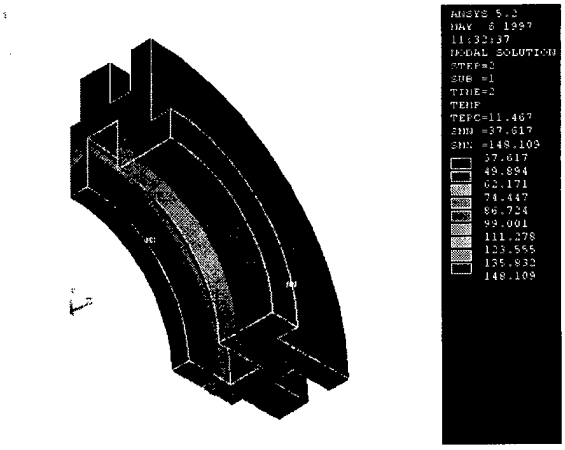



**Fig 3b**. Plot of surface temperature of load choke **with** circular polarization. At the same power level as Fig. 3a, the maximum surface temperature is 148 °C.

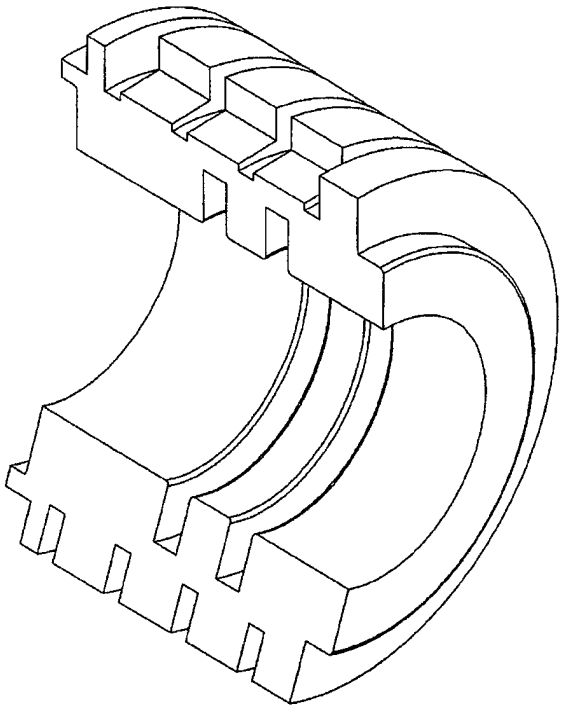


**Fig. 4** Choke-pair cell in position 8.

## SUMMARY

Although the 11 cell load has not yet been high power tested, it is expected perform comfortably up to 150 MW peak and 6 KW average power based on design calculations.

## REFERENCES


[1] W. R. Fowkes, R. S. Callin, A. E. Vlieks: "High Power RF Window and Waveguide Component Development and Testing above 100 MW at X-band". Proc. 1992 Linac Conf., vol. 1, pp 184-186.

[2] S. G. Tantawi and A. E. Vlieks, "Compact X-band High Power Load Using Magnetic Stainless Steel", Proc. 1995 Particle Accelerator Conf., p. 2132.

# THE NEXT LINEAR COLLIDER TEST ACCELERATOR'S RF PULSE COMPRESSION AND TRANSMISSION SYSTEMS

S.G.Tantawi, C. Adolphsen, S. Holmes ,T. Lavine, R.J. Loewen, C. Nantista, C. Pearson, R. Pope, J.Rifkin, R.D. Ruth, A.E. Vlieks
Stanford Linear Accelerator Center, Stanford University, Stanford, CA, 94309, U.S.A.

*Abstract*

The overmoded rf transmission and pulsed power compression system for SLAC's Next Linear Collider (NLC) program requires a high degree of transmission efficiency and mode purity to be economically feasible. To this end, a number of new, high power components and systems have been developed at X-band, which transmit rf power in the low loss, circular TE01 mode with negligible mode conversion. In addition, a highly efficient SLED-II* pulse compressor has been developed and successfully tested at high power. The system produced a 200 MW, 250 ns wide pulse with a near-perfect flat-top. In this paper we describe the design and test results of the high power pulse compression system using SLED-II.

## 1 INTRODUCTION

The NLC rf systems use low loss highly over-moded circular waveguides operating in the $TE_{01}$ mode. The efficiency of the systems is sensitive to the mode purity of the mode excited inside these guides. We used the so called flower petal mode transducer [2] to excite the $TE_{01}$ mode. This type of mode transducer is efficient, compact and capable of handling high levels of power.

To make more efficient systems, we modified this device by adding several mode selective chokes to act as mode purifiers. To manipulate the rf signals we used these modified mode converters to convert back and forth between over-moded circular waveguides and single-moded WR90 rectangular waveguides. Then, we used the relatively simple rectangular waveguide components to do the actual manipulation of rf signals. For example, two mode transducers and a mitered rectangular waveguide bend comprise a 90 degree bend. Also, a magic tee and four mode transducers would comprise a four-port-hybrid, etc. We will discuss the efficiency of an rf transport system based on the above methodology.

We also used this methodology in building the SLED-II pulse compression system. At SLAC we built 4 of these pulse systems. In this paper we describe the SLED-II system and compare the performance of these 4 systems at SLAC. We report the experimental procedures used to measure their performance as well as the results of high power tests.

## 2 CHOKED MODE CONVERTER

The flower petal mode converter is described in details in [2]. The measured level of power in spurious TE modes is ~0.5%. Simulations show similar levels of contamination due to TM modes. Although these levels of contamination are small, experimental measurements observed in a transmission line composed of a 7.442 cm diameter waveguide surrounded by two mode converters are high.

These losses are due to the mode conversion-reconversion phenomenon observed in over-moded waveguides used in communication systems[3]. Since the mode converter is efficient, for a spurious mode the circular waveguide with the two mode converters represents a high quality factor cavity. Because the line is large compared to the wavelength, there is a large number of resonating modes in the frequency band of interest. These resonant modes are coupled to the input signal because of the small mode contamination produced by the mode converters.

We basically have two choices in order to reduce the mode conversion losses. We can either reduce the coupling to spurious modes by improving the mode converter or reduce the quality factors of these resonating modes by inserting mode filters. Vacuum compatible mode filters are expensive and hard to make. We therefore tried to improve the performance of the mode converter by using mode selective chokes.

According to [2] the modes $TE_{11}$, $TE_{41}$, and $TM_{11}$ represent the main components of the mode contamination produced by the flower petal. The output waveguide of the mode converter has a diameter of 4.737 cm. Except for the $TE_{41}$ mode this guide size will not allow $TE_{4n}$ modes to propagate. Hence, a single choke designed to reflect $TE_{41}$ mode at the operating frequency of 11.424 GHz will greatly reduce the contamination from this mode. Also, if the choke width along the waveguide axis is less than the free space half wavelength it will not affect the $TE_{01}$ mode. Since the modes $TE_{11}$, $TM_{11}$, and $TE_{12}$ have the same azimuthal variations, any choke, designed to reflect any of them, will produce some mode conversion to the other modes. However, several chokes, properly spaced, can act as an effective reflector for all modes.

We added three chokes to the flower petal mode converter, one for the $TE_{41}$ and two for the $TM_{11}$ and $TE_{11}$ modes. This reduced the number and depth of these resonant modes.

0-7803-4376-X/98/$10.00 © 1998 IEEE

## 3 IMPLEMENTATION OF SLED II

Figure 1 shows the pulse compression system. It uses two 35.35 to 37.5-meter long cylindrical copper waveguides as delay lines, each 12.065 cm in diameter and operating in the $TE_{01}$ mode. In theory, these over-moded delay lines can form a storage cavity with a quality factor $Q > 1x10^6$. Each of the delay lines is terminated by a shorting plate whose axial position is controllable to within ±12 μm by a DC motor with a position-monitor feed back system. The input of the line is tapered down to a 4.737 cm diameter waveguide at which the mode $TE_{02}$ is cut-off; hence, the circular irises that determine the coupling to the lines do not excite higher order modes provided that they are perfectly concentric with the waveguide axis. A choked mode converter excites the $TE_{01}$ mode just before each iris. Both mode converters are connected to the coplanar arms of a high-power WR90 magic tee. The arms differ in length by a quarter wavelength at the operating frequency of 11.424 GHz. Therefore, the reflection from the lines exits through the H-arm when the input to the lines enters from the E-arm. The distance from the irises to the center of the magic tee has been adjusted to within ±13 μm to maximize this transmission.

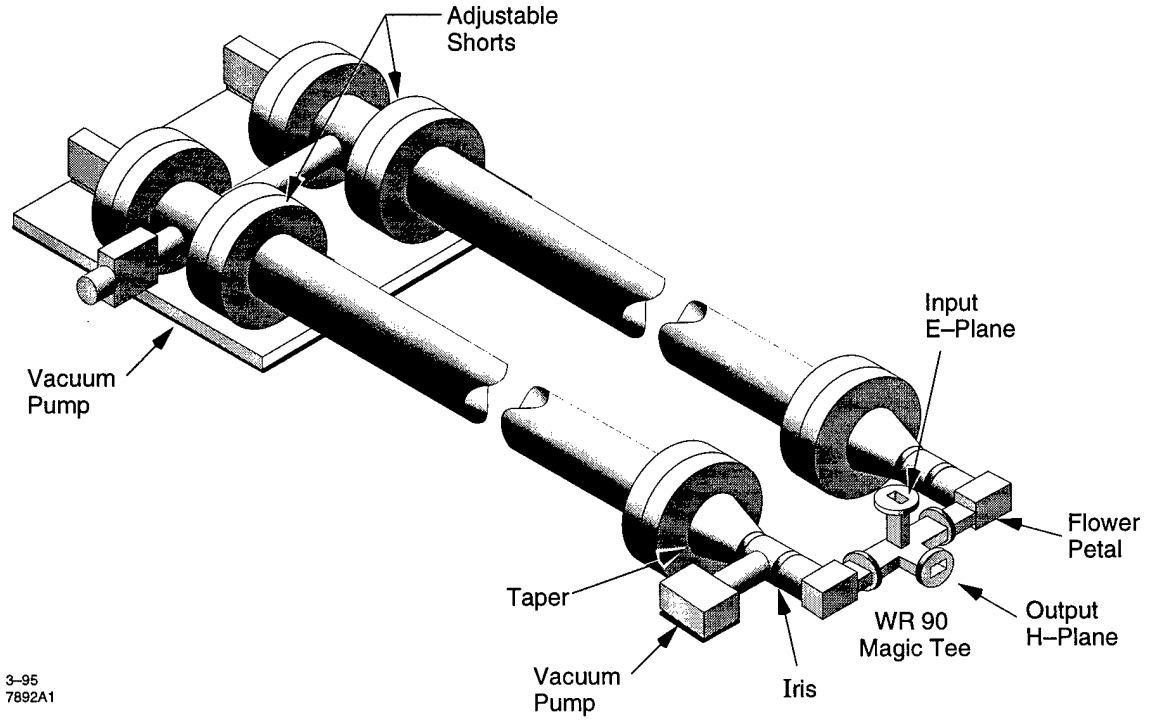



Figure 1. SLED-II Layout. It has two 12.065 cm diameter waveguides, 35.35 m in length (223 nS round-trip time.)

## 4 MEASUREMENTS

All measurements were performed using an HP8510C network analyzer with the results examined in the time domain using a PC. The frequency domain measurements were transferred to the PC via a GPIB link and multiplied by the FFT of a maximally flat pulse modulating an 11.424 GHz signal. This pulse has a limited frequency response that is smaller than the measurement's frequency span.

The time domain output is produced by taking the IFFT of this frequency domain product. Note that once we obtain the frequency characteristics of the system from the network analyzer, we can calculate the time domain response for any arbitrary input pulse. Furthermore, the phase reversed pulse required for SLED II can be sensitized by linear addition of two maximally flat pulses.

## 5 EXPERIMENTAL RESULTS

### *5.1 Transmission Line Measurements*

The transmission line that connects the output of the first pulse compressor in the NLCTA to the injector section of the accelerator is 19.86 meters long. It contains two 90 degree bends and two mode converters, one at each end. To measure the performance of that line one end was shorted. We measured the response of this system with the technique described in the above section. Figure 2 shows the reflected pulse after a round trip through the line. The one way *theoretical* power loss through the line due to the circular waveguide, which has a 7.442 cm diameter, is 1.4%. Then from the measurements the one way losses of the line is 5.82%. Hence, because the system contains 6 mode converters, an upper limit for the losses per mode converter can be set to 0.74%.

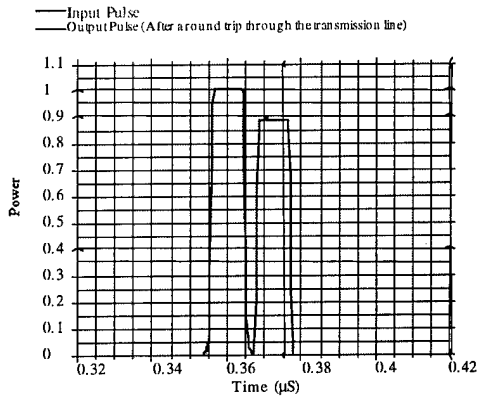



Figure 2. Performance of the transmission line that connects the pulse compressor to the accelerator.

*5.2 SLED II Measurements*

Figure 3 shows the response of the NLCTA injector system to a 1.338 μS pulse. The last 223 nS of the pulse have 180 degree phase shift. (A compression ratio of 6). The measured efficiency of the system is 67.5%. It also compares the high power measurements to the cold test results.

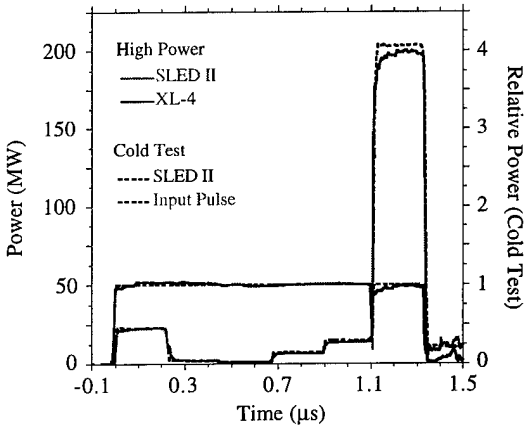



Figure 3. Measured Output of the NLCTA's First RF Pulse Compressor.

The power gain was measured for a series of compression factors. A least-squares fitting of these measurements to theoretical response [4] is shown in Figure 4. The round trip power loss was found to be 1.51%, indicating an intrinsic Q for the lines of $1.05 \times 10^6$. The theoretical value for the round trip losses is 1.15%. This low level of losses in the lines indicates that an extremely pure $TE_{01}$ mode is being excited in these lines. The external losses are 6.89%, and the iris reflection coefficient is 0.70. The iris was designed using a mode matching code to have a reflection coefficient of 0.685, the optimum value for a compression ratio of 6.

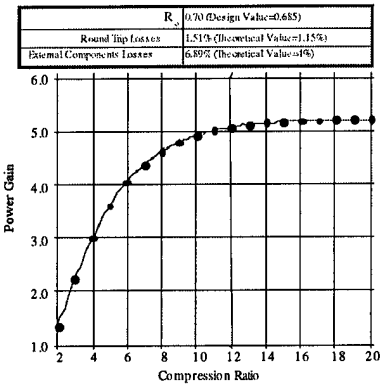



Figure 4 The points are measured power gains. The above table shows the fitting parameters.

This procedure was repeated for all 4 systems built at SLAC. Table I shows a comparison between all these systems.

| | Test Lab SLED II | NLCTA Station #0 | NLCTA Station #1 | NLCTA Station#2 |
|---|---|---|---|---|
| Compression Ratio | 8 | 6 | 6 | 6 |
| Pulse width (nS) | 150 | 223 | 245 | 245 |
| Delay Line Losses/100nS (%) | 1.63 | 0.68 | 0.52 | 0.59 |
| Intrinsic Q | $4.3 \times 10^5$ | $1.05 \times 10^6$ | $1.37 \times 10^6$ | $1.21 \times 10^6$ |
| Total Delay Line Losses (%) | 5.05 | 3.63 | 2.34 | 2.39 |
| External Losses (%) | 4.85 | 6.89 | 6.36 | 5.26 |
| Total Efficiency (%) | 58.6 | 67.5 | 68.6 | 69.3 |

Table I. Comparison Between the 4 SLED II Systems at SLAC

## 6 CONCLUSION

We have demonstrated efficient transport and pulse compression rf systems suitable for the NLC program. These systems are based on an efficient and compact mode transducer. The implemented systems approached the theoretical design values. We also demonstrated measurement techniques capable of measuring rf systems with very small losses.

## 7 ACKNOWLEDGMENT

This work is supported by the US Department of Energy under contract DE-AC03-76F00515.

## REFERENCES

[1] P. B. Wilson, Z. D. Farkas, and R. D. Ruth, "SLED II: A New Method of RF Pulse Compression," Linear Accelerator Conference, Albuquerque, NM, September 1990; SLAC-PUB-5330.

[2] S. G. Tantawi et al., "Numerical Design and Analysis of a Compact TE10 to TE01 Mode Transducer," Conference on Computational Accelerator Physics, Los Alamos, NM, 1993, AIP Conference Proceedings 297, pp. 99-106.

[3] S. E. Miller, "Waveguide as a Communication Medium," The Bell System Technical Journal, Nov. 1954, pp. 1209-1265.

[4] S. G. Tantawi et al, " Active Radio Frequency Pulse Compression Using Switched Resonant Delay Lines," Nuclear Instruments & Methods in Physics Research Section A, Vol. 370 (1996) pp. 297-302.

# UPGRADE OF THE SLAC SLED-II PULSE COMPRESSION SYSTEM BASED ON RECENT HIGH POWER TESTS*

A.E.Vlieks, W.R. Fowkes, R.J.Loewen and S.G.Tantawi
Stanford Linear Accelerator Center, Stanford University, Stanford, CA 94309 U.S.A.

*Abstract*

In the Next Linear Collider (NLC) it is expected that the high power rf components be able to handle peak power levels in excess of 400 MW. We present recent results of high power tests designed to investigate the RF breakdown limits of the X-band pulse compression system used at SLAC. (SLED-II). Results of these tests show that both the $TE_{01}$-$TE_{10}$ mode converter and the 4-port hybrid have a maximum useful power limit of 220-250 MW. Based on these tests, modifications of these components have been undertaken to improve their peak field handling capability. Results of these modifications will be presented.

## 1 INTRODUCTION

As part of an international effort to develop a new 0.5-1.5 TeV electron-positron linear collider for the 21st century, SLAC has been working towards a design, referred to as "The Next Linear Collider" (NLC), which will operate at 11.424 GHz and utilize 50 -75 MW klystrons as rf power sources. One of the major challenges in this design, or any other design, is how to generate and efficiently transport extremely high rf power from a source to an accelerator structure. SLAC has been investigating various methods of "pulse compressing" a relatively wide rf pulse ($\geq 1$ μs) from a klystron into a narrower, but more intense, pulse. Currently a SLED-II pulse compression scheme [1] is being used at SLAC in the NLC Test Accelerator (NLCTA) and in the Accelerator Structures Test Area (ASTA) to provide high rf power for accelerator and component testing. In ASTA, a 1.05 μs pulse from a 50 MW klystron was successfully pulse compressed to 205 MW with a pulse width of 150 ns.

Since operation in NLC will require generating and transporting rf power in excess of 400 MW it was decided to test the breakdown limits of the SLED-II rf components in ASTA with rf power up to the maximum available of 400 MW. This required the combining of power from two 50 MW klystrons and feeding the summed power into the SLED-II pulse compressor. Results from this experiment demonstrated that two of the key components of SLED-II; the Magic Tee and the "Flower Petal" mode converter (converts between $TE_{10}$ rectangular and $TE_{01}$ circular modes), were not robust enough at higher power levels. Because of this, a major effort is underway to upgrade the existing devices to operate stably at the higher power levels, and also to investigate new components, which have inherently low field enhancement in their design and therefore more robust.

## 2 DUAL KLYSTRON TEST

In order to have sufficient rf power to stress the critical components beyond that of earlier tests it was necessary to combine the power of two 50 MW klystrons using a 3-dB hybrid (Magic Tee). The drive signals to the two klystrons were phased so that the unused, terminated arm of the hybrid had a minimal signal. The combined power was then fed into the SLED-II 3-dB hybrid as shown in figure 1.

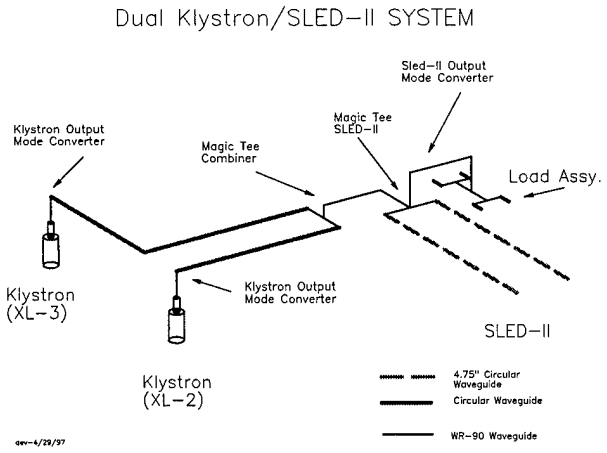



*Figure1. Dual Klystron Test Setup*

In order to absorb the total power from SLED-II, the output power was split equally into four all-metal choke loads [2] using three Magic Tees operating in parallel. Three water-cooled "grapefruit" loads [3] were used to terminate the unused arm of each Magic Tee. Forward and reflected rf power was measured at the input and output of SLED-II with side-coupled directional couplers and an HP-8990A Peak Power Analyzer. In order to minimize rf losses (and improve vacuum pumping efficiency), the rf was transported through overmoded circular waveguide in the $TE_{01}$ low loss mode. Conversion between the circular and rectangular waveguides was accomplished by "Flower Petal" $TE_{10}$-$TE_{01}$ mode converters.

RF conditioning was initially rather slow because of outgassing in the long lengths of new waveguide, mode

* Work supported by Department of Energy contract DE-AC03-76SF00515.

0-7803-4376-X/98 /$10.00 © 1998 IEEE

converters and combiner added upstream of the SLED-II Magic Tee. It required approximately 5 weeks of conditioning to reach 180 MW. In order to separate the conditioning of the new components from the high power testing of SLED-II, the 180° phase switching (PSK) of the klystron input signal was initially not used. In this way the output power of SLED-II was kept low (power gain of ≈2) while the klystrons were brought up to full power. (a combined power of ≈90 MW). Once this section of the system was conditioned and operated stably, the klystron power was lowered, the PSK was made operatonal and the SLED-II system was operated at its normal 4:1 power gain. At this point essentially all vacuum and rf break-down activity occurred at the SLED-II output mode converter and Magic Tee. Radiation levels at this mode converter exceeded 10 mR/hr for output SLED-II power levels of 225 MW and became higher as the power was raised further. After two additional weeks of conditioning, peak power levels of up to 300 MW were measured at pulse repetition rates of 10 pps. (see fig. 2.)

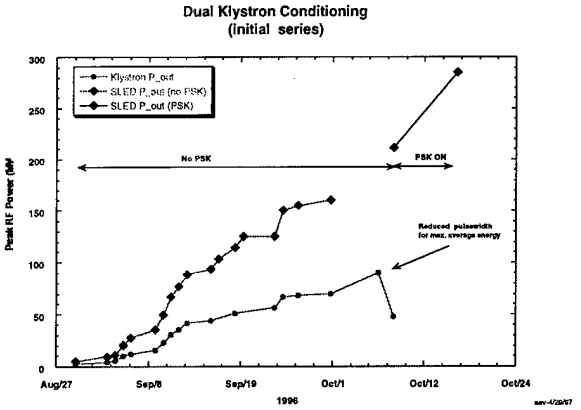



*Figure 2. Initial System Conditioning*

These power levels, however, could not be maintained for more than a few seconds at a time before rf breakdown occurred. At power levels of 275 MW the system could operate for minutes at a time and below 250 MW the system operated stably. Since most of the breakdown occurred at the output mode converter it was decided to open up the system and investigate the condition of this component. Damage to the device was obvious on initial inspection. The end of the bifurcation in the rectangular guide was severely eroded as was the opposing wall. Since this mode converter was an early model which had no deliberate radius at the bifurcation tip, it was decided to replace the component with a new model which had a 0.8 mm radiused edge. Testing was then resumed. Progress was rapid until power levels of 220 MW was reached. Above this level, breakdown in the new mode converter limited progress and the peak power level attained was ≈280 MW. Completely stable operation was only possible at 220-250 MW. After reopening the system, the new mode converter showed damage similar to the first one. In order to test other components in the system it was decided to eliminate the mode converters and connect the load assembly directly to the SLED-II Magic Tee. Repeating the experiment showed that the Magic Tee became the dominant source of breakdown. Surprisingly, the limiting power level was near the other previous values. ≈265 MW. At this point the experiment was concluded and the entire SLED-II system was inspected. It was found that the SLED-II Magic Tee was badly eroded in two trouble spots; the sharp corners on three sides of the opening into the E arm and the rounded tip of the single ended matching post in the throat of the four-port junction. No other component showed severe erosion or damage.

## 3 HIGH POWER COMPONENTS

Results of these tests clearly showed a need for improved component performance at the power levels required by NLC. Accordingly, efforts are underway at SLAC to improve the performance of some of the existing key components and to develop new components for NLC which are inherently robust at high peak fields.

### *3.1 Modified Components:*

We have developed modifications to the Magic Tee and Flower Petal mode converters, based on the damage observed from tests and from HFSS computer simulations, which have reduced field levels at critical locations. Figure 3 shows a model of the new Magic Tee design.

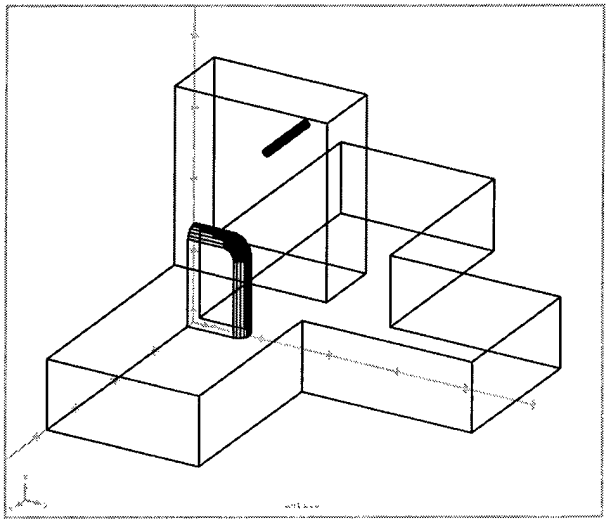


*Figure 3. Modified Magic Tee Design*

Magic Tee simulations using HFSS [4] indicate that a "fat" fin in the throat and an inductive element in the E-arm would result in a reduction in rf electric field by approximately a factor of two below the original SLAC design. A 1.2 mm radius was machined on three sides of the waveguide opening into the E-arm reducing the local surface electric field at this other trouble spot. The new Flower Petal mode converter design also has lower fields than the original design, and the region of high field is

much reduced. The reduction is not as significant as for the Magic Tee, however. The exact breakdown mechanism in the mode converter is not as clear as for the Magic Tee since, even in the original design, the rf electric field enhancement at the erosion locations does not appear particularly high according to HFSS simulatons. It is speculated that poor vacuum and perhaps a multipactor phenomenon involving forward scattered electrons may be taking place but no conclusive analysis has been performed. This new design also improves the vacuum pumping in the critical areas. Cold-testing of the new design has been completed.

*3.2 New Components:*

New, planar devices (H-plane) are also being investigated to provide components with minimum field enhancement. These include a short-slot hybrid (see figure 4) and an array of H-plane three port junctions specially matched to form a planar bridge structure.

The Riblet short slot hybrid has low maximum RF electric field for a given power compared with other four-port hybrid designs. The theory for this device is well documented [5]. High directivity and equal power division have been very difficult to achieve in the past because of critical dimensional tolerances. Precise optimization relied ultimately on cut-and-try machining and the addition of a matching element in the slot region. The success of the design depends on simultaneously controlling the phase advance and match of both the $TE_{10}$ and $TE_{20}$ modes in the slot region. The phase advance of these two modes, including the reverse shift due to the slot end effects, must differ by exactly 90° to give equal power split. At the same time the slot length is very critical to achieve a good match and hence directivity. In addition, the slot region width must necessarily be narrower than twice the single waveguide width to avoid exciting the TE30 mode.

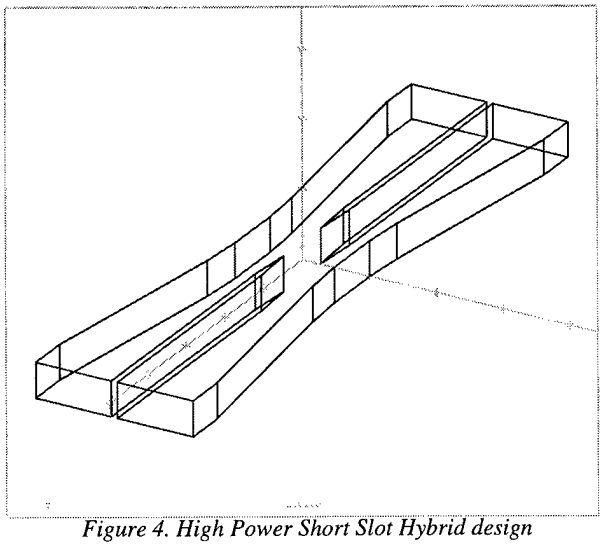


*Figure 4. High Power Short Slot Hybrid design*

Today using codes such as HFSS and MAFIA very good directivity, match and power division can be modeled and optimized before cutting any metal. A paper design for a 3 dB short slot hybrid that requires no matching elements has been completed. See figure 4.

The maximum RF electric field is somewhat higher than the field in the waveguide ports feeding the device.

A new "wrap-around" mode converter [6] (see figure 5) has also been designed with 40% lower peak electric fields than the original "Flower Petal". Recent cold-test results show excellent performance and also in complete agreement with calculation.

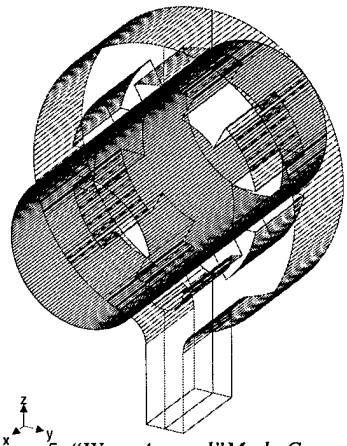



*Figure 5. "Wrap Around" Mode Converter*

## 4 CONCLUSION

We have designed and are building new high power rf components which, according to simulation, will have lower peak electric field than their existing counterparts in NLCTA and ASTA. These new components are direct replacement parts and should permit higher power operation for these facilities. In addition, we are completing the design of a new family of components which will have intrinsically, the lowest field enhancement possible for a given rectangular waveguide dimension. They will find their application in the NLC.

## REFERENCES


[1] S.G.Tantawi et Al: 'The Next Linear Test Accelerator's RF Pulse Compression and Transmission Systems, 7P.58, PAC'97

[2] Sami G. Tantawi and A. E.Vlieks: 'Compact X-band High Power Load Using Magnetic Stainless Steel', p.2132 Proceedings of the 1995 Particle Accelerator Conference and International Confrence on High Energy Accelerators.

[3] W.R. Fowkes, R.S. Callin, A.E. Vlieks: 'High Power RF Window and Waveguide Component Development and Testing above 100-MW at X-Band'. SLAC-PUB-5877, Aug 1992. 3pp., 1992, Proceedings, Linear accelerator Conference, vol. 1 184-186

[4] HFSS is Hewlett-Packard's "High Frequency Structure Simulator" software package.

[5] Riblet,H. J., 'The Short-Slot Hybrid Junction', Proc. I.R.E., 1952, **40**, p. 180.

[6] S. Tantawi, K.Ko, V. Srinivas and A.E.Vlieks, 'A Compact High Power $TE_{01}$ to $TE_{10}$ Mode Converter., 7P.57, PAC'97

# MULTIPACTOR DISCHARGE ON A DIELECTRIC

R. A. Kishek and Y. Y. Lau, Department of Nuclear Engineering and Radiological Sciences, University of Michigan, Ann Arbor, MI 48109-2104

*Abstract*

This paper proposes a novel theory of a single-surface multipactor discharge on a dielectric, such as an rf window. Using a Monte Carlo simulation, we obtain the susceptibility diagram, applicable to a wide range of materials, in terms of the rf electric field and of the DC electric field that may result from dielectric charging. The electron multiplication mechanism assumes realistic yield curves of secondary electrons, including distributions of emission velocities and angles for these electrons. The susceptibility diagram thus constructed allows an immediate assessment of the range of rf power over which multipactor may be expected to occur. A simple analytic theory which corroborates the simulation results is presented.

Multipactor discharge is an ubiquitous phenomenon observed in a multitude of devices that employ microwaves [1]. In the worst scenario, its presence leads to destruction of ceramic rf windows [1-2], erosion of metallic structures, melting of internal components, and perforation of vacuum walls [1]. Multipactor may occur when a metallic gap or a dielectric surface is exposed to an AC electric field under some favorable conditions, and its avoidance has been a major concern among workers on high power microwave sources, rf accelerators, and space-based communication systems [3].

In this paper, we present a theory of single-surface multipactor discharge on a dielectric, significantly extending the only existing theoretical treatment [2] on this subject known to us. We shall evaluate the combined action of an rf electric field that is parallel to the dielectric surface, and of a DC electric field normal to the surface that is assumed to be present as a result of dielectric charging. This surface charging has been experimentally verified, with the resulting electric field measured to be as high as 4 kV/cm [1-2]. We shall compute the multipactor growth, using realistic yield curves of secondary electron emission. A Monte Carlo simulation is performed to account for the distributions of the emission velocities and emission angles of the secondary electrons. We ignore the space charge effects, rf loading by the multipactor, and the saturation mechanism (if any).

The geometry for this type of single-surface multipactor is shown in Fig. 1. Electrons emitted with a random velocity, $v_o$, and a random angle, $\phi$, with respect to the positive y-axis, are subjected to forces imposed by the electric fields. The rf electric field, of magnitude $E_{rfo}$ and frequency $\omega$, acts only in the y-direction and imparts energy to the multipactor electrons, as well as translates them along the y-axis. The DC electric field, $E_{DC}$, does not impart any energy to the electrons. An electron emitted from the surface with a non-zero emission velocity is bent back by the restoring DC electric field and strikes the surface at a later time. During its transit, the electron gains energy only from the rf electric field, in a direction parallel to the surface. Thus upon impact, the electron strikes with much larger energy, and therefore emits a number of secondary electrons. This process repeats and, eventually, a large amount of energy gained from the rf electric field will be deposited on the surface, possibly leading to surface damage or breakdown.

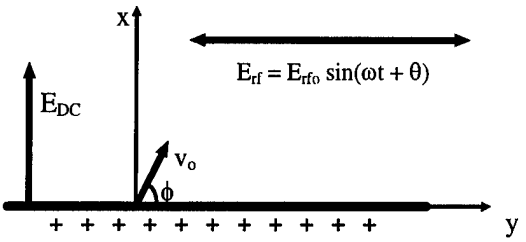



Fig. 1 Model of a single-surface multipactor in a parallel rf and normal DC electric fields.

The secondary electron yield, $\delta$, is a function of the impact energy of the primary electron, $E_i$, and the angle to the normal, $\xi$, at which it strikes the surface. For the dependence of yield on impact energy, we will adopt Vaughan's empirical formula [4] which is characterized by two material-dependent parameters: the maximum yield, $\delta_{max}$, and the energy at which it occurs, $E_{max}$. Two values of impact energy, termed the first and second crossover points, $E_1$ and $E_2$ respectively, result in a yield of 1, while $\delta > 1$ in between.

For impact at an angle, the parameters $E_{max}$ and $\delta_{max}$ are adjusted in calculating the yield, according to the following equations [4]:

$$E_{max} = E_{max0}\left(1+\frac{k_s\xi^2}{\pi}\right)$$
$$\delta_{max} = \delta_{max0}\left(1+\frac{k_s\xi^2}{2\pi}\right) \quad \textbf{(1)}$$

Here $E_{max0}$ and $\delta_{max0}$ are the parameters for an impact angle of 0° (i.e. normal to the surface), and $k_s$ is a surface smoothness factor ranging from 0 for a rough surface to 2 for a polished surface. In this paper we set $k_s = 1$, representing a typical dull surface [4]. It is worth noting that in this situation, since the electrons gain their energy from the parallel rf, most impacts will be at almost grazing incidence ($\xi = \pi/2$).

0-7803-4376-X/98/$10.00 © 1998 IEEE

In the following analysis we shall use the following normalization scales: $1/\omega$ for time, $E_{max0}$ for energies, $u = \sqrt{E_{max0}/m}$ for velocities, and $F = (\omega/e)\sqrt{mE_{max0}}$ for electric fields, where $e = 1.602 \times 4^{-19}$ C and m is the electron mass. Consider an electron launched at $t = 0$ from the surface at $y = 0$. It experiences a force due to the rf electric field, $E_{rfo} \sin(\omega t + \theta)$, which has a phase $\theta$ at the time of launch. The emission velocity, $v_o$, and angle from positive y-axis, $\phi$, are assumed to be random. Solving the equations of motion for the electron gives an expression for the impact energy:

$$E_{ix} = \tfrac{1}{2} v_o^2 \sin^2\phi$$

$$E_{iy} = \frac{E_{rfo}^2}{2}\left[\cos\left(\frac{2v_o \sin\phi}{E_{DC}} + \theta\right) - \cos(\theta) + \frac{v_o \cos\phi}{E_{rfo}}\right]^2, \quad \textbf{(2)}$$

where $E_{ix}$ and $E_{iy}$ are the x and y components, respectively, of the impact energy. The impact angle is then:

$$\xi = \arctan\left(\sqrt{\frac{E_{iy}}{E_{ix}}}\right). \quad \textbf{(3)}$$

Given the impact energy and angle, the yield is determined.

To estimate the growth rate of the multipactor discharge, we follow the trajectory of a weighted macroparticle over a large number of impacts in a Monte Carlo simulation. The initial rf phase, $\theta$, is uniformly distributed over $0 < \theta < 2\pi$. Each time a macroparticle leaves the surface, we assign it a random initial energy $E_o = \tfrac{1}{2} v_o^2$ and angle $\phi$, according to the following distributions:

$$f(E_o) = \frac{E_o}{E_{om}^2} e^{-E_o/E_{om}}, \quad \textbf{(4a)}$$

$$g(\phi) = \tfrac{1}{2}\sin\phi, \quad \textbf{(4b)}$$

where $E_{om}$ is the peak of the distribution of emission energies [note that the expected value of $E_o$ is $2E_{om}$, and that $\int g(\phi)d\phi = 1$ over $0 < \phi < \pi$].

Substituting the random values of initial energy (velocity) and angle into Eqs. (2) and (3), we obtain the impact energy and, hence, the secondary electron yield for that transit. We use this value of the yield to adjust the charge on the macroparticle, then emit it again with a random velocity. Observing the time evolution of the charge on the macroparticle over a sufficiently long time, we can see either an exponentially growing or an exponentially decaying trend, depending on the external parameters chosen ($E_{DC}$, $E_{rfo}$, and $\delta_{max0}$. A growth rate of zero identifies a point on the boundary of the multipactor region.

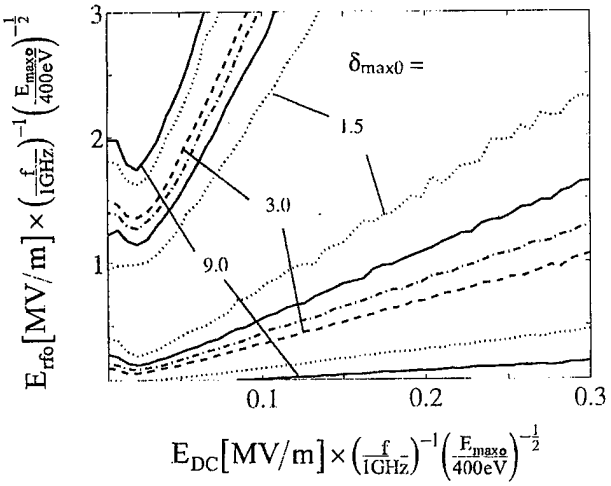



Fig. 2 Composite plot of multipactor region boundaries in the plane of ($E_{DC}$, $E_{rfo}$) for various values of $\delta_{max0}$ [from the innermost boundaries, $\delta_{max0}$ = 1.5, 2.0, 2.5, 3.0, 6.0, and 9.0], assuming $E_{om} / E_{max0} = 0.005$.

Figure 2 shows the boundary regions for selected values of $\delta_{max0}$, corresponding to typical materials used in rf windows [see Table 1]. This susceptibility curve can be quite useful. A glance at Figure 2 indicates the range of rf power over which the window may be subject to multipactor. If the design parameters lie within the multipactor boundaries (positive growth rate) then multipactor is possible and the design needs to be modified. This can be done, for example, by changing the rf level, or by adding a slightly conductive coating to the window to reduce the static charge accumulation and the resulting DC field. Alternatively, the window may be coated with a material having low $\delta_{max0}$ (e.g., TiN). These measures have been employed in practice [1-2], although perhaps not systematically but rather by trial and error.

Table 1 Typical secondary electron emission parameters for materials commonly used in rf windows [adapted from ref. 5].

| Material | $\delta_{max0}$ | $E_{max0}$ (eV) | $E_1 / E_{max0}$ (grazing incidence) | $E_2 / E_{max0}$ |
|---|---|---|---|---|
| $Al_2O_3$ (alumina) | 1.5-9 | 350-1300 | 0.23-0.011 | 10.2-24.5 |
| Quartz-glass | 2.9 | 420 | 0.072 | 15.6 |
| Pyrex | 2.3 | 340-400 | 0.107 | 13.7 |
| Technical glasses | 2-3 | 300-420 | 0.136-0.068 | 12.6-15.9 |
| $SiO_2$ (quartz) | 2.4 | 400 | 0.099 | 14.1 |

Following is the physical explanation for the shape of the susceptibility curves [Fig. 2]. For any given values of the fields, the growth rate is determined by the average value of the secondary electron yield, averaged over the random emission energy and angle distributions [Eqs. (4a) and (4b)]. Changing the magnitude of the rf

electric field changes the amount of energy the electron gains. Changing the DC field changes the amount of time spent in flight, and hence also the amount of energy gained. Since the secondary electron yield is above unity only for impact energies in between the two crossover points, if the rf electric field is too high or too low, then the amount of energy gained will vary accordingly, and thus the impact energy will fall outside of this region, where $\delta < 1$. This explains the existence of upper and lower boundaries. Now if the DC field is increased, the electron spends less time in flight, and so the rf electric field must be increased to maintain the same impact energy and yield. Preist and Talcott mention experimental evidence for the existence of the lower bound ($E_{rfmin}$) and predict the existence of an upper bound ($E_{rfmax}$) [2].

The preceding physical understanding of the phenomenon is useful in constructing an analytic solution for the susceptibility curve boundaries. First, we assume that all electrons are emitted normal to the surface, with an energy equal to the average energy of the emission energy distribution ($E_o = 2\,E_{om}$). As will be seen, this assumption does not qualitatively change the solution. Hence, substituting $E_o = 2\,E_{om}$ and $\phi = 90°$ into Eq. (2), averaging over $\theta$, and setting the resulting average impact energy equal to $E_1$, then $E_2$, we obtain the following equations for the lower and upper boundaries, respectively:

$$E_{rf\,min} = \sqrt{\frac{2E_1}{1-\cos\left(4\sqrt{E_{om}}/E_{DC}\right)}} \qquad \textbf{(5a)}$$

$$E_{rf\,max} = \sqrt{\frac{2E_2}{1-\cos\left(4\sqrt{E_{om}}/E_{DC}\right)}} \qquad \textbf{(5b)}$$

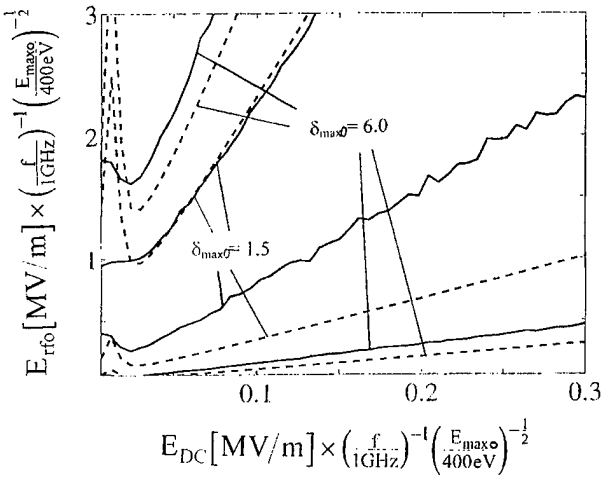



Fig. 3 Multipactor regions derived analytically (dashed) compared with ones obtained through Monte Carlo simulations (solid) for $\delta_{max0} = 1.5$ and $\delta_{max0} = 6.0$. Here, $E_{om} / E_{max0} = 0.005$.

These boundaries are compared in Figure 3 to the ones obtained from Monte Carlo simulations. We assume $E_{om} = 0.005$. As can be seen, the agreement is reasonably good, considering all the approximations involved. The slopes of the curves in Fig. 3, in the limit of large $E_{DC}$, are $\frac{1}{2}\sqrt{E_{1,2}/E_{om}}$, as easily deduced from Eqs. (5a) and (5b). Since impact is close to grazing, $\xi = \pi/2$, the values of $E_1$ and $E_2$ for grazing incidence should be used in Eqs. (5a) and (5b) [these values are listed for some materials in Table 1].

Finally, we note some differences between multipactor on a dielectric and on a metal surface. Since the impact angles of multipactor electrons on a dielectric are close to the grazing angle, the secondary electron yield would always be higher than that on a metal surface. In the steady state, multipactor on a metal surface has a secondary yield hovering around unity at the first cross-over point $E_1$ [3]. Our simulations so far cannot predict whether multipactor on a dielectric would saturate, but they seem to indicate that as the multipactor grows, the impact energies tend to prefer $E_{max}$, at which $\delta$ is maximum. Moreover, single-surface multipactor on a dielectric is less sensitive to the resonance condition that characterizes the 2-surface multipactor; it can therefore occur over a wider range of rf electric fields and phases. All of these, together with the poor heat conduction on a dielectric, perhaps partially explain the well-known vulnerability of ceramic windows to rf breakdown.

We wish to acknowledge Professor Ronald Gilgenbach and Agust Valfels for many valuable discussions. We also wish to thank Amadi Nwakanpa and Ghassan Shahin for computational support. This work was supported by the Multidisciplinary University Research Initiative (MURI), managed by the Air Force Office of Scientific Research and subcontracted through Texas Tech University, by the Department of Navy Grant N00014-97-1-G001 issued by the Naval Research Laboratory, and by the Northrop Grumman Industrial Affiliates Program.

## REFERENCES

[1] J. R. M. Vaughan, IEEE Trans. **ED-8**, 302 (1961); **ED-15**, 883 (1968); **ED-35,** 1172 (1988).

[2] D. H. Preist and R. C. Talcott, IRE Trans. **ED-8**, 243 (1961).

[3] R. A. Kishek, Y. Y. Lau, and D. Chernin, Phys. Plasmas, **4**, 863 (1997); R. A. Kishek, Ph.D. Thesis, University of Michigan, Ann Arbor (1997).

[4] J. R. M. Vaughan, IEEE Trans. **ED-36**, 1963 (1989).

[5] O. Hachenberg and W. Brauer, "Secondary Electron Emission from Solids", *Advances in Electronics and Electron Physics* **XI**, 413-499 (1959).

# OVERVIEW OF HOT TOPICS IN INSERTION DEVICE DESIGN

Kem E. Robinson, STI Optronics, Inc., 2755 Northup Way, Bellevue, Washington 98004, USA

*Abstract*

Emphasis in insertion devices (undulators and wigglers) is evolving. Conventional designs account for the majority of devices in use as synchrotron radiation (SR) or free-electron laser (FEL) sources, but more is being demanded with each succeeding application. Totally passive field compensation, gap independence, and the perfecting of phase and spectral properties are areas of major interest. However, the shift toward specialty designs is increasingly important. Designs are tailored to achieve specific radiation characteristics. These range from SR sources with time-dependent polarization capabilities to long devices optimized for FEL operation in the X-ray regime. Strong focusing and other beam dynamics related characteristics are becoming extremely important for the next generation of FEL devices. As electron beam quality continues to increase, small-gap, small period, and unconventional field profiles are becoming necessary for compact sources. These areas of increased interest are examined.

## 1 INTRODUCTION

Since the last Particle Accelerator Conference in 1995 more than 140 papers concerning insertion device technology have been published [1]. As the recent literature is examined in detail, emphasis in insertion device work can be grouped into two broad categories. The areas can be referred to as conventional devices and specialty devices. This paper, being part of the section on magnet technology, will stress those devices that fall into this technology area. Wigglers and undulators based on plasma waves [2], electromagnetic waves including lasers [3], etc., are beyond the scope of this paper and will not be discussed.

## 2 CONVENTIONAL DEVICES

Conventional devices can be defined as those whose technology and geometry have been previously demonstrated and consistently implemented. Recent work in this area has emphasized improved performance characteristics from both spectral and beam dynamics aspects. There are three general technology areas that fall into this category: permanent magnet (PM), superconducting (SC), and electromagnet (EM) technologies.

PM technology has become the "workhorse" of insertion devices and accounts for the vast majority of devices being integrated at this time. Both pure-PM [4] and hybrid [5] (containing soft permeable material) are being regularly used. Improvement of spectral properties has been a major concern as more operational experience at major synchrotron radiation facilities continues [6-10]. Delivery of undulators with 1–2 degrees of optical phase error are becoming standard [11]. Passive compensation of undulators has become a major topic with an emphasis on gap independence while preserving good-field region. Illustrative of this is work done recently at STI [12]. Whereas, powered electromagnet coils were often used in the past, work has progressed so that by adjusting the final two magnets in a hybrid device a trajectory with near zero displacement from the axis results from entrance and exit field contributions. This has been achieved without loss of periods contributing to useful radiation or FEL interaction. Figure 1 plots the measured second integral of the field (proportional to the trajectory) of several gaps showing the lack of displacement from the axis over a wide range of gaps. The undulator is the APS U55#13, a 55-mm period hybrid device. By contrast, an "ideal undulator," one with a perfect sine wave and half amplitude first kick, produces an entrance offset proportional to 80% of the wiggle amplitude. Such enhancements simplify the integration of insertion devices for both SR and FEL applications.

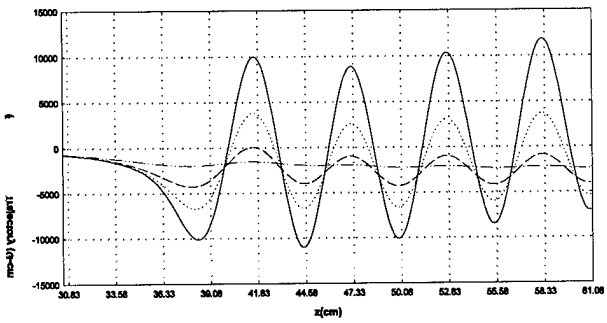



Figure 1: Entrance trajectories measured at several gaps for the APS U55#13 showing the gap independent zero-displacement configuration.

Another area that has received attention during the interim between conferences is the effect of ambient fields on performance. Magnetic performance has improved to the point that ambient field interaction is now a consideration. Pure rare-earth permanent magnet (REPM) devices are essentially transparent to ambient fields as the differential permeability of fully polarized REPM is only $\mu = 1.05$. The presence of highly permeable material in hybrid devices, on the other hand, changes the characteristics of the ambient field as the gap

0-7803-4376-X/98 /$10.00 © 1998 IEEE

is changed. The poles enhance the component of the ambient field that is in the principal field direction. The poles effectively shunt the ambient cross-field component. Figure 2 plots the relative enhancement of gap dependence of the change in the ambient field caused by a hybrid device. At minimum gap, the principal moment is increased by a factor of ~1.8 and the cross-field component is effectively shunted to zero. In addition to measurements this behavior has been confirmed in operational experience at APS and ESRF [13].

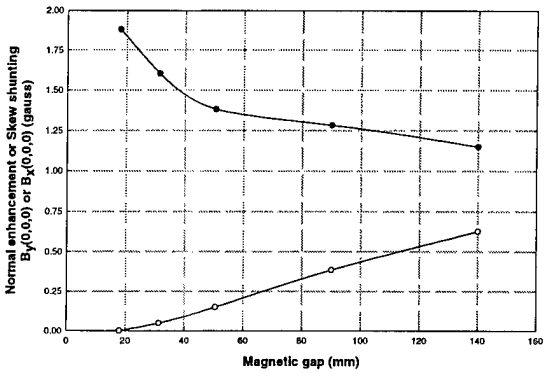



Figure 2: Plot of the relative enhancement for principal and shunting of skew ambient fields in a hybrid undulator.

In PM technology, additional work has been done in the phasing of multiple short devices mounted on the same straight section [14].

Superconducting devices are of interest in two major areas. They have proven useful as wavelength shifters in order to produce substantial quantities of hard x-rays on lower energy synchrotron radiation storage rings [15-17]. In FELs, small period superconducting undulators are being implemented to allow access into field regimes not well served at present by PM technology [18,19].

Additional aspects relating to conventional devices is the push toward small gap devices and very long straight sections for synchrotron radiation applications [20-23]

One application of undulators that have received more attention recently is their use as beam diagnostic devices. The magnetic performance has improved to the point that devices are being built and installed which are specifically dedicated for this purpose [24,25].

## 3 SPECIALTY DEVICES

Though progress and achievements in performance of conventional devices has been notable, activities in specialty devices have increased dramatically. These devices are optimized and designed for specific spectral or interaction characteristics. Three main areas appear among these devices: elliptical polarization devices for SR sources, devices optimized for self amplified spontaneous emission (SASE) FELs and compact source undulators for both FEL and SR sources.

Elliptical polarization devices have dramatically increased in number and application. These include pure REPM systems [26,27] which provide continuous or near CW elliptical polarization and electromagnet and hybrid combinations that are capable of polarization modulation of order 100 Hz or better [28-30].

SASE FEL undulators are another hot topic in insertion device technology. These devices are characteristically long, approaching 100 meters in length [31,32]. The issues associated with long undulators were first explored in the context of high power FEL oscillators and amplifiers [33,34]. Issues identified in that context remain significant concerns. Diagnostics that ensure tight overlap between the electron and photon beam are essential. If such diagnostics cannot simultaneously measure both photon and electron beams, alignment tolerances become extremely tight. The long undulators must provide, or allow, strong focusing to maintain interaction strength. This focusing is provided within the undulator structure or with external quadrupoles. External quadrupoles can either superimpose the focusing, in the case of pure-REPM designs, or be provided in longitudinal gaps in the undulator. Such gaps, whether for focusing, diagnostics, or vacuum pumping are a source of concern in SASE FEL design [35,36]. Focusing can also be provided by either arrangements of magnets within the undulator or the shaping of poles either longitudinally or transversely [37-41].

Another topic of interest is the push toward compact sources. Two areas of the many being explored for compact sources are micro-undulators and optical mode tapering. Micro-undulators are loosely defined as those devices with a period less than 10 mm. Activity in this area has extended over several years. Several approaches have been pursued including the use of LIGA technology [42-44].

Optical mode tapering is a specific application of constant resonant-energy tapering [45]. In normal tapering of undulators and wigglers the period and/or field is adjusted to change the resonant photon wavelength or electron energy subject to the resonance equation:

$$2\gamma^2\lambda_p = \lambda_w\left(1+K^2/2\right) \qquad (1)$$

In constant resonant-energy (CRE) tapering the period, $\lambda_w$, and magnetic field, B, of the wiggler, ($K = eB\lambda_w/2\pi mc$) are adjusted in order to maintain the product of the square of the electron energy, $\gamma$, and optical wavelength, $\lambda_p$, constant. This formulation of the resonance equation assumes an essentially constant period undulator. If one examines the general wiggler field and particle motion equations and maximizes the on-axis spontaneous emission, there is a modification of the wiggler parameter K,

$$K = \sqrt{\left(\frac{eB\lambda_w}{2\pi mc}\right)^2 - \left(\frac{\lambda_w}{2\pi}\frac{dK}{dz}\right)^2} \qquad (2)$$

This divides constant resonant energy tapers into two broad categories: one where the changes in B and $\lambda_w$ are small within a wiggler period (and the derivative term can be ignored), and the other where changes are large within a wiggler period.

Optical mode tapering (OMT) is a specific application of CRE to address two problems related to the operation of compact FELs. The gap of the undulator used in an FEL is often limited by the size of the optical beam at the ends of the undulator. The length of the optical cavity is often dictated by matching to the undulator and maintaining a large spot size on the resonator mirrors to limit damage. By adjusting the undulator gap throughout its length to be as small as permitted by the optical mode the interaction strength and number of periods in an undulator can be maximized. The variation in period and field needed to maintain resonance is not significant until the Rayleigh range is on the order of the undulator length or smaller.

To illustrate the types of performance enhancement that can be achieved with OMT, it is useful to examine an analytical system with a nominal values: 1 meter undulator length, $L_w$, a photon wavelength, $\lambda_p$ = 10 μm, an electron beam energy $\gamma$ = 50, and a mode limitation that the local gap must not be less than 4 times the optical mode radius. For illustration the system is assumed to have low gain and the mode is described by a $TEM_{00}$ mode. With this example system, one can examine two regimes: the Rayleigh range for a fixed undulator length, and the undulator length for a fixed Rayleigh range. Figure 3 is a plot comparing the small signal gain of the fixed 1-meter OMT undulator and the equivalent-length uniform-gap device. The optimum Rayleigh range for the uniform gap device is ~$L_w$/3 whereas the OMT optimizes at ~$L_w$/5. The maximum gain of the OMT is 40% higher than that of the uniform gap and the Rayleigh range can be shortened by more than a factor of 3 without losing gain compared to the maximum for the uniform gap device. Figure 4 plots the small signal gain for a fixed Rayleigh range = 0.5 meter for both the OMT and uniform-gap undulators. With the uniform-gap device as periods are added the K must decrease to accommodate the optical mode. The loss of the wiggler length eventually exceeds the benefit of the additional periods. For the OMT as periods are added the interaction strength of the central periods are not diminished and a stronger interaction is maintained so gain is enhanced for a significantly longer undulator. This continues until the additional periods have such a weak field that they no longer contribute to the gain.

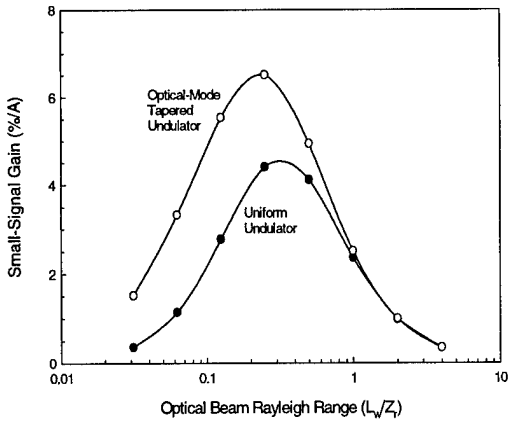



Figure 3: Small signal gain for OMT and uniform undulator for a 1-meter wiggler for various Rayleigh ranges.

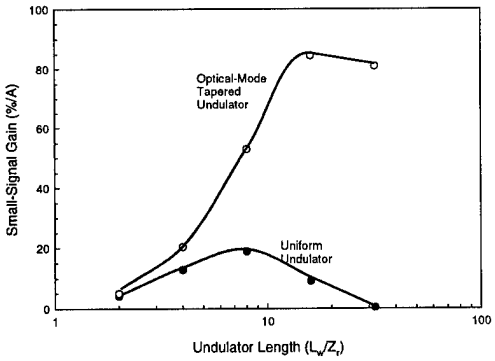



Figure 4: Small signal gain as a function of undulator length for the OMT and uniform undulator for a fixed Rayleigh range of 0.5 m.

## 4 CONCLUSION AND ACKNOWLEDGMENTS

From an examination of the activities in undulators and wigglers it is clear that it is an area still alive with interest and a great deal of potential for progress in providing radiation sources and diagnostics with improved characteristics. The technology has advanced and the variety of approaches increased that devices specialized for specific characteristics are becoming more commonplace. One area that is also important to gauging the success of an insertion device is the development of precise measurements that accurately determine its optical characteristics [46].

This paper can only scratch the surface of the activity and the works cited are illustrative only and must not be viewed as all encompassing. The absence of a citation in no way indicates the author's opinion of its significance to the field.

The author would like to acknowledge the many stimulating conversations and insights that he has received with many of the researchers in this area. He also would like to acknowledge the contributions and stimulating environment provided by his colleagues, S. C. Gottschalk and D. C. Quimby at STI Optronics, and acknowledge the work of B. Hertz in the preparation of this paper.

## REFERENCES

[1] Current Contents 1995–1996, Physical, Chemical & Earth Sciences, Institute for Scientific Information, Philadelphia, PA, USA.

[2] One recent example: Ikehata, T., Suzuki, Y., Nagai, R., Sadamoto, Y., Sato, N.Y., Mase, H., "A novel laser technique for constructing a plasma micro-undulator and a compact X-ray source," Nuclear Instruments & Methods in Physics Research Section A - Accelerators Spectrometers Detectors and Associated Equipment, 1996, 383, 3-Feb, pp. 605-609.

[3] One recent example: Csonka, P.L., "Optical beam-energy modulators," IEEE Journal of Quantum Electronics, 1997, 33, 2, 138-146.

[4] Halbach, K., "Physical and Optical Properties of Rare Earth Cobalt Magnets," Nucl. Instr. Meth., 187 (1981), pp. 109-117.

[5] Halbach, K., "Permanent Magnet Undulators," J. Phys. (Paris) Colloq. C1, 44, C1-211 (1983).

[6] Nikitina, Y.M., Pfluger, J., "Influence of magnetic field errors on the spectrum of the PETRA undulator," Nuclear Instruments & Methods in Physics Research Section A - Accelerators Spectrometers Detectors and Associated Equipment, 1995, 359, 2-Jan, 89-92.

[7] Shastri, S.D., R.J. Dejus, D.R. Haeffner, and J.C. Lang "Performance of Advanced Photon Source insertion devices at high photon energies (50–300 keV)," Rev. Sci. Instrum. 67 (9), September 1996, C02.

[8] Gottschalk, S.C., Robinson, K.E., Quimby, D.C., Kangas, K.W., Vasserman, I., Dejus, R., and Moog, E., "Multipole and Phase Tuning Methods for Insertion Devices ," Rev. Sci. Instrum. 67 (9), September 1996, C08.

[9] Chavanne, J., P. Elleaume, P. Van Vaerenbergh, "Status of the ESRF insertion devices," Rev. Sci. Instrum. 67 (9), September 1996, C01.

[10] Walker, R.P., B. Diviacco, D. Zangrando, "Operation of Insertion Devices in ELETTRA," these proceedings.

[11] STI Magnetics Group, APS U55#13, APS U33#19, APS U33#22, TJNAF U27 Certification Documentation, STI Optronics, Inc., Technical Data Sets, unpublished.

[12] Gottschalk, S. C., Robinson K. E., Quimby, D. C., "End Field Compensation on Hybrid Undulators," manuscript in preparation for submission to Rev. of Sci. Instrum.

[13] E. R. Moog, Private Communication, Advanced Photon Source.

[14] Chavanne, J., Elleaume, P., VanVaerenbergh, P., "Phasing multi-segment undulators," Journal of Synchrotron Radiation, 1996, 3, 93-96.

[15] Mikkonen, R., Soderlund, L., "A 6 T superconducting wiggler for synchrotron radiation'" IEEE Transactions on Magnetics, 1996, 32, 4, 2617-2620.

[16] Grudiev, A.V., Djurba, V.K., Kulipanov, G.N., Khlestov, V.B., Mezentsev, N.A., Ruvinsky, S.I., Shkaruba, V.A., Sukhanov, S.V., Vobly, P.D., Koo, Y.M., Kim, D.E., Sohn, Y.U., "Superconducting 7.5 tesla wiggler for PLS," Nuclear Instruments & Methods in Physics Research Section A - Accelerators Spectrometers Detectors and Associated Equipment, 1995, 359, 2-Jan, 101-106.

[17] Sugiyama, S., Ohgaki, H., Mikado, T., Yamada, K., Chiwaki, M., Suzuki, R., Sei, N., Ohdaira, T., Noguchi, T., Yamazaki, T., Isojima, S., Usami, H., Suzawa, C., Masuda, T., Keishi, T., Hosoda, Y., "Design and manufacture of a 10-T superconducting wiggler magnet at TERAS," Review of Scientific Instruments, 1995, 66, 2, 1960-1963.

[18] Ingold, G., BenZvi, I., Solomon, L., Woodle, M., "Fabrication of a high-field short-period superconducting undulator," Nuclear Instruments & Methods in Physics Research Section A - Accelerators Spectrometers Detectors and Associated Equipment, 1996, 375, 3-Jan, 451-455.

[19] Bordovitsyn, V.A., Epp, V.Y., Kozhevnikov, A.V., Zalmezh, V.F., "An undulator for a FEL based on a solenoid with superconducting diaphragms," Nuclear Instruments & Methods in Physics Research Section A - Accelerators Spectrometers Detectors and Associated Equipment, 1995, 359, 2-Jan, 47-49.

[20] Stefan, P.M., S. Krinsky, "Experience with small-gap undulators," Rev. Sci. Instrum. 67 (9), September 1996.

[21] Andersson, A., Werin, S., Meinander, T., deBrito, A.N., Aksela, S., "Experiences with the narrow gap undulator at MAX-lab," Nuclear Instruments & Methods in Physics Research Section A - Accelerators Spectrometers Detectors and Associated Equipment, 1995, 362, 3-Feb, 586-591.

[22] "4th Generation Radiation Source Workshop," ESRF, Grenoble, France, January 1996.

[23] "30-meter Straight Section Workshop," Spring-8, April 1996.

[24] Yang, B.X., A.H. Lumpkin, G.A. Goeppner, S. Sharma, E. Rotela, I.C. Sheng, E. Moog, "Status of the APS Diagnostics Undulator Beamline," these proceedings.

[25] Ponds, M.L., Feng, Y., Madey, J.M.J., OShea, P.G., "Non-destructive diagnosis of relativistic electron beams using a short undulator," Nuclear Instruments & Methods in Physics Research Section A - Accelerators Spectrometers Detectors and Associated Equipment, 1996, 375, 3-Jan, 136-139.

[26] Marks, S., C. Cortopassi, J. DeVries, E. Hoyer, R. Lenbach, Y. Minamihara, H. Padmore, P. Pepersky, D. Plate, R. Schlueter, A. Young, "The Advanced Light Source Elliptically Polarizing Undulator," these proceedings.

[27] Carr, R., Kortright, J.B., Rice, M., Lidia, S., "Performance of the elliptically polarizing undulator on SPEAR," Review of Scientific Instruments, 1995, 66, 2, 1862-1864.

[28] Montano, P.A., Knapp, G.S., Jennings, G., Gluskin, E., Trakhtenberg, E., Vasserman, I.B., Ivanov, P.M., Frachon, D., Moog, E.R., Turner, L.R., Shenoy, G.K., Bedzyk, M.J., Ramanathan, M., Beno, M.A., Cowan, P.L., "Elliptical multipole wiggler facility at the Advanced Photon Source," Review of Scientific Instruments, 1995, 66, 2, 1839-1841.

[29] Walker, R. P., D. Bulfone, B. Diviacco, P. Michelini, L. Tosi, R. Visintini, G. Ingold, F. Schaefers, M. Scheer, G. Wuestefeld, M. Eriksson, S. Werin, "Design of an Electromagnetic Elliptical Wiggler for ELETTRA," these proceedings.

[30] E. Gluskin, "Elliptical multipole wiggler for the production of variably polarized radiation," abstract, Rev. Sci. Instrum. 67 (9) 1996.

[31] Rossbach, J., "The TESLA Free Electron Laser," these proceedings.

[32] Tatchyn, R., Arthur, J., Baltay, M., Bane, K., Boyce, R., Cornacchia, M., Cremer, T., Fisher, A., Hahn, S.J., Hernandez, M., Loew, G., Miller, R., Nelson, W.R., Nuhn, H.D., Palmer, D., Paterson, J., Raubenheimer, T., Weaver, J., Wiedemann, H., Winick, H., Pellegrini, C., Travish, G., Scharlemann, E.T., Caspi, S., Fawley, W., Halbach, K., Kim, K.J., Schlueter, R., Xie, M., Meyerhofer, D., Bonifacio, R., DeSalvo, L., "Research and development toward a 4.5-1.5 angstrom linac coherent light source (LCLS) at SLAC," Nuclear Instruments & Methods in Physics Research Section A - Accelerators Spectrometers Detectors and Associated Equipment, 1996, 375, 3-Jan, 274-283.

[33] Robinson, K.E., Quimby, D.C., and Slater, J.M., "The Tapered Hybrid Undulator (THUNDER) of the Visible Free-Electron Laser Oscillator Experiment," IEEE J. Quant. Electron., QE-23 (9), pp. 1497-1513 (1987).

[34] Quimby, D. C., S. C. Gottschalk, F. E. James, K. E. Robinson, J. M. Slater, and A. S. Valla, "Development of a 10-Meter Wedged-Pole Undulator," Nucl. Instrum. And Methods in Phys. Res. A285, pp. 281-289 (1989).

[35] Kim, K.J., Xie, M., Pellegrini, C., "Effects of undulator interruptions on the performance of high-gain FEL amplifiers," Nuclear Instruments & Methods in Physics Research Section A - Accelerators Spectrometers Detectors and Associated Equipment, 1996, 375, 3-Jan, 314-316.

[36] Vinokurov, N.A., "Multisegment wigglers for short wavelength FEL," Nuclear Instruments & Methods in Physics Research Section A - Accelerators Spectrometers Detectors and Associated Equipment, 1996, 375, 3-Jan, 264-268.

[37] Pfluger, J., Nikitina, Y.M., "Planar undulator schemes with strong focusing properties for the VUV-FEL at the TESLA test facility," Nuclear Instruments & Methods in Physics Research Section A - Accelerators Spectrometers Detectors and Associated Equipment, 1996, 381, 3-Feb, 554-559.

[38] Varfolomeev, A.A., Bouzouloukov, Y.P., Gubankov, V.V., Ivanchenkov, S.N., Khlebnikov, A.S., Osmanov, N.S., Tolmachev, S.V., "Development of focusing undulators on the basis of side magnet arrays," Nuclear Instruments & Methods in Physics Research Section A - Accelerators Spectrometers Detectors and Associated Equipment, 1995, 359, 2-Jan, 85-88.

[39] Schlueter, R.D., "Undulators for short wavelength FEL amplifiers," Nuclear Instruments & Methods in Physics Research Section A - Accelerators Spectrometers Detectors and Associated Equipment, 1995, 358, 3-Jan, 44-47.

[40] Quimby, D. C. and J. M. Slater, Proc. SPIE 453, 92 (1984).

[41] Neil, V. K. "Emittance and Transport of Electron Beam in a Free Electron Laser," SRI International Report JSR-79-10 (December 1979).

[42] Choi, J.S., Heo, E.G., Lee, S.H., Choi, D.I., "The magnetoresonance operation of microwiggler using a piezoelectric with a strong magnetic guide field," Nuclear Instruments & Methods in Physics Research Section A - Accelerators Spectrometers Detectors and Associated Equipment, 1996, 375, 3-Jan, 370-372.

[43] Catravas, P., Stoner, R., Bekefi, G., "Characteristics of the MIT microwiggler for free electron laser applications," Nuclear Instruments & Methods in Physics Research Section A - Accelerators Spectrometers Detectors and Associated Equipment, 1996, 375, 3-Jan, 412-415.

[44] Turner, L.R., Nassiri, A., Mills, F.E., Kim, S., Feinerman, A., "A micro-undulator fabricated by LIGA processes," IEEE Transactions on Magnetics, 1996, 32, 4, 2602-2604.

[45] Robinson, K. E., S. C. Gottschalk, D. C. Quimby, and T. D. Hayward, "Constant Resonant Energy Tapering in Free-Electron Lasers," Proc. Free Electron Laser Conf. 1996, Rome, Italy, to be pub. Nucl. Instrum. & Methods in Phys. Res. A.

[46] Hahn, U., SchulteSchrepping, H., Balewski, K., Schneider, J.R., Ilinski, P., Lai, B., Yun, W., Legnini, D., Gluskin, E., "Measurements of emittance and absolute spectral flux of the PETRA undulator at DESY Hamburg," Journal of Synchrotron Radiation, 1997, 4, , 5-Jan.

# EXPERIMENTS AND CYCLING AT THE LHC PROTOTYPE HALF-CELL

R. Saban, J. Casas-Cubillos, P. Collier, P. Cruikshank, K. Dahlerup-Petersen, B. Desforges, B. Hilbert, G. Krainz, F. Momal, A. Rijllart, F. Rodriguez-Mateos, R. Schmidt, L. Serio,
CERN, Geneva, Switzerland

## 1 INTRODUCTION

The first version of the LHC Prototype Half-Cell [1,2] has been in operation since February 1995. It consists of one quadrupole and three 10-m twin aperture dipole magnets which operate at 1.9 K. One electrical circuit powers all the magnets in series. This experimental set-up has been used to observe and study phenomena which appear when the systems are assembled in one unit and therefore influence one another.

## 2 EXPERIMENTS

Two experimental runs have been performed in the two years since commissioning began in December 1994 [2]. RUN2 started with the addition of a third dipole and a structural modification to the cryogenic system [3]. The LHC half-cell systems, the experiments and their results have been described and reported in detail in specialized conferences [4,5,6]: what follows is a concise report of the experiments carried-out with the facility.

The 1.9 K superfluid helium cooling scheme was experimentally validated in steady state conditions and during transients [7]. The thermohydraulic effects of a resistive transition of a string of magnets have been investigated. A model was developped and was extrapolated to a full-cell of LHC [8]; this allowed the reduction the number of valves and definition of their technical characteristics. Heat loads on the cryogenic system have been measured in steady state and with degraded insulation vacuum [9]. They confirmed the calculated heat loads and in some cases highlighted possible improvements.

The quench detection and magnet protection system [10,11] was experimentally validated. Quench propagation between magnets has been studied by provoking a quench in the quadrupole and observing its propagation to the adjacent dipole [12].

Experiments to determine the upper limit on pressure in the insulation vacuum enclosure prior to cool-down have confirmed that positive displacement pumps achieving a pressure of 1 Pa are sufficient [13]. The limited propagation speed of a helium leak along a cryogenically cooled tube has been measured on the 1.9 K cold bore beam tube [14] showing agreement within 20% of the theoretical model. Accidental loss of insulation vacuum has been studied by venting the cold LHC Prototype Half-Cell to atmospheric pressure.

The displacements of the magnet cold masses relative to their cryostats, for long term stability measurements, during quenches and during electrical cycles were monitored [15].

## 3 THE CYCLING EXPERIMENT

The cycling experiment was performed in order to reveal eventual flaws of components of the half-cell which could only be seen after some time of operation of the collider.

After 18 months of routine current ramping to 12.5 and 13.1 kA, the half-cell was electrically cycled from 800 A to 12.5 kA repeatedly in a cycle that lasted approximately 43 minutes. The ramp rates (10 A/s) were similar to those which will be experienced by the magnets during the acceleration phase. Assuming 200 days of operation per year and one injection per day, the experiment simulated 10 years of operation of the collider.

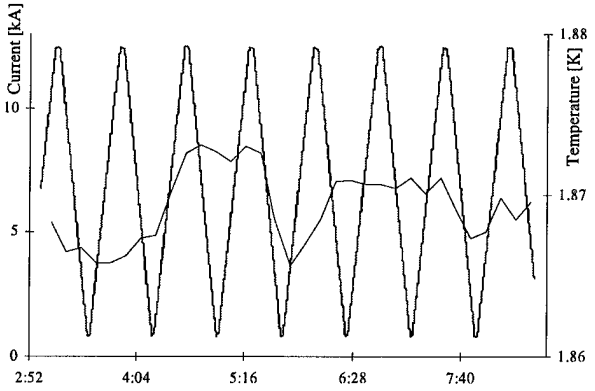



Figure 1: Current and temperature stability

### 3.1 Conditions of the experiment

The experiment was conducted from the accelerator control room under the supervision of the operators who are involved in the running of SPS and LEP. Therefore, the procedures for cycling the LHC Prototype Half-Cell had to be simple, secure and efficient to be executed by non-specialised personnel.

The area was closed with fences and video cameras were installed for remote visual inspection of the site. Two X-terminals were used to monitor the cryogenics, the vacuum and the power converter. Only limited control of the cryogenics system was available to prepare for cycling or put the cryogenic system in stand-by mode.

0-7803-4376-X/98 /$10.00 © 1998 IEEE

The program controlling the power converter allowed the operator to start, stop or interrupt the continuous cycling. A completely linear downwards ramp at -10 A/s was achieved despite the inverse voltage limitation set by the free-wheeling diodes of the power converter. Authorization for powering was granted only by the magnet protection team at the beginning of a cycling period or after the interlocks had been broken.

All the systems (vacuum, cryogenic, magnet protection, power converter, general mains) were hardware interlocked. Depending on the gravity of a failure of any of the systems, the string was either slowly discharged or the magnets were quenched by firing the protection heaters.

The experiment, which lasted eleven weeks, was conducted 24 hours a day and seven days a week; it was only interrupted by access requirements to the restricted area of the LHC Prototype Half-Cell or the unavailability of peripheral systems (e.g. central refrigeration plant). The access procedure was remotely controlled by the accelerator control room operators: it mainly involved the lowering of the current to 50 A. The power converter was rarely turned-off because the operation would break the interlock chain.

*3.2 Incidents*

Although a number of minor incidents occurred during the cycling experiment, all were adequately handled either by the emergency systems which had been engineered for this purpose, or by the control room operators.

3.2.1 Interruption of the Cryogenic Supply

On several occasions, the liquid helium level in the main dewar supplying the LHC Prototype Half-Cell among other users, fell below a threshold. The operators were informed by an alarm signal and were advised to stop cycling in order to avoid quenching the magnets due to loss of nominal cryogenic conditions.

3.2.2 Quench Heater Power Supply Failure

Capacitor banks which are discharged in the protection heaters when a quench occurrs are continuously monitored. Two different internal power supplies failed on two occasions when the magnets were at 12.5 kA and 1.8 kA. As a result, the interlock chain was broken and the magnets slowly discharged.

3.2.3 Mains Failure

A mains failure on the electricity grid occurred during the falling phase of the cycle when the magnets were excited at 9.8 kA. The protection heaters were fired and the magnets were quenched. The emergency procedure during the cycling experiment foresees this in order to simplify the recovery.

*3.3 Observations*

Before the experiment started, the highest current level attained without quenching any of the magnets on two occasions was 13.5 kA. A number of cycles were executed and then the current raised to the same value: if a magnet quenched before 13.5 kA, a degradation of the quenching magnet was assumed.

After a relatively low number of cycles (184), the 13.5 kA limit could not be attained; the third dipole quenched just below 13.5 kA. Instead of trying to confirm this quench level, it was decided to double the number of cycles (300) before the second dipole was quenched at 13.2 kA. The number of cycles were increased first to 500 then to 1000 before the test quench. They all confirmed a degradation in the quench level of the second dipole. The cycling experiment was ended after 2152 cycles.

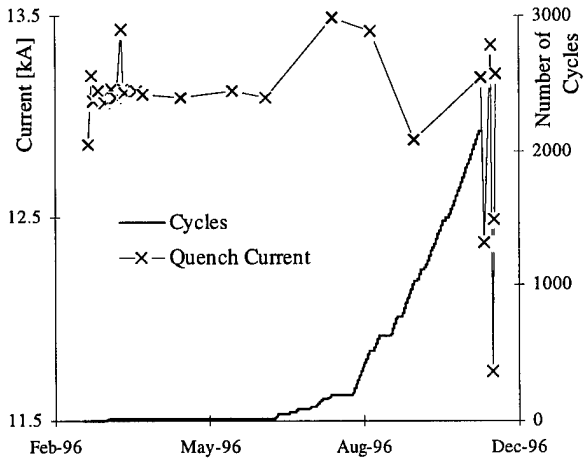



Figure 2 : Quench Current and Number of Cycles versus time

The degradation of the second dipole was investigated by repeatedly pushing the LHC Prototype Half-Cell to its highest natural quench. All the quenches which were observed during this campaign occurred in the first pole of the first aperture of the second dipole. The most salient pattern is the erratic quench behaviour characterized by quenches approaching the highest limit (13.2 kA) followed by quenches at much lower level (11.7 kA). In some cases, during the raising phase, intermediate higher current levels were attained; this wrongly suggested a retraining of the dipole (see Figure 3). The highest difference in current for two consecutive quenches was 1.6 kA. In total 10 natural quenches were caused during this campaign.

In the course of the campaign it was suggested that the quenches might be caused by a non-uniform current distribution in the superconducting cable [16]; this would start a persistent current loop which could saturate one of the strands and cause the quench. A number of attempts to highlight this effect were made, but all failed.

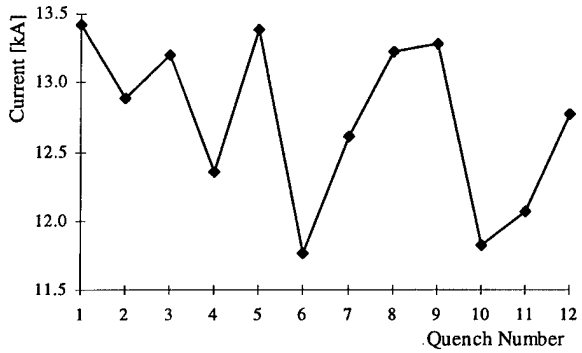



Figure 3 : Quench pattern after the cycling experiment

It was decided to remove the second dipole from the LHC Prototype Half-Cell during the shutdown following the cycling experiment. The dipole (MBL1A2) was exchanged with a spare (MBL1N1) which had been recently re-assembled and measured on the LHC Magnet Test Bench.

MBL1A2 has been since then measured on the LHC Magnet Test Bench [17]. Preliminary data, which has not yet been thoroughly analyzed, confirm what has been observed after the cycling experiment: the quenches are almost always localized to the same region of pole 1. Any attempt to identify the effects of cycling on MBL1A2 remains, so far, speculative.

Other than the degradation of the second dipole, no other effect of the cycling experiment has been identified. In the coming run, cycling will be resumed both to continue the artificial ageing of the components and, to eventually reveal other effects which might be hiding behind the degradation of the second dipole.

It is worthwhile mentioning that 85 natural or provoked quenches were performed during the two experimental runs: 45 of these were at nominal current or above. Another 15 quenches at nominal current or above were experienced by the magnets of the LHC Magnet Test Bench. This is far more than any dipole is expected to experience in the lifetime of LHC.

## 4 RUN3A

RUN3A will start in early June 1997. Following the shutdown which lasted five months, the LHC Prototype Half-Cell is now equipped with additional cryogenic instrumentation: wetting indicators in the longitudinal heat exchanger, level meter in the phase separator, flow meters in the discharge line and additional thermometers. The first beam screen [1] has been installed in the third dipole. The installation of diode directly on the bus-bars entering the third dipole will permit investigation of quench propagation between dipoles.

## 5 THE SECOND GENERATION TEST FACILITY

After RUN3, the present LHC half-cell will be dismantled. The construction of a second generation test facility will commence beginning 1999. It will include the separate cryogenic supply line and new generation 15-m dipoles with all the corrector magnets. For the year 2000 it is planned to start experimenting with a full 106-m LHC cell including three 12.5 kA circuits: one for the main dipoles, one for the focussing quadrupoles and one for the defocussing quadrupoles. Twelve additional 600 A circuits will power the multipole corrector and lattice magnets attached to the main magnets of the regular cell of an LHC arc.

## 6 ACKNOWLEDGMENTS

The authors wish to thank the operators of the Cryogenic Plant in SM18 and the operators of the Prévessin Control Room for their active participation: their autonomy during the experiment has given an insight on the reliability of the systems of the LHC Prototype Half-Cell.

## REFERENCES

[1] The Large Hadron Collider, Conceptual Design, CERN 95-05, October 1995
[2] P.Faugeras for the String Team, Assembly and Commissioning of the LHC Test String, 1995 PAC '95, Dallas, Texas, May 1995
[3] A.Bézaguet et al., Cryogenic Operation and Testing of the Extended Prototype Magnet String, paper presented at the ICEC16, Kitakyushu, Japan, May 1996.
[4] R.Saban et al., The Control and Data Acquisition of the LHC Test String, ICALEPCS, Chicago, Illinois, November 1995.
[5] Specification for a Data Acquisition System for the LHC String, CERN-AT Group Note 94-02 (IC)
[6] R.Saban et al., The LHC Test String: First Operational Experience, EPAC '96, Sitges, Spain, June 1996.
[7] A.Bézaguet et al., The Superfluid Helium Cryogenics System for the LHC Test String: Design, Construction and First Operation, Cryogenics Engineering Conference, Columbus, Ohio, July 1995.
[8] M.Chorowski et al., Thermohydraulics of resistive transitions on the LHC prototype magnet string: theoretical modelling and experimental results - to be presented at the CEC/ICMC 97 - Portland USA
[9] G.Riddone, Theoretical Modelling and Experimental Investigation of the Thermal Performance of the Prototype Lattice Cryostats, Doctoral Thesis, Politecnico di Torino, January 1997.
[10] F.Rodriguez-Mateos et al., Electrical Performance of a String of Magnets Representing a Half-Cell of the LHC Machine, MT14, Tampere, Finland, June 1995.
[11] G.Krainz, Quench Protection and Powering in a String of Superconducting Magnets for the Large Hadron Collider, Doctoral Thesis, Technical University of Graz, February 1997.
[12] L.Coull, D.Hagedorn, G.Krainz, F.Rodriguez-Mateos, R.Schmidt, Quench Propagation Tests on the LHC Superconducting Magnet String, EPAC '96, Sitges, Spain, June 1996.
[13] P.Cruikshank et al., Investigation of Thermal and Vacuum Transients on the LHC Prototype Magnet String, paper presented at the ICEC16, Kitakyushu, Japan, May 1996.
[14] E.Wallen, Experimental Test of the Propagation of a He Pressure Front in a long, Cryogenically Cooled Tube, LHC Division Vacuum Group Internal Note 96-12
[15] D.Missiaen, Metrology of Superconducting Magnets, Fourth International Workshop on Accelerator Alignment, Tsukuba, Japan, November 1995.
[16] A. Verweij, Current Redistribution in the Cables of the LHC Magnets, LHC Project Note 90, May 1997
[17] A.Siemko et al., paper in preparation for Magnet Technology MT15, Beijing, China, October 1997

# QUENCH PERFORMANCE AND FIELD QUALITY MEASUREMENTS OF THE FIRST LHC LOW-$\beta$ QUADRUPOLE MODEL

R. Ostojic, G.A. Kirby, R. Schmidt, T.M. Taylor
CERN, 1211 Geneva 23, Switzerland
S. Milward, J. Morris, S. Nobes, K. Smith, A. Street, M. Townsend, J. Treadgold, J. Wiatrzyk
Oxford Instruments, Oxfordshire, OX8 1TH, England
S.A. Gourlay, J.B. Strait
Fermilab, Batavia, IL 60510, USA

*Abstract*

As part of the LHC magnet development program, CERN in collaboration with Oxford Instruments has designed, built and tested a one metre model of a 70 mm aperture low-$\beta$ quadrupole. The magnet features a four layer coil, and is designed for 250 T/m at 1.9 K. We review the results of the magnet training and quench propagation studies performed at 4.3 K and 1.9 K, and report on the magnetic field measurements.

## 1 INTRODUCTION

As part of the LHC magnet development program, CERN in collaboration with Oxford Instruments, England, has designed built and tested a one metre model of a 70 mm aperture quadrupole for the LHC low-$\beta$ triplets. The magnet [1] has a four layer coil wound from two 8.2 mm wide NbTi cables. Two layers are wound and cured at a time, with the transition between the two cable types in the middle of the second layer. The magnet is assembled using 10 mm wide stainless steel collars and a four-piece yoke, which transmits the compression from a set of aluminium force rings with stainless stell collets.

During the first test in March 1995 [2], the magnet reached a maximum current of 3780 A at 4.3 K, after which the performance became erratic and it was not possible to train further. All quenches occurred in layers 3 and 4 of one quadrant, but the instrumentation was insufficient to locate the quenches more precisely. After the disassembly of the magnet a multi-turn short was found, caused by scissoring in the ramp between layers. The size and location of the short precluded repair and a replacement coil was wound with a modified layer ramp. This modification was also made to all the other coils to prevent similar damage. Due to availability of material, the rewound coil incorporated an insulation system which was 9 $\mu$m thicker per turn than in the other coils. To compensate for the increased thickness the size of the copper wedges at the pole was reduced. The magnet was rebuilt with a modified set of voltage taps and all the ground plane insulation replaced. In all other ways the magnet was identical to the first build.

After the rebuild the magnet was tested on two occasions, in January and October 1996, when it was trained to 4920 A at 1.8 K, and a field gradient of 238 T/m measured. In this paper we summarise the results of the magnet training and quench propagation studies, and report on the transfer function and field multipole measurements.

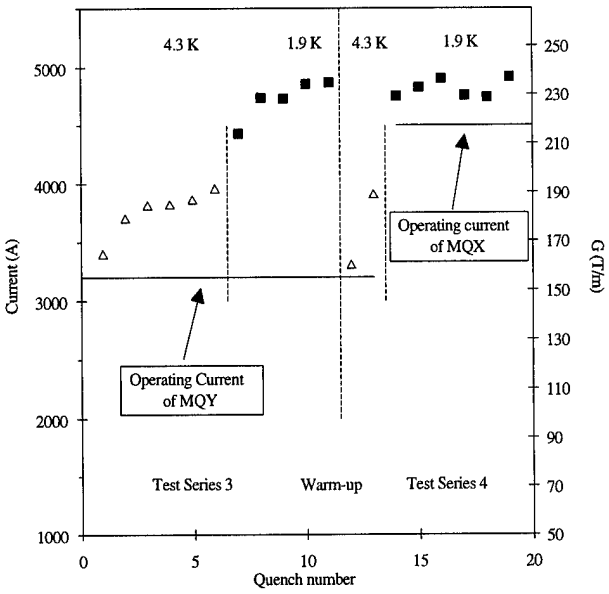



Figure 1: Training history of the model magnet.

## 2 TRAINING HISTORY

The training history is displayed in Figure 1. The maximum operating gradient of the low-$\beta$ quadrupole (MQX) of 215 T/m at 1.9 K is also shown, as well as the required gradient of 160 T/m at 4.3 K of the two-in-one quadrupole (MQY), which uses the same coil and is installed in the injection and dump insertions.

In the January 1996 test (Test 3) the magnet was initially trained at 4.3 K. The first quench occurred at 3400 A, and in the next three quenches it passed the plateau of the March 1995 test. In view of possible conductor limitation, the magnet was pumped to 4.0 K and energised with a quench at 3860 A, less than the expected gain by cooling. In the next two quenches it reached 3960 A, corresponding to 98% of the short sample limit. Throughout this stage quenches occurred in all the coils except in the rebuilt coil.

The first quench at 1.9 K occurred at 4440 A, and the next two recorded at 4745 A, with a change in quench location. Subsequently, the quench current increased to

0-7803-4376-X/98 /$10.00 © 1998 IEEE

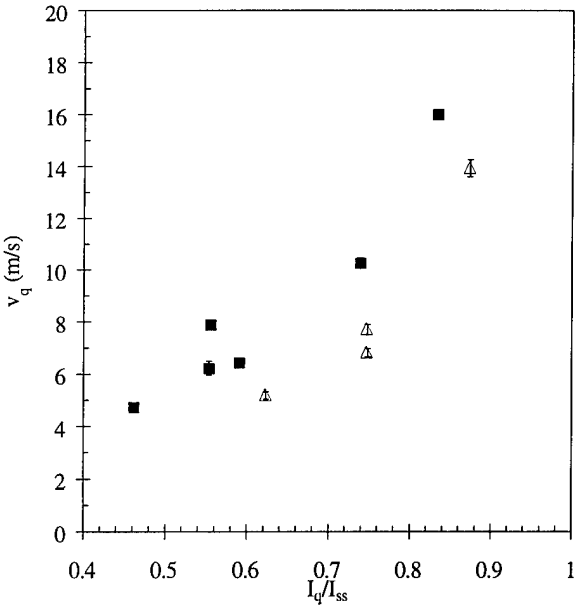



Figure 2: Quench velocity for spot heater induced quenches at 4.3 K (open symbols) and 1.9 K (full symbols). The estimated conductor limits are 4000 A at 4.3 K and 5400 A at 1.9K.

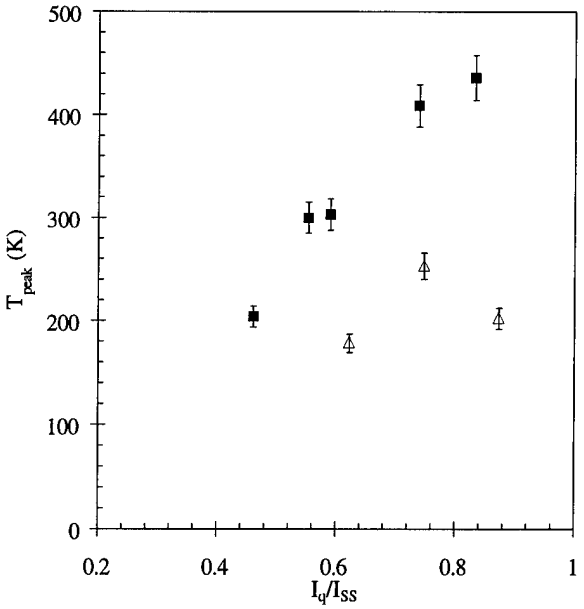



Figure 3: Peak conductor temperature for induced quenches at 4.3 K (open symbols) and 1.9 K (full symbols).

over 4850 A, indicating that the magnet has not reached a plateau. The test was discontinued in order to install the field measurement coils, and the training of the magnet resumed in October 1996 (Test 4).

A total of six training quenches were performed at 1.9 K during Test 4. The first quench current was close to that of the last quench of Test 3. All others showed a gradual increase of the current, the final quench recorded at 4920 A, corresponding to 91% of the short sample limit. In the middle of the quench series the magnet had to be warmed up to about 90 K, to unblock a faulty needle valve. A slight decrease in quench current followed, confirming the tendency of the magnet to detrain on warm up, a feature that was also noted after a long period at room temperature between January and October 1996.

At both test temperatures, the magnet has achieved a gradient above the the nominal values required for the LHC. The last quench at each temperature was in layer 2, where conductor limited quenches are expected to occur, but the instrumentation was insufficient to determine if these quenches occurred at the high field point.

## 3 QUENCH PROPAGATION STUDIES

An important objective of the tests was to measure the dependence of the quench velocity $v_q$ and of the peak conductor temperature $T_{peak}$ on the magnet current $I_q$, in order to help design a quench protection system for the full-length magnet. For these studies a special spot heater was used, located in the second layer near the high field point. A set of voltage taps defined two measurement sections. The first one, 125 mm long with the spot heater in the centre, was used for resistance measurements. The other, 585 mm away from the spot heater, was used for time of flight measurements.

The quench velocity $v_q$ for induced quenches measured by time of flight is shown in Figure 2 as function of quench current normalised to the conductor short sample limit. For both 4.3 K and 1.9 K, $v_q$ grows from about 5 m/s at low currents to 15 m/s at 85% of the conductor limit. For spontaneous quenches, the quench heater used for these measurements was still triggered as part of the protection system. The quench velocities obtained from these quenches display the same trend as in Figure 2, with the quench velocity approaching 65 m/s for highest currents. For both temperatures the relative increase of the quench velocity is well explained by the adiabatic theory. However, the measured quench velocities are systematically a factor of three smaller than predicted. A possible explanation may be in the fact that the all-polyimide insulation used in the coil construction is highly permeable, and that the assumption of adiabatic quench propagation is not fulfilled.

Quench velocities were also independently measured on the basis of the initial resistance growth dR/dt in the 125 mm section. These measurements relate to quench development over the first 10 ms, while those based on the time of flight give an average velocity over the time needed for the quench to propagate over 585 mm, typically 30-40 ms. The two methods agree well for low velocities. However, systematic differences were observed at higher fields, suggesting possible acceleration of the quench front at 4.3 K and deceleration at 1.9 K. These indications will be further investigated on the next quadrupole model, presently under construction.

Figure 3 shows the $T_{peak}$ for induced quenches mea-

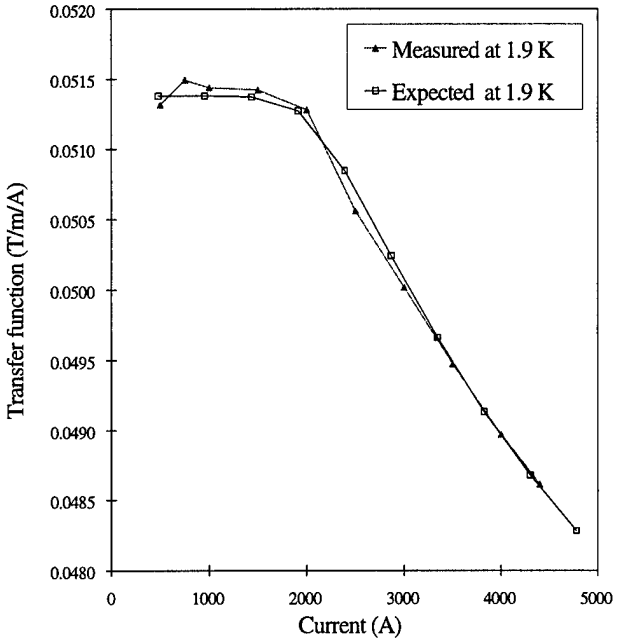



Figure 4: Measured and calculated transfer function in the body of the quadrupole at 1.9 K.

sured without energy extraction, obtained by measuring the final resistance of the 125 mm cable section. At 4.3 K, $T_{peak}$ has a maximum of about 250 K which occurs at 75% of the conductor limit. At 1.9 K, $T_{peak}$ steadily rises and reaches 430 K at 85% of the conductor limit, with an indication that a point of inflexion has been reached. This agrees well with the 465±40 K calculated on the basis of $\int I^2 dt$, where the error includes uncertainties in the start time and in the value of B at the quench location. For these conditions the magnet absorbs safely its own energy.

## 4 MAGNETIC FIELD MEASUREMENTS

The magnetic field of the quadrupole was measured using a harmonic coil system developed at CERN [3], consisting of four sets of compensated coils covering the straight section and the end regions of the magnet. The measurements were done at 4.3 K and 1.9 K, but runs were also performed at room temperature and 90 K. The measured transfer function in the body of the magnet is shown in Figure 4. The measurements performed at different temperatures agree well, and are well reproduced by the calculations which take into account coil deformation.

The measured relative field errors, given in Table I, are dominated by the low order multipoles. As remarked above, a 10% thicker insulation system was used for the replaced coil, and as a consequence, the perfect quadrupole symmetry of the magnet has been partially lost. The expected multipoles that take into account the larger size of the replaced coil are also given in Table I. They are important for all normal and skew terms up to the dodecapole and are comparable to the measurements. Higher

TABLE I
RELATIVE MULTIPOLE ERRORS AT 1.9 K AND 4600 A.
(REFERENCE RADIUS = 10 MM, IN UNITS OF $10^{-4}$)

| Multipole | Measured | | Expected | |
|---|---|---|---|---|
| | $b_n$ | $a_n$ | $b_n$ | $a_n$ |
| 3 | -0.278 | 0.492 | 0.126 | 0.126 |
| 4 | -0.393 | 0.598 | 0. | 0.197 |
| 5 | 0.647 | 0.071 | -0.041 | 0.041 |
| 6 | -0.463 | -0.028 | -0.414 | 0. |
| 7 | -0.009 | -0.002 | -0.001 | -0.001 |
| 8 | -0.002 | -0.008 | 0. | 0. |
| 9 | 0.001 | 0.005 | 0. | 0. |
| 10 | -0.006 | -0.001 | -0.006 | 0. |

order multipoles are relatively insensitive to individual coil size and block positioning. The relative $b_{10}$ multipole of $-0.006$ units was consistently measured at all temperatures and currents, and is in very good agreement with the design value.

The difference between the measured and expected multipoles may be attributed to the errors in positioning of the coil blocks. As the coil sensitivity matrix is known, the radial and angular block displacements which reproduce the residual multipoles could be determined. It was found that the displacements follow a normal distribution, indicating that the residual multipoles are due to random errors in positioning of the coil blocks. The rms errors of coil positioning are 0.02 mm and 0.04 mm for the radial and azimuthal directions respectively, and confirm the validity of the winding and curing techniques employed in the construction of the magnet.

## 5 CONCLUSIONS

The first one metre model of the 70 mm aperture low-$\beta$ quadrupole was trained to 193 T/m at 4.3 K and 238 T/m at 1.9 K, in excess of the operating current required for the LHC. Quench velocities and peak conductor temperatures have been measured, confirming that the magnet safely absorbs its energy. The measured transfer function and field harmonics are in very good correspondence with the design values, confirming the coil construction technique.

## 6 REFERENCES

[1] R. Ostojic T.M. Taylor and G.A. Kirby, "Design and Construction of a One-Metre Model of the 70 mm Aperture Quadrupole for the LHC Low-$\beta$ Insertions", *IEEE Trans. Magn.* **30** pp 1750-1753, 1994.

[2] S.R. Milward et al., "Progress in the Development of the 1-m Model of the 70 mm Aperture Quadrupole for the LHC Low-$\beta$ Insertions" Proc. 1996 Appl. Superconductivity Conf, August 1996, Pittsburgh, USA, LHC Project Report 68.

[3] J. Billan et al., "Design and Test of the Benches for the Magnetic Measurements of the LHC Prototype Dipoles", *IEEE Trans. Magn.* **30** pp 2658-2661, 1994.

# TEST RESULTS FOR A HIGH FIELD (13T) Nb3Sn DIPOLE

A.D. McInturff, R.Benjegerdes, P. Bish, S. Caspi, K.Chow, D. Dell'Orco, D. Dietderich, R. Hannaford, W. Harnden, H. Higley, A. Lietzke, L. Morrison, M. Morrison, R. Scanlan, J. Smithwick, C. Taylor, and J. van Oort
Lawrence Berkeley National Laboratory, Berkeley, California 94720

*Abstract*

A $Nb_3Sn$ dipole magnet (D20) has been designed, constructed, and tested at LBNL. Previously, we had reported [1] test results from a hybrid design dipole which contained a similar inner $Nb_3Sn$ and outer NbTi winding. This paper presents the final assembly characteristics and parameters which will be compared with those of the original magnet design [2]. The actual winding size was determined and a secondary calibration of the assembly pre-load was done by pressure sensitive film. The actual azimuthal and radial D20 pre-loading was accomplished by a very controllable novel stretched wire technique. D20 reached 12.8T(4.4K) and 13.5T(1.8K) the highest dipole magnetic fields obtained to date in the world.

## I. INTRODUCTION

The LBNL "Advancement of Accelerator Magnet Technology" program has concentrated on development of magnet construction techniques applicable to brittle superconductors. $Nb_3Sn$ was chosen as the typical brittle superconductor due to its more extensive data base, and because presently it is the only superconductor with practical current density($J_c$) in the field range of 11T to 16T. This paper will compare important design parameters previously published [2] with those achieved so far by a development $Nb_3Sn$ dipole "D20". The dipole testing has produced several surprises which summarized were a) excellent ramp rate quench performance, b) excellent thermal stability (>20 watts;12T), and c) the magnet trained up to much higher fields in contrast with earlier $Nb_3Sn$ dipole test histories [3, 4, 5]. The dipole had good high field performance 12.8T(4.4K) and 13.5T(1.8K), but at 1.8K was clearly not limited by it's critical current performance. The previous high field dipole record by Twente University group was 11.03T reached by an LHC model "MSUT" magnet [4]. The highly interdependent coil fabrication steps of $Nb_3Sn$ require a more integrated approach to cabling, insulating, stepped multi-phased heat treatment, similar expansion and contraction materials, protection heaters, epoxy impregnation, assembly, and pre-loading due to the larger temperature range that the winding must operate compared to NbTi. There is a large body of $Nb_3Sn$ data that indicates a substantial $J_c$ loss with increasing perpendicular strain, which up to fields of 13.5T did not appear to be the limit in the present configuration of D20.

Manuscript received May 16, 1997.
The work is supported under contract # DE-AD03-76SF00098 by Director, Office of Energy Research, Office of High Energy Physics, US Dept. of Energy.

## II. DESIGN

D20 is a four layer graded cable cosine Θ winding distribution 50mm bore dipole. The inner two layers (1&2) used one size cable (37-0.75mm dia strands) with a 1.57mm (1.65mm-meas.) thickness and a 14.66mm (14.66mm-meas.) width under a load of 34.5 MPa. These cable strands were made by two different manufacturers-Teledyne Wah Chang and Intermagnetics General. The outer two layers (3&4) use another size cable (47-0.48mm dia strands) with a 1.12mm (1.30mm-meas.) thickness and a 11.89mm (11.91mm-meas.) width under a load of 34.5MPa. These cable strands were manufactured by Teledyne Wah Chang. All of the cabling was done at the LBNL cabling facility. The coil design numbers as well as the maximum values attained to date are given in Table I and II.

| D20 Design@4.35K | Central Field (T) | I. Layer Field (T) | O. Layer Field (T) |
|---|---|---|---|
| 6400 A | 13 | 13.3 | 10.45 |
| 7000 A Short Sample (SS) | 14. | 14.4 | 11.2 |
| 6925 A @ 4.5 K SS-11% (Degrad 140 MPa) = 6525 A | 13.2 | 13.5 | 10.6 |
| D20 @ 4.5 K Reached 6300 A | 12.8 | 13.1 | 10.29 |
| @1.8 K Reached 6712 A | 13.5 | 13.8 | 10.75 |

Table I Magnetic Field versus $I_c$ or $I_q$

| D20 @ 13T 6400 A | Inner Cable IGC | | Outer Cable TWCA | |
|---|---|---|---|---|
| | Design | Reached | Design | Reached |
| $J_{cu}$ (A/mm²) | 1302 | 1367 | 1462 | 1535.1 |
| $J_{non\ cu}$ (A/mm²) | 559 | 587 | 1550 | 1627.5 |
| $J_{overall}$ (A/mm²) | 276 | 290 | 479 | 503 |

Table II Current Densities

Cable insulation is composed of single glass sleeve 0.12mm thick in the straight sections and then wrapped with extra glass tape 0.28mm thick around the ends to prevent shorts. The original fiberglass sizing is evaporated off the fabric before being replaced with the special palmitic acid and ethanol sizing and then drawn over the unreacted cable in preparation for winding. Wedges, pole pieces and end pieces are coated with alumina (0.13mm thick) for extra insulation. The training results indicate the pole surfaces are a problem. Due to the locations and sequence of the first quench set we conclude that an excellent insulation with a weak shear strength is needed(i.e. mica) between conductor and pole. There is a layer of fiberglass tape between the mandrel and the inner coil heater/ voltage tap kapton/stainless steel (ss) composite plane. There is a second layer of glass tape between coil layers 1 and 2, then the coil layer 2 heater/voltage tap kapton / ss composite plane outside

0-7803-4376-X/98 /$10.00 © 1998 IEEE

layer 2. The final layer of the double winding package is a layer of fiber glass cloth. During the heat treatment, the heater/voltage tap composite space is occupied by an ss shim. The special sizing is evaporated before the start of the bronze/$Nb_3Sn$ formation heat treatment sequence. The process was repeated for each of the double winding packages. Each of these reacted double winding packages had both $Nb_3Sn$/NbTi splices fabricated in the reaction fixture prior to voltage tap connection and the transfer to the potting fixture. The various electrical splices were monitored during the performance testing and the results are given in Table III.

| Location | Type of Joint | R(nano·ohms) |
|---|---|---|
| | | |
| Top/Mid | NbTi/NbTi | 1.0 |
| Mid Magnet | NbTi/NbTi | 0.5 |
| Bottom/Mid | NbTi/NbTi | 1.0 |
| T-4 | NbTi/$Nb_3Sn$ | 0.7 |
| B-3 | NbTi/$Nb_3Sn$ | 0.8 |
| T-3 | NbTi/$Nb_3Sn$ | 0.9 |
| T-2 | NbTi/$Nb_3Sn$ | 0.5 |
| T-1 | NbTi/$Nb_3Sn$ | 0.7 |
| B-4 | NbTi/$Nb_3Sn$ | 0.8 |

Table III Joint Resistances

After potting, the four double winding packages were placed back into the potting fixture with a pressure sensitive film replacing one or more insulation layers on the appropriate loading surfaces. These fixtures were then loaded to moderate levels(few MPa) to determine the surface profiles as well as the size of the packages. This sizing information along with design numbers and component measurements were used to make an assembly of the entire magnet exclusive of the yokes and structure located radially outside them. In this assembly once again a pressure sensitive film replaced insulation layers on appropriate surfaces to check for the appropriate fit and to allow an independent check of the maximum load applied. All of the pole strain gauges were monitored and the bronze collared coil structure was wrapped with ss wire at the calculated tension up to about half the desired preload. The final wrap was 304 stainless steel 3mm x 1mm round edge wire 14 kilometers long in 18 layers(actual space for 25 layers) at a tension of 850N. These results then lead to the loading numbers of the final assembly within the yokes. See figure 1 for the final preload for D20. End plates held the magnet winding in axial compression up to 30% of the total Lorentz force (820 kN). Ten end loading bolts had strain gauges on them which were pre-calibrated and eight were monitored throughout the assembly and during testing.

## III. EXPERIMENTAL RESULTS

The principal goals of the four layer Nb3Sn dipole were: a) explore the 12T-14T range, b) validate the technology required at these field levels, and c) provide a test facility to test insertion coils made with higher current density conductor or newer conductors and winding geometries in

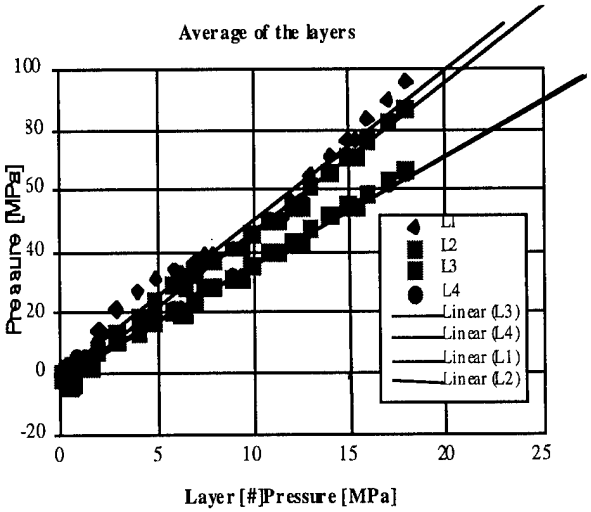



Figure 1 Winding layer Load versus stretched wire layer #

this field range. D20 was protected by heaters with a photo-etched geometry so that coil voltages would be minimum, and temperature increases be as uniform as possible. After the magnet reached LHe temperatures a series of protection heater tests were performed to measure their effectiveness similar to those reported earlier [6] except each layer was checked independently at 3.5T. The time delay after firing the heaters and the onset of resistance was 20 to 30 ms at 3.5T and <10 ms above 12.0T. The peak adiabatic heater temperature was 285K(layer 1) and 170K for the others with a peak surface power of 75 w/cm$^2$ and 26.5w/cm$^2$ respectively. The highest average winding temperatures after quench were in the outer layers(between 182K-203K). When the quench originated in an outer turn the highest hot spot estimate was 264K. By comparison, the inner two layers averaged 120K - 132K and if the quench originated there the highest temperature estimate was 168K. The maximum number of Miits(Million-ampere squared - seconds) absorbed during a quench during the test was 7.6. This maximum however did not occur at the highest field but was 12T - 13T. After nominal heater parameters were established, the actual spontaneous quench testing started. Figure 2 shows the quench history of D20.

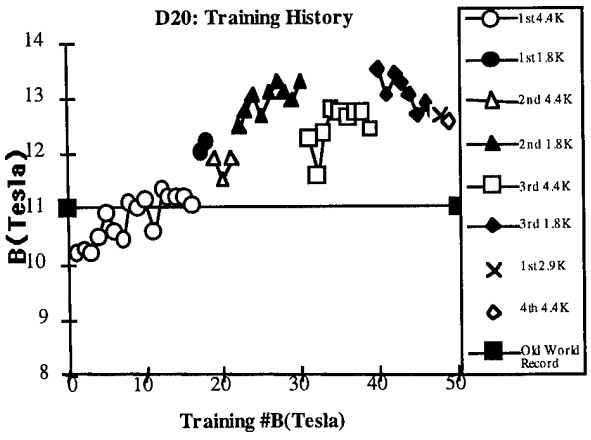



Figure 2. D20 Quench History

Unlike previous $Nb_3Sn$ dipoles (3,4,5) D20 has trained to date 25% higher than the initial quench. The rate at which D20 trained was temperature dependent. The present training at 1.8K is in a length of conductor going to an outer layer lead splice in a low field region. Usually when warmed up (>4K) after low temperature (1.8K) training the coil's 4K performance has increased substantially. A full warm up/cool down cycle has yet to be completed to room temperature. D20 displayed reasonable heat input tolerance for a completely impregnated structure. When using the inner protection heater as a source it required more than 20 watts to quench the magnet at 12T(2K). D20 appears to be presently operating near its short sample at 4.5K, and it is quenching in the ramp between the pole turns of the inner coil pair. The ramp rate dependence of the quench current at 4.4K was excellent and is shown in Figure 3, compared with existing or proposed accelerators.

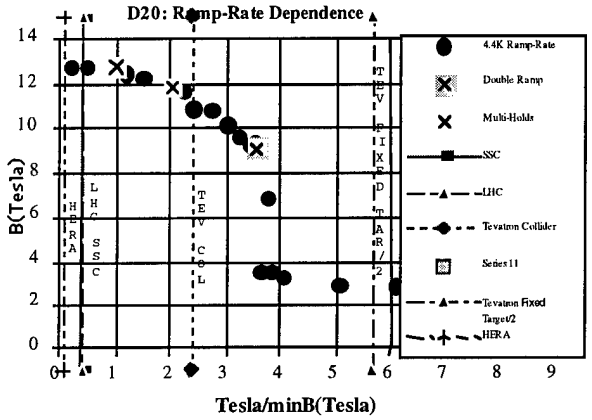



Figure 3. Ramp Rate Quench Current Values at 4.4K

The thermal margin of D20 was determined by ramping to a field level, holding, then rapidly ramping at (Eddy Current heating) 100 to 200 A/sec(12T~24T/min) and ploting the current change. The intercept of the zero current increase indicates that at least a few(0.4→0.8T) tenths of a tesla margin remains in the thermally quenched areas. However, within a millisecond most of a given layer turns are quenching together during these tests. The plot is shown in figure 4.

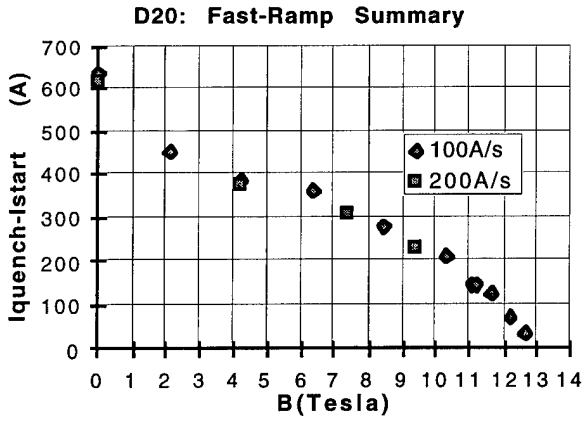



Figure 4. Thermal margin in Amperes as a function of Magnetic field (6400 amps ~ 13T)

Therefore, either the cable is damaged or the pole turn is separating from the post along the 1st layer to 2nd layer transition and the coil will have to be trained further. Afterwards, D20 should transition at the high field point. The reasons for the superfluid low field lead quench may be related to the change in geometry of that particular lead. Due to a splice box misalignment, the distance of the copper splice block and the straight section had to be made shorter. This shortening causes the splice block to end right at the edge of the end shoe. This produces a radial plane in that area such that the cable is not rigidly supported across that boundary with the metal filler pieces as is the normal case.

## IV. CONCLUSIONS

The operation of D20 up to fields of 13.5 T certainly indicates that the strain limitations of the $Nb_3Sn$ conductor up to this point have not been a limiting factor. Apparently the mechanical structure is adequate for this field range. There is still reasonable doubt that there was enough prestress once the magnet was cold. The excellent ramp rate behavior of the magnet has put added pressure to measure field quality, harmonics as function of time, as well as quantity which is planned in the next operational period. The D20 cryostat is presently being modified for extra current leads for sample coils. There is also a re-entrant cryostat (warm bore tube) being fabricated for the harmonic analysis equipment. Certainly it appears that fields up to 13.5 T and above are within reach. So far most of the ramp rate problems with the previous dipoles are not present in D20. This means strand to strand coupling is low. The application of high field $Nb_3Sn$ dipole looks very promising.

## V. ACKNOWLEDGMENTS

This project would not have been completed without the skills and contributions of the following people: D. Byford (magnet test electronics), S. Dardin (coil reaction), Ron Oort (coil winding), and J. Remenarich (coil impregnation).

## REFERENCES

[1] A.F. Lietzke et al. "Test Results for a $Nb_3Sn$ dipole Magnet"
[2] Proc. Applied Superconductivity Conference '96,
[3] Pittsburgh, PA., August 1996. To be published.

[4] D. Dell'Orco et. al. " Design of the $Nb_3Sn$ Dipole D20" IEEE Trans. on Appl. Superconductivity 3 , #1, March 1993, pp. 82-86.

[5] A. Asner, R. Perin, S. Wienger and F. Zerobin "First $Nb_3Sn$ 1m-long Superconducting Dipole Model Magnet for LHC Breaks the 9.5T Threshold", Proc. of MT-11, Tsukuba, 1992, p.36.

[6] A. den Ouden, S. Wessel, E. Krooshoop, and H. ten Kate, "Application of $Nb_3Sn$ Superconductors in High-Field Accelerator Magnets, Proc. ASC'96, Pittsburgh, PA. To be published.

[7] C. Taylor et al."A $Nb_3Sn$ Dipole Magnet Reacted after Winding",IEEE Trans. on Mag., MAG-21, March 1985, pp 967 - 970.

[8] A. McInturff et. al., "Superfluid Performance of Tevatron "IR" Quad Heaters". IEEE ASC Proc., Applied Superconductivity Conference, Pittsburgh, PA, August 1996. To be published.

# LOW FIELD MAGNETS WITH HIGH TEMPERATURE SUPERCONDUCTORS FOR AN UPGRADE OF CESR*

G. Dugan, J. Rogers, Laboratory of Nuclear Studies, Cornell University, Ithaca, NY 14853

*Abstract*

An upgrade to the CESR electron-positron storage ring is being considered in which the single ring machine is replaced with two rings capable of storing high currents to provide high luminosity symmetric electron-positron collisions. This paper considers the implementation of the two rings using dual bore quadrupoles fabricated with high temperature superconductors (HTS). The use of HTS provides the required high current density needed to achieve the small (81 mm) inter-beam spacing, with a simpler and more efficient cryogenic system than would be required with conventional low-temperature superconductors. Concepts for the quadrupole magnetic and cryostat design are discussed. A concept for dipole magnets using $Nb_3Sn$, integrated with a warm beam tube vacuum system, is also discussed.

## 1 MOTIVATION FOR THE DUAL-BORE SUPERCONDUCTING QUADRUPOLE

The requirement for closely-spaced dual bore quadrupoles in the two ring symmetric collider[1] arises from the desire to minimize, as much as possible, the separation of the beams in the two rings. In the current design , the two beams share all the dipoles in the ring. The width of the dipoles, and consequently their cost and complexity, is thus minimized by keeping the beam centerlines relatively close together. The limited space available in the existing tunnel for the new rings provides an additional motivation to keep the overall dipole and quadrupole cross section small. Furthermore, the difficulties of beam separation as the beams emerge from the interaction region is minimized with a small beam separation. The goal for the beam-to-beam separation in the current ring design, 81 mm, requires a sufficiently high current density that a normal-conducting solution would have prohibitively large operating costs. Thus a superconducting coil design is the only practical and affordable choice.

## 2 DUAL-BORE QUADRUPOLE DESIGN

### *2.1. Requirements*

Table I presents the general requirements. Fig. 1 shows a layout of a design of a dual-bore quadrupole which satisfies these requirements, using a high temperature superconducting coil.

Table I: Dual-bore quadrupole requirements

| Parameter | Requirement |
|---|---|
| Length | 380 mm |
| Field gradient | 10 T $m^{-1}$ |
| Good field diameter | 54 mm |
| Field quality @ r=27 mm | $<4x10^{-4}$, all harmonics |
| Bore-to-bore separation | 81 mm |

### *2.2 Conductor and coil*

The conductor parameters are given in Table II.

Table II: Quadrupole conductor parameters

| Parameter | Requirement |
|---|---|
| Conductor material | BSCCO 2223 or 2212 |
| Coil inner diameter | 70 mm |
| Coil cross section | 4mm x 16mm |
| Engineering current density | 8500 A $cm^{-2}$ |
| Operating temperature | 25-30° K |
| Peak field in coil in "bad" direction | 0.34 T |
| Tolerance on coil cross section dimensions | +/- 0.1 mm |

The conductor material is currently available in the form of tapes, roughly 3-4 mm wide by 0.1-0.2 mm thick. The tapes would be wound into a coil of the shape shown in Fig. 1. The operating temperature is chosen to place the peak field below the irreversibility line for BSCCO, so that sufficient critical current density is assured. In order to satisfy the field quality requirements, the coil must be of the saddle-coil form. Extensive studies were made of the possibility of using a flat racetrack coil, but no solution was found which satisfied both the geometric constraints associated with the 81 mm bore-to-bore separation, and the field quality requirement.

The principal issue in the fabrication of a saddle coil is related to the strain produced while winding the coil ends. The bending radius in the end is about 20 mm; in addition, there is a strain produced by the twist required to form a saddle coil. Tapes made from the oxide superconductors degrade rapidly with bending strains in excess of a few tenths of a percent. For this reason, it will probably be necessary to fabricate the coils using a wind-and-react approach. If sufficiently thin multifilamentary tape is available, a react-and-wind coil would be possible.

*Supported by the National Science Foundation

0-7803-4376-X/98 /$10.00 © 1998 IEEE

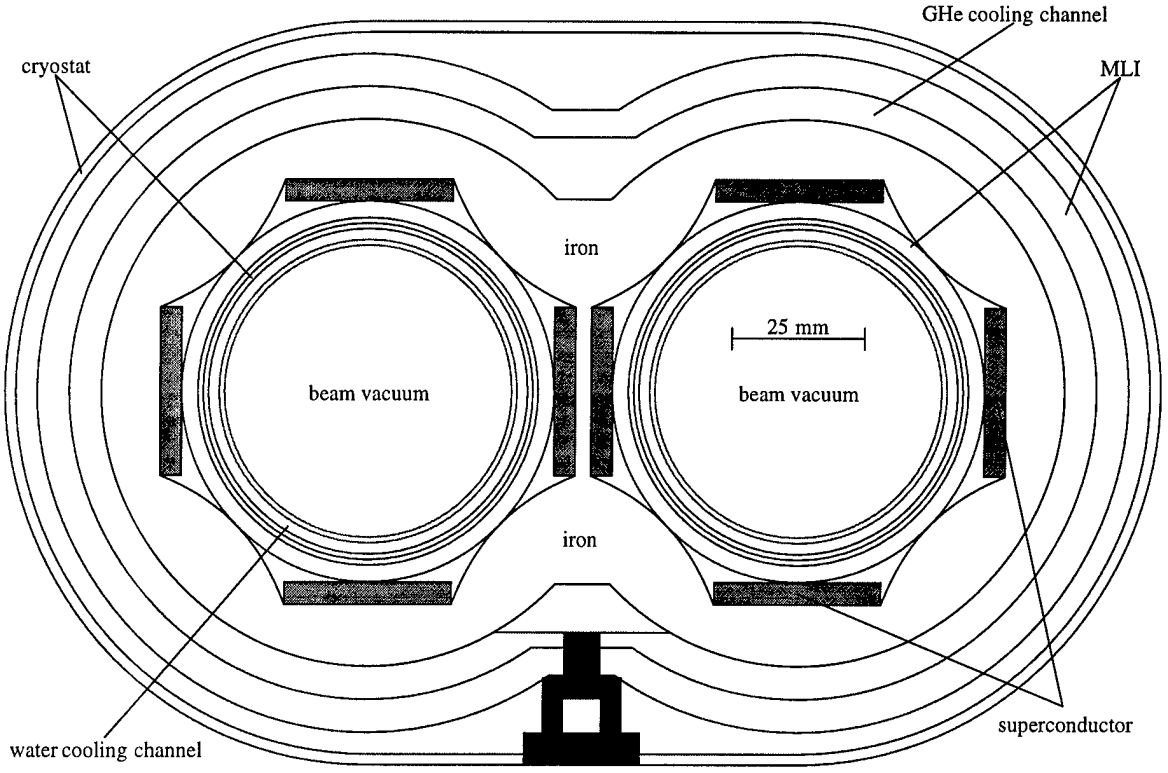



Fig. 1: Layout of the dual-bore superconducting quadrupole

*2.3 Iron design*

The pole tip shape shown in Fig. 1 is hyperbolic. The combination of a rectangular coil, and a hyperbolic iron pole tip, produces excellent field quality [2]. The outer radius of the iron, 50 mm, is chosen to ensure that the iron is not driven into saturation.

The septum between the two quadrupole bores is 2 mm thick. This is sufficient to allow the quadrupoles to be operated with up to 10% difference in current, without affecting the field quality (within the specifications).

*2.4. Cryostat*

The cryostat is illustrated in Fig. 1. The 54 mm diameter copper beam vacuum tube is warm and water-cooled, to handle the synchrotron radiation from the beam. Within the cryovacuum, the superconductor is thermally shielded from the inner bore of the cryostat with 3 mm of standard multilayer insulation. The superconductor is conduction cooled, using gaseous helium at 25°K which passes through a plenum around the outside of the cold iron. Between this plenum and the outer housing of the cryostat, there is another layer of multilayer insulation, 6 mm in thickness. No nitrogen shields are foreseen. The magnet is supported near both ends with two low-heat-leak supports, as shown in Fig. 1 The total heat leak for the quadrupole from 25°K to room temperature is estimated at about 1.6 W.

## 3 DIPOLE DESIGN

*3.1 Requirements*

Table III presents the general requirements for the dipole. Fig. 2 shows a layout of the design of a warm iron dipole which satisfies these requirements, using a $Nb_3Sn$ single-turn superconducting coil.

Table III: Dipole requirements

| Parameter | Requirement |
|---|---|
| Length | 3200 mm |
| Field | 0.24T |
| Good field diameter | 54 mm |
| Field quality @ r=27 mm | $<4\times10^{-4}$, all harmonics |
| Gap dimensions | 70mm x 281mm |

*3.2 Conductor, coil and cryostat*

The conductor parameters are given in Table IV.

Table IV: Dipole conductor parameters

| Parameter | Requirement |
|---|---|
| Conductor material | $Nb_3Sn$ |
| Coil width | 270 mm |
| Coil cross section | 8mm x 8mm |
| Engineering current density | 11,700 A $cm^{-2}$ |
| Operating temperature | 10-15° K |
| Peak field in coil | 0.42 T |

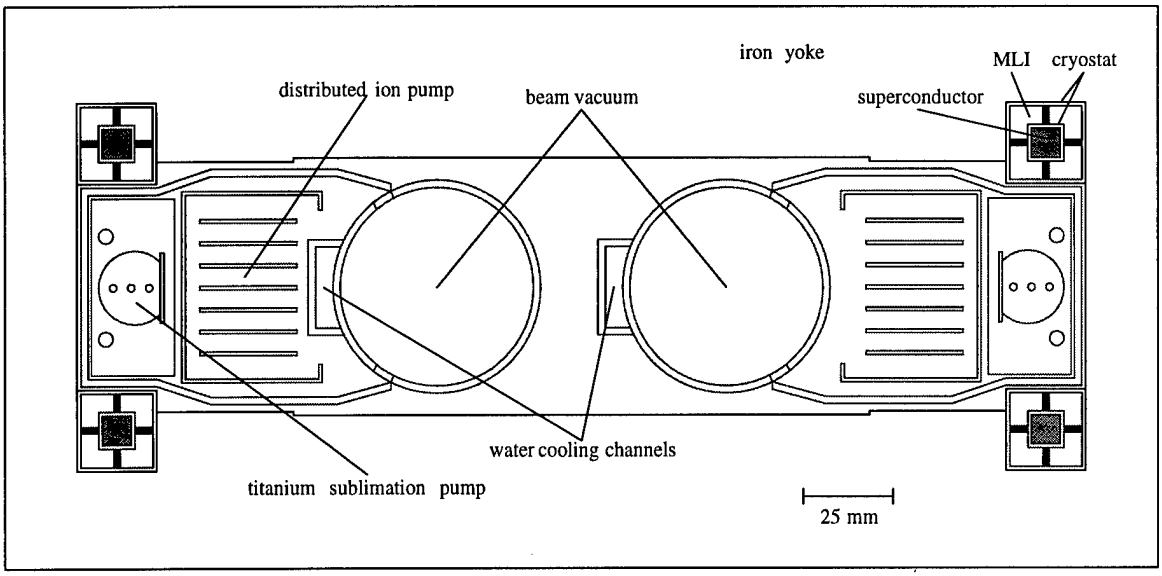



Fig. 2: Layout of the superconducting dipole

The choice of $Nb_3Sn$ for the conductor is motivated by several considerations. This material is (currently) considerably less expensive than BSCCO. Although it must be operated at a lower temperature than BSCCO, it is still substantially more cryogenically efficient than NbTi.

As shown in Fig. 2, the conductors are of the cable-in-conduit form, with each conductor encased in its own mini-cryostat. The cables carry 7500 A in a single turn. The conduits are envisioned to run in series from one dipole to the next, carrying both current and GHe cooling. Within each cryostat, the single conductor, encased in a sheath to contain the GHe cooling, is surrounded by 4 mm of MLI and supported from the cryostat walls with ceramic spacers. The total heat leak is estimated to be about 4 W per dipole.

At the ends of each magnet, the cryostats carrying opposite currents must be brought together, to limit stray fields, and routed past the quadrupoles. Since the bending radius required is quite large, issues related to the strain sensitivity of $Nb_3Sn$ should not be serious.

The pole tips are shaped to achieve the required field uniformity specified in Table III. The width of the return yoke iron is 20 mm; this is sufficient to prevent saturation.

*3.4 Beam vacuum*

Fig. 2 shows a possible design for a vacuum chamber. The circular cross section required in the dual aperture quadrupoles is maintained in the dipole magnets to minimize the coupling impedance. To maintain a beam-gas lifetime of 3 hours at an ultimate photodesorption coefficient of $2\times10^{-6}$, the average linear pumping speed in the storage ring arcs must be 230 l $s^{-1}$ $m^{-1}$. Pumping is provided by a distributed sputter ion pump, and by a distributed Ti sublimation pump which provides faster pumping at low pressures. The conductance of the pump slots is well in excess of that needed to maintain the necessary linear pumping speed.

An alternative pumping scheme is the use of a linear cryopump, consisting of a pipe containing He liquid or gas at a temperature near or less than 10 K, surrounded by several layers of slotted radiation shields. One such design has a calculated speed of 560 l $s^{-1}$ $m^{-1}$ (pump only) and a heat leak of 0.125 W $m^{-1}$. A practical difficulty with such a cryopump is the release of adsorbed gases should it become necessary to allow the cryopump to warm for maintenance or repair.

## 4 CONCLUSION

Two superconducting magnet concepts have been described. These concepts are options for main arc quadrupoles and dipoles for a new two ring symmetric 5.2 GeV electron-positron collider. The quadrupole magnet utilizes currently available high temperature superconducting tape (BSCCO), and has a relatively simple cryostat. The dipole magnet is driven by small cross section $Nb_3Sn$ cable-in-conduit, and has an integrated distributed pumping system to handle the photodesorbed gas from the beam's synchrotron radiation. Both magnets use gaseous helium cooling, and can operate at temperatures well above $4^oK$, offering the promise of a relatively simple and inexpensive cryogenic system for the whole machine.

## 5 REFERENCES

[1]. D. Rubin, G. Dugan, A. Mikhailichenko, J. Rogers, "Dual Aperture High Luminosity Collider at Cornell", contribution 6B10 to this conference

[2]. A. Mikhailichenko, D. Rubin, "Concentric Ring Colliding Beam Machine with Dual Aperture Quadrupoles", CLNS 96/420 (Cornell University)

# VIBRATING WIRE FIELD-MEASURING TECHNIQUE *

Alexander Temnykh †
Laboratory of Nuclear Studies, Cornell University, Ithaca NY, USA

The *Vibrating wire field-measuring technique* presented here is dedicated to the problem of alignment of quadrupole magnets and is based on the following principle. The stretched wire has vibrational modes consisting of the fundamental mode and higher harmonics. The half wave length of the fundamental mode is equal to the length of the wire. Suppose there is a transverse magnetic field surrounding wire. If the frequency of the current in the wire is an eigenmode frequency of wire vibration, it will excite a corresponding harmonic. The strength and phase of excitation will depend on the field distribution along the wire. Using various frequencies and measuring amplitudes and phases of the resulting vibrations, one can extract information about the field distribution in order to reconstruct it. The field in turn shows the misalignment of quadrupoles.

In comparison with the pulsed-wire method, see [1]-[4], the vibrating wire technique does not require the wire length to be longer than the length of the test region, and due to its extraordinary sensitivity it does not require the higher voltage for the long wire scheme. Therefore, it may be more appropriate for some projects.

## 1 THEORY

Figure 1 displays the setup used in experiments and in calculations below. A wire with tension $T$ and length $l$ has the fixed ends at $x = 0$ and $x = l$. The current, I(t), in the wire, i.e., driving current, depends on time as $I(t) = I_0 exp(i\omega t)$. The wire crosses a region with horizontal magnetic field, $B_y(x)$, which is zero at the ends, $B_y(0) = B_y(l) = 0$. Consider the vertical plane. There are two forces affecting the wire. They are gravity $g \cdot \mu$, where $\mu$ is mass of wire per unit of length, and the Lorentz force $B_y(x) \cdot I(t)$.

The equation for vertical wire position, $U(x,t)$, will be:

$$\mu \frac{\partial^2 U}{\partial t^2} = T \frac{\partial^2 U}{\partial x^2} - \gamma \frac{\partial U}{\partial t} - \mu g + B_y(x) \cdot I_0 exp(i\omega t) \quad (1)$$

With boundary condition:

$$U(t,0) = U(t,l) = 0 \quad (2)$$

Here term $\gamma \frac{\partial U}{\partial t}$ describes damping. A general solution may be written in the form:

$$U(x,t) = U_g(x) + U_d(x,t)$$
$$U_d(x,t) = U_b(x) \cdot exp(i\omega t) \quad (3)$$

Where $U_g(x)$ is the gravity term and $U_d(x,t)$ is the dynamic term caused by the interaction between the magnetic field and the driving current. An approximate expression for $U_g(x)$ is:

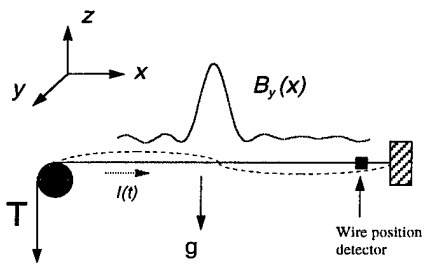



Figure 1: Scheme of vibrating wire experiments.

$$U_g(x) = -\frac{\mu g}{2T} x(x - l) \quad (4)$$

Note that at the point $x = l/2$ function $U_g(x)$ reaches its minimum which is the sag, S.

$$S = -\frac{\mu g}{8T} l^2 \quad (5)$$

Function $U_b(x)$, determined by magnetic field, may be found in the following way. As $U_b(x)$ satisfies the condition $U_b(0) = U_b(l) = 0$, it can be represented by Fourier sine series:

$$U_b(x) = \sum_{n=1}^{\infty} U_n \sin\left(\frac{\pi n}{l} x\right) \quad (6)$$

The magnetic field $B_y(x)$, with similar boundary conditions, may be represented in the same way:

$$B_y(x) = \sum_{n=1}^{\infty} B_n \sin\left(\frac{\pi n}{l} x\right) \quad (7)$$

Substituting 3,4,6 and 7 into equation 1 we set:

$$\sum_{n=1}^{\infty} U_n \cdot \left(\omega^2 - \omega_n^2 + i\gamma\omega\right) \sin\left(\frac{\pi n}{l} x\right) = \sum_{n=1}^{\infty} \frac{I_0 B_n}{\mu} \sin\left(\frac{\pi n}{l} x\right) \quad (8)$$

$$\omega_n = 2\pi \frac{n}{2l} \sqrt{\frac{T}{\mu}} \quad (9)$$

Combining expression 9 with the formula for sag, (see 5), one can find a simple relation between sag and the fundamental mode frequency:

* Work supported by the National Science Foundation
† On leave from BINP, Novisibirsk

0-7803-4376-X/98/$10.00 © 1998 IEEE

$$S = \frac{g}{32}\left(\frac{2\pi}{\omega_1}\right)^2 \qquad (10)$$

This means that to obtain the sag we only need to measure the fundamental frequency and using $g = 9.80665\, m/sec^2$ we can precisely calculate the sag.

By comparing the right and left sides of equation 8 one can find a connection between coefficients $U_n$ and $B_n$ and write the dynamic part of the general solution of equation 1 as:

$$U_d(x,t) = \sum_{n=1}^{\infty} \frac{B_n \sin\left(\frac{\pi n}{l}x\right)}{(\omega^2 - \omega_n^2 + i\gamma\omega)} I_0 exp(i\omega t) \qquad (11)$$

Consider how to obtain coefficients $B_n$ of expansion 7 and reconstruct the magnetic field knowing the wire motion at the sensor location. Suppose the wire position sensor is located at the point $x = x_s$. Let us construct the function $\mathcal{F}(\omega)$ which is the time average of the product of wire position, $U_d(x_s,t)$, and driving current, $I(t)$:

$$\mathcal{F}(\omega) = \frac{1}{T}\int_0^T U_d(x_s,t)I(t)dt = \sum_{n=1}^{\infty}\mathcal{F}_n(\omega) \qquad (12)$$

$$\mathcal{F}_n(\omega) = \frac{B_n I_0^2}{2\mu}\sin\left(\frac{\pi n}{l}x_s\right)\frac{(\omega-\omega_n)}{4\omega(\omega-\omega_n)^2+\omega\gamma^2} \qquad (13)$$

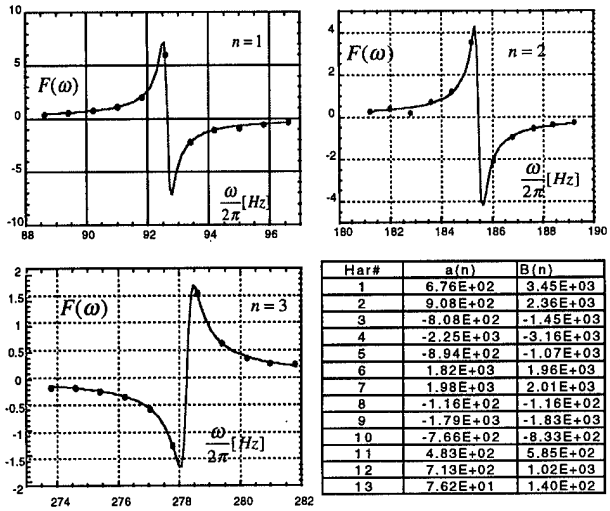
Note that due to weak damping the wire motion has a high quality factor $Q$. It causes strong resonance amplification, and if the frequency of driving current is near $\omega_n$, i.e., $\omega \approx \omega_n$, the resonance term $\mathcal{F}_n$ in equation 12 will dominate over the rest, i.e. , $\mathcal{F}(\omega) \approx \mathcal{F}_n(\omega)$. Suppose we scan the driving current frequency through one of resonance frequencies, $\omega_n$. By recording both the driving current and signal from wire position sensor and doing numerical integration, (see formula 12), we can measure function $\mathcal{F}_n(\omega)$. Then we have to fit this measurement with the formula:

$$\mathcal{F}_n(\omega) = a_n\frac{(\omega-b_n)}{4\omega(\omega-b_n)^2+\omega c_n^2} \qquad (14)$$

where $a_n$, $b_n$, $c_n$ are free parameters. Component $B_n$ is obtained from $a_n$ as:

$$B_n = a_n\frac{1}{\sin\left(\frac{\pi n}{l}x_s\right)}\frac{2\mu}{I_0^2} \qquad (15)$$

Repeating this procedure for various $\omega_n$, and using equation 7, we will reconstruct the magnetic field profile along the wire. Note that the resolution of reconstruction will depend on how many harmonics will be used and will be approximately equal to the shortest wavelength of the excited modes. Motion in the horizontal plane does not differ from vertical motion except for the gravity term. The next sections describe model measurements and the practical application of the vibrating wire technique.




| Har# | a(n) | B(n) |
|---|---|---|
| 1 | 6.76E+02 | 3.45E+03 |
| 2 | 9.08E+02 | 2.36E+03 |
| 3 | -8.08E+02 | -1.45E+03 |
| 4 | -2.25E+03 | -3.16E+03 |
| 5 | -8.94E+02 | -1.07E+03 |
| 6 | 1.82E+03 | 1.96E+03 |
| 7 | 1.98E+03 | 2.01E+03 |
| 8 | -1.16E+02 | -1.16E+02 |
| 9 | -1.79E+03 | -1.83E+03 |
| 10 | -7.66E+02 | -8.33E+02 |
| 11 | 4.83E+02 | 5.85E+02 |
| 12 | 7.13E+02 | 1.02E+03 |
| 13 | 7.62E+01 | 1.40E+02 |

Figure 2: Measured function $\mathcal{F}(\omega)$ and coefficients $a_n$ obtained from fitting. Points show measurements, lines are fits with formula $\mathcal{F}_n(\omega) = a_n\frac{(\omega-b_n)}{4\omega(\omega-b_n)^2+\omega c_n^2}$

## 2 MEASUREMENT

Wire used in the experiments was $100\,\mu m$ diameter made with alloy of copper-beryllium. A phototransistor-LED assembly, (Motorola H21A1), was deployed as a wire position monitor. This kind of device was widely used in previous work, (see for example [2] and [4]). Note that the assembly may be oriented in such way that it will effectively sense wire motion in one plane, in horizontal or in vertical . To detect motion in other plane the assembly must be rotated by 90 degrees. Macintosh Quadra 800 with LabNB Interface Board provided almost all needs of the measurements. An application program created in LabVIEW scanned the driving current frequency, recorded and manipulated signals, made fits and etc. The final output yields the magnetic field measured along wire.

A one meter long wire was used in the first modeling measurement. The wire motion detector was placed 7.5 cm from one of the ends. A small permanent magnet placed along the wire created a magnetic field for testing. The strength of the field was controlled by the distance between magnet and wire.

Figures 2 and 3 illustrate the description given in the previous section. Plots in figure 2 show the results of excitation of the first three harmonics out of thirteen which were used in the measurement. Points show the measured function $\mathcal{F}(\omega)$ defined in the theoretical section. A line is fit to formula 1. There is a good agreement between the measurement and fitting in all cases. The table on figure 2 shows the parameters $a_n$ obtained from fitting all 13 harmonics. and coefficients $B_n$ calculated from $a_n$. The field distribution reconstructed by equation 7 is plotted in figure 3. It shows a very clear signal from the magnetic field. Note that the width of the signal, $\sim 10\,cm$, is determined by the shortest harmonic wavelength used in the measurement.

The next experiment was to find the magnetic center of permanent magnet quad using a longer wire. Available setup space allowed use of wire of $3m$ length. The test

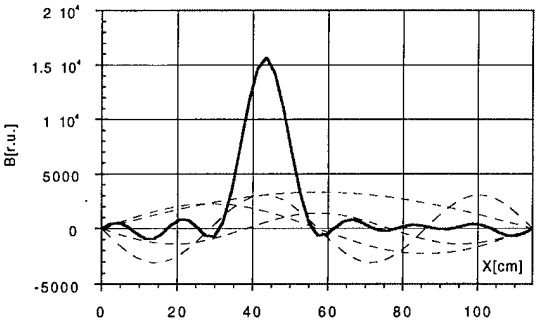



Figure 3: Components $B_n$, (see plot a), calculated from coefficients $a_n$ and reconstructed magnetic field, (see plot b). Dotted lines show the first 5 harmonics corresponding to $B_n$.

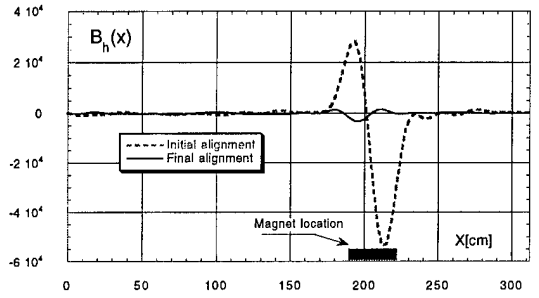



Figure 4: Horizontal magnetic field along wire after conventional alignment, (see dotted line), and after vertical alignment with vibrating wire technique, (see solid line).

permanent magnet quad was 30 $cm$ long with a $14.8\,T/m$ gradient.

In the beginning, the mechanical center of quad was adjusted to the wire position with traditional measuring tools, i.e., using rulers. The precision of this alignment was approximately 0.1 $mm$. Note that magnetic center of the quad may differ from its mechanical center.

The vibrating wire measurement gave the horizontal field distribution shown by the dotted line in figure 4. The square at the bottom shows the location and size of the test magnet. In the measurement 30 harmonics were used, with shortest wavelength equal to 20 $cm$. This wavelength is 1.5 times shorter than the length of the test magnet and allowed us to see details of the field generated by magnet. This plot shows two unequal maxima of different polarities which correspond to the magnet ends. This kind of field distribution is due to a combination of tilt and shift of magnetic axes in the vertical plane relative to the wire. The solid line on figure 4 shows the final field distribution after a few iterations of measurement and adjustment of vertical quad position. The maximum amplitude is approximately 10 times less than it was in the beginning.

After the quad's magnetic center was adjusted to the wire position in the vertical and horizontal plane, using high precision optical instruments it was found that the misalignment between geometrical and magnetic center was in range between 125 $\mu m$ and 500 $\mu m$.

## 3 DISCUSSION AND CONCLUSION

Consider the time needed for measurement. The weak damping of wire vibration which gives the enormous sensitivity of the technique slows the process of measurement. After each frequency change one must wait for about 3-5 seconds to reach equilibrium of wire motion and then record signals. Due to this delay the measurement consisting of many harmonics may take a relatively long time. For example, the time for measurement consisting of 13 harmonics with 11 steps of frequency scan for each of them, (see figure 3), was about 10 minutes. Another example, (figure 4), consisting of the analysis of 30 harmonics required 25 minutes. However the magnet alignment described above, did not require analysis of so many harmonics. Only two of them, most sensitive to the magnet shift and tilt, were used during this procedure. The full measurements, i.e. using 30 harmonics, were done just in the beginning and at the end to verify final result.

The another aspect is the effect of non-zero field at one of the ends of wire. One can suspect that this field may have propagated an effect along wire. This arrangement has been simulated with software "Mathematica" for Macintosh and two important conclusions have been derived. The difference between "real" and "measured" field profiles is localized around the wire end in a length of region approximately equal to that of the shortest wave length and a non-zero field at the wire end does not have an effect on the determination of the field profile away from this end.

Theoretical consideration and experiments reported above demonstrate that the vibrating wire technique is a convenient method for the precise alignment of magnetic centers of a series magnetic elements. It has enormous sensitivity and does not require any special equipment.

In comparison with the pulsed-wire technique it does not need more space than the length of the test region and does not require generating very high voltage pulses on a long wire.

## 4 ACKNOWLEDGMENT

I thank James Welch, who motivated me to study the problem of magnet alignment. I am also very grateful to Boyce McDaniel, David Rice, David Rubin and Scott Chapman for help and to Alexander Mikhailichenko for useful comments.

## 5 REFERENCES

[1] R. Warren and C. Elliot, *New System for Wiggler Fabrication and Testing*, Los Alamos National Laboratory, LA-UR 87-2981, (1987)

[2] R.W. Warren, NIM A272 (1988) 257-263

[3] C.M. Fortgang, et.al., *Pulsed Taut-Wire Alignment of Multiple Permanent Magnet Quadrupoles*, 1990 LINAC Conference, Albuquerque, NM, Sept. 1990.

[4] J.G. Melton, et.al., *Pulsed Taut-Wire Measurement of Magnetic Alignment of the ITS Induction Cells*, in Proceedings of the 1993 IEEE Particle Accelerator Conference, Catalog No. 0-7803-1203-1/9303.00, p. 2944

# THE ADVANCED LIGHT SOURCE ELLIPTICALLY POLARIZING UNDULATOR

S. Marks, C. Cortopassi, J. DeVries, E. Hoyer, R. Leinbach, Y. Minamihara, H. Padmore, P. Pipersky, D. Plate, R. Schlueter, A. Young, Lawrence Berkeley Laboratory, Berkeley, California

*Abstract*

An elliptically polarizing undulator (EPU) for the Advanced Light Source (ALS) has been designed and is curently under construction. The magnetic design is a moveable quadrant pure permanent magnet structure featuring adjustable magnets to correct phase errors and on-axis field integrals. The device is designed with a 5.0 cm period and will produce variably polarized light of any ellipticity, including pure circular and linear. The spectral range at 1.9 GeV for typical elliptical polarization with a degree of circular polarization greater than 0.8 will be from 100 eV to 1500 eV, using the first, third, and fifth harmonics. The device will be switchable between left and right circular modes at a frequency of up to 0.1 Hz. The 1.95 m long overall length will allow two such devices in a single ALS straight sector.

## 1 INTRODUCTION

A facility dedicated for magnetic microscopy and spectroscopy at the ALS [1] will eventually include a complement of three EPU's of the type first proposed by Sasaki [2]. The first of these (EPU5.0) is a 1.95 m long device, with 37.5 periods of 5.0 cm [3]. The EPU5.0 is designed to produce very bright photon beams with variable polarization in the spectral range of 100 eV to 1500 eV. The EPU facility will eventually include a second EPU5.0 and an EPU8.0 to access lower photon energies. The device length is chosen to allow two insertion devices to be placed in tandem in a single straight. The third device is accommodated by use of a transverse stage on which one of the EPU 5.0's will be mounted along with the longer period device. This arrangement will allow users to switch between the sources. A three magnet chicane system will separate the photon beams from the two in-line insertion device stations by 2.53 mrad.

## 2 PRINCILE OF OPERATION

The magnetic structure consists of four identical quadrants as shown schematically in Figure 1. Q1 and Q3 are fixed; Q2 and Q4 are allowed to translate parallel to the magnetic axis. The relative translation, called the quadrant phase, $\chi$, of the magnetic quadrants changes the strength of the vertical and horizontal magnetic field components, $B_x$ and $B_y$. This changes the ellipticity of an electron orbit passing through the device,. and thus the polarization of the emitted radiation. When $\chi = 0$, the magnetic structure is equivalent to a standard linear undulator, with $B_y$ the only on axis component, and the radiation is linearly polarized in the horizontal plane. When $\chi = \lambda/2$, where $\lambda$ is the undulator period, only $B_x$ is produced on axis, and radiation is linearly polarized in the vertical plane. When $\chi$ has any other value both $B_x$ and $B_y$ are produced on axis, and the radiation is elliptically polarized. When $B_x = B_y$, radiation is circularly polarized.

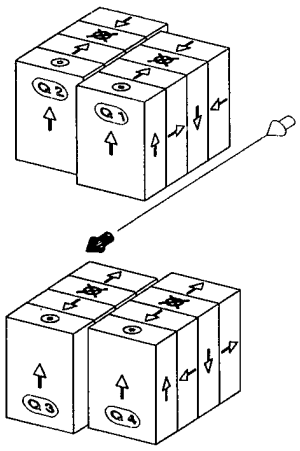



**Figure 1: Four quadrant schematic of EPU.**

## 3 SPECTRAL PROPERTIES

The EPU 5.0 will operate in various polarization modes: horizontal and vertical linear polarization, circular and elliptical polarization. The design energy ranges for these modes are summarized in Table 1 below. To achieve acceptable performance at 1500 eV for elliptical, horizontal, and vertical polarization modes, the EPU has to produce a high degree of circular polarization and high brightness in the 5th spectral harmonic.

**Table 1**

| Polarization Mode | Energy Range |
|---|---|
| Circular | 130 - 600 eV |
| Elliptical | 100 - 1500 eV |
| Horizontal | 90 - 1500 eV |
| Vertical | 170 - 1500 eV |

0-7803-4376-X/98/$10.00 © 1998 IEEE

Figure 2 shows the merit function brightness, $M_b$, for elliptical and circular polarization modes as a function of photon energy. Merit function brightness is defined as $M_b = BP_c^2$, where $B$ is the spectral brightness, and $P_c$ is the degree of circular polarization.

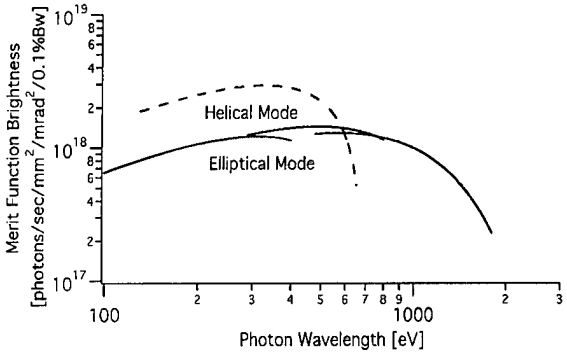



**Figure 2: Merit Function Brightness for EPU.**

## 4 MAGNETIC STRUCTURE

The four magnetic quadrants are attached to separate backing beams which allow Q2 and Q4 to translate axially relative to Q1 and Q3, which are fixed. Each quadrant has a magnetic structure length of 1.95 m, including 37.5 full magnetic periods, the ends for achieving a gap-independent steering and displacement free entrance and exit, and magnetic trim sections for correction of integrated multipoles.

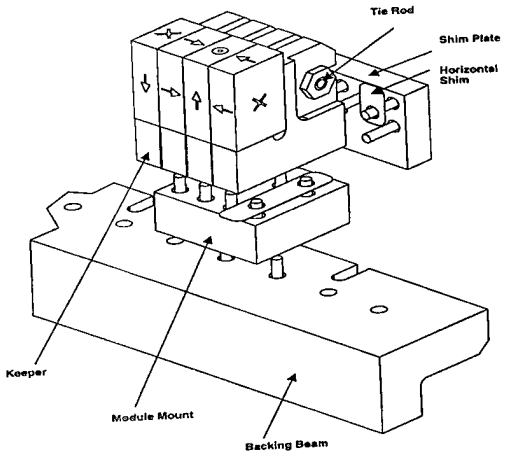



**Figure 3: EPU periodic module structure.**

Within each quadrant, the basic assembly unit is a four block, one period, module. Figure 3 shows an exploded view of a four block and keeper module and its interface to the backing beam. Each block within the module is bonded to an aluminum keeper. The set of four blocks and keepers are held together with a tie rod. A keeper's vertical position is held with two bolts. The horizontal position is held with a shim plate that is bolted to each keeper and to the backing beam. Each keeper's vertical and horizontal position can be adjusted with the use of shims between the keeper and module and the keeper and the shim plate, respectively. The design allows for a total adjustment range of ±0.25 mm. One of the four keepers in each module is keyed with a pin which, in combination with a slot in the backing beam, provides longitudinal registration of the module. The tie rod and shim plate holds the four keepers within a module together to allow individual modules to be removed from the magnetic structure for adjustment or for swapping with other modules. Field errors may be first minimized by vertical and horizontal shimming. Optical phase errors may be further reduced by module swapping.

## 5 SUPPORT STRUCTURE AND DRIVE SYSTEM

Figure 4, an elevation and side view of the EPU structure, illustrates the support structure and drive systems. The support structure is an "I" frame design. Two vertical columns are mounted to a common base with two horizontal members connecting them. The vertical columns support two roller screw assemblies, each assembly includes one right hand and one left hand roller screw coupled together at the midplane. Each roller screw has a 2 mm pitch thereby providing 4 mm of total gap movement per roller screw revolution. The roller screws are chosen to also act as a guide shaft with linear/rotary bearings mounted to the upper and lower backing beams via a vertical gap drive support. The vertical gap drive support is fastened to the stationary upper and lower backing beams which are at opposite quadrants (Q2 and Q4) of the magnetic structure. The stationary backing beam also supports the moving backing beams via a set of crossed roller slides. This allows the backing beams in Q1 and Q3 to move relative to the backing beams in Q2 and Q4.

The vertical gap is moved via a chain drive system connecting a 25:1 wormgear reduction box and servo-motor to the two roller screw assemblies. A glass engraved linear encoder is mounted to the magnetic structure to provide direct feedback to the vertical gap drive system. The longitudinal drive system is a similar system using a smaller roller screw with a 2 mm pitch directly coupled via a 3:1 planetary gear box and servo-motor. There will be two longitudinal drive systems: one for the upper magnetic structure and one for the lower magnetic structure. The motor/gear box and roller screw will be mounted to the stationary backing beams in Q2 and Q4. The roller screw nut will be mounted to the movable backing beams in Q1 and Q3. A linear encoder will be mounted to each backing beam to provide positive feedback as to the offset of the different quadrants.

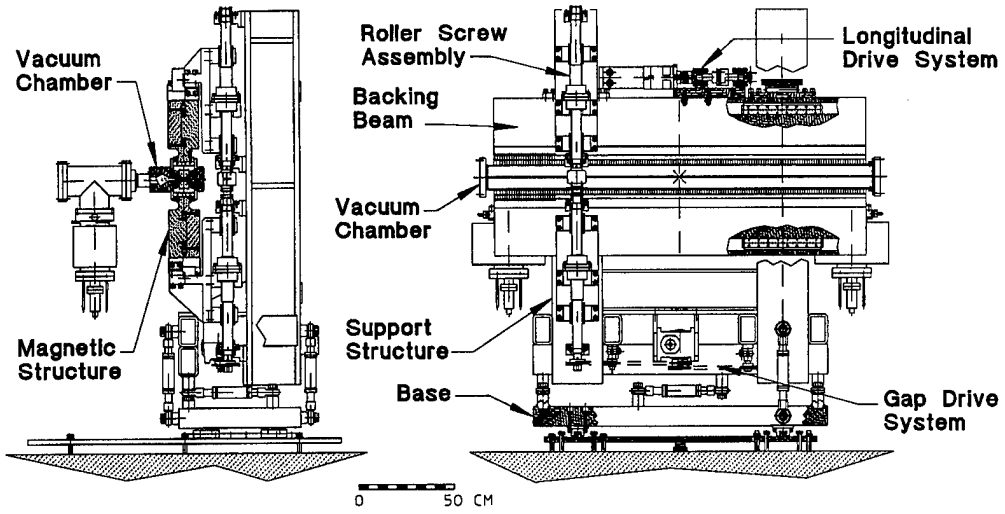



**Figure 4: EPU elevation and side view.**

## 6 VACUUM SYSTEM

The vacuum systemconsists of two 2.1 m long EPU chambers, machined in two halves out of 5083-H321 aluminum and welded together, and three smaller transition chambers to accomodate the chicane system. The EPU chambers are machined to achieve a nominal 9.4 mm vertical aperture and a 1.3 mm wall thickness. This leaves 2.5 mm for fabrication and alignment tolerances and magnetic adjustments to achieve a 14.5 mm minimum magnetic gap. A water cooled photon absorber is located in the upstream chamber to absorb radiation from the upstream bend magnet and to protect the downstream chamber. A 60 l/s ion pump and 600 l/s titanium sublimation pump combination is located at the ends of each chamber. Calculations for the vacuum configuration predict an average pressure of less than $3\times10^{-9}$ Torr after 40 A-hrs of operation in the storage ring.

## 7 CHICANE SYSTEM

A three magnet chicane system is used to steer the electron beam through two EPU's with orbit correction and to provide an angular seperation in the two photon beams. The first magnet steers the electron beam from the straight sector centerline inward 1.25 mrad, the second magnet steers the electron beam outward 2.53 mrad and the third magnet steers the electron beam 1.28 mrad back onto the centerline of the straight sector. Inward beam displacement is 3.05 mm at the center magnet. Vertical steering capability of each magnet is +/-0.20 mrad.

The magnets are conventional with water cooled coils designed to carry 80 A. Peak horizontal and vertical field integrals for the central magnet are 0.0158 T-m and 0.0079 T-m respectively. The designs are identical for the three magnets except that the central magnet has four horizontal steering coils wrapped around its poles whereas the end magnets have just two coils each. The vertical coils cover the pole faces, are inside the horizontal coils and wrap around the top and bottom of the yoke. Coils are wound from 1/8" OD × 1/16" ID copper tubing; they are insulated with fiberglass and impregnated with epoxy. Core construction is with C-shaped laminations of 1.6 mm thickness that are bonded together with epoxy. To control the magnet fringe fields, field clamps are provided on both the entrance and exit ends of the magnet. Overall magnet length is 0.15 m. Magnet support and adjustment is proviced by 6 strut assemblies mounted onto tubular pedestals. Each magnet is powered with two bi-polar power supplies; current regulation is 1 part in $10^3$.

## 11 ACKNOWLEDGEMENTS

This work was supported by the Director, Office of Energy Research, Office of Basic Energy Sciences Division, U. S. Department of Energy, under Contract No. DE-A03-76SF00098.

## REFERENCES

[1] A. Young, E.H. Hoyer, S. Marks, V. Martynov, H.A. Padmore, D. Plate, R. Schlueter, "Elliptically polarizing undulator beamlines at the Advanced Light Source", Rev. Sci. Instrum., 67 (1996) 3372.

[2] S. Sasaki: 'Analyses for a planar variably-polarizing undulator',Nucl. Instr. And Meth. A 347 (1994) 83.

[3] 'EPU5.0 Elliptical Polarization Undulator Conceptual Design Report', to be published.

# MAGNETIC PERFORMANCE OF INSERTION DEVICES AT THE ADVANCED PHOTON SOURCE

E.R. Moog, I. Vasserman, M. Borland, R. Dejus, P.K. Den Hartog, E. Gluskin, J. Maines, and E. Trakhtenberg, Advanced Photon Source, Argonne National Laboratory, Argonne, IL 60439

*Abstract*

The insertion devices (IDs) at the Advanced Photon Source have been magnetically tuned to minimize the integrals of the field through the devices and to minimize the variation of those integrals with gap, with a goal of not perturbing the stored particle beam. Measurements of the particle beam motion as the ID gap was changed found that the closed-orbit distortion was better than the requirement and agreed well with predictions based on magnetic measurement results. Another goal of the magnetic tuning is to ensure high brilliance in the low-order harmonics by keeping the rms phase error small.

## 1 INSERTION DEVICES AT THE APS

The Advanced Photon Source (APS) has 23 insertion devices (IDs), of which 18 are installed on the storage ring. Thirteen of the installed devices are 33-mm-period undulators. Other installed undulators have periods of 27 mm, 55 mm, and 18 mm; an 85-mm-period wiggler and an elliptical wiggler with a 160 mm period complete the list of installed devices. The elliptical wiggler was built jointly by the Budker Institute of Nuclear Physics (Novosibirsk, Russia) and APS; all the rest of the IDs were built and tuned to demanding specifications by STI Optronics (Bellevue, WA). The IDs have undergone further refinement of their magnetic field at APS since their delivery. The straight sections where the IDs are installed are long enough to accommodate two standard-length (2.4-meter) IDs, but only the sector that is occupied by the 55 mm and a 33 mm undulator has more than one ID installed at present.

An early conceptual version of the 33-mm-period undulators was intended to have a minimum gap of 11.5 mm. The tuning curve for this undulator, however, predicted a decrease in brilliance of about a factor of 3 when moving at constant photon energy from the third harmonic at closed gap to the first harmonic at a more open gap. The users preferred not to have such a large discontinuity in brilliance as the photon energy was scanned. In order to eliminate this jump, two things were done: the undulator magnetic design was changed to increase the magnetic field so the third harmonic would extend to lower energy, and tighter tolerances were placed on the straightness of the vacuum chamber so that the undulator would be able to go to smaller gap. The undulators currently installed can all go to a minimum gap of 10.5 mm.

## 2 MEASUREMENTS OF THE FIRST AND SECOND FIELD INTEGRALS

It is important that the integrals of the field through the ID not change by much as the ID gap is changed, so that the net effect of a gap change on the particle-beam closed orbit is small. The first and second field integrals of both the horizontal and vertical components of the magnetic field must be small enough to meet the APS requirement that the particle beam be stable to within 10% of its emittance. If compensation by local storage-ring steering correctors is relied upon, this translates into first field integral changes of no more than 100 G-cm and second field integral changes of no more than 100000 G-cm$^2$ [1]. Without compensation, the requirement is a vertical first field integral change less than 26.5 G-cm, a horizontal first field integral change less than 11.2 G-cm, a vertical second field integral change less than 37400 G-cm$^2$, and a horizontal second field integral change less than 11200 G-cm$^2$.

Measurements of the first and second integrals of the vertical and horizontal components of the magnetic field through each ID were made as a function of gap; one goal of the magnetic field refining was to minimize the changes in these integrals. The development of magnetic tuning techniques is an ongoing process at APS. New techniques are applied to IDs that are subsequently tuned or retuned. The total range spanned by the field integrals as the gap is changed is shown in Fig. 1 for the APS IDs as they are presently configured.

Changes in the field integrals as measured in the magnetic measurement facility may differ from the changes when the ID is installed in the storage ring, however, due to different environmental magnetic fields [2]. The vanadium permendur poles in these hybrid IDs can serve as field shunts, either removing horizontal components of the environmental field at small gap or focusing a vertical environmental field across the gap at small gap.

Measurements of changes in the first and second field integrals, and of changes in the tune, were also made using the particle beam in the storage ring. These measurements are complicated by other sources of orbit and tune motion, particularly because the gap change is relatively slow (approx. 1 min.) and the undulator-induced orbit and tune changes are quite small. To deal with this, we measure the difference in orbit and tune between two states of an undulator: "large" gap, typically 45 mm, and "small" gap, typically 11 mm. We take, typically, 10 measurements per state, alternating randomly between

0-7803-4376-X/98 /$10.00 © 1998 IEEE

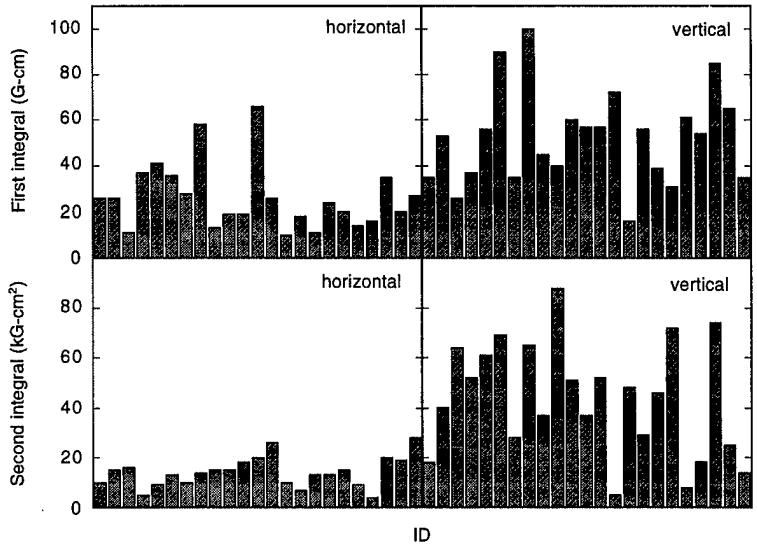



Figure: 1 First and second integrals of the vertical and horizontal components of the magnetic field through each of the IDs, as measured in the APS magnetic measurement facility.

states to reduce the effect of drifts. These two gaps were chosen because the extrema in field integrals as measured in the lab often occur at these gaps. Each measurement consists of acquiring the orbit (heavily averaged to reduce electronic noise and fast beam motion) and the spectrum around the vertical tune line (which is easier to measure precisely than the horizontal tune).

The orbit difference is determined after processing the orbits for each state to remove spikes that sometimes occur due to malfunctioning beam position monitors [3]. The undulator error field is modeled in the accelerator simulation program ELEGANT using two angle kicks per plane of beam motion, one at each end of the ID. The first integral is related to the sum of the kicks for a single plane, while the second integral is related to the value of the upstream kick. This provides exact modeling of the first and second integrals by giving the simulation control of the change in slope and angle due to passage through the device. Fig. 2 shows a typical result for displacement in the vertical plane, along with the fit from the simulation.

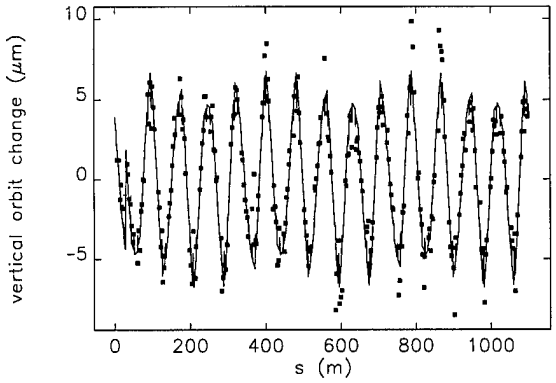



Figure: 2 Difference in vertical orbit for two different ID gaps, as a function of position around the ring. The points are the measured displacement values, and the line is the fit from the simulation. The ID is located at about 25 m.

While orbit displacement data can be measured easily and accurately, the small tune changes that result from changing an ID gap are not readily measured. We have found that in general the vertical tune change is less than 0.001, which is close to the limit of our ability to measure.

Measurements of the changes in the first and second integrals made using this beam-based technique agree with the results of magnetic measurements of the IDs that were carried out before the ID was installed on the storage ring.

## 3 PHASE ERRORS

Phase errors are another measure of the quality of an undulator magnetic field. A small rms phase error is needed in order to produce high-brilliance peaks in the undulator spectrum, although the effect of a large rms phase error is greater for high harmonics than for low ones. The IDs undergo tuning to decrease the phase errors, and, as with the field integrals, progressively better results are being achieved. The phase errors for all the 3.3 cm undulators are shown in Fig. 3. The phase is tuned primarily by placing shims on top of the magnets on the undulators. The magnets are recessed slightly (<0.5 mm) as compared to the poles in these hybrid IDs, so there is space to place shims without affecting the minimum gap. It has proved very useful in the tuning of these devices to have shims that are near-pure, i.e., that affect only the phase or only the trajectory. A standard trajectory shim would be one that covers half of the magnet in the beam direction and the whole magnet in the transverse direction. (Four of these would commonly be used together: one on each side of each of the two poles that face one another across the gap.) This shim serves to weaken the kick given by the pole and thereby changes the angle of a

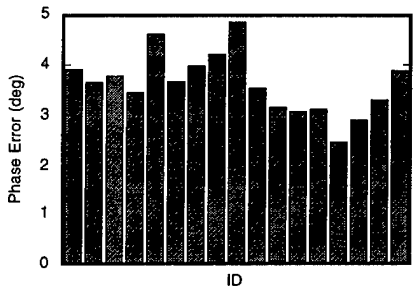



Figure: 3 Rms phase errors of all the APS 33 mm undulators, at a gap of 11.5 mm.

particle's trajectory through the ID. This shim, however, also has a strong direct effect on the phase, as can be seen by placing two such shims adjacent to one another with the opposite correction. The net effect on the phase will be large, particularly for IDs that have small magnet recesses, whereas there will be no net effect on the trajectory angle. If the length of the shim in the beam direction is made shorter, however, the direct effect on the phase will be much smaller compared to the effect on the trajectory [4]. For many of the undulators, it was found that there was no need to separately adjust the phase. Once the trajectory was corrected using the non-phase-altering trajectory shims, the rms phase error was already adequately small (less than 4 degrees).

Calculations have been made to predict the effect of the remaining phase errors on the spectral quality of the emitted photon beam, and to determine what the effect would be of making further improvements in the phase. The on-axis brilliance was calculated for the undulator with the smallest rms phase error (2.5 degrees) and for an undulator with a large rms phase error (4.6 degrees). The calculations are for an undulator gap of 11.5 mm and include representative values for the APS beam emittance and energy spread, and a coupling of 4.4%. The ratios of the intensities for the first, third, and fifth harmonics are 1, 0.98, and 0.90, respectively. The effect on higher harmonics is more pronounced, as can be seen in Fig. 4. The present phase errors meet the original design intention for the standard 33-mm-period undulator because they were intended to be used in the 1st, 3rd, and occasionally 5th harmonics. Should a user want to use higher harmonics, however, an undulator with a smaller rms phase error would be advantageous.

## 4 SUMMARY

The IDs at the APS more than meet the requirements for magnetic field quality, so that users are now allowed to change their gaps freely. The requirements will become more demanding in the future as the quality of the stored beam is improved or as users do more work at higher energy. We are developing techniques and applying them to IDs to further refine the magnetic field quality. The long-term magnetic performance of the IDs may be affected by radiation damage, though no effect has been seen yet. This is under experimental investigation [5].

## 5 ACKNOWLEDGEMENTS

This work is supported by the U.S. D.O.E., BES-Materials Sciences, under Contract # W-31-109-Eng-38.

## REFERENCES

[1] Y-C. Chae and G. Decker, Proceedings of the 1995 Particle Accelerator Conference (IEEE 1996), p. 3409.
[2] This effect has been observed at ESRF. P. Elleaume and J. Chavanne, private communication.
[3] L. Emery, et al., "Advancements in Orbit Drift Correction in the Advanced Photon Source," these proceedings.
[4] I. Vasserman, "A Shimming Technique for Improvement of the Spectral Performance of APS Undulator A," ANL/APS Light Source Note LS-253, Jan. 1996.
[5] E.R. Moog, et al., to be published in the proceedings of the SRI'97 National Conference, June 17-20, 1997, Cornell.

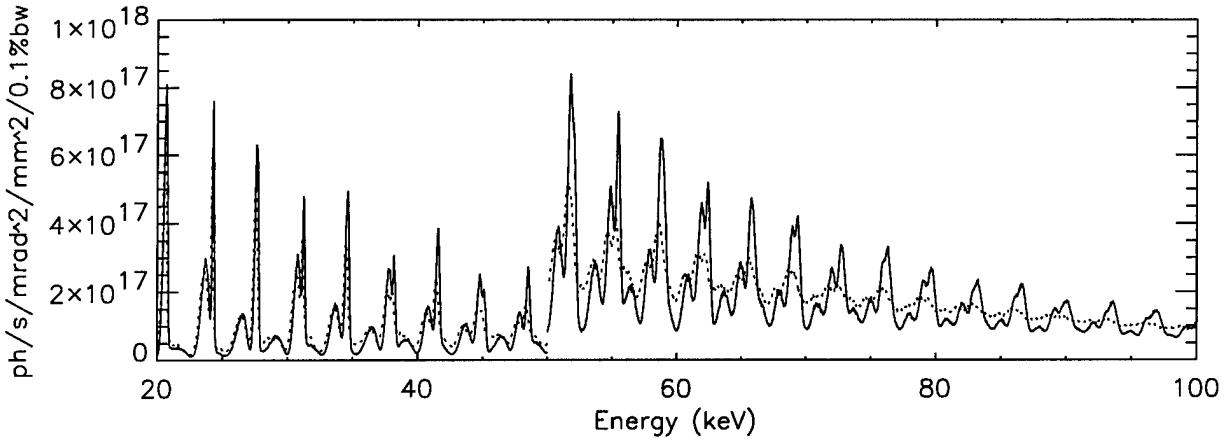



Figure: 4 Calculated on-axis brilliance, beginning at the 6th harmonic. The solid line is for the 33-mm-period undulator with the smallest rms phase error (2.5 degrees), and the dotted line is for an undulator with an rms phase error of 4.6 degrees, at 11.5 mm gap. *The brilliance above 50 keV has been multiplied by a factor of 4 for clarity.* While this difference in rms phase error has no effect at lower energies, it would affect the brilliance at higher energy.

# TEMPERATURE COMPENSATION OF NdFeB PERMANENT MAGNETS

S. H. Kim and C. Doose
Advanced Photon Source, Argonne National Laboratory,
9700 South Cass Avenue, Argonne, Illinois 60439

*Abstract*

Permanent magnet blocks of NdFeB have a relatively high maximum energy product. Because of its relatively low Curie temperature, however, NdFeB has a large temperature coefficient for its residual induction. The temperature coefficients of the relative magnetic fields $(\Delta B/B)/\Delta T$ in the air gap of NdFeB dipole magnets were reduced from $-1.1 \times 10^{-3}$/°C to less than $2 \times 10^{-5}$/°C under operating temperatures of ± 6°C. This was achieved passively by using 1.25-mm-thick strips of 30%-Ni-Fe alloy as flux shunts for the NdFeB blocks. The magnets with soft-steel poles and flux-return yokes were assembled and measured in a temperature-controlled environment.

## 1 INTRODUCTION

Stable permanent magnets could be used for charged-beam storage rings and for other new magnetic devices which require system reliability and lower construction and operation costs. One drawback of permanent magnets for these types of applications, however, is maintaining the required magnetic field when the residual induction and coersive forces change due to the ambient temperature variation.

The bulk magnetization of a permanent magnet is the result of a collective alignment of atomic spins within magnetic domains. As the temperature increases, thermal fluctuations induce random variations in individual atomic spin orientations. At Curie temperature $T_C$, all the spins are randomly oriented and the bulk magnetization disappears. Therefore, at ambient temperature, a permanent magnet with higher $T_C$ has a lower temperature coefficient for the variation of the magnetization.

Permanent magnet blocks of neodymium-iron-boron (NdFeB) have relatively high maximum energy-product in the demagnetizing quadrant compared to other permanent magnets such as Alnico, ferrite, and rare-earth cobalt [1]. Because of its relatively low Curie temperature of approximately 300°C, NdFeB has a high temperature coefficient for its residual induction.

The purpose of this work is to reduce the temperature coefficient of the magnetic fields of NdFeB permanent magnets better than $10^{-4}$/°C within the range of an operation temperature using parallel flux-shunts. At lower temperatures the shunt permeability increases, enabling the shunt to carry or divert more flux from the air gap of the magnet. At higher temperatures, the reverse condition exists: the shunt permeability decreases and less air-gap flux is diverted. In order to have higher temperature sensitivity, the shunt material should have a Curie point close to ambient temperature. Shunt materials made of Curie alloys (30-32% Ni-Fe) and Montel alloys (67% Ni-Cu-Fe) have relatively low Curie temperatures of less than 100°C. Temperature compensations for ferrite permanent magnets have been extensively studied at Fermilab for use at relatively low magnetic field [2].

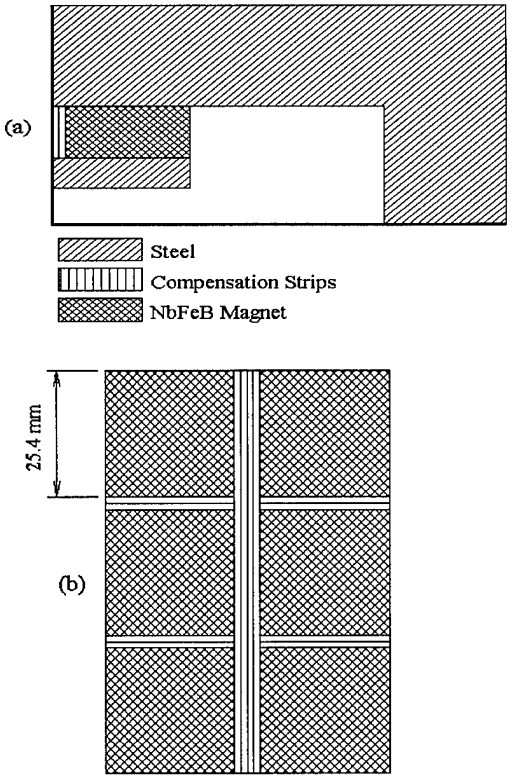



Figure 1: (a) Symmetrical cross section of a quadrant of a dipole magnet with a soft-steel pole and flux-return yoke. The NdFeB block is magnetized in the vertical direction. (b) Top view for the arrangement of the permanent magnet blocks and the temperature compensation strips inserted between the blocks.

## 2 TEMPERATURE COMPENSATION

The symmetrical cross section of a quadrant of a typical dipole magnet used for this study is shown in Fig. 1. The major components of the magnets are NdFeB permanent magnet blocks, magnetic flux shunts for temperature compensation, flux-return yokes, and soft-steel poles for field-shaping. The NdFeB blocks have a cross section of $25.4 \times 25.4$ and a thickness in the magnetized direction of

0-7803-4376-X/98/$10.00 © 1998 IEEE

12.7 mm. The residual induction and coercive force of the blocks were approximately 1.1 T and 10.5 kOe, respectively. For the temperature compensation flux shunts, 1.27-mm-thick and 25-mm-wide strips of 30%-Ni-Fe alloy were used. The alloy has a Curie temperature of 60°C and saturation induction of 0.22-0.1 T at 20-45°C.

First a dipole magnet without temperature compensators was put in a temperature-controlled incubator and its temperature and the magnetic field in the air gap were measured. The magnet was assembled using six NdFeB blocks in each of the top and bottom poles. Figure 2 shows that the temperature coefficient for the relative magnetic field $(\Delta B/B)/\Delta T$ in the air gap was $-1.1 \times 10^{-3}$/°C in the temperature range of 25-45°C. The Hall probes used for the magnetic field measurements were calibrated to $\pm 10^{-5}$ of reading/°C with a resolution of 0.2 G. The temperature measurement has an absolute accuracy of 0.5°C with a resolution of 0.1°C.

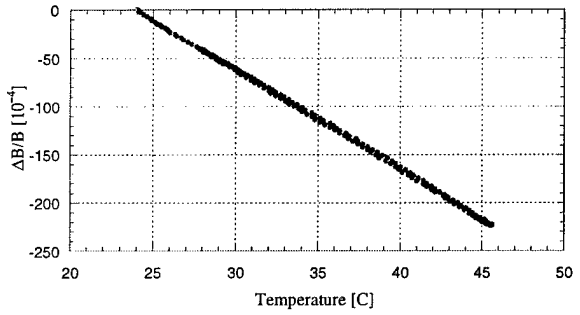
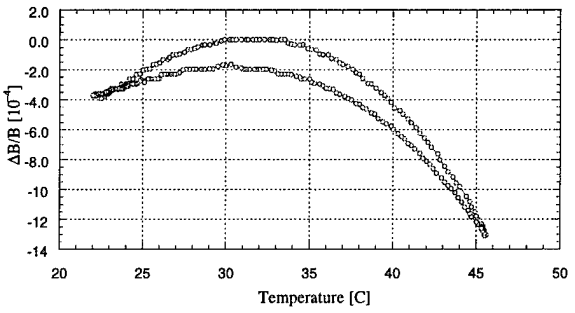



Figure 2: Magnetic field data under a slow thermal cycle for a NdFeB permanent dipole magnet. Temperature coefficient for the relative magnetic field in the air gap was $(\Delta B/B)/\Delta T = -1.1 \times 10^{-3}$/°C in the temperature range of 25-35°C.

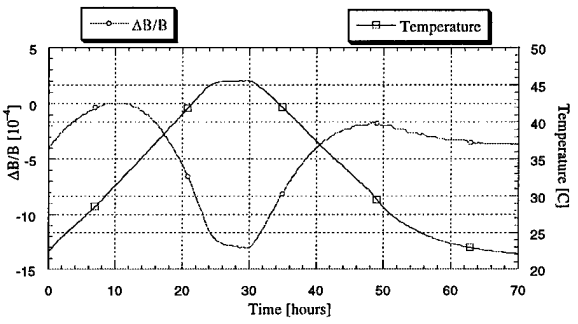
The data shown in Fig. 3 are measurements of a magnet with an optimum number of temperature compensation strips. The volume ratio of the strip/NdFeB for the magnet was 20%. In this magnet the compensation strips were inserted between the gaps of the NdFeB blocks as shown the top view in Fig 1(b). The strips cannot be distributed uniformly, but the magnetic field distribution in the air gap can be adjusted by the geometry of the magnet poles. The measured data show that within the relative field variation of $2 \times 10^{-4}$, the temperature coefficient was less than $2 \times 10^{-5}$/°C in the temperature range of 31 ± 6°C. (For better control of the temperature inside the incubator, the temperature at the compensation field was set higher than the room temperature.) In the whole range of the thermal cycle the coefficient was less than $1 \times 10^{-4}$/°C. During measurement the temperature was controlled at a rate of approximately 0.8°C/hr to ensure the uniformity of the magnet temperature.

Ideally the magnetic field in the air gap can be calculated from the magnetomotive force of the NdFeB blocks as well as the reluctances of the air gap and the compensation strips. Because of the nonlinear magnetic properties of the strips, however, the temperature range for a fully compensated field is limited. The relative magnetic permeability of the strips in the magnet was calculated to be less than 5.

Figures 4(a) and (b) show the effects of consecutive thermal cycles on the compensated field and temperature. The temperature of the magnet was controlled rather slowly at a rate of only 0.15°C/h. The compensated relative magnetic field increased by approximately $1 \times 10^{-4}$ (0.5 G) for the first to the third cycle. On the other hand, the temperature at the compensated field decreased approximately 1°C. After an additional seven thermal cycles, the compensated fields and temperatures remained within 0.1 G and 0.5°C, respectively.

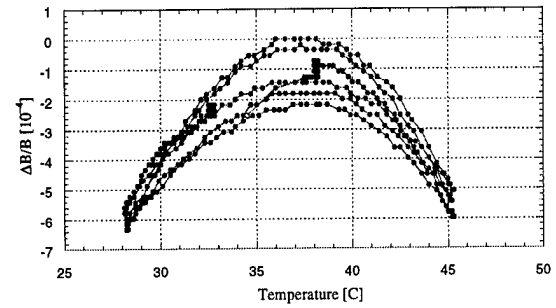



(a)

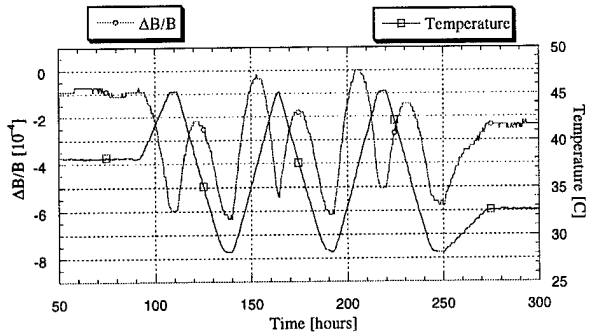



(b)

Figure 3: Temperature compensation of a dipole magnet with a volume ratio of the compensation strip/NdFeB of 20%, the temperature coefficient was $1.7 \times 10^{-5}$ in the temperature range of 31 ± 6°C. (a) ΔB/B vs. temperature and (b) ΔB/B and temperature vs. time.




(a)




(b)

Figure 4: Three thermal cycles of a compensated dipole magnet at a thermal cycle rate of 0.15°C/h (a) ΔB/B vs. temperature and (b) ΔB/B and temperature vs. time.

## 3 SUMMARY

The temperature coefficients of NdFeB permanent magnets were reduced from $-1.1 \times 10^{-3}$/°C to less than $2 \times 10^{-5}$/°C under operating temperatures of ± 6°C by passively using Ni-Fe alloy as flux shunts for the NdFeB blocks. After the initial increase of the compensated field by $1 \times 10^{-4}$ in the first three thermal cycles, the field remained within $2 \times 10^{-5}$ after an additional seven thermal cycles. The effects of thermal cycles, aging, and radiation have to be investigated further.

## 4 ACKNOWLEDGMENTS

This work was supported by the U.S. Department of Energy, Office of Basic Energy Sciences, under Contract No. W-31-109-ENG-38.

## 5 REFERENCES

[1] Rollin J. Parker, *Advances in Permanent Magnetism*, John Wiley & Sons, New York, 1990.

[2] K. Bertsche, J.-F. Ostiguy, and W. B. Foster, "Temperature Considerations in the Design of a Permanent Magnet Storage Ring," Proc. of the 1995 Particle Accelerator Conference, IEEE 95CH35843, pp. 1381-1383 (1996).

# THE STAR DETECTOR MAGNET SUBSYSTEM*

R.L. Brown, A. Etkin, K.J. Foley, W.J. Leonhardt, J.A. Mills, I. Polk, E.S. Rodger, J.A. Scheblein
Brookhaven National Laboratory, Upton, NY 11973
R.D. Schlueter
Lawrence Berkeley Laboratory, Berkeley, CA 94720

*Abstract*

The RHIC (Relativistic Heavy Ion Collider) Accelerator currently under construction at Brookhaven National Laboratory will have large detectors at two of its six intersection regions. One of these detectors, known as STAR (Solenoidal Tracker At RHIC), weighs 1100 tons and is being built around a large solenoid magnet. The magnet is 7.32 m in diameter, 7.25 m long and utilizes three different sizes of room temperature aluminum coils. The magnet will operate with a field set from 0.25 T to 0.5 T and have a field uniformity of better than 1000 ppm over a portion of its interior region. This paper describes the magnet design, fabrication and assembly requirements and presents the current construction status.

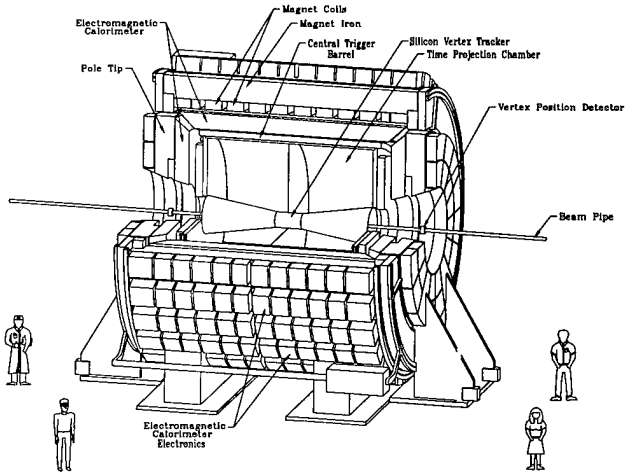



Figure 1

## 1 INTRODUCTION

The Solenoidal Tracker At RHIC (STAR) will search for signatures of quark-gluon plasma (QGP) formation and investigate the behavior of strongly interacting matter at high energy density. To accomplish this, a flexible detection system that can simultaneously measure many experimental observables is being constructed. The system contains several subsystems such as the Time Projection Chamber (TPC), Silicon Vertex Tracker (SVT), Forward Time Projection Chamber (FTPC) and the Electro-Magnetic Calorimeter (EMC) as shown in Figure 1. These subsystems operate in a magnetic field generated by the Magnet subsystem (MAG) which is an iron dominated, conventional (room temperature) solenoid magnet. The field can be varied from 0.25 T to 0.5 T with a uniformity better than 1000 ppm over the entire TPC volume.

## 2 PHYSICS REQUIREMENTS & COMPUTER SIMULATION

The momentum resolution requirements of STAR dictate that everywhere in the TPC volume

$$\mathfrak{I}_r \equiv \int_{z=2100}^{z} \frac{B_r}{B_z}\,dz \le 7.0 \text{ mm}, \quad \mathfrak{I}_\theta \equiv \int_{z=2100}^{z} \frac{B_\theta}{B_z}\,dz \le 2.5 \text{ mm}$$

$$(r,\theta,z) \in \; 0 \le r \le 2000 \text{ mm}, \; 0 \le \theta \le 2\pi, \; 0 \le |z| \le 2100 \text{ mm}$$

The magnet must provide a uniform magnetic field over its operating range $0.25 < B_z < 0.50$ T, while simultaneously minimizing radiation length to and providing structural support for the electro-magnetic calorimeter, provide a hole in the end poles at pseudorapidity $\eta = 2.0$ to allow particle transmission to external detectors, accommodate EMC fiber bundle routing to external electronics, and, most importantly, minimize STAR's capital cost. A cross section of the quasi-axisymmetric magnet is shown in Figure 2.

The magnetic design achieves a 0.5 T field with uniformity characterized by: $\mathfrak{I}_r \le 2.3$ mm and $\mathfrak{I}_\theta \le 1.0$ mm over the entire TPC volume by using a combination of a Poletip Trim and Space Trim coils to appropriately compensate and straighten field lines.

Radiation lengths to the EMC are minimized by positioning the coils radially outside the calorimeter, though at the expense of additional iron and conductor weight. The regularly spaced pancake coil design allows

*This research was supported by the U.S. Department of Energy under Contract Nos. DE-AC02-76CH00016.

0-7803-4376-X/98 /$10.00 © 1998 IEEE

for both calorimeter support to backlegs and EMC fiber bundle routes to external electronics. An end cap gap allows fiber bundle extraction through the ends. Flux density is $B \leq 1.4$ T everywhere at full coil energization, resulting in an excitation independent field uniformity.

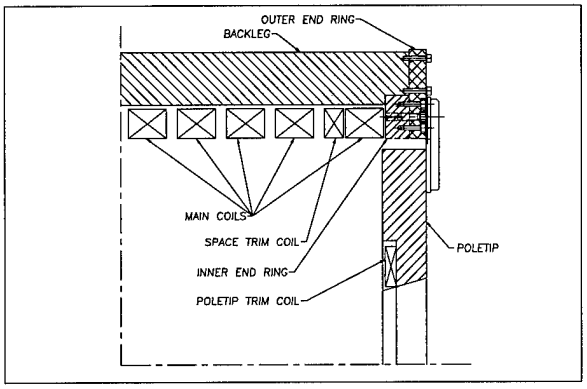



Figure 2 Magnet Quarter Section

Using poletip trim coils instead of shaping the poletip enables attainment of much better TPC field uniformity ($\Im_r|_{max}$ = 2.3 mm), well worth the additional coils and power supplies. The additional desirable feature of a flat machined poletip, with an unobtrusive trim coil recessed into the iron pole face, is incorporated into the design without impacting the attainable field uniformity.

Code calculations indicate that this robust design is capable of maintaining field uniformity even in the event of coil mispositionings by adjusting Poletip Trim and Space Trim coil settings. Current plans are to adapt the field mapping apparatus used to map the Aleph magnet at CERN. STAR and Aleph are similar in size and shape, therefore adapting the existing apparatus to the STAR geometry is not judged to require much effort.

## 3 MAGNET STEEL DESIGN

The Solenoidal Magnet steel is a cylindrical structure weighing 1,100 tons on axis with the collider beam and consisting of 30 flux return bars (backlegs), four end rings, two pole pieces, and support structures. The 6.85 m long flux return bars are trapezoidal in cross-section, and weigh 18 tons each. They form the outer cylinder wall encompassing the main and space trim excitation coils and are attached to an inner and outer end ring pair at each end of the magnet. The inner rings have a 5.27 m I.D. with thirty chord surfaces on the 6.28 m O.D. to control the azimuth location of each flux return bar, with an axial thickness of 285 mm, weighing 25 ton each. The outer rings are the structural connection between the ends of the flux return bars and the outer face of each inner ring and have the same I.D. as the inner rings with a 7.32 m O.D. and 203 mm axial thickness, weighing 35 ton each. Each pole piece weighs 73 ton and is on axis with, and supported by, the end rings and has a conical I.D. at $\eta$ = 2 with a 525 mm axial thickness a 5.06 m O.D. and a counter bore on the inner face for the pole tip trim excitation coil. A 107 mm annular gap exists between end ring I.D. and pole piece O.D. for utility routing to internal detector elements.

The main support structure consists of two cradles weighing 36 tons each supporting the lower nine flux return bars of the magnet cylindrical yoke. The main support structure is on Hillman Roller systems and hydraulic jacks and is supported and guided on two rails embedded into the floor, thus allowing the magnet to be moved via hydraulic jacks between experimental hall and assembly building as required. In addition to the main support structure there are two external pole piece support structures weighing 100 tons each that permit removal of the pole pieces for installation or maintenance of internal detector elements. All magnet yoke material was specified as AISI 1008 killed steel that is vacuum degassed with a fully annealed heat treatment allowing for a minimum yield strength of 172 MPa; while the support structure material was specified as ASTM A36.

The magnetic field quality required that deflections in the magnet structure be minimized to less than 1 mm. This was accomplished with precise fabrication of magnet components and the use of high strength bolted and pinned connections between mating components. The prime contractor for fabricating the magnet steel was Precision Components Corp., York, PA., and materials for the magnet yoke were procured from Creusot-Marrel, France, for the flux return bars and end rings and Japan Steel Works, Japan, for the pole pieces. All components were provided as one piece forging except for the outer rings which were formed from four flame-cut arcs of flat rolled steel electroslag welded together to form each ring. Final fabrication of each component was performed either at PCC or their subcontractor Gec Alsthom, Canada. End ring pairs were aligned and match pinned to insure accurate assembly and structural integrity. High strength threaded inserts were used in this low yield strength material along with Expansion Bolts, Torque Bolts, and Mechanical Tensioners from Superbolt Corp., Carnegie PA. The use of these high strength fasteners allowed us to achieve the fixed end bolted connections needed to minimize deflection of the steel structure with accurate bolt tension using standard hand held torque wrenches. This also eliminated the need for anchor points in the steel to support much heavier mechanical or hydraulic torque wrenches used on standard hex-head fasteners.

## 4 COIL DESIGN

The magnet contains three separate designs of coils each wound using aluminum conductor and insulated with fiberglass cloth vacuum impregnated with epoxy.

Main and Space Trim coils - These coils are built up from two layer pancakes wound two-in-hand (bifilar) fashion containing 13 turns. The pancakes are wound in both a "right-hand thread" and a "left-hand thread" manner and are assembled in an alternating thread manner to cancel out

undesired field components from the layer-to-layer winding transitions. The conductor used in the pancakes measures 53.9 mm by 47.5 mm with a 16.8 mm diameter central water hole. Each pancake contains two parallel water circuits measuring approximately 120 m in length.

The magnet contains ten Main coils, each with four pancakes, and two Space Trim coils containing two pancakes each. These coils are all connected in series electrically, however all the water circuits (88) are in parallel. At the nominal 0.5 T magnet field, the current through these coils is 4744 amps with an additional 10% current through the Space Trim coils.

The nominal dimensions for these coils are as follows: 5.3 m I.D. by 6.0 m O.D. with an axial thickness of 0.45 m for the Main coils and 0.23 m for the Space Trim coils. Weights are approximately 6.8 tons for the main and 3.4 tons for the Space Trim coils. These coils have been fabricated by Tesla Engineering, Ltd. of Storrington, England.

Poletip Trim coils - Each poletip requires a trim coil to help preserve magnetic field uniformity. These coils contain six layers and are wound three-in-hand (trifilar) fashion giving 118 turns per coil. Each two layers contains three separate water circuits giving a total of nine circuits per coil. Water circuits are approximately 95 m long. The conductor measures 22.2 mm square with a 12.3 mm diameter central water hole.

Each coil is 1.8 m I.D. by 2.8 m O.D., has an axial thickness of 0.14 m and weighs about 1.2 tons. At the nominal 0.5 T magnet field, current through the Poletip coils will be 1441 amp. A vendor for these coils has not yet been chosen.

## 5 ASSEMBLY

The 6 o'clock experimental hall at RHIC has an Assembly Building (AB) in which the detector will be assembled and tested prior to rolling into the experimental hall. Assembly began with the installation of the base rails in a 1 m thick reinforced concrete floor running from the AB to the experimental hall. The two main support cradles were set atop the rails with one cradle being guided and the other as the follower. The lower nine flux return bars were installed, aligned, and welded to the main support cradles to form a monolithic support for the remaining magnet yoke and detector elements. Each end ring pair was then installed by first setting the inner ring in the cradle formed by the nine chord surfaces of each flux return bar. Then the outer ring was lifted and locked to the inner ring using taper pins and expansion bolts, and, to the ends of the lower nine flux return bars, using Torque Bolts. With end rings in place an additional six flux return bars were installed to mid-plane to form the lower half of the magnet yoke cylinder. The main and space trim excitation coils are then installed into the lower magnet yoke half starting from each end ring and finishing at the axial mid-point of the magnet. When the coils have been aligned and locked into place, the remaining fifteen upper flux return bars are installed to complete the assembly of the magnet core. The two pole pieces will be individually installed to complete the magnet assembly.

## 6 POWER SUPPLIES

There are 5 separate power supplies required for proper magnetic field shaping as shown in Figure 3. Due to the balanced nature of the power supply loads, ground potential on the main supply will be midway between the output terminal voltages. Power supplies (except for the booster) are separated into two parts, transformers, from NWL, Inc., Boardentown, NJ and rectifier control sections from Macroamp, Ukiah, CA.

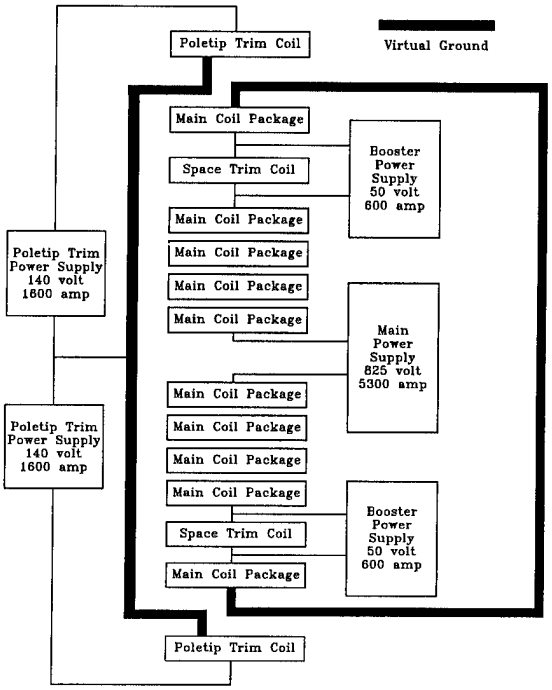



Figure 3 STAR Electrical Connections.

## 7 CURRENT STATUS

The magnet subsystem is 75% complete with the remainder to be completed in FY98. Both Main & Space Trim coil procurements are completed and the Pole Tip Trim coils are due for delivery the first quarter of FY98. All magnet steel fabrication is complete except fabrication of the pole tip supports and delivery to BNL is planned for the second quarter of FY98. Delivery of the Power Supply System of transformers and rectifiers is expected in the first quarter of FY98.

# MAGNETS FOR THE NATIONAL SPALLATION NEUTRON SOURCE ACCUMULATOR RING

J. Tuozzolo*, J. Brodowski, G. Danby, J. Jackson, W. Meng
Brookhaven National Laboratory, Upton, New York 11973

*Abstract*

The National Spallation Neutron Source Accumulator Ring[1] will require large aperture dipole magnets, strong focusing quadrupole magnets, and smaller low field dipole, quadrupole, and sextupole correcting magnets. All of the magnets will provide a fixed magnetic field throughout the accumulator's fill/storage/extraction cycle. Similar fixed field magnets will also be provided for the beam transport systems. Because of the high intensity in the accumulator, the magnets must be designed with high tolerances for optimum field quality and for the high radiation environment which may be present at the injection/extraction areas, near the collimators, and near the target area. Field specifications and field plots are presented as well as planned fabrication methods and procedures, cooling system design, support, and installation.

## 1 INTRODUCTION

The performance requirements for the magnets have been defined and the magnet cross sections have been designed. Table 1 provides a listing of the DC magnets required for the ring, the high energy beam transport[2] (HEBT) line from the Linac to the ring, and ring to target transport (RTBT) line from the ring to the target. Wherever possible magnets will be shared between the three different systems. The cross-sections for the major magnets are shown in figure 1.

| MAGNET TYPE | Location | Aperture x Length | Field kG | Qty. |
|---|---|---|---|---|
| Dipole | Ring | 17x45x150 | 7.1 | 32 |
| Dipole | HEBT | 8x30x250 | 3.0 | 13 |
| Dipole | RTBT | 17x45x250 | 7.1 | 1 |
| Quad. | H&L | 12x50 | 2.7 | 25 |
| Quad. | Linac | 12x50 | 2.7 | 2 |
| Quad. | R, H, RT | 20x50 | 3.4 | 77 |
| L. Quad. | Ring | 30x50 | 4.5 | 8 |
| VL. Quad. | RTBT | 36x80 | 3.6 | 2 |
| Corrector | HEBT | 12x12x20 | 0.3 | 27 |
| Correctors | R, H, RT | 20x20x30 | 0.2 | 77 |

Table 1

*Work performed under the auspices of the U.S. Department of Energy.

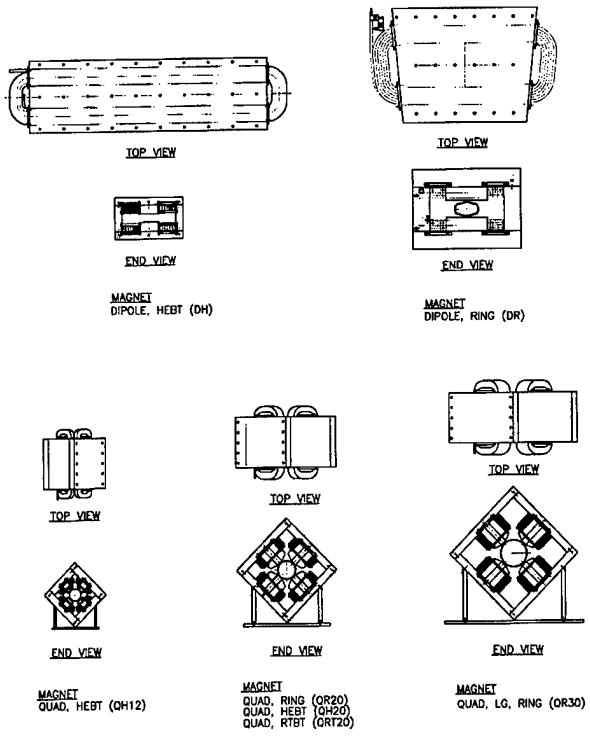



Figure 1: Major Magnet Cross Sections

Preliminary studies of the magnetic field[3] in the gaps have been completed. All of the magnets are conservatively designed to achieve the required field accuracy without expensive machining, special quality steel, or heat treating of the steel after fabrication. The magnet pole tips will have to be machined to a tolerance of $\pm$ .05 mm. The mating pieces in the magnet must be within $\pm$ .05 mm. 1006 steel will be used throughout the core including the pole tips. Figures 2 and 3 are field plots for the ring dipole and standard ring 20 cm. quadrapole.

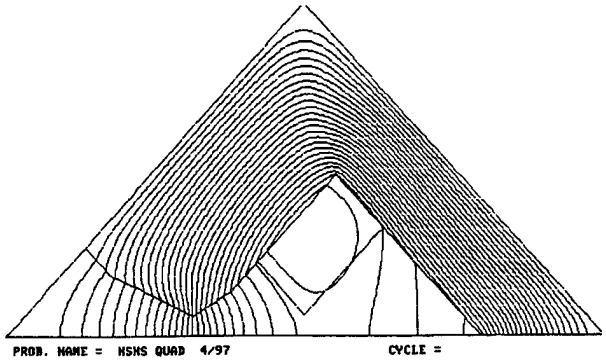



Figure 2: Ring 20cm Quadrupole Field Plot

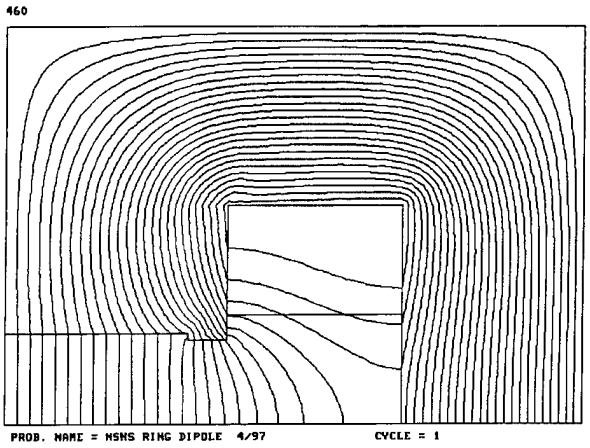



Figure 3: Ring Dipole Magnet Field Plot

*1.1 Magnet Core Design*

The magnetic cores must be accurate, inexpensive, reliable in a high radiation environment and easy to maintain. Low carbon steel cores manufactured from solid plate will meet these requirements. This method was used to fabricate the large core for the G-2 experiment superconducting magnet and is used throughout the AGS for the DC magnets used in the beam transfer lines. With computer numerically controlled machine tools the steel cores can be machined to high accuracy and repeatability. The solid cores are rigid requiring minimum stiffening from the support structure. The magnets will be built so they can be "split" for easy installation of the coils and vacuum chambers. This will allow the chambers to be built in separate clean rooms with no welding required after magnet assembly. The coils and heater blankets will also be accessible should they fail during initial testing.

For the small quantities required for the various sizes and shapes in the accumulator the solid core is significantly less expensive then a laminated core magnet. The RHIC injection transfer line magnets were built with 1.1 x $10^6$ lbs. of steel laminated cores which cost $2.75/lb in 1990. The G-2 ring which contains 1.6 x $10^6$ lbs. of solid steel block of various sizes and shapes was built for $1.75/lb at the same time. The magnets in the accumulator rings and transfer lines will require ~1.4 x $10^6$ lbs. of steel.

*1.2 Magnet Coil Design*

The magnets will be designed with low current density (>350 amps/cm$^2$) copper coils wherever possible. The low current density will reduce the resistive energy loss in the coils and keep the voltage drop across the magnets low. This will reduce the possibility of turn to turn shorts occurring in the coil should the insulation be damaged by radiation. The low current density will also reduce the resistive heat loss in the magnet system. This will lower the power consumption of the accumulator and will reduce the load on the water cooling systems. All of the coils will have a single pass water cooling passage which will reduce the number of water fittings which can leak or fail to a minimum. The exception to this rule will be the high field quadrupoles. Space limitations at the ends require current densities of up to 450 amps/cm$^2$ but these magnets will be sized for single pass coils.

The coils will use a modified epoxy/glass insulation which is used on AGS magnets in high radiation areas. Radiation protection will be provided by wrapping the coils with the glass tape which has a Kapton$^R$ layer. Manufactured by August Krempel Co. Stuttgart, Germany, this material provides the radiation protection of Kapton$^R$ with the bonding ability of glass fiber and epoxy. Because the manufacturing method for this insulating material is the same as a standard glass wrap insulation the increase in the coil costs will be small.

Magnesium Oxide mineral insulation has been used for very high radiation resistant coils in special areas[4]. The most common commercial use for this type of cable material is high temperature resistant heaters but it is sold with copper conductors. The coil material is expensive and it must be carefully formed with large radius bends to prevent damage to the insulation. The mineral insulating materials are very hydroscopic and will break down if exposed to humid air for extended lengths of time. The cable comes with a grounded metal cover which must be terminated with a brazed ceramic feedthrough to keep the coil insulation sealed. Because of the complexity of this type of coil it will only be used in areas where high dose rates are expected such as the last focusing magnets in the RTBT transfer line near the spallation target.

## 2 THE CORRECTOR MAGNETS

The corrector magnets are based on the new low field magnets used in both the AGS and the AGS Booster[5]. They will be air cooled window frame magnets. Kapton$^R$ coated wire will be wrapped around the steel leg of box or diamond shaped magnets. Each magnet will provide either horizontal or vertical dipole correction. In addition, the correctors in the accumulator ring will be wound to provide quadrapole, skew quadrapole, or sextupole correction.

## 3 WATER COOLING REQUIREMENTS

For radiation resistance and reliability, metal fittings and tubing will be used to carry the cooling water to and from the coils. The coil water lines will be mounted on insulated stand-offs and routed to a common water manifold on the magnet stand which will have an insulated ceramic break. The integrity of the water system will be monitored by klixon temperature sensors on each coil and flow switches on each of the return lines on the manifold.

All of the magnets will be cooled by the closed loop ring water system. This system will also provide cooling for the RF cavities, special injection magnets, and special extraction magnets. The water system will only see copper coils, copper cooling plates in the RF cavities, and stainless steel water pipe so corrosion in the system should not be a problem. The collimators and beam dumps which contain steel and much higher activation products will be on a separate systems. The pumps, heat exchangers, and other ancillary equipment for the ring water systems will be located in a separate water services building outside of the tunnels. Activated water from the ring will be kept in the tunnel or the service building during normal operation.

## 4 MAGNET MEASUREMENT

In addition to detailed field mapping of the first article magnets, all of the magnets built for the NSNS magnet systems be field tested after final assembly. This will serve as a final check on the quality of all aspects of the magnet assembly: the coils, the steel core, and the correct connection of the leads.

## 5 STANDS AND INSTALLATION

The magnets will be installed on the support frames outside of the accumulator ring. In the 90° bends each large dipole bending magnet will be mounted with the corrector magnet and a quadrapole. In the straight areas the quadrapole will be mounted with a corrector magnet. This assembly will allow installation of a single vacuum chamber within all of the magnets without unnecessary flange joints. All of the magnets can be aligned on the support frame with the vacuum chamber and the associated beam position monitors outside of the ring. All of the magnets on an individual frame will be plumbed onto a single water manifold on the support frame, all of the coil heat sensors will be wired into a common wiring block, and the radiation monitors will be installed on the frame assembly as well. The completed frame assemblies with magnets and instrumentation can then be transported to the tunnel and moved around the tunnel to their final position using the tunnel crane. The frames will be placed on positioning jack stands and then surveyed into final position. All of the magnets for the Accumulator System will use similar frames for installation and support as shown in figure 4.

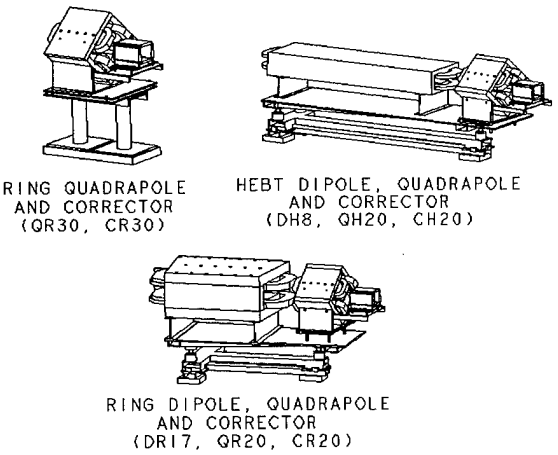



Figure 4. Magnets and Stand Assemblies

## 6 CONCLUSIONS

The magnets for the NSNS accumulator will be conservativily designed for reliability in a high radiation environment and ease of maintenance based on experience gained during the AGS Booster construction and upgrades to the AGS facility.

## 7 ACKNOWLEDGEMENTS

The authors would like to thank the design help of R. Ritter and C. Longo and the engineering help and advice provided by J. Cullen, C. Pearson, and A. Soukas.

## REFERENCES

[1] W.T.Weng, et al, "Accumulator Ring Design for the NSNS Project", (these proceedings).
[2] D. Raparia, et al, `The NSNS High Energy Beam Transport Line", (these proceedings).
[3] M.T. Menzel, "POISSON User's Guide", LAUR-87-115, January 1987.
[4] "Moun g-2 Design Report", Brookhaven National Laboratory, AUI, Upton, NY 11973, AGS 821 July 1992.
[5] A. Harvey, "Radiation Hardened Magnets Using Mineral Insulated Conductors", LA-5306-MS, LANL, June 3, 1973
[6] C. Gardner, et al, "Analyis of Resonance Driven Imperfections in the AGS Booster", The 4th European Accelerator Conf. 1994

# PERMANENT MAGNET QUADRUPOLES FOR CESR PHASE-III UPGRADE *

W. Lou, D. Hartill, D. Rice, D. Rubin, J. Welch
Lab of Nuclear Studies, Cornell University, Ithaca, NY 14853

*Abstract*

The CESR Phase-III upgrade plan includes very strong permanent magnet quadrupoles in front of the cryostat for the superconducting quadrupoles and physically as close as possible to the interaction point. Together with the superconducting quadrupoles, they provide tighter vertical focusing at the interaction point. The quadrupoles are built with Neodymium Iron Boron (NdFeB) material and operate inside the 15 kG solenoid field. Requirements on the field quality and stability of these quadrupoles are discussed and test results are presented.

## 1 INTRODUCTION

The Cornell Electron Storage Ring (CESR) phase-III luminosity upgrade plan includes very high gradient, 27.6 cm long permanent magnet quadrupoles (PMQ's) followed by a pair of superconducting quadrupoles[1]. These permanent quadrupoles are located 33.7 cm away from the interaction point. This quadrupole scheme of the interaction region permits reduction of beta function at the interaction point $\beta_v^*$ to 1 cm or less and also helps to reduce the vertical beta function at the first parasitic interaction point which occurs 2.1 m from the IP, as well as the peak vertical beta which reduces aperture requirements and vertical chromaticity. By reducing the effects of parasitic crossings adjacent to the interaction point, it allows the operation with bunch spacing of 14 ns. The luminosity after the upgrade will be increased dramatically due to the extra beam current implied by 9 x 5 bunches made possible by reducing the bunch spacing and the tighter vertical focusing at the interaction point. Although it is designed for flat-beam crossing angle collision operation, the phase-III IR quadrupole scheme is compatible with the possible round beam configuration[2].

## 2 PERMANENT MAGNET QUADRUPOLE CONSTRUCTION

The permanent magnet quadrupole is made of three 9.2 cm long sections which are assembled individually, then bolted together for the full quad. The whole assembly is mounted to the drift chamber of the CLEO detector. The cross-section view of the quadrupole assembly sketch is shown in Fig. 1

The permanent magnet quadrupoles extend from 337 to 616 mm from the interaction point, have a constant inner radius of 3.35 cm and a two-step outer radius. The dimension of the quadrupole is designed in such a way that the strength of the PMQ is as strong as possible and physically as close as possible to the interaction point in the limited space available for the PMQs. They will operate inside the 15 kG solenoid field of the experimental detector. They are built with Neodymium Iron Boron (NdFeB) material because of its cheaper price, higher commercially available remnant field $B_r$ and intrinsic coercivity $H_{ci}$ comparing with Samarium Cobalt (SmCo) material. The quadrupoles are built with sixteen azimuthal segments.

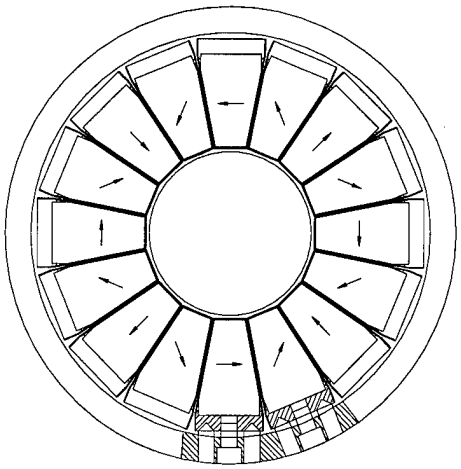


Figure 1: Phase-III Permanent Magnet Cross-section view.

Magnet pole-pieces were ordered with 3 easy-axis orientations (0,45, and $90^0$) and magnetized as shown in Fig. 1. The focusing strength of a permanent magnet quad is influenced by remnant field ($B_r$), inner "pole-tip" radius ($r_i$), and the ratio of outer to inner radius ($r_o/r_i$). This last parameter, $r_o/r_i$, must be limited to avoid subjecting parts of the magnetic material to excessive demagnetizing fields, which could seriously degrade field quality. According to the numerical analysis with the Pandira code and reverse magnetic field knock-down test with the magnet material, it is found that the $r_o/r_i$ of 2.1 is appropriate to the magnet material with $H_{ci}$ of 21 kOe and $B_r$ of 12 kG.

The magnet pole-pieces were supplied by Magnet Sales and Manufacturing Inc. The material is Shin-Etsu 36SH Neodymium Iron Boron. The typical magnetic and mechanical characteristics of this material is listed in Table. 1

The mechanical assembly of the quadrupole is similar to the existing REC quads operating in the storage ring

* WORK SUPPORTED BY THE NATIONAL SCIENCE FOUNDATION

0-7803-4376-X/98/$10.00 © 1998 IEEE

| | |
|---|---|
| Remnant Field $B_r$ | 12.2 kG |
| Coercive Force $H_c$ | 11.7 kOe |
| Intrinsic Coercive Force $H_{ci}$ | 23 kOe |
| Maximum Energy | 36 MGOe |
| Recoil Permeability | 1.05 |
| Density | 7.5 g/cm$^3$ |
| Electric Resistivity | $2.0 \times 10^{-4}\Omega \cdot cm$ |
| Temp coefficient of $B_r$ | $-0.1\ \%/^0C$ |
| Curie Temperature | $310\ ^0C$ |

Table 1: Typical characteristic for NdFeB 36SH.

| | $r_i$ cm | $r_o$ cm | Pole Field kG | k $m^{-2}$ |
|---|---|---|---|---|
| Front Section | 3.35 | 6.40 | 9.7 | 1.64 |
| Outer Section | 3.35 | 7.04 | 10.7 | 1.81 |

Table 2: Quadrupole magnetic strength.

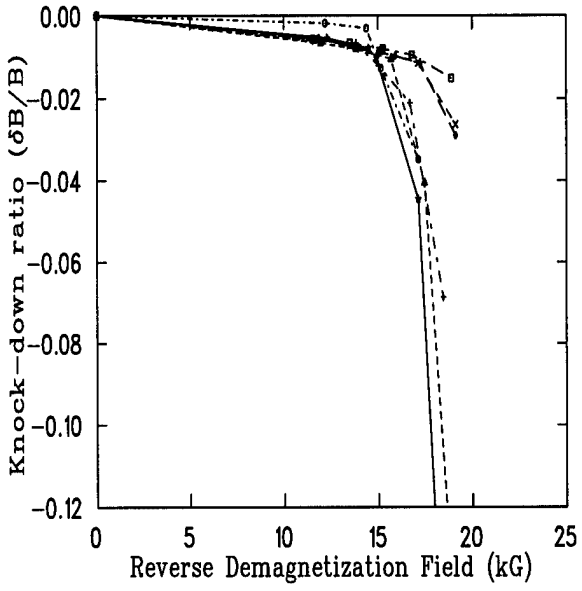



Figure 2: Knock-down ratio vs the applied external reversal field for several magnet pieces.

[3, 4, 5]. The permanent magnet pole-pieces are affixed to a stainless backing plate using high temperature adhesive and covered by a stainless steel skin spot welded to the backing plate for extra protection. The backing plate with magnet was then screwed fast to the support shell. The weight of each quadrupole assembly is about 100 pounds. At 5.289 GeV, the predicted quadrupole strength is listed in Table. 2.

## 3 FIELD QUALITY AND STABILITY

The interaction region quadrupole requires extremely precise control of magnetic field so the magnet field quality and stability requirements are especially severe. The permanent magnet must maintain a constant flux output over a long period of time during the operation. Many factors can affect the magnet and tend to alter the magnet flux which would change the field quality and quadrupole strength in our application. These influences have been studied and the flux change of the magnet have been predicted. The change of the magnetization of the magnet during the operation could be minimized by exposing the magnet to influence in advance and rendering the magnet insensitive to subsequent change in service.

### *3.1 Resistance to the Irreversible Demagnetization*

The permanent magnet maintains its magnet flux because there are lots of small magnet domains aligned by crystal anisotropy. A very high external magnetic field tends to disturb the domain alignment. When the magnet pole-pieces are assembled into the quadrupole, some regions of the magnet material operate in a very strong anti-parallel magnet field. For the case of our design, it is found that this anti-parallel magnet field could be as high as 13 kG according the Pandira simulation. Several different magnet samples were tested for the knock-down ratio of the remnant field $B_r$ with the applied reverse external field. The knock-down ratio was defined as the ratio of the magnetization change before and after the exposure of the external field over its original magnetization. It was found that the intrinsic coercivity of 21 kOe was sufficient to limit the amount of demagnetization to a few percent with 13 kG reverse external field. Fig.2 shows the the amount of demagnetization vs the reverse external field for the NdFeB 36SH material we used. It was found that the material we are using could sustain to 15 kG of the reversal external field.

The quadrupole magnet will operate immersed in a 15 kG axial solenoid field (perpendicular to the NdFeB permanent magnet easy axes) of the experimental detector. Several magnet pole-piece were exposed to external 20 kG perpendicular field, no demagnetization was found after the exposure.

### *3.2 Temperature Stability*

The properties of the magnet material changes with temperature and time. The magnet can be stabilized by heating it to the temperature well above the operating temperature. This process speeds up the initial aging and slows down the rate of change thereafter.

All magnet pole-pieces were thermally stabilized for three hours at 100 $^0C$, which was the maximum temperature without the irreversible loss of coercive force. The losses of the magnetization during this procedure were measured to be less than 1% of the original magnet moment. Several thermal stabilized magnet sample pieces

were remeasured after being stored on self for eight months and no magnetization changes were found.

It is also important that heat stabilization be performed when the magnets are in a field similar to that which they will see during operation. We will do the temperature stabilization process for the assembled quadrupole. Since the quadrupole is operated at the room temperature, it is reasonable to do the temperature stabilization process for the quadrupole assembly at 60-70 $^0C$ for one or two hours. The quadrupole strength will be decreased very slightly (less than 0.5% since the magnet material has very high intrinsic coercivity and all the magnet pieces have been heat stabilized to 100 $^oC$.

Since the the Curie temperature of the NdFeB material is much lower than the SmCo material used in the CESR's present IR quads, the temperature coefficient of $B_r$ was measured to be almost three times higher. This means the quadrupole strength is also almost three times more sensitive to the temperature. Fortunately, the Phase III quads focal length is longer (weaker focusing) due to its shorter physical length and the beta functions are lower, making the machine optics much less sensitive to changes in quad strength. It was estimated that the quadrupole temperature should be controlled to within 0.2 $^oC$ to limit the storage ring vertical tune shift within 0.0005 integer. The temperature of the quadrupole will be controlled by running coolant through a 1/4 inch tubing on the out shell to remove heat from the silicon detector electronics.

### *3.3 Corrosion and Surface Oxidation*

NdFeB material is more subject to oxidation and corrosion than the SmCo material. All surfaces of the magnet piece were coated with Cadmium Chromate coating for corrosion and oxidation resistance.

### *3.4 Radiation Damage*

There are several reported studies about the radiation damage due to the neutrons and photons ($\gamma$ and X-rays)[6, 7, 8, 9]. Those data suggested that the integrated neutron fluences of $5 \times 10^{14}$ n/cm$^2$ and 50 MR of bremsstrahlung radiation is needed to show sizeable damage to the NdFeB material. The radiation level in the electron/positron storage rings is mainly due to the gamma bremsstrahlung and the synchrotron radiation. For CESR, it is estimated that the integrated dose of photons in the interaction region where the PMQs are located is a few MR for 5 years of operation. The present CESR neutron level is measured at about $2 \times 10^9$ n/cm$^2$ a year. Both neutron and photos radiation level for the 5 years of CESR phase-III operation are estimated much lower than the threshold level to show significant radiation damage. Several magnet sample pieces were exposed to a dose of 6 MR of gamma radiation in a Cobalt-60 chamber and no magnetization change were found after the exposure.

### *3.5 Field Quality*

The effect of nonlinearities in the permanent magnet quadrupoles is evaluated by a tracking study. The dynamic aperture is computed for trajectories with initial energy offset 0, 5, and 10 $\sigma_E/E$ for both the error free machine and a machine with errors. It is found that a field error of less than $1 \times 10^{-3}$ at a radius 3 cm is required.

The multipole field could be caused by magnet piece to piece variations in magnetization, errors in positioning the magnet and the anti-parallel demagnetization by the local field observed by some of the magnet pieces when the magnet are assembled into the quadrupole.

The variation of $B_r$ and magnetization angle error of all the magnet pieces were measured. It was found the the $B_r$ variation is less than $\pm 2\%$ and the angle error of the easy axis is within $2^0$. The field error will be reduced by matching magnets with similar properties and a tuning procedure to adjust a small amount of radial motion of each magnet piece to cancel the measured multipole field. A rotating coil measurement system was built to measure the multipole field to the accuracy of 1 part in $10^4$ of quadrupole field at radius of 3 cm. It is expected that quadrupole with $5 \times 10^{-4}$ of multipole field error at 3 cm radius will be achieved.

## 4 ACKNOWLEDGMENTS

The authors would like to thank John Greenly and the Lab of Plasma Studies at Cornell for providing and helping with the capacitor bank power supply. Many thanks are due to Ted Vandermark and Richard Rice for helping with the tests and assembly. Special thanks are given to Jeff Cherwinka for helpful discussions.

## 5 REFERENCES

[1] J. Welch *et al.*, The Superconducting Interaction Region Magnet System for the Phase-III Upgrade, these proceedings (PAC97).

[2] R. Talman, Phys. Rev. Lett. 74, p 1590, 1995.

[3] S. Herb, Proc. 1987 IEEE Part. Accel. Conf., p. 1434, 1987.

[4] S. Herb, Cornell Collide Beam Note CBN85-9, 1985.

[5] K. Halbach, Nucl. Instr. and Meth. 198, p 213, 1982.

[6] H Luna *et al.*, Nucl. Instr. and Meth. A285, p 349, 1989.

[7] W. Hassenzahl *et al.*, Nucl. Instr. and Meth. A291, p 378, 1990.

[8] J. Pfluger *et al.*, Rev. Sci. Instrum. 66, p 1946, 1995.

[9] J. Cost *et al.*, Mat. Rev. Soc. Symp. Proc. 96, p 321, 1987.

# THE USE OF CORRECTING COILS IN END MAGNETS OF ACCELERATORS

L. R. P. Kassab, Faculty of Technology, São Paulo, Brasil and
P. Gouffon, Linear Accelerator Laboratory, Institute of Physics, University of São Paulo
C.P. 66318, 05315-970, São Paulo, SP, Brasil

*Abstract*

The end magnets of the race-track microtron booster [1], which is the second stage of the 30.0 MeV cw electron accelerator under construction at IFUSP, play a fundamental role in terms of the beam quality. The use of correcting coils, based on the inhomogeneities of the magnetic field and attached to the pole faces, assured uniformity of $10^{-5}$ . We present the performance of these coils when operating the end magnets with currents that differ in ±10% from the one used in the mappings that originated the coils copper leads. For one of the magnets, adjusting conveniently the current of the correcting coils, made it possible to homogenize field distributions of different intensities, once their shapes are practically identical to those that originated the coils. For the other one, the shapes are changed and the coils are less efficient. This is related to intrinsic factors that determine the inhomogeneities. However, in both cases we obtained uniformity of $10^{-5}$ , much better than necessary.

## 1 INTRODUCTION

The end magnets of the IFUSP race-track microtron booster were designed, with the aid of numerical field computations (Poisson code) and of ray-tracing calculations (Ptrace code), to deflect an electron beam of 5.1 MeV in a semicircular trajectory of about 36.0 cm diameter. They incorporate active field clamps [2] that avoid the vertical defocusing and the radial displacement of the beam. The method of correction employed [3,4] to homogenize the IFUSP race-track microtron booster accelerator magnets assured uniformity of $10^{-5}$ in an average field of 0.1 T, over an area of 700 $cm^2$. Several tests were done to investigate the behavior of these inhomogeneities and the performance of the correcting coils when the magnets are operated with currents that differ in ±10% from the one (27.4 A) that was used in the mappings that originated them.

## 2 EXPERIMENTAL PROCEDURE

The magnetic field measurements were done with differential Hall probes connected to a gaussmeter (F.W.Bell model 640) with resolution given by ±1.5μT. The magnets were submitted to a well defined cycling procedure, empirically determined. This cycle provided reproducibility of $10^{-5}$ for a magnetic field distribution of about 0.1 T. Stability of the same order was obtained.

For each magnet, the correcting coils were obtained by the arithmetic mean of four field maps taken in different planes, two situated 12 mm above and two 12 mm bellow the middle plane [1] and with 27.4 A for the current of operation. The coils were made of etched printed circuit boards and the copper leads ($4x10^{-5}$ m thickness) were shaped like the lines of equal magnetic field separated by a distance of 7.4μT. Two identical double sided etched circuits, done for each magnet, were placed at their pole faces. In each point of the coils, an adequate current density provided tangential magnetic field components, identical to those that have to be compensated. Figures 1 and 2 show the two magnets correcting coils.

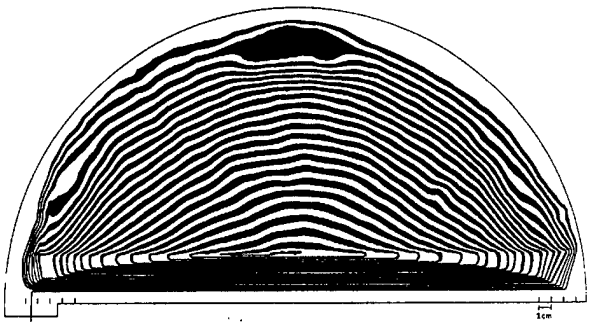


Figure 1 - The correcting coils used for the first magnet. The interval between the copper leads is 7.4μT.

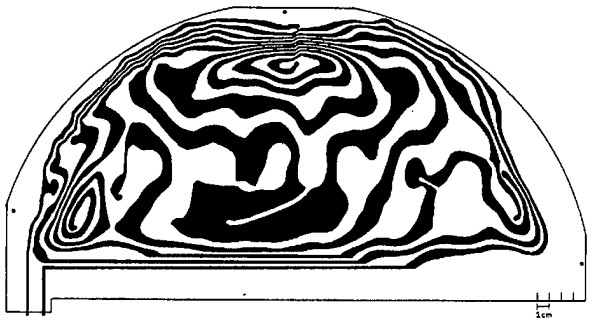


Figure 2 - The correcting coils used for the second magnet. The interval between the copper leads is 7.4μT.

## 3 THE PERFORMANCE OF THE CORRECTING COILS

Figures 3 and 4 show field distributions in the middle plane between the pole faces of the magnets operated at 27.4 A (the points indicate the coordinates, in millimeter, of each magnetic field difference measurement). The magnets exhibit differences in terms of the shape and magnitude of their inhomogeneities. In the first one,

0-7803-4376-X/98 /$10.00 © 1998 IEEE

$\Delta B / B = \pm 1.4 \times 10^{-3}$ and in the other $\Delta B / B = \pm 6 \times 10^{-4}$. The optimal currents for the correcting coils of each magnet, 122.2 mA for one of them and 115.7 mA for the other one, were found empirically and are in good agreement with the theoretical value (117.8 mA).

The standard deviation, 65.1μT, for the field distribution shown in figure 3, becomes 1.8μT (figure 5a) using for the correcting coils the optimal current value, 122.2 mA . Although the shape of the inhomogeneity changes almost nothing when the current of operation is altered, there is variation in its intensity. Then we adjusted conveniently the current of the correcting coils in order to obtain field distributions as uniform as the one for 27.4 A .

When the current of operation is raised from 27.4 A up to 30.0 A, the correction done by 122.2 mA current becomes increasingly excessive as can be seen by the growth of the standard deviations (figure 6). Then we used for the correcting coils currents successively smaller and always lower than 122.2 mA (figures 7). On the other hand, when the current of operation is raised from 24.7 A up to 27.4 A, the correction performed by 122.2 mA current becomes decreasingly insufficient, as shown by the lessening of the standard deviations (figure 6), and what explains the need for currents successively smaller but always higher than 122.2 mA (figure 7) to compensate this effect. The results obtained for this magnet lead us to conclude that the field distributions, before the corrections, for currents of operation higher than 27.4 A are closer to those that originated the correcting coils and of smaller variation. Figure 6 reveals the performance of the coils in the situations exposed and uniformity of $10^{-5}$ for all the cases as the standard deviation does not exceed 3.1μT.

Figure 4 shows the field distribution in the middle plane of the second magnet operated at 27.4 A , in which the standard deviation, 17.8μT, becomes 2.5μT (figure 5b), using the optimal value 115.7 mA for the correcting coils. When the current of operation is altered the shape of the inhomogeneity is changed, specially for currents smaller than 27.4 A . Even so, we adjusted the current of the correcting coils. Nevertheless we found few differences between the results (figure 8) mainly for currents smaller than 27.4 A, where the standard deviations are practically superimposed. When the magnet is operated with currents greater than 27.4 A the distributions of the difference field measurements are more similar to those that originated the correcting coils but of greater variation. This explains the achievement of the best corrections revealed by the standard deviations and the need to increase the correcting coils current in this interval of operation (figure 9). Contrarily to the other magnet, in this case, the shape of the correcting coils copper leads does not exactly correspond to the inhomogeneity that has to be compensated and that is why the correction performed by the coils is less efficient. However, the uniformity obtained is of about $10^{-5}$ .

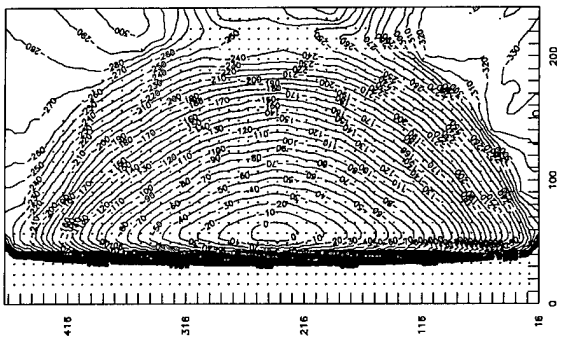


Figure 3 - Field distribution in the middle plane of the first magnet. Difference between two lines is 10μT.

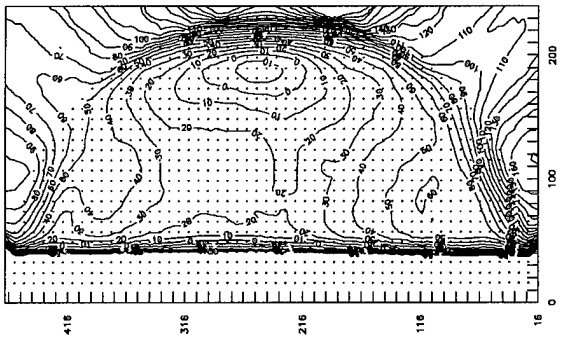


Figure 4 - Field distribution in the middle plane of the second magnet. Difference between two lines is 10μT.

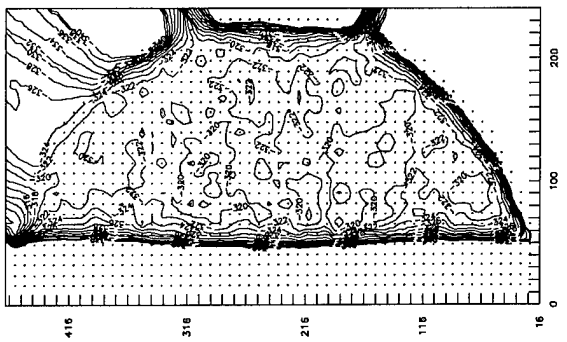


Figure 5a - Field distribution in the middle plane of the first magnet using for the correcting coils the optimal current (122.2 mA). Difference between two lines is 2μT.

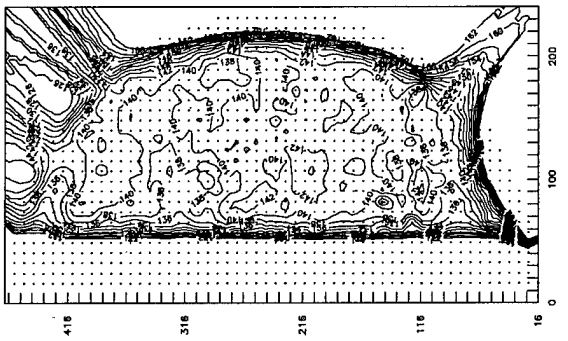


Figure 5b - Field distribution in the middle plane of the second magnet using for the correcting coils the optimal current (115.7 mA). Difference between two lines is 2μT.

## 4 CONCLUSIONS

The magnets present inhomogeneities that differ in terms of their shapes and strenghts what lead them to behave differently when the current of operation is altered.

Through the results obtained we come to the conclusion that the success of the method of correction employed is related to the fact that the correcting coils must represent copies of the inhomogeneities. Once the shape of the inhomogeneities is not altered, intensity changes can be compensated adjusting conveniently the correcting coils current as it was done for the first magnet. For the second magnet the change in the inhomogeneity shape compromises the performance of the correcting coils. Besides, we should add that the first magnet, with a well defined inhomogeneity, in spite of being initially less uniform, is more susceptible to the correction but less to changes in the shape of the field distribution. This suggests that a greater uniformity represents a tendency of a less stable field distribution. These effects are related to intrinsic factors that determine the inhomogeneities. However both of the recirculating magnets present uniformity of $10^{-5}$ when operated in the interval studied.

## 5 ACKNOWLEDGMENTS

We would like to express our thanks to Dr. Marcello Damy de Sousa Santos, Dr. Giorgio Moscati, Dr. Maria V.P. Heller and Dr. Ursula Ludwig Mertin, for important suggestions during this work, as well as to Dr. Manoel T. F. Cruz, A. Malafronte, J.C.A. Alcon and E. Monteiro, for having gently developed the automated system used to map the end magnets. We also express our thanks to Dr. Marcos N. Martins, manager of the race-track microtron project and Dr. Paulo Pascholati, coordinator of the IFUSP Linear Accelerator Laboratory in the accomplishment of this work. We thank Faculty of Technology (FATEC-SP) for its encouragement during this work. We acknowledge the financial support from FAPESP, CNPQ and FINEP.

## REFERENCES

[1] L.R.P. Kassab: 'Projeto, construção e teste do sistema de ímãs principais do acelerador microtron booster do IFUSP', PhD Thesis, IFUSP (1996).

[2] H.Babic, M.Sedlacek: 'Nuclear Instruments and Methods', 56,170 (1967).

[3] U.Czok, G.Moritz, H.Wollnik, 'Nuclear Instruments and Methods', 140, 135(1977).

[4] J.Friedrich, L.Tiator, Jahresbericht, Institut Fur Kernphysik, Johannes Gutenberg, Universitat Mainz (1986 -1987).

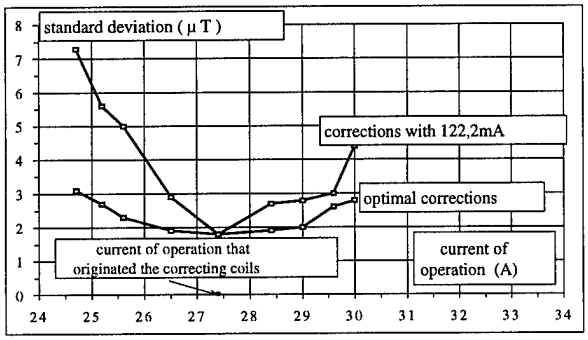



Figure 6 - Standard deviations of magnetic induction difference measurements for different currents of operation (first magnet).

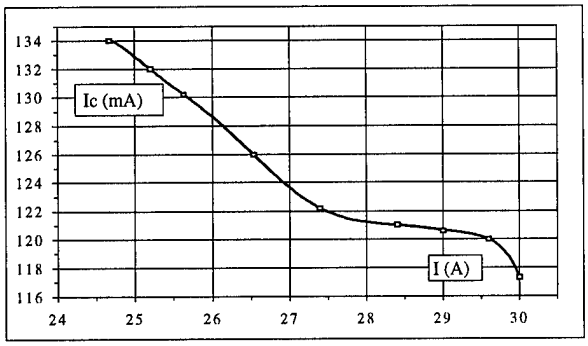



Figure 7 - Correcting coils currents for different currents of operation (first magnet).

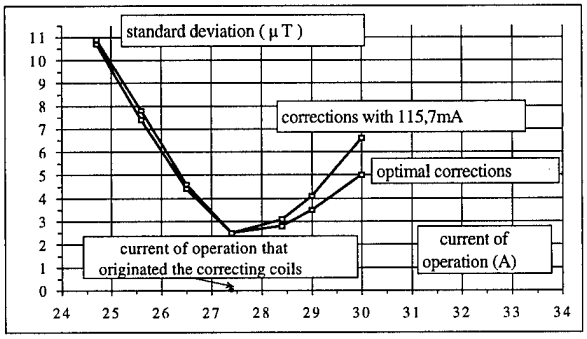



Figure 8 - Standard deviations of magnetic induction difference measurements for different currents of operation (second magnet).

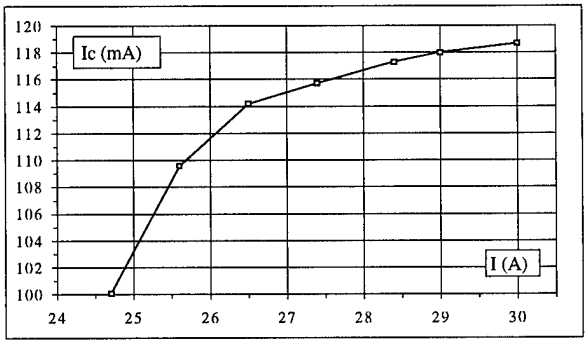



Figure 9 - Correcting coils currents for different currents of operation (second magnet).

# MAGNETIC FIELD MEASUREMENTS OF THE MAIN INJECTOR SEXTUPOLE MAGNETS

C. M. Bhat, B. C. Brown, D. J. Harding,
Si J. Fang, P. S. Martin, H. D. Glass, J. W. Sim and D. G. C. Walbridge
Fermi National Accelerator Laboratory* P.O. Box 500, Batavia, IL 60510

*Abstract*

The Fermilab Main Injector (MI) will accelerate (decelerate) protons and anti-protons from 8.9 GeV/c to 150 GeV/c (150 GeV/c to 8.9 GeV/c). To achieve high intensity stable beam in the MI throughout the acceleration or deceleration mode, two families of chromaticity compensation sextupole magnets are planned. The operating schemes for the chromaticity compensation systems will be different for the two modes because of the hysteresis of the sextupole magnets and the changed sign of the sextupole field component from beam tube eddy currents in the dipoles. Hence we have carried out detailed magnetic field measurements on some sextupole magnets. Here we present the results of the measurements and their implications on the acceleration and the deceleration cycles of the MI.

## 1 INTRODUCTION

High quality performance of the Main Injector (MI) is important for the success of high energy $p\bar{p}$ collider physics programs at the Fermilab Tevatron and for several proposed fixed target experiments using the Main Injector beam[1]. The Main Injector is primarily used to accelerate high intensity protons and anti-protons ($\bar{p}$) from 8.9 GeV to 150 GeV for Tevatron injection and protons to 120 GeV for $\bar{p}$ production. Recently we have decided to use MI to decelerate the un-used $\bar{p}$s from the Tevatron and store them in the Recycler Ring[2] at 8.9 GeV/c. The mode of operation for acceleration and the deceleration of the beams will be significantly different because of the hysteresis of the magnets.

The natural chromaticity of the MI is about -33 units in both horizontal and vertical planes. Particle tracking studies carried out in the MI at 8.9 GeV(injection energy) and at 120 GeV[1] showed that a tune spread $\Delta\nu \leq 0.0075$ is acceptable for stable operation of the beam. The $\frac{\Delta p}{p}$ of the beam at injection from the Fermilab Booster is about $1.5 \times 10^{-3}$. Then the chromaticity requirement

$$\Delta\nu = \chi\frac{\Delta p}{p},$$

where $\chi$ is the chromaticity, implies that $\chi \leq 5$. Similar value of chromaticity is suggested by the head-tail instability growth rate. To achieve the required chromaticity, two sets of 54 sextupole magnets[1],[3] will be inserted in the MI lattice. Also, to avoid head-tail instability after the transition energy of 20.49 GeV, a chromaticity jump is introduced. A model of chromaticity compensation scheme in the presence of beam-pipe eddy current, dipole saturation and static sextupole field have been developed[4] and subsequent improvements[5] have been made to include remnant fields of the sextupole magnets for different operating scenarios. Implementation of the fast ramps with $\dot{\gamma} \approx 267$ sec$^{-1}$near transition, has resulted in dominance of the eddy current contribution to sextupole components at low momenta. Some of our studies indicate that below transition the focusing set of sextupole magnets may have to run in bi-polar mode (Fig. 1(a)) i.e., at 8.9 GeV the sextupole current will be positive and for a short time during acceleration the sextupole current need to be negative to compensate for the large positive eddy current contribution to the sextupole field (Fig. 1(b)). Hence it is essential to study the low momentum behaviour of the MI chromaticity correction system.

Figure 1 shows a comparison between sextupole strength requirements for acceleration and a deceleration cycle up to 45 GeV/c. The cases shown here have slight differences in their $\dot{\gamma}$ near transition, *viz.*, $\dot{\gamma}$= 267 sec$^{-1}$ for the acceleration cycle and $\dot{\gamma}$= -250 sec$^{-1}$ for the deceleration cycle. However, it is evident that the eddy current contributions have opposite signs in these two cases.

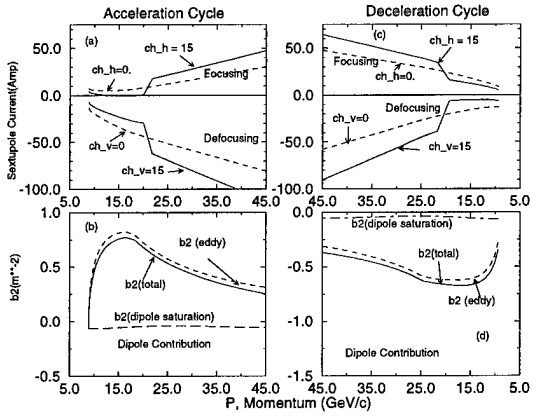



Figure 1: Main Injector sextupole current ramps as a function of the momentum for acceleration "a" and deceleration "c" cases. The sextupole contributions from the dipole magnets and contributions arising from the beam pipe eddy currents are shown in "b" and "d".

Figure 2 illustrates the sensitivity of the chromaticity as a function of the sextupole current. We notice that for focus-

* Operated by Universities Research Association, Inc. under contract No. DE-AC02-76CH03000 with the U. S. Department of Energy

0-7803-4376-X/98/$10.00 © 1998 IEEE

ing sets of sextupole magnets a current change of 1 A will introduce ≈4.5 units of chromaticity change at 8.9 GeV. So, if the chromaticity needs to be controlled to better than one unit then sextupole strength error should be less than 0.2 Tm/m$^2$. This would be difficult because of the non-linear component of the sextupole field in the sextupole magnets.

To understand the low field behavior of the MI sextupole magnets extensive measurements have been undertaken at the Fermilab Magnet Test Facility (MTF). This paper presents data on the low field measurements of randomly selected sextupole magnets.

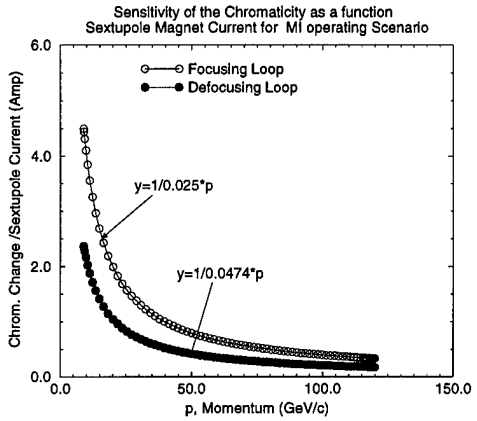



Figure 2: Sensitivity of the horizontal and vertical chromaticity as a function of the momentum.

## 2 MEASUREMENTS AND RESULTS

### 2.1 *Power Supply*

A special purpose power supply has been built to make detailed magnetic field measurements of the MI sextupole magnets at the MTF. The power supply is capable of providing -40 A to 350 A current with a maximum error of 100 mA below 10 A and 1% current regulation in the remaining current range. The power supply was built with two 20 V/250 A power supplies connected in master-slave configuration to supply forward current up to 350 A. The reverse current is supplied by another 30 V/65 A power supply with summing power diodes. The maximum voltage swing of the test power supply is ±15 V and the maximum current slew rate is set at 400 A per second.

### 2.2 *Field Measurements*

The magnets are measured at MTF using a rotating Morgan coil with the data base-controlled software[6]. The coil is rotated at the center of the magnet at a constant current. Sextupole field measurements are performed under different conditions of Main Injector operating scenarios except for the rate of change of field. Since the dipole saturation at high field provides as high as 60 units of negative chromaticity in horizontal plane, the measurement scheme also emphasizes the high field characteristics of the dipoles. During MI operation the magnets have to be ramped to their

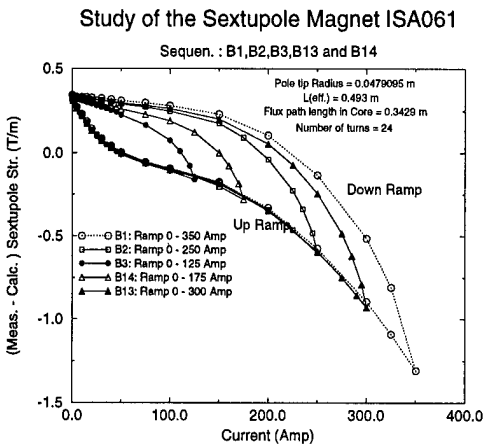



Figure 3: Remnant field as a function of sextupole current.

full strength up and down in about two to three seconds. Depending upon the details of the Fermilab accelerator "super cycle", the operating field strengths of the magnets will correspond to either 120 GeV or 150 GeV. However, the time required for each measurement with the rotating coil system mentioned above is about 0.5 min. Hence measurements under exact conditions are not possible. At low fields, measurements are carried out in the range of −40 A to 20 A in steps of 1 A. To understand the hysteresis effects at low fields we ramped the magnets to different maximum currents.

### 2.3 *Results of Data Analysis*

The magnetic field data analysis done here is based upon the formalism described in Refs. [7]. There are mainly two steps involved in the data analysis. In the first step, three data sets corresponding to sextupole currents below 100 A are used to determine the true magnetic aperture $A$ of the sextupole magnets. They are found to vary within 0.06% for the magnets studied here. In the second step, the non-linear components of the magnetic field is determined according to,

$$B_{non-linear} = B_{meas} - \frac{\mu_0 3 N L_{eff} I}{2A^3}. \qquad (1)$$

where $B_{meas}$ is the measured integrated sextupole strength, $N = 24$ is number of coil turns driving gap, $I$ is the current, $L_{eff}$ is the effective length of the magnet.

Some typical results of measurements are shown in Figs. 3 to 6. Figure 3 displays non-linear components of the sextupole magnets for five different maximum currents, *viz.*, 125, 175, 250, 300 and 350 A. In all these cases the ramps start at 0.0 A. We find that the paths followed during up-ramp is the same within 0.025 Tm/m$^2$ for all maximum current, while during down-ramps they differ significantly. The addition of the deceleration cycles of $\bar{p}$ to the MI operating scenarios suggests the necessity of use of these data (or fitted curve to these data) in the MI sextupole magnets

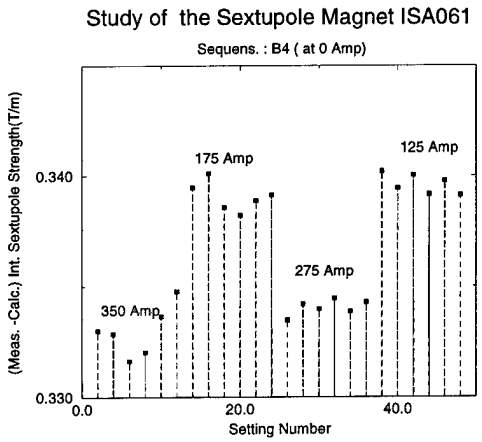



Figure 4: Remanent field for different maximum sextupole magnet current.

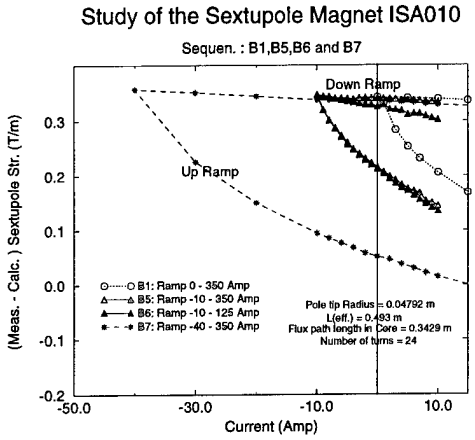



Figure 5: Remanent field for different bi-polar operation.

power supply control system[8]. In Fig. 4, the remanent field as a function of maximum ramp current is shown. The maximum deviation is about 0.005 Tm/m$^2$ which will not have any noticeable effect on the chromaticity. The data taken for negative currents are shown in Fig. 5. The open triangles showing – 10 A to 350 A data and filled triangles showing – 10 A to 125 A data follow almost identical paths during up-ramp, while they follow quite different paths during down ramps. This feature is very similar to the data shown in Fig. 3 where the minimum current is 0.0 A.

Data taken in a sequence where current is changed from (i) 10 A to 0 A to 20 A and, (ii) 10 A to – 10 A to 20 A are shown in Fig. 6. This data is very crucial in establishing the performance of the chromaticity correction in the energy range 10 GeV/c to 21 GeV/c because the sextupole strength versus momentum response curve shown in Fig. 1(a) (Focusing) has negative slope.

## 3 SUMMARY

We have carried out detailed measurements on several chromaticity compensation sextupole magnets to understand the non-linear behavior of these magnets at low magnetic fields. Since the chromaticity of the MI beam has to be controlled within a few units these data (or a fitted curve to these data) will be down-loaded to MI control system.

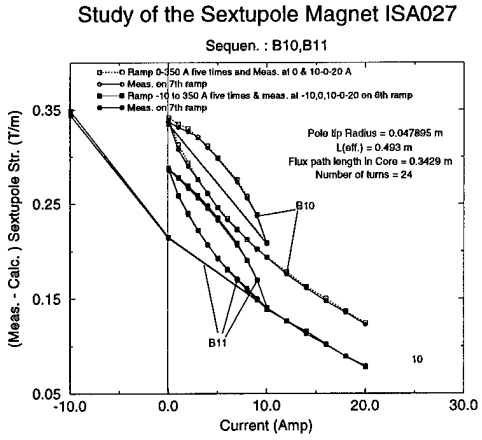



Figure 6: Remanent field for (B10) 10 A to 0 A to 20 A and, (B11) 10 A to -10 A to 20 A.

Authors would like to thank the MTF personnel for their help during the magnet measurements.

## 4 REFERENCES

[1] The Fermilab Main Injector Technical Design Handbook (1994, updated 1997) (unpublished).

[2] "Fermilab Recycler Ring Technical Design Report",edited by G. Jackson, FERMILAB-TM-1981

[3] D.J. Harding *et al., IEEE Proceedings of the 1993 Particle Accelerator Conference, Washington D.C.* (IEEE, New York, 1993), p. 2826

[4] S.A. Bogacz, *IEEE Proceedings of the 1993 Particle Accelerator Conference, Washington D.C.* (IEEE, New York, 1993), p. 77.

[5] C.M. Bhat *et al., IEEE Proceedings of the 1995 Particle Accelerator Conference, Dallas, Texas* (IEEE, New York, 1996), p. 1334.

[6] J.W. Sim *et al., IEEE Proceedings of the 1995 Particle Accelerator Conference, Dallas, Texas* (IEEE, New York, 1996), p. 2285.

[7] B.C. Brown, "Analysis of Magnet Strengths from Steel B-H Curves and Geometry" MTF-94-0078 (1997).

[8] B.C. Brown *et al.,*, "Design for Fermilab Main Injector Magnet Ramps Which Account for Hysteresis" this proceeding.

# DESIGN FOR FERMILAB MAIN INJECTOR MAGNET RAMPS WHICH ACCOUNT FOR HYSTERESIS

B.C. Brown, C.M. Bhat, D.J. Harding, P.S. Martin, G. Wu
Fermi National Accelerator Laboratory *
Batavia, IL 60510-0500

*Abstract*

Although the dominant fields in accelerator electromagnets are proportional to the excitation current, precise control of accelerator parameters requires a detailed understanding of the fields in Main Injector[1][2]magnets including contribution from eddy currents, magnet saturation, and hysteresis. Operation for decelerating beam makes such considerations particularly significant. Analysis of magnet measurements and design of control system software is presented. Field saturation and its effects on low field hysteresis are accounted for in specifying the field ramps for dipole, quadrupole and sextupole magnets. Some simplifying assumptions are made which are accepted as limitations on the required ramp sequences. Specifications are provided for relating desired field ramps to required current ramps for the momentum, tune, and chromaticity control.

## 1 INTRODUCTION

Control of the momentum ($p$), tune ($\nu_x, \nu_y$) and chromaticity ($\xi_x, \xi_y$) of the accelerated beam is maintained through the interaction of several power supply systems and the rf system. Within the controls systems one must describe these variables as well as the currents and perhaps the voltages in the power supply loops. To simplify the interactions among these systems, we will rely on the beam variables rather than such secondary properties as the magnet currents or rf phases. This should allow us to deal with subtleties, such as the history dependent hysteresis of the magnets, in only one place.

We will relate these parameters to the fields of the primary magnet systems, ignoring contributions from correction and specialty magnets. The magnet systems[2]which must be considered in this context include the main dipole (IDA, IDB, IDC and IDD) system, the focusing and defocusing main quadrupole (IQB, IQC, IQD) systems, and the chromaticity sextupole (ISA) system which also has two families of sextupoles. We reference IDA, IQB and ISA magnet properties and design effective length ratios to prescribe the accelerator properties. The measured properties will be used to establish these parameters using suitable averages over all of the magnets in each circuit.

## 2 EQUATIONS

The equations will apply to particles on the design orbit which we will assume passes through the transverse centers of the dipole, quadrupole and sextupole magnets. If we integrate through the dipoles along a complete circumference $C$ around the ring, the momentum, $p$, of the particles is

$$p = \frac{e}{2\pi}\int_C B_y\, ds = e(B\rho) \qquad (1)$$

where $e$ is the elementary charge, and $B_y$ is the vertical component of the magnetic field. This expression defines $B\rho$ where $\rho$ is a characteristic bending radius. We have $p = (e/\theta_D)B_1 L_{eff}$ for an IDA dipole which bends by $\theta_D = 2\pi/(30\,1/3)$,

The lattice design programs (such as MAD[3])describe the focusing properties of the lattice in terms of momentum-normalized gradients, $k_1$, and effective lengths, $L_{eff}$ of the quadrupoles. If we take $k_{1f}(k_{1d})$ as the gradient in an IQB quadrupole on the focusing (defocusing) magnet circuit, we find the design betatron tunes $(\nu_x, \nu_y)$ are given by

$$\begin{pmatrix}\nu_x\\ \nu_y\end{pmatrix} = \begin{pmatrix}Q_{11} & Q_{12}\\ Q_{21} & Q_{22}\end{pmatrix}\begin{pmatrix}k_{1f}\\ k_{1d}\end{pmatrix} \qquad (2)$$

where $k_{1f}(k_{1d})$ is the design gradient for focusing (defocusing) IQB quadrupoles. We write this more compactly as $\underline{\nu} = \underline{Q}\,\underline{k_1}$. The similar description of the chromaticity[4],$\underline{\chi}$, must include not only the sextupole magnets but also the sextupole fields in the dipole magnets. We describe this using the normalized sextupole $k_2$ as $\underline{\chi} = \underline{\chi_0} + \underline{S_D}k_{2D} + \underline{S}\underline{k_2}$ or

$$\begin{pmatrix}\chi_x\\ \chi_y\end{pmatrix} = \begin{pmatrix}\chi_{x0}\\ \chi_{y0}\end{pmatrix} + \begin{pmatrix}S_{Dx}\\ S_{Dy}\end{pmatrix}k_{2D} + \begin{pmatrix}S_{11} & S_{12}\\ S_{21} & S_{22}\end{pmatrix}\begin{pmatrix}k_{2f}\\ k_{2d}\end{pmatrix}. \qquad (3)$$

$\underline{\chi_0}$ is the natural chromaticity of the lattice, $k_{2f}(k_{2d})$ is the sextupole focusing near focusing (defocusing) quadrupole locations in the lattice, $k_{2D}$ is the dipole contribution to sextupole expressed as the contribution of an IDA dipole. The column vector $\underline{S_D}$, and the matrices $\underline{Q}$ and $\underline{S}$ characterize the design lattice and are determined from lattice design programs.

For the quadrupoles, the relation between tune and focusing is not linear. Perturbations about the design $\underline{\nu}$ will require a different set of coefficients which can also be calculated from lattice simulations. We will therefore supplement $\underline{\nu} = \underline{Q}\,\underline{k_1}$ with $\delta\underline{\nu} = \delta\underline{Q}\,\delta\underline{k_1}$. $\delta\underline{\nu}$ is the (time dependent) difference between the tune specified in the base design and the tune desired by the machine operators, $\delta\underline{k_1}$ is the required change in the magnet focusing, and $\delta\underline{Q}$ expresses the coefficients for this differential change[1].

* Work supported by the U.S. Department of Energy under contract number DE-AC02-76CH03000.

[1] We also expect that the real machine will imperfectly match the simulations and may also express the measured tune *vs.* current differentials with an additional such equation.

0-7803-4376-X/98/$10.00 © 1998 IEEE

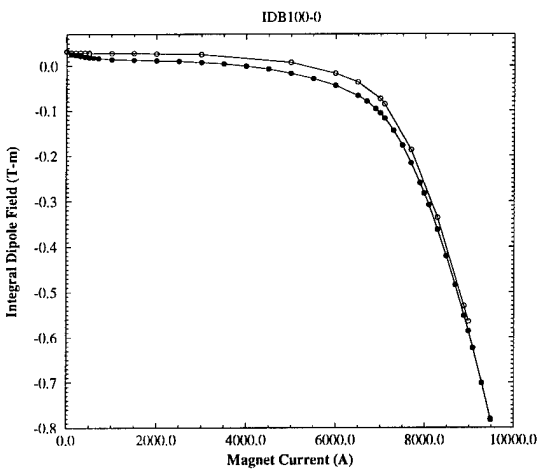



Figure 1: Nonlinear portion of integrated dipole strength for 6-m Main Injector dipole as measured by the Harmonics measuring system.

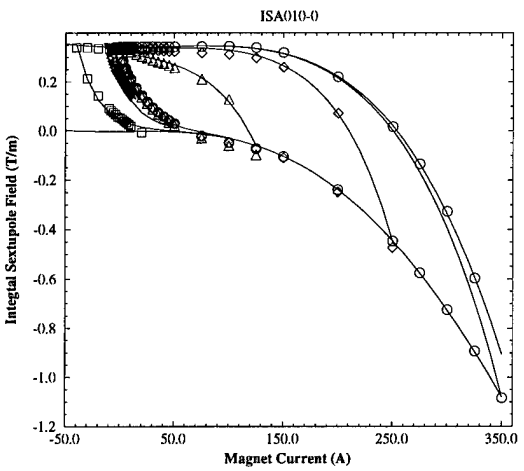



Figure 2: Nonlinear integral sextupole strength. Symbols represent measured data with a variety of ramps. Lines are analytic representations where ${}^{ramp}BL_N$ is represented by a 4th order polynomial and ${}^{trans}BL_N = ({}^{dn}BL_N - {}^{up}BL_N)Exp(-|I - I_{reset}|/I_{char})$ with the up-down difference evaluated at the reset current. $I_{char}$ is 20 A for up ramp transitions and 45 A for downramp transitions.

The focusing functions are defined in terms of the fields[2];

$$k_{N-1}L_{eff} = \frac{(N-1)\int B_N\, ds}{(B\rho)}. \quad (4)$$

The integrals are over a path along the transverse centerline and integrate through the length of the magnet. For the sextupole contribution of the dipole we have

$$k_{2D}L_D = \frac{2\int B_{3D}\, ds}{(B\rho)} = 2b_3\frac{\int B_{1D}\, ds}{(B\rho)a^2} = 2b_3\frac{\theta_D}{a^2}. \quad (5)$$

where the final expression employs the normalized sextupole harmonic to describe these fields.

Since we seek to specify the desired machine parameters and derive the required fields, we must invert these relations.

$$\underline{k_1} + \delta\underline{k_1} = \underline{Q}^{-1}\underline{\nu} + \delta\underline{Q}^{-1}\delta\underline{\nu}. \quad (6)$$

$$\underline{k_2} = \underline{S}^{-1}(\underline{\chi} - \underline{\chi_0} - \underline{S_D}2b_3\frac{\theta_D}{L_D a^2}). \quad (7)$$

## 3 SEXTUPOLE FROM DIPOLE MAGNETS

We neglect field errors (harmonics) except for the sextupole in the dipole magnets, described as $b_3 = b_3^{static} + b_3^{eddy}$.

The static sextupole field of the dipole magnets (measured at fixed current) is governed by a combination of the pole shape and contributions due to the iron. Measured hysteresis is negligible. $b_3$ measurements are obtained with two complimentary systems on each dipole[6].The contribution can be described either with a fitted function or a simple lookup table.

[2]Harmonic quadrupole fields, $B_2$, and sextupole fields, $B_3$ are defined following Glass[5].The factor of $N-1$ in the numerator is because MAD considers field derivatives rather than field harmonics as its basis of description.

The significant term due to eddy currents is created in the dipole beam pipe. Calculations[7]and measurements[8]have been carried out with rectangular shapes and with the actual beam pipe. Good agreement has been achieved. In the case of a rectangular approximation, the sextupole term is independent of the width of the pipe and the normalized sextupole harmonic is given by

$$b_3^{eddy} = \frac{\mu_0\sigma t a^2}{g}\frac{\dot{B}}{B} = P_{eddy}\frac{\dot{B}}{B} \quad (8)$$

where $\mu_0$ and $\sigma$ are the permeability and conductivity of the beam pipe material, $t$ is the beam pipe thickness and $g$ is the dipole gap height. $\dot{B}$ is the time derivative of the dipole field $B$. We use $P_{eddy}$ to account for small corrections due the actual geometry.

## 4 CALCULATION OF REQUIRED FIELDS

Field integrals of a multipole electromagnet are given[9]by

$$B_N L_{eff} = \frac{\mu_0 N N_g L_{eff} I}{2A^N} - \frac{N\mathcal{L}L_{eff}}{2A^N}\mu_0 < H_{steel} > . \quad (9)$$

where $N$ is the harmonic number (1 for dipole), $N_g$ is the number of turns per gap in the coil, $A$ the pole tip radius ($g/2$ for a dipole), $\mathcal{L}$ is the length of a flux line in iron with average $H$ along the path of $<H_{steel}>$. $I$ is the current through the coil. We note that the first term is proportional to $I$ and it represents the field created in idealized iron by the magnet current. The second term describes the field lost in driving the iron. All saturation and hysteretic terms due to iron remanence are described by $<H_{steel}>$. In

Figs. 1 and 2 we show this quantity for the Main Injector dipole[9]and sextupole[10]magnets, respectively. Describing how these fields depend upon magnet excitation and excitation history is required to enable one to control the fields in situations where a variety of magnet ramp cycles are required.

These figures suggest that the iron can be driven to an up ramp (lower $B$ field) hysteresis state or a down ramp (higher $B$ field) hysteresis state. Reversing the sign of $\dot{B}$ by reversing $\dot{I}$ will begin a transition from one hysteretic state to the other. In accordance with Equation 9 we define the non-linear field integral, $(B_N L)_{nl}$, by

$$(B_N L_{eff})_{nl} = -\frac{N\mathcal{L}L_{eff}}{2A^{N-1}}\mu_0 < H_{steel} > \quad (10)$$

$$= {}^{ramp}BL_N(I) - {}^{trans}BL_N(I - I_{rev}, I_{rev}) \quad (11)$$

where the first term takes values of ${}^{up}BL_N(I)$ and ${}^{dn}BL_N(I)$ for up ramp and down ramp segments, ${}^{trans}BL_N(I - I_{rev}, I_{rev})$ describes the transition between the two hysteretic states, and $I_{rev}$ is the current of the most recent reversal of $\dot{I}$. To describe the $I$ required to produce a given $B$ requires knowledge of the previous direction of the current ramp and the current level at which the most recent change of ramp direction occurred. These functions also have a weak dependence on the maximum and minimum currents in recent ramp cycles. In Fig. 2 we illustrate hysteresis curves using polynomial for the ramp state term and exponentials for the transition term.

## 5 RAMP CONTROL ISSUES

For the Fermilab Main Ring, one assumed that the momentum was proportional to the dipole current. Magnetic fields are scaled by momentum to set tune and chromaticity, while all the fields experience saturation and hysteresis. The addition of anti-proton deceleration cycles to the repertoire of the Main Injector makes hysteresis considerations especially significant and saturation at high fields is greater for Main Injector operation. Precise control of beam parameters requires a comprehensive new strategy.

Since the hysteresis effects depend on details of the ramp cycles, power supply control will be carried out by specifying the desired momentum ($p$), tune ($\nu_x, \nu_y$) and chromaticity ($\xi_x, \xi_y$) of the accelerated beam for a given operating mode, calculating the required fields, and determining current ramps in the 5 main current buses which achieve the required fields whenever beam is present. These calculations will be most effectively carried out in a single application which can then download the required current ramps to the real time power supply control system. In this fashion, the description of the hysteretic state is localized to an application program and is recalculated only when the operational requirements change. One may utilize special 'reset' ramp segments to establish a hysteretic state of magnets which simplifies efforts to match requirements over the balance of the cycle. Since we expect a mixture of 120 GeV and 150 GeV operating modes to be required in succession, we are concerned that a given mode may depend upon what current ramp was used in the previous mode. We will provide for a special reset segment at the end of each ramp cycle where each current bus can be required to execute some current changes which produce an approximately consistent magnetic state at the end of any magnet ramp.

## 6 LIMITATIONS AND ASSUMPTIONS

This model for power supply control assumes that the critical fields are controlled by these five magnet current systems and that the requirements depend only upon the specified beam quantities. It is known that the coherent Laslett tune shift[11]depends, instead, on the accelerated current in the ring. The tune control system will have to account for this in real time. Another exception is tune control for resonant extraction. But these need not upset the control of the hysteretic state which this system will achieve.

Other systems could affect the momentum, tune, and chromaticity. We assume that either by design or by operational control the dipole correctors and harmonic quadrupole correctors will not create net changes of $p$ or $\nu$.

## 7 REFERENCES


[1] Stephen D. Holmes. Status of the Main Injector and Recycler, Invited paper at PAC'97.

[2] *The Fermilab Main Injector Technical Design Handbook.* Fermilab (1994,1997).

[3] H. Grote and C. Iselin. The MAD Program Users Reference Guide. Sl 90-13(AP), CERN (1990).

[4] S.A. Bogacz and S. Peggs. Chromaticity Compensation - Main Injector Sextupole Strengths. Main Injector Note MI-0056, Fermilab (April 1991).

[5] Henry D. Glass, Measurement of Harmonic Amplitudes and Phases Using Rotating Coils. Technical Report MTF-94-0004 1.1, Fermilab (March 1994).

[6] D.J. Harding *et al.* Magnetic Field Measurements of the Initial Production Main Injector Dipoles. In *Proceedings of the 1995 IEEE Particle Accelerator Conference, Dallas, May 1-5, 1995*, p. 1340, Institute of Electrical and Electronic Engineers (1995).

[7] Jean-Francois Ostiguy. Eddy Current Induced Multipoles in the Main Injector. Main Injector Note MI-0037, Fermilab (October 1990).

[8] D.G. Walbridge *et al.* Measurements of Beam Pipe Eddy Current Effects in Main Injector Dipole Magnets. *Int. J. Mod. Phys. A (Proc. Suppl.)*, 2B:617 (1993).

[9] B.C. Brown *et al.* Results on Fermilab Main Injector Dipole Measurements. *IEEE Trans. on Magnetics*, 32:2186 (1996).

[10] C.M. Bhar *et al.* Magnetic Field Measurements of the Main Injector Sextupole Magnets (PAC'97).

[11] C. Moore, R. Gerig and S. Pruss. Measurement and Compensation of Coherent Laslett Tune Shifts in the Fermilab Main Ring. *IEEE Transactions on Nuclear Science*, NS-28:2486 (1981). 1981 Particle Accelerator Conference.

# MAGNET DEVELOPMENT FOR THE BRF POSITRON EMISSION TOMOGRAPHY ACCELERATOR

N. Chester, A. Makarov, P. Schlabach, I. Terechkine,
D. Walbridge, T. Wokas, V. Yarba
Fermi National Accelerator Laboratory*
D.J. Larson
Science Applications International Corporation

*Abstract*

A collaboration involving the Biomedical Research Foundation, Science Applications International Corporation, Fermi National Accelerator Laboratory, and the University of Washington is developing an accelerator for producing isotopes for Positron Emission Tomography (PET) scans. The Medium Energy Beam Transport (MEBT) section of this accelerator takes a small beam from a first RFQ acceleration device and matches it into a small 3D-acceptance at a second RFQ section. The beam transport system was designed to prevent beam losses due to emittance growth. The system includes two bending dipoles and seven quadrupoles of three different types.

This report contains a brief description of the MEBT magnets and their electric, magnetic and thermal properties. The magnet measurements show that each of the magnets meets the system requirements.

## 1 INTRODUCTION

The alternative method of isotope production for PET scans uses Radio-Frequency Sections to accelerate **3He**$^{++}$ particles up to 10.5 MeV [1]. The linac transport system consists of low energy, medium energy, and high energy parts. One 1 MeV, 212.5 MHz RFQ section and three 425 MHz RFQ sections bring the beam energy up to the target 10.5 MeV value. The MEBT, medium energy part of the accelerator (figure 1), is designed to accept the beam from the first RFQ section and insure proper beam transverse size and desired bunch longitudinal size at the entrance aperture of the second RFQ section. System requirements and space limitations resulted in a specific design for the bending dipoles and for each of the three quadrupole types used in the MEBT.

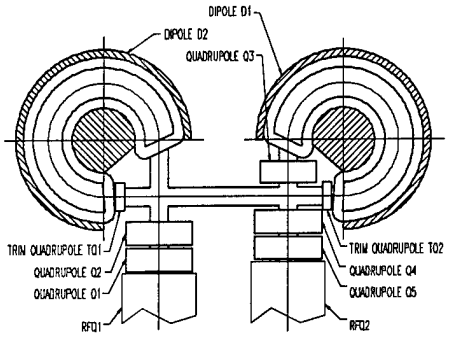



Figure 1. PET MEBT layout.

## 2 BENDING GRADIENT DIPOLES

Two 270° gradient dipoles were inserted into the MEBT to allow magnetic rebunching between the first and the second RFQ sections, and to reduce the accelerator length. The dipoles have a central line radius R = 304.8 mm, a pole width w = 158.75 mm, and a central line pole gap g = 30.48 mm. The central line, central plane (plane of symmetry) magnetic field required for the transportation of 1.0 MeV **3He**$^{++}$ particles is $\mathbf{B_0 = 4101\ G}$, but the dipoles were designed to allow $\mathbf{B_0 = 8202\ G}$ to have a possibility for **3He**$^{+}$ ion transportation through the MEBT channel. The magnetic field has to be a linear function of radius with field index **n** at central line ($R = R_0$)

$$n = -\frac{R_0}{B_0}\cdot\frac{dB}{dR} = 0.53.$$

The magnet pole ends were shaped for additional focusing to reduce the number of required additional focusing devices. The two magnets used in the MEBT system are identical except for their mirror symmetry. The magnet main parameters are listed below:

diameter and height - Ø0.96 m x 0.33 m;
weight - 1400 kg;
wire used - 5.79 mm square wire with Ø 3.2 mm hole for cooling water;
total number of turns per magnet - 112;
maximum current - 180 A ($B_0$ = 8202 G);
nominal wire resistance at 20° C - 0.270 Ohm;
calculated low-frequency inductance - 0.12 H;
maximum power losses at 180 A - 9300 W;
water temperature rise at 180 A - 30° C;
minimum water flow required at 180 A - 4.6 l/min.;
number of parallel water circuits per magnet - 8;

For proper system operation, only ±3.2 G difference is allowed between the real and ideal magnetic field in a

* Operated by Universities Research Association Inc. under contract with the U.S. Department of Energy.

region **254 mm < R < 355 mm** at nominal field strength.

A tolerance analysis made using the OPERA-2D program has shown that in order to meet this requirement, it is necessary to machine the magnet pole surfaces with an accuracy of about 10 μm. Figure 2 shows the difference between the measured (or calculated) and ideal magnetic field that is plotted against the radial position. Calculations were based on the measured pole profile.

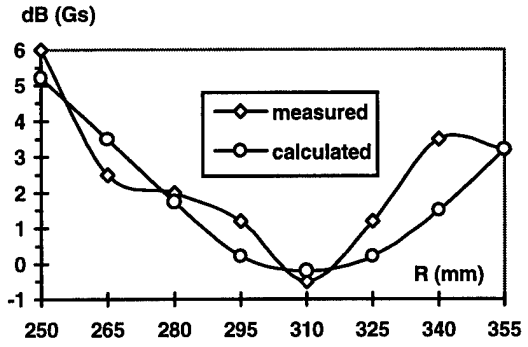



Figure 2. The Dipole Field Quality. $B_0$=8200 G.

The dipole excitation curve is practically a linear function of current, but about 100 G magnetic field hysteresis exists.

## 3 QUADRUPOLES

The MEBT quadrupoles focus the beam transverse dimensions inside an allowed range at the entrance into the dipole D1 and into the RFQ-2 (figure 1). Five main and two trim quadrupoles are installed in the MEBT beam-line. Table 1 below shows the required integrated strength for the main quadrupoles.

Table 1

| | Q1 | Q2 | Q3 | Q4 | Q5 |
|---|---|---|---|---|---|
| G*L (T) | 0.72 | 0.66 | 0.15 | 0.92 | 1.28 |

All quadrupoles should have an aperture R≥38 mm. The length of the main quadrupoles must be less than 125 mm. The width of Q1, Q2, Q4, and Q5 can't be larger than 400 mm; the width of Q3 should be less than 300 mm. Trim quadrupoles should have minimum integrated strength G*L = 0.04 T, their length should not exceed 50 mm and width - 150 mm. Because of the relatively large integrated strength of Q1, Q2, Q4, and Q5, only water-cooled coils can be used. Trim quadrupoles and Q3 were made with air-cooled coils.

### *3.1 Water-cooled quadrupoles*

The cores for the Q1, Q2, Q4, and Q5 quadrupoles were made from the laminations that were used for the Fermilab 3Q-120 quadrupole production in the 1980's. To meet the integrated strength requirements the core length was chosen equal to 50 mm.

The main water-cooled quadrupole parameters are listed below:

wire used - 5.79 mm square wire with Ø 3.2 mm hole for cooling water;
number of turns per pole - 48;
nominal quadrupole resistance - 0.04675 Ohm;
low-frequency magnet inductance - 7 mH;
power losses at integrated strength 1.3 T - 5000 W;
minimum water flow required - 1.2 liter/min.
temperature rise at minimum water flow - 60° C;
number of parallel water circuits per magnet - 2.

Figure 3 shows the difference between the calculated and ideal magnetic field, which is a linear function of X, for the gradient G = 2000 G/cm corresponding to the integrated strength required for the Q5 quadrupole.

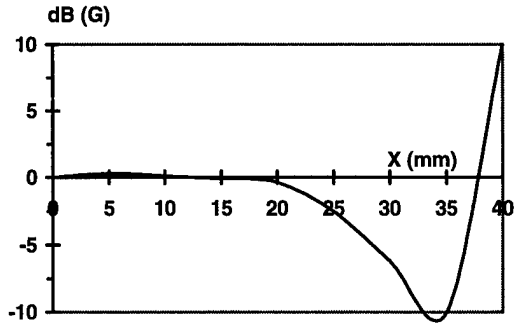



Figure 3. Water-cooled quadrupole field quality.

As the quadrupole excitation curve (figure 4) shows, the current required to achieve the Q5 maximum integrated strength (table 1) is about 1.7 times larger than that for the quadrupole with an ideal core.

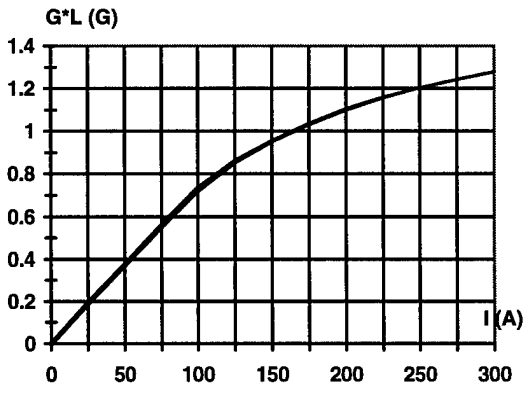



Figure 4. Q5 quadrupole excitation curve.

2D magnetic modeling can explain only 30% of the current rise due to the steel nonlinearity. This difference originates from the very short length of the quadrupole: the end flux of the quadrupole becomes comparable with the useful flux. The problem can be corrected by

making the pole tip length as large as possible within the allowed quadrupole total length limit.

*3.2 Air-cooled quadrupoles*

Except for required maximum field strength and dimensions, Q3 and the trim quadrupoles have a similar design (figure 5).

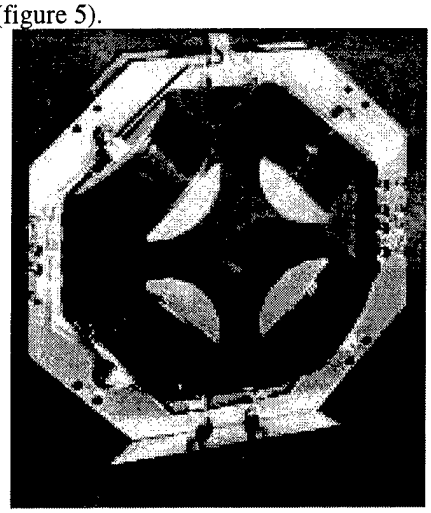


Figure 5. Air-cooled Quadrupole.

To make air-cooling possible, the pole length was made as large as the space limitation allowed. Poles were manufactured from solid steel; flux returns were assembled from two halves to allow quadrupole mounting around the PET beam-pipe. Coils were wound on cylindrical bobbins using solid round insulated copper wire. Coil-pole assemblies were mounted into a flux return frame using assembly tooling that insured proper pole positioning. The main design parameters for the trim quadrupoles are listed below:

wire - film coated ∅ 0.7 mm round copper wire;
number of turns per coil - 315;
quadrupole resistance - 7.0 Ohm;
nominal current - 1.1 A;
quadrupole low-frequency inductance - 0.2 H;
power losses at nominal current - 9.0 W;
maximum coil current allowed - 3.0 A;
surface temperature at maximum current - 95° C.

Figure 6 shows the excitation properties of the trim quadrupole. Analysis of this excitation curve reveals a significant reserve in the integrated strength, but this reserve is too small to use a trim quadrupole instead of Q3. The Q3 quadrupole has a larger length and steel cross-section in order to meet the integrated strength requirement. The design parameters for Q3 are listed below:

wire - film coated ∅ 1.15 mm round copper wire;
number of turns per coil - 1190;
quadrupole resistance - 19.1 Ohm;
nominal current - 0.64 A;
quadrupole low-frequency inductance - 6.7 H;
power losses at nominal current - 8.0 W;
maximum coil current allowed - 4.0 A;
surface temperature at maximum current - 95° C

The excitation curve for Q3 is shown in figure 7.

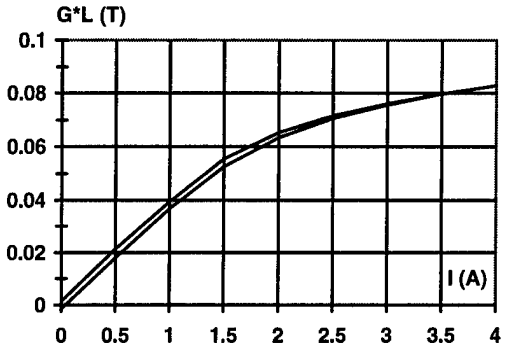



Figure 6. Trim quadrupole excitation curve.

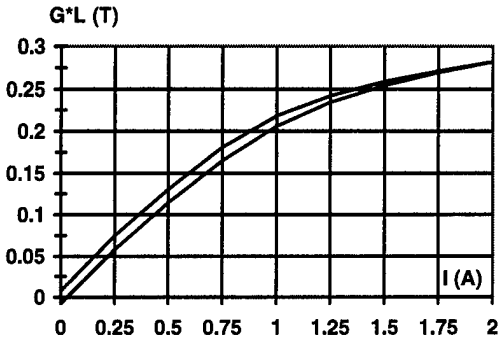



Figure 7. Q3 quadrupole excitation curve.

## 4 CONCLUSION

A set of magnetic devices was designed, manufactured and tested at Fermilab for the PET Medium Energy Beam Transport System. The magnets' properties are close to what was expected. The recent PET accelerator beam experiments [2] have shown that the MEBT meets the system requirements.

*References.*

1. D.J. Larson, P.E. Young, D Sun, at al.,
Ion Optical Design of the BRF-FNAL-SAIC-UW PET Accelerator. PAC-97, 4V.18.
2. Ralph Pasquinelli,
A $3He^{++}$ RFQ Accelerator for the Production of PET Isotopes. PAC-97, 9B.09

# ANALYSIS AND MEASUREMENTS OF EDDY CURRENT EFFECTS OF A BEAM TUBE IN A PULSED MAGNET

S. Fang and W. Chou
Fermi National Accelerator Laboratory
P.O. Box 500
Batavia, Illinois 60510, USA

*Abstract*

The power supply design of the $\gamma_t$ - jump system in FNAL Main Injector uses a resonant circuit[1]. A critical design parameter is the ac losses of the beam tube in a pulsed quadrupole. This paper gives an analysis to this problem. An equivalent circuit model based on the impedance measurement was established. The measured and calculated losses are in agreement. Another effect of the eddy current is the distortion of the magnetic field inside the beam tube. A Morgan coil was used for field measurements up to 10 KHz. These results are presented in this paper.

## I INTRODUCTION

The power supply of FNAL Main Injector $\gamma_t$ - jump system requires a pulsed magnet string as part of its resonant circuit. The total ac losses of magnet string is critical on designing the power supply. The ac losses come from coil winding resistance, laminations and beam tube due to eddy current effects. The transfer function of magnetic field and magnet current is no longer a constant. Magnetic field attenuation inside of the beam tube and the time delay between the field and current increase as frequency increases. The ac losses of the beam tube and the associated effects on magnetic field are the focus of this paper.

## II BEAM TUBE AC LOSSES

In order to study the AC losses of a beam tube in a pulsed magnet, an air core quadrupole magnet called QXR with a circular stainless steel beam tube was used for analysis and measurements. The core losses from this air core quadrupole magnet are very small and can be neglected. The sources of the ac losses come from the beam tube due to eddy current effect and winding dc resistance.

The first approach for estimating the ac losses of a beam tube is the electrical equivalent circuit based on impedance measurement.

Figure 1 shows a circuit basic model for a magnet with a beam tube. The degree of the circuit complexity is dependent on the impedance measurement data. The values of the frequency independent circuit elements are selected such that the basic model matches the impedance measurement data both in magnitude and phase. The resulting basic circuit model can be converted and simplified to the circuit model shown in figure 4. The $R_w$ represents the winding dc resistance of the magnet. $L(f)$ is the equivalent inductance of the magnet and $R(f)$ represents the beam tube ac losses due to eddy current. The $L(f)$ and $R(f)$ are frequency dependent variables and they are determined by the impedance of the magnet.

$$L(f) = \frac{4\pi^2 f^2 {L_{eq}}^2 + {R_{eq}}^2}{4\pi^2 f^2 L_{eq}} \tag{1}$$

$$R(f) = \frac{4\pi^2 f^2 L^2{}_{eq} + {R_{eq}}^2}{R_{eq}} \tag{2}$$

where $R_{eq} = \mathrm{Re}(Z) - R_w$, $L_{eq} = \mathrm{Im}(Z)/2\pi f$. Perform simple circuit analysis on the circuit in figure 4, the power dissipated in $R(f)$, which represents the beam tube ac losses, is obtained by

$$P_{BeamTube} = \frac{4\pi^2 f^2 L(f)^2}{R(f)} {I_{mag}}^2 \tag{3}$$

and the power dissipated in $R_w$ is

$$P_{Winding} = [1 + \frac{2\pi f L(f)}{R(f)}]^2 R_w {I_{mag}}^2 \tag{4}$$

where $I_{mag}$ is the magnet inductance current and it is directly related to the magnetic field inside the beam tube.

The impedance data taken from the measurement for the QXR magnet are shown in figure 2. The measured $R_w$ is $140\,m\Omega$. The frequency independent circuit elements in figure 1 were selected such that the basic circuit model matches the data (R1=$8\,\Omega$, R2=$400\,\Omega$, R3=$20\,\Omega$, L1=$420\,\mu H$, L2=$230\,\mu H$, L3=$230\,\mu H$). The

Operated by the University Research Association Inc., Under contract number DE-AC02-76CH03000 with the U.S. Department of Energy.

0-7803-4376-X/98/$10.00 © 1998 IEEE

basic circuit model is then converted to the simplified model as shown in figure 4. The $L(f)$ is plotted in figure 5 by using equation (1). Figure 5 shows the QXR inductance decreases as frequency increases. This is because the flux is reduced by the eddy current induced B field. The ac losses of the beam tube is generated by equation (3) in figure 3 with beam tube ac losses in watts per ampere squared as function of frequency. As seen in figure 3, the beam tube ac losses rise linearly as a function of $f^2$ below 2 KHz. There is a fall off from this linear relationship above 2 KHz. This is partly due to the decrease of $L(f)$ as frequency increases as explained above.

The second approach for estimating the ac losses of the beam tube is theoretical calculation based on the quadrupole field and the properties of the beam tube. When a circular beam tube is placed in a varying quadrupole field, the eddy current induced field is

$$B'_{ed} = \frac{1}{2}\ \mu_o \frac{dB'}{dt} \sigma\ t\ r \qquad (5)$$

The ac losses due to the eddy current is

$$P_{ed} = \frac{1}{4}\ \pi(\frac{dB'}{dt})^2 \sigma\ t\ r^5 l_{tube} \qquad (6)$$

where $\mu_o$ is the permeability of air, $B'$ is quadrupole field gradient, $\sigma$ is the conductivity of tube material, $t$ is the thickness of the tube, and $l_{tube}$ is the length of the tube. The field gradient of an air core quadrupole is:

$$B' = \frac{1}{2}\frac{\mu_o N I_{mag}}{A^2} \qquad (7)$$

where $N$ is number of turns per gap which is twice the number of turns per pole, $A$ is the radius of inscribed circle of the magnet poles. The inductance is

$$L = \frac{1}{4}\ \pi\mu_o N^2 l_{mag} \qquad (8)$$

where $l_{mag}$ is the length of the magnet. From equation (6), (7), and (8), one gets the beam tube ac losses due to eddy current:

$$P_{ed} = \pi^2 f^2 \mu_o L \sigma t r \frac{l_{tube}}{l_{mag}} I_{mag}^{\ 2} \qquad (9)$$

Equation (9) uses the fact that $A$ is about the same as $r$ in the measurement. For a given set of beam tube data and the measured magnet inductance, the calculated ac losses of the beam tube is obtained by equation (9) and the result is plotted in figure 3. It is seen that the results from the two different approaches agree with each other up to 2 KHz.

## III MAGNETIC FIELD DISTORTION

In order to understand the possible associated distortion of the quadrupole field, a Morgan coil is placed inside the stainless steel beam tube of the QXR magnet. The coil has a set of pickups that can probe various multiple components of a varying field, including dipole, normal quadrupole, skew quadrupole, sextupole, octupole, decapole,12-pole and 20-pole.

The coil is positioned manually at the center of the beam tube such that the normal quad signal reaches maximum while the dipole and skew quad signals minimum with a sinusoidal excitation current at 130 Hz. The measurement was carried out in the frequency range from 130 Hz to 10 KHz. The results are shown in figure 6. In an ideal situation, the normalized ratio of magnetic field and current B/I, which is proportional to the ratio of pickup signal to time derivative of magnetic field, should be a constant as frequency increases. The actual decline of B/I is believed to be the result of the eddy current in the beam tube.

Almost all the error field signals remain to be small (< 3%) in this frequency ranges shown in figure 7. These error fields are probably mainly due to the position error of the coil rather than from the eddy current effect. One exception is the 12-pole. This is the first allowed (by symmetry) error field. It reaches about 12% of the normal quad field at 10 KHz.

## IV CONCLUSION

The ac losses of the beam tube due to eddy current has been analyzed by using impedance measurements and theoretical calculations. The agreement between these two approaches below 2 KHz gives us confident on estimating beam tube ac losses as functions of current and frequency for the $\gamma_t$ - jump system design. The magnetic field distortion due to eddy current effect on a stainless steel beam tube is small.

## V ACKNOWLEDGEMENTS

The authors would like to thank H. Pfeffer and B. Brown of Fermilab for their helpful suggestions on the work.

## REFERENCES

[1] W. Chou et al., 'The Design of a $\gamma_t$-Jump System for the FNAL Main Injector', This conference.

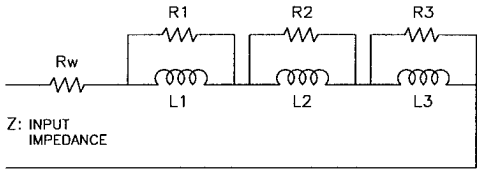



Fig 1 Magnet Equivalent Circuit General Model

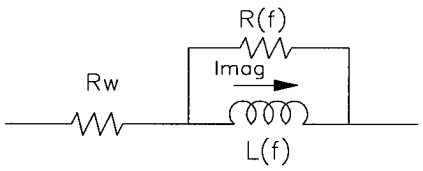



Fig 4 Magnet Circuit Model

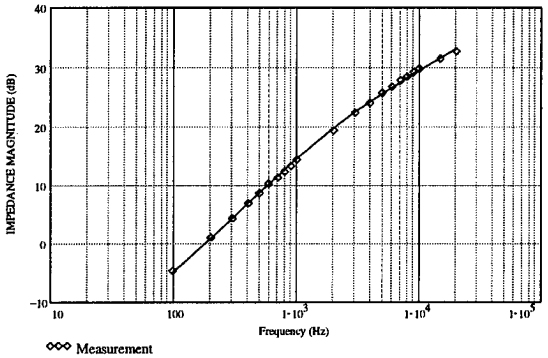



Fig 2 Impedance Plot

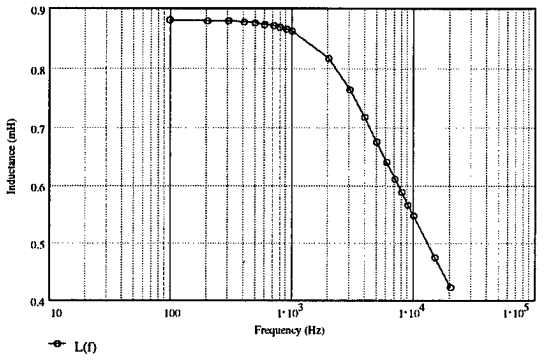



Fig 5 Inductance Plot

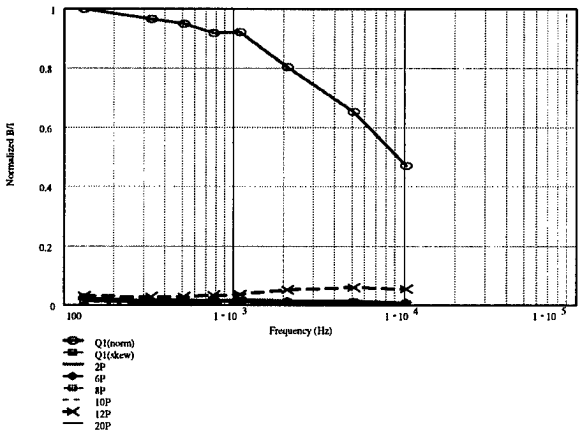



Fig 6 Magnetic Field and Current Transfer Function

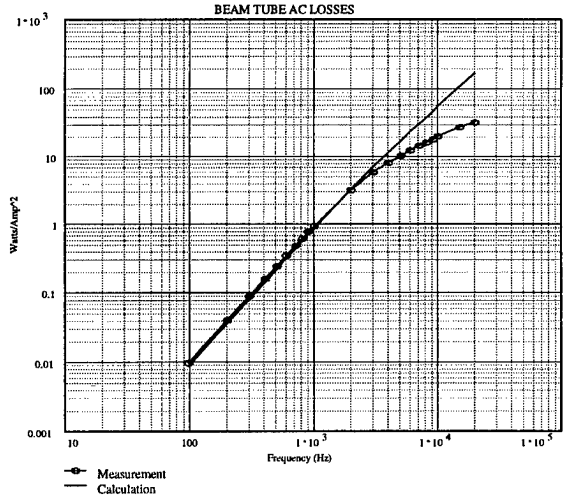



Fig 3 Beam Tube AC Power Losses Plot

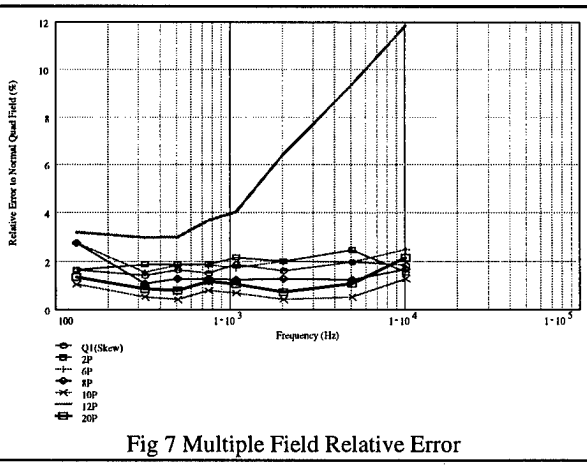



Fig 7 Multiple Field Relative Error

# EXPERIENCE WITH THE PROCUREMENT OF FERRITE AND TEMPERATURE COMPENSATOR FOR PERMANENT MAGNETS FOR ACCELERATORS

William B.Fowler, Bruce Brown, and James Volk, Fermi National Accelerator Laboratory* *, P.O. Box 500 Batavia, IL 60510

*Abstract*

The use of permanent magnets for transporting the 8 GeV proton beam from the Fermilab Booster to the new Fermilab Main Injector accelerator has been implemented and the magnets for a new 8 GeV ring to be installed in the Main Injector tunnel for increasing the luminosity of pbar/p collisions in the Tevatron are about to start being produced. Strontium oxide ferrite was selected for the magnets due to it's low cost and satisfactory magnetic properties for the 1.5 kilogauss fields required in the 2-inch gap magnets. Fermilab has received 96,000 pounds of ferrite and by working with the Vendor (HITACHI, Edmore, MI) improved uniformity of Residual Induction (Br) has reached 3905 gauss ±0.65%. Further details are given in the paper. Overcoming the magnetic field variation when the temperature of the magnets changes is accomplished by incorporation of approximately 30% nickel steel alloy. The ferrite changes approximately -o.2% per degree C, which is compensated for by the 13% by volume of compensator alloy incorporated in the magnet. Fourteen thousand (14,000) pounds of this material has been received and in order to obtain sufficient uniformity we mixed equal amounts from each batch into each magnet. Results of this process are given in the paper.

## 1 INTRODUCTION

Fermilab has added to the Main Injector Project a fixed 8 GeV storage ring called the Recycler. It is to be located in the Main Injector tunnel directly above the Main Injector magnets near the ceiling of the tunnel. The construction schedule calls for the installation of the Recycler ring during the completion of the Main Injector. This is made possible by the use of permanent magnets. The primary benefits of the Recycler are:

1) Facilitates the attainment of Tevatron collider goals by relieving the Antiproton Source of the responsibility for maintaining high stacking rates at high stacks.
2) Provides potential for a factor of two in Tevatron Luminosity by allowing recovery of unspent antiprotons at the end of stores.

Since there was very little experience in the use of permanent magnets at Fermilab it was decided to convert the 8 GeV beam transport line from the Booster to the Main Injector from electro magnets to permanent magnets similar to those required by the Recycler. The 8 GeV line of about 100 magnets required 80,000 pounds of Ferrite.

## 2 FERRITE

Type 8 Strontium Ferrite was chosen based on cost, availability and stability. There are three major manufactures of Strontium Ferrite in the United States each with a capacity of several million pounds per year. The Material is used in automobiles, speakers and lifting devices. Recently it has been used in permanent magnet magnetic imaging applications. A standard brick size was selected and in order to incorporate the bricks into the Recycler magnet design attention was given to dimensional tolerances. Fig. 1 shows the variation of the six inch length dimension of a brick in a typical sample of 40 bricks. Fig. 2 shows the variation in the four inch width dimension in the same sample of 40 bricks and Fig. 3 the variation of the one inch thickness dimension.

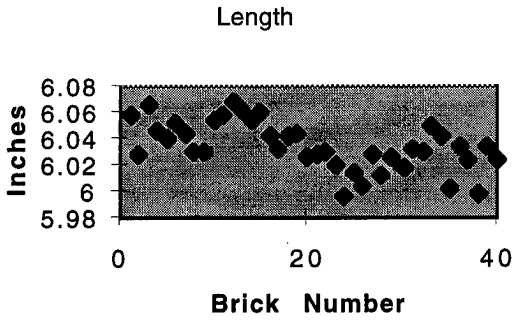



Fig. 1 Variation in Brick length for 40 Bricks

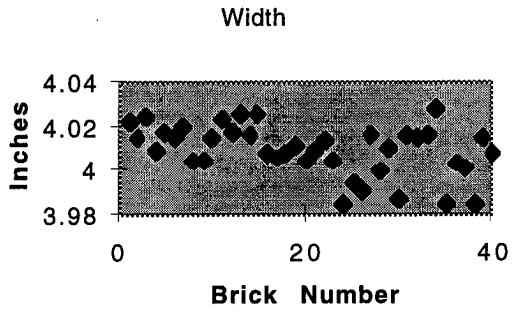
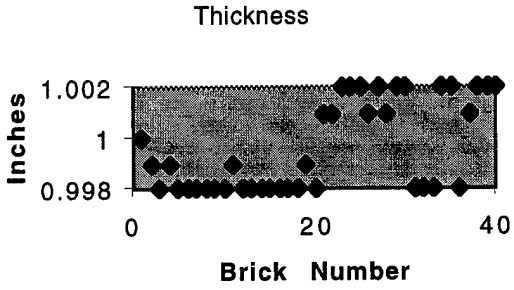



Fig. 2 Variation in Brick width for 40 Bricks

* Operated by Universities Research Association under contract to the United States Department of Energy

0-7803-4376-X/98/$10.00 © 1998 IEEE




Fig, 3 Variation in Brick thickness for 40 Bricks

Table I presents this data in comparison with the specification. In order to achieve the smallest possible dimensional variation a three cavity die was constructed by the successful Vendor, HITACHI METALS(Edmore, MI) and all of the Strontium Ferrite bricks for Fermilab are produced with this die. Of interest to note is that the production rate with this three cavity die is three bricks every two minutes and 15 seconds. This yields about 1600 bricks per 20 hour day.

Table 1: Specification vs. Measurements
Brick Dimensions in inches

| **Specifications** | | |
|---|---|---|
| Length | 6.000 | +.090 |
| | | -.090 |
| Width | 4.000 | +.060 |
| | | -.060 |
| Thickness | 1.000 | +.005 |
| | | -.005 |
| | | |
| **40 Brick Measurements** | | |
| Length | 6.000 | +.070 |
| | | -.000 |
| Width | 4.000 | +.030 |
| | | -.015 |
| Thickness | 1.000 | +.002 |
| | | -.002 |

One note of caution in using the tighter tolerances as determined from the 40 brick data should be expressed. This restricted set of bricks did not include the entire range of possible dimensions over the production run of 70,000 bricks so it may not correspond to the maximum variation one might encounter. However the important conclusion is that it is probably not necessary to use the range of the generally accepted specification if a single die is used and by measuring the total range of brick dimensions a tighter tolerance can be used for the permanent magnet design.

Recycler magnets are required to have an integrated field strength accuracy that can only be achieved by adjusting the amount of Ferrite in each magnet after it is constructed. This then overcomes the inherent variation in Ferrite magnetic properties. However in order to minimize the magnitude of the trimming operation it is beneficial to reduce the Ferrite brick differences in Br and Hci to the extent possible. Type 8 Ferrite nominal Br is 3850 Gauss with 3050 Gauss for Hci. The accepted tolerance on Br is ±5% and ±8% on Hci. By restricting the brick processing to the more uniform temperature portion of the kiln during the Sintering operation the variation in Br has been reduced to ±0.65%. Of interest is the tracking studies that Fermilab has carried out from batch to batch of Ferrite received. Fig.'s 4 and 5 summarize magnetic tests performed by the Vendor on a randomly selected brick from each 400 bricks shipped. Five shipments are shown. The two earliest consisted of 10 tests from a total of 4000 bricks each. The three latest shipments contained 6000 bricks with 15 tests each.

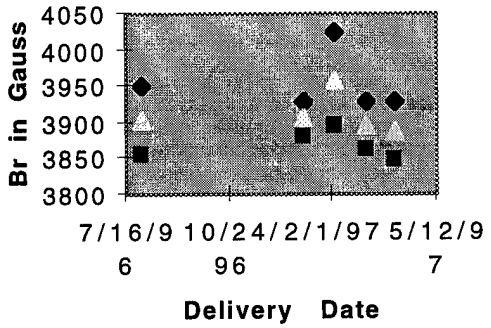



Fig. 4 Trend Analysis of Ferrite Bricks Received by Fermilab (Br)

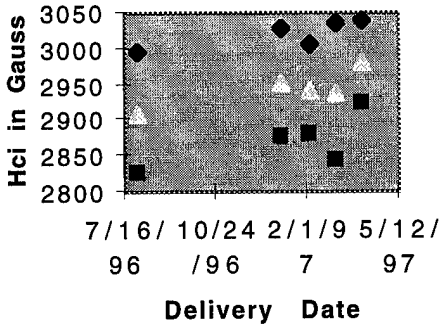



Fig. 5 Trend Analysis of Ferrite Bricks Received by Fermilab (Hci)

## 3 COMPENSATOR

Overcoming the Recycler magnets change in magnetic field due to unavoidable tunnel temperature changes is accomplished by incorporating 13% by volume of 30% nickel steel alloy. Recent measurements of the temperature coefficient of three separate Ferrite bricks showed -0.187%,0.184% and -0.189% per degree C. Therefore some of the magnetic field change can come from variation in the Ferrite properties. Compensator alloy measurements supplied by the Vendor (TELCON,

Crawley, England) show a variation of $\Delta B/\Delta T$ of 61 to 78 Gauss/degree C. These measurements are at 50 Gauss. Recent measurements at 1500 Gauss, the field that the Recycler magnets operate at were similar. The variation seems to depend on the work hardening that occurs after a final heat treatment. We have avoided the complication of the need to change the percentage of compensator in each magnet by mixing compensator batches. the mixing included mixing different melts of material and also mixing compensator from the ends and middle of a roll of material. For instance some measurements from the two ends of a roll are identical while in other cases the measurement from the two ends of a roll vary by 10%.

The Recycler permanent magnets are primarily combined function magnets, that is they combine a dipole field and a quadrupole field by using tapered pole tips. The compensator is incorporated as two inch wide by six inch long strips each 50 mils thick. Per four inch brick there are ten compensator strips. Since these packets of compensator are assembled into the magnet as it is constructed it is important to not have to adjust the number of strips. To do so requires the magnet to be taken apart. Investigations are continuing to be sure that our mixing procedure avoids this complication even though during the last stages of 8GeV beam line magnet production no magnets had to be redone.

# PERMANENT DIPOLE MAGNETS FOR THE 8 GEV TRANSFER LINE AT FNAL

H.D. Glass†, B.C. Brown, G.W. Foster, W.B. Fowler, J.E. Haggard, D.J. Harding, G.P. Jackson, M.P. May, T.H. Nicol, J.F. Ostiguy, P. Schlabach, G.A. Smith, J.T. Volk, Fermi National Accelerator Laboratory, Batavia, IL 60510

*Abstract*

The transfer line that will serve to transport 8 GeV protons from the Booster to the new Fermilab Main Injector has been built using permanent magnets. A total of 46 horizontal bend dipoles and 5 vertical bend dipoles were built for this beamline; 67 gradient magnets [1] were also built. The magnets were built using magnetized strontium ferrite bricks. Thermal compensation of these bricks was effected by use of a nickel-iron alloy. The dipole magnets were built with a mean integrated strength of 0.56954 T-m, and an rms spread of 0.06%. The magnets were thermally cycled from 20°C to 0°C to condition the ferrite against irreversible thermal losses, and the compensation was measured with a flipcoil. The magnet strength was adjusted by varying the number of bricks installed at the magnet ends. Details of the assembly process and a summary of magnetic measurements are presented here.

## 1 THE 8 GEV TRANSFER LINE

The design of the Fermilab Main Injector (FMI) calls for protons to be extracted from the existing Boster at 8 GeV and transported 756 m for injection into the FMI [1]. This transfer line is comprised of three major sections; the long central section, consisting of a long string of periodic FODO cells, is made entirely of permanent magnet dipoles, quadrupoles, and gradient magnets. The motivation for employing permanent magnets wherever possible in the line was primarily to acquire the manufacturing and operating experience necessary to ensure the success of the future Recycler Ring [2].

### *1.1 8 GeV beamline permanent magnets*

The 8 GeV line uses four types of permanent magnets: a gradient (combined function) dipole [3] used in the normal arc cells, a normal quadrupole [4] used in the reverse bend cells near the beginning of the line, a short dipole used for horizontal bends in the arc cells, and a vertical bend dipole used to pitch the beam down coming out of the Booster. The horizontal and vertical bends are very similar in design, and are the focus of this paper.

| Type | $L_{mag}$ (m) | ∫Bdl (T-m) | ∫ gdl (T) | N |
|---|---|---|---|---|
| Horizontal bend | 2.464 | 0.56953 | 0 | 45 |
| Vertical bend | 3.556 | 0.8220 | 0 | 4 |
| Gradient | 4.00 | 0.56953 | 1.851 | 65 |
| Quadrupole | 0.508 | 0 | 1.481 | 9 |

### *12 Permanent magnet design*

We have elected to use "hybrid" permanent magnets in the 8 GeV line; in this type of design, the field is driven by permanent magnet material and the field shape is determined by the geometry of steel pole pieces. For reasons of stability and cost, we use strontium ferrite as the permanent magnet material. A drawing of the double dipole (horizontal bend) magnet end view is shown in Fig. 1; the permanent magnet bricks drive flux into the pole tips from the top and sides.

The pole tips are supported by an aluminum spacer which determines the height of the magnetic gap. The pole assembly plus bricks are contained in a flux return shell that is 1.91 cm thick. We use solid bar stock components for the poles and flux returns rather than laminations. The pole tip steel is 1008 low carbon steel. A NiFe temperature compensation alloy is used for cancellation of the –0.2%/C temperature coefficient of the ferrite, and in the dipole magnets is inserted into the sides of the magnet aperture.

In order to limit stray flux from leaking out, the end fields of the magnet are terminated by flux clamp / end plate assemblies which are magnetically connected to the flux return shell. An aluminum retainer plate immobolizes the beam tube and protects the magentic pole tips from magnetic debris. The end plates are removable to permit access to the ends of the pole pieces for shimming operations. The flux return extends 5.08 cm past the ends of the pole pieces at each end; the end plates are 1.27 cm thick; therefore, the mechanical length of these magnets are 12.7 cm longer than the magnetic (pole piece) length.

† Work suported by the U.S. Department of Energy under contract number DE-AC02-76CH03000.

0-7803-4376-X/98/$10.00 © 1998 IEEE

The magnets are designed to fit around an elliptcial beam pipe with inner dimensions under vacuum of approximately 4.57 cm (vertical) x 9.91 cm (horizontal). A transition to a 10.16 cm round pipe has been provided on all magnets.

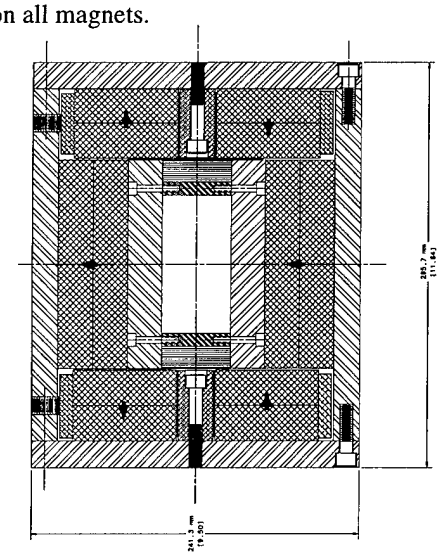


Figure 1. Cross section of the vertical bend dipole.

## 2 MAGNET ASSEMBLY

### *2.1 Magnetization of bricks*

Ferrite bricks are shipped unmagnetized from the foundry and are magnetized shortly before assembly using a 2 T electromagnet. The ferrite is purchased in standard size 1"x4"x6" bricks, with the 1" dimension ground to ±0.005" flatness and the 4"x6" dimensions left at a tolerance of ±0.060". The dipole side bricks are cut in half before magnetization. In the early stage of the production run, the magnetic strengths of the bricks were individually measured; this measurement became superfluous as the production line became more efficient.

### *2.2 Mechanical assembly*

The assembly process begins with the machining of the pole tips from solid bar stock. The pole tip spacing is set by bolting them down against aluminum pole tip supports at either edge. Magnetized bricks are then glued with epoxy to the flux return plates. Both the vertical and horizontal bends employ a "double-dipole" design in that two layers of bricks are used behind each pole, providing 5.08 cm total thickness of magnetic material. A double layer of bricks are also glued onto the side flux return plates. The flux return plates are then lowered carefully onto the pole tip assembly using mechanical fixturing to control the magnetic forces [6]. A steel end plate is bolted onto each end of the magnet to terminate the flux lines.

### *2.3 Strength trimming*

The magnet is designed so that a fully-loaded magnet having bricks of nominal strength will be 3-5% stronger than required. Dummy bricks, fractional bricks, and spacers are used to control the total strength and to correct for brick-to-brick and lot-to-lot variations. A final strength trim was performed at the magnet factory using a flip coil system to measure the integrated strength. Trimming is accomplished by removing or adding bricks or partial bricks to the magnet ends as required. The trimming tolerance, as measured with the flip coil, was 0.1% for the dipole magnets. The strength measurements were independently verified using a rotating harmonics coil at the Fermilab Magnet Test Facility.

## 3 DIPOLE MAGNET DESIGN

The horizontal and vertical bend dipoles are identical in cross section but differ in length and integrated strength. A cross section of the magnet is shown in Fig. 1. The horizontal dipoles (PDD) provide a 20 mrad bend and a nominal bend field of 0.23 T. This higher strength is achieved by stacking the ferrite bricks two deep behind the poles and at the sides of the magnet. The vertical bends (PVB) are longer versions of the PDDs, which are mounted on their sides to provide the bends in the vertical drop region of the 8 GeV line.

The dipoles use a flat pole tip fabricated from a single piece of Blanchard-ground bar stock. No edge shims are needed on the pole face to provide adequate field quality because of the field shaping provided by the side bricks. This represented a significant cost savings over a custom ground pole profile.

A significant design choice for the dipoles was the placement of the compensator material at the edges of the magnet gap region. This is in contrast to the interspersed method used with the gradient magnets. The advantages of the gap comepnsator are 1) the design is more magnetically efficient, since none of the ferrite space behind the pole tip is wasted, 2) less total compensator is used since it only spans the 1" half-gap of the magnet, and 3) the compensator strips run longitudinally and can easily be replaced after magnet assembly. The disadvantage of the gap compensator is a slight sensitivity of the field shape to both compensator placement and temperature. Both effects are accepatble for the 8 GeV line but undesirable for the more stringent requirements of the Recycler.

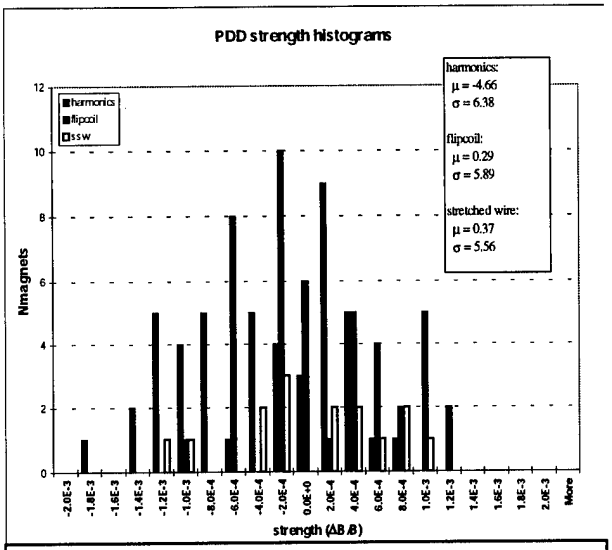



Figure 2. Histogram of dipole strengths as measured by 3 different probes.

## 4 THERMAL CYCLING AND COMPENSATION

### *4.1 Freezing to condition against irreversible losses*

Strontium ferrite can be demagnetized by exposure to low temperatures, due to the positive value of $dH_c/dT$. This is a one-time loss which depends only on the lowest temperature to which the magnet has been exposed. Typical demagnetizations are 0.1% at 0°C and 0.2% at -20°C. There is a lot-to-lot variation of ±10% in $H_c$. For these reasons we froze each magnet to 0°C in a custom built refrigerator in the magnet factory prior to final trimming. The refrigerator was large enough to freeze up to 18 magnets overnight. Magnets were measured for strength at room temperature prior to freezing, and were measured again immediately after being removed from the freezer. They were remeasured one last time after they had warmed up to room temperature. The strength losses from freezing were typically 0.1% as expected, and no anomalous strength losses were noted. We warmed a sample of magnets using heating blankets up to 40°C, and as expected, observed no irreversible losses on the magnets.

### *4.2 Temperature compensation*

The intrinsic thermal coefficient of strontium ferrite, -0.2%/°C, is reduced to nearly zero by inserting a compensating NiFe alloy (~30% Ni) in the vicinity of the ferrite. This alloy is characterized by a low Curie temperature (~50-70°C), and therefore the permeability is a strong function of temperature. The alloy shunts flux away from the magnet aperture in a temperature dependent manner, and by adjusting the proportion of ferrite to compensator, one can null out the overall thermal dependence of the field strength. The degree of temperature compensation is linearly related to the amount of compensator material in the magnet. By adjusting the number of compensator strips, we were able to reduce the temperature coefficient to <0.01%/°C.

The thermal coefficient of all the magnets was measured at the magnet factory by comparing the strength at 0°C and after warmup to room temperature. We also measured this coefficient on ~20% of the magnets by heating and measuring the change in strength with a rotating coil.

The observed variation in the temperature dependence of the permeability of the NiFe alloy as received from the vendor was ±10%. This made it necessary to iterate the temperature compensation in production. In the dipoles, the compensator strips run longitudinally in the magnet gap, and it was straightforward to adjust the number of strips after initial assembly. This procedure converged in most cases immediately, requiring only an additional cooldown cycle to verify the compensation

### *4.3 Transient thermal effects*

A rapid thermal transient (e.g., condensation from exposure of a frozen magnet to a warm, humid environment) is observed to produce a large strength transient in the magnet (see Fig. 2). This is most probably due to a temporary mismatch between ferrite and compensator temperatures. The thermal transients that produce these effects are much larger than one expects in the 8 GeV tunnel, and is not likely to be an operational difficulty.

## REFERENCES

[1] The Fermilab Main Injector, Technical Design Handbook. FNAL, Nov. 1995.
[2] G.W. Foster, "The Fermilab permanent magnet antiproton Recycler ring," this conference.
[3] H.D. Glass et al., "Permanent gradient magnets for the 8 GeV transfer line at FNAL," this conference.
[4] S.M. Pruss et al., "Hybrid permanent quadrupoles for the 8 geV transfer line at Fermilab," this conference.
[5] S.D. Holmes, "Status of the Main Injector and Recycler," this conference.
[6] Nicol, T.H. & A.B. Knauf, "Permanent magnet assembly tooling for the 8 GeV transfer line and Recycler Ring at Fermilab," this conference.

# STABILITY TESTS OF PERMANENT MAGNETS BUILT WITH STRONTIUM FERRITE

H.D. Glass, BC. Brown, G.W. Foster, W.B. Fowler, R. Gustafson, G.P. Jackson, J.-F. Ostiguy, and J.T. Volk, Fermi National Accelerator Laboratory, P.O. Box 500, Batavia, IL 60510

*Abstract*

Permanent magnets built using strontium ferrite bricks have been tested for stability against demagnetization. Ten test dipoles were built to monitor ferrite behavior under a variety of stressing conditions, including irradiation, mechanical shock, extreme thermal excursions, and long term magnetization stability. The test magnets were geometrically similar to, but much shorter than, the magnets built for the 8 GeV transfer line at FNAL. No loss of magnetization was observed for bricks exposed to a proton beam, and a magnet exposed to several Gigarads of $Co^{60}$ gamma radiation suffered no measurable demagnetization. The magnet strength was observed to decrease logarithmically with time, consistent with the expected effect of thermal fluctuations. Irreversible demagnetization of ~0.1% was seen in cooling magnets to 0°C, and the loss was ~0.2% for magnets cooled to -20°C. No additional demagnetization was seen on subsequent cycling to 0°C. Finally, one of the long dipoles built for the 8 GeV line was periodically tested over the course of 3 months, and showed no measurable demagnetization.

## 1 MAGNETS FOR THE 8 GEV LINE

The new Fermilab 8 GeV transfer line connecting the Booster to the Main Injector has been built using hybrid permanent magnets [1,2]. This beamline is designed to have an operating lifetime of 30 years. The magnets will be operated at an ambient tunnel temeparture between 20°C and 35°C. They must also be capable of storage between 5°C and 50°C. We also require that the magnets be resistant ($\Delta B/B < 0.05\%$) to shock and vibration under normal handling. We also impose a reasonable requirement for radiation resistance, demanding that $\Delta B/B < 1\%$ for an exposure of 1 GigaRad. Finally, a long operational lifetime imposes a temporal stability requirement of $\Delta B/B < 0.02\%$ per year, measured from the first month after initial magnetization.

### *1.1 Permanent magnet material*

We chose Type 8 Strontium Ferrite as the material to be used for making our permanent magnets [3]. This choice was driven by low cost, consideration of stability over time, temperature, and radiation. Strontium ferrite is the material of choice in automotive and other industrial applications, and is available from vendors in standard grades and sizes.

## 2 THEORY

The phenomenon of decrease in magnetization with time, often and incorrectly referred to as aging (it has nothing to do with long term chemical or structural changes in the material) is qualitatively well understood. The theory was developed by Louis Néel [4] and by Street and Wooley [5]. It was initially applied to Alnico magnets, but was later shown to apply to ferrites as well [6].

Hard ferrites are composed of small ferromagnetic regions or "grains" generally about 1 μm in size, closely packed and separated by non-ferromagnetic media. Each grain is constituted at most of a few domains whose walls are pinned by various imperfections. Thermal fluctuations induce local strain variations and changes in the magnetic anisotropy constant resulting in wall nucleation and changes in the net magnetization of the grains. Regardless of the exact nature of the mechanism, the energy required to irreversibly change the magnetization can be seen as the activation energy for the grain.

It is supposed that at some time $t = t_0$, a certain number of grains have their net magnetization vector in metastable orientations and fluctuations in thermal energy induce irreversible magnetization rotation in small volumes of the material.

Consider the number $N$ of domains characterized by activation energies between $E$ and $E+dE$ at the time $t$

$$N(E,t) = f(E,t)\,dE \qquad (1)$$

The rate of change of $N$ due to thermal activation a temperature $T$ is

$$\frac{dN}{dt} = -Cf(E,t)e^{-E/kT}dE \qquad (2)$$

where $C$ is a constant which depends on the material and $f$ is a distribution function. Equation 2 is satisfied by

$$\begin{aligned} N(t) &= f(E,t_0)e^{-\lambda(E)t}dE \\ &= f_0(E)e^{-\lambda(E)t}dE \end{aligned} \qquad (3)$$

where

$$\lambda(E) \equiv Ce^{-E/kT} \qquad (4)$$

0-7803-4376-X/98/$10.00 © 1998 IEEE

If each activation contributes an average amount $m$ to the magnetization, then the activation of $dN$ regions results in a mean decrease of the magnetization $M$

$$dM = -mCf_0(E)e^{-\lambda t}e^{-E/kT}dEdt \qquad (5)$$

Integrating over all values of the activation energy

$$\frac{dM}{dt} = -mC\int_{E_0}^{E_m} f_0(E)e^{-\lambda t}e^{-E/kT}dE \qquad (6)$$

In practice, the detail of the distribution $f_0(E)$ and the limits $E_0$ and $E_m$ are not known, but it is reasonable to assume that $f_0(E)$ should vanish beyond a maximum energy $E_m$.

For a simple impulse distribution at $E=E_m$ one obtains after integrating,

$$\Delta M = -mN_0\left[1-e^{-\lambda_m t}\right] \qquad (7)$$

where

$$\lambda_m = e^{-E_m/kT}/t \qquad (8)$$

For a more realistic rectangular distribution where all activation energies are between $E_0$ and $E_m$

$$\Delta M \cong -mN_0\frac{kT}{(E_m-E_0)}\left[\log\frac{t}{t_0}-\lambda_0(t-t_0)\right],$$

$$\text{for } \lambda_0(t-t_0)<<1 \qquad (9)$$

$$\cong -mN_0\frac{kT}{(E_m-E_0)}\left[\log\frac{t}{t_0}\right],$$

$$\text{for } \lambda_0(t-t_0)>>1 \qquad (10)$$

Thus, the theory predicts that after a brief more or less linear drop, the magnetization decays logarithmically with time.

## 3 STABILITY TEST MAGNETS

To study the long term behavior of magnets built with strontium ferrite, we built a set of 0.5 m long dipoles having a cross section similar to the design used for the production 8 GeV magnets. In Table 1 we list a description of the properties and testing history of each magnet. Magnets were built from strontium ferrite bricks supplied by several vendors, including Hitachi and Crucible. The magnets were thermally compensated using NiFe alloys obtained from vendors Telcon and Carpenter. All magnets listed in the table were made using Hitachi bricks and Carpenter compensator , unless otherwise noted. The bricks were fully magnetized (100% saturation), except for magnet 5.

| *magnet* | *description* |
|---|---|
| 1 | standard reference |
| 2 | same as #1 |
| 3 | Crucible bricks |
| 4 | Telcon compensator |
| 5 | bricks @ 95% saturation |
| 6 | cooled to –20°C |
| 7 | heated to 45°C |
| 8 | Co-60 irradiation |
| 9 | identical to #1 |
| 10 | no side bricks |

Table 1. Properties of the 10 stability test magnets.

All of magnets were built using a single layer of full-size bricks (4" x 6") on the top and bottom poles, and using half-size bricks (4" x 3") on the sides, with the exception of magnet #10. For this magnet, we left out the side bricks in order to study whether these bricks aged at a different rate than the top/bottom bricks.

## 4 AGING RESULTS

All of the magnets showed a slight degree of aging consistent with the logarithmic model discussed above. The main loss of magnetization, generally around the level of 0.1%, occurred within the first few weeks after magnetization. After that period of time, very little additional loss was observed. Some examples of the decrease in magnet strength vs time are shown in the accompanying figures. All of the observations are within the allowable limits for operation of the 8 GeV beamline and Recycler. No significant differences were seen in the behavior of ferrite or compensator from different vendors.

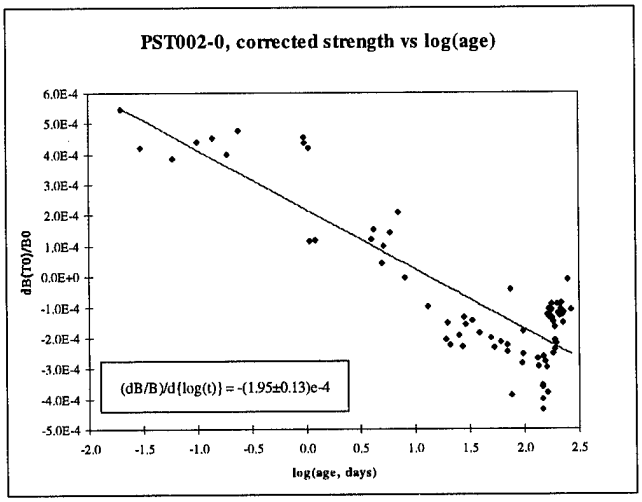



Figure 1. Stability of test magnet #2 as a function of the log of its age. The magnetic strength loss is 0.02% per "decade".

In Fig. 1, a fit is shown for (dB/B)/d(log t) vs log(t), where time is measured in days. The interpretation of the result is that the magnet is observed to lose 0.02% in strength after its first 10 days of existence (after magnetization); a subsequent loss of 0.02% after the next 100 days; and an extrapolation that over the next 1000 days, the loss will be an estimated 0.02% additional loss.

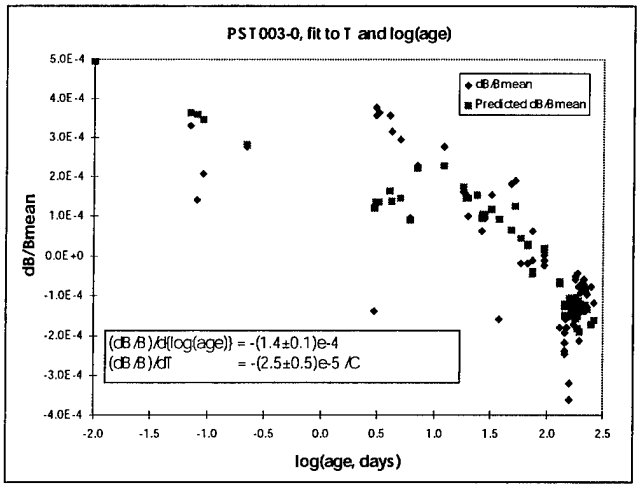



Figure 2. Stability of test magnet #3 as a function of both temperature and time. This fitting accounts for thermal effects due to imperfect temperature compensation.

A slight complication in the analysis of the aging of the magnets was to properly account for temperature effects. In constructing these magnets, we attempted to correctly balance the compensator to ferrite ratio so that there was a minimal temperature dependence to the magnet strength. Compensation was not perfect (although generally less than 0.01%/C), and could provide an important source of systematic error in the measurement of aging. Figure 3 shows the result of fitting the magnetic strength to a functional form dB/B = k1*T + k2*log(t). The fitting for temperature and temporal effects simultaneously are shown in the figure.

*4.1 Other stability results*

Magnet #8 was exposed to several gigarads of gamma radiation from a Cobalt-60 source. The magnet strength was monitored with an NMR probe over the course of the exposure, which lasted several months. There was no observed loss of strength that could have been attributed to radiation damage; i.e., the observed losses were consistent with aging with log(t).

Magnet #7 was heated to 45 C. As with other magnets which we have heated, only reversible changes in strength with temperature are observed. Magnet #6, on the other hand, was cooled first to 0 C, and we observed a strength loss of 0.1%. A second cycle down to 0 C saw no additional loss. This was followed by a cooling down to a temperature of 20 C, and the loss was 0.2% from the original strength. A second cooldown to 20 C saw no further loss. This series of tests led us to cool all our production magnets for the 8 GeV line to 0 C as a conditioning against thermal losses.

## CONCLUSION

We have studied the temporal stability of a number of model magnets over an 8 month period. These data are consistent with logarithmic aging at a level of $2 \times 10^{-4}$ / decade. This corresponds to a field degradation of 0.06% between 10 days and 30 years after initial magnetization. Aging at this level can be easily accomodated by occasional recentering of the gradient magnets over the lifetime of the 8 GeV line.

## REFERENCES


[1] The Fermilab Main Injector Technical Design Handbook, Fermilab, 1995.

[2] 'Status of the Main Injector and Recycler,' S.D. Holmes, this conference.

[3] Type 8 Strontium Ferrite data sheets & specifications from Hitachi, Edmore, MI.

[4] Néel, Louis, 'Théorie du Trainage Magnétique des Substances Massives dans le Domaine de Rayleigh,' *J. de Phys. et Radium*, **11**, 49-61 (1950).

[5] Street R. and Wooley, J.C.: 'A Study of Magnetic Viscosity,' *Proc. Phys. Soc.* **A62**, 562-572, (1949).

[6] Kronenberg K.J. and Bohlmann M.A.: 'Long Term Stability of Alnico and Barium Ferrite Magnets,' *J. Applied Physics* **31**, 82S-84S (1960).

# PERMANENT GRADIENT MAGNETS FOR THE 8 GeV TRANSFER LINE AT FNAL

H.D. Glass[†], K.J. Bertsche[*], B.C. Brown, G.W. Foster, W.B. Fowler, J.E. Haggard, D.J. Harding, G.P. Jackson, M.P. May, T.H. Nicol, J.F. Ostiguy, P. Schlabach, G.A. Smith, and J.T. Volk, Fermi National Accelerator Laboratory, Batavia, IL 60510

*Abstract*

The 8 GeV transfer line feeding protons into the new Fermilab Main Injector has been built using strontium ferrite permanent magnets. This article addresses the design and manufacture of the 67 combined function magnets; permanent horizontal and vertical bend dipoles [1] and quadrupoles were also built. The combined function magnets were built with a mean integrated strength at midaperture of 0.56953 T-m (central field nominally 0.15 T), and a gradient of 3.23% per cm relative to the dipole strength (nominal gradient = 0.48 T/m). Thermal compensation of these bricks was effected by use of a nickel-iron alloy. The magnets were thermally cycled from 20°C to 0°C to condition the ferrite against irreversible thermal losses; the compensation was measured with a flipcoil and verified with a rotating harmonics coil. We present details of the magnet assembly process and also summarize the magnetic measurements.

## 1 GRADIENT MAGNET DESIGN

An overview of the 8 GeV transfer is described elsewhere at this conference [1], and details regarding the general permanent magnet design strategy is discussed in [2]. In this article we focus our attention on the gradient, or combined function, magnets. The basic design of the gradient magnet is a 0.16 T gradient dipole with a vertical gap of 5.08 cm and an 8.89 cm good-field aperture in the bend direction (physical horizontal aperture is 13.97 cm). Overall dimensions are 19.1 cm high by 24.1 cm wide by 4.10 m long. The weight is 910 kg. The magnets are straight, and the sagitta of the beam inside the magnet is 1 cm.

### *1.1 Side bricks*

A significant design decision made in the 8 GeV line magnets was to include side bricks which drive flux into the pole tips from the sides. These provide a more magnetically efficient design than one without side bricks, since the field strength drops ~40% when they are removed. This compact design provides the 0.15 T average bend field needed to follow the 8 GeV line tunnel. The side bricks also provide field shaping at the edges of the aperture.

While the side brick design proved economical and more than adequate for meeting the 8 GeV line field quality requirements, a number of design and production issues have since arisen which argue against the use of side bricks in higher-quality storage ring magnets (e.g., the Recycler Ring [3]).

One difficulty observed with the side brick design was the magnet-to-magnet variation in the field shaping due to small variations in the side brick positions. Another difficulty was that some multipoles (especially the normal 6-pole) exhibited an undesirable temperature dependence. This is caused by the placement of the compensator, which is interspersed with the top and bottom bricks but not the side bricks, with the result that the field shaping from the side bricks has a temperature dependence.

## 2 MAGNETIC MEASUREMENTS

### *2.1 Thermal measurements*

Thermal measurements were made on every magnet using a flip coil to measure the change in strength between 0°C and room temperature. Figure 1 shows the distribution in relative strength change with temperature (dB/B)/dT in units of $10^{-4}$ /°C. We attempted to adjust the amount of compensator to limit the maximum variation to ±1.0 units/°C, but some magnets were allowed to go beyond this limit.

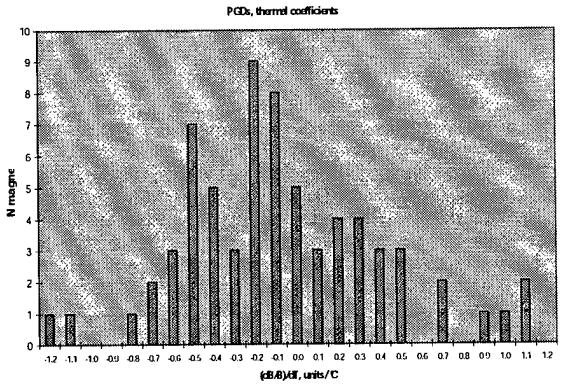



Figure 1. Histogram of thermal coefficients for the gradient magnets.

[†] Work supported by the U.S. Department of Energy under contract number DE-AC02-76CH03000.

[*] Present address: Siemens Medical Systems, Concord, CA 94520

0-7803-4376-X/98/$10.00 © 1998 IEEE

*2.2 Strength measurements*

The magnet strength was measured using two different instruments. We first used a flipcoil to measure the integrated dipole strength; this information was then used to trim the amount of ferrite needed to bring the magnet strength within 0.01% of the target value (0.56953 T-m). The magnet was then measured again, this time using a rotating Morgan coil. This coil not only gave us the strength, but also the low order harmonics up to 14-pole. Figure 2 shows the distribution in magnet strength, and the agreement between the two different probes is satisfactory. Most of the magnets fall within the desired strength tolerance.

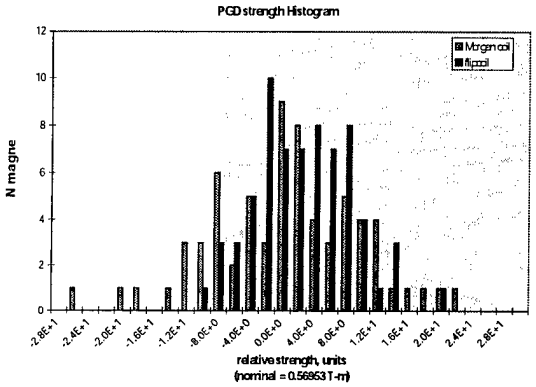



Figure 2. Strength histogram of the gradient magnets.

*2.3 Harmonics measurements*

The field quality specification for 8 GeV beamline dipoles and gradient magnets was set to 10 units (0.10%) of the total measured $B_y$ vs. x along the midplane as measured by a rotating Morgan probe placed at the center of the aperture. Since the observed field defect is dominantly a gradient error arising from non-parallelism of the pole tips, this scales roughly to $\Delta B/B = 0.2\%$ over the good field region (4.45 cm vertical x 8.89 cm horizontal). This specification represents a compromise between the minimum field quality required for adequate performance of a transfer line (where ~0.5% would be adequate) and the Recycler permanent magnet field quality [3], which must be in the range of $1\text{-}2\text{x}10^{-4}$ over a 2.54 cm aperture.

Table 1 shows the systematic and random harmonics for the ensemble of gradient magnets. Figure 3 shows the typical field shape along the midplane (reconstructed from harmonics b3 – b7); also shown are the best and worst cases among all the magnets. Even the magnet with the worst field shape is within the 8 GeV tolerance. A histogram of the normal gradient ($b_2$) is shown in Fig. 4.

| PGD harmonics | *mean* | *std deviation* |
|---|---|---|
| b2 | 8.23E-02 | 4.32E-04 |
| b3 | 2.39E-04 | 1.60E-04 |
| b4 | -3.89E-04 | 1.65E-04 |
| b5 | -1.24E-04 | 1.51E-04 |
| b6 | 3.62E-04 | 1.44E-04 |
| b7 | -5.10E-05 | 1.60E-04 |
| a2 | 6.73E-05 | 2.55E-04 |
| a3 | 3.78E-05 | 1.59E-04 |
| a4 | -3.04E-05 | 9.31E-05 |
| a5 | -1.70E-05 | 8.55E-05 |
| a6 | -5.90E-06 | 7.13E-05 |
| a7 | -2.59E-08 | 6.33E-05 |

Table 1. harmonic coefficients through 14-pole for the 68 PGD magnets.

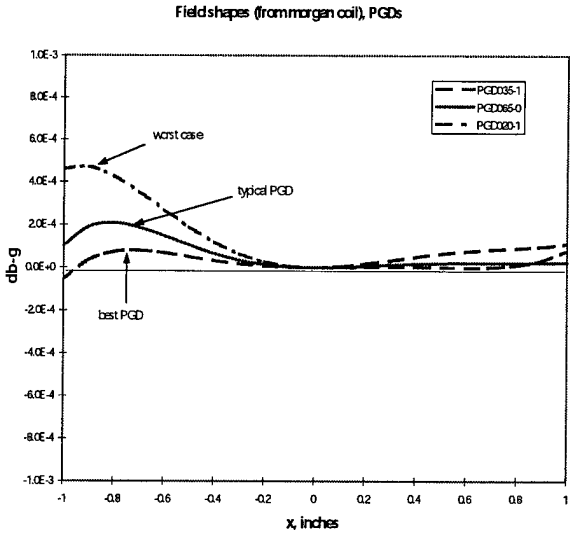



Figure 3. Field shapes of typical and extreme cases in the gradient magnets.

Our basic manufacturing strategy was to specify machining tolerances of typically 75 μm for the steel pole tips, which is sufficient to obtain roughly 0.1% field defect over the aperture. The dominant source of field error arose from assembly tolerances in the parallelism of the pole tips, producing a gradient error of roughly $1\text{x}10^{-4}$ for a mismatch of 25 μm between the two pole tip side supports.

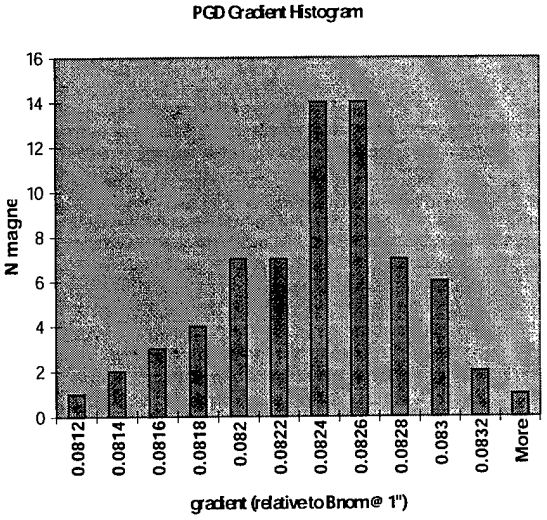



Figure 4. Histogram of normal quadrupole (gradient) for the PGD magnets.

*2.4 Longitudinal bend centers*

Some care had to be taken during magnet assembly to insure that the longitudinal bend center of the magnet was near the physical center. In the early stages of production, as experienced with the double dipoles [2], bricks were laid down on the pole tip beginning at one end, and proceeding down the length to the other end. This sometimes resulted in a longitudinal gradient (dB/dz nonzero). To avoid this phenomenon, we modified the assembly procedure for the gradients so that we first laid bricks down in the center of the pole tip, and then proceeded outward towards both ends. This resulted in a more uniform distribution of B(z). We mapped the longitudinal profile of each magnet with a Hall probe, and used these data to determine a bend center relative to the physical center. The distribution is shown in Figure 5.

The requirement was to keep the bend center within 1 cm of the physical center, and the figure shows that this was achieved for nearly all of the magnets.

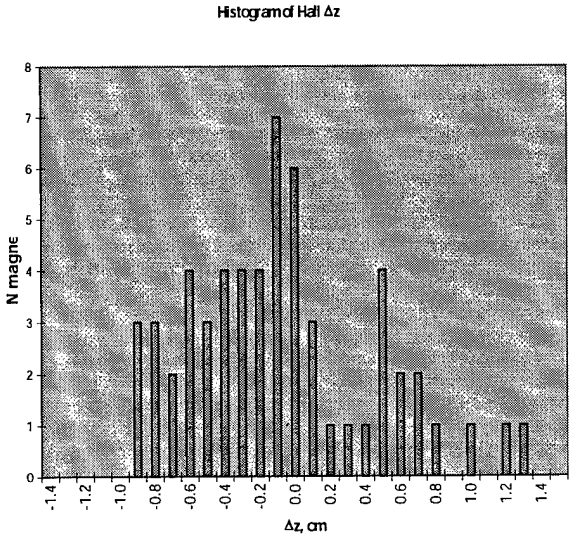



Figure 5. Distribution of longitudinal bend center for the gradient magnets.

## REFERENCES

[1] S.D. Holmes, "Status of the Main Injector and Recycler," this conference.

[2] H.D. Glass et al., "Permanent dipole magnets for the 8 GeV transfer line at FNAL," this conference.

[3] G.W. Foster, "The Fermilab permanent magnet antiproton Recycler ring," this conference.

# AUTOMATED PERMANENT MAGNET MAGNETIZATION SYSTEM FOR 8 GEV TRANSFER LINE AND RECYCLER RING PRODUCTION AT FERMILAB*

Eric Haggard, Fermi National Accelerator Lab, Batavia, Illinois 60510

*Abstract*

The Recycler antiproton storage ring and the 8 GeV beam transfer line between the Fermilab Booster and the Main Injector are constructed using permanent magnet ferrite bricks surrounding a steel pole and housed inside a steel flux return shell. The transfer line consists of 51 dipoles, 67 gradient magnets, and 8 quadrupoles. The Recycler ring consists of approximately 350 gradient magnets and 60 quadrupoles. These magnet assemblies are being produced at Fermilab currently and as a part of the tooling required to produce these assemblies we have designed, built and put into production an automated permanent magnet magnetization system. The system includes a conventional B-2 type dipole, a Programmable Logic Controller (PLC) controlled brick mover, a hall-probe measurement station and an IBM Compatible P.C. for data acquisition. The system has been used in the production of the 8 GeV beam transfer line magnet assemblies each requiring several hundred individual permanent magnets. This paper describes and illustrates the design of the automated system, the data acquisition, use of FEA analysis in the design, and the experience we have had using this production system.

## 1 INTRODUCTION

The Fermilab Permanent Magnet Magnetizer System was developed to produce saturated permanent magnet bricks to be used in the construction of permanent magnet assemblies for the 8 GeV Line and the Recycler Ring for the Main Injector Project. The new system replaces an existing manual system for the saturation and measurement of YBM-2b Permanent Magnet Bricks. There are several sizes of bricks used in the construction of the magnet assemblies, namely 4" x 6" x 1", 3" x 4" x 1" and 2" x 6" x 1". The magnetizer system is designed to shuttle an unsaturated permanent magnet brick into the aperture of a conventional dipole, energize the dipole, saturate the brick, shuttle the brick to a measurement fixture, and record the field measurement. The system also provides operator feedback to sort acceptable bricks from those which lie outside the required field strength range. The Fermilab Permanent Magnet Magnetizer System was put into operation on July, 30th 1996 and has been useful in magnetizing all the bricks used in the 8 GeV Transfer Line which operated successfully at Fermilab on February 20th, 1997.

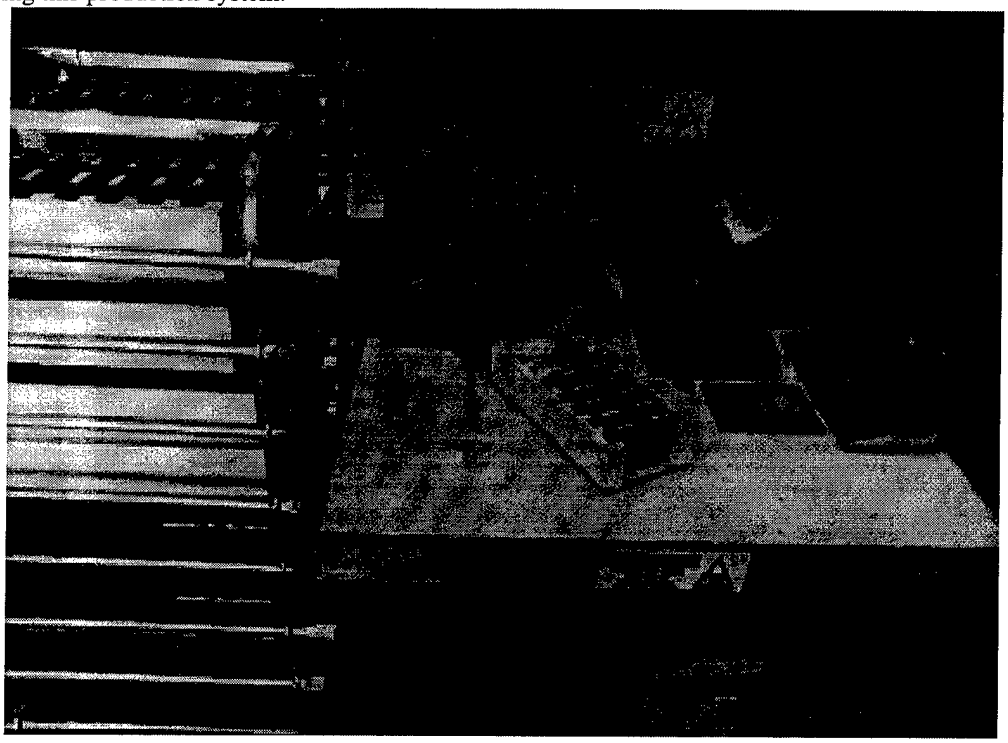


**FIGURE 1. MAGNETIZATION SYSTEM AT FERMILAB**

* Operated by Universities Research Association, Inc. under contract with the U.S. Department of Energy

0-7803-4376-X/98 /$10.00 © 1998 IEEE

## 2 THE CONTROL SYSTEM

The automatic control of the mechanism is accomplished using a GE-Fanuc Series 90-30 programmable logic controller (PLC). The system also has a Personal computer for data logging. We have used an IBM 386 clone in this case. The PLC has an ASCII BASIC module which runs a small basic language program to supply the Hall probe readings to the PLC registers. The PC runs a program written in MS-Quick Basic which communicates with the registers of the PLC to read and record the current hall probe measurements. The PC has several programs written in MS-BASIC which run the machine in automatic mode for saturation, automatic mode for measurement only and a small program to toggle the PLC run states. The small program to toggle the PLC from Stop/Outputs Disabled mode to Run/Outputs Enabled is used if the PLC shut down on an interlock violation. A conceptual drawing of the control system follows as figure 2.

## 3 THE MECHANISM

The brick shuttle mechanism includes a half horsepower DC motor which drives a timing belt to which is attached an aluminum carriage running on aluminum rails. The carriage contains the permanent magnet brick and has a sliding cover which captures the brick in its entirety. The cycle starts with the brick holder carriage at its home position where a brick is loaded into the carriage and the cover closed. After the cover is closed, the operator hits the cycle start buttons and the carriage begins to travel into the dipole aperture. The carriage moves at a high rate of speed until it hits a downslope switch which sets a lower speed and slows the carriage down to a soft stop at the end of travel micro switch. The conventional dipole is energized automatically and the brick is saturated. After a short time, the carriage is driven to the measurement fixture where a Hall probe measures the field strength and this data is sent to the PLC. The data is then logged to a PC from the PLC, the carriage returns to the home position using the same high speed-low speed method used at the dipole position where the operator then unloads the saturated brick and inserts an unsaturated brick. And the cycle begins again. The current cycle time excluding brick handling time is 13 seconds per brick.

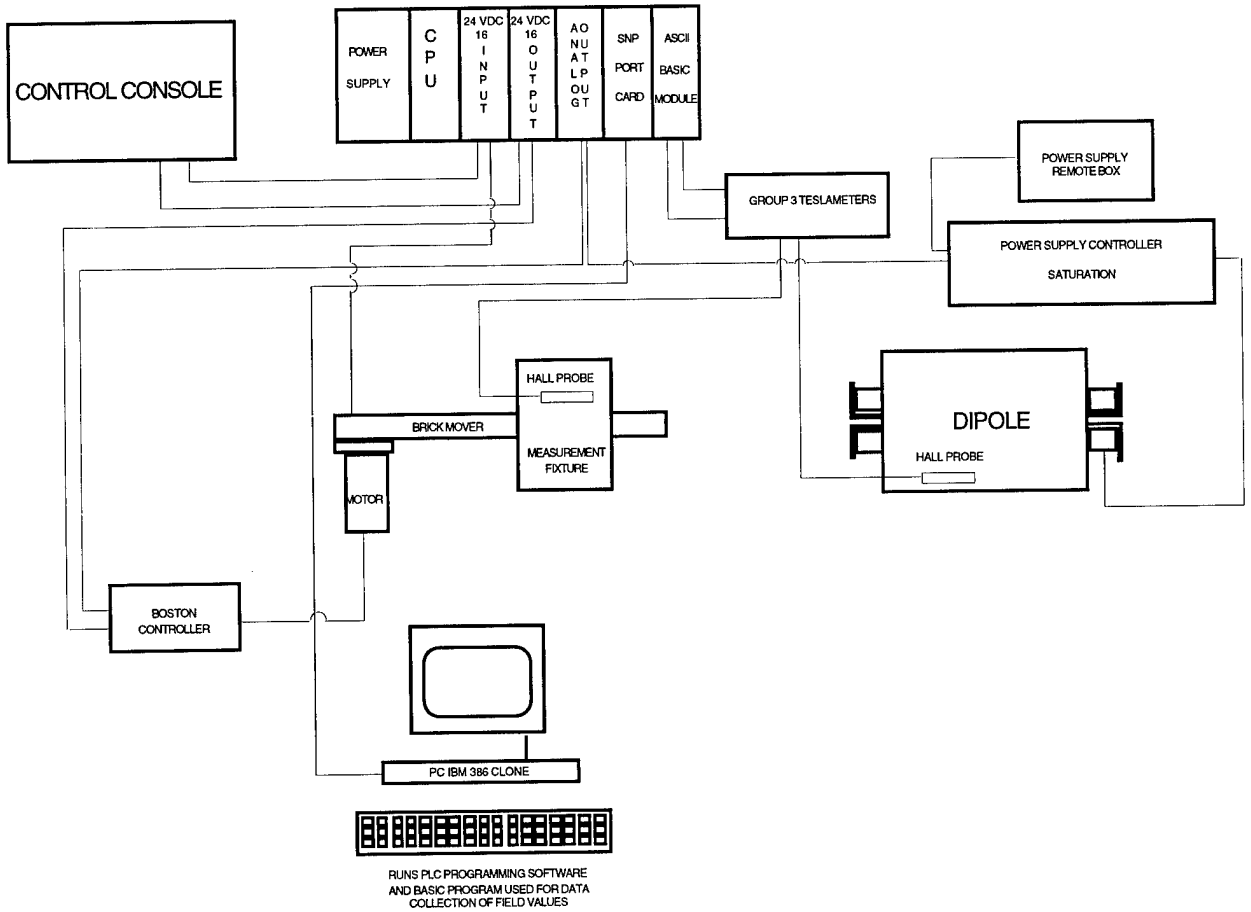



**FIGURE 2. MAGNETIZATION CONTROL SYSTEM CONCEPTUAL LAYOUT**

## 4 MAGNETIC MEASUREMENTS

Finite Element Analysis (Ansys) was employed to aid in the design of the measurement fixture. The flux return for the measurement fixture was made out of conventional Main Injector ring dipole lamination steel. The steel was plentiful at Fermilab and its magnetic properties were well understood. The original pole piece for the fixture was a laminated design which was discovered to have a positional sensitivity of 20 gauss per inch of carriage travel due to the fact that air between lamination layers has the effect of bunching the flux in the center of the fixture and no hard stops are employed to stop the brick holder carriage precisely at the measurement fixture. The measurement fixture pole piece was replaced with a solid steel pole which distributed the flux more uniformly but also had the effect of lowering the magnitude of the average magnetic flux density measurement from 920 gauss to 813 gauss. The position sensitivity went from 20 gauss per inch to 2.5 gauss per inch or less than 1% error due to positional inaccuracies. Finite element analysis was also used to verify that the magnitude of the magnetic flux density measurement was reasonable. The magnetic inductance was found by analysis to be 813 gauss and the average measured at the Fermilab production facility was 786 gauss which is within 3.5%.

## 5 FUTURE DIRECTION

This system works well and was used in the production of the saturated permanent magnet bricks for use in the 8 GeV line permanent magnet assemblies. These magnet assemblies were produced at the rate of 2 magnets per day and required about 200 bricks per magnet. Fermilab is currently designing a higher capacity production system which is based upon this design without measurement capability for the Recycler Ring bricks. The carriage in this particular version will be designed to carry 4 bricks into the dipole aperture. The new system is scheduled to be completed in July of 1997.

# MAGNETIC FIELD STRENGTH AND SHAPE MEASUREMENTS OF THE FERMILAB MAIN INJECTOR QUADRUPOLES

D.J. Harding, B.C. Brown, J. DiMarco, H.D. Glass, T.K. Kroc,
P.S. Martin, C.S. Mishra, D.G.C. Walbridge, E.G. Pewitt, Fermilab*,
P.O. Box 500, Batavia, IL 60510 USA

*Abstract*

All of the new quadrupoles for the Fermilab Main Injector ring have been built and measured. The magnets are 2.95 m and 2.54 m in length with a 41.7 mm bore. In operation, the magnets run from 1.61 T/m at 8.9 GeV/c to 15.7 T/m at 120 GeV/c and 19.6 T/m at 150 GeV/c. These points correspond to injection, Main Injector fixed target physics and antiproton production, and extraction for transfer to the Tevatron. Good field uniformity is required to ensure a stable beam over the whole acceleration cycle. A significant octupole is included to assist in resonant extraction. The performance of these quadrupoles, in both integrated strength and field uniformity, is presented. All magnets produced meet the accelerator requirements.

## 1 MAGNETIC REQUIREMENTS

The Fermilab Main Injector is a new proton and antiproton accelerator currently under construction at Fermi National Accelerator Laboratory [1]. It will replace the existing Main Ring in all functions. While many of the quadrupoles used in the Main Injector will be reused from the Main Ring, the lattice requires some new quadrupoles of the same design but different lengths to run on the same busses. Some key design parameters are shown in Tables 1 through 3. The performance requirements of the quadrupoles have been studied extensively [2] [3] [4]. The two significant areas of magnetic performance are the magnet-to-magnet variation in the integrated magnetic field ("strength") and the variation of the strength as a function of transverse position ("shape"). These are discussed here separately.

| Parameter | Value |
|---|---|
| Pole Radius | 41.68 mm |
| Number turns / pole | 4 |

Table 1: Basic Main Injector magnet parameters.

| Magnet Type | IQB | IQD | IQD |
|---|---|---|---|
| Steel length (m) | 2.134 | 2.540 | 2.946 |
| Effective length (m) | 2.118 | 2.522 | 2.930 |
| Number in Ring | 128 | 32 | 48 |

Table 2: Lengths of Fermilab Main Injector quadrupoles.

| | Injection from Booster | FMI Fixed Target and P-Bar Production | Extraction to Tevatron |
|---|---|---|---|
| Momentum | 8.9 GeV/c | 120 GeV/c | 150 GeV/c |
| Gradient | 1.20 T/m | 16.15 T/m | 20.19 T/m |
| B at pole | 0.0500 | 0.6744 T | 0.8430 T |
| Current (A) | 207 | 2830 | 3560 |

Table 3: FMI quadrupole strengths..

### *1.1 Strength*

We define the strength to be $\int_{-\infty}^{\infty}(dB_y/dx)dz$ The integral is taken at the center of the aperture. When discussing relative strengths we quote fractional differences in "units" of parts in $10^4$. The majority of our tracking studies have assumed a root mean square deviation of the strength of 24 units.

A systematic difference from nominal in the ratio of IQD strength to IQC strength of 25 units produces a negligible beta wave, and up to 50 units would be tolerable.

### *1.2 Shape*

We define the shape to be the variation in the strength as a function of position. We characterize the field by its harmonic decomposition. The normal component of a quadrupole's field can be reconstructed as

$$B_y(x) = B_1(b_1 + 1(\frac{x}{r_0})^1 + b_3(\frac{x}{r_0})^2 + b_4(\frac{x}{r_0})^3 + \ldots),$$

where $B_1$ is the quadrupole strength, $b_n$ are the normal harmonic components. We quote the components at $r_0$=25.4 mm and in "units" of parts in $10^4$. Properly centered, the dipole component $b_1$ is zero.

From the symmetry of the magnet design we expect the field to have significant quadrupole, octupole, and twelve-pole components. For our tracking studies we have assumed distributions of the forbidden components that are consistent with the measured spread in values.

Given the known octupole component in the existing Main Ring quadrupoles, we chose the octupole of the new quads to meet the beam dynamics needs. The octupole has two demands placed upon it. One need is that the dynamic aperture be large enough to meet the accelerator requirements. The beam

* Work supported by the United States Department of Energy under contract No. DE-AC02-76CH0300

0-7803-4376-X/98 /$10.00 © 1998 IEEE

should not fall out of the machine on its own. The other need is that the beam be close enough to the edge of stability so that the existing trim octupoles can bring the beam to the point of slow extraction. Based on simulations, an average of 4 to 8 units appears to satisfy both requirements. Magnet-to-magnet variations are not significant dynamically.

The tracking studies assume 12-pole components based on old measurements of a sample of Main Ring quadrupoles. The simulation uses -1.49 ±0.63 units at 8.9 GeV/c and -1.86 ±0.16 at 120 GeV/c.

## 2 MEASUREMENT SYSTEMS

All magnets were measured with a rotating Morgan-style coil, and most were also measured with a single wire stretched wire system to provide redundancy and a better absolute calibration.

The Morgan coil extends through the length of the magnet. The probe has two orthogonal dipole coils, two orthogonal quadrupole coils, and one each sextupole, octupole, decapole, 12-pole, and 20-pole coils. One quadrupole coil is used to measure the strength of the magnet. The other coils measure the harmonic components while suppressing the signal from the quadrupole field. The rotating coil measurements are performed at multiple currents on every magnet, measuring on both the up ramp and the down ramp.

The single stretched wire system moved a single wire to multiple positions in the magnetic field. The field was measured at a limited number of currents for each magnet, providing a constant cross-check of the rotating coil data.

## 3 MEASUREMENT DATA

We present data on the IQC and IQD magnets. The IQB magnets, the 84 inch Main Ring Quadrupoles, are still in use in the Main Ring. All of the quadrupoles that will be used in the Main Injector will be measured after they have been removed from the tunnel and refurbished.

### *3.1 Strength*

We have averaged the strength over all magnets of each type, excluding only the first seven IQC's. There are slightly larger strength variations among those magnets due to experimental modifications to the laminations. The mean can be compared to a strength calculated assuming infinite permeability. These differences are plotted in Figures 1 and 2. We also calculated the RMS deviation from the mean of the magnets of each type and display the results in the same figures. This spread in strengths is well within the acceptable range.

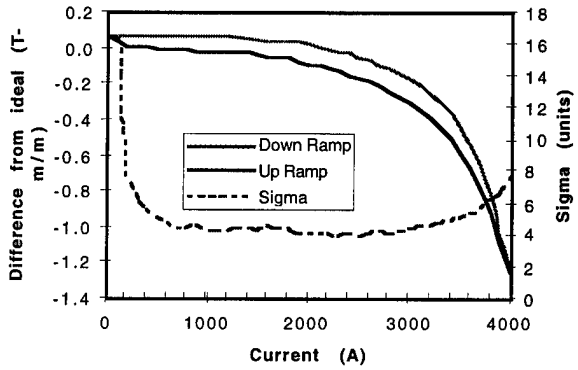



Figure 1. IQC strength.

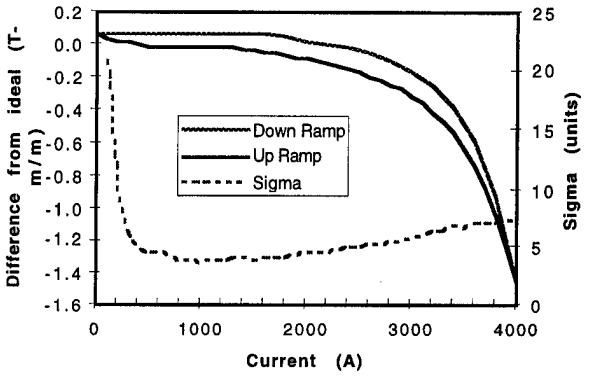



Figure 2. IQD strength.

We write the fractional difference between the design strength ratio and the measured strength ratio:

$$\frac{\left(\frac{S_{IQC}}{S_{IQD}}\right)_{measured} - \left(\frac{S_{IQC}}{S_{IQD}}\right)_{nominal}}{\left(\frac{S_{IQC}}{S_{IQD}}\right)_{nominal}} x10^4$$

This quantity is plotted in Figure 3. It is everywhere well under the specified 25 unit threshhold for paying attention to it.

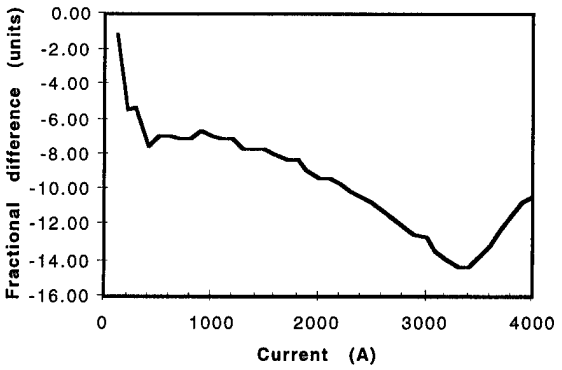



Figure 3. Fractional difference between measured IQC/IQD ratio and nominal.

*3.2 Shape*

Figure 4 shows the mean octupole component of the newly constructed quadrupoles as a function of current. The value falls comfortably in the allowed range. The sigma of the distribution is everywhere less than the value used in the tracking studies.

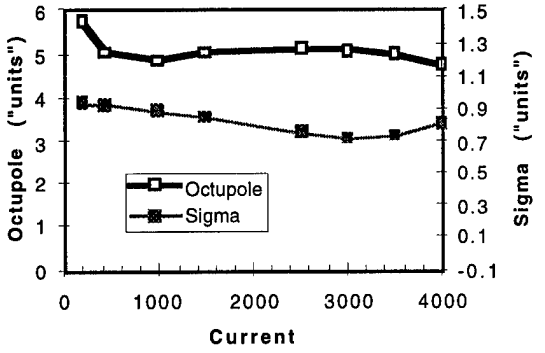



Figure 4. Octupole component of quadrupoles.

Figure 5 shows the mean 12-pole component of the newly constructed quadrupoles as a function of current. The mean value at injection is slightly higher than has been used in the tracking studies, but the spread in values is much tighter. Further studies will be required.

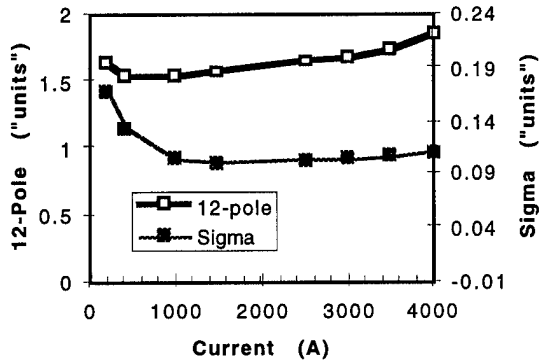



Figure 5. 12-Pole component of quadrupoles.

*3.3 Hysteresis*

In general we want to be able to run an arbitrary mix of accelerator cycles, intermingling ramps to 120 GeV/c and 150 GeV/c. At injection the magnets are at a low enough field (pole tip field 0.0500 T) that hysteretic effects can be noticeable, so we must pay attention to the history of the magnet. At the end of each ramp cycle we expect to lower the current below the injection level to a "reset level", then return to the injection level. The further below the injection excitation we make the reset level, the less memory the magnet has of the maximum excitation level on the previous ramp cycle when we return to the injection level.

To study this effect we have measured the strength of a quadrupole at the injection excitation after each of several ramp cycles to different maximum excitation and with different reset levels. This is not a perfect measurement, because the power supplies currently in use at the Fermilab Magnet Test Facility do not "invert", or generate a negative voltage to drive the current down as fast as the FMI ramp will run. None the less, we believe that in these magnets the effect of overshoot due to eddy currents in the laminations is small.

Figure 6 demonstrates that at injection we are insensitive to the energy of the previous ramp cycle even if we do not use a reset level below the injection field. Each data point was taken at 200 A, approximately the 8.9 GeV/c injection current, after running the magnet up to a maximum current $I_{max}$ then down to reset current $I_{min}$. For each reset current five cycles to the 120 GeV/c level were followed by five cycles to the 150 GeV/c level. We are sensitive to the reset level used, and must control this carefully to maintain a stable tune at injection. The effect of running the current to OA before each super-cycle is clearly seen in the first data point at each $I_{min}$.

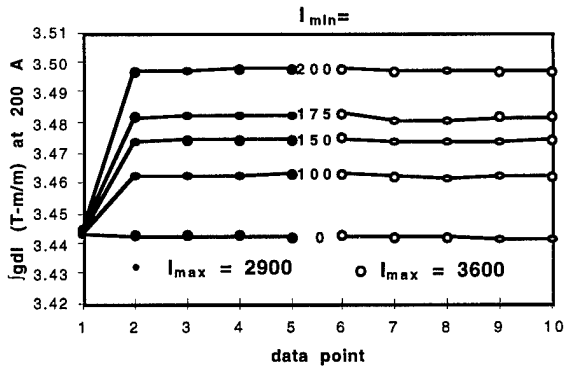



Figure 6. IQD052-0, ∫gdl at 200 A.

## 4 CONCLUSIONS

We have constructed and measured all of the new quadrupoles that we will build for the Fermilab Main Injector Ring. They meet our expectations and do not appear to offer any serious problems to the operation of the Main Injector.

## REFERENCES


[1] S.D. Holmes, et. al. "Status of the Main Injector and Recycler," *these proceedings.*

[2] C.S. Mishra P.S. Martin D.J. Harding, H.D. Glass and B.C. Brown. Fermilab Main Injector Magnet Acceptance Criteria," *Proceedings of the Particle Accelerator Conference (1995).*

[3] C.S. Mishra. "Requirement of the Fermilab Main Injector Quadrupole Strength Matching," *Proceedings of the Particle Accelerator Conference (1995).*

[4] C.S. Mishra. "Fermilab Main Injector Quadrupole Placement Scheme," *Proceedings of the Particle Accelerator Conference (1995).*

[5] J.W. Sim, et. al. "Software for a Database-Controlled Measurement System at the Fermilab Magnet Test Facility," *Proceedings of the Particle Accelerator Conference (1995).*

# DESIGN AND MAGNETIC MEASUREMENTS OF THE FERMILAB MAIN INJECTOR LAMBERTSON

D.E. Johnson, J.E. DiMarco, D.J. Harding, P.S. Martin, J.-F. Ostiguy, D.G.C. Walbridge, R. Baiod *
Fermi National Accelerator Laboratory†, P.O. Box 500, Batavia, IL 60510

*Abstract*

A new 1.1 Tesla Lambertson for Main Injector injection/extraction and Tevatron injection has been designed and the magnetic properties of the first production magnet have been measured. The Main Injector Lambertsons will be used for injection of 8.9 GeV/c antiprotons from the Antiproton Source and 150 GeV/c antiprotons recycled from the Tevatron, and the extraction of 120 GeV/c protons for antiproton production, 150 GeV/c protons for Tevatron Injection, 120 GeV/c resonant extraction, and the Main Injector abort. This magnet must accommodate Main Injector and Tevatron circulating beam in its field free region while the field region is at all excitation levels with minimal impact on the circulating beam. The design specifications and results of magnetic measurements in both the field region and field free region for the first production magnet are discussed.

## 1 MAGNET GEOMETRY AND MAGNETIC REQUIREMENTS

The Lambertson has a ±8 inch field region with a 2 inch gap. The field free region is 2.5 inches wide with a 78 degree opening. The septa thickness is 0.157 inch and has a 0.2 inch radius. The magnet is composed of 4 quarter cores: 2 inner cores (which are encased in a stainless steel vacuum skin, one with a field free region and the other without) and 2 outer cores which make up the return yoke. The inner core assembly extends approximately 4.3 inches beyond the outer core. The last 4.3 inches of the inner quarter core without the field free region is made with non magnetic material (stainless steel laminations and end plate) and has a magnetic length the same as the outer core. This produces an inner quarter core with the field free region which a magnetic length of 8.6 inches longer that the other inner quarter.The outer core length is 110.25 inches (2.8 meters) and the complete magnet has a flange to flange length of 128.375 inches. A 3 inch magnetic mirror plate is located between the end of the inner core assembly and the vacuum flange. The magnet is powered by a 24-turn single saddle coil. A nominal current of 2000 Amp. produces the required integrated field of 3.0 T-m. Figure 1 shows a cross section and longitudinal end view.

The magnetic requirements of a Lambertson septa for use in the Main Injector project have been presented elsewhere. [3] The first three requirements pertain to the bending field and effects either the extracted or injected beam.

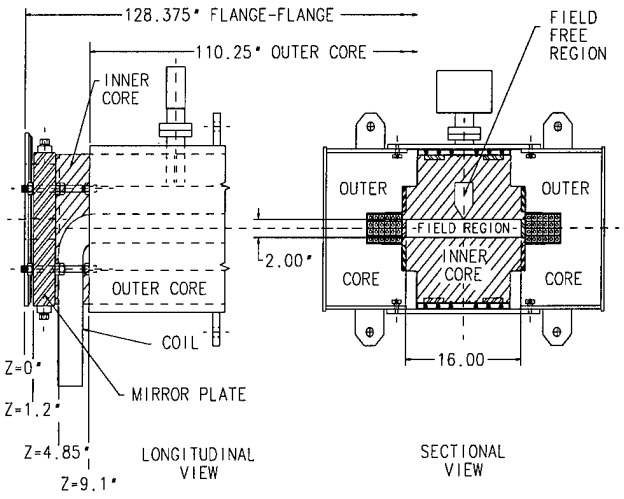



Figure 1: Geometry of the Lambertson

The last three requirements impact the behavior or the circulating beam in both the Tevatron and Main Injector. The final specifications used to build the production magnet are listed in Table 1.

TABLE 1: Magnetic Specifications

| | | |
|---|---|---|
| Nominal field | 1.072 | Tesla |
| Good field height | ±6 | inches |
| Field Uniformity | < 0.28 | percent |
| Leakage Field | < 0.0114 | T-m |
| Leakage Gradient | < .1 | Tesla-m/m |
| Leakage Sextupole | < 9 | Tesla-m/m2 |

## 2 MAGNETIC MODEL

### 2.1 *Two Dimensional Model*

Magnetic 2-D modeling, with OPERA 2-D [1] was used to determine the detailed geometry of the Lambertson (i.e. the opening angle and radius of curvature of the field free region septum, the septum thickness, the pole tip shim in the dipole region, the height of the dipole region, and the placement of the stainless steel skin and tie bars) to minimize the leakage of the field from the steel into the field free region and maintain a high uniformity in the field region.

### 2.2 *Three Dimensional Model*

Early in the design of the end geometry of the Lambertson a 3D finite element code, TOSCA [1], was used to guide the end extension/mirror plate design. [5] A three foot prototype Lambertsons was constructed to test the magnetic design. The model was able to successfully predict the results of magnetic measurements from various end configu-

* Present address: AT&T Corp., Middletown, NJ.

† Operated by the Universities Research Association under contract with the U. S. Department of Energy

0-7803-4376-X/98/$10.00 © 1998 IEEE

rations of the prototype and allow a better understanding of the the saturation effects in the end plate.

Subsequently, the 3D finite element model was updated to reflect the exact geometry of the production Lambertson including a realistic description of the permeability of the steel components. This model was used to calculate the dipole field (and its integral) through the end of the magnet for comparison with measured data.

## 3 MAGNET MEASUREMENTS

The Lambertson was oriented on the test stand at the Magnet Test Facility in orientation shown in Figure 1 such that a positive current produced a positive $B_y$. The coordinate system was defined such that x,y=0 is in the center of the bend region and z=0 is at the face of the vacuum flange (positive z is inside the magnet). Various measurement techniques were used to measure the fields in both the bending and field free region to confirm the design and compare with the 2-D and 3-D models.

## 4 FIELD REGION MEASUREMENTS

The field in the bending region was characterized using several methods to measure the integrated field, the field uniformity, and longitudinal extent of the dipole field over a 0 to 2500 A range. The dipole field in the bend region showed a 10 % falloff over the last 2 inches of the outer core and was down by a factor of 100 at the outside face of the mirror plate.

### *4.1 Strength and Hysteresis*

The excitation curve for the Lambertson was measured to 2500 A after a set of hysteresis ramps to the same maximum current. The field is quite linear up to 1500 A which corresponds to an integrated field of 2.4 T-m. The design integrated field of 3.0 T-m is achieved at 2000 A and deviates from the linear by roughly 6%. The maximum integrated field measured was 3.5 T-m at 2500 A. The integrated remnant field after the 2500 A hysteresis ramp is 42 Gauss-meter.

### *4.2 Field Uniformity*

The field uniformity along the x direction in the bending region was measured over $\pm 7$ inches at y = 0 and 0.5 inches using a 2-Wire Stretched Wire (2WSW) system which has a wire loop, separated by precision quartz rods at each end, stretched within the magnet aperture. Since the width of the wire loop is constant, the change in flux as the loop moves across the magnet aperture measures the variation in field strength as a function of position (field uniformity). The field at y = 0 inches (not shown) is uniform to within 0.05% over the full $\pm 7$ inches for all currents up to 2500A. Figure 2 shows the measured uniformity over the region from x=0 to +8 inches for y=0.5 inches, since it is symmetric in x. Here the field is uniform to within 0.1% out to $\pm 6$ inches for all currents up to 2500 A, well within the specification. These measurements include both body and end contribution to the integral. The predictions from the 2-D model include *only* the body field at 2000 A.

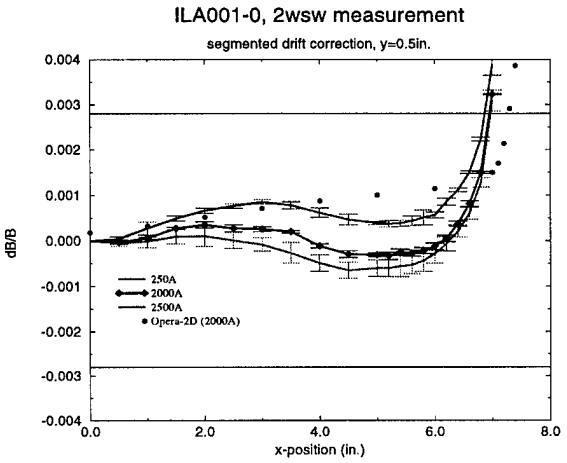



Figure 2: Comparison of the measured and 2D model field uniformity in the bend region at y=0.5 inches.

## 5 FIELD FREE REGION

The fields in the field free region impact the circulating beam and therefore must be controlled. Contributions from both the body and the ends *must* be taken into account. By minimizing the integrated dipole, other harmonic terms will be minimized as well.

### *5.1 End Field Shape*

The magnitude of the dipole field on axis (x=0) at approximately .35" from the septum was measured with a hall probe as a function of longitudinal position z. The probe consists of a Hall element and readout device which was operated under computer control. The readout device was programmed to read field values in Tesla using a full range of 3 Tesla. These probes have a precision of $\pm 0.006\%$ of full range, and a resolution of $\pm 0.5$ gauss on the 3 Tesla range. Positioning the probe was accomplished through the use of x and y stages. Probe motion was automated in the z direction.

The dipole field was measured using the hall probe at 1/2 inch intervals from a value of z= -8 inches outside the end of the vacuum flange to z=+14 inches, about 5 inches inside the body of the magnet. Measurements were taken at various excitations bracketing the expected operating range. Figure 3 displays the measured end field shape at 500 A, compares the measured end field shape with the prediction of the 3D model at 2000 A, and shows the integration of the 2000 A data from -8 inches to +9.1 inches. The effect of the mirror plate can be seen in the region between 4.35 and 4.85 inches, the gap between the end of the field free inner core and the steel mirror plate. Instead of jumping to the opposite pole, the leakage flux is channeled into the mirror plate around the field free hole and returned to the opposite pole. In this 1/2 inch region, the field has a transverse component (as seen by the large negative and positive fields

at the two surfaces, but the integrated effect cancels due to symmetry. Provided the plate remains out of saturation, the plate surface remains at a constant magnetic potential, and there should be no field outside the plate.

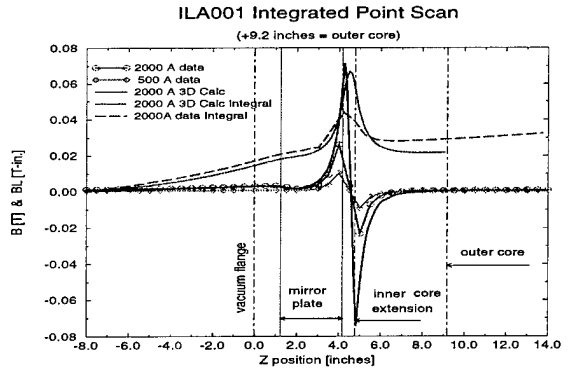



Figure 3: Comparison between the measured end dipole field and the predictions of the 3-D magnetic model as a function of z in the field free region at x=0,y=1.5. The z dimensions may be referenced to the orientation in figure 1.

### 5.2 *Integrated Dipole*

The integrated dipole in the field free region of the first production magnet was measured using several techniques. Figure 4 shows a comparison between the measured dipole field integral as a function of current for the various measurements and the predictions of the end field from the 3-D model. The first set of data shows the results of integrating the point scan data (in figure 3) through the magnet. The contribution to the total integral (2*end+body) from the body and the end are displayed. The agreement between the measured end contribution (boxes) and the predictions from the 3D model is quite good with values between 5 and 7 G-m at 2000A. Both show a linear dependence. Uncompensated, the contribution to the dipole field integral from the magnet end surpassed 300 G-m.[5] Note that the major contribution to the total integral at the higher currents comes from the body field leakage and not the end field.

The next two sets of data were measured using a single stretched wire at the approximate the same location at point scan data. The Single Stretched Wire (SSW) system consists of moving a single wire stretched through the magnet aperture using high precision x-y stages while measuring the integrated voltage induced in the wire (flux). The return wire which completes the 'loop' is held fixed external to the magnet. Since the magnetic vector potential depends only on the wire position within the magnet, the change in flux through the loop only depends on the motion of the wire. The distance the stages move are measured to 1 micron accuracy by linear encoders, and so the absolute accuracy of the measured integrated field strength is a few times 10-4. This system was used to map the integrated field due to both the body and ends as a function of x and y inside the notch. The difference between the two data sets, taken on two different days, reflect a systematic uncertainty in the measured value. The third set of data was obtained by integrating the dipole field using a rotating coil over each half of the magnet and summing the result. This data shows the effect of the hysteresis on the leakage between the up and down ramp. The up ramp data agrees well with the point scan data (taken at increasing currents).

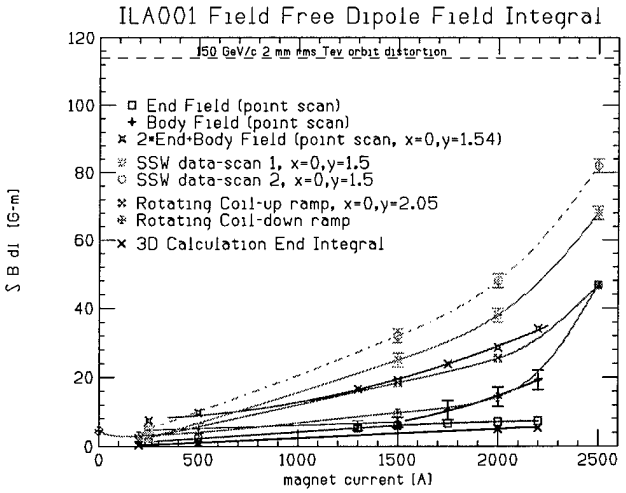



Figure 4: Comparisons between various measurements of the integrated dipole (at x=0,y=1.5 inches) and the prediction of the 3-D model.

### 5.3 *Harmonic Analysis*

The harmonic content in the field free region was measured on axis, x=0, at three different values of y using a rotating coil. These measurements were done using a tangential coil probe with coil radii of 0.01219 meters and a length of 2.286 meters. This probe uses a dipole Morgan coil to measure the dipole integrated strength. Higher order harmonic components were obtained by monitoring the signal from a dipole bucked tangential coil. [4] The induced voltage in the coil was integrated for all coil configurations by a precision digital integrator. Data were captured over two complete probe rotations at 256 readings/rotation. The results to the rotating coil measurements showed the integrated harmonics for normal and skew quad and sextupole were well within the required specifications.

## 6 REFERENCES


[1] Vector Fields, Oxford, England.

[2] The Fermilab Main Injector Technical Design Handbook, August 1994.

[3] D.E. Johnson, et.al. "Design of the Fermilab Main Injector Lambertson", proceedings 1995 PAC.

[4] Henry D. Glass, "measurements of Harmonic Amplitudes and Phases Using Rotating Coils", MTF Note MTF-94-0004, 1994.

[5] J.-F. Ostiguy and D.E. Johnson, "3D End Effects in Iron Septum Magnets", proceedings 1995 PAC.

# VARIATIONS IN THE STEEL PROPERTIES AND THE EXCITATION CHARACTERISTICS OF FERMILAB MAIN INJECTOR DIPOLES

P.S. Martin, D.J. Harding, E.G. Pewitt, A.D. Russell
Fermi National Accelerator Laboratory*
Batavia, Illinois 60510

*Abstract*

The Fermilab Main Injector project is building 344 dipoles, for which over 7000 tons of steel are required. Budgetary and logistic constraints prevented purchasing all of the steel required prior to production. Run to run variations in the magnetic properties of the steel have produced variations in the excitation curves of the dipoles. The variations in the B(H) curves for the steel as a function of run number, and the excitation characterisitics of the dipoles, are discussed.

## 1 INTRODUCTION

The Main Injector accelerator [1] will be constructed using new conventional dipole magnets [2-3]. An extensive R&D program was carried out [4] to assure the quality of the magnets and to determine the desired end geometry to minimize the effective length variation with excitation and the sextupole content of the ends. Twelve full-length, pre-production dipoles (six six-meter and six four-meter dipoles) were then built and measured. The FMI project was then ready to begin fabrication of the production magnets, and a contract was awarded for approximately fourteen million pounds of steel. This contract consisted of a (i) base quantity of 3,339,000 pounds to be delivered at a rate of 556,500 pounds per month over six months during calendar year 1993; (ii) an option for 7,813,000 pounds for delivery over twelve months spanning most of 1994: and (iii) an option for 3,562,000 pounds for delivery over eight months in 1995. The delivery schedule in the procurement contract was necessitated both by a lack of funding and by a lack of storage space for the steel.

The steel specification included two aspects regarding the magnetic properties: the coercive force was specified to be less than 1.0 oersted and to fall within a range relative to the running average of all previous batches, and the permeability at 100 Oe was specified to be between 176 and 181. The steel specifications were written with the goal of producing magnets with strength variations over the production which would be a random distribution with a root mean square deviation of less than 0.1%.

*Work supported by the U.S. Department of Energy under contract number DE-AC02-76CH03000.

All of the steel that was received was within our specification. There were, however, some changes in the characteristics of the B(H) curves of the steel during the production runs which will be described below.

## 2 STEEL PRODUCTION

The steel, a standard low-silicon electrical steel, was produced by LTV Steel Company at their Cleveland Works. The steel was produced in a total of thirteen "runs" over the course of three years. Each run involves the consecutive processing of a number of coils through their Continuous Anneal Line (CAL). The number of coils processed at a time ranged from 8 to 86. These coils in turn came from a number of "heats", with a given heat having a particular chemistry and producing seven to ten coils. Coils from a given heat were generally, but not always, processed during a single run. LTV demonstrated very good control over the chemistry throughout the production. Between the melting and casting and the CAL runs, the steel is hot- and cold-rolled to the final thickness. Subsequent to the CAL, the master coils are coated, slit into five strips the proper width for stamping with minimum waste, and then shipped to the lamination stamper (under separate contract to Fermilab).

The CAL consists of seven stages: direct-fired furnace, radiant tube heater, radiant tube soak, gas jet cooling, over-aging furnace, final jet cooling, and final water cool. An eighth stage, the roll quench, was not used for processing our steel. Prior to processing any steel for the FMI project, the CAL processed transition coils until the desired temperatures were attained. The temperatures at the various points in the CAL were also controlled very well. As the coils were exiting the CAL, samples of steel were taken from the head and tail of each coil and longitudinal and transverse specimens were prepared according to ASTM A343. These were measured by LTV Steel at their Technical Center in Independence, OH, and then forwarded to Fermilab where the samples were remeasured. The Fermilab measurement results were forwarded to the accelerator physics group which was responsible for the assignment of the "recipes". The recipe assignment [6] used both the magnetic information and measurements which were made of the gap as the laminations were being stamped. The recipes were formulated for half-cores, with the intention to be able to mix any pair of half-cores together during the final assembly. Only in a few cases were two specific half-

0-7803-4376-X/98/$10.00 © 1998 IEEE

cores assigned for assembly within a given dipole, and this was driven by the desire to investigate some property of the steel rather than from some limitation in the ability to formulate recipes.

Given the production schedule outlined above, and the project schedule requirements which required us to commence production as early as possible, the first 13 magnets assembled at Fermilab used steel exclusively from Run 1. After that, steel from different runs was generally mixed together within half-cores, although again, there were instances where dipoles were intentionally fabricated containing steel from only one run.

## 3 DIPOLE STRENGTH COMPARISONS

The first twenty-five to thirty magnets demonstrated a very narrow spread in their integrated strengths at all excitations. The rms of the distribution was about 0.03%. These magnets were all composed of steel from runs 1-3, although very little from run 2. (Run 2 steel was primarily used for the quadrupoles for the FMI project.) As steel from run 4 began being used in magnets, the strength of the dipoles began increasing, and the difference in strength was approximately proportional to the fraction of run 4 steel in the magnet. The strength variation was current-dependent, indicating a difference in magnetic properties of the steel, as opposed to a geometric effect which should be current independent. The change in strength peaked at about 13.8 kG, with a maximum change of about 0.5% being observed; this is shown in Figure 1.

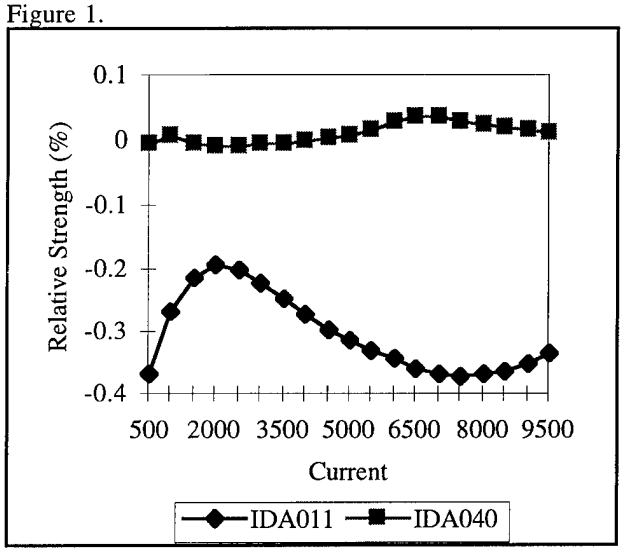



Figure 1. Strength variation vs. excitation for two dipoles, one early and one later in production.

In this figure, the relative strengths of two dipoles are plotted as a function of current, where the strength is relative to the later "production average". As production continued, it became evident that the later steel runs were the normal ones, and steel from the first three runs produced magnets which were anomalously weak. Figure 2 shows the strength at 13.8 kG of the early magnets produced using LTV Steel; data on all magnets produced to date can be found elsewhere [6]. Up through the first fifty or so magnets, the production of the magnet half-cores and the final assembly of the magnets (and their subsequent magnetic measurements) proceeded together as a well-matched chain of parallel processes. After the first fifty magnets, with the half-core stacking proceeding more rapidly, the correlation between production date and the run number of the steel used in the half-cores became less distinct as half-cores were used randomly rather than in order of their production (which would have required additional handling.) Records on what steel was used in each magnet are maintained.

These magnet-strength variations led to numerous, lengthy discussions between Fermilab and LTV Steel to better understand the production process and its influence on the magnetic properties of the steel. A consultant was hired to assist Fermilab and he was present at many of the discussions and witnessed several of the subsequent runs through the CAL; he provided reports [7] of his observations both to Fermilab and to LTV Steel. Much of the information on temperature control in the CAL discussed in section 2 above is derived from our consultant's reports. One result of these discussions was that all subsequent steel production had a minimum as well as a maximum speed specified during the CAL processing. Although an explanation for the difference in steel properties exists, namely differences in residual strain in the steel, there is no clear understanding of where in the

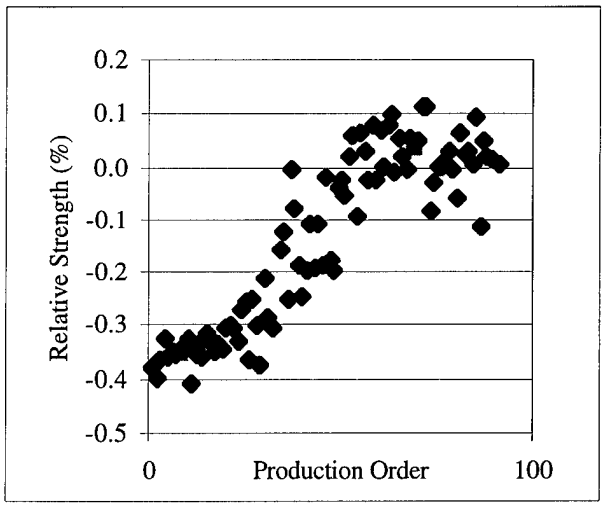



Figure 2. Relative strength at 13.8 kG for the dipoles for the early dipoles, in order of production. The two dipoles shown in Figure 1 are denoted with different symbols.

processing of the steel these differences arise. Much of the discussion between Fermilab and LTV Steel focussed on our desire to have the remaining steel as uniform as possible. To a very large extent, that desire was realized.

During the period these discussions were taking place, much effort at Fermilab was also being devoted to understanding the phenomenon through magnetic field calculations. The measurements of the steel samples from each coil are maintained in a database so the information is readily available for analysis. The variations between all the coils within a run exhibit a spread on the order of ±200 Gauss at H > 20 Oe, which is larger than the differences from run to run, for runs 4 through 13. Plots of the average B(H) curve for each of the thirteen runs are shown in Figure 3; an analytic function was fit to the data for run 6, and subtracted from each of the other runs to make the differences between runs more visible. The difference between the first three runs and the remaining runs is significant, particularly in the region H < 40 Oe.

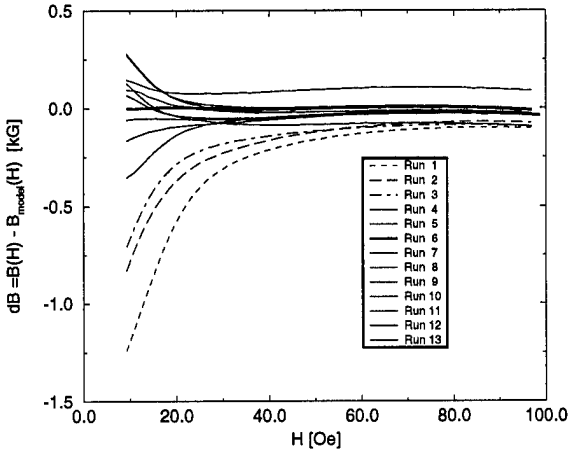



Figure 3. B(H) curves averages for each of the thirteen runs of steel, relative to a fit to run 6.

Using the averages (over each run) of the measured B(H) curves for run 1 and run 4 steel as input to the magnetic field calculation program OPERA2D predicts differences in dipole strength that are very similar to what we observe. It is perhaps of interest to note that the differences in the B(H) curves that contribute most to the strength differences are in the vicinity of 15 Oe, around the "knee" of the B(H) curve, and that in order to achieve uniform magnet strengths one would have to specify the B(H) curve in this range as well. Specifying only the high and low ends is insufficient.

A number of other aspects of the production process were also studied. A measurable correlation is observed between magnet strength and the fraction of steel which came from the edges of the master coil. Although the magnitude of the effect was small, all subsequent recipes were formulated with the goal of maintaining 20-60% edge-slit laminations. Packing factor, i.e. the density of the half-core relative to the maximum obtainable, was measured for about 10% of the magnets. The correlation between strength and packing factor is small: a 1% change in packing factor is expected to produce roughly a 0.1% change in magnetic strength. The packing factor of the half-cores did increase somewhat as the vendor fabricating them gained experience, but the change was less than 0.5%.

The Main Injector lattice has a phase-advance per cell of nearly ninety degrees, which allows using anomalously strong (or weak) dipoles in pairs, producing only a local closed orbit distortion. By assigning magnets, the strength differences described above are expected to have only minimal impact upon the Main Injector closed orbit, as discussed more fully in reference 6.

It should be stressed that all the steel which LTV Steel produced was within our specification, and exhibited excellent magnetic and mechanical properties. The Fermilab Main Injector project management would like to acknowledge the dedication of the LTV Steel Company, and of R. Blotzer in particular, to producing a high-quality steel for use in our magnets, and the cooperative spirit of the LTV Steel personnel in our extensive discussions with them. Our consultant, E. W. Collings of Ohio State University, provided much valuable guidance during our discussions. The authors would also like to acknowledge the many contributors who were essential to this effort, including G. Kobliska and W. Pritchard in the Fermilab Technical Division, J.-F. Ostiguy and B.C. Brown in the Beams Division, and many others too numerous to acknowledge individually.

## REFERENCES

1. S.D. Holmes, et al. "Status of the Main Injector and Recycler", these proceedings.

2. B.C. Brown, et al., "The Design and Manufacture of the Fermilab Main Injector Dipole Magnet", EPAC 92, Proceedings of the 1992 European Particle Accelerator Conference (1992).

3. D.J. Harding, et al., "Magnetic Field Measurements of the Initial Fermilab Main Injector Production Dipoles", Proceedings of the 1995, IEEE Particle Accelerator Conference.

4. D. J. Harding, et al., "Design Considerations and Prototype Performance of the Fermilab Main Injector Dipole", Conference Record of the 1991 IEEE Particle Accelerator Conference (1991).

5. A.D. Russell, et al., "Selecting Magnet Laminations Recipes Using the Method of Simulated Annealing", these proceedings.

6. P.S. Martin and C.S. Mishra, "Excitation Characteristics of FMI Dipoles and Magnet Assignment to Reduce Closed Orbit Errors", these proceedings.

7. E.W. Collings, "Influence of Process Parameters on the Magnetic Properties of LTV-Processed Steel" (May, 1995, unpublished), "Site Inspection of the LTV Steel Continuous Anneal Line", (August, 1995, unpublished) and subsequent reports.

# MODIFICATIONS TO THE EXCITATION CHARACTERISTICS OF FERMILAB MAIN INJECTOR DIPOLES BY MACHINING

P.S. Martin, R. Baiod†, D.J. Harding, J.F. Ostiguy, A.D. Russell
Fermi National Accelerator Laboratory*
Batavia, Illinois 60510

*Abstract*

Twelve dipole magnets were built under the R&D phase of the Fermilab Main Injector project using steel from a different vendor than the production vendor. These dipoles exhibited an excitation-dependent difference in strength relative to the production magnets, with a maximum difference of about 1% observed at high field. This difference was too large to allow them to be used in the project. From calculations based on the differences in the B(H) curves of the two types of steel, the high-field strength of the twelve R&D dipoles was reduced by machining the back-legs of the cores. The machining technique will be described, and excitation curves before and after machining will be compared.

## 1 INTRODUCTION

The Main Injector accelerator [1] will be constructed using 344 new conventional dipole magnets [2-3]. An extensive R&D program was carried out [4] to assure the quality of the magnets and to determine the desired end geometry to minimize the effective length variation with excitation and the sextupole content of the ends. Twelve full-length, pre-production dipoles (six six-meter and six four-meter dipoles) were built using steel supplied by Armco. When the FMI project was ready to begin fabrication of the production magnets, LTV Steel submitted the low bid and was awarded the production contract for approximately fourteen million pounds. The steel specification is discussed elsewhere [5].

## 2 STRENGTH COMPARISONS

The twelve pre-production dipoles were quite uniform in strength. The six, 6-m dipoles had a full width of about 0.14% at 1.38 T, while the spread in strengths of the 4-m dipoles was even less. There was, however, a difference at all fields of about 0.08% between the average of the 6-m dipoles and one and one-half times the average of the 4-m dipoles. This effect was corrected in the production magnets by reducing the stacking length of the 4-m dipoles by about 3 mm. However, compared to the production dipoles, the pre-production ones were stronger by as much as 0.9%, in a current-dependent manner. The averages of the strengths of the 6-m and the 4-m dipoles, relative to the strength of the production magnets, are shown in Figure 1; the upper two curves in that figure show the dipole strengths before the modifications which are discussed below. The impact on the closed orbit distortion in the Main Injector ring was determined to be too large to allow using these magnets.

Since the strength deviation is a function of current, the cause is a difference in the magnetic properties of the steel as opposed to a geometrical difference. The permeability of the Armco steel was somewhat higher than the LTV steel at all values of H. Based on this difference, it was plausable to try to reduce the strength of the pre-production dipoles by removing steel.

Although several locations on the cores were candidates, the easiest location to access while still maintaining symmetry was the backleg at the parting plane. According to Ampere's law, the field in the gap is given by:

$$B_{gap} = \frac{\mu_o}{gap}\left[nI - \int \frac{B_{steel}}{\mu_{steel}} dL\right]$$

where the integral is over the steel along a flux line. We can manipulate the value of B in the gap by changing B in a section of steel with length $L$:

$$\Delta B_{gap} \approx -\frac{\mu_o}{gap} L \; \Delta\left(\frac{B_{steel}}{\mu_{steel}}\right)$$

Modifying the cross-section of the backleg such that

$$B_{steel} \times (backleg \;\; width) \approx B_{gap} \times (poletip \;\; width/2)$$

( flux conservation) we obtain a variation of B in the gap that depends upon the length of the section of backleg which is reduced in width. Also, one sees that at low excitation, where $\mu$ is large the change in B is small, but that as the excitation increases the effect increases.

The above equations suggest the starting point. It was determined through OPERA2D calculations that removing a rectangular region 2.69 cm wide by 5.08 cm high on each backleg (see Figure 2) should reduce the field at 1.38 T by the desired amount. The width of the flux-carrying region in the steel in the backleg, taking into account the keyway on the parting plane, was reduced from 13.0 cm to 10.3 cm. Removing steel from a rectangular region was done for simplicity of machining. While the height of the cut determines the absolute change in strength and mostly shifts the strength curve vertically, the depth of the cut controls its general shape, i.e. the level of current at which saturation effects become important.

† Present address AT&T Corp., Middletown, NJ

*Work supported by the U.S. Department of Energy under contract number DE-AC02-76CH03000.

0-7803-4376-X/98/$10.00 © 1998 IEEE

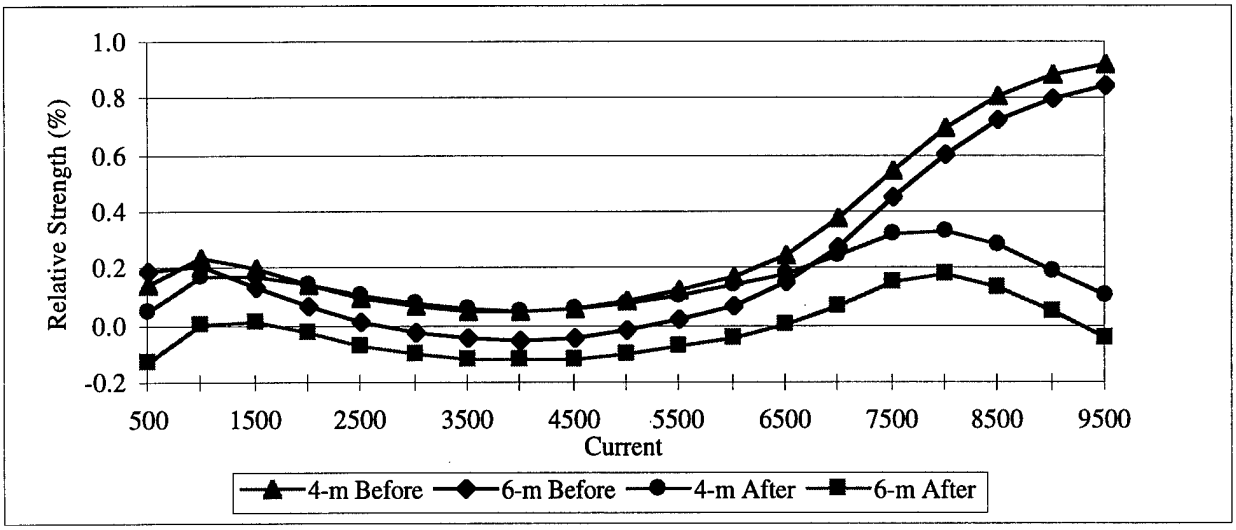



Figure 1. Dipoles strengths, relative to production magnets, for the pre-production magnets before and after machining.

The method chosen for removing the steel in the backleg was to remove twenty-six of the thirty tie plates which join the half-cores together (sixteen of twenty for the 4-m dipoles), leaving one tie plate in each of the four corners. After machining, the magnet was reclamped in the assembly press and stainless steel tie plates were welded to fasten the half-core together. It was verified during the modification of the first dipole that if the tie plates are replaced with steel tie plates after machining, the reduction in field in the gap is much smaller than expected; i.e. the presence of a parallel flux path drastically diminishes the reduction in field. However, simply replacing the tie plates on a dipole which has not yet been machined has almost no effect on the field. Leaving the corner tie plates in place allowed shipping the magnet with the coils still intact. The machining was done by outside firms at a total cost of less than 5% of the value of the magnet, including Fermilab labor.

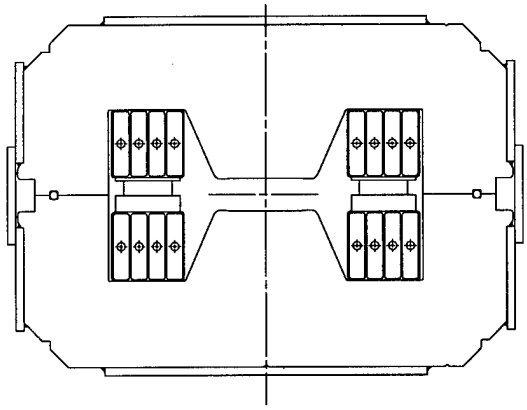


Figure 2. Cross-section of machined dipole. For scale, the lamination is 78.1 cm x 26.7 cm.

The procedure was first tested on one of the two prototype dipoles which were totally unsuitable for use in the ring: the endpacks were bolted on rather than being an integral part of the cores, and had the wrong profiles; the coils were not of the final configuration, and their impregnation was inferior. They were, however, fabricated from the same steel as the twelve pre-production dipoles. When this test proved to be successful, the same procedure was done to one of the pre-production dipoles. In both cases, the machining was done as a series of straight cuts which approximated the 15 mm sagitta of the dipole in 3 mm steps. For the remaining eleven pre-production dipoles, a different vendor was found who had larger capacity, and whose machines could follow the sagitta precisely. In both cases, the machining was done over the length of the cores except for the last 24 cm on each end where the tie plates were still in place.

Figure 1 also shows the strength deviation as a function of excitation for the machined dipoles, again relative to the production dipoles. The dipoles were reduced in strength very close to the desired amount. The residual strength variation is not a problem: by placing them in pairs the local closed orbit distortion is about 2 mm, which is less than the expected errors due to misalignment, and is within the range of the individually-powered correction dipole system to correct.

## REFERENCES

1. S.D. Holmes, et al. "Status of the Main Injector and Recycler", these proceedings.

2. B.C. Brown, et al., "The Design and Manufacture of the Fermilab Main Injector Dipole Magnet", EPAC 92, Proceedings of the 1992 European Particle Accelerator Conference (1992).

3. D.J. Harding, et al., "Magnetic Field Measurements of the Initial Fermilab Main Injector Production Dipoles", Proceedings of the 1995, IEEE Particle Accelerator Conference.

4. D.J. Harding, et al., "Design Considerations and Prototype Performance of the Fermilab Main Injector Dipole", Conference Record of the 1991 IEEE Particle Accelerator Conference (1991).

5. P.S. Martin, et al., "Variations in the Steel Properties and the Excitation Characteristics of FMI Dipoles", these proceedings.

# THE DESIGN AND CONSTRUCTION OF THE PERMANENT MAGNET LAMBERTSON FOR THE RECYCLER RING AT FERMILAB

M. P. May, G. W. Foster, G. P. Jackson, and J. T. Volk
Fermi National Accelerator Laboratory, Batavia, Illinois 60510

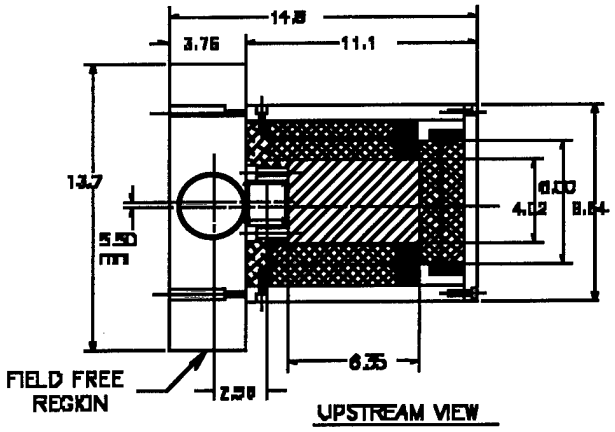
*Abstract*

This paper will show and discuss the simple design of a permanent magnet Lambertson used to extract and inject 8 GeV. beam from the Fermilab Main Injector Ring to the Recycler Ring, and from the Recycler Ring to the Main Injector. Pictures will show how four different magnets used to form the injection and extraction double dog legs are made from one universal design. Detailed assembly drawings will illustrate the construction techniques using solid pieces of steel instead of laminations. The field strength in both the bending region and the field free region will be discussed along with temperature compensation of the strontium ferrite magnetic bricks.

## 1 INTRODUCTION

The idea of using permanent magnet Lambertsons for injection and extraction from the Main Injector ring to the Recycler ring was an extension of the idea to use permanent magnets wherever we have a fixed energy of 8 GeV. The Recycler storage ring will be installed in the Main Injector ring at a nominal height of 84 inches from the floor. The Main Injector ring is at 27 inches from the floor.

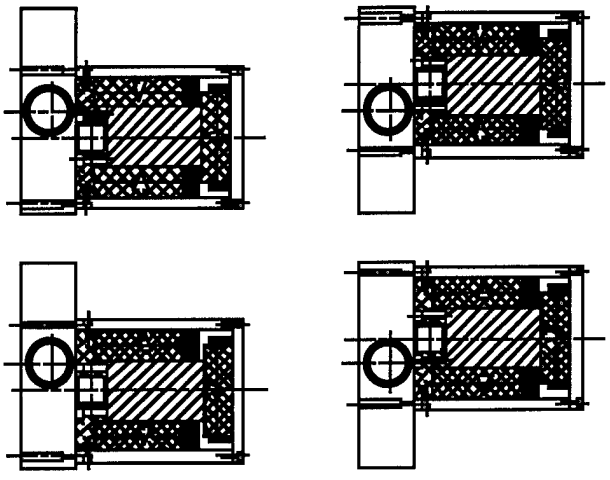
The Recycler ring was the first large scale machine built with permanent magnets. We built a couple of successful prototypes for the Recycler ring and concluded that it would be a good idea to use as many permanent magnets as seemed reasonable in our 8 GeV transfer line which runs from the Booster ring to the Main Injector ring. The permanent magnets that were constructed for the 8 GeV transfer line and the Recycler ring have strengths which range from 1.5 to 2.0 Kg-m. The more permanent magnets we built, the wiser we became in the methods of building these types of magnets, and from this the permanent magnet Lambertson evolved.




## 2 THE PERMANENT MAGNET LAMBERTSON

The permanent magnet Lambertson is unique in that it uses solid bar stock and plates for its construction. The field free region is constructed using a gun boring technique. In laminated magnet construction, the field free region is located at a fixed point in relation to the bending region, and the bending region has to be designed with a wide enough aperture to bend the beam in the good field region. Having the field free region made in a separate piece of steel allows the bending region to be positioned bending upward or downward in relation to the field free region. Since we are able to angle the bending region in the direction of the bend, the width of the bending region is greatly reduced.

Having this mechanical capability of bending up or down, the permanent magnet bricks can be arranged such that the field direction of all the bricks is pointing in the direction of the center poll piece or away from the center pole piece. Thus, with one mechanical design, four different Lambertson configurations can be constructed. The specifications of the permanent magnet Lambertson are as follows: The pole tip length is 160 inches. The base plate length is 168 inches. The bending angle is 22mr, and the field strength is 1,607kg-m. The field free region has a 3 inch OD X .049 wall
steel vacuum tube, and the bending region has a 2 X 2 X .065 wall stainless steel vacuum tube. (See the illustrations of the four types of magnets.)

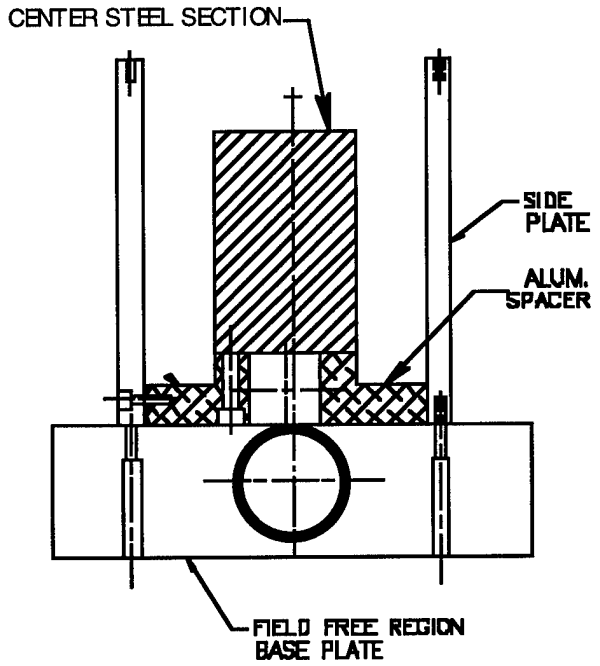


0-7803-4376-X/98/$10.00 © 1998 IEEE

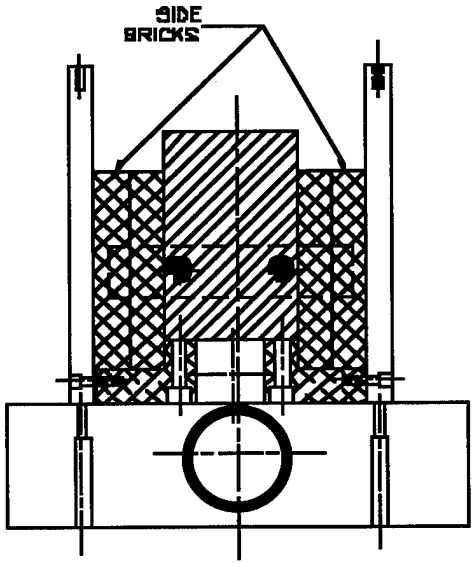
## 3 LAMBERTSON ASSEMBLY SEQUENCE

The sequence for assembling a permanent magnet Lambertson goes in the following manner:

1. The 1X4X6 strontium ferrite bricks are fully magnetized.
2. The type of Lambertson to be constructed is selected: Extracting protons or anti-protons. Bending up or bending down.
3. The center pole piece and the side plates are assembled to the base plate which has the field free region in it, in the appropriate bending direction.

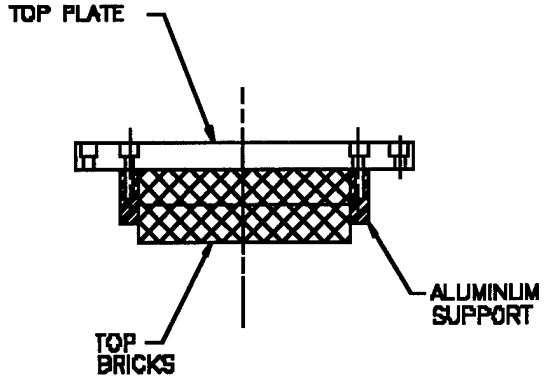



4. The side bricks are slid into the magnet between the side plates and the center pole piece, working equally on both sides and starting at one end of the magnet.



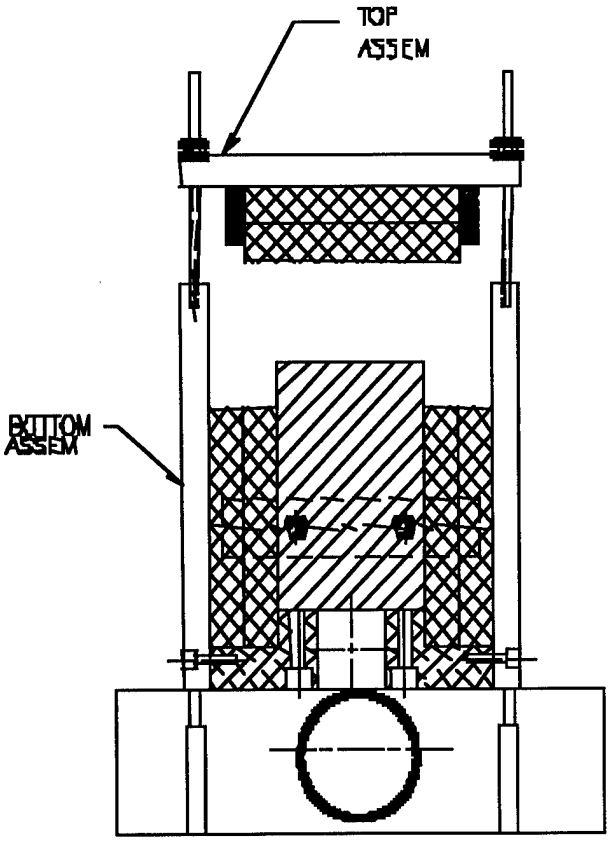

ADD SIDE BRICKS

5. The top plate is a sub-assembly which is constructed on a separate table. The magnetized bricks are glued to each other and then glued to the top plate. They are located on the steel top plate by aluminum bars which run down the length of the top plate.

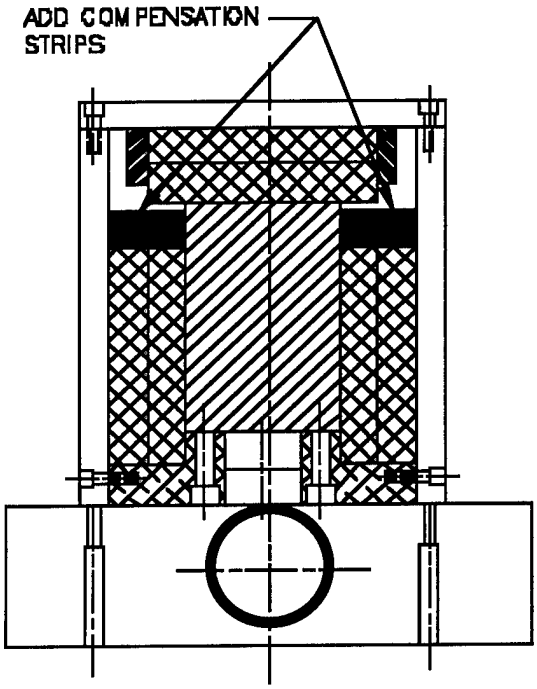



TOP PLATE W/ BRICKS

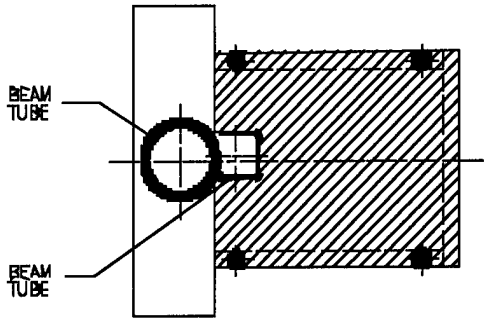
6. The top plate is rotated 180 degrees, and lowered on to the magnet sub-assembly. Guide rods are used to keep the top plate centered as it is forced into its final position. There is a very strong repulsion force until the top plate and the side plates get close enough to make magnetic contact. At this point the magnetic circuit is completed and the force becomes one of attraction.



7. The magnetic compensation strips are now installed, and the end plates are added.




8. The magnet is now magnetically measured for field strength using a flip coil. After measurements, the magnet is place in a freezer where it's temperature is lowered to 32 degrees F. The magnet is again measured at this temperature to insure that the correct amount of temperature compensating material has been added to the magnet. Once the magnet has warmed up to room temperature, another set of measurements are again taken to finalize the magnet strength and temperature compensation of the magnet.
9. The magnet is now ready for a final painting and the vacuum beam pipes are installed.




UPSTREAM VIEW
W/ COVER

## 4 ACKNOWLEDGMENTS

Special credit is due to Tom Nicol, Tom Schmitz, Glenn Smith, and Dan Snee for their help and suggestions in the design and construction of the first prototype magnet.

# DESIGN AND FABRICATION OF AN ACHROMATIC BEND FOR MEDIUM ENERGY ELECTRON COOLING AT FERMILAB

M.W. McGee, P.G. Hurh and K.J. Bertsche*
Fermi National Accelerator Laboratory, Batavia, Illinois 60510†

*Abstract*

The use of an achromatic bend for a medium energy electron cooling beamline in the new Recycler Ring at Fermilab is required to ensure a stable beam position. This first order 180° achromat consists of two 90° dipoles with a 61 cm bend radius and a central dispersion-suppressing quadrupole flanked symmetrically by a weak solenoid and an air-core cos(2θ) quadrupole. The mechanical design and technique of fabrication for each bend component is discussed. Each of the air cooled mechanical designs are simple yet precise in terms of construction technique. The results of magnetic field measurements are also presented.

## 1 INTRODUCTION

Medium energy electron cooling for the Recycler Ring requires a highly parallel electron beam with less than 20 μrad divergence. The beam transport system must be carefully designed and constructed to preserve these parameters. Achromatic bends have been adopted, and these are designed so that components and beam profiles are symmetric about the midpoint.

A simple first-order achromatic bend is achieved by splitting the bend equally in two bend magnets and placing a quadrupole lens between them[1]. The quadrupole cancels dispersion by imaging the center of the first bend magnet onto the center of the second. This places the two bend magnets 180° apart in horizontal betatron phase and causes particles of different energies to emerge at the same point and with the same angle, to first order.

Achromatic bends not only stabilize the trajectory against energy spreads or energy fluctuations in the beam, they also stabilize the trajectory against power supply fluctuations (assuming magnets separated by 180° are operated on common supplies). For a relativistic beam, achromatic transport is also isochronous. This is essential for electron cooling if a recirculating electrostatic accelerator is used. Otherwise, energy fluctuations would affect the timing and modulate the instantaneous beam current, tending to destabilize the system.

For beam symmetry about the midpoint of the system, there should be a vertical waist at the center of the central quadrupole. Most of the vertical focusing to accomplish this comes from the edges of the dipole magnets. Additional small adjustments of vertical and horizontal focusing are provided at each end of the achromat. Because of the small lens strength required, weak solenoid lenses and cos(2θ) quadrupoles are used. Figure 1 displays the layout for the achromat.

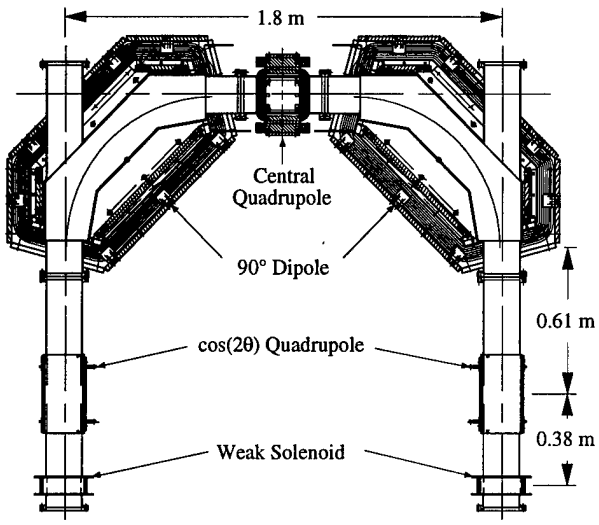



Figure 1. Top view of achromat.

## 2 MECHANICAL DESIGN

### *2.1 90° Dipoles*

The 90° dipoles are designed to satisfy several magnetic and geometric criteria. For a bend radius of 61 cm and a 5 MeV electron beam, a 300 Gauss field is required. In addition, in order to counter the strong horizontal focusing associated with a 90° dipole, the use of edge angles on the pole ends is desired. For a total beam separation of 1.8 m between the entry and exit beam lines, a 15° edge angle provides nearly enough focusing to focus the beam both vertically and horizontally at the center of the dispersion-suppressing central quadrupole. The body field of each dipole is desired to be as uniform as practically possible (less than ±0.5% variation) and the beam trajectory field integral of both dipoles are desired to match each other within ±0.1% to ensure symmetry of the bend when dipoles are run in series on the same power supply.

To accommodate electron cooling in the Recycler Ring, the vacuum chambers in the dipoles must allow for a 15.2 cm diameter aperture. This sets the dipoles' pole tip gap at 16.5 cm (allowing for vacuum chamber wall thickness). In addition the vacuum chambers must provide an entrance/exit path for the cooled ion beam. This requires a large opening in the flux return steel of the dipoles.

Figure 2 shows an end view of a dipole magnet. The 90° dipoles are designed with a simple, bolted together

*Currently with Siemens Medical Systems, Concord, California 94520.

†Work supported by the US Department of Energy under contract number DE-AC02-76CHO3000.

0-7803-4376-X/98 /$10.00 © 1998 IEEE

construction method using solid steel (1010) plates rather than laminations. The pole pieces are 5.1 cm thick and flux return pieces are 1.9 cm thick. All pieces are ground flat to 50 μm where they mate together and on the pole faces. The pole plates are spaced apart with precisely machined brass blocks featuring dowel pins to align the pole pieces to each other within 100 μm. The ends of the magnet feature field clamps to control the field fall-off and removable steel pieces which may be re-machined to eliminate some of the second order aberration terms. Small field shim strips are also added to the edges of the pole pieces to ensure flat field across the aperture.

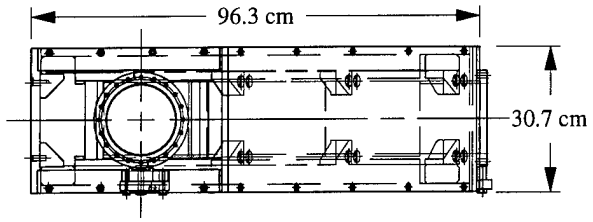



Figure 2. End view of 90° dipole magnet.

Coils are constructed of 119 turns of #6 magnet wire layered with epoxy resin tape. They were cured at 149° C for several hours and then wrapped with glass fiber tape and painted with room temperature curing epoxy. The coils fit tightly around the pole pieces and are secured in place with several brass brackets.

The completed dipole pole faces were mechanically measured using a coordinate axes measurement machine and found to be parallel to each other within 180 μm in the worst case. This is equivalent to 0.1% of the magnet aperture.

The field variation across the aperture of the dipoles was measured using a conventional hall probe. Figure 3 shows the variation at the centers of the magnets to be less than 0.14% ±0.12% of the full field (303 Gauss at 17.36 A). Figure 4 shows a typical field fall-off for a magnet end along the beam trajectory. Using the measured field integrals along the beam trajectory, the effective lengths of the magnets are found to differ by 0.38%. This difference can be reduced in practice by using a shunt to regulate the current in one of the dipoles.

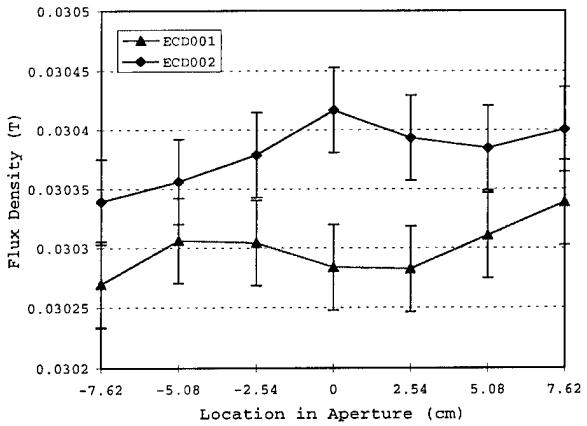



Figure 3. Field versus transverse position at dipole center.

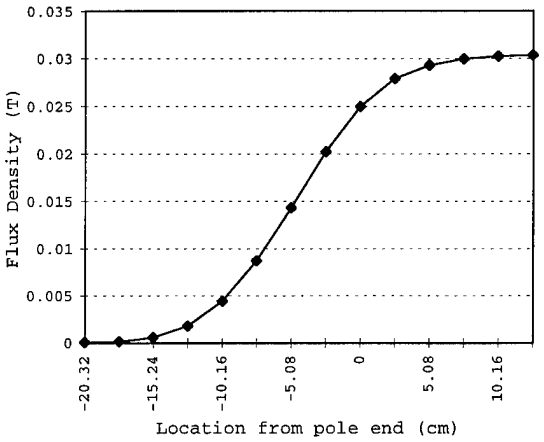



Figure 4. Typical field fall-off for 90° dipole magnet.

### 2.2 *Central Quadrupole*

Due to space constraints, the central quadrupole is very short, with a ratio of bore diameter to iron of 1.22. A pole tip field strength of 400 Gauss is required, which corresponds to a gradient of 0.469 T/m. The steel structure of the quadrupole consists of 4 yoke plates and pole pieces made of (1018) and (1008) steel, respectively. The pole tips have a circular cross-section, with a diameter 1.15 times the aperture diameter to eliminate the 12-pole component of the body field[2]. Figure 5 shows a combined cross-section and end view of the central quadrupole.

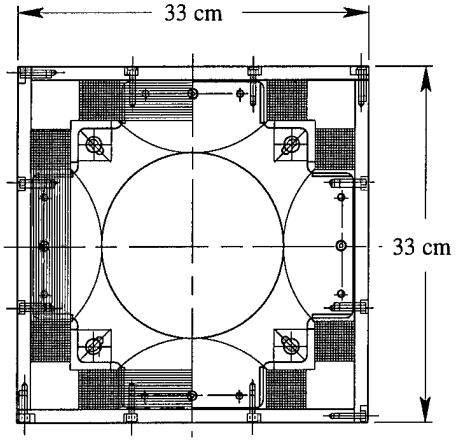



Figure. 5 End view of central quadrupole.

To eliminate the 12-pole component of the end fields, each pole was corrected with a 45° chamfer as described by Hassenzahl[3]. The integrated multipole fields were measured with a Morgan coil before trimming, after trimming one end, and finally after the other end was trimmed. The second measurement confirmed the correctness of the chamfer depth. The chamfer chord length divided by bore diameter was 0.097.

Stainless steel alignment plates located on each end ensured the repeatability of quadrupole assembly. The placement of each pole piece was indexed from one

reference dowel pin location with respect to the bore center. The dual alignment plate feature of the mechanical design allowed for an iterative process of pole trimming described above. An alignment mandrel was placed in the center to ensure relative pole positioning during initial assembly and assist in pole end trimming.

Each pole piece was ground flat on five surfaces and each pole radius was cut using an electrodischarge machining (EDM) process with a 250 μm diameter wire. The yoke and alignment plates were also ground to flatness within 25 μm.

Each coil consists of 225 turns of #12 solid square conductor. Between each layer an epoxy resin filled tape provides added insulation. The coils were cured over a duration of three hours in a 177° C oven. The design gradient was obtained with 4.5 A.

The mechanical design could be improved by increasing the thickness of each alignment plate to maintain dimensional stability. The results of the magnetic measurements of the integrated fields at 25 mm provided in Table 1 show the virtual elimination of the 12-pole component $B_6$. The sextuple $A_3$ is higher than anticipated but adequate for present needs; the source is presumably effects of an asymmetric support stand which uses some ferromagnetic steel.

Table 1. Results of quadrupole magnetic measurement.

| | |
|---|---|
| $N = \int B_2 dl[T]$ | 6.545e-2 |
| $\int A_3 dl / N[1/m]$ | -3.920e-4 |
| $\int B_6 dl / N[1/m^4]$ | -5.282e-5 |

### *2.3 cos(2θ) Quadrupole*

Weak quadrupoles in the non-dispersive region outside the bend are required to provide some focus adjustment both vertically and horizontally. The effective pole tip field for these quads is so weak (20 Gauss) that remnant fields in the iron of traditionally designed quadrupoles could be problematic. Thus the outer quadrupoles are constructed without iron pole tips using wire conductors alone lying on a circular cross-section with a cos(2θ) density distribution.

Figure 6 shows an end view of the weak quadrupole design. Wire conductors (#12 magnet wire) are pressed into grooves in the outer surface of a precision machined nylon tube. The wires are arranged into 4 coils of 6 turns each on a diameter of 16.5 cm. The act of pressing the wire into the grooves actually straightens the relatively thin conductor to within ±30 μm. The assembled coils are inserted into a steel shielding tube (30.5 cm long by 0.5 cm wall thickness), and the coil ends are wrapped back over the edges of the steel to shield the aperture from the coil end effects. Alignment fiducials are attached to the outside of the steel shielding tube for use in aligning the quads to the beam line. For a magnet of this design, an excitation current of 12 A should develop a gradient of 0.024 T/m.

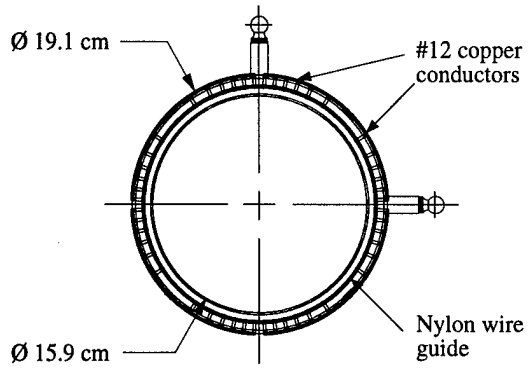



Figure 6. End view of cos(2θ) weak quadrupole.

Two weak quadrupoles of this design have been constructed and are currently undergoing magnetic measurements. It should be noted that because of the very weak nature of the desired gradient, stray fields are very problematic.

### *2.4 Weak Solenoid*

The weak solenoid's bore diameter is 17.2 cm and 7.6 cm in length, enclosed by 6 mm thick permeable iron. The solenoid coil is made of #14 square conductor with 300 turns. This design will provide a focal length of 100 m when excited with 5A.

## 3 CONCLUSIONS

The magnetic measurement results to date indicate the design success of those components tested. Also, the sensitivity of the magnetic tests to the surrounding environment demonstrates that great care in shielding the beam line and all components will be required. This bend is designed for medium energy electron cooling at Fermilab and will be tested using a proton analog beam during September of 1997.

## 4 ACKNOWLEDGMENTS

Thanks to Jim MacLachlan for his help. Technical support for the device was given by Mike Frett, Fred Saffrahn, Jim Wilson and Chih-Wen Yang.

## REFERENCES

[1] John J. Livingood, "The Optics of Dipole Magnets," Academic Press, New York, 1969.
[2] A. P. Banford, "The Transport of Charged Particle Beams," London:Spon, 1966.
[3] W. V. Hassenzahl, "Proceedings of 4th International Conference of Magnet Technology," BNL, 1972.

# HYBRID PERMANENT QUADRUPOLES FOR THE 8 GEV TRANSFER LINE AT FERMILAB

S.M. Pruss, B.C. Brown, G.W. Foster, H.D. Glass, D.J. Harding, G.P. Jackson, M.P. May, J.-F. Ostiguy, J.T. Volk (Fermilab)

*Abstract*

Hybrid Permanent Magnet Quadrupoles for specialized portions of the 8 GeV transfer line from the Fermilab Booster to the new Main Injector have been built, tested and installed. These magnets use a 0.635 m long iron shell and provide an integrated gradient of 1.48 T-m/m with an iron pole tip radius of 0.0416 m. and pole length of 0.508 m. Bricks of 0.0254 m thick strontium ferrite supply the flux to the back of the pole to produce the desired 2.91 T/m gradient. For temperature compensation, Ni-Fe alloy strips are interspersed between ferrite bricks to subtract flux in a temperature dependent fashion. Adjustments of the permeance of each pole using iron between the pole and the flux return shell permits the matching of pole potentials. Magnetic potentials of the poles are measured with a Rogowski coil and adjusted to the desired value to achieve the prescribed strength and field uniformity. After these adjustments, the magnets are measured using a rotating coil to determine the integral gradient and the harmonics. These measurements are used to calibrate the production Rogowski coil measurements. Similar quadrupoles are included in the design of the Fermilab Recycler.

## 1 MAGNET DESIGN

These magnets serve both as necessary components of the 8 Gev transfer line and as production prototypes for the quadrupoles needed for the Fermilab Recycler. All the of Fermilab permanent magnets are of the "hybrid" type in which the field is driven by permanent magnet bricks and the field shape is determined mainly by iron pole pieces [1]. The advantage of this design is low cost due to the use of the same type of permanent magnet material (Type 8 Strontium Ferrite) as many automotive and other commercial applications. The magnets made in this way are also very stable over long time periods and are not affected by radiation. The disadvantage is the brick to brick strength variation which must be tuned out of each magnet based on measurements of assembled magnets. The intrinsic temperature coefficient of the Ferrite material (-0.18% / °C) is canceled by interspersing a "compensator alloy" between the ferrite bricks. In this application an amount of compensator about 14% of the brick in volume is required.

## 2 MAGNET ASSEMBLY

Assembly of these magnets from purchased parts is straightforward and requires two technicians for only two hours. The four precision pole pieces are assembled to two precision stainless steel end spacers and four aluminum spacer bars. The ferrite bricks and compensator strips are inserted along one side with one channel length having its field pointing into a pole and the other with its field pointing out of the adjecent pole. A steel flux return side is layed over the bricks and the assembly rolled 90°. This procedure is repeated for the remaining three sides, taking care to maintain the proper brick polarity. The four sides are bolted together but are not attached to the pole assembly. The flux return end pieces are installed and bolted to the sides, but again not to the pole assembly. The magnetic forces hold the pole assembly strongly to the flux return shell and prevent it from moving longitudinally. Nevertheless, we plan to have retainer spacers between the flux return end pieces and the pole assembly in the Recycler quadrupoles to prevent movement if the magnet is mishandled. A total of ten magnets were built, nine used in the beamline and one prototype/spare.

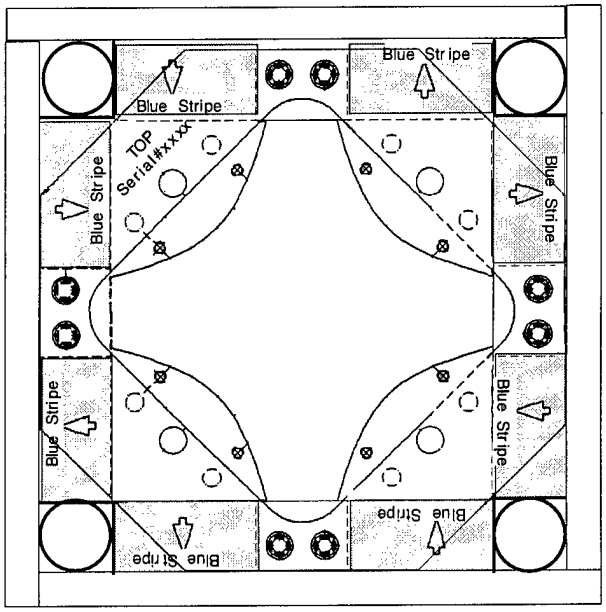



Figure 1 Magnet Cross Section, ferrite bricks are dotted.

## 3 ROGOWSKI MEASUREMENTS AND TRIMMING

After each magnet is assembled, the magnetic potential is measured at both ends of all four poles with a Rogowski coil [2,3]. The magnet is then put in a freezer overnight and cooled to 0° C. The magnet is removed from the freezer, wrapped in a thermal blanket in such a

0-7803-4376-X/98 /$10.00 © 1998 IEEE

way that the ends are accessable, and the magnet temperature and the magnetic potential is quickly remeasured. After the magnet has completely returned to room temperature, the temperature and magnetic potential are remeasured. The freezing typically causes a very small increase in strength (~0.05%) in these magnets. While other types of hybrid permanent magnets have had seen variability of the temperature compensator material, because all the material for these magnets was from one lot, no variation was seen and all the magnets were stable over the temperature range.

In order to qualify the Rogowski measurement technique, a prototype magnet was measured 22 times over a one month period. The strength of the magnet, averaged over the eight points measured, had an RMS variation of 0.018% even though the RMS variation of the eight individual points was 0.18%. If this were a statistical error problem, one would expect the error of the average of eight measurements to be a factor of square root of 8 (= 2.8) smaller than the error of the individual measurements. The greater variation of the individual points suggests some slow variation with time in the distribution of flux lines within the magnet leaving the overall strength relatively more stable. However, this variation is small enought to allow use of this quick and simple measurement technique for trimming the individual pole variations. This was believed to be necessary to reduce the field errors which give higher order multipole components, especially sextupole and skew sextupole. The magnets were built with enought ferrite to give ~2.7% more integrated gradient than we calculated would be required to allow for brick variation. In fact, the brick variation was quite small and the actual magnet RMS variation before trimming was 0.17%. The trimming was done by loading steel washers onto stainless steel threaded rods and inserting these rods into the stainless steel tubes in the four corners of the magnet. Varying the number of washers changed the amount of flux shunted out the back corner of the pole into the flux return. One washer in one corner reduced the total magnet strength by about 0.007%, a quite reasonable least change. Of course the pole that the washer was behind was reduced more than four times that while adjacent poles were strengthened slightly. After a sufficient distribution of washers had been added to the magnets to produce the desired Rogowski readings, the magnet was shipped to the Fermilab Magnet Test Facility where a full length rotating harmonic coil was used to measure the integrated gradient and the higher order harmonics[4]. Only after this process had been performed on several prototype magnets did we determine the appropriate Rogowski readings to aim for. The average of the six magnets built to that aiming point were 0.1% stronger than desired as measured by the harmonic coil. They had an RMS variation of 0.06% in strength. The average sextupole component (normalized to the quad at 0.0254m) was 2e-5 for the normal component and 3.8e-4 for the skew with an RMS of 6e-4 for both normal and skew. Because the poles are cut off squarely at the ends with no chamfer, the magnets have an average 12-pole of -7.9e-4, again normalized to the quadrupole at 0.0254m. The RMS of this 12-pole is 2.7e-5. This can be fixed for the Recycler Ring magnets either by a small chamfer or by adding two small screws with a few washers to each pole.

## REFERENCES


[1] 'Recycler and 8 GeV Line Permanent Magnets Reference Design & Performance Requirements', by G.W.Foster. FNAL Main Injector Note #150.

[2] 'A Modified Rogowski Coil for Measurements of Hybrid Permanent Magnets', by Kirk Bertsche. FERMILAB-Conf-95/190.

[3] 'Rogowski Coil Measurements of PQP003 and PQP004', by B.C.Brown, S.M.Pruss, FNAL Main Injector Note #193.

[4] 'Software for a Database Controlled Measurement System at the Fermilab Magnet Test Facility', by J.W.Sim, R.Baiod, B.C.Brown, E.Desavouret, H.D.Glass, P.J.Hall, D.J.Harding, C.S.Mishra, J.M.Nogiec, J.E.Pachnik, A.D.Russell, K.Trombley-Freytag, D.G.C.Walbridge. Proceedings of the 1995 IEEE Particle Accelerator Conference.

# SELECTING MAGNET LAMINATIONS RECIPES USING THE METHOD OF SIMULATED ANNEALING

A. D. Russell, R. Baiod*, B. C. Brown, D. J. Harding, P. S. Martin
Fermi National Accelerator Laboratory †, Batavia, IL 60510-0500

*Abstract*

The Fermilab Main Injector project is building 344 dipoles using more than 7000 tons of steel. There were significant run-to-run variations in the magnetic properties of the steel. Differences in stress relief in the steel after stamping resulted in variations of gap height. To minimize magnet-to-magnet strength and field shape variations the laminations were shuffled based on the available magnetic and mechanical data and assigned to magnets using a computer program based on the method of simulated annealing. The lamination sets selected by the program have produced magnets which easily satisfy the design requirements. This paper discusses observed gap variations, the program structure and the strength uniformity results for the magnets produced.

## 1 INTRODUCTION

The Main Injector [1] is a high performance 150 GeV synchrotron which is being built at Fermilab to provide high quality, high intensity beams. Design studies [2] from which requirements were established, assumed a magnet-to-magnet uniformity of the bend strength of $10^{-3}$. Efforts to improve on that minimum goal have been directed toward minimizing commissioning and operating efforts by reducing the use of correction magnets.

The bend strength of a dipole may be characterized [3] by

$$BL_{eff} = \int B_y ds = \frac{\mu_0 L_{eff}}{g}(N_g I - \mathcal{L}\langle\mathcal{H}\rangle) \quad (1)$$

where $I$ is the current (per turn) in the coil, $N_g$ is the number of turns linked by a flux line which crosses the gap in the good field aperture, $g$ is the gap height, $\mathcal{L}$ is the length of the flux path in the core, $L_{eff}$ is the effective length of the magnet, and $\langle H\rangle$ is the average of $\vec{H}$ along the flux line in iron. The parameters which can be controlled during manufacture are the (effective) length, the gap, and $\langle H\rangle$.

The steel received from the manufacturer, LTV Steel, was of high quality and met all contract specifications. Nonetheless, there were run to run variations [4] in the properties of the sheet steel which resulted in variations in the gaps of the stamped laminations and in the magnetic properties at high fields.

To produce the half cores, laminations from different production heats and runs were mixed taking into account their magnetic properties, their average gap height and their transverse taper, Figure 1. Control of $L_{eff}$ was obtained by stacking laminations to a fixed length with a minimum pressure which was sufficient to flatten the laminations. The half cores produced had sufficiently uniform magnetic and mechanical properties that matching of half cores was not required.

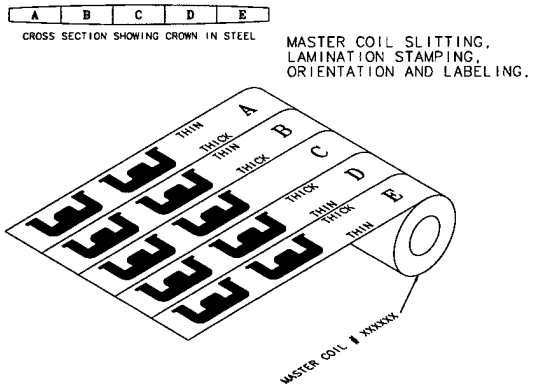



Figure 1: Master coil and slit structure.

## 2 STEEL AND LAMINATION PROPERTIES

The 55″ wide steel master coils, Figure 1, were cut into 5 $10\frac{7}{8}$″ slit coils to minimize waste during stamping. Each slit coil yielded about 800 laminations. It was necessary, because of the crown in the master coils, to balance the amounts of A and E slits and B and D slits in each half core to insure that the core ends were sufficiently parallel.

The lamination shape is shown in Figure 2. The shape of the pole sets the high order field properties of the magnet and is quite reproducible across all steel lots. The half height of the gap is the distance of the pole feature from a reference line across the backleg features on each

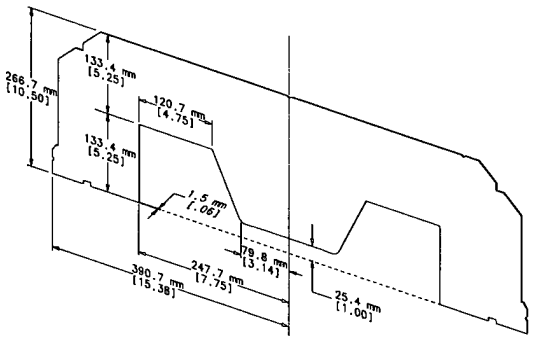



Figure 2: Main Injector dipole lamination.

* Current address: AT&T Corp., Middletown, NJ 07748-4801

† Work suported by the U.S. Department of Energy under contract number DE-AC02-76CH03000.

0-7803-4376-X/98/$10.00 © 1998 IEEE

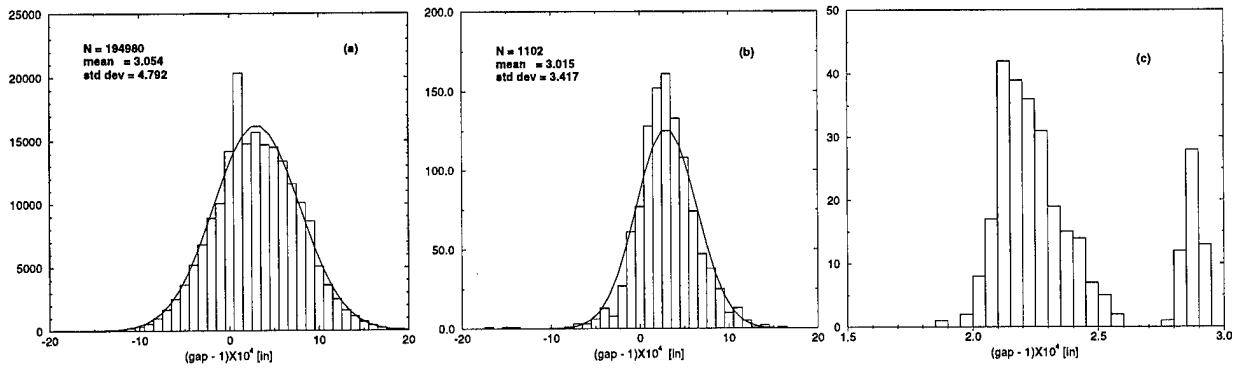



Figure 3: Measured gap (half) height distributions. (a) All measured laminations. (b) Averaged over slit coils. (c) Average gaps for half core recipes.

side. However, the half gap height created in the lamination stamping die is modified by stress relieving deformations which vary from coil to coil. Occasional die adjustments were required to maintain the required gap height by compensating for die wear.

The lamination shape was monitored by measuring a 0.2% sample of the laminations with a coordinate measuring machine (CMM) and a 2% sample with a gap monitoring system. The CMM confirmed in detail the shape of the laminations. The gap monitoring system used three mechanical sensors[1] to measure the pole position at the center and 2.00″ to either side of center. The selected lamination was placed with a reference surface supporting the back legs and the three distances to the pole were recorded.

The target range for the average gap of a half core was 1.0002″ to 1.0003″. Figures 3a and 3b show the measurement data for the laminations. The standard deviations of the distributions are 0.00048″ (12$\mu$m) and 0.00034″ (8.6$\mu$m) respectively, significantly larger than the target range. Figure 3c shows the gap distribution for a set of half core recipes generated by the simulated anneal program, some of which were eliminated on other grounds. Figure 4 shows the time sequence of the average gaps for this set of half core recipes.

## 3 SIMULATED ANNEALING PROGRAM

To meet the required magnet specifications it was necessary to control the average gap and average $H_c$ for each half core. The spread in the distribution of each was several times greater than allowed. (Pre-production, it was anticipated that the spreads would be even larger than was actually realized.) As noted above, it was also necessary to compensate for the taper of the slits used to make the laminations.

A program based on the simulated annealing [5], [6] method was used to generate the lamination recipes from which the half cores were assembled. The recipes were computed in batches, typically of 20–80, depending on the inventory of laminations available. Simulated annealing is based on the observation that when a metal is heated and cooled slowly (annealed), the resulting solid is highly ordered. We can think of the available energy states in the metal as obeying a Boltzman distribution, $e^{-E/kT}$. The probability that a state with energy $E_i$ will change to a state with energy $E_j$ is $P_{ij} = e^{-(E_j - E_i)/kT}$ if $E_j > E_i$ and $P_{ij} = 1$ if $E_j < E_i$. The important observation is that there is a non-zero probability that the final state will have higher energy than the initial. The system can escape from a local energy minimum.

The simulated anneal program adjusted 4 parameters for each half core: the total number of laminations, the A-E and B-D slit imbalance, the average gap, and the average $H_c$. Each box of laminations was characterized by its slit type, A–E, the number of laminations (typically between 350 and 450), $N$, the average gap, $\overline{g}$, and the average coercive force, $\overline{H_c}$. The optimization specified tolerances on the total number of laminations in the half core, on the slit-type imbalance, and the deviations of $\overline{g}$ and $\overline{H_c}$ from the

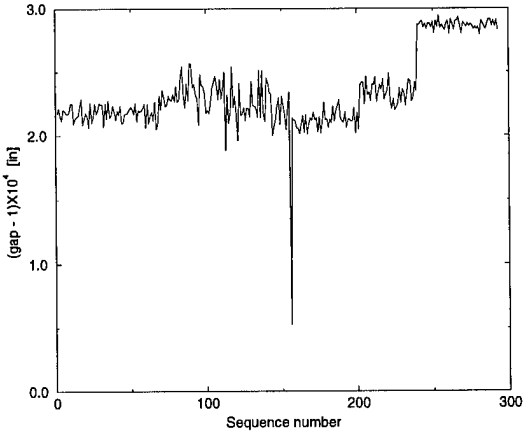



Figure 4: Time evolution of the average gaps for the same set of 6 meter half core recipes. This plot shows the improvement obtained as the cooling program was refined.

[1] Mitutoya Digamatic Indicator Model IDC112C. The sensor has a resolution of 0.0001″ (2.5 $\mu$m) with an accuracy of 0.00015″ (3.8 $\mu$m).

inventory averages. The "energy" for a half core recipe is

$$E = \left(\frac{\sum N(n) - N_{nom}}{\delta N}\right)^2 + \left(\frac{\sum b(n)}{\delta b}\right)^2 + \left(\frac{\sum \overline{g}(n) - \overline{g}_0}{\delta g}\right)^2 + \left(\frac{\sum \overline{H_c}(n) - \overline{H_{c0}}}{\delta H_c}\right)^2 \quad (2)$$

where the sums run over the boxes of laminations included in the recipe. $N_{nom}$ is the target number of laminations and $\sum b(n)$ is the total slit-type imbalance. The quantities $\overline{g}_0$ $\overline{H_{c0}}$ are the average gap and $H_c$ for the total inventory from which the half cores are being selected. The "cooling" is achieved by slowly reducing the denominators in each term while shuffling the box assignments to produce half cores which meet the criteria. (Before starting the program, the inventory is adjusted to ensure that the slit balance, the average gap and the average coercive force will allow the specifications to be met. Over- and undersized laminations were used to make the end packs. This helped us maintain the average gap of the pool in the target range without significant waste.)

## 4 MAGNET PROPERTIES OBTAINED

The magnet fabrication system has been monitored by a program of mechanical and magnetic measurements. The results are recorded in, and easily retrieved from, a comprehensive relational database. The 1.5 mm lamination thickness provides a least step size in the magnet length. Mechanical measurements of the half core lengths are consistent with having this as the dominant limitation on length uniformity. As we see in Equation 1, the strength variation due to geometry is governed by $L_{eff}/g$. To evaluate this we fit the low field (below 0.8 T) downramp excitation curve [3] to a linear function and multiply the inverse slope by $\mu_0 N_g$ to determine $g/L_{eff}$. The correction for finite $\mu_{dr}$ is expected to be less than 0.5% and nearly independent of the steel sample involved. Results are shown in Figure 5. We note that the initial production of 6 m dipoles had a larger and less uniform gap, but the late 6 m dipoles and the full production run of 4 m dipoles had remarkable uniformity. Statistics are shown in Table 1.

| *Series* | | $\langle g/L_{eff} \rangle$ | $\sigma$ | $\sigma/\langle g/L_{eff} \rangle$ |
|---|---|---|---|---|
| IDA | all | 0.008349 | 3.859e-06 | 4.622e-4 |
| IDB | all | 0.008347 | 3.476e-06 | 4.614e-4 |
| IDC | all | 0.012520 | 2.572e-06 | 2.054e-4 |
| IDD | all | 0.012519 | 2.920e-06 | 2.333e-4 |
| IDA | early | 0.008354 | 2.602e-06 | 3.114e-4 |
| IDA | late | 0.008347 | 1.544e-06 | 1.850e-4 |
| IDB | early | 0.008353 | 2.632e-06 | 3.152e-4 |
| IDB | late | 0.008352 | 2.632e-06 | 3.152e-4 |

Table 1: Average $g/L_{eff}$, $\sigma$, the rms spread, and the ratio for the different magnet populations shown in Figure 5.

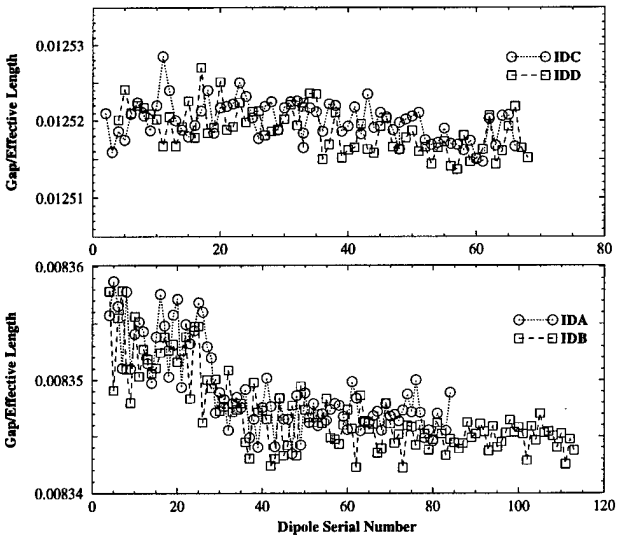



Figure 5: $g/L_{eff}$ for 6 m (below) and 4 m (above) dipoles *vs.* production serial number. The apparent change after IDA028 and IDB025 and the subsequent improved uniformity is believed to be due to several improvements in the half core manufacture and magnet assembly procedures. The relative change in $g/L_{eff}$ is $\approx 10^{-3}$.

## 5 SUMMARY

In the face of significant materials variations we have produces a remarkably uniform set of magnets. The simulated annealing method provided a very robust and efficient tool to assign laminations to magnets to obtain desired and tightly controlled properties,

## 6 ACKNOWLEDGEMENTS

The authors want to thank S.L. Beverley, W. Pritchard and R.W. Riley who have handled large quantities of material and data with diligence and good humor. The original programming was by R. Dixon.

## 7 REFERENCES

[1] Holmes, S. D., et al. Status of the Fermilab Main Injector and Recycler, this conference

[2] Harfoush, F. A., B. C. Brown, H. D. Glass, C. S. Mishra, S. Peggs, Defining the Systematic and Random Multipole Errors For Mail Injector Tracking, Proceedings of the 1993 IEEE Particle Accelerator Conference, pp 351–353, 1993

[3] B. C. Brown *et. al.*, Results on Fermilab Main Injector Dipole Measurements, IEEE Trans. on Magnetics, **32**, 2186 (1996)

[4] Martin, P. S., D. J. Harding, E. G. Pewitt, A. D. Russell, Variations in the Steel Properties and the Excitation Characteristics of FMI Dipoles, this conference.

[5] Kirkpatrick, S., C. D. Gelatt, Jr., M. P. Vecchi, Optimization by Simulated Annealing, Science, **220**, 671 (1983)

[6] Numerical Recipes in C, 2nd ed., W. H. Press, S. A. Teukolsky, W. T. Vetterling, B. P. Flannery, Cambridge Univ. Press, 1988

# AIR-COOLED TRIM DIPOLES FOR THE FERMILAB MAIN INJECTOR

D.J. Harding, J.A. Carson, N.S. Chester, J.D. Garvey,
G.E. Krafczyk, A. Makarov, I. Terechkine, V.A.Yarba.
Fermi National Accelerator Laboratory *

*Abstract*

New horizontal and vertical trim dipoles have been designed for the Fermilab Main Injector (FMI) and are being assembled in the Fermilab Technical Division. Magnets are 42.6 cm in length (30.5 cm steel length) and have similar cross-section dimensions. The horizontal (vertical) magnet gap is 50.8 mm (127 mm) and the target integrated strength is 0.072 T*m (0.029 T*m). The major design effort lay in making air cooling possible for these magnets.

This report presents the magnets' thermal and magnetic properties and discusses the limitation on excitation current.

## 1 INTRODUCTION

The FMI lattice includes 104 horizontal and 104 vertical trim dipoles that perform fine close orbit correction [1]. The accelerator operation with 120 GeV energy requires 0.072 T*m integrated strength for the horizontal trim dipole and 0.029 T*m for the vertical one, but the dipoles must generate larger magnetic strength for 150 GeV operation, which will last about 10 minutes a day. The current duty factor, which is the ratio of the r.m.s. current to the maximum one, is 0.7.

The magnets must be less than 0.43 m long to allow their fitting into the space between the FMI dipoles and quadrupoles.

To simplify the mounting procedure and to increase reliability, the magnets were made air cooled. Maximum core temperature of 50° C was accepted to meet the safety requirements.

For air-cooled magnets, the surface temperature is a result of a balance between the coil power consumption and the power lost from the surface by radiation and convection. A simple estimate shows that if a magnet design uses traditional surface shaping, the coil total copper wire cross-section and the magnet core dimensions must be unreasonably high to meet the temperature specification.

## 2 THE DESIGN PRINCIPLES

The most obvious way to reduce the dipole coil cross-section is to increase significantly the magnet core surface. This was done by building the cores from E-shaped laminations with different width of flux return legs. The dipole half-cores were assembled from lamination packs. Each pack is 15 mm in thickness and contains 24 laminations die-stamped from 0.625 mm M15 ARMCO silicon steel sheets with two-side type C3 insulating coating. When being stacked together in a stacking fixture, alternating lamination packs were turned around the pole axis of symmetry. Due to the different widths of the flux return legs, this procedure resulted in half-cores with increased vertical surface. Prior to stacking, each lamination was coated with a thin epoxy layer. Curing in an oven in a stacking fixture with pressure applied to the whole assembly produced solid half-cores that were ready for the final assembly.

The coil has a simple racetrack configuration, rectangular 8 x 4 $cm^2$ cross-section, and is wound using ML-coated 6.56 $mm^2$ square copper wire. The coil leads are made using flexible insulated wires. After the coil was wound, it was ground insulated, vacuum impregnated with epoxy, and cured in an oven in a curing fixture. To avoid any air layers between the coil and the core, coils are glued into the core using room-cure epoxy. Figures 1 and 2 show the dipoles after final assembly.

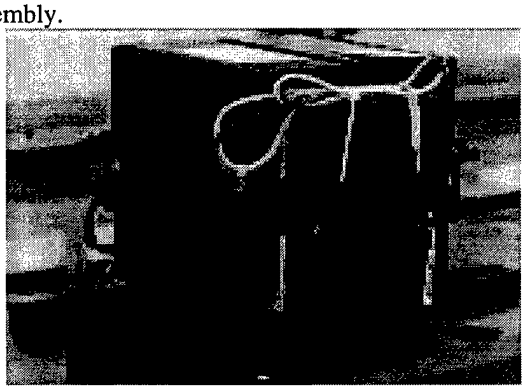


Figure 1: Horizontal Trim Dipole

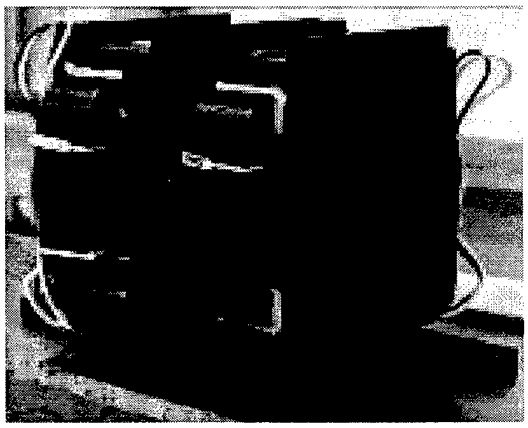


Figure 2: Vertical Trim Dipole

* Operated by the Universities Research Association Inc. under contract with the U.S. Department of Energy.

0-7803-4376-X/98/$10.00 © 1998 IEEE

The table 1 below presents the dipoles main parameters.

Table 1

| Feature Description | Horizontal Dipole | Vertical Dipole |
|---|---|---|
| Magnet size: (mm) | | |
| length | 426 | 426 |
| width | 295 | 380 |
| height | 280 | 305 |
| Core length (mm) | 305 | 305 |
| Magnet weight (kg) | 180 | 220 |
| Coil cross-section (mm) | | |
| width | 40 | 40 |
| height | 80 | 80 |
| Average wire turn length (m) | 1.02 | 1.12 |
| Number of turns per magnet | 812 | 812 |
| Total copper weight (kg) | 50 | 55 |
| Magnet resistance (Ohm) | 2.2 | 2.4 |
| Magnet inductance (H) | 1.1 | 0.9 |
| Nominal power (W) | 180 | 200 |
| Cooling surface area ($cm^2$) | 8200 | 9300 |

## 3 MAGNETIC PROPERTIES

Figures 3 and 4 show the relative magnetic field distribution in a transverse (X, Y) plane for the horizontal and vertical trim dipoles found using the OPERA-2D magnetic modeling program. The integrated field measurement performed using a rotation coil have shown that the magnet end field adds some negative sextupole to the body field harmonic content. It makes the integrated field distribution differ slightly from the body field distribution. Nevertheless (and partly due to this effect), for both dipoles, the magnetic field meets the field quality requirement. Due to relatively low field level, the magnets do not have saturation problems.

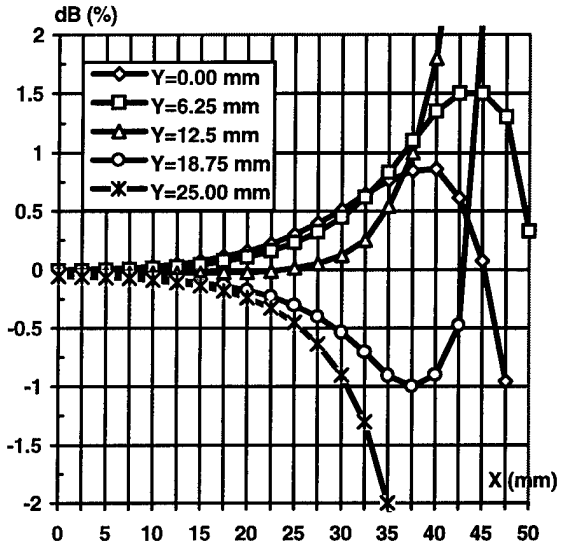



Figure 3 Horizontal trim dipole magnetic field.

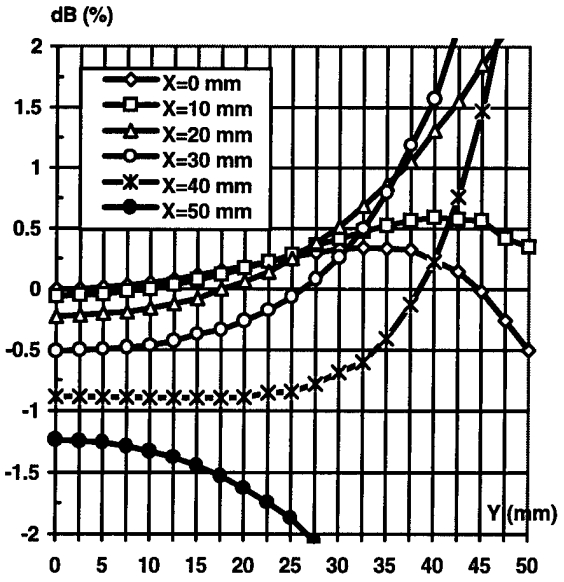



Figure 4 Vertical trim dipole magnetic field.

## 4 STATIC THERMAL PROPERTIES

The factor that can put a natural limit to the magnet strength is the coil temperature. The normal regime current density for both of the magnets is approximately 1.8 $A/mm^2$, so it is necessary to insure proper coil cooling to avoid overheating. The maximum temperature inside the coil

$$T_m = T_{core} + \frac{p \cdot a}{2} \cdot \left[\frac{a}{k_{eff}} + \frac{g}{k_{ins}}\right], \qquad (1)$$

where **p** ($W/m^3$) is the coil power consumption; **a** (m) is the coil thickness; **g** (m) is the gap between the coil and the core, filled with a material with a thermal conductivity $\mathbf{k_{ins}}$ ; $\mathbf{k_{eff}}$ is the effective thermal conductivity of the coil. Calculating the power consumption, one should apply all the coil power to the coil volume inside the core, because thermal conductivity of the coil along wire layers is much larger than that across the coil. For the dipoles' normal operation, the coil power consumption $\mathbf{p} = 41000\ W/m^3$. The effective thermal conductivity $\mathbf{k_{eff}}$ can be found if we know thickness **d** and thermal conductivity **k** of copper and insulating layers:

$$\frac{d_{Cu} + d_{epoxy} + d_{ML}}{k_{eff}} = \frac{d_{Cu}}{k_{Cu}} + \frac{d_{epoxy}}{k_{epoxy}} + \frac{d_{ML}}{k_{ML}}. \qquad (2)$$

Table 2 lists the thermal conductivity values for the materials used in the coil [2]:

Table 2

| Material | Units | Value |
|---|---|---|
| Copper | W/(m*°C) | 386 |
| Dupont Pyre-M.L. | W/(m*°C) | 0.155 |
| Epoxy | W/(m*°C) | 0.65 |
| Air | W/(m*°C) | 0.024 |

The average epoxy layer thickness can be calculated using the data from Table 1: $d_{epo}$ = 0.45 mm. The thickness of the wire insulation $d_{ML}$ = 0.1 mm. Then, the estimate of the coil effective thermal conductivity

$$k_{eff} = 1.6 \text{ W/(m*°C)}.$$

It is relevant to say that for an epoxy-impregnated coil, the wire film insulation has two times larger thermal resistance than the epoxy filled gap between the wires. If we do not use epoxy to fill the gaps, the air layers will dramatically increase the coil thermal resistance. With no epoxy inside the coil, we would have a maximum coil temperature of about 300°C, which is not acceptable from the point of view of the wire insulation reliability.The same effect will take place if we leave air gaps between the coil and the core after the coil is installed into the core. Assuming that these gaps are equally distributed and filled with epoxy ($g_{av}$= 2.3 mm), using (1), we can estimate the coil temperature rise as ΔT = 23°C. So, using the epoxy impregnation technique, and eliminating any air gaps between the coil and the core, we can eliminate the problem of coil overheating.

To evaluate the magnet static thermal properties, measurements were performed at different current levels for the Horizontal and Vertical trim dipoles. The measurement results are in a reasonably good agreement with predicted numbers. The table 3 below compares the measured and calculated coil and core temperatures for the Horizontal trim dipole tested using 15 A D.C. excitation current. The coil power consumption in this case was almost 4 times larger than the magnets nominal power. The measured average coil temperature in the table was calculated based on the measured rise of the coil resistance. Surface-to-air heat transmission coefficient α = 13 W/(m$^2$ °C) was used for the core surface temperature rise calculation [3].

Table 3

| Feature | Calcul. | Measured |
|---|---|---|
| Power consumption at 15 A. | 714 W | 720 W |
| Core surface temp. rise (above ambient) | 64°C | 62°C |
| Core surface temperature | 84°C | 82°C |
| Maximum coil temperature | 148°C | -- |
| Average coil temperature | 127°C | 105°C |

As it is possible to see from the table 3, the core temperature is the main component contributing to the coil maximum temperature. The magnet design and manufacturing technology helped to reduce the problem of coil overheating. On the other hand, as it was mentioned earlier, the yoke cross-section, which was chosen to insure the magnet rigity, can tolerate much more magnetic flux without saturation. It provides a significant reserve for the magnets integrated strength increase. By accepting higher core surface temperature, or by using forced air flow or water for additional core cooling, we can significantly increase the average current before degradation to the magnet would occur.

## 5 DYNAMIC THERMAL PROPERTIES

The dynamic thermal properties of the magnets can be described by the heating characteristic time index τ, which provides a scale to the exponential temperature change, according to the expression

$$\Delta T(t) = \Delta T_0 \cdot (1 - e^{-\frac{t}{\tau}}), \qquad (3)$$

where $\Delta T_0$ is the maximum temperature rise. For the coil, which mainly releases deposited energy into the core, the estimate that takes into the account the numbers from the table 2 gives for both magnets $\tau_{coil} \approx$ 25 min. For the steel core, $\tau_{St}$= 130 min. Because $\tau_{coil} << \tau_{St}$, we can expect that the coil maximum temperature will follow the core temperature after about 25 minutes of a magnet operation. The core temperature after t minutes of the magnet operation with the increased current can be found from the expression:

$$\Delta T(t) = \Delta T_{nom} \cdot \frac{I_m^2 - I_{nom}^2}{I_{nom}^2} \cdot \frac{t}{\tau_{St}}, \qquad (4)$$

where $I_{nom}$ and $I_m$ are nominal and increased current values, and $\Delta T_{nom}$ - the core temperature rise at nominal current. Calculation gives ΔT(10 min)=0.73°C.

Dynamic temperature measurements performed with the Horizontal Trim Dipole gave the results that are in very good agreement with the calculated predictions. Measured coil-core characteristic time was about 25 minutes, core heating time - 2 hours; core temperature rise after 10 minutes of operation with the increased current was less than 1°C.

## 6 CONCLUSION.

A strict limit on the magnet core temperature forced us to increase the magnet's cooling surface, arranging vertical air passages along the core sides. Using epoxy for the coil impregnation and gluing the coil into the core nest with epoxy compound helped to keep maximum wire temperature at a reasonable low level. The dipole cores saturation properties allow operation at more then twice the nominal field. The 15 A DC horizontal dipole operation with the power consumption almost 4 times as larger than at the nominal 12 A maximum current (0.7 duty factor) operation has confirmed the magnet reliability.

*References:*

[1] - Fermilab Upgrade: Main Injector. Technical Design Handbook, August,1994.

[2] - Handbook of Chemistry and Physics, Thirtieth Edition, Chemical Rubber Publishing Co., Cleveland, Ohio, 1947.

[3] - R. Baiod, private communication.

# A COMBINED FUNCTION MAGNET FOR A COMPACT SYNCHROTRON

M. Tadokoro, J.I. Hirota, K. Hiramoto, M. Umezawa, S. Kakiuchi,
Hitachi, Ltd. Hitachi shi, Ibaraki 317, Japan
Y. Iwashita, A. Noda, T. Shirai and M. Inoue
Institute for Chemical Research, Kyoto University, Uji shi, Kyoto 611, Japan

*Abstract*

At Kyoto University, a compact proton synchrotron with combined function lattice has been proposed for cancer therapy facility, KUMPF (Kyoto University Medical Proton Facility). KUMPF provides proton beam in the energy range of 70-250 MeV with average current of about 10 nA. The synchrotron consists of six identical combined function magnets, each of which deflects the proton beam 60 degrees. The magnet has an FDF structure where focusing (F) and defocusing (D) sectors deflect the beam 15 and 30 degrees, respectively. In order to realize the tune value of (1.75, 1.75 ), n-values of -5.856 and 6.164 are required for F and D sectors, respectively. In the present paper, the detailed design of the combined function magnet will be presented.

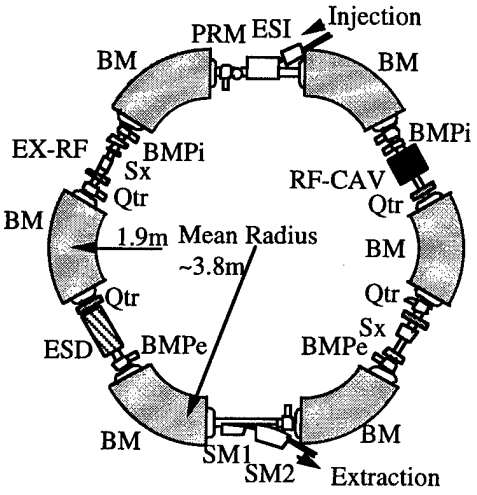
## 1. INTRODUCTION

At present, a particle therapy using protons and heavy ions has been recognized as a powerful tool to treat malignant tumor due to the Bragg peak effect which serves a sharp dose distribution in human body. From this effect, the particle therapy is also expected to satisfy the requirement for keeping the shape and function of the human body from the point of view of the QOL(Quality Of Life) of the patients. A medical accelerator, however, system should be able to be operated easily and acceptable in size in public hospitals.

Based on this conditions, a compact proton synchrotron dedicated for medical use composed of combined function magnets with circumference of about 23m had been proposed for KUMPF(Kyoto University Medical Proton Facility) [1][2]. To realize clinical beam energy from 70 to 250MeV for therapy in compact size, the bending field is required from 0.2 to 1.28T and the necessary focus and defocus quadrupole field are 1.71 and $-1.62(1/m^2)$ at 1.28T, respectively. Construction of such a combined function magnet with high K-values are not so easy. A new design method to introduce vacant portions in the magnet core so as to improve a shape of the magnetic field in the combined function bending magnet has been developed. An outline of the compact synchrotron for KUMPF and a design principle of the combined function bending magnet are described in section 2 and 3, respectively.

## 2. OUTLINE OF THE COMPACT SYNCHROTRON

Figure 1 shows the compact synchrotron with combined function lattice in KUMPF. And typical operation parameters are shown in Table 1.




BM : Combined Function Bending Magnet
BMP : Bump Magnet
ESD : Electrostatic Deflector
ESI : Electrostatic Inflector
EX-RF : RF Electrode for Extraction
Qtr : Trim Quadrupole Magnet
PRM : Profile Monitor
RF-CAV :Untuned type RF Cavity
SM1,SM2 : Septum Magnets
Sx : Resonance Exciter Sextupole Magnet

Fig.1 Structure of the Combined-Function Synchrotron

A proton beam is injected from a linac with 7MeV. The injection energy was chosen to reduce an effect of the space charge force. The proton beam is accelerated up to 70-250MeV and extracted to the treatment room. This operation is conducted in repetition rate of 0.5 Hz. The mean radius and the circumference of the synchrotron are 3.8m, 23.9m, respectively. The combined function magnet consisting of an FDF structure was adopted for the merit of easy operation. Especially no need of tracking procedure between dipole and quadrupole magnets is a large merit. In this structure, F and D denote focus and defocus sectors in horizontal direction, respectively.

0-7803-4376-X/98/$10.00 © 1998 IEEE

The radius of curvature and the bending angle of the combined function bending magnet is 1.9m, and 60 degrees, respectively. The maximum field is 1.28T at the central orbit.

Moreover, an untuned type RF cavity using ferro-magnetic material named FINEMET with multiple power feeding[3] and the constant separatrix extraction with broad band RF noise are also adopted in this compact synchrotron[4].

Table1 Kyoto University synchrotron operation parameters

| particle | proton |
|---|---|
| Beam Energy (MeV) | |
| Injection | 7 |
| Extraction | 70-250 |
| Repetition Rate (Hz) | 0.5 |
| Dose Rate (Maximum) | 5 Gy per min |
| Circumference (m) | 23.9 |
| Tune | |
| horizontal $\upsilon x$ | 1.75 |
| vertical $\upsilon y$ | 1.75 |

## 3. THE COMBINED FUNCTION BENDING MAGNET

Figure 2 shows the schematic view of the combined function bending magnet for KUMPF. The present bending magnet is an FDF type. The deflection angles of F and D sections are 15 and 30 degrees, respectively. The curvature radius is 1.9m. Then, the maximum magnetic field on the design orbit is 1.28T for 250MeV. Figure 3 and 4 show the cross sectional view of the magnet poles of the F and D regions, respectively. As shown in the figures, the gap height of both the sections is 67mm on the design orbit. This value has been determined based on the analysis of the beam size in the synchrotron. The n-values of the F and D regions are -5.865 and 6.1641, respectively. The specifications of the present bending magnet are listed in Table 2. In order to adjust the field gradient integrated along the design orbit, the one turn correction coil with air cooling is applied. This correction coil is twisted in the transition regions between the F and D sectors. A few percents of the integrated field gradient can be tuned by using the present correction coil .

The present bending magnet is designed in such a way as there are some vacant portions, hereafter called the air slots, in the magnet poles. The magnetic susceptibility of the air slots in the magnet poles is much lower than that of the iron core. This results in an increase of the magnetic flux in the iron region. In the present combined function bending magnet, the air slots in the larger gap section makes the magnetic flux in the larger gap region increase and the characteristics of the magnetic field distribution is improved. Accordingly, by adjusting the position, shape and volume of the air slots, the maximum magnetic field , that is, the beam energy range of the synchrotron is increased with keeping the size of the synchrotron constant. It is expected that the air slots in the magnet pole are also effective for the control of the magnetic field distribution in the usual dipole bending magnet as well as the combined function magnets. An intensive study to apply this effect to a conventional type bending magnet is now carried out.

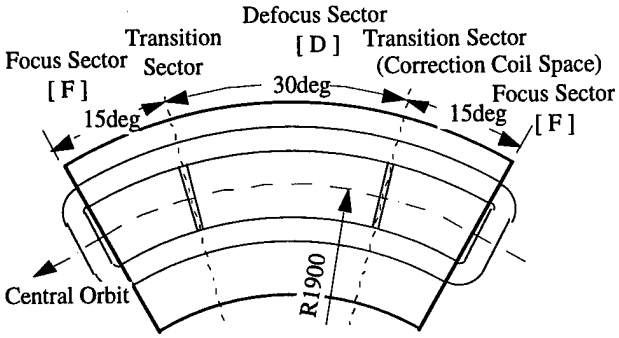



Fig.2 Top View of the Unit Magnet

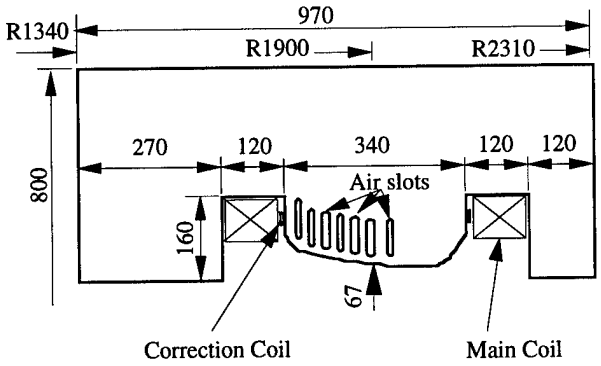



Fig.3 Cross-sectional View of the Focus Sector

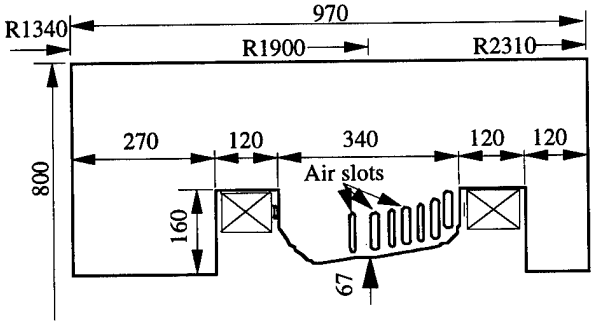



Fig.4 Cross-sectional View of the Defocus Sector

The shape of the magnet pole has been determined by the following equation.

$$y(1+b_1 x)-\frac{1}{6}\frac{b_1}{\rho}y^3=y_0-\frac{1}{6}\frac{b_1}{\rho}y_0^3 \qquad (1)$$

$b_1$ : quadrupole component (1/m)

$\rho$ : curvature radius(m)

$y_0$ : half gap height on the design orbit(m)

Table 2 Specifications for the Bending Magnet

| | |
|---|---|
| Bending Angle | 60deg (15deg[F]-30deg[D]-15deg[F]) |
| Radius of Curvature | 1.9m |
| Center Gap Height | 67mm |
| Magnetic Field Strength (at the central orbit) | 0.2T (7MeV) to 1.28T (250MeV) |
| n-value D sector<br>F sector | 6.1641<br>-5.8560 |

Figure 5 shows the two dimensional magnetic field distribution obtained by numerical analysis. The horizontal axis shows the radial distance from the design orbit and the vertical axis shows the deviation of the magnetic field strength from the design value. As shown in the figure, the difference between the calculated and design values is smaller than 0.02% at even the magnetic field of 1.35T for the horizontal width of 120mm. Since the curvature radius of the present bending magnet is 1.9m, the proton beam can be accelerated up to about 275 MeV.

For the comparison, the two dimensional magnetic field distribution of the conventional combined function magnet without air slots is shown in Fig. 6.

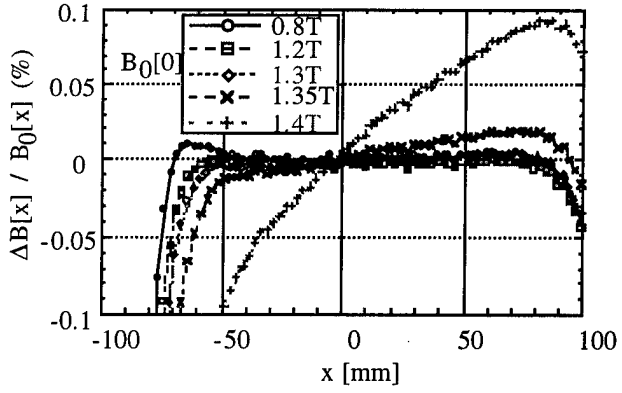



Fig.5 Two dimensional magnetic field distribution of the present combined function magnet. (D Sector)

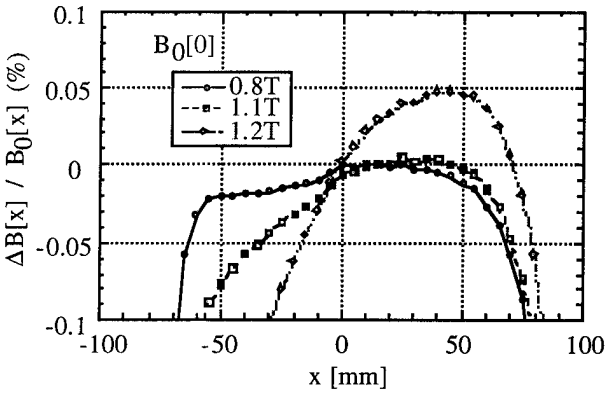



Fig.6 Two dimensional magnetic field distribution of the conventional combined function magnet.

In the conventional combined function bending magnet, the saturation effect of the magnet pole in the narrower gap region deforms the magnetic filed distribution. This effect limits the maximum magnetic field used in the synchrotron. As shown in the figure, although the good field region of 120mm width is obtained up to the magnetic field of 0.8T, the widths of the good field region are rapidly decreases to 40mm for 1.1T and to about 20mm for 1.2T.

## 4. CONCLUSION

The combined function bending magnet for the proton synchrotron of KUMPF has been presented. The circumference of the synchrotron is 23.9m. The acceleration of the proton beam to 250 MeV requires the maximum magnetic field and n-values to be 1.28T and -5.8560 for F, 6.1641 for D sectors respectively. A new magnet pole in which there are some vacant portions has been applied to realize the needed n-values up to the designed magnetic field. The results of the numerical analysis showed that the sufficiently good field region is obtained at 1.28T and the present bending magnet can be applied to the magnetic field up to 1.35T.

## ACKNOWLEDGMENTS

This work presented here was partly supported by Grant-in-Aid for Scientific Research from Ministry of Education, Science, Sports and Culture of Japan.

## REFERENCES

[1] A. Noda et al., Contribution Paper to the 6th China-Japan Joint Symposium on Accelerators for Nuclear Science and Their Applications Chengdu, Sichuan, China, October 21-25,1996

[2] A.Noda, et al., Proc. of the NIRS, International Workshop on Heavy Charged Particle Therapy and Related Subjects, P.292, Chiba, Japan, 1993

[3] K.Saito, et al., Beam Science and Technology, Vol.2, P.15(1997), Published by Institute for Chemical Research, Kyoto University

[4] K.Hiramoto, et al. ,Nucl. Instr. and Meth. A322, P.154(1992)

# FIELD MEASUREMENT OF PEP-II LER DIPOLES AND QUADRUPOLES AT IHEP

R. Hou, F. Ren, Y. Hao, Y. Han, G. Ni, L. Li, J. Sun, L. Zheng,
M. Wang, B. Yin, Q. Peng, G. Zhao, J. Zhang, J. Li, Y. Li and W. Chen
IHEP, Chinese Academy of Sciences
P.O. Box 918(9), Beijing 100039, China

*Abstract*

The field measurement of 209 dipoles and 320 quadrupoles for PEP-II LER will be finished at IHEP in June 1997. This paper covers the details of the magnetic measurement devices developed to measure these magnets as well as the results of the measurements.

## 1 INTRODUCTION

Four individual measurement devices have been developed at IHEP with the aim to perform precise, fast and reliable measurement of production dipoles (63.5 mm gap height and 45 cm effective length), production quadrupoles (50 mm bore radius and 43 cm effective length) and their prototype magnets for PEP-II LER. The field properties including transfer fuction and line integral uniformity for 140 dipoles, multipole error contents and offset of magnetic center for 280 quadrupoles as well as magnet-to-magnet reproducibility have been measured by now.

## 2 FIELD MEASUREMENT OF DIPOLES

Two separate measurement devices were made for field measurement of dipoles.

### *2.1 Hall probe mapping device*

It is used for mapping field distribution of prototype magnet and calibration of long coil probes. This device consists of a Digital Teslameter (DTM-141) and a positioning mechanism used to move the Hall probe in three directions, the precision of the positioning is $\pm 0.01$ mm, $\pm$ 0.02 mm and $\pm 0.025$ mm along x, y and z axis respectively, by means of the digital controller and servomotors. The measurement precision of magnetic field with this device is better than $2 \times 10^{-4}$.

### *2.2 Ramp (or step) current method*

(1) Magnet-to magnet reproducibility
The measurement principle and procedure are described as follows:

- Choosing one magnet as bucking magnet(B-magnet) and another one as reference magnet(R-magnet), and others as testing magnet(T-magnet).
- Two pickup long-coil of 90cm long with about 400 turns each are connected in bucked configuration, one coil is fixed on the horizontal center plane of B- magnet and the another one into R- magnet . B-magnet and R-magnet are connected in series and powered by ramp (or step) exciting current. The relative deviation of line integral between B-magnet and R-magnet can be written as follows:

$$\frac{\triangle \int B(0)dl_{R-B}}{\int B(0)dl_R} = \frac{\int B(0)dl_R - \int B(0)dl_B}{\int B(0)dl_R} \quad (1)$$

where $\triangle \int B(0)dl_{R-B}$ and $\int B(0)dl_R$ can be measured separately.

- In the same way, all T-magnets are measured in turn, so we can also obtain

$$\frac{\triangle \int B(0) \cdot dl_{T-B}}{\int B(0) \cdot dl_R} \quad (2)$$

Based on above, the relative deviation of all T-magnets from the R-magnet can be calculated . In addition , the effect of remanent field can be extra added.

(2) Line integral uniformity
In practice, it is much the same way that two pickup long-coil as above are connected in bucked configuration , one coil is fixed on the horizontal center plane of B-magnet and the other one into T-magnet, B-magnet and T-magnet are connected in series and powered by ramp (or step) exciting current. When the T- magnet is moved laterally at different positions the induced signals from two pickup long-coil are fed to PDI 5025 Digital Integrater and then process data by microcomputer via RS232 and GPIB interface. The transverse distribution of line integral field can be obtained.

## 3 FIELD MEASUREMENT OF QUADRUPOLES

### *3.1 Harmonic Measurement System*

The measurement system is based on the harmonic coil method. It consists of rotating long coil assembly, step motor controller and data aquisition system. While the coil assembly rotates in the aperture of the magnet, the induced voltage in coils is digitally integrated over equally spaced angular intervals by using a digital integrator. IBM computer controls the measurement procedure and performs the FFT analysis. Some of its features are as the follows :

- Measurement coil assembly is made with high bucking ratio(>300) in order to get a high sensitivity for higher harmonics. It is wound with adequate number of turns such that the voltage signals anticipated in both configurations, unbucked and bucked, are large compared to the ambient electrical noise and insensitive to both the dipole and quadrupole components of the measured field in bucked

0-7803-4376-X/98/$10.00 © 1998 IEEE

configuration. The rotating coil assembly consists of a support structure made of G10 and two measurement coils, main coil (r=40 mm, r=-30 mm and N =200turns) and bucking coil (r=22.5 mm, r=-12.51 mm and N =400 turns).
• The barrel construction for the measurement coil assembly is chosen for positioning it in aperture of magnet easily and rapidly.
• Higher resolution and accuracy of measurement are obtained by using a precision Digital Integrator (PDI 5025), an Angular Encoder(5VN278AZ, 14Bit) and the slow rotating long coil assembly (0.5 sec/rev).
• A switch box is used to change the coil configurations and improve the bucking ratio by the precision potentialmeters. The induced voltage signals to be collected with a permanently connected wire rather than a brush and a slip ring are drift corrected and then analyzed through FFT.
• A cycle of the measurement including data acquisition and processing can be finished automatically in only a few minutes.

### *3.2 Step current measurement device*

The relative deviation of transfer function of the production quadrupoles from reference magnet that are excited in series by the step current is measured by using the same method as that in the dipole measurements. Instead of long-coils there are two long coil pairs to be used. It is simpler in match of the measurement coils and rapid to obtain the measurement results.

## 4 MEASUREMENT RESULTS OF DIPOLES

### *4.1 The line integral uniformity*

The line integral uniformity at mid-current of 578.9 Amps for 140 dipoles is below the limit of of the central field for $-4.5\ cm \leq X \leq 4.5\ cm$. The average curves for different group A, B and C are shown in Fig. 1, and the results show that their standared deviations are less than $1 \times 10^{-4}$.

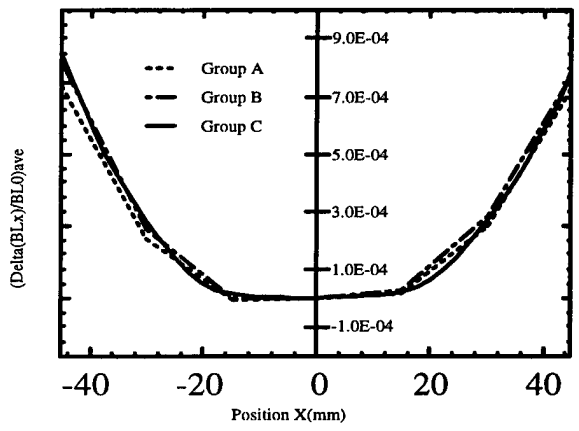



Figure 1: Average curve of field uniformity.

### *4.2 Magnet-to-Magnet Reproducibility*

The integral field dispersion relative to the reference magnet for 140 dipoles is shown in Fig. 2, and its standard deviation is $1 \times 10^{-4}$. After shimming the magnet to magnet the reproducibility of 137 dipoles is $\leq 1 \times 10^{-3}$. The relationship between integral field and the ratio of core length to the gap height is shown in Fig. 3.

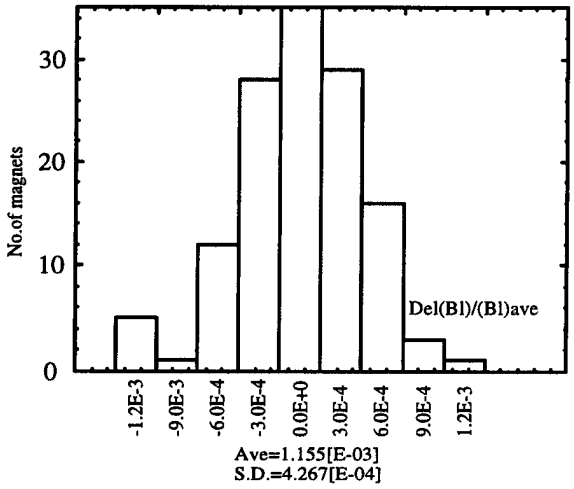



Figure 2: Integral field dipersion of 140 dipoles.

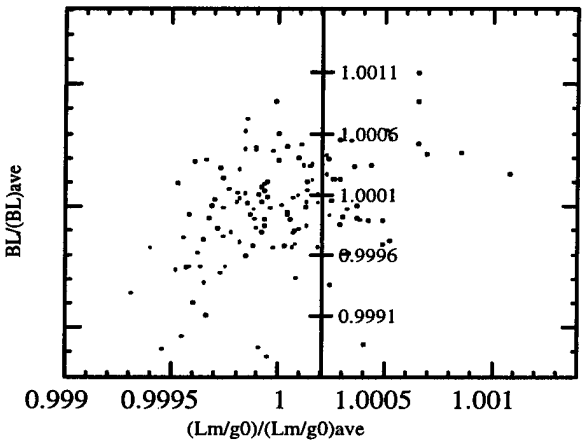



Figure 3: Integral field with core length/gap width.

## 5 MEASUREMENT RESULTS OF QUADRUPOLES

### *5.1 Magnet Field Quality*

The average values of relative multipole error contents of 150 quadrupoles with 15-turn aluminum coil at mid current of 355 A are summarized in Table 1, and their spectrogram is shown in Fig. 4. It is shown that the standard deviations of high harmonics are less than $1 \times 10^{-4}$. Systematic and random multipole error contents for 280 quadrupoles are below the limit of $1 \times 10^{-3}$ and $5 \times 10^{-4}$ of the fundamental field respectively.

| | (Bn/B2)ave | S.D. |
|---|---|---|
| B1/B2 | 3.775E-04 | 1.723E-04 |
| B2/B2 | 1 | 0 |
| B3/B2 | 7.656E-05 | 4.48E-05 |
| B4/B2 | 1.74E-04 | 7.61E-05 |
| B5/B2 | 1.902E-05 | 1.08E-05 |
| B6/B2 | 5.797E-04 | 1.86E-05 |
| B7/B2 | 8.531E-06 | 4.72E-06 |
| B8/B2 | 1.062E-05 | 5.6E-06 |
| B9/B2 | 5.271E-06 | 2.89E-06 |
| B10/B2 | 3.386E-04 | 3.91E-06 |
| B11/B2 | 4.999E-06 | 3E-06 |
| B12/B2 | 5.537E-05 | 7.84E-06 |
| B13/B2 | 1.173E-05 | 7.12E-06 |
| B14/B2 | 6.31E-05 | 9.2E-06 |

Table 1: Average values of spectrum of 150 quads.

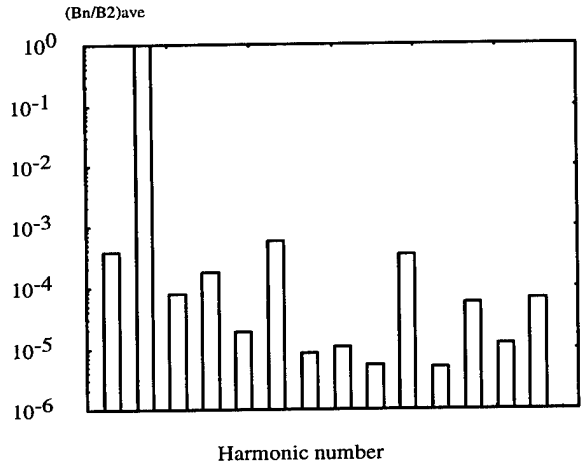



Figure 4: Spectrogram of 150 quads.

### 5.2 *Magnet-to-Magnet Reproducibility*

The integral field gradient dispersion of 150 quadrupoles with 15 turn aluminum coil at 355 A is shown in Fig. 5. The standard deviation is $4.12 \times 10^{-4}$.The magnet-to-magnet reproducibility of 280 quadrupoles is $\leq 1 \times 10^{-3}$.

### 5.3 *Displacement of Magnetic Center*

The radial displacements of magnetic center $\triangle r$ of 280 magnets are below the limlt of 0.05 mm, and their average value is 0.022 mm and the standard deviation is 0.01 mm.

## 6 CONCLUSION

The field performance of all magnets clearly met the specification requirement for PEP-II LER dipoles and quadrupoles except for several dipoles which are slightly out of reproducibility of $1 \times 10^{-3}$. Corrections of these magnets, shorter or longer, were made by changing the shims located at the matching surfaces in between the two

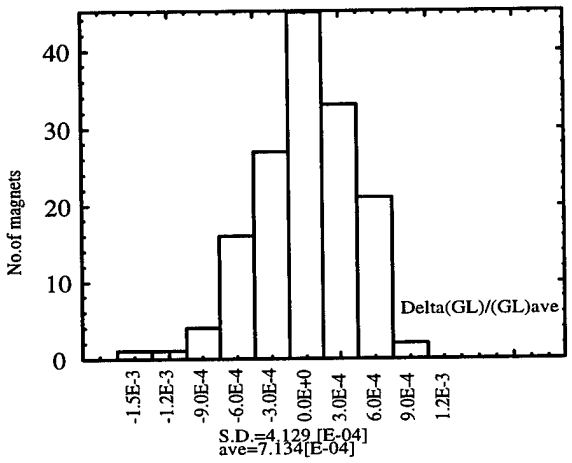



Figure 5: Integral field gradient dispersion of 150 quads.

half cores. The measurement results show that the relative accuracy of four sets of measurement devices is better than $2 \times 10^{-4}$.

## 7 ACKNOWLEDGEMENTS

We would like to express many thanks to Prof. Z. Cao and Z.S. Yin for giving us a lot of invaluable help. We also thank all members of Magnet Group and colleagues in IHEP for their helps.

## 8 REFERENCES

[1] J. Tanabe *et al.*, Magnetic Measurement Coil Design, LBL, Jan. 22, 1990.

# THE FABRICATION OF QUADRUPOLE MAGNETS FOR PEP-II LER

Fuhe Huang, Yaolin Sun, Xiaoping Wang, Dunan Zhang, Bingsong Huang, Lan Dong
(IHEP, Beijing, China)

*Abstract*

There are eight types of precision quadrupole magnets, total 320 for the PEP-II Low Energy Ring (LER) of SLAC B factory project. For this job, IHEP utilized some special technical measures, fabricated more than 40 types (about 70 sets) of precision technical equipment, fixtures and specially tooling. A high-precision die-set has been made which punched 560 thousand of laminations successfully. By the end of April of 1997 309 qualified quadrupole magnets have been completed.

## 1 INTRODUCTION

A total of 320 PEP-II LER quadrupole magnets which are designed by LBNL in collaboration with IHEP are being fabricated by the IHEP machine-shop. The fabrication began in December, 1994, and the prototype magnet was finished in July 1995. Currently, 309 quadrupole magnets have been completed; 261 of them have been shipped from IHEP to LBNL. The magnetic measurement of all magnets is carried out by IHEP, and some measurements are repeated by LBNL. The results show that all magnets satisfy the prescribed specifications.

The LER Quadrupoles are divided among eight types (Table 1); they have the same contour size: 461mmx646mmx617 mm, and the weight of each is about 1,200kg.

Table 1. Quantity of Each Type of Magnet

| Type | QTY | QF | QD | A | B | C | D |
|---|---|---|---|---|---|---|---|
| Q43-15-Al-1 | 150 | 77 | 73 | 77 | 73 | | |
| Q43-58-Al-1 | 4 | 2 | 2 | | 2 | 2 | |
| Q43-58-Al-2 | 16 | 6 | 10 | | 4 | 8 | 4 |
| Q43-58-Al-4 | 87 | 44 | 43 | 3 | 1 | 70 | 13 |
| Q43-58-Cu-2 | 13 | 8 | 5 | | | | 13 |
| Q43-58-Cu-4 | 18 | 7 | 11 | | | | 18 |
| Q43-52-Al-4 | 12 | 120 | | | | | 12 |
| Q43-52-AL-8 | 20 | 8 | 12 | | | | 20 |
| TOTAL | 320 | 164 | 156 | 80 | 80 | 80 | 80 |

The fabrication precision requirements are very high. The gap requirement between the adjacent pole tips is 34.88+/-0.05mm; the deviation of the magnetic center with respect to the mechanical center must be less than 0.05 mm; the dispersion of the effective length between magnets must be less than or equal to $1 \times 10^{-3}$. Details of the quadrupole magnets design are reviewed in an earlier paper [1].

To fulfill this mission in high quality and speed professionally, IHEP machine shop set up a production line and laid down a technological process which was approved by LBNL; meticulously designed and fabricated a variety of tooling; set up a Quality Control and Quality Assurance system according to ISO 9000 standard.

## 2 TOOLING

To assure the production quality and consistency, 40 types (about 70 sets) of precision technical equipment, fixtures and tooling were designed and fabricated including punching die-set for core laminations, core lamination stacking fixtures, coil epoxy potting molds, end-pack stacking & curing fixtures, pole tip chamfer machining fixtures, end plate machining fixture, drilling fixtures, welding fixtures, bussing bending fixtures, lifting tooling for core handling and so on. The production practice shows that all these tooling components play very important roles in QA and QC. It is worth mentioning that the punching die set has a high precision and long life. The total 560,000 laminations for the 320 magnets have been punched with one set of punching die set. All the laminations satisfy the uniformity requirement 0.02 mm and the burr requirement 0.03 mm (Fig.1). This is the first time for IHEP to have made this kind of punching die set that has such a long life in practice.

## 3 CORE FABRICATION

The shuffling process is a very important program to assure the reproducibility of magnets. The method we adopt is to distribute the laminations punched from different packets of steel sheet with different magnetic properties to each half core and to distribute the laminations punched early and late to each half core.

Stacking is a key process. We control the half core weight difference among magnets in the range not to exceed the weight of one lamination (≈ 500g). Stacking pressure is more than $3kg/cm^2$. Stacking factor is more than 97.5%. The geometrical sizes of every half core are controlled strictly. For instance, the flatness of yoke and pole is less than 0.03 mm (the design requirement is 0.05mm). The length deviation of half core is within the range of +0.25mm to -0.13mm (the design requirement is +/- 0.50 mm).

Welding the core is the last key process for the half core fabrication. We adopt a reasonable welding standard, and the welding deformation is less than 0.02mm.

0-7803-4376-X/98/$10.00 © 1998 IEEE

Until now, among the 638 half cores (for 319 magnets) the rate of finished products is 100%.

## 4 COIL FABRICATION

The coil fabrication is very complicated. Among the procedures, the vacuum impregnation procedures are the most important and key ones. For the LER Quadrupoles, we adopt the potting procedures which were used for BEPC project in 1980's. The production practice shows that the procedures can satisfy the requirements well. The main difference of these procedures from the procedures which were used by LBNL, is the different potting mold design. Our mold design uses the mold itself as the vacuum sealing container; LBNL's mold was placed separately into a big vacuum tank.

There are four kinds of coils; they are as follows:

| Material | Cross Sec. | W Channel | Turns | W Circuits |
|---|---|---|---|---|
| | (inch) | (ID inch) | | |
| Al | 0.5x0.5 | 0.25 | 15 | 1 |
| Al | .25x.25 | 0.124 | 58 | 1,2,4 |
| Al | .25x.25 | 0.124 | 52 | 4,8 |
| Cu | .25x.25 | 0.124 | 58 | 2,4 |

During the fabrication of coils, some coil cracking occurred. After we found the causes we have solved the problem. There are several main causes that made some coils crack.

1. The thickness of epoxy at the root of the coil lead is too thick. When we open the mold after potting and curing, the outer force makes the thick epoxy at the lead root crack.

2. The contour size of the wound coil is too big, and it caused difficulty in putting the coil into mold. After we forced the coil into the mold, the coil accumulated some stress. When the potted coil was taken out of the mold, the stress releases caused the epoxy to crack.

## 5 MAGNET ASSEMBLY

The gaps between the pole tips of upper half core and low half core are adjustable with shims.

When we carry out the pre-assembly, we chose two half cores which have similar lengths, adjust the gaps within the tolerance (+/- 0.04 mm), and ensure the clamp torque of the two half cores is identical with others.

Last, we assemble all the parts including the four coils, bussing, water hose, and so on, and remeasure the gaps precision as mentioned above.

So far, all the quadruple magnets we produced satisfy the specifications [ see Figure 2, 3, 4 and 5].

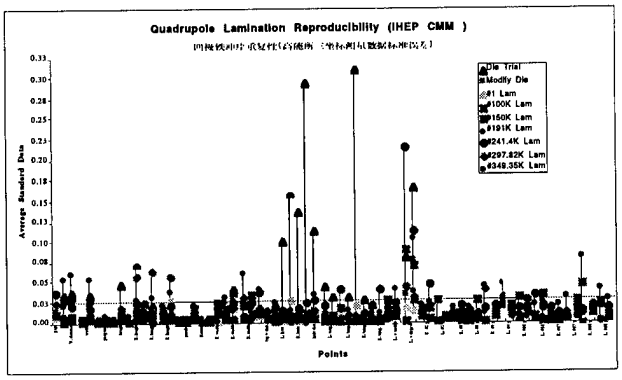



Figure 1: Quadrupole Lamination CMM Data

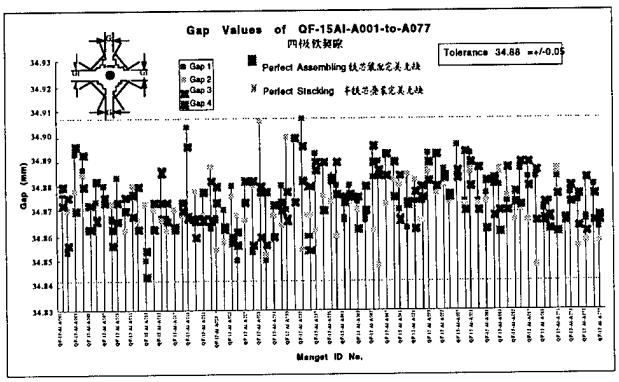



Figure 2: Gap Values of 77 Quadrupoles

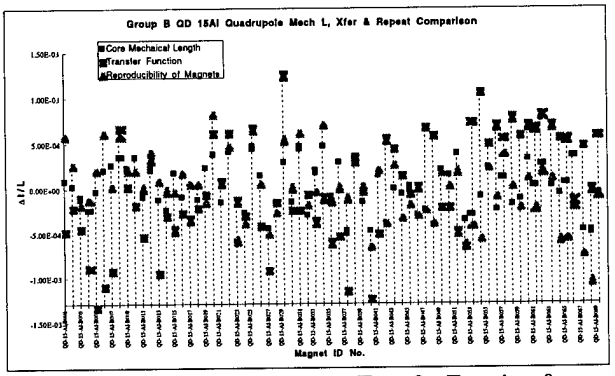



Figure 3: Mechanical Length, Transfer Function & Reproducibility Comparison of 69 B Group Quadrupoles

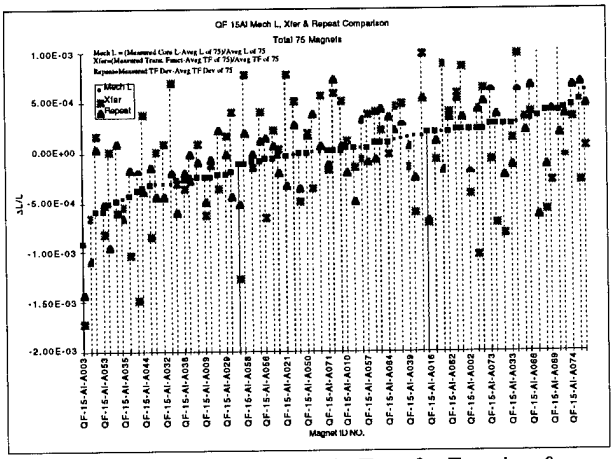



Figure 4: Mechanical Length, Transfer Function & Reproducibility Comparison of 75 Quadrupoles

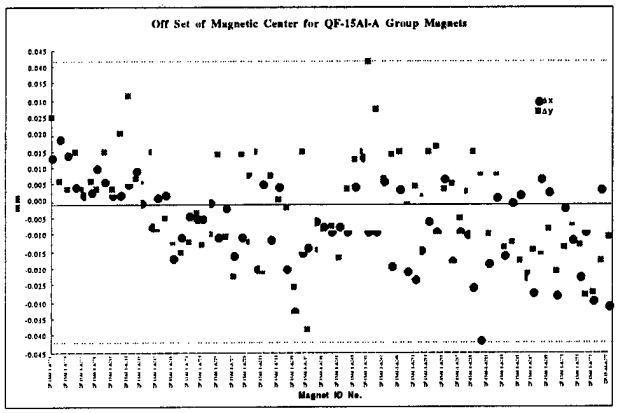



Fig. 5 A Group Quadrupole Magnetic Center Off Set

## REFERENCES

1. J. Tanabe, J. Osborn, N. Li, D. Yee, Standard 43 cm Quadrupole Engineering Design, LBNL Mechanical Engineering Note M7498A, October, 1994

# 3D DESIGN, CONSTRUCTION, AND FIELD ANALYSIS OF CIS MAIN DIPOLE MAGNETS

G. P. A. Berg, W. Fox, D. L. Friesel, and T. Rinckel
Indiana University Cyclotron Facility, 2401 Milo B. Sampson Lane, Bloomington, IN 47405

*Abstract*

Four normal conducting main dipole magnets were designed and built for the Cooler Injector Synchrotron CIS allowing proton acceleration up to 220 MeV with a magnetic field of $B_{max} \approx 1.78$ T. Field calculations in two (2D) and three (3D) dimensions were used to optimize magnet laminations and end packs. Endpacks are designed to determine edge angle, effective field length (EFL) and to compensate hexapole components. The magnets are assembled of machined laminated wedges to accommodate the strong curvature. Field maps were performed in the range of B = 0.25 T - 1.8 T. The magnet parameters are well within expected specifications and initial tests at injection energy of CIS were conducted successfully.

## 1 INTRODUCTION

The main objective of CIS [1] is to replace the present Cyclotron injection to fill the IUCF Cooler up to about $10^{11}$ protons within a few seconds. The CIS circumference of 17.384 m allows bucket-to-bucket injection into the Cooler. The lattice for CIS requires four laminated 90° main dipole magnets with bending radius $\rho$ = 1.273 m, EFL = 2 m, and edge angles of 12°. Initial operation of 1 Hz, with later upgrade to 5 Hz is planned and eddy current effects were taken into account.

With the availability of improved finite element electromagnet design programs [2] with 3D capability, faster computers and new materials for magnet construction it has become feasible to design magnets optimized for special purposes without costly and time consuming prototyping. This has allowed us to design high field dipole magnets for a very compact and cost efficient synchrotron. Despite the best field calculations there are remaining uncertainties in the produced magnets resulting from uncertainties in materials, fabrication, construction details and other approximations which cannot be or which are impractical to be modeled in the calculations.

We adopted the following guide lines for the design.

1) Consider and determine construction methods.

2) Calculate axisymmetric radial sections to determine the laminations and to evaluate higher order components inside the magnet. Evaluation of dynamical aperture for magnet without end effects.

3) Study end block parameters using 2D calculations.

4) Compensate hexapole components developing along the magnet and at the ends by designing final end blocks using 3D calculations.

5) Model complete magnet in 3D and verify dynamical aperture using field integrals $\int Bdl$ along beam rays.

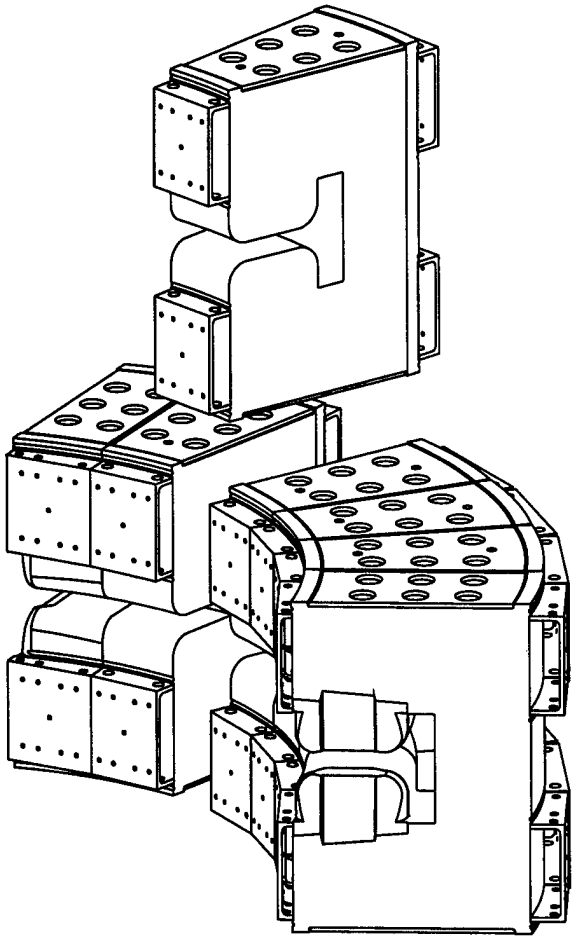


Figure 1: Isometric plot of CIS dipole magnet assembly. For better viewing one wedge is moved up and the coil is removed.

## 2 MAGNET DESIGN AND CONSTRUCTION

For cycling rates up to 5 Hz lamination thickness of 1.519 mm was found to be sufficient. The large bend of 90° prevented application of usual stacking methods. We decided to stack and cure lamination blocks and machine appropriate wedges, assembled as shown in Fig. 1. This was possible because of the availability of B-stage epoxy, which is dry and allows stacking of large blocks which is not possible using the wet-laying method. Bonding of the B-stage epoxy is done subsequently by curing at 150°. The electrical insulation is also provided by the epoxy. We decided to build C-magnets because of several potential problems with H-frame magnets in this design, e.g. field distortions from lamination severely cut at the thin side of the wedge.

The magnet consists of five machined wedges and two

0-7803-4376-X/98/$10.00 © 1998 IEEE

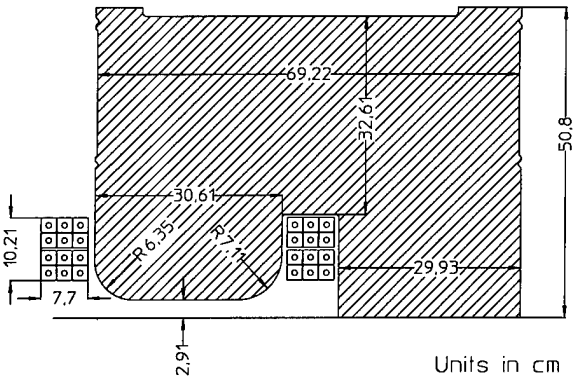



Figure 2: Upper half of CIS lamination and coil cross section.

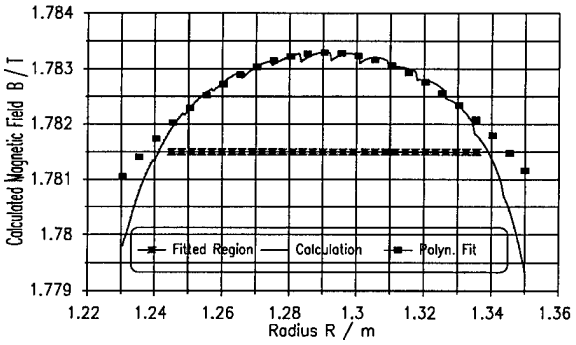



Figure 3: Axisymmetrical field calculation at high field and fit.

end blocks. The pole piece ends show a Rogowsky profile in the center and extrusions ( "noses" ) at the sides. Plates and U-shaped brackets were welded on the bocks for mechanical stability. While the five inner wedges are welded together at the joining brackets, the end blocks are bolted to the assembly for easy removal if necessary. Not shown in Fig. 1 is the strong support to which all block are bolted. No prototyping was done except for one initial end block which was slightly remachined with simple cuts at the "noses" for optimization. A low carbon soft steel with B = 1.8 T at H = 72 Oe was chosen to provide a high saturation limit. The coercive force of about 3.1 Oe was acceptable for our application with hysteresis losses below approximately 1 kW per magnet for the acceleration of protons up to 220 MeV at 5 Hz. The steel was cold rolled in a continuous process and came from a single steel ingot. This eliminated otherwise necessary randomization of laminations during stacking.

In the final calculations we used a B(H) curve deduced from measurements with an Epstein facility for the actual material purchased. Fig. 2 shows the lamination geometry. Also shown are cross sections of the coils which consist of two pancakes with 6 windings in two layers. The pancakes fit through the vertical gap of g = 5.82 cm for assembly. Maximum current is 4.2 kA.

## 3 AXISYMMETRIC FIELD CALCULATIONS

The lamination geometry was optimized using axisymmetrical field calculations with the finite element code MagNet which solves the Laplace equation in 2D and 3D geometries. We optimized the size of the return, inner and out radii of the sides of the pole pieces R = 6.35 cm and 7.11 cm, respectively and the location of the coils slightly above the midplane to avoid eddy current effects from fringe fields in the coil conductor. We compared the circular pole edges and a Rogowsky profile and found that in saturation the circular profile provides a 1 - 2 cm wider good-field region. Shims on the pole pieces in the gap were found to be inefficient at high fields and are therefore not used.

Calculations were performed in the field range from B = 0.34 - 1.78 T. The field as function of the radius $\rho$ in the midplane was fitted by the lower terms of a Taylor series $B(x) = B_0 + B_1(x\text{-}x_0) + 1/2B_2(x\text{-}x_0)^2 + 1/6B_3(x\text{-}x_0)^3$. Field calculation and fit at a high excitation are shown in Fig. 3. The range of 9 cm from radius $\rho$ = 1.245 m to 1.335 m was used in the fit. The fitting results are $x_0$ = 1.291 m, $B_0$ = 1.7833 and $B_2$ = -1.22277 T/m$_2$

No improvement of the $\chi^2$ could be achieved by including quadrupole $B_1$ and octupole $B_3$ components except for a small $B_1 < 0.00035$ T/m for the lowest fields. Therefore these terms where omitted in all fits. Also the inclusion of a $B_4$-term and higher order terms was not necessary in the fitted range of 9 cm.

The fitting results of $k2 = B_2/B\rho$ for all calculations are summarized below in Fig. 6 denoted by the label "Axisym". The hexapole component k2 is negative and quite constant up to about 1.5 T when saturation effects set in as visible in Fig. 3.

## 4 2D AND 3D ENDPACK CALCULATIONS

The end blocks of the magnet assembly are parallel blocks of bonded laminations but required machining of the pole piece ends to adjust EFL, edge angle and hexapole component. Around the central ray a Rogowsky profile in beam direction (see Fig. 1) was chosen to provide an effective field boundary EFB close to the mechanical length of the pole pieces. The effect of the "noses" were studied in 3D calculations and edge angle and hexapole components were optimized. The $\int Bdl$ is the field quantity which determines the path of the circulating particles. We analyzed the calculated 3D field in the midplane of the magnet and calculated $\int Bdl(\rho)$ as function of radius $\rho$. The calculated $\int Bdl(\rho)$ values were compared to the same quantity of an ideal magnet with a constant field within the EFB and zero field outside. This allowed us to define the average quantities of hexapole, EFL and edge angle shown in Figs. 4,5, and 6.

The average hexapole k2 calculated in this way is plotted in Fig. 4 as solid line and labeled "Endpack". The effect of the hexapole component "Axisym" inside the magnet is compensated to better than $|k2| < 0.1\ m^{-3}$ up to a field of about 1.4 T. Then k2 becomes more negative due to saturation effects and is about k2 = - 0.55 $m^{-3}$ at 1.8 T field.

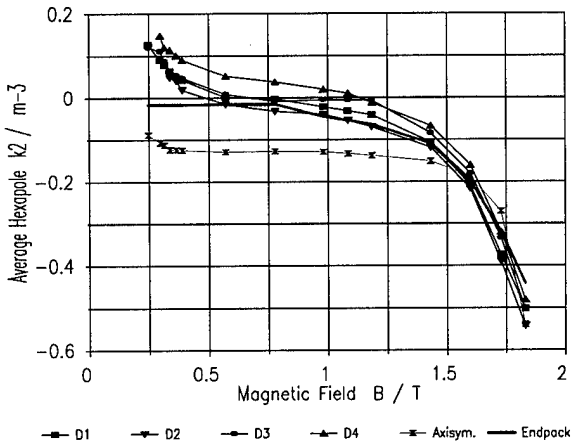



Figure 4: Hexapole component as function of field B.

## 5 FIELD MEASUREMENTS AND ANALYSIS

The fields of all four dipole magnets were mapped with a 16 Hall probe array mounted on the arm of a large x-y table. All Hall probes were calibrated relative to each other within about $10^{-4}$ precision. Absolute calibration was established by comparison to NMR probe measurements to similar precision. Midplane measurements were taken on a 1.27 cm Cartesian grid inside the gap and about 40 cm outside in beam direction for several excitations. Analysis of relevant parameters from the data are performed in the same way as for the calculations. Results for dipoles D1-4 are shown in Figs. 4 - 6. All measured quantities

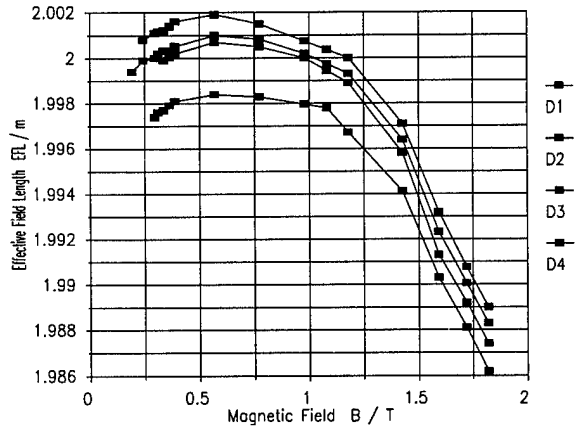



Figure 5: Effective field length as function of magnetic field B.

show some deviation which can be expected from uncertainties in the manufacturing process. The calculated and measured hexapole component shown in Fig. 4 agrees well within manufacturing uncertainties except for a rise of k2 $\approx 0.1\ m^{-3}$ at or slightly below injection field. The effect of the end pack compensation is clearly visible at fields up to 1.5 T. The EFL shown in Fig. 5 agrees within the thickness of one lamination well with the design value of 200.0 cm up to a field of about 1.2 T. For higher fields the EFL decreases by about 1 cm for the highest field of 1.8 T.

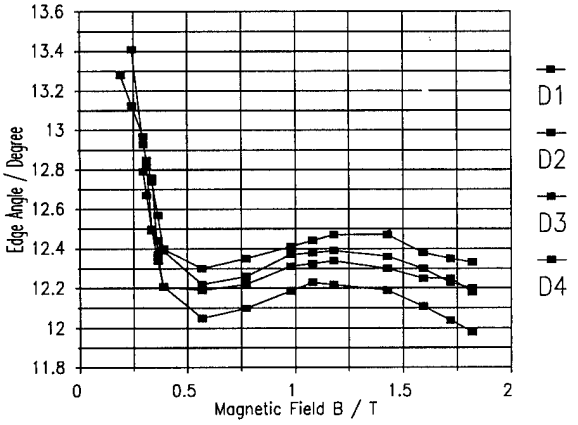



Figure 6: Edge angle as function of magnetic field B.

In Fig. 6 the edge angle is shown. The average value is about 12.25° slightly higher than the design value of 12° for fields higher that 0.35 T. This could be corrected in the magnet design but was not done because it can be compensated easily with the trim quadrupoles, as mentioned before. An increase at lower fields is observed and several measurements were taken below injection field to study this effect, the nature of which is not understood.

## 6 CONCLUSIONS AND SUMMARY

The four normal conducting CIS main dipoles with several new design and construction methods perform as designed and were tested at injection energy for CIS. Detailed field measurements and analysis show that these magnets will enable the synchrotron to operate up to about 220 MeV just below the transition energy of the present lattice design.

## 7 ACKNOWLEDGEMENTS

We want to acknowledge the advise and help, which we received from Fermilab, Brookhaven National Laboratory, the Advanced Photon Source, and the Budker Institute of Nuclear Physics, Novosibirsk which has enabled us to find quickly a successful design for our dipole magnets. We also would like to thank the technical staff of IUCF for their assistance in all stages of the project.

## 8 REFERENCES

[1] Conceptual Design Manual for CIS, Internal Report, Indiana University Cyclotron Facility, Jan. 30, 1995.

D.L. Friesel and S.Y. Lee, "Status of the IUCF Cooler Injector Synchrotron", this publication.

[2] In this design we used the computer code MagNet, Infolytica Corp., Montreal, Quebec.

D.A. Lowther, P.P. Silvester, Computer Aided Design in Magnets, Springer-Verlag, New York 1986.

# MAGNETS AND THEIR POWER SUPPLIES OF JHF 50-GEV SYNCHROTRON

M.Muto, K.Niki and Y.Mori,
Accelerator Laboratry, High Energy Accelerator Research Organization,
Tanashi-shi, Tokyo 188, Japan

*Abstract*

The JHF 50-GeV Synchrotron [1], high intensity proton synchrotron, consists of 96 bending magnets, 176 quadrupole magnets and 48 sextupole magnets. The design study of the magnets is now in progress. Also, the conceptual design study of the power supply system has been started. The bending magnet is of a modified window frame type, 6.2 m in length and 1.8 T in magnetic field in peak. Field gradient of the quadrupole magnet is 20 T/m in peak and the bore radius is 66 mm. The total active power of bending and quadrupole magnets is estimated to be 80 MW in peak.

Recent results of the design studies of magnets and power supply system are described in this paper.

## 1 MAGNET DESIGN

The JHF 50-GeV synchrotron ring consists of 96 bending magnets, 176 quadrupole magnets and 48 sextupole magnets. Main parameters for magnet design of the bending and quadrupole magnets are summarized in Table 1. Based on these requirements, the bending magnet and the quadrupole magnet have been designed.

Table 1. Main Parameters for Design of 50 GeV Synchrotron Magnets

| | |
|---|---|
| Injection | 3 GeV |
| Maximum | 50 GeV |
| Circumference | 1442 m |
| Repetition Rate | 0.29 Hz (~3 Hz in future) |
| Bending Magnet | |
| Magnetic Rigidity | 12.76 - 170 Tm |
| Field | 0.135 T (for 3 GeV) |
| | 1.8 T (for 50 GeV) |
| Length | 6.2 m |
| Number | 96 |
| Quadrupole Magnet | |
| Max. Field Gradient | 20 T/m |
| Length | 1.5 - 2 m |
| Total Number (8 families) | 176 |
| Magnet Aperture (full width) | |
| B-Magnet | 106 $mm^h$ |
| | (x $106^W$ for useful) |
| Q-Magnet | 132 $mm^\phi$ |

### *1.1 Bending Magnet*

Figure 1 shows a cross sectional view of the bending magnet. The side slopes of the pole are determined carefully to avoid partial magnetic saturation in the pole. In order to reduce a magnet size and an excitation power requirement, the bending magnet is designed as to be of a sector type one.

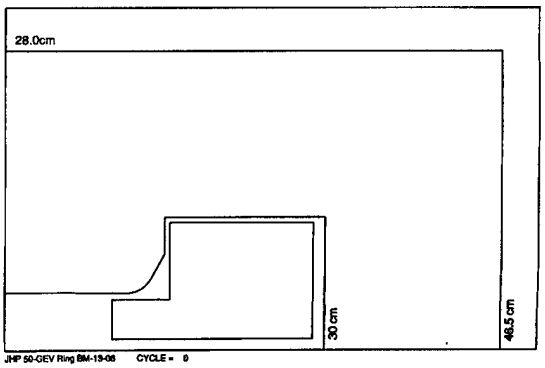



Fig. 1. Cross sectional view of the bending magnet

Figure 2 shows field distributions at the field level of 0.135, 0.5, 1.0, 1.5 and 1.8 T calculated with the program code of Poisson. Vertical beam sizes in the bending magnet at the energy of 3 GeV and 50 GeV is estimated to be about 50 mm and 18 mm in half, respectively. In these regions, the field distortion is suppressed to the level of +- 0.02 % or less as be seen in the figure. The main parameters of the bending magnet are listed in Table 2.

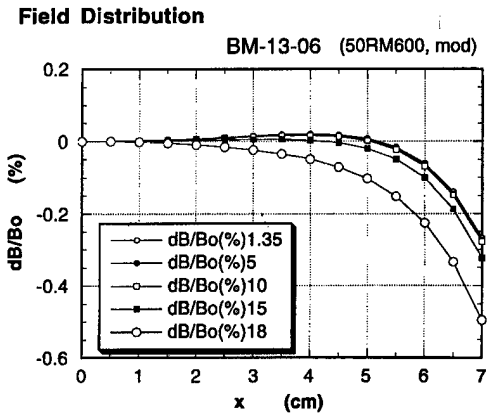



Fig. 2. Field distributions of the bending magnet

0-7803-4376-X/98 /$10.00 © 1998 IEEE

Table 2. Main Parameters of Bending Magnet

| | |
|---|---|
| Magnet Size | |
| Length | 6.2 m |
| Width (iron yoke) | 93 cm |
| Height (iron yoke) | 56 cm |
| Coil | 17 turns x 2 |
| Weight | 25 ton |
| Excitation Current | |
| Injection (3 GeV) | 336 A |
| Maximum (50 GeV) | 4978 A |
| Power | |
| Active Peak Power | 54.0 MW |
| Dissipation Power | 12.0 MW |
| Cooling Water | 8.5 ton/min. |

*1.2 Quadrupole Magnet*

Figure 3 shows a cross sectional view of the quadrupole magnet and figure 4 shows a distributions of calculated field gradient at the excitation level of 0.15, 1.0, 1.5, 1.8 and 2.0 T/m. Some quadrupole magnets in the section of a slow extraction straight are designed separately, because the extraction orbit will be sfifted from the center and beams go through the region of coil and/or return yoke of the normal design.

The main parameters of normal bending magnet are listed in Table 3.

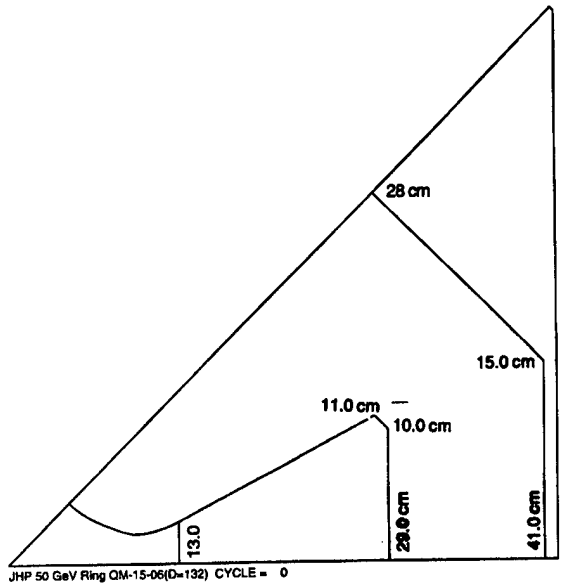



Fig. 3. Cross sectional view of the quadrupole magnet

Table 3. Main Parameters of Quadrupole Magnet

| | |
|---|---|
| Magnet Size | |
| Length | 1.5 and 2.0 m |
| Width (iron yoke) | 82 cm |
| Height (iron yoke) | 82 cm |
| Weight | 6.7 ton |
| Excitation Current | |
| Injection (3 GeV) | 2630 AT |
| Maximum (50 GeV) | 48430 AT |
| Power | |
| Active Peak Power | 24.0 MW |
| Dissipation Power | 7.0 MW |
| Cooling Water | 5.0 ton/min. |

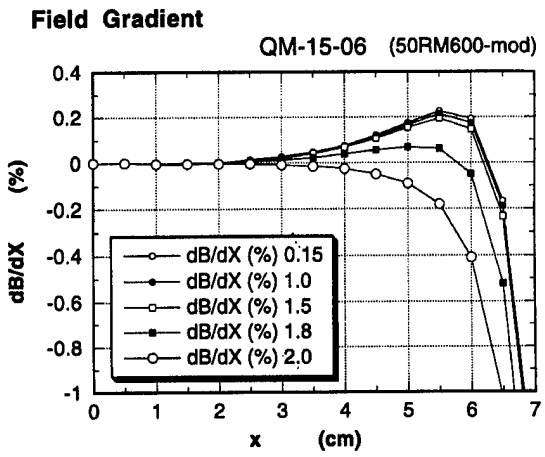



Fig. 4. Distributions of field gradient view of the quadrupole magnet

## 2 POWER SUPPLIES

Figure 5 shows an example of an excitation pattern of the bending magnet operated up to the peak energy of 50 GeV.

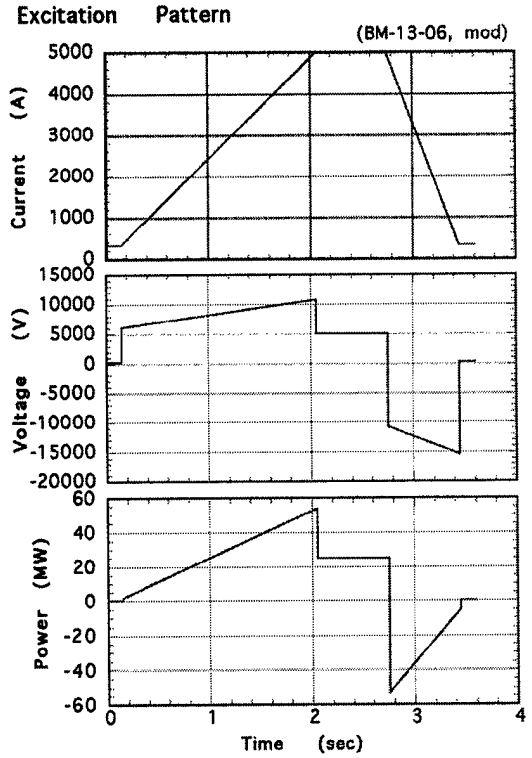



Fig. 5. An example of an excitation pattern of the bending magnet

As seen in Tables 2 and 3, the total peak active-power becomes about 80 MW. In a case of a power supply like this, a SCR system is generally used to convert electric power from AC to DC and to generate trapezoidal wave form current. However, as well known, it makes very large reactive peak power and significant higher-order AC current, and as a result, it gives rise to a problem of serious voltage fluctuation in an external AC line. In our case, a voltage fluctuation has been estimated to become about 8 - 10 %, which exceeds an allowable level. Therefore, in order to connect a power supply with a large SCR system to an external AC line directly, a very large reactive power compensator and many filters to reduce higher-order current components in the AC line are required inevitably.

On the other hand, the 50 GeV synchrotron is to be constructed in the KEK campus in which there exist some big accelerators, namely the 2.5 GeV electron linac, the PF ring and, in near future, KEK-B. From this circumstances, it is strongly expected to smooth the variation of active power itself as long as possible.

To resolve these difficulties, a power supply system shown in the figure 6 is investigated optionally as a power supply for the bending magnet of the JHF 50-GeV synchrotron ring. By using a rotating machine between an external AC line and a SCR system, problems of the very large reactive power and higher order AC current in the AC line are removed perfectly and, furthermore, the variation of active power is smoothed significantly.

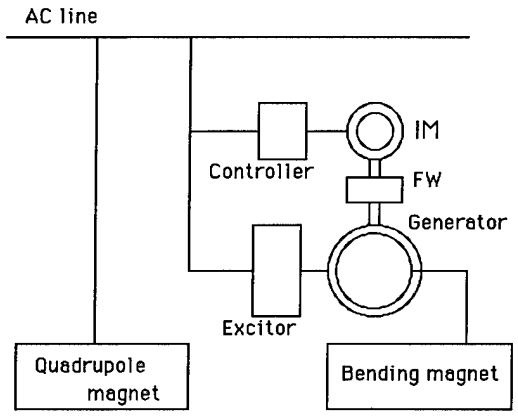



Fig. 6. One idea of a power supply system for the bending magnet

The principal parameters of the rotating machine are listed in Table 4.

Table 4. Principal Parameters of Rotating Machine

| | |
|---|---|
| Induction Motor | |
| Input Power | 17 MW |
| Voltage | 6.6 kV |
| Generator | |
| Output Power | 70 MVA |
| Voltage | 6.6 kV |
| Rotating Frequency | 600 Hz +- 5 % |
| Total Weight | 200 ton |

On the other hand, for the quadrupole magnet, it is studied to use IGBT (Insulated Gate Bipolar Transistor) as an element of power convertor from AC to DC of a power supply and connect it to the external AC line directly. By using IGBT, it becomes possible to construct a power supply which generate no reactive power in spite of forming a trapezoidal wave-form current. If using a SCR for this case, a reactive peak power is estimated to become about 20 Mvar with corresponding to the active peak power of 24 MW (total of 8 families, see Tables 1 and 3).

Eight power supplies using IGBT will be installed because the 176 quadrupole magnets are divided into 8 groups (families). In which, the largest power rate of active peak power is about 5 MW.

By employing a rotating machine and IGBT power supplies, the voltage fluctuation of the external AC line is finally expected to be suppressed to the level of about 1 %.

## 3 ACKNOWLEDGEMENTS

The authors would like to thank Prof. H.Sato for his many usefull disussions and suggessions.

## REFERENCES

[1] to be reported elsewhere in this conference.

# MAGNETIC DESIGN AND MEASUREMENT OF NONLINEAR MULTIPOLE MAGNETS FOR THE APT BEAM EXPANDER SYSTEM*

D. Barlow, R. Shafer, R. Martinez, Los Alamos National Laboratory, Los Alamos, NM 87545
P. Walstrom, Northrop Grumman Corp.
S. Kahn, A. Jain, P. Wanderer, Brookhaven National Laboratory

*Abstract*

Two prototype nonlinear multipole magnets have been designed for use in the 800-MeV beam test of the APT beam-expansion concept at LANSCE. The iron-dominated magnets each consist of three independent coils, two for producing a predominately octupole field with a tunable duodecapole component, and one for canceling the residual quadrupole field. Two such magnets, one for shaping each transverse plane, are required to produce a rectangular, uniform beam current density distribution with sharp edges on the APT target. This report will describe the magnetic design of these magnets, along with field measurements, and a comparison to the magnetic design.

## 1 INTRODUCTION

Static beam-expansion systems made up of a combination of linear and nonlinear magnets have been proposed for various accelerator-driven neutron sources such as the Accelerator Production of Tritium (APT) facility[1]. The static beam-expansion system proposed for APT accepts a nearly round Gaussian beam with a mean radius of a few millimeters and produces a 0.16 m by 1.6 m rectangular beam distribution on the target. Inside the rectangle, the current density is nearly constant, while outside, the current density drops off sharply to essentially zero. The nonlinear expansion is accomplished in a two-stage process. Quadrupoles and drifts are first used to produce a beam that is highly elongated in the $y$ direction, with a waist in the $x$-$z$ plane. The first nonlinear magnet is placed at this waist. The leading term in the multipole expansion for the central field of this magnet is an octupole term; the higher terms that are present modify the octupole behavior at larger distances from the axis. The effect of the first nonlinear magnet is to fold in the tails of the distribution in $y$-$y'$ phase space, while leaving the $x$ phase-space distribution substantially unchanged. The first nonlinear magnet is followed by quadrupoles and drifts that produce a beam that is elongated in the $x$-$x'$ phase space, with a waist in the $y$-$z$ plane. A nonlinear magnet at the second waist that is similar to the first one, but somewhat larger and rotated 90°, folds in the tails of the $x$-$x'$ phase-space distribution. Finally, quadrupoles and drifts are used to produce the desired expanded beam size on the target.

As a test of this concept, two nonlinear magnets have been designed and built for use in a beam-expansion experiment using the 800-MeV proton beam of LANSCE.

*Work supported by the US Department of Energy

## 2 FIELD DESCRIPTION

In initial particle-tracking simulations of the beam expander, the fields of the nonlinear magnets were described by truncated multipole expansions with a leading octupole term followed by higher order terms, i.e.,

$$B^* = B_x - iB_y = -ig_8 z^3 (1 + az^2 + bz^4 + cz^6), \quad (1)$$

where $z=x+iy$, $g_8$ is the octupole gradient, $a$ adds a duodecapole component, etc[2]. The coordinates in Eq. 1 refer to the local magnet coordinates; they are the same as the beamline coordinates for the second nonlinear magnet and are rotated 90° for the first nonlinear magnet. Typical values of the parameters for the two magnets that gave good results for particle-tracking simulations of the 800 MeV beam expansion experiment at LANSCE are listed in Table I, along with the magnet lengths and clear beam apertures. Since the magnets are long in comparison to their apertures, a two-dimensional field description is entirely adequate for simulation purposes. The nonlinear magnets built for the experiment at LANSCE and planned for APT are variable-profile magnets for which Eq. 1 can be only an approximate description of the various possible field profiles. Indeed, apart from the leading octupole behavior and the fact that the field strength levels off to a value lower than a pure octupole field at larger $x$, there is nothing fundamental about the form of Eq. 1. From the point of view of the present beam-expansion scheme it is merely a convenient form to use for field-profile optimization. For the parameter values of both the LANSCE experiment and the APT design, contours of constant flux-density around the axis for the two magnets are oval-shaped and elongated in the same direction as the beam cross section. It would not be feasible to produce these fields with round-aperture magnets. Fortunately this is not necessary in view of the elongated beam profiles. Since the magnets have an aperture with a large width-to-height ratio, a single power-series expansion, e.g. Eq. 1, cannot

Table I
Field shape parameters, dimensions of the beam envelope, and length of the two nonlinear magnets.

| Magnet | First | Second |
|---|---|---|
| $g_8$ | $6.498\times10^4$ T/m$^3$ | $1.979\times10^4$ T/m$^3$ |
| $a$ | $-1.847\times10^3$ 1/m$^2$ | $-7.072\times10^2$ 1/m$^2$ |
| $b$ | $1.279\times10^6$ 1/m$^4$ | $1.876\times10^5$ 1/m$^4$ |
| $c$ | $-3.936\times10^8$ 1/m$^6$ | $-2.211\times10^7$ 1/m$^6$ |
| beam height | 3 mm | 5 mm |
| beam width | 25 mm | 40 mm |
| length | 500 mm | 500 mm |

0-7803-4376-X/98/$10.00 © 1998 IEEE

be used to describe the field over the entire volume occupied by the beam because the radius of convergence is limited to the distance from the origin to the nearest iron. Accordingly, a more sophisticated field description has been developed to parameterize the two-dimensional field in a way that can be used in particle-tracking simulations[3]. This field description uses a set of overlapping triangular dipole density distributions uniformly distributed on the surface of fictitious poles. The poles are planes of infinite extent and permeability and are located outside the beam envelope, but not substantially more than the minimum magnet gap. Weights for the triangle source elements are found by a least-squares fit to the field data.

## 3 MAGNETIC DESIGN

It is possible to design iron pole-piece magnets that produce a field that closely approximates the truncated power series of Eq. 1. for fixed parameter values $g_8$, $a$, $b$, and $c$. The design approach is based on the fact that high-permeability pole pieces are very nearly contours of constant scalar magnetic potential. The scalar magnetic potential is the real part of the complex potential obtained by integrating Eq. 1, i.e.,

$$\Phi = -ig_8 z^4 \left(\frac{1}{4} + a\frac{z^2}{6} + b\frac{z^4}{8} + c\frac{z^6}{10}\right), \qquad (2)$$

Pole-tip profiles are obtained by choosing contours of constant real scalar potential that clear the beam pipe. Although the full plot of the scalar potential of Eq. 2 has 20 lobes, in practice only 8 lobes (two per quadrant) are needed for a practical magnet, since distant lobes affect the field inside the beam envelope negligibly. The ampere-turns required to excite the poles are obtained by dividing the respective scalar potentials by the permeability of free space. Unfortunately, an eight-fixed-pole magnet cannot be used if the parameters of Eq. 1 (or other field descriptions) are to be substantially varied by varying only the currents, since the constant-potential contours for one set of parameters do not coincide with the contours for another set of parameters. In order to allow field-profile variation, we have adopted a different design approach, employing twelve poles instead of eight in a variable-profile magnet that provides a range of leading octupole strengths and varying rates of departure from the octupole field at larger $x$. In the design of the 12-pole magnet, contours of constant scalar potential for the limits of parameter variation of Eq. 1 were plotted and initial pole-piece shapes that could, when appropriately energized, approximate the limiting contours were found. Flat pole-tip surfaces were used to simplify the modeling and fabrication of the magnet. The inner, middle, and outer poles were energized by inner, middle, and outer windings respectively. In finding the final pole-piece shapes, the midplane field was calculated for various combinations of currents with a two-dimensional finite-element code and compared with the desired range of field profiles. Since the quadrupole component of field at the origin is supposed to be zero in the present expansion scheme, there are effectively two degrees of freedom in varying the field profile. The current in the inner winding required to null out the quadrupole field is very nearly a constant times the current in the middle winding and almost independent of the current in the outer winding. Incremental changes were made to the pole tip shapes until the difference between the desired and calculated fields was minimized over the width of the beam. The resulting cross section for the first magnet, including the conductors, is shown in Fig. 1. A comparison of the midplane field for the first magnet calculated with a finite-element code and the fields from Eq. 1 using the parameter values of Table I is shown in Fig. 2.

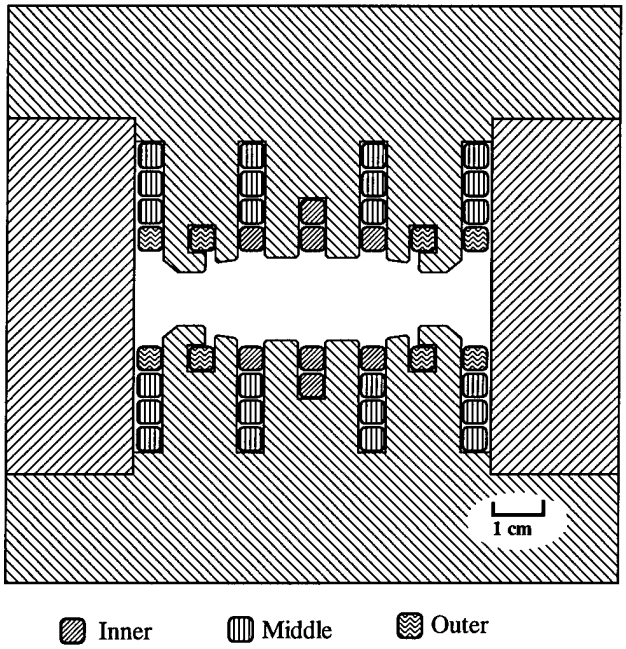



Fig. 1 Cross section of the first nonlinear magnet showing the inner, middle, and outer windings.

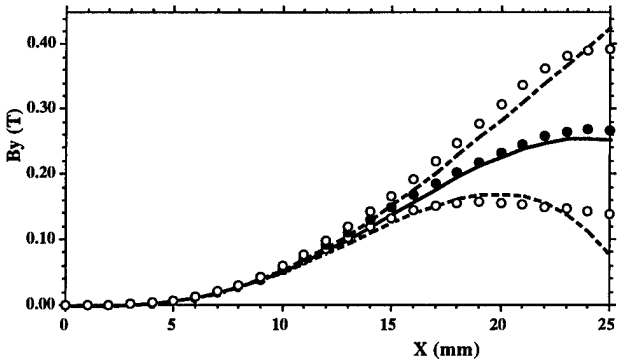



Fig. 2 Comparison of the desired and calculated midplane fields of the first nonlinear magnet for the nominal setting (solid curve and solid points respectively). Also shown are the desired and calculated midplane fields at the limits of the field profile variation (dashed curves and open points respectively). The normal field component (By) is antisymmetric in $x$.

The desired field shape of the second magnet was similar enough to that of the first that its pole-tip profile was simply a scaled-up version of that of the first magnet.

## 4 MECHANICAL DESIGN AND FABRICATION

Both the nonlinear magnets were built with the same mechanical design and fabrication procedures. The pole tip profile was machined by electron-discharge machining (EDM) followed by a light grinding of the pole tips and other critical dimensions to achieve the desired tolerance on the pole tip profile and spacing. Due to limitations in the EDM machining the 50 cm-long iron core was machined in two 25 cm-long segments. After machining, the two segments were aligned and held together by stainless steel strongbacks. Iron yokes on either side maintained the spacing between the top and bottom halves of the magnets. As shown in Fig. 1 the first nonlinear magnet was wound with just 1, 3, and 1 turns of hollow-core copper conductor for the inner, middle, and outer windings respectively. The larger size of the second nonlinear magnet made it possible to quadruple the number of turns per winding. The windings were formed on a mandrel, fit into their respective spaces, and potted with epoxy. The corresponding windings in each quadrant were connected in series allowing the magnet to be energized by three independent power supplies.

## 5 MAGNETIC MEASUREMENTS

The central field of the first nonlinear magnet was measured at the Los Alamos National Laboratory (LANL) using a small calibrated Hall probe mounted on a three-axis measuring machine. Measurements were made of the normal field component in the midplane at the center of the magnet for the three windings energized separately as well as simultaneously. Some typical measurement results for the first nonlinear magnet are shown in Fig. 3. Also included in Fig. 3 are the results of the two-dimensional field calculations for the nominal current settings. The fields from the three windings energized separately were found to vary linearly with current. This linearity implies that, to a good approximation, the field with all three windings energized simultaneously equals the sum of the fields with the windings energized separately. Hence it is sufficient to characterize the field for the windings energized separately. In addition to the Hall probe measurements, the integral field of the first nonlinear magnet was measured at the Brookhaven National Laboratory (BNL) using a rotating coil system. The rotating coil was wound with tangential windings at a radius of 7.4 mm from the axis of rotation. The rotating coil measured the integral field as it was stepped in 3 mm intervals across the width of the magnet. These measurements provided a harmonic description of the magnetic field, from which both the integral of the normal and transverse field components could be calculated at any point of interest over the area measured. As shown in Fig. 4 the rotating coil measurements are in good agreement with the two-dimensional field calculations on and above the midplane.

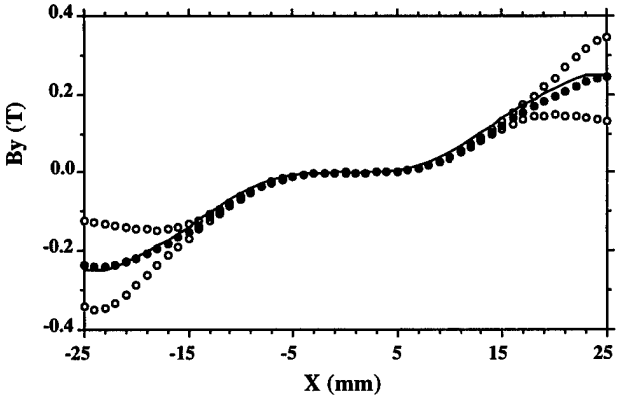



Fig. 3 Calculated and measured midplane field at the center of the first nonlinear magnet for all three windings at their nominal values (solid curve and solid points respectively). Also shown are the midplane fields measured at the limits of the current range of the outer winding, (open points).

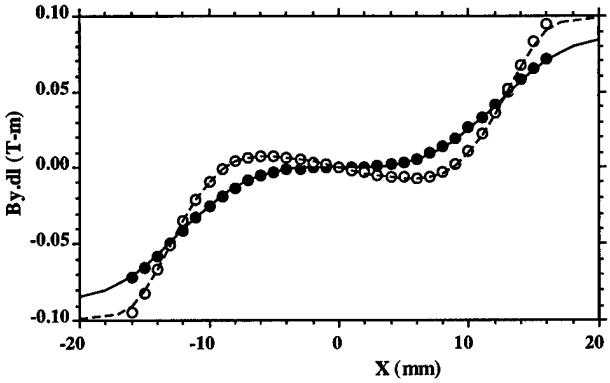



Fig. 4 Results of the rotating coil measurements of the first nonlinear magnet showing the integral field 5 mm above as well as on the midplane for a typical current setting (open and solid points respectively). Also shown are the integral fields for the same conditions estimated from the two-dimensional field calculations (curves). The integral fields were estimated from the two-dimensional results by multiplying by the 0.5 m length of the magnet.

The second nonlinear magnet was measured at LANL with a Hall probe and three-axis measurement machine with similar agreement between the measured and calculated fields.

## 6 CONCLUSIONS

Two nonlinear multipole magnets have been designed, fabricated and measured. The calculated and measured fields for both magnets were found to be in good agreement. The magnets are presently being installed in the first experiment at LANSCE.

## 7 REFERENCES

[1] B. Blind, Nucl. Instr. and Methods, B57, p1099 (1991).

[2] P. Walstrom, AOT-1:TN-95-109, LANL internal report (1995).

[3] P. Walstrom, LANL, LA-CP-97-13, (1997).

# OPTIMIZATION OF THE PEP-II LOW-ENERGY RING DIPOLES

P. Barale, N. Li, J. Osborn, J. Tanabe, R. B. Yourd, and M. S. Zisman
Lawrence Berkeley National Laboratory*, Berkeley, CA 94720 U.S.A.

Y. Sun and X. Xu
Institute of High Energy Physics, Beijing, PRC

*Abstract*

The PEP-II Project [1], a collaboration of SLAC, LBNL, and LLNL, began construction in January 1994. Dipoles for the PEP-II Low-Energy Ring (LER) are being fabricated in China in collaboration with the Institute of High Energy Physics (IHEP) in Beijing. The LER design calls for short dipoles ($l_{eff}$ = 450 mm) with a 63.5 mm gap. As a result, magnetic properties are dominated by end effects and a proper end chamfer must be developed. Magnetic measurements using both integral coil and rotating coil techniques were carried out at LBNL on an early dipole prototype to determine the sensitivity of various allowed multipoles to the end chamfer shape. Dynamic aperture studies were carried out in parallel to explore the sensitivity of the lattice to these multipoles. By interpreting the measurement results in terms of differences from the baseline chamfer, a prescription was developed to "transfer" the results to another prototype dipole more representative of the production magnets. The optimized end chamfer shape was validated with a pre-production dipole and full production is under way.

## 1. INTRODUCTION

The design for the LER arc dipoles was developed [2] in collaboration with IHEP and these magnets are now being fabricated in Shanghai, China. Main parameters for the dipole are given in Table I. Although the LER circumference is 2200 m, the desire for enhanced radiation damping led to the use of short, high-field dipoles (see Fig. 1). For a short dipole having a large gap, the magnetic properties are heavily influenced by the end fields.

Table I. PEP-II LER dipole parameters.

| | |
|---|---|
| Nominal energy [GeV] | 3.1 |
| Energy range [GeV] | 2.4–3.5 |
| Effective length [m] | 0.45 |
| Bend radius [m] | 13.75 |
| Gap [mm] | 63.5 |
| Nominal field [T] | 0.752 |
| Core length [m] | 0.382 |
| Nominal current [A] | 580 |
| Magnet power [kW] | 4.5 |
| RMS strength variation, $\Delta B/B$ | 0.001 |
| Allowed multipoles, $b_n/b_1$ @ 30 mm | $\leq 1 \times 10^{-4}$ |

*Supported by the U.S. Department of Energy under contract DE-AC03-76SF00098.

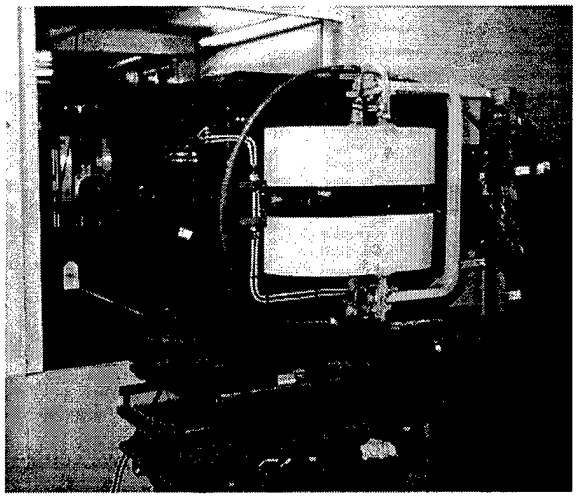


Fig. 1. LER dipole being measured at IHEP.

Measurements of two early prototypes (the first with removable end chamfer inserts) indicated that the multipole content was somewhat too high; this was confirmed by tracking studies of the LER dynamic aperture. Dipole field optimization required development of a chamfer to reduce these unwanted field components, particularly the sextupole ($n$=3) contribution. Though we did carry out some 3-D magnetic analyses [3], the development work consisted mainly of shimming the end chamfers to determine empirically the changes in multipole content of the first prototype magnet. Measured differences were then applied as adjustments to the second magnet. We were guided in the shimming by Halbach's analytical approach [4], which permits exploring the problem of canceling more than one multipole with the end chamfer.

## 2. PROTOTYPE RESULTS

Integral-coil measurements made at LBNL on the first prototype dipole (Fig. 2), fabricated by an initial industrial partner of IHEP, showed marginally satisfactory multipole content with the baseline chamfer obtained from 3-D calculations with the AMPERES code [5].

After IHEP transferred dipole production activities to Kelin Company, an industrial partner in Shanghai, a second prototype was produced, measured at IHEP, and sent to LBNL for verification. Though the second magnet was nominally identical to the first, it showed (Fig. 3) more pronounced field dependence and higher multipole content. Laminations for the two dipoles were from the same batch, and were punched with the same die, so the

0-7803-4376-X/98/$10.00 © 1998 IEEE

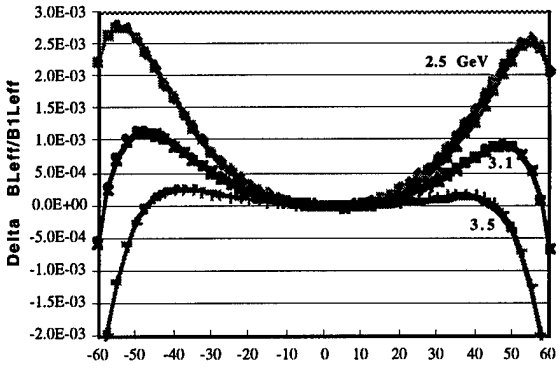



Fig. 2. Prototype 1 integral-coil results.

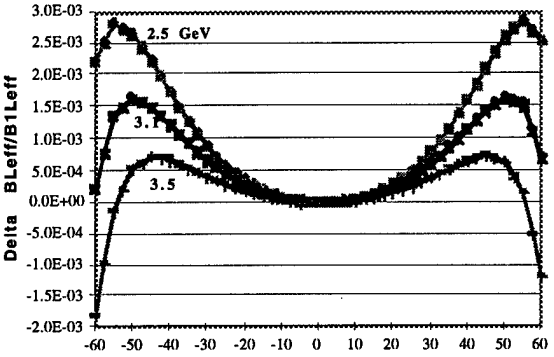



Fig. 3. Prototype 2 integral-coil results.

difference between magnets could only be attributable to the solid steel end plates.

Comparing Figs. 2 and 3, it appears that the original magnet shows saturation effects. Subsequent investigation showed that the steel used in the end plates of the original prototype had lower magnetic quality than that used in the second magnet, consistent with our observations.

Although the first magnet was built with removable inserts for the end chamfer—which proved invaluable in the optimization work described below—the second and subsequent dipoles had a fixed chamfer. For this reason, we made many of the measurements with modified chamfers only on the original prototype.

## 3. MEASUREMENT APPROACH

Measurements on both prototypes were initially carried out at IHEP using a long coil to measure ∫Bdl across the mid-plane of the dipole. After air shipment to LBNL, equivalent measurements were repeated with a finer grid. Both sets of measurements gave consistent results. Multipole coefficients were extracted from the long coil results by fitting a polynomial to the data. (Though this is straightforward in principle, care was taken to avoid numerical problems that appeared in several fitting routines we tried.) Unfortunately, it is difficult in practice to reliably measure a sextupole coefficient of $b_3/b_1 \leq 1 \times 10^{-4}$ by this technique, as the changes in integral field close to the magnetic axis ($x$=0) are very small.

To determine the multipole content of the magnet reliably, we resorted to a technique not commonly applied to dipoles—rotating coil measurements. A bucked "quadrupole" measurement coil with a length of 0.75 m and a radius of 25 mm was employed. The data reduction routine was suitably modified to produce coefficients normalized to the dipole, rather than the quadrupole, term.

Because the coil was slightly too short to give a reliable integral measurement, all measurements were performed by inserting the coil from each end of the dipole to the longitudinal center and then combining the results vectorially. It was observed that there was a significant difference in the harmonic content of the magnet at the lead end and the non-lead end. We have not studied this aspect in detail, but there is some evidence that the longitudinal asymmetry is due to different coupling between core and coil associated with the coil crossover geometry.

As a verification of our rotating coil measurements, the multipoles so obtained were used to reconstruct the integral coil measurements by means of Eq. (1).

$$\frac{\Delta B_y l_{eff}}{B_1 l_{eff}} = \sum_{n=3}^{\infty} \left(\frac{b_n}{b_1}\right)_{r_0} \left(\frac{x}{r_0}\right)^{n-1} \qquad (1)$$

The comparison clearly demonstrated that the two techniques produce equivalent results, giving us confidence that we are accurately determining the low-order multipoles with the rotating coil.

## 4. MEASUREMENT RESULTS

Based on the rotating-coil data, we proceeded to modify the chamfer to reduce the multipole content. In view of the strong field dependence visible in Fig. 3, our focus was on the intermediate case of 580 A, corresponding to nominal 3.1 GeV operation of the LER. It is clear from inspection of Fig. 3 that the original chamfer was too deep in the center, so magnetic material had to be added in this region. To determine the sensitivity, thin steel shims of different thickness were glued in turn to the end plate chamfers and measurements made with the rotating coil to see the effects on the $n$=3,5,7 components. We verified experimentally that identical shims on the two dipoles modified the allowed multipoles ($n$=3,5,7) in a similar fashion, that is, the *change* in, say, the $n$=3 multipole was the same when the same shims were added to either dipole, though the starting points were different in the two cases. Thus, we predicted multipoles for the second prototype from Eq. (2)

$$\left(\frac{b_n}{b_1}\right)_{2,\mathrm{mod}} = \left(\frac{b_n}{b_1}\right)_{2,\mathrm{nom}} + \left(\frac{b_n}{b_1}\right)_{1,\mathrm{mod}} - \left(\frac{b_n}{b_1}\right)_{1,\mathrm{nom}} \qquad (2)$$

where the subscripts 1 and 2 denote the first and second prototype, respectively, "nom" denotes the nominal baseline chamfer, and "mod" denotes a modified chamfer, either shimmed or machined.

Our main goal was to reduce the sextupole component to $b_3/b_1 \approx -0.5 \times 10^{-4}$. The preference for a slightly negative $b_3$ coefficient comes from the tracking results [6]. It is related to the fact that, in the nominal lattice, the SD sextupole families are stronger than the SF families. A positive $b_3$ in the dipoles further increases the required strength of the SD families and reduces the dynamic aperture margin. A negative $b_3$ produces the opposite effect and results in a larger dynamic aperture.

With regard to the $n$=5 and 7 components, we found that the chamfer depth had little effect on either. Using Halbach's approach, we used "split" shims (two shims on each end plate with a gap between, see Fig. 4) to attack the two higher terms. We found that we were able to affect the $n$=5 and 7 terms independently of the sextupole term, but the shims essentially traded $n$=5 for $n$=7. We could interchange the two strengths, or find shims that made both terms the same. Because tracking results [6] showed no strong sensitivity to any of the configurations, we ultimately chose to avoid the complication of the split shim configuration for the production magnets.

We took advantage of the removable end chamfers on the first dipole to confirm the results from the shims by fabricating new inserts on an NC milling machine. A comparison of the original and modified profile are shown in Fig. 5. Note that the change in the chamfer depth to give the desired result was only about 0.5 mm.

## 5. PRODUCTION STATUS

Dipole magnet production is in full swing, at a rate of 30 magnets per month. Each dipole is characterized magnetically at IHEP prior to shipment to LBNL. To date, coil fabrication is completed and about 150 dipoles have been produced, of which 67 have been received at LBNL, another 40 have been measured at IHEP and await shipment, and the remainder are awaiting measurement. To fully characterize their multipole content, some of the magnets are being remeasured at LBNL with the rotating coil system. Thus far, the measured $b_3$ coefficient is small and slightly negative, as desired.

The integrated strength of each dipole with respect to an arbitrarily chosen "reference" magnet is also measured

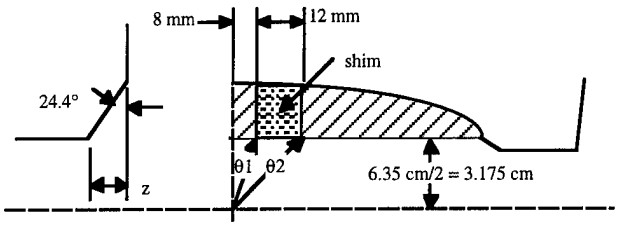



Fig. 4. Dipole chamfer geometry for the split shim case.

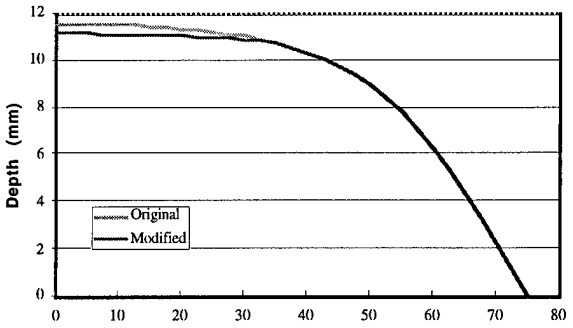



Fig. 5. Depth of original chamfer and modified version adopted for production dipoles.

at IHEP. With half of the dipoles measured, almost all magnets are within the strength tolerance specified in Table I. For the magnets on the extremes of the distribution, a sorting procedure has been defined to minimize the resultant orbit distortion. A few magnets have been determined to be beyond tolerance, and these will be reshimmed at IHEP to adjust their gap to bring the strength within specification.

## 6. ACKNOWLEDGMENTS

The professionalism and hard work of the members of the IHEP and Kelin team were critical to a rapid and successful completion of the dipole chamfer optimization. We thank Z. Cao and especially R. Hou and her talented and dedicated magnetic measurement group at IHEP for assistance. We are grateful for their continued support and enthusiasm. We also appreciate the strong support from the IHEP Director, Z. Zheng and Deputy Director, S. Wang, without whom the logistics of dealing with remote production might have been insurmountable. Finally, we thank D. Van Dyke for yeoman service in performing magnetic measurements at LBNL.

## REFERENCES

[1] PEP-II: An Asymmetric B Factory, Conceptual Design Report, SLAC-418, June 1993.

[2] T. Henderson *et al.*, "Design of the PEP-II Low-Energy Ring Arc Magnets," Proceedings of 1995 Particle Accelerator Conference, Dallas, May 1–5, 1995, p. 1322.

[3] J. Osborn and J. Tanabe, LBNL Mechanical Engineering Note M7512A, March, 1995.

[4] K. Halbach, Nucl. Instrum. Meth. 74, 147 (1969); K. Halbach and R. Yourd, "Tables and Graphs of First-Order Perturbation Effects in Iron-Dominated Two-Dimensional Symmetric Multipoles," UCRL-18916, UC-34 Physics, TID-4500 (54th Edition), May 1969.

[5] AMPERES© Integrated Engineering Software, 46-1313 Border Place, Winnipeg, Manitoba, Canada, R3H0X4.

[6] Y. Cai and M. Donald, unpublished tracking studies (private communication, 1997).

# HARMONIC CORRECTION RINGS FOR THE PEP-II I.R. QUADRUPOLE MAGNETS

D. Humphries, R. Schlueter, Lawrence Berkeley National Laboratory†

*Abstract*

Two harmonic corrector ring magnet designs have been developed to correct field error harmonics generated by quadrupole magnets in the interaction region of PEP-II [1]. They consist of circular arrays of cylindrical permanent magnet pairs which can be both arbitrarily oriented and counter-rotated for strength. This arrangement allows the correctors to be tuned to generate a correction field with arbitrarily selected combinations of harmonics. These correctors are designed such that they can be pre-fabricated and then tuned after the quadrupole magnets have been built and their residual harmonic error content ascertained. The correctors can thus be used to cancel any residual combination of error harmonics in the completed quadrupoles.

## 1. GENERAL

The theory of harmonic corrector rings (HCRs) is a recent development which is described in mathematical detail in reference [2]. Harmonic correctors are an outgrowth of permanent magnet (PM) multipole theory which describes pure permanent magnet multipole magnets, usually constructed of fixed trapezoidal elements, with orientations which give the particular desired multipole field. [3]

These magnets are generally constructed from "analytic" material, i.e. samarium cobalt or neodymium- iron boron which is linear in the second quadrant of the B-H curve with $\mu_r \cong 1$. These structures can be immersed in high fields from adjacent magnets without being significantly affected. When combined with other PM structures, their fields superimpose nearly linearly.

While it is possible to utilize a series of multipole magnets to correct integrated multipole errors, it is expensive and the mix of multipoles in need of correction cannot generally be ascertained until the magnetic system to be corrected is built and measured.

## 2. A PRACTICAL APPROACH

To achieve a more practical mechanism, we use cylindrical magnet elements rather than the usual fixed trapezoidal segments of the standard PM multipole magnet. This immediately allows us to tune the magnet array to any harmonic N up to N=M/2 where M is the number of cylindrical elements. The magnitude of the generated harmonic depends on the number of elements M, the length of the elements L, the radius of the circular magnet array R and the radius of the individual cylindrical elements $r_c$.

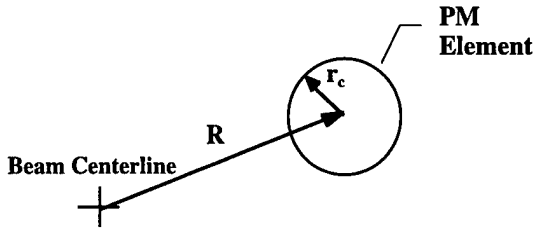



Fig. 1. Corrector array primary geometric variables.

We could now fix M, R and $r_c$ and create a series of multipole corrector magnets whose strengths vary by the length of their respective elements. These arrays could be stacked together to produce a given desired corrector field. Since M, R and $r_c$ are the same, at each element position we have a superimposed set of magnetic vectors which are equivalent to a single cylindrical PM element with a resultant orientation vector and a length which is in general not equal to the sum of the individual element lengths.

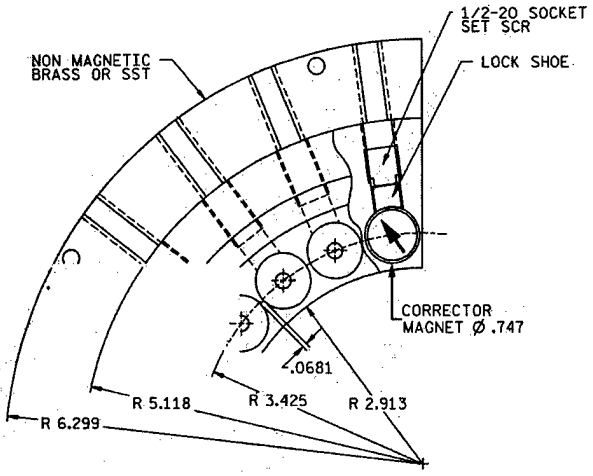



Fig. 2. One quadrant of Q1 HCR showing housing and locking mechanism. Dimensions are in inches.

Thus the stacked arrays could be replaced with a single array of unequal length PM cylinders having the same M, R and $r_c$ as the original arrays. The final step in achieving a practical system is to now replace the unequal length single cylinder array with an array of pairs of same length cylinders. The two cylinders of each pair are placed end to end and counter-rotated to achieve the same integrated

†Work supported in part by the US Department of Energy under contract number DE-AC03-76SF00098.

0-7803-4376-X/98/$10.00 © 1998 IEEE

multipole field as the unequal length single cylinder array.

We now have a system that can be designed and built to accommodate the expected approx. error range of the field we desire to correct. The length of the corrector pairs can be fixed to provide a reasonable total harmonic capacity and the HCR can be tuned to provide the exact harmonic content required to correct the error fields immediately after magnetic measurements are performed.

Other practical geometries ( e.g., with coaxial inner PM cylinders and outer PM annuli ) are described in [2].

## 3. APPLICATIONS

### Q1 Harmonic Corrector

In the B-Factory interaction region, harmonic correctors are applied to both the Q1 and the Q2 quadrupoles [4],[5]. The Q1 magnets are pure permanent magnet structures that reside in the solenoid field of the Babar detector. These are 24 element HCRs with an array radius R of 8.7 cm, an element radius $r_c$ of 1.0 cm and a magnetic length of 6 cm.

The integrated correction capacity of this configuration is given in the graph of figure 3. This graph gives integrated capacity per harmonic per unit length of corrector element. To determine the total required corrector length for multiple error harmonics we add the lengths required to correct maximum expected individual harmonics. This graphical approach to capacity allows us to easily calculate the total required corrector length for any combination of error harmonics.

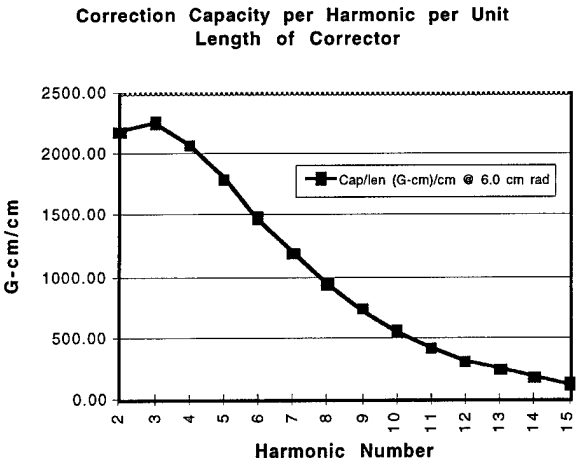



Fig. 3. Q1 HCR integrated correction capacity curve.

### Feed-Down Harmonics

In the course of generating a corrector field, the harmonic corrector will also generate higher order feed-down harmonics. These are shown in figure 4 for the Q1 HCR configuration. They are represented in similar fashion to the corrector capacities, i.e., they are given as a function of generator harmonic per unit length of corrector.

The lowest order feed-down harmonic is the number of the lowest order corrector harmonic plus M, the number of elements in the corrector array. Thus for the Q1 HCR which has 24 elements, the lowest order feed-down harmonic possible is N=25. As is shown in figure 4, these feed-down harmonics are small and decay rapidly as $r_p$, the calculation radius, is reduced.

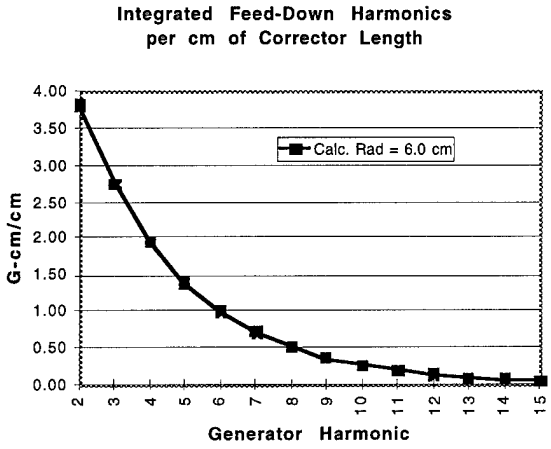



Fig. 4. Q1 HCR integrated feed-down harmonics.

### Q2 Harmonic Corrector

The Q2 quadrupoles reside in the interaction region outboard of the Q1 quads. They are conventional electromagnets with rigorous field quality requirements. These magnets span the two converging beams of the accelerator with a high current density septum which isolates the high and low energy beams.

A two stage harmonic corrector ring is under developement for use in conjunction with these magnets. The first stage or primary Q2 HCR is intended to correct residual field errors which are produced by the Q2 magnet. The secondary HCR is designed to correct harmonics that may be generated by interaction between the detector solenoid stray fields and the body of the Q2 magnet.

While all error harmonics could be corrected with a single HCR, installation logistics dictates that the Q2 magnets be tuned with the primary HCR prior to installation. The secondary HCR is adjusted and installed within a limited

time frame after solenoid effects on the installed Q2 are determined.

The Q2 HCRs are concentrically configured around the low energy beam and are enclosed by a cylindrical ferromagnetic shield which isolates their effect from the adjacent high energy beam.

Integrated correction capacity curves are shown in figure 5 for both correctors. The nominal dimensions of the Q2 HCRs are given in Table I.

Table I. Design Parameters for Q2 HCR.

| | Primary | Secondary |
|---|---|---|
| Array Radius R cm | 5.95 | 7.75 |
| Element Radius $r_e$ cm | 0.65 | 0.5 |
| Number of Elements | 24 | 24 |

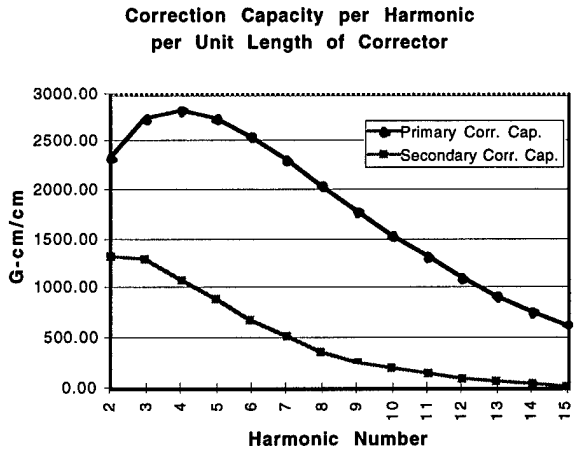



Fig. 5. Q2 HCR integrated correction capacity curves.

## 4. MECHANICAL DESIGN

The mechanical design of the HCRs is relatively simple. The magnetic elements or cylinders must be contained in a non-magnetic housing which allows for tuning of the system by rotating the elements and locking them in position afterwards. Half of the aluminum housing for the Q1 HCR is shown in figure 6. A longitudinal retaining ring to prevent the escape of the magnets during tuning can also be seen in the figure.

A system of dual locking mechanisms can be seen in figure 2. After rotation to the appropriate orientation, individual magnetic elements are locked in place by redundant friction mechanisms which consist of a set screw which bears on a follower or shoe which in turn bears on the PM element. PM materials are inherently fragile and so the PM element is encased in a thin stainless steel tube to prevent damage by the locking shoe.

A thin disk is bonded to the end of each element which has slotted features aligned to the transverse magnetization axis of the cylindrical element. This disk allows for positive engagement of an orienting tool and also protects the magnet.

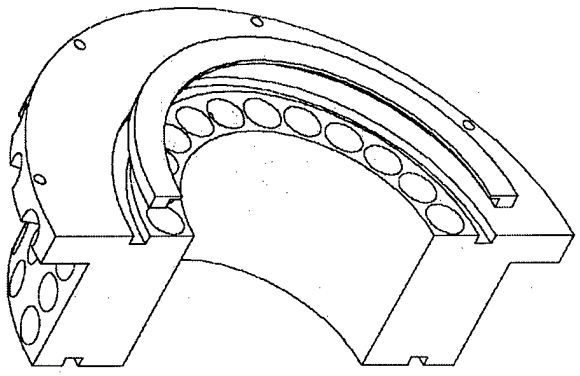


Fig. 6. Upper half of Q1 HCR housing and longitudinal retainer ring.

## REFERENCES


[1] PEP-II: An Asymmetric B Factory, Conceptual Design Report, June 1993.

[2] R.D. Schlueter, D. Humphries, J. Tanabe, "Pure Permanent Magnet Harmonics Corrector Ring", *Nuclear Instruments and Methods in Physics Research A*, LBNL Report 38629, April 1996.

[3] K. Halbach, "Design of permanent multipole magnets with oriented rare earth cobalt material", *Nucl. Instr. and Meth.*, Vol. 169, p. 1, 1980.

[4] M. Sullivan, et al, "Interaction region design at the PEP-II *B* Factory", *Proceedings of the 5th European Particle Accelerator Conference (EPAC96)*, p. 460, Sitges (Barcelona), Spain, June 1996.

[5] J. Osborn, et al, "Design of the PEP-II interaction region septum quadrupole", *Proceedings of the 17th Particle Accelerator Conference*, Vancouver, B.C., Canada, May 1997.

# PERFORMANCE OF THE PEP-II LOW-ENERGY RING QUADRUPOLES*

N. Li, J. Osborn, J. Tanabe, D. Yee, R. Yourd, M.S. Zisman, *Lawrence Berkeley National Laboratory, Berkeley, CA, USA 94720,* and Z. Cao, R. Hou, Y. Sun, *Institute for High Energy Physics, Beijing, P. R. C.*

*Abstract*

Production quantities of quadrupoles for the PEP-II Low-Energy Ring (LER) have been fabricated and measured in China in collaboration with IHEP (Beijing). The LER design specification calls for short quadrupoles ($L_{eff}$ = 430 mm) with a bore radius of 50 mm. End effect corrections, using a chamfer geometry originally developed for the ALS quadrupoles at LBNL, were verified in a prototype magnet prior to release of the design for production of the 320 quadrupoles (including spares) required for the LER. Rotating coil measurements were carried out at IHEP yielding multipole error spectra, magnetic center distribution and transfer function behavior for the full production quantity of magnets. Separate measurements were made to determine the reproducibility of magnets connected together in a series string by measuring the individual magnets against a reference magnet using a bucking magnet. Measurement results of all the magnets indicate that the error multipole spectra satisfy the field quality requirements, reproducibility requirements for magnets in a power supply string are satisfied and the spatial distribution of the magnetic center with respect to the mechanical magnet center falls within a radius which is substantially smaller than the transverse alignment tolerance specified for the quadrupoles.

## 1 INTRODUCTION

LER ring quadrupoles are divided among four different designs. 150 have coils wound with 15 turns of aluminum conductor per pole. These are connected in two power supply strings QF and QD. In addition to requirements for field quality, they must satisfy reproducibility requirements. The balance of the magnets are connected singly, in pairs, or in series strings which contain four magnets. These magnets are wound with 58 and 52 turns of either aluminum or copper conductor.

Details of the core and coil designs and operating parameters are reviewed in previously published papers[1,2]. The LER will operate at a positron energy of 3.1 GeV. However, the magnet design parameters and performance requirements are specified for energies ranging from 2.4 to 3.5 GeV.

| | |
|---|---|
| No. Required: | 316 |
| Bore Radius: | 50 mm |
| Effective Length: | 430 mm |
| Excitation Range: | $0.67 \le B' \le 13.91$ T/m |
| String Magnet Excitation: | 4.5 T/m @ 3.1 GeV |
| Reproducibility: | $\le 1 \times 10^{-3}$ |
| Systematic Multipoles: | $\le 1 \times 10^{-3}$ •B2 @50 mm r |
| Random Multipoles: | $\le 5 \times 10^{-4}$ •B2 @50 mm r |

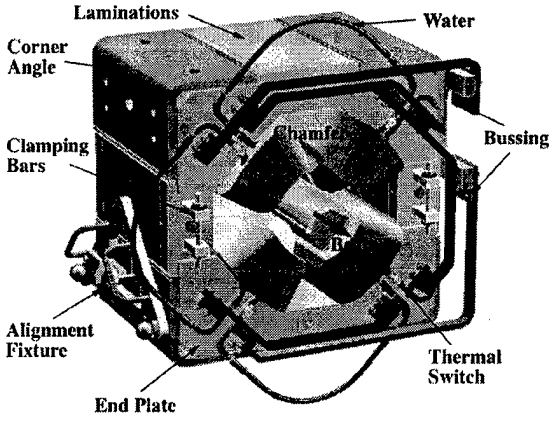



Fig. 1. PEP II LER Quadrupole.

At the writing of this paper, all the 15 turn magnets and most of the 58 turn aluminum conductor magnets have been manufactured, measured and received at LBNL. This paper summarizes the performance of some of the quadrupoles received from IHEP.

## 2 MAGNETIC MEASUREMENTS

A compensated line integral coil was designed at IHEP. Three coils were fabricated by a vendor in China selected by IHEP. A MetroLab® Integrator and a PC based computer were purchased and a data acquisition system was designed and assembled at IHEP. Two of the coils were retained at IHEP and the third was delivered to LBNL so that measurements can be verified.

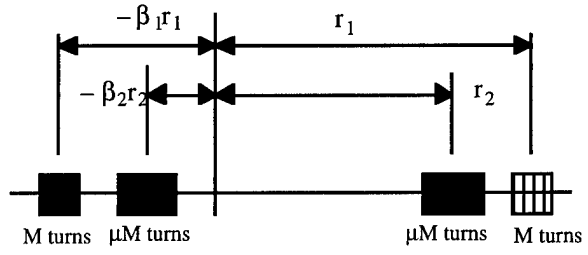



Fig. 2. Compensated coil schematic.

| | |
|---|---|
| $r_1$=40.05 mm | $\beta_1 r_1$=30.05 mm |
| $r_2$=22.58 mm | $\beta_2 r_2$=12.63 mm |
| M=342/190 turns | μM=684/380 turns |
| Coil length | 897 mm |

*Work supported in part by the U.S. Department of Energy under contract number DE-AC03-76SF00098.

0-7803-4376-X/98 /$10.00 © 1998 IEEE

*Magnetic Centers*

The deviation of the magnetic center with respect to the axis of the coil is calculated using the dipole field measured by the rotating coil.

$$\Delta x = \left(\frac{b_1}{|B_2|}\right)_{@r_0} r_0 \quad \Delta y = \left(\frac{a_1}{|B_2|}\right)_{@r_0} r_0$$

This measured center is related to the mechanical center of the quadrupole since a cylinder with the exact diameter of the rotating coil housing is used to define the center axis of the quadrupole during fiducialization. Figure 2 illustrates the center distribution for 77 QF magnets. Distribution plots for the QD and the 58 turn magnets display similar patterns.

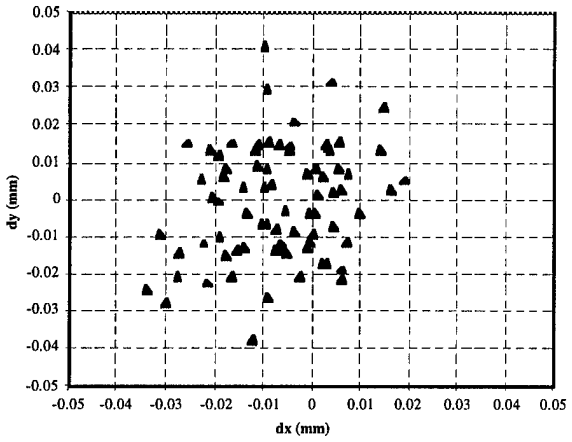



Fig. 3. Magnetic axis distribution for 77 QF quadrupoles.

Integrated error multipole data for all the magnets satisfy the reqirements. In Figs. 4 and 5 bar graphs are presented for five multipoles measured for a sample of 25 of the QF magnets thus far received. These spectra are typical of the spectra for the balance of the magnets. Two different bar graphs are presented.

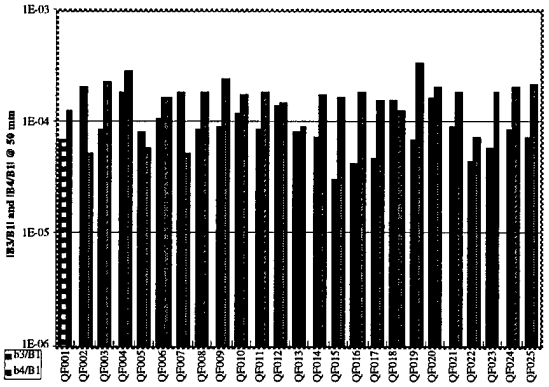



Fig. 4. Random multipoles for 25 QF quadrupoles.

The unallowed random multipoles (Fig. 4) result from small errors in core manufacture or assembly

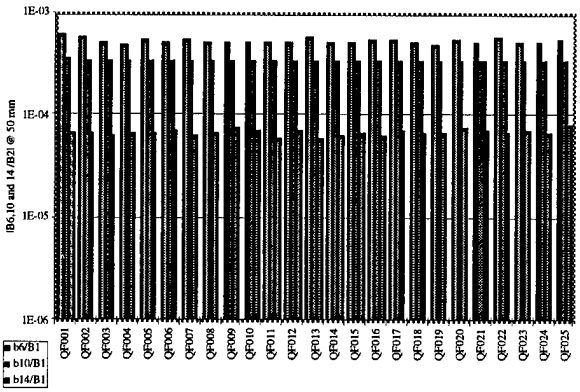



Fig.5. Systematic multipoles for 25 QF quadrupoles.

The systematic "allowed" multipoles (Fig. 5) are primarily introduced in the magnet fringe fields. The magnitudes of the "unallowed" random multipole errors have a fairly wide variation from magnet to magnet. The "allowed" multipoles are reproducible within a narrow range for all the magnets. Measurements are collected for individual magnets at various levels of excitation. Although the individual magnet excitation required for 3.1 GeV LER operation is narrowly specified, measurements were made for a range of excitation broader than the required current. These measurements were made since the individual magnets in the LER ring vary over wide ranges in excitation and since performance at different LER energies (for future upgrades) must be anticipated. Typically, the magnet center varied $\leq\pm 10$ μm and the individual multipoles varied $\leq\pm 3\text{x}10^{-6}$ from their average values over the range of current values for which the measurements were performed.

*Transfer Functions*

For the QF magnets, the power supply is cycled three times to 760 Amps (for conditioning) and ramped to the prescribed currents where the measurements are made with increasing current. A final measurement is made with the current reduced to 355 Amps. The change in the function at 355 Amps is due to the magnet operating on a different load line due to hysteresis in the iron.

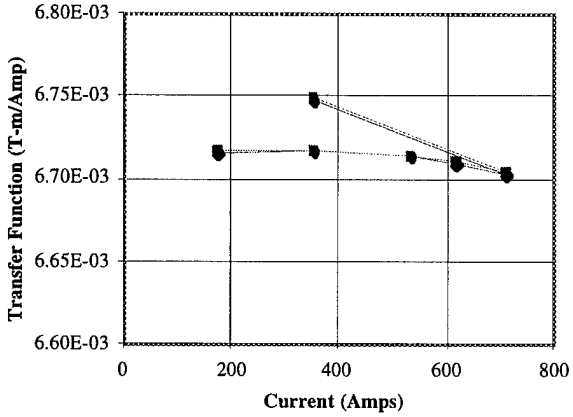
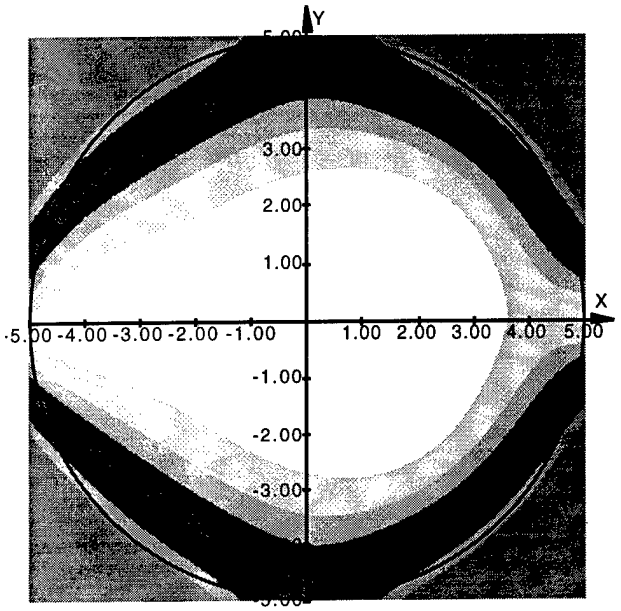



Fig. 6. Transfer function for QF01.

The transfer function data are not used to determine the reproducibility of the collection of magnets since the measurements are not sufficiently repeatable. Lack of stability of electronic components and environmental factors (temperature variations) contribute to errors in the measurement greater than the required precision to identify magnet repeatability to less than the specification ($\leq 1 \times 10^{-3}$).

*Magnetic Field Reconstruction*




QF001 IHEP Measurement

Units: CM
Current: 355.00A
Ref. Radius: 5.00

Err ≤ 1.0E-04
1.0E-04 < Err ≤ 2.0E-04
2.0E-04 < Err ≤ 3.0E-04
3.0E-04 < Err ≤ 4.0E-04
4.0E-04 < Err ≤ 5.0E-04
5.0E-04 < Err ≤ 6.0E-04
6.0E-04 < Err ≤ 8.0E-04
8.0E-04 < Err ≤ 1.0E-03
1.0E-03 < Err ≤ 2.0E-03
Err > 2.0E-03

Pole Radius: 5.00

| N | BN/B2 | PHI | N | BN/B2 | PHI |
|---|---|---|---|---|---|
| 3 | 6.28e-05 | 346.1 | - | - | - |
| 4 | 1.67e-04 | 176.9 | - | - | - |
| 5 | 5.54e-06 | -3.8 | - | - | - |
| 6 | 6.35e-04 | 0.4 | - | - | - |
| 7 | 1.74e-06 | 152.0 | - | - | - |
| 8 | 5.51e-06 | 35.0 | - | - | - |
| 9 | 1.09e-05 | 151.3 | - | - | - |
| 10 | 3.53e-04 | 178.9 | - | - | - |
| 11 | 6.01e-06 | 170.9 | - | - | - |
| 12 | 5.19e-05 | 177.7 | - | - | - |
| 13 | 1.29e-05 | 296.0 | - | - | - |
| 14 | 6.51e-05 | 178.6 | - | - | - |

Fig. 7. Typical iso-error curve reconstructed from multipoles.

A table of multipole error amplitudes and their phases are difficult to interpret when evaluating the quality of a magnet. An analog method of reconstructing the field was developed which maps the field error in space and helps evaluate the quality of the magnetic field within the prescibed good field region. The algorithm for reconstructing the field error map is simple.

$$\left(\frac{\Delta B_{\substack{\text{azimuthal}\\ \text{radial}}}}{B_2}\right)_{r,\theta} = \sum_{n=3}^{n=14}\left(\frac{\Delta B}{B_2}\right)_{r_0}\left(\frac{r}{r_0}\right)^{n-2}\begin{matrix}\cos\\ \sin\end{matrix}\left(n\theta+\psi_n\right)$$

$$\left|\frac{\Delta B}{B_2}\right|_{x,y} = \sqrt{\left(\frac{\Delta B_{\text{azimuthal}}}{B_2}\right)^2_{x,y} + \left(\frac{\Delta B_{\text{radial}}}{B_2}\right)^2_{x,y}}$$

*Magnet Reproducibility*

Magnet reproducibility was measured at IHEP by placing identical coils in a bucking magnet and the measured magnet connected in opposition and ramping the magnets connected in series. This null measurement was compared with the null measurement from a reference magnet. The figure compares the reproducibility data (trIangles) with mechanical length measurements of the quadrupoles (squares) which are ranked from shortest to longest. In general, the quadrupoles satisfy the requirement of magnet reproducibility $\leq \pm 1 \times 10^{-3}$.

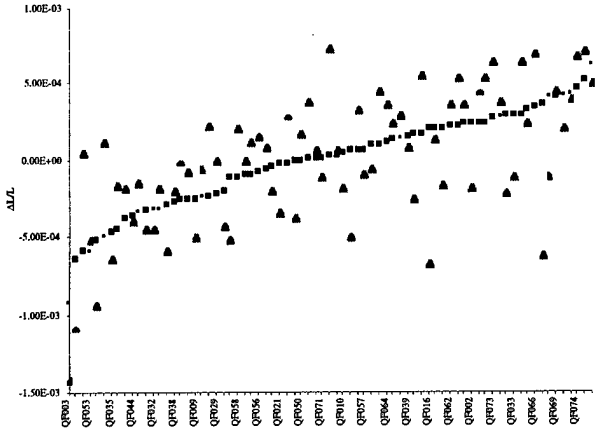



Fig. 8. QF magnet reproducibility.

## 3 STATUS

Quadrupole magnet production will be complete by the end of June, 1997. Magnetic measurement results have been routinely delivered to LBNL for evaluation from IHEP as magnets are delivered. All magnets thus far delivered have met or exceeded the performance specifications set forth at the beginning of the project.

## 4 ACKNOWLEDGMENTS

The PEP-II project is grateful for the hard work and professionalism of the team of scientists, engineers, and craftspersons at IHEP. Approximately 200 of the 316 quadrupoles required for installation in the LER have been received. Measurements have indicated that the excellent field quality demonstrated by the prototype has been maintained and that the craftsmanship evident in the early magnets continues. We would also like to thank the team of technicians and scientists working for Ms. R. Hou at IHEP for the thorough and careful measurements of all the magnets.

## 5 REFERENCES

[1] J. Tanabe, J. Osborn, N. Li, D. Yee, "Standard 43 cm Quadrupole Engineering Design", LBL Mechanical Engineering Note M7498A, October, 1994.

[2] T. Henderson, N. Li, J. Osborn, J. Tanabe, D. Yee and R. Yourd, "Design of the PEP-II Low Energy Ring Arc Magnets", Proceedings of the IEEE Particle Accelerator Conference (PAC), Dallas, TX, May 1995, pp. 1322-1324.

# DESIGN OF THE PEP-II INTERACTION REGION SEPTUM QUADRUPOLE

J. Osborn, J. Tanabe, D. Yee, F. Younger, Lawrence Berkeley National Laboratory[†]

*Abstract*

The PEP-II QF2 magnet is one of the final focus quadrupoles for the Low-Energy Ring (LER) and utilizes a septum aperture to accommodate the adjacent High-Energy Ring (HER) beamline. The LER lattice design specification calls for an extremely high field quality for this magnet. A conventional water-cooled copper coil and laminated steel core design was selected to allow adjustment in the excitation. The close proximity between the LER and HER beamlines and the required integrated quadrupole strength result in a moderately high current density septum design. The QF2 magnets are imbedded in a confined region at each end of the BaBar detector, thus requiring a small magnet core cross section. Pole face windings are included in the QF2 design to buck the skew octupole term induced by the solenoidal fringe field that leaks out of the detector. Back-leg windings are included to buck a small dipole component induced by the lack of perfect quadrupole symmetry in this septum design. 2D pole contour optimization and 3D end chamfers are used to minimize harmonic errors; a separate permanent-magnet Harmonic Corrector Ring compensates for remaining field errors. The design methods and approach, 2D and 3D analyses, and the resulting expected magnet performance are described in this paper.

## 1. REQUIREMENTS

The QF2 magnet along with the Q1, Q4, and Q5 magnets require the highest field quality of any magnets in PEP-II. The lattice requirements for the QF2 magnet combine high field quality with moderately high field strength and places the magnet in a congested region at each end of the BaBar detector. A permanent magnet design option was investigated in addition to the conventional design. The conventional design utilizing water-cooled copper coils and a laminated steel core was selected to allow adjustment in the excitation. Table I gives a summary of design requirements[1].

## 2. DESIGN PARAMETERS

The QF2 inboard end is about 3.1 meters from the interaction point. This places the magnet in a part of the lattice where the LER and HER beamlines are very close together, about 9.5 cm apart at the inboard end of QF2. In addition, the shape of the LER beam stay clear is changing and its center is shifting over the length of the magnet, particularly at the inboard end.

Table I. Design requirements for QF2.

| | |
|---|---|
| Nominal gradient [T/m] | 7.7 |
| Adjustment [%] | +3.5/-5 |
| Effective length [m] | 0.62 |
| Allowed multipoles, main aperture, bn/b2 @ 4.23 cm | $\leq 1 \times 10^{-4}$ |
| Allowed multipoles, septum aperture, bn @ 2.2 cm [T-m] | $\leq 2 \times 10^{-4}$ |

These considerations led to the selection of a quadrupole bore aperture radius of 47.8 mm with a 3x3 coil package of 5 mm square conductor. The core length was determined based on the required effective length and an estimate of the fringe integral including the shortening due to the end chamfers.

To achieve the required field strength in this tight package, a moderately high current density of 52 Amps/mm$^2$ and ample cooling is required. Though two-turn water circuits would achieve the desired cooling, single-turn circuits were selected for a lower ambient temperature within the support raft and to reduce the required cooling flow velocity. Table II summarizes the QF2 design parameters. Note that only 8 turns are energized in the 3x3 package; this is discussed below.

## 3. MECHANICAL DESIGN

Though utilizing conventional water-cooled copper coils and a laminated steel core, the QF2 design incorporates several additional features to meet its demanding requirements. Figures 1 and 2 show 3D representations which point out many of these features.

Table II. Design parameters for QF2.

| | |
|---|---|
| Design gradient [T/m] | 8.47 |
| Core length [m] | 0.61 |
| Bore radius [mm] | 47.8 |
| Estimated efficiency [%] | 96 |
| Design excitation [Amp-Turns] | 8021 |
| Turns per coil | 8 |
| Design current [A] | 1003 |
| Design current density [A/ mm$^2$] | 52 |
| Magnet resistance [mΩ] | 52.6 |
| Magnet power [kW] | 52.9 |
| Conductor size [mm] | 5.0 |
| Conductor hole diameter [mm] | 2.5 |
| Conductor corner radius [mm] | 1.0 |
| Cooling circuits per coil | 8 |
| Length per circuit [m] | 1.7 |
| Design pressure [mPa] / [psi] | 2.07 / 30 |
| Flow velocity [m/s] / [ft/s] | 4.4 / 14.5 |
| Magnet flow [l/s] / [gpm] | 0.7 / 11 |
| Temperature rise [°C] | 18.2 |

[†]Work supported in part by the US Department of Energy under contract number DE-AC03-76SF00098.

0-7803-4376-X/98/$10.00 © 1998 IEEE

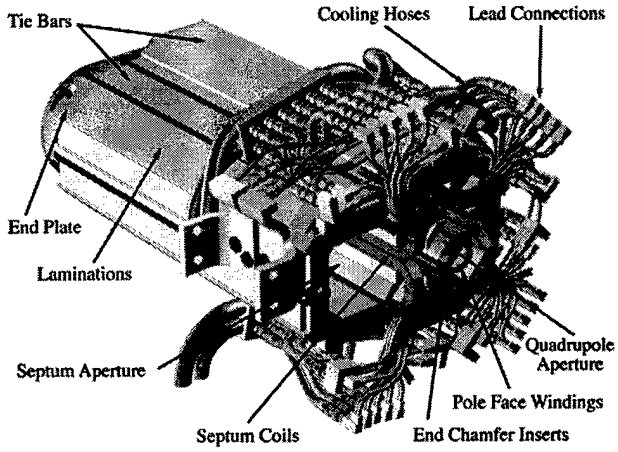



Fig. 1. Outboard from detector end of QF2.

In addition to the main quadrupole coils, there are three sets of trim windings. Back-leg trim windings are used to compensate for a small dipole and sextupole term in the quadrupole aperture, which is due to a small flux imbalance arising from the non-quadrupole symmetry in this design. 2D magnetic analyses were used to verify that when the back-leg trim windings are excited to the proper level (which is proportional to the main coil excitation), the magnet behaves like a symmetric quadrupole. Pole-face windings are used to induce a skew octupole term in the quadrupole aperture to buck the skew octupole term induced by the solenoidal field leaking out of the detector. Similarly, septum aperture windings are used to buck a skew-dipole term induced in the septum aperture by the detector's fringe field.

The QF2 design also incorporates a field-clamp with two bores at the inboard end of the magnet. The purpose of the field clamp is to absorb some of the solenoidal leakage field from the detector. In addition, the main aperture in the field clamp may be shaped so as to induce a skew octupole of the opposite sign to that induced in the core[2]. As yet unproved, this technique is promising as it potentially corrects for skew octupole passively without inducing higher order harmonics as do the pole-face windings.

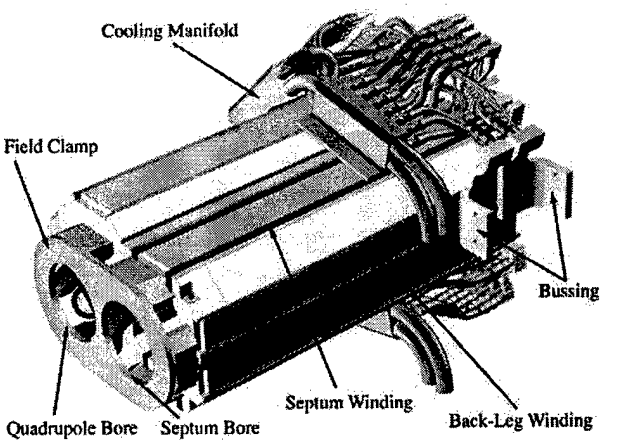



Fig. 2. Inboard towards detector end of QF2.

Since the shaped bore would be four-fold symmetric, only allowed harmonics are introduced, most notably N=6. So slightly different end-chamfers may be required.

## 4. 2D MAGNETIC ANALYSES

Because the good field radius of 4.23 cm is large compared to the bore radius of 4.78 cm, there is not enough pole overhang to allow 2D optimization utilizing only pole bumps. Additionally, since the septum coil is tightly constrained in size and position, the coil is close to the aperture. Consequently conductor position has a significant effect on the multipole content. These factors led to a design in which a combination of conductor displacement into the aperture, the deactivation of one of the conductors in the nominal 3x3 package, and pole corner bumps were all used to achieve the desired field quality requirements. Figure 3 shows a close up cross-section of the coil and pole corner.

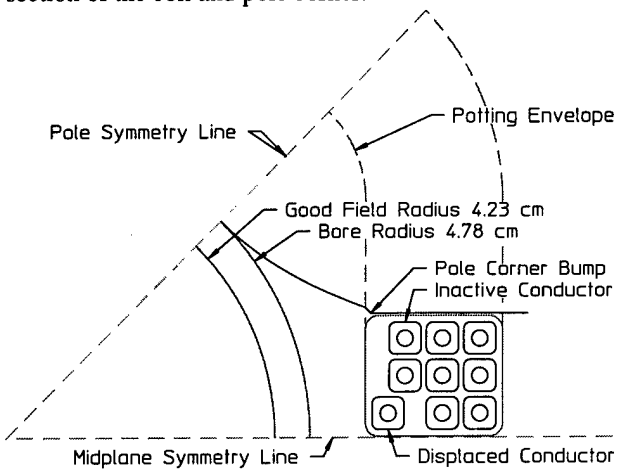



Fig. 3. Close-up view of coil and pole corner.

The pole corner bump geometry was selected to allow installation and removal of the coils and simultaneously to provide 45 degree flats for convenient measurements between opposing poles in the assembled magnet. The distance that this corner is pulled into the aperture from a nominally hyperbolic pole contour was used as one parameter in the 2D optimization.

It was determined that a very helpful reduction in the N=6 term resulted when the conductor closest to the pole corner was deactivated. The displacement of the midplane conductor closest to the aperture was used as the second parameter in the 2D optimization. The complete 2D optimization strategy combines the conductor deactivation with a suitably sized pole corner bump and a suitable displacement of the midplane conductor.

In order to determine the optimal pole corner bump size and midplane conductor displacement, a grid study was performed using the Poisson/Superfish group of codes[3]. A series of iso-contours were calculated from interpolations of the grid cases for values of constant multipole content. The iso-contours show combinations

of bump size and conductor displacement where a given normalized multipole has a value of zero, $1x10^{-4}$, or $-1x10^{-4}$. For a given multipole, the band between these extremes can be interpreted as the locus of acceptable designs. The optimum combination can be determined from where the bands of N=6, 10, and 14 cross in the same region. Figure 4 shows the results of this study at the nominal excitation. Other grids were created using a variety of materials and excitations to determine that the design was insensitive to these changes. The final selected combination is where the N=10 and N=14 zero iso-contours cross. This leaves a residual N=6 term of about $1x10^{-4}$ which will be trimmed along with the fringe field using end chamfers.

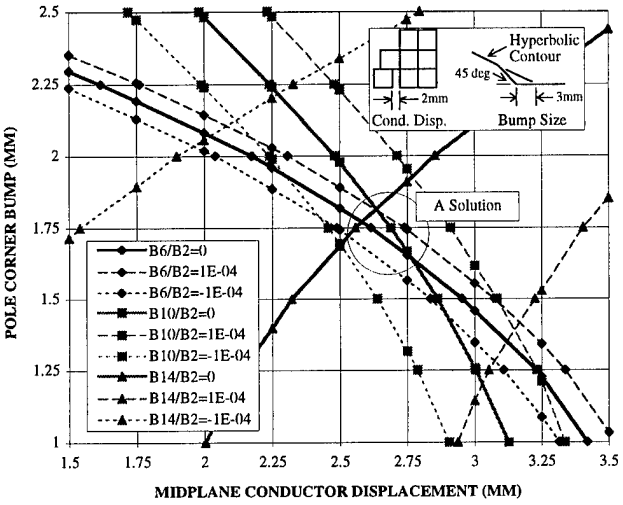



Fig. 4. 2D multipole iso-contours for various pole bumps and conductor displacements, nominal excitation, normalized @ 4.23 cm radius.

## 5. 3D MAGNETIC ANALYSES

To verify that the proposed chamfer inserts are large enough to allow trimming of the fringe field and the residual N=6 from the 2D portion of the magnet, a similar grid study was performed in 3D for a series of simple notch end chamfers. The two parameters varied for these chamfers are the height along the pole axis (X-Y Direction) and the longitudinal depth (Z Direction). Figure 5 shows the notch depth and height convention.

The 2D Poisson performance with optimum pole bump and midplane conductor displacement was used to model the central 51 cm of 2D body harmonics, while the 3D integrated performance for the remaining fringe portion of the field was modeled with Amperes©[4]. Figure 6 shows the results of this study in format similar to Figure 4. A solution is evident where the bands of $\pm 1x10^{-4}$ for the various integrated normalized multipoles cross. The actual final 3D end chamfer geometry will be determined empirically after the magnet is built, by means of rotating coil measurements. It is expected that the required allowed multipole content of $\leq 1x10^{-4}$ will be achieved with careful fabrication and trimming.

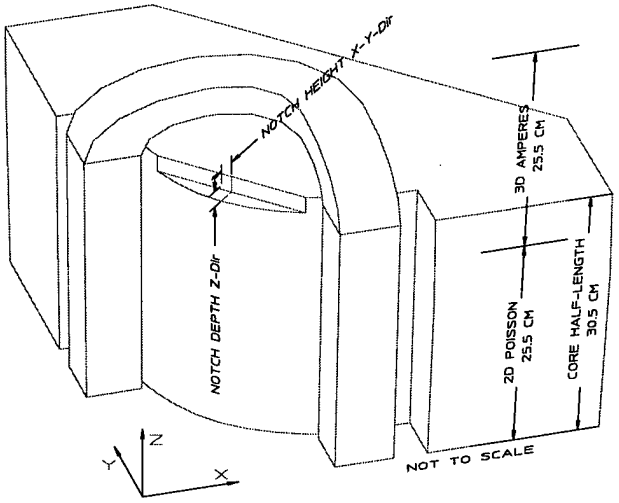



Fig. 5. Notch chamfer convention.

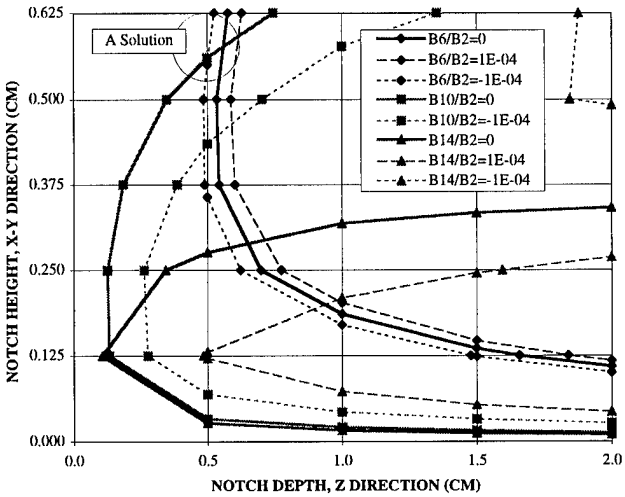



Fig. 6. 3D integrated multipole iso-contours for various notch end chamfers, nominal excitation, normalized @ 4.23 cm radius.

## 6. ACKNOWLEDGMENTS

The authors would like to thank all of the individuals working on the Interaction Region in PEP-II. This magnet is tightly constrained in many ways. The final design would not be possible without the professional cooperation between many competing interests in several collaborating laboratories.

## REFERENCES

[1] PEP-II: An Asymmetric B Factory, Conceptual Design Report, June 1993.

[2] Supplement to: Magnetic Field Calculation in the BaBar Detector, by S. Mikhailov et al., BaBar Note, December 25, 1996.

[3] Poisson/Superfish Group of Codes, maintained by Los Alamos National Laboratory, contact: Robert Ryne, (505) 667-2839.

[4] Amperes© Integrated Engineering Software, 46-1313 Border Place, Winnipeg, Manitoba, Canada, R3H0X4.

# PULSED SEPTUM FOR THE LNLS INJECTOR

A.R.D. Rodrigues[†] , R. H. A. Farias, M. J. Ferreira, F. S. Rafael and G. Tosin,
LNLS Laboratório Nacional de Luz Síncrotron - LNLS/CNPq
Caixa Postal 6192 -- 13081-970 Campinas - SP - Brazil.

*Abstract*

The design and construction of a pulsed thin septum for the LNLS UVX injection system are presented. The injection system uses two septa and three kickers to inject the 120 MeV electron beam from the Linac into the storage ring. The present system uses two d.c. septa. A pulsed thin septum is under construction in order to reduce the septum wall thickness from the present 5.5 mm to 1.5 mm, thus improving the injection efficiency. A prototype has been built with a 1.5-mm-thick copper septum wall which is now being measured. The magnet is driven by a 1.6-kA half-sine wave current pulser. It is constructed of a 0.4 m manganese-zinc ferrite yoke and is being tested in passive and active configurations. The magnet will be housed inside vacuum and has been designed to operate at up to 200 MeV.

## 1 INTRODUCTION

The injection system of the LNLS 1.37 GeV electron storage ring consists of an underground 120 MeV Linac operating at 2856 MHz and a 20.03 metre long transport line [1]. The storage ring has a wide dynamic operational range: the electrons are injected at 120 MeV, stacked and then ramped to the final energy.

At the end of the transport line, the final deflection of the injected beam towards the storage ring is carried out by two septa deflecting the beam in the plane of the stored beam orbit. Both septa are conventional non-staggered laminated C-core d.c. magnets. The thin septum has an active shielding provided by a four-turn water cooled coil. At 120 MeV the current density is 11 A/mm$^2$ and the coil shows good thermal behaviour. However, for higher injection energies the cooling system of the coil has inevitably to be improved. The total septum thickness, composed of the coil, the cooling system and the vacuum chamber of both the storage ring and the transport line, amounts to 5.5 mm. The thick septum is a non-cooled passive-like dc magnet built to work at an injection energy injection up to 250 MeV. Shielding is accomplished by properly wrapping the storage ring vacuum chamber with low-carbon iron laminations.

The replacement of the present thin septum by a pulsed one is motivated by the increase of the Linac energy to 170 MeV, to be performed during the last quarter of 1997. Since an extra effort ought to be applied to the development of a new refrigerated coil, the substitution of the current septum by a new pulsed one has been decided. Besides allowing the injection at the increased energy, the new septum can be made considerably thinner. In fact, a prototype has been built and is now under measurement with a total 1.5 mm thick septum wall. With the reduced septum thickness an increase in the injection efficiency is expected. Another reason is the huge dependence of the stray field upon the accuracy in the manufacture and positioning of the coil in the present septum. Even though the effects of the dc leakage fields on the beam can be partially corrected by using the steering magnets the effect of the multipolar components are hazardous to the dynamic aperture and can not be compensated.

In this paper the design and the preliminary measurements of the new pulsed septum are presented. At a first stage the present thick septum is not going to be substituted but just repositioned in order to fit the optical characteristics of the transport line. A new active water-cooled dc thick septum, based on the same principle of current sheet, has been designed notwithstanding.

## 2 PULSED THIN SEPTUM

The main characteristics of the pulsed thin septum are shown in table 1. To choose between a passive 'eddy current' and an active 'current sheet' septum, a prototype has been built allowing both configurations. These configurations are easily interchangeable and measurements are now under way.

In the design of the septum the usual requirements have been aimed at: the thinnest septum, low leakage

| | |
|---|---|
| Deflection angle (mrad) | 52.4 |
| Physical length (m) | 0.4 |
| Aperture height (mm) | 22 |
| Aperture width (mm) | 45 |
| Nominal Field (T) | 0.09 |
| Nominal Excitation Current (kA) | 1.6 |
| Maximum repetition rate (Hz) | 7.5 |
| Pulse width (μs) | 10 |
| Self-inductance (μH) | 1 |
| Septum wall thickness (mm) | 1.5 |

Table 1 - Main characteristics of the thin septum (@200 MeV)

[†] Also at Departamento de Física de São Carlos, Universidade de São Paulo.

0-7803-4376-X/98/$10.00 © 1998 IEEE

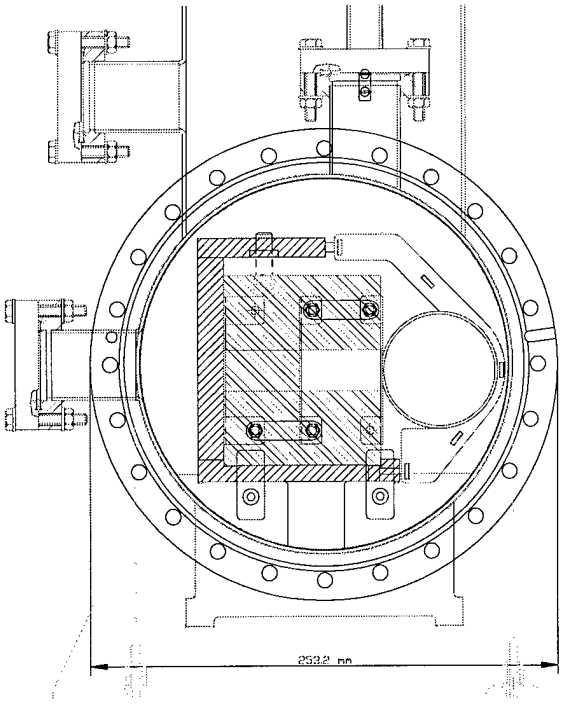


Figure 1 - Section of the thin septum magnet inside the vacuum tank

field, good field homogeneity along the gap. Some additional constraints have also been set out. The use of a solid state based power pulse circuit limited the peak voltage of the pulser to below 1.8 kV. To avoid using a ceramic chamber it was decided to put the septum in vacuum. This makes a thinner septum easier to be achieved but special care has to be taken so as to attain u.h.v. quality in the vacuum tank. The magnet should be able to work at a maximum beam energy of 200 MeV. Moreover, any cooling system should be avoided.

The main requirement refers to the leakage field. The 120 MeV beam is very sensitive to any spurious field. An integrated leakage field of 2 Gauss·m along the septum wall deflects the beam by 0.5 mrad. Beam optics considerations show that keeping the integrated field in the 'field free' region below 0.4 Gauss·m @120 MeV (0.1% of the field in the gap) is a quite safe threshold.

Figure 1 shows a cross section of the septum magnet inside the vacuum tank. The vacuum tank includes both the septum and the storage ring vacuum chamber. In the storage ring side a copper tube is allocated to minimize impedance effects and also to provide an additional shielding to the leakage fields. Pumping slots have been introduced in the tube.

The magnet is constructed of a manganese-zinc ferrite yoke. A stainless steel housing is used to keep the ferrite blocks in the required position. The shielding is provided by a 1.0 mm thick indented copper plate. The storage ring copper tube is tapered in the point it leans against the shielding to a minimum thickness of 0.5 mm. The

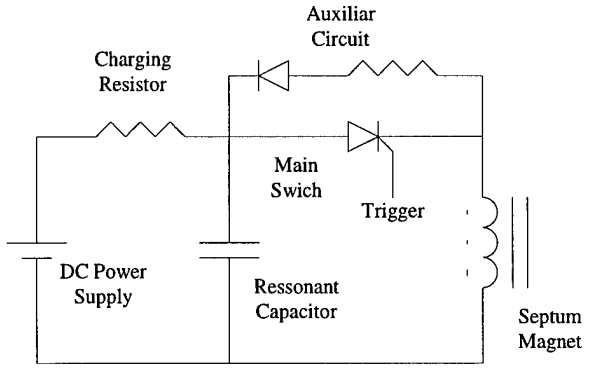



Figure 2 - Diagram of the septum magnet pulsed power supply

insulation is provided by a 20 μm thin kapton layer placed in between the tube and the copper plate.

In both passive and active configurations a single turn coil is used. In the passive case both the winding conductor in the gap and the external return conductor have the same cross section (20×1mm²). The 'eddy current' shield is a 1 mm thick indented copper blade (skin depth ≈ 0.3 mm). In the active configuration, the indented blade is the active septum with an effective 20×1mm² cross section. In both cases forced cooling is not necessary due to the low power dissipation (the average power is 0.4 W at the most demanding operational condition).

At the very end of the transport line the pulse duration of the beam coming from the Linac is about 150 ns. For a 10 μs current pulse the 'flat top' of the magnetic field in the aperture is 300 ns for 0.1% field homogeneity.

## 3 SEPTUM POWER SUPPLY

The septum is driven by a sub-damped resonant circuit, the impedance and the pulse duration of which are basically determined by the magnet self-inductance. The main characteristics of the circuit are:

- Maximum charging voltage 1.6 kV
- ½-sine pulse width 10 μs
- Peak current 2.0 kA

The charging supply is formed by a high voltage d.c. power supply and a charging resistor. Such configuration can be used due to the low repetition pulse rate applied to the magnet (7.5 LINAC PRR) and the resulting low power dissipation in the charge.

The auxiliar circuit attached to the main thyristor switch makes the resonant circuit overdamped. The backswing reaches 35% of the main pulse amplitude and dies out after 10 μs.

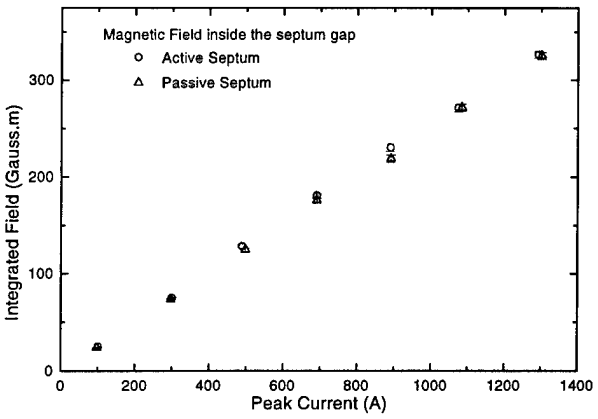



Figure 3 - Integrated magnetic field along the septum aperture($i_p$ = 1.1kA, $B_{int}$=280 Gauss.m).

## 4 MEASUREMENT RESULTS

Magnetic field measurements have been performed using an assembly consisting basically of a Fluke osciloscope PM3382A and a geometrically well known measuring coil. The field is obtained by numerical integration of the voltage induced in the sensitive coil. The time interval for each signal acquisition is 40 ns. Preliminary measurements have been made of the septum in both the active and passive configurations. Up to now, the septum has been measured up to the present injection energy (120 MeV).

The peak magnetic field in the central region of the gap has been measured with a 99.80×19.65 mm single turn rectangular coil. The integrated field in the gap region has been measured with a 40.41×600.0 mm single turn coil in order to include the end fields (Figure 3). The mapping of the field in the gap region has shown good field homogeneity (1% in the region 7-35 mm inward the core).

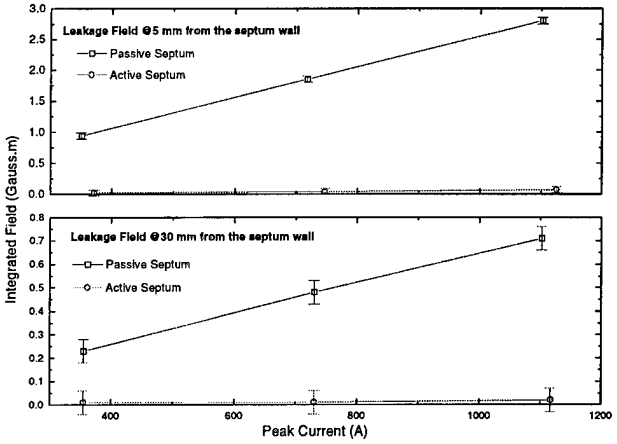



Figure 4 - Integrated leakage field at two points in the stored beam region($i_p$ = 1.1kA, $B_{int}$=280 Gauss.m).

In order to measure the integrated leakage field a 698×10.13 mm 10-turn search coil has been used. The field was measured close to the septum wall (@5 mm) and in the centre of the vacuum chamber (@30 mm). Due to the weak induced voltages special care had to be taken so as to minimize the effects of high-frequency oscillation signals induced over the averaged signal.

As expected, the shielding provided by the active configuration is by far more efficient. Close to the septum wall the leakage field is 40 times smaller in the active configuration for 1.1 kA peak current (Figure 4). In that case the integrated field in the gap region is about 280 Gauss·m in both configurations. At 5 mm from the septum wall the field is atenuated to 1% of its value in the gap in the passive configuration and to less than 0.05% in the active case. For the active septum the required 0.1% leakage field has been achieved. For the passive septum the field is 10 times stronger and modifications in the septum wall are necessary in order to improve the shielding efficiency. Two possible choices are to increase the septum thickness or to introduce a magnetic shield.

## 5 CONCLUSIONS

Preliminary measurements carried out on the prototype of the thin septum now under construction at LNLS shows that the active "current sheet" configuration delivers the level of performance which is demanded of it. Due to the low repetition rate and relatively low peak current the average power dissipated in the septum wall is small and no special cooling system is required. Parallel to the tests performed on the septum prototype the vacuum tank is already projected and under construction.

The authors would like to thank P. Marin, M. Sommer (LURE) and D. Gough (SSRL) for their valuable suggestions.

## REFERENCES

[1] R. H. A. Farias, Liu Lin and G. Tosin *"Magnetic Design of the LNLS Transport Line"*, PAC95

# EDDY CURRENT EFFECT OF VERY LONG TIME CONSTANT OF BLOCK MAGNETS

M.Kumada [1], H.Ogawa [2], K.Sato [3], M.Kase [4] and H.Okuno [4]
e-mail kumada@nirs.go.jp
[1] National Institute of Radiological Sciences(NIRS), 4-9-1 Anagawa, Inage, Chiba, 263 Japan
[2] AEC, [3] RCNP, University of Osaka, [4] RIKEN

*Abstract*

We have observed a transient effect of a magnetic field in a gap of block magnet with very long time constant, which extends to an e-folding time of an hour. It was confirmed that not only a response of the magnetic field strength but also the field gradient changes. This phenomena could be accounted for the eddy current field induced in iron core and yoke of the magnet. An attempt was made to explain by analytical expressions and by a numerical computation. Details of the data and analysis are presented.

## 1 INTRODUCTION

In a cyclotron, it is known that during a start-up a sophisticated initialization of magnets is necessary. The way of initialization seems to vary from institute to institute. In spite of extensive efforts, it is common that operators have to wait for more than a couple of hours until a beam stabilizes. The reason is not clearly understood but is usually ascribed to a magnetic after-effect, a warm-up effect of magnet iron, or a temperature change of the cooling water. Recently it was found at RCNP that the effect of the temperature of cooling water of trim coil is of vital importance [1] to stabilize the beam. In the cyclotron of JAERI Takasaki, it was found that the beam stability is related with long time constant [2] of two distinct components. One of the time constant of an order of day seems to indicate the effect of the temperature change. Another time constant of several hours seems to indicate the presence of the effect of eddy current. Its effect in a spectrometer magnet was first mentioned by K.Halbach [3]. He pointed out that a block magnet has a long time constant and could give an effect to an accuracy of the energy resolution. It has been known that the spectrometer magnet had a puzzlingly unstable long drift. Knowing this work, a large DC magnet of Mainz Microtron (MAMI) was divided into several parts so that the effect of the eddy current is weakened [4]. In spite of an extensive field mapping in MAMI, the experimental confirmation of the eddy current effect has not been done [5]. Looking for the examination of the experimental observation, the effect of the ramp rate of the excitation current to the magnitude of the residual field of the DC magnet at KEK Photon Factory was found [6]. The evidence of the eddy current in cyclotron block magnet was dug out from the old data as an effect of trim coil at ring cyclotron magnet [7] at RIKEN. The size of the sector is about 3.1m × 3.9m in roughly triangular shape.

It may be surprising that the eddy current effect can not be negligible even in laminated magnets of synchrotron. The field delay from the excitation current has been observed in GSI [8] and KEK [9] and also at HIMAC [10] beam line pulse magnet. More measurements and numerical calculation are under progress and will be reported elsewhere [11].

## 2 EVALUATION OF EDDY CURRENT EFFECT

In a DC block magnet, a transient phenomena appears as an eddy current effect at start-up of the power supply or also at a change of current settings. The time constant of the field change is proportional to a square of the width of magnet and to the conductivity of the iron.

The analytical expression was given by K.Halbach, P.J.Bryant [12] and K.Sato. Here we use the formulation by Bryant for a rectangular magnet. The governing equation for the dipole magnet of the gap length $g$ and the path length $l$ in the iron is,

$$\frac{\partial B^2}{\partial x^2}+\frac{\partial B^2}{\partial z^2}=\frac{l}{g+l/\mu_r}\sigma\mu_0\frac{\partial B}{\partial t}. \tag{1}$$

This equation is a diffusion equation in the magnet. For simplicity, we consider the case when the excitation current is abruptly turned off. The equation (1) has a solution of,

$$B=\sum_m\sum_n B_{mn}\cos[\alpha_m x]\cos[\beta_n z]e^{-\frac{t}{\tau_{m,n}}} \tag{2}$$

where the time constant $\tau_{m,n}$ of the mode $m$ and $n$ for coordinate $x$ and $z$ is written as

$$\frac{1}{\tau_{mn}}=\frac{g+l/\mu_r}{l}\sigma\mu_0\left[\left(\frac{m\pi}{a}\right)^2+\left(\frac{n\pi}{b}\right)^2\right]. \tag{3}$$

It is instructive to relate the time constant to the skin depth $\delta$ as

$$\frac{1}{\tau_{mn}}=\frac{\omega}{2}\delta^2\left[\left(\frac{m\pi}{a}\right)^2+\left(\frac{n\pi}{b}\right)^2\right] \tag{4}$$

where in $\delta$ the path length factor of the first term in eq.(3) is taken account. As we see, the effect of the eddy current causes a cosine distribution. This distribution is like a "hat" and is called "a hat effect" as Halbach first coined it. In the case of turning-on the excitation current, the distribution has "a dish" shape. These distributions are caused as the magnetic field near the coil responds faster and that of at the center responds slower. This changes of

0-7803-4376-X/98/$10.00 © 1998 IEEE

field gradient is the cause of the change of focussing force and effects the beam stability. For the evaluation of the time constant for lower mode number, that of the size up to 5 m was plotted in Fig.1. In the calculation we have assumed that the $l/g \approx 200$ and the conductivity of the iron is $10^{-7}$ ohm. Note the amplification factor $l/g$ in the time constant. It is shown that for the principal mode ($m$=1), the time constant exceeds 1752 sec (30 minutes) above 4 m size magnet. This means to reach a field level below 10-4 accuracy one need 2 hours for this size of magnet.

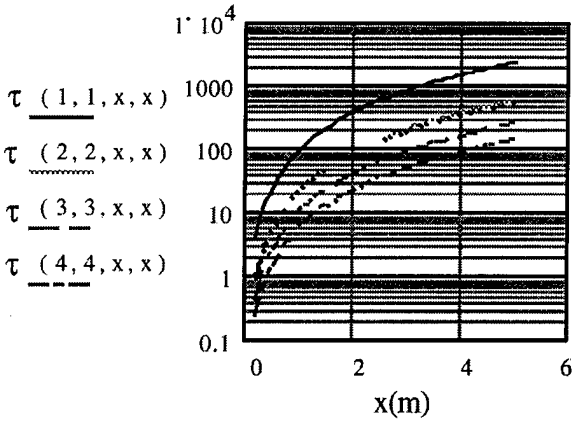



Fig.1 Size dependence of the time constant up to $m$=$n$=4 for the size of up to 5m. τ in sec and x in meter.

The numerical calculation was performed using Opera2D(Vector Field) for cylindrical pole of 1 m radius and shown in Fig.2. The time constant of a principal mode at $r$=624 mm is 500 sec. Figure 2 clearly shows the hat and dish effects. Fig.3 shows a residual current density 700 sec after the turn-off of the excitation current. It is interesting to see opposite direction of the current co-exists, which is due to the trapezoidal excitation having opposite $dB/dt$.

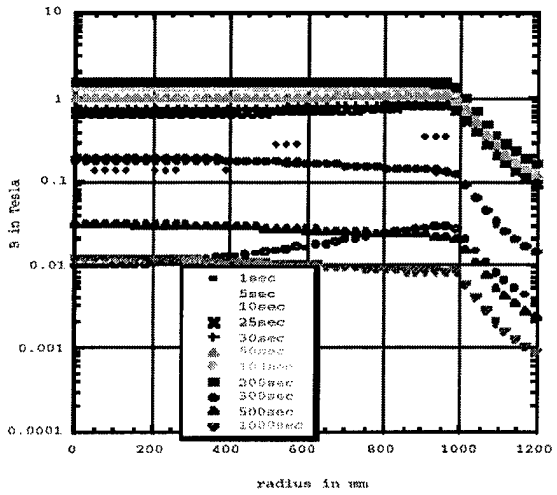



Fig.2 Transient response of field distribution for trapezoidal current excitation (100sec rise, flat top and fall).

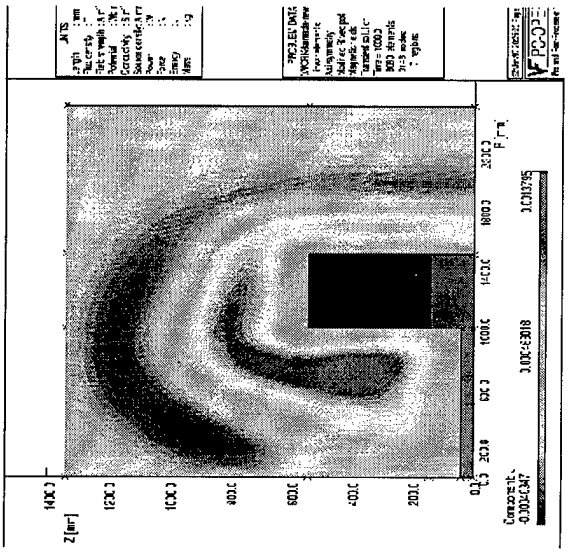


Fig.3 Distribution of current density at $t$=1000 sec. Excitation current is turned off at $t$=300 sec. The figure is rotated by 90 degree.

## 3 OBSERVATION OF EDDY CURRENT EFFECT

Transient response of the magnetic field at three points in the gap of various size of magnet from steering magnet to ring cyclotron magnet were measured using FW Bell hall probe and NMR probe where excitation current was always simultaneously monitored. Due to an insufficient measuring apparatus capability, the ratio of the magnetic field at three locations were measured instead of monitoring the whole distribution. Fig.4 shows the transient response of the magnetic field and its ratio. The ratio indicates the change of field distribution. It should be noted that eddy current effect is responsible for a huge hysteresis effect. They are shown as a field strength and as a ratio of the field as in Figs.5 and 6.

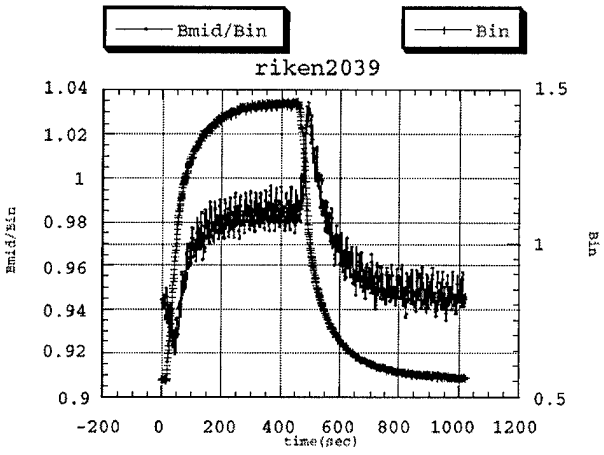



Fig.4 Response of magnetic field and the ratio at two locations, at a middle and inside each 10 cm apart.

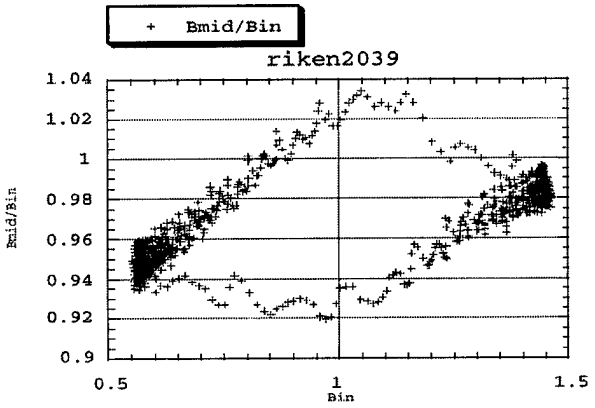



Fig.5 Hysteresis effect of the field ratio as in Fig.4.

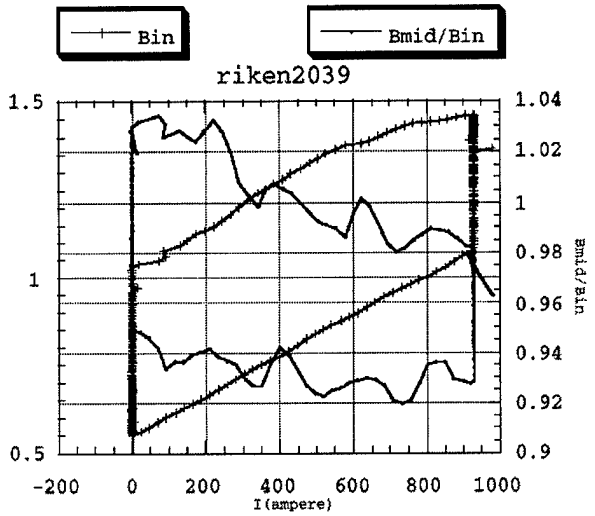



Fig.6 Hysteresis effect of the field strength and the field ratio as in Fig.4.

The measured time constant of the principal mode of ramp-down current is 4900 sec for ring cyclotron magnet shown in Fig.7. The scaling factor of 3 in size could account for this time constant from the calculation of Opera2D.

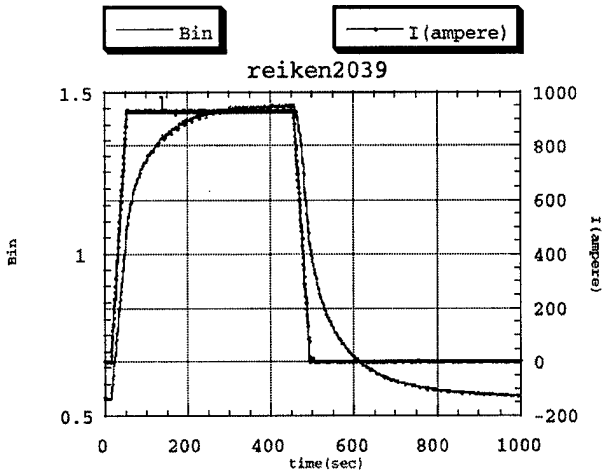



Fig.7 Excitation current and its response of the field strength in RIKEN ring cyclotron magnet.

## 4 ACKNOWLEDGEMENT

The authors would like to express their thanks to accelerator staff members of HIMAC, Drs.Torikoshi, Takada, Noda, Kanazawa,Yamada, Kitagawa, and those of AEC for helping measurements and discussions. The authors also express thanks for having an opportunity for the development and the study of this research to director Dr.K.Kawachi.

## REFERENCES

[1] T.Saito et. al., The XVI RCNP Osaka International Symposium, March 12-14,1997.
[2] K.Arakawa(JAERI), private communication
[3] K.Halbach, NIM, 107(1973) pp529-540.
[4] K.Kaiser, private communication, Institute of Kernphysics of Johaness Gutenberg University
[5] P.Zinnercker, Institute of Kernphysics of Johaness Gutenberg University,KPH 13/89.
[6] N.Kumagai( SPRING 8), private communication.
[7] A.Goto(RIKEN), private communication
[8] B.Langenbeck and R.Steiner(GSI), private communication, also GSI Scientific Report, 1988,p.385.
[9] T. Sueno(KEK), private communication.
[10] M.Kumada, The XVI RCNP The XVI RCNP Osaka International Symposium, March 12-14,1997.
[11] M.Kumada et al., to be presented at MT-15 in Beijin,China,1997.
[12] P.J.Bryant,CERN 92-05,1992,pp52-69.

# RESULTS FROM A PROTOTYPE PERMANENT MAGNET DIPOLE-QUADRUPOLE HYBRID FOR THE PEP-II *B*-FACTORY*

M. Sullivan, G. Bowden, S. Ecklund, D. Jensen, M. Nordby, A. Ringwall, Z. Wolf
Stanford Linear Accelerator Center, Stanford University, Stanford, CA 94039 USA

*Abstract*

We describe the construction of a prototype hybrid permanent magnet dipole and quadrupole. The magnet consists of two concentric rings of $Sm_2Co_{17}$ magnetic material 5 cm in length. The outer ring is made of 16 uniformly magnetized blocks assembled as a Halbach dipole and the inner ring has 32 blocks oriented in a similar fashion so as to generate a quadrupole field. The resultant superimposed field is an offset quadrupole field which allows us to center the field on the high-energy beam in the interaction region of the PEP-II *B*-factory. The dipole blocks are glued to the inside surface of an outer support collar and the quadrupole blocks are held in a fixture that allows radial adjustment of the blocks prior to potting the entire assembly with epoxy. An extensive computer model of the magnet has been made and from this model we developed a tuning algorithm that allowed us to greatly reduce the n=3–17 harmonics of the magnet.

## 1 INTRODUCTION

Obtaining high luminosity from modern colliding beam accelerators generally requires magnetic components to be within 2 m of the collision point. Accelerator elements this close to the interaction point (IP) are invariably inside a detector solenoidal magnetic field. This restricts the choice of technologies for these elements to either superconducting or permanent magnet (PM).

For PEP-II, the *B*-factory being designed and built by a collaboration from SLAC, LBNL, and LLNL[1,2], the 9 and 3.1 GeV beams collide head-on and then are horizontally separated by a bend magnet (B1) positioned between 0.2 and 0.7 m from the IP. Separation continues when the two beams travel through the next magnetic element Q1, a horizontally defocusing quadrupole extending between 0.9 and 2.1 m from the IP. The separation of the beams is maximized if the high-energy beam (HEB) travels through the magnetic center of Q1. Both B1 and Q1 are inside the magnetic field of the detector and are therefore made from PM material.

## 2 Q1 MAGNET DESIGN AND BLOCK SPECIFICATIONS

The Q1 magnet is the vertically focusing quadrupole of the final focus doublet for the low-energy beam (LEB) with a gradient of 106 kG/m. The field quality of this magnet must be very good; we are asking for the strength of each higher harmonic to be less than $1\times10^{-4}$ of the quadrupole strength at a radius that contains the beam-stay-clear (BSC) apertures of both the LEB and the HEB. This requirement is especially demanding at the back of the magnet where the beams are farthest apart (a circle encompassing both BSCs has a radius of 5.9 cm at this position). The BSC is defined as $15\sigma+2$ mm where $\sigma$ is the calculated beam size using uncoupled emittance for x and fully coupled emittance for y[3].

In order to minimize the space taken up by the Q1 magnet, we decided to horizontally shift the magnetic center of Q1 about 2 cm by superimposing a 2.1 kG dipole field over the quadrupole field. This positions the magnetic center of Q1 over the HEB orbit and keeps both beams relatively close to the mechanical center of the magnet thus minimizing harmonic feed-down effects.

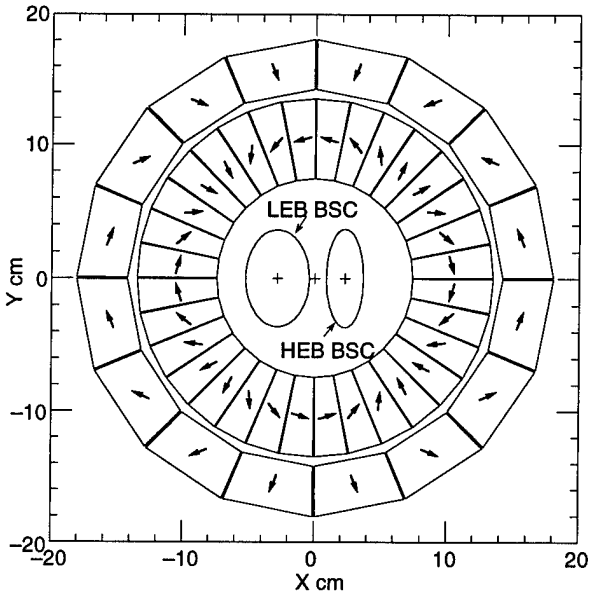



Figure 1. Block dimensions and magnetization angles of the blocks that make the field in the Q1 magnet. The BSC ellipses are at the end farthest away from the IP (z=2.1 m).

Figure 1 shows the positions and magnetization angles of the blocks. Q1 is made up of uniformly magnetized blocks of $Sm_2Co_{17}$ PM material. The magnet is divided into 5 cm thick slices with each slice containing 32 blocks oriented and magnetized according to the method de-

* Work supported by U.S. Department of Energy, under contract number DE-AC03-76SF00515.

0-7803-4376-X/98 /$10.00 © 1998 IEEE

scribed by Halbach[4] to make a quadrupole field. Outside of the ring of 32 blocks is another ring of 16 blocks oriented and magnetized to make a horizontal dipole field. Because of the limited space for this strong magnet, the blocks are held in place with epoxy. The inside radius of the magnetic material is 7.4 cm.

A computer model of the magnetic blocks has been made which computes the magnetic field for each magnetic block according to the Halbach formulas and sums up the individual block fields to get the total magnetic field of a slice. This program structure allows one to model inaccuracies in block placement, dimensions and magnetization. The introduction of errors in the block parameters allows us to determine the expected harmonic content of a magnet slice. The program was used to help define the tolerance ranges for the magnetic blocks.

The unallowed higher harmonics in a Halbach style magnet stem from the block inaccuracies mentioned above. There are also allowed harmonics at n=m+N where m is the number of blocks in the magnet (m=32 for the quadrupole and 16 for the dipole in this case) and N=1 for a dipole and 2 for a quadrupole. To minimize the unallowed higher harmonics, we set fairly tight tolerances on the manufactured blocks.

The magnet blocks were machined from a Shin-Etsu material (R26HS) with a very high intrinsic coercive force (in excess of 18 kOe). Each magnetized block was thermally stabilized in an open circuit condition at 150°C. The magnetization strength of all blocks had to be within 2% of the average value with no block below 10.4 kG. The magnetization angle had to be within 2° of the correct value. The block dimensions were specified assuming a nominal block strength of 10.4 kG with tolerances on the block dimensions of ±200 μms. We attempted to position the dipole blocks to within ±200 μms radially and ±400 μms in azimuth of the correct location.

To verify the quality of the blocks, the dipole moment and magnetization angle of each block were measured using a rotating table positioned in the center of a Helmholtz coil. The magnetic moment measurement precision is 0.1% for the magnitude and 0.1° for the direction.

## 3 MAGNET ASSEMBLY

The first step in the assembly of a magnetic slice is to glue aluminum tabs to the inside and outside radial surfaces of the magnetic blocks. The adhesive is a fast-cure, high-temperature, modified acrylic (Loctite®325). Part of these tabs protrude above the block and allow for a fixture to bolt to these extensions holding the block rigidly. The fixture, with magnetic block, is then mounted on an xyz table for insertion into an aluminum collar mounted on a rotating table. The collar has been faceted on the inside diameter using a wire EDM to accommodate the 16 dipole blocks. The dipole blocks are glued to the inside of the collar with the Loctite®325 adhesive.

Once the dipole blocks are mounted in the collar, the quadrupole blocks can be placed into position. The 32 quadrupole blocks are prepared in the same manner as the dipole blocks. In this case, a brass block bolts to the two glue-tabs and this assembly is mounted into a slot in a support arm that positions the quadrupole block in the bore of the dipole magnet. The brass block is secured in the slot in the arm with a shoulder bolt that can be positioned radially with set screws. This mechanism allows us to independently adjust the radial position of each quadrupole block prior to epoxying the entire assembly. Once the slice is epoxied, the fixtures are removed and the tops of the glue-tabs machined off.

## 4 MAGNET TUNING AND HARMONIC MEASUREMENTS

The harmonics of a magnet slice are measured with a rotating bucking coil. The rotating assembly consists of three coils. Two coils are bucking coils, one designed to buck out the dipole field and the other to buck out the quadrupole field. The third coil measures the higher harmonics. The coil is 100 cm long with an effective radius of 6.35 cm and is mounted vertically on a set of rails so that it can be easily and quickly lifted out of the bore of the magnet. This gives us access to the bore to make adjustments to the quadrupole blocks. The signal from the rotating coil is fed to an integrator and then read out by a PC. The system has a sensitivity of 0.003% of the quadrupole signal for the higher harmonics.

The program that models the block tolerances can also simulate a perfect magnet slice. One can then introduce a sinusoidal variation (as a function of azimuth) of the radial position of the quadrupole blocks. This results in the generation of a pure sextupole and dipole harmonic. Introducing a radial block motion with a $\sin 2\theta$ azimuthal dependence produces a pure octupole (n=4) harmonic. The amplitude of the radial motion is directly proportional to the strength of the harmonic. The skew and normal harmonics can be independently generated by adjusting the phase of the radial block motion (e.g. $\sin\theta$ and $\cos\theta$). Inverting this process, one can compute the radial block motion needed to cancel measured harmonics in a magnet slice; the final block motion being the sum of the motions computed for each harmonic. This procedure works for a total of 32 normal and skew components; harmonics n=3 through 17, both skew and normal, and n=18, skew component only. One can also adjust the quadrupole normal harmonic by moving all of the blocks radially in or out. The normal component of n=18 cannot be changed because this harmonic produces a block motion function that matches the block segmentation in azimuth and therefore all blocks are located where the radial oscillation function crosses zero.

According to the computer model algorithm, the largest block motion needed to correct the harmonics prior to tuning was about 1 mm. The initial block adjustments

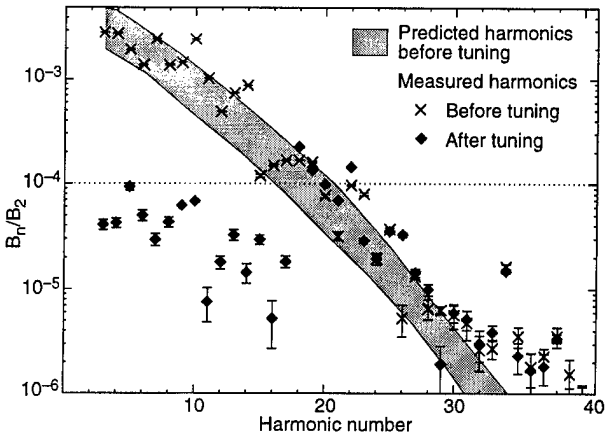



Figure 2. The harmonic content of the prototype magnet before and after the quadrupole blocks are radially adjusted. The quadrupole and dipole harmonics are off-scale and hence not shown. The inner radius of the magnetic material is 7.4 cm. These harmonics are shown at a radius of 5.9 cm. The gray area is the region for the harmonics predicted by the computer model before tuning.

were made by observing the set screw motion (counting bolt head flats). After the block displacement was reduced to less than about 250 μms, we used a capacitive readout sensor to monitor the motion of the blocks. This sensor is attached to a fixture that can be directed to the face of any one of the quadrupole blocks and can measure a difference in block position of less than 2 μms. Using the sensor, we were able to reduce the maximum block displacement to 28 μms (five blocks had displacements greater than 20 μms, the rest had values that were less than 15 μms). The harmonics of the magnet before and after tuning are shown in Figure 2. It should be noted that this procedure will tune out harmonics from any source. In particular, some of the harmonics from the dipole blocks are present in the magnet aperture and these harmonics have also been tuned out by adjusting the positions of the quadrupole blocks.

After tuning, the entire magnet (quadrupole and dipole) was potted with a slow-curing, low-viscosity, casting epoxy (Epic®R1055/H5039, a highly cross-linked thermoset which contains a silica filler). We saw no change in the harmonic content of the slice after the epoxy had set and the fixtures had been removed. Figure 3 is a picture of the potted magnet. Some small changes (about $3\times10^{-5}$ at a radius of 6.35 cm) in some of the harmonic values were observed after about one month which we attribute to magnetic aging, but the following month saw no further change in the harmonics of the slice.

## 5 SUMMARY

We have constructed a 5 cm thick prototype permanent magnet quadrupole with a superimposed dipole field. The

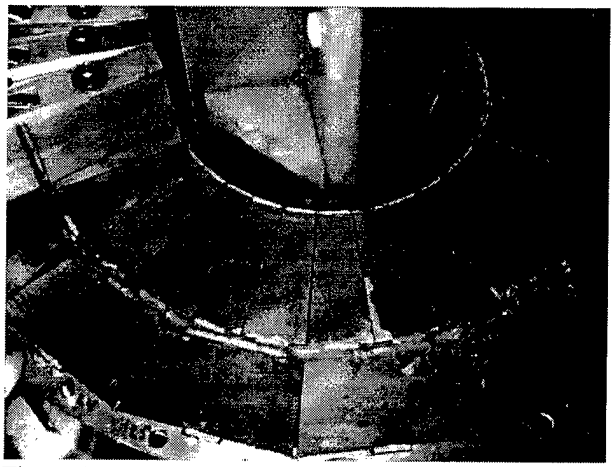


Figure 3. The prototype slice with the harmonic measuring coil in place. The Al tabs have been machined off. Some of the quadrupole block support arms are shown on the left side of the picture.

magnet is made of two concentric rings of uniformly magnetized blocks–16 for the dipole field and 32 for the quadrupole field–magnetized and oriented according to the Halbach formulas. A computer model of the magnet has been made that accurately predicts the harmonic quality of the magnet. The magnetic blocks are held in place with epoxy due to limited radial space for the magnet. Prior to potting, the quadrupole blocks are held in a fixture that allows the blocks to be radially adjusted. This ability is used to lower the harmonics (n=3–17) of the magnet to below $1\times10^{-4}$ of the quadrupole strength at a radius of 5.9 cm (80% of the magnet aperture).

## 6 ACKNOWLEDGMENTS

We would like to thank the machine shop and support staff at SLAC for their assistance in this study. We also thank the designers and technicians who helped us, especially Joe Stieber, who was the lead designer and Bruce Anderson, who was instrumental in helping us with the magnet assembly.

## REFERENCES

[1] "PEP-II an Asymmetric *B* Factory," Conceptual Design Report, CALT-68-1869, LBL-PUB-5379, SLAC-418, UCRL-ID-114055, UC-IIRPA-93-01, June 1993.

[2] M. Sullivan, *et al.*,"Interaction Region Design at the PEP-II *B* Factory," European Particle Accelerator Conference, p. 460 (1996).

[3] M. Sullivan, S. Ecklund, J. Seeman, U. Wienands (SLAC), M. Zisman (LBNL), "BSC Definition of the PEP-II *B* Factory," EPAC, p. 463 (1996)

[4] K. Halbach, "Physical and Optical Properties of Rare Earth Cobalt Magnets," Nucl. Inst. and Methods 187, pp. 109-117 (1981).

# MAGNETIC MEASUREMENTS OF THE PROTOTYPE DIPOLE FOR THE IR-FEL AT THE THOMAS JEFFERSON NATIONAL ACCELERATOR FACILITY

J. Karn, G. Biallas, A. Guerra, and L. Harwood
Thomas Jefferson National Accelerator Facility
12000 Jefferson Avenue, Newport News, VA 23606 USA

*Abstract*

Magnetic measurements have been performed on the prototype dipole for the high power IR-FEL presently under construction at the Thomas Jefferson National Accelerator Facility. The optics-driven requirements for these magnets include low fields, large horizontal apertures, tight field homogeneity, absolute setability of core field & integrated field, and control of the horizontal & vertical focusing terms designed into the magnets. A prototype dipole was fabricated and underwent several iterations of mechanical adjustment and magnetic measurement. Measurements were made to quantify the effects of field clamps on vertical focusing terms and effective length. Additional tests were made using various applications of Purcell gaps and high permeability materials in order to achieve the required homogeneity. Results from the prototype have been integrated into the design of the seven families of dipoles needed for the FEL.

## 1 INTRODUCTION

A 1 kW infrared free-electron laser is under construction at the Thomas Jefferson National Accelerator Facility. The injector for the accelerator produces a 10 MeV, 5 mA CW electron beam. The injected beam is accelerated to 42 MeV using a single CEBAF-style SRF cryomodule. A wiggler and optical cavity produce light in the 3 to 6.6 micron range. A transport arc recirculates the beam exiting the wiggler back through the cryomodule for energy recovery. A potential upgrade to a beam energy of 75 MeV would produce light in the 1 micron range.

## 2 DIPOLE DESIGN REQUIREMENTS

The lattice design of the IR-FEL was tightly constrained due to the low energy, high current, and the 5% relative momentum spread of the recirculated beam [1]. The accelerator requires a total of 29 bending dipoles consisting of 7 different families. The recirculation dipoles will be engineered for beam energies from 33 to 75 MeV. Injector dipoles will cover injection beam energies from 8 to 12 MeV. Table 1 summarizes the 7 families and their field strength requirements.

| Dipole Family | Quantity | Core Field Range (kG) | Effective Length (m.) |
|---|---|---|---|
| DU | 7 | 0.45 - 0.67 | 0.21 |
| DV | 2 | 0.45 - 0.67 | 0.43 |
| DX | 4 | 1.10 - 2.64 | 0.51 |
| DQ | 4 | 1.10 - 2.64 | 0.51 |
| DW | 8 | 1.04 - 2.48 | 0.41 |
| DY | 2 | 1.10 - 2.64 | 3.14 |
| DZ | 2 | 0.92 - 2.20 | 0.21 |

Table 1: Dipole strength specifications

In the designed lattice, the dipoles are also used to manage dispersion and the beam envelope in the recirculation arc. To provide horizontal focusing four of the dipole families have wedge shaped cores with included angles ranging from 7.7° to 20.0°. Important to vertical focusing is the end-field roll-off integral defined as:

$$K_1 = \int_{-\infty}^{\infty} \frac{B_y(z)\left[B_0 - B_y(z)\right]}{gB_0^2} dz$$

where g is the height of the gap and $B_0$ the field strength in the center of the magnet.

The specifications for the horizontal and focusing terms are listed in Table 2 [2].

| Constraint | Tolerance |
|---|---|
| End-field roll-off integral (K1) | $0.27 \pm 0.05$ |
| Field integral slope tolerance | $6.25 \times 10^{-4}$/m x Bρ |
| Relative field integral flatness | $1 \times 10^{-4}$ |

Table 2: Dipole focusing specifications (rms)

Excitation errors in the dipoles could lead to undesirable steering and focusing effects. This puts constraints on the reproducibility of the magnets and the knowledge of the absolute core field and integrated field. Since several of the dipole families are powered in series by a common power supply, the variance of magnets within a family is important. Excitation tolerances are listed in Table 3 [2].

0-7803-4376-X/98/$10.00 © 1998 IEEE

| Constraint | Tolerance |
|---|---|
| Reproducibility of integrated field | $1x10^{-4}$ |
| Accuracy of core field | $1x10^{-3}$ |
| Accuracy of integrated field | $1x10^{-3}$ |
| Tracking within dipole family | $1x10^{-3}$ |

Table 3: Dipole excitation error tolerances (rms)

## 3 CONSTRUCTION OF PROTOTYPE DIPOLE

A single prototype dipole (Figure 1) was fabricated to help quantify the above mentioned tolerances for all seven dipole families. The magnet was a window frame design with a AISI 1006 low-carbon steel core and two saddle-style coils. The coils were 27 turns each, wound from 0.25 inch hollow-core copper conductor, and encased in glass epoxy.

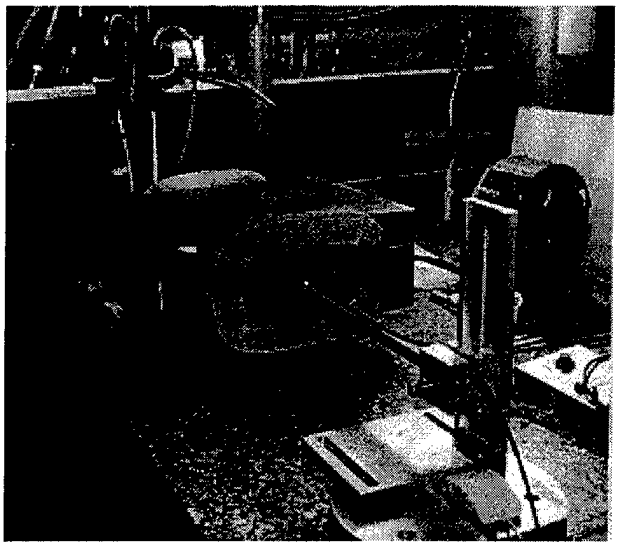


Figure 1: Prototype Dipole

## 4 MAGNETIC MEASUREMENTS

### *4.1 Measurement Setup*

The measurements described below were performed using a Group 3 Hall Effect Probe and a Metrolab NMR Teslameter. The probes were attached to a cart that provided transverse and longitudinal motion. The cart referenced off a granite surface plate to maintain a constant probe orientation with the magnet. A PC-based data acquisition system recorded the probe values at the selected position steps.

### *4.2 Longitudinal Measurements*

There were three areas of interest to study from longitudinal profile measurements: fringe fields, effective length, and the field roll-off integral. The extent of the fringe field was important due to the compact design of the lattice and the close proximity of the dipoles to other beamline elements. Determining the effective length to an accuracy better than $1x10^{-3}$ was needed to meet the core field and field integral tolerances for all dipole families. Determination of the field roll-off integral was required to finalize the lattice design. (The lattice designer graciously left this value flexible to accommodate magnet design.)

Once fringe fields could be brought to an acceptable level, measurements could be made to quantify the effective length and the field roll-off integral. The first measurements revealed the field dropped of to 0.1% at a distance of 37.0 cm from the end of the iron core. To minimize the extent of fringe fields, various designs of field clamps were tested. The final design was a clamp of 0.5 inch thick steel surrounding the coil and connected to the iron core. This setup resulted in the field dropping to 0.1% at a distance of 15.0 cm from the iron core. Figure 2 shows the change in field fall-off with the addition of the field clamp.

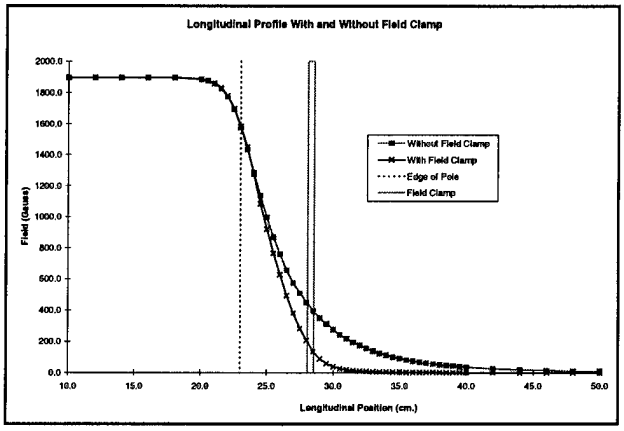



Figure 2: Longitudinal field fall-off with added field clamp.

With the design of the field clamp finalized, measurements were taken to determine the effective length and the field roll-off integral. Longitudinal profiles were made over the operating ranges needed for the 7 families of dipoles. The effective length was calculated to be 25.396 ± 0.004 cm. ($1.6x10^{-4}$ relative) over the operating range. The field roll-off integral was calculated to be 0.31 ± 0.01 over the operating range. Both values were within the tolerances defined in Section 2.

### *4.3 Transverse Measurements*

Measurements were made to study the transverse field homogeneity inside the core. These measurements would be the first step in achieving the $1x10^{-4}$ integrated field flatness defined in Section 2. The first measurements revealed a relative deviation from flatness of ± $1x10^{-3}$, an order of magnitude larger than the requirements. The

transverse profile is plotted in Figure 3 at several core fields.

To improve field flatness, the dipole was modified by the addition of Purcell gap plates. This consisted of adding a 1.5 mm. plate of high permeability material (Vacoperm 70 - mumetal) to each pole, but separated from the iron by a 1.6 mm. plate of aluminum. The return legs of the core were shimmed with iron in order to maintain the 2 inch mechanical gap. Measurements with the Purcell gap showed a relative deviation from flatness of $\pm$ 1x10$^{-4}$, a drastic improvement in field homogeneity (Figure 4.)

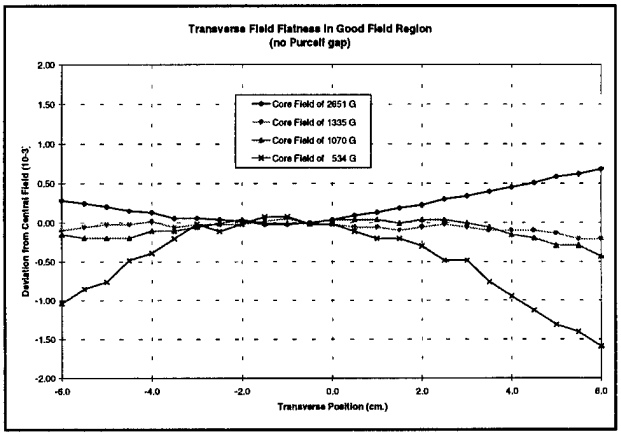



Figure 3: Relative Transverse profile at various core fields before addition of Purcell gap plates.

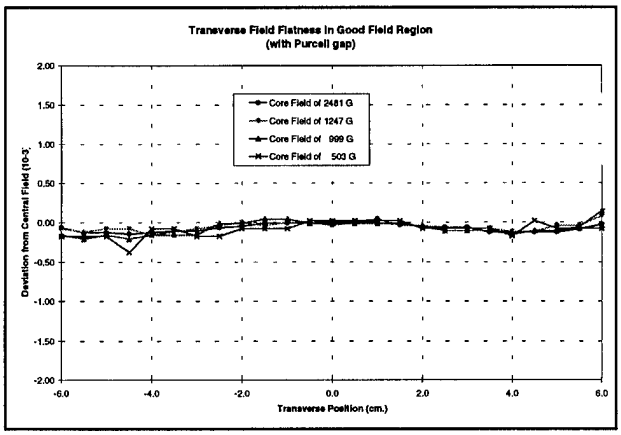



Figure 4: Relative Transverse profile at various core fields with the addition of Purcell gap plates.

## 5 DESIGNING THE PRODUCTION DIPOLES

The seven families of dipoles vary in their aperture, effective length, and the width of their good field region. Extrapolations were made from the experimental data obtained from the prototype to the design of the production magnets. The effective length value obtained from the prototype was used to obtain a scaling factor for changes in aperture. This resulted in:

(Effective Length) = (Core length) + (0.995)(aperture)

Similarly, measurements on the prototype with the Purcell gap plates showed the good field region started at a distance of 2.3 cm. from the coils. This offset was scaled by the aperture of the production dipoles and the required core widths calculated to achieve the desired good field regions.

## 6 PRODUCTION MEASUREMENT PLANS

At the writing of this paper, several of the dipole families were being fabricated at outside vendors and the remaining families were in final design. All dipoles will undergo magnetic measurement before being installed in the accelerator enclosure. The core field, field integral, and field roll-off integral will be determined using the Hall and NMR probe stand described in Section 4.1.

To determine the transverse integrated field profile and the variation in field integral within a family, a specialized stand is under construction. This stand will use the same technique, and share common hardware, with the setup used to measure the CEBAF dipoles [3]. This method uses two pickup coils that are driven simultaneously across the aperture of two magnets of a given family. The induced signals are bucked against each other and thus measure the difference between the two magnets. This method produced a precision of 1x10$^{-5}$ in measuring the relative transverse profile of the CEBAF arc dipoles [4].

## 7 CONCLUSIONS

The optics requirements of the IR-FEL accelerator result in tight tolerances on the design and measurement of the seven families of main bending dipoles. A prototype was built and went through several iterations of mechanical adjustments and magnetic measurements. The final measurements met the required specifications and were integrated into the design of the production dipoles. Design and fabrication of the production dipoles is almost complete and plans are underway for their eventual magnetic mapping.

## 8 ACKNOWLEDGMENTS

This work was supported by the U.S. DOE under contract number DE-AC05-84ER40150.

## REFERENCES

[1] D. R. Douglas, *Lattice Design for a High-Power Infrared FEL,* these proceedings.

[2] D. R. Douglas, *Error Estimates for the IR FEL Transport System,* Jefferson Lab Tech Note # 96-035, 1996.

[3] L. Harwood, *Beam Transport Magnet Measurement,* Jefferson Lab Tech Note # 187, 1989.

[4] L. Harwood and J. Karn, *Measured Field Performance of CEBAF Beam transport Magnets,* Proceeding of Vancouver Magnet Conference, Vancouver, British Columbia, Canada, 1993.

# MAGNETS FOR THE CERN PS BOOSTER TRANSFER LINE

George S. Clark, Alan J. Otter, and Paul Reeve, TRIUMF 4004 Wesbrook Mall, Vancouver, B.C., Canada V6T 2A3

*Abstract*

TRIUMF is building 22 magnets for the CERN PS Booster Transfer Line as part of the Large Hadron Collider (LHC) upgrade. These magnets replace similar existing magnets in the transfer line but have higher fields as the maximum proton energy is being increased from 1 GeV to 1.4 GeV. The magnets, 12 quadrupoles and 10 dipoles, are laminated for pulsed operation with a 1.2 second cycle time. The original magnets operated DC. The new magnets must fit within the existing space envelopes and mate to existing support stands.

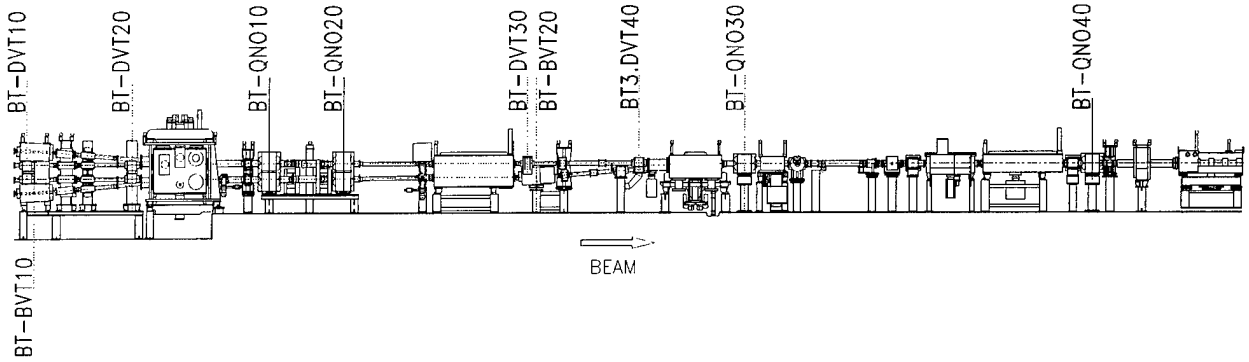



**Figure 1 The CERN PS Booster Transfer Line**

## 1 INTRODUCTION

TRIUMF is participating in a collaboration with CERN to upgrade the Large Hadron Collider. As part of this project TRIUMF is supplying 12 quadrupole and 10 dipole magnets. These magnets are to replace existing magnets in transfer lines connected to CERN's PS Booster. The new magnets must fit within the space envelope of the original magnets despite the maximum proton energy increasing from 1 to 1.4 GeV. The change from DC to pulsed operation with 1.2 second cycle time required the magnets be laminated.

Figure 1 shows the PS Booster Transfer Line and the locations where TRIUMF supplied magnets are to be installed.

The first four dipoles in the Booster Transfer Line will be supplied by TRIUMF. One side of this front end region is very close to the Booster so that space is extremely tight. Figure 2 shows the magnets of the front end region. The lower BVT10 bender supports two DVT dipoles and a second BVT10 bender. The upper bender is cantilevered.

## 2 THE BENDERS

The DVT magnets [1] are small window frame correction dipoles with the field oriented horizontally to give a vertical bend. To fit the magnet into the allowed space the coil leads had to exit from inside the coil. This coupled with the CERN requirement that the coils are splice free, forced the coil manufacturer to wind the saddle shaped coils from the outside-in. TRIUMF is supplying five magnets for installation and two spares.

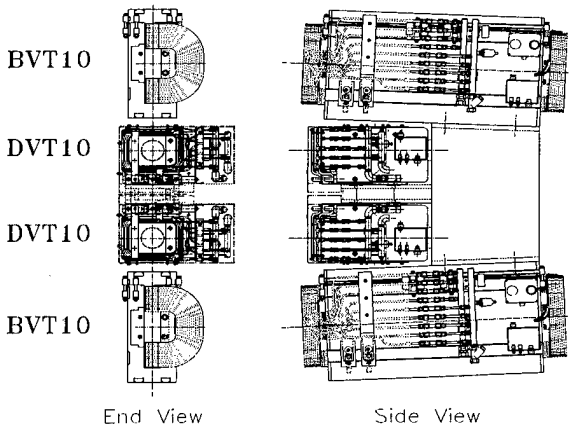



**Figure 2 Front End Region**

TRIUMF is supplying the two BVT10 benders [2,3] in the front end and a single BVT20 bender [2,3] further down the transfer line. These window frame dipoles share a common coil design.

0-7803-4376-X/98/$10.00 © 1998 IEEE

**Table 1 Bender Parameters**

| Type | Overall Length | Effective Length | Aperture | DC Current at 1.4 GeV | Field at 1.4 GeV | Bend Angle 1.4 Gev | Turns Per Coil | Magnet Resistance | Magnet Inductance |
|---|---|---|---|---|---|---|---|---|---|
| | m | m | m | A | T | Radian | | Ohms | H. |
| DVT | 0.4 | 0.383 | 0.102 | 248 | 0.191 | 0.01 | 32 | 0.1 | 0.003 |
| BVT10 | 0.98 | 0.908 | 0.062 | 273 | 0.608 | 0.077 | 112 | 0.24 | 0.043 |
| BVT20 | 0.98 | 0.927 | 0.120 | 234 | 0.542 | 0.07 | 112 | 0.48 | 0.092 |

**Table 2 Quadrupole Parameters**

| Type | Overall Length | Effective Length | Aperture | Max. Energy | DC Current at Max E | Gradient at Max E | Turns Per Coil | Magnet Resistance | Magnet Inductance |
|---|---|---|---|---|---|---|---|---|---|
| | m | m | m | eV | A | T/m | | Ohms | H. |
| BI | 0.57 | 0.462 | 0.150 | | 17 | 1.79 | 159 | 0.83 | |
| BT | 0.6 | 0.466 | 0.150 | 1.4 G | 258 | 6.57 | 57 | 0.16 | 0.041 |

Stresses imposed by lifting and supporting the magnets was not a problem for the original thick yoked BVT benders. The lifting and stand attachment points of the original magnets had to be reproduced in the new laminated magnets. For the BVT magnets these attachment points are not at stress minimizing locations, so considerable work was put into the mechanical design [4,5]. Thick tension straps recessed into the magnet were positioned to accept the attachment points. The thickness of the weld attaching the tension strap to the laminations varies along the length of the magnets.

Table 1 shows the bending magnet parameters.

## 2 THE QUADRUPOLES

TRIUMF is supplying twelve quadrupole magnets in three configurations that share a common steel design. These magnets are a figure-of-eight design [6,7]. Five air-cooled BI-Quadrupoles have been measured at CERN and installed in the Linac Transfer Line leading to the PS Booster. At 15 A the measured gradient is 1.077 T/m and the measured effective length is 0.4598 m.[8].

Seven water cooled BT-Quadrupole magnets are currently under construction. Four of the BT-Quads will be assembled in stacked pairs, one at top the other. The position of the apertures in the pairs is held to a 0.1 mm tolerance. TRIUMF is now field mapping three of the BT quadrupoles.

Table 2 shows the quadrupole magnet parameters.

## REFERENCES


[1] Alan Otter, 'A Review of CERN DVT Dipole Magnets', TRIUMF Design Note TRI-DN-96-5, April 1996.

[2] Alan Otter, 'CERN BV Benders Upgraded for 1.4 GeV Pulsed Operation', TRIUMF Design Note TRI-DN-95-32, November 1995.

[3] Alan Otter, 'CERN BV Benders -- OPERA-2D Calculations', TRIUMF Design Note TRI-DN-96-1, February 1996.

[4] G.S.Clark, 'Mechanical Calculations for the TRIUMF/CERN BV1 Bender', TRIUMF Design Note TRI-DN-96-20, September 1996.

[5] G.S.Clark, 'Mechanical Calculations for the TRIUMF/CERN BV2 Bender', TRIUMF Design Note TRI-DN-96-25, November 1996

[6] Paul A. Reeve, 'Design of BT/BI Quadrupole for CERN Booster Beam Lines', TRIUMF/University of Victoria Design Note VPN-95-3, December 1995

[7] G.S.Clark, 'Mechanical Stress Calculations for the BT/BI Quadrupole for CERN', TRIUMF Design Note TRI-DN-96-4, April 1996

[8] R. Chritin, D. Cornuet, and G. Patron, 'Mesures magnetiques en courant continu d'aimants quadripoles de type BI', CERN Note Technique SL-MS/Note 97-15, Fevrier 1997

# REMOVAL OF AXIAL TWIST IN RHIC INSERTION QUADRUPOLE MAGNETS*

J. Cozzolino, M. Anerella, A. Jain, W. Louie, J. Muratore, P. Wanderer,
Brookhaven National Laboratory, Upton, New York 11973, USA

*Abstract*

The focusing triplets located on either side of the six interaction points of RHIC each consist of three 13cm aperture quadrupoles with magnetic lengths of 1.44m (Q1), 3.40m (Q2), and 2.10m (Q3). The field quality and alignment of these magnets are critical to the performance of the accelerator. The maximum allowable axial twist of the cold mass, defined as the standard deviation in the quadrupole roll angle, is 0.5 mrad. This requirement has occasionally exceeded the capabilities of the assembly fixturing and the procedures used to complete the axial welding of the shell halves around the cold mass yoke. A corrective shell welding technique has been successfully employed to remove excessive axial twist of the 13cm quadrupoles. This "custom straightening" method is described along with the mechanical inspection data before and after straightening. The magnetic results which confirm the untwisting procedure are also discussed.

## I. INTRODUCTION

The ultimate luminosity of the Relativistic Heavy Ion Collider (RHIC) at Brookhaven National Laboratory depends largely on the field quality in the 13cm insertion quadrupole magnets. These 72 quadrupoles have magnetic lengths of 1.44m (Q1), 3.40m (Q2), and 2.10m (Q3). They are the heart of the focusing triplets and must be held to a level of axial twist such that the variation in field angle along the length of each cold mass does not exceed 0.5 milliradian (rms). Axial twist data from mechanical inspection is acquired on each individual quadrupole unit after shell seam welding, and warm magnetic measurements are performed on the final cold mass assembly (Q1, Q2 mated with a single corrector, or Q3 mated with two correctors). Therefore, an opportunity exists to make corrections for twist after shell welding, and for twist and straightness after final cold mass assembly.

## II. WELDING PROCEDURE FOR PRODUCTION

The 13cm quadrupole helium containment vessel includes a two piece stainless steel shell, 6.35mm thick, with longitudinal seams at the twelve and six o'clock locations[1]. The shells of all twelve 13cm quadrupole units installed in Sextant #5 (comprising the first sextant test in January, 1997) have been manually seam welded at BNL using TIG welding equipment and a procedure which calls for two welders operating simultaneously on either side (the cold mass is rotated 90 deg. while clamped straight and securely on the welding platform). It is generally believed that undesirable degrees of twist or bending of the containment vessel can result from an imbalance induced during the welding process (e.g., unequal heat input or rate of filler wire consumption from side-to-side), uneven weld shrinkage, variations in shell straightness, variations in shell weld gap, or the presence of asymmetric welds and discontinuities on the containment vessel necessitated by the placement of such items as fiducials, mounting brackets, cover patches on the shell, or repairs, etc. In the case of the 13cm quadrupoles, the twist and straightness requirements can and often do exceed the practical design limitations of the shell assembly tooling, and cold mass assembly techniques. Experience has shown that despite the fact that the cold mass is firmly clamped against strong and precise fixturing which is designed to keep it straight throughout the duration of the welding process, the cold mass may "spring" upon removal from the fixturing. Much effort has gone into designing the tooling and tailoring the process with one of the primary goals being the control and minimization of this springing.

Most 13cm insertion quadrupoles installed in the tunnel after the first sextant test will have shells that are seam welded via automatic MIG welding utilizing computer controlled wire feed and progression of the weld head. This will involve using the same unit that was previously used successfully to weld all 8cm CQS assemblies at BNL. Although machine welding is clearly a tremendous time saver compared to manual welding, presently it is not yet known whether or not it will result in a reduction of axial twist or bending of the cold masses.

## III. REMOVAL OF AXIAL TWIST

Removal of excessive cold mass twist via "flame straightening" methods was first successfully employed by Northrop-Grumman Corp. on 8cm dipole DRG567. This method of "counter-twisting" has since been refined at BNL and is used to efficiently and reliably reduce axial twist of the 13cm quadrupoles to within acceptable limits. A twist bridge is used to monitor the change in inclination of the cold mass at locations where holes in the shell allow access to the flat survey surfaces on the outside diameter of the iron yoke. The twist bridge consists of a precision aluminum frame onto which an electronic level sensor or

* Work supported by the U.S. Department of Energy under Contract No. DE-AC02-76CH00016.

0-7803-4376-X/98 /$10.00 © 1998 IEEE

inclinometer is rigidly mounted. The inclinometer has a range of ±20 mrad and is accurate to within .05mrad. The two lower contact surfaces of the twist bridge engage the yoke survey notches which serve as indicators of the mechanical center and level of the magnet. The basic procedure for twist removal is outlined below:

1. Set the cold mass on two pairs of precision steel rollers spaced at approximately 1/4 and 3/4 overall cold mass length. Place the twist bridge on the cold mass so it engages the survey notches at the top pair of shell holes closest to the lead end.

2. Level the cold mass so that the twist bridge reads zero. Use suitable means to lock the cold mass so that this first shell hole location remains level and does not rotate during the untwisting process.

3. Move the twist bridge to the next shell hole location and determine inclination. If the twist is deemed excessive, apply a TIG weld bead between the two shell hole locations and about the horizontal midplane, and angle it approximately 30 deg. in the chosen area to be untwisted. Do the same except in the reverse orientation on the exact opposite side of the cold mass in order to maintain weld symmetry side-to-side and to preserve axial straightness. The length, number of weld beads, and filler wire input depend on the demonstrated effectiveness (i.e., the degree to which they mitigate axial twist in a particular instance). Fig. 1 illustrates the general concept.

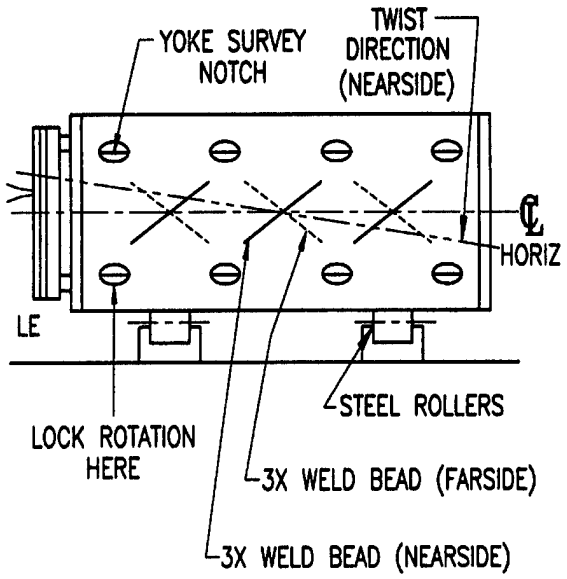



Figure 1. Schematic showing the procedure used to remove axial twist.

4. The twist condition existing at each region between adjacent sets of shell holes is corrected separately and individually. Only a single welder is necessary but weld length, size and filler wire input must be identical on opposite sides or the cold mass will bend.

5. Observe the twist bridge display while welding is in progress so that it is continuously clear that the desired results are being achieved and that no more weld is being laid than is absolutely necessary. Successive welds must be in matched pairs of equal length on both sides and must be adjacent to but not overlapping previous welds. The amount of counter-twist generated by each pair of angled welds is governed by their length and not by varying the angle or size (filler wire input) of the weld, once it is established. Weld lengths should be shortened if necessary to ensure that a matching weld of identical length may be applied on the opposite side of the cold mass.

6. After the cold mass has cooled completely, obtain final twist data by taking inclination measurements at each available shell hole location to verify that the overall twist is within the specified tolerance.

## IV. RESULTS

Referring to Fig. 2, it is observed that Q3 quadrupole QRJ114 has an initial twist exceeding 1 mrad rms (dotted line). The corresponding solid lines show that the final twist of QRJ114 after flame straightening is within 0.5 mrad rms. Fig. 3 shows twist measurements on Q2 quadrupoles. Both QRK103 and QRK107 had large twist initially (dotted lines). QRK103 with an initial twist of over 2 mrad rms received three pairs of corrective welds. The final twist of this cold mass was reduced to well within 0.5 mrad rms. A similar result was also obtained for QRK107.

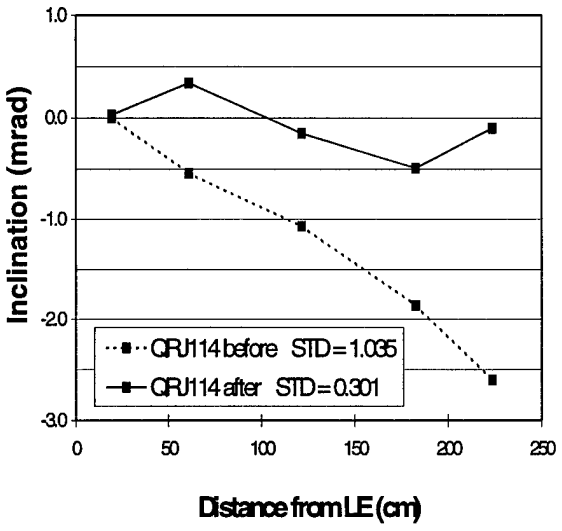



Figure 2. 13 cm Q3 Quardupole Twist Data.

The magnetic field angles of the completed quadrupole assemblies were measured with a 0.91m long rotating coil system. Only one measurement of field angle was possible in the straight section of the Q1 and Q3 magnets so no information on twist could be obtained. In the Q2 magnets the field angle was measured at three axial locations, thus allowing an estimate of the actual twist. The field angle plot shown on Fig. 4 clearly demonstrates that the room temperature magnetic measurements correspond closely to

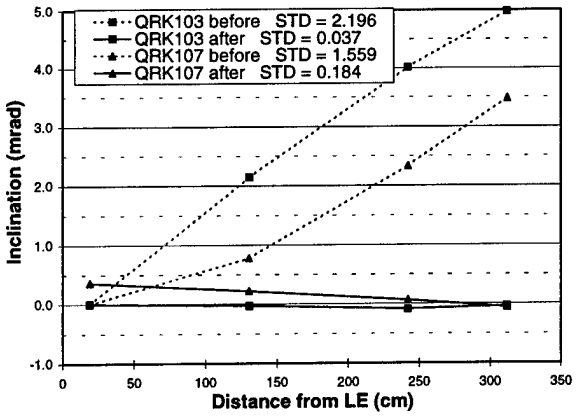



Figure 3. 13 cm Q2 Quadrupole Twist Data.

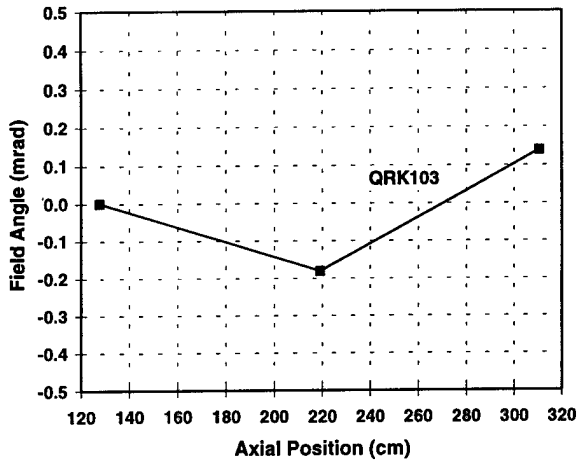



Figure 4. Field angle measured with a 0.91m long rotating coil at three axial locations in the straight section of the Q2 magnet QRK103.

the mechanical data as far as overall axial twist of the cold mass is concerned. In the case of QRK103, the field angle is held to within 0.4 mrad after twist removal. These measurements verify that the yoke is a good indicator of the magnetic field angle, as expected, thereby validating the corrective procedure. Furthermore, this suggests that even in the absence of mechanical means of measurement (the yoke survey notches may no longer be accessible) the variation in magnetic field angle may be read directly and reduced as needed, by careful application of corrective welds.

## V. CONCLUSION

A procedure is described to remove axial twist in magnets based on mechanical measurements of the iron yoke and application of corrective welds. Magnetic measurements of twist are in agreement with the mechanical measurements. Therefore, either may be used to reliably monitor the effect of the twist removal process.

## REFERENCES

[1] R. Gupta et al., "Large Aperture Quadrupoles for RHIC Interaction Region," Proc. 1993 Particle Accelerator Conf., Washington, DC, p.2745.

# PARAMETERIZATION AND MEASUREMENTS OF HELICAL MAGNETIC FIELDS

W. Fischer* and M. Okamura
Brookhaven National Laboratory, Upton, NY 11973, USA

*Abstract*

Magnetic fields with helical symmetry can be parameterized using multipole coefficients $(\tilde{a}_n, \tilde{b}_n)$. We present a parameterization that gives the familiar multipole coefficients $(a_n, b_n)$ for straight magnets when the helical wavelength tends to infinity. To measure helical fields all methods used for straight magnets can be employed. We show how to convert the results of those measurements to obtain the desired helical multipole coefficients $(\tilde{a}_n, \tilde{b}_n)$.

## 1 INTRODUCTION

The magnetic field inside straight magnets can be parameterized in terms of multipole coefficients $(a_n, b_n)$. We will present such a parameterization first. Fields of helical magnets (see Fig. 1) can be described in a similar way, by means of multipole coefficients $(\tilde{a}_n, \tilde{b}_n)$. We give a notation for the $(\tilde{a}_n, \tilde{b}_n)$ for which the $(a_n, b_n)$ are the limiting case when the helical wave length tends to infinity. A Cylindrical coordinate system $(r, \theta, s)$ is used where $s$ denotes the longitudinal direction.

We then assume that a magnetic field measurement device always parameterizes its measurements in terms of $(a_n, b_n)$, and give formulae to obtain the coefficients $(\tilde{a}_n, \tilde{b}_n)$ when a helical magnetic field is measured. Three types of measurement devices are treated: rotating "radial" coils, rotating "tangential" coils and rotating Hall probes (see Fig. 2 (a), (b) and (c) respectively).

## 2 MAGNETIC FIELD PARAMETERIZATION

### 2.1 *Straight Magnetic Fields*

In a current free region in vacuum where the electrical field $\vec{E}$ is constant, the magnetic field $\vec{B}$ can be derived from a scalar potential $\psi$ as $\vec{B} = -\nabla\psi$. We consider a magnet of infinite length, thus neglecting fringe fields. The symmetry condition of such an element is $\psi(r, \theta, s) = \psi(r, \theta, s+\Delta s)$ with $\Delta s$ arbitrary. Therefore, the potential $\psi$ is independent of $s$, $\psi(r, \theta, s) = \psi(r, \theta)$.

Having a main field $B_0 \sin\theta$ the solution of the Laplace equation $\Delta\psi = 0$ can be written as

$$\psi(r,\theta) = -B_0 \sum_{n=0}^{\infty} \frac{1}{n+1} \frac{r^{n+1}}{r_0^n} \times \times \left[ a_n \cos\Big((n+1)\theta\Big) + b_n \sin\Big((n+1)\theta\Big) \right]. \quad (1)$$

The $b_n$ are called "normal" and the $a_n$ "skew" multipole coefficients. Here, the subscript "0" denotes a dipole, "1" a quadrupole etc. $r_0$ is a reference radius.[1]

From $\vec{B} = -\nabla\psi$ and Eq. (1) the magnetic field can be obtained. We have

$$B_r = B_0 \sum_{n=0}^{\infty} \left(\frac{r}{r_0}\right)^n \left[ a_n \cos\Big((n+1)\theta\Big) + b_n \sin\Big((n+1)\theta\Big) \right], \quad (2)$$

$$B_\theta = B_0 \sum_{n=0}^{\infty} \left(\frac{r}{r_0}\right)^n \left[ b_n \cos\Big((n+1)\theta\Big) - a_n \sin\Big((n+1)\theta\Big) \right], \quad (3)$$

$$B_s = 0. \quad (4)$$

### 2.2 *Helical Magnetic Fields*

We consider again a magnet of infinite length and neglect fringe fields. The symmetry condition for a helical magnet is $\psi(r, \theta, s) = \psi(r, \theta - k\Delta s, s + \Delta s)$, where $\Delta s$ is arbitrary.

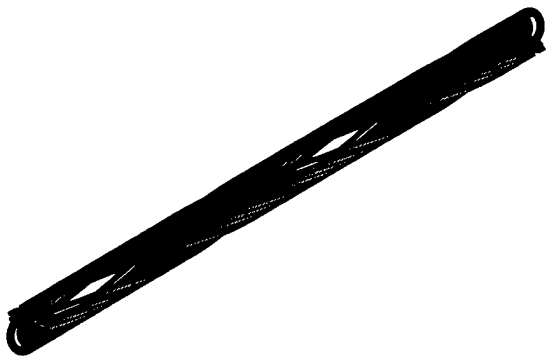


Figure 1: The conductor of a helical dipole (one helical wavelength long). This magnet will be used for proton spin manipulation in RHIC.

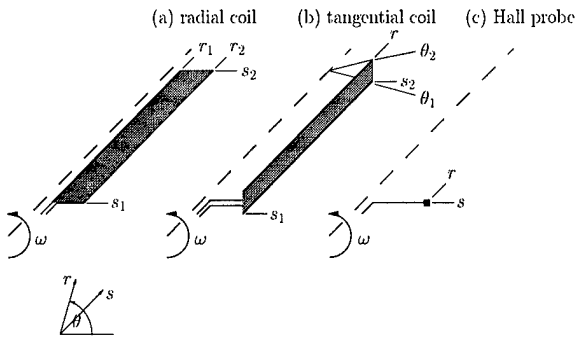



Figure 2: Three methods to measure magnetic multipole coefficients.

[1]Note that the European notation (see for example Ref. [1]) differs from the American one presented here. The transformation is $b_{n,American} = b_{n+1,European}$ and $a_{n,American} = -a_{n+1,European}$.

* Work performed under the auspices of the US Department of Energy

0-7803-4376-X/98/$10.00 © 1998 IEEE

In other words, $\theta - ks = const.$ $k = 2\pi/\lambda$ is the wave number and $\lambda$ the wave length of the helix. $k$ shall have a positive sign for right-handed and a negative sign for left-handed helices. Introducing the new variable $\tilde{\theta} = \theta - ks$, the symmetry condition leads to a potential $\psi$ which is only dependent on $r$ and $\tilde{\theta}$, $\psi(r, \theta, z) = \psi(r, \tilde{\theta})$. The tilde shall remind the reader of the fact that $\tilde{\theta}$ in a helix is similar to $\theta$ in an ordinary dipole. Using $(r, \tilde{\theta})$ as coordinates and having a transverse helical main Field $B_0 \sin\tilde{\theta}$ a solution of the Laplace equation $\Delta\psi = 0$ is

$$\psi(r,\tilde{\theta}) = -B_0 \sum_{n=0}^{\infty} \frac{f_n}{k(n+1)} I_{n+1}\Big((n+1)kr\Big) \times \times \left[\tilde{a}_n \cos\Big((n+1)\tilde{\theta}\Big) + \tilde{b}_n \sin\Big((n+1)\tilde{\theta}\Big)\right] \quad (5)$$

where $I_n$ are modified Bessel functions and the $f_n$ are defined as

$$f_n = \frac{2^{n+1}(n+1)!}{(n+1)^{n+1}} \frac{1}{r_0^n k^n}. \quad (6)$$

The $\tilde{b}_n$ are called "normal" and the $\tilde{a}_n$ "skew" helical multipole coefficients (with respect to the main field $B_0$). The subscript "0" denotes a helical dipole, the subscript "1" a helical quadrupole etc. $r_0$ is again a reference radius.

The factors in (5) are chosen in such a way as to obtain the potential (1) when the helical wave length tends to infinity. In this case $k \to 0$, $\tilde{\theta} \to \theta$ and the Bessel function can be approximated by $I_n(z) \approx \frac{1}{2^n}\frac{z^n}{n!}$ (cf. Ref. [2]). Now, the magnetic field can be computed as

$$B_r = B_0 \sum_{n=0}^{\infty} f_n I'_{n+1}\Big((n+1)kr\Big) \times \times \left[\tilde{a}_n \cos\Big((n+1)\tilde{\theta}\Big) + \tilde{b}_n \sin\Big((n+1)\tilde{\theta}\Big)\right], \quad (7)$$

$$B_\theta = -\frac{1}{kr} B_s, \quad (8)$$

$$B_s = -B_0 \sum_{n=0}^{\infty} f_n I_{n+1}\Big((n+1)kr\Big) \times \times \left[\tilde{b}_n \cos\Big((n+1)\tilde{\theta}\Big) - \tilde{a}_n \sin\Big((n+1)\tilde{\theta}\Big)\right]. \quad (9)$$

where $I'_n$ denotes the derivative with respect to the argument of the Bessel function.

Since the Bessel function is nonlinear, a magnetic field with helical symmetry is nonlinear too, even the field of a perfect helical dipole. In addition, there is a longitudinal field component off the $s$-axis. Fig. 3 shows an example for the field inside a helical dipole.

## 3 MEASUREMENTS OF HELICAL FIELDS

While the multipole measurements with rotating coils are obtained from the field within the coil area (shaded in Fig. 2), the multipole coefficients of Hall probe measurements are obtained from the field on the circumference of a circle with given radius $r$. For rotating coils the magnetic flux is computed for both parameterizations $(a_n, b_n)$ and $(\tilde{a}_n, \tilde{b}_n)$. The results are stated in a form that allows a direct comparison. For Hall probe measurements the magnetic fields in both parameterizations are also stated in a form that allows a comparison. For all cases conversion formulae from $(a_n, b_n)$ to $(\tilde{a}_n, \tilde{b}_n)$ are given in the same form.

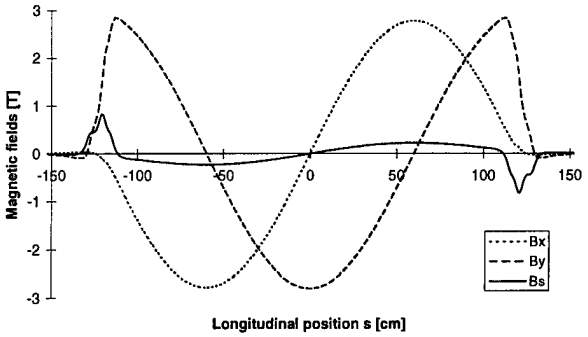



Figure 3: Magnetic field components along the $s$-axis with $x$=0 cm and $y$=31 cm for the magnet shown in Fig. 1. Note that end effects are not treated in this article.

### 3.1 *Rotating Coils*

The magnetic flux through a coil is

$$\Phi(\theta) = N \int \vec{B}(r,\theta) \cdot d\vec{a} \quad (10)$$

where N is the number of coils windings. For rotating coils one has $\theta = \omega t$ and the induced voltage $U = -d\Phi/dt$ is proportional to the angular velocity $\omega$.

#### 3.1.1 Radial Coils

The area of a flat rotating radial coil ranges from $r_1$ to $r_2$ and from $s_1$ to $s_2$ (cf. Fig. 2). The magnetic flux (10) through the coils is

$$\Phi(\theta) = N \int_{s_1}^{s_2} \int_{r_1}^{r_2} B_\theta(r,\theta)\, dr\, ds. \quad (11)$$

Using (3) the magnetic flux (11) for straight magnets becomes

$$\left.\begin{aligned} &\Phi(\theta) = NB_0(s_2 - s_1) \sum_{n=0}^{\infty} K_n \Big[b_n \cos\Big((n+1)\theta\Big) - a_n \sin\Big((n+1)\theta\Big)\Big] \\ &\text{with} \quad K_n = \frac{r_0}{n+1}\left[\left(\frac{r_2}{r_0}\right)^{(n+1)} - \left(\frac{r_1}{r_0}\right)^{(n+1)}\right]. \end{aligned}\right\} \quad (12)$$

With (8) the flux for helical fields is

$$\left.\begin{aligned} &\Phi(\theta) = NB_0(s_2 - s_1) \sum_{n=0}^{\infty} R_n \Big[\hat{b}_n \cos\Big((n+1)\theta\Big) - \hat{a}_n \sin\Big((n+1)\theta\Big)\Big] \\ &\text{with} \quad R_n = f_n \int_{r_1}^{r_2} \frac{1}{kr} I_{n+1}\Big((n+1)kr\Big)\, dr. \end{aligned}\right\} \quad (13)$$

In (13) new magnetic multipole coefficients

$$\begin{aligned} \hat{a}_n &= +\tilde{a}_n T_n + \tilde{b}_n S_n, \\ \hat{b}_n &= -\tilde{a}_n S_n + \tilde{b}_n T_n. \end{aligned} \tag{14}$$

are used for which

$$S_n(s_1,s_2) = -\frac{2}{\Delta s(n+1)k} \sin\frac{(n+1)k\Delta s}{2} \sin\frac{(n+1)k\Delta s}{2} \tag{15}$$

and

$$T_n(s_1,s_2) = +\frac{2}{\Delta s(n+1)k} \sin\frac{(n+1)k\Delta s}{2} \cos\frac{(n+1)k\Delta s}{2} \tag{16}$$

with $\Delta s = s_2 - s_1$ have been defined.

#### 3.1.2 Tangential Coils

The magnetic flux through this type of coil is (cf. Fig. 2)

$$\Phi(\theta) = N \int_{s_1}^{s_2} \int_{\theta_1}^{\theta_2} B_r(r,\bar{\theta})\, r d\bar{\theta}\, ds. \tag{17}$$

The difference $\Delta\theta = \theta_2 - \theta_1$ is fixed and one can assume that $\theta_1 = \theta - \Delta\theta/2$ and $\theta_2 = \theta + \Delta\theta/2$ hold. With (2) the magnetic flux in straight magnets becomes

$$\left.\begin{aligned} \Phi(\theta) &= NB_0(s_2-s_1)\cdot\frac{2}{n+1}\sin\frac{(n+1)\Delta\theta}{2}\times \\ &\times\sum_{n=0}^{\infty} K_n\left[a_n\cos\Big((n+1)\theta\Big) + b_n\sin\Big((n+1)\theta\Big)\right] \\ \text{with}\quad K_n &= \frac{r^{n+1}}{r_0^n} \end{aligned}\right\} \tag{18}$$

and for helical fields one obtains with (7)

$$\left.\begin{aligned} \Phi(\theta) &= NB_0(s_2-s_1)\cdot\frac{2}{n+1}\sin\frac{(n+1)\Delta\theta}{2}\times \\ &\times\sum_{n=0}^{\infty} R_n\left[\hat{a}_n\cos\Big((n+1)\theta\Big) + \hat{b}_n\sin\Big((n+1)\theta\Big)\right] \\ \text{with}\quad R_n &= f_n\, r\, I'_{n+1}\Big((n+1)kr\Big). \end{aligned}\right\} \tag{19}$$

The $(\hat{a}_n, \hat{b}_n)$ are defined by (14) and the $(S_n, T_n)$ needed in this definition in (15,16).

### *3.2 Hall Probes*

For Hall probe measurements the magnetic fields, either tangential or radial, can be compared directly.

#### 3.2.1 Tangential Field Components

The tangential field in a straight magnet is (cf. Eq. (3))

$$\left.\begin{aligned} B_\theta(\theta) &= B_0\sum_{n=0}^{\infty} K_n\left[b_n\cos\Big((n+1)\theta\Big) - a_n\sin\Big((n+1)\theta\Big)\right] \\ \text{with}\quad K_n &= \left(\frac{r}{r_0}\right)^n \end{aligned}\right\} \tag{20}$$

and in a helical field (cf. Eq. (8))

$$\left.\begin{aligned} B_\theta(\theta) &= B_0\sum_{n=0}^{\infty} R_n\left[\hat{b}_n\cos\Big((n+1)\theta\Big) - \hat{a}_n\sin\Big((n+1)\theta\Big)\right] \\ \text{with}\quad R_n &= \frac{1}{kr} f_n I_{n+1}\Big((n+1)kr\Big). \end{aligned}\right\} \tag{21}$$

The $(\hat{a}_n, \hat{b}_n)$ are again defined by equations (14) and the $(S_n, T_n)$ needed in this definition by equations (15,16).

#### 3.2.2 Radial Field Components

The radial field in a straight magnet is cf. Eq. (2))

$$\left.\begin{aligned} B_r(\theta) &= B_0\sum_{n=0}^{\infty} K_n\left[a_n\cos\Big((n+1)\theta\Big) + b_n\sin\Big((n+1)\theta\Big)\right] \\ \text{with}\quad K_n &= \left(\frac{r}{r_0}\right)^n \end{aligned}\right\} \tag{22}$$

and in a helical field cf. Eq. (7))

$$\left.\begin{aligned} B_r(\theta) &= B_0\sum_{n=0}^{\infty} R_n\left[\hat{a}_n\cos\Big((n+1)\theta\Big) + \hat{b}_n\sin\Big((n+1)\theta\Big)\right] \\ \text{with}\quad R_n &= f_n I'_{n+1}\Big((n+1)kr\Big). \end{aligned}\right\} \tag{23}$$

Also in this case the $(\hat{a}_n, \hat{b}_n)$ are defined by equations (14) and the $(S_n, T_n)$ by equations (15,16).

### *3.3 Conversion*

It is now assumed that a device parameterizes the measured magnetic field in terms of multipole coefficients $(a_n, b_n)$ for straight magnets. If the measured magnetic field has helical symmetry, the coefficients $(\tilde{a}_n, \tilde{b}_n)$ can be derived by comparing (12) with (13), (18) with (19), (20) with (21) or (22) with (23). One obtains for all cases

$$\begin{aligned} K_n b_n &= R_n \hat{b}_n, \\ K_n a_n &= R_n \hat{a}_n. \end{aligned} \tag{24}$$

With (14) it follows that

$$\boxed{\begin{aligned} \tilde{a}_n &= \frac{K_n}{R_n}\cdot\frac{a_n T_n - b_n S_n}{S_n^2 + T_n^2}, \\ \tilde{b}_n &= \frac{K_n}{R_n}\cdot\frac{a_n S_n + b_n T_n}{S_n^2 + T_n^2}. \end{aligned}} \tag{25}$$

## 4 ACKNOWLEDGMENTS

We are thankful to the members of the RHIC spin collaboration group for discussions.

## 5 REFERENCES

[1] J. Rossbach and P. Schmüser, "Basic course on accelerator optics", Fifth General Accelerator Course, University of Jyväskylä, Finland, CERN 94-01 (1994).

[2] M. Abramowitz and I. Stegun, "Handbook of Mathematical Functions", Dover, New York (1972).

# A COMMON COIL DESIGN FOR HIGH FIELD 2-IN-1 ACCELERATOR MAGNETS*

Ramesh Gupta, RHIC Project, Brookhaven National Laboratory, Upton, NY 11973 USA

*Abstract*

A common coil design concept for 2-in-1 superconducting accelerator magnets is presented. It practically eliminates the major problems in the ends of high field magnets built with either high temperature superconductors (HTS) or conventional superconductors. Racetrack coils, consisting of rectangular blocks built with either superconducting tapes or cables, are common to both apertures with each aperture containing one half of each coil. The ends are easy to wind with the conductors experiencing little strain. The overall magnet design, construction and tooling are also expected to be simpler than in the conventional cosine theta magnets. The concept is also suitable for superferric and combined function magnet designs. A modular design for an HTS based R&D magnet is also presented.

## 1 INTRODUCTION

The recent advances in high temperature superconductors have raised the expectations of using them in a high field (10T-15T) magnet design for high energy hadron colliders [1]. Conventional cosine(θ) designs may not be suitable for such magnets. In particular, problems arise in containing the large Lorentz forces and winding the coil ends since, like $Nb_3Sn$, HTS material exhibits poor mechanical properties. The proposed common coil design for 2-in-1 magnets overcomes these problems and offers a conductor-friendly way of making magnets. The design is well suited for coils made with tapes using the "React and Wind" technique. The conductor is wound in the easy direction and the bend radius is large. This paper is intended to present a concept rather than a detailed engineering design.

## 2 COMMON COIL MAGNET DESIGN

### *2.1 Basic Geometry*

A schematic of the proposed 2-in-1 design for the main coils is shown in Fig. 1. The main coils are common to both apertures, and hence the name, 'Common Coil Magnet Design'. A set of racetrack coils, operating in series, are placed vertically on the left and right side of the two apertures producing field in opposite directions.

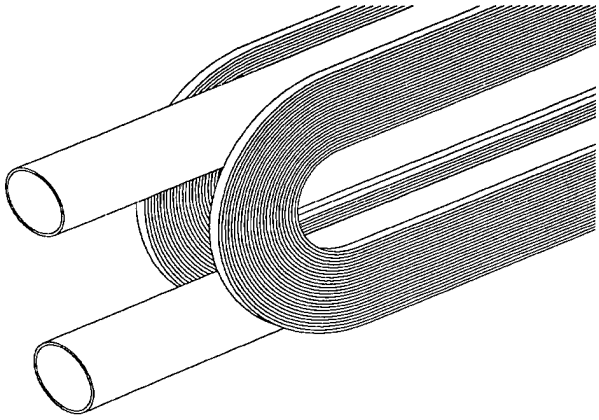


Fig. 1: The main coils in the 2-in-1 common coil design concept. The coils on the left and on the right sides of the beam tubes are common to both top and bottom apertures.

### *2.2 A High Field Magnet Cross-section*

A preliminary magnetic design of a 50 mm aperture, 15 tesla magnet is shown in Fig. 2. The separation between the two apertures is 120 mm and the outer yoke diameter is 400 mm. The design is based on a conductor having a width of 6 mm and an overall or engineering current density ($J_c$) of 3 kA/mm$^2$. It is assumed that conductors with such performance will be available in the future. A lower current density requires a few centimeter increase in yoke diameter.

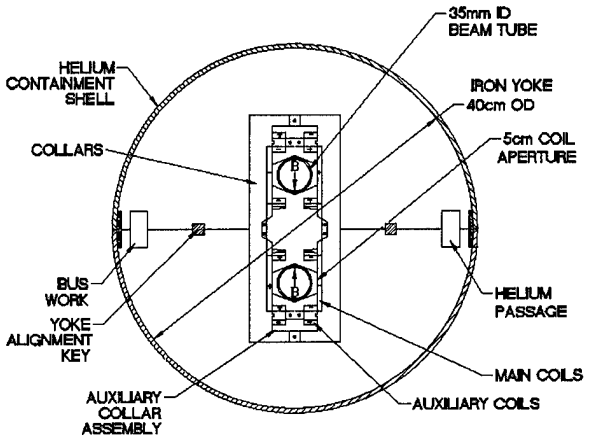



Fig. 2: A preliminary design of a 15 tesla magnet showing the main and auxiliary coils.

* Work supported by U.S. Department of Energy under contract No. DE-AC02-76CH00016.

0-7803-4376-X/98/$10.00 © 1998 IEEE

In addition to main coils, there are also auxiliary coils at/near the poles. The main coils are primarily responsible for the magnitude of the field and the auxiliary coils for the field uniformity. The auxiliary coils are made with the same conductor as the main coils and are powered in series. The main coils and the auxiliary coils which are closer to the yoke midplane (lower coils of the top aperture and upper coils of the bottom aperture) are common to both apertures.

The auxiliary coils which are away from the yoke midplane (upper coils of the top aperture and lower coils of the bottom aperture) are placed in such a way that the other side of the coils returns in the same aperture. The separation between the two sides of this coil is determined by the acceptable value of the bend radius in the ends. It may be noted that though the other side of this coil makes a small negative contribution to the central field, it has a large influence in reducing the exterior field and hence reducing the yoke outer diameter. The yoke outer diameter to contain flux at 15 tesla central field is only 400 mm which is about half the size required in conventional 2-in-1 magnets. For example, the yoke diameter in 8.4 tesla, 56 mm aperture LHC 2-in-1 dipole is 550 mm. Moreover, the collar width at the midplane can be increased to contain large Lorentz forces ($\propto B^2$) without increasing the overall size, as the magnetic design does not require maximum yoke width at the midplane.

This design has an inherent up-down asymmetry which creates skew harmonics. The details of the conductor configuration are optimized to minimize the normal and skew harmonics. For the purpose of this conceptual study, the harmonics were minimized to only the $10^{-3}$ level at a reference radius of 10 mm. A computer model and the field lines at 15 tesla are shown in Fig. 3.

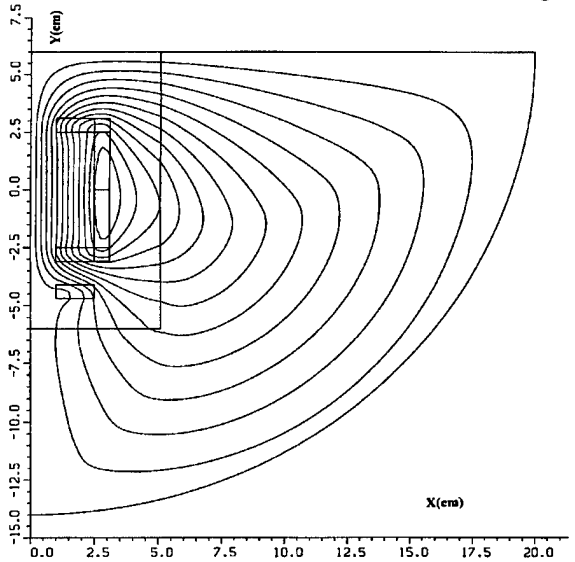



Fig. 3: The field lines at 15 tesla field in the lower-right quadrant of the proposed common coil design magnet. The coldmass is shown in ~1/3 scale.

*2.3 Assembly and Mechanical Support in Magnet Body*

An assembly of the main and auxiliary coils and a conceptual mechanical support structure are shown in Fig. 2. In the proposed configuration, all coils are first individually collared in a simple structure where a small pre-load is applied. The coils are then assembled in a final collared assembly and a horizontally-split yoke and shell are placed around them. In this design, the large component of the Lorentz forces is in the horizontal direction (outward) which is taken by a mechanical system consisting of stainless steel collars, yoke and the stainless steel shell. A small vertical pre-load is applied to overcome the vertical component of the Lorentz forces. The vertical component is similar to the azimuthal component of Lorentz forces in the conventional cosine theta designs, but the accumulated value is smaller here.

*2.4 Magnet Ends*

The ends are usually the biggest problem in the magnets, particularly those built with conductors having poor mechanical properties. The proposed design significantly reduces this problem as the tapes (or cables) are not wound in the hard direction, and furthermore, the bend radius is large. The ends can be fully supported by a simple 2-d structure. This structure can either be made of a solid piece or with laminations placed perpendicular to the body laminations of the magnet. The ends will be supported/loaded after the straight section is collared. To support from the inside, a wedge can be inserted between the body and end laminations and to load from the outside one can apply compression as is done presently in the conventional designs. The skew and normal harmonics in the ends can be minimized by optimizing the lengths and internal configuration of the various coils.

*2.5 A Combined Function Magnet Design*

In the proposed design the coils on the left side and right side of the aperture can have an independent geometry. Therefore, one can make a magnet where the two sides have a different number of turns, etc. In this case a combined function magnet design can be optimized where the harmonics other than dipole and quadrupole are small.

## 3 A HIGH FIELD R&D MAGNET DESIGN

A magnet built with the geometry used in the design described in last section but using commercially available high temperature superconductors will produce only ~2 tesla field. For near term R&D purposes, a moderate field (8T-10T at 1.8 K), 45 mm aperture, hybrid magnet using both HTS tape and normal superconducting cable, as shown in Fig. 4, is proposed. This will allow a study of the issues which are critical to making a high field magnet using high temperature superconductors, namely coil windings with HTS, mechanical support structure and the

performance under the conditions that will be present in an actual magnet.

The innermost pair of coils are made with 6 mm wide HTS tapes and the outer two layers are made with 12 mm wide flat Nb-Ti cable. All six racetrack coils (three pairs) are wound on a stainless steel structure which plays an integral role in the mechanics of the magnet. Each coil and its support structure form a separate module within the magnet. A moderate amount of vertical pre-compression is applied. The coils may be potted on the horizontal plane and/or an small pre-compression may be applied to support and to ensure that no voids are left. The coil modules are installed into existing yoke laminations (with aperture modified), support shells, etc.

The modularized approach, described above, will allow an upgrade of this magnet (or replace components) when, for example, a better conductor, perhaps having a different geometry, becomes available. Various design options/principles can also be investigated without having to design and build a completely new magnet. For example, the magnet aperture and/or support structure can be changed. An adequate amount of space is left between the outermost coil and the yoke aperture to allow sufficient flexibility for such studies. For example, four HTS coils may be used to investigate a large (160 mm) single aperture quadrupole within the same overall structure.

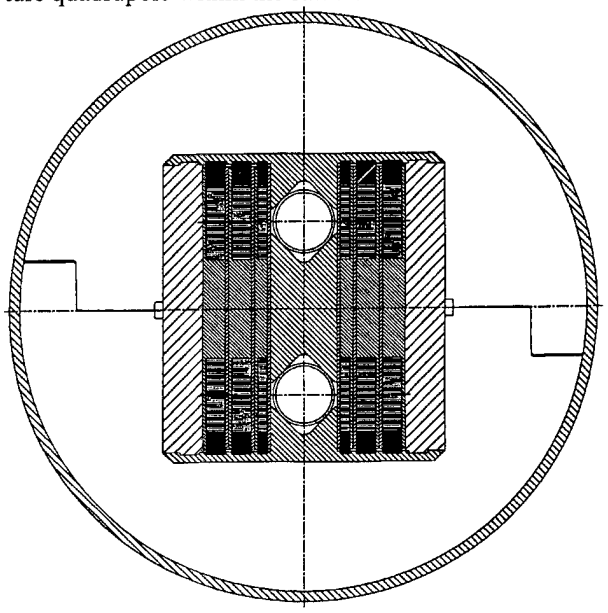


Fig. 4: A proposed R&D magnet design. The inner-most layer is made with HTS tape and the outer two with flat cables made with Nb-Ti superconductor.

## 4 A LOW FIELD IRON DOMINATED MAGNET

The common coil design concept offers advantages to the low field design option which are similar to those offered to high field magnets. In this case the stainless steel support structure between the two apertures will be replaced by an iron yoke to enhance the field. A magnetic design of a 2.3 tesla 2-in-1 magnet with an horizontal aperture of 45 mm and vertical aperture of 25 mm is shown in Fig. 5. The design uses a 6 mm wide tape having an overall current density of 400 A/mm$^2$ at 4.2 K. This is a value which, according to manufacturers [2], should be available shortly in commercially supplied high temperature superconductors. An adequate space is left for a small coil containment/support structure. The flux lines are contained in a 120 mm x 140 mm yoke.

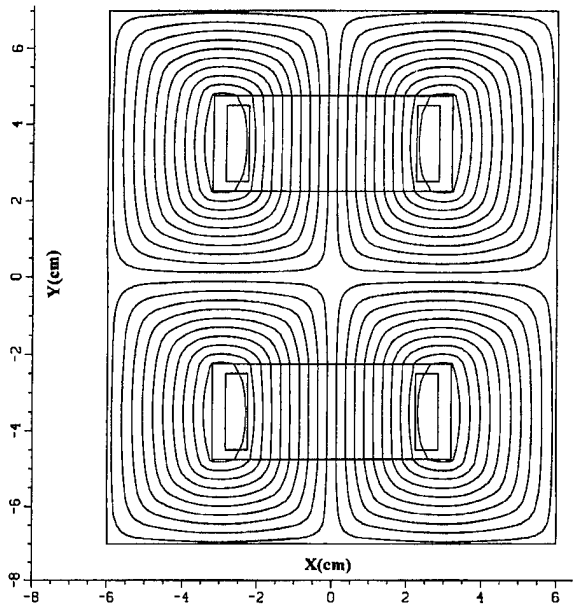



Fig. 5: A proposed low field iron dominated 45 mm x 25 mm aperture 2-in-1 magnet based on the common coil design. The coldmass is shown ~½ scale here.

## 5 CONCLUSIONS

The common coil magnet design concept offers a conductor friendly way of building compact high field magnets based on racetrack coils in a block configuration. High temperature superconductors have reached a stage where a serious R&D effort can be planned. The proposed modularized design approach for an R&D magnet should provide an ideal vehicle for investigating various design concepts and high temperature superconductors.

## 6 ACKNOWLEDGEMENTS

The motivation for the high field HTS magnet design was provided by Mike Harrison. Contributions from and discussion with M. Anerella, A. Ghosh, M. Harrison, G. Morgan, W. Sampson, M. Suenaga, P. Wanderer and E. Willen are highly appreciated.

## REFERENCES

[1] S. Peggs, et al., "Lattice Optimization for Really Large Hadron Collider, RLHC", 1996 European Particle Accelerator Conference, Sitges, Spain (1996), p. 377.

[2] A. Ghosh, private communication.

# CHANGE IN FIELD HARMONICS AFTER QUENCH AND THERMAL CYCLES IN SUPERCONDUCTING MAGNETS*

R. Gupta, A. Jain, J. Muratore, P. Wanderer, E.Willen, BNL, Upton, NY 11973 USA and
C. Wyss, CERN, Geneva, Switzerland

*Abstract*

A change in field harmonics after quench and thermal cycles has been observed in superconducting magnets for the Relativistic Heavy Ion Collider (RHIC). This paper presents the results of a systematic investigation of this effect in a number of RHIC dipole and quadrupole magnets. These changes in field harmonics may limit the ultimate field quality and its reproducibility in superconducting magnets. A change in pre-stress has also been observed after quench and thermal cycles. A possible link between these two changes is explored.

## 1 INTRODUCTION

To satisfy high field quality requirements in RHIC interaction region (IR) quadrupoles, a magnetic tuning shim method is used to compensate harmonic errors after measurements [1]. However, it has been observed that the harmonics changes after quenches and thermal cycles are larger than the capability of the tuning shim correction. The stability and resolution of the measurement system is known to be sufficient for the observations. In the following sections we present the results of a systematic study made to understand and quantify this effect.

The skew ($a_n$) and normal ($b_n$) components of field harmonics are defined as follows :

$$B_y + iB_x = 10^{-4} B_R \sum_{n=0}^{\infty} [b_n + ia_n] \left[\frac{x+iy}{R}\right]^n ,$$

where $B_x$ and $B_y$ are the components of the field at $(x,y)$ and $B_R$ is the magnitude of the field of the fundamental harmonic at a reference radius $R$.

## 2 CURRENT DEPENDENCE

During the calibration runs to obtain the harmonics produced by tuning shims at the design field, it was discovered that two runs produced two different harmonics. The magnetization of the tuning shim iron was ruled out as a possible source because the difference in harmonics between two runs was nearly the same at all currents. To confirm this inference, the tuning shims were removed and the measurements were repeated with a number of interleaving quenches and thermal cycles. Fig. 1 shows the variation in integral $b_5$ at 40 mm reference radius as a function of current during six up ramps in 130 mm aperture RHIC IR quadrupole QRK102. Each ramp was preceded by either a quench or a thermal cycle or both. The $b_5$ change is independent of current. This eliminates yoke saturation and persistent currents as possible sources as both would produce a current dependent change. A similar current independent change is seen in other harmonics as well. This observation indicates that the change in harmonics is related to the change in magnet geometry.

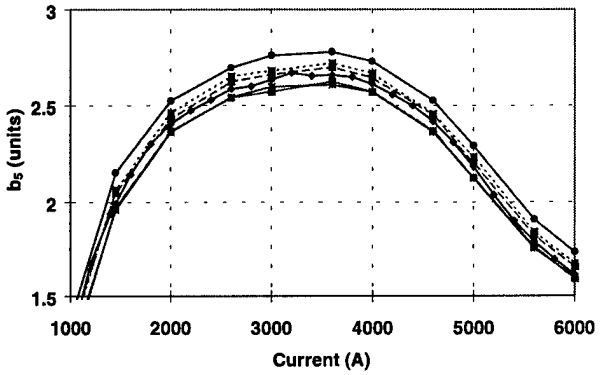



Fig. 1 : The current dependence in $b_5$ during six up ramps (separated by quench and/or thermal cycles) in 3.4 m long 130 mm aperture RHIC IR quadrupole QRK102.

## 3 HARMONIC CHANGES IN DIPOLES

The mechanical design and assembly of RHIC quadrupoles are similar to those of the dipoles. For example, the quadrupole yoke and collaring scheme has a two fold symmetry. Therefore, the dipoles may also show a corresponding change in harmonics. This indeed was found in both 80 mm aperture and 100 mm aperture dipoles in terms of the observed changes in $a_1$, the skew quadrupole harmonic, which is related to up-down asymmetry.

Fig. 2 shows a significant change in integral $a_1$ at 31 mm reference radius in RHIC 100 mm aperture insertion dipole DRZ106 after a number of quenches and thermal cycles. No change was, however, observed in repeated up and down ramps (dc loops) which is important for a stable accelerator operation. "LN2 Run" are the measurements in the range of 20-90 K and represent the change in geometry due to cooldown. Persistent current induced harmonics are not expected as the cable is in a non-superconducting state. Warm harmonics return to their original values. This has been seen in many (but not all) magnets.

* Work supported by U.S. Department of Energy under contract No. DE-AC02-76CH00016.

0-7803-4376-X/98/$10.00 © 1998 IEEE

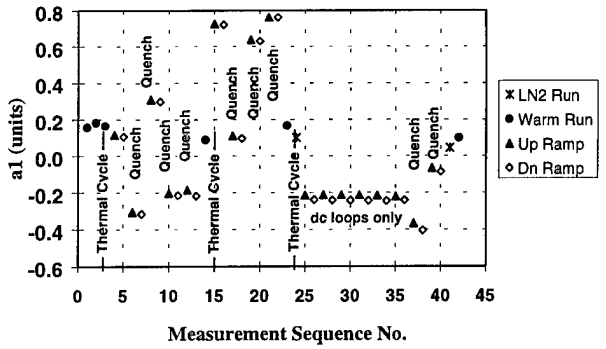



Fig. 2 : Variation in integral $a_1$ at 31 mm reference radius in RHIC 100 mm aperture dipole DRZ106 from quench and thermal cycles.

## 4 AXIAL DEPENDENCE OF CHANGE

In Fig. 3, we show the measured $a_1$ before and after a thermal cycle (thin lines) and the change between the two (thick line) in five sections of magnet DRZ106. This axial scan was done to determine if the changes are lumped locally or distributed uniformly. The large $a_1$ in the first position is from the lead end. The change in harmonic is about the same at all locations. This means that the coil as a whole is changing its geometry.

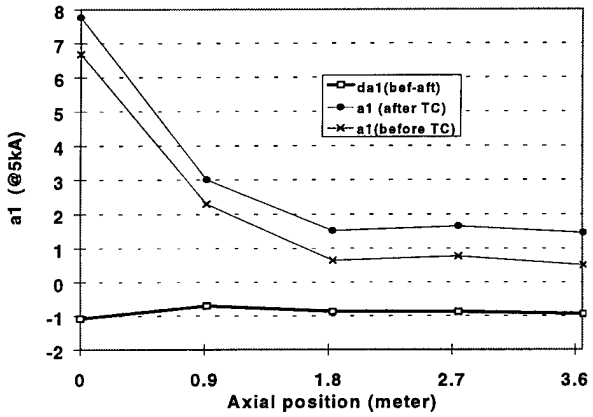



Fig. 3 : Axial dependence of the change in $a_1$(@31 mm) caused by a thermal cycle in DRZ106.

## 5 CHANGE IN A SERIES OF MAGNETS

In this section the results of measurements in eight 1.44 meter long 130 mm aperture Q1 magnets are presented to statistically quantify this effect. Since the issue is most critical in IR quadrupoles a number of these magnets were measured before and after quench and thermal cycles. Fig. 4 shows the change in integrated harmonics from quench and Fig. 5 from thermal cycle. The solid line represents the mean and the dashed line one sigma around the mean. One can see that generally a thermal cycle generates smaller changes than a quench. The magnitudes of the observed changes in harmonics are acceptable in RHIC [2].

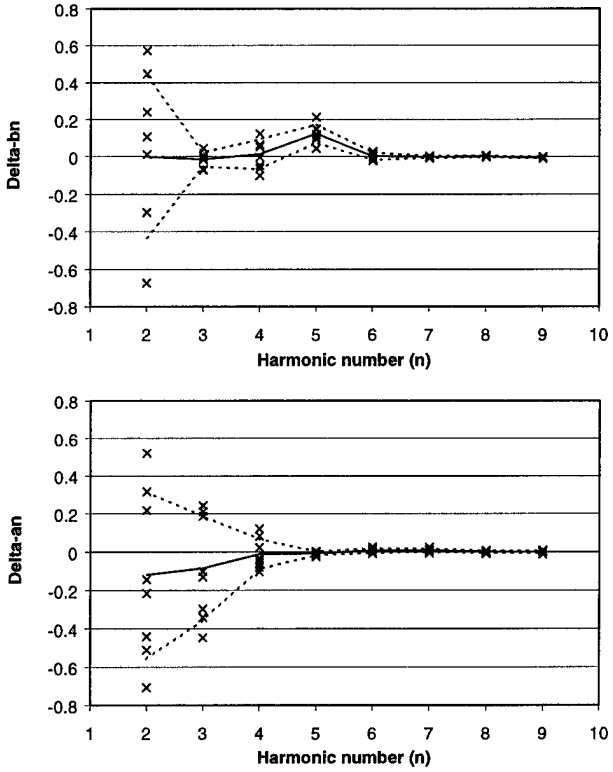



Fig. 4 : Change in harmonics in eight 130 mm aperture insertion quadrupoles caused by a quench.

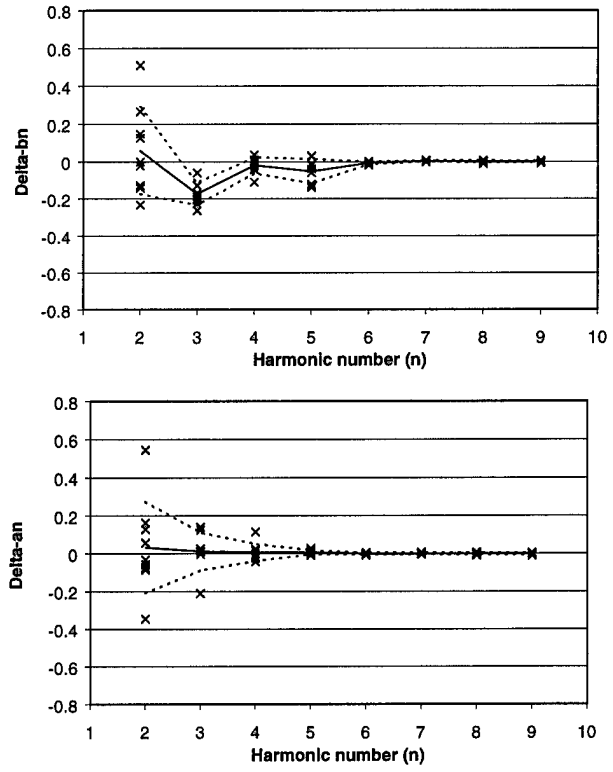



Fig. 5 : Change in harmonics in eight 130 mm aperture insertion quadrupoles caused by a thermal cycle.

For quenches (Fig. 4), the changes are of random nature except for a small systematic $b_5$ (the first allowed harmonic in quadrupoles). A similar behavior is also seen in dipoles where the change in all harmonics except for a small systematic $b_2$ (the first allowed harmonic in dipoles) is of a random nature.

In the case of thermal cycles (Fig. 5), the changes are of a random nature except for a systematic $b_3$ (always a negative change). The magnet QRI105 was subjected to five thermal cycles to further study $b_3$. The net drop stabilized at 0.3 units after three thermal cycles meaning that the collared coil geometry stabilized. This magnet had showed small change in other harmonics (~0.1 unit or less) after first thermal cycle. The change remained small (~0.1 unit or less) during the remaining thermal cycles.

## 6 CHANGES IN AZIMUTHAL STRESS

A change in azimuthal coil stress on pole faces has also been observed after quench and thermal cycles. We examine the change in azimuthal stress as independent evidence of the change in coil geometry. In Fig. 6, we have plotted the azimuthal coil stress on four pole faces (dashed lines) after successive quenches together with a thermal cycle in between in 100 mm aperture dipole DRZ105. The magnet was cold but not powered. We have also plotted the average stress on four pole faces (solid line) and the difference between the average of top two and bottom two (thick solid line). Though the absolute values of these stresses (measured by strain gauges) may not be reliable to a few hundred psi, the relative change is. One can clearly see a change in behavior after each quench. Most interesting is the difference between top and bottom (thick solid line) as this is related to change in $a_1$ harmonic (Fig. 2 and Fig. 3). A one to one correlation can not be established between $a_1$ and stress as the stress measurements were done in DRZ105 and the magnetic measurements in DRZ106. However, both the harmonic and stress changes can be explained, depending on the computer models, by a geometric change which is of the order of 0.001'' (25 μm).

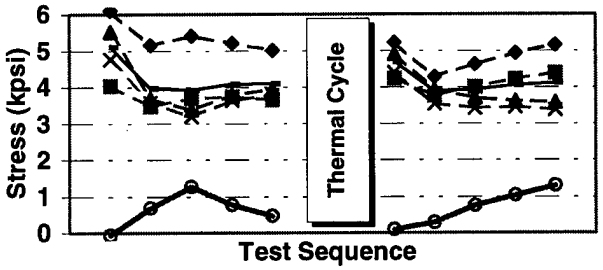



Fig. 6 : The azimuthal stress on pole faces (dashed lines), average (solid) and difference between top and bottom (thick solid line) after successive quenches together with a thermal cycle in between in the magnet DRZ105.

## 7 DISCUSSION

In addition to the 130 mm aperture quadrupole and 100 mm aperture dipole magnets, harmonic changes of similar magnitude have also been observed in 80 mm aperture dipole and 80 mm aperture quadrupole magnets for RHIC. All these magnets were made using a similar design and construction techniques. Therefore, it implies that it is a common phenomenon in such magnets. These changes are larger than the measurement uncertainties. The changes are smaller than the RMS variations in harmonics in a series of magnets. The effect, though of smaller magnitude, has also been observed in SSC dipole magnets [3]. The SSC design was based on stainless steel collars, whereas the RHIC magnets use the yoke as a collar and phenolic spacers (which are not as strong as stainless steel) between coil and yoke. Though this is an important difference, we can not say definitely that this is the sole reason for smaller changes in SSC dipole harmonics. SSC magnets also had a smaller aperture. Moreover, we have examined this effect in only one magnet.

The following mechanism may explain the observed changes. Quenches and thermal cycles generate a pressure shock which may cause a change in the internal geometry of the collared coil by a small amount (~25 μm). Unless overcome by large mechanical forces (such as another shock), this small change may get locked into a new and slightly different coil geometry, particularly when the magnet is cold and the stresses are small. A uniform change in the $a_1$ harmonic along the magnet length (see Fig. 3) means that effectively the coil midplane moves as a whole.

In most cases (but not all), the harmonics returned to their original values when the magnet was warmed up to room temperature. The azimuthal stresses are much larger when the magnet is warm as compared to when it is cold. It is possible that larger azimuthal stresses at room temperature are enough to overcome the friction to bring the magnet back to its original geometry.

## 8 CONCLUSIONS

The ultimate field quality in superconducting magnets may be limited by the dynamic changes caused by quench and thermal cycles. These changes are much larger than the resolution of tuning shims and as such can not be compensated by the static nature of tuning shim correction. The measured harmonic changes, though significant, are acceptable in RHIC magnets.

## REFERENCES


[1] R. Gupta, et al., "Tuning Shims for High Field Quality in Superconducting Magnets", Proc. of MT-14, IEEE Transaction on Magnetics, Vol. 32, No. 4, July 1996.

[2] S. Peggs and J. Wei, private communication.

[3] P. Wanderer, et al., "Partial Lifetime Test of an SSC Collider Dipole", MT-13, Sep. 1993.

# MAGNETIC DESIGN OF SUPERCONDUCTING QUADRUPOLES FOR A SC LINAC FOR APT

S. Kahn and P. Wanderer
Brookhaven National Laboratory, Upton, NY 11973

*Abstract*

This paper describes the magnetic design for superconducting quadrupoles to be used in the superconducting option of the proton linac for the Accelerator Production of Tritium (APT) project. The quadrupole magnets provide the focusing for a singlet FODO lattice used in the linac. The magnets have a 16 cm (13 cm) aperture in the hi-$\beta$ (medium-$\beta$) section of the linac. The proposed design is a coil dominated magnet with an iron yoke at a larger radius to shield the magnetic field from other parts of the accelerator. The field performance, field quality, peak field and forces on the conductor are discussed.

## 1 INTRODUCTION

The proton linac for the APT project is likely to have superconducting RF cavities for the medium energy, $\beta = 0.64$, and high energy, $\beta = 0.82$, regions of the machine. Two options have been considered for the quadrupole focusing in the linac. One is to position a single superconducting quadrupole (either focusing or defocusing) between each of the SC RF cavities. The magnets would be placed in the same cryostat as the RF cavities. Each medium-$\beta$ (high-$\beta$) cryostat would contain 3(4) RF cavities and 4(5) SC quadrupoles. There are 30 medium-$\beta$ and 78 high-$\beta$ cryostats in the linac. The other option is to place only the RF cavities into the cryostat and use a room temperature quadrupole doublet (one focusing and one defocusing) between each of the cryostats. The SC quadrupole in the singlet lattice design provides a higher gradient and shorter period length than the room temperature doublet design. The singlet linac with the SC quadrupoles would reduce the beam size by about half in each of the transverse dimensions. The Conceptual Design Report for the APT project [1] uses the singlet design with the SC quadrupoles. The APT project is now favoring SCRF design with the separate room temperture quadrupole doublet. This report discusses the superconducting singlet design with SC quadrupoles.

Certain requirements for the SC quadrupoles are dictated by the linac design. These are summarized in Table 1 . Because of the large beam current in the accelerator a large aperture is chosen to keep the number of particles hitting the beam pipe to a minimum so that hands on maintainance will be possible. The gradient requirements for the quadrupoles are modest for a superconducting magnet. This allows conservative operation at about half of the quench current. Since the APT accelerator is intended to be operated with an uptime efficiency of 85%, good quadrupole reliability is essential. Another design concern is that the field from the quadrupole should not interfere with the proper operation of the RF cavity. The requirement is stated that the field from the quadrupole must be less than 1 gauss at the RF cavity wall. This requirement is easily met.

Table 1: Superconducting Quadrupole Parameters.

| Parameter | Medium-$\beta$ section | High-$\beta$ section |
|---|---|---|
| Aperture radius (cm) | 6.5 | 8.0 |
| Lattice half period (m) | 1.70 | 2.03 |
| Quadrupole length (m) | 0.305 | 0.459 |
| Effective length (m) | 0.294 | 0.338 |
| Integrated gradient (T) | 3.30 | 3.26 |
| Nominal gradient (T/m) | 11.2 | 9.6 |
| Operating temperature (K) | 4.3 | 4.3 |
| Number of quadrupoles | 120 | 390 |

## 2 MAGNET DESIGN

The proposed quadrupole is coil dominated with the iron yoke at approximately twice the coil radius so that most of the magnetic flux is returned in the space between the coil and yoke. The iron yoke remains essentially unsaturated for optimum shielding. Fig. 1 and Fig. 2 show the transverse and axial views of the quadrupole cold mass. The iron yoke surrounds stainless steel laminations which register the coil position and support transverse components of the coil forces. A stainless steel shell exterior to the yoke along with the bore tube contains the helium.

The coil is of a planar racetrack design and is wound with 460 (264) turns for the medium-$\beta$ (high-$\beta$) design. The construction technique for the coil is the same as used for the sextupole and trim quadrupole magnets for the RHIC project at BNL. [2] The coil consists of alternate layers of insulated wire and epoxy-impregnated fiberglass wound in a rectangular form. The wire is a 25.5-mil diameter NbTi superconducting strand, and is the same as that used in the the outer cable of the Superconducting Supercollider dipole magnets. The wire has a copper to superconductor ratio of 1.8 to provide conductor stability. The coils are conservatively designed to operate at one half the quench current. The magnet should be self-protecting and will not be damaged by overheating during a quench, because of its fast normal-zone propagation velocity and the short coil length. The peak field at the coil limits the current that a wire can carry. The field at the coil is calculated using the 3D mag-

†Work performed under Contract No. DE-AC02-76CH00016 with the U.S. Department of Energy.

0-7803-4376-X/98/$10.00 © 1998 IEEE

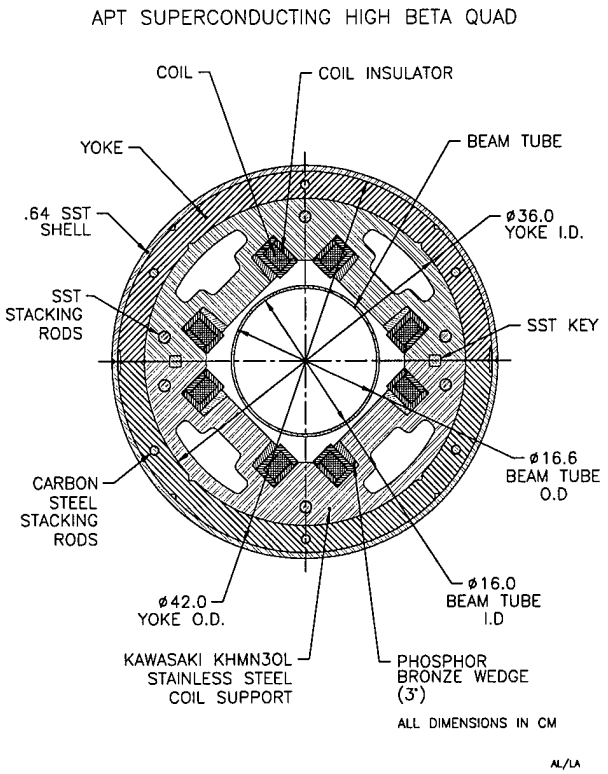



Figure 1: Cross section of the high-$\beta$ quadrupole.

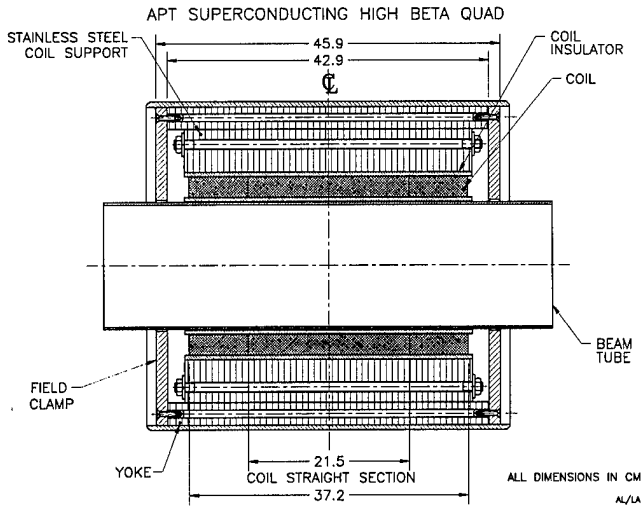



Figure 2: Longitudinal section of the high-$\beta$ quadrupole.

Table 2: Coil Parameters for the Superconducting Quadrupoles.

| | Medium-$\beta$ | High-$\beta$ |
|---|---|---|
| $B_{peak\ coil}$, T | 3.0 | 2.0 |
| Amp-turns | 111578 | 82650 |
| $I_{wire}$, Amp | 243 | 314 |
| $N_{turns}$ | 334 | 264 |
| Inductance,H | 0.126 | 0.133 |

netic field finite element program TOSCA. [3] Table 2 lists the design parameters of the coil. The RF cavities will operate at 1.9K with superfluid He. There would be a 50% increased quench margin if the magnets were operated at the same conditions. However without increased refrigeration, the helium surrounding the magnets would be just above the superfluid state, which is an unstable operating point. 4.3K is the likely operating temperature at this point. Skew and normal trim dipole coil windings for beam steering can be mounted in the magnet poles.

## 3 FIELD PERFORMANCE

The SC quadrupoles should exhibit good field quality for the linac. Deviations from perfect field quality can come from systematic design errors, random construction errors and magnet alignment errors. The largest contributor to the field error is likely to come from the magnet-to-magnet variation of the integral gradient, $G \cdot L$. The first harmonic allowed in magnets built with perfect quadrupole ($2\theta$) symmetry is the duodecupole ($6\theta$) term. The azimuthal angle subtended by the coil can be chosen to make the $6\theta$ term negligible. A conductor placement accuracy of 4 mils (100 $\mu m$) gives non-allowed harmonics that are less than 0.0004 of the integrated gradient at $R_{ref} = 5$ cm.

Table 3 summarizes the estimates of the various contributions to the field quality that can be expected. The harmonics are calculated at a reference radius of 5 cm. The table indicates that a good field radius of 5 cm where $\frac{\Delta B}{B} < 0.001$ is achievable. These estimates are based on construction and placement errors obtained with the RHIC accelerator magnets. The alignment errors in Table 3 are estimated from RHIC magnet field measurements relative to external markers on the magnets. They do not include the additional contribution from magnet installation errors.

One of the major design concerns for the SC quadrupoles that share the same cryostat with the SCRF cavities is whether the magnetic field from the magnets will interfere in any way with the operation of the cavities. The field from the SC quadrupoles at the cavity wall is estimated to be less than 50 mG with the magnets operating. This estimate is without the use of $\mu$-metal shielding which will be present to shield the cavities from the earth's magnetic field.

Table 3: Estimates of contributions to RMS field errors. For the evaluations of the field harmonics a reference radius of 5 cm is chosen.

| Contribution | Error |
|---|---|
| $\frac{\Delta GL}{GL}$ | 0.003 |
| $\frac{C(6\theta)}{GL}$ | $< 10^{-4}$ |
| Random Harmonics | $< 4 \times 10^{-4}$ |
| Angular Alignment | 0.6 mrad |
| Center Alignment | 75 $\mu m$ |

Table 4: Calculated Lorentz Forces for the APT Linac quadrupoles. Side forces are *lbs per inch* and the end force is given in *lbs*.

| Forces | Medium-$\beta$ | High-$\beta$ |
|---|---|---|
| Side Forces in plane | 367 | 220 |
| Side Forces out of plane | 4 | 4 |
| Total End Forces | 5957 | 4638 |

## 4 MECHANICAL ISSUES

Because of the intense beam, the large aperture of the beam pipe is necessary to keep the number of particles hitting the pipe to a minimum so that hands on maintainance will be possible. Large aperture magnets typically have a large Lorentz force acting on the coils. The end forces in particular are proportional to the stored energy which has a radial dependance, $F_{ends} \sim r_{bore}^4$. However the gradient requirements of the APT linac quadrupoles are low enough that the stress in the NbTi is less than that in other magnets of similar construction. Table 4 summarizes the side and end forces that are expected to be seen in the quadrupoles. The side forces are separated into the component in the coil plane and perpendicular to it. The perpendicular component measures the interaction of the coil with the other coils and with the iron yoke. It tends to be small when the magnet is not iron dominated. The total end force is summed over all four coils. The side forces are supported by the stainless steel laminations holding the coils. Whether to support the coil ends has not been decided. The force per wire in the coil end is modest enough that end support may not be needed. Table 5 shows the axial force per wire and tensile stress on NbTi. Since the Lorentz forces elongate the wires and since NbTi is stiffer than copper, it is assumed the entire force strains the NbTi and that limits the performance.

The reliability of the SC magnets inside the same cryostat as the RF cavities is of great concern since the APT is expected to operate with minimal downtime in production. The APT is also expected to function for 40 years. Estimates of the reliability of these magnets can be made using the operational experience of the Fermilab Tevatron and DESY HERA accelerators. The correction magnets in both facilities are similar in construction to these

Table 5: End force per wire and stress on NbTi for the APT linac quadrupoles and other magnets of similar construction. *Field Level* indicates whether the forces are at the operating value or at conductor limit. Force and stress are in *lbs* and *Kpsi* respectively.

| Magnet | Field Level | Axial Force per wire | NbTi Stress |
|---|---|---|---|
| Medium $\beta$ | Operating | 4.6 | 12.0 |
| High $\beta$ | Operating | 4.4 | 12.2 |
| RHIC trim quad | Operating | 1.1 | 3.5 |
| RHIC trim quad | Current Limit | 4.5 | 14.2 |

quadrupoles. Each of these accelerators has more corrector magnets than are needed for APT. The Tevatron corrector magnets, which have been in operation for 13 years, have an average mean time between failure (MTBF) of $3 \times 10^6$ hours. The MTBF for the Tevatron correctors is increasing with time. The HERA correctors, which have been in operation for six years, have an a MTBF of $3 \times 10^7$ hours. Cold testing 100% of the superconducting magnets would remove the infant mortality failures. SC quadrupole failures should not limit the APT availability.

## 5 ACKNOWLEDGEMENTS

The authors would like to thank P. Walstrom and T. Wangler for much discussion relevant to this study.

## 6 REFERENCES

[1] Accelerator Production of Tritium Conceptual Design Report, 1997 Los Alamos Document LA-UR96-4847, APT-Doc-005.

[2] P. Thompson et al., Superconducting Sectupoles and Trim Quadrupoles for RHIC, Proceedings of the 1996 Particle Accelerator Conference, Dallas, p 1396 (1995).

[3] TOSCA is a computer code marketed by Vector Fields, Inc.

# TEST RESULTS FROM THE COMPLETED PRODUCTION RUN OF SUPERCONDUCTING CORRECTOR MAGNETS FOR RHIC*

J. Muratore, A. Jain, G. Ganetis, A. Ghosh, A. Marone,
A. Morgillo, W. Sampson, P. Thompson, P. Wanderer
Brookhaven National Laboratory, Upton, New York 11973, USA

*Abstract*

The production run of all 432 superconducting 8 cm corrector magnets required for the Relativistic Heavy Ion Collider (RHIC) has been completed at Brookhaven National Laboratory (BNL). All have been tested at 4.35 K for quench performance and at room temperature for magnetic field quality. In addition, magnetic field measurements at 4.35 K have been done for a 20% sample of these. Summaries of the harmonic and quench test results are presented. A comparison of the quench performance for magnets made with different coil preload tensions is also shown.

## 1 INTRODUCTION

All 432 superconducting 8 cm aperture corrector magnets have been manufactured and tested at Brookhaven National Laboratory (BNL) for the Relativistic Heavy Ion Collider (RHIC), now under construction at BNL. These correctors will provide magnetic field corrections to random and systematic errors in the main dipole and quadrupole magnets and be used to help determine beam dynamics in the two superconducting collider rings. A previous paper[1] has described in detail the design and construction features of these magnets and presented test results available for the 65% of the magnets that had been tested up to that time. The present paper summarizes the final test results for quench performance and field quality for all the 8 cm correctors at the end of the successful production run, and compares the quench performance of correctors which were made with different coil prestress loads.

## 2 GENERAL MAGNET DESCRIPTION

For details of the design and construction features of RHIC 8 cm correctors, our previous paper[1] should be consulted. Only a brief description of these features will be presented here. Each corrector may include either one ($a_0/b_0$) or four ($a_0/b_0$, $a_1/b_1$, $b_3$, $b_4$) multipole elements, where $a_n$ denotes a skew, and $b_n$ a normal, multipole; and the subscript $n$ = 0, 1, 3, 4 refers to dipole, quadrupole, octupole, and decapole symmetries, respectively. Each multipole element is constructed by winding 0.33 mm diameter multifilament Cu/NbTi (ratio 2.5:1) wire in flat winding patterns (one racetrack-shaped winding for each pole) on a kapton/epoxy/fiberglass substrate by a technique known as the Multiwire process, using a computer-controlled stylus. The wires are wound in double layers, with the top layer wires nested in between the wires of the bottom layer. The coil substrate is then wrapped around and epoxy-bonded to a cylindrical stainless steel support tube. Next, the mounted coil windings are wrapped with a single layer of epoxy/fiberglass cloth and a double layer of Kevlar yarn at a specified tension in order to provide mechanical clamping and minimize movement of the wires by Lorentz forces during magnet excitation. The dipole coil consists of three double layers of windings and the other multipole coils have one double layer.

The four completed coil-tube assemblies are mounted concentrically in order of decreasing multipolarity with the highest order harmonic (decapole) at the innermost, smallest diameter and the lowest order harmonic (dipole) at the outermost, largest diameter. This is shown in the magnet cross-section of Fig. 1. The two outermost tubes have thicker walls to withstand the stronger Lorentz forces of the higher field strengths of the dipole and quadrupole coils. In order to provide mechanical stability and a return path for the magnetic flux, the finished multiple tube assembly is surrounded by a laminated iron yoke with the same outer configuration and diameter as the other 8 cm magnets. Each corrector is then assembled with a main quadrupole and trim sextupole, or trim quadrupole, magnet in a combined assembly, where they share a common cold beam tube and outer helium-containment/support shell. These so-called CQS units are then installed in their own cryostats and subjected to various diagnostic tests before acceptance and delivery to the collider rings.

## 3 EXPERIMENTAL PROCEDURE

Because of the stresses imposed on the thin superconducting wires during the coil winding process, it was considered necessary, as part of the acceptance procedure, to cold-test all individual correctors before insertion into CQS assemblies. This would screen out any coils that may have sustained wire damage which could lower the maximum current limit. Cold-testing was performed by fitting the yoked coil assemblies with temporary support shells and hanging them in vertical dewars filled with liquid helium at 4.35 K (nom). The magnets and test system were instrumented to provide data for quench and electrical analysis. Among experimental parameters which were monitored during testing were dewar temperature and pressure, coil and lead voltages, power supply current and voltage, and quench detector signal data.

* Work supported by the U.S. Department of Energy under Contract No. DE-AC02-76CH00016.

0-7803-4376-X/98/$10.00 © 1998 IEEE

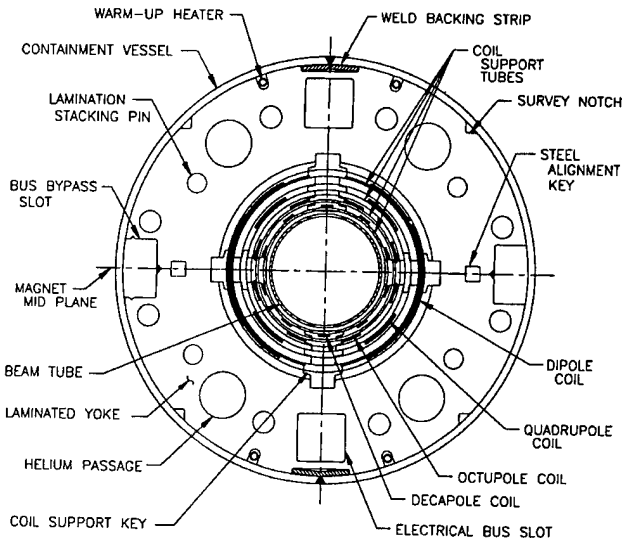



Figure 1: Cross-section of corrector magnet with four multipole coils.

All magnets were subjected to at least the following minimum test procedure:

1. Ramp the dipole coil to +70 A, then to -70 A, then back to 0; this is repeated at least two more times;

2. With the dipole at +70 A, each of the other three coils is ramped to +100 A, then -100 A, then back to +100 A, then back to 0.

If any coil quenched in the course of these ramp tests, the ramps for that coil were started over again and repeated until the above ramping scheme could be performed without a quench. In most cases, magnets were subjected to more rigorous testing, with more bipolar ramps, occasionally one hour tests at maximum test current, and sometimes ramps to quench. The maximum test current of 100 A for ramp tests was selected to provide 100% quench margin above the design corrector operating current of 50 A (nom). This was reduced to 70 A for the dipoles to avoid quenches that might overheat the conductor wire. This caution was necessary because of the high inductance of the dipole coils and the nature of the quench detection system being used. All corrector coils have a conductor limit above 130 A for all operating conditions at the RHIC temperature of 4.6 K.

## 4 QUENCH PERFORMANCE

It is convenient to discuss the test results grouped according to the four types of corrector coils regardless of the type of assembly. Also, in order to provide a uniform comparison among all the coils of each type, only performance during the initial test ramps, as described above in the minimum test procedure, will be shown. The initial tests were common to all magnets. Results from more extensive testing and quench tests will not be included here.

The results are presented in Table 1 and are grouped according to coil type and performance category. For each type, the first column denotes 1) total coils tested, and the number of coils which 2) did not quench, 3) trained smoothly (monotonically), 4) trained erratically, 5) failed due to wire damage, and 6) had an initial quench below 50A but trained acceptably. A coil was rejected if its current limit was low due to wire damage (Row 5) or if its quench behavior was judged to be too erratic.

Table 1: Quench Performance Results of RHIC Arc Corrector Coils (Multipoles tested with dipole at +70 A).

| Performance | Dipole | Quadrupole | Octupole | Decapole |
|---|---|---|---|---|
| total | 420 | 273 | 268 | 268 |
| no quenches | 288 | 207 | 197 | 226 |
| smooth training | 124 | 53 | 62 | 33 |
| erratic training | 6 | 11 | 9 | 9 |
| failed | 2 | 2 | 0 | 0 |
| $I_{init} < 50$ A | 28 | 2 | 5 | 1 |

As can be seen from the table, 69% of the dipole coils and 76% of the quadrupole coils did not quench at all during initial ramp testing, while 74% and 84% of octupole and decapoles, respectively, did not quench. All other coils had one or more quenches but trained satisfactorily, except for two dipoles, four quadrupoles, and a decapole; each of these was removed from its corrector assembly and replaced by coils which tested satisfactorily.

The two dipoles and two of the quadrupoles which failed were conductor-limited at low currents, probably because of wire damage during winding. The other two rejected quadrupoles and decapole exhibited quench behavior judged too erratic. It should also be noted that one of the quadrupoles which quenched erratically was rejected on the basis of its performance in extended testing while one of the acceptable erratic decapoles was accepted because of extended testing results.

32 (2.6%) of the accepted coils exhibited some erratic quench behavior but were acceptable for collider operations. Also shown in the table are the numbers of each coil type where the first quench was below the RHIC maximum operating current of 50 A but trained acceptably afterwards. Of these 36 coils, 15 had initial quenches between 25 A and 40 A, while the others quenched above 40 A.

During the course of the production testing run, quench experiments by Ghosh[2] on single multipole coils without iron yokes showed that quench performance could be improved by increasing the pre-tension of the Kapton yarn wrapping from the initial design specification of 97 kPa to at least 152 kPa, which then became the new loading specification for all coils built afterwards. 61% of the 1229 coils in Table 1 were made with the higher pre-tension loading, and if the results are separated into two groups for low and high pretension, significantly improved performance when using the higher tension can be shown. Table 2 shows the percentage improvement in each category for each coil type.

Table 2: Comparison of Quench Performance Results of RHIC Arc Corrector Coils Assembled with Low and High Tension Kevlar (Multipoles tested with dipole at +70 A).

| Performance | Dipole | | Quadrupole | | Octupole | | Decapole | |
|---|---|---|---|---|---|---|---|---|
| | LO | HI | LO | HI | LO | HI | LO | HI |
| no quenches | 45% | 84% | 56% | 89% | 67% | 77% | 77% | 89% |
| smooth training | 51% | 16% | 36% | 9% | 26% | 21% | 16% | 10% |
| erratic training | 3% | 0.4% | 7% | 2% | 7% | 1% | 7% | 1% |
| $I_{init} < 50$ A | 12% | 3% | 1% | 1% | 3% | 1% | 1% | 0 |

## 5 FIELD QUALITY MEASUREMENTS

All the corrector magnets were measured warm to determine the integral transfer function, various normal and skew multipoles, and the offsets of the magnetic centers of individual layers relative to the mechanical center of the iron yoke. These measurements were carried out using a rotating coil of radius 35.6 mm whereas the reference radius used for calculating the multipoles in these magnets was chosen to be 25 mm. All warm measurements were carried out at a current of 0.2 A. The contribution from remnant field is significant at such low excitation and was subtracted by making measurements at both positive and negative currents. The measuring coil was radially centered in the iron yoke using a well-aligned fixture. The magnetic centers are derived from feed-down and are generally within 0.25 mm of the center of the iron yoke.

The results of the warm measurements are summarized in Table 3. The integral transfer functions are expressed in T.m/kA at a reference radius of 25 mm. The standard deviations in the transfer functions are partly due to the use of several different winding patterns in the early stages of production. The largest harmonic error terms are well below 1% of the main harmonic for the dipole and the quadrupole coils and are below 2% of the main harmonic for the octupole and the decapole coils. These error levels are quite acceptable for the accelerator.

Table 3: Corrector Field Quality.

| Layer Type | Transfer Function T.m/kA @25 mm (Warm) | Std. Dev. in T.F. | Change in T.F. on Cool-down | Harmonics as Fraction of the Fund. Field |
|---|---|---|---|---|
| $b_0/a_0$ | 5.5549 | 0.16% | +1.0% | <0.3% |
| $b_1$ | 0.7627 | 0.18% | +0.7% | <0.6% |
| $a_1$ | 0.7570 | 0.09% | +0.7% | <0.6% |
| $b_3$ | 0.1920 | 0.53% | +0.9% | <2% |
| $b_4$ | 0.1494 | 0.48% | +1.2% | <2% |

The correctors were tested at liquid helium temperature for quench performance. Most of these cold tests were performed in a 2-in-1 dewar to reduce the test time. Field quality measurements on cold correctors could not be performed in this dewar. However, roughly 20% of the correctors were cold-tested individually in other dewars where field quality measurements using a rotating coil could be made. There is good correlation between the warm and the cold measurements. The only significant effect is a change in the transfer function as a result of cool down, as given in Table 3. The standard deviation of the warm-cold difference in the integral transfer function is less than 0.1% of the transfer function for the dipole and quadrupole coils and is ~0.3% for the octupole and decapole coils.

## 6 CONCLUSION

The results and experience of the testing of 432 superconducting corrector magnets, roughly 2/3 of which consisted of four multipole layers, have shown how such a large production test run may succeed within an allotted time and budget and, more importantly, accomplish the two main goals of 1) acceptance testing of the magnets for use in a working collider, and 2) provide a set of parameters which characterizes the behavior of each magnet for efficient operation in the collider. The use of higher pre-tension for improved quench performance, as described above, is a good example of how, even during a production test run of a large number of magnets, when basic R&D testing has finished, improvements to the design and/or assembly process may still be implemented when careful monitoring of data is carried out during testing. This experience was also seen in the production runs of other types of magnets for RHIC. From the quench performance results, it can also be seen that, in the case of these particular magnets, the decision to cold-test all correctors was important in screening out those magnets, though few, which did not meet the acceptance criteria due to damage during the delicate but efficient winding process used for these wire coil magnets. Other types of magnets, such as the main dipoles and quadrupoles, whose coils were wound with cable in a very different process, did not require 100% cold-testing for the acceptance process.

## 7 REFERENCES


[1] A. Morgillo, *et al.*, "Superconducting 8 cm Corrector Magnets for the Relativistic Heavy Ion Collider (RHIC)", Proc. 1995 Part. Accel. Conf., p. 1393 (1995).

[2] A. Ghosh, private communication.

# RHIC D0 INSERTION DIPOLE DESIGN ITERATIONS DURING PRODUCTION*

J. Schmalzle, M. Anerella, G. Ganetis, A. Ghosh, R. Gupta, A. Jain, S. Kahn, G. Morgan,
J. Muratore, W. Sampson, P. Wanderer and E. Willen,
Brookhaven National Laboratory, Upton, New York 11973, USA

*Abstract*

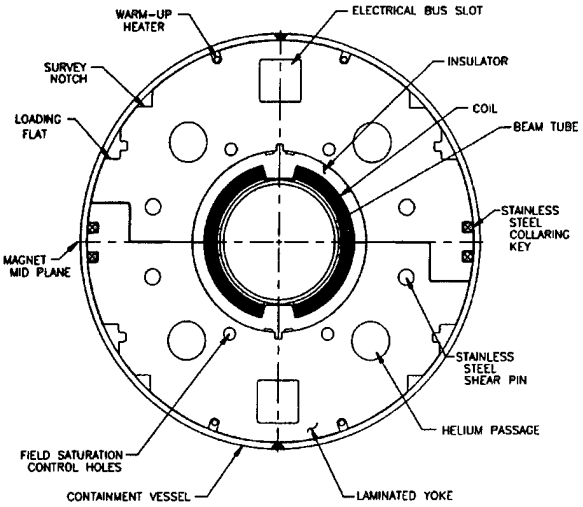
Iterations to the cross section of the Relativistic Heavy Ion Collider (RHIC) D0 Insertion Dipole magnets were made during the production. This was included as part of the production plan because no R&D or pre-production magnets were built prior to the start of production. The first magnet produced had the desired coil pre-stress and low field harmonics in the body of the magnet and is therefore being used in the RHIC Machine. On the first eight magnets, iterations were carried out to minimize the iron saturation and to compensate for the end harmonics. This paper will discuss the details of the iterations made, the obstacles encountered, and the results obtained. Also included will be a brief summary of the magnet design and performance.

## I INTRODUCTION

There are twenty-four D0 insertion dipole magnets required in the RHIC machine. These magnets are being built at BNL, with the production broken into two stages. The first stage consisted of six magnets (four plus two spares) required for the first sextant and the second stage consists of the remaining magnets. The coil design uses 40 turns of 30 strand superconducting cable and 4 wedges. The cold mass design is very closely based on the 8cm arc dipole cold mass [1] adjusted for the increase in aperture. A cross section of the cold mass is shown in Fig.1 and the basic design parameters are as follows:

| | |
|---|---|
| Coil ID | 100 mm |
| Coil OD | 120 mm |
| Number of turns per pole | 40 |
| Magnetic length | 3.6 m |
| Iron inner diameter | 139.4 mm |
| Iron outer diameter | 310 mm |
| Shell thickness | 6.35 mm |
| Operating temperature | 4.6 K |
| Design current | 5.0 kA |
| Design field | 3.5 T |
| Quench current | 7.4 kA |

The D0 production plan called for cold mass production to begin without the benefit of any R&D or pre-production magnets. Several features were therefore incorporated into the design of these magnets that would allow iterations to the cross section to be made during the course of production in order to improve the field quality. Machined G-10 shims were used at the pole and filled Kapton [2] caps were used as spacers between the coil midplanes. Having various sizes of these two parts in stock would allow changes to be made without significantly interrupting production.




The field harmonics are defined in the following relation:

$$B_y + iB_x = 10^{-4} B_0 \sum_{n=0}^{\infty} [b_n + ia_n] \left( \frac{x+iy}{R_0} \right)^n ,$$

where $B_x$ and $B_y$ are the components of the field at $(x,y)$ and $B_0$ is the central field. $a_n$ are the skew harmonics and $b_n$ are the normal. $R_0$ is the normalization radius which is chosen to be 31mm in these magnets.

## II TEST ASSEMBLY

Past magnet building experience has shown that the first magnet does not usually have the desired pre-stress and/or the desired low field harmonics ($b_2$ and $b_4$). First article inspection sample yoke lamination were used to collar a portion of the straight section of two test coils in order verify the coil pre-stress and check the field harmonics in the body of the magnet prior to commencing production. The coils were collared with the design pole shim and midplane caps. This section was then measured at room temperature using a rotating coil to check the field harmonics. The measurements indicated that the pre-stress was low by 2000 psi and that $b_2$ and $b_4$ were unacceptable. Based on these results, the sample was disassembled and

* Work supported by the U.S. Department of Energy under Contract No. DE-AC02-76CH00016.

0-7803-4376-X/98/$10.00 © 1998 IEEE

the thickness of the midplane caps was increased by 0.005". The reassembled section was re-measured to determine if the desired shift in harmonics was achieved.

## III PRODUCTION CROSS SECTION ITERATIONS

Based on the results of the test collaring and warm measurements some changes were made to the baseline cross section design. The thickness of the smallest wedge was increased by 0.004" by adding an additional layer of Kapton [2] wrap, the midplane cap thickness was increased by an additional 0.001", and the pole shim thickness was increased by 0.001". At this point coil production started, thereby limiting any future changes to small variations in pole shim and midplane cap thickness. Cold mass production of the first magnet was accelerated so that test data could be analyzed before the second magnet was assembled. The results of the first magnet confirmed this iteration. The desired pre-stress was obtained and the body harmonics at 2000 Amps were within one standard deviation of ideal values. Fig. 2 shows the relative field error dBy/B on the x-axis based on these measurements. The errors are $<10^{-4}$ within 60% of the coil radius and $<4 \times 10^{-4}$ at 80% of the coil radius. This is the best one can expect given the general manufacturing tolerances. Since the first magnet had the desired coil pre-stress and low field harmonics in the body of the magnet it has been installed in the RHIC ring.

The test assembly helped to get the desired geometric harmonics. However the saturation induced harmonics and the end harmonics were measured for the first time when the first magnet tested. The end harmonics could only be measured at room temperature because the meas. coil for 4.2K tests was not yet available. The saturation induced harmonics were an order of magnitude smaller than in the first arc dipole magnet, but they were still larger than desired. To reduce them in the following magnets, steel rods were inserted into the saturation suppression holes in the yoke. To compensate for the end harmonics observed, the thickness of the midplane caps was increased by 0.002" for the remaining magnets.

The test results from the next magnet showed that the desired changes had been obtained both in geometric and saturation induced harmonics (see Fig. 3). However, the saturation in the end harmonics, which was being measured for the first time, was found to be large. This prompted a decrease in pole shim thickness of 0.004" which was incorporated into the fifth and sixth cold masses. This geometric change in cross section was made to give the desired field quality at the design field.

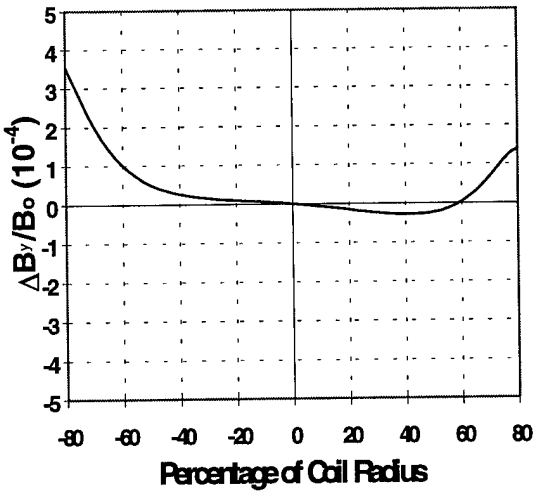



**Figure 2.** Geometric Field Errors on x-axis of DRZ101 body.

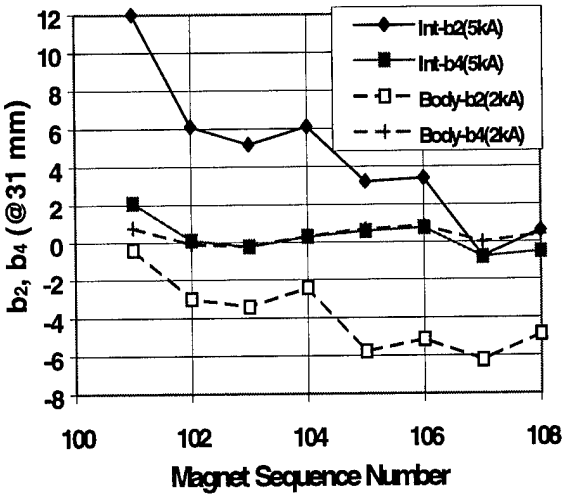



**Figure 3.** Plot showing $b_2$ and $b_4$ by magnet.

During the planned break in the production after the sixth cold mass, a change to the stamping die was made to remove the saturation suppression holes and thereby eliminate the need to fill the void with steel rods at cold mass assembly. The computer calculations indicated that this would reduce the $b_2$ saturation. A small integral $b_2$ which was seen in the fifth and sixth magnets was eliminated in the following magnets. No further changes are expected for the remainder of the production run.

Listed below in Table 1 are the thicknesses of the midplane caps and pole shims for the various assemblies.

**Table 1.** Midplane cap and pole shim data.

| | Test Assy. 1 | Test Assy. 2 | Prod. Assy. 1 | Prod. Assy. 2-4 | Prod. Assy. 5-6 | Prod. Assy. 7-24 |
|---|---|---|---|---|---|---|
| Midplane Cap Thickness (inches) | .008 | .013 | .014 | .016 | .016 | .016 |
| Pole Shim Thickness (inches) | .033 | .033 | .034 | .034 | .030 | .030 |

The measured integral harmonics at the design field in magnets DRZ103-DRZ108 are summarized in Table 2. Mean $b_2$ is expected to be reduced in the rest of the production as per the iterations described earlier. "Quench data will be reported in a later paper."

**Table 2. Integral Harmonics at 5kA (up ramp) in D0 Dipoles.**

| Harmonic ($n$) | Mean $b_n$ (units) | Std. Dev. in $b_n$ | Mean $a_n$ (units) | Std. Dev. in $a_n$ |
|---|---|---|---|---|
| 1 | 0.03 | 0.58 | 0.53 | 1.88 |
| 2 | 2.90 | 2.73 | -2.98 | 0.25 |
| 3 | 0.05 | 0.12 | 0.02 | 0.37 |
| 4 | -0.01 | 0.68 | 0.51 | 0.06 |
| 5 | 0.01 | 0.04 | 0.01 | 0.08 |
| 6 | 0.96 | 0.13 | -0.23 | 0.01 |
| 7 | 0.00 | 0.01 | 0.01 | 0.02 |
| 8 | -0.15 | 0.01 | 0.06 | 0.00 |
| 9 | 0.00 | 0.01 | 0.00 | 0.01 |
| 10 | -0.15 | 0.01 | -0.02 | 0.00 |

## IV CONCLUSION

The production of the D0 magnets has demonstrated that with the help of a test assembly, the first magnet can be built with the desired pre-stress and field harmonics in the body of the magnets. It has also been shown that a number of design adjustments can be made during production without changing the coil geometry or significantly interrupting magnet production.

## REFERENCES


[1] P. Wanderer et al., "Construction and testing of arc dipoles for RHIC" 1995 International Particle Accelerator Conference (PAC'95), Dallas.

[2] Kapton is a registered trademark of the DuPont Corporation.

# HELICAL DIPOLE MAGNETS FOR POLARIZED PROTONS IN RHIC

M. Syphers†, E. Courant, W. Fischer, A. Luccio, F. Mariam, S. Peggs, F. Pilat, T. Roser, S. Tepikian, N. Tsoupas, E. Willen, Brookhaven National Laboratory, Upton, NY, USA,
T. Katayama, U. of Tokyo, Japan, K. Hatanaka, Osaka U., Japan,
T. Kawaguchi, M. Okamura, T. Tominaka, H. Wu, RIKEN, Saitama, Japan, and
V. Ptitsin, Y. Shatunov, BINP, Novosibirsk, Russia

*Abstract*

Superconducting helical dipole magnets will be used in the Brookhaven Relativistic Heavy Ion Collider (RHIC) to maintain polarization of proton beams and to perform localized spin rotations at the two major experimental detector regions. Requirements for the helical dipole system are discussed, and magnet prototype work is reported.

## 1 SNAKES AND SPIN ROTATORS IN RHIC

The Relativistic Heavy Ion Collider at Brookhaven National Laboratory allows for the unique possibility of colliding high energy polarized proton beams. To maintain polarization during the acceleration process, two full "Siberian Snakes" are to be inserted on opposite sides of the RHIC lattice for each of the two counter-rotating rings. In addition, spin rotators will be located on each side of the two major interaction points (again, for each ring) which allow the spin orientation to be altered from the vertical direction to the longitudinal direction. Superconducting magnets are used in order to contain the magnetic elements for a Snake within a 10 m longitudinal space so as to fit within available room in the RHIC lattice. The use of a helical dipole field as part of a Siberian Snake in a synchrotron was first suggested by Courant[1]. A system made completely of four identical length helices was first proposed by Ptitsin and Shatunov[2]. Four right-handed helical dipole magnets, each 2.4 m long and operating near 4 T or less can produce a Siberian Snake for RHIC. The strong helical fields reduce the orbit excursions normally produced by interleaved horizontal and vertical dipole magnets. Hence, the magnet apertures can be similar to those found elsewhere in RHIC. Furthermore, a combination of right-handed and left-handed helical dipole magnets also within a 10 m space can perform the desired local 90° rotations of the spin at the major detector regions.

### *1.1 Helical Magnets for Spin Control*

Let $x$ and $y$ be the transverse coordinates, $z$ the longitudinal coordinate, and $k \equiv 2\pi/L$, with $L$ the repeat period of the helix. Then the magnetic field of a helical dipole magnet in which the field begins in the vertical direction (at $z = 0$) can be described to lowest order in Cartesian coordinates according to[3]

$$B_x \approx -B_0\left\{\left[1+\frac{k^2}{8}\left(3x^2+y^2\right)\right]\sin kz-\frac{k^2}{4}xy\cos kz\right\}, \quad (1)$$

$$B_y \approx B_0\left\{\left[1+\frac{k^2}{8}\left(x^2+3y^2\right)\right]\cos kz-\frac{k^2}{4}xy\sin kz\right\}, \quad (2)$$

$$B_z \approx -B_0 k\left\{1+\frac{k^2}{8}\left(x^2+y^2\right)\right\}\left[x\cos kz+y\sin kz\right], \quad (3)$$

The twisting current distribution introduces intrinsic nonlinear terms into the field. To first order, the trajectory through the helical field above is just

$$x(z) = x_0 - \frac{B_0}{(B\rho)}\frac{1}{k^2}(1-\cos kz) + x'_0 z, \quad (4)$$

$$y(z) = y_0 + \frac{B_0}{(B\rho)}\frac{1}{k^2}\sin kz + (y'_0 - \frac{B_0}{(B\rho)}\frac{1}{k})z. \quad (5)$$

We see that for a complete 360° helix, the effect on the particle trajectory is simply a vertical "shift" in the orbit by an amount $\delta = -B_0 L/k(B\rho)$. We also note that the handedness of the helix is given by the sign of $k$, positive is right-handed, negative is left-handed. By pairing identical length 360° helical magnets of the same strength but opposite field directions (or, equivalently, with equal strength but opposite handedness), the overall orbit distortion outside the system will be zero. With four magnets, this allows one to choose two independent field strengths for control of the spin rotation angle and axis of rotation. A third parameter is needed to completely define the rotation, but by providing the system with reflection symmetry, the axis of rotation is constrained to lie in the horizontal plane.

The spin precession through a helical dipole magnet is most easily found by using the spinor formalism and solving the equation of motion for the first-order field expressions[4],[5]. For the field description given above the axis of rotation, $\boldsymbol{n}$, and angle of rotation, $\mu$, can be written as

$$\mathbf{n} = \frac{\mathbf{x}_1 + \left(\frac{\kappa}{k}\right)\mathbf{x}_3}{\sqrt{1+\left(\frac{\kappa}{k}\right)^2}} \quad \text{and} \quad \mu = -2\pi\sqrt{1+\left(\frac{\kappa}{k}\right)^2} \quad (6)$$

† Work performed under the auspices of the U.S. Department of Energy and partially supported RIKEN, Japan.

0-7803-4376-X/98/$10.00 © 1998 IEEE

where $\kappa = (1+G\gamma)B_o/(B\rho)$, and $\mathbf{x}_1$, $\mathbf{x}_3$ are unit vectors in the longitudinal and vertical directions, respectively. With Eqs. 4-6, the first-order orbit and spin behavior through a system of helical dipole magnets can be readily studied and optimized.

### *1.2 RHIC Helical Magnet System*

In the present RHIC design Snake helical dipoles are all 360° right-handed helices whose fields begin pointed vertically upward or downward. The "Rotator" magnets are either left-handed or right-handed, but each begins with its field pointed in the horizontal plane.

| **Snake** | inj. orbit dev: | 32 mm | |
|---|---|---|---|
| Length | start/end | helicity | max. field |
| 2.4 m | vertical | RH | 1.2 T |
| 2.4 m | vertical | RH | -3.9 T |
| 2.4 m | vertical | RH | 3.9 T |
| 2.4 m | vertical | RH | -1.2 T |
| **Rotator** | inj. orbit dev: | 24 mm | |
| Length | start/end | helicity | max. field |
| 2.4 m | horizontal | RH | 3.4 T |
| 2.4 m | horizontal | LH | 3.1 T |
| 2.4 m | horizontal | RH | 3.1 T |
| 2.4 m | horizontal | LH | 3.4 T |

Table 1: Helical Magnet Parameters for Siberian Snakes and Spin Rotators in RHIC.

The field strengths of the Snake magnets are kept constant during the acceleration process, while the appropriate fields in the Rotator magnets are beam energy dependent. This is due to the fact that there is a net horizontal bending of $\theta$ = 3.7 mrad between the spin rotator location and the interaction point. Hence once the spin vector is rotated into the horizontal plane by the spin Rotator system, it will undergo further precession of $G\gamma\theta$ about the vertical by the time it reaches the interaction point.

Table 1 shows the magnet parameters of the system. The Rotator fields are for 250 GeV proton operation. The maximum orbit deviations listed in each case, however, are for an injection energy of 25 GeV. The magnet fields, particle trajectories, and spin precession for a Siberian Snake are shown in Figure 1. Figure 2 shows a plot of the required values of the two independent magnetic fields in the spin Rotators for various RHIC energies[6].

The effects on RHIC operation of helical dipole magnet error fields and misalignments have been studied. In contrast to a "regular" dipole magnet error which can be thought of as producing a kink in the slope of the particle trajectory at the source of the error, a "helical" dipole error will introduce a step in the trajectory. To keep the vertical orbit distortions under control, the helical dipole field errors *ΔBL/(BL)* should be kept reasonably below 1%, and rotational misalignments should be less than about 10 mrad[7]. Another important parameter will be the total integrated field strength ( $\int B_x ds$, $\int B_y ds$) which should be zero, or equivalently the total effective integrated twist of the magnet should be 360°. With careful orbit correction in the vicinity of the helical dipoles, it is expected that this effective twist angle should be 360° ±2° [8]. The ends of the magnets will need to be carefully designed to obtain not only the desired integrated field strength but also the desired total field twist.

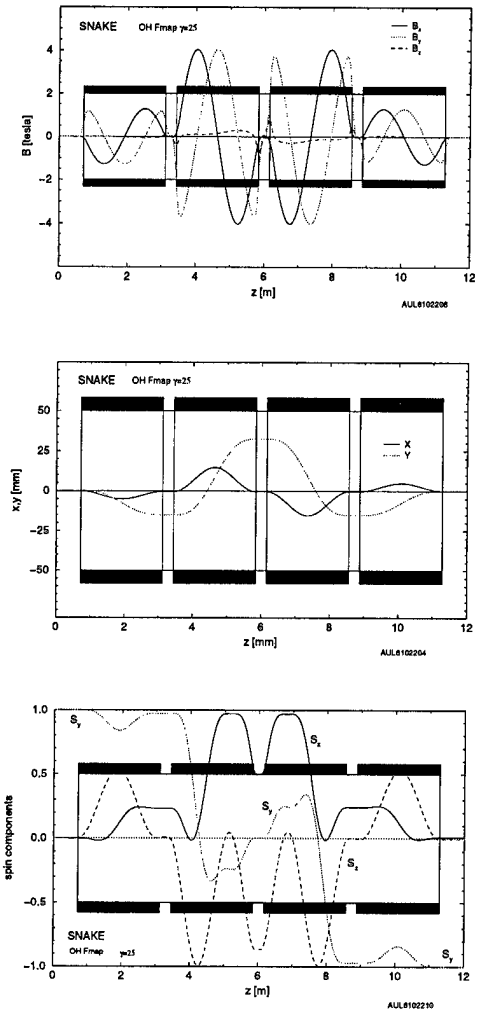



Figure 1: Magnetic field, 25 GeV proton trajectory, and proton spin components versus distance through a RHIC Siberian Snake.

Field quality is also an issue for the helical magnets. The intrinsic twist of the helices in addition to the magnet design and construction errors generate nonlinear fields. While the nonlinear field components tend to average to zero over the length of the helical dipole, the protons follow a trajectory which is not centered within the magnet. Thus, one expects to see feed-down effects. For example, a sextupole component in the magnet will generate a tune shift due to the off-centered orbit.

Analytical estimates indicate that the intrinsic tune shift at 25 GeV due to two Snakes in RHIC is on the order of $\Delta\nu = 0.015$, and that a sextupole component in the magnet design of strength $b_2 \approx 2\times10^{-4}/cm^2$ will give approximately the same tune shift[9],[10]. Particle tracking results are in qualitative agreement with these estimates[11]. It may be possible to design the magnet cross-section with multipole moments which help compensate the intrinsic nonlinear field[12].

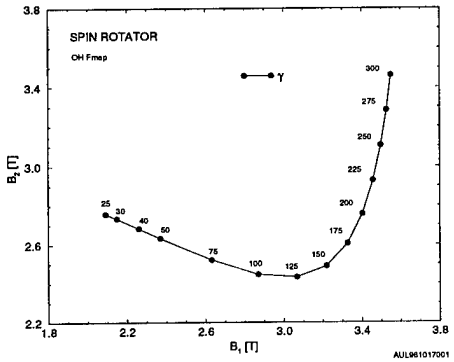



Figure 2: Spin Rotator field strengths for various RHIC beam energies.

## 2 PROTOTYPE MAGNET DEVELOPMENT

A total of 48 individual full-helical dipole magnets will be required for the project. The four magnets needed to create one Snake or one Rotator will be mounted inside of a single cryostat. The magnets will be constructed with hundreds of turns of superconducting cable to minimize both the required current and the associated heat leak through the power leads. At present, two possible techniques for producing helical coils are being investigated. (See Figure 3.) The first, called the "slotted" coil method, is based upon established BNL technology used to produce the RHIC sextupole magnets.

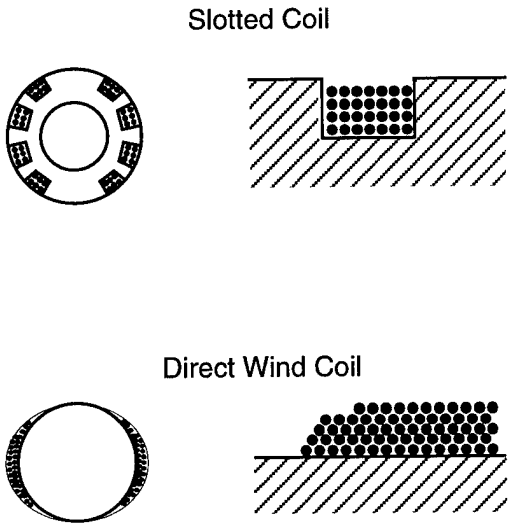



Figure 3: Possible Magnet Technologies.

It consists of an ordered wound cable placed into helical grooves that have been milled into a thick-walled aluminum cylinder. Thin sheets of epoxy-loaded fiberglass are placed between layers, and the entire assembly is cured at elevated temperature and with radial pressure to produce a compact, strong wire matrix. The second, called the "direct-wind" coil method, consists of the same type of cable being bonded directly onto a stainless steel cylinder in multiple layers. The cable is wound into a helical pattern using a computer controlled multiple-axis winding machine. This direct-wind process holds the promise of a low cost production method.

Half-length prototype helical dipole magnets have been manufactured using both processes. The first prototype produced using the direct wind method, was completed by AML, Inc., of Palm Bay, FL, and tested at BNL in November, 1996. This magnet reached 475 A (approximately 4 T) at a temperature of 4.35 K. This was the first time a low current direct-wind magnet reached this field level, the previous mark being roughly 2.5 T. The magnet experienced significant training, which was later diagnosed as being due to voids in the cable-epoxy matrix along the first cable layer near the poles. A solution to this problem has been proposed, and a second prototype magnet is scheduled to be built in the near future.

The first complete slotted magnet prototype was constructed at BNL and tested in February, 1997. After two training quenches, the magnet plateaued at its short-sample current of 400 A, corresponding to a field of 4.8 T. The coil for this prototype magnet was wound by hand, and methods for automating the winding process are being investigated. Further details of each of these magnet designs and their performance can be found elsewhere in these proceedings[13],[14]. The prototype magnets have been modeled in 3-D to examine the end effects and to assist in the final magnet parameterization. Results can be found elsewherein these proceedings[15].

## REFERENCES


[1] E. D. Courant, 8th Intl. Symp. on High Energy Spin Physics, AIP Conf. Proc. 187, 1085 (1989).
[2] V. I. Ptitsin and Yu. M. Shatunov, BNL Report BNL-52453, 15 (1994).
[3] J. P. Blewett and R. Chasman, J. App. Phys. **48**, 2692 (1977).
[4] E. D. Courant, BNL AGS/RHIC/SN-010, June, 1995
[5] M. Syphers, BNL AGS/RHIC/SN-020, Feb. 1996.
[6] A. Luccio, BNL AGS/RHIC/SN-042, Nov. 1996.
[7] M. Syphers, BNL AGS/RHIC/SN-016, Dec. 1995.
[8] M. Syphers, BNL Report, in preparation.
[9] M. Syphers, BNL AGS/RHIC/SN-015, Nov. 1995.
[10] T. Katayama, BNL AGS/RHIC/SN-038
[11] W. Fischer, BNL AGS/RHIC/SN-034, Aug. 1996.
[12] K. Tominaka, BNL AGS/RHIC/SN-054, Apr. 1997.
[13] R. Meinke, et al., these proceedings.
[14] E. Willen, et al., these proceedings.
[15] M. Okamura, et al., these proceedings.

# A HELICAL MAGNET DESIGN FOR RHIC*

E. Willen, R. Gupta, A. Jain, E. Kelly, G. Morgan, J. Muratore, R. Thomas
Brookhaven National Laboratory, Upton, NY 11973

*Abstract*

Helical dipole magnets are required in a project for the Relativistic Heavy Ion Collider (RHIC) to control and preserve the beam polarization in order to allow the collision of polarized proton beams. Specifications are for low current superconducting magnets with a 100 mm coil aperture and a 4 Tesla field in which the field rotates 360 degrees over a distance of 2.4 meters. A magnet meeting the requirements has been developed that uses a small diameter cable wound into helical grooves machined into a thick-walled aluminum cylinder.

## 1 INTRODUCTION

In order to control the spin of polarized protons in the Relativistic Heavy Ion Collider (RHIC), it is necessary to use a system of dipole magnets arranged to precess and rotate the particles' spin direction. Helical magnets, in which the dipole field rotates along the axis of the magnet, offer several advantages for this purpose compared to standard, rotated magnets: minimum beam orbit excursion, orbit excursion independent of separation between magnets, and good control of spin rotation and the spin precession axis orientation. A system using only helical magnets was first proposed by Shatunov and Ptitsin [1], although others had earlier proposed systems using a combination of helical and standard dipole magnets. Studies at Brookhaven confirm the advantages of a pure helical system and that is the system now planned for RHIC [2].

In the system chosen for RHIC, two Snakes and four Rotators are required in each ring. Snakes keep both intrinsic and imperfection resonances from depolarizing the beam by flipping the spin from up/down to down/up twice on each orbit around the machine. Rotators rotate the spin to beam-parallel or beam-antiparallel for experiments. Each Snake and Rotator is made up of four, 2.4 m long, 100 mm coil aperture magnets in which the field rotates through 360° over the length of the magnet. These magnets are all able to operate up to 4 T but depending on location, may operate at lower fields. At the entrance to the magnet the field may be either vertical or horizontal, and the sense of the helix may be either right-handed or left-handed. Four of these magnets are encased in a stainless steel tube to provide structural support and helium containment. A beam position monitor is installed at the center of each assembly. The resulting integrated cold mass is mounted into a cryostat and the assembly replaces dummy sections in the RHIC lattice. Because the field in each magnet must be individually controlled in order to achieve maximum operational flexibility, the current leads could become a significant heat load on the system; the operating current of the magnets is therefore specified at ≤500 A. The design of the system of magnets is intended to minimize the variety and therefore the cost of the magnetic elements that are needed. A companion paper [3] summarizes the magnet parameters for the various Snakes and Rotators in RHIC.

## 2 DESIGN CONCEPT

The basic structure of the helical coil, shown in Fig. 1, uses a new concept: conductor in helical slots milled into thick-walled aluminum cylinders to give a cos θ current distribution in a two-dimensional section. Two of these cylinders, concentric with one another, are assembled to

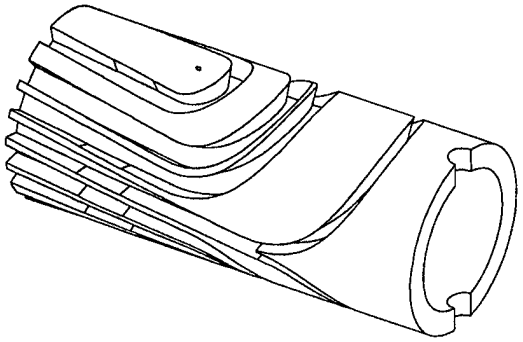


Figure 1 An isometric view of the end of the inner coil cylinder showing slots ready to accept conductor.

give the required field of 4 T. A cross section of the design is shown in Fig. 2.

The Lorentz forces are contained initially by the strength of the aluminum cylinders and the compressive force exerted by an overwrap of Kevlar and fiberglass/epoxy around the circumference of each coil. At high field, the cylinders distort into an elliptical shape, growing outward on the midplane. After deflecting a fraction of a millimeter, they reach the stop provided by the next tube or the iron yoke. These small elastic motions are not expected to affect the quench performance of the magnet nor to distort the field in any significant way.

* Work performed under the auspices of the US Department of Energy

0-7803-4376-X/98/$10.00 © 1998 IEEE

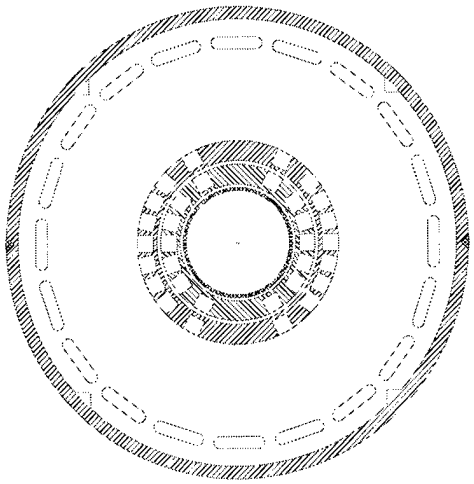


Figure 2 A cross section of the slotted coil helical magnet cold mass showing two concentric coils, the iron yoke, and the containment shell. The diameter of the iron yoke is 14 inches (355.6 mm).

## 3 CONDUCTOR

The conductor is a twisted cable made of seven strands of the 0.330 mm superconductor wire (Cu/non-Cu: 2.5/1) developed for the RHIC corrector program. This cable, nearly 1 mm in diameter, carries 314 A to produce a 4 T field in the present design. A cable is preferable to a single wire: if a break in a wire of the cable should occur, the magnet would very likely still operate satisfactorily. In addition, a cable is more flexible than an equivalent wire and therefore eases the manufacturing of the coils. The required Kapton insulation is wrapped onto the cable in the cable-manufacturing operation.

The cable is made with a 6-around-1 geometry, which results in a cable in which the center wire is not transposed along the length of the cable. Eddy currents are generated in this wire when the magnet current is ramped. They generate heat and have a measurable effect on quench performance above a ramp rate of 2 A/s. However, since these magnets are not required to ramp with the machine, this design feature is not detrimental to the required performance.

The Kapton wrap on the cable allows space for helium inside the wrap, in direct contact with the wires. This is a desirable feature for enhancing the stability of the superconductor. It is estimated that somewhat over 10% of the volume is available for helium inside the Kapton wrap.

Fig. 3 shows the field vs. current characteristic for the magnet and the superconductor as designed.

## 4 MECHANICAL CONSTRUCTION

The cable is laid in an ordered pattern into the Kapton-lined slots milled into the aluminum cylinders. A piece of fiberglass cloth impregnated with a B-stage epoxy is placed between each layer of wires in the slots. The slots continue around the ends in a layout designed to minimize undesired harmonics. When all the turns have

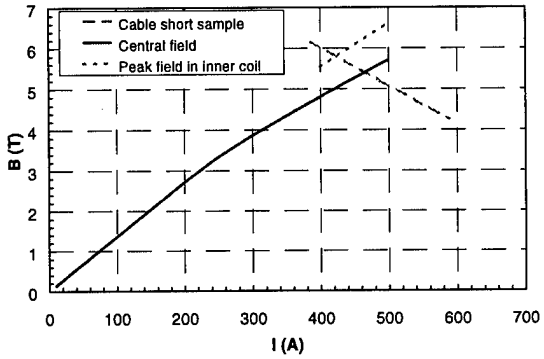



Figure 3 Field vs. current for the slotted coil helical magnet. The central field is 4 T at 314 A. The peak field determines the quench current, estimated at ~420 A.

been wound into the slots, G10 fiberglass pusher plates 3.18 mm thick are placed on top of the turns. Then the assembly is temporarily compressed with Kevlar that is wrapped onto the cylinder under tension. The entire assembly is next placed into an oven for curing, thereby forming a series of current blocks around the cylinder in which each wire is firmly supported in a fiberglass/epoxy matrix. After curing, any voids in the ends are filled with a mineral-loaded epoxy.

The finished diameter of a cylinder is achieved by over-wrapping each cylinder with new Kevlar strand to compress the current blocks and then with layers of fiberglass/epoxy, followed by grinding to size after curing. The two cylinders are fitted into an iron yoke supported at one end by a plate that aligns the cylinders to a fixed position. Only a slight clearance (~0.1 mm) exists between finished cylinders. The yoke is made up of one-piece laminations having a ring of elongated holes on the outside perimeter. Tie-rods through these holes in four places provide axial restraint for the assembly (but are not required to restrain the axial Lorentz forces). Holes are also necessary for the passage of the helium coolant and the electrical buswork. The holes are designed to minimize field irregularities as the field rotates along the length of the magnet. The inner radius of the yoke is increased in the ends to reduce the peak field on the conductor. A helium containment shell is welded in place around the yoke later when the magnet is assembled into a complete helical Snake or Rotator.

A summary of mechanical parameters is given in Table 1.

## 5 ELECTRICAL FEATURES

The 16 separate windings of the two coils are connected in series at the end of the magnet. These interconnections generate a small but manageable amount of heat. A low-value resistor is connected across each of the windings for protection against excessive temperature and voltage during a quench. Resistors provide a current

Table 1 Selected mechanical parameters of the slotted coil helical magnet.

| Parameter | Value Inner, Outer |
|---|---|
| Number of cylinders | 2 |
| Num of current blocks per cylinder | 7, 9 |
| Num of cable turns per layer | 12, 12 |
| Num of layers per current block | 9, 9 |
| Num of cable turns per block | 108, 108 |
| Num of cable turns per cylinder | 756, 972 |
| Total turns | 1728 |
| Coil inner radius (mm) | 49.7, 68.6 |
| Coil outer radius (mm) | 60.0, 78.9 |
| Helix, magnetic length (mm) | 2400 |
| Helix, rotation (deg) | 360 |
| Yoke IR in straight section (mm) | 84.5 |
| Yoke IR in ends (mm) | 114.4 |
| Yoke outer radius (mm) | 177.8 |

bypass as coil resistance builds following a quench. Without these resistors, a quench in a winding could absorb too much of the stored energy of the magnet and possibly lead to conductor damage. Since these magnets do not have a ramp rate requirement, resistors are the best choice---diodes could be used if there were a need to ramp the magnets during operation. The stored energy of the magnet at 4 T is 240 kJ (2.4 m effective length) and the inductance is 4.8 H.

## 6 PROTOTYPE MAGNET & TEST RESULTS

A half-length prototype magnet of the slotted coil design was built and tested at Brookhaven. This magnet followed an earlier coil prototype that was built to test the concept and to evaluate the requirements of this novel coil design. The windings in the prototype magnet were placed by hand, a laborious process because of the tight dimensions of the slots; this task will be automated for production magnets. Other features of the prototype were close to those intended for production magnets.

The quench performance of the prototype magnet was excellent, as shown in Fig. 4. After two low quenches, believed to have originated in inadequately supported leads, the magnet quenched only at the level expected from prior tests on the cable. A shift in dewar temperature, and a variation in ramp rate, both moved the quench current in the expected direction---independent confirmation that the magnet was operating at the short sample limit. The current for all four quenches at the nominal test temperature (4.35 K) and ramp rate (0.1 A/s) was 398 A (4.8 T). At 4.6 K, the magnet quenched at 378 A. Not shown are several quenches with a dual current configuration powering the coils that reached 5.0 T, indicating that the design is not mechanically limited. Detailed field measurements using a Hall probe system are in progress.

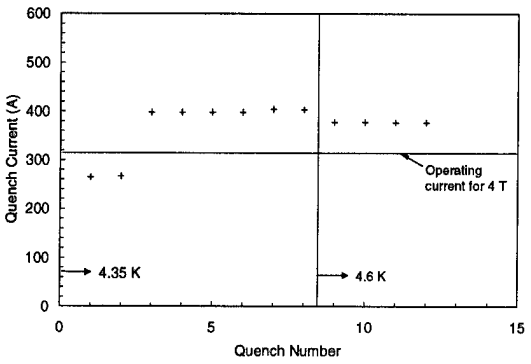



Figure 4 Quench performance of the magnet. Following two low quenches believed to have originated in the leads, the magnet quenched on a stable plateau following ramps at 0.1 A/s. Quenches 7 and 8 were slightly higher (6 A) because of the higher ramp rate used (1 A/s).

Measurements of temperature rise during quench (maximum recorded 490 °C) on the earlier coil prototype indicated tolerable limits.

## 7 SUMMARY

The test results confirm the adequacy of the slotted coil design. A full-length model using a slightly modified turn layout to adjust the field harmonics will be built in the coming year. The coils in this model will be fabricated with an automated wiring machine, currently under construction. Some additional tests in the next model are needed to measure the temperature rise in the final coil during quench. The design provides a field margin of ~20% under operating conditions in RHIC.

## 8 ACKNOWLEDGEMENTS

The authors thank Mike Harrison for his support and encouragement of this development effort. We also thank T. Roser and M. Syphers for their continued interest and support.

## REFERENCES

[1] V. I. Ptitsin and Y. M. Shatunov, Helical Spin Rotators and Snakes, Proc. Third Workshop on Siberian Snakes and Rotators (A. Luccio and T. Roser, Eds.) Upton, NY, Sept. 12-13, 1994, Brookhaven National Laboratory Report BNL-52453.

[2] Preliminary Design Report, Polarized Proton Collider at RHIC, Brookhaven National Laboratory, January 28, 1997.

[3] M. Syphers et al., Helical Dipole Magnets for Polarized Protons in RHIC, Proc. PAC97, Vancouver, BC, May, 1997.

# DYNAMIC FIELD QUALITY OF LHC/SACLAY ARC QUADRUPOLE MAGNET PROTOTYPE

A. Devred, J. Belorgey, J. Deregel, B. Gallet, P. Genevey, F. Kircher, J.M. Rifflet, J.C. Sellier, and P. Védrine
CEA Saclay, DSM/DAPNIA/STCM, 91191 Gif-sur-Yvette Cedex, France
J. Billan – CERN, LHC/MMS, 1211 Genève 23, Switzerland
T. Ogitsu – KEK, National Laboratory for High Energy Physics, 1–1 Oho, Tsukuba-shi, Ibaraki-ken 305, Japan

## ABSTRACT

As part of the magnet R&D program for the Large Hadron Collider (LHC), CEA Saclay has designed and built two 3-m-long, 56-mm-twin-aperture arc quadrupole magnet prototypes. Extensive field quality measurements were performed during the cold-test of the second prototype. A review of the field quality data as a function of ramp rate is presented. The observed field distorsions are explained in terms of inter-strand coupling currents arising from low and non-uniform resistances at the crossovers between the strands of the two-layer Rutherford-type cable. Last, the distribution of crossover resistances within the quadrupole magnet coil is determined.

## INTRODUCTION

The field produced by superconducting particle accelerator magnets has three main components: 1) a component, $B_t$, resulting from the transport current, $I$, 2) a component, $B_m$, resulting from persistent magnetization currents arising in the superconducting filaments, and 3) a component, $B_c$, resulting from cable coupling currents. $B_t$ only depends on the coil geometry and is expected to vary linearly as a function of $I$. $B_m$ is dominated by the superconductor critical current density, which depends on temperature and magnetic field, and which decreases as a function of $I$. $B_c$ only appears when the current is ramped and is expected to be independent of $I$ and to vary linearly as a function of ($dI/dt$). In addition, magnetization of the surrounding iron yoke enhances each of the field components. The iron contribution is expected to follow the same dependence as the coil contributions, except at high transport currents, where saturation effects may occur.

In a previous paper,[1] we reviewed selected field quality data from a 3-m-long, 56-mm-twin-aperture quadrupole magnet prototype developed for the LHC arcs. The magnet, which relied on a two–layer, cos($2\theta$) coil, wound from a Rutherford-type cable, reached its nominal gradient of 252 T/m at 15060 A with little training.[2,3] The geometric field errors, estimated from magnetic measurements at constant current and various axial positions along the magnet length, appeared to be quite small. The contributions from persistent magnetization currents, determined from measurements at a given axial position during the successive plateaus of a staircase current loop were consistent with predictions from standard theoretical models. Finally, a slight field-dependence of the magnetic permeability of the stainless steel collars used to constrain the magnet coil was held responsible for unexpected non-linear variations as a function of $I$ observed on the geometric field component. (For the LHC/Saclay quadrupole magnet, the iron saturation effects are negligible.)

In this paper, we complete our review by discussing magnetic measurement data taken at a given axial position while ramping the current up and down continuously at various ramp rates. Such data allow one to estimate the contributions from cable coupling currents. Large field distorsions as a function of ramp rate were observed on a number of dipole magnet prototypes developed for the Superconducting Super Collider (SSC).[4] Detailed analyses of the SSC magnet ramp rate sensitivity led to the elaboration of a model of cable interstrand coupling currents.[5,6] The same model is applied here to interpret the data from the LHC/Saclay quadrupole magnet prototype.

## MULTIPOLE FIELD EXPANSION

In the quadrupole magnet straight section, the field can be considered as two dimensional and is conveniently represented by a multipole expansion

$$B_y + iB_x = \sum_{n=1}^{+\infty} (B_n + iA_n)\left(\frac{x+iy}{R_{ref}}\right)^{n-1} \quad , \quad (1)$$

where $B_x$ and $B_y$ are the $x$- and $y$- components of the field, $B_n$ and $A_n$ are the *normal* and *skew* $2n$-pole field coefficients, and $R_{ref}$ is the reference radius. (For LHC magnets, $R_{ref}$ = 1 cm). The symmetries of a cos($2\theta$) conductor distribution are such that only the $B_{4k+2}$ field coefficients, also called *allowed* multipole field coefficients, are expected to be non zero. Furthermore, it can be shown that, in first approximation, the persistent magnetization currents only affect the allowed multipole coefficients.

## MEASURING DEVICE AND PROCEDURE

The multipole field coefficients are measured using a 700-mm-long rotating coil array.[1] The coils are connected to a voltage switching unit which allows the read-out of selected coil combinations and which includes several stages of amplifiers. The output voltage is sent to a voltage-to-frequency converter which integrates the signal between trigger pulses given by an angle encoder located at one end of the coil array. The fact that the current, hence the field, is varying during the measurement is corrected by recording the time of each trigger pulse and by considering a set of successive rotations. The data from the different rotations corresponding to a same angle interval are fitted as a function of time. The fits determined for the different angle intervals are then used to

0-7803-4376-X/98 /$10.00 © 1998 IEEE

interpolate the data at a number of selected times (one per rotation). Last, the interpolated data at each selected time are processed by mean of a discrete Fourier transform and converted into multipole field coefficients. The rotation period is 5 s.

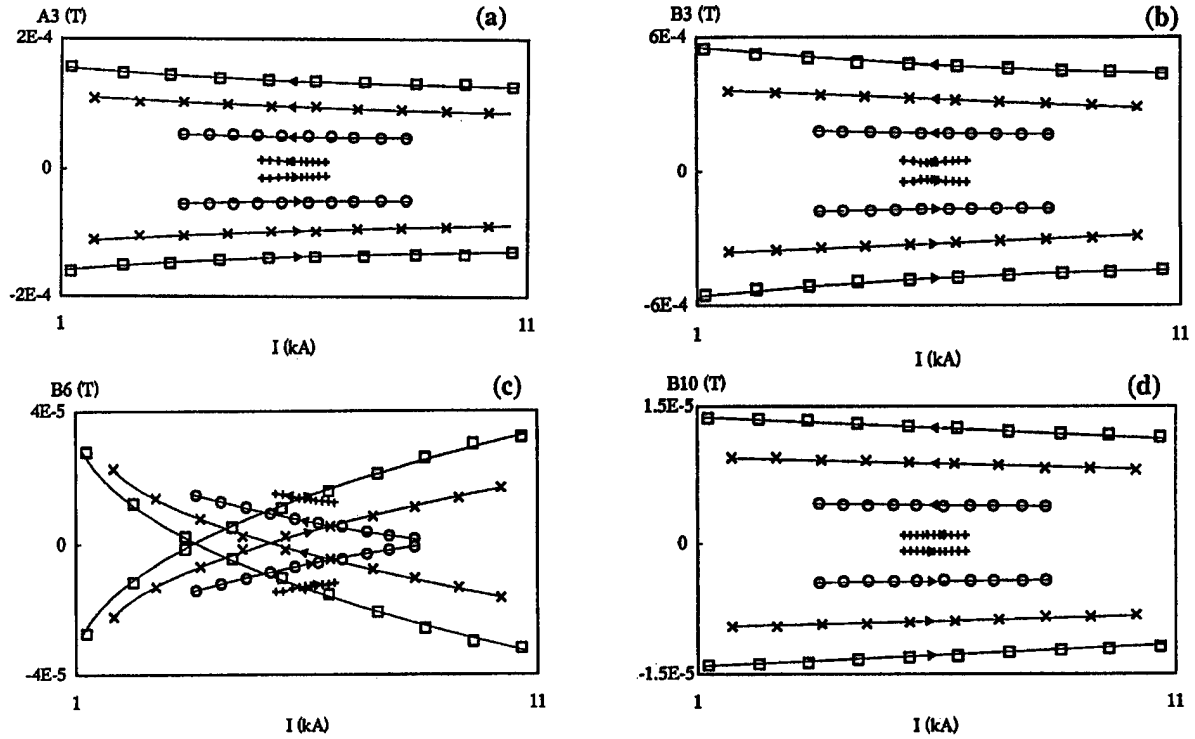



Figure 1. Rescaled multipole field coefficients as a function of current for a series of sawtooth ramps at increasing ramp rates (5 A/s (+), 20 A/s (o), 40 A/s (x), and 60 A/s (□)): a) skew sextupole field coefficient ($A_3$), b) normal sextupole field coefficient ($B_3$), c) normal dodecapole field coefficient ($B_6$), and d) normal 20-pole field coefficient ($B_{10}$). The field coefficients are in tesla.

## MEASUREMENT RESULTS

Figures 1(a) through 1(d) display typical measurement results taken during series of sawtooth current ramps at increasing ramp rates. The coil array was located at the axial center of one aperture. For each ramp rate, the multipole field coefficients, $A_{n,r}$ and $B_{n,r}$, reported in the figures are rescaled in order to substract the geometric terms using

$$A_{n,r}(I) = A_n(I) - (A_{n,u} + A_{n,d})/2 \qquad (2a)$$

and

$$B_{n,r}(I) = B_n(I) - (B_{n,u} + B_{n,d})/2 \qquad (2b)$$

where $A_{n,u}$ and $B_{n,u}$ designate the multipole field coefficient values at $I$ during the up-ramp and $A_{n,d}$ and $B_{n,d}$ designate the multipole field coefficient values at $I$ during the down-ramp.

In a quadrupole magnet, the first multipole field coefficient expected to be affected by persistent magnetization currents is $B_6$. It appears in Figs. 1(a) and 1(b) that the re-scaled skew and normal sextupole field coefficients both exhibit sizable hystereses as a function of current, even at 5 A/s. It appears also that the hystereses widths are roughly constant as a function of current, but increase quasi linearly as a function of ramp rate. Similar observations can be made for most un-allowed multipole field coefficients.

Turning now to Fig. 1(c), it appears that the rescaled $B_6$ describes hystereses whose widths vary as a function of current. Furthermore, at 5 A/s, the lower branch of the plot corresponds to the current up-ramp, while the upper branch corresponds to the current down-ramp. As the ramp rate is increased, the up-ramp branch moves upward while the down-ramp branch moves downward. The two branches cross each other a little below 8 kA at 20 A/s. The crossing current decreases to 4.2 kA at 40 A/s and 2.6 kA at 60 A/s, where the hysteresis is described almost entirely in a direction opposite to that observed at 5 A/s. In addition, it can be verified that, at a given current, the hysteresis width varies quasi linearly as a function of ramp rate. The behavior of the rescaled $B_{10}$ shown in Fig. 1(d) resembles that of the sextupole field coefficients, but the amplitudes of the effects are smaller.

The data presented here exhibit the same features as the magnetic measurement data from the SSC dipole magnet prototypes mentioned in introduction.[4-6] The behaviors of the rescaled un-allowed multipole field coefficients are consistent with what can be expected from the effects of

cable coupling currents. Coupling currents also affect the allowed multipole coefficients. They appear to compete with the effects of persistent magnetization currents in the case of the rescaled $B_6$ but are largely predominant in the case of the rescaled $B_{10}$.

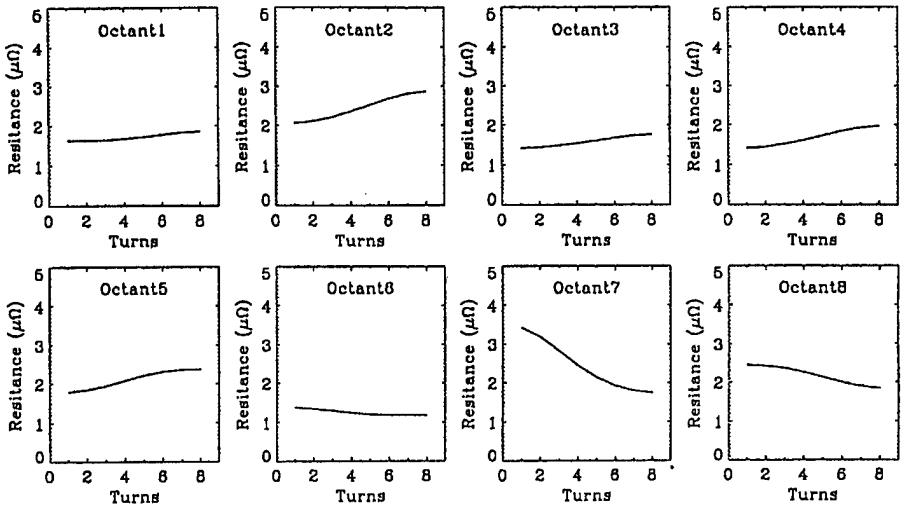



Figure 2. Estimated crossover resistance as a function of turn number in the various octants of one aperture of a LHC/Saclay arc quadrupole magnet prototype. The optimization process was carried out using magnetic measurement data as a function of ramp rate taken at the magnet axial center. The crossover resistances are in ohm.

## DATA ANALYSIS

As for SSC dipole magnet prototypes, the dynamic field behavior of the LHC arc quadrupole magnet prototype seems to be dominated by cable interstrand coupling currents. The LHC prototype uses a flat, two-layer, slightly keystoned Rutherford-type cable with a radial width of 13.05 mm and a mid-thickness of 1.93 mm. It is made of 24 strands (strand diameter: 1.09 mm) which are coated with *staybrite* (a silver-tin coating). The cable pitch length is 100 mm.

During cabling, the strands are deformed heavily and large contact areas are created at the crossovers between the strands of the two layers. Furthermore, during and after magnet assembly, large pressures are applied perpendicularly to the cable which put the strands firmly in contact. If the contacts are good, the crossovers may provide low resistance paths for interstrand coupling currents to flow from one strand to another when the cable is subjected to a varying field.

Such a cable can be described by a network model where the strands are connected by resistances at each crossover points.[5] Representing every turn of a magnet coil by a network model, and knowing all the values of crossover resistances, it is then possible to determine the interstrand coupling current distribution and the resulting field distorsions. Conversely, having measured the field distorsions attributed to interstand coupling currents, one can attempt, by an optimization process, to determine the crossover resistance distribution within the magnet coil.

Figure 2 presents the results of such an optimization. The followed process was identical to the one developed to interpret the SSC data and is described elsewhere.[6] It assumes that the crossover resistance is uniform within the coil outer-most layer and within every turn of the coil inner-most layer, but

that, for the inner layer, it can vary from turn to turn. The crossover resistance appears to vary from 1.2 μΩ to 3.2 μΩ, with an average value of the order of 2 μΩ. The distribution is more uniform than the ones determined for the SSC dipole magnet prototypes, but the average value is somewhat smaller. The strands used in SSC cables were not coated.

## CONCLUSION

The observed dynamic field behavior of the LHC/Saclay quadrupole magnet prototype can be explained in terms of cable interstrand coupling currents, with a rather uniform distribution of low crossover resistances.

## REFERENCES


[1] A. Devred, *et al.*, "Field Quality of LHC/Saclay Arc Quadrupole Magnet Prototype," Proc. 5th Eur. Part. Acc. Conf., pp. 2225-2227 (1996).

[2] J.M. Rifflet, *et al.*, "Cryogenic and Mechanical Measurements of the First Two LHC Lattice Quadrupole Prototypes," Proc. 4th Eur. Part. Acc. Conf., pp. 2265-2267 (1994).

[3] P. Genevey, *et al.*, "Cryogenic Tests of the First Two LHC Quadrupole Prototypes, IEEE Trans. Appl. Super., Vol. 5(2), pp. 202-205 (1995).

[4] T. Ogitsu, *et al.*, "Influence of Cable Eddy Currents on Magnetic Field Harmonics," KEK–Proc. 92–14, pp. 23-27 (1992)

[5] T. Ogitsu and A. Devred, "Ramp Rate Sensitivity of SSC Magnets," *Frontiers of Accelerator Magnet Technology*, S.I. Kurokawa, M. Month, S. Turner, eds., World Scientific, pp. 184-308 (1996).

[6] T. Ogitsu, *et al.*, "Influence of Inter-strand Coupling Currents on Field Quality of Superconducting Accelerator Magnets," submitted to Particle Accelerators.

# MECHANICAL DESIGN AND LAYOUT OF THE LHC STANDARD HALF-CELL

J.C. Brunet, P. Cruikshank, W. Erdt, M. Genet, V. Parma, A. Poncet, P. Rohmig, B. Skoczen, R. Van Weelderen, J. Vlogaert, U. Wagner, L.R. Williams, CERN, Geneva, Switzerland

*Abstract*

The LHC Conceptual Design Report issued on 20th October 1995 [1] introduced significant changes to some fundamental features of the LHC standard half-cell, composed of one quadrupole, 3 dipoles and a set of corrector magnets. A separate cryogenic distribution line has been adopted containing most of the distribution lines previously installed inside the main cryostat. The dipole length has been increased from 10 to 15 m and independent powering of the focusing and defocusing quadrupole magnets has been chosen. Individual quench protection diodes were introduced in magnet interconnects and many auxiliary bus bars were added to feed in series the various families of superconducting corrector magnets. The various highly intricate basic systems such as: cryostats and cryogenics feeders, superconducting magnets and their electrical powering and protection, vacuum beam screen and its cooling, support and alignment devices have been redesigned, taking into account the very tight space available. These space constraints are imposed by the desire to have maximum integral bending field strength for maximum LHC energy, in the existing LEP tunnel. Finally, cryogenic and vacuum sectorisation have been introduced to reduce downtimes and facilitate commissioning.

## 1 INTRODUCTION

The Large Hadron Collider (LHC) to be installed in the LEP tunnel at CERN will produce two proton beams of 7 TeV energy for head on collisions in 4 points around the circumference. The machine is subdivided into 8 octants, each one comprising a standard arc composed of 54 optical half-cells housed in a common cryostat (Arc cryostat), flanked on each side by specific insertion optics for the various experimental areas and functions of the machine (injection, ejection, cleaning, RF, etc.).

The standard 914 mm diameter arc cryostat, of an octant 2.7 km long, is bounded at each extremity by electrical current feedboxes (DFB) allowing the numerous families of superconducting magnets to be powered in series. The cryogenic distribution line (QRL) housing various headers servicing the main stream of cryomagnets runs parallel to the arc cryostat, and as for the main electrical supplies is fed at the 4 even points of the machine from cryoplants installed at ground level. The basic repetitive segment of the arc is the half-cell of 53.4 m length providing 90° phase advance for the beams. It is composed of 3 two-in-one 8.3 T dipoles of 15 m length, one two-in-one quadrupole and various sets of correcting magnets. The so-called Short Straight Section (SSS) housing the quadrupole, sextupole, octupole, dipole orbit correctors, and beam position monitors (BPM) is flanked by a cryogenic service module housing service piping for quench discharge into the QRL, phase separation for 1.9 K heat exchanger cooling, etc.

The half-cell length occupancy has been optimised to provide maximum bending field length, taking into account the various functions and elements of the machine.

## 2 CRYOSTAT

The string of superconducting magnets operates in a static 1.9 K superfluid helium bath pressurised at 1 bar absolute [2]. The heat load budget to 1.9 K is composed of static heat losses through cryostat components (radiation, conduction through support posts, vacuum barriers, etc.) and dynamic loads resulting from resistive heating in splices between cables, beam losses into the 1.9 K bath and synchrotron radiation and RF image current power deposited on the beam screen. To minimise the static heat load to the 1.9 K level at which the cost of refrigeration is 3 to 4 times higher than at 4.5 K, two actively cooled aluminium screens operating at 5-10 K (radiative shield) and 50-75 K (thermal shield) are interposed between the 293 K and 1.9 K levels. These shields are made of polished aluminum sheets welded onto 15 m long structures, extruded together with the cooling channels.

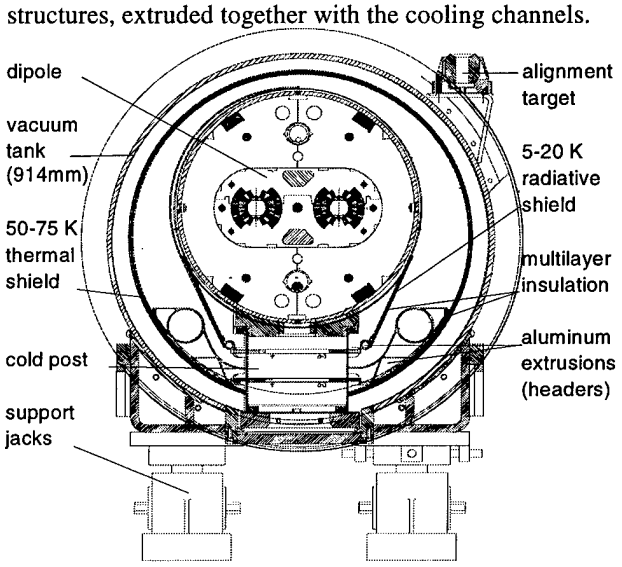



Figure 1: LHC Dipole Cryostat

0-7803-4376-X/98/$10.00 © 1998 IEEE

The radiative shield carries 10 layers of MLI to thermally protect the system in case of degraded vacuum.

The thermal shield is covered by 30 layers of MLI pre-fabricated blankets to reduce thermal radiation load.

The calculated static thermal loads are given in Table 1.

The transverse dimensions of magnet cold masses with their shields have been minimised to fit in an insulating vacuum vessel of diameter 914 mm (36" standard pipe dimension).

## 3 SHORT STRAIGHT SECTION CRYOGENIC MODULE AND JUMPER CONNECTION

The Short Straight Section which houses the quadrupole, chromatic correction elements, a set of orbit correctors and beam position monitors, also incorporates a cryogenic service module which connects the cryogenic distribution line to the main cryostat out every cell [3].

An intricate set of components finds its place in a reduced volume: the phase separator of the 1.9 K heat exchanger cooling a full cell, the connecting pipes housing the bus bars with manifolds tubes to the QRL allowing filling and discharge of a stretch of cells, the beam position monitors, beam pipes, sectorisation valves, and quadrupole protection diodes, accessible for repair via the interconnect. A set of 50 A current leads installed in the cryogenic module feeds the closed orbit dipole corrector magnets. Low heat in-leak insulating vacuum separation barriers are installed between the quadrupole cold mass and the vacuum enclosure every two cells. This facilitates vacuum pump down, leak testing by confining leaks. The vacuum hardware is attached to the SSS.

To permit an easy and precise alignment of the SSS, it must be mechanically decoupled from the QRL. For this purpose, a set of interconnecting bellows in the jumper connection gives the necessary flexibility and compensation for forces due to atmospheric pressure.

## 4 ELECTRICAL DISTRIBUTION

Apart from the orbit correctors, all superconducting magnets of the Arc are powered in series from the main electrical feed box installed at the even points. The focusing and defocusing quadrupole pairs of 12.5 kA bus bars run through the two upper slots in the magnet yokes. The main dipole 12.5 kA circuit occupies a third slot, and dipoles have two different types of electrical connections built into the cold masses, lodging alternatively (every half-cell) the magnet inductance on the go and return bus bars in order to limit voltages to ground during a discharge. 40 to 80 auxiliary superconducting cables rated at 600 A run through the magnet cold masses and are electrically connected at each magnet intergap. This represents a total of more than 80'000 electrical connections for the whole machine, which must be carried out within a tight electrical specification concerning insulation breakdown voltage (5 kV) and connection resistance ($10^{-8}$ Ohms).

To minimise erroneous connections and to reduce manpower costs at installation, special multichannel connectors and distributors are envisaged and developed. Furthermore, the electrical connection of auxiliary magnets in the interconnect gap is being studied, as this would specialise SSS only at the installation stage.

Alternative designs currently being studied consider the routing of uninterrupted cable bundles through the cold masses of a half-cell to feed the chromatic magnet correctors installed in the SSS.

Bus bars are routed through 4 slots and 4 interconnecting tubes in and between the cryomagnets.

## 5 MAGNET SUPPORT AND ALIGNMENT

The superconducting magnets of the arc are positioned by column-type supports. The stringent positioning precision for magnet alignment and the high thermal performance for cryogenic efficiency are the main conflicting requirements which have lead to a trade-off design. An additional function requested of the support system is the suspension of the thermal and radiative screens in the cryostat.

A three point support is chosen for the 15 m long, 30 ton dipoles, where the support spacing limits the maximum vertical sagitta to 0.25 mm; only two support points are needed for the shorter (6 m) and lighter (6 ton) cold mass of the SSS to keep the maximum vertical sagitta below 0.23 mm.

The support is made of a main composite column bolted to stainless steel pads previously welded on the magnet cold masses. The fixations on the vacuum vessels allow sliding of the supports to free the thermal contractions and to leave free the required degrees of freedom.

The thermal performance of the supports is improved by intercepting most of the residual heat conduction at two intermediate temperature levels (one in the 50-75 K and the other in the 4.5-20 K range). These intercepts consist of aluminum plates, glued to the composite column and welded to the thermal and radiative shields via flexible aluminium straps.

The heat loads reported in table 1 are estimated from measurements made on previous supports.

| | Temperature level | | |
|---|---|---|---|
| Watts | 1.9 K | 4.5-20 K | 50-75 K |
| Cryomagnet support posts | 0.5 | 9 | 44 |
| Vacuum barrier Instrumentation capillaries, BPM | 3.1 | 0.2 | 18.6 |
| Cryostat | 0.3 | 3.2 | 165.4 |
| Total for LHC standard half-cell | 3.9 | 12.4 | 228 |

Table 1: Estimated half-cell static heat loads (Watts)

The composite column of the support is made of a 4 mm thick tube with integrated top and bottom flanges. A glass fibber/epoxy composite system was chosen for its high stiffness-to-thermal-conduction ratio, allowing minimisation of the cross section and, as a consequence, of conduction heat loads. A long-fiber, woven fabric lay-up technology is chosen to achieve the highest stiffness.

The initial positioning precision of the magnet cold masses is ±0.5 mm with respect to the cryostat axis and ±1 mm in the longitudinal direction. This precision is achieved by a tight chain of mechanical tolerances. Under the worst hypothesis of residual mechanical loads, the present design of the support system for magnets gives a stability of ±0.2 mm in the radial and vertical plane.

## 6 INTERCONNECTIONS

The interconnections between cryomagnets contain a number of structural components which are designed to assure a continuity and provide maximum security to different systems integrated within the accelerator : vacuum systems [4], cryogenics , and electrical distribution. In order to extend the magnetic length of the LHC magnets as much as possible the interconnection space is reduced to a strict minimum. This requirement imposes longitudinal and radial limitations on the interconnect components and implies a compact design compatible with the existing tunnel as well as the established transport and installation procedures [5].

The combination of a relatively high pressure of 20 bar (which may develop during the cool-down procedure or a quench) with a necessity of assuring leak tightness for all the superfluid helium transfer systems leads to a choice of all welded assemblies.

In order to keep up with the LHC project requirements in terms of system reliability, automatic welding, cutting and control procedures were proposed. The stringent space requirements for the welding and cutting tools was restricted to 50 mm. To reduce the helium consumption at 1.9 K the electrical connections will be brazed and the ohmic resistance limited to some $10^{-8}$ . The large number of bus bar connections (80,000) imposes a high level of reliability as well as strict procedures for manufacture, installation and control.

The interconnect space is determined to a large extent by the superconducting cable overlap length of 120 mm and the necessary length of the bellows expansion joints which compensate for the thermal contraction of the magnets (around 50 mm). In order to reduce the length of the expansion joints and their axial stiffness a special optimisation program has been developed. It aims at reducing the global forces between the magnets (transmitted to the support posts) in the installation phase and during the LHC operation.

Protection diodes constitute some of the critical components of the LHC machine. The present design provides an easy access to the diodes in case they need to be replaced. The access to the box containing the diodes will be possible through the interconnection space, after the removal of the large diameter bayonet sleeve of the vacuum vessel and of the thermal shields.

## 7 SECTORISATION OF SUB-SYSTEMS

The 2.7 km LHC arc cryostat has a cold mass weight of more than 6000 tons. One cryoplant at the corresponding even point will be able to cool-down and warm-up such a mass via the QRL in about 44 days.

Taking advantage of a separate parallel cryoline naturally decoupling the feeding of cryogens from the main stream of magnets, the arc is cut in four sub-sectors. Insulating vacuum barriers separate the QRL from the main cryostat at each jumper connection and sectorise the main cryostat every two cells [6]. High vacuum valves and cryogenic separation valves are installed at each sector boundary and additional cryogenic valves complete the separation of the QRL from the main cryostat at each jumper connection. Finally, so-called bus bar plugs are installed every two cells in magnet gap interconnects to sectorise the 1.9 K cold mass cryogenic volume. This sectorisation allows the partial and independent warm-up and cool-down of small stretches of a few cells. This will yield a factor 2 reduction in the time required for most interventions for repair.

## 8 ACKNOWLEDGEMENTS

A large design, development and testing effort is being actively pursued to integrate all LHC intricate systems in the LHC arc cryostat. Technical choices are regularly tested on the LHC prototype test String [7].

Particular credit must be attributed to R.Saban (LHC test string), W.Cameron,, M.Genet, Th.Renaglia, Ph.Trilhe and to many other people in the LHC team,and CEA and CNRS teams.

## REFERENCES

[1] The Large Hadron Collider, conceptual design, CERN/AC/95-05 (LHC)
[2] Ph.Lebrun, Superfluid Helium Cryogenics for the LHC, ICEC 15, 1994, CERN AT/94-18
[3] L.Tavian et Al, A. simplified cryogenic Distribution Scheme for the LHC to be published to CEC/ICMC'97, Portland, USA, August 97.
[4] O.Gröbner, The LHC Vacuum System, this conference.
[5] J.C.Brunet, Space Management at the LHC Dipole Magnet Ends and in the Interconnections, LHC Project Note 33
[6] Cryogenic and Vacuum Sectorisation of the LHC Arcs, M.Bona et Al, LHC Project Report 60
[7] R.Saban et Al, Experiments and Cycling at the LHC prototype half-cell, this conference.
[8] The Short Straight Sections for the LHC, M.Peyrot et Al, this conference

# STATE OF THE LHC MAIN MAGNETS

R. Perin for the LHC Magnet Team

*Abstract*

The main features of the dipole magnet design have been frozen in 1996 and important steps for the preparation of their series production are being taken in the current year.

To finalize the technical specifications of the superconducting cables and other components, a number of detail variants are being validated with the construction and test of short and long magnets. Thus, beside a number of 1 m long models, four 10 m long models of the main dipoles and two 14.2 m prototypes are being assembled in industry and at CERN. The fabrication of a further set of 3 full length dipoles is also starting in industry to verify the reproducibility of production and performance.

The lifetime and fatigue test of the String Test Facility, consisting of three dipoles and one quadrupole and simulating the basic periodic cell of the LHC, has been successfully concluded. The String was repetitively cycled between the injection field of 0.6 T and the operational field of 8.4 T, 24 hours per day, and has accumulated more than 2100 cycles, corresponding to about ten years of machine operation.

The final design of the main quadrupoles, based on the use of the dipole coil outer layer cable, is being worked out by CEA, Saclay and the construction of two new prototypes has been launched.

## 1 INTRODUCTION

The main magnetic components of the LHC i.e. the 1232 dipoles and the 386 quadrupoles of the lattice have already been described in several publications [e.g. 1,2], so that only the recent evolution in their design and the present state of advancement towards their procurement are reported here.

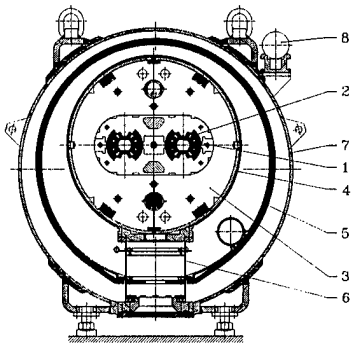
## 2 DIPOLES

### *2.1 Design evolution*

Since 1995 the design of the magnets, though maintaining the main features, evolved partly to adapt to changes in the design of the machine and partly as a result of the R&D programme on short and long magnets.

*Inter-beam distance*

The distance between the centres of the two apertures has been increased from 180 mm to 194 mm. This change was motivated by space considerations in the RF sections and by the desire to diminish both the spring back of the collars when releasing the press after collaring and the tensile stress concentration around the central dowel rod hole. In fact the collar central "leg" appeared to be rather weak as compared to the side "legs". With this modification the final pre-stress in the central and in the lateral parts of the coils is better balanced and the spring back after collaring has been reduced by 20 %. This allows to apply a lower compression under the press with less danger of damaging the coils and easier production. This increase of the inter-beam distance did not require an increase of the overall cold mass diameter which remains unchanged (ø 570 mm) (fig. 1).




1. Beam Screen, 2. Cold bore, 3. Cold mass at 1.9 K, 4. Radiative insulation, 5. Thermal shield (55 to 75 K), 6. Support post, 7. Vacuum vessel, 8. Alignment target

Figure 1: Cross-section of LHC dipole

*Dimensions of the superconducting cables*

The compaction of the previous cables was found to be too high especially at the thin edge where it was difficult to avoid sharp edges that could damage the insulation. A slight reduction in compaction was also found to be favourable to penetration of liquid helium and better wetting of the strands, thus improving heat transfer to helium and heat capacity and consequently increasing the amount of energy needed to provoke a quench [3]. The compaction was, therefore, reduced by about 2 % and at the same time the keystoning angles were also slightly diminished, resulting at present 1.25° in the inner shell cable and 0.90° in the outer shell cable. The new parameters of the cables are listed in table 1.

| | Inner layer | Outer layer |
|---|---|---|
| *Strand* | | |
| Diameter (mm) | 1.065 | 0.825 |
| Cu/Sc ratio | 1.6 | 1.9 |
| Filament size (μm) | 7 | 6 |
| Twist pitch (mm) | 25 | 25 |
| Critical current (A) | | |
| at 10 T, 1.9 K | ≥515 | - |
| at 9 T, 1.9 K | - | ≥380 |
| *Cable* | | |
| Number of strands | 28 | 36 |
| Cable dimension | | |
| width (mm) | 15.1 | 15.1 |
| thin/thick edge (mm) | 1.736/2.064 | 1.362/1.598 |
| Transposition pitch (mm) | 110 | 100 |
| Critical current (A) | | |
| at 10 T, 1.9 K | ≥13750 | - |
| at 9 T, 1.9 K | - | ≥12950 |

Table 1: Dipole strand and cable characteristics

0-7803-4376-X/98/$10.00 © 1998 IEEE

*Field quality*

The problems related to field quality are continuously studied from the points of view of beam optics and dynamics and magnet construction. Understanding is improving with the growing information from tests and measurements of short and long model magnets. Data are accumulating and being analysed on the effects of persistent currents, eddy currents, time dependence and influences of previous history and excitation cycle. It has been decided to compensate the $b_5$ (decapole), $b_7$ (14-pole) and $b_9$ (18-pole) field multipoles produced by persistent currents at injection by modifying the conductor distribution in the cross-section which was then re-optimised for this purpose. It is recalled that small sextupole and decapole magnets located at each dipole end can compensate systematic errors of those two components.

*2.2 State of R&D programme*

The R&D programme, which has validated the main design features, will continue until the start of the series production of the final dipoles with the aims to improve quench behaviour, field quality and economy of construction. It will terminate with the final trimming, in particular of the coil geometry to obtain the wanted field quality, during the production and measurement of the pre-series magnets.

*Superconducting cables*

About 10 t of superconducting cable of the new design have been produced by industry, thoroughly measured and qualified. They meet the specifications in all respects, current carrying capacity, dimensional tolerance and mechanical characteristics, and have also been tested in short dipole models. This has permitted to order a quantity sufficient to start the pre-series production of the final magnets. Investigations are still intensively carried out on different coatings of the strands, so as to obtain a uniform and reproducible interstrand resistance in the range 10 to 20 $\mu\Omega$ per crossing contact, necessary to limit field errors and heat generation by eddy currents at ramp. The interstrand resistance is difficult to control as it depends not only on the coating material, but also on storage conditions, temperatures and pressures in the curing cycle and pre-stress in the coils [4]. At present the best results are obtained with staybrite (Ag 3.5 %, Sn 96.5 %) coating and a special heat treatment in argon atmosphere.

*Conductor insulation*

Several conductor insulation systems have been investigated from the points of view of heat transfer and porosity to helium to take advantage of its excellent cooling properties [5], while ensuring a good dielectric barrier between turns. An all polyimide system has been chosen, but different tapes and layouts (thickness, width, overlap, spacing) are still being tested in short model magnets with the aim to further improve permeability to superfluid helium.

*Models and prototype magnets*

The programme of magnet construction proceeds in parallel on three lines: short (1.3 m long) models, 10 m long models and prototypes of the final length (magnetic length 14.2 m). At CERN a dedicated workshop manufactures single and twin aperture short models [6]. The so called Coil Test Facility, in fact a single aperture magnet structure conceived for easy assembly and disassembly, is a time-and-cost-effective means of studying different versions of coil construction as e.g. different types of end spacers, layer jumps, conductor insulation systems, strand coating and assembly methods. One important observation, which confirms earlier finding in the SSC magnet development program [7], is that in some of the best behaving magnets the azimuthal compression in the coil at the coil collar pole interface had completely disappeared at fields well below the field finally reached by the magnet. An investigation has, therefore, been started to determined the optimum pre-stress to be applied since there is no point to collar coils at pre-stress values above what is needed, as this can only make the fabrication more difficult and increase the risk of damaging the insulation.

As previously reported [8, 9, 10], other successful dipole development was carried-out by collaborating laboratories, as the CERN-Finnish-Swedish version 1 m model, the models built by KEK and Japanese industry and the $Nb_3Sn$ high field model of Twente University.

Last year an assembly facility for full length dipoles has been put into operation at CERN. This is now used to assemble 10 m long models starting from coils wound and collared in industry and will be soon employed to assemble final length magnets. The main purpose of this work at CERN is to study and finalize important details of the assembly procedures, such as e.g. economical and efficient welding methods for the shrinking cylinder, the way to obtain the wanted curvature of the magnets, the optimization of the electrical connections.

Four 10 m long magnets of the second generation (aperture 56 mm) are at present being completed, the first one, mounted in a cryostat of the first generation dipoles, is already being tested. A second one will follow at a month interval and the other two will be tested in the second half of the year.

The first full length (~ 15 m, magnetic length 14.2 m) prototype, funded and built in the framework of a collaboration with Istituto Nazionale di Fisica Nucleare (INFN), is in advanced state of construction (fig. 2) and is expected to be delivered to CERN in October 1997. It will be followed by four collared coil assembly manufactured in industry, which will be finally assembled into finished magnets partly at CERN and partly in industry.



Figure 2: Collared coils of the first 15 m long magnet (courtesy of Ansaldo Energia S.p.a.)

*LHC prototype half-cell*

A major milestone in the project has been the assembly of a magnet string facility, consisting of one short straight section and three 10 m dipole magnets connected electrically and cryogenically together on a slope of 1.4 %, in simulation of the LHC conditions. The string has undergone already several thousand hours of operation with more than 80 provoked quenches and several thermal cycles with full success. It has been powered with LHC like ramping cycles between injection and 8.4 T field for more than 2'000 cycles simulating about 10 years of the collider operation [11].

*2.3 Towards the series production*

Final drawings and detailed technical specifications are being prepared for the main magnet cables and for the manufacturing of the magnets. An important order for the supply of 50'000 tonnes of low-carbon steel sheet for all main dipoles and quadrupoles has already been placed. It is hoped to order the superconducting cables before the end of this year. Market surveys for several other materials and components as well as for the supply of the main dipole cold masses have already been carried out and calls for tenders are expected to be issued in the course of this and next year.

The LHC planning, largely dominated by the main dipole magnets, foresees to place the main orders for their supply in 1998. They will include the manufacturing of a number of pre-series magnets (at least 10 per manufacturer) whose delivery to CERN will start in 1999 and terminate in the year 2000. After their thorough test, measurement and evaluation, the green light for mass production could be given by mid 2001.

## 3 QUADRUPOLES

The main parameters of the quadrupoles are gradient 223 T/m, coil aperture 56 mm and magnetic length 3.1 m. Their cross-section is shown in fig. 3.

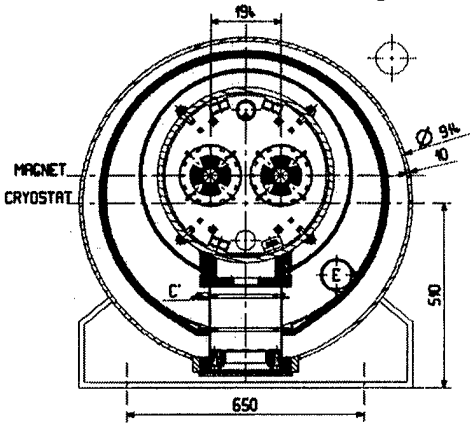



Figure 3: Cross-section of the LHC main quadrupole

The design [12] is based on the use of the same cable as for the dipole outer layer. This should result in some saving because possible broken length of dipole cables could be used for the quadrupoles which require much shorter stretches of conductor.

Their main constructional features are: two layer coils made from a single stretch of cable, austenitic steel collars supporting the full electromagnetic forces and a "two-in-one" yoke structure held by an outside stiffening cylinder, which also serves as helium vessel and support for the correction magnets and other components of the short straight sections. The 12-pole field error component produced by persistent currents at injection is for a large part (> 80 %) compensated by a special layout of the conductors in the cross-section.

The development of the quadrupoles has been from the beginning entrusted to CEA, Saclay in France. This has resulted in the construction of two 3.06 m (magnetic length) real size quadrupoles which have been successfully tested at Saclay and delivered to CERN. In the frame of a special contribution of France to LHC, CEA will ensure the development and test of two further prototype of the new design. CEA will then be responsible for the technical specification and the follow up of fabrication in industry of the series quadrupoles. The remaining R&D programme foresees delivery to CERN of the two new prototypes, already tested, in autumn 1998.

## 4 REFERENCES


[1] The LHC Study Group, The Large Hadron Collider, Conceptual Design, CERN/AC/95-05 (LHC).

[2] R. Perin, Superconducting Magnets for the Large Hadron Collider, CERN LHC Project Report 52, 8 October 1996.

[3] M.N. Wilson, W.B. Sampson and A.K. Ghosh, Experimentally measured Minimum Quench Energies of LHC cables, CERN LHC Project Report 86, 15 January 1997.

[4] D. Richter et al., DC Measurement of Electrical Contacts between Strands in Superconducting Cables for the LHC Main Magnets, Proc. 1996 Applied Superconductivity Conference, Pittsburg, 25-30 August 1996.

[5] L. Burnod et al., Thermal Modelling of LHC Dipoles functioning in Superfluid Helium. Proc. EPAC'94 Conference, London and CERN AT/94-21.

[6] N. Andreev et al., The 1 m long Single Aperture Dipole Coil Test Program for LHC, Proc. EPAC'96, Sitges, (Barcelona), June 1996.

[7] P. Wanderer et al., Effect of Prestress on Performance of a 1.8 m SSC R&D Dipole, presented at ISSC Atlanta, March 13-15, 1991.

[8] J. Ahlbäck et al., Construction of a 56 mm Aperture High-Field Twin-Aperture Superconducting Dipole Model Magnet, Proc. MT14, IEEE Trans. on Magnetics, Vol. 30, July 1994.

[9] T. Shintomi et al., Development of a 56 mm aperture Superconducting Dipole Model Magnet for LHC, Proc. 1996 Applied Superconductivity Conference, Pittsburg 25-30 August 1996.

[10] A. den Ouden et al., An Experimental 11.5 T $NB_3Sn$ LHC Type of Dipole Magnet, Proc. MT13, IEEE Trans. on Magnetics, Vol. 30 No. 4, July 1994.

[11] R. Saban et al., Experiments and cycling at the LHC Prototype Half-Cell, PAC'97, Vancouver, 12-16 May 1997.

[12] T. Tortschanoff et al., The Short Straight Sections for the LHC, PAC'97, Vancouver, 12-16 May 1997.

# THE SHORT STRAIGHT SECTIONS FOR THE LHC

T. Tortschanoff, V. Parma, P. Rohmig, CERN, Geneva, Switzerland,
M. Peyrot, J.M. Rifflet, P.Védrine, CEA-Saclay, France and D. Vincent CNRS, Orsay, France

*Abstract*

During more than five years a close collaboration between CERN and CEA-Saclay led to the development and construction of two prototype quadrupole magnets and the integration of one of them into the short straight section of the LHC half-cell test string at CERN. In the frame of the special host country contribution to the LHC project this collaboration has been extended to the CNRS laboratory in Orsay and covers besides the quadrupole magnets the complete cold mass assembly (CEA) and the integration into the short straight section cryostat (CNRS). The short straight sections include not only the main lattice quadrupoles with their protection diodes, they also house different corrector magnets and the beam position monitors. Further, they provide the cryogenic feed units for a half-cell with all the magnet interconnections and the jumper connection to the separate cryo-line. The paper will show the general lay-out of these complex units and elaborate the different aspects of their assembly.

## 1 INTRODUCTION

The major effort in the development of the LHC magnet system has been put into the design and construction of the dipole magnets. Since 1989, however, a collaboration with CEA-Saclay in France was started for the development of the lattice quadrupole magnets for the LHC. This resulted in the successful construction and testing of two prototype quadrupole magnets [1] of which one has been integrated into a short straight section unit forming the first cryo-magnet unit in CERN's test string operated since 1994 [2].

Following the approval of the LHC project a new collaboration for the design, prototyping and industrial series production was concluded between CERN and two French laboratories, CEA-Saclay and CNRS in Orsay. While the CEA is looking after the cold masses of the short straight sections CNRS has been entrusted with the work for the cryostating of these units.

Although much shorter than the 15 m long dipole units [3] the short straight sections are of much higher complexity. As their main magnetic component they contain the 3.25 m long twin aperture lattice quadrupole magnets. Further, on one end of the quadrupole the combined sextupole-dipole corrector magnets for each beam are placed, while on the other end a pair of octupole corrector magnets is mounted or, depending on their location in the arc, a pair of tuning quadrupoles. For the short straight sections which will be located in the dispersion suppresser regions and near the insertion points other types of correctors will be used like long tuning quadrupoles, skew quadrupoles or eventually skew octupole magnets.

## 2 LAY-OUT OF THE SHORT STRAIGHT SECTIONS FOR LHC

The cold mass of the earlier short straight section designed for the LHC test string consisted of two parts. One, the main twin aperture quadrupole magnet with its stiffening inertia tube, the other with all the correction elements, placed in a separate inertia tube: The two halves were aligned and joined together, both mechanically and electrically to form the cold mass of the prototype straight section.

The new LHC design features now among other modifications a symmetric arrangement of the quadrupoles with respect to the dipole magnets. This implies that the corrector magnets have to be on both sides of the quadrupole. Furthermore, the quadrupoles are powered independently from the dipoles thus reducing the integrated length of the tuning quadrupoles significantly. The inertia tube into which all magnets must be aligned, will no more be made out of two halves but in one single piece. It has to be rigid enough to guaranty the geometrical stiffness under the weight load and in all operating conditions.

The cryostat which has been simplified with respect to earlier versions [4] by the implementation of a separate cryogenic feed line, will be completed on one end by the cryogenic technical service module. The functions of this module are multiple. Each module will house the beam position monitors, the protection diodes of the quadrupole magnets and the cold mass instrumentation capillaries. Every second will contain in addition the cryogenic interconnection and the liquid helium separator. On the opposite end of the short straight section the interconnection is practically identical to those of the standard dipole magnets.

An important feature of the short straight section design is the sectorisation of the insulation vacuum [5]. This implies that the short straight section has a vacuum barrier which in the present design will be mounted every second cell, i.e., every fourth short straight section. This helps in the leak testing during installation and makes short intervention, like the exchange of a diode, possible. It permits in case of a major intervention, like the replacing of a magnet, to warm up one sector only. The liquid helium flow in between cold masses is also sectored by means of pressure plugs placed in the bus-bar connection tubes for every second cell.

0-7803-4376-X/98/$10.00 © 1998 IEEE

## 3 MAIN QUADRUPOLE MAGNETS

The new quadrupole design follows the line of the earlier concept. The main parameters of this twin aperture magnet are summarised in table 1.

**Table 1: LHC Main Quadrupoles Parameters**

| | | |
|---|---|---|
| Nominal temperature | 1.9 | K |
| Nominal gradient | 223 | T/m |
| Margin on load line | 19.7 | % |
| Nominal Current | 11870 | A |
| Magnetic length | 3.10 | m |
| Beam separation distance (cold) | 194.0 | mm |
| Inner coil aperture diameter (warm) | 56 | mm |
| Outer coil diameter | 118.6 | mm |
| Outer yoke diameter | 452 | mm |
| Collar material | Stainless steel | |
| Yoke length including end plates | 3250 | mm |

The super-conducting cable of the quadrupole magnets will be the same as the key-stoned cable used for the outer coil layer in the main dipole magnets. By this it is hoped to achieve savings not only because of standardisation but especially since the unit cable length for a quadrupole coil is considerably shorter than that for the dipoles.

Fig. 1 shows the cross-section of the quadrupolein its cryostat. Since the electromagnetic forces in a quadrupole are significantly lower than in a dipole no contribution of the yoke is needed to pre-stress the coils. This is ensured by the independent stainless steel collars which themselves are centred inside the single piece yoke laminations by longitudinal keys. The cut-off on top or bottom of every second yoke laminations allows to press and key them such that the coil collar units are well fixed and aligned inside the yoke apertures. The centring of the yoke inside the inertia tube is again provided by a series of keys which are blocked from the outside of the tube by a series of bolts. Welded covers over these series of bolts have to make sure that the inertia tube is helium leak tight to an operational maximum pressure of 20 bar and fulfils its function as helium vessel. The upper of the two 60 mm diameter holes in the yoke will house the heat exchanger tube which runs through all elements of one machine cell and where the cooling down to 1.9 K takes place [6]. The lower one will be used for the passage of cables, especially for instrumentation and eventually for corrector magnet wiring.

## 4 CORRECTOR MAGNETS

Each short straight section will have on the end, opposite to the connections, the sextupole- dipole corrector magnets. While the sextupole coils of this combined units will be powered in series to currents up to nominally 500 A the corrector dipole magnets, alternatively either horizontally or vertically deflecting ones, will be powered individually which means that they have to have their current passage between 1.9 K and room temperature in every short straight section. Their maximum operational current will be 32 A. The yoke

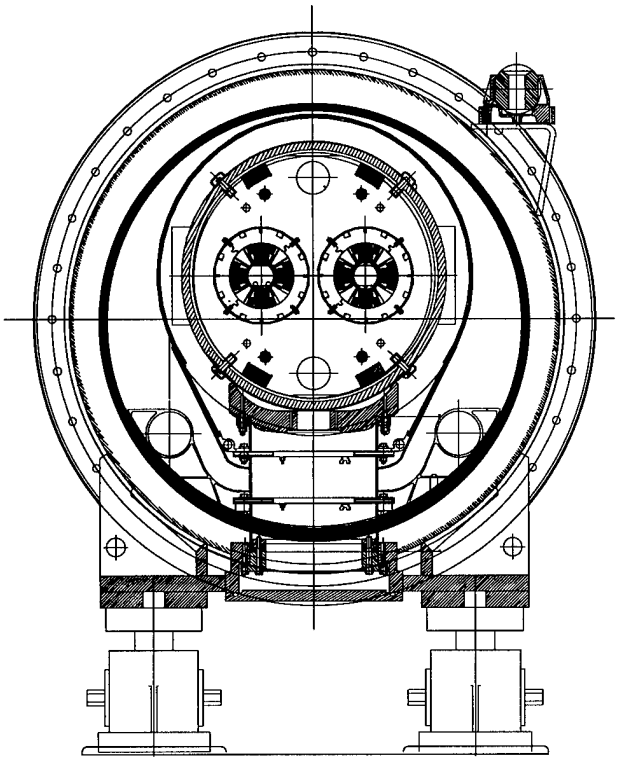


Figure 1 - Cross-section of the LHC lattice quadrupole in its short straight section cryostat

length of these units will be 1.26 m, the sextupole strength is 1500 T/m$^2$ over a magnetic length of 1.10 m the corrector dipole field is 1.5 T over 1.03 m. These coils will be assembled in a common yoke and fixed inside the inertia tube similar to the main quadrupoles.

On the connection side of the quadrupole, most short straight sections will have two octupole corrector magnets of 380 mm overall length, including a magnetic shield around them. Their strength will be $6.7.10^4$ T/m$^3$ over a magnetic length of 320 mm. Their outer diameter will not be more than 117 mm and thus they will be mounted separately and fixed by a pair of plates inside the inertia tube. The nominal current will be 600 A.

The short straight sections near the ends of the arc will have tuning quadrupoles in place of the octupoles. With the same amperage and overall length they will have a larger outer diameter of 170 mm. Their field gradient will be 120 T/m. In some of the short straight sections in the dispersion suppresser region their yoke length will be 1700 mm. Because of their high number and their similitude to the corrector magnets in the dipoles cold masses a semi-automized coil fabrication is envisaged for all corrector magnet coils.

## 5 CRYOSTAT

The short straight section cryostat has been conceived together with the dipole cryostat. With the separated cryo line in the tunnel its cross-section had been simplified considerably. As a variation to the dipole cryostat the sectorisation must be mentioned. This item will have to take not only differences in pressure and

assure leak tightness it must also allow for all the dimensional variations during cool-down and operation. Further, it must be mountable in the short straight section cryostats where needed and interface well with the cryostat, the cold mass, the tubes and the shielding inside the cryostat. Two techniques have been pursued, one with an all steel membrane and one with a composite membrane in collaboration with industry [7].

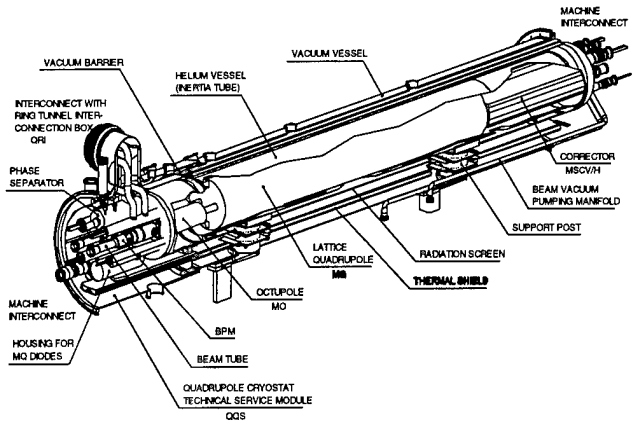



Figure 2 - Perspective view of the cold mass in cryostat together with cryogenic technical service module

Only two cryogenic pipes remain inside the cryostat which are the one for thermalising the thermal shield at 50 K and that for thermalising the upper part of the support posts to 5 - 10 K. One of the two support posts, positioning the cold mass inside the cryostat, will be fixed, the other one will be allowed to slide to compensate thermal contraction. Fig. 2 shows a perspective view of the cold mass in the cryostat.

## 6 CRYOGENIC TECHNICAL SERVICE MODULE

The short straight section is completed by a cryogenic technical service module. This will contain the two beam position monitors attached to their beam screens and bolted to the endplate of the cold mass, the quench protection diodes in their container. Every second module will have its cryogenic jumper connection to the separate cryogenic supply line and a helium phase separator. which provides for all cryogenic but also electrical interconnections. This implies that there will be two major types of these modules.

The magnet to magnet linking must provide the continuity of the currents and helium flow or of the plugging of the latter one where required. In this area will also be placed the interconnections for the auxiliary bus-bars and their leads to the corrector magnets of the short straight section in question. Further, there must be passages of the instrumentation wiring from the cold-mass interior to the capillaries which leads them to outside of the cryostat. All this makes this service module a very complex unit the study of which is not yet finalised.

## 7 CONCLUSIONS

The short straight sections of the LHC are vital units for the operation of the machine. Their complexity is given by the multitude of magnetic and other machine components. The presence of the cryogenic technical service module with its variants and different combinations of function complicates the still ongoing design even further. CERN is however confident to realise these units in the great number of their different versions with the active help of the collaborating laboratories, CEA-Saclay and CNRS in Orsay.

## REFERENCES


[1] K. Henrichsen et al., Cryogenic and mechanical measurements of the first two LHC lattice quadrupole prototypes, Proc. EPAC 94, London, UK, 27 June to 1 June 1994.

[2] A. Bézaguet et al., The LHC test string: first operational experience, Proc. EPAC 96, Sitges, Barcelona, Spain, 10 to 14 June 1996.

[3] R. Perin, Super-conducting magnets for the Large Hadron Collider, Proc. EPS 10, Trends in Physics, Seville, Spain, 3 to 13 Sep. 1996.

[4] W. Cameron et al., Design and construction of a prototype super-fluid helium cryostat for the short straight section of the CERN Large Hadron Collider (LHC), Proc. Int. Cryogenic Engineering Conf. (CEC), Albuquerque, NM, USA, 12 to 16 July 1993.

[5] M. Bona et al., Cryogenic and vacuum sectorisation of the LHC arcs, CERN-LHC-Project Report 60.

[6] V. Benda et al., Conceptual design of the cryogenic system for the Large Hadron Collider (LHC), Proc. EPAC 96, Sitges, Spain, 10 to 14 June 1996.

[7] B. Jenny, P. Rohmig, J.-M. Uriarte, A Composite Vacuum Barrier for the LHC Short Straight Section, Proc. Cryogenic Engineering Conf. (CEC), Columbus-Ohio, USA, 17 to 21 July 1995.

# TOWARDS SERIES MEASUREMENTS OF THE LHC SUPERCONDUCTING DIPOLE MAGNETS

L. Walckiers, Z. Ang, J. Billan, L. Bottura, A. Siemko, P. Sievers, R. Wolf,
CERN, 1211 Geneva 23, Switzerland

*Abstract*

Extensive power tests of the LHC dipole magnets required the development of new techniques to study the quench and training behaviour. Magnetic measurements of short and long model dipoles have allowed to understand and quantify the time dependent behaviour of the field quality during the current flat top needed during beam injection. The experience gained is employed for the design of the measuring tools presently under construction for the series measurements of the LHC dipole magnets. The economically important issue of how many magnets have to be measured in the superconducting state is addressed in view of the field quality required for the performance of the LHC.

## 1 INTRODUCTION

The experience from previous accelerators based on superconducting magnets stresses the difficulty to control the beam during injection and beginning of the acceleration due to time dependent effects of the sextupole component of the field. Furthermore studies of the dynamic aperture of the LHC accelerator [1] pointed to stringent specifications for higher harmonics. The main dipole field is only 0.54 T at injection for a nominal field of 8.3 T at collision energy.

Seven 10 m long twin aperture magnets based on the previous design and more than ten 1 m long models with the present structure were tested in cold conditions. The measured training characteristics and the magnetic measurements performed are analysed to give detailed arguments to specify the extend of the costly cold measurements of the series magnets.

## 2 POWER TESTS

### *2.1 Training of the 1 m long dipole models*

Cold tests of ten 1 m long single and twin aperture models, thoroughly instrumented, allow to classify the training quenches of the magnets in two ranges of behaviour. Their construction is described in [2].

Some magnets show a training (less than 3 quenches) starting below or around the nominal field of 8.3 T and going to about 8.8 T, corresponding to 90 % of the cable limit. All these quenches start in specific weak points of the winding located either in the ends of the coils windings, or in the "splice-layer jump" region (ramp of the inner layer conductor to the outer layer and connection to the outer layer cable). These findings have allowed to improve that area in the last magnets tested.

A second part of the training, starting at the range of 8.8 T has about the same average slope for all magnets built with the nominal structure (Fig. 1). Although the same specific regions of the windings are generally involved, recent tests show that changes in the structure are likely to improve this behaviour: decrease the sensitivity of the cable to local energy deposition [3], lower the average compression of the winding or change the material of the collars. This regular training is again found after a thermal cycle to room temperature.

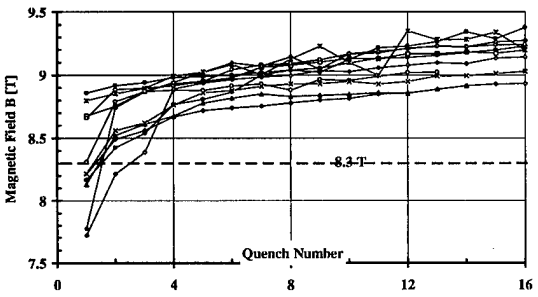



Figure 1: Training curves of the 1 m long model magnets tested.

### *2.2 Defining the power tests for the series*

Voltage taps are the simplest tool to localise where a training quench starts in the winding. Series magnets will however not be equipped with them and even full length prototype magnets to come will have a limited number of voltage taps.

Dedicated 'Quench Antenna' coils help to determine where the training quenches start and to deduce the weak points in the magnets coils. They provide as well some information about the mechanism generating these early quenches [4]. The 15 m long shaft, fitted with modular coils and built for the magnetic measurements will as well serve for quench localisation (see section 4).

Since the first part of the training is of concern for magnets to be installed in the LHC, the first quench of any series magnet will be recorded with fully debugged instrumentation and in condition of temperature and current cycles as near as possible to machine conditions.

The integrity of the superconducting cable is systematically verified by a quench at 4.3 K after the training since its value is confidently related to the limit at superfluid temperature [5]. The RRR (ratio of the

0-7803-4376-X/98 /$10.00 © 1998 IEEE

electrical conductivity of the copper matrix between room and low temperature) is also systematically measured because of its importance for protection of the magnets during the quenches. The sensitivity of the quench level to the current ramp rate is established.

## 3 FIELD QUALITY MEASUREMENTS

### *3.1 Expected field harmonics*

The three following sources of field imperfections can degrade the performances of the beam:

- Geometric: accuracy in the positioning of the coils.
- Decay: amplitude of the decay with time at the injection plateau [6]. The snap-back at the start of the acceleration has the same value but with an opposite sign. The data of table 1 come from the measurements of 6 single aperture 1 m long models measured.
- Ramp: harmonics created by the coupling current between the strands of the superconducting cable for the nominal ramp of 8 T in 20 min. The data are obtained from measurements of 5 apertures of the first generation 10-m long models. They are scaled to the present magnets structure and apply for injection field.

| | Geometric | | Decay | | Ramp | |
|---|---|---|---|---|---|---|
| | σ | Unc. | σ | Unc. | σ | Unc. |
| $a_2$ | 1. | 0.3 | 0.5 | 0.2 | 1. | 0.4 |
| $b_3$ | 0.5 | 0.3 | 0.3 | 0.13 | 0.2 | 0.08 |
| $b_4$ | 0.1 | 0.05 | 0.04 | 0.015 | 0.04 | 0.02 |
| $a_4$ | 0.1 | 0.05 | 0.13 | 0.05 | 0.11 | 0.05 |
| $b_5$ | 0.05 | 0.05 | 0.1 | 0.04 | 0.04 | 0.02 |

Table 1 : Standard deviations (σ) and uncertainties on the averages (Unc.) per octant expected for the LHC dipole magnets. The $b_n$, $a_n$ are the normal and skew harmonics of the field errors relative to the main field at a reference radius of 10 mm, given in units of $10^{-4}$.

Table 1 gives the present estimation of the standard deviation of the harmonics of the field for the LHC main dipoles. The uncertainties of the averages due to possible systematic effects on a production line of magnets are also given. Magnets coming from a given manufacturer and having superconducting cables from the same production line will be assembled in the same octant of the machine. Beam stability calculations are based on the hypothesis that the uncertainties of the average per octant are equal to the expected maximum for a production line.

Values for the averages of the non-allowed harmonics indicated for the ramp and decay effects are probably pessimistic with the lack of statistics. Recent developments to increase and stabilise the interstrand resistance will lead to further improvements [7].

### *3.2 Comparison with tolerances from the beam optics*

The coupling between the vertical and horizontal betatron tunes has to be controlled during the beam acceleration to within 0.003, corresponding to 0.025 unit for the integrated $a_2$. Similarly a specification of a maximum excursion of 2 unit in chromaticity requests a control of the integrated sextupole, $b_3$, to 0.015 unit. The dynamic aperture remains satisfactory if the octants average of both octupoles terms are lower than 0.015 unit and if the control of the integrated decapole with the help of the end correctors is within 0.03 units.

| | Geometric | | Decay | | Ramp | |
|---|---|---|---|---|---|---|
| | Δ/σ | Δ/Unc. | Δ/σ | Δ/Unc. | Δ/σ | Δ/Unc. |
| $a_2$ | 0.03 | 0.08 | 0.05 | | 0.03 | |
| $b_3$ | 0.03 | 0.05 | 0.05 | 0.1 | 0.08 | 0.2 |
| $b_4$ | 0.15 | 0.3 | 0.4 | | 0.4 | |
| $a_4$ | 0.15 | 0.3 | 0.1 | | 0.14 | |
| $b_5$ | 0.6 | 0.6 | 0.3 | 0.5 | 0.8 | 1 |

Table 2 : Tolerances specified for beam stability (Δ) divided by the standard deviations (σ) or uncertainties of the averages (Unc.) per octant.

Table 2 indicates the relative accuracy to which the standard deviation and the average per production line should be measured for the series of the LHC dipole magnets. Measurements of the coupling and chromaticity during the beam acceleration are difficult to realise for a correction in closed loop. Tables to predict the skew quadrupole and the normal sextupole are therefore needed with the accuracy expressed in table 2. These predictions will require to measure all magnets in cold conditions unless the standard deviations of the Decay and Ramp imperfections are found to be smaller than those of Table 1 for the preseries magnets.

Some care will also be needed during the magnets production to ensure that the Decay and Ramp effects do not introduce systematic octupoles that can be detrimental for the dynamic aperture.

### *3.3 Reproducibility needed for the harmonic content*

In addition to the spread and the bias over a series of magnets, the stability with respect to previous or external conditions (current history, quenches, helium bath temperature) was also studied on the existing magnets.

The reproducibility of 0.015 unit for the normal sextupole $b_3$ corresponds to the following variations around injection field: temperature change of the superconductor of 0.04 K or current overshoot in the magnet in the range of 0.1 A. Furthermore the time previously spent at high field or below injection current influences the decay of $b_3$ at injection current within a range of 1 unit. We have measured that these variations are larger for long magnets than for the 1 m long models tested. Therefore prediction laws for magnets from

different manufacturers or wound with cables having different properties will have to be measured with the accuracy quoted above to choose reference magnets.

The correction of the decapole term will however be much easier to control since it varies by less than 0.08 unit, taking into account all of these effects.

## 4 TOOLS FOR THE SERIES MEASUREMENTS

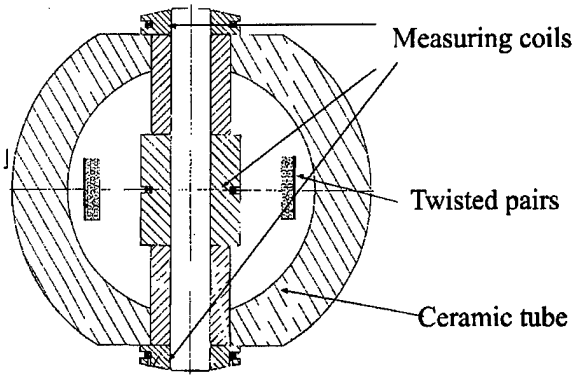



Figure 2 : Cross-section of the harmonic coils for the cold magnetic measurements and quench localisation.

Early it appeared that scanning the pair of 14.2 m long apertures of each dipole piece wise with a single coil would need too much time, in particular the measurement of time dependent behaviour. Based on the experience gained with long and slender ceramic shafts, driving measuring coils, an integral coil is now under construction. It consists of 13 identical modules each 1.26 m long and mechanically assembled into one long shaft spanning the total length of the aperture. Each module consists of a ceramic pipe, providing the necessary rigidity, onto which the tangential measuring coils are mounted (Fig. 2). Between each module a length of 110 mm is required to house the rotating bearings and the cable interconnects. Careful calibration and sorting of the individual coils allow to achieve a rejection of the main harmonic to better than 500 without electronic bucking. Each coil is read out individually. That requires finally 39 micro-pin connectors and strands of twisted pairs, designed and verified that noise picked up during the rotation of the shaft by residual loops of wires is negligible. Each coil within the fully assembled unit will be calibrated with respect to harmonics and orientation via a resistive reference dipole magnet. Using one long shaft in each aperture allows to measure simultaneously within about 10 s the harmonics along the whole magnet, very efficient for the study of dynamic effects and their local and integral behaviour. Moreover, quench detection and localisation is readily provided by these coils.

### *4.1 The inactive lengths along the measuring shaft*

The length not covered by measuring coils has to be chosen as near as possible to the transposition pitch of the cable to avoid errors from the strong longitudinal periodic pattern of the field. 12 transposition pitches will therefore be missing in the measured field corresponding to about 10 % of the effective length of the magnet. The transposition pitch of the LHC cable is expected to stay within 105 to 110 mm. Some residual beating of the periodic pattern will occur with the constant 110 mm of hole length. Estimations based on the measured magnets give a maximum error of 0.03 units for the skew quadrupole component at injection field. The variation of the harmonics along the magnet axis, after averaging the contribution of the periodic pattern, has been measured to be small enough to guarantee an error of less than 1 % on the values expected.

## 5 CONCLUSION

Power tests of the dipole magnets will be needed to prove that the weak points in the coils windings do not lead to quenches below the nominal field of the LHC machine. Sufficient statistics must be accumulated on the dynamic behaviour of the field harmonics before deciding on the amount of LHC dipoles to be tested cold. A prototype 15 m long measuring shaft is presently being assembled to address both of these types of measurements.

## REFERENCES

[1] The Large Hadron Collider - Conceptual Design, CERN/AC/95-05,1995.

[2] N. Andreev et al., 'The 1 m long single aperture dipole test program for LHC', Proc. of 5th European Particle Accelerator Conference, Sitges, June 1996.

[3] A.K. Ghosh et al., 'Minimum quench energies of Rutherford cables and single wires' *IEEE Trans. Of Appl. Sup.*, 7, to appear, 1997.

[4] A. Siemko et al., "Power tests results of the first LHC second generation superconducting single aperture 1 m long dipole models', Proc. of 16th International Cryogenic Engineering Conference, pp. 837-842, Kitakyushu, May 1996, Elsevier Science.

[5] L. Walckiers et al., 'Power tests of single and twin aperture superconducting dipole models for LHC', Proc. of 14th Magnet Technology Conference, Tampere, June 1995.

[6] L. Bottura, L. Walckiers, R. Wolf, 'Field errors decay and snap-back in LHC model dipoles', *IEEE Trans. Of Appl. Sup.*, 7, to appear, 1997.

[7] D. Richter et al., 'DC measurement of electrical contacts between strands in superconducting cables for the LHC magnets, *IEEE Trans. Of Appl. Sup.*, 7, to appear, 1997.

# FORCES ON INTERACTION REGION QUADRUPOLES AND DIPOLES DUE TO A DETECTOR SOLENOID MAGNET *

James J. Welch and Gerald F. Dugan
Wilson Laboratory, Cornell University, Ithaca NY

One feature of today's high energy physics experiments is a detector with a large scale solenoid magnet for measurement of transverse momenta of charged particles [1]-[6]. Another is the demand for very high luminosity. To meet luminosity demands accelerator designers need to put insertion magnets close to the interaction point, even within the detector solenoid field. Such designs have lower chromaticity, smaller peak beta functions, require less aperture and basically allow tighter focussing of the beams. However, the insertion magnets become more difficult and complicated to design since they are so closely coupled with the detector magnetically and mechanically.

Only insertion magnet designs that use superconductors or rare earth permanent magnets are practical within the detector volume. Detector magnetic fields are typically 1.5 T and can overload any steel placed within them. Furthermore, steel within the solenoid field would generate large perturbations of the fields that would be difficult to predict or control accurately due to hysteresis. Permanent magnets tend to have less interaction with the detector solenoid than superconducting magnets. The fringe field of permanent magnets rapidly falls off with radial distance, especially if a large number of segments are used [7]. With superconductors there are typically no special coils to cancel the external fields, (though in principle that would be possible at the cost of substantial radial space and complication), so the problems of interaction with the solenoid are maximal. In this paper we will only discuss the forces on superconducting magnets.

Superconducting magnets are often designed to support large internal Lorentz forces generated by their self-fields. However when immersed in the external field of a solenoid the Lorentz forces can produce large net forces and torques on a magnet as a whole. This leads to problems supporting the magnet, coupling the magnet to the helium vessel, and supporting the cryostat. Support is critical because the beam is particularly sensitive to motions of insertion magnets due to the relatively high gradients and large beta functions in the interaction region.

## 1 DETECTOR SOLENOID FIELD

We will only discuss detector solenoids which have a main component $B_z$ as well as a radial fringe field component $B_r$, but no azimuthal component. Both components can produce substantial Lorentz forces on the accelerator magnet coils. In the body of the magnet coils, where the current is only in the $\pm z$ direction, the solenoid $B_z$ component generates no force — only the radial component does. However both components can contribute to generate forces in the coil ends.

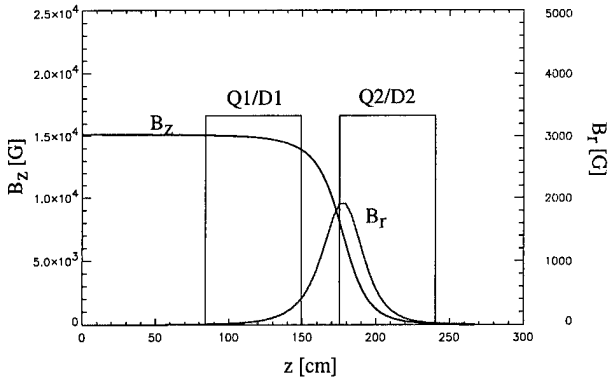



Figure 1: The calculated longitudinal and radial components of the magnetic field of the CLEO solenoid are plotted as a function of the distance from the interaction point, for a constant radii equal to the average coil radius. Superimposed are the locations of the superconducting quadrupole magnets.

As an example, consider the CLEO detector solenoid. The calculated $B_z$ and $B_r$ components are shown in Figure 1. Also shown in the plot are outlines of insertion quadrupoles and concentrically wound dipoles which are being built for the CESR phase III upgrade [2]. The forward quadrupole magnet Q1 is entirely immersed in an almost uniform solenoid field with only a small radial component near the outermost end. The second magnet coil Q2 starts where the radial component of the solenoid field is near maximum and $B_z$ has dropped to about one-half its central value.

## 2 SYMMETRIES

The symmetries of external electromagnetic forces acting on dipole and quadrupole coils are shown in Figures 2—5. Forces due to the $B_z$ and $B_r$ components are separately plotted for clarity. One force vector is shown for the end of each coil and one is shown for each magnet straight section. Only near-side forces are shown in each view.

*Dipole Symmetries*

In Figure 2 we can see that from the longitudinal component of the solenoid field a dipole coil experience forces only at the coils ends. The resulting torque can be large since the end forces are separated by the entire length of the magnet. There will also be a net force to the extent

* Work supported by the National Science Foundation

0-7803-4376-X/98/$10.00 © 1998 IEEE

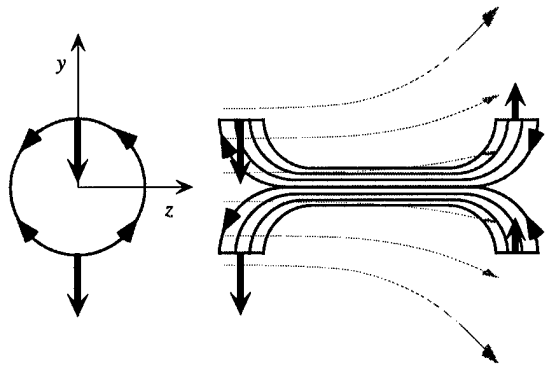



Figure 2: Forces acting on a dipole magnet due only to the $B_z$ component of the solenoid field

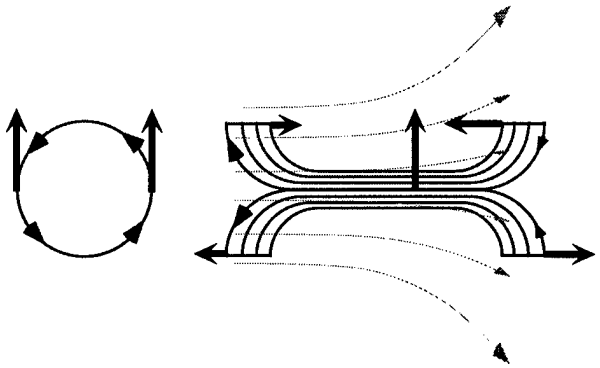


Figure 3: Forces acting on a dipole magnet due only to the $B_r$ component of the solenoid field

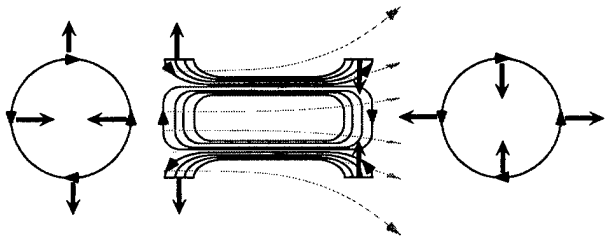


Figure 4: Forces acting on a quadrupole magnet due only to the $B_z$ component of the solenoid field

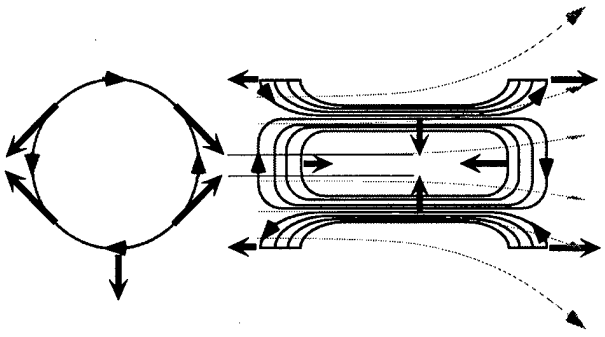


Figure 5: Forces acting on a quadrupole magnet due only to the $B_r$ component of the solenoid field

that $B_z$ is different at the two ends. The direction of the force is either parallel or anti-parallel to the field the dipole generates.

In Figure 3 the dipole coils shown produce a dipole field downward just as in Figure 2. One can see that $B_r$ produces an upward force in the body which is centered at a location determined by $\int zB_r dz$. This force is only partially canceled by the forces generated in the ends by the $B_z$ component shown in Figure 2. The $B_r$ component will also generate torques in the coil ends which partially cancel each other to the extent that $B_r$ is the same at the two ends.

*Quadrupole Symmetries*

Perfectly aligned quadrupole coils experience no net forces or torques due to $B_z$ or $B_r$. This is easily seen in Figure 4 and Figure 5. Generally the force on each coil part is canceled by an equal and opposite force on the corresponding part of the opposing coil.

Even though there are no net forces or torques, the forces can be important to the magnet design. The net solenoid generated force on the ends may be $\sim 1/3$ as much as the quadrupole self-field generated forces. [1] But the symmetry of the solenoid generated force on the ends is much more unfavorable. The solenoid force tends to crush the end of the coil while the internally generated forces attempt the much more difficult operation forcing the coils into a square shape. Adequate collar stiffness has to be provided to resists this crushing force.

*Misaligned Magnets*

A substantial force can be generated for a quadrupole asymmetrically placed with respect to nearby detector steel (not shown). For example the Q2 magnet in Figure 1 is surrounded by the CLEO solenoid yoke steel. Two dimensional ANSYS calculations indicate that for a 3 mm offset of the quadrupole center with respect to the hole in the pole, an 1100 lb force is generated which tries to pull the magnet toward the steel. This force could be in any transverse direction and would be proportional to the current in the quadrupole coils. Similarly large forces can be generated by asymmetrically adding large holes to the steel yoke even if the quadrupole is perfectly positioned.

If the solenoid field is tilted with respect to the quadrupole or dipole axes, or vice versa, many more forces and torques are introduced.

## 3 CALCULATION OF FORCES

Direct 3D integration of the Lorentz force per unit volume over the coil geometry can provide values for the total forces and torques on elements of the coils. Forces due to $B_r$ are best obtained by this method, though the integration over the coil end geometry can be difficult. However,

[1] Typical solenoid fields are 1.5 T and typical quadrupole self-field is $\sim 5$ T.

within the approximation of $\vec{B} = B_0\vec{e}_z$ where $B_0$ is constant there are several simple analytic methods which can be quite accurate in determining forces on the coil ends.

We start by calculating the forces on a single turn. In this case there is no force on the wire in the straight portion of the coil because the current and the solenoid field are in the same direction — all the forces are generated in the ends. The force on a infinitesimal length of a wire $d\vec{s}$, with current $I$ in the uniform field is:

$$d\vec{F} = IB_0 d\vec{s} \times \vec{e}_z \quad (1)$$

$$= IB_0(-dx\vec{e}_y + dy\vec{e}_x) \quad (2)$$

The total force on the coil end is obtained by integrating $d\vec{F}$ along the wire around the end. The integral is trivial and the result is simply that the net force on the single wire is $\vec{F} = IB_0(-\Delta x\vec{e}_y + \Delta y\vec{e}_x)$, where $\Delta x(\Delta y)$ is the net change in the $x(y)$ coordinate of the wire. The actual path the wire takes does not matter, only the net change in position contributes to the total force on the end. Applying this result to the coil as a whole we have that the total force on a coil end is:

$$\vec{F} = \sum_{wires} IB_0(-\Delta x\vec{e}_y + \Delta y\vec{e}_x) \quad (3)$$

So the problem remains only to add up the contributions from all the wires. This is best done with a set of $x, y$ positions of all the wires. Such data can be put into a spreadsheet and the resulting force immediately calculated via equation 3.

Even more convenient would be a simple analytic expression. We will derive four. The first two are for a quadrupole idealized as a $\cos 2\theta$ current sheet or as a 30° sector current sheet. (To better represent the real coil the radial dependence should be taken into account.) In the former case the density of turns per unit angle $n(\theta) = 2N\cos 2\theta$, where $N$ is the number of turns per coil. We will express $\Delta x$ and $\Delta y$ in terms of the radius of the current sheet $R$ and $\theta$. Assuming the coil is wound symmetrically about a central post, $\Delta x = R(\cos(\frac{\pi}{2} - \theta) - \cos\theta)$ and $\Delta y = -\Delta x$. The force on the coil may now be obtained by integrating over $\theta$ from 0 to $\pi/4$.

$$\vec{F}_{coil\ end} = -\frac{2}{3}NIB_0R(\vec{e}_y + \vec{e}_x) \quad (4)$$

$$F_{radial,\ coil\ end} = \frac{2\sqrt{2}}{3}NIB_0R \quad (5)$$

which is the desired result for the $\cos 2\theta$ quadrupole.

For example, a quadrupole with $NI = 450,000$ ampere turns, with a coil radius of $R = .092$ m in a solenoid of $B_0 = 1.5$ T, the radial force on each pole is 58,548 N or 13,130 lbs.

For 30 degree sector idealization of a quadrupole the density of turns is simply a constant: $n(\theta) = 6N/\pi$. The expressions $\Delta x$ and $\Delta y$ are the same so the force integral is just

$$\vec{F}_{coil\ end} = -\frac{B_0NIR3(\sqrt{3}-1)}{\pi}(\vec{e}_y + \vec{e}_x) \quad (6)$$

$$F_{radial,\ coil\ end} = -\frac{3\sqrt{2}(\sqrt{3}-1)}{\pi}NIB_0R \quad (7)$$

The force is $\frac{9}{2\pi}(\sqrt{3}-1) = 1.05$ times larger than for the $\cos 2\theta$ approximation.

Expressions for the force on dipole coils can be derived in exactly the same manner using equation 3 and current distributions for a dipole. For a $\sin\theta$ dipole coil idealization we have that $n(\theta) = N\sin\theta$. For a symmetrically wound dipole producing a horizontal field, $\Delta x = 0$ and $\Delta y = 2R\sin\theta$. Replacing the summation with an integral and integrating yields

$$\vec{F}_{dipole\ coil} = B_0I\int_0^{\pi/2} N\sin\theta 2R\sin\theta\vec{e}_x \quad (8)$$

$$= \frac{\pi}{2}B_0RNI\vec{e}_x \quad (9)$$

For the 60 degree sector approximation for a dipole we have $n(\theta) = 3N/\pi$. This distribution yields

$$\vec{F}_{dipole\ coil} = \frac{3\sqrt{3}}{\pi}B_0RNI\vec{e}_x \quad (10)$$

For illustration, consider a dipole at radius 0.144 m and with $NI = 28,400$ ampere turns, in a uniform solenoid field of 1.5 T. The $\sin\theta$ idealization yields a horizontal force per coil end of 9636 N or 2161 lbs, for total force on the magnet end of 4,322 lbs. The 60 degrees sector approximation result is again only about 5% higher.

## 4 REFERENCES


[1] J.J.Welch, G.F. Dugan, E. Nordberg, D. Rice, Cornell University, *The Superconducting Interaction Region Magnet System for the CESR Phase III Upgrade*, these proceedings (PAC97)

[2] D.L. Rubin, *CESR Status and Plans*, Proc. 1995 Particle Accelerator Conference, (PAC95), vol. 1, pp 481f, http://www.lns.cornell.edu/public/CBN/1995/cbn95-8.ps

[3] T.M. Taylor, *Technological Aspects of the LEP Low-Beta Insertions*, IEEE Trans on Nucl. Sci. Vol NS-32, No. 5, October 1985

[4] W.W. Ash, et. al., *Superconducting Final Focus for the SLC Linear Collider*, Proc. 14th Int. Cryogenic Engineering Conf., June 1992

[5] K. Tsuchiya, T.M. Kobayashi, T. Haruyama, Y. Ajima, Y. Doi, KEK, *Superconducting Magnets in the Interaction Region of the KEK B-Factory*, proc. 13th Intl. Conf. Magnet Tech., Victoria Canada, Sept 1993

[6] C.E. Taylor, S. Caspi, and N. Saho, *A Final-Focus Magnet for PEP-II*, LBL, report LBL-35421, proc. Applied Superconductivity Conference, Boston MA, October 1994.

[7] K. Halbach, *Design of Permanent Multipole Magnets with Oriented Rare Earth Cobalt Material*, Nucl. Instr. and Methods, vol 169, pp 1, (1980)

# THE SUPERCONDUCTING INTERACTION REGION MAGNET SYSTEM FOR THE CESR PHASE III UPGRADE *

James J. Welch, Gerald F. Dugan, Emery Nordberg, and David Rice,
Wilson Laboratory, Cornell University, Ithaca NY

## 1 INTRODUCTION

In 1998 CESR and the CLEO detector will commence another major upgrade to bring their performance up to B factory levels. New interaction region (IR) insertion magnets were designed to allow the highest possible luminosity from an equal energy, crossing angle, bunch train configuration of CESR [1][2]. With the new magnets the IR limited luminosity is expected to be at least $3 \times 10^{34}\ cm^{-2}s^{-1}$ — well above the phase III luminosity goals of $1 - 3 \times 10^{33}\ cm^{-2}s^{-1}$. The new magnets will have the focussing capability of running with smaller $\beta_y^*$, crossing angles large enough to accommodate beams from two separate rings, or even round beams — ideas which conceivably could take CESR into the $10^{34}$ range [3][4].

Compared with previous IR magnets for CESR, the new superconducting magnets will have higher gradients, larger apertures and shorter focal lengths. The high gradients and short focal lengths allow the magnets to be placed closer to the interaction point (IP) at near optimal locations, largely mitigating the effects of long-range beam-beam interactions. The close-in location also improves the optical quality of the lattice which could improve the tune shift limit. Increased physical aperture provides more room for larger crossing angles which allows for better beam separation and higher long range beam-beam current limits. More aperture also makes room for carefully chosen orbit offsets which can reduce detector backgrounds thereby improving the quality of the data, lengthening the lifetime of the detector and increasing the data taking time by making tuning faster.

The new magnets will have some unusual capabilities such as nested skew and dipole coils for coupling and orbit correction, and a cryostat positioning system which can adjust the position of the magnets during operation. So we expect to see increases to the data taking time due to the higher functionality: energy changes, coupling correction, magnet alignment and positioning, and beam steering will be far easier and faster. However, the intimate magnetic and mechanical coupling with CLEO solenoid has caused design complications as well.

## 2 IR LUMINOSITY OPTIMIZATION

Generally luminosity can be increased by raising the stored beam current and the most straightforward way to do this is to increase the number of bunches in each beam. However as more and more bunches are stored the long range beam-beam interaction (LRBBI) eventually reduces the beam lifetime and effectively limits the current. In a crossing angle configuration, the crossing angle at the IP generates orbit separation at the nearby crossing points where the beams pass by each other but do not actually collide. The bigger the angle the larger the separation and the higher the long range beam-beam current limit. Phenomenological models based on a series of measurements on CESR [6] indicate that beta functions and beam separations at the nearby crossing points ought to be kept to values similar to those in the arcs, otherwise they become the dominant source of LRBBI and limit the current in the machine. The minimum feasible bunch spacing, (14 ns, set by the relative frequencies of the synchrotron injector and the CESR storage ring [5]), determines the first crossing point to be only 2.1 m from the IP. Thus the optimum IR optics design should have an overall focal length in both planes of about 2.1 m or less, so the magnet design was driven toward very short high gradient magnets, with large aperture, located as close to the IP as possible.

The long range beam-beam interaction, together with countless magnet engineering, detector mechanical and background constraints, were simultaneously optimized for maximum luminosity [7]. The optimization program indicated that for our application superconducting magnets (SC) have a large advantage over permanent magnets (PM) in that they have the best combination of high gradient and large aperture. Nevertheless, because PM's can be placed closer to the IP than SC magnets (SC magnets need radial and axial space for thermal insulation) it was advantageous to also use short, 24 cm long, vertically focussing PM's starting 337 mm from the IP [8].

The bulk of the focussing starts at 842 mm with a 650 mm long vertically focussing SC quadrupole labeled Q1 (See Figure 1). This magnet lies completely within the 1.5 T solenoid field of CLEO detector. Very close to Q1 is Q2, a horizontally focussing quadrupole mechanically identical to Q1 and situated in the fringe field of CLEO solenoid. The resulting beam optics has beta functions that never get larger than 80 m, even for $\beta_y^*$ of 1 cm. (See Figure 2). The worst crossing point is the first, at 2.1 m from the IP, where we have $\beta_y = 24$ m and $\beta_x = 34$ m — comparable with typical arc values. At other IR crossing points the beta functions are less. Thus the LRBBI in the IR is largely mitigated.

## 3 MAGNET DESIGN AND SPECIFICATIONS

To a great extent the design and specifications of the quadrupole coils were based on the LEP interaction region quadrupoles recently installed as part of the energy

* Work supported by the National Science Foundation

0-7803-4376-X/98/$10.00 © 1998 IEEE

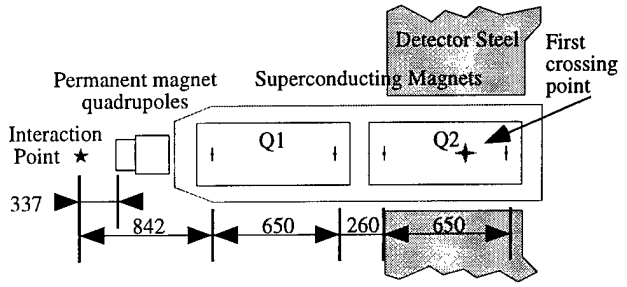



Figure 1: Schematic showing outlines of superconducting IR magnets and their proximity to the IP.

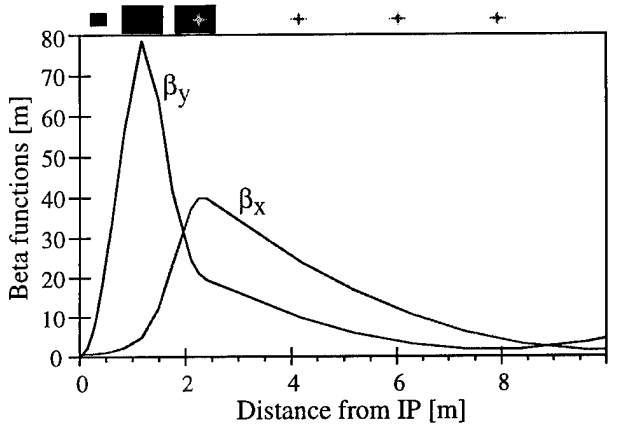



Figure 2: Beta functions for IR limited luminosity. Crossing points and magnet positions are shown at the top. $\beta_y^*$ is 1 cm.

upgrade to LEP 200 [11]. Considerable effort was made to avoid taxing any engineering requirements, such as conductor position tolerance, peak field, or current margin; so that relatively little R&D would be needed. Likewise, Q1 and Q2 were specified to be identical to reduce the design and tooling time, although a smaller aperture would have sufficed for Q1. General magnet parameters are given in Table 1.

We required a field quality of $< 5 \times 10^{-4}$, for all harmonics, at 50 mm radius. This was based on dynamic aperture considerations. Since the beams are on separated orbits through the quadrupoles, and the lattice functions change significantly along the magnet's length, the magnet has been designed to satisfy the field quality requirement in both the ends and body separately; that is, there is no end-body cancellation of unwanted harmonics. The specified level of field homogeneity provides a dynamic aperture greater than the physical aperture (with the pretzel on) in collision optics, with $\beta_y^* = 1$ cm.

The quadrupole's design current margin (along the load line) has been specified to be at least 30% above short-sample, under worst-case conditions as described above (peak field 6.3 T). Since there is neither the time nor resources available for a great deal of development effort in prototyping this magnet, a relatively generous design margin has been required. The magnets are required to reach the design field gradient, possibly with some training: they are required not to need retraining after thermal cycling.

| | | |
|---|---|---|
| **Cryostat** | | |
| ID Warm Bore | [mm] | 145 |
| OD Cryostat | [mm] | 500 |
| **Main Quadrupoles** | | |
| Gradient Maximum | [T/m] | 48.4 |
| Gradient Operating Q1/Q2 | [T/m] | 44.0/27.6 |
| **Skew Quadrupoles** | | |
| Gradient Maximum | [T/m] | ±4.8 |
| **Correction Dipoles** | | |
| Field Maximum | [T] | ±0.13 |

Table 1: General specifications for the various magnet coils at nominal rotation (not 4.5 degree, see text).

The maximum vertical correction dipole field of 0.13 T is specified to allow some tolerance for vertical quadrupole alignment errors. Such a field can correct for up to 3 mm of vertical positioning error. Horizontal positioning error is less critical and can be handled by warm correction dipoles outside the interaction region as well as by the magnet positioning system.

*Coupling Compensation*

The CLEO detector solenoid couples the horizontal and vertical beam trajectories. To produce a flat beam at the IP, and to avoid a family of coupling resonances, the coupling must be compensated before the beams collide. This is done by a combination of variable skew quadrupole coils concentrically wound around the main quadrupoles, a fixed rotation angle of 4.5 degrees of all magnetic elements including the main quadrupole, and warm sqew quadrupoles located just outside the IR. This scheme has sufficient flexibility to allow decoupling even with round beam optics [1].

*Round Beam Limitations*

As designed the IR magnets will accommodate round beam optics with $\beta^*$ of 3 cm. An additional electromagnet would be located just outside the CLEO yoke, and the relative sign of the focussing of the permanent magnet versus the SC magnets would change. The round beam apertures are actually less restrictive than than for flat because they do not include a crossing angle.

*CLEO Interaction*

The stray fields from the quadrupoles and other coils significantly add to the CLEO detector solenoid field and create regions of reduced uniformity which must be taken into account when tracking. [9]

[1]For round beam optics, the beams are decoupled at the IP but the eigen-planes are not exactly horizontal and vertical.

The CLEO solenoid field causes large forces and torques on the various coils. It tends to crush the ends of the quadrupoles (effectively with 26,000 lbs of clamping force) and put large torques on the dipole coils (nearly 10,000 ft-lbs). Because one end of one dipole is shielded from the solenoid, it experiences a net horizontal force of over 4000 lbs. A 3 mm misalignment of the quadrupole within the steel yoke causes a 1100 lbs force of attraction toward the steel [10]. These forces are larger than the weight of the magnets and cryostat. The torques and net forces must be borne by the cryostat, rails, and support pylon with very little overall distortion.

*Support and Positioning System*

Because of the high gradients, small misalignments of the quadrupoles can cause very large and uncorrectable closed orbit distortions. To be able to adequately correct the orbit using warm corrector magnets outside the IR we will need to have the quadrupole magnetic centers within about 0.1 mm vertically and 0.5 mm horizontally of the design axis. The tolerance on run-to-run stability needs to be an order of magnitude tighter. Vibration amplitudes should be less than $\sim 1$ $\mu$m. For this reason a beam-based positioning system was designed which can precisely realign the quadrupoles while beam is stored. This system is somewhat redundant with the set of dipole coils. However, the dipole coils only provide correction for vertical offsets, and are thought to be somewhat risky at this time because of the large torques and forces they cause through their interaction with the CLEO solenoid. The dipole coils can be used to effectively align the magnetic and mechanical centers if needed. Also the dipoles have more effective range than the positioning system.

The cryostat will be kinematically mounted on a set of eccentric cams. Stepper motors control the angle of the cams and allow smooth ($\sim 5$ $\mu m$ resolution) independent positioning of the center of eac magnet over a range of roughly 1 mm in all directions. The cams are held by bimetallic rails attached to a thick steel pylon which is suspended from CLEO detector steel. The rails are made of 316L stainless welded to magnet iron so as not to perturb the detector solenoid field. The CLEO pole-end has a cutout corresponding to the pylon giving it a keyhole shape. In this manner good access to the detector electronics can be provided by pulling back the pole-end without having to disassemble the superconducting magnets.

*Cryogenic Design*

A rigidly attached current leads box will be located right above the main part of the cryostat just outside the CLEO detector. The warm to cold transition will be vertical which considerably simplifies a bath cooled cryogenic design. It is expected that the dominant liquification load will be from the 12 power leads for each cryostat. The overall specified cooling limit is a linear combination of 60 W for gas returned cold and 0.66 g/s liquification; was set primarily by the available refrigeration power at Cornell. Roughly 1200 W of refrigeration will be available for the superconducting RF systems, the CLEO solenoid, and the IR quadrupoles; the quadrupoles are allotted 10% of this capacity.

Quench onset of the magnet is expected to be determined by the peak field in the quadrupole coil. The peak field due to the quadrupole current (alone) occurs in the coils ends. In addition to the quadrupole's field, the skew quadrupole, correction dipole, and especially the CLEO solenoid fields must also be considered. Quench protection will be passive as large peak quench temperatures are not anticipated.

## 4 ACKNOWLEDGMENTS

The authors wish to thank the generous help and guidance we received from A. Ijspeert and T. Taylor, both of CERN.

## 5 REFERENCES

[1] *The CESR/CLEO Upgrade Project*, CESR and CLEO staff, report of the Laboratory of Nuclear Studies, Cornell University, CLNS 93/1265, (1993)

[2] D.L. Rubin, *CESR Status and Plans*, Proc. 1995 Particle Accelerator Conference, (PAC95), vol. 1, pp 481f, http://www.lns.cornell.edu/public/CBN/1995/cbn95-8.ps

[3] D.L. Rubin, G.F. Dugan, A. Mikhailichenko, J. Rogers, *Dual Aperture High Luminosity Collider at Cornell* these proceedings (PAC97)

[4] G.F. Dugan, J.R. Rogers, *Low Field Magnets with High Temperature Superconductors for an Upgrade of CESR*, these proceedings (PAC97)

[5] M. Billing, *Thoughts on Injection into CESR, Configured with a Different Harmonic Number*, report of the Laboratory of Nuclear Studies, Cornell University, CON 90-15, (1990)

[6] A.B. Temnykh, J.J. Welch, D.H. Rice, *The Long Range Beam-Beam Interaction at CESR — Experiments, Simulation and Phenomenology*, Proc. 1993 Particle Accelerator Conference, (PAC93), vol 3, pp 2007f.

[7] James J. Welch, *The Interaction Region Optimization for CESR Phase III*, report of the Laboratory of Nuclear Studies, Cornell University, CBN 95-18, (1995), http://www.lns.cornell.edu/public/CBN/1995/

[8] W. Lou, D. Hartill, D. Rice, D. Rubin, J. Welch, *Permanent Magnet Quadrupoles for CESR Phase-III Upgrade*, these proceedings (PAC97)

[9] G.F. Dugan and J.J. Welch, *Stray Fields in CLEO from the Phase III Superconducting Quadrupoles*, CBN 96-4, http://www.lns.cornell.edu/public/CBN/1996/CBN96-4/cbn96-4.ps

[10] J.J. Welch, G.F. Dugan, *Forces on Interaction Region Quadrupoles and Dipoles to a Detector Solenoid Magnet*, these proceedings (PAC97)

[11] M. Begg *Tesla Engineering*, A. Ijspeert, T.M. Taylor, *CERN, Construction and Test of Superconducting Quadrupoles for the LEP200 Low-Beta Insertions*, EPAC'94, London (1994) CERN AT/94-27 (MA), LEP2 NOTE 94-14

# CONFIGURATION OF THE PROPOSED DIAMOND SUPERCONDUCTING DIPOLE MAGNET

N. Marks, J.A. Clarke, CLRC, Daresbury Laboratory
and E. Baynham, R. Coombs, CLRC, Rutherford Appleton Laboratory.

*Abstract*

Whilst the majority of the dipole magnets in the proposed UK synchrotron source DIAMOND will be of conventional design, the option of including a small number of superconducting magnets, to provide hard radiation, is currently under consideration. The required field strength of 4.35 T is modest, but the large horizontal aperture and the short magnetic length place unusual demands on the design. To meet these, a number of possible configurations have been examined. These include a straight cylindrical arrangement, with cosine theta coil distribution and cold iron, and a rectangular coil configuration, with warm iron. The reported work is not a full design exercise, but rather a preliminary investigation to identify the most suitable configuration and for use in a more detailed study in the future.

## 1 SPECIFICATION OF THE S.C. DIPOLES

It is common for synchrotron sources to make use of superconducting technology for wavelength shifting wigglers; now a number of recent studies for new sources have also explored the use of superconducting dipoles as bending magnets at a small number of lattice positions. These magnets will produce s.r. beams with higher critical energy than the conventional bending magnets, with the minimum expenditure in r.f. power.

### *1.1 The DIAMOND requirements*

A feasibility exercise for the proposed new U.K. source, DIAMOND, is nearing completion. This includes the possibility of replacing at least two of the 32 dipole benders by superconducting magnets. These would have the same deflection as the conventional dipoles but, with a much higher field, would be physically much shorter.

The problems associated with the design of the dipole are demonstrated by the parameters in Table 1. The field strength of 4.35T determines the very short magnetic length of 450mm. In the horizontal plane, space is required radially outside the standard 'beam stay clear' region, both to allow the full radiation fan from the s.c. magnet to emerge and also to house the absorber which receives the radiation from the up-stream dipole. This gives an asymmetrical horizontal aperture which is significantly greater than the vertical aperture and appreciable compared to the magnetic length.

| | | |
|---|---|---|
| Machine energy | 3.0 | GeV |
| Total number of dipoles | 32 | |
| Number of s.c. dipoles | at least 2 | |
| Field in s.c. dipole | 4.35 | T |
| Magnetic length | 450 | mm |
| Field homogeneity | $\pm 2 \times 10^{-4}$ | |
| Horizontal good field | $\pm 20$ | mm |
| Vacuum vessel type | warm bore | |
| Vertical aperture | $\pm 20$ | mm |
| Radial outer aperture | 75 | mm |
| Radial inner aperture | 31 | mm |
| Magnet sagitta | 11 | mm |

Table 1: Parameters of the DIAMOND superconducting dipoles.

### *1.2 Possible Configurations*

The standard superconducting dipole in high energy accelerators has a cylindrical coil geometry located close to a cold iron yoke; the cosine theta distribution of the conductors then provides a high quality dipole field. This arrangement is usually associated with magnets having lengths one to two orders of magnitudes greater than their aperture, so that end effects are negligible. Whilst the above geometry does not readily match this arrangement, the cylindrical configuration represents the 'classical' design, with well understood magnetic and mechanical behaviour. The cylindrical design was therefore regarded as a possible option and was investigated by the Rutherford-Appleton Laboratory team. At Daresbury Laboratory, an alternative solution, using rectangular coils in an approximate Helmholtz configuration, with warm iron, was investigated.

## 2 THE CYLINDRICAL MAGNET SOLUTION

### *2.1 Geometry*

The layout developed to meet the geometric constraints used a fully symmetrical cylindrical design for the warm bore, cryostat, coil and the cold steel yoke; the arrangement therefore gave a vertical aperture in the beam tube that was significantly larger than the specified minimum value of $\pm$ 20mm. The geometric parameters of this magnet are given in Table 2.

0-7803-4376-X/98/$10.00 © 1998 IEEE

| | | |
|---|---|---|
| Warm bore radius | 75 | mm |
| Coil inner radius | 95 | mm |
| Iron cylinder inner radius | 155 | mm |
| Iron cylinder outer radius | 355 | mm |
| Cryostat outer radius | 500 | mm |

Table 2: Cylindrical magnet geometric parameters

*2.2 Adjustments to obtain an acceptable field integral.*

The machine requirements given in section 1.1 dictate a winding aperture which is large compared to the good field region. Field quality at the beam will therefore be insensitive to high order harmonics produced by the coil. A simple 60° winding will eliminate sextupole errors in two dimensions and this was taken as the starting point for the design. The field quality of this arrangement was checked in two dimensions using the code, OPERA 2D; as expected, field which met the quality criteria was obtained. However, three dimensional non-linear modelling indicated that the end fields had a large negative sextupole component, which contributed strongly to the integrated field. These end effects were therefore balanced by introducing positive sextupole into the central section. It was found that by terminating the conductor at 45°, good integrated field was obtained through the magnet. Fig 1 shows the cross section through the magnet with this geometry, whilst Fig 2 presents an orthographic view of the complete magnet, showing the saddle arrangements at the ends of the coils.

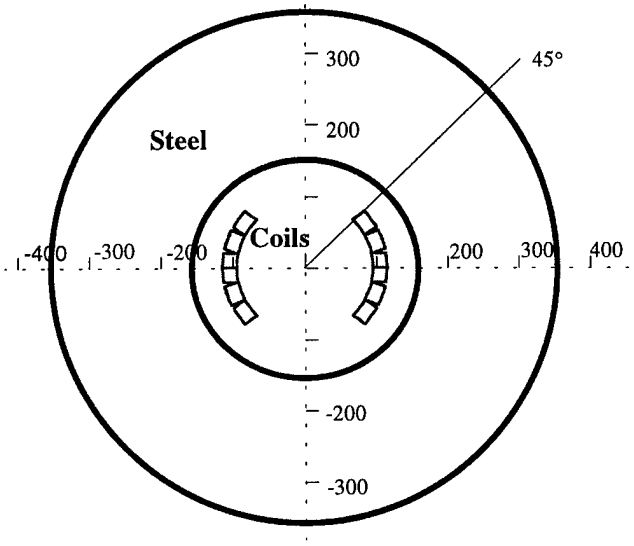



Fig: 1 Cross section through cylindrical design magnet showing coil and iron radial distribution.

The resulting field quality is presented in Fig 3 as a plot of integrated field through the magnet as a function of horizontal position. It can be seen that the integrated field is close to specification, with an error of +0.06% at 20mm. Additional optimisation to the coil configuration is expected to result in further improvements.

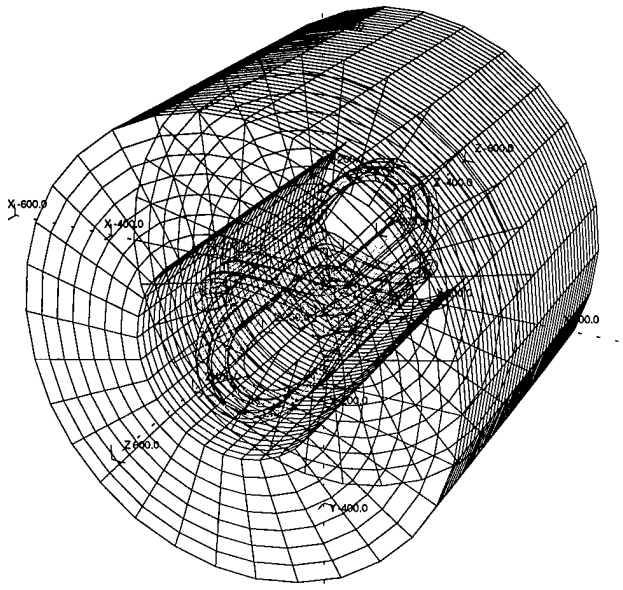


Fig: 2 Orthographic projection showing cylindrical magnet coil and iron geometry.

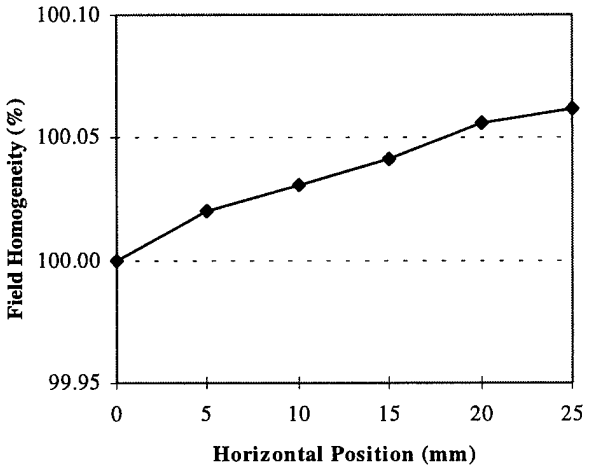



Fig: 3 Homogeneity of integrated field through the cylindrical magnet design as a function of horizontal position.

## 3 THE HELMHOLTZ COIL SOLUTION

This configuration is based on the 'classical' Helmholtz coil, with steel added to provide a flux return path. The central warm bore is of rectangular or elliptical cross section, with the two quasi-rectangular coils located in the cryostat and supported above and below the beam. The outer face of the cryostat is cylindrical and is surrounded by a substantial warm iron cylindrical yoke, to enhance the central field and minimise leakage.

*3.1 Optimisation of coil geometry*

It is known that, in the absence of iron, the 'classical' Helmholtz configuration gives good quality field on axis. However, the steel yoke and the curved corners at the coil ends distort the field and adjustments to the coil geometry are required to regain this quality. The arrangement shown in Fig 4 was used to model the magnetic behaviour in three dimensions, using the code OPERA 3D, and the radial coil position was adjusted to improve the integrated field distribution through the magnet. Table 3 gives the dimensions of the basic magnet geometry together with the coil positions that provided a closest match to the specification.

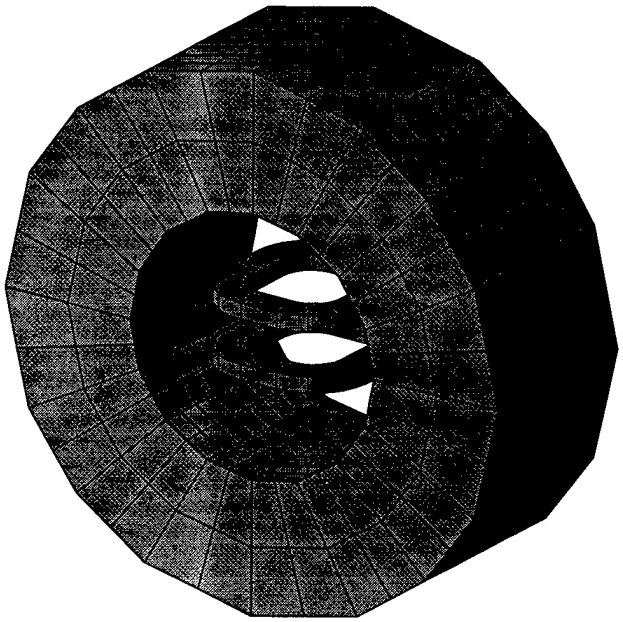


Fig: 4 Orthographic projection showing Helmholtz configuration magnet in three dimensions.

| | | |
|---|---|---|
| Warm bore width | +75, -31 | mm |
| Warm bore height | ± 20 | mm |
| Coil centre horiz. position | 170 | mm |
| Coil centre vert. position | 82 | mm |
| Coil width | 80 | mm |
| Coil height | 44 | mm |
| Coil current density | 250 | $A/mm^2$ |
| Cryostat outer radius | 350 | mm |
| Steel inner radius | 355 | mm |
| Steel outer radius | 720 | mm |

Table 3: Helmholtz configuration magnet parameters.

The homogeneity of integrated field through the magnet is shown in Fig 5. This rises to 100.02%, before falling to 99.97% at the edge of the aperture. It was also found that with 4.35 T at the beam, the cylindrical yoke geometry resulted in a maximum flux density in the steel of the order of 1.6 T; the magnet was therefore very linear both in amplitude and field distribution.

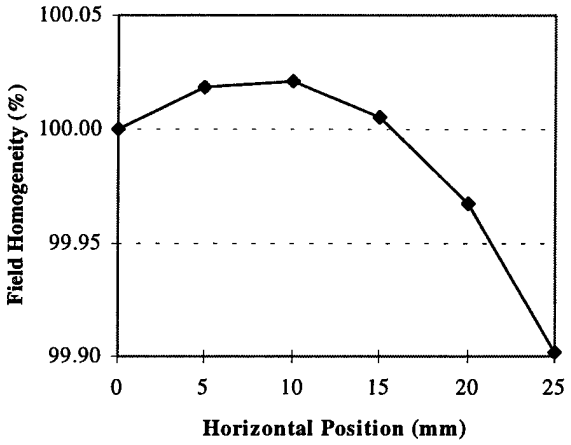



Fig: 5 Homogeneity of integrated field through the Helmholtz configuration magnet as a function of horizontal position.

## 4 CONCLUSION

The features of the two different arrangements are contrasted in Table 4. As the cylindrical arrangement is close to a well proven arrangement, there is confidence that a full design would result in an efficient, economic design. However, the alternative configuration, with its smaller cryostat, presents some advantages, whilst also presenting difficulties. It has therefore been decided to pursue the Helmholtz design further, to determine whether this will result in a cheaper and more flexible design, whilst holding the classical solution in reserve.

| Feature of mag | Cylindrical magnet | Helmholtz magnet |
|---|---|---|
| Warm bore | Circular, symmetrical | Rectangular or elliptical - asymmetrical if required |
| Cryostat outer radius | Large - 500 mm | Smaller - 350 mm |
| Shape in axial direction | Straight | Could be curved |
| Steel | Cold - close to coil | Warm- remote from coil |
| Cold mass | Large - includes steel | Small - excludes steel |
| Asymmetrical forces, coil/steel | Directly reacted | Reacted through cryostat walls. |

Table 4: Design features of the alternative configurations.

# QUENCH PROTECTION OF SC QUADRUPOLE MAGNETS

S. Feher, R. Bossert, J. DiMarco, D. Mitchell, M.J. Lamm, P.J. Limon, P. Mazur,
F. Nobrega, D. Orris, J.P. Ozelis, J.B. Strait, J.C. Tompkins, A.V. Zlobin,
Fermi National Accelerator Laboratory*, P.O. Box 500, Batavia, IL 60510, USA
A.D. McInturff, Lawrence Berkeley National Laboratory*, Berkeley, CA USA

*Abstract*

The high gradient quadrupole (HGQ) being developed for the LHC interaction regions by the collaboration of FNAL/LBNL/BNL[1], relies on the use of quench protection heaters. As part of the HGQ R&D program at Fermilab, Tevatron low-$\beta$ quadrupoles installed with quench protection heaters were tested in normal and superfluid helium. This paper focuses on heater operation time delay and quench propagation velocity measurements since these are important input parameters for designing the quench protection system of the HGQ.

## 1 INTRODUCTION

The energy stored in a superconducting (SC) accelerator magnet is dissipated after a quench in the normal zones, heating the coil and generating a turn to turn and coil to ground voltage drop. The propagation velocity of the normal zone is usually low relative to the heating rate of the cable and the cable temperature will rise so high that it will damage the cable. Quench heaters are used to protect the SC magnet by greatly increasing the coil normal zone thus allowing the energy to be dissipated over a larger conductor volume making the protection to be less dependent on the quench propagation velocity. Such heaters will be required for the HGQ.

Without overheating the cable or developing too high voltages, the ellapsed time between the quench origin and the start time of the stored energy dissipation in the heater quenched part of the coil is usually quite short, for HGQ this value is in the order of a few millisecond[2]. This time depends mainly on the quench propagation velocity and the time delay of the heater operation. The study of these important parameters in normal and superfluid helium as part of the HGQ R&D program has been started at Fermilab on low-$\beta$ (LBQ) quadrupoles[3, 4]. This paper presents experimental results on a LBQ (R54002) heater operation time delay and quench propagation velocity.

## 2 MAGNET DESCRIPTION

The magnet R54002 for this study is a modified 1.4 m long Tevatron low-$\beta$ quadrupole. Details of the baseline design have been described elsewhere[5, 6]. This cold iron superconducting quadrupole has two layer coils with a 76 mm diameter bore. There are copper wedges in the inner coils whose primary purpose is to minimize the geometric 12- and 20-pole harmonics. Four inner to outer coil splices are located in the magnet lead end radially beyond the outer coil and are made through pre-formed solder-filled cable originating from the lead end pole turn.

The inner and outer coils are made from 36 strand Rutherford cable. The strands are 0.528 mm in diameter and contain 13 $\mu$m filaments. The cable insulation is made of 25$\mu$m thick and 9.53 mm wide Kapton tape covered both side with B-stage epoxy. Kapton tape is wrapped with 67% overlap forming three layer of insulation with total thickness of 75$\mu$m and 1-1.5 mm gaps in the outer insulation layer.

The coils are supported in the body by aluminum collars. The coil lead and return ends are clamped with a 4 piece G-10 collet assembly enclosed in a tapered cylindrical can. Iron yoke laminations surround the coil in the body region, and stainless steel laminations surround the end region cylindrical can. A welded stainless steel skin surrounds the yoke.

The quench protection heaters are 25$\mu$m thick and 12.5 mm wide stainless steel strips and are located radially beyond the outer coil, in the middle of four layers of 125 $\mu$m Kapton sheets. One heater covers approximately 12 turns of two midplane-adjacent outer coils. This is accomplished by running the heater longitudinally along the body of the magnet and making appropriate folds on the heater in the magnet return end region. Two heaters oriented 180 degrees apart provide coverage for one side of each of the four outer coils. The resistance of the heater for coils A and B was 5.5 $\Omega$, and that for C and D was 5.0 $\Omega$. The system resistance (including cabling from the Strip Heater Firing Unit (SHFU) to the magnet) was 3.0 $\Omega$ , which means that $\sim$85.5 % of the SHFU voltage was deposited directly to the heaters.

The 69 voltage taps that instrumented R54002 allowed for localization and determination of propagation velocity for most quenches. Magnet was tested at the Fermilab Technical Division horizontal test facility[7].

## 3 HEATER TIME DELAY

The heater time delay ($t_{fn}$) is the time from protection heater current initiation to the presence of a detectable quench voltage in the outer coils. Figure 1 shows the time diagram of the heater and magnet voltage and an example of the $t_{fn}$ determination.

The heater time delay as a function of voltage applied to heaters is shown in Figure 2. As one can see, at the lower heater energies (close to $V_{min}$) the $t_{fn}$ increases rapidly

* Supported by the U.S. Department of Energy

0-7803-4376-X/98/$10.00 © 1998 IEEE

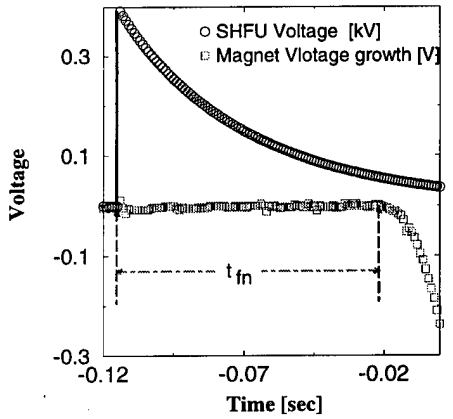



Figure 1: Heater and magnet voltage vs. time.

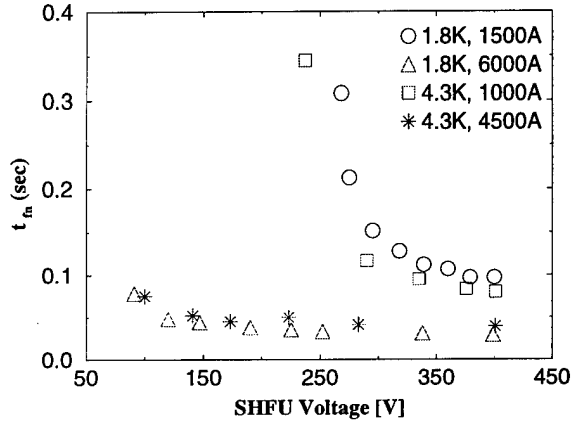



Figure 2: $t_{fn}$ vs. the heater voltage.

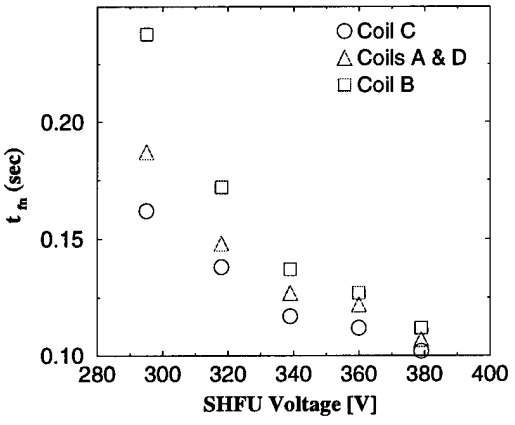



Figure 3: $t_{fn}$ is plotted for each of the four coils in contact with the heaters vs. SHFU voltage at $I/I_c = 0.2$

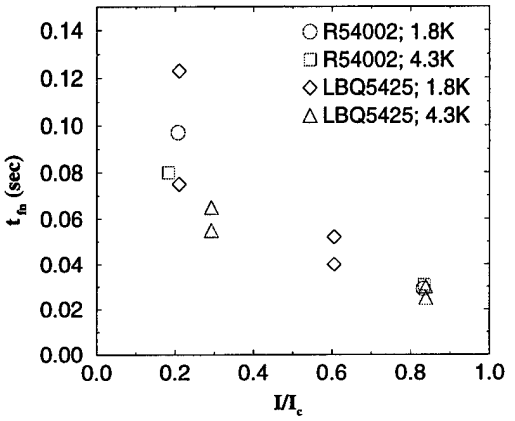



Figure 4: $t_{fn}$ as function of $I/I_c$. R5425 is a previously tested Tevatron low-$\beta$ quadrupole[4].

while at higher energies $t_{fn}$ levels off. At sufficiently large SHFU voltage (> 300 V), $t_{fn}$ does not change significantly with changes in SHFU voltage and magnet operating temperature.

In Figure 3 we plotted $t_{fn}$ for each of the four coils in contact with the heaters as a function of the SHFU voltage. These data are at 1.8K He bath temperature and 1500A magnet current. At low SHFU voltages, the coils show quite a large absolute spread in their $t_{fn}$ values. It could be indicative of small differences in the magnet construction favoring the quenching of some coils over others. At larger SHFU voltages this spread decreases and all four coils quench with similar $t_{fn}$. Therefore to avoid an unreasonably large spread of the individual coil $t_{fn}$ values, the SHFU voltage should be set sufficiently high with respect to the coil which has the largest $t_{fn}$.

In Figure 4 heater time delay is plotted as a function of normalized current ($I/I_c$) at a fixed and relatively high SHFU voltage. The $I_c$ used in the plots for current normalization, correspond to the expected short sample limit of the magnet (5400A @ 4.3K and 7150A @ 1.8K)[3]. It shows an order of magnitude decrease of the heater time delay as magnet current approaches the critical value. At operating currents 10-15% below the $I_c$ the time delay becomes rather small, less than 20-30 ms. This suggests that the heater time delay does not depend significantly on the magnet operation temperature. The penetration of superfluid helium in the coil (if it indeed takes place) does not affect the value of the heater time delay at high operating currents.

## 4 QUENCH PROPAGATION VELOCITY

The quench propagation velocity was determined using a "time of flight" technique. The basic idea of this technique is to determine the time needed for the quench to propagate between voltage taps separated by a known distance. Figure 5 shows the signals collected with voltage taps during a magnet spontaneous quench. The start time of a quench in a voltage tap segment was determined by tracing back the voltage rise in the segment to the first point $3\sigma$ above the

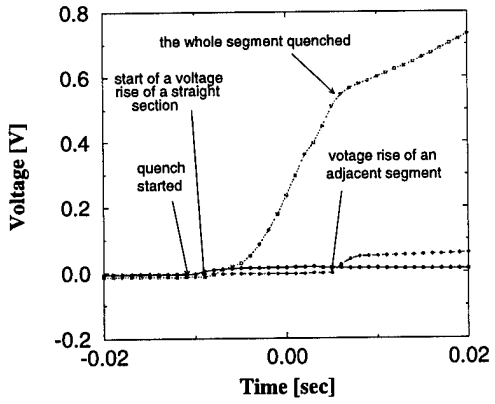



Figure 5: Voltage rise diagram.

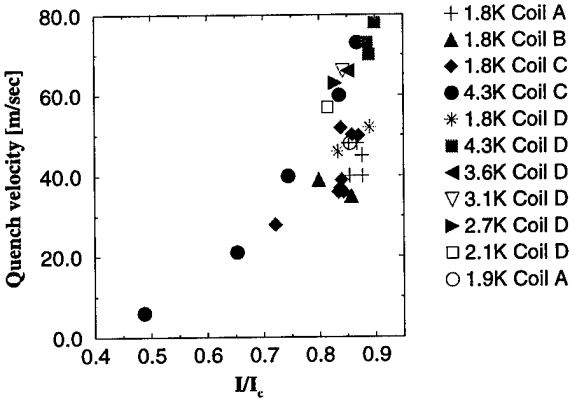



Figure 6: Quench velocity as a function of $I/I_c$.

noise. In some cases the end time was determined by the change of the slope of the voltage growth in the segment where the quench was initiated, rather than the difference between the start times in adjacent segments.

Longitudinal quench propagation velocity as a function of the normalized current ($I/I_c$) is plotted in Figure 6. It is increasing with the magnet operating current and 15% below the magnet critical current it is already quite high, more than 60 m/sec. From Figure 6 one can conclude that the longitudinal quench propagation velocity as a function of the normalized current does not change with temperature in the interval between 2.1-4.3K. However, dramatically lower values were observed at superfluid helium temperatures between 1.8-1.9K. This effect might be explained by the better cooling condition of the cable in superfluid He.

Quenches which occurred close to voltage tap located near the pole turn of the coil could be used to measure turn to turn quench propagation velocity using the voltage taps on the next turn. The turn to turn quench propagation times as a function of the normalized current at quench are shown in Figure 7. The turn to turn quench propagation time de-

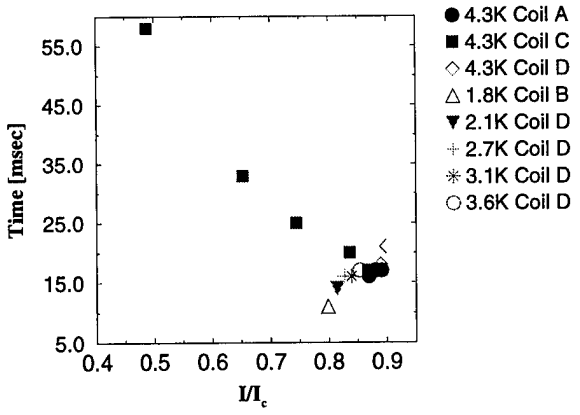



Figure 7: Turn to turn quench propagation time as a function of the normalized current at quench.

creases as the operating current aproaching the magnet critical current. The experimental data obtained at relatively high normalized current ($I/I_c \sim 0.8 - 0.85$) indicate that turn to turn quench propagation time monotically decreases as the temperature is droping from 4.3K to 1.8K.

## 5 CONCLUSIONS

It was observed that at sufficiently large heater energies the heater time delay does not change significantly with changes in the applied heater energy and magnet operating temperature. Significantly lower longitudinal quench propagation velocity was observed for quenches taken at 1.8-1.9K temperature range relative to those taken at 2.1-4.3K. At fixed normalized current value the turn to turn quench propagation velocity however increases as the temperature decreases from 4.3 to 1.8K.

## 6 REFERENCES

[1] R. Bossert et. al., "Development of a High Gradient Quadrupole for the LHC Interaction Regions", ASC'96, Pittsburg (1996).

[2] A.V. Zlobin,"Quench Protection of a High Gradient Quadrupole for the LHC Interaction Regions", ASC'96, Pittsburg (1996).

[3] R. Bossert et. al., "Test of Fermilab Low-$\beta$ Quadrupoles", ASC'96, Pittsburg (1996).

[4] A. Lietzke et. al., "Superfluid Performance of Tevatron IR Quad Heaters", ASC'96, Pittsburg (1996).

[5] "D0 Low-$\beta$ Quadrupole Requirements and Specifications #10," Fermilab Technical Support Section Internal Document, February 15, 1990.

[6] A.D. McInturff et. al.,"The Fermilab Collider D0 Low-$\beta$ Sustem", EPAC, Rome, Italy, Vol.2, p.1264, June 1988.

[7] J. Strait et. al.,"Fermilab R&D Test Facility for SSC Magnets", Supercollider 1, p. 61 (1989).

# DESIGN AND OPERATION OF AN EXPERIMENTAL "DOUBLE-C" TRANSMISSION LINE MAGNET

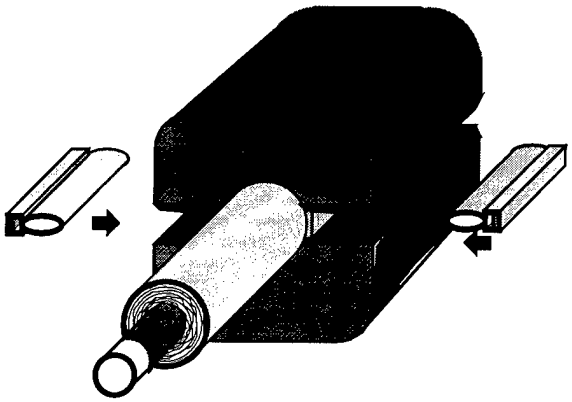
G.W. Foster, P.O. Mazur, T. Peterson, C.D. Sylvester, P. Schlabach,
Fermi National Accelerator Laboratory, PO Box 500 Batavia IL 60510

*Abstract*

The "Double-C" transmission line magnet is a warm-iron warm-bore single turn 2-in-1 superferric magnet designed to provide a significant reduction in magnet costs for future hadron colliders. Construction and first operational tests of a prototype magnet system are described.

## 1 INTRODUCTION

The transmission line magnet development program[1] has the goal of demonstrating a magnet with construction and operating costs (per Tesla-meter) which are an order of magnitude below current (cosine theta) superconducting magnets.



*1.1 Transmission Line Magnet Design*

Fig. 1 - The Transmission Line Magnet is a single-turn warm iron superferric magnet built around a superconducting 75kA DC transmisssion line.

A "Double-C" magnet yoke placed around the transmission line provides twin gaps with opposite bend fields for two counter-rotating proton beams. Alternating gradients of the iron pole tips eliminate quadrupoles and most costs associated with magnet ends. The current is returned in a cryogen distribution line located nearby.

Other design features include:

- Crenelated iron pole tips[2] which maintain acceptable field quality up to ~2 Tesla in an alternating-gradient design.
- An peak operating field at the conductor of ~0.8T. This translates to a very high current density and/or a high allowable operating temperature. Superconductor costs (for today's NbTi conductors operated at 7K) are in the range of $1M/TeV.
- A very simple and low heat leak cryogenic structure[3] from the transmission-line geometry. This translates into low cryogenic operating costs.
- A small cold mass (0.7kG/m or ~7 tonnes/TeV).
- An absence of large cold-to-warm magnetic forces due to the symmetry of the "Double-C" design.
- An Invar cryogenic pipe for the center conductor which eliminates bellows for thermal shrinkage.
- An inexpensive warm-bore vacuum system [4,5] using extruded aluminum and NEG pumping.
- Low Magnetic Stored Energy (60MJ/TeV). This translates into small power supplies for ramping and a simple quench protection system [6].

## 2 PROTOTYPE SYSTEM

In the last year a proof-of-principle 50kA Transmission Line Magnet system was constructed. To avoid the cost and complexities of high current leads, a current transformer approach with a floating superconducting secondary loop was used. The "Double-C" iron structure was mounted on the 5m long secondary loop which served as both the experimental transmission line and the curent return.

*2.1 Current Transformer*

The current transformer yoke was the iron structure from an accelerator magnet. The primary windings were the 24 turn x 2.5kA water-cooled copper windings of that magnet. The copper windings were driven by a 15V 2.5kA conventional SCR power supply.

Under ideal conditions a single turn shorted secondary should develop 24 x 2.5kA = 60 kA according to the turns ratio of the current transformer. Nearly ideal coupling can be expected as long as the iron yoke of the transformer does not saturate. The current at which the yoke saturates depends on the inductance of the load plus the stray inductance of the secondary loop. Calculations of the expected electrical and magnetic behavior of the prototype are detailed in [7].

0-7803-4376-X/98/$10.00 © 1998 IEEE

### 2.2 *Superconducting Secondary*

The superconducting secondary consisted of 7 turns of surplus SSC dipole inner coil cable, and was located in a loop cryostat 5m long which serves as the prototype transmission line. The SSC Cable was looped through the cryostat 7 times and then spliced to itself by soldering over a length of ~40cm. This approach reduced the effective resistance of the joint by a factor of seven, since the current only passes through the splice every 7$^{th}$ time around the loop. An L/R decay time of order 10 hours is expected for the current in the superconducting secondary.

The superconductor was supported inside the 2.5cm diameter helium cryopipe at ~10cm intervals by UHMW form-fitting spacers which were clamshelled around the conductor and tied in place by twisted steel wire. Less than 10% of the cross sectional area was available for helium flow.

The superconducting line is supported in symmetric positions and accurately centered in both the transmission line magnet and drive transformer to avoid large magnetic forces. The drive transformer has a pair of copper primary coils which are placed on either side of the superconducting secondary to maintain the symmetry. In the "Double-C" magnet the conductor experiences nominally zero force but a decentering "negative spring constant" of approximately 100 kgf per mm of displacement per meter of transmission line. In the drive transformer the decentering force is about half of this.

### 2.3 *Cryogenic System*

The system consisted of a loop cryostat cooled by a convective "bubble pump" from a 30" high x 12" diam. LHe filled Dewar at one end. Liquid Helium enters the loop from the lower end of the Dewar, is heated (and perhaps vaporized) by the heat leak along the length of the transmission line loop. Bubbles travel upward in the U-turn region at the far end of the loop, and 2-phase flow is forced back out the top (return) half of the loop and back into the Dewar. The flow is convective and needs no special pumps, etc. for a system of this size.

The loop cryostat consists of a 2.5cm diameter Helium-filled stainless cryopipe with a 180-degree bend at the far end (5m from the Dewar). The 180-degree bend used a rigid U-tube 60cm in diameter. The cryopipe was enclosed in a vacuum jacket consisting of 2.5" stainless pipe and a 4" diameter flexible stainless bellows hose in the region of the U-turn. The cryopipe was superinsulated and supported from the vacuum jacket by G-10 "spiders". The spacing of the supports was ~30cm along the length of the cryopipe and ~15cm in the region underneath the test magnet where conductor forces are greatest.

Helum was provided to the system from a 500L Dewar. Liquid level in the experimental Dewar was monitored by a superconducting liquid level probe which was also used to control the automatic transfer system.

### 2.4 *Instrumentation*

Temperature measurements were made 3 places along the loop cryostat and two places inside the Dewar using. Pressure in the Dewar was logged and there were 4 voltage taps on the 7-turn winding for quench detection and studies.

Current in the secondary was monitored with a Hall probe fixtured ~10cm away from a clear section of the drive conductor. A secondary Hall probe was used to monitor the field in the gap of the test magnet as well as various stray fields which were monitored for safety reasons.

Rapidly changing data (currents, voltages, pressures) were logged with a Sony DAT data logger. Slowly changing data (temperatures and fill levels, etc.) were logged using a computerized slow-scan system from Fermilab's Magnet Test Facility.

## 3 PRELIMINARY TEST RESULTS

The initial running of the prototype took place a few days prior to this conference (PAC97).

### 3.1 *Cool Down of Loop Cryostat*

Cooldown began by initiating a transfer of liquid helium into the dewar at room temperature. A liquid level was quickly established and regulated ~60cm above the bottom line of the loop cryostat (i.e. near the level of the return line of the loop). Cooldown of the loop was initially very slow. After 3½ hours the far end of the loop cyostat was still at room temperature as the "cold wave" propagated slowly down the lower half of the loop. Shortly after this the cold wave reached the far end of the loop, travelling at ~2m/hr. as it passed the temperature transducers at the turnaround. The cooldown of the top (return) half of the cryoloop was much faster, taking only ~1/2 hour for the entire 5m return leg to reach 4.3K.

The system operated very stably after initial cooldown had been achieved. Recovery following quenches was also rapid (<2 mins), indicating that the convective flow, once established, has significant excess capacity to keep the system cool.

### 3.2 *Electrical and Magnetic Measurements*

The magnet was cooled down with the power supply off, so that nominally zero flux was trapped in the superconducting loop. The primary was then energized to various DC current levels and the currents and magnetic fields were observed. At low excitation (10kA of secondary current) the expected 24:1 current transformer ratio was observed. The transfer function between transmission line curent and B-field in the gap of the Transmission Line Magnet structure was measured to be 25kA/Tesla and agreed with calculations. Stray fields

were recorded for ES&H reasons and agreed with estimates based on 2-d calculations.

In the initial running of the prototype the iron size of the coupling transformer yoke limited the circulating current in the secondary to 25kA. This behavior was calculated in advance, and served the useful side purpose of limiting the maximum energy which could be transferred to the cryogenic system until preliminary tests were completed. A larger transformer yoke is under construction which should allow us to reach the full 50kA/2T design goal in the next run.

*3.3 Quench Behavior*

At full current in the prototype, the SSC Cable used for the conductor is being run at a small fraction (~20%) of the nominal short-sample current carrying limit at 4.3K and 1 Tesla. However, there were (and are) concerns due to the fact that the conductor is very loosely clamped in the transmission line cryopipe, which could make the device prone to quenches induced by mechanical motion of the drive conductor. Thus the quench behavior is interesting even at the half-current tests run to date.

A conservative calculation [8] indicated a final conductor temperature following a quench of less than 300K, and hence no protection was necessary. Nonetheless quench detection and protection circuitry was included in the prototype to permit quench studies and protect against unforseen circumstances.

Two 60cm long stainless heater strips were embedded between cables of the superconducting loop and connected to Tevatron Quench Heater Firing Units to allow manual initiation of quenches. The heater units had 2/3 of the capacitance removed to limit the energy delivered to the heater tapes. In practice it was not possible to induce a quench by firing the heater tapes with the secondary current at 10kA or below. At ½ current (25kA) firing the heater tapes induced a quench which blew off only ~ 3 liters of LHe. No spontaneous quenches have been observed.

## 4 SUMMARY AND FUTURE PLANS

The first goal of the next run is operation of the system at the full 50kA design current. This requires a larger transformer yoke which is currently under fabrication. If still higher current is to be achieved, a polarity reversing switch on the copper primary would allow a 4 Tesla swing of the iron in the transformer yoke and a doubling of the load inductance which can be driven. The ultimate current limit of the existing setup is ~60kA given by the ideal turns ratio of the coils.

The full-current quench behavior and decay time will be studied, as well as any effects from decentering conductor forces in the Double-C magnet iron.

The present Double-C magnet iron test structure does not have contoured pole tips and hence no precision magnetic field quality measurements are planned. An interesting measurement which can be made is the ramp rate dependence of the sextupole arising from eddy currents in the solid-iron Double-C magnet yoke. This measurement is important since we anticipate substantial cost savings from using solid extruded/cold drawn steel yokes instead of laminations for the full scale machine.

A potential follow-on use of the test setup will be to evaluate persistent-current switches to extend the range of the transformer coupling technique to longer (higher inductance) prototypes. If feasible, this technique could allow dewar-based operation of prototype magnets with lengths up to ~100m.

## 5 ACKNOWLEDGEMENTS

The authors thank the Fermilab Technical Divison (especially B. Bianchi, J. Garvey, J. Sim, D. Sorensen, and D. Validis) and the staff of the Magnet Test Facility for their support during this project. Thanks also to M. May, D. Snee, and J. Volk of the FNAL Beams Division for fabrication Double-C magnet structure and the coupling transformer. Alvin Tollestrup is thanked for useful discussions in the initial stages of this project.

## REFERENCES

[1] 'The Pipetron, a Low-Field Approach to a Very Large Hadron Collider', selected reports submitted to the Proceedings of the DPF/DPB Summer Study on New Directions in High-Energy Physics (Snowmass '96), compiled by Ernie Malamud (malamud@fnal.gov) Jan 1997. Current project information can be found at http::://www-AP.fnal.gov/PIPE and ../VLHC

[2] G.W.Foster, 'Magnetic Calculations for the Pipetron Transmission Line Magnet', in Ref. 1. The crenelation technique was described by R.R. Wilson in Snowmass 1982 and evaluated numerically by S. Snowdon in a 1983 Fermilab TM.

[3] M. McAshan, P.O.Mazur, "Cryogenic Systems for the Low Field RLHC Study Cases", in Ref. 1.

[4] H. Ishimaru, "Conceptual Design for a Very Low Cost Aluminum Alloy Vacuum Chamber in a High Energy Low-Field Collider", in Ref. 1.

[5] William C. Turner, "Beam Tube Vacuum in Low Field and High Field Very Large Hadron Colliders", in Ref. 1, also LBNL-39482, UC-414.

[6] K. Koepke, A Zlobin, G.W. Foster, "Power Circuit and Quench Protection for the Pipetron Transmission Line Magnet", in Ref. 1.

[7] G.W. Foster "Magnetic Calculations for the Transmission Line Magnet and Current Transformer Test Setup", FNAL Tech. Div. Note #TD-97-014

[8] A. Zlobin, contribution to FNAL Tech. Div. Electrical Safety Review documentation for transmission line magnet protoype system.

# A NEW FACILITY TO TEST SUPERCONDUCTING ACCELERATOR MAGNETS*

M.J. Lamm, J. DiMarco, E. Desavouret, S. Feher, J.D. Garvey, C. Hess, P.J. Limon, J.M. Nogiec, D.F. Orris, J. Pachnik, T. Peterson, S. Sharonov, J. B. Strait, C. Sylvester, J.W. Sim, M. Tartaglia, J.C. Tompkins, A.V. Zlobin
Fermi National Accelerator Laboratory, Batavia, Illinois 60510-0500

*Abstract*

Future high energy accelerators such as the Large Hadron Collider require accelerator magnets with the highest possible fields. For NbTi conductor magnets, this means operating at superfluid helium temperatures in the range of 1.8-1.9K. As part of Fermilab's superconducting magnet R&D program, we have built a facility to test magnets in a vertical dewar of superfluid liquid helium. The dewar is designed for magnets up to 4 m length and 620 mm diameter, with a temperature range of 1.8 K to 4.4 K and 1 atmosphere helium. The power system consists of 10 kA and 8.8 kA power supplies operating in parallel, with bus work and an extraction circuit that can accommodate up a 18kA excitation current. A description of the facility as well as operational experience from the first magnet tests are presented.

## 1 INTRODUCTION

Testing superconducting accelerator magnets in a vertical dewar can be time and cost effective since it eliminates the need for the construction and installation of a magnet-specific cryostat. Thus the development of a new facility to accommodate large diameter, high current magnets in a vertical dewar was an early consideration for Fermilab's participation in the LHC high gradient quadrupole (HGQ) program [1].

There are three major components to this new vertical magnet test facility (VMTF): 1) a dewar capable of efficient operation over a wide range of temperatures, 2) a high current power system with an energy extraction circuit and protection heater firing units and 3) hardware and software for control and monitor of the dewar, power supply and magnet instrumentation.

In preparation for the first HGQ magnet, VMTF has been commissioned through the tests of Tevatron Low beta quadrupoles (LBQ) [2].

## 2 VERTICAL DEWAR

Figure 1 shows a cross section of the vertical dewar [3]. The top of the dewar is recessed 1 meter from the VMTF floor to achieve the crane hook height required for manipulating 4 meter long magnets. The helium shell is separated from the outer vessel by a vacuum space and superinsulation, and an 80K shield. The helium volume is divided into two chambers, a 4.2K, 1 atm helium space for the vapor cooled leads and helium reservoir for the heat exchanger, and the lower space for the magnet at 1 atm and 1.8K-4.4K.

The lambda plate which separates these chambers consists of a G-10 plate bonded with epoxy to a tapered stainless steel ring. This ring is matched to a corresponding tapered surface on the dewar inner wall. Imperfections in the lambda plate-dewar seal have been improved by bonding a layer of stycast to the lambda plate between the stainless steel surfaces.

There are several penetrations through the lambda plate, for instrumentation, superconducting power leads and pressure relief valves. The lambda plate supports the weight of the magnet. The maximum length (diameter) of a magnet that can be tested is 4 m (620 mm). For small magnets, the helium volume can be significantly reduced by using a closed-cell foam displacer [4].

The temperature of the volume below the lambda plate is controlled through a built-in heat exchanger. This heat exchanger consists of 4 m long OFHC copper tubes in direct contact with the 1 atm helium in the lower chamber. The temperature of the liquid helium in the heat exchanger is controlled by a vacuum pump system, which is capable of removing 30 W of heat at 1.8K.

## 3 HIGH CURRENT POWER SYSTEM

Power system as shown schematically in figure 2 consists of two high current power supplies, an energy extraction circuit and water cooled copper bus. The power supplies

* Work supported by the U.S. Departement of Energy.

0-7803-4376-X/98/$10.00 © 1998 IEEE

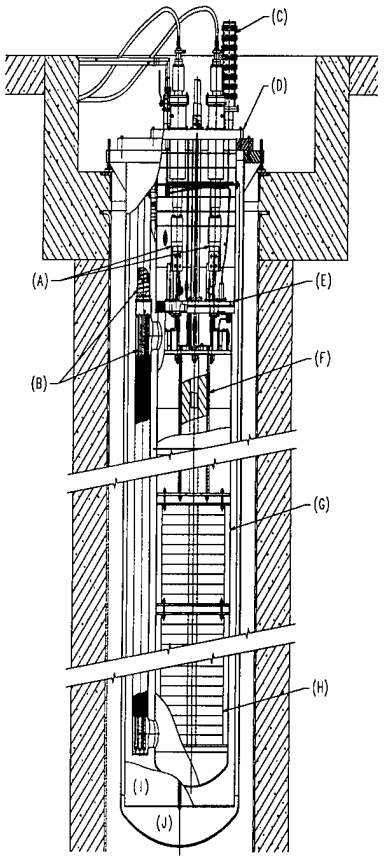



Figure: 1 Vertical dewar is located in a fiberglass lined concrete pit which is recessed 1 meter from the floor: (A) Vapor cooled leads (B) Heat exchanger, (C) Instrumentation tree, (D) Top Plate, (F) Magnet, (G) Helium Shell, (H) Displacer, (I) 80K Shield, (J) Vacuum shell

are Dynapower[5] 12 phase 40 V supplies. For these first commissioning tests, only one supply 10kA was required as the quench current for LBQ magnets is approximately 7kA at 1.9K. The power supply is controlled through a Fermilab built interface board [6].

The extraction circuit consists of a dump switch, a dump resistor and a personnel protection interlock system (shown in figure 3). The dump resistor consists of 12 90 mΩ stainless steel coils that are configured through parallel and series connections. A typical setting of 60 mΩ has a maximum energy deposition limit of 3 MJ/extraction. The dump switch[7] contains 10 parallel 1800 A SCR's in parallel with the dump resistor. Current is diverted from the SCR's to the dump resistor by removing the SCR gate and discharging the negatively biased 9000 μF capacitor bank across the SCR's.

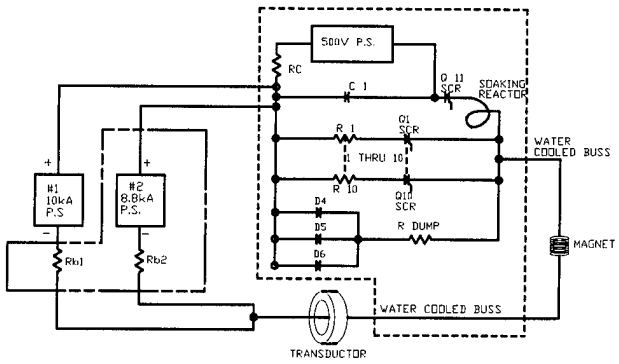



Figure: 2 High Current Power System Dashed line represents 18kA energy extraction circuit. Phantom lines represent upgrade to 18.8kA (Summer 1997).

## 4 INSTRUMENTATION AND SOFTWARE

Instrumentation is used to monitor cryogenic status and mechanical strain transducers, detect and characterize quench propagation in the superconducting magnet, and control power supply and cryogenic operation. Magnetic measurements are not yet fully implemented and will not be discussed.

Like tasks were group together into VME crates controlled by Motorola MVE167 processors. For example, thermometry and strain gauge control and monitoring is performed through programmable current sources, and read out through a FET based MUX.

Figure 3 shows the flow diagram for the quench detection and characterization electronics. The system includes 100kHz data loggers for recording quench voltages[8], a Change of State Module (COS) which records the time of various TTL level changes and relay contact closures[9] , a combined function digital IO,DAC and ADC board for heater power supply control [10] and a Fermilab built Quench Logic Module (QLM). The QLM performs the following tasks:

1) Checks the status of the extraction and power supply interlocks to give permission for power supply turn on.
2) Scans for change of states in the quench detection circuits for indications of a quench or otherwise fault condition and
3) Issues the commands subject to programmable time delays to phase off the power supply, fire the dump switch capacitor bank, fire the quench protection heaters and trigger the quench characterization data loggers.

The software monitoring and control system is described in another contributed paper [11]. The system includes graphical user interfaces, archivers, a data acquisition subsystem and direct control components.

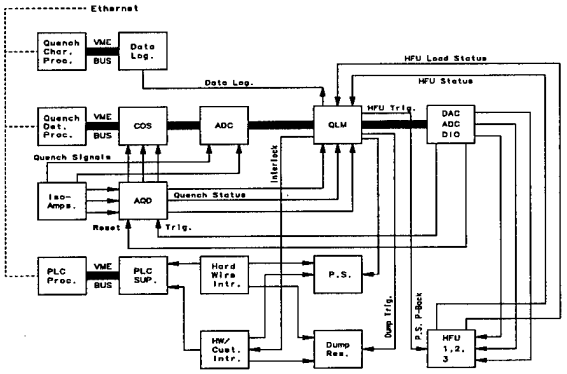



Figure: 3 Block diagram of quench detection-quench characterization circuit

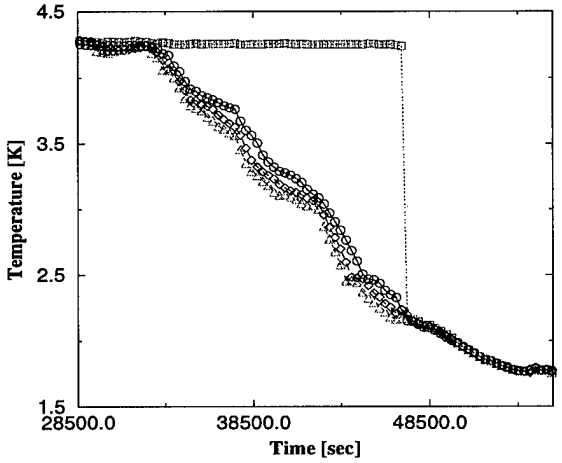



Figure: 4 Cooldown from 4.2K to 1.8K as measured by thermometers at different vertical positions under the lambda plate. The top thermometer (squares) is located directly below the lambda plate. Time scale is arbitrary.

## 5 COMMISSIONING WITH THE TEVATRON LBQ

Two commissioning runs were performed. For these runs, helium was supplied through portable 500L Helium dewars. In the near future we plan to connect the VMTF helium supply to the magnet test facility liquifier. During December 1996, the cryogenic operation of VMTF was commissioned. A 1.4m Tevatron Low Beta Quadrupole was successfully cooled to 1.9K. As a result of this study, improvements to the facility were made including a larger diameter helium transfer line and a better lambda plate seal.

In the April-May 1997 run, a newly constructed 1.4m Tevatron Low Beta Quadrupole was tested in VMTF. The cryogenic part of the program included determining heat loads as well as gaining operational experience in Helium I and Helium II. The magnet evaluation part of the program includes quench studies, splice resistance measurements, strain gauge transducer studies and quench protection heater studies.

Figure 4 shows the cool down from 4.2 K to 1.8K. Note that the thermometer below the lambda plate is above the heat exchanger and thus does not benefit from convection cooling. At the lambda point, all thermometers converge to the superfluid temperature.

## 6 CONCLUSIONS

We have successfully tested a Fermilab Tevatron Low Beta quadrupole in our new magnet test facility. The dewar operates well in both normal and superfluid helium. In this test with approximately 800 L of helium underneath the lambda plate, we reached a temperature of 1.9K from 4.2 K in about 4 hours; A bath temperature of 1.7K has also been achieved. For 3.7K operation, a vertical gradient of 10 mK or less over a 4 meter dewar length was possible due to the convection flow through the dewar heat exchanger. The VMTF instrumentation, a combination of commercially available and in-house designed and built, was successfully operated through graphical user interfaces on UNIX work stations.

.

## 7 ACKNOWLEDGEMENTS

The authors would like to acknowledge the support of the Magnet Test Facility staff, in particular Clark Reid, Al Rusy, Bill Mumper, Steve Helis and Ed Schmidt, and the Fermilab Beams and Particle Physics Power Systems Groups.

## REFERENCES

[1] R. Bossert et al., "Development of a High Gradient Quadrupole for the LHC Interaction Regions", ASC 1996, Pittsburgh (1996)
[2] A. D. McInturff et al., "The Fermilab Collider D0 Low-β System", EPAC, Rome, Italy, Vol. 2. p. 1264, June 1988.
[3] Manufactured and co-designed with Fermilab by Meyer Tooling and Manufacturing, Oaklawn IL
[4] Rohacell, Rohm Gmbh, Darmstadt
[5] The Dynapower Corp. Burlington, VT.
[6] S. Sharonov et al. "An Embedded Power Supply Controller", presented at this conference.
[7] A. Visser, "Design Note of a 10,000V, 1,000Vdc Solid State Dump Switch for the Magnet Test Facity, Fermilab TM-1692.
[8] Pentek 4201A-004 MIX baseboard with 4275 ADC's
[9] VMIVME-1160A VME Microsystems International Corp, Huntsville, AL
[10] MD-DAADIO, Matrix Corp, Raleigh, NC
[11] J.D. Nogiec et al., "A Distrubuted Monitoring and Control System" presented at this conference.

# MAGNETIC DESIGN OF A HIGH GRADIENT QUADRUPOLE FOR THE LHC LOW-$\beta$ INSERTIONS

G. Sabbi, S.A. Gourlay, J. Kerby, M.J. Lamm, P.J. Limon, F. Nobrega, I. Novitski, J.B. Strait, A.V. Zlobin, FNAL[1], S. Caspi, R. Scanlan, LBNL[1], A. Ghosh, R. Gupta, BNL[1]

*Abstract*

Fermilab, Lawrence Berkeley National Laboratory and Brookhaven National Laboratory have formed a consortium to provide components for the Large Hadron Collider (LHC) to be built at CERN. The U.S. contribution includes half of the high gradient quadrupoles (HGQ) for the inner focusing triplets. In this paper a description of the HGQ magnetic design is given, including short sample limit for field gradient, sources and expected values of systematic and random field errors, and possible strategies for field quality correction.

## 1 INTRODUCTION

In order to achieve a luminosity in excess of $10^{34}$ cm$^{-2}$s$^{-1}$ at the LHC, special high gradient quadrupoles are required for the final focusing triplets [1]. These magnets must provide a field gradient of 235 T/m over a 70 mm bore, with a sufficient margin in order to withstand the heavy heat load due to secondary particles from beam-beam collisions. At the same time, due to large and rapidly varying values of the $\beta$-function, a high field quality is required. To meet these severe constraints, a design based on a two-layer coil geometry has been proposed [2]. The magnet uses SSC-type NbTi superconducting strands and operates in superfluid helium. The first short model of this design is being fabricated and will be tested this fall. In this paper, the magnetic design for the HGQ straight section is discussed.

## 2 MAGNET DESIGN

The HGQ design is based on four two-layer coils connected in series, surrounded by collar and yoke laminations. A thick-wall stainless steel beam tube also serves as an internal beam absorber. With respect to the last status report [2], the coil prestress is now entirely provided by the collars. For this purpose the collar material has been changed from aluminum to stainless steel, and the collar width at the midplane has been increased from 20 to 25 mm. The yoke inner radius at the midplane is now 92.56 mm while the outer radius remains unchanged at 200 mm. The yoke lamination features four round holes for the HeII heat exchanger and four rectangular holes for electrical connections, as well as special cutouts for magnet fabrication. In the pole regions, eight rectangular gaps between collars and yoke house tuning shims for field quality adjustment [3]. The resulting HGQ cross section is shown in Figure 1.

The cables for the magnet models are made of SSC NbTi strands with a critical current density of 2.75 kA/mm$^2$ at 5 T and 4.2 K. The SSC strands will eventually be replaced with improved ones that are now under development, with the goal of increasing the critical current density to 3.4 kA/mm$^2$ at 5 T and 4.2 K. Table 1 shows the HGQ short sample limits at 1.9 K operating temperature, calculated for both existing and new strands.

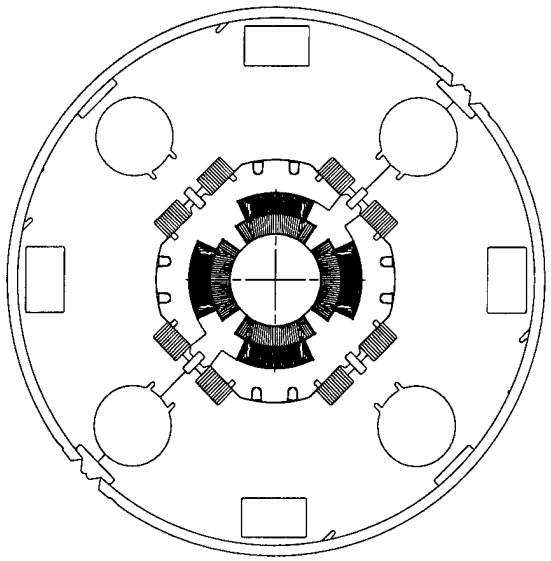


Figure 1: HGQ cross-section

Table 1: Short sample limits.

| $J_c$(5T, 4.2K) kA/mm$^2$ | $G_{ss}$ T/m | $I_{ss}$ kA | $B_{max}^{(inner)}$ T | $B_{max}^{(outer)}$ T |
|---|---|---|---|---|
| 2.75 | 253.8 | 14.2 | 9.9 | 8.2 |
| 3.4 | 270.2 | 15.2 | 10.4 | 8.8 |

The operating current is 0.8 kA at injection and 13.1 kA at nominal gradient. At nominal current, the magnet will operate at 93% along the load line with the SSC conductor and at 87% with the improved one.

## 3 FIELD QUALITY ANALYSIS

The design low-order harmonics for the HGQ central field, resulting from the cross-section optimization with a circular yoke of infinite permeability, are $b_6$=-2·10$^{-3}$, $b_{10}$=-1.3·10$^{-5}$. All other normal and skew harmonics with n<14 are zero. The harmonics here and below are given in units of $10^{-4}$ of the main quadrupole field at 1 cm reference radius.

[1]Supported by the U.S. Department of Energy.

0-7803-4376-X/98/$10.00 © 1998 IEEE

### 3.1 *Field error sources*

Mechanical effects. Due to insufficient keystoning of the cables, the coil curing mandrels do not provide a perfect radial constraint for some of the turns. It is expected that after curing the turns will be aligned to the outer mold radius. The validity of this assumption will be checked as part of the model magnet program. The uncertainty range corresponds to alignment of all turns to the inner mandrel radius.

The collared coil deformation during cooling down and springback under nominal prestress, as well as its deformation under Lorentz forces with respect to the warm unstressed geometry produce additional field errors. The Lorentz force effect is negligible at injection and maximal at collision.

Deviations from nominal prestress and turn/coil block displacements due to manufacturing tolerances contribute to the random errors.

Magnetization effects. The coil magnetization is determined by the critical current density in the superconductor, filament diameter, Cu/Sc ratio, etc. This effect is maximal at injection and becomes negligible at collision. The uncertainty is related to the accuracy of the model and the parameters of the conductor under development.

The magnetization of the stainless steel collars and beam absorber produces current independent harmonics which depend on geometry and magnetic permeability. A collar permeability of 1.003 is expected. However, depending on the exact chemical composition and the heat treatment, larger values up to 1.006 may be obtained. A beam absorber with 27 mm inner radius, 6 mm thickness and magnetic permeability 1.005 has been analyzed. Both the systematic effect and the random contribution due to misalignment were found to be negligible if the offset is below 0.5 mm.

The yoke cross section was optimized to minimize the change in the harmonics due to iron saturation and to compensate the harmonics due to collar magnetization. The uncertainty is related to a precise knowledge of the iron B-H characteristic.

Iron is the material of choice for the cryostat vacuum vessel. The cold mass is placed off-center with respect to this shell. The effect on the harmonics has been analyzed and found to be negligible.

Magnetic measurements. The field quality of each HGQ magnet will be determined during magnetic measurements. Measurement errors contribute to the uncertainty in the systematic harmonics and to the harmonic RMS spread. Since the measurement system is still being designed, the estimates have been done based on data available in [4, 5].

### 3.2 *Systematic effects*

Table 2 shows the main contributions to the $b_6$ harmonic component. Since all the contributions represent small perturbations to the main field, they are treated as independent effects. The total value of $b_6$ is -0.09 [-0.14,+0.04] at injection and +0.01 [-0.14,+0.02] at collision. For the $b_{10}$ component the same approach has been used and the following values have been obtained: +0.0001 [-0.0011,+0.0009] at injection and +0.0003 [-0.0011,+0.0009] at collision.

Table 2: Systematic $b_6$.

| Effect | Expected | Uncertainty |
|---|---|---|
| Coil optimization | -0.002 | |
| Turn alignment | 0.000 | -0.134, +0.0 |
| Prestress at 1.9 K | 0.027 | |
| Lorentz forces | -0.017 | |
| Coil magnetization | -0.11 | ±0.03 |
| Collar magnetization | -0.018 | -0.018, +0.0 |
| Yoke geometry | 0.016 | |
| Iron saturation | 0.005 | ±0.001 |
| Measurements | 0.000 | ±0.02 |

Table 3 shows the expected uncertainty in the systematic errors resulting from the accuracy of magnetic measurements.

Table 3: $a_n$, $b_n$ measurement uncertainty.

| $n$ | $a_n$, $b_n$ uncertainty (±) |
|---|---|
| 3 | 0.16 |
| 4 | 0.085 |
| 5 | 0.042 |
| 6 | 0.020 |
| 7 | 0.0095 |
| 8 | 0.0044 |
| 9 | 0.0020 |
| 10 | 0.00087 |

### 3.3 *Random effects*

The RMS spread of geometrical harmonics due to manufacturing tolerances, prestress changes and radial alignment, as well as the RMS spread which has been assumed for the magnetic measurements are reported in Table 4.

Table 4: HGQ random errors (RMS spread).

| $n$ | Coil geometry | | Measurement |
|---|---|---|---|
| | $b_n$ | $a_n$ | $b_n$ & $a_n$ |
| 3 | 0.97 | 0.96 | 0.080 |
| 4 | 0.35 | 0.33 | 0.042 |
| 5 | 0.089 | 0.090 | 0.021 |
| 6 | 0.026 | 0.023 | 0.010 |
| 7 | 0.0066 | 0.0067 | 0.0047 |
| 8 | 0.0018 | 0.0016 | 0.0021 |
| 9 | 0.00041 | 0.00040 | 0.00098 |
| 10 | 0.00010 | 0.00010 | 0.00044 |

As can be seen, the random errors are dominated by the geometrical component for n<8, while for higher order harmonics the spread due to measurement errors dominates.

Figure 2 shows a comparison between the total estimated random errors for the HGQ normal harmonics and the results of measurements for the FNAL LBQ [4] and HERA

arc quadrupoles [5]. Both magnets have a two-layer coil and a bore radius comparable to HGQ. The measured data have been rescaled to 1/3.5 of the bore radius (1.09 cm for LBQ and 1.07 cm for HERA quads). As can be seen, rather good agreement is found between calculated and measured values.

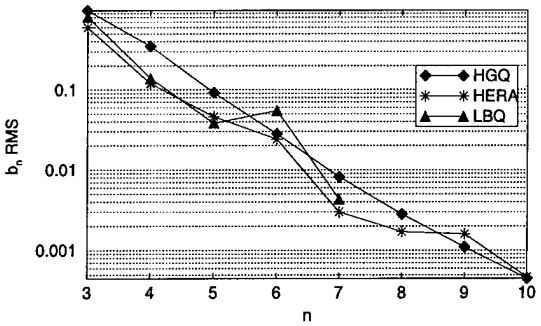



Figure 2: Random errors comparison (normal components).

### *3.4 Field quality correction*

The correction scheme relies on modification of the coil geometry using pole and midplane shims in each octant, independently for the inner and outer layer. Larger corrections may be obtained by changing the thickness of the bearing strips, while for fine tuning of the harmonics insulation layers 25 $\mu$m thick can be added or removed. The analysis shows that corrections of the systematic harmonics at nominal gradient within the predicted range of variation are possible using the existing tuning capability. Should larger effects appear, a cross-section iteration may be considered.

The RMS spread in the harmonics may be reduced either by coil reshimming after warm magnetic measurements or by the use of iron tuning shims. The first method provides a current-independent correction, but it is labor-intensive and subject to some uncertainty as the harmonics are not exactly reproducible after collared coil reassembling. The second method is very attractive in terms of required effort and reproducibility, but the resulting correction is current-dependent due to saturation effects. Preliminary calculations indicate that only 50% of the correction capability at low current is preserved at nominal gradient. The tuning shim correction scheme will be studied as part of the model magnet program.

## 4 ERROR TABLES

Based on field quality measurements carried out on the series of model magnets, correction schemes will be applied to make the average error at full excitation equal to zero. Some residual uncertainty applies due to the limitations of the correction scheme as well as the measurement accuracy. The harmonics at injection are then determined by the current dependent effects, with some additional uncertainty on $b_6$ related to the contribution from coil magnetization. The resulting systematic errors are listed in Table 5.

Table 5: Systematic errors.

| $n$ | $a_n$, $b_n$ mean | $a_n$, $b_n$ uncertainty ($\pm$) |
|---|---|---|
| 3 | 0.0 | 0.2 |
| 4 | 0.0 | 0.09 |
| 5 | 0.0 | 0.04 |
| 6 | 0.0 (-0.1*) | 0.02 (0.04*) |
| 7 | 0.0 | 0.01 |
| 8 | 0.0 | 0.004 |
| 9 | 0.0 | 0.002 |
| 10 | 0.0 (-0.0001*) | 0.0009 |

(*) data for $b_n$ at injection.

To generate the random error table, first the maximum between the estimated RMS spread of each HGQ harmonic component and the corresponding measured value from the LBQ and HERA quad productions was chosen. Then, for the low order non-allowed harmonics, and for all the higher order harmonics (where the measurement errors dominate), the normal and skew RMS errors have been made equal to the largest between the two. The resulting values are shown in Table 6.

Table 6: Random errors (RMS spread).

| $n$ | $b_n$ | $a_n$ |
|---|---|---|
| 3 | 1.3 | 1.3 |
| 4 | 0.4 | 0.4 |
| 5 | 0.09 | 0.09 |
| 6 | 0.06 | 0.03 |
| 7 | 0.008 | 0.008 |
| 8 | 0.003 | 0.003 |
| 9 | 0.0016 | 0.0016 |
| 10 | 0.0005 | 0.0005 |

## 5 SUMMARY

The HGQ maximum gradient exceeds the LHC low-$\beta$ quadrupole design specification with a good margin. A detailed field quality analysis has been carried out, and estimates of the systematic and random field errors for the production magnets have been generated in a form suitable for dynamic aperture studies.

## 6 REFERENCES


[1] 'Large Hadron Collider Conceptual Design', CERN AC/95-05 (LHC), 1995.

[2] R. Bossert et al., 'Development of a High Gradient Quadrupole for the LHC Interaction Regions', ASC '96, Pittsburgh, August 1996.

[3] R. Gupta et al., 'Tuning Shims for High Field Quality in Superconducting Magnets', MT-14, Finland, June 1995.

[4] R. Hanft et al., 'Magnetic Performance of New Fermilab High Gradient Quadrupoles', IEEE Particle Accelerator Conference (PAC91), S. Francisco, May 1991.

[5] J. Perot, J. M. Rifflet, 'Measurement Data Taken During the Industrial Fabrication of the HERA Superconducting Quadrupoles', Supercollider 3, Plenum Press, NY, 1991.

# A MU MU COLLIDER CAPTURE SOLENOID SYSTEM FOR PIONS FROM A TILTED TARGET*

M. A. Green[a], and R. B Palmer[b]
a. Lawrence Berkeley National Laboratory, Berkeley CA 94720, USA
b. Brookhaven National Laboratory, Upton NY 11973, USA

*Abstract*

In order to generate muon beams for a muon Collider, pions produced in a target must be captured before they can go through phase rotation and decay into muons. A 20 T solenoid with a clear bore of 150 mm can capture particles with a transverse momentum of 225 MeV/c or less. As captured particles leave the capture solenoid, the induction is decreased to 5 T while the beam pipe diameter increases to 300 mm. Phase rotation and decay of the pions will occur at 5 T. The capture solenoid and the solenoids just downstream from the capture solenoid are subject to high heat loads (up to 2.4 MW). The conventional inner solenoid of the 20 T hybrid magnet system and the water cooled absorber will absorb most of the beam power from the protons thus protecting the superconducting solenoid system from heating. Tilting the target and the incoming beam about 150 milliradians with respect to the solenoid axis appears to increase the net pion capture by about sixty percent. This paper describes approaches for capturing muons from a tilted target while getting rid of the spent proton beam.

## I. BACKGROUND

Capture of the pions from the target can occur in a solenoid of any induction provided the solenoid bore is large enough[1,2]. A capture induction of 20 T within a radius of 75 mm is needed to capture pions with a transverse momentum up to 225 MeV/c. Once the pions have been captured in the solenoidal field, the channel solenoidal induction is reduced to 5 T. Because some of the particle transverse momentum is transferred to forward momentum, the clear bore radius of the 5 T solenoid is only 150 mm. The pions are transferred to a system of phase rotation rf cavities that speed up the low momentum particles and slow down the high momentum particles so that the particles travel bunched in time to the muon cooling system. Ninety-nine percent of the pions decay to muons within the first 80 meters.

The hybrid capture magnet option was selected for the following reasons: 1) When a superconducting outsert solenoid is used the operating power for the water cooled solenoid is lower. 2) The current density in the water cooled solenoid can be low enough to insure that its life time will be long (at least 25000 hr 3) Additional space inside the water cooled solenoid can be made available for a heavy metal water cooled shield, which reduces the incident energy from the target into the water cooled solenoid and the surrounding superconducting solenoid.

* This work was performed with the support of the Office of High Energy and Nuclear Physics, United States Department of Energy under contract numbers DE-AC03-76SF00098 and DE-AC02-76CH00016

## II. THE TILTED TARGET

Calculations of pion yield from a target suggest that tilting the incident proton beam and target with respect to the solenoid axis increases the pion yield for a given input proton intensity to the target. Pions produced in the upstream end of the target are not recaptured by the target downstream from the point where they were created. Simulations of pion production suggest that the pion production is maximized at a tilt angle of about 150 milliradians (see Figure 1). Above the 150 milliradian tilt angle the transverse momentum of some of the pions in the target becomes too high for capture to occur.

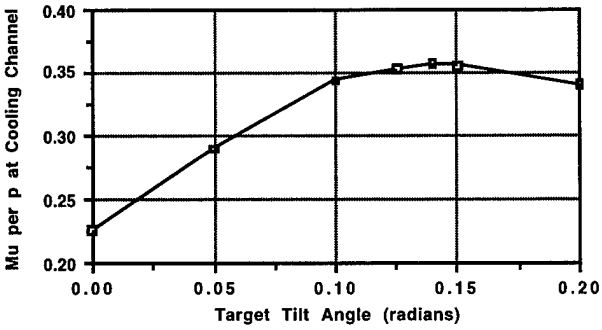



Figure. 1. Muon Production at the Cooling Channel Entrance for Optimized Targets as a Function of Target Tilt Angle

An increase in the yield of pions from the target means that the input beam power from the driver can be reduced, for instance, from 3.8 MW to about 2.4 MW. Even with improved efficiency, a copper target will absorb about 230 kW of energy from the proton beam. Cooling the target is a difficult proposition, which will not be addressed here. Tilting the target and the input proton beam allows virtually all of the beam energy that has not been transferred to the captured pions to be absorbed in the capture solenoid. The superconducting magnet will absorb less than 500 W of the energy from the beam.

## III. BITTER SOLENOID INSERT

In this study, a Bitter solenoid insert that has an inner radius of 120 mm has been assumed. The extra inner bore radius allows a water cooled heavy metal (tungsten or some other high Z, high density metal) shield that is 30 mm thick to be inserted around the target region. An extra 15 mm on the inside of the solenoid is allotted for water cooling channels for the shield. The Bitter solenoid insert outer radius has been set at 345 mm. The superconducting outsert solenoid cryostat starts at a radius

0-7803-4376-X/98/$10.00 © 1998 IEEE

of 370 mm. The 25 mm between the Bitter solenoid and the cryostat wall is allocated for water cooling. Much of the space at the ends of the Bitter insert solenoid should be filled with a water cooled shield to protect the superconducting solenoids on the outside from particles coming from the target.

The Bitter solenoid insert is divided along its length into three regions, each with a different current density[4]. The gradation of the current density in the windings allows for the magnetic field to be shaped along the solenoid axis, in the high field region. The current density in the Bitter solenoid section can be changed by changing the thickness of the plates in the solenoid. Thick palates have a lower current density than thin plates.

A Bitter solenoid is characterized by a current density in the winding that varies inversely as radius. The highest current density is found on the inside radius of the solenoid The highest current density part of the highest current density coil has a current density of 108.8 A per square mm, which is lower than the highest current density sections of some of the high field hybrid solenoids[5]. Most of the magnet power is dissipated in the highest current density section. The cooling system must handle about 15.6 MW (13.3 MW of resistive heating plus 2.3 MW of beam power).

## IV. SUPERCONDUCTING OUTSERT SOLENOID

The water cooled Bitter insert solenoid is surrounded by a superconducting outsert solenoid system. The combination of the Bitter magnet insert and the superconducting outsert generated a magnetic induction of 20 T in the region of the target. The superconducting outsert is defined as the three coils that are immediately outside of the Bitter magnet insert. Other superconducting solenoids downstream from the outsert coils form the transition region that shapes the magnetic field between the target and the phase rotation system. Within the transition region solenoids, the spent beam from the target must be dealt with. The energy absorber must be thick enough to prevent heating of the superconductor in the outsert and transition region coils. As a result, the energy absorber will extend some distance downstream from the target. The material that absorbs particles from the target will become radioactive. The superconducting magnet around the target, the Bitter solenoid and energy absorption material should be split so that it can be taken apart so that the radioactive material inside magnet can be dealt with. The split in the magnet could occur at the end of the transition solenoids.

The outsert solenoid cryostat starts at a radius of 370 mm. The outsert coil alone is will produce a central induction of about 7.5 T. Operating under this condition, the outsert solenoid can be made from niobium titanium in a copper matrix operating at 2.0 K. The outsert solenoid has three coils with an inner radius of 400 mm. The outer radius of these coils is about 540 mm. The peak magnetic induction in the outsert coil is about 8.3 T.

## V. TRANSFER SOLENOID SYSTEM

The transfer solenoid system guides the magnetic field so that the magnetic induction decreases in a smooth fashion from 20 T to 5 T at the start of the phase rotation channel. A transfer of the captured pions from the 20 T target region to the 5 T beam transport and phase rotation region requires an increase in the minimum beam pipe radius to 150 mm.

Once the solenoid magnetic induction has been brought down to the field in the pion decay channel or phase rotation channel, the diameter of the solenoid coils must be changed to match the diameter of the coils in the decay channel solenoids or the solenoids in the phase rotation cavities. The change in solenoid diameter must be accomplished without altering the desired induction along the solenoid axis.

The option shown in Figure 2 has the final 5 T solenoid coil inside diameter set at 375 mm. The system is suitable for transfer into phase rotation cavities that have their 5T solenoids inside the cavities. Solenoids inside the cavities is suitable if the acceleration gaps in the cavity are kept relatively small (below 110 mm). This option shows the spent proton being captured within the superconducting transition magnet section.

A plot of magnetic induction along the axis of the capture and transfer solenoids as a function of distance from the end of the target is shown in Figure 3. Figure 3 shows that there is a smooth transition of the magnetic induction from the end of the target to the start of the first phase rotation cavity (with a 5 T solenoid within it).

Table 1 shows some parameters for the capture and transfer solenoid options. About 15.5 MJ of the system stored magnetic energy is due to the current that flows in the water cooled Bitter insert coils. The Bitter solenoid is inductively coupled with the superconducting solenoids. A shut down of the Bitter solenoid will increase the current in the superconducting magnets. This effect should be tolerable provided the superconducting solenoids are well cooled. A loss of current in the Bitter solenoids system will probably cause the superconducting solenoids to turn normal.

Table I: Capture Solenoid Parameters

| | |
|---|---|
| Magnet Length to x = 3 m(m) | 3.92 |
| Cryostat OD at x = 0 (m) | 1.50 |
| Cryostat OD at x = 3 m (m) | 0.70 |
| Bitter Magnet OD (m) | 0.69 |
| Induction at Target (T) | 20.32 |
| Induction at Target from Bitter Magnet (T) | 12.86 |
| Induction at Target from S/C Magnet (T) | 7.46 |
| Target Region Length (m) | 0.23 |
| Bitter Magnet Peak Current Density (A mm) | 108.8 |
| Bitter Magnet Power (MW) | ~13.0 |
| Beam Tube ID at x = 0 (m) | 0.15 |
| Beam Tube ID at x = 3 m (m) | 0.30 |
| Transition Length (m) | 1.10 |
| Transport Channel Induction (T) | 5.0 |
| Stored Energy to x = 3 meters (MJ) | 59.2 |
| Stored Energy S/C Magnet to x = 3 m (MJ) | 43.7 |

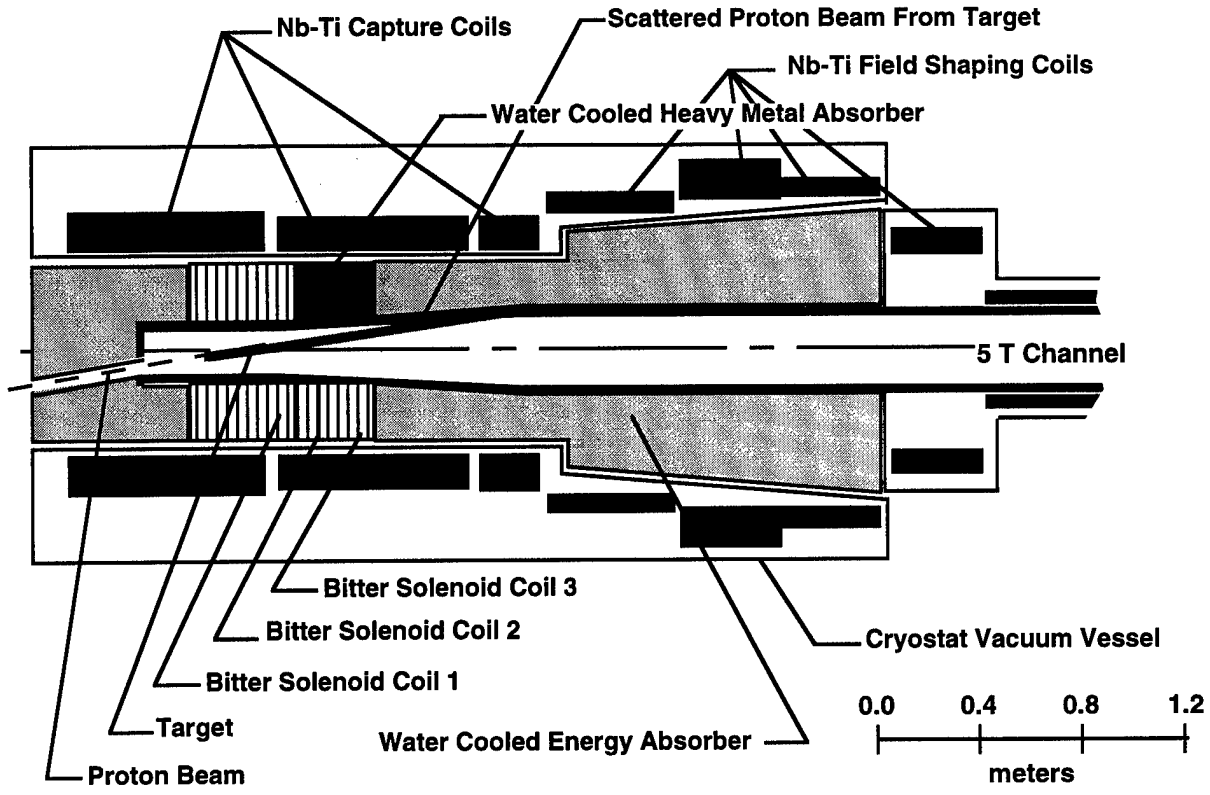



Figure 2 A 20 T Hybrid Capture Solenoid with a Transfer Solenoid System to 5 T in Phase Rotation RF Cavities

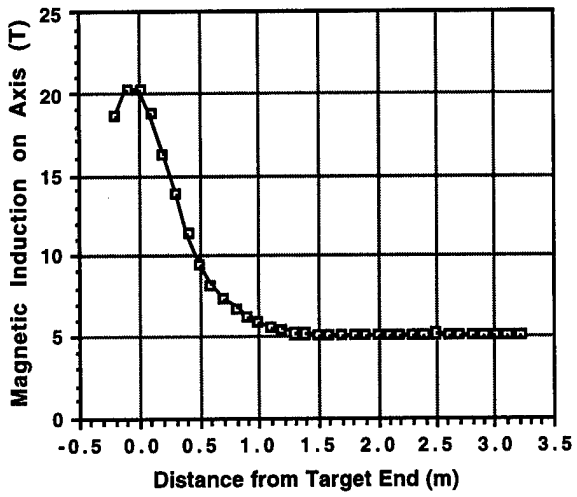



Figure 3 The On Axis Magnetic Induction as a Function of Distance from the Target in the Capture Solenoid System

## IV. CONCLUSIONS

A hybrid solenoid that uses a Bitter water cooled solenoid combined with a superconducting outsert solenoid appears to be an attractive magnet system for capturing and transporting pions generated in a target struck by a high energy proton beam. The hybrid solenoid permits one to shape the magnetic field in a way that is desirable for pion capture and transport to a phase rotation system. Tilting the target will increase the number of pion captured by about sixty percent. The problem of high heat loads from uncaptured particles can be solved with enough water cooled absorber inside of the superconducting magnet system. The water cooled insert solenoid is part of the energy absorption system. An advantage of the tilted target system is that the spent proton beam and any high energy electrons produced at the target are disposed of before they reach the phase rotation system.

## REFERENCES


[1] N. V. Mokhov, R. J. Noble and A. Van Ginneken, "Targetry and Collection Optimization for Muon Colliders," AIP Conference Proceedings **372** (1996)

[2] M. A. Green, "Some Options for the Muon Collider Capture and Decay Solenoids," AIP Conference Proceedings **372** (1996)

[3] "$\mu^+ \mu^-$ Collider, A Feasibility Study," by the $\mu^+ \mu^-$ Collider Collaboration, BNL-52503, July 1996

[4] R. J. Weggel, Collector Magnets for $Mu^+$ - $Mu^-$ Colliders, an unpublished report concerning preliminary design studies of capture magnets system for 2 TeV on 2 TeV and a demonstration collider

[5] J. R. Miller, M. D. Bird, S. Bole, et al, "An Overview of the 45T Hybrid Magnet System for the National High Field Magnet Laboratory," IEEE Trans. Mag **30**, No. 4, p 1563, (1994)

# TUTORIAL ON SUPERCONDUCTING ACCELERATOR MAGNETS*

M. J. (Penny) Ball, Carl L. Goodzeit, M J B Consulting, DeSoto, TX.

*Abstract*

A multimedia CD-ROM tutorial on the physics and engineering concepts of superconducting magnets for particle accelerators is being developed under a U.S. Dept. of Energy SBIR grant. The tutorial, scheduled for distribution this year, is intended for undergraduate junior or senior level science students, and portions will also be useful as resources for high school science classes. However, the unified presentation of the broad range of issues involved in the design of superconducting magnets for accelerators will also be of value to staff of research institutes and industrial concerns with an interest in applied superconductivity or magnet development. The source material is based on the worldwide R&D programs to develop superconducting accelerator magnets. A description of the content material and how it has been organized to be an effective educational presentation is discussed.

## 1. FOREWORD

In response to an SBIR solicitation to enhance the educational value of DOE funded technology, MJB Consulting was awarded Phase I and Phase II grants to develop a multimedia CD-ROM tutorial on Superconducting Accelerator Magnets. The material has been divided into five basic units, with the following themes: (1) Introduction to magnets and accelerators; (2) Superconductors for accelerator magnets; (3) Magnetic design methods for accelerator magnets; (4) Electrical, mechanical, and cryogenic considerations for the final magnet package; (5) Performance characteristics and measurement methods.

Technical and student reviews are in progress. Distribution for industrial users is planned for later this year; the educational version with a teacher guide is expected within six months of the initial release. The product will be available first as a CD-ROM set for the Windows platform; a Macintosh version is expected at a later date. Status information will be available from our web site [1].

## 2. SUBJECT AREAS

This tutorial material is organized in a structure that can be used as a complete course, as individual lessons to supplement physics and engineering courses, or as a reference that can be browsed. The content is organized so that a linear progression through the lessons provides a logical development of the material. However, all material is available at any time; it is possible to jump between topics as need for information dictates. The content of Units 1 and 2 is primarily concepts with minimal mathematics; Units 3, 4 and 5 present the detailed mathematical procedures related to the design and testing of magnets. The content for the five units includes the following topics:

*Unit 1: Introduction to Magnets and Accelerators*

- Introduction to particle physics and accelerator laboratories.
- Types of particle accelerators. Forces on charged particles in a magnetic field.
- Characteristics of dipole and quadrupole magnets for accelerators and how they act on particle beams.
- Function of principal parts of magnets; field line diagrams for normal and skew multipoles.
- Particle beam optics and the analogy between magnets and lenses; aberrations and errors in magnets and how they affect the beam.
- Introduction to superconductivity and the superconducting state. Types of superconducting materials suitable for accelerator magnet application.
- Types of magnet designs used for accelerator dipoles. Description and data for dipole magnets for RHIC, Tevatron, HERA, SSC, and LHC.
- Magnet construction and assembly procedures with videos of RHIC dipole construction at Northrop Grumman and SSC dipole construction at FNAL.
- Factors affecting the choice between superconducting and resistive magnets for accelerator applications.
- Magnet design issues, including structural, electrical insulation, coil cooling, environmental effects, superconductor development.
- Future superconducting magnet applications with overview of MagLev, MHD, SMES.

*Unit 2: Superconductors for Accelerator Magnets*

- Description of the manufacture of NbTi wire and cable.
- Short sample properties for NbTi materials, empirical formula for computing Jc at B and T, calculation of expected magnet performance with a given conductor.
- Manufacture and characteristics of Rutherford cable.
- Properties and present development status of superconducting materials for magnets (including HTS). Calculation of Jc of $Nb_3Sn$ at B and T.
- An interactive program for computing some mechanical, electrical, and thermal properties of materials commonly used in accelerator magnet construction.

* Work supported by U. S. Dept. of Energy under grant DE-FG05-94ER-81813.

0-7803-4376-X/98/$10.00 © 1998 IEEE

*Unit 3: Magnetic Design Methods for Accelerator Magnets*

- Computing 2-D fields from current lines
- How fields are calculated with current shells.
- The effect of the iron yoke on the magnetic field. Iron saturation effects.
- Methods for optimizing the magnetic design using multiple shells and wedges. Calculating the optimum amount of superconductor. An interactive procedure is included for computing fields and multipoles in single layer dipole and quadrupole coils with an optional wedge and yoke.
- Methods used to calculate the magnetic fields produced by cos θ type coil ends. End spacers and their design.
- Discussion of available public domain and proprietary software for calculating magnetic fields in accelerator magnets.

*Units 4 and 5*

The content material of the last two units is not yet in place. However, the following topics will be included:

*Unit 4: Electrical, Mechanical, and Cryogenic Considerations for the Final Magnet Package*

- Mechanical aspects of the cold mass design, such as Lorentz, thermal, and assembly loads.
- Design concepts and methods for collars and yokes.
- Data on mechanical properties of cold mass materials, including conductor stacks.
- Thermal design of magnets, with pool boiling and supercritical helium. Diffusion and cross flow cooling schemes for the cold mass.

*Unit 5: Performance Characteristics and Measurement Methods*

- Magnet quench and performance testing. Methods of locating quench origins. Training data from actual magnet tests.
- Quench protection methods for magnet strings and calculation of the maximum temperature from a quench.
- Magnetic performance measurements and techniques for dipoles and quadrupoles.
- Mechanical performance measurements, such as coil size, pre-stress, and end forces.

## 3. EDUCATIONAL APPROACH AND EXAMPLES

### *3.1 Educational approach*

The guidelines for the technical level of this tutorial were that it should be suitable for a junior or senior level college course. Thus, we have attempted to keep the mathematical treatment of the material consistent with that objective. Most of the mathematical based presentations are in Unit 3, which deals with the magnetic design of the magnets. Here we have treated the material on a level that requires only the use of trigonometry and an understanding of the basics of differential and integral calculus. A useful reference for the development of this section was the 1989 paper by Mess and Schmüser [2].

To accommodate users with widely varying technical backgrounds, frequent use is made of "hot words" and "buttons" that can be clicked to give access to screens with more details, basic explanations, and background material. The tutorial thus also serves as a reference source that would be useful for those interested in superconductivity or magnet development because much technical data is available in these button accessible "sidetracks".

### *3.2 Visuals*

A major advantage of a multimedia presentation is the ability to include video clips and animation sequences, in addition to many photographs. Unit 1 includes a lesson that shows all steps in the production of a magnet, starting from the cable cleaning. This lesson has many video clips and is supplemented by animations that illustrate details. For example, Figure 1 shows part of the sequence that explains the steps in assembly and insulation of the superconducting coils into the cold mass. Unit 2 illustrates the steps in production of superconducting wire and cable with many animations.

These materials are intended to give students a good understanding of the complexity of making these large but extremely precise devices. This content will also be interesting for industrial staff, including technicians and engineers, so that they can appreciate where their particular specialty fits into the complete magnet construction process.

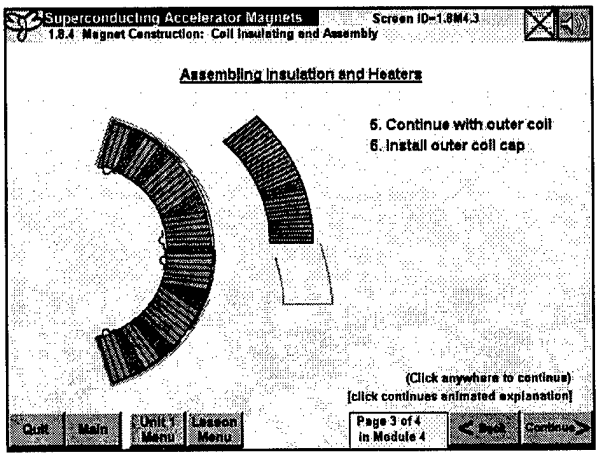



Figure 1

### *3.3 Exercises and Examples*

The educational value of the tutorial is enhanced by the use of numerous exercises / examples: problems (with their solution available on a succeeding screen) or information about actual magnets. Some of these exercises are interactive, allowing the user to move

symbols or input data values. Other exercises are to be solved off-line.

One interactive exercise in Unit 1 tests the student's understanding of the role of dipoles and quadrupoles in accelerators. The screen for this is shown in Figure 2. Diagrams are shown for dipole and quadrupole magnets, which must be placed in their correct positions on the diagram of two intersecting beams to produce the bending and focusing as shown.

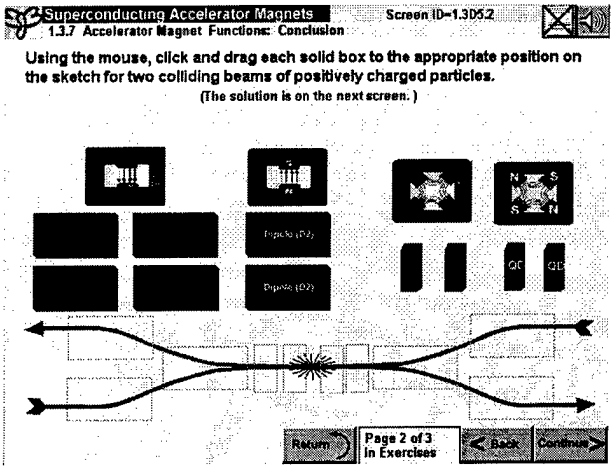



Figure 2

Unit 1 also contains labeled cross section diagrams of the RHIC dipole assembly and cold mass. When the label for a part is clicked, a pop-up box with an explanation of the function of that part is displayed. This interactive example is demonstrated on our web page [1].

Illustrative examples are used to complete the understanding of key issues and provide useful reference points. For example, in Unit 2 formulas are presented for the relationship between critical current, field, and temperature in NbTi superconductor. Then their use is illustrated by the following examples:

Problem: The critical current of the superconducting wire used in the RHIC magnets is 264 A in a field of 5 T and at 4.2 K. If the maximum field on the superconductor in the magnet is 5.3 T and the associated maximum temperature is 4.5 K, what would be the expected critical current of the wire under these conditions?

Problem: Calculate the critical current for $Nb_3Sn$ with a net strain of -0.001 at the point where the peak field is 13.1 T and the conductor temperature is 4.35 K.

Figure 3 shows an example from Unit 3, which is used to illustrate principles of magnetic field calculation.

Also in Unit 3, a detailed example is used to illustrate the process of optimizing the superconductor in a magnetic design. Stepping through this example provides the user with a basic understanding of the principles involved in achieving a magnetic design.

Problem: Develop the magnetic design for a 50 mm diameter aperture dipole magnet using a NbTi conductor, with an iron yoke, that will produce a central field of 9 T at a maximum operating temperature of 2.0 K. Assume that the maximum field in the conductor is 5% greater than the central field. A reasonable assumption to keep the amount of superconductor to a minimum is to assume that the operating margin is 15%.

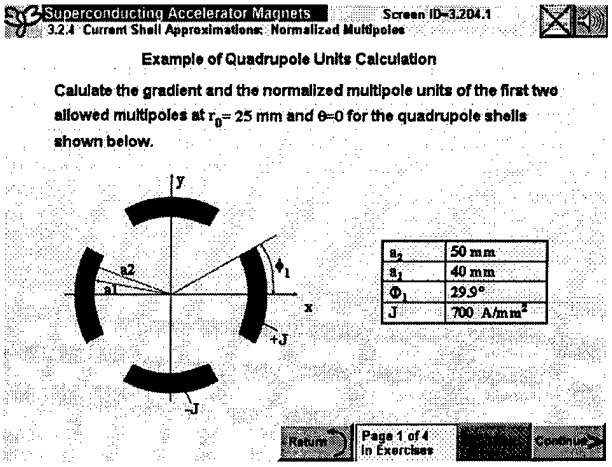



Figure 3

## 4. SOURCE MATERIAL AND ACKNOWLEDGEMENTS

The initial inspiration for the tutorial was the lecture material developed by Arnaud Devred for the Superconducting Super Collider (SSC) magnet program. Presentations from CERN Accelerator Schools have been important sources also. Magnet developers and superconductor scientists at laboratories and industrial firms, both U.S. and international, have supplied valuable data that has enabled completion of the technical content.

The following institutions have also supplied material: Northrop Grumman; Lockheed Martin; Oxford Instruments; Fermi National Accelerator Laboratory; Brookhaven National Laboratory, Lawrence Berkeley National Laboratory, Applied Superconductivity Center-University of Wisconsin-Madison, Texas Center for Superconductivity- University of Houston.

## REFERENCES

[1] The URL for the web page is: http://web2.airmail.net/mjb1

[2] K.-H. Mess and P. Schmüser: 'Superconducting Accelerator Magnets', CERN 89-04, CERN Accelerator School – Superconductivity in Particle Accelerators, Proceedings, CERN, Geneva 1989, p 87.

# SUPERCONDUCTING SOLENOIDS FOR THE POLARIZED ELECTRON SPIN CONTROL SYSTEM OF THE MIT-BATES SOUTH HALL RING (SHR)

R. Averill, K. Dow, J. Dzengeleski, C. Sibley MIT-Bates;
Y. Shatunov, P. Vorobiev, P. Klimine, A. Smirnov, Budker Institute of Nuclear Physics.

## I. INTRODUCTION

A scientific collaboration between MIT-Bates and the Budker Institute of Nuclear Physics (BINP) has produced a design for a magnetic insertion, aka "Siberian Snake", into the SHR lattice, which allows for spin control of 0.3 to 1.0 GeV polarized electron beams for planned internal and external target physics. This report describes the design, construction and testing at BINP and the final testing at MIT-Bates for the two superconducting solenoids, which make up part of the "Snake". The solenoids each have the following specifications for 1.1 GeV polarized electron spin manipulation; 7.0 cm dia. warm bore, LOA of 104 cm, Bz (max) of 7.27 Tesla @290 A and an integrated axial field strength of 5.764 Tesla-meter @ 290 A. The magnetic insertion is 4.8 meters long and consists of two pairs of skew quadrupoles each with Leff=0.3 meter and a central quadrupole with a Leff=0.5 meter. Alternatively, the solenoids could be placed on the extraction line and be used for spin control of the extracted polarized electron beam should the SHR be operated simply as a stretcher ring. See Figure 1 for elevation view of the insertion.

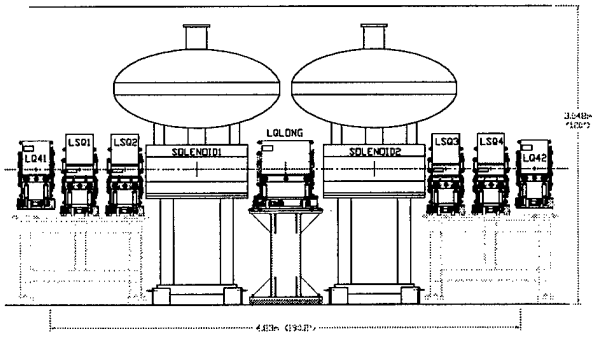



Fig. 1. SHR proposed layout of solenoids

## II. DESIGN PARAMETERS

Mechanical specifications concerned the physical size of the units and the limitations of the space available in the SHR tunnel for the insertion to be installed easily. Since the tunnel has a height limitation of 120 inches and the overall length of the insertion was to be minimized, the maximum field was specified to be 7.27 Tesla and allow the standard 2.5 inch diameter beam pipe to pass through with a radial clearance of about 3 mm. The stray field was specified to be <10 Gauss at 1 meter from the ferromagnetic shield, which encloses the cryostat for the solenoid coils. A special BINP designed support stand allows each unit to be assembled and installed before raising the solenoid to the SHR beam height of 54" above the tunnel floor.

Magnetic specifications were set to operate the solenoids at up to 300 A. The solenoidal field is produced by five shorter (160mm long) solenoids assembled on a fixed mandrel and connected electrically in series. See Figure 2.

The superconductor is wound under a pretension so that the coils are in compression when unpowered and use both sides of the increased strain range available when powered fully. The field varies along the axis as in Figure 3.

The number of turns of the 0.87 mm diameter conductor wound on each sub coil is about 3170 turns over 17 layers and the solenoid total inductance is calculated to be

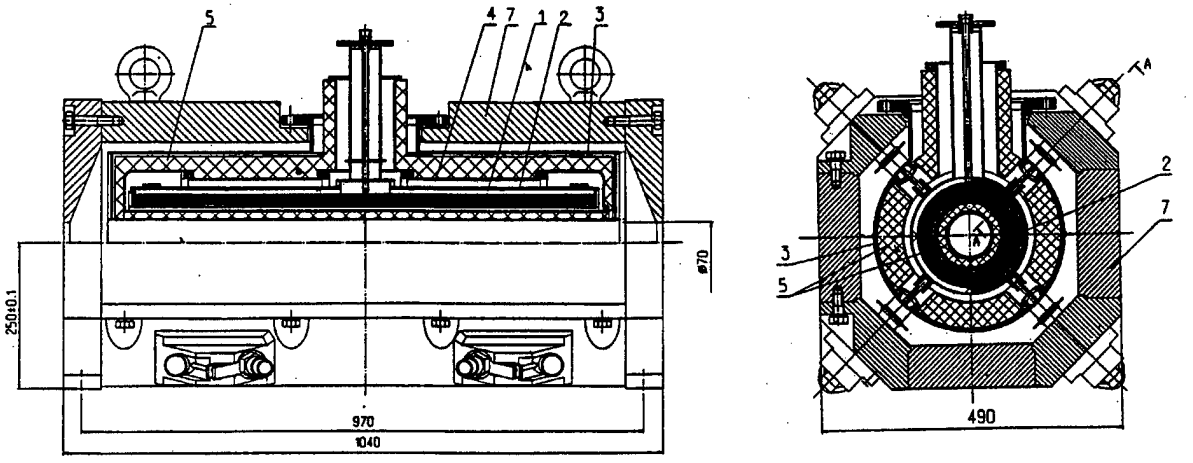
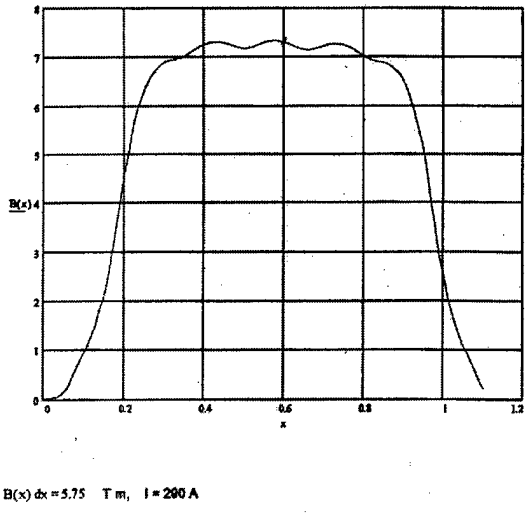



Fig. 2. Superconducting Solenoid (side and end view).

0-7803-4376-X/98/$10.00 © 1998 IEEE




$\int_0^{1.14} B(x)\,dx = 5.75$ T m, I = 200 A

Fig 3. Solenoid $B_{(x)}$ vs. x; $B_{(x)}$ = tesla, x = meter

4.5 Henry. The magnetic shield is made of a low carbon steel and also serves to support the internal components. The magnetic forces between the coils and the shield is exactly zero provided all subcoils have the same excitation. In a quench scenario studied for a single subcoil the solenoid suspensions easily handle all unbalanced axial forces. BINP technical staff calculated the magnetic fields and forces using a software called MERMAID. MIT-Bates independently had the fields and forces calculated using the software program called ANSYS. The agreement between the programs was excellent and is the basis for the approved magnetic design.

Cryogenic specifications included only liquid helium be used for the cooldown and operating the coils in the superconductive state. The boil off rate for LH2 was set at < 1.38 Liters/hr (1 watt) for each solenoid. The rate measured in testing so far has been about 1.2 watts, but the systems may not have reach final equilibrium during those short test periods. The design includes a storage dewar which attaches to the solenoid cryostat from above and has an ellipsoidal shape to allow the volume of about 400 liters to be fit into the SHR tunnel.

Quench protection circuitry was designed to bring out some of the energy stored into external resistors by a means of a discriminator circuit that looks at the voltage across the coils and inserts a resistance if the voltage is above a preset level. This circuit includes the subcoil leads (10) being brought out of the cryostat and connected in a way that reduces the quench energy in the cryostat and the amount of LHe that is boiled off during a quench. Several quenches imposed by the designers during testing demonstrated this approach to work well. The storage cryostat when connected as designed to the solenoid cryostat allows LHe to be fed to the bottom of the solenoids during cooldown, but after a level is established above the solenoid, the tube feeding the LHe is withdrawn a few cm and then fills the upper storage dewar. All leads into the solenoid enter through the top of the storage dewar and have a relatively long thermal path between room temperature and LHe temperatures.

Controls and Instrumentation specifications included the power supplies to be supplied by MIT-Bates. Controller for the power supplies were also of the standard type in use at MIT-Bates. Collaboration between the electrical engineers of the two laboratories allowed this interface to be jointly designed so that preliminary testing could take place at BINP and then at MIT-Bates using the final power supplies selected. All internal instrumentation for monitoring temperature of the coils, the copper shields of the solenoid cryostat and the storage dewar were required to be redundant to insure alternate monitors be available should one fail. Carbon resistors were used to measure the temperature of the coils and platinum resistors are used to measure the 90k temperature of the heat shield screen at several places. There is a pressure transducer which samples the pressure in the cryostat. Four Hall probes are installed inside the ferromagnetic shield and provide a measurement of 73 mv/Tesla and is proportional to the axial field, which is linear with current. All controls and instrumentation have been designed to be compatible with the SHR computer system known as the RCS. At this time only one set of controls exists at MIT-Bates in December 1996. Plans are to complete the controls system for the second solenoid system and run both systems again for training and magnetic field measurements at more levels than earlier measured.

## III. MEASUREMENTS AT BINP

MIT-Bates technical staff visited BINP in June 1996 and witnessed factory acceptance tests over a 10 day period for the two solenoid systems. A full set of planned measurements was taken for both systems and the factory acceptance testing was successfully completed without any significant problems.

Cooldown measurements indicated that about 60-80 liters of LHe was necessary to bring a single cryostat's internals to the 4.2 Kelvin level. Additional cryogen then began filling the storage dewar above the solenoid to a level sufficient to operate the unit for several days. A limitation in the availability of LHe caused the tests to be run in series for the two solenoid systems, but both behaved similarly during their respective cooldowns. Some effort was expended to determine the boil-off rate of LHe and using a gas meter over a period of time the volume of liquid gas boiled off was determined to be about 1.6 liters per hour or 1.2 watts, exceeding the specification by about 20%. Later measurements on the loss rate could be somewhat lower since the system had not reached its final thermodynamic equilibrium during the testing period. Pressure and resistive temperature sensors monitored the status of the cryostat during the cool down to 4.2 Kelvin. The resistance of the solenoid leads was monitored by a meter in order to verify the state of the coil as it was cooled.

Axial field measurements were made every cm along the full solenoidal field extent at various currents. See Figure 3. A similar plot was taken parallel to the on axis field at r = 1.5 cm and the data obtained showed no significant difference from the on axis measurements. Meas-

urements at r = 1.5 cm and at multiples of 30 degrees confirmed the cylindrical symmetry of the solenoidal field. The axial field was calibrated against a NMR probe and showed a linear relationship with current over the 0 to 290 A range. The magnetic field maximums at a distance of about 1 meter from the iron shield were about 3 gauss satisfying the <10 gauss specification when the axial field level was 7.3 Tesla.

## IV. TESTS AT MIT-BATES

In mid November 1996 a team of five BINP technical staff arrived to assemble, test and provide training to the MIT-Bates staff in the solenoid systems operation. The work went forward rapidly and the first solenoid was cooled down in two weeks. Interfacing of the control system and instrumentation allowed proper control of the unit. MIT-Bates staff made magnetic measurements along the axis at several field levels and determined that the systems magnetic design was achieved. Assembly of the units is demanding particularly at the connection points between the solenoidal and the storage dewar where several joints between the 0.87mm diameter NbTi/Cu superconductor wire are made. These leads run up through the storage dewar and then to the control/quench systems. The second unit was assembled and tested without any problems completing the MIT-Bates acceptance tests required. This acceptance testing was completed within a four week period. Figure 4 shows the arrangement at MIT-Bates during acceptance tests in December 1996.

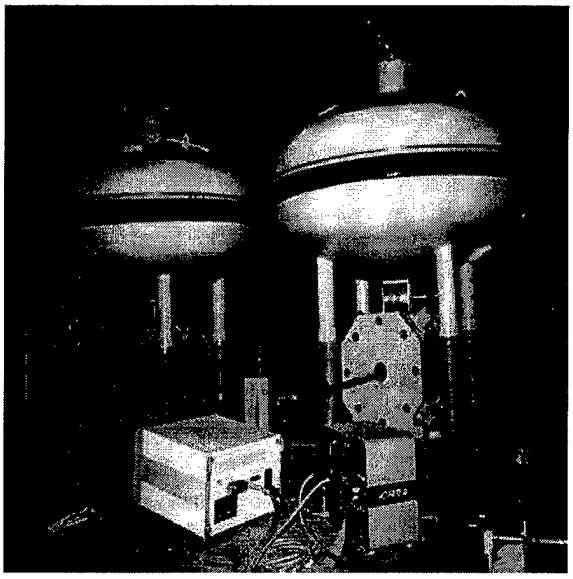


Fig. 4 Solenoids under test at MIT-Bates, Dec. 1996.

## V. CONCLUSIONS

The scientific collaboration between BINP and MIT-Bates has produced a set of superconducting solenoids to provide spin control of a polarized electron beam in the SHR. The collaboration also provides for BINP technical staff to assist MIT-Bates in the commissioning of the "Siberian Snake" when it is installed in the SHR lattice some time in the future. The cooperation of all parties in the project is acknowledged and was important to the success achieved to date. The authors acknowledge the major contribution of V. Seleznev of BINP to the completion of acceptance testing at Novosibirsk and Bates and of S. Ottaway of MIT-Bates during the testing at the Laboratory. See Table 1 for a tabular listing of magnetic specifications.

**Table 1. Solenoid Parameters**

| | |
|---|---|
| Integrated Field Strength on axis @290A | .5.764 T-m |
| Peak Magnetic Field @290A | 7.27 T |
| Effective Length | 803 mm |
| Outside axial length f-f | 1040 mm |
| Conductor diameter | 0.87 mm |
| Superconductor fill factor | 0.43 |
| Average critical current at 7.3 Tesla | .310 A |
| Number of sub section coils in solenoid | 5 |
| Number of turns per sub section coil | 3170 |
| Total number of turns for solenoid | 15,850 |
| Inductance of solenoid | 4.5 Henry |
| Solenoid stored energy @290A | 189,000 Joules |
| ID of coils | 124 mm |
| OD of coils1 | 60 mm |
| Build of coils | 18 mm |
| Length of sub coils | 160 mm |

## VI. REFERENCES


[1] P.M. Ivanov, Yu.M. Shatunov, G.T. Zwart; A Universal Superconductive Spin Rotator for MIT-Bates South Hall Ring., Technical Report No. B/SHR 93-10, MIT-Bates

[2] R.J. Averill; Technical Specification for Superconducting Solenoids for the MIT-Bates South Hall Ring. October 1, 1993[3] I.Koop, Yu.M. Shatunov, P. Vorobiev,

[3] Superconducting Solenoid of Spin Rotator for MIT Bates Linear Accelerator Center. Technical Design, BINP, Novosibirsk, 1995

[4] P. Vorobiev, A. Smirnov & BINP technical staff, Superconducting Solenoid for Spin Rotator, Description

# MEASUREMENT OF YOUNG'S MODULUS AND SHIM CALCULATION FOR LHC PROTOTYPE DIPOLE MAGNETS

F. G. Eysselein, W. Gärtner, Noell-KRC Energie- und Umwelttechnik GmbH, 97064 Würzburg, Germany and
J. Vlogaert, D. Perini, CERN

*Abstract*

The superconducting coils of LHC prototype dipole magnets wound from a Nb-Ti cable of the Rutherford type are assembled in an Aluminium clamping structure, the so called collars. The coils have to be prestressed in order to avoid movements of the superconductor during operation, which may cause quenches. The exact value of the prestress and the uniformity of the prestress over the length are adjusted by the thickness of inserted shims.

The basis for prestressing the dipole coils is the precise measurement of the size and the Young's modulus of the winding. Based on the measurements shims are calculated ensuring the specified prestress of the coil. During shim calculation several corrections of the shim thickness have to be taken into accopunt e.g. corrections due to the deformation of collars.

The measurement of Young's modulus and the shim calculation will be presented.

## 1 INTRODUCTION

Superconducting coils have to be prestressed in order to avoid movements of the superconductor during operation. The value of the prestress is calculated by finite element analysis. The prestress is 55 MPa for the inner and outer layer of the actual prototype dipole magnets.

The coils are prestressed by inserting shims in the collaring structure. The thickness of the shims is based on the required prestress, the Young's modulus measurements and the actual size of the coils

## 2 MEASUREMENT EQUIPMENT

The coil will be compressed hydraulically in a special mould and the deformation measured by inductive gauges and recorded via PC.

Using different inserts of the mould the following positions are measured:

a) the straight part of a single layer
b) the coil ends of a single layer
c) the layer jump of the assembled

## 3 MEASUREMENTS

For prototype manufacturing the straight part and the coil ends of single layers are measured. After the assembly of a pole the layer jump of the assembled pole is measured.

This method has to be reviewed for series production.

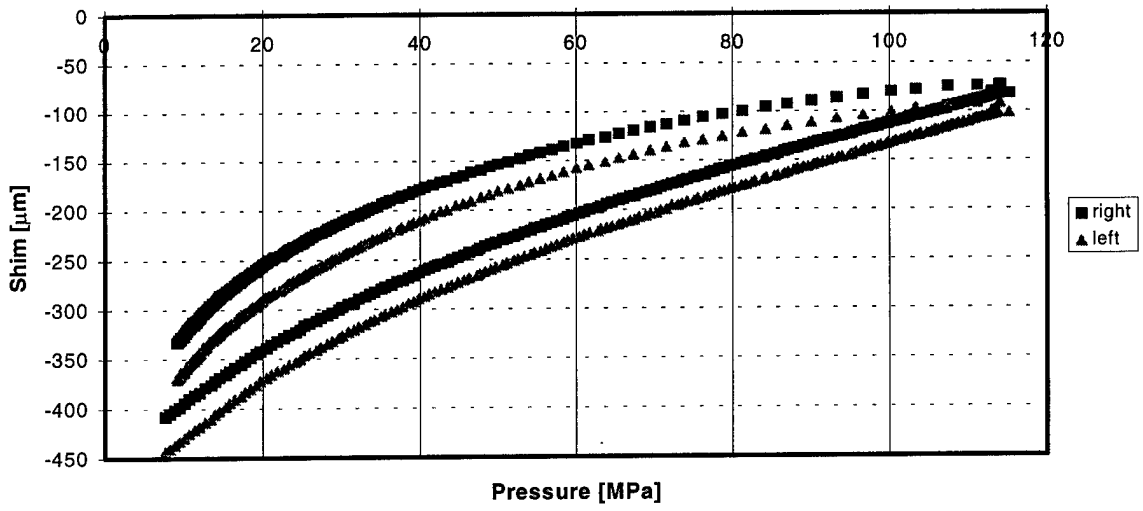



Figure 1: Measurement of inner layer

0-7803-4376-X/98/$10.00 © 1998 IEEE

The coils are compressed five times and the fifth load cycle is recorded. The applied load varies between 0 MPa and 120 MPa for the straight part and the layer jump or 0 MPa and 30 MPa for the coil ends respectively.

The deformation of the left and right side of the coils is measured and recorded for increasing and decreasing load.

The coils are measured at nine positions of the straight part, at one position of each coil end and at one or two positions respectively of the layer jump.

Figure 1 shows a typical measurement graph of an inner layer with the curves for increasing and decreasing load.

## 4 CALCULATION OF SHIMS

There are two different ways of shim calculation with regard to the collar deformation.

The first way is to take for specified prestress of 55 MPa of the coil the shim thickness from each graph for decreasing pressure at 55 MPa. Then the values are averaged over left and right side and over the nine measurement positions of the length.

To this averaged shim thickness the corrections due to the collar deformation, the elastic behaviour of the ground insulation, the size of the gauge pieces and the tolerances of the collars are added.

A second way is to take from each graph the shim thickness at 110 MPa under consideration that there is a reduction of the prestress due to the collar deformation of approx. a factor of two (factor obtained by FE analysis and tests on models). The values are averaged and the remaining corrections for ground insulation, gauge pieces and tolerances of collars are added.

Both methods show the same results for the shim thickness within approx. 3/100 mm.

## 5 RESULTS

Figure 1 shows the measurement of an inner layer at measurement position 5 of the straight part. Negative values of the shim have to be subtracted from the nominal shim

The measured Young's moduli of the layers wound from superconducting cable with a prepreg insulation vary between 18,000 MPa and 22,000 MPa.

Fig. 2 shows the distribution of the coil size over the 10m length of 4 different outer layers. The tolerance of the coil size over the length is ± 4/100 mm.

The difference between the layers 009, 010 and 011, 012 is due to different superconducting cable. The cable of layers 009 and 010 is coated, the cable of layers 011 and 012 is not coated

The graphs of the 4 different coils are nearly parallel which indicates that the variations are caused by the tooling.

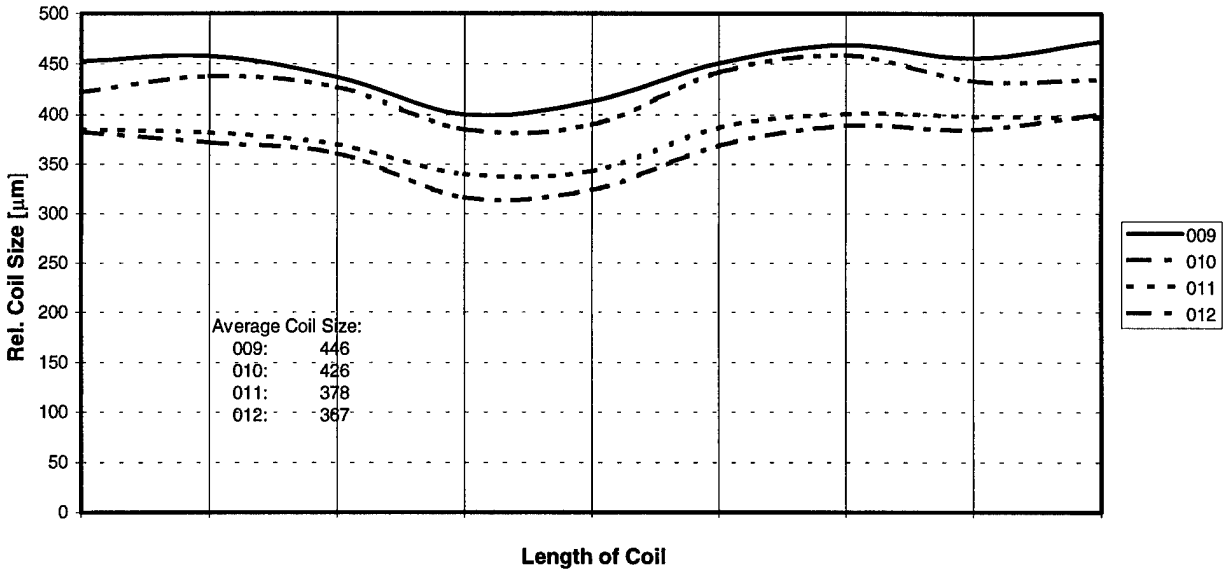



Figure 2: Distribution of coil size

The remaining prestress of the coil after collaring is verified by measuring the deformation of the collars. The higher the prestress of the coil the larger the deformation of the collars.

For this purpose the dependence of the deformation of the collars on the prestress of the coils was determined in several ways. Collars were loaded hydraulically or by screws and their deformation measured. Short models of coil sections were collared with different inserted shims for different prestresses and in each case the deformation of the collars measured. The measured datas resulted in a curve for calibration.

Figure 3 shows the measurement of the collar deformation over the length of the coil as an indication of the prestress of the collared coils. The distribution is homogenous over the length. The minor collar deformation in the coil ends shows the required lower prestress.

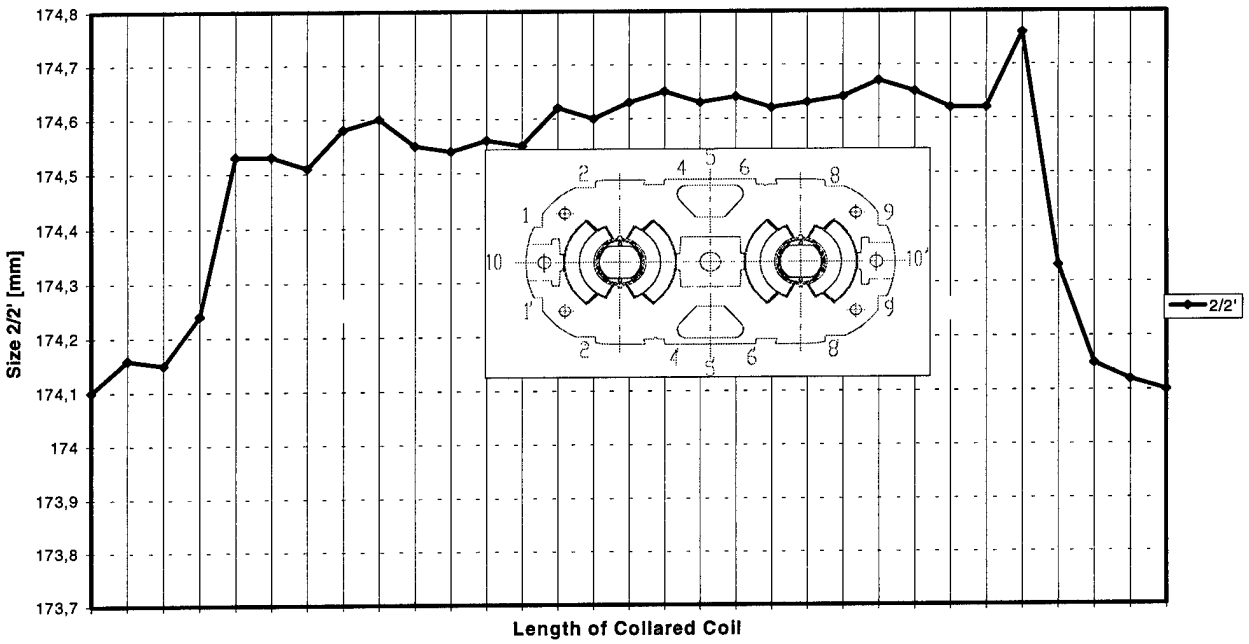



Figure 3: Deformation of collars

The measured collar deformation shows that the specified prestress could be achieved within the tolerances.

## 6 CONCLUSIONS

The presented method for Young's modulus measurements and shim calculation give reliable results for obtaining the correct thickness of the shims for a specified prestress of the collared coils.

By the measurement of the collar deformation the remaining prestress of the collared coil after collaring is controlled. The measurements show a homogenous stress distribution over the length of the coil.

It has to be checked if the measurement procedure has to be improved for series production of the magnets by measuring assembled poles.

# PROGRESS IN THE DESIGN, MANUFACTURE AND TESTING OF THE KLOE SOLENOID FOR THE DAΦNE RING AT FRASCATI

D.E. Andrews, A.J. Broadbent, M. Greenslade, S.M. Harrison, D.M. Jenkins, J.S.H. Ross, K.D. Smith, A.J. Street, C. Timlin, J.M. Wiatrzyk (Oxford Instruments, United Kingdom),
KLOE Collaboration: Spokesperson P. Franzini (INFN, Frascati, Italy)

*Abstract*

Oxford Instruments took over the manufacture of the 5.8 m outer diameter 4.4 m long 0.6 T Solenoid for the KLOE detector on the DAΦNE ring when the Austrian company ELIN closed its magnet manufacturing plant. The paper begins by briefly discussing the magnet design before describing the approach Oxford Instruments has taken to the completion of the magnet. The results of system testing at Oxford Instruments will be described along with the proposed installation schedule.

## 1 INTRODUCTION

In January 1994, ELIN (an Austrian electrical company) was awarded the contract for the design and manufacture of the KLOE solenoid for the DAΦNE ring at Frascati. Until December of that year the company had worked on the design and procurement of elements of the system before the holding company decided to close its superconducting magnet manufacturing plant in Weiz, Austria. Oxford Instruments took over completion of the system at this time as sub-contractors to ELIN with INFN's agreement.

The superconducting magnet is designed, in conjunction with its iron yoke, to produce 0.6 T over a 4.3 m long 4.8 m diameter volume to act as a detector in the search for the solution to the "matter - anti matter" imbalance. The magnet specifications are below.

Table 1 - magnet specifications

| | |
|---|---|
| Central magnetic field | 0.6 T |
| Vacuum case length | 4.4 m |
| Vacuum case inner diameter | 4.86 m |
| Vacuum case outer diameter | 5.76 m |
| Coil shell inner diameter | 5.19 m |
| Cold mass | 10 tonnes |
| Vacuum case mass | 26 tonnes |
| Iron return yoke mass | 475 tonnes |

## 2 DESIGN

The design constructed by Oxford Instruments is shown in the schematic below.

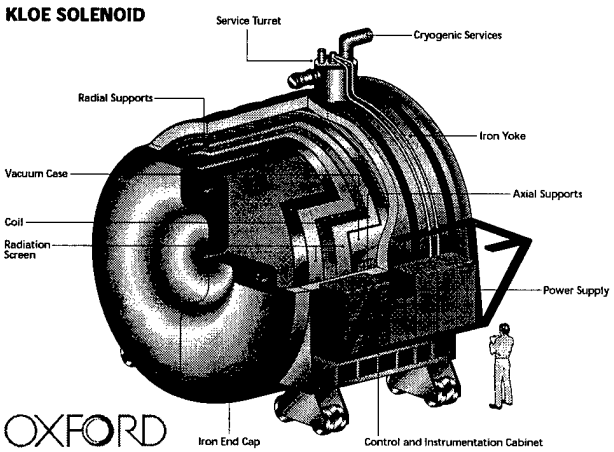



Figure 1 - KLOE schematic

### *2.1 Coil Shell and Conductor*

Oxford Instruments took over responsibility for the shell after the coil shell made by Elin was rejected by INFN; Oxford Instruments changed the design to one fabricated from a number of 12 mm thick aluminium sheets and cooling channels. The new design relied on achieving the diametrical tolerances (eased by INFN to ± 8 mm) by fabricating it on an adjustable spider that allowed the ribs to be moved around until the tolerances were met. The inner skin was fully welded to the ribs whilst the outer was partially welded. No machining took place on the shell although the inner welds were all hand dressed. This approach was very successfully carried out by Vosper Thorneycroft (Southampton, UK).

This new design of coil shell was designed, manufactured and delivered in 6 months thus minimising the delay to the system manufacturing schedule.

The conductor is a 10 mm by 5 mm composite consisting of a Rutherford cable co-extruded with high purity aluminium. The conductor, provided by LMI, was cleaned and then wrapped with two half lapped layers of 0.125 mm glass tape.

The two layer coil was wound inside the coil shell by rotating the shell on motorised rollers in a controlled manner whilst the conductor was fed in and directed on to the shell face from a spool mounted off the winding machine. The conductor was wound on flat and between the two layers 1 mm thick high purity aluminium sheets were placed in order to improve propagation velocities and reduce the peak quench temperatures.

0-7803-4376-X/98/$10.00 © 1998 IEEE

After winding, the coil was lined with aluminium, to act as an impregnation vessel, before being turned axis vertical and placed inside a 7 m cubic impregnation oven. The aluminium liner was supported against collapse by a fabricated support structure before the coil space was evacuated, filled with epoxy and then cured at 100° C for 48 hours. The major coil parameters are listed in Table 2.

Table 2 - coil parameters

| | |
|---|---|
| Layers | 2 |
| Turns/layer | 368 |
| Ampere-turns | 2.14 MA-T |
| Operating current | 2902 A |
| Stored energy | 14.3 MJ |
| Inductance at full field | 3.4 H |
| Discharge voltage | 250 V |
| Peak quench temperature | 80 K |

*2.2 Radiation Screen*

The radiation screen will be cooled by helium gas from the DAΦNE refrigerator.

The inner and outer radiation screen cylinders are simple end cooled screens each constructed from eight pre-fabricated panels - each panel consists of three components - two 1 mm thick flat aluminium sheets and one 1 mm thick corrugated aluminium sheet. The three components are all bonded and riveted together on a former of the correct diameter in a sandwich construction consisting of flat sheet - corrugated sheet - flat sheet. The cooling pipe is welded to the panels over a length equivalent to 30 % of their circumferential extent. This minimal approach to the cooling of the radiation screens is possible only as a result of the extremely low radiant and conducted heat loads. The guaranteed heat load is given in Table 3. The screen is supported from the vacuum case by stainless steel cables.

Table 3 - guaranteed heat load

| **Source** | **Heat load** |
|---|---|
| Current leads | 0.6 g/s |
| 4 K Radiation and conduction | 55 W |
| 70 K Radiation and conduction | 530 W |

*2.3 Service Turret*

Little design work had taken place before contract hand over and the refrigerator contractor was not selected until early in 1996: as a result many design issues were not finalised until then.

The space available for the service turret is very restricted due to the need to minimise the cut out in the iron and the very restricted height. The service turret provides the following functions:

- supply and control of liquid helium
- 150 litre helium storage volume
- supply and control of 70 K helium for radiation screens
- gas cooled 3,000 A current leads from 300 K
- instrumentation connections to the coil and radiation screens

The delay in the settlement of some of the design issues meant that connections to the refrigerator were finalised after the service turret was in manufacture. This, coupled with a lack of space forced by the need to minimise the iron cut-out, has led to a need for a separate valve box. This will be mounted on top of the iron and contains a number of valves to facilitate safe and easy connection to the refrigerator.

The system is now complete and the cryogenic guaranteed parameters are summarised in Table 3.

*2.4 Power Supply and Control Instrumentation*

The power supply was originally to be a thyristor controlled switch mode system. However, because of concern about electromagnetic interference with the experimental detectors a series regulated supply designed for low EMI has been provided.

The control and instrumentation can be subdivided as shown in Table 4.

Table 4 - controls & instrumentation

| **Functions** | **System Component** |
|---|---|
| Overall control + monitoring | Labview running on Pentium PC |
| Temperature measurement | Oxford Instruments ITC-600 |
| Helium valve control | Weka valve controlled by Labview driver |
| Current leads control | Northvale Korting Bossmatic valve controlled by separate PID controller |

The system has distributed control with centralised monitoring via Labview.

## 3 WORKS TEST

The system was assembled in January 1997 ready for the works test which began in February. The system components tested consisted of the following:

- Magnet and Cryostat
- Service Turret
- Power Supply
- Control and Instrumentation
- Valve Control Panel

The additional valve box was not subject to a cryogenic works test and the iron yoke was not involved.

The coil cooling system and radiation screen were externally connected in series so that they could be cooled by a single controlled flow of nitrogen. The system took nineteen days to cool from 300 K to 77 K and used 36 tonnes of liquid nitrogen. After pumping and flushing with helium, the coil and service turret were cooled to 4 K in a further two days using 3,000 litres of helium. Magnet energisation and heat load tests took a further day before the system was actively warmed, using the power supply and by airing up the vacuum space with nitrogen gas, back to room temperature in a further 6 days.

The 4 K heat load was found by monitoring the boil off gas flow rate. The test was performed with the coil at 4.3 K, with liquid in the service turret, the transfer siphon (used to fill the service turret from transport dewars) removed from the service dewar and the coil energised at a steady 1,000 A. The radscreen was at a steady temperature of 83 K throughout the test. The steady boil off measurement, after removing the current lead contribution, was 1.38 g/s and produces a 4 K heat load of 27.6 W - compared with a guaranteed value of 55 W. The current lead boil off for both leads was 0.12 g/s at 1,000 A which compares well with the scaled guaranteed value of 0.2 g/s.

The system was energised to 1,000 A at a charge rate of 1.4 A/s (specified rate is 0.5 A/s) without problem and the magnet operated at this current during other system tests. The quench detector, power supply, contact breaker, free wheel diodes and dump resistors were all checked along with all the safety interlocks.

The magnet proved to be difficult to quench. Even after drying out the helium in the service turret and coil cooling channels and warming the coil the conductor had still not quenched two hours after all helium had been removed. The current lead protection system took over when the lead temperature exceeded its threshold and the magnet ran down on the power supply resistor.

The 77 K heat load was measured after removing all cryogens from the radscreen by monitoring the mid screen temperatures over a 48 hour period. The temperature rose from 85 K to 104 K which, given a mass of 1,250 kg and enthalpy change of 8,650 J/kg, gave an equivalent heat load of 62.6 W at 77 K. This compares favourably with the guaranteed value of 530 W.

## 4 COMPLETION SCHEDULE

Subsequent to the status report and schedule reported in [1] the completion schedule has advanced significantly and it is now expected that commissioning and acceptance will be over by July 1997 rather than October 1997.

## 5 CONCLUSION

Many detailed and some major design and manufacturing changes have been made to the original ELIN design. The system has been assembled and successfully tested at reduced current at Oxford Instruments' facility in Eynsham UK. Testing at Oxford Instruments took place in early 1997 and delivery to Frascati took place in March 1997. Full tests will take place at Frascati in the iron return yoke ready for handover by mid 1997, assuming the INFN test facilities are available as scheduled.

## 6 ACKNOWLEDGEMENTS

Oxford Instruments would like to thank the KLOE collaboration for their help and support throughout the period since contract handover in 1994.

Thanks are also due to the ELIN engineering and commercial teams who dealt with the information transfer in a very professional manner.

## REFERENCES

[1] K.D. Smith, A.J. Broadbent, M. Greenslade, S.M. Harrison, D.M. Jenkins, J.S.H. Ross, A.J. Street, M.C. Townsend and J.M. Wiatrzyk "Progress in the Design and Manufacture of the KLOE Solenoid for the DAΦNE ring at Frascati", *ASC*, August 1996.

# MAXWELLIAN FIELD EXPANSION OF HELICAL MAGNET

K. Hatanaka, T. Katayama*, and T. Tominaka**
Research Center for Nuclear Physics, Osaka University, Ibaraki, Osaka 567, Japan
*Research Center for Nuclear Science, University of Tokyo, Tanashi, Tokyo 188, Japan
**The Institute of Physical and Chemical Research (RIKEN), Wako, Saitama 351-01, Japan

*Abstract*

Three dimensional (3D) magnetic field calculated by the computer code TOSCA was analyzed including the fringing field region. The magnetic field in the median plane was well simulated by a simple function. Off median plane, contributions from the coils should be taken into account.

## 1 INTRODUCTION

Superconducting helical dipole magnets will be used in RHIC as Siberian snakes and rotators[1]. Extensive investigations are performed on the orbit and spin trackings to examine whether the spin polarization of the proton will be conserved up to the highest energies with the help of Siberian snakes. During the first stage, the numerical tracking was performed using an analytical expression for the magnetic field in the snake. It is now required to use a more realistic description for the magnetic field in the snake. Beam trajectory and spin motion can numerically be calculated, provided that the magnetic field map is given along the beam path. However, it is not practical to store the whole field strengths along the helical magnets. Besides, the map has usually some errors. Calculated or measured magnetic field maps may not always satisfy Maxwell's equations. This causes errors in numerical calculations of the orbit and spin matrices; orbit matrices should be symplectic, and spin matrices be unitary. There are following three methods to improve the situation. (1) An approximately symplectic matrix calculated from a field map is transformed into an exactly symplectic one, (2) Small modifications to the field values are performed so as to bring the field satisfy Maxwell's equations, (3) The field is made more Maxwellian by reading only one or two field components from the map and deriving the other components by using appropriate expansion coefficients.

The method (3) is physically more sound[2] and should produce a more symplectic matrix. This strategy was applied to examine three dimensional (3D) magnetic field calculated by the computer code TOSCA includind the fringing field region.

## 2 MULTIPOLE EXPANSION OF THE MAGNETIC FIELD

### 2.1 Cartesian Coordinate System

In a current free region in vacuum where the electric field $\vec{E}$ is constant, the magnetic field $\vec{B}$ can be derived from a scalar potential $\Psi$ as

$$\vec{B} = -\nabla\Psi. \tag{1}$$

In a Cartesian coordinate system, the scalar potential is expanded in power series of $x$ and $y$ coordinates:

$$\Psi = \sum_{m=0}^{\infty}\sum_{n=0}^{\infty} A_{m,\,n}(z)\frac{x^n}{n!}\frac{y^m}{m!}, \tag{2}$$

where $z$ is a coordinate of axis. If the magnetic field has a median plane symmetry, $\Psi$ is an odd function of $y$; i.e., $m = odd$[3]. The Laplace equation, $\Delta\Psi = 0$, gives the following recurrent relation between coefficients:

$$A_{m,\,n+2}(z) + A_{m+2,\,n}(z) + A^{(2)}_{m,\,n}(z) = 0. \tag{3}$$

Coefficients, $A_{0,\,n}(z)$ and $A_{1,\,n}(z)$ are obtained as functions of $z$, from the expansion of $B_x(x,0,z)$ and $B_y(x,0,z)$ in the median plane in series of $x$ at each $z$-position. Therefor, all the coefficients are determined from the analysis of measured/calculated magnetic field distributions only in the median plane:

$$A_{0,\,n} = -\left(\frac{\partial^n B_x}{\partial x^n}\right)_{x=y=0}, \tag{4}$$

$$A_{1,\,n} = -\left(\frac{\partial^n B_y}{\partial x^n}\right)_{x=y=0}, \tag{5}$$

$$A^{(k)}_{m,\,n} = \frac{d^k A_{m,n}}{dz^k}. \tag{6}$$

With these coefficients, $B_x(x,y,z)$, $B_y(x,y,z)$ and $B_z(x,y,z)$ are calculated off median plane as below:

$$B_x = -\frac{\partial\Psi}{\partial x} = -\sum_{m=0}^{\infty}\sum_{n=0}^{\infty} A_{m,\,n+1}(z)\,\frac{x^n}{n!}\frac{y^m}{m!}, \tag{7}$$

$$B_y = -\frac{\partial\Psi}{\partial y} = -\sum_{m=0}^{\infty}\sum_{n=0}^{\infty} A_{m+1,\,n}(z)\,\frac{x^n}{n!}\frac{y^m}{m!}, \tag{8}$$

$$B_z = -\frac{\partial\Psi}{\partial z} = -\sum_{m=0}^{\infty}\sum_{n=0}^{\infty} A'_{m,\,n}(z)\,\frac{x^n}{n!}\frac{y^m}{m!}. \tag{9}$$

### 2.2 Cylindrical Coordinate System

In the central region of a helical dipole magnet or for a helical magnet of infinite length, the magnetic field has a cylindrical symmetry and a solution of the Laplace equation $\Delta\Psi = 0$ is given by[4]

$$\Psi = -B_0\{\sum_{n=0}^{\infty}\frac{2^{n+1}(n+1)!}{(n+1)^{n+2}}\frac{1}{r_0^n k^{n+1}} I_{n+1}((n+1)kr)$$

$$\times\,[\,\tilde{a}_n\cos((n+1)\,\tilde{\theta}) + \tilde{b}_n\sin((n+1)\,\tilde{\theta})]\}, \tag{10}$$

0-7803-4376-X/98/$10.00 © 1998 IEEE

where $I_n$ are modified Bessel functions and $\tilde{\theta}$ is defined as

$$\tilde{\theta} = \theta - kz, \tag{11}$$

where $k = 2\pi/\lambda$ and $\lambda$ is the wave length of the helix. Modified Bessel functions are expanded in the form of the ascending series of $r$,

$$I_{n+1}((n+1)kr) = \sum_{j=0}^{\infty} \frac{1}{j!(n+j+1)!} \left(\frac{(n+1)kr}{2}\right)^{2j+n+1}. \tag{12}$$

Now, the magnetic field can be computed as

$$B_r = B_0\{\sum_{n=0}^{\infty} \frac{2^{n+1}(n+1)!}{(n+1)^{n+1}} \frac{1}{r_0^n k^n} I'_{n+1}((n+1)kr)$$

$$\times [\, \tilde{a}_n \cos((n+1)\,\tilde{\theta}) + \tilde{b}_n \sin((n+1)\,\tilde{\theta})]\}, \tag{13}$$

$$B_\theta = B_0\{\sum_{n=0}^{\infty} \frac{2^{n+1}(n+1)!}{(n+1)^{n+1}} \frac{1}{r_0^n k^n} \frac{1}{kr} I_{n+1}((n+1)kr)$$

$$\times [\, \tilde{b}_n \cos((n+1)\tilde{\theta}) - \tilde{a}_n \sin((n+1)\tilde{\theta})]\}, \tag{14}$$

$$B_z = -krB_\theta, \tag{15}$$

$$B_x = B_r \cos(\theta) - B_\theta \sin(\theta), \tag{16}$$

$$B_y = B_r \sin(\theta) + B_\theta \cos(\theta). \tag{17}$$

Multipole coefficients, $\tilde{a}_n$ and $\tilde{b}_n$ are related with $a_n$ and $b_n$ in a two-dimensional approximation (or a straight magnet)[5]:

$$a_n = \tilde{a}_n \cos((n+1)kz) - \tilde{b}_n \sin((n+1)kz), \tag{18}$$

$$b_n = \tilde{a}_n \sin((n+1)kz) + \tilde{b}_n \cos((n+1)kz). \tag{19}$$

If we expand vertical magnetic field components, $B_y$, in series of $r$, we obtain

$$B_y/B_0 = [\, 1 + \frac{1}{4}(kr)^2 + (\text{higher order of } r^n)\,] \cdot b_0$$

$$+\{[\, b_2 - \frac{1}{8}(kr_0)^2 \cdot b_0\,](\frac{r}{r_0})^2 + (\text{higher order of } r^n)\} \cos(2\theta)$$

$$+\{\text{higher multipoles}\} \tag{20}$$

Helical dipoles have sextupole components originating from the structure[6]. When the magnet length, $\lambda = 240\ cm$ and the reference radius, $r_0 = 3.5\ cm$, then the sextupole contribution from the dipole field becomes

$$\frac{1}{8}(kr_0)^2 \simeq 1 \times 10^{-3}. \tag{21}$$

## 3 NUMERICAL ANALYSIS

### 3.1 Fitting Procedure

In order to analyze the magnetic field calculated by Okamura[7], the scalar potential was assumed to be expanded as

$$\Psi = -B_0 \sum_{n=0}^{\infty} (\frac{1}{r_0})^n$$

$$\times\{[\sum_{j=0}^{\infty} \frac{r^{n+1}}{n+2j+1} (\frac{r}{r_0})^{2j} \cdot a_{n,j}(z)\,] \cos((n+1)\theta)$$

$$+[\sum_{j=0}^{\infty} \frac{r^{n+1}}{n+2j+1} (\frac{r}{r_0})^{2j} \cdot b_{n,j}(z)\,] \sin((n+1)\theta)\}. \tag{22}$$

Here, $a_{n,j}(z)$ and $b_{n,j}(z)$ are functions of $z$, and they are $\cos((n+1)kz)$ - or $\sin((n+1)kz)$ - like functions for an infinitely long magnet. The order of magnitude of their derivatives are estimated as

$$a_{n,j}^{(2m)}(z) = \frac{d^{2m}}{dz^{2m}} a_{n,j}(z) = o(((n+1)k)^{2m}) \cdot a_{n,j}$$

$$\sim o(10^{-3m}(n+1)^{2m}) \cdot a_{n,j}. \tag{23}$$

From the Laplace equation, $\Delta\Psi = 0$, coefficients, $a_{n,j}(z)$ and $a_{n,j}(z)$, satisfy following relations

$$a_{n,j+1} = -\frac{n+2j+3}{4(j+1)(n+j+2)} \cdot \frac{1}{n+2j+1} \cdot a_{n,j}^{(2)}, \tag{24}$$

$$b_{n,j+1} = -\frac{n+2j+3}{4(j+1)(n+j+2)} \cdot \frac{1}{n+2j+1} \cdot b_{n,j}^{(2)}. \tag{25}$$

In the analysis, coefficients, $a_{n,j}(z)$ and $b_{n,j}(z)$, were determined by fitting the radial field $B_r$ and the azimuthal field $B_\theta$ in the median plane ($\theta = 0$ or $\pi$), respectively. In the fitting procedure, the maximum value of $n$ was taken 6 and odd $n$ values were also included. The $j$'s were taken to be zero except for $n = 0$ (dipole component). Only the second derivatives of $a_{0,0}$ and $b_{0,0}$ were taken into account and higher order derivatives were negrected. This assumption is reasonable from the previous estimation of the order of magnitudes for coefficients $a_{n,j}$ and $b_{n,j}$ in (23). Following expansion was used in the fitting procedure,

$$B_r = -\frac{\partial\Psi}{\partial r}$$

$$= B_0\{[a_{00} + a_{01}(\frac{r}{r_0})^2] \cos(\theta) + [b_{00} + b_{01}(\frac{r}{r_0})^2] \sin(\theta)$$

$$+ \sum_{n=1}^{6} (\frac{r}{r_0})^n [a_{n0} \cos((n+1)\theta) + b_{n0} \sin((n+1)\theta)]\}, \tag{26}$$

$$B_\theta = -\frac{\partial\Psi}{\partial\theta}$$

$$= B_0\{[\, b_{00} + \frac{1}{3} b_{01}(\frac{r}{r_0})^2] \cos(\theta) - [\, a_{00} + \frac{1}{3} a_{01}(\frac{r}{r_0})^2] \sin(\theta)$$

$$+ \sum_{n=1}^{6} (\frac{r}{r_0})^n \, [\, b_{n0} \cos((n+1)\theta) - a_{n0} \sin((n+1)\theta)]\}. \tag{27}$$

The longitudinal field $B_z$ was "predicted" with derivatives of coefficients obtained above,

$$B_z = -\frac{\partial \Psi}{\partial z}$$

$$= B_0 \cdot r\{[a'_{00}+\frac{1}{3}a'_{01}(\frac{r}{r_0})^2]\cos(\theta) + [b'_{00}+\frac{1}{3}b'_{01}(\frac{r}{r_0})^2]\sin(\theta)$$

$$+ \sum_{n=1}^{6} \frac{1}{n+1}(\frac{r}{r_0})^n \, [\, a'_{n0} \cos((n+1)\theta) + b'_{n0} \sin((n+1)\theta)]\}. \tag{28}$$

### *3.2 Results*

At each $z$-position, coefficients $a_{n0}(z)$ and $b_{n0}(z)$ were determined by fitting the 3D-calculated field $B_r$ and $B_\theta$ in the median plane ($y = 0$) with equations (26) and (27). The 3D-field was calculated from $x$, $y = -35\ mm$ to $35\ mm$ in $5\ mm$ step including the iron core[7]. Consequently, 14 coefficients were determined by fitting the calculated fields at 30 points with the Simplex minimizing procedure. Differences between the 3D calculated and fitted/predicted fields are shown in Fig. 1. In the median plane, the 3D-field $B_x$ and $B_y$ are well approximated including the fringing field region by the function assuming a cylindrical symmetry. The longitudinal field $B_z$ was "predicted" with the equation (28) and it agrees with the 3D-field very well.

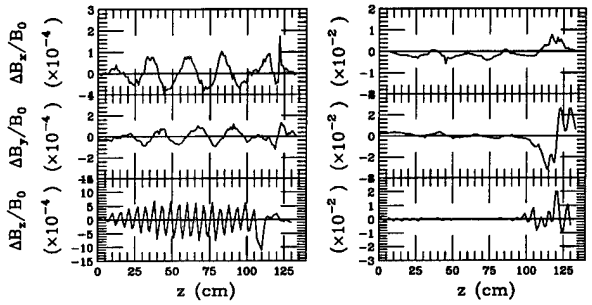



Figure 1: Differences between the 3D-calculated and fitted/predicted fields normarized by $B_0$, left: in the median plane $x = 3\ cm$ and $y = 0\ cm$, and right: off median plane $x = 0\ cm$ and $y = 3\ cm$.

Off the median plane, for example along the line $x = 0\ cm$ and $y = 3\ cm$, relatively large differences are observed between 3D-results and our approximation, especially at the magnet edge. The magnetic field generated by a current parallel to the $x$-axis at $y = y_0$ and $z = z_0$ is given by

$$\vec{B} \propto (0, \frac{z - z_0}{[(y - y_0)^2 + (z - z_0)^2\,]^{\frac{3}{2}}}, \frac{y_0 - y}{[(y - y_0)^2 + (z - z_0)^2\,]^{\frac{3}{2}}}). \tag{29}$$

The fitting errors observed for the $B_y$ field at the magnet edge are well described by the sum of three terms with the functional form (29) corresponding to a magnetic field generated by a line current parallel to the $x$-axis[8]. Fitting errors for the $B_z$ field at the edge is also described by the functional form derived from three line currents at the same positions, if the these currents are reduced by a factor of four[8]. At the edge of a helical magnet, there are currents not only parallel to the $x$-axis but also those parallel to the $z$-axis. The latter cause additional $B_y$ field but do not have $B_z$ component. Altough the field (29) overestimates the contribution for $B_z$ due to such a simplification, it shows that we have to take account of the effects of the coil at the end of a magnet. Inside the magnet, on the other hand, magnetic field is well described by a simple function of cylindrical symmetry including the fringing field region.

## 4 SUMMARY

Calculated 3D-field was analyzed to obtain the analytical expressions satisfying Maxwell equations. In the median plane, the field $B_x$ and $B_y$ were well expanded with simple functons of a cylindrical symmetry including the fringing field region. The longitudinal field $B_z$ was also well "predicted" with coefficients determined from fitting $B_x$ and $B_y$. Off median plane, on the other hand, effects of coils parallel to the $x$-axis were required to explain the difference between 3D-field and the "predicted" field from the analysis. Present procedure can be also applied to analyze measured magnetic fields for helical magnets.

## 5 ACKNOWLEDGEMENTS

The authers acknowledge M. Okamura for the results of his 3D calculations, and T. Kawaguchi and A. Luccio for discussions.

## 6 REFERENCES

[1] E. Courant et al.: 'The Use of Helical Dipole Magnets in the RHIC Spin Project', AGS/RHIC/Spin Note, BNL, No. 40 (1996).

[2] A. Luccio: 'Field Map Generated Matrices for Spin Tracking', AGS/RHIC/Spin Note, BNL, No. 41 (1996).

[3] K.L. Brown: 'A First- and Second-Order Matrix Theory for the Design of Beam Transport Systems and Charged Particle Spectrometers', SLAC Report, No. 75 (1967).

[4] G.H. Morgan: 'Computation of the Harmonics in a Helically Wound Multipole Magnet', AGS/RHIC/Spin Note, BNL, No. 9 (1995).

[5] W. Fischer: 'On Measurements of Helical Magnetic Fields Using Devices for Straight Magnets', AGS/RHIC/Spin Note, BNL, No. 32 (1996).

[6] T. Katayama: 'Multipole Field Expansion of Helical Magnet', AGS/RHIC/Spin Note, BNL, No. 38 (1996).

[7] M. Okamura: private communication.

[8] K. Hatanaka: 'Magnetic Field Analysis of Helical Magnets', AGS/RHIC/Spin Note, BNL, No. 37 (1996).

# DESIGN OF THE SECTOR MAGNETS FOR THE RIKEN SUPERCONDUCTING RING CYCLOTRON

T. Kawaguchi, T. Kubo, T. Mitsumoto, H. Okuno, T. Tominaka, J. W. Kim, S. Fujishima, K. Ikegami, N. Sakamoto, S. Yokouchi, T. Morikawa, Y. Tanaka, A. Goto, and Y. Yano
The Institute of Physical and Chemical Research (RIKEN), Wako, Saitama, 351-01, Japan

*Abstract*

Design study of the superconducting sector magnets for the RIKEN superconducting ring cyclotron is described. Structures, magnetic forces, superconducting coils and a cryogenic system are discussed. Special features are, the cold pole arrangement, the supporting structure for huge magnetic forces, and the cryogenic stable coils.

## 1 INTRODUCTION

The RIKEN Superconducting Ring Cyclotron (SRC) is one of the main accelerators for the "RIKEN RI Beam Factory".[1] Six units of superconducting sector magnets[2] are used as the main components of the SRC. Each of sector magnets must generate a maximum magnetic field of 4.5 T in the beam orbital area. We use superconducting main coils and also superconducting trim coils to obtain compactness in size and to save electric power and cooling water. A yoke and poles made of magnetic soft iron are arranged in the sector magnet to reduce ampere turns of the superconducting coils and to minimize a leakage magnetic flux. Table 1 shows main parameters of the sector magnets.

Table 1. Parameters of the sector magnets.

| | |
|---|---|
| Average radii of beam injection | 3.56 m |
| extraction | 5.36 m |
| Sector angle of main coil | 25 degree |
| Maximum magnetic field | |
| in the beam orbital area | 4.5 T |
| in the main coil | 5.5 T |
| in the trim coil | 5.0 T |
| Main-coil's ampere turns per magnet | 6.0 MA |
| Coil cooling method | LHe bath cooling |
| Magnetic stored energy for 6 magnets | 450 MJ |
| ( 75 % in air, 17 % in poles, 8 % in yokes) | |
| Maximum operation currents | |
| for main coil | 5,000 A |
| for trim coil | 500 A |
| Iron weight of 6 magnets | |
| poles | 216 tons |
| yokes | 3,630 tons. |

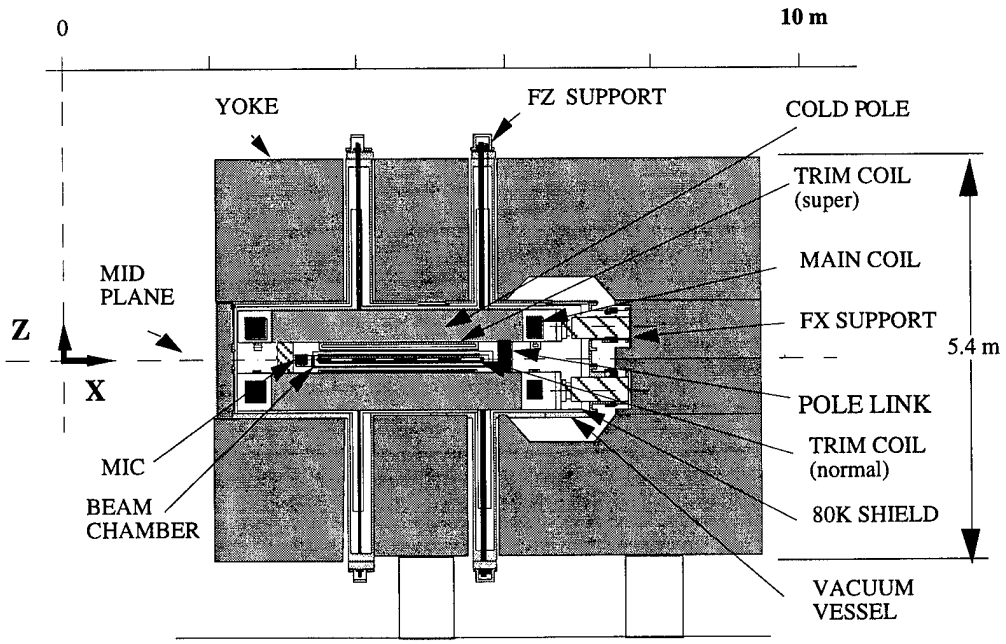



Fig. 1. Cross-sectional view of the sector magnet.

0-7803-4376-X/98/$10.00 © 1998 IEEE

## 2 STRUCTURES OF THE SUPERCONDUCTING SECTOR MAGNET

Figure 1 shows a cross-sectional view of the sector magnet. Main components of the magnetic elements are superconducting and normal conducting coils, poles and a yoke. We use two kinds of superconducting coils: a pair of main coils and a group of trim coils. Both coils are located upper and lower sides with respect to the mid plane. A group of normal conducting trim coils is also arranged in the upper and lower sides of the beam chamber, to obtain a strictness of isochronous fields.

A special feature is the cold-pole arrangement. This arrangement gives an easier mechanical support against the huge magnetic forces of the main coils, and gives the reductions of ampere-turns and of magnetic forces, compared with a warm-pole arrangement. A vertical magnetic force (Fz) is supported with two pole links which are attached to the upper and lower cold poles.

We have invested two ways of supporting a magnetic shifting force (Fx) in the radial direction. One way is to arrange a pair of cold rings which connect the cold masses (coils and cold poles) of the six sector magnets in 4.5 K region. A problem of the cold ring support system is the central space for the cyclotron. This space is limited for arranging the beam injection elements. The other way is to use large size thermal insulated supports made of high strength material like as titanium alloy, in between the cold mass and the yoke using the outer space of the sector magnet. The problems of this support system are its large heat leak, and its mechanical deflection which causes a position shift of the magnetic field. After optimization for decreasing the shifting force Fx, we have almost decided to use the thermal insulation support system as shown in Fig. 1.

## 3 MAGNETIC FORCES

Table 2 shows the calculated magnetic forces on the main coil and cold pole at an ampere turns of 6 MA per magnet (or per two coils). The vertical force Fz of 1,154 tons will make a bending deflection of 2 mm in the normal direction to the cold pole of 465 mm in thickness. The shifting force Fx of 104 tons will make the coil position change by 1 mm in the radial direction. This force Fx is generated by the arrangement of six sector coils and the asymmetric configuration of the coils and irons.

## 4 SUPERCONDUCTING COILS

The superconducting main coil has a triangle shape with two long straight sections of about 3.5 m long. The magnetic force on the main coil is supported by the coil vessel and the cold pole. We apply a cryogenic stabilizing method for the main coil and the trim coil to prevent coil quench. Their average current densities are 34 A/mm$^2$ and 41 A/mm$^2$, respectively.

We considered two materials for the stabilizer of the superconducting wire. One was pure copper having rough surface, and another was pure aluminum having flat surface. We have decided to use pure aluminum stabilizer with a reason of the price. Therefore more considerations about the electrical and mechanical properties, the thermal contraction from room temperature to 4.5 K, and the quench protection, were necessary. Specifications of the superconducting wires are shown in Table 3.

## 5 CRYOGENIC SYSTEM

Figure 2 shows the cooling diagram. Two refrigerators having a capacity of 500 W each at 4.5 K will be used for cooling of the six sector magnets plus the beam injection and extraction superconducting magnets.

Table 2. Magnetic forces exereted on the main coil and the cold pole

unit: ton

| | Fx | Fy | Fz |
|---|---|---|---|
| For half main-coil | | | |
| No. 1 element | -87 | 0 | -9 |
| No. 2 | -166 | 132 | -25 |
| No. 3 | -185 | 940 | -254 |
| No. 4 | 160 | 205 | -84 |
| No. 5 | 310 | 21 | -115 |
| Sum. | 32 | 1298 | 87 |
| For one cold-pole | -12 | 0 | -180 |
| For half cold-mass ( one main-coil and one cold-pole) | 52 | 0 | -1154 |
| For one cold-mass (one magnet) | 104 | 0 | 0 |

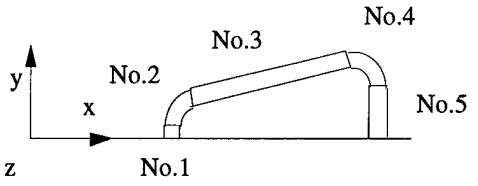



Table 3. Specifications of the superconductors

| | [Main Coil] | [Trim Coil] |
|---|---|---|
| Max. operation current (A) | 5,000 | 500 |
| Critical current (A) at 6T, 4.5K | 10,000 | 1,000 |
| Cryogenic stabilizing current (A) | 6,000 (partial stab.) | 550 (full stab.) |
| Cooling surface ratio | 50 % | 40 % |
| Outer dimensions (mm) | 8 X 15 | 2.9 X 3.6 |
| Material | NbTi/Cu-Al | NbTi/Cu-Al |
| Al/Cu /NbTi section area ratio | 17/1/1 | 15/1/1 |
| Surface treatment | non | non |
| Total length for 6 magnets (km) | 77 | 47 |

The cold-mass weight of the six sector magnets is 360 tons, and it will take one and a half months for cooling the cold mass from room temperature to 4.5 K. We expect to operate the superconducting ring cyclotron for more than 6,000 hours a year. Therefore, the cold mass should be kept in low temperature as long as possible. When one refrigerator breaks down, the magnets can be kept at 5 to 6 K with the other refrigerator. We will have one or two days of power off a year for the power system maintenance, and at that time a recovery compressor with an emergency power source will recover the evaporated helium gas to buffer tanks. We will use no liquid nitrogen in this cryogenic system for simplicity of the cooling system.

## 6 R&D ITEMS

We have measured and plan to the following items for verifying our design before constructing the real sector magnets.

1) Heat flux characteristics of superconductors.

Heat flux characteristics of the main and trim coil conductors, which are important parameters for cryogenic stabilizing, were already measured in liquid helium. The results satisfied the design.

2) Cryogenic stabilizing currents.

The cryogenic stabilizing currents of the main and trim coil conductors will be measured using small circular coils under 6 T magnetic field with a bias superconducting coil in liquid helium.

3) Mechanical properties of aluminum stabilizing superconductor.

We have not enough mechanical property data about aluminum stabilizing superconductor. Tensile strength, fatigue strength, and creep characteristics are being measured using the main coil superconductor.

4) A real-size model magnet.

The biggest R&D item is a real-size model sector magnet. We are now constructing the model magnet. The details are given in Ref. 3.

5) Unbalanced magnetic forces.

Unbalanced magnetic forces in the radial, vertical and azimuthal directions can be calculated with 3-D finite element computer program. But these calculated values are less than 2 % of the total magnetic force. Hence, the accuracy of the calculated value should be carefully considered. We plan to measure these unbalanced forces using three sets of small size sector magnets, each consisting of copper coils, poles and a yokes.

## 7 SUMMARY

A basic design of the superconducting sector magnet for the RIKEN superconducting ring cyclotron has been carried out. We are currently studying the details and making the optimization, doing many kinds of R&D.

## REFERENCES


[1] Y. Yano et al.: 'RIKEN RI Beam Factory Project', Proc. of 14th Cyclotrons and Their Applications, 1995.

[2] T. Mitsumoto et al.: 'Design Study of Sector Magnets of Superconducting Ring Cyclotron for the RIKEN RI Beram Factory', Proc. of 14th Cyclotrons and Their Applications, 1995.

[3] T. Kubo et al.: 'Design of a Model Sector Magnet for the RIKEN Superconducting Ring Cyclotron', these proceedings.

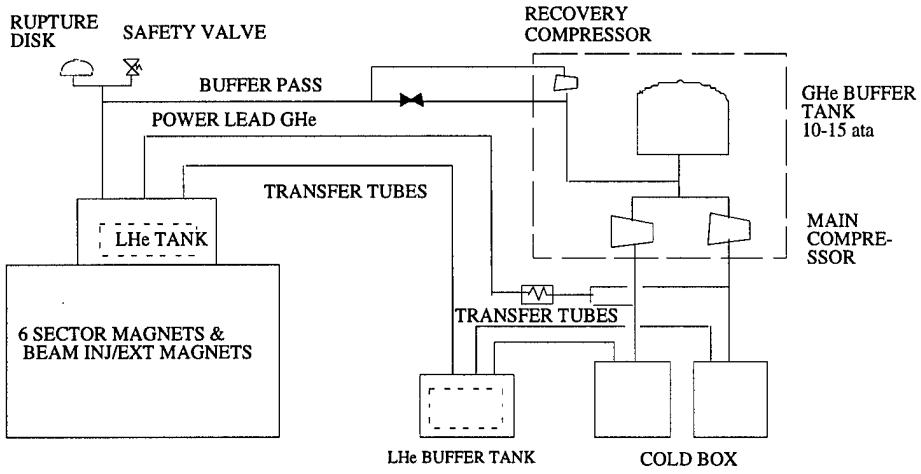




Fig. 2 Cooling diagram for 6 secter magnets and beam injection/extraction magnets

# TRIM COIL SYSTEM FOR THE RIKEN SUPERCONDUCTING RING CYCLOTRON

J.W. Kim, A. Goto, T. Mitsumoto, T. Kubo, H. Okuno, T. Kawaguchi, T. Tominaka, S. Fujishima, K. Ikegamai, N. Sakamoto, S. Yokouchi, T. Morikawa, and Y. Yano
RIKEN, Saitama, Wako, 35-01 Japan

*Abstract*

A superconducting ring cyclotron proposed as a booster of the existing RIKEN Ring Cyclotron (RRC), is composed of six superconducting sector magnets. In each sector magnet, the pole pieces are placed at 4 K to be used as a support structure of the coil vessel against large electromagnetic forces and also to enhance magnetic flux efficiently. The field trimming system suitable for such a cyclotron is thought to be a combination of superconducting and normal trim coils. Considering their differing properties, optimization of a trimming system has been carried out using numerical methods. The trimming system is required to isochronize the magnetic fields for various ions in a wide range of beam energy. Features of the trim coils and the results of optimization are described.

## 1 INTRODUCTION

A superconducting ring cyclotron with six sectors (SRC-6) is under design at RIKEN as the final booster of the primary beam in a cyclotron complex of the Radio Isotope (RI) Beam Factory [1]. Heavy ions such as $^{238}U^{58+}$ will be accelerated from 58 MeV/u to 150 MeV/u, and light ions such as $^{16}O^{7+}$ from 126 MeV/u to 400 MeV/u for efficient RI beam production using a projectile fragmentation method.

Variable energy cyclotrons need an efficient magnetic field trimming system, which requires optimization of its location, current, and so on. Regarding to the location, room temperature ring cyclotrons usually have their trim coils placed on the pole faces. However, in a superconducting ring cyclotron the location of resistive trim coils is restricted to either near the beam chamber or near the yoke due to the presence of a cryostat [2]. In both cases, the trimming capability solely by resistive trim coils is poor, partly also due to pole saturation. The SRC-6 will utilize both superconducting and normal trim coils. A major portion of field trimming is carried out with five sets of superconducting trim coils. Normal trim coils are then used for fine field tuning, keeping their power dissipation relatively low.

There have been design attempts to reduce the contribution from the trim coils by modifying the magnetic fields from the main sector magnet [3]. In our case, however, the superconducting trim coils easily make most of the correction, leaving the error fields less than $\pm 15$ gauss with a vertical space occupation of 2 cm.

## 2 DESIGN OF THE TRIM COIL SYSTEM

Figure 1 shows the isochronous fields and fields from the sector magnets of SRC-6, in which the fields are azimuthally averaged. Three representative cases have been used in designing the trim coil system, covering the major operation field region. The case of $^{16}O^{7+}$ accelerating to 400 MeV/u requires a maximum correction by the superconducting trim coils.

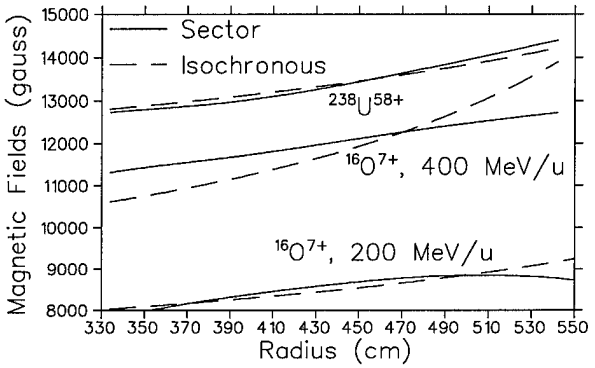



Figure 1: Isochronous fields and fields from the six sector magnets of SRC-6.

The locations of the trim coils are shown in Figure 2. The superconducting trim coils are enclosed with an independent liquid helium vessel from the main coil vessel [4]. The vacuum jacket of the resistive trim coils is separated from the beam chamber, and they comprise a room-temperature penetration through the midplane.

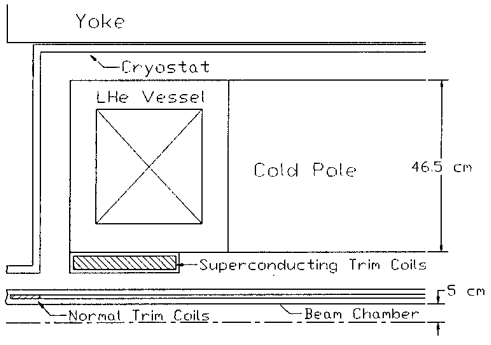



Figure 2: A schematic view of trim coil locations.

### 2.1 *Superconducting Trim Coils*

The superconducting trim coils are accommodated on the cold pole faces so that some vertical support is provided. However, fastening the trim coil vessel onto the pole will

0-7803-4376-X/98/$10.00 © 1998 IEEE

be limited to along the pole center line in order to reduce the thermal stress generated from thermal contraction difference between iron of the pole and stainless steel of the coil vessel.

Figure 3 shows a configuration of the superconducting trim coils. This is not the final shape, but it shows the main features such as no negative curvature. The number of independent excitation is five in the present design, and further details on this number are given in section 2.3.

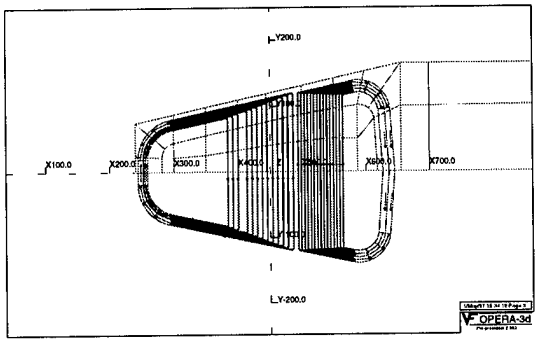



Figure 3: Configuration of the superconducting trim coils.

Among five sets three sets are wound around the nose of the sector, and two around the back of the sector. This configuration appears to be effective in field trimming in view of the shape of pure sector and isochronous fields as shown in Figure 1; the separation point of coil winding direction roughly matches with the intersection of the sector and isochronous fields of $^{16}O^{7+}$. The field distributions of the five-set trim coil system are given in the lower graph of Figure 4 when the sector field is 4.5 T.

Depending on the maximum current required on each set, the total number or the size of each coil has to be varied. Figure 3 shows the case of using a large number of coils in each set. The size of each coil is 1.3×2.3 cm, in which 24 turns can be wound. The coil will be cryogenically stabilized, and high-$T_c$ material current leads will be used.

Superconductor is manufactured by Furukawa wire company with the maximum operation current of 500 A. Some parameters of the wire are listed in Table 1. Performance of the trim coils will be tested with the model sector magnet under construction [5].

Table 1: Parameters of the superconducting trim coil

| | |
|---|---|
| $J_{ave}$ | 4100 A/cm$^2$ |
| $I_{op}$ | 500 A |
| Superconducting Wire | 2.9 × 3.6 mm<br>Al/(Cu/NbTi)> 10<br>RRR > 400<br>$I_c$=1200 A at 6 T, 4.3 K |

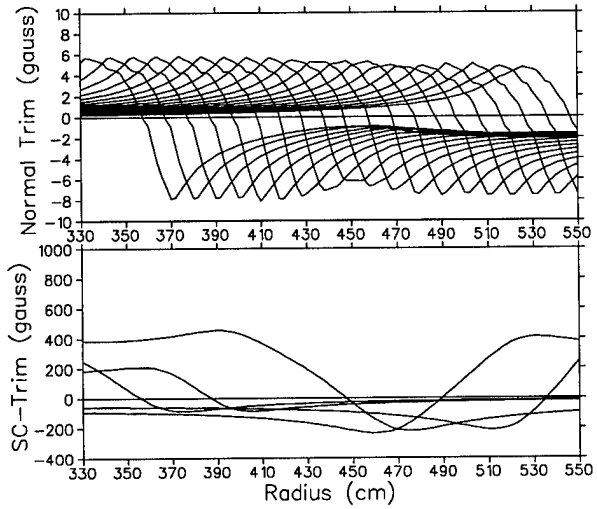



Figure 4: Upper Graph: field distributions of twenty normal trim coils at 500 A when the sector field is 3.8 T, and Lower Graph: field distributions of five superconducting trim coils when the sector field is 4.5 T

### 2.2 *Normal Trim Coils*

The structure of the normal trim coils will be similar to that of the present RRC [6]. Figure 5 shows a layout. Arcs of copper plates insulated with aluminum oxide coating are enclosed with an auxiliary vacuum jacket. At the ends of arcs the copper tubes are welded as both leads and cooling channel.

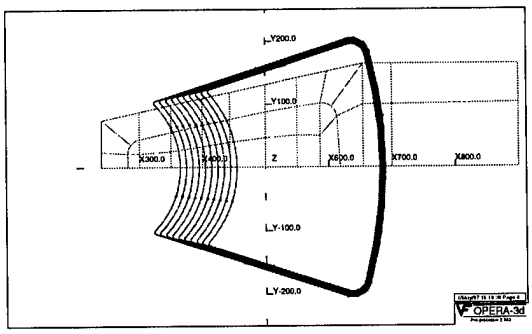



Figure 5: Configuration of the normal trim coils. Trim coils of only inner radii are plotted here.

The upper graph of Figure 4 shows the azimuthal average fields of the normal trim coils at the current of 500 A when the sector field is 3.8 T. Since the normal trim coils are located distant from the pole, the field shapes are not much different from those of the air core fields.

### 2.3 *Optimization of the Trim Coil system*

The criterion of optimization is not well defined as two different kinds of trim coils are involved. The condition of minimum power dissipation which is often adopted for the resistive trim coil optimization is not equally applicable to

the superconducting trim coil. Figure 4 in fact implies that it may be advantageous to use a large number of superconducting trim coils since the field profile of the normal trim coil is not so optimal as a correction coil due to the cancelation effect on adjacent coils. However, the number of the superconducting trim coils is limited by available space for the current leads with a vertical space of 2 cm.

The program used in optimization is the same as used for the design of previous RIKEN cyclotrons [7], utilizing a least square fitting routine. The design ion first used is $^{16}O^{7+}$ in the energy range of 58-400 MeV/u because of the maximum correction field required. As a function of the superconducting trim coil number, the error fields are calculated and shown in Figure 6. With use of 5 sets, the error field reduced within ± 15 gauss, or ±0.13 % of the isochronous field. The case of 6 trim coils didn't improve the fitting so much in the present calculation.

Twenty sets of normal coils were then tested with uniform spacing of 10 cm at radii between 365 cm and 555 cm. Figure 7 shows the leftover error fields after fitting. The orbital frequency error calculated with the EO code is less than ±0.02 %. This error will produce the phase excursion of about 10°, allowing a low beam energy spread. Fitting was also performed for the case of $^{16}O^{7+}$ accelerating to 200 MeV/u. The orbital frequency error could be kept within ±0.025 %, with which the phase excursion is also about 10° because of smaller number of turns.

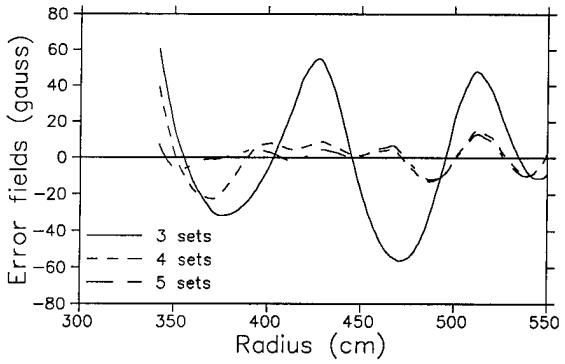



Figure 6: The error fields remained after fitting with different number of sets of the superconducting trim coils for $^{16}O^{7+}$.

In the present design the normal coils which are uniformly spaced can tune the fields well with even distribution of currents as a function of radius. The maximum current needed is about 500 A. The power dissipation is estimated to be 100 kW for 400 MeV/u $^{16}O^{7+}$, which is obtained by scaling the power loss of the present RRC trim coils.

### *2.4 Harmonic Field Effects*

A major field perturbation in the SRC-6 is the first harmonic component coming from the stray fields of injection and extraction elements. The magnitude of the first harmonic is expected to be about 100 gauss on the first turn

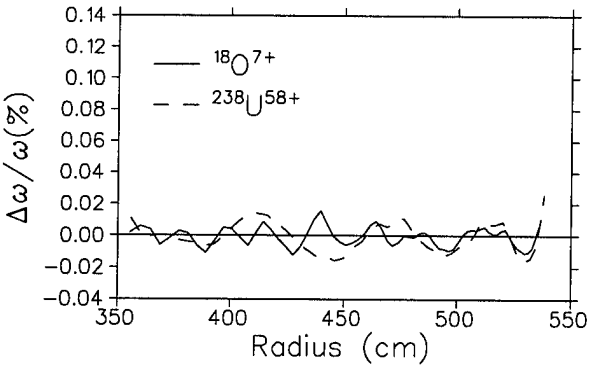



Figure 7: Orbital frequency error after fitting with normal trim coils

with active shielding employed. To compensate for this rather strong stray field, it seems that the innermost and the outermost radius sets of the superconducting trim coils need to be harmonic coils.

The first harmonic field is often used for orbit centering and for off-centering acceleration to increase the extraction efficiency. The estimated off-centering is 0.2 mm/gauss for $^{16}O^{7+}$, which means the first harmonic of about 10 gauss may be needed to move the orbit center. Resistive harmonic coils can handle this magnitude.

## 3 CONCLUSION

For the SRC-6 five sets of superconducting trim coils can effectively correct most of the error fields. The leftover fields can be easily corrected with twenty normal trim coils in the present calculation. The power loss on the normal trim coils is estimated to be around 100 kW for 400 MeV/u $^{16}O^{7+}$. The cryo-stability of the superconducting trim coils will be tested with the model sector magnet under construction.

## 4 REFERENCES


[1] A. Goto et al., The Superconducting Ring Cyclotrons for the RIKEN RI Beam Factory, in these proceedings.

[2] T. Mitsumoto et al., Design Study of Sector Magnets of Superconducting Ring Cyclotron for the RIKEN RI Beam Factory, Proc. of 14th Int'l Conf. on Cyclotrons and Their Applications, (1995) 237

[3] F. Marti, Magnetic Design for a Separated Sector Cyclotron, Proc. of 1994 Euro. Partl. Accel. Conf. (1994) 2304

[4] T. Kawaguchi et al., Design of the Sector Magnets for the RIKEN Superconducting Ring Cyclotron, in these proceedings.

[5] T. Kubo et al., Design of a Model Sector Magnet for the RIKEN Superconducting Ring Cyclotron, in these proceedings.

[6] S. Motonaga, et al., The Sector Magnet for the RIKEN SSC, RIKEN Accel. Progr. Rep. **15** (1981) 162

[7] H. Takebe et al., Design of the Trim Coils for the RIKEN SSC, RIKEN Accel. Progr. Rep. **15** (1981) 173

# A SUPERCONDUCTING SOLENOID FOR HEAVY ION BEAM FOCUSING

J.W. Kim, T. Kubo, T. Kawaguchi,
RIKEN, Saitama, Wako-shi, 351-01 Japan
Y. Imai, T. Minato, and K. Seo,
Mitsubishi Electric Corporation, Wadasaki-cho, Hyogo-ku, Kobe, 661 Japan

*Abstract*

A 6 T superconducting solenoid has been constructed to focus heavy ion beams on the production target of radio isotope beams. The design field on axis is 6.2 T with an average current density of 9,600 A/cm$^2$. The overall coil length is 1.1 meter, and the coil is divided into three equal-length sections to ease winding and to reduce IR drop through diode connection. A main feature of the system is that the solenoid is conductively cooled by a cryocooler directly attached onto the center coil without liquid helium involved. The solenoid was successfully trained to 6.2 T, and its optical properties were tested in the beamline at RIKEN. The design features and the test results are presented.

## 1 INTRODUCTION

The accelerator research facility at the Institute of Physical and Chemical Research (RIKEN) in Japan has provided high current radio isotope beams for nuclear physics research [1]. To produce isotope beams a projectile fragmentation method is being used. By bombarding a production target with heavy ion beam, fragments of the projectile are produced. The Radio Isotope Projectile Separator (RIPS) located downstream then selects the desired beam [2].

Until recently the primary beam has been focused on target using quadrupole lens, the resulting beam spot being larger than 1.5 mm, which meets usual experimental requirements. However, a need for higher precision measurements has demanded even smaller beam spot. After some computational studies and comparison works, a superconducting solenoid was chosen to increase the focusing power with a slight modification of the existing beamline. A quadrupole triplet was also an option, but the solenoid appeared to be more attractive in the aspect of its versatile uses. One example of its uses is that with a production target placed upstream from the solenoid, the solenoid can accept and focus the produced fragments on another production target downstream.

The solenoid was manufactured by Mitsubishi Electric Corporation, and was installed in the beamline at RIKEN in January, 1997. The axial field reached 6.2 T after several quenches. The first focusing test was performed using 95 MeV/u $Ar^{17+}$ beam, which is the highest rigidity beam from RIKEN Ring Cyclotron (RRC).

## 2 SUPERCONDUCTING SOLENOID DESIGN

The superconducting solenoid is designed as a focusing element in the beamline. Since no present beamline magnets at RIKEN are superconducting, it was thought to be inconvenient to add a new component which requires using liquid helium. A conduction cooling method was preferred to bath cooling. A compact refrigerator of a Gifford-McMahon type and a high-$T_c$ material current leads are the major components of such system as in other similar systems [3]. (The current leads is made of high-$T_c$ material between 50 K and 4.5 K, and of copper between 300 K and 50 K.) Figure 1 shows the system configuration. Design parameters of the solenoid and the superconductor are listed in Table 1.

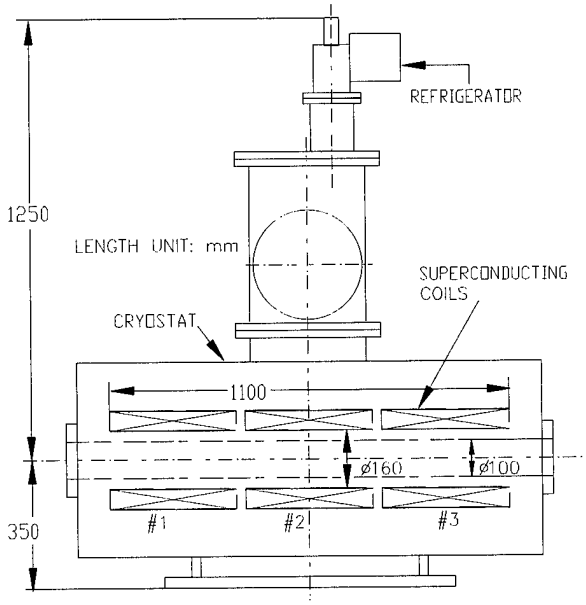



Figure 1: A schematic view of the superconducting solenoid.

The solenoid is divided into three equal-length coils as shown in Fig. 1. Its main purpose is to reduce the maximum IR drop. Each coil is connected to a diode so that the maximum IR drop during quench is reduced approximately by one third compared to without coil division. The electric circuit incorporating quench protection is plotted in Figure 2. Three diodes are located inside the cryostat, and there is another diode used at room temperature in series with a resistor which are in a parallel connection with the power supply. Because of these connections quench characteristics are rather complicated. A detailed analysis is given in the next section.

The voltage of power supply is $\pm 4$ volts, taking about 90 mins to reach the design current. It is, however, not a

0-7803-4376-X/98/$10.00 © 1998 IEEE

Table 1: Parameters of the 6 T Solenoid

| | |
|---|---|
| $B_{max}$ on axis | 6.2 T |
| $\int B \cdot dl$ | 6.8 T·m |
| $J_{ave}$ | 9,800 A/cm$^2$ |
| Amp·turn | 5.5 MA·turn |
| $I_{op}$ | 40 A |
| Stored Energy | 450 kJ |
| Inductance | 534 H |
| Superconducting Wire | Cu/NbTi=1.3, $\phi$ =0.60 mm |

significant inconvenience in our case because the current is usually fixed for many hours during experiments.

The cold mass of the solenoid is about 300 kg, and the cooling capacity of the refrigerator is 0.5 W at 4.5 K with 30 W being provided to the thermal shield at 45 K. It takes 9 days to cool the coil from 300 K to 4.5 K. This seems a rather long time, but is acceptable since experiments are usually scheduled well in advance.

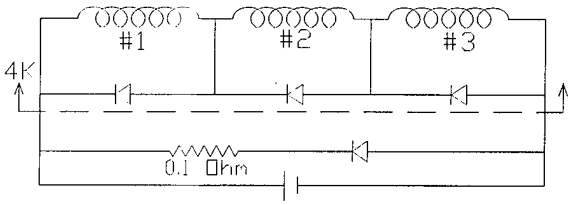



Figure 2: A circuit diagram. Three diodes are located inside the cryostat, and one more diode at room temperature for quench protection.

## 3 SOLENOID TEST AND FIELD MEASUREMENT

The solenoid reached the design field of 6.2 tesla after training. Among the three coils, two (#1 and #3 in Figure 1) were tested in a liquid helium dewar prior to assembly. The coil #1 quenched at the current of 48.3 A, and the coil #3 didn't even at 49.1 A, which proved the quality of coil winding. Test of the third coil was skipped. After the solenoid was fully assembled, it was first tested at the factory site. And then the test continued after the solenoid was installed in the beamline of RIKEN. Twelve quenches in total were needed to train the solenoid to the design field. This number is larger than expected. The quench occured at the coil #3 for the first 4 quenches, and then at #1 for the following 7 quenches. Since these two coils passed individual tests, the quality of winding should not be the cause of these quenches. Moreover, the coil joints are extra-cooled by means of separate copper strips extended from the cold head of the refrigerator. We think that the change of coil force direction from individual coil tests is the probable cause.

During quench tests variations of the following physical parameters have been measured: 1) voltages on each coil, 2) magnetic fields, and 3) solenoid current. The magnetic fields were measured using three hall probes temporarily attached to the outside of vacuum jacket around each coil. A typical result is shown in Figure 3 when a quench occured at the coil #1. As shown in the upper three curves, the voltages on #2 and #3 coils are opposite to that on the coil #1, which is forced by the warm diode. The gate voltage of the diode at 4.5 K is measured to be around 10 volts which is the maximum voltage on each coil. The middle three curves show the magnetic fields of each coil which are equivalent to the currents of each coil. The current of the coil #2 increases due to magnetic induction before its own quenching. This kind of behavior is usually observed when a quench occurs to the coils which are magnetically coupled but electrically independent.

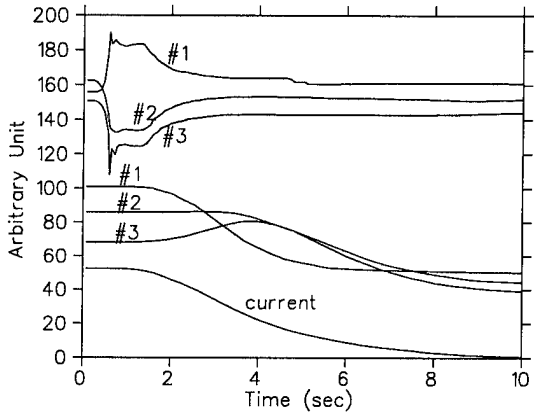



Figure 3: Variations of physical parameters measured as a function of time during coil quench testes. The upper three curves show the coil voltages, the middle three displaying magnetic fields measured at the outside of the vacuum jacket around each coil, and the lower curve shows the decay of the solenoid current.

The magnetic field was measured at the factory site using a hall probe positioned by a three dimensional mover. The magnetic center was found from the measurements, and it agrees with the mechanical center. Magnetic field measured along the axis is shown in Figure 4 together with the calculation result using TOSCA [4].

## 4 BEAM FOCUSING TEST

The main design parameters of the solenoid and its location were chosen to focus heavy ion beams with a spot diameter of 0.4 mm when beam emittance is 3 $\pi$mm·mrad. The beam envelopes were calculated using TRANSPORT [5], and shown in Figure 5. The beam envelopes are enlarged by the quadrupoles upstream from the solenoid, and their upper limits are determined by the clear bore size ($\phi$8 cm) of the last quadrupole. Aberrations on the solenoid are not the limiting factors in producing the spot size of 0.4 mm.

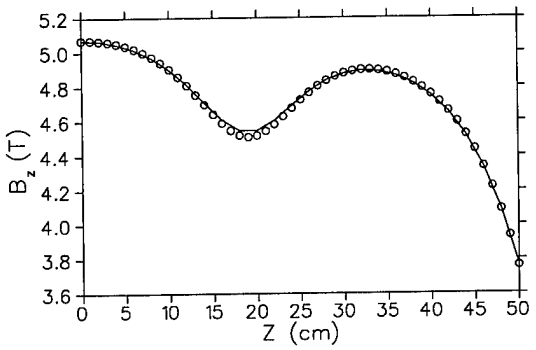



Figure 4: Magnetic fields calculated with TOSCA drawn by the curve and measured with a hall probe indicated by circles

The first beam test was carried out using 95 MeV/u $Ar^{17+}$ beam. The spot was observed on a ZnS target at the location of the production target of radio isotope beams. The beam diameter was around 0.3 mm when the beam-line magnets were adjusted according to the TRANSPORT calculations. The optics calculation agreed with measurements, and the transmission efficiency was near 100 %.

The beam spot can be easily shaped with control of three upstream quadrupole doublets as well as solenoid current. With the solenoid inductance of 534 H and the power supply voltage of 4 volts, the adjustment of the solenoid current takes five minutes per amp. Therefore, it is quicker to control the currents of the quadrupoles as long as the transmission efficiency doesn't deteriorate.

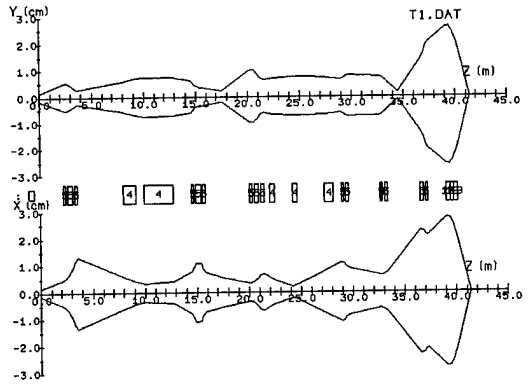



Figure 5: Beam envelopes calculated with TRANSPORT. The upper and lower graphs show the envelopes of two transverse planes, respectively.

## 5 CONCLUSION

The solenoid reached the design field of 6.2 tesla, and the beam test was successfully carried out. The number of quench before reaching the design field was larger than expected, but it was understandable considering training against the changes in coil stress distributions from the individual coil tests.

It appears easy to operate a superconducting magnet using conductive cooling. A further application of this kind of system is under consideration.

## 6 REFERENCES

[1] I. Tanihata, RIKEN Accelerator Research Facility, Nuclear Physics News, V5, No1 (1995) 5

[2] T. Kubo et al., The RIKEN Radioactive Beam Facility, B70 NIM (1992) 309

[3] T. Ogitsu et al., Superconducting focusing solenoid for X-band klystron, Proceedings of 1995 Partl. Accel. Conf. (1995) 1405

[4] Vector Fields Limited, Oxford, England

[5] K. Brown et al., TRANSPORT. A Computer Program for Designing Charged Particle Beam Transport System, CERN 73-16 (1993)

# DESIGN OF A MODEL SECTOR MAGNET FOR THE RIKEN SUPERCONDUCTING RING CYCLOTRON

T. Kubo, T. Kawaguchi, T. Mitsumoto, T. Tominaka, S. Fujishima, J.-W. Kim, Y. Tanaka, K. Ikegami, N. Sakamoto, S. Yokouchi, T. Morikawa, A. Goto and Y. Yano
The Institute of Physical and Chemical Research(RIKEN)
2-1 Hirosawa, Wako, Saitama 351-01, Japan

*Abstract*

A six-sector superconducting ring cyclotron is to be built in the RIKEN RI-beam factory project as one of post accelerators of the existing K540 ring cyclotron. This paper reports on a full-scale model sector magnet for the superconducting ring cyclotron.

## 1 INTRODUCTION

In the RIKEN RI-beam factory project, it is planned to build two new ring cyclotrons as post accelerators of the existing K540 ring cyclotron [1]. The first new cyclotron we call IRC has a K-value of 950 MeV, consisting of four normal-conducting sector magnets. Its mean injection and extraction radii are designed to be 2.77 m and 4.15 m, respectively. The second one we call SRC is a superconducting ring cyclotron with a K-value of 2,500 MeV, consisting of six superconducting sector magnets whose sector angle is 25 degrees and maximum field is 4.3 T. Its mean injection and extraction radii are designed to be 3.56 m and 5.36 m, respectively. The cascade operation of these cyclotrons boosts energies of heavy ion beams up to: e.g. 400 MeV/nucleon for light heavy ions like carbon, 300 MeV/nucleon for krypton ions, and 150 MeV/nucleon for uranium ions.

Here we report on a design of a model superconducting sector magnet for the SRC. The design of the SRC is reported elsewhere in these proceedings [2, 3].

## 2 MODEL SECTOR MAGNET

A full scale model is to be built so that we can make sure the design of sector magnet under the condition as close to the real one as possible. Figure 1 shows a schematic drawing of the model sector magnet. The cold pole method has been adopted to support the huge electromagnetic force due to the large magnetic field and coil current [3]. Figure 2 shows some details of the main coil vessel and cold pole.

### *2.1 Cold Pole and Main-coil Vessel*

As seen from Figs. 1 and 2, the iron pole pieces are separated from the iron yoke and are cooled down together with the main coils in the cryostat. Two coil vessels that accommodate the main coils are attached to the side of the upper and lower pole pieces, which are linked each other by pole links. This arrangement allows the pole pieces to work as a mechanical support against the huge force excerted on the mail coils or the coil vessels.

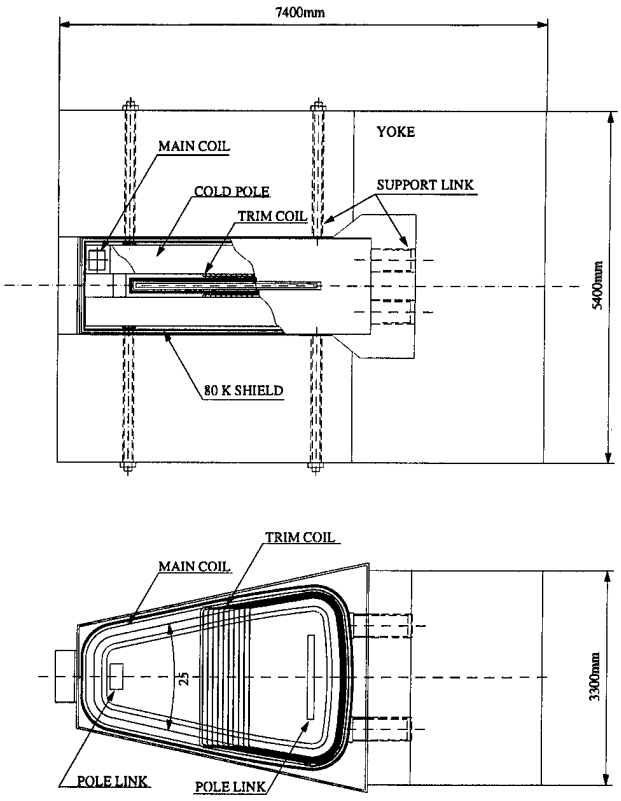



Fig. 1. Schematic drawing of the model sector magnet: a side view (upper figure); a top view (lower figure).

The pole gap is designed to be 380 mm, considering sizes of the trim coils and of the magnets for injection and extraction to be installed in the gap space. The cold-mass weight is estimated to be about 50 tons. The coil vessels are made of stainless steel. One of the important issues in the design is how to fix the coil vessel to the side of pole piece. Figure 3 shows two alternative methods that we considered. The scheme shown in the upper part of Fig. 3 uses sort of "hook" to fix the coil vessel to the pole. The coil vessel and the "hook" are assembled by

0-7803-4376-X/98/$10.00 © 1998 IEEE

welding. The second scheme shown in the lower part of Fig. 3 uses screws to fix the coil vessel to the pole as well as to assemble the coil vessel. We plan to adopt the former scheme for the upper coil and the latter one for the lower coil, and to examine in the test operation of model magnet which scheme is better.

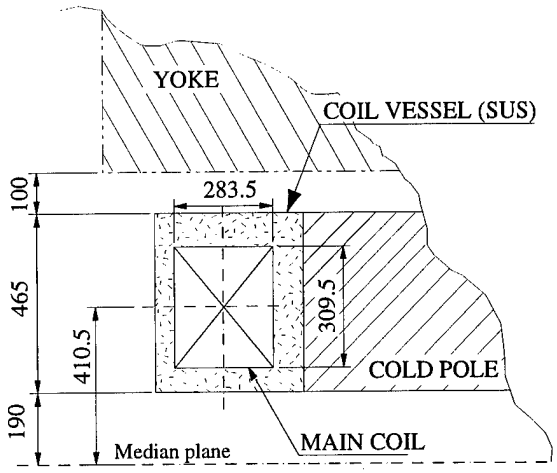



Fig. 2. Some details of the main coil and cold pole.

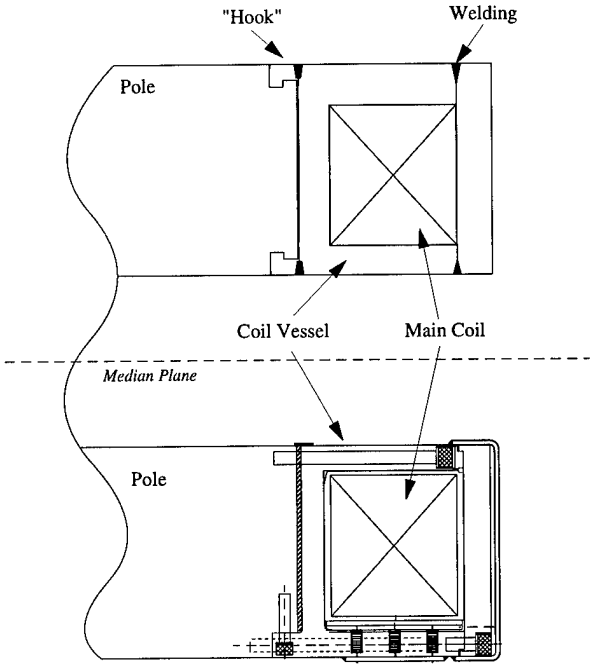



Fig. 3. Two alternative schemes to fix the coil vessel to the cold pole.

*2.2 Main Coil and Conductor*

A cryogenically-stabilized superconductor has been designed based on Maddock's criterion, and is used for the main coil in order to prevent it from quenching. The conductor has a rectangular shape, consisting of a Rutherford-type NbTi cable located at the center of conductor and a stabilizer housing. The conductor's cross-sectional sizes are horizontally 8 mm and vertically 15 mm. The Rutherford-type cable is composed of ten NbTi superconducting wires of 1.25 mm diameter and 1.05 Cu/SC ratio. The diameter and twisting pitch of the filaments contained in each wire are 27 and 18 mm, respectively. Critical currents of the wire at 4.3 K is greater than 14,500 A at 5 T, 11,500 A at 6 T, and 8,500 A at 7 T. The Rutherford-type cable has a rectangular cross-section of 2.35 mm x 6.35 mm and has a twisting pitch of 55 mm. The stabilizer material has been chosen to be pure aluminum with a residual resistivity ratio greater than 500. The condition of the stabilizer surface is flat. The Al:Cu:SC ratio of the conductor is 17 : 1.05 : 1. The conductor is cryogenically stable up to a current of 6,000 A when the applied magnetic field is 6 T and the cooling efficiency is assumed to be 50%.

The main coil is cooled by the liquid-helium bath cooling method. Cross-sectional area of the main coil is 283.5 mm x 309.5 mm, as shown in Fig. 2. The number of turns is 600 for each coil. The main coil is wound by the solenoid winding method in such a way that it has 30 layers in the horizontal direction and 20 turns in the vertical direction. The conductor length is estimated be 6.4 km/coil. The cooling gaps in horizontal and vertical directions are chosen to be 1.5 mm and 0.5 mm, respectively. A heat-flux measurement has shown that these gap-widths are large enough to achieve the designed heat flux. The spacers of FRP (Fiber Reinforced Plastic) are placed in the gaps in such a way that 50 % of conductor surface is exposed to the liquid helium. We plan to excite the main coil with currents lower than 5,000 A, considering deterioration of cooling which may happen in some parts of the coil. The current density at 5,000 A is estimated to be about 34 A/mm$^2$. The total ampere-turn is 6 MA at 5000 A, which is large enough to generate the design field strength of the sector magnet.

*2.3 Test Trim Coils*

Test trim coils, which correspond to a part of real trim coil, are to be fabricated and installed in the pole gap space as shown in Fig. 1. The conductor of trim coil has been designed to be cryogenically stable, based on Stekly's criterion. It is a rectangular conductor whose cross-sectional sizes are horizontally 2.9 mm and vertically 3.6 mm, and consists of a stabilizer housing of pure aluminum and a superconducting wire located at the center of conductor. The superconducting wire is the same as that used for the Rutherford-type cable of main-coil conductor. The cooling gaps of trim coil are taken to be 0.25 mm. The cooling efficiency is estimated to be 40 % considering the spacers placed in the gaps. The trim coil is stable up to 550 A at 6 T. We plan to excite it with currents lower than 500 A for safety. The current density at 500 A is estimated to be about 41 A/mm$^2$. The trim

coil vessel is connected in series to the main coil vessel, so that the trim coil can be cooled by liquid helium provided by a common refrigerator.

## 3 SCHEDULE

Fabrication of the conductors has been finished this March. Fabrication of the model magnet will be soon placed an order with manufacturers. The cold mass and cryostat will be completed in a year.

## REFERENCES

[1] Y. Yano: 'RIKEN RI Beam Project', These proceedings.
[2] T. Mitsumoto et al.: 'Orbit Analysis for the RIKEN Superconducting Ring Cyclotron', These proceedings.
[3] T. Kawaguchi et al.: 'Design of the sector magnets for the RIKEN Superconducting Ring Cyclotron', These proceedings.

# THREE DIMENSIONAL FIELD ANALYSIS OF HELICAL MAGNET FOR RHIC SIBERIAN SNAKE

M. Okamura, T. Kawaguchi, T. Tominaka, The Institute of Physical and Chemical Research (RIKEN), Wako, Saitama, Japan
T. Katayama, Center for Nuclear Study, University of Tokyo, Tanashi, Tokyo, Japan / RIKEN

*Abstract*

Siberian Snakes that consist of four helical dipole magnets will be installed in the Relativistic Heavy Ion Collider (RHIC) to preserve the polarization of the proton beam. To promote this project we are collaborating with Brookhaven National Laboratory (BNL) in studying helical magnet designs. At present, two types of helical magnets are being developed. One is being designed by the BNL magnet group, and the other by Advanced Magnet Technology (AML), Inc. These magnets use the same superconducting cable but have different shapes especially in the end regions. We are evaluating the performance of both magnet designs using the three dimensional (3D) magnetic field analysis code TOSCA. In particular, saturation effect, field strength, multipole component and magnet quenching features will be discussed.

## 1 INTRODUCTION

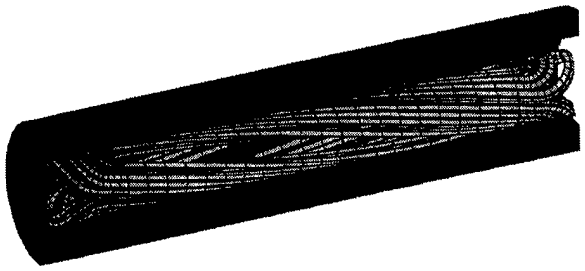
We have studied the Siberian Snake[1] for the RHIC-Spin project and the development of the super conducting helical dipole magnets are one of the key issues to the success of this project. Two types of designs for these magnets are being evaluated and the half length model magnet of each type was recently fabricated and the quench performances were tested. The first, called the Slotted Type[2], was designed by the BNL magnet group and the other, called the Direct Wind Type[3], was developed by the AML. Using TOSCA, we have calculated 3D magnetic fields of both built models and investigated these characteristics.

## 2 DEMANDED PERFORMANCES

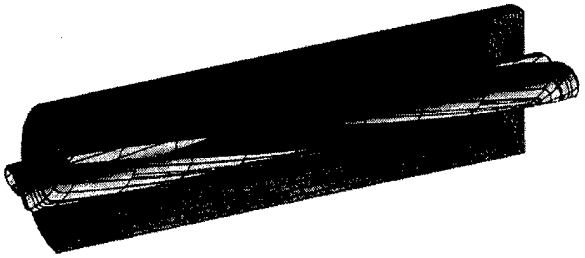
The Siberian Snake magnets adopted by RHIC are a type called Full Snake, and have to flip the spin direction by 180 degrees without any influences to the beam orbit. Using the helical dipole magnet twisted by 360 degrees, the transverse magnetic fields the accelerated particles feel are cancelled and the deflection of the beams is eliminated. Furthermore the symmetric combination of the helical dipole magnets, as sequence of 1.2 T, -3.9 T, 3.9 T and -1.2 T fields, can evade the shift of the beam orbit. Therefore the required performances for each helical dipole magnet are to achieve more than 3.9 T of the field strength and zero transverse fields when integrated along the particle trajectories. The optimization of the multipole components is also important to avoid a tune shift. From the cryogenic point of view, in RHIC, it is needed to minimize the heat leak from these magnets. On this account, the Rutherford type cable which is used for usual magnets is not adopted, and a thin cable of 1 mm diameter comprise of seven wires will be applied. As a result, the design of the helical dipole magnets became different from a conservative design.

## 3 TWO TYPES OF THE MAGNET DESIGNS

As mentioned above, there are two types of magnet designs, the Slotted Type and the Direct Wind Type, for the superconducting helical dipole. The fabricated models have half sized length, and these are twisted by 180 degree. Figure 1 shows these magnets.



Slotted Type



Direct Wind Type

Figure: 1 The half length models for the Siberian Snake. Only halves of the yokes are drawn not to hide the coils.

In Slotted Type construction, the cables are wound along the slots machined on a column of aluminum, and finally pressuring radial direction, wound cables are hardened with epoxy in the slots. The coil winding was done by hand work basically, and mastery of skills and long production time are necessary. A study of the automation winding for this type was just begun at BNL. On the contrary, the coils of Direct Wind Type are wound by a numerically controlled machine and this procedure is completely automated. At first, a cylinder wrapped with fiber grass is

0-7803-4376-X/98/$10.00 © 1998 IEEE

grooved along the location of first layer cable. Then the cable of first layer is wound up on the groove, and the second or next layer is wound up on the gap from previous cables. Thus, the positions of each cable are fixed, once the groove on the cylinder was decided. As a result, a packing factor of the conductor is maximized. In addition, a turn number of upper layer is always less than that of lower layer. Most important difference between these models is in the shape of the coil end. As for Slotted Type, the coil end is divided into upper side and lower side and this configuration is the same as ordinary magnets. On the other hand, as for Direct Wind Type, all of the conductors turn around on one side, upper or lower, without being divided. Accordingly, length of end gets longer comparatively. About the magnetic fields at the end, non-symmetric distribution is expected. It is possible to adopt a design of the end divided into up and down as same as Slotted Type. However, in this case, the coil at the body region also should be divided into two coils. Since wound cables at the median plane except the first layer can not be accumulated, then the cables are not wound efficiently at the area which contributes most effectively to induce the dipole magnetic field.

## 3 3D ANALYSIS OF THE FIELDS

### *3.1 Peak fields survey*

In both half length models, the peak field strength at body region and the end region were estimated using TOSCA. The results are shown in Table 1.

Table: 1 Peak fields in helical dipole magnets.

| | Center Field | Peak Field in Body (Ratio) | Peak Field in End (Ratio) |
|---|---|---|---|
| Slotted Type | 4.16 T | 4.67 T (1.12) | 4.59 T (1.105) |
| Direct Wind Type | 3.91T | 4.74 T (1.21) | 4.43T (1.13) |

In both magnets, the peaks of the bodies are found at inner edge of the coil which is nearest to the poles, and the peak of the end found at the most inside edge of the curved coils. If we can fix entire coils of the helical magnets in an ideal condition, the Slotted Type coil will reach a critical current with the body part, and the Direct Wind Type with the end part. The relationship between the critical current of the cable and expected peak fields are shown in Fig. 2. In the Slotted Type, a cable in the body part reaches a critical current at 395 A, and then the dipole field strength near beam axis becomes 5.3 T. In Direct Wind Type, a cable at the end part reaches critical current at 480 A, at that time the field strength near the axis is 4.4 T. The Slotted Type magnet was designed to be used two currents, 9 to 11, and in order to increase the maximum field strength around the axis, the coils in stronger field have a lower current. The operation current, at high field slots, for 4.0 T is expected to be 280 A. On the other hand the operation current of the Direct Wind Type is 430 A. The reason of high field in the end section of Direct Wind Type is its yoke geometry. The point at which the high peak occurs is covered by the yoke. If the length of the yoke is shorter, the strength of peak field can be reduced.

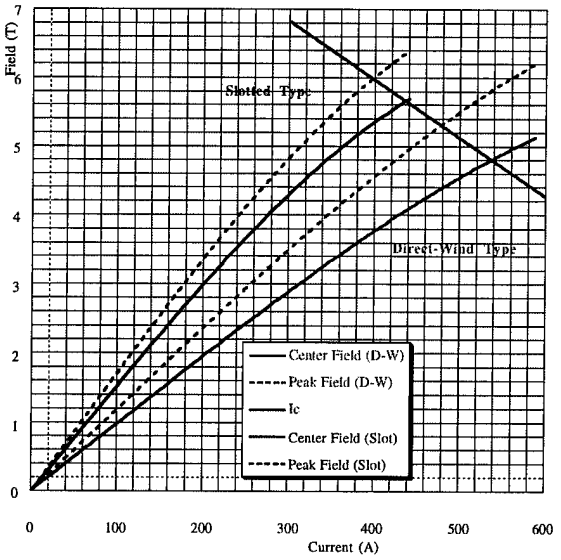



Figure: 2 Expected field strengths

### *3.2 The field uniformity*

In the helical structure, strong longitudinal fields will be induced at off axis area. We can optimize the helical dipole magnet to eliminate the azimuthal angle dependence of the fields, however we cannot expel radial dependence[5,6,7]. Accordingly, the definition, which has been used for a two dimensional magnet, cannot be applied. Then, we calculated the multipole component of these model magnets using the Fourier expansion of the $B_y$ component along the circle of 3.1 cm radius. The results are indicated in Table 2.

Table: 2 The expected multipole component.

| | Low Current | | High Current | |
|---|---|---|---|---|
| Slotted Type Two-Current | C.F. | 0.44 T | C.F. | 4.16 T |
| | 6P | -0.128 % | 6P | -0.133 % |
| | 10P | 0.011 % | 10P | 0.016 % |
| Slotted Type One-Current | C.F. | 1.36 T | C.F. | 4.03 T |
| | 6P | -0.609 % | 6P | -0.701 % |
| | 10P | 0.063 % | 10P | 0.033 % |
| Direct Wind Type | C.F. | 0.40 T | C.F. | 3.91 T |
| | 6P | -0.907 % | 6P | -0.278 % |
| | 10P | -0.951 % | 10P | -0.948 % |

C.F. : Center Field
6P: Sextupole component
10P: Decapole component

In Slotted Type magnet, not only two current mode but also uniform current mode is computed. In case of one current mode, of course, the multipole component is larger. We can control the multipole component by changing the ratio of two currents in the Slotted Type. In Direct Wind Type, the effect of the iron saturation to the sextupole component is large by reason of small clearance between the yoke and the coil. Anyhow, it is needed to study the adequate field strength which should be referenced by the optimization of the multipoles.

### *3.3 Magnetic field distribution*

As mentioned above, there are longitudinal fields in the helical magnet. The more the distance from the axis is, the stronger the longitudinal field is. The beam orbit will not be influenced much by the longitudinal magnetic field, but the spin motion is. Figure 3 shows the calculated field distributions on the axis in the two types of model magnet. In Direct Wind Type, strong longitudinal fields were expected in end region even on axis due to the non-symmetric coil end structure.

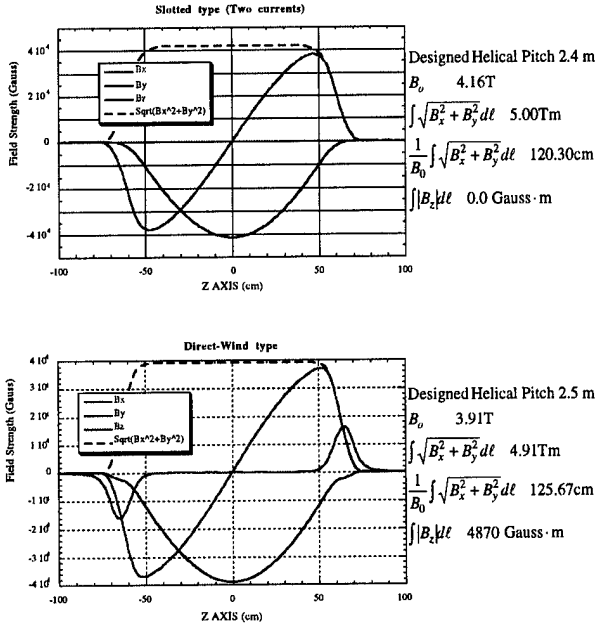



Figure: 3 Field distributions along the beam axis.

In Siberian Snake magnets in RHIC, the maximum orbit excursion will become 3 cm at injection energy of polarized proton beam. So, Fig. 4 shows field distribution at 3.0 cm above the axis. In Slotted Type, which has the symmetric end configuration, longitudinal field in yhe body and that in the end tend to be canceled. In Direct Wind Type, the non-symmetric ends make strong longitudinal field especially in the area close to the coil. Besides, this field is too strong to be canceled by the longitudinal field in the body. The longitudinal field in the end of other side emphasizes the longitudinal field of the body. So the direction of coil end in Direct Wind Type should be chosen carefully to avoid this effect. In case of both magnet types, we plan to optimize longitudinal field using modification of the yokes.

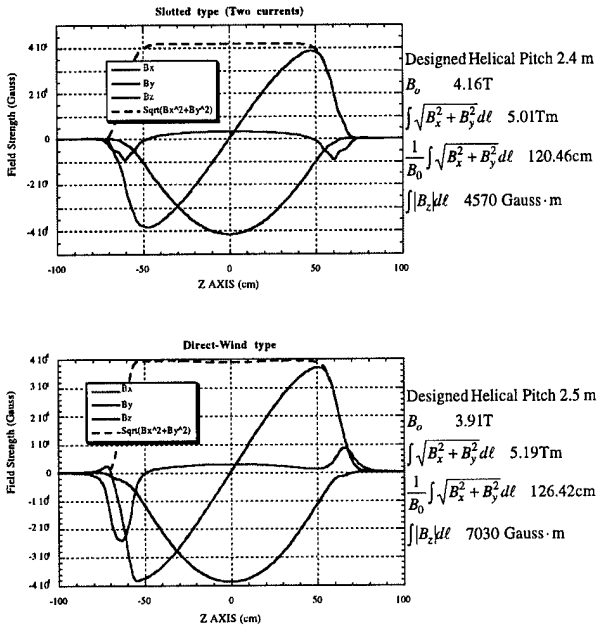



Figure: 4 Field distribution 3.0 cm above the beam axis.

## 4 CONCLUSION

Using 3D calculations, the two types of model magnet which are candidates for RHIC Spin project were analyzed, and the characteristics were predicted. We will optimize the design of coils and the shape of the yoke comparing the field measurement which will be held soon.

## 5 ACKNOWLEDGMENTS

We wish to thank BNL accelerator group, magnet group and AML., Inc. and also grateful to M. Syphers for discussions and reading this manuscript.

## REFERENCES

[1] M. Syphers, et al., these proceedings.
[2] E. Willen, et al., these proceedings.
[3] R. Meinke, et al., these proceedings.
[4] M. Okamura, et al.,'Three Dimensional Field Analysis of Helical Snake Magnets for RHIC' Proc. EPAC96
[5] M. Okamura, BNL AGS/RHIC/SN-46, Nov. 1996.
[6] T. Tominaka, BNL AGS/RHIC/SN-54, Apr. 1997
[7] M. Okamura, et al., RIKEN Accel. Prog., Vol 30 1997

# MULTIPOLE EXPANSION FOR A SINGLE HELICAL CURRENT CONDUCTOR

T. Tominaka, K. Hatanaka*, and T. Katayama**
The Institute of Physical and Chemical Research (RIKEN), Wako, Saitama, 351-01, Japan
*Research Center for Nuclear Physics, Osaka University, Ibaraki, Osaka, 567, Japan
**Center for Nuclear Study, School of Science, University of Tokyo, Tanashi, Tokyo, 188, Japan

*Abstract*

Various helical coils such as helical dipole magnets, multifilamentary superconductors and superconducting strands have something in common with the helical structure. In this paper, we discuss the analytical expression for the magnetic field of a single helical current conductor. In addition, the comparison between the analytical and numerical calculations is made.

## 1 INTRODUCTION

The magnetic field of helical coils has been examined by several authors. [1,2,3,4,5,6] In this paper, the multipole expansion for a single helical current conductor is derived as the extension of the case for a single straight current conductor. [7] Then, the comparison between the analytical and numerical calculations is made for a single helical current conductor. [6] The Cesàro's method of summation is applied for this multipole expansion.

## 2 MULTIPOLE EXPANSION FOR A SINGLE HELICAL CURRENT CONDUCTOR

3-dimensional (3D) Laplace's equation in circular cylindrical coordinates is as follows,

$$\nabla^2\psi = \frac{\partial^2\psi}{\partial r^2} + \frac{1}{r}\frac{\partial\psi}{\partial r} + \frac{1}{r^2}\frac{\partial^2\psi}{\partial\theta^2} + \frac{\partial^2\psi}{\partial z^2} = 0 \qquad (1)$$

Since the winding is periodic in z with a pitch length L, the general solution is, [8]

$$\psi_h(r,\theta,z) = \sum_{n=1}^{\infty}\left(c'_n I_n(nkr) + d'_n K_n(nkr)\right)\times \left\{a'_n\cos\left(n(\theta - kz)\right) + b'_n\sin\left(n(\theta - kz)\right)\right\} + \left(e'\ln r + f'\right)\times\left(g''\theta + h''kz + i'\right) \qquad (2)$$

where $k = 2\pi/L$, and $I_n(nkr)$ and $K_n(nkr)$ are the modified Bessel functions of the first and second kind of order n, respectively. For the interior scalar potential of helical coil, we can define the following form for $r < a$,

$$\psi_{h,in}(r,\theta,z) = \frac{\mu_0 I}{2\pi}\sum_{n=1}^{\infty}(n-1)!\left[\frac{2}{n k a}\right]^n I_n(n k r)\times \left\{-a_n(k)\cos\left(n(\theta - k z)\right) + b_n(k)\sin\left(n(\theta - k z)\right)\right\} - \frac{\mu_0 I}{2\pi}k z \qquad (3)$$

Then, the asymptotic form for this scalar potential as $k \to 0$ ($L \to \infty$) is,

$$\lim_{k\to 0}\left[\psi_{h,in}(r,\theta,z)\right] = \psi_{2d,in}(r,\theta) \qquad (4)$$

$$\psi_{2d,in}(r,\theta) = \frac{\mu_0 I}{2\pi}\sum_{n=1}^{\infty}\frac{1}{n}\left(\frac{r}{a}\right)^n\sin(n(\theta - \varphi)) \qquad (5)$$

$$= \frac{\mu_0 I}{2\pi}\sum_{n=1}^{\infty}\frac{1}{n}\left(\frac{r}{a}\right)^n(-a_n\cos(n\theta) + b_n\sin(n\theta))$$

where $\psi_{2d,in}(r,\theta)$ is the interior scalar potential of 2D non-spiral coil. From this scalar potential, the interior ($r < a$) magnetic field of helical coil is,

$$\begin{cases} B_r(r,\theta,z) = -\dfrac{\partial\psi_h}{\partial r} = -\dfrac{\mu_0 I}{2\pi}\displaystyle\sum_{n=1}^{\infty} n!\left[\frac{2}{n k a}\right]^n k\, I'_n(n k r)\times \left\{-a_n(k)\cos\left(n(\theta - k z)\right) + b_n(k)\sin\left(n(\theta - k z)\right)\right\} \\ B_\theta(r,\theta,z) = -\dfrac{1}{r}\dfrac{\partial\psi_h}{\partial\theta} = -\dfrac{\mu_0 I}{2\pi}\displaystyle\sum_{n=1}^{\infty} n!\left[\frac{2}{n k a}\right]^n\frac{I_n(n k r)}{r}\times \left\{a_n(k)\sin\left(n(\theta - k z)\right) + b_n(k)\cos\left(n(\theta - k z)\right)\right\} \\ B_z(r,\theta,z) = -\dfrac{\partial\psi_h}{\partial z} = -\dfrac{\mu_0 I}{2\pi}\displaystyle\sum_{n=1}^{\infty}(-k)\, n!\left[\frac{2}{n k a}\right]^n I_n(n k r)\times \left\{a_n(k)\sin\left(n(\theta - k z)\right) + b_n(k)\cos\left(n(\theta - k z)\right)\right\} + \dfrac{\mu_0 I}{2\pi}k \end{cases} \qquad (6)$$

On the other hand, for the exterior scalar potential of helical coil, we can define the following form for $r > a$,

$$\psi_{h,ex}(r,\theta,z) = \frac{\mu_0 I}{2\pi}\sum_{n=1}^{\infty}(n-1)!\left[\frac{2}{n k a}\right]^n\frac{I'_n(n k a)}{K'_n(n k a)}K_n(n k r)\times \left\{-a_n(k)\cos\left(n(\theta - k z)\right) + b_n(k)\sin\left(n(\theta - k z)\right)\right\} - \frac{\mu_0 I}{2\pi}\theta \qquad (7)$$

Then, the exterior ($r > a$) magnetic field of helical coil is,

$$\begin{cases} B_r(r,\theta,z) = -\dfrac{\mu_0 I}{2\pi}\displaystyle\sum_{n=1}^{\infty} n!\left[\frac{2}{n k a}\right]^n k\,\frac{I'_n(n k a)}{K'_n(n k a)}K'_n(n k r)\times \left\{-a_n(k)\cos\left(n(\theta - k z)\right) + b_n(k)\sin\left(n(\theta - k z)\right)\right\} \\ B_\theta(r,\theta,z) = -\dfrac{\mu_0 I}{2\pi}\displaystyle\sum_{n=1}^{\infty} n!\left[\frac{2}{n k a}\right]^n\frac{I'_n(n k a)}{K'_n(n k a)}\frac{K_n(n k r)}{r}\times \left\{a_n(k)\sin\left(n(\theta - k z)\right) + b_n(k)\cos\left(n(\theta - k z)\right)\right\} + \dfrac{\mu_0 I}{2\pi}\dfrac{1}{r} \\ B_z(r,\theta,z) = -\dfrac{\mu_0 I}{2\pi}\displaystyle\sum_{n=1}^{\infty}(-k)\, n!\left[\frac{2}{n k a}\right]^n\frac{I'_n(n k a)}{K'_n(n k a)}K_n(n k r)\times \left\{a_n(k)\sin\left(n(\theta - k z)\right) + b_n(k)\cos\left(n(\theta - k z)\right)\right\} \end{cases} \qquad (8)$$

0-7803-4376-X/98/$10.00 © 1998 IEEE

On the situation that the currents are confined to lie on the surface of a circular cylinder of radius a, the surface currents will give rise to a discontinuity of the components $B_Z$, $B_\theta$, at the interface of radius a, but the radial component $B_r$ will pass continuously through this interface. The values of $a_n(k)$, $b_n(k)$ can be determined for the current element. Applying Ampere's law for a closed path on z=constant plane enclosing the current element at radius a, we can obtain the following equation,

$$\left(B_{\theta,out} - B_{\theta,in}\right)\big|_{r=a} = \mu_0 j_z \Delta a \qquad (9)$$

Then, the coefficients an(k) and bn(k) are obtained with the Wronskian relation, [9] as follows,

$$\begin{cases} a_n(k) = -\dfrac{2}{I}\dfrac{1}{(n-1)!}\left(\dfrac{n\,k\,a}{2}\right)^n k\,a^2\,K_n'(n\,k\,a)\,\Delta a \displaystyle\int j_z \sin n\theta\, d\theta \\ b_n(k) = -\dfrac{2}{I}\dfrac{1}{(n-1)!}\left(\dfrac{n\,k\,a}{2}\right)^n k\,a^2\,K_n'(n\,k\,a)\,\Delta a \displaystyle\int j_z \cos n\theta\, d\theta \end{cases} \qquad \text{- - - (10)}$$

For a helical line currents : current +I , radius a, angle $\varphi$, the coefficients $a_n(k)$, $b_n(k)$ can be calculated. The following relation between the current and the current density is used with the real cross section S of the conductor and the cross section $S_Z$ (=S/sin$\alpha$) of the conductor on the z=constant plane. $\alpha$ is the pitch of the winding so that the relationships between the above-mentioned k and $\alpha$ are $k = 1/(a \tan \alpha)$. Then, we can obtain the following expression,

$$j_z = j \sin\alpha = \frac{I}{S}\sin\alpha = \frac{I}{S_z} \qquad (11)$$

$$\begin{cases} a_n(k) = \dfrac{2}{(n-1)!}\left(\dfrac{n\,k\,a}{2}\right)^n \left(k\,a\,K_{n-1}(n\,k\,a) + K_n(n\,k\,a)\right)\sin n\varphi \\ b_n(k) = \dfrac{2}{(n-1)!}\left(\dfrac{n\,k\,a}{2}\right)^n \left(k\,a\,K_{n-1}(n\,k\,a) + K_n(n\,k\,a)\right)\cos n\varphi \end{cases} \qquad \text{- - - (12)}$$

When n is fixed and $k \to 0$, the limiting forms for small arguments of the modified Bessel function of the second kind of order n, $K_n(nkr)$ are as follows, [9]

$$\begin{cases} K_0(k\,a) \approx -\ln(k\,a) \\ K_n(n\,k\,a) \approx -\dfrac{1}{2}\Gamma(n)\left(\dfrac{2}{n\,k\,a}\right)^n, \qquad n \geq 1 \end{cases} \qquad (13)$$

Then,

$$\begin{cases} \lim_{k\to 0}\left[a_n(k)\right] = a_n = \sin n\varphi \\ \lim_{k\to 0}\left[b_n(k)\right] = b_n = \cos n\varphi \end{cases} \qquad (14)$$

As a result, the interior magnetic field of a single helical conductor with the current +I, located at radius a and angle $\varphi$ is for r < a,

$$\begin{cases} B_r(r,\theta,z) = \dfrac{\mu_0 I}{\pi} k^2 a \displaystyle\sum_{n=1}^{\infty} n\,K_n'(n\,k\,a)\,I_n'(n\,k\,r) \times \\ \qquad \sin\left(n(\theta - \varphi - k\,z)\right) \\ B_\theta(r,\theta,z) = \dfrac{\mu_0 I}{\pi} k\,a \displaystyle\sum_{n=1}^{\infty} n\,K_n'(n\,k\,a)\dfrac{I_n(n\,k\,r)}{r} \times \\ \qquad \cos\left(n(\theta - \varphi - k\,z)\right) \\ B_z(r,\theta,z) = -\dfrac{\mu_0 I}{\pi} k^2 a \displaystyle\sum_{n=1}^{\infty} n\,K_n'(n\,k\,a)\,I_n(n\,k\,r) \times \\ \qquad \cos\left(n(\theta - \varphi - k\,z)\right) + \dfrac{\mu_0 I}{2\pi} k \end{cases} \qquad (15)$$

Then, the transverse field magnitude at axis of the helical winding B(r=0,$\theta$,z=0) is obtained as follows,

$$\begin{aligned} &B_y(r=0,\theta,z=0) \\ &= \frac{\mu_0 I}{\pi}\left(k\,a\,K_0(k\,a) + K_1(k\,a)\right) \times \\ &\left\{\frac{k}{2}\left\{\cos(2\theta - \varphi) - \cos\varphi\right\} + \frac{k}{2}\cos(2\theta - \varphi)\right\} \\ &= -\frac{\mu_0 I}{2\pi} k\left(k\,a\,K_0(k\,a) + K_1(k\,a)\right)\cos\varphi \end{aligned} \qquad (16)$$

This result coincides with that obtained with the Biot and Savart's Law. [10] Similarly, the expression for the exterior (r > a) magnetic field of a single helical conductor is obtained. The above expression for the magnetic field of helical coil is the function of r and $\theta$ - kz, and is helically symmetric. However, the helical symmetry of the coil structure does not demand that the scalar potential is invariant to the transformation $\theta$ - kz = constant.

## 3 COMPARISON BETWEEN THE ANALYTICAL AND NUMERICAL CALCULATIONS FOR A SINGLE HELICAL CURRENT CONDUCTOR

The sum $\Sigma$ to a finite order of the above expressions of the interior and exterior magnetic fields do not approach the same value at r=a, as shown in Fig.1. This discontinuity of the magnetic field at r=a can be overcome with application of the Cesàro's method of summation, as shown in Fig.2. [11] As a result, the interior (r < a) magnetic field of a single helical conductor with the current +I, located at radius a and angle $\varphi$ is expressed as follows,

$$\begin{cases} B_r(r,\theta,z) = \dfrac{\mu_0 I}{\pi} k^2 a \dfrac{1}{N}\displaystyle\sum_{m=1}^{m=N}\left\{\sum_{n=1}^{n=m} n\,K_n'(n\,k\,a)\,I_n'(n\,k\,r) \times \right. \\ \qquad \left. \sin\left(n(\theta - \varphi - k\,z)\right)\right\} \\ B_\theta(r,\theta,z) = \dfrac{\mu_0 I}{\pi} k\,a \dfrac{1}{N}\displaystyle\sum_{m=1}^{m=N}\left\{\sum_{n=1}^{n=m} n\,K_n'(n\,k\,a)\dfrac{I_n(n\,k\,r)}{r} \times \right. \\ \qquad \left. \cos\left(n(\theta - \varphi - k\,z)\right)\right\} \\ B_z(r,\theta,z) = -\dfrac{\mu_0 I}{\pi} k^2 a \dfrac{1}{N}\displaystyle\sum_{m=1}^{m=N}\left\{\sum_{n=1}^{n=m} n\,K_n'(n\,k\,a)\,I_n(n\,k\,r) \times \right. \\ \qquad \left. \cos\left(n(\theta - \varphi - k\,z)\right)\right\} + \dfrac{\mu_0 I}{2\pi} k \end{cases} \qquad \text{- - - (17)}$$

For a single helical conductor with current I = 100 A, radius a = 0.33 mm, angle $\varphi$ = 30° and pitch length L = 9.51 mm, the comparison between the analytical and numerical calculations was made. Since an agreement was confirmed between the analytical and numerical calculations, the field was calculated for the whole space except for the singular point occupied by a single helical conductor, as shown in Fig.3.

## 4 CONCLUSION

An analytical expression for the magnetic field of a single helical coil is obtained. This expression will be useful to estimate the various electromagnetic characteristics of helical coils.

## 5 ACKNOWLEDGMENTS

The authors are indebted for helpful discussions and comments to the RIKEN RHIC spin accelerator group and Prof. T. Watanabe and Prof. J. Todoroki of National Institute for Fusion Science, Japan.

## REFERENCES

[1] J. P. Blewett and R. Chasman, "Orbits and fields in the helical wiggler", J. Appl. Phys. 48 pp.2692-2698 (1977).
[2] S. Caspi, "Magnetic Field Components in a Sinusoidally Varying Helical Wiggler", SC-MAG-464, LBL-35928, (1994).
[3] G. H. Morgan, "Computation of the Harmonics in a Helically Wound Multipole Magnet", AGS/RHIC/SN No.9, April 26, (1995).
[4] Kenro Miyamoto, "Plasma Physics for Nuclear Fusion", Revised ed. The MIT Press, pp.29-33 (1989).
[5] T. Tominaka, "Magnetic Field Calculation of Helical Dipole Coils", AGS/RHIC/SN No.24, April 29, (1996).
[6] T. Tominaka, "Multipole Expansion for a Single Helical Current Conductor", AGS/RHIC/SN No.49, December 18, (1996).
[7] K. -H. Mess, P. Schmüser and S. Wolff, "Superconducting Accelerator Magnets", World Scientific, p.44-53 (1996).
[8] H. Margenau and G. M. Murphy, "The Mathematics of Physics and Chemistry", Van Nostrand (1943).
[9] M. Abramowitz and I. A. Stegun (eds.), "Handbook of Mathematical Functions", Dover, pp.374-376 (1970).
[10] William R. Smythe, "Static and Dynamic Electricity", McGraw-Hill, pp.296-297 (1968), (Revised Printing (1989) by Hemisphere Publishing Corporation).
[11] E. T. Whittaker and G. N. Watson, "A Course of Modern Analysis", 4th ed. Cambridge University Press, p.155 (1927).

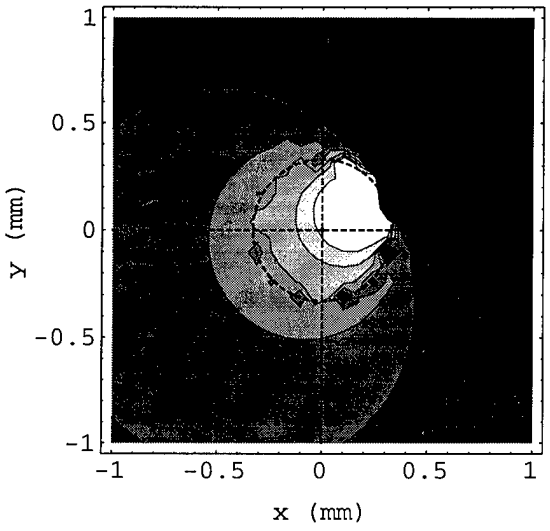



Fig. 1. Contour plot of $B_Z$ at z=0 analytically calculated with Eq.(15) to n=20.

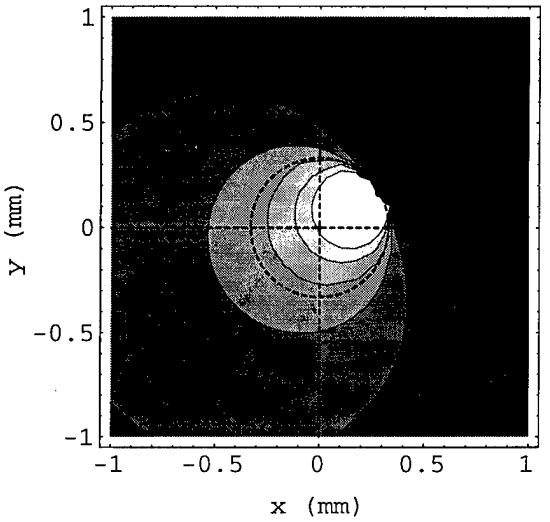



Fig. 2. Contour plot of $B_Z$ at z=0 analytically calculated with Eq.(17) to N=20.

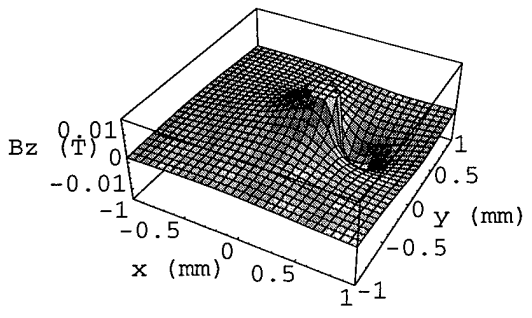



Fig. 3. 3D plot of the analytically calculated $B_Z$ at z=0, which is consistent with the numerical calculation with Biot-Savart Law.

# ANALYTICAL FIELD CALCULATION OF HELICAL DIPOLE MAGNETS FOR RHIC

T. Tominaka, M. Okamura*, and T. Katayama**
The Institute of Physical and Chemical Research (RIKEN), Wako, Saitama, 351-01, Japan
*Brookhaven National Laboratory, Upton, NY 11973-5000, USA
**Center for Nuclear Study, School of Science, University of Tokyo, Tanashi, Tokyo, 188, Japan

*Abstract*

The analytical expression for the magnetic field of helical coils is presented. In particular, the multipole coefficients are introduced for helical dipole magnets, which are essential components of Siberian Snakes and spin rotators for polarized proton acceleration at RHIC. In addition, the comparison between analytical and numerical calculations is presented for simple helical dipole magnets.

## 1 INTRODUCTION

Using the expression of multipole expansion for a single helical current conductor[1], the magnetic field of helical dipole coil with an infinite length is derived as the summation of four(4) helical line currents with dipole symmetry, deriving the helical multipole coefficients. [2,3] The helical multipole coefficients are defined so that the non-twist helical multipole coefficients are equal to the 2-dimensional multipole coefficients. As a result, the dependence of helical multipole coefficients upon the twist parameter is derived. With the comparison between the analytical and numerical calculations, it is confirmed that the helical multipole coefficients derived from the analytically calculated field are consistent with those calculated numerically.

## 2 ANALYTICAL EXPRESSION FOR THE MAGNETIC FIELD OF HELICAL DIPOLES

Using the expression of the multipole expansion for a single helical current conductor, the magnetic field inside the helical coils with an infinite length can be derived as the summation of four(4) helical line currents with dipole symmetry as follows, [1,2,3]

$$\begin{cases} B_r(r,\theta,z) = B_{ref}(k)\, r_0 \sum_{n=1}^{\infty} n! \left[\frac{2}{n\,k\,r_0}\right]^n k\, I_n'(n\,k\,r) \times \\ \quad \{-a_n(k)\cos(n(\theta - k\,z)) + b_n(k)\sin(n(\theta - k\,z))\} \\ B_\theta(r,\theta,z) = B_{ref}(k)\, r_0 \sum_{n=1}^{\infty} n! \left[\frac{2}{n\,k\,r_0}\right]^n \frac{I_n(n\,k\,r)}{r} \times \\ \quad \{a_n(k)\sin(n(\theta - k\,z)) + b_n(k)\cos(n(\theta - k\,z))\} \\ B_z(r,\theta,z) = B_{ref}(k)\, r_0 \sum_{n=1}^{\infty} (-k)\, n! \left[\frac{2}{n\,k\,r_0}\right]^n I_n(n\,k\,r) \times \\ \quad \{a_n(k)\sin(n(\theta - k\,z)) + b_n(k)\cos(n(\theta - k\,z))\}, \end{cases} \quad (1)$$

$$\begin{cases} \lim_{k\to 0}[B_{r,h}(r,\theta,z)] = B_{r,2d}(r,\theta) \\ = B_{ref}\sum_{n=1}^{\infty}\left(\frac{r}{r_0}\right)^{n-1}(-a_n\cos n\theta + b_n\sin n\theta) \\ \lim_{k\to 0}[B_{\theta,h}(r,\theta,z)] = B_{\theta,2d}(r,\theta) \\ = B_{ref}\sum_{n=1}^{\infty}\left(\frac{r}{r_0}\right)^{n-1}(b_n\cos n\theta + a_n\sin n\theta) \\ \lim_{k\to 0}[B_{z,h}(r,\theta,z)] = B_{z,2d}(r,\theta) = 0 \end{cases} \quad (2)$$

Therefore, the normal and skew multipoles due to many helical line currents with current $I_i$, radius $a_i$, angle $\varphi_i$ are,

$$\begin{cases} B_n(k) = B_{ref}(k)\, b_n(k) = -\frac{\mu_0}{\pi}\frac{1}{2^n(n-1)!\, r_0}(n\,k\,r_0)^n \times \\ \quad \sum_i I_i\left(k\,a_i\, K_{n-1}(n\,k\,a_i) + K_n(n\,k\,a_i)\right)\cos n\varphi_i \\ A_n(k) = B_{ref}(k)\, a_n(k) = -\frac{\mu_0}{\pi}\frac{1}{2^n(n-1)!\, r_0}(n\,k\,r_0)^n \times \\ \quad \sum_i I_i\left(k\,a_i\, K_{n-1}(n\,k\,a_i) + K_n(n\,k\,a_i)\right)\sin n\varphi_i \end{cases} \quad (3)$$

where $k = 2\pi/L$, and $I_n(nkr)$ and $K_n(nkr)$ are the modified Bessel functions of the first and second kind of order n, respectively. With the definition of $b_1(k) = 1$ (=constant), naturally $B_{ref}(k) = B_1(k)$. Then, the asymptotic forms for the reference field $B_{ref}(k)$ and for these helical multipole coefficients $a_n(k)$ and $b_n(k)$ are given in the limit $k \to 0$ (or $L \to \infty$) by,

$$\begin{cases} \lim_{k\to 0}[B_{ref}(k)] = B_{ref} \\ \lim_{k\to 0}[a_n(k)] = a_n \\ \lim_{k\to 0}[b_n(k)] = b_n \end{cases} \quad (4)$$

## 3 COMPARISON BETWEEN ANALYTICAL AND NUMERICAL CALCULATIONS

### *3.1 Calculation for four helical line currents*

Following numerical values are assumed in the calculation for four helical line currents with dipole symmetry.

Radius of helical line current: a = 50 mm,
Angle of helical line current: $\varphi = \pm\pi/6$, or $\pm 5\pi/6$,
Current: $I = -1 \times 10^5$ A,
Pitch length: L = 2 m,
$k = 2\pi/L = 1/(a\tan\alpha) = \pi$,

0-7803-4376-X/98/$10.00 © 1998 IEEE

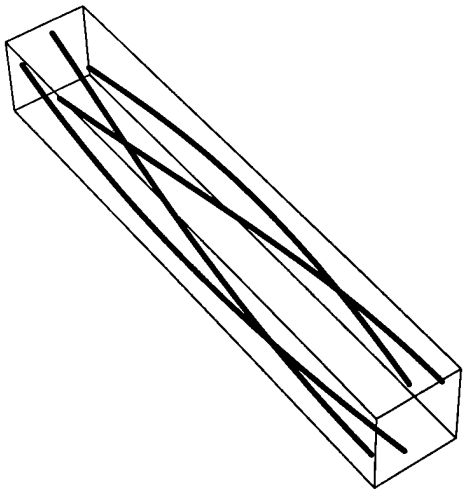


Fig. 1. 3D view of a four currents' helical dipole.

Table 1. Normal multipole coefficients for a infinitely long four line currents' helical dipole.

| n | Pole | bn-theta | bn(k) |
|---|---|---|---|
| (Bref) | | 1.411 | 1.411 |
| 1 | dipole | 0.9998 | 1. |
| 3 | sextupole | $-2.859\ 10^{-10}$ | 0 |
| 5 | decapole | -0.1239 | -0.1243 |
| 7 | 14-pole | -0.04386 | -0.04419 |
| 9 | 18-pole | $-1.721\ 10^{-10}$ | 0 |

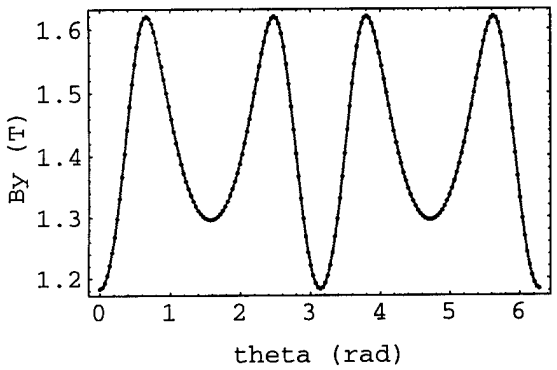



Fig. 3. Distribution $B_y$ on the circle of r = 30 mm, with the comparison between the numerical (black dots) and analytical (gray line) calculations.

Pitch of the winding: $\alpha = \tan^{-1}(1/0.05\,\pi)$,
Reference radius for multipole: $r_0 = 30$ mm,

as shown in Fig.1. Both of the numerical and analytical calculations for the helical dipoles with the infinite length, are made, using Mathematica [4]. Both calculated helical multipole coefficients are listed in Table 1. The

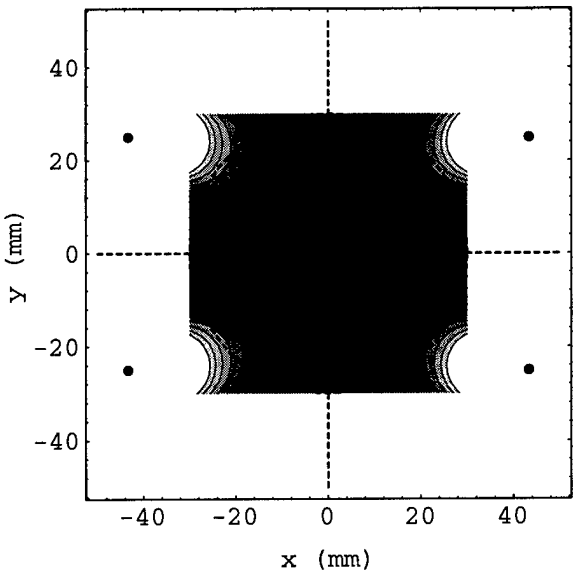



Fig. 2. Contour plot of dipole field $B_y$.

bn-theta and $b_n(k)$ correspond to the normal multiple coefficients derived from the angular component of numerically calculated field $B_\theta$ and analytically calculated helical coefficients, respectively. The analytically calculated contour plot of the dipole field $B_y$ (r, θ, z=0) is shown in Fig.2. Both analytical (gray line) and numerical (black dots) calculations for the dipole field $B_y$ (r=30 mm, θ, z=0) are also shown in Fig.3. As a result, it is confirmed that the agreement between the analytical and numerical calculations is quite good in the interior region of helical coils. The twist dependence of the dipole field $B_{ref}$ is also shown in Fig.4.

### *3.2 Calculation for four helical current shells*

Similarly, the magnetic fields are calculated for a four helical current shells with dipole symmetry of current density $\pm j_z$, radii $a_1$, $a_2$, limiting angles $\pm\varphi_1$, $\pm\varphi_2$, with,

Inner radius of helical line current: $a_1 = 50$ mm,
Outer radius of helical line current: $a_2 = 60$ mm,
Inner angle of helical line current: $\varphi_1 = 0$, or $\pi$,
Outer angle of helical line current: $\varphi_2 = \pi/3$, or $2\pi/3$,
Coil length: L = 2 m,

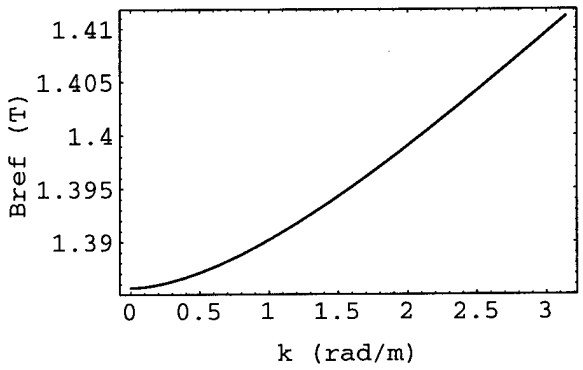



Fig. 4. Twist dependence of the dipole field $B_{ref}$.



Fig.5. 3D view of a four helical current shells' dipole.

Table 2. Normal multipole coefficients for a 2 m long, 4 helical current shells' dipole.

| n | Pole | bn-theta | bn(k) |
|---|---|---|---|
| (Bref) | | 2.463 | 2.456 |
| 1 | dipole | 1. | 1. |
| 3 | sextupole | $-1.001\ 10^{-6}$ | $1.369\ 10^{-17}$ |
| 5 | decapole | -0.01727 | -0.01734 |
| 7 | 14-pole | 0.003718 | 0.003743 |
| 9 | 18-pole | $-3.246\ 10^{-6}$ | $3.775\ 10^{-19}$ |

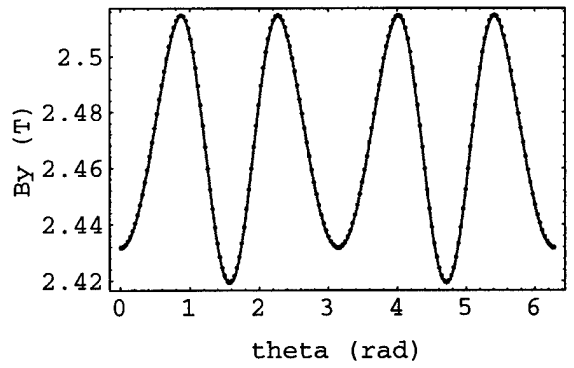



Fig. 6. Distribution of By on the circle of r = 30 mm.

Current: $I = -2 \times 10^5$ A,

Current density: $j_z = 347$ A/mm$^2$

$k = 2\pi/L = 1/(a \tan\alpha) = \pi$,

Pitch of the winding: $\alpha = \tan^{-1}(1/0.05\ \pi)$,

Reference radius for multipole: $r_0 = 30$ mm,

as shown in Fig.5. The numerical calculation for the helical coil with the finite length of one period is made, using the code 'OPERA-3d'. [5] Both analytical (gray line) and numerical (black dots) calculations for the dipole field $B_y$ (r=30 mm, θ, z=0) is shown in Fig.6. The 3D

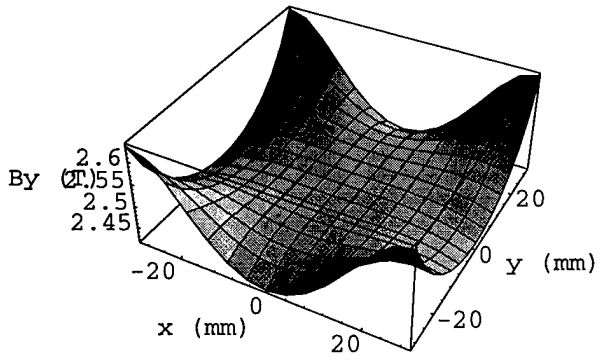



Fig. 7. 3D plot of dipole field By.

plot of the analytically calculated dipole field $B_y$ (r, θ, z=0) is shown in Fig.7. Both of the analytically and numerically calculated helical multipole coefficients are also listed in Table 2. In addition, this analytical method was applied for two helical magnet of different type. [6,7,8]

## 4 CONCLUSION

As an extension of single helical current conductor, the magnetic fields of helical dipole magnet are derived and helical multipole coefficients are presented. In addition, it was confirmed that this analytical calculation is consistent with the numerical calculation by the 3D magnetic field numerical code, OPERA-3d/TOSCA

## 5 ACKNOWLEDGMENTS

The authors are indebted for helpful discussions and comments to the RIKEN RHIC spin accelerator group.

## REFERENCES

[1] T. Tominaka et al., "Multipole Expansion for a Single Helical Current Conductor", in this proceedings.

[2] T. Tominaka, "Multipole Expansion for a Single Helical Current Conductor", AGS/RHIC/SN No.49, December 18, (1996).

[3] T. Tominaka, "Magnetic Field Calculation of Helical Dipole Coils", AGS/RHIC/SN No.24, April 29, (1996).

[4] Stephen Wolfram, "Mathematica, A system for Doing Mathematics by Computer", Addison-Wesley Publishing Company, Inc., (1991).

[5] Vector Fields Limited, Oxford, England.

[6] T. Tominaka, "Analytical Field Calculation of the Slotted Helical Dipole", AGS/RHIC/SN No.47, November 12, (1996).

[7] T. Tominaka, "Analytical Field Calculation of the Direct Wind Helical Dipole", AGS/RHIC/SN No.48, December 18, (1996).

T. Tominaka, " Relation between Field Homogeneity and Multipole Coefficients for a Helical Dipole", AGS/RHIC/SN No.54, April 25, (1997).

# DESIGN STUDY OF THE INJECTION AND EXTRACTION ELEMENTS FOR THE RIKEN SUPERCONDUCTING RING CYCLOTRON

T. Tominaka, H. Okuno, S. Fujishima, T. Mitsumoto, T. Kubo, T. Kawaguchi, Y. Tanaka, J. -W. Kim, K. Ikegami, N. Sakamoto, S. Yokouchi, T. Morikawa, A. Goto, and Y. Yano
The Institute of Physical and Chemical Research (RIKEN), Wako, Saitama, 351-01, Japan

*Abstract*

The injection system for the RIKEN 6-sector superconducting ring cyclotron (SRC) consists of four bending magnets (BM1, BM2, BM3, BM4), three magnetic inflection channels (MIC1, MIC2, MIC3), and an electrostatic inflection channel (EIC). The four bending magnets and one of the three magnetic channels are superconducting. In this paper, the status of the design study of the BM1 is reported.

## 1 INTRODUCTION

The injection and extraction systems of the RIKEN 6-sector superconducting ring cyclotron (SRC) are designed. [1,2,3,4] It is required that the disturbance due to the bending magnets in the acceleration region should be less than 100 G. Two types of bending magnets - with an iron yoke or a shield coil - have been studied. A stray field up to 0.6 T is anticipated in the area of the BM1 due to the saturation of iron yoke of the main SRC's sector magnet, depending on ions. Then, if the BM1 has an iron yoke, the iron yoke saturates due to the stray field. Such saturation of the iron yoke was simulated by the field calculation, with 3D electromagnetic calculation code TOSCA, for the complete configuration of 6-sector magnets. As a result, it was found that the iron yoke is ineffective due to the stray fields of up to 0.6 T from the sector magnets, and an active-shield type magnet, which is equipped with shield coils, is adopted for the BM1 close to the sector magnets. The magnetic inflection channels are also designed to be an active shield type. In this paper, we discuss about the design of the injection bending magnet BM1, in particular about the optimization of the cross-sectional shape of the BM1. Major parameters of BM1 are shown in Table 1.

Table 1. Major parameter of BM1

| | |
|---|---|
| Bending field | 4.0 T |
| Bore size | 40 (H) × 20 (V) mm$^2$ |
| Uniformity (excluding quadrupole) | $1 \times 10^{-3}$ |
| Bending radius | 1.32 m |
| Effective magnetic angle (length) | 52° (1.20 m) |
| Stray field | < 100 G at 0.5 m |

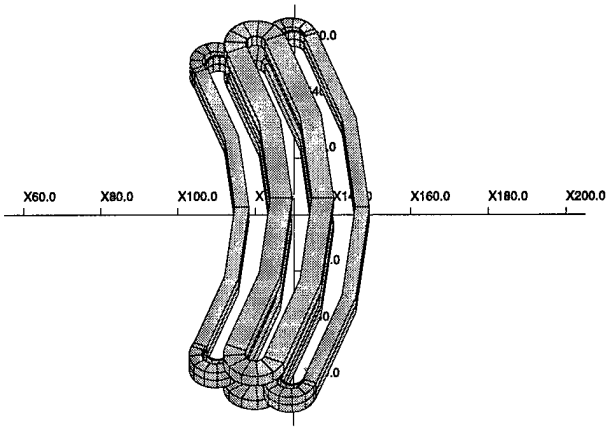



Fig. 1. Schematic view of the bending magnet (BM1)

## 2 OPTIMIZATION OF CROSS SECTIONAL SHAPE FOR BM1

The BM1 is planned to be composed of rectangular coil blocks. Then, the procedure of the optimization for the cross sectional shape is as follows:
1) calculation of the multipoles determined from the cross sectional configuration of coil,
2) search of the minimum value of field uniformity from these multipoles

### *2.1 Calculation of the Multipoles*

For four helical current blocks, current density $\pm j_z$, x-coordinate $\pm x_1, \pm x_2$, y-coordinate $\pm y_1, \pm y_2$, with dipole symmetry, the interior normal multipoles $B_n$ for $r < \sqrt{x_1^2 + y_1^2}$, are given as follows, [5,6,7]

$$\begin{cases} B_1(x_1,x_2,y_1,y_2) = B_{ref}(x_1,x_2,y_1,y_2) = \\ B_1(x_2,y_2) - B_1(x_1,y_2) - B_1(x_2,y_1) + B_1(x_1,y_1) \\ B_n(x_1,x_2,y_1,y_2) = B_n(x_2,y_2) - B_n(x_1,y_2) - \\ B_n(x_2,y_1) + B_n(x_1,y_1), \qquad n=3,5,\cdots \end{cases} \tag{1}$$

where

$$\begin{cases} B_1(x,y) = B_{ref}(x,y) = \\ -\dfrac{\mu_0 j_z}{\pi}\left\{2 x_0 \tan^{-1}\left(\dfrac{y}{x}\right) + y_0 \log\left(\dfrac{x^2+y^2}{x^2}\right)\right\} \\ B_n(x,y) = \dfrac{2\mu_0 j_z}{\pi} \dfrac{1}{(n-1)(n-2)} \dfrac{r_0^{n-1}}{\sqrt{x^2+y^{2n-2}}} \times \\ \sin\left[(n-2)\tan^{-1}\left(\dfrac{y}{x}\right)\right], \qquad n=3,5,\cdots \end{cases} \tag{2}$$

0-7803-4376-X/98/$10.00 © 1998 IEEE

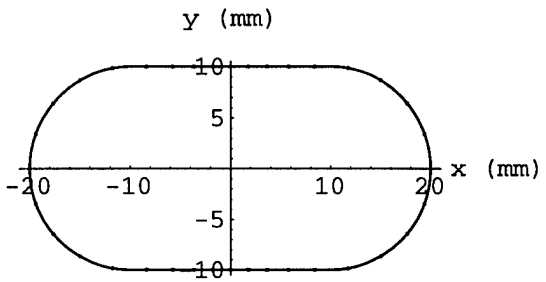


Fig. 2. Required region of the uniform field.

where $r_0$ is the reference radius, and the normal multipole coefficients $b_n$ is defined as $b_n=B_n/B_1$.

*2.2 Relation between Field Uniformity and Multipole Coefficients for Dipole Coils*

The interior magnetic field of 2-dimensional dipole coil with the infinite length is given as follows, on the European definition, [8]

$$B_y(r,\theta) = B_{ref}\sum_{n=1}^{\infty}\left(\frac{r}{r_0}\right)^{n-1}\{a_n \sin[(n-1)\theta] + b_n \cos[(n-1)\theta]\}. \quad (3)$$

Then, for the case with the dipole symmetry, $a_n=b_{2n}=0$ for n=1, 2, 3, ... , ∞, the y component of field, $B_y(r,\theta)$ becomes, with $b_1=1$,

$$B_y(r,\theta) = B_{ref}\sum_{n=1,3,5}^{\infty}\left(\frac{r}{r_0}\right)^{n-1} b_n \cos[(n-1)\theta] = B_{ref}\left(1 + b_3\left(\frac{r}{r_0}\right)^2 \cos 2\theta + b_5\left(\frac{r}{r_0}\right)^4 \cos 4\theta + b_7\left(\frac{r}{r_0}\right)^6 \cos 6\theta + \ldots\right) \quad (4)$$

Then,

$$\left|\frac{B_y(r,\theta)-B_{ref}}{B_{ref}}\right| = \left|\frac{B_y(r,\theta)-B_{y0}}{B_{y0}}\right| = \left|b_3\left(\frac{r(\theta)}{r_0}\right)^2 \cos 2\theta + b_5\left(\frac{r(\theta)}{r_0}\right)^4 \cos 4\theta + b_7\left(\frac{r(\theta)}{r_0}\right)^6 \cos 6\theta + \ldots\right| \quad \text{- - - (5)}$$

The required condition of multipole coefficients depends on the shape of the uniform region where the field uniformity is prescribed. The shape of the uniform field region for BM1 is shown in Fig.2. Therefore, the requirement condition for the normal multipoles can be calculated from the prescribed uniformity of the dipole field $B_y$ at the boundary points of the region shown in Fig.2, using Eq.(5). For the coil with the dipole symmetry, the resultant satisfying regions of sextupole and decapole, ($b_3$, $b_5$) of $|(B_y - B_{y0})/B_{y0}|$ of < 0.1 %, in the case of $b_7$, $b_9$, ⋯ = 0, is shown as the central white

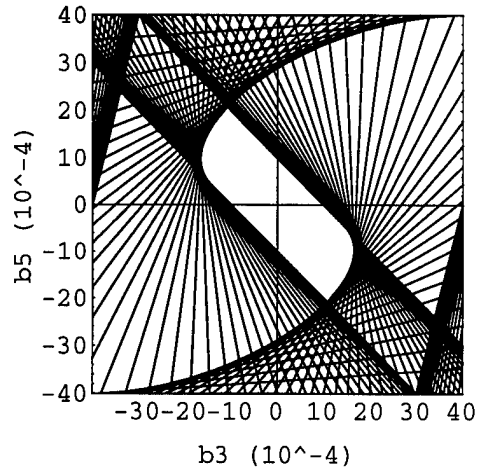


Fig. 3. ($b_3$, $b_5$) region of < 0.1% of |(By-By0)/By0| with $b_7$=0 and, $b_9$, $b_{11}$,...=0.

zone in Fig.3. As a result, the field uniformity U, which is defined as the maximum value of $|(B_y(r,\theta)-B_{y0})/B_{y0}|$, can be obtained as a function of the multipoles, that is, U=U($b_3$,$b_5$, ... ). In addition, it is realized that the structure of this function, U($b_3$,$b_5$, ... ) depends on the shape of the uniform region, e.g. circle, ellipse, etc. For the case as shown in Fig.2, the field uniformity U can be expressed approximately with $r_0$ = 20 mm,

$$U(b_3,b_5,b_7,\ldots) = \mathrm{Max}\left(\left|\frac{B_y(r,\theta) - B_{y0}}{B_{y0}}\right|\right) = \approx \mathrm{Max}\left(\left|b_3 + b_5 + b_7\right|, \left|-\frac{b_3}{3} + \frac{b_5}{3} + \frac{b_7}{2}\right|, \left|b_7\right|\right) \quad (6)$$

*2.3 Search of the Minimum Value of Field Uniformity from Multipoles*

For the BM1, the contour plot of the approximated field uniformity U=U($b_3$,$b_5$, ... ), as a function of the horizontal coordinates $x_1$ and $x_2$ of the upper main coil and lower main coil from the initial coil configuration, is shown in Fig.4. From this figure, the optimal value of ($x_1$, $x_2$) is easily obtained.

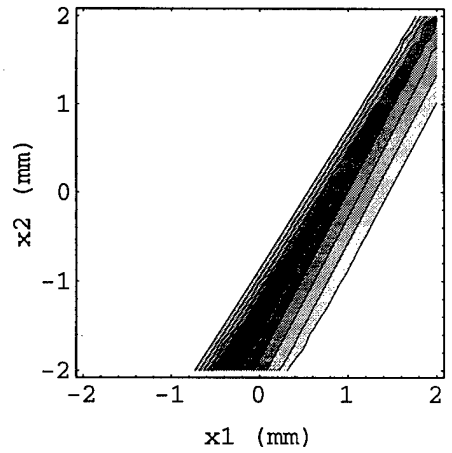


Fig. 4. Contour plot of field uniformity of < 0.2% of |(By-By0)/By0.

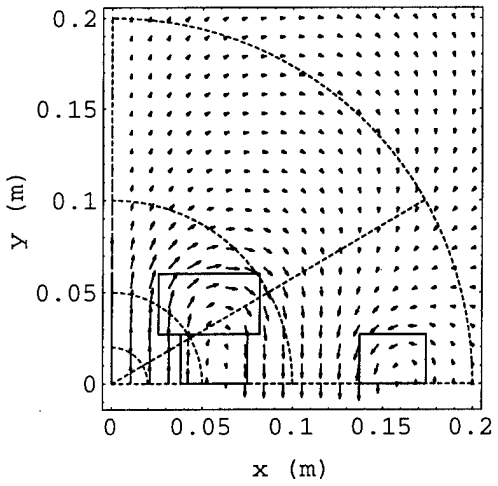



Fig. 5. Field distribution without the bias field and cross section of a active shield bending magnet.

## 3 FIELD ANALYSIS

In this field analysis, it is assumed that both main and shield coils are fabricated from the superconducting wire which permits the overall current density of 200 A $mm^{-2}$. For the case without the vertical bias field of -0.6 T, the distribution of field vectors is shown in Fig.5, together with the cross sections of coils. The inversely vertical bias field $-B_{bias}$ increases the total field between the main coils and the shield coils, and changes the location of the maximum field and the magnetic forces acting on each coil. The contour plot of $|(B_y-B_{y0})/B_{y0}|$ is shown in Fig.6 The white region corresponds to the larger region of $|(B_y-B_{y0})/B_{y0}|$, while the black region corresponds to the smaller region. The contour plot of |B| is also shown in Fig.7 The maximum field of coils is 5.5 T. Supporting structure for the magnetic forces should be optimized. The mechanical and cryogenic design are currently under study. Since the installation space for the bending magnet (BM1) is so limited, a compromise between the compactness for the whole structure and the easiness for the coil fabrication must be made.

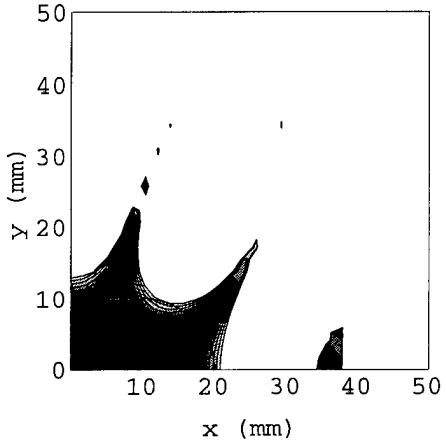



Fig. 6. Distribution of |(By-By0)/By0| of < 0.1 %.

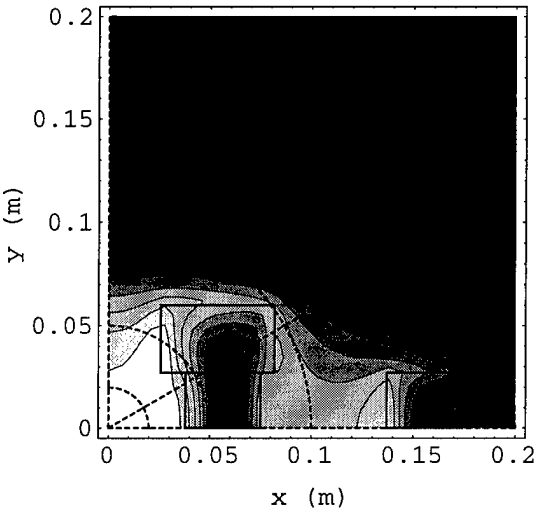



Fig. 7. Contour plot of |B| on the case without the bias field.

## 4 CONCLUSION

The relation between field uniformity and multipoles of dipoles was approximately obtained for the specific uniform region. It was recognized that this relation will be useful to optimize the cross-sectional shape of dipole coils such as the injection and extraction bending magnets of the SRC.

## REFERENCES

[1] Y. Yano et al., "RIKEN RI-Beam Factory project", in this proceedings.

[2] T. Mitsumoto et al., "Orbit Analysis for the RIKEN Superconducting Ring Cyclotron", in this proceedings.

[3] H. Okuno et al., "Design Study of the Injection and Extraction Systems for the RIKEN Superconducting Ring Cyclotron", in this proceedings.

[4] S. Fujishima et al., "Numerical Analyses of the Injection and Extraction Trajectories for the RIKEN Superconducting Ring Cyclotron", in this proceedings.

[5] K. Halbach, "Fields and First Order Perturbation Effects in Two-dimensional Conductor Dominated Magnets", Nucl. Instr. and Meth. 78 (1970) pp.185-198.

[6] H. Hirabayashi et al., "A Design Proposal for High Field Dipole Magnet", KEK 81-1 (1981).

[7] J. Rossbach and P. Schmüser, "Basic Course on Accelerator Optics", CAS, CERN94-01 pp.17-88 (1994).

[8] K. -H. Mess, P. Schmüser and S. Wolff, "Superconducting Accelerator Magnets", World Scientific, pp.45-63 (1996).

# STRESS MANAGEMENT IN HIGH-FIELD DIPOLES

N. Diaczenko, T. Elliott, A. Jaisle, D. Latypov, P. McIntyre, P. McJunkins, L. Richards, W. Shen, R. Soika, D. Wendt, Dept. of Physics, Texas A&M University, College Station, TX 77843
R. Gaedke, Dept. of Physics, Trinity University, San Antonio, TX 78212

*Abstract*

The management of Lorentz stress and preload forces is the biggest single challenge in the effort to develop collider dipoles with ever greater field strength. Were the Lorentz forces permitted to accumulate through a coil, they would exceed the limit for strain degradation for the A15 and high-temperature superconductors which are capable of sustaining such field strength.

A strategy has been devised for intercepting Lorentz stress within the coil to overcome this problem in high-field block-coil dipoles. The coil is fabricated in multiple independent shells, in which a high-strength structure and a soft-modulus spring are used to bypass stress between succeeding layers. Finite-element analysis and experimental studies have demonstrated that this strategy can limit the maximum stress anywhere in a coil so that it nowhere exceeds strain degradation limits for fields at least to 20 Tesla.

## 1 STRESS IN A SUPERCONDUCTING DIPOLE

The field strength and field quality of superconducting dipoles are the primary challenge in extending the energy reach of hadron colliders. The design field of colliders has increased over the past two decades from 4.5 Tesla (4.2°K, Fermilab) to 8.65 Tesla (1.9°K, LHC) for NbTi cos θ dipoles. The state-of-the-art has now reached 11 Tesla (Twente) and 13 Tesla (LBL) for $Nb_3Sn$ cos θ dipoles at 4.2 °K. Today groups at BNL, KEK, LBL, and Texas A&M are developing new approaches to high-field dipoles, aimed at 16 Tesla and beyond. A primary challenge in that effort is stress management.

The Lorentz stress in a coil accumulates through its thickness, with $\vec{\nabla} S_L = \vec{j} \times \vec{B}$, where $j$ is the current density and $B$ the field in the coil. If the coil is supported only at its boundaries, this stress accumulates to at least the stored energy density $S_0 = B^2 / 2\mu_0$ At 16 Tesla, $S_0$ = 100 MPa, which is the limit for strain degradation of $Nb_3Sn$ even when the coil is vacuum impregnated to provide isostatic support of cable elements. The problem is compounded if we contemplate the use of high-temperature superconducting (HTS) inserts to extend operation beyond 16 Tesla, because the limits for strain damage of HTS is ~40 MPa, less than half that of $Nb_3Sn$. If this accumulation of stress within the coil were not intercepted, it would not be feasible to operate a dipole to fields greater than about the current 13 Tesla limit.

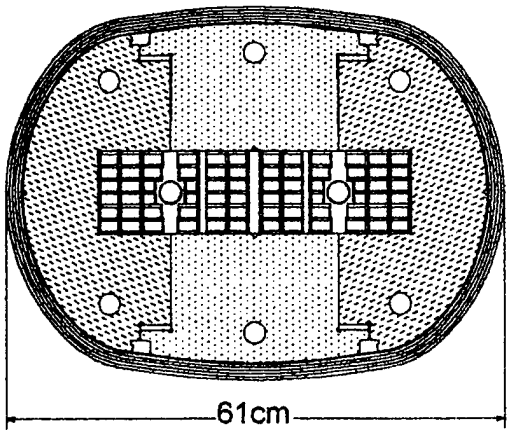



Figure 1. Block-coil dual dipole: 16 Tesla @ 4.2°K.

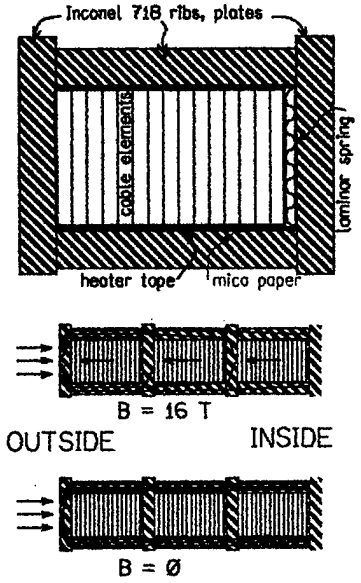



Figure 2. Detail of stress management in a coil block.

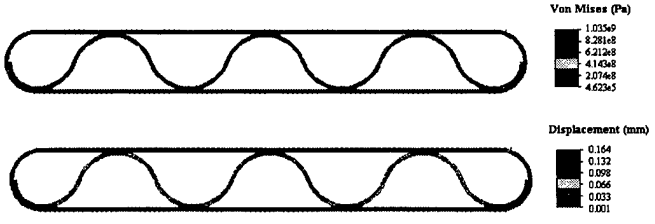



Figure 3. Laminar spring under 15 MPa load: stress and strain distributions.

0-7803-4376-X/98/$10.00 © 1998 IEEE

## 2 STRESS MANAGEMENT STRATEGY

Figure 1 shows a block-coil dipole in which the coil stress is managed by introducing a structural matrix within the coil. The matrix intercepts the Lorentz stress from the inner coil elements and shunts it past the outer coil elements. No coil element sees more than the Lorentz stress in its own coil layer, ~40 MPa.

In order for this strategy of stress management to be feasible, three important elements must be incorporated into the coil assembly, as shown in the detail of Figure 2: a support matrix which has much greater yield strength than the coil package; a spring element which has much lower elastic modulus than either the coil or the support matrix; and a shear relief layer that releases shear between the sides of the coil and the support matrix when the ribs are compressed. Table I presents the materials used in each of these functional units and their mechanical properties.

One last requirement of the strategy is particularly demanding: *all elements of the coil assembly must be added as the coil is wound; so all elements must survive the reaction bake (650°C for $Nb_3Sn$, 800°C for HTS) and subsequent epoxy impregnation.* The complete coil assembly then can be fabricated in one operation, passed through reaction bake (when both superconductor and insulation are extremely fragile), and then immediately epoxy impregnated without intermediate disassembly and handling.

### *1.1. Preload*

Preload is delivered by wrapping banding around the magnet structure as shown in Figure 1. The resulting circumferential stress is transformed into a horizontal compression of the two side segments of the flux return structure. In the stress management strategy, the ribs are compressed by this preload, and by the magnetic load when the magnet is energized. A preload of ~1.5 $S_0$ is required in order to prevent coil motion from the magnetic load. The preload is optimally divided between two strain patterns in the magnet (Figure 1): ~1/3 of the preload compresses the ribs within the coil assembly; the remaining 2/3 compresses the steel flux return assembly. The sharing of preload is controlled by a vertical gap separating the center and side sections of the flux return. Thus we deliver only part of the preload into the coil assembly at room temperature, and hold most of it in reserve in the steel, available as required to counter Lorentz stress.

### *1.2. Ribs and plates*

A pattern of Inconel ribs and plates is integrated into the coil package to provide the path by which stress developed in one block of the coil can bypass the next block. The ribs and plates are able to sustain the concentration of preload and magnetic loading to ~1 GPa. This bypass strategy is complicated by the fact that the rib and the coil block form parallel elements in the stress circuit. The elastic modulus of the impregnated coil is about half that of the ribs, while the span between ribs is ~5 times the rib thickness. In order to decouple the coil package from the strain in the ribs when they are under load, there must also be a soft-modulus element at the inner end of each coil block. We have devised the laminar spring shown in Figure 3 for this purpose.

Table I. Material properties of the coil structure.

| element | material | modulus GPa | yield strength MPa |
|---|---|---|---|
| impregnated cables | $Nb_3Sn$, Cu, epoxy | 40 | 100 |
| ribs, plates | Inconel 718 | 210 | 1.300 |
| laminar spring | Inconel X750 | 210 | 900 |
| flux return | 1008 steel | 170 | 200 |

### *1.3. Laminar spring*

The springs are constructed of 75 μm thick Inconel X-750 foil, and are laser welded to form a sealed assembly. The spring has an overall thickness of 1.5 mm, a working range of 0.2 mm, and an effective modulus of 100 MPa - 400 times smaller than that of the coil assembly. Thus as a rib is compressed by the magnet stresses, the spring compresses likewise so that the load on each coil block is just its own Lorentz stress (<35 MPa) plus the spring preload (~5 MPa).

A spring is located at the inner boundary of each coil block, and compressed sufficiently to deliver ~5 MPa preload. When the coil is vacuum impregnated with epoxy, the springs are sealed so that they are not impregnated and retain their spring moduli. The springs are later opened at the magnet ends, and provide a second benefit as helium cooling channels throughout the coil.

We have built and tested models of the laminar spring. We cold-formed a 1 mm thick, 2-convolute spring from annealed foil, laser-welded the assembly, then performed a re-annealing and precipitation hardening. The spring was then constrained across its wide dimension and cycled in face-loading on a dynamometer. Figure 4 shows a 10,000 cycle test, in which the spring exhibited some creep but retained most of its spring memory. We have since improved the design to a 1.5 mm thick, 3-convolute spring to reduce peak stress in the foil of the spring and to increase its elastic stroke to 0.2 mm.

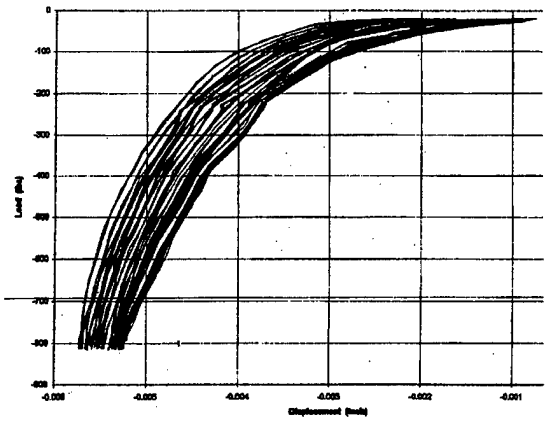


Figure 4. Laminar spring stress/strain: 10,000 cycles.

### *1.4. Shear relief*

As a rib is stressed under preload and Lorentz loading, it strains longitudinally. Even though the spring decouples the linear stress in the adjacent coil block, there would be unrelieved shear at the side interface between coil block and rib. Such shear is a potential source of stick-slip friction as the magnet is energized, which can cause training.

Inspired by the technology developed at MIT for $Nb_3Sn$ solenoid coils, we relieve this shear by inserting a layer of mica paper between the coil block and the rib, as shown in Figure 2. We selected a particular mica paper which does not produce smoke or ash during a reaction bake. We assembled a prototype coil block, and passed it through the processes of reaction bake and epoxy impregnation. We then mounted the block in a 2-axis dynamometer and measured the shear required to release the mica paper to be 4 MPa. This shear would be provided in the first preloading of the completed coil, so that the coil blocks would be released from shear even before the first cooldown.

## STRESS DISTRIBUTION

We have implemented the above strategy in an optimized design for a 16 Tesla dual dipole for future hadron colliders, shown in Figure 1. The coil is configured in rectangular block elements which can be wound as pancake coils. The coil is segmented into three current circuits, and the circuits are separately current-programmed to produce collider-quality field (all multipoles $b_n < 10^{-4}$ $cm^{-n}$) over a 20:1 dynamic range of field strength. Figure 5 shows the field distribution at full field, calculated using the code PE2D.

We used the code ALGOR to calculate the distribution of stress and strain in the magnet, including the effects of preload, differential contraction during cooldown, operation of the laminar springs, and shear relief at the mica paper boundaries. The results are shown in Figure 6 for three cases: preload at room temperature, cooldown to 4.2 °K, and operation at 16 Tesla.

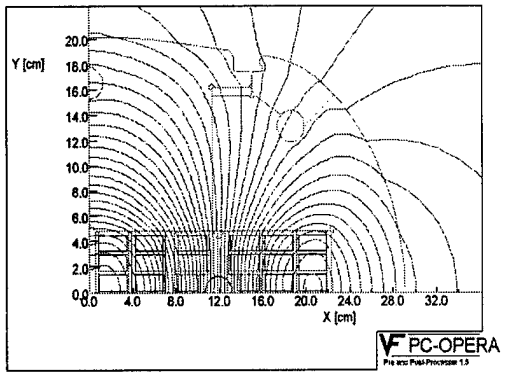
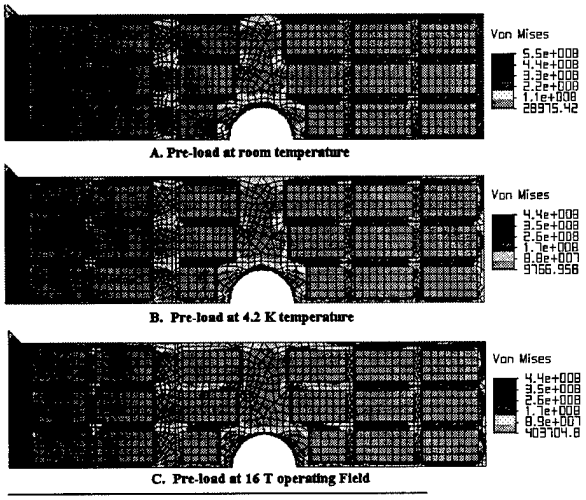



Figure 5. Calculated field distribution in 16 Tesla block-coil dual dipole.




| | Pre-load | Temperature | Magnetic Field | Maximum Stress (MPa) Cable | Inconel Alloy |
|---|---|---|---|---|---|
| A | 65 Mpa | 300 K | 0 | 33.8 MPa | 290 MPa |
| B | 65 Mpa | 4.2 K | 0 | 27.0 MPa | 206 MPa |
| C | 65 Mpa | 4.2 K | 16.0T | 33.0 Mpa | 220 Mpa |

Figure 6. Finite-element calculations of the stress and strain distributions in the 16 Tesla dual dipole.

In no case does the stress in any coil element exceed 40 MPa, the sum of the maximum Lorentz stress in a single block and the spring preload. This stress level would be comfortable for impregnated $Nb_3Sn$ cable, and is even tolerable for HTS conductor. The same strategy could be employed for fields well beyond 16 Tesla, simply by adding additional blocks.

## ACKNOWLEDGMENTS

It is a pleasure to acknowledge material help, many ideas, and helpful criticism by our collaborators in the Supercon group at LBL, particularly R. Scanlan and C. Taylor. This work was supported by U.S. Dept. of Energy grant # DE-FG03-95ER40924.

# QUENCH SIMULATION FOR 16T DIPOLE BUILT AT TEXAS A&M UNIVERSITY

Damir Latypov, Peter McIntyre and Weijun Shen
Department of Physics, Texas A&M University, College Station, TX

## 1. QUENCH CODE

A 16 Tesla $Nb_3Sn$ block-coil dual dipole and its prototype are being developed at Texas A&M University [1]. Quench protection system for the magnet is, of course, one of our concerns. Although there is a number of quench codes reported in literature, most of them are written to model a specific magnet. To our knowledge, the only commercially available quench codes are OPUS [2] and QUABER [3]. In OPUS the magnetic field calculations and the quench simulator are incorporated in one finite element package. The local magnetic fields and inductive couplings of the coils are accurately recalculated during the quench. However, being otherwise very general and robust OPUS deals only with the solenoidal magnets. QUABER has only been used at CERN and we have not yet had an opportunity to evaluate it. Therefore to facilitate the design of quench protection we have developed a new code for a magnet of general geometry with an arbitrary number of coils and with the provision for heaters and switches.

The algorithm is based on adiabatic assumption which allows to integrate the equation for the temperature distribution in a coil and express it as an implicit function of miits. This function is tabulated for each coil and is used to calculate the peak temperature in the coils. Quench propagation is described in terms of time-dependent longitudinal quench velocities and transversal turn-to-turn quench jump steps. The circuit equations are solved by inverting the circuit inductance matrix and integrating the resulting set of equations by the Runge-Kutta method. The average magnetic fields seen by the coils are calculated using the transfer functions.

This algorithm is rather standard and closely resembles the one implemented in QUCERN [4]. However, in implementing it the care has been taken to parametrize the data so that the program can be used for different magnets with little further programming.

To check our code we have simulated the coil described in [2]. As with any quench code the results of simulations depend critically on the input assumptions. To make a meaningful test of our program we therefore used the same input data as had been used in [2] for OPUS simulation. We found our results to be in a good agreement with both, OPUS and the experiment.

## 2. QUENCH RESULTS

The prototype 16T dipole is 1 m long, has two bores with three coils and stored energy of 1.03 MJ per bore. A 2D view of the magnet with the field lines is shown in Fig.1.

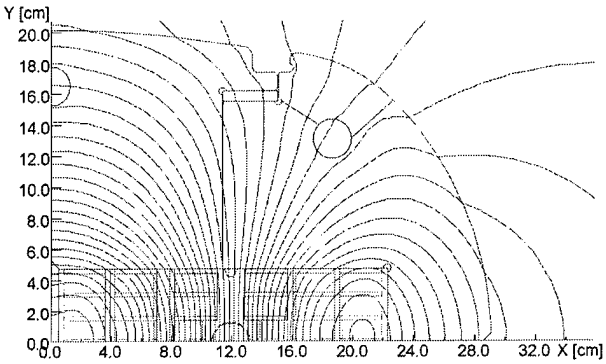



Fig.1. 2D view of the magnet with the field lines.

Main coil parameters are summarized in Table 1. The data on cable which will be used for the winding of coils are given in the Table 2.

Table 1. Coil Parameters.

| Coil | Outer | Middle | Inner |
|---|---|---|---|
| Op. Current (A) | 8650 | 8650 | 8650 |
| Peak field (T) | 9.45 | 13.29 | 16.18 |
| J in $Nb_3Sn$ ($A/mm^2$) | 2300 | 1462 | 592 |
| Turns per bore | 102 | 96 | 50 |
| Inductance per bore (mH) | 11.496 | 6.948 | 1.078 |

Table 2. Cable Parameters.

| Cable | Outer | Middle | Inner |
|---|---|---|---|
| Strand diameter (mm) | 0.6081 | 0.6950 | 1.1583 |
| Cu/Sc ratio | 2.095 | 1.244 | 0.515 |
| Filament size (μm) | 6 | 6 | 6 |
| Number of strands | 40 | 35 | 21 |
| Cable thickness (mm) | 1.2571 | 1.4178 | 2.2749 |
| Cable width (mm) | 12.537 | 12.537 | 12.537 |

0-7803-4376-X/98/$10.00 © 1998 IEEE

The calculated miits curves for the coils are shown in Fig.2. The cable of the inner coil being substantially thicker can take more miits than the cable of outer and inner coils.

Electrical circuit adopted for the quench protection circuit is shown in Fig.3. Besides the dump resistors each coil has a stainless-steel heater tape attached to it (not shown in the figure) which quenches all the turns at the end of a coil once the quench has been detected. Three current supplies are used in order to operate the dipole in a dynamic range of 1 to 20 by means of current programming. At 16T field the current in all coils is the same, 8650A and power supplies PS1 and PS2 are disconnected.

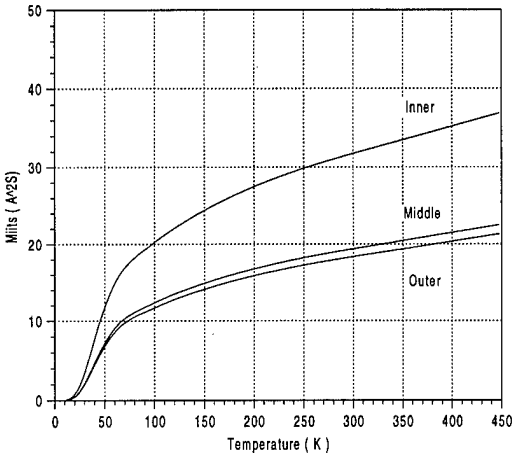



Fig.2 Miits curves.

Our simulations at 16T field indicate that the quench circuit in Fig.3 will adequately protect the coils within some range of the values of the dump resistors. The peak terminal voltage is defined by the value of the dump resistor R3 and therefore it should be of the order of 0.1 Ohm or less in order to keep the voltage below 1kV. The hot spot temperature rise, current in the coils and the coils resistances of the magnet with R1=1, R2=0.5 and R3=0.1 Ohm are shown in Figs. 4, 5 and 6. In this simulation the quench has been started in the inner coil. The heaters have been fired in 10 ms and quenched 10 cm long portion of every turn of all three coils. The power supply has been disconnected 50 ms after the quench initiation.

With these conservative assumptions the highest temperature in the conductor is only 112K, peak terminal voltage is 832V and peak resistive voltage is 118V. Approximately 20% of the stored energy is dissipated in the coils and the rest is taken mostly by the resistor R3.

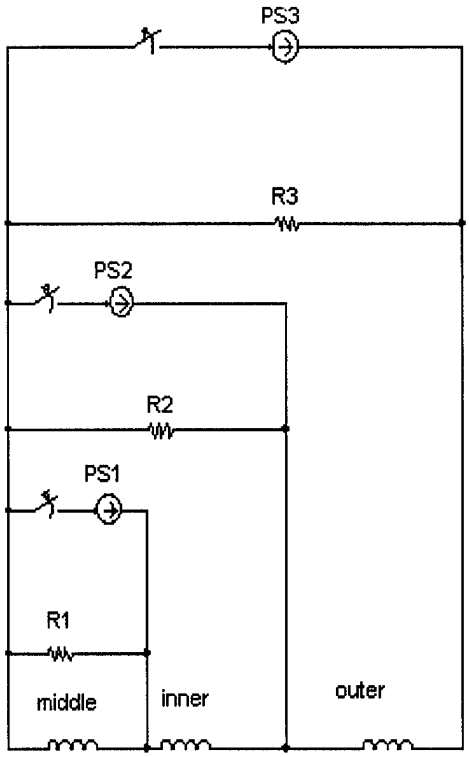



Fig.3 Quench circuit.

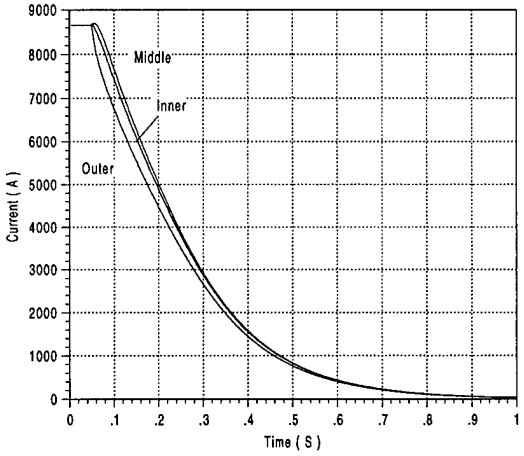



Fig.4 Current profiles.

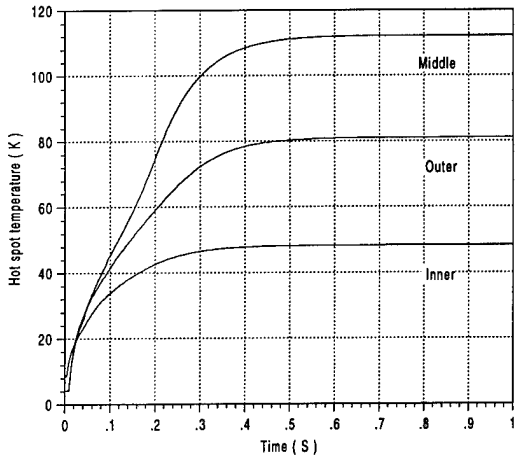



Fig. 5 Temperature rise.

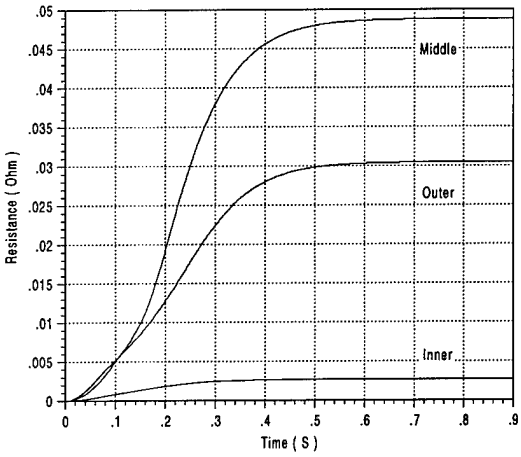



Fig. 6 Coil resistances.

The simulations of the 15 m long version of the dipole with the same circuit show that in order to keep the temperature low, the heaters must initiate quench at a larger part of the coils. The calculated peak temperature in the extreme case when the entire stored energy is evenly dissipated into the coils is 125K. Faster quench will however lead to a problem of large induced and resistive voltages. At this point we note that the stress management design of the magnet utilizes a laminar spring to control the preload given to each block of coil in the support lattice [1, 5]. The spring is sealed so that it is not filled with epoxy during impregnation. If we open the springs at each end of the magnet after the impregnation, they can provide a distributed matrix of helium flow channels which carry helium exactly where it is most needed. This configuration forms in effect an open-geometry cable-in-conduit coil geometry with its advantages for the quench protection.

## 3. SUMMARY

The results of the quench simulations of 16T 1m long prototype dipole being developed at Texas A&M University are presented. The protection of the prototype doesn't seem to be a difficult problem and can be accomplished by means of the dump resistors and heaters. Protection of the longer version of the dipole is a more difficult task. However, the laminar springs introduced into the each coil block for the stress management [5] can also provide cooling channels which should bring liquid helium into thermal contact with the cable. This effect might simplify the task of quench protection but experimental measurements are needed before we can draw any conclusions.

## 4. REFERENCES

[1] T. Elliot et al. "16 T $Nb_3Sn$ Dipole Development at Texas A&M University" to be published in IEEE Trans. on Applied Superconductivity.

[2] S. Pissanetzky, D.M. Latypov, "Full featured implementation of quench simulation in superconducting magnets", Cryogenics, 1994, **34**, p.795.

[3] D. Hagedorn and F. Rodriguez-Mateos, "Modelling of the quenching process in complex superconducting magnet systems", IEEE Trans. MAG-28 (1992) 336.

[4] A.D. McInturff, "QUCERN users manual", CERN, Internal Note EMA 89-12, 1989.

[5] P.M. McIntyre et al., "Stress management in high field magnets", in Proceedings of this conference.

# OVERVIEW OF THE ATR POWER SUPPLIES [1]

D. Bruno, A. Soukas, and F. Toldo, R.F. Lambiase, Brookhaven National Laboratory
Associated Universities, Inc., Upton, Long Island, New York 11973

*Abstract*

The AGS to RHIC transfer Line (ATR) transports a variety of beams from the Alternating Gradient Synchrotron (AGS) which gets its input from the Booster Synchrotron. In turn, the Booster receives input beams from either a Tandem Van de Graaff (heavy ions) or a Linac (protons). The AGS extracts beam bunches, up to a rate of 30 Hertz, to the ATR which feeds the Relativistic Heavy Ion Collider (RHIC) starting with the sextant test in January of 1997. The ATR is made up of the upgraded U line and the new W, X and Y lines. A test in 1995 transported beam to the end of the W line. During normal operation, a pulsed switching magnet at the end of the W line will bend the beam into the X line or the Y line so that the two storage rings in RHIC are filled with counter rotating beams. The ATR line is comprised of 80 power supplies (PS's), 17 of which are upgraded AGS PS's. The remaining 63 PS's were newly purchased. These PS's range from bipolar 600 watt linear type trim magnet PS's to 1 Megawatt, thyristor, dipole PS's. Results of the commissioning runs will be presented, as well as descriptions of regulation, filtering, and analog and digital controls.

## 1 INTRODUCTION

Figure 1 is a layout of the AGS, ATR Line and RHIC. The upgraded U-line starts out with 7 magnets in the AGS ring. These magnets consist of 3 quadrupoles, 2 trim dipoles, and 2 gradient type dipoles. The 2 gradient dipoles are connected in series and make up the 4.25° degree bend. The ATR line has a total of 5 big horizontal bends (4.25°, 8°, 20°, 90°, 90°). The remaining magnets in the upgraded U-line in the ATR tunnel are 10 quadrupoles, 7 trim dipoles, and 4 gradient type dipoles connected in series which make up the 8° bend. The U-line then leads into the W-line which is made up of 6 quadrupoles, 6 trim dipoles, 2 pitching dipoles, and 8 gradient type dipole magnets which make up the 20° bend. The W-line then feeds both the X and Y lines. The X and Y lines are mirror images of each other. Each one contains 6 quadrupoles, 6 trim dipoles, one vertical pitching magnet and 32 gradient type dipoles. The 32 dipoles make up the 90° bend. The repeatability of all the PS's is generally ±0.01% for the large dipoles and quadrupoles and ±0.1% for the trim dipoles. This specification applies to short and long term regulation and ripple. Five PS houses (see figure 1) are utilized for the ATR line PS's with all of the controls ultimately getting back to the AGS main control room.

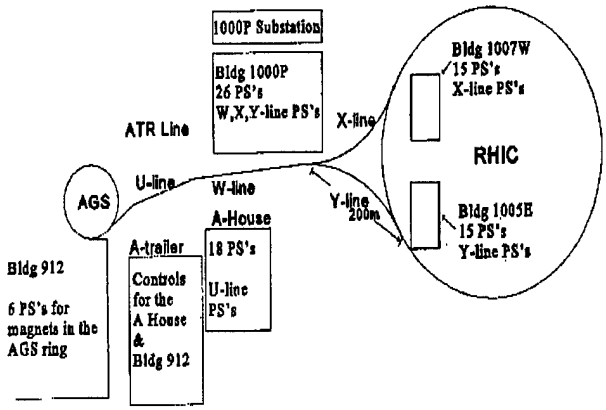



Figure:1 AGS-ATR Line-RHIC Layout

## 2 PS DESCRIPTION

Table I categorizes the PS's into 3 major groups, New Purchases, Upgraded and Constructed In-House.

### *2.1 Upgraded PS's (14)*

The following are modifications for the Quad and Dipole PS's (7). A dc current transformer (DCCT) replaced a shunt for improved regulation. The regulator card was modified to accept the DCCT input and new reference. The PS controls were upgraded. The PS's were modified for OFF/STANDBY/ON operation and they were interfaced to an ALLEN BRADLEY (AB) programmable logic controller (PLC) 5/12. This PLC contains a redundant main interlock string to protect the PS.

The Trim Dipole PS's (7) had the same control modifications made as above, however, these did retain their shunt, and mechanical reversing switches were purchased and installed so they could be used as bipolar PS's for vertical or horizontal trim magnets.

### *2.2 Constructed In-House PS's (3)*

For the SCR Dipole PS's (2), the old transformers (2400V/300V) were replaced with new outdoor oil filled transformers (13.8kV/300V) which were purchased. Refurbished contactors (outdoor, 13.8kV) from the old AGS RF system are now the switches for the primary AC power. The SCR bridges were not altered since they were installed new in 1985. New ripple filters were designed, installed and tested. A more sensitive ground fault circuit was designed to protect the large string of 32 dipole

0-7803-4376-X/98 /$10.00 © 1998 IEEE

magnets. In order to improve the regulation, a DCCT was installed and a feedback loop analysis was performed on these PS's. They were also interfaced to a PLC.

| NEW PURCHASES | UPGRADED | CONSTRUCTED IN-HOUSE |
|---|---|---|
| SCR-quads | SCR-quads | SCR-dipoles |
| 50V/500A(17) | 125V/400A(2) | 350V/3200A(2) |
| 50V/300A(14) | 90V/2400A(2) | |
| LINEAR-trim-dipoles | SCR-trim-dipoles | SCR-reversible-dipole (SWM PS) |
| ±30V/±20A(28) | ±40V/±400A(7) | ±125V/±3000A(1) |
| ±20V/±100A(4) | | |
| | SCR-dipoles | |
| | 50V/3000A(1) | |
| | 130V/3000A(1) | |
| | 125V/3600A(1) | |

Table I. Power Supply Groups

A special, pulsed switching magnet (SWM) PS is required to inject beam into each arc. Since this PS has to reverse polarity in a variety of timing modes to enable flexibility in the RHIC injection process, it was decided to construct it in house from an existing unit. It turned out the enclosure and a filter choke are the only remaining original parts. The new items designed, procured or fabricated and installed in house were a new contactor, ac fusing, step-down rectifier transformer, full wave secondary SCR bridge, a DCCT, a passive damped LCRC filter and a solid-state SCR reversing switch. The reversing switch needed newly-designed trigger and protection circuits. The PS received standard (RHIC) digital and analog controls based on the Waveform Generator (WFG) and interfaced via a PLC.

A network of PLC's was set up to monitor and send commands to all of the power supplies in the entire ATR line. AB PLC's were used. The 5/12 PLC was used to control up to 4 p.s.'s. The 5/12's then communicated with a higher level PLC 5/40 which acts as a master to the 5/12 slaves. This communication is via the AB Remote Input/Output Network (R I/O). The 5/40 is a VME type PLC which acts as an interface between the VME and the 5/12 field devices. There are a total of 4-5/40's, and 25-5/12's in the ATR line. All of the PLC's are connected on the AB Data Highway Plus (DH+) network. The VME crates include the AGS/RHIC Sun networked front end computers that control the beam line via the high-level application code (pet pages). The DH+ network ties all the PLC's together and allows a computer, running the AB software to monitor and/or program the PLC's from any network location.

For the analog setpoint control and monitoring, several boards were developed, that have as their basis the implementation of embedded D/A and A/D converters within the PS's. The communication between a WFG and the embedded controller is via 2 fiber optic connections. A PLD chip(s) is used to receive and convert the serial transmissions. Monitored readbacks include the D/A reference, the PS output voltage and current, the regulator error, the magnetic field (where available), and A/D $^{1}/_{4}$ and $^{3}/_{4}$ reference points. These are multiplexed and fed back to a fiber in 2 groups of 4 readbacks each. The differences between the trim PS's and the other higher precision units are that the trims do not have the above analog readbacks, (they are monitored through the MADC (see below)), and their precision is ± 11 bits as opposed to ±15 bits.

The MADC (multiplexed A/D converter system) [2] is a large digital waveform monitoring system for the RHIC accelerators. It is intended for machine fault analysis (e.g. after quenching). All the ATR PS's have isolated, buffered, analog channels that feed the local MADC via copper cables. The accuracy of this system is typically ±10 bits. The digitization rate is typically 720Hz.

A network analyzer was used to determine the closed loop bandwidth of the voltage loop and the current loop of the Constructed In-House SCR Dipole PS. A model was built in a circuit analysis program (Microcap IV) (TM) to confirm the measured results. This model will also help to predict different closed loop bandwidths based on different compensation settings for different loads without exhaustive PS testing.

The voltage loop closed loop 3dB bandwidth (BW) was measured as 10Hz at a gain of -1.233dB. The simulation of the voltage loop has a 3dB BW of 12Hz and a gain of -1.494dB. Figure 2 is a photo of the measured Frequency and Phase Response of the current loop. The photo shows a closed loop 3dB (BW) of 4Hz and a gain of +0.03195dB. Figure 3 is the result of the circuit simulation which shows a 3dB BW of 3.525Hz and a gain of -0.027dB.

All of the Constructed In-House PS's had new passive damped, filters designed and installed. The 350V/3200A PS's require a regulation of ±0.01% of maximum. The ripple filters were designed for ±0.002% maximum peak-to-peak current ripple near the final operating point. At the operating current of 3200A the 360Hz voltage ripple was measured before the
filter. This voltage ripple before the filter was 160V peak to peak and the 360Hz voltage ripple after the filter was 6V peak to peak. This is an attenuation of approximately -28.5dB at 360Hz and along with the time constant of the magnets this well exceeds the specification.

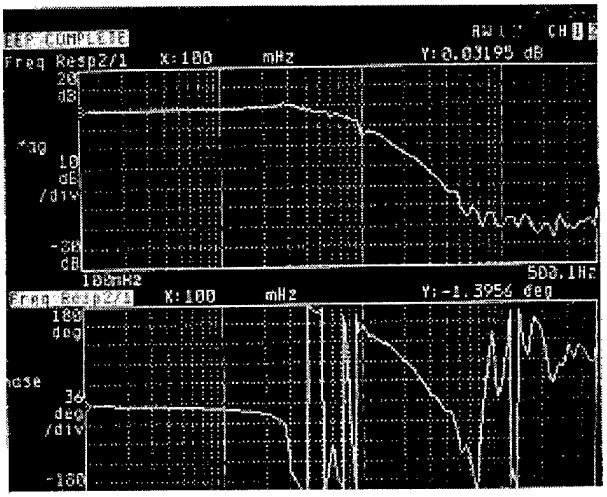



Figure: 2 Current Loop Measured Frequency and Phase Response

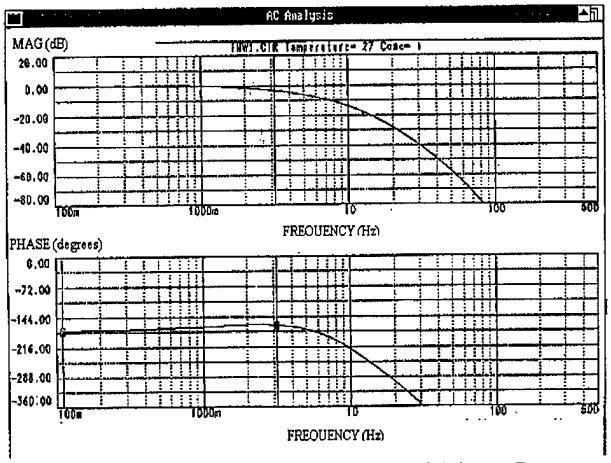



Figure: 3 Current Loop Frequency and Phase Response Simulation

## 3 PS COMMISSIONING RESULTS

During the ATR run in 1995 some problems were encountered. The PS for the 4.25° bend tripped off on a ground fault. After making an access into the AGS ring it was determined that a metallic water hose was touching the magnet core. The filter damping resistor in the new SCR quad PS's needed to be replaced because the power rating was too low. One of the AC breakers in the new SCR quad PS's overheated and was replaced because the AC connections were loose.

During the ATR run of January 1997 the switching magnet PS had a bad temperature sensor on the filter choke which was replaced. In one instance during a security system tripout, both of the large Dipole PS's tripped off and the substation breakers tripped off as well. The cause of this still needs to be determined. We suspect an AC line transient. Two of the Linear PS's had some of their MOSFETS short-out when all the PS's in the ATR line were sent to their maximum current due to a network problem that occurred. The MOSFETS were replaced after spare PS's were installed.

The performance of the ATR PS's has been excellent. Both stability and reproducibility readings with an accurate DVM have shown better than the required or anticipated results, for both the short and long term. Comparisons between accurate references, shunts and DCCT's have been very good. The ultimate test has been the beam. During both runs the beam positions and beam sizes have been measured [3],[4] and have shown the system to have met the specifications very well.

## 4 CONCLUSION

The two commissioning runs of 1995 and 1997 have proven very successful. The beam has been transported down to the end of the of the W line in 1995 and through one sextant of RHIC in 1997. Much has been learned about the operation of the PS's. The last test of the ATR line will be in 1999 when the X-ARC PS and the switching magnet PS will be completely tested. The switching magnet PS was used as a DC PS for the 1997 run. In 1999 the PS will be required to reverse the current through the magnet so as to bend the beam down the Y-ARC and then down the X-ARC.

## 5 ACKNOWLEDGMENTS

The authors would like to thank Jim Makoulis, Neil Wade and his group for all of their work in the construction process, Bill Anderson's group - especially Ken Wokosky for all the help in testing the ATR PS's, and Joe Drozd for continuing to test the PS's and maintain them during commisioning.

## REFERENCES

[1] Work performed under Contract No. DE-AC02-76CH00016 with the U.S. Department of Energy.

[2] R. Michnoff, "RHIC General Purpose Multiplexed Analog to Digital Converter System", Proceedings of the 1995 Particle Accelerator Conference, p.2229, Dallas, Texas.

[3] W.W. Mackay et al. , "AGS to RHIC Transfer Line: Design and Commissioning", Proceedings of the 1996 European Particle Accelerator Conference, p 2376. , Sigtis, Spain.

[4] T. Satogata et al., "Physics of the AGS-to-RHIC Transfer Line Commissioning", Proceedings of the 1996 European Particle Accelerator Conference, p 2379. , Sigtis, Spain.

# POWER SYSTEMS FOR THE RHIC FIRST SEXTANT TEST [1]

C. Schultheiss, D. Bruno, P. K. Feng, T. Haque, R. F. Lambiase
Brookhaven National Laboratory, Associated Universities, Inc., Upton, New York 11973

*Abstract*

The first sextant test of the RHIC project is an opportunity to evaluate the many systems that must work together for the accelerator to operate. For the main dipole string, the actual main quadrupole power supply with its DSP regulator and output circuit compartment will be used. Temporary supplies will be used for the main quadrupole string, quadrupole offset, and quadrupole shunt supplies. This will let us both measure the performance of the main supply as well as determine the interaction among other power elements in the circuit. Correction elements will also be powered. The actual gamma-T power supplies will be used, as well as temporary supplies for the dipole correctors and sextupole supplies. Some of these units are required for beam to be transported, others are to be operated without beam to measure their performance, and how they interact with their superconducting loads. The power supply equipment, and that of other systems, required an infrastucture of AC power and output cable distribution in the RHIC tunnel, outlying service buildings, and interconnecting the tunnel to the service buildings. This note will describe the performance of the RHIC power supply systems during the sextant test, and the experience gained from this exercise.

## 1 MAIN POWER SUPPLIES

Each of the main power supplies consists of a single regulator controlling two power modules. The "ramp" power module has a high output voltage and is used to ramp the current from injection level to storage level. The "flattop" power module has a lower output voltage and is used to maintain the current at fixed levels. When the commanded current slope exceeds 10 Amps/sec the regulator automatically switches from the flattop to the ramp power module, this is referred to as "cross-over".

The regulator uses digital firing boards to time the firing pulses to the SCRs. Loop compensation and real-time sub-harmonic correction of the output voltage are carried out by a digital signal processor (DSP). The DSP calculates a firing count that is sent to the firing board at a 720 Hz rate. Twelve correction counts, one for each SCR pair, are calculated and sent to the firing board at a 3 Hz rate. The firing board adds the appropriate correction to the firing count and uses this adjusted value to fire the SCR pairs.

The sextant test provided an opportunity to test the stabilty, cross-over, and sub-harmonic correction capabilities of the power supplies on a load approximating that of the main quadrupole string.

The regulator used during the sextant test was a prototype. The digital boards had been fabricated as printed circuit boards, but the analog signal conditioner boards used were the prototype boards. The final regulator will be housed in a temperature controlled enclosure, this was not available for the sextant test.

### *1.1 Stability*

The stability of the prototype power supply was measured using Hewlett Packard 3458 DVMs. Data was collected at a 60 Hz rate over a period of three hours. The short term stability was 3 ppMrms, this should be improved by the analog printed circuit boards. The long term stability was 20 ppM. This was dominated by the ambient temperature change, the temperature controlled enclosure will significantly reduce this drift.

### *1.2 Cross-over*

The regulator contains two firing boards, one dedicated to each of the power modules. The firing board's outputs are gated; enabling the DSP to select the power module that will be active. When the DSP detects the current slope threshold is crossed it turns on the power module that will supply the current, it then turns off the power module that had been supplying the current. This process is timed to occur between the SCR firings. The voltage loop is not broken during the cross-over, only a scaling factor in the voltage-to-phase angle conversion is altered. The maximum error during cross-over was measured and found to be 40 ppM. Adjusting the scaling factors in the voltage-to-phase angle conversion will reduce this error. In addition, adjustments to the power modules fault detection circuits were found to be necessary to accommodate the cross-over.

### *1.3 Sub-Harmonic Correction*

Sub-harmonic correction was measured during the sextant test. The degree of sub-harmonic reduction vs. frequency is depicted in the table. Better reduction was achieved in the middle of the frequencies of interest. The reason for this is still being investigated. The sub-harmonic correction algorithm was coded in "C", coding the algorithm in the DSP's assembly language will increase the correction rate.

0-7803-4376-X/98/$10.00 © 1998 IEEE

**Sub-Harmonic Correction Acheived**

| Frequency (Hz) | Power Reduction (dB) |
|---|---|
| 60 | -1.09 |
| 120 | -19.64 |
| 180 | -15.08 |
| 240 | -19.72 |
| 300 | -1.13 |

## 2 GAMMA-T POWER SUPPLY

RHIC needs a Gamma-T jump to move rapidly through transition. This will be accomplished by pulsing the series connected quadrupole windings in the magnet corrector package. The current in this circuit will be allowed to rise to a planned operating value just prior to the "jump" and then forced to a negative value in a specified amount of time. During the sextant test the string of CQ6 and CQ8 series connected quadrupole magnets in alcove A were pulsed. The current in this quadrupole winding was ramped up slowly to a value of +40 amps. The current was then forced to transition from +40 amps to a value of -40 amps in 0.06 seconds. The parameters are shown below.

**Gamma-T jump parameters**

| ITEM | DESIGN VALUE |
|---|---|
| Jump Current | +40 A to -40 A |
| Jump Time | 0.06 seconds |
| dI/dT during jump | 1333 A/sec |

The core of the Gamma-T power supply was a 3 Kwatt (55A at 55V) unipolar switcher which was used to ramp the current in the magnet to 40 amps. At the initiation of the jump the switcher was disconnected from the 58 millihenry quadrupole magnet using MOSFET switches. The magnet was then allowed to resonate in parallel with a 6278uF capacitor for 60msec. The resonant frequency of this parallel LC circuit is 52.4 rad/sec ( period 0.12 sec ). Therefore, after 0.06 seconds the current in the magnet was forced to -40 amps and this allowed the switcher to be reversed and catch the magnet current at this negative value.

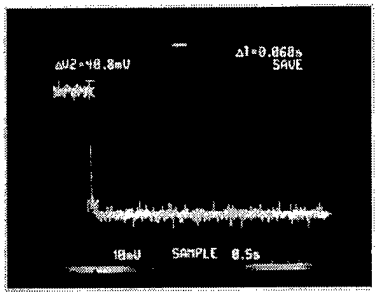


Figure 1 Current Reversal in Gamma-T Magnet

## 3 OUTPUT CIRCUIT COMPARTMENT

The output circuit compartment (10'x8'x9'H) contains the passive ripple filter, two pole DC contactor, two pole DC thyristor switches, DCCT head and regulator.

The frame of the compartment is made of AMCO aluminum structural framing system. The air-core inductor and DC contactor are mounted directly on the concrete floor. All the devices are natural convection except the DC thyristor switch main heatsink assembly which uses forced air cooling. In order to break the magnet flux path of the air-core inductor, magnet breaks are provided for the frame and roof surrounding the air-core inductor. In order to maintain the inductance of the air-core inductor nonmagnetic material are used at the vicinity of the air-core inductor. The housing of the ripple filter capacitor is stainless steel. The proper distance from the DCCT head to the air-core inductor is also maintained so that the stray flux does not exceed the manufacturer's limit.

The 100 micro-H 5500ADC air-core inductor made by NEELTRAN consists of two half coils with total DC resistance of 197 micro-Ohms at 26 degree C temperature. The total weight is 5000 lbs. Proper air ducts between the layers of the coil windings are used to ensure that the maximum winding temperature is not exceeded. The filter capacitor made by CSI Technologies consists of 11 units of 6333 micro-F capacitors. The two-pole 6000A DC contactor with mechanical latching device is made by MICROELETTRICA SCIENTIFICA in Italy, the total resistance between the main terminals per pole is 8.6 micro-Ohms at 6000A and the contact resistance is 1.72 micro-Ohms at 6000A.

### *3.1 Design of the Output Switching Circuit for the Main Power Supplies*

The ramp and flattop power modules share the same output circuit switches. The switches include the main SCR switches at the two legs of the outputs, the two pole electrical-mechanical contactor, and the free-wheel circuit self-triggering SCRs. The main SCR switches include the associated Pulse-forming-network turn-off SCRs. The two pole switch design isolates the main power supply from the magnet string so that the transient during operation does not propagate to the power supply. For example , the return circuit to ground voltage would rise to 512V when the free-wheel circuit is activated. The two pole design also reduces the voltage stress of the switching devices. The switches work with the main power supplies, if there is a high current fault or quench fault the power supplies will turn off and the main switches will open. DC ground fault monitoring will be installed to monitor the whole magnet string. The system will be grounded at both legs by the high impedance sensing network of the ground fault monitoring relay.

The main SCR switches serve two main purposes. They lengthen the life of the electrical-mechanical contactor. During normal operation the SCR switch makes and breaks the current, therefore the contactor switches without a load. The SCR switch also turns off faster than contactor, it takes about 300 μs to interrupt the current while the contactor requires 20 ms to open.

When the SCR switch or contactor opens, the magnet current continues to flow, first it reverses the ripple filter capacitor voltage and then activates the self-triggering circuit of the free-wheel circuit SCRs. The energy stored in the magnet is then disspated in the energy dump resistors in the free-wheeling circuit. Because the time constant of the energy dump circuit is about 10 seconds, the speed of the main SCR switch is not important. Without the ripple filter capacitor, the voltage would rise so fast that it would exceed the system maximum allowable voltage before the self-triggering circuit and free-wheeling circuit SCRs conduct.

The main power supplies are capable of operating in invert mode, to avoid activating the free wheel circuit during invert the free-wheeling circuit firing voltage should be higher than the maximum system invert voltage. This is done by properly selecting the self-triggering circuit breakover voltages.

The main switch consistes of 6 SCRs in parallel; each SCR is in series with two paralleled stainless steel resistors.

The 1.3 milliohm resistor is used to force balanced current sharing between the SCRs, and to support the minimum anode to cathode turn on voltage. The SCRs were selected so that conduction voltage (about 1.2 V) is within 70 mV range for static current sharing. An SCR conducting monitoring circuit is provided to detect over-current of any single SCR.

## 4 POWER SUPPLY CONTROL SYSTEM

The power supply control system consists of two distinct paths. The setpoints are provided by waveform generators and are sent in digital serial format over fiber optic cables. Discrete control and status is provided by Programmable Logic Controllers (PLC) connected by serial networks. A central VME based PLC resides in a Control System Rack and communicates with the Front-End Computers over the VME backplane. This PLC then communicates with other PLCs on the local area network. The main power supplies use Allen-Bradley PLCs and the AB Data Highway Plus network. The VME PLC can globally turn on all the power supplies on its network, and can reduce the status information before passing it on to the control system. This system worked well during the sextant test.

## 5 ATR POWER SUPPLIES

The performance of the ATR PS's has been excellent. Both stability and reproducibility readings with an accurate DVM have shown better than the required or anticipated results, for both the short and long term. Comparisons between accurate references, shunts and DCCT's have been very good. The ultimate test has been the beam. During both runs the beam positions and beam sizes have been measured and have shown the system to have met the specifications very well.

## 6 CONCLUSIONS

The various components that make up the RHIC power supply system worked well together. The minor problems associated with the systems' interaction will be remedied with little difficulty.

## REFERENCES

[1] Work performed under Contract No. DE-AC02-76CH00016 with the U.S. Department of Energy.

# THE POWER SUPPLY SYSTEMS FOR ELLIPTICAL MULTIPOLE WIGGLERS

A.S. Medvedko, Yu.A. Evtushenko, B.A. Dovgenko, S.P. Petrov, V.F. Veremeenko,
Budker Institute of Nuclear Physics, 630090, Novosibirsk, Russia
E. A. Medvedko,
Argonne National Laboratory, Argonne, Ill, 60439, USA, (now at SLAC)
Om Vir Singh,
Brookhaven National Laboratory, Upton, NY. 11973, USA

*Abstract*

The Elliptical Multipole Wiggler (EMW; 3.4 meter-long) and its Prototype (0.8 m) had been built by the joint team of INP (Novosibirsk, Russia), ANL (Argonne, USA), and BNL (Upton, USA). These Wigglers are supplied by the DC or trapezoidal shape AC current with variable frequency. Current is in 200 A to 1200 A range. Two different PSs were developed: for Prototype – with the frequency range up to 100 Hz, for EMW – up to 10 Hz. The PSs have the original circuit for current polarity forced switching. These circuits allow us to get the rise/fall time twenty times faster than that determined by magnet time constant: it became 1.5 ms for Prototype and 5 ms for EMW. Top of the pulses have the flatness better than 0.01, current difference for both polarities better than 0.001. Prototype is under the operation at the NSLS (BNL) during two years. EMW has been installed, tested and first beam for users would be taken out soon at the APS (ANL).

## 1 INTRODUCTION

The EMW generates elliptically polarized photons in the energy range of 0.1–10 keV with AC modulation of polarization helixity. This type of wigglers will make it possible to detect the very weak signatures of circular dichroism and other effects associated with right- left- handedness of some physical systems [1]. To increase the measurement accuracy of the asymmetry between the effect of left and right circularly polarized radiation, the modulation frequency should be located in the range with the minimum spectrum power density of closed orbit noise. From this point of view, it was determined that the preferable modulation frequencies are: 0 ¡ Fmod ¡ 10 Hz and F $\sim$ 100 Hz. The EMW includes a vertical hybrid permanent magnet structure and a horizontal electromagnet structure. Prototype wiggler (0.8 m length, 27 mm aperture) has a magnetic field period of 160 mm with seven poles. Field value is of 0.83 T for hybrid structure and of 0.12 T – for electromagnet [2]. The EMW has 36 poles with period of 80 mm and the aperture of 71 mm with closely the same field values. The core of electromagnet is fabricated from the laminated iron to operate with a switching frequency up to 100 Hz.

## 2 MAGNET PARAMETERS

The electromagnet structures of EMW and of Prototype are the inductive loads with the Resistance 5.6 mOhm (3 mOhm, Prototype) and Inductance 500 $\mu$H (100 $\mu$H), operating current range 200–1200 A. So the electromagnet structure of EMW can store 360 J of energy (75 J). Load time constant is approximately 90 msec (33 msec). It was desired to have changeable polarity of current with the trapezoidal in-time shape of current with operating frequency range from zero up to 10 Hz for EMW and up to 100 Hz for the Prototype. The top part of the current need to have the flatness better than 1%, current difference for both polarities better than 0.1%.

## 3 POWER SUPPLY OPERATION PRINCIPLE

The Function Diagram of the PS is presented at the Fig.1. The input AC power is going to the primary windings of the voltage reducing Transformer. The secondary Transformer coils are connected to the gate controlled Thyristor Rectifier Bridge with RLC–filter. Transformer, Rectifier, and RLC–filter form the "V–1000 Thyristor Rectifier".

The V–1000 output DC current with variable value from 200 A up to 1200 A is going through the choke L1, Direct Current Current Transformer DCCT–1 and Commutating choke L2 to input diagonal of the Thyristor Bridge–Inverter SW1–SW4. Its output diagonal is connected to the EMW Electromagnet Coil with Capacitor C1 in parallel. Commutating choke has two secondary coils, connected into both current buses, and one primary joined with Commutator's output.

Let us say that the Bridge–Inverter has the initial position with SW1 and SW4 Thyristors are switched on (into the conducting mode), but SW2 and SW3 are switched off (into the isolation mode). The Electromagnet current direction is shown at the Fig.1 by left arrow. For current polarity changing we need to switch off the SW1, SW4 and to switch on the SW2, SW3 Thyristors. The Commutator with choke L2 is used for realizing this process. Time Diagrams of switching processes are presented at the Fig.2.

The Commutator Thyristor SWcm, being driven by Clock external signal via Switch Controller, connects the Capacitor Ccm to the primary coil of choke L2. This Capacitor had been charged preliminary. The Capacitor discharging process applies the pulse with the reversed

0-7803-4376-X/98/$10.00 © 1998 IEEE

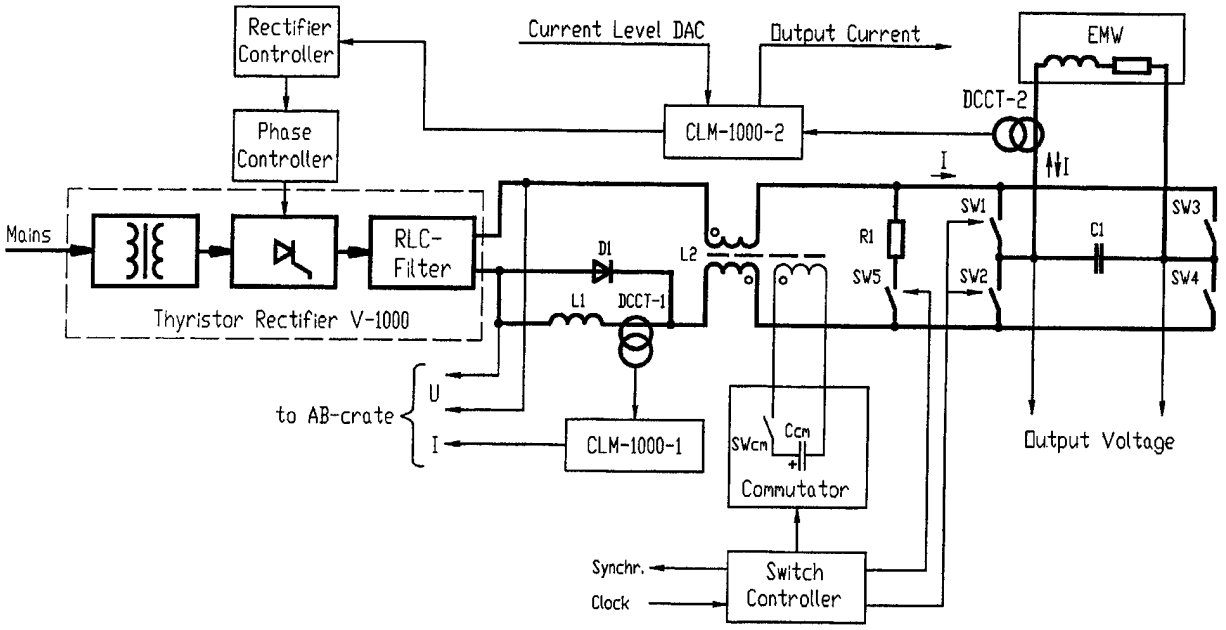



Figure 1: EMW function diagram.

(closing) polarity to input diagonal of the Bridge–Inverter. This time interval corresponds to positive polarity pulse at the time diagram. This pulse cause breaking current through the Switches SW1 and SW4. It need approximately 15 $\mu$sec for Thyristors to switch off the current. So, after this time duration the Bridge–Inverter became switched off. The resonant circuit formed with Electromagnet coils and Capacitor C1 became isolated, so the energy stored in the Electromagnet magnetic field begins to recharge the capacitor and after that – to reverse the current polarity. It needs approximately half of free oscillating period (5 to 6 msec for EMW and 1.5 msec for Prototype) of this circuit for Electromagnet current polarity reversing. One can see that due to this oscillating process the voltage on the resonant circuit increases up to 300–350 Volts for the 1000 A input current (DC voltage on the coil is approximately 6 V ). This method of current switching is some time named like "Forced Switching".

The isolated ideal LC circuit has no energy dissipation so it reverses the polarity of 100% of Current. Real RLC circuit with Electromagnet coil of EMW and capacitor C1 have quality factor:

$$Q = (\sqrt{L/C})/R \approx 10\,,$$

that determines the relatively noticeable level of the energy dissipation during the half of free oscillation period. As a result, the coil reversed current value at the end of this time interval (Fig.2) became equal to:

$$I_{rev} = I_{ini}(1 - \delta/2), \text{ where}$$

$$\delta = \pi R\sqrt{C/L}\,.$$

In our case we had got $I_{rev} \approx 0.85 I_{ini}$ for EMW and $0.9 I_{ini}$ for the Prototype; $I_{ini}$ – initial Current value.

During the transient process and all time later the Switch Controller generates the pulses to fire the Switches SW2 and SW3. These Switches come into conducting mode when the voltage applied to them became in conducting direction that means the end of free oscillation process. This moment determines the switching on of the negative feedback loop that helps to output current to get the required level $I_{rev} = I_{ini}$. Sign of feedback did not depend on the output current polarity because of circuit configuration.

By the way, all the firing pulses of Switches SW1–SW4 are taken away by the Clock pulse front for more reliable switching off of the Bridge–Inverter. The next stage of process of current polarity changing occurs with the next Clock pulse. During this stage SW2 and SW3 became switched off but SW1 and SW4 became switched on. As a result the period of current polarity changing is twice longer than the period of Clock pulses.

One can see that switching off of the Bridge–Inverter Thyristors cause the break of its input current. To avoid the V–1000 output current break the shunting Switch SW5 with resistor R1 is installed in parallel with the Bridge. This Switch comes into the conducting mode at the beginning of the switching process and switches off when Bridge–Invertor became conducting. Two transistors (KS621K60 type, Powerex) with driving circuit perform the role of SW5. The Fast Diode D1 and Choke L1 are installed to protect the DCCT–1 against the short pulsed current of switching process and to support this process. DC Current Transformer DCCT–2 is installed at the output bus to measure and to stabilize the Electromagnet current.

PS for the Prototype and for the EMW have closely the

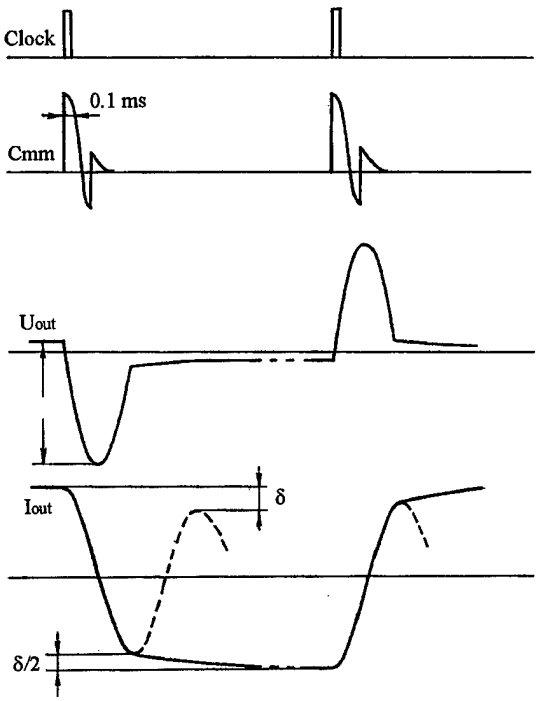



Figure 2: Current switching diagrams.

same frame dimentions: 1200 mm (front width)x900 mm (depth)x 2200 mm (height).

## 4 PECULIARITIES

Power Supply for the Prototype and for the EMW have some peculiarities in circuitry, design and operation. First of all, the current stabilizing loop of the EMW is organized with measuring of the current at the bus behind the Bridge–Inverter (Fig.1), but for the Prototype it was organized with the help of DCCT installed before it. This is determined by the difference in load time constant and in switching frequency. As a result the system for the Prototype is to stabilize the current "in long time mode" only but the feedback loop of the PS for EMW took part in transient processes at the top part of the current and slightly helps to shorten the time duration of its "$\delta/2$-part". Of course, the feedback loop of the PS for EMW need to re-reverse the DCCT–2 signal polarity (to make it unipolar). Another difference between PSs is in design of the Commutator: we need to apply the recuperation for charging the Capacitor for the Prototype because of high maximal operational frequency and relatively simple circuit with direct capacitor charging – for the EMW. Computer control of the PS for Prototype is organized without special interface module inside PS frame but the frame of the EMW PS includes the AB (Allan–Bradley) Crate. Both systems have the analog and digital status control, of course. Systems were successfully incorporated into the computer control systems of the Storage Rings. Both PSs need the external Clock pulses and they have three types of output pulses to synchronize the external devices like, for example, correcting magnet PS and magnetic field measuring system [3].

## 5 RESULTS AND CONCLUSIONS

The described PS for Prototype had been developed and tested at the 1994. It is under the AC mode of operation with frequencies 2 Hz, 10 Hz, and 100 Hz at the NSLS from January, 1995. The PS for the EMW had been developed, tested and shipped to ANL from INP at May, 1996. EMW with this PS were installed to APS storage ring at December, 1996 and the first experimental runs with the beam were successfully done.

## 6 ACKNOWLEDGEMENTS

Authors are gratefully acknowledged to Drs. Gennady Kulipanov (INP), Efim Gluskin (ANL), and Sam Krinsky (BNL) for so interesting task and for the high attention to this work.

## 7 REFERENCES

[1] A. Fridman, S. Krinsky, E. Blum, K. Halbach, in Proc. of IEEE Part. Acc. Conf., Washington, DC, May, 1993, p. 1599.

[2] E. Gluskin et al., "The elliptical multipole wiggler project", in Proc. of IEEE 1995 Part. Acc. Conf., Dallas, TX, May, 1995, p.1427.

[3] D. Frachon et al.,"Results of Magnetic Measurements and Field Integral compensation for the Elliptical Multipole Wiggler", in Proc. of IEEE 1995 Part. Acc. Conf., Dallas, TX, May, 1995, p.1429.

# FAILURE STATISTICS OF DESY POWER SUPPLIES IN 1996

Hans-Joerg Eckoldt, DESY Hamburg, Germany

*Abstract*

The HERA machine delivered good results in 1996. This was possible due to a higher availability of the technical subsystems than in the years before. Here the failures of the power supplies during 1996 will be analysed and a statistic of the failures of the accelerators will be shown. This will be compared to the failures of the last years to see what improvements had the most succes. A preview onto the next changes will be given and the introduction of new tools (software and hardware) will be explained.

## 1 INTRODUCTION

One of the subsystems in particle accelerators are the magnet power supplies. Due to the large number of components a high reliability is required. This is not only the availability which is the number of failures multiplied by the repair time of the sub-system, but also the number of failures is important in machines with long filling times. In DORIS the beam is filled within a few minutes after the end of repair whereby in HERA not only the repair time of the power supply is important but also the time of refilling the beams and optimisation for the luminosity run. A failure that is repaired in 10 minutes will have a down time of the machine and the experiments of several hours. To detect systematical errors an analysis of the failures of the power supplies at DESY is made annually and will be presented here. By this systematical errors have been detected and eliminated.

## 2 SOURCE OF INFORMATION

Beside the machine control room operators a technical shift crew of two persons is working in three shifts when the machines are running. This shift crew is responsible for the repair of the power supplies, part of the water cooling system and the rf-high voltage supplies. Each failure that occurs is written into a log book with time, the assumed reason of failure and with a description of the repair action. This material was used as data base. Additional information about the machine status can be found in computer archives and the control room log books. The HERA machine coordinator tracks down the trips as well in combination with beam loss and down time.

## 3 NUMBERS OF FAILURES

Over the time period from May 15th till December 23rd the shift crew was called 574 times to solve a problem. This is the actual time when the HERA electron machine was commissioned till it was turned off for the winter shut down. The problems to be solved are from simple reset of an electronic up to a several hours lasting repair of the power parts, which is luckily not very often.

The first statistic of this type was made in 1993. That result and the numbers of the last years is shown in table 1.

Table 1: Number of events when technical shift crew had to react.

| | 1996 | 1995 | 1993 |
|---|---|---|---|
| HERA | 238 | 248 | 252 |
| PETRA | 114 | 165 | 143 |
| DORIS | 87 | 81 | 184 |
| DESY II / III | 43 | 113 | n.n. |
| transport lines preaccelerators | 92 | 131 | n.n. |
| analysed period | 5304 hrs | 6720 hrs | n.n. |

## 4 STATISTICS

The availabilty of the subsystem power supply can be calculated by

$$AV = \frac{MT - (NOF * TOR)}{MT} * 100\%$$

with AV = availability
MT = machine time
NOF = number of failures
TOR = time of repair

The average repair time for the power supplies is assumed as 45 min per failure. Pushing a reset button is much shorter whereby the repair in the power parts takes much longer.

0-7803-4376-X/98/$10.00 © 1998 IEEE

The MTBF mean time between failure of the machines is given by the formula:

$$MTBF_M = \frac{MT}{NOF}$$

The failure distribution of power supply failures at DESY can be seen in table 2. P and e indicate the proton or electron machine of HERA whereby the e + p is the sum of both.

Table 2: Power supply failures in the machines, Mean TimeBetweenFailure, AVailability

| | problems | MTBF_M hrs | AV |
|---|---|---|---|
| HERA e+p | 238* | 22.3 | 96.6% |
| HERA p | 163 | 32.5 | 97.6% |
| HERA e | 84 | 63.1 | 98.8% |
| PETRA | 114 | 46.5 | 98.3% |
| DORIS | 87 | 61 | 98.7% |
| DESY II / III | 43 | 123.3 | 99.4% |
| transport lines preaccelerators | 92 | 57.6 | 98.6% |
| entire DESY | 574 | 9.2 | 91.9% |
| analysed period | 5304 hrs | | |

The availability in table 2 includes all failures that appeared and is just the availability of one subsystem. It does not give the number for the performance of the machine. In comparison the actual time between two beam costing failures due to power supplies in HERA is 56 hours.

MTBF of the power supplies in the machines

$$MTBF = \frac{MT * NOPS}{NOF}$$

with NOPS = number of power supplies

Here two numbers are calculated. One is the overall value including every fault that appeared and the power supply was turned off. The second value is with only the problems of the power supply. External interlocks and failures as grid disturbances have been substracted.

Table 3: MTBF of the power supplies

| | Number of PS | MTBF_PS overall | MTBF no external failures |
|---|---|---|---|
| HERA e+p | 1166 | 25985 | 29310 |
| PETRA | 269 | 12515 | 13988 |
| DORIS | 93 | 5669 | 8968 |

## 5 KATEGORIES OF FAILURES

The data material was sorted to the failures of the machines and categorised. The categories are:

1) unknown -failures that could not be sourced down
2) work induced -due to work a failure was produced
3) single interlocks -interlocks from exterior eg. thermoswitch of magnet. (not really failure but turn off of the supply)
4) Electronic malfunction -error that is due to a malfunction of electronic without a physical failure in the electronic
5) Electronic component -a physical failure in the electronic or survey elements
6) ELS -electronic protection in the choppers. The voltage drop over the MOSFET transistors in the switched mode supplies is monitored. In case of short circuit or break down of a transistors this turns the power supply off. (one of the major problems in HERAe in 1995)
7) Shorts to ground -low impedance to ground within the magnets or the power supplies
8) Semiconductors, fuses -failure of the power semiconductors eg. SCRs, diodes and power fuses. A 100 mA fuse would be an electronic component.
9) mechanical switches - contactors, circuit breakers and polarity switchers
10) PSC, controles -power supply controllers, programmable logical controllers, main computer in the control room
11) transformers -transformers, chokes etc. also the circuit breakers for the transformer protection
12) connections -bad connections of circuitboards, plugs up, bad soldering points, bad screwing of copper bars
13) water cooling plant - failures in the cooling system. An error causes several power supplies to trip
14) water/air cooling in the supplies - only the supplies of one water circuit trip. One to maximum four supplies of the choppers.

## 6 FAILURES IN THE MACHINES

When looking at the failures each machine has it's own pattern of failure due to the different types of supplies and also the age of the units. The failures can be seen in table 4.

* Please note that the sum of failures of HERA e + HERA p is higher than the value of HERA e+p. Grid disturbances were conted for both machines. In the sum only one event is counted per machine

Table 4: Failures in the machines

| | HERA e | HERA p | PETRA | DORIS |
|---|---|---|---|---|
| unknown | 1 | 4 | 0 | 1 |
| work | 0 | 4 | 1 | 2 |
| Single interlocks | 11 | 8 | 3 | 21 |
| Electronic malfunction | 11 | 21 | 21 | 22 |
| Electronic component | 2 | 6 | 24 | 5 |
| ELS | 14 | 5 | | 0 |
| Short to ground | 0 | 4 | 2 | 0 |
| Semiconductor, fuses | 0 | 0 | 3 | 0 |
| mech. switches | 9 | 71 | 4 | 0 |
| grid disturbances | 9 | 9 | 9 | 9 |
| PSC, controls | 4 | 22 | 8 | 4 |
| Transformers | 0 | 0 | 0 | 0 |
| connections | 7 | 4 | 14 | 5 |
| Water cooling plant | 1 | 2 | 1 | 2 |
| Water, cooling | 4 | 3 | 10 | 6 |
| correctors | 12 | 0 | 14 | 8 |
| | | | | |
| sum | 85 | 163 | 114 | 84 |

*HERA p*

Still a systematic failure is in the system. The problem is the mechanical polarity switcher of the chopper supplies. The auxiliary contacts of the contactors become high resistive. During polarity switching the magnet is shorted by the switch. A build in electronic waits for this status to continue which due to the bad contacts will not be detected. The polarity switcher stops in the middle of the action.

*HERA e*

No really overwhelming problem is seen in these statistics. Systematic errors appear to have been eliminated, leaving random errors to be dealt with. The largest problem of the last year, the aging of MOSFETs, has been eleminated by exchanging the MOSFETs.

*PETRA*

The year was good. The major problems of the previous year been eliminated. Still the number of damaged electronic components might be a sign for the aging of the power supplies.

*DORIS*

The power supplies worked well this year. The number of failures is constant to the previous year, whereby one quarter of the failures were turn offs by external interlocks. The electronics problem was mainly to one power supply where the failure was extremly hard to find.

*DESY II / III*

The number of failures decreased rapidly. In 1995 it was a problem with a bad contact of a high voltage switch. The problem was fixed.

*BEAM TRANSPORT LINES*

Here the number of failures decreased with only routine maintenance.

## 7 NEW TOOLS FOR MAINTENANCE

When looking at the investment and operating costs of accelerators the demand for short maintainance period and long runs gets stronger. This is usually in contradiction to the technicians view who wants to maintain the power supplies for a failure free next run. Therefore new methods and tools have to be found to decrease the time of working at the units with the same amount off quality.

One fairly simple attempt was made to control the accuracy of the supplies. By a computer program a group of power supplies is driven with a slow ramp procedure and the data of the monitored current is stored. With an EXCEL-spreadsheet this data is visualized. Errors in the Digital/Analog Converter (DAC) or the DigitalVoltMeter (DVM) can easily be detected. This program is used also to control suspicious power supplies during ramping of HERA .

In 1997 an infrared thermo camera will be taken to supervise the power supplies. By this it is possible to check connections and operation of power parts during normal run conditions of the accelerator. On a vendors presentation of such a camera some bad connections where found. This promises good results.

## 8 SUMMARY

When comparing the numbers of the events the last year did not look much better than the 1995 year though the impact of the failures to the machine run time was smaller. The supplies had more failures during turning on time or massage times than during the actual run time. These failures have to be solved in the next shut down. For several machines the obvious systematic errors seem to be eliminated. The consequence is that the future failures have to be investigated even closer to guarantee a better run.

# FOUR QUADRANT DC TO DC SWITCHING SUPPLY FOR THE FERMILAB MAIN INJECTOR

L. Bartelson, G. Krafczyk, H. Pfeffer, D. Wolff
Fermi Nationl Accelerator Laboratory
P.O. Box 500
Batavia IL, 60510

## Abstract

The Fermilab Main Injector (FMI) will require 248 ramped corrector power supplies for the operation of the accelerator. The design and prototype test results will be described in this paper. The 3 main design goals for these supplies are: 1) eliminate failure due to thermal fatigue that has plagued similar systems at FNAL, 2) utilize PWM technology to attain good efficiency and small size, and 3) minimize conducted and radiated noise typically generated by PWM systems. The power supplies operate at 30kHz switching frequency and are rated for +/-150 Volts and +/-15 Amps at 95 percent switching duty cycle and 95 percent efficiency into a 1 Henry magnet load. The FMI requirements call for a ramp cycle of 1 - 2 seconds. During the cycle, the maximum temperature swing, junction to heat sink, of the power components is less than 30 degrees centigrade. The output voltage ripple is less than 1 Volt RMS.

## INTRODUCTION

The Fermilab design uses the PWM technology using 4 FETs in an H-bridge configuration for 4 quadrant operation. The switching frequency of 30 kHz was chosen due to accelerator beam interaction considerations. The switching scheme does not use a 50/50 technique. The scheme chosen permits the bottom FET on one side of the H-bridge to be ON continuously. This accounts for less power dissipation since testing showed that the switching losses in the FET are about twice the DC losses. The analog closed loop controls include an inner voltage loop and an outer current loop using a transducer for current feedback. The voltage loop has a response of 5kHz and the current loop has a response of 300 Hz. A block diagram of the unit is shown in Figure 1.

## SWITCHING SCHEME

| | QUADRANT | |
|---|---|---|
| | 1 & 2 | 3 & 4 |
| S1 | PWM | OFF |
| S2 | PWM | ON |
| S3 | OFF | PWM |
| S4 | ON | PWM |

Figure 2, Switching Scheme

The switching scheme chosen is shown in Figure 2. The FETs on one side of the bridge are pulse width modulated while the devices on the opposite side are held

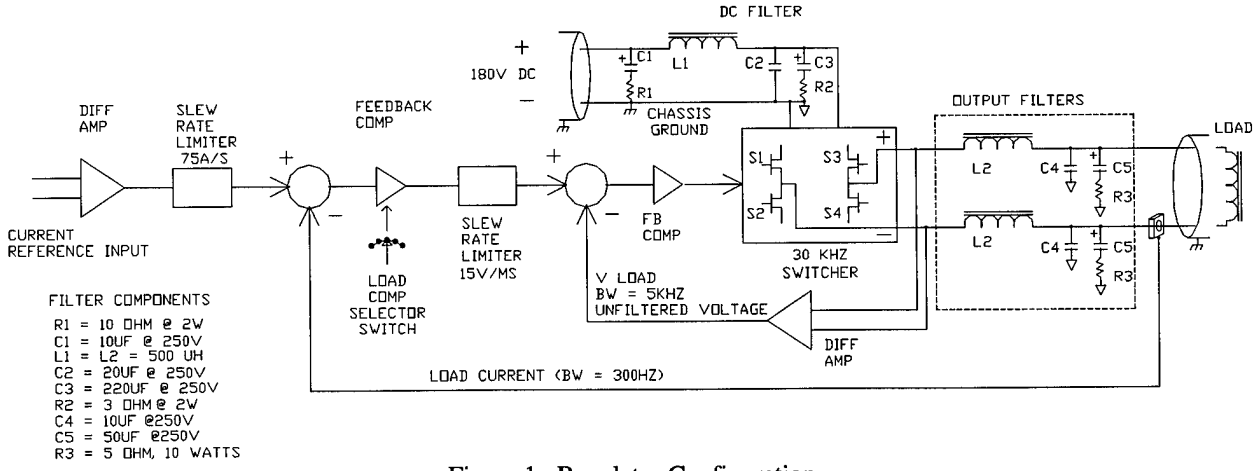



Figure 1, Regulator Configuration

0-7803-4376-X/98/$10.00 © 1998 IEEE

ON, for the lower device, or OFF for the upper . As mentioned above, this technique is used to reduce the switching losses in the bridge. The power dissipation data shown in Figure 3 is for a negative output current of 15 amps, a switching ON time for S3 of 90%, and S2 is ON continuously:

| FET | Power (W) |
|---|---|
| S1 | 0 |
| S2 | 20.9 |
| S3 | 42.6 |
| S4 | 0.9 |
| Total Power | 64.4 |

Figure 3, Device Dissipation

The data in Figure 3 shows that the switching side has about twice the power dissipated compared to the static side. This is due to the predominance of dynamic switching losses over ohmic losses. Data was also taken with 10 and 50% ON times of the top switching FET operating at 15 amps. In both cases the total power dissipated in the FETs never drops below 50 watts. Power consumed by one filter is 5 watts at 15 amps. The maximum total power in the FETs and the chokes is 74.4 watts. This calculates to be 3.3% of the total 2250 watts of output power.

The FET dissipation was measured in the switching mode using calorimetry. First the case to heat sink thermal impedance was determined for the FETs by operating them in DC mode where power dissipation could be easily measured. Then the case to sink temperature differences were measured while operating in switch mode. The thermal impedance determined under DC conditions was then used to calculate the device dissipation under switching conditions.

Considerable time was invested in getting the temperature data. Copper blocks were added and insulated which made an electrostatic shield between the FET case and the heat sink. This was done because the temperature probes would pick up switching noise that affected the accuracy of their readings. The copper blocks provided more area to clamp thermocouples to and provided a stable time constant for temperature measurements.

## FET MOUNTING

Testing was done on different mounting techniques of the FETs and the effects on temperature. The FET used has a TO-247 case with a single hole mount and the case is common to the drain. This obviously requires an insulator which raises the overall thermal impedance. Measurements indicated that a lower thermal impedance on the FET can be achieved if a clamp is used on the case versus the single hole for mounting.

Isolation pads that are commercially available have a large thermal impedance. The combination of a beryllium insulator under each FET and a bar clamp across all 4 devices was the final configuration arrived at. The mounting technique reduced the case to heat sink thermal impedance from 0.85 to 0.2 °C/W. The thermal impedance rating of the FET from junction to case is 0.34 °C/W. Therefore the total impedance junction to heat-sink is 0.54 °C/W. The maximim junction temperature using figure #3 is 42.6 watts times 0.54 °C/W or 23 °C plus the heat sink temperature. A small amount of air flow over the heat sink is needed to limit the maximum junction temperature to 80 °C. Tests in the lab resulted in a maximum heat-sink temperature of 47.8 °C while switching at 15 amps.

## FET REVERSE CURRENT

Testing was done on the bottom FET when current is flowing through it in the reverse direction. The normal current path is through the intrinsic diode. However it was observed that when the current is less than 12 amps a lower voltage drop occurs if you turn the gate of the FET on. Reverse current can be forced to flow in the FET, bypassing the intrinsic diode and reducing the voltage drop. Lower switching losses can be obtained during this cycle of operation.

## NOISE GENERATION

The switching supply generates noise by nature of the operation. During switching when the top FET turns on, a large current shoots through the top and bottom FET until the intrinsic diode shuts off. When operating at 15 amps output current, this shoot through current is on the order of 50 amps with a duration of 200ns. In order to keep the noise radiated to a minimum the power section was shielded separate from the rest of the power supply. The authors are aware of more elaborate schemes of putting a fast recovery diode in series and another in parallel with the bottom FET. The disadvantage is power dissipated in the series diode making the total losses greater.

The other large items in the power section sheilded were the chokes and caps which make up a Praeg filter [1]. The design specification stated that the 30 kHz 150 volt output switching signal must be reduced to 1 volt RMS at the supply output terminals. This requires a filter with 40 dB per decade roll-off and a break frequency of 1 kHz. The filter chokes selected had an inductance of 500 μH.

## FET DRIVERS

The power section uses opto coupled devices to send ON/OFF signals to the FET driver. The driver uses a commercially available device that has it own isolation scheme for the top FET drive. The top FET drive energy

is developed by a bootstrap circuit. The proper use of this device requires the designer to pay strict attention to input gating and minimum pulse widths. It was observed that if a signal less than 50 ns to the lower gate drive, the chip will lock up until it receives another pulse. To ensure lock-up will not occur, the gate logic circuits were designed to produce a minimum pulse of 200 ns.

## CONTROL LOOPS

The voltage loop feedback is taken on the H-Bridge side of the the Praeg filters. This signal is edge filtered using an RC time constant of 10μs. A differential amplifier is used to subtract the 2 output legs, and feed an error amplifier that compares the output voltage and the current loop output. The error signal is then integrated to generate a signal that controls the ON time of the top FET from 200 ns to 31.7μs (95% of total time). The voltage loop also determines the direction control, which determines if the output voltage is negative or positive.

The current loop is outside the voltage loop and uses a 50 amp LEM current head for isolated feedback. The LEM is sensitive to external magnetic fields and dv/dt signals on the wire. The head was moved to the front of the 23 inch chassis to remove it from the power section, and reduce magnetic pickup. Early testing was done using differential amplifiers and current shunts. However, these scheme had serious common mode problems at frequencies above 500Hz.

The current loop reference goes through a slew rate limiter (SRL) set to 75 amps per second. The SRL smooths out the steps in the output of a D/A reference card which keeps the power generated in the damping resistor in the filter to a reasonable value. The compensation parameters for the current loop are set up for 5 different load settings ranging from a L/R ratio of 0.95/5 to 0.030/2. The closed loop frequency response for the 1 Henry magnet is 250 Hz. All other magnets have a 300 Hz bandwidth.

## PROTECTION & MONITORS

The supply has several internal interlocks that force the supply into the inhibit mode. These signals are dc overcurrent, RMS current, ground fault current, heat sink temp, filter temp, and external permit. The unit also has alarms for low input supply voltage and tracking error. All these faults and alarms are sent to the control system as digital status.

The analog monitors are the program reference, output current, output voltage, RMS current, and current error x100. All the analog signals except the last one are sent to the control system.

Each supply is isolated from the main DC power supply by a 25 amp circuit breaker. Each magnet load has a MOV installed at the power terminals to absorb the inductive stored energy under fault conditions, such as cables being unplugged or power supply failures.

## SIZE & AIR FLOW

The units are air cooled and measure 5.25"H x 4.188"W x 23"D.. A total of 4 units are mounted side by side in a standard 19" relay rack crate. A group of 16 supplies will be mounted 4 wide by 4 high. A fan pack will be used to blow air up through the group of 16.

## CONTROL POWER

The supplies use +/- 15V, and +5V in each regulator. This power is daisy chained at each unit and comes from a common distribution supply.

## MAIN DC POWER SUPPLY

The main supply is designed to provide 180 VDC power to 48 units. This supply consists of a 3 phase transformer with a 480 volt input, a 3 phase full wave bridge rectifier, and a passive filter. The nominal current from the 48 units is estimated to be 120 amps.

## PROJECT STATUS

Several prototypes have been operating since last October. Currently 24 units are being built for extended testing in a Main Injector Service Building. After a satisfactory run, any necessary changes will be made and the total quantity needed (275) made to print.

## REFERENCES

[1] Praeg, W., A High Current Low Pass Filter For Magnet Power Supplies, pp 16-22,IEEE Transactions On Industrial Electronics and Control Instrumentation, Volume IECI-17, Number1, February, 1970

# AN EMBEDDED POWER SUPPLY CONTROLLER

S.Sharonov and J.M.Nogiec,
Fermi National Accelerator Laboratory*, P.O.Box 500, Batavia, IL 60510

*Abstract*

Several different models of high current power supplies are used to test accelerator magnets at the Fermilab's Development and Test Department (D&TD). Department-wide standardization of current control and monitoring has been achieved by embedding a proprietary intelligent device into each of these power supplies. The device is based on a highly integrated Intel 87C196 microcontroller that is used to control and monitor current, collect status information, issue control signals and communicate with a host computer. The controller interfaces with a power supply via onboard high precision ADC and DAC converters, and digital I/O registers. Some of the advanced features of the system include: downloading and interpreting of complex ramp profiles, built-in parabolic waveform approximation, external triggering, and fiber-optic communication media. Network access is enabled by an extensive set of UNIX tools such as GUI, ramp profile simulator, API library, and shell programming tools.

## 1 POWER SUPPLIES FOR ACCELERATOR MAGNETIC SYSTEMS

Modern particle accelerators employ a large number of high current power supplies to drive their magneto-optical systems. These supplies are capable of achieving thousands of Amps of current and maintaining it with the accuracy of better than 100 ppm. Accelerator physics as well as the inductive nature of the load dictate sophisticated waveforms of the magnet current. In contrast, most of the supplies, that come from the factory, are equipped with a minimal interface; it is usually comprised of an input for the analog reference signal and a digital I/O to transmit status and to accept control signals. As a result, an external control system is required to make a power supply usable in a fully automated environment.

## 2 D&TD POWER SYSTEMS

High current power supplies have been always an integral part of the Development and Test Department magnet test facility. The are used for both conventional and superconducting magnet tests.

### *2.1 Former Systems*

In 1994 two different power control systems coexisted at the Fermilab's Development and Test Department. One of them was based on a VAX computer and used the CAMAC interface, whereas the other was a UNIX-based system and used the VXI interface. The VAX-based system was about to become extinct and UNIX system had severe drawbacks:

- The system did not allow users to generate controllable ramps because of the non-deterministic characteristics of the Unix system.
- The system did not provide sufficient means for automatic/remote control of power supply and for logging the current and power supply histories.
- The long analog cable runs deteriorated the signal quality in the industrial environment.
- Multiple analog and digital cables between the power supply and the measurement system created ground loops.
- User interfaces were not adequate.
- The information about a power supply status or cause of exception was not available via computer interface.

### *2.2 New System Design*

The new Fermilab Development and Test Department control system [1] was designed to overcome the above mentioned drawbacks and to provide a uniform interface for every power supply in service. This standardization was achieved via encapsulation of the control functions into an intelligent controller that is embedded into each power supply. The controller is accessed by conventional methods from the host computer through a serial interface. Server software that is running on the host computer, fans out the connection to the multiple local and remote clients.

### *2.3 Hardware*

The controller module consists of several subsystems (Fig.1):

- 87C196KR processor with integrated peripherals, 64 kBytes of external FLASH ROM, 64 kBytes of external SRAM.
- High precision isolated 16 bit DAC used for the ramp profile generation.

Operated by the Universities Research Association under contract with the U.S. Department of Energy

0-7803-4376-X/98/$10.00 © 1998 IEEE

- High precision isolated 24 bit ADC for digitizing the power supply current.
- Digital I/O with 32 input and 16 output lines for status readout and application of the control.
- Input and output external trigger lines for synchronization of the external measurement system with the current profile.
- Fiber-optic interface for communication with the host computer.

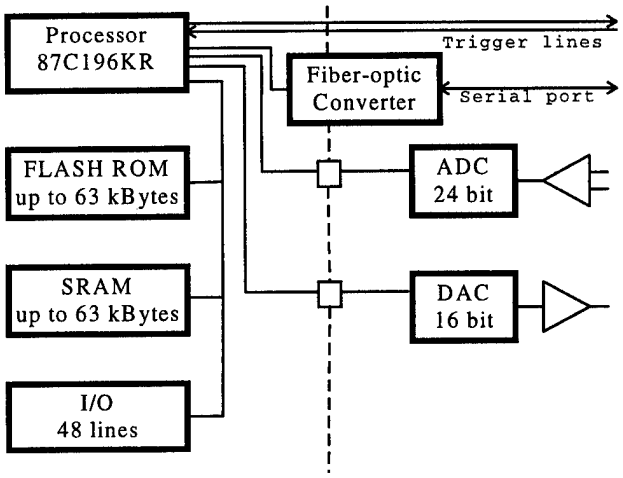



**Figure 1 Controller Block-Diagram**

The 87C196KR [2] is a 16-bit microcontroller designed especially for the high speed event control. Its primary components include a CPU, several types of memory, six I/O ports, two timers, A/D converter, two serial I/O devices and an event processor array.

Special care was taken to eliminate the possibility of ground loops and to preserve the integrity of the analog signals. This was achieved by taking the following measures: the controller communicates with the external world via a fiber-optic link, the ADC and DAC are isolated by means of separate DC/DC converters and the ADC has a balanced differential input.

Both the DAC and the ADC use external high precision references that exhibit an extremely low temperature drift of only 0.6 ppm/C.

AD7710 ADC [3] employs a sigma-delta conversion technique to realize up to 24 bits of no missing code performance, and an integration time of one power line cycle has been programmed for improved noise rejection. The ADC is used in a background calibration mode that removes both zero scale and full-scale errors while still allowing for 10 samples/s acquisition rate.

*2.4 Firmware*

Firmware consists of a simple monitor and power supply controller code. The monitor is used primarily for debugging and offers the capability to view/modify memory locations, and to download user code into SRAM and execute it.

C language and the compiler from BSO Tasking [4] was used to implement the most part of the firmware.

A proprietary serial protocol was developed for the reliable communication with the host computer over a serial line.

The controller recognizes a set of 28 commands including, among others, downloading and executing complicated profile tables and storing and retrieving of up to 1024 ADC readings. A typical profile table consists of a number of segments, where the segment may be one of the following types:

- Parabolic ramp segment described by the destination current, initial ramp rate and acceleration.
- Hold segment which allows the controller to wait for the software or hardware trigger.
- Wait segment (delay).
- Unconditional jump segment for the jumps inside the profile table.
- Repeat segment for organizing the loops.
- Trigger segment used to issue a synchronization signal for the external recipient.

The ADC buffer is set up as a FIFO and may be controlled by the host computer or via the profile table. For example, ramping to a specific current, taking a requested number of measurements and disabling the FIFO for further readout.

In addition, software readable id provides a means of identification of the controller/supply system, which enables the application of the appropriate calibration constants and constraints.

*2.5 Software*

An extensive set of the software components has been developed to provide a convenient and easy to use interface to the power supply control system. It consists of the following elements:

- A server that may run under the Unix or VxWorks [4] operating system.
- A GUI that provides easy access to all main features of the power supply control system.
- A simulator for developing and debugging profile tables on a Unix workstation without actually running a power supply.
- A simple trace client for archiving ADC data.
- An API comprised of a reach set of functions that give the user application full control over the power supply.
- Shell programming tools that allow the user to write standard Unix scripts and to access the main controller features without the need for C programming.

## SUMMARY

The power supply control system has been deployed in all T&DD test stands and has proved to be a reliable and full-featured system with a user-friendly interface. It has been successfully used in our cryogenic and conventional test stands being fully capable of generating precision ramps ranging from a fraction of an Amp/s up to 18000 Amps/s. In addition, adopting a parabolic form of the ramp segments was invaluable for improving of the transient response of the SCR-based high current supplies.

## REFERENCES

[1] 'An Open Distributed Monitoring and Control System',
J.M.Nogiec, E.Desavouret, J.Pachnik, S.Sharonov, J.Sim, Proceedings of CHEP'97, April 1997, Berlin
[2] '8XC196KR Users Manual', Intel Corporation
[3] '1994 Design-In Reference Manual', Analog Devices, Inc., 1994
[4] '80C196 C Compiler User's Guide', Boston Systems Office Tasking
[5] 'VxWorks Programmer's Guide 5.2', Wind River Systems, Inc., 1995

# MAGNET POWER SUPPLY SYSTEM FOR KEK B-FACTORY

Tadashi Kubo , Masato Yoshida

High Energy Accelerator Research Organization
Oho , Tsukuba-Shi , Ibaraki-Ken , 305 , Japan

*Abstract*

A number of magnet power supplies have to be newly prepared for KEK B-Factory accelerator except for a small number of power supplies recycled from TRISTAN. High stability and low long term drift of magnet current must be guaranteed for these new power supplies from the requirement of accelerator design. Many R&D works have been put into practice from two years ago. Finally the type of power supplies with small and medium power has been decided to be switch mode.

## 1 INTRODUCTION

Power supplies for KEKB-Factory will be installed in 4 small and 4 large existing power supply stations used for TRISTAN. For R&D we have manufactured unipolar 20kW and bipolar 300W switch mode power supplies. Many measurements have been carried out as to these power supplies. A lot of useful data have been obtained.

We have designed new power supply system being based on these R&D works. Other construction works for power supply system have been going well in parallel at present. The companies that manufacture power supplies and other electronic parts on this year will be fixed on this May end. The outline of design concept and configuration etc. of the magnet power supply system for KEK B-Factory will be described in this paper.

## 2 SPECIFICATION OF POWER SUPPLIES

Table 1. shows required specifications of magnet current and magnetic field ripple content inside Cu vacuum chamber.

| Power Supplies for | Current Stability (P-P) | Magnetic Field Ripple Content(P-P) |
|---|---|---|
| Superconducting Quadrupole Mag. | $1 \times 10^{-4}$/year | $1 \times 10^{-5}$ |
| Quadrupole Mag. | $1 \times 10^{-4}$/year | $1 \times 10^{-5}$ |
| Bending Mag | $1 \times 10^{-4}$/year | $1 \times 10^{-5}$ |
| Sextupole Mag. | $5 \times 10^{-4}$/year | $5 \times 10^{-4}$ |
| Steering Mag. | $5 \times 10^{-4}$/year | $5 \times 10^{-5}$ |

Table 1. Required Specification for Magnet Current and Magnetic Field Ripple Content (P-P)

Small value of long term current stability has been adopted to guarantee the stable accelerator operation through the year. But this requirement is very severe for designing a hardware block diagram of a current control of power supply, because temperature change from winter to summer is about 40 degrees(Centigrade) in KEK.

Table 2. shows the rough parameters of power supplies estimated from lattice design, magnet resistance and voltage drop of the DC cable.

| Ring | Magnet Type | Current (A) | Voltage (V) | Number of Units | Total Units |
|---|---|---|---|---|---|
| LER | Dipole | 1250 | 30-800 | 4 | |
| | | 1000 | 110 | 3 | |
| | | 800 | 30-110 | 7 | |
| | | 600 | 50 | 2 | |
| | | 500 | 20-70 | 4 | |
| | | 5 | 10 | 3 | |
| | Wiggler | 1000 | 750 | 4 | 27 |
| | Quadrupole | 800 | 20-40 | 2 | |
| | | 500 | 20-130 | 109 | |
| | | 350 | 350-600 | 7 | |
| | | 200 | 30-40 | 8 | 126 |
| | Sextupole | 425 | 40-60 | 54 | 54 |
| | Steering | 10 | 50 | 58 | |
| | | 5 | 45-65 | 860 | 918 |
| HER | Dipole | 840 | 20-600 | 5 | |
| | | 500 | 10-20 | 2 | |
| | | 10 | 10-70 | 13 | 20 |
| | Quadrupole | 3500 | 60 | 1 | |
| | | 1600 | 60 | 1 | |
| | | 800 | 50 | 1 | |
| | | 600 | 20-450 | 24 | |
| | | 500 | 10-1000 | 83 | |
| | | 300 | 60 | 1 | |
| | | 200 | 30-40 | 12 | 123 |
| | Sextupole | 425 | 40-80 | 52 | 52 |
| | Steering | 10 | 50 | 41 | |
| | | 5 | 60-100 | 831 | 872 |
| Colliding Point (Superconducting) | | | | | |
| | Quadrupole | 3500 | 15 | 1 | |
| | Solenoid | 650 | 30 | 2 | |
| | Steering | 50 | 20 | 6 | |

Table 2. List of magnet power supplies prepared for KEK B-Factory.

0-7803-4376-X/98/$10.00 © 1998 IEEE

## 3 R&D WORKS

Various investigations have been carried out to satisfy the performances given in the specifications. The performance of power supply will be under the control of the performance of DAC, Error Amp., Shunt Resistor or Burden Resister of DCCT.

### *3.1 Room Condition of the Power Supply Installation Area*

Room temperature of existing 8 power supply stations varies remarkably through the year, because the power supply stations have not air-conditioner. But it will be possible to keep the room temperature in the range of 10 to 40 degrees through the year by on/off control of ventilation fan [1].

### *3.2 Electronic Parts*

All magnet current data set through control network are 16 bits, and are converted into analogue reference by DAC in the power supply. As a result of measurements, the temperature coefficients of DACs of a few companies proved to be below 5 ppm/degree. However, except for steering magnet power supply temperature control of DAC will be necessary to satisfy the performance of power supply.

The measured temperature coefficients of a few types of operational amplifier proved to be below 0.1 ppm/degree. These data will be enough to satisfy the performance of power supply.

Steering magnet power supply will be kept in natural room temperature to reduce the production cost. Therefore, the shunt resistor must have low temperature coefficient. Fortunately from many kinds of measurements it seems that it is possible to get such resistors from a few companies.

DCCT will be used for comparatively high current power supplies such as bending, quadrupole and sextupole magnet power supplies. Burden resistor has a function of converting a current signal of DCCT to a voltage signal. Measured temperature coefficient of typical burden resistors have been below 5 ppm/degree. In this case temperature control of burden resister will be necessary.

### *3.3 R&D of Power Supply*

R&D of the power supply started from two years ago. Three companies joined to fabricate both unipolar 20kW and bipolar 300W switch mode power supplies. To realize the specification the control circuit including DAC, error amplifier and burden resistor for DCCT has been separated from hardware power unit and installed in air-conditioned room. This was a first plan of the power supply configuration of KEK B-Factory. Detail discussion has been made in the report [1]. Table 3. and Table 4. show the measured performances of the R&D power supplies respectively.

| Company | Current Stability (P-P) | Current Ripple Content(P-P) |
|---|---|---|
| A | 40ppm/89h | 14.8ppm(5.9Hz) |
| B | 110ppm/65h | 5.1ppm (50Hz) |
| C | 102ppm/43h | 20.8ppm (50Hz) |
| | Load : | 20 mH, 0.0755 ohm |

Table 3. Measured Data of 20kW(40V,500A) Power Supplies

| Company | Current Stability (P-P) | Current Ripple Content(P-P) |
|---|---|---|
| A | 250ppm /89h | 1.2ppm(50Hz) |
| C | 10ppm /69h | 50ppm(50Hz) |
| | Load : | 3.4 H, 8 ohm |

Table 4. Measured Data of 300W(60V,5A) ,Bipolar Power Supplies

It proved to be that to satisfy the required specifications have not been easy, but will be in our hands before long when the mass production of power supply starts on this fiscal year.

## 4 DESIGN OF TOTAL POWER SUPPLY SYSTEM

The estimation of R&D power supplies have finished on this March end. The size of power supplies has been reduced remarkably in comparison with usual SCR + Transistor Dropper type power supply. Consequently, all power supplies for KEK B-Factory can be installed in existing power supply stations.

Figure: 1 shows a final configuration of the power supply system. The delicate electronic parts in control circuit will be temperature controlled by putting Peltie semiconductor on the cooling fin and will be assembled in power supply hardware unit in stead of separating. Figure: 2 shows a block diagram of temperature compensator.

## 5 SCHEDULE

All the power supplies will be manufactured within two years from this fiscal year. The manufacturers that product the power supplies on this year will be fixed on this May end. The wiring of power cable will be finished on this July end. Current monitor system and sequence controller will be ordered on this May end. Almost all of hardware devices except for the remaining power supplies will be installed up to the end of this fiscal year.

The actual adjustment of the power supply system from a point of view of both hardware and software systems will start from the beginning of next fiscal year. The preparation works for accelerator operation will be completed up to the end of September of next fiscal year.

## 6 CONCLUSION

The design of power supply system started from three and a half years ago and the varieties of R&D works started from two years ago. The final design of the power supply system has been greatly indebted to these R&D works.

## REFERENCE

[1] Ta. Kubo et al.,"Design of Magnet Power Supplies for KEKB Accelerator",Proc. of the 10th Symp. on Acc. Sci. and Tcch.,118(1995)

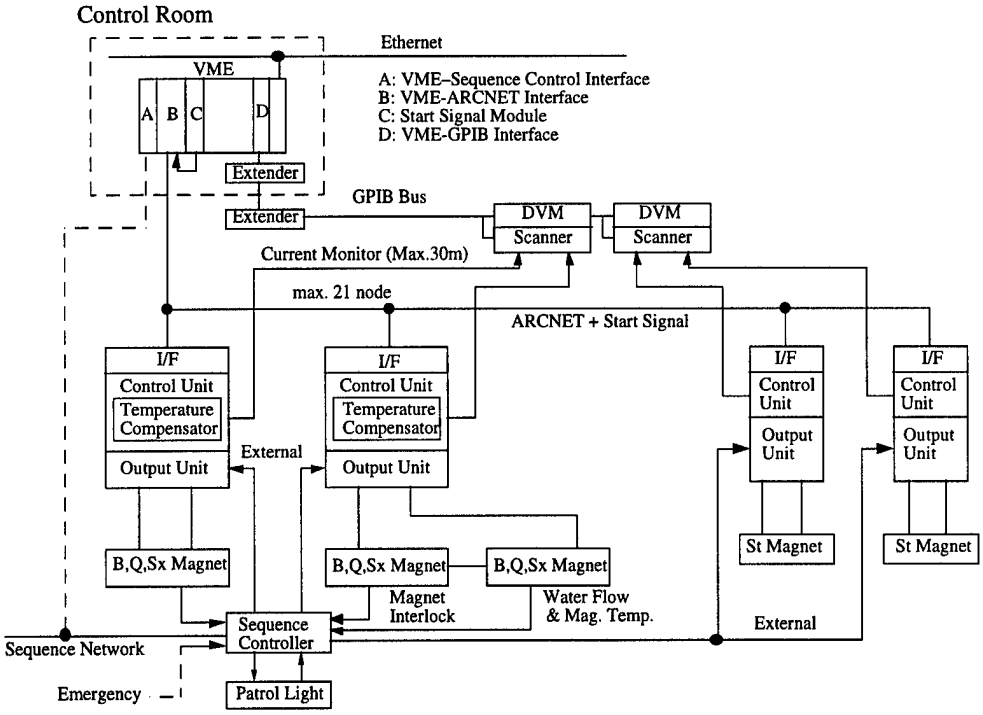



Figure: 1 Control System for Magnet Power Supply

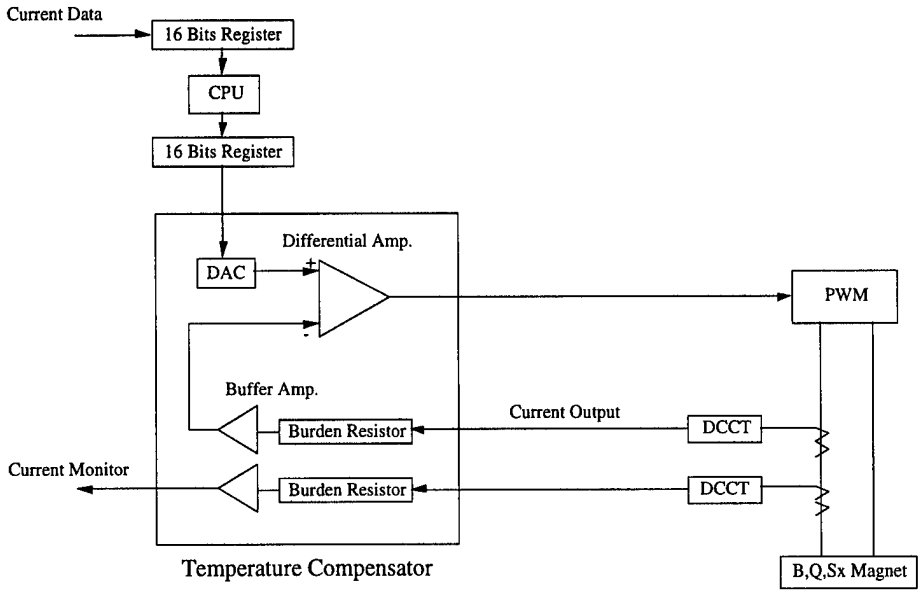



Figure: 2 Temperature Compensator for B and Q Magnet Power Supplies

# EFFECT OF SOURCE VOLTAGE SUBHARMONICS ON A RAPID CYCLING SYNCHROTRON POWER SUPPLY

F.Q. Zhang, The Graduate Univ. for Advanced Studies, KEK, Tsukuba, Japan
T. Adachi and K. Endo, High Energy Accelerator Research Organization, KEK, Tsukuba, Japan

*Abstract*

In a 50 Hz rapid cycling power supply, the resonant ac current of the synchrotron magnet is modulated by the subharmonics of the source voltage rectified in 12 pulses with SCR. The modulation is found to be caused by the fluctuation of the pulsed power that is transferred to the magnet circuit via a choke transformer due to the cycle-to-cycle unequal charging of the capacitor located just after the rectifier. This phenomena is observed when there is a mismatch between frequencies of the power line and resonant magnet circuit. In this paper, the modulation behavior is analyzed and the experimental results are given as well as those of the circuit computations.

## 1 INTRODUCTION

In fast-cycling synchrotrons, a pulsed power supply is commonly used as power source for resonant network as shown in Fig.1.

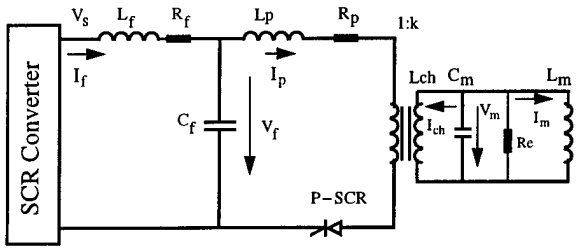



Figure 1: Pulsed power supply and resonant network for a fast cycling synchrotron.

Generally, the resonant magnet current is not easily affected by the source voltage disturbances owing to the large stored energy in the resonant network, but it is never immune from the disturbances. In a 50Hz rapid cycling power supply system [1, 2], modulation of the resonant current was observed and found to be caused by the harmonics, especially the subharmonics of the source voltage generated by a 12-pulse SCR rectifier. In this paper, the investigation on the effect of the source voltage on the resonant output is performed by both computation and experiment. To the best of our knowledge, the existing analyses [3, 4] were all carried out on an assumption of harmonics-free source voltage. This suggests a new approach that has to be developed to investigate the system response to source voltage harmonics. The approach described in this paper is based on the general method on the analysis of linear circuits containing periodically operated switches. The properties predicted by the computation are well justified by the experimental observations.

## 2 EFFECT OF SUBHARMONICS ON RESONANT CURRENT

The pulsed supply and its resonant network fit into the category of linear time-varying networks. Because of the periodical switching operation, the circuit reduces to the special class of linear, periodically time-varying networks. The response y(t) of a linear time varying system to an input x(t) with Fourier transform X(ω) is defined by

$$y(t)=\frac{1}{2\pi}\int_{-\infty}^{\infty} H(\omega,t)X(\omega)e^{j\omega t}d\omega$$

where H(ω, t) is the transfer function of the system [5]. For linear periodically time varying networks of period T, the system function is periodic with respect to the period T: H(ω, t+T)=H(ω, t). Therefore, it may be expanded in a Fourier series,

$$H(\omega,t)=\sum_{-\infty}^{\infty} H_n(\omega)e^{j(2\pi nt/T)}.$$

$H_0$ may be regarded as an averaged time varying system function. Evidently the remaining Fourier coefficients represent system responses at sidebands around $n\omega_s=n(2\pi/T)$. The analyses on periodically switched linear networks can be found in [6-9]. This paper follows Liou's approach [7]. We first present the system response to an sinusoidal or exponential input in time domain and describe the properties of the response. Then an analysis in frequency domain shows the sidebands containing in the pulse current $I_p$ and resonant current $I_m$.

### *2.1 Time domain*

#### 2.1.1 Approach

Generally the circuit can be described by the following differential equations with respect to the periods of switching-off and switching-on as follows,

$$\dot{X}_{n,k}(t)=A_kX_{n,k}(t)+B_ku(t) \quad (1.a)$$

$$y_{n,k}(t)=C_kX_{n,k}(t)+D_ku(t) \quad (1.b)$$

where $X_{n,k}$ is a state vector, u an input vector, $y_{n,k}$ an output vector, n the n-th operation and k=1, 2 means the state of switching off and on, respectively. Fig.2 illustrates the notations for the n-th switching period.

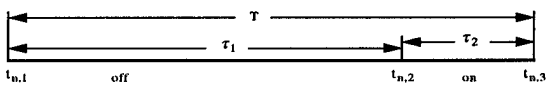



Figure 2: Notations for n-th switching period.

At the switching instants $t_{n,2}$ and $t_{n,3}$, the boundary conditions can be described by the state transient matrices

0-7803-4376-X/98/$10.00 © 1998 IEEE

$F_2$ and $F_3$ as follows.

$$X_{n,2}(t_{n,2})=F_2X_{n,1}(t_{n,2})+G_2u(t_{n,2}) \quad (2.a)$$

$$X_{n+1,1}(t_{n,3})=F_3X_{n,2}(t_{n,3})+G_3u(t_{n,3}) \quad (2.b)$$

Assuming $u(t)=ve^{pt}$, where v is a constant and p is a complex number, the solution is given by

$$X_{n,k}(t) = \exp[A_k(t-t_{n,k})] \cdot [X_{n,k}(t_{n,k}) + \alpha_k(t_{n,k})] - \alpha_k(t) \quad (3.a)$$

$$\alpha_k(t)=(A_k-pI)^{-1}e^{pt}B_kv \quad (3.b)$$

The solution (3), together with (2) can be computed successively from a given initial vector to get the response, but a useful result about the boundary conditions is obtained as follows by manipulating further.

$$X_{n,1}(nT)=M^n[X_{0,1}(0)-Jv]+Je^{pnT}v \quad (4)$$

where $J=[e^{pT}I-M]^{-1}H$, $M=F_3e^{A_2\tau_2}F_2e^{A_1\tau_1}$ (5)

and

$$H = F_3e^{A_2\tau_2}F_2(A_1-pI)^{-1}(e^{A_1\tau_1}-e^{p\tau_1}I)B_1 + F_3(A_2-pI)^{-1}(e^{A_2\tau_2}e^{p\tau_1}-e^{pT}I)B_2 + F_3e^{A_2\tau_2}G_2e^{p\tau_1}+G_3e^{pT} \quad (6)$$

It is noticed from (4) that $X_{n,1}(nT)$ consists of two terms. The first term represents the transient mode while the second is the steady-state mode. For $n\to\infty$, $M^n\to 0$ and we get the steady-state result,

$$X_{n,1}(nT)_{ss}=Je^{pnT}v. \quad (7)$$

From the repetitive computations of equations (2)-(7), the response in time domain is obtained.

### 2.1.2 Numerical results

#### 2.1.2.1 System parameters

Considering the circuit of Fig.1, we have:

$X_{n,1}=[i_f \quad v_f \quad i_L \quad v_m]^T$ and

$X_{n,2}=[i_f \quad v_f \quad i_p \quad i_L \quad v_m]^T$,

where $i_L=i_{ch}+i_m$. In charging period (k=1),

$$A_1=\begin{bmatrix} -R_f/L_f & -1/L_f & 0 & 0 \\ 1/C_f & 0 & 0 & 0 \\ 0 & 0 & 0 & 1/L \\ 0 & 0 & -1/C_m & -1/(C_mRe) \end{bmatrix}$$

$B_1=[1/L_f \quad 0 \quad 0 \quad 0]^T$, and $i_p=0$.

In pulse period (k=2),

$$A_2=\begin{bmatrix} -R_f/L_f & -1/L_f & 0 & 0 & 0 \\ 1/C_f & 0 & -1/C_f & 0 & 0 \\ 0 & 1/L_p & -R_p/L_p & 0 & -1/(kL_p) \\ 0 & 0 & 0 & 0 & 1/L \\ 0 & 0 & 1/(kC_m) & -1/C_m & -1/(C_mR_e) \end{bmatrix}$$

$B_2=[1/L_f \quad 0 \quad 0 \quad 0 \quad 0]^T$,

$$F_2=\begin{bmatrix} 1 & 0 & 0 & 0 \\ 0 & 1 & 0 & 0 \\ 0 & 0 & 0 & 0 \\ 0 & 0 & 1 & 0 \\ 0 & 0 & 0 & 1 \end{bmatrix}, \quad F_3=\begin{bmatrix} 1 & 0 & 0 & 0 & 0 \\ 0 & 1 & 0 & 0 & 0 \\ 0 & 0 & 0 & 1 & 0 \\ 0 & 0 & 0 & 0 & 1 \end{bmatrix}, \quad G_2=0 \text{ and } G_3=0,$$

where $L_f$=0.268H, $C_f$=0.6mF, $L_p$=1.86mH, $L_{ch}$=10.4mH, $L_m$=4.7mH, $L=L_{ch}L_m/(L_{ch}+L_m)$, $R_f$=5mΩ, $R_p$=1mΩ, k=2, $C_m$=3.2mF, and $R_e$~70. Re is a pseudo-resistance representing the ac loss. Accordingly, the resonant frequency (i.e. switching frequency) is $f_s$~50Hz, $\tau_1=5\tau_2$ and $\tau_1+\tau_2=T$ (=switching period). Resonant network quality factor is: $Q=\omega_sC_mR_e$~70. The resonant condenser $C_m$ is adjustable in both calculation and experiment for our purposes.

#### 2.1.2.2 System response to source voltage harmonics

The source voltage is provided by a 12-pulse SCR rectifier, of which output contains both characteristic and non-characteristic harmonics that arise from "unideal" converter operation. The non-characteristic harmonics called subharmonics are the components with lower frequencies than the converter's fundamental frequency. Assuming the power line frequency $f_0$, the subharmonics are of frequencies $hf_0$, where h is an integer. For the model system under discussion, $f_0$=50Hz and h<12. The calculation shows that the subharmonics appear as a modulation with frequency $f_m=h\Delta f$ in resonant output as shown in Fig.3, where $\Delta f=|f_s-f_0|$ and $f_s$ is the switching frequency.

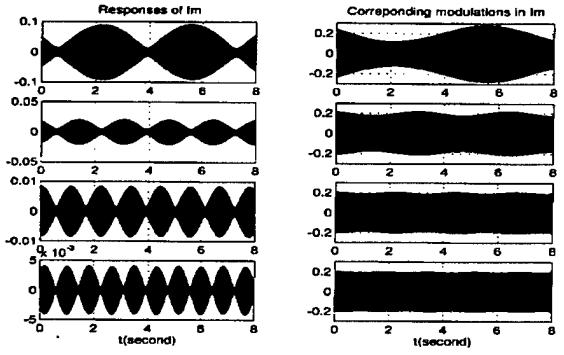



Figure 3: Modulations by subharmonics. Scaled responses (left) to unit amplitude with $nf_0$ (n=1,2,3 and 4 from top to bottom) in resonant current $I_m$ for $f_s$=49.85Hz are added to the unperturbed $I_m$ in the exaggerated ways (right).

Modulation frequencies can be determined by investigating the variation mode in the boundary condition. For an input subharmonic $v_s=e^{jh2\pi f_0t}$ according to (7), the state vector is given at each beginning instant of switching period for steady-state operation as:

$$X_{n,1}(nT)=Je^{jh2n\pi f_0/f_s}.$$

It is seen that $X_{n,1}(nT)$ varies at a quasi-periodic mode with frequency $f_m=h\Delta f$, accordingly the system outputs will

also vary with the same way. $f_m$ is not a rigid frequency but always holds a value close to $h\Delta f$.

### 2.2 *Frequency domain*

Frequency domain formulations are obtained by performing the Laplace transform of the state vector given by (3) then deriving the Laplace transformation for output y(t). Finally the following results are obtained,

$$Y(s)\Big|_{\substack{p=j\omega_0\\ s=j\omega}} = Y(\omega)=T(\omega)\frac{1}{j[\omega-(\omega_0+n\omega_s)]}v,$$

$$T(\omega_0+n\omega_s)=\sum_{k=1}^{2}\{C_k e^{-j(\omega_0+n\omega_s)\eta_{k-1}}R_k(\omega_0+n\omega_s)-$$

$$\frac{e^{-jn\omega_s\eta_{k-1}}(1-e^{-jn\omega_s\tau_k})}{jn\omega_s}[C_k(A_k-j\omega_0 I)^{-1}B_k-D_k]\}/T$$

for $n\neq 0$, and

$$T(\omega_0)=\sum_{k=1}^{2}\{C_k e^{-j\omega_0\eta_{k-1}}R_k(\omega_0)$$

$$-\tau_k[C_k(A_k-j\omega_0 I)^{-1}B_k-D_k]\}/T$$

for n=0, where $\eta_0=0$ and $\eta_1=\tau_1$. $R_k$ is complex matrix comprising the circuit configuration matrices and switching transformation matrices in (1) and (2), respectively. It is concluded that for a subharmonics $hf_0$, the output contains sidebands: $nf_s\pm h\Delta f$ plus lower-frequency $h\Delta f$, where n=1,2,3,... Fig.4 is a typical calculation result showing the spectra of $I_p$.

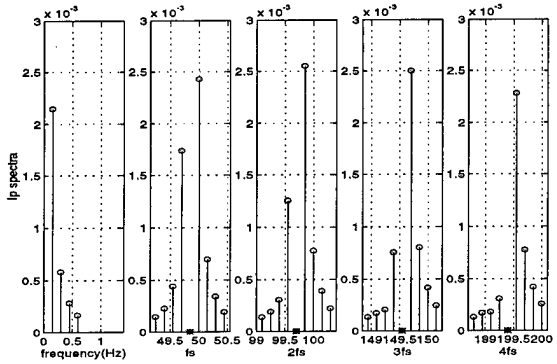



Figure 4: Calculated spectra of $I_p$, $f_s$=49.85Hz.

## 3 EXPERIMENTS

The modulation in resonant current was measured and the relation to the subharmonics of 100Hz was obtained as in Fig.5. In the model pulsed power supply, the prominent subharmonic frequency is 100Hz due to the configuration

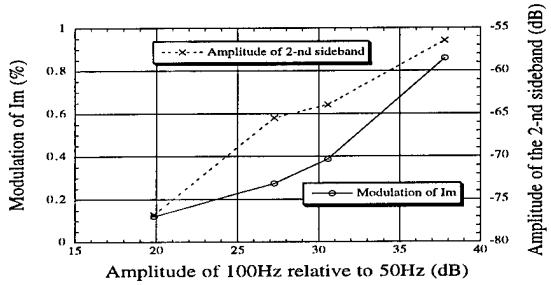



Figure 5: Modulation by 100Hz subharmonics

of the firing circuit for the 12-pulse rectifier, while 50Hz is very low and almost unchanged. The measured spectra of $I_p$ and $I_m$ in Fig.6 support the analyses made above. Sidebands of $I_p$ appear at both sides of $nf_s$ (n=1,2,...), while those of $I_m$ at both sides of only $f_s$. This is because the latter sidebands at higher frequency is suppressed by the decreased amplitude response of the transfer function of $I_m/I_p$.

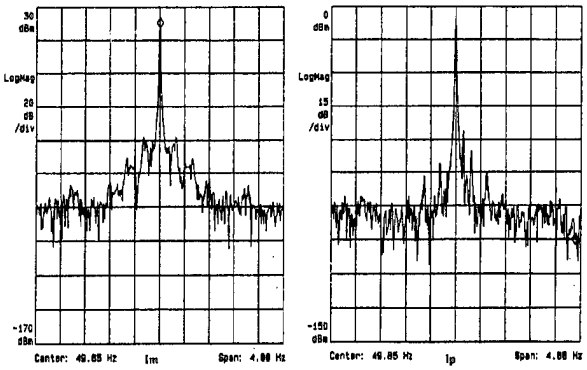



Figure 6: Measured spectra of $I_p$ and $I_m$.

## 4 CONCLUSIONS

Analytical model based on the Liou's approach is used to adapt for the periodically operated SCR switch in the linear time-varying circuit whose frequency is different from the line frequency. This approach explains the experimental observations on the amplitude modulated ac current of the fast cycling synchrotron magnet quite well.

## 5 REFERENCES


[1] K. Endo, Y. Ohsawa, W.M. Zhou and T. Yamagishi, "50Hz Power Supply for B-Factory Booster Synchrotron," 1993 IEEE Conf. Record Nuclear Science Symp. & Medical Imaging Conf., San Francisco, 1993, pp.385-9.

[2] F.Q. Zhang K. Endo and Y. Irie, "Feedback Control of 50Hz Power Supply," EPAC96, Barcelona, 1996, pp.2343-5.

[3] J.A. Fox, "Resonant magnet network and power supply for the 4 Gev electron synchrotron Nina," Proc. IEE Vol. 112, 1965, pp.1107-26.

[4] A. Sreenivas e, G.G. Karaday and H.A. Thiessen, "A General Method for Resonance Power Supply Analysis," IEEE Trans., Vol. NS-39, 1992, pp.29-34.

[5] M.R. Aaron, "Application characterization, and design of switched filters" in Modern Filter Theory and Design, G.C. Temes, and S.K. Titra. Eds. New York: John Wiley & Sons, Chap. 10.

[6] W.R. Bennett, "Steady-state transmission through networks containing periodically operated switches." IRE Trans., Vol. CT-12, 1955, pp.17-21.

[7] M.L. Liou, "Exact analysis of linear circuits containing periodically operated switches with applications," IEEE Trans., Vol. CT-19, pp.146-154.

[8] T. Stroem and S. Signell, "Analysis of Periodically Switched Linear Circuits," IEEE Trans., Vol. CAS-24, 1977, pp.531-41.

[9] A. Opal and J. Vlach, "Analysis and Sensitivity of Periodically Switched Linear Networks," IEEE Trans., Vol. CAS-36, 1989, pp. 522-32.

# DEVELOPMENT OF A HIGH SPEED CROWBAR FOR LANSCE*

C. Friedrichs, J. Lyles, J. M. Doub
Los Alamos National Laboratory

*Abstract*

Each of the four 200 MHz Final Power Amplifiers (FPAs) in the LANSCE proton linac has its own capacitor bank and crowbar. The dissipation in the 10Ω crowbar limiting resistor is as high as 67 kW, and oil cooling is used. Our stated upgrade goal was to substantially reduce the limiting resistor dissipation and eliminate the oil cooling. Early tests showed that the fault energy quickly rose to unacceptable levels as the current limiting resistance was reduced. FPA arcs are normally quenched by interrupting the FPA modulator current, and the crowbar waits 10 μs for this to occur. The successful upgrade strategy was to replace the 10Ω resistor with a 3Ω air cooled resistor and to add a high speed crowbar circuit which operates only if there are simultaneous arcs in the FPA and its modulator. This paper describes the high speed circuit and its interface with the existing crowbar. Test results are also given.

## 1 INTRODUCTION

The 200 MHz amplifiers in the LANSCE linac are currently being operated with 838 μs pulses at 120 pps. The first module is a low power (400 kW) segment, while the second, third, and fourth modules operate at the 3 MW level. The plate current for each 3 MW FPA is typically 250 A peak and its Intermediate Power Amplifier (IPA) plate current is typically 10 A peak. Both currents are drawn from a common capacitor bank. While the average current delivered by the capacitor bank is only 26 A, its RMS value is 82 A. The remainder of this paper will present the parameters relevant to the second, third and fourth modules only.

When an arc occurs in one of the RF amplifiers, the preferred method of protecting the RF amplifier is to interrupt the remainder of the plate modulator output pulse rather than to fire the crowbar. Normal operation can then resume at the next pulse. The existing crowbar design allowed approximately 10 μs for current interruption to occur before crowbar triggering was initiated.

A typical crowbar circuit will contain a crowbar current limiting resistor between the capacitor bank and the crowbar. This resistor keeps the crowbar current within the limits of the crowbar device. A second resistor must be placed between the crowbar and the load it is protecting. Without this second resistor, a load arc would short out the voltage across the crowbar, and under that condition it would be very difficult or impossible to fire the crowbar device. The existing crowbar circuit used a 5Ω, Ohm-Weve® resistor in each of these positions. The total dissipation in both resistors during normal operation is 67 kW. High dissipation as well as dust precipitation on the resistors rendered air cooling impractical, so oil cooling was included in that design.

## 2 CIRCUIT DEVELOPMENT

A simplified crowbar circuit is shown in figure 1. The capacitor bank is made up of forty eight 4.6 μF capacitors in parallel, resulting in a total bank capacitance of 221 μF.

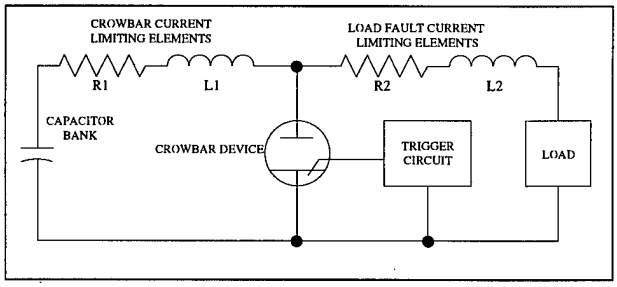



Figure 1: Simplified diagram of a typical crowbar circuit.

### *2.1 Limiting Resistor Selection*

Early in the development program, we elected to use a bank of Carborundum® resistors to make up the crowbar limiting element. This resistor bank is made up of ninety six (two per capacitor) 115Ω resistors in parallel. The total bank resistance is 1.2Ω. Each resistor is 18 inches long and is rated at 150 W, 43,000 J, and 150 kV. During normal operation, each resistor will dissipate 84 W. During the crowbar operation, with a 32 kV capacitor bank voltage, each resistor will dissipate 1200 J of energy. The value of the load fault limiting resistor, R2, could not be predetermined because we wanted its value to be as low as possible. We built a 2.5Ω experimental resistor, using Nichrome® wire in an Ayrton-Perry winding configuration. We then shorted out sections of the resistor to see how low we could go without compromising load protection. Our fault test device is made up of a high voltage switch which shorts out the load through a 60 cm length of 30 ga. copper wire. If the wire remains intact after the test, adequate protection has been demonstrated. After numerous tests, we settled on a value of 2Ω for the load fault limiting resistor. The Ayrton-Perry winding configuration consists of two parallel windings in opposite directions on the same form.

* Work supported by the U. S. Department of Energy

0-7803-4376-X/98/$10.00 © 1998 IEEE

Each winding consists of 3 strands of 12 ga. Nichrome® wire in parallel. Each winding is made up of 40 turns on a 36 inch circumference with a coil length of 70 inches.

*2.2 Inductance Considerations*

The loop inductances, L1 and L2 will affect the performance of the crowbar, and a reasonable effort to estimate their values is imperative. The following equation, which predicts the inductance of a circular loop was used to estimate loop inductance.

$$L_0 \cong r\mu\left[\ln\left(\frac{8r}{a}\right)-2\right]H \quad [1]$$

$r$ is the loop radius, $a$ is the conductor radius, and $\mu$ is the permeability of free space.

The loop for L1 was assumed to be equivalent to a 2 meter diameter circle, the loop for L2 was assumed to be equivalent to a 4 meter diameter circle, and the loop conductor was assumed to be 0.025 meters in diameter. These assumptions were based on the actual rectangular geometries of the loops. Calculations based on these dimensions result in 5 μH for L1 and 12 μH for L2. It is important that both the L1 loop and the L1+L2 loop be over damped. If an under damped condition exists, ringing will occur and the crowbar device may extinguish well before the capacitor bank energy is dissipated. In order for the overdamped condition to exist, the following inequality must be true.

$$L < 0.25 * R^2 * C$$

The limiting value for L1 is 79 μH and the limiting value for L1+L2 is 565 μH. Based on the estimated inductance values, both loops appear to be very well damped.

*2.3 Crowbar Device*

The existing crowbar used a 7703EHV mercury vapor ignitron. This device is rated up to 50 kV, 100 kA, and 30 coulombs in crowbar service. The 7703EHV has a 0.5 μs ionization time, and requires a 3 kV trigger pulse. All of these parameters are well suited to the high speed crowbar upgrade, so this device is incorporated into the new design.

*2.4 Trigger Circuit*

The high speed crowbar triggering threshold is designed to be about 3000 A; a value slightly above the emission capability of both modulator tubes. This high threshold allows the existing crowbar circuit to function as it was originally intended. The requirement for high speed triggering exists when both the RF tube and the modulator arc simultaneously and the fault currents are determined by the limiting elements. Based on early tests to determine the value of R2, 3 μs was established as the time limit from fault current inception to full conduction of the ignitron. In order to meet this requirement, we sought to optimize a simple trigger circuit which has been used in various crowbars for at least 30 years. The circuit is shown in figure 2 along with the interface with the existing crowbar. The high voltage diodes serve a dual purpose. They act both as steering diodes to accept a trigger from either circuit and as voltage clippers to prevent negative voltage from appearing on the ignitor.

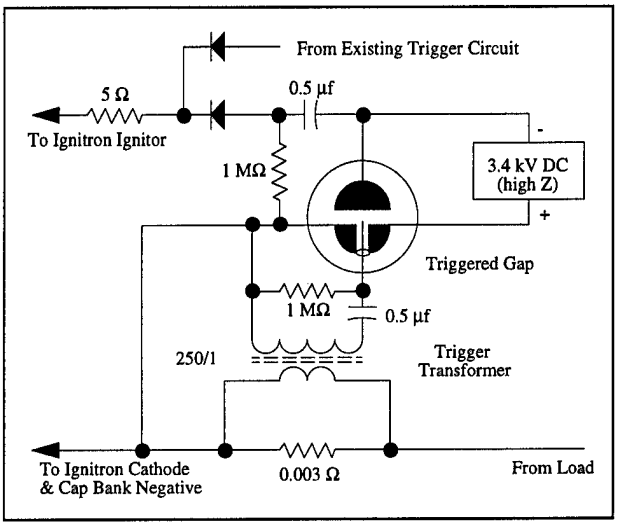



Figure 2: Simplified diagram of the High Speed Crowbar Trigger Circuit.

In order to get the best performance from this circuit, we went through several iterations to select the proper trigger transformer and triggered gap combination. The fault sampling resistor is made up of 6 strands of 12 ga. Nichrome® wire in parallel, 2.15 inches long. During the optimization process we found that better performance was obtained when the six strands were placed in a close cluster about 1 cm in diameter.

The final configuration uses an EG&G® TR1647 trigger transformer and an EG&G® GP 90 triggered spark gap. Normally, one would couple the gap output to the ignitron input using a 1:1 pulse transformer; however by applying a negative voltage to the opposite electrode, capacitive coupling may be used to provide the required positive pulse to the ignitron input. The EG&G application notes for the GP90 recommend a positive trigger and positive polarity on the opposite electrode. Our configuration, which applies a positive trigger and negative voltage to the opposite electrode, was approved by EG&G applications engineering for crowbar service.

## 3 AIR COOLING

The Carborundum® resistors which make up R1 are positioned vertically and distributed throughout the capacitor bank such that two resistors are located immediately above each capacitor. The wire wound resistor, R2 is positioned horizontally, close to the capacitor room ceiling, between the capacitor bank output and the capacitor room DC output cables. Two exhaust fans are positioned in the capacitor room ceiling immediately above the wire wound resistor, R2. Each fan will exhaust 2250 cfm through an exhaust area of 1.9 square feet. Air is drawn into the capacitor room through four 1 micron filters, each with an area of 2.1 square feet. Two of the filters are positioned such that their air is drawn over the Carborundum® resistors, and the other two filters are positioned low on the vertical wall below the wire wound resistor. The temperature of the resistors is maintained well below their operating limits, and dust accumulation within the capacitor room is minimal. Annual cleaning of the capacitor bushings is sufficient.

## 4 RESULTS

The most important result of the High Speed Crowbar Development is that the upgraded circuit has been in service in Module 2 at LANSCE for all of the present run cycle. There has been no degradation in Module 2 performance after 4 months of continuous operation. If the crowbar circuit were deficient, erratic performance would be expected in the RF tubes.

As mentioned earlier, our test for crowbar adequacy is to short the capacitor room output through a 60 cm length of 30 ga. copper wire. The test circuit has been operated numerous times, and the crowbar has never failed to protect the wire.

The voltage across the ignitron is shown in figure 3. The initial drop in voltage results from the fault which shorts the load. After about 1.5 μs, the ignitron goes into full conduction, and the voltage falls to zero.

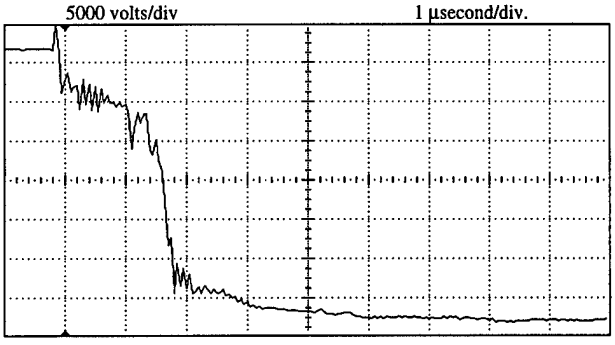


Figure 3: Ignitron voltage during fault.

The output of a current transformer placed in series with the fault test is shown in figure 4.

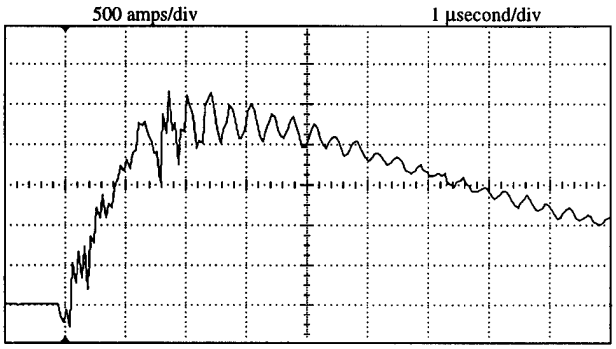


Figure 4: Current through the fault test wire.

The effects of the loop inductances are readily apparent. The fault current rises monotonically to about 2500 A, at which time the ignitron fires, then decreases monotonically back to zero. If no inductance were present, the current would rise abruptly to 10,000 A, then decrease abruptly to zero when the ignitron fired. The energy dissipated in the wire is less with the inductance than it would be without it. The information learned from this picture suggests that if some of our loop 2 inductance could be transferred to loop 1, the value of R2 could be reduced below 2 Ω. Since the performance of the high speed Crowbar is adequate, no further investigation is anticipated.

## ACKNOWLEDGMENTS

The authors wish to thank all of the people who helped in the development and installation of the components making up the module 2 air-cooled capacitor room. We would like to particularly recognize Steven Archuletta and Luis Lopez whose dedication and hard work brought this project to completion in time for the next LANSCE run cycle.

## REFERENCES

[1] Simon Ramo and John Whinnery, *Fields and Waves in Communication Electronics,* John Wiley and Sons, 1965, p311.

# COMMISSIONING AND FIRST YEAR OPERATION OF THE LNLS MAGNET POWER SUPPLIES

D. Wisnivesky°, A. C. Lira, A. R. Silva, F. C. Arroyo and L. H. Oliveira.
Laboratório Nacional de Luz Síncrotron - LNLS/CNPq
Cx Postal 6192, 13083-970 Campinas SP Brazil
°also IFGW/ UNICAMP

*Abstract*

We describe the commissioning and operation of over 100 power supplies used in the LNLS injector, transport line and storage ring. In particular, we discuss the power supply characteristics required for low energy injection and ramping as well as for high energy operation. Low current ripple and stability at injection energies as well as repeatability and performance at high beam energy are specially considered.

## 1 INTRODUCTION

The light source of the Laboratório Nacional de Luz Síncrotron (LNLS) [1], in Campinas, SP Brazil, includes an electron linear accelerator (linac), a transport line and a booster-storage ring. To achieve the characteristics of a high-quality light source, a total of 163 magnets are used. These magnets require 49 dc current power supplies for the storage ring, 26 for the transport line and 28 for the linac, adding up to 103 power supplies [2]. The LNLS accelerators were commissioned during the first semester of 1996 and the machine has been in normal operation since then.

Injection and electron current accumulation in the storage ring is done at low energy, 120 MeV. After accumulation, the current is ramped up to 1.37 GeV. This represents a very large dynamic range for the power supplies and special requirements on current repeatability. At initial energy, the magnet remnant magnetic field in the quadrupoles and dipoles is significant. Furthermore, operation at low energy is done with horizontal and vertical tunes which are very close to an integer [3], 2.09 $ß_{VER}$ and 5.05 $ß_{HOR}$. This requires that the power supply have a small ripple-to-mean-value ratio at low as well as at nominal current.

The final electron energy is limited by the saturation of the dipoles. The final current is 12 times the initial one, in particular the dipole power supply changes from 25 A at injection up to 300 A at final energy. To allow for different modes of operation of the storage ring, the magnets are split in to several families. The quadrupoles and sextupoles are arranged in 17 different power supply families. Thus, in order to guarantee that the six fold symmetry of the ring be preserved, the precision and repeatability of the power supply settings become important. During ramping, the power supplies track the 16-bit references along energy and tune space. At the same time, along the ramp the 12-bit orbit corrector power supply references are adjusted so that the orbit distortion is kept under control. At high energy, periodical adjustments of the steering magnet power supplies allow the orbit of the stored beam to be maintained within 30 μm of the specified trajectory.

## 2 POWER SUPPLY LAY OUT

A power supply room, next to the accelerator's control room, houses all linac, transport line and storage ring power supplies, with the exception of the storage ring steering magnet power supplies This arrangement allows measurements in the power supplies to be performed while the accelerators are in operation. The room is air conditioned with temperature and humidity control (25 ± 1 °C, 65 % relative humidity). The power supply' input and output cabling run under the removable floor, through cable trays along the underground linac tunnel and into the inside of the storage ring. To avoid unnecessarily long cables, the steering coil power supplies for the storage ring are placed in 6 racks around the inside perimeter of the ring. All power supplies have been developed and built in house. Many of these supplies have innovative topologies that allow for simple, reliable and precise operation [4, 5]. They have been designed to operate with high efficiency so that air cooling suffices to keep the cabinets' inside temperature and most sensitive electronic components below 40 °C. No water cooling is necessary in the power supply room. This has the additional advantage of avoiding any possible water leakage in to the cable bed. All power supplies have local and remote computer control options. In the second case, operation is possible using a PC. Remote control permits a power supply to be turned on and off, sets its current reference, reads the set current value and knows the status of the equipment operating conditions. Figure 1 shows the power supply room. The storage ring power supplies are arranged in three rows. The first two cabinets on the front left correspond to the 12-dipole supply, followed by several 2-quadrupole supplies. On to the right are the sextupole power supplies. At the back, to the left is the linac and to the right the transport line power supplies.

0-7803-4376-X/98/$10.00 © 1998 IEEE



Figure 1: power supply room

## 3 POWER SUPPLY PERFORMANCE

The 12 storage ring dipoles are fed from a single power supply. It is an association of 2 converters: a 12-pulse SCR rectifier with 910 V maximum output in series with a switching Buck converter which uses 10 parallel connected IGBT [4]. The SCR converter supplies 90 % of the load power and the low power switching supply trims the current variations to the required ripple and stability values. Output current can vary from 3 to 300 A in 12 s with zero tracking error. The current ripple is determined by the DCCT sensibility and its frequency by the load characteristics. When operating with the 12-dipole load, the current is forced to oscillate around the mean value at about 2 kHz. This produces a magnetic field ripple of 0.1 G pp, equivalent to a $4.10^{-5}$ variation at injection energy and $3.10^{-6}$ at full energy. Communication with the control computer comprises 16-bit writing and reading analog signals, one turn on/off and 33 status digital signals.

The storage ring quadrupoles are divided in to 14 families involving 12 two-quadrupole families for the low-dispersion sections of the storage ring and 2 six-quadrupole families for the disperse sections. The splitting of the storage ring quadrupoles in so many families allows for several different modes of operation of the ring. The specification of the power supplies was done in order to accommodate those various high energy modes. The quadrupole power supplies are IGBT Buck converters, operating at 8 kHz @ 220 A, maximum current. This produces a $2.10^{-5}$ maximum variation in the magnetic field. Nevertheless, low-energy accumulation adds extra requirements to the quadrupole power supplies. The best operating conditions for low-energy accumulation are a combination of a large number of factors which were defined during the commissioning of the accelerators. In particular, it was found that for significant current accumulation in the machine, both vertical and horizontal fractional betatron tunes are very small. Correspondingly, the power supply ripple at low current must also be small to guarantee a magnetic gradient variation of $\pm\ 2.10^{-4}$. Measurements indicated the need to modify the original design of the two-quadrupole family power supplies to reduce the magnetic field ripple when operating with 12 A, corresponding to injection energy. Consequently, an output damped LC filter was added to the 12 power supplies .This causes a 10-fold reduction in the current ripple and also in the switching frequency, which varies from 1 kHz @ 12 A up to 3 kHz @ 220 A.

The power supplies for the 6 quadrupole and sextupole families are 220 A, 50 V current sources constructed using a novel design developed at LNLS [5]. The new topology combines an SCR rectifier which supplies the power to the load and a two-switching transistor active filter which regulates the load current within specified limits. The novelty of the design is that

the active filter handles not only a small fraction of the load power but also a very small current, less than 1 A @ 220 A load current. The active filter operates at 15 kHz and the ripple in the magnetic field gradient is 5 ppm. Figure 2 shows the measured mean current long-term stability for the 6 quadrupole supply and indicates a 2 ppm variation for a room temperature change of 5 °C.

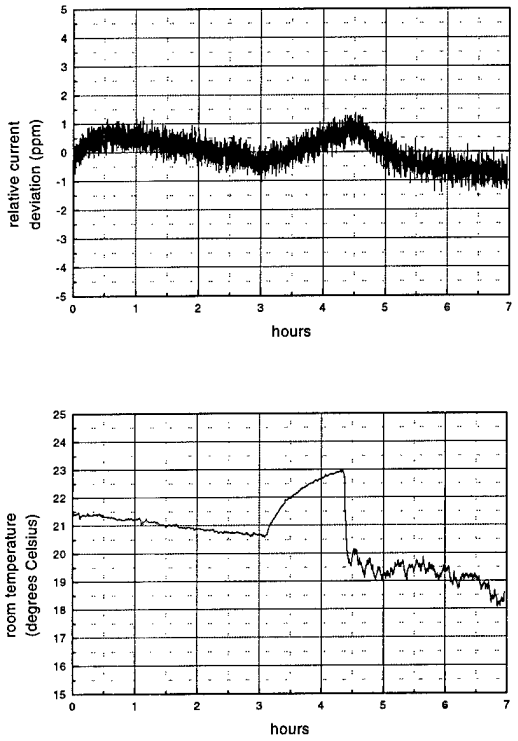



Figure 2: load current deviation (top) and room temperature (bottom) measured during a long time-stability test of the six-quadrupole power supply.

Calibration and operation of all these power supplies guarantee a maximum difference of 1 mV between written and read set point, which corresponds to $10^{-5}$ precision in the current repeatability.

The 30 storage ring steering magnet power supplies are bipolar, series-transistor controlled with ± 10 A, 10 V maximum output. The betatron tune set, needed for significant current accumulation at 120 MeV, and the high current orbit stability impose strong requirements on current stability and ripple for these supplies. The high energy orbit is adjusted between injections to 20 μm to comply to the beam line user needs. The steering coil supplies are stable to 0.1 % and the 180 Hz ripple is 2 mA, which corresponds to 1 bit of the 12-bit DAC.

## 4 CONCLUSIONS

The LNLS accelerator power supplies have been in operation for over 1 year. During this period, the actual operation parameters and conditions have been defined and the power supplies adjusted accordingly, when necessary. In particular, the injection and accumulation at low energy have demanded stringent new operating conditions for the power supplies, which were designed mainly according to high current specifications. At present, the system performance is adequate and reliable for all the needed types of operation of the accelerators: cycling, injection, low energy accumulation and storing.

## REFERENCES

[1] A. R. Rodrigues et al. "LNLS Commissioning and Operation". In these proceedings.

[2] D. Wisnivesky et al. "Power Supply System for the LNLS Magnets". Proceedings of the 5th European Particle Accelerator Conference EPAC 96, p. 2349.

[3] A. R. Rodrigues et al. "Ramping Efficiency Studies in the LNLS Synchrotron Light Source". In these proceedings.

[4] J. A. Pomílio, D. Wisnivesky and A. C. Lira "A New Topology for the Bending Magnets Power Supply at LNLS". IEEE Transactions on Nuclear Science vol. 39, N. 5. P 1506-1511, Oct. 1992.

[5] D. Wisnivesky and A. C. Lira "A New High-Precision Current Supply for Magnets". IEEE Transactions on Nuclear Science, vol. 42 N. 4, August 1995.

# A HIGH CURRENT SHUNT REGULATOR FOR QUADRUPOLE MAGNETS IN PLS 2GeV STORAGE RING

S.H. Nam, J. H. Suh, K. M. Ha, J. Y. Huang, and I. S. Ko
Pohang Accelerator Laboratory, POSTECH, Pohang 790-784, Korea

*Abstract*

Total 144 quadrupole magnets are installed in the PLS. The magnets are connected in series with groups of two or 24. Each group is powered by a high-precision constant-current DC power supply. For the purpose of the beam based alignment of beam position monitors in the PLS, it is necessary to adjust the current of each quadrupole independently. To achieve this, a high current shunt regulator is designed. It can shunt a maximum 50 A of the quadrupole magnet current. The shunt regulator is programmable and the current amplitude can be varied linearly with a 12-bit resolution. Power transistors are used in the current shunt regulator. The operation of transistors is in linear region. The RS232C protocol is used for remote control and status report of the shunt regulator to the main control centre of the PLS. Preliminary result indicates that the calibration accuracy of the beam position monitor can be achievable in less than 10μm.

## 1 INTRODUCTION

In an electron storage ring, the luminosity and performances of stored beam are mainly determined by precise alignment of quadrupole magnets. The stored beam is designed to pass through the centre of quadrupole magnets. Even though quadrupole magnets of the PLS storage ring are carefully aligned, there still exists residual offsets between beam position monitors (BPM) and the magnetic centre of the quadrupole magnets. To measure and correct this offset, a method of the beam based alignment (BBA) is commonly used [1]. However, in the PLS storage ring, quadrupole magnets are grouped by two or 24 and connected in series to their power supplies. So the individual control of each quadrupole magnet current is not possible. By introducing a high current transistor shunt regulator, the individual control of magnet current for BBA is successfully achieved.

## 2 PLS QUADRUPOLE MAGNET

Quadrupole magnets in the PLS storage ring are categorised in 6 different types: Q1, Q2, Q3, Q4, Q5, and Q6. The PLS storage ring consists of 12 superperiods, and two magnets of each quadrupole type are installed in a superperiod. Hence, there are total 144 quadrupole magnets in the storage ring. For Q1, Q2, and Q3 magnets, two magnets in each superperiod are grouped together. For Q4, Q5, and Q6 magnets, all 24 magnets are grouped. Each group is connected in series and powered by single power supply. Therefore, total number of power supplies for quadrupole magnets is 39. Since the quadrupole magnets are connected in series in groups of two or 24, the current of individual magnet is not controllable. However, individual control of the quadrupole magnet current is required for the BBA operation. In Table 1, important characteristics of quadrupole magnets are listed. A resistance of magnet is given in a column of ***R***, and a maximum output voltage of magnet power supply is given in a ***V Max.*** column. Current (I) and voltage drop (V Drop) in Table 1 are values for a 2 GeV operation.

Table 1: Characteristics of PLS Quadrupole Magnets

| Mag -net | Qty. | R [Ω] | V Max. [V] | I [A] | V Drop [V] |
|---|---|---|---|---|---|
| Q1 | 24 | 0.257 | 83.9 | 35.5 | 9.10 |
| Q2 | 24 | 0.429 | 133.5 | 83.4 | 35.76 |
| Q3 | 24 | 0.318 | 101.4 | 95.85 | 30.43 |
| Q4 | 24 | 0.021 | 326.2 | 339.7 | 6.97 |
| Q5 | 24 | 0.027 | 421.7 | 415.7 | 11.16 |
| Q6 | 24 | 0.016 | 268.0 | 186.0 | 3.05 |

## 3 SHUNT REGULATOR

### *3.1 Design Approach*

A shunt regulator is typically connected in parallel with a magnet to shunt a desired current while maintaining the neighbouring magnet current constant. Important design requirements of the current shunt regulator are following: The regulator

- shunts 5 to 10 % of magnet current,
- should be able to adjust each quadrupole current independently,
- has a remote control capability,
- maintains stability (<±0.005%) and ripple (<±0.05%) of magnet main current while operating the shunt,
- should not kill the stored beam from turn on and off transients.

As listed in Table 1, the magnet current varies from 36 A to 416 A. We select two types of the shunt. They are 15 and 50 ampere shunts that can commonly accommodate the required shunt current. The 15 A shunt is for Q1, Q2, and Q3 quadrupoles. The 15 A unit is also used for Q6 because of its low voltage drop. The 50 A unit is used for Q4 and Q5 quadrupoles. Except the Q6 unit, the regulators are capable of shunting the required current in 2.0 GeV as well as 2.5 GeV operations. For the shunt regulator, a power transistor is employed as a linear switching device. The transistor operates in its linear

0-7803-4376-X/98 /$10.00 © 1998 IEEE

active region. In this design, it is easy to control the current amplitude remotely. Quadrupole magnet power supplies have the stability and the ripple better than ±0.005 % and ±0.5 %, respectively. The power supply has its own controlling ability to maintain the required stability and ripple. As long as the shunt regulator current varies within the main current dynamics, the power supply preserves its characteristics. However, during turn on and off of the shunt, transients exist and may affect the main current dynamics. Therefore, it is necessary to adopt slow start and stop functions in the shunt control circuit which can be realized with hardware as well as software routines. The shunt circuit also has a current regulation function by using a current feedback loop. The transient phenomenon appears more significantly on Q1, Q2, and Q3 than Q4, Q5, and Q6. This is because, for the Q1, Q2, and Q3, small number of magnets is connected in series and thus shunt current variations can easily be detected by the power supply controller. Since the operating voltage of quadrupoles is as high as 422 V as listed in Table 1, an electrical isolation of the shunt circuit is considered in the design of the regulator.

*3.2 Configuration of Shunt Regulator*

A detailed circuit of the transistor shunt regulator is shown in Fig. 1. The power module that handles the shunt current is consisted of fifteen MJ5015 transistors. The transistor has 15 A, 120 V, 180 W specifications. Its typical current gain is about 70. The power module is mounted on a heat sink and electrically isolated from the metal case. Forced air cooling is selected to simplify the electrical isolation. In order to balance current sharing among transistors, a high precision 0.1Ω resistor is connected in series with each transistor. A free-wheeling diode module is also connected in parallel with the magnet. The transistors in the power module are commonly driven by a Darlington pair. The shunt current amplitude is detected by a DC current transducer (LAM Module LA50-P) and a bulk metal foil resistor (Vishay VHP-3, 100 Ω). The current transducer has an accuracy of ±0.5 %, an isolation voltage of 2 $kV_{rms}$, and a linearity of ±0.1 %. The resistor has a tolerance of ±0.01 %, and a temperature coefficient of resistance of ±5 ppm/°C. The sampled current is amplified and fed back to an error amplifier. At the amplifier, the feedback current signal is compared with a DAC reference. Then, the error amplifier output drives the Darlington pair to achieve the current regulation of the shunt. A gain-bandwidth product of the error amplifier is chosen as 1.592 kHz in order to minimise a high frequency noise response of the shunt controller. A high frequency switching noise exists in the main power supply current. There is also a soft start circuit when the shunt is turned on. This reduces turn-on transients that can influence the control dynamics of the main power supply. The soft start can also be realized by a control software of DAC reference.

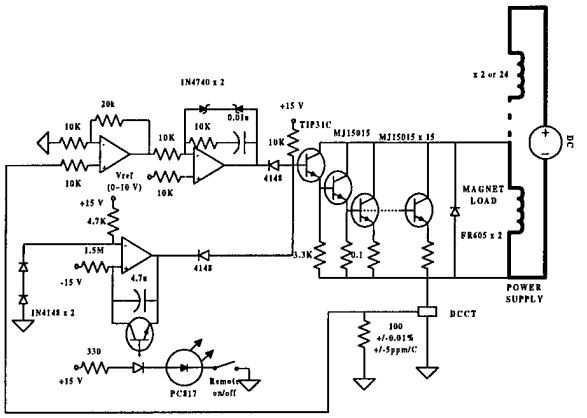


Figure 1: Transistor shunt regulator circuit.

The whole shunt assembly that includes the power module as well as the feedback control board is floated and electrically isolated. The electrical isolation between internal and external circuits is achieved by using PC817 photo-couplers (5 $kV_{rms}$ isolation), ISO122P isolation amplifiers (1.5 $kV_{rms}$ isolation), and transformers. In the shunt regulator, there are also self protection functions such as over-current and over-heating. It also contains a 12-bit DAC to generate a current set value. These functions are not shown in Fig. 1.

*3.2 Shunt Regulator Controller*

Each shunt regulator controller is assembled as a separate unit. The controller sends various commands to the shunt via a parallel data bus. It also receives a current reading and status from the shunt. In addition, the controller communicates with the PLS main control computer via a RS232C port. A TMS320C32 DSP is used for the controller. It can function as an independent processor unit, and local as well as remote operations are possible.

## 4 EXPERIMENTAL RESULTS

A plot of Q2 quadrupole current change is shown in Fig. 2 when the shunt regulator is turned on and off. The result is obtained at the 2 GeV operation. At this energy, the Q2 current is 83.352 A. The shunt current amplitude in Fig. 2 is 0.871 A or 1.04 % of Q2 current. As shown in the figure, there exist transients at the turn on and off instances. However, the transients do not kill or significantly affect the stored beam current. With the shunt operation, the magnet current stability is maintained except during the transients. The stability requirement of quadrupole current is better than ±0.005 %.

A ripple oscillograph of the Q2 current is shown in Fig. 3. In the figure, two waveforms are compared. The top ripple is measured when the shunt is off and the bottom is measured when the shunt is on. The waveforms are obtained during 2.0 GeV beam operation. The quadrupole current is 83.43 A, and the shunt current is 8.75 A which shunts 10.48 % of the quadrupole current. From Fig. 3, we can realize that no considerable ripple

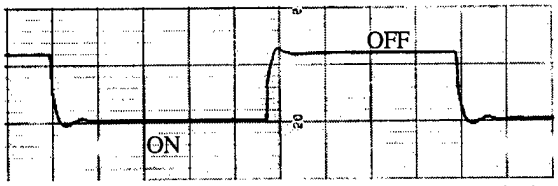



Figure 2: Variation of Q2 quadrupole current during a shunt regulator operation (3.0 sec/Div.). The Q2 current is 83.352 A with shunt-off and 82.481 A with shunt-on.

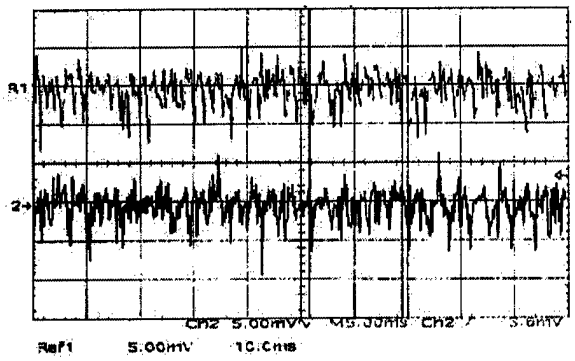


Figure 3: Ripple of Q2 quadrupole current (0.075 A/Div., 5 ms/Div.). Top: Shunt off, Bottom: Shunt on.

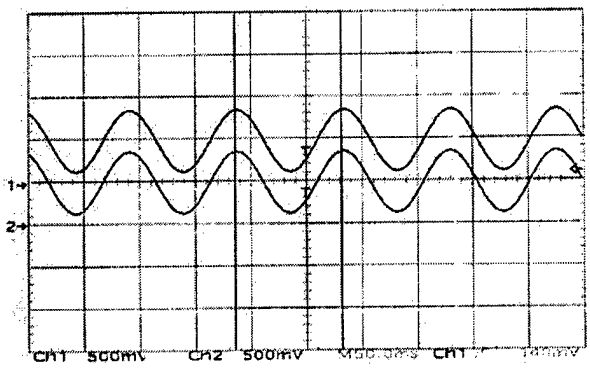


Figure 4: Comparison of a command signal (top) and a shunt current (bottom) of Q2 at a 10 Hz AC operation. Q2 current: 83.36 A, DC offset shunt current: 1.22 A, AC current: 1.8 A.

increment is detected. The ripple requirement of quadrupole is better than ±0.005 %.

The shunt can be operated in DC as well as AC modes. Even though the AC mode operation is not necessary for the BBA, we test the shunt in the AC mode to extend its capability that can be useful for other applications. In Fig. 4, a result of the AC mode operation is shown. The top wave in the figure is a shunt command, and the bottom is the measured shunt output current. As seen in the figure, the shunt current follows the command signal very smoothly and precisely. Due to the time constant limit of the quadrupole magnet, a useful operating frequency is expected to be less than 10 Hz. During the AC mode operation, a ripple is also measured. The AC shunt current gives some effect on the ripple content of the main magnet current. About 10% of the shunt current is superposed on the ripple.

In the PLS, total 108 BPMs are installed to collect beam position data. Preliminary measurement of BPM offset with the shunt regulator shows better than a 10 μm calibration accuracy. The enhancement of BPM calibration is also beneficial to the reduction of the closed orbit distortion. At present, the overall closed orbit distortion is no better than 500 μm (rms). Our goal is to enhance the electrical offset of all BPM less than 10 μm (rms) and also the closed orbit distortion less than 50 μm (rms) [2].

## 5 CONCLUSION

In order to enhance a calibration accuracy of BPM in the PLS storage ring, a BBA system is developed and installed. To realize the BBA system, it is required to control each quadrupole magnet current independently. However, the quadrupoles are grouped and connected in series, and each group is powered by a power supply. Therefore, a transistor-type high current shunt regulator is developed to perform the BBA function. It can shunt more than 10 % of main magnet current while maintaining current specifications. The shunt regulator shows satisfactory performance during preliminary tests. It also performs nicely in an AC mode operation. Preliminary calibration of a BPM using the shunt is also carried out. The result shows that a BPM calibration accuracy of less than 10 μm (rms) can be achievable. The result also indicates that the closed orbit distortion of less than 50 μm (rms) is also possible. The 50 μm (rms) is about an order of magnitude improvement from the present value of closed orbit distortion.

## 6 ACKNOWLEDGEMENTS

This work is supported by POSCO and MOST of Korea. We are grateful to our colleagues, especially Mr. S. H. Jung, and Mr. S. H. Han at PAL, for their support during the work.

## REFERENCES

[1] I. Barnett et. al., "Dynamic Beam Based Alignment," 2nd European Workshop on Beam Diagnostics and Instrumentation for Particle Accelerators, DESY M-95 07, pp. 38, 1995.

[2] J.Y. Huang, D.H. Jung, S.H. Nam, M. Yoon, I.S. Ko, "Beam Based Offset Calibration of the PLS BPM," in this proceeding.

# A UNIQUE POWER SUPPLY FOR THE PEPII KLYSTRON AT SLAC

R. Cassel & M. N. Nguyen [†], Stanford Linear Accelerator Center

*Abstract*

Each of the eight 1.2 MW RF klystrons for the PEP-II storage rings require a 2.5 MVA DC power supply of 83 Kv at 23 amps. The design for the supply was base on three factors low cost, small size to fit existing substation pads, and good protection against damage to the klystron including klystron gun arcs. The supply uses a 12 pulse 12.5 KV primary thyristor "star point controller" with primary filter inductor to provide rapid voltage control, good voltage regulation, and fast turn off during klystron tube faults. The supply also uses a unique secondary rectifier, filter capacitor configuration to minimize the energy available under a klystron fault. The voltage control is from 0-90 KV with a regulation of <0.1% and voltage ripple of < 1% P-P, (< 0.2% RMS.) above 60 KV. The supply utilizes a thyristor crowbar, which under a klystron tube arc limits the energy in the klystron arc to < 5 joules. If the thyristor crowbar is disabled the energy supplied is < 40 joules into the arc. The size of the supply was reduced small enough to fit the existing PEP transformer yard pads. The cost of the power supply was < $140 per KVA.

## 1 DESIGN CONSIDERATIONS

The SLAC PEP-II storage rings require eight 1.2 MW RF klystrons powered by eight 2.5 MVA DC power supply at 83 Kv, 23 amps. The design consideration besides low cost were: 1) Small size so as to fit on existing PEP transformer pads. 2) Good protection against damage to the klystron from RF and klystron gun arcs. 3) Rapid Voltage adjustment to accommodate changes in beam loading and rapped conditioning of the cavities. 4) Good voltage regulation for stability with the stored beam. In addition the power supply was designed to accommodate a Depressed Collector Klystron if it were to be developed for power efficiency
reasons

## 2 CONFIGURATION SELECTION

The supply configuration chosen was the use of a Primary SCR controlled rectifier operating at 12.5kv the existing site wide distribution voltage. This chose reduces the size of the Power supply over more conventional VVT adjusted power supplies as well as provides for fast voltage adjustment and fault protection. The SCR's were configured in the so-called star point controller configuration with the filter inductor in the primary. A configuration commonly used in Europe in fusion research [1]. This configuration is ideally suited for an inductive capacitor filtered supply were bypassing of the stored energy in the filter inductor is important.
The rectifier configuration is a unique arrangement which prevent/ reduces the dumping of the stored energy in the filter capacitor into the klystron under a klystron arc Figure 1.

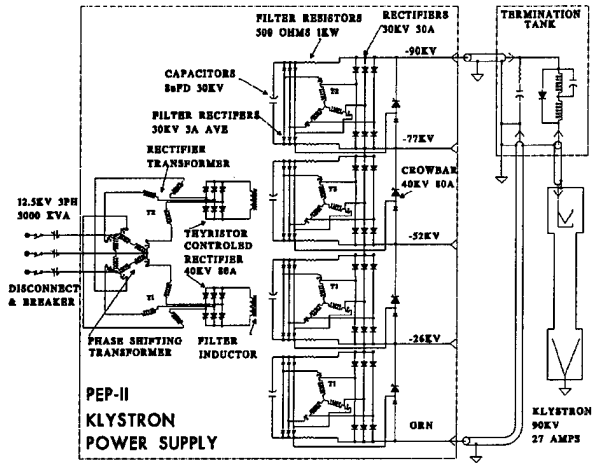



Figure 1: Power supply schematic

The primary 12.5Kv enters without a Manual Load breaker disconnect used for Safety lock and tag disconnection for maintenance. The supply is energized by way of a full fault rated Vacuum breaker used as a contactor. The breaker has independent overcurrent relaying and transformer sudden pressure lockout in case of a transformer or SCR fault. To reduce the amount of power line harmonics to meet the industrial standards a 12-pulse configuration was chosen. To accomplish the 12-phase operation with a Wye connected primary controller a phase shifting transformer is used. The use of a delta with extension windings to produce the ±15° was selected because the phase shifted output voltages are only 4% larger than the incoming line voltages. The nominal size of the phase shifting transformer is less than 15% of the full load MVA. The rectifier transformers consist of two, open Wye primary dual Wye secondaries, transformers used to step up the voltage. The SCR

[†] *Work supported by DOE, contract DE-AC03-76SF0051

0-7803-4376-X/98/$10.00 © 1998 IEEE

controller is connected to the open Wye, with the filter inductor on the primary side. The secondary windings are taped with main power rectifier connected in a full wave bridge configuration to the full current rated taps The 5% voltage extension is used by the filtering rectifier which is a low current full wave bridge configuration. The filter rectifiers is loaded by the filter capacitor, which is coupled to the output load by way of high ohmage resistors which limits the current in the filter rectifier to approximately 1 amp maximum. This is enough current to bleed off the voltage on the filter capacitor to allow for complete voltage filtering of the supply at 60Kv output voltage.

Figures 2 & Figure 3 show the output voltage, filter inductor ripple voltage, and the secondary transformers line to line voltage waveforms.

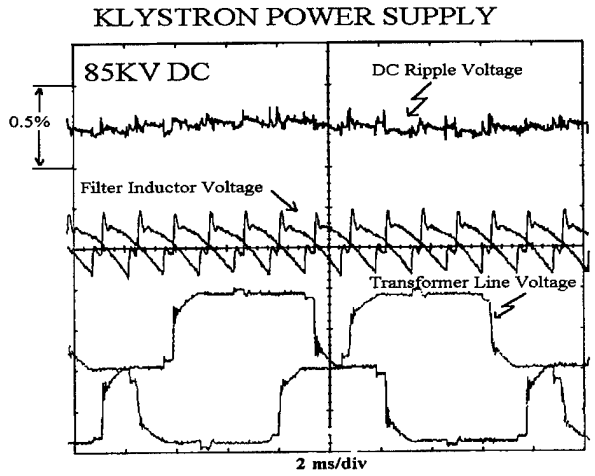



Figure 2: Output ripple 85Kv

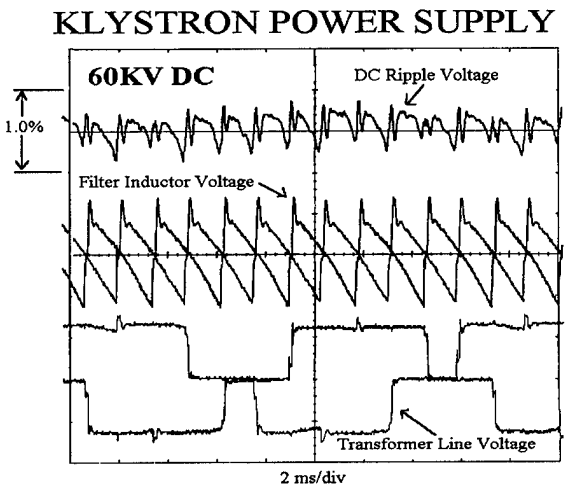



Figure 3: Output ripple at 60KV

The output voltage ripple is greater at 60kv due to the larger ripple voltage across the filter inductor caused by phasing back the SCR's. The ripple voltage is still less than the specifications of 1% Peak to Peak voltage ripple.

A SCR Crowbar is connected across the output rectifier to crowbar the supply in the event of a klystron arc.

## 3 KLYSTRON ARC PROTECTION

Protection of the klystron tube under a klystron arc is of extremely important. The klystron is very expensive and will probably arc at some time. To protect the klystron under arc condition the joules delivered by the power supply should not exceed 60 Joules or an $I^2t$ of 40 $amp^2seconds$ [2]. In conventional supplies this is accomplished by use of fast crowbar and a series resistor. The series resistor is typically 10-50 ohms which results in vary large power losses at high voltages. If the crowbar fails in anyway the klystron would be destroyed because of the large amount of energy involved.

With the new design although there is a slower SCR crowbar, failure of the crowbar or any other single point failure will not result in the destruction of the klystron. The main stored energy from the capacitor back is isolated by use of the filter capacitor and isolating resistors which in the event of a crowbar failure results in only 50 amps for 4 milliseconds and a $I^2t$ of <15 $amp^2seconds$ with less than 40 Joules in a arc to the klystron. The Primary star point control with filter inductor allows for the bypass of the filter inductors energy under klystron fault conditions by turn on both SCR's in one phase and turning off all the other SCR's. The result is the isolating of the load from the power line and the discharge of the energy in the filter inductor into its resistance. The result of an arc is seen in figure 4 on the klystron and figure 5 on the primary line current.

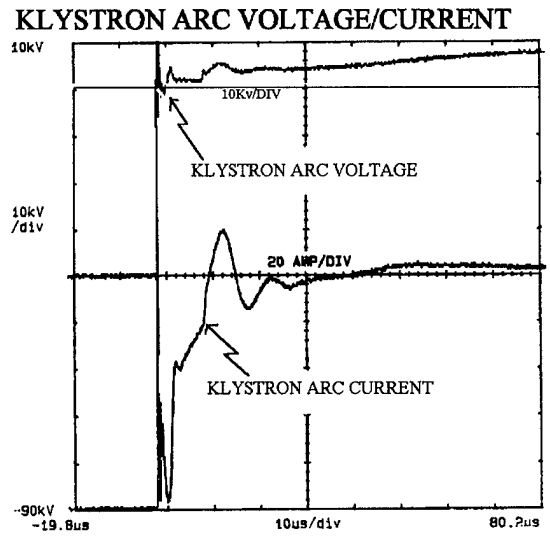



Figure 4: Klystron Arc current & voltage

The distribution cable discharge current is reduced as well as a forced current zero by the use of small 200 uhy inductors in the termination tank. With the crowbar his combination allows less than 5 joules to reach the

klystron and less than 20 joules without the crowbar operating. The crowbar has a delay time of approximately 10 microseconds before it conducts current.

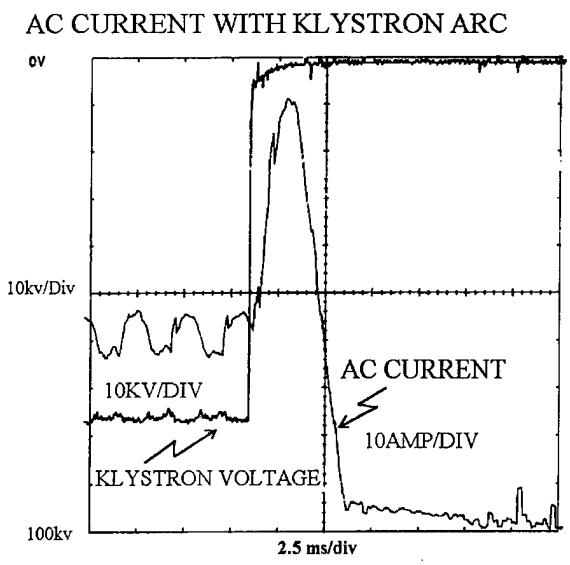



Figure 5: Klystron arc line current

When the klystron arcs the primary current rate of rise is limited by the primary filter inductor until the inductor is bypassed and the primary SCR's are turned off. The complete interruption of current on the primary side last from 4 to 8 milliseconds depending on the exact time of the arc with respect to the firing of the SCR's. As you can see the primary current only double under this fault condition for 2 milliseconds.

## 4 POWER SUPPLY SIZE

Because of size constraints and the fact that all the components would be at high voltage and high power the SCR Primary controller and SCR Crowbar were mounted in the transformer oil tank in isolated oil tanks. The tanks have oil to oil high voltage feed through to prevent cross contamination of the oil in the event a crowbar or SCR stack would need maintenance.

The crowbar tank consists of 4 SCR stacks with snubber network to match the output cable impedance. In addition there are two voltage dividers to monitor the high voltage output.

The SCR Primary control tank consist of 12 SCR stacks with 12 snubber networks to limit the rate of rise of voltage and damp the stray capacitance ringing.

The transformer tank contains two filter inductors two power transformers, one phase shifting transformer, 4 filter diode rectifier stack, 4 filter capacitors, 8 filter resistors loads, and 4 power diode rectifier stacks. See figure 6.

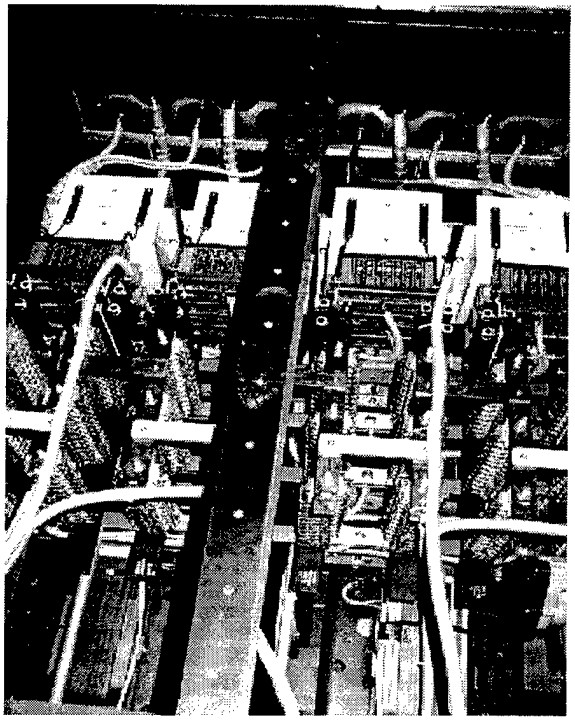


Figure 6: Internal power supply tank parts

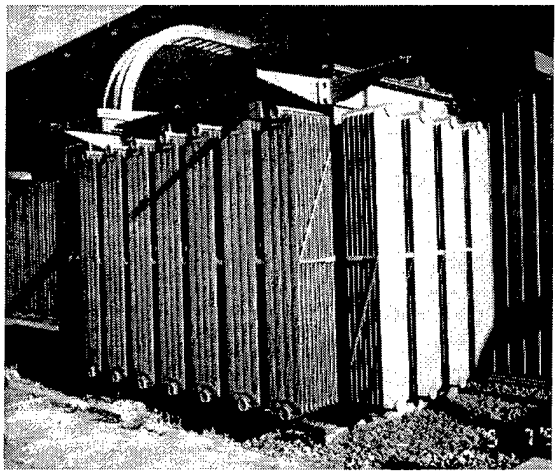


Figure 7: Power supply installation

crowbar was manufactured and tested by SLAC and installed by NWL into their transformer tanks.

## REFERENCES

[1] 'HV-Power Supply for Neutral-Injection Experiments Wendelstein VII and ASDEX' by D Hrabal, R. Kunze, W. Weigand, Proceedings of the 8th Symposium on Engineering Problems of Fusion Research, IEEE Pub No. 79CH1441-5 NPS. Page 1005-1009

[2] 'Installing and Operating Klystron YK1360' PHILIPS manual, Issue #1 May 1996, Rev. Sept 1996 page 11.

# PEP II 16-CHANNEL CORRECTOR CONTROLLER USING BITBUS

R. Olsen, Stanford Linear Accelerator Center, P.O. Box 4349, Stanford, CA 94309

*Abstract*

A 16-channel controller has been implemented to control the PEP II corrector switching power converters. The design and performance are discussed.

## 1 INTRODUCTION

The PEP II injection and storage rings require more than 1000 corrector magnets. In order to economically meet this requirement, a new power converter termed MCOR12 was designed[1]. It is equipped with 16 switching power converter modules rated at +/- 50 volts, 12 amperes. A bulk power converter supplies the raw DC power to a number of MCOR's. The 16 switching converters are housed in a 17-slot, 6U Eurocard crate with non-standard module spacing. The 17th slot is standard single-width, and is occupied by the controller module. Control of each power converter is by means of a control voltage input with a range of +10 to -10 volts for full scale current of each polarity. Readback is provided by primary and secondary shunt circuits with outputs of the same voltage range. A status bit is provided from each converter to indicate that the converter is on-line, and the controller provides a reset and inhibit function common to all converters.

## 2 DESIGN REQUIREMENTS

A fundamental requirement of the controller was that it be able to ramp the 16 channels simultaneously on demand using a cosine function after the appropriate control information had been downloaded. This requirement, to a substantial degree, determined the architecture of the system and the use of a DSP to perform the main control functions. Communication was to be at a high level, and setpoints would be specified using current and timespan. Accuracy of the control voltage outputs and shunt readbacks was to be 0.1% minimum.

## 3 COMMUNICATION PROTOCOL

Communication with the controller is by means of BITBUS, a subset of SDLC [2]. The individual packet length is limited to 43 bytes due to limitations in the 8044 on-chip SRAM. Superimposed on the basic protocol is a high-level protocol devised by the SLAC controls group [3].

This protocol provides the mechanism to send commands to multiple channels in each message, and to send multiple packets in a single message block. The protocal is designed to make maximum use of available bandwith in the signalling channel. In order to effectively synchronize the ramp function between multiple controllers, hardware ramp start, ramp stop, and reset lines are included in the BITBUS interconnect cable.

## 4 ANALOG CONTROL VOLTAGE OUTPUTS

Severe constraints on available volume to package the requesite functions dictated that one DAC per channel, although the simplest configuration, was not a viable alternative. Thus, the configuration chosen was a single 16-bit DAC feeding 16 individual sample and holds through a 16-channel isolation switch. The 16-channels are refreshed once per millisecond using a serial port on the TMS320C31. The serial data stream contains a 16-bit data field, a 4-bit address field, and a 4-bit control field. The control field selects the main DAC or one of two 12-bit DAC's used to adjust the offset and gain of the main DAC. The data stream is demultiplexed by a pASIC which contains all the logic necessary to control the refresh and calibration functions.

## 5 ANALOG READBACKS

### *5.1 Data Aquisition*

There are a total of 56 readback channels in four blocks. These are:

1) 16 control voltages
2) 16 main shunts
3) 16 secondary shunts
4) 8 calibration functions

These signals are carried through 16 to 1 FET switch multiplexers, to an instrumentation amplifier. This amplifier feeds the selected signal to a CS5016 analog to digital converter. This ADC is a self-calibrating stand-alone system which is able to maintain high accuracy over a wide temperature. Control of the analog data aquisition is under control of a subroutine executed in ISR1 at the 1 ms. interval. One sample is acquired each millisecond. Multiple samples are aquired for each channel. To capture all channels requires approximately 2 seconds.

Work supported by the Department of Energy under contract No. DE-AC03-76SF00515

0-7803-4376-X/98/$10.00 © 1998 IEEE

*5.2 Calibration and Monitoring*

In addition to sampling the 48 signal channels, the following parameters are converted

1) + reference
2) reference inverted
3) ground
4) control DAC output
5) reference sample and hold
6) ground fault setpoint
7) ground current
8) bulk power converter voltage

By using a combination of the first five parameters, the offset and gain of each channel is dynamically controlled. Since the control voltage outputs must remain fixed, a 17th sample and hold is provided such that a first order correction may be performed based on the gain of the sample and hold which is approximately 0.9997

## 6 PROCESSORS

The controller uses two processors. An INTEL 8044 is used as the BITBUS slave, and a TI TMS320C31 is used to provide control and computational functions and to refresh the sample and holds.

*6.1 TMS320C31 Main Processor*

The TMS320C31 has a number of features which made it an attractive choice. It is a 32-bit floating point processor with a 32 Mhz clock with an instuction cycle time of 120 ns. (in this application). It has 4 external hardware interrupts, an on-chip boot loader, a serial port, two timers, a DMA channel, and 2K of on-chip SRAM. All of these features were used in the implementation of the multi-channel BITBUS controller. The front panel holds 17 LEDS which display status information and two 9-pin connectors for two serial ports for local control and status display.

*6.1.1 Basic System Organization*

The system refreshes the sample and holds once per ms. by a service routine ISR1 on interrupt level 1 under control of TIMER1. All other periodic functions are performed by the same routine. ISR1 executes from internal SRAM and refreshes the sample and holds over the serial port using the DMA channel. In this way, bandwidth on the main memory bus is conserved. All memory access and control functions are performed by a pASIC.

*6.1.2 Boot Loading the Controller*

The controller is equipped with two 64K*8 EPROM's in the region 400000h-41ffffh of 'C31 address space. In the current implementation, one holds the code for the 'C31 the other code for the 8044 although overlap is possible. Boot loading is initiated by a reset or power-up. After reset, the shared SRAM is mapped to f00000h, the 8044 is held reset, the 'C31 is in the boot loader mode, and an interrupt is applied to INT1 which initiates 8-bit mode to 400000h. Upon completion of the 'C31 load cycle, control is passed to a routine in the on-chip SRAM which remaps the SRAM to start at location 00h and branches execution to the SYSINIT routine in main memory. With the 8044 held reset, the 'C31 has access to its program store which is first cleared, then loaded with the executable code copied from the EPROM. The 8044 is then released from the reset state which gives it control of its program store and it then proceeds through its initialization.

*6.1.3 Inter-Processor Communication*

The two processors exchange messages by means of shared memory. The controller is equipped with 32K of SRAM in the 'C31 address space. The lower 32K bytes of 8044 data store is mapped into the top 8K words in the 'C31 address space. The 8044, of neccessity, operates asynchronously. When the 8044 accesses the shared memory space, a hold request is issued to the 'C31 which replies with a hold acknowledge. Since it cannot be guaranteed that memory access will be granted in the time required by the 8044 bus cycle, a dummy read always prefixes any access. Since the 8044 only requires shared memory access to transfer blocks of data, a hold request will not be relinquished at the end of the current cycle. For each access to shared memory, a release timer is reset. If no further accesses are made, the timer will time-out in 340 us. Memory is normally released by writing to a specific memory location. The timer is provided to allow the 'C31 to regain control in the event of a failure in the 8044. Several hardware flags are provided which are used to synchronize message passing without the neccessity of accessing shared memory.

*6.2 I8044 BITBUS Slave processor*

An INTEL 8044 functions as the BITBUS slave. This device consists of an 8051 core processor along with the serial port hardware and control firmware in an on-chip PROM necessary to implement the BITBUS protocol. It has a Harvard architecture, with a program store and a data store. The program store is read-only, and no instuctions are provided which can write to it. The 8044 has no capabilty for either WAIT or HOLD states. In addition, severe constraints in on-chip ram restrict the message buffer size to two 43-byte buffers.

In this application, the program store is an SRAM which is loaded from the TMS320C31 during the boot loading process. In order to facilitate debugging using an emulator, the chip is configured to use external memory only. The executeable code was copied from the the on-chip prom and is loaded to program store during the boot loading proceedure.

*6.2.1 Basic System Organization*

The 8044 runs under control of the INTEL DCX51 operating system. Four tasks are defined. TASK0 performs the serial I/O and the BITBUS protocol and is hidden from the user. TASK1 is invoked by TASK0 when a message has been received. It copies the message from the buffer in the memory pool RAM, saves it in 1 of 16 temporary buffers in data store, and deallocates the buffer to return it to the memory pool. TASK3 is invoked from the 'C31 by ISR1 to test for the presence of any waiting messages. If a message is waiting, it will be copied to the shared memory. TASK2 is is invoked by the 'C31 when processing of the current message is completed. The reply is copied from shared memory the an assigned buffer in the memory pool, and a request is sent to TASK0 to send the reply message to the master.

## 7 INTERLOCKS

*7.1 Power Converter Module Interlocks*

The MCOR12 system is provided with a number of interlocks to assure safe and reliable operation. Each power converter module is equipped with a latching over-current and under voltage detector. An over-current failure in a converter is latched and the status bit returned to the controller is set

*7.2 Controller Interlocks*

A daughter board is used to provide controller interlock functions. This board contains a ground fault detector and the controller fault latches.

*7.2.1 Under Voltage*

The bulk power converter voltage is monitored and returned to the control system. In addition, the power converter must be reset with a minimum voltage present on the supply bus before the converter will become active

*7.2.2 Ground Current*

Each MCOR12 has a ground current resistor. This current is monitored and returned to the control system.

*7.2.2 Ground Fault*

The ground fault detector will latch a fault if this current exceeds a preset value.

*7.3 System Interlock Handling*

When an interlock occurs, the appropriate bit is set in the controller status word. The next message requesting device status will inform the system of the failure. A message RESET INTERLOCK may be sent to reset. If the reset is not reset, the affected channel(s) will remain off-line. A successful reset will return them to service.

## ACKNOWLEDGEMENT

The authour wishes to express gratitude to Dave Brown, Mike Brown, Mark Crane, Linda Hendrickson, Tom Himel, Dave Macnair, Jeff Olsen, and Lee Ann Yasukawa for their able assistance in finding a number seemingly intractable problems. We also wish to express our appreciation to Len Genova for his continued support of this project.

## REFERENCES

[1] G.E. Leyh, A.R. Donaldson, SLAC, Stanford CA 94309

[2] "8-Bit Embedded Controllers", Intel order number 270645

[3] Lee Ann Yasukawa, "PEP II BITBUS Power Supply Interface Control Document", SLAC internal document

# NEW POWER SUPPLY CONTROL INTERFACE AND ENERGY RAMPING DESIGN IN SRRC

C. S. Chen, Jenny Chen, J. S. Chen, C. J. Wang, K. B. Liu, C. Y. Liu, J. T. Sheu, K. T. Hsu
Synchrotron Radiation Research Center
No. 1 R&D Road VI, Hsinchu Science-Based Industrial Park, Hsinchu, Taiwan, R.O.C.

*Abstract*

For the purpose of lattice optimization, eighteen individual quadrupole power supplies was installed in the SRRC storage ring in March 1997 to replace the three quadrupole family power supplies. In order to accomodate newly installed and already existed power supplies, the control interface of Taiwan Light Source (TLS) has been rejuvenated recently. The new control interface has improved drastically on control speed in comparison with the existed interface. Operation of the power supply system from device level to system level is reorganized to make control and access easier. This new control interface provides capability from complex operation such as lattice file loading, magnet degaussing, to file energy ramping scheme, etc. Performance of this power supply control interface including hardware components and software applications is presented.

## 1 INTRODUCTION

The new power supply control interface implemented for the storage ring quadrupole magnet in SRRC is important task within March 1997. The new power supply control interface has been integrated into SRRC control system, providing remote control function: the digital input and output for power supply status control and reading, the analog input and output for power supply current setting and reading, and other complex operation. This new power supply control interface is a VMEbus based crate containing the digital-to-analog converter, analog-to-digital converter, digital input and output modules. All these modules, together with a PowerPC VME cpu module, are running with LynxOS real time operation system.

## 2 SYSTEM DESCRIPTIONS

The new control interface is a part of the SRRC control system, Figure 1 shows the environment of the new power supply control interface in SRRC. Hereinafter, we will illustrate the new control interface hardware configuration and software structure with some important considerations to accommodate "new" and "old" power supplies control interface [1].

### *2.1 TLS power supplies control interfaces*

There are three VME crates to connect all power supplies of TLS as shown in figure 1. In the VME crate #1, it is composed of digital-to-analog (DAC) output modules, analog-to-digital input (ADC) module, digital input and output boards, and a powerful new generation VMEbus processor module. The DAC provides analog output with 16 bits high resolution, it is used for power supply output current control. A high performance 16 bits ADC board is chosen to monitor power supply output current, the ADC module board provides wide dynamic range, high analog input channel density, and many other operating modes. Digital input and output board are software configured to control power supply operation and status monitor. A new and powerful cpu module is introduced to improve the control interface performance in terms of speed. We use a GPIB interface in crate #2 to control the power supply for dipole, sxtupole, and a Q4 quadrupole. About eighty correction power supply are controlled and monitored by the DAC and ADC modules in crate #3. The digital control for correction power supply operation is in crate #2.

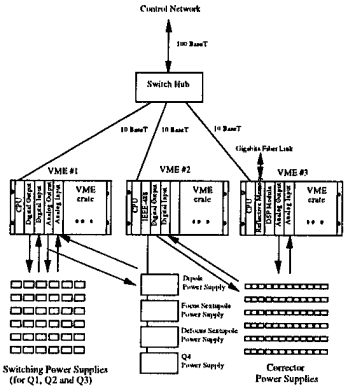



Figure: 1 TLS power supply control environment

### *2.2 The control software*

The SRRC control environment is a two-layer network connected via Ethernet. The upper layer has several workstations and a control server, the lower layer is VME crate based intelligent local controller interfacing with various devices. Low level control functions for power supplies are built in VME crates. These functions include setting and reading tasks, interpolation, and slew rate control. There are also equipped in dipole, quadrupole, sextupole power supplies. Reading data is

0-7803-4376-X/98 /$10.00 © 1998 IEEE

periodically updated to upper layer computers in every 100 msec. Setting is issued by the high level applications. Power supply control related high level applications are running on workstations and control server. Cold start and shutdown processes are typical examples of this application. Lattice management, energy ramping and data archiving are already in service [2].

## 3 PERFORMANCE

### *3.1 Power supply ripple*

Power supply ripple tolerance for dipole, sextupole and quadrupole magnet power supplies are listed in table 1. Performance of power supplies cooperating with new control interface have been measured. Figure 2 shows the current spectrum of one of a Q2 power supply. The setting is 116 Amp, 60 Hz peak is 0.22 mA in rms. The corresponding ripple is less then 10 ppm. The other power supplies have similar performance.

Table: 1 specifications of power supply

| PS-Type | Dipole | Quadrupole | Sextupole |
|---|---|---|---|
| Ripple | $<5\times10^{-5}$ | $<5\times10^{-5}$ | $<2\times10^{-4}$ |
| Long-term stability | $<5\times10^{-5}$ | $<5\times10^{-5}$ | $<2\times10^{-4}$ |

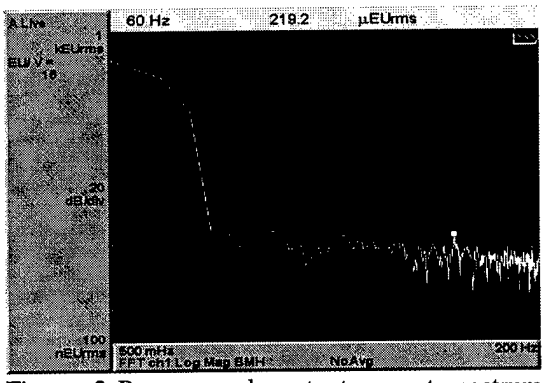



Figure: 2 Power supply output current spectrum of Q2 working at 1.5 GeV setting point. EU on the figure denote engineering unit. 1 EU corresponds to 1 Ampere.

### *3.2 Linearity of control channel*

Linearity is important for power supplies control in a storage ring with variable energy. The linearity of the power supply control channel is measured with high precision, high linearity DCCT. Different linearity were observed on various power supply control. Figure 3 is a monitoring data for R56QPS1 power supply linearity. It shows the difference of the output of power supply DCCT and the Output of DAC. Both are directly and individually connected to ADC. DAC linearity is less than 1 least significant bit. The measured result shows that the phenomena observed in figure 3 is contributed by the power supply.

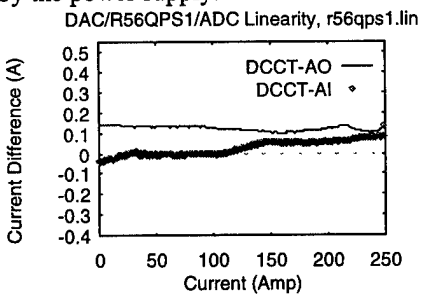



Figure: 3 Linearity of the control channel

### *3.3 Long-term stability*

Long term stability test at full power to their final loads has been intensively tested. In cold start procedure, these swithching power supply (SPS) have a better performance in long-term stability then the "old" power supply, SPS only needs half hour to get into steady state compared with a couple of hours of the old quadrupole power supplies. During five hours operation of R61QPS2 power supply in normal operation shift, it shows that the long-term stability is well within the specification.

### *3.4 Calibration for power supply control*

In order to control the output current of power supply precisely, a high precision, stability, and linearity DC current transform (DCCT) was taken as a reference current reading to find the correlation between the power supply output current and the digital setting. this will provide system conversion between the actual output current and the requested current. The offset measurement is also an important factor in the whole calibration procedure. All the calibration scheme is based on the specification of the power supply linearity.

### *3.5 Control performance of the correctors system*

The corrector system in SRRC storage ring has about eighty correction power supplies, we use the new power supply control interface to improve the control performance in speed, precision and stability. In order to support a high level stability output, the new control interface is needed. The control resolution is better then 1mA which corresponds to sub-µrad kick setting .

## 4 HIGH LEVEL APPLICATION

There are several high level applications which support the operation of the power supply system [3].

### *4.1 Lattice file related applications*

The main purpose of the lattice file, when it is loaded, is to make the power supplies operation easy. The functions of the loading lattice include setting current to zero, to maximum, and power supplies slew rate control. Slew rate control mechanism is built in VME crate to support smooth change between different operating lattices.

*4.2 Energy ramping scheme design*

File ramping scheme is used for varying energy of TLS because of its high flexibility. Energy range had been tested from 650 MeV to 1.5 GeV successfully. Ramping application at workstation is able to set output current of the power supplies 10 times per second. The VME crate performs linear interpolation in every 10 μs step to ensure the setting of power supplies is smooth enough. All power supplies are set within 20μs so as to guarantee good tracking among various power supplies. Setting of correctors can be scaled proportional to the beam energy during ramping. Ramping from 1.3 GeV to 1.5 GeV has been achieved within 5 seconds. Ramping time is basically limited by the magnet inductance and the characteristic of power supplies. Presently, the ramping duration is set to be 30 seconds [4].

*4.3 Tune correction*

In order to keep constant tune during energy ramping, open loop tune correction scheme has been tested. Figure 4 shows typical tune drift for energy ramping from 1.3 GeV to 1.5 GeV and then backs to 1.3 GeV without tune correction. The tune variation is mainly caused by magnetic hysteresis in dipole magnet [5].

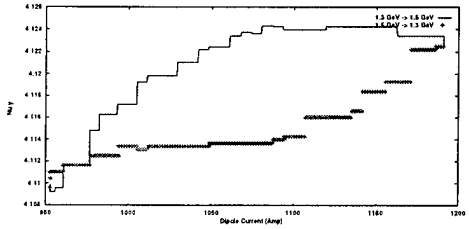


Figure: 4 Vertical betatron tune evolution during ramping - before correction.

Before SPS was installed, the relationship between tune change and Q1, Q2 current is displayed as the following relation [6]:

$$\begin{bmatrix} \Delta\nu_x \\ \Delta\nu_y \end{bmatrix} = \begin{bmatrix} -0.056 & 0.080 \\ 0.028 & -0.019 \end{bmatrix} \begin{bmatrix} \Delta I_{Q1} \\ \Delta I_{Q2} \end{bmatrix}$$

A mdified the ramping file, based on the above information, is used in order to keep $\nabla$nx and $\nabla$ny small. The correction is then applied to ramping the beam energy from 1.3 to 1.5 Gev and the result is shown in figure 5. It shows that $\nabla$ny can be kept within 0.002 peak-to-peak.

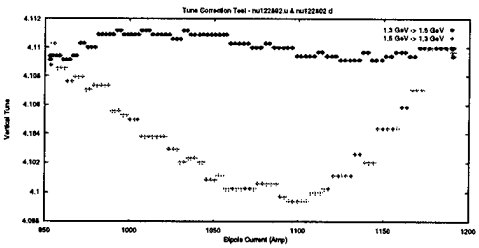


Figure: 5 Vertical betatron tune evolution during ramping - after correction

## 5 CLOSING REMARKS

Power supply control plays a crucial role in the operation of the accelerator system. The new power supply control interface has been commissioned successfully. Accomplished performance of the power supply system and related support control applications were satisfactory. A lot of works which are related power supplies operation will be finished in the future, a tune feedback system is under development for further improvement.

## 6 ACKNOWLEDGMENTS

The author thanks Drs. Richard Sah, C. C. Kuo for their continue encouragement. The authors would like to show their appreciation to all the staff of the power supply group and the instrumentation and control group of SRRC for their help in setting up the system.

## REFERENCES

[1] R. Richter, R. Visintini, "Performance of the ELETTRA Storage Ring Main Power Supplies" Proceedings of the 1994 European Particle Accelerator Conference, June 1994.

[2] D. Bulfone, et al., "Controls in the Past Year of ELETTRA Operation", ICALEPCS'95, 1995.

[3] D. Bulfone, M. Lonza, P. Michelini, L. Pasquali, "The Design of the Energy Ramping System for ELETTRA", Proceedings of the 1994 European Particle Accelerator Conference, June 1994, p. 1809.

[4] J. A. Carwardine, S. V. Milton, "Power Supply Ramp Control in the APS Booster Synchrotron", EPAC'96, 1996.

[5] S. V. Milton, J. A. Carwardine, "Ramp Tuning of the APS Booster Synchrotron Magnet Power Supplies", PAC'95, 1995.

[6] K. J. Cassidy, S. Howry, "Development of a Model for Ramping in a Storage Ring", AIP conference Proc. No. 325, P. 144, 1992.

# AN ELECTROMAGNETIC MICRO-UNDULATOR

A. Nassiri
Advanced Photon Source
L. R. Turner
Energy Technology Division
Argonne National Laboratory, 9700 South Cass Avenue, Argonne, Illinois 60439 USA

*Abstract*

Microfabrication technology using the LIGA (a German acronym for Lithography, Electroforming, and Molding) process offers an attractive alternative for fabricating precision devices with micron-sized features. One such device is a mm-sized micro-undulator with potential applications in a table-top synchrotron light source for medical and other industrial uses. The undulator consists of a silver conductor embedded in poles and substrate of nickel-iron. Electromagnetic modeling of the undulator is done using the eddy-current computer code ELEKTRA. Computations predict a field pattern of appropriate strength and quality if the current can be prevented from being shunted from silver by the nickel-iron poles either through insulation or through slotted poles. The design of the undulator along with the computational results are discussed.

## 1 INTRODUCTION

Development of table-top synchrotron light sources for medical applications and industrial usage have been recognized by many in the synchrotron radiation community to play a key role in providing compact, reliable, and cost-effective accelerators for these applications. Compact table-top synchrotron radiation sources have many applications ranging from hospital-based medical diagnostic imaging, cancer therapy, biological crystal studies, surface and catalytic studies, to x-ray lithography for microcircuit production. Also medical applications of free-electron lasers (FELs) with their variable-output-wavelength property, have attracted the interest of researchers in medicine and biology. With variable wavelength FEL, one may ascertain that a given wavelength may be more readily absorbed by one tissue type than by another. It is thus possible to identify critical wavelengths for biomedical use. Such wavelengths could then be incorporated in the design of chemical or other lasers for use in clinical therapies. Toward this goal, a group of researchers have begun to study methods of producing synchrotron radiation using compact accelerator devices [1].

An important part of these studies is the design, construction, and testing of a "micro-undulator" with a period of one millimeter. Undulators and wigglers are devices that are inserted into an electron or positron beam to produce x-rays. The magnetic field of such an insertion device is transverse to the beam direction and alternates periodically along the beam direction. The field causes the particles of the beam to oscillate and thereby generate x-rays.

## 2 DEEP X-RAY LITHOGRAPHY

The undulator will be fabricated using the deep x-ray lithograhy (LIGA) process [2]. In LIGA, x-rays with a wavelength less than 1 nm are used to expose a photosensitive layer, typically polymethylmethacrylate (PMMA). The PMMA is usually applied over a plating base, and when the exposed PMMA regions are removed in a highly selective developer, metal can be electroplated into the PMMA recesses defined by the x-rays. The short wavelength minimizes diffraction, and the metal features can be electroplated several hundred microns high with edge runouts of less than 0.1 microns [3].

## 3 MICRO-UNDULATOR

The undulator can operate in the electron beam from the linac of the Advanced Photon Source (APS) at Argonne National Laboratory. With the positron target retracted from the beamline, the linac could accelerate electrons to an energy of 650 MeV. The material properties of this undulator are given in section III of Ref. [3]. A summary of the micro-undulator geometrical and operating parameters are shown in Table 1.

Table 1: Micro-undulator Parameters

| **Parameter** | **Value** |
|---|---|
| Period | 1.0 mm |
| Gap | 0.6 mm |
| Pole height | 0.2 mm |
| Pole thickness | 0.3 mm |
| Pole width | 0.7 mm |
| Beam energy | 650 MeV |
| Deflection parameter | 0.047 |
| Field strength | 0.5 T |
| Excitation current | 280 A |
| Excitation pulse length | 10-20 μsec |

A 40-micron slot is cut in each 0.3-mm-wide pole to prevent current from the silver conductor shorting across the nickel-iron pole. The winding pattern is shifted one half period between the top and bottom halves of the undulator

0-7803-4376-X/98/$10.00 © 1998 IEEE

so that for the two halves, the currents in the beam direction oppose each other, but in the transverse direction, currents flow in the same direction. Earlier designs with current in the same direction top and bottom led to a field gradient across the central region of the undulator. The geometry of one period of the micro-undulator, in perspective view, is shown in Figure 1. In this figure, the silver conductors are arranged so that currents above and below the poles flow in opposite directions axially but in the same direction transversely. The slots in the nickel-iron poles prevent current flowing across the poles.

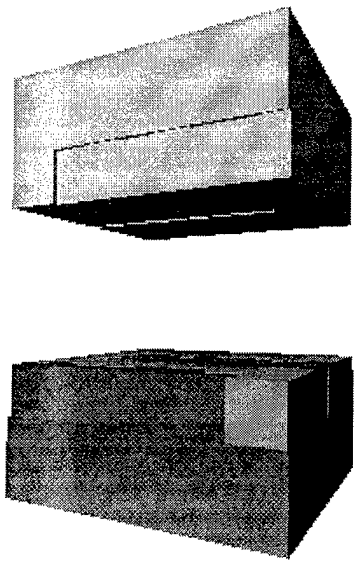


Figure 1: Perspective view of one period of the micro-undulator.

## 4 ELECTROMAGNETIC MODELING

Numerical computations were performed with the 3-dimensional eddy-current code ELEKTRA. One period of the micro-undulator was modeled axially by applying a flux-tangential boundary condition on the two faces of the undulator one period apart. Current was determined by using boundary conditions to specify a difference in electric scalar potential (voltage) between the two faces. Since the silver conductors, the nickel-iron poles, and the substrate are conducting, current can flow from one into the other. Were it not for the slots in the poles of the undulator, considerable current would flow through the poles, greatly impairing its behavior as an undulator. The Lorentz-Gauge solution option of ELEKTRA was used to determine the solution for the steady-state AC problem.

An earlier computation, treating the silver as a driven conductor with a specified current and the nickel-iron as a vector potential region with no net current, was used to consider the situation where the silver was insulated from the substrate, but that approach could not treat current sharing and current shunting between the materials.

Because of the high current densities involved, the undulator will be run only in a pulsed mode; in the modeling it was driven by a 50-kHz steady-state AC source.

## 5 COMPUTATIONAL RESULTS

Since the gap of this undulator (0.6 mm) is larger than the half-period (0.5 mm), the undulator is not efficient; the mid-plane field is small compared to the average pole-to-pole field. Within the mid-plane, the field is fairly uniform transversely across the central region. Figure 2 shows a contour plot of the flux density over one period. Lines show contours of equal $B_y$ in the x-z plane. Figure 3 shows a contour plot of the flux density over one period. Lines shows contours of equal $B_y$ in the y-z plane. Figure 4 shows field variation in the beam direction (arbitrary vertical scale).

## 6 THE TEN-SCALE MODEL

As described in Ref. [4], a seven-period, ten-times scale model was designed and fabricated by EDM (Electrode Discharge Machining) using 1010 steel for the substrate and insulated copper wire for the conductor. The model was measured using a Hall probe along the beam-axis of the undulator. In the design, no effort was made to correct end effects, so the measurements were taken only over the central four periods. Results from the measurements are summarized in Figure 5. The model was driven with a current of 10 A from a DC power supply to avoid overheating of the iron. This gave a peak field of 25.5 G, in agreement with the 26.6 G predicted by a 2-dimensional computation.

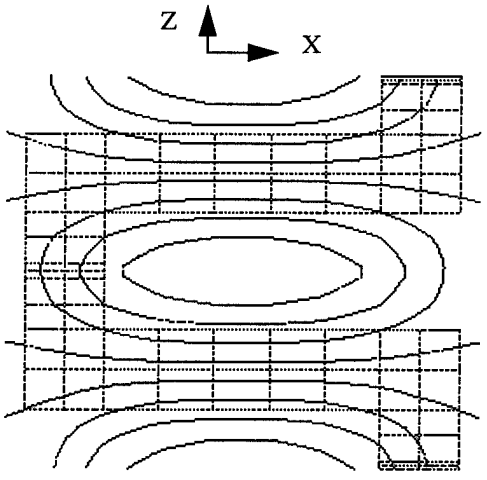



Figure 2: Contour plot of the flux density over one period. Lines show contours of equal $B_y$ in the x-z plane.

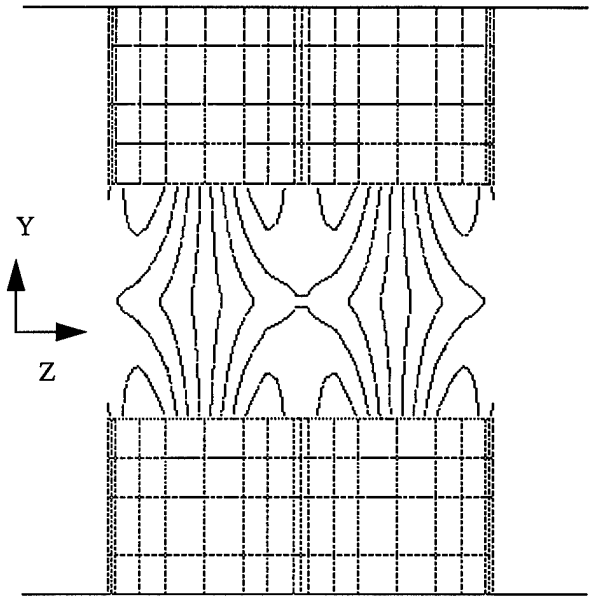



Figure 3: Contour plot of the flux density over one period. Lines show contours of equal $B_y$ in the y-z plane.

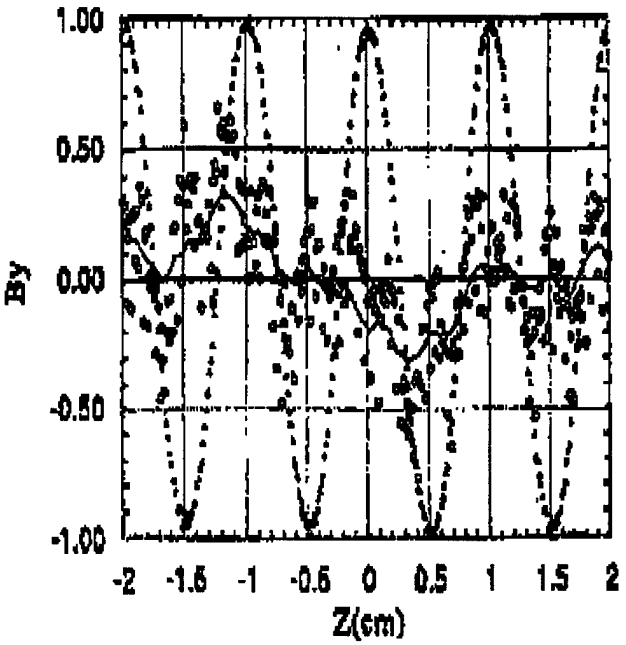



Figure 5: Measured field over the central region of the undulator. Circles show the measured field with a field of cosine variation subtracted, multiplied by a factor of ten. The solid line shows a smoothed fit to the circles.

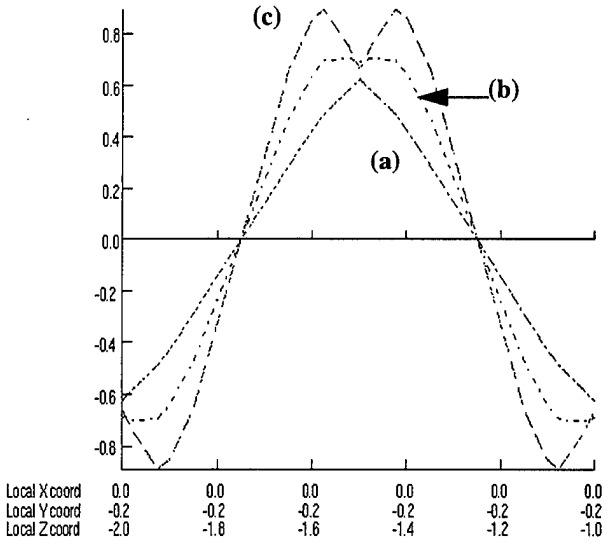



Figure 4: Field variation in the beam direction over one undulator period. Curve (a) is the field variation in the mid-plane. Curve (b) shows field variation 0.1 mm above or below the mid-plane. Curve (c) shows field variation 0.2 mm above or below the mid-plane. The field is weaker in the mid-plane since the gap between the poles (0.6 mm) is not small relative to the period of the undulator (1 mm) or the width of the poles (0.7 mm). The dip in the curve is due to a slot in the pole.

## 7 ACKNOWLEDGMENTS

This work was supported by the U. S. Department of Energy, Office of Basic Science, under Contract No. W-31-109-ENG-38. The first author would like to thank R. Kustom and J. Galayda for their support and encouragement. We also greatly benefited from various discussions with F. E. Mills of the Advanced Photon Source.

## 8 REFERENCES

[1] A. Nassiri, et. al., "A 50 MeV mm-Wave Electron Linear Accelerator System for Production of Tunable Short Wavelength Synchrotron Radiation," Proc. of the IEEE International Electron Devices Meeting, Washington DC, pp. 116-120, December, 1993.

[2] W. Ehrfeld, F. Gotze, D. Munchmerer, W. Schelb, and D. Schmidt, "LIGA Process: Sensor Construction Techniques via X-Ray Lithography," Technical Digest, IEEE Solid-State Sensor and Actuator Workshop, pp. 1-4, 1988.

[3] H. Guckel, T.R. Christenson, K.J. Skrobis, D.D. Denton, B. Choi, E. G. Lovell, J. W. Lee, S. S. Bajikar, and T. W. Chapman,"Deep X-Ray and UV Lithographies for Micromechanics," Proc. of the IEEE Solid State Sensor and Actuator Workshop, pp. 118-122, 1990.

[4] L. R. Turner, A. Nassiri, F. E. Mills, S. Kim, and A. D. Feinerman,"A Micro-undulator Fabricated by LIGA Process," IEEE Transactions on Magnetics, Vol. 32, No. 4, pp. 2602-2605, July 1996.

# A SUPERCONDUCTING WIGGLER MAGNET FOR THE NSLS X-RAY RING

E.B. Blum, D.R. Lynch, P. Mortazavi, O.V. Singh, W. Thomlinson, and M.H. Woodle
Brookhaven National Laboratory, Upton, NY 11764 USA

A.J. Broadbent, M.C. Coates, S.R. Milward, E.J.F. Moor, and K.D. Smith
Oxford Instruments Accelerator Technology Group
Unit 14 Oakfield Industrial Estate, Eynsham, Witney, Oxon OX8 1TH UK

*Abstract*

The superconducting 5 pole, 5 Tesla wiggler which has been operating in the X-17 straight section of the x-ray storage ring at the National Synchrotron Light Source (NSLS) since 1989 will soon be replaced by a new wiggler being built by Oxford Instruments with lower operating costs, higher reliability, and greater performance. The new wiggler has three modes of operation: the full wiggler with 11 poles producing 3.0 T, the partial wiggler with 5 poles at 4.7 T, and the wavelength shifter with a single pole producing 5.5 T. The full wiggler, optimized for the digital subtraction radiography program, will produce the same x-ray flux at the 33 KeV iodine K-edge as the existing wiggler operating at 4.7 T but will reduce the higher energy harmonics delivered to the target. The partial wiggler will deliver the same flux for solid state physics experiments as the existing wiggler, and the wavelength shifter will provide an elliptically polarized x-ray beam that is not now available.

## 1 INTRODUCTION

A 4.7 T, five pole superconducting wiggler[1] has been operating in the X-Ray storage ring at the National Synchrotron Light Source since 1989. The existing wiggler has been an important source of radiation for material science, high pressure research, and biomedical studies including, especially, digital subtraction angiography. The wiggler and its associated electronics and cryogenics systems, however, are aging and no longer represent the state of the art. Oxford Instruments is now building a new wiggler that will exceed all of the capabilities of the current wiggler but will be more reliable and less expensive to operate. The wiggler, shown schematically in fig.1, will have 13 iron poles that are excited by superconducting NbTi coils. Some important characteristics of the wiggler are listed in Table 1.

Table 1. Superconducting Wiggler Characteristics

| | | |
|---|---|---|
| Beam Energy | 2.584 | GeV |
| Maximum Beam Current | 438 | mA |
| Period | 17.16 | cm |
| Number of Poles | 13 | |
| Maximum Field | 5.5 | T |
| Horiz. Beam Aperture | 59.5 | mm |
| Vert. Beam Aperture | 19.5 | mm |

The wiggler will have three different modes of operation: full wiggler, partial wiggler, and wavelength shifter. In the full wiggler mode, the central 11 poles will be excited to produce a field of 3.0 T on the beam axis and the two end poles will produce half of that field to close the trajectory. In the partial wiggler mode, the poles labeled 0, ±1, and ±2 in fig. 1 will produce 4.7 T on-axis, poles ±3 will be powered to half-strength and the remaining poles will be unpowered. In the wavelength shifter mode, pole 0 will produce 5.5 T, poles ±1 will be powered to half-strength, and the remaining poles will be unpowered. Switching between the modes will be accomplished by changing the connections of the magnet leads to the

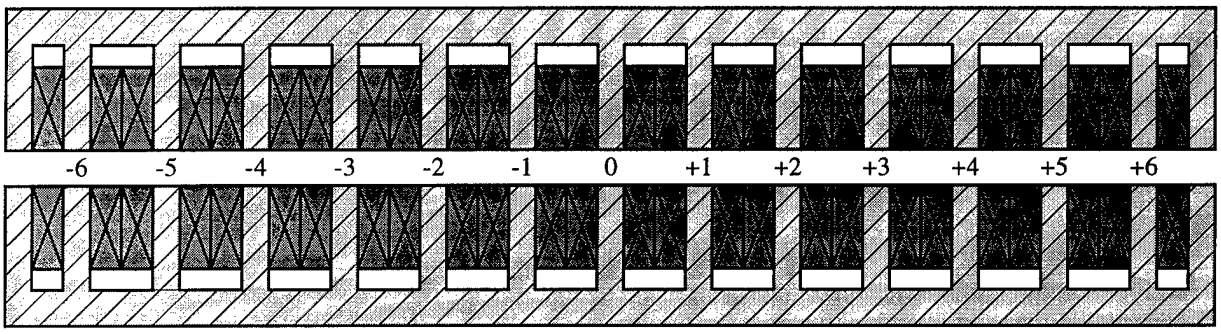



Figure. 1. Schematic cross section of the superconducting wiggler. The iron poles are indicated by diagonal lines and the superconducting coils by crossed, diagonal lines.

0-7803-4376-X/98/$10.00 © 1998 IEEE

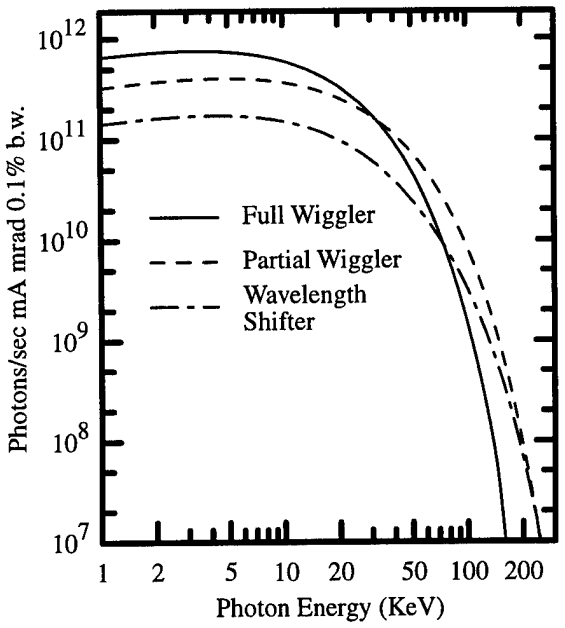



Figure. 2. On-axis flux in each wiggler operating mode.

power supply. A plot of the on-axis flux produced by the wiggler as a function of photon energy in each of the three operating modes is shown in fig. 2.

The full wiggler mode will be used for high intensity imaging experiments. In particular, it will be used for the coronary angiography and computed tomography medical programs. The 3.0 T peak field has been chosen because the critical energy is low enough that the higher energy harmonics in the (nearly) monochromatic beam that can be produced by diffracting the wiggler radiation in Si(111) crystals does not contaminate the images. The 11 poles produce the maximum allowable power level in the white beam, thereby maximizing the available flux at the 33 KeV iodine absorption edge used in digital subtraction imaging.

In the partial wiggler mode, the wiggler will produce the same flux as the present wiggler. This option will be used by high pressure materials science researchers in experiments using both high volume presses and diamond anvil cells. The higher fields raise the critical energy and hence the available energy spectrum for transmission through the cells for diffraction experiments. Most diffraction experiments will also use this field value as will other experiments where high flux above about 40 KeV is desirable.

The wavelength-shifter mode is designed for experiments where beam polarization is an important parameter. In particular, scattering and absorption by magnetic materials may be dependent on the polarization. Although the polarized radiation from bending magnet sources is readily available for surface diffraction experiments, the elliptically polarized, high energy photons from the wavelength shifter will permit measurements in transmission.

## 2 WIGGLER CONSTRUCTION

A warm bore–cold iron design was chosen in which the poles and coils are mounted in a 4.5 K liquid helium (lHe) bath and an insulated bore tube is provided for the electron beam. Heaters are incorporated to keep the temperature of the beam tube above 0° C so that water vapor will not freeze on the tube in the event of a vacuum leak in the storage ring. To minimize the heat leak, the stainless steel cryostat incorporates a 20 K shield cooled by the boiled-off helium vapor and a liquid nitrogen cooled 80 K shield. High temperature superconducting leads are used for the magnet current to further reduce losses. In steady operation, the wiggler will use 0.35 l/hr of LHe. The LHe will be supplied from a pressurized dewar by an automatic transfer system.

The magnet poles are constructed of a special low carbon steel called REMKO B in order to minimize the residual magnetization. The superconducting coils are made from round wires of NbTi stabilized with copper. The ratio of NbTi to Cu is 1:1. The coil around each pole is divided into two sections in order to reduce the current density in the high field region nearest the pole. The wire diameter in the inner coil is 1.0 mm and it is 0.7 mm in the outer coil. The maximum current is approximately 295 A and the current densities are 485 A/mm$^2$ in the outer coil and 285 A/mm$^2$ in the inner. The maximum stored energy in the wiggler is170 KJ.

The magnetic field of the wiggler must be ramped to accommodate storage ring injection. Electrons are injected into the ring at an energy of 750 MeV. After the desired current is stored, the ring energy is ramped to 2.584 GeV. The wiggler was designed so that it can be ramped between an injection level of 1.1 T and the maximum operating field in each mode at a rate of 1.14 T/min. The maximum voltage required to achieve this rate is 16.5 V.

The coil design, small ramping voltages, and low stored energy permit the use of passive quench protection. Diode–resistor networks are placed across the coil leads inside the cryostat to absorb the stored energy in the event of a quench. Calculations have shown that the magnet power supply can safely remain on during a quench.

## 3 WAVELENGTH SHIFTER POLARIZATION

It is well known[2] that the synchrotron radiation from the electrons in a bending magnet is linearly polarized in the bending plane and elliptically polarized out of the plane, with the polarization growing increasingly circular with the vertical angle $\psi$. In most wigglers, the transversely polarized component of the radiation from alternate poles cancels, resulting in radiation that is linearly polarized in the bending plane at all vertical angles. In a wavelength shifter, however, the transversely polarized radiation from the strong central pole is only partially canceled by the

radiation from the half-strength end poles, leaving strong elliptical polarization off-axis.

We will now estimate the degree of circular polarization from the wavelength shifter. When the wiggler parameter K>>1 most of the radiation observed with an energy that is near or above the critical energy is emitted from the portions of the electron trajectory that are tangential to the axis of observation.[3] Because the emitting regions are small they can be approximated by circular arcs. The radiation from the wiggler magnet can therefore be approximated as the radiation from a series of bending magnet sources. This is called the *bend source* approximation.[4] The wavelength shifter will hence be modeled by a magnet with bending radius $\rho$ sandwiched between two magnets with radius $2\rho$.

The degree of circular polarization from a radiation source can be defined in terms of the Stokes parameters as[3]

$$P_C = S_3 / S_0$$

where

$$S_3(\rho) \propto \frac{8}{3}\rho^2\psi\left(\psi^2 + 1/\gamma^2\right)^{3/2} K_{1/3}(\eta)K_{2/3}(\eta)$$

is the intensity of the circularly polarized radiation,

$$S_0(\rho) \propto \frac{4}{3}\rho^2\psi^2\left(\psi^2 + 1/\gamma^2\right)K_{1/3}^2(\eta) + \frac{4}{3}\rho^2\left(\psi^2 + 1/\gamma^2\right)^2 K_{2/3}^2(\eta)$$

is the total radiation intensity,

$$\eta(\rho) = \frac{E}{2E_C(\rho)}\left(1+\gamma^2\psi^2\right)^{3/2},$$

$$E_C(\rho) = 3\hbar\gamma^3 c / 2\rho$$

is the critical energy, $E$ is the photon energy, $\gamma$ is the Lorentz parameter, $\psi$ is the angle at which the radiation is observed relative to the bending plane, $K_{1/3}$ and $K_{2/3}$ are modified Bessel functions. The direction of polarization is opposite for the central and end poles. The degree of circular polarization of the radiation from the wavelength shifter is therefore

$$P_{C,total} = \left[S_3(\rho) - 2S_3(2\rho)\right] / \left[S_0(\rho) + 2S_0(2\rho)\right].$$

Fig. 3 shows a plot of the degree of circular polarization of the radiation shifter as a function of photon energy for a series of vertical angles. The circularly polarized component of the radiation from the central pole becomes predominant at energies above critical as the angle approaches $1/\gamma$. The polarization at low energies is dominated by the half-strength end poles and is in the opposite direction. This is not normally of much interest because wavelength shifters are built as a source of high energy radiation. The dependence of the intensity of the circularly polarized radiation on photon energy will not be discussed in this paper.

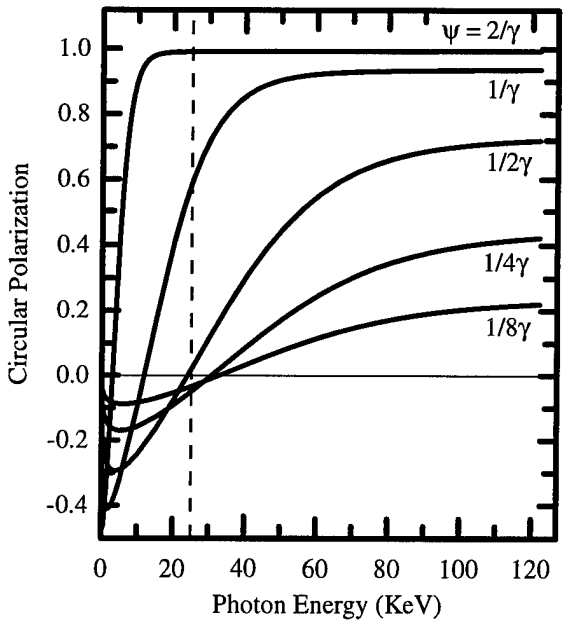



Figure 3. Degree of circular polarization for the wavelength shifter mode at various vertical angles. The broken line represents the critical energy for the central pole.

## 4 PLANS FOR INSTALLATION

The wiggler is now under construction at Oxford Instruments. Delivery at Brookhaven National Laboratory is expected in the Fall of 1997 and installation in the NSLS X-Ray Ring is planned for December 1997.

## 5 ACKNOWLEDGEMENTS

The authors thank Florin Staicu for his assistance. Support was provided by the U.S. Department of Energy under contract No. DE-AC0276CH00016 and the U.S. Advanced Research Projects Agency under contract No. AO:B228.

## 6 REFERENCES

[1] W. Thomlinson, D. Chapman, N. Gmür, and N. Lazarz, Nucl. Instr. Meth. **A266**, p. 226, 1988.

[2] G.K. Green, *Spectra and Optics of Synchrotron Radiation,* BNL Report BNL-50522, 1976.

[3] A. Friedman, S. Krinsky, and E. Blum, *Polarized Wiggler for NSLS X-Ray Ring Design Study*, BNL Report BNL-47313, 1992.

[4] S. Yamamoto, T. Shioga, S. Sasaki, and H. Kitamora, Rev. Sci. Instrum. **60**, p. 1834, 1989.

# MAGNETIC MEASUREMENTS ON AN IN-VACUUM UNDULATOR FOR THE NSLS X-RAY RING*

G. Rakowsky, J.J. Aspenleiter, W.S. Graves, L. Solomon and P.M. Stefan
NSLS, Brookhaven National Laboratory, P.O. Box 5000, Upton, NY 11973-5000, USA

*Abstract*

Magnetic measurements have been performed on the In-Vacuum Undulator (IVUN), built jointly by BNL and SPring-8 for the NSLS X-Ray Ring. The IVUN magnet has a Halbach-type, pure-permanent magnet structure with a period of 11 mm and a minimum gap of 2 mm. Results of magnetic measurements utilizing Hall probe, moving wire and pulsed wire techniques will be presented and compared.

## INTRODUCTION

A short-period, In-Vacuum UNdulator (IVUN) is being developed in a collaboration between Spring-8 and NSLS for installation in the NSLS X-Ray Ring [1]. This magnet builds on experience gained in the successful development and operation of the in-vacuum undulator for the KEK Accumulator Ring [2] and the Prototype Small-Gap Undulator (PSGU)] in the NSLS X-Ray Ring.[3]. Studies with the PSGU have demonstrated minimal beam lifetime reduction in the X-Ray ring with apertures as small as 3mm in low-beta straight sections. With an in-vacuum device, the magnet array itself, rather than the vacuum chamber, can be the limiting aperture. The IVUN design explores this new parameter regime. Details of the IVUN design are presented by Tanabe [4] elsewhere in these Proceedings. Installation of IVUN in the NSLS X-Ray Ring is scheduled for May, 1997.

The magnet arrays were assembled, mapped, trimmed, vacuum baked and remeasured at SPring-8 before shipment to NSLS. The magnet array support structure and vacuum chamber were designed and built at NSLS. Upon arrival at the NSLS, the magnet arrays were mounted to the support structure and gap drive system for magnetic measurements. This paper reports the results of these measurements.

## 1 DESIGN HIGHLIGHTS

The IVUN magnet design employs a pure-permanent magnet, Halbach-type structure with four blocks per period. The arrays are 30.5 periods long with +3/4, -1/4 type (displacement-free) terminations. With a design gap of 3.3 mm and a period of 11 mm, the IVUN magnet achieves a peak field of 0.7 Tesla and a K value of 0.72., The design fundamental peak is at 4.6 keV (2.7Å) for the X-Ray Ring energy of 2.584 GeV. High-temperature neodymium-iron-boron magnets (Sumitomo NEOMAX 32EH) were used, allowing bakeout at up to 125°C.

The magnet arrays, with their water-cooled backing beams, are each supported by a single post via bellows through the rectangular vacuum chamber flanges. The variable-gap drive and support structure are nearly identical to that of the PSGU. The gap is adjustable from 10 mm down to 1 mm, but will be limited to 2 mm by controls, limit switches and hard stops.

Electron beam image currents are carried from the Conflat end flanges to the gap region by flexible transitions and bellows liners of a design developed for the PSGU. In the gap region the current will be carried by high-purity, annealed nickel foil strips, 0.1 mm thick, laid directly on the magnet pole surfaces.

## 3 MAGNETIC MEASUREMENTS

The magnetic measurements at NSLS had a three-fold objective: (1) to verify that the magnet assembly had not been damaged in transit, (2) to perform measurements complementary to those already done at Spring-8, and (3) to measure the effect of the nickel image-current continuity sheets on magnet performance.

Visual inspection of the magnet arrays upon arrival at NSLS showed no damage in transit. However, soon after, a magnet broke spontaneously. This raised concerns about possible additional magnet failures, particularly since a magnet had also broken at Spring-8 during vacuum-compatibility bakeout testing. A magnet breakage in an in-vacuum device such as IVUN is much more serious than in a conventional insertion device. Therefore, in parallel with the magnetic measurements, a detailed modeling study was undertaken to analyze the forces and stresses involved. As a result, each pair of magnet block retaining clips was systematically loosened and retorqued, so as to limit the maximum stress in the NdFeB to 50% of its tensile strength. As a further precaution, the reassembled magnet was then cycled over 100 times between 9.5 mm and 2 mm gap, without any further magnet failures.

### *3.1 Hall Probe Measurements*

Hall probe measurement of the IVUN magnet was done on a granite mapper using a miniature Group3 transverse Hall probe with built-in temperature correction. The probe's response was calibrated against NMR probes in a standard dipole magnet. A fifth-order polynomial was used to fit the Hall probe voltage vs. field data. Only the vertical (y) component of B was mapped with the Hall probe system.

Field maps were taken in the midplane (Y=0) at X=0, ±2 and ±4 mm, at the nominal 3.3 mm gap. On-axis field

0-7803-4376-X/98 /$10.00 © 1998 IEEE

maps [X=0, Y=0) were taken at several gaps between 3.3 and 9.5 mm. To help correlate certain trajectory features with either the upper or lower magnet array, off-midplane scans were also taken at the 9.5 mm gap, with the probe at X=0 and Y=±3.1 mm, i.e., at 1.65 mm from each array, the same distance as in the midplane scan at 3.3 mm gap.

First integrals of these Hall probe scans show that the integrated dipole varies from about 30 to 70 gauss-cm for -2mm<X<+2mm. The quadrupole error is about 100 gauss, exceeding the design goal of 10 gauss. These results differ significantly from Tanabe's data, which will be discussed in the following paragraph.

The second integral of the field is proportional to the e-beam trajectory and reveals the location of non-cancelling field errors. The on-axis trajectory, calculated from Hall probe data, is shown in Figure 1 and is in good agreement with Tanabe's result. The off-axis trajectories (not shown) show local dipole errors which vary with X, and which suggest that various magnet blocks may have large multipole errors. Comparison of off-axis trajectories with Tanabe's data show local deviations in the region of the block replaced at NSLS. This suggests that the replacement block may have significantly different multipoles from the broken one, which would account for the discrepancy in integrated multipoles reported above.

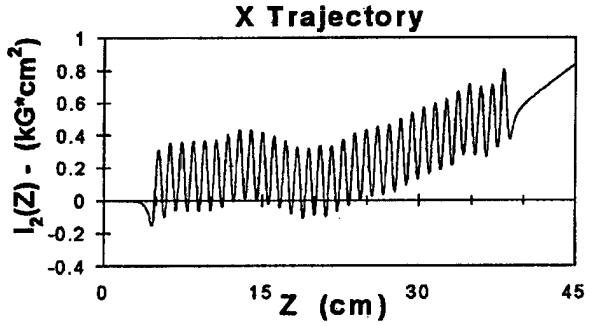



Figure 1. IVUN on-axis trajectory at 3.3 mm gap.

*3.2 Nickel Continuity Sheets.*

The effect of the nickel continuity sheets was measured by mapping the field with and without the foils at a gap of 3.3 mm. As expected, field amplitude decreased due to shunting of flux from pole to neighboring pole. At a field amplitude of about 0.7 Tesla, the decrease in peak field varied between 20 and 30 gauss, with larger deviations near the zero crossings. Because the effect is symmetric, the trajectory plots and the phase error plots appear virtually identical, so there should be no degradation of performance.

*3.3 Moving-Wire Measurements*

The small gap led us to choose a moving wire integrator, similar to a design reported by Zangrando and Walker, [6] to measure integrated fields. The wire was a 43-strand Litz cable formed into a loop, with the strands connected in series. The leg of the loop passing through the undulator is stretched between supports mounted on motorized translation stages. Integrated dipole profiles are obtained by measuring the voltage induced in the loop with an integrating voltmeter, as the wire is translated through the magnet in increments of DX. Due to random drift in the integrating voltmeter, voltage readings were averaged over many repetitions to achieve adequate signal-to-noise. As with the Hall probe, only normal (By) field integrals were measured, due to the restricted gap.

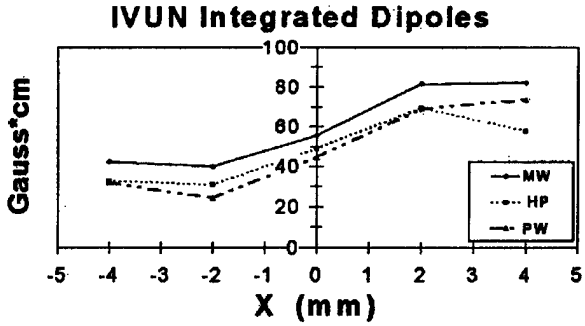



Figure 2. Integrated dipoles in IVUN from Hall probe (HP), moving wire (MW) and pulsed wire (PW) data.

Integrated dipoles were measured in the midplane (Y=0) at 2 mm intervals from -4mm to +4mm, at several gaps, with DX=2mm. Figure 2 compares the integrated dipole profiles at 3.3mm gap obtained from the moving wire with those computed by numerical integration of Hall probe data. These profiles agree qualitatively and indicate a strong quadrupole and octupole.

*3.4 Pulsed Wire Measurements*

The pulsed wire bench is modeled after the Los Alamos design developed by Warren and Fortgang [7], with the addition of viscous damping. Its main advantage is rapid visualization of both X and Y trajectories. In this case, it was our only means of measuring the Y trajectory.

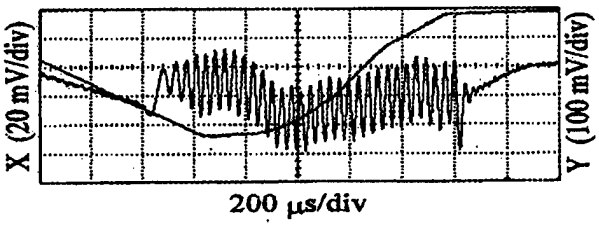



Figure 3. X and Y trajectories from pulsed wire.

Figure 3 shows a "snapshot" of the on-axis X and Y trajectories in IVUN at a gap of 3.3mm. The X trajectory agrees quite well with the trajectory shown in Figure 1, both in terms of the distinctive features discussed earlier, and in terms of the integrated dipole, (computed graphically from the entry and exit trajectory angles.) The distortion observed at the ends of the sinusoidal waveform is due to dispersive properties of the BeCu wire.

The Y trajectory exhibits a peak deviation of about 2.3 mm, equivalent to 9 wiggle amplitudes. This large trajectory error undoubtedly resulted from optimizing only the X trajectory, without benefit of an on-line, Y trajectory diagnostic. The Y trajectory shows distinct kinks which point to localized sources of Bx fields. Integrated dipoles calculated graphically from exit and entry trajectory angles are also in good agreement with those obtained from Hall probe scans and moving wire measurements (Figure 2). The Y trajectories also exhibit variation with off-axis position, indicating the presence of significant skew multipoles.

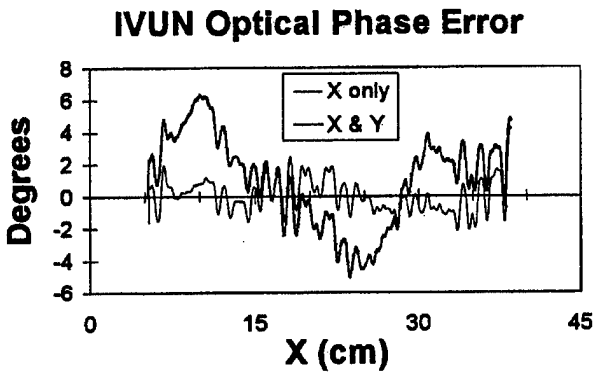



Figure 4. Optical phase error due to (a) X trajectory only, and (b) both X and Y trajectory components.

*3.5 Phase Shake Analysis*

Optical phase error is an excellent measure of undulator quality since it is strongly correlated to loss of spectral brightness.[5] It is calculated by integrating the difference between the path length along the actual trajectory and a best-fit sinusoidal trajectory, expressed in degrees at the fundamental optical wavelength. Phase error calculated from our on-axis By field maps is shown by the "X only" curve in Figure 4. It shows rms phase shake of less than 2 degrees, predicting excellent spectral performance. Tanabe's data gives similar phase error results. However, phase error is also affected by Y trajectory errors due to Bx. The "X+Y" curve shows the phase error when both By and Bx are taking into account. As can be seen, the phase excursions have increased to ±5°. The actual spectral brightness will therefore be lower than would be expected due to phase shake from X motion alone.

The phase error plot reveals mechanical alignment errors, particularly gap taper. This produces a field taper and results in a "chirp" in the resonant wavelength. Its effect on the optical spectrum is to smear the spectral lines. The presence of taper is revealed by a parabolic phase profile. For IVUN, a gap taper error of only 25 μm (0.001 in) resulted in a noticeable chirp of several degrees. This level of precision is just below the threshold of standard optical survey instruments, so the phase error plot becomes the best remaining diagnostic of magnet array alignment.

## 4 CONCLUSIONS

Magnetic field measurements on the IVUN undulator have been completed at NSLS. The Hall probe, moving wire and pulsed wire techniques proved to be mutually complimentary and the three sets of measurements are in good agreement. Intercomparison with measurements done earlier on this device at Spring-8 show generally good agreement in the X trajectories, except at the location where a broken magnet was replaced. Disagreement in multipole measurements can be attributed to differences in multipole characteristics of the replacement magnet from the broken one. Using the pulsed wire bench as an on-line diagnostic, it should be straightforward to find a better replacement magnet and also to retrim IVUN to minimize the Y trajectory errors and integrated multipoles.

## 5 ACKNOWLEDGEMENTS

The authors thank T. Tanabe for a fruitful and collegial collaboration; M. Lehecka, R. Scheuerer and the survey crew for assistance in setups; and Sam Krinsky for guidance and encouragement during this project. This work is supported by the U.S. Department of Energy under Contract No. DE-AC02-76CH00016.

## REFERENCES

[1] P. Stefan, et al., 'Insertion Device Development in the X13 Straight of the NSLS X-Ray Ring', these Proceedings.
[2] S. Yamamoto et al., Rev. Sci. Instr., 63 (1), p.400, (1992).
[3] P.M. Stefan et al., Proc. 1995 Part. Accel. Conf., Dallas, TX, p.2435, (1995).
[4] T. Tanabe, et al., 'Development of an In-Vacuum Minipole Undulator', these Proceedings.
[5] B.L. Bobbs et al., Nucl. Instr. and Meth., A296, p.574, (1990).
[6] D. Zangrando and R.P. Walker, Nucl. Instr. and Meth., A376, p.275, (1996).
[7] R.Warren and C. Fortgang, Nucl. Instr. and Meth., A341, p.444, (1994).

# SIBERIAN SNAKES FOR ELECTRON STORAGE RINGS

V.Ptitsin and Yu.Shatunov, BINP, 630090, Novosibirsk, Russia

*Abstract*

Applying a Siberian snake to obtain longitudinally polarized electron beam is discussed. Depolarization effects are analysed and spin matching conditions to decrease the depolarization are derived.

## 1 INTRODUCTION

Siberian snake was invented at mid-70th mainly as a mean against spin resonances which can destroy the beam polarization in circular accelerators[1]. Recently this concept has been tested and confirmed practically in a series of experiments carried out at the IUCF cooler ring[2].

However, there is another important area of the snake application, it is for obtaining longitudinal polarization at an interaction point. First longitudinally polarized electron beam was obtained at the energy of 27 Gev on the HERA electron ring where a pair of spin rotators was installed around the interaction point[3]. However, such the method is difficult to apply when beam energy is lower than 10 Gev because dipole magnets of the rotator will provide enormous orbit excursions inside the rotators. The Siberian snake is a special kind of a spin rotator which rotates particle spin by 180° angle around a direction lying in the horizontal plane. This direction is called by snake axis. An insertion of Siberian snake with longitudinal snake axis provides automatically the longitudinal beam polarization on a ring azimuth opposite to the snake insertion. Such a snake can be naturally performed with the use of solenoidal magnets. For a compensation of betatron modes coupling introduced by the solenoids, the snake must contain also quadrupole lenses (normal and/or rotated)[1]. The first experiments with the solenoidal Siberian snake for obtaining longitudinally polarized electrons was carried out at the AmPS storage ring at NIKHEF[4, 5]. and demonstrated the success of the given method.

The AmPS ring is operating in 300-900 Mev energy range. When using a Siberian snake at higher energies one must take into account a sharp depolarization increase with energy.

## 2 SPIN MATCHING CONDITIONS

In fact, the use of one Siberian snake leads to an unusual situation when the direction of the beam polarization is in horizontal plane everywhere over a ring excepting the snake itself. In this case the Sokolov-Ternov self-polarizing mechanism does not work and, on the other hand, a depolarization mechanism caused by quantum fluctuations of synchrotron radiation is considerably enhanced. Thus a special care must be taken to keep the beam polarization decay as slow as it is required by experiment needs. The depolarization rate is described by the well-known DK formula[7] as:

$$\tau^{-1} = \frac{5\sqrt{3}}{8}\frac{e^2\hbar\gamma^5}{m^2c^3}\,\alpha_+$$

$$\text{with} \qquad \alpha_+ = \Big\langle \frac{1}{|\rho|^3}\Big[1 - \frac{2}{9}(\hat{\mathbf{n}}\hat{\mathbf{v}})^2 + \frac{11}{18}|\mathbf{d}|^2\Big]\Big\rangle \quad (1)$$

where $\hat{\mathbf{n}}$ is a periodical spin solution, $\mathbf{d} = \gamma\frac{\partial\hat{\mathbf{n}}}{\partial\gamma}$ vector, $\rho$ is bending magnet curvature, $\hat{\mathbf{v}}$ is an unit vector in the direction of particle velocity. The average is taken over the ring azimuth $\theta$ and, generally, over beam distribution.

The reduce of the depolarization time $\tau$ is completely determined by the value of the spin-orbit coupling vector $\mathbf{d}$. At the first-order approximation the $\mathbf{d}$ vector is orthogonal to $\hat{\mathbf{n}}$: $\mathbf{d} = \mathrm{Re}(iD\hat{\eta}^*)$ where $\hat{\eta}$ is an eigen solution of spin motion equation orthogonal to $\hat{\mathbf{n}}$. In general case the $D$ function can be represented as a sum of two contributions: $D = D_\gamma + D_\beta$. Here $D_\gamma$ comes from the direct dependence of the vector $\hat{\mathbf{n}}$ on the particle energy while $D_\beta$ results from a jump of betatron amplitudes during an emission of a quanta.

We consider a practical case when there is no dispersion in the insertion region ($\psi_x = \psi_z = 0$) and the coupling introduced by the solenoids is fully compensated by the insertion quadrupoles. For the snake located at $[\theta_1; 2\pi]$ we obtain the expressions for $D_{\gamma,\beta}$ outside the snake insertion. The $D_\gamma$ does not depend on internal structure of a snake:

$$D_\gamma = -\frac{\pi}{2}\sin(\pi\nu_0) + i\nu_0\left(\pi - \int_0^\theta \frac{H_z}{< H_z >}d\theta'\right)$$

where $H_z$ and $< H_z >$ are the vertical field and its average value over ring azimuth, $\nu_0 = \gamma a$.

The form of the expression for $D_\beta$ depends on a number of solenoids used in the snake. For instance, for a snake containing one solenoid:

$$D_\beta = -\frac{\nu_0\pi}{2\cos(\pi\nu_x)}\Big[\cos(\pi\nu_0)\,\mathrm{Im}\big(\mathrm{e}^{i\pi\nu_x}J(\theta)f'^*_{Iz0}\big) - i\,\mathrm{Im}\big(\mathrm{e}^{i\pi\nu_x}f'^*_{Ix0}J(\theta)\big)\Big]$$

where $f'_{Ix0}$ and $f'_{Iz0}$ are first mode Floquet function derivatives taken at the midpoint of the solenoid and $J(\theta) = f_{Ix}\psi'_x - f'_{Ix}\psi_x$.

Two solenoids snake was applied at the AmPS storage ring This compact snake, designed and builded at BINP (Novosibirsk), uses two superconducting solenoids with up to 7.5 T field and five compensating quadrupoles:

[1] A general method of solenoid compensation is described in[6]

0-7803-4376-X/98/$10.00 © 1998 IEEE

**sq1 sq2 sol q sol -sq2 -sq1**

Here (**sol**) stands for solenoid, (**sq1,sq2**) are quads rotated by 45° and (**q**) is a normal quadrupole. For two solenoids snake one finds:

$$D_\beta = -\frac{\nu_0\pi}{4\cos(\pi\nu_x)}\Big[\cos(\pi\nu_0)\,\mathrm{Im}\big(e^{i\pi\nu_x}J(\theta)G^*_{Ix}\big) + \\ + \; i\,\mathrm{Im}\big(e^{i\pi\nu_x}G^*_{Iz}J(\theta)\big)\Big] \qquad (2)$$

where $G_{Ix,z} = f'_{Ix,z(out)} - f'_{Ix,z(in)}$ is the difference of the first mode Floquet function derivatives at the entrance of the first solenoid and at the exit from second one. Also each solenoid has been treated here as having infinitely short edges. In the above expression a point just after the first edge is called by the solenoid entrance and a point just before the second edge is called by the exit.

Unlike the $D_\gamma$, the $D_\beta$ contribution depends on lattice functions. In particular, this fact causes the dependence of the depolarization time on horizontal betatron tune and on any manipulation with optics of the storage ring. For example, in the Figure 1 $\tau$ is drawn versus horizontal tune for AmPS snake for two possible sets of gradients of compensating quadrupoles.

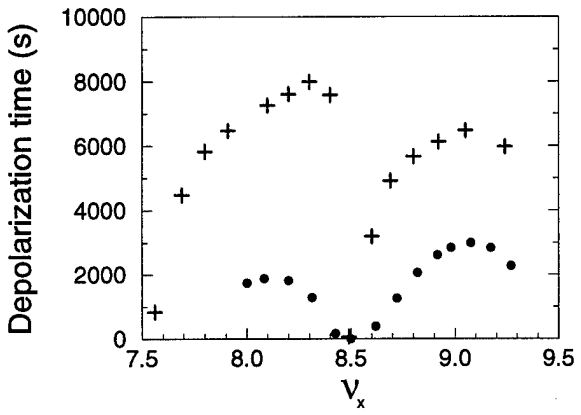



Figure 1: The dependence of depolarization time on the horizontal betatron tune, $E = 0.9$ Gev, $\nu_z = 7.25$. Circles for normal scheme, pluses for reversed gradient scheme.

The contribution of $D_\beta$ term to the depolarization time can be comparable or even larger than the contribution resulting from $D_\gamma$. Figure 2 demonstrates the $|\mathbf{d}|$ variation along azimuth of AmPS ring again for the two possible sets of snake quadrupoles. At the top picture the $D_\beta$ causes large oscillations of $|\mathbf{d}|$ in the magnets on background of smooth variation of $D_\gamma$. At the bottom picture $D_\beta$ is small enough and this variant provides considerably larger depolarization time.

In order to increase the depolarization time and avoid its dependence on the ring optics one should apply snake scheme that cancels $D_\beta$ term. For the case of two solenoids snake such the snake must provide $G_{Ix} = G_{Iz} = 0$ and,

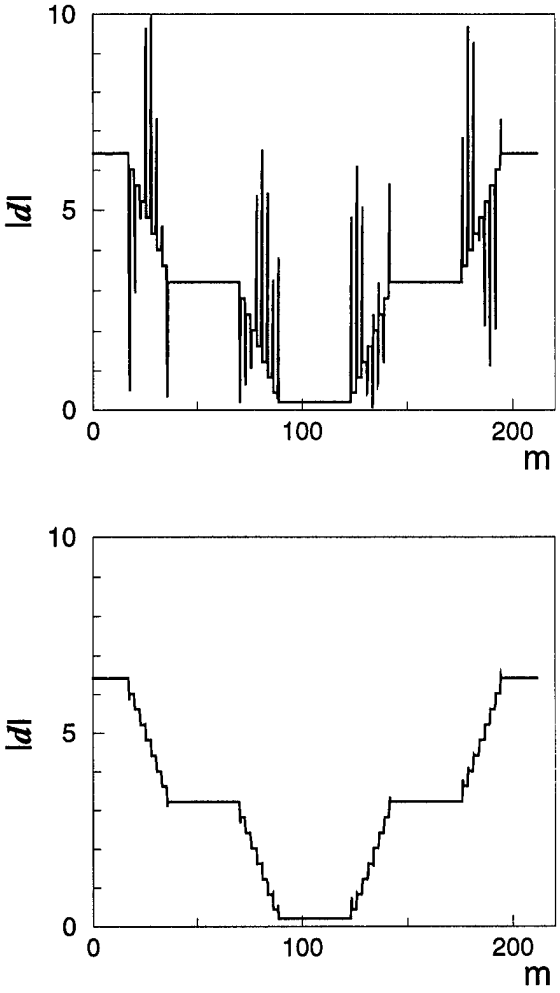



Figure 2: $|\mathbf{d}|$ along azimuth of the AmPS ring for normal (top) and reversed (bottom) gradient scheme.

therefore:

$$f'_{Ix(out)} = f'_{Ix(in)}, \quad f'_{Iz(out)} = f'_{Iz(in)} \qquad (3)$$

It provides some relations on elements of transport matrix between the solenoids. Such a snake can be called a spin matched snake on the analogy with spin matching concept, introduced for spin rotators [3]. Actually in the considered case we have only partial spin matching since it is not possible to cancel the contribution of $D_\gamma$.

The simplest variant of spin matched snake is a scheme where the coupling compensation is carried out by six normal quadrupoles (**q1-6**) inserted between two solenoids:

**sol q1 q2 q3 q4 q5 q6 sol**

From the relations (3), taking into account the transformation of optical Floquet functions on solenoid edges, one can find that a transport matrix of the whole snake must have a form:

$$\begin{pmatrix} I & 0 \\ 0 & -I \end{pmatrix}$$

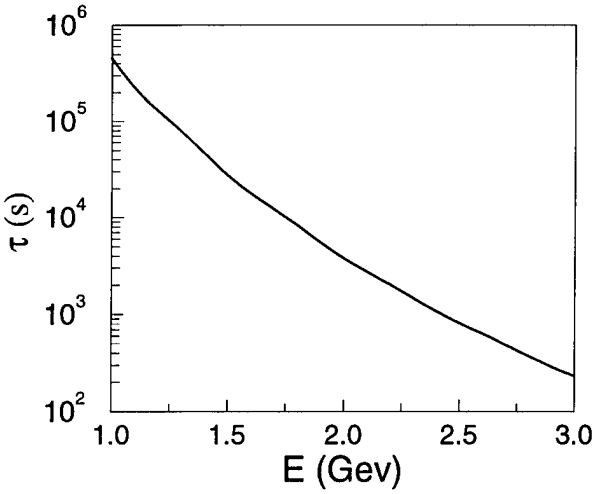



Figure 3: The depolarization time versus beam energy for the VEPP-4 with matched snake.

where $I$ is the identity matrix. The strengths of the insertion quadrupoles are choosen to provide such the matrix.

Applying the matched snake increases the depolarization time. Nevertheless the depolarization time decreases rapidly with energy:

$$\tau \simeq \frac{54}{11}\frac{1}{\nu_0^2\pi^2}\,\tau_p \sim \frac{1}{E^7}$$

where $\tau_p$ is self-polarization time calculated when the snake is switched off.

For example, in the Figure 3 the dependence $\tau$ on beam energy is shown for the VEPP-4 storage ring with the spin matched snake. Thus for typical electron storage rings in this energy range the use of this method of obtaining longitudinally polarization is restricted to the energies below 3 Gev.

## 3 KINETIC POLARIZATION

As follows from DK formulas[7], though Sokolov-Ternov polarizing mechanism does not work, the equilibrium polarization should differ from zero level due to so-called kinetic polarizing mechanism caused by the dependence of synchrotron radiation probability on a spin projection on a field direction:

$$P_{eq} = -\frac{8}{5\sqrt{3}}\frac{\alpha_-}{\alpha_+} \quad \text{with} \quad \alpha_- = -\left\langle \frac{\hat{\mathbf{b}}\cdot\mathbf{d}}{|\rho|^3}\right\rangle$$

$\alpha_+$ is given by (1) and $\hat{\mathbf{b}}$ is an unit vector in the direction of magnetic field.

This mechanism, predicted theoretically, has been never observed yet. A storage ring with a Siberian snake provides the unique possibility to confirm its existence. The kinetic polarization is driven by the vertical projection of $\mathbf{d}$ vector in bending magnets. For a snake with two solenoids this projection is:

$$d_z = -\frac{\pi\sin(\pi\nu_0)}{2} + \frac{\nu_0\pi\cos(\pi\nu_0)}{4\cos(\pi\nu_x)}\,\mathrm{Im}\left(e^{i\pi\nu_x}J(\theta)G_{Ix}^*\right)$$

Thus the value of polarization and its sign depends both on the beam energy and, for an unmatched snake, on the ring optics. In the Figure 4 the equilibrium polarization dependence on energy is demonstrated for two variants of AmPS optics.

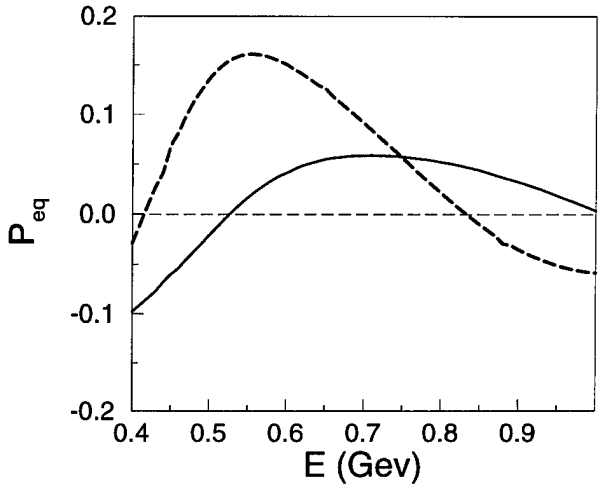



Figure 4: The equilibrium polarization versus beam energy for two variants of the AmPS ring with $\nu_x = 8.3$ (solid) and $\nu_x = 9.2$ (dashed).

Spin-matched Siberian snake provides higher level of the equilibrium polarization, but even in this case at energies higher than 1 Gev the equilibrium polarization level becomes very small:

$$P_{eq} \simeq \frac{72\sqrt{3}}{55}\,\frac{\sin\nu_0\pi}{\nu_0^2\pi} = 0.72\,\frac{\sin\nu_0\pi}{\nu_0^2}$$

## 4 REFERENCES


[1] Ya.S.Derbenev and A.M.Kondratenko, Part.Accel. **8**, 115 (1978).

[2] A.D.Krish et al., Phys.Rev.Letters **63**, 1137 (1989).

[3] D.P.Barber et al., Phys.Lett. **B 343**, 436 (1995).

[4] I.Passchier et al., Report presented on Worksh. on High-Energy Electron Polarimeters, Amsterdam, (1996).

[5] C.W. de Jager, V.Ptitsin and Yu.M.Shatunov, Report presented on 12th Intern. Symp. on High Energy Spin Physics, Amsterdam, (1996).

[6] A.A.Zholents, V.N.Litvinenko, Preprint INP 81-80, 1981.

[7] Ya.S.Derbenev and A.M.Kondratenko, Sov.Phys.JETP **37**, 968 (1973).

# THE MAGNETIC DESIGN OF A HIGH FIELD PERMANENT MAGNET MULTIPOLE WIGGLER FOR THE SRS

J. A. Clarke, CLRC Daresbury Laboratory, Warrington, WA4 4AD, UK

*Abstract*

Two new insertion devices will be installed as part of the Daresbury SRS upgrade project. The devices are multipole wiggler magnets with a peak field of 2 T. This paper describes the complete magnetic design of these permanent magnet devices which has been carried out in both 2 and 3 dimensions. The design has been optimised to generate the highest fields with the shortest possible period to fully utilise the limited space available in the SRS.

## 1 INTRODUCTION

The SRS is a 2 GeV, 2nd generation synchrotron radiation source operating in the UK. It was designed to use the main dipole magnets as the primary source of radiation. Nevertheless during its life three insertion devices have been installed, two superconducting wavelength shifters [1,2] and one undulator [3]. An upgrade project has recently been funded that will add two more insertion devices to the lattice [4]. These two identical insertion devices will be hybrid multipole wigglers designed to provide high flux levels at about 10 keV. The free straight section available for the IDs is just over one metre so there is great pressure to reduce the period of the MPWs as much as possible to give the greatest flux output for the beamlines. With this in mind the vertical aperture has been assessed in detail with beam scrapers [5] and it has been concluded that the total internal beam stay clear region in the straight section could be reduced from the present 36 mm to 15 mm without reducing the beam lifetime by more than about 15%. The insertion device vacuum vessel has been designed so that the gap between the steel poles is minimised [6]. A prototype titanium vessel has been built and measured that will allow the magnet gap to reach 19.2 mm.

The peak magnetic field specified for the MPWs is 2.0 T since this provides a high critical energy of 5.3 keV and also provides enough angular spread in the electron beam to allow 2 stations to be built on each beamline. An initial assessment quickly concluded that an electromagnetic device was feasible but with a longer period than would be possible from a permanet magnet hybrid device. The specification for the MPWs is given in Table 1.

Table 1. Specification of the Multipole Wigglers

| | |
|---|---|
| Peak Field on axis | 2 T |
| Minimum Gap | 19.2 mm |
| Period | 200 mm |
| K value | 37.4 |
| Number of full strength poles | 9 |
| Maximum length available | 1.1 m |

## 2 MAGNET DESIGN

The magnet design has been carried out in both 2 and 3 dimensions to give as accurate a model as possible. The computing time is much shorter for 2D studies and so as much of the design as possible has been carried out in this regime and then final checks made with a full 3D simulation. Typical execution time for the complete 3D simulation is about 30 hours with 150,000 nodes on a Unix workstation. The 2D models have been generated with Opera-2D [7] and Pandira [8], the 3D models were created with Opera-3D running Tosca [7].

### *2.1 Longitudinal Design*

Simple ¼ period models were initially investigated to check the feasibility of the specification. These concluded that the specification required would be challenging but possible if the highest grade materials were assumed. High saturation field strength vanadium permendur steel has been chosen for the pole pieces, in common with other projects requiring very high field strengths. A high remanent field permanent magnet material has also been assumed (NdFeB with Br=1.35 T, Hc = 1020 kA/m). An optimum geometry for the steel and permanent magnet material has been found by manual iteration. The main permanent magnet block extends beyond the steel pole piece by 34 mm to increase the on-axis field. The vertical gap between the pole pieces is 19.2 mm but the gap between the permanent magnet blocks must be larger than this to provide room for strengthening ribs on the vacuum vessel (see figure 1). The permanent magnet blocks are separated by a vertical gap of 27.2 mm. An additional permanent magnet piece was initially placed on top of the steel but it was concluded that this only had a small effect on the peak field. The corner of the steel pole is chamfered at 45 degrees to reduce steel saturation in this area. More

0-7803-4376-X/98/$10.00 © 1998 IEEE

complicated steel profiles have not been found to be necessary.

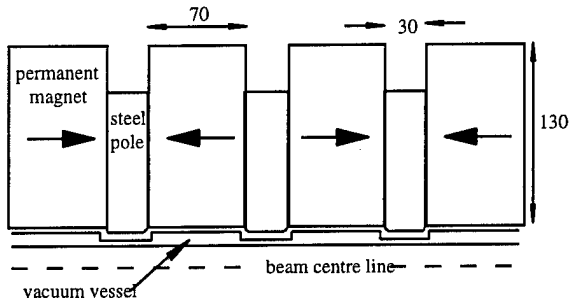



Figure 1. Longitudinal cross-section though a part of the top array. The arrows indicate the direction of magnetisation. Dimensions are in mm.

*2.2 Transverse Design*

Although the extra permanent magnet material above the steel was found to be inefficient, additional permanent magnet material side pieces do provide a significant contribution to the field on axis. These extra side pieces are found to reduce the flux leakage in the transverse plane. This is seen in figure 2 where the effect of leaving out the side pieces is illustrated. The width of the main permanent magnet blocks is extended well beyond that of the steel in common with most hybrid designs. As with the longitudinal profile, the steel corner is removed in the transverse plane with a 45 degree chamfer to reduce steel saturation problems.

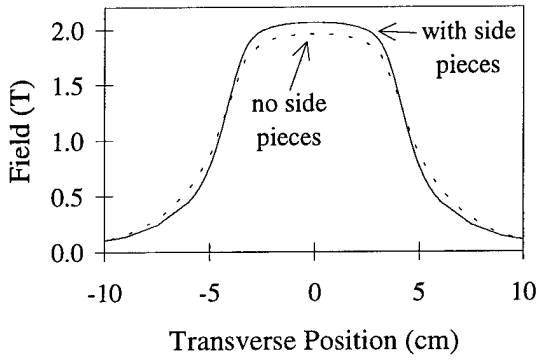



Figure 2. The on-axis vertical magnetic field as a function of transverse position underneath the pole. The dotted line shows the effect of not using permanent magnet side pieces.

*2.3 End Design*

Since the number of main poles is only 9, the 2 end poles can make a significant contribution to the photon output. For this reason the field in the end poles has been forced to be as high as possible whilst still terminating the magnet correctly with zero angle and displacement of the electron beam. A slim steel end pole and half main permanent magnet block are found to give a peak field of about 1.8 T. No side permanent magnet pieces were included as they were unnecessary. The vertical magnetic field along the electron beam axis is given in figure 3. An air-cooled trim coil will be wound around each array to provide fine tuning of the electron beam steering through the MPW.

A view of one complete array of the MPW assembled onto a backing beam is given in figure 4. A summary of the design parameters for the MPW is given in Table 2.

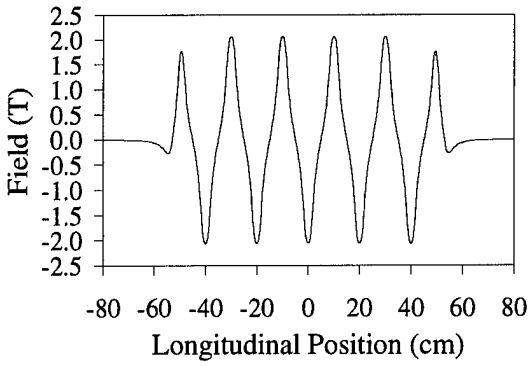



Figure 3. The on-axis vertical magnetic field through the MPW.

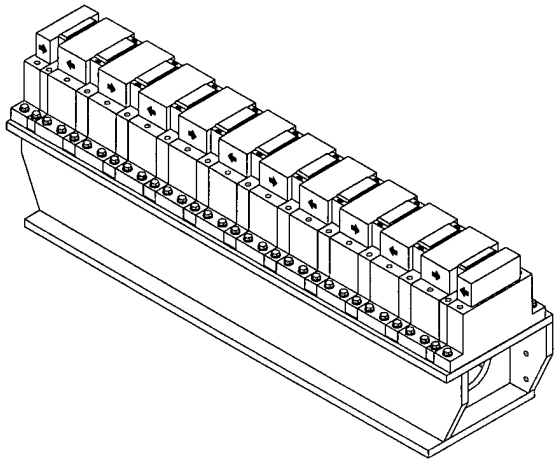


Figure 4. A complete magnet array of the MPW. The arrows indicate the direction of magnetisation.

Table 2. Design parameters for the MPW.

| | |
|---|---|
| Pole Material | Vanadium Permendur |
| Permanent Magnet Material | NdFeB |
| Remanent Field | 1.35 T |
| Pole Dimensions | 100 x 80 x 30 mm |
| Main PM Block Dimensions | 130 x 120 x 70 mm |
| Side PM Block Dimensions | 96 x 10 x 30 mm |
| Total Length of Magnet | 1.078 m |
| Gap Setting Accuracy | < 10 μm |
| Gap Resolution | < 5 μm |
| Parallelism of Two Arrays | < ±40 μm |
| Force at Minimum Gap | 50 kN |
| Trim Coil Ampere Turns | 450 At |

## 3. PHOTON OUTPUT

The magnetic field model has been used to calculate the synchrotron radiation output from the multipole wigglers. The most interesting feature is the influence of the non-sinusoidal longitudinal field shape. This has the effect of decreasing the angular spread of the radiation in the horizontal plane from what would be expected of a pure sinusoidal field. The photon flux at 10 keV has been calculated as a function of horizontal angle from the beam centre line. This is compared with an ideal sinusoidal device in figure 5. The power levels from the devices are also significantly affected by the non-sinusoidal field shape, these are summarised in Table 3.

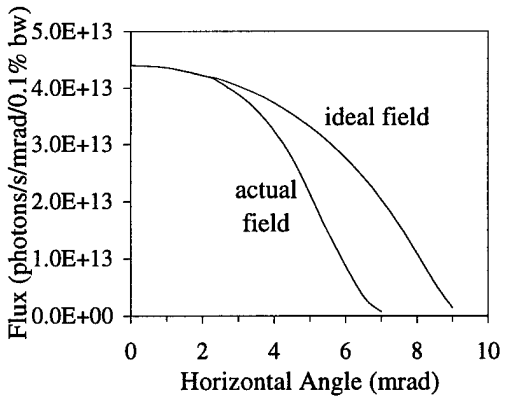



Figure 5. Photon output as a function of horizontal angle. A beam current of 300 mA has been assumed.

Table 3. Predicted power levels form the multipole wiggler assuming a beam current of 300 mA.

| | |
|---|---|
| Total Power | 2.4 kW |
| Vertically Integrated Power | 220 W/mrad |
| Peak Power Density | 1130 W/mrad$^2$ |

## 4. FUTURE WORK

A new magnet measurement facility is now being assembled to make detailed measurements of the two devices. Two measurement benches will be available in an air-conditioned environment. The first will provide point by point field measurements using a Hall plate and the second will provide integrated field measurements with either a rotating coil or a scanning wire.

The design of the multipole wigglers is now complete and it is intended that manufacturing should start in the Summer of 1997 with the two devices available for magnet testing in the Summer of 1998. It is intended to install the two devices at the start of 1999 and to have operational beamlines later that year.

## REFERENCES


[1] V P Suller et al, "SRS behaviour with a superconducting 5 Tesla wiggler insertion", Proceedings of the 1983 IEEE Particle Accelerator Conference, Santa Fe, p3127.

[2] M W Poole et al, "A second superconducting wiggler magnet for the Daresbury SRS", Proceedings of the 1989 IEEE Particle Accelerator Conference, Chicago, p1250.

[3] M W Poole and R P Walker, "An undulator source for the SRS at Daresbury", Proceedings of the 1985 IEEE Particle Accelerator Conference, Vancouver, p3374.

[4] J A Clarke and M W Poole, "Upgrading the Daresbury SRS with additional insertion devices and its implications for the storage ring layout", Proceedings of the 5th European Particle Accelerator Conference, Sitges, 1996, p623.

[5] J A Clarke and H L Owen, "Operation of the Daresbury Synchrotron Radiation Source with reduced vertical aperture", Proceedings of the 5th European Particle Accelerator Conference, Sitges, 1996, p620.

[6] N Bliss and C L Dawson, "The design, construction and testing of a multipole wiggler magnet titanium vacuum chamber for the SRS", these proceedings.

[7] Vector Fields Ltd, 24 Bankside, Kidlington, Oxford, UK.

[8] Los Alamos Accelerator Code Group, Los Alamos National Laboratory, USA.

# RECENT DEVELOPMENTS OF INSERTION DEVICES AT THE ESRF

J. Chavanne, P. Elleaume, P. Van Vaerenbergh, European Synchrotron Radiation Facility,
B.P. 220, F-38043 Grenoble Cedex, France

*Abstract*

After 4 years of user operation, the ESRF is operating 44 segments of Insertion Devices serving 25 beamlines. Recent developments in the technology of Insertion Devices are discussed such as the design of passive phasing sections for both the pure permanent magnet and hybrid type undulator. A novel design of a short period variable polarization helical undulator is presented. It is made of both permanent magnets and coils. It will cover the photon energy range from 1 to 15 keV with a flipping time of a few milliseconds between left and right circular polarization. Finally, some perturbations induced by ambient residual field on hybrid insertion devices are reported.

## 1 STATUS OF INSTALLATION

The European Synchrotron Radiation Facility (ESRF) is a third generation synchrotron source optimized to produce hard X-rays in the 1 to 100 keV range. The majority of the beamlines use an insertion device (ID) as a source point which generates high fluxes and brilliance. The source is routinely operated with a stored current of 200 mA, an horizontal emittance of 4 nm and a coupling smaller than 1% resulting in a record brilliance reaching $10^{20}$ phot./sec/.1%/mm2/mrad2 around 5 keV. The Facility has been in user operation for more than 4 years and the number of IDs has gradually increased to reach 44 segments serving 25 beamlines (Table 1). All IDs except the 4T superconducting wiggler are made of permanent magnets with magnet blocks in the air on both sides of the vacuum chamber. Each segment is 1.6 meters long and three segments can be installed on a single straight section. 15 (9) beamlines operate with a minimum magnetic gap of 16 mm (20 mm). A prototype undulator chamber with 10 mm external aperture has been successfully tested which does not degrade the vacuum of the ring and therefore the lifetime of the stored beam (> 50 hours at 200 mA). These new chambers will gradually replace the existing ones. All permanent magnet IDs have been mechanically and magnetically designed and field measured at ESRF.

A special multipole and spectrum shimming [1] has been developed and systematically applied. Multipole shimming eliminates the need of dipole or multipole correction on all conventional undulators. The spectrum shimming reduces the phase error from one period to the next allowing nearly ideal spectral performance of each segment on harmonics # 1 to 15.

| ID # | Type | Period [mm] | Field [T] | Techno. |
|---|---|---|---|---|
| 1 | Wiggler | 70 | 0.85 | hybrid |
| | Undulator | 42 | 0.56 | ppm |
| 2 | Undulator | 46 | 0.48 | ppm |
| | Undulator | 26 | 0.16 | ppm |
| 3 | Undulator | 42 | 0.56 | ppm |
| | Undulator | 42 | 0.56 | ppm |
| 6 | Undulator | 46 | 0.48 | ppm |
| 9 | Wiggler | 70 | 0.85 | hybrid |
| | Undulator | 46 | 0.62 | ppm |
| | Undulator | 26 | 0.27 | ppm |
| 10 | Undulator | 46 | 0.48 | ppm |
| | Undulator | 26 | 0.71 | ppm |
| 11 | Wiggler | 125 | 1.20 | hybrid |
| | Undulator | 34 | 0.70 | ppm |
| 12A | Helic. Und. | 85 | 0.51 | ppm |
| 12B | Helic. Und | 52 | 0.36 | ppm |
| 13 | Undulator | 46 | 0.65 | hybrid |
| 14 | Undulator | 42 | 0.56 | ppm |
| | Undulator | 23 | 0.20 | hybrid |
| 15A | Asym. Wigg | 220 | 1.8 | hybrid |
| 15B | SuperCond. | 200 | 4 | superc. |
| 16 | Undulator | 42 | 0.56 | ppm |
| | Undulator | 42 | 0.56 | ppm |
| | Helic. Und. | 52 | 0.36 | ppm |
| 17 | Wiggler | 150 | 1.9 | hybrid |
| 18 | Undulator | 23 | 0.21 | ppm |
| | Undulator | 34 | 0.42 | ppm |
| 19 | Wiggler | 150 | 1.9 | hybrid |
| 20 | Asym. Wigg | 210 | 1 | ppm |
| | Undulator | 48 | 0.5 | hybrid |
| 21 | Wiggler | 80 | 0.81 | hybrid |
| | Wiggler | 80 | 0.81 | hybrid |
| 22 | Undulator | 42 | 0.56 | ppm |
| 23 | Undulator | 48 | 0.65 | ppm |
| | Undulator | 46 | 0.62 | ppm |
| | Undulator | 44 | 0.59 | ppm |
| 24 | Undulator | 42 | 0.56 | ppm |
| 26 | Undulator | 42 | 0.56 | ppm |
| | Undulator | 42 | 0.56 | ppm |
| 30 | Undulator | 40 | 0.52 | ppm |
| | Undulator | 40 | 0.52 | ppm |
| | Wiggler | 70 | 0.82 | hybrid |
| 32 | Undulator | 48 | 0.50 | ppm |
| | Undulator | 40 | 0.40 | ppm |

Table 1: Type, spatial period, peak field and technology used to build the 44 IDs presently in operation.

0-7803-4376-X/98 /$10.00 © 1998 IEEE

The spectrum shimming has routinely been applied over the last three years to all undulators. Figure 1 presents the rms phase error at a 16 mm gap as well as the maximum rms phase error for any useful gap on the last 13 ndulators produced.

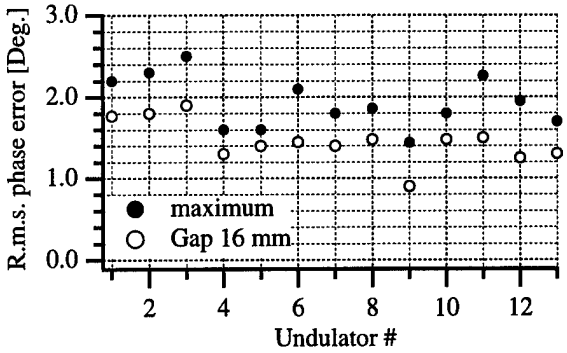



Figure1: rms phase error of the last 13 Undulators produced at ESRF.

## 2 UNDULATOR PHASING

### *2.1 Generalities*

The motivation for the phasing between the undulator sections is to ensure that a three segment assembly produces the same spectrum as a 5m long single piece ID. The magnet termination should be carefully designed to minimze the field integral induced as one varies the gap of one segment while maintaining the other unchanged. The proper operation of such a termination allows the user to vary the length of its undulator by switching between one, two or three segments at any time, therefore optimizing the heatload conditions in the beamline to the ring current and photon energy.

### *2.2 Pure Permanent Magnet Assemblies*

The first attempt to phase the undulator segments was tested on a pure permanent magnet assembly in 1995 [2]. It is now in use on 4 beamlines each operating two undulator segments of identical periods.

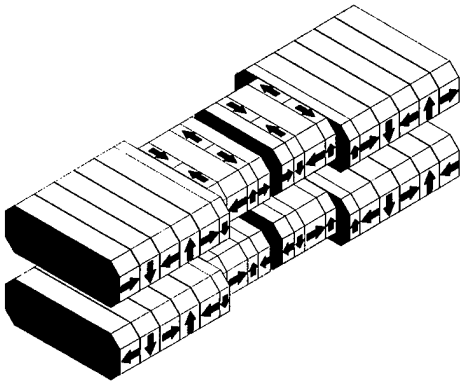


Figure 2: Phasing section for Pure Permanent Magnet. The distance between the magnet array is 6 mm (3 mm) for a period of 42 mm (20 mm).

The magnetic assembly is presented in Figure 2. The measured field integral produced at the junction between the segments is smaller than 30 Gcm for any gap combination of the segments (as low as 15 mm). These phasing sections are robust and inexpensive. They also allow the proper phasing of undulators of slightly different field or periods. As a result, almost all undulators produced at ESRF over the last two years are equipped with phasing sections.

### *2.3 Hybrid Assemblies*

Recently, an attempt was made to phase three long period undulators for the ID21 microscopy beamline. The requirements were the operation of a single segment in the undulator regime at small gap and large field in order to lower the energy of the fundamental around 0.28 keV and to operate the three segments simultaneously above 2 keV. The large field and long period required for the low energy operation resulted in selecting the hybrid technology for the magnet assembly with a period of 80 mm. The difficulty met at the design phase in maintaining both the phase variation and the field integrals independent of the magnetic gaps was significant because of the large susceptibility of the iron poles. It required a large number of 3D magnetic field simulations performed with the code Radia[3]. The configuration retained is presented in Figure 3.

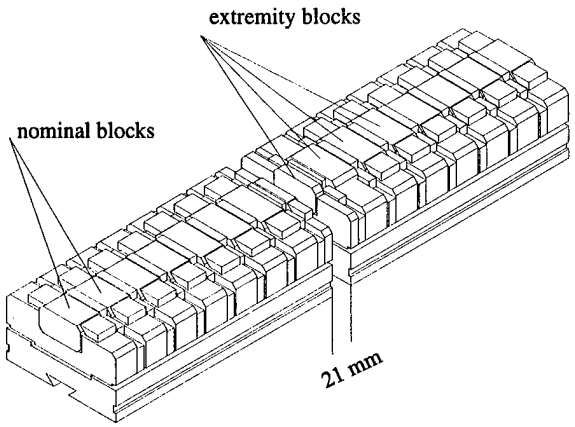



Figure3: Phasing section for an Hybrid Undulator. Due to the large interaction between magnet arrays, the distance between the arrays is increased to 21 mm resulting in some variations of the phase as a function of the magnetic gap.

The last magnet blocks have slightly larger dimensions than those in the middle of the undulator. To limit the differential field integral variation vs. gap to 125 G-cm, a large air gap of 21 mm between the segments has been selected. Due to this large distance between segments, the phase between the segments varies between 0 and 20 degrees in the useful gap range (35 to 100 mm) where

phasing is required. This is sufficient to ensure the constructive interference for harmonic 1 but some degradation of brilliance takes place on harmonics 3 and 5 depending on the magnetic gap. To conclude, three phased undulator segments have been built with the hybrid technology, the effort required was much greater than for phasing pure permanent magnet devices and the performances achieved significantly poorer.

## 3 FAST SWITCHING HELICAL UNDULATOR

Producing circularly polarized radiation from insertion devices has always been a major priority at ESRF. The hard X-ray range (between 20 and 500 keV) is covered by three asymmetric wigglers installed on ID15A, ID15B and ID20 while the low energy (0.5 to 10 keV) is covered by three variable polarization helical undulators installed on ID12A, ID12B and ID16 which are among the beamlines the most demanded by the user community. These undulators are unique in the world. They produce an ellipsoidal magnetic field with an independent control by the user of the amplitude and phase of the vertical and horizontal magnetic fields [4].

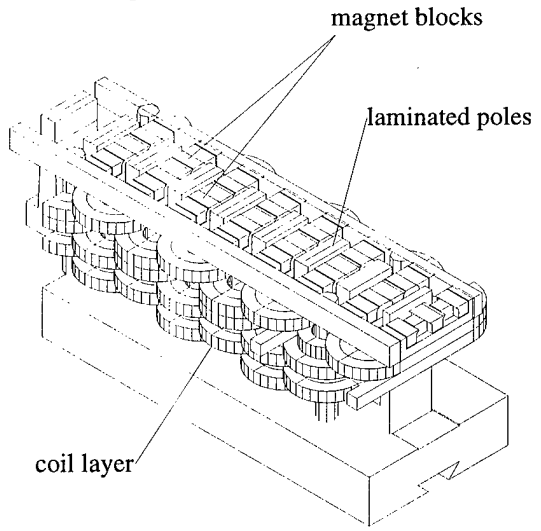



Figure 4: Design of the central part and termination of a novel type permanent -magnet / electro-magnet variable polarisation helical undulator.

During the three years of user operation, the most frequently performed field adjustment concerns the phase inversion which results in a flipping of the circular polarization between left and right. Such a flip takes a few seconds which is incompatible with the detection of a dichroism signal as low as $10^{-4}$. To overcome this limit, a new variable polarization helical undulator presented in Figure 4 is being built. The vertical magnetic field is produced by a coil and laminated iron structure while the horizontal magnetic field is produced by an array of $Sm_2Co_{17}$ permanent magnets located between the poles. Its period is 80 mm and its horizontal and vertical peak field is 0.21 T resulting in a deflection parameter K of 2.2. It covers the 1 to 15 keV range using harmonics 1 to 5. The horizontal (vertical) fields are tuned by changing the magnetic gap (coil current). The fast flipping of the polarization is achieved by inverting the current in the coil. A special power supply is being built which produces square shaped current between 300 and -300 Amp with a flipping time of a few milliseconds at a repetition rate from dc to 10 Hz. The magnetic field and field integrals in the central part and termination have been simulated and optimized using Radia.

## 4 AMBIENT FIELDS

The residual field observed in the ring tunnel can have significant consequences on the radiation and operation of the IDs. This field comes from the earth, ion pump and power cables of the dipoles, quadrupoles... It has been observed on ID16 that a 0.5 G horizontal component of field can bend the trajectory and reduce the undulator brilliance of a two segment device by 10% around 30 keV. Moreover for hybrid devices, this residual field magnetizes the iron poles resulting in a field integral on the electron beam which depends on the magnetic gap. For the same field of 0.5 G, we have observed (and confirmed with Radia) field integral variations larger than 100 Gcm over a 1.6 m segment when the magnetic gap is changed between 16 and 200 mm. This corresponds to an unacceptable displacement of the closed orbit by half the beam size in the vertical plane (on average). Proper measures have been taken to minimize this residual field , but because of this, active electro-magnet correctors are nevertheless required on a large number of hybrid devices.

## REFERENCES

[1] J. Chavanne, P. Elleaume, Undulator and Wiggler Shimming, Synchrotron Radiation News, Vol. 8, No. 1 , 1995 , p 18. See also J. Chavanne, P. Elleaume, Insertion Devices at the ESRF, Rev. Sci. Instrum. 66 (2) 1995, p 1868.

[2] J. Chavanne, P. Elleaume, P. VanVaerenbergh, ESRF, Proceedings of the 1995 Particle Accelerator Conference, Dallas May 1995, p 1319

[3] P. Elleaume, O. Chubar, J. Chavanne, "Computing 3D Magnetic Field from Insertion Devices", This proceedings.

[4] P. Elleaume, HELIOS a New Type of Linear/Helical Undulator, J. Synchr. Rad. (1994), Vol.1, p 10-26.

# COMPUTING 3D MAGNETIC FIELDS FROM INSERTION DEVICES

P. Elleaume, O. Chubar, J. Chavanne, ESRF, B.P. 220, F-38043 Grenoble CEDEX, France

*Abstract*

A 3D magnetostatics computer code optimized for Undulators and Wigglers is described. The code uses a boundary integral method and makes extensive use of analytical expressions for the field and field integrals along a straight line. The code outperforms currently available finite element packages in the area of simple data input, CPU time of the solver and accuracy reached for the estimation of field integrals. It is written in C++ and takes advantage of object-oriented programming. The code is interfaced to Mathematica [1]. Pre- and post-processing of the field data is done in the Mathematica Language. It has been extensively benchmarked with respect to a commercial finite element code. All ESRF Insertion Devices built during the last 4 years have been designed using this code or an older version.

## 1 INTRODUCTION

The most common approach used to compute the magnetic field produced by an ensemble of permanent magnets, iron pieces and current coils is based on the Finite Element Method (FEM). The popular code POISSON which computes magnetic fields in 2D geometry belongs to this category. Several 3D packages are available commercially. Their development typically requires several man-years of programming. The input of geometry, materials and proper meshing requires significant skills and time from users.

In this paper we present an alternate approach based on the Boundary Integral Method (BIM) [2]. The Radia code has been continuously developed by the authors over the past 8 years representing a total effort of 1.5 man-year. During the development, the code has been regularly and successively checked against a commercial 3D FEM package called FLUX3D [3] and against field and field integral measurements made on real magnetic devices built in the ESRF Insertion Device laboratory. The code consists in a set of functions implemented in C++ and available in the Mathematica programming environment. The Mathematica language is used for pre- and post-processing. Versions of the code are currently available for Power Macintosh and Windows 95/NT [4].

## 2 PRINCIPLES OF THE CODE

A user of Radia creates several types of objects and combines them to solve the problem. The basic type of objects are the source objects capable of creating magnetic fields. This includes magnetized volumes, current coils of various shapes and container objects. The magnetized volumes can be subdivided into smaller objects of the same kind with independent magnetizations. Another type of object describes material properties through the magnetization vs field law which can be a linear anisotropic (as for NdFeB or SmCo) or nonlinear isotropic (as for iron). The next type of objects are space transformations such as translation, rotation or plane symmetry. After creating the necessary objects, the user builds the model by linking the objects together.

The essential step consists in solving the problem in terms of magnetizations in all the volumes with particular material properties. This is done by creating in memory a large matrix also called an Interaction Matrix and applying a relaxation scheme to it. After the relaxation, magnetic field and field integrals can be computed anywhere in space by summing the field created by all the sources. The field from each source is computed with efficient analytical formulas. The accuracy of the computed field only depends on the level of segmentation of the iron and magnet pieces.

### *2.1 Analytical Expressions for Field and Field Integrals*

Magnetic field **H** produced by an object of arbitrary shape with its volume uniformly magnetized according to the vector **M** can be expressed by a matrix relation

$$\mathbf{H} = \mathbf{Q}\mathbf{M}. \tag{1}$$

If the object is a rectangular parallelepiped block with faces parallel to XY, XZ and YZ planes of the Cartesian frame, the components of the matrix **Q** are represented by the well-known formulas

$$Q_{xx} = \frac{1}{4\pi}\sum_{i,j,k=1}^{2}(-1)^{i+j+k+1}\tan^{-1}[x_i^{-1}y_j z_k (x_i^2+y_j^2+z_k^2)^{-1/2}],$$
$$Q_{xy} = \frac{1}{4\pi}\ln\left[\prod_{i,j,k=1}^{2}[z_k+(x_i^2+y_j^2+z_k^2)^{1/2}]^{(-1)^{i+j+k}}\right], \tag{2}$$

where

$$x_{1,2} = x_c - x_0 \mp w_x/2,\quad y_{1,2} = y_c - y_0 \mp w_y/2,\quad z_{1,2} = z_c - z_0 \mp w_z/2, \tag{3}$$

$(x_c, y_c, z_c)$ are Cartesian coordinates of the block's center, $(w_x, w_y, w_z)$ the block's dimensions, $(x_0, y_0, z_0)$ coordinates of an observation point. $Q_{yy}(Q_{zz})$ is deduced from $Q_{xx}$ by exchanging $x \leftrightarrow y$ ($x \leftrightarrow z$) in (2); $Q_{xz}(Q_{yz})$ is deduced from $Q_{xy}$ by exchanging $y \leftrightarrow z$ ($x \leftrightarrow z$). In addition,

$$Q_{ll'} = Q_{l'l},\quad l, l' = x, y, z. \tag{4}$$

In accelerator physics, the magnetic field integrated along a straight line from -∞ to +∞ is of major importance. Numerical integration of the field is time consuming and fundamentally inaccurate. In Radia, the

0-7803-4376-X/98 /$10.00 © 1998 IEEE

field integrals are computed from an analytical integration except for a few cases when such expressions cannot be derived easily.

Let **I** be the field integral along a line parallel to a vector $\mathbf{v}=(v_x,v_y,v_z)$, $|\mathbf{v}|=1$, and passing through a point $\mathbf{r}_0$. For a rectangular parallelepiped block with faces parallel to XY, XZ and YZ planes and uniform magnetization **M**, **I** can be expressed as

$$\mathbf{I} \equiv \int_{-\infty}^{+\infty} \mathbf{H}(\mathbf{r}_0 + \mathbf{v}s)ds = \mathbf{GM}, \tag{5}$$

$$G_{xx} = \frac{1}{2\pi}\sum_{i,j,k=1}^{2}(-1)^{i+j+k}\left[(v_z z_k u_y^{-1} - v_y y_j u_z^{-1})\tan^{-1}\left[\frac{u_x x_i - (v_y y_j + v_z z_k)v_x}{v_z y_j - v_y z_k}\right] + \right.$$

$$+ v_x x_i\left[u_y^{-1}\tan^{-1}\left[\frac{u_y y_j - (v_x x_i + v_z z_k)v_y}{v_x z_k - v_z x_i}\right] + u_z^{-1}\tan^{-1}\left[\frac{u_z z_k - (v_x x_i + v_y y_j)v_z}{v_x y_j - v_y x_i}\right]\right] +$$

$$\left. + [(v_x y_j - v_y x_i)v_z u_z^{-1} + (v_x z_k - v_z x_i)v_y u_y^{-1}]\,L_{ijk}\right],$$

$$G_{xy} = \frac{1}{2\pi}\sum_{i,j,k=1}^{2}(-1)^{i+j+k}\left[(v_y x_i - v_x y_j)u_z^{-1}\tan^{-1}\left[\frac{u_z z_k - (v_x x_i + v_y y_j)v_z}{v_x y_j - v_y x_i}\right] + \right.$$

$$\left. + [(v_x x_i + v_y y_j)v_z u_z^{-1} - z_k]\,L_{ijk}\right],$$

$$L_{ijk} = \ln[(v_x y_j - v_y x_i)^2 + (v_x z_k - v_z x_i)^2 + (v_z y_j - v_y z_k)^2]/2, \tag{6}$$

$$u_l = 1 - v_l^2, \quad l = x,y,z,$$

where $x_{1,2}$, $y_{1,2}$, $z_{1,2}$ are given by (3) with $(x_0,y_0,z_0)$ now being coordinates of the point $\mathbf{r}_0$ on the line along which the integration is done. The other components of the matrix **G** can be derived using the same rules as for the corresponding components of the matrix **Q** (the exchanging procedure concerns now also the components of the vector **v**). Eqs. (6) only apply if the line does not cross the body of the block. If $v_x = v_z = 0$ (integration along the y edge), Eqs. (6) reduce to

$$G_{xx} = \frac{w_y}{2\pi}\sum_{i,k=1}^{2}(-1)^{i+k}\tan^{-1}(x_i z_k^{-1}),\ G_{zz} = \frac{w_y}{2\pi}\sum_{i,k=1}^{2}(-1)^{i+k}\tan^{-1}(x_i^{-1} z_k),$$

$$G_{xz} = \frac{w_y}{4\pi}\ln\left[\frac{(x_1^2+z_2^2)(x_2^2+z_1^2)}{(x_1^2+z_1^2)(x_2^2+z_2^2)}\right],\ G_{yy} = G_{xy} = G_{yz} = 0. \tag{7}$$

The linearity of (1) and (5) is the general property applicable to any shape. The specificity of the shape only appears in (2) and (6). The corresponding Matrices **Q** and **G** derived for the general case of a volume enclosed by a set of planar polygons will be detailed in a future publication. At present, Radia handles the rectangular parallelepipeds and any volumes defined by a thick polygon (straight prism with a polygonal base).

The formulas analogous to (1)-(3), for the case of a current carrying rectangular parallelepiped block with constant current density can be found in [5]. We have also implemented a current carrying arc element with constant rectangular cross-section (details to be published later). Finally, the vector potential can be computed on request for all the elements using the corresponding analytical formulas.

### *2.2 Space Transformations*

Space transformations are used for orientation of field source elements in space as well as for simulation of boundary conditions by mirroring. There are four basic space transformations in use: translation, plane symmetry, rotation around an arbitrary axis, and field inversion. Several space transformations can be combined (through matrix multiplication) into a new space transformation. Let **T** be a transformation that applies to a point **r** or to a source object *S*, **H**(**r**,*S*) be the field produced by the object *S* at the point **r.** The field produced by the transformed object **T***S* can be computed by means of the following identity:

$$\mathbf{H}(\mathbf{r}, \mathbf{T}S) = \mathbf{T}\mathbf{H}(\mathbf{T}^{-1}\mathbf{r}, S). \tag{8}$$

It is important to note that **T** applies not only to the point **r**, but also to the field components. The laws of the transformation may differ for various types of vectors. Radial and axial vectors transform differently.

A transformation **T** may be applied to a source *S* with some multiplicity *m*. $m = 2$ is typically used to simulate a boundary condition, while $m > 2$ may be used to simulate a multipole field symmetry. In such a case, the field produced by *S* results in the sum of the fields created by the objects $\mathbf{T}^i S$ with *i* varying from 0 to *m*-1. Applying transformations with a multiplicity can be understood as an efficient use of the symmetries in the model being solved. This results in a minimum number of degrees of freedom and therefore dramatically reduces the memory requirements and CPU time needed for the solution.

### *2.3 Interaction Matrix and Relaxation*

Let us consider *N* source objects having magnetization vectors $\mathbf{M}_i$, $i=1,2,\ldots,N$. Let $\mathbf{H}_i$ be the field strength in the center of object *i*. Due to the linearity of the Eq. (1), $\mathbf{H}_i$ can be expressed as

$$\mathbf{H}_i = \sum_{k=1}^{N}\mathbf{Q}_{ik}\mathbf{M}_k + \mathbf{H}_{\mathbf{ex}i}, \quad i = 1,2,\ldots,N, \tag{9}$$

where $\mathbf{H}_{\mathbf{ex}i}$ is an external field in the center of the object *i*. $\mathbf{Q}_{ik}$ with $i,k=1,2,\ldots,N$ gives the Interaction Matrix. For each particular *i* and *k*, $\mathbf{Q}_{ik}$ itself is a 3 x 3 matrix. In the simplest case of a rectangular parallelepiped with no symmetries its components are defined by the Eqs. (2) - (4). If a space transformation with some multiplicity *m* was applied to the source object *k*, then $\mathbf{Q}_{ik}$ is the sum of *m* contributions deduced from Eqs. (2) - (4) after series of transformations of the observation point and field.

For each of the *N* objects, the magnetization $\mathbf{M}_i$ is related to the field strength $\mathbf{H}_i$ by a material relation:

$$\mathbf{M}_i = \mathbf{f}_i(\mathbf{H}_i), \quad i = 1,2,\ldots,N. \tag{10}$$

Eqs. (9) - (10) describe the problem. They can be solved by an iterative procedure that must be properly

selected to ensure rapid convergence. We use the following procedure where the magnetization $\mathbf{M}_{i,p}$ and field strength $\mathbf{H}_{i,p}$ in each object $i = 1,2,\ldots,N$ at iteration $p$ are deduced from the collection of $\mathbf{M}_{i,p-1}$ and $\mathbf{H}_{i,p-1}$ derived for all the objects at the iteration $p$-1 by:

$$\begin{aligned}
\tilde{\mathbf{H}}_{\mathrm{ex}i,p} &= \mathbf{H}_{\mathrm{ex}i} + \sum_{k=1}^{i-1} \mathbf{Q}_{ik}\mathbf{M}_{k,p} + \sum_{k'=i+1}^{N} \mathbf{Q}_{ik'}\mathbf{M}_{k',p-1}, \\
\mathbf{H}_{i,p} &= [\mathbf{E} - \mathbf{Q}_{ii}\chi_i(\mathbf{H}_{i,p-1})]^{-1}(\tilde{\mathbf{H}}_{\mathrm{ex}i,p} + \mathbf{Q}_{ii}\mathbf{M}_{\mathrm{r}i}), \\
\mathbf{M}_{i,p} &= \mathbf{f}_i(\mathbf{H}_{i,p}),
\end{aligned} \tag{11}$$

where $\mathbf{E}$ is the 3 x 3 unit matrix, the function $\chi_i(\mathbf{H})$ gives the local susceptibility tensor, $\mathbf{M}_{\mathrm{r}i}$ is the remanent magnetization in the object $i$. For a linear material, $\chi_i$ does not independ of $\mathbf{H}$. For a non-linear isotropic one with the material relation being $\mathbf{M} = f_i(|\mathbf{H}|)\,\mathbf{H}/|\mathbf{H}|$,

$$\begin{aligned}
\chi_i(\mathbf{H}) &= \begin{cases} [f_i(|\mathbf{H}|)/|\mathbf{H}|]\,\mathbf{E}, & |\mathbf{H}| \neq 0, \\ f_i'(0)\,\mathbf{E}, & |\mathbf{H}| = 0, \end{cases} \\
\mathbf{M}_{\mathrm{r}i} &= \mathbf{0}.
\end{aligned} \tag{12}$$

The iterations are stopped when the magnetizations $\mathbf{M}_{i,p}$ ($i = 1,2,\ldots,N$) are stable to a specified precision. For almost all cases of linear and non-linear materials that we have studied and all sorts of subdivisions, the iterative solution (11) - (12) was found to be fast and stable such that no additional relaxation parameter was needed.

## 3 COMPARISON WITH MEASUREMENTS

The Radia code has been systematically and quite successfully used in the past few years for the design of Insertion Devices at ESRF. Figure 1 presents a comparison of a peak field and field integral measured on a real device and computed with Radia. For almost any ID that we have designed, the computed peak field agrees with the measurement within 2%. The discrepancies come essentially from partially unknown material properties.

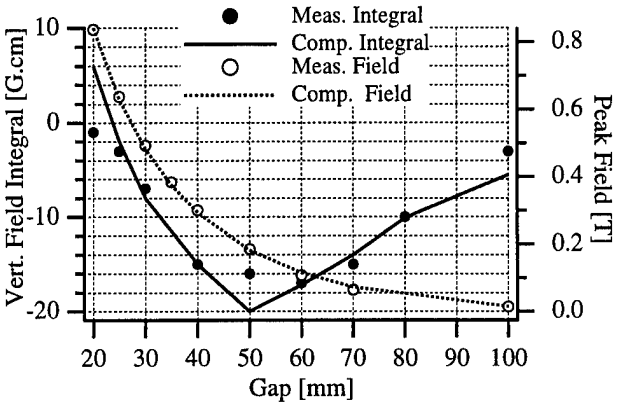



Figure 1: Comparison of the peak field and field integral predicted by Radia and measured on a 70 mm period hybrid wiggler. The computed and measured small variations of the field integral with the gap are in good qualitative agreement.

## 4 COMPARISON WITH FEM CODES

The proposed approach presents a number of advantages over FEM codes.

+ Geometries opened to infinity are more easily simulated.

+ The geometry creation requires only a few lines of the Mathematica code.

+ For the same precision, the number of elements and CPU time required to compute the central field of an undulator is roughly 20 times smaller in our approach than with second order tetrahedron elements in FEM codes. For example, the peak field of a hybrid undulator can be obtained with a precision better than 1% in less than 10 seconds on a PowerMac 4400, while it would take a few minutes with an FEM code.

+ The precision of the field integral computation only depends on the level of segmentation of the iron, but not on the field sampling and boundary conditions applied at infinity as is the case with FEM codes. Taking the example of a hybrid 2T wiggler, we obtain reliable estimation for the field integrals within several minutes of CPU time (PowerMac 4400) which is extremely difficult (may be impossible) with an FEM code. The design of termination of a hybrid wiggler can therefore be optimized over one night by a systematic exploration of a few geometrical parameters.

There are nevertheless some weak points as well.

- In the present version of the code, the memory required scales proportionally to the square of the number of elements. For example, one roughly needs 100M (25M) bytes of memory to solve a geometry made of 1000 (500) elements. We plan to improve this in a future version.

- Another drawback is a discontinuity in the value of the magnetic field inside subdivided iron objects, occurring at the boundary between any adjacent sub-objects. It is harmless if one is interested in the field sufficiently far outside the iron. This will also be improved in future versions.

## REFERENCES


[1] Mathematica is a registered trademark of Wolfram Research, Inc.

[2] For basics of the FEM and BIM see, for example, T. Tortschanoff: 'Survey of Numerical Methods in Field Calculations', IEEE Trans. on Magnetics, vol. MAG-20, No.5, 1984, p.1912.

[3] FLUX3D, Copyright Cedrat Recherche, CEDRAT SA, 10, Chemin du Pre Carre ZIRST 4301 38943 MEYLAN Cedex FRANCE.

[4] For more information see "http://www.esrf.fr/machine/support/ids/Public/index.html".

[5] L.K. Urankar: 'Vector Potential and Magnetic Field of Current-Carrying Finite Arc Segment in Analytical Form, Part III: Exact Computation for Rectangular Cross Section', IEEE Trans. on Magnetics, vol. MAG-18, No.6, p.1860.

# CONCEPTUAL AND EXPERIMENTAL FEASIBILITY STUDY OF A SUPERCONDUCTIVE MICRO-UNDULATOR

T. Hezel, R. Rossmanith, B. Krevet, H. O. Moser
Forschungszentrum Karlsruhe, Projektgruppe Errichtung ANKA,
Postfach 3640, D-76021 Karlsruhe, Germany

*Abstract*

Generating synchrotron radiation from conventional undulators in the hard X-ray region requires high electron energies. In order to open this spectral region for sources with smaller electron energy, such as ANKA (2.5 GeV), the period length of the undulator has to be decreased. In this paper the concept and the first successful tests towards constructing a superconductive micro-undulator with a period length of 3.8 mm are described. The structures were built with a commercially available NbTi wire. It was possible to run about 1000 AmpËre through the undulator coil at 4 K. A full prototype of a superconductive undulator is now under construction.

## 1 INTRODUCTION

This study was stimulated by various ideas on how to build a micro-undulator (an undulator with a period length significantly less than 1 cm) [1, 2]. Since a first design study of a superconductive micro-undulator in 1991 [3, 4], the interest in micro-undulators has grown very considerably [5, 6].

### *1.1 The Principle*

Fig. 1 shows a schematic drawing of the design presented in this paper. The wire is wound in grooves around a cylinder. The direction of the current alternates along the electron trajectory.

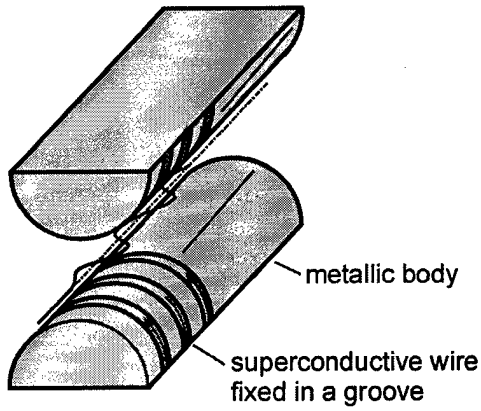



Fig. 1: Principle of the superconductive micro-undulator.

In this first prototype the metallic body of the undulator has a cylindrical form to save machining cost. In a later version the metallic body will have a flat profile similar to conventional undulators.

According to the law of Biot-Savart, an electrical current in a wire generates a circular magnetic field. The vertical field components add in the middle of the gap and result in a magnetic field alternating in the vertical direction along the beam axis.

### *1.2 Emitted Spectrum*

Insertion devices can expand the spectral region of storage rings to higher energies. The photons emitted by an ANKA [7] bending magnet have a critical energy of about 6 keV. According to the standard formula for the fundamental wavelength $\lambda$ of an undulator (period length $\lambda_u$=3.8 mm)

$$\lambda = \frac{\lambda_u}{2\gamma^2}\left[1+\frac{K^2}{2}+\gamma^2\Theta_0^2\right]; K \approx 0.934 \cdot B_0[T] \cdot \lambda_u[cm] \quad (1)$$

$\lambda$ is 0.8 Å (≈15 keV) at an energy of 2.5 GeV.

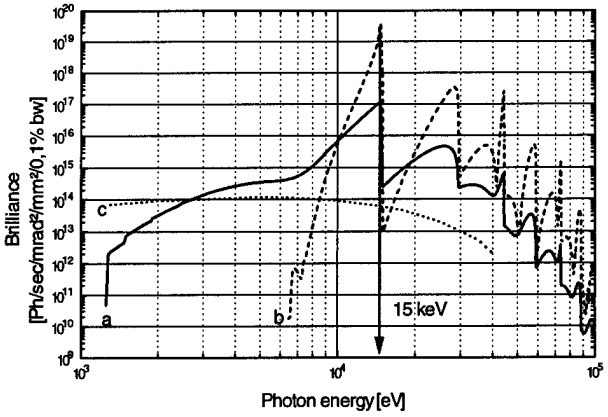



Fig. 2: Brilliance of a 100-period undulator: I=400 mA, $\lambda_u$=3.8 mm, $\beta_x$=1.5 m, $\beta_y$=0.5 m, $B_0$= 1 T and E=2.5 GeV calculated with URGENT [8]. a) $\varepsilon$=80 nmrad; b) $\varepsilon$=5 nmrad; c) ANKA bending magnet at $\varepsilon$=80 nmrad.

## 3 CURRENT LIMITATION

For the undulator prototype a commercially available NbTi superconductor with a cross-section of 1.25 x 0.80 mm$^2$ (including insulation) has been chosen [9]. Since superconductors are usually used in a high magnetic field environment, the quench behaviour in the low field region (where the undulator operates) is not well documented. Therefore, the quench behaviour was measured as a function of an external field.

0-7803-4376-X/98/$10.00 © 1998 IEEE

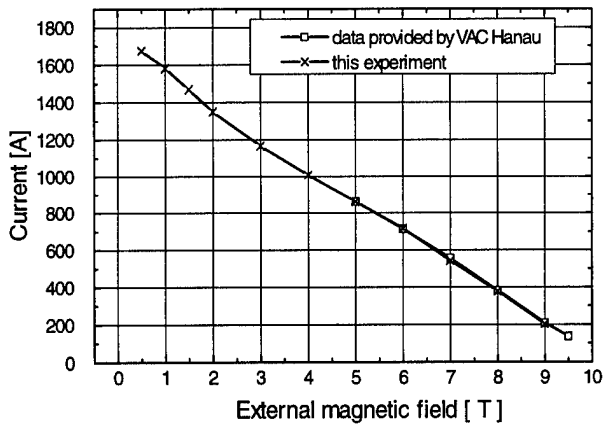



Fig. 3: Measurement of the quench current as a function of an external magnetic field.

## 4 WIRE ARRANGEMENT

The wire described in chapter 3 can be arranged in various ways (fig. 4). Each arrangement will result in a different maximum field in the gap, a different maximum field in the wire package (and therefore in a different current limit according to fig. 3) and a different undulator period.

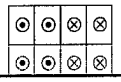
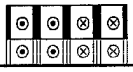
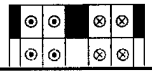
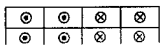
| case no. | geometry | period length [mm] | electr. current [A] | gap [mm] | field in the gap [T] |
|---|---|---|---|---|---|
| 1 |  | 2.96 | 1300 | 0.5<br>1.0 | 0.7<br>0.44 |
| 2 |  | 3.2 | 1300 | 0.5 | 0.67 |
| 3 |  | 3.8 | 1350 | 0.5<br>1.0 | 0.94<br>0.65 |
| 4 |  | 3.8 | 1470 | 0.5<br>1.0 | 0.82<br>0.56 |
| 5 |  | 4.76 | 1300 | 0.5<br>1.0 | 1.22<br>0.90 |

Fig. 4: Various possible wire arrangements in an undulator. The geometry is shown for one period only. The shaded areas represent insulation material. The first layer is fully drawn, the second partly, the third and fourth layers are omitted. The calculations were performed with MAFIA [10].

## 5 QUENCH TEST FOR AN UNDULATOR WINDING

In the first test the simple wire arrangement shown in fig. 5 was used.

This wire arrangement has the advantage that it is easier to coil, but the disadvantage that the achievable field strength in the gap is lower compared to all other wire arrangements shown in fig. 4.

The experiment proved that it was possible to run 1000 A through the undulator winding.

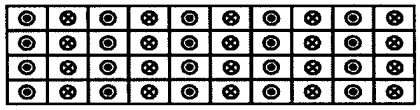


Fig. 5: Wire arrangement used for the quench test of the undulator winding. The measured quench current was 1000 A.

## 6 UNDULATOR PROTOTYPE WITH IRON

After this first test a 100-period undulator with a period length of 3.8 mm was built by using the winding configuration no. 4 from fig. 4. In order to increase the field strength in the gap, iron was used. The undulator body consists of six different parts: a copper core, an iron and four aluminium half-cylinders (figs. 6 and 7).

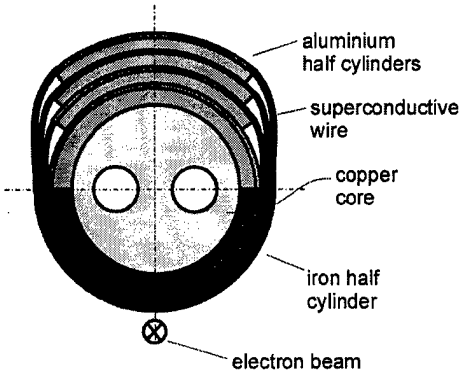



Fig. 6: Cross-section of the assembled undulator. A copper core cooled by liquid helium is located in the center. The iron half-cylinder is placed next to the electron beam.

The copper core contains two tubes through which the liquid helium flows. The iron half-cylinder has straight grooves perpendicular to the electron beam, whilst the aluminium parts have helical grooves. The grooves keep the superconductive wire fixed.

The maximum field strength in the 1 mm gap is 1 T. Calculations performed with MAFIA [10] have shown that the peak field close to the wires is about three times higher than the maximum field in the center of the gap (fig. 8).

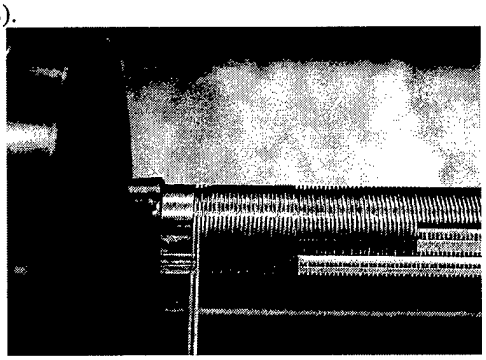


Fig. 7: Photograph of the undulator prototype during coiling.

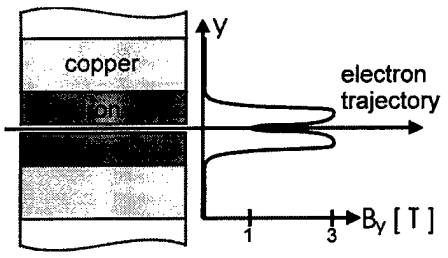



Fig. 8: Vertical cut through the undulator and corresponding vertical magnetic field calculated with MAFIA.

## 7 THE CRYOSTAT

Fig. 9 shows the cryostat of the superconductive undulator. The cryostat is presently under construction.

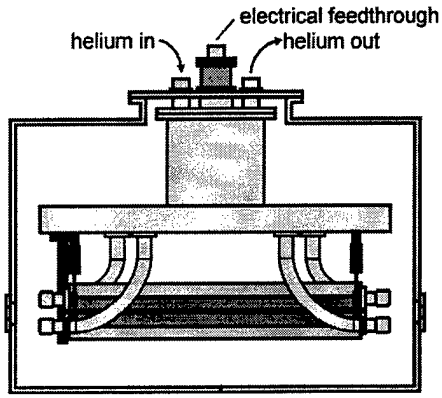



Fig. 9: Sideview of the cryostat (under construction).

The undulator is housed in a vacuum tank. The container for the helium (shown in grey) is in the upper part of the tank. From this container the helium flows via flexible tubes into the body of the undulator. A current in excess of 1000 A, which is needed to operate the undulator, is transported through a large number of copper wires located in the He-tank. This arrangement reduces the heat transport from outside and, in addition, reduces the electrical resistance of the copper wires. At their cold end, the copper wires are soldered to two hollow, helium-filled copper cylinders. The ends of the cylinders are positioned in close proximity to the undulator.

Also, in order to reduce the heat transport, the undulator is mechanically fixed to the helium tank. The undulator gap can be varied by several millimeters.

Thin metal sheets fixed to the helium container (not shown in fig. 9) protect the undulator from the heat radiated from the walls of the vacuum tank.

If an arrangement is envisaged in which the undulator and the accelerator vacuum system are separate, a thin metal foil (<50 μm) can be inserted between the two systems. Since the pressure difference between the two vacuum systems is small, the mechanical force acting on this foil is almost negligible.

## 8 SUMMARY

It was experimentally shown that an undulator with a period length of 3.8 mm built with superconductive wires can produce a maximum field of 1 T. At the moment a 100-period prototype undulator is under construction which is soon to be tested. The undulator is housed in a vacuum tank which can be either part of the accelerator vacuum system or, if required, the tank and the accelerator vacuum system can be separated by a thin metal foil.

## REFERENCES

[1] V. L. Granatstein et al., Small-period electromagnet wigglers for free-electron lasers, Appl. Phys. Lett. 47 (6), Sept. 1985

[2] R. Tatchyn et al., Attainment of Submillimeter Periods and a 0.3-T Peak Field in a Novel Micropole Undulator Device, Appl. Phys. Lett. 50(7), pp. 377-379, 1987

[3] H. Holzapfel, Diploma thesis, Entwurf eines supraleitenden Mikroundulators zur Erzeugung harter Synchrotronstrahlung, Universit‰t Karlsruhe, 1991

[4] H. O. Moser, B. Krevet, H. Holzapfel, Mikroundulator, Patentschrift DE 4101094 C1, Kernforschungszentrum Karlsruhe, 1991

[5] P. M. Stefan, L. Solomon, S. Krinsky, G. Rabowski, NSLS Prototype Small-Gap Undulator (PSGU), Proc. IEEE Part. Accel. Conf., San Francisco, CA, 1991, p. 1096

[6] 10th ICFA Beam Dynamics Panel, Workshop, General presentation of ESRF Insertion Devices, p. WG7-1, 1996, ESRF

[7] D. Einfeld et al., ANKA Status, these proceedings

[8] URGENT, R. P. Walker, B. Diviacco, Proc. 4th Int. Conf. Synchrotron Radiation Instrumentation, Chester, July 1991

[9] VAC Hanau, Germany, private communication

[10] MAFIA, CST Gesellschaft f‚r Simulationstechnik mbH, Darmstadt, Germany

# DEVELOPMENT OF AN IN-VACUUM MINIPOLE UNDULATOR

Toshiya Tanabe [1], Hideo Kitamura [1] and Peter Stefan [2]

1) JAERI-RIKEN SPring-8 Project Team, Kamigori, Ako-gun, Kyogo 678-12, JAPAN
2) National Synchrotron Light Source, Brookhaven National Laboratory, Upton, NY 11973

*Abstract*

An in-vacuum minipole insertion device [1] is currently being developed in collaboration between and the National Synchrotron Light Source (NSLS). The magnetic array is constructed by SPring-8 and it will be installed in a chamber with mechanical parts in the X-ray ring (E=2.584 GeV) at the NSLS. The device is made of permanent magnets with 31 periods and the length of the period is 11mm. It is to produce the fundamental radiation at 4.6 KeV which will be mainly used for X-ray photo-correlation spectroscopy (XPCS), and modest value of deflection parameter (K=0.7@3.3mm gap) enables higher harmonics to be used for a variety of experiments. We describe technical difficulties of constructing this type of device as well as the outline of our collaboration.

## 1 INTRODUCTION

With the advent of the third generation light source, vertical emittance of electron beam (e-beam) has become small enough to accommodate sub-centimeter magnet gap without sacrificing e-beam life-time. Unlike conventional insertion devices whose minimum gap is limited by the thickness of vacuum chambers, in-vacuum insertion devices allow magnetic gap to be closed up to the value allowed by beam dynamics limit. With a value of K not much smaller than unity, the use of higher harmonics and modest tunability are also viable.

## 2 ARRAY DESIGN

In-vacuum minipole undulator imposes extra constraints and difficulties compared to conventional IDs in design of magnet pieces primarily due to the following reasons: (1) It requires higher machining accuracy simply because of its small physical dimensions. (2) As the minimum allowable size of good field region (horizontal field roll-off is less than 0.5 %) for stable ring operation remains the same, horizontal dimension of the magnet cannot be decreased indefinitely. (3) Due to baking process of magnets the permeance of a magnet piece should not be lower than a certain value that is determined by the material. In general, stocky piece is more favorable than thin one, which contradicts the requirement (2).

A type of construction with independent magnet holder and clamp is not appropriate as relative errors in machining with respect to block size become larger and a large number of gaps created by the structure may result in poor vacuum. Hence, we have developed a novel structure to place and hold small magnet pieces in precise locations, and it is delineated in Figure 1.

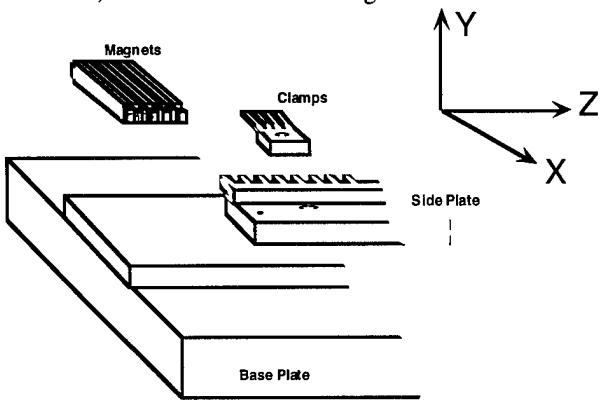



Figure 1. Magnet and holder structures

## 3 MAGNETIC FIELD MEASUREMENT

A picture of our magnetic field measurement facilities are shown in Figure 2. There are two types of systems; a Hall probe field mapping system which includes a moving stage on a granite bench, holders for magnet arrays and a base plate, and a rotating coil field integral measurement system which is seen at the upper right corner in the picture.

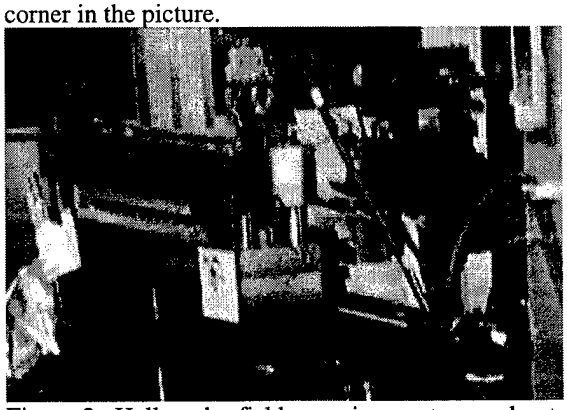


Figure 2. Hall probe field mapping system and rotating coil system.

As for the Hall probe, we use AREPOC HHP-MP which has an active area of 100μm × 100μm, and the thickness of enclosure is 1mm. It is placed in 1.5mm thick copper plate and sandwiched by Kapton tapes. Even though there is no temperature controlling device in the enclosure of the probe, sufficiently low ($3.0 \times 10^{-4}$ / K) temperature coefficient of the probe with software

0-7803-4376-X/98 /$10.00 © 1998 IEEE

compensation and reasonable ambient temperature control ensure the accuracy of the measurement. Extra attention was paid to the straightness and flatness of travel. The center of the probe has been found to stay on axis within a range of ± 1 μm vertically, and ± 7 μm horizontally. The rotating coil device is the same one as is used for SPring-8 IDs [2] except for narrower coil width (1.5mm) and shorter length (1.6m.) Magnetic field correction was made by first using simulated annealing [3] for coarse correction, then inserting magnet chips on the back of magnets for fine adjustment. A stainless chip is always inserted between a main magnet and chip magnets to warrant removability, in case it becomes necessary. The multipole components are measured within a range of x = ±4mm. They are derived from polynomial fitting of the first integral distribution along horizontal axis using the following formula.

$$\int_{-\infty}^{\infty} (B_y + iB_x)\, dz = \sum_{n=0}^{\infty} (b_n + ia_n)(x + iy)^n \qquad (1)$$

where $b_n$ are normal components and $a_n$ are skew ones. Integrated multipole requirements for NSLS X-ray ring and our measurement results are presented in Table 1. Figure 3-(a) and (b) show gap dependence of measured integrated dipole, quadrupole, respectively.

Table1. Integrated multipole requirements for NSLS X-ray ring versus the results of magnetic field measurement of IVUN arrays at 3.0mm gap

| (n) Normal / Skew | Goal (Abs) | Measurement |
|---|---|---|
| (0) Dipole | 100 G*cm | 77 / -70 G*cm |
| (1) Quadrupole | 10 G / 100G | -25 G / -192 G |
| (2) Sextupole | 50 G/cm | 161 / 41 G/cm |
| Norm. 2nd Integral | 8 G*m$^2$ | 0.031 G* m$^2$ |
| Skew 2nd Integral | 8 G*m$^2$ | N.A. |
| RMS Phase Shake | 2 degrees | 1.45 degrees |

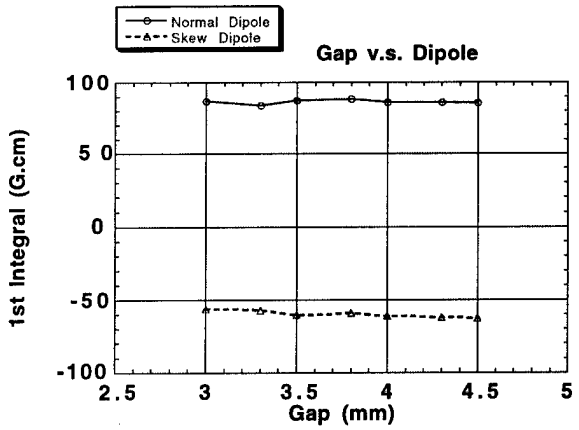



Figure 3-(a). Gap versus dipole components of the field

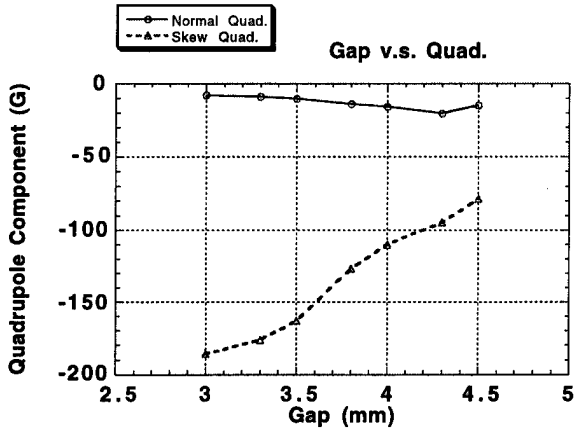



Figure 3-(b). Gap versus quadrupole components of the field.

## 4 ID PARAMETERS AND SPECTRUM

Pertinent ID parameters are presented in Table 2. Predicted radiation spectrum is shown in Figure 4 and peak brilliance with varying K is found in Figure 5.

Table 2 Selected ID parameters

| | |
|---|---|
| Type | Linear (4 block) |
| Period Length ($\lambda_u$) | 11.0 mm |
| Number of Period | 31 |
| $B_y$ , ( K ) @ 3.3 mm | 0.688 T (0.707) |
| Packing Factor | 0.992 |
| Fundamental Rad ($\lambda_1$ ) | 2.688 Å |
| Magnetic Material | NEOMAX 32 EH |
| Coating Material | TiN (5mm) |

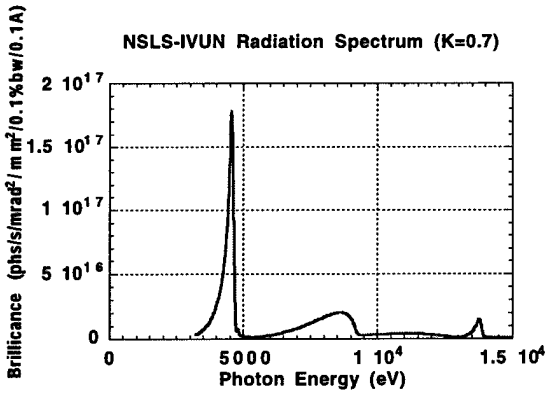



Figure 4. NSLS-IVUN radiation spectrum

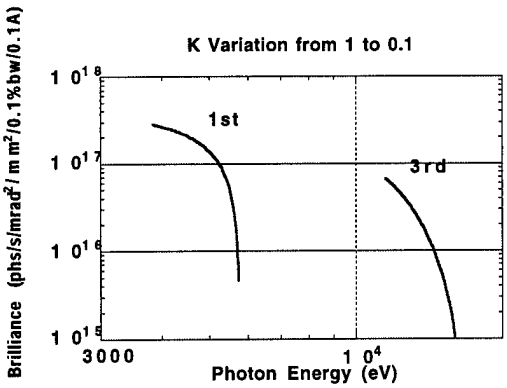



Figure 5. Peak brilliance with varying K

## 5 TRANSITION AREA

According to Reference [4], there are three predominant beam dynamic effects caused by small gap aperture of the minipole undulator and aperture change due to transition from outer vacuum chamber to ID. They are power dissipation due to longitudinal impedance, transverse coupled bunch instability / strong head-tail instability due to transverse resistive impedance and transverse geometric impedance. Power dissipation turns out to be modest. It can be shown that for gap being smaller than 2mm transverse resistive impedance becomes dominant as it is inversely proportional to the third power of the gap length, whereas geometric one is only to the first power. Two transverse effects are comparable when the undulator is operated at the gap of 3.3mm.

## 6 UHV TEST

After magnetic field correction was finished, a vacuum test in UHV minichamber was conducted to make sure of no degassing elements in the magnet-arrays before installation. Figure 6 shows schematic of the vacuum testing facility. The final value of vacuum reading by an extractor gauge (IONIVAC IM520, Leybold) reached $2 \times 10^{-9}$ Pa, which indicates sufficient ultra-high-vacuum (UHV) compatibility of the arrays.

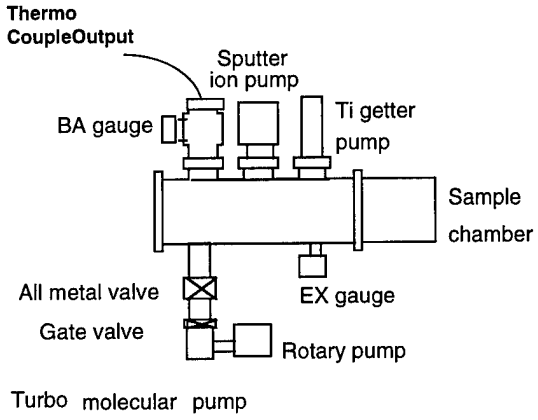



Figure 6. Schematic of the vacuum testing facility

## 7 MECHANICAL SUPPORT AND VACUUM SYSTEM (BNL)

IVUN is comprised of three major components: a rectangular vacuum chamber with bellows feedthroughs, magnet array units with drive system, and an elevator base stage, upon which all of the above components are supported.

The chamber is equipped with three forms of pumping, a 300 l/s ion pump, a titanium sublimator, and a non-evaporable getter. Precise alignment of the magnet arrays is facilitated by removable top and bottom rectangular flanges on the chamber: With the central section of the vacuum chamber removed, the magnet arrays are precisely aligned, with full access to the arrays. Then, using auxiliary pneumatic cylinders on the magnet drive, the magnet gap is opened to nearly 300 mm, and the central section of the vacuum chamber is replaced, without disturbing any of the adjustments.

The undulator magnet arrays are mounted on the water-cooled beams of the drive system, directly in the accelerator ultra-high vacuum. The drive system enables magnet gaps between 1 mm and 10 mm. The elevator base stage provides mounting fixtures for the IVUN vacuum chamber and the undulator magnet drive. In addition, it provides a 3 mm vertical translation of the combined chamber/magnet assembly about the nominal beam height.

## 8 CONCLUSION

With in-vacuum structure, a minipole undulator having modest tunability and harmonics has been constructed. The magnetic field quality is found be satisfactory after spectral and mutipole correction, and the magnet arrays show excellent UHV compatibility. A clever design of vacuum chamber greatly improves accessibility of magnet arrays. A complete device is expected to be installed in the X13 R&D straight section of the NSLS X-ray Ring in May 1997.

## 9 ACKNOWLEDGEMENTS

The authors wish to thank Dr. T. Tanaka of SPring-8 for help in vacuum testing and Mr. S. Okada of Sumitomo Special Metal Co. for his support.

## 10 REFERENCES

[1] T. Tanabe et al, SPring-8 Annual Report 1995, 173
[2] Insertion Device Handbook '96, (SPring-8 OPSRR 1996-0003)
[3] A. Cox and B. Youngman, Proc. SPIE 582, 91
[4] K. Bane and S. Krinsky, "Impedance of the NSLS Prototype Small-Gap Undulator Vacuum Chamber," BNL Informal Report, BNL-48792

# NOVEL STRUCTURE OF SHORT-PERIOD TWISTED UNDULATOR SPONTANEOUS EMISSION PROPERTIES

A.V. Smirnov and A.S. Khlebnikov
Russian Research Center `Kurchatov Institute`, 123182 Moscow, Russia

*Abstract*

A novel short-period undulator scheme is developed. The geometry looks like helical transformation applied to an original linear undulator structure and provides a combination of fast and slow oscillations of the electron beam. The following properties of the radiation are considered: i) reduction of relative content of higher odd harmonics as the `slow` helical field increases; ii) radiation enhancement as the number of helical turns increases; iii) spectral line splitting and intensity adjustability along with circular polarization of the radiation for the short-period twisted structure.

## 1 INTRODUCTION

Undulators with two or more frequencies are attractable from many points of view. One of them is insertion devices with special radiation characteristics.

We are considering here a somewhat new kind of two-frequency motion that could combine useful radiation properties of both linear microundulator and helical undulator. It can be implemented in a real construction as depicted in fig. 1. As it was discussed in [1] such schemes can be regarded as belonging to a new class of `twisted linear undulator`.

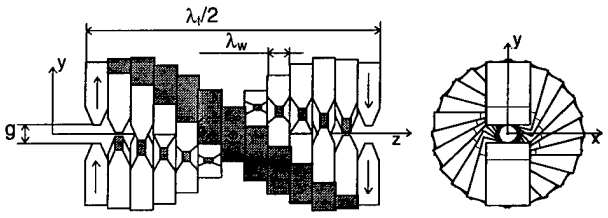



Fig. 1. Schematic drawing of the twister undulator structure.

## 2 UNDULATOR FIELDS

It was found in [2] the solution of Laplace`s equation for magnetic potential $\Delta\psi=0$ satisfying the condition of superimposed helical `slow` transformation to the original linear undulator structure:

$B_x=(B_w cosh_w z+B_t)sin(k_t z)$,

$B_y=(B_w cosh_w z+B_t)cos(k_t z)$,

where $k_t<<h_w$ and $h_w r<<1$, $B_w$ and $B_t$ are the amplitudes of the original linear (`microundulator` contribution) and `helical` undulator fields with periods $\lambda_w$ and $\lambda_t$ respectively, $h_w=2\pi/\lambda_w$ and $k_t=2\pi/\lambda_t$.

Under these assumptions one can derive:

$$\psi(r,j,z)=Re\sum_{m=-1}^{m=+1}\begin{pmatrix} C_m I_1(r(mh_w+k_t))\times \\ exp(i(j+(mh_w+k_t)z))\end{pmatrix},$$

where $C_0=\frac{2iB_t}{k_t}, C_{\pm 1}=i\frac{2B_w}{k_t\pm h_w}$

## 3 ELECTRON TRAJECTORIES

Equations of motion for a single electron were solved assuming $Kk_w r<<\gamma/2\pi$, where $K_t=eB_t/k_t mc$.

For the twisted undulator having zero first and second integrals and $\gamma>>1$ one can obtain

$$\vec{r}_\perp(z)=\frac{K_t}{\gamma k_t}\begin{pmatrix}\cos k_t z\\ -\sin k_t z\end{pmatrix}+\sum_{\pm}\frac{K_w^{\pm}}{\gamma\sqrt{2}}\begin{pmatrix}\cos(k_t\pm h_w)z\\ -\sin(k_t\pm h_w)z\end{pmatrix}\frac{1}{k_t\pm h_w}$$

$$r_z(t)=\beta_{\|}ct-\frac{1}{\gamma^2 h_w}\begin{bmatrix}\frac{K_w^+K_w^-}{\sqrt{2}}\sin 2h_w z(t)\\ +K_t\left(K_w^+ + K_w^-\right)\sinh_w z(t)\end{bmatrix}, \qquad (1)$$

where $\beta_{\|}=1-\frac{1}{2\gamma^2}\left(1+K_t^2+\frac{1}{2}\left(K_w^{+2}+K_w^{-2}\right)\right)$, and

$K^{\pm}_w=eB_w/mc(k_t\pm h_w)\sqrt{2}$.

The last coupling term in (1) containing $\sin h_w z$ can be comparable with the term containing $\sin 2h_w z$ and does not appear for a conventional planar undulator. Hence one can expect appearance of even harmonics for on-axis view of spontaneous emission.

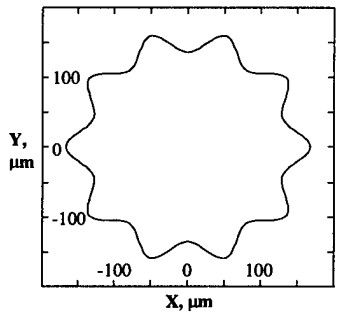



Figure 2. Electron trajectory view in transverse plane. E=500 MeV, $B_w$=10kG, $B_t$=1kG, $\lambda_w$=1cm, $\lambda_t$=10cm.

0-7803-4376-X/98/$10.00 © 1998 IEEE

## 4 SPONTANEOUS EMISSION RADIATION RELATIONSHIPS

Energy radiated per unit solid angle ($d\Omega$) per unit frequency ($d\omega$) per electron was investigated numerically for both zero and non-zero imposed helical `slow` field $B_t$.

We separate two components of spectral angular density of radiation for spherical frame with $\theta$ and $\varphi$ coordinates:

$$\frac{d^2I}{d\omega d\Omega} = \frac{d^2I_\theta}{d\omega d\Omega} + \frac{d^2I_\varphi}{d\omega d\Omega}.$$

Substitution of the equations of motion (1) into the simplified formula for $d^2I/d\omega d\Omega$ expressed in [3] through the product $[\mathbf{n}[\mathbf{n}\beta]]$ neglecting `near-field` effects gives the following general expression containing products of five sums of Bessel functions:

$$\frac{d^2I_{\theta,\varphi}}{d\omega d\Omega} = \frac{(e\omega L)^2}{4\pi^2 c^3}\left|\sum_{j,k,l,m,n=-\infty}^{\infty}\begin{pmatrix} J_j(a_t)J_k(a_w^+)J_l(a_w^-)\times \\ J_m(a_w)J_n(a_{tw})F^{\theta,\varphi}_{j,k,l,m,n}\end{pmatrix}\right|^2, \quad (2)$$

where:

$$\begin{pmatrix} F^{\theta}_{j,k,l,m,n} \\ F^{\varphi}_{j,k,l,m,n}\end{pmatrix} = (-1)^{m+n} i^{j-k-l} e^{i\varphi(j+l+k)} \times$$

$$\begin{pmatrix} \cos\theta(u_{j,k,l,m,n}\cos\varphi + v_{j,k,l,m,n}\sin\varphi) - \beta_{\|}Sn_{j,k,l,m,n}\sin\theta \\ u_{j,k,l,m,n}\sin\varphi - v_{j,k,l,m,n}\cos\varphi\end{pmatrix},$$

$$\begin{pmatrix} u_{j,k,l,m,n} \\ v_{j,k,l,m,n}\end{pmatrix} = -\frac{1}{\gamma}\begin{pmatrix} Ss_{j\pm1,k,l,m,n} & Ss_{j,k\pm1,l,m,n} & Ss_{j,k,l\pm1,m,n} \\ Sc_{j\pm1,k,l,m,n} & Sc_{j,k\pm1,l,m,n} & Sc_{j,k,l\pm1,m,n}\end{pmatrix}\begin{pmatrix} K_t \\ K_w^+/\sqrt{2} \\ K_w^-/\sqrt{2}\end{pmatrix},$$

$$Ss_{j\pm1,k,l,m,n} = \frac{1}{2i}(Sn_{j+1,k,l,m,n} - Sn_{j-1,k,l,m,n}),\ Sn(x) = \frac{\sin x}{x},$$

$$Sc_{j\pm1,k,l,m,n} = \frac{1}{2}(Sn_{j+1,k,l,m,n} + Sn_{j-1,k,l,m,n}),\ a_t = \frac{K_t}{\gamma}\nu\frac{k_x}{k_t}\sin\theta,$$

$$Sn_{j,k,l,m,n} = Sn\left(N_t\pi\left(\frac{h_w}{k_t}(\nu + k - l - 2m - n) - j - k - l\right)\right),$$

$$a_w^{\pm} = \frac{K_w^{\pm}}{\gamma}\frac{\nu k_s/\sqrt{2}}{k_t \pm h_w}\sin\theta,\ a_w = \frac{K_w^+K_w^-}{4\gamma^2}\frac{\nu k_s}{h_w}\cos\theta,\ N_t = L/\lambda_t,$$

$$a_{tw} = \frac{K_w^+ + K_w^-}{\sqrt{2}\gamma^2}K_t\frac{\nu k_s}{h_w}\cos\theta,\ k_s = \frac{h_w}{1-\beta_{\|}\cos\theta},\ \nu = \omega/k_s c.$$

We consider below specific properties of the radiation compared to the conventional planar undulator, i.e. in the vicinity of $\nu \approx n$. We do not consider here the radiation features corresponding to helical undulator component (i.e. when $K_t \geq 1$ and $\nu \approx nk/h_w$) because in practice we have $K_w^2 << K_t^2$ and the influence of the `twisted undulator` component is negligible.

As it can be seen from (2) the main maxima of $d^2I/d\omega d\Omega$ spectral distribution correspond to the frequencies $\omega = \frac{(nh_w \pm k_t)/c}{1-\beta_{\|}\cos\theta}$, where $n$ is integer.

## 5 PERFORMANCE FEATURES OF THE TWISTED UNDULATOR

The results given below refer to on-axis radiation ($\varphi$=0, $\theta$=0) emitted by a single electron having energy 500 MeV. Some results corresponding to non-axis radiation ($\theta \neq 0$) can be found in [1]. The first five harmonics are analyzed here at the frequencies $\nu = n + \lambda_w/\lambda_t$. The properties of radiation at the frequencies $\nu = n - \lambda_w/\lambda_t$ are qualitatively similar. The parameters of the undulator considered numerically (see the figs. 3-7) were the following: $L$=30cm, $\lambda_w$=1cm, $B_w$=6kG, $N_t$=3 with the exception of the figs. 3, 5, where $N_t$ is a variable.

A number of features occurs in the twisted structure. The first is spectral line splitting mentioned above and demonstrated in ref. [1].

The second general feature is circular polarization of the on-axis radiation at $N_t = L/\lambda_t > 1$, where $L$ is the undulator length. To obtain pure circular polarization it is enough to provide $N_t = 0.5$ in `half-turn twisted` structure (see fig. 3). The degree of circular polarization is very close to unity at $N_t = n/2$ and almost does not depend on harmonic number or helical field $B_t$ (see fig. 4). The on-axis radiation of the first harmonic corresponds to pure circular polarization (deviation equals zero).

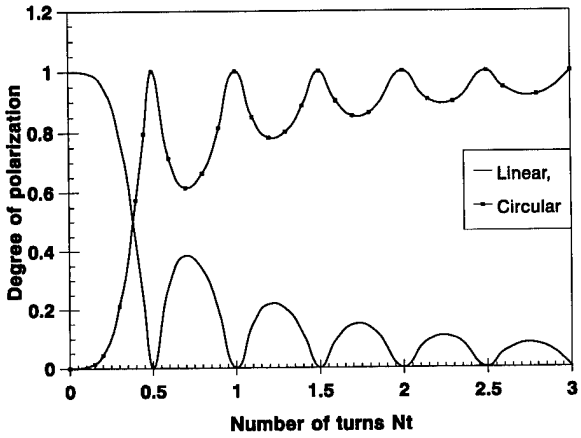



Figure. 3. Degree of linear and circular polarization as a function of number of turns $N_t = L/\lambda_t$. $B_t$=0, $\nu$=1.1.

The third feature is possibility of spectral-angular intensity increase compared to the source (untwisted) linear undulator. One can see from fig. 5, that when $\lambda_t/\lambda_w$ is less then 5.9 (or number of turns per undulator length exceeds 5.1) the first harmonic density exceeds that value for equivalent linear undulator.

Relative change of odd harmonics is depicted in fig. 6 as a function of helical field $B_t$. The density for each harmonic is normalized to its value at $B_t$=0. These dependencies demonstrate decrease of higher harmonic relative content as the helical field increases.

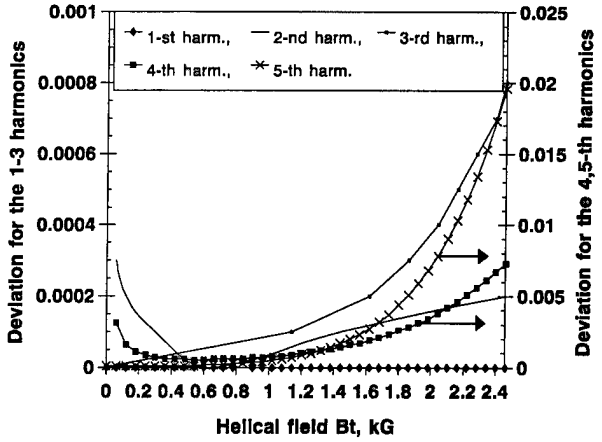



Figure. 4. Deviation of the degree of polarization from unity as a function of $B_t$ for different harmonics. $N_t$=3.

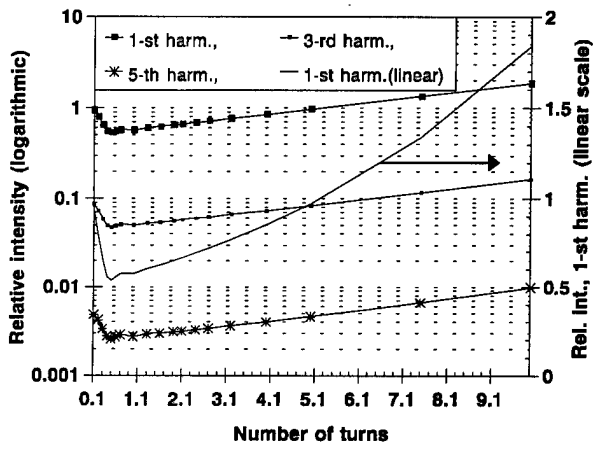



Figure 5. Spectral angular on-axis density for odd harmonics related to that for the first harmonic of linear undulator versus $N_t=L/\lambda_t$. $B_t$=0.

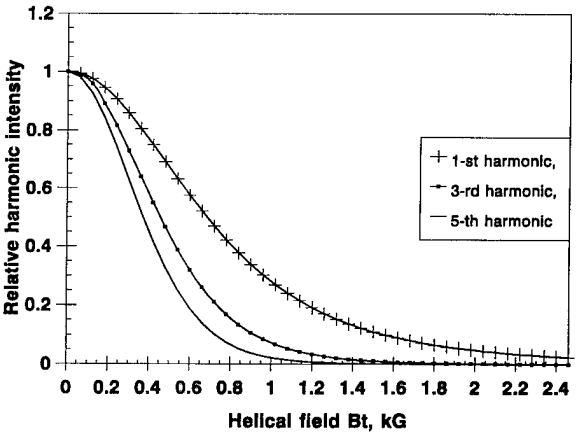



Figure 6. Spectral angular on-axis density for odd harmonics related to that values of corresponding harmonics for conventional linear undulator versus helical field $B_t$.

On-axis radiation of the even harmonics predicted in the previous section has the maxima close to $B_t \sim B_w\lambda_w/\lambda_t$, however its intensity is negligible compared to the odd harmonics (see fig. 7).

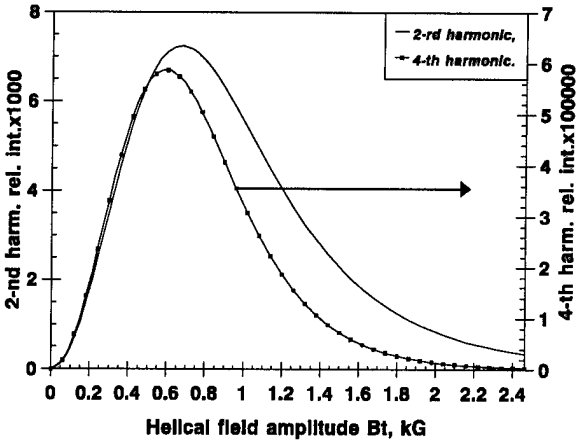



Figure 7. Spectral angular on-axis density for even harmonics related to that for the first harmonic of linear undulator versus helical field.

## 6 DISCUSSION

The twisted undulator structure combines some properties of both helical and linear undulator. The main features are circular polarization, spectral line splitting, and continuous adjustability of the radiation intensity by the helical field variation. The structure can be considered also as a `twisted microundulator` providing radiation with circular polarization.

Although the insertion device proposed can not be used in FELs, it is of potential interest for applied research of plasma beat waves and in solid state physics, e.g. circular dichroism.

## REFERENCES

[1] Yu.P. Bouzouloukov, V.V. Gubankov, A.S. Khlebnikov, N.S. Osmanov, A.V. Smirnov, N.V. Smolyakov and S.V. Tolmachev. Short-period planar undulators development towards twisted structures, Proc. of the 18-th. Int. Free-Electron Laser Conf., Rome, Italy, August 26-31, 1996 (Th P23).

[2] A.V. Smirnov, On the Analytical Representation of Magnetostatic Periodic Fields, these Proceedings (3V34)

[3] J.D. Jackson, *Classical Electrodynamics*, 2nd ed. (Wiley, New York, 1975).

# DESIGN OF AN ELLIPTICAL UNDULATOR AND X-RAY BEAM LINE AT DSR OF RIKEN RI BEAM FACTORY PROJECT

M. Wakasugi and T. Katayama*

RIKEN, The Institute of Physical and Chemical Research, Wako, Saitama 351-01, Japan
*Center for Nuclear Study, School of Science, University of Tokyo, Tanashi, Tokyo 188, Japan

*Abstract*

According to requirements from the X-ray - RI collision experiment at DSR that is proposed in the RIKEN RI beam factory project, an undulator for elliptically polarized X ray was designed. An Apple-II type of the undulator was adopted so that both the X-ray energy and the polarization are continuously changed at the same time. The photon flux of more than $10^{15}$ photons/s/0.1%b.w. is calculated for any polarization in the energy range of 30 - 800 eV.

## 1 INTRODUCTION

The X-ray - RI collision experiment proposed in the RIKEN RI beam factory project [1,2] requires on the X ray as follows. The X-ray energy is 30 -800 eV and it can be continuously scanned with the step of less than 0.1 eV. Any polarization of the X ray can be chosen. The polarization should be kept during the energy scanning. The X-ray beam intensity is as large as possible, and the energy resolution is also as high as possible.

For the experiment, the higher energy resolution is essential because the isotope shifts in the X-ray transitions of the Li-like RI ion beam have to be resolved [3]. Since the resolution of the X ray from the undulator is not enough, the X-ray spectrometer having high energy resolution of about $\Delta E_e/E_e = 10^{-4}$ should be used. The X-ray beam line including the X-ray spectrometer is inserted between the undulator and the X-ray - RI colliding section. To get the X ray beam intensity of more than $10^{12}$ photons/s/0.01%b.w. at the colliding section, output photon flux from the undulator has to be more than $10^{15}$ photons/s/0.1%b.w.

In this paper, the design of the magnetic structure, calculated X-ray spectra and the mechanical design of the undulator for elliptically polarized X ray are reported.

## 2 SPECIFICATIONS OF ELECTRON BEAM IN DSR

The intensity and the polarization of photon beam strongly depend on the electron beam quality in the DSR. To make low emittance electron beam, DBA lattice is adopted in the arc section of the DSR [4]. As described in Ref. [3], the electron beam having the energy of 0.3 - 2.5 GeV is stored in the DSR. The calculated electron beam specifications are listed in Table 1. The averaged current is 0.5 A. The beam emittance is obtained to be $\varepsilon_x/\varepsilon_y$ = 7.8/13.9 nmrad at the maximum energy of 2.5 GeV. Since the beta function value at the undulator section is about 5 m, the electron beam size at the undulator section is smaller than $\sigma_x/\sigma_y$ = 197/264 μm.

## 3 DESIGN OF APPLE-II TYPE UNDULATOR

### *3.1 Magnetic Structure*

Figure 1 shows the schematic view of the magnetic structure of the Apple-II type of the undulator proposed by Sasaki et al. [5]. This has two pairs of planer permanent magnet (Nd-Fe-B) arrays above and below the electron beam plane. The X-ray energy is scanned by changing the gap width. The polarization is changed by shifting the relative position of pairs of magnetic arrays. On-axis magnetic field produced by the phase shifting makes helical and sinusoidal motions of the electron beam. The magnetic field in horizontal and vertical directions are shown in Fig. 2 at three different phases. The linear polarization in horizontal and vertical directions are obtained at the phase shifts D = 0 and D = $1/2\lambda_u$, respectively, where $\lambda_u$ is the length of a magnetic period. the circularly polarized X ray can be get at D = 3/8 $\lambda_u$ as shown in the figure.

Table 1. The specification of the electron beam in the DSR.

| | | | | | | | |
|---|---|---|---|---|---|---|---|
| Electron Beam Energy | $E_e$ | (GeV) | 0.3 | 1 | 1.5 | 2 | 2.5 |
| Radiation Loss | U | (keV/turn) | 0.1 | 10.6 | 53.2 | 169.1 | 412.7 |
| Emittance | $\varepsilon_x$ | (n m rad) | 0.11 | 1.24 | 2.8 | 4.97 | 7.76 |
| | $\varepsilon_v$ | (n m rad) | 0.2 | 2.22 | 5.01 | 8.92 | 13.9 |
| Energy Resolution | $\Delta E_e/E_e$ | ($10^{-4}$) | 0.82 | 2.7 | 4.1 | 5.5 | 6.9 |
| Bunch Length | $\sigma_z$ | (cm) | 0.006 | 0.033 | 0.061 | 0.095 | 0.134 |
| Damping Time | $\tau_x$ | (sec) | 6.2 | 0.17 | 0.05 | 0.02 | 0.01 |
| | $\tau_v$ | (sec) | 6.1 | 0.17 | 0.05 | 0.02 | 0.01 |
| | $\tau_e$ | (sec) | 3.1 | 0.17 | 0.03 | 0.01 | 0.005 |
| Toushek Lifetime | $\tau$ | ($10^6$sec) | 0.008 | 0.16 | 8.1 | 180 | 2.7 |

0-7803-4376-X/98/$10.00 © 1998 IEEE

### 3.2 Minimum Gap and Length of a Period

The minimum gap width depends on the size of the vacuum tube inserted in the gap. Taking the vertical tube size of 10 mm, the 2-mmx2 tube thickness and the 3-mm x2 spacing between the tube and magnet, the minimum gap width was decided to be 20 mm.

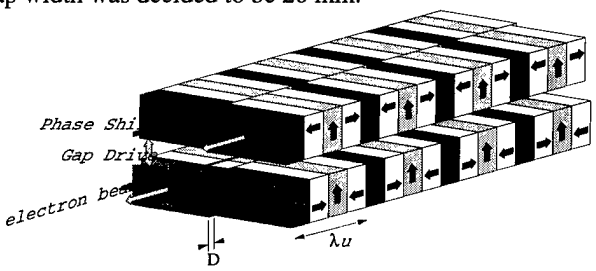



Fig. 1. Magnetic structure of the Apple-II type undulator.

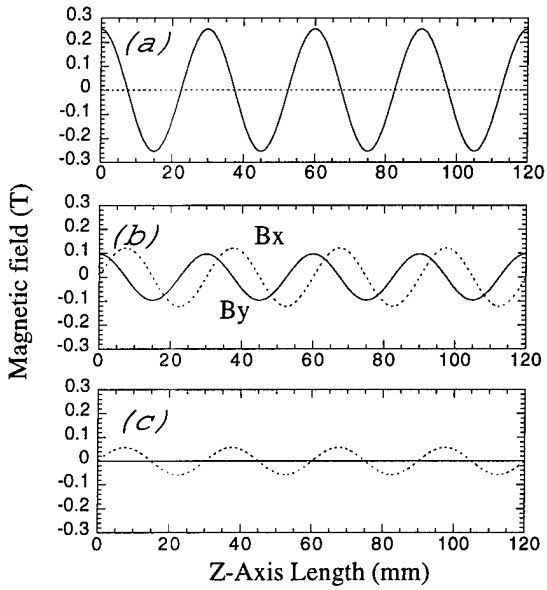



Fig. 2. Magnetic field on the electron beam axis. (a), (b) and (c) correspond to the phase shifts of 0 mm, 11.25 mm and 15 mm, respectively.

When the length of period is decided, the followings have to be considered. The whole system of the undulator is inserted in the limited space of 6.7-m length. The photon flux of more than $10^{15}$ photons/s/0.1%b.w. has to be obtained using the electron beam having the energy of more than 0.3 GeV and the gap width of more than 20 mm over the X-ray energy range of 30 - 800 eV. Thus the length of the period was decided to be 3 cm. In this case, the maximum K value is 0.712 by assuming the magnetic field strength of 1.3 T at the pole tip of the Nd-Fe-B magnet. The X ray having the energy of 30 - 800 eV can be produced by changing the gap width from 20 to 26.7 mm and the electron beam energy of 0.3 - 1.7 GeV.

### 3.3 Magnetic Field along the Beam Axis

The calculated magnetic fields are shown in Fig. 2, and the relations between the gap width, the phase shift and the maximum field are shown in Fig. 3. The maximum magnetic field is 0.245 T. For any gap width, the circularly polarized X ray is obtained at the phase shift is around 11 mm. To keep the circular polarization during the energy scanning, both the gap width and the phase have to be simultaneously changed along the arrow in the figure.

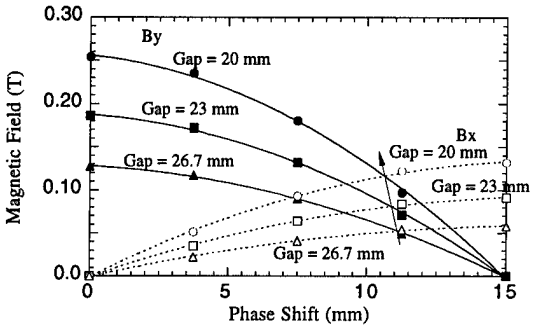



Fig. 3. Maximum magnetic field as a function of the phase shift.

### 3.4 Photon Flux

The photon flux is calculated for both case of the linear polarization (K=0.712) and the circular polarization ($K_x$=$K_y$=0.328), and they are shown in Fig. 4. The fluxes are larger than $10^{15}$ photons/s/0.1%b.w. for both cases in the whole energy range. The requirement from the experiment will be completely satisfied. The flux for the case of the linear polarization is about three times larger than that for circular polarization because of larger magnetic field.

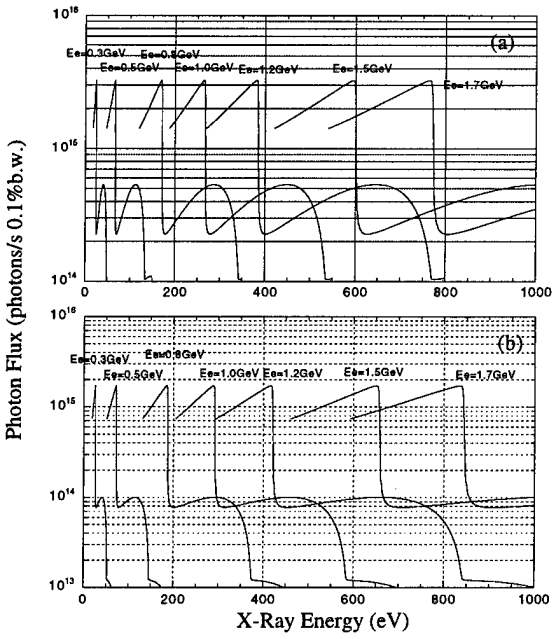



Fig. 4. Photon flux for the linearly polarized X ray (a) and the circularly polarized X ray (b).

## 4 MECHANICAL DESIGN

### *4.1 Mechanical Structure*

Whole system of the undulator having the total length of 6.24 m is divided into two undulator units because it is too long to construct a 6-m undulator with high accuracy. Both are exactly the same and they are coupled at a distance of 60 mm. The undulator unit consists of the magnet array, array holders, support stands, a vacuum tube, correction magnets, valves, and gap and phase driving system. In one unit, the length of the magnet array is 2400 mm and the number of periods is 80. Total weight is about 7.5 t per unit.

### *4.2 Vacuum Tube*

The vacuum tube inserted in between the magnets has special form because not only the low emittance electron beam but also the heavy ion beam are stored in the DSR depending on the operation mode [4]. The tube has three rooms; those are for the low emittance electron beam, for the heavy ion beam and for the NEG pump as shown in Fig. 5. When the DSR is used as the heavy ion storage ring, the tube is moved without breaking vacuum after expanding the gap width to 300 mm.

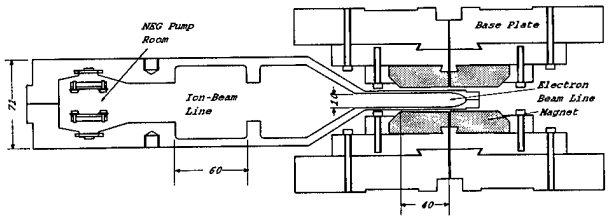



Fig. 5. Cross section of the vacuum tube inserted in between the magnets.

### *4.3 Gap and Phase Driver*

The gap driving system consists of a servomotor, two decelerator, a gear box, four linear guide, position sensors and interlock system. The magnetic force acting on a magnet array is calculated to be about 1 t in the horizontal direction, 0.2 t in the vertical direction and 0.8 t in the beam direction. The accuracy of the gap driving can be achieved to be less than 5 μm that comes from the requirement of the minimum X-ray energy scanning step of 0.1 eV. The driving system has a feed back system from the position sensors, and it can keep the gap width within 3 μm. The phase driver has the same kind of the system.

### *4.4 X-ray Beam Line*

The X-ray beam line including the X-ray spectrometer will be inserted in between the vertically bending magnets at the merging section of the DSR [4]. The design of the spectrometer, which is based on the constant-length spherical grating (CSG) type, is now in progress.

## REFERENCES


[1] Y. Yano et al., Proc. 5th European Particle Accelerator Conf., p. 536 (1996).

[2] T. Katayama et al., Proc. 5th European Particle Accelerator Conf., p. 563 (1996).

[3] M. Wakasugi et al., Proc. 5th European Particle Accelerator Conf., p. 611 (1996).

[4] N. Inabe et al., Proc. 5th European Particle Accelerator Conf., p. 926 (1996).

[5] S. Sasaki et al., Nucl. Instrum. Meth. **A331**, 763 (1993).

# OPERATION OF INSERTION DEVICES IN ELETTRA AND PLANS FOR FUTURE DEVICES

R.P. Walker, B. Diviacco and D. Zangrando, Sincrotrone Trieste, Italy

*Abstract*

Recent improvements in the technique used to minimize the effect of undulator gap change on the closed orbit in ELETTRA are presented. Plans for future devices, which include four sections with variable polarization as well as an in-vacuum device, are also summarised.

## 1 INTRODUCTION

Five insertion devices are presently operational in ELETTRA out of a total number available of 11. The table below summarizes the main parameters of these devices including the maximum field and K value at the operational minimum gap. The four undulators (U) have a pure permanent magnet configuration, while the multipole wiggler (W) is of the hybrid type. Each device except one (ID#7) consists of 3 separate sections based on a standard 1.5 m support structure. The design and construction of the first 3 devices has been presented previously [1-3] and the initial operation was reported in [4]. A sixth device, an electromagnetic elliptical wiggler, is presently under construction [5]. In this article we discuss recent improvements in the technique used to minimize closed orbit effects due to undulator gap changes, as well as plans for future devices.

| ID# | Type | N | Gap (mm) | Bo (T) | K |
|---|---|---|---|---|---|
| 2 | U5.6 | 81 | 27.0 | 0.44 | 2.3 |
| 3 | U12.5 | 36 | 28.0 | 0.51 | 5.9 |
| 5 | W14.0 | 30 | 22.0 | 1.50 | 19.6 |
| 6 | U12.5 | 36 | 26.0 | 0.55 | 6.4 |
| 7 | U8.0 | 19 | 26.0 | 0.71 | 5.3 |

## 2 CLOSED ORBIT CORRECTION

Each undulator sub-section contains two sets of correction coils, one at either end of the carriage [6]. Each set of 4 coils allows either a horizontal or vertical field to be generated, depending on the inter-connections. In order to compromise on the total number of correction channels, a 4-channel power supply is used for each complete undulator. For the 3-section undulators the 4 channels are connected so as to produce a horizontal field at the entrance and the exit of the complete ID, and a vertical field at the two interfaces between sections. This allows both first and second field integrals to be compensated in both planes, with a local correction of the vertical field component that arises due to the interaction between two sections as a result of the non-unit permeability [7]. The correction capacity is up to 1.2 (1.6) Gm per channel in the horizontal (vertical) plane at 20 mm gap. In the case of the single section undulator full compensation is also possible, however in this case each channel affects both horizontal and vertical planes. The power dissipation for each coil is sufficiently small (< 2 W) to produce negligible temperature rise.

An automatic compensation of the orbit changes due to the undulators has been implemented using the correction coils. Based on a table of values of coil current as a function of gap, the VME crate controlling each ID automatically sets the required currents dynamically during gap changes. Initially the optimum coil settings were determined by manual adjustment of the sum and difference of the two coil currents for each plane, for separate correction of the first and second field integrals respectively. In this way it was possible to reduce the maximum (rms) displacement in the closed orbit at any point in the ring to about 15 μm (8 μm) in both planes.

The limitation of the original method of correction was the drift in the orbit in the time needed to perform the manual correction. Recently significant effort has gone into improving the correction with a view to giving control of ID gaps to the users. To achieve this a special program has been written to automate the correction procedure. In this way the correction is both more accurate and more rapid, thus reducing the effect of orbit drift.

The program works as follows : after recording the orbit at maximum gap, the gap is then brought to the first required value and the coils are calibrated by applying a fixed excitation (1 A) to each set in turn and recording the change in orbit. The required currents to minimize the difference orbit are then obtained using a least-squares method, either separately for the horizontal and vertical planes (ID#2, 3, 6) or for both planes simultaneously (ID#7). The program iterates the correction until a specified level of correction has been reached (2 μm rms). To eliminate non-physical changes that sometimes occur BPM's that indicate a change in difference orbit greater than 2σ are discounted from the calculation.

The new program has allowed the correction to be applied to many more gap values and in a reduced time interval : typically 10 gap values can be corrected in 25 mins. Figure 1 shows the results obtained in two cases, which are typical also of the results obtained with the other devices.

The results that are presently obtained show an rms difference orbit at the level of 2 μm horizontally, 1 μm vertically, roughly a factor of 5 better than previously obtained. The maximum displacement in position and angle at the ID location can be estimated from these values as follows :

$$\frac{\Delta_{max,ID}}{\Delta_{rms}} = \sqrt{\frac{2\beta_{ID}}{\bar{\beta}_{mon.}}} \qquad \Delta'_{max,ID} = \frac{\Delta_{max,ID}}{\beta_{ID}}$$

where the mean β values at the monitor positions are (9.2, 6.3) m and the β values at the ID location are

0-7803-4376-X/98/$10.00 © 1998 IEEE

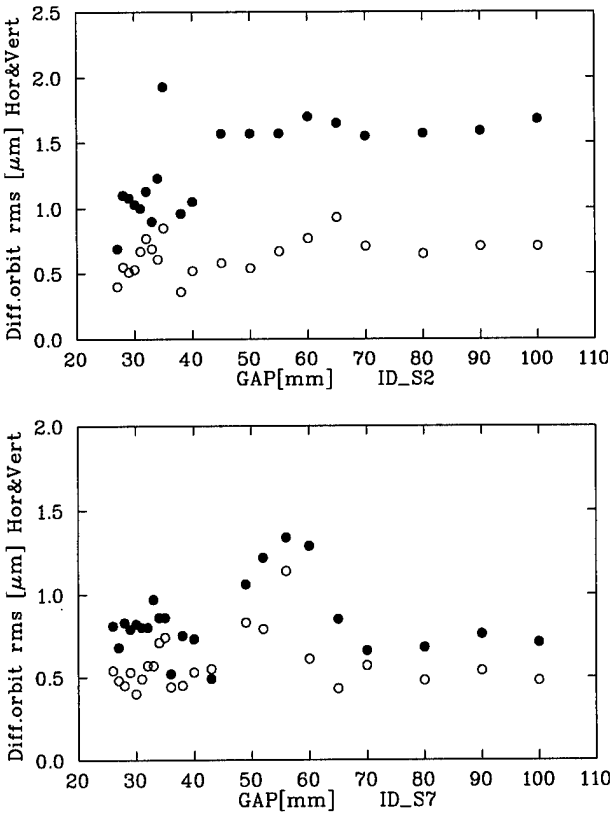



Figure 1. Residual change in orbit (rms) due to gap changes of ID#2 (upper ) and ID#7 (lower) after correction coil calibration; solid circles - horizontal plane, open circles - vertical plane.

(8.2, 2.6) m in the horizontal and vertical planes respectively. The table below shows the corresponding maximum displacements and angular deviations at any ID.

| ID orbit changes | horiz. | vert. |
|---|---|---|
| $\Delta_{max}$ (μm) | 2.6 | 0.90 |
| $\Delta'_{max}$ (μrad) | 0.32 | 0.35 |
| $\Delta_{max}/\sigma$ (%) | 1.1 | 6.7 |

Also shown is the ratio of displacement to rms beam size (= ratio of angular deviation to beam divergence) assuming the natural horizontal emittance of 7 $10^{-9}$ m rad and the estimated 1 % coupling. The present correction accuracy should therefore be sufficient to allow user control of the ID gaps.

## 3 PLANS FOR FUTURE DEVICES

A number of new beamlines are being planned for ELETTRA following a recent call for proposals by the CNR (National Research Council) and INFM (National Institute for the Physics of Materials) funding bodies. At the present time two new beamlines involving insertion devices have been approved for construction by INFM and Sincrotrone Trieste, and others may be approved in due course. Here we give preliminary details of these two devices, together with one of the other proposals for an in-vacuum undulator.

### *3.1 Variably polarized undulators*

Two separate beamlines are proposed for advanced dichroism and photoemission studies both of which require circularly polarized as well as linearly polarized radiation. Both beamlines are designed to cover a wide photon energy range, one from 35 eV to 1.5 keV, the other from 10 eV to 2 keV. To cover such a wide range requires the use of two undulators with different period lengths in each case.

| | EU4.6 | EU6.0 | EU7.6 | EU12.5 |
|---|---|---|---|---|
| Period (mm) | 46 | 60 | 76 | 125 |
| No. periods | 47 | 36 | 28 | 17 |
| Length (m) | 2.162 | 2.160 | 2.128 | 2.125 |
| $K_{max}$ - vertical | 2.4 | 4.2 | 6.3 | 8.8 |
| - horizontal | 1.4 | 2.8 | 4.5 | 6.9 |
| - helical | 1.2 | 2.3 | 3.6 | 5.4 |

A preliminary optimization of parameters has been carried out based on the APPLE-II structure [8] resulting in the values shown in the table above. Two magnets of length in the range 2.1 - 2.2 m can be accommodated in the straight section allowing sufficient margin for longitudinal displacement of the magnet arrays. A minimum gap of 18 mm is assumed for the first three devices based on a new vacuum chamber design [9]. In the case of EU12.5 a longer period and lower field than could be achieved were chosen in order to reduce the radiation opening angle and hence power loading problems.

Figure 2 shows the performance of the two pairs of devices in the circular polarization mode. For each photon energy the magnet gap and longitudinal phase have been adjusted to maximize the product of total flux and the square of the degree of circular polarization, calculated using the usual analytic approximations. Two new features can be seen with respect to standard undulator tuning curves. Firstly, the circular polarized flux drops off rapidly at low photon energies, reflecting the fact that the highest field, and hence lowest photon energies, are obtained in the linearly polarized mode. Secondly, there is a much reduced figure-of-merit for the higher harmonics compared to the fundamental, since the flux is zero for pure circular polarization, and maximum for pure linear polarization.

A particular aspect of the implementation of these devices that is presently under study is the problem of the heat load on the downstream bending magnet vacuum chamber. The large vertical divergence of the radiation means that a significant radiation power can be intercepted on the walls of the 10 mm high slot, 6.2 m downstream from the ID centre, particularly in the case of the longer period and higher K value devices. Finite element calculations show that temperatures in excess of 500 °C could be experienced (2 GeV, 400 mA) in the worst cases (EU7.6 and EU12.5) with the present method of external cooling, which is however adequate both for the present linear devices and the elliptical wiggler. Two solutions to the problem are being investigated in parallel: improving

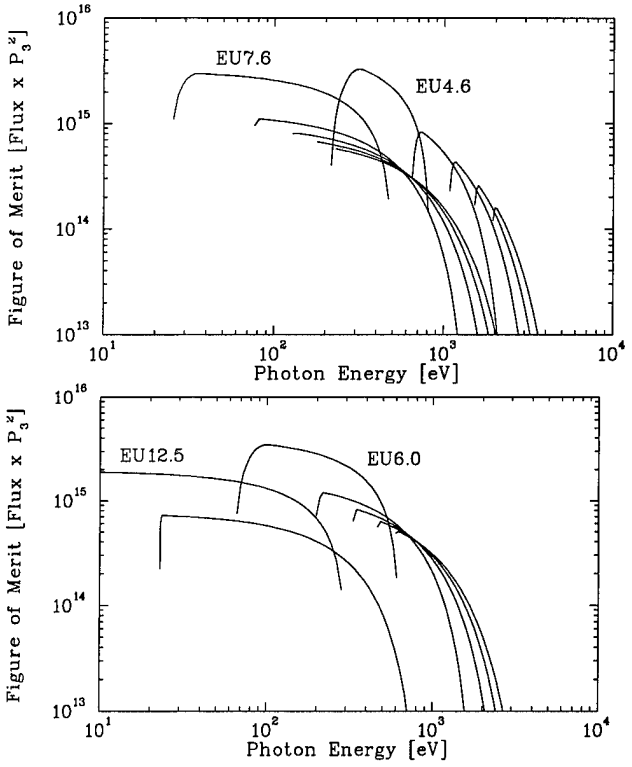



Figure 2. Performance of the proposed elliptical undulators in the circular polarization mode (2 GeV, 0.4 A).

the cooling of the existing chamber and design of a new Al chamber with integral cooling. Initial calculations show that the latter solution would eliminate completely the problem, whereas in the former case it may be necessary to relax the magnetic parameters somewhat by choosing a slightly longer period and hence smaller field value than those given in the table.

In the case of the lowest photon energy device (EU12.5) there is strong interest in the possibility of removing the rational harmonics in the linearly polarized mode. Accordingly we have made some preliminary studies [10] of a version of the APPLE-II structure which contains quasi-periodic arrays both of the type introduced in [11] as well as a new type based on a conventional 4-block per period pure permanent magnet device with vertical block displacements. The initial conclusion of this work is that it seems feasible to generate variably polarized radiation with a quasi-periodic spectrum in this way. Further calculations for a specific design will be made in due course.

*3.2 In-vacuum undulator*

In order to satisfy the needs of some experimenters for high brightness radiation at higher photon energies than presently available at ELETTRA a short period

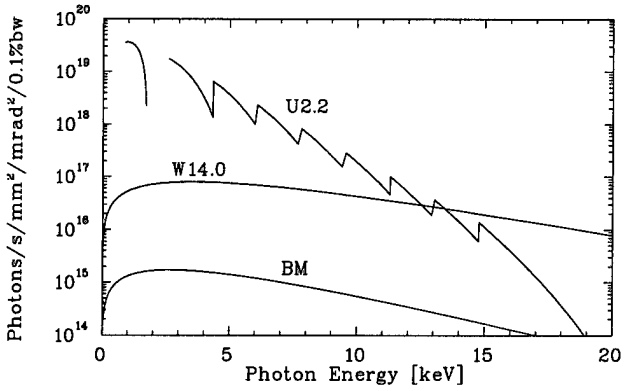



Figure 3. Performance of a mini-gap undulator in ELETTRA (2 GeV, 0.4 A, $\varepsilon_x = 7\ 10^{-9}$ m rad, $\kappa = 1$ %).

device is being studied. The in-vacuum technology is considered the most appropriate in the present case and tentative parameters for such a device are an operational gap of 7 mm, period length of 22 mm, K = 1.4, N = 136, length = 3 m. The predicted brightness of such a device is shown in fig. 3 compared to that of the W14.0 multipole wiggler at 20 mm gap (1.6 T) and a bending magnet source. The undulator brightness has been computed using the URGENT program, and includes the nominal electron beam emittances and energy spread. It can be seen that such a source would give 100 times higher brightness at 5 keV, and 6 times at 10 keV, compared to the existing multipole wiggler, and 400-3000 times higher than a bending magnet.

## REFERENCES

[1] R.P. Walker et al., Proc. 1993 Particle Accelerator Conference, IEEE Catalog No. 93CH3279-7, p. 1587.
[2] B. Diviacco et al., Proc. 4th European Particle Accelerator Conference, World Scientific (1994), p. 2250.
[3] A. Codutti et al., ibid. p. 2253.
[4] R.P. Walker and B. Diviacco, Rev. Sci. Instr. 66 (1995) 2708.
[5] R.P. Walker et al., these Proceedings.
[6] B. Diviacco et al., Rev. Sci. Instr. 63 (1992) 388.
[7] B. Diviacco and R.P. Walker, Proc. 1993 Particle Accelerator Conference, IEEE Catalog No. 93CH3279-7, p. 1593.
[8] K. Kakuno and S. Sasaki, JAERI-M 92-157 (1992).
[9] C.J. Bocchetta et al., "ELETTRA Performance and Upgrades", these Proceedings.
[10] B. Diviacco and R.P. Walker, Sincrotrone Trieste Internal Report, ST/M-TN-97/11 (March 1997).
[11] S. Sasaki et al., Rev. Sci. Instr. 66 (1995) 1953.

# DESIGN OF AN ELECTROMAGNETIC ELLIPTICAL WIGGLER FOR ELETTRA

R.P. Walker, D. Bulfone, B. Diviacco, W. Jark, P. Michelini, L. Tosi and R. Visintini,
Sincrotrone Trieste, Italy
G. Ingold, F. Schäfers, M. Scheer and G. Wüstefeld, BESSY, Berlin
M. Eriksson and S. Werin, MAX-lab, Sweden

*Abstract*

The main aspects of the design of the electromagnetic elliptical wiggler under construction for ELETTRA are summarized.

## 1 INTRODUCTION

An electromagnetic elliptical wiggler (EEW) was first proposed for ELETTRA in 1991 as a source of circularly polarized VUV/Soft X-ray radiation with variable helicity [1,2], but due to funding limitations was not able to be constructed at that time. The present project commenced in February 1996 with partial European Commission funding as a collaboration between Sincrotrone Trieste, BESSY and MAX-lab. The project also includes the construction of a soft X-ray polarimeter which will be used to make a complete analysis of the polarization properties of the source in the 80-1000 eV range.

The detailed mechanical design and construction of the EEW is presently being carried out by Danfysik A/S, Denmark. The power supplies are under construction by OCEM SpA, Italy, while the control system and dynamic correction system are being developed at Sincrotrone Trieste. Following a period of magnetic testing at Trieste in September/October the device will be installed in ELETTRA and commissioning will start in November.

## 2 MAIN DESIGN PARAMETERS

| | |
|---|---|
| Period | 212 mm |
| No. vertical poles | 32 |
| No. horizontal poles | 31 |
| Length | 3.332 m |
| Gap | 18 mm |
| Max. vertical field | 0.5 T |
| Max. horizontal field | 0.1 T |

The original parameters of the device were 12 periods of 230 mm with maximum vertical and horizontal field of 0.6 T ($K_y$=13) and 0.046 T ($K_x$=1) respectively. A review of these parameters was firstly carried out in order to optimize performance in the 5-1500 eV range, using both undulator and wiggler modes of operation, but within the constraints imposed by the existing beamline design [3] of not increasing significantly either the radiation power or the vertical source size. A better optimum proved to be with a reduced period length and an increased number of poles, with a reduced vertical field strength of 0.5 T. The maximum vertical deflection angle was also increased to $\pm 1.5/\gamma$ in order to provide more circularly polarized flux at low photon energies in the wiggler mode. The final parameters are listed in the table above.

The vertical field component will be powered with d.c., but three different operating modes are required for the horizontal field : d.c., trapezoidal from 0.1-1 Hz and sinusoidal from 10-100 Hz, to enable different types of data acquisition methods to be used in order to maximize the dichroism signal detection.

## 3 MAGNETIC DESIGN

The initial concept of the EEW was a combination of a vertical permanent magnet to generate a wiggler field and a horizontal electromagnet in order to provide the possibility of switching the helicity of the radiation. A new requirement however was the need to operate also in the undulator mode, requiring low vertical field strengths and therefore a large vertical gap. In order to avoid potential problems with field quality under these conditions, it was decided to investigate solutions involving two electromagnets. A scheme proposed by E. Gluskin of the APS was first studied which uses 3-poles to generate the horizontal field and therefore has the advantage that it is open on one side of the device [4]. It was found however that the asymmetric structure leads to small field gradients on the beam axis which might have unwanted beam dynamics effects in lower energy machines. From this we then developed the idea of a symmetric planar structure which is open on both sides of the median plane, as shown in fig. 1.

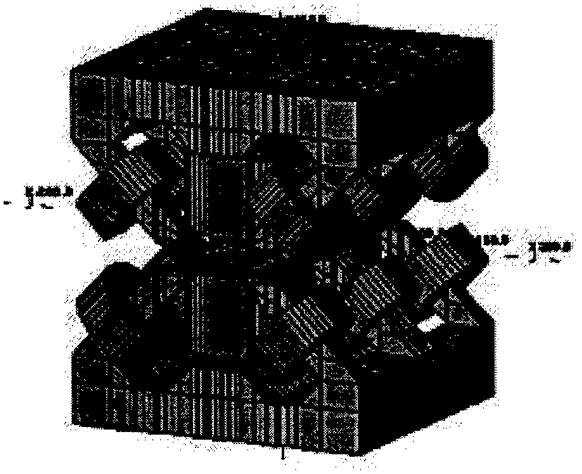


Figure 1. One-period model of the EEW for 3D field calculations.

0-7803-4376-X/98 /$10.00 © 1998 IEEE

A longitudinally anti-symmetric arrangement was chosen for the vertical field in order to have an equal number of positive and negative poles and hence a symmetric distribution of circularly polarized flux with respect to the median plane (when $K_X \neq 0$) to avoid any intensity differences between positive and negative excitation in the event of a vertical misalignment. A symmetric horizontal field is therefore demanded in order to give equal vertical deflections to corresponding vertical poles. "No displacement" terminations will be used for both field components to avoid variation or oscillation in the beam position with excitation, by means of a 1/4, -3/4, 4/4 end-pole sequence.

Although some initial calculations were successfully carried out using the 2D code POISSON, all subsequent calculations were carried out using OPERA-3D [5] because of the strong three dimensional nature of the problem. The magnetic design had to satisfy many often contradictory requirements :

- a small horizontal pole gap gives a higher horizontal field amplitude;
- to obtain a good transverse field homogeneity requires a wide vertical pole (for By) and not too small a horizontal gap (for Bx);
- to minimize saturation requires wide and long poles - this is important in order to reduce hysteresis losses and also to reduce the variation of field integrals with excitation, due to differences between central and end poles;
- to minimize the interaction between the horizontal and vertical fields requires a narrow vertical pole, a wide horizontal pole gap and short poles;
- it is important to reduce the inductance of the horizontal coils to minimize the power supply requirements, which requires a compact pole and coil design.

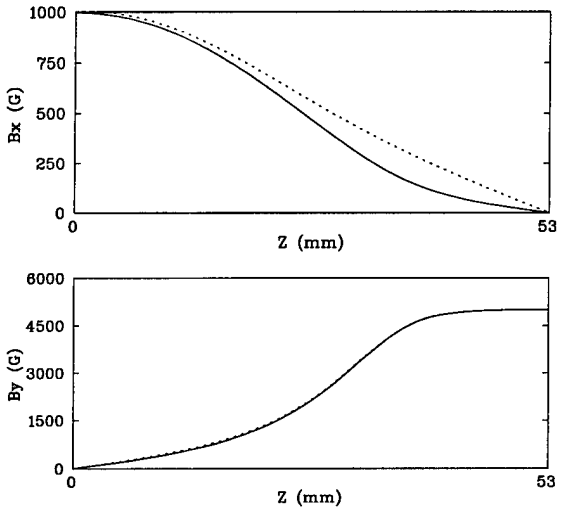



Figure 2. Field distributions in the final EEW design (solid lines) and in the case with only poles of a single type present (dotted lines).

Figure 2 shows the influence of the vertical poles on the horizontal field and vice-versa in the final design. The vertical field is affected very little by the presence of the horizontal poles both in amplitude (< 0.1%) and shape. As might be expected however the horizontal field is affected more, but not so much in peak amplitude (~ 1%) as in the shape in the region of the vertical pole. The resulting reduction in field integral means that a 32 % higher horizontal field is required (0.1 T) compared to a pure sinusoid to obtain the required vertical deflection angle. Further calculations have demonstrated that the effect of interaction is limited to the iron geometry : the additional effect on one component due to switching on the other is negligible, since the flux paths generated by the two sets of coils are to a large extent independent.

Due to the large period/gap ratio and relatively small pole length the vertical field also deviates significantly from a pure sinusoid (see also fig. 3).

The number of turns in the coils was chosen so as to have reasonable values of voltage and current for the power supply construction, as well as being a multiple of 4 to facilitate the implementation of the termination sequence. A small cross-section conductor was chosen (5.8 mm x 3.7 mm, $\phi$ = 2.5 mm) in order to produce a compact design and to reduce eddy-current effects but without too high a current density. The table below gives the final parameters required to meet the field specification, including an extra margin of about 10% on current.

| Electrical parameters | Vertical field | Horizontal field |
|---|---|---|
| Number of turns/coil | 24 | 8 |
| Maximum current (A) | 175 | 300 |
| Maximum power/coil (W) | 190 | 140 |
| Inductance, total (mH) | - | 2.44 |
| Maximum voltage (V) | 66 | 516† |

† at 100 Hz.

In order to reduce eddy current effects in the steel, a laminated construction is necessary. The steel finally selected is 0.35 mm thick STABOCOR M 270-35A from EBG, Germany. By integrating $B^2$ over the poles and scaling the manufacturer's data for core loss of 2.3 W/kg at 1.5 T, 50 Hz the estimated maximum hysteresis + eddy current losses are estimated as 12 W/pole at 100 Hz with maximum current, which is acceptable. Eddy current losses in the copper have been estimated as 1 W/coil for the horizontal coils, negligible in comparison to resistive losses. For the 1.5 mm thick elliptical stainless steel vacuum chamber a calculation was carried out using the ELEKTRA program [5] which gave a maximum eddy current loss of 10 W/m.

An interesting feature of the present design is the fact that magnetic flux circulates both in the plane of the laminations (generated principally by the horizontal field coils) and also perpendicular to it (due mainly to the vertical field coils). Since the effective permeability in the transverse direction reduces very rapidly as the packing factor decreases, the packing factor was optimized by choosing a steel that is supplied with a thin lacquer ("Stabolit 70") providing both electrical insulation and bonding between laminations. The expected packing factor after block curing is 97 %, which causes an acceptably

small reduction of 2.6 % (0.5 %) for the vertical (horizontal) field amplitudes respectively.

Modelling the end-termination required extensive cpu-time. Both terminations with an outer vertical pole and outer horizontal pole were calculated. The latter has the advantage that the 3/4 vertical poles receive an equal deflection angle to that of the central poles, however it was found that the horizontal field integral was much larger in this case. The alternative arrangement was therefore selected, which results in only about 5 % less flux in the wiggler mode. Figure 3 shows the final computed field distribution and trajectory in the entrance region. It can be seen that the trajectory is well compensated with the oscillation axis coincident with the magnetic axis.

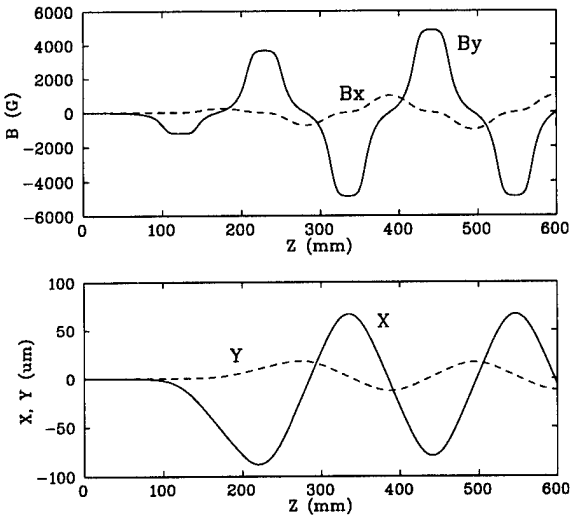



Figure 3. Field distributions (upper) and electron trajectory (lower) in the entrance region of the EEW.

Various pole profiles giving different transverse field distributions were studied and their effect on the beam dynamics properties investigated [6]. Despite earlier indications to the contrary, the pole profile was not found to have a significant influence on the dynamic aperture and so of the solutions investigated the ones giving the best magnetic performance, i.e. minimum field levels in the steel, were chosen.

## 4 MAIN POWER SUPPLIES AND CONTROL SYSTEM

The vertical field requires a conventional mono-polar d.c. supply, while the horizontal field requires a special bi-polar design capable of operating both in d.c. or a.c. modes with various waveforms. The solution that has been adopted is the use of two switch-mode power supplies in the same cabinet.

Special attention has been given to the stability of the power supplies since it affects directly the detectability of small changes in absorption/scattering etc. due to the change in helicity of the radiation. Calculations show that in the worst case, at the highest photon energies in the wiggler mode (1.5 keV), a given fractional change in either field level causes a similar change in the Stokes parameters that describe the polarization of the emitted radiation. Small ripple and short term stability have therefore been specified ($\pm$ 5 $10^{-5}$ $I_{max}$), a performance that has already been met for the existing ELETTRA d.c. supplies. In addition, in the a.c. modes the symmetry of the positive and negative current values is also critically important. Special attention will therefore be given to achieving this level of d.c. offset in the a.c. modes.

In order to achieve the specified stability levels requires an even more stable reference signal to drive the power supplies. For the d.c. modes this can be provided by the standard DAC boards used for the ELETTRA power supplies. For the a.c. modes however a suitable waveform generator could not be identified giving the required performance, particularly in terms of d.c. offset. To resolve this problem a novel solution has been developed. The output signal of a standard DAC board has been synchronized with the pulse from a programmable timer located on the main cpu of the control system interface, thus allowing pre-defined waveforms to be generated step-by-step. Initial tests with a 10-100 Hz sinusoidal waveform show that a practical resolution of 150 μs can be obtained, and that the signal has very good amplitude stability ($\pm$ 10 ppm of full-scale/$^{o}$C).

## 5 DYNAMIC CORRECTION SYSTEM

In order to guarantee that the operation of the EEW in the a.c. mode will not disturb the closed orbit and so not affect other users, a correction system is being developed that is capable of dynamically correcting the field integral errors. The system will have 4 channels for powering horizontal and vertical correction coils at the entrance and exit of the magnet. Suitable air-cored coils have been designed that provide a correction of 7.2 Gm in both planes at 4A excitation, with an inductance of 2.3 mH per coil pair. The coils will be supplied by 4 power modules (Copley mod. 412) integrated in the main supply cabinet which will allow the above current to be produced up to at least 1 kHz. The four channels will be driven using a single VME module (Analogic DVX 2901) containing 4 independently programmable 16-bit, 200 kHz, waveform generators, synchronized to the main power supply.

## ACKNOWLEDGEMENTS

The contributions of L. Barbina (controls) and M. Vento (power supplies) of Sincrotrone Trieste are gratefully acknowledged.

## REFERENCES

[1] C. Poloni et al., Proc. 1991 Particle Accelerator Conference, IEEE Catalog No. 91CH3038-7, p. 2712
[2] R.P. Walker and B. Diviacco, Rev. Sci. Instr. 63 (1992) 332.
[3] A. Derossi et al., Rev. Sci. Instr. 66 (1995) 1718.
[4] E. Gluskin, Proc. 10th ICFA Beam Dynamics Panel Workshop, 4th Generation Light Sources, ESRF, Grenoble, Jan. 1996, p. WG1-56.
[5] Opera-3D, Vector Fields Ltd., Oxford, England.
[6] L. Tosi et al., these Proceedings.

# DESIGN FEATURES OF A PLANAR HYBRID/PERMANENT MAGNET STRONG-FOCUSING UNDULATOR FOR FREE ELECTRON LASER (FEL) AND SYNCHROTRON RADIATION (SR) APPLICATIONS*

R. Tatchyn
Stanford Synchrotron Radiation Laboratory, Stanford Linear Accelerator Center, Stanford, CA 94309, USA

*Abstract*

Insertion devices for Ångstrom-wavelength Free Electron Laser (FEL) amplifiers driven by multi-GeV electron beams generally require distributed focusing substantially stronger than their own natural focusing fields. Over the last several years a wide variety of focusing schemes and configurations have been proposed for undulators of this class, ranging from conventional current-driven quadrupoles external to the undulator magnets to permanent magnet (PM) lattices inserted into the insertion device gap. In this paper we present design studies of a flexible high-field hybrid/PM undulator with strong superimposed planar PM focusing proposed for a 1.5 Angstrom Linac Coherent Light Source (LCLS) driven by an electron beam with a 1 mm-mr normalized emittance. Attainable field parameters, tuning modes, and potential applications of the proposed structure are discussed.

## I. INTRODUCTION

Å-wavelength LCLS undulators driven by multi-Gev elecron beams generally require superimposed focusing [1,2]. Since it is typically optimal to induce 1 full betatron oscillation over the length of the undulator, the required strength of the focusing field (for a fixed undulator K and fundamental output wavelength) varies inversely with the required undulator length. But since the undulator length required to attain saturation varies roughly inversely with e-beam emittance, the required focusing gradient for, say, a FODO lattice of given period and quadrupole length, also varies inversely with the minimum attainable emittance. This dependency is illustrated by the LCLS design study recently undertaken at SLAC [3], which projects a net emittance of approximately 1.5 mm-mr at the undulator entrance. The LCLS parameters from this study are contrasted in Table 1 with those from an earlier study [4], which presupposed a net attainable emittance of 1 mm-mr.

The focusing strength (viz., gradient Q) that can be attained in a FODO lattice superimposed on the undulator field inside the gap is highly dependent on the technique employed. For $Q \leq 45$ T/m, for example, external quadrupoles can be employed in pure-permanent magnet (PM) designs [5], and pole wedging, staggering, and canting can be employed with hybrid/permanent magnet (hybrid/PM) technology [6]. If the details associated with shimming are disregarded, the latter technology has the advantage of utilizing a minimal number of elements per period. For $Q \geq 45$ T/m, alternative techniques need to be employed [7-10]. In this paper, the planar-PM multipole technology proposed in recent years [7,8] is explored as a basis for a strong-focusing LCLS undulator field design [4,11]. The r&d associated with this work anticipates the eventual development of photocathode (pc) rf guns and linac-based compressor/transport systems that will deliver emittances of 1 mm-mr or less to the LCLS insertion device.

**Table 1.** LCLS Parameters.

| | Earlier study | Current Study |
|---|---|---|
| Radiation wavelength [Å] | 1.5 | 1.5 |
| Norm. emitt. $\gamma\varepsilon$ [mm-mrad] | 1 | 1.5 |
| Bunch Charge (initial) [nC] | 0.94 | 0.94 |
| Peak current $I_p$ [kA] | 5 | 3.4 |
| Electron beam energy $E$ [GeV] | 14.55 | 14.35 |
| $\sigma_E / E$ [%] | 0.02 | 0.02 |
| Pulse duration $\sqrt{2\pi}\sigma_\tau$ [fs] | 260 | 250 |
| Repetition rate [Hz] | 120 | 120 |
| Undulator period $\lambda_u$ [cm] | 3.0 | 3.0 |
| Peak field $B_u$ [T] | 1.3 | 1.3 |
| Saturation length[a] $L_u$ [m] | 60 | 100 |
| Focusing beta [m/rad] | 10 | 18 |
| Peak spontaneous power [GW] | 66 | 81 |
| Peak coherent power* [GW] | 50 | 9.3 |
| Average coherent power [W] | 0.64 | 0.09 |
| Energy/pulse [mJ] | 5 | 0.75 |
| Coherent photons/pulse ($x10^{12}$) | 12.2 | 1.4 |
| Approx. Bandwidth (BW) [%] | 0.1 | 0.1 |
| Peak brightness** ($x10^{31}$) | 5.1 | 61.7 |
| Average brightness** ($x10^{21}$) | 1.7 | 20.6 |
| Transverse size [m, FWHM]*** | 30 | 30 |
| Diverg. angle [mrad, FWHM]*** | 10 | 5 |

[a] Sufficiently small field errors assumed;
*Output fully transversely coherent;
**Photons/s/mm2/mrad2/0.1%BW;
***At exit of undulator

## II. A HIGH-FIELD LCLS UNDULATOR DESIGN WITH STRONG PLANAR-PM FOCUSING

The basic undulator construction, schematized in Fig. 1, is seen to consist entirely of PM and permeable pole pieces with rectangular cross sections. The easy axes of all the PM pieces are, in each piece, perpendicular to two

* Work supported in part by the Department of Energy Offices of Basic Energy Sciences and High Energy and Nuclear Physics, and Department of Energy Contract DE-AC03-76SF00515.

0-7803-4376-X/98 /$10.00 © 1998 IEEE

opposed faces. This not only optimizes the ease and accuracy of component fabrication and undulator construction, but provides a left-right symmetry in the undulator's dipole field structure that can be exploited for shimming and tuning purposes. In addition, the geometrical symmetry allows the axially magnetized PM material to be brought as close as possible to the undulator axis, allowing for the utmost maximization of the on-axis field strength.

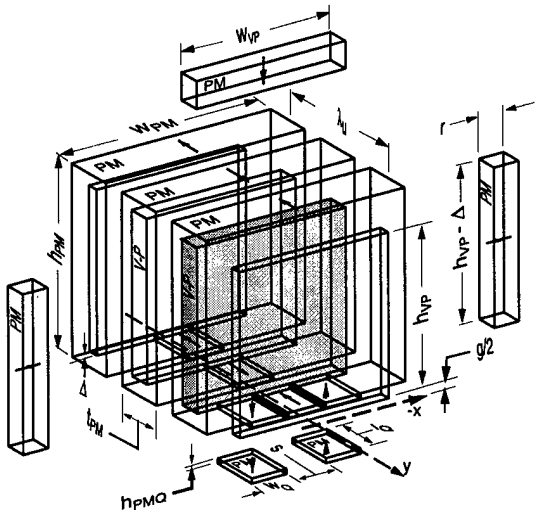



Figure 1. Undulator components and design options (structure mirror-symmetric with respect to the x-y plane; top half shown). To maximize or shim the on-axis field, each pole piece can have one top and two side bias pieces appended to it. Bevels on pole surface edges not shown. For the recessed PMQs, $l_Q=t_{PM}$ and $s=w_{smin}$.

The proposed structure is seen to be of the "separated-function" type, allowing the quadrupole focusing to be implemented basically independently of the dipole field structure [11]. There are a number of possible implementations; for some of these the axially-magnetized PM material immediately above the axis can: 1) be excluded. 2) comprise individual PM pieces (as depicted in Fig. 1), or 3) comprise continuous extensions of the large axial PM magnet blocks. First, the axial PM blocks can be recessed back from the plane of the permeable pole faces by a distance $\Delta$ ($>h_{PMQ}$), leaving room for the insertion and full variation of the PMQ's lateral gap parameter s ($\geq 0$). Second, if s can be bounded by some minimum value $w_{smin}$, the axial PM blocks can be cut with lateral indents allowing for both the lateral insertion of the PMQ pieces and the extension of the axial PM block material down toward the plane of the pole faces. Third, the PMQ pieces can be made with $l_Q>t_{PM}$ and extended (below the pole faces) along distances of several periods. Here, $s \geq w_{smin}$, and the PMQ pieces could be either affixed to the vacuum duct and tuned with linear wire currents [4], or moved into the gap laterally with high-precision mechanical movers. Finally, the dipole structure could be implemented with periodic drift spaces [12], and the PMQ pieces could be installed thereinto, again with mechanical or wire-current tuning of their gradients.

In view of their large spontaneous power output, LCLSs of the class being considered here can induce energy chirps in the electron bunch substantially larger than the the natural linewidth of the FEL (see Table 1). In this case, it could be advantageous to be able to induce a compensating chirp in the undulator field strength. As shown in Fig. 2, this can be accomplished with the proposed design by moving two planar shunt bars into locations at equal distances above and below the undulator structure.

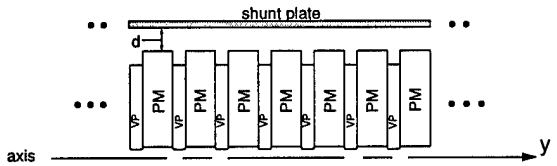



Figure 2. Scheme for tailoring the field profile of the strong-focusing LCLS undulator using two monolithic field shunts (top half of full structure shown). The shunt can be segmented and each segment can be canted along the entire FEL. It can also be segmented, with each segment placed parallel to each gain length (as depicted) at an incrementally varying distance. PMQ pieces not shown.

## III. FIELD SIMULATIONS

Comprehensive field design studies were conducted with the AMPERES [13] modeling package. Here we present results for a selected number of configuration cases (see Table 2), with $\lambda_u$=3cm, $t_{PM}$=10.5mm, $h_{PM}$=34mm, $w_{PM}$=4cm, $t_{VP}$(=($\lambda_u$-2$t_{PM}$)/2)=4.5mm, $h_{VP}$=3cm, $w_{VP}$=3cm, r=5mm, $w_Q$=7mm, $l_Q$(=$t_{PM}$)=10.5mm, $h_{PMQ}$=0.95mm, $\Delta$=1mm, and g/2=3mm. The model consists exactly of the configuration shown in Fig. 1, extended by symmetry reflections in the x-y and x-z planes. The pole material is Vanadium Permendur and $B_r$=1.25T ($H_c$~11900 Oersted) for the PM (Nd/Fe/B).

**Table 2.** Four configurations modeled with AMPERES.

| | Lateral PM Bias Blocks | $s \geq w_s$ (Axial PM Near Axis) | Shunt Plate | PMQs recessed |
|---|---|---|---|---|
| Case I | Yes | Yes | No | Yes |
| Case II | No | Yes | No | Yes |
| Case III | No | No | Yes | Yes |
| Case IV | No | No | No | Yes |

In Fig. 3 Cases I, II, and IV are plotted to show the corresponding range of attainable on-axis fields. A harmonic analysis of the curves confirms a field amplitude in the fundamental of 1.3 T or more for Cases I and II. In Fig. 4, $B_z$ is plotted vs. x between the middlemost poles of the symmetry-extended structure. Both curves show homogeneous central field regions of >2mm extent, fully adequate for the given LCLS beam. In Fig. 5, $B_z$ is plotted

vs. x directly under the axial center of a recessed PMQ (Case I) for spacings s of 5mm and 2mm. The curves reveal gradients of 19T/m and 55T/m, respectively, to be contrasted with a maximum value, for s=0, of ~62T/m. With $h_{PMQ}$ increased to 3mm, this maximum could be increased to ~200T/m. Finally, in Fig. 6 the effects of parallel shunt plates (Case III) on the on-axis field amplitude is plotted for three different spacings d (see. Fig. 2). A reasonable sensitivity to field control over the $10^{-1}$-$10^{-4}$ range, adequate for strong tapering through low-level chirp correction, is indicated.

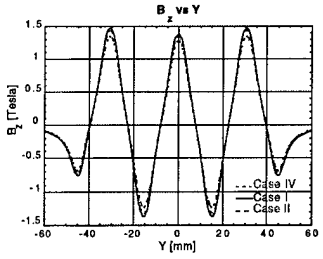



**Figure 3.** Modeled on-axis dipole field $B_z(y)$.

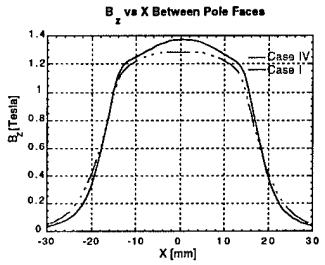



**Figure 4.** Modeled transverse field $B_z(x)$ under central pole face.

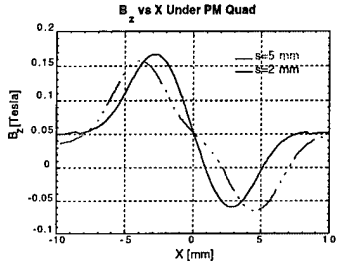



**Figure 5.** Transverse field $B_z(x)$ under the axial center of a PMQ.

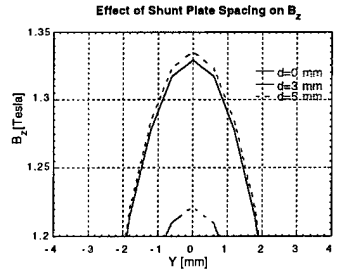



**Figure 6.** $B_z(y)$ about the undulator's central peak field for 3 different shunt plate spacings.

## IV. CONCLUSIONS

We have described selected structural and field features of a simple high-field, strong-focusing LCLS undulator design developed at SSRL over the 1993-1996 period. These were motivated by the requirements for minimizing the length and cost while maximizing the field strength and quality of the structure. The proposed technology and design are also of interest for the development of long (viz., $>>\beta$), short-period, small-gap insertion devices for storage ring straights, a recognized direction for attaining 4th generation increases in brightness over conventional 3rd generation storage rings [14]. Future work will include further design refinement, including the simulation of wire-current quad field correction, planar-PM sextupole focusing, and the development of small prototypes.

## V. REFERENCES


[1] C. Pellegrini, "A 4 to 0.1 nm FEL Based on the SLAC Linac," in *Proc. Workshop on 4th Generation Light Sources*, M.Cornacchia and H. Winick, eds., SSRL, Feb. 1992. p. 364 ff.

[2] R. Tatchyn, "Optimal Insertion Device Parameters for SASE FEL Operation," ibid., p. 605 ff.

[3] M. Cornacchia et al, "Performance and design concepts of a free-electron laser operating in the x-ray region," SPIE Proceedings 2988, 1997, paper 2988-01.

[4] R. Tatchyn et al, "Research and development toward a 4.5-1.5 Å Linac Coherent Light Source (LCLS) at SLAC," NIM A 375, 274(1996).

[5] R. Tatchyn, R. Boyce, K. Halbach, H.-D. Nuhn, J. Seeman, H. Winick, and C. Pellegrini, "Design Considerations for a 60 Meter Pure Permanent Magnet Undulator for the SLAC Linac Coherent Light Source (LCLS)," in Proceedings of the 1993 Particle Accelerator Conference, IEEE Catalog No. 93CH3279-7, 1608(1993).

[6] R. Schlueter, "Undulators for short wavelength FEL amplifiers," NIM A 358, 44(1995).

[7] R. Tatchyn, "Selected applications of planar permanent magnet multipoles in FEL insertion device design," NIM A341, 449(1994).

[8] R. Tatchyn, "Permanent Magnet Edge-Field Quadrupole," US Patent 5,596,304.

[9] A. A. Varfolomeev, A. H. Hairetdinov, "Advanced hybrid undulator schemes providing enhanced transverse e-beam focusing," ibid., p. 462.

[10] G. Travish, J. Rosenzweig, "Strong sextupole focusing in planar undulators," NIM A345, 585(1994).

[11] Caspi, R. Schlueter, R. Tatchyn, "High-Field Strong-Focusing Undulator Designs for X-Ray Linac Coherent Light Source (LCLS) Applications," in Proceedings of the 1995 Particle Accelerator Conference, Dallas, TX, May 1-5, 1995; SLAC-PUB-95-6885.

[12] N. A. Vinokurov, R. Dejus, H. Friedsam, E. S. Gluskin, J. Maines, S. V. Milton, E. R. Moog, E. M. Trakhtenberg, I. B. Vasserman, "Design considerations for the magnetic system of a prototype x-ray free electron laser," SPIE Proceedings No, 2988, 64(1997).

[13] Integrated Engineering Software,Inc.,Winnipeg, Manitoba.

[14] R. Tatchyn, in Proceedings of the ESRF Workshop on 4th Generation Light Sources, Grenoble, 1/22-25/96, p. WG7-116 et ff.

# LINEAR BEAM DYNAMICS EFFECTS OF THREE DIMENSIONAL STATIC MAGNETIC FIELDS OF INSERSION DEVICES AT SRRC

Peace Chang, M.H. Wang, Chaoen Wang, C.C. Kuo, and C.S. Hsue*
Synchrotron Radiation Research Center, Hsinchu 300, Taiwan, R.O.C.
*Department of Physics, National Tsing Hua University, Hsinchu 300, Taiwan, R.O.C.

*Abstract*

To understand the effects of the insertion devices on beam dynamics, Hamiltonian equations of charged particles in the presence of the insertion devices have been studied. Fields with insertion devices are considered to be periodic in the longitudinal direction with period length $\lambda_s$. The magnetic fields of the different types of magnet structure, namely AGID, APID and EPU, are derived and discussed. The linear beam dynamics effects for different kinds of insertion devices can be obtained directly from the canonical equations of the Hamiltonian mechanics.

## 1 INTRODUCTION

Various types of insertion devices (IDs) have been designed for generating specific light sources. In particular, adjustable gap insertion devices (AGIDs) are the most popular IDs. Special insertion devices such as adjustable phase insersion devices (APIDs) and elliptically polarizing undulators (EPUs) are being designed and realized for providing light sources of special properties. At SRRC, W20 wiggler and U10P, U5, U9 undulators are AGIDs, the testing purpose APU9P undulator belongs to the APID, and the EPU-5.6 is an EPU. Since these IDs are installed in the storage ring, the influence of the magnetic fields of IDs upon the stored electron beam should be concerned. Here, we study the linear beam dynamics effects of IDs by the Hamiltonian equations of a 3-dimensional periodic magnetic field.

## 2 TRANSVERSE EQUATIONS OF MOTION

We consider the general 3-dimensional magnetic field

$$\begin{aligned}
B_x &= \sum_n \Big[ f_{1n}(x,y)\cos(nk_s s) + f_{2n}(x,y)\sin(nk_s s) \Big] \\
B_y &= \sum_n \Big[ g_{1n}(x,y)\cos(nk_s s) + g_{2n}(x,y)\sin(nk_s s) \Big] \\
B_s &= \sum_n \Big[ h_{1n}(x,y)\cos(nk_s s) + h_{2n}(x,y)\sin(nk_s s) \Big],
\end{aligned}$$

which is a periodic function in the longitudinal direction, i.e., $\hat{s}$ of the curvilinear coordinate system $(x, y, s)$, with wave vector $k_s = \frac{2\pi}{\lambda_s}$. Using Maxwell's equations $\nabla \cdot \mathbf{B} = 0$ and $\nabla \times \mathbf{B} = 0$, we have four equations to solve for the $f_{1n}$, $f_{2n}$, $g_{1n}$, $g_{2n}$, $h_{1n}$, and $h_{2n}$. For convenient, we set $c_{mnu} \equiv \cosh(nk_{mnu}u)$ and $s_{mnu} \equiv \sinh(nk_{mnu}u)$, where $m = 1, 2$ and $u = x, y$. We obtain

$$\begin{aligned}
h_{1n} &= k_s(\alpha_{1n}c_{1nx} + \beta_{1n}s_{1nx})(\gamma_{1n}c_{1ny} + \delta_{1n}s_{1ny}), \\
h_{2n} &= k_s(\alpha_{2n}c_{2nx} + \beta_{2n}s_{2nx})(\gamma_{2n}c_{2ny} + \delta_{2n}s_{2ny}), \\
f_{1n} &= -k_{2nx}(\alpha_{2n}s_{2nx} + \beta_{2n}c_{2nx})(\gamma_{2n}c_{2ny} + \delta_{2n}s_{2ny}), \\
f_{2n} &= k_{1nx}(\alpha_{1n}s_{1nx} + \beta_{1n}c_{1nx})(\gamma_{1n}c_{1ny} + \delta_{1n}s_{1ny}), \\
g_{1n} &= -k_{2ny}(\alpha_{2n}c_{2nx} + \beta_{2n}s_{2nx})(\gamma_{2n}s_{2ny} + \delta_{2n}c_{2ny}), \\
g_{2n} &= k_{1ny}(\alpha_{1n}c_{1nx} + \beta_{1n}s_{1nx})(\gamma_{1n}s_{1ny} + \delta_{1n}c_{1ny}),
\end{aligned}$$

and

$$k_{mnx}^2 + k_{mny}^2 = k_s^2.$$

For charged-particles in such a magnetic field, the Hamiltonian in Frent-Serret coordinate system[1, 2] is given as

$$G = \frac{-e}{c}A_s - \left(1 + \frac{x}{\rho(s)}\right) p_0^{\text{mech}} \left[ \left(1 + \frac{\Delta p^{\text{mech}}}{p_0^{\text{mech}}}\right)^2 - \left(\frac{P_x}{p_0^{\text{mech}}} - \frac{eA_x}{cp_0^{\text{mech}}}\right)^2 - \left(\frac{P_y}{p_0^{\text{mech}}} - \frac{eA_y}{cp_0^{\text{mech}}}\right)^2 \right]^{1/2},$$

where "$P$"s represent canonical momenta and $p_0^{\text{mech}}$ means the (relativistic) mechanical/kinetic momentum. The radius of curvature at long straight sections is $\rho(s) \to \infty$. Furthermore, comparing with $p_0^{\text{mech}}$, the transverse mechanical momenta of the electron beams in a storage ring are small, i.e.,

$$\frac{p_u^{\text{mech}}}{p_0^{\text{mech}}} = \left(\frac{P_u}{p_0^{\text{mech}}} - \frac{eA_u}{cp_0^{\text{mech}}}\right) \ll 1$$

with $u = x, y$. Therefore we expand the Hamiltonian $G$ in a Taylor series up to 2nd order of transverse mechanical momenta

$$G \simeq \frac{-e}{c}A_s - p_0^{\text{mech}} \left[ 1 + \frac{\Delta p^{\text{mech}}}{p_0^{\text{mech}}} + \frac{1}{2}\left(\frac{\Delta p^{\text{mech}}}{p_0^{\text{mech}}}\right)^2 - \frac{1}{2}\left(\frac{P_x}{p_0^{\text{mech}}} - \frac{eA_x}{cp_0^{\text{mech}}}\right)^2 - \frac{1}{2}\left(\frac{P_y}{p_0^{\text{mech}}} - \frac{eA_y}{cp_0^{\text{mech}}}\right)^2 \right].$$

The canonical equations of the Hamiltonian are

$$\begin{cases} \dfrac{dx}{ds} = \dfrac{\partial G}{\partial P_x} \simeq \dfrac{P_x}{p_0^{\text{mech}}} - \dfrac{eA_x}{cp_0^{\text{mech}}}, \\ \dfrac{dy}{ds} = \dfrac{\partial G}{\partial P_y} \simeq \dfrac{P_y}{p_0^{\text{mech}}} - \dfrac{eA_y}{cp_0^{\text{mech}}}. \end{cases}$$

From the relation, $\mathbf{B} = \nabla \times \mathbf{A}$, we can select $A_s = 0$ and solve $A_x$ and $A_y$ to get the transverse equations of motion:

$$\begin{cases} \dfrac{d^2x}{ds^2} \simeq \dfrac{d}{ds}\left(\dfrac{cP_x - eA_x}{cp_0^{\text{mech}}}\right) \simeq \dfrac{e}{cp_0^{\text{mech}}}\left(B_s\dfrac{dy}{ds} - B_y\right) \\ \dfrac{d^2y}{ds^2} \simeq \dfrac{d}{ds}\left(\dfrac{cP_y - eA_y}{cp_0^{\text{mech}}}\right) \simeq \dfrac{e}{cp_0^{\text{mech}}}\left(B_x - B_s\dfrac{dx}{ds}\right). \end{cases}$$

0-7803-4376-X/98/$10.00 © 1998 IEEE

Dividing $u$ into two parts $u_0 + u_1$ with $u = x, y$, we set

$$\begin{cases} \frac{d^2x_0}{ds^2} = \frac{-e}{cp_0^{\text{mech}}} B_y, & \frac{d^2x_1}{ds^2} = \frac{e}{cp_0^{\text{mech}}} B_s \frac{dy}{ds}, \\ \frac{d^2y_0}{ds^2} = \frac{e}{cp_0^{\text{mech}}} B_x, & \frac{d^2y_1}{ds^2} = \frac{-e}{cp_0^{\text{mech}}} B_s \frac{dx}{ds}. \end{cases}$$

Since $\frac{du}{ds} \ll 1$ for $u = x, y$, we can apply an iteration/successive approximation[3]

$$\begin{cases} \frac{d^2x}{ds^2} \simeq \frac{d^2x_0}{ds^2} + \frac{e}{cp_0^{\text{mech}}} B_s \frac{dy_0}{ds} \\ \frac{d^2y}{ds^2} \simeq \frac{d^2y_0}{ds^2} - \frac{e}{cp_0^{\text{mech}}} B_s \frac{dx_0}{ds}. \end{cases}$$

The effects of different kinds of IDs on the electron beam can then be obtained after their periodic 3-dimensional magnetic fields are determined by writting down the parameters $k$'s, $\alpha$'s, $\beta$'s, $\gamma$'s, and $\delta$'s.

## 3 AJUSTABLE GAP INSERTION DEVICES

Common properties of AGID structure are

$$B_y(-y) = B_y(y) \Longrightarrow \gamma_{1n} = \gamma_{2n} = 0,$$

$$\left.\begin{array}{l} B_x(-x) = -B_x(x) \\ B_y(-x) = B_y(x) \\ B_s(-x) = B_s(x) \end{array}\right\} \Longrightarrow \beta_{1n} = \beta_{2n} = 0.$$

### 3.1 $B_y$ is symmetric in $\hat{s}$ direction

The W20 wiggler and U10P undulator of SRRC have the property $B_y(-s) = B_y(s)$, which implies $k_{1ny}\alpha_{1n}\delta_{1n} = 0$. The magnetic field becomes

$$\begin{aligned} B_x &= \sum_n -k_{2nx}\alpha_{2n}\delta_{2n}s_{2nx}s_{2ny}\cos(nk_s s) \\ B_y &= \sum_n -k_{2ny}\alpha_{2n}\delta_{2n}c_{2nx}c_{2ny}\cos(nk_s s) \\ B_s &= \sum_n k_s\alpha_{2n}\delta_{2n}c_{2nx}s_{2ny}\sin(nk_s s). \end{aligned}$$

The second order differential equations of $x$ and $y$ expaned near the $s$-axis become

$$\begin{aligned} \frac{d^2x}{ds^2} &\simeq \frac{e}{cp_0^{\text{mech}}} \sum_n k_{2ny}\alpha_{2n}\delta_{2n}\cos(nk_s s) + \mathcal{O}(2), \\ \frac{d^2y}{ds^2} &\simeq -\left(\frac{e}{cp_0^{\text{mech}}}\right)^2 \left[\sum_n nk_{2ny}\alpha_{2n}\delta_{2n}\sin(nk_s s)\right] \\ &\quad \cdot \left[\sum_n \frac{k_{2ny}}{n}\alpha_{2n}\delta_{2n}\sin(nk_s s)\right] \cdot y + \mathcal{O}(2), \end{aligned}$$

where $\mathcal{O}(2)$ are terms of orders equal to or higher than second order in $x$ and $y$. The effective focusing strengthes are $K_x = 0$ and

$$\overline{K}_y = \frac{-1}{2}\left(\frac{e}{cp_0^{\text{mech}}}\right)^2 \sum_n (\alpha_{2n}\delta_{2n}k_{2ny})^2.$$

### 3.2 $B_y$ is anti-symmetric in $\hat{s}$ direction

On the other hand, the U5 and U9 undulators of SRRC are the types with $B_y(-s) = -B_y(s)$. We get $k_{2y}\alpha_2\delta_2 = 0$ and

$$\begin{aligned} B_x &= \sum_n k_{1nx}\alpha_{1n}\delta_{1n}s_{1nx}s_{1ny}\sin(nk_s s) \\ B_y &= \sum_n k_{1ny}\alpha_{1n}\delta_{1n}c_{1nx}c_{1ny}\sin(nk_s s) \\ B_s &= \sum_n k_s\alpha_{1n}\delta_{1n}c_{1nx}s_{1ny}\cos(nk_s s). \end{aligned}$$

The differential equations of $x$ and $y$ near the $s$-axis are

$$\begin{aligned} \frac{d^2x}{ds^2} &\simeq \frac{-e}{cp_0^{\text{mech}}} \sum_n k_{1ny}\alpha_{1n}\delta_{1n}\cos(nk_s s) + \mathcal{O}(2), \\ \frac{d^2y}{ds^2} &\simeq -\left(\frac{e}{cp_0^{\text{mech}}}\right)^2 \left[\sum_n nk_{1ny}\alpha_{1n}\delta_{1n}\cos(nk_s s)\right] \\ &\quad \cdot \left[\sum_n \frac{k_{1ny}}{n}\alpha_{1n}\delta_{1n}\cos(nk_s s)\right] \cdot y + \mathcal{O}(2). \end{aligned}$$

We obtain the effective focusing strengthes $K_x = 0$ and

$$\overline{K}_y = \frac{-1}{2}\left(\frac{e}{cp_0^{\text{mech}}}\right)^2 \sum_n (\alpha_{1n}\delta_{1n}k_{1ny})^2.$$

For AGIDs, the linear beam dynamics effects are clear and only non-linear effects should be controlled carefully. In the horizontal plane, the oscillation term comes from the $B_y$ field. The effective focusing strength in the vertical plane is caused by the interaction of the horizontal oscillation motion and the $B_s$ field.

## 4 AJUSTABLE PHASE INSERTION DEVICES

With the APID structure, we have the condition

$$\left.\begin{array}{l} B_x(-x) = -B_x(x) \\ B_y(-x) = B_y(x) \\ B_s(-x) = B_s(x) \end{array}\right\} \Longrightarrow \beta_1 = \beta_2 = 0.$$

The linear properties of beam dynamics of APID are more complex than the case with AGID. There exist oscillations and coupling/mixing of motions in the horizontal and the vertical planes. If the phase of APID defined as $\phi \equiv 2\pi\frac{\Delta s}{\lambda_s}$ is zero, then $\gamma_1 = \gamma_2 = 0$, and APID becomes AGID disscussed in section 3.

By setting $\delta_1 = \gamma_2 = 0$ and $B_x = 0$, our 3-dimensional magnetic field can be reduced to the 2-dimensional field discussed by Roger Carr [4, 5]. The equations of motion become

$$\begin{aligned} \frac{d^2x}{ds^2} &\simeq \frac{e}{cp_0^{\text{mech}}}\left[\sum_n k_s\alpha_{2n}\delta_{2n}\cos(nk_s s)\right] - \\ &\frac{e}{cp_0^{\text{mech}}}\left[\sum_n nk_s^2\alpha_{1n}\gamma_{1n}\sin(nk_s s)\right] \times y + \cdots \end{aligned}$$

and

$$\frac{d^2y}{ds^2} \simeq -\left(\frac{e}{cp_0^{\text{mech}}}\right)^2 \left[\sum_n \alpha_{1n}\gamma_{1n}\cos(nk_s s)\right] \times \left[\sum_n \frac{k_s}{n}\alpha_{2n}\delta_{2n}\sin(nk_s s)\right] - \left(\frac{e}{cp_0^{\text{mech}}}\right)^2 k_s^2 \times \left\{\left[\sum_n \alpha_{1n}\gamma_{1n}\cos(nk_s s)\right]^2 + \left[\sum_n n\alpha_{2n}\delta_{2n}\sin(nk_s s)\right] \times \left[\sum_n \frac{1}{n}\alpha_{2n}\delta_{2n}\sin(nk_s s)\right]\right\} \times y + \cdots.$$

There is an intrinsic oscillation in the $y$ plane, though the quantity of the oscillation amplitude is quite small. A particle tracking of $(\frac{1}{4}, \frac{-3}{4}, 1, -1, \cdots, 1, \frac{-3}{4}, \frac{1}{4})$ structure also shows a small vertical drift besides the tiny oscillation. The drift is proportional to the period number of APID. If we take the average of the x and y terms in the differential equations of motion, the horizontal linear coupling term is cancelled and the vertical average effective focusing strength is

$$\overline{K}_y = \frac{-1}{2}\left(\frac{e}{cp_0^{\text{mech}}}\right)^2 (B_{y0}^2 + B_{s0}^2) = \frac{-k_s^2}{2}\left(\frac{e}{cp_0^{\text{mech}}}\right)^2 \left[\sum_n (\alpha_{1n}\gamma_{1n})^2 + \sum_n (\alpha_{2n}\delta_{2n})^2\right],$$

where $B_{y0}$ and $B_{s0}$ are the amplitudes of $B_y$ and $B_s$. For SRRC's APU9P, $B_{y0}^2 + B_{s0}^2$ does not keep constant such that the vertical tune shift appears when phase is changed. Experiment has confirmed that the vertical tune shift is proportional to $B_{y0}^2 + B_{s0}^2$.

## 5 ELLIPTICALLY POLARIZING UNDULATOR

The condition $B_s(s, x = 0, y = 0) = 0$ of EPU gives $\alpha_{1n}\gamma_{1n} = \alpha_{2n}\gamma_{2n} = 0$. Furthermore, from the structure of SRRC's Sasaki-type EPU-5.6, we have

$$\left.\begin{array}{l} B_x(x,y) = B_x(-x,-y) \\ B_y(x,y) = B_y(-x,-y) \\ B_x(-x,y) = B_x(x,-y) \\ B_y(-x,y) = B_y(x,-y) \end{array}\right\} \Longrightarrow \beta_{1n}\delta_{1n} = \beta_{2n}\delta_{2n} = 0.$$

Comparing with the on-axis magnetic field of Sasaki type EPU[6]

$$B_x = \left(\hat{B}_x \sin^2\frac{\phi}{2}\right)\sin k_s s - \left(\hat{B}_x \sin\frac{\phi}{2}\cos\frac{\phi}{2}\right)\cos k_s s$$
$$B_y = \left(\hat{B}_y \sin\frac{\phi}{2}\cos\frac{\phi}{2}\right)\cos k_s s + \left(\hat{B}_y \cos^2\frac{\phi}{2}\right)\sin k_s s,$$

we have $n = 1$ and

$$k_{11x}\beta_{11}\gamma_{11} = \hat{B}_x \sin^2\frac{\phi}{2},\ k_{21x}\beta_{21}\gamma_{21} = \hat{B}_x \sin\frac{\phi}{2}\cos\frac{\phi}{2},$$
$$k_{11y}\alpha_{11}\delta_{11} = \hat{B}_y \cos^2\frac{\phi}{2},\ k_{21y}\alpha_{21}\delta_{21} = -\hat{B}_y \sin\frac{\phi}{2}\cos\frac{\phi}{2}.$$

The equations of motion become

$$\frac{d^2x}{ds^2} \simeq \frac{e}{cp_0^{\text{mech}}}(k_{2y}\alpha_2\delta_2\cos k_s s - k_{1y}\alpha_1\delta_1\sin k_s s) - \left(\frac{e}{cp_0^{\text{mech}}}\right)^2 (k_{1x}\beta_1\gamma_1\cos k_s s + k_{2x}\beta_2\gamma_2\sin k_s s)\cdot (k_{1y}\alpha_1\delta_1\cos k_s s + k_{2y}\alpha_2\delta_2\sin k_s s)\cdot y - \left(\frac{e}{cp_0^{\text{mech}}}\right)^2 \cdot (k_{1x}\beta_1\gamma_1\cos k_s s + k_{2x}\beta_2\gamma_2\sin k_s s)^2 \cdot x + \mathcal{O}(2)$$

and

$$\frac{d^2y}{ds^2} \simeq \frac{e}{cp_0^{\text{mech}}}(-k_{2x}\beta_2\gamma_2\cos k_s s + k_{1x}\beta_1\gamma_1\sin k_s s) - \left(\frac{e}{cp_0^{\text{mech}}}\right)^2 (k_{1x}\beta_1\gamma_1\cos k_s s + k_{2x}\beta_2\gamma_2\sin k_s s)\cdot (k_{1y}\alpha_1\delta_1\cos k_s s + k_{2y}\alpha_2\delta_2\sin k_s s)\cdot x - \left(\frac{e}{cp_0^{\text{mech}}}\right)^2 \cdot (k_{1y}\alpha_1\delta_1\cos k_s s + k_{2y}\alpha_2\delta_2\sin k_s s)^2 \cdot y + \mathcal{O}(2).$$

The equations of motion contain oscillation terms and linear coupling terms and make the linear beam dynamics effects becomes complex. The oscillation terms come from the interaction of $v_s$ and the transverse magnetic fields $B_x$ and $B_y$. The longitudinal magnetic field $B_s$ couples the transverse oscillations in both planes.

## 6 CONCLUSION

The 3-dimensional periodic magnetic field discussed here can cover the AGID, APID, and EPU in a unified way by adding suitable structure conditions. AGID is the most popular type of IDs and its influence on the stored beam is well known and clear. A detail linear beam dynamic effects of APU with 2-dimensional field form have been achieved and discussed in section 4.

The analytical solutions of the differential equations of motion for EPU can not be written down in a simple form. Numerical calculation/simulation is by far the easiest way to study the EPU's effects on beam dynamics.

## 7 REFERENCES


[1] E. D. Courant and H. S. Snyder, "Theory of the Alternating-Gradient Synchrotron", Annals of Physics, **3**, p. 1 - 48, 1958.

[2] Henri Bruck, "Circular Particle Accelerators", 1966.

[3] C. C. Lin and L. A. Segel, "Mathematics Applied to Deterministic Problems in the Natural Sciences", Macmillan Publishing Co., Inc., New York, ISBN 0-02-370720-8.

[4] Roger Carr, "Adjustable phase insertion devices as X-ray sources", Nuclear Instruments and Methods in Physics Research, A306, 391-396, 1991.

[5] Roger Carr and Heinz-Dieter Nuhn, "Design study for an ajustable phase undulator", Rev. Sci. Instrum., **63** (1), January 1992.

[6] Shigemi Sasaki, "Analyses for a planar variably-polarizing undulator", Nuclear Instruments and Methods in Physics Research, A 347, p. 83-86, 1994.

# MAGNET SORTING ALGORITHMS FOR A PROTOTYPE OF THE SRRC EPU

T. C. Fan, C. S. Hwang, C. H. Chang, Ch. Wang
Synchrotron Radiation Research Center, Hsinchu 30077, Taiwan

*Abstract*

The Synchrotron Radiation Research Center (SRRC) is constructing a prototype of Sasaki-type elliptically-polarizing undulator (EPU) characterized by its four longitudinal movable magnet rows, whose shifting determines the polarization of synchrotron radiation. A total of 280 pure NdFeB blocks with square cross-section of 40 mm x 40 mm and thickness of 14 mm are magnetized into two types identified by the main field orientation. To minimize field errors, the blocks are sorted and assigned appropriate locations on the rows. Due to the special symmetry of the blocks, the 40 mm x 40 mm square face, and rows structure, the orientation and locations of blocks can be assigned freely. However the cutting on one pair of opposite angles on each square face for rigid clamping reduces the freedom of permutation. Moreover, the perturbation of the field from the shifting of rows must be taken into account. The authors would like to present the sorting algorithm and address its contribution to field performance.

## 1 INTRODUCTION

The Synchrotron Radiation Research Center (SRRC) will construct a 3.9 meter long Sasaki-type elliptically-polarizing undulator (EPU). The period length of this device is 56 mm. Therefore we name it EPU 5.6. A prototype of one meter long is being fabricated to evaluate the concept design [1]. The schematic view of one period (of length $\lambda_u$) of the magnetic structure for generating the elliptically polarizing light is provided in Fig. 1. Each of the four magnet rows can move with a range of ± 28 mm, i.e. one quarter period along two opposite direction each, independently. Therefore all the combination of the rows movement, and all kinds of planar- and elliptically-polarized X-rays with various energies can be achieved [2]. A gap adjustment mechanism supported by a drive train system can also tune the magnetic field strength.

The EPU 5.6 is a pure type device using NdFeB permanent magnet blocks with square cross-section of 40 mm x 40 mm and thickness of 14 mm. For rigid clamping under the strongly magnetic force, there are cuttings on one pair of opposite angles on each square face. Due to the special symmetry of the blocks, they need to be magnetized into only two types, V- and H- types, identified by the main field orientation. Because of the 40 mm x 40 mm square face, and arrays structure, the orientation and locations of one type of blocks can be assigned freely. However, the angle cuttings mentioned above and the periodical magnetic structure reduce the freedom of permutation. In Fig. 2 we summarize the allowed rotation of each type.

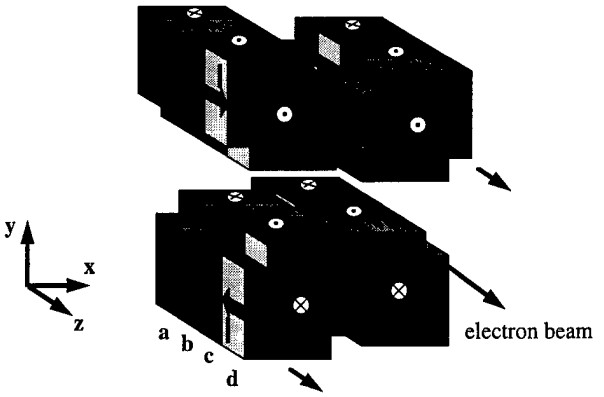



Figure 1: One period of magnets: The magnet blocks can be located at four quadrants (I, II, III and IV) and four quarter periods (a, b, c and d). The small bars indicating the series numbers and broad arrows are marked by vendor.

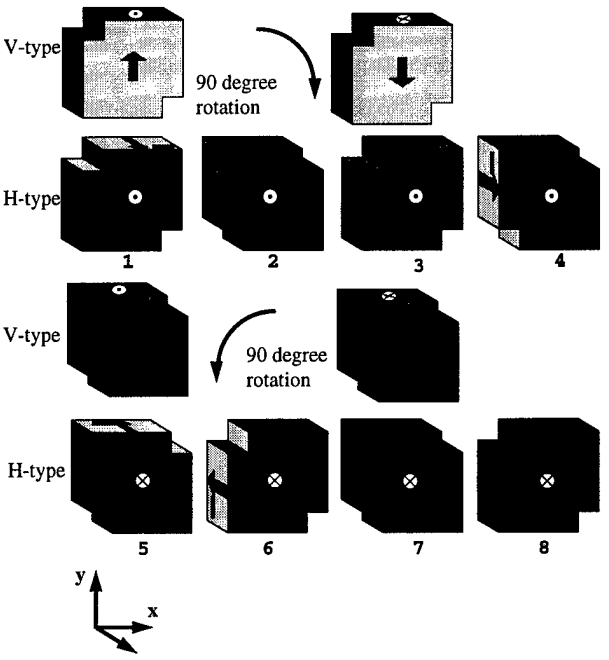



Figure 2: The allowed block rotation of two types of magnetization.

The demand on the quality of magnet blocks and the sorting results are diverse at different laboratories. Some purchase the best magnet blocks commercially available but costly. Some develop sophisticated sorting code with enormous measurement data and tremendous computer

0-7803-4376-X/98 /$10.00 © 1998 IEEE

running time. There are also a few laboratories put much effort on shimming or field correction techniques [3-4]. Though the passive field correction is most demanding, most of the field correction techniques are effective only when the field error is reasonable small. Under the limited budget, the suitable sorting algorithms are quite feasible.

For insertion devices with hybrid structure, there is a magnet sorting algorithm to establish uniform pole excitation by reducing the deviation of the average Mz of each unit cell [5]. Mz is the magnetic moment in the direction of magnetization. Each unit cell comprises one pole and six magnet blocks. However, in such non-iterative algorithms, the multipole field can not be controlled effectively. Therefore, that algorithm has been improved to control the effect from minor components [6]. On the other hand, the techniques of annealing have been applied to magnet sorting [7].

In pure permanent magnet structures such as EPU 5.6, we have an advantage of ignoring the nonlinear component. The field distribution can be calculated by superposition of the magnet field. In this prototype, we will try two approaches of sorting. One is just to use the magnetic moments measured by Helmholtz to minimize the total magnet moments, the other is to sort the magnets by multipole field measured by flip coil eliminate the field error.

## 2 SORTING CONSIDERATION

Before the algorithm of sorting for the prototype EPU 5.6 is deduced, we have some considerations as the following:

### *2.1 About the Magnet Blocks*

An amount of 174 V-type and 176 H-type magnets have been purchased for this prototype EPU. Only 280 of them will be used. The maximum principal dipole variance and inclination angle is required to be ± 1% and 2° respectively. Fig. 3 shows an example of the population of the magnetic moment My of V-type magnets. By removing the magnets with extremely high or low field, we can get an acceptable group to sort. The magnetic moment was measured by a Helmholtz coil system with a resolution and reproducibility of 4 Gauss. With the sorting of a large amount of magnets, it is evident that an average effect will diminish a part of effect from measurement error.

A magnet keeper is designed to allow easy adjustments in the vertical and transverse positions. This adjustment can also serve as magnetic field tuning.

### *2.2 First Stage Sorting*

To simplify the modeling, we separate the sorting algorithm into two stages. At first stage, we try to make a reduction of first integral of field at the axis of electron beam as the following steps:

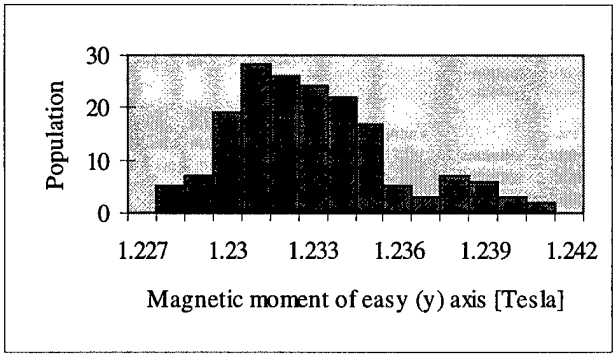



Figure 3: The vertical magnetic moment of V-type blocks. The total number of the blocks is 174.

1) The V- and H-type blocks are monotonically ordered in ascending values of My and Mz respectively.
2) The V-type blocks are assigned to rows I and II alternatively from upstream to downstream in proper order. The left ones are assigned to rows III and IV in the similar way, but from downstream to upstream.
3) The H-type blocks are assigned to rows in reverse order, i.e. to rows III and IV from upstream to downstream in proper order and to rows I and II from downstream to upstream.

If we can ignore the minor moments, Mz and Mx for V-type but My and Mx for H-type, we would have a beautiful sinusoidal vertical and horizontal fields at each period of each row by calculation. Because of the linearity of the magnets, the "row phase shift" will keep the sinusoidal fields with field phase shift. The "yaw phase shift" and "pair phase shift" also have sinusoidal fields only with the amplitude change. The terminology of these three "phase shifts" are defined in [2].

If the minor moments have no dependence on the main moment, the order of the main moment at each quarter period would not cause any systematic errors of multipole fields. This dependence has been checked. The example in the Fig. 4 is the only one, which can be identified. The correlation between the main and minor moments is quite weak however.

### *2.3 The Second Stage*

After all the magnets are assigned to locations and the zeroth order of field is constructed, the next step is to face the multipole problem. To look at one period as a unit, we can exchange the locations or rotate the orientation of magnets in each unit. In order not to destroy the sinusoidal field obtained at the first step, some exchange and rotation are forbidden. The rules of permutation and rotation turn out be as follows:

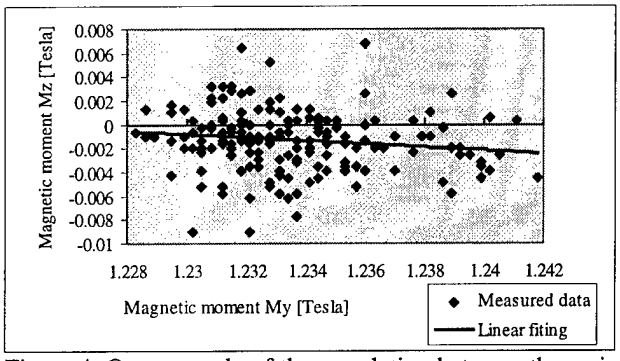


Figure 4: One example of the correlation between the main and minor moments.

1) The upper rows (upper jaw) of magnets can not be interchanged with the lower rows owing to the large difference of Main moments. The magnets of the same jaw can, since the difference is quite small according the first stage ordering.
2) There are 4! / (2! x 2!) permutations of V-type permutation in each period of upper or lower row. After an iteration of calculation of all combination, one can find an optimum of the three total moments (so that the absolute value is closest to null). The interchanged configuration shall be recorded for the final step.
3) Besides the same 4! / (2! x 2!) permutations of H-type permutation in each period of each jaw, there are two more 180° rotation freedoms along z-axis. So the total number of permutation is 12. The calculation and recording is the same as item 2).
4) In each period of each jaw, by reversing the process of 2) or 3) according to the record, one may find a less number.
5) In each jaw, one can reverse some period process according to the record to find a minimum multipole field.

### *2.4 Multipole Field Sorting*

Similar to the two-stage sorting of the magnet moments, we can measure and calculate the dipole field at the axis of electron beam and take the place of Mz. We can use the same permutation procedure to minimize the multipole field.

## 3 CONCLUSION

Although there are many complicated phase shift modes in EPU, thanks to the linearity of the pure permanent magnets, it is feasible to sort the magnets directly to reduce the error effect on the spectrum and beam dynamics.

## 4 REFERENCE

[1] Ch. Wang et al., "SRRC EPU-5.6 Conceptual Design Report", July 26, 1996.
[2] Steve Lidia and Roger Carr, "An elliptically-polarizing undulator with phase adjustable energy and polarization", NIM in Physics research A 347,1994.
[3] J. Chavanne and P. Elleaume, "Undulator and Wiggler Shimming ", Synchrotron Radiation News", Vol. 8 No. 1, 1995.
[4] E. Hoyer, S. Marks, P. Pipersky, and R. Schlueter, "ALS Multiple Trim Magnets, or 'Magic Fingers', for Insertion Device Field Integral Correction", 5th International conference on Synchrotron Radiation Instrumentation, 1994.
[5] D. Humphries, E. Hoyer, B. Kincaid, S. Marks, and R. Schlueter, "Magnet Sorting Algorithms for Insertion Devices for the Advanced Light Source", proceedings of the 13th International Conference on Magnet Technology
[6] D. Humphries, F. Goetz, P. Kownacki, S. Marks, R. Schlueter, " A multiple Objective Magnet Sorting Algorithm for the Advanced Light Source", 1994
[7] S. Lidia, R. Carr, "Faster magnet sorting with a threshold acceptance algorithm", Rev. Sci. Instrum. 66, 1985.

# INSERTION DEVICES CONTROL DEVELOPMENT AT SRRC

K. T. Pan, Jenny Chen, J. S. Chen, C. J. Wang, C. S. Chen, K. H. Hu,
Chaorn Wang, C. H. Chang, C. S. Hwang, T. C. Fan, K. T. Hsu
Synchrotron Radiation Research Center, Hsinchu, Taiwan

*Abstract*

Insertion devices are the most important gadget of the third generation Taiwan Light Source at SRRC. These insertion devices include the turn-key systems and in-house developed systems in SRRC. The corresponding control configurations are different due to historical reason. However precision, fastness, simplicity, and uniformity in insertion devices control are the most desirable from practical viewpoint. The proposed uniform control systems are first applied successfully to undulator U10 prototype and experimental one meter length adjusted polarizing undulator. The new system provides several features which are not available in existed insertion device control system. The residual field compensation procedure can be done with 100 times per second. The compensation table is updated from the server of the control system. The software design supports the beamline users to adjust gap after granting permission from the control room operator. The detailed descriptions about the features and performances will be presented in this report.

## 1. INTRODUCTION

There are three installed insertion devices systems, wiggler (W20), undulator (U5, U10P). Two of them are turn-key systems (W20, U5). The undulator U10P is homemade. There are two insertion devices in development phase in house, elliptically polarizing undulator (1 m EPU prototype and 4 m EPU). The undulator U9 has contracted with vendor. The control system of the U10P is built to achieve the simplicity, minimum man power and good performance that are prospects of insertion devices control at SRRC.

## 2. SYSTEM CONFIGURATION

The VME crate controller is the core of the control system configuration for all insertion devices. The W20 [1] and the U5 [2] are similar configuration. The VME crate controller connects with personal computer (PC) through GPIB bus, using the PC as local controller to control motion controller and motor drivers and to monitor encoders via GPIB bus or RS232. The control system of the undulator U9 will be similar to the undulator U10Pofthe SRRC. It integrates the intelligent motion controller in the VME crate controller without PC. Figure: 1 represents the software structure on U10P controller.

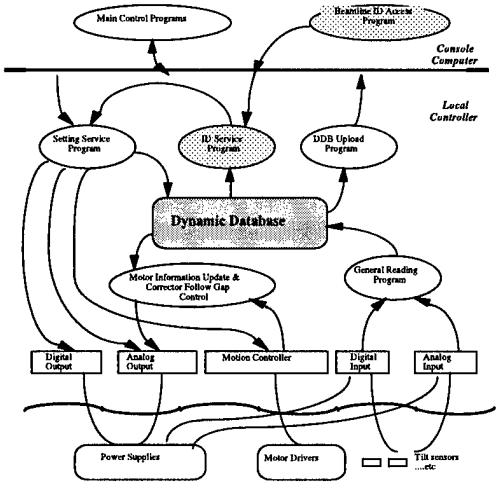



Figure: 1 Software structure on U10P controller

## 3. ISSUES OF INSERTION DEVICES CONTROL

### 3.1 *Motion control*

The motion control is a key point in insertion device control. It needs the requirements of the high precision, good reproducibility and multiple axes synchronization as well as fast control response.

### 3.2 *Residual field compensation mechanism*

The residual field compensation mechanism provides a easy operation and maintenance for machine physicist. The compensation table which the setting of the end-pole correction power supplies follows the corresponding gap value is a text file and saves on a NFS (network file system) server. The machine physicist needs to edit a table file on server and issues an updating event via graphic user interface on main control system. The new compensation table will be rebuilt and the compensation procedure can be done 10 ms per step [3][4][5]. For the W20 system, the residual field compensation table is stored on the PC. The gap and phase information will be included in the table for the EPU system.

### *3.3 Homing*

When the power which provides to the incremental encoder is lost, the incremental encoder information will be lost. There is an optional method which saves the

0-7803-4376-X/98 /$10.00 © 1998 IEEE

information on non-volatile RAM or harddisk to avoid information lost. If the position information is lost by accident, the homing procedure is necessary to recover the information. The U10P control system is with four incremental linear encoders. The encoder inform- ation is stored in the user accessible area of the non-volatile RAM. Whereas, the encoder information is saved on harddisk for the W20 control system. For the system of the U9 and the 4 m EPU, the absolute linear encoder will be used to measure the gap information. Hence, no homing procedure is needed.

### 3.4 *Protection and interlock*

The safety of the system is the one of the important considerations. For the U10P system, there are the tilt and slip detection, software limits protection, maximum and minimum limit switches. If one of the these interlocks is active, the four motors would be immediately stop. The controller supports error recovery functions used by the operator to eliminate errors. For the W20, U5, U9 and EPU are similar to the U10P.

## 4. CONTROL ROOM OPERATOR INTERFACE

The operator interface is a graphic mode interface. Normal operation page includes the setting and reading of the gap position and end-pole corrector power supplies, the monitoring of the tilt sensors, limit switches and drivers status and motors stop function. For the critical functions such as errors recovery, reset motor controller, homing procedure and updating the residual field compensation table are hidden in another page.

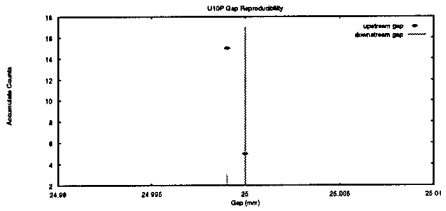
## 5. PERFORMANCE ISSUES

There are several control performance issues about insertion devices of the SRRC such as gap or phase resolution, reproducibility, two axes tracking. Table: 1 lists the performance of the U5, U10P and 1 m EPU [6]. The output signals of motion controller for the U10P are TTL pulse counts which represent the corresponding target position only. Thus the position errors are corrected at target position by using the encoder tracking function of the motion controller. It possesses a good reproducibility (shown in Figure: 2 (a)) but has not a good dynamic tracking on synchronous moving in multiple axes (shown in Figure: 3 (a)). For the U5 system, the reproducibility is worse than the U10P (shown in Figure: 2 (b)). For the 1 m EPU, the output signals of motion controller to motor drivers are analog voltages corresponding to the position error. It needs to optimize the proportional, integral and derivative parameters on feedback control system. Although it is more complexity than the U10P control, it offers the advantage of the good dynamic tracking. According to the resolution of the encoder is 5m, the two axes tracking performance is shown in Figure: 3(b). If the resolution of the encoder is 1 m, it will be achieved to several microns for the two axes tracking. The control response is hoped to achieve mechanical limitation. So far the response time of the U10P is about 1.2 sec per 0.1 mm.

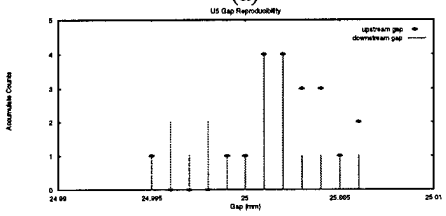
Table. Performance of the insertion devices for SRRC

| Item \ insertion device | U5 | U10P | 1m EPU |
|---|---|---|---|
| encoder resolution | 1 um | 0.5 um | 5 um |
| gap/phase resolution | – | ~ 2 um | – |
| reproducibility | +/- 6 um | +/- 1 um | +/- 5 um |
| two axes tracking | +/- 30 um | +/-30 um | +/- 10 um |

Table 1. Performance of the insertion devices

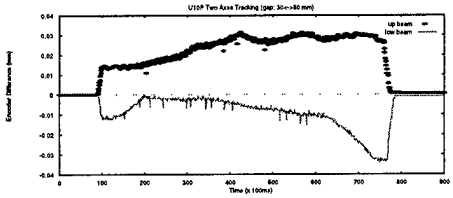



(a)

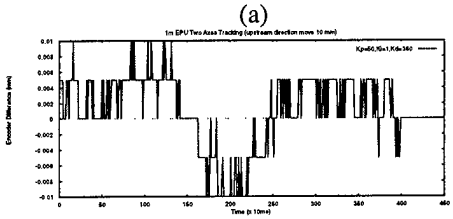



(b)

Figure: 2 Gap setting from different gap position to 25 mm (a) reproducibility of the U10P (b) reproducibility of the U5




(a)




(b)

Figure: 3 (a) Two axes tracking (upper beam and lower beam) of the U10P (b) Two axes tracking of 1 m EPU for phase only

## 6. BEAMLINE USER INTERFACE

The U10P controller possesses to accept the capability of issue commands from end-station computer to change gap directly via Ethernet. To execute the requests coming from the end-station, the controller should be granted by control room operator. Then the end-station

user can send a command to U10P controller and monochromator system simultaneously. For the U5 control system, RS422 is used to communicate with the end-station (shown in Figure: 4). Figure: 5 is the simulation of the beamline request gap change scenario for the operation of U10P.

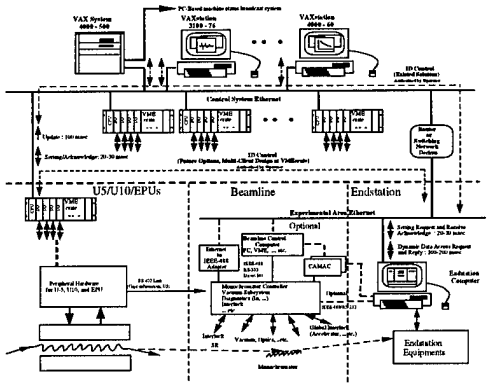



Figure: 4 Relation between main control system, U10P controller and the beamline end-station

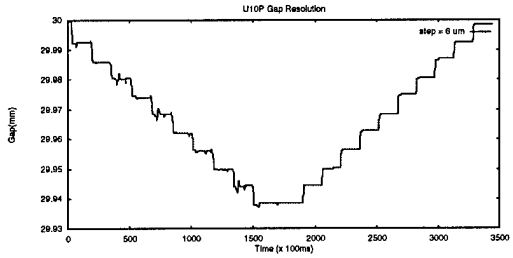



Figure: 5 Simulate beamline request gap change scenario for U10P

## 7. DISCUSSION

The effects of stepper mode and servo mode for the SRRC insertion devices control are as the follow :

a. *Dynamic tracking*

For the stepper mode, the output signal is pulse with constant motion profile that follows the acceleration, deceleration, velocity and target position counts. The position errors with varying time can not be corrected during moving. The feedback correction occurs only at target position. For the servo mode, output signal is a analog voltage, it can be changed following the position errors. It possesses a good dynamic tracking function.

b. *Overshoot*

Using the servo mode control on servo motor such as 1 m EPU prototype, it can improve the overshoot by adjusting the control parameters to critical damping region.

c. *Response time*

The response time of the U5 system is longer than the U10P system. Because the U5 need spend time on communication between personal computer and VME controller whereas the U10P need not. For the 1 m EPU, it adjusts the control parameters to achieve the optimum response. The fast response will be foreseeable.

d. *Protection, error reporting and recovery*

For the W20 system, according to the transmission structure was failed to result in the beam tilt. However it could not supply the tilt information to control system. The tilt sensors will be provided to increase the judgment of the W20 system working well or not. In the future, the information of the system status during the movement will be saved in the intelligent motion controller. If the error occurred, these information would be dumped as error analysis reference. And there will be a error reporting to suggest troubleshooting method.

## 8. ACKNOWLEDGMENTS

Thanks are extended to Elizabeth R. Moog of APS, the staff of the instrumentation and control group and the magnetic construction and measurement group. The help of top management at SRRC are also highly appreciated.

## REFERENCES

[1] D. C. Quimby, K. E. Robinson, D. R. Jander, "Personal-Computer-Based Control System for a 1.8 T Hybrid Wiggler", Rev. Sci. Instrum. 66, 1949(1995).

[2] "Detail design report of undulator U5 system" , designed by Danfysik in Jyllinge, Denmark (1995).

[3] P. Walker, B. Diviacco, "Initial operation of insertion devices in ELETTRA", Rev. Sci. Instrum. 66, 2708 (1995).

[4] Brgl, et al., "Controller Area Network (CAN) - a Field Bus Gives Access to the Bulk of BESSY II Devices", Proceedings of the ICALEPCS'95.

[5] J. Chavanne, P. Elleaume, "Insertion devices at the ESRF", Rev. Sci. Instrum. 66, 1868 (1995).

[6] Bahrdt, A. Gaupp, G. Ingold, M. Scheer, "Status of the Insertion Devices for BESSY II", Rev. EPAC96, 2535

# THE LHC VACUUM SYSTEM

O. Gröbner, CERN, 1211 Geneva 23, Switzerland

*Abstract*

The Large Hadron Collider (LHC) at CERN, involves two proton storage rings with colliding beams of 7 TeV. The machine will be housed in the existing LEP tunnel and requires 16 m long superconducting bending magnets. The vacuum chamber will be the inner wall of the cryostat and hence at the temperature of the magnet cold bore, i.e. at 1.9 K and therefore a very good cryopump. To reduce the cryogenic power consumption, the heat load from synchrotron radiation and from the image currents in the vacuum chamber will be absorbed on a 'beam screen', which operates between 5 and 20 K, inserted in the magnet cold bore. The design pressure necessary for operation must provide a lifetime of several days and a further stringent requirement comes from the power deposition in the superconducting magnet coils due to protons scattered on the residual gas which could lead to a magnet quench. Cryopumping of gas on the cold surfaces provides the necessary low gas densities but it must be ensured that the vapour pressure of cryosorbed molecules, of which $H_2$ and He would be the most critical species, remains within acceptable limits. In the room temperature sections of the LHC, specifically in the experiments, the vacuum must be stable against ion induced desorption and ISR-type 'pressure bumps'.

## 1 INTRODUCTION

The Large Hadron Collider (LHC) [1] will be installed in the existing 27 km underground tunnel of the Large Electron Positron collider (LEP) at CERN in Geneva. The main element of the new accelerator/storage ring will be a string of superconducting magnets, dipoles and quadrupoles, which bend and focus the two counter rotating proton beams with a design energy of 7 TeV. The bending radius is 2784 m and the magnetic field will be 8.3 T. The dipole magnets are mounted in a 'two-in-one' configuration within the same cold iron yoke and in the same common cryostat. The two inner tubes of this cryostat, in direct contact with the 1.9 K helium, fulfil the function of the vacuum chamber for the machine. With this design, the LHC will be the first high energy storage ring with a vacuum system at cryogenic temperature which is exposed to intense synchrotron radiation emitted from proton beams. The design intensity of each beam is 0.53 A (but only about 0.053 A during the first period of operation). Due to the very high energy of the proton beams and since the 'cold-bore' beam pipe is a very effective cryopump, a number of novel design requirements as well as constraints will have to be met. The general design of the vacuum system for LHC [2, 3, 4] has been presented at several conferences and, therefore, only the most important characteristics and the results from some recent studies will be described here. A detailed description of the insulation vacuum for the cryomagnets can be found in reference [5].

## 2 SYNCHROTRON RADIATION

Synchrotron radiation in LHC is a dominant factor for the design of the vacuum system. At 7 TeV, the critical energy of the synchrotron radiation spectrum is 44 eV and the radiated power represents a heat load of 0.2 W/m per beam. To prevent this heat load reaching the 1.9 K cryogenic system, it has been proposed, since the early design phase, to install inside the cold-bore a 'beam screen' which can be operated at a temperature in the range of 5 to 20 K. However, the additional advantage of this beam screen is that it intercepts not only the synchrotron radiation, but removes also the resistive losses dissipated by the beam induced wall currents which are of comparable magnitude. The beam screen can also remove the more recently identified heat source by photoelectrons [6]. In the course of the experiments which were started for the SSC Project to study in detail the synchrotron radiation induced gas desorption in a cold vacuum system, it became evident that in the LHC, this screen had to be partially transparent so that $H_2$ molecules desorbed by the beam could be pumped permanently on the 1.9 K cold bore surface. Figure 1 shows a section of the circular cold-bore vacuum chamber (49 mm I.D.) and of the perforated beam screen, which has a carefully optimised section for both the horizontal (44 mm) and vertical (36 mm) apertures. Also shown in the figure are the pumping holes which represent approximately 4% of the surface. A more detailed discussion of the function of these pumping holes will be given later.

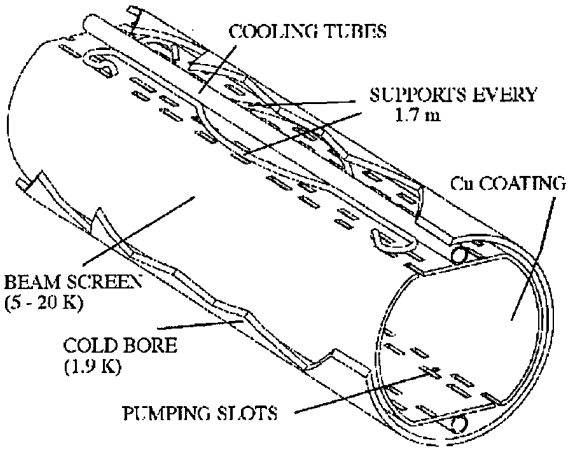



Figure: 1 Beam screen installed in the magnet cold-bore. Cooling pipes and supports are located in the vertical plane above and below the beam where the resulting aperture reduction can be accepted.

The beam screen is held in position with respect to the cold-bore by regularly spaced supports and cooled by two longitudinal helium pipes placed in the vertical plane above and below the beam. For mechanical and magnetic

0-7803-4376-X/98 /$10.00 © 1998 IEEE

reasons, the screen will be made of a low permeability stainless steel, approximately 1 mm thick. A detailed description of the required electric, magnetic and mechanical characteristics of the beam screen has been presented previously [7] and the most recent developments are presented in a separate contribution [8]. The inner wall, exposed to the electric field of the beam, will be coated with a 0.05 mm layer of high conductivity copper to keep the electric impedance low [9]. With this mechanical design of the beam screen an optimum compromise has to be found between several conflicting requirements. For example, the good electric conductivity of the copper conflicts with the magnetic forces produced by eddy currents during a magnet quench. These forces have been evaluated at several tons per m and impose the mechanically strong structure of the screen.

## 3 DYNAMIC VACUUM

The synchrotron radiation which strikes the inner copper coated surface of the beam screen is expected to produce a significant amount of desorbed gas in spite of the relatively low critical energy photon spectrum when compared with conventional synchrotron light sources. The linear photon flux (photons $s^{-1}$ $m^{-1}$) depends on the beam current I(A) and the beam energy E(TeV) and the bending radius, in LHC it is given by $2.5 \times 10^{16}$ I E . It is interesting to note that LHC will have a larger linear photon flux then LEP2 or the SSC. The resulting flow of photo-desorbed gas is proportional to the photon flux and to the molecular desorption yield. Over the last years, an intensive program of measurements has been undertaken, using mainly an external photon beam line on the EPA storage ring in CERN to obtain reliable data for the molecular desorption yields for representative vacuum chamber surfaces at the relevant photon energies and covering the temperature range from room temperature to 4.2 K [10], as shown in Table 1.

Table 1
Molecular desorption yield (molecules/photon) for copper plated stainless steel and for 45.3 eV critical energy photon spectrum at perpendicular photon incidence. From reference [10].

| T (K) | $H_2$ | $CH_4$ | CO | $CO_2$ |
|---|---|---|---|---|
| 300 | $5.0\ 10^{-4}$ | $1.6\ 10^{-3}$ | $2.5\ 10^{-4}$ | $2.2\ 10^{-4}$ |
| 77 | $2.5\ 10^{-4}$ | $4.0\ 10^{-6}$ | $1.5\ 10^{-5}$ | $7.0\ 10^{-6}$ |
| 4.2 | $3.5\ 10^{-5}$ | $8.0\ 10^{-7}$ | $6.0\ 10^{-6}$ | $7.0\ 10^{-6}$ |

These latest results indicate a decrease of the molecular desorption yield with temperature but at 4.2 K, the observed yields are still significant. In addition, the effect of the grazing photon incidence in LHC has yet to be included. This dependence on photon incidence has been studied by measurements on a photon beam line at the VEPP-2M storage ring at INP in Novosibirsk [11]. There it was found that the molecular desorption yield for $H_2$ from a copper coated surface at about 10 K and under grazing incidence (~10 mrad) is approximately $5.10^{-4}$ molecules per photon (measured after an initial exposure to a photon dose of $2\ 10^{21}$ photons/m), hence a factor of 14 larger than the corresponding value in Table 1.

## 4 NUCLEAR SCATTERING

Beam loss due to nuclear scattering on the residual gas represents a non-negligible heat load in LHC. Since these losses are due to interaction of high energy protons with the residual gas, the secondaries are sufficiently energetic to escape from the vacuum chamber and deposit their energy in the cryomagnets. There are two limits to the residual gas density, the first due to a concentrated, local heat load which could quench a magnet and the second from the distributed, total load to the cryosystem. The first limit applies to a local region with a high pressure (e.g. as it could be caused by a helium leak) while the second can be expressed in terms of the average gas density around the machine or more conveniently by the nuclear scattering beam lifetime $\tau$(h).

$P_{ns}$ (W/m) = 0.93 E(TeV) I(A)/$\tau$(h).

The design of the LHC includes a nuclear scattering allowance of ~0.1 W/m for the two beams and this specifies a lower limit for the beam-gas lifetime of 69 hours; thus a 'lifetime limit' of 100 hours has been chosen to design the vacuum system. The local 'quench limit' on gas density, depending on the efficiency of the collimation system, is expected to be at least a factor 100 higher.

Gas densities are related to beam lifetime $\tau$ through the relation $1/\tau = \sigma\ c\ n$ , where $\sigma$ is the total nuclear scattering cross section at 7 TeV, n the gas density and c the velocity of light. For $H_2$ and for the other molecular species in the residual gas Table 2 gives the relative nuclear scattering cross sections with respect to $H_2$ and the densities ($m^{-3}$) corresponding to a100 h beam life time.

Table 2
Relative nuclear scattering cross sections with respect to $H_2$ and densities corresponding to a100 h beam life time in LHC

| Molecules | $\sigma_i/\sigma_{H2}$ | n ($m^{-3}$) $\tau$=100h |
|---|---|---|
| $H_2$ | 1 | $9.8\ 10^{14}$ |
| He | 1.26 | $7.7\ 10^{14}$ |
| $CH_4$ | 5.4 | $1.8\ 10^{14}$ |
| $H_2O$ | 5.4 | $1.8\ 10^{14}$ |
| CO | 7.8 | $1.2\ 10^{14}$ |
| $CO_2$ | 12.2 | $3.0\ 10^{14}$ |

The 100 h beam lifetime limit requires an equivalent $H_2$ density < $10^{15}$ $m^{-3}$ . At the temperature of the beam screen (average ~10 K), this corresponds to $10^{-9}$ Torr.

## 5 BEAM INDUCED HEAT LOAD

The justification for a beam screen to intercept the power from the various beam related sources which otherwise would reach the cold bore and load the 1.9 K cryogenic system can be seen in Figure 2. Apart from the resistive losses in the beam screen all other heat loads increase with the beam energy. The contribution from photoelectrons will be discussed in a subsequent section.

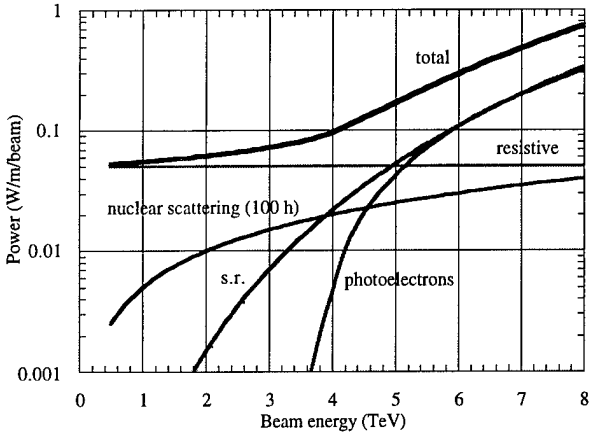



Figure: 2 Estimated and assumed beam induced losses in LHC. The contribution from photoelectrons will be discussed in a later section. Nuclear scattering is the only part which can not be removed by the beam screen.

## 6 VAPOUR PRESSURE

The cold length of the LHC vacuum system (some 80% of the circumference) relies on the cryopumping of the 1.9 K vacuum chamber through the perforated beam screen. Among the desorbed gases, hydrogen, which has the largest molecular desorption yield, is the most critical species for which the vapour pressure is high and the pumping capacity of the beam screen, operated between 5 and 20 K, is very small. Without the pumping holes, the cryopumping of the beam screen would not provide any useful capacity for LHC operation. In fact, the equilibrium vapour density at 5 K for a monolayer of hydrogen exceeds by several orders of magnitude the acceptable limit [12]. With the concept of pumping holes in the beam screen, hydrogen, and even more so all other gas species, can be pumped on the 1.9 K surface with a negligibly low saturated vapour density and hence in practical an unlimited capacity. Effectively, the pumping holes provide a constant pumping speed, proportional to the surface area of the holes and which can be optimised for different requirements. However, one important exception is He since even at 1.9 K, only a small amount of this gas can be accommodated and this highlights the importance of a perfect leak tightness for the beam vacuum system.

## 7 RECYLING OF PHYSISORBED GAS

Due to the photon flux which strikes the inner surface of the beam screen, cryopumped gas molecules on the screen may be re-desorbed. Measurements of this 'recycling' coefficient (secondary desorption) for hydrogen [13] give values increasing in proportion to the surface coverage and reaching approximately 1 molecule per photon at a monolayer. For any significant molecular coverage of the beam screen, this secondary effect for $H_2$ is several orders of magnitude larger than the primary desorption. The global result of thermal desorption and recycling will be that a limited equilibrium quantity of gas can be accommodated on the inner surface of the beam screen. Thereafter all the primary desorbed gas load will be transferred through the pumping holes to the 1.9 K vacuum chamber wall with a pumping speed now determined by the total hole area. A schematic picture of this process is illustrated in Figure 3.

The recycling coefficients for the important heavier gases, $CH_4$, CO and $CO_2$ have also been measured and it was found that even for thick physisorbed layers (10-20 monolayers) these coefficients are small and can not be distinguished from the respective primary photodesorption coefficients [14] i.e., they range below $10^{-3}$ molecules/photon. Fore these gases the recycling will be small and the pumping speed will remain, in contrast to $H_2$, at the level determined by the screen area and the respective sticking coefficient.

This behaviour of the vacuum system is illustrated in Figure 4 which shows experimental results from a prototype beam screen at the VEPP-2M photon beam line. The data have been scaled to the photon flux in the LHC at 1/10 of the nominal current. With a ~2% area of pumping holes, hydrogen saturates at ~3 $10^{13}$ $m^{-3}$, well below the specified lifetime limit.

An important parameter for the design of the LHC vacuum system is also the total amount of desorbed $H_2$. This quantity has been estimated as 2.6 monolayers during the initial year of operation and as 10.5 monolayers during the second year at the full nominal beam current. This large quantity of gas should not pose a problem with the present design of the LHC vacuum system since the molecules can diffuse through the pumping holes and be adsorbed on the 1.9 K cold bore with a negligible vapour pressure.

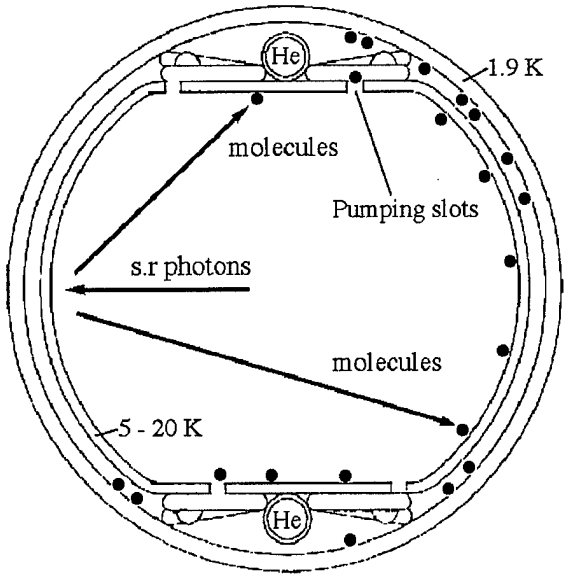



Figure: 3 Beam screen function with primary desorption and recycling of physisorbed gas. Permanent adsorption occurs on the 1.9 K cold-bore surface, protected by the beam screen from synchrotron radiation and photoelectrons.

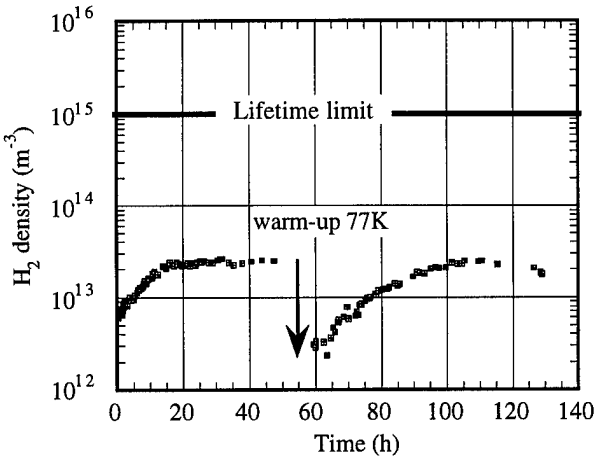



Figure: 4 Evolution of the molecular density of $H_2$ during photon exposure in an experiment at VEPP-2M with a perforated beam screen to simulate LHC during the first running year with 1/10 of the nominal beam current. During the experiment, the screen has been warmed-up to 77 K, while maintaining the cold-bore at ~3K, to the remove cryosorbed hydrogen and thus to demonstrate the repetition of the recycling effect.

## 8 ION INDUCED PRESSURE INSTABILITY

In the LHC, the ionisation of the residual gas molecules will produce ions which then are repelled by the positive beam potential and accelerated towards the beam screen or the vacuum chamber wall. The final energy of the ions may be up to 300 eV. As for the photons, the energetic ions can desorb tightly bound gas molecules with a molecular desorption yield, $\eta_i$ (molecules per ion). Desorbed molecules will in turn be ionised and participate in the desorption process. This positive feedback can lead to the so-called 'ion induced pressure instability' known from previous experience with the Intersecting Storage Rings (ISR) at CERN. The pressure runaway depends critically on the local cleanliness of the surface, via the ion induced molecular desorption yield, and on the local pumping speed. The stability limit is expressed by the condition that the product of beam current I and of the molecular desorption yield $\eta_i$ must be less than a limit given by the pumping speed

$$\eta_i I < \frac{e}{\sigma} S_{eff}$$

where $e$ is the electron charge, $\sigma$ the ionisation cross section of the residual gas molecules for high energy protons (typically 20 barn for hydrogen) and Seff is the effective linear pumping speed. In the cold sections of the LHC, a well defined, lower limit of the pumping is determined by the cryosorption on the 1.9 K vacuum chamber surface through the pumping holes. The safe condition for vacuum stability for the cold sections is defined by the area $A_f$ of pumping holes per unit length

$$\eta_i I < \sqrt{\frac{kT}{2\pi m}} \frac{e}{\sigma} A_f$$

with $k$ the Boltzmann constant and $m$ the mass of the molecules.

With the parameters of LHC, the stability limit for hydrogen is $\eta_i I = 10^3$ A. Since a typical primary ion desorption yield for an unbaked surface is of order unity, and since the large recycling coefficient for hydrogen does not permit the formation of a thick layer of $H_2$ on the screen, the cold sections of LHC will operate well inside this stability limit. However, this situation will be different in the room temperature sections, where the conventional, external pumping system is limited through the conductance of the beam pipe. The control of the $\eta$-parameter by appropriate surface preparation and by bakeout will be essential.

## 9 PHOTOELECTRONS AND MULTIPACTING

Beam induced multipacting [15] which may arise through synchronous motion of photoelectrons and low energy secondary electrons bouncing back and forth between opposite vacuum chamber walls with successive proton bunches represent a potential problem for the machine [16]. In the LHC the beam screen radius $r_p$ = 22 mm, the bunch intensity $N_b$ = 1 $10^{11}$ protons and the bunch spacing $L_{bb}$ = 7.5m are such that the wall-to-wall multipacting threshold, given by

$$N_b = \frac{r_p^2}{r_e L_{bb}} \quad , \ (r_e \text{ the classical electron radius}),$$

can be reached at about 1/4 only of the nominal intensity [6].

An additional effect attributed to synchrotron radiation is the production of photoelectrons a source which largely dominates electrons from residual gas ionisation. Measurements on the photon beam line at EPA [17] with an LHC test chamber give a photo-yield of typically 0.02 electrons/photon for the synchrotron radiation spectrum in LHC. Due to the strong electric field of the proton bunches these electrons can be accelerated across the beam pipe and transfer energy to the beam screen. A first, still very approximate estimate of this effect gives 0.2 W/m [6]. An additional consequence of these photoelectrons will be enhanced outgassing which will add to the photo-desorption.

## 10 MECHANICAL DESIGN

The mechanical design of the cold arc vacuum system requires a large number of interconnections for the beam vacuum between the beam screens of adjacent magnets. Following the proven design of the LEP-type RF-finger contacts a new concept has been developed which takes into account the large thermal contraction (approx. 45 mm) between room temperature and operating temperature. An important design criterion to be met is the requirement of installation and alignment of the long cryomagnets without the risk of damaging the delicate finger contacts. The principle of the proposed novel solution is shown in Figure 5 where the R.T. and the cold positions of the RF-bridge are drawn on the lower and on the upper section respectively18 [18].

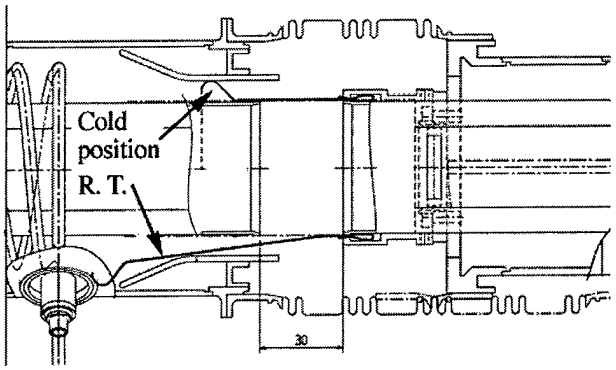



Figure: 5 Beam vacuum interconnection between magnets with a novel RF-bridge design to guarantee flexibility during installation and alignment. Lower section shows room temperature (R.T.) position, upper section shows the contact position at cryogenic temperature.

Only once the final cold position is reached, will the required smooth and well defined electric contact be established with a controlled contact force.

## 11 ACKNOWLEDGEMENTS

The description of the LHC vacuum system presented here reflects the status of the LHC Project as given in the design report [1] and updated according to more recent work by many colleagues in the LHC Vacuum Group. The important contributions, in particular from the groups LHC-CRI and EST-SM, are also gratefully acknowledged.

## 12 REFERENCES

[1] CERN/AC/95-05 (LHC), 20 October 1993.
[2] Mathewson, et al., EPAC 94, London, June 1994.
[3] Mathewson, et al., PAC 95, Dallas, 1995.
[4] Gröbner, Vacuum, 46, 767 (1995).
[5] Cruikshank, G. Engelmann, W. Koelemeijer, N.Kos, A.G. Mathewson, 5th European Vacuum Conference, Salamanca, 23-27 September, 1996.
[6] Gröbner, contribution to this conference.
[7] Poncet et. al., EPAC 94, London, June 1994.
[8] Cruikshank, et al., contribution to this conference.
[9] Ruggiero, R. Caspers, M. Morvillo, contribution to this conference.
[10] Vincent Baglin, Doctoral thesis, Université Denis Diderot Paris 7, UFR de Physique, Paris, May 1997.
[11] Calder, O. Gröbner, A.G. Mathewson, V.V. Anashin, A. Dranichnikov, O.B. Malyshev, J. Vac. Sci. Technol. A 14(4), Jul/Aug 1996.
[12] Wallén, J. Vac. Sci. Technol. A 15(2), March/April 1997.
[13] Anashin, O. Malyshev, V. Osipov, I. Maslennikov, W.C. Turner, 40th National Symposium AVS, Orlando, November 1993.
[14] Calder, O. Gröbner, A.G. Mathewson, V.V. Anashin, O.B. Malyshev, 5th European Vacuum Conference, Salamanca, 23-27 September, 1996.
[15] Gröbner, 10th Int. Conf. on High Energy Accelerators, Protvino, July 1977.
[16] Zimmermann, LHC Project Report 95, 27 February 1997.
[17] Goméz-Goñi, O. Gröbner, A.G. Mathewson, J.Vac.Sci. Technol. A 12(4), July/August 1994.
[18] Brunet, P. Cruikshank, P. Lepeule, I. Nikitine, C. Reymermier, G. Schneider, R. Veness, unpublished, April, 1997.

# DUST IN ACCELERATOR VACUUM SYSTEMS

Darren R.C. Kelly, DESY, Notkestr.85, 22603 Hamburg, Germany

*Abstract*

Many accelerators of electron beams are susceptible to persistent beam lifetime disruptions, with correspondingly reduced performance. One distinguishes between three prevailing explanations of these disruptions: (1) trapping of positive atomic ions in the negatively charged beam; (2) trapping of small highly positively ionised micro-objects ("dust") in the negatively charged beam; (3) disruptions due to stray magnetic objects trapped in the magnetic field of undulators.

The lifetime disruption of certain electron storage rings that employ ion-getter pump systems are attributed by most researchers to explanation (2), the trapped dust hypothesis. Systematic experimental studies of HERA, PETRA and DORIS reinforce the suspicion that specifically this type of pump system is the culprit.

Examples of beam lifetime disruptions are presented, together with a summary of observations and experiments performed at various afflicted storage rings to investigate dust trapping and the connection between ion getter pumps and dust particle release. Observations of the disrupted beam are found to agree with the dust trapping hypothesis.

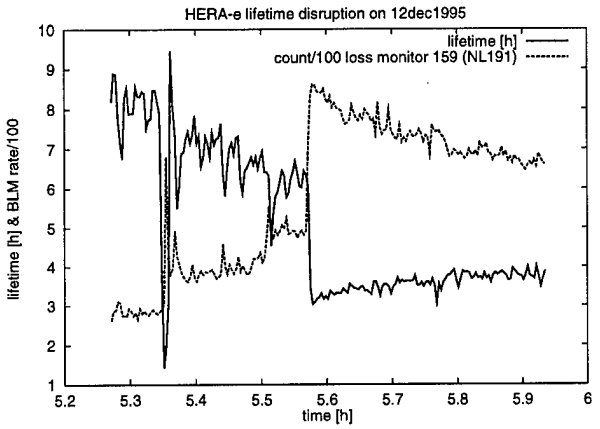



Figure 1: Example of the reaction of a beam loss monitor during a lifetime disruption in HERA-e at injection energy 12 GeV on 12 Dec 1995. The beam loss monitor count $R_{i,j}$ divided by 100 for monitor NL191 (number j=159) and the lifetime $\tau$ in hours are shown against time $t_i$. Reductions in the lifetime coincide with local loss rate increases.

## 1 INTRODUCTION

Various electron storage rings are afflicted by a spurious reduction of the beam lifetime – apparently caused by the deflection of beam electrons by positively charged dust particles of size order $1\mu$m trapped in the electric field potential of the negatively charged beam: Super-ACO [1], TRISTAN AR [2], CESR [3], HERA-e, PETRAII, DORISIII [4, 5], PF [6]. The complementary experience at these machines has built a consistent picture of the symptoms of macroparticle lifetime disruptions, and this picture agrees quantitatively with the dust trapping model detailed in [3, 4].

This *electron beam lifetime problem* is beam charge dependent, i.e. it only occurs with electron beams, as evidenced by the problem-free switch to positron operation in HERA and DORIS.

Observations confirm that the ion getter pumps of all above-mentioned machines are implicated in casting dust particles into the beam pipe. The lifetime disruption can be provoked by switching an ion getter pump on and off, or by abruptly increasing the pump voltage, when a discharge within the pump can be sometimes be observed.

Such lifetime disruptions are not observed in the non-evaporative getter (NEG) pump based storage ring LEP or at ESRF (with NEG pumps and auxilliary lumped ion pumps), with the exception of the possible capture of magnetic dust in undulators [7]. Trials over a limited region of HERA with NEG pumps indicate a strong if not complete reduction of the release of disrupting particles within this NEG pump region.

It will be illustrated in this report that the extensive observations of beam lifetime disruptions in a number of accelerators are well described by the trapped dust hypothesis. However, the formation or liberation of dust particles within the complicated environment of the ion-getter pump chamber is poorly understood. Relatively few direct observations of the processes within these pumps systems are available, whereas many observations of pump configurations and operating conditions conducive to the onset of beam lifetime disruptions have been performed, in particular with HERA, PETRA and DORIS. Such observations are however not sufficient to form a causal model of dust particle release into the beam pipe; our knowledge of the processes on the pump side of the vacuum chamber gas conduction slits is as poor as the available diagnostics. A number of interesting observations and experiments of dust-like disruptions at other afflicted storage rings will also be discussed.

## 2 AN EXAMPLE OF LIFETIME DISRUPTIONS IN HERA-E

Of all available diagnostics of the disrupted beam, the 214 beam loss monitors of HERA [8] are perhaps the most revealing. In Fig. 1 we see an example of a typical life-

0-7803-4376-X/98/$10.00 © 1998 IEEE

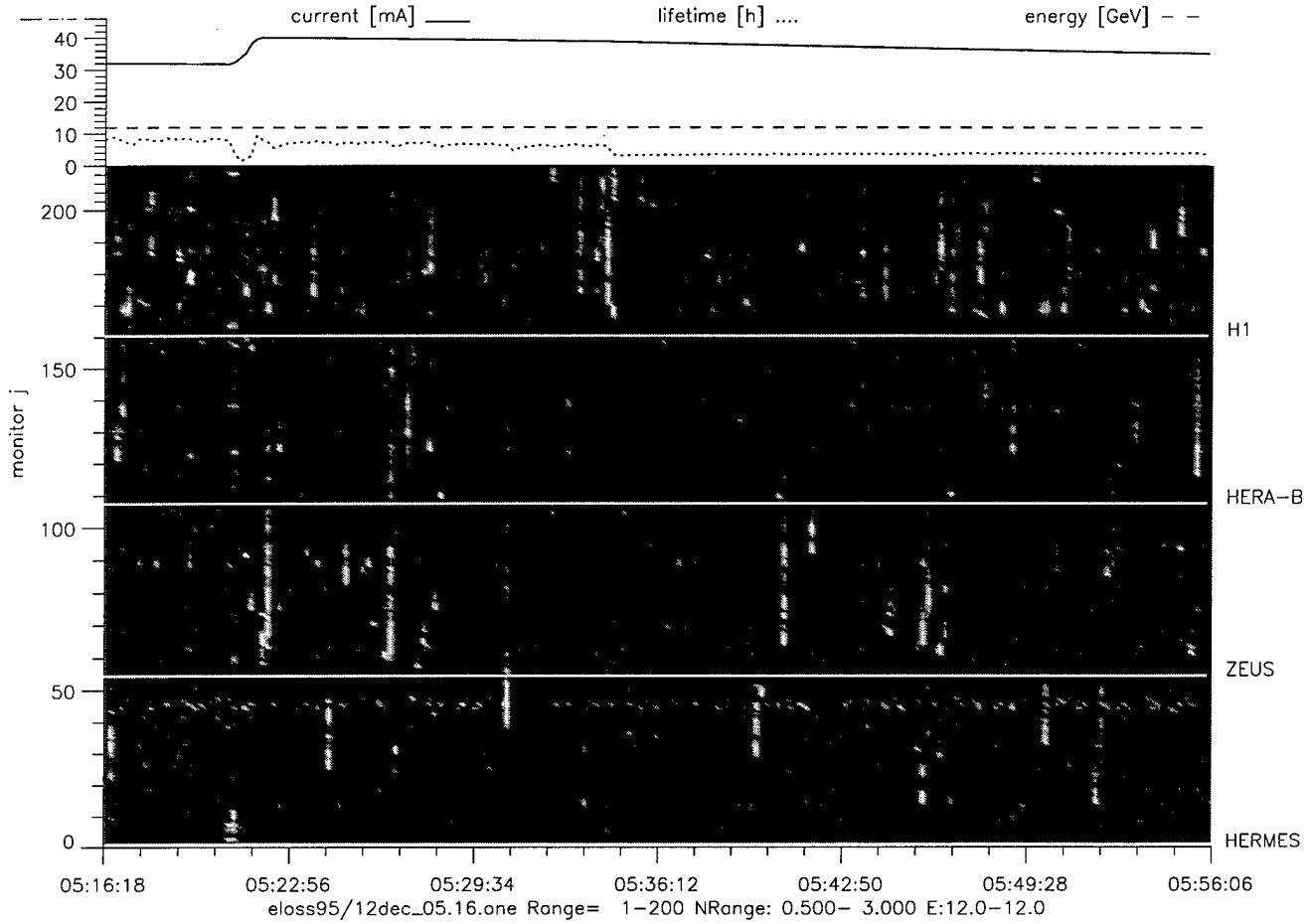



Figure 2: The beam loss monitor count ratio $N_{i,j} = R_{i,j}/R_{i-1,j}$ reveals the influence of dust particles moving longitudinally around the HERA electron ring. The grayscale corresponds to a range 0.5...3 in $N_{i,j}$ at 12 GeV, where 1 represents background (no change). The ratios are plotted over the $(i,j)$-plane of BLM monitor numbers $j = 1 \ldots 214$ for the entire machine against time $t_i$. Current in mA, energy 12 GeV and lifetime in h are shown on an extended scale

time disruption in HERA-e at injection energy 12 GeV[1]. In this particular HERA-e run a number of abrupt beam lifetime reductions seemed to correlate with increases in the rate $R_{i,j}$ of beam loss monitor number $j$=159 at position NL191 over times $t_i$.

More global insight into the dust trappings is obtained when the time development of the beam loss monitor count ratio $N_{i,j} = R_{i,j}/R_{i-1,j}$ of all monitors $j = 1 \ldots 214$ around the machine is displayed simultaneously in one diagram for a range of times $t_i$. Thus *changes* in the reaction of each monitor are reflected by departure from $N_{i,j} = 1$, which value then represents predominantly the synchrotron radiation background and beam electron losses due to deflection from residual gas molecules in the vacuum chamber. In Fig. 2 the count ratio is associated with grey shades for a range 0.5 – 3 in $N_{i,j}$ for the same HERA-e run on 12 Dec 1995 at 12 GeV . *The reader will be rewarded by taking a few minutes to peruse and understand this somewhat overwhelming diagram, which illustrates most of the important aspects of the dust trapping problem.* A number of features of the disrupting particles can be identified in this diagram:

- The longitudinal flight of many particles can be easily discerned as bright flight trails, and their velocities can be measured to be around 10 to 100 m/s (in HERA-e at beam energy 12 GeV and current 30-40 mA).
- Both transient and instransient disruptions of the lifetime can be seen to correspond with particles entering the beam. The lifetime is plotted against time on the extended axis.
- It can be seen that there are hundreds to thousands of particles passing through the beam per hour, only a handful of which are permanently trapped. Many

[1]In HERA-e at 12 GeV the beam loss monitor reaction to scattered electrons dominates over the loss monitor's reaction to synchrotron radiation, permitting easy recognition of events, whereas at e-p luminosity energy 27.5 GeV transient reactions *can* be identified but at 3% of the count are difficult to resolve against the dominant synchrotron radiation background, so examples in this paper are restricted to injection energy 12 GeV .

particles do not survive their flights along an arc, perhaps due to thermal, structural or dynamic instability. There is clearly a narrow stability window.

- The reaction of monitor number 159 (position NL191) shown individually in Fig. 1 can be identified at the instant of lifetime reduction (extended axis).

## 3 THE TRAPPED DUST HYPOTHESIS

Most if not all symptoms of the electron beam lifetime disruption can be quantitatively explained by the prevailing *dust trapping model* as detailed in [3, 4], which I summarise briefly. Macroparticles, perhaps of $SiO_2$ or metallic oxides from the beam pipe and ion pump surfaces, are cast into the beam pipe by numerous ion pumps at frequent intervals, where they are rapidly ionised and drawn into the electron beam by the beam's strong electric field. The particles are transversely trapped and rapidly reach an equilibrium charge determined by competition between ionisation by beam electrons and deionisation through field evaporation and photoelectron capture. The equilibrium charge obtained by $SiO_2$ particles of sizes $0.1 - 1$ $\mu$m – as computed by integration of a trapped particle's equation of motion [12] with charge development after [4] – is listed in Table 1 for current 20 mA and energy 27.5 GeV in HERA-e. The particles oscillate transversely at frequencies of a few kHz. Particles of low mass-to-charge ratio, i.e. of radius $\ll 0.1\mu$m are transversely unstable.

The macroparticles are driven downstream by Mœller scattering at about 12 $ms^{-2}$ [4] until they are possibly trapped in horizontally defocussing quadrupoles by restoring kicks due to the longitudinal asymmetry of the beam bunches from the $\beta$-function gradient there [3]. In HERA particles of radius $< 1\mu$m achieve an equilibrium charge meeting this longitudinal trapping criterion.

Table 1: Charge number $Q$, mass number to charge number ratio $Q/A$, and and transverse oscillation frequencies obtained by particles of different radii $R$ trapped in the core of the HERA electron beam at 20 mA current at 27.5 GeV.

| $R$ [$\mu$m] | $Q$ | $A/Q$ | $f_x$ [Hz] | $f_z$ [Hz] |
|---|---|---|---|---|
| 1.0 | 5.81E+06 | 1.04E+06 | 1510.88 | 3152.41 |
| 0.5 | 4.75E+06 | 1.58E+05 | 3863.99 | 8062.09 |
| 0.3 | 4.04E+06 | 4.02E+04 | 7668.93 | 16001 |
| 0.1 | 2.72E+06 | 2.23E+03 | 32576.5 | 67969.8 |

Particles of size $0.1 - 1$ $\mu$m should be thermally stable in HERA-e at typical current 40 mA and energy 27.5 GeV , although [4] has predicted that these particle might be thermally unstable at very high electron currents $\gg$ 40 mA.

In view of this model the myriad of activity in the beam loss monitor diagram Fig. 2 becomes understandable. A large number of dust particles with a distribution of sizes are cast into the beam pipe at many locations in the machine. Only the handfull of particles per hour meeting the transverse, longitudinal and thermal stability conditions survive to cause intransient lifetime disruptions, the others leaving merely brief trails of losses as they are swept downstream before melting, falling out of the beam, or becoming structurally unstable.

## 4 EXPERIMENTAL INVESTIGATIONS

A number of chance observations and machine studies at various institutes have added greatly to our knowledge of the lifetime disruption problem, some of which are now briefly described.

Since the inception of CESR sudden lifetime drops have been observed and by comparison of the magnitude of the observed lifetime drops with a model of a trapped macroparticle's equilibrium charge as a function of particle mass the typical particle size was estimated to be of order 1 $\mu$m [3].

At TRISTAN AR dust particles were dropped into the beam pipe via a 1 mm nozzle to see whether macroparticles could indeed be trapped in an electron beam [14]. Metal particles consisting of Cu, Al, Ti (sizes 0.1-8 $\mu$m) were not trapped, whereas metallic oxides such as Cu0 (0.35 $\mu$m), $TiO_2$ (0.3 $\mu$m), and the NEG compound Zr-V-Fe ($\sim$ 1 $\mu$m) were trapped for many minutes at currents order 10 mA and energy 6.5 GeV. Particles of diameter 0.5 $\mu$m consisting of C (diamond), SiC and $Al_2O_3$ were trapped even at very low currents (less than 0.1 mA).

Surprisingly, the TRISTAN AR beam lifetime was found to be poor *after* dumping and refilling, and bremsstrahlung signals and electron losses typical of trapped particles were still observed. This "hysteresis" effect has also been observed at HERA, and is not yet understood. Simple considerations predict that the image charge force on a dust particle exceeds the beam electric field force within a few mm of the vacuum chamber wall for both HERA and TRISTAN AR [3, 15].

During dust trapping investigations at TRISTAN AR bremsstrahlung observations with $\gamma$-ray detectors [15] suggested both longitudinal motion and transverse oscillations of dust particles.

At CERN a troublesome ion pump installed above an electrostatic separator was reported [7]. The pump was found to arc frequently. When the pump was moved below the separator and around a 90$^o$ elbow the problem disappeared.

At Super-ACO a CCD camera 10 m from an ion pump in a beam-line from Super-ACO was found to be "sand-blasted" with titanium and stainless steel after an accidental gas inlet [7].

The degree and frequency of beam lifetime disruptions seems to increase with higher beam energy and beam current. This correlation has been systematically studied in HERA-e [9]. Analysis of the correlation reveals that dozens of particles of radius 0.3 $\mu$m are typically trapped

in HERA at current 20 mA and energy 27.5 GeV resulting in a total lifetime reduction from 10 h to about 3 h.

It has been suggested [16] that the likelihood of spontaneous ion pump discharge and consequent macroparticle release is related to the number of photoelectrons released per metre from the vacuum chamber surface, a quantity approximately proportional to the product $E \times I$ where $E$ and $I$ are the beam energy and current respectively. This defines a locus for onset of the disruptions, although clearly one is dealing with a stochastic phenomenon not a sharp threshold. There were no indications of lifetime disruptions due to macroparticles at the NEG-pump based LEP storage ring with beam current 8 mA at 45 GeV[19], whereas lifetime disruptions are prevalent at HERA at current 30 mA at 12 GeV and at current 13 mA at 27.5 GeV.

Investigations in PETRA showed that a range of adapted ion pumps were capable of causing lifetime disruptions [17], either spontaneously or by abrupt switching of the pump high-voltage. These pump variations included: (1) a regular PETRA ion pump where many cylindrical Penning cells share a common cathode; (2) a regular HERA ion pump where perforated anode foils offer an open discharge region to the side; (3) a HERA ion pump with a baffle between the gas conduction slits and the pump anode, blocking the direct route to the beam pipe; (4) an "inverted" pump with high negative voltage attached to the cathode instead of the anode. A "dummy" pump with a closed, inactive rectangular tube replacing the cylindrical Penning cells did not give rise to lifetime disruptions.

A possible mechanism for dust particle release from ion pumps is the liberation of pump material such as titanium by strong discharges known to occur spontaneously within the pump cells, and provokable by abrupt switching of the pump high voltage. Resistors of strength 100 MΩ were installed before integrated dipole pumps in HERA in the hope of dissipating the energy of the discharge sufficiently to prevent liberation of particles [18]. However beam lifetime disruptions where found nevertheless to occur frequently and analysis of beam loss monitor responses did not show a reduction in the frequency of particle release into the beam pipe.

It has been shown that both strong repeated beam kicks and a carefully tuned beam excitation sweep with a feedback kicker can restore the disrupted beam lifetime of PETRA and HERA [17, 11, 12]. In HERA, where the lifetime is "multiply-disrupted", presumably by dozens of disrupting particles, the lifetime and the rates in particular beam loss monitors and experiment detectors could be seen to improve in discrete steps as the parameters of the beam excitation were scanned, providing strong support for the dust trapping model. Bremsstrahlung detector observations at PETRA likewise indicated discrete beam disruption.

A clearing field constructed using beam position monitors button electrodes immediately downstream from HERA's horizontally defocussing quadrupoles was shown to deflect the longitudinal flights of particles travelling sufficiently slowly past the clearing field [13]. The location of the BPMs is not suitable for construction of a clearing field capable of improving the beam lifetime in HERA by removing particles trapped within horizontally defocussing quadrupoles, but the experiment provides further support for the dust trapping model. The installation of general clearing-field electrodes to improve the HERA-e beam lifetime is a technically cumbersome option.

## 5 CONCLUSION

A wealth of experimental and observational information has been gathered by researchers at many electron storage rings afflicted by spontaneous beam lifetime disruptions, most of which is consistent with the model of macroparticles (dust) of size order 1 $\mu$m being trapped in the electron beam.

Yet despite this consistent picture of the symptoms, the cause is not fully understood. As researchers of viral infections know, the tiniest creatures can be responsible for the greatest grievances and warrant the most extensive combat. An elegant, inexpensive solution to the electron beam lifetime problem compatible with general machine operation in HERA is not yet available. Trials indicate that replacing the ion getter pump system with NEG pumps will likely restore good electron beam lifetime. But a deeper understanding of dust generation/liberation in accelerator *pump* systems would be welcome now that so much is known about dust in electron accelerator beam pipes.

## 6 ACKNOWLEDGEMENTS

Thanks to DESY colleagues and other electron storage ring colleagues too numerous to list for discussions and communications.

## 7 REFERENCES

[1] P. Marin. 'Microlosses of beam current on Super-ACO operated with electrons', *LURE, ORSAY* RT/90-01 (1990)

[2] H. Saeki, T. Momose, and H. Ishimaru. 'Observations of dust trapping phenomena in the TRISTAN accumulation ring and study of dust removal in a beam chamber', *Rev. Sci. Instrum.* **62**, 874 (1991)

[3] D. Sagan. 'Mass and charge measurement of trapped dust in the CESR storage ring', *Nucl. Instrum. Methods.* **A330** 371 (1993)

[4] F. Zimmerman. 'Trapped dust in HERA and prospects for PEP-II', *Technical Report PEP-II AP* Note No.: 8-94, (Stanford Linear Accelerator Center, 1994).

[5] D. R. C. Kelly. 'Characterisation of lepton beam lifetime behaviour in HERA', *Technical Report DESY HERA 95-01'*, (Deutsches Elektronen Synchrotron, 1995).

[6] K. Fuke 'Photon Factory activity report #6',R-1, 1988

[7] P. Marin. 'Problems encountered with stray micro-objects in various ultra-high vacuum systems', *LURE, ORSAY* RT/93-04 (1993)

[8] Bialowons, W., Ridoutt, F., and Wittenburg, K. (1994), 'Electron beam loss monitors for HERA', in *Fourth European Particle Accelerator Conference (EPAC94)*, Vol. 2, p. 1628, World Scientific

[9] D. R. C. Kelly. 'Many-event lifetime disruption in HERA and DORIS', *Technical Report DESY HERA* 95-02, (Deutsches Elektronen Synchrotron, 1995).

[10] D. Sagan. 'Some aspects of longitudinal motion of ions in electron storage rings', Nucl.Instrum.Meth. **A307** 171 (1991)

[11] D. R. C. Kelly. 'The effect of beam excitation on the HERA electron beam lifetime disruption'. In *Fifth European Particle Accelerator Conference (EPAC96).*

[12] D. R. C. Kelly. 'The effect of transverse beam excitation and kicking on the HERA electron beam lifetime disruption'. To be submitted to *Nucl. Instrum. Methods.A* (1997)

[13] D. R. C. Kelly. 'The effect of a static clearing field on trapped dust particles in the HERA electron ring', To be submitted to *Nucl. Instrum. Methods.A* (1997)

[14] K. Kanazawa, (TRISTAN) pers.communication, (1995)

[15] H. Saeki, T. Momose, and H. Ishimaru. 'Motions of trapped dust particles around the electron beam in the TRISTAN accumulation ring', *Rev. Sci. Instrum.* **62**, 11 (1991)

[16] J. Kouptsidis,'Lebensdauerprobleme in Elektronenspeicherringen', in *HERA Seminar, Bad Lauterberg* DESY (1995)

[17] H. Ehrlichmann,'Untersuchung zur Elektronenlebensdauer in PETRA', in *HERA Seminar, St.Englmar* DESY (1996)

[18] W. Bialowons,'HERA Betrieb mit Elektronen', in *HERA Seminar, Hamburg* DESY (1997)

[19] CERN, LEP machine study 10 June 1995: S. Myers, F. Willeke, J. Kouptsidis, W. Bialowons, H. Ehrlichmann, K. Wittenburg, D. Kelly.

# APS STORAGE RING VACUUM SYSTEM PERFORMANCE

J.R. Noonan, J. Gagliano, G. A. Goeppner, R.A. Rosenberg, and D. R. Walters
Advanced Photon Source, Argonne National Laboratory
9700 South Cass Avenue, Argonne, IL 60439

*Abstract*

The Advanced Photon Source (APS) storage ring was designed to operated with 7-GeV, 100-mA positron beam with lifetimes > 20 hours. The lifetime is limited by residual gas scattering and Touschek scattering at this time. Photon-stimulated desorption and microwave power in the rf cavities are the main gas loads. Comparison of actual system gas loads and design calculations will be given. In addition, several special features of the storage ring vacuum system will be presented.

## 1 INTRODUCTION

The Advanced Photon Source (APS) is a high-intensity, hard x-ray synchrotron light source that is currently being commissioned and operated. The APS storage ring is designed to store up to 100 mA of 7-GeV positrons for up to 20 hours. In order to achieve the design goal for the stored beam lifetime, the accelerator vacuum system must achieve ~ 1-2 nanoTorr average pressure with the beam on. In fact, the storage ring has already achieved up to 37 hours lifetime for 100-mA beams of 7 GeV positrons.

The paper will discuss the design and fabrication of the storage ring chamber, absorbers, and special features. The storage ring chambers were fabricated from aluminum extrusions, then machined and welded to achieve the proper design. The photon absorbers presented special design and fabrication problems. The mechanical engineering group developed elegantly simple solutions to the high heat load problems associated with the absorbers.

Several problems encountered during the installation and operation of the storage ring vacuum system will also be discussed. Finally, the current performance and vacuum history will be presented.

## 2 VACUUM SYSTEM CONFIGURATION

The 1104-m circumference storage ring is divided into 40 sectors, each sector has six vacuum chambers. Each sector can be isolated with all-metal gate valves that have rf continuity through flexible stainless steel "fingers." The vacuum group was responsible for fabricating 235 of the 240 chambers. The five remaining sections were devoted to rf cavities (four sets of four cavities are used) and to the injection region. Thirty-five chambers will be replaced by insertion device vacuum chambers—to date 14 insertion devices have been installed.

Each sector has two bending magnet girder assemblies, three focusing magnet girder assemblies, and a drift chamber—some of the drift chambers have been replaced by rf cavities, an injection region, and insertion devices. The configuration provides two beam exit ports per sector, one for dipole radiation and one for insertion device radiation. The chamber and the photon absorbers were critical components to design and fabricate in order to achieve the design performance of the storage ring.

Each chamber has ports to install photon absorbers, vacuum pumps, vacuum diagnostics, and x-ray beam transmission. The pumping philosophy was to install non-evaporable getter (NEG) strips in the pumping antechamber along the chamber lengths and to install large capacity NEG cartridge pumps and ion pumps at locations near the photon absorbers. In the initial design the NEG material would act as the principal UHV pumps and the ion pumps would trap chemically unreactive gases. As will be discussed later, the NEG pumps are primarily used after bake-out and in early commissioning of a sector. The ion pumps can capture sufficiently the stimulated desorption gas load during beam operation.

## 3 CHAMBER FABRICATION

Fabrication of the storage ring vacuum chamber with aluminum (Al) and the use of Al Conflat flanges was an early design choice. Although there are many advantages of Al vacuum systems such as low cost extrusions, high thermal conductivity, low radiation activating, and low magnetic permeability, aluminum vacuum systems presented several technical challenges. Extruding the chamber to tolerances as demanding as the APS design had not been done before. Achieving reproducibility in machining, welding, forming, and cleaning the chambers presented a number of challenges. Finally, since an ultra-high vacuum system required bake-out to 150°C, bake-out procedures needed to be developed to maintain vacuum integrity of aluminum-to-stainless steel Conflat flange joints

The chamber extrusions were made of 6061 aluminum. A cross section of the extrusion is shown in Fig. 1. The elliptical area is the stored beam region, and the pentagonal area is the pumping antechamber. The connecting region allows the x-rays to pass through and across chambers. The slots in the antechamber are to capture carrier strips that hold the NEG strip, and the three holes are for water cooling channels.

The gap of the beam exit channel needs to be maintained very accurately. In addition, the distance from the beam chamber center to the antechamber wall is critical. After a number of die trials, extrusions were successfully made to hold the channel gap to 0.428 ± 0.010" and the cross chamber length to 11.05" ± 0.015".

The second major problem was reproducibly welding vacuum parts to the chamber. An extensive weld development program was established that devised self-aligning

0-7803-4376-X/98/$10.00 © 1998 IEEE

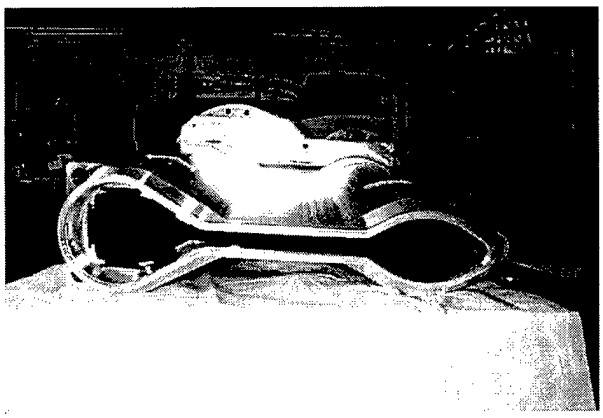


Figure 1: View of the APS storage ring Al extrusion used for vacuum chambers.

weld joints and used automatic welding systems to provide the repeatability. Over the production cycle reliability the vacuum-tight welds improved from 90% to better than 98%—and all weld leaks were repairable by manual welding. The major cause of leaks was oxide precipitation in the weld. A major breakthrough was the discovery that the Al feed wire introduced hydrogen to the weld. Subsequently, the Al wire was formed to thickness in an inert atmosphere.

Finally, cleaning the chamber presented yet more major problems. A KOH caustic wash was used in the initial development. However, the KOH was incompatible with 2219 Al used in the Al conflat flanges. Since 2219 Al is an alloy using 6% copper to harden the Al, KOH forced the copper to segregate to the surface where it then oxidized. It would be impossible to clean an assembled and welded vacuum chamber with KOH.

Use of an alkaline detergent and ultrasonic cleaning not only resolved the problem, but also provided a thinner oxide layer. The stimulated desorption rate from the detergent-cleaned chambers has been measured on a white light beamline at the NSLS x-ray ring at 2.5 GeV. The desorption coefficient curves for selected residual gases are shown as a function of photon flux in Fig. 2 [1]. The desorption coefficients are similar to Al surfaces with other surface treatments. As will be discussed later, gas load measurements from initial operation of the APS are poor because the storage ring vacuum system was unbaked during initial commissioning studies. The present system has a desorption rate of ~ 2-5 × $10^{-11}$ Torr per mA.

## 4 PHOTON ABSORBERS

The most demanding engineering problem for the storage ring vacuum system was the heat load on the photon absorbers, especially the absorbers at the bending magnet chamber. The x-ray power on these absorbers is greater than 5 kW, and the linear power density is greater than 100 W/mm. Engineers in the mechanical engineering group developed and fabricated an absorber that not only can withstand 12 kW, but is elegantly simple [2].

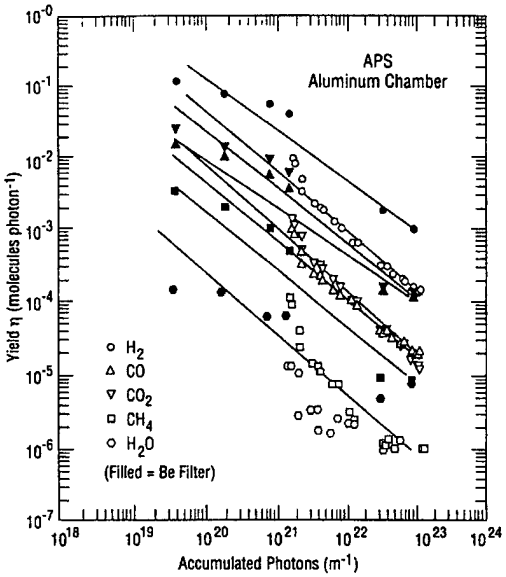



Figure 2: Simulated desorption coefficients for $H_2$, $H_2O$, CO, $CO_2$, and $CH_4$ as a function of integrated "white" x-ray beam from a 2.5-GeV electron beam [1].

The absorber is manufactured using GlidCop [3]—copper stabilized with 0.15% $Al_2O_3$. The internal water channels are cut using electric discharge machining (EDM), and a plug is brazed in to direct the inlet and outlet flow. The face is cut at an angle to disperse the power, and slots are machined to further spread the heat over the absorber surface. The absorber for the dipole chamber is shown in Fig. 3.

## 5 INITIAL PROBLEMS

During installation of the storage ring vacuum system, two problems developed that limited operation of the accelerator. Corrosion damaged the chamber water fittings and prevented bake-out of the sectors. A design flaw with the carriers for the NEG strip caused the strip to short to the chamber and prevented the NEG strip from being activated. This section details the problems and the redesign. These discussions are included for two reasons: to clarify misconceptions that have developed, and to highlight how seemingly minor changes can be disastrous in large vacuum systems.

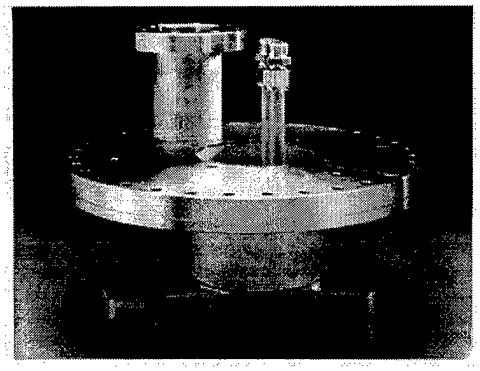


Figure 3: View of the APS absorber in chamber 2.

Soon after the problems of corrosion and NEG electrical shorts, the group learned that there were rumors in the accelerator community that the APS would have to replace its entire vacuum system. To illustrate how extravagant the rumors were, the problems were identified and the repairs completed in seven months. It would be a Herculean task to fabricate, install, and commission the complete vacuum system in seven months. The actual modifications undertaken by the vacuum group were daunting enough.

The first problem developed in a bi-metal joint between stainless steel and aluminum. The joint was welded to the chambers to connect the water headers to the chamber water channels. The water was deionized (DI) to 16 MΩ when the system was filled, but the conductivity fell to 500 kΩ. A galvanic cell developed across the bi-metal joint and the corrosion caused the joint to disintegrate. Without water circulating in the chambers, bake-outs could not be performed. This left the system base pressure in the low to mid $10^{-8}$ Torr range. Once it was determined that the principal failure was due to corrosion, the redesign was straightforward. A new chamber connector was made using 6061 aluminum, and the aluminum was connected to the stainless steel header system at a demountable flange. The flange used elastomer gaskets and jacket to electrically isolate the aluminum from the stainless steel at the joint. In addition, the water was continuously deionized and filtered to maintain a minimum resistivity of 3 MΩ. The major lesson learned from the failure analysis is that the water must be continuously deionized.

At the same time a second problem developed that also kept the system pressure high. The NEG strip that was installed in all of the chambers was to be activated by resistively heating the strip to 450° C. In fact, the strip was activated in the individual chambers during testing and certification. However, when the strips were electrically connected in series so that the NEG strip in a full sector could be activated at one time, the strip shorted to ground.

The electrical problem was traced to subtle changes in the design of the NEG electrical circuit. In order to install the NEG strip in the chambers and be able to pass current through the strip, stainless steel carriers were riveted to the strip through a ceramic electrical break (see Fig. 4). The carriers were connected together by fitting a tab in a slot on the adjacent carrier. The carriers were then captured by the channels in the extrusion antechamber. Tests showed that the "railroad car" connections could be pushed into the chambers. Although the carriers worked and were tested, there was significant friction when installing the carriers over the length of the chamber—especially the curved (dipole) chambers. The carriers were "improved" by using a pin inserted into a hole instead of the tab-and-slot design. Unfortunately, this new design was not tested in a full sector assembly. Because of the friction, one carrier could be galled in the chamber channel. The adjacent carrier would flex due to thermal expansion during NEG activation, the pin would push through the hole and the carrier would move over the adjacent carrier. Now the distance between electrical breaks was shorter than the NEG strip at 450° C, and the strip would buckle and short to the chamber.

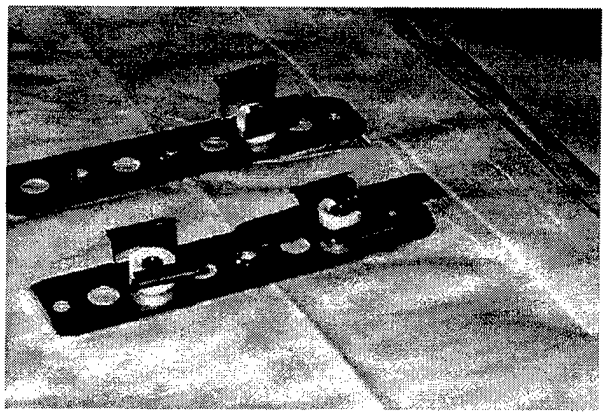


Figure 4: View of an old carrier for NEG strip (top); view of a new carrier for NEG strip (bottom).

The redesigned distributed NEG pump has layered protections. The new carriers were designed so that the carriers could not ride over adjacent carriers (Fig 4). The strip at temperature could not touch the chamber at the minimum span. In addition, a cantilevered plate coated with aluminum oxide blocked the strip from the carrier. The power supply was also rewired to have a ground fault circuit interrupt. If the strip somehow shorted out, the strip could not be overheated. Finally, new power supplies were built to activate individual chambers—also with ground fault indicators. So even in the event of a strip shorting to one chamber, the NEG pumps in a sector could still be activated. The new design is successful—the NEG strips have been installed around the ring, there are no shorted NEG strips in any chamber, and the strip can be activated in a full sector with one power supply.

## 6 ALUMINUM SYSTEM BAKE-OUT

The reinstallation of the water fittings and NEG strips created a third major problem that inhibited acceptable system base pressures. The bake-out of aluminum chambers with aluminum Conflat flanges mating with stainless steel flanges often opened a gasket seal. The problem was not significant when the individual chambers were being tested and certified; the failure rate was approximately one vacuum leak out of 30 or 40 flanges when baking the sector to 150°C. However, when an entire sector was being baked, the problem was significant because there are almost 50 flange seals in a sector. At least one gasket seal developed a leak in two out of three sector bake-outs.

Tests determined that gasket leaks could develop when the differential temperature was greater than 12°C. Obviously the larger the gradient, the more likely that the gasket seal would fail. Techniques were developed in which thermal insulation was wrapped around the alumi-

num-stainless steel flange assembly to minimize the temperature gradient. All but four flange assemblies could be protected with this passive temperature control. The two beam exit beam tubes and the two sector isolation valves required additional electrical heating to keep the flange temperatures within the 12°C range. The ion pumps were also electrically heated to at least 150°C.

## 7 SYSTEM PERFORMANCE

The new DI water system, NEG distributed pumps, and bake-out procedures have been successfully implemented. Since October 1995 the storage ring vacuum system has base pressures below $4 \times 10^{-10}$ Torr. Today, 32 out of 40 sectors have base pressures below $1 \times 10^{-10}$ Torr. With the new bake-out procedures, a gasket leak does not develop until after more than 10 sector bake-outs.

The dynamic system pressure is adequate at this time in commissioning/operation. The average ring pressure is below 2 nTorr at 100 mA. The beam lifetime at 100-mA stored current is more complex because the lifetime is a convolution of Touschek lifetime and residual gas scattering. In recent operating cycles with 100 mA in 200 bunches the lifetime was 37 hours. When 100 mA are stored in 60 bunches, the lifetime was only 14 hours. It is clear that the residual gas scattering lifetime and the Touschek lifetime are on the same order.

The high pressure regions of the storage ring are the rf cavities and the injection girders. The injection chamber is difficult to bake because it is surrounded by the magnet laminations and is potted in cement. Long bake-outs of the region are required in order to improve the base pressure. Plans to upgrade the vacuum system in the rf cavities are being finalized. Better system conditioning, and additional static and dynamic pumping will be added.

## 8 ACKNOWLEDGMENTS

As in any major project, the authors alone did not design, fabricate and install the accelerator vacuum systems. The mechanical engineering group under the supervision of Sushil Sharma was responsible for design, analysis, and fabrication of major components, such as the photon absorbers. The group technicians were essential to the successful system—especially the enormous work performed in a short time to re-install the water system, the NEG pumping, and perform sector bake-outs. Finally this work was supported by the U.S. Department of Energy, Office of Basic Energy Sciences, under Contract No. W-31-109-ENG-38.

## 9 REFERENCES

[1] C.L. Foerster, C. Lanni, J.R. Noonan, and R.A. Rosenberg, J. Vac. Sci.Technol. A 14, p. 1273, 1996.

[2] C. Sheng, S. Sharma, E. Rotella, J. Howell, Proceedings of the 1993 Particle Accelerator Conference, Washington D.C., p. 1497 (1993).

[3] Glidcop is manufactured by SCM Metal Products, Research Triangle Park, NC.

[4] R. Dortwegt, R. Benaroya, Proc. of the 1993 Particle Accelerator Conference, Washington D.C., p. 3857 (1993).

# ADVANCED PHOTON SOURCE EXPERIENCE WITH VACUUM CHAMBERS FOR INSERTION DEVICES

P. K. Den Hartog, J. Grimmer, E. Trakhtenberg, G. Wiemerslage, S. Xu,
Argonne National Laboratory, 9700 S Cass Avenue, Argonne, IL 60439 USA

*Abstract*

During the last five years, a new approach to the design and fabrication of extruded aluminum vacuum chambers for insertion devices was developed at the Advanced Photon Source (APS). With this approach, three different versions of the vacuum chamber, with vertical apertures of 12 mm, 8 mm, and 5 mm, were manufactured and tested. Twenty chambers were installed in the storage ring and successfully integrated into the APS vacuum system. All have operated with beam, and 16 have been coupled with insertion devices. Two different vacuum chambers with vertical apertures of 16 mm and 11 mm were developed for the BESSY-II storage ring and 3 of the 16 mm chambers were manufactured.

## 1 INTRODUCTION

A number of considerations in the design of undulators, such as a desire for high brilliance and a large tuning range, drive the design of the vacuum chamber to small gaps. On the other hand, particle beam transport considerations require the largest possible aperture. The competing requirements demand a vacuum chamber design with a minimum chamber wall thickness, close tolerances for straightness and flatness to enable precision alignment, and mechanical and thermal stability. Specialized insertion devices (IDs) often demand additional features in order to accommodate individual geometries.

Extruded chambers are economical for large accelerators such as the APS that can amortize the development costs over a large number of chambers. We have built a variety of long chambers, that have small vertical gaps, are straight and flat across the surface to within 50 μm, and that have performed well within the APS storage ring. The design depends on a rigid strongback that limits deflection of the chamber under vacuum despite a thin wall. All of these vacuum chambers have a wall thickness of $1.0 \pm 0.1$ mm at the beam orbit position, an elliptical beam chamber and a pumping antechamber with ST707 non-evaporable getter strips (NEG). Alignment of the vacuum chamber on its support is routinely accomplished with a precision of ± 75 μm over the entire surface, allowing minimum insertion-device pole gaps.

## 2 VACUUM CHAMBER TYPES

Versions of the vacuum chamber, with vertical apertures of 12 mm and 8 mm, and lengths of 2.5 meters and 5 meters were manufactured and tested [1]. Twenty aluminum chambers were installed in the storage ring and successfully integrated into the APS vacuum system. All but one have 8 mm vertical apertures (APS8). Of these, all are 5 m long and can accommodate two APS 2.4-meter long standard IDs. One 12-mm-aperture chamber is used with a 2.4-m-long wiggler (APS12). One stainless steel chamber has been built and installed for a specialized elliptical multipole wiggler (EMW)[2]. All have operated with beam, and 16 have been coupled with IDs, including the EMW. Additional chambers using the same approach but with 11 mm and 16 mm vertical apertures have been built for the BESSY II storage ring in Berlin (see Table 1).

| | Vert. Aperture (mm) | Horiz. Aperture (mm) | Length (m) | Min. ID Gap (mm) |
|---|---|---|---|---|
| APS5 | 5 | 30 | 5.59 | 7.5 |
| APS8 | 8 | 40 | 5.59 | 10.5 |
| APS8 | 8 | 40 | 2.92 | 10.5 |
| APS12 | 12 | 51 | 2.92 | 14.5 |
| BESSY | 11 | 45 | 4.53 | 13.5 |
| BESSY | 11 | 45 | 3.70 | 13.5 |
| BESSY | 16 | 60 | 4.53 | 18.5 |
| EMW | 19.6 | 66.6 | 3.10 | 23.0 |

Table: 1. Dimensions of ID vacuum chambers built at the APS. All are machined aluminum extrusions except the last, which is the EMW chamber described below.

### *2.1 APS8 and APS12 chambers*

The chambers are fabricated by extruding 6063 T6 aluminum alloy to form a tube with the desired internal shape and machining the exterior to the final dimensions. The extrusion process must be tightly controlled in order to yield a chamber with the straightness and wall thickness uniformity that is needed. This is accomplished first by proper design of the die to maintain a balanced mass flow and by fine tuning the die through a series of test extrusions. Two or three die trials are usually necessary before the production run. The extruded tube is cut to length and stretched 5% while still warm and plastic to reduce warps and kinks.

As delivered, the extrusion is quite straight and uniform, with a variation of only ±0.150 mm over the entire length, but even greater straightness is required before machining in order to assure a constant thickness profile. The chamber is shimmed and straightened with a large bed hydraulic press and then the interior profile is probed to

0-7803-4376-X/98/$10.00 © 1998 IEEE

determine the axis of the ellipse that will serve as the reference for the final machining. The thickness of the chamber is repeatedly checked with an ultrasonic thickness monitor during the machining.

The chamber is inspected after machining and prepared for welding. Using an automatic welding machine, it is welded to 304 stainless steel boxes at each end with ports for vacuum diagnostics, an ion pump, and a 220 l/s NEG cartridge pump. The end boxes also accommodate rf transition sections and a photon absorber.

### *2.2 5-mm-aperture ID vacuum chamber*

A 5-mm-aperture extrusion was designed and fabricated and successfully machined to the same exacting tolerances as the standard 8-mm-aperture chamber. The chamber end geometry was tapered to 12 mm aperture to enable use of the standard end box. The chamber was welded, assembled, certified for vacuum, and completely prepared for installation into the storage ring. This chamber can be used with the standard APS undulator down to a gap of 8.5 mm or possibly with a new ID with a shorter period down to 7.5 mm. The small fixed aperture places severe constraints on the beam orbit during injection. Current plans call for a test installation in the storage sometime during late 1997 or early 1998.

### *2.3 ID vacuum chambers for BESSY II*

BESSY II is a synchrotron light source facility under construction in Berlin. The APS has collaborated with scientists and engineers from this facility to design and fabricate the ID vacuum chambers for a 1.7 GeV storage ring.

The chambers are similar to the APS standard chambers but without the internal NEG pumping and without the attached diagnostic end boxes. Two different vacuum chambers with vertical apertures of 16 mm and 11 mm were developed. Pumping is provided by 6 ion pumps attached to the back of the chamber through stainless steel Conflat flanges. These flanges and the SS end flanges are welded to the chamber through Al-SS bimetallic transitions. Three of the 16 mm chambers were manufactured, tested, and delivered to Berlin. The extrusions for the 11-mm-aperture chamber have been fabricated and machining has begun, with delivery scheduled for late 1997.

### *2.4 EMW Vacuum Chamber*

The elliptical multipole wiggler (EMW) utilizes both a vertically oriented permanent magnetic field and a horizontally oriented electromagnetic field. The design incorporates a 3100-mm-long stainless steel vacuum chamber of rectangular cross section, with outer dimensions of 69 mm wide by 22 mm high and a wall thickness of 1.3 mm. The magnet structures completely surround the chamber on all four sides, positioned only 1 mm from the chamber when in use. This precludes use of an antechamber, as used in the standard ID vacuum chamber.

Given the constraints of the magnet geometry and the chamber length, two approaches were pursued for effective UHV performance. Both approaches utilize lumped NEG and ion pumping at either end of the chamber. One approach uses no additional pumping over the length of the chamber, relying on thorough cleaning and baking to minimize surface outgassing. The other method uses strips of sintered NEG material in diagonally opposed corners of the chamber top and bottom. The NEG material is activated by heating the chamber. Both approaches are complicated by the need to bake the vacuum chamber inside the EMW magnet structures. The system for *in situ* heating must maintain the temperature of the permanent magnet structures below 35 °C. Activation of the NEG strips requires heating the NEG material to at least 250 °C.

The heating system uses copper plates in contact with the outside of the vacuum chamber. A total of four plates are used, covering most of the chamber length on the top and bottom. A 1 kW heater is mounted to each copper plate. Reliable thermal contact is maintained with a number of clamps. Insulating boxes encapsulate the heating assembly. These boxes are made of thin stainless steel and filled with ceramic foam. The entire heating and insulating system can be installed within the EMW structure after the magnet assemblies have been retracted.

While an acceptable pressure for installation was achieved with the NEG-pumped chamber, it was not clear that the heat-activated NEG material provided a clear benefit. Heating the NEG material from the outside meant that the activated NEGs were subjected to heavy outgassing from the hot chamber, reducing their pumping speed and capacity upon cooling. Thus, the second test focused on the chamber without NEG pumping. The chamber was heated to 150 °C, the heaters were at 225 °C, and the outside of the insulating box reached a maximum of 61 °C. With ion pumping and activation of the other NEGs, a pressure of $1.7 \times 10^{-10}$ torr was obtained, comparable to the level of the NEG-pumped chamber. This chamber was used for the EMW installation.

## 3 PERFORMANCE

### *3.1 Vacuum measurements*

The ultimate pressure achievable during testing was $5.0 \times 10^{-11}$ torr. Each chamber was certified at a pressure below $2.0 \times 10^{-10}$ torr prior to installation. Initial installed pressure without beam is typically 1 to $5 \times 10^{-10}$ torr. Photodesorption from synchrotron radiation raises the pressure to about $2 \times 10^{-9}$ torr. After several weeks of beam conditioning, pressure with a beam declines to $< 1 \times 10^{-9}$ torr.

The ESRF observed [3] that dust particles of ferromagnetic material, possibly from the ST707 NEG strip, levitate into the beam aperture of the ID vacuum chamber during movement of the ID gap. The expected signature is a sudden drop in the lifetime of stored beam due to collisions with the levitated particles. No evidence of this effect has been observed at the APS.

### 3.2 *Chamber heating*

In order to be able to use the same style end box with various sized vacuum chambers, the transition necks down to a 12 mm ellipse. Each aluminum vacuum chamber is machined to provide a smooth transition from the chamber aperture to the 12 mm aperture of the end box. Consequently, a small fraction of bending magnet radiation can fall on the aluminum chamber if the beam is severely missteered in the vertical direction. The temperature has been monitored with thermocouples and heat sensitive tapes. Most chambers have never seen an increase beyond ambient temperature but a few have experienced transient rises to > 65 °C, the maximum limit of most of the installed tapes. In one case a higher range tape showed a temperature of 106 °C. No negative impact of this temperature rise has been observed or is expected.

### 3.3 *Deflection measurements*

Critical to the performance of the vacuum chambers is the rigidity and resistance to collapse under atmospheric pressure when evacuated. The width of the pumping slot between the beam chamber and the antechamber collapses about 100 μm, but this has a negligible influence on the conductance. Of more importance is the vertical aperture at the beam position (shown in figure 1). For the APS vacuum chambers, the 8 mm chamber has the largest deflection because the size of the pumping slot was chosen to be 6.35 mm to achieve the best conductance. Consequently, the area with the thin wall is rather extended. The BESSY chambers have greater deflections because the horizontal aperture is so large. The deflection is somewhat less for the 11 mm chamber. In addition, the 11 mm extrusion has been designed with a thicker root to reduce the collapse. During fiducialization prior to installation, the deflection is measured for each chamber in order to be able to precisely locate the center of the ellipse on the beam axis.

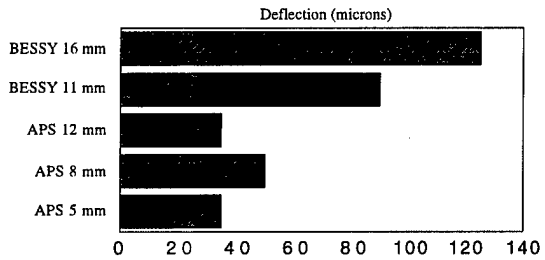



Figure: 1. Deflection of the center of the aperture of ID vacuum chambers under atmospheric pressure (per wall). The deflection of the 11 mm BESSY chamber is estimated.

### 3.4 *Sealing vacuum leaks*

A common feature of the ID vacuum chambers is the use of bonded aluminum and stainless steel in bimetallic transitions, which allow the joining of stainless steel and aluminum parts. A roll bond joint formed with a layer of 304 stainless steel alloy, a layer of pure aluminum, and a layer of 2219 aluminum alloy, provides a transition from the main chamber body to the stainless steel.

In the process of vacuum testing, several small vacuum leaks were discovered in the bonds. Sandwich plate was used for fifty-two standard end joints and for twenty-four circular ports. Of the fifty-two standard end joints, we have detected leaks in five. Of the twenty-four circular ports, leaks were detected in six.

To repair these leaks for an ultrahigh vacuum and a high radiation dose environment, a completely new method was tested using high velocity oxygen fuel (HVOF) metal powder spray deposition. An HVOF system accelerates a powder of the selected material to supersonic velocities. A variety of coating materials can be used including many metals and alloys, as well as ceramics. The high momentum of the particles creates a deposit with high adhesion, fine grain, and low porosity. The desired seal must introduce no contaminants into the system, particularly hydrocarbons, must seal after repeated bakeouts at 150 °C, and must be immune to radiation damage. To test the feasibility of the process, leak samples were prepared. One of the samples was sealed completely with a $Cr_3C$/NiCr coating.

The HVOF process is subject to a great number of variables including surface preparation, powder mixture, gas mixture and consumption rates, deposition rate, and substrate temperature. Each of the ID vacuum chambers was sprayed under different conditions with different results. Results vary from sealing the leak, to no change, to actually increasing the size of the leak (probably due to thermal effects). Given the proper set of conditions, however, it has been shown that it is possible to seal vacuum leaks for ultrahigh vacuum requirements. Further tests are planned to define the best parameters.

## 4 ACKNOWLEDGMENTS

The authors wish to thank J. Gagliano for assistance with the aluminum welding, and K. Knoerzer, J. Attig, T. Roberts, and R. Otto for their excellent work in assembling, testing, and installing the chambers.

This work was supported by the U.S. Department of Energy, Office of Basic Energy Sciences, under Contract No. W-31-109-ENG-38.

## REFERENCES

[1] E. Trakhtenberg, *et al.*, The Vacuum System for Insertion Devices at the Advanced Photon Source, Proc. of the 1995 Particle Accelerator Conf., Dallas, TX, Apr 30 - May 5, 1995

[2] P. Den Hartog, *et al.*, Design of the Vacuum System for the Elliptical Multipole Wiggler at the Advanced Photon Source, Proc. of Synchrotron Radiation Instrumentation Conference, Oct. 17-20, 1995, Argonne, IL

[3] N. Rouviere, ESRF Newsletter, No. 24, June 1995, pg. 15-16

# MASSIVE TITANIUM SUBLIMATION PUMPING IN THE CESR INTERACTION REGION*

N.B. Mistry, R. Kersevan and Yulin Li,
Laboratory of Nuclear Studies, Cornell University, Ithaca, NY 14853 USA

*Abstract**

The residual gas pressure within 30 m of the interaction point (IP) at the $e^{\pm}$ collider CESR is maintained in the low nanotorr range, despite the high gas loads produced by the intense flux of synchrotron radiation, in order to minimize the experimental backgrounds due to beam gas scattering. Within 12 m of the IP, the vacuum chambers incorporate large pumping plenums with massive titanium sublimation pumping to provide the necessary pumping speed and capacity. Operating experience over the last two years has shown that this method of pumping is efficient and inexpensive.

## 1. INTRODUCTION.

Lost particles generated by the 5.3 GeV $e^{\pm}$ beams in the collider CESR interacting with the residual gas are a major source of background in the CLEO High Energy Physics detector. They could also lead to radiation damage of sensitive components such as the new Silicon Vertex Detector (SVX) electronics installed around a two-centimeter radius thin beryllium beampipe.[1]

An aggressive R&D program to increase the luminosity of CESR has led to successive upgrades of the storage ring, which is now producing peak luminosities of $4x10^{32}$ $cm^{-2}$ $s^{-1}$ at a beam energy of 5.3 GeV, well beyond its original design specification. The main objective of the 1995 upgrade to Phase-II was to allow storage of up to 300 mA per beam. Increased current produces increased desorption of gases by synchrotron radiation (SR), so that the beam-gas background in the detector could increase proportional to the *square* of the current if the pressure were allowed to increase in proportion. The detector at the interaction point (IP) is most sensitive (in the present optics) to lost particles produced by beam-gas bremssstrahlung in the region up to about 30 m from the IP. The region up to 12 m was in particular need of increased pumping, to keep the pressure below about 2 ntorr at 300 mA.

For Phase-II, the vacuum chambers from the IP up to 12 m were replaced by new chambers, most of them incorporating massive titanium sublimation pumping (TiSP) plenums. The secret to maintaining high distributed pumping speed is, of course, large conductance to the pumping surfaces. The SR is absorbed on water-cooled copper bars and high-conductance slots lead to the pumping surfaces lining the plenum in each chamber. Right after flashing fresh Ti, the sticking coefficient is about 0.7 for CO. The net pumping speed is dominated by the slot conductance and gradually decreases as the Ti surface saturates. The TiSP speed is quite appreciable even when the sticking coefficient has fallen to 0.1. However, we flash again when the operating pressure with beams is about 2 ntorr.

There is another factor that affects the dynamic pressure rise and the flashing interval. It is well known[2] that the SR induced desorption coefficient $\eta_{SR}$ decreases steadily from its initial high value after intervention. Thus the dynamic pressure rise, $dP/dI$, expressed in nanotorr per mA of beam, continues to decrease with beam dose $D$, expressed in Amp-hours. Correspondingly, the flashing interval increases steadily. Eventually, we find that $\eta_{SR}$ levels off due to the overall equilibrium between desorption and readsorption of the molecules on the cleaned surfaces during steady operation at a particular beam current. This phenomenon has also been observed directly as "wall-pumping", contributing very significant distributed pumping in regions of intense SR flux.

The variation in desorption yield at any given location is well described by a power law $\eta_{SR} = \eta_{in} D^{\alpha}$, with $\alpha$ of order $-1$. The initial yield, $\eta_{in}$, immediately after start up of the accelerator can be as high as 0.1 molecule/photon and $\eta_{SR}$ reaches values as low as $2x10^{-6}$ mol/photon after exposure to $10^{24}$photons/m.

## 2. CHAMBERS NEAR THE IR.

Immediately surrounding the IP is a 50 cm long, 2 cm radius thin beryllium beam-pipe. A silicon vertex detector, the most sensitive part of the detector, surrounds this pipe. The first pump is the Q1 TiSP at 2.3 m from the IP. A tapered, slotted beam-pipe incorporates water-cooled copper absorber bars in the horizontal plane and is surrounded by a 20 cm radius TiSP plenum. The total conductance of the slots leading to the plenum is 620 l/s for $N_2$. Three Ti-sublimation cartridges, each with three filaments, are installed on demountable conflat flanges, baffled from each other and from direct line-of-sight to the beam tube. The next pump is a 220 l/s "noble-diode" sputter-ion pump (SIP) at 6 m. This serves to keep the partial pressure of noble gases and methane in control. Although methane is desorbed by the beam, the intense photon and electron flux is efficient at cracking methane ($CH_4$) to $CH_3$ and H which are then pumped by the TiSP, and no buildup of $CH_4$ is observed.

Figure 1 shows the "ISP chamber" which occupies the region from 6.4 m to about 8.6 m. From the end nearest the IP, there is a section of 1 m long

* Work Supported by the National Science Foundation

0-7803-4376-X/98/$10.00 © 1998 IEEE

copper beam chamber with pumping slots and holes ( of total conductance 9,000 l/s) surrounded by a cylindrical pumping plenum of 0.4 m diameter with three Ti-filament cartridges. A total surface of about $10^4$ cm$^2$ is covered by Ti during flashing. A CCG is installed on top of the pumping plenum.

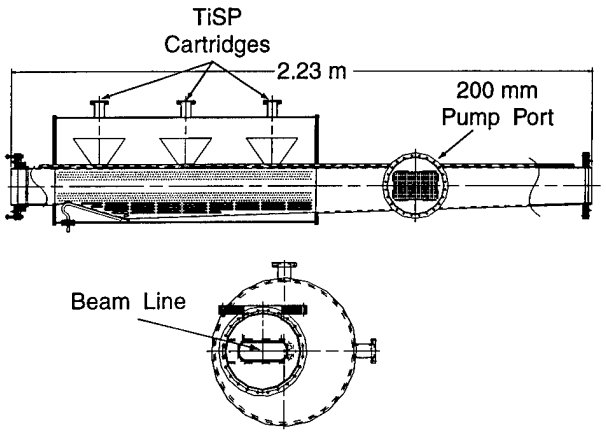



Figure 1. The ISP Chamber with Ti pumping plenum.

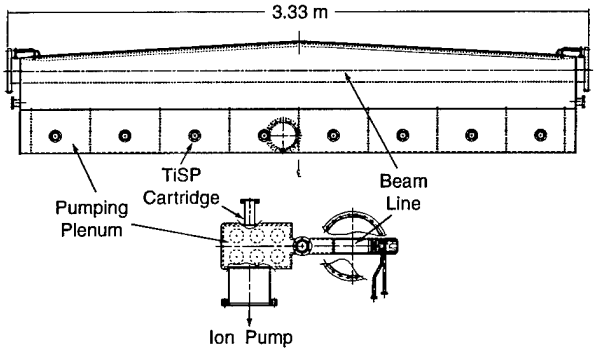



Figure 2. The Soft-Bend Chamber. Top view (above) and cross-section showing Ti pumping plenum.

The 3.3 m long "Soft-Bend" vacuum chamber, (Figure 2) sees the intense SR radiated by the beam in the "Hard Bend" (HB) magnets upstream. The absorber is a 3.2 m long copper bar bent to a chevron shape, with wedge-shaped absorbing steps. A slotted wall of about 7,800 l/s conductance leads to a large rectangular copper pumping plenum, 15 cm high by 25 cm wide, running the full length of the chamber. Nine vertical baffles give rigidity and increase the surface covered by titanium. Eight Ti-filament cartridges are equally spaced in the pumping plenum, covering about 25,000 cm$^2$ with Ti during flashing. A 110 l/s noble-diode sputter-ion pump is mounted on the pumping plenum. A CCG is installed near the beam line.

In Table 1 we give an estimate of the CO gas load obtained in different regions of the IR when the photodesorption yield in the HB region of most intense flux gets down to $\eta_0 = 1.8 \cdot 10^{-6}$ mol/photon. We use this "ultimate" value of $\eta_{SR}$ to predict the vacuum performance of CESR when the vacuum system is fully conditioned and use it to model pressure profiles below.

TABLE I. Synchrotron Radiation Flux and Gas Load in the CESR IR for 300 mA $e^{\pm}$ Stored Beams.

| Location | Flux Density (Photon/s/m) | Total Flux (Photons/s) | CO GasLoad [Torr-l/s] |
|---|---|---|---|
| Q1-Pump | $1.3 \cdot 10^{18}$ | $2.5 \cdot 10^{17}$ | $7.9 \cdot 10^{-8}$ |
| ISP absorb. | $1.1 \cdot 10^{19}$ | $1.9 \cdot 10^{18}$ | $2.0 \cdot 10^{-7}$ |
| Soft-Bend | $3.3 \cdot 10^{18}$ | $3.5 \cdot 10^{18}$ | $6.7 \cdot 10^{-7}$ |
| Hard-Bend | $6.9 \cdot 10^{18}$ | $2.3 \cdot 10^{19}$ | $1.3 \cdot 10^{-6}$ |

## 3. PUMPING SPEED AND CAPACITY.

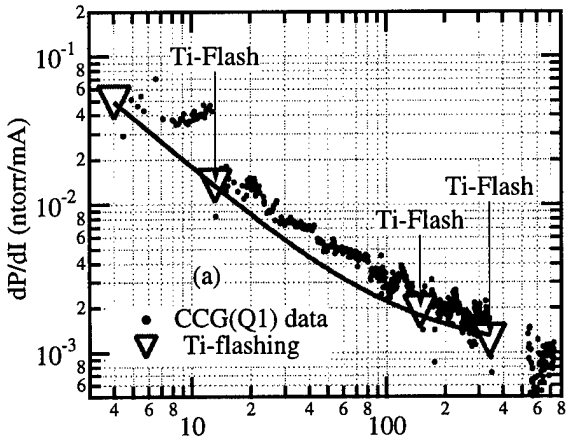
Each pumping chamber was treated as follows before installation in CESR: leak check; bakeout and degassing of all Ti filaments and gauges; saturation of the bare walls with either CO or $N_2$ using calibrated leaks; flashing of Ti cartridges; slow saturation of the Ti surface using CO and/or nitrogen calibrated leaks with continuous monitoring of pressure and gas composition. The effective pumping speeds at each stage were determined from the data. The experience obtained with the Soft-Bend chamber is quite illustrative and typical. After bakeout and degassing of filaments, initial pumping speeds of the *bare walls* were $S_{N2}$= 957 l/s and $S_{CO}$= 4,400 l/s and absorbed a dose of 0.29 torr-liter of nitrogen! Significant partial pressure peaks of $CH_3$, $CH_4$ and Argon showed clear evidence of passive gettering action. After flashing all eight Ti -cartridges for 2 minutes each at 220 W, the pumping speeds for CO and $N_2$ were measured as a function of nitrogen load. Initial pumping speeds at zero load were: $S_{N2}$= 1,571 l/s and $S_{CO}$= 8,420 l/s (higher sticking coefficient for CO). After absorbing 2.2 torr-liters of $N_2$ $S_{CO}$ was still as high as 3,500 l/s and decreased to 1,500 l/s after 0.4 torr-liter of CO was absorbed.

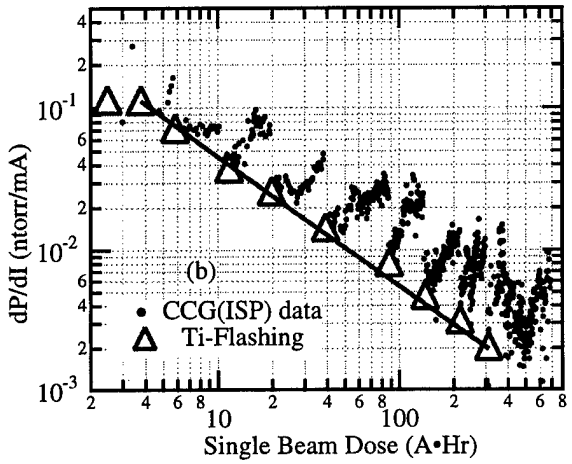
Saturation of the Q1 pump chamber with CO showed that the pumping speed falls by five at about 0.6 torr-l/s. In CESR, this is a region of low SR gasload, 8 x $10^{-8}$ torr-l/s with 300 mA beams, so the ultimate flashing interval for Q1 should be ~ 90 days. The data for the ISP chamber show that saturation occurs at 1.0 torr-liter of CO. The ultimate expected SR-induced gasload at 300 mA per beam is 2 x $10^{-7}$ torr-l/s, so we expect a flashing interval of about 60 days to maintain pressures below a few nanotorr.

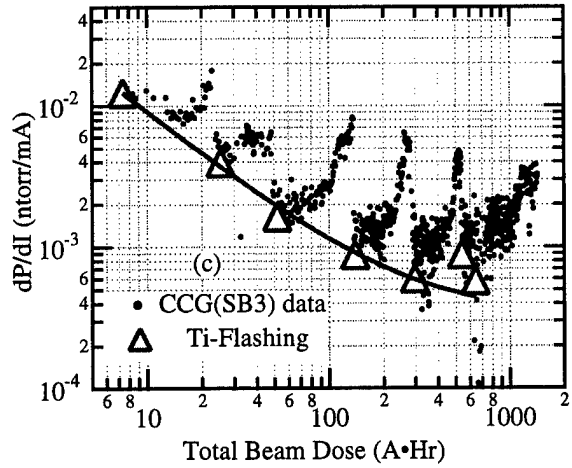
## 4. DYNAMIC PRESSURE RISE IN CESR.

The new IR chambers were installed and Phase-II operation started in November 1995. The dynamic pressure rise with beam, ($dP/dI$ ), at various locations in the IR is shown in the Figure 3 as a function of beam dose in Amp-hrs. Single beam dose or total beam dose is used as appropriate for each geometry. Ti-flashing points are shown (triangles) and

the subsequent points show the slow saturation of the TiSP. The plots include data recorded up to March 3, 1997, representing approximately 14 months of operation. The clean-up due to the beams is very apparent in all plots and shows the characteristic dose dependence of the gas load, $N_{gas} = N_{phot} \cdot (\eta_0 + \varepsilon \eta_{in} D^{\alpha})$, with $\alpha \approx -1$ for all plots. Here $\varepsilon$ is the fraction of photons scattered from the primary SR stripe which is assumed to have reached the ultimate coefficient $\eta_0$.



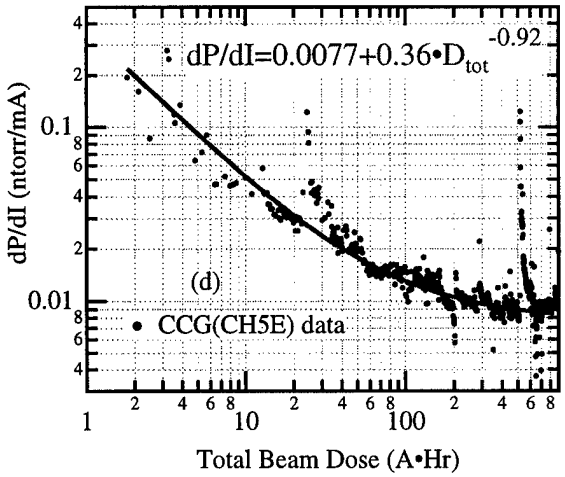




Figure 3. The beam induced dynamic pressure rise, (*dP/dI*), at various locations in the IR. (a) At Q1E chamber; (b) on the beamline next to the ISP chambers, and (c) for the soft-bend chambers. (d) shows *dP/dI* for a gauge within the hard-bend sector pumped only by distributed ion pumps, where the SR flux and gas load are the most intense.

The scattered photons then continue to clean up the rest of the chamber. In the high-intensity HB region (Figure 3d) we see that after about 100 Amp-hrs of total beam, the dynamic pressure rise has levelled off to $N_{phot}\eta_0$, indicating the equilibrium between desorption by the beam and readsorption by the cleaned surfaces, leading to a constant effective $\eta_{SR}$.

## 5. CONCLUSIONS.

Ti sublimation pumping on an extensive scale has been used successfully in the interaction region of CESR, to keep pressures at a few nantorr level despite the intense SR flux. Present operation of CESR with two beams of 150 mA each results in operating pressures of between 1.5 ntorr and 3.5 ntorr in most of the IR. This pressure profile is sufficient to keep detector backgrounds at acceptable levels. In the near future, we will install more chambers similar in design to the soft-bend chambers further down the line in the bend region. We expect the pressures to be maintained at the low nanotorr level as the beam currents are raised to 300 mA and beyond.

## 6. REFERENCES.


[1] S.Henderson, "The CESR High Luminosity IR", these Proceedings.

[2] O.Groebner et al., Vacuum **33**, 397 (1983).

[3] R. Kersevan, "MOLFLOW, a 3D Monte-Carlo Code for the simulation of molecular flow", available from the author, Laboratory of Nuclear Studies, Cornell University, Ithaca, NY, 14853.

# INTERACTION REGION VACUUM SYSTEM DESIGN AT THE PEP-II *B* FACTORY

L. Bertolini, O. Alford, P. Duffy, R. Holmes, L. Mullins
Lawrence Livermore National Laboratory, University of California, Livermore, CA 94550 USA
C. Ng, M. Sullivan
Stanford Linear Accelerator Center, Stanford University, Stanford, CA 94309 USA

*Abstract*

The Interaction Region Vacuum System in the PEP-II *B*-Factory at SLAC must produce average pressures in the $10^{-10}$ Torr range. Low beamline pressures will minimize the background radiation encountered by the BaBar Detector. A combination of copper and stainless steel vacuum chambers with continuous antechambers are used to make up the beam tubes. Linear Non-Evaporable Getter (NEG) pumps are used to produce distributed pumping along the length of these beam tubes. High conductance "microwave" type screens provide RF shields between the beam aperture and the NEG pumps. In this paper the design features of the beam tubes, NEG pumps, and RF pump screens are described and the vacuum and impedance analyses conducted in support of the design are discussed.

## 1 INTRODUCTION

The Interaction Region (IR) is the heart of the PEP-II storage ring. Since the BaBar Detector is located at the IR there is a more stringent pressure requirement for the vacuum system. This pressure requirement is intended to minimize background radiation caused by bremsstrahlung gas-beam interactions viewed by the detector. Gas-beam intereactions produce off-energy particles which are swept into the detector by the bend magnets near the Interaction Point (IP). The average beamline pressure in the IR must be below 1 nTorr (nitrogen equivalent) [1]. This pressure requirement applies to the "mid-IR", defined in the High Energy Beam (HEB) at 2-40 meters upstream of the IP and the Low Energy Beam (LEB) at 2-30 meters upstream of the IP.

Producing sub-nTorr average pressures is especially difficult considering the copius amounts of synchrotron radiation that are deposited along the walls of both incoming beamlines. The gas load is estimated to average $10^{-7}$ Torr-liters/second/meter throughout the mid-IR. To achieve an average pressure of $10^{-10}$ Torr, distributed vacuum pumping is required on the order of 1000 liters/second/meter. This is especially difficult to accomplish without producing a high impedance which causes beam instabilities and higher-order-mode heating.

## 2 VACUUM SYSTEM DESIGN

The majority of Interaction Region vacuum chambers are constructed from oxygen-free copper extrusions. There

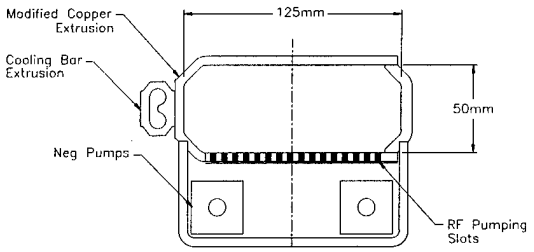



Figure 1. Cross-section of the HEB IR Chamber

are some special HEB chambers where the sychrotron radiation power is high. These chambers are constructed from stainless steel with GLIDCOP absorbers. The standard cross-section of the HEB IR chamber is shown in Figure 1. It has an octagonal beam aperture with a pumping plenum attached below the beam. The pumping plenum communicates with the beam aperture through an array of slots (Figure 2). On the backside of each set of slots is a 1 mm thick screen with 3 mm wide slots. These slots are oriented 90° to the main slots and their purpose is to block the transmission of transverse electric (TE) modes of RF power into the pumping plenum.

The cross-section of the LEB IR chamber is shown in Figure 3. The LEB chamber has the pumping plenum adjacent to the beam aperture, but separated by a "microwave type" RF pumping screen. The pumping screen for the LEB IR chambers is shown in Figure 4.

The vacuum pump chosen for the IR is the Non-evaporable Getter (NEG). The design of the distributed NEG pumps for the PEP-II IR is an innovative departure from conventional NEG designs. SAES ST707 strip is laser cut into individual "wafers" and stacked onto a stainless steel tube with 1 mm spacers between wafers. The stainless steel tube wall serves as both the vacuum barrier and support for the NEG. A commercial tubular heater is inserted into the tube and used to activate the NEG. The heater is outside the vacuum system, so

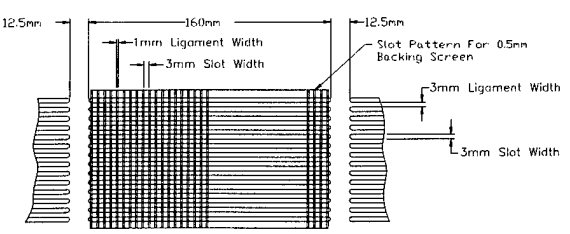



Figure 2. HEB IR pumping slots

penetration of the vacuum barrier with an electrical feedthrough is not required. With this design feature, a failed heater can be replaced with the chamber under vacuum. Each pump within the IR contains the equivalent of 18 meters of NEG strip per meter of pump length. This provides a distributed pumping speed in the range of 1000 liters/second/meter with a getter capacity of 1.8 Torr-liters CO/meter. Estimates show that with this pumping capacity, after initial beamline "clean-up" regeneration will be required only on an annual basis. The distributed NEG pumps are also supplemented by discrete ion pumps to pump hydrocarbons during machine operation and to pump hydrogen during NEG activation.

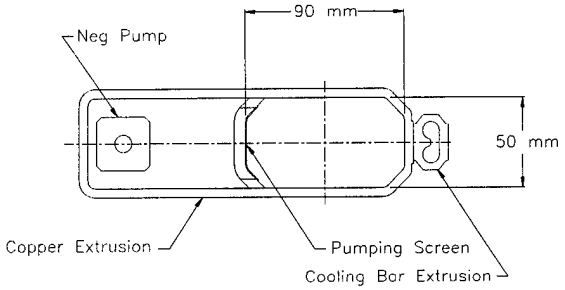



Figure 3. Cross-section of the LEB IR Chamber

## 3 VACUUM ANALYSIS

To produce an average beamline pressure in the $10^{-10}$ Torr range, it is essential to determine the locations and extent of the gasloads generated by the circulating beams. The major source of outgassing in the IR is due to photo-desorption, that is, gas expelled from the chamber walls by synchrotron radiation. Early in the PEP-II project, photo-desorption tests were conducted at Brookhaven National Laboratory. Prototype PEP-II copper vacuum chambers that had been ultrahigh vacuum processed were exposed to synchrotron radiation. Outgassing due to photo-desorption was measured to assess "clean-up" time and determine the photo-desorption outgassing coefficient (referred to as "η", with units of molecules/photon). The design value for "η" was determined in these tests and was found to be 2.0 x $10^{-6}$ molecules/photon after 40 Amp-hours of exposure [2].

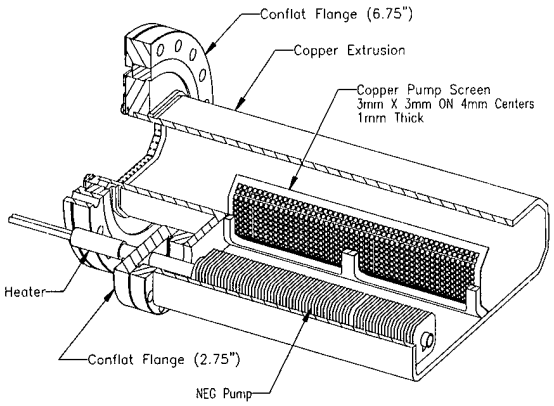



Figure 4. LEB IR pumping screen.

Both of the HEB and LEB beamlines were laid out on CADD workstations and ray traces were made of the synchrotron radiation "fans" generated by the bend magnets. From the ray traces, profiles of the synchrotron radiation power incident on the walls of the chambers were calculated. Distributed gas loads were calculated by converting the synchrotron radiation power profiles to gas load profiles (in nitrogen equivalent) using the empirical photo-desorption data.

Pumping speed and sorption capacity for SAES ST707 NEG material is well known. Manufacturer's data for carbon monoxide pumping speed was extrapolated for the actual surface area of the NEG material in the IR pumps. Prototype pumps were built and tested to verify the design calculations. The results of these tests are reported in reference [3].

It is one thing to design a high speed UHV pump, it is quite another to deliver high "net" pumping speed to the beam aperture where it is required. The design of the high conductance/low impedance RF pumping screens were the most challenging aspect of the project. Several iterations were made between the vacuum engineer and the electromagnetic physicist to come up with a compromise design that satisfied all of the design criteria.

Calculating the molecular conductances of the RF pumping screens was done analytically. As a check, a two-dimensional Monte Carlo model was made of the screens [4]. The model was compared to a benchmark model of the PEP-II High Energy Ring arc screen design which had been protoyped and measured. The calculated molecular conductance of the HEB IR pumping slots is

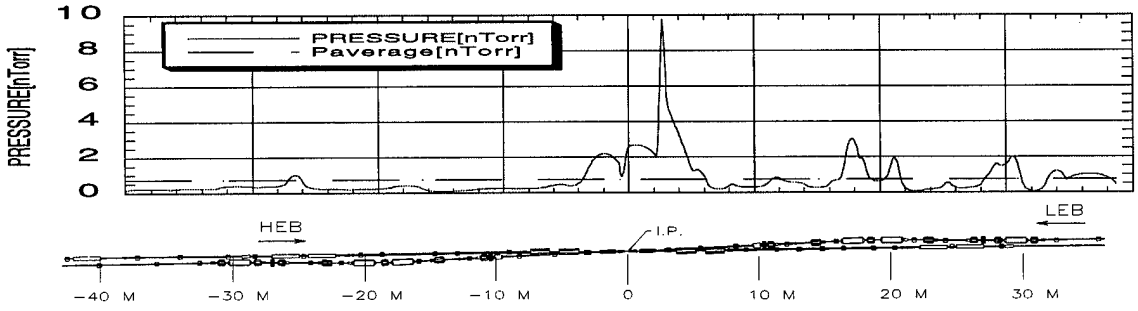



Figure 5. Interaction Region Plan and Pressure Profile

2000 liters/second/meter (nitrogen equivalent). The calculated molecular conductance of the LEB IR pumping screen is 1600 liters/second/meter.

With the gasloads and the net pumping speeds calculated, the next step was to generate a one-dimensional beamline pressure profile. This was done with the use of pressure pipeline code developed for vacuum beamlines [5]. Each discrete section of beamline was characterized by its length, axial conductance, gasload, and pumping speed. Once the beamline model was built, it was straightforward to make changes to address localized pressure problems. The final pressure profile for the upstream sections of the HEB and LEB are shown in Figure 5. There is a sharp pressure peak the IP due to low beamline conductance and the absence of pumping. This pressure peak is not expected to produce significant background radiation. The average beamline pressure in the HEB mid-IR is 0.75 nTorr. The average beamline pressure in the LEB mid-IR is 1 nTorr after 40 Amp-hours of machine operation.

## 4 IMPEDANCE ANALYSIS

From a beam impedance point of view, long slots are preferred over holes, since the main contribution to the impedance comes from the ends of the slots. However, long slots allow TE power to penetrate into the pumping plenum which can cause excessive heating to the NEG pump. The ideal situation is to place a screen with small holes at the back of the slots to block TE power penetration. In this manner, the hidden holes produce only a small impedance. However, here in the IR, vacuum conductance considerations required the RF screen to be placed directly at the beam chamber wall increasing the impedance substantially. In this case an optimized design had to accomodate both beam impedance and vacuum conductance requirements.

The HEB IR pumping slots (Figure 2) contribute an inductance of 0.15 nH, which is small compared with the overall High Energy Ring impedance budget of 50 nH. The IR upstream high energy beam dump chambers have about 76,000 holes (3 mm square) located at the bottom of the beam chamber. They contribute an inductance of 3.41 nH, which is still a relatively small fraction (7%) of the impedance budget. The LEB IR pumping screen (Figure 3) creates an inductance of 1.2 nH, which is also relatively minor. Hence, the two pumping screen designs for the HEB IR and the LEB IR will have a small effect on the beam impedance.

The effectiveness of both the long slots and the "microwave screen" designs in shielding the TE power is evaluated by transmission calculations of a $TE_{10}$ mode propagating in the beam chamber. The results are shown in Figure 6. The deviation of the transmission coefficient from unity represents radiation penetrating through the screen. The HEB slots allow negligible penetration over a broad range of frequencies. The slots are long enough to interrupt the azimuthal current of the TE mode. In contrast, the screen design is opaque to TE penetration at all frquencies with 100% transmission down the beam aperture.

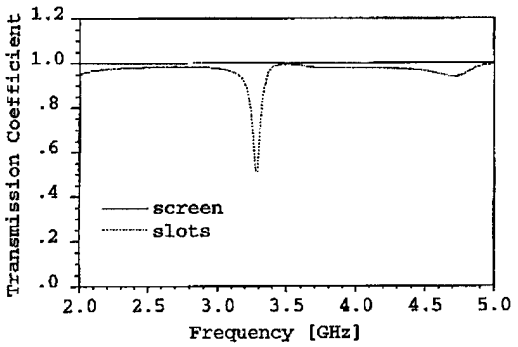



Figure 6. TE Mode Transmission Spectrum for pumping slots and screen.

## 5 SUMMARY

The design and analysis of the vacuum system for PEP-II Interaction Region has been described. The IR vacuum system performance has been shown to produce average beamline pressures at or below 1 nTorr. The pumping screens have been shown to be minor contributors to the overall machine impedance budgets and to protect the NEG pumps from TE radiation.

## 6 ACKNOWLEDGEMENTS

This work was supported by the Director, Office of Energy Research, Office of High Energy and Nuclear Physics Division, of the U.S. Department of Energy under contracts DE-AC03-76SF00098 and W-7405-ENG-48-(LLNL).

## 7 REFERENCES

[1] "PEP-II an Assymmetric *B* Factory," Conceptual Design Report, CALT-68-1869, LBL-PUB-5379, SLAC-418, UCRL-ID-114055, UC-IIRPA-93-01, June 1993.

[2] "Photon Stimulated Desorption (PSD) Measurements of Extruded Copper and of Welded Copper Beam Chambers for the PEP-II Asymmetric *B* Factory," Foerester et al.

[3] "MONTE," Tanabe and Osborn, December 1995.

[4] "Design of the Linear Non-Evaporable Getter Pump for the PEP-II *B* Factory," Bertolini et. al., these proceedings.

[5] "A Method for Calculating Pressure Profiles in Vacuum Pipes," PEP-II AP Note No. 6-94, March 1994.

# SURVEY OF ELECTRONIC SAFETY SYSTEMS IN ACCELERATOR APPLICATIONS

K. Mahoney
Thomas Jefferson National Accelerator Facility, Newport News, Virginia 23606

*Abstract*

This paper presents the preliminary results and analysis of a comprehensive survey of the implementation of accelerator safety interlock systems from over 30 international labs. At the present time there is not a self consistent means to evaluate both the experiences and level of protection provided by electronic safety interlock systems. This research is intended to analyze the strength and weaknesses of several different types of interlock system implementation methodologies. Research, medical, and industrial accelerators are compared. Thomas Jefferson National Accelerator Facility (TJNAF) was one of the first large particle accelerators to implement a safety interlock system using programmable logic controllers. Since that time all of the major new U.S. accelerator construction projects plan to use some form of programmable electronics as part of a safety interlock system in some capacity.

## INTRODUCTION

To date, there are no basic requirements or generally accepted standards for the design of safety interlock systems in accelerators. Some specialized industries, such as medical accelerators have general guidance for interlocks for oncology machines, and more guidelines are under development (ref1,2). Some standards which could be applied to safety interlock system design (ref.3) are under development but there are no guidelines or requirements for the application of these standards for accelerators.

The purpose behind a survey of accelerator safety system implementations was to provide some foundation for comparing "good practice" within the industry. To this end several different types of accelerators were chosen in order to have a comprehensive picture of the practices involved. Specific goals were to:

- Gather a wide variety of data on safety system applications within the accelerator community.
- Get an idea of the implementation methods used by safety system designers in diverse applications.
- Compare methods used in the design of accelerator safety interlock systems to those in other high risk industries.
- Compare attributes such as complexity, cost, reliability, and customer satisfaction between different machines.
- Form a basis of "Good Practice" which may then be used to develop standards and guidance applicable to accelerator safety systems.

The intended audience for the survey were the persons directly involved in the design, maintenance, and supervision of safety interlock systems. The focus of the survey was on those systems used to interlock prompt ionizing radiation hazards.

## SURVEY DESIGN

The survey was broken up into 100 questions, divided into 4 categories.

- Background - what type of accelerator(s), energy, current, particles, ... etc.
- Safety System Design Architecture - What types of design architectures are used. Redundant? Electronic? Relay based?...etc.
- Documentation - What type of documentation was used in the design, fabrication, review, testing,...etc.
- Administration - what policies are used in the administration of the system. What type of management support, funding, ...etc does the interlock system get?

## SOME PRELIMINARY RESULTS

There were over 40 respondents out of 150 surveys mailed. The respondents included a wide cross section of accelerator applications. Table 1 gives a breakdown of the type of applications

| Application | # Responding |
|---|---|
| Fundamental research | 22 |
| Applied Research | 17 |
| Industrial Research | 14 |
| Medical Applications | 12 |
| Other Applicants | 1 |

**Table 1. Applications**

Table 1 includes responses from multipurpose labs which may have more than one application for the accelerator.

There are a few basic attributes which can be compared among safety interlock system implementations:

- Technology
- Redundancy
- Layering (multiplicity of devices)
- Diversity of components

Each of these attributes may or may not add to the safety or availability of a system. Some are a matter of practice.

Typically, in fields which are highly competitive or under great scrutiny, the implementations are optimized for performance - both availability and safety. Examples of such applications may be a the airline industry or nuclear power stations. For both to be economically viable, the safety system must be extremely reliable and also free of false trips. In applications which are less competitive,

0-7803-4376-X/98/$10.00 © 1998 IEEE

such as research physics accelerators, safety systems vary greatly in the implementation. Availability has historically not been a driving consideration in these designs.

## TECHNOLOGY

A basic theme of one section of the survey was to determine what type of technology was used in the design of the system. Until recently, almost all safety interlock systems were designed using relay based systems. In contrast, the newer designs are using the advantages of programmable electronic based designs. In particular, programmable logic controller (PLC) based designs are becoming prevalent in the nuclear physics accelerators, while microprocessor based systems are used in industrial and medical applications. A pivot of 1990 was used to look at the breakdown of electronic vs. electromechanical (relay) based systems.

| Implementation | Electronic/Programmable | Relay/Switch |
|---|---|---|
| Before 1990 | 13 % | 18 % |
| After 1990 | 40 % | 29 % |

**Table 2. Safety Interlock System Technologies**

A majority of the electronic systems implemented after 1990 were electronic or programmable systems. Most of the relay based systems implemented after 1990 were extensions or upgrades to existing systems.

The trend is to replace relay based systems with electronic systems when the cost and increased availability can be justified.

## ARCHITECTURE

The most common architecture for accelerator safety interlock systems is the dual redundant arrangement. There are varying degrees of isolation between the two chains, however, there are typically two independent systems.

| Architecture - Redundancy | | | |
|---|---|---|---|
| Single Channel | Dual Redundant | Triple Redundant | Other |
| 32% | 62% | 3% | 3% |

**Table 3. Safety System Redundancy**

Most of the safety systems use layering of devices which are interfaced to, or controlled by the safety system. Layering of protection devices is used to achieve a diversity between protection devices so that the system is less susceptible to common cause failure modes. An example of layering vs. redundancy is shown in figure 1.

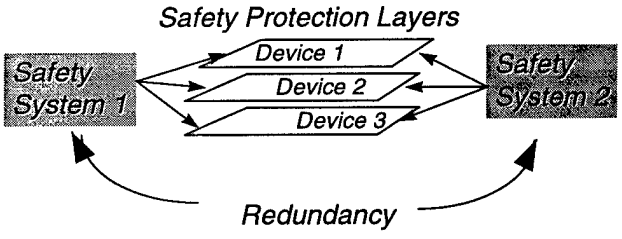



**Figure 1. Redundancy vs. Layering**

| Architecture - Layering | | | |
|---|---|---|---|
| Single Layer | 2 Layers | 3 Layers | 4 Layers |
| 6% | 59% | 29% | 6% |

**Table 4. Safety System Layering**

The trend in layering is to have n+1 layers, where n is the level of redundancy. For example, a newly designed dual redundant safety system would tend to have 3 devices used to stop beam. Likewise, even a single channel system would use 2 different means to block or shut off beam.

## DESIGN BASIS

The technology involved in the implementation of safety systems was relatively well understood. One of the survey questions asked "Was there a design goal for safety system reliability?" There were three basic types of responses. The most prominent were the qualitative response of "no failures," with 86% of those responding. The next two most common answers were quantitative with 14 % giving a number of $10^{-6}$ failures per year and 4 % giving a number of 0.5 - 1 failure per year. The disparity between the requirements again points to a lack of a common definition of safety reliability within the accelerator community.

## CUSTOMER SATISFACTION

Two of the questions had to do with the satisfaction with the safety system. 100% of the respondents were satisfied with their safety system. The validity of this response comes into question when compared with some quantitative measure of satisfaction. For example, 20% of the respondents thought that their system was difficult to operate or to trouble shoot. Thirty-five percent had not done any type of reliability analysis of their system or the potential failure mechanisms. What was most surprising was that, while the majority of respondents set a criteria of "no failures" and were "completely satisfied" with their system, 26% have actually uncovered unsafe failures in their system.

## COMPARING TO OTHER INDUSTRIES

Table 5 compares the approach taken by several different industries which use safety interlock systems for life safety. An important distinction between the applications is not necessarily the quantitative risk associated with the hazard, but rather the perception of the risk in the general public's eye.

Note that the increased redundancy of the aircraft, nuclear power, and chemical applications is not necessarily to achieve an increase in the reliability of the safety system, but rather to achieve an increase in the availability of the system. A typical 3x redundant system would use a voting arrangement such that if one of the systems failed, the other two would still maintain the safety interlocks.

## ADMINISTRATION

Administration of safety systems is an important factor when and if one considers incorporation of the system into a total quality management (TQM) frame work. It is a must if one considers working to the ISO 9000 series of standards. Only 6% of the respondents were ISO 9000 certified. Another 17% were either considering ISO certification or actively working toward ISO standards.

Other questions in the administrative section dealt with issues such as satisfaction with current funding (79%), and management support (95%).

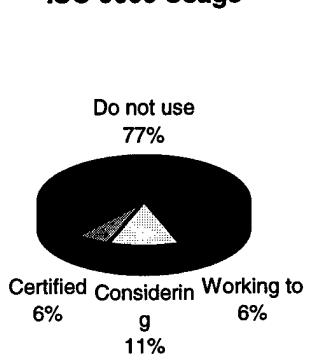



**Figure 2. Usage of ISO 9000 among accelerators**

## CONCLUSIONS

The conclusions of the survey of safety interlock systems in accelerator applications are still preliminary. Much more analysis is required to come to a comprehensive understanding of the data. However, the following conclusions are evident from the data at the time of this publication:

- The trend in technology for the implementation of safety interlock systems is toward programmable electronic systems. The most predominant type of hardware is the industrial programmable logic controller (PLC).
- The architecture generally used is the dual redundant system with at least two safety layers. The trend in new designs is to use dual redundant/3 layers.
- Requirements for system reliability are not well defined or understood in many cases.
- Perception of safety provided by a safety system is not always based on analysis or metrics of system performance.
- Safety System personnel are generally satisfied with management support and funding.

## ACKNOWLEDGEMENTS

The author would like to thank all those individuals who took the time to complete and return the survey sheets. This work was supported by the U.S. DOE under contract number DE-AC05-84ER40150.

## REFERENCES

[1] 'Design Control Guidance for Medical Device Manufacturers', March, 1997 US Food and Drug Administration, Center for Devices and Radiological Health.

[2] 'ODE Guidance for the Content of Premarket Submission for Medical Devices Containing Software', US FDA Draft 1.3, August 1996.

[3] K. Mahoney, "Emerging Standards with Application to Accelerator Safety Systems," 1997 Particle Accelerator Conference, Vancouver, B.C., Canada.

| Application | Particle Accelerator | Aircraft | Chemical Plant | Nuclear Power Plant |
|---|---|---|---|---|
| Type of hazard | Prompt Radiation | Loss of Control/ Power | Chemical Release/ explosion | Radioactive Release/ exposure |
| Potential Consequences | Catastrophic to limited number of individuals. No long term hazard. | Extremely Catastrophic to hundreds of individuals. No long term hazard. | Extremely Catastrophic to potentially thousands of individuals. Possible long term hazard. | Very Catastrophic to potentially hundreds of individuals. Possible long term hazard. |
| Examples of accident | Therac 25 | Several | Bhopol | Chernobyl |
| Relative importance of Reliability | Very | Extremely | Very | Extremely |
| Public Acceptance of risk | Completely | Grudgingly | Grudgingly | None |
| Importance of machine availability | 50 - 95 % | 100 % | 80-98 % | 98 - 100 % |
| Safety System Architecture | Dual Redundant | 3-4x Redundant | 2-3x Redundant | 2-3x Redundant |
| Hardware Diversity | Sometimes | Yes | Yes | Sometimes |
| Software Diversity | Sometimes | No | No | Yes |

**Table 5. Comparison of accelerator safety system criteria with that of other industries.**

# TiN COATING OF THE PEP-II LOW-ENERGY RING ALUMINUM ARC VACUUM CHAMBERS

K. Kennedy, B. Harteneck, G. Millos, *Lawrence Berkeley National Laboratory*
M. Benapfl, *Lawrence Livermore National Laboratory*
F. King and R. Kirby, *Stanford Linear Accelerator Center†*

*Abstract*

The PEP-II Low-Energy Ring will operate at a nominal energy of 3.1 GeV with a positron beam current of 2.1 A. Design parameters for vacuum components are 3.5 GeV at 3 A. The arc vacuum system is based on an aluminum antechamber concept. It consists of 192 pairs of 2 m long magnet chambers and 5.5 m long pumping chambers. Titanium nitride coating of the entire positron duct is needed in order to suppress beam instabilities caused by multipactoring and the "electron-cloud" effect. An extensive R&D program has been conducted to develop coating parameters that give proper stoichiometry and a suitable thickness of TiN. The total secondary emission yield of TiN-coated aluminum coupons has been measured after the samples were exposed to air and again after electron-beam bombardment. A coating facility has been built to cope with the large quantity of production chambers and the very tight schedule requirements.

## 1 Introduction

An instability was observed at the Photon Factory [1] which was later analyzed [2] and attributed to trapped "electron clouds." The origin of these clouds is thought to be the amplification of photo-electrons by secondary electron multiplication at the surface of the vacuum chamber. The tendency for this amplification can be predicted from the total secondary electron yield (SEY) which, for most metals (when averaged over primary energies of 0 to 1000 volts), is slightly above 1. The yield for aluminum, with its native oxide, tends to be much greater than 1 (typically 3-5 at peak yield). The PEP II Low Energy Ring (LER) will have 3 A of positrons with aluminum vacuum chambers in the arcs, conditions which are expected to show the cloud effect.

A SEY-lowering coating is needed on the chamber walls, if electron clouds are to be avoided. This coating will constitute the inner surface of the vacuum system and must have properties consistent with that role. These include: 1) low vapor pressure , 2) moderately good electrical conductivity, 3) good thermal stability and, 4) low ion-induced gas desorption yield. Titanium nitride (TiN) has the needed properties.

## 2 Titanium Nitride

TiN has a boiling point above 3000K and an electrical conductivity above that of titanium. The nitrogen is covalently-bonded to the titanium without destroying electrical conductivity. TiN has been used previously in storage rings, in places where a low SEY is necessary such as rf cavities. TiN can have a SEY that averages below one.

A thin coating of TiN must be put on all surfaces of the arc vacuum chambers that are effected by the electric field of the positrons. The coating must be thin because the thermal expansion of TiN is one third that of aluminum. A thick coating would create high stress between the TiN and the aluminum. The coating must, however, be thick enough to resist "20 years of ion bombardment". A 50 nm TiN film has been calculated to withstand such primarily hydrogen-ion bombardment, using conservative assumptions.

Thermal dissociation of TiN makes an evaporative coating process impractical; however, titanium itself can be deposited by sublimation or sputtering and reacted with nitrogen gas to form a TiN deposit. Sputtered titanium ions arrive with some kinetic energy at the wall and adhere better than thermal energy atoms. This is the preferred choice for a stable coating.

## 3 Vacuum Chambers

The LER vacuum system has six arc regions made of two types of 6063 aluminum alloy vacuum chambers. The profiles are shown in Figure 1. The magnet chamber is 2 m long with a 1.875° bend and the pumping chamber 5.5 m long. The positrons circulate in the elliptical chamber, with their electrical field the largest on the minor axis dropping off rapidly in the antechamber.

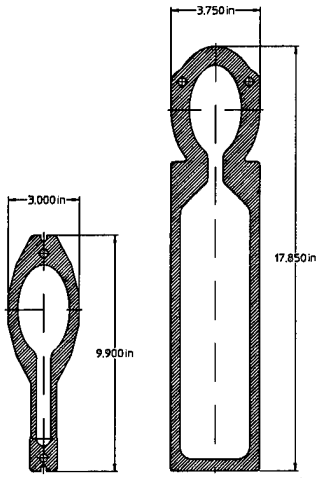



Figure 1: Magnet and Pumping chambers

## 4 Sputtering

*4.1 Selection Process*

The sputtering method chosen needed to be able to readily coat 5.5 m-long chambers with 100 nm or so of TiN with

Work supported by the US. Department of Energy under contract numbers DE-AC03-76SF00098 (LBNL), W-7405-Eng-48 (LLNL), and DE-AC03-76SF00515 (SLAC).

0-7803-4376-X/98/$10.00 © 1998 IEEE

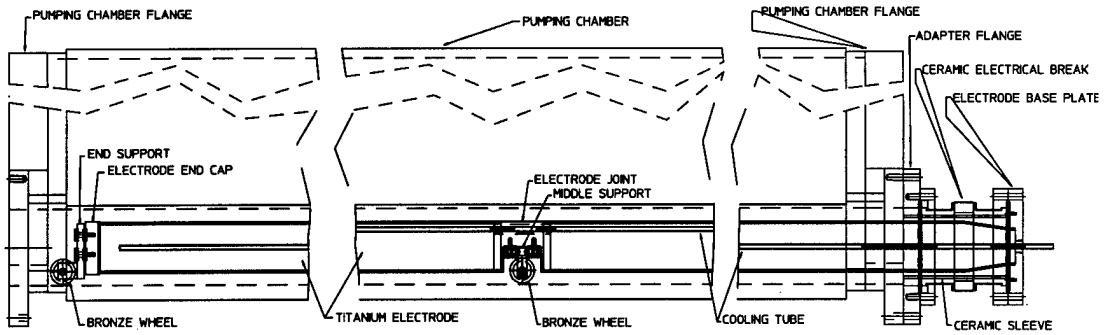


Figure 2: Titanium cathode shown in vacuum chamber

the sputtering source being easily reproducible for high production rate use and with reliable operating parameters. DC diode sputtering with a shaped-crossection cathode met the requirement. The cathode can be made virtually any length needed provided it can be centered, supported and insulated. The shape of the cathode determines the deposition rate ratio for the major and minor axis.

*4.2 Cathode design and fabrication*

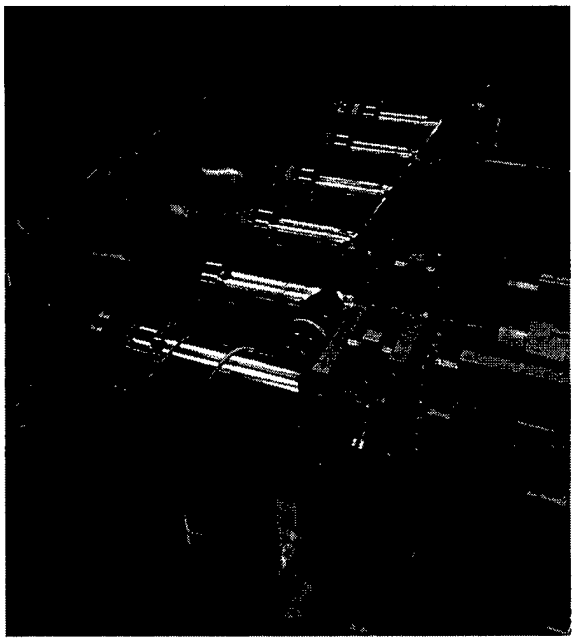
The sputtering cathode has to reflect the shape of the substrate being coated. To get a uniform coating thickness, however, the perfect cathode shape would take into account the effect of radius of curvature on electric field. A constant gap between the cathode and inside surface of the beam duct gives adequate thickness uniformity and was adopted for our purposes.

The cathode was made by forming a round 48 mm titanium tube in a closed die to make an elliptical tube that would create a uniform annulus with the vacuum chamber. The space left for a sputtering plasma, 15 mm, is very small and created the need to run at relatively high pressure. To increase the gap between the cathode and the vacuum chamber wall by only 5 mm would decrease minor diameter of the cathode to an unusable 15 mm.

The 2 meter cathode could be supported at the ends and have an acceptable deflection in the center. The vacuum feedthrough created one of the insulating supports and an insulating wheel at the end of the electrode was the other support. The 5.5 meter electrode for the pumping chamber needed an additional center support as shown in Figure 2.

*4.3 Vacuum system*

The vacuum chambers had to be baked before and possibly after coating, so coating and baking facilities were combined. Processing multiple chambers is required to achieve the production goal of 8 chambers per week The vacuum system was built around a manifold that could accommodate 6 chambers and was pumped by a 250 l/s turbo pump and a 400 l/s ion pump. Attached to the manifold was an ion gauge, an RGA and a capacitance manometer as shown in Figure 3. Up to 6 chambers can be installed over permanently attached electrode. The process gas is introduced to each vacuum chamber at the end opposite the vacuum manifold. The process gas is regulated by a piezoelectric valve controlled by the capacitance manometer. After the piezoelectric valve reduces the process gas pressure to 250 mTorr the gas passes through a liquid nitrogen trap to remove any water.


Figure 3: TiN coating oven

*4.4 Operation*

The vacuum chambers are installed in the coater/bakeout oven, baked into the turbo for 4 hrs and baked into the ion pump for 60 hr. The system is then pumped by the turbo through a 2 mm orifice, the pressure controller is set for 224 mTorr, the premixed 20% $N_2$-80% Ar is turned on and liquid $N_2$ is added to the trap. When pressure equilibrium is established, the electrodes are energized. A single variable-voltage 1500 V power supply powers the multiple electrodes. Each electrode has a 250 Ω resistor that limits the current from arcs. The power supply voltage is adjusted until the current to each electrode averaged 1.5 A. The current distribution to the electrodes was uniform to about ±5%. After 16 hours the process gas is turned off and the system pumped by the ion pump to remove any argon and verify that the chamber is leak free.

Process Parameters

| | |
|---|---|
| Process Gas Composition | 80%A-20% $N_2$ |
| Current Density [A/cm$^2$] | $2x10^{-4}$ |
| Cathode Potential [V] | 1000 |
| No. of N Atoms Entering [/sec/cm$^2$] | $2.7x10^{+13}$ |
| No. of Molc of TiN Formed [/sec/cm$^2$] | $1.2x10^{+13}$ |
| No. of Ions [/sec/cm$^2$] | $1.2x10^{+15}$ |
| No. of $N_2$ Molc. Landing [/sec/cm$^2$] | $1.0x10^{+20}$ |
| Time to Form a 100 nm Film [sec] | $4.3x10^{+4}$ |

## 5. Film Characterization

*5.1 Stoichiometry*

Measurements of the film stoichiometry, thickness and secondary yield were done with sectioned pieces of coated chamber and, routinely, aluminum witness coupons mounted in the beam-position-monitor ports of the chambers being processed/coated. Stoichiometry was measured by x-ray photo-electron spectroscopy (XPS) [3] with Ti/N ratios consistently in the 0.9-1.1 range. The information depth for this method is a few nanometers.

*5.2 Film Thickness*

Film thickness was determined in the same analytical unit by low-energy x-ray fluorescence spectrometry (LEXRF), a technique originally developed [4] to measure ultra-thin silicon oxide layers on silicon. In the present application of this method, the exciting x-ray energy is tuned to just-above the absorption energy edge of the titanium K-alpha x-ray emission line, thereby maximizing its fluorescence yield. The absorption length of the now-excited titanium x-ray is large compared to the film thickness and, if suitable TiN thickness standards are available, a linear calibration plot of fluorescence intensity vs. film thickness can be constructed. Then, measuring an unknown film thickness under identical conditions readily gives a non-destructive measurement. Coating runs of 16 hrs gave thicknesses in the range of 90-140 nm, depending on the coupon location in the chamber and the accuracy with which the cathode was radically located. Thicknesses above 30 nm were sufficient to completely obscure the aluminum substrate to XPS.

*5.3 SEY Measurements*

After the as-coated and exposed-to-air non-surface-modifying measurements described above, the coated pieces were transferred to a second system where the SEY measurements [3] were made. The total SEY was measured, for normal incidence, from 50-1000 eV primary energy at very low current density (to minimize surface modification effects). The as-deposited /air-exposed very low-electron-dose yield (Figure 4, inset) is determined by the presence of an adventitious surface water layer. Electron bombardment of this layer, similar to the initial processing expected during machine-commissioning, desorbs the layer and also causes electron-induced adsorption of carbon from carbon-containing residual-gas molecules. The water desorption and small amount of carbon deposition serve to reduce the peak SEY to near 1 (Figure 4, graph). This yield is near the expected in-situ as-deposited value [3].

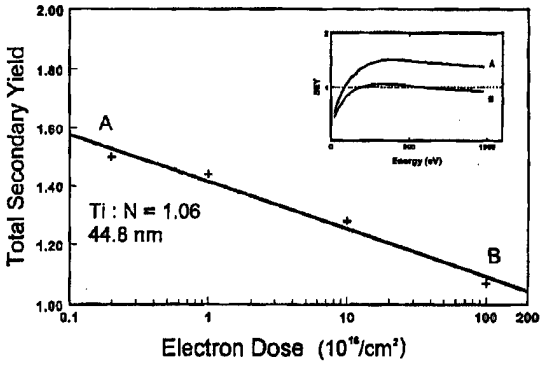



Figure 4: Secondary electron yield as a function of electron dose and primary energy

## REFERENCES


[1] M. Izawa, Y. Sato and T. Toyomasu, Phys. Rev. Lett. **74**, 5044 (1995).

[2] K. Ohmi, **Proc. EPAC96**, Barcelona, Spain, June 10-14, 1996, p. 1042.

[3] E.L. Garwin, F.K. King, R.E. Kirby and O. Aita, J. Appl. Phys. **61**, 1145 (1987).

[4] R.E. Kirby, D. Wherry and M. Madden, J. Vac. Sci. Technol. **A11**, 2687 (1993).

# BREMSSTRAHLUNG MEASUREMENTS AT THE ESRF

P. Berkvens, P. Colomp, ESRF, BP220 38043 Grenoble Cedex, France

*Abstract*

Increased bremmstrahlung radiation levels were observed around several ESRF beamlines, which had been equipped with new insertion device vacuum vessels with a reduced vertical aperture. In order to understand the origin of this increased radiation, detailed bremsstrahlung measurements have been carried out on several beamlines. This paper describes the results of these measurements. The measurements allowed the dose levels originating from the gas-bremsstrahlung component to be quantified. However, precise vertical profile measurements have clearly indicated the presence of a second bremsstrahlung component, due to a scraping effect of the electron beam at these reduced vertical apertures. It was shown that the latter component could easily be the predominant one in the radiation dose levels observed around the beamlines. The curing effect of changing the storage ring optics from a high β to a low β optics was clearly demonstrated.

## 1 INTRODUCTION

People working on the beamlines in the Experimental Hall of the ESRF are not considered as workers exposed to radiation. Therefore the shielding of the beamline hutches must guarantee dose rates below 2.5 μSv/h. In order to allow for a certain error in the dose measurements, as well as anticipating new legal dose limits (based on ICRP 60), our aim is not to exceed measured levels of 0.3 to 0.4 μSv/h.

The use of an X-ray shielding computer code, developed at the ESRF, as well as a by now well-established hutch construction standard, has resulted indeed in such low dose rates.

However, in 1995, increased radiation levels were measured around a number of beamlines, which had been equipped with new 5 metre long insertion device vessels, with a reduced vertical aperture (11 mm internal gap). This increased radiation, although still relatively low (a few μSv/h) presented a big problem in view of our general radiation protection policy.

This paper describes the origin of this radiation, as well as the solutions which were adopted to solve the problem.

## 2 SHIELDING REQUIREMENTS FOR ESRF BEAMLINES

Synchrotron beamline hutches must provide shielding against two distinct radiation sources: synchrotron radiation and bremsstrahlung. In the case of the ESRF the lateral shielding of these hutches will be determined by the synchrotron radiation. Indeed, the high power of the synchrotron sources (both insertion devices and bending magnets) and the high critical energies (up to several 10 keV) imply that a lot of scattered radiation is produced on the various optical elements. The bremsstrahlung radiation on the other hand, although highly penetrating, requires essentially shielding in the forward direction. Scattering at larger angles is due to multiple scattering of electrons and delta-ray production. These processes are much weaker than the Compton scattering of hard X-rays. Shielding against bremsstrahlung therefore essentially requires the addition of a typically 1 $m^2$ wide, 10 cm thick lead wall on the hutch back wall, centred around the 0° beam axis.

The spectrum below, measured with a Ge detector behind the side wall of a hutch, shows indeed a pure X-ray spectrum. One sees the primarily Compton scattered X-ray contribution, lower energy, multiple scattered X-rays (mainly in the shield wall) and the lead fluorescent rays.

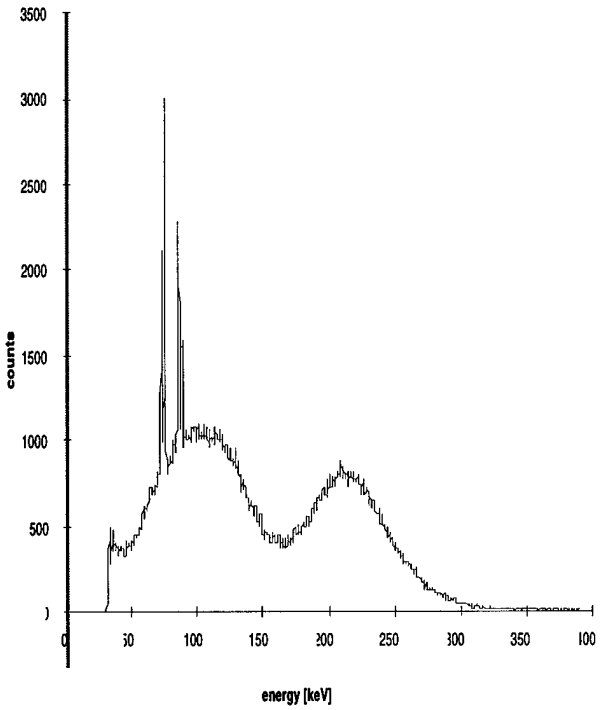



Figure 1: Example of a measured X-ray spectrum behind an optics hutch side wall.

When in 1995 new insertion device vacuum vessels, with smaller vertical aperture (11 mm internal gap) were installed, increased radiation levels outside the beamline hutches were measured (of the order of a few μSv/h). It turned out that this radiation, after an initial period needed

0-7803-4376-X/98/$10.00 © 1998 IEEE

for the vacuum conditioning of these new vessels, persisted only on insertion device beamlines, installed on high β straight sections. This radiation was clearly identified as bremsstrahlung. Indeed, spectra measured with a Ge detector showed the presence of high energy photons. As an example we show one of these spectra. The presence of 511 keV annihilation photons is a clear footprint of bremsstrahlung photons. It is clear that, because of the decreasing detector efficiency with increasing energies, the measured dose rates are mainly due to these high energies.

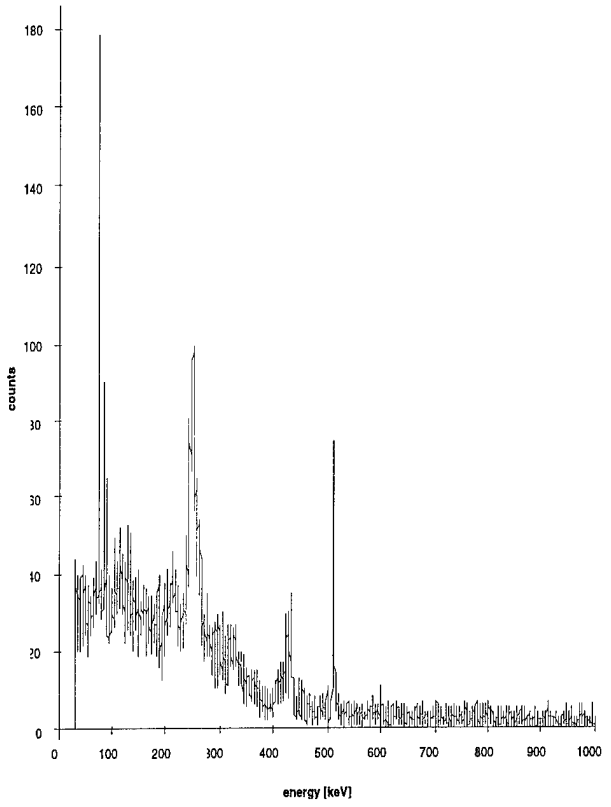



Figure 2: Example of a bremsstrahlung dominated spectrum, measured behind an optics hutch side wall.

## 3 BREMSSTRAHLUNG MEASUREMENTS

Initially some confusion existed about the origin of this radiation. Either it was gas bremsstrahlung, due to increased vacuum level inside the 5 metre long vessels (pumping is only foreseen at the two extremities of the vessel, and a higher gradient could not be excluded due to a reduced conductance) or the bremsstrahlung originated from a more direct interaction mechanism between the electrons and the reduced aperture ("scraping" effect).

Therefore, in order to identify the source of this increased radiation, more detailed measurements were carried out. Bremsstrahlung profiles were measured using a small ionisation chamber (0.6 $cm^3$ Farmer type chamber). This chamber was scanned vertically through the bremsstrahlung beam, behind a 3 cm thick lead wall. This lead wall eliminated possible scattered synchrotron radiation from the upstream and downstream dipole, and also provided sufficient dose build-up for the high energy radiation.

Several measurements were made. One measurement was carried out on a low β straight section, following the evolution of the bremsstrahlung during the vacuum conditioning of a newly installed 11 mm vessel. This measurement proved a normal behaviour, with a correct vacuum conditioning, and the bremsstrahlung intensities were completely proportional with the product of pressure and current.

The presence of another bremsstrahlung source on high β beamlines was clearly demonstrated by measurements done with various scraper settings. There are two sets of horizontal and vertical scrapers installed on the ESRF storage ring. The measurement shown below was carried out on a high β beamline, which in terms of phase advance is normally well-protected by these scrapers. One can see that, when opening the scrapers completely, a drastic increase in bremsstrahlung was observed. This measurement proved unambiguously the presence of a "scraping" effect made by these new vessels. Monte Carlo calculations would indicate that even with the scrapers in their nominal position, part of the radiation is still due to this scraping effect.

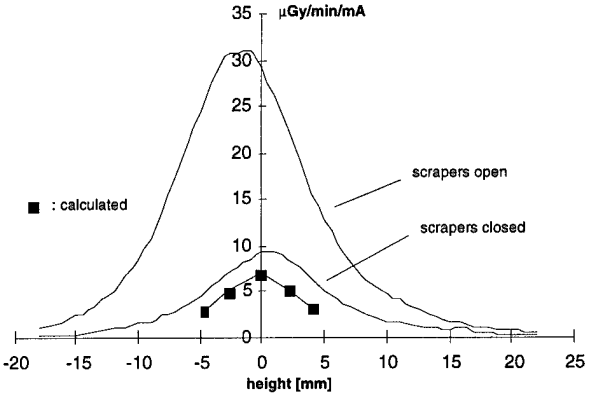



Figure 3: Measured vertical bremsstrahlung profiles for two extreme scraper settings. The expected dose profile from Monte Carlo calculations is also shown.

When looking at these 2 profiles in more detail, one observes a clear vertical offset between the two, indicating indeed a different origin (beam axis for the gas bremsstrahlung, vessel wall for the "scraping" induced bremsstrahlung).

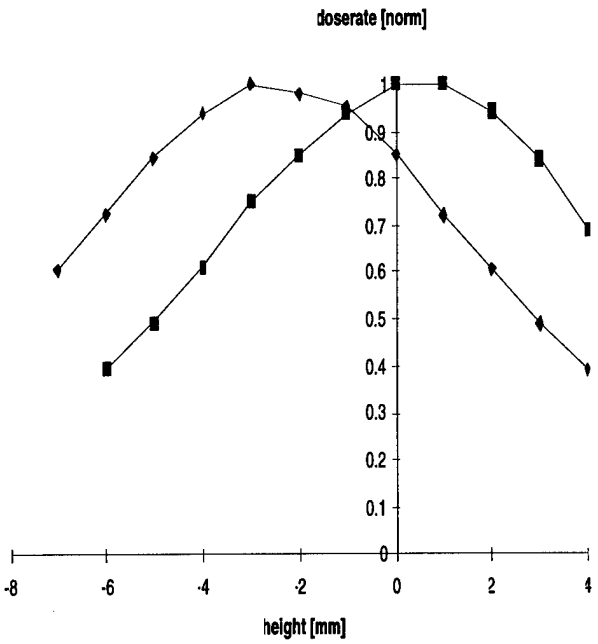



Figure 4: Vertical offset between the two bremsstrahlung profiles.

## 4 LOW BETA OPTICS

As mentioned above, the increased radiation levels only remained after the initial vacuum conditioning period on those beamlines installed on high β straight sections. The ESRF lattice alternates low β ($\beta_{vertical}$ = 3.51 m) with high β ($\beta_{vertical}$ = 12.85 m) cells. A new lattice was tried out, putting all the cells into low beta optics. The measurements reported above were repeated on the same beamline, with the storage ring operated in this new low beta optics, and the results are shown below. As can be seen, there is no more effect of the scraper position on the measured bremsstrahlung profiles. Also, these new profiles are now slightly lower, corresponding very well with the calculated levels shown in figure 3. This result therefore clearly shows that with this new low β optics, the bremsstrahlung originating from the "scraping" effect completely disappears, and that the residual bremsstrahlung spectrum can be completely attributed to gas bremsstrahlung.

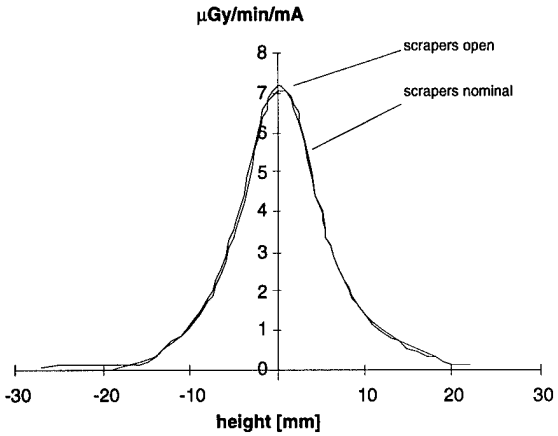



Figure 5: Measured vertical bremsstrahlung profiles for two extreme scraper settings, for the new low β lattice.

We also verified that no extra radiation was measured on the originally low β beam lines.

Since the end of 1996 the storage ring is now permanently operated in this new low β optics, and the bremsstrahlung problems on all the beamlines have dissapeared.

## 5 CONCLUSION

This experience at the ESRF clearly demonstrated the radiation problems that can be caused by localised beam losses in the straight sections used for beamlines. In the case of the ESRF, the local beam losses were caused by the bottleneck effect produced by the reduced vertical aperture of the new insertion device vacuum vessels. The bremsstrahlung produced by these "scraping" effects can be much higher than the expected gas bremsstrahlung, and produces radiation which is vertically off-centred with respect to the synchrotron beam.

At present new insertion device vacuum vessels are being tested at the ESRF, with a further reduction of the vertical aperture (9 mm internal gap). Up to now bremsstrahlung measurements carried out show a correct vacuum conditioning of these vessels, as well as no evidence of any scraping effect. Further measurements will be carried out before these vessels are installed on operational beamlines.

# DESIGN AND ANALYSIS OF A BE WINDOW FOR THE APS DIAGNOSTICS UNDULATOR BEAMLINE

I. Ching Sheng, B. X. Yang and S. Sharma
Advanced Photon Source, Argonne National Laboratory
9700 South Cass Avenue, Argonne, Illinois 60439 USA

*Abstract*

The design of a beryllium (Be) window for use under the extremely high heat load of an undulator beam is one of the challenges for third-generation synchrotron radiation beamlines. A novel design of a Be window is presented for the Advanced Photon Source (APS) diagnostics undulator beamline, whose beam has a peak power density of 150 W/mm$^2$ (7 GeV/100 mA stored beam). The window has a double concave profile with a thickness of 0.5 mm at the center and is brazed to a water-cooled oxygen-free, high-conductivity (OFHC) copper manifold. Finite-element thermal analysis of the Be window is also presented.

## 1 INTRODUCTION

The APS diagnostic insertion device (ID) beamline uses both bending magnet and undulator radiation for beam imaging. To maintain the vacuum integrity of the storage ring, windows are required to separate the beamlines from the ring. Since the power density of the undulator beam is extremely higher than that of the bending magnet, the following design criteria are considered:

- Reduced absorption of x-ray beam power.
- Enhanced conductive and convective cooling to reduce the temperature gradient.
- Ability to withstand vacuum force in case of leak in the beamline.
- Large window stiffness to increase thermal buckling threshold.
- Ease of fabrication.

To satisfy the above design considerations, we utilize Be as the windows material for its low absorption of x-ray and high material strength. A concave-shaped window is introduced to meet the other goals above. With a thickness of 0.5 mm, Be absorbs 5% of the 800 W total power of the diagnostic undulator at 100-mA beam current in APS. For the bending magnet radiation a second window, consisting of a 1-mm flat disk of Be, is used because it absorbs much less power.

## 2 DESIGN AND FABRICATION

Previous studies have shown that the major cause of failure of a Be window in an x-ray beamline is thermal buckling. The design of a conventional, flat Be window is often the result of compromise between two considerations:

- Thicker windows increase the thermal conduction as well as flexural stiffness.
- Thicker windows increase absorbed power.

We introduce a double concave window which significantly improves the thermal conduction and flexural stiffness without increasing the absorbed power. We use 99.4% pure beryllium in our design. As shown in Figure 1, the 0.2-mm undulator beam will pass through at the center of the Be window, where the thickness is only 0.5 mm. This concave Be window has three advantages: it absorbs less power when beam is aligned, it provides larger conductive area for heat flow, and it is structurally stiff which prevents thermal buckling.

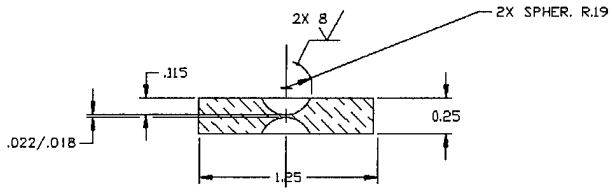



Figure 1: Cross section of the double concave Be window (dimensions are in inches).

The Be window assembly is shown in Figure 2. Two 50-mm 304 stainless tubes are brazed with a water-cooled OFHC copper manifold; Be windows are then diffusion-brazed on the counterbores of the manifold by using silver-copper-based alloy. Three circular water channels are drilled in the copper block for cooling. The assembly is machined and brazed by Brush Wellman Company. Two of the window assemblies are mounted in series (as shown in Figure 3) with an ion pump in between for pumping.

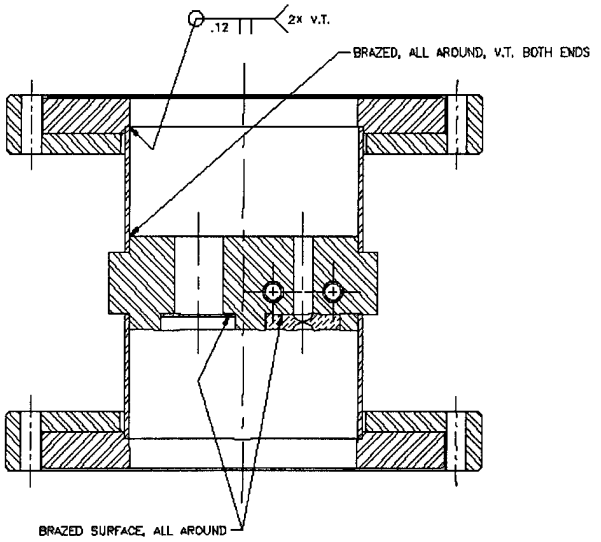



Figure 2: Cross-section view of the Be window assembly.

0-7803-4376-X/98/$10.00 © 1998 IEEE

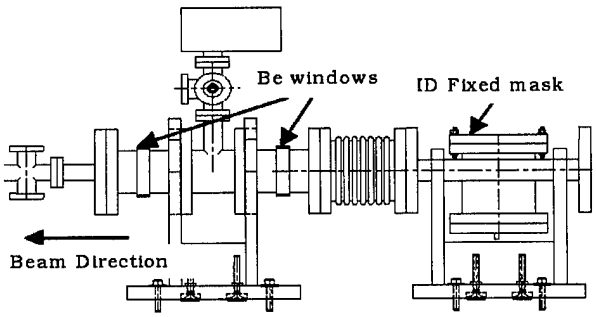



Figure 3: Be windows assembly.

## 3 THERMAL ANALYSIS

### *3.1 Thermal Analysis - Beam at Center*

An axisymmetric finite-element model is used to calculate the temperature rise, assuming a constant temperature of 0°C at the brazed joint. The results are plotted as temperature contours in Figure 4. A peak temperature rise of 61°C is obtained at the center of the double concave area.

The temperature rise between the braze joint and water channels is determined by a simplified one-dimensional model. The brazing area can be treated as a heating strip with area of 1 cm (width) × 9.2 cm (height, parallel to the cooling channel), with incident total power of 40 W. An equilibrium power density (q) on this heating strip is 4.3 W/cm$^2$. The average conductance path (l) from the braze joint to the water channel is 1 cm. Using 1 W/(cm$^2$ k) for the water film coefficient (h), the temperature rise between the braze joint and cooling channels is determined as [1]

$$\Delta T = q\left(\frac{l}{k}+\frac{1}{h}\right) = 4.3\left(\frac{0.9}{3.6}+1\right) = 5.4\ ^\circ C,$$

where k=3.6 W/(cm °C) is the thermal conductivity of the OFHC copper. Summing up the two temperature increases, the peak temperature rise on the Be window is approximately 66°C.

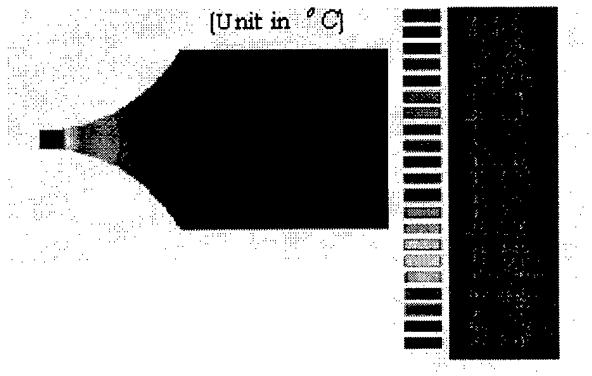



Figure 4: Axial symmetrical temperature contours on a Be window.

The critical buckling load on a circular plate [2] is proportional to $t^3/a^2$, where t is the thickness and a is the radius of the plate. Since the outer thickness of the Be window is large (6.4 mm) compared to that at the center (0.5 mm), the effective radius a reduces from 32 mm to approximately 3 mm. The buckling threshold is therefore increased by 100 times compared to that of a flat plate with the same 0.5-mm thickness. Detailed analysis for thermal buckling of circular disks under x-ray heating are presented in [3] and [4].

### *3.2 Thermal Analysis - Missteered Beam*

A beam missteering situation is also analyzed. We assume that the undulator beam is incident off-centered on the window. A higher percentage of the undulator power is absorbed (30%, or 240 W) because of the increase in Be thickness in the beam path. Figure 5 shows the temperature contour plot where the peak temperature rise is 147°C. Further investigation is in progress to determine the maximum safe temperature rise.

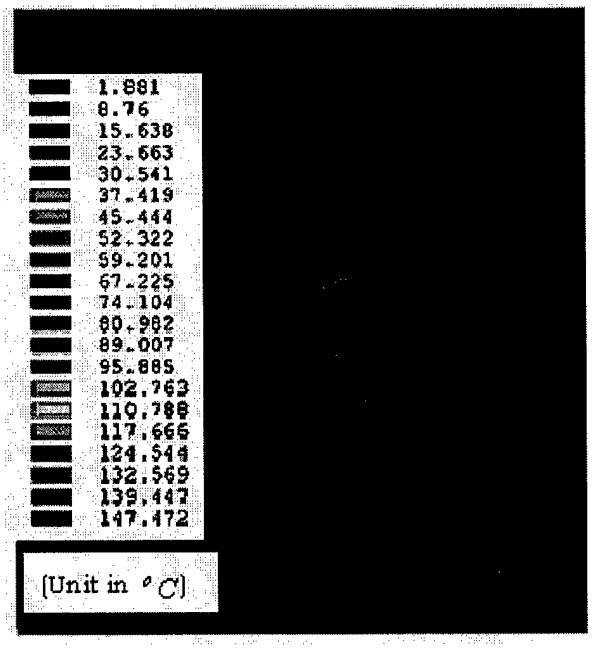



Figure 5: Temperature contours in a Be window due to beam missteering.

## 4 CONCLUSION

A novel Be window design of double concave geometry has been presented. In this window geometry the absorbed beam power is reduced at the thinner center while heat conduction is increased at the thicker outer periphery. The double concave shape is structurally stiff and prevents thermal buckling. The window has been installed and used in the APS diagnostics undulator beamline.

## 5 ACKNOWLEDGMENTS

The authors would like to thank Ms. Catherine Eyberger for editing this paper. The work is supported by the U.S. Department of Energy, Office of Basic Energy Sciences, under Contract No. W-31- 109-ENG-38.

## 6 REFERENCES

[1] J. P. Holman, *Heat Transfer*, McGraw-Hill Book Company, 1977.

[2] S. P. Timoshenko and J. M. Gere, *Theory of Elastic Stability*, McGraw-Hill Book Company, 1961.

[3] H.L. Nian, T. M. Kuzay and I. C. Sheng, "Thermal Buckling Parametric Analysis for a Diamond Disk for an X-ray Beamline at the Advanced Photon Source," *Rev. Sci. Instrum.* **67** (9), September 1996.

[4] I. C. Sheng, B.X. Yang and S. Sharma "A Be Window on an APS Diagnostic Beamline," to be published in SPIE97 conference proceedings.

# IN SITU MEASUREMENT OF CERAMIC VACUUM CHAMBER CONDUCTIVE COATING QUALITY

C. Doose, K. Harkay, S. Kim and S. Milton
Advanced Photon Source, Argonne National Laboratory
9700 South Cass Avenue, Argonne, Illinois 60439 USA

*Abstract*

A method for measuring the relative surface resistivity and quality of conductive coatings on ceramic vacuum chambers was developed. This method is unique in that it allows one to test the coating even after the ceramic chamber is installed in the accelerator and under vacuum; furthermore, the measurement provides a localized surface reading of the coating conductance. The method uses a magnetic probe of wire wound on a ferrite and an LCR meter. The probe is calibrated using the measured DC end-to-end resistance of the tube under test and by comparison to a high quality test surface. The measurement method has also been verified by comparison to high frequency impedance measurements. A detailed description, results, and sensitivity of the technique are given here.

## 1 INTRODUCTION

The Advanced Photon Source (APS) is a national facility dedicated to the generation of highly-brilliant X-rays for use in scientific and industrial research [1]. The facility consists of four machines: a linear accelerator capable of generating 450-MeV positrons, a positron accumulator ring, a booster synchrotron for accelerating the positron beam up to 7 GeV, and the 7-GeV storage ring. The three circular machines use fast-pulsed kicker magnets for injection, extraction, and beam diagnostics. Ceramic vacuum chambers, coated internally with a conductive material, are used at the location of these kicker magnets. The conductivity of the coating is adjusted to allow the kicker magnetic fields to penetrate the vacuum chamber wall while at the same time providing a relatively low resistance path for the beam image charges.

Two storage ring kicker vacuum chambers overheated during the first high-beam current runs of 100 mA. It quickly became clear that the conductivity of the ceramic chamber coatings was either damaged or significantly lower than desired. Since these chambers were installed in an operational machine, a new method to measure their conductivity in situ was developed in order to test the coatings without opening the ring vacuum system.

## 2 CONDUCTIVE COATING ON CERAMIC CHAMBER

A typical ceramic vacuum chamber for the storage ring is made of 99.7% pure alumina. Figure 1 shows a typical cross section of the chamber, with a sensor coil on top. The chamber has a wall thickness of 3.2 mm, an axial length of 74 cm, and an inner circumference of approximately 23 cm. Details of the chamber and coating procedure are described in reference [2].

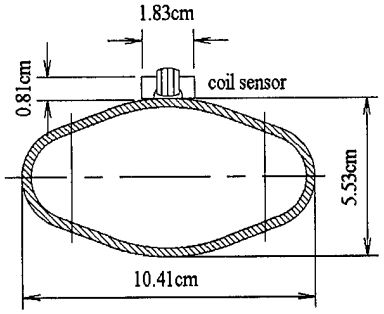



Figure 1: Ceramic chamber cross section showing the sensor coil.

The coatings of the ceramic vacuum chambers are subjected to both eddy currents due to the kickers' pulsed magnetic fields, and the beam image currents. A compromise is needed in coating thickness and conductivity in order to adequately conduct image currents while not significantly shielding the kicker magnetic field. If care is not exercised in the selection of the conductivity, the power and current densities can become quite high and damage the coating or ceramic. The choices of conductivity and thickness of the coatings used on the ceramics were based on a number of factors, with the first being a minimization of the power density seen by the coating. After arriving at this initial value, the conductivity was adjusted to insure that the impact on machine performance or the kicker magnet field itself were not seriously compromised [2], or approaching any damage threshold of the coating.

The coating chosen for the storage ring ceramic vacuum chambers is a resistor paste commonly used in the semiconductor industry, Heraeus Cermalloy type 410 resistor material. The paste when applied and sintered as per the application specification, has a surface resistivity of 0.1 Ω/square, and a bulk resistivity of $2 \times 10^{-6}$ Ω-m.

0-7803-4376-X/98/$10.00 © 1998 IEEE

Given the dimensions of the ceramic chamber the DC end-to-end resistance is roughly 0.3 Ω when the coating is properly applied.

## 3 MEASUREMENT SYSTEM AND CALIBRATION

The sensor coil shown in Figure 1 is essentially a metal detector. It was constructed to provide a means to measure the local surface resistivity of the coating with the ceramic vacuum chamber still installed in the ring. The sensor consists of a 200-turn coil wound on the bottom of a "U" shaped ferrite core 2.86 cm long, 1.83 cm wide, and 0.81 cm high. Because the coil is effectively an eddy current sensor, the geometry of the core was chosen in an attempt to maximize the magnetic coupling between the coil and the coating. It was found that high-Q sensor coils, although more sensitive, had poor measurement stability. The use of manganin wire, with a resistance of 11.8 Ω/m and a diameter of 200 μm, "de-Q'd" the sensor coil and so improved the stability of the measurements. Also, because of its' relatively low temperature coefficient of resistivity, the use of manganin wire improved temperature stability of the AC resistance measurements compared to the use of copper wire.

The sensor coil is placed on the exterior surface of the ceramic chamber, and an AC signal (100 kHz, 1 V rms) is applied to the sensor coil using a Hewlett Packard 4263A LCR meter. By comparison, the effective frequency of the pulsed kickers is 143 kHz (3.5 μsec pulse-width). The AC field generated by the coil penetrates the conductive coating and creates eddy currents. The induced eddy currents, in turn, create a field that opposes the driving coil field. The change in effective impedance of the sensor coil, when coupled to the coating, is equivalent to adding a series impedance (coupled impedance) to the sensor coil. The measured impedance of the coil is then the nominal coil impedance (the ACR is 200 Ω and XL is 2.3 kΩ at 100 kHz) plus the coupled impedance $Z_c$. For coating thickness less than approximately one tenth of the skin depth at the measurement frequency, the eddy current density is essentially uniform throughout the coating, and the coupled resistance, $R_c$, is therefore proportional to the surface conductivity. Due to the local extent of the sensor coil field, approximately 28 cm$^2$, compared to the area to be measured of 1732 cm$^2$, the method makes it possible to measure the local surface resistivity of the chamber coating and so map out the quality of the coating over the entire ceramic surface.

The equivalent circuit of the sensor coil coupled to a conductor is shown in Figure 2. The resistive and reactive components of the coupled impedance due to a conductor are given by:

$$R_c = \frac{R_2 \cdot (\omega \cdot M)^2}{R_2^{\,2} + (\omega \cdot L_2)^2}$$

$$X_c = -j\omega \cdot \left[ \frac{L_2 \cdot (\omega \cdot M)^2}{R_2^{\,2} + (\omega \cdot L_2)^2} \right]$$

where $R_2$ and $L_2$ are the effective resistance and inductance of the coating. The mutual inductance, $M$, is a function of coil geometry, distance from the coil to the conductor, and conductor thickness.

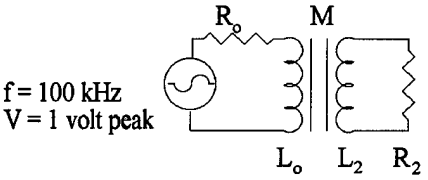



Figure 2: Schematic of sensor coil coupled to a conductor.

Measurements were performed to confirm the linearity of the measured coupled resistance to surface resistivities near 0.1 Ω/square. The coupled resistance and reactance were measured for different thickness of stainless steel sheets. The surface resistivity of a 12.7 μm sheet, using a bulk-resistivity of $\rho = 7 \times 10^{-7}$ Ωm, is approximately 0.06 Ω/square (60 % of the desired value of the chamber coating). As shown in Figure 3, the increase of the coupled resistance is approximately linear to the thickness of the sheets, with a slope of 2.7 Ω/μm for thickness less than 100 μm. This is equivalent to surface resistivities of greater than 0.007 Ω/square.

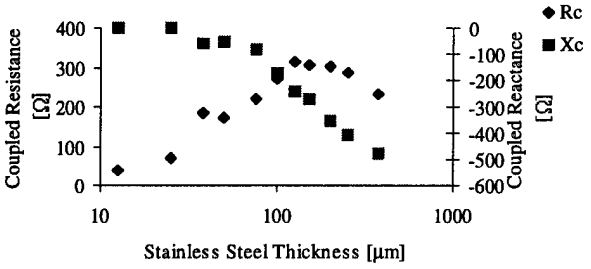



Figure 3: Measurement of coupled impedance vs. stainless steel sheet thickness.

To determine the effects of chamber wall thickness variations on the coupled resistance, measurements were performed to determine the sensitivity to height above a 12.7-μm-thick stainless steel sheet. Figure 4 shows the relationship of the coupled resistance vs. height above the sheet. The measured coupled resistance in the region within 3 mm of the sheet falls off at a rate of roughly 7 Ω/mm. With a measurement resolution of 1 Ω and a coating surface resistivity of 0.1 Ω/square the system is insensitive to ceramic vacuum chamber wall thickness variations of less than approximately 0.3 mm.

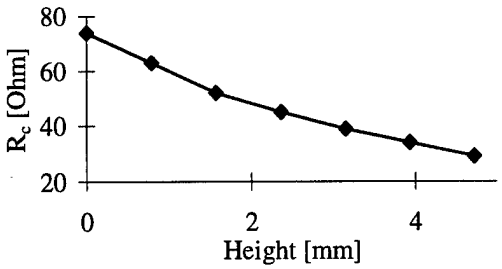



Figure 4: Measurement of the coupled resistance vs. height above a 12.7-μm stainless steel sheet.

Coupled resistance measurements of the coating on a good quality chamber (reference chamber) were compared to measurements of the installed chamber coatings. The reference chambers' end-to-end DC resistance was known to be 0.4 Ω ±0.05 Ω. The average coupled resistance value for the reference chamber was 13 Ω with a standard deviation of 2.5 Ω. Given the end-to-end DC resistance and the chamber geometry, an average surface resistivity of 0.13 Ω/square (with an uncertainty of ±10%) was calculated for the reference chamber. The maximum surface resistivity measurable with this system when the coil is 3 mm from the coating surface is approximately 1.3 Ω/square.

## 4 CERAMIC CHAMBER MEASUREMENTS

In situ measurements on the suspect ceramic vacuum chambers using the sensor coil revealed the cause of the heating to be a lack of sufficient conductive coating. In fact, the coating surface resistivity was so large on two chambers that it was beyond the measurement resolution of the sensor coil system. After removal from the storage ring it was found that the end-to-end DC resistance of one chamber was greater than 1 MΩ. The second chamber's DC resistance was 320 Ω, these are to be compared to the desired value of 0.3 Ω.. Measurements on new spare chambers, before their installation into the machine, revealed another defect, and that was uneven coating along the length of the chamber as shown in Figure 5. This was caused due to sagging of the liquid coating during the initial curing process of the coating on the chamber (the chamber had been mounted vertically). After correcting the sagging problem, subsequent chamber coating quality has met design requirements as shown in Figure 6.

The sensor coil results were also verified on the bench using a high-frequency transmission measurement. Probes were inserted through plates on either end of the chamber to form a cavity and a network analyzer was used to excite the cavity modes. The widths, or quality factors, of these modes are determined by the surface resistivity of the chamber coating and the volume and surface area of the cavity. The calculated surface

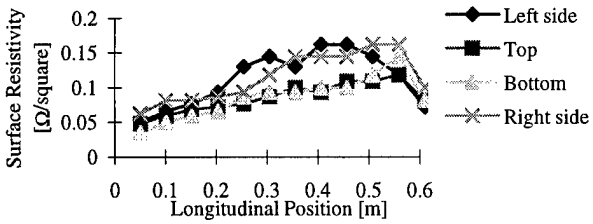



Figure 5: Uneven coating surface resistivity.

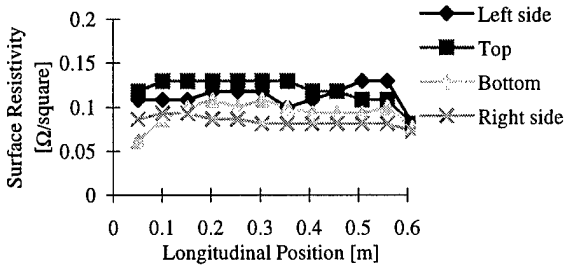



Figure 6: Relatively even coating surface resistivity.

resistivity for the chamber depicted in Figure 6 is between 0.06 and 0.3 Ω/square. The surface resistivity for the two defective storage ring chambers was more than a factor of 200 higher.

## 5 SUMMARY

Using readily available materials and laboratory equipment a simple detector was constructed which allowed in situ measurements and surface quality mapping of the conductively coated ceramic chambers used in the APS machines. Its use revealed problems with some of the chambers used in the storage ring. It was also used for new chamber quality control. The measurement system is simple, non-invasive and inexpensive; however, at present our implementation is somewhat crude and could be optimized to increase the sensitivity for a particular type of coating and application.

## 6 ACKNOWLEDGMENTS

The Authors wish to thank Klaus Halbach for his insight. D. Erickson, J. Pace, and C. Putnam for all their help related to the ceramic vacuum chamber assemblies, and J. Song for his assistance with the high frequency measurments. This work was supported by the U.S. Department of Energy, Office of Basic Energy Sciences, Under Contract No. W-31-109-ENG-38

## REFERENCES

[1] "7-Gev Advanced Photon Source Conceptual Design Report," Argonne National Laboratory, ANL-87-15, 1987.

[2] S. Milton, D. Warner, "The APS Ceramic Chambers," EPAC'94 pp. 2494-2496

# AN ANCILLARY PUMPING SYSTEM FOR THE APS VACUUM SYSTEM

D. Walters, J. Noonan, J. Gagliano, G. Harris, V. Svirtun
Argonne National Laboratory, Advanced Photon Source
9700 South Cass Avenue, Argonne, Illinois 60439 USA

*Abstract*

An ancillary pumping system has been designed and installed in the Advanced Photon Source (APS) storage ring. This vacuum system has the ability to pump sectors of the storage ring down from room pressure to ultra-high vacuum (UHV). The ancillary system is a "dry" system that uses a combination of turbomolecular pumps and oil-free roughing pumps. The benefits of this system are the reduction of equipment needed for in-tunnel maintenance, essential for the operation of a UHV storage ring; rapid response to vacuum emergencies; and a guard to accidental exposures to hydrocarbon contamination. The operational logic and the pump interlock and controls are described.

## 1 INTRODUCTION

The Advanced Photon Source is a facility for material science research. It provides users with a source of x-rays at an energy of 7 GeV. The main positron beam is contained within the storage ring that is two-thirds of a mile in circumference. The storage ring is divided into 40 sectors with isolation valves between each sector.

## 2 APS VACUUM SYSTEM

To achieve an average pressure of $10^{-11}$ Torr without beam and $10^{-9}$ Torr with beam, the main vacuum system uses a combination of ion and non-evaporable getter (NEG) pumps. The NEG pumps handle the majority of the gas load within the system. One characteristic of the NEG pumps that mandates the use of ion pumps is their ability to only pump active gases, such as water, oxygen, carbon dioxide, carbon monoxide, and hydrogen. However, the NEG pumps do not pump inert gases such as helium, neon, and argon, and are poor pumps for stable gases like methane and nitrogen. Ion pumps can, to a much greater extent, pump these inert and stable gases.

An additional technique used to achieve UHV in the storage ring is to bake it. This is done at 150°C where pressurized, heated water flows through the water cooling channels in the storage ring vacuum chamber. At this temperature the pressure is very high and would constitute a high gas load to the NEG pumps. For this reason, external pumps are attached to the system during the bake to remove gas from the system, and the ion and NEG pumps are not started until the system has started cooling down after the bake. This is done to preserve the life of both the NEG and ion pumps. Before this system was put into place the external pumps were in the form of movable carts at each end of the sector. The permanently installed ancillary pumping system is located at one end of the sector.

## 3 DESCRIPTION OF THE ANCILLARY VACUUM SYSTEM

### *3.1 System Overview*

The ancillary vacuum system is organized into 20 subsystems for each pair of sectors in the storage ring (see Fig. 1). Sectors 1 and 2 make up the first installation, sectors 3 and 4 make up the next, and so on around the 40 sectors of the ring. Each installation is made up of two turbo pumps, a dry roughing pump, interconnecting vacuum lines, and controls. Each sector has its own turbo pump

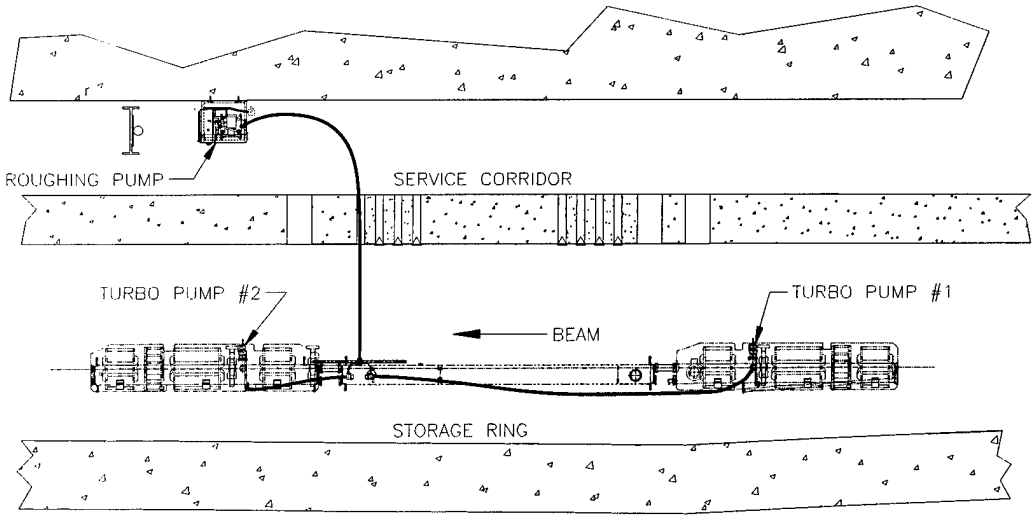



Figure 1: APS storage ring with ancillary pumping system.

0-7803-4376-X/98/$10.00 © 1998 IEEE

attached to an all-metal valve on the storage ring chamber.

### *3.2 Turbo Pump*

A turbomolecular pump was chosen because it represents a good balance of features and capabilities, and can be obtained for a reasonable price. The turbo pump is a throughput type pump that moves gas through it rather than storing the gas on the pump walls like an ion pump does. It is very useful on systems that are being baked out or for a second pumping stage after initial pump out.

The turbo pumps used at the APS are called hybrid turbo pumps because they have an additional drag pump stage that expands the capability of the pump. A standard turbo pump has a roughing pump in series with it to take in the turbo pump's exhaust. This exhaust line, called a foreline, needs to be at $10^{-2}$ Torr in the standard pump; in the hybrid pump, the foreline is now 20 Torr. The pressure difference that the pump can hold off has been greatly expanded by the drag stage. Since the hybrid pump can have a roughing pump with a much higher base pressure (a potential cost savings), it can use several types of dry pumps that have high base pressures. In the case of this system which has a roughing pump with a base pressure of $10^{-2}$ Torr, the turbo pump can reach base pressures of $10^{-10}$ Torr. Turbo pumps are very low in vibration and have a relatively high natural frequency. Given that the reaction mass of the storage ring is very high, the turbo pumps can be run under regular conditions. In the early conditioning of the storage ring this in fact did happen on one or two occasions.

We use an Alcatel ATS 100 hybrid turbo pump. With a 6" vacuum flange, the pump is rated to 125 liters/second. The drag stage is very effective because it has a tolerable foreline pressure of 20 Torr. This has two primary ramifications for this installation: the pump can be started at a higher pressure, and in the event the roughing pump becomes inoperative, the turbo pump can still run (~ 3 hours) while the roughing pump is replaced. In this application the converter in on top of the tunnel shielded from the radiation in the storage ring.

### *3.3 Roughing Pump*

One roughing pump services two turbo pumps in this system. When the pressure in the storage ring is down to $10^{-4}$ Torr the amount of gas flowing out of two turbo pumps is small enough that it can easily be handled by one roughing pump. We considered a number of pumps from various manufacturers, all having a minimum speed of 9 cfm of speed and base pressure lower than 50 mTorr. All the pumps were some sort of dry pump, with no oil or grease lubricants exposed to the vacuum. We chose a Vacuum Research 2 × 9 dry piston pump with a pumping speed of 9 cfm at room pressure and a base pressure of approximately 30 mTorr. This two-piston pump has one piston in series with the other to produce the low base pressures, and can rough the 360-liter volume of the sector in 35 minutes to a pressure where the turbo pump can take over. In spite of the approximately 40 feet of hose that connects the roughing pump to the turbo, this has become a useful part of the system.

## 4 DETAILS OF THE ANCILLARY SYSTEM

### *4.1 Turbo Pump Subsystem*

Shown in Fig. 2 is the turbo pump subsystem. In each installation there is a manual all-metal valve connected to the storage ring vacuum chamber. Between the turbo pump and the valve is a double-sided flange where a small all-metal valve is attached. This valve allows the sector to be pumped down with the flow going around the pump. After some in-house testing it was determined that there is a very large penalty for roughing the sector down through the turbo, and even a small valve can make a large difference. The valve and the turbo are joined together in a common manifold that is then connected to the main roughing hose.

### *4.2 Roughing Pump Connection*

The hose connecting the turbo to the Y manifold mounted on the ceiling is made by Swaglok™. The hose connector is modified by welding an NW-25 long flange onto it. All the connections are standard NW-25 where the O-ring is silicone rubber rather than Viton. The silicone has better radiation resistance than Viton. The Y manifold contains two aluminum right angle valves with silicone vacuum O-rings. The valves allow pump-down of each sector separately. The hose extends outside the tunnel to the rough pump platform.

### *4.3 Roughing Pump Subsystem*

The platform is made up of three main subassemblies: the pump itself, the remote relay box, and the pneumatic box piggy-backed onto the remote relay box (see Fig. 2). On the pump is a manifold elbow on which is mounted the main valve, the vent valve, and the low vacuum gauge. The gauge and the vent valve are between the pump and the main valve. The remote relay box houses the motor starter and a number of control logic relays. Mounted on the remote relay box are external lights to indicate power and faults and an elapse time meter to show the hours on the roughing pump. The 208-V disconnect is part of this box. If an emergency occurs, the roughing pump can be turned off without having to go to the local control box on top of the tunnel. The pneumatics are in an external box on the back of the remote relay box; also on the platform is the delay volume. The two needle valves together with the volume establish a circuit that delays the opening of the vent valve for a period of 3 to 6 seconds. Part of the operation of this system is that the vent valve opens after the main valve closes. This allows ample time for the main valve to shut before the vent valve opens.

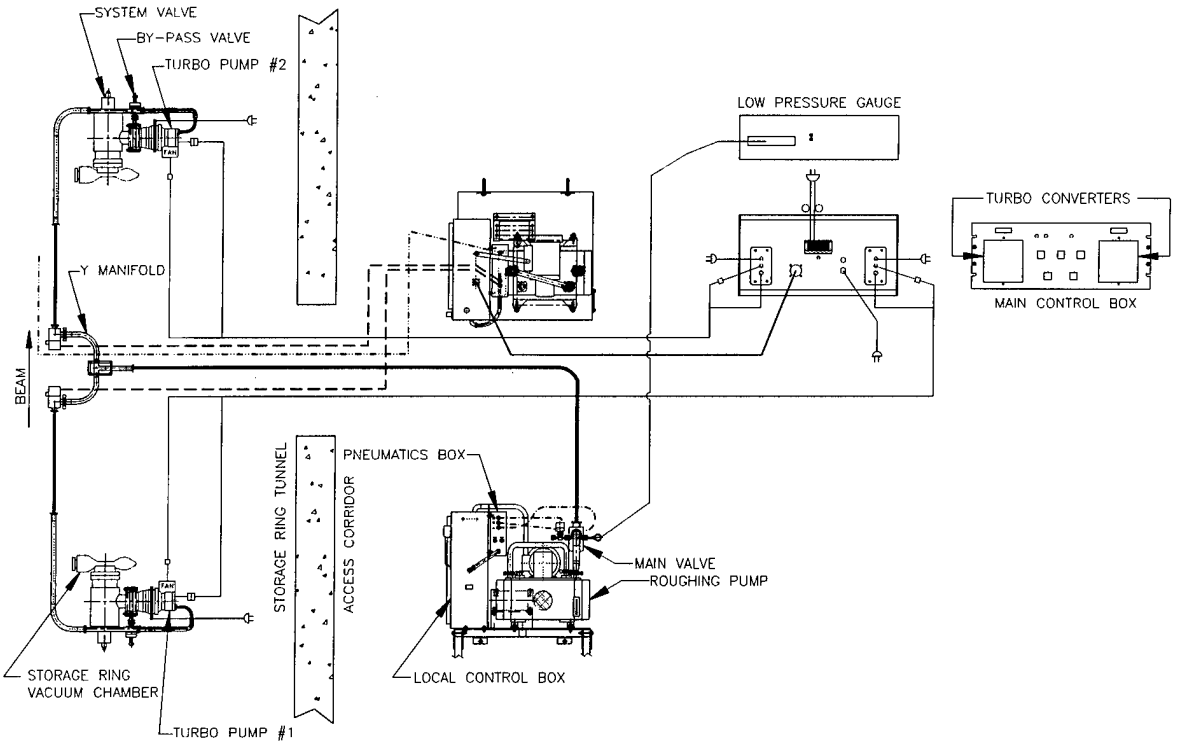



Figure 2: Ancillary pumping system.

*4.4 System Controls*

The main control box is in the rack on top of the tunnel. The relays are part of a logic control whereby if the main control box, connecting cable, remote relay box, or roughing pump should become inoperative, the main valve will close and protect the turbo pump. Part of the logic behind this is the assumption that the roughing pump is able to generate a pressure lower than the setpoint on the low-vacuum gauge, thus guaranteeing that the pump is working. As described above, if the roughing pump becomes inoperative, the main valve will close and the vent valve will automatically vent the pump and gauge. When the pump begins to operate again, the main valve will only open after the gauge has reached its setpoint. The gauge will latch a relay so that if it goes to high pressure later the main valve will not close. The two turbo controllers (converters) are in the main control box connected to the meters. The meters serve two functions: feedback to the operators that the turbo has started to spin up and information on the pumps spinning down. Only when the turbos are at a *complete* stop can the roughing pumps be valved out and turned off. The main control box has remote indicators for the main APS control room to monitor the turbo pump system for the following conditions: turbo pump on, turbo pump at full speed, roughing pump on, and the roughing pump pressure.

## 5 CONCLUSIONS

This system is currently installed at the Advanced Photon Source. It is used on a regular basis for system maintenance and system baking.

## 6 ACKNOWLEDGMENTS

This system was designed, assembled, and installed by a group larger than just the authors. Ron Kmak was instrumental in the design and documentation of this system. The mechanical engineering group provided support for the component installation in the storage ring. The vacuum group as a team provided the assembly, installation, and ongoing maintenance of this system that allows it to be used on the regular basis. This work was supported by the U.S. Department of Energy, Office of Basic Energy Sciences, under Contract No. W-31-109-ENG-38.

# STRESS RUPTURE CONSIDERATIONS IN THE DESIGN OF LARGE APERTURE, LOW MASS COMPOSITE VACUUM WINDOWS*

W.J. Leonhardt, J.R. Cullen and P.F. Gill
Brookhaven National Laboratory, Upton, NY 11973

*Abstract*

Large vacuum vessels are often employed in High Energy and Nuclear Physics experiments to provide a volume for particle traverse in the absence of air molecules. The ends of these vessels generally have a large aperture which is closed with a thin membrane known as a vacuum window. To minimize the vacuum window mass, composites of Kevlar and Mylar have been used in window construction. Historically, these windows have been designed based on the ultimate tensile strength of the materials, however, following the costly failure of a 193 cm x 86 cm window, other design methods emerged. This paper reviews the history of window design and describes the window failure and possible causes. It further presents the phenomenon of *stress rupture* and describes the analytical and experimental work carried out to improve composite window design methods.

## 1 INTRODUCTION

Several experiments utilizing protons and heavy ions in the BNL-AGS employ large vacuum vessels as part of the beamline apparatus. Generally, these vacuum vessels have a portion or portions of their wall made thin so as to have the minimum impact on particles passing through them. These thin areas are known as vacuum windows.

Vacuum windows are fabricated from materials where the density is minimized yet sufficient strength is provided so the windows operate safely and reliably for long periods of time. Several materials have been considered [1,2], however BNL utilizes dry combinations of Kevlar™ and Mylar™ exclusively.

## 2 ANALYTICAL APPROACH

### *2.1 Timoshenko Relations*

Design of rectangular Kevlar/Mylar composite windows has traditionally been based upon classical Timoshenko [3] formulas for thin plates where membrane stresses dominate. The stress formula is:

$$\sigma = K_1\left(E\left(\frac{pa}{t}\right)^2\right)^{1/3}$$

Transverse and angular deflections are calculated using respectively:

$$\delta = K_2\left(\frac{pa^4}{Et}\right)^{1/3} \text{ and, } \theta = K_3\left(\frac{pa}{Et}\right)^{1/3}$$

Modulus of elasticity (E), pressure (p), length of the short side (a), and thickness (t) of the membrane take on any consistent set of units. $K_1$ $K_2$ and $K_3$ are coefficients which depend upon the ratio of the length of the long side to short side of the window and range in value from 0.273 to 0.346 for $K_1$, 0.320 to 0.360 for $K_2$, and 1.280 to 1.440 for $K_3$. For rectangular windows the Kevlar fabric is oriented such that the weave is parallel to the window edge. Membrane thickness is taken as the equivalent solid thickness of the fibers running perpendicular to the window edge.

Experience has shown that these formulae do not accurately predict the pressures at which window assemblies fail. This is probably due to the large deflections of these windows. Consequently, designers have come to rely upon an iterative process of testing to failure then applying a suitable factor of safety in a subsequent design.

### *2.2 ANSYS*

More recently the ANSYS finite element program has been applied to the analysis of these problems to both improve the accuracy beyond Timoshenko's relations and give a better idea of the stress distributions in a given geometry.

Generally a 2-D plane model is sufficient. To create the model a geometric quarter section is generated taking advantage of symmetry. SHELL41 elements with membrane option are used. A second layer of elements is placed over the first to model the Mylar layer. In this way stresses can be obtained for both the Kevlar and Mylar. This is useful since in some window designs the thickness of the Mylar not the Kevlar is the limiting factor in the

*This research was supported by the U.S. Department of Energy under Contract Nos. DE-AC02-76CH00016.

0-7803-4376-X/98/$10.00 © 1998 IEEE

design. A solution is obtained using stress stiffening and large deflection options available in the program. Results of these analyses more closely predict failure stresses as is shown in the following section.

*2.3. Experimental Data*

Several windows with various geometries have been analyzed and tested to destruction. They are listed in Table I. Window rectangular dimensions are 1930 mm x 860 mm except as noted.

TABLE I
WINDOW FAILURE PRESSURE AND CALCULATED STRESS

| Dimensions Kevlar/Mylar (mm) | Pressure @ Failure (MPa) | Calculated Stress Timoshenko (MPa) | Calculated Stress ANSYS (Mpa) | Kevlar Strength (MPa) |
|---|---|---|---|---|
| 0.43/0.13 | 0.276 | 2350 | 2575 | 2925 |
| 0.43/0.05 | 0.248 | 2190 | 2470 | 2925 |
| 0.41/0.13 | 0.308 | 2970 | 3110 | 3380 |
| 0.38/0.13 | 0.262 | 2570 | 2810 | 2925 |
| 0.38/0.13[a] | 0.324 | 2340 | 2570 | 2925 |
| 0.30/0.13[a] | 0.248 | 2175 | 2330 | 2925 |
| 0.30/0.05[a] | 0.227 | 2050 | 2280 | 2925 |
| 0.25/0.05[b] | 0.379 | 2600 | 2565 | 3000 |

[a] 1220 mm x 610 mm [b] 457mm dia.

For rectangular shapes, the Timoshenko expression results in stresses which are about 10% below ANSYS results which are in turn 10%-20% below the actual Kevlar fiber strength. Although ANSYS results appear to more accurately represent failure stresses, the reason for apparent differences is not well understood, therefore, at the present time, testing to failure with application of a suitable safety factor for the specific window is still necessary.

## 3 WINDOW DESIGN

Specific details of window design are given elsewhere [1,2] and are briefly repeated here for convenience. Components of a typical window assembly are shown in Figure 1. In this figure, the Mylar vacuum membrane and the Kevlar are fabricated to fully cover the aperture and the area under the clamp flange, while the Mylar ring has the aperture cut out and exists under the clamp flange. The Kevlar and Mylar are assembled dry, that is without any epoxy impregnating the Kevlar except for an epoxy bead opposite the o-ring seal to prevent edge leakage while under vacuum. The aluminum wire serves as an aide in clamping.

## 4 BNL WINDOW HISTORY

BNL has utilized circular composite windows of 343, 457, 914 and 965 mm diameter and rectangular windows measuring 1220 mm by 610 mm, 1930 mm by 860 mm, 2119 mm by 429 mm and 2776 mm by 500 mm. The thickness of the Kevlar and Mylar material used in these designs was determined by considering the material's ultimate tensile strength and then specifying a thickness to provide an adequate margin of safety. Experimental testing of windows to failure was accomplished to confirm the analytical strength predictions.

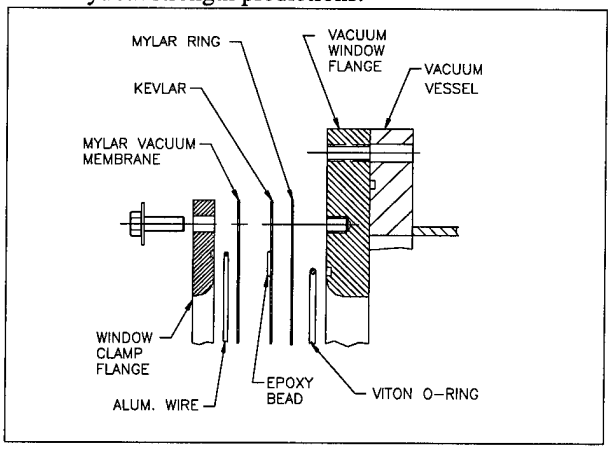



Figure 1 Typical Window Assembly

In the spring of 1995, the 1930 by 860 window failed while operating under full vacuum. Fortunately, this implosion caused no personnel injury however approximately a quarter of a million dollars of experimental equipment was lost. A post failure investigation identified two possible causes for the failure. The first was the presence of a metal chip trapped in the window material near the clamp flange. This chip may have caused a stress concentration in one or both materials, resulting in the failure. The second possible cause was that the Kevlar material failed due to a phenomenon known as stress rupture. Stress rupture lifetimes are not accurately predictable, however the failed window was analyzed and it was judged that stress rupture could have been a contributing cause.

## 5 STRESS RUPTURE PHENOMENON

"Stress rupture is the sudden failure (break) in a material held for long periods of time under loads which are less (sometimes considerably less) than the nominal tensile strength of the material. The greater the load, the more quickly failure occurs. Inversely, even the smallest load could theoretically cause stress rupture if enough time were allowed. The stress rupture properties of wet and dry yarns are the same."[4] Values of the stress rupture properties of Kevlar yarns are shown in Figure 2.

## 6 STRESS RUPTURE TESTING

Although stress rupture data was available for Kevlar yarns, it was decided to perform independent

measurements on the stress rupture performance of the

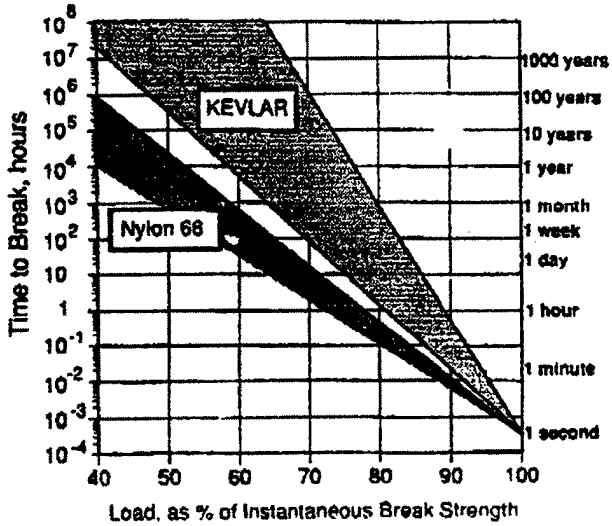



Figure 2 Stress Rupture of Kevlar Yarns [4]

Kevlar cloth. Samples of Kevlar 129 fabric were loaded in tension using a standard Instron tensile testing machine with custom made gripping fixtures to hold the cloth. This setup is essentially the same as is used to measure the tensile strength of cloth samples except, in stress rupture testing, the force on the sample is kept constant.

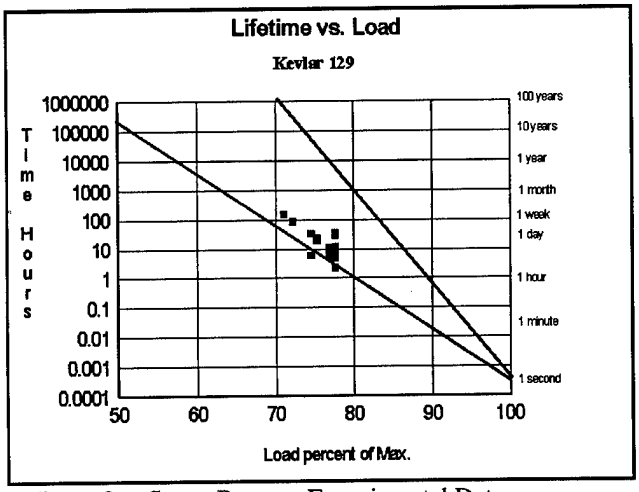



Figure 3 Stress Rupture Experimental Data

Alignment and uniform loading systematics were minimized empirically by loading the samples to failure and comparing differences in the ultimate tensile strength. It was discovered that removing edge fibers increased the ultimate tensile strength since there could be damage during cutting and distortion in the fabric near the free edge. The final width of all samples tested was 37 mm. This technique also has the advantage of enhanced sample reproducibility by maintaining a constant number of fibers between samples.

The results of the stress rupture measurements are shown in Figure 3. The measuring period for the data taken is between one hour and one week. The data show good agreement with the DuPont values shown in Figure 2 and the lines plotted in Figure 3 are the upper and lower bounds from Figure 2. The data also show good agreement with a study performed by Chiao,, et. al. [5] of Kevlar49/epoxy pressure vessels which found that vessels loaded to 50% of their burst pressure had no failures in 9 years.

## 7 SUMMARY

Composite vacuum windows are an extremely useful piece of experimental apparatus that need to be designed carefully. In the design process, it is imperative to consider both the Kevlar ultimate tensile strength and its stress rupture lifetime. Experiments have shown that the catalog values for stress are reasonable and it is recommended that the most conservative values be used. Since experimental sensitivity is also important, current BNL policy is to provide windows with a minimum of a 100 year lifetime (which corresponds to a stress level of approximately 47% of the strength) and to replace the window after one year under load. A ten year lifetime is allowable with special review.

## 8 ACKNOWLEDGMENTS

The authors wish to acknowledge valuable input on stress rupture and finite element modeling from J. Kilmer and A. Lee of Fermi National Accelerator Laboratory.

Kevlar and Mylar are registered trademarks of E.I du Pont de Nemours and Co., Inc.

## 9 REFERENCES

[1] W.J. Leonhardt and M. Mapes, "Design of Large Aperature, Low Mass Vaccuum Windows," Proc. of 1993 Particle Accelerator Conf. pp 3882-3884.

[2] M. Mapes and W.J. Leonhardt, "Design of Large Aperature, Low Mass Vacuum Windows," J. Vac. Sci Technol. A, 11(4), Jul/Aug 1993, pp 1587-1592.

[3] S. Timoshenko and S. Woinowsky-Krieger, Theory of Plates and Shells, McGraw Hill, N.Y., 2/e, 1959.

[4] Data Manual for Fiber Optic and Other Cables, E.I du Pont de Nemours and Co., Inc., July 1991

[5] T.T. Chiao and R.L. Moore, "Fiber/Epoxy Filament-Wound Vessels Final Report," Report UCID-20845 Lawrence Livermore Labratory, August 1986

# MECHANICAL DESIGN ASPECTS OF THE LHC BEAM SCREEN

P. Cruikshank, K. Artoos, F. Bertinelli, J.-C. Brunet, R. Calder, C. Campedel, I. Collins, J.-M. Dalin, B. Feral, O. Grobner, N. Kos, A. Mathewson, L. Nikitina, I. Nikitine, A. Poncet, C. Reymermier, G. Schneider, I. Sexton, S. Sgobba, R. Valbuena, R. Veness, CERN, Geneva, Switzerland.

*Abstract*

Forty-four kilometers of the LHC beam vacuum system [1,2] will be equipped with a perforated co-axial liner, the so-called beam screen. Operating between 5 K and 20 K, the beam screen reduces heat loads to the 1.9 K helium bath of the superconducting magnets and minimises dynamic vacuum effects. Constructed from low magnetic permeability stainless steel with a 50 μm inner layer of high purity copper, the beam screen must provide a maximum aperture for the beam whilst resisting the induced forces due to eddy currents at magnet quench. The mechanical engineering challenges are numerous, and include stringent requirements on geometry, material selection, manufacturing techniques and cleanliness. The industrial fabrication of these 16 metre long UHV components is now in its prototyping phase. A description of the beam screen is given, together with details of the experimental programme aimed at validating the design choices, and results of the first industrial prototypes.

## 1 INTRODUCTION

The LHC layout is defined by the existing 27 km LEP tunnel geometry. The two 7 TeV counter-rotating proton beams are separated horizontally in the arcs and channelled through twin-bore superconducting magnets. The two beam vacuum tubes, or cold bores, are the interface between the 1.9 K magnet baths of superfluid helium and the ultra high vacuum system. Synchrotron radiation power emitted by the proton beams (up to 0.32 W/m per beam), together with a comparable power dissipated by beam image currents, would represent an excessive heat load to the 1.9 K cryogenic system. In addition, an unacceptable gas density, and hence beam lifetime, would result from the dynamic equilibrium between cryopumped and desorbed (photon and ion induced) gas. The beam screen overcomes these problems by intercepting the heat loads at a higher and more thermo-dynamically efficient temperature. Also, by shielding the 1.9 K cryopumping surfaces from synchrotron radiation, gas in the beam aperture may be effectively cryopumped via holes (pumping slots) in the beam screen wall.

## 2 DESCRIPTION

The present design of the beam screen (Figure 1) is based on a 1 mm thick, ultra-low magnetic permeability stainless steel tube coated on its inner surface with a 50 μm layer of high electrical conductivity Cu. Two stainless steel cooling tubes, which maintain the beam screen temperature between 5 K and 20 K are positioned to optimise the available aperture [3]. A nominal annular gap of 1.5 mm between cold bore and beam screen is proposed to avoid thermal shorts and to accomodate the low thermal conductivity spring supports located at 1.7 metre intervals. Pumping slots on the flat zones of the beam screen body, representing some 4.4% of the inner surface area, have a randomised pattern which repeats every 500 mm ± 10 mm.

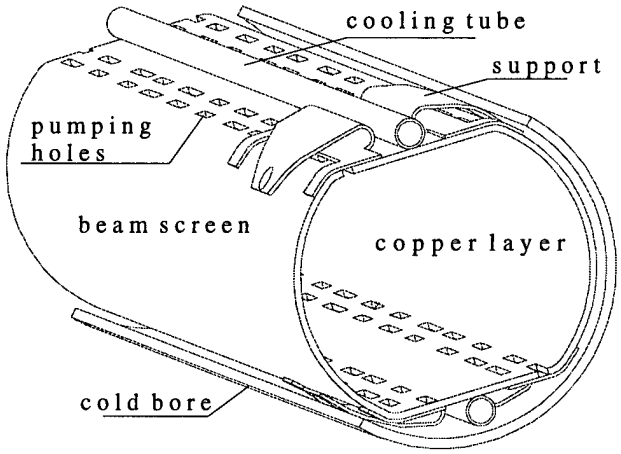



Figure: 1 The LHC beam screen

## 3 TECHNICAL REQUIREMENTS

### *3.1 Material Selection*

To minimise resistive wall losses and coupling impedance, the inner surface of the beam screen must be of high electrical conductivity material [4]. High purity Cu with a relative resisitivity ratio (RRR) of approximately 100 is proposed. However, the large eddy current forces created during a magnet quench (section 3.2), imply that this Cu layer must be minimised and have excellent adherence to a high strength support structure, the beam screen body, which in turn must have an optimum thickness to maximise beam aperture. For the given geometry, it has been shown that a magnetic permeability of less than 1.005 (in the temperature range 5 K to 20 K) is required [5] to avoid significant magnetic field distortions. Conventional AISI 300 series stainless steels have permeabilities well in excess of this value.

0-7803-4376-X/98 /$10.00 © 1998 IEEE

Several other vacuum compatible materials have been discounted due to their low temperature characteristics which show ferro-magnetic transitions ( Ni superalloys - inconel, monel, etc.), fragility (titanium), or low strength (aluminium). Grades of austenitic stainless steel alloyed with Mn and Ni, having magnetic permeabilities < 1.005 at the operating temperature of the beam screen, such as Armco Nitronic 40, Ugine UNS 21904, Aubert & Duval X20MD are commercially available (typically 4 to 9% Mn, 7 to 10% Ni). However, laser welding trials have shown unacceptable levels of ferrite formation [6] due to nitrogen depletion in the weld bath. In collaboration with the steel industry, experimental batches of optimised higher alloyed grades (12% Mn, 11% Ni) have been produced and tested, showing excellent austenitic stability and ferrite free welds [7].

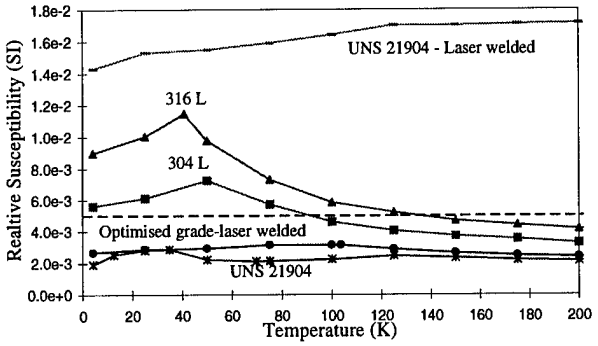



Figure: 2 Magnetic susceptibility of various stainless steels as a function of temperature.

*3.2 Quench forces*

A rapid decay of the 8.4 T magnetic field in the superconducting dipole magnets occurs during a resistive transition (quench) of the magnet windings. Large eddy currents are induced in the beam screen Cu layer, resulting in horizontal outward forces. The beam screen Cu layer must remain undamaged after repeated quenches. The maximum horizontal elastic deflection of the beam screen body must not exceed the annular gap between it and the cold bore, as the latter is simultaneously subjected to large external helium pressures [8]. Finite element quench calculations show good agreement with experimental beam screens (prior geometry with 304L stainless steel body) tested in 1 metre long model magnets [9,10]. Further testing of 11 metre beam screens in the LHC Prototype Half-Cell [11], together with the data from material testing will be used to optimise the stainless steel wall thickness.

*3.3 Geometrical Tolerances*

The manufacture tolerances specified for the beam screen x-section (0.2 mm), straightness (0.5mm/m) and twist between extremities (1°), are target values based upon manufacturing techniques and results of prototypes. Loss of beam aperture due to concentricity errors between cold bore and beam screen have been estimated [12].

*3.4 Interconnections*

Beam screens will be joined at magnet extremities by flexible RF sleeves which allow alignment and thermal contraction displacements. For security, helium to vacuum welds have been prohibited on the beam vacuum system and the seamless cooling tubes must traverse the cold bore envelope into the insulation vacuum at each magnet interconnect. Thermal transients imply that the cooling tubes must accept large movements (up to 44mm) with respect to the cold bore.

## 4 MANUFACTURE

The method of construction must consider the technical constraints as well as the necessity to economically produce 44 km of beam screen in lengths of 16 metres. For each step in the manufacturing process, many different techniques are possible. Figure 3 shows the methods of construction that have been retained.

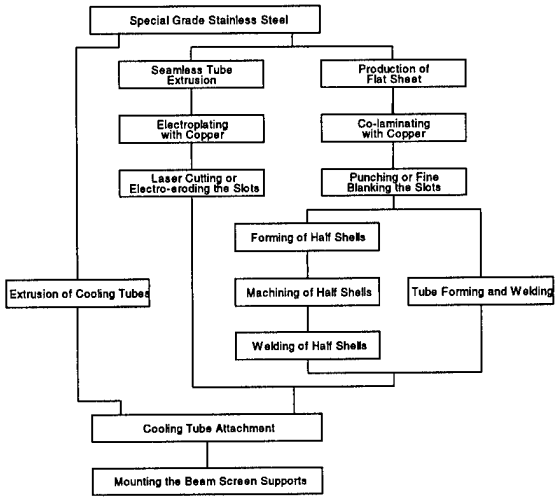



Figure: 3 Methods of construction

A key issue in the manufacturing process is the application of the Cu layer. It has been shown that prolonged heat treatment of electrodeposited Cu layers on stainless steel substrates above 550 °C will reduce the RRR to unacceptable values[13]. Therefore, once the Cu layer has been applied, high temperature brazing, welding with large heat input (TIG) or high temperature vacuum degassing are excluded from the manufacturing process, and extreme care is necessary to avoid mechanical damage or contamination of this soft Cu layer.

*4.1 Attachment of the copper layer*

Two methods are under investigation; electrodeposition and colamination (or roll-bonding). The former may be performed on both a closed geometry or a flat sheet.

*4.1.1 Electroplating*

Cu electroplating using a Ni strike increases the magnetic permeability of the beam screen; a 0.5 μm Ni layer

remains acceptable. Electrodeposited Cu layers on 1.2 metre beam screens have been characterised [14]. Eleven metre long prototype beam screens have been manufactured and installed at the Prototype Half-Cell.

*4.1.2 Colamination*

The colamination of stainless steel with Cu is obtained by cold rolling, followed by heat treatment to improve adhesion. First trials using UNS 21904 resulted in blistering of the Cu layer due to aluminium oxide contaminants at the stainless/Cu interface. Particles from the abrasive belts used to grind the stainless steel prior to colamination, had become embedded in the surface of the high strength alloy ($R_m$ ~ 800 MPa). Subsequent trials have shown that the elimination of the grinding step produces acceptable colaminated material. During the heat treament cycle (which also moderates the steel properties) the RRR peaks at > 180 before decreasing sharply. Glow discharge optical spectroscopy has shown a diffusion of Mn into the Cu [15]. A compromise between Cu heat treatment (RRR ~ 60) and stainless steel annealing ($R_p$ 0.2 ~ 600 MPa) is possible using a short heat treatment cycle (7.5 mins at 920 °C). The finished product shows excellent surface finish (Cu ; Ra < 0.2 μm) and thickness tolerances (Cu ; 50 ± 10 μm, St. Steel. ; 1.00 ± 0.02 mm). Further trials will be made with optimised stainless steel grades.

*4.2 Beam screen body and cooling tubes*

Production trials of seamless cooling tubes and beam screens in experimental grades of high manganese stainless steel have given acceptable results for the former, but failure for the latter due to high inclusion levels in the steel and the low ratio of wall thickness to diameter. Further tests using commercial grades are continuing. Sample beam screen bodies made from welded half shells have been manufactured in UNS 21904 (1.5 m) and AISI 316L (5.5 m). The technique of continuous tube forming from flat sheet may be applied for the beam screen body, and hence exploit the availabilty of colaminated material. Trials have been conducted using AISI 304L sheet, proving the feasibility for the beam screen geometry. The required geometrical tolerances (x-section, straightness, twist) go beyond the values obtained for industrially produced tubes. The use of sheet with good thickness tolerance, in-line laser welding and continous on-line dimensional control is expected to give improved results. Prototype beam screens of 16 metres length have been ordered in colaminated UNS 21904.

*4.3 Pumping slots*

Colaminated sheet can be on-line punched prior to forming. The narrow slot width (1.5 mm), high strength steel and limited lubrication choices (UHV compatibility) present challenges. Trial punching from the Cu side of colaminated sheet has shown fully ductile shearing with limited burr formation. For slot production on finished beam screen bodies, alternative methods (laser, laser with water jet, abrasive water jet, chemical etching, spark erosion) have also been evaluated [16].

*4.4 Attachment of cooling tubes*

Good thermal contact is required between the cooling tube and beam screen. Intermittent laser welding has been investigated (~ 500 spots/m), producing ferrite free welds with no measurable deformation to the beam screen body or visible damage to the Cu layer.

## 5 CONCLUSIONS

The LHC beam screen design continues to be optimised. Suitable materials have been developed and the joining techniques mastered. Progress has been made on each of the manufacturing techniques to be employed. Prototype 16 m beam screens have been ordered from industry.

## 6 REFERENCES


[1] The Large Hadron Collider, Conceptual Design, CERN, 95-05, October1995.

[2] O. Grobner, The LHC Vacuum System, PAC'97, Vancouver, Canada, May 1997.

[3] Y. Baconnier et al., LHC beam aperture and beam screen geometry, LHC Note 326, June 1995.

[4] F. Ruggiero et al., Surface resistance measurements for the LHC beam screen, PAC'97, Vancouver, Canada, May 1997.

[5] G. Houtappel, Multipoles in the magnets for LHC, caused by piping, air gap in yoke, cryostat, asymetric excitations and bus-bar currents, LHC-MMS, Internal Note 96-11, Sept. 1996.

[6] C. Boudot, S. Sgobba, Welding of Stainless Steels, International, Colloquium "Processing of Stainless Steels", Le Mons (B), 29-30 April 1997, page14-1ff.

[7] S. Sgobba, Techniques laser de soudage pour l'ecran de faisceau du grand collisioneur protonique (LHC), proceedings du Cycle Metaux et Procedes, Tremelan (CH), 4-8 Nov. 1996, vol. Journee soudage - page 8/1-10.

[8] M. Chorowshki et al., Thermohydraulics of resistive transitions on the LHC prototype magnet string: theoretical modelling and experimental results,-to be presented at CEC/ICMC 97, Portland, USA.

[9] K. Artoos et al., Mechanical and thermal measurements on a 1 m long beam screen. LHC Project Note 35, March 1996.

[10] R. Valbuena, Comparison de resultats de mesures realisees sur un ecran test et ceux donnes par le calcul, EST Technical Note EST-ESI 31/10/96, October 1996.

[11] R. Saban et al., Experiments and cycling at the LHC Prototype Half- Cell, PAC97, Vancouver, Canada, May 1997.

[12] N. Kos et al., Beam screen - cold bore concentricity, Vacuum Technical Note 96 - 24, December 1996.

[13] J.-M. Dalin, J. Hague, The effect of the temperature and duration of heat treatment on the electrical resistivity of electrodeposited copper, EST Internal Report MT-SM/93-06, April 1993.

[14] J.-M. Dalin, Caracterisation du depot de cuivre a l'interieur de l'ecran de faisceau du LHC, EST Internal Report EST-ESI 96-09-15, September 1996.

[15] Swiss Federal Laboratories for Materials Testing and Research EMPA, Test Report 165593, October 1996.

[16] G. Jesse, Examen metallurgique de differentes decoupes dans des toles inox avec une couche de cuivre colaminee pour l'ecran de faisceux LHC, EST Internal report, EST/MI/11/1/96, Jan. 1996.

# BEAM INDUCED MULTIPACTING

O. Gröbner,
CERN, CH - 1211 Geneva 23, Switzerland

*Abstract*

Beam induced multipacting driven by the electric field of successive bunches, as first observed in the ISR proton-proton storage ring [1] may arise from a resonance motion of a cloud of secondary electrons bouncing back and forth between opposite walls of the vacuum chamber. Under conditions where the average secondary electron yield of this process exceeds unity, the electron cloud may increase exponentially. A consequence for the vacuum system is strong electron stimulated gas desorption and the associated pressure increase which may affect the beam lifetime. A simple criterion for the onset of multipacting and an estimate of the average secondary electron yield is derived and will be applied to typical vacuum chambers and to the specific conditions found in the LHC.

## 1 INTRODUCTION

Electrons from ionisation of the residual gas which are accelerated by the electric field of the successive proton bunches and which can build up to a cloud of electrons due to the generation of secondary electrons at the vacuum chamber, have first been observed at the ISR [1]. The most striking detrimental effect for the operation of the machine has been the very fast pressure rise due to electron stimulated gas desorption from the wall of the vacuum chamber. The particular condition under which this electron multipacting effect was observed involved a beam pipe made of aluminium alloy instead of the conventional stainless steel used elsewhere in the machine. Due to its much larger secondary electron coefficient (seec) as compared to stainless steel, the $Al_2O_3$ surface exhibited - under specific beam conditions - a strong multipacting effect. In LHC, the dominant source of electrons will be photo-electrons from synchrotron radiation. The effects of an electron cloud on the stability of the beam has been studied recently [2].

## 2 MODEL

A set of basic equations can be derived which applies to locations in the machine without magnetic field. The electric field of a circular beam in a concentric, circular beam pipe can be expressed as

$E(r) = \frac{\lambda}{2\pi\varepsilon_o\, r}$ where $\lambda$ is the line charge of the bunch

$\lambda = \frac{e\,N_b}{c\,\tau}$ with $\tau$ the bunch duration, $N_b$ the particles per bunch, c the velocity of light and e the electron charge. The momentum transfer by one bunch to a stationary electron at a radial position r, is

$$\Delta p = e\,E(r)\,\tau = \frac{e^2\,N_b}{2\pi\varepsilon_o\,c\,r}$$

and hence independent of the bunch length. From this follows the velocity increment

$$\Delta v = \frac{\Delta p}{m} = \frac{e^2\,N_b}{2\pi\varepsilon_o\,m\,c\,r} = 2c\,r_e\,\frac{N_b}{r}$$

introducing the classical electron radius $r_e$. The electrons must cross the vacuum pipe, with radius $r_p$, in synchronism with the bunches to be able to multipactor. This condition requires that the transit time must be less than or equal to the time between successive bunches $\frac{2r_p}{\Delta v} \le t_{bb}$. Introducing the bunch distance $L_{bb} = c\ t_{bb}$ the wall-to-wall transit time condition, determining the threshold beam intensity becomes

$$N_b = \frac{r_p^2}{r_e\,L_{bb}}.$$

A further, necessary condition to be met is that the energy of the electrons when they hit the vacuum chamber wall is sufficiently large to produce, on average, more then 1 secondary electron. This energy, corresponding to the kick by a bunch, can be obtained from

$$\Delta W = \frac{\Delta p^2}{2\,m} = 2\,\frac{mc^2}{e}\,r_e^2\left(\frac{N_b}{r}\right)^2 (eV)$$

Compared with this simple, stationary electron model, more realistic results can be obtained by introducing the following two generalisations:

i) the radial distribution of the beam charge is assumed gaussian, with the parameter $r_b$, thus giving

$$E(r) = \frac{\lambda}{2\pi\varepsilon_o}\,\frac{1-e^{-\left(r/r_b\right)^2}}{r}$$

ii) the electrons are not stationary but move during the passage of the bunch. This requires the integration of the equation of motion $m\ddot{r} = e\,E(r)$ from which the velocity $\dot{r}(\tau)$ after the passage of the bunch can be computed. The corresponding energy is

$$\Delta W = \frac{m\,\dot{r}(\tau)^2}{2}.$$

In a strong magnetic field, the net momentum transfer will be confined along the field lines. For a concentric, circular geometry, it can be shown that the transit time condition is unchanged [3].

0-7803-4376-X/98/$10.00 © 1998 IEEE

## 3 APPLICATION TO THE LHC

Typical parameters for the LHC are [4]: $N_b = 1\ 10^{11}$ p/bunch, $\tau = 0.25$ ns, $t_{bb} = 25$ ns or $L_{bb} = 7.5$ m. The beam radius in the arcs is typically 1.1 mm and the vacuum chamber (the beam screen) radius is 22 mm. In LHC, the threshold for multipacting corresponds to an intensity of only $2.3\ 10^{10}$ p/bunch and at the nominal intensity the transit time condition for wall-to-wall multipacting is met for vacuum chamber radii less than 47 mm.

A comparison between the energy gain of a stationary (dotted curve) and of a moving electron for the nominal bunch length of 0.25 ns as well as for 0.1 and 0.5 ns is shown in Figure 1 where it can be seen that apart from the central region, close to the beam, the approximation for a stationary electron is quite satisfactory. In the LHC an electron created at the wall receives an energy of about 190 eV and electrons which have drifted closer to the beam may gain several keV up to a maximum of about 13 keV.

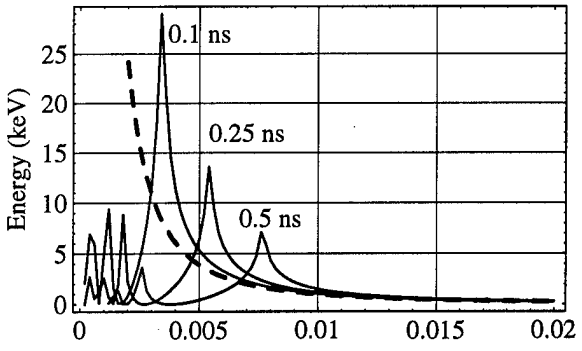



Figure: 1 Electron energy after the passage of a bunch in LHC versus the initial radial position for 0.1, 0.25 and 0.5 ns bunch length. The dotted curve is calculated for the stationary electron approximation.

The secondary electron coefficient (seec) as a function of incident electron energy and for different materials and surface treatments applicable to typical vacuum chambers has been studied extensively by N. Hilleret and co-workers [4]. Figure 2 shows data for technical surfaces at perpendicular electron incidence for aluminium ($Al_2O_3$), copper plated stainless steel (LHC beam screen), stainless steel and titanium. The important result of these measurements is that, apart from Ti, a seec of unity is exceeded at energies well below the energy range in the LHC and that the seec remains above unity up to many keV. Therefore, the basic conditions for the multiplication of the secondary electron cloud are met.

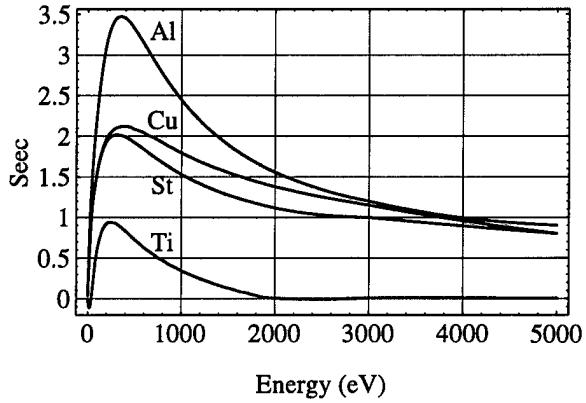



Figure: 2 Secondary electron yield (seec) as a function of primary electron energy for perpendicular incidence and for technical surfaces representative for vacuum chambers (provided by N. Hilleret, extrapolated for energies >2 keV)

Combining the energy dependence on the radial position and the dependence of the seec on incident electron energy gives the secondary electron coefficient as a function of the radial position in the vacuum chamber shown in Figure 3.

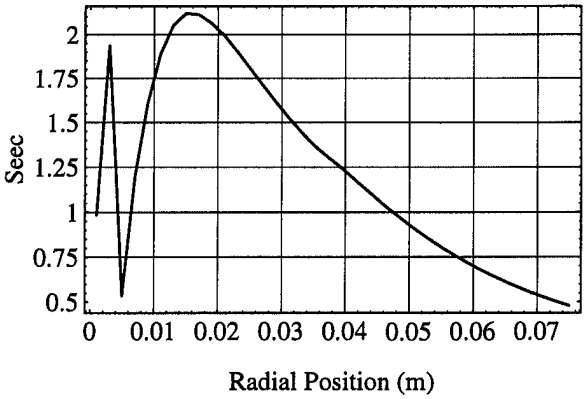



Figure: 3 Seec versus radial position for nominal LHC parameters and for copper plated stainless steel.

Whether an electron cloud remains limited or will grow exponentially, depends on the secondary electron coefficient averaged over the cloud <seec>. To compute this average the following simplifying assumptions have been made :

i) electrons which are kicked by the bunch must meet the transit time condition, i.e. they must reach the opposite side of the vacuum chamber before the next bunch arrives.

ii) secondary electrons drift with a given energy (e.g. 5 eV) and are lost when they reach the opposite wall before the next bunch arrives.

iii) under steady state conditions, the electron cloud is uniformly distributed over the vacuum chamber aperture.

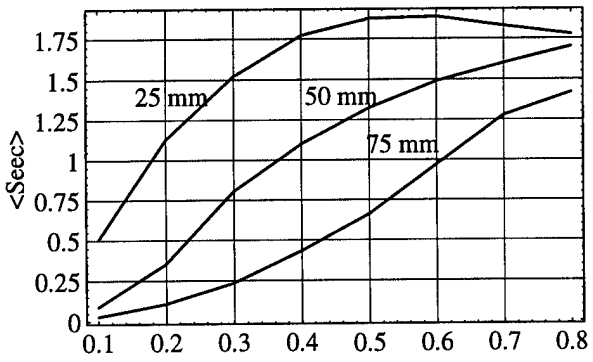



Figure: 4 < seec> versus beam current for different beam pipe dimensions and for copper plated stainless steel.

From Figure 4 it can be seen that the average yield of unity can be exceeded at beam currents below the nominal value in LHC for small beam pipes. The validity of the assumptions in this model has been cross-checked with results from the ISR. From this comparison one may conclude that the multipacting threshold corresponds to a computed <seec> of 1.3 rather than unity. Figure 5 illustartes the importance to use a vacuum chamber material with a low secondary electron coefficient.

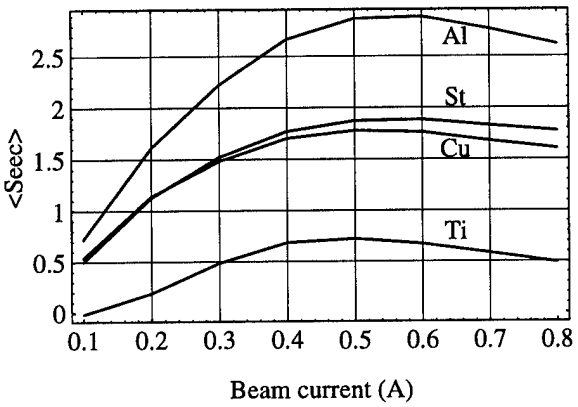



Figure: 5 <seec> for different materials versus beam current for a 25 mm beam pipe

## 4. HEAT LOAD DUE TO PHOTO-ELECTRONS

For LHC where the dominant source of electrons are photo-electrons from synchrotron radiation, an additional aspect is the power dissipated on the beam screen and thus the heat load to the cryogenic system which results from the energy transfer to the electron cloud. The average energy transfer to the uniformly distributed electron cloud by a single bunch passage can be calculated from Figure 1 as 700 eV. The photo-yield as a function of the critical photon energy has been measured with a copper plated test chamber in the EPA synchrotron radiation beam line at CERN [5]. When these data are converted to LHC conditions one finds that up to 4 TeV the photo-yield is negligible but it increases to 0.02 at 7 TeV. The specific linear photon flux as a function of the beam current I(A) and beam energy E(GeV) is $2.65.10^{13}$ I E photons/s/m. The production of photo-electrons is shown in Figure 6.

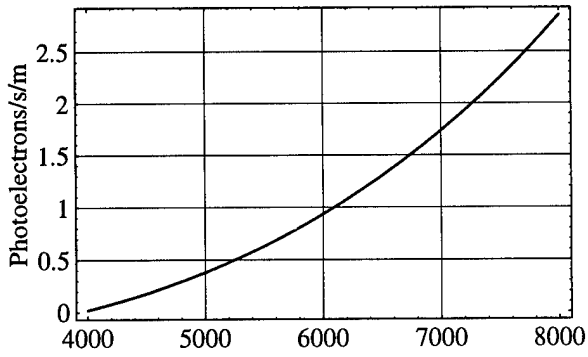



Figure: 6 Production of photo-electrons in LHC (units of $10^{15}$) versus beam energy for 0.53 A beam current.

Assuming that each photo-electron in the cloud receives just one kick with an average energy transfer, computed from Figure 1 as 700 eV, this would give a linear power dissipation -on the beam screen- of approx. 0.2 W/m.

## 5 CONCLUSIONS

Bunch induced multipacting is a potential problem for LHC but may be avoided by constructing the vacuum chambers and the beam screen from materials with low secondary electron coefficient (seec). The influence of the magnetic field has still to be studied in more detail but first estimates tend to show that its effect is small. Wherever possible, beam pipes with sufficiently large size should be chosen to avoid wall-to-wall multipacting. The power dissipation by photo-electrons represents a significant and, so far, not included contribution to the thermal budget.

## 6 ACKNOWLEDGMENTS

The basic data for the secondary electron coefficients of technical surfaces have been provided by N. Hilleret and I. Bojko. Numerous stimulating discussions with R. Calder, A.G. Mathewson from CERN, M. Furman from LBL and F. Zimmermann from SLAC are gratefully acknowledged.

## 7 REFERENCES

[1] O. Gröbner, 10th Int. Conf. on High Energy Accelerators, Protvino, July (1977).
[2] F. Zimmermann, LHC Project Report 95, 27 February, 1997.
[3] R. Calder, private communication, 1997.
[4] N. Hilleret, I. Bojko, unpublished, 1997.
[5] J. Gómez-Goñi, O. Gröbner, A.G. Mathewson, J. Vac. Sci. Technol. A 12(4), July/August 1994.

# OPERATION OF CESR DISTRIBUTED ION PUMPS AT REDUCED VOLTAGE

Yulin Li, R. Kersevan, N.B. Mistry
Laboratory of Nuclear Studies, Cornell University, Ithaca, NY 14853 USA

*Abstract**

A transverse single-beam instability is observed in CESR which has been found to arise from the DC static electric field leaking into the beam chamber from distributed ion pumps (DIPs). Further, a very large photoelectron current is measured in the DIPs which may impose a potential problem in future CESR upgrades. The purpose of this study was to investigate the possibility of lowering the DIP operating voltage without sacrifice of DIP pumping speed. A relatively constant DIP pumping speed was measured with the anode voltage ranging from the 'normal' operating voltage of 7.6 kV to as low as 1.8 kV, when there is beam stored in CESR. On the other hand, a higher (5 kV) minimum DIP anode voltage is needed to sustain effective pumping speed without beam present. A simple model is proposed to describe the operation of DIPs under the influence of the stored beam. As the result of this study, the majority of CESR DIP controllers have been modified to enable remote switching of the DIP anode voltage between 2.2 kV (for normal beam operation) and 6.6 kV for start-up or for long periods without stored beam.

## 1. INTRODUCTION

Ultrahigh vacuum is a necessity for a storage ring system to provide required good beam lifetime. Both lumped noble diode ion pumps (LPs) and distributed ion pumps (DIPs) are employed in the arc regions of CESR to keep the beam chambers at typically $2\sim3\times10^{-9}$ torr with total stored electron and positron beam currents more than 300 mA. The detailed description of the DIPs can be found in references [1]. All the DIP anodes had been operating at 7.6 kV for more than 15 years prior to this study. It has become desirable to reduce the operating DIP anode voltage for the following two considerations. First, a transverse single-beam instability was observed in CESR. Studies[2] indicated that this transverse instability has been caused by the interaction between the stored bunched particles and photoelectrons trapped by the DC static electric field leaking into the beam chamber from DIPs. The growth-rate of the instability is observed to peak at some intermediate beam current, which imposes a difficulty during beam injection. It is also found that the growth-rate decreases with lower DIP anode voltage. Secondly, we have measured very high DIP pump current with beams stored in CESR. For some DIPs, the pump current are as high as 5 mA per 100 mA of stored beams, which may extrapolate to a power dissipation of more than 370 W in those DIPs at planned CESR Phase III upgraded operation at total stored beam current of 1A. This is very likely to impose a potential operation problem in future CESR upgrades. As will be discussed in the paper, this high DIP pump current is due to scattered photoelectrons and does not reflect pressure in the pump chamber. It is observed that the DIP current may be reduced at lower DIP anode voltage.

The practical purpose of this study is to explore the possibility of reduction of DIP anode voltage without degradation of pumping performance. Thus we measured the relative DIP pumping speed as a function of anode voltage, with and without stored beams. The DIP current is also studied to understand the pumping behavior of the DIPs under the influence of stored beams in CESR.

## 2. DIP PUMPING SPEED

Most of the measurements were carried out in a special sector of CESR, which consists of one long straight chamber and four bending chambers, which is densely instrumented for pressure readout. The schematic layout of the instrumentation section is given in Figure 1. The power supplies for the four DIPs in the section were modified to enable remote control of DIP anode voltage from 0 to 7.6 kV. Nine cold cathode gauges (CCGs) and one residual gas analyzer (RGA) are installed in the

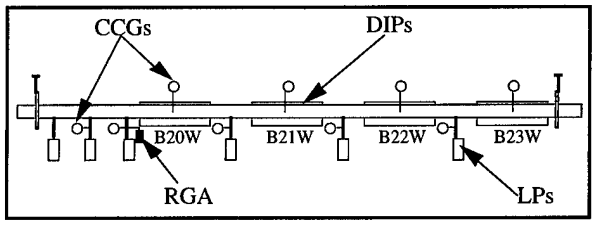



Figure 1. Vacuum Instrumentation Sector Layout

section to measure pressure and gas composition in the beam chamber. Prior to the study, the vacuum chambers in the test section had been subjected to more than 250 Amp•Hours total beam dose so that the variation of vacuum conditions due to beam-conditioning in the section during this study can be ignored. Most of the data shown below were taken during CESR high energy physics (HEP) runs, in very stable conditions.

Measuring absolute DIP pumping speed is no easy task, as detailed information is required of the pressure, pumping speed and gas-load distributions along the beam chambers, as well as the gas conductance of the beam chambers. However, for the practical purpose of this study, we were interested only in the relative DIP pumping speed as we vary the DIP anode voltage. One can calculate the relative DIP pumping speed from measured pressure at the center of the bending chamber[3]. The relative DIP pumping speed is defined

* Work supported in part by the National Science Foundation

as $S^i_{DIP}/S^H_{DIP}$, where $S^i_{DIP}$ and $S^H_{DIP}$ are the DIP pumping speed at anode voltages of $V_i$ and at the 'nominal' higher setting 7.6 kV, respectively. In Figure 2, the measured relative DIP pumping speed for the four DIPs in the section is shown as a function of DIP anode voltage.

The relative DIP pumping speed was also measured without stored beam in CESR, and the result is shown in Figure 3. One can see that the behavior of the DIPs without stored beam is very different from that with stored beam. With stored beam in CESR, the DIP pumping speed is rather insensitive to the anode voltage from 1.8 kV to the 'normal' operating voltage of 7.6 kV. In fact, we can gain about 20% higher pumping speed by operating the DIPs between 2 to 6 kV. However, without stored beam in CESR, the DIP pumping speed drops rapidly when the anode voltage is reduced below 5 kV. These measurements clearly indicate that stored beam in CESR has a significant effect on the DIPs.

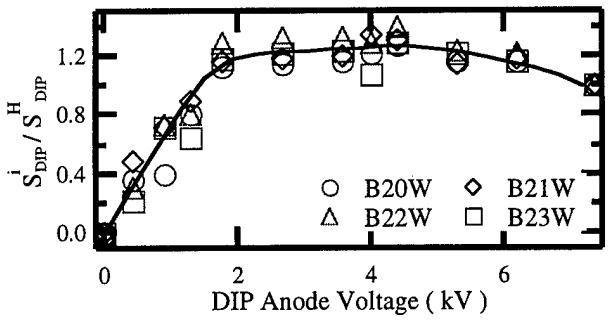



Figure 2. Relative DIP pumping speed vs. DIP anode voltage, with 300 mA total stored beam in CESR.

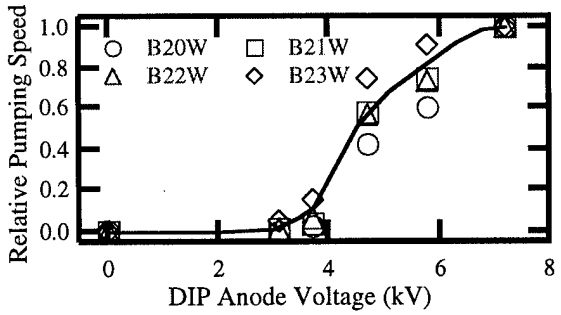



Figure 3. Relative DIP pumping speed Vs. DIP anode voltage, without stored beam in CESR.

The measured chamber pressures changed from 0.4 to 1.1 ntorr with no stored beam and from 1.0 to 3.0 ntorr with stored beam, as the DIP anode voltages were decreased over the full range. No significant change in the residual gas composition was observed at all tested anode voltages, with and without stored beam.

## 3. DISCUSSION

We have measured very large pump current (milli-amperes) in the DIPs when there is stored beam in CESR, and have found the pump currents have no correlation with the pressures in the pumps. In figure 4, the measured DIP current is plotted as a function of anode voltage with total stored beam of 320 mA in CESR, for a typical DIP, B20W. As can be seen in figure 4, the DIP current increases with increasing anode voltage approximately linearly with stored beam in CESR. In contrast, the DIP current is small (microamps) and is found to depend on the anode voltage exponentially when there is no stored beam in CESR. It is clear that the rather large DIP current is induced by a coupling between the stored beam and the DIP. One measure of the coupling at any given beam current is the slope of the pump current vs the anode voltage, as in Fig. 4, or the DIP 'conductance'. As shown in Figure 5, this coupling is proportional to the total stored beam current.

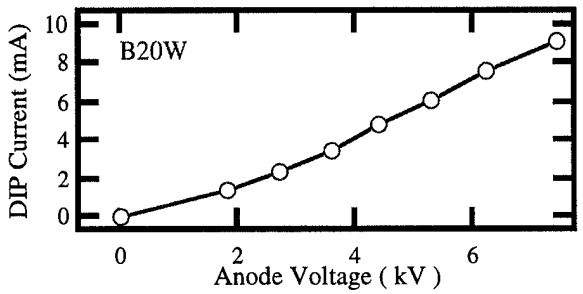



Figure 4. Measured DIP current as a function of the anode voltage with 320 mA total stored beam in CESR.

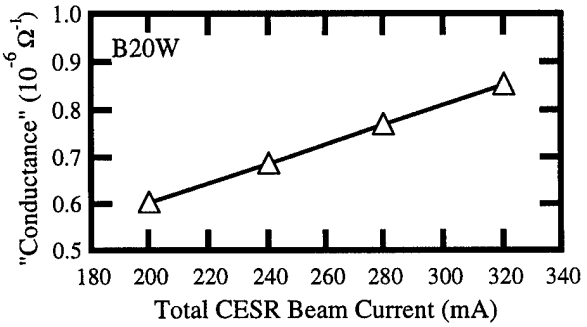



Figure 5. DIP 'conductance' vs. total stored beam current.

There may be two possible coupling mechanisms: (a) higher-order-mode (HOM) RF coupling which is sensitive to bunch structure and orbit of the stored beam; (b) photoelectrons produced in the DIPs by scattered synchrotron radiation (SR) photons. The photoelectron current depends on the total stored beam current and is insensitive to the beam bunch structure. To differentiate between the two mechanisms, we measured the DIP current with two different beam bunch structures, namely, 9-trains of one bunch (or 9x1), and 9-trains of two bunches (or 9x2). The results, as shown in Figure 6, indicate that DIP current is insensitive to the beam bunch structure. Considering the linear dependence of the coupling on the total beam current (see Figure 4),we can conclude that the large DIP current with stored beam is dominated by the photoelectron current induced by scattered SR photons.

Among many factors which affect the pumping speed of an ion pump, there are two fundamental

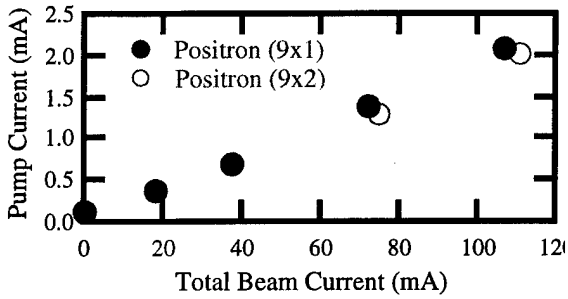


Figure 6. DIP current vs. stored beam current with different bunch structures of the stored beam (see text).

parameters for a given sputter-ion pump: electron cloud density in the pump cell and the sputtering yield of energetic ions on the pump cathode. At low pressures, the pumping speed can be expected to be proportional to electron density and sputtering yield. As is shown above, a sufficient high electron cloud density is always maintained in the DIP due to the photoelectrons when there is stored beam in CESR. In this case, the pumping speed is limited by the sputtering yield of ions on the pump cathode. As a matter of fact, the dependence of relative DIP pumping speed on the anode voltage (Fig. 2) almost resembles the ion-energy-dependence of sputtering yield[4] of typical residual gas ions on a titanium cathode (as in CESR). On the other hand, without stored beam in CESR, the DIP current, proportional to the electron cloud density in the pump cells, is observed to decrease exponentially when the anode voltage is reduced. As a result of the decrease of the electron density in pump cells, the pumping speed of DIPs drops rapidly at lower DIP anode voltage.

## 4. DIP CONTROLLER MODIFICATION AND OPERATIONAL EXPERIENCE AT REDUCED ANODE VOLTAGE

To summarize the above results: we have observed very different pumping behavior of the DIPs with and without stored beam in CESR. With stored beam, the DIP pumping speed is insensitive to the DIP anode voltage from 1.8 kV to 7.6 kV. On the other hand, with no stored beam in CESR, lower DIP pumping speed always results if the anode voltage reduced, and the DIPs virtually stop pumping when the anode voltage is decreased below 4 kV. Based on the results of this study, we have modified DIP controllers for over 80 DIPs in CESR. The CESR DIPs are grouped in twenty stations, and DIPs in each station may be remotely switched between a 'HIGH' state at 6.6 kV and a 'LOW' state at 2.2 kV. During normal CESR operation with stored beam, all the DIPs may be switched to the 'LOW' state to suppress the transverse beam instability, without sacrifice of DIP pumping speed. However, the DIPs will be set to the 'HIGH' state for long periods without stored beam or during start-up after any maintenance or upgrade shutdown, to provide effective pumping.

This modified DIP operation mode has been in place for more than a year in CESR. Both vacuum data and beam lifetime data have shown no degradation in DIP pumping speed and vacuum condition in the CESR arc regions. Meanwhile, the transverse instability has been greatly reduced from operating the DIPs at the reduced anode voltage.

However, we have observed pressure bursts in some DIPs which have operated at the reduced anode voltage over long periods. This has raised some concerns about metal-deposition from ion-sputtering, or so-called 'whisker' growth in the DIPs when operating at reduced anode voltage. At higher anode voltage filamentary metallic growth on the cathode is inhibited due to the higher discharge density and higher kinetic energy of sputtered ions in the DIP pumping elements.

Two proposals are currently under investigation to condition the DIPs in CESR after operating at lower anode voltage and to prevent possible 'whisker-growth' in the DIPs. One is to operate DIPs one to two stations at a time at higher voltage with stored beam over certain time periods, and cycle through all DIPs stations on a regular schedule. As the beam instability induced by DIPs in a few stations is usually relative small, this way of DIP-conditioning will have minor impact on the CESR HEP operation. But the effectiveness of this conditioning has yet to be evaluated. The other proposed conditioning method is to operate DIPs periodically at higher anode voltage under a relative high pressure (typically in $10^{-5}$ torr range) of $N_2$ or Ar gases. Though this method is reportedly[5] effective, it poses a much greater impact on CESR operation. The high-pressure conditioning can only be carried out during an accelerator shutdown period, and it usually conflicts with other shutdown activities.

## 5. CONCLUSION

We have measured DIP pumping speed at various anode voltages with and without stored beam in CESR. As a result of this study, most of the CESR DIPs are routinely operated at a much lower anode voltage. This has greatly suppressed a transverse beam instability induced by the DIPs and has also reduced photoelectron current in the DIPs. Long term DIP operation at the reduced anode voltage shows no degradation of vacuum condition and beam lifetime.

## 6. REFERENCES

1. N.B.Mistry, "Ultrahigh Vacuum Systems for Storage Rings and Accelerators",AIP Conference proceedings No.153, Physics of Particle Accelerators, American Institute of Physics, New York, 1987
2. J.T.Rogers and T.Holmquist, CEIBA Workshop, Tsukuba, 1995
3. Y. Li, R. Kersevan and N.B. Mistry, CESR Notes, 1997, CBN 97-11, Cornell University, Ithaca, NY
4. H.H.Anderson and H.L.Bay, in *Sputtering by Particle Bombardment I,* ed. (Springer-Verlag, 1981) by R.Behrisch, compiled sputtering yield data for Titanium, p.170;
5. Y. Suetsugu, *Vacuum*, **45**, 133 (1994)

# A TITANIUM SUBLIMATION CONTROL SYSTEM FOR THE CESR INTERACTION REGION

Yulin Li, Benjamin Manvell, William Lucas and Nariman Mistry
Laboratory of Nuclear Studies, Cornell University, Ithaca, NY 14853 USA

*Abstract**

Titanium sublimation pumps (TiSPs) are used to achieve ultrahigh vacuum in the interaction region (IR) of phase II. This paper describes a Ti sublimation control system developed to provide convenient and efficient control of 28 TiSP cartridges with 84 Ti filaments in the IR. The control system consists of RF filter networks, control cable networks, a PC controlled mobile power supply and multiplexer, and a LabView-based graphic control program. The RF filter network is necessary to block any RF pick-up from the stored beam by the TiSP filaments. The TiSP flashing is done using a constant power scheme.

## 1. INTRODUCTION

In the upgraded CESR phase II interaction region (IR), massive titanium sublimation pumping (TiSP) is employed to keep average pressure below 2 nano-torr at 300 mA of stored beam[1]. The extreme low residual pressure in the IR is essential to the Phase II operation as the scattered particles from the residual gas not only produce background in the CLEO high energy detector, but could also damage sensitive electronic components in the detector.

Six new vacuum chambers[1] with TiSP plenums are installed symmetrically on both sides of the interaction point (IP). There are a total of 28 TiSP cartridges (Model ST-22, Vacuum Generator Inc.) with a total of 84 Ti filaments (85%Ti/15%Mo alloy, Ø2.0 mm wire) installed on these new vacuum chambers. During the commissioning of Phase II, especially in the early stage of the operation, we anticipated a large synchrotron radiation desorbed gas load which would saturate titanium film deposited on the pumping plenum. A TiSP control system is called for to provide convenient and efficient re-activation of all the TiSP cartridges in the CESR IR.

## 2. SYSTEM DESCRIPTION

### *2.1. System Requirements*

(1)RF seal and filtering network

The TiSP filaments in the pumping plenum may couple RF power from the bunched beam to the environment. The RF leakage through the TiSP cartridge may produce noise or even cause damage to electronic components. The system must contain and filter out the RF power by at least 60 dB.

(2)Mechanical protection of vacuum feedthroughs of the TiSP cartridges.

(3)Multiplexing and central control

Multiplexing and control cable network of the system should enable control of all the Ti filaments on the 28 TiSP cartridges, which are distributed over 12 meters on each side of the IP, from one or two stations.

(4)Ti Flashing Control

A programmable power supply with PC-based control software to allow an operator to control and monitor the activation (or Ti flashing) process.

### *2.2. RF Seal and Filtering*

Mechanical protection, RF seal and filtering are provided by home-made TiSP boxes mounted on each of 28 TiSP cartridges, as shown in Figure 1. The box is divided into two compartments. The compartment A is made to be RF-tight with silver-brazed seams and wire-mesh gasket sealed joints. The TiSP filaments are connected to the compartment B via capacitance filter power feedthroughs (MTK Electronics, Inc.), which have a cut-off frequency of 10 MHz and a DC voltage drop of less than 10 mV at 50 A DC current. Further filter networks are included in the compartment B for the Ti flashing power line and Ti filament voltage monitoring lines, respectively, to filter out frequencies above 10 kHz.

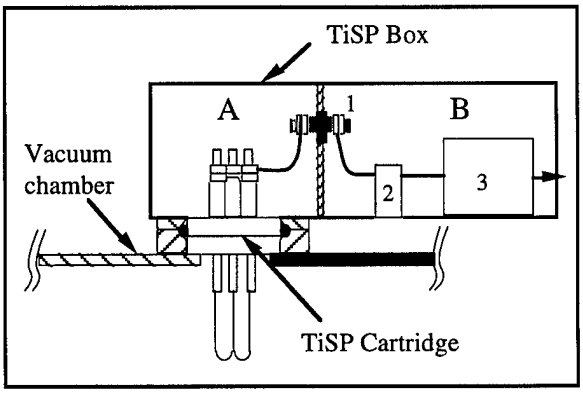



Figure 1. Schematic of CESR interaction region TiSP box. (1)Capacitance feedthroughs; (2)DC contacts (3)LC / RC filter networks

### *2.3. Multiplexing and cabling*

Cable network connect all the TiSP cartridges and Ti filaments to two TiSP flashing terminals, located about 15-m away from the IP on either side of the IP. Selection of TiSP chambers is done by plugging into corresponding power and control terminals, and selection of TiSP cartridges and Ti filaments is accomplished by a set of rotary switches on a multiplexing box.

* Work supported by the National Science Foundation

0-7803-4376-X/98/$10.00 © 1998 IEEE

*2.4. TiSP flashing controller*

A mobile TiSP flashing controller consists of a programmable DC power supply, a multiplexing switching box and a control PC. The computer reads back Ti filament current and voltage, and controls the power delivered to the filament through a multi-functional data acquisition plug-in card (National Instruments, LabPC+). TiSP flashing control software, developed with the graphic programming tool LabView (National Instruments, Inc.), allows an operator to set Ti flashing control parameters and monitor the flashing process in real-time. A *constant-power* Ti flashing mode is adopted in CESR. Measurements carried out by the authors[2] indicated that the constant power Ti flashing mode yields many more flashing cycles before filament failure while providing comparable Ti sublimation rate as compared to a *constant current* Ti flashing mode.

The Ti flashing process includes the following steps:

(1) TiSP cartridge and filament selection. The Ti flashing parameters are preset for all the TiSPs in the CESR IR, and these parameters are listed in Table 1.
(2) Filament test. A 100 mV voltage is applied to the selected filament. The flashing process ceases if the filament current at the testing voltage is less that 1A, as a typical filament resistance is much less than 0.1Ω.
(3) Power Ramp-up. A one-minute power ramp-up follows the filament test. The smooth power-ramp is designed to avoid current surge and thermal shock to the filament.
(4) Ti sublimation for assigned period.
(5) Record average sublimation current and voltage.

Table 1. TiSP Flashing Parameters for Phase II CESR IR

| Chamber Name† | Q1 | ISP | SB3 |
|---|---|---|---|
| Distance from IP (m) | 2.2-2.5 | 6.4-7.6 | 8.8-12.1 |
| Flashing Power (W) | 195 | 205 | 205 |
| Flashing Time (min.) | 2 | 2 | 2 |

†see ref. [1] for description of the chambers

Each of the six TiSP pumping vacuum chambers is equipped with a cold cathode gauge (CCG). The TiSP chamber pressure is monitored during the power ramp-up and the Ti sublimation, and an "Over-Pressure" (pressure set-point, typically $10^{-5}$ torr) will terminate the flashing process. The average sublimation current and voltage are recorded for each filament for every flashing, in order to document the filament resistance change. As discussed below, the filament resistance and the resistance change from each flashing cycle is a good measure of filament status and Ti sublimation rate.

## 3. Ti FILAMENT CHARACTERIZATION

Since the installation of the CESR phase II IR vacuum chambers in late 1995, some of the Ti filaments have been subjected to many flashings due to the large gas load created by the intense synchrotron radiation. It is important to be able to characterize the status of a Ti filament installed in the IR vacuum system. We have conducted extensive measurements of Ti sublimation rate, by measuring the pumping speed and pumping capacity of the Ti film in a test vacuum chamber. These measurements show that one can characterize the status of a Ti filament by its resistance. The details of the measurements are reported in Reference [2], with major results summarized as below.

*3.1. Filament lifetime vs. filament resistance*

One of the important parameters of a Ti filament is its ultimate lifetime, or total number of flashing cycles before failure of the filament. During the test, Ti filaments are repeatedly flashed at either constant current mode or at constant power mode in a testing setup until the failure of the filaments. In the *constant current* mode, the filaments were flashed at a current of 55 Amps for two minutes for each cycle with 1-minute ramp-up. In the *constant power* mode, the filaments were flashed at 205W for 2 minutes for each cycle with a 1-minute ramp-up. Two filaments were tested under the constant current mode, and four were tested under the constant power mode. The resistance of the filaments were recorded for each flashing, and the typical results are given in Figure 2. Several conclusions may be drawn from the results. First, a Ti filament lasts more than 200 activation cycles for the constant current mode and nearly 800 cycles for the constant power mode. This assures us that there is no need for concern about the lifetime of the Ti filaments used on the TiSP cartridges installed in the CESR IR at normal situation, as we expect to flash less than 100 times over a 5-year operation period. Second, the characteristic resistance curves for the two activation modes are somewhat similar. For comparison, the rates of resistance change are plotted in Figure 3. Initially, the filament resistance increases with number of activation cycles at a

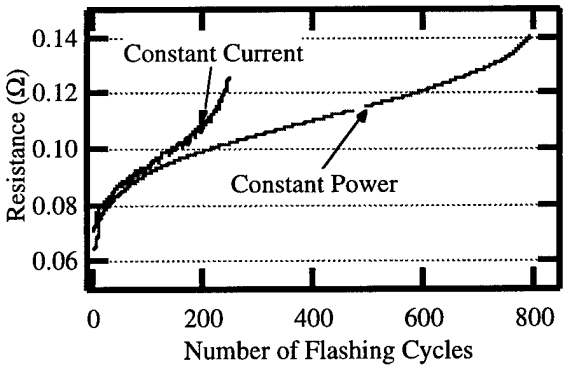



Figure 2. Resistance of Ti filaments during Ti flashing

very large rate for both activation modes, and the rate of resistance change drops rapidly with the activation cycles. After certain activation cycles, the Ti filaments reach a

stable condition and the rate of resistance change levels off at a smaller constant rate. Lastly, the rate of resistance changes starts to increase rapidly before a filament opens up. This is the case for both activation modes. In practice, one may use this feature to predict when a Ti filament is about to fail, so that one can switch to another filament before the filament opens up, as an open Ti filament may short the other filament(s) on the same TiSP cartridge.

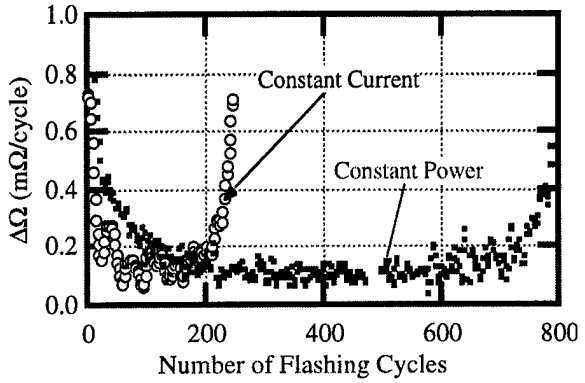



Figure 3. Resistance change rate of Ti filaments, as derived from the results shown in Figure 2.

*3.2. Sublimation rate vs. filament resistance*

Another important parameter of a Ti filament is the Ti sublimation rate at a given flashing power. As direct measurement of the absolute sublimation rate is rather difficult, we choose to measure relative sublimation rate by measuring pumping capacity of the sublimated Ti film, since, in practice, we are interested in how the Ti sublimation rate, hence the pumping capacity, changes with the filament condition. In Figure 4, the measured relative Ti sublimation rate is plotted as a function of the filament resistance. We found that the sublimation rate of a Ti filament can be characterized very well by its resistance. For the filament (85%Ti/15%Mo, Ø2.0 mm dia., 12 cm long) used in the CESR IR and tested here, the sublimation rate first increases with the filament resistance, simply due to the increased power dissipation on the filament as the filament diameter decreases. After reaching a maximum sublimation rate at the filament resistance of ~70 mΩ, the rate decreases relative rapidly as the Ti filament resistance increases beyond 70 mΩ. The sublimation rate levels off as the Ti filament resistance gets further higher. It is reported[3,4] that a metallurgical transition occurs in the Ti/Mo alloy due to the relative composition change in the alloy. This metallurgical transition results in a "micro-crystalline" surfaces with higher emissivity and therefore lower Ti filament temperature at a given sublimation power. The decrease in the Ti sublimation rate, with Ti filament resistance between 70 to 85 mΩ, may be due to this metallurgical transition of the Ti filament. The Ti sublimation rate levels off at a rate which is 5 to 6 times smaller than at its peak value with its resistance higher than 90 mΩ. Also shown in Figure 4 is the Ti filament resistance change rate as a function of filament resistance. It is expected that the resistance change rate scales with the sublimation rate, as the resistance change rate reflects the loss of Ti from sublimation.

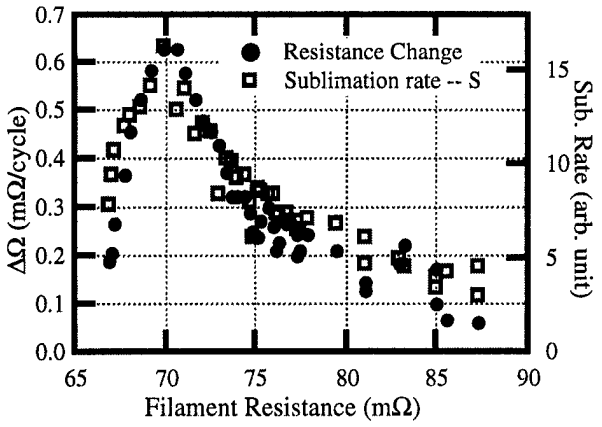



Figure 4. Resistance change rate and relative sublimation rate as a function of Ti filament resistance.

## 4. CONCLUSION REMARKS

A Ti sublimation control system is developed for the CESR phase II IR. This system successfully meets the requirement of the CESR phase II operation. The laboratory tests showed that one can keep track of a Ti filament status and its sublimation rate by documenting its resistance and resistance change rate.

## *Acknowledgment*

Authors would like to thank Ilkka Koskelo for assistance in laboratory tests.

## REFERENCE

1. N.B. Mistry, R. Kersevan and Y. Li, "Massive Titanium Sublimation Pumping in the CESR Interaction Region", these Proceedings
2. Y. Li, LNS Notes, CBN-97-9, 1997, Laboratory of Nuclear Studies, Cornell University, Ithaca, NY 14853 USA.
3. R.W. Lawson and J.W. Woodward, *Vacuum*, **17**, 205 (1967)
4. K.M.Welch, Capture Pumping Technology, p185-223 Pergamon Press, 1991.

# THE DESIGN, CONSTRUCTION AND TESTING OF A MULTIPOLE WIGGLER MAGNET TITANIUM VACUUM CHAMBER FOR THE SRS.

N. Bliss and C.L. Dawson, CLRC Daresbury Laboratory, Warrington, WA4 4AD UK.

*Abstract*

A vacuum chamber is required for two new insertion devices (IDs) at the SRS. The chamber has been designed, finite element analysis performed, and a prototype constructed and successfully tested. The chamber is 1208 mm in length, it has an internal aperture of 134 mm x 16 mm and a minimum wall thickness of 1 mm. The chamber has been precision machined in two halves from titanium alloy and electron beam (EB) welded in order to meet the demanding tolerances. Titanium alloy was selected in preference to more conventional ultra high vacuum (UHV) materials, due to its electron beam weldability, low distortion and outgassing rates. The design, construction and processing has been conducted to UHV standards to achieve a working pressure of 1 x $10^{-9}$ mbar.

## 1 INTRODUCTION

An upgrade to the 2 GeV, 2nd generation synchrotron radiation source operating in the UK is planned, which will reconfigure existing components of the storage ring to create space into which two new IDs will be installed [1].

The devices will provide photon beams of high flux and medium brightness at about 10 keV and allow up to 2 new stations to be built on each beamline. The magnet design is a hybrid multipole wiggler consisting of Neodymium-Iron-Boron permanent magnets and Vanadium Permendur pole pieces which has been optimised [2] to produce a high peak on-axis magnet field of 2.0T with the shortest possible period providing photons with a critical energy of 5.3 keV.

In order to realise the high field strength and reduce the volume of permanent magnet material a minimum magnet gap is required. To achieve this the amount of vacuum chamber material at the critical location between the electron beam-stay-clear zone and the poles of the ID must be minimised. In addition, the storage ring electron beam stay clear vertical aperture at the location of the ID has been assessed [3] and it has been concluded that it can be reduced, from the present 36 mm to 15 mm, without reducing the beam lifetime by more than about 15%.

## 2 DESIGN

Careful consideration has been given to the chamber design, material selection and construction technique, in order to meet the ID requirements and allow full integration into the SRS, Table 1.

Austenitic stainless steels grades 304LN and 316LN are often chosen as the material for fabricated storage ring UHV chambers due to low magnetic permeability requirements within magnet apertures (better than 1.005) and their high proof stress. Aluminium alloys such as 6063 T6 are also widely used, especially when an extruded chamber is the more cost effective approach. Since only two production chambers of this design are required at only 1208 mm in length, a fabricated vessel construction is preferred.

Table 1. Specification for the Vacuum Chamber

| | |
|---|---|
| Magnet gap | 19.2 mm |
| Maximum external chamber size at poles | 18.8 mm |
| Horizontal electron beam stay clear | ± 53.0 mm |
| Vertical electron beam stay clear | ± 7.5 mm |
| Horizontal photon beam stay clear | + 79.0 mm |
| Chamber length | 1208 mm |
| Vacuum pressure with e⁻ beam on | 1 x $10^{-9}$ mbar |

The chamber needs to be a precision construction to meet the stringent technical requirements on size and geometric shape, therefore the design chosen is a precision machining in two halves with full penetration EB welds along each side of the chamber to reduce distortion to a minimum, Figure 1.

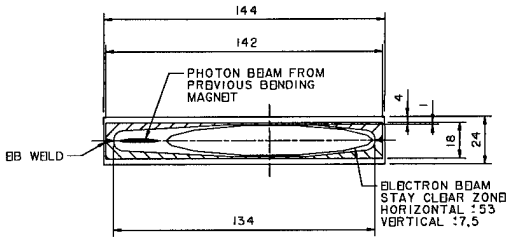



Figure 1. Section through Chamber

Low magnetic permeability stainless steels have low ferrite content and consequently higher nitrogen content making electron beam welding difficult but not impossible [5]. Titanium alloy grade Ti-6AL-4V was chosen in preference to stainless steel mainly because of its electron beam weldability. Smooth welds are possible with less than half the weld distortion compared to stainless steel due to its high welding speed and low coefficient of thermal expansion. Titanium alloys have a low out gassing rate [6], high proof stress and low density. A disadvantage is its lower modulus of elasticity which results in a greater deflection due to vacuum loading. Table 2 shows a comparison of mechanical properties for Stainless steel 316LN, Aluminium alloy 6063 T6 and Titanium alloy Ti-6AL-4V. The magnetic permeability of all three materials is better than 1.005.

0-7803-4376-X/98/$10.00 © 1998 IEEE

Table 2. Material Property Comparison [4]

| Property | Aluminium Alloy Gd. 6063 T6 | Stainless Steel Gd. 316LN | Titanium Alloy Gd. Ti-6Al-4V |
|---|---|---|---|
| 0.2% Proof Stress (MPa) | 60-180 | 316 | 900-970 |
| Young's Modulus (GPa) | 67 | 201 | 105-120 |
| Thermal Expansion (/°C) | $22x10^{-6}$ | $17x10^{-6}$ | $7.9x10^{-6}$ |
| Hardness HB | 75 | 197 | 255 (measured at DL) |
| Density ($kg/m^3$) | 2690 | 7900 | 4420 |

It is extremely difficult to weld stainless steel to titanium alloy, therefore the vacuum flanges were also made from titanium alloy Ti-6AL-4V which has a measured hardness of 255 HB compared to the 170 HB required for a good knife-edge.

The cross-section of the vessel is asymmetric to clear the photon beam on one side of the chamber and maintain a minimum span, as seen in Figure 1. To keep as much rigidity as possible in the chamber the 1mm wall section has been restricted to the pole areas only.

Finite Element Analysis of the chamber was performed using PTC Mechanica with P-type solid elements used with general convergence set to 10% on global RMS strain energy. The chamber has two lines of symmetry, therefore it was only necessary to construct a one quarter model.

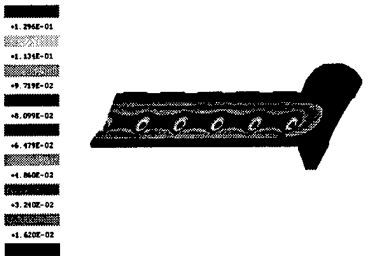


Figure 2. Deflection Contour Plot

The maximum Von Mises Stress due to atmospheric pressure loading and self weight was relatively low at 67 $N/mm^2$ and the maximum deflection at the centre of the thin wall section was predicted to be 0.15 mm, as shown in Figure 2.

## 3 CONSTRUCTION

The ID chamber manufacturing procedure consists of the following steps:

(i) Pre machining of vacuum chamber halves (VCH)
(ii) stress relieving of VCH
(iii) final machining of the VCH with length oversize
(iv) UHV clean the VCH and welding fixture
(v) electron beam weld the two longitudinal welds
(vi) UHV clean and vacuum leak test
(vii) machine weld preparations for the VC and flanges
(viii) UHV clean the VC, flanges and fixture
(ix) electron beam weld the 2 orbital flange welds
(x) UHV clean and vacuum leak test.

Machining of titanium alloy was similar to that of an alloy steel with the same strength level. Rigidity of both the work piece and the cutting tool was essential. Titanium alloy has a lower modulus of elasticity than steel resulting in spring-back when machining, which limited the achievable thin wall section. To reduce this effect fixtures were used to support both sides of the chamber halves.

Titanium also has a tendency to gall and smear onto other metals. Cutting tools need to have a good surface finish with machine speeds low and feeds as high as practical for the various operations. Special care was needed in following procedures for handling the swarf as under certain circumstances it is inflammable.

The stress relieving and EB welding of the chamber halves was conducted on a rigid flat stainless steel fixture, as shown in Figure 3.

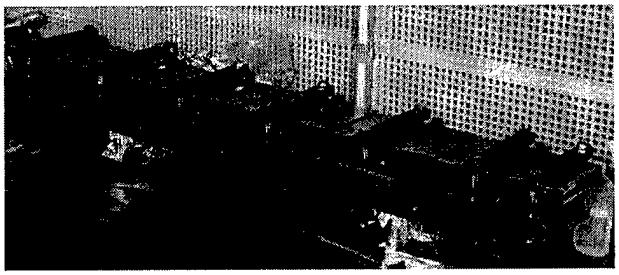


Figure 3. Vacuum Chamber on the Welding Fixture

Weld test pieces for both longitudinal and orbital flange welds were conducted to establish optimum EB welding machine settings, to achieve acceptable UHV quality internal weld beads. The longitudinal full penetration welding of the two chamber halves was conducted using a 40 mA beam at 2000 mm/min and the orbital EB welds between the pipe ends and the knife edge flanges was conducted using a 10 mA beam at 1000 mm/min to produce a 3 mm penetration depth. All welding was performed at TWI in machine EBII with gun type 100kW RF at a vacuum pressure < $5x10^{-3}$ mbar.

All machining, assembly, measurements and testing of the chambers was conducted in-house.

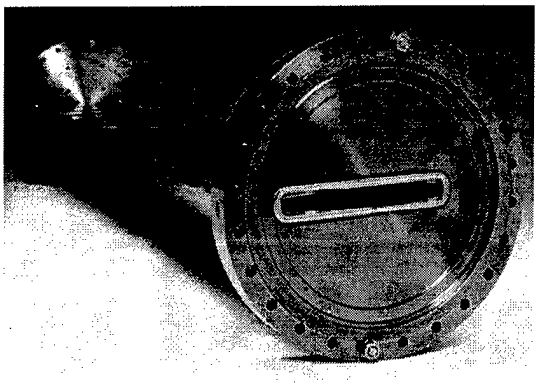


Figure 4. Completed Chamber

## 4 TESTING

The external faces at the position of the 11 poles have been measured on both sides of the chamber along three lines: line 2 along the centre-line of the chamber and lines 1 and 3 at the edges. Figure 5 shows the results for both sides of the vacuum chamber.

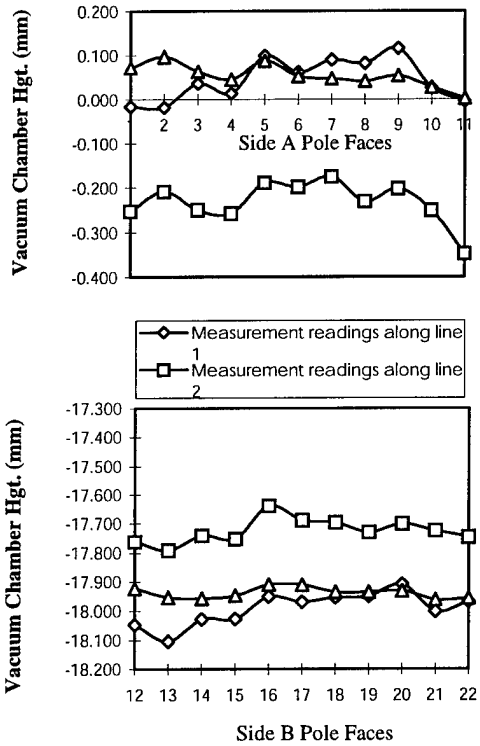



Figure 5. Flatness Measurements

Flatness of the external faces of the chamber in the area covered by the 11 pole faces, under vacuum loading was 0.3 mm. The maximum parallel plane measured over the poles occupied by chamber material without twisting the chamber was 18.2 mm, 0.6 mm less than the specified value of 18.8 mm. Table 3 shows a summary of the achieved specification.

Table 3. Achieved Specification

| | |
|---|---|
| Magnet gap | 19.2 mm |
| Maximum external chamber size at poles | 18.2 mm |
| Minimum internal chamber size at c/line | 15.3 mm |
| Flatness tolerance over 11 pole faces | 0.3 mm |
| Vessel wall thickness at pole locations | 1.00-1.15 mm |

The maximum deflection measured at the thin wall area of the chamber under atmospheric pressure was 0.13 mm on each side, which is in good agreement with the theoretical value of 0.15 mm, reported in section 2.

The EB welds and titanium alloy knife-edge sealing flanges have successfully passed all vacuum leak tests to $1x10^{-9}$ mbar l/s, before and after a 250°C vacuum bake. Vacuum outgassing rate tests are currently being undertaken and a programme of repetitive making and breaking of titanium alloy test flanges is underway, to assess the lifetime of the titanium alloy knife-edges.

Future developments to the prototype vessel include adding four titanium alloy electron beam position monitors, two at each end of the chamber in a small space available between the magnet array and the chamber flanges. The modification is planned to be complete by November 1997 and two new production chambers by April 1998.

## 5 ACKNOWLEDGMENTS

The authors would like to thank a large number of Daresbury staff that have been involved with the project especially, although not exclusively, C. Hill and S. D. Postlethwaite for their contribution to the design; to C. Hodgkinson and G. D. Markey for manufacturing; and to R. J. Reid for his expertise in vacuum technology.

## REFERENCES

[1] J A Clarke and M W Poole, "Upgrading the Daresbury SRS with additional insertion devices and its implications for the storage ring layout", Proceedings of the 5th European Particle Accelerator Conference, Sitges, 1996, p623.

[2] J A Clarke, "The Magnetic Design of a High Field Permanent Magnet Multipole Wiggler for the SRS", these proceedings.

[3] J A Clarke and H L Owen, "Operation of the Daresbury Synchrotron Radiation Source with reduced vertical aperture", Proceedings of the 5th European Particle Accelerator Conference, Sitges, 1996, p620.

[4] N A Waterman and M F Ashby, "Elservier Materials Selector", Elservier Science Publishers Ltd., 1991.

[5] C S Punshon, TWI, Cambridge, UK. Private Communication, 18 January 1996.

[6] Michio Minato and Yoshio Itoh, "Vacuum Characteristics of Titanium", Journal of Vacuum Science & Technology A, Second Series, Vol. 13 No. 3, May/June 1995.

# FNAL MAIN INJECTOR $\gamma_t$-JUMP SYSTEM BEAMTUBE DESIGN

J. R. Leibfritz
Fermi National Accelerator Laboratory*, P.O. Box 500, Batavia, IL 60510, USA

*Abstract*

The design of the FNAL Main Injector $\gamma_t$-jump system calls for a special beamtube that is to be placed inside the pulsed magnets. The requirements for this beamtube include: an elliptical shaped tube that mates with the existing vacuum system, high electrical resistivity for reducing the eddy current effects, high strength for withstanding the vacuum load, and a design that facilitates simple fabrication and installation. Inconel 718 was selected to meet these criteria. Results obtained from analytical calculations, 2-D and 3-D finite element modeling, and testing of prototypes were in general agreement. The design process, analysis results, and final specifications are discussed.

## 1 INTRODUCTION

The pulsed magnets in existing $\gamma_t$-jump systems have typically contained round beamtubes made of ceramic materials. This type of beamtube is used because of the unique requirements of a $\gamma_t$-jump system [1], which include: a high electrical resistivity to minimize eddy current effects, high strength to withstand the vacuum load, and the need to mate with the existing vacuum system. The FNAL Main Injector (MI) vacuum system consists of a stainless steel 316L beamtube with a somewhat elliptical shape. Because of the shape of the MI beamtube, using a round (ceramic) beamtube for the $\gamma_t$-jump magnets would introduce significant transition problems in the system. As a result, an effort was made to develop a metal beamtube with an elliptical cross-section that satisfied all the necessary requirements of the $\gamma_t$-jump system. In addition to solving the transition problems, such a design would also simplify the fabrication and installation processes.

Based on the Main Injector $\gamma_t$-jump system requirements described above, a metal (Inconel 718) beamtube with an elliptical cross-section has been developed. Data from analytical calculations, 2-D and 3-D finite element modeling, and measurements of prototypes were used in the development of the final design.

## 2 DESIGN PROCESS

### *2.1 Material Selection*

Of all the materials available for use in fabricating the MI $\gamma_t$-jump system beamtube, one material was found that seemed ideally suited to meet all the necessary requirements, Inconel 718. The properties that make this material attractive for this application include its: high electrical resistivity, good machineability and weldability, and high mechanical strength. Figure 1 provides a comparison of selected material properties for Inconel 718 and stainless steel 316L.

| Property | Inconel 718 | S.S. 316L |
|---|---|---|
| Electrical Resistivity ($\rho$) ($\mu\Omega$-cm) | 125 | 73 |
| Tension Modulus (E)·(psi) | $29.8 \times 10^6$ | $28.0 \times 10^6$ |
| Poisson's Ratio ($\nu$) | 0.284 | 0.290 |
| Yield Strength (ksi) | 150 - 220 | 35 |
| Ultimate Strength (ksi) | 180 - 230 | 80 |

Figure 1: Selected material properties of Inconel 718 and stainless steel 316L.

### *2.2 Eddy Current Effects*

Eddy current effects have a negative impact on the field inside the beamtube. The extent of these effects is directly proportional to the conductivity of the beamtube. As a result, it is preferable to use a beamtube with a low conductivity. The conductivity of an elliptical beamtube can be approximated using the following equation:

$$\gamma = (1/\rho) \times t$$

where ($\gamma$) is the conductivity in $\mu\Omega^{-1}$, ($\rho$) is the resistivity in $\mu\Omega$-cm, and (t) is the thickness in cm. The beamtube used in the Main Injector accelerator is made of stainless steel 316L and has a wall thickness of 0.060" (0.152 cm). Using the above equation, the conductivity of the existing MI beamtube is 0.002 $\mu\Omega^{-1}$. Whereas, the conductivity for a 0.025" (0.064 cm) thick beamtube made of Inconel 718 is 0.0005 $\mu\Omega^{-1}$. By using a thin Inconel beamtube for the $\gamma_t$-jump system magnets, the conductivity can be reduced by a factor of four. For a detailed discussion of the eddy current effects of a beamtube in a pulsed magnet, see [2].

### *2.3 Mechanical Analysis*

Once a suitable material had been found, the next step in the design process was to study the mechanical characteristics associated with various geometries of elliptical beamtubes made from Inconel 718. Analytical calculations [3] were used to model the effects (deflections and stresses) an external vacuum load of 14.7 psi (1 atm)

* Operated by Universities Research Association, Inc., under Contract No. DE-AC02-76CH03000 with the U.S. Department of Energy

0-7803-4376-X/98 /$10.00 © 1998 IEEE

would have on various sized elliptical beamtubes. Three equations were used for these calculations:

$$|\sigma_2|_{max} = \left|\frac{6K_2pa^2}{t^2}\right| + \left|\frac{pa}{t}\right|$$

$$\delta_y = 2C_1\left(\frac{pa^4}{D}\right)$$

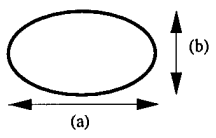
$$\delta_x = 2C_2\left(\frac{pa^4}{D}\right)$$

where ($\sigma_2$) is the maximum stress, ($\delta_y$) and ($\delta_x$) are the maximum vertical and horizontal deflections, respectively, (p) is the internal pressure, (a) is half the major diameter, (t) is the wall thickness, (D) is the flexural rigidity, and ($C_1$), ($C_2$), and ($K_2$) are geometry dependent functions of the ellipse being studied (see [3] for values of $C_1$, $C_2$, and $K_2$).

The goal of these calculations was to find a geometry that would deform, under vacuum, to the vertical aperture of the MI beamtube, while not exceeding the maximum allowable bending stress of the material, [0.6 x (yield strength)]. The following values were used in the above equations for this analysis: p = -14.7 psi, a = 1.950", t = 0.025", D = 42.2 in-lb., $C_1$ = 0.0407, $C_2$ = 0.0248, and $K_2$ = 0.166.

Once a desirable geometry was found, a 2-D finite element model was created, using ANSYS, to verify the analytical calculations and confirm the feasibility of such a design. The ANSYS results agreed (within an acceptable error) with the analytical calculations and were within the acceptable limits (see Figure 2).

Material: Inconel 718
Wall Thickness: 0.025"
Major Diameter (a): 3.90"
Minor Diameter (b): 2.50"
Internal Pressure: -14.7 psi




| Results | Analytical | ANSYS (2-D) |
|---|---|---|
| Maximum Stress | 90,223 psi | 87,799 psi |
| Vertical Deflection | -0.410" | -0.442" |
| Horizontal Deflection | 0.250" | 0.269" |

Figure 2: Analytical and (2-D) finite element results of elliptical beamtube under vacuum load.

*2.4 Fabrication of Prototypes*

Based on the results of the analytical and 2-D ANSYS calculations, prototype beamtubes were fabricated for testing. The material used to make the prototypes was 0.025" thick, Inconel 718. Three 36" long pieces of material were cut to size and rolled into round tubes. Two of these 36" long tubes were made to achieve the cross-section used in the analytical calculations. The third tube was made to a slightly larger cross-section. The round tubes were then electron-beam welded along their length. After welding, the prototype tubes were vacuum leak checked to ensure the quality of the weld. The round tubes were then cut into 18" lengths and pressed into the desired elliptical shape using a device developed at Fermilab. Once the desired elliptical shape was achieved, the tubes were annealed and age-hardened. The annealing process relieves any stresses that may have developed from welding and forming the material. The age-hardening process gives the material the high mechanical strength required to withstand the vacuum loads placed on it.

*2.5 Testing of Prototypes*

The deflections, under vacuum, of the 18" long prototypes were measured to test the validity of the analytical calculations and to see if the design would work. All the prototypes deflected significantly less than the calculations had predicted. These results raised some questions as to the validity of the models used. As a result, all the variables used in the models were verified. The exact thickness of the material was checked, the material properties of the prototypes were experimentally confirmed, and the model was redone using the exact geometry of the actual prototypes. None of these tests uncovered any significant variations from the data used in the original model.

The only other possibility was that because of the short length of the prototypes (18"), end effects from the vacuum-test setup were affecting the results. Because the analytical and 2-D finite element models assume an infinitely long tube, end effects are not taken into consideration. To account for these end effects, a 3-D ANSYS model was created. This model consisted of an 18" long beamtube, having the same geometry and end constraints as the test setup. The results of the 3-D model agreed (within an acceptable error) with the measurements of the prototype (see Figure 3). These results confirmed that the end effects do play a significant role in the amount of deflection of the beamtube.

Major Diameter (a): 4.289"
Minor Diameter (b): 2.846"

| Results | (3-D) ANSYS | Test Measurements |
|---|---|---|
| Maximum Stress | 41,400 psi | Not Measurable |
| Vertical Deflection | -0.231" | -0.242" |
| Horizontal Deflection | 0.139" | 0.132" |

Figure 3: Prototype measurements and (3-D) finite element results of elliptical beamtube under vacuum load.

*2.6 Transition Flanges*

Because Inconel 718 can be welded directly to stainless steel, the connection of the $\gamma_t$ beamtube to the existing Main Injector beamtube can be easily accomplished using a minimum amount of space. Thin (1/8") metal flanges could be welded to each end of the mating tubes. These flanges can then be welded together, creating a vacuum tight connection.

A set of Inconel flanges, that matched the elliptical profile of the prototype beamtube, was fabricated and welded to each end of the $\gamma_t$ beamtube. (During the welding process, it is critical that the material is clean and an argon purge used to prevent any oxidation of the welded surfaces.)

The final step in the design of the prototype was to ensure that the Inconel to stainless steel connection could be made and that the resulting system would be vacuum tight. To verify this, two stainless steel blank flanges (one with a pump-out port) were fabricated and welded to the Inconel flanges. The same welding procedure was followed as before. The prototype beamtube was vacuum leak checked to $1.6 \times 10^{-10}$ mm Hg (torr) and the deflections measured. No leaks were detected in the system and the measured deflections agreed (within an acceptable error) with the 3-D ANSYS model (modified to incorporate the flanges) results (see Figure 4).

Major Diameter (a): 4.289"
Minor Diameter (b): 2.846"

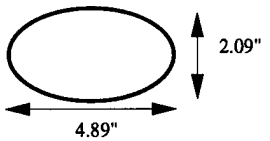
| Results | (3-D) ANSYS | Test Measurements |
|---|---|---|
| Maximum Stress | 51,460 psi | Not Measurable |
| Vertical Deflection | -0.143" | -0.169" |
| Horizontal Deflection | 0.092" | 0.100" |

Figure 4: Prototype measurements and (3-D) finite element results of elliptical beamtube (with flanges) under vacuum load.

## 3 FINAL DESIGN

The last step in the design process was to determine the final geometry for the $\gamma_t$ beamtube, so that it mates properly with the existing Main Injector beamtube. Because all the measured data of the prototypes agreed very closely with the results of the 3-D ANSYS model, it was assumed that if the 3-D ANSYS model was modified to the correct final geometry, these results could be used for the final design. By making this assumption, the need to fabricate a final prototype to these exact dimensions would be eliminated. The ANSYS results showing the calculated geometry, deflections, and stresses of the final design of the FNAL Main Injector $\gamma_t$-jump system beamtube are shown in Figure 5.

Material: Inconel 718
Wall Thickness: 0.025"
Internal Pressure: -14.7 psi




| Results | (3-D) ANSYS |
|---|---|
| Maximum Stress | 62,210 psi |
| Vertical Deflection | -0.156" |
| Horizontal Deflection | 0.063" |

Figure 5: Geometry and finite element results of final Main Injector $\gamma_t$ beamtube design.

The maximum stress (62,210 psi) for this design is well below the allowable bending stress [(0.6)(yield strength) = 90,000 psi] for Inconel 718 and the deflections are acceptable. An isometric drawing of the final design for the FNAL Main Injector $\gamma_t$-jump system beamtube is shown in Figure 6.

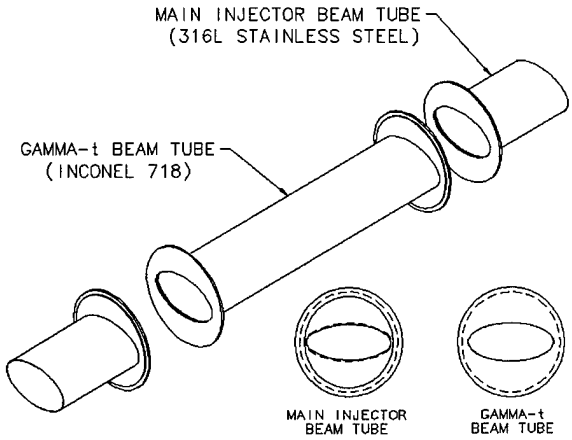



Figure 6: Isometric drawing of FNAL Main Injector $\gamma_t$-jump system beamtube design.

## 4 CONCLUSION

Based on the work described above, the design of an elliptical beamtube, made from Inconel 718, for the FNAL Main Injector $\gamma_t$-jump system seems to be a feasible alternative to the traditional ceramic design. In addition to meeting all the required design parameters, this design also provides for easy fabrication and installation with the existing Main Injector vacuum system.

## 5 ACKNOWLEDGMENTS

Technical support for the design of this beamtube was provided by B. Brown, W. Chou, M. May, K. Ng, P. Martin, M. Rauchmiller, B. Rush, L. Sauer, D. Snee, and S. Wesseln.

## REFERENCES

[1] W. Chou et al., "The Design of a $\gamma_t$-Jump System for the FNAL Main Injector," this conference.

[2] Fang, W. Chou, "Analysis and Measurements of the Eddy Current Effects of a Beamtube in a Pulsed Magnet," this conference.

[3] Avery, G. Tidrick, "Structural Analysis of an Elliptical Chamber with a Uniform Pressure Loading," Engineering Note, UCID-3215, LBL Berkeley, 1968.

# COMPARISON OF THE QUALITY OF TWO ECRIS VACUUM STANDS*

J.Pivarč†, K.D.Tumanov, V.B.Kutner, A.I.Ivanenko, J.Pivarč, jun.‡
Joint Institute for Nuclear Research, Flerov Laboratory of Nuclear Reactions
141980 Dubna, Moscow region, Russia

*Abstract*

The DECRIS (Dubna Electron Cyclotron Resonance Ion Source) and ECR-4M (GANIL ECRIS) high vacuum systems are described and compared. The test results of the vacuum systems are presented with respect to desorption and leakage characteristics. Also illustrated are the construction of two stands.

## 1 INTRODUCTION

The vacuum system (VS) of the ECR ion source is one of the main components of every source. Whereas the operating pressure ranges for the vacuum systems of accelerators are $10^{-4}$ - $10^{-9}$ Pa [1] the required operating pressure range for the vacuum system of the ECR ion source is $10^{-2}$ - $10^{-5}$ Pa, respectively. Basically, it consists of stainless steel or cooper beam tubes pumped with turbomolecular, cryopumps combined with rotary pumps and adsorption traps. A combination of turbomolecular and rotary pumps was used in the first DECRIS - 14 ion source. Another combination is being used for the ECR-4M ion source. It is mainly based on a combination of turbomolecular, cryopumps and rotary pumps.

In this paper there are presented two ECR ion source vacuum stands. Given are the constructions of the stands as well as measured residual gas analyser spectra and desorption rates and leakages.

## 2 DESCRIPTION OF THE STANDS

About 40 ECR ion sources stands have been built in different countries. Their performances are steadily improved over the last decade.

### *2.1 DECRIS-14 ion source vacuum stand*

One main and two auxiliary pumping units are used providing clean, safe pumping with the pressure monitoring of the DECRIS-14 ion source vacuum stand. It is designed in order to produce an average dynamic pressure of $10^{-4}$ Pa. Basically, it consists of 7 cm dia stainless steel, 4 cm dia copper, 10 cm dia steel and 4 cm dia duralumin beam tubes pumped by a combination of 500 l $s^{-1}$ turbomolecular pumps (VMN - 500) [2] and a rotary pump (BL-90) [3]. The pumping units are spaced at about 1.5 m intervals and contain besides the pumps, high vacuum gauges, electrodes and various beam diagnostic elements. The total length of the high vacuum beam tubes is about 3 m. The high vacuum volume of the stand is about 38 l.

After 20 h of pumping the leak rate of the DECRIS-14 vacuum system is bellow 5 x $10^{-3}$ Pa l $s^{-1}$. The results of the desorption rate and leakage measurements are shown in Figure 1. The best vacuum conditions are obtained after a 200 h pumping.

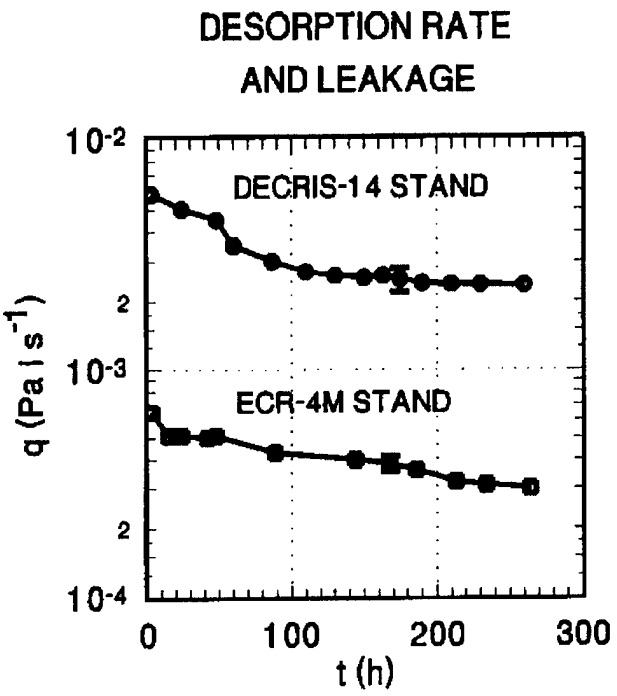



Figure 1: Measured desorption rates and leakages q of the DECRIS-14 and the ECR-4M vacuum stands as a function of pumping time 't'.

Figure 2 shows the mass spectrum of the residual gases which are evolved from the DECRIS-14 VS. A mass spectrometer MX 7304 gauge [4] was placed in the region of cube $C_2$. The spectrum is taken at a pressure of 1.75 x $10^{-5}$ Pa. By spectrum analysis one can see the subsequent contamination by hydrocarbons and other organics. The peak sets of 27,29; 39,41,43; 55,57; 69; 79; 89; 109; 119; 149 from the Rubber 7889 are shown. However, some of these hydrocarbons are also observed in the spectrum of the rotary pump oil and other elastomer seals such as 'O' ring seal VITON Roumania (peak sets: 27,29; 39,41,43; 55; 149). The spectrum illustrates the expressive water vapour contamination. All these effects could be, however, reduced by using two or more adsorption traps in sequential operation above the rotary pumps.

* Work supported by the VEGA L3 Ltd. firm, Nezábudková 20, SK-821 01 Bratislava, Slovak Republic.

† Permanent address: Institute of Physics, Slovak Academy of Sciences, Dúbravská cesta 9, SK-842 28 Bratislava, Slovak Republic.

‡ Working-place address: Martin-Luther-University, Dept. of Physics, NMR Group, Friedemann-Bach-Platz 6, D-06108 Halle/Saale, Germany.

0-7803-4376-X/98/$10.00 © 1998 IEEE

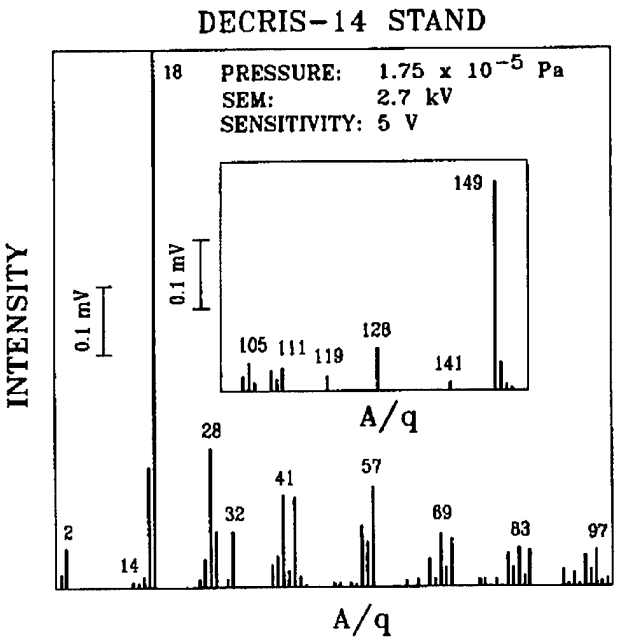



Figure 2: Measured mass spectrum of the residual gases from the DECRIS-14 vacuum stand.

### 2.2 *ECR-4M ion source vacuum stand*

The ECR-4M stand is designed to pump not only the vacuum chamber of the ECR-4M ion source but also to pump the U-400 cyclotron axial injection system with a beam analyzing magnet, diagnostic elements and vacuum gauges. It is based on double stage rotary and turbomolecular pumps but also cryopumps and an ion getter pump are used. The total pumping speed of the VS is about 7000 l $s^{-1}$, which allows one to produce a working pressure of about $10^{-4}$ Pa and $10^{-5}$ Pa in the region of the first stage of the ECR-4M ion source and in the region of the beam transport lines, respectively.

The VS consists of three sections:

1. The injection line section of the gases and vapours of the solid state samples ($\approx$ 5 l).
2. The ECR-4M ion source and extraction beam line section ($\approx$ 30 l).
3. The transport lines, beam analyzing and bending section ($\approx$ 45 l).

All three sections are designed similarly from the point of view of vacuum technology. The first one is evacuated by Balzers TMH-064 (30 l $s^{-1}$) turbomolecular and double stage DUO-1.5 (0.5 l $s^{-1}$) forvacuum pumps.

The second one is pumped by Balzers TPH-520M (500 l $s^{-1}$), TMH-064 turbomolecular pumps, double stage DUO-008 (2.5 l $s^{-1}$) and DUO-1.5 rotary pumps, a CTI-Cryogenics CRYO-Torr 8 cryopump (1500 l $s^{-1}$), an Omsk NVK-3.2 (2400 l $s^{-1}$) cryopump and a Vacuum Prague IPT-200 (200 l $s^{-1}$) ion getter pump, respectively. The TPH-064 turbomolecular pump is connected to the ECR-4M high frequency input. The TPH-520M turbomolecular and CRYO-Torr 8 pumps are pumping the extraction region of the ECR-4M ion source. The NVK-3.2 cryopump and IPT-200 ion getter pump are connected to the first beam diagnostic block.

The third section is pumped by Balzers TMH-520 (500 l $s^{-1}$) turbomolecular and DUO-008 rotary pumps, Omsk NVK-1.5 (1200 l $s^{-1}$) and NVK-3.2 cryopumps, respectively. The beam transport line consists of two beam tubes of 6 cm inner diameter, three diagnostic blocks, a 102° analyzing magnet and a 90° bending magnet deflecting the beam from the horizontal to vertical direction, i.e. to the center part of the U-400 cyclotron.

In order to evacuate the beam lines and the cryopumps to forvacuum as well as to pump the cryopumps during regeneration a Balzers DUO-016 (5 l $s^{-1}$) rotary pump is used. Three stages are used in order to produce suitable operation vacuum in the beam lines and the other parts of the VS. At the beginning the system is pumped to a pressure of 1 Pa and then the turbomolecular pumps are switched on. During pumping (3 h) by the turbomolecular pumps, the cryopumps are parallelly regenerated and then the cryopumps are also switched on. At the end the VS is pumped only by the cryopumps and the TMH-064 turbopumps. In this case it is possible to attain pressures of about $10^{-5}$ Pa and $10^{-6}$ Pa after a 5 h pumping and after a 30 h pumping, respectively. At the same time a pressure of about $10^{-5}$ Pa was produced in the first section.

This VS mainly consists of nonmagnetic stainless steel vacuum chambers, ion beam tubes and vacuum volume channel connections. VITON 'O'-rings are used as a sealing material for the main parts of the VS but OFHC cooper gasket rings are also used in the first section. The total volume of the VS is approximately 80 l. The mass spectra of the residual gases which were evolved from the surfaces of the VS are shown in Figures 3 - 4. A mass spectrometer MX 7304 was again used [4]. The spectra were taken at pressures of (2.8 - 4.5) x $10^{-5}$ Pa. By spectrum analysis one can see no contamination by hydrocarbons and other organics from the rotary pump oil. However, the spectrum illustrates the expressive water vapour contamination.

The results of the desorption rate and leakage measurements for the ECR-4M stand are shown in Figure 1. The best vacuum conditions are obtained after a 200 h pumping.

The vacuum monitoring is provided from 0.1 MPa to $10^{-6}$ Pa by using a combination of Pirani and Penning gauges. A Balzers Total Pressure Controller TPG-300 (3 pc) and TPR 010 Pirani (8 pc), IKR 020 coaxial Penning cold cathode gauge heads (4 pc) are used.

Because of the permanent working of the VS imergency interlockings have been installed. It causes to close immediately all the electropneumaticall gate valves at a pressure of 5 x $10^{-2}$ Pa. At the same pressure the gate valve which separates section three from section two will also be closed. The VS is safequard yet from the side of the U-400 high VS by means of another interlock. The gate valve separating the U-400 beam line tube is interlocked by the U-400 high VS.

The service regime of the VS is secured by the IPT 200 ion getter pump. In this case pressures are about $10^{-4}$ Pa

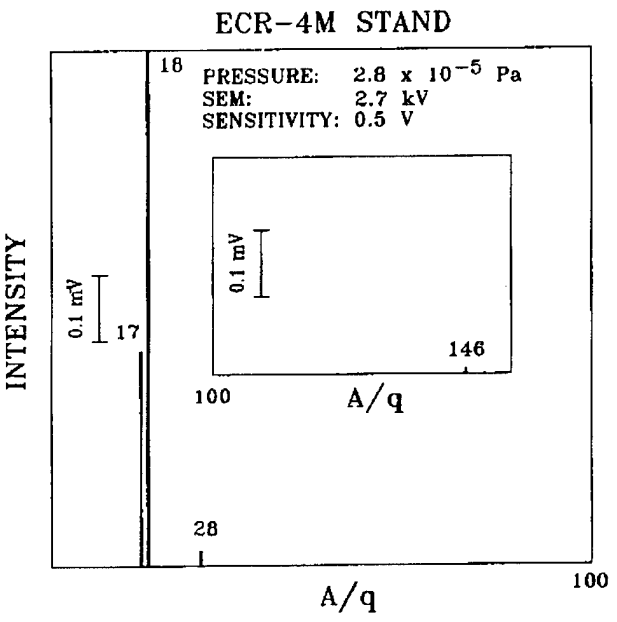



Figure 3: Measured mass spectrum of the residual gases from the ECR-4M vacuum stand.

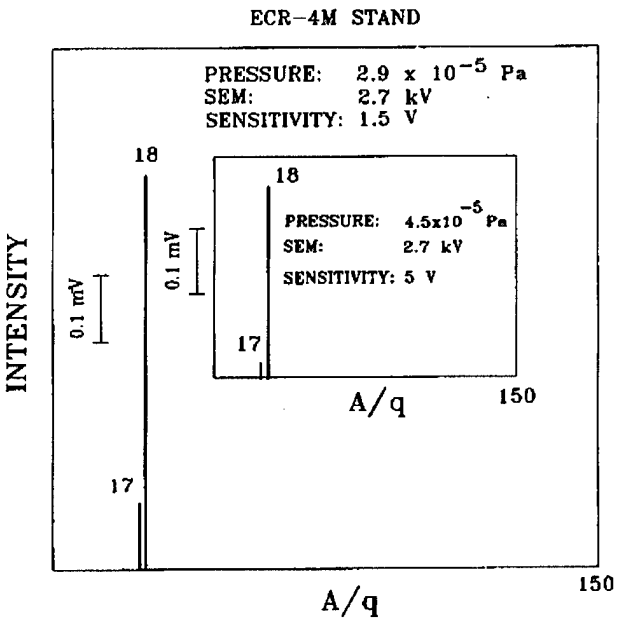



Figure 4: Other measured mass spectrum of the residual gases from the ECR-4M vacuum stand.

and $10^{-3}$ Pa in the extraction region of the ECR-4M ion source and in the first section, respectively.

The VS is also controled remotely from the control desk of the U-400 cyclotron. The system permits total and partial pressure readings and full operation of all the electropneumaticall valves. The valves and pumps are operated and controled from the own autonomous control desk placed at about 15 m from the 90° bending magnet.

## 3 COMPARISON OF THE STANDS

The minimum desorption rates and least pressures producable in testing experiments of the DECRIS-14 and ECR-4M vacuum stands are shown in Table 1. It is seen that the ECR-4M vacuum stand is better than the DECRIS-14 one by a factor of 10. It follows not only from the quality of the materials used in the construction of the VS but also from the cleanliness of the pumping units. It is known that a VITON 'O' ring is better than a RUBBER 7889 ring by a factor of 15 and RAMSAY fet is worse than APIEZON 'L' grease by a factor of 100. The worst materials are PERBUNAN - N, TEXTIT, TEFLON and RUBBER 7889 (TU MCHP 7889) and the worst grease is RAMSAY fet.

In addition to the spectra expressive water vapor contamination is observed in both VS.

## 4 CONCLUSIONS

The present work provides new data on the desorption rates and the mass spectra of the residual gases for the ECR-4M ion source stand which is now used as the axial injection vacuum system of the U-400 cyclotron. Taken together, all these data show that it may be impossible to obtain the suitable operation vacuum ($10^{-5}$ Pa) and the necessary cleanliness of the VS if the vacuum exposed surfaces have higher desorption rates than $10^{-3}$ Pa l s$^{-1}$.

Table 1: Minimum desorption rates and least pressures producable in testing experiments of the DECRIS-14 and the ECR-4M vacuum stands.

| DECRIS-14 | | ECR-4M | |
|---|---|---|---|
| Desorption rate (Pa l s$^{-1}$) | Pressure (Pa) | Desorption rate (Pa l s$^{-1}$) | Pressure (Pa) |
| 2.35 x $10^{-3}$ | 1.5 x $10^{-5}$ | 3 x $10^{-4}$ | 3.4 x $10^{-6}$ |

## 5 REFERENCES


[1] J. Pivarč, J. Vac. Sci. Technol. A12(5), 2716, 1994.

[2] Turbomolecular pump VMN-500, 126024 Kostroma, Plant "LUCH", Russia.

[3] Rotary pump BL 90, Zakład Techniki Prozniowej, Koszalin, ul. Przemysłowa 1/3, Poland.

[4] Mass Spectrometer MX 7304 (monopol), Industrial Association SPO "ELECTRON", 244030 Sumy, ul. Komsomolskaja 68a, Ukraine.

# VACUUM BEAM LOSSES IN THE AXIAL INJECTION SYSTEMS OF THE FLNR HEAVY ION CYCLOTRONS

M.N. El-Shazly, M.V. Khabarov, A.I. Ivanenko, G.G. Gulbekian, FLNR, Joint Institute for Nuclear Research, Dubna, Moscow region, 141980 Russia

*Abstract*

A simulation program was carried out to calculate the pressure distribution and the beam loss due to the charge exchange cross section in order to optimize the vacuum system parameters of the heavy ion transmission lines. A series of measurements was set up to evaluate the beam loss in the axial injection systems of the FLNR cyclotrons. The pressure measurements were compared with the program.

## 1 INTRODUCTION

The isochronous cyclotrons U-400M and U-400 [1] have been equipped with ECR ion sources provided with axial injection systems. They were located atop the cyclotron magnets [2,3]. This paper presents a model for calculating the pressure distribution and the beam losses due to the charge exchange with the residual gasses in the axial injection system. The result of the calculations made are compared with those of some pressure measurements. Also Investigated the manner in which the heavy ion beam transmission factor of the ion guide pipe depends on the following parameters: the diameters of its parts, the pumping speed, the gas loading from the ECR ion source, and the gas desorption rate.

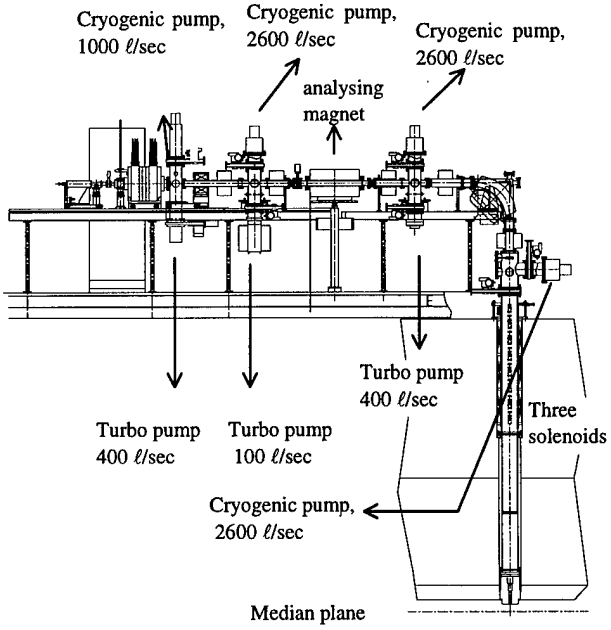



Figure 1. The axial injection system of the U-400 cyclotron

## 2 VACUUM SYSTEM

Figs. 1 and 2, show the vacuum system of the U-400 and U-400M axial injection systems.

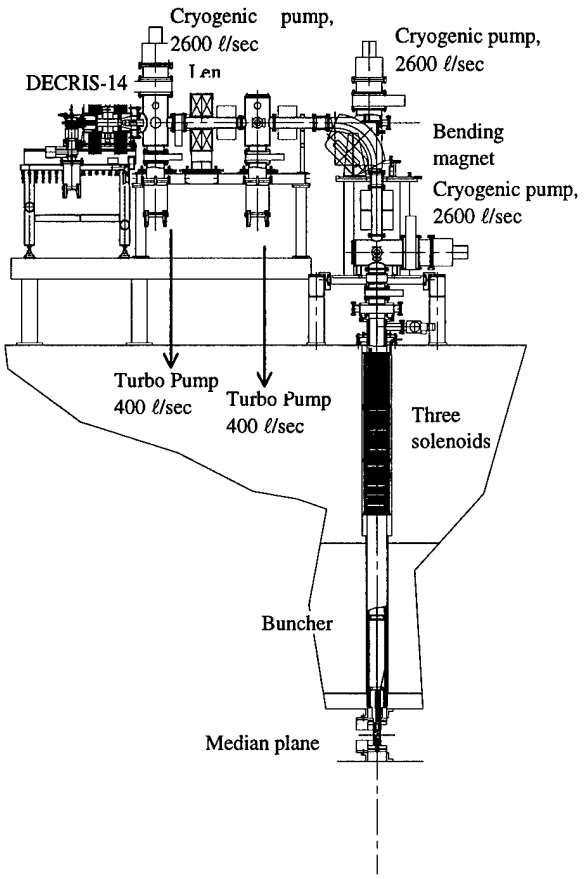



Figure 2: The axial injection system of the U-400M cyclotron

In any vacuum system, the first important gas source is formed by the static or thermal outgassing of weakly adsorbed molecules and diffusion of gasses like $H_2$, $N_2$, $H_2O$,...etc. from the material of ion guide pipe and through the seals.

The systems concerned have specific static outgassing rate ranging from $1.3\times10^{-7}$ to $1.3\times10^{-6}$ Pa ℓ/sec/cm$^2$ depending on the pumping time. Choosing the design of the ion guide pipe and the treatment of the material is very important to decrease the static outgassing and, consequently, the pumping time. Responsible for the second important gas source is the dynamic outgassing in the presence of the beam, which results from two causes. The first cause is accounted by the gas loading of $N_2$, $O_2$, $CO_2$, ..., Xe from the ECR ion source, this parameter is expected to range from $3\times10^{-3}$ to $1.6\times10^{-2}$ Pa ℓ/sec. The second cause lies in strongly adsorbed molecules being released because of the lost ion beam striking the ion guide pipe. This means that the dynamic outgassing also depends on the material and the material treatment of the ion guide pipe. The ion guide pipes concerned are made of stainless steel. Used for the seals are VITON 'O' rings. The vacuum systems were created by the JINR in collaboration with Vacuum-Praha (The Czech Republic).

0-7803-4376-X/98/$10.00 © 1998 IEEE

## 3 PRESSURE DISTRIBUTION

A simulation program was developed estimating the pressure distribution through the ion guide pipe and the ion beam transmission efficiency in relation to the pressure distribution pattern. The program proposed is capable of calculating the pressure distribution through the ion guide pipe comprising any number of parts of various forms and gas molecular conductivity. Within the molecular flow regime the flow of molecules through the ion guide pipe is expressed by the equations

$$Q(x) = -w\frac{dp}{dx} \quad \text{and} \quad \frac{dQ}{dx} = -Aq \tag{1}$$

where

| | |
|---|---|
| $Q$ (Pa $\ell$/sec) | gas flow. |
| $A$ (cm$^2$ /m) | specific surface area . |
| $q$ (Pa $\ell$/sec/cm$^2$) | specific static outgassing rate. |
| $p$ (Pa) | pressure. |
| $w$ (m$\ell$/sec) | specific molecular conductance. |

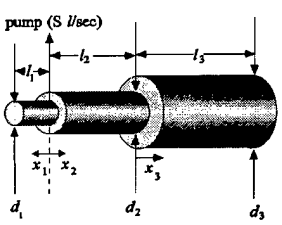



Figure 3.

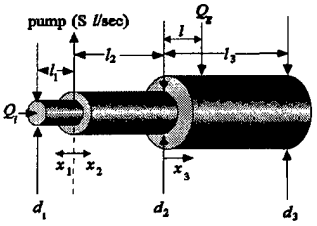



Figure 4.

To explain the mathematical algorithm of the program let us divide our vacuum chamber into three parts each part being of length $l_i$, and diameter $d_i$. The specific static outgassing in the $i$-part will be $q_i$, $i$=1,2,3 (see Fig. 3). Granted that there is only one pump and no beam, just only the static outgassing, the pressure distribution along the coordinates $x_1$, $x_2$, and $x_3$ is defined by the equations [5].

$$P_q(x_1) = \frac{q_1\pi d_1 l_1}{S} + \frac{q_2\pi d_2 l_2}{S} + \frac{q_3\pi d_3 l_3}{S} + \frac{q_1\pi d_1 x_1}{12d_1^3}\left(l_1 - \frac{x_1}{2}\right) \tag{2 A}$$

$$P_q(x_2) = \frac{q_1\pi d_1 l_1}{S} + \frac{q_2\pi d_2 l_2}{S} + \frac{q_3\pi d_3 l_3}{S} + \frac{q_3\pi d_3 l_3 x_2}{12d_2^3} + \frac{q_2\pi d_2 x_2}{12d_2^3}\left(l_2 - \frac{x_2}{2}\right) \tag{2 B}$$

$$P_q(x_3) = \frac{q_1\pi d_1 l_1}{S} + \frac{q_2\pi d_2 l_2}{S} + \frac{q_3\pi d_3 l_3}{S} + \frac{q_3\pi d_3 l_3 l_2}{12d_2^3} + \frac{q_2\pi d_2 l_2^2}{24d_2^3} + \frac{q_3\pi d_3 x_3}{12d_3^3}\left(l_3 - \frac{x_3}{2}\right) \tag{2 C}$$

where

| | |
|---|---|
| S ($\ell$/sec) | is the pump speed |

Not only there is static outgassing but also dynamic outgassing in the ion guide pipe, the latter being formed by two sources. The gas loading from the ECR ion source is responsible for the first gas source and stimulated desorped gases caused by the lost ions makes up the second source. The gas desorption rate due to the lost beam was calculated according to the next equation [4].

$$Q_g = 1000\frac{I}{Z}\gamma_i KT \tag{3}$$

where

| | |
|---|---|
| $Q_g$ (Pa $\ell$/sec) | the gas desorption rate due to lost beam |
| $I$ (A) | the lost beam intensity |
| $Z$ (coulomb) | the average charge state of the lost ions |
| $\gamma_i$ (mol./ion) | the gas desorption yield |
| $K$ (Joul/°K) | Boltzmann constant |
| $T$ (°K) | gas temperature |

The gas desorption yields from the ion guide pipe at room temperature are considered to lie between 2 and 3 mol/ion. Granted that the system configured as shown in Fig. 4 is only of one pump and static outgassing-free, the gas loading from an the ion source being $Q_i$ and the gas desorption due to beam losses $Q_g$, then the pressure distribution through the vacuum chamber concerned will be as follows:

$$P_Q(x_1) = \frac{Q_g}{S} + Q_i\left(\frac{x_1}{12d_1^3} + \frac{1}{S}\right) \tag{4 A}$$

$$P_Q(x_2) = \frac{Q_i}{S} + Q_g\left(\frac{x_2}{12d_2^3} + \frac{1}{S}\right) \tag{4 B}$$

$$P_Q(x_3) = \frac{Q_i}{S} + Q_g\left(\frac{l_2}{12d_2^3} + \frac{1}{S} + \frac{x_3}{12d_3^3}\right) \quad \text{if } x<l \tag{4 C}$$

$$P_Q(x_3) = \frac{Q_i}{S} + Q_g\left(\frac{l_2}{12d_2^3} + \frac{1}{S} + \frac{l}{12d_3^3}\right) \quad \text{if } x>l \tag{4 C'}$$

If there is in addition static outgassing the pressure distribution is founded by combining equations (2) and (4).

$$P_j(x_i) = P_q(x_i) + P_Q(x_i) \tag{5}$$

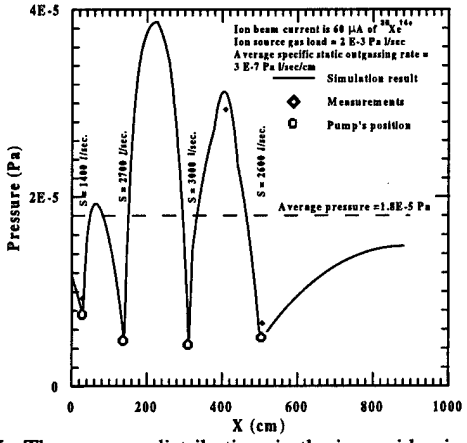



Figure 5: The pressure distribution in the ion guide pipe of the axial injection system of the U-400 cyclotron.

To return to the axial injection systems of the U-400 and U-400M cyclotrons, as shown in Figs. 1 and 2 there are more than one pump located at four sites along the length of each ion guide pipe. The pressure distributions due to these pumps were calculated according to the next equation:

$$\frac{1}{P(x_i)} = \sum_{j=1,4}\frac{1}{P_j(x_i)} \tag{6}$$

The pressure was measured at three points in each system at various beam current intensities and varying the number of pumps in operation. The results of the measurements were compared with those of the simulations. The results of the simulation and measurements are shown in Figs. 5 and 6.

## 4 TRANSMISSION FACTOR

The transmission factor depends on the pressure distribution and the charge exchange cross section between the beam ion

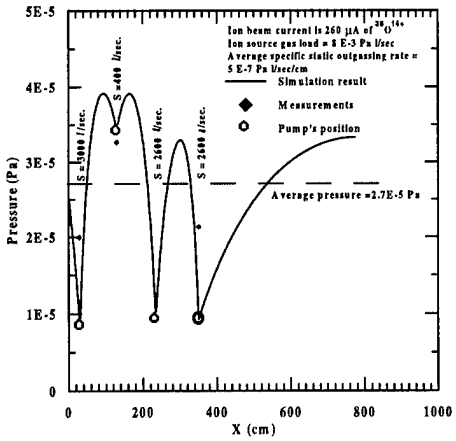



Figure 6: The pressure distribution in the ion guide pipe of the axial injection system of the U-400M cyclotron.

considered as a projectile and residual gas considered as a target. The pressure distribution can be founded as indicated above. The ECR ion source injection voltage lies 12-25 kV range depending on the ion beam charge-to-mass ratio. In this energy range, the single-electron capture cross section is much higher than that of single-electron loss cross section and of multi-electron capture cross section, it depends on the first ionization potential of the target (residual gas), varies in direct proportion to the ion charge, and is independent of energy. An approximate scaling rule can be used for this energy range [6].

$$\sigma_{z,z-1} = 1.43\times10^{12}\, z^{1.17}\, R^{-2.76} \qquad (7)$$

where

| | |
|---|---|
| $\sigma_{z,z-1}$ (cm$^2$) | the electron capture cross section |
| $z$(coulomb) | the ion (projectile) charge |
| $R$(eV) | the first ionization potential of the target (residual gas). |

In this case, the transmission factor for any ion in our ion guide pipe can be obtained easily using the next formula:

$$\tau = \frac{100}{\exp\left(2.69\times10^{16}\sigma_{z,z-1}\int_0^L P(x_i)dx_i\right)} \qquad (8)$$

where

| | |
|---|---|
| $\tau$ | transmission factor |
| $\sigma_{z,z-1}$(cm$^2$) | the single electron capture cross section |
| $P$ (Pa) | pressure |

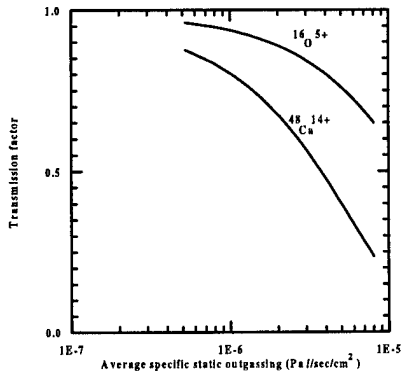



Figure 7: The specific static outgassing effect on the transmission factor through the axial injection system of the U-400M cyclotron.

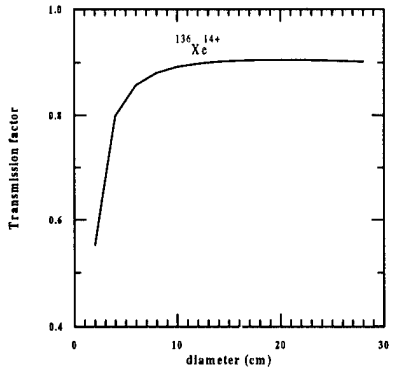



Figure 8: The transmission factor due to the variation of the diameter of the ion guide pipe in the axial hole of the U400 cyclotron magnet.

The transmission factor is seen to depend on the average pressure only. On this basis, the relationships between the transmission factors and the vacuum system's parameters were investigated under the conditions that are written in Figs. 5 and 6. For example, in the axial injection system of the U-400M cyclotron, where $^{16}O^{5+}$ and $^{48}Ca^{14+}$ 260μA beams were being considered and the gas loading from the ion source was being taken to be about $8\times10^{-3}$ Pa $\ell$/sec, the relation between the transmission factor and the specific static outgassig rate is presented in Fig. 7. In the axial injection system of the U-400 cyclotron, the diameter of the of the ion guide pipe in the axial hole of the magnet first was varied from 2cm to 20cm. The diameter dependence of the transmission factor is shown in Fig. 8.

## 5 CONCLUSION

The investigation of various parameters affecting the pressure distribution and the transmission factor of the axial injection systems of the U-400 and U-400M cyclotrons shows that:

- The most important parameter is the static outgassing.
- The second cryopump of the axial injection system of the U-400M has an insignificant effect on the average pressure and, consequently, on the beam intensities.
- The pumping speed is an important parameter from the stand point of reaching the required level of the static outgassing as quickly as possible.
- The transmission factor increases insignificantly with the diameters of the ion guide pipe for the values of the diameters greater than those of the existing configuration.
- The gas load from the ECR ion source has not great effect on the transmission factor because of the two pumps that are installed after the ECR ion source.
- It is possible to increase the ion beam current up to 1 mA and the beam losses will not be much higher.

The simulation program is useful to optimize the vacuum parameters of the transmission lines and linear accelerator after chosing the cross section formula in their range of energies.

## REFERENCES


[1] Gulbekian G. et al., 13th Inter. Conf. on Cyclotrons and Their Application, Vancouver, 1992, p.11
[2] Efremov A. et al., Rev. Sci. Inst., V. 65 (4), 1994, p.1084.
[3] Gulbekian G. et. al., Axial injection
[4] Gröbner O, CAS, CERN, V. 2, 85-19, 27 Nov. 1985, p489.
[5] Kalinin Yu Zh. et. al., Vacuum, V. 46, No. 7, 1995, p.717.
[6] Müller A. et al., Inst. Phys. Conf. , No. 38, 1978, Chapter 4.

# BEAM LOSS DUE TO THE CHARGE EXCHANGE WITH THE RESIDUAL GAS IN THE FLNR HEAVY ION CYCLOTRONS

G.G. Gulbekian, M.N. El-Shazly, A.V. Tikhomirov, B.N. Gikal,
FLNR, JINR, 141980 Dubna, Russia

*Abstract*

A simulation program was developed to calculate the pressure distribution and the beam loss due to the charge exchange cross section in the FLNR heavy ion cyclotrons. A series of measurements was carried out to evaluate the beam loss. These measurements and the pressure distributions were compared with the program results.

## 1 INTRODUCTION

The compact type cyclotrons U-400 and U-400M provide accelerated heavy ion beams (with ion charge-to-atom mass ratio z/A from 0.03 to 0.2 for U-400 and from 0.1 to 0.5 for U-400M and over a wide range of energy per nucleon up to 20 MeV/amu and 100 MeV/amu respectively). At present, these two cyclotrons are being equipped with ECR ion sources and axial injection systems [1]. Previously PIG ion sources were used, which can now be used as alternative sources for the U-400 cyclotron. The loss of the intensity of the beam due to its charge-changing collisions with the residual gas molecules is determined by the cross sections for the loss process over a wide range of energy and depends on the pressure distribution in a cyclotron. The average pressure inside the cyclotron is a function of the vacuum chamber's conductivity, the pumping speed of the pumps, the gas loading from the internal ion source such as a PIG source and the outgassing. Five oil diffusion pumps (both for the U-400 and for the U-400M cyclotron) with a total pumping speed of 20000 l/s are used in order to provide an average pressure of $(0.5\div1)\cdot10^{-6}$ Torr inside each cyclotron.

The computer simulation program VACLOS using EXCEL has been developed to determine the beam loss caused by the charge-changing collisions between various heavy ions and residual gas molecules in a cyclotron. This program includes the following main parts:

– the determination of the pressure distribution inside the cyclotron;

– the evaluation of the ion charge changing cross section;

– the calculation of the transmission factor for different ion beams.

## 2 RADIAL PRESSURE DISTRIBUTION

The total gas loading in the cyclotron vacuum chamber involves the following main components:

– the working gas flow from the internal ion source (usually for a PIG source, $Q\cong(3\text{-}6)\cdot10^{-3}$ Torr·l·sec$^{-1}$ for Xe or Kr working gas and $Q\cong(6\text{-}9)\cdot10^{-3}$ Torr·l·sec$^{-1}$ for Ar or $N_2$),

– the thermal outgassing from the surfaces of the constructional materials (the specific static outgassing $q\cong1\cdot10^{-5}$ Torr·l·sec$^{-1}$·m$^{-2}$ in the steady state),

– the atmospheric gas flow through the micro-defects in the vacuum chamber (it was found experimentally to be no more than 10% of the thermal outgassing [2]).

We can disregard the ion stimulated desorption, because in the optimal regime of beam focusing it is significantly less than the thermal outgassing for ion beam intensities of $1\cdot10^{11}\div1\cdot10^{15}$ s$^{-1}$.

For the case of the cyclotron geometry with azimuth symmetry and an internal gas flow inside the cyclotron, the pressure profile is expressed by the equation:

$$P(r) = P_0 + \frac{Q}{G_{R-r}}, \qquad (1)$$

where $P_0=P(R)$ is the pressure at the pump's positions, Q is the gas flow rate due to the ion source, $G_{R-r}$ is the gas flow conductivity, R is the vacuum chamber radius.

The radial gas flow conductivity inside the vacuum chamber of the cyclotron can be obtained from the Knudsen formula:

$$G_{R-r} = \frac{4}{3}\nu_a \frac{1}{\int_r^R \frac{\Pi(x)}{F^2(x)}dx}, \qquad (2)$$

where $\nu_a$ is the molecular average thermal velocity, $\Pi$, F are the perimeter and cross section of the azimuth periodic segment (hill and valley of the magnet poles) of the vacuum chamber.

From equations (1) and (2), we can get the pressure profile resulting from the gas loading of the internal ion source:

$$P(r) = P_0 + \frac{3nQ}{2\pi\nu_a}\frac{1}{h^2}\left[\ln\frac{R}{r} + \frac{nh(R-r)}{\pi Rr}\right], \qquad (3)$$

where n is the number of the pole sectors, h is the axial gap between the magnet poles.

The pressure produced by the thermal outgassing is presented by:

$$P'(r) = P'_0 + \int_r^R \frac{q\Pi}{G'_{R-r}}dx + \frac{1}{G'_{R-r}}\int_0^r q\Pi dx, \qquad (4)$$

where q is the specific static outgassing, and $P_0$ or $P_0'$ is the pressure at the pump's position.

Equation (4 ) leads to:

0-7803-4376-X/98/$10.00 © 1998 IEEE

$$P'(r) = P'_0 + \frac{3nq}{\pi h^2 v_a}\left[\frac{\pi}{4n}\left(R^2 - r^2\right) + \right.$$
$$+ \frac{3}{2}h(R - r) + \frac{nh^2}{\pi}\ln\frac{R}{r}\frac{\pi}{2n}R_0^2\ln\frac{R}{r} -$$
$$- hR_0\ln\frac{R}{r} - \frac{hR_0^2(R - r)}{2Rr} -$$
$$\left. - \frac{nh^2R_0(R - r)}{\pi Rr}\right] \qquad (5)$$

where r changes from $R_0$ to R.

Then the average pressure in the periodic segments (hill, valley and regarding the dee's position) of the vacuum chamber was calculated. The results are in good accordance with the previous measurements [3].

The intervals of working pressure for the U-400 cyclotron equipped with either an ECR or a PIG ion source are presented in Figure 1.

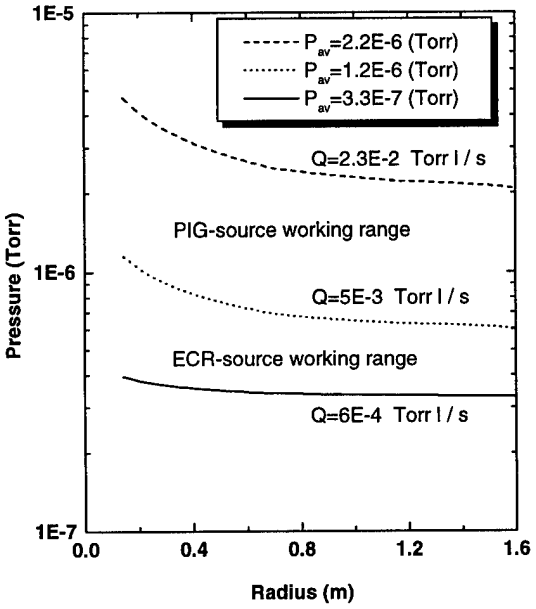



Figure 1: The calculated radial pressure distribution for the U-400 cyclotron, being equipped with an ECR or a PIG ion source, at the corresponding average pressure at the extraction radius R=160 cm ($q = 1\cdot10^{-5}$ Torr·l·sec$^{-1}$·m$^{-2}$) for $_{14}N$ beams.

## 3 ION BEAM LOSS

In the case of beam losses due to the charge exchange between the ions and the residual gas the transmission efficiency T of an accelerator over pathlength L is:

$$T = \exp\left\{-3.3 \times 10^{16}\int_0^L P(\ell)\sigma(\beta)\cdot d\ell\right\}, \qquad (6)$$

where P is the pressure in Torr, $d\ell$ is an element of the pathlength in cm, $\beta$ is the relative velocity (v/c) and $\sigma$ is the sum of all the relevant capture and loss cross-sections in cm$^2$/molecule.

Several analytical and semi-empirical models [4-9] have been applied to the calculation of the cross-sections, and, obtained as a result, the transmission factors of every model were compared with the experimental data on the vacuum losses of accelerated heavy ions in the U-400 and U-400M cyclotrons.

The best accordance with the experimental data has been found for the joint model of the two following models :

$$\text{I.} \quad \sigma_C = 2 \times 10^{-15} z^2 (137\beta)^{-5} \qquad (7)$$

$$\sigma_L = 2 \times 10^{-15}(1 + z)^2(137\beta)^{-5} \times$$
$$\times \exp\left(-\frac{2(z - \bar{z}) + 1}{2d^2}\right) \qquad (8)$$

Where the mean charge value $\bar{z}$ is approximated by $\bar{z} = Z_p\left\{1 - C\cdot\exp(-137\beta\delta)\right\}$, $C\cong1$ has a very weak dependence on the atomic number $Z_p$, $\delta = 0.3443 - 0.0667\ln(Z_p)$ and the standard deviation is given by $d = 0.27\sqrt{Z_p}$ in a residual gas such as $N_2$ or

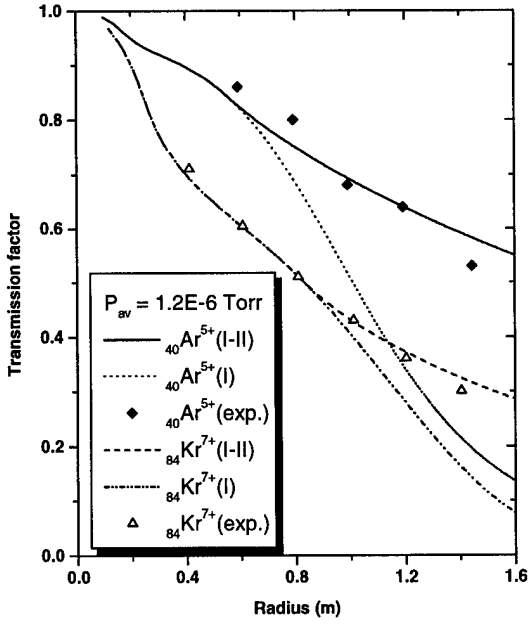



Figure 2: The transmission factor for the cyclotron equipped with a PIG ion source, calculated in accordance with the two models (joint I-II and I), as compared with the experimental data for accelerated ions $_{40}Ar^{5+}$ (up to 9 MeV/amu, $Q=6.5\cdot10^{-3}$ Torr·l·s$^{-1}$) and $_{84}Kr^{7+}$ (up to 4 MeV/amu, $Q=6\cdot10^{-3}$ Torr·l·s$^{-1}$) at an average pressure of $P_{av}=1.2\cdot10^{-6}$ Torr (considering radial pressure distribution) at the extraction radius R=160 cm.

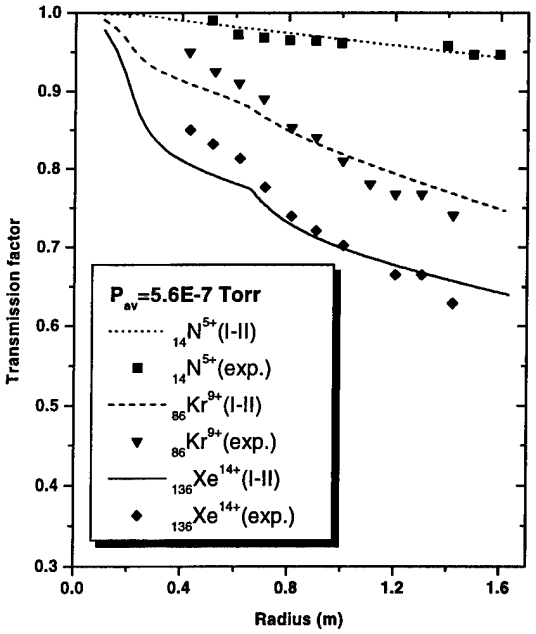



Figure 3: The transmission factor for the cyclotron equipped with an ECR ion source, calculated in accordance with joint model I-II, as compared with the experimental data for accelerated ions $_{86}Kr^{9+}$ (up to 6 MeV/amu) and $_{136}Xe^{14+}$ (up to 6 MeV/amu) in the U-400 cyclotron and $_{14}N^{5+}$ (up to 53 MeV/amu) in the U-400M cyclotron at an average pressure of $P_{av}=5.6\cdot10^{-7}$ Torr (considering radial pressure distribution) at the extraction radius R=160 cm.

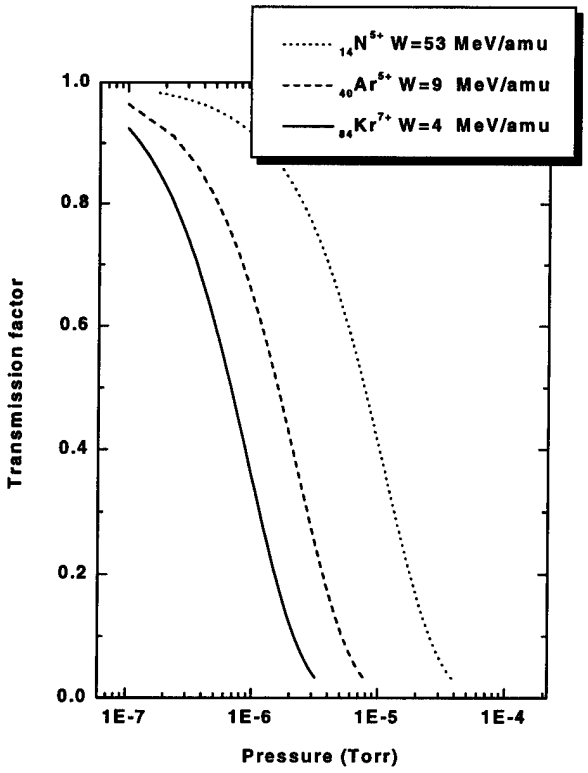



Figure 4: The transmission factor calculated by the joint I-II model versus the average pressure at the extraction radius R=160 cm for accelerated ions $_{40}Ar^{5+}$ (up to 9 MeV/amu) and $_{84}Kr^{7+}$ (up to 4 MeV/amu) in the U-400 cyclotron and $_{14}N^{5+}$ (up to 53 MeV/amu) in the U-400M cyclotron.

air [4];

II. $$\sigma_C \cong 3 \times 10^{-28} z^{5/2} \beta^{-7} \qquad (9)$$

$$\sigma_L \cong 9 \times 10^{-19} z^{-2/5} \beta^{-2} \qquad [5]. \qquad (10)$$

In the joint (I-II) model we used the first (I) model for ions energy up to 1.5 MeV/amu and the second (II) model for higher energy. For other residual gases except $N_2$ we used this joint model for cross section calculation with a factor of $\sqrt{M / M_0}$, where $M / M_0$ is the ratio between the molecular masses of the gas and $N_2$.

Such an approach allowed us to obtain quite satisfactory accordance with the experimental data as shown in figures 2-3. Figure 2 also shows the comparison between the two models. Figure 4 represents the examples of the estimations based on the joint (I-II) model for the acceleration of $_{40}Ar^{5+}$ up to 9 MeV/amu and $_{84}Kr^{7+}$ up to 4 MeV/amu in the U-400 cyclotron and $_{14}N^{5+}$ up to 53 MeV/amu in the U-400M cyclotron.

## 4 CONCLUSION

The above described vacuum loss simulation program VACLOS allows one to estimate quite satisfactorily the transmission factors of any accelerated ions in a wide range of ion energy and gas loading in different operation regimes both with an ECR and with a PIG ion source, that is important for analyzing and forecasting the efficiency of a cyclotron with the definite vacuum system.

## REFERENCES


[1] G. Gulbekian et al., 14th Int. Conf. on Cyclotrons and their Application, Cape Town, 1995, p.95.

[2] Yu. Zh. Kalinin et al., Vacuum, v. 46, 1995, p.717.

[3] G. Gulbekian et al., JINR, P9-83-451, Dubna, 1983.

[4] E. Baron, M. Bajard and Ch. Ricaud., Nuc. Inst. Meth., v. A328, 1993, p. 177.

[5] H.C. Hseuh, I. Feigenbaum, M Manni, P. Statel, R. Skelton, IEEE Trans. Nuc. Sci., v. NS-32, No. 5, 1985, p. 3797.

[6] B. Franzke, IEEE Trans. Nuc. Sci., v. NS-28, No. 3, 1981, p. 2116.

[7] F. Becchetti et al., IEEE Trans. Nuc. Sci., v. NS-28, No. 2, 1981, p. 1437.

[8] H.D. Betz, Rev. Mod. Phys., v.44, No.3, 1972, p. 467.

[9] Y. Nakamura et al., 14th Int. Conf. on Cyclotrons and their Application, Cape Town, 1995, p. 276.

# THE VACUUM SYSTEM FOR THE SYNCHROTRON RADIATION SOURCE ANKA

E.Huttel, D.Einfeld, Forschungszentrum Karlsruhe, ANKA, PO Box 3640, 76021 Karlsruhe, Germany

*Abstract*

ANKA, a 2.5 GeV Synchrotron Radiation (SR) source with a circumference of 110.4 m, an emittance of 40-73 nmrad and a nominal current of 200 mA, is dedicated for micro-fabrication and analytics purposes. The vacuum chamber will be made of stainless steel. An in situ bake out is not foreseen. Most of the synchrotron radiation will be absorbed by discrete absorbers (two per bend) in ante chambers. Here 500 l/s and 300 l/s diode pumps will be installed. The pumping will be done by lumped ion pumps (diodes) with a total nominal pumping speed of 18800 l/s, respectively 13000 l/s at $10^{-9}$ mbar. The installation of Titanium sublimator or NEG pumps is foreseen as back up. Assuming a desorption coefficient of $10^{-6}$ mol/ph the expected gas load is 1.5 $10^{-5}$ mbar l/s. Pressure profile calculations show that the foreseen pumping speed should be sufficient to obtain a pressure of 3 $10^{-9}$ mbar, necessary to get a lifetime of more than 12 h.

## 1 GENERAL REQUIREMENTS

In ANKA the lifetime of the electron beam is mainly determined by the scattering of the electrons at the residual gas. A status report of ANKA is given in a separate contribution to this conference[1]. Measurement at KEK showed that a pressure of $10^{-9}$ mbar is necessary in order to get a lifetime of about 20 h [2], in accordance with own calculations. Most of the gas load is produced during operation, when the synchrotron radiation hits the wall of the vacuum chamber. The number of molecules $N_{mol}$ desorbed by the synchrotron radiation is proportional to the number of the emitted photons $N_{ph}$ and to the desorption coefficient $\eta$, which depends on the wall material and decreases as a function of the absorbed photon dose (d).

$N_{mol} = N_{ph}\,\eta(\text{mat., dose})$

Desorbed molecules are mainly $H_2$, CO, $CO_2$ and $CH_4$. In general the $H_2$ gas load is by an order of magnitude larger than the gas load from CO and $CO_2$ and by two orders of magnitude larger than the gas load of $CH_4$. The desorption coefficient of aluminum is at least at the beginning an order of magnitude larger compared to stainless steel and copper [3].The number of photons is given by the following formula [3]:

$N_{ph} = 8\ 10^{+17}\ I\ (mA)\ E\ (GeV)$ $\qquad$ $1Ah \sim 7\ 10^{24}$ ph

Desorption coefficient for stainless steel measured at the 2.5 GeV e-storage ring at KEK [4] were extrapolated for the calculations given in Table 1 ($\eta$ (7 $10^{23}$ ph/m) = $10^{-4}$ mol/ph). Furthermore the following assumptions were used:

a) 90% of the photons hit the main absorbers (10m) in the bend, 10% hit the vacuum wall (100m) in the straight sections. Thus the dose for the main absorbers in the bend is a factor 10 higher compared to the straight sections and the desorption coefficient is a factor five lower.

b) The effective pumping speed (S) is about $10^4$ l/s.

c) $\eta \sim d^{-0.7}$

$1Ah \sim$ 7 $10^{23}$ ph/m (bend) $\rightarrow$ $\eta_b = 10^{-4}$

7 $10^{22}$ph/m (straight) $\rightarrow$ $\eta_s = 5\ 10^{-4}$

$p[mbar] = 3.7\ 10^{-20}\ N_{ph}(0..9\ \eta_b + 0.1\ \eta_s) / S[l/s]$

Table 1 Expected pressure and lifetime behavior for ANKA, $\eta$ is given for the main absorbers.

| dose[Ah] | $\eta_b$[mol/ph] | p/I[mbar/A] | $\tau$I[Ah] |
|---|---|---|---|
| 0,01 | 2,50E-03 | 2,6E-05 | 0,001 |
| 0,1 | 5,00E-04 | 5,2E-06 | 0,004 |
| 1 | 1,00E-04 | 1,0E-06 | 0,02 |
| 10 | 2,00E-05 | 2,1E-07 | 0,1 |
| 100 | 4,00E-06 | 4,1E-08 | 0,5 |
| 1000 | 8,00E-07 | 8,3E-09 | 2,4 |

The thermal desorption for prebaked stainless steel after 1000 h pumping time is in the order of $10^{-11}$ mbar l / (s $cm^2$). A surface of the vacuum system of about 3 $10^5$ $cm^2$ thus leading to an additional gas flow of 4 $10^{-6}$ mbar l / s and an additional pressure rise of 3 $10^{-10}$ mbar.

## 2 MATERIAL FOR THE VACUUM CHAMBERS

As material for the vacuum chamber of SR sources stainless steel, aluminum and copper is used. The advantages and disadvantages of these materials are well known and discussed. The final decision using stainless steel 316 LN for ANKA was done since almost all possible manufacturers in Europe are experienced in this material.

0-7803-4376-X/98/$10.00 © 1998 IEEE

## 3 DESIGN OF THE VACUUM CHAMBER

The design of the vacuum chamber of ANKA follows the ante chamber concept of the recently built SR sources. In the region of the dipole and the following sextupole, respectively quadrupole, the e-beam is circulating in one chamber and the synchrotron radiation passes through a small gap into the ante chamber where it is absorbed by discrete absorbers. Since the length of these absorbers are small compared to the circumference of the ring, the outgassing is obtained in a shorter time. Furthermore the desorbed gases are immediately pumped away by a pump close to the absorber.

Figure 1 shows the design of the dipole vacuum chamber consisting of the e-beam chamber, the ante chamber at the dipole and the ante chamber at the following sextupole, respectively quadrupole. The e-beam chamber and the ante chamber are separated by a slot 10 mm high and 30 mm wide. The chamber is welded out of 3 mm thick stainless steel plates. The e-beam chamber is 70 mm wide and 32 mm high. Most of the synchrotron radiation is absorbed by two discrete absorbers made of OFHC copper, the first positioned in the ante chamber of the dipole covers the radiation from 0° to 11°, the second in the adjacent ante chamber covers the range from 11° to 20°. Close to the absorbers diode pumps are installed with a nominal pumping speed of 500 and 300 l/s, respectively. In addition a small 150 l/s ion pump is installed in the middle of the chamber for pumping the e-beam chamber.

In the following section the vacuum chamber is a straight tube and the synchrotron radiation is absorbed on the wall of the chamber which is indirectly cooled. A copper plating of a 1m long section behind the dipole is foreseen in order to reduce the temperature step.

The disadvantage of the ante chamber design is the large width of the vacuum chamber which has to sustain the atmospheric pressure, especially in the case of ANKA, where the width is up to 500 mm. An unsupported chamber with a wall thickness of 3 mm would result in an unacceptable large deformation. Thus the chamber must have supporting ribs. The deformation and the stress of chamber have been calculated by means of finite elements (ANSYS) and the geometry of the chamber is optimized in order to get a deformation of less than 0.5 mm.

## 4 VACUUM PUMPS FOR STORAGE RINGS

Generally ion and getter pumps are used at storage rings. Concerning ion pumps, two types exist: diodes and triodes. The pumping speed of a diode in the $10^{-9}$ mbar range is nearly twice as large as a triode for all reactive gases (CO, $CO_2$, $H_2$,). Noble gases are not pumped by conventional diodes. But diode pumps with tantalum electrodes can pump noble gases. Since noble gases are not desorbed by synchrotron radiation conventional diode pumps are foreseen close to the absorbers. Using noble

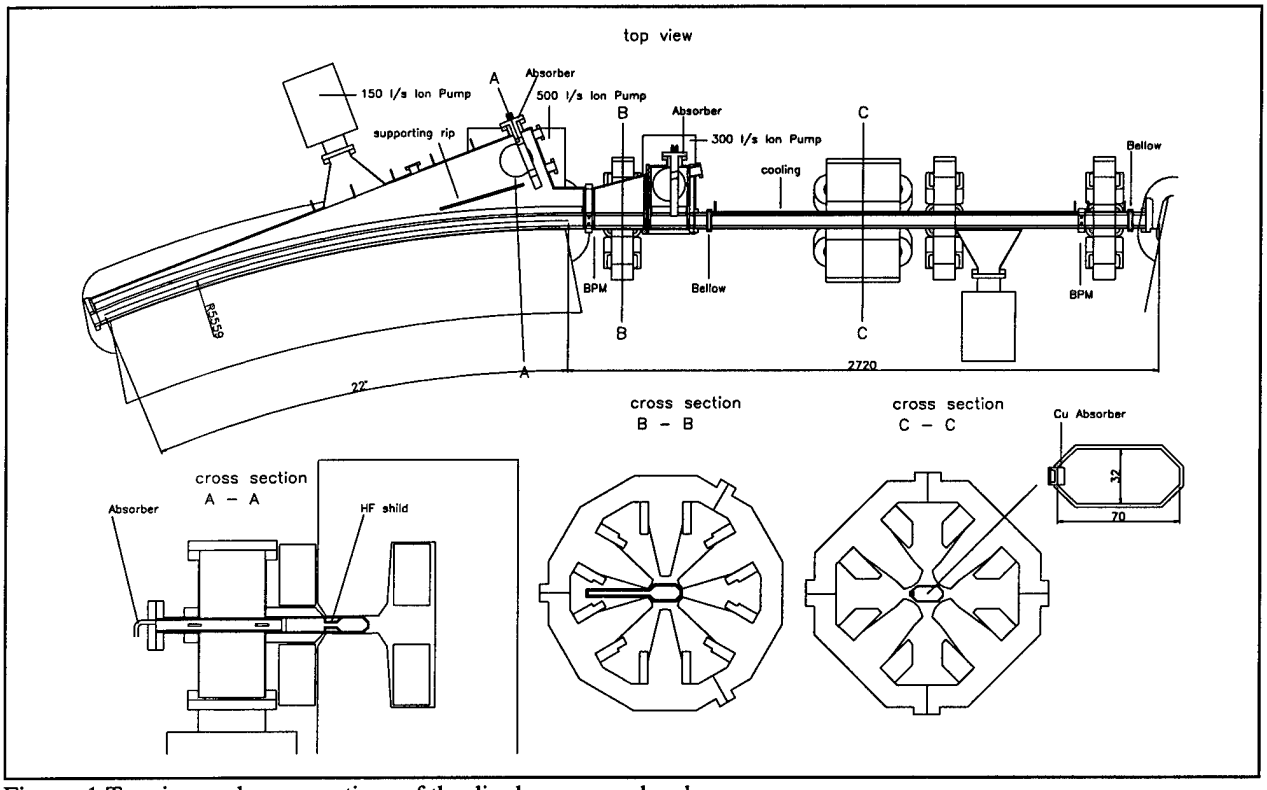



Figure: 1 Topview and cross sections of the dipole vacuum chamber.

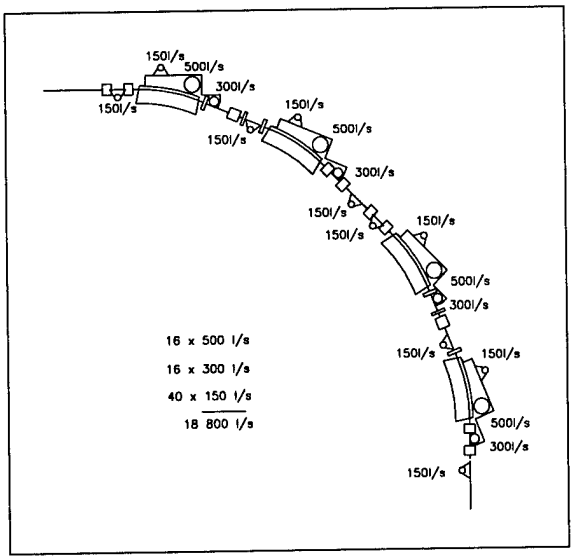



Figure: 2 Pumping scheme for a quarter of ANKA.

diodes elsewhere might be a compromise between optimum pumping speed and not excludable leaks.

Concerning getter pumps both titanium sublimator (TS) and NEG pumps (Non Evaporable Getter) are used at storage rings. Both pumps have a considerable pumping speed for hydrogen, they pump all reactive gases but do not pump noble gases and hydro carbons at all. Since the pumping speed decreases when a certain amount of gases has covered the surface of the pump, (After 10 h for a TS at 3 $10^{-9}$ mbar) the getter must be regenerated periodically.

At ANKA only diode ion pumps will be used at the beginning. It is foreseen to install lumped NEG's or titanium sublimator on top of the ion pumps later on if this turns out to be necessary. The foreseen pumping scheme is shown in Figure 2.

## 5 PRESSURE PROFILE

For calculating the pressure profile of the vacuum chambers and optimizing the pumping configuration a program similar to the one described by P.C.Chen et.al.[5] was used. Figure 3 shows the pressure profile in the e-beam chamber for one quarter of ANKA. A gas load of 3.5 $10^{-5}$ mbar l/s and an effective pumping speed of 15000 l/s (both numbers refer to the complete ring) were used for this calculation.

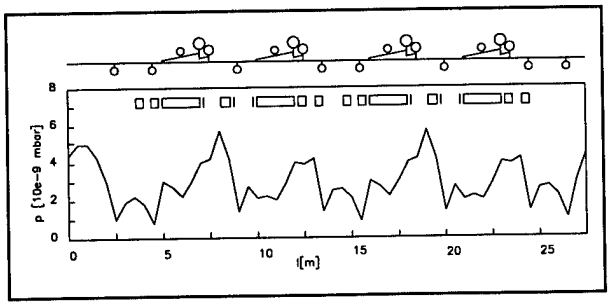



Figure: 3 Pressure profile for one quarter of ANKA.

## 6 THERMAL LOAD

The total power of the synchrotron radiation (2.5 GeV, 200 mA) of 123 kW leads to a power per length of 130 W/cm for the main absorbers. The maximum wall temperature, calculated with ANSYS is in the order of 95°C.

Behind the second absorber the synchrotron radiation is absorbed on the wall of the e-beam chamber. The thermal conditions of this wall are shown in Figure 4 as a function of the distance from the dipole.

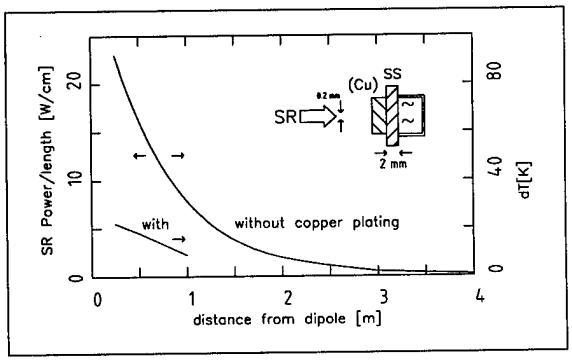



Figure: 4 Absorbed power and temperature step inside the vacuum wall (E=2.5 GeV, I=200mA).

## 7 BAKING

Nearly all SR sources have an insitu baking system. It's merits: getting a cleaner vacuum (i.e. no water content), having a faster commissioning and a faster recovery after vacuum break down are well established. On the other hand due to the experiences at ELETTRA it's necessity is now discussed [6]. Costs for heating jackets and insulation can be saved, the gap of the magnets can be made smaller and thus the current reduced. The bellows need only compensate the mechanical tolerances. Due to the budget limitations of ANKA, it was decided not to install an insitu baking system. Instead the chambers will be cleaned and only be baked before installation.

---

[1]D.Einfeld et al, this conference

[2] Y.Hori, M.Kobayashi,Y.Takiyama, Vacuum47(1996)617

[3] O.Grödner, A.G.Mathewson, H.Störi, P.Strubin, R.Souchet, Vacuum 33(1983)397

[4] S.Ueda, M.Matsumoto, T.Kobari, T.Ikeguchi, M.Kobayashi, Y.Hori, Vacuum 41(1990)1928

[5] P.C.Chen,G.Y.Hsing and J.R.Chen, J.of Vac.Soc.R.O.C. 1(1987)24

[6] J.Miertusova, F.Giacuzzo, 5.EPAC(1996)2527

# EXPERIENCE WITH THE ULTRA-HIGH-VACUUM PROTECTION SYSTEM FOR THE SYNCHROTRON RADIATION BEAM LINES WITH HIGH-POWER WIGGLERS/UNDULATORS AT THE PHOTON FACTORY

Noriichi Kanaya, Seiji Asaoka, Shogo Sakanaka and Hideki Maezawa Photon Factory
High Energy Accelerator Research Organization (KEK) 1-1, Oho, Tsukuba, 305,Japan

*Abstract*

There are six high-power wiggler/undulator beam lines at the2.5-GeV synchrotron radiation source at the Photon Factory. In the case of an instantaneous vacuum failure at such a beam line, a normal Fast-Closing-Valve (FCV) system is incapable of functioning to protect the Ultra-High-Vacuum (UHV) of the beam lines and the synchrotron radiation source, since a meltdown of the titanium-alloy FCV is caused by intense photon flux radiation. To avoid such a case, a dedicated UHV protection system has been built where all FCV systems for the high power beam lines have been linked, using high-speed communication links to RF klystrons to allow the FCV systems to initiate blade closure after dumping the positron beam by tuning off the RF power. In this paper, experience with the UHV protection system for the wiggler/undulator beam lines is discussed.

## 1 INTRODUCTION

There are six high-power wiggler/ undulator beam lines (BL-2, BL-13, BL-14, BL-16, BL-19 and BL-28) and sixteen normal bending-magnet beam lines installed around the 2.5- GeV positron storage ring at the Photon Factory at the National Laboratory for High Energy Physics. The six high-power wiggler/ undulator beam lines are simultaneously in operation, producing very intense synchrotron radiation beams. The high-power beam lines are distributed along the long circumference of the storage ring. These beam lines feed synchrotron radiation to the experimental hall where experiments such as surface physics, x-ray lithography, microscopy and crystal structure analysis are simultaneously carried out.

The pressures in the storage ring and the beam lines are maintained at anUltra-High-Vacuum (UHV) of less than 10 -10 Torr. In order to protect the Ultra-High Vacuum of the storage ring against an instantaneous vacuum failure, fast-closing valve systems (FCV) [1,2] have been installed in the wiggler/undulator beam lines as well as normal bending- magnet beam lines. The FCV system can close a guillotine blade (1.2-mm thick titanium-alloy) in ~ 0.01 seconds. A vacuum failure would be caused by a rupture of the beryllium windows (~200 mm-thick) at an x-ray beam line due to an intense thermal load, or by an instantaneous gas leakage downstream of the VUV (Vacuum Ultra Violet) branch line [4]. Such a failure could result in fatal damage to the components of the storage ring, including the vacuum chambers, beam position monitors, pressure gauges and the doughnut.

The wiggler/undulator can produce synchrotron radiation with a high power density, two orders of magnitude higher than that obtained with a bending-magnet source [4]. At such a high-power wiggler beam line, the impingement of intense photon flux on the closing blade of the FCV causes a melt-down within 0.1 seconds before a water-cooled heat-absorber closes (~1 sec) [5]. Thus, the FCV can not protect the storage ring vacuum for the wiggler/undulator beam lines. There has been no protection system that allows many high-power wiggler/undulator beam lines to simultaneously protect the Ultra-High Vacuum of the synchrotron radiation source from an instantaneous fatal vacuum failure. To avoid such case, the authors have designed and built a dedicated vacuum protection system for the high-power wigger/undulator beam lines [6]. In this paper, the first experience with the UHV protection system for such high power wiggler/undulator beam lines is discussed.

## 2 SYSTEM CONFIGURATION

In order to ensure that the blade can avoid intercepting intense radiation, the protection system allows any high-power beam line to instantaneously turn off the beam upon the detection of a vacuum failure, by switching off the RF power in the four remote RF cavities. The response time is much less than the closing time of the FCV (~11 ms), preferably less than 0.1 ms. Figure 1 shows a block diagram of the protection system. Each beam li ne has a Fast -Cl osi ng-Val ve syst em wi t h a vacuum sensor. The Fast-Closing-Valve systems are connected to RF klystrons with optical-fiber links. The communication links comprises a high-speed optical transmitter and receiver wi t h a transmi ssi on rat e of 76 MHz. Upon an instantaneous vacuum failure at the experimental hall, the pressure signal of the vacuum detector is transmitted to the Fast-Closing-Valve system. This system initiates a cut-off signal, thereby requesting the RF klystrons to turn off the RF power. At the same time, it simultaneously requests the computer of the beam line control system to shutdown the water-cooled absorber mask (closing time ~ 1sec).

After the RF power in the klystrons is removed, the status signal of the RF power is transmitted to the Fast-Closing-Valve system, notifying the removal of the RF

0-7803-4376-X/98 /$10.00 © 1998 IEEE

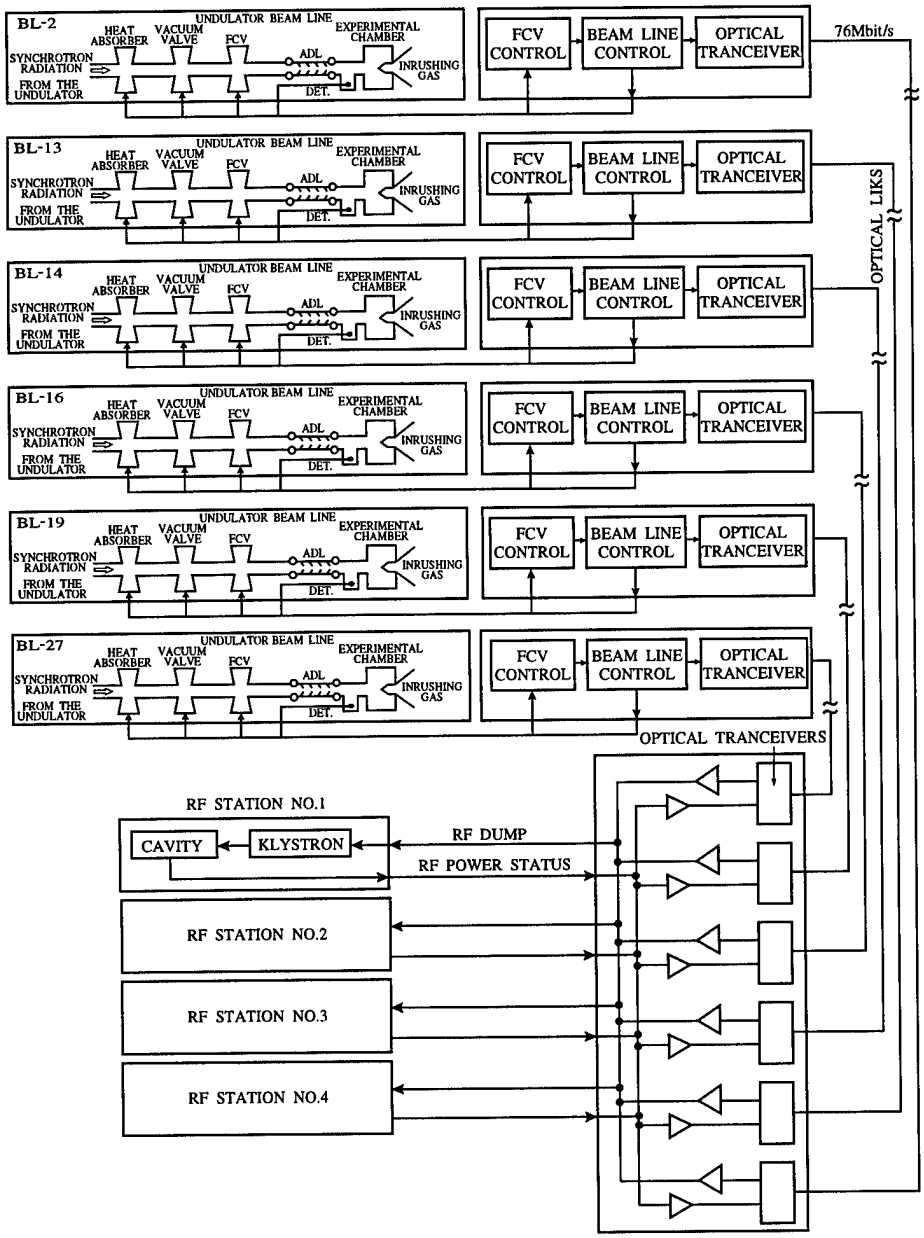



Figure 1 Block diagram of the Ultra-High-Vacuum protection system for synchrotron radiation beam lines with multiple wiggers and undulators

power, and the synchrotron radiation beam. The status signal from the RF klystrons can reach the beam line within 100 microseconds after being sent to the beam line. Upon receiving the status signal from the RF klystrons, the Fast-Closing-Valve system can close its titanium blade in 10 ms to block any inrushing shock wave from the experimental hall. The total response time measured between a vacuum failure and the closure of the Fast-Closing-Valve blade is 12ms. The water-cooled absorber mask can completely close in 1 second after being initiated. Then, the computer of the beam line control system closes the backup vacuum valves (closing time ~ 1sec) to completely close the beam line.

## 3 ACTURAL VACUUM FAILURE

In April, 1996, there was an actual instantaneous vacuum failure at wiggler beam line BL-19 in the experimental hall. The positron beam current was 366 mA at 2.5 GeV, and the wiggler was providing the intense beam to the experimental hall at BL-19.

Upon an instantaneous vacuum failure, the protection system detected it, and immediately turned off the RF power in the klystrons and then closed the titanium blade of the Fast-Closing-Valve. The positron beam was dumped at the RF klystrons, which, in turn, transmitted a status signal of the RF power in the klystrons to the

protection system. The protection system initiated the closure of the FCV blade to block any inrushing shock wave from the experimental hall at the BL-19. The record in the on-line database [7] shows how these protection procedures were successfully achieved.

The pressure in the middle point of the beam line reached almost atmospheric pressure. However, it was found that there was no effect on the pressure at the connecting point of the upstream end of the beam line and the storage ring. The pressure has been successfully protected below $1.1\times 10^{-10}$ Torr, the same pressure value before the incident. It allowed the storage ring to resume operation immediately after reinjection of a positron beam, and start synchrotron radiation experiment.

## 4 CONCLUSION

Experience with the Ultra-High-Vacuum protection system is discussed concerning the high-power wiggler/undulator beam lines at the 2.5 GeV synchrotron radiation source at the Photon Factory. The actual operation for an instantaneous vacuum failure proved that the dedicated UHV protection system can protect the UHV of the storage ring by initiating the Fast Closing Valve after dumping the positron beam by cutting off the RF power in the RF klystrons, using high-speed communicati on links. The system allows the synchrotron radiation source since to avoid an instantaneous vacuum failure during synchrotron radiation experiments under intense photon flux radiation.

## 5 ACKNOWLEDGEMENTS

The authors wish to express their gratitude to the staff of the Photon Factory Light Source Division for operating the beam liens and the storage ring.

## REFERENCES

[1] N.Kanaya, S.Sato, K.Nakajima and S.Hayashi, "Pneumatically-driven Fast Closing Valve System for Synchrotron Radiation Sources," IEEE Trans. Nucl. Sci., Vol.NS-33, No.3, pp.1071-1077,June, 1986.

[2] N.Kanaya, S.Sato, S.Asaoka, K.Nakajima, S.Hayashi and S.Kurita, "Pneumatic Fast-Closing Valve for Synchrotron Radiation Beam Lines at the Photon Factory," IEEE Trans.Nucl.Sci. Vol.36, No.4, pp.1391-1395,Aug.1989.

[3] N.Kanaya,"Photon Factory Activity Report 1992," Photon Factory, KEK, pp.R-16-17,1993.

[4] H.Kitamura, "Photon Factory Activity Report 1993," Photon Factory, KEK, 1993.

[5] N. Kanaya, S. Sakanaka, S. Sat o, T. Koi de and S. Asaoka, "Vacuum Protection System using an Interlocked Fast-Closing Valve for a High-Power Wiggler Beam Line," IEEE Trans. on Nucl. Sci. Vol. 37, No. 1, pp. 2-6, Feb, 1990.

[6] N.Kanaya, in preparation (noriichi.kanaya@kek.jp).

[7] N. Kanaya, S. Asaoka and H. Maezawa, "Operat i on Logging System using Database for Synchrotron Radiation Beam Lines at the Photon Factory," in these proceedings.

# STATUS OF THE PEP-II LOW-ENERGY RING VACUUM SYSTEM

D. Cheng, D. Hunt, H. Hsieh, J. Meneghetti, K. Kennedy, T. Stevens, G. Jones, T. Miller,
D. Colomb (LBNL, Berkeley, CA 94720), L. Bertolini, C. Belser, J. Kerns
(LLNL, Livermore, CA 94550), E. Daly (SLAC, Stanford, CA 94309)

*Abstract*

The PEP-II *B* Factory* Low-Energy Ring (LER) will operate at 3.1 GeV with 2.1 A; design specifications are based on 3.5 GeV at 3 A. The vacuum system, 2200 m long, consists of 6 arcs and 6 straights. The arc vacuum system is based on an aluminum antechamber pumped by titanium sublimators located directly under discrete photon stops, supplemented by 110 l/s ion pumps near the end of each dipole. The straight sections serve various utility functions, including emittance control with a wiggler, injection, and an interaction region (IR). Vacuum chambers in most of the straight sections are circular stainless steel pipe with external copper plating to facilitate heat transfer to cooling tubes brazed to the outside wall. The wiggler chicane vacuum system uses both aluminum and stainless steel technology, along with a 24 m long distributed copper photon dump. The IR vacuum system is mainly based on copper extrusions. LER vacuum system components are either in the late stage of prototyping or already in full production.

## 1 INTRODUCTION

The vacuum system of the PEP-II *B* Factory LER is designed to maintain a <10 nTorr pressure storing a 3 A positron beam current at 3.5 GeV, although the nominal operating conditions will be 2.1 A at 3.1 GeV. Both the High Energy Ring (HER) and LER are made of 6 arc sections and 6 straight sections, with the LER located 35" (0.889 m) above the HER, each having a total circumference of about 2200 m. The straight sections provide for various functions such as beam injection, damping and emittance control with wigglers, and the IR where the beams collide in a detector. Vacuum calculations were conducted with VACCALC, a pipeline pressure computer code developed by M. Sullivan [1], showing the peak pressures to be ~7 nTorr, and average pressures below 3 nTorr during operation. LBNL, LLNL, SLAC are involved with the various designs and fabrication of the LER vacuum system components.

## 2 ARC REGIONS

Each of the six arc regions of the ring uses extruded aluminum antechambers, making up sixteen standard cells. A half-cell, shown in Figure 1, consists of a magnet chamber with a slotted appendage to pass the photon beam that is connected to a ~6 meter length of pumping chamber. On the far end is a discrete photon stop and titanium sublimation pump (TSP) mounted from the antechamber. Additional pumping is achieved with a 110 l/s ion pumped placed near the string of magnets.

### *2.1 Vacuum chambers*

Figure 2 shows the extrusion profiles of both types of chambers. The magnet chambers are currently being processed at LBNL, including the coating of the inside surface with a 1000-2000 Angstrom layer of titanium nitride. Due to the high positron current in the LER and the positron instability first seen at the KEK Photon Factory [2], it was decided that a TiN coating was needed to reduce secondary electron emission in these elliptical profile beam chambers. More details on this process can be found in another article at this conference [3]. The pumping chambers are being built at SLAC, while R&D work on coating these chambers with TiN has been completed at LBNL. A 3/4-cell mock-up of the arc vacuum system has been finished to test the assembly and installation procedures of these components into the tunnel (see Figure 3).

### *2.2 Photon Stops*

At the design value of 3.5 GeV, 3 A $e^+$ beam, each 45 cm dipole will produce 15 kW of synchrotron radiation power, which will be absorbed by photon stops approximately 6 meters from the dipole. These stops are made of grooved Glidcop®, optimized using the ANSYS finite-element code, absorbing the photons at a 70 mrad angle to the beam. The maximum thermal stresses are about 23 ksi (von Mises), well below the 39 ksi yield limit of brazed Glidcop® for a $\Delta T$ of ~130 °C, initial cooling water being 35 °C. The preliminary designs incorporated wire-brazing of the OFE copper backing plate to the stock copper-cladding around the Glidcop® with Nicusil-3 or equivalent. However, since the interface at the cladding cannot be guaranteed to function as a structural joint, a costlier brazing method of 25/75 Au-Cu foil was adopted, joining the backing plate directly to the Glidcop®, now plated with a 0.0015" cyanide copper barrier. Final designs of the photon stop are now complete and production is beginning.

### *2.3 Titanium Sublimation Pumps*

Located directly below the photon stops are TSPs, chosen for their high pumping speed and low cost. Active surfaces of the pump are fins of extruded 6063 Al, increasing the surface area by a factor of ten. The estimated pumping speed of these pumps is 8,000 liters

* Work Supported by U.S. Dept. of Energy contract nos. DE-AC03-76SF00098 (LBNL), DE-AC03-76SF00515 (SLAC), W-7405-Eng-48 (LLNL).

0-7803-4376-X/98 /$10.00 © 1998 IEEE

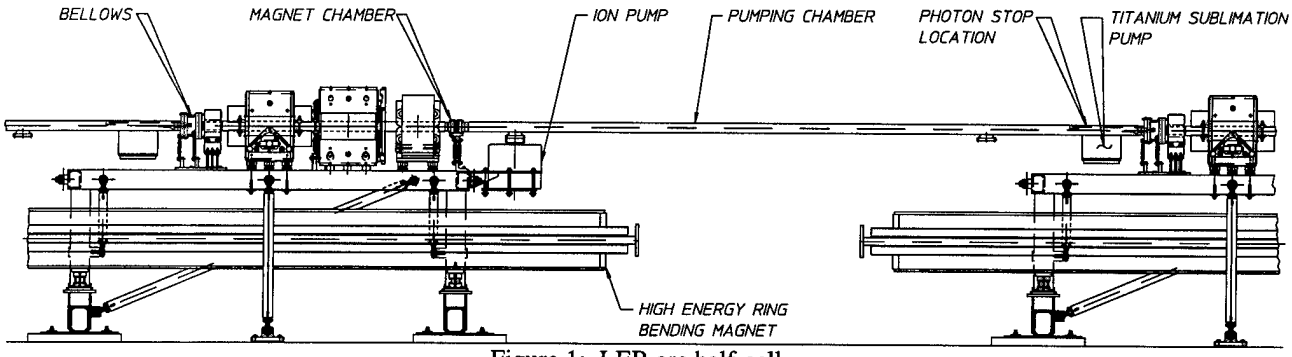


Figure 1: LER arc half-cell.

per second. The inital pumpdown of the chamber will be done with ion pumps, followed by activation of the TSPs. It is anticipated that the time between activations will be greater than three months. At these intervals, a 20 year lifetime for these filaments is expected.

### *2.4 Arc Bellows Shields*

The arc regions, with elliptical chamber profiles, will use a bellows design that has 0.030" thick RF contact fingers, held in contact to a Glidcop® rider stub by Inconel spring fingers (see Figure 4). This design is based on the HER arc bellows design, which is discussed in [4]. This bellows shield must allow an expansion of up to 3 cm (at 150 °C bakeout) plus alignment tolerances of ±0.25". The design was finalized in April 1997, and fabrication is slated to begin in May.

## 3 STRAIGHT SECTIONS

Because the straight section vacuum system does not have to absorb much synchrotron radiation power, the standard vacuum chambers are round, water-cooled, 3.5" I.D. stainless-steel tubing. These are the same chambers used in the HER, with a few geometric differences in lengths and in the locations of water cooling lines. With the lattice components frozen and additional vacuum hardware set, the lengths of all the drift tubes have been set and are now in production at SLAC, where the HER chambers were also fabricated. After fabrication, they will be glow discharge cleaned at LLNL before installation into the tunnel.

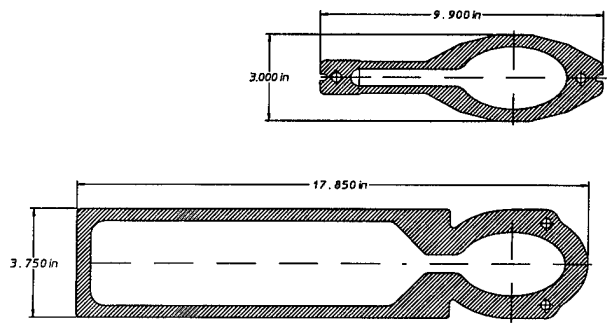


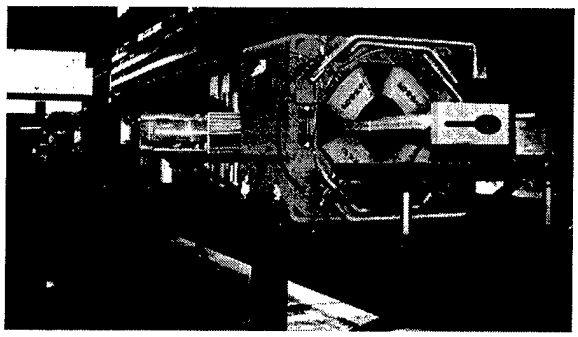
Figure 2: Magnet and Pumping chamber extrusions.

### *3.1 Interaction Region*

The Interaction Region (IR) is where the orbiting electrons of the HER collide with the LER positrons. The positrons are directed down to the elevation of the HER orbit by vertical bend magnets, collide head-on with electrons, then are directed back to the normal orbit elevation. Due to the highly non-standard nature of this region, the vacuum chambers are primarily HER-type copper extrusions to mask and absorb the radiation power in both the horizontal and vertical planes. Currently, prototyping is complete and the mechanical detailing of the chambers is just beginning. The IR bellows is also similar to the HER arc bellows [4]; detailed design of the IR bellows has been completed and it is ready for production.

### *3.2 Wiggler Chamber*

Two straight sections in the ring are fitted with chicanes to allow the placement of a wiggler since additional emittance control in the LER is necessary [5]. However, only one of these regions will be fitted with a wiggler at startup, since it was determined that sufficient control is achieved with only one. The wiggler vacuum chamber is approximately 25 meters long, composed of five 5 m long machined copper sections. Synchrotron radiation produced by the wiggler is absorbed by the water-cooled beam dumps on the walls of the chamber. The desorbed gases will also be continuously pumped by NEG pumps, which are described more in detail in [6]. The mechanical design was completed mid 1996, and the rough machining of the chambers has also been completed. The e-beam


Figure 3: 3/4-cell mock-up of the LER arc vacuum and supports.

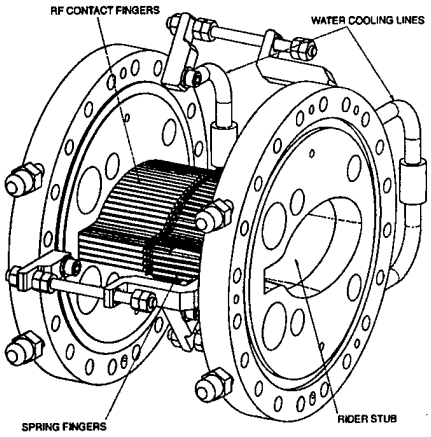



Figure 4: Arc bellows shield module (without bellows convolutions).

welding is about 50% complete, and the final machining has just begun in March 1997.

### *3.3 Injection Region*

The Linac beam will be injected vertically into both rings; therefore, as much as possible, the LER injection region is to be a twin of the already-designed HER injection region, using common vacuum components. This region is also highly non-standard, making use of 8" chambers to accommodate the beam-stay-clear of the aborted beam trajectory, and 2.5" ID ceramic chambers (and their corresponding bellows for mechanical compliance). The LER injection region layout was finalized in January 1997, and since most of the component designs have been finalized for the HER, production of components in tandem will allow the LER to undergo injection tests in the fall of 1997.

### *3.4 Straight Section Bellows Shields*

Since the chambers in the standard LER straight sections are of the same design found in the HER straights, the original intention was that the same bellows shields of HER straights were to be used as well. This bellows shield used a "Curly-Q" finger design that is described with more detail in [7]. However, during vacuum processing of the HER bellows, the initial bakeout at 200°C at its nominal position caused the spring fingers to relax and, under certain conditions, could then be made to lose RF contact with the stub. Whereas HER operating procedures guard against the bellows seeing such conditions, it was decided that with minimal effect to cost and schedule the bellows shields in the LER straights would be modified to the RF and spring finger/rider stub design, similar to that of the HER and LER arcs. See Figure 5. This change was finalized at the beginning of 1997 and components are currently in production.

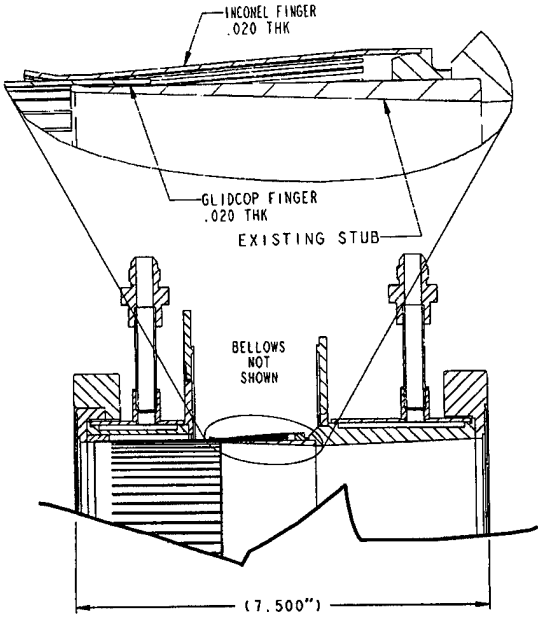



Figure 5: Detail and cross section of the LER straight section bellows module.

## 4 SUMMARY

The major components have been designed and are currently in production, so the LER vacuum system is progressing toward its commissioning target of spring 1998. Storage tests will follow, and first collisions are expected in the summer of 1998. The close-working of the three-lab LER design team, LBNL, LLNL, and SLAC, has been, and will continue to be the key factor in meeting these milestones.

## 5 REFERENCES

[1] M. Sullivan, "A Method for Calculating Pressure Profiles in Vacuum Pipes," PEP-II AP Note No. 6-94, Mar. 1, 1994.

[2] M. Izawa, Y. Sato, and T. Toyomasu, Phys. Rev. Lett 74, 5044 (1995).

[3] K. Kennedy, et al., "TiN Coating of the PEP-II Low-Energy Ring Aluminum Arc Vacuum Chambers," these proceedings.

[4] N. Kurita, A. Kulikov, J. Corlett, "Final Design and Manufacturing of the PEP-II High Energy Ring Arc Bellows Module," these proceedings.

[5] J. Heim, et al., "Wiggler insertion of the PEP-II B-Factory LER," in Proc. of 1995 PAC, Dallas, May, 1995, p.533.

[6] L. Bertolini, et al., "Design of the Linear Non-Evaporable Getter Pump for the PEP-II B Factory," these proceedings.

[7] J. Berg, et al., "High Current RF Shield of PEP-II Vacuum System Expansion Joint," in Proc. of 1996 EPAC, Barcelona, Spain, June, 1996, p. 1090.

# DESIGN OF THE LINEAR NON-EVAPORABLE GETTER PUMP FOR THE PEP-II *B* FACTORY

L.Bertolini, D. Behne, J. Bowman, D. Hathaway, K. Kishiyama, M. Mugge, T.Swan
Lawrence Livermore National Laboratory, University of California, Livermore, CA 94550 USA

*Abstract*

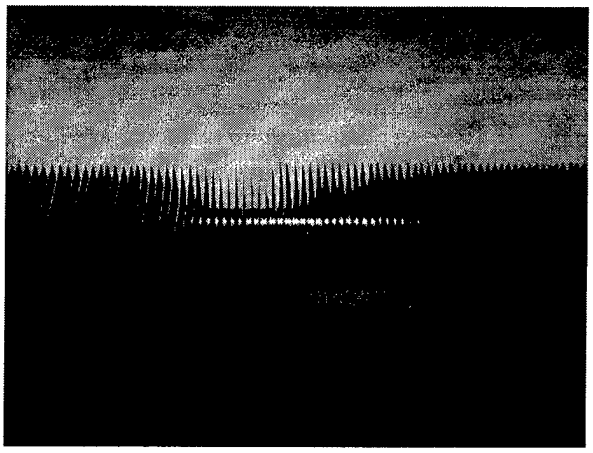
There are several regions in the PEP-II *B* Factory at SLAC that require distributed pumping to deal with large photo-desorbed gas loads or to produce very low pressures($<10^{-9}$ Torr). These regions include the Low Energy Ring Wiggler dump chambers, the transitions between the High Energy Ring arcs and straight sections, and most importantly the Interaction Region. We have designed a compact Non-Evaporable Getter pump using commercial getters that combines high pumping speed and high sorption capacity. We describe the design features of the NEG pumps, and our test results from prototype pumps. In addition, we discuss future variations of this style of NEG pump.

## 1 INTRODUCTION

The PEP-II Asymmetric B Factory collider is made up of two counter-circulating storage rings. The High Energy Ring (HER) circulates electrons at an energy of 9 GeV and a current of 1 Amp. The Low Energy Ring circulates positrons at an energy of 3.1 GeV and a current of 2.1 Amps. The Interaction Region (IR) vacuum system where the two beams collide requires very low average beamline pressures ($<10^{-9}$ Torr). High gasloads generated by the synchrotron radiation striking the vacuum chamber walls necessitates a vacuum pumping system with high pumping speed and high sorption capacity. In addition, the low beamline conductance requires that the vacuum pumping be of a distributed or linear nature.

The vacuum pumping solution in the HER arcs is the Distributed Ion Pump (DIP). The HER arcs have 5.4 meter long dipole magnets to bend the electron beam in an arc. The DIPs conveniently make use of the residual magnetic field from the magnets to provide uniform distributed pumping along the beam aperture. DIPs however, are not a viable option in the Intraction Region. The pumping speed of ion pumps decreases as pressure decreases. In a region where sub-nTorr pressures are the goal, this is not a desirable characteristic. In addition, the magnets in the IR do not provide enough coverage along the length of beamline to provide for continuous vacuum pumping.

Our solution is to use Non-evaporable Getters (NEG). The task is to configure the NEG in a way to maximize linear pumping speed and sorption capacity. The high pumping speed will produce the low beamline pressure we desire and the high sorption capacity will allow us to operate the NEGs for long periods of time before regenerating them. The NEG activation mechanism is also a concern. Activation by baking the chambers is not possible since the chambers are extruded half-hard, oxgen-free copper which will anneal at activation temperatures. Activation by ohmic heating requires continuous lengths of NEG and presents thermal expansion problems.



Two main concerns have been expressed about the use of NEGs within PEP-II. First, NEGs are inherently "dusty" devices to install into a high current electron storage ring. There was concern that the phenomena experienced at the HERA storage ring would occur at PEP-II. HERA experienced beam interactions with "macro-particles" which caused severely shortened beam lifetimes. The second concern was that high gas loads would result in unreasonably short regeneration intervals.

Once we developed an acceptable getter configuration, we found other regions within PEP-II where the NEG pump design could be applied. Figure 1 shows a plan view of PEP-II with the NEG locations identified. The PEP-II NEG pump design is used in the IR, the LER Wiggler vacuum chamber, and the HER arc-to-straight transition chambers.

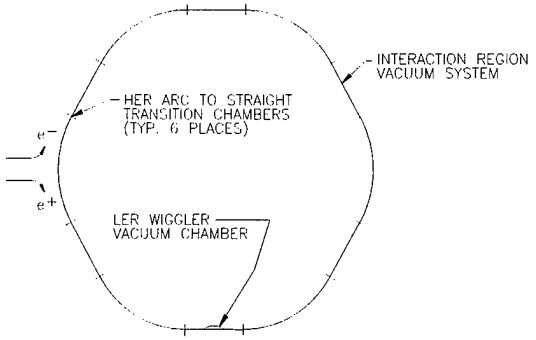



Fig. 1. NEG Pump Locations within the PEP-II *B* Factory

0-7803-4376-X/98/$10.00 © 1998 IEEE

## 2 PUMP DESCRIPTION

The pumping speed and sorption capacity of a NEG pump are proportional to the surface area of NEG material in the pump. For this reason it was important to find a way to maximize the surface area within the small volumes allocated for pumps in the beam tubes. We have decided to increase surface area in the same manner an engineer increases convective heat transfer area in a automobile radiator, by using "fins". We cut individual "wafers" from SAES ST707/CTAM/30D strip using a laser welding machine. The laser is used to produce as clean a cut as possible. We found that precision shearing dies produced torn edges which tended to increase dust generation from the NEG. Cutting the NEG with the laser (under a nitrogen gas purge) produced a clean edge without damaging the nearby granules of getter alloy.

A cross-section of the pump is shown in Figure 2. Individual NEG wafers are strung on a 0.375" o.d., 0.035" wall stainless steel tube. Adjacent wafers are separated by stainless steel wire spacers. The width of the spacers can be varied to adjust the speed and capacity of the pump. Typically, the NEG spacing ranges from 0.040" to 0.120". The stainless steel tube has a 0.125" square key attached along its length. The purpose of the key is to prevent rotation of the square NEG wafers. On each end of the pump are slip-on tube clamps that keep the wafer array compressed. The stainless steel tube has a cap on one end and a conflat flange on the other end. The tube acts as both a support for the NEG wafers and part of the vacuum barrier. The pump is inserted into a pumping antechamber within a PEP-II vacuum chamber and bolts to a conflat flange on the end of the chamber. Figure 3 shows a cut-away view of a NEG pump installed in an IR vacuum chamber. There are supports located every 20" along the stainless steel tube which stand the pump off the walls of the antechamber. The supports and the NEG wafers are sized to allow a conflat gasket to be slipped over the pump to seal the end flange.

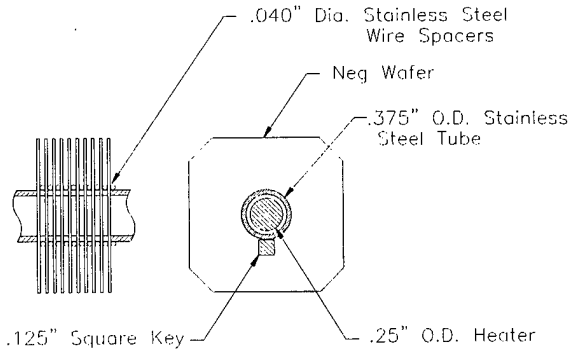



Fig 2. Cross-section of a PEP-II NEG Pump

Using a wafer spacing of 0.040", we have built vacuum pumps with the equivalent of 18 meters of NEG strip per meter of pump length. That quantity of NEG can sorb several Torr-liters of gas before needing to be regenerated. After machine commissioning, we are predicting that the NEG pumps will only require annual regeneration.

Activation of the NEG is accomplished with a 0.25" o.d. commercial tubular heater. The heater is inserted into the stainless steel tube from outside of the vacuum system. With the heater outside the vacuum there is no need for an elecrical feedthrough. If a heater fails, it can be

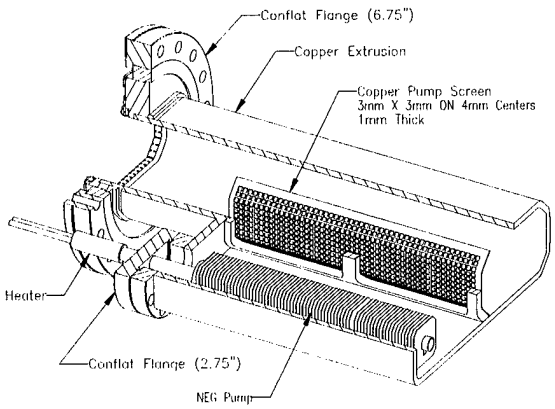



Fig. 3. NEG Pump in an IR Chamber

replaced without venting the vacuum system. Since this pump is heated from the center there is a significant radial temperature variation across each wafer. For a 1.18" square wafer the temperature can vary as much as 180°C. The published activation parameters for ST707 are 450°C for 45 minutes [1]. If we heat the NEG wafers to a minimum temperature of 450°C the center portion of each wafer will be approximately 600°C. In previous activation tests [2] we have found the NEG alloy will suffer catastrophic delamination from the constantan substrate at approximately 710°C. For this reason it is important to characterize the heater parameters well to avoid overheating and damaging the NEG.

## 4 TESTING

There were two goals in testing the prototype PEP-II NEG Pump. First of all we wanted to verify the pumping speed and sorption capacity of this new configuration. Sorption tests were conducted for prototype pumps with different wafer spacings. Figure 4 shows the sorption curve for a pump with 0.040" spaces between wafers. Also shown is a calculated sorption curve based on the NEG manufacturer's published data [1].

The second goal of the tests was to characterize the heater parameters required to adequately activate the NEG. Since the pumps installed in PEP-II will not be equipped with internal thermocouples it is essential that we know what heater parameters will produce the proper NEG temperature. The prototype pump was outfitted with two thermocouples, one on the outer edge of a NEG wafer and one attached to the outside of the stainless steel tube. Between sorption tests we activated the pumps and

monitored the temperatures. Figure 5 shows the temperature profile of the NEG and stainless steel tube during a typical activation.

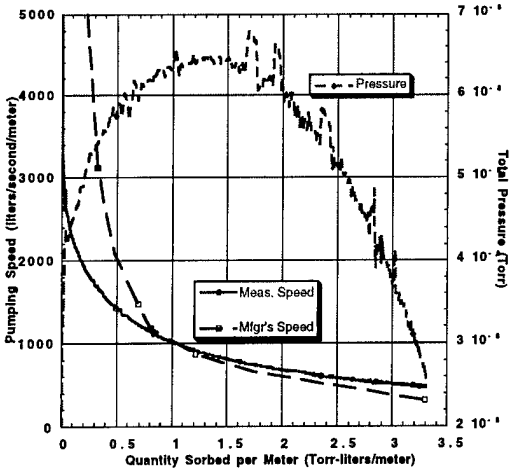



Fig. 4. Sorption Curve for a PEP-II NEG Pump

## 5 DUST

There were two separate issues regarding "dust production" and NEGs. As we have mentioned earlier, we were concerned about the production of macro-particles that potentially could interact with the beams. But a second issue came up during the project. The European Synchrotron Radiation Laboratory (ESRF) experienced lifetime problems because of magnetic contaminants from ST707 interacting with their stored beam [3]. We not only worked to minimize dust production, but we also attempted to deal with magnetic dust production too. The best solution for both problems was to use a sintered NEG alloy. The alloys used in sintered configurations are not required to go through a ball mill where the magnetic contaminates are introduced. Sintering also produces much stronger adhesion than does the roll bonding process used on ST707 strip. Unfortunantly, the cost of the sintered NEGs was prohibitive for the project and therefore not an option. We were left with utilizing ST707 and trying to minimze dust production wherever possible. As mentioned earlier, we cut the individual NEG wafers with a laser to produce a clean edge. We also worked with SAES Getters S.p.A. to process all of our NEG by multiple passes through a magnetic sieve. These processes will not eliminate dust production, however, they may decrease it to an acceptable level. In chambers where our NEG pumps will experience changing magnetic fields, we may have to revisit sintered NEGs if we encounter problems.

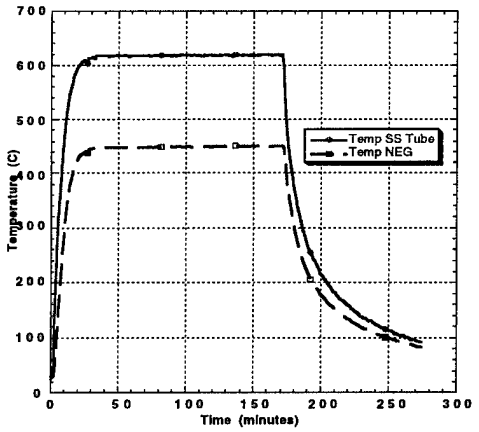



Fig. 5. Temperature Plot of Typical NEG Activation

## 6 SUMMARY

We have designed a linear NEG pump to solve a variety of vacuum problems within the PEP-II machine. The pump utilizes an innovative configuration of commercial getter strips to produce high pumping speed an high sorption capacity. The pump design allows us to vary the quantity of getter and thus vary the linear pumping speed.

## 7 ACKNOWLEDGEMENTS

This work was supported by the Director, Office of Energy Research, Office of High Energy and Nuclear Physics Division, of the U.S. Department of Energy under contracts DE-AC03-76SF00098 and W-7405-ENG-48-(LLNL).

## REFERENCES

[1] SAES ST707 Product Data.
[2] "NEG Cyclic Tests," Holdener, Kishiyama, Mugge, and Stoeffel, LLNL, October 1994.
[3] "New Undulator Vacuum Chambers without Distributed Pumping," N. Rouviere, ESRF Newsletter, June 1995.

# APT/LEDA RFQ VACUUM PUMPING SYSTEM

S. Shen, K. Kishiyama, J.M.Parker,
Lawrence Livermore National Laboratory, Livermore, CA and
N. G. Wilson, AMPRO, Inc., Los Alamos, NM and
D. Schrage, Los Alamos National Laboratory, Los Alamos, NM

*Abstract*

This paper describes the design and fabrication of a vacuum pumping system for the APT/LEDA (Low Energy Demonstration Accelerator) RFQ (Radio Frequency Quadrupole) linac [1]. Resulted from the lost proton beam, gas streaming from the LEBT (Low Energy Beam Transport) and out-gassing from the surfaces of the RFQ cavity and vacuum plumbing, the total gas load will be on the order of 7.2 x $10^{-4}$ Torr-liters/sec, consisting mainly of hydrogen. The system is designed to pump on a continual basis with redundancy to ensure that the minimal "operating vacuum level" of 1 x $10^{-6}$ Torr is maintained even under abnormal conditions. Details of the design, performance analysis and the preliminary test results of the cryogenic pumps are presented.

## 1 INTRODUCTION

The APTLEDA RFQ consists of four resonantly coupled two meter segments. The over-riding requirement for the APT/LEDA RFQ vacuum pumping system is that it be capable of pumping the combined gas load from the lost proton beam, gas streaming from the LEBT (Low Energy Beam Transport) and out-gassing from the surfaces of the RFQ cavity and vacuum plumbing. The total gas load will be on the order of 7.2 x $10^{-4}$ Torr-liters/sec. The main gas to be pumped will be hydrogen and the system must be able to pump hydrogen on a continual basis. Vacuum pumps are to be completely oil-free (both high-vac and roughing) and a single pump type must pump all other species of gas ($O_2$, $N_2$ and any outgassed mixture). Redundancy must be provided in the system pumping and gauging to ensure that the minimal "operating vacuum level" of 1 x $10^{-6}$ Torr is maintained despite pump failures in the system. All pumps, valves and gauges must be replaceable without bringing the RFQ cavity up to atmospheric pressure.

## 2 DESIGN

### *2.1 Design Requirements*

Tables 1 and 2 summarize the vacuum parameters and pumping system requirements for the APT/LEDA RFQ respectively.

| PARAMETER | VALUE |
|---|---|
| Surface Outgassing Rate | $2.4 \times 10^{-9}$ Torr-liters/cm$^2$-sec<br>$2.4 \times 10^{-4}$ Torr-liters/sec |
| LEBT Gas Load ($H^+$) | $1.1 \times 10^{-4}$ Torr-liters/sec |
| $H^+$ Beam Loss (10 mA) | $1.0 \times 10^{-3}$ Torr-liters/sec |
| $H_2^+$ & $H_3^+$ Injection (2mA) | $4.0 \times 10^{-4}$ Torr-liters/sec |
| Total $H_2$ Gas Load | $1.4 \times 10^{-3}$ Torr-liters/sec |
| TOTAL GAS LOAD | $7.2 \times 10^{-4}$ Torr-liters/sec |
| Pumping Ports | 36 6-slots each<br>140 liters/second each |
| Pumping Plenums | 3 @ Section A1<br>3 @ Section A2<br>3 @ Section C2 |

Table 1: Vacuum Parameters

| PARAMETER | VALUE |
|---|---|
| Prototype for APT | System Must be Fully Suitable for APT Operation |
| Operating Pressure | $\leq 1.0 \times 10^{-6}$ Torr |
| System Time Constant | $\leq$ 0.1 second |
| Pump Down Time | $\leq$ 30 minutes |
| Concurrent Regeneration | Regeneration Must Occur During Operation |
| Installed Redundancy | System Must Operate with a Pump Failure During Regeneration |
| Redundant Gauging | False Positives Must be Detected |
| Standalone Operation | System Must Operate Independently of LEDA Control System |
| Control System Interface | System Must Accept Commands & Provide Signals to LEDA Control System |
| RF Window Vacuum | System Must Allow for Vacuum Pumping of 12 RF Windows |
| Safety/Codes | System Must Meet All Codes & Present No Safety Hazards |

Table 2: Pumping System Requirements

### *2.2 Design Approach*

Since the intent of the LEDA is that it will be a working prototype for the APT accelerator, it is imperative that the vacuum pumping system for the APT/LEDA RFQ be fully suited for actual APT operation. In developing the conceptual design for the vacuum pumping system we strove to meet the requirements set forth in the scope of work, and also expanded on those requirements by utilizing a "3 R's" approach in the design. We made a conscious effort to build in a *robustness* that will guarantee adequate pumping during all operating conditions of the accelerator.

0-7803-4376-X/98/$10.00 © 1998 IEEE

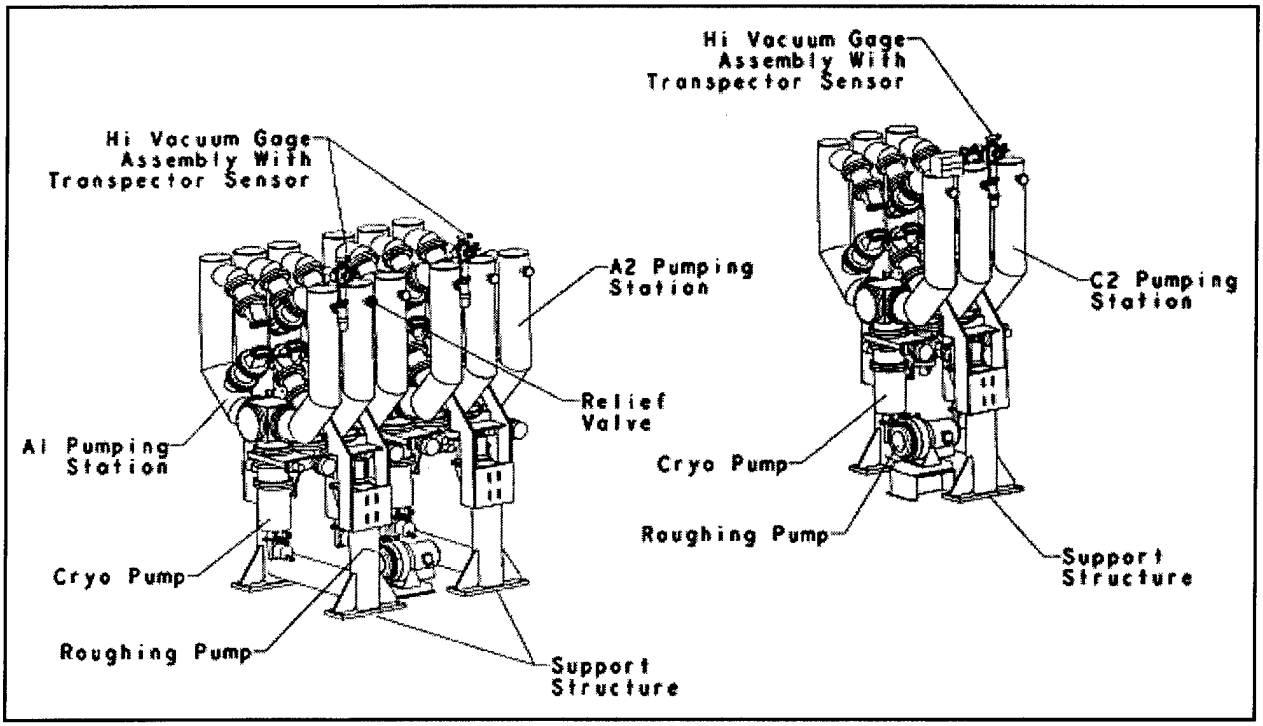



Fig. 1 RFQ Vacuum Pumping System

This was accomplished by researching and specifying *reliable* components in the system to safeguard against possible failures. In addition, we installed *redundancy* to counteract any unforeseen operating conditions or vacuum failures in the system.

*2.3 System Design*

Figure 1 shows the layout of the pumping stations and roughing system for sections A1, A2 and C2 of the RFQ. We opted to use cryopumps based on dynamic analysis of performance during both nominal and abnormal operations, as well as total system pumping speed versus cost. Two Varian DS-600 Dry Scroll Pumps were chosen for the roughing system. These pumps provide a total pumping speed of 1000 L/min atatmospheric pressure with an ultimate total pressure of $10^{-2}$ Torr and are totally hydro-carbon free as required. The system can be pumped down to below the cross-over pressure (~ 100 mTorr) of the cryopumps in such an arrangement within 30 minutes.

The majority of the pumping is located in sections A1 and A2 of the RFQ as most of the gas load occurs in the first two meters. Two 2200 L/s (for hydrogen) cryopumps are attached to the pumpstation at section A1, while section A2 has one 2200 L/s cryopump and a 500 L/min roughing pump. The vacuum headers of A1 and A2 are plumbed together via an 8" spool to allow cross-pumping between the two stations. The pumpstation at segment C2 of the RFQ is similar in configuration to that of A1 and A2, but contains two 2200 L/s cryopumps and one 500 L/min roughing pump.

Having a total of five cryopumps and two roughing pumps in the vacuum system guarantees the ability to individually regenerate cryopumps during accelerator operation. In addition, as shown in the analysis summary, the redundancy ensures that the "operating pressure" is maintained should one pump fail while another is in its regeneration cycle.

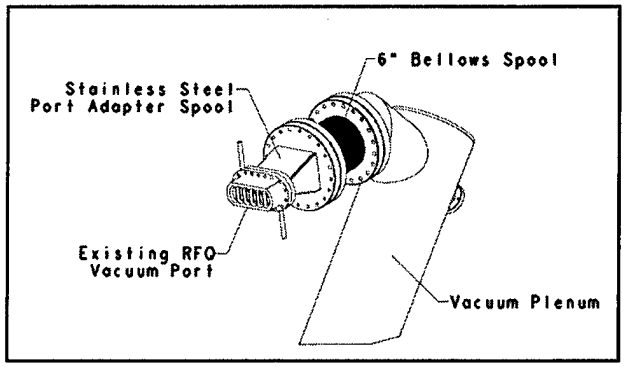



Fig. 2 RFQ Vacuum Port Adaptor Spool & Bellows Assembly

The port adapter spool shown in figure 2 is constructed from 304 stainless steel plate and an 8" conflat flange. It provides the transition from the RFQ vacuum port to the plenum. The 6 slot configuration of the RFQ vacuum port flange has the poorest conductance of any component in the system and the aggressive taper from the oval shape of the vacuum port flange to the circular plenum flange has a significantly higher conductance than would a straight oval or rectangular

spool transition piece. Since the RFQ cavities are fabricated from copper, it is difficult to provide a metal seal between the adapter spool and vacuum port. An o-ring groove, designed to accept a standard sized o-ring, is machined into the mating face of the adapter spool and a viton o-ring will provide the seal. This is the only connection in the high-vac system that will not have a metal seal. However, the RFQ vacuum port is water cooled to a temperature suitable for viton use.

## 3 SYSTEM ANALYSIS

Dynamic system analysis were carried out for pumpdown, nominal operation and under abnormal conditions. This was done by solving the coupled differential Heat-Load Equations described for each segment:

$$-V_i \frac{dP_i}{dt} = -Q_i + C(P_i - P_j) + K(2P_i - P_{i+1} - P_{i-1})$$

where $V_i$, $Q_i$ and $P_i$ represents the volume, gas load and pressure in segment i respectively. C is the total effective conductance of the RFQ pump ports, and K is the conductance of the coupling plates between two segments. $P_j$ is the effective pressure at the port adaptor described by the equation for pump station j as:

$$-V_j \frac{dP_j}{dt} = S_j P_j - Q_j + C(P_i - P_j)$$

where $S_j$ is the effective pump speed at the pump ports with all the conductance of the plumbing taken into account. One example of the analysis results is shown in Fig. 3. Description of the sequence of events is listed in Table 3.

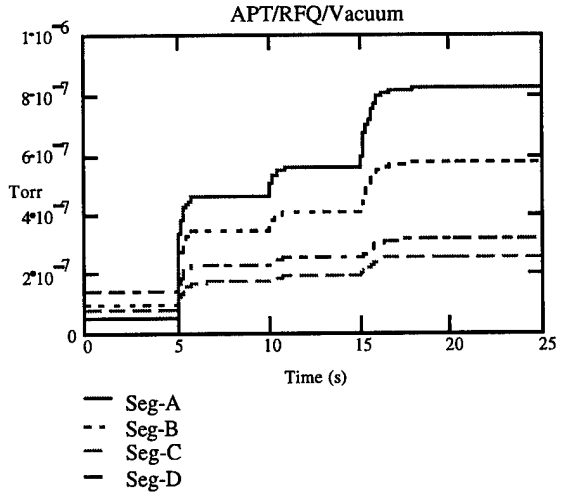



Fig. 3 Analysis Results of Simulation of Loss of Pumps in Segment A.

| Time Interval (s) | Description |
|---|---|
| 0 - 5 | Base pressure with out-gassing load |
| 5 - 10 | With gas streaming from LEBT |
| 10 - 15 | With one pump out of service |
| 15 - 25 | With two pumps out of service |

Table 3 Description Sequence of Events in Fig. 3

It is clearly shown that the minimum operating pressure of $10^{-6}$ Torr can be maintained even if two out of three pumps were taken out of service.

## 4 CRYOPUMP TEST

To verify the major design parameters, we have started a series of performance tests on the cryopumps procured for the system (Ebara ICP 200Q). Major tests include the measurements of $H_2$ pumping speed and $H_2$ capacity. We have adopted the standard test arrangement (AVS Procedure 4.1) [2]. Preliminary results of measured hydrogen pump speed are shown in Fig. 4. It should be notd that the measured value of 2700 L/s exceeds the vendor's specified value of 2200 L/s. Results of the pump speeds with $H_2$ quantity sorbed up to 30 L will be published at a later date.

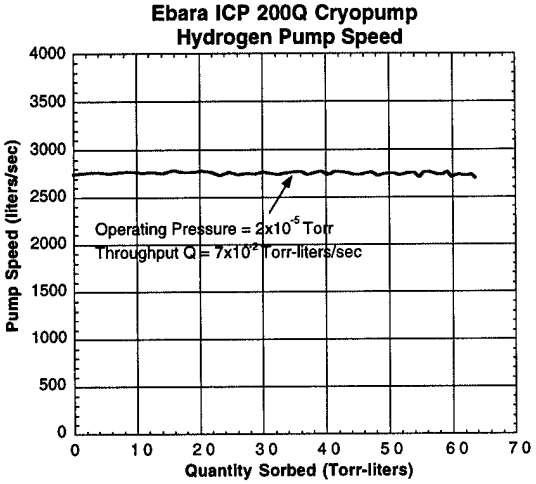



Fig. 4 Measured Pump Speed vs $H_2$ Quantity Sorbed

## 5 ACKNOWLEDGEMENTS

This work was performed under the auspices of the U.S. Department of Energy by Lawrence Livermore National Laboratory under Contract W-7405-Eng-48.

## REFERENCES

[1] D. Schrage: `A 6.7 Mev CW RFQ Linac', ibid., (2W.25)

[2] M.H. Hablanian: `Recommended Procedure for Measuring Pumping Speed', J. Vac. Sci. Technol. A5(4), July/Aug 1987, 2552

# LNLS VACUUM SYSTEM COMMISSIONING

M. J. Ferreira, R. O. Ferraz, F. A. Minuzzi, and M. B. Silva
Laboratório Nacional de Luz Síncrotron - LNLS/CNPq
Caixa Postal 6192 - Campinas - SP - Brazil.

*Abstract*
The Brazilian National Synchrotron Light Laboratory, LNLS, operates a synchrotron light source consisting of a 1.37 GeV electron storage ring and a 120 MeV injector. A summary of the commissioning and operation performance of the vacuum system for the linear accelerator (LINAC), transport line, RF system and storage ring is presented. The performance of the sub-systems is described including the photon induced desorptions (PID) and the effects on the beam lifetime.

## 1. INTRODUCTION

Commissioning of the injector LINAC started in December 1995 with and commissioning of the storage ring (at low energy) started on May 1st 1996. Full energy operation has first achieved in August 1996. The description of the vacuum system is given elsewhere (2). At present 10.0 Ah of accumulated beam dose in the storage ring has been achieved. The average dynamic pressure in the LINAC, transport line and storage ring is in the $10^{-7}$ Pa range, whereas in the LINAC RF system the pressure is in the $10^{-6}$ Pa range. All parts of the system were opened at least once, during modifications and improvements. This allowed us to check the short recovery time. Today if any one of the 6 cells of the ring needs ventilation to atmospheric pressure, 6 hours later it is possible to inject at low energy without baking. The transport line can be operated after 4 hours of pump down under the same conditions. The most sensitive is the LINAC RF system. The rectangular copper wave guides need baking (400 K, 24 hours) after ventilation. The copper accelerating structures of the LINAC are not bakeable and 24 hours of pump down are necessary after ventilation before operation.

## 2. LINEAR ACCELERATOR

After 15 months of operation the linear accelerator had to be vented for removing the ceramic RF window near the gun. The window ceramic had been eroded by sparks, developing a leak and turning the LINAC operation unstable. The LINAC had to be vented a second time since we did not have at the time a spare window available. Almost at the same time, the gun cathode had to be replaced and the gun ion pump was replaced by a new 25 l/s model. After this maintenance we used the normal baking procedure in the gun and heated up the LINAC to 333 K using the hot water stabilizing system of the accelerating tubes. The final static and dynamic pressure in the gun reached $2.8 \times 10^{-7}$ Pa and $6.0 \times 10^{-7}$ Pa respectively. In the LINAC the static and dynamic pressure are $4.1 \times 10^{-7}$ Pa and $6.6 \times 10^{-7}$ Pa, respectively.

## 3. LINAC RF SYSTEM

The LINAC RF system has no gauges and uses the current in the power supplies for the interlock system. A current bellow 500 μA ($\approx 5 \times 10^{-4}$ Pa) in the ion pump enables the system to work. Each time we opened one of the "arms" of the system, we needed baking for 24 hours at 453 K against a turbo-molecular pump. We tried to condition the system with the RF only, but were a lot of sparks in the ceramic windows and the operation became unstable. In normal operation conditions the maximum current is 10 μA ($\approx 1 \times 10^{-5}$ Pa).

## 4. TRANSPORT LINE

We have built a new septum chamber very similar to the already installed one but with some improvements, such as providing more space for the injection angle. Changing the chamber took one day. The chamber was not baked it and we used only the beam cleaning capability. A slit was installed to help a better control of the energy dispersion during the injection. The main computer, in the control room, operates the slit.

## 5. STORAGE RING

The storage ring chambers were baked for 10 days right after installation in April 1996. During the following 4 months of commissioning, the vacuum chamber was opened several times and 3 beam lines were installed. In order to prepare the ring for the installation of the remanding 4 beam lines, the machine was baked again without the NEG activation. After the second baking the ring started to operate without interruptions and the average pressure started to decrease. Figure 1 shows the time evolution progress of the accumulated beam dose at 40 mA and the lifetime of the beam. The lifetime is the time it takes for the current to fall to 1/e of its initial value. During the last month of operation the beam dose increased from 5.4 Ah to 10.0 Ah. In the conceptual

0-7803-4376-X/98 /$10.00 © 1998 IEEE

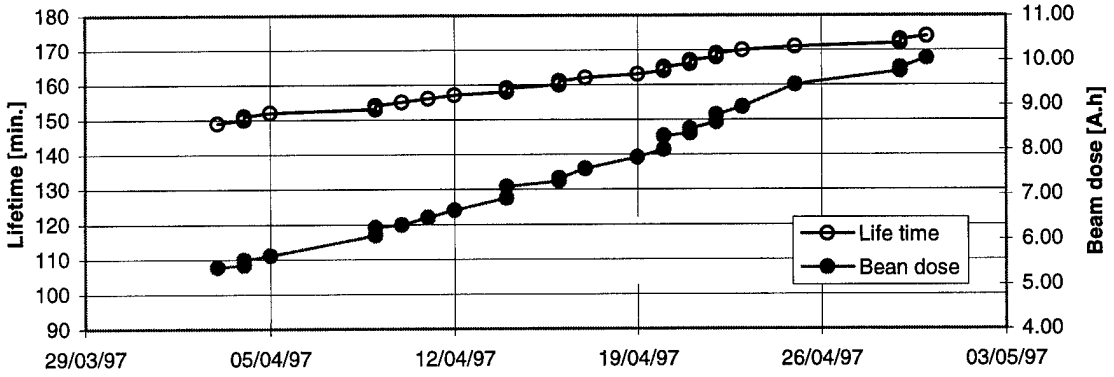



Figure 1: Beam lifetime at 40 mA and the integrated beam dose

design we estimated 100 Ah of beam dose (3,4) to attain the specified lifetime of 7 hours at 100 mA. The averaged pressure readings of the ring are 4 x $10^{-8}$ Pa without beam, 8 x $10^{-8}$ Pa at a beam current of 70 mA. This is the dominant factor to the beam lifetime limitation. The pressure rise per unit of electron beam current ($\Delta P/I$), as a function of the bean dose, at pump stations near the bending and a straight section are shown in fig. 2.

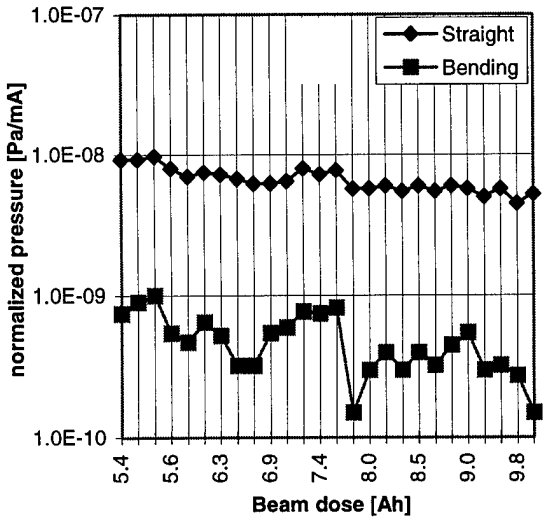



Figure 2: Normalized pressure at bending and straight chambers

The experimental results show that the decrease of the normalized pressure in the bending magnet chamber is only about a fact of 2 lager than the straight section. Since the linear photon power density at the location of bending chambers is many times higher than in the case of the straight section chamber, we have expected a much lager difference rate. We believe the reason of this is the high temperature on the exit port of the bending chamber (430 K). Examining the conceptual design of the bending chamber, we found an inadequate cooling rate on the photon absorber in this position. A new device has been design and a prototype is ready for the test. The design of a wiggler chamber and the new bending chambers for the insertion devices incorporate this detail.

## 6. CONCLUSION

After one year of commissioning and an accumulated beam dose of 10.0 Ah, the average dynamic pressure has reached 6.0 x $10^{-7}$ Pa at 40 mA beam current. The limitation of the lifetime is the elastic scattering on the residual gas. This pressure was obtained without NEG activation. The inefficient cooling rate at the bending magnet chambers has been identify and a new cooling device was designed. A new baking with NEG activation will be performance in the next shutdown period, a long with the change of the septum (5).

## 7. REFERENCES

(1) A. R. D. Rodrigues et al, "Commissioning and Operation of the Brazilian Synchrotron Light Source, these Proceedings.
(2) M. J. Ferreira et al, "LNLS Vacuum System", EPAC 1996.
(3) P. A. P. Gomes, "LNLS UVX Storage Ring Vacuum System: Requirements and pumping", MET-10/91.
(4) B. A. Tricket, Vacuum 38, 8-10, p.607, 1988
(5) A. R. D. Rodrigues et al, "Pulsed Septum for the LNLS Injector", these Proceedings.

# INTERNAL GAS TARGETS IN AmPS

A.P. Kaan[1], J.F.J. van den Brand[1,2], M. Doets[1], E. van Leeuwen[1], and O. Postma[1]

[1] NIKHEF, P.O. Box 41882, 1009 DB Amsterdam, The Netherlands
[2] Dept. of Physics and Astronomy, Vrije Universiteit, Amsterdam, The Netherlands

## 1 INTRODUCTION

Measurements of spin-dependent electron scattering have the potential to greatly enhance our understanding of nucleon and nuclear structure. For example, spin observables in electron scattering from polarized hydrogen in the $\Delta$-region are sensitive to a possible d-wave admixture in the quark wave functions of the nucleon or $\Delta$-isobar. Measurements of elastic and quasi-elastic scattering from deuterium and $^3$He are predicted to provide important information on the effects of S'- wave and D-wave components in the ground state of $^2$H and $^3$He and the largely unknown charge form factor of the neutron. Furthermore, a combination of measurements on polarized hydrogen, deuterium, and $^3$He targets in deep-inelastic lepton scattering can be applied to measure the spin structure functions of the nucleon and to verify the Björken sum rule.

The measurement of analyzing powers and spin-correlation parameters in spin-dependent electron scattering from polarized nuclei is optimally performed by scattering electrons from a pure and highly polarized target. Polarized internal gas targets in electron storage rings have the advantage that spin-dependent scattering from chemically and isotopically pure atomic species of high polarization can be realized. They offer rapid polarization reversal and flexible orientation of the nuclear spin direction by using low magnetic holding fields, a low thickness at high luminosity which allows for the detection of low-energy recoiling hadrons, and access to a broad kinematic range by using large acceptance detectors. For polarized deuterium one has the additional ability to reverse the tensor polarization, $P_{zz}$, at fixed vector polarization, $P_z$, and vice versa. Subsequently, small systematic errors can be expected.

This technique is currently exploited at the Amsterdam Pulse Stretcher (AmPS) storage ring[1] at NIKHEF, where ultrapure polarized hydrogen, deuterium, and $^3$He targets are available. In this presentation, we want to discuss the implications of the use of gas targets for the vacuum in the storage ring, and the strategy that was used at NIKHEF to optimize the luminosity by balancing between the conflicting requirements of dense gas targets and high electron beam life time.

In section 2 the polarized internal gas targets are briefly described. In section 3 the implementation of the gas targets in the vacuum system of the ring is discussed.

## 2 POLARIZED GAS TARGETS

Figure 1 shows a schematic layout of the experimental setup with the hydrogen/deuterium target. An atomic beam source provides the polarized hydrogen or deuterium atoms. The molecules are dissociated into atoms, and an atomic beam is formed at the nozzle, which is cooled to 70 K. The hyperfine states with electron spin down are rejected in the sextupole magnets. With RF-transition units between and after the sextupole magnets, an arbitrary selection of hyperfine states can be made, in such a way that the nuclear polarization can be chosen freely. The atomic beam is injected into a T-shaped, open-ended storage cell, which is cooled to 100 K. The use of such a storage cell gives an increase of target thickness at the place of the electron beam of more than two orders of magnitude for the present configuration. Ions, produced by the electron beam, can be extracted by using a combination of electrostatic lenses, a spherical deflector, a Wien filter, and an ion collector, consisting of a tritiated titanium foil (see Fig. 1). The reaction $^3$H(d,n)$^4$He was applied to monitor the polarization of the target gas *in situ* [3]. More details on the experimental setup can be found in Refs. [4, 2].

For the experiments on $^3$He, a metastability-exchange optical pumped target is used. A fraction of the $^3$He gas in a glass pumping cell is brought into the $2^3S_1$ metastable state. These metastables can be polarized by pumping with circularly polarized laser light (1.083 $\mu$m) to a 2P state. The atoms in the ground state are polarized by metastability exchange collisions. A fraction of the gas in the pumping cell is injected via a capillary into a cylindrical storage cell, which is cooled to 20 K in order to increase the target thickness at the beam, while keeping the flow limited. For the target currently employed at NIKHEF, we obtained 60 % polarization for a flow of $10^{17}$ atoms/s. Since the flow for the $^3$He target is larger than for the deuterium/hydrogen target, and since He is more difficult to pump, we will discuss the vacuum system for the latter target in the next section.

## 3 VACUUM SYSTEM AT THE TARGET AREA

The use of gas targets may compromise the vacuum in the storage ring. This will deteriorate the beam life time and may introduce unwanted background from interactions with the rest gas. In the case of the NIKHEF storage ring, the vacuum has to be of high quality (better than $10^{-8}$ mbar) especially downstream from the target area, since there a Laser-Compton Backscattering polarimeter is used to measure the polarization of the electron beam. The main background for this polarimeter is due to interactions of the beam with rest gas. Furthermore, the pumps in the ring outside the target region are titanium getter pumps, which cannot handle excessive loads of helium gas. The capacity for helium for the pumps in the AmPS ring (Varian Starcell

0-7803-4376-X/98/$10.00 © 1998 IEEE

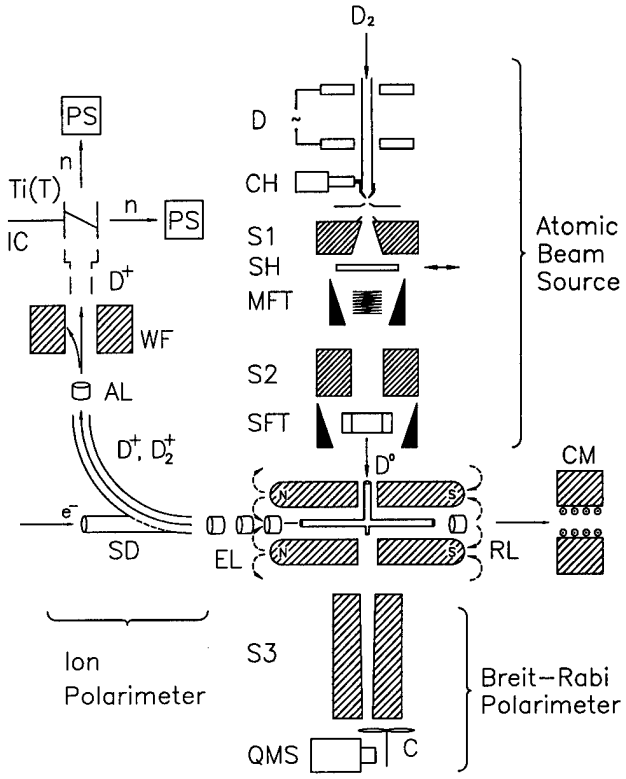



Figure 1: Schematic outline of the atomic beam source, Breit-Rabi polarimeter, internal target, and ion-extraction system. All components, except the target holding field, the neutron detectors (PS), and the correction magnets (CM), are inside the vacuum system. D: RF dissociator; CH: cold head; S1, S2, S3: sextupole magnets; MFT, SFT: medium- and strong-field transition units; SH: shutter; C: chopper; QMS: quadrupole mass spectrometer; RL: repeller lens; EL: triplet of ion-extraction lenses; SD: spherical deflector; AL: electrostatic lens; WF: Wien filter; IC: ion collector.

919-0103) is limited to about 1 mbar*l per pump. It is clear, that one wants to minimize the gas load of the target to the ring vacuum. Therefore a differential pumping system has been developed. The sections are separated by (movable) conductance limiters, which have a circular aperture through which the electron beam can pass. The positions and diameters of the conductance limiters are optimized for the boundary conditions set by the $\beta$ functions of the electron beam and the ratio between ballistic and molecular flow (where the ballistic flow consists of atoms leaving the storage cell at such small angles with respect to the electron beam that they can pass the conductance limiters without a single wall collision).

Figure 2 shows the setup in the target area. Monte-Carlo studies were performed to choose the optimal solution in terms of costs and pumping speed for the target area section [5]. The target chamber is pumped by two pumping stations containing 3200 l/s turbo pumps (2200 l/s for $N_2$, 3200 l/s for He). The ring is separated by the target chamber by three sets of conductance limiters. The first and second differential pumping stage contain 1450 l/s and 300 l/s turbo molecular pumps, respectively. All turbo molecular pumps are backed up by a turbo drag pump to obtain a high enough compression ratio. In order to assure an oil-free vacuum, membrane roughing pumps are used. Figure 3 shows the helium pressure profile for an experiment with a flow of $4.2 \times 10^{16}$ $^3$He atoms/s. In a region of 1.5 meter the gas pressure drops by 5 orders of magnitude. Note, that the base pressure of the AmPS storage ring (without the presence of a gas target) is about $10^{-9}$ mbar.

Studies of the gas pressure in the ring and in the target region for different gas flows demonstrated, that the Monte Carlo code predicts the local pressure correctly within better than a factor of two.

In summary, the requirements of dense gas targets and high vacuum in the storage ring have been met by designing a three-stage differential pumping system. The system is capable to reduce the gas load of the target to the storage ring sufficiently, obtaining a decrease in pressure of five orders of magnitude in only 1.5 meter. The system has been tested in the ring and performs in accordance with the specifications.

## 4 REFERENCES


[1] G. Luijckx *et al.*, in *Proceedings of the 1995 Particle Accelerator Conference and International Conference on High-energy Accelerators*, (Dallas, May 1995).

[2] Z.-L. Zhou *et al.*, Nucl. Inst. Meth. **A364**, 44 (1995).

[3] Z.L. Zhou sl et al., Nucl. Inst. Meth. **A379**, 212 (1996).

[4] M. Ferro-Luzzi *et al.*, Phys. Rev. Lett. **77**, 2630 (1996).

[5] O. Postma, NIKHEF internal report MT 96-3 (March 1996).

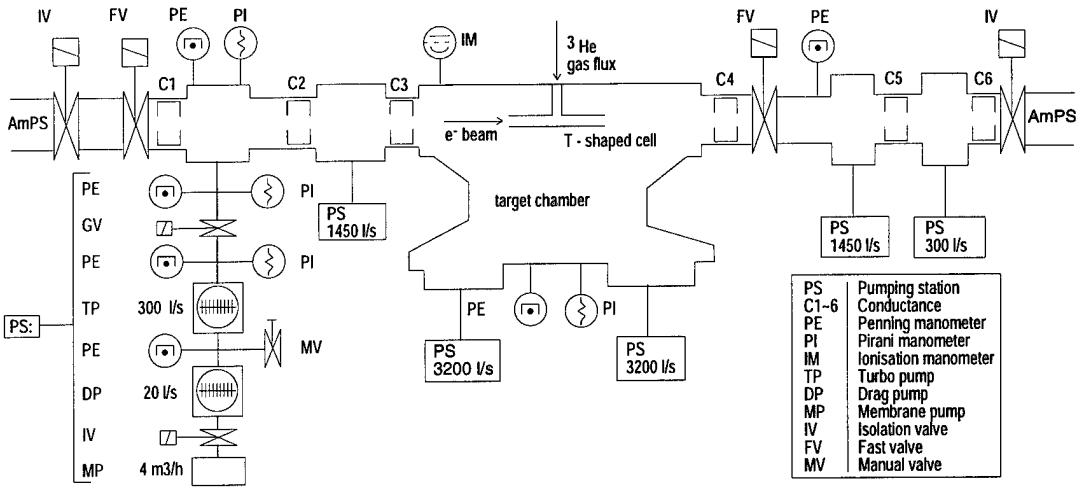



Figure 2: The differential pump system in the target area

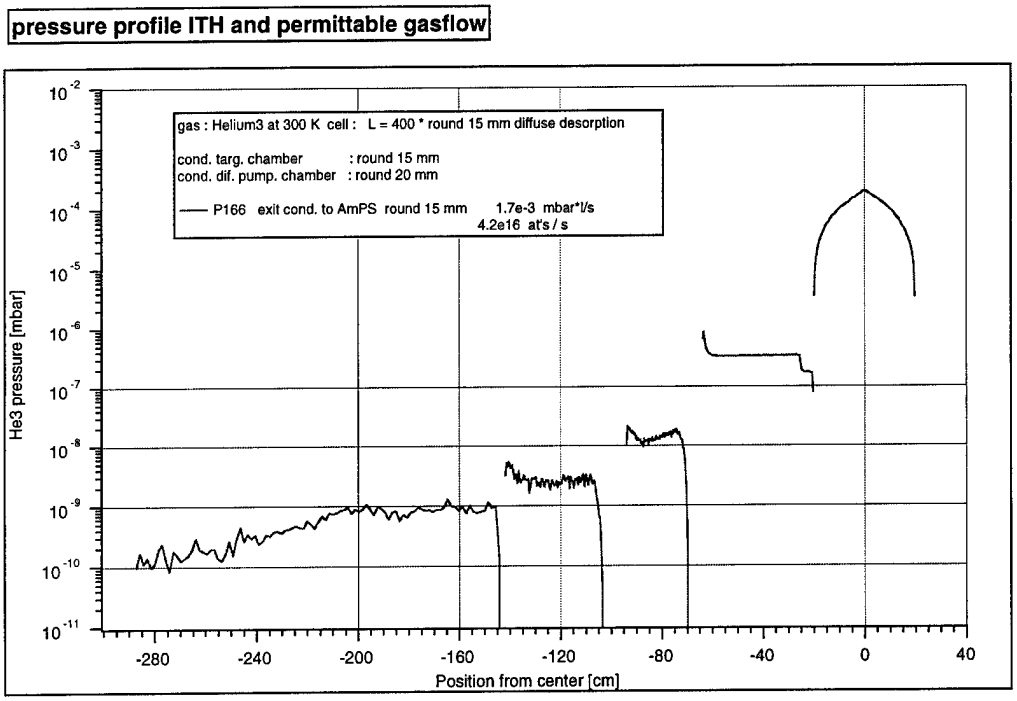



Figure 3: The pressure profile for an experiment, flowing $4.2\times10^{16}$ atoms/s of helium gas

# OPERATION EXPERIENCES FOR PLS VACUUM SYSTEM*

D. Park, Y. J. Han, C. K. Kim, S. M. Chung, and I. S. Ko
Pohang Accelerator Laboratory, POSTECH, Pohang 790-784, Korea

*Abstract*

The ultra-high vacuum system of the PLS electron storage ring was successfully commissioned in July 1995. Since then, it routinely provides a dynamic pressure of about $7x10^{-10}$ Torr. The measured beam lifetime is more than 10 hours with 100 mA beam at 2 GeV. The rapid recovery of normal operation after installation of new components is achieved without *in-situ* bakeout by using a dry venting system. We present operation experiences with the NEG pumps and the performance of the vacuum system.

## 1 INTRODUCTION

The Pohang Light Source (PLS) of the Pohang Accelerator Laboratory is a third generation synchrotron light source with a nominal electron beam energy of 2 GeV. The PLS started its commissioning in September 1994. The PLS was successfully commissioned in July 1995 and opened to users in September 1995. The storage ring (SR) vacuum system of the PLS has been operated since September 1994. The design, fabrication, testing and installation of the vacuum system have been reported elsewhere [1,2]. In brief, the vacuum system is made of either machined A5083 and extruded A6063 aluminum alloy vacuum chambers. The system is mainly pumped by combination pumps which consist of non-evaporable getter (NEG) pumps and sputter ion pumps (SIPs). The PLS vacuum is now so good that improving it would have almost no effect on beam lifetime; lifetime is mainly limited by intra-bunch scattering of electrons, not by electrons scattering with residual gas molecules. The average pressure of the SR is around $3x10^{-10}$ Torr without beam and about $7x10^{-10}$ Torr with 100mA of stored beam at 2 GeV. In this article, the operation experiences of the vacuum system, including NEG operations, recovery works, and the performance of the vacuum system are described

## 2 COMMISSIONG OF THE VACUUM SYSTEM

The installation of the SR vacuum system was completed on June 7, 1994. The vacuum system underwent two operational phases according to the storage ring commissioning [3]. At the SR phase I commissioning, the vacuum system was pumped only by SIPs without NEG activation and without bakeout. Before the first beam injection on September 1, 1994, the ultimate static vacuum reached about $8x10^{-9}$ Torr. With the beam stored, the pressures increased abruptly due to the photon induced gas loads (PIDs). The specific pressure rise was measured as high as $2x10^{-7}$ Torr/mA initially and reduced to $1x10^{-9}$ Torr/mA at the end of phase I commissioning.

After the phase I commissioning, efforts were made to improve beam lifetime due to the gas scattering in two ways; by enhancing the pumping speed and by accumulating beam dose. Firstly, the SR vacuum system was baked at about 90°C for 48 hours. Although the PLS aluminum vacuum chambers could be baked to 150°C by using pressurized hot water, the transverse deflection at the end of the chamber was so large that the bakeout temperature was reduced practically to less than 100°C to prevent RF shielded bellows from breaking down. The NEG pumps were activated at 450°C for about 45 min. at the end of bakeout period. The average static vacuum was then low $10^{-10}$ Torr, and the specific pressure rise due to the PID decreased immediately after the NEG activation. The phase II commissioning began on April 4, 1995. During this period, the beam was stored as high as possible in the night in order to clean up the photon irradiating surfaces by accumulating the beam dose and hence to lower beam-gas scattering. As a result, a rapid increase in lifetime from 150 min. to 10 hours at 100 mA was achieved at the end of the phase II commissioning.

On September 1, 1995, the first beam was delivered to users. During the user service period, there was a machine shut down due to the water leak at the brazed interface with copper to stainless steel in the strip photon absorber on October 19, 1995. The machine resumed to store beam on November 13, 1995 after the repair work. An operation efficiency of the scheduled beam time was 65% in 1995 due to the water leak. But the system has been in normal operation since 1996 and an operation efficiency of more than 90% is routinely achieved.

## 3 VACUUM PERFORMANCE

Fig. 1 shows the reduction of specific pressure rise due to the PID measured as a function of the accumulated beam dose (Amp.hr). The specific pressure rise was $6x10^{-9}$ Torr/mA at 1 AH and gradually reduced due to the beam self-cleaning effect to $1x10^{-9}$ Torr/mA at 7 AH where the system was pumped by SIPs only. After the NEG activation, the specific pressure rise reduced immediately to $1x10^{-10}$ Torr/mA at 12 AH and finally reached $3x10^{-11}$ Torr/mA with a slope of about -0.7 at the end of commissioning.

Fig. 2 shows the residual gas spectra with and without the beam. The composition of the residual gas

0-7803-4376-X/98 /$10.00 © 1998 IEEE

has drastically changed with the beam stored. The gases desorbed were, in order of importance, $H_2$ followed by CO, $CO_2$, and $CH_4$ with small traces of Ar. After enough beam dose(>600AH), $H_2$ was still the predominant component, followed by CO, $CO_2$, and $CH_4$, while $H_2O$ was effectively cleaned up.

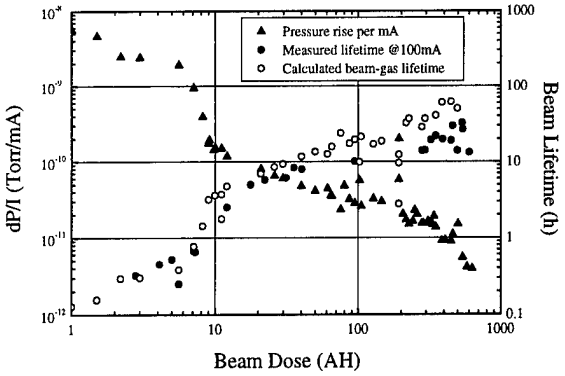



Figure 1: Reduction of pressure rise along with measured beam lifetime with respect to the accumulated beam dose.

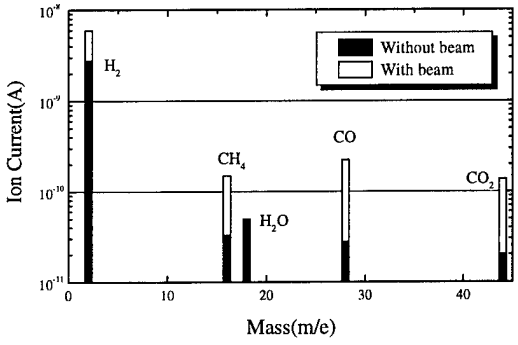



Figure 2: Typical residual gas spectra; without beam and with 100mA stored beam.

Fig. 1 also shows the measured and calculated beam lifetimes. The beam-gas lifetime calculated with the gas compositions described in Ref 3. The measured lifetime at 100mA beam current was in good agreement with the calculated one for low beam dose, meaning that the beam lifetime was limited by beam-gas scattering, *i.e.*, Coulomb and Bremsstrahlung scatterings. The measured lifetime during the phase I commissioning was less than 50 min. at 100mA. After the chamber bakeout and the NEG activation, the lifetime jumped to about 150 min. and finally reached to about 10 hours with 100 mA beam by the end of the commissioning.

As shown in Fig. 1, the vacuum system reached its designed value of low $10^{-9}$ Torr with lifetime in excess of 10 hours after the accumulated beam dose of 50AH. The scattered data in lifetime between 200~600 AH reflects the machine operation parameters. For example, the beam lifetime increases to more than 30 hours when the filling pattern of the electron beam is uniformly distributed, and decreases to about 10 hours at 100mA when the machine is operated to reduce the beam instability. After the beam dose of 400AH, the lifetime does not vary with the pressure, which strongly suggests that the lifetime is limited by pressure independent Touschek effect.

## 4 NEG OPERATION

The lumped NEG wafer module(WP950) used for the PLS is ST707( made by SAES Getters. The NEG is activated typically at 450°C for 45min. Since the installation of the vacuum system in September 1994, the NEG pumps of the complete ring have been reconditioned twice. The first time was after the phase I commissioning (after 7 AH of beam dose) with *in-situ* bakeout, and the second time was after about 320 AH accumulated beam dose. Additional reconditionings have been carried out in sectors opened for repairs and new beamline front-end installations.

After the absorption of 0.1 Torr(1 per module, the pumping speed of the NEG drops below 60% of its initial value with the gas composition of 90% $H_2$ and 10% CO [2]. Assuming the total operation time about 5,000 hours per year, the sorbed quantity is comparable to the point where the speed drops to 60% of its initial speed. And the distributions of the gas loads, and hence pressures, are somewhat varies around the SR due to the thermal load, leaks, and the PID. So, the periodical regeneration is necessary to keep the maximum performance. The reconditioning is planed yearly in the summer maintenance period.

The reconditioning procedure consists of closing of sector valves and switching off the SIPs to avoid the degradation of its performance. The typical operation takes about 4 hours. The NEG pumps are activated by heating them gradually to the predefined temperature. The NEG modules are connected each other in series to keep the current low from one power supply. The current is set at 37 amps to activate NEG at 450°C. After the ion gauges are degassed, the SIPs are switched on at pressures below $10^{-7}$ Torr. A mobile pumping system is then disconnected at about $5x10^{-9}$ Torr due to the poor $H_2$ compression ratio of a magnetic turbo pump backed by a dry mechanical pump.

In order to find an optimum regeneration condition, we have made several measurements with different activation temperatures. The regeneration is carried out as a function of the activation temperature. The results are shown in Fig. 3. The NEG pumping speeds are restored when the regeneration temperature is higher than 310°C and the pressure improvements are comparable with various temperatures. However, the pressure improvement after reconditioning is significant when the pressure before reconditioning is in the range of $10^{-10}$ Torr. This means that the pumping speed of some parts of the SR drops to a very low value. It can be seen from Fig. 3 that the periodic regeneration is necessary and the regeneration at 350°C for about 45 min. is the most effective way to restore the NEG pumping speed.

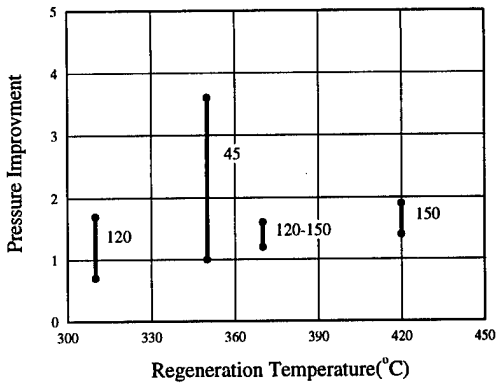



Figure 3: Pressure improvement; the ratio of pressure before the regenerations to pressure after the regenerations. Numerics stand for the duration of regeneration in min.

## 5 VACUUM RECOVERY

The PLS requires extremely clean vacuum and the normal operation condition should be recovered even without bakeout in a reasonably short time. Backfilling of the vacuum system should be done with a moisture-free nitrogen gas. To meet this requirement, a dry venting system (DVS) has been used since the machine start-up [4]. Recently, new DVS has been developed in the laboratory. It consists of a $LN_2$ Dewar, an evaporator, and a diffuser. The DVS works without bakeout in such a way that moisture is frozen out at $LN_2$ temperatures and then pure $N_2$ gas is introduced into the chamber. Fig. 4 compares typical pump down curves measured with different venting gases; ambient air, liquid nitrogen boil-off, and dry nitrogen. The venting effectiveness is apparent as seen from Fig. 4. So far, 10 sectors have been let up to dry nitrogen for repairs and new components installations. The relatively rapid recovery could be obtained using a procedure that includes dry venting, heating of SIPs, 1 hour NEG activation at 450°C and subsequent 24-hour pump down. It usually takes two or three days. After 1~2 AH of accumulated beam dose in case of a photon absorber replacement, the beam lifetime was almost the same as before the venting as shown in Fig. 5. This means that the dry venting is quite good and only PID from the new component appears to cause the pressure rise. Further to minimize the new component effect, a special surface treatment for the vacuum components is necessary and its study is under way.

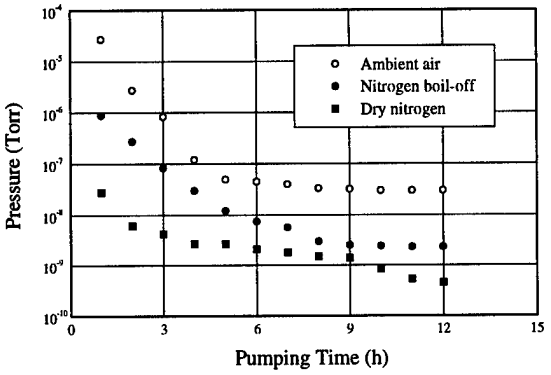



Figure 4: Pump down curves with different venting gases.

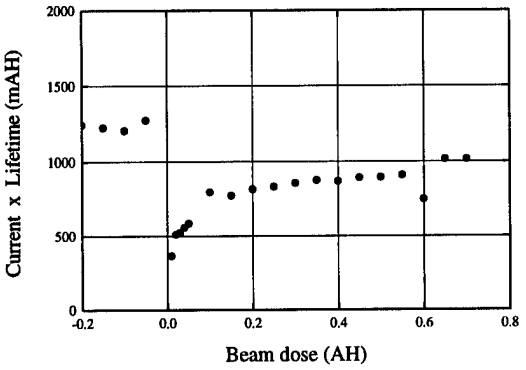



Figure 5: Typical recovery of beam lifetime after a photon absorber replacement

## 6 SUMMARY

The operation experiences as well as the performances of the vacuum system for the PLS storage ring have been described. The relatively fast recovery of normal operation condition is achieved by a dry venting without bakeout. But we often perform a mild bakeout after a long shut down. Now 10-hour beam lifetime is achieved within 4 days with the stored beam of 100 mA at 2 GeV.

## REFERENCES

* Work supported by MOST and POSCO fund.

[1] C. K. Kim, G. H. Kill, W. C. Choi, and S. Y. Park, J. of Korean Vac. Sci. Tech., 1, 24(1992).

[2] C. D. Park, Y. J. Han, H. J. Kim, H. S. Youn, and W. C. Choi, J. of Korean Vac. Sci. Tech., 1, 336 (1992).

[3] C. D. Park and C. K. Kim, EPAC96, Barcelora.

[4] S. I. Ru, S.S. Lee, J. W. Chung, and S. M. Chung, J. of Korean Vac. Sci. Tech., 1, 332(1992).

# VACUUM SYSTEM DESIGN USING SYMBOLIC NUMERIC PROCESSORS

Wayne D. Cornelius, Scientific Solutions, PO Box 500207, San Diego CA 92150

*Abstract*

The widespread availability of software for the personal computer (Maple, MathCAD, Mathematica, etc.) provides a convenient means of analyzing the design of vacuum systems for large and small facilities. The overall vacuum system is easily expressed as a matrix equation that includes surface outgassing and vacuum pumping rates and can include such effects as opening and closing of valves. Once the matrix equation has been defined, it is a simple matter to derive pressure solutions as a function of the different variables and to determine the effects of opening or closing valves. Thus one can derive the vacuum pressure in each section of the entire system as a function of these variables and quickly optimize the overall vacuum system design.

## 1. INTRODUCTION

Because of the relative uniqueness of each accelerator facility, the designs of their associated vacuum systems also tend to be unique. Often a great deal of effort goes into the overall system design and relatively little of this accumulated analysis effort can be applied to the following generations of facilities, in some cases because the technology has changed and in other cases because the facilities are not compatible. Some of these vacuum design efforts have been archived into relatively crude vacuum-design programs that are generally too narrowly focused or are difficult to adapt and are not widely used within the community. The purpose of this paper is to introduce a mathematical formulation for the design of a vacuum system that is compatible with analysis using one of the symbolic numeric processors now available for the personal computer.

In the past, this author has been involved in the design of several vacuum systems. Virtually all of these designs were started from scratch because no coherent design framework survived the gap between projects. The vacuum design system was reinvented with each new project, usually in the form of rough calculations performed with the help of a calculator. More recently, some assistance in the form of computer-assisted characterization of various components has helped the design process [1], but these codes are generally limited in their flexibility and the relatively small number of allowed elements is particularly inconvenient for the analysis of the large and complicated systems generally associated with accelerator facilities.

The widespread availability of symbolic numeric processor environments for the personal computer (such as MathCAD [1], Maple [2], Mathematica [3], Macsyma [4], etc.) now provides a convenient framework to support the design of large and complicated vacuum systems. The mathematical model introduced below provides a framework for using symbolic processors to design both simple and complex vacuum systems.

## 2. MATHEMATICAL FRAMEWORK

All vacuum systems can be modeled as a series of chambers or segments comprised of outgassing surfaces with mutual conductances between adjacent segments. In each segment, n, the mass flow of gas, $Q_n$(Torr-liters/sec) is equal to the outgassing from the surfaces of that segment, $R_n$, plus the gas conducted in from the adjacent segments minus the gas conducted out into the adjacent segments and minus any vacuum pumping, V, connected to that segment:

$$Q_n = R_n + (P_{n-1} - P_n)\cdot C_{n-1,n} + (P_{n+1} - P_n)\cdot C_{n+1,n} - V_n \cdot P_n ,$$

where $P_n$ is the pressure in segment n and $C_{n,m}$ is the conductance (liters/sec) between segment n and segment m. Since $C_{n,m} = C_{m,n}$, we can write:

$$Q_n = R_n + C_{n-1,n}\cdot P_{n-1} - (C_{n-1,n} + C_{n+1,n})\cdot P_n + C_{n+1,n}\cdot P_{n+1} - V_n \cdot P_n .$$

Conservation of mass ensures that these flow rates balance and the net mass flow is zero, $Q_n \rightarrow 0$. Therefore the vacuum system can be modeled as the sum of a tri-diagonal conductance matrix, **C**, and a sparse diagonal vacuum pumping matrix, **V**, multiplying a pressure vector, P, being equal to a gas-effusion rate vector R:

$$(\hat{C} + \hat{V})\cdot \vec{P} = \vec{R} . \qquad (1)$$

The vacuum pressure vector, and hence the vacuum pressure in each segment of the system, is given by the solution of Equation 1. Conservation of mass also shows up in the conductance matrix by requiring the sum of all elements in a row to be zero. This feature is a useful cross-check to ensure that the conductance matrix has been properly defined.

Since the conductance is generally a strong function of pressure, Equation 1 is non-linear except in the molecular-flow pressure region. The examples used in

0-7803-4376-X/98 /$10.00 © 1998 IEEE

this paper are restricted to that regime where the conductance is constant. Since the goal of the vacuum system design is usually to compare the ultimate pressures in the system with the vacuum requirements, the pumpdown characteristics are usually addressed after the design is more or less complete. Hence the solution of Equation 1 in the molecular flow region is the primary focus of this paper.

In principle Equation 1 can be solved in the higher pressure regions by an iterative schemes follows. The conductance at a particular pressure is used to derive an initial conductance matrix. That conductance matrix and the vacuum pumping speed at that pressure are used to derive a new pressure vector using Equation 1. That new pressure vector is then used to derive new conductances etc. This scheme can be used bootstrap the system from atmospheric pressure into the molecular flow region and hence derive the pumpdown characteristics of the system.

Deriving solutions to Equation 1 is relatively simple using one of the symbolic numeric processor packages. The examples used in this paper were produced using MAPLE V, Release 3. Although MAPLE provided quick solutions to the problems posed, Release 3 lacks the capability of saving the results in any format except the MAPLE environment. This feature is particularly inconvenient for translating results into written reports or in producing output that can be copied into other environments such as word processors or spreadsheets. Apparently more recent versions of MAPLE support cross-platform compatibility in the Windows environment.

## 3. EXAMPLES

The first example, illustrated in Figure 1, is a simple 10-element beam transport line with three potential locations for vacuum pumps. The beam line is comprised of 61 cm lengths of 10 cm ID tubing and the pump boxes are 30 cm cubes with 100 l/sec ports for attaching vacuum pumps. The outgassing rates were taken from Appendix C of reference 5. The pressures expected from placement of a single 100 l/sec pump in segment 3, 6, or 10 are illustrated in figure 2.

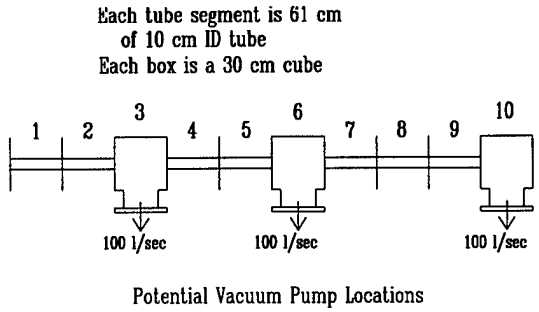



Figure 1. Example 1 beamline consisting of ten segments with potential pumping ports in segments 3, 6, and 10.

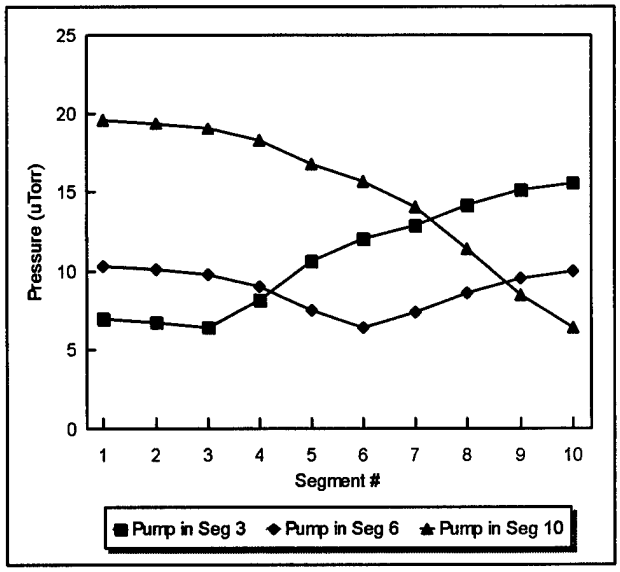



Figure 2. Plot of vacuum pressures of the Example 1 vacuum system for different pump configurations.

The second example is a 70-250 MeV proton beam transport line comprised of two sections, a switching magnet, and in-line valves (Figure 3). The beam exiting a cyclotron is directed by a pair of 30° bends towards the switchyard and proton therapy treatment gantries. The beam transport line is comprised of 6 cm ID tubing with 8 cm by 4 cm rectangular tubing in the dipole magnets. The vacuum system design model is comprised of 43 elements. Each segment in the model consists of an outgassing surface connected to adjacent regions by the effective conductances computed from formulae in reference 5. A closed valve is represented by zero conductance between segments.

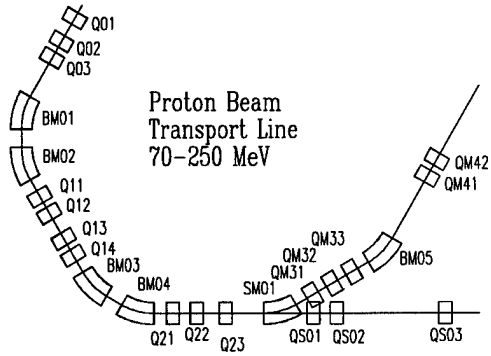



Figure 3. Beamline geometry of example 2. This beamline is comprised of two branches with in-line valves.

The goal of this particular vacuum system design was to minimize the number and size of vacuum pumps while maintaining a low level of scattering from the residual gas atoms in the vacuum.

Equation 1 was modeled in MAPLE using the various conductances, outgassing surfaces, and vacuum pump configurations. Table I provides a matrix of solution parameters and the resulting vacuum profiles are illustrated in figure 4. Figure 4 is notable not because of the information displayed, but because all nine different vacuum configurations were analyzed within a few seconds. The conclusion that can be drawn from figure 4 is that only three vacuum modes are important and the pressure profiles fall within one of these three categories. The final vacuum system design consists of two 100 l/sec vacuum pumps in the Q22 and Q34 segments and no pumping elsewhere in the system.

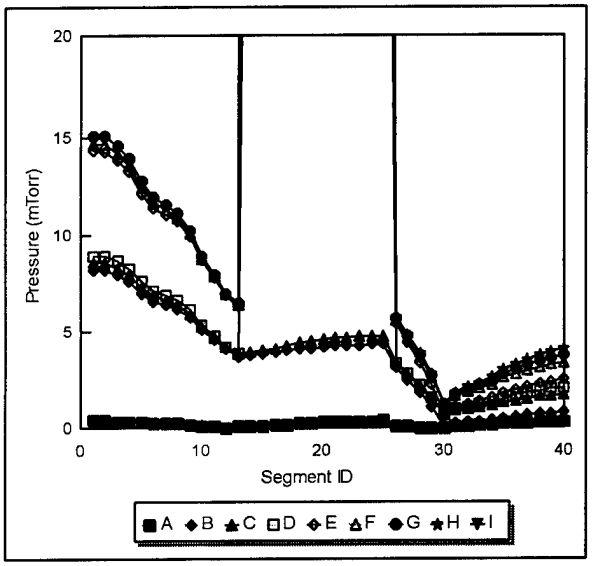



Figure 4. Vacuum pressure solutions of example 2 for the conditions listed in Table I. Segments 13-26 represent the left-hand branch of the beamline while Segments 27-43 represent the straight-through branch. The gap in the left-hand branch pressure values illustrates the result of closing the in-line valve to that branch.

## 4. SUMMARY AND CONCLUSIONS

A mathematical description of a generic vacuum system was derived. This matrix formulation is easily implemented in one of the symbolic numeric processors available for the personal computer thus facilitating the analysis and design of simple and complex vacuum systems as illustrated in the examples. Although these examples illustrate ultimate vacuum pressures in the molecular flow pressure region, the mathematical framework can be used to derive pump-down characteristics.

Table I. The beamline vacuum system model was solved for the following configurations:

| Config ID | Q22 Pump Status | Q34 Pump Status | Valve #1 Status | Valve #2 Status |
|---|---|---|---|---|
| A | OFF | ON | OPEN | OPEN |
| B | OFF | ON | OPEN | OPEN |
| C | ON | OFF | OPEN | OPEN |
| D | ON | ON | CLOSED | OPEN |
| E | OFF | ON | CLOSED | OPEN |
| F | ON | OFF | CLOSED | OPEN |
| G | ON | ON | OPEN | CLOSED |
| H | OFF | ON | OPEN | CLOSED |
| I | ON | OFF | OPEN | CLOSED |

## 5. REFERENCES


[1]for example VACTRAN, a product of Professional Engineering Computations, Livermore CA

[2]MathCAD is a product of MathSoft Inc, Cambridge MA

[3]Maple is a product of Waterloo Maple Software, Waterloo, Ontario Canada

[4]Mathematica is a product of Wolfram Research Inc, Champaign IL

[5]Macsyma is a product of Macsyma Inc, Arlington MA

# FINAL DESIGN AND MANUFACTURING OF THE PEP-II HIGH ENERGY RING ARC BELLOWS MODULE*

Nadine R. Kurita, Artem Kulikov, Martin Nordby,
Stanford Linear Accelerator Center, Stanford, CA USA
John Corlett, Lawrence Berkeley National Laboratory, Berkeley, CA USA

*Abstract*

An update on the Arc bellows module for the PEP-II High Energy Ring is presented. Final design, manufacturing issues, material and coating selection, and tribological and RF testing are discussed. Performance and operational requirements are also reviewed. The RF shield design has been proven during assembly to allow for large manufacturing tolerances without reducing the mechanical spring force below required values. In addition, the RF shield maintains electrical contact even with large misalignments across the module.

## 1. INTRODUCTION

A novel RF shield bellows module developed at SLAC has been successfully manufactured and installed in the PEP-II High Energy Ring (HER). Tests indicate that the module meets its performance and operational requirements. The primary function of the bellows module is to allow for thermal expansion of the chambers and for lateral, longitudinal and angular offsets due to tolerances and alignment, while providing RF continuity between adjoining chambers.

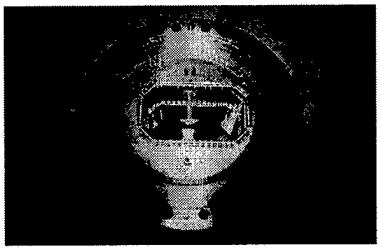


Figure: 1 HER Arc Bellows Module

To make a more robust design and reduce RF shield failure, a "double finger" mechanism was developed. This improves on previous designs by keeping high temperature areas away from high stress areas. The hot RF shield does not provide the contact force, but is held by lower temperature backing fingers. Alumina-dispersion strengthened copper (GlidCop®) and Nickel-chromium alloy (Inconel®) were the materials selected.

## 2. ARC CELL DESIGN

The HER circumference is 2.2km and stores 3000mA of 9GeV electrons [1]. The HER is hexagonal, with six arc regions 240 m in length and six straight regions 120m in length. A cell consists of two dipole magnets, separated by a quadrupole/sextupole doublet with 16 cells per arc. The dipole and quadrupole chambers are made from octagonal copper extrusions, and the bellows module bridges the gap between the dipole and the quad chamber.

## 3. DESIGN DESCRIPTION

The design employs a silver plated high conductivity GlidCop Al-15 RF shield finger which slides and makes electrical contact on the outside wall of a Rhodium plated GlidCop Al-25. This assembly preserves the chamber profile to create a uniform beam pipe. A welded bellows maintains vacuum and allows for travel with lateral offset.

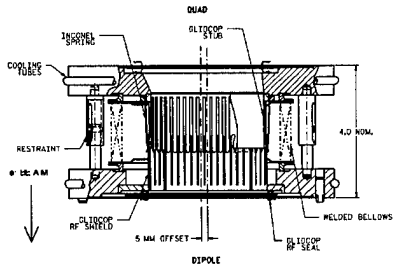



Figure 2: Bellows Module Assembly Drawing

The bellows module is designed to satisfy several key requirements. First, it allows for thermal expansion of an arc half cell. Table 1 lists the different scenarios for thermal motion. It is also requires that the module compress 19mm for installation. The major concern during installation is to consistently seal the flanges and to install the module without damaging the delicate RF seals on each end. In addition, a lateral offset of ±1mm and 25mrad of angular misalignment is required for fabrication and chamber alignment tolerances. Note that the lateral offset is limited by the welded bellows and not the RF shield.

| Scenario Description | Travel | Cycles |
|---|---|---|
| Max. Compression, Installation | 19 mm | 100 |
| Max. Extension, | 1.3 mm | 20 |
| In-Situ Bake (150°C) | 11 mm | 10 |
| Beam Off/On | 5 mm | 10,000 |
| Filling | 3.8 - 5 mm | 200,000 |

Table 1: Thermal and Installation Travel Scenarios

Another primary function is maintaining a continuous chamber and electrical conduction path to minimize beam instability and impedance. RF shield failure could result in creating a cavity which produces a trapped mode. The RF shield fingers slide on the outside wall of the stub, which ensures that potential failure will not result in the fingers falling into the beam tube. The sliding joint produces an inward 1.5mm step which eliminates the potential for mode trapping. The size of the

* Work supported by the U.S. Department of Energy under contract number DE-AC03-768F00515

step is driven by two features: the mechanical stability of the stub wall and the rounded contact surface at the tip, which ensures that the shield finger will not make a secondary contact on the stub.

The module also required masking to be from intercepting a synchrotron radiation strike of up to 1170W/cm$^2$. An offset of 5mm between the Dipole and Quadrupole chamber was used to shadow the module with minimal change to the volume of the beam passage. The offset was produced by tapering the upstream flange. The module produces a calculated 0.061nH inductive impedance [2].

For every RF shield finger there is a mating Inconel 718 spring finger which applies an average of 170g of force to provide sufficient electrical contact. Previous RF shield designs had dual purpose fingers which served as both the spring and the shield. However, this is extremely difficult to implement successfully since conductive materials do not exhibit the mechanical properties of high temperature springs.

The conductivity of the materials used for electrical contact joints are key parameters in its current carrying capacity. Numerous designs in the past utilized Beryllium Copper (BeCu) for the RF shield. The thermal conductivity of GlidCop Al-25 is 90% of copper, and a factor of two higher than BeCu. Also, the mechanical properties of BeCu are extremely sensitive to the precipitation age hardening process conducted after forming. Due to the hardening process, BeCu is also susceptible to overaging, which significantly lowers the strength properties at slightly elevated temperatures. The yield strength of GlidCop is slightly reduced to 448MPa at 1000°C [3], which is the braze temperature for the RF shield sub-assembly. This decrease in yield strength is not sufficient to cause permanent distortion due to lateral offsets across the fingers. Stress relaxation at elevated temperatures does occur in GlidCop, but does not affect the contact force.

## 4. THERMAL/STRUCTURAL ANALYSIS

### *4.1 Thermal Loading*

There are four primary sources of heat: 0.25 W/cm$^2$ scattered SR, 0.04W/cm$^2$ from ohmic losses, 0.07W/cm$^2$ from HOM Heating and localized heating due to high frequency and large image currents *in vacuo* from contact resistance. The total heat load applied on the inside perimeter is 0.36W/cm$^2$

### *4.2 RF Shield/Spring Finger*

GlidCop was used for the stub and shield for its high thermal and electrical conductivity, its mechanical stability at high temperatures, and manufacturabilty. The temperature at the tip of the shield finger is balanced against structural loading. Thin shield fingers are stressed by the lateral and angular offsets across the module. Required finger length determined by the total travel of the module is 30 mm. The thickness and width of the RF shield is optimized to decrease tip temperature, keep the bending stress at the base below yield, maintain the force due to operational bending stress below 28g and prevent buckling. ANSYS calculations show that the cooling on the flange will keep the base of the majority of shield fingers at 65°C. The majority of the fingers could reach 91°C based on 0.5W/cm$^2$ of heat flux, with a few of the tip temperatures slightly exceeding 100°C. Test data indicates minimal stress relaxation in GlidCop at 300°C [3]. The consequences of a high tip temperature are reduced by the independent Inconel spring fingers. These isolate the high-temperature region at the ends of the shield fingers from the high-stress area at the base of the spring fingers.

When the module is fully compressed during installation and has a lateral offset of 1.3mm, the bending stress is only slightly below yield. If handled properly it would be difficult to apply the full lateral offset allowed by the module restraints. A 1.3mm offset during normal operation produces 83MPa stress at the root and less than 10g of force. This bending stress does not significantly affect the contact force because the spring fingers are 15 times stiffer.

Calculations indicate that the critical buckling force for the RF shield is two times higher than the load. Analysis assumed pinned ends and a coefficient of friction of 1 for Silver on Rhodium in vacuum. To confirm that buckling is not a problem in this design, a test at the worst case extension and highest load was performed. Buckling was not observed.

The pre-deflection on the Inconel spring applies 85 to 200g on the shield finger and is relatively insensitive to manufacturing tolerances. The bending stress at the root is nominally 60 percent of yield. Inconel 718 was selected for the spring because of its high strength, high temperature capabilities and ease of manufacture.

### *4.3 Stub*

ANSYS calculations using a stainless steel stub and 1W/cm$^2$ heat flux produces a maximum temperature of 273°C. GlidCop Al-15 was used instead to increase the conductivity, which reduces the heat flux to 0.5W/cm$^2$ Calculations for the GlidCop stub produced an acceptable peak temperature of 45°C.

## 5. TESTING

### *5.1 Plating*

Plating adhesion is critical for solid lubrication and for dust reduction. An acid etch test was used to confirm that the adhesion between the Rhodium and the base material was acceptable. No surface asperities were observed when the plating was brought to 500°C. The adhesion of the silver plating was also verified prior to and during manufacturing by firing the part at 900°C.

*5.2 Sliding Joint Tribology*

The tribology of the sliding joint *in vacuo* is a concern for three reasons: overheating or galling at the contact joint could cold-weld a finger to the stub, insufficient or excessive lubricity from silver plating could produce excessive dust, and plated surfaces could behave below expectation at elevated temperatures. Initial tests were performed at SLAC using 4.7mm of travel for 200,000 cycles. Forces from 55 to 200g were applied using various silver plating thicknesses at ambient temperature and 200°C. Results indicated that a combination of 5μm of rhodium plating on the stub and 13 μm of silver on the shield and produced an acceptable sliding joint.

Final cyclic testing was performed using the correct geometry, materials, and plating thickness. The fingers were cycled to traverse a distance equal to 150,000 cycles of 1.3mm travel. Qualitative analysis showed no indication of wear to the base metal and negligible dust production. The shield was plated with 13μm of silver and the Rhodium was plated with 2.5μm.

*5.3 RF Contact Integrity*

The integrity of the RF contact was confirmed for the full lateral, angular and longitudinal motion of the bellows module. No configurations were found where contact was lost between the finger and stub.

*5.4 Welded Bellows Cyclic Testing*

The lateral offset of the bellows module was limited by the cyclic lifetime of the welded bellows. Calculations indicated that the maximum allowable offset was only 0.76 mm. Results of cyclic lifetime testing found that an offset of 1.3 mm was acceptable.

*5.5 Resonances in Bellows Module*

Possible resonances of the bellows module were tested at LBNL by studying TE and TM modes propagating along the beam pipe. A poorly coupled TE mode resonance was found at 2.48 GHz. This resonance corresponds to a half-wavelength between the bellows flanges. It was estimated that only 20 percent of the propagating TE mode power will be lost to this resonance. Measurements showed no significant resonances coupled to the TM modes.

*5.6 Power Testing*

The goal of this test was to determine if the contact load is sufficient to transfer RF current without significant heating due to the contact resistance between the RF shield and the beam pipe. Previous experiments found that conductivity is an important parameter for high current carrying capacity across an RF joint [4]. The higher the conductivity, the lower the contact resistance and the lower the local temperature at the contact. A low temperature at the contact is desired to reduce cold welding of the two materials.

The test apparatus built at SLAC employed the Straight Section bellows module. The materials and contact forces of the RF shield fingers and stub plating were the same for the HER Arcs bellows module. Therefore, the test results pertaining to contact force and current carrying capacity is applicable.

The bellows module was subjected in vacuum to 1.5 times higher current than is expected at 3 A circulating current for PEP-II. The contact showed no signs of damage from this test.

*5.8 Residual Gas Analyzer (RGA) Scans/Bake Out*

RGA scans were performed to ensure that the part was compatible for ultra high vacuum. After 24 to 48 hours at 200°C, there were no peaks above mass 44. The bellows module showed no indication of mechanical failure or reduction of contact force.

## 6. MANUFACTURING

Minimal fixturing was necessary during final assembly of the bellows module. The springs were deflected away from the mating stub using dowel pins and the RF shield was inserted. The spring fingers went through numerous inspections during their manufacturing process to ensure that the pre-deflection was in the range needed for the spring force. All forces inspected were greater than 85g and the average was approximately 170g.

## 7. INSTALLATION

The inner chamber profiles from each end of the module were aligned using precision dowel pins, these pins were also used as datums to align the Dipole with respect to the Quad chamber. Furthermore, the pins aided in mating the RF Seals by reducing any transverse motion while being compressed between the two flanges. To mitigate potential problems during the early stages of installation, approximately 15% of the chambers were boroscoped for RF continuity.

## 8. FUTURE WORK

The HER Arc RF shield bellows module has been adapted for several different areas of the ring. Bellows for the Interaction Region are similar in design. The design has also been modified for a round chamber in the abort line and is currently being assembled. PEP-II is working on applying this design for the LER Arc bellows and the LER Straight Section bellows which will be installed at the end of this year.

## 9. REFERENCES


[1] M. Zisman, ed., "PEP-II: An Asymmetric B Factory: Conceptual Design Report", SLAC Report 418, 1993.

[2] S. Heifets, et al, "Impedance Study for PEP-II B Factory", PEP-II AP Note No 99.

[3] SCM Metal Product, Inc., "GlidCop Product Information", North Carolina.

[4] Bigham, C.B.,"Sliding Contacts for Tuners in High Power RF Resonators", Atomic Energy of Canada Limited, Chalk River.

[5] M. Nordby, N. Kurita, et al, "Bellows Design for the PEP-II High Energy Ring Arc Chambers", US PAC95 Conference Proceedings, Dallas, Texas.

# PHOTON STIMULATED DESORPTION PHENOMENA AT THE TAIWAN LIGHT SOURCE VACUUM SYSTEM

G.Y. Hsiung, Y.J. Hsu, Synchrotron Radiation Research Center, Hsinchu, Taiwan, and
J.R. Chen, Synchrotron Radiation Research Center, also at Institute of Nuclear Science, National Tsing Hua University, Hsinchu, Taiwan,

*Abstract*

The photon stimulated desorption (PSD) by the synchrotron radiation irradiated from the Taiwan Light Source (TLS) vacuum chambers were analyzed. The desorption behavior of the various gas species were compared by either adjusting the electron beam orbit and hitting the photons on the fresh chamber walls or turning off the pumps. The dominated gases during the earlier years' operation are the $H_2$, in concentration of > 90%, followed by other gases, e.g. CO, $H_2O$, $CH_4$, etc.. However, some of the massive gas species, e.g. CxHy, CxFy, were observed after replacing the new vacuum parts or unsuitable baking the O-ring gate valves in higher temperature. The contaminated gases are to be reduced by beam-self cleaning treatment. Planning in upgrading the storage ring vacuum system is also described.

## 1 INTRODUCTION

In the Taiwan Light Source (TLS) of the Synchrotron Radiation Research Center (SRRC), three insertion devices, W20 wiggler (1.8 Tesla, 25 poles), U10P undulator (1.04 Tesla, 37 poles), and U5 undulator (0.675 Tesla, 75 poles), have been built and installed in the 1.3 GeV electron storage ring since the spring of 1995 to the spring of 1997[1]. The long straight section vacuum chambers were replaced by the new vacuum chambers for the insertion devices[2,3]. The photon stimulated desorption (PSD) phenomenon is continuously monitored by the residual gas analyzers located near the new chambers, and the performance of the vacuum system after installing the new chambers were also compared[4,5]. Several upgrading works to improving the performance of the TLS vacuum system are planned during the periods of the installation. The PSD phenomenon and the upgrading programs will be reported in this article.

## 2 PHOTON STIMULATED DESORPTION

The photon stimulated desorption (PSD) by the synchrotron radiation were measured by the quadrupole mass spectrometers located near the bending chambers. The dominated gases desorbed from the vacuum chamber

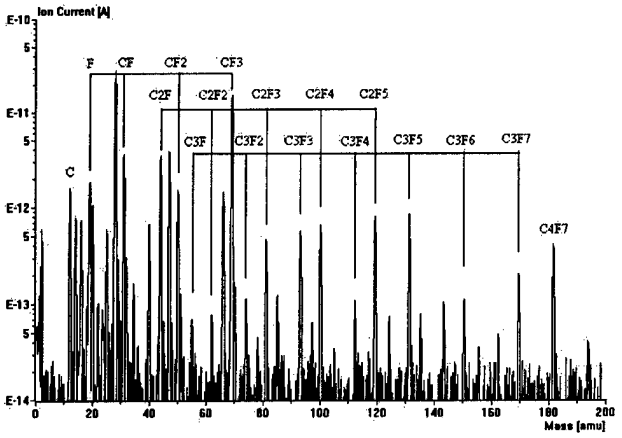



Figure 1:Mass spectrum near the bending chamber closed to the O-ring gate valve at a stored beam.

during the currently routine operation are the $H_2$, in concentration of > 90%, followed by other gases, e.g. CO, $H_2O$, $CH_4$, etc.[6]. However, an unsuitable baking an O-ring sealed gate valve to a temperature of 300 ℃ was occurred at once of baking a bending chamber in the storage ring by the end of 1996. Unlike other sections of the storage ring, some of the massive gas species, e.g. CxFy, were clearly observed at the bending chamber closed to the over-baked gate valve after baking as well as during a stored electron beam. Figure 1 shows the mass spectrum near the bending chamber at a stored beam which reveals the families of the cracked molecular ions decomposed from the CxFy molecules. The $CF_3^+$ ion, with mass number of 69, was selected as a better role to represent the behavior of the families of $CxFy^+$ cracking ions for easier illustrating the PSD phenomenon in various conditions in this article. Figure 2 shows the intensity of $CF_3^+$ ion observed near the contaminated area in three different conditions, the electron beam was injected and stored (region a), the nearby sputtered ion pump (IP) and the distributed ion pump (DIP) were switched off (region b), and the nearby non-evaporable getter (NEG) pumps were activated (region c). The increase of the intensity of $CF_3^+$ ion at a stored beam (region a) shows the observed outgas species of CxFy molecules were stimulated by the synchrotron photons and desorbed from the bending chamber wall near the contaminated area. The dramatic peaks appeared in

0-7803-4376-X/98 /$10.00 © 1998 IEEE

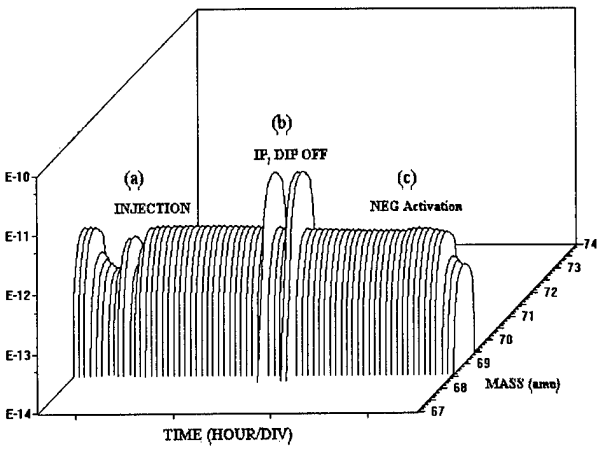



Figure 2:Intensity of $CF_3^+$ ion, mass [69], observed near the contaminated area at a stored beam.

region (b), when switching the IP and DIP off, reveal the pumping effect to the CxFy molecules is so efficient with the sputter ion pumps be operated. In region (c), no severe pumping effect to the $CF_3^+$ ions was observed during activating the NEG pump.

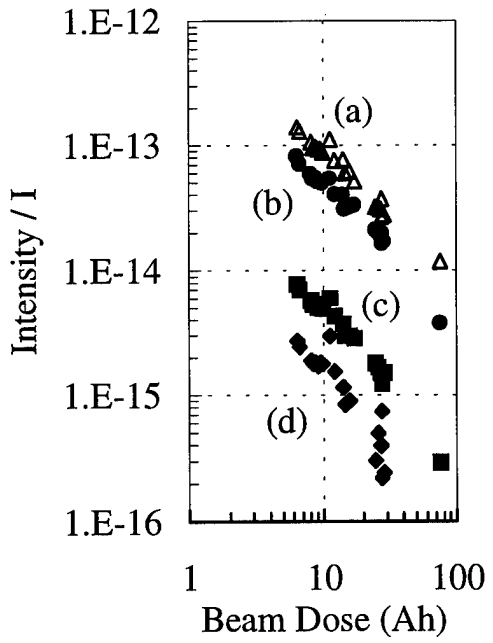



Figure 3:Curves of intensity of various gases, (a)[28], (b) [69], (c)[12], and (d)[2], per electron beam current as functions of the accumulated beam dose.

Figure 3 shows the curves (a) to (d) which represent the intensity of various gases with mass-over-charge ratio of [28], [69], [12], and [2], respectively, per electron beam current as functions of the accumulated beam dose. The behavior of the curve (b), [69], is similar to other curves which decay during the continuous beam running that reveals a fact that the contaminated gases could be effectively reduced by continuous exposure to the synchrotron radiation, which is so called beam-self cleaning treatment.

## 3 PLANNING IN UPGRADING THE TLS VACUUM SYSTEM

The planning to upgrade the vacuum system of the TLS electron storage ring, started from 1996, is to reduce the vacuum pressure, to reduce the impedance of the vacuum chambers, to remove the vibration source, etc.

### *3.1 Reduction of the Vacuum Pressure*

The nuclear scattering between the electron beam and the gas molecules in the beam chamber will shorten the life time and induce the instability of the circulated electron beam. To maintain a vacuum pressure under $10^{-10}$ Torr in the beam chamber is necessary. The sources of the gas species contained in the vacuum chamber include (1) surface desorption from the vacuum chamber by the PSD process, (2) leakage, (3) outgas from the contaminated parts, etc. The observed outgas species in the TLS vacuum system can be classified as (1) $H_2$, (2) carbonate gas, e.g. CO, $CO_2$, CxHy, CxFy, etc., (3) leakage gas, e.g. $N_2$, $O_2$, Ar, etc., and (4) $H_2O$. Since the installed vacuum chambers in the storage ring had pre-cleaned by the oil-less machining, chemical cleaning, and the vacuum baking processes. Although the surface desorption induced by the synchrotron radiation can be effectively reduced by continuous exposure to the synchrotron light. However, it takes long time to reach the goal. It is necessary to improve the machining and the pre-cleaning processes if we want to reduce the carbonate gases.

The current undergoing works are reported as following mentioned processes. The gate valves sealed with viton or kalrez O-ring which have potential problems to produce the massive molecules, e.g. CxFy, come from the O-ring materials will be replaced by the all metal sealed gate valves. Increase the effective pumping to the $H_2$ and CO gases by adding the quantity of the non-evaporable getter (NEG) pumps into the vacuum chambers. Most of the leakages come from the sealing gasket between the stainless steel flange and the aluminum alloy flange after the baking process. The reason to induce the leakage is not so clear. However, the leak parts will be replaced during the shutdown periods.

### *3.2 Reduction the RF impedance of the Chamber*

The chambers for the screen monitors will be replaced by the new designed chambers. The calculated rf impedance of the new chamber is 1% less than the original chamber for the screen monitor.

### *3.3 Remove the vibration source from the Chamber*

Since the turbo-molecular pumps (TMP) and the dry pumps (DP) are the potential vibration sources to the vacuum chambers. On the other hand, it takes much effort to prevent the vacuum chambers from the back streaming contaminated outgas from the TMP and DP. Thus all the TMP and DP will be removed from the vacuum system after completing the roughing process and the vacuum baking by these pumps.

## 4 SUMMARY

The photon stimulated desorption phenomena and the future planning to improve the vacuum system of the TLS synchrotron light source is reported in this article. The contamination of the massive gas species, CxFy, was observed after an unsuitable baking an O-ring gate valve to 300 ℃ near a bending chamber. The families of the CxFy molecular ions clearly appeared when the electron beam was stored, which reveals a fact of the outgas species coming from the kalrez O-ring material. The outgas molecules were stimulated by the synchrotron photons out of the vacuum chamber wall near the O-ring gate valve. The contaminated gas molecules can be reduced by beam self-cleaning treatment during a long period beam operation. Due to the poor conductance of the vacuum beam pipes and the effective evacuation to the CxFy gas by the sputter ion pumps, no evidence was shown that the CxFy molecules had propagated to another sections of the storage ring. Future planning to upgrade the TLS vacuum system will improve the machining and the cleaning processes for the vacuum chambers, replace the new vacuum chambers with lower rf impedance, remove the vacuum parts contained the O-ring material, remove the vibration sources, e.g. TMP, DP, etc., increase the NEG pumps, and replace the leakage vacuum parts.

## 5 ACKNOWLEDGEMENTS

The authors would like to thank their colleagues in the SRRC vacuum group for their invaluable contribution to this work. Special thanks also go to Dr. J. C. Lee for his assistance in adjusting the electron beam orbit and valuable discussions.

## 6 REFERENCES

[1] Y. C. Liu, J. R. Chen, C. H. Chang, K. T. Hsu, C. C. Kuo, W. K. Lau, G. H. Luo, K. K. Lin, Ch. Wang, and W. T. Weng, Proceedings of the Fifth European Particle Accelerator Conference EPAC96, Barcelona, Spain, p.700 (Institute of Physics Publishing, Bristol, UK,1996) .

[2] D. J. Wang, J. R. Chen, G. Y. Hsiung, J. G. Shyy, J. R. Huang, S. N. Hsu, K. M. Hsiao, and Y. C. Liu, J. of Vac. Sci. & Technol. A14(4), 2624 (1996).

[3] G. Y. Hsiung, D. J. Wang, J. G. Shyy, S. N. Hsu, K. M. Hsiao, and J. R. Chen, J. of Vac. Sci. & Technol. A15 (1997). (in press)

[4] G. Y. Hsiung, J. R. Huang, D. J. Wang, J. G. Shyy, J. C. Lee, R. J. Sheu, H. S. Tzeng, S. N. Hsu, S. Y. Perng, K. M. Hsiao, W. D. Wey, J. R. Chen, and Y. C. Liu, J. of Vac. Sci. & Technol. A13(5), 2569 (1995).

[5] G. Y. Hsiung, J. R. Huang, J. G. Shyy, D. J. Wang, J. R. Chen, and Y. C. Liu, J. of Vac. Sci. & Technol. A14(6), 3275 (1996).

[6] G. Y. Hsiung, J. R. Huang, J. G. Shyy, D. J. Wang, J. R. Chen, and Y. C. Liu, J. of Vac. Sci. & Technol. A12(4), 1639 (1994).

# CLOSED ORBIT FEED-BACK FROM LOW-BETA QUADRUPOLE MOVEMENTS AT LEP

F. Tecker, RWTH Aachen, Germany,
W. Coosemans, A. Marin, K. Rybaltchenko, J. Wenninger, CERN, Geneva, Switzerland

*Abstract*

Left and right of each of the four LEP interaction points superconducting low-beta quadrupole magnets are installed to squeeze the vertical beam size at the interaction points. These magnets are the dominant source of vertical closed orbit drifts at LEP because of their strength, the large vertical beta function and their support. Hydrostatic Levelling Systems and resistor-based position sensors were installed to measure the vertical movements of these magnets continuously. The correlation between the mechanical movements and closed orbit variations has been studied. The analysis has shown that the orbit can be kept stable by acting on one correction dipole per low-beta quadrupole pair. This has led to a feed-back system which uses the mechanical measurements to correct the closed orbit and to prevent large orbit variations.

## 1 INTRODUCTION

Since the beginning of LEP operation the vertical closed orbit has been found to be drifting with time. This required frequent orbit corrections by the operation crew. The distribution of corrector magnets used for the corrections showed that the correctors near the low-beta quadrupoles (QS0) or with a phase advance of $n\pi$ nearby were used for the majority of corrections.

The superconducting low-beta quadrupoles are vertically focusing and have a quadrupole strength ($k = -0.16\,\mathrm{m}^{-2}$) 10 times larger than other magnets in LEP to obtain the small beam size at the interaction point. Their strength and the large vertical beta function at this location make the closed orbit very sensitive to any vertical mechanical displacement of these magnets. In addition, the mounting of the magnets makes it likely that they can actually move.

Hydrostatic levelling systems (HLS) and potentiometer-based position sensors were installed to measure the movements of the magnets continuously. A first analysis of the observed movements and their correlation to orbit drifts can be found in [1]. This analysis was extended and led to a feed-back system for the vertical orbit.

## 2 MECHANICAL INSTALLATIONS

The schematic layout of one of the four experimental interaction point (IP) is shown in Fig. 1.

The low-beta quadrupoles are mounted on a cantilever support structure which extends into the experimental detectors. Since it is not supported on the inner side, it is possible that the magnets move with the support. Hydrostatic Levelling Systems [2, 3] are installed to monitor the movements. They consist of vessels with capacitance-based hydrostatic sensors and temperature sensors connected by communicating tubes. These vessels are placed at different locations on the magnets and supports. One system with horizontal tubes is installed on each support for the QS0 and the next closest magnets (QS1). Since the tubes are horizontal, local temperature differences do not introduce a measurement error and the precision is better than 1 $\mu$m. A different system of communicating vessels is connecting the supports and the ground on both sides of a detector. It was not possible to install the tubes in a horizontal plane and the precision is limited to $\mathcal{O}(10)$ $\mu$m. The HLS at one interaction point (IP 8) which was installed as a pilot system has also non-horizontal tubes and hence a lower precision.

In addition potentiometer-based systems measure the position of the magnets with respect to reference points in the experimental detectors with precision of a few $\mu$m.

## 3 OBSERVED MOVEMENTS

Fig. 2 shows a typical vertical movement of a low-beta quadrupole measured by the hydrostatic levelling system.

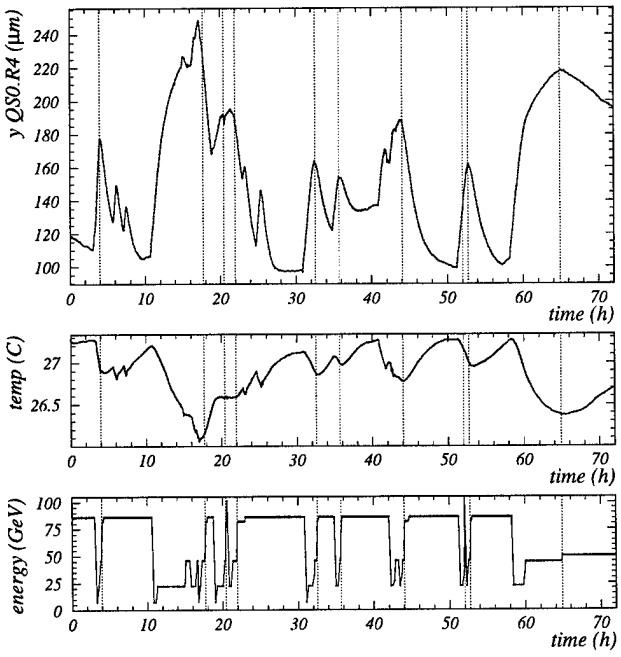



Figure 2: Movement of a low-beta quadrupole (QS0.R4) for a period of three days (top), the temperature measured at the support of this magnet (middle) and LEP beam energy (bottom). The vertical dashed lines indicate the end of the ramp to collision energy.

In general, the pattern of the movement in time is the

0-7803-4376-X/98 /$10.00 © 1998 IEEE

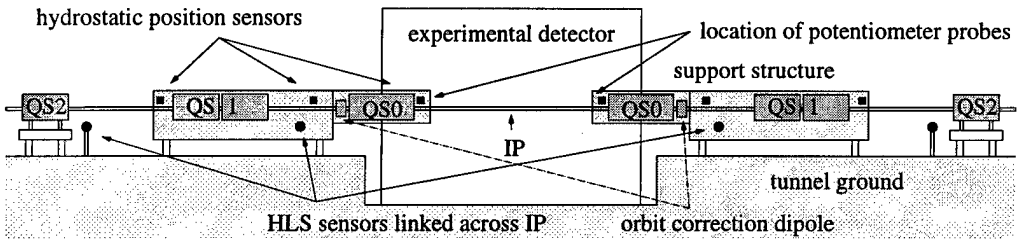



Figure 1: Schematic view of the low-beta insertion around an experimental detector. The QS0 are the superconducting low-beta quadrupole magnets. The layout of one IP is slightly more complicated since the inner magnets (QS0,QS1) and the inner parts of the detector are mounted in a support tube (not shown).

same for all QS0 magnets. The movement is correlated with temperature changes of the support. When the temperature rises, the magnets start moving downwards. The temperature changes are mainly caused by the operation cycle of LEP. The temperature starts rising after LEP has been ramped to higher energy. This can be understood by the higher current heating up the current feed-throughs which traverse the support. The time constant of the thermally driven movements is of the order of a few hours and a short refilling time keeps the amplitude of the movements smaller.

## 4 ORBIT ANALYSIS

The vertical orbit drifts were studied in detail to determine the contribution from the movements of the low-beta QS0 magnets. A movement $\Delta y_Q$ of a quadrupole at location $s_0$ creates an angular kick $\Delta y'(s_0) = kl\Delta y_Q$ which changes the closed orbit at any location $s$ by $\Delta y(s)$ according to

$$\Delta y(s) = \frac{\sqrt{\beta(s)\beta(s_0)}\cos(|\mu(s)-\mu(s_0)| - \pi Q)}{2\,\sin(\pi Q)} \cdot \Delta y'(s_0). \quad (1)$$

$\beta$, $\mu$ and $Q$ are the betatron function, phase advance and tune, respectively. Since both $k$ and $\beta(s_0)$ are large for the QS0, the movement $\Delta y_Q$ of a single QS0 generates a RMS change of the vertical closed orbit $\sigma_{\Delta y}$ 40 times larger than the mechanical movement. This factor is only 2 for a regular lattice quadrupole.

The beta function is symmetric around the interaction point and the vertical betatron phase advance between the two magnets is nearly $\pi$. Eq. 1 shows that the effect on the orbit nearly cancels if both magnets move by the same amount in the same direction. A common movement of $\Delta y_Q = 10\mu$m for both QS0s results in a RMS orbit change of only $\sigma_{\Delta y} = 7\mu$m.

Fortunately, the pairs of QS0s at the different interaction points tend to move in a similar way. Eq. 1 also implies that the differential movement of the QS0 pair can be corrected with only one orbit correction dipole (see Fig. 1) at each IP.

The differential movement can be seen in the closed orbit. Orbits logged during physics data taking were used to calculate the *'bare orbit'*[1] from the measured orbit $y_{meas}$

[1]The closed orbit if all correction magnets were switched off.

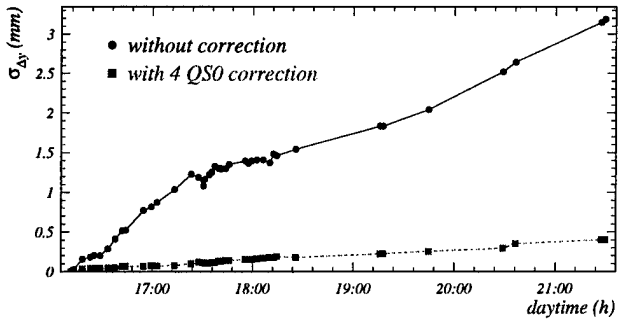



Figure 3: RMS of the difference of bare orbits during a physics fill relative to the first physics orbit before and after orbit correction with only 4 QS0 correctors. A typical vertical orbit has a residual RMS of about 500$\mu$m.

by

$$y_{bare} = y_{meas} - \frac{\sqrt{\beta_{bpm}}}{2\sin(\pi Q)} \sum_{cor} \sqrt{\beta_{cor}}\cos(|\mu_{cor} - \mu_{bpm}| - \pi Q)\cdot\theta_{cor} \quad (2)$$

where the sum is taken over all vertical correctors. $\theta_{cor}$ is the kick angle for the corrector, $\beta_{cor}$ and $\mu_{cor}$ are beta function and phase at the corrector, $\beta_{bpm}$ and $\mu_{bpm}$ at the beam position monitors, respectively. This procedure removes the effects of all corrector magnets. The difference of two bare orbits shows the orbit changes from other sources than corrector magnets and can be used to localise the source of the changes.

The bare orbit of the first orbit acquired after the physics experiments start taking data is used as a reference for each fill. For all subsequent orbits the bare orbit is calculated and the RMS of the difference from the reference $\sigma_{\Delta y}$ is evaluated. This represents the movements of the orbit if no orbit corrections had been made.

An example of the movements during a fill is given in Fig. 3.

If the QS0 magnets are the source of the drifts then it should be possible to correct most of the effect with only one orbit corrector magnet per IP. This was done with the COCU package [4] using the MICADO algorithm [5]. The result showed that this correction is very effective, taking away about 70–90% of the orbit movements (Fig. 3). This

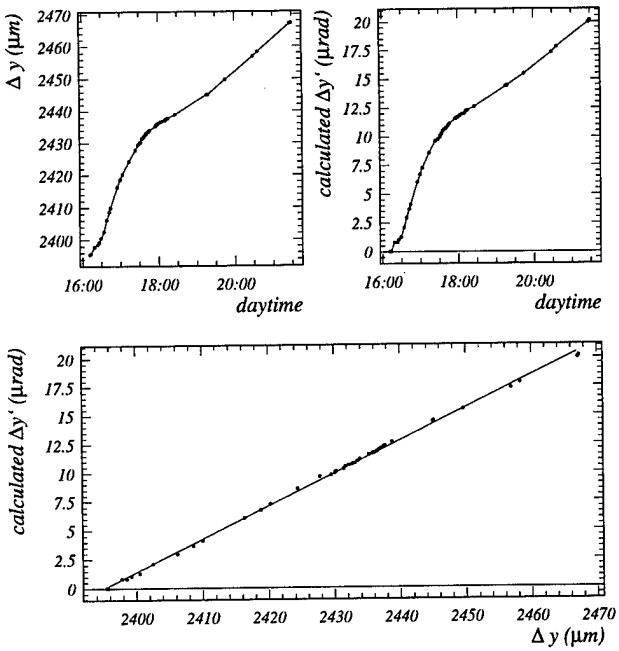



Figure 4: Example of the mechanical movement (top left), the calculated orbit correction kick (top right) and their correlation (bottom) at one IP during a fill with large quadrupole movements.

proves that the superconducting low-beta magnets are indeed the major source of the drifts.

## 5 CORRELATION AND FEED-BACK

The calculated orbit correction kick $\Delta y'$ should be proportional to the differential movements of a QS0 pair. This was examined for the different interaction points. Only the HLS with horizontal connecting tubes on the supports are used for the analysis. Due to the lower precision, including the HLS system connecting the supports on both sides of the IP does not improve the correlation. An example is shown in Fig. 4.

A proportionality constant between the correction kick and the differential movement was derived for each QS0 pair from this correlation. A software feed-back was developed which reads the mechanical position of the magnets and calculates the necessary correction kick from the differential movement. Whenever the correction kick exceeds a certain threshold, it is sent to the orbit corrector. The HLS is used except for IP 8 where the potentiometers are more precise than the pilot HLS.

The feed-back has been running very successfully at the end of the 1996 operation period of LEP. Fig. 5 shows an example.

The feed-back was compensating well for the movements of the orbit. The potentiometer system used at IP 8 is less precise than the HLS but still capable of tracking the movements. The feed-back significantly reduced the number of orbit corrections that had to be made by the operator.

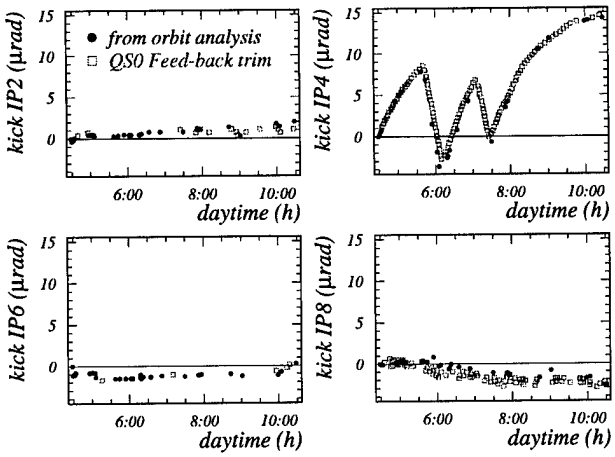



Figure 5: Example of the feed-back during one fill. The correction kicks sent by the feed-back are compared to the corrections calculated from the off-line orbit analysis.

Another application of the QS0 measurements is the reload of a previously stored set of corrector excitations of an orbit which gave high luminosity and good background conditions. The positions of the QS0 magnets of storage and reload time are compared and the necessary correction is incorporated. An experiment was performed and it demonstrated that the orbit with the incorporated correction had a significantly lower RMS excursion. This reduces the risk of accidental beam loss when an old set of corrector settings is reloaded.

## 6 CONCLUSIONS

The superconducting low-beta quadrupoles are the major source of vertical orbit drifts at LEP. Hydrostatic Levelling Systems with horizontal connecting tubes measure the vertical movements of these magnets very precisely. A feed-back system based on the measurements has been implemented and prevents large orbit variations during the physics data taking. The HLS at IP 8 will be upgraded this year and the more precise HLS measurements will be used for the feed-back at all IPs.

## 7 REFERENCES

[1] F. Tecker, Low-Beta Quadrupole Movements as Source of Vertical Orbit drifts at LEP, 1996, CERN-SL/96-40 (BI).

[2] Fogale Nanotech, 190, Parc Georges Besse, 30000 Nimes, France, *Sensors and Actuators for alignment of large machine components*.

[3] LEP Hydrostatic Levelling Systems, http://www.cern.ch/-CERN/Divisions/SL/groups/bi/hls/WelcomeHLS. html.

[4] D. Brandt, W. Herr, J. Miles, and R. Schmidt, A new Closed Orbit Correction Procedure for the CERN SPS and LEP, *Nucl.Instr.Meth.*, A(293):305–307, 1990.

[5] B. Autin and Y. Marti, Closed Orbit Correction of A.G. Machines using a limited number of Magnets, 1973, CERN ISR MA/73-17.

# BEAM POSITION MONITOR OFFSET DETERMINATION AT LEP

F. Tecker, RWTH Aachen, Germany,
B. Dehning, P. Galbraith, K. Henrichsen, M. Placidi, R. Schmidt, CERN, Geneva, Switzerland

*Abstract*

For the performance of an electron positron storage ring it is important that the beam orbit passes well centred through the quadrupole magnets. Beam position monitors (BPM) aligned relative to the magnets can still have a residual mechanical or electronical offset with respect to the magnetic axis. A beam-based method is used at LEP to measure these offsets. During the machine operation for physics the gradient of selected quadrupoles is modulated with low frequencies (few Hz) and very small amplitudes (of the order of $10^{-4}$). The effect on the beam is observed with a high sensitivity pick-up. The observed effect passes through a minimum when the beam is centred in the quadrupole. Offsets for about 70 different BPM's were determined. Systematically different offsets were found for different type of BPM electronics and different types of quadrupoles. Simulations based on the past results show that the level of spin polarisation can be increased by further offset measurements.

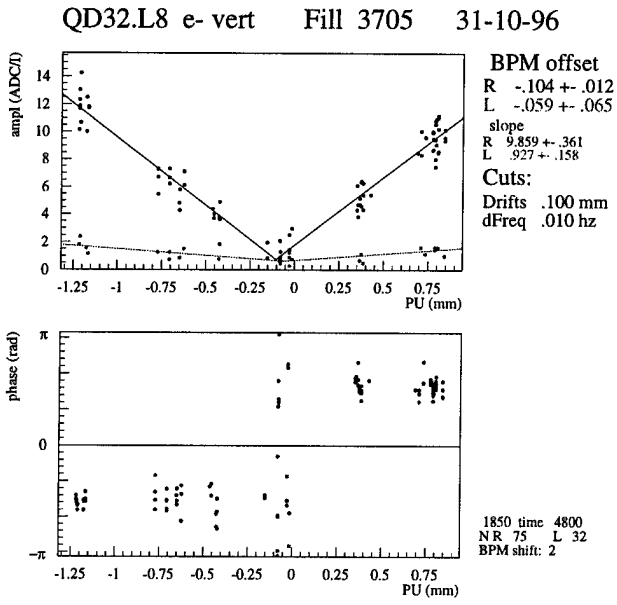



Figure 1: Oscillation amplitude (top) and phase (bottom) measured by the two couplers as a function of the beam position monitor reading

## 1 INTRODUCTION

An important issue for the successful operation of a particle accelerator is an efficient control of the closed orbit. Luminosity, background in the physics experiments and the degree of beam polarisation depend strongly on the vertical closed orbit. The best performance is achieved if the quadrupoles are well aligned and the beam travels through the magnetic centre of the quadrupoles.

The quadrupole magnets form a reference system for the beam and are aligned with high precision. Beam position monitors (BPM) at the quadrupoles can have a mechanical or electronical offset with respect to the magnetic centre of the magnets. This offset is measured by a beam based method [1].

## 2 PRINCIPLE OF BEAM BASED ALIGNMENT

The principle of the methods for beam based alignment is based on the fact that the magnetic field inside a quadrupole magnet increases linearly with the distance from the centre. When the gradient is varied, the field change is proportional to the distance from the magnetic axis of the quadrupole. An off-axis beam travelling through the magnet receives an additional deflection depending on its position. The gradient changes are slow compared to the betatron frequency. The closed orbit variation can be measured at nearly any location in the ring. This effect vanishes when the beam passes centred through the quadrupole. A more detailed description of the method used at LEP can be found in [2].

The strength of the quadrupole magnet is modulated periodically at frequencies in the range from 0.7 to 16 Hz. Since most of the magnets are powered in series, additional (back leg) winding have been installed to change the gradient of individual quadrupoles. The quadrupoles in all straight sections and in one of the eight LEP arcs were equipped with back leg windings. The modulation depth is smaller than $10^{-3}$ and the measurements can be performed in parallel to the physics experiments' data taking. The offsets of several BPMs can be measured simultaneously using different excitation frequencies.

The induced beam oscillations are measured by two sensitive beam position monitors (couplers) close to an odd multiple of $\pi/2$ phase advance apart to be able to detect every oscillation with acceptable sensitivity. A harmonic analysis of the signal determines the oscillation amplitude at the excitation frequency. This amplitude is proportional to the distance from the axis of the quadrupole with the modulation and shows a V-shaped behaviour when plotted as function of the beam position in the quadrupole. The position changes due to orbit drifts [3] or by intentional amplitude variations of local closed orbit bumps.

Fig. 1 shows the results of an offset determination by the two couplers. The measurement points show some scatter since beam oscillations from other sources than the mod-

0-7803-4376-X/98/$10.00 © 1998 IEEE

ulation are always present. Different cuts are applied to improve the data quality. A three parameter fit gives the offset of the BPM. The amplitude for one of the couplers is smaller due to a less favourable betatron phase advance between magnet and coupler, and the results are less precise. Since the modulation of the magnet current and the measurement are synchronised, one can determine the phase of the orbit oscillation with respect to the modulation. The measured phase changes by $\pi$ when crossing the symmetry plane of the quadrupole which gives an additional cross-check.

## 3 DISTRIBUTION OF OFFSETS

The beam position monitor system of LEP uses two different types of electronics, a narrow band and a wide band system. The BPMs close to the interaction points have the wide band electronic to cope with the shorter time separation between the counterrotating bunches. The wide band BPM have different gain settings depending on the beam current. All other BPMs, in particular the BPMs in the arcs of LEP, have narrow band electronics which is independent of the beam current.

Eight quadrupoles (QS0) at the four interaction regions of LEP are superconducting magnets to achieve the strong gradient needed for the focusing at the interaction points. The associated BPMs are of the wide band type. Their offsets were found to be significantly larger than for any other BPMs. The first generation of superconducting quadrupoles at LEP had systematic offsets up to nearly 2 mm. After replacing these magnets with the new generation of quadrupoles for LEP2, the measured offsets were below 1 mm. The wide band BPMs show different offsets for different gain settings and for the two particle types. Differences of up to 300 $\mu$m were measured. This implies that the offset is partially caused by the BPM processing electronics.

The wide band BPMs at normal conducting magnets show smaller offsets than those at the superconducting quadrupoles. A calibration was performed for a large number of arc quadrupoles with narrow band electronics BPMs. In general, the offsets are smaller than for the wide band electronic and the differences between the two particle types are less important. Table 1 compares the offsets for the different categories. The measured offsets are included as a correction to the BPM readings whenever an orbit is acquired.

| | | RMS [$\mu$m] | mean [$\mu$m] |
|---|---|---|---|
| wide band | QS0 | 250 | −600 |
| | other | 350 | −220 |
| narrow band | | 185 | −90 |

Table 1: Characteristics of offset distribution for different magnet types and BPM electronics

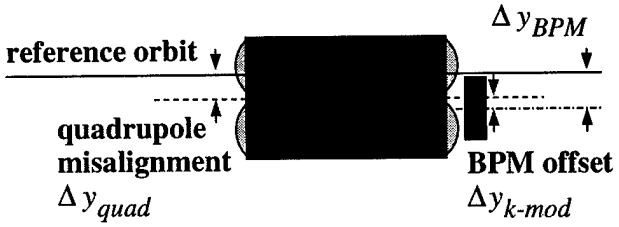



Figure 2: Relevant offsets for the BPM misalignment relative to the reference plane

## 4 IMPACT ON POLARISATION LEVEL

The vertical orbit is of particular importance for a high level of beam polarisation. The spins of the particles in an electron-positron storage ring tend to polarise in the vertical direction with time. Horizontal fields from vertical corrector dipoles and a beam passing off-centre in the quadrupoles can create depolarising resonances. The depolarising effects become significantly stronger at higher beam energies [4].

In order to maximise the degree of polarisation, the resonances can be compensated by so-called Harmonic Spin Matching (HSM) [5]. Two different variations of HSM exist:

**deterministic HSM:** A Fourier analysis of the vertical closed orbit [6, 7] gives the strength of the necessary orbit bumps (4 parameters).

**empirical HSM:** The 4 parameters of the bump amplitudes are varied and the changes in the polarisation level are observed.

In principle, empirical HSM could be used to find the best compensation for the depolarising resonances. In practical application it is very tedious and time consuming since one has to find the optimum in a four-dimensional parameter space and the build-up time for the polarisation is slow. If the initial polarisation level is too low, it is even impossible to observe changes of the polarisation level when the parameters are varied.

For this reason the deterministic HSM has to be applied. The precision of the calculated parameters depends strongly on the BPM offsets relative to a reference plane. Simulations with the SITF [8] module of MAD [9] were performed to study the effects in detail. In the simulations, the quadrupoles were misaligned with an RMS value of $\sigma(\Delta y_{quad}) = 150\,\mu$m which corresponds to the value measured by the geometrical survey. The RMS values of the BPM offsets $\sigma(\Delta y_{k\text{-}mod})$ to the quadrupole axis was varied between 0 and 700 $\mu$m. The different offsets are illustrated in Fig. 2.

The offset of the BPM relative to the reference orbit in a plane is

$$\Delta y_{BPM} = \Delta y_{quad} + \Delta y_{k\text{-}mod}. \qquad (1)$$

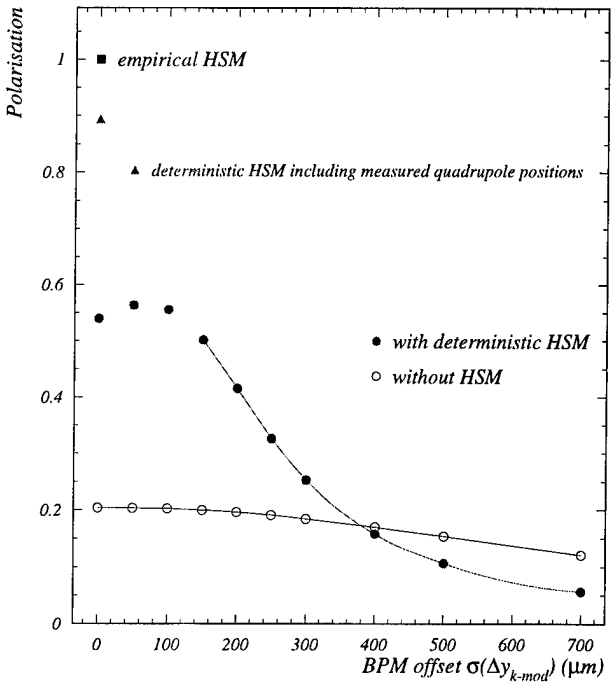



Figure 3: Influence of the vertical offset between BPM and quadrupole axis on the polarisation level.

Ten different random distributions were used for each RMS value of the offsets. The orbit was corrected to the best possible value. The harmonic content of the vertical BPM readings were analysed. The polarisation level in linear approximation was determined by SITF before and after applying HSM.

The linear calculations of SITF do not give a realistic absolute value of the polarisation level. Higher orders can be included [4]. This was done for a few samples. Therefore the average value of the ten random seeds for the linear results are normalised to the average level of polarisation obtained by empirical HSM. This is the highest level of polarisation achievable for a given energy and set of tunes. The polarisation level for empirical HSM was calculated in the simulations by deterministic HSM taking the beam position with respect to the reference orbit without errors. The results for the beam energy of 55 GeV are shown in Fig. 3.

The polarisation level without HSM is only slightly dependent on the BPM offsets. The polarisation level with deterministic HSM increases with decreasing BPM offset but saturates at about 0.55 for $\sigma(\Delta y_{k\text{-}mod}) < 150\ \mu$m. This can be understood since then the error of the position of the BPM relative to the reference plane $\sigma(\Delta y_{BPM})$ is dominated by the misalignment of the magnets $\sigma(\Delta y_{quad})$ since

$$\sigma(\Delta y_{BPM}) = \sqrt{\sigma(\Delta y_{quad})^2 + \sigma(\Delta y_{k\text{-}mod})^2}. \qquad (2)$$

The vertical mechanical misalignment of the quadrupole is measured with a precision of about 50 $\mu$m at LEP. This information can be used to get a more precise knowledge of the BPM relative to the reference plane. The achievable error of the offset determination by the beam based alignment has the same magnitude. The deterministic HSM including the geometrical alignment data was simulated (see again Fig. 3).

The polarisation level does not show the saturation effect and 0.8 of the level by empirical HSM can be obtained with $\sigma(\Delta y_{k\text{-}mod}) = 50\ \mu$m. This value can be achieved if all BPM offsets in the arcs of LEP are measured. The gain in polarisation will be only minor when the mechanical measurements are included without the offset determination since then the error $\sigma(\Delta y_{BPM})$ is dominated by the BPM offsets.

## 5 CONCLUSIONS AND OUTLOOK

The Harmonic Spin Matching technique becomes more precise by measuring the offsets of all BPMs in the arcs of LEP and including the measured misalignment of the quadrupole magnets at LEP from the geometrical survey. Simulations show that the optimum level of polarisation for a given energy can nearly be reached by deterministic HSM. The remaining optimisation can be performed by empirical HSM.

Presently, the all quadrupoles at LEP with an associated BPM are being equipped with back leg windings. It is envisaged to measure the offsets of all BPMs during the 1997 running period.

## 6 REFERENCES


[1] D. Rice et al., Beam Diagnostic Instrumentation at CESR, *IEEE Transitions on Nuclear Science*, NS-30(4):2190, 1983.

[2] I. Barnett, A. Beuret, B. Dehning, P. Galbraith, K. Henrichsen, M. Jonker, M. Placidi, I. Reichel, R. Schmidt, F. Tecker, L. Vos, and J. Wenninger, Dynamic Beam Based Calibration of Orbit Monitors at LEP, In *Proceedings of the Fourth International Workshop on Accelerator Alignment, KEK Proceedings 95-12*, pages 421–426, 1995, CERN SL/95-97 (BI).

[3] W. Coosemans, A. Marin, K. Rybaltchenko, F. Tecker, and J. Wenninger, Closed Orbit Feed-Back from low-beta Quadrupole Movements at LEP, this Conference.

[4] A. Blondel, M. Böge, B. Dehning, A. Drees, M. Placidi, F. Tecker, and J. Wenninger, Transverse Polarization beyond the Z Energy at LEP, this Conference.

[5] R. Rossmanith and R. Schmidt, Compensation of Depolarizing Effects in Electron Positron Storage Rings, *Nucl. Instr. Meth. Phys. Res.*, A(236):231, 1985.

[6] R. Assmann, *Optimierung der transversalen Spin-Polarisation im LEP-Speicherring und Anwendung für Präzisionsmessungen am Z-Boson*, PhD thesis, Ludwig-Maximilians-Universität München, 1994.

[7] R. Assmann et al., Polarization Studies at LEP in 1993, CERN SL/94-08 (AP).

[8] J. Kewisch et al., *Phys. Rev. Lett.*, 62:419, 1989.

[9] H. Grote and F. Iselin, *The MAD program*, CERN SL/90-13 (AP).

# ALIGNMENT OF THE HIGH BETA MAGNETS IN THE RHIC INTERACTION REGIONS *

D. Trbojevic, A. Jain, S. Tepikian, R. Grandinetti, G. Ganetis, J. Wei, and F. Karl,
Brookhaven National Laboratory, Upton, NY, 11973, USA

*Abstract*

The betatron functions inside the triplet quadrupoles in the Relativistic Heavy Ion Collider-RHIC are of the order of 1500 m, necessitating additional attention in the alignment procedure. On each side of the interaction regions eight cryogenic elements (six quadrupoles and two horizontal bending dipoles) are placed inside large cryostats. The quadrupole magnetic centers are obtained by "antenna" measurements with an accuracy of $\pm 60\mu$m. The signals from the "antenna" were cross calibrated with the colloidal cell measurements of the same magnet. The positions of the fiducials are related to the magnet centers during the "antenna" measurements. Elements are positioned warm inside the cryostats, with offsets to account for shrinkage during the cool down. The supports at the middle of the two central quadrupoles are fixed, while every other element slides longitudinally inside the cryostat during cool down or warm up.

## 1 INTRODUCTION

Two rings of the Relativistic Heavy Ion Collider cross each other in the horizontal plane at six interaction points. Twelve very large cryostats, located one on each side of the six interaction regions, house eight cryogenic elements- six quadrupoles and two dipoles. In the two interaction crossings (six o'clock and eight o'clock, at the RHIC detectors "STAR" and "PHENIX", respectively), the beams are focussed very tightly with the betatron functions of $\beta^*$=1 m. This is why special attention to the properties and alignment of the strong focusing quadrupoles, and dipoles close to them, is essential. Due to the large values of the amplitude betatron functions in these quadrupoles ($\sim$ 1500 m) their influence on the beam properties is 5.5 times magnified with respect to the regular arc quadrupoles (where $\beta \sim 50m$). There are three packages of multi-layer correction magnets between the triplet magnets. Two are directly connected to the Q3 while one is connected to the Q2 magnet (see Figure 1). During production the magnetic centers of the correctors are measured and their positions optimized.

The magnetic field angles (rolls) are obtained from rotating coil measurements with an accuracy of $\pm 0.1$ mrad. In addition to collisions of heavy ions, the RHIC accelerators will do spin physics experiments with two proton beams. The spin physics puts additional constraints on the alignment.

* Work performed under the auspices of the U.S. Department of Energy

## 2 "COLD"AND "WARM" ELEMENT POSITIONS

Positions of the supports or *insulating posts* of the large magnets inside the IP cryostats were established at room temperature. They remain unchanged with respect to the temperature conditions. Every magnet is installed at room temperature. Their longitudinal and vertical positions change during the cool-down when the temperature drops from 300K down to the operating temperature of 4K.

### 2.1 *Vertical Shrinkage*

The vertical positions of the quadrupole and dipole centers were estimated to shrink for $\Delta l$=2.743 mm. The vertical shrinkage of the RHIC arc quadrupoles was estimated, by the same method, to be $\Delta l$=1.905 mm. Difference in the vertical positions of the RHIC arc quadrupole magnetic centers between room and 4K temperature has been determined by four sets of measurements. The surveying instruments were used under the same conditions in both cases. It was important to allow 5 days cooldown period to establish correct and stable conditions. The value of $\Delta l$=1.905 mm was confirmed with an rms value of $\pm 38$ $\mu$m.

### 2.2 *Longitudinal Positions*

The "D0-dipoles" are located at the end of the cryostat toward the interaction point. There are additional dipoles named as the "DX-dipoles", which belong to both rings. They bend one beam from the IP towards the D0 dipole and the other one from the D0 dipole towards the IP. The available aperture of the D0 dipole is not larger than $\pm 6\sigma$ of the beam. The D0 dipole bends the beam either from the IP toward the DX magnet or it bends the beam from the DX magnet toward the triplet magnets. In the two interaction regions where the $\beta^*$= 1 m the amplitude betatron functions at the D0 dipoles are six times larger than at the regular bending dipoles in the RHIC arcs, although they are much shorter than the regular RHIC dipoles. The D0 dipoles are only 3.6 m long.

The largest quadrupole in the IP region is the central "Q2" quadrupole. Every cryogenic element in the cryostat is supported by two *posts*. Their large *"cold masses"* are mechanically connected tightly to each other. The Q2 quadrupole *cold mass* has the side towards the IP fixed to the *post* below (see Figure 2). All other magnet supports are allowed to slide at the top of the *cradles*. A connection of the *cold masses* to the *posts* is provided by the *cradles*. All the *cradles*, with the exception of the one with the fixed position at the Q2 magnet, allow the *cold masses* to slide due to the shrinkage or expansion at lower or higher

0-7803-4376-X/98/$10.00 © 1998 IEEE

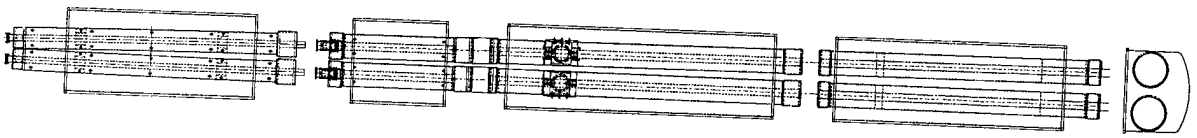


Figure 1: The layout of the high beta magnets.

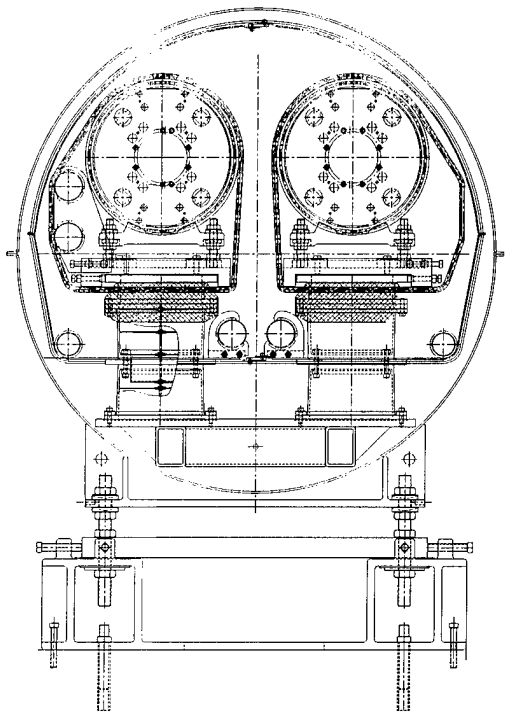


Figure 2: The cryostat cross section of the High Beta Magnets. The insulating posts and the stands are shown.

temperatures. Longitudinal positions of the *cold masses* at the *posts'* connections change as much as 22.7 mm at the magnet Q3, and 23.19 mm at the D0 dipole from the temperature difference between 300K and 4K. A shrinkage constant of $\alpha = (L_{300K} - L_{4K})/L_{300K} = 0.0031378$ has been experimentally established. The sliding was allowed with a special design of the *cradles* using the brass plates on both sides of the stainless steel blocks. A tolerance of $\pm 30$ $\mu$m between the block and the brass sides is achieved by two adjustable bolts on one side of the block. The D0 magnet is a sector dipole with a curvature. The sagitta of the magnet is obtained from the mechanical measurements at five positions along the length. The holding blocks at the *cradle* positions of the D0 magnet were positioned with angles with respect to the straight beam line through the triplet magnets to get an optimum for the magnet position.

## 3 MEASUREMENTS OF THE MAGNETIC CENTERS

The colloidal cell magnetic measurements of the RHIC quadrupoles are reported elsewhere [1]. A survey *antenna* system also has been developed to measure the magnetic centers of quadrupoles as well as various corrector layers. The antenna has several harmonic windings to measure dominant harmonic and the feed down terms. Fiducials are placed on the antenna to locate the magnetic centers relative to the magnet fiducials. Magnetic centers are measured and electronically recorded in every RHIC quadrupole by either the "antenna" or colloidal cell measurements. Accuracy of the direct field center determination is within $\pm$ 60 $\mu$m. Positions of the "antenna" coil or ferro-fluidic colloidal cell with respect to the outside fiducials are determined by the optical survey using a portable Leica ManCAT system with four theodolites. All data are transferred electronically and stored and used by the SYBASE data system. Only the best D0 dipoles and triplet magnets are assigned to the $\beta^* = 1m$ locations. In the process of magnet selection other important magnet properties like: alignment of the correctors, harmonic content, roll angles, quench performance, etc. are included. A prefiducialization of the high beta magnets is performed at the same magnet position. A relationship between the center of the magnetic field and the harmonic-antenna coil, or ferro-fluidic colloidal cell is obtained by using the ManCAT system at the same time and in the same local coordinate system.

### *3.1 Location of the Beam Position Monitors*

There are two beam position monitors (BPM's) per ring (four inside the cryostat). One is located at the end of the quadrupole Q3, attached to the end plate. The other is between the D0 dipole and Q1 quadrupole attached to the end plate of the quadrupole Q1. A separate RF antenna system has been built for determining positions of the BPM's in

the triplet magnets. A high frequency signal of 50 MHz is sent to a rod placed close to the center of the BPM. Three positions of the rod with respect to the center of the BPM are used to accurately determine the position of the BPM's. The BPM plates provide signals which determine the position of the rod with respect to the plates. Part of the rod outside the triplet quadrupole cold mass vacuum flange has two fiducials. These are used to determine the rod position with respect to the outside cryostat fiducials by using the already mentioned ManCat system. The accuracy of the BPM position with respect to the outside fiducials is estimated to be $\pm 0.13mm$. During the calibration procedure it was found that the reproducibility and accuracy of the measurements was $\pm 50\mu m$. The BPM positions are electronically transfered to the SYBASE and used by the high level BPM application code to correct for the real BPM positions.

## 4 SURVEY AND ALIGNMENT

The primary network of monuments in the tunnel had been established before [1]. The secondary network in the tunnel provides eight monuments on the floor, four on both sides of each triplet cryostat. Eight elements are brought to the tunnel after they had been presurveyed in the magnet production facility. They are positioned at the top of the *posts* with only the lower side of the cryostat built. The top of the cryostat, the bus connections, the 80K cryogenic shield, vacuum and beam pipe connections, etc. are built after the survey is completed.

The survey and alignment of the high beta elements were performed by using eight theodolites at the same time which are electronically connected to a Compaq 486c portable computer. Adjustments of the magnet positions are performed until the difference between the required and established positions in readings of at least four instruments are less than $\pm 25$ $\mu$m.

## 5 CONCLUSIONS

A development of two new techniques, colloidal ferrofluidic cell and "antenna"measurements, allowed a very precise location of magnetic field centers within quadrupole magnets. Accuracy achieved in the center determination is $\pm$ 60 $\mu$m. Special attention to the presurvey, alignment and control of the roll angle of the high beta elements in RHIC is expected to provide better operation and higher luminosity of the colliding beams.

## 6 ACKNOWLEDGEMENTS

We would like to thank Mike Goldman who developed the ferrofluidic technique, Peter Cameron for developing the BPM antenna measurement system, Richard Thomas, Wing Louie, Andrew Marone for implementing measuring techniques, Mike Hemmer and Gerry Trahern for organizing the data analysis and transfer from the SYBASE to the ManCAT system, David McChesney for his contribution to the presurveying, James Cammarata and Sue Norton for providing the presented drawings, and the surveyors' teams who did a marvelous job surveying and aligning these elements.

## 7 REFERENCES

[1] D. Trbojevic, P. Cameron, G.L. Ganetis, M.A. Goldman, R. Gupta, M. Harrison, M.F. Hemmer, F.X. Karl, A. Jain, W. Louie, S. Mulhall, S. Peggs, S. Tepikian, R. Thomas, and P. Wanderer, "Alignment and Survey of the Elements in RHIC", Proceedings of the 1995 PAC and International Conference on High Energy Accelerators, held May 1-5, 1995, Dallas, Texas, TAA009, pp.2099-2101.

# THE SUPERCONDUCTING INTERACTION REGION MAGNET POSITIONING SYSTEM FOR THE CESR PHASE III UPGRADE *

James J. Welch, David L. Rubin, and Alexander B. Temnykh †,
Wilson Laboratory, Cornell University, Ithaca NY

*Abstract*

Due to the extraordinary sensitivity of beams to misalignments of the superconducting high gradient interaction region magnets for the Phase III upgrade, a beam-based alignment and active positioning scheme has been designed and is being constructed. Using cams and kinematic mounting, the magnetic centers of the four quadrupole magnets will be independently positioned over a radial range of 1 mm with a resolution below 10 $\mu$m. Beam measurements of the closed orbit will determine where to set the position. In principle realignment can be done while beams are stored. The positioning system must withstand considerable dynamic forces due to the interaction of the CLEO detector solenoid field with the current in the dipole windings. It is located almost entirely within the CLEO detector and has a special transition from non-magnetic to magnetic materials so as not to disturb the uniformity of the solenoid field. It allows for retraction of the CLEO pole from the detector without interference.

## 1 BACKGROUND

In 1998 the CLEO detector will complete another major upgrade to bring its performance up to B factory levels. Taking advantage of the opportunity presented by the re-design of most of the detector, new interaction region focussing and correcting elements were designed to allow the highest possible luminosity [1][2]. To ameliorate the effects of the long range beam-beam interaction at crossing points near the interaction point, the new magnets are designed to be quite short with high gradients.

## 2 MISALIGNMENT TOLERANCE

Machine performance depends critically on the alignment of the superconducting interaction region quadrupoles. Sensitivity to vertical misalignments is enhanced due to the high gradient, high $\beta$, and rapid phase advance through the interaction region. The result of misalignments is closed orbit errors, and loss of effective physical aperture, and vertical dispersion, that will dilute vertical beam size.

A 1 mm vertical misalignment of one of the vertically focussing quadrupoles, if uncorrected, generates an 80 mm closed orbit error, nearly four time the physical aperture of the machine. Vertical dispersion is most severe when the relative misalignment of quadrupoles on either side of the interaction point is such as to create a closed orbit bump. Since the betatron phase advance between the vertically focussing magnets is approximately 180 degrees, a nearly closed bump is produced when the magnets are displaced vertically in equal but opposite directions.

Because of the large chromaticity in the interaction region, phase advance, and therefore bump closure depends strongly on energy. If the four magnets are alternately displaced vertically by $\pm 1$ mm, peak vertical dispersion in the machine arcs is closed to 7 m. If the orbit error is corrected with steering magnets located 1 m outboard of the cryostat, the residual vertical dispersion is reduced to an unacceptably high 70 cm. (Significant dilution of vertical beam size is evident if vertical dispersion is greater than 5-10 cm.)

While vertical beam size and aperture are quite sensitive to vertical misalignments, effects of horizontal misalignment are much less severe. The strength of the horizontally focussing quadrupoles and the horizontal $\beta$ in them are both smaller than their vertical counterparts. In addition, the horizontal dispersion in the machine is near 4 m by design, while the vertical dispersion is nominally zero. Finally, horizontal correction near the IR is easier than vertical because of the larger horizontal beta functions there.

Taking into account the sensitivity of the closed orbit and the limited ability of existing corrector magnets to accommodate quadrupole position errors, we have have designed a magnet positioning system that should be able to put the magnetic centers of the quadrupoles on the correct axis to within 100 $\mu$m vertically and 500 $\mu$m horizontally under all conditions. The run to run tolerance should be an order of magnitude less and vibration amplitudes should be less than 1 $\mu$m.

## 3 DESIGN

Holding and accurately positioning cryostats containing the superconducting magnets is problematic: they must be deeply inserted into the CLEO detector, there is little space available, there are large electromagnetic forces, materials must be either highly non-magnetic or good magnet steel depending on location within the detector and its steel yoke, and there must be semi-frequent personnel access to the interior of the CLEO detector for maintenance and repair of the electronics. The basic design choice is to either use a cantilevered support [3][4], or to use some portion of the CLEO pole with a column or pylon support. Detector access has been provided for by longitudinally extracting the end poles. Cantilevered support would have to extend over a distance of about 5 meters and would occupy a space that might someday be needed for round beam quadrupoles or two-ring separators. Cantilevered support also implies that the transition from cold to warm cryostats occurs horizontally, which complicates the cryogenics[3]. We chose

* Work supported by the National Science Foundation
† On leave from BINP

0-7803-4376-X/98/$10.00 © 1998 IEEE

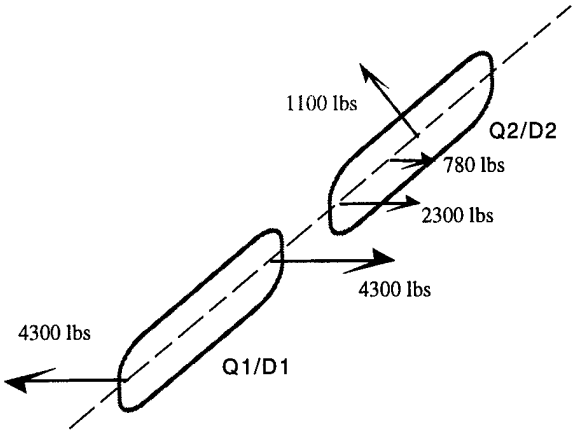



Figure 2: Electromagnetic forces acting on the dipole and quadrupole magnets which must be taken up by the positioning system. The dipole forces are in the horizontal plane, while the quadrupole force could be in any transverse direction.

instead cut a vertical slot out of the pole pieces and suspend each cryostats on a thick steel pylon which hangs from the fixed portion of CLEO return yoke. See Figure 1. The pylon remains in place when the pole is retracted for access. Cryogenics utility lines are located immediately behind the pylon so there is no need to modify or move the interaction region magnets to obtain access to the detector. A pylon rather than a column is preferable for bath cooling of the magnets.

*Pylon Mount*

Detailed finite element studies were carried out to ascertain the stiffness of various pylon designs [6]. The main cause of flexure was found to be due to twisting of the ring to which the pylon is attached when the CLEO solenoid magnetic load (43,000 lbs) is turned. The twisting is greatly reduced by strategically coupling the inner ring to the next outermost ring. With this improvement the transverse flexure of the pylon and CLEO magnet is kept to less than about 0.005 inches when the CLEO solenoid is energized. Other loads due to the interaction region magnets reacting with the CLEO solenoid produce substantially smaller displacements.

*External Forces*

In addition to the usual gravitational loads, there are several rather large external forces acting directly on the superconducting magnets which are the result of the CLEO solenoid field acting on the currents in the dipole and quadrupole coils. These forces, which are dynamic, must be carried by the helium vessel, the cryostat and the positioning system. There is also a more or less static force on Q2 due to the nearby steel detector yoke which is due to misalignment of the yoke with respect to the quadrupole [7]. These forces are shown in Figure 2.

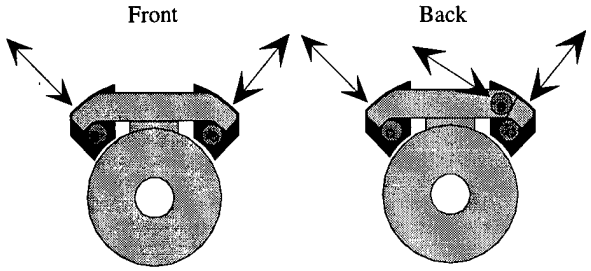



Figure 3: Cam arrangements at the front and back of the cryostat.

The weight of each cryostat/magnet assembly is expected to be about 4000 lbs. The electromagnetic forces are larger though to some extent they cancel. Detailed mechanical analysis shows that under some possible conditions the cyrostat could lift off the cams unless an additional 4000 lbs vertical load is applied. These loads will be supplied via pre-loaded spring assemblies. Gas cylinders will be used to energize the springs because they have good force/volume characteristics and are non-magnetic.

*Cam Configuration*

Bearings mounted eccentrically on a shaft (cams) offer several advantages as positioning devices in our application:

- Fine control and limited range of motion
- Heavy load carrying ability
- Simple and tested [5].

By providing kinematic mounting of the cryostat, the axis connecting the magnetic centers of the two quadrupoles can be uniquely and precisely positioned independent of the variable forces that will be borne Of course, cam's have some disadvantages too: the system will have to be preloaded to insure positive contact at all cam contact points under all load conditions. Also it is somewhat difficult to understand the range of motion of a cam based system, and the range is not exactly suited to the application.

These considerations led to a choice of cam configurations which minimizes the excess motion of the cryostat. The configuration is shown in figure 3. There are two longitudinal planes where the cams are located. The front plane at, 1324 millimeters from the IP, has two cams that are 90 degrees from each other and control the position of one end of the cryostat axis. The back plane of cams, located 2492 millimeters from the IP, is the same except for an additional 'theta cam' which controls the rotation about the cyrostat axis. The theta cam is not independent of the other cams. That is when the cryostat axis is moved the theta cam angle must be adjusted just to keep the rotation about the axis constant.

Two tee shaped brackets attached to the cryostat are set on the cam bearings so that the cryostats effectively hangs on the bearings. If it were not for the theta cam, the cryostat would roll freely about its center. Conceptually it is helpful

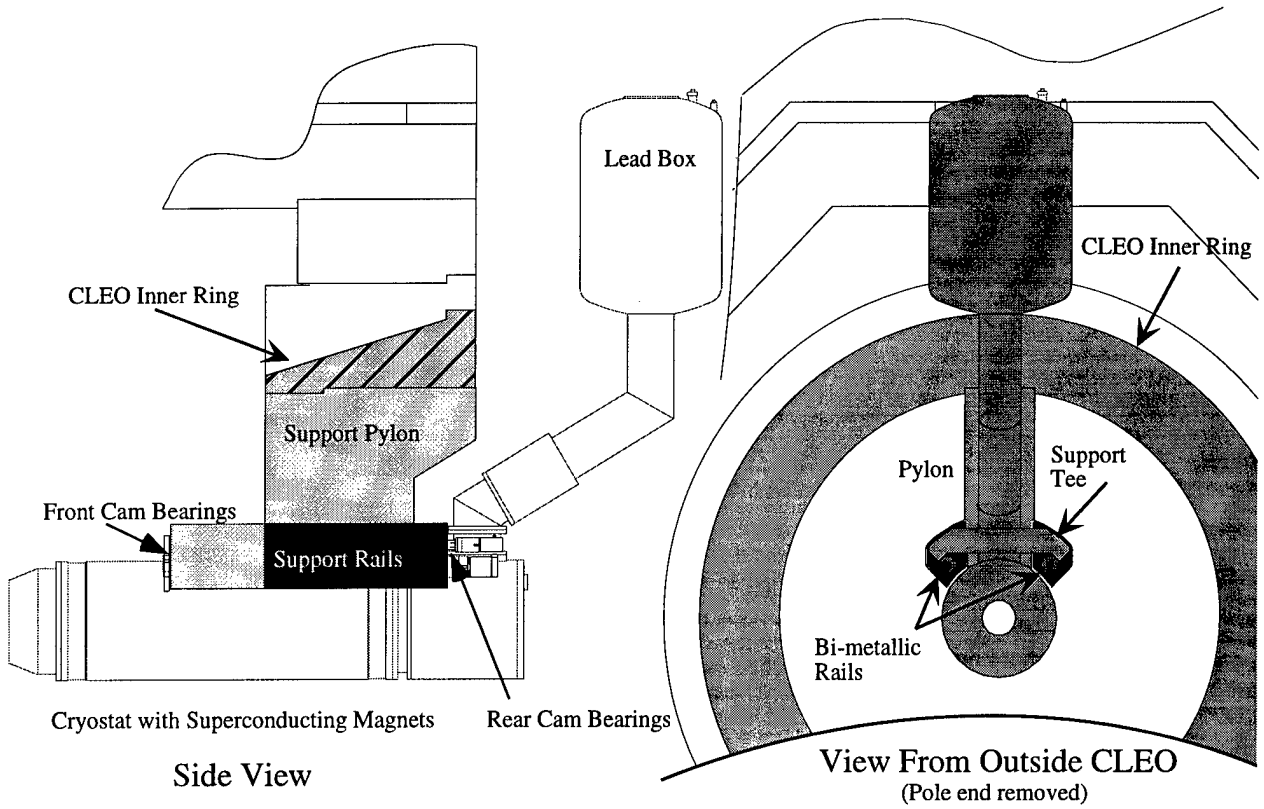



Figure 1: A thick steel pylon attached to the inner steel ring of the CLEO solenoid magnet yoke holds the cryostats containing the superconducting interaction regions magnets. The remaining 'keyhole' shaped portion of the CLEO pole is not shown. It can roll out for detector access. The cryostat is kinematically held by rolling contacts on five cam bearings and one spherical bearing contact for longitudinal location.

to imagine the cam bearings to be in rolling contact with a circle centered on the cryostat center and cut into tees attached to the top of the cryostat. Since the bearings are mounted eccentrically on a fixed shaft, the center of the bearings can be moved by changing the shaft angle. This directly translates into a motion of the cryostat center. In practice the difference between a flat rolling surface and a circular one centered on the cryostat is negligable since only small $\sim 1$ millimeters motions are encountered.

Hence we have five degrees of freedom (the shaft angles) controlling all possible motions of the cryostat except its longitudinal position. The longitudinal position is set at assembly time by the pre-load device. It constrains the longitudinal location of a point on the mounting bracket with only second order constraints on the transverse position or rotation of the cryostat. The second order constraint leads to small but negligable longitudinal motion when a transverse motion is introduced.

## 4 ACKNOWLEDGEMENTS

We gratefully acknowledge the generous and knowledgeable help from Gordon Bowdon of SLAC and Jeffery Cherwinka at Cornell.

## 5 REFERENCES

[1] *The CESR/CLEO Upgrade Project*, CESR and CLEO staff, report of the Laboratory of Nuclear Studies, Cornell University, CLNS 93/1265, (1993)

[2] D.L. Rubin, *CESR Status and Plans*, Proc. 1995 Particle Accelerator Conference, (PAC95), vol. 1, pp 481f, http://www.lns.cornell.edu/public/CBN/1995/cbn95-8.ps

[3] T.M. Taylor, *Technological Aspects of the LEP Low-Beta Insertions*, IEEE Trans on Nucl. Sci. Vol NS-32, No. 5, October 1985

[4] W.W. Ash, et. al., *Superconducting Final Focus for the SLC Linear Collider*, Proc. 14th Int. Cryogenic Engineering Conf., June 1992

[5] G. Bowdon, SLAC, personal communications

[6] Philip C. Farese, note *Quad Support Study Followup*

[7] J.J. Welch, G.F. Dugan, *Forces on Interaction Region Quadrupoles and Dipoles to a Detector Solenoid Magnet*, these proceedings (PAC97)

# A WIRE POSITION MONITOR (WPM) SYSTEM TO CONTROL THE COLD MASS MOVEMENTS INSIDE THE TTF CRYOMODULE

D. Giove, A. Bosotti, C. Pagani and G. Varisco, INFN Milano
LASA, Via F.lli Cervi 201, Segrate (Mi), Italy

*Abstract*

A system able to measure, on-line, movements and vibrations of the Cold Mass (CM) during cool down and steady state operation has been developed and installed inside the first TTF Cryomodule. The system includes two independent lines, with 18 WPMs each, and an improved version of BPM type.
read out and data analysis. Laboratory tests on a shorter prototype have shown that the system is able to monitor the CM displacements with a few micron sensitivity, the absolute error being less than 50 microns in the range of +/- 2.5 mm. Fast read out and FFT technique allow also to detect and analyze possible CM vibrations.

## 1 INTRODUCTION

The TTF facility will consist of four 12 m long cryounits each with eight 9-cell superconducting cavities operating at 1.3 Ghz and one focusing quadrupole. Beam tests will be carried out at about 500 MeV.
The test program for the first cryounit of TTF includes measures of the cryomodule alignment stability and reproducibility during cool-down/warm up operations.
The required alignment tolerances for the elements inside a cryomodule are 0.5 mm for the RF cavities and 50 μm for the quadrupole. After final assembly inside the cryomodule, the stability of the axis position must be monitored on line during thermal cycles with a resolution of 10 μm. Fig. 1 shows a cross section of the first cryounit.

## 2 METHOD

The stretched wire alignment system has been discussed in detail in literature since it has been used for the precise measurement of transport components in beam lines [1]
Taking as a reference such an experience we have designed a measuring system able to monitor on line positions and vibrations of objects from room temperature down to LHe temperature[2]. Desy laboratory has designed the components necessary to install this measuring apparatus inside a cryomodule to monitor the RF cavity axis stability.
The measuring system consists of detectors, called WPMs (Wire Position Monitors), similar to beam position monitors. Each one contains 4 antennas and the differential signal strength received from opposite pairs is the quantity of interest. The WPMs receive their signal from a stretched wire excited by a 140 Mhz RF signal and centered inside a tube. The wire provides the fixed reference with respect to the lab frame while the detectors are fixed to the CM elements to monitor.
The TTF design foresee two sets of 18 transducers fixed along two straight sections inside the cryomodule to provide a complete 3D analysis of the displacements. The system had to take into account many constrains due to the peculiar operating conditions. The most important have been the wide range of temperature (from room temperature up to the operating 2K), the need to contain the overall power consumption at 2K (few Watts) and the fact that the system, after the final assembly, will be inaccessible.

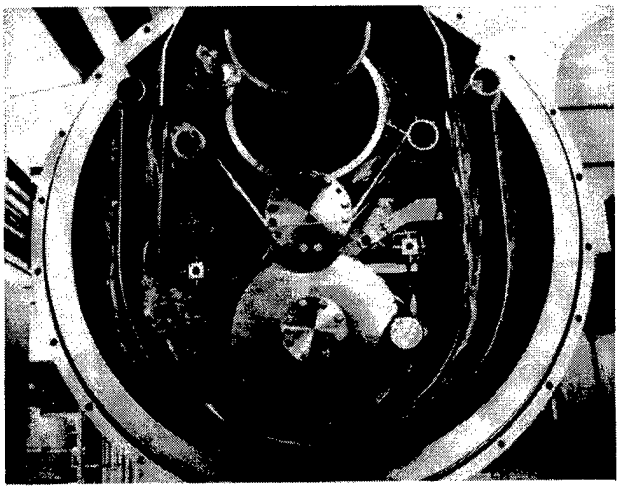


**Figure 1 - Cross section of the cryounit**

## 3 DETAILS OF THE APPARATUS

### *3.1 The WPM*

A schematic layout of two WPMs with their supporting frames, is shown in fig. 2.
The detector is of the stripline kind with four electrodes matched to 50 Ω and symmetrically placed at 90° each other. The downstream end of each stripline (relative to RF propagation) is terminated to 50 Ω and the clear aperture is of 12 mm. The wire-stripline coupling and the

0-7803-4376-X/98/$10.00 © 1998 IEEE

crosstalk between adjacent striplines have been measured as 39 dB and >55 dB respectively.

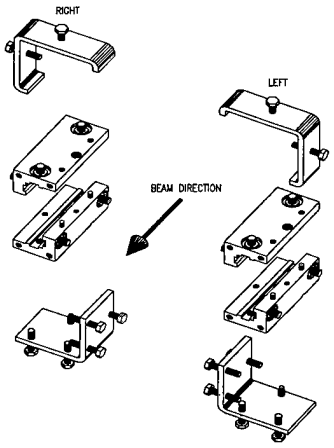



**Figure 2 - Schematic layout of two WPM**

*3.2 The wire and the coaxial tube*

The wire employed is a 0.5 mm diameter beryllium copper wire coated with EV-13 to provide electrical insulation. The choice of the material has been imposed by the need to use amagnetic materials and the possibility to stretch the wire with an high tensile stress (of the order of 100 Kg/mm$^2$). This will reduce, under the operating conditions, the overall sag of the wire at 2.07 mm.

*3.3 RF coaxial cable and connectors*

The choice of the connectors and RF coaxial cables to transport the signal from WPM to the external of the cryomodule has been a major technological challenge.
The radioactive environment and the cryogenic compatibility have posed severe limitations on materials for connectors and cables. The final choice has been to use a Suhner cable mod. P02182 and special designed SMA connectors and 50 Ω terminations with PEEK dielectric and amagnetic spring.

*3.4 Read out electronics*

The electronics which handles the signals coming from the WPMs has been developed according to the VXI format, in order to improve noise immunity and to take advantage of the larger board size. Each board will accommodate the components for the control of two WPMs.
The RF signal sensitivity is of -65 dBm with a dynamic range of 40 dB and a linearity of the order of 0.1% in a 20 dB range[3]. The BPM detector cannot process the signal in less than 50 μs, so the maximum rate of acquisition is of the order of 20 Khz for a single stripline. Under operating conditions the acquisition rate for a whole set of detectors is of 1 Khz.

*3.5 Data acquisition and analysis system*

On line control of the detector electronics and handling of data acquisition from each one of the two structures is performed by a VME 68040 CPU fitted inside each VXI crate. Raw data acquisition, averaging and corrections with polynomial curve are performed at this level. A local storage of data has been provided before a transfer will occur toward a dedicated NFS server. This machine allows to share data between consumer processes.
A PC with a LabVIEW based application provides console functionality for the whole system. On line monitoring of each set of WPM along with analysis of the displacement of each WPM versus time may be done using a menu driven interface. Advanced data processing (frequency analysis, power spectrum of any instability, etc.) is available as a powerful tool to analyze the possible vibrations of the structure.

## LABORATORY MEASUREMENTS

A test fixture has been constructed for studying the response of the single WPM or of a string of 3 WPMs. The detectors are assembled on a two axis translation stage and can be positioned anywhere within their aperture with respect to the fixed wire. The absolute accuracy of the positioning system is repeatable to about 4 μm. The electronics reading chain is the same as the final one. The more relevant aspects which have been investigated are the following:

- mapping of the response of the WPM over its aperture
- reproducibility of the measurements after a mechanical disassembling of the detector
- tolerance to errors in mechanical positioning of the detector on its support arm
- long term stability
- characterization of the full set of detectors.

The dependence of the response with respect to the position of the wire can be described by a 3rd order bidimensional polynomial, where the even and cross terms of the 2D polynomial expressions take into account mechanical tolerances and inter-electrode coupling. A mapping of each WPM has been performed in order to determine the polynomial coefficients. These coefficients have been computed fitting the experimental data using Mathematica. The results of these fits shows that the functions describing the wire vertical (Y) and horizontal (X) positions have a strong dependence on the odds terms, whose coefficient has higher weight than the even ones. Moreover odd term coefficients are almost equal for all WPMs, while even term coefficients vary in a random way either when we change the monitor or repeat the measurement of the same device after a disassembling. This suggests us to describe a WPM using only odd

terms. A simulation based on a 2D electrostatic model of the WPM has been performed to investigate this behavior. In this model the wire is simulated by a point charge and the signal induced on an infinitely long microstrip is computed. The results have shown that the functional dependence of the picked up signals with respect to a generic wire position can be described by a superposition of Arcsinh(x,y) functions, whose expansion may be stopped at the 3rd order. A graph of the error in position measurement is shown in figure 3. An error of less than 40 μm has been measured within a 2.0 mm range. The same set of coefficients has been applied to the analysisi of the measures for all the WPMs. The error in the reconstructed position has been of the order of 50 μm in the range of +/- 2.0 mm.

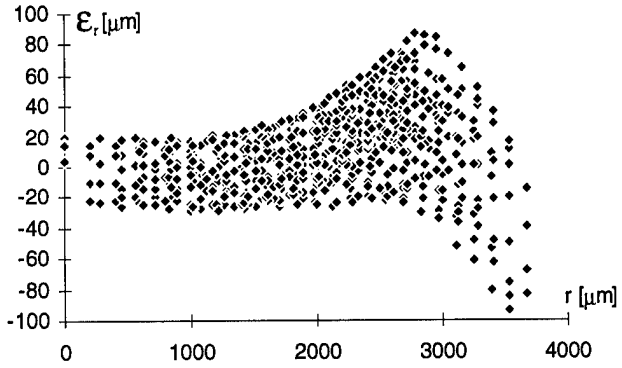



**Figure 3 - Errors in position measurements**

Tests carried out over a period of 2 month of operation on the 3 WPMs string have shown no significant deviation in the readings (less than .1 mm), assuring a good long term stability of the system.

Misalignment effects of the order of 1.0 mm over the detector dimensions have been studied. The mapping of the response function have shown negligible modifications with respect to that taken with the detector in the reference position. This makes the assembling procedure inside the cryostat less critical.

## INSTALLATION AT DESY

In February 1997 the measuring system has been installed into the first cryounit at Desy. A close view of a WPM assembled on its support arm is shown in fig. 4.

The WPMs has been assembled following the catenary sag at each position with a precision of the order of 20 μm. The performance of the WPM system has been assessed measuring the sag of the cryostat under its own weight releasing the central post support on the alignment fixture. Fig. 5 shows the reconstructed position of the detectors in this circumstance. Once the normal position of the cryostat has been recovered the monitors return to their rest measurements within an error of 5 μm.

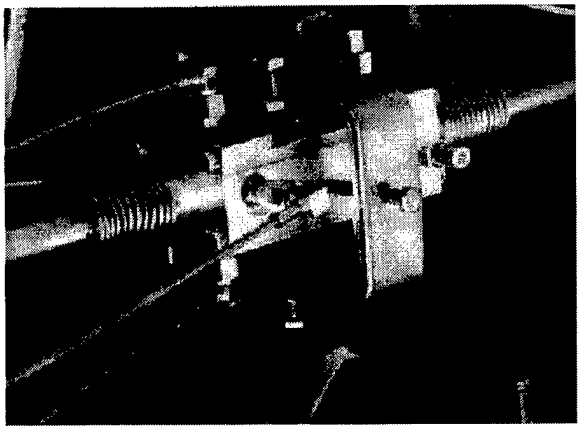


**Figure 4 - A WPM installed in the cryounit**

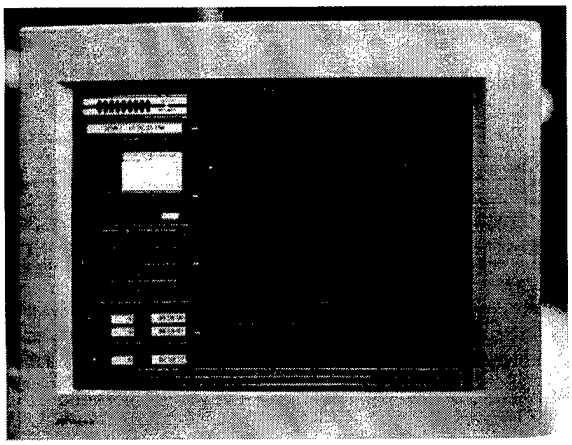


**Figure 5 - Console front panel**

## CONCLUSIONS

We have developed a system able to measure displacements over a range of 6 mm with resolutions up to 10 μm. Components have been designed and tested for operation at 2 K. The final system has been installed in Desy and it will be operative during the first cooldown in May 1997.

## REFERENCES

[1] V.E. Bressler et al., Overview of the Final Focus Test Beam Alignment System, Proc. PAC 1991, p. 2736

[2] D. Giove et al., The On Line Monitoring System for the Cold Mass of the TTF Cryostat, Tesla Report, to be published

[3] R. De Monte et al., Elettra BPM System (Hardware and Software): First Results, Proc. EPAC 1994, pag. 1530

# GROUND MOTION STUDIES FOR LARGE FUTURE LINEAR COLLIDERS

Shigeru Takeda, Noboru Yamamoto, and Katsunobu Oide
KEK, High Energy Accelerator Research Organization
Oho, Tsukuba, Ibaraki 305, Japan

## 1 INTRODUCTION

The future large accelerator, such as a TeV linear collider, should have extremely small emittance to perform the required luminosity. Precise alignment of machine components is essential to prevent emittance dilution. The ground motion spoils alignment of accelerator elements and results in emittance growth. This paper discusses about ground motion and its effect on the main linac. The ground motion in the frequency range of seismic vibration is mostly coherent in the related accelerator. But the incoherent diffusive or Brownian like motion may become dominant at frequency region less than seismic vibration. Shiltsev reviewed many studies of ground motion and discussed about the diffusive motion [1]. Sery discussed about the ground motion focusing on the effects to the main linac of linear collider [2]. This paper intends to start from the power spectrum of the $ATL$ model [3], then show typical parameters of main linacs and consider measured data including excavated effects.

## 2 POWER SPECTRUM OF $ATL$ MODEL

Th $ATL$ model can be formulated using an auto correlation function $\langle y(t+\tau)y(t)\rangle_{av}$, as

$$\begin{aligned}\Delta_y(\tau)^2 &= 2\langle y(t)^2\rangle_{av} - 2\langle y(t+\tau)y(t)\rangle_{av} \\ &= A\cdot L\cdot\tau. \end{aligned} \quad (1)$$

Here, $\langle X\rangle_{av}$ means an ensemble average of $X$. Using the definition of a power spectral function,

$$P(f) = \int_{-\infty}^{\infty} df\,\langle y(t+\tau)y(t)\rangle_{av}\, e^{-2\pi i f\tau}, \quad (2)$$

Eq. 1 becomes,

$$A\cdot L\cdot\tau = 4\int_{-\infty}^{\infty} df P(f)\sin^2(\pi f\tau). \quad (3)$$

If we assume that the power spectral function is proportional to the inverse of squared frequency,

$$P(f) = \frac{K}{4\pi^2 f^2}, \quad (4)$$

we can carry out integration in the the right hand side of Eq. 3,

$$4\int_{-\infty}^{\infty} df P(f)\sin^2(\pi f\tau) = K\cdot\tau. \quad (5)$$

Putting this result into Eq. 3, we find the power spectral function of $ATL$ model as,

$$P(f) = \frac{A\cdot L}{4\pi^2 f^2}. \quad (6)$$

## 3 LINAC AND GROUND MOTION

Let us estimate emittance growth due to the drift in the transverse alignment of the accelerating structures caused by the $ATL$ model. Although the drift of the ground also affects the transverse alignment of the focusing elements, the orbit can be maintained as a straight line from the injection point to the extraction point with beam-based techniques. We assume that the orbit correction is so perfect that the orbit is an ideal straight line with an injection angle created by an achromat kicker placed at the entrance of the linac. Thus only the misalignment of accelerating structures is the source of the emittance blow-up in this case. Here we concentrate on the single bunch effect due to the dipole wake of the structures.

The transverse displacement of the beam at the end of linac caused by a misaligned accelerating structure $\delta y(s)$ is written as

$$\Delta y_1(z) = \int ds \frac{Ne^2 w(z)}{E(s)} \times\sqrt{\frac{\gamma(s)}{\gamma_1}\beta_1\beta(s)}\sin(\psi_1-\psi(s))(\delta y(s)-y(s))\,, \quad (7)$$

where $w(z)$ is the transverse wake function per unit length, $N$ the number of particles per bunch, $E(s)$, $\gamma(s)$, $\beta(s)$, $\psi(s)$ are the beam energy, Lorents factor, $\beta$-function, and betatron phase at location $s$, respectively. Suffices 0 and 1 denote the values of those functions at the entrance and the exit of the linac. We set the origin of the coordinate at the entrance of the linac as $s_0 = 0, y(0) = 0$. The orbit $y(s)$ is always maintained to be linear in $s$, *i.e.*,

$$y(s) = y_1 s/L\,, \quad (8)$$

where $L = s_1$ is the total length of the linac.

The expected value of square of the orbit is written as

$$\langle\Delta y(z)^2\rangle = \left(\frac{Ne^2w(z)}{E_0}\right)^2\int ds\int ds' \times\frac{\beta_1\beta_0\gamma_0^{1/2}}{\gamma_1(\gamma(s)\gamma(s'))^{1/4}}\sin(\psi_1-\psi(s))\sin(\psi_1-\psi(s')) \times\langle(\delta y(s)-y(s))(\delta y(s')-y(s'))\rangle\,, \quad (9)$$

where we have assumed a scaling of focusing as $\beta(s) = \beta_0\sqrt{\gamma(s)/\gamma_0}$. The $ATL$ model gives the correlation of displacements between at $s$ and $s'$ or $s$ and $s_1$:

$$\begin{aligned}\langle\delta y(s)\delta y(s')\rangle &= At\times\min(s,s') \\ \langle\delta y(s)y_1\rangle &= Ats\,. \end{aligned} \quad (10)$$

0-7803-4376-X/98/$10.00 © 1998 IEEE

The betatron phase is expressed as

$$\psi(s) = \int_0^s \frac{ds}{\beta(s)} = \frac{2\sqrt{\gamma_0}}{g\beta_0}(\sqrt{\gamma(s)} - \sqrt{\gamma_0}) , \qquad (11)$$

where $g$ is the acceleration gradient $g \equiv d\gamma/ds$. Putting Eqs. 8, 10, and 11 into Eq. 9, we obtain the expected value of the relative blow-up of the beam as

$$\epsilon \equiv \frac{\langle \Delta y(z)^2 \rangle}{(\beta_1 \varepsilon_{Ny}/\gamma_1)} \approx At\frac{N^2 e^4 w(z)^2}{4g^2 E_0^2 L \varepsilon_{Ny}} \beta_0^3 \gamma_0^{1/4} \gamma_1^{11/4} , \qquad (12)$$

where $\varepsilon_{Ny}$ is the invariant emittance. We have approximated $(\gamma(s)\gamma(s'))^{1/4} \approx (\gamma_0\gamma_1)^{1/4}$, and have assumed $g\beta \gg 1$, etc.

**TABLE** 1: Parameters of typical linear collider linacs.

| | | "X-band" | "C-band" | |
|---|---|---|---|---|
| Beam energy entrance/exit | $E_0/E_1$ | 10/500 | | GeV |
| Particles/bunch | $N$ | 0.8 | 1.0 | $10^{10}$ |
| Inv. emittance | $\varepsilon_{Ny}$ | 30 | | nm |
| Bunch length | $\sigma_z$ | 80 | 200 | $\mu$m |
| $\beta$ at entrance | $\beta_0$ | 4 | | m |
| Rf frequency | $f$ | 11.4 | 5.7 | GHz |
| Acc. gradient | $dE/ds$ | 45 | 32 | MeV/m |
| Iris radius/ Wavelength | $a/\lambda$ | 0.16 | 0.14 | |
| $ATL$ coeff. | $A$ | 1 | | $\mathrm{nm}^2/\mathrm{m/s}$ |
| Stable time for $\epsilon = 0.1$ | $t$ | 3 | 24 | hours |

Equation 12 gives the duration time $t$ for the emittance blow-up remains within an amount $\epsilon$. The actual magnitude of $t$ thus depends on the parameters of the linac. As an example we calculate for two cases of X-band and C-band. We assume the focusing parameters are same in two cases. We applied an approximation by K. Yokoya for the wake function $w(z)$ to calculate the blow-up factor $\epsilon$ in Eq. 12:

$$w(z) \approx w'\sigma_z \approx 1.55\frac{cZ_0}{\pi a^4}\left(\frac{a/\lambda}{0.14}\right)^{0.179}\sigma_z \qquad (13)$$

where $a$, $\lambda$, $Z_0$ are the iris radius, the rf wavelength, and the vacuum impedance, respectively. The parameters in Table 1 may be different from existing designs in detail, but the essential characteristics are not much far from "real" designs.

## 4 PROPERTIES OF GROUND MOTION

In the frequency range $f < 0.1$ Hz, the measured power spectrum of ground motion can be characterized by $k/f^2$ . This coefficient $k$ has site dependence and changes from 1 to $10^2$ $\mathrm{nm}^2/Hz$. The sources of the ground motion are the atmospheric activity, change of underground water, ocean tide, earth-tides, temperature variation of the surface ground etc [5, 6, 2]. At high frequency $f > 0.1$ Hz, the power spectrum decreases very rapidly with frequency being proportional to $1/f^4$. The motion consists of seismic activity, that is elastic motion. Correlation measurements show that the motion has good correlation in quiet sites [6, 2].

The motion at $f < 0.1$ Hz, however, is very different. Dominant part of the ground motions is inelastic motion, though the elastic motion presents in this frequency range. The earth-tides, one of the elastic motion in this low frequency range, becomes cause of inelastic motion through its dissipation. One of the models describing this inelastic ground motion is the $ATL$ model mentioned above [3]. The $ATL$ model means that slow relative ground motion is random and the number of discrete breaks appearing between two points is proportional to the distance and the passed time. These discrete breaks consist of random popping up/down of fragmented rocks. The duration times and the amplitudes of popping motion of the rocks are not complete random phenomena, then this two-dimensional covariance function and the white noise correlation are not equivalent. The $ATL$ model is one of the mathematical approximation for this covariance function provided the process of random motion including slow variable component. The parameter $A$ should be influenced dominantly by the earth properties, providing the source of inelastic motions is dissipation of the elastic motion. In other words, the value of $A$ should depend on the degree of fragmentation of the rock. Observed parameter $A$ is smaller in the tunnel of solid rock than in the broken rock [1]. The excavation

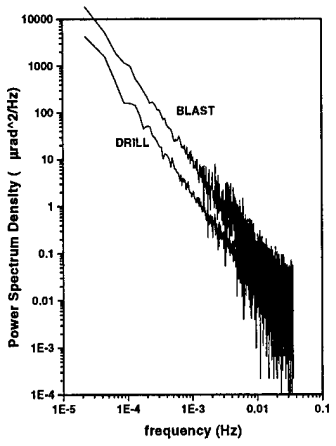



**FIGURE** 1: Power spectrum densities in the tunnel excavated by Drill or Blast.

method of the tunnel also affects significantly the value of $A$, as shown in Fig. 1 [5]. Although the tunnel excavated by use of dynamites gives $A \cong 5$ $\mathrm{nm}^2/\mathrm{m/s}$ , the tunnel bored by a machine gives $A \cong 1$ $\mathrm{nm}^2\mathrm{m/s}$. This difference shows probably because of artificial fragmentation of the rock occurred during construction. Our experimental results and recent report on the excavation clarify that application of TBMs is better excavating method than NATM

(Drill + Blast) for accelerator tunnel to prevent emittance dilution [5, 7].

NATM (New Austrian Tunnelling Method) is a excavating method with distributed dynamites and drills. Many rockbolts are essential to prevent relaxation of the rock on NATM. TBM (Tunnel Boring Machine) is a name of tunneling tool which is a very big drilling machine. Excavation using TBMs in the massive hard rock eliminates overbreak on the surface of the tunnel and no tunnel support may be possible. On the other hands, NATM gives relaxation in the surface layer of the rock caused by blast, then utilization of many rockbolts becomes essential to support the surface [7]. Fragmentation of the rock through this relaxation gives the increase in $A$.

**TABLE** 2: Typical values of $A$ in the $ATL$ model

| | $A$ : nm$^2$/m/s | | |
|---|---|---|---|
| Laboratory Site | | Other Site | |
| UNK | 100 | Pinon Flat | 0.1 |
| SLAC | 100 | Esashi | 0.3 |
| CERN | 10 | Sazare | 0.05 |
| KEK | 40 | | |

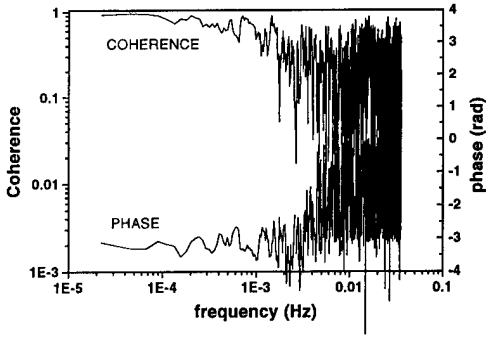



**FIGURE** 2: Coherence and phase difference obtained in the tunnel excavated by NATM. Two levels were set up 46 meters apart.

The tolerance for errors of the linear collider strongly depends on the design of the machine. We summarize the typical data of $A$ in Table 2, in order to clarify the severe tolerance of the machine. The natural level of seismic vibrations has been usually considered as seriously affecting machine operation. They are assuming that slow ground motion much less than characteristic frequency of an accelerator gives complete space and time coherence of the machine displacements. Our experimental results, however, suggests being frequency dependent structure for the space coherence in the low frequency range [5]. We have observed the slow ground motion in the tunnels which were excavated using different methods. Figures 2 and 3 show the coherence and phase difference between the two points separated by a distance 46 m. The followings are found out from the figures:

1. The parameter $A$ is found about 5 times difference.
2. The coherence decreases in the frequency range of $5 \times 10^{-4}$ Hz or more in Fig. 2, on the other hand, Fig. 3 shows good coherence for almost all frequency range.
3. The phase relation has a big difference between them. In Fig. 2, the phase changes in the whole frequency range and it becomes at random in the frequency range of $3 \times 10^{-3}$ Hz or more, though it is almost stable in Fig. 3. Out of phase in the low frequency range of Fig. 2.
4. The tunnel is divided into the block and our obtaining result is information on the movement of the block.
5. The size of the block depends on the the method of excavating the tunnel and/or geological property.

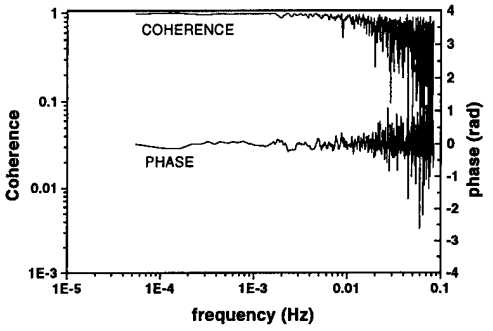



**FIGURE** 3: Coherence and phase difference obtained in the tunnel excavated by TBM. Two levels were set up 46 meters apart.

## 5 REFERENCES


[1] V. Shiltsev 'Space-Time Ground Diffusion: Space- Time Ground Diffusion: The $ATL$ Model for Accelerators', Proc. IWAA95, KEK, Nov. 14-17 (1995) pp. 352-381. Many references are there.

[2] A. Sery 'Ground Motion Studies with Respect to Linac Performance', Proc. of LINAC96, CERN96-07 pp. 621-625.

[3] B. Baklakov, P. Lebedev, V. Parkhomchuk, A. Sery, A. Sleptov and V. Shiltsev, INP 91-15; Tech. Ph. 38, 894, (1993).

[4] K. Yokoya, private communications.

[5] Shigeru Takeda et al., Proc. of EPAC96, 1996. ; S. Takeda, K.Kudo, Y. Funahashi, A. Akiyama and Y. Kanazawa 'Slow Ground Motion and Alignment System', Proc. EPAC94, London, June 3 (1994) pp. 2564-2566; S. Takeda and M. Yoshioka 'Ground Motion at KEK', KEK Preprint 95-209 Feb. 1996.

[6] S. Takeda, A. Akiyama, K.Kudo, H. Nakanishi and N. Yamamoto 'Slow Drift and Frequency Spectra on Ground Motion', Proc. 3rd Int. Workshop on Accelerator Alignment, Sept. (1993) pp. 225-232.

[7] P. J. Tarkoy 'Comparing TBMs with Drill+Blast Excavation', Tunnels and Tunnelling Oct. (1995) pp41-44.

# PRECISION SURVEYING AND SMOOTHING ANALYSIS FOR POHANG LIGHT SOURCE

K. W. SEO, A. H. MAENG, S. C. LEE, and I. S. KO
Pohang Accelerator Laboratory, Pohang 790-784, Korea

*Abstract*

The Pohang Light Source (PLS), a 2 GeV synchrotron radiation source, started its operation from August 1994. The magnets of the storage ring were aligned to a designed beam path with a relative positional error of 0.15mm(rms) in 1994. Since then the storage ring tunnel has moved by 1.0mm and 3.0mm per year(average) in the horizontal and the vertical directions, respectively. The deformation by the ground motion gives rise to the maximum offsets from the designed beam path. We introduce a smoothing analysis using a low-pass filter method in order to estimate the relative positional errors close to the actual beam path. Based on the measurement of the machine deformations and daily machine operational status, we come up with an idea of the allowable maximum offset of 2.0mm from the designed beam path. The relation between boundary conditions of the smoothing analysis and estimated maximum offset is also studied.

## 1. INTRODUCTION

Allowable tolerances of relative position errors (rms) for quadrupoles and sextupoles of the PLS storage ring are 0.15mm in both horizontal and vertical directions. To achieve this goal, we have introduced various precision surveying techniques such as a non-contact 3-dimensional surveying system with theodolites, conventional surveying techniques, and a GEONET program for data analysis and data base management. The positional errors (rms) of 0.15mm was obtained in positioning the quardrupoles and sextupoles in 1994. Since then, the floor of the storage ring tunnel has settled about 3.0mm per year unevenly around the tunnel. In order to estimate the floor settlement and offset errors of magnets in the storage ring, we have studied various smoothing schemes and developed a smoothing analysis using a low-pass filtering method. This technique was applied to the PLS storage ring magnet alignment successfully in August 1995, August 1996, and March 1997. Based on the smoothing analysis and daily machine operational status, we come up with an idea of the allowable maximum offset of 2.0mm from the designed beam path, and we suggest the 6 MHz of allowable filtered frequency.

## 2. STORAGE RING ALIGNMENT

The PLS storage ring has a 12-period Triple Bend Achromat (TBA) lattice. Its circumference is 280.56m. There are 36 bending magnets, 144 quadrupoles, and 48 sextupoles. The allowable positional errors (rms) for quadrupoles and sextupoles are $\Delta x$=0.15mm and $\Delta y$=0.15mm.[1] The alignment process of the storage ring consists of magnet fiducialization, vacuum chamber prealignment, girder rough-setting, magnet rough-setting, fine positioning, and smoothing analysis. A magnet fiducialization is the process of establishing machine coordinates by coordinate measuring machine (CMM) measurement. A pre-alignment of vacuum chamber is the process of establishing girder coordinates and aligning vacuum chamber to the girder within the maximum offset of 0.5mm using a non-contact 3-dimensional surveying system. A girder rough-setting is the process of bringing the vacuum chamber and girder assembly into the storage ring tunnel and setting it to the designed position on the basis of a storage ring tunnel survey network. A magnet rough-setting is the process of positioning magnets by adjusting 6 struts. Applying an intersection method using two theodolites, the magnets are aligned horizontally as accurately as possible. Magnet fine positioning processes which consist of surveying and adjustment are repeated 4-5 times until the positional errors of magnets are reduced within tolerance. Positional errors consist of positioning errors and offset errors. While the positioning errors in the horizontal positioning, which represent reading errors in the form of standard error ellipses, are calculated by GEONET program, those in the vertical positioning are derived from the statistics of elevation survey data. The offset errors, which are mainly described in this paper, indicate the magnet alignment status. This is the standard deviation of magnet offset values from the electron beam path.

When the magnets of the storage ring were aligned in 1994, the magnets were aligned to the designed electron beam path. Since then, we found some positional changes of the magnets and tunnel deformations. Magnet offset errors is then increased to out of tolerance which is estimated from the designed beam path. Therefore, it is necessary to study a method of estimating reasonable errors, which are called relative positional errors, based on the actual beam path, because

0-7803-4376-X/98 /$10.00 © 1998 IEEE

the machine operation shows a normal condition in spite of magnet positional changes.[2]

## 3. TUNNEL DEFORMATION

The tunnel deformation is estimated by surveying the survey networks in the storage ring tunnel. The survey network of the PLS is composed of a surface net and tunnel nets. These are linked with one another that they provide the global coordinate of the PLS. The surface net consists of 10 geodetic control points around the PLS site. The tunnel net is composed of TNET and ENET. It is linked to the surface net. Control monuments of TNET are installed on the inner wall. The TNET controls the horizontal locations of the magnets. In order to control the elevation, control points of the ENET are embedded in the tunnel floor. Fig. 1 shows that the storage ring tunnel has settled unevenly about 3.0mm per year, and deformed horizontally about 1.0mm.

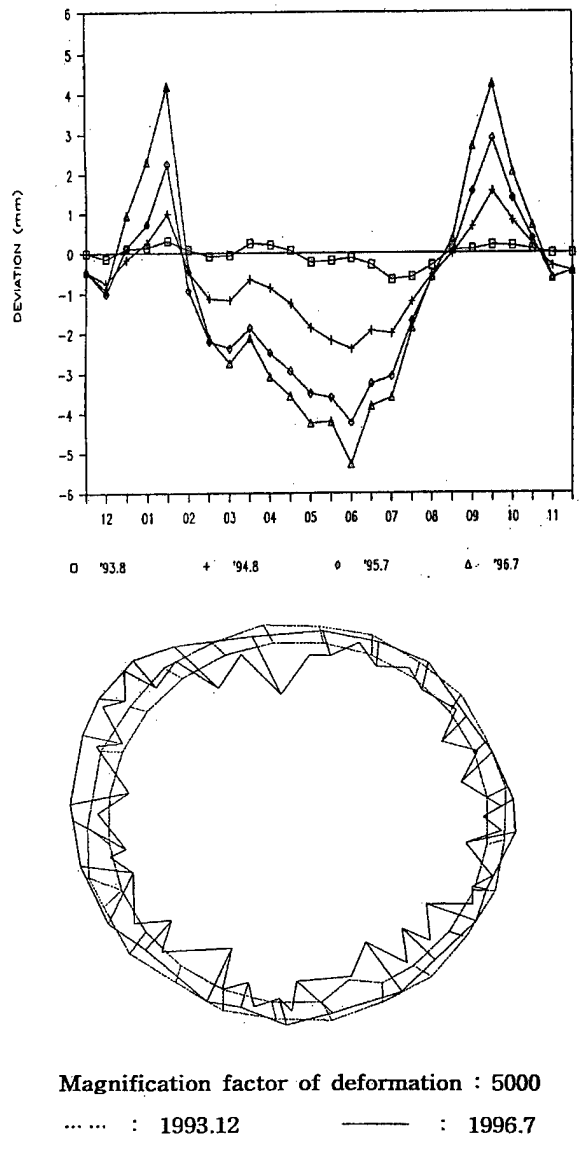



Figure 1 : Deformation of the PLS storage ring tunnel.

## 4. SMOOTHING ANALYSIS

A Smoothing analysis is the process of estimating a storage ring electron beam path to the actual electron beam path as closely as possible. The actual electron beam path is shown in the form of a smoothed curve by analysing the offset values of quadrupoles from the designed path. In this case, the offset errors of magnets are estimated on the basis of the smoothed curve. A smoothing analysis using a low-pass filtering method was developed and applied in August 1995. Table 1 shows that, while the offset errors on the basis of designed electron beam path are increased to out of tolerance, the errors from the smoothed curve remain within the tolerance.[3]

Table 1 : Estimation of offset errors (rms) by smoothing analysis in PLS storage ring quadrupole magnets.

| Year | Offset errors(in mm) on the basis of designed path | | Offset errors(in mm) on the basis of smoothed curve | |
|---|---|---|---|---|
| | Δx | Δy | Δx | Δy |
| 1994 | 0.139 | 0.075 | - | - |
| 1995 | 0.388 | 0.365 | 0.127 | 0.118 |
| 1996 | 0.542 | 1.103 | 0.136 | 0.130 |
| 1997 | 0.456 | 1.087 | 0.131 | 0.122 |

Applying the smoothing analysis, we investigate the relationship between allowable filtered frequency range and the offset errors of magnets. As the filtered frequencies are increased by 1 MHz step, the relative positional errors, Δx and Δy, are decreased dramatically as shown in Table 2.

Table 2 : Estimation of filtered frequencies for smoothing analysis in the PLS storage ring quadrupole magnet alignment from August 1996 to March 1997.

| Freq. (MHz) | Relative positional error (rms) (unit : mm) | | | | Remark |
|---|---|---|---|---|---|
| | 1996 | | 1997 | | |
| | Δx | Δy | Δx | Δy | |
| 0 | 0.456 | 1.087 | 0.162 | 0.698 | |
| 1 | 0.300 | 0.742 | 0.144 | 0.427 | |
| 2 | 0.250 | 0.538 | 0.142 | 0.336 | |
| 3 | 0.218 | 0.294 | 0.140 | 0.224 | |
| 4 | 0.171 | 0.199 | 0.140 | 0.202 | |
| 5 | 0.153 | 0.162 | 0.131 | 0.166 | |
| 6 | 0.136 | 0.130 | 0.131 | 0.122 | ≤0.15 |
| 7 | 0.130 | 0.127 | 0.130 | 0.109 | |

When the filtered frequency is 6 MHz, the errors become smaller than the positional tolerance of 0.15mm (rms). In order to maintain the allowed position tolerance, we expand the boundary condition of allowable filtered frequency to 6 MHz. Previously, the filtered frequency was estimated as 3 MHz in August 1995. Fig. 2 shows a smoothed curve, which is derived from analysing the offsets of quadrupole magnets in August 1996, and magnet distributions along the curve. Also, the maximum offsets of 2.0mm from the designed electron beam path is shown in this figure.[4][5]

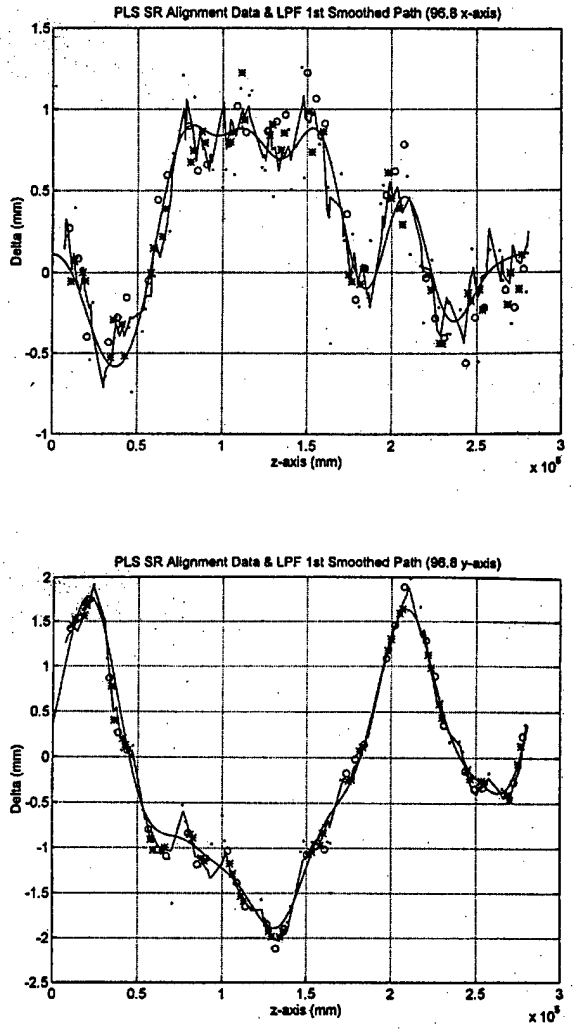



Figure 2 : Smoothed curve and magnets distribution of the PLS storage ring.

## 5. SUMMARY

Since the magnets of the PLS storage ring were aligned to the designed electron beam path with the positional error of 0.15mm(rms) in 1994, magnet movements due to the tunnel deformation are monitored in order to estimate when and how much the magnets of the storage ring are to be realigned. A smoothing analysis is studied and developed in order to estimate an actual electron beam path. It is shown in the form of smoothed curve, and offset errors from the estimated path. With several case studies over 1995 and 1996 period, we can understand the situation that the machine operation shows normal condition while the maximum offsets of magnet are increased as much as 2.0mm from the designed electron beam path.

## REFERENCES


[1] Design Report of Pohang Light Source, PAL, January, 1992.

[2] A. H. Maeng, K. W. Seo, J. G. Yoon and S. C. Lee, "Survey and Alignment of Pohang Light Source," presented at the 4th International Conference on Synchrotron Radiation Sources and 2nd Asian Forum on Synchrotron Radiation, Korea, Oct. 25-27, 1995.

[3] J. G. Yoon and S. C. Lee, "Smoothing Analysis of PLS Storage Ring Magnet Alignment," presented at the 4th International Workshop on Accelerator Alignment, KEK, Nov. 14-17, 1995.

[4] Annual Report, PAL, Postech, 1995.

[5] Annual Report, PAL, Postech, 1996.

# SURVEY AND ALIGNMENT OF SLAC'S B-FACTORY

M. Pietryka, M. Gaydosh; Stanford Linear Accelerator Center, Stanford, CA 94309, USA.

*Abstract*

The survey and alignment of SLAC's B-factory injector and high energy ring will be complete in March 1997. Modern digital electronic surveying tools are contributing to new, efficient alignment procedures. A laser tracker was used to fiducialize almost 300 quadrupole magnets. Digital levels were used to pre-set base plate elevations. Theodolites with very accurate co-axial distance meters were used for everything from layout to 3D magnet positioning to network surveys, all in free stationing mode. A number of procedures and measurement results are outlined.

## 1 FREE STATIONING

Laser trackers and a new breed of "total station" are designed specifically for industrial metrology. They both combine arc-second angle accuracy with better than 100 micron distance accuracy in a package with co-axial optics. They are, essentially, portable coordinate measuring machines and have changed the face of surveying at SLAC. While the laser tracker's power and versatility is now familiar, most B-factory work was performed with the Leica TC2002 total station. The TC2002 is much more robust and portable, much less expensive, and ideally suited to discrete point measurements.

Total station technology was introduced by HP twenty years ago. The key to metrology application was improvement of distance meter technology. Unlike the laser tracker, which uses interferometry, this class of distance meter emits a modulated infrared signal that is reflected back to the instrument by a retro-reflective target. The differential phase angle between the exiting and returning signals yields a distance equal to a fraction of the modulation wavelength. The additional integer number of wavelengths comprising the distance is then determined by switching to a lower frequency to repeat the measurement. A few years ago the most accurate total station distance meters, after extensive calibration, could approach 1mm. Today, certain Leica total stations achieve 0.1mm right out of the box. Figure 1 shows differences between distances measured with four TC2002s and SLAC's interferometer. Distances from 1 to 30 meters were measured at one-meter intervals. Figure 2 shows a Fourier model of the differences between TC2002 and interferometer distances measured at intervals of 0.1 meter over 6 meters. The model reduced the measurement standard deviation from 73 to 52 microns.[1]

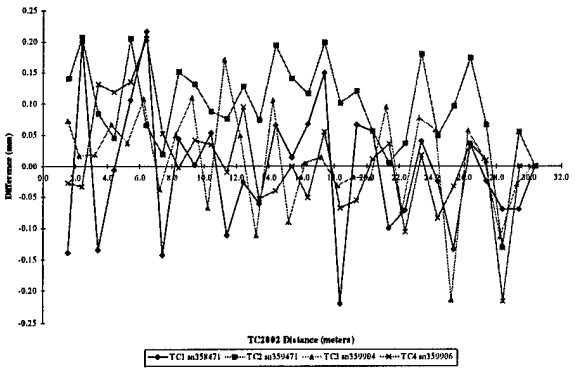


**Figure 1 TC2002 vs. Interferometer**

The total station allows dramatic changes in routine surveying procedures. Formerly, special forced-centering hardware was erected and centered over floor monuments to receive separate angle and distance measuring instruments. Distance measurements were very slow, many minutes per observation, and differential leveling was required to deliver the third dimension. With the total station, activities ranging from network data collection to bolt pattern layout are conducted in "free stationing" mode. Free stationing means that the instrument is not force-centered over a monument, but located in a general area where all points of interest are visible. Monuments are no longer confined to the floor, but more conveniently located on walls and even ceilings. Monument designs vary, but all are some form of cup made to accept sphere-mounted

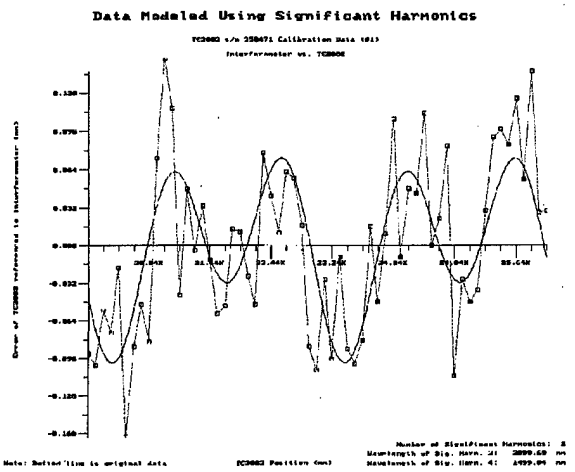



**Figure 2 Fourier Cyclic Error Model**

0-7803-4376-X/98/$10.00 © 1998 IEEE

targets(SMT) and retro-reflectors(SMR). Trackers and total stations both use commercially available 1.5 inch sphere targeting. The reference point is the center of the sphere in the monument. A much denser monument pattern can be installed since distances require only a few seconds each and measurements are taken in 3D. The instrument measures 3D vectors, horizontal angle, vertical angle, and distance, from its center of optics to each point of interest. For network or mapping surveys, the measurements are simply stored on the data collector for processing in the office. For alignment work, the surveyor first takes observations to several monuments, a data collector program solves for the instrument position and orientation, then component positioning proceeds.

## 2 HER QUAD FIDUCIALIZATION

The fiducialization measurements were performed with SLAC's CMS 3000 laser tracker. The liabilities of the tracker's 80-pound weight, large power supply, bulky cabling, and delicate nature are mitigated when it can be set up in a laboratory environment for gross data collection. An area in the magnet warehouse was cleared so that the tracker could be rolled on its stand all the way around the magnets. Monuments were installed in the floor around the perimeter of the cleared space. Six fiducial bushings were welded onto each magnet, four on the top and two on the aisle side, to accept removable magnetic mounts for 1.5 inch sphere targeting. The magnet engineer designed a one-meter-long mandrel that registered on two pole tips, projected through the magnet, and held a magnetic sphere mount on axis on each end.

The magnets were measured six at a time. They were arranged in a line, in three groups of two to facilitate mandrel handling, as shown in Figure 3. The tracker was situated adjacent to the first pair, on the "aisle" side, and measurements were recorded to all floor monuments, the fiducials and exposed lamination edges on magnets 1 and 2, and the mandrel in magnets 1and 2 in four different positions each. With bungy cords and shims the mandrel was forced into contact with each pair of pole tips for four different positions. In turn, the tracker was moved into position next to the aisle side of each magnet pair and then measurements were taken to the monuments, fiducials, and the mandrel positions. Then the tracker was rolled to the "wall" side and another data set was recorded next to each magnet pair. One surveyor in one shift measured this large, six-magnet data set. On the swing shift, another six magnets were moved into position to be measured the next day.

The day's measurements were processed in one big adjustment. The common monument observations made for a very redundant, geometrically strong network. The resulting coordinates were parsed into individual magnet data sets for further processing. Each magnet data set was used to generate magnet-centered fiducial coordinates. The beamline axis was defined by the axis of a best-fit cylinder through the mandrel coordinates, magnet center by the average of magnet end positions, and remaining coordinate axis orientation by a best-fit plane through lamination edge coordinates.

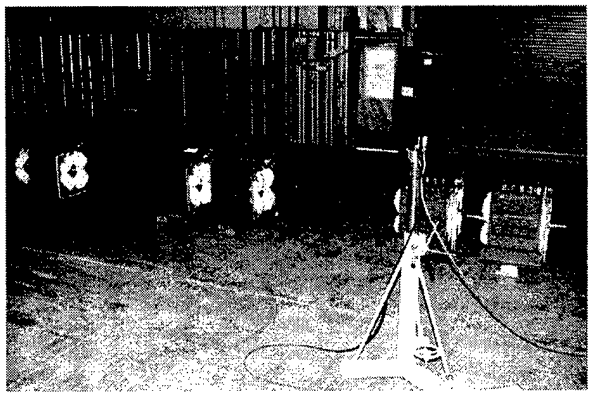


**Figure 3 Six magnets ganged for fiducialization**

## 3 TOTAL STATION WORK

To do alignment work with the total station, whether bolt pattern marking or component positioning, the surveyor arrives on scene with the instrument and a data collector loaded with surveyed monument coordinates and component ideal coordinates.[2] The instrument is set up on a portable tripod where several monuments and the area to be worked are visible. The monument positions are considered known and are used to solve for the instrument position. Distances and angles are measured to a number of monuments, some upstream and some downstream. While two monuments would give a unique solution for the instrument position, it is good practice to observe four or five monuments. This is enough data to identify possible problems with the monument coordinates and provide a redundant solution. SLAC's software displays measurement residuals and calculated standard deviations to help evaluate the quality of the solution. With a good solution in hand, alignment begins.

### *3.1 Layout and Stand Alignment*

Some simple custom hardware facilitates layout and stand alignment. A layout block is a piece of steel 3 by 5 by 1 inches with a through-hole in its center. Pressed flush into one end of the hole is a drill bushing, while the other end is beveled to form a cup for the 1.5 inch SMR. The floor is marked by removing the SMR and inserting a center punch sized for the bushing. For stand alignment, special magnetic SMR cups were built to occupy critical component/stand interface positions. The surveyor enters the point name in the data collector and the position of the SMR in the block or cup is observed with the total station. For low precision work, it is adequate to aim the instrument at the apparent SMR apex and record a single measurement. The software computes a position and returns the difference between the observed and ideal positions. The difference cab be displayed in the beam-

following coordinate system or in a system oriented to the line between the point and the instrument. The block or stand is moved toward the ideal position, perhaps aided by a pocket tape, and another observation is made. This process is repeated until the difference between observed and ideal is within tolerance, typically 1 or 2mm. If doing layout, the SMR is removed, and the center punch is inserted to mark the point. For stand alignment, there may be several points to check to verify stand orientation and special spirit levels can be very handy as well.

The HER quad raft installation required a second layout step. The hole patterns were drilled, the threaded anchor studs and steel mounting plates were installed, the surveyors leveled the plates, and the plates were grouted. The second layout was for mating pins in the mounting plates. The same procedure was used, but with a 0.5mm tolerance. After the surveyors punch-marked the steel plates the ironworkers followed with a magnetic base drill to make the mating holes. The mating pins controlled a quad raft's position and orientation. Table 1 displays how effective this scheme proved to be. The left side shows the surveyed positions of quads in region five before alignment. The residuals represent the sum of errors resulting from mating hole marking and drilling, and quad raft assembly.

| Quad | DZmm | DXmm | Dymm | DXmm | DYmm |
|---|---|---|---|---|---|
| 1 | -0.15 | -0.31 | -0.29 | -0.03 | -0.12 |
| 2 | -0.40 | -0.27 | -0.03 | 0.01 | 0.06 |
| 3 | -0.18 | -0.52 | -0.36 | 0.10 | 0.14 |
| 4 | -0.45 | -0.47 | -0.02 | 0.10 | 0.01 |
| 5 | -0.19 | -0.62 | -0.11 | 0.04 | 0.04 |
| 6 | -0.01 | -0.38 | -0.73 | -0.39 | 0.20 |
| 7 | -0.99 | -0.37 | -0.13 | -0.18 | 0.13 |
| 8 | -1.01 | -0.36 | -0.43 | -0.10 | -0.04 |
| 9 | -0.43 | -0.55 | 0.13 | -0.22 | 0.11 |
| 10 | -0.10 | -0.65 | -0.12 | -0.23 | -0.02 |
| 11 | -0.62 | -1.07 | -0.37 | 0.07 | -0.15 |
| 12 | -0.79 | -0.35 | -0.23 | -0.10 | 0.04 |
| 13 | -0.61 | -0.37 | -0.18 | 0.02 | 0.03 |
| 14 | -0.31 | -0.53 | -0.21 | 0.19 | -0.13 |
| 15 | -0.15 | -0.19 | -0.01 | 0.11 | 0.08 |
| 16 | -0.78 | -0.68 | -0.04 | 0.07 | 0.20 |
| 17 | -0.33 | -0.99 | -0.15 | 0.13 | 0.08 |
| 18 | -0.47 | 0.07 | -0.77 | 0.10 | 0.11 |
| 19 | | | | 0.09 | 0.07 |
| 20 | -1.06 | -0.62 | -0.06 | 0.24 | -0.04 |
| 21 | | | | 0.19 | 0.08 |
| 22 | -0.21 | 0.05 | 0.37 | -0.01 | 0.01 |
| 23 | -1.07 | -0.51 | 0.30 | 0.04 | 0.00 |
| 24 | -0.94 | -0.28 | -0.13 | -0.01 | 0.02 |
| 25 | -0.62 | -0.16 | -0.02 | 0.02 | 0.02 |
| 26 | -0.79 | -0.38 | -0.04 | 0.03 | 0.01 |
| 27 | -0.33 | -0.02 | 0.41 | -0.14 | -0.10 |
| 28 | -0.25 | -0.52 | 0.48 | -0.07 | -0.01 |
| 29 | -1.34 | 0.00 | 0.25 | -0.03 | -0.01 |
| 30 | -0.16 | -0.16 | 0.09 | 0.07 | -0.08 |
| 31 | | | | 0.05 | -0.01 |
| 32 | | | | -0.06 | 0.06 |
| std. dev.= | 0.36 | 0.28 | 0.30 | 0.13 | 0.09 |

**Table 1 Region 5 Residuals Before and After First Alignment**

### *3.2 Magnet Alignment*

At a glance, the magnet alignment procedure looks the same as that for layout or stands. The tighter tolerances dictate a few refinements, however. First, the single set of monument observations is replaced by two or three sets to better determine the optical center. This yields benefits not only statistically, but also mechanically by compensating for instrumental errors. Second, it is more accurate to aim at a separate sphere-mounted SMT and then switch to the SMR for distance measurement. Finally, the light hardwood tripod is replaced by a heavy optical tooling-style stand, which is rolled from place to place.

Magnet fiducial observations started with single pointings to SMRs; no sense looking for microns until the millimeters were worked out. In the HER, the surveyors shot the four top fiducials first to get a look at magnet orientation. They adjusted pitch and roll to zero to de-couple orientation and translation, then worked Z, Y, and X struts to bring the magnet into position. Typically, this took several iterations of survey and alignment. The SMT and reverse pointings were not brought into play until the magnet was very close to its ideal position, say 100 to 200 microns.

After all HER quads were aligned, the tracker was used to map the quads and BPMs. This was another great application for the tracker; gross data collection in a protected environment where it could be rolled from magnet to magnet all around the ring. The right side of Table 1 shows results of that map. The residuals are from a smooth curve fit through the differences between surveyed and ideal magnet centers.[3] They represent the sum of errors from the monument network and the total station measurement procedure.

## 4 ACKNOWLEDGEMENTS

The authors recognize that they are reporting the accumulated knowledge and experience of the entire SLAC alignment team.

Work supported by the U.S. Department of Energy under contract number DE-AC03-768F00515.

REFERENCES

[1] B.C. Fuss: 'FOURIER: A Harmonic Analysis Program to Model Periodic Data', SLAC, 1994.

[2] W.A. Oren: 'Ideal Coordinate Calculations', SLAC.

[3] H. Friedsam, W. Oren: 'The Application of the Principal Curve Analysis Technique to Smooth Beamlines', Proceedings of the First IWAA, SLAC, 1989.

# ACCESS CONTROL AND INTERLOCK SYSTEM AT THE ADVANCED PHOTON SOURCE

J. Forrestal, R. Hogrefe, M. Knott, W. McDowell, D. Reigle, L. Solita, R. Koldenhoven, D. Haid
Advanced Photon Source, Argonne National Laboratory,
9700 South Cass Avenue, Argonne, Illinois USA 60439

*Abstract*

The Advanced Photon Source (APS) consists of a linac, position accumulator ring (PAR), booster synchrotron, storage ring, and up to 70 experimental beamlines. The Access Control and Interlock System (ACIS) utilizes redundant programmable logic controllers (PLCs) and a third hard-wired chain to protect personnel from prompt radiation generated by the linac, PAR, synchrotron, and storage ring. This paper describes the ACIS's design philosophy, configuration, hardware, functionality, validation requirements, and operational experience.

## 1 INTRODUCTION

Personnel protection from prompt radiation produced by the APS accelerators is provided using four PLC-based ACISs. The first system covers the linac/PAR, the second the booster synchrotron, the third the rf area of the storage ring (designated Zone F), and the fourth covers the remaining zones (A-E) of the storage ring. In addition, each of the 70 beamlines uses PLCs for their Personnel Protection Systems (PSSs). The PSSs interface to the Zone F ACIS and storage ring ACIS. This paper describes the four ACISs.

## 2 DESIGN PHILOSOPHY

All the ACISs are designed to the same criteria:

- they must fail-safe so that any single fault leaves the system in a safe beam-inhibiting state,
- they offer redundant and independent protection so that any component or subsystem failure leaves the system in a safe state,
- they monitor beam enclosure tunnel security and prevent beam operations if any unsafe or potentially unsafe condition is detected, and
- they incorporate built-in testing to facilitate biannual validation of all functions.

PLCs are special-purpose microprocessor-based controllers which interface to "real-world" input and output devices. They monitor the input devices, execute user-written logic, and update output devices based on the result of these logic functions. Allen-Bradley PLC5 series PLCs were chosen to implement the ACIS logic for several reasons:

- higher reliability than comparable relay-based systems,
- ease of programming and self documenting,
- built-in features for testing, system monitoring, and diagnostics,
- easy interfacing of external control devices,
- modular design, wide variety of compatible devices, and
- field proven operation, mature technology.

## 3 CONFIGURATION

Each ACIS monitors its specific accelerator and communicates with its neighboring ACISs. Figure 1 illustrates the relationship among the four ACISs, their relationship to each other, and then the relationship to the PSSs. Two independent PLC chains (A and B) and a third, "hard-wired" chain C, monitor tunnel security and system integrity. If any system trips, the equipment controlled by the ACISs is disabled and beam is inhibited. Controlled equipment consists of rf amplifiers, modulators, steering/focusing magnet power supplies, and the electron gun.

The ACISs also send permissives to partitions which are installed between the accelerators. Closed partitions prevent beam from entering a downstream area or prevent radiation from "back streaming" to an upstream area. The partition between the linac/PAR and synchrotron consists of three movable beam blocks. Each block is monitored by both chains of the linac/PAR and synchrotron ACIS. Permits to open are granted by both ACISs as long as each machine is in the same operating mode. The partition between the synchrotron and Zone F consists of steering magnets which direct the beam to a dump or towards Zone F for injection into the ring. The status of these magnets is sensed by magnetic gap switches installed in the magnet and by current monitors installed on the outputs of the magnet's power supplies. This partition is monitored by the Zone F ACIS (both chains).

Ultimately 70 beamlines will connect to the storage ring. The front-end section of a beamline is located inside the storage ring's tunnel and contains photon and safety shutters. When closed, these shutters protect the experimental area outside the storage ring wall from stored beam radiation. The closed positions of the shutters are monitored by both PLC chains and their status is sent to the beamlines for use by the PSSs.

## 4 HARDWARE

ACIS hardware consists of emergency shutdown buttons, controlled access key switches, radiation monitors, beam current monitors, limit switches, relays, watchdog timers, control panels, message displays, magnetic locks, and controlled equipment interface panels. The PLC processors are installed in the main control room (MCR) and are connected to remote input/output (I/O) crates via fiber optic cables. All racks containing ACIS equipment are

0-7803-4376-X/98 /$10.00 © 1998 IEEE

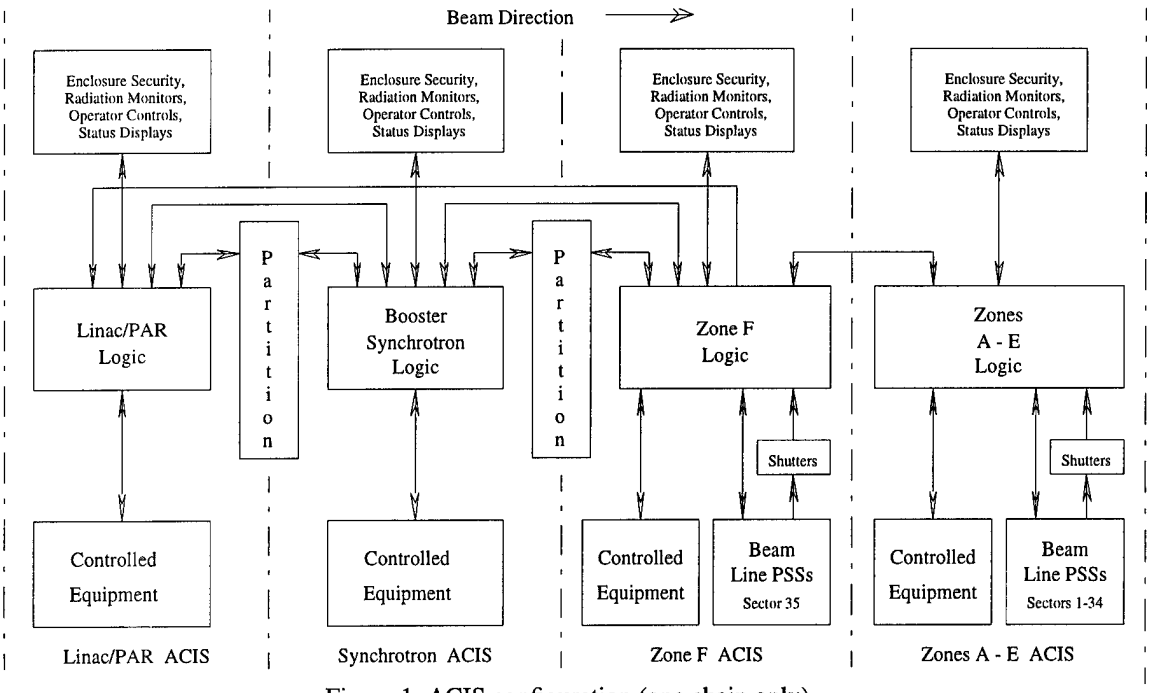



Figure 1: ACIS configuration (one chain only).

locked and tamper-monitored. ACIS cables are labeled and protected by separate cable tray and conduit.

Figure 2 is a typical interface to the controlled equipment. Enables are granted the equipment if two normally-open relay contacts wired in series are closed. The relay coils are independently driven by chain A and chain B. In addition to asserted PLC outputs, other conditions must be met before the relays energize: chain C (the hard-wired chain) must be complete, a beam permit signal from the MCR must be on, and watchdog timers must be energized. For testing and system validation, key-operated switches are installed to direct the ACIS permissives from "real" controlled equipment to test loads.

The MCR beam permit signal is driven by a key switch on the ACIS control panel. It is monitored by the PLC and independently sends a pulse train to the receivers in the interface panel. If the pulses are present, the contacts, which are in series with the output relays, close and the relays are energized. The watchdog timers receive pulses from their respective PLC chain via a local output module. The contacts are closed as long as the PLC programs are running. If a program ceases to execute its periodic scan, the pulses stop, the contacts open, and the output relays de-energize.

## 5 FUNCTIONALITY

As shown in Figure 3, the ACISs are state machines with the five operating modes. The modes escalate from Authorized Access to Beam Permit, and have the following meaning:

AUTHORIZED ACCESS MODE: tunnel access is allowed on an unrestricted basis. It is entered upon initial program execution, a system reset, a normal transition from Controlled Access Mode, or a trip.

SEARCH / VERIFICATION MODE: A search is enforced to verify no personnel are in the beam enclosure tunnels. As the tunnel is searched, buttons located on the beam shutdown station (BSS) boxes are pressed to indicate that area was visited by the search team. The search must be completed in a preset time. If the time is exceeded, or if a button is hit out of order, a trip to Authorized Access Mode is generated.

CONTROLLED ACCESS MODE: This mode is entered after the successful completion of the tunnel search. It is implemented to allow personnel into the tunnels on a limited basis without requiring another search. While in the tunnels, personnel are required to carry a controlled access key. If any key is out, the ACIS cannot transit to the next higher mode. This mode may be re-entered from Beam Permit Pending Mode or by a Controlled Access Mode trip.

BEAM PERMIT PENDING MODE: Entry from Controlled Access Mode requires a 1-minute warning message initiated by the MCR operator. This message is announced in the tunnel by audible alerts and red strobe beacons installed in the BSS boxes. At the end of the warning, the alerts silence but the strobes remain flashing.

BEAM PERMIT MODE: To enter this mode the MCR operator inserts a key in the beam permit key switch and selects the "Enable" position. The PLCs monitor this switch and, if all other conditions are met, energize the ACIS output relays. At the same time, a pulse train is transmitted to the beam permit receivers in the output relay panels.

Authorized Access or Controlled Access Modes are unconditionally entered if a fault is detected. The types of faults are listed in Figure 3.

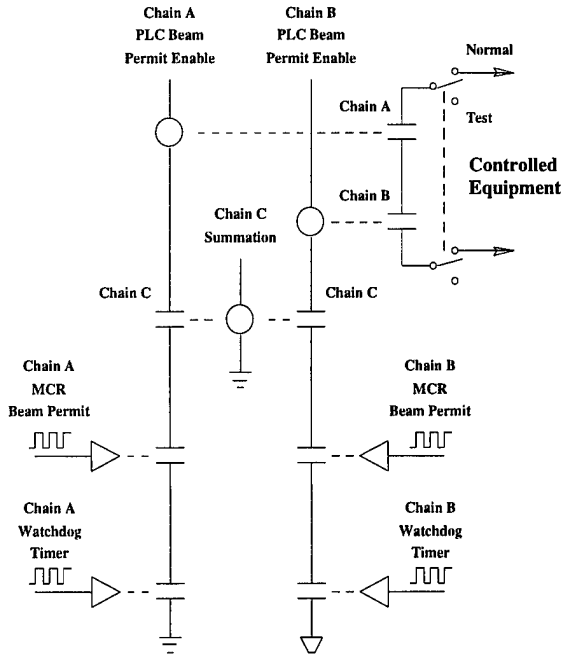



Figure 2: ACIS output interface.

Permits to open the partitions and permissives to energize the controlled equipment are only granted by the ACISs. Other commands to open the partitions or energize equipment must be sent by MCR operators. For additional protection, the ACIS monitors the state of the controlled equipment. If the feedback signal indicates the equipment is on while being disabled, or if the interface cable is disconnected, the ACIS declares a "No Shutdown Verification" alarm. This alarm locks access doors to prevent entry and activates the in-tunnel strobes to alert personnel to evacuate.

The ACISs are designed to eliminate the use of physical jumpers for testing. A test mode—which can only be entered if all sets of controlled equipment are disconnected and a test mode key-operated switch is on—is provided to allow bypassing of certain functions. Since chains A and B cross trip each other and chain C influences the final permissives, the validation procedure must prove system independence. Test features include disabling influences from other chains, providing a "quick search," inhibiting watchdog timers, and masking tampers.

## 6 VALIDATION REQUIREMENTS

The ACISs are validated every six months or whenever the interlock software is modified. The PLC processors calculate checksums unique to their application programs. These checksums are used to identify the program version, and any change to the checksum requires revalidation of the system. ACIS validation involves exercising all I/O devices and verifying that the interlock logic performs as specified, ACIS status is properly displayed, and the controlled equipment shuts down when disabled. Validation results are recorded in the validation test procedure along with the checksum of the software being validated. Completed procedures are archived in the APS's Document Control Center.

## 7 OPERATIONAL EXPERIENCE

The linac/PAR ACIS became operational in July 1993, the synchrotron ACIS (including most Zone F hardware) in February 1994, and the Zone F and storage ring ACISs in February 1995. To date there have been no failures of PLC hardware. However, some external devices have failed, namely an intermittent relay socket, a failed watchdog timer, sluggish operation of a beam stopper's control cylinder, and intermittent trips from a radiation monitor. Every ACIS challenge has resulted in a successful shutdown, and no unsafe failures have occurred.

## 8 CONCLUSION

The four ACISs were designed and installed over a four-year period based on the APS's construction schedule. PLC system modularity and flexibility was vital in meeting construction and commissioning goals and provided full protective functionality during commissioning. The troubleshooting capabilities of the PLCs are valuable tools in diagnosing system operation and correcting malfunctions. The PLC-based ACISs have exceeded all operational expectations.

## 9 ACKNOWLEDGMENTS

Work is supported by the U.S. Department of Energy, Office of Basic Energy Sciences, under Contract No. W-31-109-ENG-38.

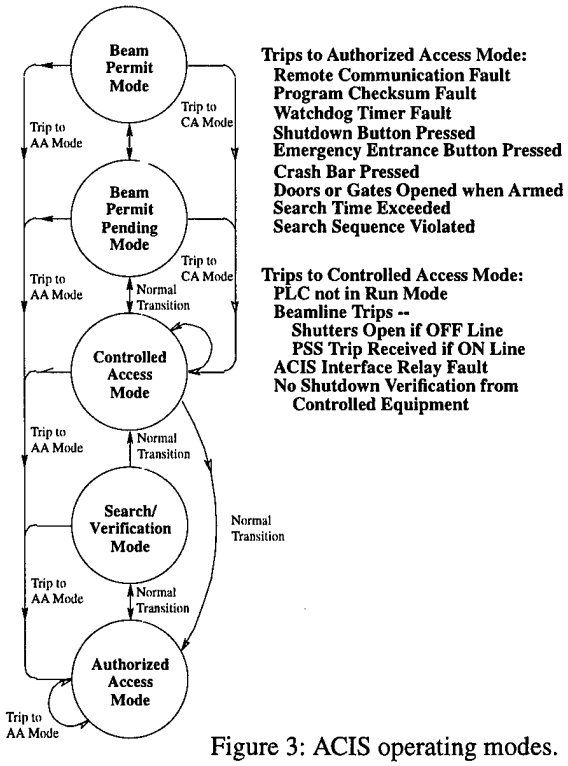



Figure 3: ACIS operating modes.

# RADIATION LEVELS AROUND THE FERMILAB MAIN INJECTOR EXTRACTION SEPTA

C. M. Bhat and N. V. Mokhov
Fermi National Accelerator Laboratory*
P.O. Box 500, Batavia, IL 60510

*Abstract*

The Fermilab Main Injector extraction system will be capable of delivering a uniform 120 GeV beam of $\sim 3 \times 10^{13}$ protons per spill to the fixed target experiments ( with spill time of 1 sec). Up to 2% of the beam is expected to be lost at the extraction septum and the Lambertson magnet. As a result, one expects increased radiation levels around the septa compared to other parts of the Main Injector. Realistic Monte-Carlo simulations have been performed to estimate the instantaneous and residual radiation levels in the beam extraction region. The results of these studies are presented and implications are discussed.

## 1 INTRODUCTION

The Fermilab Main Injector (MI) is being built as a high intensity 150 GeV proton and antiproton injector to the Tevatron [1]. The MI is also capable of providing year-round 120 GeV proton beam with fast spill with a spill time of 0.04 sec, and a slow spill with a spill time of $\approx$ 1 sec [2]. In both of these cases the final extraction takes place at the MI52 straight section. During the extraction we expect beam induced radioactivity in the extraction septa and the down-stream beamline elements due to unavoidable beam losses at the septum wires. In this paper we present the estimated radioactivity in the vicinity of the extraction septa arising from the slow resonant extraction of the beam and its consequences on the operation of the MI.

The design beam intensity of the MI for the fixed target experiments with slow spill operation mode is $3\times10^{13}$ for every 2.9 sec. The accelerator is also capable of providing beam in mixed modes where only about 80 % of the beam is extracted in slow extraction mode. However, we take the worst case beam loss scenarios for our calculations.

## 2 EXTRACTION SEPTA AND THE BEAM LOSSES IN MI

The extraction system comprises of three 12 ft long electrostatic septa, Lambertson magnets and a "C" magnet. Each of the electrostatic septa is designed to produce about 200$\mu r$ kick on 120 GeV beam. A schematic view of the extraction region near MI52 location of MI is shown in Fig. 1. Two of the three extraction septa are located in straight section of MI-52. The third septum is situated at MI-30 which is at about n$\times$360$^o$ phase (or $\approx$ 920 meters up-stream of MI52) away from either of the two. This arrangement is done because there is not enough space to install all three septa at MI-52.

Each septum has a wire plane 3.048 m long with a high voltage gap of 10 mm. These wires are made of tungsten-rhenium and are of 0.1 mm dia. The maximum voltage gradiant in the septum gap is about 70 kV/cm.

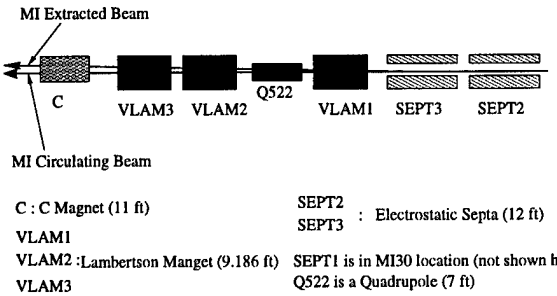



Figure 1: A schematic view of the Main Injector slow extraction region at MI52 straight section. One of the electrostatic septum is located in MI30 straight section and not shown here. The longitudinal dimension of each of the devices are also shown. The total extent of this region is about 60 meters.

The displacement of one of the septum magnet may be beneficial because the beam loss will be less local. Also, the part of the beam kicked by the electrostatic septum at MI-30 will gain a displacement of dx = $\theta\sqrt{\beta_{sept}\beta_Q}\ sin(\Delta\phi)$. Hence by selecting proper phase advance $\Delta\phi$ at MI-52, we can choose dx $\geq$0.1 mm ($\approx$ diameter of the septum wire). This helps to reduce or eliminate the beam losses at the MI-52 extraction region. However in our estimation of the beam loss and the induced radioactivity, rearrangement of the exectrostatic septa mentioned above are ignored. Also in reality, all particles that hit the septum wire may not be entirely lost during extraction process. Hence results presented here are highly conservative.

The particles that hit the septum wire are taken to be the extraction losses and this defines the extraction inefficiency. The minimum extraction loss, $\zeta_{min}$ (percentage loss), is related to the aperture between wire and the cathode $\Delta x$, and the wire size $w$ [3].

$$\zeta_{min} = \frac{2w}{\Delta x}$$

In the present case $\Delta x$ = 10 mm and the wire size $w$ = 0.1 mm. Hence, we expect a minimum of about 2 % beam loss for steady-state density distribution of the particles. Alternatively it has been shown [2] that quantity $\zeta_{min} \approx w\sqrt{\beta\epsilon}$ which indicates that the inefficiency can be reduced only by increasing the emittance and/or $\beta$ before extraction.

* Operated by Universities Research Association, Inc. under contract No. DE-AC02-76CH03000 with the U. S. Department of Energy

0-7803-4376-X/98/$10.00 © 1998 IEEE

## 3 MONTE CARLO CALCULATIONS AND RESULTS

### *3.1 Monte Carlo Code - MARS*

The Monte Carlo code MARS [4] employs inclusive simulation of the hadron-nucleus interactions and uses statistical weights method. A phenomenological description [5] of the inclusive particle distributions is adopted and on the average the energy-momentum conservation is satisfied. This program is most suitable for evaluating shielding problems encountered in high-energy (E≥10 GeV) accelerators. For the cases discussed here, the primary proton energy is 120 GeV. The hadron energy cutoff and star prouction energy cutoff are taken to be 14.5 MeV and 300 MeV, respectively. The properties of the septum wires are externally supplied to the code during the calculations. The atomic number and the mass are taken to be 74 and 180, respectively. Since the wires in the septa are widely separated, their effective density is taken as 0.31 g/cc. For other beamline materials the calculations use the necessary information from the MARS code.

### *3.2 Conversion Factors*

The instanteneous and residual radioactivity of the beamline components are determined by using calculated energy deposition densities and hadron fluxes. The required conversion factors have been extracted in a seperate set of Monte Carlo calculations performed with incident proton energy 120 GeV on material of the beamline elements such as Fe, Cu and Al. The quantities are extracted from locations of shower maximum. The results of these calculations have been listed in Table I. It is important to note that the dose equivalent ( i.e., Rem/p) in this table is valid in tissue like region only.

Table 1. Useful conversion factors from MARS. p.p stands for per incident proton.

| Type of Conversion | Fe | Cu | Al |
|---|---|---|---|
| $\frac{Hadron flux/cm^2}{GeV/gm\ p.p}$ | 110.28 | 133.6 | 88.4 |
| $\frac{Star/cc}{GeV/cc\ p.p}$ | 2.11 | 2.31 | 1.53 |
| $\frac{Rem/p}{GeV/gm\ p.p}$ | 6.11E-5 | 6.0E-5 | 4.8E-5 |

### *3.3 Instanteneous Radiation Dose*

To estimate instantaneous (and residual) radioactivity we have used exact geometry of the electrostatic septa and the Lambertson magnet in our model. The quadrupole magnet is assume to have cylindrical symmetry. The kick on the beam induced by electric field of the wire is replaced by equivalent magnetic field. The magnetic fields are $B_x = 0.0265$ Tesla and $B_y = 0.0$ Tesla. The extracted beam is bent vertically in the Lambertson magnet. The corresponding x and y components of the field in the Lambertson are $B_x = 0.0$ Tesla and $B_y = 0.749$ Tesla, respectively. In the program MARS the instanteneous dose is determined assuming time of irradiation $T_i = \infty$ and cooling time $T_c = 0$.

Table 2. Instantaneous maximum radiation dose in the down-stream quadrupole. The nomenclature : "S" for septum magnet, "Q" for quadrupole magnet and "o" for drift space.

| Configuration | Drift Space (Meters) | Instantaneous Dose (KRad) |
|---|---|---|
| SooQ | 6.9 | 5.8 |
| oSoQ | 3.7 | 6.4 |
| ooSQ | 0.4 | 6.5 |
| oSSQ | 0.4 | 6.5 |
| Lambertson[a] | 0.4 | 1880.0 |

[a]Maximum dose near the intersection of no field and field region

Presently the exact location of the electrostatic septum in the MI30 straight section is not well determined. But we know that it will be installed between MI-quadrupoles Q305 and Q306 which are separated by a distance of approximately 17.3 meters. Depending upon the location of the electrostatic septum, the down-stream quadrupole will be activated differently. The maximum dose for different configurations are shown in Table 2. The Main Injector enclosure is built with a minimum radiation shielding of 7.5 m of soil equivalant which provides sufficient radiation shielding at the surface.

### *3.4 Residual Activity of the Extraction System*

Estimation of the induced radioactivity of an irradiated target involves detailed calculation of production of various types of radioactive nuclei and their dacay. Previously such a calculation has been carried out to the Fermilab antiproton production target [6] and compared with experimental data. Here we adopt a method described by Barbier[7] which states that the dose rate $\dot{D}$ is given by,

$$\dot{D} = \frac{\Omega}{4\pi} \times \Phi \times I \times danger\ parameter$$

where $\Omega$ is the solid angle at the source and $\Phi$ is the hadron flux calculated using MARS. The quantity $I$ is the beam inensity. The *danger parameter* is a function of the target material, duration of exposure of the material to the primary radiation ($T_i$) and total cooling time ($T_c$). The quantity $\frac{\Omega}{4\pi} = 0.5$ if radiation level is measured at contact. Figure 2 displays the worst case residual radioactivity in the downstream quadrupole which is adjacent to the first electrostatic septum (configuration ooSQL). Four different scenarios of $T_i$ and $T_c$ are indicated.

Figure 3 shows the cross-sectional view of the Lambertson magnet. Various partitions (in the first 10 cm depth) examined by Monte Carlo calculations are numbered as separate regions. The residual activity as a function of region number is shown in Fig. 4. We find that after continuous extraction of the beam for 30 days and cooling it for one day, one expects a maximum radiation level to be about 10 Rad/hour around the region number 14. The radiation dose

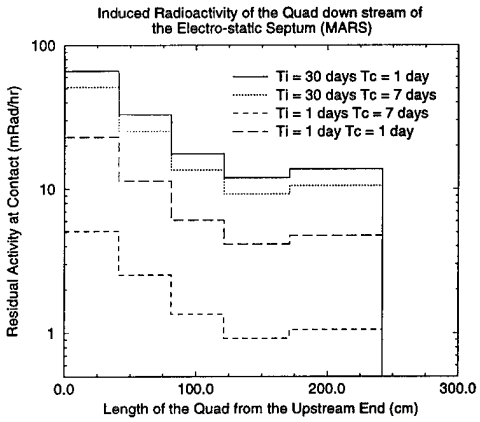



Figure 2: Worst case residual activity of the down-stream quadrupole magnet due to the beam extraction loss at the electro static septum. The data shown are radiation dose as a function of the distance along the magnet.

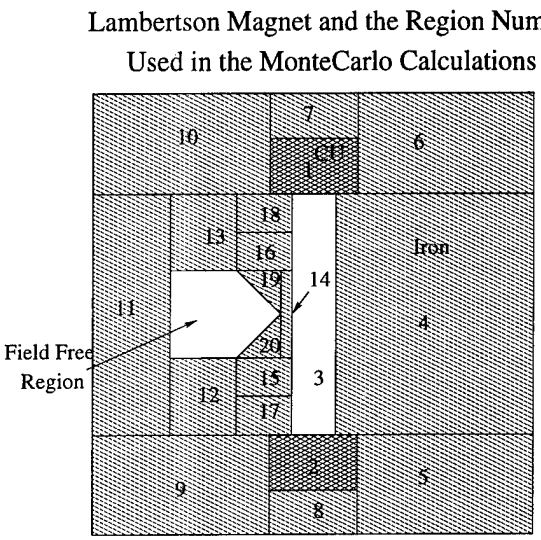



Figure 3: Schematic view of the Lambertson magnet and the partitions used in the Monte Carlo calculations.

on the body of the Lambertson at contact is found to be less than 10 mRad.

## 4 SUMMARY

We have performed detailed Monte Carlo calculations of the radioactivity at three different devices in the Main Injector extraction system. We find that the instantaneous and the residual activity of the extraction devices do not pose any potential problem from the point of view of operation.

Authors would like to thank P.S. Martin for useful discussions.

## 5 REFERENCES

[1] The Fermilab Main Injector Technical Design Handbook (1994, updated 1997).

[2] J. A. Johnstone, MI note MI-0091, Sept. 1993.

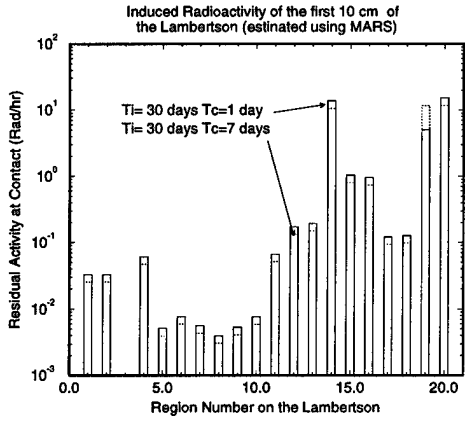



Figure 4: Radiation dose in the first 10 cm length of the Lambertson magnet. The region numbers are shown in Fig. 3.

[3] M. Harrison, "Physics of Particle Accelerators",AIP Conference Proceedings 184, AIP New York, (1989) p 2010.

[4] N.V. Mokhov, MARS users guide (1994,updated in 1997).

[5] A.N. Kalinovskii, N.V. Mokhov and Yu. P. Nikitin, "Passage of High-Energy Particles through Matter", Translated by S.J. Amoretty, AIP NewYork (1985).

[6] C.M. Bhat and J. Marriner, Proc. IEEE Particle Accelerator Conference, 1991 San Franscisco, CA (1991) p 831.

[7] M. Barbier, "Induced Radioactivity" North Holland Publishing Company (1969).

# RADIATION PROTECTION IN THE NLC TEST ACCELERATOR AT SLAC[1]

Theodore L. Lavine and Vaclav Vylet
Stanford Linear Accelerator Center, Stanford University, Stanford, California 94309

*Abstract*
This report describes the ionizing radiation protection and safety issues in the design of the Next Linear Collider Test Accelerator (NLCTA), a high-gradient, 1-GeV, X-band linac at SLAC.

## 1 INTRODUCTION

The Next Linear Collider Test Accelerator (NLCTA) is a high-gradient, X-band linac at SLAC designed to validate 2.6-cm microwave linear accelerator technology for a future high-energy linear collider (the Next Linear Collider).[2] This report describes the ionizing radiation protection and safety issues in the design of the NLCTA, including power limits, shielding, and safety systems.[3]

The NLCTA beam line (Fig. 1) consists of an injector, chicane, linac, and spectrometer. The injector contains a 3-A, 150-kV, pulsed thermionic-cathode gun and two 0.9-m-long X-band accelerator sections.[4] The sections are energized by a single 50-MW klystron, and boost the beam energy by up to 90 MeV (50 MV/m). The gun pulse has 0.125-ms duration. The repetition rate is variable up to 10 Hz. The net current loss in the injector is approximately 30%.

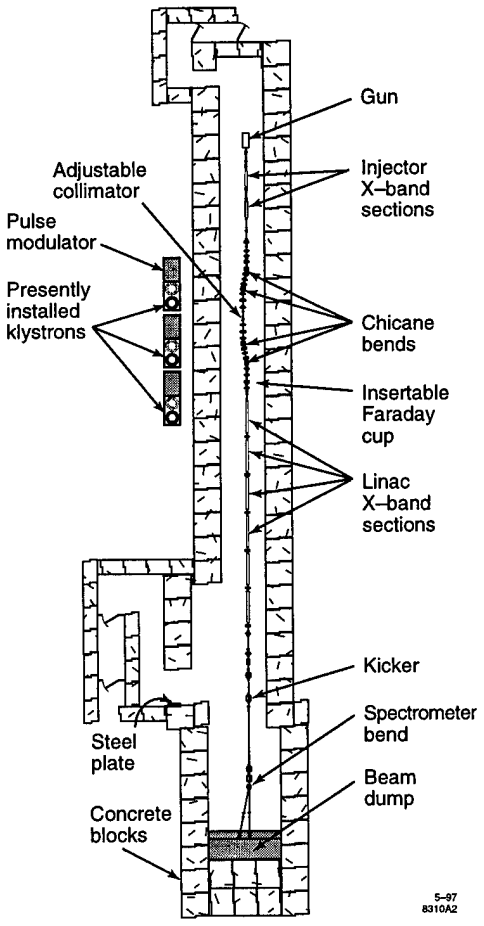



Fig. 1. Plan view of the NLC Test Accelerator. The length of the beam line from gun to dump is 43 m.

Downstream from the injector is a magnetic chicane containing an adjustable collimator. The dominant sources of radiation in the chicane are beam losses in the bends and collimator, for which 30% is assumed.

Downstream from the chicane is an insertable, re-entrant tungsten Faraday cup followed by an X-band linac.

The linac is designed to contain up to three pairs of 1.8-m-long X-band accelerator sections. (At present, two pairs are installed.) Each pair is powered by a single 50-MW klystron, and boosts the beam energy by up to 180 MeV (50 MV/m). The dominant source of radiation in the linac is expected to be small, distributed beam losses. The net loss is expected to be much less than 0.5%, consistent with experience in the SLAC linac and Final Focus Test Beam. However, for the purpose of estimating the radiation doses, a point loss of 0.5% in the linac is assumed.

A future upgrade of the rf system is planned in which the rf power will be tripled by replacing each 50-MW klystron with a pair of 75-MW klystrons, which will increase the gradient in the injector and linac by $\sqrt{3}$. A future upgrade of the injector is also planned which would double the peak current and change the micropulse structure for NLC accelerator-development studies. Because of the upgrade plans, the beam dump and shielding were designed for the future, upgraded beam power, with losses as described above.

## 2 ALLOWED BEAM POWER

Allowed Beam Power (ABP) is limited by an electronic limit on the gun rep rate, and physical limits on the duration of the high-power rf pulses and the accelerating gradient.

The maximum gun rep rate is limited to 10 Hz by three re-triggerable, monostable multivibrator circuits which limit the rep rate by virtue of their finite re-charging times. The three devices have independent power systems and are not subject to common-mode failure.

The duration of the accelerated beam pulse (nominally 0.125 ms) is limited to 0.2 ms by the duration of the high-power rf pulses (which is determined by the physical length of the SLED-II delay-line waveguides[5]) and by the filling time of the X-band accelerator structure.

The accelerating gradient is limited by the available microwave power. If the pulse current exceeds its

0-7803-4376-X/98/$10.00 © 1998 IEEE

nominal value, the beam power is further limited by current-dependent loading of the X-band gradient. The steady-state current-loaded gradient ($V$) in a section of the X-band structure is

$$V \approx V_0\{1-0.25[I/(0.74\text{A})][(50\text{MV/m})/V_0][L/(1.8\text{m})]\}, \quad (1)$$

where $I$ is the average pulse current, $V_0$ is the unloaded accelerating gradient, and $L$ is the length of the section. $V_0$ is 50 MV/m before upgrade, and 87 MV/m after upgrade. $L$ is 0.9 m for the two sections in the injector, and 1.8 m for the six sections in the linac. Consequently, the pulse power ($IV$) is maximized for the finite pulse current,

$$I^* = 2\ (0.74\ \text{A})\ [V_0/(50\ \text{MV/m})]\ [(1.8\ \text{m})/L].$$

Since the ABP is obtained when the current is twice nominal and the loaded gradient is two-thirds nominal, the ABP is only one-third greater than the nominal beam pulse power, for equal pulse durations. If the pulse current of the gun increases to twice the nominal value, the beam loading doubles, and the beam energy drops to 2/3 nominal.

The net effect of the increased pulse duration (×0.2 ms/(0.125 ms)), increased pulse current (×2), and decreased beam energy (×2/3) due to increased loading is that the ABP exceeds the nominal beam power by a factor of 2.1. ABP after upgrades is 3.1 kW.

## 3 MAXIMUM CREDIBLE BEAM POWER

The maximum credible beam power (MCBP) is obtained if the electronic rate-limiting devices that limit ABP fail in such a way that the beam rate increases to 180 Hz. For rates from 10 Hz up to 180 Hz, the MCBP is limited by a fail-safe electronic circuit that limits the average current to less than 11 mA. [6]

Beam loading does not significantly limit MCBP. The MCBP is attained at nearly the highest possible energy since the average current limit applies to the product of pulse rate, pulse duration, and peak current. At the maximum possible pulse rate (180 Hz) and pulse duration (0.2 ms), the 11-mA average gun current limit corresponds to a peak pulse current of only 0.3 A, which loads the gradient by only a few per cent (eq. 1).

MCBP after upgrades, calculated assuming nominal current losses, is 5.7 kW at 1070 MeV. The "safety envelope" corresponds to 100% loss of the MCBP either in the chicane, the insertable Faraday cup, the spectrometer, or the beam dump.

## 4 SHIELDING

The shielding was designed to limit the continuous dose rate at the surface of the shield in occupied areas to 2 mrem/h, assuming the ABP after upgrade, nominal beam-loss fractions, operation for 1000 h per year, and an occupancy factor of 50%. Since the ABP exceeds the nominal beam power by a factor of approximately two, operation at the nominal upgraded beam power is compatible with 100% occupancy.

The shielding-design calculations indicate the potential for some unoccupied areas, such as the roof of the enclosure and beam dump, to experience doses greater than 5 mrem/h. This is because the concrete roof is thinner than the walls, and because of vertical penetrations, offset from the beam axis, for waveguides and cables. Additionally, there are unoccupied utility tunnels, below the chicane and spectrometer areas, where continuous dose rates may approach 5–15 mrem/h. Areas receiving dose rates above 5 mrem/h are designated as "radiation areas," and are identified by appropriate signs and barriers. No areas outside the shielding are expected to be "high-radiation areas," where continuous doses exceed 100 mrem/h.

Considering the magnitude of expected losses, it is practical to divide the beam line into two regions: (1) the injector, chicane, and insertable Faraday cup, where a large fraction of the beam may be lost; and (2) the linac and spectrometer, where losses will be less than 0.5%. The thickness of the lateral concrete shielding is the same in all regions: 6-ft walls, and a 4-ft roof. The walls and roof are constructed from blocks that interlock in order to prevent direct streaming of radiation.

After the planned upgrades, the dose rate outside the walls is estimated to be 0.5 mrem/h near the chicane and Faraday cup. The dose rate on the roof, away from any penetration, is estimated to be 10–15 mrem/h above the chicane and Faraday cup. The dose rate at the nearby roof penetration will be less than 100 mrem/h.

The highest dose rates under normal conditions are expected at the end of the linac. The continuous dose rate after upgrades is estimated to be 0.9 mrem/h outside the walls, and 3 mrem/h on the roof.

## 5 BEAM DUMP

The beam dump is a stack of horizontal iron slabs. The beam impinges on only one slab (which will become activated). The power-handling capability of the dump, cooled only by natural convection and thermal radiation, is adequate for the MCBP.[7] The dump is surrounded by 6–12 ft of concrete laterally, on top, and forward.

The nuclides of greatest concern in the activated dump are $^{46}$Sc, $^{48}$V, $^{51}$Cr, and $^{54}$Mn, which have half-lives of 16–303 days, and gamma-ray energies of 0.8–1.3 MeV. The saturation dose rate will be approximately 2 rad-m$^2$/kWh. Assuming nominal beam power of 1.5 kW after upgrade, the estimated dose rate inside the housing, 50 cm from the point of impact, will be 1 rad/h. In order to permit access to the housing near the dump, the middle slab of iron contains a 70-cm deep, re-entrant recess for a (radially) 20-cm thick Pb collar surrounding the beam pipe. This collar reduces the gamma dose rate below 1 mrem/h outside the beam pipe.

## 6 AIR ACTIVATION AND OZONE PRODUCTION

Beam loss may result in activation of air and ozone production in the housing if some of the energy deposited

by the beam leaks out into the air as ionizing radiation. The saturation level of the build-up of activation products and ozone in the housing was estimated from the ratios of the production and decay rates. Our estimates of these effects are conservative in that they assume minimal attenuation of the ionizing radiation in the "target" (which may be quite thick), no ventillation, and whole-body exposure. Beam losses assumed for estimating these effects were 230 W at 125 MeV in the Faraday cup, and 7.5 W at 800 MeV.

The most significant nuclides for air activation are $^{13}N$ ($T_{1/2}$ = 10 min) and $^{15}O$ ($T_{1/2}$ = 2 min). The saturated concentrations are in the range of 10–20% of the limits allowed by DOE ("Radation Protection for Occupational Workers," DOE Order 5480.11, 1988) for these species, 5% of the limit for $^{41}A$ ($T_{1/2}$ = 110 min) produced from $^{40}A$ by thermal neutrons from the Faraday cup, and less than 1% of the limits for other nuclides including $^{3}H$ and $^{7}Be$.

The dose at the site boundary due to airborne transmission of air-activation products was estimated for compliance with the Environmental Protection Agency's National Emissions Standards for Hazardous Air Pollutants (40CFR61, H). The effective dose equivalent to the maximally exposed individual of the general public was found to be $1.5 \times 10^{-4}$ mrem/y, well below the 10-mrem/y limit.

To estimate the production rate for ozone ($T_{1/2}$ = 50 min) at the end of the linac, it was conservatively assumed that 0.4 W escapes into the air in the form of 10-MeV electrons. The estimated production rate of $4 \times 10^{7}$ molecules $cm^{-3}$ $s^{-1}$, results in a saturated concentration of $10^{11}$ molecules $cm^{-3}$, which is 5% of the threshold limit for ozone. Ozone production at the Faraday cup is about 50 times less because of greater self-attenuation and the lower energy.

## 7 SITE BOUNDARY DOSE

The SLAC site boundary, 400 m away from the NLCTA, is continuously monitored by active and passive detectors which are sensitive to neutrons and gamma rays. The predominant source of boundary dose from NLCTA is secondary radiation from the primary beam, in the form of neutrons that leak through the 4-ft-thick concrete roof and scatter in air. This source is estimated to result in an annual boundary dose of less than 0.04 mrem.

The klystrons used to generate the microwave power for the accelerator can be sources of 400-keV X rays. The klystron dose rates are 0–25 mrem/h at 30 cm. The klystron dose at the site boundary is negligible.

## 8 PROTECTION SYSTEMS

A Beam Containment System (BCS), is designed to limit the beam losses to the 0.5% level. The BCS utilizes eight Protection Ionization Chambers (PICs) deployed inside the housing along the beam line between the chicane and the beam dump. The individual PICs act redundantly in that radiation from a point loss is detected by more than one PIC. PIC readings that correspond to a 1-mrem/h dose outside the shielding cause a 10-fold reduction in the gun trigger rate to allow for operator intervention. PIC readings that correspond to a 2-mrem/h dose outside the shielding cause the BCS to inhibit triggers to both the gun and the klystron pulse modulators.

The Personnel Protection System (PPS) is designed to detect radiation doses outside the shielded housing, and to control access to the housing. The PPS utilizes 10 Beam-shut-off Ionization Chambers (BSOICs) deployed outside the shielding. The trip levels of the BSOICs at ground level are set at 10 mrem/h. Three of the BSOICs are positioned in potential radiation areas on the roof and in a utility tunnel, and are set to trip at 100 mrem/h. BSOIC trips or access violations cause the PPS to turn off the high voltage for both the gun and the modulators, and inhibit the modulator triggers.

The BCS also includes physical devices designed to contain the beam at the chicane and spectrometer bends, where an unanticipated drop in energy (due to klystron failure) could cause the beam to over-bend, escape the vacuum chamber, and hit the concrete shield, which cannot absorb the maximum power. The BCS devices designed to prevent this mishap are protection collimators capable of absorbing the MCBP.

The vertical kicker has the potential to steer the beam into a pole of a spectrometer matching quad, which may result in excessive dose rates in an underlying utility tunnel (3–10 rem/h for 1.5–5.7 kW). To limit the duration of such rates, a BSOIC with a 100-mrem/h trip threshold is located in the tunnel. This BSOIC will shut off the beam if losses exceed 50 W. Since simultaneous dose rates of 0.6 rem/h outside the walls and 2.5 rem/h on the roof are anticipated, the scenario is mitigated also by three other BSOICs and two PICs, which will shut off the beam at 25-W loss.

Full functionality of the BCS and PPS interlocks and devices, and other radiation safety items, is maintained by routine testing, inspection, and configuration controls.

### REFERENCES


[1] This paper was prepared for the Department of Energy under contract number DE-AC03-76SF00515.

[2] See Ronald D. Ruth *et al.*, "Results from the SLAC NLC Test Accelerator, " in these proceedings.

[3] More details are available in Vaclav Vylet and Theodore Lavine, "Radiation Protection in the NLCTA," NLCTA-Note #46.2, revised 12/5/95.

[4] W. Wang *et al.*, "RF System for the NLCTA," in these proceedings.

[5] S.G. Tantawi *et al.*, "The NLCTA's RF Pulse Compression and Transmission," in these proceedings.

[6] M.. Browne, unpublished.

[7] D. Walz, unpublished.

# MODULAR RELIABILITY MODELING OF THE TJNAF PERSONNEL SAFETY SYSTEM

J. Cinnamon, K. Mahoney, Thomas Jefferson National Accelerator Facility, 12000 Jefferson Avenue, Newport News, VA, 23606

*Abstract*

A reliability model for the Thomas Jefferson National Accelerator Facility (formerly CEBAF) personnel safety system has been developed. The model, which was implemented using an Excel spreadsheet, allows simulation of all or parts of the system. Modularity of the model's implementation allows rapid "what if" case studies to simulate change in safety system parameters such as redundancy, diversity, and failure rates. Particular emphasis is given to the prediction of failure modes which would result in the failure of both of the redundant safety interlock systems. In addition to the calculation of the predicted reliability of the safety system, the model also calculates availability of the same system. Such calculations allow the user to make tradeoff studies between reliability and availability, and to target resources to improving those parts of the system which would most benefit from redesign or upgrade. The model includes calculated, manufacturer's data, and Jefferson Lab field data. This paper describes the model, methods used, and comparison of calculated to actual data for the Jefferson Lab personnel safety system. Examples are given to illustrate the model's utility and ease of use.

## 1 BACKGROUND

### *1.1 Need for Safety Analysis*

The Jefferson Lab PSS is responsible for preventing several types of danger to personnel. This system must detect unsafe conditions during the lifetime of the accelerator. An analysis of an accelerator safety system is a necessary requirement in determining if the system meets the original design specifications. If a safety system exceeds the failure rate of its design, changes can be made to improve physical implementation. A reliability study not only allows a system engineer to determine the system's current reliability, but also to identify the "weak links". The expense of unnecessary improvements can also be avoided by having realistic "before and after" data about the effects of any changes.

### *1.2 Scope of Study*

The reliability model of the TJNAF Personnel Safety System (PSS) was developed to predict the safe and unsafe failure rates ($\lambda_s$ & $\lambda_u$), availability, and actual TJNAF in-field failure information for PSS systems. The model uses the industry accepted reliability modeling techniques of the military standard MIL-STD-756B. This information is used to determine the true safety the PSS system.

## 2 METHOD

The TJNAF PSS system was modeled using Microsoft Excel™ as a platform to calculate reliability. The actual implementation of the study was done using a common-sense approach. Instead of the usual formula-focused method, the PSS was studied using a more graphical approach. The entire PSS system was drawn in block diagram form. Each major block was reduced into its constituents, and the resulting blocks were further reduced to the individual component level.

At this point, a special spreadsheet was built to contain the calculated reliability values for all PSS components. This master sheet was used as a reference source for information on each PSS part. Having a single source of reliability data greatly simplifies the process of developing the study. These values were then referenced whenever needed via pointers to the cell in the master database.

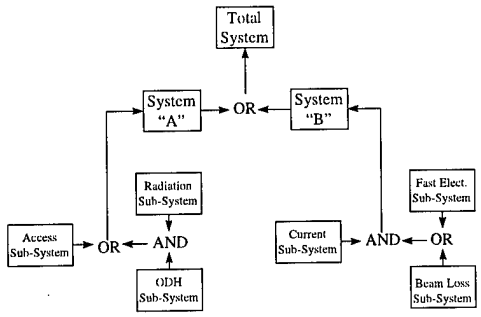
## 3 DEVELOPMENT

### *3.1 Preparation*

The first step in beginning a reliability analysis is to develop a drawing of the system you wish to model. This drawing should be a schematic showing each major part of the system in block diagram form. The major sections of the system should show any interconnections between sub-systems to provide any information about interdependence. The each block of the system diagram should be separate and discreet from other blocks.

The level of detail at this point is very low. All that is needed is an understanding of what is to be under focus in the reliability study. Often, there are areas of an accelerator safety system which cannot or need not be included in the analysis.

0-7803-4376-X/98/$10.00 © 1998 IEEE




The purpose of the system picture is to logically group components of the system into blocks. These major blocks are used to determine the final system reliability. Each of the major sub-systems under investigation is further broken down into its sub-systems and components.

### *3.2 Identifying all components of the study*

After the sub-system drawings are completed, a list of each unique component should be made. This is a time consuming process, but a necessary one. A single database should be constructed in a spreadsheet program capable of calculating complex formulas. The TJNAF PSS used Microsoft EXCEL™ because of the high availability of the program and ease in use of formulas.

### *3.3 Gathering information about components*

The method for determining the individual component reliability begins by researching the component for information on proven reliability. This is information which the manufacturer has obtained after thorough research and experience. The values are usually dependent on the frequency of use and operating environment. It should be noted that the manufacturer's reliability quotes are often much better than the component's actual field reliability, so field data is also used.

### *3.4 Calculating Component Reliability Values*

If the reliability value for a given component is already known, the numbers can be directly entered into the Master database. If this is not the case, the values must be determined using what information is available.

If the *Failure rate* is available,
Failure Rate ($\lambda$) = 1/MTBF in Failures per Hour
Single-Component Reliability = Exp(-$\lambda$ * time interval)

If the *MTBF* is given,
MTBF = Mean Time Between Failure (in Hours)
Failure Rate ($\lambda$) = 1/MTBF in Failures per Hour
Single-Component Reliability = Exp(-$\lambda$ * time interval)

If the *Minimum Operations* information is given,
Minumum Operations Lifetime = # of ops.
MTBF = (in Hours)
Failure Rate ($\lambda$) = 1/MTBF in Failures per Hour
Single-Component Reliability = Exp(-$\lambda$ * time interval)

### *3.5 Inclusion of Values in Database*

Once the individual component reliability is determined, the value is entered into the Master database. The MTBF values may be calculated and entered for use in *Availability* determination. A column containing the actual in-field MTBF values for a component is kept for reference. A value for the Mean Time to Repair is entered into the MTTR column. This represents the time needed to replace or repair the component in the field. The time interval of the study is also an important factor in determining reliability. This value should be the time between system re-certifications, usually 6 months or 1 year.

## 4 ARRANGING COMPONENTS TO SIMULATE SYSTEM

The components are arranged in a spreadsheet model according to their pattern of usage in the actual system. This technique for reliability modeling allows the system under study to be easily examined for current reliability, and later dynamically improved as new components are put into service. In addition, the use of component "pointers" instead of numbers in the sub-system modeling make updates easier.

### *4.1 Previous Methods of Analysis*

The more common approach to modeling an area is to write out a formula such as the one below. This shows the reliability as equal to the product of the reliability values of each of its constituents.

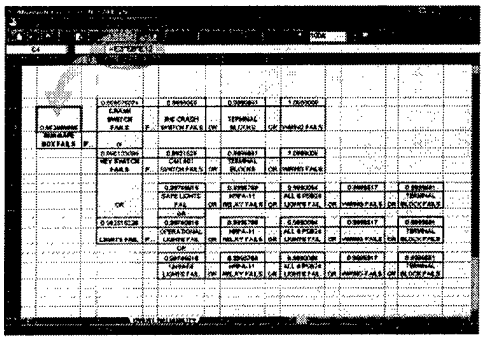
$$R_{system}=((R_{unit\ 1})\ OR\ (R_{unit\ 2})\ AND\ldots(R_{unit\ n}))$$

### *4.2 TJNAF Method*

The method used in the TJNAF reliability analysis involved the use of spreadsheet blocks to produce a more visual and easily modified picture of a system. The formulas are the same, but in a more graphical arrangement. This use of spreadsheet cells provides unique advantages when calculating large systems.

When information about a part is entered into the master database, often only certain information is needed to calculate reliability. The rest of the information may clutter the view of the important material. Pointers were used to reference the master database reliability values wthout displaying every piece of information about the part.

Spreadsheets of several systems can be opened together and interlinked using "drag and drop" pointers. These pointers consist only of the cell location of the information needed.



*4.3 Linking sub-systems*

When the reliability of a single component or individual system is determined, the process of interconnecting with other systems begins. The larger system groups are formed by linking the reliability values from individual system sheets to a single sheet. The values are arranged as they exist in-field and a single value for the larger system is produced. As more and more systems are unified, the reliability of the complete system is approached.

The key benefit of using a modular model in a spreadsheet is having the ability to quickly change things. As the size of a study expands, the need for an easier and less time consuming approach expands exponentially.

## SUMMARY

The methods used be the TJNAF Safety System Personnel involved in the study have proved to be valuable and worth mention to other accelerator safety groups. The modularity affords a great deal of flexibility in generating scenarios of system revision and investment. This study has allowed our engineers to determine the cost-to-improvement ratio for upgrades on the TJNAF system. This has provided the Safety group with the data needed to save countless dollars on unnecesary "improvements", and permitted the components truly needing attention to be seen.

## FUTURE

Sometime in the future, the analysis of the study will be expanded to include a Markov Analysis. This will be instrumental in providing more realistic information about safety and availability issues.

## REFERENCES


[1] MIL-217F Standards Document

[2] MIL-756B Standards Document

[3] U.K. Department of Health and Social Serices. Functional safety of programmable electronic system: generic aspects. London: DHSS; 1987.

[4] Petschenik, N.H. Practical priorities in system testing. IEEE Software 2(5):18-23; 1985.

[5] Simmons, J.M. Safety shutdown systems. *Advances in Instrum.* 42(1): 115-122; 1987

# JEFFERSON LAB PERSONNEL SAFETY FAST BEAM KICKER SYSTEM

K. Mahoney, O. Garza, E. Stitts, H. Areti, M. O'Sullivan
Thomas Jefferson National Accelerator Facility, Newport News, Virginia 23606

*Abstract*

The CEBAF accelerator at Thomas Jefferson National Accelerator Facility (Jefferson Lab) uses a continuous electron beam with up to 800 kilowatts of average beam power. The laboratory beam containment policy requires that in the event of an errant beam striking a beam blocking device, the beam must be shut off by three methods in less than 1 millisecond. One method implemented is to shut off the beam at the gun. Two additional methods have been developed which use fast beam kickers to deflect the injector beam on to a water cooled aperture. The kickers designed and implemented at Jefferson Lab are able to deflect the injector beam in less than 200 microseconds. The kicker system includes self-test and monitoring capabilities that enable the system to be used for personnel safety.

## INTRODUCTION

The CEBAF accelerator personnel safety system (PSS) is segmented into six geographical areas to allow flexibility in operation and maintenance of the machine. "Critical Devices" were defined which are used to ensure that beam cannot be transported from a segment under beam operations to a segment which may be open for access. Copper beam stoppers were chosen as one of the methods to ensure that beam cannot reach an occupied area. Control of arc transport magnets was another.

The CW nature of the CEBAF beam is such that no single device other than a very high power beam dump can withstand beam indefinitely. A beam current monitor system was incorporated into the personnel safety system to ensure that beam detected at a beam stopper would result in the immediate shutdown of the beam at the source **[1]**.

The beam current monitor system can shut off the beam in less than five-hundred micro seconds using three different methods. The first method is to clamp the electron gun modulation source to a cutoff potential.

The second method chosen was to implement fast beam kickers in the 100keV injector beam line.

The requirements for the beam kickers included the ability to deflect the injector beam out of the beam transport path and on to a water cooled aperture within 200 micro seconds. The system had to be fail safe and incorporate self test and integrity monitoring as well. Just as importantly, the kicker system must not degrade the quality of the electron beam optics in a very sensitive part of the accelerator.

The area chosen for the kicker was in between two emittance defining apertures in the 100 kV section of the CEBAF injector (Figure 1.). Placement at this point relaxed the requirements on the magnetic elements as well as provided a convenient point to dissipate the beam power when deflected out of the beam transport path.

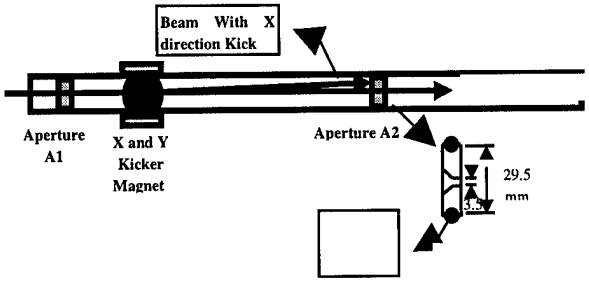



**Figure 1. Kicker Beam Line layout**

The kicker magnets were placed one half meter up stream of the second aperture. Because the aperture was used to collimate beam, the kicker requirements had to take into account a beam diameter greater than the aperture diameter. Measurements confirmed a beam diameter of approximately 4 mm at this point.

In order to achieve the required level of redundancy in the kicker function, there are actually 2 kicker magnets, one for the X plane and one for the Y plane.

## SYSTEM DESCRIPTION

The kicker system is designed to have minimal effect on the beam optics when there is no fault, i.e. no kick, and to quickly and efficiently kick the beam out of the beam line when there is a fault. To achieve this, the system was designed such that normally there is equal current in two oppositley biased coils (Figure 2).

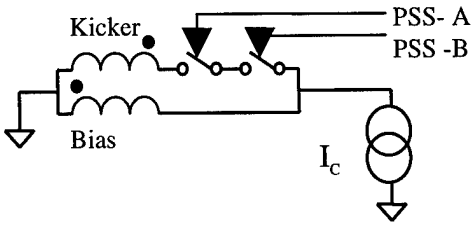



**Figure 2. Kicker Coil Arrangement**

0-7803-4376-X/98/$10.00 © 1998 IEEE

A constant current source ensures that the current is regulated and does not vary more than 0.1 %. When there is a fault the current is removed from one of the two coils, leaving a net magnetic field, and thus, a kick. Using the constant current source as the bias element also has another advantage. Normally, one half of the total current is through any one coil. This minimizes the effect of residual fields due to coil mismatch. When one of the coils is open circuited, the current in the other coil is doubled to maintain a constant current. This provides the maximum kick.

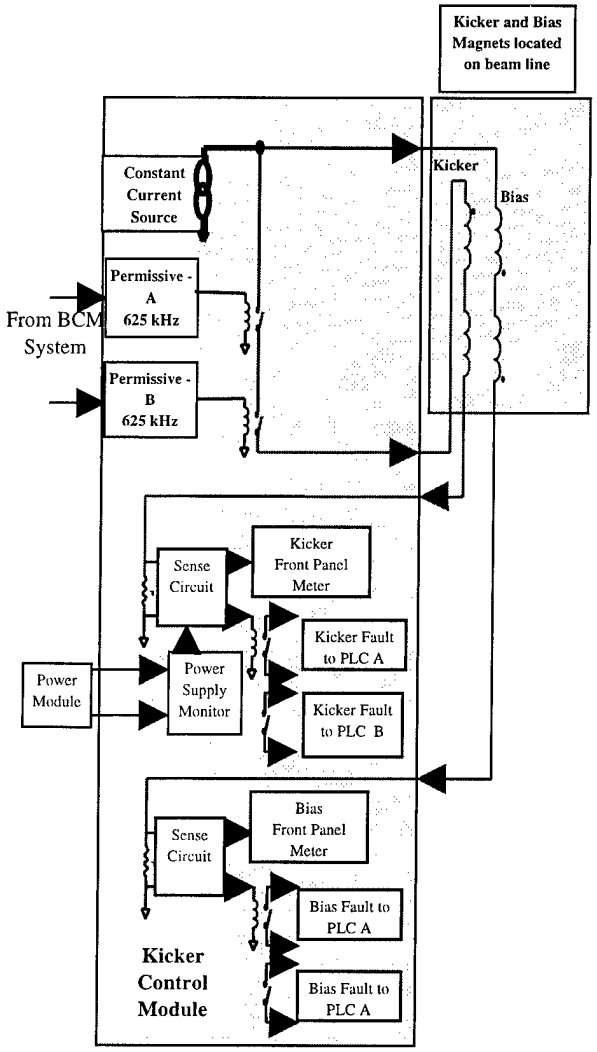



**Figure 3. Kicker System Block Diagram**

## SYSTEM HARDWARE

The kicker system (Figure 3.) is composed of a 3-U electronics card cage located in the upstairs service building and the kicker magnet assembly located on the beam line in the tunnel. The electronics for both the X and Y kicker are identical. Each is composed of a power module, a kicker control module and a fiber optic fan-out module.

The power module houses DC power supplies which provide power to the control module. The power can be turned off by a keyswitch located on the back of the chassis.

The control module contains the PSS decoding circuitry, the constant current source, and the fault detection circuitry. The decoding circuitry looks at a 625 kHz squarewave input from each of the redundant beam current monitor systems. Loss of the signal or the signal stuck at one level is interpreted as a fault. Any fault will then open the kicker current line.

The control module uses fast reed relays to switch off the kicker coil curtrent. These relays have a switch off time of less than 100 us. Figure 4 shows the timing of the decoder circuitry. The top trace is the kicker and bias coil current. The bottom trace is one of the two permissive inputs. Once the permissive is off, the kicker coil opens within 160 us. The kicker coil current goes to zero while the constant current source then doubles the current in the bias coil.

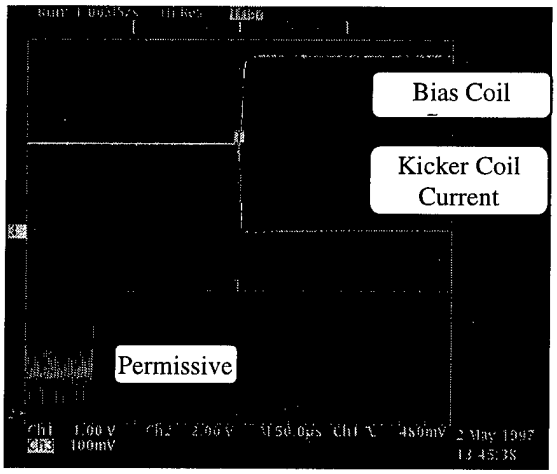



**Figure 4. Kicker Timing**

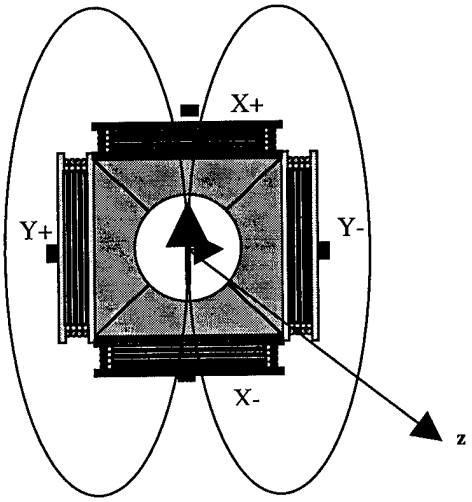
Fault detection circuitry on the control module measures current in each coil. A window detector looks for out-of-tolerance conditions. The detector is set to detect open circuits or shorted turns on the magnet coils.

An additional set of relays on the control module is connected to the personnel safety system. Any fault on the kicker system will also fault the personnel safety interlock system.

## THE KICK

The magnet design is based on a flat solenoid disk electro magnet. The required kick is achieved when one of the two windings is open circuit. Figure 5 shows the magnet assembly. Each of the disks has both kicker and bias coil windings. The magnets are split in two (top-bottom,

right-left) in order to reduce the current required to achieve the net kick in the center of the beam pipe.




**Kicker Magnet layout showing field orientation for X direction kick**

**Figure 5.**

The magnet assembly was designed for easy mounting and orientation on the beam line. An aluminum block holds both the X and Y kicker windings.

The required bending angle to deflect the beam onto thte aperture can be approximated as :

$$\Delta\theta = \tan^{-1}\left(\frac{\Delta x}{L}\right) = \frac{5.87 \times 10^{-4}}{\gamma\beta_z} BL \text{ rad} \quad [2]$$

where $\gamma\beta_z$ for the 100 kV injector beam is approximately 0.6426.

The bending power of the kicker magnet was confirmed to be approximately 110 G-cm/A. To ensure that the beam is kicked completely onto the aperature the current is set to 200 mA. This means that the normally the current in each coil is 100mA. When there is a fault the current in the bias coil increases to 200 mA whie the kicker current is switched to zero.

## EXPERIENCE

The Personnel Safety System Fast Beam Kicker has been in service for over a year. During this time there have been no failures or false trips of any kicker components. More importantly, the kicker current has remained at the original setpoint without any adjustments required. Tests in situ with beam have shown that the kicker has no effect on the beam optics in the "no fault" state. These tests also show that, when tripped, the current is fully deflected onto the aperture, regardless of upstream steering or beam properties.

## SUMMARY

A fail-safe fast beam kicker has been developed at Jefferson Lab which is able to deflect the injector beam onto a water cooled aperture. Deflection time has been measured at much less than the required 200 us. The kicker has no effect on the injector beam properties when there is not a fault condition. Fault monitoring circuitry ensure that no undetected failure modes exist during operation.

## ACKNOWLEDGEMENTS

This work was supported by the U.S. DOE under contract number DE-AC05-84ER40150.

## REFERENCES

[1] R. Ursic et al, "CEBAF Beam Loss Accounting", Proceedings of the 1995 Particle Accelerator Conference, Volume 4.
[2] From Geoffrey Krafft, CEBAF Operator Training material.

# EMERGING STANDARDS WITH APPLICATION TO ACCELERATOR SAFETY SYSTEMS

K.L. Mahoney, H.P. Robertson
Thomas Jefferson National Accelerator Facility
12000 Jefferson Avenue, Newport News, VA 23606

*Abstract*

This paper addresses international standards which can be applied to the requirements for accelerator personnel safety systems. Particular emphasis is given to standards which specify requirements for safety interlock systems which employ programmable electronic subsystems. The work draws on methodologies currently under development for the medical, process control, and nuclear industries.

## INTRODUCTION

The CEBAF accelerator was one of the first large DOE labs to use programmable controllers for personnel safety applications. At the time the CEBAF Personnel Safety System (PSS) was designed, there were few documents which could be used as guidance to incorporate a PLC into the system.

Input was sought from experts at other labs in the design of accelerator radiation protection systems **[1]** in order to ensure that the appropriate steps were taken in evaluating the new system's reliability. A relatively new standard, developed by the U.K Health and Safety Executive **[2]** for the chemical process and petroleum industries, was also used as a guidance in the application of PLCs in the personnel safety system.

Over the last ten years several non-industry specific documents (consensus standards) have been developed which may be applied as guidance to the design of accelerator safety interlock systems. In addition to the general specifications there are also several industry specific documents which still provide a good measure of "best practice" applications of safety system design. Areospace, nuclear, and militarty fields are an example of industries that have had to incorporate electronic safety systems in life-safety applications. Other "low profile" industries such as train signaling systems are another source of industry specific safety system standards.

## GENERALIZED SAFETY SYSTEM STANDARDS

ISA-S84.01-1996 from the Instrumentaiton Society of America **[3]** is one of the most comprehensive general documents to be recently released. S84 covers the definition and requirements for electrical/electronic/ and programmable electronic based safety systems. Because the document is generic, it may be applied to both programmable based and conventional switch-relay based safety systems in a variety of applications.

The S84 standard defines requirements for the design, development, operation, and maintenence of a safety system which must meet a given safety integrity level (SIL). The safety integrity level is based on the probability of the safety system failing to respond to a demand (PFD)**[4]** to mitigate a hazard. Table 1 gives the PFD for the three safety integrity levels defined in S84.

| Safety Integrity Level | 1 | 2 | 3 |
|---|---|---|---|
| SIS Performance requirements | Safety Availability Range | | |
| | 0.9 to 0.99 | 0.99 to 0.999 | 0.999 to 0.9999 |
| | PFD Average Range | | |
| | $10^{-1}$ to $10^{-2}$ | $10^{-2}$ to $10^{-3}$ | $10^{-3}$ to $10^{-4}$ |

Table 1. SIL levels defined in S84.

The safety availability (1-PFD) is related to the safety reliability of the system $R_s$ by

$$R_s = 1 - \int_0^t \text{PFD}\, dt$$

Where t is the time interval over which the reliability is being measured.

The $R_s$ that the safety system is required to achieve over a period of time is usually defined at the beginning of the safety system design process. The combination of the PFD, the rate that the safety system may be challenged (demand), the severity of a the outcome of an accident, and the length of time the hazard persists **[5]** define the overall risk of the process. Usually the last three steps are minimized before the SIL of the safety system is defined. Not doing so leads to overly complex safety systems. PFD is specifically addressed by the S84 standard. Other factors that influence the overall safety of the system including design, commissioning, maintenance, and management of change, are also included in the standard.

A companion document to S84, Technical Report dTR84.0.02 is in draft from. TR84 gives examples of several methods which may be used to calculate the safety integrity level of a given safety system design.

Depending on where one is in the design process, they may need to define the SIL required, the $R_s$, the PFD, the mean time to failure (MTTF), or the system

0-7803-4376-X/98 /$10.00 © 1998 IEEE

failure rate ($\lambda_s$). For a constant failure rate model, these components are related by:

$$PFD = R_s\lambda_s = \lambda_s \exp(-\lambda_s t) \qquad \text{eq. 1}$$

where t is the time period over which the safety system is required to perform. This assumes any errors found during test are repaired and the "clock" is set zero. Most accelerator safety interlock systems are dual redundant systems in which both systems must fail simultaneously in order to allow a hazard to persist. The probability that both systems fail (PFD) within a given time period, t is given by the relation:

$$R_s = 2\exp(-\lambda t) - \exp(-2\lambda t) \qquad \text{eq. 2}$$

where $\lambda$ is the failure rate of one of two systems.

If given the required safety reliability of the redundant system:

$$\lambda = \frac{-1}{t}\ln(1-\sqrt{1-R}) \qquad \text{eq. 3}$$

This would give the requirement for the failure rate for each of the redundant legs of the system.

Note that for a dual redundant system the MTTF is $\neq 1/\lambda$, but rather MTTF $= 1.5/\lambda$.

Examples and methods for evaluating several types of safety system architectures are given in TR84. TR84 also includes more complicated reliability models which include effects like common cause failures and mean time to repair. For example, when one considers common cause factors for a dual redundant system:

$$PFD = \lambda^{DU} t\left[\lambda^{DU} t/3 + \lambda^{DD}\,MTTR + \beta + \frac{\lambda^{D}_{f}}{2\lambda^{DU}}\right] \qquad \text{eq. 4}$$

The superscripts DU and DD separate the failure rates into "Dangerous Undetected" and "Dangerous Detected" faults. $\lambda^{D}_{f}$ is the dangerous common mode (systematic fault ) failure rate.

Systematic failures are items such as specification errors, software errors, or other design errors which equally effect both channels of a redundant system. $\beta$ is a factor which represents the percentage of failures that impact more than one channel of the system. An example of a failure that may affect both channels of a redundant system are such factors as enviromental stress, lightning, or electromagnetic interference (EMI) **[6]**.

The S84 standard was designed to eventually be incorporated into a another more general standard, IEC-1508, currently under development by the european standards ageny IEC. The IEC-1508 covers all aspects of a safety system lifecycle for any safety related system. It also covers requirements for sensors and final elements used in safety system implementations. S84 does not cover sensors and final elements specifically. Chapter 12 of the S84 standard lists the current differences between S84 and IEC draft standard 1508. S84 will eventually become a process control industry specific standard, IEC-1511, which will fall under the umbrella of IEC-1508.

IEC-1508 is currently divided into seven parts.

1. General Requirements
2. Requirements for Elec./Electr./Programmable Electronic Safety Systems
3. Software Requirements
4. Definitions and abbreviations of terms
5. Guidelines for applicaiotn of part 1
6. Guidelines for applicaiton of parts 2 and 3
7. Bibliography of techniques

IEC-1508 also defines a SIL 4, probability of fail on demand of $10^{-3}$ to $10^{-4}$.

One U.S. military standard, MIL-STD-883C **[7]**, published in 1993 may be genericly applied to the management of the safety system process and the management of safety systems in general. MIL-STD-883 defines the requirements fo evaluating hazards and steps that should be taken to make sure the hazards are properly tracked and addressed.

## INDUSTRY SPECIFIC STANDARDS

Until the advent of S84 and IEC1508, almost all standards up to this time have targeted a specific industry or application. To date, these standards have been applied mostly to the obvious "high risk" industries such as the nuclear and aerospace industries. Over the last 10-15 years more emphais has been placed on other areas with less obvious, but potentially just as high risk. Industries such as medical instrumentation, mining equipment and chemical processing all have specific standards for the use of programmable safety systems.

### *Nuclear Industry*

Standards which describe the requirements for safety systems in the nuclear industries have been in circulation for several years. In an attempt to keep up with the rapid advance in programmable logic controllers and microprocessors, these standards are undergoing constant change. IEC880 **(8)**, is an especially good example of a safety related software standard.

The US Nuclear Regulatory Commission is currently taking comments on a draft of NUREG-0800 section 7, **[9]** which deals specifically with the use of programmable controllers in nuclear safety applications.

### *Medical Industry*

The U.S. Food and Drug Administaration (FDA) has prepared new documents which provide guidance to the design and manufacture of medical instruments. "Design Control Guidance for Medical Device manufacturers" **[10]** provides guidance for the manufacture of medical electronic devices. Other FDA draft documents **[11]** address the use of software in medical devices specifically.

## SAFETY LIFECYCLE MODEL

A common factor found in many of the new standards is the concept of the safety lifecycle model. The safety lifecycle model describes a process by which the a safety system is defined, designed, and maintained through out the lifetime of the applicaiton. Feedback from the major steps are defined for all models.

Figure 1 shows a safety lifecycle model appropriate for application to an accelerator programmable electronic safety system. Note that the model applies specifically to the safety system and not other ancilliary or non-safety systems.

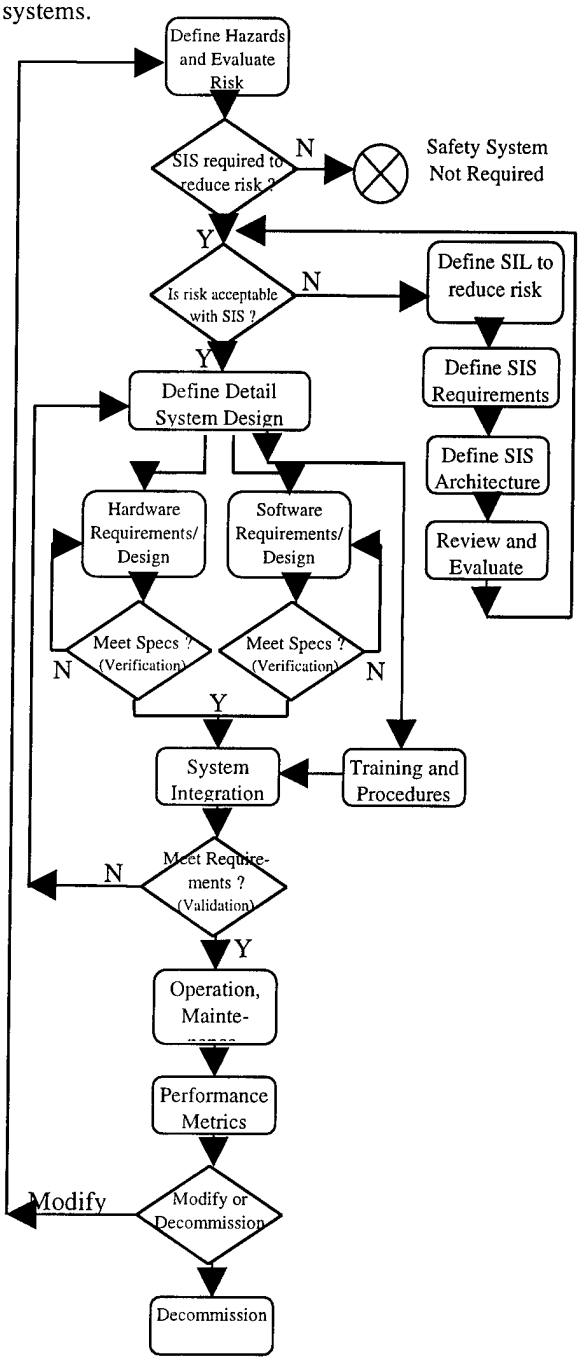



Figure 1. Safety Lifecycle Model Applicable to Accelerator Safety Systems

The safety lifecycle model is used as a framework to identify each step in the evolution of the safety instrumented system. In practice, each of the steps would have a detailed process associated with it. For example, the box titled "Define SIS Architecture" would involve the design tradeoffs of redundancy, diversity, and technology.

## SUMMARY

There are currently several international standards which may be adapted to accelerator safety systems. While several of the standards are intended for a specific industry, the approach taken to the safety system design is very similar in each case. The different approaches may be condensed into a safety system life cycle model appropriate for accelerators.

## ACKNOWLEDGEMENTS

This work was supported by the U.S. DOE under contract number DE-AC05-84ER40150.

## REFERENCES

[1] `Workshop on Personnel Safety Interlocks' CEBAF TN-90-233
[2] 'Programmable Electronic Systems in Safety Applications', 1987, U.K. Health and Safety Executive, Library and Information Services,
Broad Lane, Sheffield S3 7Hq, U.K.
[3] ANSI/ISA-S84.01-1996, 'Application of Safety Instrumented Systems for the Process Control Industry', February 1996, Instrumentation Society of America, 67 Alexander Drive, P.O. Box 12277, Research Triangle Park, North Carolina, 27709
[4] ANSI/ISA-S84.01-1996, pp21.
[5] N.G. Leveson, 'Safeware: System Safety and Computers', Addison-Wesley, 1995, pp179.
[6] ISA-dTR84.02 'Electrical/Electronic/Programmable Electronic Systems - Safety Integrity Level (SIL) Evaluation Techniques', March 1997, Instrumentation Society of America, 67 Alexander Drive, P.O. Box 12277, Research Triangle Park, North Carolina, 27709
[7] MIL-STD-883C, "System Safety Program Requirements", January, 1993.
[8] IEC-880 'Software for Computers in the Safety Systems of Nuclear Power Plants' 1986, IEC, Geneva, Switzerland.
[9] NUREG-0800 Section 7, Draft
[10] 'Design Control Guidance for Medical Device Manufacturers', March, 1997 US Food and Drug Administration, Center for Devices and Radiological Health.
[11] 'ODE Guidance for the Content of Premarket Submission for Medical Devices Containing Software', US FDA Draft 1.3, August 1996.

# DESIGN AND CONSTRUCTION OF A 1-MW, 352-MHZ RF TEST LOAD

D. Horan, Y. Kang
Advanced Photon Source, Argonne National Laboratory
9700 South Cass Avenue, Argonne, Illinois 60439 USA

*Abstract*

A 1-MW, 352-MHz rf load was built at Argonne National Laboratory for performance testing the klystrons used as final amplifiers at the Advanced Photon Source (APS). The load utilizes four CERN-type 300-kilowatt coaxial water loads which are fed from a single WR2300 waveguide using a four-way power splitter consisting of a WR2300 hybrid-T junction and two WR2300 waveguide-to-dual-6-1/8" coaxial transitions. The load system is cooled using deionized water at a nominal flow rate of 160 GPM. The entire load system is mounted on a wheeled carriage which allows for rapid relocation to specific areas of the APS klystron gallery. The metering and interlock system will be described. The load has logged approximately 250 hours of use and has demonstrated accuracy in flow and temperature measurement sufficient to allow calorimetric rf power measurement.

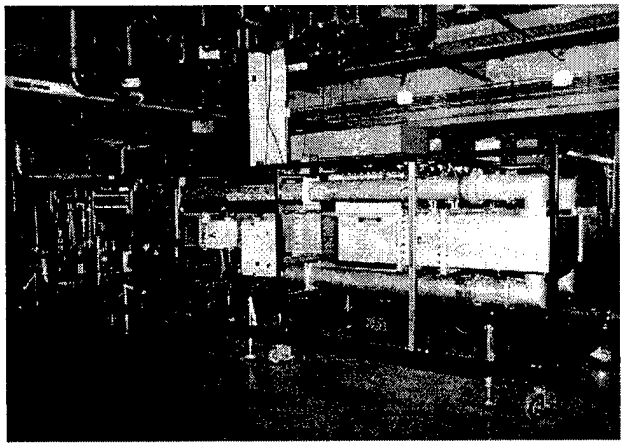


Figure 1: Side view of the rf load.

## 1 CAPABILITY REQUIREMENTS

A high-power rf test load capable of dissipating 1.2 MW at 352 MHz was built for full-power testing of the APS 352-MHz klystrons. The test load was designed with features which shorten required set-up time, thereby reducing rf system downtime when klystron testing or troubleshooting is necessary. The load system is a one-piece design with outside dimensions that allow for mobility to specific areas of the APS klystron gallery where the klystron rf output flanges are accessible. The existing APS deionized water system is used as a coolant source and features hose connections that provide rapid connections to the water supply and return lines at various locations in the building. The load has an interlock system which can protect each of the coaxial water loads individually against insufficient water flow and excessive return water temperature, and excessive voltage standing wave ratio (VSWR) on the H-plane outputs of the hybrid-T junction. The interlock system provides a dry contact for control of the high-voltage power supply (HVPS) used during klystron testing and rapid PIN-diode rf source switching to inhibit the rf drive to the klystron in the event a high-VSWR condition exists at either output of the hybrid-T junction.

## 2 DESIGN DETAILS

The rf power circuit of the load forms a four-way power divider, with the input power dissipated in four individual water-cooled rf loads (see Figure 1). A hybrid-T junction [1] was chosen as the first power divider in order to keep the overall width of the load system under 60 inches. The rf power input to the load is a standard WR2300 waveguide flange that terminates at the input of a WR2300 H-plane hybrid-T junction at either the H-plane or E-plane port, depending on orientation to the rf system output flange. Each of the two H-plane outputs of the junction are fed through WR2300 waveguide directional couplers to WR2300-to-dual-6-1/8" coaxial transitions. The orthogonal port of the hybrid-T junction is terminated with a shorting plate or a 50-ohm matched load to dissipate reject power due to load phase imbalance. Each 6-1/8" coaxial transition output is terminated with a 6-1/8" coaxial input water load.

The individual water loads were designed and manufactured at CERN. Each load consists of a coaxial line, made from stainless-steel components, shorted at one end with a plate that also provides for water inlet and outlet connections. Each load is capable of a maximum rf power dissipation of 300 kW, with a maximum outlet water temperature of 60°C. The water circuits of the load consist of 4" hose fittings which terminate into supply and return manifolds (see Figure 2). Four individual parallel water circuits, one for each coaxial rf load, complete the path between the supply and return water manifolds. The water circuit to each individual load includes flow throttling valves on both the inlet and outlet lines plus temperature and flow measurement devices. The outlet water flow for each load is measured using an electronic flowmeter and is also passed through a direct-reading float-type flowmeter for independent confirmation of the electronic flow measurement. Outlet water temperature of each load is measured using platinum RTD thermistors. Thermometer wells are provided on each load outlet line to allow use of standard mercury thermometers for independent confirmation of the electronic temperature measurement. The inlet

0-7803-4376-X/98/$10.00 © 1998 IEEE

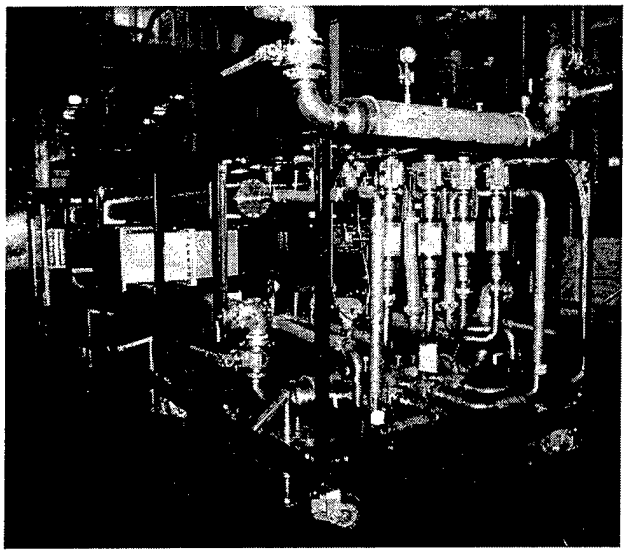


Figure 2: The rf load water system.

water temperature is measured using an RTD thermistor mounted in the inlet water manifold.

The load interlock systems protect against cooling water temperature and flow problems, and excessive VSWR conditions. The water interlock uses the programmable alarm-setpoint form-C dry contacts internal to each flow and temperature measurement meter to configure a series interlock circuit which provides a form-C dry contact for control of the HVPS supplying beam power to the klystron under test. If an under-flow or over-temperature condition exists on any of the individual coaxial water loads in the rf load system, the HVPS will be immediately shut down, removing beam power from the klystron under test. VSWR protection for the load system is provided by using the reflected-power outputs of the WR2300 directional couplers at each H-plane output of the hybrid-T junction. Each of these outputs is peak-detected and used to trigger the DC input of a PIN-diode fast rf switch controller, which removes the rf drive from the klystron in the event a high VSWR is detected at the input of either coaxial transition. Both interlock systems latch in the tripped state and require a manual operator reset to clear.

The load assembly is constructed on a unistrut frame equipped with wheels for easy mobility within the APS klystron gallery. The load carriage is also equipped with leveling jacks around the frame perimeter to assist in waveguide flange alignment when mating to the fixed rf output flange of the klystron under test.

## 3 PERFORMANCE MEASUREMENTS

The 1-MW rf test load system has logged approximately 250 hours of use to date during power-testing of klystrons and other high-power rf transmission components at the APS facility. It has demonstrated adequate stability in both impedance and power handling characteristics to be an effective load at the 1-MW power input level. However, during initial high-power tests of the load system, the power division between the four individual coaxial loads would occasionally become unbalanced at intermediate power levels. This resulted in one or two of the coaxial loads reaching their individual maximum power handling capability prematurely, thereby limiting the total dissipation of the load system to well under 1 MW. This power imbalance phenomenon was random in nature and suddenly occurred at various input power levels between 600 and 900 kW.

Thermal effects were the suspected cause of this power imbalance. As the rf impedance of the individual rf loads varied with water temperature (see Figure 3), a power imbalance between the loads began to appear. The impedance differential on the outputs of the hybrid-T junction further promoted imbalance of the system, and the phenomenon avalanched into greater power imbalance. Thermal expansion of the waveguide-to-coaxial transition components may have been responsible for the initial power imbalance. This original subtle difference then increased to greater power differential as the individual load temperatures change. During continued investigation of this phenomenon, it was noted that the power balance improved and remained much more stable if the inlet water temperature to the load system was raised from 25°C to approximately 30.5°C, and fans were positioned to cool the external surfaces of the waveguide coaxial transitions. With these changes, the load system became stable and power balance between the four coaxial loads remained close enough to allow 1-MW operation.

The rf input impedance of the load system varied with water temperature and provided a better match as the total power dissipation rose (see Figure 3). The best VSWR performance observed was 1.18:1 at a power input level of 928.1 kW. This VSWR is only marginally sufficient for direct-terminating load on the APS klystrons and, at lower power input levels, the load system match would exceed the maximum VSWR specification for the APS klystrons.

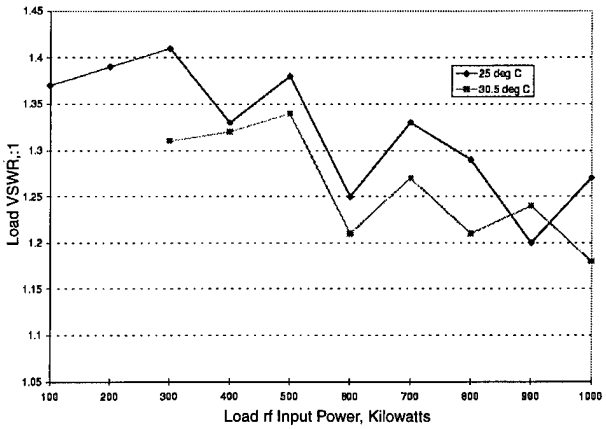



Figure 3: Load VSWR vs. water temperature.

Therefore, this load must be used in conjunction with a 1-MW Y-junction circulator when testing klystrons. The 3-dB return-loss bandwidth of the load system was measured under "cold" conditions and found to be approximately 3 MHz, exceeding the 1-dB power bandwidth of the klystrons.

The calorimetric power data with 1 MW of output power is shown in Table 1; the close power balance between the individual coaxial loads is apparent. The klystron output power was measured using a power meter on a WR2300 directional coupler immediately after the klystron output flange. Assuming waveguide and circulator transmission power losses of 15.5 kW and 40.1 kW, respectively, the calorimetric power calculation of the load power is within 2 percent of the total klystron rf output power, an accuracy sufficient to verify electronic power measurement data.

## 4 CONCLUSION

The 1-MW rf load system has proven to be adequate for high-power testing of the APS klystrons and rf transmission components. Future improvements to the load system include an on-board computer to perform real-time calorimetric calculations of the power dissipation for each coaxial load directly from the water flow and temperature data and to provide remote status readout capability over an RS232 data link. Permanent fans will also be installed on the load system to enhance the cooling of the coaxial transition components.

## 5 ACKNOWLEDGMENTS

The authors would like to thank Eugene Swetin and Andy Kelly of the APS Mechanical Engineering Group for their assistance in the design and assembly of the water system and support structure of the load. Work is supported by the U.S. Department of Energy, Office of Basic Energy Sciences, under Contract No. W-31-109-ENG-38.

## 6 REFERENCE

[1] R. E. Collin, *Foundations for Microwave Engineering*, McGraw-Hill, pp. 435-437, 1992.

Table 1: Calorimetric Power Data at 1 MW rf Input Power

| | **Load 1** | **Load 2** | **Load 3** | **Load 4** |
|---|---|---|---|---|
| **Flow Rate** | 40 gpm | 40 gpm | 40 gpm | 40 gpm |
| **Supply Temp, °C** | 30.6 | 30.6 | 30.6 | 30.6 |
| **Return Temp, °C** | 52.2 | 52.8 | 52.4 | 52.6 |
| **Water Power, kW** | 228.09 | 234.43 | 230.20 | 232.32 |
| Total water heat = 925.04 kW<br>Estimated total waveguide transmission losses = 15.5 kW<br>Estimated circulator rf transmission losses = 41.0 kW<br>TOTAL rf power = 981.54 kW | | | | |

# DESIGN AND CONSTRUCTION OF THE ADVANCED PHOTON SOURCE 352-MHZ RF SYSTEM SWITCHING CONTROL

D. Horan, L. Solita, D. Reigle, N. Dimonte
Advanced Photon Source, Argonne National Laboratory
9700 South Cass Avenue, Argonne, Illinois 60439 USA

*Abstract*

A switching control system has been designed and built to provide the capability of rapidly switching the waveguide and low-level cabling between different klystrons to operate the Advanced Photon Source storage ring in the event of a failure of a klystron system or to perform necessary repairs and preventative maintenance. The twelve possible modes of operation allow for complete redundancy of the booster synchrotron rf system and either a maximum of two storage ring rf systems to be completely off-line or one system to be used as a power source for an rf test stand. A programmable controller is used to send commands to intermediate control panels which interface to WR2300 waveguide switches and phase shifters, rf cavity interlock and low-level rf distribution systems, and klystron power supply controls for rapid reconfiguration of the rf systems in response to a mode-selection command. Mode selection is a local manual operation using a keyswitch arrangement which prevents more than one mode from being selected at a time. The programmable controller also monitors for hardware malfunction and guards against "hot-switching" of the rf systems. The rf switching control system is monitored via the Experimental Physics and Industrial Control System (EPICS) [1] for remote system status check.

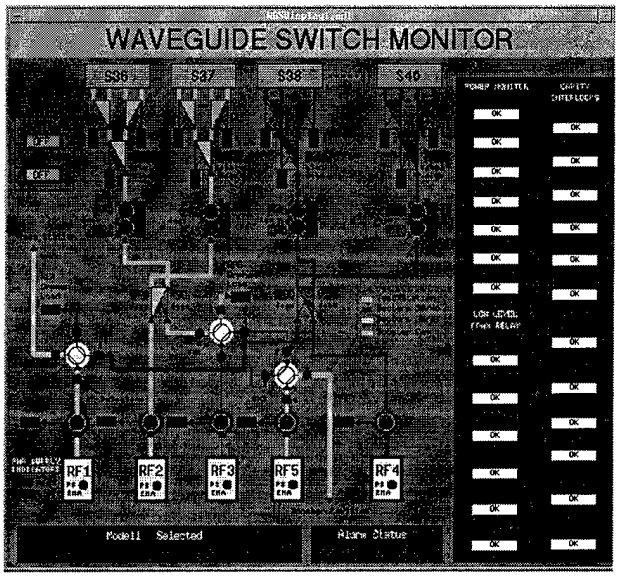



Figure 1: The APS rf system switching control screen.

## 1 RF SYSTEM SWITCHING OVERVIEW

The Advanced Photon Source has five 1-MW, 352-MHz klystron rf systems installed. The storage ring can operate with either two, three, or four rf stations online, using hybrid combiners/3-dB splitters to operate two rf stations in parallel (see Figure 1). One of the storage ring rf systems can also serve as an operational spare for the booster synchrotron rf system, and another can be used as a power source for a 1-MW rf test stand.

The rf stations can be combined in a variety of ways to provide twelve distinct modes of operation that require changes in waveguide rf circuit configuration, interlock system delegation, and low-level rf signal distribution to permit proper operation of the rf systems. The rf system switching controls execute and verify the required circuit changes for each mode automatically in response to a manual operator command and provide system monitoring functions. Motor-driven WR2300 waveguide switches are used to route the rf output of specific rf stations to a designated load, or to take the systems off-line in the event of a failure or for maintenance. Motor-driven WR2300 phase shifters are used to correct for output port phase differences when the 3-dB hybrids are used as combiner/splitters with rf stations in parallel, or as power dividers when a single rf system is used. The cavity and klystron interlock signals for each rf system are routed and delegated, respectively, by the switching control system to insure that all interlock circuits required by the accelerator hardware are routed to the rf system supplying the power.

The heart of the rf system switching control is an Allen-Bradley programmable logic controller (PLC) that is interfaced to the existing rf system hardware by eight intermediate relay interface panels (see Figures 2 and 3). The PLC accepts manual mode requests from operations personnel via a keyswitch panel, executes all necessary system changes required by the selected mode, and monitors overall system status.

## 2 SYSTEM CONTROLLER PROGRAM

The PLC operating program is written to provide a user-friendly interface to the complex task of reconfiguring multiple electrical circuit paths when an rf system operating mode change is requested. It also verifies correct hardware responses to system controller commands and can display error conditions on a local screen as a system troubleshooting diagnostic aid. The program also prevents "hot switching" of rf components by verifying that all rf power is off before any circuits are reconfigured. Mode selection commands are input to the system via the mode

0-7803-4376-X/98/$10.00 © 1998 IEEE

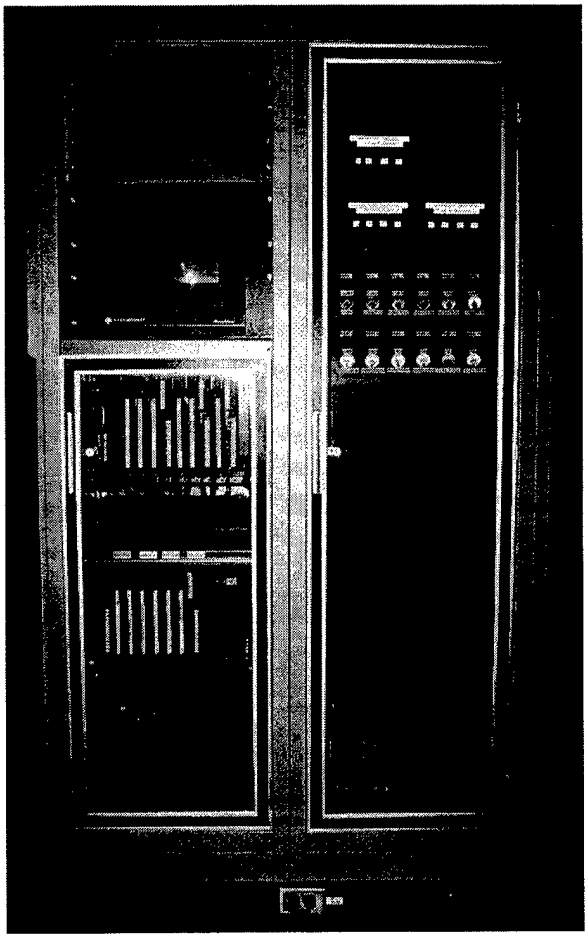


Figure 2: PLC hardware and mode keyswitch.

selection keyswitch panel (see Figure 2), which provides for administrative control of the switching system and prevents selection of more than one mode at a time. The output of the selection switch panel is continuously monitored by the PLC and triggers the PLC to begin the process of mode switching.

The mode selection sequence of events begins with mode-change recognition, where the PLC sends an immediate shutdown command to all rf high-voltage poser supply (HVPS) units, followed by a check for rf presence in all waveguide switch ports to insure all high-power rf is off. The PLC then refers to look-up tables to determine the correct configuration of waveguide switches, phase shifters, cavity interlock delegation, rf power monitor delegation, and low-level rf signal distribution required to support the selected mode. The waveguide switches and phase shifters are first commanded to move to their required positions, with a time limit imposed to trigger an error indication and abort the mode change command in the event a mechanism is balky or not moving. Once these movements are complete and home positions match the truth table values, the interlock, low-level rf, and power monitor circuits are delegated to match their truth table values for the selected mode. These circuits are configured within one second, as this action requires merely the activation of delegation relays. Once all status indicators match the truth table values for all circuits, the PLC sends an enable command to the rf HVPS units that clears them for manual turn-on by system operators.

During rf system operation, the PLC continuously monitors the status of all waveguide switches and phase shifters for unauthorized movement and immediately shuts down the rf HVPS units if such a condition is detected. The status of all intermediate relay interface panels is also monitored to detect any unauthorized change in state, which is indicated as an error message on the PLC screen. The rf detector output at the waveguide switch ports is compared with a truth table of expected locations of rf power for a given mode; any discrepancies generate an error message on the PLC screen.

## 3 SOFTWARE AND SYSTEM MONITORING

The PLC system interfaces rf system input and output devices to a programmable logic processor, which is user-programmed using an IBM-compatible computer running a "ladder-logic" editor. The editor displays the status of input and output devices as relay contacts and coils. These displays are used to build logical relationships implemented by the program algorithm. Ladder logic is an

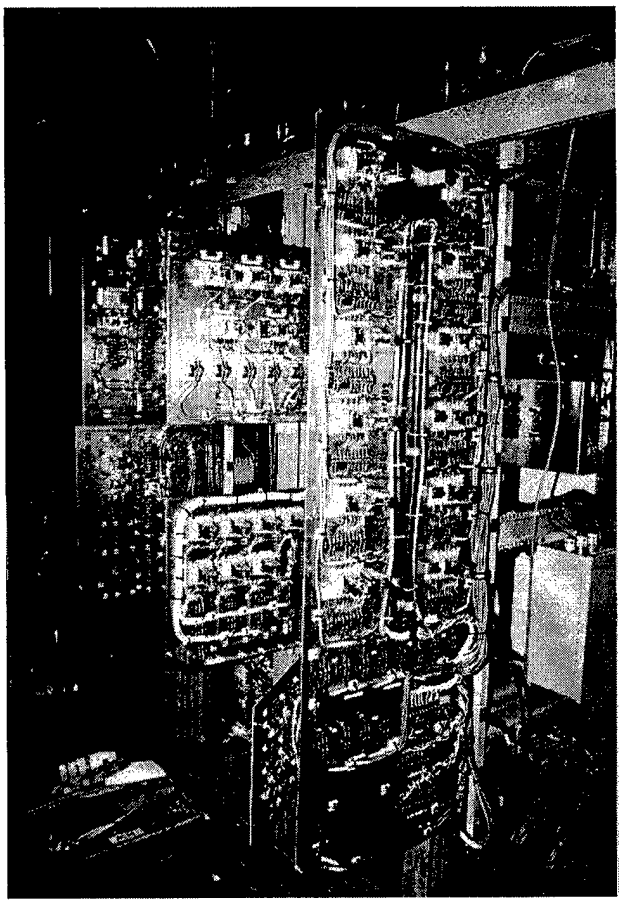


Figure 3: System interface relay panels.

interpretative programming language and displays PLC states in real time on the computer. Simple logic functions are easily programmed as are more complex functions such as timers, counters, file manipulation, sequencers, and interfaces to display devices like Panelview. The PLC processor constantly calculates a checksum that is unique to each application program.

The Allen-Bradley Panelview provides a local status display of the rf HVPS units, waveguide switches and rf detectors, phase shifters, and delegation relays for the cavity interlock, rf power monitor, and low-level coaxial relay systems. Each of these system components is represented on the screen by an identifying icon. As these devices move to their correct position for the operational mode selected, they appear red on the screen. When all devices are in the correct position, the entire status screen is green, and the PLC will enable the five rf HVPS units so they can be energized by operations personnel. The power supplies remain enabled until another mode is selected or the PLC detects that a waveguide switch or phase shifter has moved from its correct position.

For system troubleshooting, diagnostic screens are provided on the Panelview. Faults are latched and time-date stamped to help detect intermittent failures. The operator can select a real-time diagnostic screen for comparison to a reference screen to identify faults. The fault information is retained until another trip is detected. The status of the PLC processor is also displayed, including the program checksum, memory battery status, program scan time, and force status. EPICS is also used to display system status remotely (see Figure 1). This display screen indicates rf system status, waveguide switch and phase shifter position, and present operational mode. The EPICS alarm handler alerts operators to abnormalities in mode status and errors detected in delegation relays for each rf subsystem the PLC controls.

## 4 HARDWARE INTERFACE DESIGN

The PLC communicates with the rf hardware using intermediate relay panels for each subsystem requiring control and monitoring (see Figure 3). These subsystems include waveguide switch control, waveguide phase shifter control, rf HVPS control, cavity interlock contact sum delegation, rf power monitor delegation, low-level rf signal routing, rf presence detectors, and mode selector keyswitch panel. Each of these panels is supplied 24-volt DC control power from a central distribution chassis that supplies both continuous and switched 24-volt DC outputs. The switched output is enabled only when the PLC watchdog tuner indicates that the operating program is running. The watchdog-switched 24-volt output disables any critical control function of the switching system when the PLC program is not running.

The motorized waveguide switches and phase shifters use 120-volts AC for motor power; this voltage is accessed locally to each device through individual circuit breakers. This AC power is then looped through local relays which are energized by the PLC only when switch or phase shifter movement is required. In this way, the possibility of unintentional movement of the rf hardware through accidental short circuits is reduced. Home-position limit switches inside each waveguide switch and phase shifter provide contact closures which supply the PLC with position indications. The PLC also verifies the correct operation of all other intermediate control relays by monitoring their auxiliary contacts.

The rf detector system uses waveguide directional couplers and peak detectors, located close to each waveguide switch port, to generate a proportional DC voltage which is converted to a 4- to 20-mA current signal for routing to an adjustable alarm module. This module converts the 4- to 20-mA signal to a dry contact closure which supplies an input to the PLC when rf is present in the switch port waveguide. These rf detectors are used as a last check for the presence of high-level rf in all waveguide switch ports before the PLC sends the command to change switch or phase shifter positions.

## 5 CONCLUSION

The rf switching control system designed and installed at the Advance Photon Source provides accelerator operators with a user-friendly interface capable of reconfiguring complex rf systems rapidly in the event of a system failure, thereby reducing accelerator down time. It provides redundancy for both the storage ring and booster synchrotron rf systems and provides remote system status information for diagnostic purposes.

## 6 ACKNOWLEDGMENTS

I would like to recognize Nick Dimonte of the APS Controls Group for his efforts in developing the EPICS display screen for this project, and also Mike Phelan, Gian Trento, and Carl Gonzalez of the APS RF Group for their work building and installing the interface hardware. This work was supported by the U.S. Department of Energy, Office of Basic Energy Sciences, under Contract No. W-31-109-ENG-38.

## 7 REFERENCES

[1] L. R. Dalesio, M. R. Kraimer, A. J. Kozubal, "EPICS Architecture," Proc. of ICALEPCS '91, Tsukuba, Japan, KEK Proceedings 92-15, pp. 278-282 (December 1992).

# SUPPORTS AND INSTALLATION SYSTEM OF THE RHIC SUPERCONDUCTING MAGNETS

Rudy Alforque, Brookhaven National Laboratory, Upton, New York 11973
and
Jim Cammarata, Bill DeVito, Frank Karl, Tom Muller,
Steve Kane, Gary McIntyre, Ray Savino, and Jack Sondericker,
Brookhaven National Laboratory, Upton, New York 11973

*Abstract*

The Relativistic Heavy-Ion Collider that is currently under construction at Brookhaven National Laboratory is composed of hundreds of superconducting magnets. A careful study was done in order to support and install these magnets inside the RHIC tunnel systematically and efficiently. A basic systems-approach was pursued and primary consideration was given to develop a system that would not be only both economical and efficient but also well-suited to a fast-paced production environment. This report will present a description of the design of the magnet stands and the magnet transport and installation system, the procurement and fabrication phase, and then finally, the experience gained in implementing the system. In summary, the system turned out to be very efficient and cost-effective far beyond our expectations.

## 1 MAGNET STANDS

Although the original plan was to provide three vertical supports for the 6-ton, 33-ft. long arc dipoles, i.e. two end stands and one in the center, after a thorough finite-element study, I recommended eliminating the center support since the results showed a reasonably acceptable vertical sag. (The dipole cold mass, however, still retained its 3-point vertical support inside the vacuum vessel). Without the center support, the savings would be significant owing to the fact that there would be a few hundred dipoles.

The recommendation was accepted, but in addition, it was also decided that all the magnets may have the same stands. Therefore, although, there were a few design alternatives that were considered and studied, for an optimized, cost-effective design geared towards production quantities, the most attractive choice was a *casting*.

### *1.1 Design, Fabrication, and Procurement*

The primary structural requirement was to support the magnet dead weight as well as the axial forces that might result from a worst-case scenario triggered by a magnet quench, vacuum failure, etc. The dipole was estimated to weigh 6 tons; the worst-case axial force was estimated to be also about 12,000 lbs. Based on these loads, a conceptual casting design was made, and a finite-element study was undertaken. I chose ductile iron, specifically ASTM A536 Gr 80-55-06, owing to its superior strength and corrosion resistance over gray iron.

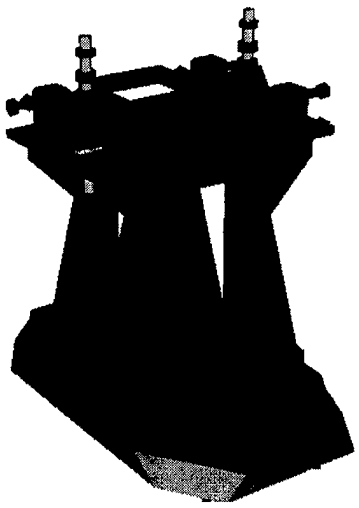


**Figure 1: Magnet Stand (Solid Model)**

The solid model of the casting is shown in Fig. 1. The figure shows also the adjusting slider and the x-y-z adjusting screws that would enable the surveyors to position the superconducting magnets accurately.

When the design was approved after the final design review, detailed fabrication drawings were made, and then the procurement process began. Without going into details, which would be irrelevant for this report anyway, the magnet stands were finally fabricated and delivered well on schedule by a reputable company in Orange, Massachussets, U.S.A., called Rodney Hunt Co. who did an excellent job for us.

### *1.2 Installation*

The installation of the magnet stands was done by the Collider Ring Division's Survey Group. First, they laid out the Rhic ring, and then using a template of the magnet stand footprint they installed the 3/4-inch Hilti-Drop-In anchors, and subsequently, the anchor bolts. At some

0-7803-4376-X/98/$10.00 © 1998 IEEE

locations, special "maxibolts" from Drill-Co, another company from Long Island, New York, were added in order to absorb the expected greater pull-out loads due to a large unbalanced force on the warm-to-cold transition. Next, the magnet stands were positioned into place, leveled, and then set to a specified elevation. Subsequently, the base was grouted to the tunnel floor.

The installation group added the additional hardwares, i.e. the adjusting sliders and the x-y-z jacking screws. After this last step, the stands were ready to accept the magnets.

By the end of June, 1995 all of the required magnet stands were fully installed.

## 2 TRANSPORTERS

Having completed the design of the magnet stands, the next step was to design the magnet transporters. There would be no overhead cranes available inside the Rhic tunnel for magnet installation, so the transporters would serve also as the main installation mechanism to install the magnets into the stands.

The primary parameters in the design of the transporters were the following:

•Structural integrity: The transporters should not only be strong, durable and rugged enough to carry repeatedly the prescribed load, they should be designed to assure safety of the personnel who would be installing the magnets,

•Adjustability and maintainability: The transporters should be modular, adjustable, and maintainable since they would be subjected to repeated load cycles as hundreds of Rhic magnets were going to be installed; In addition, they would have to be usable in the future, when a necessity might arise to remove and replace some ring magnets,

•Cost-effectiveness: The transporters should be simple, and easy and convenient to use in order to minimize actual magnet installation time, thus maximising the number of magnets that could be installed in a given day to save installation labor cost. Considering the difficulties facing us then, the design objective was to install at least 2 magnets in an 8-hr. day.

Another aspect that also controlled the transporter design was the fact that there are only 3 specific locations, namely 4:00 o'clock, 8:00 o'clock, and 12:00 o'clock, that would allow us to install/remove magnets. These entry/removal points are all located in the inner part of the ring.

### *2.1 DIPOLE MAGNET TRANSPORTER*

As I mentioned earlier, the arc dipole magnets were the heaviest magnets, about 6 tons in weight, to install as a unit. Each one was also about 35 ft. long, including all the cryo pipes and wires protruding at both ends, and it would be a major challenge to transport and maneuver it inside the tunnel.

But the arc dipoles were also the first ones to be available for installation. Hence, the dipole transporter was the first one to be designed and fabricated.

After the final design review, we fabricated the transporter in-house. Then we proof-tested the whole assembly by loading it with a fully assembled arc-dipole plus 25% more extra load. During the test, the actuators performed as expected and it was approved and commissioned for service by the safety representative.

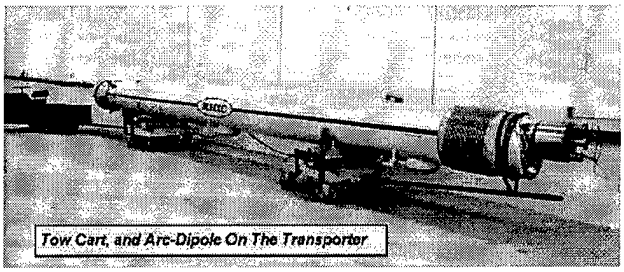



**Figure 2: Arc Dipole On Transporter**

Figure 2 above shows a dipole cradled by the transporter being pulled by a small electric Taylor-Dunn cart inside the Rhic tunnel. The cart had been modified and re-geared in order to limit its speed below 6 mph for personnel safety. The two transporter carts shown at each end of the magnet are mirror images of one another, and both have electrically-driven actuators that are simultaneously controlled from a main control box; These mechanical screw actuators would allow vertical adjustability. Furthermore, alathane wheels were used for their durability and ruggedness.

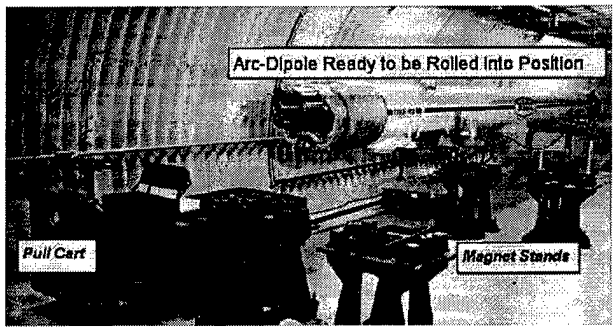



**Figure 3: Dipole Installation**

Figure 3 above shows the arc-dipole in its raised position a little above the magnet stands. From this position, the wheels would be rotated 90° and then the whole assembly would be pushed carefully to a nominal position directly over the stands. The mounting holes on the magnet support base would be aligned with the vertical mounting bolts on the stands and then the magnet

would be lowered down until it would hit a prescribed nominal vertical position. The magnet would now be safely resting on its support and the transporter assembly could now be rolled out. The entire process of trucking and transporting a magnet from the storage area to the ring and then completing the whole installation would take a little over an hour. In an 8-hr. day, six (6) arc-dipoles could be fully installed, or three-fold from the original design objective!

### *2.2 ADJ-LENGTH MAGNET TRANSPORTER*

The arc-CQS (CQS: Corrector, Quadruple, Sextuple) magnets are much shorter and lighter than the arc-dipoles. Aside from the arc-CQS's, there are also several other magnets with various different lengths in the insertion region. Therefore it was decided to design and fabricate an adjustable-length transporter in order to accommodate all the CQS's and the insertion magnets.

It should be noted, however, that based on the concept of the dipole transporter, the installation group also made a dedicated CQS transporter/installer out of a lift table that fitted well in between the stands of the arc-CQS. Although this lift table transporter would have limited use in the removal/replacement of arc-CQS's, it certainly served very well in the installation phase like the dipole transporters.

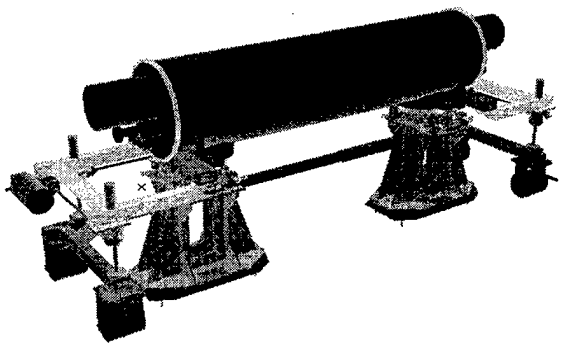


**Figure 4: Adj-Length Transporter (Solid Model)**

The adjustable-length transporter would have a load-carrying capacity of about 1/3 that of the dipole transporter. But unlike the dipole transporter that fits "in-between" the stands, this new transporter would have to go "around" the magnet stands since the stands of the shorter magnets were very close to one another. Figure 4 shows the conceptual layout of the adjustable-length transporter as a CQS magnet was installed into position. Again, this transporter was fabricated in-house, and upon completion, it was first proof-tested before it was put in service.

Unfortunately, a short insertion dipole turned out to be significantly heavier than the arc-CQS. Although the mechanical actuators and other components were designed to handle the excess load, the horsepower of the drive motor was not sufficient enough. After replacing the drive motor, however, the whole system worked well as planned.

## 3 MAGNET INSTALLATION PROCEDURES

The final selection and sorting of the magnets was done by the Rhic Accelerator Physics (RAP) group. All magnets were serialized and assigned to specific locations inside the Rhic ring based on a general project-wide nomenclature and naming convention.

A database was created to automate the generation of traveller sheets that went with each magnet. The database was published on the Rhic Accelerator Systems webpage for easier access and was updated at least once a week as new magnets were accepted and assigned to their respective locations in the ring.

The magnet acceptance crew would print out the necessary information relevant to a particular magnet. They would attach this information to the magnet before turning it over to the installation crew. This process was done at the magnet storage area where the magnets would be loaded unto the transporter on top of a flatbed truck and then moved to one of the three loading docks in the inner periphery of the Rhic ring as indicated in the traveller sheet. It should be noted that a given magnet would have to be at a specific orientation as it was pulled out from the flatbed towards the tunnel since there was no room inside the tunnel to turn it around.

## 4 CONCLUSION

The experience in installing the superconducting magnets in the Rhic ring had shown that a basic systematic approach in planning and designing the support and transport system proved quite beneficial in the long run. Computer modelling and simulation contributed significantly in visualizing basic concepts especially in checking and verifying interferences. Costly proto-typing was essentially avoided.

We started installing arc dipoles in August, 1994, and by the end of February, 1996, all 264 arc-dipoles were installed; Installation of the arc-CQS started around March, 1995 and as of April, 1997, 98% were already installed. The main constraint now is simply the availability of magnets that are ready for installation.

For further information, check the Rhic collider ring installation webpage at the following address:
http://www.collider.bnl.gov/installation/installation.html

# SYSTEMS LAYOUT OF THE LOW-$\beta$ INSERTIONS FOR THE LHC EXPERIMENTS

R. Ostojic, T. M. Taylor and S. Weisz,
CERN, CH-1211 Geneva 23, Switzerland

*Abstract*

The LHC experimental insertions consist of a low-$\beta$ triplet, a pair of separation dipoles, and a matching section of four quadrupoles. The superconducting low-$\beta$ quadrupoles must accommodate separated beams at injection, provide high field gradients and low multipole errors for colliding beams, and sustain considerable heat load from secondary particles generated in the high luminosity ATLAS and CMS experiments. In the other two proposed experiments, ALICE and LHC-B, the separation dipoles and matching sections share the available space with the injection equipment. In this report we present the systems layout of the experimental insertions for the LHC, and review the requirements for the superconducting magnets.

## 1 INTRODUCTION

The layout of the Large Hadron Collider comprises eight straight sections available for experiments and major machine systems [1]. The two high luminosity p-p experiments, ATLAS and CMS, are located on the symmetry axis of the machine, at interaction points 1 and 5. The other two proposed experiments, ALICE and LHC-B, are at points 2 and 8, where beam injection will occur. In these four insertions the two beams are guided onto crossing orbits by a pair of recombination-separation dipoles.

The final focus in the low-$\beta$ insertions is achieved with a inner triplet together with a matching section of four quadrupoles. In the low-$\beta$ triplets the beams travel in a single beam tube, and must be sufficiently separated at all times. Besides providing high gradients in a sufficiently wide aperture, the superconducting low-$\beta$ quadrupoles must sustain considerable heat load from secondary particles generated in the high luminosity collisions. At points 2 and 8, the luminosity is lower but the matching section and separation dipoles share the available space with the injection equipment, creating further constraints.

## 2 HIGH LUMINOSITY INSERTIONS

The layout of the left half of a LHC high luminosity insertion is shown in Figure 1. The ATLAS and CMS insertions are identical, and are mirror symmetric around the interaction point. The insertion consists of a low-$\beta$ triplet, a pair of recombination-separation dipoles, D1-D2, and a matching section of four quadrupoles, Q4-Q7. It is designed for a collision $\beta^*$ of 0.5 m, corresponding to the nominal LHC luminosity of $10^{34}$ cm$^{-2}$s$^{-1}$ at 7 TeV. At injection energy, the insertion is detuned by adjusting the matching section to a $\beta^*$ of 12 m. The low-$\beta$ triplets do not participate in the tuning, except to keep the phase advance of the insertion constant. The matching section has enough reserve to adjust the $\beta^*$ of the insertion beyond the nominal range.

### 2.1 *Low-$\beta$ Triplets*

The low-$\beta$ triplets, shown in Figure 2, consist of four wide aperture superconducting quadrupoles powered by a common power supply. The outer two quadrupoles, Q1 and Q3, are 6.3 m long, while the central one is divided for convenience into two identical units, Q2a and Q2b, 5.5 m each. The low-$\beta$ triplet is 23 m from the interaction point, and is preceded by a 1.8 m long copper absorber (TAS), located within the front shielding of the experiments.

One of the most important issues in the design of the low-$\beta$ triplets is the protection of the superconducting quadrupoles against the high flux of secondary particles emanating from the p-p collisions at nominal luminosity. This issue has been studied by several groups [2, 3], and it has been found that the Q2a quadrupole, where the power density due to the secondaries is the highest, can be better protected by optimising its distance from Q1. Based on these studies, the separation between Q1-Q2a has been set to 2.5 m, sufficient to place a supplementary 1.5 m absorber. Protection of the triplet as a whole may be further improved by increasing the thickness of the quadrupole cold bore.

The space of 1 m between Q2a and Q2b is required for the combined horizontal-vertical orbit corrector. In this location the $\beta$-function has a maximum in one plane, while the maximum in the orthogonal plane occurs upstream of Q3, where an additional orbit corrector is envisaged. The space between Q2b and Q3 is used to adjust the optics of the single parameter low-$\beta$ triplet to that of the matching section. The resulting drift of 3.5 m is slightly longer than otherwise needed for magnet interconnects, a BPM and multipole spool pieces.

The single aperture quadrupoles Q1-Q3 are considered the most demanding magnets in the experimental insertions. Besides accommodating fully separated beams at injection, they must provide a high field gradient and low multipole errors required for the colliding beams, and sustain high power density of the secondary particles. A 70 mm aperture quadrupole with a design gradient of 240 T/m adequately fulfils these requirements. A magnet development program for the low-$\beta$ quadrupole is in progress in CERN, Fermilab and KEK [4, 5, 6]. The successful test of the first low-$\beta$ quadrupole model [7], indicates that the chosen operating gradient of the triplet, 200 T/m at 7 TeV, provides an adequate operational margin at full luminosity.

0-7803-4376-X/98/$10.00 © 1998 IEEE

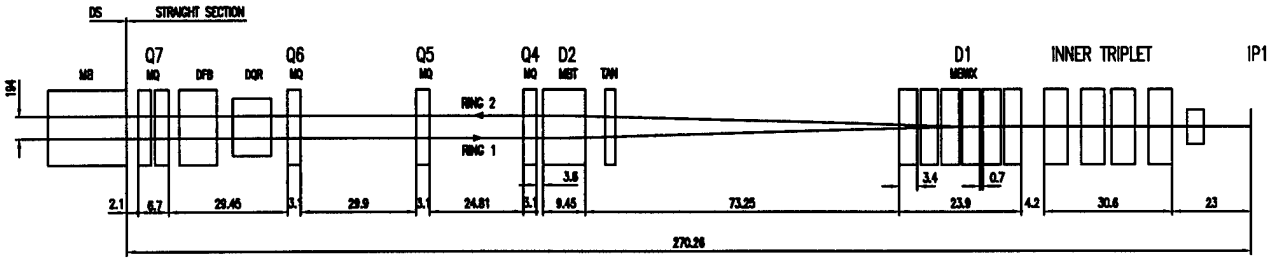



Figure 1: Schematic layout of the left half of the LHC high luminosity insertion. The layout is symmetrical with respect to the IP, and is identical for the ATLAS and CMS experiments.

### 2.2 *Separation Dipoles and the Matching Section*

The separation of the beams must be made as close as possible to the interaction point in order to avoid long range parasitic crossings, which occur every 3.75 m in the common vacuum chamber. The separation is accomplished with a pair of bending magnets, D1 and D2. It has been proposed in [1] that both D1 and D2 be superconducting magnets using identical coils. This solution has been a matter of concern since similarly to the low-$\beta$ triplet, D1 is also submitted to intense irradiation by the secondaries. Its magnetic field deviates the charged particles into its own coil, so that its aperture has to be larger than 80 mm in order to avoid excessive energy deposit [3]. On the other hand, a coil aperture greater than 90 mm seems to be incompatible with a bore separation of 194 mm in the two-in-one D2. An alternative, retained in this proposal, is to use a resistive D1, which is made possible by the larger separation between the dipoles than proposed in [1]. The neutral secondaries are not deviated by D1 and are stopped in a dedicated absorber (TAN) placed a few metres downstream of the two-in-one superconducting D2. D2 has a coil aperture of 80 mm and is located 155 m from the interaction point.

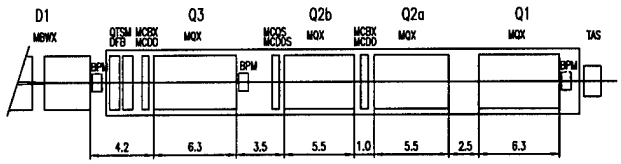



Figure 2: Schematic layout of the LHC low-$\beta$ triplet.

The matching section of the high luminosity insertion consists of four twin aperture quadrupoles, Q4-Q7. These are standard LHC arc quadrupoles with independent powering of apertures. In the nominal tuning range, the gradients of the matching quadrupoles vary down to 35% of the nominal gradient of 210 T/m.

### 2.3 *Crossing Scheme and Geometrical Acceptance*

The nominal LHC luminosity is achieved with the beams colliding at a full crossing angle of 200 $\mu$rad [1]. At injection, and similarly at top energy prior to collision, the beams need to be separated in the common part of the vacuum chamber, typically by 10 $\sigma$. The separation scheme consists of imposing a crossing angle at the interaction point, together with a parallel separation of the beams in the plane orthogonal to the crossing plane. The crossing plane may be additionally rotated around the longitudinal axis in order to limit the effects of the long range interactions [8]. As a result, the beams follow complicated trajectories in the low-$\beta$ triplets, so that the beam separation and the geometrical acceptance of the triplets depend on all parameters of the scheme.

The method used for calculating the acceptance of LHC magnets is based on fitting the normalised beam halo, which is the result of multi-turn beam cleaning, to the shape of the magnet cold bore [9]. Specific conditions in each magnet, such as $\beta$-functions, closed orbit errors, mechanical tolerances and alignment, are taken into account, and the acceptance calculated in terms of the equivalent primary collimator aperture. For the nominal primary collimator at 5.5 $\sigma$, an acceptance greater than 7 $\sigma$ is required everywhere in the insertions. In Figure 3, the beam separation and the acceptance of the low-$\beta$ triplet are shown for the injection $\beta^*$ of 12 m and full crossing angle of 400 $\mu$rad. In this particular case, the beam separation is larger than 10 $\sigma$, and the acceptance of the triplet is greater than the required primary collimator equivalent of 7 $\sigma$. The acceptance minimum occurs in between Q2a and Q2b, as shown in Figure 3, or at the upstream end of Q3 if the crossing plane is rotated by 45 degrees. An analysis of different sets of crossing parameters leads to the conclusion that the 70 mm aperture of the low-$\beta$ quadrupole is large enough to accommodate crossing angles of up to 450 $\mu$rad, both at injection and collision energies.

These results correspond to the optics studied to date. Recent layout studies indicate that the low-$\beta$ triplet could be advanced by about 0.5 m towards the IP, without modifications to the experiments. As a result, the acceptance of the triplet would be increased, and $\hat{\beta}$ in Q2-Q3 reduced. For the purpose of operating margin, 10 cm longer low-$\beta$ quadrupoles should be foreseen.

## 3 EXPERIMENTAL INSERTIONS COMBINED WITH BEAM INJECTION

The layout of the low-$\beta$ insertions for the ALICE and LHC - B experiments follows the same general approach of the high luminosity insertions, i.e. a matching section of four quadrupoles is used to tune the low-$\beta$ triplets. The

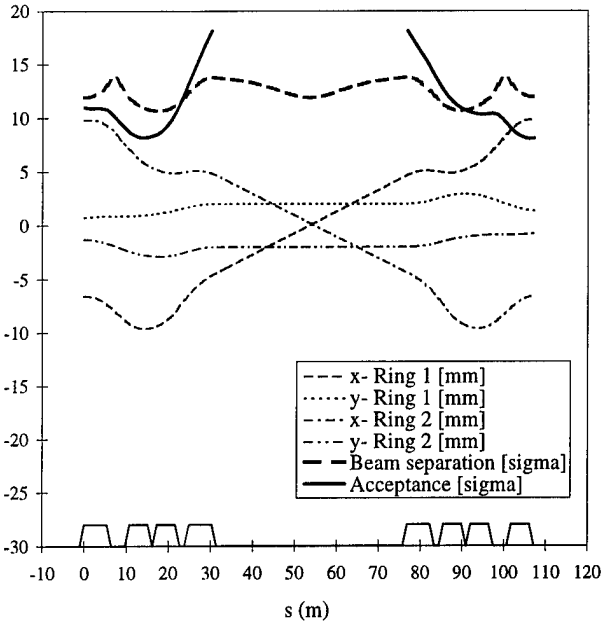



Figure 3: Trajectory of the two beams in the low-$\beta$ triplets for a horizontal plane at full crossing angle of 400 $\mu$rad and vertical separation of 4 mm. The separation of the beams and geometrical acceptance of the quadrupoles are also shown for these conditions.

important difference comes from the fact that in both insertions the layout of the matching section must satisfy the severe requirements of the beam injection system. For example, long warm drifts between the quadrupoles must be provided for the injection kicker and septum magnets, whose position is related to the geometry of the beam injection tunnels. Furthermore, strict requirements must be fulfilled in order to protect the low-$\beta$ triplets and the rest of the machine against badly injected or accidentally kicked circulating beams. Although these requirements substantially limit the flexibility of the insertion, it is nevertheless continuously tunable from the injection $\beta^*$ of 12 m to a collision value of 0.5 m. To allow ALICE runs with p-p collisions, the $\beta^*$ can be detuned up to 250 m. The difficulties in fulfilling the injection requirements are partially offset in LHC-B where the interaction point is displaced by 11.25 m from the centre of the insertion, leaving more space between the injection magnets and the matching quadrupoles. The layout then provides a tuning range of 5-50 m for the LHC-B experiment.

The low-$\beta$ triplets in ALICE and LHC-B insertions are identical to those in the high luminosity insertions, except that the front absorber is not required. Due to the shortage of space, both D1 and D2 are 9.45 m long superconducting dipoles. While the aperture of D1 is determined by the separation scheme, that of D2 must be large enough to allow the passage of miskicked beams. It has been determined that in both cases a coil aperture of 80 mm is sufficient, leading to a proposal where identical coils are used in both the single aperture D1 and two-in-one D2, and the two dipoles could possibly be powered in series.

The matching section quadrupole Q5 has a particular role as the beam is injected through it at vertical angle of 0.35 mrad. Similarly, Q4 must be big enough to let pass accidentally kicked beams. In both cases, it is proposed to use twin aperture quadrupoles with a coil aperture of 70 mm [10]. These quadrupoles have sufficient acceptance to cope with these situations, but constrain the placement of dipole correctors used for the crossing scheme. The other quadrupoles in the matching section are standard LHC arc quadrupoles, except that the cryostat of Q6 has to be adapted for the passage of injection lines.

## 4 CONCLUSIONS

The design of the LHC low-$\beta$ insertion has advanced to the point where the requirements of experiments could be harmonised with the flexibility of the collider operation and superconducting magnet performance. In this report we have reviewed the systems layout of the experimental insertions, and specified the requirements for the superconducting magnets.

## 5 REFERENCES


[1] The LHC Study Group, *The Large Hadron Collider, Conceptual Design*, CERN/AC/95-05.

[2] A. Morsch, R. Ostojic, T.M. Taylor, "Progress in the Systems Design of the Inner Triplet of 70 mm Aperture Quadrupoles for the LHC Low-$\beta$ Insertions", Proc. 4th European Part. Accel. Conf., London, England, 1994, pp. 2274-2276.

[3] J. Strait and N. M. Mokhov, "Optimisation of the LHC Interaction Region With Respect to Beam-Induced Energy Deposition", 5th European Part. Accel. Conf., Barcelona, Spain, 1996, LHC Project Report 43.

[4] R. Ostojic T.M. Taylor and G.A. Kirby, "Design and Construction of a One-Metre Model of the 70 mm Aperture Quadrupole for the LHC Low-$\beta$ Insertions", *IEEE Trans. Magn.* **30** pp 1750-1753, 1994.

[5] R. Bossert et al., "Design of a High Gradient Quadrupole for the LHC Interaction Regions", 1996 Appl. Superconductivity Conf, August 1996, Pittsburgh, USA.

[6] A. Yamamoto et al., "Design Study of a Superconducting Insertion Quadrupole Magnet for the Large Hadron Collider", 1996 Appl. Superconductivity Conf, August 1996, Pittsburgh, USA, LHC Project Report 75.

[7] R. Ostojic et al., "Quench Performance and Field Quality Measurements of the First LHC Low-$\beta$ Quadrupole Model", presented at this Conference.

[8] J. Miles, private communication.

[9] J.B. Jeanneret and T. Risselada, "Geometrical Aperture in LHC at Injection", LHC Project Note 66

[10] G. Kirby et al., "Design of the 70 mm Twin Aperture Superconducting Quadrupole for the LHC Dump Insertion", 1996 Appl. Superconductivity Conf, August 1996, Pittsburgh, USA, LHC Project Report 66.

# HIGHER ORDER MODES POWER LOSS IN THE VERTICAL SEPARATORS AT CESR

S. Greenwald *
Laboratory of Nuclear Studies, Cornell University, Ithaca, NY 14853

*Abstract*

CESR upgrade "phase III" is designed to operate with a total current of 1.0 ampere. It was clear to us that the "old" separators, built in 1978, will not be able to handle this amount of current. Therefore, the vertical separators were re-designed and three new separators were build. Two are installed in the north side of CESR. In order to study if the new separators will be able to support the high current beams designed for phase III, an accurate calorimetric system was designed and built on one of the vertical separators, 48E. Using this system we were able to study the total higher order modes power dissipation in each component of the separator and estimate the total HOM power loss at the higher currents.

## 1 INTRODUCTION

At CESR the two 2.7 meter long vertical separators are used to separate the two beams at the symmetric point in the north and are also used for luminosity tuning. In each separator the gap between the two high voltage electrodes is 55 mm, which is only 10% wider than the vertical beam pipe dimension. The width of the electrodes is 203 mm. The electrodes were put 1.4 inches away from the outer vacuum tank edge on each side in order to prevent a voltage breakdown between the high voltage electrodes and the outer tank. This 1.4 inches gap is the main cause of the higher order modes power loss. Using an accurate calorimetric system, the higher order modes power dissipated in each component of the separator was measured for various CESR operation conditions. The loss parameter $k$ of the separator was calculated from the measured dissipated power.

## 2 HIGHER ORDER MODES LOSSES IN THE VERTICAL SEPARATOR

The vertical separator cross section can be seen in Figure 1. The high voltage feeds-through are insulated from the outer tank via a cylindrical insulator (9 inches long and 6 inches in diameter) which is enclosed by a stainless steel tube (10.5 inches in diameter). The 7 inch flange that is mounted on top on the insulator introduces a large mismatch in impedance for the HOM power that is coupled out. The $S_{11}$ parameter of the insulator and the enclosing stainless steel tube wasmeasured to be about -1 dB and almost all the power will be reflected back into the separator. This will increase significantly the heat load of the electrodes and lower the safe high voltage operation. To avoid this, 40 blocks of ferrite ( 1.5 inches by 2.0 inches) were glued inside the stainless steel tube below the top flange of the insulator. The $S_{11}$ parameter of the insulator configuration including the ferrite blocks is about -7.5 dB. In this case only about 50% of the HOM power that is coupled outside through the feed-through is reflected back. As was mentioned above, most of the HOM power loss will occur at the gap between the electrodes ends and the end plates of the outer tank. The total HOM power loss can be calculated using the following equation.

$$P = \frac{k(\sigma_z, Pr) \cdot I_b^2 \cdot N_b}{10^{-12} \cdot Frev} Watts \qquad (1)$$

Where: $k(\sigma_z, Pr)$ is the loss factor $(V/pC)$, $\sigma_z$ is the bunch length (m), $Pr$ the horizontal beam offset at the separator due to the close orbit distortion "pretzel" that is needed for multibunch operation, $I_b$ bunch current in (A), $N_b$ number of bunches, $Frev$ revolution frequency (Hz). Since the gap between the electrode ends and the end plates is of the same order as the bunch length the loss factor $k$ will depend inversely on the bunch length. Also, the high voltage electrode ends are made from 180 degrees, 6 inches in diameter elbows; therefore the gap seen by the beam is larger as the beam offset amplitude is increased and the HOM power loss will depend on the size of the closed orbit distortion as is given by the horizontal pretzel amplitude. The HOM beam power loss in the separator is dissipated in the electrodes, the outer vacuum tank and the part that is coupled outside, in the ferrite and the inductive load on the high voltage cables.

## 3 THE CALORIMETRIC SYSTEM

The cooling of the separator is done by two different coolant systems, one is using CESR 85°F water and the other is using freon which is cooled via a heat exchanger by the 85°F water. The water system is used to cool the outer tank, the ferrites in the top and bottom insulator can and the high voltage cables' inductive loads. The freon is used to cool the top and bottom high voltage electrodes. In order to be able to measure the dissipated power in each one of the seven components of the separator, the cooling is done in parallel. High resolution thermistors are imbedded, using a spacial housing, in each one of the input and output coolant pipes. These thermistors are measuring the temperature of the coolant at the input and output with resolution of 0.005°C. The flow rate of the coolant to each one of the components was measured. By knowing the coolant flow rate and the temperature difference between input and output the dissipated power in each component of the separator can be calculated.

* Work supported by the National Science Foundation

0-7803-4376-X/98/$10.00 © 1998 IEEE

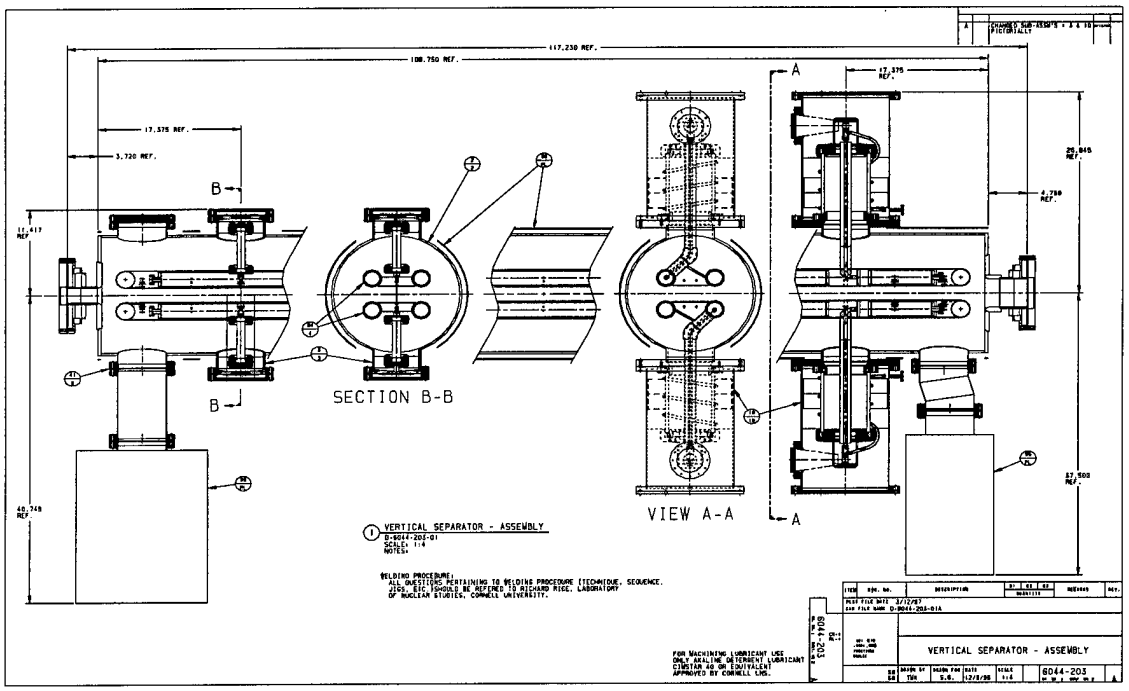



Figure 1: The vertical separator cross section

## 4 H.O.M POWER LOSS MEASUREMENTS

Using the calorimetric system we have measured the HOM power loss in the vertical separator for different CESR operation parameters :

A. The dependence of the HOM power loss on horizontal beam offset as is determined by the horizontal closed orbit distortion and is given by the pretzel amplitude ,can be seen in the upper part of Figure 2. The HOM losses increase as the horizontal pretzel amplitude is increased since the gap seen by the beam is larger. For example, when going from zero pretzel, beam on axis, to HEP pretzel which shifts the beam horizontally at the separator by about 1 inch, the gap seen by the beam changes from 1.4 inches to 1.53 inches and the HOM power loss increases by 10%.

B. The measurements described above were repeated with the two wigglers closed, as can be seen in the lower part of Figure 2. The power loss for the case when the wigglers were closed was lower by about 8% compared to whe n the wigglers were open. The reason for this is that the bunch length is elongated by the wigglers by 8% as was also seen with a streak camera[1]. In HEP condition, wigglers closed and full pretzel, the increase in the HOM power loss due to the horizontal beam offset is partly cancelled by the elongation of the bunches by the wigglers, since both effects are of the order of 8%.

C. The HOM power loss as function of the number of bunches in a train, can be seen in Figure 3. It was found that the loss factor $k$ increases by about 17% when the number of bunches in each train was increased from 1 to 3. The increase in power loss is probably caused by the interaction of the trailing bunches with the HOM power induced by the leading bunches in the train. (The spacing between the bunches was 14 and 28 nsec while the spacing between the trains is about 280 nsec.)

D. The change in the HOM power loss as function of the bunch length, can be seen in Figure 4. The bunch length was changed by changing the RF Accelerating voltage[1]. The HOM power loss is proportional inversely to the bunch length.

The distribution of the HOM power loss in the different components of the separator as function of current per bunch can be seen in Figure 5. The percentage of the total

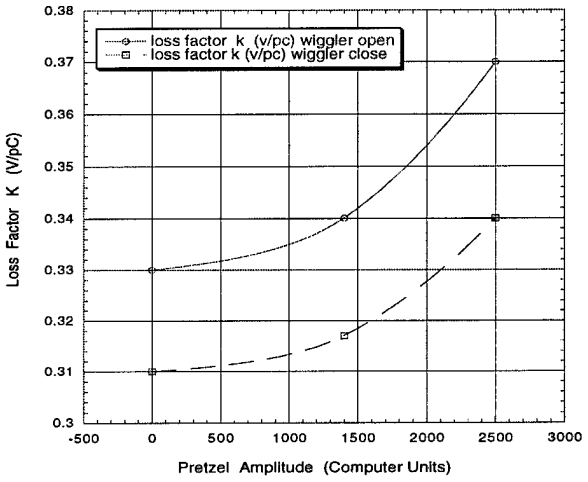



Figure 2: HOM power loss as function of the horizontal beam offset determined by the pretzel amplitude for open and closed wigglers. 2500 computer units correspond to about 25 mm off center beam shift.

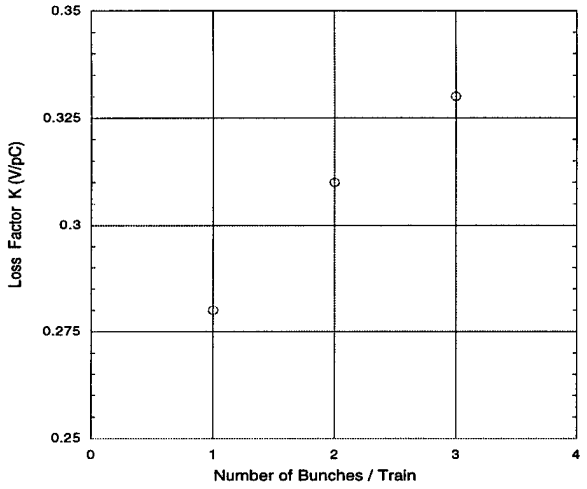



Figure 3: HOM Power Loss as Function of the Number of Bunches in a Train, Beam on Center Wigglers Open

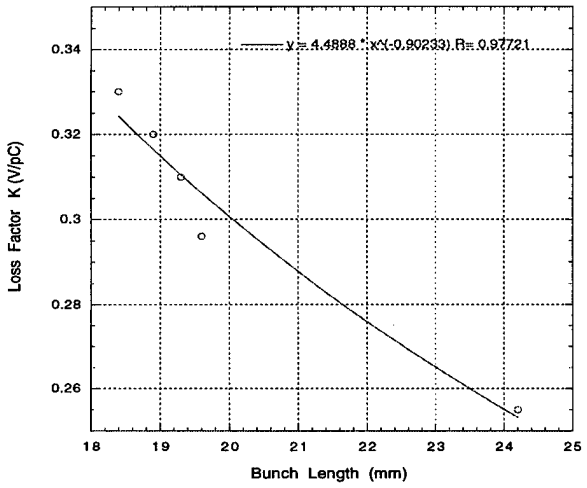



Figure 4: HOM power loss as function of the bunch length, beam on center, wigglers open

power dissipated in each component is independent of the current. Fifty seven percent of the total HOM loss power is coupled out through the feed-through of which fifty percent is dissipated by the ferrite blocks and eight percent in the inductive load of the high voltage cables, thirty percents is dissipated in the electrodes and about thirteen percent is dissipated in the outer tank.

## 5 CONCLUSION

Only thirty percent of the total HOM power loss is cooled by the freon system and the remaining seventy percent by the water system. This reduces significantly the heat load on the freon system which is much less efficient than the water system. Ninety percent of the HOM power that is coupled outside through the feed-through is absorbed by the ferrite blocks and the rest by the inductive load. Thus

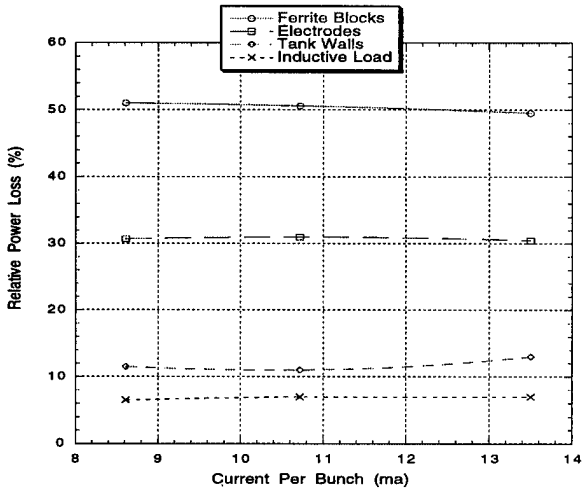



Figure 5: The distribution of the HOM power loss in the different components of the separator as function of current/bunch

there is hardly any power dissipated on the high voltage cables and connectors. This increases the reliability of the high voltage cables and connectors. The loss factor $k$ for the separator in colliding condition with two bunches per train is $0.32 \pm 0.01$ V/pC, while for three bunches per train it is $0.34 \pm 0.01$ V/pC. The expected HOM power loss in future upgrades of CESR with three bunches per train with total of 600 ma will be $5.6KW$, while for five bunches per train with total current of 1.0 ampere it will be $9.5KW$. The vertical separators will be able to handle this power with any problems.

## 6 ACKNOWLEDGMENT

We would like to thank David Rice for very helpful discussions.

## 7 REFERENCES

[1] R.Holtzapple and D. Hartill Streak Camera Measurenents at CESR to be published.

# PHOTOCURRENTS IN THE VERTICAL ELECTROSTATIC SEPARATORS AT CESR

S. Greenwald *
Laboratory of Nuclear Studies, Cornell University, Ithaca, NY 14853

*Abstract*

At CESR a pair of vertical separators are used to separate the two beams vertically at the symmetry point, in the north, of the interaction point in the south. They are 2.7 meter long and each one is providing a 1.0 mrad kick for a differential voltage of 100 KV between the electrodes. One side of each separator is exposed to the high flux of synchrotron radiation from a soft bend, 140 meter radius, magnet and a hard bend, 34.8 meter radius, magnet. The radiation generates large amount of photoelectrons which are converted to a large photocurrent . For a beam current of 150 ma the photocurrent is 1.2-1.5 ma. It caused,a few times a day, a partial drop in the high voltage which caused a vertical beam blow up and beam loss. In addition the photocurrent was increasing the heat load of the positive electrode by 25 percent. In the paper we will show how we were able to suppress the photocurrent almost to zero. As a result we have seen an increase in the life time of the beams and as well an increase in the luminosity.

## 1 INTRODUCTION

The main sources of synchrotron radiation that enters the vertical separator that is located to the east of the symmetry point are the two bending magnets B47E1 (R=140.62 m) and B47E2 (34.817 m), while for the separator that is located to the west of the symmetry point it is B47W1 and B47W2. The electrons which travel from east to west radiate into the east separator and the positrons which travel from west to east radiate into the west separator. When operating CESR with large horizontal closed orbit distortion "pretzel" that is needed for multibunch operation in colliding condition, synchrotron radiation from positrons generated in B47W1&2 can also enter the east separator and synchrotron radiation from electrons generated in B47E1&2 can also enter the west separator. This occurs because of the large beam offset in the bending magnets; some of the radiation misses the radiation absorber and thus is able to reach the other separator. When the synchrotron radiation enters the separators there are four different possibilities to generate photoelectrons but only two of them will lead to photocurrents. A. If the photons hit the outer tank near the positive voltage electrode the emitted photoelectron will be accelerated to the positive electrode and photocurrent, that is supplied by the positive electrode power supply, will be generated. B. If the photon hit the high voltage positive electrode the photoelectron will not be able to escape and it will be pulled back by the high positive voltage of the electrode and no photocurrent is generated. C. If the photon hit the outer tank near the negative electrode the photoelectron will not be able to escape and no photocurrent is generated. D. If the photon hit the high voltage negative electrode the photoelectron will be accelerated either to the outer tank which is at ground potential or to the high voltage positive electrode. In both cases a photocurrent is generated. If the the photoelectron is accelerated to the outer tank the photocurrent is supplied by the negative electrode power supply. On the other hand if the photoelectron is accelerated to the positive electrode the photocurrent is supplied by the negative and the positive high voltage power supplies. For summary, the current we measure on the high voltage positive power supply is the sum of the photocurrent generated by the photons hitting the outer tank near the positive electrode and the photocurrent generated by photons hitting the negative electrode. While the current we measure on the high voltage negative power supply is equal to the photocurrent generated by the photons hitting directly the negative voltage electrode.

* Work supported by the National Science Foundation

## 2 THE MEASURED PHOTOCURRENTS IN THE EAST AND THE WEST VERTICAL SEPARATORS

The vertical separator cross section can be seen in Figure 1. In the separators the top electrode is positive while the bottom electrode is negative. The measurements were carried out in three steps. First we measured the effect of the electron beam only, second we measured the effect with positron beam only and last we measured it with both beams. In all the three measurements each beam had eighteen bunches composed of nine trains two bunches per train, with eight ma per bunch. The measurements were done in colliding conditions which had large horizontal closed orbit distortion. Each electrode has its own high voltage power supply that can be regulated independently. The results of the measurements of the photocurrents with 144 ma of one beam in CESR at a time can be seen in the upper part of table 1, while the results for both beams in CESR at the same time with 144 ma per beam can be seen in the lower part of table 1.

## 3 METHOD TO SUPPRESS THE PHOTOCURRENTS

From the results of the measurements with electrons only, which are shown in the second row of table 1, we can also see photocurrent in the west separator. That means that some of the synchrotron radiation generated in the east

0-7803-4376-X/98/$10.00 © 1998 IEEE

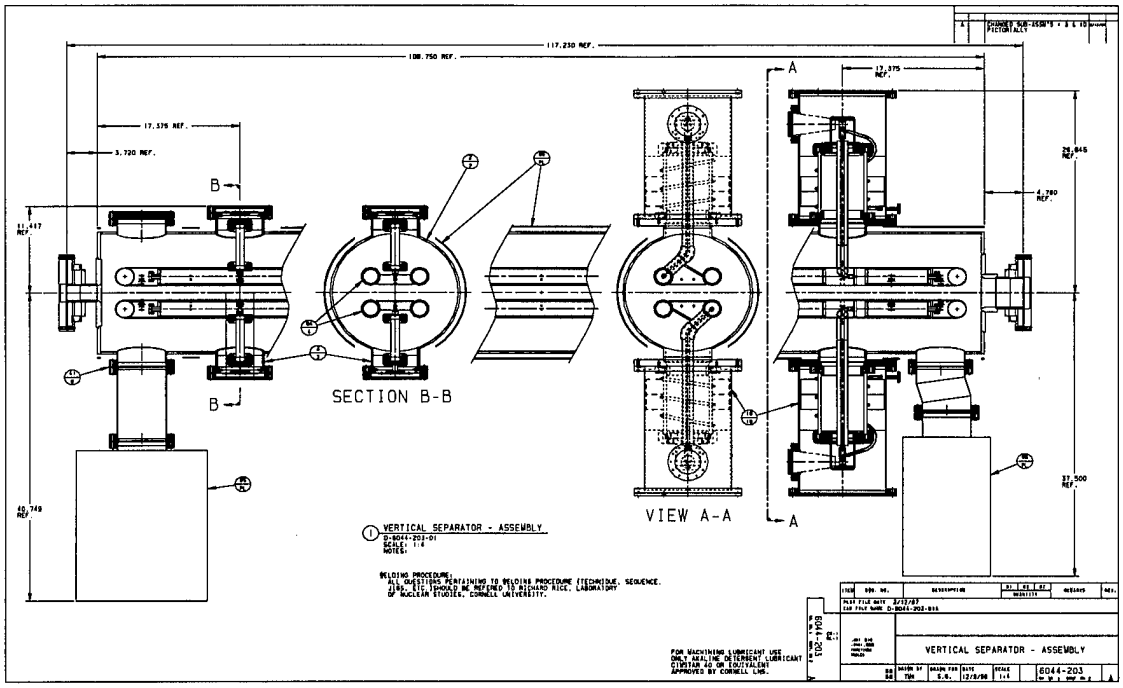



Figure 1: The Vertical Separator Cross Section

| *Beam* | *EAST* | | *WEST* | | Conditions |
|---|---|---|---|---|---|
| in CESR | $TopEle.(ma)$ | $Bot.Ele.(ma)$ | $TopEle.(ma)$ | $Bot.Ele.(ma)$ | |
| e - | 0.75 | 0.10 | 0.20 | 0.10 | $OFF\ Energy\ (Oct.8.96)$ |
| e - | 0.70 | 0.10 | 0.40 | 0.00 | $ON\ Energy\ (Oct.15.96)$ |
| e + | 0.15 | 0.10 | 0.80 | 0.00 | $ON\ Energy\ (Oct.15.96)$ |
| e+& e - | 1.35 | 0.60 | 1.10 | 0.07 | $ON\ Energy\ (June.17.96)$ |
| e+& e - | 0.90 | 0.15 | 1.10 | 0.00 | $ON\ Energy\ (Oct.5.96)$ |
| e+& e - | 0.90 | 0.15 | 1.10 | 0.10 | $OFF\ Energy\ (Oct.8.96)$ |

Table 1: The Measured Photocurrents in the Top(+) and the Bottom (-) Electrodes in the East and the West Vertical Separators, with only one Beam in CESR Upper part of the Table and Two Beams in CESR lower part of the Table

bending magnets B47E1&2 entered the west separator hitting its south end. The resulting photoelectrons were drawn to the top (positive) electrode generating 0.4 ma of photocurrent (option 1). While from the measurements with the positrons, the photocurrents in the east separator are low meaning that very little of the synchrotron radiation generated by the positrons in the west bending magnets enters the east separator. From the measurements that were done on June 17, 96, with both beams in CESR, it can be seen that the bottom (negative) electrode of the east separator had 0.6 ma of photocurrent. This photocurrent is generated by photons that are hitting directly the negative electrode. We have found that the source of these photons are the positrons in the west (option2). The effect of the electrons on the west separator and the positrons on the east separator depend on the optic lattice that is used. We have found that we can reduce by more than 70% the photocurrents induced by the opposite beam by introducing local vertical bumps in the bending magnets in the positrons optics in the west and in the electron optics in the east. The Oct. 5, 96, measurements had such bumps which reduced the photocurrent of the negative electrode of the east separator from 0.60 ma to 0.15 ma. At the same time the photocurrent of the positive electrode decreased by the same amount from 1.35ma to 0.9 ma, as can be seen in lower part of table 1. This indicate that the photoelectrons from the negative electrode are accelerated to the positive electrode and not to the ground. In the vertical separators the radiation absorber is made of copper block with a shallow grove and is water cooled. The center of the absorber in the vertical direction coincide closely with the zero potential plane which is located in the mid plane between the positive and negative electrodes. As a result of this the top half of the absorber is in a positive electrical field regime while the lower half is in a negative electrical field regime. Because the grove in the absorber is shallow, any photoelectron generated by photon hitting the top half of the absorber is able to escape and be drawn to the positive electrode. An

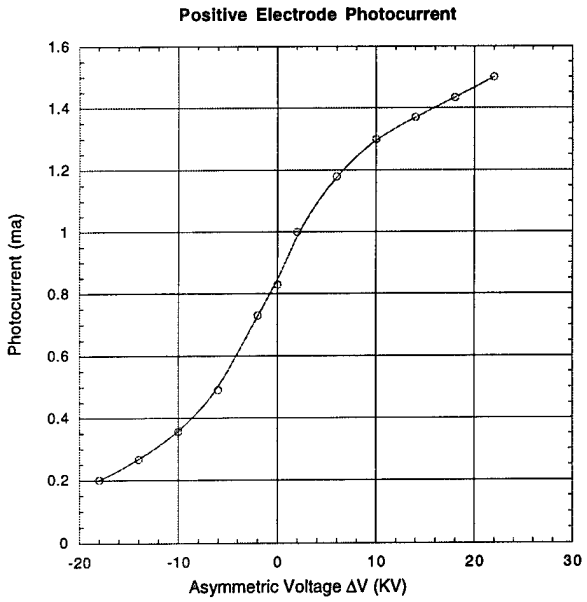



Figure 2: The Measured Photocurrent of the Positive Electrode as Function of the Asymmetric Voltage $\Delta V = V^+ - V^-$

effective way to stop the photoelectrons from reaching the positive electrode is to move the zero potential plane up so the whole absorber will be in the negative electrical field regime and the photoelectrons will not be able to escape. One way to achieve this is to operate the separator in an asymmetric mode i.e., increase the voltage of the negative electrode (bottom) and by the same amount decrease the voltage of the positive electrode (top) so that the vertical kick to the beams will be the same but the zero potential plane will move up. Results of such an asymmetric mode of operation of the separator can be seen in Figure 2, where by moving the zero potential up the photocurrent of the positive electrode was reduced from 0.83 ma to 0.22 ma. On the other hand, when we moved the zero potential plane down by increasing the positive voltage and decreasing the negative voltage by the same amount, the photocurrent of the positive electrode was increased from 0.83 ma to 1.5 ma. Another way to stop the photoelectrons from reaching the positive electrode is by placing an external magnet across the absorber. When operating in symmetric mode $\pm 45$ KV with an external dipole magnet, which has 230 Gauss at the center, across the absorber the photocurrent of the positive electrode was reduced from 0.75 ma to 0.20 ma. The photocurrent was further reduced to 0.1 ma by changing the electrode voltages from $\pm 45$ KV to -50 KV and + 40 KV.

## 4 SUMMARY AND CONCLUSION

Any time a new optic lattice is implemented in CESR, the effect of the synchrotron radiation generated by the opposite beams, i.e. positron beam on the east separator and electron beam on the west separator, is reduced by introducing local closed vertical bumps in the lattice (a bump in the west for the positrons and a bump in the east for the electrons). As we have shown above, each one of the methods; moving the zero potential plane up or the external dipole magnet across the absorber, is very successful in suppressing the photocurrents in the vertical separator. But the combination of both methods has a number of advantages because of the following reasons: A. using only asymmetric voltages on the electrode will require more then 20% increase in the voltage of the negative electrode compare to symmetric voltages, which will limit the maximum vertical kick that the separators will be able to provide. B. In addition, by moving the zero potential plane up by a large amount, the electrical fringe fields at the ends of the separator will be stronger at the beam location. Thus having larger effect on the beam dynamic. On the other hand using the external magnets only will not stop the photoelectrons generated by the radiation hitting the other end of the separator generated by the opposite rotating beam. Operating CESR with electrons and positrons in collide mode with total current of 150 ma per beam the photocurrents in both separators were reduced to less then 0.2 ma for the positive electrode and 0.1 ma for the negative electrode. This was achieved by using an external magnet across the absorber combined with asymmetric voltage. These remaining photocurrents are mainly generated by scattered photons from the beam chamber into the separator either by mirror scattering which will hit the inside tank wall and the photoelectrons will be drawn to the positive electrode or Rayleigh large angle scattering where part of them will hit the negative electrode and generate photocurrent in both electrodes. Since the photoelectrons from the negative electrode will be accelerated to the positive Electrode. The estimated photocurrents for CESR upgrade "phase III" which is designed to have 500 ma per beam are; 0.65 ma for the positive electrode and 0.35 ma for the negative electrode. We have measured the effect of the external magnet and the asymmetric voltage on the electrodes in three different ways: 1. We did not see any measurable changes in the beams orbit. 2. The horizontal and the vertical tunes did not change by more than 30 Hz. 3. The vertical chromaticity did not change. On the other hand we saw improvements in the beam life time and more important the number of beam losses due to high voltage micro arcs in the vertical separators became very small. As a result the total integrated luminosity was increased.

# REC BEAM PIPE TEMPERATURE CONTROL

Z. Greenwald, S. Greenwald and D. H. Rice *
Laboratory of Nuclear Studies, Cornell University, Ithaca, NY 14853

*Abstract*

In CESR the clearance between the beam pipe and the REC (Rare Earth Cobalt) magnet is only 1 mm. The 160 cm beam pipe in this section is sloped and has steps to mask the detector from radiation. During high energy operation the beam pipe temperature increases due to synchrotron radiation, higher order modes power loss and image current, and effects the temperature of the REC magnet via convective and radiative heat transfer. The temperature change is proportional to the beam current. This causes a current dependent change in the REC magnetic field strength, resulting in a betatron tune shift of about $\Delta Q$ =0.011/°C for each quadrupole. To prevent the temperature changes of the beam pipe in this section, a sensitive temperature control cooling system was developed. The temperature of the beam pipe is stabilized within ±0.1°C. The loss parameter of the sloped pipe and power dissipated by synchrotron radiation was calculated from temperature measurements and used to estimate performance at higher current.

## 1 INTRODUCTION

The REC Quadrupole $Sm_Co_5$ material has a magnetization temperature dependence of $-0.04\%°C$ (see reference [1]). In order to avoid a shift in the vertical tune due to changes in the REC magnetic field the temperature of the inner side of the REC must be controlled to within ±0.1°C. The main source of heating the inner side of the REC is the beam pipe whose temperature changes with the beam. Since the outer radius of the beam pipe inside the REC is only 1 mm smaller then the inner radius of the REC, the beam pipe inside the REC must be kept at constant temperature with fluctuation smaller then ±0.1°C during all times with or without beam in CESR.

## 2 TEMPERATURE CONTROL

A block diagram of the control system is shown in *Figure* 1. The coolant (PF 200) temperature is measured at the output of the beam pipe section (point 2 on *Figure* 1) by a thermistor with high resolution (see *Appendix I*) and maintained constant by changing the coolant temperature at the input (point 1 on *Figure* 1) when the beam pipe is heated by synchrotron radiation and higher order modes. *Figure* 2*b* shows the profile of the input temperature needed to keep the pipe temperature constant for the beam current shown in *Figure* 2*a*. A constant shift of about 0.3°C exists between the input and the output thermistors due to electronic offset. The coolant temperature

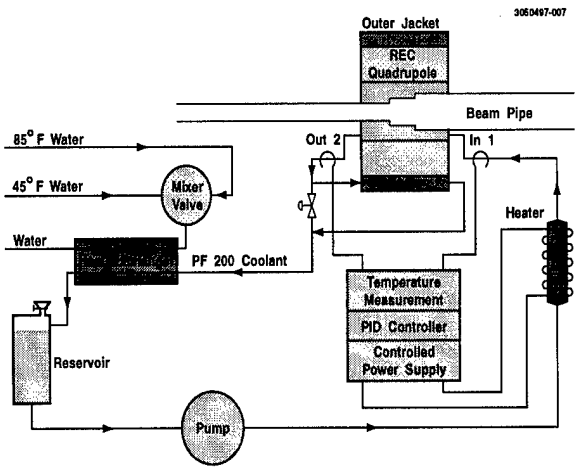



Figure 1: Block Diagram of the Control System

is regulated by a heater which also mixes the fluid making its temperature more uniform. The control system was designed to have a time constant of 3 minute in order to have a stable closed loop feedback and minimize the amount of walking. During injection when the filling rate is few ma per minutes the system is able to keep the beam pipe temperature very stable. In the case of a beam loss or total beam damp it takes the control system about 5 minutes to restabilize the beam pipe temperature, but even in this case the deviation in the beam temperature is only 0.1°C as can be seen from *Figure* 2*b*.

### 2.1 *The Heater*

The heater is built out of two concentric pipes 55 inches long, with a spiral divider in between. The coolant flows between the two pipes in a 0.1 inch gap along the spiral divider. Three heat tapes (1.5 $KWatts$ each), connected to the regulating power supply, are wrapped on the outer pipe. The regulated voltage for the heat tapes that corresponds to the heating of the beam pipe due to the beam current shown in *Figure* 2*a*, is seen in *Figure* 2*c*. Note that the controlled voltage has to compensate not only for the heating due to the beam current but also the changes in the $45°C$ and $85°C$ water mix which cools down the coolant via a heat exchanger.

### 2.2 *The Controller*

The controller is regulating the power supply of the heater. It uses of an OMEGA PID[2] unit and a variable DC level shifter [3]. The DC shifter converts the desired REC beam

* Work supported by the National Science Foundation

0-7803-4376-X/98/$10.00 © 1998 IEEE

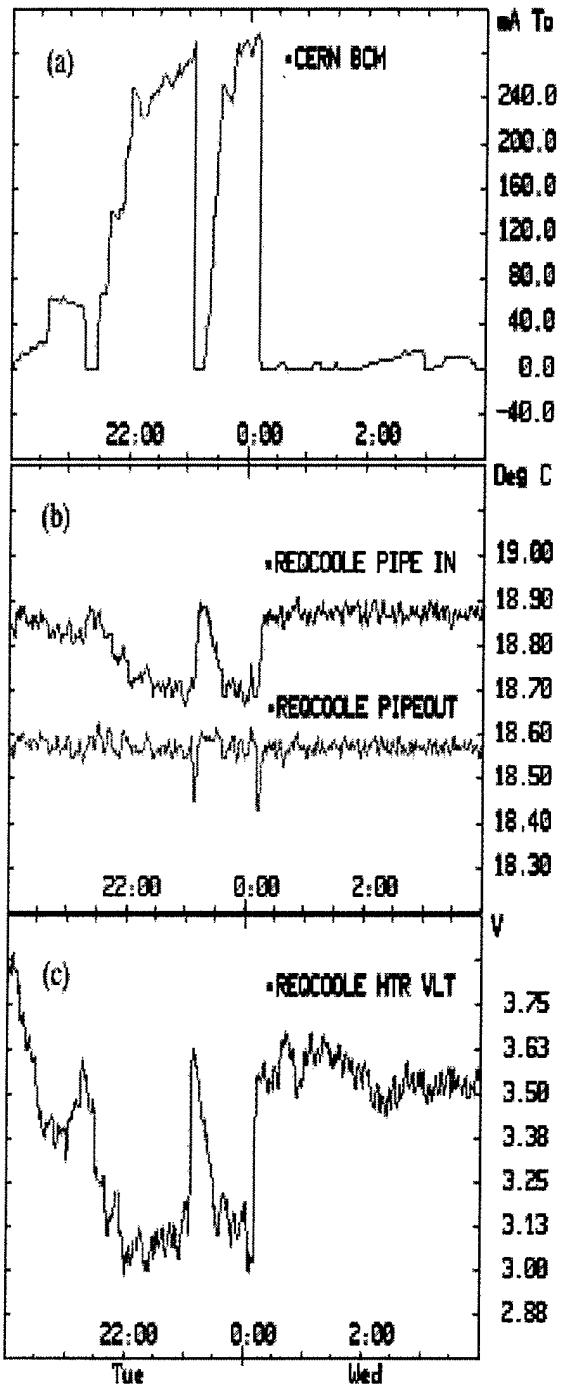



Figure 2: a. Positrons Current in the Storage Ring. b. Profile of the coolant input temperature needed to keep the pipe temperature constant, and the corresponding coolant output temperature. c. Regulated voltage corresponds to the heating due to the current in part a. Time scale is in hours.

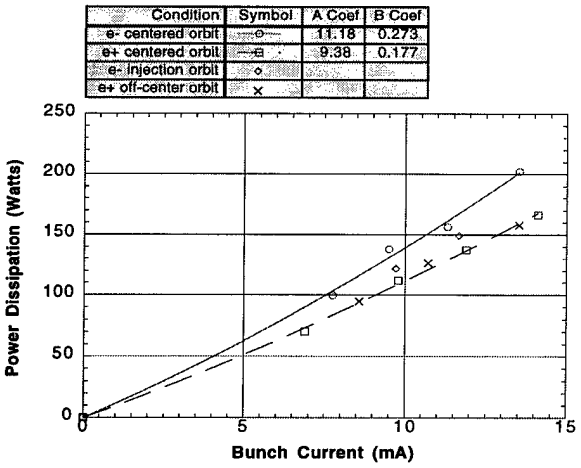



Figure 3: Power Dissipated in the WEST REC pipe by electrons and in the EAST REC pipe by positrons

pipe temperature to 2.5 $Volts$, which is the center of the PID $(0-5)V$ operating range. When the beam pipe is heated up by the beam, or the water temperature changes, the PID controller output can change up to $\pm 2.5\ V$ corresponding to $\pm 10°C$.

## 3 REC OUTER JACKET COOLING

Some of the REC beam pipe stabilized coolant at the output side is diverted to the REC copper external jacket with brazed on tubes in order to stabilize the outer temperature of the REC magnets. This temperature is not as critical as the beam pipe temperature.

## 4 MEASURED PRESENT POWER DISSIPATION

As explained above, the temperature decrease in the input compensates the heating of the pipe, and thus the input temperature change is directly proportional to the power dissipated in the pipe . The power dissipation in the west REC pipe by electrons and in the east REC pipe by positrons, for several beam currents (18 bunches / beam), going through the center of the pipe is shown in Figure 3. The data were fitted to the function: $P = A \cdot I_b + B \cdot I_b^2$; $A, B$ are constant. $I_b$, is the bunch current. The term $A \cdot I_b$ represents the dissipated power due to synchrotron radiation (linear with bunch current), and the term $B \cdot I_b^2$ represents the power loss due to higher order modes (proportional to square of the bunch current). At these currents the heating due to image currents is about 5 Watts [4]. The second set of data corresponds to the power dissipated in the pipe when the electron beam was displaced by a sine-like closed orbit distortion (generated by electrostatic separators to avoid parasitic beam-beam interactions).

| CESR Upg-rade | $Nb$ | $Ib$ (ma) | WEST | | EAST | |
|---|---|---|---|---|---|---|
| | | | $P_{HOM}$ (W) | $P_{SR}$ (W) | $P_{HOM}$ (W) | $P_{SR}$ (W) |
| Ph II | 27 | 11.1 | 50.6 | 186.3 | 32.7 | 156.3 |
| Ph III | 45 | 11.1 | 84.4 | 310.5 | 54.6 | 260.5 |

Table 1: Estimated Power Dissipation in the REC Magnet for the Planed CESR Upgrades.

## 5 CALCULATED FUTURE POWER DISSIPATION

The above power dissipation was measured for 18 bunches. A general expression as function of the number of bunches $N_b$ is derived.

### 5.1 Loss Parameter Calculation

It is assumed that all the power measured is generated by heating in the REC itself. The Loss Parameter $k$ is calculated from $B$ extracted by the curve fitting to the data in Figure 3. $f_{REV}$ is the revolution frequency, and $I_B$ bunch current.

$$P_{HOM} = k \cdot \frac{N_b}{f_{REV}} \cdot I_B^2 = B \cdot I_B^2 \quad (1)$$

$$k = \frac{B \cdot f_{REV}}{N_b} \quad (2)$$

$k_{West} = 5.94 \cdot 10^{-3} V/pC$
$k_{East} = 3.85 \cdot 10^{-3} V/pC$
$P_{HOMWest} = 1.52 \cdot 10^4 \cdot N_b \cdot I_B^2 watts$
$P_{HOMEast} = 0.983 \cdot 10^4 \cdot N_b \cdot I_B^2 watts$

### 5.2 Synchrotron Radiation Calculation

The constant $A$ extracted from figure 3 was measured with 18 bunches. Thus the contribution from radiation is:

$$P_{S.R.} = \frac{A \cdot N_b}{18} \cdot I_B \quad (3)$$

$P_{S.R.West} = 621. \cdot N_b \cdot I_B watts$
$P_{S.R.East} = 521. \cdot N_b \cdot I_B watts$

### 5.3 Future Estimation of Power Dissipation in REC pipe

We plan to have a total of $300ma/beam$ carried by 9 trains with 3 bunches in a train in CESR phase II, and $500ma/beam$ carried by 9 trains with 5 bunches in a train in CESR phase III. The distribution of the calculated dissipated power in the WEST REC pipe due to the electron and in the EAST REC pipe due to positrons are summarized in Table 1.

## 6 CONCLUSIONS

After installing the temperature control system of the REC pipe we did not have any more fluctuations in the vertical tune due to temperature changes in the REC quadrupoles. The estimated total heating of each REC beam pipe will include also HOM heating by the other species. That means that the expected total power dissipation in Phase II will be 290 and 220 Watts for the WEST and EAST REC beam pipe respectively. In Phase III the expected total power dissipation will be 480 and 370 Watts for the WEST and EAST REC beam pipe respectively (Assuming we will be using similar optics in CESR). The main reason for the difference between the west and the east is due to different beam bumps of both sides of the interaction point that are put in to minimize the radiation into CLEO.

## 7 APPENDIX

### 7.1 High Resolution Temperature Measurement

The resolution of the measured temperature should be of the order of hundredth of a degree in order to stabilized the temperature with a 0.1°C. A YSI 44005 precision thermistor was connected to $R = 3\ K\Omega$ resistor bridge, to balance the resistance of the thermistor at the center of the desired temperature range (25°C in this case). The bridge output voltage was connected to a difference amplifier. See reference [5]. The output voltage is:

$V_o = V_b \left(1 + \frac{2 \cdot R_2}{R_1}\right) \left(\frac{R - R_{th}}{R + R_{th}}\right)$

where $V_b$ is a stabilized DC power supply, and $R_1, R_2$ are the amplifier high precision resistors.

for $R_{th} = R + \Delta R_{th}$ with $R >> \Delta R_{th}$ the output voltage

$V_o = V_b \left(1 + \frac{2 \cdot R_2}{R_1}\right) \left(\frac{-\Delta R_{th}}{2R + \Delta R_{th}}\right) \cong -G \Delta R_{th}$

is linear with the temperature. The gain $G$ can be adjusted to give high resolution.

## 8 REFERENCES


[1] S. W. Herb, "Construction and Measurement of Large Permanent Magnet Quadrupoles",IEEE PAC 1987, catalog no. 87CH2387-9.

[2] CN76000 "Microprocessor - Based Temperature Controller" by OMEGA.

[3] D. Sagan, "REQ Beam Pipe Temperature Stabilization",CON 94-15 June,1194.

[4] Z. Greenwald, "REC Pipe Temperature Control"' drawing no. 6058-001 (05-1995).

[5] Z. Greenwald, "REC Temperature Readout"' drawing no. 6056-021 (06-1995).

# IMPROVED MEASUREMENT OF ELECTRIC FIELD UNIFORMITY IN HORIZONTAL ELECTROSTATIC SEPARATORS *

Alexander B. Temnykh† and James J. Welch, Wilson Laboratory, Cornell University, Ithaca NY

*Abstract*

An improved technique for measuring the uniformity of the electric field between the deflecting plates of a electrostatic separator was developed and applied to the measurement of a horizontal separator at CESR. The effect of stray charge was found to be limiting accuracy in previous measurements. Appropriate shielding has eliminated the problem.

## 1 INTRODUCTION

While magnetic field quality measurement techniques have advanced to a fine art for accelerator magnets, the measurement of the uniformity of electric fields is still in its infancy, perhaps because electrostatic elements are relatively uncommon [1]. Nevertheless, electrostatic separators are being employed at various accelerator laboratories and provide substantial kicks to the beams so as to obtain closed orbit distortions that are opposite for oppositely charged particles; i.e. beam separation. Nonuniformity of the electric field can cause unwanted tune shifts, coupling, etc. Such effects will have a different symmetry with respect to the charge of the beams than analogous effects from magnetic corrector elements. Also, magnetic correctors elements are usually used to correct for unavoidable errors in the closed orbit and so their strengths tend to be centered about zero, while separators are usually powered to obtain a constant effect on the beams and tend to be near maximum values. So it would seem worthwhile to try to obtain more information about the actual uniformity of the electric field in a separator than can be provided by a 2D design solution.

A measurement technique based on zeroing out the induced charge on a stretched wire held between the separator plates was discussed in [2]. The original measurement showed apparent nonlinearities whose origin was not understood. Since then we have improved the technique and the previously observed large nonlinearities are no longer observed.

## 2 DESCRIPTION OF METHOD

The basic technique we used was to stretch a long thin wire along a hypothetical particle trajectory between the deflecting plates and adjust the potential of the wire relative to the plate potentials to zero out the net induced charge on the wire. The induced charge is observed by varying the plate voltages so that the resulting induced currents can be seen on an oscilloscope. Once the wire potential is determined the wire can be translated a precise amount and the process repeated. The electric field is obtained by taking the derivative of the wire potential data with respect to the position of the wire. The theory supporting this technique worked out in [2].

Because only the total induced charge on the wire is observed, we need to avoid inducing any charge on the wire except due to electric field of the plates. However, as the wire is moved to measure the field off-axis, its potential becomes further from ground potential. So any grounded surfaces near the wire will induce charge on the wire and influence the measurement of the electric field due to the plates. The improvement we made to the basic technique is to add a shield which is at the wire potential which effectively prevents grounded surfaces from inducing charge on the wire.

## 3 MEASUREMENT DESCRIPTION

The measurement scheme is shown in figure 1. We used the following equipment:

- signal generator "Wavetek",
- two precision voltmeters DVM1 and DVM2,
- potentiometers P1 and P2,
- digital oscilloscope "Scope",
- switch SW,
- two linear translation stages PS1 and PS2.

The scheme worked in the following way: The Wavetek produced square-wave with voltage amplitude $V_0$, floating with respect to ground. This voltage was precisely measured by DVM1 and we applied it directly to separator's plates. Potentiometer P2 was used to divide this voltage in half. The center tap of P2 was connected to the vacuum chamber (separator ground). This results in the plates having $\pm V_0/2$ voltage relative to the vacuum chamber as it is under normal operating condition. A stretched wire was strung through the separator and connected through the Scope to the central tap of the other potentiometer P1. The Scope indicated electric charge flowing through the wire caused by the voltage difference between wire and middle point of $P1$. The measuring procedure was the following. For a given wire position, say $x$, we adjusted potentiometer P2 to eliminate the signal seen on scope in at the beginning of the each pulse. The voltage measured with DVM2, $V_w$ gave us the potential at the wire location while DVM1 gave us the voltage, $V_0$, between plates. The ratio $V_w/V_0$ as function of wire position gives the potential distribution. Taking the derivative with respect to wire position gave the electric field profile. In earlier measurements we found very strong disturbing factor. Near the separator's

* Work supported by the National Science Foundation

† On leave from BINP, Novosibirsk

0-7803-4376-X/98/$10.00 © 1998 IEEE

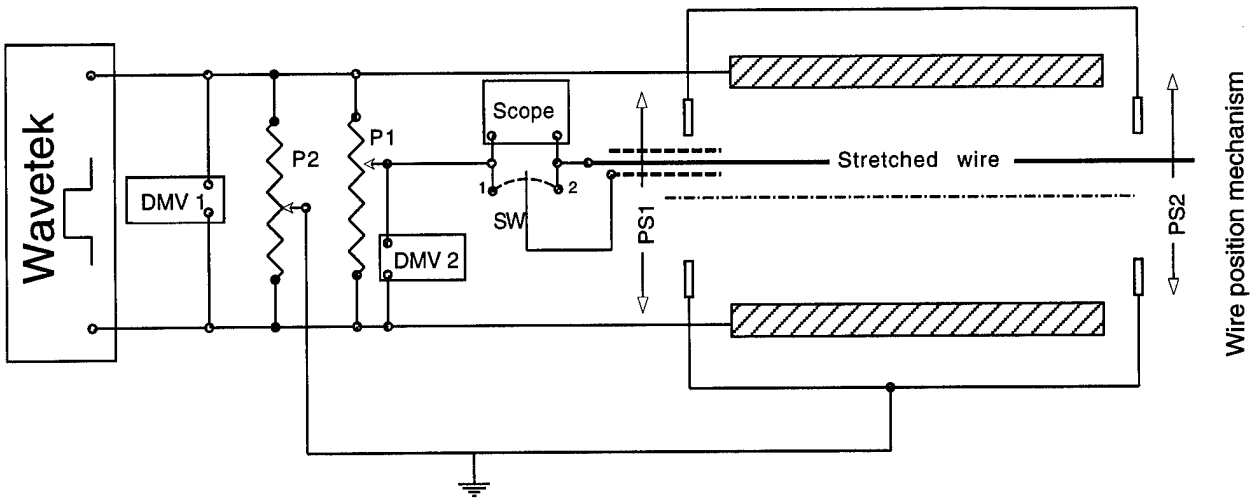



Figure 1: Schematic of electric field uniformity measurement setup.

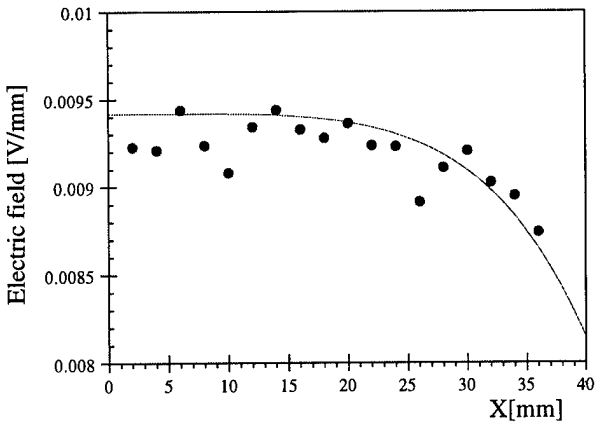



Figure 2: Measured and calculated with POISSON electric field distribution between plates.

ends the stretched wire was close to the vacuum chamber flanges. The voltage difference between wire and these flanges caused additional electrical charge flow which affected the measurement. To fix this problem we made the following improvement. One of the wire ends had been shielded with copper foil in the region close to one flange as shown in Figure 1. Shielding was connected either to point 1 or to point 2 shown on the schematic. In the first case, when the shielding was connected to point 2, we had two ends effect, in the second there was only one end effect. Combining these measurements we obtained end effect data and then using it we calculated the potential profile and excluded the end effects. The electric field was calculated as a difference in voltage measured at two adjacent wire positions divided by the distance. Figure 2 shows the measured electric field, corrected for end effects, in comparison with field calculated with the POISSON program. Here one can see quiet reasonable agreement between calculation and measurements.

## 4 REFERENCES

[1] A.A. Mikhailichenko, *On the Measurement of Electric Fields Using a Rotating Probe*, Novosibirsk, Institute of Nuclear Physics preprint 84-126 (1984), In Russian

[2] *Measurement of Electric Field Uniformity in a Electrostatic Separator*, Weiran Lou and James J. Welch, proc. Particle Accelerator Conference, PAC95, pp 2138, Houston TX, (1995)

# PERMANENT MAGNET ASSEMBLY TOOLING FOR THE 8 GEV TRANSFER LINE AND RECYCLER RING AT FERMILAB

T.H. Nicol and A.B. Knauf, Fermi National Accelerator Laboratory, Batavia, IL, USA

*Abstract*

Magnets for the beam transfer line between the Fermilab Booster and Main Injector and the Recycler antiproton storage ring are constructed using permanent magnet ferrite bricks surrounding a steel pole and housed inside a steel flux return shell. The transfer line consists of 51 dipoles, 67 gradient magnets, and 8 quadrupoles. The Recycler ring consists of approximately 350 gradient magnets and 60 quadrupoles. Positioning and handling large steel plates lined with magnetized ferrite bricks pose several challenges to the design of assembly tooling. Large attractive forces between mating magnet sub-assemblies must be controlled in order to minimize personnel hazards. Positioning of subassemblies must be precise to allow insertion of mechanical fasteners and to maintain consistent magnetic performance in all similar magnets and provisions must be made for magnet disassembly in the event that repairs or adjustments are indicated by magnetic measurements. This paper describes and illustrates the assembly tooling designed and fabricated to facilitate construction of all of the nearly 500 dipole and gradient magnet assemblies in the 8 GeV beam transfer line and Recycler ring.

## 1 INTRODUCTION

Unlike their conventional and superconducting counterparts, there is very little about permanent magnet accelerator magnets that is mechanically sophisticated. Their beauty lies in their simplicity and their uniqueness lies in the way they are assembled. Since they can't be magnetized after assembly, all of the components are either magnetic prior to assembly or strongly attracted to other magnet components during assembly. Anyone who has tried to maneuver two strongly magnetic elements in close proximity to one another can appreciate the unique handling problems one encounters in large permanent magnet assemblies.

Attractive forces vary widely due to differing geometries. For the strontium ferrite bricks used in the 8 GeV transfer line and Recycler, we use 200 kg/meter of magnet length for a row of single ferrite bricks and 400 kg/meter for a double row as the attractive force between two magnetic components in a magnet assembly. These forces are based on calculations and tests conducted during the R&D phase of the 8 GeV transfer line.[1] For magnets like those being built for the Recycler, this translates to an attractive force of nearly 1800 kg between, say the top plate and pole assembly. Forces of this magnitude are both difficult to control during assembly and constitute a serious pinch hazard to personnel. For both of these reasons, to control the forces and to minimize the personnel hazard, we opted early in the R&D phase of the permanent magnet development to fabricate tooling that could be used throughout the R&D and production phases of both the 8 GeV transfer line and Recycler.

## 2 MAGNET DESIGN

Seven different gradient and dipole magnet designs exist for the 8 GeV beam transfer line and Recycler storage ring, each with different cross sections, lengths, strengths, and magnetic characteristics, but all containing similar mechanical features. It is beyond the scope of this paper to describe each of the designs in detail, however, a brief overview serves as background for a description of the tooling design.

Figures 1 and 2 illustrate a cross section and an exploded isometric projection of one of the gradient magnets being developed for the Fermilab Recycler. It is representative of all the permanent magnet assemblies built for the 8 GeV transfer line and Recycler and consists of a low carbon steel pole assembly surrounded by magnetized ferrite bricks, all housed in a steel flux return shell. Spacers between the individual poles and between the pole assembly and flux return are aluminum. The ferrite bricks are 101.6 mm wide, 152.4 mm long, and 25.4 mm thick. All of the magnets are of similar size, 24 to 30 cm wide and 19 to 25 cm high. Magnet lengths vary from 2.4 to 4.7 m.

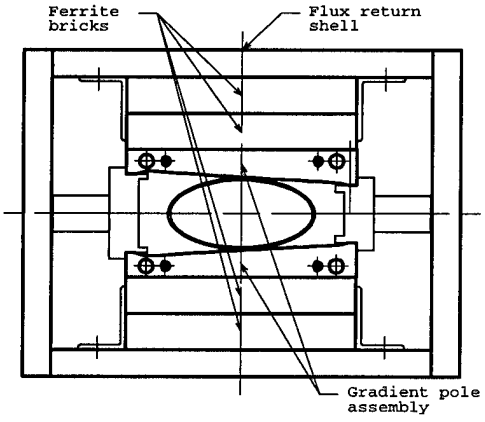



Figure 1: Recycler gradient cross section

0-7803-4376-X/98/$10.00 © 1998 IEEE

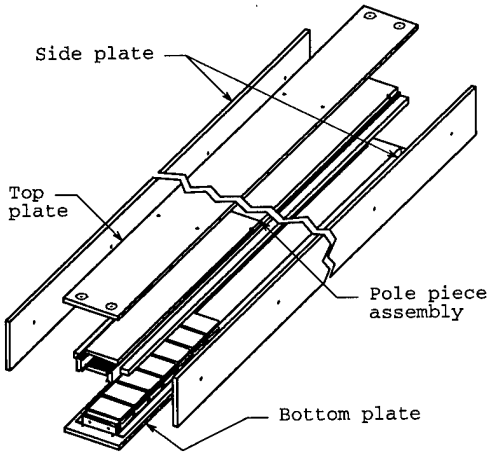



Figure 2: Recycler gradient exploded view

## 3 TOOLING DESIGN

The design goals for the assembly tooling were apparent during early efforts building R&D magnet assemblies. Controlling the attractive and repulsive forces, aligning mating magnet components, and ensuring personnel safety at all times were the key elements we sought to achieve. Speed of operation was not a strong consideration due to the relative few magnets being built and the fact that final assembly represents only a small fraction of the total time producing any one complete assembly. For these reasons, a high degree of automation was not necessary. A simple set of hand operated controls with appropriate fixturing were more than adequate in the initial design studies and proved to be so in production.

Figure 3 illustrates the result of this design effort. The tooling consists of four key pieces, all of which work together in building each magnet assembly. The main component is the table itself shown in profile on the left side of figure 3. With the exception of guide pins, actuators, bearings, and fasteners, the table is constructed entirely from 6061-T6 aluminum plate and structural members. The table serves as the main work surface and contains guides and motion control devices for the remaining parts. Shown above the table is a lifting fixture used first to lower the pole assembly onto the bottom plate then to lower the top plate onto the pole assembly. The lifting fixture contains features to accurately position the pole assembly and top plate and serves as a stiffener to prevent bending of the subassemblies being lowered as the attractive forces between mating parts increase. It also contains Teflon bushings which align with and slide over precision guides attached to the assembly table. Linear actuators at either end of the table connect to the lifting fixture once it is in position over the table and allow it to be lowered toward the table surface.

Two aluminum channels on either side of the main table are removable and are used as the base for assembly of both side plates. Once complete, the side plates with the attached aluminum channels are lowered onto two stainless steel pins on either side of the table. These pins are connected to handwheel actuated drive mechanisms which allow both side plates to be moved toward the center together.

The upper lifting fixture and side channels have been designed to accommodate all of the various magnet assemblies. Wherever possible, standard spacing has been used for fastener locations in the magnet top, bottom, and side plates to minimize the rework in the assembly tooling between production of the various magnet types.

## 4 ASSEMBLY PROCEDURE

### *4.1 Magnet Assembly*

Regardless of the magnet type; gradient, dipole, vertical

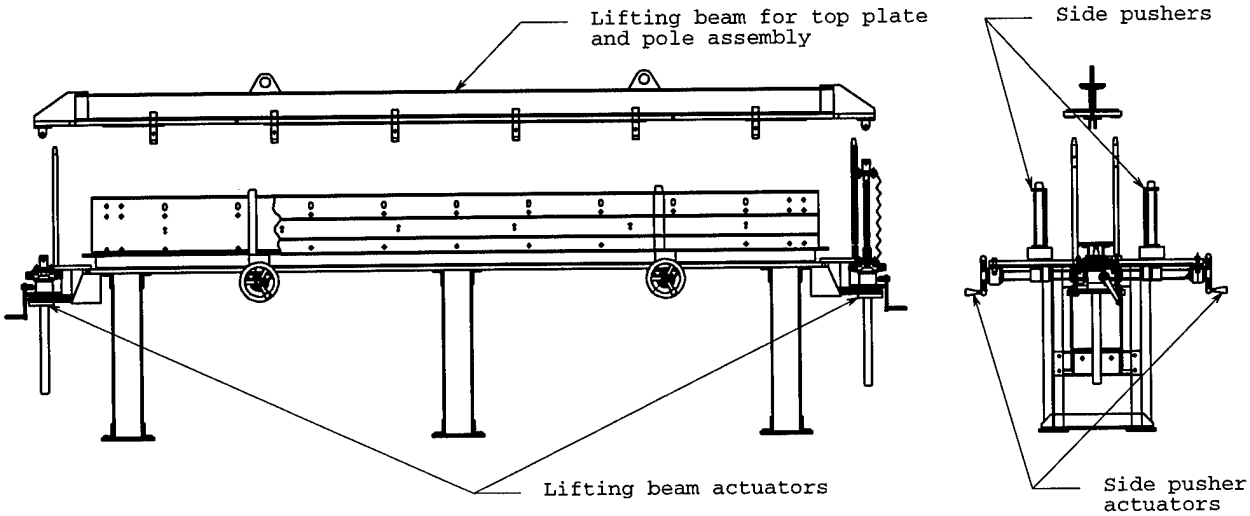



Figure 3: Permanent magnet assembly tooling

bend or dispersion suppressor, the assembly procedures are nearly identical. Each of the four main subassemblies; top, bottom, and two side plates, are completed on separate nonmagnetic work stations. After completion of these subassemblies, each is brought to the magnet assembly table in turn. First the bottom plate with attached hardware and ferrite bricks is attached to the base of the table. Next the pole piece assembly is lifted using the lifting fixture and lowered onto guide rods attached to the table. The lifting fixture positions the pole precisely over the bottom plate and prevents the attractive forces between the pole and bottom plate from bending the pole assembly. Once the pole is in place, the top plate is similarly lowered onto the subassembly of the bottom plate and pole. Finally, each of the two sides, complete with their respective aluminum channel stiffeners are lowered onto vertical guide rods on the assembly table. Once in position, the guide rods are moved uniformly toward the center. An attempt is made to ensure that each side plate contacts the center assembly at the same time.

Once all four plates are in position, mechanical fasteners are installed through clearance holes in the side aluminum channels. When complete, the channels are removed, the magnet assembly is unbolted from the assembly table, the end plates are attached, and the competed assembly is moved to the test area.

### *4.2 Magnet Disassembly*

Although not anticipated in the early design stages, it became apparent early in production that the assembly tooling would be just as valuable for magnet disassembly as it was for assembly. During the R&D phase of each particular magnet design, several attempts are typically necessary to find the exact ratio of ferrite to temperature compensator. There was no way to determine this in advance due to the lack of homogeneity in the bricks and batch variations in the compensator. Complete magnets are built and tested in order to evaluate the degree to which the design field and temperature coefficients are met. If measurements indicate that an adjustment is needed, disassembly is required. Typically, we have had to disassemble at least one magnet at each lot change in temperature compensator. Attractive forces are at a maximum when the gaps between parts are closed as in a completed assembly which makes disassembly without this tooling not only time consuming, but hazardous. Magnets requiring rebuild are fastened to the table and disassembly proceeds in exactly the reverse order from the assembly described earlier.

## 5 SUMMARY

The assembly tooling developed for the 8 GeV beam transfer line and Recycler ring has proven itself to be both versatile and flexible. More importantly, however, it has allowed us to control the inherent forces which exist in these assemblies, routinely assemble magnets with the required precision, and to do both with minimal hazards to personnel.

## REFERENCES

[1] "Ferromagnetism", Richard M. Bozorth, IEEE Press, New York, 1978.

# A DISTRIBUTED MONITORING AND CONTROL SYSTEM

J.M.Nogiec, E.Desavouret, D.Orris, J.Pachnik, S.Sharonov, J.Sim,
J.C.Tompkins, K.Trombly-Freytag
Fermi National Accelerator Laboratory*, P.O.Box 500, Batavia, IL 60510

*Abstract*

A monitoring and control system designed and implemented by Fermilab's Development and Test Department is presented. The system consists of a set of configurable communicating distributed objects. It includes graphical user interfaces, archivers, a data acquisition subsystem, and direct control components. The system is open and its functionality can be altered by: a) selecting modules that plug into an event-based software bus, b) developing new modules with help of the existing APIs to access system resources, and c) modifying system configuration data. This paper presents the system architecture, discusses its unique features, and describes applications of the system to control tests of superconducting accelerator magnets.

## 1 INTRODUCTION

The challenge the system designers faced was to produce an integrated system to serve as both a general-purpose monitoring and control system and a measurement tool. It means that the requirements traditionally imposed on the monitoring and control systems were accompanied by an additional requirement: to measure a multitude of intrinsically different process variables with varying accuracy, speed, and dynamic range. The system is required to monitor and control the environment while performing special tests and measurements.

At the same time the R&D environment calls for a system that is flexible, reconfigurable, extendible, and scalable. In response to these requirements an open software platform for building multi-user distributed control and monitoring as well as test and measurement systems has been developed.

## 2 SYSTEM ORGANIZATION

The Distributed Monitoring and Control System (DMCS) is a configurable set of communicating distributed objects. The following components constitute the core of the system: memory resident real-time data base, scan system with on-line processing capabilities, event and message communication subsystem, data archival subsystem, off-line analysis tools, and various user interfaces.

The system is decentralized and, unlike in many other systems, no single computer assumes a central role. As a result, a failure of any single computer will not bring the whole system down.

From the hardware point of view the DMCS is a multi-platform system consisting of a set of distributed computers connected via a local area network. Functionally, the system follows the traditional, hierarchical approach: graphical user interfaces and data analysis applications run under Unix while data acquisition and direct control run on so-called process control computers under the VxWorks [4] real-time operating system. Most of the system components are available on both platforms and there are plans to extend this functionality into the Windows-NT environment.

The system accesses various hardware modules via the VME and GPIB instrumentation buses and transparently integrates PLC-based I/O systems.

## 3 MODEL OF PROCESS UNDER CONTROL

The state of the process under control is monitored and altered through manipulations on a set of process variables (PVs). Some process variables (*input process variables*) reflect directly measured process parameters, whereas other contain control values used to regulate the process *(output process variables*). Still other process variables called *software process variables* may contain system control parameters, internal system variables, statistics, long-term trends, etc.

All PVs have calculations assigned to them. Each input and output PV is additionally associated with a data acquisition channel, signal conditioning device, and a sensor.

## 4 SYSTEM OPERATION PRINCIPLES

The system configuration is described using the Data Base Definition Language (DBDL). Currently, the system description includes four classes of objects: scans, process variables, devices, and calculations. DBDL enables the user to define all of the objects present in the system. The result configuration is loaded to the process control computers for interpretation. All objects are kept in the memory resident *real-time data bases* (RTDB) located in each of the process control computers.

Operated by the Universities Research Association under contract with the U.S. Department of Energy

0-7803-4376-X/98/$10.00 © 1998 IEEE

### *4.1 Real-time Data Base*

RTDB is a fast memory-resident object-oriented data base. It provides transparent access to local and remote objects via names, indices, and object attributes. It also contains a caching mechanism for remote objects and a locking mechanism to control access to the objects.

### *4.2 Scan System*

Monitoring, control, and data saving features of the DMCS are implemented through an elaborate scanning system offering coherent, device-independent I/O and powerful synchronization capabilities. The scan system links the real-time data base with the process under control by uniformly accessing devices and pseudo-devices and passing the data to and from the RTDB. Advanced features of the scan system include time-driven and event-driven data acquisition and control, PV-based or device-based scanning lists, data saving scans, and PID control scans. All scans and their attributes are user-configurable and can be monitored and manipulated in real-time.

### *4.4 Communication and Synchronization*

Scans, servers, and control clients communicate and synchronize through exchange of messages and events.

The DMCS offers transparent system-wide event-based communication and synchronization. Events are exchanged using a concept of a software bus where objects can communicate with each other without having direct knowledge of each other. In this scheme any active object (e.g., data acquisition scan) that wants to receive events, registers its interest in specific types of events. Events are multicast to all interested parties in a local computer as well as in remote computers. The mechanism of events is a primary way of synchronizing actions of all system active components- essentially all data acquisition scans and special measurement-type programs.

The DMCS also provides uniform message-oriented data access based on a client-server model of cooperative computing.

### *4.5 Continuous control*

Continuous control is provided by the system through closed loop control using a PID algorithm. The PID algorithm is implemented as a calculation attached to a controlled process variable. The calculation is triggered whenever a new value of the process variable is requested, which happens periodically with a period defined for the appropriate scan. The system includes a dedicated user interface to tune and examine PID loops.

Since implementing another control algorithm is as simple as adding a new calculation to the system the authors plan on supplementing the PID algorithm with a set of fuzzy logic control algorithms.

## 5 INTERACTIVE CONTROL

Modern data monitoring and control systems require sophisticated graphical user interfaces. Since X Windows and Motif are currently the dominant technologies for visualization on Unix workstations, they are the basis for the user-system dialog implementation. However, due to the advent of Java-enabled systems and the growing amount of Windows NT systems we are forced to consider a multi-platform user interface for future releases of the system.

The DMCS provides users with several readily available universal user interfaces as well as with a set of tools to enable rapid development of animated process schematics and *ad hoc* user interfaces. The universal tools enable selecting and displaying values and attributes of any set of process variables, either graphically or numerically.

Specialized user interfaces are developed with the help of graphical user interface builders, which significantly accelerates the development process. Examples of specialized user interfaces developed with these tools are fast data logging control panels, power control and monitoring user interfaces [3], quench detection, and magnet protection control panels.

## 6 BATCH CONTROL

Special tests, non-standard operation sequences, and required system actions can be performed with the help of scripts. The scripts can be executed from any authorized Unix workstation. A set of programs has been specially created to facilitate the script development that enable event signaling, remote real-time data base accesses and inserts, remote invocation of VxWorks-resident functions, and current control. These programs constitute a powerful toolset to control the system in a batch mode.

## 7 DATA MANAGEMENT AND ANALYSIS

In order to satisfy the real-time, as well as data archival and retrieval requirements, the DMCS adopts a hierarchical storage model. The model includes light-weight in-memory data bases to satisfy real-time requirements (RTDB), file system based intermediate storage, a commercial data base for day-to-day data management, and optical storage for long term data archival. At the current phase of system development the last two levels of the storage system are still under construction.

Data collected by the DAQ subsystem is processed in real time before entering the RTDB. Therefore, all process variables can be monitored in real-time without any data processing on the client side.

Archived data can be subjected to off-line processing and analysis.

*7.1 Chunk Format Standard*

The Chunk Format Standard, or CFS, is a hierarchical multi-object file format for storing diverse scientific data. The main requirement addressed in the design of CFS is the extensibility for future enhancements and capability to store any data. CFS enables easy merging of data by simply appending one CFS file at the end of another. Current implementation of the Chunk Format Standard includes both the Unix (SunOS) and VxWorks platforms.

*7.2 On-line data processing*

The software system provides for real-time conversion of measured input voltages to engineering units, by applying calibrations and performing calculations. This on-line processing includes a mechanism similar to triggers found in relational data bases: Calculations of some quantities can in turn trigger automatic re-calculation of other quantities. This mechanism constitutes a powerful tool for implementing any algorithm and processing hierarchy while maintaining access to all required partial results.

*7.3 Off-line data analysis*

Archived data can be interactively analyzed and visualized with the help of a universal data analysis program. This program can be used for plotting waveforms of individual data channels as well as for performing simple mathematical operations on single or combined waveforms prior to visualization. The user can extend the processing capabilities of this tool by adding any custom algorithms that later can be selected and applied interactively.

Specialized data analysis and report generating tools that access data through the use of an appropriate API can be also constructed. A program to generate a quench summary for each accelerator magnet quench event is one of the examples of such tools.

## 8 APPLICATIONS OF THE SYSTEM

The DMCS system has been successfully applied for monitoring and controlling the Horizontal and Vertical Magnet Test Facilities in the Fermilab Technical Division. The system is also expected to be used to control the Magnet Test Facility cryogenic plant.

*8.1 Horizontal Magnet Test Facility*

The DMCS was incorporated in the horizontal magnet test facility as an early application. This test facility includes the following: an SSC 15 meter magnet test stand modified to perform 1.8K quench tests of a low beta quadrupole magnet, a standard Tevatron magnet test stand used to re-test Tevatron dipole magnets at 4.6K, and another Tevatron magnet test stand modified to include corrector magnets as part of a special cryogenic accelerator magnet heat leak study. In all three applications the parameters being measured were cryogenic temperatures, pressures, helium flow, helium vapor pressure, magnet current, and Idot. In addition, the low beta quad measurements also included strain gauges.

*8.2 Vertical Magnet Test Facility*

The vertical magnet test facility [2] is another application of the DMCS system. This four meter vertical dewar is capable of testing superconducting magnets over a temperature range of 1.8K to 4.6K and can power these magnets up to 18kA. Helium valves are regulated through a feedback loop to control liquid helium level and temperature. In addition, a fast high voltage data logging system (quench characterization), a magnet quench detection and magnet quench protection system, and a power supply control and hardware interlock system are integrated to provide complete magnet power control and data acquisition.

## CONCLUSIONS

Despite the fact that the full version of the DMCS is not yet available, the system has been already successfully applied to control and monitor several installations. The authors' experience from running the systems based on DMCS confirmed that the openness and flexibility of the design pays off when confronted with constantly changing R&D environment and tight schedules.

## ACKNOWLEDGMENTS

The authors would like to thank all the users of the system for their valuable remarks, especially M.Lamm, T.Peterson, J.DiMarco, and M.Tartaglia.

## REFERENCES

[1] 'An Open Distributed Monitoring and Control System', J.M.Nogiec et al. Proc. of the International Conference on Computing in High Energy Physics CHEP'97, April 1997, Berlin

[2] 'A New Facility to Test Superconducting Accelerator Magnets in Superfluid Helium', M.J.Lamm et al. Proc. of the 1997 Particle Accelerator Conference, Vancouver, Canada

[3] 'An Embedded Power Supply Controller', S.Sharonov, J.M.Nogiec, Proc. of the 1997 Particle Accelerator Conference, Vancouver, Canada

[4] 'VxWorks Programmer's Guide 5.2', Wind River Systems, Inc., 1995

# PULSED MAGNETIC FIELD MEASUREMENT USING A FERRITE WAVEGUIDE IN A PHASE BRIDGE CIRCUIT

W. Pellico,P. Colestock, Fermi National Accelerator Laboratory †, P.O. Box 500, Batavia, Ill., USA, 60510

*Abstract*

There are several standard methods used for measuring pulsed magnetic fields. However the induction or Hall probe methods have limited bandwidth and experience reflection problems. The integrated magnetic field can only be found by measuring along the entire length of the magnet. Problems with reflections, noise and bandwidth will limit the accuracy of measurement. Presented in the following paper is a method for measuring pulsed fields without the typical noise errors and bandwidth limitations. This paper will describe a phase bridge network that relies upon the permeability of a ferrite waveguide to accurately measure the integrated field of a Main Injector kicker magnet. We present some data taken with the system, a first pass at the analysis of this data, and discuss some possible design variations.

## 1 INTRODUCTION

In pulsed magnetic systems, the measurement the integrated magnetic field is a difficult process, which usually results in limited accuracy. One method of ascertaining the integrated magnet field is by taking current probe data from both ends of the kicker and integrating. Another method is to use a shielded coil loop to measure a changing magnetic field. Both methods will result in limited accuracy due to the large electric field present in kickers, reflections over the probe length and bandwidth limitations of the measuring device. These problems can be eliminated (or greatly reduced) if the probe's susceptivity to electric fields and signal reflections along the conductor are reduced. The choice of ferrite with high intrinsic impedance makes it an ideal probe for pulsed field measurement.

### *1.1 Phase Bridge System*

The ferrite probe is actually a waveguide, which acts as one of the legs in a phase bridge circuit. A radio frequency (RF) signal is split down both legs of the circuit. One of the signals is coupled into the ferrite guide and the other is sent into a delay line. The ferrite is placed inside the center of the kicker aperture. The emerging ferrite guide is then coupled back into cable and mixed with the delay line signal. The DC mixing term is then low passed before being measured on a fast digitizing oscilloscope. In the absence of an externally applied magnetization, the phase bridge is measured and balanced. When the magnetization pulse occurs a phase unbalance develops between the two legs of the phase bridge. The unbalance is a result of the magnetization of the ferrite, which changes the wave velocity of the guided RF signal.

### *1.2 System Specification*

The quality of the measurement will depend largely upon choice of ferrite. There are numerous types of ferrite and each have material characteristics that need to be matched for the particular pulsed magnetic system. The ferrite(s) used in this testing was based upon the specifications of the Main Injector kicker. Since the shifting of the wavelet velocity will result is a phase shift, the greater the phase shift the larger the resulting mixed DC component.

Another key factor is the frequency of the signal used in the system. The higher the frequency, the larger the number of waves inside the ferrite which results in higher sensitivity. The RF will also determine the bandwidth of the measurement system and should be well above the highest frequency component in the pulsed magnet waveform. The magnetization pulse was calculated to have a frequency spectrum of DC to 100 MHz. The high frequency is also a requirement for single-mode operation in a ferrite guide, which must have small cross-sectional dimensions. Listed below are several of the kicker system specifications, which were used in determining the choice of ferrite and RF:

- Nominal Field 136 gauss
- Magnetic Length 0.83 meters
- Field Rise Time ~50 nsec.
- Flattop Time 1600 nsec
- Aperture H,V 101.6mm x 50.8mm

The frequency chosen for our measurement was an X-band (9 to 10 GHz) signal. Two ferrites which complied with the requirements and used in the system are G-1009 and G-250, both are manufactured by Trans-Tech, Inc. The table below lists several of the two ferrite materials characteristics. The data comes from a 1992 Trans-Tech microwave materials data book.

† Operated by the Universities Research Association, Inc. under contract with the U.S. Department of Energy.

0-7803-4376-X/98/$10.00 © 1998 IEEE

| | | |
|---|---|---|
| • FERRITE | G-1009 | G-250 |
| • Saturation M | 179 g | 250 g |
| • Permeability | 11 | 34 |
| • Dielectric | 13.8 | 13.8 |

The choice of mixer was determined by its passband flatness and expected power levels Choice of components were also based upon availability and cost.

## 2 LAYOUT

The phase bridge system is shown in figure 1. The RF source was a network analyzer with an output power of +12 dBm (A 150 MW 10 GHz Gunn source was also tried.) The signal launched into the waveguide was approximately +8dBm. The waveguide to ferrite coupler was a machined Aluminum block with quarter wave steps on the input end and a flared output on the output end for impedance matching. After passing through the kicker, the ferrite was then again coupled back into coax. Both upstream and downstream launches were identical. A waveguide isolator was attached at both ends of the launch. The upstream waveguide section also had a waveguide phase shifter attached. This allowed for about 400 degrees of phase tuning. The phase shifted signal was then mixed with the delayed line RF signal and then low passed filtered. We did use an IF amplifier in some of the test runs but found it wasn't necessary in all cases. The low pass filter cutoff of 200 MHz was well above the harmonic content of the magnetic field pulse but still eliminated noise spikes and other higher order terms of the mixing. The DC to 100 MHz signal was then sampled on a fast oscilloscope and saved to disk for analysis. The scope needed to be housed in a shielded cage for EMI reduction (not shown in figure 1).

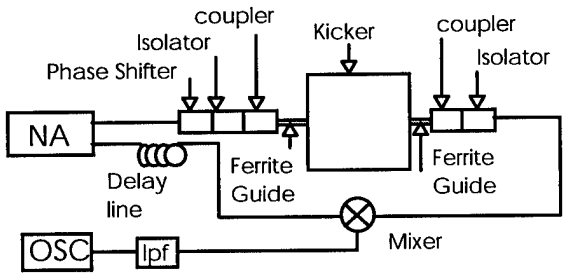



Figure 1:Phase Bridge Measurent Setup

## 3 MEASUREMENTS

Measurements of the pulsed kicker system were taken over a two week period. Small modifications to the measurement system continued throughout the testing period. Prior to using the ferrite probe system, a printed circuit field coil and capacitive pickup probes were used to measure the pulsed magnetic field [1]. Although those measurements were affected by some noise and ringing, the results can give a fairly accurate magnetic field profile against which to compare the ferrite probe data.

The phase bridge measurements were taken with various kicker voltage and reservoir settings. The tests were to confirm the performance of the phase bridge system as well as the pulse magnet.

### *3.1 Flattop Measurement*

A critical aspect of kicker systems is the flattop stability. We took two sets of flattop data. The first set was a measurement of the flattop field verses various kicker voltage settings to see if the measured magnetic field scaled properly (see figure 2.) The second data set measured the kicker flattop when the impedance matching of the kicker and its termination load was being changed. The idea is to measure the flattop when the kicker is terminated in a matched load to that of a slightly different load value. This was done by heating the load with a higher pulse rate.

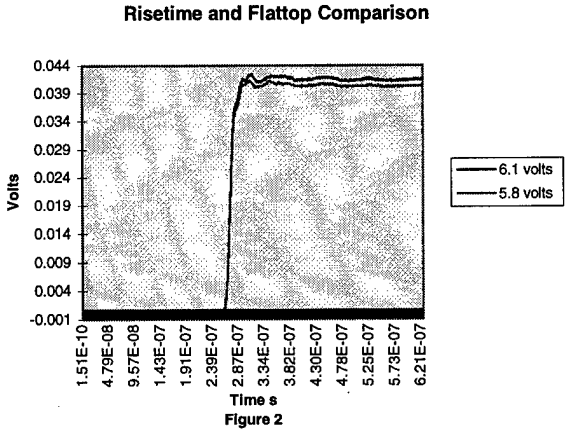



Figure 2

The data from the first set of measurements shows an ability to measure voltage changes to better than 2%. This is more a test of relative change rather then a measure of absolute field value. Since the only way to get absolute values is to DC test the ferrite and trace out the characteristic B-H curve for the given ferrite waveguide. This test is being done at the writing of this paper.

The second set of data shows evidence of a kicker mismatch. The flattop has developed a small perturbation with a period related to the load and kicker length. The impedance mismatch is not accurate enough to be used as a calibration. But the flattop measurement was able to detect a 3% change in load resistance (see figure 3.)

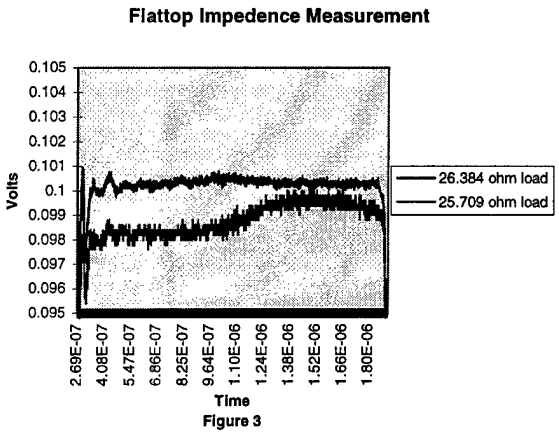


Figure 3

3.2 Risetime Measurements

Another critical aspect in kicker performance is the magnetic field risetime. The risetime was measured from base line to when the integrated field has reached flattop. The Main Injector kicker is specified to have a 50 ns risetime.

We measured the risetimes as a function of kicker voltage settings and at various tube gas pressures. The phase bridge circuit measured a risetime at nominal kicker settings of approximately 30ns. The comparison with that of a current probe showed a 12ns faster risetime. This difference can be partly explained by the systemic error of the two systems. The current probe is coupled through a ~30 pf capacitor and shows signs of being critically damped. This reduction in bandwidth could result in a longer risetime.

## 3 SYSTEM DESIGN ALTERNATIVES

We used a network analyzer as a source. A high loss ferrite may require an additional amplifier. An IF amplifier could be attached before the mixer. Another option is to mix down the X band signal before passing through a log amplifier. The log amplifier will reduce errors associated with amplitude variations.

## 4 CONCLUSION

Preliminary field measurement data shows the possibility of using a ferrite rod as a waveguide in a phase bridge setup. The accuracy of the field measurement will be proven with beam tests when the Main Injector comes on line. The agreement with standard measurement techniques shows that the phase bridge system is a viable measurement. Used in conjunction with standard methods, a more accurate magnetic field profile is obtained. More testing will need to be done to improve upon the accuracy, but the present system can deliver 1 to 2 % accuracy.

## 4 ACKNOWLEDGMENTS

The authors acknowledge Bruce Hanna for his assistance in the project. We would also like to thank Peter Bagley

## 5 REFERENCE

[1] D. Quenell, "Kicker System for 8Gev Proton Injection", PAC 97, These Proceedings

# LONGITUDINAL IMPEDANCE MEASUREMENTS OF AN RK-TBA INDUCTION ACCELERATING GAP

S. Eylon, E. Henestroza, J.-S. Kim, Fusion and Accelerator Research, San Diego, CA 92122
T.L. Houck, G.A. Westenskow, Lawrence Livermore National Laboratory, Livermore, CA 94551
S.S. Yu, Lawrence Berkeley National Laboratory, Berkeley, CA 94720

*Abstract*

Induction accelerating gap designs are being studied for Relativistic Klystron Two-Beam Accelerator (RK-TBA) applications. The accelerating gap has to satisfy the following major requirements: hold-off of the applied accelerating voltage pulse, low transverse impedance to limit beam breakup, low longitudinal impedance at the beam-modulation frequency to minimize power loss. Various gap geometries, materials and novel insulating techniques were explored to optimize the gap design. We report on the experimental effort to evaluate the rf properties of the accelerating gaps in a simple pillbox cavity structure. The experimental cavity setup was designed using the AMOS, MAFIA and URMEL numerical codes. Longitudinal impedance measurements above beam-tube cut-off frequency using a single-wire measuring system are presented.

## 1 INTRODUCTION

A greatly simplified gap, using high-gradient insulator (HGI) technology, has been designed for the induction modules of a proposed RK-TBA rf power source [1]. These insulators, comprised of finely spaced, alternating dielectric and metal layers, have demonstrated factors of 1.5 to 4 times the vacuum surface flashover capability of insulators made from a uniform dielectric [2,3]. HGI's have maintained similar capability in the presence of an electron beam [4]. These characteristics allow more flexibility in the positioning of the insulator and the overall gap design. In typical induction accelerator designs [5], the gap is shaped to accommodate an extended insulator that is hidden from line-of-sight view of the beam. The shape of the gap must be carefully designed to minimize field stress on vacuum surfaces. An issue that needs to be addressed concerning the placement of a stacked insulator in an accelerating gap involves the interaction impedance of the integrated module/insulator with the beam. The concern is that the multilayered stacked geometry would generate additional resonances compared to a solid insulator, and that these new resonances would have unacceptable impedance. The transverse impedance characteristic of accelerating gaps using HGI's is presented elsewhere in these proceedings [6]. In this paper we present experimental and computational measurements of the longitudinal impedance of a pillbox cavity with a HGI insulator.

## 2 SIMULATIONS OF HGI PERFORMANCE

URMEL simulations were performed to provide an intuitive feel for the effect of electrodes placed in an insulator. The gap design simulated was a simple pillbox cavity with the same geometry used in the impedance measurements. A schematic of the pillbox geometry is given Fig. 1. . The simulated insulator varied in the number of electrodes (conducting disks), but maintained overall dimensions of width 1.3 cm with inner/outer radius of 2.4/4.9 cm. A summary of results of the simulations for the lowest modes is given in Table I. The cutoff frequency for the simulated cavity is 4.8 GHz. The URMEL results indicate that while additional resonances are generated, their R/Q is not significant. Impedance spectrums generated by AMOS simulations of similar cavities including rf absorbers displayed no additional impedance peaks. Comparison of AMOS simulations and experiments are presented below.

## 3 EXPERIMENTAL SETUP

Longitudinal impedance measurements up to 20 GHz were performed on a pillbox cavity configuration using a wire transmission line system developed by LBNL [7]. Special techniques were implemented in the system to allow the frequency range to be extended well above the beam tube cutoff frequency. These techniques also allow accurate measurements of very low impedance in the heavily damped acceleration gap structures. The absolute error can be kept to less than 2 ohms. Both features are important. For the RKTBA application, the beam pipe cut off frequency is about 4 GHz while the longitudinal modulation of the beam current is 11.424 GHz. In

Table I. Summary of pillbox cavity modes from URMEL simulations for different numbers of intermediate electrodes in the insulator. Although more resonances are created with increasing number of electrodes, their R/Q's are negligible.

| Solid | | One Electrode | | Three Electrodes | | Five Electrodes | |
|---|---|---|---|---|---|---|---|
| Freq (GHz) | R/Q (Ω) | Freq (GHz) | R/Q (Ω) | Freq (GHz) | R/Q (Ω) | Freq (GHz) | R/Q (Ω) |
| 0.986 | 16.2 | 0.958 | 15.2 | 0.894 | 13.3 | 0.814 | 11.4 |
| 2.820 | 6.95 | 2.841 | 6.38 | 2.893 | 5.23 | 2.940 | 4.13 |
| ---------- | ---------- | ---------- | ---------- | ---------- | ---------- | 3.483 | 0.027 |
| ---------- | ---------- | ---------- | ---------- | 3.576 | 0.007 | 3.636 | 0.000 |
| 4.182 | 3.35 | 4.165 | 3.18 | 4.140 | 2.798 | 4.097 | 2.35 |

0-7803-4376-X/98/$10.00 © 1998 IEEE

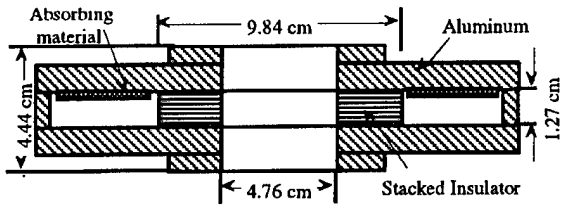



Figure 1. Illustration of the test pillbox cavity.

addition, the desired impedance at 11.424 GHz is only 2.5 Ω. Fig. 2 shows a schematic of the impedance measurement setup. The pillbox is positioned between two sections of transmission line with a characteristic impedance ZL of 160 Ω. The transmission line inner diameter is 4.76 cm and the center wire diameter is 0.32 cm. To ensure accurate positioning, a Styrofoam guide is used to centered the wire in the beam line. Two conical, electroformed Chebyshev tapers are used for matching the transmission line impedance to the 50 Ω lines attached to the inputs of a HP8510B network analyzer.

In the above wire measurement, the matching tapers have been design to be free of TEM reflections over the range of 100 MHz to 20 GHz. The tapers, however, are not matched for traveling waveguide modes (TWs). TWs could be reflected from the tapers and lead to standing waves in the system producing erroneous results. To prevent TW reflections, absorbing material (Emerson & Cuming Eccosorb AN73) was placed between the pillbox and the tapers. The transmitted TEM signal is also attenuated, but the network analyzer has sufficient dynamic range to accommodate the reduced signal.

For test cavities occupying a limited length of the transmission line, the impedance, $Z_B$, is calculated from:

$$Z_B = 2Z_L\,(S_{21ref}/S_{21obj} - 1), \text{ where}$$

$S_{21ref}$ is the system response when replacing the test cavity with a smooth tube having the same longitudinal length, $S_{21obj}$ is the test cavity (pillbox) response, and $Z_L$ is the characteristic impedance (160 Ω) of the beam tube transmission line.

The test pillbox cavity represents a simplified version of an induction accelerator module and gap. Refer to the illustration in Fig. 1. The geometry of the pillbox was varied by including a metallic ring, ID/OD 14.9/16.2 cm, attached to one wall of and extending 1 cm across the cavity dividing the pillbox into two chambers. Absorbing materials in the form of ferrite tiles or foam bands (Emerson & Cuming Eccosorb AN73) were inserted in the pillbox to suppress trapped resonances. A solid rexolite insulator was used to establish a base impedance for the pillbox. The stacked insulators were alternating layers comprised of thin washers (flatten toroids) of mylar (7.5 mils per washer) and copper (5 mils per washer). The number of washers of mylar and copper per layer could be varied. For the majority of the measurements, the inner diameter of the rexolite and stacked insulators was equal to that of the pillbox, 4.76 cm, and the outer diameter was 9.84 cm. Measurements were also taken for a solid rexolite insulator recessed into the pill box with inner diameter of 7.30 cm and outer diameter of 9.84 cm.

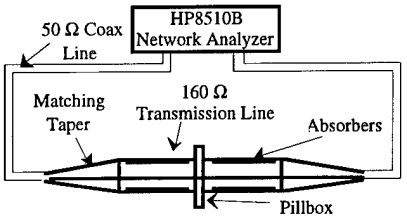



Figure 2. Impedance measurement setup.

## 4 MEASUREMENTS

Samples of the measurements are shown in Fig. 3, 4, and 5. For these measurements, the pillbox arrangement is as illustrated in Fig. 1. The absorbing material was a mosaic of ferrite tiles placed to approximate a solid toroid. Figure 3 compares three different gaps widths using a stacked insulator with a 1.5:1 ratio (alternating layers of 7.5 mil mylar and 5 mil copper) of insulator to conductor. Copper washers, with radii equal to the insulator washers, were stacked in the gap to adjust the width. Peak impedances of resonances below the cutoff frequency vary linearly with gap width. Above cutoff, the peak impedances varied from this scaling.

An important purpose of the measurements was to validate the induction cell design code, AMOS, for simulation results above the beam pipe cut-off frequency. Two difficulties were encountered when attempting to simulate the measurements. First, the rf characteristics of the damping ferrites were not known. The simulations modeled the TDK PB11b ferrite which appeared to be more efficient at damping than the actual ferrite used in the pillbox. Also, the rectangular ferrite tiles used as rf absorbers could not be tightly packed and only approximated the toroid modeled in the simulations. This could also explain some of the difference in damping between the simulated PB11b ferrite and the actual ferrite. Qualitative agreement can be seen between measurements and simulations in Fig. 4 and 5. The simulation results were adjusted about 4% in frequency to match resonant peaks. The measurements in Figure 5 were a more demanding test as the stacked insulator was included in the simulation.

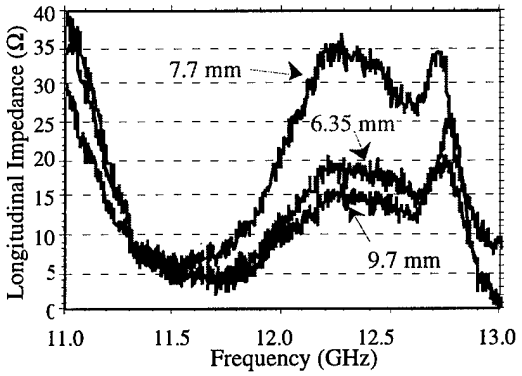



Figure 3. Effect of different gap widths on $Z_L$. Above the cutoff frequency, peak impedances did not obey the linear scaling with gap width predicted by analytical theory.

## 5 CONCLUSIONS

Observations made during the measurements include:

(1) Analytical theory for impedances above cutoff has addressed resonant peak impedances [8]. In general, the theory is in agreement with the measurements performed where the gap width is taken to be the insulator width minus the conducting layers. Theory is not useful for estimating the impedance spectrum between peaks.

(2) Changes to the geometry of the interior of the pillbox (adding an intermediate ring to change the effective OD) had negligible effect on the impedance spectrum well above cutoff.

(3) Reducing the gap width generally reduced resonant peaks with minimal effect on the "valleys" between peaks, and did not shift peaks, or valleys, in frequency.

(4) The placement of the conducting layers in the insulator does not have a significant effect on the impedance spectrum of the pillbox.

(5) Recessing the insulator from the beam tube reduced the impedance in general.

(6) Increasing the damping can lower the peak resonant values, but tends to increase the minimum value of the "valleys" between peaks.

Two primary objectives were accomplished. Very low longitudinal impedances (~ 2 ohms) were obtained and measured for the cavity geometry of interest. Also, consistent qualitative agreement was found between measurements and AMOS simulations.

## 6 ACKNOWLEDGMENTS

Measurements were performed at the LBNL Beam Electrodynamics Laboratory with the invaluable assistance and guidance of J. Corlett and D. Lozano. The work was performed under the auspices of the U.S. Department of Energy by LBNL under contract AC03-76SF00098, LLNL under contract W-7405-ENG-48, and FAR under SBIR Grant DE-FG03-96ER82179.

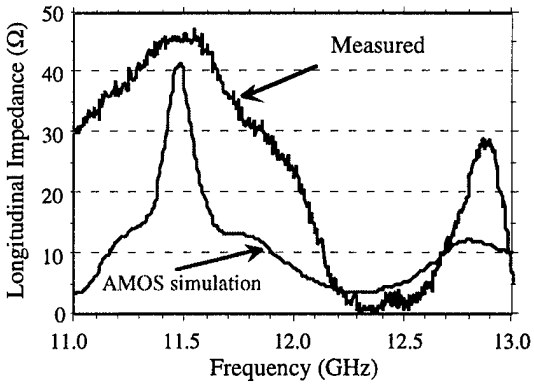



Figure 4. Comparison of measurement and simulation for a solid rexolite insulator.

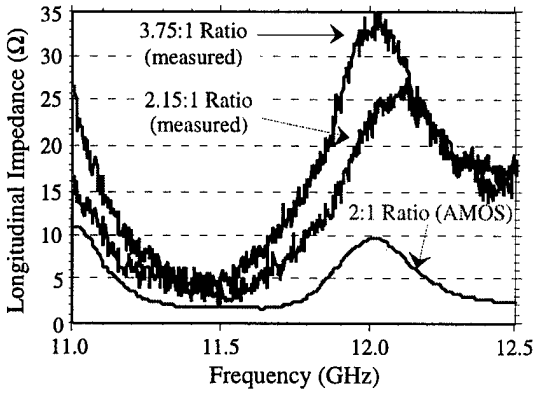



Figure 5. Comparison of ratios of insulator to conductor thickness in the stacked insulator. Decreased effective gap width generally reduced resonant peaks with minimal effect on the "valleys" between peaks.

## 7 REFERENCES

[1] J-S Kim, et al., "Stacked Insulator Induction Gaps", these proceedings.

[2] Juan M. Elizondo and A.E. Rodriguez, "Novel High Voltage Vacuum Surface Flashover Insulator Technology," Proceedings of the XVth International Symposium on Discharges and Electrical Insulation in Vacuum, Vde-Verlag, Berlin, Germany, pp. 198–202 (1992).

[3] S. Sampayan, et al., "High-Performance Insulator Structures for Accelerator Applications", these proceedings.

[4] S. Sampayan, et al., Proceedings 1995 Particle Accelerator Conference, (IEEE), New York, N.Y., pp. 1269–1271.

[5] M. Burns, et al., Proceedings 1991 Particle Accelerator Conference, (IEEE), New York, N.Y., pp. 2958–2960.

[6] T.L. Houck, "Measured and Theoretical Characterization of the RF Properties of Stacked, High-Gradient Insulator Material", these proceedings.

[7] G.R. Lambertson, et al., "Technique for Beam Impedance Measurements Above Cutoff", Proceedings 1990 European Particle Accelerator Conference, Nice, France, June 12-16, 1990.

[8] S. Chattopadhyay (ed.), "Special Edition on Impedance Above Cutoff", *Part. Accel.*, **25** (1990).

# STACKED INSULATOR INDUCTION ACCELERATOR GAPS

T.L. Houck, G.A. Westenskow, Lawrence Livermore National Laboratory, Livermore, CA 94551
J.-S. Kim, S. Eylon, E. Henestroza, Fusion and Accelerator Research, San Diego, CA 92122
S.S. Yu, D. Vanecek, Lawrence Berkeley National Laboratory, Berkeley, CA 94720

*Abstract*

Stacked insulators, with alternating layers of insulating material and conducting film, have been shown to support high surface electrical field stresses. We have investigated the application of the stacked insulator technology to the design of induction accelerator modules for the Relativistic-Klystron Two-Beam Accelerator program. The rf properties of the accelerating gaps using stacked insulators, particularly the impedance at frequencies above the beam pipe cutoff frequency, are investigated. Low impedance is critical for Relativistic-Klystron Two-Beam Accelerator applications where a high current, bunched beam is transported through many accelerating gaps. An induction accelerator module designs using a stacked insulator is presented.

## 1 INTRODUCTION

Induction accelerators are a unique source for high-current, high-brightness, charged particle beams. Induction accelerators are used to drive very high-power microwave sources such as free electron lasers and relativistic klystrons, as intense-xray sources for radiographic applications, and as intense beam sources for material processing. Induction accelerators also are expensive, and the higher energy induction accelerators have been limited to major national laboratories. For these accelerators to become commercially viable, the basic unit of the accelerator, the induction module, must be made more compact, efficient, and less costly.

Novel accelerating gap designs for induction modules based on developing insulator technology provide an opportunity to move induction accelerators from expensive research devices into commercial applications. These novel high-gradient insulators (HGI's), comprised of finely spaced, alternating layers of dielectric and metal, have demonstrated much greater (factors of 1.5 to 4 times) vacuum surface flashover capability than insulators made from a uniform dielectric [1,2]. The HGIs also maintained similar capability in the presence of a cathode and electron beam [3]. The high field stress level in the presence of a beam can permit greatly simplify designs for accelerating gap. In typical induction accelerator designs [4], the gap is shaped to accommodate an extended insulator that is hidden from line-of-sight view of the beam. The shape of the gap must be carefully designed to minimize field stress on the vacuum surfaces.

The rf characteristics of the gap are an important consideration. The transverse interaction impedance of the gap with the beam can lead to collective beam instabilities. The longitudinal impedance can also be an important parameter in some applications, e.g. RK-TBA's. Recent measurements [5,6] of simplified gaps including stacked insulators have shown that the HGI's can improve the rf characteristics over that of a solid insulator.

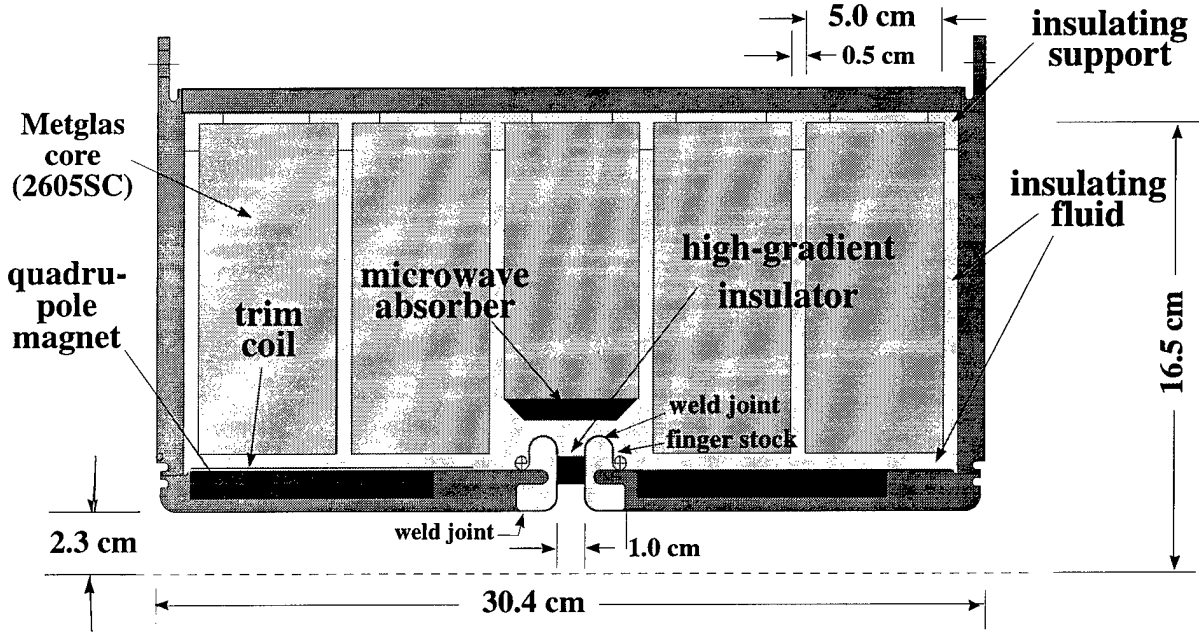



Figure 1. Schematic of an accelerator induction module using a high-gradient insulator.

0-7803-4376-X/98/$10.00 © 1998 IEEE

## 2 ACCELERATOR MODULE DESIGN

We have designed an induction module suitable for use in the proposed TBNLC relativistic klystron [7]. The performance specifications for the TBNLC induction module are comprehensive and demanding, and, prior to our design, no design had met all the specifications. An illustration of our module design is shown in Figure 1. The design must also be consistent with the beam focusing scheme that uses periodic quadrupole magnets.

### *2.1 RF Characteristics*

The transverse impedance for a cavity can be estimated from $Z_\perp = 120\ \eta\ w/b^2$ ohms/m [8], where w is the gap width and b is the beam pipe radius. $\eta$ is a design quality factor of order unity and determined by the de-Q-ing of the cavity. In our design, w = 1 cm and b = 2.3 cm. The desired $Z_\perp$ is $\leq$ 5,400 Ω/m. This leads to a modest value of 2.3 for $\eta$ (most designs have $1.3 < \eta < 1.9$). The desired longitudinal impedance, $Z_L$, is less than 2.5 Ω at 11.4 GHz, a difficult value to achieve. Changing $\eta$ to reduce $Z_\perp$ tends to increase the minimum value of $Z_L$.

The transverse impedance was initially studied with URMEL to determine the field structure of the trapped dipole modes. This information was used to determine appropriate locations for placement of absorbing (de-Q-ing) material within the cell. An induction module design code, AMOS, was then used to calculate the impedances of the module with ferrite absorbers. Results of AMOS calculations are shown in Fig. 2 and 3. $Z_\perp$ decreases to a negligible level above 7 GHz. $Z_L$ is shown over the range of interest. The power spectrum of the modulated current is only significant at 11.424 GHz ± 10 MHz.

### *2.2 Transverse Beam Dynamics*

Transverse beam dynamics were examined with the MBBU code [9] using AMOS generated wakefields. The wakefield associated with the impedance in Fig. 2 is shown in Fig. 4. Shown are the transverse wakefields of a 11.4 GHz gaussian bunch with standard deviation length of 1.875 mm for the distribution. For clarity, wakefields up to about 114 bunch spacings are shown. The open circles indicate the wakefields at bunch centers. Higher

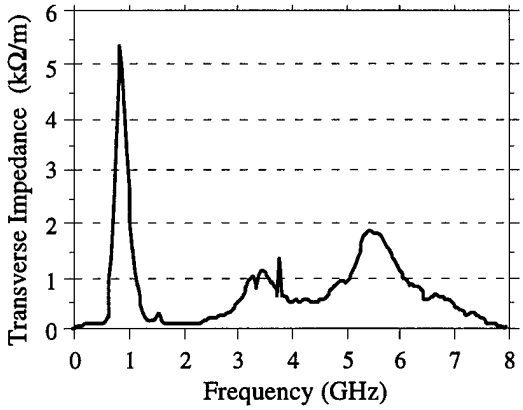



Figure 2. Transverse impedance spectrum.

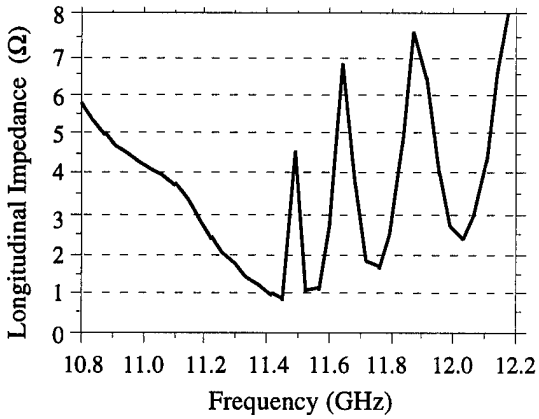



Figure 3. Longitudinal impedance spectrum.

wakefields are seen for the shorter bunches. Since BBU is cumulative over many bunches and structures, a small increase in wakefield magnitude results in a large growth in transverse motion. The effect of bunch length needs to be considered with respect to BBU growth.

In Fig. 5, we summarize the BBU growth for 1,000 bunches using the MBBU code for the wakefield of the Gaussian bunch (solid line in Fig. 4). The initial beam displacements were assumed to be uniform with no transverse momentum. An average beam current of 600 A with energy of 10 MeV, and betatron length of 2 m are considered.

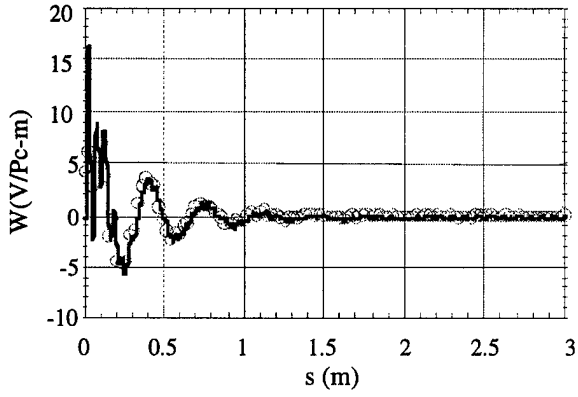



Figure 4. Dipole wakefield for impedance in Fig. 2.

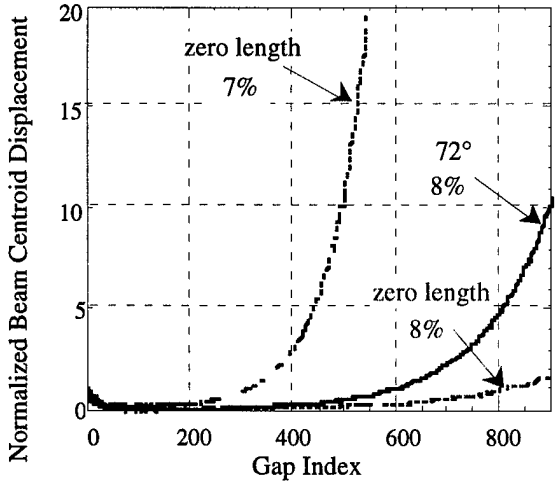



Figure 5. BBU growth for different energy spreads and different bunch lengths.

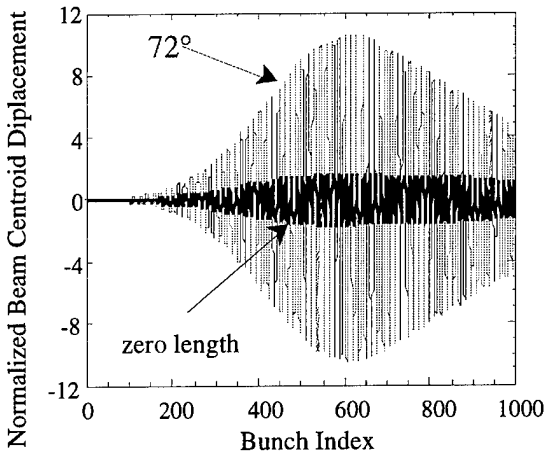



Figure 6. Beam centroid displacements at 900th gap exit.

The dotted lines in Fig. 5 summarizes the BBU growth for various energy spreads. For energy spreads of $\geq \pm 8\%$, the BBU is reduced to an acceptable level over 900 structures by Landau damping. The solid line in Fig. 5 includes the wakefield effect within a bunch; each bunch is uniformly divided into 3 slices over 72° of a bunch wavelength. Each slice is represented by 30 microparticles for all cases. Fig. 6 shows normalized beam centroid displacements at the exit of the 900th gap.

*2.3 Electric Field Stresses*

Poisson was used to determine electrical field stresses in the gap. An equipotential plot for the gap design is shown in Fig. 7. The highest vacuum electrode fields are 120 kV/cm along the entrance to the gap and are acceptable for 300 ns pulses [10]. The electric field across the stacked insulator is a uniform 100 kV/cm. We expect that the stacked insulator will support nearly 200 kV/cm without breakdown. The method of assembling the gap in the cell readily allows for special treatment, e.g. electropolishing, of the high field stress surfaces if a greater safety margin is desired. On the oil side of the gap, the highest surface electric field is 135 kV/cm near the top of the gap.

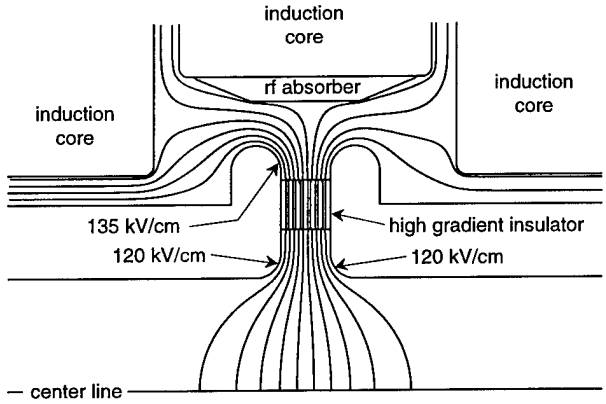



Figure 7. Equipotential lines in vicinity of module gap.

*2.4 Mechanical Design Considerations*

The insulator is comprised of seven 1 mm layers of polycarbonate alternating with six 0.5 mm layers of conductor. This configuration was also used in the AMOS and Poisson simulations. The insulator fabrication procedure will incorporate additional, larger conductors on either end that are used for mounting the insulator into the gap. These two conductors will be preformed with a 0.5 cm radius of curvature, 90° bend on the inner radius and welded to the beam line at a point of low surface electric field stress to create the vacuum seal. On their outer radius, the conductors have a 180° bend terminating in an electrical slip connection that rides on the magnet housing. This arrangement reduces stress on the insulator due to module housing motion or thermal expansion.

The microwave absorber is segmented ferrite sections epoxied to the inner radius of the center core support mandrel. The AMOS simulations used a TDK PB11b ferrite model.

## 3 SUMMARY

An induction module has been designed that meets the stringent requirements of the TBNLC relativistic klystron. The demonstrated performance of stacked insulators was a critical factor in achieving a satisfactory design. An important feature of these insulators is their ability to withstand high field stress in the presence of intense electron beams. This allowed for a greatly simplified gap design for the specific application presented and can readily be applied to other induction module designs.

## 4 ACKNOWLEDGMENTS

The work was performed under the auspices of the U.S. Department of Energy by LLNL under contract W-7405-ENG-48, LBNL under contract AC03-76SF00098, and FAR under SBIR Grant DE-FG03-96ER82179. S. Sampayan (LLNL) and M. Krogh (Allied Signal) provided helpful information on the performance and application of high-gradient insulators.

## 5 REFERENCES

[1] Juan M. Elizondo and A.E. Rodriguez, "Novel High Voltage Vacuum Surface Flashover Insulator Technology," Proceedings of the XVth International Symposium on Discharges and Electrical Insulation in Vacuum, Vde-Verlag, Berlin, Germany, pp. 198–202 (1992).
[2] S. Sampayan, et al., "High-Performance Insulator Structures for Accelerator Applications", these proceedings.
[3] S. Sampayan, et al., Proceedings 1995 Particle Accelerator Conference, (IEEE), New York, N.Y., pp. 1269–1271.
[4] M. Burns, et al., Proceedings 1991 Particle Accelerator Conference, (IEEE), New York, N.Y., pp. 2958–2960.
[5] T.L. Houck, et al., these proceedings.
[6] S. Eylon, et al., these proceedings.
[7] T. Houck, et al., *IEEE Trans. Plasma Sci.*, vol. 24, p. 938, 1996.
[8] R.J. Briggs, et al., *Part. Acc.*, **18**, pp.41-62, 1985.
[9] J.-S. Kim, .et al., Proceedings 1993 Particle Accelerator Conference, (IEEE), New York, N.Y., pp. 3288–3290.
[10] Birx, D., Phase II Final Report of Contract DAA H01-89-C-0201, 1991.

# RESONANT RING FOR TESTING OF ACCELERATOR RF WINDOWS

E. Gerken, J. M. Gahl*, D. Rees, W. Roybal, and K. Cummings

Los Alamos National Laboratory, Los Alamos, New Mexico, USA
and the *University of New Mexico, Albuquerque, New Mexico, USA

Abstract

A klystron-driven resonant ring has been designed and assembled at the Los Alamos National Laboratory for use in the Accelerator Production of Tritium Project (APT). The ring was built to test rf windows for the 700 MHz section of the APT accelerator. The ring has been designed to apply an effective power of approximately 1 MW on test windows. Details of ring design, operation and performance will be presented.

## 1 INTRODUCTION

A resonant ring, also known as a traveling wave resonator, is a loop of waveguide which can amplify apparent power through the coupling of waves at its input. Resonant rings can be used for high power breakdown tests, unidirectional filters, or pulse-shaping techniques. The Lansce-5 group at the Los Alamos National Laboratory has built a resonant ring to test radio frequency windows at high powers for the Accelerator Production of Tritium (APT) project.

The first step in this experiment is the characterization of the resonant ring at low power. The ring was designed for a power gain of 12.5, allowing for the application of an effective power of approximately 1 MW on test windows with currently available 700 MHz klystrons. With the impending delivery of 1 MW, 700 MHz klystrons to APT, windows and other rf components could be tested at extremely high rf power levels.

Power gain, at low power levels, has now been measured as a function of ring attenuation. The insertion of various microwave absorbers into the ring mimicked the attenuation of rf windows and components under test in the ring. These low power tests have increased confidence that the ring will operate as designed in high power testing.

## 2 THEORY

Figure 1 shows a basic resonant ring circuit.

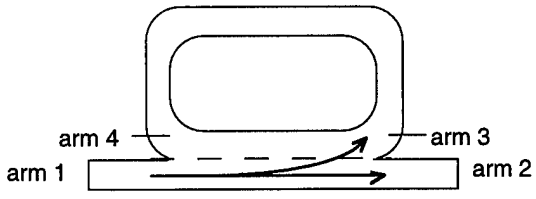



Figure 1: Basic Resonant Ring Circuit

Power is input to the first arm and then coupled into the ring through the third arm. Uncoupled waves continue through the second arm, which is usually terminated by a load, and the waves in the ring continue to travel through the third and fourth arms. With the proper ring length and matching, the waves add constructively. This creates a voltage increase and acts as a power gain in the ring.

Several variables factor into the ring's performance: loop gain, coupling coefficient, attenuation in the ring, transmission coefficient, and electrical length. Some of these variables are dependent on one another.

The transmission coefficient is the ratio of the voltage of the wave that passes through a junction to the voltage before the junction. In the ring the "junction" is the load imposed upon the ring by attenuation which causes the voltage to drop.

If the electrical length of the ring is properly related to the frequency of the coupled energy, it will reinforce previously coupled energy and place the ring in a state of resonance [1]. In order for this to occur, the length of the ring must be an integral number of guide wavelengths of coupled wave.

The amount of power input to the ring from the primary arm is determined by the voltage coupling coefficient. The coupling coefficient (usually designated as C) is defined as the ratio of the voltage coupled into the ring to the incident voltage from the main guide when all arms but the one with incident voltage are terminated in matched loads [2].

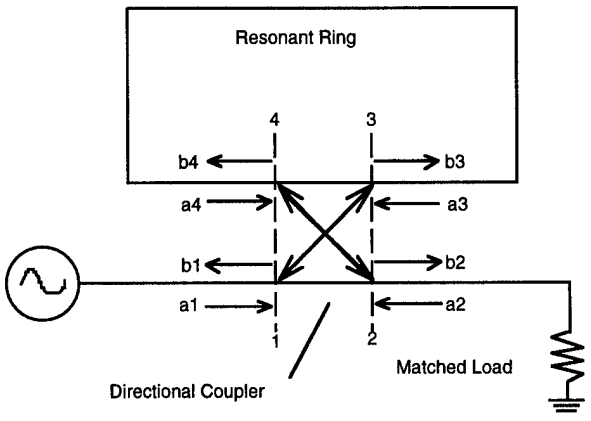



Figure 2: Forward and Reflected Waves in a Resonant Ring Circuit

To calculate the coupling coefficient it is necessary to make use of the scattering matrix of a directional coupler. The matrix can be derived from one

0-7803-4376-X/98/$10.00 © 1998 IEEE

solution to the standard transmission-line differential equations for the voltage and current as a function of distance along such a line. From Miller [3], the total loop power gain $(b_3/a_1)^2$ is found by using the fact that $a_4=b_3 e^{-\gamma l}$, where $\gamma=(\alpha+j\beta)$.

Referring to Figure 2, voltage loop gain, or multiplication, is defined as the ratio of the voltage of $b_3$ (the forward traveling wave in the loop) to the voltage of $a_1$ at the input arm of the coupler. Since power meters can be easily used to measure ring performance, it is often the loop power "gain" that is of interest (proportional to the square of the voltage gain).

$$\text{Power Gain} = \left|\frac{b_3}{a_1}\right|^2 = \left|\frac{jC}{1-e^{-\gamma l}\sqrt{1-C^2}}\right|^2$$

$$= \frac{C^2}{\left|1-Te^{-\beta l}\sqrt{1-C^2}\right|^2}$$

T is the transmission coefficient and accounts for the attenuation in the circuit (attenuation = $e^{-\alpha l}$). When the ring is in resonance, $\beta l$ will be an integral number of $2\pi$ and the $e^{-j\beta l}$ phase shift term will drop out, leaving:

$$\text{Power Gain} = \frac{C^2}{\left|1-T\sqrt{1-C^2}\right|^2}$$

Because this equation relies on three variables, the coupling coefficient, the ring attenuation, and the desired power gain, it can be plotted in several different ways. In Figure 3, gain is plotted versus attenuation for two different values of the coupling coefficient.

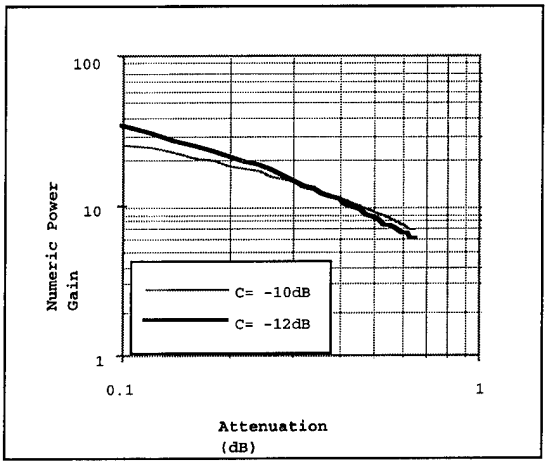



Figure 3: Power Gain vs Attentuation

## 3 RESONANT RING DESIGN

A klystron-driven resonant ring was designed as shown schematically in Figure 4. 3 1/8 inch coax is used at the outputs of the klystrons and also to connect to the water loads. The coax is connected to waveguide through transition pieces. The waveguide sections are WR1500 which operates in a frequency range of 490 MHz - 750 MHz. Straight waveguide sections are used to connect the other waveguide components (such as the sweeps and couplers) in order to give the traveling wave some settling space. These pieces are made at least one wavelength long. The 50 Ω water loads in the ring can handle up to 300 kW. A circulator is used to protect upstream devices in a circuit, such as amplifiers, that could be damaged by reverse power.

The ring loss can be estimated by summing the losses of the individual components along the length of the ring. It is estimated that the rf windows will contribute 0.1 dB of loss. Based on the manufacturer's test data for the loss of the ring components, the total loss of the ring can be approximated as 0.3 dB. The two 700 MHz klystron transmitters now available can deliver 80 kW CW of rf power to the resonant ring. The desired power level in the resonant ring is 1MW. This is a numeric power gain of 12.5.

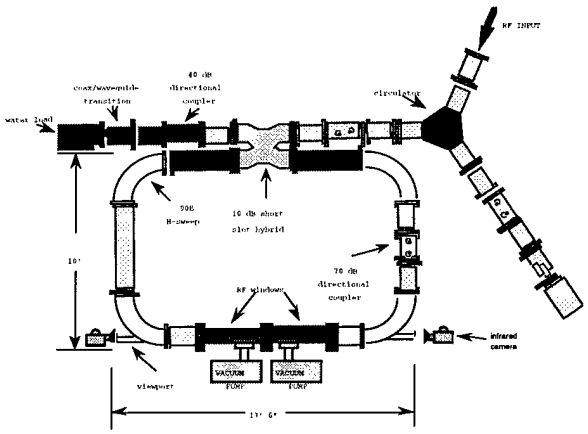



Figure 4: Resonant Ring Test Stand

## 4 RESULTS

The objective of this work was first to derive mathematically how the ring should behave and then prove it experimentally. For a ring attenuation of 0.3 dB and a power gain of 12.5, the information in Figure 3 indicates that a 12 dB coupler would be a better choice than the 10 dB coupler. However, the 12 dB coupler falls off faster than the 10 dB coupler for larger values of ring loss. Since the ring loss was approximated to have a least 0.3 dB of attenuation due to the uncertainty of the rf test windows and other components, the 10 dB short slot coupler was chosen.

From the graph of the power gain equation, it was evident that only 0.2 dB to 2 dB of attenuation would be useful. Graphite, nickel, and tin first seemed like good choices for coating the inside of the ring, but after running these conductivities, permeabilities, and permittivities through the attenuation calculations, it was shown that even if the entire ring were coated, not enough attenuation would be provided. Finally, one-inch thick sheets of graphite-coated "horsehair" were chosen as the microwave absorber. To obtain different attenuation values, different sizes of absorber sheets were placed into the resonant ring.

To test the circuit, the ring was first tuned to resonance by finding the frequency which produced the most forward power in the ring. The resonant frequency varied from about 704 to 706 MHz. The daily temperature flux of the laboratory contributed to this variation. The empty ring's Q-factor was high enough that a few degrees of temperature change could change the resonance by 0.5 MHz or more. Once the data were gathered, the measured power gains were plotted versus the inserted attenuation. Using the forward power in the ring divided by the input power as the power gain produced the following graph (Figure 5).

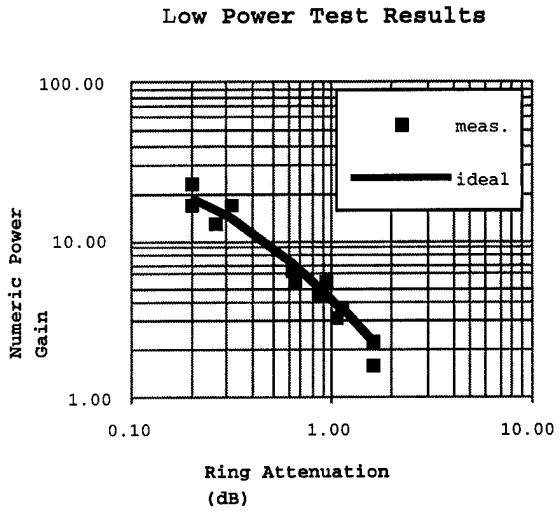



FIGURE 5 : Measured and Ideal Results

## 5 CONCLUSIONS

As can be seen from Figure 5, the resonant ring did follow the theoretical predictions of the power gain equation. The low power resonant ring test improves confidence that the resonant ring will have sufficient gain to test rf windows at high apparent power. The deviations from the ideal values could have been caused by any number of measurement errors, however it is apparent that these errors are quite small. The next step in this project is to operate the high power resonant ring test stand for the testing of rf windows and other rf components.

## 6 ACKNOWLEDGEMENTS

Work supported by the United States Department of Energy.

## REFERENCES

[1] "Theory and Application Instruction Manual for the Resonant Ring" I-T-E Circuit Breaker Company, Special Products Division, Philadelphia 34, Pennsylvania.

[2] R. Veltrop and W. Shelton, "Application of a traveling wave resonant ring circuit for voltage-breakdown testing of microwave components."

[3] S. J. Miller, "The Traveling Wave Resonator and High-Power Microwave Testing," The Microwave Journal, Vol. x, No. x, September, 1960, pp. 50-58.

# BEAM EXPANSION WITH SPECIFIED FINAL DISTRIBUTIONS*

Andrew J. Jason and Barbara Blind, Los Alamos National Laboratory, and
Klaus Halbach, Lawrence Berkeley National Laboratory

*Abstract*

The formation of nearly uniformly distributed beams has been accomplished by the use of multipole magnets. Multipole fields, however, are an inappropriate basis for creating precise distributions, particularly since substantial departures from uniformity are produced with a finite number of multipole elements. A more appropriate formalism that allows precise formation of a desired distribution is presented. Design of nonlinear magnets for uniform-beam production and the optics of an accompanying expansion system are presented.

## 1 INTRODUCTION

We consider the general problem of providing an arbitrary spatial beam distribution at a point starting from a given input beam. Such a technique is of interest in matching and for applications where material or power deposition must conform to a particular distribution. For some purposes the requirement is simply to sharply limit the beam extent on a target to prevent undesired radioactivation of surrounding areas. Often a uniform distribution is desired for medical purposes or for minimizing the cooling on a target. Other distributions may be useful in maximizing neutron flux from a spallation target. Although we here concentrate on producing a uniform distribution, the extension to other distributions is straightforward.

The problem of producing a uniform distribution has previously been attacked by using a multipole series to provide a nonlinear field that folds the beam in phase space [1-4]. The results of such processing of an initially gaussian beam by application of a strong octupole field and subsequent magnification optics are shown in Fig. 1.

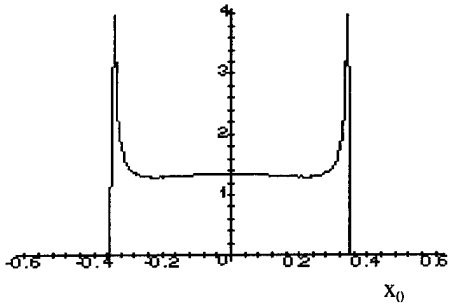



Fig. 1 Beam distribution versus transverse distance after nonlinear focusing by an octupole. Units are arbitrary.

In this process, the beam is expanded within the octupole in, say, the x dimension so that it is very narrow in y to eliminate coupling terms. for sufficient expansion, the effect of the emittance is small and the $x, x'$ phase space may be represented by a line, as was done in the creation of Fig. 1. Figure 2 shows the phase space for the distribution of Fig 1. The "ears" on the distribution are caused by the fold shown in Fig. 2 and are smaller for finite emittance and momentum spread. The distribution is well confined except for the wings that form the lower and upper branches of the field. If further multipoles are added the confinement can be improved.

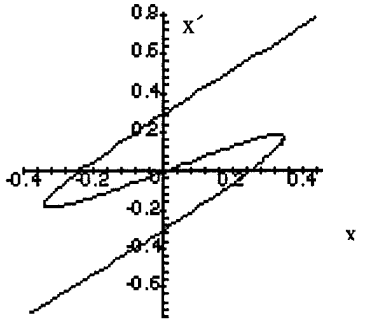



Fig. 2 Phase space for the distribution of Fig. 2. The ordinate is the position in Fig. 1 and the abscissa is the divergence in arbitrary units.

It has been noted [5] that a series of multipoles can be configured to tend toward an analytically exact uniform distribution, but the convergence is slow. We consider a magnetic element that is capable of providing the precise distribution required.

## 2 MAGNETIC FIELD

Since it is possible to effectively decouple the two transverse phase planes, a one-dimensional treatment is adequate. Beam in an element $dx_0$ contained in a distribution $\rho_0(x_0)$, described by initial phase-space coordinates $x_0$ and $x_0'$, transformed to a set of coordinates $x$ and $x'$ obeys the relation $\rho(x)\,dx = \rho_0(x_0)\,dx_0$ if the two distributions are single valued. Thence,

$$\rho(x) = \frac{\rho_0(x_0)}{dx/dx_0}. \qquad 1)$$

This relation follows Batygin [5] and others.

We consider a small-emittance beam, extended in $x_0, x_0'$ phase space with slope $a = dx_0'/dx_0$ and with small extent in y, that passes through a magnet of length $l$ with y-directed magnetic field $B(x_0)$ on the $x_0$ axis. A subsequent linear optical system described by a matrix

* Work supported by the U.S. Department of Energy

0-7803-4376-X/98 /$10.00 © 1998 IEEE

**R** transports the beam to the location described by the $x$ coordinates. Transformation between $x$ and $x_0$ is

$$x = (R_{11} + aR_{12})x_0 + l\,R_{12}B(x_0)/B\rho \qquad 2)$$

where $B\rho$ is the beam rigidity. Inserting this relation into Eqn. 1), the derivative of the magnetic field with respect to $x_0$

$$B'(x_0) = \frac{\rho_0(x_0) - (R_{11} + aR_{12})\rho(x)}{l\,\rho(x)R_{12}} B\rho. \qquad 3)$$

Integrating, the field becomes

$$B(x_0) = \frac{B\rho}{l\,R_{12}} \int_0^{x_0} du\, \frac{\rho_0(u)}{\rho[x(u)]} - \frac{B\rho(R_{11} + aR_{12})}{l\,R_{12}} x_0. \qquad 4)$$

Thus for various choices of beam transport, the fields required to produce a given distribution will vary by a linear term. One natural choice, given a limited beam distribution, is to minimize the peak field by adjusting the linear term. An attractive alternative sets

$$R_{11} + aR_{12} = 0, \qquad 5)$$

i.e., a point focus on the target.

For the case of a uniform target distribution of width $2w$, Eqn. 4) becomes

$$B(x_0) = \frac{2w\,B\rho}{l\,R_{12}} \int_0^{x_0} du\, \rho_0(u). \qquad 6)$$

Note that for a limited initial distribution and the choice of Eqn. 5), the field at large $x_0$ is constant, a convenient field for magnet design. We consider an initially gaussian-distributed beam with rms width $\sigma$ to obtain a field

$$B(x_0) = \frac{w\,B\rho}{l\,R_{12}} Erf\left(\frac{x}{\sqrt{2}\sigma}\right). \qquad 7)$$

An alternative choice for the initial distribution is $\sim 1/\cosh^2(x/c)$ which yields $w\tanh(x/c)/(2R_{12}c)$, a very similar function to 7) (along the $x_0$ axis) for $c \sim 1.25\sigma$, differing by only 3% in a limited range. The significance of this is that the latter distribution has been noted to represent a beam that is poorly matched in a linac whereas the gaussian distribution is representative of a well matched beam. Hence, a nonlinear magnet with some adjustability can presumably deal with a range of observed beams.

## 3 BEAM OPTICS

### *3.1 One-Dimensional Optics*

Consider a drift of length $L$ as an example of an optical system. Then $R_{11} = 1$ and $R_{12} = L$; accordingly set $a = -1/L$. For a given $L$ the peak value of the magnetic field $B_0$ can be set from the asymptotic value of Eqn 7). Choosing $L$=1 and w=1 sets $a = -1$ and $B_0 l/B\rho = 1$. Setting $\sigma = 0.1$, the angular deflection through the magnet as a function of $x_0$ is shown in Fig. 3.

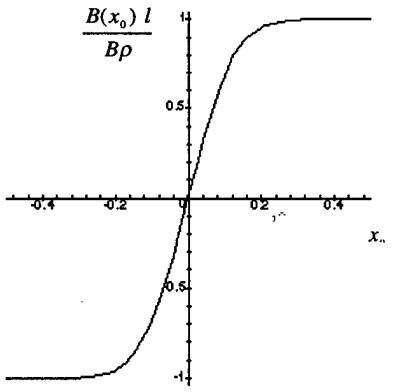



Fig. 3 Plot of the magnetic field along the $x_0$ axis needed to produce a uniform distribution for the parameters given in the text.

The phase space loci just after the nonlinear magnet and at the target are given in Fig. 4, where the calculation is limited to $6\sigma$. Note that, at the target, the central $2\sigma$ of the beam is transformed to within $x = \pm 0.95$ while the remainder of the beam is placed at $|x| > 0.95$ along the trajectory tending asymptotically to the lines $|x| = 1.0$.

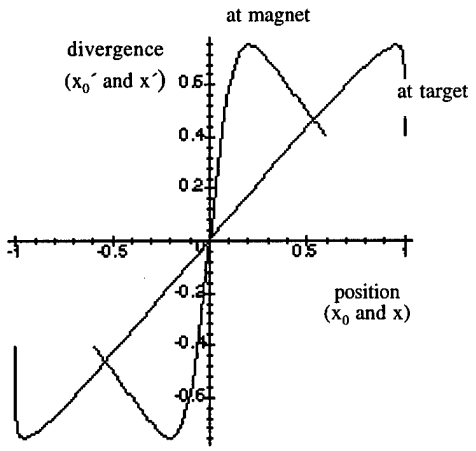


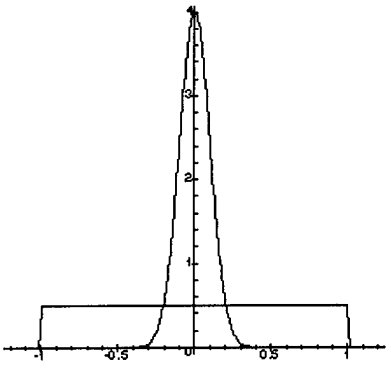

Fig. 4. Phase space at the nonlinear magnet and at the target for the example cited in the text.

Initial and final distributions are shown in Fig. 5. The final distribution departs negligibly from constant within $-w \le x \le w$. Finite bin sizes in the calculation blur the final-distribution edges slightly.

### *3.2 Errors*

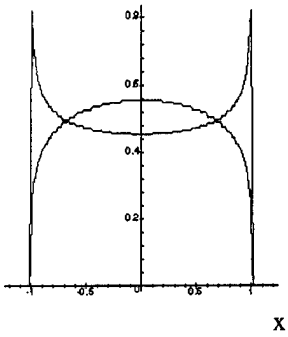
We consider two possible errors that affect the final distribution. The first is departures from the initial distribution. In general, if the initial distribution is "wider" than the distribution for which the magnet was constructed, the final distribution will grow "ears" (as in

Fig. 1); "narrower" distributions will experience rounding on top. This is illustrated in Fig. 6 that shows the output distributions for $\sigma = 0.09$ and 0.11. If a $1/\cosh^2$ input distribution is used, similar changes occur in the distribution.



x and $x_0$

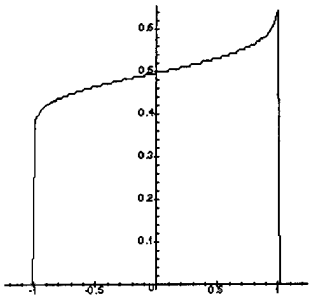
Fig. 5 Normalized initial and final distributions.



x

Fig. 6 Final distributions for ±10% width errors in the initial distributions.

Steering errors also change the distribution. This is shown in Fig. 7 where the beam enters the nonlinear magnet off axis by $0.1\sigma$.



x

Fig. 7 Final distribution for a steering error of $0.1\sigma$.

Note that despite marked changes in the distribution, the beam remains entirely confined for both these cases because of the well-defined beam limits due to the vertical part of the phase-space trajectory seen in Fig. 4.

*5.3 Two-Dimensional Optics Design*

Two nonlinear magnets are used in producing a beam that has a given two-dimensional profile on the target. In the first magnet, the beam is made small in the y dimension so that interplane coupling by the field x components is negligible and the beam is made large in the x dimension with large correlation and slope $a$. A subsequent focusing section provides condition 5) in the x direction with small $w$ in the second linear magnet that is rotated 90° from the first. This limits the beam in the magnet gap. The beam in the y direction is highly correlated (as specified in the x direction of the first magnet). A second focusing section provides the condition 5) from the second magnet to the target in the y direction and from the first magnet to the target in the x direction. For each plane, the values of $R_{12}$ and $R_{34}$ are determined by the desired values of $w$ and the value of $B_0$, in the respective planes. Such simulations have verified the calculations shown here.

For a given value of $B_0$ four quads are in general needed in each focusing section to meet all conditions. The number of quads may be reduced by using symmetry, system lengths, and choice of input beam.

## 5 MAGNET DESIGN

We treat the magnet design only briefly. The magnet has quadrupolar symmetry. For sufficiently low fields, the pole shape along a scalar equipotential is determined from the field in the complex plane. The complex potential provides the conformal map into a dipole geometry, to be used in specifying the pole width or shimming that provides a homogeneous field to the extreme particles of the beam. Variability in the magnet field shape to fit off nominal distributions is provided by dividing the pole into individually excited segments or by current sheets on the pole surfaces.

## REFERENCES


[1] Andrew J. Jason, Barbara Blind, Ernest M. Svaton, "Uniform Ribbon-Beam Generation for Accelerator Production of Tritium," Proceedings of the 1988 Linear Accelerator Conference, CEBAF Report 89-001, 192 (1989).

[2] E. Kashy and B. Sherrill, Nucl. Instr. and Meth. "A Method for the Uniform Charged Particle Irradiation of Large Targets, B26, 610 (1987).

[3] B. Sherrill, J. Bailey, E. Kashy, and C. Leakas, Use of Multipole Magnetic Fields for Making Uniform Distributions, Nucl. Instr. and Meth., B40/41, 1004 (1991).

[4] B. Blind, "Production of uniform and well-confined Beams by Nonlinear Optics," Nucl. Instr. and Meth., B56/57, 1099 (1991).

[5] Y. K. Batygin, "Beam Intensity Redistribution in a Nonlinear Optics Channel," Nucl. Instr. and Meth., B79, 770 (1993).

# DEVELOPMENT OF A FAST TRAVELING-WAVE BEAM CHOPPER FOR THE NATIONAL SPALLATION NEUTRON SOURCE*

Sergey S. Kurennoy, Andrew J. Jason, Frank L. Krawczyk, and John Power,
LANSCE-1, Los Alamos National Laboratory, Los Alamos, NM 87545, USA

*Abstract*

High current and severe restrictions on beam losses, below 1 nA/m, in the designed linac for the National Spallation Neutron Source (NSNS) require clean and fast — with the rise time from 2% to 98% less than 2.5 ns to accommodate a 402.5-MHz beam structure — beam chopping in its front end, at the beam energy 2.5 MeV. The R&D program includes both modification of the existing LANSCE coax-plate chopper to reduce parasitic coupling between adjacent plates, and development of new traveling-wave deflecting structures, in particular, based on a meander line. Using analytical methods and three-dimensional time-domain computer simulations we study transient effects in such structures to choose an optimal chopper design.

## 1 REQUIREMENTS

The NSNS, to be constructed at Oak Ridge National Laboratory, is a next-generation pulsed spallation neutron source designed to deliver 1 MW of beam power on the target at 60 Hz in its initial stage [1]. It consists of a 1-GeV 28-mA linear $H^-$ accelerator and an accumulator ring. The NSNS project is a collaboration of 5 national laboratories. Los Alamos National Laboratory is responsible for the linac design and the chopping system of its front end.

Beam injected into the NSNS accumulator ring must be chopped at near the ring-rotation frequency 1.189 MHz in order to leave a gap for the kicker rise time during one-turn ring extraction. The duty factor of the injected beam has been set at 0.65. Chopping is to be done in the Medium Energy Beam Transport (MEBT) line that transports 28-mA of peak beam from a 2.5-MeV 402.5-MHz RFQ to a drift-tube linac. A 0.5-m space is currently allocated for the chopper that deflects beam into a collimator during the 35% beam-off time. In case of a partial chopping or small errors in the timing system, an identical "anti-chopper" is placed in the line at an optically symmetric point from the chopper in order to return uncollimated beam to the axis.

Using a planar structure, with a half gap of 1 cm and a 900-V deflection voltage on each plate, the chopper will provide a beam deflection of 9 mrad. The gap between plates can be further reduced, down to a half gap of 7.5 mm or even 5 mm. A small tilt of the chopper structure in the vertical plane will be required in the last case to avoid beam hitting the plates. A traveling-wave structure, with the pulse phase velocity along the beam path matching the beam velocity ($\beta$=0.073), will be used to avoid transit-time effects. The chopper is required to rise from 2% to 98% (and fall) in 2.5 ns to accommodate the 402.5-MHz beam structure. Partial chopping of a micropulse would cause decreased charge in the transmitted pulse with subsequent variation of the linac-output Twiss parameters and increased loss in the transport line and ring.

An additional function of the chopper is pulse width modulation of the beam. At the start of the macropulse, it is necessary to increase the beam intensity from zero to full to accommodate linac beam loading. This is done by decreasing the width of the chopper deflection pulse from full to nominal 35%. This function can be also used in experiments that require fractional ring filling or simply to modulate beam intensity.

## 2 PRESENT STATUS

The present chopper system [2] at Los Alamos Neutron Science Center (LANSCE) was constructed for the Proton Storage Ring (PSR). It works at the beam energy 750 keV and provides the rise time of approximately 7 ns with a larger contribution from the pulse modulator. The current structure itself is capable of providing a pulse front slightly longer than 2 ns, with an overshoot on the 10% level ringing for a few nanoseconds. This coax-plate structure is 1-m long and consists of two parallel plates each interfaced with many small strips which are connected with coaxial cables on the reverse side of each plate to form a circuit that is continuous along the structure (Fig. 1).

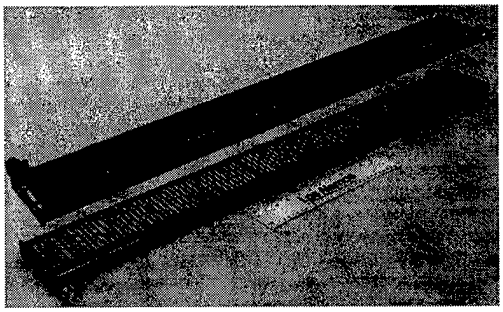


Figure 1: Photograph of the traveling-wave chopper struc-ture used at LANSCE.

* This work is supported by the US Department of Energy under contract DE-AC05-960R22464.

0-7803-4376-X/98/$10.00 © 1998 IEEE

The voltages on the upper and lower plates are synchronized and have opposite signs so that the resulting vertical electric field deflects the beam.

## 3 STRUCTURE DEVELOPMENT

### *3.1 Coax-plate structure*

The major limitations on the structure rise time for the existing coax-plate design are caused by stray capacitance between the electrode segments and by multiple coax-to-plate transitions. A similar structure for the higher energy, 2.5 MeV, would have slightly better rise and fall times, simply because one can use wider strips and make wider gaps between strips in the structure to match the higher beam velocity. Wider gaps reduce strip-to-strip coupling. As an additional way to reduce this parasitic coupling between adjacent strips, guard barriers (or separators) rising from the ground plane have been proposed.

### *3.2 Meander-line structure*

A promising alternative design under consideration is a meander line with separators, see Fig. 2, instead of the coax-plate current structure. Such a design has no transitions, and the meander bends can be properly chamfered to avoid pulse reflections. It is also easier to manufacture. The meander line parameters are calculated analytically to match the beam velocity and provide the line characteristic impedance $Z_c$=50 Ω. It results in the strip width $w$ = 5 mm, strip-to-strip gap $g$ = 2 mm, the full meander width $b = (w+g)(1/\beta-1)$ = 89 mm, and the distance between strips and the ground plate $h$ = 1 mm. The chamfering cuts are triangles $w \times w \times w\sqrt{2}$. For structures with separators, $h$ should be slightly increased, to 1.25 mm for the separators as high as $h$, to keep $Z_c$ fixed.

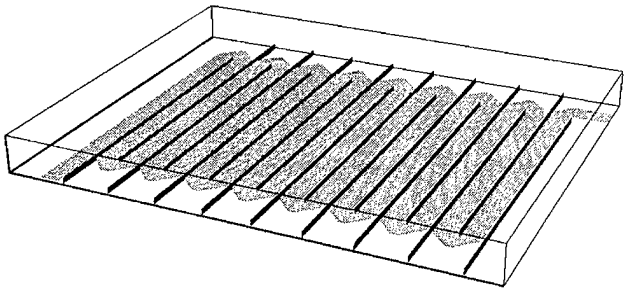


Figure 2: The meander structure (one quarter of the total length) with separators (dark) used in MAFIA simulations.

Transient effects in meander structures have been studied thoroughly using time-domain 3D simulations with the code package MAFIA [3]. The structure is fed with a TEM-wave pulse whose amplitude can be switched on as an arbitrary function of time, e.g., an abrupt or smoothed step, or a pulse of a finite time-length. It allows us to simulate any modulator pulse voltage. The pulse propagates along the strip and its vertical electric field on the beam path is recorded as a function of time. Figure 3 presents results of transient-effects simulations in the structure with the length of about 25 cm along the beam, one half of the full chopper length. The signal amplitude versus time in this case was a slightly smoothed step (squared *sin* with the full rise in 0.15 ns). It can be seen that even without separators the meander structure can provide a rise time about 2-2.5 ns, while with separators the rise time can be reduced down to 1-1.25 ns, depending on the separator height.

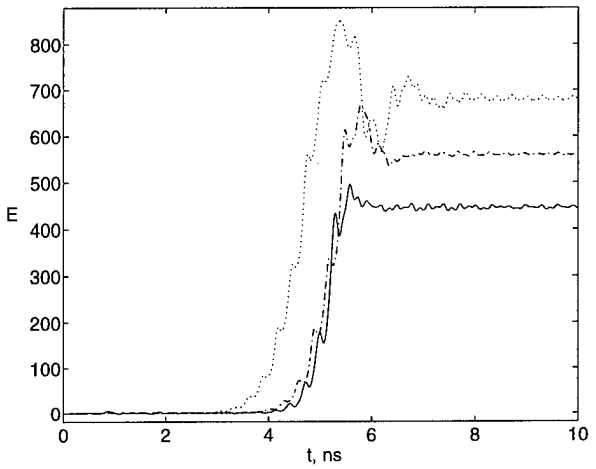



Figure 3: Vertical electric field, in arbitrary units, at a fixed point on the beam path versus time in the half-length meander structure with separators $h_s = 2h$ (solid), $h_s = h$ (dash-dotted), and without them (dotted).

Simulations have also been performed for meander structures having small low-dielectric (ε=2-4) posts used as supports. The support influence was found negligible.

The structure efficiency η can be defined as a ratio of the deflecting field to that produced by continuous plates under the same voltage. The designed meander line without separators has η = 0.94. The separators reduce the effective field on the beam path, as one can see in Fig. 3. The η-decrease can also be easily calculated by solving an electrostatics problem; it depends on the separator height $h_s$, being about 10-12% for $h_s = h$ and almost 20-25% for $h_s = 2h$. This should be compensated either by reducing the gap or by increasing the voltage.

We have completed the transient-effect simulations for the quarter-length, half-length, and the full-length (50 cm long) current structures, including simulations with a finite pulse rise time. The results are similar to those shown in Fig. 3, except that the pulse slightly deteriorate closer to the end of the long structure, mostly by developing some ringing overshoot about 1-2 ns long. The structure fall time was found in all simulations to be about the same as the rise time. Figure 4 illustrates the propagation of a 4-ns long pulse along the quarter-length meander structure. One can see a small overshoot developing as the pulse reaches the structure end. The front and back pulse edges remain well within 1 ns.

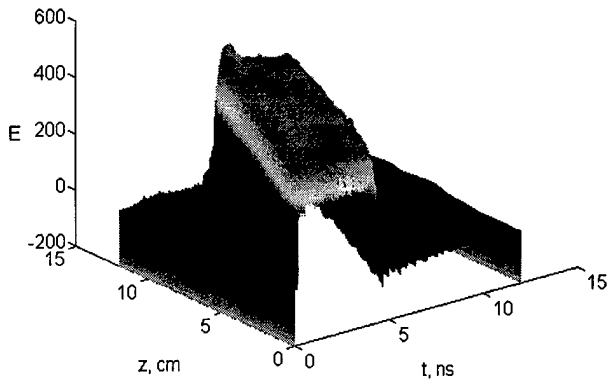



Figure 4: Vertical electric field at the beam path due to a 4-ns long pulse propagating along the meander structure.

To check our simulation results, a simple model structure with a meander line on a printed-circuit board (PCB) has been manufactured at LANL. The PCB with the meander on its bottom surface was placed on 1.25-mm barriers-separators sticking out of the aluminum ground plane. The prototype length is about 12 cm. The transient effects in the prototype have been measured with a TDR and were found to agree well with the MAFIA simulations for that case, with all transitions within a 2-ns range.

### *3.3 Notched meander-line structure*

Another way to increase the efficiency is to use a notched strip line in the meander instead of a straight one [4]. The magnetic field of the wave propagating along the notched strip is concentrated closer to the strip center, and the wave phase velocity is less then $c$ due to the inductive loading by notches.

This design reduces a strip-to-strip magnetic coupling. It also allows us to have a larger ratio of the strip width to the width of the gap between adjacent strips, which increases the efficiency $\eta$. On the other hand, the notched line has some additional dispersion that can worsen the rise and fall times. Analytical calculations and simulations of the notched-strip meander structure are underway.

## 4 PULSE GENERATOR

The LANSCE pulse modulator was originally a vacuum-tube-driven device. It has been revised to a solid-state model, easier to maintain at peak performance, but with a slower rise time. The modulator rise time is largely limited by semiconductor limitations and inaccuracies in matching. It appears likely that the fastest speeds possible with the present-day FET technology will be on the order of 4 ns. This speed limitation is largely independent of voltage and limited to around 900 V across 50 Ω.

The main problem is to satisfy the requirements of the fast pulse fronts, high repetition rate, and high voltage simultaneously. A modest program with semiconductor manufacturers for development of fast FET semiconductors is believed necessary. A simplified schematic of the proposed pulser design is shown in Fig. 5. It uses a combination of two switches, one to generate a fast rise time and a second to clamp the end of the output pulse to provide a faster fall time.

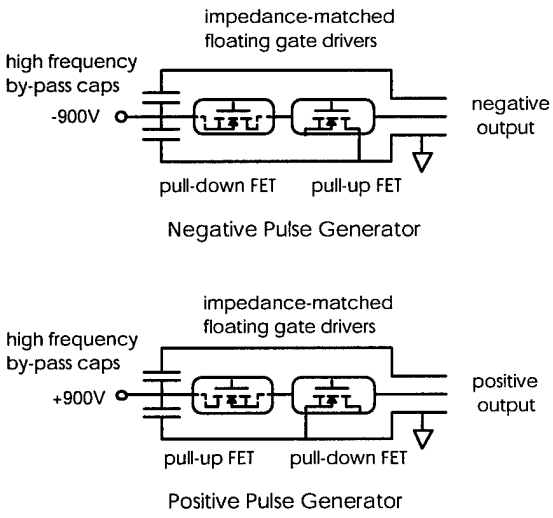



Figure 5: Simplified FET-based chopper-pulse generators.

## 5 SUMMARY

From considerations above we can conclude that at least two traveling-wave structures — the coax-plate design and the meander line, both with additional separators, — can be used as the chopper current structure with the required rise and fall times in the 1-ns range. The measurement results for the prototype meander structure agree well with our computations, and further simulations will be performed to optimize a final design.

The existing FET technology for the pulse modulator is capable of providing a 4-ns rise time. Some development of fast power FET semiconductors should permit the desired 2.5-ns device.

The authors would like to gratefully acknowledge useful discussions with R.K. Cooper and G.R. Lambertson.

## REFERENCES

[1] B.R. Appleton, *et al.*, in *Proceed. of EPAC* (Barcelona, 1996), p.575 – IOP Publishing, Bristol, 1996.
[2] J.S. Lundsford and R.A. Hardekopf, IEEE Trans. **NS-30,** 2830 (1983).
[3] M. Bartsch, *et al.*, Computer Physics Comm. **72**, 22 (1992).
[4] The notched-line approach was suggested to the authors by G.R. Lambertson, LBNL (March 1997).

# DESIGN OF QUASI-TRAVELING WAVE PINGER MAGNET FOR BEAM DIAGNOSTICS ON THE ADVANCED LIGHT SOURCE

D.E. Anderson and G. Stover , Lawrence Berkeley National Laboratory, 1 Cyclotron Rd., Berkeley, CA 94720

*Abstract*

A beam diagnostic tool to modify single bunch orbits in all four quadrants is proposed for measuring various machine physics parameters at the Advanced Light Source (ALS). Quasi-Traveling Wave pinger magnets were chosen to provide programmable bipolar horizontal and vertical kicks of sufficient duration while providing negligible deflection on subsequent beam revolutions in the storage ring. This magnet technology, originally investigated at the SSC[1], provides a cost-effective method of achieving the moderately fast pulse requirements of the pinger application. The design of the pinger magnet and associated pulsed power drive unit will be presented. Electrical response results of initial pinger magnet prototypes and ceramic beampipe coatings will be given.

## 1 INTRODUCTION

An orthogonal set of horizontal and vertical fast kicker magnets and their requisite pulse forming networks, termed the "pinger" system, are currently being constructed for installation in the ALS storage ring. The pinger system was specifically designed to apply a single one turn kick to an orbiting bunch in the storage ring. The kick is intended to provide an independently adjustable change in the single bunch's transverse momentum. Following the kick, 1024 subsequent turns of transverse bunch motion can be captured by an existing circumferential array of 96 BPM's operating in the "fast acquisition data" mode.

Comparison of actual bunch motion orbits with computer simulations should provide improved parameter definition for the model and refine measurements of critical machine parameters that should lead to improved storage ring performance. The necessary parameters to accomplish this task are shown in table I below.

Table I—Pinger Magnet System Parameters

| | |
|---|---|
| Horizontal Bdl Kick | ±2.5-157.5 Gauss-m |
| Vertical Bdl Kick | ±6.25-80 Gauss-m |
| Magnet Aperture | 91mm × 91mm |
| Magnet Length | 475mm V&H |
| Field Uniformity | ±5% |
| Pulse flattop duration | ≥25ns |
| Post-pulse Oscillations | ≤±1% $B_{max}$ after 650ns |

## 2 MAGNET TECHNOLOGY OPTIONS

Various magnet technologies were considered to meet the requirements for the pinger application. C-magnets and window-frame magnets were considered and compared. System topologies considered included lumped inductance, 1% underdamped series RLC, traveling-wave, and quasi traveling-wave. In an effort to minimize system cost and complexity, it was desirable to build each horizontal and veritcal kicker with a single 475 mm magnet and to maintain operating voltages below 35 kV (single-gap thyratron).

### *1.1 C- vs. Window-frame magnets*

Window-frame magnets, with a septum decoupling the two halves of the magnet, are advantageous in reducing the overall magnet inductance when the two halves are driven in parallel. However, this magnet type becomes an integral part of the beam line once installed, since removal of the magnet requires complete disassembly of the magnet. C-magnets can be removed from the beam line with a minimal effort by removing the return conductor plate and sliding the assembly away from the beampipe.

### *1.2 System topology considerations*

Lumped inductance magnets were considered first because of their relative simplicity. A peak operating voltage of 35kV with a current peak of 2400A dictates a maximum driving impedance of 7.3Ω. An impedance of 6.25Ω was chosen to maintain charge voltages at 30kV and still allow for operation 10% over specification. At this impedance level with a 600nH kicker magnet inductance, the time constant is 96ns, making any flattop unachievable.

An underdamped RLC circuit, allowed to reverse 1% within the 650ns post-pulse oscillation period, was also considered. The condition for this case is $R=1.7(LC)^{0.5}$. Circuit simulations were run to determine the system topology. The inductance and capacitance of the cables connecting the magnet to the pulser were found to have a profound effect on the circuit performance. A solution was found which used a 3Ω cable, but post-pulse ringing in the cable was ~5%, and thus deemed unacceptable.

Traveling-wave magnets were investigated, and could easily meet the system parameters. Their high

0-7803-4376-X/98 /$10.00 © 1998 IEEE

manufacturing cost made them unattractive, so other alternatives were investigated.

Quasi traveling-wave magnets, consisting of a lumped ferrite magnet with shunt capacitors placed along its length, approximates a transmission line, and thus should produce a moderately fast risetime with minimal reflections. The magnet topology is shown in Figure 1. The risetime is limited by some percentage of the magnet inductance (which is a function of the number of discrete capacitors incorporated) which the forward-going pulse initially sees upon arrival at the magnet.

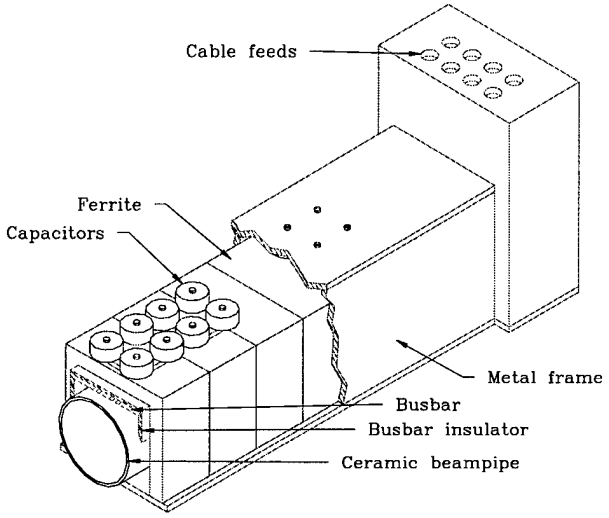



Figure 1—Quasi Traveling-Wave Pinger Magnet Geometry. Load not shown for clarity.

## 3 PINGER SYSTEM DESIGN

Design of the pinger system is closely coupled to the design of the magnet. The initial inductance seen by the forward-going wave as it arrives at the magnet affects the risetime of the ∫Bdl signal and subsequent post-pulse reflections. These effects influence the choice of number of stages in the quasi traveling-wave magnet, the length of the cable isolating the pulser from magnet and the pulse-forming network (PFN) topology.

The forward-going wave, upon arriving at the magnet, is partially reflected back toward the pulser by the initial magnet inductance. After transiting through the cable and PFN, the reflected energy is then transformed into ∫Bdl signal following the main pulse. To first-order, the sum of the two-way transit times through the magnet to pulser cable and PFN is equal to the bunch transit time in the ring minus the risetime of ∫Bdl (the duration of the reflected pulse). To maintain post-pulse levels below 1% in the pinger application, this resulted in a three section magnet with 120ns and 100ns one-way cable and PFN transit-times, respectively, in the optimized system. Figure 2 shows the system schematically.

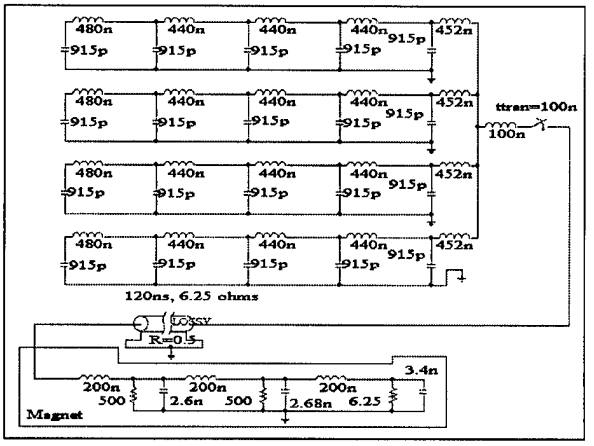



Figure 2—Pinger System Schematic used in Circuit Simulations

The inclusion of a resistively-coated ceramic beampipe is necessary to carry beam return currents in a low-impedance configuration. The high resistivities required for magnetic field diffusion into the beampipe result in moderate power dissipation generated by the beam image currents. The penetration time constant, given by $\tau_p=2\pi a/R$ ns, where a is the pipe radius in cm and R is the surface resistivity (Ω/□), must be much less than the risetime of the external magnetic field[2].

The permitted ±5% variation in field over the duration of the flattop of the pulse permitted the use of a pulse-forming network for driving the magnetic field. The ability to "float" the PFN also allowed for a relatively low inductance output structure, an important feature to achieve sub-100ns risetimes at 6.25Ω impedance. Bipolar operation is achieved through the use of two identical PFNs connected to the same switch. The unutilized PFN is shorted and connected to ground, thereby referencing the anode or cathode of the thyratron to ground. The PFN outputs are connected, via a high-voltage custom SPST switch on a 6.25Ω stripline transmission line, to a common set of output connectors. Cables then feed into one of two π-network high-voltage stripline attenuators. Use of these attenuators allows for vertical and horizontal low and high range operation with the same pulser units.

The remote connection to the ALS computer control system is accomplished through the standard Intelligent Local Controller (ILC)[3] module. The module is connected to the control system via standard 422 serial fiber optic link. All analog and digital controls and monitors are provided by the ILC. All digital and +24V chain signals to and from the pinger are also optically isolated from the ILC.

Basic trigger timing (Storage Ring Orbit Clock) will be transmitted to the pinger racks via fiber optics. Trigger delay control will be provided by a commercial timing delay generator controlled through an IEEE interface to the ILC.

## 4 PROTOTYPE RESULTS

To verify the suitability of a quasi-traveling wave magnet for the pinger application, a prototype magnet was built and tested. The prototype used Stackpole C11 NiZn ferrite, had an 88mm×88mm aperture, and was 530mm long. Ceramic doorknob capacitors were located equally-spaced at three locations on the structure. The ALS kicker magnet test stand, an 8.33Ω system with 20ns risetimes, was used to drive the 6.25Ω pinger magnet through a 6dB attenuator/impedance-matching π network. This prototype magnet was used to measure the electrical response of quasi-traveling wave magnets and to quantify penetration time effects of resistively-coated beampipes.

### *4.1 Electrical response of prototype magnet*

A 50Ω stripline B-dot probe, 600mm long, was constructed to monitor the magnetic field in the magnet. The signal generated was then integrated using the digitizer integration package. The result for the prototype magnet is shown in Figure 3.

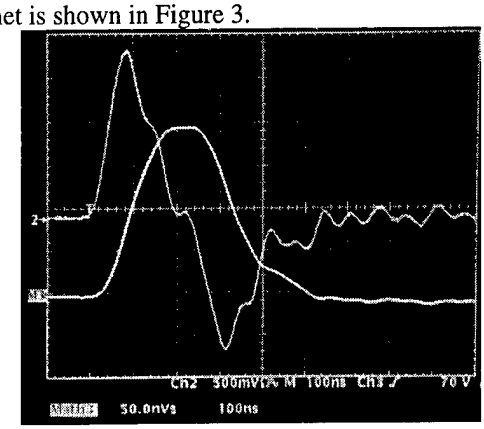



Figure 3—Pinger Magnet Prototype Electrical Response. Signals are a) direct B-dot signal and b) software integrated ∫Bdl (pulse).

The magnet produced an ∫Bdl risetime (10-90%) of 120ns, with 53ns of flattop at ±0.5%. The calculated one-way transit-time through the magnet of 107ns agrees well with the measured risetime minus the input pulse risetime. The poor falltime with the long "foot" is due to the energy reflected off the magnet after returning from the PFN. The peak value of the dB/dt signal agrees well with that expected for the calculated magnetic gain at the measured dI/dt.

A higher impedance magnet structure was also tested. This 8.33Ω magnet, with identical physical dimensions, was also pulsed. The risetime was reduced to 106ns, which agrees well with the 80ns one-way transit-time through the magnet. Other aperture size magnets were also tested with predictable results.

### *4.2 Beampipe coating and penetration measurements*

The inside surface of the ceramic vacuum chamber (137mm length and 72mm dia.) was coated with thermally sublimed titanium in a nominal vacuum of $6\times10^{-6}$ Torr. The coating process was driven to an estimated center tube resistivity of 2.0Ω/□. The actual longitudinal resistivity profile was parabolic in form. Thus the average resistivity for the total tube was measured at 2.7Ω/□. This value was chosen to minimize excessive eddy current shielding effects of the fast rising (100ns) magnet field and reduce the thermal heating of the tube from beam image currents. Calculations indicate a maximum of 110 watts will be dissipated in the tube at nominal storage ring energies and currents.

Magnetic field penetration measurements were performed on the 6.25Ω magnet using the stripline B-dot probe. Figure 4 shows the measured waveforms for various resistivity coatings.

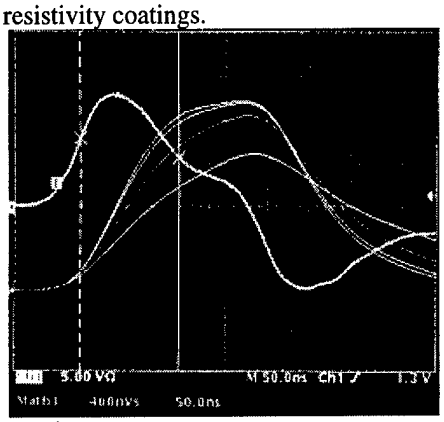



Figure 4—∫Bdl for Various Resistivity Beampipe Coatings. Beampipe I.D. 60.3mm with a) infiniteΩ/□ ($\tau_p$=0), b) 1.941Ω/□ ($\tau_p$=9.8ns), c) 0.572Ω/□ ($\tau_p$=33.1ns), and d) 0.180Ω/□ ($\tau_p$=105.2ns) coating resistivities.

## REFERENCES

[1] D. Anderson and L. Schneider, "Design and Preliminary Testing of the LEB Extraction Kicker Magnet at the SSC", Proceedings of the 1993 Particle Accelerator Conference, May 1993, pp.1354-6.

[2] Peterson, J.M., "Requirements for Resistive Coating on Ceramic Tubes in Kicker Magnets", *Single Pass Collider Memo CN-49*, April 1981.

[3] Magyary, S. and et al, "The Advanced Light Source Control System", LBL-28412, LSEE-067.

# TiN COATING OF ACCELERATOR BEAMLINE CHAMBERS*

K.N. Leung, Y. Lee, A. Mashaw, D. Wutte[a)] and R. A. Gough
Lawrence Berkeley National Laboratory
University of California
Berkeley, CA 94720

*Abstract*

A titanium nitride (TiN) coating can reduce multipactoring problems in vacuum cavities and also reduce photoemission electrons from beam-pipe surfaces. A new technique is being explored at LBNL that will allow an efficient way to coat differently-shaped surfaces with TiN. In this technique, an rf-induction discharge with an exposed Ti induction antenna is employed. Tests are being performed using argon, nitrogen, and a mixture of argon and nitrogen gases. It is found that the characteristics of the TiN coating depends on the processing time and the gas that forms the discharge plasma.

## I INTRODUCTION

One of the problems encountered in many high-power rf systems is multipactoring inside vacuum rf cavities. The potential for multipactoring occurs whenever the secondary electron emission coefficient of the surface exceeds unity. Under this condition, electrons can be accelerated by the rf fields onto the surface, causing more electrons to be emitted than the number impinging upon them. The electron current becomes amplified within a few rf cycles, not only absorbing a large percentage of the rf power, but depositing that power as heat in a very localized area. Multipactoring can be a serious problem in high-power rf cavities, often preventing not only sustained operation, but in many cases, preventing satisfactory operation altogether.

The secondary electron emission coefficient of titanium Ti is always less than unity. [1] A thin layer of Ti on the rf component surfaces should eliminate the potential for multipactoring. However, pure Ti is very reactive and it forms an oxide when exposed to air or water vapor. The titanium-oxide layer is not durable and has a higher secondary electron emission coefficient than pure Ti. On the other hand, a titanium-nitride layer is very stable and it has a secondary electron emission coefficient similar to pure Ti.

## II TIN COATING METHODS

Several methods have been tested for TiN coating of vacuum chambers. In one approach, Ti is first evaporated from a hot Ti filament and the Ti neutrals are deposited on the substrate surfaces. Ammonia gas $NH_3$ is then introduced into the system and the gas molecules interact with the Ti to form TiN. [2] The drawback for this technique is that the Ti vapor lands on the substrate surfaces softly with very low energy. As a result, the TiN coating is not strongly bonded to the surface and the coating comes off quite easily. Second, the thickness and stoichiometry of the coating (i.e. ratio of Ti:N) cannot be controlled accurately. In the plasma discharge technique, a Ti electrode is used as the cathode while the metal chamber wall acts as the anode. A plasma is formed when a high voltage is applied between the anode and the cathode. The filling gas is normally a mixture of argon and nitrogen. This technique enables one to deposit both Ti and N on the substrate surfaces in the form of positive ions. Not only the deposition rate is higher, but the ions acquire some energy (several or tens of eV) as they cross the anode sheath. For this reason, stronger bonding between the TiN coating and the substrate can be achieved.

The new TiN coating technique described in the following section employs rf induction discharge instead of dc discharge. The Ti neutrals are sputtered from a bare Ti antenna coil and the plasma (Ar or a mixture of Ar and $N_2$) is generated by rf discharge. The experimental setup is simple and easy to operate. As the implant ion dose rate is high, the processing time is much faster than the dc discharge or the evaporation method. In addition, this technique allows an efficient way to coat differently shaped surfaces.

## III EXPERIMENTAL SETUP

Figure 1 is a schematic of the experimental setup. The test chamber is a section of the B-factory low-energy booster-ring beamline chamber. It is made of aluminum and has water cooling channels built into it. The rf antenna is water-cooled and is fabricated from 2-mm-OD titanium tubing. The tubing is wound to match the oval shape of the chamber (Fig. 2). Two water-cooled copper plates are installed on top and bottom of the antenna so as to limit the volume of the discharge plasma. The entire antenna unit can be moved in and out with an electric motor attached on top of the setup. Both the water and gas inlets and the pumping port are located at the top flange.

The rf supply is a 13.56 MHz generator with a maximum output power of 2.5 kW. The rf power is coupled into the plasma through a matching network which is connected to the leads of the rf antenna. In normal discharge operation, the capacitor in the matching circuit is adjusted to minimize the reflected rf power. Although the rf supply is capable of delivering 2.5 kW

* The work is supported under contract # DE-AD03-76SF00098 by Director, Office of Energy Research, Office of High Energy Physics, US Dept. of Energy.
[a)] also with the Institut für Allgemeine Physik, Technical University Vienna.

0-7803-4376-X/98 /$10.00 © 1998 IEEE

output power, only 1 kW of output power is used for this test.

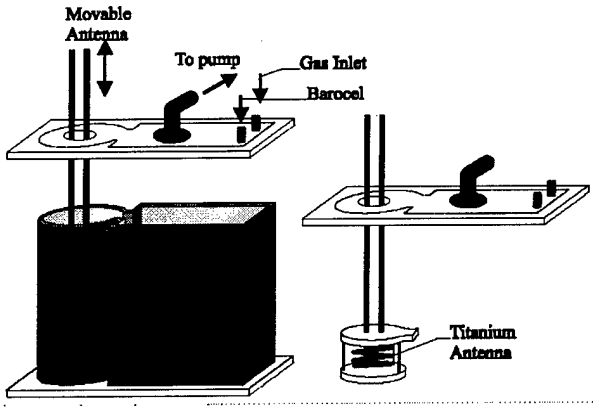



Fig. 1 Experimental setup for TiN coating of a B-factory beamline chamber

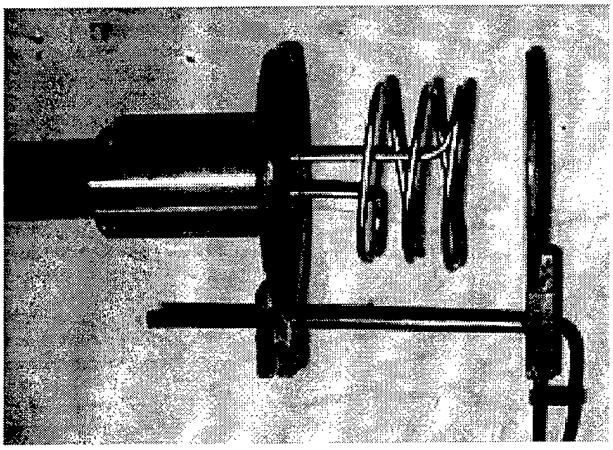


Fig. 2 A picture showing the water-cooled titanium rf induction antenna.

## IV EXPERIMENTAL RESULTS

In order to investigate the characteristics of the TiN coating, three aluminum disk samples are installed on the chamber as illustrated in Fig. 3. The inner surface of the chamber as well as the sample disks are chemically cleaned to remove the oxide layer. The chamber is initially evacuated to a base pressure of about $2\times10^{-6}$ Torr. Argon, nitrogen or a mixture of argon and nitrogen gas is then introduced into the chamber until the pressure reaches ~20 mTorr. The output power of the rf supply is gradually increased until a plasma is formed. The rf reflected power is minimized by adjusting the capacitor of the matching network.

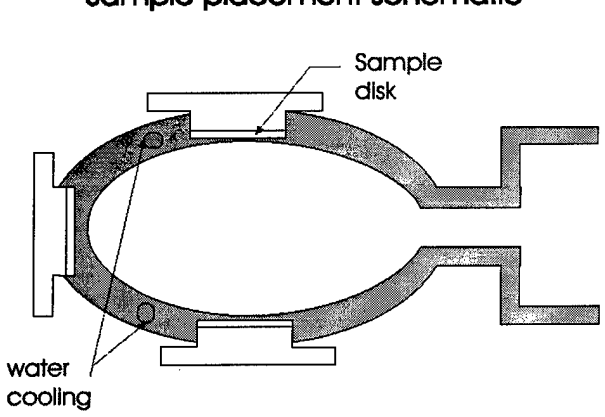



Fig. 3 A schematic diagram showing the locations of the three sample disks when they are mounted in the beamline chamber.

Disk samples and the beam pipe have been TiN coated with several different operating conditions. In general, a reasonably thick TiN coating can be achieved if the system is first operated with a pure argon plasma. The argon ions can sputtered the Ti from the antenna due to the high negative potential. Some of the Ti atoms are ionized and they are implanted into the chamber surface with energies in the order of tens of eV (due to the high plasma potential of rf discharge). After about 20 minutes, the argon plasma is turned off and is replaced with a nitrogen plasma. The $N^+$ and $N_2^+$ ions as well as the neutrals then react with the Ti on the walls to form TiN.

Table I shows the analyzed results for three sample disks under different processing conditions. It is found that the color of the TiN coating varies from blue to gold, depending on the thickness as well as the stoichiometry of the film. By first operating the system with argon for 15 min followed with a mixture of $Ar/N_2$ (30% $N_2$) for another 15 min, the stoichiometry (Ti/N) ratio is unity and the thickness of the coating exceeds 500 nm.

Table I.

| Discharge gas (nm) | Ti/N Stoichiometry | Thickness |
|---|---|---|
| $Ar/N_2$ (15% $N_2$) (48 min) | 1.08 | 12.6 |
| Ar (32 min) $N_2$ (16 min) | 0.74 | 779 |
| Ar (15 min) $Ar/N_2$ (30% $N_2$) (15 min) | 1.02 | 555 |

In this experiment, movement of the antenna is limited to the length of the beamline chamber which in this case is ~30 cm. It has been demonstrated that a dense plasma can be generated even when the coaxial cable between the matching network and the antenna is 6 meters long. Thus, this TiN coating technique can easily be applied to long beamline chambers typically found in synchrotrons and storage or accumulator rings.

## ACKNOWLEDGMENT

We would like to thank T. Elioff, K. Kennedy, J. DeVries and S. Wilde for all the technical assistance and R. E. Kirby at SLAC for analyzing the samples. One of the authors (D. Wutte) gratefully acknowledges the support by the Schrödinger Fellowship granted by the Fonds zur Forderung der wissenschaftlichen Forschung in Österreich under contract number J01220-PHY.

## REFERENCES

[1] D. Ruzic, R. Moore, D. Manos, and S. Cohen, J. Vac. Sci. Tech. 20, 1313 (1982).

[2] W. D. Cornelius and R. J. Grieggs, Los Alamos National Laboratory Report No. LA-UR-84-2489.

# RAMPING EFFICIENCY STUDIES IN THE LNLS SYNCHROTRON LIGHT SOURCE

R.H.A. Farias, L.C. Jahnel, Liu Lin, A.R.D. Rodrigues* and P.F. Tavares
Laboratório Nacional de Luz Síncrotron LNLS, Campinas, Brazil

*Abstract*

The 1.37 GeV LNLS UVX electron storage ring has a 120 MeV injector LINAC. Once stored, the electron beam must be ramped up to the nominal operation energy. In order to minimize current loss, orbit and tune corrections have been implemented along the energy ramp. In this report, we present a description of the energy ramping process, performance, orbit and tune corrections.

## 1 INTRODUCTION

The LNLS synchrotron light source is composed of a 1.37 GeV electron storage ring and a 120 MeV injector LINAC. Commissioning of the storage ring started in May 1996 and the latest results as well as other details on the machine are presented in a separate contribution to this conference[1]. Beam accumulation at injection energy and energy ramping have proven to be the most challenging part of the commissioning.

To achieve a ramping efficiency up to 80% it was necessary to implement a versatile ramping system which allows several ramp parameters to be easily changed by the operator. These parameters include:

- intermediate optical configurations;
- RF gap voltage ramp;
- varying ramping speeds along the ramp and
- varying energy step sizes along the ramp.

This report describes how the energy ramping process has been implement and shows illustrative experimental results.

## 2 RAMPING SYSTEM

### *2.1 Hardware*

During the energy ramp, 47 power supplies must have their current increased simultaneously. In order to achieve the necessary synchronism among power supplies during the ramp, it is not possible for the main control computer to control directly all ramped power supplies. Rather, during the ramp, control is temporarily passed on to distributed local controllers that step along a precalculated table of set points as they receive trigger signals from a master clock. These trigger signals produce a hardware interruption in the local controller's CPU bypassing any other process that might be running at that time. The main control computer must calculate all set points along the ramp and send them to the local controllers' memory before the ramp is started. The ramp master clock is directly controlled by the main control computer and is used to provide different ramping speeds. A counter board connected to one of the three outputs of the master clock board is used to monitor the ramping progress.

The number of points in each ramping table was determined by a compromise between the desired resolution of the energy ramp, the amount of memory available in the local controllers for storage of the ramp tables and the time needed to send those tables to the controllers. At present the dipole, quadrupole and sextupole power supplies have 4096-point ramp tables whereas the orbit corrector power supplies have 1024-point tables and the total time to send a complete set of ramp tables to the local controllers is about 2 minutes.

### *2.2 Software*

Figure 1 shows the main window of the ramping application. Intermediate optical configurations (sets of quadrupole, sextupole and corrector strengths) may be set up so that the ramping software interpolates linearly between those configurations. This allows the tune and orbits to be controlled along the ramp. Different ramping speeds may also be chosen. Three different RF gap voltage ramps may be used: no ramp (normally used when ramping to low energy, i.e. 300-400 MeV), linear ramp (with a given initial and final setpoints) and an arbitrary set of points given in a separate text file. The ramp software registers the beam current, beam orbits and possibly the beam tunes along the ramp for off-line analysis.

* also at IFSC, Universidade de São Paulo.

0-7803-4376-X/98 /$10.00 © 1998 IEEE

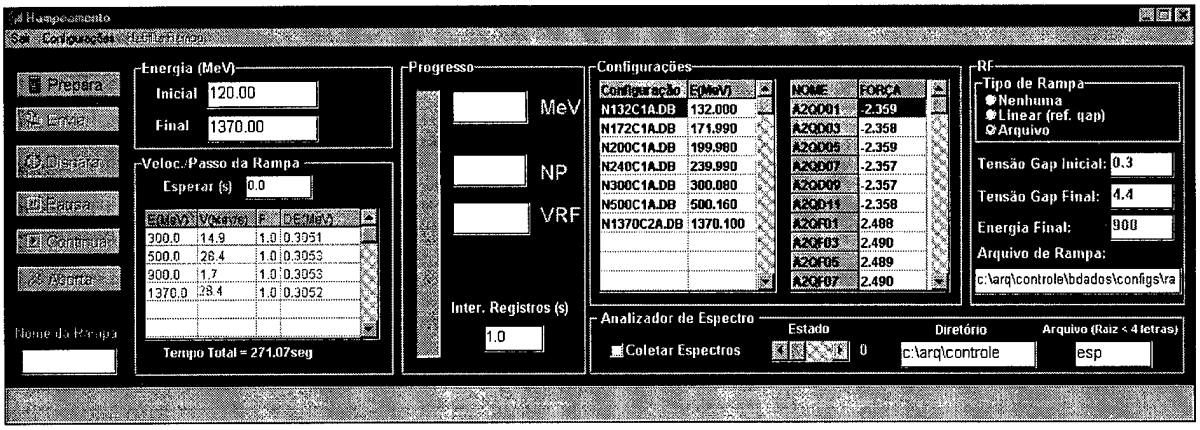



Figure: 1 Main window of the ramping application.

## 3 EXPERIMENTAL RESULTS

Many different ramping parameters have been tried and these had to be changed often as the commissioning proceeded and higher beam intensities were stored at injection energy.

Due to the fact that the horizontal and vertical tunes at injection energy ($\nu_x$=5.05 and $\nu_y$=2.09) are different from the tunes at 1.37 GeV ($\nu_x$=5.27 and $\nu_y$=2.17)[1], it is necessary to find a suitable path in tune space from one point to the other. We have found it necessary to keep the tunes low up to until about 500 MeV when the beam is damped and rigid enough to withstand the change in tune. In order to keep the tunes constant up to 500 MeV, it is necessary, due to remnant field effects, to change quadrupole strengths and six intermediate optical configurations had to be set up. Figure 2 shows the tune variations during the ramp.

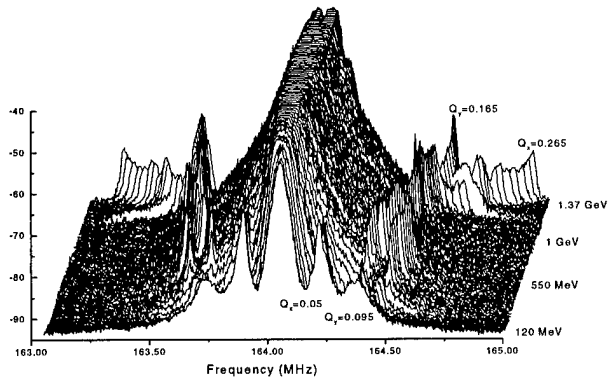



Figure 2: Tune variations during the ramp.

Figure 3 displays the difference between the initial and the six intermediate optical configurations of quadrupole and integrated sextupole strengths and figure 4 shows the strengths of correctors ACH07A and ACV07A along the ramp until 500 MeV.

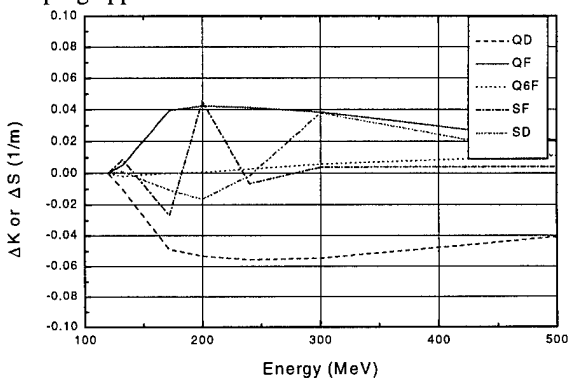



Figure 3: Variations of quadrupole and integrated sextupole strengths along the energy ramp.

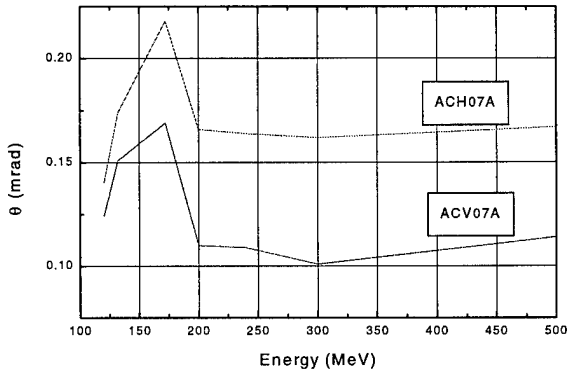



Figure 4: Strengths of correctors ACH07A and ACV07A along the energy ramp.

Orbit correction along the ramp is necessary partly due to remnant field effects but also because of the influence of the (DC) thin septum magnet leakage field on the stored beam orbit which is only properly corrected at injection energy. Orbit correction has been done with two different methods: (a) by ramping to an intermediate energy and correcting the orbit and (b) by acquiring orbit data dynamically along the ramp, calculating corrections off-line and then implementing corrections for the next ramp. The second method, although more laborious, takes into account the effect of Foucault currents on the orbit distortion. The difference between the orbit corrected with these two methods is around ±2 mm in the horizontal and

±1 mm in the vertical. Figure 5 shows the corrected orbits during the ramp.

The RF power must also be ramped since beam accumulation is only possible at 120 MeV with at most 60 kV gap voltage (this is due to the excitation of large energy oscillations as a result of the large phase spread of the injected beam). The start of the RF ramp is delayed to until 300 MeV to avoid the excitation of synchrotron oscillations (and corresponding current loss) and the gap voltage reference is taken to its full value at 500 MeV. The ramping speed is then decreased to allow for the cavity power in the cavity to stabilize at high level.

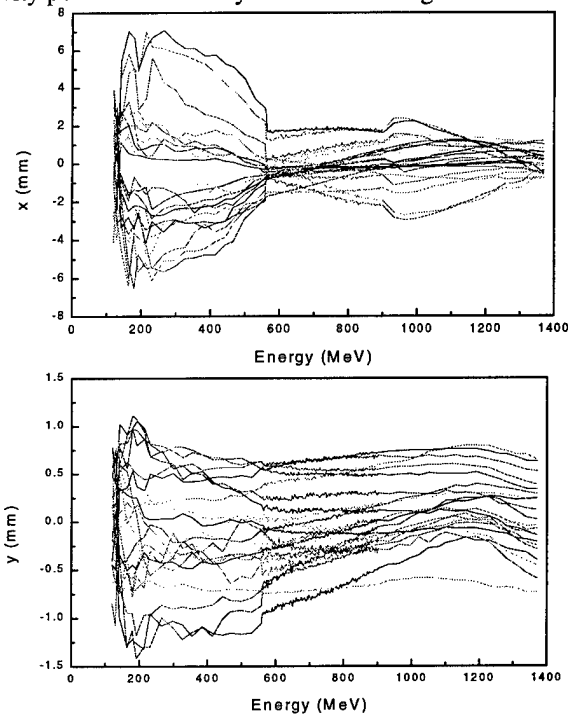



Figure 5 - Orbits during ramp.

The RF ramp has proved to be the most critical part of the ramping process. Initial conditions such as the cavity temperature and tuner positions play an important role in the determination of the overall ramping efficiency[2].

Three different speed regimes (Table 1) are used during the ramp. In the low energy part, we proceed as fast as possible to avoid losses due to the low lifetime. At intermediate energies, we proceed slowly in order to allow the RF system to stabilize with RF power. Finally above 900 MeV we proceed quickly to the nominal energy. The total ramping time is about 4 minutes.

| E (MeV) | v (MeV/s) |
|---|---|
| 120 - 300 | 15 |
| 300 - 500 | 28 |
| 500 - 900 | 2.5 |
| 900 - 1370 | 28 |

Table 1: Values of ramping speed.

Ramping efficiency is lower for higher stored currents and some ramping parameters (especially in the RF system) have to be changed according to the stored beam intensity.

Figure 6 shows the variation of current as function of energy during ramping process, where the speed of ramping is given in table 1 and figure 7 shows the variation of RF gap voltage and gap reference during the same ramping process, as function of the time.

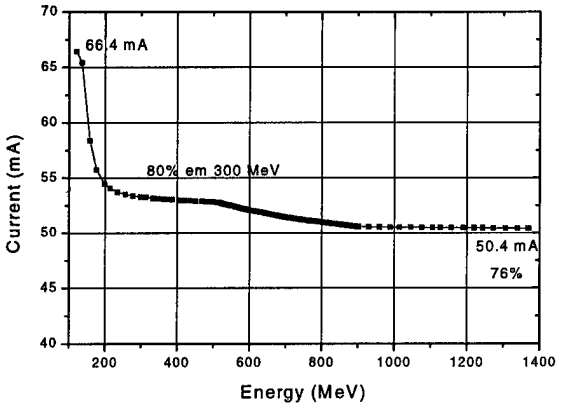



Figure 6: Current vs. energy during ramping process.

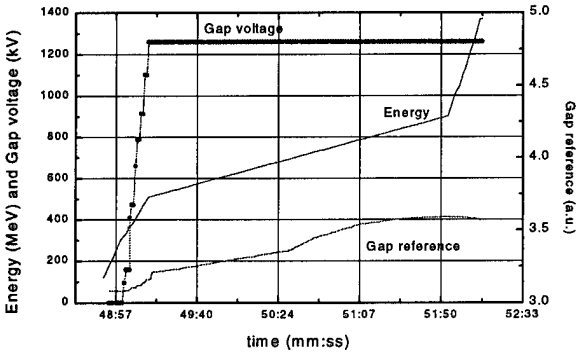



Figure 7: Variation of RF gap voltage, gap reference and energy as function of the time during ramp.

## 4 CONCLUSIONS

The energy ramping system of the LNLS electron storage ring has proven to be capable of ramping electrons from 120 MeV to 1.37 GeV with an efficiency ranging from 65% to 80%, depending on the initial beam current.

Possible improvements include changing the cavity detuning during the ramp and implementing a feedback loop for the RF gap voltage.

## REFERENCES

[1] A.R.D. Rodrigues et al., 'Commissioning and Operation of the Brazilian Synchrotron Light Source', these proceedings.

[2] D. Wisnivesky et al.,'Operation of the LNLS Storage Ring RF System', these proceedings.

# POWER FACTOR CORRECTION AT THE MIT-BATES LINEAR ACCELERATOR CENTER WITH PULSED LOADS OF UP TO 180 MW PEAK (2.7 MW AVERAGE)

R. Averill, K. Hatch, C. Sibley, MIT-Bates Linear Accelerator Center
R. Gross, PLM, Inc.

## I INTRODUCTION

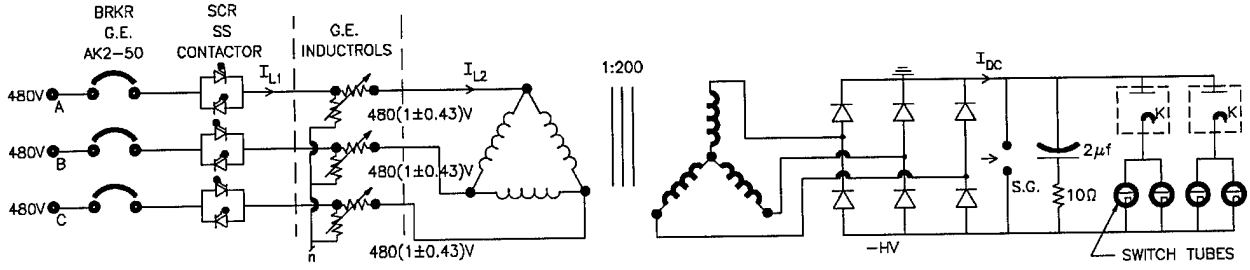
Power demand charges to MIT-Bates are based on a fixed rate times the greater of kWatt or 0.9 (kVolt A) called for in a 15 minute period within a billing cycle. There have been a number of months in a year when the power factor (PF) was less than 0.9 lagging, resulting in the increase in the demand charges to MIT by the Middleton Municipal Electric Department (MMED). A study resulted in a decision to correct the PF to >0.9 in order to minimize the demand charges. This action would save about $3500 per month in demand charges. Other benefits would also be realized by MIT-Bates and MMED, depending on the installation location. Information obtained on operational AC power requirements for the pulsed loads was obtained by measuring current and voltages at the 480V inputs to the pulsed loads and at the incoming 22,900V line input to the facility. A review of the harmonics generated in the voltage and current waveforms at both voltage levels for several operating levels allowed completion of an engineering analysis, which resulted in the selection of a 1200 kVAR switchable capacitor bank to be installed in a wye connection at the 22,900V incoming line point just after the metering equipment. This paper describes the results of the harmonic studies of the AC power, the pulsed loads required as measured at 480V, and the resultant overall harmonics generated at the 22,999V level by the pulsed loads when combined with the other normal AC loads at the Laboratory.

## II 480 VOLT TRANSMITTER STUDIES

Jomitek, Inc. made a series of measurements on the five 480V substation distribution system. The information (Ref. 1) obtained was very useful to the MIT-Bates technical staff due to a lack of instrumentation which prevented observation of the normal operating loads for these substations. A report submitted to MIT-Bates by Jomitek focused on a power monitoring system proposal and additionally discussed the correction of the PF at the 480V or at the 22,900V level.

Current and voltage measurements were taken for a single transmitter operating at several different levels and repetition rates (PPS).

This information showed the harmonic levels to be maximum at the highest operating conditions. Various commercial companies have been offering power monitoring systems with increased measurement capabilities and attractive pricing.




TYPICAL OPERATING CONDITION
600 pps, 23μS

| MODE | 2 KLYSTRONS | | HVDCPS | | INDUCTROL OUT | | 480V IN | P + jQ | KVA |
|---|---|---|---|---|---|---|---|---|---|
| | $I_{PK}$(A) | $E_{PK}$(kV) | $E_{DC}$(kV) | $I_{DC}$(A) | $E_L$(V) | $I_L$(A) | $I_L$(A) | (kw) $K_{VAR}$ | |
| LOW | 70 | 107 | 120 | 1.93 | 473 | 381 | 467 | 319 + j 221 | 388 |
| NORMAL | 76 | 113 | 130 | 2.09 | 493 | 397 | 521 | 360 + j 240 | 433 |
| MAX | 95 | 131 | 153 | 2.62 | 610 | 500 | 664 | 500 + j 333 | 600 |

GENERAL SCHEMATIC FOR ONE OF SIX TRANSMITTERS

NOTE: TX6 HAS VVT, NOT INDUCTROL

Fig. 1. The schematic for a typical transmitter.

0-7803-4376-X/98/$10.00 © 1998 IEEE

One transmitter was instrumented with current and voltage measurements on the primary and secondary of a G.E. Inductrol unit and the input AC requirements for the HVDCPS transformer rectifier was determined for the present operating levels, which are lower than the original design specifications. The nominal pulsed parameters for an operating transmitter are: 23• S pulse width, 600 pps, and peak currents of 76A for each of the two paralleled klystrons being driven. Figure 1 shows the schematic for a typical transmitter.

Additional transmitter harmonic measurements were taken using a METROSONICS commercial package on a single transmitter operating at the nominal operating conditions. Waveform and harmonic spectrum for the pulsed load typical 480V line current can be seen in Figure 2. The voltage waveforms are not very distorted and are not shown to save space. The voltage waveforms have a total harmonic distortion expressed as a percent of the fundamental (THD%) of 3.5%, while the current waveforms were measured to have a THD of 22.5%.

## III 22,900 VOLT LINE MEASUREMENTS

PLM, Inc. an engineering firm specializing in providing service to the utility firms in New England, and in particular to MMED over the past several years on an as-needed-basis, was hired to determine if it was possible to implement a PF correction system at the MIT-Bates Laboratory, and if so where would be the best place on the power distribution system to install the equipment. PLM was given the earlier data and used some of this data to review the case for installation of the PF correction at the 480V level.

It was determined that the harmonic levels generated at the 480V level by the transmitters would require more analysis and there would be more risk, but with more benefits within the MIT-Bates distribution system. Certain filters would need to be determined and installed to prevent unwanted resonances peculiar to the variable harmonics generated by the nearby pulsed loads.

In order to study the voltage and current harmonics at the 22,900V level, measurements of the harmonics generated at the incoming metering point were necessary. PLM then could evaluate the extent of these harmonics and the effects of a capacitor bank installed on MMED's transmission line. The typical harmonic spectrum for line voltages and currents is shown in Figure 3 at the 22,900V level. PLM engineers then performed an analysis (Ref.3) of the system under several scenarios. A one-line diagram of the approximately 5 mile long transmission line is shown in Figure 4 with all impedances shown referenced to the 22,900V level. The system resonance frequencies for a 1200kVAR and 1800kVAR banks were determined with a worst case operating voltage level 5% above nominal (under normal system impedance) and under a 20% increased system impedance. The installation of a 1200kVAR capacitor bank and the resulting harmonic currents flowing through the capacitors would not exceed

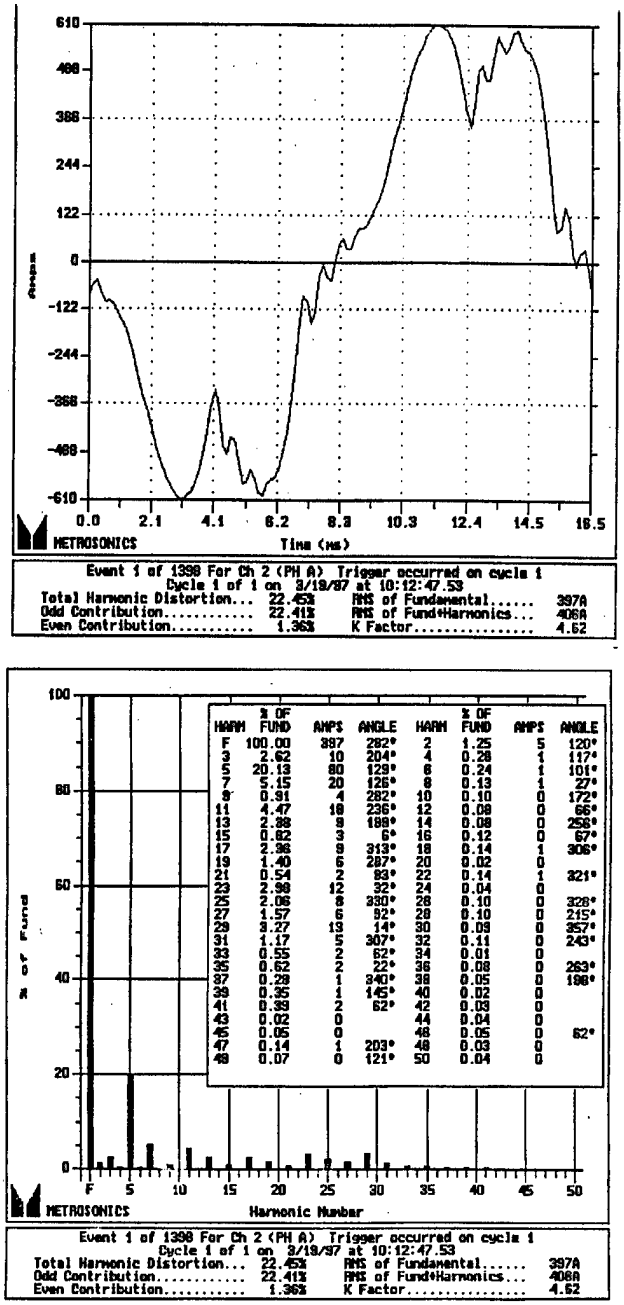






Fig. 2. Typical transmitter line currents at 480V-3Ph-60Hz.

the manufacturer's ratings of the capacitor units. For this proposed installation at the nominal system impedance, the system resonance frequency was calculated to be 604.25 Hz. The bank would operate at 95.52% of the RMS capacitor voltage rating with a 3.52% THD. The capacitor RMS current was calculated to be 61.5% of the manufacturer's capacitor current rating. PLM, Inc. then proposed and MIT-Bates agreed to install a 1200kVAR PF correction system at the incoming 22,900V level as being the simplest most economical and least risk approach to solve the main goal of increasing the load PF to >0.9 and avoid the demand charges associated with PF <0.9.

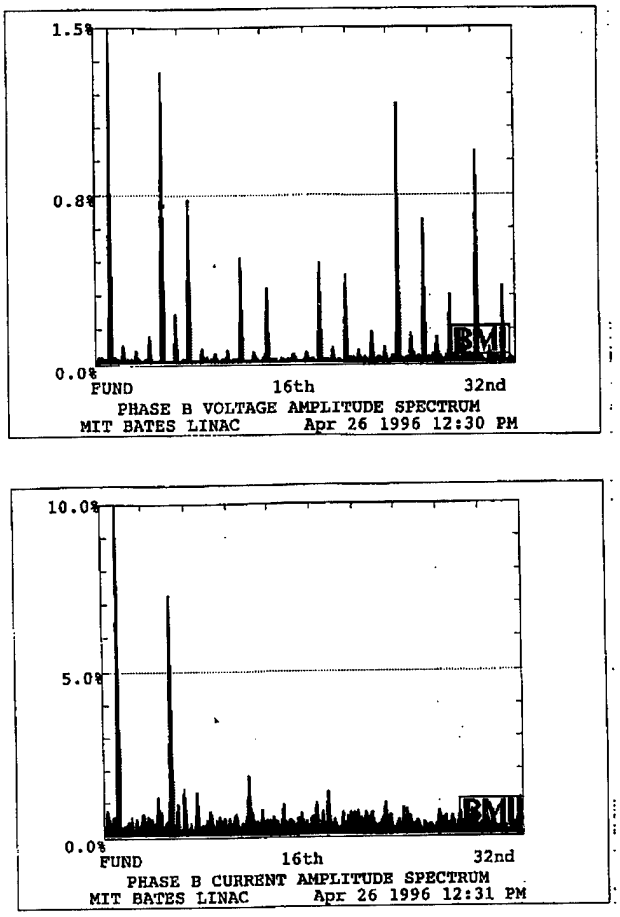



Fig. 3. Typical harmonics for line voltages and currents at 22,900V and 4.0 MVA, 0.8 PF with 6 transmitters operating

PLM then was charged to specify the PF correction equipment (Ref. 4) and to review the bids obtained. An order was placed with the low bidder for a Cooper Industries rack mounted switchable capacitor bank to be pole mounted after the incoming line metering point. The system was delivered in January 1997 and awaits an installation window of time for which the Laboratory power must be interrupted for about 4 hours to install and connect the equipment. MMED personnel have been given an installation contract including the pole, mounting the capacitor/switch assembly and connecting the capacitors to the 22,900V line.

## IV CONCLUSION

The project to correct the MIT-Bates PF to > 0.9 is almost complete. Remaining work is to mount the capacitor switch assembly on the already installed pole, connect the units to the 22,900V lines and make a final checkout of the installation. Excellent cooperation between MIT-Bates technical staff, PLM, Inc. engineer and the MMED technical staff was an important part of the solution selected for implementation. The authors would like to thank the following persons for their contributions to the project: John J. Marczewski, Principal Engineer, PLM, Inc. and Paul Kilroy, Facility Coordinator, MMED.

## V REFERENCES

[1] Power Factor Study for the MIT-Bates Linear Accelerator Laboratory, Jomitek Systems, Inc. Poughkeepsie, NY 12601 January 21, 1993, Lawrence Fish, President
[2] BMI Harmonic Survey for MIT-Bates, UPG,Inc.Brockton, MA 02401, Jay Donadio, Project No. U059613, April 26, 1996
[3] PLM, Inc. Harmonic Analysis, Proposed 23kV Capacitor Bank, Report/Letter, June 23, 1996, John J. Marczewski, P. E.
[4] PLM, Inc. Specifications for power factor correction at MIT-Bates Laboratory, June 7, 1996, Richard C. Gross, P. E.

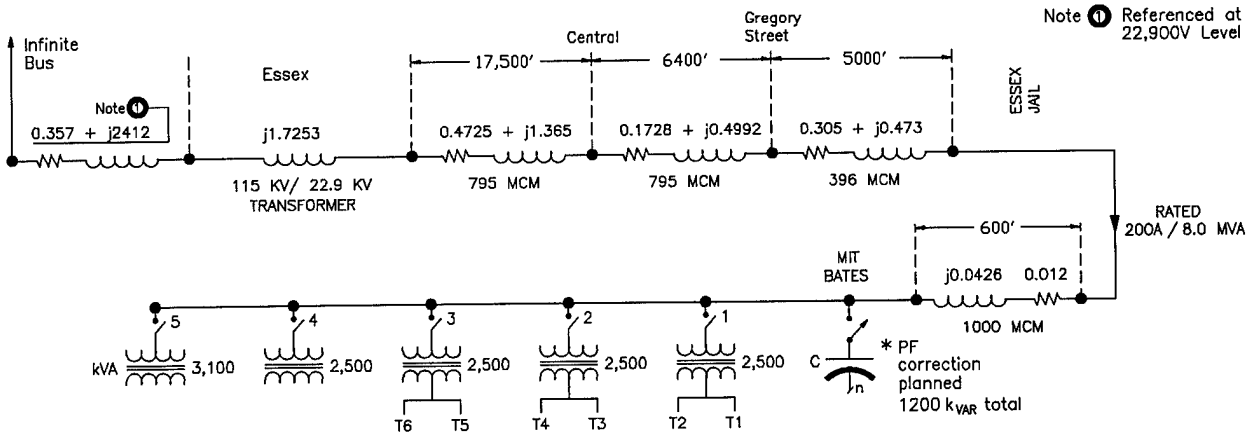



Fig. 4. Diagram of transmission line.

# HARMONIC RESONANCE ANALYSIS FOR PEP-II POWER FACTOR CORRECTION UPGRADES*

C. Corvin, Stanford Linear Accelerator Center, Stanford University, Stanford, CA 94309 USA

*Abstract*

Recent upgrades to the high voltage utility distribution network at the Stanford Linear Accelerator Center have been accompanied by the installation of a large number of power supplies associated with the PEP-II B Factory project. These power supplies include a diverse assortment of single and three phase units, in two, six and twelve pulse configurations with chopped, pulsed and continuous loading. Viewed as harmonic power sources in a range from a hundred to several kilohertz, they have the potential to be in resonance with the utility system network, a condition to be avoided. This paper analyzes and evaluates these resonance conditions with a view toward adding electric power factor correction upgrades to achieve substantial cost savings associated with power factor penalty avoidance. Similar studies and upgrades at SLAC in the past have reduced electric power costs over time by several hundred thousand dollars thus providing the incentive to evaluate the recent upgrades to the PEP-II network.

## I. INTRODUCTION

Since June 1994, electrical power factor correction systems at the Stanford Linear Accelerator Center, SLAC, have included a fixed capacitor bank and a synchronous condenser, both operating at 12,470 volts. The capacitor bank operates continuously to correct base load power factor and the condenser operates with a variable output to correct power factor for varying experimental loads. The site power factor for peak loads during SLC and SLD experimental operations have been consistent at 0.90 at roughly 52 megawatts. For synchronous condenser operations alone, the total of avoided power factor billing penalties from June 1994 until recently have exceeded $400,000. With the substantial completion of the PEP-II B Factory 12.47 kilovolt electric utility network in 1997, an evaluation of future site power factors at SLAC has been possible. Power factor levels will clearly change from those experienced during the SLC-SLD era. Unlike prior SLC-SLD operations, new modulator power supply loads for klystrons in PEP-II will have substantial power factor excursions associated with beam loading. This variable, and a near resonant 12 kilovolt distribution network, add complexity to upgrades for power factor control. This paper evaluates the technical risks associated with PEP-II power factor correction upgrades and suggests effective technical solutions to avoid future substantial power billing penalties.

## II. OVERVIEW

Budgetary projections of future PEP-II loads assume that in late 1997, the site power factor will be 0.93 at 67 megawatts, an increase of 15 megawatts and 0.03 in power factor over the 0.90 power factor and 52 megawatts of recent SLC-SLD operating experience. A technical summation of the major new PEP-II loads describe a more complex view of the future as compared to the budgetary averages. The primary PEP-II load additions are ring magnet loads and modulator power supplies for klystron RF. The magnet loads should be quite good totaling 3.4 megawatts and 0.96 power factor. The klystron modulator power supplies are not as good however and vary depending on beam loading. At full load they should total 16 megawatts at 0.80 power factor and at minimum load they may operate as low as a total of 8 megawatts at 0.55 power factor. Summing these with other site loads yields 60 to 68 megawatts total, at 0.87 to 0.89 power factor depending on beam loading. To assure that site power factor does not degrade below the most recent level of 0.90, and instead improves, an additional source of leading reactive power should be added to the utility distribution network.

The fundamental change to the electrical utility distribution network brought on by the upgrade to the PEP-II high voltage circuit configuration is to increase the total installed length of 15 kilovolt class power cable that feeds power to the PEP-II IR halls. This cable is nearly all 750 kcmil copper cable with 220 mils of ethylene propylene rubber insulation. The center conductor with the surrounding insulation and grounded outer shield form a series inductance with a shunt capacitance. Each power cable circuit then effectively establishes a low Q resonant transmission circuit. In general, industrial power circuits such as these are either too short or too long to create a resonant condition that would be of concern. The new

* Work funded by Department of Energy contract DE-AC03-76SF00515

0-7803-4376-X/98 /$10.00 © 1998 IEEE

PEP-II circuits however are somewhere in between. The effect of increasing power to the PEP IR halls and adding miles of new cable has been to lower the circuit resonant frequencies substantially. Shunt capacitors added to the PEP-II network can not only improve power factor but be used to shift otherwise harmful resonant conditions to more benign frequencies. The goal of this first study has been to identify the areas of risk and the best locations for the addition of shunt capacitors at 12.47 kilovolts.

A complete engineering solution for power factor correction during PEP-II operations is not within the scope of this paper but is the logical next step. It would of necessity include attention to switching transient response, grounding, voltage regulation, and insulation coordination as well as the control scheme(s) for site power factor management.

## III. TECHNICAL

The PEP-II electrical utility network consists of four high voltage circuits each operating at a nominal voltage of 12.47 kilovolts and radiating out of the SLAC master substation to the various PEP-II IR halls. Each of the circuits is a combination of series and parallel cable runs that total almost 8 miles of installed cable plant. The electrical circuit lengths are substantially greater than the physical routes of the right of ways which are almost entirely in underground cable duct banks. Per unit circuit constants used to model the cable network are typical for standard cables, and are: 0.038 ohms inductive reactance per 1000 feet at 60 hertz, 0.0171 ohms resistance per 1000 feet at 60 hertz, and 416.6 ohms capacitive reactance per 1000 feet at 60 hertz. These values are typical for the 133 percent MV-90 design cable in use. The dielectric constant of the cable insulation varies by manufacturer and the date of manufacture (age). It is between 2.7 and 3.0 . The X/R ratio is about 2.2 . For the preliminary results included here, mutual inductive reactance has been left out. As of the date of this paper some sections of cable plant are yet to be connected, with some being parallel and electrically floating, and some being long stubs, connected at only one end.

The PEP-II harmonic power sources supplied by the utility feeders are power supplies located at the IR halls. By origin, 2nd order harmonics (of a 60 hertz fundamental) are produced by small single phase supplies but are often modest in magnitude. Single phase supplies in three phase groupings often sum to cancel most second harmonic content through one or more upstream delta-wye transformations. The triplen 3rd and 9th order harmonics appear in unbalanced supplies of any type. This three-nine signature is useful for locating faulty power supply regulator controls and thyristor trigger circuits. The 5th and 7th order harmonics appear in six pulse power supplies and the 11th and 13th orders dominate in 12 pulse power supplies. Higher order harmonics are also generated but are of lesser magnitude. For other frequencies, modulation of the power system power feeder circuits can occur at the chop, pulse and repetition rate frequency needed to supply their respective loads. PEP-II magnet power supplies are planned to chop at 20,000 hertz. Listing these harmonic sources gives orders of 2, 3, 5, 7, 11 and 13, plus 333. Since the addition of shunt power factor capacitors will lower resonant frequencies, the 4th and 8th orders, 240 hertz and 480 hertz respectively, are the lowest desirable frequencies of interest for power factor correction resonance as they avoid the source frequencies above. The addition of capacitors might seek to drive the final operating circuit resonant frequency center point there, or close to it, ideally 240 hertz if possible . The possible installation of 60 hertz inductors along with power factor capacitors is not considered here in that it does not consider the circuit impedances and resonances already installed and it adds unnecessary cost.

The ideal location of power factor capacitors is usually recommended to be between one-third and one-forth of the total length of a distribution circuit taken from the circuit load end. This generally manages and distributes the voltage rise associated with pulling leading reactive power through lagging inductive cable circuit impedances. As the four PEP-II circuits are not accessible along their complete length some alternative location may have to be considered including placement at the circuit ends , at a PEP-II IR hall.

## IV. RESONANT UTILITY CIRCUITS

As the utility network must at times be operationally switched, no single model is really correct for all conditions. Various configurations of cable circuit impedances are possible, however those models that combine to produce the lowest frequencies are of the most interest. Summations that maximize shunt capacitance and series inductance are listed in Table 1, below. For reference, the frequencies of the nearest harmonics, the 9th, 10th and 11th orders, are also listed in bold type.

Of first concern are IR-2 and IR-4 which bracket the 11th harmonic at 660 hertz and are resonant at 698 and 602 hertz respectively. Power factor correcting capacitors should be considered for those locations to shift resonance to a lower frequency. Of less concern are IR-10 and IR-6 which bracket the 9th harmonic of 540 hertz, at 501 and 551 hertz respectively. As the triplen ninth harmonic only

appears as a source under abnormal unbalanced conditions, IR's ten and six would not be primary locations for power factor capacitors. Shifting these circuit resonances as low as 240 hertz would require a sizable installation of capacitors. However a large installation may be both technically indicated and also the cost effective solution.

| PEP-II Locations, Harmonic Orders | Net Circuit Length (ft) | Resonant Frequency (Hz) |
|---|---|---|
| IR-10 | 12585 | 501 |
| **9th Harmonic** | | **540** |
| IR-6 | 11440 | 551 |
| B-750, SLD-SLC | 11040 | 571 |
| IR-12 | 11000 | 573 |
| **10th Harmonic** | | **600** |
| IR-4 | 10480 | 602 |
| **11th Harmonic** | | **660** |
| IR-2 | 9040 | 698 |
| IR-8 | 5365 | 1176 |

Table 1: Lowest possible resonance frequency of PEP-II 12.47 kilovolt utility supply circuits with selected power supply harmonic sources shown in bold type.

## V. AVOIDED POWER PENALTIES

Monthly power factor penalties are incurred at SLAC based on power factor and peak megawatt demand. The current maximum contracted rate of delivery, CRD, is limited to 53.903 megawatts [1] . PEP-II operations will exceed this maximum. Penalties will be set as power factor varies at peak demand above 53.9 megawatts. Table 2 describes the potential magnitude of these penalties.

| Demand (mw) | $ Max Penalty per month | Power Factor |
|---|---|---|
| 60.0 | $ 32,342 | 0.87 |
| 68.0 | $ 24,795 | 0.89 |
| 68.0 | $ 0 | 0.95+ |

Table 2: Possible maximum SLAC power factor penalties for PEP-II operations.

The quantity of new additional leading reactive power needed for PEP-II varies from a minimum of 3.5 megavars to maintain 0.90 power factor, to 11.0 megavars to achieve 0.95 power factor. A simple per-unit cost for capacitors in this quantity, neglecting switching, transient suppression, and site related costs, is estimated at 7 cents per volt-ampere reactive. The most aggressive proposal for power factor improvement would then be 0.95 power factor at a capacitor (only) cost of $ 770,000. Simple payback from avoided penalties considering the costs of other equipment and related project costs would be less than 5 years. The penalty for not correcting power factor at all would run about $ 200,000 a year for eight months of annual PEP-II operations at peak demand.

## VI. SUMMARY

PEP-II high voltage power distribution circuits are configured to present a potential resonant condition with non-linear PEP-II loads. Power factor capacitors can reduce the risk of an undesirable resonant condition and also reduce PEP-II operating costs for electric power. A project for a PEP-II power factor upgrade is indicated at a cost of about $ 1,000,000 with a simple return on investment of about 5 years.

## VII. REFERENCES

[1] Western Area Power Administration, *Central Valley Project Notice of Rate Order* No. WAPA-59 (July 2, 1993). Federal Register, vol. 58, no. 126, pp. 35948–35949.

# A DYNAMIC LOCAL BUMP SYSTEM FOR PRODUCING SYNCHROTRON RADIATION WITH AN ALTERNATING ELLIPTICAL POLARIZATION

K. T. Hsu, C. H. Kuo, K. H. Hwu, K. K. Lin, C. S. Chen, J. S. Chen, J. Chen, C. T. Chen
Synchrotron Radiation Research Center
No.1 R&D Road VI, Hsinchu Science Based Industrial Park
Hsinchu 300, TAIWAN

*Abstract*

To facilitate high sensitivity soft-X-ray magnetic circular dichroism experiments, we have developed a dynamic local bump system at the SRRC storage ring. This system was devised to vary dynamically the vertical slope of electron beam in a bend magnet, producing, in the electron orbit plane, soft-X-rays with an alternate elliptical polarization. The local bump was created by using two pairs of vertical correctors located on each side of the bend magnet. Bump strength coefficient was obtained from both calculated estimation and measured beam response matrix. Control electronics for proper bump strength settings was designed to incorporate the existed orbit corrector function. Corresponding graphic user interface was implemented so that bump amplitude can be easily adjusted. Performance of this system is presented. Disturbance on the stored electron beam orbit was observed while flipping of corrector polarity during EPBM operation. A local feedback loop developed to eliminate such disturbance on other beamlines is also described.

## 1 INTRODUCTION

The prospect of obtaining element- and site-specific magnetic information has stimulated a good number of experiments taking advantage of circularly polarized synchrotron radiation [1]. These magnetic circular dichroism (MCD) experiments, whether performed in absorption or reflection, offer the possibility of determining the magnetic moment of each element in the material being investigated. It is expected to have an elliptical polarization from bending magnet (EPBM) operation mode which provides adjustable degree of polarization with polarity switching frequency of 0.5 Hz. This report describes the design and preliminary test result of a dynamic local bump system for producing synchrotron radiation with an alternate elliptical polarization.

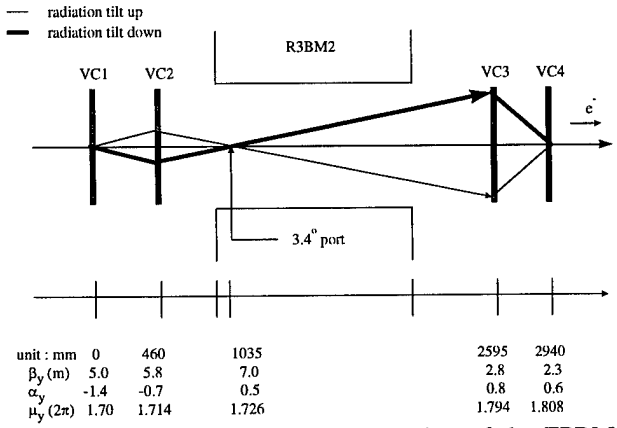



Fig.1. Operational schematic illustration of the EPBM system.

## 2 TECHNICAL FEATURES

### *2.1 Spatial Arrangement*

The schematic illustration of EPBM mode operation isshown in Fig.1. The SRRC storage ring lattice structure is a triple bend achromat with six-fold symmetry and the EPBM beamline is situated at the second bending magnet of the section three achromat. As shown in the figure, the R3BM2 stands for the second bending magnet of ring section 3. VC1, 2, 3, 4 represent vertical correction magnets associated with the EPBM local bump generation. The electron beam trajectory can be either flipped up or down depending on the bump magnet polarity chosen.

Since the EPBM configuration was new to the storage ring lattice, locations for installing extra correction magnets was limited by existing elements in the lattice structure, such as magnets, diagnostic and vacuum components. A compromised solution ends up with the arrangement given in Fig.1.

### *2.2 Bump Coefficient Determination*

With a specified user shift machine lattice, bump coefficient and strength can be determined by matching vertical beam position and slope at the intersection of lattice beam centerline and photon beamline.

Estimated bump coefficient can be verified under DC mode operation and some fine adjustment may be practically needed. Example of an EPBM DC bump was shown in Fig.2 for illustration. A local bump in the R3BM2 region is added onto the regular user shift beam trajectory along the storage ring. One can also use the orbit difference monitoring tool to display beam orbit

0-7803-4376-X/98 /$10.00 © 1998 IEEE

change before and after the AC bump was applied with persistent option. The detail of this beam instrumentation tool is described elsewhere [2].

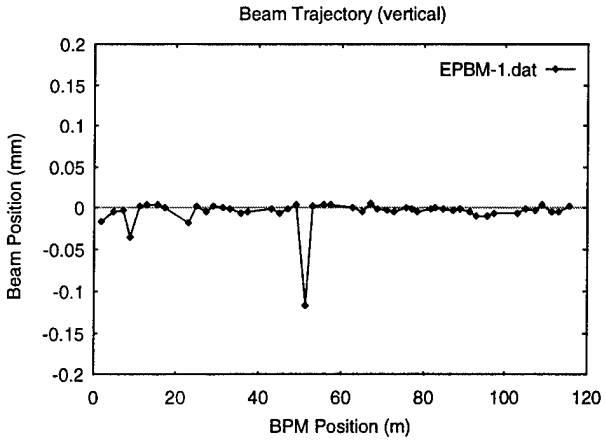



Fig.2. An EPBM local bump was generated in the storage ring section 3 under regular user shift lattice.

*2.3 Beam Response Matrix*

Another method to determined bump coefficient is using the measured beam response matrix [3,4]. The details of determining this EPBM local bump is described elsewhere [5]. This bump shape adjustment provides capability of convenient tuning in the future beamline commissioning, therefore the measured response matrix method was used for producing EPBM bump in this experiment.

## 3 IMPLEMENTATION AND TEST RESULTS

*3.1 Control Electronics*

Functional block diagram is given in Fig.3.

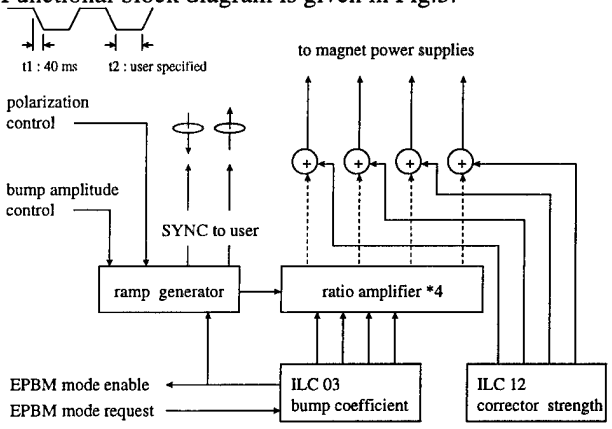



Fig.3. Functional block diagram of EPBM control electronics.

As shown in the figure, these bumpers act also as correction magnets. Consequently, the EPBM control electronics was designed to be able to provide independent corrector strength adjustments for both routine orbit correction and EPBM local bump generation. In switching the local bump polarity, a ramp generator was applied so as to keep polarity transient duration longer than the magnet response time of 25 ms. Tuning of bump amplitude was achieved by adjusting the bump amplitude control knob and the polarity switching frequency is determined by an external square wave function generator.

*3.2 Graphic User Interface (GUI)*

The EPBM graphic user interface was designed to provide easy adjustment of degree of polarization. The EPBM control page is shown in Fig.4.

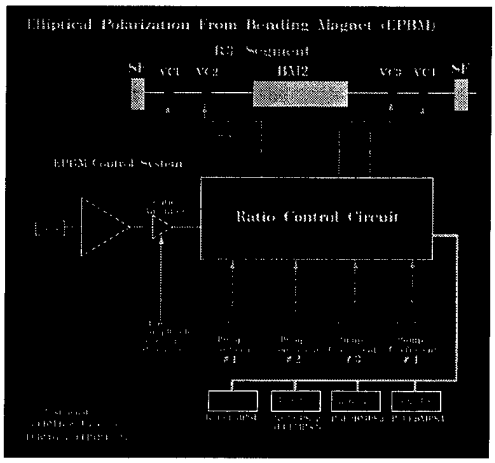



Fig.4. Display of present EPBM graphic user interface.

Tuning knob settings of bump coefficient for four magnets were determined from measured response matrixes. These values have also been cross-checked through simulation and will be determined during EPBM beamline commissioning.

*3.3 Mismatch of the Eddy Current Effect due to Bellow in the Third Corrector And Its Phase Compensation*

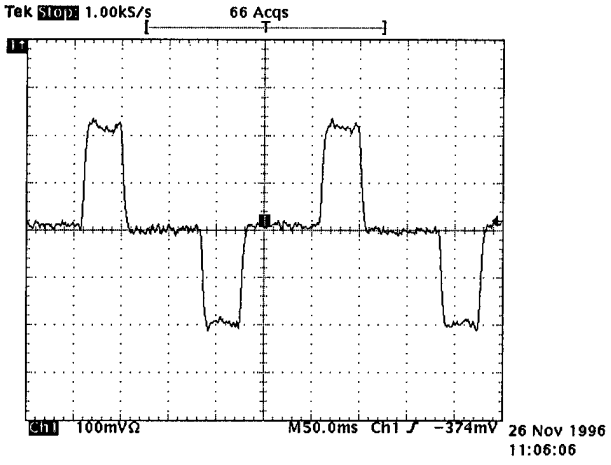



Fig.5. A 40 ms beam orbit shift was observed during EPBM bump polarity transient period.

When EPBM was tested in AC mode, beam orbit disturbance was observed outside the EPBM local bump. After careful examination, it was found that the beam orbit disturbance was occurred during the transient of bumper polarity change. As shown in Fig.5, the vertical position of the electron beam monitored at one of the

BPM located outside the EPBM bump gives about 50 μm beam position shift for 40 ms. This 40 ms period corresponds to the transient duration set by the control electronics and was caused by bump phase mismatch of the third bumper magnet. The vacuum chamber, where the third bumper magnet is located at, is a bellow type which is different from what the other three bumper magnets are associated with, a 5 mm thick aluminum chamber, was responsible for this bump mismatching. A compensation circuit was then built into the control electronics for the third magnet channel in order to compensate the mismatch due to eddy current.

### *3.4 Beam Test Result with Local Feedback Loop*

Although the compensator in the EPBM control electronics provides reduction of orbit disturbance on the beam orbit during polarity transient period, further improvement is still desirable. In order to fulfill this requirement, a local feedback loop on the beamline of interest was put to test in stabilizing beam trajectory at upstream of the beamline. As illustrated in Fig.6, with EPBM control electronics operating at 0.5 Hz, a local feedback loop was setup for stabilizing beamline of R2BM3, whereas EPBM beamline is located downstream of R3BM2.

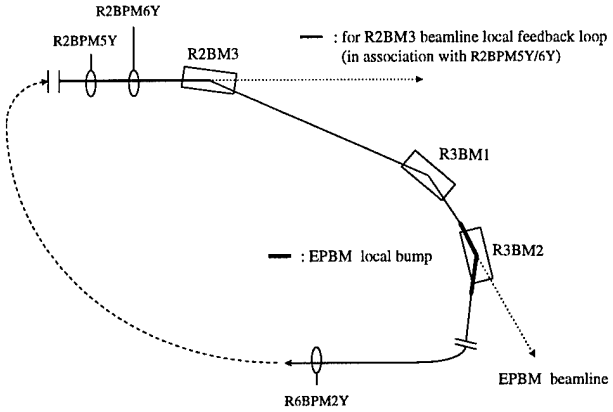



Fig.6. Schematic layout of the test run of EPBM with local feedback loop.

As shown in Fig.7, beam position monitors within the region of applied feedback loop (R2BPM5Y, R2BPM6Y) and the outside one (R6BPM2Y) give beam position during this experiment. At the beginning of this experiment, beam position readings were recorded under normal operation mode. Then, the EPBM control electronics was turned on in order to observed its influence to the beam position fluctuation at upstream BPMs of a selected beamline. The local feedback loop was turned on three minutes later in order to suppress beam position fluctuation induced by EPBM operation. This experimental result indicates that with EPBM in operation, other beamlines may be disturbed by EPBM local bump mismatch during flipping of correctors polarity [3]. Beam position fluctuation of 40 μm (R2BPM5Y), 70 μm (R2BPM6Y), 30 μm (R6BPM2Y) were observed while EPBM was operating. This implies that beamlines located downstream of (R2BPM5Y/R2BPM6Y) and that of R6BPM2Y were greatly disturbed by this EPBM operation. However, when local feedback loop installed in the region where (R2BPM5Y/R2BPM6Y) located was turned on, the beam position was stabilized to have fluctuation within 15 μm, 15 μm, and 25 μm, correspondingly.

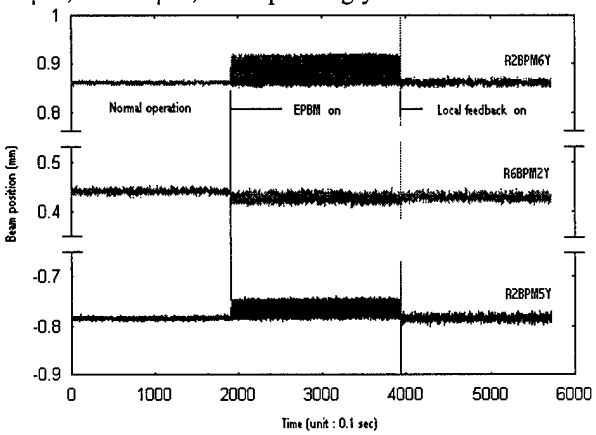



Fig.7. Monitoring beam position fluctuation while EPBM is operating and then is suppressed by local feedback loop.

This indicates that installing the local feedback loop at the beamlines of interest can do a great help in stabilizing beam position at its upstream.

## 4 CONCLUSIONS

In order to fulfill a dynamic EPBM local bump operation requirement, a control electronic system has been developed for this purpose and the test results are presented. The EPBM bump coefficients were determined based on the measured response matrix and calculation. Beam orbit disturbance was observed due to phase mismatch among bumper magnetic field. It is shown that this phase mismatch can be greatly reduced with a built-in compensator in the control electronics. The residual orbit disturbance on other beamline can be further suppressed in cooperation with an associated local feedback loop.

## REFERENCE


[1] See for examples, G. Schutz et al., Phys. Rev. Lett. 58, 737(1987); C. T. Chen, et al., Phys. Rev. B 42, 7262 (1990); T. Koide el al., ibid. 44, 4697 (1991); and the Proc. of the 7th XAFS Conf. In Jpn. J. Appl. Phys. 32, Suppl. 32-2 (1993).

[2] J. Chen, C. S. Chen, C. H. Kuo, K. K. Lin, K. T. Hsu, these proceeding.

[3] C. H. Kuo et al. Conf. Proc. of EPAC96, Barcelona, 10-14 June, 1996. P.1923-1925.

[4] S. Krinsky, J. Bittner, A. M. Fauchet, E. D. Johnson, J. Keane, J. Murphy, R. J. Nawrocky, J. Rogers, O. V. Singh, L. H. Yu, Chap.6 & 7 of AIP Conf. Proc. 249, 1992.

[5] C. H. Kuo, K. T. Hsu, J. Chen, K. K. Lin, C. S. Chen, R. C. Sah, these proceedings.

# A METHOD OF PRODUCING VERY HIGH RESISTIVITY SURFACE CONDUCTION ON CERAMIC ACCELERATOR COMPONENTS USING METAL ION IMPLANTATION

F. Liu and I. Brown, Lawrence Berkeley National Laboratory, University of California, Berkeley, CA 94720 and L. Phillips, G. Biallas and T. Siggins, Thomas Jefferson National Accelerator Facility, 12000 Jefferson Ave., Newport News, VA 23606

*Abstract*

An important technique used for the suppression of surface flashover on high voltage DC ceramic insulators as well as for RF windows is that of providing some surface conduction to bleed off accumulated surface charge. We have used metal ion implantation to modify the surface of high voltage ceramic vacuum insulators to provide a uniform surface resistivity of approximately 5 x $10^{10}$ Ω/square. A vacuum arc ion source based implanter was used to implant Pt at an energy of about 135 keV to doses of up to more than 5 x $10^{16}$ ions/cm$^2$ into small ceramic test coupons and also into the inside surface of several ceramic accelerator columns 25 cm I. D. by 28 cm long. Here we describe the experimental set-up used to do the ion implantation and summarize the results of our exploratory work on implantation into test coupons as well as the implantations of the actual ceramic columns.

## 1 INTRODUCTION

The voltage hold-off capability of a high voltage ceramic insulator in vacuum is poor compared to that of the ceramic material or the vacuum itself. Electronic processes lead to a discharge over the ceramic surface commonly referred to as "surface flashover".[1] The electrons originate from the negative end of the insulator assembly, most often at the "triple junction" (metal-ceramic-vacuum junction). The number of secondary electrons produced per incident primary electron is high (≈10 for aluminum oxide at normal incidence) creating a net positive charge on the ceramic surface which increases the electric field gradient. Consequently the field-emitted current increases yet further. When the gradient exceeds the hold-off voltage in the vacuum, surface flashover results.

After design measures used to reduce flashover such as polished corona rings are exhausted, flashover onset may be further retarded by adding a tolerable level of surface conductivity to the ceramic to bleed the charge away. The Photo Emission Electron Gun [2] for the Injector Test Stand at Thomas Jefferson National Accelerator Facility (Jefferson Lab) requires the application of this technique.

The design voltage for the gun is 500 kV. Two ceramic insulating cylinders, in series, 28 cm in length by 25 cm I. D. are used to stand off this voltage. Most methods for producing bleed coatings do not have high enough resistance for use at these very high electric fields. The excessive energy dissipated would heat the ceramic to unacceptably high temperatures. The coatings on insulators (Figure 1) in the photo emission gun are limited to resistances at the tens of Giga-Ohm level.

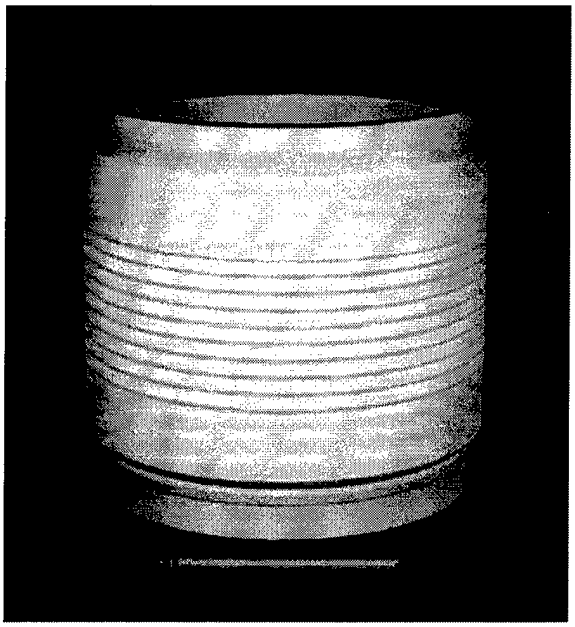


Figure 1
Ceramic Insulating Cylinder

In an earlier version of the gun, a chromium sesquioxide, vanadium pentoxide system [3] was used for the bleed coating. For all insulating cylinders using this process, we found that the resistance values varied widely, were nonuniform and were not able to be adjusted to target values. The technique of metal ion implantation of the ceramic surfaces[4] proved to be a successful alternate technology. The ion implantation process was generally predictable and could be adjusted to target values during the process.

## 2 ION IMPLANTATION

An LBNL broad-beam, multiple-cathode, vacuum arc ion source was used to produce Pt ion beams for the implantations discussed here. The source and implantation facility have been described in detail elsewhere [4-7]. Small implantation targets can be mounted on a radially moveable target holder. A magnetically suppressed Faraday cup that is temporarily moved into the beam path near the target location prior to beginning the implantation run is used to measure the beam current, and the required implantation dose is then accumulated by running for a pre-calculated number of beam pulses. Briefly, in typical operation, the metal ion beam is produced in pulses of 250 or 500 μsec duration at a repetition rate of several (typically 1 to 20) pulses per second. The mean energy of the ions in the beam is usually in the range 50-150 keV, and the beam current

0-7803-4376-X/98/$10.00 © 1998 IEEE

delivered to the downstream target is several hundred mA peak with the mean on-target beam current less than this by the chosen duty cycle, typically of order 1%.

Note that the implantation is done in a broad-beam mode. The diameter of the ion beam formation electrodes ("extractor grids") is 10 cm and the initial beam diameter is almost the same. In this mode of ion implantation, the broad area ion beam propagates line-of-sight from ion source to target; there is no magnetic analysis or beam bending, and the target is implanted over its complete forward-exposed surface at one time, in contrast to the conventional swept, focused beam approach used widely in the semiconductor industry. Important also is that this facility and mode of implantation are accompanied by an 'automatic' charge neutralization feature – the broad area ion beam propagates in a self-produced sea of cold electrons that can provide more than enough neutralization for the potential charge build-up on the ceramic surface by the positive ion beam [8].

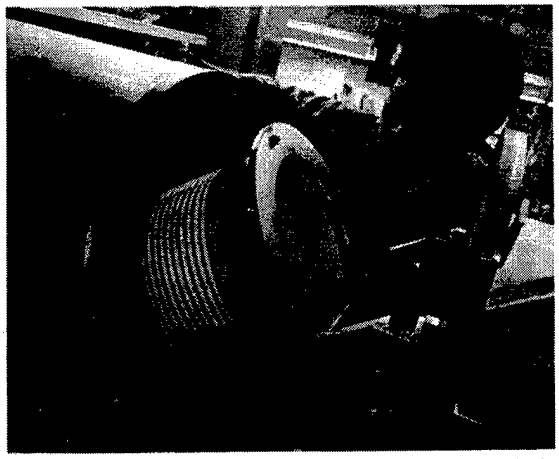


Figure 2, Rotisserie Detail with Ceramic Insulating Cylinder in Implanting Position

For the work described here we fabricated an appendage to the implanter in which the ceramic insulating cylinder was housed and which allowed the cylinder to be continuously rotated while implanted. A rotating cradle (the "rotisserie") held the cylinder at an appropriate angle (35°) to the incident energetic ion flux while continuously, slowly rotating it about its axis so that the entire inside surface was implanted. The mechanism was insulated and high voltage resistance was monitored at selected times during the processing. For this geometry the entire surface area of the cylinder was exposed to the beam and implanted, but in order to maximize the implantation dose symmetry and uniformity we turned the cylinder 180° lengthwise in the cradle halfway through the implantation process.

The type of ceramic used throughout this work was 97% alumina with a surface finish of a few micro inches rms. Ion source extraction voltage was 65 kV, which for the Pt mean ion charge state [6,9] of 2.1 gives a mean ion beam energy of 135 keV. Note that for the 55° angle of incidence, the ion energy normal to the surface is 135cos35° or 77 keV. The source-to-target distance was ~2.5 m for this implantation set-up.

The dc surface resistivity of the samples was measured using a 0-100 kV high voltage power supply and a current meter accurate to a few pA; most of the measurements were done with the sample (either small ceramic coupon or the actual cylinder) in vacuum, and at a voltage gradient of from 1 to 10 kV/cm.

## 3 RESULTS

We first investigated the effect of implantation parameters on the surface resistivity of small ceramic coupons of dimension 1 cm x 2 cm. The metal ion species investigated were Ti, Au and Pt; ion energy was varied from 50 keV to 135 keV; dose was varied from 1 x $10^{14}$ $cm^{-2}$ to 5 x $10^{16}$ $cm^{-2}$; and the angle of incidence of the ion beam upon the ceramic substrate was either 0° (i.e., normal incidence) or 45°; not all cells of this parameter array were tested. The most important and quite basic result from this preliminary exploration was that indeed the surface resistivity could be controlled in this way. Small surface cracks in the ceramic coupons, possibly introduced in the grinding stage of sample preparation and not at all easily visible in the unimplanted ceramic, were found to be a frequent cause of apparent irreproducibility; Interestingly, the cracks were considerably more visible after implantation. The dependencies of the resistivity on ion species, ion energy, and angle of incidence were small (over the range investigated), and the resistivity decreased with increasing implantation dose.

After the work on samples, we chose to do implantation on the cylinders using Pt at 135 keV, and to mount the cylinder at the angle required so as to expose the entire inner surface to the beam. Platinum does not oxidize and is a good cathode material for the vacuum arc ion source. Our small samples indicated (with much scatter) that Pt was slightly more effective than the nearest competitor, gold. Future work would certainly address further the issue of the effect of implanted species.

The surface resistivity as a function of implantation dose, under the conditions of the cylinder implant, is shown in Figure 3. In this processing we monitored the total number of implantation pulses, and the dose as shown in the figure is estimated from the pulse count based on RBS (Rutherford Backscattering Spectrometry) measurements [10] of the Pt dose implanted into small silicon coupons mounted in place of the cylinder during a calibration run. The required resistivity of approximately 50 GΩ/square was achieved for a dose of about 2 x $10^{16}$ ions/$cm^2$. The data point in Figure 3 that shows an apparent rapid drop in resistivity as a function of applied dose seems to be real; we speculate that resistivity tailoring by ion implantation is a complicated physical phenomenon that may lead to a highly non-linear resistivity vs. dose relationship, and that considerably lower resistivities than achieved (and wanted) here may be obtainable. No knowledge of the conductivity mechanism exists, but a negative resistance coefficient with respect to temperature leads to speculation that the mechanism is a semiconductor effect.

We have not measured the Pt ion implantation dose or profile in the alumina. Measurement in the usual way,

by using RBS, is not feasible because of the surface roughness of the alumina, but we can make a good estimate of the profile using the TRIM code [11], which carries out a Monte Carlo calculation of the transport of ions in matter. For Pt into alumina at 77 keV, the range (distance below the surface to the peak of the distribution) is 220 Å and the straggling (HWHM of the distribution) is 44Å

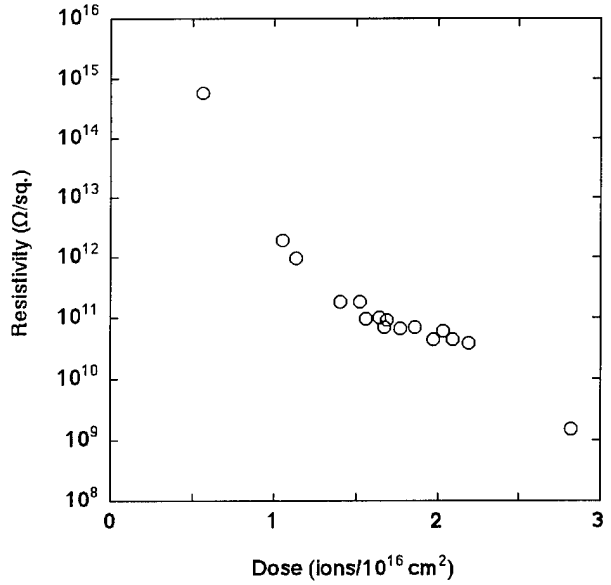



Figure 3 Resistivity vs. Dose

Three "production" cylinders were implanted. Each acquired nearly the desired resistance at 18 GΩ +- 5% (54 GΩ/square). A negative temperature effect was observed with a rise in resistivity of 50% upon cooling from the 60 C implantation temperature to room temperature. The resistance at 20 C should dissipate 3.5 W per cylinder at design voltage, well below a power that could cause a thermal run-away. Two cylinders have been assembled into an insulating column assembly, installed in the gun, baked out at 250 C for several days and subsequently conditioned up to 420 kV. In situ resistance measurement of one cylinder, with vacuum on the inside and room air on the exterior, yielded a value of approximately 13 GΩ. The nearly 1/3 drop is considered an effect of the conditions of measurement and attachment. No voltage dependence was seen in the in situ measurements using voltages of 10 to 100 kV.

Using a conservative approach, the gun has subsequently been run at 350 kV for collection of a data set at this value. (Before upgrade to the new ceramic insulating cylinders, the data sets were taken at 250 kV and 300 kV.) Conditioning the gun at 500 kV+ and operation at 500 kV awaits production of a spare ceramic cylinder set and success at intermediate voltages.

## 4 DISCUSSION AND CONCLUSION

Unlike the original methods tried, Metal Ion Implantation achieved the goal of obtaining the tens of GΩ value resistance required. The accuracy achieved was of a different class than the original methods, far more accurate because of the ability to monitor the decreasing resistance during the process. The method is also well suited to be the final process in a production sequence, where risky value-added features are already applied to ceramics before this high-value-added step. Note that before the continuous resistance monitoring feature was installed on the rotisserie, an implantation attempt undershot the target resistance. The cylinder was recovered to original condition by a simple sanding with diamond grit. The ion implantation method also appears to be well suited to the gun application, withstanding the bakeout and exhibiting no voltage dependence. However, more running experience would allow a firmer statement. The steep negative temperature dependence could result in thermal runaway for applications that have too low initial resistance and inadequate cooling. The investment in hardware and experience is now substantial and the ion implantation group at LBNL is ready to use this method in other applications.

## 5 ACKNOWLEDGMENTS

Work was supported by the U.S. DOE under Contract Number DE-AC05-84ER40150 and the LBNL group was supported by the U.S. DOE, under Contract Number DE-AC03-76SF00098. F. Liu was supported as a visiting scientist at LBNL from Beijing Normal University by the University of California Education Abroad program.

## REFERENCES

[1] R. V. Latham, "High Voltage Vacuum Insulation: The Physical Basis", Academic Press, Inc. (London) Ltd. (1981).

[2] C. K. Sinclair, "A 500 kV Photoemission Electron Gun for the CEBAF FEL", *Nucl. Instrum. Methods* **A318**(1992) p.# 410.

[3] US Patent #3,729,575 granted to Maynard C. Harding & Joseph A. Payne, Litton Systems Inc., filed October 28, 1971, granted April 24, 1973.

[4] S. Anders, A. Anders, I. G. Brown, "Surface Resistivity Tailoring of Ceramic Accelerator Components", Proc. 1993 Particle Accelerator Conf., Washington D.C., IEEE (1993) p.# 1390

[5] I. G. Brown, M. R. Dickinson, J. E. Galvin, X. Godechot and R. A. MacGill, "Versatile high current metal ion implantation facility", *Surf. Coat. Technol.* 84 (1992) 529.

[6] I. G. Brown, "Vacuum arc ion sources for particle accelerators and ion implantation", *IEEE Trans. Plasma Sci.* 21, 537 (1993).

[7] I.G. Brown, A. Anders, S. Anders, M. R. Dickinson, R. A. MacGill and E. M. Oks, "Recent advances in vacuum arc ion sources", *Surface and Coatings Technol.* 84, 550-556 (1996).

[8] F. Liu, O. R. Monteiro, K. M. Yu and I.G. Brown, "Self-Neutralized Ion Implantation into Insulators", submitted to *Nucl. Instrum. Meth. B.*

[9] I.G. Brown and X. Godechot, "Vacuum arc ion charge state distributions", *IEEE Trans. Plasma Sci.* PS-19, 713 (1991).

[10] See, for instance, L.C. Feldman and J. W. Mayer, *Fundamentals of Surface and Thin Film Analysis*, (North Holland, NY, 1986).

[11] J. P. Biersack, S. Berg and C. Nender, *Nucl. Instrum. Meth. Phys. Res.* B59/60, 21 (1991).

# INTERACTIVE TROUBLESHOOTING GUIDE FOR ACCELERATORS

R. Legg, B. Dunham, S. Higgins, R. Kazimi, D. Kehne and T. Oren
Thomas Jefferson National Accelerator Facility, 12000 Jefferson Ave., Newport News, USA

*Abstract*

Modern accelerators face the challenge of supporting increased machine complexity and higher levels of utilization while relying on downsized maintenance and support groups. To improve system availability, reduce reliance on system experts and provide a systematic approach to problem solving, an interactive troubleshooting guide has been implemented for the CEBAF injector at Jefferson Lab. This guide, which uses a tree structure with appropriate hypertext links, traces problems from a set of "symptoms," through a series of diagnostic tests, to a specific corrective action. This guide is used in conjunction with an active parameter monitoring system that is part of the EPICS control system tool kit. The monitoring system generates operator alarms when injector RF or magnet parameters fall outside pre-set windows. Operators receive immediate feedback when injector components vary from their standard values and the troubleshooting guide provides a systematic means to identify and ultimately correct the problem.

## 1 INTRODUCTION

CEBAF, the Continuous Electron Beam Accelerator Facility[1], is a five-pass, recirculating, superconducting RF linac designed to provide a 4 GeV, 200 μA CW beam of exceptional quality. It is made up of an injector, two 400 MeV linacs and nine recirculation arcs having a total beamline length of more than 4.5 kilometers. There are presently over 40,000 control points and more than 120,000 database records in the control system[2].

During commissioning of the injector, problems affecting the electron beam parameters occurred on a regular basis. In order to minimize disruptions to the program, these problems had to be corrected as quickly as possible. To address this need, a group of personnel with injector expertise was assembled and placed on-call 24 hours a day on a rotating basis. Once the commissioning phase was completed, however, the use of accelerator physicists to troubleshoot routine injector problems proved to be an intolerable drain on resources. A way for the operations crews to troubleshoot problems without the intervention of system experts was needed.

The requirements for the system were that it should not require any special knowledge of beam dynamics, it should be easy to use with a point-and-click interface and hypertext links, and it should have an underlying structure that would guide the user from a specific symptom through a set of tests that would help identify the specific problem and, finally, to some corrective action. The goal of the guide was not to eliminate the experts, but to answer the most frequently asked questions that account for 80–90% of the injector problems.

## 2 THE PROCESS

The first step in the creation of the troubleshooting guide was to define a set of symptoms that could then be passed on to the original on-call personnel for "solution." To gather the symptoms a search of the Daily Activity Log, the log book kept by the machine operations group, was conducted. This search led to three broad categories of problems commonly encountered in the injector. 1) an irregular or 'bad' spot on the beam viewer at a dispersed point immediately prior to injection into the first linac, 2) an injector orbit that was offset by more than ±0.5 mm, and 3) "Something's wrong with the injector"—a generic problem category. This last problem usually indicated an odd beam envelope downstream from the injector, suggesting that the injector beam phase space was no longer matched into the first linac.

The second step in the process was to pass the list of "symptoms" out to the experts, who then generated flowcharts that specified a set of diagnostic tests to determine the possible cause for each symptom. As a cross check of the experts, an additional search of the Daily Activity Logs generated a list of actual injector problems that had been encountered in the control room and how they had ultimately been solved.

The next step was to take the flowcharts for diagnosing the symptoms and break them down into steps while seeking commonality between the different flow charts. Once identified, these common elements could be written only once and then, using hypertext links, shared between the various diagnostic tests. This shared module approach led, however, to one long term problem: it made the overall "tree" a hyper-object with a structure that was not intuitively obvious without a diagram. As different people made changes to the tree to upgrade the guide or reflect changes in the injector itself, over time, the inconsistencies grew in number. This non-intuitive structure made maintenance of the guide difficult for new authors assigned to the task.

The result of the flowcharts was a list of the precise procedures needed to diagnose the symptoms. Many of the procedures already existed among the 100 or so that had been written for the commissioning effort, although most were not in the form needed. In those cases, the directories of procedures were searched and the appropriate documents were rewritten. In some cases, new software was written to allow the required tests to be done more easily. Some of the procedures for diagnostic tests were written from scratch. Once written, these procedures went through a formal review process by the operations department and were corrected to reflect the recommended changes. As these modules were

0-7803-4376-X/98 /$10.00 © 1998 IEEE

completed and corrected, they were collated for use in the final tree structure.

At this point, we had a set of written procedures within a tree framework leading from a set of symptoms to possible solutions. Finally, it was time to decide on a delivery system for the troubleshooting guide—a way to get the information to the end user in the control room. We needed a system that allowed hypertext pointers from one document to another and a point and click interface that would be easy for the operators to use. The initial thought was to use the Worldwide Web and HTML to post the troubleshooting guide as a series of linked pages; however, the setup procedures written during the commissioning phase were in Framemaker© and a translation to HTML format would be very time consuming and make updating the documents more cumbersome. If the original procedures were not translated, however, they would not be available to a web browser, and if the operator needed the original procedure they would be forced to open the original word processing application.

While the problem of what document delivery system should be used was studied, a preliminary test of the troubleshooting guide was performed using HTML. A copy of the tree was drawn out by hand and the corresponding HTML files were set up on a local web server. This system was deliberately very crude, with no graphics and little discussion, but it did provide the hypertext pointers and the basic Symptom-to-Diagnostic Test-to-Solution structure. This allowed us to look for dead ends and inconsistencies in the procedures that didn't show up while looking just at the tree or at the procedures alone. This test did not, however, settle the question of how to implement the final version and also raised the issue of change control for the pages in the guide. During the creation of the troubleshooting guide, multiple authors worked simultaneously, with multiple updates occurring in some instances.

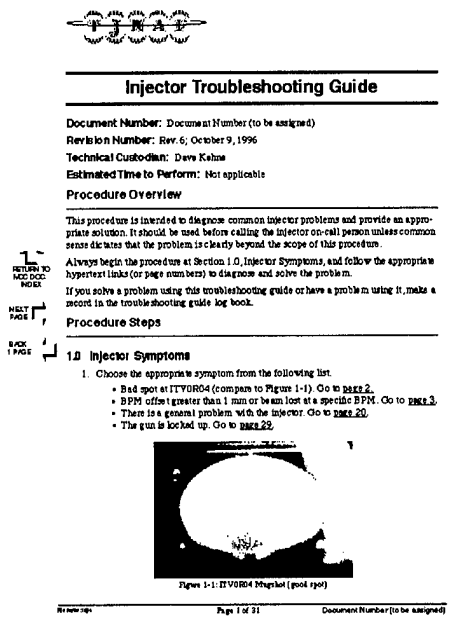
As the prototype system was going through testing, another group was working with the Alarm Handler, an EPICS tool, to generate a system that would passively monitor the signals generated by the injector and send the operators an audible and visual signal when the injector parameters went out of tolerance. The Alarm Handler was already being used to monitor the major accelerator systems during operation, and in its simplest form provided a set of window comparators looking at control signals defined within a tree-like hierarchy. When a signal moves outside a user-defined range, the Alarm Handler trips and the fault propagates up the tree to the top node and sets off an alarm. The injector Alarm Handler differs by comparing the signals in the injector to a pre-defined set of values. It ignores the question of whether the hardware is working properly and is only concerned with whether the signals are at a preset value. The allowed beam orbit through the injector becomes an alarm parameter, along with the magnet and RF settings. The idea was not only to provide a troubleshooting guide to solve problems after they occurred, but to give the operators a monitoring capability that would alarm as the beam or the hardware began to drift away from the nominal settings. This system was implemented and has worked well within its limitations.

## 3 IMPLEMENTATION

The tests of the original HTML implementation of the troubleshooting guide revealed several problems with using the HTML format. There were questions about the stability of HTML as a language, since vendors freely added their own extensions to the language and these extensions were not serviced by all web browsers[3]. There were also concerns about document management, particularly with the large number of image and text files required to create the HTML pages. There was also the issue of control system security if operators were going to access the Worldwide Web from X terminals on the controls subnet. If the guide was made local to the subnet, then no external browser could view it. Finally, in the spring of 1996 the available tools for generating HTML were not well suited to such a large word processing task and long term maintenance of the raw HTML files was seen as a potential problem. To address these concerns, Adobe Acrobat© was adopted to act as a delivery system.

Acrobat is freeware published by Adobe Systems, Inc. and is widely used to distribute on-line documents. This conference's proceedings, for example, will be published using Acrobat. Acrobat runs on most platforms. It handles Portable Document Files (PDF)—an Adobe standard—that are created from any Postscript file using an Acrobat distiller[4]. Acrobat supports hypertext links within the document and uses a controlled file standard. FrameMaker and Acrobat are a powerful combination; hypertext links and cross references created in FrameMaker are automatically converted to hypertext links in the PDF files during the Postscript-to-PDF conversion process. The on-screen version of a PDF document looks just like the final printed version, allowing for off-line review and use of the document. Basic document control elements such as page numbers and header an footer information match the original document, and the fidelity of graphics and type fonts is also maintained. In addition, Acrobat acts as a plug-in for all major web browsers, allowing PDF files to be read as Worldwide Web documents (see Figure 1).

One by one, Acrobat addressed our concerns. Since it uses a proprietary controlled file specification (the PDF file format), unlike HTML, there is no question about the long term stability of the file format and how it will be "extended" by other vendors. Acrobat is widely accepted as an emerging standard in the on-line publishing industry. It leverages the popularity of the Postscript page description language, and provides a convenient, reliable means of converting existing graphically rich document files for on-line display, without having to convert to HTML. Document control becomes much easier because one person controls the distiller that converts the files into PDF format. This person acts as a final quality assurance step in the documentation creation and revision process and provides a level of document



Injector Troubleshooting Guide

Document Number: Document Number (to be assigned)
Revision Number: Rev. 6; October 9, 1996
Technical Custodian: Dave Kehne
Estimated Time to Perform: Not applicable

Procedure Overview

This procedure is intended to diagnose common injector problems and provide an appropriate solution. It should be used before calling the injector on-call person unless common sense dictates that the problem is clearly beyond the scope of this procedure.

Always begin the procedure at Section 1.0, Injector Symptoms, and follow the appropriate hypertext links (or page numbers) to diagnose and solve the problem.

If you solve a problem using this troubleshooting guide or have a problem using it, make a record in the troubleshooting guide log book.

Procedure Steps

1.0 Injector Symptoms

1. Choose the appropriate symptom from the following list.
   - Bad spot at ITV0R04 (compare to Figure 1-1). Go to page 2.
   - BPM offset greater than 1 mm or beam lost at a specific BPM. Go to page 3.
   - There is a general problem with the injector. Go to page 20.
   - The gun is locked up. Go to page 29.

Figure 1-1: ITV0R04 Mugshot (good spot)

Page 1 of 31 Document Number (to be assigned)

Figure 1

control by tracking revisions and maintaining consistency between documents.

The authors have access to the original word processor documents in their original format and thus can use familiar, powerful document editing and formatting tools when document revisions are necessary. When changes are needed, the original document is updated and then reconverted to a PDF file—a short, very predictable process that avoids the unpredictable, labor-intensive conversion to HTML. The question of network security is also no longer a problem since Acrobat runs in a stand alone configuration on the controls network. These same PDF files can also be viewed remotely from a web browser. The only thing passed between the networks are the read-only PDF files.

## 4 PROBLEMS

There are two types of problems associated with the injector troubleshooting guide and the injector Alarm Handler: 1) the elements in the injector do not reproduce, and 2) the injector itself changes. The first problem is typified by the performance of a 100 keV 90° bending magnet. This magnet runs at such a low field that it is very difficult to remove hysteretic effects at the 0.01% level necessary to insure that the orbit through the magnet is reproduced on a day-to-day basis. This error, though small, changes the downstream orbit, which then sets off the Alarm Handler. To prevent this, the values in the Alarm Handler are updated when the device setpoints are changed, and efforts continue to improve the reproducibility of the devices.

The second problem occurs as a result of ongoing work to make the injector more useful and reliable, such as the addition of a polarized electron source. Such changes can fundamentally change the tree structures of the troubleshooting guide and, since no single person is responsible for maintaining the troubleshooting guide, there is a need for periodic general updates of the document. As changes are made to the underlying hyper tree, it is important to carefully consider how these changes will affect the procedure as a whole. Past difficulties with maintaining the troubleshooting guide have lead to the creation of an overall flow chart of the document. Though it is never seen by the operators using the troubleshooting guide, the flow chart is maintained as a way to identify potential problems with the hypertext link structure and simplify document maintenance.

## 5 RESULTS

The injector Alarm Handler and the troubleshooting guide have proven to be a very successful combination and have reduced the amount of time spent troubleshooting the thermionic injector. This trend is evidenced the fact that the number of physicists supporting the thermionic injector has been cut in half without affecting injector performance and reliability.

## REFERENCES


[1] Work supported by USA DOE#DE-AC05-84ER40150

[2] K. White, D. Kehne, "Operational Experience with the CEBAF Control System", Proceeding of ICALEPS 1995

[3] Jesse Berst, "Three Overlooked Problems That Threaten the Internet", ZDNet AnchorDesk, Nov. 25, 1996

[4] Acrobat Distiller, Adobe Systems Incorporated, 1585 Charleston Road, Mountain View, CA 94039

# RUNTIME ACCELERATOR CONFIGURATION TOOLS AT JEFFERSON LABORATORY

M. G. Tiefenback, L. Doolittle, and J. F. Benesch,
Thomas Jefferson National Accelerator Facility,
12000 Jefferson Avenue, Newport News, VA, USA, 23606

*Abstract*

RF and magnet system configuration and monitoring tools are being implemented at Jefferson Lab to improve system reliability and reduce operating costs. They are prototype components of the Momentum Management System [1] being developed. The RF is of special interest because it affects the momentum and momentum spread of the beam, and because of the immediate financial benefit of managing the klystron DC supply power. We describe present and planned monitoring of accelerating system parameters, use of these data, RF system performance calculations, and procedures for magnet configuration for handling beam of any of five beam energies to any of three targets.

## 1 INTRODUCTION

The Continuous Electron Beam Accelerator Facility (CEBAF) consists of two 1497 MHz recirculating electron linacs and the associated beam transport lines. Each linac provides a nominal energy gain of 400 MeV, for a final beam energy of 4 GeV after five acceleration passes. The injector provides three interleaved 499 MHz electron pulse trains, one for each of the three experimental halls. The machine typically operates at a fixed linac energy for weeks at a time, with most of the magnets in the system held at a constant field during such times. The major exceptions are orbit feedback correctors and the magnets and RF separators used for selecting the number of acceleration passes for the pulse train destined for each hall.

The present implementation is file-based, using a collection of awk, perl, and tcl scripts [2]. The user interface unifies these from an operator's perspective, but has been used so far only for generating RF and magnet parameters. Configuration data generated is downloaded by operators with the standard tools used during accelerator operations.

## 2 TYPICAL CONFIGURATION TASKS

The configuration needs of the accelerator, generally in order of frequency of execution, are:

- Configure linac gradient distribution respecting:
  - RF cavity performance
  - RF system line power consumption
  - available klystron power
- Switch beam destinations
- Switch pass count of beam to a hall (coarse momentum control)
- Provide variable acceleration per pass (fine momentum control)

We have delivered beam from our polarized source for checkout of the source and polarimeters, and will soon be adding polarization to the configuration tasks.

The overall goal is to provide a unified interface with minimal execution time and error rate for:

- RF reconfiguration
- changing beam destination or pass count
- changing acceleration per pass
- setting on-target polarization

The most mature of the configuration tools is the RF gradient calculation. It is used to determine usable gradients for the RF cavities at the expected total beam loading, which are then used to distribute gradient along the linacs.

## 3 REGIONS OF THE ACCELERATOR

The accelerator is naturally divided into regions successively occupied by the beam as it is accelerated and extracted (see Figure 1). Interlocks for devices such as valves and vacuum pumps must be enabled while carrying beam, but may be disabled for maintenance. Information defining the active portions of the machine for system configuration is exactly that needed to support an advisory (and possibly control) interface with the machine protection system.

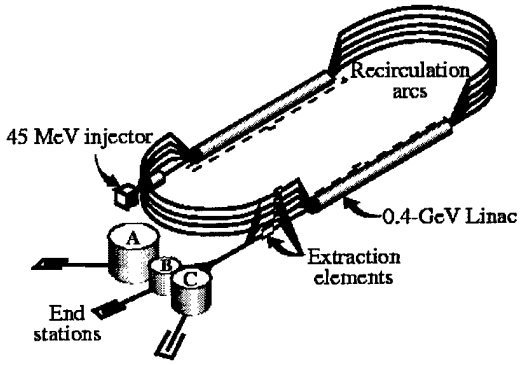



Figure 1: The accelerator is naturally divided into the segments between branch points occupied by the beam on its path to the experimental halls.

With respect to magnet configuration (generally parallel to the machine protection system), these regions are:

- injector (momentum, current, polarization on target)
- linac quadrupoles (matched to RF acceleration profile)
- beamline for each of the first four acceleration passes to the extraction septum

0-7803-4376-X/98 /$10.00 © 1998IEEE

- extraction line (with RF separators) for each of the first four passes
- fifth pass transport including the final extraction line
- destination switching in the beam switchyard
- hall transport lines (variable momentum)

## 4 RF HANDLING

The primary goal of line power management is provision of adequate beam power within constraints set by the electrical utility's demand charge schedule, rather than incremental reduction of energy use. Excessive power demand increases the billing rate for all site power usage. The power usage is adjusted by a combination of reducing the klystron DC supply voltage and reducing the cathode current (using the klystron modulation electrode). The system characterization required for efficient use of the available capacity also results in early identification of weak components. Reducing the klystron cathode current also allows reduction of the filament temperature without running the cathode in emission-limited conditions. This increases tube lifetime and decreases maintenance costs and frequency of online failures.

### *4.1 Limitations on RF Gradient*

The calculation of maximum gradient for each RF system outlined below uses both generic and individually measured characteristics. Measurements for individual RF systems include the rms acoustic vibration level and loaded $Q$. Generic dependences on klystron voltage and cathode current are used to extrapolate from measured conditions to other configurations. The information required for RF configuration is:

- Klystron DC HV and cathode current
- Active cavity complement
- Required energy gain per linac
- Anticipated beam loading
- Limiting gradient for each cavity

Assuming that the cavity accelerating voltage $\vec{E}$ itself is fixed, the fields in the cavity satisfy the vector equation:

$$\left(1 - j\frac{\omega_d}{\omega_f}\right)\vec{E} = 2\vec{K}\sqrt{\frac{R_c}{l}} - R_c\vec{I} \qquad (1)$$

where $\vec{K}$ is the incident wave amplitude in $\sqrt{\text{Watts}}$, $R_c$ is the coupling impedance $Q_L \cdot (r/Q)$, $\omega_d$ is the (time varying) frequency error, and $\omega_f = \omega_0/2Q_L$. The detuning angle $\phi$ is given by

$$\tan(\phi) = \frac{-\omega_d}{\omega_f}$$

The circulating beam current $\vec{I}$ (the sum of current for each experimental hall times the pass count) is used to calculate the maximum gradient each RF system can support.

For any given machine setup, the available gradient $|\vec{E}|$ is computed on a cavity by cavity basis, given an assumed current $|\vec{I}|$. The power available from the Klystron is derived by scaling from available measurements by (cathode voltage)$^{5/2}$, and then derated if the cathode current is reduced by use of the modulation electrode of the klystron. The value of $\omega_d/\omega_f$ is conservatively estimated to cover three sources of detuning: 1.) 3.5 times the measured rms acoustically driven detuning for that cavity, 2.) a 10° allowance for the deadband of the mechanical tuner control and 3.) an 8° allowance for drift and other tuner control loop errors. The machine is assumed to be operated with perfect cresting ($\vec{I} \parallel \vec{E}$).

The final value for available $\vec{E}$ for each cavity is limited to the maximum rated gradient for that cavity. These maximum usable gradients are downloaded into the control system as limits on the gradient setpoint for each RF system. The actual gradient setpoints are subsequently calculated online [3] as needed, the operators providing any additional limits appropriate from time to time (due to 2K region waveguide vacuum degradation, or instability of the RF regulation, as common examples). All operational cavities not used for feedback energy stabilization are set to the same fraction of their available gradient. An empirical scaling factor input by the operators for all cavities in a linac (typically between 1 and 1.01) allows for beam setup even with some of the cavities off-crest. The total energy available from all cavities in the linac is compared with the desired machine setup; we call any available $E$ beyond that required for setup of each linac our headroom. Headroom values less than 10% of the desired linac energy gain have been operationally difficult, given the remaining uncertainty in the calculations and demands on this reserve as cavities are taken offline for maintenance.

### *4.2 Additional RF Optimizations*

Minimizing the momentum spread of the beam delivered to the experimental halls requires on-crest acceleration of the beam in each RF cavity. Once the crested phase setpoint is determined, the cavity must be run near resonance for greatest efficiency of coupling RF power into the beam. Both of these parameters are measured periodically at CEBAF [4, 5], as the regulation systems for both have residual drifts from thermal effects and aging of components.

The relative phase of the RF drive field $\vec{K}$ and cavity field probe signal $\vec{E}$ in Eq. 1 is a monitored as the detuning angle. For cavities properly crested and on resonance, $\vec{K}$, $\vec{E}$, and $\vec{I}$ are aligned. The beam loading dependence of the detuning angle allows for passive monitoring of the difference of these two parameters during normal operation. Interruption of the delivery of as little as 100 $\mu$A of total circulating current, whether due to a system fault or deliberately, causes a shift in detuning angle from which the phase relationship of the beam loading and the klystron drive power may be calculated. This provides individual monitoring for each cavity in the system. Independent drift of either parameter can be detected, and the periodic cresting and cavity tuning measurements mentioned above will

detect accidentally coincident drifts. Shifts in both of these parameters have been observed in the past due to degraded cabling or to internal RF module faults. Early detection and correction are very desirable.

## 5 MAGNET HANDLING

The control parameter used for the magnets is the straight-line path integral of magnetic field (G cm) for dipoles or of gradient (G) for quadrupoles. Future plans are to provide a beam momentum value for each point in the system, so that the control system can calculate the required magnet current from geometrical parameters such as lens strength or bending angle. Scaling the system to various energies is expected to be possible using a master template. As we develop experience with the machine at different energies, we expect to be able to separate the corrections required for static perturbations like the earth's field. We have had ia few occasions to use linac energy gains other than 400 MeV, and scaling all magnetic fields with the beam momentum has provided a good starting point for final tuning.

### *5.1 Beam Switchyard and Recombiners*

During most accesses to the experimental halls, we divert beam to the beam switchyard (BSY) tuning dump for use in commissioning tests or in system checkout and retuning. At other times, we prepare for delivery of beam of a different energy to an experimental target by changing the number of acceleration passes for the beam before it is directed to the BSY dump. These switchings of beam destination and pass count are simple in concept but have been demanding in practice. The switchyard consists of a vertical recombiner mirroring the spreader near the extraction elements at one corner of the main accelerator (see Fig. 1) and a 3-aperture Lambertson magnet which directs the beam to the three experimental hall transport lines.

By design, the vertical dipoles of the recombiner should be set for fixed bending angles for the beam, with switching among the various destinations effected by referring to a lookup table for the necessary settings. We have found anomalous steering variations of the scale of 50 microradians at the exit of each of the similar recombiners feeding the linacs, potentially associated with variations in the relative timing of cycling the drive currents of these closely spaced dipole strings for remanent field control. These (along with distributed but identified problems with the individual quadrupole and steering magnet channels) are the largest remaining sources of irreproducibility in the machine setup. We are presently searching for sources of coupling between the various magnet strings in these areas, and hope soon to have fixed steering settings for these critical regions.

## 6 SUMMARY

The CEBAF accelerator will be delivering beam simultaneously to all three experimental halls in the coming weeks, and needs comprehensive system monitoring and reliable setup tools. We are identifying the remaining uncontrolled parameters in the system, instituting monitors for early identification and correction of systems which are prone to drifts, and removing the last major obstacles to high reliability operation of CEBAF for nuclear physics research. The processes unifying the configuration interface for major accelerator subsystems (magnets, RF, and the machine protection system) will ultimately be greatly improved over the prototypes being implemented, but those future developments will be significantly aided by the multi-system integration being done now.

## 7 ACKNOWLEDGEMENTS

This work is supported by the United States Department of Energy under contract DE-AC05-84-ER40150.

## 8 REFERENCES

[1] "Mom-management.doc" by B. Dunham, G. Krafft, and R. Legg, and "Software Requirements for the Momentum Management System" by Michael Tiefenback; CEBAF internal development specifications.

[2] Awk, perl, and Tcl/Tk are standard Unix scripting and interfacing tools, freely available. Perl and Tcl are becoming available on DOS/Windows platforms, as well.

[3] "Rapid Application Development Using the Tcl/Tk Language," J. van Zeijts, Proceedings of the 1995 Particle Accelerator Conference and International Conference on High-Energy Accelerators.

[4] "Automated RF Cresting at CEBAF," M. G. Tiefenback and Kurt Brown, Tech. Note CEBAF-TN-96-020; "Beam-Based Phase and Gradient Calibration of CEBAF RF Systems," these proceedings.

[5] "Parallel SRF Cavity Tuning by MO Modulation," L. Doolittle, CEBAF internal procedure.

# HIGH POWER ELECTRON BEAM DUMPS AT CEBAF

M. Wiseman, C. K. Sinclair, R. Whitney, M. Zarecky, Thomas Jefferson National Accelerator Facility, 12000 Jefferson Avenue, Newport News, Virginia 23606 U.S.A.
and R. Vetterlein, Stanford Linear Accelerator Center (retired)

*Abstract*

The CEBAF accelerator produces a very small emittance CW electron beam of up to 200 μA average current. The resulting beam power, up to 1 MW at 5 GeV, and the very high beam power density, pose challenging problems for beam dump design. Two styles of high power dumps have been developed. The first, rated for 100+ kW, is used for beam tune-up and accelerator commissioning. The beam power is entirely contained in metal in this dump, minimizing the problems associated with radioactive water handling. Full power 1 MW dumps are used with the experimental halls. In these dumps, one-third of the beam power is directly absorbed in water. Both dump designs require the beam to be rastered when the smallest beam sizes are used. Design details for each of these dumps will be presented.

## 1 COMMISSIONING AND TUNE-UP DUMP

The commissioning and tune-up dumps at Jefferson Lab were designed to help commission the Continuous Electron Beam Accelerator Facility's first linac. The same design was also employed as a tune-up dump for commissioning the entire accelerator. One dump is located at the end of the first linac and can be used to test CEBAF's injector and first linac to its full current rating of 200 μA and 600 MeV, or 120 kW. The second commissioning and tune-up dump is located in the beam switchyard just upstream of the experimental halls, which allows full accelerator operations without sending beam to one of CEBAF's three end stations. It is rated at 6 GeV and 100 kW of beam power. The full energy ratings of these dumps are given in FIGURE 1. Note that below 600 MeV the dump is current limited to protect the first copper window. The northeast stub dump has been in operation since early 1993. The beam switchyard dump has been in operation since the fall of 1994 and has been used at up to 5500 MeV and 100 kW of power. Further description of these dumps can be found in CEBAF Tech Notes [1,2].

A cross sectional view of the commissioning and tune-up beam dump is given in FIGURE 2. The dumps consist of a copper window section, 87 cm of drift space with an aluminum jacket, a solid aluminum core section and finally 29 cm of copper. The entire dump is edge cooled by two separate deionized (DI) water circuits. The first circuit supplies 0.3 L/s for the copper windows and rear copper section, and the second, 1.3 L/s for both the aluminum sections. Two individual circuits are used to avoid any galvanic corrosion resulting from copper ions and aluminum. An EGS run for 0.6 and 4.0 GeV into the dump is shown in FIGURE 3.

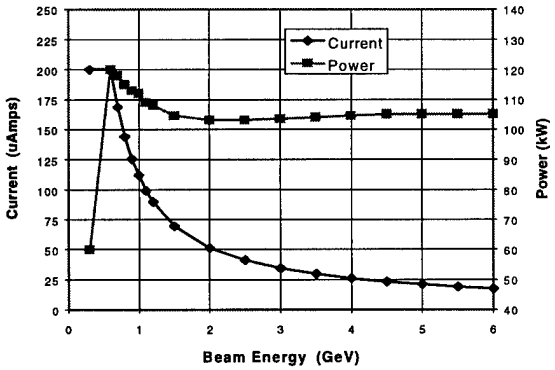



FIGURE 1. Current and power ratings for the commissioning and tune-up dumps.

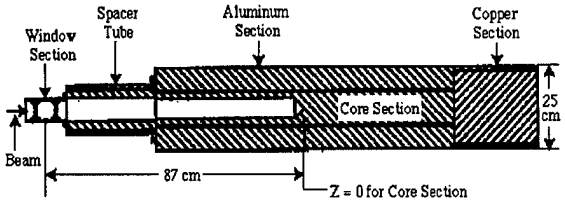



FIGURE 2. Cross sectional view of the commissioning and tune-up dump.

The window section consists of two 0.3 cm thick edge cooled windows brazed into a stainless steel jacket. The window section serves three purposes. First, it seals the accelerator vacuum. Second, the two windows scatter the beam before it reaches the main aluminum body, eliminating the possibility of melting the main body. Finally, the two windows provide a trapped gas interlock to detect a possible burn through of either window. The space between the two windows is filled with pressurized helium gas. If the first window fails, the accelerator vacuum will spoil and quickly shut down the beam. If the second window fails, a pressure transducer will detect the loss of pressure and provide an alarm. The beam is rastered on a 2 cm diameter circle at

0-7803-4376-X/98/$10.00 © 1998 IEEE

60 cps to help alleviate any possibility of any burn through. With rastering and a 200 μA beam, the average temperature in the window is 110 C.

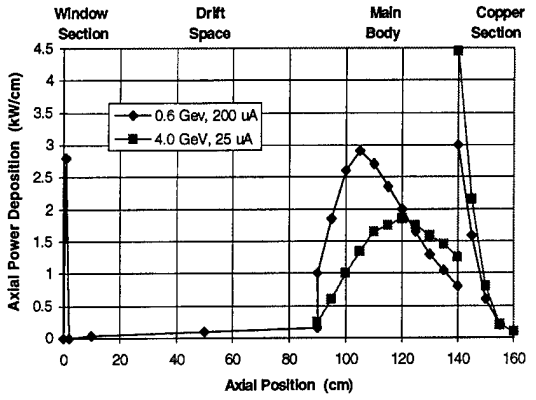



FIGURE 3. Axial power deposition in the commissioning and tune-up dumps.

The aluminum drift space region provides room for the beam to spread radially to lower the power density in the main body. The section is filled with helium gas at just over 1 atm, less than the pressure in the window section. Only scattered beam is intercepted in this region. The main aluminum body absorbs most of the beam energy. Aluminum was used for the main body to allow the beam power at 600 MeV to be distributed along the length of the dump so that the peak heat fluxes into the water were at conservative levels, no greater than 100 w/cm$^2$. For the worst case beam power of 120 kW, 200 μA and 600 MeV, the peak temperature in the aluminum section at shower maximum is predicted to be 480 C, 12.5 cm into the body of the aluminum. At the start of the main body, temperatures are predicted at 300 C, about half the melting point of aluminum.

The copper section at the rear of the dump absorbs up to 27 percent of the power at 4 GeV. This section was added at the end of the dump, were the beam is fully dispersed, to reduce the overall length of the dump. It consists of a solid cylinder of copper with machined water channels on the diameter, brazed into a stainless steel jacket. This section is not thermally stressed, with maximum heat fluxes to the water at less than 60 w/cm$^2$ at 4 GeV.

## 2 END STATION BEAM DUMPS

Two of Jefferson Lab's three experimental halls, Halls A and C, are capable of running experiments at CEBAF's design energy of 4 GeV and 200 uA. The third, Hall B operates at a much lower current. In order to safely dissipate the beam in the high power end stations, beam dumps capable of absorbing 1 MW, 5 GeV and 200 μA are used. These dumps are also capable of dissipating energies up to 10 GeV with reduced currents so that the maximum power is held constant at 1 MW. The dumps are housed at the end of 33 m, heavily shielded tunnels after the end stations. Each dump is cooled by a closed loop DI water circuit. The Hall C dump has been in service since the fall of 1994 and the Hall A dump since the fall of 1995. To date, the dumps have been used at 4.05 GeV and up to 180 μA, or 728 kW.

The cross sectional view on an end station beam dump is given in FIGURE 5. The dump consists of an internal aluminum plate heat exchanger surrounded by an all aluminum pressure vessel. Heat exchanger designs from 30% to 100% water were explored with the final design being a 50/50 ratio by volume. The final design was decided on to seek a practical maximum in the fraction of total beam power absorbed in the metal. There are 20.8 rl of aluminum and 3.1 rl of water in the heat exchanger so that 70 % of the power is absorbed directly in the aluminum. This design minimizes tritium production, hydrogen evolution, and short term activation in the cooling water, as well as the long term activation trapped in the DI filters.

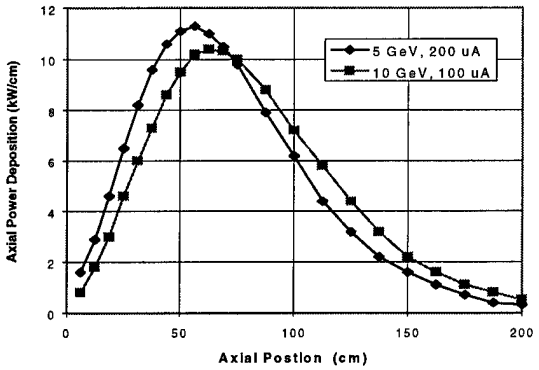



FIGURE 4. Average derivative axial power for 50% Al, 50% water by volume beam dump.

An EGS run for 5 GeV and 10 GeV beams into a 50% Al, 50% water by volume beam dump is given in FIGURE 4. During operations the beam is either rastered, or scattered so that the spot size on the dump face is a minimum 4 cm diameter to an 8 cm diameter maximum. The beam dump was designed based on a beam spot of 4 cm. The maximum power deposition occurs approximately 55 cm into the dump and is 11.3 kW/cm average, or 15.4 kW/cm in the aluminum. Using the EGS calculations, the thicknesses of the plates were sized so that the maximum heat flux to the water was less than 200 w/cm$^2$. The plates range in size from 0.48 to 2.54 cm. For the first 70 cm of the dump, the 5 GeV beam governs the plate thickness, with the remainder of the heat exchanger design based on the 10 GeV case. Peak temperature in the aluminum plates is

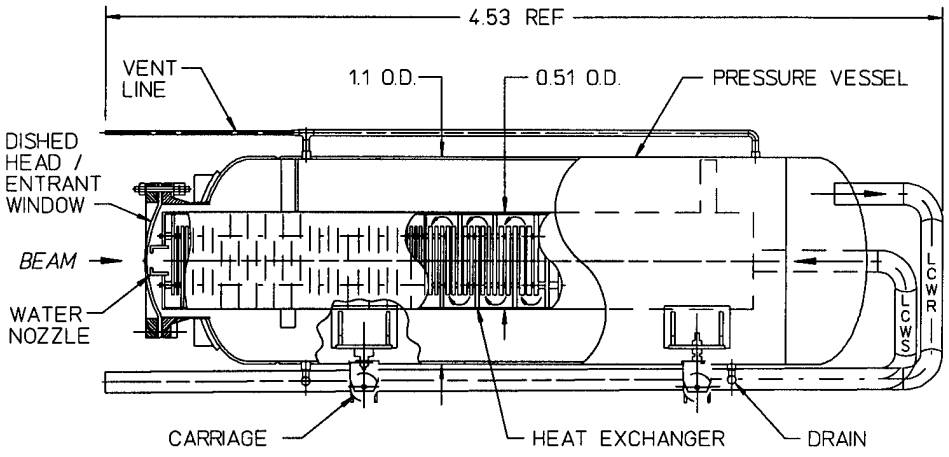



FIGURE 5. Cross sectional view of the end station beam dump.

190 C. The flow rates through the heat exchanger range from 0.9 to 2.3 m/sec with a volumetric flow of 13.9 L/s, yielding a 17.6 C rise in the water at 1 MW. A 7.6 cm nozzle at the end of the heat exchanger focuses the cooling water at 3.6 m/sec onto the entrance window of the dump. The water is then returned to the rear of the dump before being returned to the pump building.

The pressure vessel, as well as the heat exchanger, is made entirely of 6061 aluminum in the T6 condition whenever possible. Aluminum was chosen because the radiation levels in aluminum are about one-eighth of those of stainless steel within two to seven days after running beam. The vessel was designed to the ASME Pressure Vessel Code, Section VIII for an internal pressure of 1 MPa gauge at 93 C with an extra 0.16 cm external corrosion allowance added due to concerns of nitric acid evolution in the dump tunnel. In practice the dump pressures are between 0.34 and 0.41 MPa gauge.

The beam window of the dump is a fine grain forged 6061-T6 flared and dished head. The fine grain forging was used to reduce radiation damage effects which propagate at the grain boundaries [3]. It has a code required nominal thickness of 1.6 cm which is reduced to 0.95 cm for the central 10 cm of the head where the beam enters the dump. The central part of the head was reduced in thickness to lower the amount of beam energy deposited in the metal. At 1.6 cm, the calculated temperature in the window would be above that allowed for the corresponding pressure vessel stresses. At 0.95 cm, the expected power in the window from a 200 μA beam is 1.6 kW with peak temperatures in the window below 150 C. The membrane stresses in the window are then within those allowed by the code for that temperature. The window is sealed using a Helicoflex type gasket and bolted with 3.8 cm 2024-T6 aluminum studs and silicon bronze bolts. Aluminum studs were used in order to match the thermal responses of the rest of the aluminum vessel.

## 3 SUMMARY

Two types of beam dumps have been in use at Jefferson Lab for several years. The intermediate power dumps have been used successfully through their entire design rating. The end station beam dumps have seen three quarters of their design power and plans are in place to commission them to their full current rating this year.

## 11 ACKNOWLEDGMENTS

This work was supported by the U.S. DOE under contract number DE-AC05-84ER40150.

## REFERENCES

[1] Sinclair, C.K. and Vetterlien, R.J., "CEBAF Intermediate Power Beam Tune-up Dump", CEBAF TN# 93-003.

[2] Sinclair, C.K. and Vetterlien, R.J., "Operation of the Intermediate Power Beam Dumps at High Beam Energies", CEBAF TN# 94-049.

[3] Conversation with Dieter Walz, Stanford Linear Accelerator Center.

# DIAGNOSIS OF INDIVIDUAL CELL FREQUENCIES IN A COUPLED CAVITY CHAIN WITHOUT INTRODUCING OBJECTS INTO THE CAVITY

Ni Yi, Xiao Liling, Tong Dechun, Tian Bo, Jin Qingxiu and Huang Yuanzhong
(Dept. of Engineering Physics, Tsinghua Univ., Beijing 100084, P.R.China)

*Abstract*

In this paper, a new method that can diagnose the cell frequencies in a cavity without a perturbing probe is presented. The cell frequencies and couplings between cells are estimated in terms of the measured pass-band performance. This method will simplify the tuning processes and make the tuning of a sealed cavity possible. It has been well checked with some numerical examples.

## 1. INTRODUCTION

To research and manufacture a linear accelerator, it's necessary to tune the cavity carefully. In order to determine the tuning direction of each cell, the ordinary means is to insert the perturbing probe into the cavity to measure the frequency cell by cell. Therefore, it takes much time and work. It would be more inconvenient to tune a long cavity or a non-uniform one. Moreover, if a sealed cavity is out of shape while sealed or installed, its detuned state can't be dignosed with the perturbing object. On the other hand, for a superconducting cavity, its field flatness is strictly demanded, it requires more careful tuning. But when the cavity is under operating conditions and in a bath of liquid helium, it is much more complicated to measure the field with a perturbing probe. With the development of computer science, numerical computation and intelligent instrument, it will be a signficant task to develope a method that can estimate each cell's frequency without a perturbing probe.

At the early of 1980's, while testing a superconducting cavity in CERN, E.Hable and J.Tuckmantel developed a method based on coupled resonant model that can calculate each cell's frequency through measured resonant frequency of the cavity[1]. Their cavity was a uniform single period one consisting of 5 cells. Because of superconducting, loss of each cell can be ignored. The varying range of each cell's frequency is small, so it was treated as a first order perturbing problem. In article[2], a method using measured resonant frequency and its relevant field distribution to calculate each cell's frequency was described. This method can reduce tuning work, but can not be used to a sealed cavity.

Now a general object is discussed, which has a long or non-uniform chain with loss of each cell considered. The fundamental method is by means of the passband information got from RF network analyzer and computer data acquisition system to calculate each cell's frequency. The method has been well checked by some numerical examples.

## 2. FUNDAMENTAL METHOD

As shown in Fig.1, the pass-band performance of the cavity is measured from RF network analyzer. The frequency span and step can be adjusted as needed. The measured results are illustrated by the pass-band performance curve $\rho(F)$. And the measured data are analyzed by the PC computer.

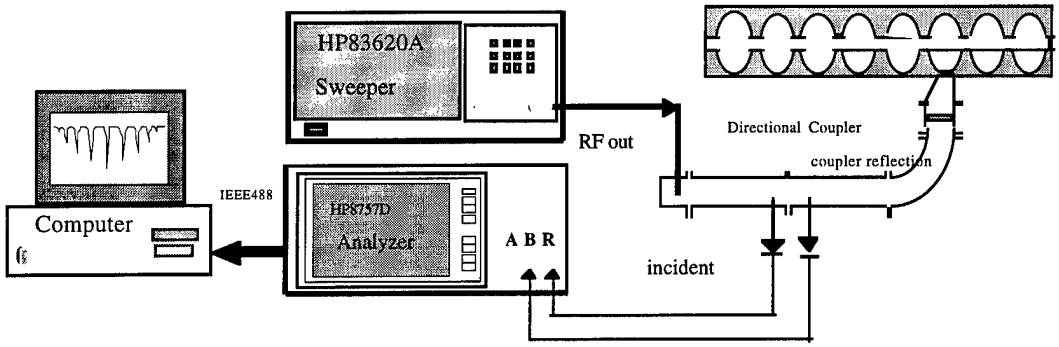



Fig.1 The data acquisition system of the pass-band performance of a coupled cavity chain

0-7803-4376-X/98/$10.00 © 1998 IEEE

In general, each pass-band performance of *N*-cell accelerating structure consists of *N* dispersion modes. A typical pass-band performance curve $\rho(F)$is shown in Fig.2.

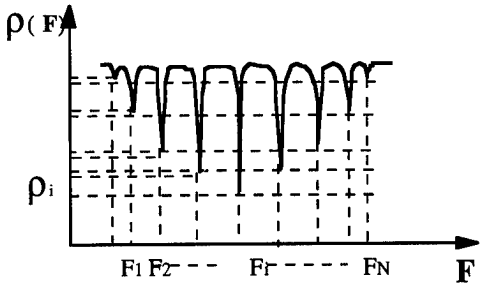



Fig.2 The typical pass-band performance curve $\rho(F)$ of coupled cavity chain

Of course, the pass-band performance $\rho(F)$ can be also calculated directly. The fundamental method is based on the equivalent circuit model of a coupled cavity [3] (shown in Fig.3)

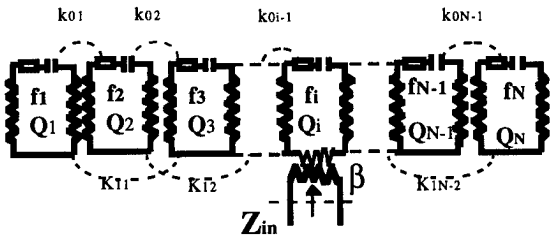



Fig.3 Equivalent circuit of a coupled cavity

$f_n$ and $Q_n$are the resonant frequency and quality factor in the n[th] cell *(n=1,2,.....N);* $k_{0n}$ *(n=1,2,.....N-1)* and $k_{1n}$ *(n=1,2,.....N-2)* are the nearest and next nearest neighbour couplings between cells, respectively. $\beta$ is the coupling factor between the input waveguide and the resonant cavity.

If $f_n, Q_n, k_{0n}, k_{1n}$, $\beta$and the position of coupler are known, $\rho_c(F)$can be calculated by solving the algebraic eigenvalue equations of the coupled cavity chain. In the following, the letters with the subscript "c" or "m" represent the calculated or measured results, respectively. The letters with bar are used to espress the related row vectors.

$$\vec{f} = (f_1, f_2, \ldots\ldots f_N) \quad \vec{Q} = (Q_1, Q_2, \ldots\ldots Q_N)$$

$$\vec{k}_0 = (k_{01}, k_{02}, \ldots\ldots k_{0N-1})$$

$$\vec{k}_1 = (k_{11}, k_{12}, \ldots\ldots k_{1N-2})$$

$$\vec{F} = (F_1, F_2, \ldots\ldots F_N) \quad \vec{\rho} = (\rho_1, \rho_2, \ldots\ldots \rho_N)$$

Now we want to solve the instrinc parameters of each cell from the measured characteristic parameters of coupled cavity chain. In mathmatical sense, this is a reverse problem of matrix's eigenvalue. If the problem can be sovled, diagnosing the cell frequencies of cavity without introducing any objects into cavity is possible.

The previous method to solve the problem was only suitable to a short single- or bi-periodic structure[4]. The cell parameters are $(f_0, Q_0, k_0, k_1)$ or $(f_1, f_2, Q_1, Q_2, k_0, k_{11}, k_{12})$. For a superconducting structure, the quality factor in each cell is very high and the loss can be ignored. If the number of cells *(N)* is more than that one of the cell parameters in a cavity, the least-squares method can be used to estimate the cell frequencies and couplings between cells from the measured *N* dispersion frequencies $\vec{F}_m$,. In this paper, a method to be suitable for a more common structure is developed, in which the measured pass-band performance $\rho_m(F)$ and the dispersion modes $\vec{\rho}_m, \vec{F}_m$ are used to estimate the cell frequencies and couplings between cells. A special computer method and program are described in next section.

## 3. DESCRIPTION OF CALCULATING METHOD

In order to simplify the numerical process and consume less time, at the beginning, it is supposed that $\vec{k}_1$ and $\vec{Q}$ are known, only *2N* parameters $(\vec{f}, \vec{k}_0, \beta)$ need to be found.

The following goal function is defined,

$$\varepsilon = \sum_{i=1}^{N} (F_{ci} - F_{mi})^2 + w \sum_{i=1}^{N} (\rho_{ci} - \rho_{mi})^2$$

where W is a weighted factor.

In our calculating program Newton[5] and Simplex[6] Methods are combined. Therefore, this program has such advantages as wide initial data, quick convergence and high precision.

First, a set of guess values $\vec{f}, \vec{k}_0$ and $\beta$ with a wide scale are taken as the initials of Simplex method. According to the error crition ($\varepsilon < EPS1$) or the limit number of iterations ($MOF$), the solutions that are close to the true one were found and taken as the initials of Newton method. Then the more accurate solutions were determined. If the divergence appear in Newton method, Monte Carlo (MTC) method will be used as a back-up tool. Because different groups of $\vec{f}, \vec{k}_0, \beta$ may get same resonant frequency and SWR, the measured pass-band performance $\rho_m(F)$ was used. If the error $\Delta\rho$ is larger than Err, the Scale and cri in Simplex method will be modified and a new cycle begin. At last, the set of paremeters $(\vec{f}, \vec{k}_0, \beta)$ whose $\rho_c(F)$ satisfy demand are found and printed out. The flow chart is shown in Fig.4.

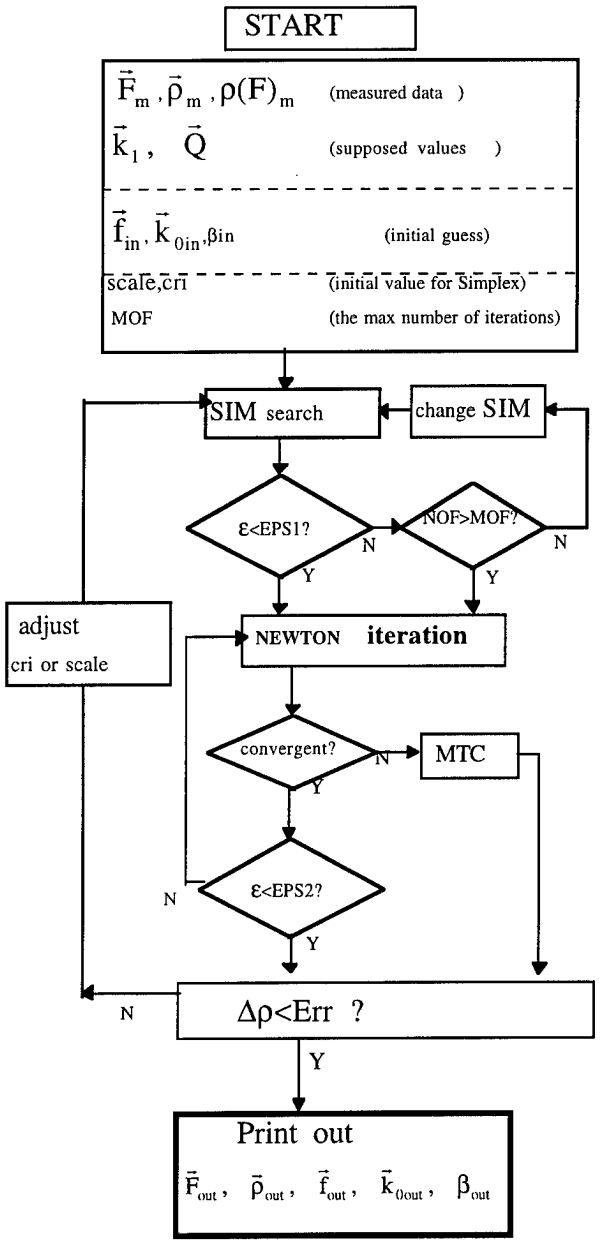



Fig.4 The flow chart of computer program

First, the method is checked by a theoretical value. The cell parameters in a S-band 11-cell non-uniform chain are known. From the matrix of coupled circuit equations consisting of these elements, the pass-band performance, resonant frequencies and related SWR are solved. Then, using these calculated characteristic information to estimate the cell parameters of the cavity, the results were agreement with the given one in advance. The max error of each cell's frequency is 210KHz..

Next, a 6MeV S-band model cavity consisting of 11 cells was analyzed. The cell parameters and the characteristic informance have been measured. Using the method, the cell frequencies and couplings between cells were estimated from the measured characteristic informance. Comparing the estimated data and the measured data, the max error of each cell's frequence is about 900KHz (measuring error<1MHz). If the $\vec{k}_1$ and $\vec{Q}$ are as unknown values and need to be diagnosed, a more precision solution can be obtained.

## REFERENCES


[1] E.Hable et al, "Tuning of a Superconducting Accelerating Cavity Under Operating Conditions" CERN/EF/RF81-5, 1981.

[2] J.Sekutowicz, et al., "A Different Tuning Method for Accelerating Cavities"

[3] D.E.Nagle et al, "Coupled Resonator Model for Standing Wave Acclerator Tanks" The Review of Scientific Instruments, Vol. 38, No.11,1967

[4] S.O. Schriber "Fitting of an Ordered Set of Mode Frequencies" Master Thesis Chalk River Nuclear Laboratories ,1970

[5] W.H.Press, et al., "Numerical Recipes in C", The Art of Scientific Computer Second Edition, Cambridge University Press 1988,1992

[6] J.A.Nelder, et al., Computer Journal, Vol.7.,1965

# A NEW MEASUREMENT METHOD OF THE DELAY LINE LENGTH IN THE X-BAND DELAY LINE DISTRIBUTION SYSTEM (DLDS)

F. Tamura, University of Tokyo, Tokyo 113, Japan, and
H. Mizuno, KEK, Tsukuba, Ibaraki 305, Japan

*Abstract*

In order to control the driving RF phase at the input of the accelerating structure of X-band linear collider main linacs, it is necessary to measure the length of the long TE01 mode delay lines of 40-80m. A new measurement scheme by using the low frequency resonant mode of the TE01mode delay line was proposed. The delay lines have the tapered guide on its both ends, thus the low frequency resonant mode around 2GHz can be the measure of the delay line dimensions. The operational principle and the elementary characteristics of this measurement method such as, sensitivity, and other basic design parameters are presented.

## 1 INTORODUCTION

Delay Line Distribution System (DLDS) is an RF pulse compression equivalent sysyetm[1]. In DLDS, long circular wave guides are used as the part of RF power distribution systrem, and RF power must travel through these long delay lines to drive the accelerating structure where RF crest synchronize to the linac beam. In X-band linear collider, allowable RF phase deviation to the beam is about or even less than 1-degree to clear the energy spread of 0.2%. This limit is determined by the energy acceptance of the final focus system and also by the physics requirement [2,3,4]. This phase diviation limit correspond to the temperature change of 0.08 degree Celsius in case of TE01 mode 118.1mm circular Cu waveguide. Table 1 shows the thermal expansion coefficient and corresponding temperature change for TE01 mode in the guide. Even with Invar that is the typical low thermal expansion material, this temperature limit is 0.6 degree. Considering the size of the delay line and the scale of the linear collider, it is clear that some measurement of the delay line length and some phase control are necessary.

| | $\alpha = \frac{1}{l_0}\frac{dl}{dT}$ | Allowable $\Delta T$ (for 40m) |
|---|---|---|
| Cu | $1.65 \times 10^{-5}$ | 0.08 deg. |
| Invar | $2 \times 10^{-6}$ | 0.6 deg. |

Table 1: Thermal expansion of material

## 2 MEASUREMENT PRINCIPLE AND BASIC PARAMETERS

### *2.1 Measurement principle*

Delay lines have the tapered circular guide on their both ends that are connected to the mode convertor from rectangular TE10 to circular TE01. Thus, this delay line works as the resonant cavity for the lower frequency than the cut off of these tapered guide. This resonant mode parameters such as the resonant frequency, the phase change of the reflected wave etc., can be the measure of the dimension change of the delay line.

Figure 1. shows the conceptual illustration of this resonant mode measurement. Low frequency RF signal is fed into the delay line that works as a resonant cavity at this frequency. Observing the shift of the resonant mode frequency and/or the phase shift of the reflected wave from the delay line, change of the delay line length could be measured.

As the X-band high power mode in DLDS is expected to be an axial symmetric TE01 mode, TE11

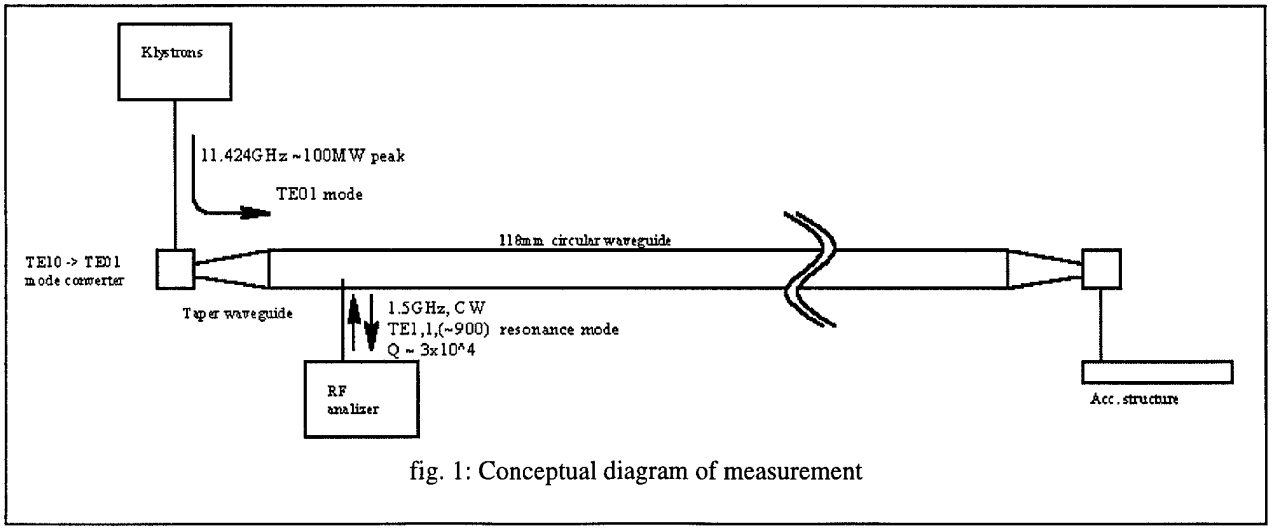



fig. 1: Conceptual diagram of measurement

0-7803-4376-X/98/$10.00 © 1998 IEEE

dipole mode was chosen as the low frequency resonant mode of the delay line. Also, single mode operation by possible in using TE11 mode.

### 2.2 *Parameters*

Severtal parameters of the low frequency mode were calculated in case of 4/3 DLDS of JLC x-band main linac [4]. Two delay lines are 118.1mm circular waveguide of 80m and 40m respectively. For calculations, following points were assumed, (1) Tapered parts were ignored, ie. for the resonant mode calculation, both ends are assumed as being shorted. (2) temperature distribution along the delay line was assumed as uniform. (3) Dimension change of the line was also assumed as uniform and both ends were free for expansion.

For the 2.25GHz TE11,900 mode of 80m 118.1mm diameter circular delay line, $Q_0$ was calculated as $\sim 40000$. The conductivity of Cu was assumed as $\sigma = 5.6 \times 10^7$ mho per meter.

Figure 2 shows the X-band phase deviation (dimension change ofthe line) vs. phase change of the reflected resonance mode frequency. The sensitivity and the amplitude of the reflected wave strongly depend on the coupling coefficiet $\beta$, and reach zero and infinity respectively at the critical coupling, $\beta = 1.0$. Figure 3 shows the coupling coefficient vs. reflected power ratio. Considering the reflected power and the sensitivity, $\beta = 0.5$ was chosen as the operating point of this method. At this point, 10% reflected power is expected. And sensitivity, which is defined as $\left|\Delta\phi_{reflected} / \Delta\phi_{X-band}\right|$, is sufficient (about 8) at this point.

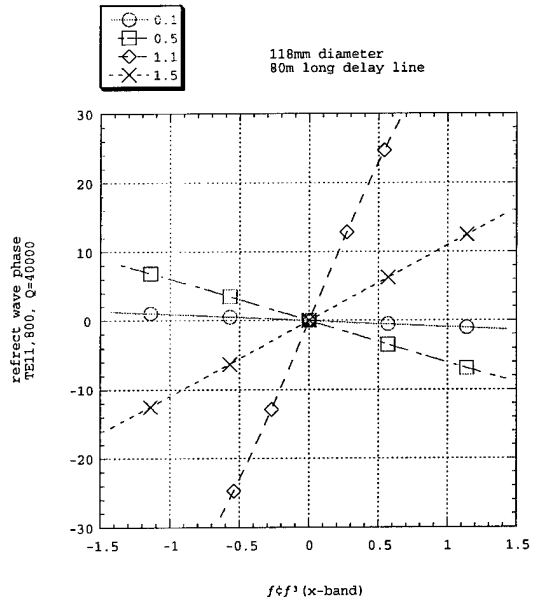



fig. 2: Phase deviation of X-band pulse vs. phase change of reflected wave. 1 degree of X-band corresponds to 70 micro meter lengh change.

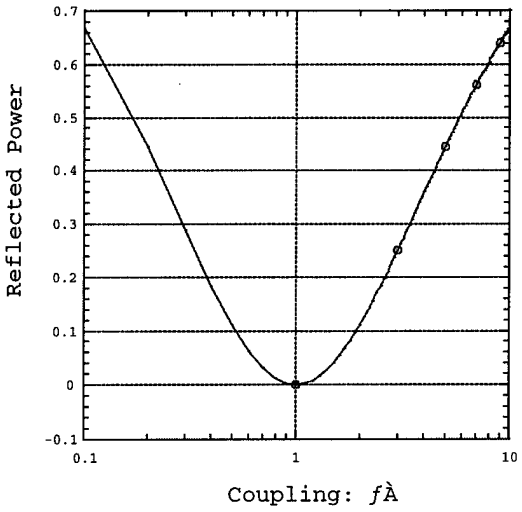



fig. 3: Coupling vs. reflected power

## 3 SIMULATION AND PRELIMINARY MEASUREMENT

Low power measurement set up with the 40m long and 69mm diameter circular wave guide system with two tapered guide and mode convertor is under preperation. The coupling slot of the TE11 resonant mode of the line must be seperated from the TE01 X-band mode. Figure 4 shows the HFSS model of the coupling slot.

SLED II theory shows the the coupling coefficient of the long line is represented by the reflection coefficient of the coupling S, as follows [5],

$$\beta = \frac{Q_0}{Q_{ex}} = \frac{-\ln s}{2\tau}$$

where:

$$Q_0 = \frac{\omega D}{4\tau},$$

$$Q_{ex} = -\frac{\omega D}{2 \ln s},$$

$\tau$ : Attenuation of wave running guide between both ends.

$s$ : Reflection coefficient into macthed circular wave guide.

$D$ : Time that run pulse between both ends.

From this, coupling coefficient of 0.5 corresponds to the s=0.92 for the coupling slot to the matched circular waveguide.

Preliminary calculation by HFSS showed that this coupling slot in Figure 4 has only small effect to the TE01 X-band mode in propagating in the circular guide. This problem must be surveyed more carefully.

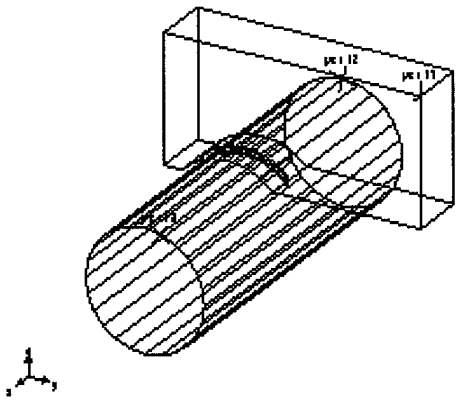


fig. 4: Monitor coupler design

## 4 DISCUSSIONS

As long as the preliminary calculation showed, this new measurement method has sufficient sensitivity and possible in principle. Several problems are to be considered as follows.

1) TE11 mode has dipole symmetry, therefore the probable rotation of its symmetry plane due to the deformation of the circular waveguide should be surveyed. This problem could be important especially in the very long resonator like this case.
2) Signal seperation from X-band TE01mode high power pulse. The preliminary calculation showed the posiibility that the design choice of the coupling slot can achieved this seperation. Also gating the X-band driving pulse could block the unnecessary X-band signal. X-band high power pulse has 500nsec width and 150Hz reptation rate, so we can spend about 5msec for this measurement. Time constant of the delay line resonator is about 4micro sec, so 5msec is enough to this measurement in principle.
3) High power related matters, such as a discharge around the coupling slot for TE11 mode, Mode purity degradation of the TE01 X-band mode and resulting loss of the power are to be surveyed.

## 5 ACKNOWLEDGEMENTS

The authors would like to thank Dr. Takata and Dr. Higo for fruitful discussions and suggestions.

## REFERENCES

[1] H.Mizuno, Y.Otake: 'A New RF Power Distribution System for X-band Linac Equivalent to an RF Pulse Compression Scheme of Factor 2n', Proc. LINAC94, 1994
[2] 'JLC-I', KEK Report 92-16, p.205,1992
[3] 'Zeroth order design report for the Next Linear Collider', SLAC Report 474, chapter 11, 1996
[4] 'JLC Design Study Report (draft)', 1997, will be printed
[5] P.B.Wilson, Z.D.Farkas, R.D.Ruth: 'SLEDII: A New Method Of RF Pulse Compression', Proc. Linear Accelerator Confference, p.204, 1990

# REVIEW OF COMPACT COMMERCIAL ACCELERATOR PRODUCTS AND APPLICATIONS

Y. Jongen, Ion Beam Applications (IBA), Louvain-la-Neuve, Belgium

*Abstract*

Application-oriented accelerators are generally built commercially, and they often emphasize other qualities than the accelerators for research. These accelerators are generally specialized for a specific application, and are therefore very simple and inexpensive to operate. The author will review some products and applications in the field of medicine, such as the production of radio-isotopes and radiotherapy, as well as in the industrial field, such as sterilization applications and the modification of materials.

## I INTRODUCTION

Historically, particle accelerators were developed initially for nuclear, then for particle physics research. From this research resulted applications of accelerators in the field of medicine and industry. These application-oriented accelerators are generally built commercially, and they often emphasize other qualities than the accelerators for research. Research frequently requires energies or beam qualities at the limit of the existing technologies. Accelerators for research offer the largest flexibility in term of particles and beam properties, but are more complex, more expensive and often require large and highly qualified staff to operate and maintain them. In contrast, most applications are done with low to moderate energy protons or electrons, but often with large average beam power. The accelerators are generally specialized for a specific application, and are therefore very simple and inexpensive to operate. In the field of medicine, typical applications include the production of radio-isotopes for medical diagnostic or the production of electrons, protons or fast neutron beams for cancer therapy. In the industrial field, high power electron beam are used for sterilization and for the modification of materials.

## II PRODUCTION OF RADIOISOTOPES FOR IMAGING AND DIAGNOSIS IN NUCLEAR MEDICINE

Radioisotopes are essential in diagnosis and study of the human functions. The access to the full range of radioisotopes used in nuclear medicine is vital to the early diagnostic and treatment of a wide variety of problems including cancer and heart disease. Various radioisotopes are produced [1] with cyclotrons, according to the organ that must be represented: Gallium 67, Iodine 123, Thallium 201, among others. To produce such radioisotopes, a medium energy cyclotron is a suitable device. In Europe, in the USA and in Japan, commercial companies operate several cyclotrons in the same facility. Many important hospitals and clinics are now also equipped with cyclotrons producing radioisotopes for their own use or for a distribution on a regional scale.

All this is possible because of the high degree of automation, reliability and simplicity characterising the cyclotrons used nowadays for radioisotope production. The evolution of the cyclotrons dedicated to this application is quite interesting [2]. The first cyclotrons produced commercially for the production of medical r.i. were "classical", positive ion, isochronous cyclotrons, similar to their counterparts built for nuclear physics research, where the beam was extracted using an electrostatic deflector. The heat dissipation limits in the deflector septum limited the extracted beam power to a couple of kW, but higher intensities, typically several hundred μA were available on internal targets. The Cyclotron Corporation (TCC), based in Berkeley (Ca), produced between 1968 and 1984 in excess of 30 cyclotrons based on this technology. A major step was made in the early 80's when TCC proposed a 42 MeV cyclotron accelerating negative ions, produced by an internal P.I.G. source, and extracting by stripping. Extracted beam currents exceeding 200 μA up to 40 MeV were available. Thanks to the stripping extraction, variable energy extracted beams could be obtained in a fixed field, fixed frequency cyclotron. The simultaneous extraction of two beams was also, in principle possible. However, the use of an internal ion source meant a poor vacuum in the cyclotron accelerating tank, and significant amounts of beam were lost in the median plane by stripping on the residual gas. The need to deal with these large beam losses resulted in a quite complex design of the dees and of the R.F. systems, and resulted, at least in the beginning, in a lower reliability. This cyclotron was, initially, a commercial success. Six CP42's were ordered and built, even before the prototype was fully tested. Delays in the commissioning of these cyclotrons contributed eventually to the bankruptcy of TCC. After this significant failure, negative ion technology was rejected by radioisotope producers for some time, in favor of more classical positive ion isochronous cyclotrons, like the MC40 model, made by the Scanditronix company in Upsala.

0-7803-4376-X/98./$10.00 © 1998 IEEE

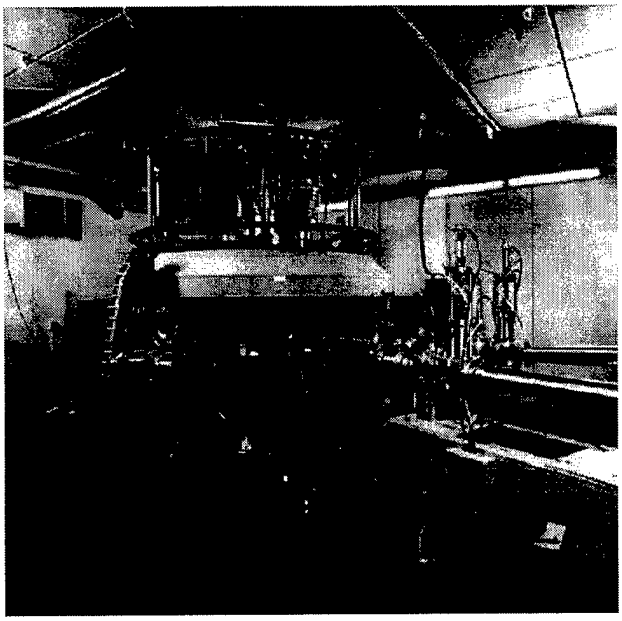


Fig. 1. A CYCLONE 30 cyclotron manufactured by IBA

The next major step in radioisotope production cyclotrons was the introduction, in 1987, by IBA, of the CYCLONE 30. It is a 30 MeV, fixed-field, fixed-frequency, $H^-$ cyclotron with extraction by stripping, dual beam and variable energy. The first major improvement of this model was the use of an external, multicusp ion source for the production of the negative ions. The ions are injected axially into the cyclotron magnet, so that the neutral gas released by the ion source can be pumped externally. The second major improvement was the introduction of the "deep valley" magnet design, combining the advantage of solid pole and separated sectors cyclotrons, and allowing to improve significantly the power efficiency of the accelerator. Typically, previous positive ion cyclotrons were using 300 kW of electricity to get 3 kW of extracted beam (1% power conversion efficiency), while the CYCLONE 30 required only 90 kW of electricity to produce 15 kW of extracted beam (16% power conversion efficiency). The CYCLONE 30 was the first cyclotron to demonstrate the possibility to have a beam loading exceeding 50% of the total R.F. power. Today, the CYCLONE 30 is the world standard for radioisotope production. A total of 17 CYCLONE 30 have been sold up to now by IBA. Since a number of years, another company, Ebco Technologies, is also proposing this type of cyclotron. Two units of their TR30 are installed around the world.

The first CYCLONE 30's used a 2 mA external multicusp ion source made by IBA, and a 25 kW output R.F. final amplifier. The extracted beam intensity 350 μA guaranteed, with actual maximum currents varying from machine to machine between 450 μA and 600 μA. There is also some interest for higher intensities, so today several high intensity versions of CYCLONE 30 are also proposed, based on more powerful RF amplifiers, four high pumping speed cryopumps, and higher intensity ion sources (7 mA or even 25 mA of $H^-$).

## III CYCLOTRONS SPECIFICALLY DESIGNED FOR POSITRON EMISSION TOMOGRAPHY CENTRES

Positron Emission Tomography (PET) is a powerful diagnostic tool at the forefront of modern medical imaging. PET images biological function and physiology instead of anatomy. It uses short-lived radioactive isotopes ($^{11}C$, $^{13}N$, $^{15}O$, $^{18}F$) which can be produced by low-energy cyclotrons (<20 MeV) accelerating protons and/or deuterons.

A cyclotron of the type of those presented in the above paragraph may also be used to produce the radioisotopes needed for PET, but the very short life-time (a few minutes half-life) of most radioisotopes used in PET makes it convenient and appropriate to place the isotope production equipment very close to the scanners. Moreover, lower energies are used compared to the 20 - 30 MeV typically needed to produce radioisotopes for nuclear medicine. A range of turn-key systems have therefore been developed by a number of companies, including targets and automated chemistry modules in addition to cyclotrons, and specifically covering each segment of the PET market. These include large manufacturers of medical equipment such as General Electric or Siemens/CTI, as well as accelerator-dedicated companies such as IBA [3] or Ebco.

Typical energies for this application are in the range of 10 to 18 MeV. Some of the cyclotrons accelerate only protons, while others produce both protons and deutons. Most of these accelerators can be self-shielded and accelerate negative ions. The extraction is done by the stripping method. Several targets can be used, located either internally or externally. Typical maximum extracted currents vary between 50 and 100 μA. The systems are fully automated, from cyclotron operation to radiochemistry, with a particular emphasis on targetry and chemistry.

## IV HIGH INTENSITY CYCLOTRONS FOR THE PRODUCTION OF RADIOISOTOPES FOR BRACHYTHERAPY

In addition to the radioisotopes used for imaging and diagnosis in nuclear medicine and PET, some radioisotopes are used for cancer therapy. The beam currents needed for the production of these isotopes are much higher and are generally expressed in milliampere. In 1992 IBA was asked to develop a very high intensity, 18 MeV cyclotron for the production of the radioisotope $^{103}Pd$. This radioisotope is marketed, in small sealed sources, for example for the local treatment of prostate cancer, by the company Theragenics in Atlanta (Ga). It can be produced by a (p,n) reaction on Rhodium, a good material for internal target. Because of the low reaction yield, the production of the $^{103}Pd$ isotope for cancer treatment requires a proton current in excess of one milliampere, at an energy of 15 to 18 MeV. An internal target being acceptable for this application, IBA designed a very high current positive ion, internal target cyclotron: the CYCLONE 18+. This cyclotron has demonstrated the possibility to provide continuous, unattended operation at

2 mA on target for one week irradiation's. An interesting feature of this cyclotron is the beam loading factor, reaching 80% of the total R.F. power, with only 20% being used to maintain the accelerating field. A 7 mA current was observed during factory tests on a beam dump at lower energy (the maximum current was actually limited by the melting of the beam dump, not by the ion source or space charge limits) [4].

## V ACCELERATORS FOR CONVENTIONAL RADIOTHERAPY

Externally produced photon beams, or X-rays, contribute to more than 80% of all radiotherapy treatments. In addition, electron-beam therapy is used in 10 to 15 percent of cases. These beams are currently produced mainly by rf linear accelerators, which have today a dominant place on the world market of medical accelerators for external beam radiotherapy. According to [5], the total number of radiotherapy electron accelerators was around 4000 in 1996. This success can be explained by the effectiveness of the treatment and by the fact that conventional radiotherapy is the less expensive method of cancer treatment compared to other modalities such as surgery or chemotherapy for example.

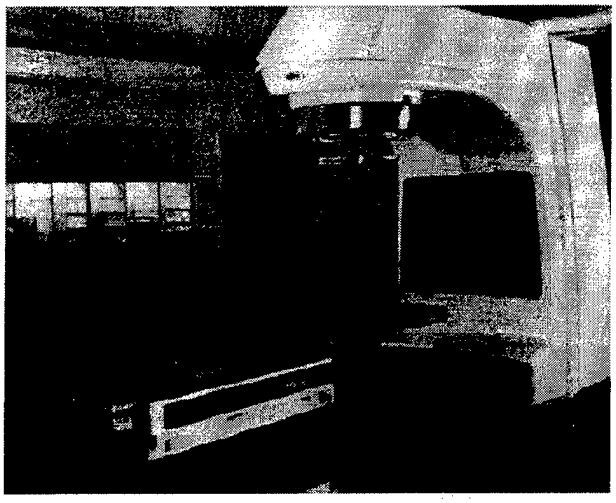


Fig. 2. RF linear accelerator manufactured by Varian [5]

The design of the first generation of Linacs in the mid-1950 was based on the in-line position of the accelerating waveguide in the movable treatment head [5]. In the sixties, the available machines had an horizontally mounted accelerating waveguide, with the advantage of generating higher energy beams but needing a 90° bending magnet. Later on, in the seventies, waveguides with a travelling wave were replaced by structures using a standing wave. This made it possible to increase the linear gradients and therefore to obtain smaller accelerators for the same energy. In the first models the accelerating structure was still horizontal and used a 270° achromatic magnet, but nowadays, some models use in-line waveguides, thus avoiding the need for bending magnets. The full rotating head of these machines include several devices such as X-rays conversion targets, collimators, dosimetry devices, etc. Multi-energy accelerators are now also available, offering the possibility of producing two photon energies as well as several electron energies. Typical values are 6 and 10, 15 or 18 MV for X-rays, and six electron energies between 4 and 20 or 22 MeV. Well known manufacturers include companies such as Varian, Siemens, Philips and General Electric, among others.

## VI ACCELERATORS FOR PROTON AND NEUTRON THERAPY

### *A Proton Therapy*

The advantage of protons in radiation therapy, especially their ballistic accuracy, is widely acknowledged. However, the development of proton therapy as a clinical tool has been hampered by the complexity, the size and the cost of proton therapy facilities. Indeed, the medical use of protons require high energy accelerators not adapted, up to now, to the hospital environment. Pioneering institutions had to work with complex, inadequate equipment designed for research in nuclear physics. Today things are changing and a number of proton therapy systems specifically designed for in-hospital operation are under installation or already in operation. One of them is the synchrotron-based proton therapy system at Loma Linda, California. It was jointly built by a team of the Fermi National Accelerator Laboratory in Chicago, Illinois, the Loma Linda University Medical Center and SAIC (Science Applications International Corporation), a private company based in San Diego. The Loma Linda system includes an accelerator as well as a beam transport system and a number of gantries allowing to irradiate the tumour from any direction. The accelerator system includes an RFQ injector (2 MeV) and a synchrotron delivering a 70 to 250 MeV pulsed beam.



Fig. 3. A 235 MeV cyclotron for proton therapy

However, the first proton therapy system specifically designed for in-hospital operation and to be installed as a commercial system is a cyclotron-based system. IBA has indeed integrated the technologies developed for its low and medium energy cyclotrons into a high energy system dedicated to proton therapy. The objective was to meet all the clinical specifications of a state-of-the-art proton

therapy facility in the most simple, reliable and cost effective manner. The main elements of the IBA integrated system are the following [5]: a compact 235 MeV isochronous cyclotron, a short energy selection system transforming the fixed energy beam extracted from the cyclotron into a variable (70 - 235 MeV) energy beam, one or more isocentric gantries fitted with a nozzle, a system consisting of one or more horizontal beam lines, a global control system including an accelerator control unit and three independent but networked therapy control stations, a global safety management system independent of the global control system, and a robotic patient positioning system. Two of these systems are presently under installation: one at the Massachusetts General Hospital of the Harvard Medical School in Boston, MA (see [6] as well as another paper presented at this conference), and another one at the National Cancer Center near Tokyo, in Japan.

*B Neutron Therapy*

Neutron therapy is more effective than conventional radiation for certain advanced tumours because it has the ability to kill tumours cells which are low in oxygen and often become resistant to the usual forms of radiation. A prototype of a Neutron Therapy System developed by Dr. Blosser at the Michigan State University is in operation since several years at the Harper Hospital in Detroit, MI. The system, which is also commercialised by IBA, consists of an ultra-compact, superconducting cyclotron which rotates around the patient. The cyclotron is indeed mounted on a rotating gantry allowing 360 degrees rotation around the patient. It accelerates deuterons up to 50 MeV to produce neutrons on an internal Beryllium target.

## VII INDUSTRIAL APPLICATIONS WITH ELECTRON BEAMS

Electron beams are used in industry for several applications including the sterilization of medical disposable, the improvement of properties of polymer materials, and food treatment. The energy of the beam, together with the product density, determines the thickness of the products which can be treated. At a fixed energy, the treatment capacity will depend on the power of the beam. The energy of an electron accelerator is therefore a key parameter for the classification of the several types of accelerators used in this field.

At very low energy (few hundreds keV), typical accelerators are single gap machines. These include machines with point cathodes and scanners which scan the beam over the surface of the product to be treated, and linear cathode machines which emit electrons from a linear cathode irradiating the product over its entire surface. Another development is the WIP (Wire Induced Plasma) system in which a stream of ions generate in a plasma secondary electrons which are consequently accelerated. The advantage of these single gap accelerators is the fact that they are self-shielded, have a small size, and produce high beam currents. They are well adapted for many surface and thin layer applications.

At low energy (say up to 3 MeV), multi-gap accelerators with electron beam tubes and scanners are used. Different high voltage generating principles can be used. Typical accelerators in this energy range include ICT (Insulated Core Transformer), dynamitrons and Cockroft-Walton generators. Well known commercial companies in this field include High Voltage Engineering, Radiation Dynamics and Nissin-High Voltage, among others. The machines are larger than those used in the very low energy field, and they need concrete radiation shielding. Some of them produce high power beams (100 kW). A typical application in this low energy range is the crosslinking of several types of industrial components (cables, pipes, ...). Accelerators in this energy range are the classical equipement in the electron beam market, with more than 100 machines in operation.

At medium energy (between 3 and 5 MeV), most of the available accelerators are of the dynamitron or the Cockroft-Walton types. Output power levels are in the range of ten to hundred kW. These machines require meter thick concrete shielding and are typically used for crosslinking and also for sterilization of packaged medical disposable products.

The high energy category includes energies between 5 and 10 MeV. Up to a few years, typical machines in this energy range were Linacs such as those proposed by AECL, Canada. These Linacs are RF devices producing pulsed beams. Today, installed systems are limited to moderate powers (10 to 50 kW). Since three years, however, IBA entered the field of high energy, high current electron accelerators for sterilization and other industrial applications with its RHODOTRON [7]. This new accelerator concept, developed at the CEA in Saclay (France), was licensed to IBA. RHODOTRON accelerators are based on an innovative concept of using a single "recirculating cavity" to provide high energy (up to 10 MeV) / high power (up to 200 kW) electron beams, with high electrical efficiency. Three Rhodotron models are now available, ranging from 25 to 150 kW guaranteed beam power at 10 MeV. The Rhodotron technology opens the doors to industrial applications for which high energy / high current electron beams are needed: cross-linking of plastics, polymerization of composite materials, sterilization of medical products, food treatment, etc.



Fig. 4. A RHODOTRON accelerator from IBA

## REFERENCES


[1] S. M. Qaim, "Nuclear data relevant to cyclotron produced short-lived medical radioisotopes", Radiochimica Acta 30, pp. 147-162, 1982

[2] Y. Jongen *et al.*, "High Intensity Cyclotrons for Radioisotope Production", Proceedings of the 14th International Conference on Cyclotrons and their Applications, Cape Town, South Africa, 1995, pp. 115-119

[3] M. Abs *et al.*, "The IBA PET-dedicated Cyclotrons: Main Features and Improvements", Proceedings of the 14th International Conference on Cyclotrons and their Applications, Cape Town, South Africa, 1995, pp. 120-123

[4] Y. Jongen, "Extremely High Intensity Cyclotrons for Radioisotope Production", proceedings of the EPAC'94 Conference, London, 1994

[5] W. Scharf *et al.*, "Medical Accelerators in Radiotherapy: Past, Present and Future", Physica Medica - Vol.XII, N.4, 1996

[6] Y. Jongen *et al.*, "The proton therapy system for the NPTC", Proceedings of the 4th European Conference on Accelerators in Applied Research and Technology, Zürich, August 1995

[7] Y. Jongen *et al.*, "Rhodotron accelerators for industrial electron-beam processing: a progress report", Proceedings of the EPAC'96 Conference, Sitges, Barcelona, 1996

# A HIGH CURRENT TANDEM ACCELERATOR FOR GAMMA-RESONANCE CONTRABAND DETECTION

B.F. Milton,
TRIUMF, 4004 Wesbrook Mall, Vancouver,
B.C., V6T 2A3, Canada

*Abstract*

TRIUMF and Northrop Grumman have developed a new system for the detection of concealed explosives and drugs. This Contraband Detection System (CDS) is based on the resonant absorption by $^{14}N$ of gammas produced using $^{13}C(p,\gamma)^{14}N$. The chosen reaction uses protons at 1.75 MeV and the gammas have an energy of 9.17 MeV. By measuring both the resonant and the non-resonant absorption using detectors with good spatial resolution, and applying standard tomographic techniques, we are able to produce 3D images of both the nitrogen partial density and the total density. The images together may be utilized with considerable confidence to determine if small amounts of nitrogen based explosives, heroin or cocaine are present in the interrogated containers.

Practical Gamma Resonant Absorption (GRA) scanning requires an intense source of protons. However this proton source must also be very stable, have low energy spread, and have good spatial definition. These demands suggested a tandem as the accelerator of choice. We have therefore constructed a 2 MeV $H^-$ tandem optimized for high current (10 mA) operation, while minimizing the overall size of the accelerator. This has required several special innovations which will be presented in the paper. We will also present initial commissioning results.

## 1 INTRODUCTION

In recent years the ease with which high explosives can be concealed and then placed on public transport such as planes has caused major concern worldwide. There is also a growing demand to reduce the transit of illegal drugs through public transport systems including the postal service. In both cases because of the required throughput and privacy requirements there is a desire for non-invasive techniques for the detection of contraband. Normal x-ray systems rely on strong density differences for identification, and have proven very successful in the detection of weapons in carry-on luggage. However while most explosives have fairly high densities, they are difficult to distinguish from other items commonly contained in luggage, particularly given the ability to shape them and/or conceal them in appropriate materials. Therefore there have been many efforts to detect contraband using methods more dependent on the exact chemical composition.

When reviewing the composition of explosives it is immediately noted that they all have a large partial density of either nitrogen or chlorine when compared with most common materials. Various techniques have been developed to measure the quantities of key constituents such as carbon, oxygen and nitrogen. In fact many techniques that exploit the specific properties of these nuclei are being pursed and are reviewed elsewhere[1][2]. Perhaps the best known of these is neutron activation.

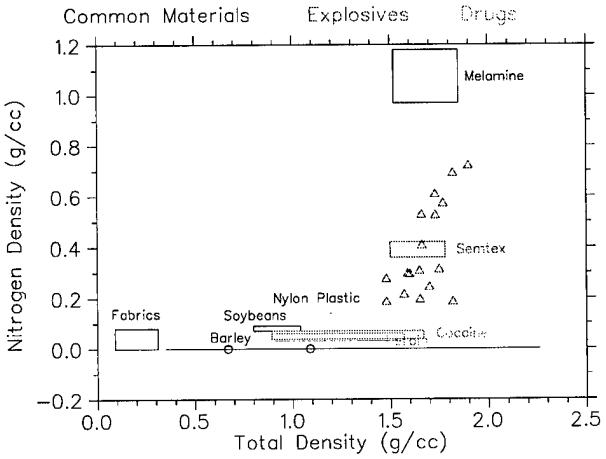



Figure 1: Explosives have a unique signature compared to common materials when nitrogen density is plotted against total density

In figure 1 the density and nitrogen partial density of a number of substances are shown. The clustering of the explosives in one part of the plot indicates how knowledge of the nitrogen partial density can lead to the identification of an explosive substance. The plot also indicates how a knowledge of both the partial nitrogen density and the total density together could be used to identify heroin or cocaine. Gamma resonant absorption (GRA) is a process that shows strong promise as a way to measure partial nitrogen (or chlorine) density.

It should be stressed that one needs to know the partial density of nitrogen in a selected volume, not the total amount of nitrogen in the overall container being inspected. For this reason it is important to have a spatially defined measurement technique, which in the case of high explosive reduces to a position resolution around 5mm. We have thus decided to combine GRA with high resolution tomography, similar to the combination of x-rays and tomography used in CAT scans. More details of the specific mission can be found in ref [3]

0-7803-4376-X/98/$10.00 © 1998 IEEE

| Production Reaction | Proton Energy | Gamma Energy | FOM |
|---|---|---|---|
| $^{14}N(\gamma,p)^{13}C$ | 1.75 | 9.17 | 1000 |
| $^{35}Cl(\gamma,p)^{34}S$ | 1.89 | 9.08 | 35 |
| $^{35}Cl(\gamma,p)^{34}S$ | 2.79 | 8.21 | 76 |
| $^{16}O(\gamma,p)^{15}N$ | 1.03 | 13.1 | 22 |
| $^{12}C(\gamma,p)^{11}B$ | 1.39 | | 10 |

Table 1: A comparison of potential gamma resonances in carbon, oxygen, nitroge and chlorine, using a Figure Of Merit normalized to 1000 for the $^{13}C(p,\gamma)^{14}N$ reaction.

## 2 GAMMA RESONANCE ABSORPTION

GRA makes use of the fact that for each element there are certain gamma energies that are strongly absorbed by the nucleus. Since the gamma energy at which this happens is specific to the target nucleus, a comparison of the absorption at the resonant energy with the absorption at an energy just off resonance will yield a measure of the sought after element. For example the reaction $^{13}C(p,\gamma)^{14}N$ has a large cross section at a gamma energy of 9.17 MeV, so by interrogating a container with gammas at this energy one could measure the nitrogen density.

From a practical point of view it is not easy to produce a near mono-energetic beam of gammas. At present the most promising approach is to use an inverse reaction to produce the gammas. For example the 9.17 MeV gammas can be produced using a beam of protons and the $^{14}N(\gamma,p)^{13}C$ reaction. Assuming favourable reaction kinematics, it is possible to find an outgoing gamma angle at which the gammas have been Doppler shifted by an amount that exactly compensates for the energy absorbed in the production reaction.

In 1994/95 the TRIUMF-Grumman team conducted an extensive study of GRA for the detection of concealed contraband. This study developed a figure of merit for evaluating various resonances. The figure of merit included factors for the strength of the resonance, the width of the resonance, gamma energy spread and other factors that affect the usefulness for imaging by tomography. The figure of merit was normalized to 1000 for the $^{13}C(p,\gamma)^{14}N$ reaction. Table 1 compares some of the considered reactions. From this the $^{13}C(p,\gamma)^{14}N$ reaction was found to be the most promising, however CDS has continued to maintain the option of using the lower energy $^{34}S(p,\gamma)^{35}Cl$ reaction, for the detection of chlorine based explosives, and the hydrochloride forms of cocaine and heroin.

One advantage of producing the required gammas using an inverse reaction is that gammas meeting the reabsorption criteria form a narrow conical fan. In the case of $^{14}N$ detection, the cone lies at 80.7 degrees, and is about half a degree wide. This results in a convenient inspection geometry as shown in figure 2. Gammas produced just outside this cone can be used to measure the non-resonant absorption, which can be used to normalize the resonant absorption for the calculation of nitrogen partial density, and for the calculation of total density.

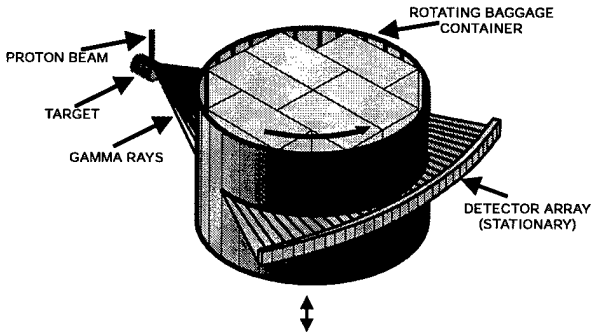



Figure 2: CDS detector and inspection geometry

## 3 ACCELERATOR REQUIREMENTS

For a practical inspection device there are several key elements affecting the choice of accelerator. They include image resolution, throughput, over all size and convenience of operation. The first two of these determine the number of gammas per second required and the quality of those gammas.

In order to maximize the efficiency of gamma production it is important that the energy spread of the beam be less than the target thickness. As well the lowest energy protons must have an energy at least as high as the resonance energy. Therefore the larger the proton energy spread, the higher the proton beam central energy that is required and the thicker the target that has to be used. This has a limit since we are interested in a target as thin as possible to avoid the excitation of other resonances which contribute only to the background. In addition, using too thick a target will affect the energy spread of the produced gammas, which in turn will decrease the resonance absorption signal.

The size of the beam spot on the target combines with the position resolution of the detectors to reduce the precision with which the flight path of each gamma is measured. Thus the larger the beam spot size the poorer the position resolution of the overall system. It is therefore desirable to choose a spot size that will make a negligible change in the image resolution given the resolution of the detectors.

Angular divergence of the proton at the target changes the angle of the produced gamma. Thus the proton beam's divergence creates an uncertainty as to the energy of a gamma ray even if its position at the detector is known precisely. Because of this uncertainty, some of the gamma rays that arrive at the detector on the locus of the resonant-energy conic section deviate from the resonant angle by an unknown amount up to the divergence of the beam. However these rays will not have meet the resonance condition when passing through the luggage. The effect of including off-energy gammas rays in the resonant image is to dilute the resonant absorption effect which causes an increase in the resonant image noise. The larger the proton beam divergence the greater the noise added to the resonant-energy image. Simulations were used to determine the beam di-

| | $^{14}N(\gamma,p)^{13}C$ | $^{35}Cl(\gamma,p)^{34}S$ |
|---|---|---|
| Proton Energy (MeV) | 1.75 | 1.89 |
| Energy Spread (keV) | $< 25$ | $< 12$ |
| Spot Size (cm) | 0.6 x 2.4 | 0.6 x 2.4 |
| Divergence(mrad) | 12 | 12 |
| Current (mA) | 10 | 12 |

Table 2: CDS accelerator requirements for the selected production reactions

vergence levels that would cause minimal increases in the false alarm rate.

Once an image resolution, a detection level, and false alarm rate have been chosen, then throughput determines the gamma flux requirement. Calculations show that in order to achieve throughput rates in the hundreds of bags per hour for the chosen configuration, the proton beam current must be in the 10 milli-ampere range.

A summary of the beam requirements as determined in the initial design study are summarized in table 3. The design study then performed a survey of methods for the production of protons up to 3 MeV. Accelerator options such as RFQs and cyclotrons were investigated. While RFQs looked very promising because of their compactness and high current capability they are not able to meet the other beam parameters. Electrostatic accelerators were really the only system capable of producing such high quality beams. However most electrostatic accelerators have two disadvantages for CDS, size and limited beam current. It was therefore decided to design a new tandem accelerator specifically for CDS. It should also be noted that a DC accelerator, when compared to a CW accelerator, creates a significantly lower instantaneous data rate in the detectors.

## 4 THE CDS SYSTEM

The layout of the CDS Proof-of-Principle system is shown in figure 3. This system has been designed to perform a laboratory proof of principle experiment and to allow for the testing and development of components that could be used in a commercial system.

The gamma production system begins with a high brightness $H^-$ ion source coupled by a short matching section to the tandem. The tandem is followed by a beam transport section that analyzes the beam and produces the correct beam spot parameters at the target. At present the target consists of a fixed water cooled target coated with carbon-13. However in order to use the full beam current a rotating target will be constructed. The high energy beam line has been constructed so that the resonant gamma cone lies in the horizontal plane in the region of the baggage carousel.

In order to acquire tomographic information the objects to be inspected are located on a carousel that is capable of rotating and elevating. Behind the carousel is located a detection system that consists of a double deck arc of segmented BGO block detectors. The arcs subtend an angle of 53 degrees and contain 44 blocks each. Standard electronics is used to collect the phototube output which is then converted into gamma position information. Image reconstruction and interpretation is then performed in separate computers. At present we are using 7 detector blocks and offline data processing and a very simple carousel in order to assess the overall system performance. In a high throughput system the carousel would rotate and elevate simultaneously.

## 5 THE CDS TANDEM

As discussed above, the CDS requires an electrostatic accelerator capable of a very high beam current, while maintaining the smallest practical size. Using a tandem allows the terminal voltage to be halved thus reducing the demands on the voltage generator, and the amount of space required to hold voltage. The trade-off is the requirement for a stripper located in the terminal that is capable of handling the current. Since the proton beam energy at the terminal will be below 1 MeV, the energy loss in a stripping foil would be quite large. Calculations show that expected foil lifetimes would be perhaps a few minutes at the design intensities. We therefore chose to use a vapour stripper. Design of this element has concentrated on providing good differential pumping between the stripper cell, and the acceleration columns. A schematic of the system is shown in figure 4. Pressure in the acceleration columns is particularly important because interactions between the residual gas and the beam will produce free electrons that will then be accelerated and generate x-rays. Significant production of high energy x-rays could lead to voltage breakdown and constitute a radiation hazard external to the accelerator. Testing to date has shown that with the stripper operating above design pressure, the pressure in the columns is in the low $10^{-7}$ range.

Obviously the overall size of a tandem can be reduced by increasing the electric fields, particularly in the acceleration region. However voltage holding problems rise steeply with electric field so we have chosen to remain at a fairly conservative 50 kV/inch in the acceleration region. By pressurizing the containment vessel to 60 PSI with $SF_6$ the distance between the vessel and the terminal has been reduced by factor of almost 10 over using unpressurized nitrogen (air). Keeping the terminal compact has also helped to reduce size. As well as the vacuum equipment for the stripper, the terminal contains two magnetic quadrupole triplets for matching beam between the acceleration regions and the stripper cell. Considerable effort has been devoted to making this region compact while still using commercial power supplies and controllers. Communication between ground and the terminal is achieved using fiber optics.

Of particular importance to CDS is a suitable power supply. In order to produce a 10 mA, 2 MeV beam, the power supply must be able to supply at least 20 mA at 1MV, meaning it must be capable of a power output greater than 20

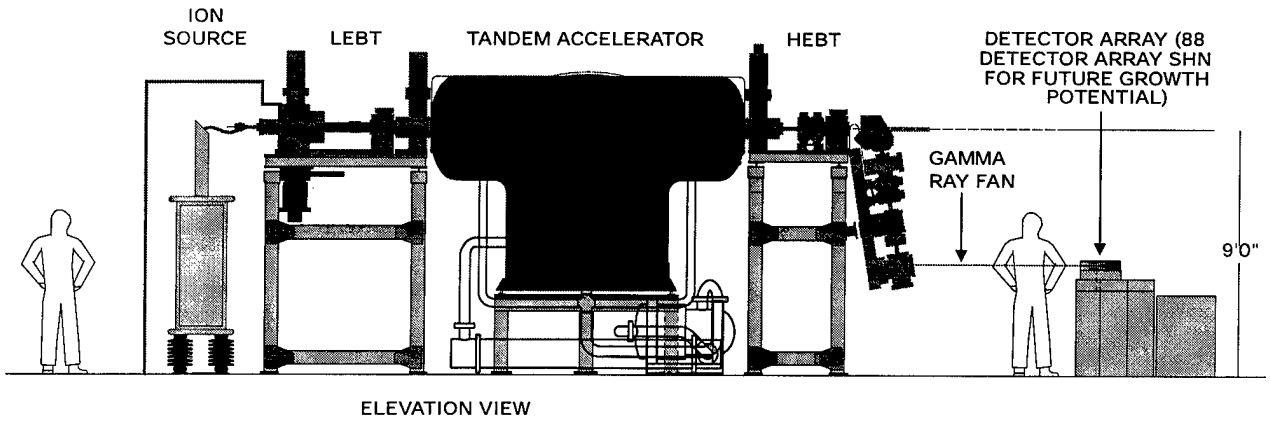



Figure 3: Side elevation of the CDS proof-of-principle device

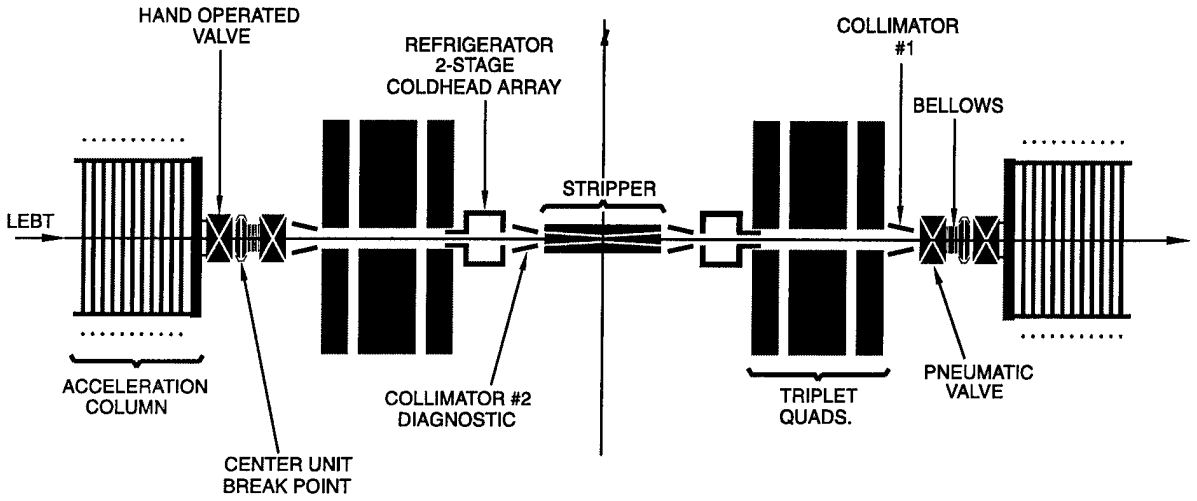



Figure 4: Schematic layout of the terminal vacuum system

kW. The preliminary CDS design study showed that most conventional power source were incapable of providing the necessary current, and those that had produced currents in the milli-Ampere range were extremely bulky. However the design study also identified a novel power supply development at the University of Waterloo that was able to meet the CDS requirements in a compact volume. Basically this system uses a high frequency isolated core transformer to couple a large number of voltage doubler circuits that are then connected in series to develop the necessary voltage. The high frequency allows relatively small conventional components to be used, with the secondary tracks and doubler circuits mounted on normal circuit boards. This supply occupies a space less than 300 $in^2$ and is under 36 inches high. In the tandem the supply sits under the terminal between the support insulators and is insulated by the $SF_6$. In the region of the voltage generation the average field is 50 kV/in. Tests of the supply using a water load have demonstrated outputs of greater than 26 kW at 1 MV.

Fine control of the power supply voltage is achieved by varying the primary frequency, allowing rapid changes. As well since the capacitance of the doublers is small, the stored energy of the supply is small when compared to the overall tandem capacitance. Tests at 860 kV without beam have shown that even with no voltage stabilization the system shows less than a $\pm 5$ kV variation. We have implemented a system that will adjust the frequency based on the terminal voltage. This appears to take care of basic beam loading effects. Eventually we expect to use feedback from the high energy beamline to adjust this loop.

At present all of the system sub-components have been tested. A resonant image has been observed with the detectors using gammas produced with a proton beam of a couple of micro-amperes on a vanderGraff. The ion source and low energy beam transport emittance has been fully characterized at 10 mA. The tandem has undergone a series of voltage tests up to 900 kV on the terminal, including full operation of the stripper while at 865 kV. Initial tests at

25 $\mu$A have indicated that the beam spot at the stripper location is as specified. On the first attempt to run beam 100 $\mu$A at virtually 100% transmission was extracted. Beam current was limited to this level by target restrictions. We are now working on parametrization of the beam and expect start basic tomographic scans of realistic phantoms in the near future.

## 6 ACKNOWLEDGEMENTS

The CDS team consists of three groups and has included many people over the last 4 years. Key players at the Northrop Grumman Advanced Technology and Development Center include; J.J. Sredniawski, T. Debiak, E. Kamykowski, J. Rathke, and S. Melnychuk. At TRIUMF they have included; P. Schmor, J. Rogers, A. Altman, J. Boyd, G. Stanford, D. Dale, R. Ruegg, L. Buchman, and J. Welz. At Scientific Innovations there is J. Brondo.

## 7 REFERENCES

[1] T. Gozani, "Nuclear based Techniques for Cargo Inspection - A Review",*Proc. of Contraband and Cargo Inspection Technology International Symposium*, Washington D.C., 1992, p. 9.

[2] D. Vartsky, *et. al.*, "A Method for detection of Nuclear Explosives Based on Nuclear Resonance Absorption of Gamma Rays in $^{14}$N", NIM, section A, (1994) P. 668.

[3] J. Sredniawski, "A New Proof-of-Principle Contraband Detection System", ONDCP Conference in Nashua N.H., Oct. 1995.

# THE ACCELERATOR PRODUCTION OF TRITIUM PROJECT

P. W. Lisowski, Los Alamos National Laboratory, Los Alamos NM 87545, USA

*Abstract*

Tritium is essential for U.S. nuclear weapons to function, but because it is radioactive with a half-life of 12.3 years, the supply must be periodically replenished. Since the last production reactor stopped operating in 1988, tritium has been recovered from dismantled nuclear weapons. This process is possible only as long as many weapons are being retired and will not work indefinitely, thus requiring the United States to bring a new tritium production capability on line. To make the required amount of tritium using an accelerator system (APT), neutrons will be generated by high-energy proton reactions with tungsten and lead. Those neutrons will be moderated, and captured to make tritium. The APT plant design is based on a 1700 MeV linear accelerator operated at 100 mA CW. In preparation for engineering design, scheduled to start in October 1997, and subsequent construction, a program of engineering development and demonstration is underway. That work includes assembly of a 20 MeV, 100 mA low-energy linac plant prototype, high-energy linac accelerating structure protoyping, radio-frequency system improvements, neutronic efficiency measurements, and materials qualifications.

## 1. INTRODUCTION

Production of tritium in a quantity large enough to supply the needs of the U.S. stockpile can only be accomplished through neutron capture by a stable isotope such as $^{3}He$ or $^{6}Li$. Presently only reactor or accelerator systems can make enough neutrons to produce tritium in the quantities needed. In a reactor, nuclear fission supplies the neutrons. In APT, neutrons are made by proton spallation of heavy metal nuclei. The use of spallation to produce neutrons makes it possible to avoid the use of fissile material, which in turn makes the system design simpler than that of a reactor and provides additional safety and environmental features.

### *1.1 Project History*

The design of an APT system was first considered by the DOE Energy Research Advisory Board (ERAB) in late 1989 and by the JASONs, an independent scientific review panel, in 1992 and 1995. Reviews of APT technology were positive, and endorsed the need for further design and for a technology development and demonstration program. As a result, from 1992 to 1994, the DOE sponsored an APT preconceptual design study using a multi-laboratory and industry team to support a DOE Programmatic Environmental Impact Statement for Tritium Supply and Recycling.

In December, 1995 the DOE announced a decision to pursue a dual track approach to obtaining a new tritium supply. That strategy initiated action to purchase an existing commercial reactor (operating or partially complete) or irradiation services with an option to purchase the reactor for conversion to a defense facility; and authorized work to design, build, and test critical components of an accelerator system for tritium production. The DOE has committed to select one of the tracks to serve as the primary source of tritium by fall, 1998. In addition, the Savannah River Site (SRS) in South Carolina was selected as the location for the APT accelerator.

A critical part of the DOE decision is the fact that the government plans to develop the technology that is not selected for tritium production as an assured backup in the event that the primary technology proves unworkable. For APT that means that the project will continue through engineering design of the plant and include sufficient Engineering Demonstration and Development (ED&D) to ensure low-risk construction and operation.

APT ED&D activities cover areas that have the greatest impact on plant cost and schedule, including an evaluation of alternative designs, and prototyping of key components and subsystems. This work is being performed with the assistance of a Prime Contractor, Burns and Roe teamed with General Atomics, which will be responsible for plant design and construction; and with the Maintenance and Operations Contractor at Savannah River, in order to assure actual plant operations experience.

### *1.2 Conceptual Design Report*

The basis of this paper is the APT Plant Conceptual Design Report (CDR) [1]. The CDR establishes the design, cost, and schedule for the entire project. It also includes technical information on Environment Safety and Health, Operations and Maintenance, Safeguards and Security, and Decontamination and Decommissioning. The report was coordinated by Los Alamos National Laboratory with contributions from Sandia, Brookhaven, and Livermore National Laboratories; the Westinghouse Savannah River Company; the APT Prime Contractor; and supporting subcontractors Northrup Grumman, and Babcox and Wilcox.

DOE requirements for the APT plant include:

- Sustained normal operation at a production rate within the range of 2 to 3 kg of tritium per year,
- Sustained operation at the higher production rate of 3 kg/yr averaged over 5 years,
- Production of 3 kg/yr no later than 2007,
- Operational lifetime of 40 years, and

Cost effective, efficient operation in the 2 to 3 kg/yr range.

## 2. SYSTEM DESCRIPTION

The APT plant has a CW proton linear accelerator [2] to produce a 170 MW proton beam that is directed onto a tungsten target surrounded by a lead blanket. Tubes filled with $^{3}He$ gas are located adjacent to the tungsten and within the lead blanket. Spallation neutrons created by the energetic protons are moderated by the lead and cooling

0-7803-4376-X/98/$10.00 © 1998 IEEE

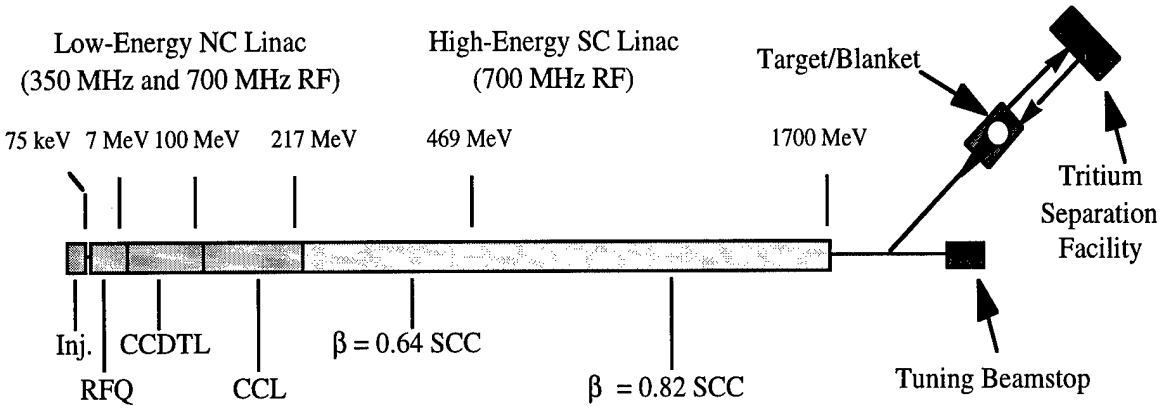



Figure 1, APT Plant Systems and Accelerator Architecture

water and are absorbed by $^3$He to create about 40 tritium atoms per incident proton. The tritium is continuously removed from the $^3$He gas. The overall APT plant is designed to operate at 71% or greater availability.

The APT design was strongly influenced by the need for efficient use of the large amount of required RF power [3]. The selection of basic accelerator parameters, such as current, energy, and accelerating gradient, was determined by the required plant production capacity, using a cost-performance model [4]. The model has an energy-dependent parameterization of spallation neutron production in high-Z targets and includes cost estimates for subsystems and consumables such as electricity. The model also includes technical constraints, such as injector current limits and maintenance requirements.

### *2.1 Linear Accelerator*

The accelerator system has been designed to provide:

- A 100-mA proton beam at 1700 MeV that can be expanded to provide a current density at the entrance window to the Target/Blanket that is less than 80 mA/cm$^2$ and uniform to within ±30%,
- Beam loss within the accelerator structure that is low enough to allow unrestricted hands-on maintenance (At the highest energy, the loss corresponds to about 0.1 nA/m.), and
- Accelerator availability during scheduled operations of ≥85%.

The APT linac uses normal conducting (NC) water-cooled copper structures [5] to accelerate the 100-mA continuous wave (CW) proton beam to 217 MeV, and niobium superconducting (SC) accelerating cavities [6] thereafter.

In order to smoothly and efficiently accelerate the proton beam without loss, there are several accelerating structures following the injector, each optimized for a specific energy range. The low-energy normal-conducting (NC) linac, which is used up to 217 MeV, consists of a 350 Mhz radio-frequency quadrupole (RFQ), a coupled cavity drift tube linac (CCDTL), and a coupled-cavity linac (CCL). Within the NC linac, the CCDTL and CCL use 48 1-MW 700-MHz klystrons. Each klystron distributes power to the accelerating structure through four 250-kW windows. The high-energy linac, consists of superconducting-cavity (SCC) cryomodules of only two designs. From 217 MeV to 469 MeV, the cavities are optimized at b = 0.64, and in the section above 469 MeV, at b = 0.82. The shapes were modeled after well-established elliptical designs used in electron machines, but compressed along the longitudinal axis in proportion to b. Each cavity has two coaxial RF couplers to supply up to 210 kW of 700-MHz RF power and uses a SC focussing lattice.

This combination NC/SC accelerator is designed to have strong focusing at low beam energy and to avoid any phase-space transitions after the RFQ that might perturb the beam. Studies [7] have shown that this is important in order to minimize emittance growth and beam halo formation. The amount of clearance between the accelerating structure and the beam core is indicated by the "aperture ratio", which is the ratio of the structure aperture diameter to the rms beam size. In order to ensure low beam loss, the linac has the largest practical aperture ratio at every energy. The ratio is achieved by having large apertures in accelerating structures and in focusing magnets, and by keeping the beam size small using strong beam focusing per unit length. The aperture ratio increases from about 20 at the end of the NC linac, to 80 at the end of the SC linac. The ratios are designed [8] to be large enough to keep beam losses low enough to allow hands-on maintenance.

Because of the SC linac can operate with accelerating cavities having only two values of b the linac output energy may be adjusted over a wide range, providing considerable operational flexibility. For example, output beam energy may be traded for beam current, if necessary, and the accelerator may be retuned for operation following an RF station or cavity failure.

Cooling for the SC linac is provided by a cryogenic plant consisting of three identical refrigerators similar in design to the one in use at the Thomas Jefferson National Accelerator Facility. This system must provide 2°K helium in the superfluid state to the superconducting cavities, 4.5°K helium for the superconducting magnets, a stream of 45°K helium gas for the cryomodule thermal shields, and liquid helium to cool the magnet current leads.

A High Energy Beam Transport (HEBT) system [9] delivers the beam to a target/blanket (T/B). The beam passes through a magnetic switchyard which directs it

either to a straight-ahead tuning beamstop or into the beam line serving the T/B assembly. This beam line terminates in a beam expander, which converts the small-diameter Gaussian-like beam distribution into a large-area rectangular uniform distribution at the target. The beam expander has two non-linear (multipole) magnets and two quadrupoles, one pair for horizontal-plane expansion, and the other for vertical-plane expansion. After 30 m of drift, the beam expands to a 16 cm by 160 cm uniformly-filled rectangular pattern at the T/B.

### *2.2 Target/Blanket*

The T/B assembly has been designed to meet tritium production requirements while maintaining a high degree of safety and reliability. Design features include a tungsten and lead assembly that stops the protons, a lead blanket containing $^3$He that produces approximately 40 tritons per incident 1700 MeV proton, low-pressure, low-temperature cooling systems with redundant heat removal systems, and welded, doubly-contained gas handling systems to retain the $^3$He and tritium.

Assembled from replaceable modules, the T/B has a beam entrance window, a centrally-located tungsten neutron source, a surrounding lead blanket, a reflector, and shielding. All modules are placed in a cavity maintained at a rough vacuum. A double-wall Inconel window isolates the T/B cavity vacuum system from the accelerator.

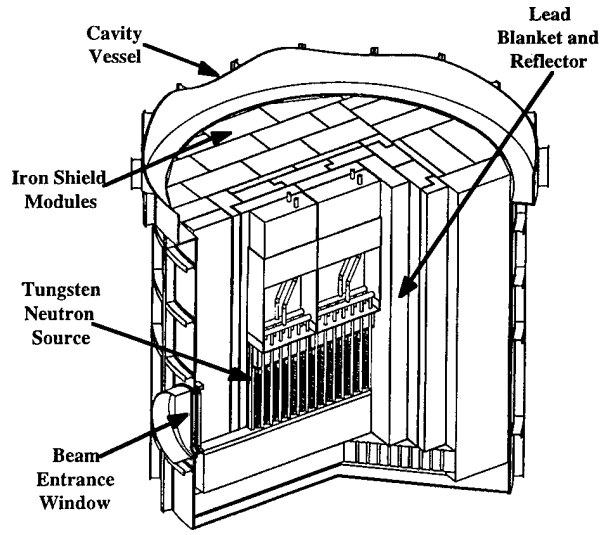



Figure 2, APT Target/Blanket System

The physics design of the tungsten neutron source maximizes the production of neutrons through nuclear spallation and allows them to leak into the blanket region with minimum loss. The tungsten neutron source consists of small heavy-water cooled, Inconel-clad tungsten rods mounted perpendicular to the proton beam axis in horizontal stainless steel tubes. The tubes are connected to vertical manifold tubes, in a ladder arrangement that is about 2 m tall. To enhance neutron leakage from this source, the tungsten is spread over a large volume. The tungsten neutron source produces approximately 21 neutrons per 1700 MeV proton. Approximately 3 neutrons are parasitically absorbed by the tungsten, and therefore, unavailable for making tritium. Surrounding the tungsten neutron source ladders is a neutron decoupler which allows high-energy neutrons and other particles to leave the central region. The decoupler also preferentially absorbs any neutrons in $^3$He that attempt to return. The decoupler has several layers of light-water cooled, $^3$He -filled aluminum tubes. Approximately 46% of the total tritium production occurs in the decoupler.

A blanket of lead, light water, and $^3$He gas surrounds the tungsten neutron source and decoupler . The blanket is 120 cm thick laterally and extends about 50 cm above the ladders. The lead in this region increases neutron production by additional spallation and (n,xn) reactions. The neutrons are moderated to low energy by collisions in the lead and light water, and are captured in $^3$He gas contained in circular aluminum tubes to produce tritium. Tritium produced in the $^3$He diffuses to a manifold, where it is carried away by flowing $^3$He. The $^3$He/hydrogen-isotope mixture is transported to the Tritium Separation Facility (TSF) for continuous tritium removal and cleanup. The lead blanket and decoupler produce an additional 26 neutrons per proton, with approximately 4 neutrons lost to structure and coolant. Fifty-four percent of the tritium is produced in the blanket. The blanket is surrounded by a water reflector holding additional aluminum tubes which contain $^3$He for reducing neutron leakage from the blanket. Of the 170 MW of beam power incident on the T/B, only 130 MW is converted to heat that must be removed by cooling systems.

The tungsten neutron source, decoupler, reflector, and blanket are mounted inside a cylindrical steel vacuum vessel that is shielded both inside and outside to reduce the radiation dose rate to less than 0.1 mrem/hour for personnel working in adjacent areas.

Target/Blanket safety is provided by multiple inherent and engineered design features. Inherent to safety is the low amount of heat that continues to evolve from the tungsten target and other components after the beam is removed. Unlike fission-based systems for tritium production, there are no delayed neutrons and no criticality concerns. Inconel cladding on the tungsten rods prevents radionuclide release in the unlikely event that the cooling water is lost and the rods must cool by radiating their decay heat. There is a highly reliable T/B fault detection system which would turn off the proton beam should an upset condition occur. Backup safety features include natural circulation heat removal, an active residual heat removal system, and the ability to flood the cavity.

### *2.3 Tritium Separation Facility*

The TSF delivers tritium in quantity and purity meeting production requirements. Spallation products in the $^3$He/hydrogen-isotope gas mixture produced in the target/blanket are removed before the gas is circulated to the TSF. There hydrogen isotopes are removed, and $^3$He is recirculated to the T/B. The hydrogen isotopes are separated by cryogenic distillation, and the tritium is sent to existing SRS tritium facilities. The TSF recovers

99.9% of the tritium transported from the T/B assembly, and chemically and isotopically purifies it to a minimum of 99% tritium.

### *2.4 Balance of Plant*

The Balance of Plant (BOP) design is driven by the need to meet the requirements of the linac, target/blanket, and tritium separation facilities. Those requirements include input electric power, waste heat to be removed, distributed utilities within the plant, shielding requirements, and remote handling of radioactive materials. About $10^6$ square meters of land area is needed to accommodate the APT plant which will be 1.5 kn long and bounded by a fence to provide access control.

Incoming ac power from a local utility is converted by an electrical switchyard to a lower voltage for distribution to the accelerator and plant systems, and is distributed via a series of sub-stations along the length of the plant. Nine Cooling towers and their associated heat exchangers are located above ground along the accelerator tunnel to serve the accelerator and its power supply components. Because of its major cooling load, the T/B facility has an additional dedicated cooling station.

The APT total electric power requirement is 486 MWe, consisting of two major loads: the RF and BOP electric power loads of 377 and 109 MWe, respectively. The ac plant distribution system will be supplied by two 100% capacity overhead lines from the local utility. Loads that must meet safety requirements are fed from both normal and three 800-kW power generators and several uninterruptible power supply (UPS) backup systems.

The accelerator tunnel and high energy beam transport buildings are housed in a concrete tunnel, with seven meters of dirt covering the linac section for shielding. The klystron gallery is a steel frame, metal building that parallels the accelerator tunnel.

The T/B building has above- and below-grade structures. Below-grade, the T/B building is reinforced concrete, while above grade it is composed of a reinforced concrete bay and a steel frame with metal siding. Remote handling equipment is used where contact handling is not practical or not permitted by personnel hazards, such as during replacement of used targets.

The BOP contains the Integrated Control System (ICS), which integrates accelerator protection and operation, ensures safe running conditions, and adjusts plant production variables. The plant will be completely operable from the main control room.

Other infrastructure support services considered within the BOP include radiation monitoring and protection, heating, air conditioning and ventilation, water supply, fire protection, communications, interfaces to SRS infrastructure, and safeguards and security.

## 3. ENGINEERING DEVELOPMENT AND DEMONSTRATION

The operation of all essential APT systems, structures, and components has been demonstrated, sometimes on a smaller scale and in different environments than will be present in the production plant. However, because the DOE dual-track approach has a critical decision in 1998, the APT Project plans to develop and demonstrate several key technologies and components at prototypic scale before that decision. These planned activities are identified in a Core Technology Plan which forms the basis for the ED&D component of the APT project. They will be carried out with the assistance of the Prime Contractor, and with the Maintenance and Operations Contractor at Savannah River, in order to assure actual plant operations experience. ED&D has substantial breadth, but there are four major technical activities underway:

- Low Energy Demonstration Accelerator (LEDA)
- Target/Blanket and materials ED&D
- Tritium separation
- High-energy accelerator ED&D

### *3.1 Low Energy Demonstration Accelerator*

LEDA activities [10] will be conducted in five stages to progressively demonstrate integrated high-power operation of the low-energy linac.

- Installation and testing of a 75-keV, 110-mA proton injector;
- Addition of a 350-MHz RFQ accelerator to accelerate a 100-mA CW proton beam to 7 MeV;
- Addition of a 700-MHz CCDTL to further accelerate the 100-mA CW proton beam to 20 MeV;
- Addition of CCDTL modules to raise the final energy of the 100-mA CW proton beam to 30-40 MeV; and
- Optional phase addition of a second parallel apparatus similar to that of Stage III, and a beam combiner to merge two 350-MHz, 100-mA, 20-MeV proton beams into a single 700-MHz, 200-mA, 20-MeV proton beam. This beam would then be accelerated with CCDTL modules to an energy as high as 40 MeV.

Of these, the first item has been completed, while construction and assembly of the RFQ [11] in the second item is underway.

### *3.2 High Energy Accelerator*

Although the high-energy linac accelerating structures are based on well proven designs, RF coupling, manufacturability, and thermal performance will be demonstrated by building and testing a prototype of the 100 MeV CCDTL section.

The SCRF development program has as its basis the successful cryomodules for electron accelerators. For proton applications there are several engineering development activities leading to pre-production prototypes suitable for manufacture that will be addressed by the following activities:

- Fabrication and high-gradient testing of several single-cell intermediate velocity proton beams Nb cavities;
- Fabrication and testing of high-power couplers for SCRF medium-velocity cavities;
- Fabrication and high-field testing of multi-cell SCRF cavities;
- Tests of multi-cell prototype SCRF cavities and couplers in beam cryostats at full power, using resistive loads to simulate the beam; and,

- Evaluation of radiation damage of a prototype Nb cavity and Nb samples.

Of these activities, the first and fifth have already been successfully accomplished.

### *3.3 Tritium and Neutron Production Efficiency*

The technology associated with generation and moderation of neutrons produced by energetic proton beams on tungsten and lead targets has been demonstrated at neutron sources worldwide. The efficiency of tritium production for an optimized T/B has a proton energy dependence very nearly the same as that of the total neutron production for range-thick targets. Measurements of tritium production from simplified prototype targets at 800 MeV and for neutron production over the proton energy range of interest for APT have been completed, confirming the predicted neutron and tritium production. Additional work is in the planning stage involving a protoypic power density system for investigating the engineering performance of a tritium-producing $^3$He loop at the LANSCE accelerator.

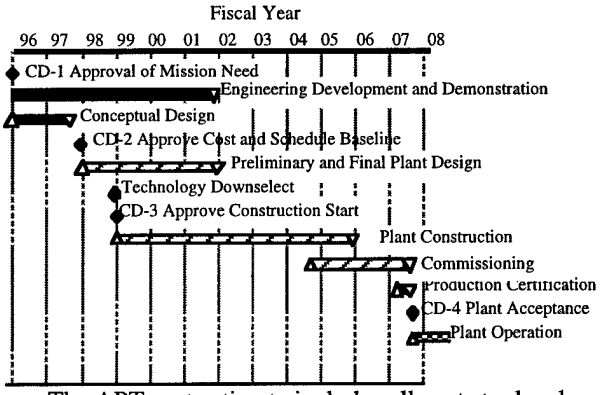
### *3.4 Materials Performance*

Candidate Target/Blanket structural materials, including Inconel, stainless steel, aluminum alloys, lead, zircaloy and tungsten, are being irradiated in the high power proton beam at 800 MeV at LANSCE. The irradiations are planned to achieve a fluence corresponding to about one full-power APT year. Included with the materials irradiation samples will be a corrosion study to determine on-line and in-situ water chemistry in which an instrumented closed-loop coolant system exposes candidate materials to a prototypic proton flux. The materials work will lead to fundamental information on the response of proposed materials to prototypic radiation environments as a function of fluence, material lifetimes, water radiolysis and spallation product mitigation requirements, and water chemistry requirements.

## 4. PROJECT COST AND SCHEDULE

The Integrated APT Project Schedule was developed to support key DOE and project specific milestones, from Critical Decision 1, "Approval of Mission Need," to Critical Decision 4, "APT Plant Acceptance." The schedule is also based on key deliverables from the ED&D program that interface with final design and procurement activities. The APT Project summary schedule shown in Figure 3, presents the major phases of the project: Engineering Development and Demonstration Conceptual Design, Preliminary and Final Plant Design, Procurement and Construction, and Operational Testing and Commissioning.

Figure 3 APT Project Summary Schedule




The APT cost estimate includes all costs to develop, engineer, construct, commission, operate, and decommission the APT plant. The Total Estimated Cost ($3.5B, with contingency and escalation) includes Preliminary and Final Design, construction costs, and all associated supporting activities such as systems and construction engineering, construction management (including inspection and testing), and all project management. Other Project Costs (OPC) ($1B ,with contingency and escalation) includes costs of the Engineering Development and Demonstration program, Conceptual Design costs, Environmental Safety and Health program costs, start-up costs, and all of the associated project management and administration costs for OPC activities. Annual operating costs for 3 kg/yr production are $150M.

## 5. REFERENCES


[1] APT Conceptual Design Report, Los Alamos Report
[2] LA-UR-97-1329, April 15, 1997.
[3] Lawrence and T. P. Wangler, "Integrated Normal Conducting/Superconducting High-Power Proton Linac for the APT Project," Proc. 1997 Particle Accelerator Conf., Vancouver (May 1997).
[4] Rees, "Design of 250-MW CW RF System for APT," ibid.
[5] Lawrence, et al., "Conventional and Supercon-ducting RF Linac Designs for the APT Project," Proc. 1996 Int. Linac Conf., Geneva, 710 (August 1996).
[6] Wangler, "New High Power Linacs and Beam Physics Issues," Proc. 1997 Particle Accelerator Conf., Vancouver (May 1997).
[7] Nath, et al., "Physics Design of APT Linac with Nor-mal Conducting rf Cavities," Proc. 1996 Int. Linac Conf., Geneva, Aug. 1996.
[8] Krawczyk, et al., "Superconducting Cavities for the APT Accelerator," Proc. 1997 Particle Accelerator Conf., Vancouver, May 1997.
[9] Nath, et al., "Beam Dynamics Design for the APT Integrated Linac," ibid.
[10] Shafer et al., "Overview of the APT High Energy Beam Transport and Beam Expanders," ibid.
[11] Schneider and K.C.D. Chan, "Progress Update on the Low-Energy Demonstration Accelerator," ibid.
[12] Schrage, et al., "A 6.7-MeV CW RFQ Linac" ibid.

# COMMISSIONING OF THE 1 MW SPALLATION NEUTRON SOURCE SINQ

G.S. Bauer, W.E. Fischer, U. Rohrer, U. Schryber, Paul Scherrer Institut, CH-5232 Villigen-PSI†

*Abstract*

First beam tests were carried out successfully on the spallation neutron source SINQ at Switzerland's Paul Scherrer Institut (PSI) in December 1996. SINQ is driven by the PSI 590 MeV isochronous cyclotron which is now operating routinely at a current level around 1.5 mA. After running at 20 μA for several hours to enable radiation surveys and neutron beam measurements on December 3, the current was raised in steps to its maximum value within 3.5 hours on December 4, making the power on SINQ the highest one ever reached on a spallation target so far.

The tests allowed measurements of neutron and gamma radiation levels around and in the extracted neutron beams and guides and included beam transport studies in the new section of the proton beam line. At the same time the whole target system including its associated cold neutron moderator was tested successfully.

## 1 THE ACCELERATOR FACILITY AT PSI

PSI has been operating a cyclotron facility for the production of intense proton beams since 1974. The accelerator complex and its evolution during two decades having been described previously (cf. e. g. [1]), only its main features will be summarized here. Protons are accelerated to their final energy of 590 MeV in an isochronous cyclotron with an injection energy of 72 MeV. Its main components are 8 sector magnets, 4 acceleration cavities (50 MHz) and 1 flat top cavity (150 MHz). The injector is also an isochronous ring cyclotron, with 4 sector magnets, 2 coaxial resonators for the acceleration and 2 flat top cavities. It is fed from a Cockcroft Walton type preaccelerator of 0.87 MeV. The 590 MeV protons from the main ring, after passing through two pion production targets in sequence used to be stopped in a beam dump.

The facility was originally designed for a current of 100 μA, but very soon was routinely operated at a level up to 250 μA with a limitation of 350 μA arising from the available RF-power. Beam dynamics considerations, however, yielded an estimated intensity limit between 1 and 2 mA. This promising outlook into a high current future at PSI stimulated the planning of a spallation neutron source, called SINQ, which would make use of the remaining beam after the targets. With a view on this new facility an upgrading program for a current up to 1.5 mA, corresponding to a beam power of almost 1 MW, was started in the late 70's. The main steps in the upgrade were:

- Replacement of the original Philips injector cyclotron by a new Injector 2, which was commissioned in 1985 and reached 1.5 mA in 1990.
- Adaptation of the two target stations (in 1986 and 1990) to the future megawatt beam and improvement of the secondary beam lines.
- Stepwise upgrade of the 590 MeV ring between 1990 and 1995 during the annual shut down periods, increasing the cavity voltages by about 50 % and the available RF-power per cavity from 200 kW to about 600 kW.
- Replacement of all injection and extraction elements, installation of improved local shielding, new beam diagnostics and upgrade of the control system.

Fig. 1 summarizes the performance of the accelerators for the period 1974 to 1996. Although the beam current and the charge accelerated per year increased by a factor of 6, the average extraction losses stayed almost constant at a level of about 0.3 μA since 1989. To date, the highest beam current measured on target was 1.7 mA.

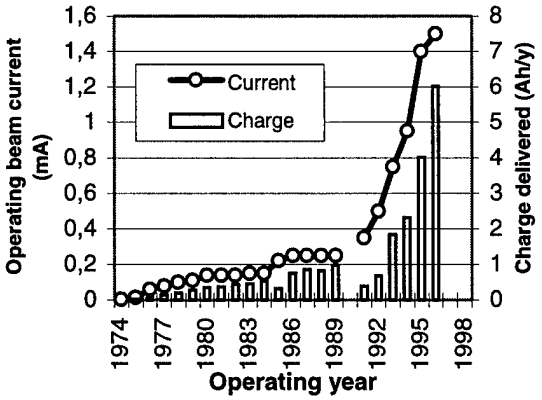



Fig1. *Evolution of the beam current of the PSI accelerators from 1974 to 1995. The bars show the total beam charge delivered per year. In 1990 one of the two target stations was completely rebuilt and the ring upgrade program was started.*

For the users of the facility, the stability of the beam and its availability are of similar importance as the beam current. The availability, as measured over periods of one week, is between 80% and 92% (in 1996). Figure 2 shows the operating current, the weekly average beam current and the number of beam trips of more than 1 min

† The authors stand for the whole project team and would like to acknowledge the continuing support by the PSI management to accomplish this goal and the enormous effort of all persons involved to get the facility ready in time for these tests.

0-7803-4376-X/98/$10.00 © 1998 IEEE

duration, which are mainly caused by voltage breakdowns in cavities and electrostatic devices

After several years of high power operation the activation of the accelerator components is still within levels for normal hands on maintenance. Only exposed components and their suroundings, such as extraction devices, beam splitters and targets are equipped with local shields and need remote handling.

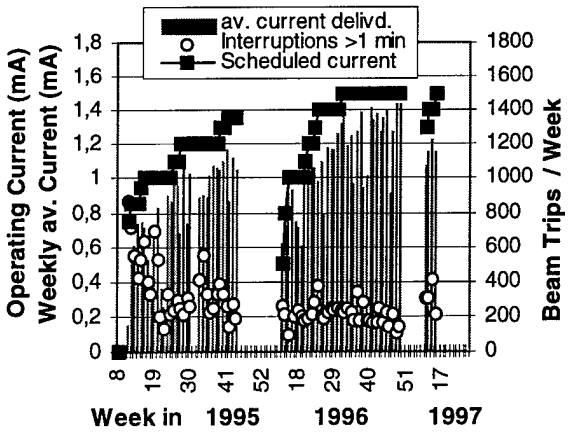



Fig. 2: *590 MeV operation of the PSI accelerators since 1995.*

## 2. THE NEW SECTION OF PROTON BEAM LINE

The new section between the second, thick target (TE) and the SINQ target, installed from 1990 onwards, is 55 m long. It features 4 bending magnets, 12 quadrupole lenses, 9 pairs of profile monitors, 5 horizontal steering magnets, 7 collimators and 3 pairs of slits. The apertures of all beam line elements are between 20 and 26 cm. This makes the magnets relatively heavy (up to 60 tons for the final 64 degree bend ). Optically this beam line consists of a long stretched "Z" and a flat "U". Because the protons enter the SINQ target region vertically from below, the beam line is rotated into a vertical plane. Just below the target, 3 collimators prevent beam line components from being activated by back scattered neutrons and avoid deposition of protons on the rim of the entrance window to the target. The position and width of the beam entering the target region can be monitored by electrically insulated electrode segments mounted in front of each of the 3 collimators.

The main components of this beam line are grouped in two regions: the first one behind TE is in the old experimental hall, and the second one in a new 11 m deep channel below the SINQ target hall. They are connected via a 12 m long drift tube passing below the foundation of the 2 adjacent halls and pointing downwards at an angle of 28 degrees.

Reshaping the beam with collimators and slits after passage through TE is important for low loss transport of the remaining part of the proton beam (60 %) to the SINQ target and in order to achieve a beam diameter of 10 cm at the target. The projected emittances in both directions are defined by the cut-off at an elliptically conical collimation system after the blow up in the 6 cm of pyrolithic graphite of the rotating wheel target. This trimming can well be seen when looking at the measured beam profiles which are all but gaussian in shape.While the beam losses at the target E, the nearby collimators and other aperture constraints add up to 40%, the losses after the 2 moveable slits (which act as beam halo scrapers) and the 12 m long drift tube were computed to be as little as 10 ppm along the last 25 m of beam line, using an enhanced version of the computer code TURTLE. First measurements of the dose deposited along the beam line and the readings of the installed ionisation chambers during beam-up time confirmed these results. This is very important for future maintenance and repair work, which

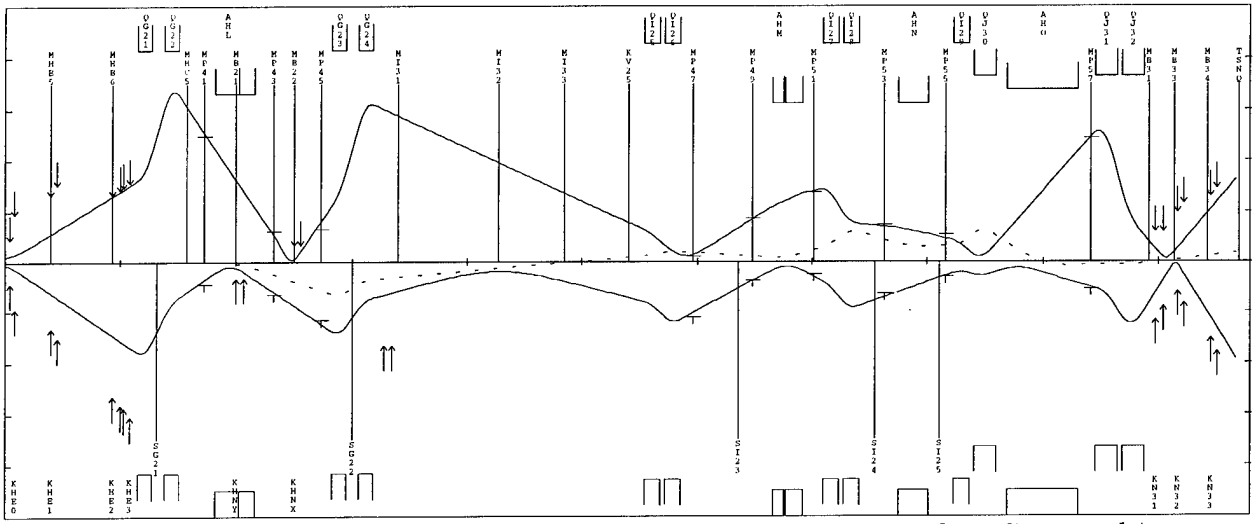


Fig 3: *Envelope fit for the 900 μA beam during the commissioning of the new proton beam line.* T *and* ⊥ *represent measured beam widths. The lower and upper half-frames show data for the vertical (bending) plane and the horizontal plane respectively. Computations were done with the code TRANSPORT. Full scale in both direction is 15 cm. The dotted line shows the assumed 1% dispersion trajectory.*↑, ↓ *symbolize slits and collimators.*

would be impossible under high activation levels in this complex environment.

## 3. THE SINQ NEUTRON TARGET STATION

At the end of its passage the remaining 60% of the proton beam hits the SINQ target from underneath with an elliptical beam spot whose half axes are about 4.5 and 6 cm (right hand side of Fig. 3). The target used for the commissioning phase is an array of 10 mm diameter Zircaloy rods, arranged perpendicular to the proton beam, in which the beam is completely stopped and which is cooled by heavy water in cross flow. Little under 60% of the beam power is deposited in the target material. The rest goes into binding and kinetic energy of the neutrons and other radiation generated and is deposited in the structures surrounding the target. About 5 neutrons per protons are generated with energies below 15 MeV, and are slowed down in a surrounding heavy water moderator to thermal energies (around 25 meV), which is what is required for neutron scattering experiments on extracted beams. Thermal neutrons are extracted through beam tubes penetrating the shielding of 4.5 m of steel and 30 cm of borated concrete and ending in the moderator in a configuration tangential to the target. A vessel containing 25 litres of liquid deuterium and placed next to the target serves as a cold moderator and feeds even lower energy neutrons into an array of 7 supermirror coated neutron guides. These guides are curved and heavily shielded over their first 30 m of length to clean the beams from unwanted fast neutron and γ-radiation and then transport neutrons in straight sections to the various neutron scattering instruments.

SINQ is unique in two ways: with its design beam power of 1 MW it has the highest power rating of any spallation neutron source world wide and, being driven by a cyclotron, it is the only continuous spallation neutron source. This makes it of interest not only for its neutrons but also in terms of its prototypic character for the technology of future high power spallation neutron sources. It was, therefore, with great interest that the results from the first beam tests were anticipated, with respect to the neutron flux level, as well as to backgrounds from fast neutrons in the beams and in the instrument halls.

A low current run at 20 μA was scheduled for the first day, Dec. 3, 1996 of the commissioning phase, enabling measurements of intensities in the neutron beams and surveys of radiation levels in the whole area. Although the need for additional shielding was identified at various locations, no serious deficiencies were detected and it was decided to run a full power test on the following day, with a limit on the total charge of 2 mAh (cf. Fig. 4)

This also enabled monitoring of the radiation levels in the cooling plant room (Fig. 5) and analysis of the cooling water activation. In general, these measurements confirmed calculated production rates.

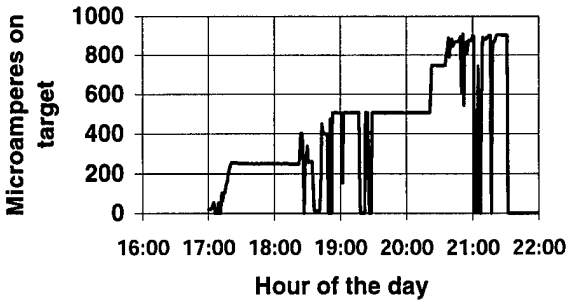



Fig. 4 *High current beam test of the SINQ target on Dec.4,1996. The beam trips were mainly caused by low levels set in loss monitors. At 21:35h the charge limit of 2 mAh was reached*

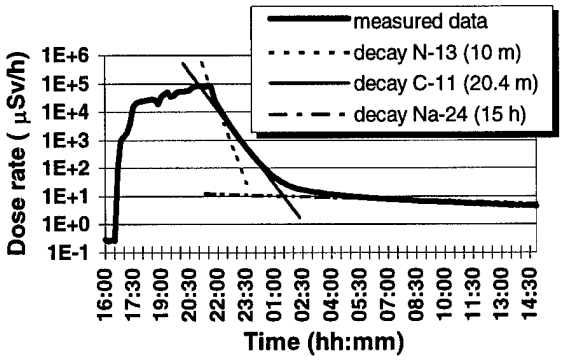



Fig. 5 *Dose rate in the SINQ cooling plant room from short lived isotopes in the cooling water during and after the high current test of Dec. 4, 1996.*

Also neutron intensities measured at the beam tubes and cold neutron guides [2] conform well with expectations based on calculations. Cold neutron currents at the guides are around 2.5 to $3.5 \times 10^8$ $cm^{-2}s^{-1}$ at the positions of the instruments and around $6.3 \times 10^8$ $cm^{-2}s^{-1}$ at the edge of the target shield. Thermal neutron currents at the beam tube exits are about 1-2 $10^{12}$ $cm^{-2}s^{-1}.sr^{-1}$. All values refer to 1 mA on target and are expected to double when the next generation target containing lead filled tubes instead of Zircaloy rods will be installed. Fast neutron contamination (>20 MeV) was checked with a $^{11}C$ detector and was found to be below $10^{-4}$ of the thermal netron flux in the beam tubes and absent in the guides.

## REFERENCES


[1] U. Schryber et al., Proc 14th Int. Conf. on Cyclotrons and their Applications, Cape Town (SA) 1995, p.

[2] W. Wagner, G.S. Bauer, J. Duppich, S. Janssen, E. Lehmann and M. Lüthy, "Flux Measurements at the New Swiss Spallation Neutron Source SINQ", to be published

# SYNCHROTRONS AND BEAMLINES FOR PROTON RADIOGRAPHY*

F. Neri and H. A. Thiessen, Los Alamos National Laboratory, Los Alamos, NM 87545
and P. L. Walstrom, Northrop Grumman, Los Alamos National Laboratory, Los Alamos NM 87545

*Abstract*
A 50 GeV accelerator complex for dynamic proton radiography, including a linac, synchrotron, and multiple isochronous beamlines is described, and critical technology development is outlined.

## 1. INTRODUCTION

Transmission radiographic images with high spatial and temporal resolution can be made when proton pulses illuminate an imploding test object that is placed in the object plane of a point-to-point magnetic quadrupole imaging system. From 2 to 16 simultaneously-illuminated views and approximately 50 time-separated exposures per view are desired. The desired beam-pulse structure should be flexible, with $10^{10}$ to $10^{11}$ protons in a 10-20 nsec-long pulse per view, and a variable time separation between pulses in a view of that is a minimum 100 nsec and a maximum of many microseconds. These requirements lead to use of a low-duty-factor, slowly cycling proton synchrotron with a flexible multipulse beam-extraction system feeding into a multistage beam-splitting and transport-line system that transmits proton pulses to the test facility. The total number of protons in the ring is approximately $3\times10^{12}$. In the paper, a conceptual point design for a system that can meet the above requirements is presented. The nominal beam energy of 50 GeV is set by object thickness and also by the thickness of the windows that must contain the blast.

## 2. SYNCHROTRON

The present study is based on use of an 800-MeV linac injecting an $H^-$ beam directly into a 50 GeV synchrotron. The synchrotron is fairly conventional, except for use of a lattice with an imaginary transition $\gamma$ and certain features of the achromatic arcs.

### *2.1 Ring acceptance*

With an injection energy of 800 MeV (the energy of the LAMPF linac at LANL), and $5\times10^{12}$ protons in the ring, a minimum 95% emittance of 4.7 $\pi$-mm-mrad is required. For calculating magnet apertures, we use a total emittance of 10 $\pi$-mm-mrad. It should be kept in mind that, with the low duty cycle, fairly high losses are tolerable. Injecting directly from the linac simplifies operation, but the dipole magnets are required to have a good field quality at the injection field of 0.04 T. At an energy of 50 GeV, the dipole field is 1.4 T. If we assume using dipoles like the ones designed for the proposed LISS synchrotron at IUCF, a maximum field of 1.7 T is possible, increasing the energy to about 60 GeV. Beyond this, the synchrotron needs to be redesigned and a booster added. Table I is a summary of the parameters for the 50-GeV ring.

Table I. Ring Description

| | |
|---|---|
| Max Momentum | 51 GeV/c |
| Circumference, harmonic no | 1710 m, 56 |
| Ring Size | 649.34 m × 361.14 m |
| Tunes | $Q_x$ = 16.23, $Q_y$ = 13.19 |
| Transition $\gamma$ | 38.839 $i$ |
| Uncorrected chromaticity | $Q'_x$ = -19.68, $Q'_y$ = -21.39 |
| Transverse Emittance Norm | $\varepsilon_x = \varepsilon_y = 5\ \pi$ mm-mrad ($4\sigma$) |
| Longitudinal Emittance | 0.15 eV-sec |
| Maximum Tune Shifts | $\Delta Q_x$ = 0.2, $\Delta Q_y$ = 0.24 |
| RF Voltage, Frequency, max | 85 kV/turn, 10 MHz |
| Extracted long. phase-space | 2 nsec, 0.13 % dp/p FWHM |
| ACHROMATIC ARCS | |
| Arc cell number | 8 (× 2) |
| Arc length | 566.8 m (× 2) |
| Arc tunes | $Q_x$ = 6, $Q_y$ = 5 |
| Arc max beta functions | $\beta_x$ = 56.6 m, $\beta_y$ = 57.7 m |
| Arc max dispersion | 4.21 m |
| STRAIGHTS | |
| Length | 288.2 m (× 2) |
| Straight cell number | 10 (× 2) |
| Straight cell phase advance | $\theta_x$ = 76.14°, $\theta_y$ = 57.42° |
| Max beta functions | $\beta_x$ = 44.8 m, $\beta_y$ = 54.4 m |
| MAGNETS | |
| Number of dipoles | 128 |
| Dipole length | 6 m |
| Dipole max B | 1.4 T |
| Number of quadrupoles | 152 |

### *2.2 Lattice design*

We are proposing a lattice for the synchrotron with a transition gamma of about $40i$. A lattice with an imaginary transition energy avoids transition and stays away from some instabilities. Figure 2 gives the lattice functions and dispersion for a quarter of the ring, including half of one of the achromatic arcs. Figure 3 shows the lattice functions and dispersion for one arc cell. A useful feature of this particular lattice is that the maximum of the horizontal beta is reached near a zero of the dispersion: this reduces the apertures required. With a full-aperture emittance of 10 $\pi$-mm-mrad, Figs. 2 and 3 show that magnets with full apertures of 8 cm should be sufficient.

### 2.3 *Extraction Kicker*

With staged beam splitting in the transport lines, only one extraction kicker is required. A straight section almost 15-m long between an F and a D quadrupole is available for the kicker. The kicked beam will pass through the following D and F quadrupoles and into a septum magnet just downstream of the following F quadrupole. The injected-beam full aperture is about 4-cm diameter at the

* Supported by the US Department of Energy

0-7803-4376-X/98 /$10.00 © 1998 IEEE

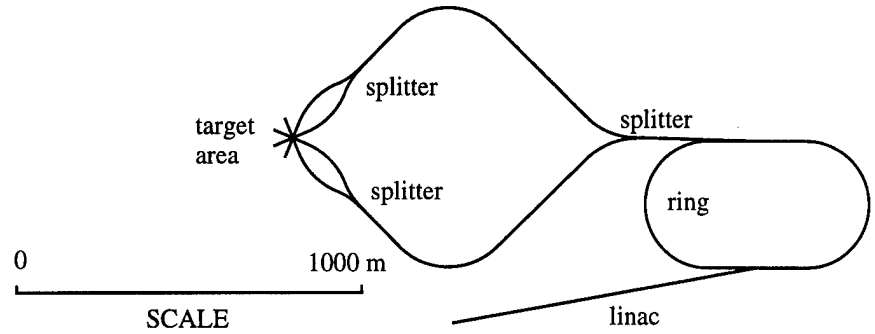



Fig: 1 Layout of the entire facility, showing the linac, synchrotron ring and beamlines.

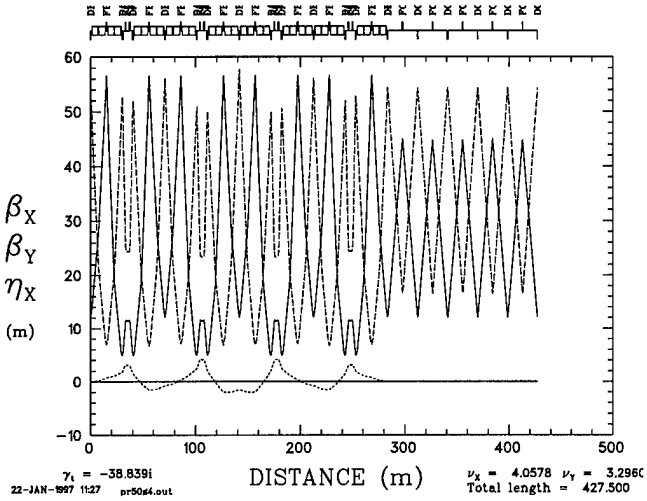



Fig: 2 Lattice functions and dispersion for a ring quadrant

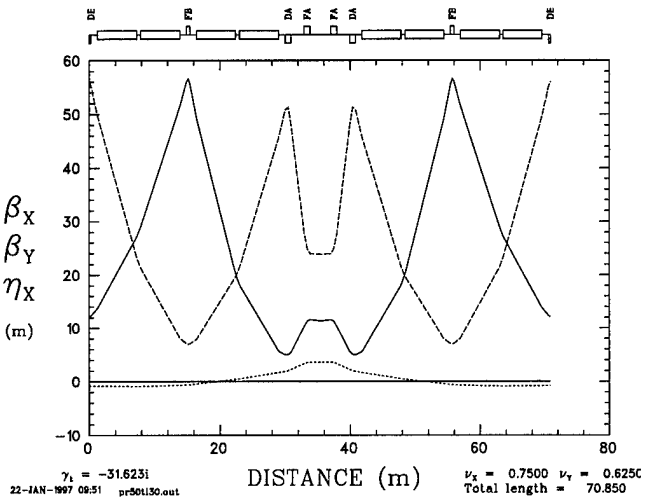



Fig: 3 Lattice functions and dispersion for an arc cell.

kicker, and shrinks during acceleration to about 1 cm diameter. If a TEM-mode (i.e., transmission-line) kicker is used, the kicker can have an aperture that is large enough for 50-GeV beam, but not large enough for the injected beam. The kicker is vertically offset from the machine midplane and steering magnets are used to move the beam up into the kicker after full energy is reached. Steering magnets are also used to bring the beam next to the septum magnet in order to minimize the required kick. Assuming that both kinds of steering are used, a kick of about 0.6 mR is needed. This can be obtained with an 8-m TEM-type kicker. A TEM-type kicker scaled from the kickers in the LANL Proton Storage Ring requires 600A at ±30 kV in a push-pull configuration. A flattop of about 64 nsec is needed for an 8-m TEM kicker (beam time-of flight+TEM pulse transit time+10 nsec beam pulse width). In order to get the total time for the kicker pulse to rise and fall, the modulator switching time for up plus down must be added to the flattop width. Using an estimated 140 nsec for this time, a total 205-nsec pulse width results. This will fit between ring pulses with 220 nsec spacing. Ringing of more than a few percent after fall time cannot be tolerated. If needed, end-of-pulse effects can be canceled by placing a properly-timed identical second kicker at a point 180 degrees in betatron phase downstream of the first kicker. A conventional pulse-forming cable (PFCs) with a thyratron switch could be used to drive the kicker if all of the particles in the entire ring were to be extracted at once (fall time is then of course not an issue). On-demand pulse extraction, in which selected pulses are to be extracted, while others are allowed to remain in the ring for later extraction, will require a modulator with a faster cycling time. A brute-force, but expensive option would be to employ multiple PFC/thyratron modulators isolated with high-voltage diodes. A more attractive possibility is to use high-power vacuum tubes. Another possibility is to use multiple lumped-inductor-type full-aperture (4 cm) kickers without bumping. These kickers would be driven with directly-coupled tubes or solid-state switches right next to the kickers.

## 3. BEAMLINES AND SPLITTERS

Both beam transport and beam splitting are performed in the beam transport system (see Fig. 1). The beamlines are achromatic and isochronous; the latter feature is enforced by symmetry. In the present study, there are 4 beamlines all in a plane illuminating the target at equally-spaced angles from 22.5° to 157.5°. At the end of each beamline, there is a 45-m target-illuminating section that includes a diffuser and magnetic quadrupoles that prepare the beam size and convergence angles for target illumination. On the opposite side of the target chamber from each target-illuminating section, there are a magnetic imaging system and detector arrays. The target-illuminating section and

imaging systems are described elsewhere in these proceedings. [1]

*3.1 Beamlines*

The basic building block for achromatic bends is 4 cells with a 90-degree betatron phase advance per cell, and with two conventional iron-pole-piece dipoles per cell. A maximum of 5.75 degrees bend per cell is assumed. This corresponds to about 1.2-T bending field in the dipoles, which occupy 14 m of each cell's length. Straight sections and bends use the same 20-m (F to F) FODO cell. Most four-cell bends are 22.5 deg., which means the field in the dipoles is a little less than the maximum. Some bend angles are slightly less than 22.5 deg. in order to direct thre beams appropriately. Straight dipoles, all of a single design, are used to minimize cost. The sagitta for the maximum bend angle is about 4 cm. With the 22.5° bend, the maximum of the dispersion function in the middle of the bend is about 6 m. With $\delta p/p$ of 0.1 %, this gives a 6 mm spread. The maximum $\beta$ function in the bends and straight sections is 36 m; the unnormalized full-aperture emittance is 0.5 $\pi$-mm-mR. A 2-in. beam pipe, curved inside the dipoles, will therefore accommodate the beam in both the bends and straights with some margin.

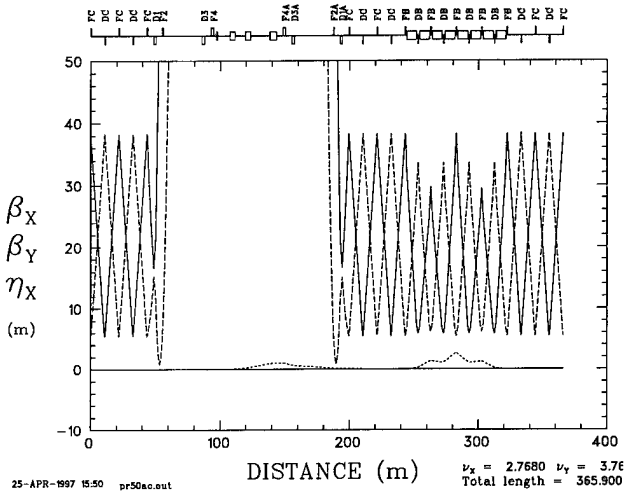



Fig: 4 The basic modules of the transport line system: the large beta insert, containing the beam splitting section on the left and the four-cell achromat on the right. The maximum $\beta_x$ in the insert is off scale and is 6250 m; the maximum $\beta_y$ is 1207m.

*3.2 Beam-splitting insert*

There are 2 stages of splitting in an 4-beam transport system. Each splitter section has a total length of 160 m and includes a 60-m expander section, a 50-m splitting section, and two parallel 60-m contractor sections. The expander section, which consists of 4 drifts and 4 quadrupoles, blows the $x$ beam width up to 10 cm and the $y$ beam width to 4 cm. The contractor sections are essentially the expander section in reverse order. The splitter section (see Fig. 5) contains a pulsed septum

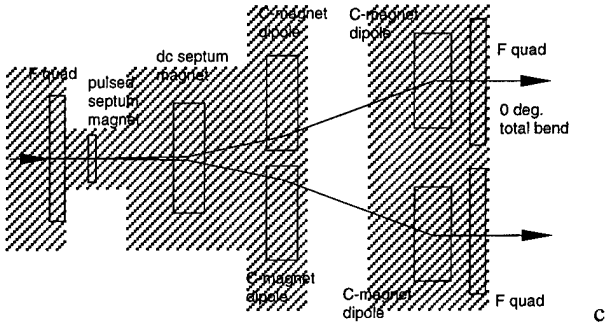



Fig: 5 Schematic of splitter section (vertical scale exaggerated by roughly a factor of 10). The first F quad in this figure is F4 in Fig. 4.

magnet, a dc septum magnet, C–dipoles, and drifts. The pulsed septum consists of a single sheet of copper 1 mm thick in a laminated iron yoke and intercepts about 3% of the beam. The septum is pulsed once for each ring cycle for a total of 2 msec. Fields are equal and opposite on each side of the septum. Each of the two legs forms an S bend. The insert is essentially achromatic because the beam has no net bend in the splitter section and the two half-beams leaving the splitter are not bent before they pass through contractor sections. Beam alignment, magnet field quality, and precision of net bend angle are critical in the insert.

*3.3 Beamline component summary*

The transport system parameters are listed in the table below. Beamline layouts with 2, 8 and 16 views with the same basic building blocks were also developed. It was found that the system length scaled very nearly linearly with the number of views.

Table II. Four-View Beamline Summary

| | |
|---|---|
| Total splitter sections | 3 |
| Total straight cells | 36 |
| Total bend cells | 96 |
| Total target illumination sections | 4 |
| Total bend length | 1920 m |
| Total straight length | 720 m |
| Total length | 3300 m |

## REFERENCES


[1] C. Thomas Mottershead, John D. Zumbro, Los Alamos National Laboratory, "Magnetic Optics for Proton Radiography", paper in 4V.16 of these proceedings.

# CLINICAL REQUIREMENTS AND ACCELERATOR CONCEPTS FOR BNCT

B. A. Ludewigt, Lawrence Berkeley National Laboratory, Berkeley, CA 94720

*Abstract*

Accelerator-based neutron sources are an attractive alternative to nuclear reactors for providing epithermal neutron beams for Boron Neutron Capture Therapy. Based on clinical requirements and neutronics modeling the use of proton and deuteron induced reactions in $^{7}$Li and $^{9}$Be targets has been compared. Excellent epithermal neutron beams can be produced via the $^{7}$Li(p,n)$^{7}$Be reaction at proton energies of ~2.5 MeV. An electrostatic quadrupole accelerator and a lithium target, which can deliver and handle 2.5 MeV protons at beam currents up to 50 mA, are under development for an accelerator-based BNCT facility at the Lawrence Berkeley National Laboratory.

## 1 INTRODUCTION

Neutron Capture Therapy (NCT) is a promising approach to cancer therapy for sites such as glioblastoma multiforme, a malignant brain tumor, where conventional radiation therapies fail. Boron Neutron Capture Therapy (BNCT) relies on a binary method for delivering a sufficient dose to the tumor cells. A pharmaceutical compound which carries $^{10}$B and concentrates selectively in the tumor cells is administered to the patient. $^{10}$B has a very large capture cross section (3830 barns) for thermal neutrons and decays into an alpha particle and a lithium nucleus, the combined ranges of which are ~10 μm, approximately one cell diameter. When a patient is irradiated with an epithermal neutron beam, the neutrons thermalized in the tissue may be captured by $^{10}$B damaging the cells in which the capture took place. The success of this therapy depends on two factors, the selectivity of the $^{10}$B carrying drug and the availability of a neutron beam with a suitable energy spectrum and sufficient intensity.

Epithermal neutron beams can be obtained at nuclear reactors. Clinical BNCT trials are ongoing at the Brookhaven Medical Research Reactor (BMRR) and at the research reactor at the Massachusetts Institute of Technology. However, because of the problems associated with reactor installations at hospitals, the development of accelerator-based neutron sources is pursued. In addition, such neutron sources can provide clinical advantages as discussed in section 3.2. Accelerator-based neutron sources consist of an accelerator, a neutron production target and a moderator and filter assembly for shaping the epithermal neutron beam. There are a number of nuclear reactions which can be exploited. The $^{7}$Li(p,n)$^{7}$Be reaction offers the highest neutron yield, but the low melting point of lithium (179 °C) is disadvantageous. On the other hand, beryllium targets have excellent mechanical properties, but higher proton beam currents or energies are required to compensate for a lower neutron yield. The evaluation of a particular reaction for BNCT requires the modeling of the primary neutron source and of the neutron transport through the moderator and filter assembly. In addition, the clinical properties of an epithermal neutron beam must be assessed by simulating the radiation transport in a phantom. Such a study, described in sections 2 and 3, led to the approach chosen for an accelerator-based BNCT facility at the Lawrence Berkeley National Laboratory (LBNL). It will be based on an electrostatic quadrupole (ESQ) accelerator capable of delivering up to 50 mA of 2.5 MeV protons onto a $^{7}$Li target.

## 2 CLINICAL CONSIDERATIONS

Radiotherapy aims at delivering a tumoricidal dose without exceeding the clinical dose limits for surrounding normal tissues and organs. In BNCT the tumor dose is boosted by a high $^{10}$B concentration in the tumor cells. However, several background reactions contribute equally to the dose in normal tissue and tumor. Thermal neutrons produce the so-called nitrogen dose ($D_N$) through the $^{14}$N(n,p)$^{14}$C neutron capture reaction and are the main contributor to the gamma dose ($D_\gamma$) via the $^{1}$H(n,γ)$^{2}$H capture reaction. Neutrons with higher energies generate recoil protons and deposit the fast neutron dose ($D_f$). $D_f$ is sensitive to the energy spectrum of the epithermal neutron beam.

### *2.1 Dose Computation*

The evaluation of the clinical efficacy of epithermal neutron beams for BNCT requires the calculation of the dose distributions in tumor and normal tissues. This task is complicated by the fact that the different kinds of radiation contributing to the total dose are of different biological effectiveness (RBE). Furthermore, the biological effectiveness of the physical dose due to neutron capture by the $^{10}$B nuclei depends on compound specific properties and a so called compound factor (CF) has been introduced. Compound factor and RBE make it possible to add the different dose components and express the total photon equivalent dose ($D_{tot}$) in gray-equivalent (Gy-Eq) units:

$$D_{tot} = CF \cdot D_B + RBE_N \cdot D_N + RBE_f \cdot D_f + D_\gamma . \qquad (1)$$

For this study the dose calculation protocol [1] developed for the BNCT clinical trial at BMRR was adopted. It established boron concentrations and compound factors for the boron compound boronphenylalanine (BPA). The values listed below were used for all dose calculations: normal tissue $^{10}$B concentration: 13 ppm; normal tissue compound factor: 1.3; tumor $^{10}$B concentration: 45.5 ppm; tumor compound factor: 3.8; fast neutron RBE ($RBE_f$): 3.2; nitrogen capture RBE ($RBE_N$): 3.2; and γ

0-7803-4376-X/98 /$10.00 © 1998 IEEE

RBE ($RBE_\gamma$): 1.0. The "rtt-MC" BNCT treatment planning code [2] developed at the Idaho National Engineering Laboratory (INEL) for use at the clinical trials at BMRR was employed to calculate in-phantom dose distributions.

*2.2 Clinical Requirements*

The discussion in this paper is based on single beam treatments of brain tumors although in practice two or more fields, e.g., parallel opposed ports, are often used. As the most important clinical requirement the dose to the normal brain must be kept within its tolerance in order to prevent radiation injuries. Following the BMRR protocol the maximum normal brain equivalent dose was set to 12.5 Gy-Eq. The maximum entrance surface dose was limited to 10 Gy-Eq in order to limit radiation injury to the scalp. Also, doses to other organs and the whole body must be considered in the actual treatment planning process since they may impose limitations and may require special beam collimation and patient shielding in particular BNCT treatments.

In treatments of glioblastoma multiforme one tries to maximize the tumor dose. Thus, the patient is irradiated until the normal tissue dose limit is reached. However, delivering a tumoricidal dose to the distal end of a deep seated tumor is, at present, not always possible. Treatment protocols specify a minimum tumor dose. For future accelerator-based BNCT facilities it is desirable to limit the treatment time to less than one hour for the following reasons: First, the boron delivery drug gets washed out of the tumor cells over time. For example, the concentration of BPA, the only drug currently approved for U.S. clinical trials, is greatly reduced after several hours. Second, patient comfort can be a limitation and, third, short treatment times are desirable at future hospital-based BNCT facilities for operational reasons.

## 3 ACCELERATOR-BASED NEUTRON SOURCES

A variety of accelerator-based neutron sources for BNCT have been proposed and investigated [3]. This paper is restricted to p and d induced reactions in Li and Be targets. Other interesting options such as neutron production near the threshold of the $^7Li(p,n)^7Be$ reaction [4] or photoneutron sources [5] are not included.

*3.1 Neutron production*

The reaction $^7Li(p,n)^7Be$ has a threshold of 1.881 MeV and displays a large resonance in the forward direction around 2.3 MeV which extends to about 2.5 MeV. Neutron double differential distributions were calculated as function of incident proton beam energy using normalized Legendre coefficients [6] for predicting the $^7Li(p,n)^7Be$ cross section [7].

Neutron yield distributions for proton and deuteron induced reactions in thick beryllium targets were taken from the literature. However, as described below, complete neutron energy and angular distributions at the energies of interest were not available and, consequently, some neutron yield distributions were extrapolated from the available data.

The angular and energy distributions of thick beryllium target neutron yields published by Brede et al. [8] for a proton energy ($E_p$) of 19.08 MeV were used as the neutron source description for an evaluation of this reaction for BNCT.

Thick target neutron yields for the Be(p,n) reaction at lower proton energies were recently measured by Howard et al. [9]. The published neutron yield energy spectra for Ep = 4.0 MeV at three angles, 0°, 40°, and 80° were used. The energy distribution at backward angles was approximated as being identical to the 80° spectrum with an upper energy cutoff at 1 MeV. The resulting total neutron yield of $6.3 \cdot 10^{11}$ n/mC is about a factor of 2 lower than the total neutron yield given by Hawkesworth [10].

The Be(d,n) reaction was included in this study since it offers higher neutron yields than the $^7Li(p,n)$ reaction at beam energies below 3 MeV. Only limited neutron yield data could be found in the literature. Meadows et al. [11] published thick beryllium target neutron spectra at 0° for incident deuteron energies between 2.6 and 7.0 MeV, and Smith et al. [12] published angular distributions for the $^9Be(d,n)^{10}B$ thick target reaction at $E_d$ = 7 MeV. Neutron yield distributions were constructed based on the 0° spectrum at 2.6 MeV and the angular distributions measured at 7 MeV. A total neutron yield of $2.3 \cdot 10^{12}$ n/mC was found compared to a yield of $1.5 \cdot 10^{12}$ n/mC given by Hawkesworth [10].

The neutron yields of the reactions listed above vary by two orders of magnitude. The $^9Be(p,n)$ reaction at $E_p$ = 19 MeV produces the highest total neutron yield of $6 \cdot 10^{13}$ n/mC (for neutrons energies $E_n > 0.7$ MeV) but the energy spectrum extends to $E_n$ ~15 MeV necessitating a thick moderator. At $E_p$ = 4 MeV the upper neutron energy limit is ~2 MeV and the neutron yield is much reduced. The neutron spectrum of the $^9Be(d,n)$ reaction at $E_d$= 2.6 MeV exhibits its highest yield at neutron energies below 2 MeV, but also features a high energy component up to about 6 MeV. The upper neutron energy for the $^7Li(p,n)^7Be$ reaction at $E_p$ = 2.4 MeV is 700 keV and the total yield is $7.69 \cdot 10^{11}$ n/mC.

*3.2 Moderator and Neutron Transport Modeling*

Modeling of the neutron beams from the production target, through a filter assembly, and into a phantom is necessary for evaluating different neutron sources for BNCT. This has been carried out in two stages. The first stage simulates the neutron beam from the production source through the moderator and filter assembly using the Monte Carlo program MCNP [13]. The same moderator and filter assembly has been used for all analyzed neutron sources. Only the moderator thickness has been varied to optimize the performance.

A cross section through the three dimensional geometry specified for MCNP is shown in Figure 1. This geometry includes a 5 cm radius flat circular neutron source, which is followed by a cylindrical moderator of variable thickness and material. Surrounding the entire moderator and production target is an $Al_2O_3$ reflector. In

all simulations a mixture of 60% Al and 40% Al/$AlF_3$ has been used as the moderator material. This material has been shown to perform well at a fission reactor [14] and for the $^7Li(p,n)^7Be$ reaction [15].

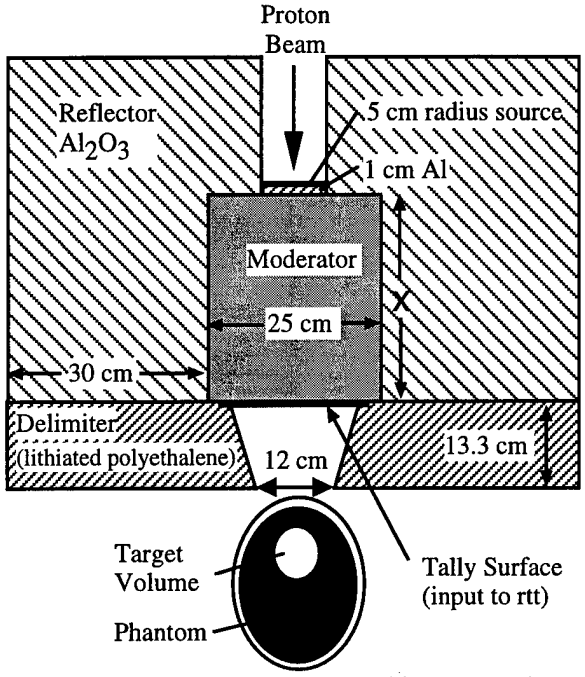



Figure 1: Moderator and filter assembly cross section with head phantom.

Analyzing the transport of neutrons and photons through a head phantom is necessary to determine the clinical properties of a beam. This has been done in the second modeling stage using the Monte Carlo-based BNCT treatment planning code, "rtt-MC" [2]. The geometry and setup is depicted in figure 1. It includes a lithiated polyethalyene beam delimiter and a head phantom. "Tally Surface" indicates the epithermal neutron source used as input to "rtt-MC'.

Figure 2 shows the total thermal neutron fluence for a treatment, which is roughly proportional to the equivalent tumor dose, as a function of depth for the accelerator beams and, for comparison, the BMRR beam. The $^7Li(p,n)$ source produces the highest thermal neutron fluences. Significantly lower thermal fluences, particularly at more than 3 cm depth, were found for the sources for which the primary neutron energy spectrum extends to higher energies, $^9Be(p,n)$ at 19 MeV, $^9Be(d,n)$, and the fission reactor. This is due to the increased moderator thickness needed for the suppression of the fast neutron dose. At a proton beam energies of 4 MeV the thermal fluence distribution for the $^9Be(p,n)$ source is closer to that of the $^7Li(p,n)$ source. Table 1 lists for each source the equivalent tumor doses at the point of maximum thermal fluence, at 5 cm depth, and at 8 cm depth. It also gives the beam currents required to match the BMRR treatment time of 40 min. The range given for the neutron sources using a beryllium target reflects the uncertainties in the neutron yield estimates.

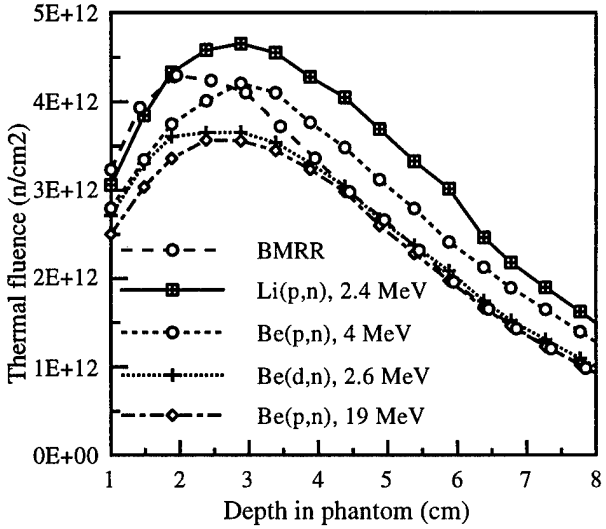



Figure 2: Thermal fluences as function of depth.

*3.3 Accelerator options*

As can be seen in Table 1 the beam current requirement is dramatically lowered when bombarding a Be-target with 19 MeV protons. Compact cyclotrons are an attractive option for providing beam currents of a few mA at energies between 10 and 20 MeV. Although such neutron sources may be suitable for BNCT, they can not match the quality of the epithermal neutron beams that can be produced at lower proton beam energies.

The neutronics study points towards an accelerator neutron source utilizing a lithium target and a proton beam of about 2.4 MeV. A number of accelerator technologies have been proposed [3] including radiofrequency quadrupole (RFQ) and other linac structures. While some of these technologies still need significant research and development, others are quite mature. A prototype tandem accelerator [16] designed for a maximum energy of 4.1 MeV and currents up to 4 mA is operated at MIT and used for BNCT related research. At

| Neutron source | $^7Li(p,n)$ | $^9Be(p,n)$ | $^9Be(p,n)$ | $^9Be(d,n)$ | BMRR |
|---|---|---|---|---|---|
| Beam energy (MeV) | 2.4 | 4.0 | 19 | 2.6 | 3 MW |
| Beam current (mA) | 27 | 40-80 | 1.5 - 3 | 50 - 100 | - |
| Moderator thickness (cm) | 34 | 42 | 70 | 70 | - |
| Eq. tumor dose (max.) (Gy-Eq) | 66 | 61 | 53 | 54 | 62 |
| Eq. tumor dose (5cm) (Gy-Eq) | 51 | 44 | 38 | 39 | 39 |
| Eq. tumor dose (8cm) (Gy-Eq) | 22 | 20 | 16 | 16 | 15 |

Table 1: Comparison of epithermal neutron sources. The treatment time for all sources is 40 min.

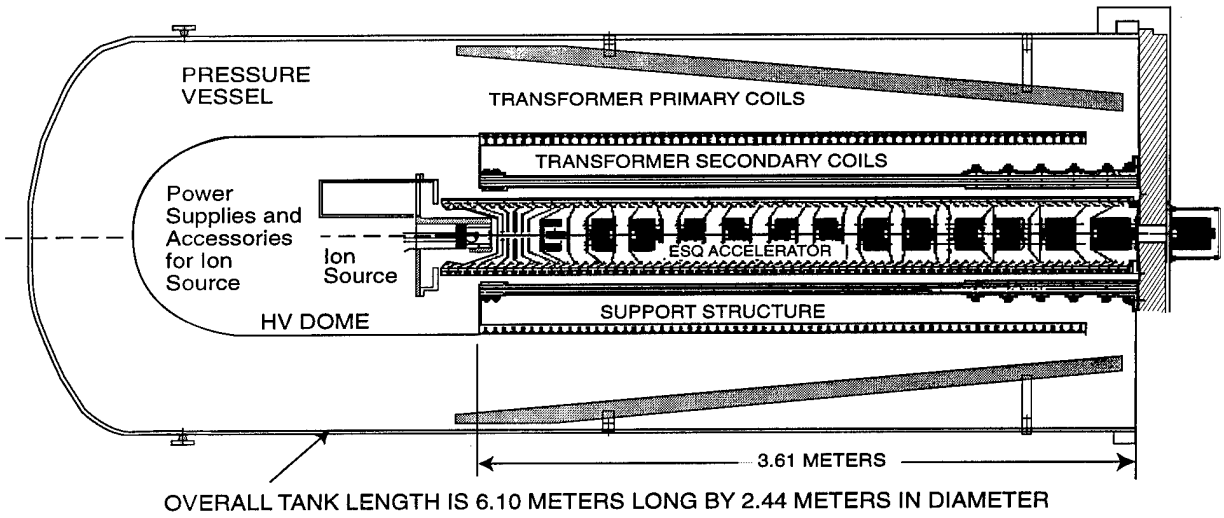



Figure 3: Schematic diagram of the 2.5 MeV ESQ accelerator

Birmingham, UK, it is planned to utilize a d.c. accelerator expected to deliver beam currents of 5 - 10 mA. However, the neutronic studies summarized in this paper indicate that higher proton beam currents are desirable for optimization of the epithermal neutron beam and increased flexibility in patient treatments. Accelerators with electrostatic quadrupole (ESQ) columns, which have been developed at LBNL for fusion applications [17], are capable of producing high current, megavolt beams and are therefore well suited for BNCT.

## 4 ESQ-ACCELERATOR BASED BNCT FACILITY

### *4.1 ESQ Accelerator*

For applications that require high average beam currents or variable beam energy, d.c. electrostatic accelerators are most suitable. Accelerators using electrostatic quadrupole (ESQ) columns can be operated with high beam current and high reliability [18]. The electrostatic quadrupole lenses in the acceleration column provide a combination of converging and diverging lenses that produces a net focusing effect on the beam. This gives the key advantage of an ESQ accelerator that the transverse focusing can be very strong without incurring a longitudinal field exceeding the breakdown limit. In addition, the secondary electrons generated within the accelerator column are quickly removed by the strong transverse electric field instead of being allowed to multiply and then develop into a column arc-down.

At LBNL the supporting structure and high pressure vessel of a decommissioned injector are reused for the construction of an ESQ accelerator for a BNCT facility. A new ESQ accelerator column will be installed and the existing power supply (Dynamitron) replaced with an air-core multistage transformer-rectifier stack [19]. Figure 3 shows a schematic diagram. Located at the front end is a multiscup ion source that can deliver positive hydrogen ion beams with monoatomic ion fraction higher than 90% [20]. Radio-frequency induction discharge is used to provide clean, reliable and long-life source operation. An extractable hydrogen ion current density of 100 mA/cm$^2$ has been achieved demonstrating that this ion source can meet the requirement for BNCT. Following the ion source is a 325 keV low energy beam transport section (LEBT) which consists of 6 electrodes. The main acceleration is done by 13 ESQ modules. The bore diameter is 6 cm. 70 alumina rings make up the 3.8 m long column. Cooling of the copper ESQ electrodes will keep the temperature rise below 100°C for a deposition of 100 W on each electrode. Computer simulation using the WARP-3D particle code showed that the column can accelerate a 125 mA beam. Further details can be found in Kwan et al. [21].

Modifications to the existing power supply for test measurements from capacitively coupled to inductively coupled have been completed. The primary to secondary coupling along the length of the acceleration column has been equalized to ±10% by adjusting the primary current density. It will ultimately be reduced to ±1% by adjusting the number of turns in the secondary coil. The low impedance of the inductively coupled system will allow operation at currents exceeding 50 mA.

### *4.2. Neutron Production Target*

The lithium neutron production target is a crucial component of the accelerator neutron source. Since metallic lithium has a low melting point of 179°C, very effective target cooling is mandatory. In our design a 50 μm thick Li layer is deposited on an aluminum backing. Applying the microchannel absorber concept, many channels are cut into the substrate for convective water cooling. The finite element code ANSI was employed to simulate the heat flow and perform a temperature and stress analysis. The results indicate that for a heat-load of ~600 W/cm$^2$ the surface temperature can be kept below 150°C. A recent heat-load test of a prototype aluminum panel, performed at the Plasma Materials Test Facility at Sandia National Laboratory, confirmed the simulations. The thermal fatigue reliability of the prototype was

demonstrated by subjecting it to 50,000 heat cycles. A V-shaped target with the panels placed at a 30° angle in respect to the beam cuts the surface heat-load in half. Further analyses showed that by optimizing the beam profile and increasing the target area up to 15 cm x 15 cm beam currents of up to 50 mA can be handled.

## 5 SUMMARY

ESQ accelerators capable of producing high d.c. current, megavolt beams are very well suited to exploit the $^{7}Li(p,n)^{7}Be$ reaction as a neutron source for BNCT. A d.c. ESQ accelerator is being designed for proton beams up to 2.5 MeV and beam currents exceeding 50 mA. The d.c. power to the ESQ electrodes is provided by an air-core transformer stack surrounding the accelerator column. A Li-target is being developed for proton beam currents up to 50 mA. The design of the moderator and filter assembly is driven by clinical requirements and geared towards high quality epithermal neutron beams while maintaining a short treatment time. Our work indicates that an accelerator-based neutron source for BNCT is practical and superior to reactor neutron sources.

## 11 ACKNOWLEDGMENTS

This paper is based on the work of many people involved in the BNCT project at LBNL. Especially, I would like to acknowledge the contributions of D.L. Bleuel, R.J. Donahue, J. Kwan, K.-N. Leung, L.L. Reginato, and R.P. Wells. This work is supported by the Director, Office of Energy research of the U.S. Department of Energy under Contract No. DE-AC03-76SF00098.

## REFERENCES

[1] Boron Neutron-Capture Therapy of Glioblastoma Multiforme at the Brookhaven medical research reactor, A Phase I/II Study (FDA IND # 43,317), Protocol #4, A.D. Chanana, M.D., Med. Dep., Brookhaven Natl. Lab., Upton, NY 11973-5000, January, 1996.

[2] D.W. Nigg et al., "Methods for Radiation Dose Distribution Analysis and Treatment Planning in Boron Neutron Capture Therapy," Int. Journal of Rad. Oncology Bio. Phys., **28**, 1121-1134, 1994.

[3] See contributions to the Proceedings of the First International Workshop on Accelerator-Based Neutron Sources for Boron Neutron Capture Therapy, Jackson, Wyoming, September 1994.

[4] F. Harmon, "Accelerator Neutron Sources for NCT using Near Threshold Charged Particle Reactions," Abstract for the 14th Int. Conf. on the Appl. of Acc. in Res. & Ind., Denton, Texas, November 1996.

[5] D. Nigg et al., "Computational and Experimental Studies of an Electron Accelerator Base Epithermal Photoneutron Source Facility for BNCT," INEL-96-0139, 1996.

[6] H. Liesken and A. Paulsen, "Neutron Production Cross Sections and Energies for the Reactions $^{7}Li(p,n)^{7}Be$ and $^{7}Li(p,n)^{7}Be^{*}$," Atomic Data and Nuclear Data Tables, **15**, 57-84, 1975.

[7] D.L. Bleuel and R.J. Donahue, "Optimization of the $^{7}Li(p,n)$ Proton Beam Energy for BNCT Application," LBL-37983, Rev. 1, May 1996.

[8] H.J. Brede et al., "Neutron Yields from Thick Be Targets Bombarded with Deuterons and Protons," Nucl. Instr. Meth. **A274**, 332-344, 1989.

[9] W.B. Howard et al., "Measurements of the $^{9}Be(p,n)$ thick target spectrum for use in accelerator-based Boron Neutron Capture Therapy," Med. Phys. **23**, 1233-1235, 1996.

[10] M.R. Hawkesworth, "Neutron Radiography: Equipment and Methods," Atomic Energy Review, **152**, 169-221, 1977.

[11] J.W. Meadows, "The $^{9}Be(d,n)$ thick-target neutron spectra for deuteron energies between 2.6 and 7.0 MeV," Nucl. Instr. Meth., A324, 239-246, 1993.

[12] D.L. Smith et al., "Neutron Emission from $^{9}Be(d,n)^{10}B$ Thick-Target Reaction for 7 MeV Deuterons," Nucl. Instr. Meth. **A241**, 507-510, 1985.

[13] "MCNP-A A General Monte Carlo N-Particle Transport Code, Version 4A," J.F. Briesmeister, Ed., LA-12625, Los Alamos Natl. Lab., 1993.

[14] I. Auterinen et al., "Design of an epithermal neutron beam for the TRIGA reactor in Otaniemi," CUNCT BNCT Workshop Helsinki 1993, TKK-F-A718, 1994.

[15] D.L. Bleuel et al., "On Optimizing the $^{7}Li(p,n)$ Proton Beam Energy and Moderator Material for BNCT," to be published in the Proceedings of the 14th Int. Conf. on the Appl. of Acc. in Res. & Ind., Denton Texas, November 1996.

[16] R.E. Shefer et al., "Tandem Electrostatic Accelerators for BNCT," Proceedings of the First Int. Workshop on Accelerator-Based neutron Sources for Boron Neutron capture Therapy, Jackson, Wyoming, September 1994, Vol. I, 89-110.

[17] J.W. Kwan et al., Proc. 14th IEEE Particle Accelerator Conf., San Francisco, CA, p. 1955, 1991.

[18] J.W. Kwan et al., Nucl. Instr. and Meth., B99,710-712, 1995.

[19] L.L. Reginato et al., "Designing Power Supplies for 2.5 MeV, 100 mA d.c. for BNCT," to be published in the Proceedings of the 14th Int. Conf. on the Appl. of Acc. in Res. & Ind., Denton Texas, November 1996.

[20] K.N. Leung, "Ion Sources for High Purity Ions," to be published in the Proceedings of the 14th Int. Conf. on the Appl. of Acc. in Res. and Ind., Denton Texas, November 1996.

[21] J.W. Kwan et al., "Design of a DC ESQ Accelerators for BNCT Application," to be published in the Proceedings of the 14th Int. Conf. on the Appl. of Acc. in Res. & Ind., Denton Texas, Nov., 1997 and LBNL #38983, 1996.

# MARKET DRIVEN DESIGN OF ACCELERATOR SYSTEMS FOR STERILIZATION OF MEDICAL PRODUCTS

K. Whitham, T. Allen, H. Anamkath, F. Gower, R. Mendonsa, H. Schaffer, A. Zante
Titan Beta, 6780-R Sierra Court, Dublin CA 94568

*Abstract*

Historically, most scientific accelerator systems are the primary ingredient of a given facility. In commercial applications of accelerators the customers needs are for a systems in which the accelerator is a part of a process. In the case of the sterilization of medical products, the accelerator is part of a process which ensures a sterile dose to FDA standards to a variety of products. The process includes a variety of hardware and specifications for parameters that are unrelated to accelerator technology. In addition, the customers are in general unfamiliar with accelerator technology. This creates the need for a different approach to design including a multidisciplined group of designers as well as the need for the design of equipment that has industrial ruggedness and reliability, so as to be usable by relatively low skill levels. In addition, the systems must be highly cost efficient, because the accelerator technology will be competing with alternative technologies which invariably are less expensive.

This paper describes the design of the TB 10/15 accelerator system which is currently being operated in several locations around the world. The description includes the market needs that were addressed and how the system was designed to meet them.

## INTRODUCTION

Sterilization of medical products was identified as a possible application for a scanned beam accelerator.

Societal pressure to check rising health care costs has resulted in demands for less expensive and more flexible methods to sterilize medical devices. This has generated interest in electron beam sterilization because it offers fast turnaround time and high efficiency compared with competing technologies. The combination provides the opportunity for lower sterilization cost. In addition, competing technologies have inherent problems which encourage the accelerator technology.

1. Cobalt 60 has high costs for the source and replacement. There is public pressure to avoid placement of large amounts of highly radioactive material in urban locations.
2. EO (ethyleneoxide) gas is toxic, carcinogenic, and explosive, and is being phased out.

The market for alternative sterilization methods need was recognized and studied to ascertain if a business could be established. The effort involved market surveys, and cost estimates based on various system designs and scenarios. The system design rapidly converged on the parameters of the Titan Scan machine.

One of the major parameters considered was beam power. The power was sized to be able to provide sterilization support on a contract service basis to a regional area of manufacturers within reasonable transport range. If the system were too large, the capital cost could not be justified because the system could not be kept busy. If it were too small, the facility could not handle the product volume and the cost per watt of beam would be too high. We converged on a 15 kW beam power operating point. We designed for 20 kW.

Another major parameter was beam energy. The FDA regulations preclude operation beyond 10 MeV, to avoid activation in some materials. 10 MeV provides a useful range of direct electrons in most medical products. The density of which is .03 - .3 g/cc.

Another parameter was the number of operating energies. In order to maximize reliability, we chose the simplest approach with the fewest components and that is a single operating energy. At that point all the parameters can be optimized for efficiency and reliability.

Another decision was to have the system dedicated to medical products and not multipurpose. The result was the Titan Scan TB 10/15 scanned beam system.

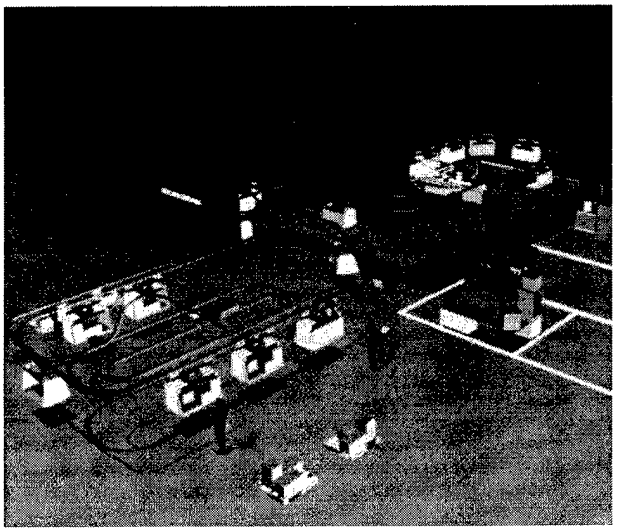


**Fig. 1.** *Artist sketch of facility.*

## FACILITY DESCRIPTION

The Titan Scan TB 10/15 facility is divided into four areas: a processing room, a modulator room, a control room and a product staging area. The processing room is a shielded concrete structure with walls and roof ranging from 2.1 m to about 3.1 m at the thickest point directly in front of the electron beam. The processing room contains a 1.4 m long standing-wave accelerating section, magnetic systems to focus and scan the 10 MeV, 15 kW electron beam, an overhead power and free transport conveyor and the under-beam process table.

0-7803-4376-X/98/$10.00 © 1998 IEEE

Power supplies and utilities are located in an adjacent modulator room, which is separated from the processing room by a shield wall so it can be occupied during operation. The control room houses the computers and subsystems that control, monitor and document the sterilization process. An isolated dosimetry lab is located in the control room area. Processed and unprocessed product is separated by a chain-link fence to prevent intermixing.

## LINEAR ACCELERATOR (LINAC)

Because the LINAC system is specifically designed to function as part of a medical product sterilization system, it is built with a component safety margin allowing continuous, 24 hour per day operations. The horizontal accelerator axis provides for easy two-sided irradiation of medical products with bulk density in the range from 0.03 to 0.30 grams per cubic centimeter. The beam is scanned into the vertical direction to accommodate packages up to 51 cm in height at the front surface of the carrier.

Figure 2 shows the vertical dose distribution profile on the surface of a 0.1 g/cc uniform density foam phantom from the top to the bottom of a carrier performed with an energy of 10.8 MeV and a repetition rate of 300 pulses per second. Figure 2 results show an average of 15.2 kGy with a coefficient of variation (CV) of 1.54%.

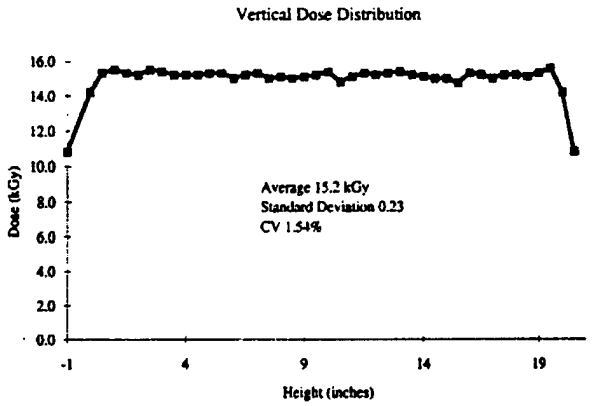



**Fig. 2.** *Vertical dose distribution (scan width) at the surface of a 0.1 g/cc uniform density foam phantom.*

## BEAMLINE

The electron gun is a Pierce geometry triode design with a dispenser cathode and is operated at 25 kV and delivers up to an ampere of peak current. It has a one square cm cathode and is operated with a one liter per second appendage ion pump.

The gun pulser is a floating deck pulser which provides the gun filament and grid bias as well as pulsing the cathode. It has an automatic filament cutback circuit which programs the filament current as a function of rep rate.

A solenoid covers the 1.4 m s-band standing waveguide to insure an acceptable beam shape can capture efficiency. With it we obtain over 300 mA of accelerated beam current. A pair of steering coils are placed under the solenoid for beam positioning.

The output of the waveguide has a fast in-line valve shutter and beam current monitor prior to the scanner.

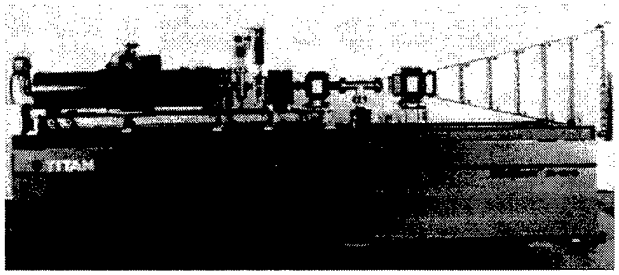


**Fig. 3.** *Accelerator beamline.*

## RF POWER

The RF power source for the TB 10/15 system is a klystron operated at up to 5.0 MW and 40 KW at 2856 MHz. It requires 120 watts of RF drive at full peak power.

An Automated Frequency Control (AFC) system utilizing waveguide Reflected power phase sensing is used to maintain frequency.

## MODULATOR

The modulator uses a 14 section Pulse Forming network (PFN) with an operating voltage of 20 kV. End-of-line clippers protect the klystron and thyratron against voltage reversals. The modulator HVPS is shown in Figure 4.

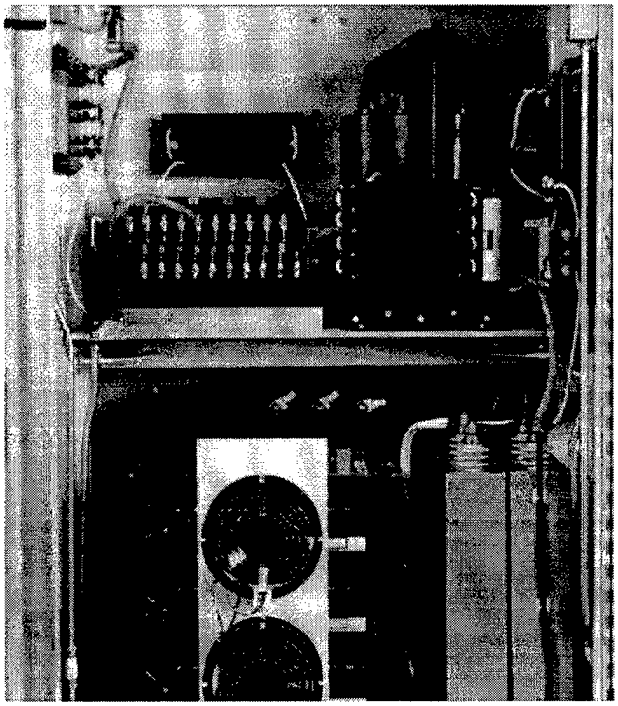


**Fig. 4.** *Modulator High Voltage Power Supply*

## CONTROLS

The system is remotely controlled from the control room. The information and control system uses a graphic based interface with a distributed architecture containing industrial PLC's and a PC control system network. The system provides real-time monitoring and control of process variables and on-line error detection and recovery.

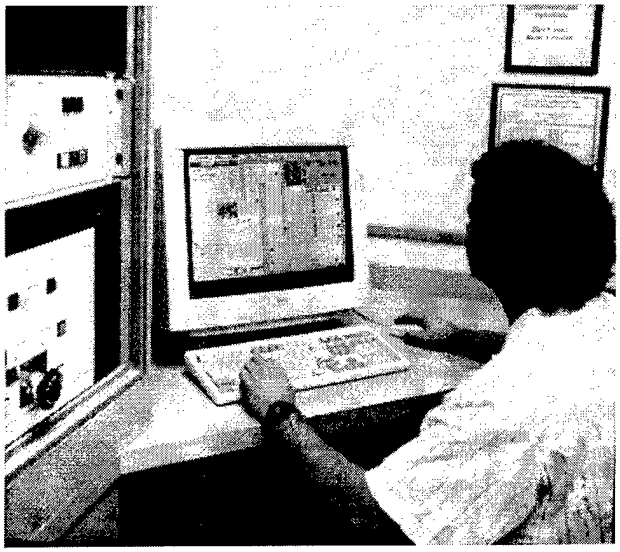


**Fig. 5.** *Operator's station in the control room.*

Local controls for system adjustment along with power supplies are in a rack near the modulator.

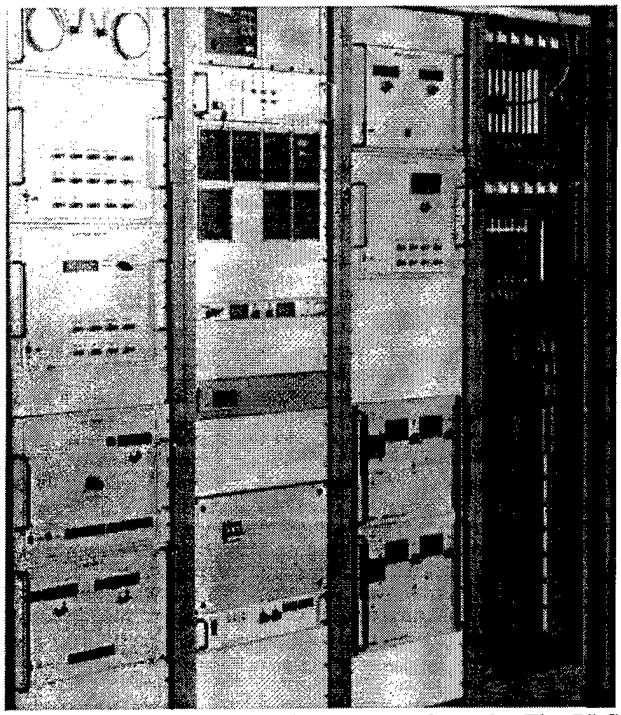


**Fig. 6.** *Local controls and power supply rack. The PLC also resides in this rack.*

## OPERATING DATA

The existing TB 10/15's are in daily operating routinely running 24 hours a day with a 4 hour per week maintenance shift. The operating parameters are as follows:

| | |
|---|---|
| RF Power | 5 MW peak |
| Beam Current | 300 mA |
| Energy | 10.0 MeV |
| Pulse Width | 16.2 μs |
| Rep Rate | 310 |
| Beam Power | 15 kW |

Medical products from a variety of medical product manufacturers are being processed daily.

## MATERIAL HANDLING SYSTEM

The material handling system employs a power and free conveyor to transport carriers between the product staging area and the process room. In the common entrance labyrinth, the inbound and outbound conveyor paths are stacked one above the other. In the process room, the 99 cm long carriers are transferred to an independent servo-controlled process conveyor table that provides and maintains a spacing of less than 2.54 cm between carriers as they are transported through the beam. The tight spacing of the carriers in front of the beam contributes positively to the beam utilization efficiency.

The process conveyor servo-motor maintains carrier speed within 0.5% of the set point and assures a highly uniform and reproducible horizontal dose distribution within the product. Figure 7 shows the horizontal dose distribution measured in polyethylene foam at the midline of the carrier.

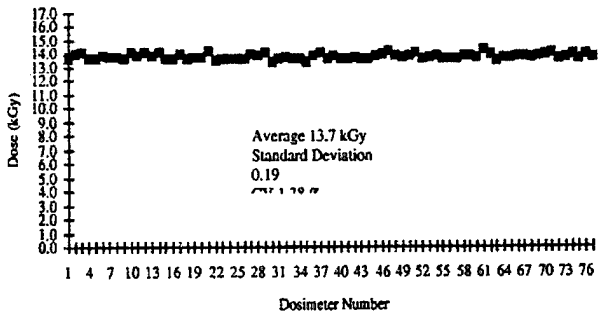



**Fig. 7.** *Horizontal surface dose profile at the carrier midline.*

A fail-safe 180° rotation mechanism located in the process room assures that each carrier receives uniform two sided irradiation. The concept of horizontal beam processing eliminates the need for cartons to be manually flipped and the associated concern with product shifting.

## PROCESS INTERRUPTS

If an event occurs triggering a shutdown of the LINAC while product is being processed, the entire system is shut down. During this shutdown interval, as the beam is turned off, the process conveyor requires additional time to reach a complete stop. It is during this interval that a potential variation in the dose delivered to the product can occur. Process integrity must be maintained at all times even during a process interrupt. To compensate for the potential decrease in dose at the point of the process interrupt, the start-up sequence is such that the beam turns on prior to start-up of the process conveyor. This results in additional beam pulses delivered to the product, compensating for the pulses lost during the shutdown interval. This restart sequence produces a positive transition dose

similar to the transit dose associated with process interrupts in a typical gamma processing facility.

During the facility commissioning and validation, simulated process interrupt tests were conducted and their effects on the absorbed dose were measured. All measurements were made in a phantom product of polyethylene foam of 0.1 g/cc density.

Figure 8 shows the effect of a process interrupt on the absorbed dose at process conveyor speed of 1.2 meters per minute. Figure 8 depicts three process interrupts on the same carrier. All three process interrupts reflect the same small transit dose as one would see in a typical gamma facility interrupt. The dose was measured in the direction of carrier travel on the front face (0 cm) of the phantom, ¼ deep (18.4 cm) into the phantom and on the center line (36.8 cm).

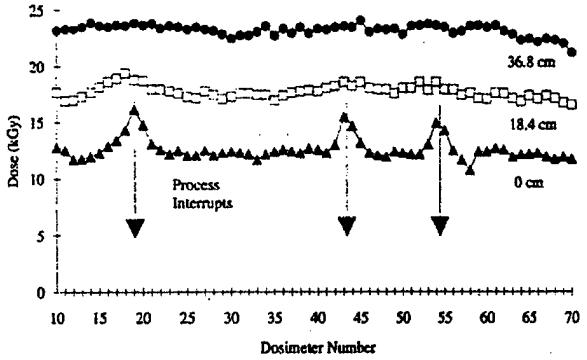



**Fig. 8.** *Effect of a series of three process interruptions at various product depths at a conveyor speed of 1.2 meters per minute.*

It is interesting to note that the effect of the process interrupt diminishes with depth into the phantom to the point where it is not observable on the center line. This behavior is the result of side scatter and diffusion of electrons in the interior of the phantom.

Using the same phantom material of 0.1 g/cc density foam as used on the interrupt tests, calculations of net beam efficiency were shown to be 56%.

## PROCESS PERFORMANCE

Monitoring of process repeatability from carrier to carrier is demonstrated in Figure 9 which depicts a thirty carrier dose map run on cases of petri dish product performed in July, 1993. The reported results are those of dosimeters placed in the standard reference monitoring position on the front of the product cases. The results demonstrate repeatability with a 0.6 kGy standard deviation and an overall coefficient of variation (CV) of 4.1%.

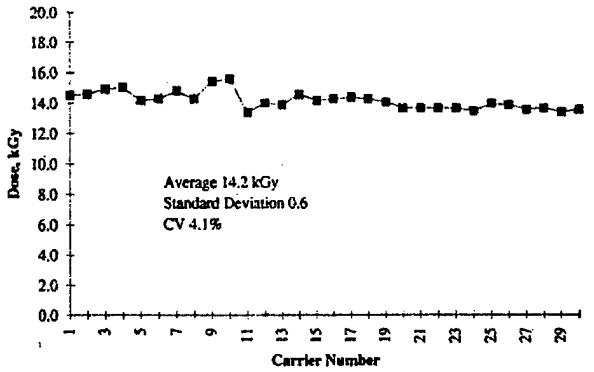



**Fig. 9.** *Results of thirty carrier measurement on a single process run measured at the reference monitoring position on the product box.*

Process reproducibility is demonstrated in Figure 10 which is an average of the dose results over a series of twelve process runs conducted over twenty days in August 1994 on the same petri dish product. Again, the standard monitoring position has been measured and the results are displayed which show a standard deviation of 0.39 kGy and a CV of 0.3%.

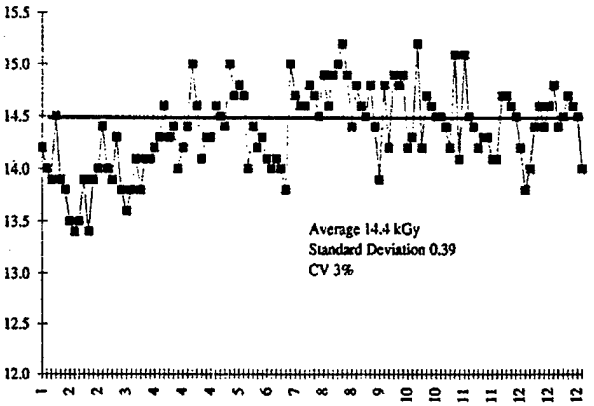



**Fig. 10.** *Dose results from twelve process runs performed over a 20 day period measured at the reference monitoring position on the product box.*

## VALIDATION MAINTENANCE

It is important in medical device sterilization to have demonstrated results which are consistent over time with the original validation of the process.

All of these issues and specifications along with many others were developed and clarified in conjunction with customer's needs as revealed in countless discussions and correspondence.

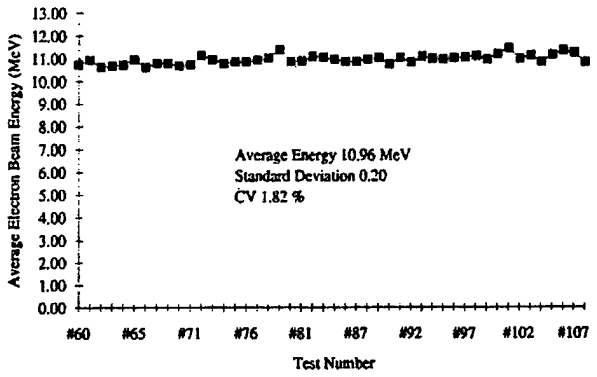



**Fig. 11.** *Plot of 47 energy determinations from penetration range measurements in aluminum block over an eight month period.*

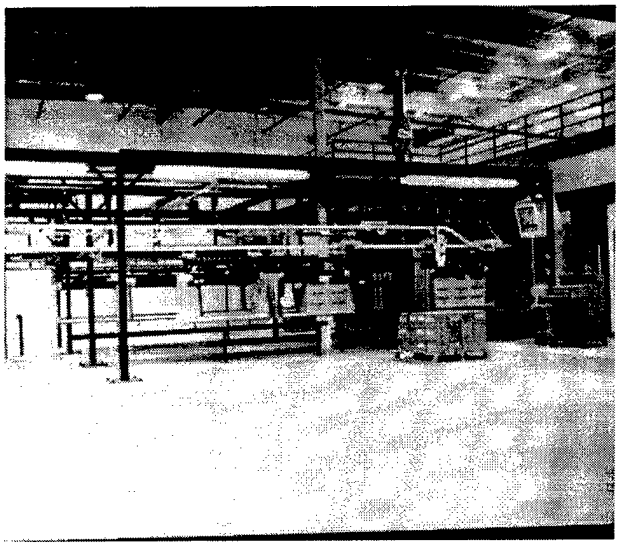


**Fig. 12.** *Product handling area of a typical system.*

## CONCLUSION

The successful application of an rf linac to the sterilization of medical products has been performed by the Titan Corporation. It required careful attention to market requirements, in order to be successful in addition to careful design and implementation of the accelerator system. The parameters that drove the system performance included beam power, energy, surface dose uniformity, process interrupt recovery without product loss, stability of energy surface dose, and depth dose with time, and high reliability. Many critical parameters were not directly accelerator related. Close collaboration of the system design team was required to reach the multidisciplined goals.

## BIBLIOGRAPHY


Allen, J.T, Calhoun, R., Helm, J., Kruger, S., Lee, C., Mendonsa, R., Meyer, S., Pageau, G., Schaffer, H., Whitham, K., Williams, C.B., Farrell, J.P., "A Fully Integrated 10 MeV Electron Beam Sterilization System", 9th International Meeting on Radiation Processing.

Anamkath, H., Gower, F., Mendonsa, R., Miller, R., Whitham, K., Zante, A., "An Industrial Application of a Pulsed Power Modulator", 22nd International Power Modulator Symposium, June 24-27, 1996.

Anamkath, H., Gower, F., Mendonsa, R., Whitham, K., Zante, A., Allen, T., Pageau, G., Williams, C.B., "10 MeV, 10 kW E-Beam Processing Linac". Application of Accelerators in Research and Industry. Duggan, J.L., ed. Nuclear Instruments and Methods, North Holland, Amsterdam.

Association for Advancement of Medical Instrumentation (1991). Guideline for Electron Beam Sterilization of Medical Devices. ANSI/AAMI ST31-1990. Arlington, Virginia.

Association for Advancement of Medical Instrumentation Sterilization of Health Care Products – Requirements for Validation and Routine Control – Radiation Sterilization. AAMI/ISO 11137 (R/2-94). Arlington, Virginia.

Boyd, A.W., Chadwick, K.H., McDonald, J.C., McLaughlin, W.L., Miller, A., (1989). Dosimetry for Radiation Processing. Taylor & Francis, London.

Cleland, M.R., O'Neil, M.T., and Thompson, C.C. (1993). Sterilization with Accelerated Electrons. Sterilization Technology. Morrisey, R.F. and Phillips, G.B., eds. Van Nostrand Reinhold, New York, 218-253.

Cleland, M.R., Pageau, G.M., (1985). Electrons vs. Gamma Rays: Alternative Sources for Irradiation Processes. FAO/IAEA International Symposium on Food Irradiation Processing. Washington D.C.

Cleland, M.R., Pageau, G.M., (1987). Comparisons of X-Ray and Gamma-Ray Sources for Industrial Irradiation Processes. Nuclear Intruments and Methods in Physics Research. North-Holland, Amsterdam, 967-971.

Kruger, S.K., Pageau, G.M., Peterson, B., Dosimetry Automation and Data Management. 4th Nordion Gamma Processing Seminar, May 26-31, 1991.

Whitham, K., Anamkath, H., Gower, F., et al., "12 MW, 100 kW, 7000 hour/year Modulator for Titan Scan", 10th IEEE International Pulsed Power Conference, Albuquerque, NM, July 10-13, 1995.

# THE GSI CANCER THERAPY PROJECT

H. Eickhoff, Th. Haberer, G. Kraft. U. Krause, K. Poppensieker, M. Richter, R. Steiner
GSI Darmstadt

*Abstract*

At the Heavy Ion Research Institute GSI in Darmstadt an experimental cancer treatment program with a five years duration has been developed. A new method for cancer treatment with ions is applied, using rasterscan method in addition to an active pulse to pulse variations of ion beam properties, including the energy, intensity and focusing.
An overview of this Cancer Therapy Project is presented, that covers both accelerator aspects to provide the required beam variations within a short time and the installations at the treatment place for rasterscan control. In addition to a description of the technical design (controlhard- and software) experimental results will be shown, containing the achieved beam properties and measurements of rasterscan performance.

## 1 INTRODUCTION

Whereas at presently existing therapy-dedicated proton- and light-ion accelerators for cancer treatment the beam-parameters (energy, intensity, optics) are constant over the treatment interval, at GSI a novel treatment concept is realized, that is based upon the 'rasterscan'-method and an active energy- and intensity-variation within the treatment time. With this method passive beam manipulations in order to perform a 3d-conformal irradiation (by means of devices for spreading and shaping the beam and sophisticated mechanical range manipulators) can be avoided [1, 2].
At the GSI in Darmstadt 350 patients will be treated within a five years experimental cancer treatment program; the first patient treatments are scheduled for this year.
The experiences within this experimental program with a novel treatment scheme will contribute to the design of a dedicated, hospital based therapy accelerator.

## 2 THERAPY REQUIREMENTS

For accelerator operation the GSI Therapy program requires reliable, fast, active variations (within a few seconds) of :

- beam energy
- beam intensity
- beam-size

within the treatment sessions. In the following table the essential beam parameters are summarized, which are the basis for the definition of the accelerator performance:

| | |
|---|---|
| • **Ion-species** | **:12 C (6+)** |
| • **Ion-source** | **: ECR** |
| • **Ion-energy** | **: 80 - 430 MeV/u** |
| • **Extraction-time** | **: 2 s** |
| • **beam-diameter** | **: 4 - 10 mm (hor., vert.)** |
| • **Intensity-Variation** | **: $2*10^6$ to $2*10^8$ Ions/spill** |
| • **No. of energy-steps** | **: 255** |
| • **No. of intens.-steps** | **: 15** |
| • **No. of focusing-steps** | **: 7** |

**Table. 1:** Therapy requirements

These requirements in connection with the enhanced safety demands imply a major change of the accelerator operation in all accelerator sections in comparison to the usual physics research mode.
The necessary parameter variations of the accelerator components have to be performed with a high degree of reliability and reproducibility. The requested beam properties for all possible parameter variations have to be accurate in the (sub-) mm range.
A second demand is the possibility of performing therapy treatment and various physic experiments sequentially within short time intervals.

## 3 MODIFICATIONS OF ACCELERATOR CONTROLS

The required large amount of parameter variation can only be handled by a major modification of control-hard and -software. Due to the tight schedule of the therapy project a concept had to be found to achieve this goal within the existing frame of accelerator operation and without influence on the experimental program. This concept is based upon the following essential features:

- the set parameters of the accelerator components have to be defined for all required parameter variations,
- the experimentally validated parameters are permanently stored within non-volatile memory of the component's control hardware,
- the reproducibility of beam parameters for identical set parameters is verified,
- during the therapy irradiation times parameter manipulations are excluded on component's level.

Within the present 'normal' accelerator operation a maximum number of 16 'virtual accelerators' (VA) can be provided for the experimental physics program. These VAs represent a complete set of different accelerator

0-7803-4376-X/98 /$10.00 © 1998 IEEE

parameters, that allow a change of beam parameters (energy, intensity,..) from pulse to pulse.
The Therapy requirements largely extend this maximal number of parameter variations (255 * 15 * 7 individual steps, see Table 1). Fortunately most components only depend upon one parameter (either energy or intensity or focusing); thus the variation possibilities are drastically reduced. Nevertheless an upgrade of memory capability was necessary. The existing Equipment Controllers (ECs) could be reused by replacing the existing memory piggi-back by a new one, providing 2 MByte of flash EPROM for the set parameters and 2 MByte of RAM for storing the actual component's parameters. [3]
Only the 'therapy accelerator' (#0) can activate subcycles within one VA for the demand of various energy-, intensity- and focus-steps. To provide the beam parameter information for the ECs in real time, there is no other means in the GSI control system but the timing system. It is connected to the irradiation place by a dedicated hardware link to receive, besides some status informations, the request for the next therapy beam according to the specific irradiation plan.
Although the patients safety will be guaranteed by the raster control system with redundant fast beam diagnosis and spill abort, additional precautions have been installed on the accelerator side:
- The stored, verified set values for the accelerator components are signed with a unique identification code; this code has to be transfered in order to activate the EPROMs set values.
- During the treatment time the accelerator is in a 'locked' state, which prohibits any components access.
- An interruption of the therapy cycle by other virtual accelerators is prohibited.
- all passive beam affecting devices (profile-grids, cups, valves,..) will be removed automatically.

## 4 THE INTENSITY CONTROLLED RASTERSCAN-METHOD

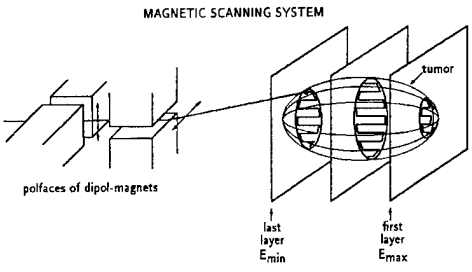



**Fig. 1** Rasterscan-Method

Fig. 1 shows the principle of the rasterscan-method [2]. The accelerated and slowly extracted beam enters 2 fast scanner magnets, that deflect the beam both in horizontal and vertical direction to cover the lateral dimensions of the tumor. Ionization chambers in front of the patient measure the number of ions at a specific irradiation point and control the scanner excitation. Fast multiwire proportional counters control the position and beam width at each scanning point. Whereas intensity measurements are performed within 13 µs, position control is done about every 150 µs.
When a required dose limit has been reached the beam extraction is interrupted very fast (0.5 ms) by locking the power supply of the two 'resonance'-quadrupoles, driving the beam smoothly into the 1/3 order betatron resonance. For safety reasons this procedure, that is well established at the synchrotron, will be extended by a second redundant spill-abort system.

## 5 EXPERIMENTS

In July 1995 the first beam was delivered to the newly installed beam line to the irradiation place ('Cave M')
In Nov. '95 the first therapy 'test cycle', consisting of 30 different energies in the range from 430 to 80 MeV/u was successfully tested after the described extensions of the control system had been installed and a new program for the data generation had been developed [4, 5]. For all required parameter variations this software calculates the set parameters for the synchrotron and the Cave-M beamline and sends them to the devices. In addition programming of the non-volatile memories and activation of different test conditions are possible.

Fig. 2 shows in the upper trace the SIS-Dipolefield for such a predefined test cycle; the lower trace shows the signal of the SIS beam current transformer.
A (low intensity) experimental pulse (1) is followed by 5 therapy preparation pulses (2) and twelve therapy pulses with decreasing extraction energies (3).

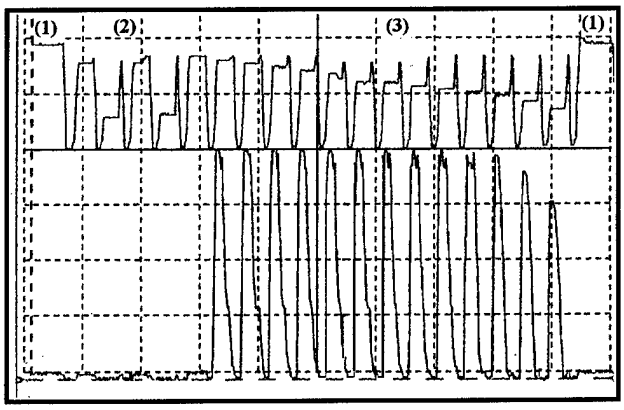



**Fig. 2** SIS-Dipole field (upper trace) and synchrotron beam current (lower trace) for a Therapy test cycle

The preparation pulses with variing magnet excitations are required to cope with magnetic hysteresis effects in

the SIS and the high energy beam line (within these pulses no beam is injected into the synchrotron).
For the same reason an additional magnet ramp after beam extraction was introduced for the therapy cycles in order to generate a constant magnet cycle that is independent from the extraction energy.
For the accelerator most of the available therapy test beamtimes within the last year were used to optimize the beam parameters in order to achieve the required specifications.

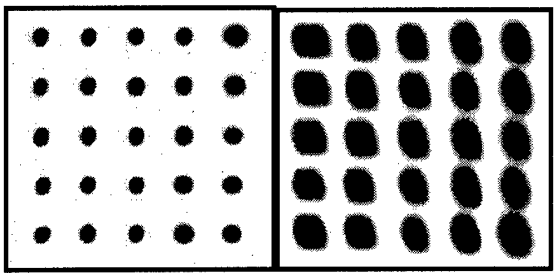


**Fig.3**: Beamspots at the isocenter for 25 energy-steps (strong and weak focusing)

Fig. 3 shows two pictures (a strongly focused beam on the left and a weak focused one on the right) of a polaroid film directly exposed to the beam at the treatment position ('isocenter'). By an appropriate programming of the scanner magnets, 25 spills with different energies were deflected in horizontal and vertical direction to individual positions with a separation of 15 mm (from 430 at the lower left side to 80 MeV/u at the upper right side).

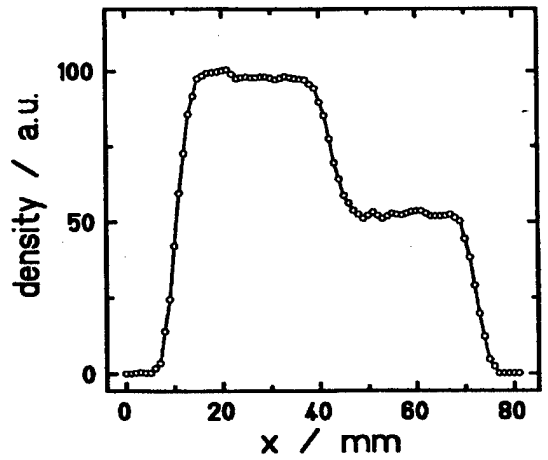



**Fig. 4** Dose profile with a factor of two step at the center

At the treatment place the main tasks were the development and test of the control system including the rasterscan and the fast beam monitor system.
Although a relatively strong intensity modulation of the extracted beam within the spill is observed, homogeneous dose distributions are achieved due to the fast intensity control of the scanning system.

Fig. 4 shows a measured dose profile of a 2-dimensional rasterscan, with a step of a factor of two in the center. The absolute homogeneity of the flat parts is in the range of ± 5 %, that is sufficient for therapy.

## 6 STATUS AND OUTLOOK

- Within the last 2 years all required modifications of the accelerator control to fulfill the therapy requirements were established and successfully tested. In addition the 'mixed operation', which means a change between therapy treatment and physic experiments, was realized.
- At the treatment place all hardware components are functional
- The reference point for the medical treatment and the central treatment beam are visualized by four laser systems; three movable x-ray systems were installed, which serve for the final inspection and documentation of the patient position with respect to the reference point.
- The Positron emission tomograph (PET) [6] has been installed at the treatment site and successfully tested in various experiments. From these experiments two modes of application of PET-imaging for quality assurance in heavy ion therapy have been deduced: the 'retrospective dose localization' and the 'treatment plan verification'.

Within the next months tests of quality assurance and diagnostic measurements have to be performed for the final approval.
After an adequate period of clinical testing first patient treatments will start.

## REFERENCES

[1] G. Kraft, G. Gademann, GSI-Report 93-23
[2] Th. Haberer et al, Nucl. Instr. Meth. A330, 296 (1993)
[3] U. Krause et al., ICALEPS 1995
[4] B. Franczak, 'Data Generation for SIS and Beam Lines for the GSI Therapy Project', this conference
[5] H. Eickhoff et al., EPAC 1996
[6] J. Pawelke et al.. Phys. Med. Biol. 41 (1996), 279

# A 3HE$^{++}$ RFQ ACCELERATOR FOR THE PRODUCTION OF PET ISOTOPES

Ralph J. Pasquinelli: Fermilab* , SAIC, BRF, UW Collaboration

*Abstract*

Project status of the 3He$^{++}$ 10.5 MeV RFQ Linear Accelerator for the production of PET isotopes will be presented. The accelerator design was begun in September of 1995 with a goal of completion and delivery of the accelerator to BRF in Shreveport, Louisiana by the summer of 1997. The design effort and construction is concentrated in Lab G on the Fermilab campus. Some of the high lights include a 25 mA peak current 3He$^{+}$ ion source, four RFQ accelerating stages that are powered by surplus Fermilab linac RF stations, a gas jet charge doubler, and a novel 540 degree bending Medium Energy Beam Transport (MEBT). The machine is designed to operate at 360 Hz repetition rate with a 2.5% duty cycle. The average beam current is expected to be 150-300 micro amperes electrical, 75-150 micro amperes particle current.

## HISTORY

The current project is a continuation of a SDIO funded effort between SAIC and University of Washington (UW) that began in 1990.[1] The use of a 3He RFQ linear accelerator to replace cyclotrons could have several advantages: no need for enriched target material, lower shielding requirements, high reliability, and ease of maintenance and operation. The project was revived in 1995 with the addition of two collaborating institutions, Fermilab and Biomedical Research Foundation of Northwest Louisiana (BRF). Fermilab is the managing partner and has the prime responsibility for building and commissioning the accelerator. SAIC is also part of the accelerator development team and will ultimately be responsible for operation of the accelerator when it is delivered to BRF late summer 1997. UW and BRF are the collaborators responsible for radiochemistry experiments which are projected to be carried out for an additional two years after the accelerator is commissioned at the BRF facility in Shreveport, Louisiana. The project is funded by the Department of Energy.

## THE ACCELERATOR

The initial SDIO funded project was a linear 8 MeV 3He$^{++}$ accelerator that would utilize three RFQ's in series. The first RFQ was chosen to operate at 212 MHz to improve capture efficiency and accelerate the 3He beam to 1 MeV where it would be stripped to a doubly charged state for more efficient acceleration in the subsequent RFQs. The following two RFQs operate at 425 MHz and require some longitudinal matching of the beam. Initial attempts to bunch rotate the beam with an RF cavity after the charge stripper failed due to the charge neutralized character of the beam.

The high average current of the accelerator requires a robust ion source. Efforts to create a doubly charged ion source were abandoned as they were beyond the scope and funding available for the project. The ion source used is a duoplasmatron that can be operated on both 4He and 3He. The source can be started and commissioned with 4He with 3He used one it has stabilized. (3He cost is $100/liter, consumption is approximately one liter per day.) Initial problems with filament burn out were overcome when the Nickel gauze was replaced with Molybdenum. Operation with 360 Hz, 2.5% duty cycle and 25 mA peak current single charge is routine. The Low Energy Beam Transport (LEBT) consists of two small steering magnets and a 5 inch beam diameter solenoid.

During the period when the project was stopped due to lack of SDIO funding and picked up again by the DOE, it was also decided to increase the energy of the beam to 10.5 MeV in an attempt to make target cross sections more viable for production of the desired isotopes and the target window (separating the targets from the accelerator vacuum) more robust. This project was not resumed on a green field as the funding for the project was limited to $10 million, needed to utilize as much of the original SDIO equipment as possible, and had to include the two years of chemistry research. The decision to increase energy necessitated a fourth RFQ for the system. The design was similar to the existing segmented vane RFQs and operates at 425 MHz.[2,3] One of the problems with the original project was a source of reliable RF power. Four surplus RF stations were available at Fermilab following the upgrade of the Fermilab Linac to side coupled cavities in 1993. The Continental Electronics RF stations served the FNAL linac faithfully for a quarter of a century and now have found a new use in the PET project. The 212 MHz station was easily converted from the 201 MHz frequency of the Fermilab Linac. The power amplifiers for the 425 MHz systems were purchased from the former GTA project at Los Alamos. We were fortunate in that the GTA amplifiers utilized the 4616 tetrode of the existing linac stations. A few mechanical changes were required to integrate the hardware into the existing relay rack enclosures. Each RF system is capable of a minimum of 120 KWatts of pulsed RF power at the rated duty cycle and repetition rate.

The charge doubler design centers on using a gas jet. The idea of using thin foils for stripping the second electron from the 3He$^{+}$ beam were quickly dismissed as the

* Operated by Universities Research Association under contract to the United States Department of Energy

0-7803-4376-X/98/$10.00 © 1998 IEEE

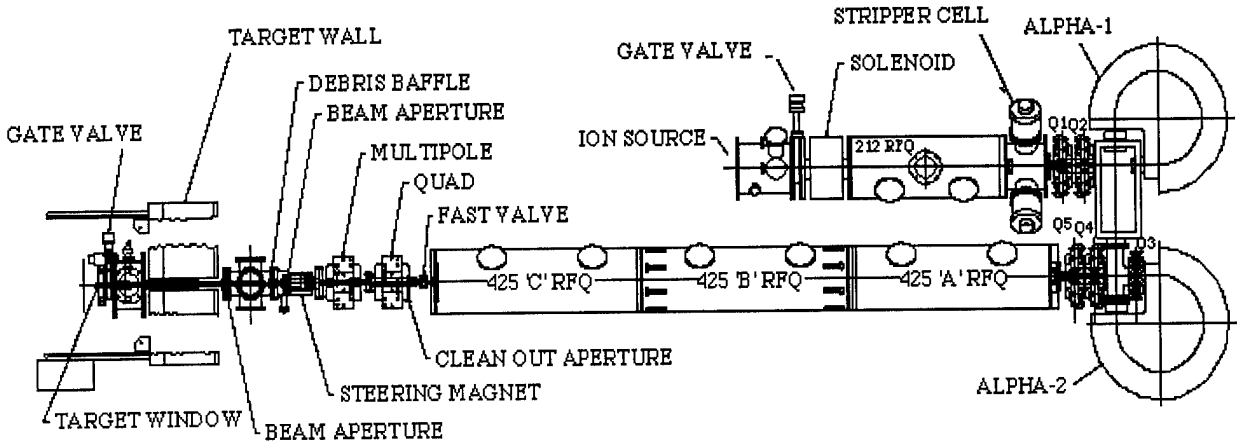



Figure 1. Layout of 10.5 MeV $3He^{++}$ PET accelerator.

thickness of the foils would be too thin to be mechanically robust. A novel idea of using an automotive fuel injector has proven to be a reliable and inexpensive solution to the problem.[4]

The linear appearance of the machine changed once the final energy was increased. The problem of longitudinal matching between RFQ's needed to be overcome and required a

non RF solution. A matching section between 212 & 425 MHz RFQs utilizes a 540 degree bend consisting of seven quadrupoles and two "alpha" 270 degree dipoles.[5] This Medium Energy Beam Transport (MEBT) changed the layout of the machine to bend back on itself. (figure 1) A side benefit

is the overall length of the machine was reduced and would easily fit into both the development area at Fermilab and the facility at BRF. The magnets for the MEBT and LEBT were designed and manufactured at Fermilab's Technical Support Division.[6] The final transport stage is the High Energy Beam Transport (HEBT) which utilizes a quadrupole, multipole and steering magnets from the original project to expand and control the beam to the required 2.5x10 centimeter size of the Havar target window.

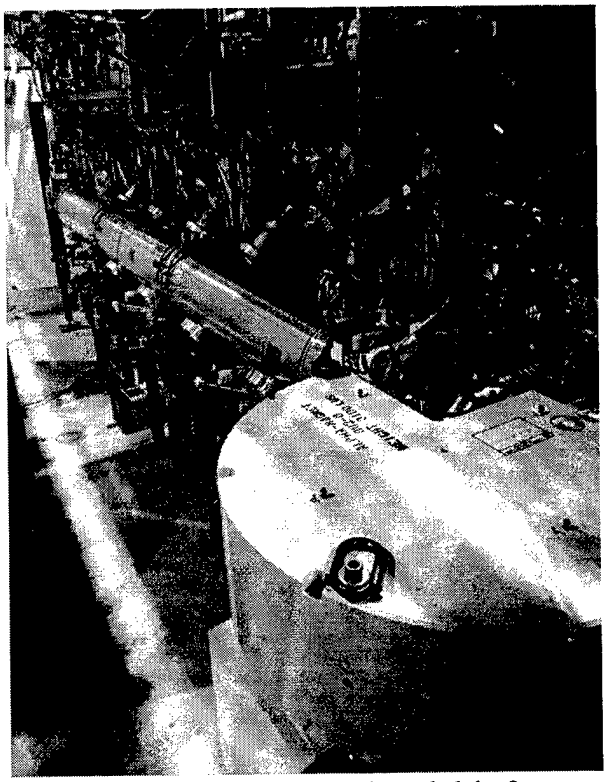


Figure 2. View of 425 MHz RFQs and alpha 2 magnet of the MEBT.

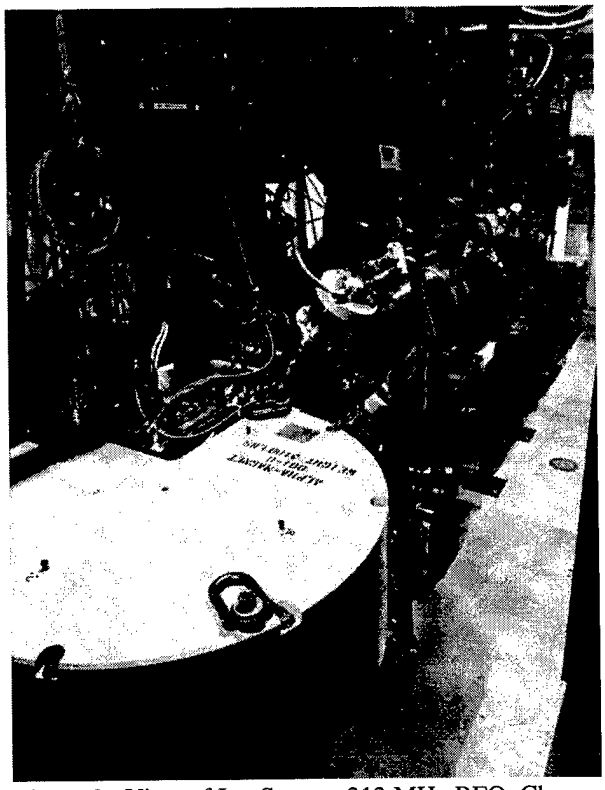


Figure 3. View of Ion Source, 212 MHz RFQ, Charge Stripper, and alpha 1 magnet of the MEBT.

A number of support systems have been specifically designed for the project. The Low Level RF system utilizes the VXI platform and provides amplitude, phase, and frequency control for all four RF systems. Frequency tuning of the RFQs is accomplished by modulating the phase of the IQ modulator removing the need for individual VCOs. The RFQs are thermally tuned via a closed loop water cooling system for each RFQ consisting of a Neslab chiller and custom electronics. The diagnostics package is complete with a number of current torroids, segmented Faraday apertures, multiwire profile monitors, thermocouples, vacuum monitors, movable target beam collimaters and targetry instrumentation. A complete Low Conductivity Water (LCW) and chilled water system are part of the stand alone design that will be shipped to the BRF facility. The control system is based on the Internet Rack Monitor (IRM) that was developed for the FNAL linac upgrade.

The entire accelerator was designed with mobility in mind as it must be transported to Shreveport after initial commissioning at Fermilab. All relay racks and RF stations are easily picked up by forklift and will be shipped with electronics intact. The major challenge will be disassembly of system cabling. The footprint at Fermilab is identical to that in Shreveport with the exception of the Anode supplies for the RF stations.

## PERFORMANCE RESULTS

Work on designing and building the accelerator began on September 1, 1995. The first six months were dedicated to characterizing the equipment from the original project and converting RF stations. It was noticed early in the project that the "light weight" requirement imposed by the SDIO funding was a source of trouble. The vacuum vessels were constructed from Aluminum and provided little shielding from x-rays produced by the RF fields in the RFQs. This problem was mitigated by placing the RFQs in 1-5/16 inch thick stainless steel vacuum enclosures. (See figure 2 &3)

The ion source has been running trouble free at full duty cycle, peak current of 25 mA, for several months with only one filament change. Cold start up time is minutes. The timing system has been set up to allow different triggering of the source and RF systems, allowing full flexibility in duty cycle while not compromising source performance.

A severe leak in the water channels of the RFQ vanes has caused an appreciable amount of delay in the project. The vanes are constructed of 7075 Aluminum which is highly sensitive to corrosion. The water cooling channels have corroded sufficiently to cause a leak to the main vacuum vessel. This problem was temporarily fixed with the use of a casting impregnation solution. All vanes for all RFQs needed to be re-fabricated. Teflon coating of the water passages and water treatment have been implemented to retard corrosion. The replacement 212 MHz RFQ is currently being fabricated.

The MEBT was commissioned over a period of weeks and found not to have any serious space charge effects. This was the most controversial aspect of the project and was rewarding to experience success.

Commissioning of the RFQ systems has proven to be a little tricky in that all of the RF stations and RFQs have a slightly different personality. The surplus linac stations have been modified to make them identical. The control system software has made operations simple. All four RF stations can be turned on and at resonance in a matter of minutes.

The HEBT has been installed and beam has been delivered to a Faraday cup in the vault. Measurements of shielding efficiency are in progress.

The current status of the machine is 6 mA peak, 25 microamperes average (electrical) 10.5 MeV beam has been accelerated to the target vault at the 120 Hz repetition rate. Increasing the duty cycle and current are the main focus of commissioning. Efforts now are directed to improving operational performance and reliability.

A six week radiochemistry program is just underway. The intent is to do a wide array of targeting of various materials at Fermilab in an attempt to fully assess the radiation produced and the shielding necessary to allow occupancy near the accelerator and target vault.

The accelerator will be shipped to the BRF facility where it will be installed in a specially prepared room in the building's physical plant. The shipping, assembly and re-commissioning at BRF is expected to take approximately two months. After that time, the accelerator will be made available for PET isotope production research. As the accelerator is not FDA approved, isotopes produced by this accelerator will not be used in the clinical PET center.

## ACKNOWLEDGMENTS

The extremely tight schedule and funding for the project required a talented group of people to carry it out. The members of the collaborating institutions have shown a dedication and professionalism that has made this ambitious project a reality.

## REFERENCES

[1] W. Hagan, A. Dabiri, D. Swenson, (SAIC), K. Krohn (UW), "A $3He^{++}$ Radio Frequency Quadrupole Accelerator for Positron Emission Tomography", Nuclear Technology Vol. 92, pp. 127-133, Oct. 1990.

[2] D. Sun, "Design and Operation of PET Radio Frequency Quadrupoles", These proceedings.

[3] W.D. Cornelius and P.E. Young, "Design of a 1 MeV He-3 RFQ for the SAIC PET accelerator facility", Nuclear Instruments and Methods in Physics Research, B79 (1993) 933

[4] Bieniosek, Anderson, Pasquinelli, Schmidt, Webber, Larson, Young, "Gas-jet Charge Stripper and MEBT for the 3He RFQ Linac", These proceedings.

[5] D.J. Larson, P.E. Young, D. Sun (SAIC), R.J. Pasquinelli, F. Bieniosek, J.-F. Ostiguy, C. Schmidt, M. Popovic (FNAL), "Ion Optical Design of the BRF-FNAL-SAIC-UW PET Accelerator", These proceedings.

[6] N. Chester, et al., "Magnet Development for the BRF Positron Emission Tomography Accelerator", These proceedings.

# A NEW INTENSE NEUTRON TOOL FOR RADIOGRAPHY AND DETECTION OF WATER AND GROUND CONTAMINANTS

C.M. Celata, M. Amman, R. Donahue, K.N. Leung, P.N. Luke, L.T. Perkins, Peter T. Zawislanski, *Ernest Orlando Lawrence Berkeley National Laboratory, Berkeley, CA* and D. Hua, *University of California at Berkeley, Berkeley, CA.*

*Abstract*

Advances in ion sources and gamma ray detection at LBNL are being applied to enhance neutron logging tools. A rf-driven plasma ion source has been miniaturized to the 2 inch diameter necessary for most underground uses. The ion current produced is >80% monatomic, and is projected to produce a neutron flux of $10^9$ - $10^{10}$ neutrons/sec, an enhancement of 1-2 orders of magnitude over the state-of-the-art. A 1.5 x 1.5 x 1 $cm^3$ CdZnTe gamma detector is also being developed for the tool. This detector has relatively high efficiency, good energy resolution, and room temperature operation. Results of 3-D Monte Carlo calculations are presented which show the enhancements in sensitivity and range possible with the new technology.

## 1. INTRODUCTION

Compact sources of neutrons are used for neutron activation analysis, radiography, and for detection of water, oil, and minerals in the subsurface. One common example is the use of neutron logging tools, 2-4 inches in diameter and a few meters in length, in the oil industry and in earth science research. These tools consist of a Penning ion source and ~100 kV accelerator column, which accelerates a mixture of deuterium and tritium ions onto a tritiated target, producing 14 MeV neutrons. Detectors in the tool measure returning neutrons, and gamma rays produced by neutron capture and inelastic scattering of neutrons from the elements of the medium. The energy of the gamma rays produced by these processes is characteristic of the nuclei impacted, enabling, in theory, an elemental analysis of the medium. In practice, the gamma-ray spectrum is often crowded with spectral lines, so that what can be detected depends heavily on the energy resolution of the gamma-ray detector and the cross section of the element being detected.

In this paper we report improvements in the components (ion source, accelerator, and gamma-ray detector) of such a neutron logging/gamma-ray spectroscopy system. The results of 3-D Monte Carlo modeling of the enhanced system for new earth science applications will also be presented. The MCNP code [1] has been used to quantify the advantages in instrument range and sensitivity resulting from the enhanced neutron flux. Calculations have also been used to look at the possibility of 3-D localization of detected substances.

## 2. ION SOURCE AND ACCELERATOR

For this project a LBNL radio-frequency-driven ion source was miniaturized to an overall diameter of 2 inches. The ion source and accelerator are described in detail in another paper in these proceedings (L.T. Perkins et al.), but a summary directed to the application will be given here. The source consists of a cylindrical volume of plasma 2.5 cm in diameter and 9 cm in length. The beam is extracted through a 2 mm aperture in the extraction electrode. Miniaturization has required the reduction of source operating pressure in order to avoid electrical breakdown in the accelerator column. The source presently runs well at 5 mTorr.

A helical rf antenna 1.5 cm in diameter is used to generate the plasma. Because of the difficulty of miniaturization, the rf power supply will be located above ground. Presently, cable losses limit source use to depths less than about 500 feet.

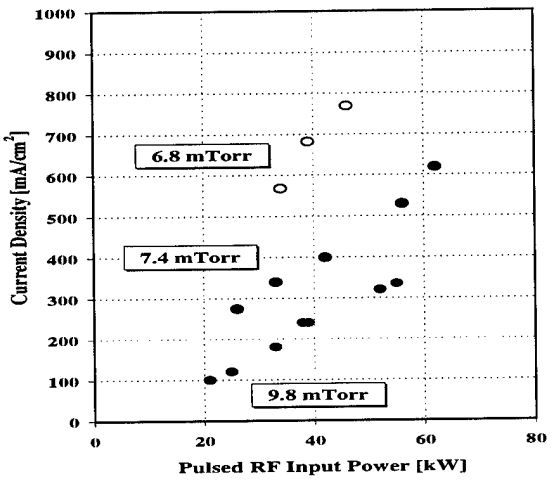



Figure 1. Peak extractable current density at three different source pressures, versus rf input power.

Measured current density is shown in Fig. 1 as a function of input rf power. The ion current densities measured are about a factor of 500 higher than those in commercial neutron logging tubes. Up to 35 mA/pulse has been produced, and this current can be increased by simply opening the 2 mm extraction aperture, since current is linearly proportional to aperture area. Minimum pulse width is about 8 μs. The beam is largely monatomic, with monatomic fraction increasing with increasing rf power. At 40 kW, the beam is 80%

0-7803-4376-X/98/$10.00 © 1998 IEEE

monatomic, and 94% at 60 kW. (For details, see L.T. Perkins et al., in these proceedings.) The monatomic fraction is particularly important because these ions will have nuclei with energies double that, for instance, of diatomic nuclei, and therefore are closer to the optimum energy for neutron production. Based on the data presented, we project a yield of $10^9$-$10^{10}$ D-T n/s, or $10^7$-$10^8$ D-D n/s, at pulse rates ≈ 1 kHz. A test of neutron production in a commercial neutron tube will be performed within the next 6 months.

A 100 kV accelerating system has been designed, using the IGUN© code to obtain the shape, potential, and positions of the accelerating electrodes. A suppresser electrode is included to minimize backstreaming electrons. This also removes ambiguity in ion current measurements. The accelerator design will minimize sputtering and produce uniform beam spreading on the target, leading to longer tube lifetime. The accelerator is presently in fabrication.

## 3. GAMMA-RAY DETECTOR

For well logging applications, gamma ray detection is usually done with scintillation detectors (e.g., NaI), or, to a lesser extent, with cryogenically-cooled germanium. For this project, we have chosen to develop a detector based on the compound semiconductor material CdZnTe, because of its high efficiency, good energy resolution, and the promise of room temperature operation. The problem of poor charge transport in this material has recently been overcome by the development of the coplanar-grid technique [2], which uses the subtraction of signals from two interdigitated grids to make detector response largely insensitive to the depth of gamma-ray interactions. Using this technique, an energy resolution of ~2% FWHM for 662 keV gamma rays has been achieved for 1 $cm^3$ CdZnTe detectors operating at room temperature [3][4]– a factor of three higher than the resolution of NaI. Resolution better than 1% FWHM (662 keV) is in principle possible [3].

Though the high thermal neutron capture cross section of Cd would normally be a problem in this application, calculations have shown that a thin layer of $^{10}B_4C$ can provide adequate neutron shielding for the detector. Another issue of some concern is detector radiation damage. Fast neutrons can damage the crystal lattice of the detector, degrading the charge collection properties and adversely affecting its energy resolution. Currently, only very limited experimental data exists on the effects of neutron damage in CdZnTe detectors [5]. More studies are needed in this area to determine whether CdZnTe detectors, and particularly those using the coplanar-grid technique, are suitable for this application.

CdZnTe detectors are currently limited to volumes of 1-2 $cm^3$, mainly due to material nonuniformity. However, because of the high atomic number of CdZnTe, the photopeak efficiency is equivalent to that of a substantially larger Ge or NaI detector, and the small size is advantageous in the limited space of the borehole. MCNP calculations show the efficiency of CdZnTe to be about three times that of the same volume of NaI or Ge in the energy range of interest [6].

The goal of the present work is to develop CdZnTe coplanar-grid detectors of approximately 2 $cm^3$ volume and energy resolution ≤1% FWHM for the energies of interest (≈ 1-10 MeV). Figure 2 shows the spectral performance of a 2.25 $cm^3$ detector made for this project. Energy resolution at 1.33 MeV is 1.6% FWHM. The detector was slightly cooled (to approximately -10°C) to reduce its leakage current so that higher bias voltages could be used. At room temperature, noise due to leakage current would dominate and significantly degrade the energy resolution. The high bias was needed to minimize the effects of nonuniform charge collection in the crystal. Room temperature operation with similar or better performance can be achieved if crystals with better uniformity are available. Alternately, further improvements in the fabrication process may lead to lower leakage current so that room temperature operation at high biases is possible without excessive leakage-current noise. A prototype hermetic detector module containing the detector and front-end electronics has been fabricated. Power consumption of the front-end electronics is less than 150 mW.

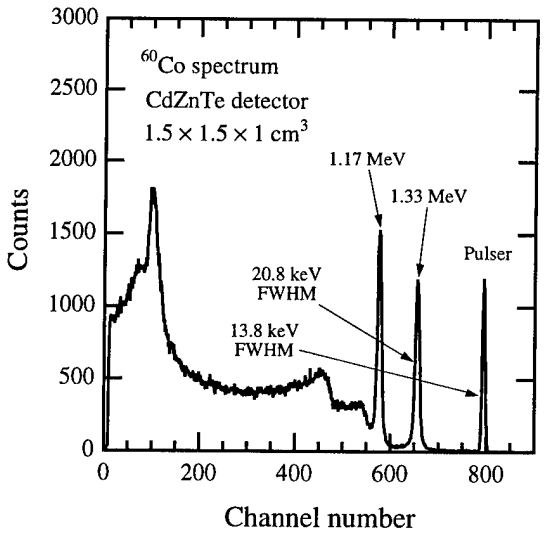



Figure 2. Spectrum of $^{60}$Co obtained using a coplanar-grid CdZnTe detector operated at a temperature of approximately -10°C and at a detector bias of 1600 V.

## 4. MODELING

The 3-D point-energy time-dependent Monte Carlo code MCNP with the ENDL60 [7] cross section library has been employed to model use of the enhanced-flux neutron logging tool with a CdZnTe detector. Previous results have shown the utility of this method for detection of water and for chlorinated solvents, which are widespread

pollutants [6]. Note that all gamma-ray spectra calculations quoted here are simulations of measurements for 14 MeV neutrons taken with the detector gated off during the neutron pulse and the 30 μs following the pulse. This is a standard technique for eliminating counts due to inelastic scattering of fast neutrons.

We present here MCNP results showing the advantages of increased source intensity for increased range of the instrument. To measure range we assume the level of minimum detectability to be 2.33σ above background [8], where σ is the standard deviation of the background counts. In the model, fractures were formed using two infinite parallel planes. Vertical fractures intersecting the center of the borehole were generally used. Very little difference was found between horizontal and vertical fractures through the borehole. Calculations showed that for 1 g/cm$^3$ TCA in a 1 cm-wide fracture, for 1000 second counting times, the range increased from 50 to 70 cm as source intensity increased from $10^7$ to $10^9$ neutrons/sec. For the same fracture filled with 0.3 g/cm$^3$ NaCl in water, the increase was from 40 to 60 cm, an increase of 50%. In both cases the 6.11 MeV chlorine capture line was used. The detector efficiency is not included in these calculations. For 1% detector efficiency, range decreases for the TCA to 20 cm at $10^7$ n/s, and 40 cm at $10^9$ n/s.

A few cases have been run to determine the effect of neutron flux on minimal detectable concentration. For TCA uniformly spread through wet sand (30% water), 2 ppm TCA is detectable with $10^7$ n/s, and 0.5 ppm with $10^9$ n/s.

We have begun to investigate the possibility of 3-D localization of detected materials. As neutron borehole tools are used today, readings are taken vs. depth, giving only location in the vertical dimension. With increased flux, some azimuthal photon collimation can also be done, without decreasing the signal below the limits of detectability. To model this, a 1 cm$^3$ spherical CdZnTe detector was assumed to be at the center of a 5 cm radius borehole. The detector was surrounded by a spherical tungsten collimator shell 3.88 cm thick. A neutron shield consisting of a 0.5 cm-thick spherical shell of $^{10}B_4C$ enclosed the detector/collimator. A 0.6 cm diameter horizontal cylindrical hole through the collimator, aimed at the detector center, allowed photons to enter the detector. A vertical fracture 1 mm wide, filled with water containing 0.3 g/cm$^3$ NaCl, intersected the borehole. Signal intensity vs. collimator position is shown in Fig. 3, as the collimator is rotated around the borehole axis. The fracture is at 0°. The photon energy spectrum is measured at the center of the detector using an MCNP biased point detector tally. The detector efficiency has not yet been taken into account. Results are shown for the 2.23 MeV gamma ray from hydrogen capture as well as the 6.11 MeV and 7.42 MeV gammas from capture in chlorine. The best results, from the 6.11 MeV line, indicate a signal-to-noise ratio of about 8. These results for such a small fracture size are quite promising. Analyses are underway to investigate the effects of collimator size and material, composition of media and fracture, and detector energy response.

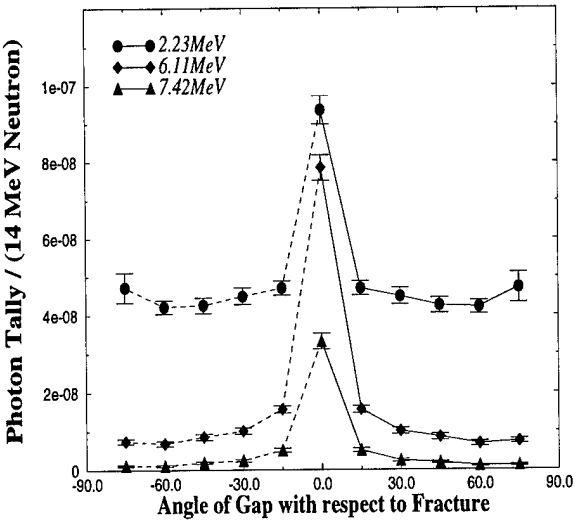



Figure 3. Calculated angular response to a 1 mm fracture in dry granite, filled with water containing 0.3 g/cc NaCl. Photon yields are normalized to the response at 0 degrees (collimator aligned with fracture).

## 5. ACKNOWLEDGEMENTS

The authors gratefully acknowledge the contributions of N. Madden and C. Cork, who designed and built the electronics and housing for the CdZnTe detector module. This work was supported by the U.S. D.O.E., contract #DE-AC 03-76SF00098.

## REFERENCES

[1] Briesmeister, "MCNP - A General Monte Carlo N-Particle Transport Code, Version 4A", Los-Alamos National Laboratory Report LA-12625 (1993).

[2] P. N. Luke, "Unipolar Charge Sensing with Coplanar Electrodes - Application to Semiconductor Detectors", IEEE Trans. Nucl. Sci., vol. 42, no. 4, pp. 207-213, Aug. 1995.

[3] P. N. Luke and E. E. Eissler, "Performance of CdZnTe Coplanar-Grid Gamma-Ray Detectors", IEEE Trans. Nucl. Sci., vol. 43, no. 3, pp. 1481-1486, June 1996.

[4] Z. He, G. F. Knoll, D. K. Wehe and J. Miyamoto, "Position Sensitive Single Carrier CdZnTe Detectors", Conference Record, 1996 IEEE Nuclear Science Symposium, vol. 1, pp. 331-335.

[5] C. M. Stahle et al., "CdZnTe Detector for Gamma-Ray Burst ArcSecond Imaging and Spectroscopy", Presented at the 9th International Workshop on Room Temperature Semiconductor A and Gamma-ray Detectors, Associated Electronics and Applications, Grenoble, France, 1995.

[6] C.M. Celata et al., "A New Intense Neutron Generator and High-Resolution Detector for Well Logging Applications", Proc. of the 1996 IEEE Nucl. Sci. Symposium, Anaheim, CA, Nov. 1996, Vol. 1, p. 29 (1997).

[7] J.S. Hendricks, S.C. Frankle, and L.D. Court, "ENDF/B-VI Data for MCNP, "Los Alamos National Laboratory Report LA-12891, 1994.

[8] L. Currie, Analytic Chemistry 40, No. 3, 586 (1968).

# ELECTRON-LINAC-BASED RADIATION FACILITIES OF THE UKRAINIAN NATIONAL SCIENCE CENTER "KIPT"

A.N. Dovbnya, M.I. Ayzatsky, Ye.Z. Biller, V.N. Boriskin, V.A. Kushnir, V.V. Mitrochenko, V.A. Popenko, Yu.D. Tur, V.L. Uvarov, E.S. Zlunitsyn, A.I. Zykov
National Science Center,
Kharkov Institute of Physics&Technology (KIPT), 310108, Kharkov, Ukraine

*Abstract*

A review is given about electron Linacs of KIPT and their some applications for research of radiation effects in reactor materials, channeling, plasma-beam interactions, geology (gamma-activation analysis of ore samples), as well as sterilization of single-use medical products, modification of polymers and semiconductors, isotope production for nuclear medicine etc.

## 1 ELECTRON LINEAR ACCELERATORS

Characteristic of the Ukraine economy of Today's transition period is the absence of stable situation on the radiation technology market. Considering this, it would be to good advantage to develop, build and make use of accelerators with a broad range of parameters, capable to meet the market's demands. This ideology is fundamental in the activities of "Accelerator" R&D Establishment of the Ukrainian National Science Center "Kharkov Institute of Physics&Technology", the leading organization in Ukraine in creation of electron linacs and applicable technologies. This paper gives a short survey of some electron linear accelerators and the results in the areas of applied physics and radiation technologies.

There are six electron linear accelerators at "Accelerator" R&D Establishment. The biggest one is the oldest linac in Europe LUE-2000 [1]. Three accelerators (EPOS, LU-10, KYT) are used for performing various radiation processes. There main parameters are represented in Tab.1.

### 1.1 Accelerator EPOS

The accelerator EPOS is a two-section linac with an extracted electron beam scanning system, built on the base of the existing equipment. EPOS has been designed to be used for radiation processing of various items, employing electron beams with energies up to 30 MeV.

The EPOS is disposed underground, horizontally, in a concrete tunnel. The accelerator layout is given in Fig. 1. The electron source is a diode-type gun with a lanthanum hexaboride ($LaB_6$) heated cathode. Electron beam (5.5 mm diameter, current up to 3A) is formed in the source upon application of 80 kV-pulsed voltage to the cathode from the HV-modulator (MG). While passing the bunching cavity (B), the beam is chopped up into separate bunches. Electron acceleration takes place in a disk-loaded waveguide (DLW) that has a homogeneous structure, the structure's a/b ratio being 0.14, with the phase shift per cell $\pi/2$, and the phase velocity equal to the speed of light. In order to suppress the beam breakup instability in the disk-loaded waveguide, thin radial cuts were made in them [2]. At the input end of the first section (AS1) there is a certain length (30 cm) with a lower wave phase velocity [3], providing the capture of more than 50% of the injected electrons. Temperature inside the DLW (37±0.5)C is self-maintained during the operation modes.

Tab.1 Basic Linacs Parameters

| | EPOS | LU-10 | KYT |
|---|---|---|---|
| Energy range, MeV | 10 -30 | 8-18 | 8-14 |
| Operation energy , MeV | 20 | 12 | 9 |
| Frequency, MHz | 2797.2 | 2797.2 | 2797.2 |
| Number of sections | 2 | 1 | 1 |
| DLW length, m | 3.05 | 3.05 | 1.23 |
| Number of klystrons | 2 | 2 | 1 |
| RF-pulse width, μs | 5 | 4 | 5 |
| RF-power input, MW | 10 | 10 | 10 |
| Current-pulse width, μs | 4 | 3.5 | 4 |
| Repetition rate, pps | 50 | 300 | 300 |
| Average current, μA | 150 | 1000 | 800 |
| Maximum Bsf, Hz | 3 | 3 | 3 |
| w×l, cm | 1 x 30 | 1 x 30 | 1 x 30 |

The rf-power input, needed for electron acceleration, is provided by two KIU-12AM-type klystrons, the first of which operated in the self-exiting mode, and the second one is excited from the first klystron [4].

RF-power from each klystron (K) - up to 10 MW- is fed through a rectangular waveguide into the DLW. The klystrons work in a pulsed mode triggered by two klystron modulators (MK) with the parameters that are given in [5].

The beam focusing is performed by two short magnetic lenses (FL1 and FL2), two DLW-coaxial solenoids (FS1 and FS2) and two quadrupole lenses (QL1 and QL2).

0-7803-4376-X/98/$10.00 © 1998 IEEE

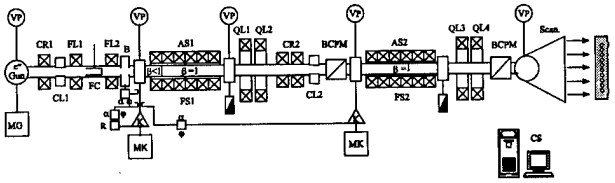


Figure 1: EPOS layout

Electron beam extraction is made through a Ti-foil 50 microns thick. In order to enlarge the irradiation area a beam scanning system (BSS) is installed at the acceleration exit, providing for beam sizes (w×l) up to the value (1×30) cm [6], the beam scanning frequency (Bsf) being 3 Hz.

Control over EPOS operation is performed by a computer-automated system, providing for the monitoring of parameters of beam and modulators, their lock-up when the assigned mode of operation is off, as well as magnetic component current adjustment and amplitude-phase tuning.

1.2 Accelerator LU-10

The LU-10 single-section electron Linac was commissioned in 1987 [7]. Up to mid-1993 it had operated with KIU-53 klystron, producing electron beam with output energy E≅10 MeV and average current I≅ 500 μA at a repetition rate F=150 Hz. In 1993 a necessity arose to increase beam energy and output power. Our studies [5] gave a reason to believe that a scheme of adding up the rf-power output from both KIU-12 klystrons should provide for a reliable operation of the accelerator and required beam parameters at F=300 Hz and the input operation power P≅(12÷13)MW from each of the two KIU-12 klystrons. A schematic layout of the accelerator LU-10 is given in Fig.2.

Since 1994 at the LU-10M research has been going on in basic and applied areas of radiation damage physics, radiation technologies and pharmaceuticals sterilization. The facility is equipped with a suspended conveyer belt, a load/unload and storage from for various items for a mass-scale radiation processing, and devices for target irradiation by large doses with necessary cooling.

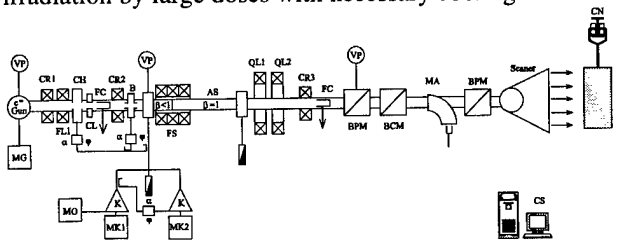


Figure 2: LU-10 layout

Accelerator has a sufficiently high long -lasting stability of beam parameters, with the 24-hour mean variations in beam energy and current not more ±1,5%. The accelerator is equipped with metrologically licensed devices [8] for energy spectrum measurements and monitoring of average and pulsed beam current.

1.3 Accelerator KYT

The KYT has been operating in NSC KFTI since September 1993 [9]. KYT consists of electron linac with the scanning and electron beam extraction device, cooling and control systems. KYT produces 8-10 MeV electron beam with power up to 10 kW and is meant for performing various radiation technological processes including sterilization of medical articles. A schematic layout of the accelerator KYT is given in Fig.3

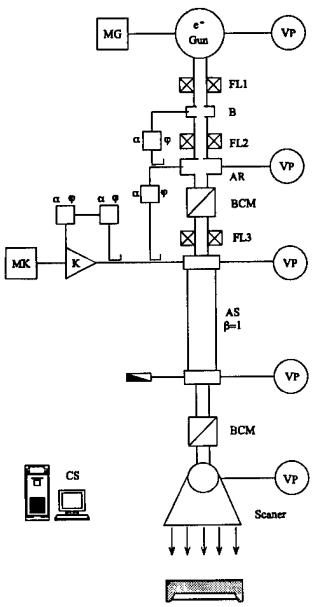


Figure 3: KYT layout

The injector is designed to inject a well-bunched (20°), well-collimated and sufficiently accelerated (E>300 keV) beam of electrons into the accelerator section. The injector consists of an electron gun, a prebuncher (B),a accelerating resonator (AR) and two magnetic thin lenses (FL1 and FL2). . The electron gun which operates at ~25 kV is of diode type with oxide cathode ∅ 15 mm.

The accelerating structure (AS) consists of the disk-loaded waveguide and input and output couplers. The disc-loaded waveguide operates at f=2797 MHz in 2π/3 mode and consists of constant impedance landings connected via four transition cells (quasi constant gradient structure).

The scanning and electron beam extraction device consists of a scanning magnet and a special system with an air-cooled exit foil.

## 2 APPLIED PHYSICS AND TECHNOLOGIES

A series of experiments has been carried out on LU-2000 accelerator to simulate radiation damage in reactor materials [10]. It was shown that electron beam with energy up to 300 MeV and beam current 80 μA produces on the irradiated area 3.5 x 10 mm a radiation flux (e,γ) equivalent to a fast neutron flux ($E_n$>0.1MeV), up to $2.\cdot10^{15}$ n/cm$^2$. This interaction will accumulate He, as a reaction product, for example in Ni and Cr, higher approximately by two orders of magnitude, then in a fast neutron reactor. This fact allows to employ electron linacs in order to simulate, very rapidly, the phenomenon of

high-temperature radiation embrittlement in advanced materials. Besides, research work on our accelerators produced important results in the studies on radiation defect aggregation in metals and high-temperature superconductors [11], as well as in the studies on electron channeling in single crystals [12].

Sterilization. Radiation processing of medical products, pharmaceutical and raw materials calls for electron and bremsstrahlung with the upper energy spectrum range $\leq$ 10 MeV and absorbed radiation dose range 5-25 kGy. LU-10 is well equipped to provide such conditions, being also outfitted with robotics for remote-control target material installation in the radiation area. For sterilization radiation dose being 25 kGy, and average material density up to 0.2 g/cm$^3$, the facility shall provide the yield up to 4 m$^3$/h with the production cost (for big batches) near \$ 35 / m$^3$ .

Semi-conductor modification. A technology has been developed for electron flux treatment of semiconductor devices and chips for Ukraine's electron industry. By way of radiation-induced defect implantation and silicon doping with Al in ($\gamma$,n) reactions, one can obtain a programmed modification of lifetimes of secondary charge carriers and on improved semiconductor device performance.

Polymer modification. With an aim of a obtaining heat-shrinking items, mainly polyethylene-based, a technology developed for their treatment in the bremsstrahlung radiation field. The characteristic range of irradiation doses various polyethylene brands and items is 50...150 kGy.

Utilization of rubber wastes. Some rubbers (mainly, butylcaoutchokc-based) can be re-cycled to new applications by way of preliminary radiation-induced devulcanization. It is achieved by electron irradiation to the dose up to 100 kGy of the wastes that have been preliminary cold-worked. The resulting product can be utilized as a raw material for fabrication of construction, water-resistant and roofing materials, and also to make tires and radioengineering materials. The ecological importance of this technology are significant.

Medical radionuclides. The most widely used radionuclide on the appropriate nuclear medicine market is $^{99m}$Tc. In 1996 we mastered a technology of environmentally pure production of $^{99m}$Tc, using a high-current linac bremsstahlung in the reaction $^{100}$Mo($\gamma$,n)$^{99}$Mo $\rightarrow$ $^{99m}$Tc. The first experimental $^{99m}$Tc yield has been successfully accomplished. The appropriate spectrometric and radio pharmaceutics studies confirmed its good quality [13].

Activation analysis. The inherent capabilities of a high-current linac, outfitted with an appropriate converter, to generate bremsstahlung radiation access a wide range of incident power and gamma-radiation energy with the needed radiation field dimensions have been applied to develop some systems for element activation express-analysis of ore samples and technological raw materials for rare - and precious metal inclusions. One of advantages of this technique is a capability of fast determination of element concentration at the level 0.1g/t in samples of irregular ores, weighing 1 kg and more with the yearly analysis flow up to $10^4$-$10^5$.

Irradiation metrology. The above applied research and technologies call, as a rule, for a rigorous control over incident irradiation characteristics. This can be achieved by equipping each radiation facility with a necessary diagnostic channel set. Calibration of such sets is done, using a reference measurement complex, created jointly by "Accelerator" Establishment and Mendeleev Institute of Metrology (St.Peterburg, Russian) [14].

## REFERENCES


[1] J. Clendenin et al. Compendium of Scientific Linacs. CERN, 1996.

[2] B.M. Levin, V.L. Smirnov. Author's License 197875, Inventor's Bulletin, N13, 1967.

[3] V.A. Vishnyakov et al. A single-section laboratory-frame electron linac, VANT: High energy physics series, 1972, Issue 1 (1), 19-21; V.A. Vishnyakov et al. Studies on a high-current linac injector, Atomic Energy, 1977, vol.42, N1, p.234-236.

[4] V.I. Beloglazov et al. Utilization of a klystron field-emitter on a two-section accelerator, VANT series: Linac, 1976, Issue 1(2), 18-19.

[5] Yu.D.Tur et al. Klystron modulator for industrial linac. Proceedings of the 1995 PAC, v.2, p.1225-1226.

[6] A.N. Dovbnya et al. Sweepout and shaping of electron beam from a multi-purpose linac at KFTI, Proc. XIV Workshop on charged particle accelerators, 25-27 October 1994, Protvino, Russia, vol.3, 130-136.

[7] V.I.Beloglazov et al. Industrial-Materials Science Accelerator Complex to Energies up to 10 MeV. VANT Series: Radiation Damage Physics and Radiation Materials, in 1(36),1986, 89-91

[8] J.V.Avdeev et.al. Metrological Studies on Parameter-Measurement Devices for Electron Radiation from the Accelerators LU-10 and LU-40 at KFTI, Preprint 91-16, Kharkov, KFTI, 1991

[9] M.I.Ayzatsky et al. KYT- Industrial Technological Accelerator. Proc.XIV Particle Accelerator Workshop, Protvino, 1994, v.4, p.259.

[10] V.F.Zelensky al. Charged particle accelerator utilization for irradiation simulation and radiation studies on materials mechanical properties of fission and fusion reactors. KFTI Preprint 90-30, Kharkov, KFTI, 1990.

[11] V.F.Zelensky et al. Effect of electron irradiation on properties of high-Tc Superconductors. Physica C. 1988, v.153-155, p.850-851

[12] D.I.Adeishvili et al. A technique for measuring angular distributions of radiation intensity of relativistic electrons, scattered in single crystals. Atomic Energy, 1987, v.63, p.258-260.

[13] N.P.Dikiy et al. Report on testing the radiopharmaceuticals based on $^{99m}$Tc. Ukr. radiolog. Jorn. 1996, N 2, p.186.

[14] S.Karasyov et al. A Beam Monitoring & Calibration system for powerful electron Accelerators. This Conference.

# A COMPACT PROTON SYNCHROTRON FOR CANCER TREATMENTS

Kazuo Hiramoto, Masumi Umezawa, Kooji Matsuda and Masatsugu Nishi
Hitachi Research Laboratory, Hitachi, Ltd.
2-1, Omika-cho, 7-chome, Hitachi-shi, Ibaraki-ken, 319-12, Japan

*Abstract*

A compact proton synchrotron for cancer treatments is presented. In the present synchrotron, the beam can be accelerated up to 270MeV for the application to proton radiography as well as cancer treatments. In order to shorten the straight section for the extraction deflector such as a septum magnet, the deflections due to the defocusing quadrupole and edge type bending magnets in the synchrotron lattice are utilized effectively. The beam is extracted by the resonant extraction scheme which features that the position and gradient of the extracted beam are constant and the rapid switching is possible. Then, the present synchrotron can be applied to various irradiation schemes such as the double scattering, wobbler and raster scanning methods.

## 1 INTRODUCTION

A high energy proton beam has been successfully applied to cancer treatments (for example [1]) and patients more than 18000 have been treated worldwide[2]. In cancer therapy, it is expected that varying the energy of the proton beam is necessary when treating a different depth in the tissue because the proton beam shows a sharp Bragg peak. Then, a synchrotron seems to have an advantage as an accelerator for cancer therapy because it can accelerate charged particle beams to various energies.

In a medical proton synchrotron, the beam energy of 250 MeV is desirable for the treatments of the tumors which depth is 30cm. The medical proton synchrotron should be kept as small as possible in order to be constructed in public hospitals. Futhermore, simple operating scheme is needed for the accelerator and irradiation systems because medical accelerator systems must be used in daily treatments. Considering these conditions, we have presented a synchrotron design of combined function lattice which satisfies the above conditions [3]. Further study is aslo presented in this conference [4].

On the other hand, it has been pointed out that the high energy proton beam can be also applied to radiography as well as cancer treatments [5]. For this application, the beam energy higher than the 250MeV is desirable. Then, we present a compact proton synchrotron of the separated function lattice in which the maximum beam energy reached is 270 MeV and the other above conditions for medical use are kept .

## 2. SYNCHROTRON

### 2.1 *Machine Parameters and Lattice*

The main machine parameters of the designed synchrotron are listed in Table 1. In the present synchrotron, a proton beam of 7 MeV is injected from a linac to the synchrotron based on the multi turn injection scheme. The maximum beam energy reached is 270MeV so that the proton radiography may be performed for various cases. The accelerated beam is extracted by the resonanat extraction in which the separatrix of the nonlinear resonance is kept constant and the RF perturbation with a narrow frequency band width is applied to make the beam diffuse to the separatrix [6]. Basically, the procedures of the injection, acceleration and extraction are repeated at 0.5Hz. When the breath synchronized treatment is

Table 1 Machine Parameters

| | |
|---|---|
| Injection Energy (MeV) | 7 |
| Extraction Energy(MeV) | 70-270 |
| Superperiodicity | 2 |
| Circumference(m) | 22.2 |
| Extracted Particle Number (ppp) | $>1.3\times10^{11}$ |
| Tune | |
| Qx | 1.72 |
| Qy | 1.74 |
| Bending Magnet | |
| Deflection Angle(deg) | 60 |
| Curvature Radius(m) | 1.4 |
| Max. Field Strength iT, | 1.8 |
| Twiss Parameters | |
| $\beta$x, max ( m) | 12 |
| $\beta$y, max (m) | 11 |
| $\eta$ max ( m) | 2.3 |
| Momentum Compaction Factor | |
| $\alpha$ | 0.36 |
| Transition Gamma | |
| $\gamma$ tr | 1.67 |
| Natural Chromaticity | |
| $\xi$ x = ( $\Delta$Qx/Qx ) / $\Delta$p/p) | -0.24 |
| $\xi$ y = ( $\Delta$Qy/Qy ) / $\Delta$p/p) | -1.78 |

0-7803-4376-X/98 /$10.00 © 1998 IEEE

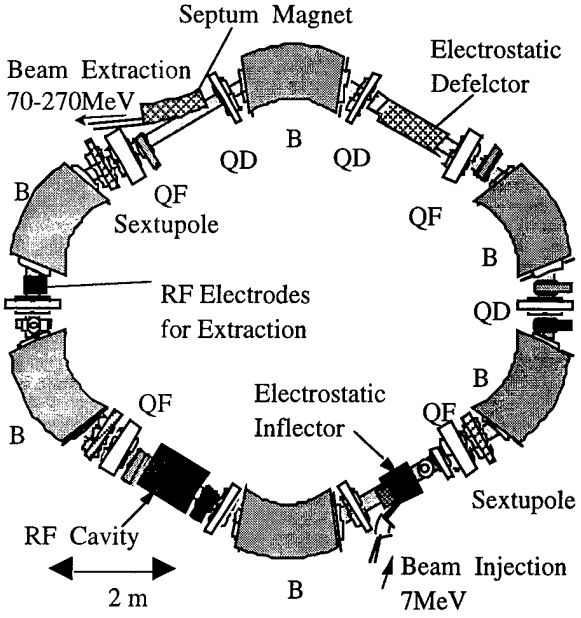



Fig. 1 The Layout of the Synchrotron

necessary, the operation period is changed flexibly and the extraction is switched by the RF perturbation based on the breathing of each patient. Figure 1 shows the lattice of the designed synchrotron. The present synchrotron employs the separated function lattice of two superpriods. Each bending magnet is an edge type and has a curvature radius of 1.4m. The deflection angele is 60 degrees. The maximum magnetic field of 1.8T is needed for the beam energy of 270MeV. The horizontal tune Qx and the vertical tune Qy are 1.72 and 1.74, respectively. There is no structure resonance near this operating point. The horizontal and vertical betatron functions are lower than about 12m and the horizontal dispersion function is sufficently low. The momentum compaction factor is 0.36. Accordingly, the transition gamma is 1.67 and this value is much higher than the maximum gamma of the beam of 1.29.

### *2.2 Injection*

Beam injection into the synchrotron is done during about 10 revolution periods by the multi turn injection scheme. We assume that the dilution factor for the emittance of the injected beam is about 50%. Then, the circulating beam current is about 5 times as large as the injection current from the linac.

### *2.3 Acceleration*

The beam energy is ramped with the current of the bending and quadrupole magnets using the radio frequency (RF) accelerating cavity. The RF acceleration is done using the untuned type cavity which employs Fe-based Nanocrystalline FINEMET cores[7]. Since the untuned RF cavity does not need control of the resonant frequency, the acceleration can be simplified significantly. Generally, the gap voltage of the untuned cavity is relatively low because of its small Q value in comparison with that of the tuned type cavity. Then, the gap voltage of the present RF cavity is increased by matching the impedances of the power source and the untuned cavity due to respective feeding of the RF power to each FINEMET core. The gap voltage for the acceleration can be easily obtained by an RF source with a rather low power.

### *2.4 Extraction*

The beam is extracted by the diffusion resonant extraction scheme in which the separatrix is kept constant and the narrow band RF noise is applied to make the beam diffuse to the separatrix[6]. The frequency of this RF noise ranges from 0.6fr to 0.7fr, where fr is the revolution frequency of the beam around the synchrotron. Since this frequency range covers the width of the frequencies of the betatron oscillations, which occurs due to the nonlinear effect and momentum spread of the beam etc., the beam diffuses due to the RF noise and the particles exceeding the separatrix are extracted. During the extraction, the intensity of the RF noise is slightly increased to obtain the constant spill. The needed maximum voltage of the RF perturbation is lower than 100V for the beam energy of 270MeV. The particles are extracted horizontally through the electrostatic deflector. Figure 2 shows the phase space trajectories at the

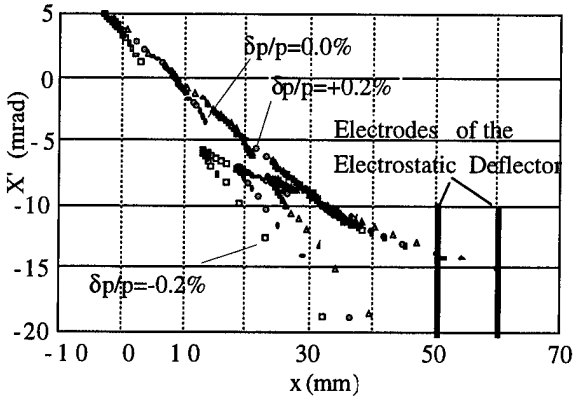



Fig. 2 Phase Space at the Electrostatic Deflector

electrostatic deflector for the particles of different momenta. It is seen that the particles of different momenta are extracted at the same gradients. Furthermore, from the effect of the constant separatrix, the orbit gradients of the extracted particles at the deflector postion are constant without dynamic control of the magnets. As a result, the beam position does not change and the time integrated emittance can be kept very low. These effects have been also studied experimentally in HIMAC[8]. Because of these effects, the present extraction scheme can be applied to various irradiation schemes such as the double scatterer, the wobbler-scatterer, and other scanning methods. Furthermore, the extraction can be switched on and off quickly by the RF perturbation. Then, the breath synchronized operation can be done easily in the present system.

The particles which exceeds the separatrix are extracted through the electrostatic deflector, the two quadrupole magnets of the defocusing type, the bending magnet in the synchrotorn lattice and the septum magnet. After the deflection by the electrostatic deflector, the extracted particles are further deflected outward by the two quadrupole magnet of defocusing type. Since the present bending magnets is an edge type, the inward deflection by the bending magnet is rather weak. Because of these effects, the separation between the circulating and the extracted particles becomes large at the entrance of the septum magnet. As a result, the septum magnet of the high magnetic field can be applied and its length can be shortened significantly.

### *2.5 Bending Magnet*

The magnetic field of the bending magnets ranges from 0.27T to 1.8T to accelerate the proton beam from 7 to 270 MeV. In order to obatin the good field distribution for the various energy levels, the magnet pole shape has been studied based on the numerical study. Although the saturation effect of the magnet occurs at the high magnetic field, the good distributions of the magnetic field are obatined for various energy levels by shaping adequately the shim of the magnet pole. Figure 3 shows the magnetic field distributions obtained by two dimensional numerical analysis. As shown in the figure, the deviations of the magnetic field from the value at the position of r=1.4m (X=0) are smaller than 0.02% for the energy levels of the injection, acceleration and extraction. Furthermore, the 3D analysis of the magnetic field has been done by using TOSCA to evaluate the nonlinear magnetic field at the circumferential edge region of the magnet. The dynamic aperture has been evaluated based on the above 3D magnetic field analysis and the results show that the sufficient dynamic aperture is kept for all the enegy levels.

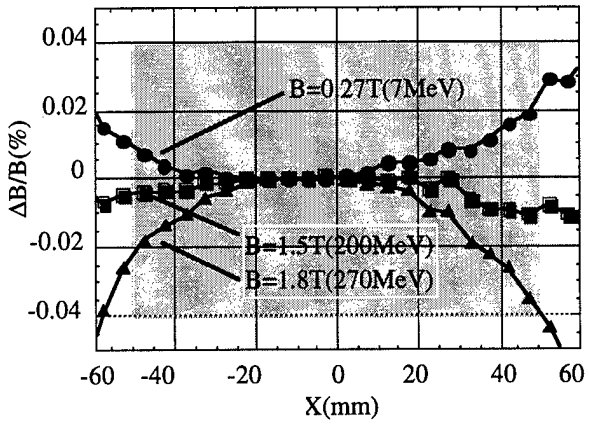



Fig. 3 The Calculated Magnetic Field Distribution of the Bending Magnet

Furthermore, we are investigating the possibility to apply a new type of the bending magnet which has the vacant portions in magnetic poles to control the flow of the magnetic flux in the magnet gap and poles. This new concept has been proposed originally in the project of the development of combined function bending magnets[4] and its effectiveness has been confirmed by the numerical study. This new concept may be useful to enlarge the dynamic range of the magnetic field, that is, the acccleration enegy range for the separated function as well as the combiend function lattices.

## 3 CONCLUSION

We presented a compact proton synchrotron of 270 MeV for cancer therapy and radiography. In the synchrotron, a separated functionlattice was applied with a slow beam extraction scheme using a transverse radio frequency perturbation of a narrow bandwidth under the contant separatrix. By utilizing the defocusing effects of quadrupole magnets and the bending magnets having an edge effect, the particles are extracted from the rather short straight section.

Since the position and gradient of the extracted beam are constant and the rapid switching on and off for the extraction are possible, the present synchrotron can be applied to various irradiation schemes such as the double scatterer, the wobbller-scatterer and other scanning methods.

## REFERENCES


[1] S. Fukumoto et al., Proc. of the NIRS International Workshop on Heavy Charged Particle Therapy and Related Subjects, p6, Chiba, Japan, 1993

[2] PARTICLES, Number 19, Jan(1997) editted by J. Sisterson

[3] K. Hiramoto et al., Proc, of the the NIRS International Workshop on Heavy Charged Particle Therapy and Related Subjects, p96, Chiba, Japan, 1993

[4] M. Tadokoro et al., in this conference

[5] W. Chu, Rev. Sci.Instrum. 64(8),2055(1993)

[6] K. Hiramoto et al., Nucl. Instrum. Methods. A322, p154 (1992)

[7] K. Saito et al., BEAM SIENCE AND TECHNOLOGY, Vol.2, p15(1997) published by INSTITUTE CHEMICAL RESEARCH, KYOTO UNIVERSITY

[8] K. Noda et al.,Nucl. Instrum. Methods. A374, p269 (1996).

# PROGRESS REPORT ON THE CONSTRUCTION OF THE NORTHEAST PROTON THERAPY CENTER (NPTC) EQUIPMENT

Y. Jongen, M. Abs, J.-C. Amelia, W. Beeckman, W. Kleeven, M. Ladeuze, G. Lannoye, S. Laycock, D. Leyman, V. Poreye, D. Prieels, D. Vandeplassche, S. Zaremba, *Ion Beam Applications (IBA), Louvain-la-Neuve, Belgium;* M. Heiberger, E. Hubbard, T. Hurn, L. Nissley, C. Silke, M. Tabor, *General Atomics (GA), San Diego, CA;* Kiyotaka Ohtomo, Masami Sano, Takemi Satoh, Toshiki Tachikawa, Takeshi Takayama, *Sumitomo Heavy Industries (SHI), Niihama-City, Japan*

*Abstract*

The IBA proton therapy system selected by the Massachusetts General Hospital (MGH) to equip its new NPTC is presently under construction and test. This paper presents a progress report on the equipment construction. The cyclotron, as well as the rest of the equipment, are being progressively installed in the NPTC building. The acceptance tests of the whole system are foreseen for the end of 1997.

## I THE IBA TEAM AND THE NPTC PROJECT

In the early 1994, a team composed by IBA, SHI and GA, with IBA as the prime contractor, was selected by MGH to construct the proton therapy system to equip its new NPTC. The main elements composing this system are:

- a 235 MeV isochronous cyclotron.
- an energy selection system transforming the fixed energy beam extracted from the cyclotron into a variable energy beam (235 to 70 MeV range).
- a beam transport and switching system connecting the exit of the energy selection system to the entrance points of a number treatment rooms.
- two complete isocentric gantries fitted with a nozzle, and a system consisting of two horizontal beam lines, the large field one being equipped with a nozzle.
- a robotic patient positioning system.
- a global control system.
- a global safety management system independent of the global control system. This safety management system uses hardwired interlocks to achieve a safety level meeting applicable standards.

## II A CYCLOTRON-BASED SYSTEM

Our goal was to meet all the clinical specifications of a state-of-the-art proton therapy facility in the most simple, reliable and cost effective way. This is the reason for our choice of a fixed energy cyclotron followed by an energy selection system.

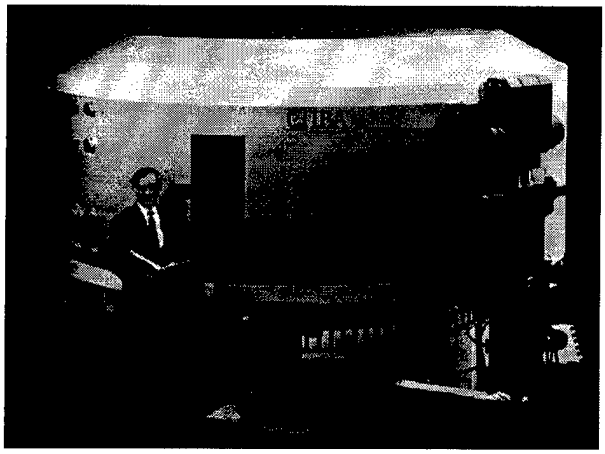


Figure 1: The 235 MeV cyclotron for proton therapy.

With this choice, we have maintained and even increased the advantages of a fixed energy accelerator while completely eliminating the perceived disadvantages. Indeed, compared to the characteristic of a synchrotron which offers the possibility to vary the energy from pulse to pulse, our energy selection system allows for a comfortable 10% energy variation within 2 seconds, with the additional advantage that the high intensity, continuous beam extracted from the cyclotron can be intensity controlled from the ion source within 15 μsec turn on/turn off time. These are essential features for the new treatment modes currently under consideration such as pencil beam scanning for example.

## III THE ENERGY SELECTION SYSTEM (ESS)

The energy variability of the system is achieved by means of a carbon wedge used as an energy degrader. As a result of the energy degradation, there is an increase in emittance and energy spread. Emittance slits are therefore used to define the emittance of the transmitted beam, while an analysing magnet system limits the energy spread. Energy changes are completed in two seconds, using laminated magnets and quadrupoles. Figure 2 presents a picture of the energy degrader.

0-7803-4376-X/98 /$10.00 © 1998 IEEE

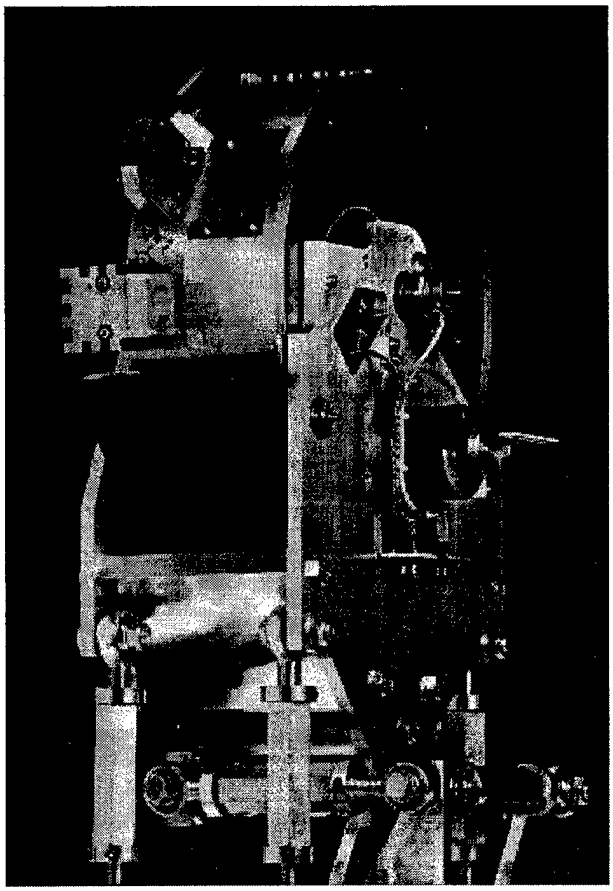


Figure 2: The energy degrader

## IV THE BEAM TRANSPORT SYSTEM

The beam transport and switching system connects the exit of the energy selection system to the entrance points of the gantries and the fixed beam lines. All bends are achromats. At strategic points along the beam transport system, the beam characteristics are monitored by grid ionisation chambers. This information can be used for automatic tuning.

## V THE GANTRIES

The gantry is the movable portion of the beam transport emerging from the cyclotron and terminating at the patient. The gantry structure is designed to minimize interference with the beam delivery system, provide maximum access to the patient, and maintain the isocenter position to within a sphere of confusion of radius 1 mm under all operating conditions, including all orientations, of the gantry. It is made up of a basic rotatable structure and a beam transport line which utilises one 45° bending magnet, one 135° bending magnet, nine quadrupole magnets, two sextupole magnets, three trim steering coils, and a nozzle. A simple rotating seal connects the moving portion of the beam transport tube to the stationary portion at the end of a 60° achromatic bend leading to the gantry.

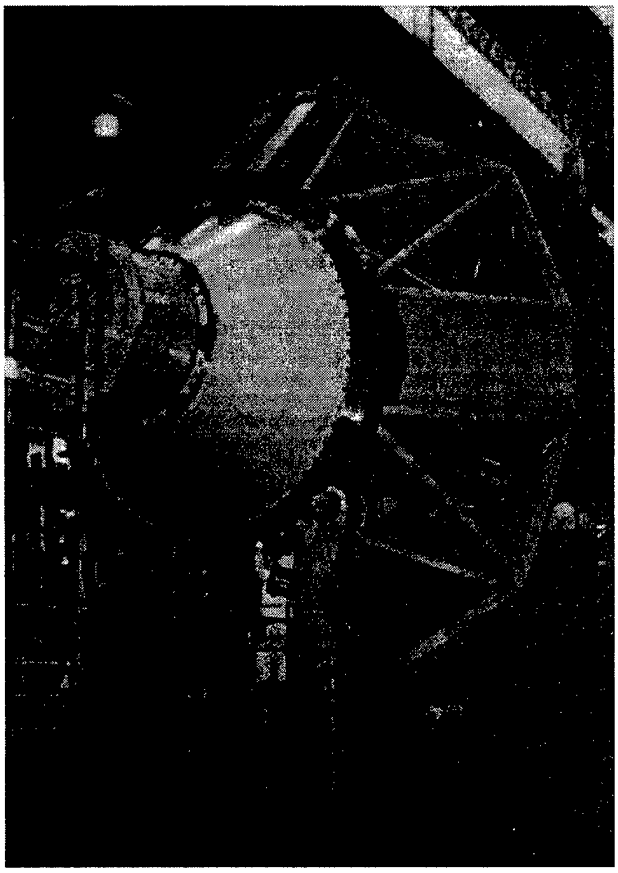


Figure 3: A gantry under construction (the gantry presented here, for illustration, is to be installed at the National Cancer Center in Japan)

The NPTC equipment includes two complete isocentric gantries. Each gantry is an achromatic system. Its optics can be tuned for either beam scattering/wobbling or for pencil beam scanning. As for the energy selection system and the beam transport system, the use of laminated magnets and quadrupoles allows for energy changes in two seconds.

## VI THE NOZZLES

The isocentric gantries and one of the horizontal beam lines, the large field one, will be fitted with nozzles. The functions of the nozzles include the 3-D beam shaping to irradiate the target volume at a constant dose, the beam monitoring and dosimetry, the help for patient positioning and field alignment verification, and the support of patient specific devices. The spreading techniques provided by the IBA nozzle are the double scattering for small to moderate fields, and the wobbling technique for the largest and deepest fields. The nozzle is compatible with a future upgrade to pencil beam scanning.

## VII THE PATIENT POSITIONING SYSTEM

The accuracy of proton therapy is such that patient positioners should be submillimeter precision instruments. Our Proton Therapy Equipment therefore includes a patient positioner specifically designed for proton therapy. It positions the patient to permit the beam

to be delivered with great accuracy to any point in the patient from any angle. Coupled with the gantry which provides 360° rotation of the beam about one vertical axis, the patient positioner must provide a minimum of four axis of motion (three translations and one rotation) to accomplish this objective. In fact, the patient positioner for the NPTC has six degrees of freedom - four axes as defined here above, and couch pitch and roll to accomplish fine scale adjustments.

## VIII THE CONTROL SYSTEM

The NPTC Control System is developed on three levels: the equipment control level where we have the process controllers close to the equipment, the management level, which is responsible for the operation of a set of high level functions, and the user interface level with the operator interface. Networks provide the connection between the different levels and between units at the same level. The process controllers, using VME card cages or industrial PLCs, are connected through a highly reliable serial bus (CANBus). An Ethernet network allows the connectivity from the equipment control level to the user interface level and the database system running on UNIX-based work stations.

## IX STATUS OF THE NPTC PROJECT

The construction of most of the subsystems is reaching completion. The cyclotron and the ESS were shipped to Boston at the end of March 1997, after successful completion of all cyclotron and ESS factory tests in IBA's assembly hall, including Bragg peak measurements. As far as the cyclotron is concerned, beam was accelerated up to the maximum energy, with extracted beam intensities up to 1 μA. This equipment arrived at the NPTC mid-April and is presently being installed.

The beam transport system will be completely mounted and ready to accept beam (on site) in September 1997.

The assembly of the gantry structure mechanical parts was done in March (vertical position). Shipment of the first gantry will take place at the end of April, after factory tests with the magnets installed. The second gantry will follow one month behind.

Some parts of the nozzle are still under final design (snout, bolus), while the other parts are under fabrication. Beam tests of the nozzles are scheduled in August and September 1997.

The patient positioning system assembly started at GA in early 1997 and the factory tests are underway.

Finally, work on the control system and on the safety system is progressing well. The computer network is installed and was connected to the available equipment in the assembly hall at IBA (before shipment). A group of seven computer scientists and engineers is developing and testing the software.

The whole system acceptance tests on site are expected to be performed at the end of 1997, and the first patient should be treated by the end of 1998.

## REFERENCES


[1] Y. Jongen *et al*, "Progress report on the IBA-SHI small cyclotron for cancer therapy", *Nuclear Instruments and Methods in Physics Research* B79 (1993) 885-889

[2] Y. Jongen *et al*, "New features in the design of the IBA-SHI proton therapy facility", Proceedings of the EPAC 94, London, May 1994

[3] Y. Jongen *et al*, "The proton therapy system for the NPTC", 4th European Conference on Accelerators in Applied Research and Technology, Zürich, August 1995

# PERFORMANCE OF PARALLEL PLATE IONIZATION CHAMBER FOR MEDICAL IRRADIATION

E. Urakabe, M. Inoue, Y. Iwashita, T. Shirai, T. Sugimura, A. Noda,
ICR, Kyoto University, Japan
M. Kanazawa, M. Torikoshi, K. Noda, S. Yamada, NIRS., Japan
M. Tadokoro, M. Nishi, Hitachi Ltd., Japan
Y. Fujita, INS, University of Tokyo, Japan

*Abstract*

We have developed *Parallel Plate Ionization Chambers (PPIC)* to measure not only the cumulative intensity but also the time structure of slow-extracted heavy-ion beams from a medical synchrotron. The characteristics of the PPIC with 3 mm and 1 mm gap distances for 760, 200, 111, and 55 Torr air were investigated with $C^{6+}$ beam (290 MeV/u) at HIMAC. The applied voltage to start the plateau region strongly depends on the beam intensity, and pressure of counter gas. The PPIC can be also used as a useful beam monitor for the time-structure measurement of heavy-ion beams.

## 1 INTRODUCTION

As a new method of radiation therapy with ion beams, the spot scanning is started at the PSI[1] and GSI[2]. We have also been planning to use the spot scanning method, at HIMAC (Heavy Ion Medical accelerator in Chiba)[3].

Intensity of beams slowly extracted from a synchrotron, in general, varies in time mainly due to the current ripple in the synchrotron magnets. To realize the accurate dose distribution, the speed controlled spot scanning should be achived. In this system the intensity of the slow-extracted beams should be measured at the upstream of the irradiation room.

As a beam monitor for the intensity measurement, a parallel plate ionization chamber (PPIC) is a good candidate, because of its stable operation and wide dynamic range for the detection of the heavy-ion beams. We have developed PPIC. In this paper, we describe on the preliminary results of performances for $C^{6+}$ beams extracted from the HIMAC.

## 2 DETECTOR CONSTRUCTION

The structure of the PPIC is shown in Fig. 1. We have used air as a counter gas. In order to keep the heavy ion beam qualities, the total effective thickness of PPIC is very thin. i.e.; about $6.15mg/cm^2$ for 760 Torr air, and about $0.52mg/cm^2$ for 50 Torr. The electrodes are square-shaped $3\mu m$-thick aluminized polypropylen ($270\mu g/cm^2$ the polypropylen and $20\mu g/cm^2$ the aluminium). These very thin electrodes are fixed in the glass-epoxy frame and set into the aluminum chamber. The gap dependence of the S/N ratios in the detector signal can investigate by using the spacer as shown in Fig. 2.

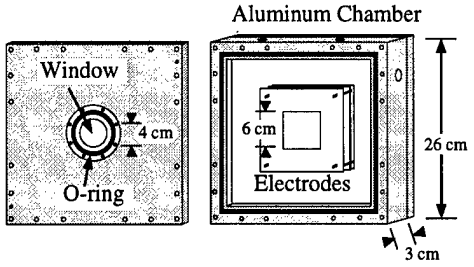



Figure 1: The PPIC. The left figure shows the front lid of the PPIC. The front and rear windows are sealed with O-rings. Three electrodes are mounted in the aluminum chamber.

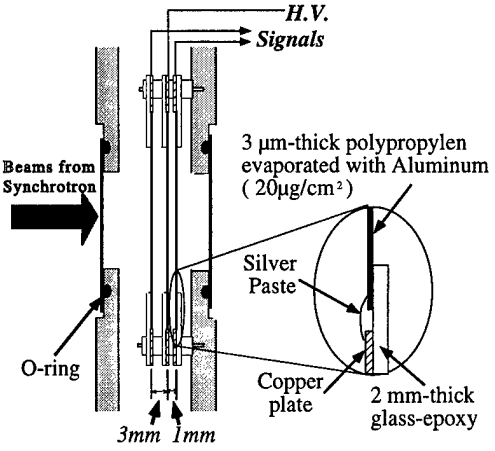



Figure 2: The cross-sectional view of the PPIC. The electrodes are the 3 $\mu$m-thick aluminized polypropylen film fixed on the 2 mm-thick glass-epoxy frame. Three electrodes can be arranged with front and rear gap distances of 3 mm and 1mm, respectively.

## 3 EXPERIMENTAL SETUP

The $C^{6+}$(290 MeV/u) beams slow-extracted from synchrotron with RF-KO method[4] at around 11/3 resonance are used in the present experiments. The setup of the PPIC experiment is shown in Fig. 3 and Fig. 4.

Before the time structure measurement, we measured the plateau characteristics under different conditions: the gap distances, the beam intensities and gas pressures of air. The picked up signals from the PPIC were integrated during 10 spills in order to reduce the statistical error. To cancel out the fluctuation of $C^{6+}$ beam intensities, we utilized the output signals from the HIMAC ion chamber, which is

0-7803-4376-X/98/$10.00 © 1998 IEEE

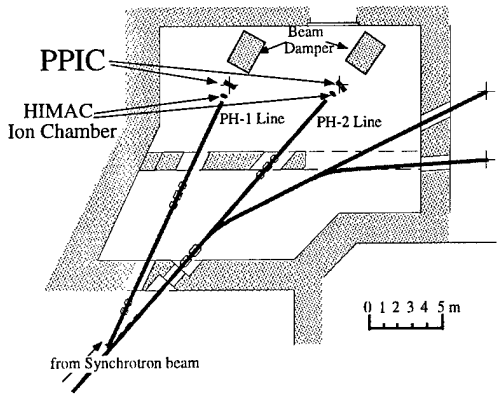



Figure 3: The plane view of the "physics and general" experimental room.

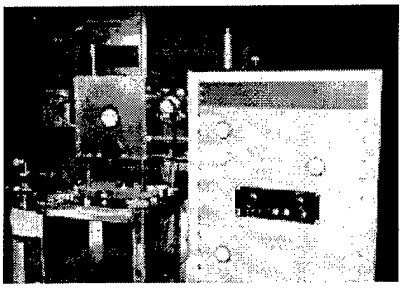


Figure 4: Photograph of the experimental setup of the beam line. From the downstream, the PPIC, the HIMAC ion chamber (the ionization chamber with a the gap distance of 2 mm) set up.

calibrated with Faraday cup.

The charges from the PPIC were converted into voltage signals with current amplifiers and observed by a digital oscilloscope (HEWLETT PACKERD 54540A) triggered by the timing signal of beam extraction. In order to investigate the time response of the PPIC, we compared PPIC signals with those of the 0.2 mm-thick plastic scintillation counter which has been used as a "Ripple Monitor" at just after the extraction point.

## 4 RESULTS

### *4.1 INTENSITY MEASUREMENT*

Normalizing the charge signal from the PPIC by that of the HIMAC ion chamber, we have obtained plateau curves for air. We have found that the plateau characteristics depends strongly on the beam intensity. Fig. 5 shows the plateau curves for the 3 mm gap distance PPIC with 759.6 Torr air. The plateau starting voltage is about 24 volts for intensity of $1.7 \times 10^6$pps, and about 362 volts for intensity of $1.3 \times 10^9$pps.

In the case of beam intensity of $1.3 \times 10^9$ pps, the plateau starting voltage is about 17 volts at 50.2 Torr air (see Fig. 6). In the case of with 759.6 Torr air, however, the operation mode can reach the plateau region for around 362 volts.

The dynamic range of the PPIC is illustrated in the top of Fig. 7. It is clear that the signal height of the PPIC

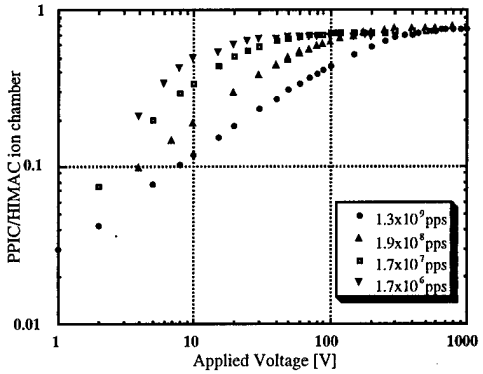



Figure 5: The plateau curve of PPIC(3mm gap distance) with 759.6 Torr air. The beams are $C^{6+}$ (290 Mev/u). The ordinate is the ratio between the output charge from the PPIC and the HIMAC ion chamber.

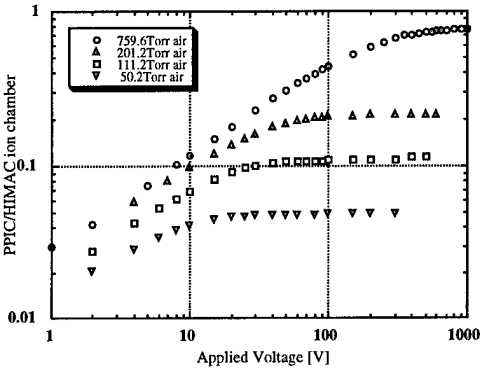



Figure 6: The plateau curve of PPIC(3mm gap distance) with air. The beams are $1.3 \times 10^9$pps $C^{6+}$ (290 mev/u). The ordinate is the ratio between the output charge from the PPIC and the HIMAC ion chamber.

are proportional to the pressure of gas density with errors of 10%. The linearity of the signal against the pressure is also confirmed by the bottom of Fig. 7. Consequently, we can deduce that the PPIC signal height is proportional to number of primary ion pairs. It is also due to the density of the primary ion pairs that the plateau characteristics differ in beam intensity and pressure of counter gas.

### *4.2 TIME STRUCTURE MEASUREMENT*

We measure the time structure of the RF-KO extracted beam with PPIC. The time structure of the RF-KO extracted $C^{6+}$ beams measured with PPIC(1mm gap distance) and Ripple Monitor is shown in Fig. 8. Both detectors have the peak of 777, 100 Hz and these linear combination in the frequency spectrum. These frequencies come from the repetition rate of frequency modulation of the RF field as usually used for the therapy at HIMAC and the ripple of AC power line.

When the frequency modulation of RF-KO is changed, the corresponding frequency component come dominant and we can study the time response of the PPIC at that frequency. With the frequency of RF-KO at 3000 Hz, the

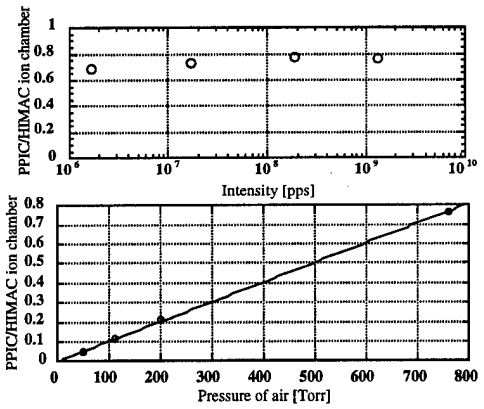



Figure 7: The PPIC signal dependence on the intensity (upper) and the pressure of the counter gas (lower).

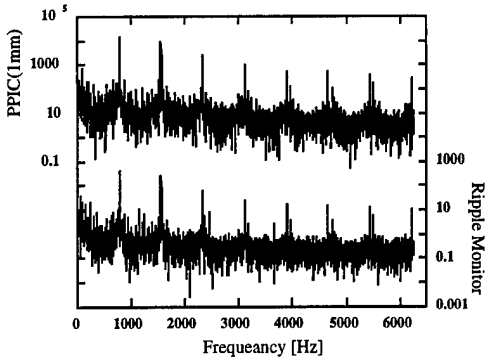



Figure 8: Frequency spectra of the signals from the PPIC(1mm) with the 759.8 Torr air (upper) and the Ripple Monitor (lower). The repetition rate of the frequency modulation of RF-KO field is 777 Hz as usually use for therapy.

frequency response of both detector is as shown in Fig. 9. Because the plastic scintillation counter is fast enough to respond beam change in kHz order, it is concluded that our PPIC system achieve the kHz order time response.

### *4.3 SUMMARY AND FUTURE PLAN*

We can summarize the present results that the PPIC with gap distances of 3mm and 1mm can be used as a useful beam monitor from both viewpoints of beam-intensity and time-structure measurements. Although the 3mm gap distance PPIC needs the higher applied voltage to reach the plateau, we will choose the gap distance of the PPIC 3mm. It is because the electrode films of 1mm gap distance PPIC pull each other by Coulomb force and reduce the effective volume by several percent.

While we continue the further basic study concerning the PPIC characteristics, we are planning to a two-dimensional beam monitor with the PPIC having stripped electrodes so as to observe the two dimensional beam profile at the same time. Because the signal from one strip electrode is smaller than the plane electrode, we choose the pressure of counter gas is 760 Torr.

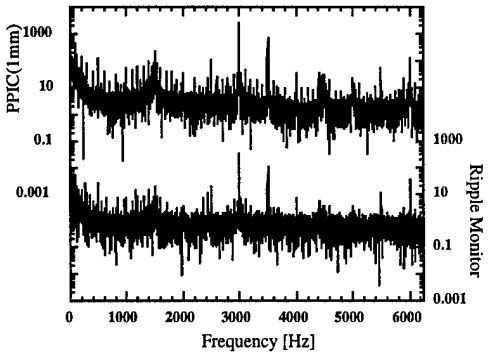



Figure 9: Frequency spectra of the signals from the PPIC(1mm) with the 759.8 Torr air (upper) and the Ripple Monitor (lower). The repetition rate of the frequency modulation of RF-KO field is 3000 Hz.

## 5 ACKNOWLEDGEMENT

The authors would like to express their gratitude to Mr. M. Hori for the fruitful discussion about the characteristics of the PPIC. They appreciate the help given by Mr. H. Tonguu. They would also like to thank to Mr. Sagarifuji (a manager of Mishima-factory of TOYO-Metalizing Co. LTD.) and the crews of AEC for the excellent supports to the present experiments. These experiments have been carried out as a Research Project with Heavy Ions at NIRS-HIMAC.

## 6 REFERENCES

[1] E.Pedroni et al., " The 200-MeV proton therapy project at the Paul Scherrer Institute: Conceptual design and practical realization ", Med. Phys. 22 (1), January 1995, 37-53

[2] B.Franczak, " Data Generation for SIS and Beam Lines for the GSI Therapy Project ",Contribution paper to the EPAC '96 H. Eickhoff et al., " Accelerator Aspects of the Cancer Therapy Project at the GSI Darmstadt ",Contribution paper to the EPAC '96

[3] Y. Hirao et al., " Heavy Ion Medical Accelerator in Chiba -A Design Summary and Update- ", NIRS-M-89, HIMAC- 001, December 1992

[4] M. Tomizawa et al., " Slow Beam Extraction at TARN II ", Nucl. Instr. and Meth. in Phys. Res. A326 (1993) 399- 406 K. Noda et al., " Slow beam Extraction by a Transverse RF Field with AM and FM ", Nucl. Instr. and Meth. in Phys. Res. A374 (1996) 269-277

# NEW SECONDARY BEAM COURSE FOR MEDICAL USE IN HIMAC

S. Kouda, M. Torikoshi, M. Kanazawa, A. Kitagawa, T. Murakami, K. Noda, Y. Sato, E. Takada, J. Yoshizawa, Y. Futami, A. Higashi, T. Kanai, N. Matsufuji, H. Tomura, S. Yamada, K. Kawachi, M. Suda, T. Tomitani and M. Kumada, National Institute of Radiological Sciences, 9-1, Anagawa 4-chome, Inage-ku, Chiba-shi 263 JAPAN, H. Ogawa, Y. Ishikawa, H. Tsubuku and T. Kato, Accelerator Engineering Corporation 2-13-1 Konakadai, Inage-ku, Chiba-shi 263, JAPAN

*Abstract*

A new beam course, a projectile fragment separator to provide radioactive beams, is under construction at HIMAC. A primary purpose of the new beam course is to study medical applications of radioactive beams. The specifications and status of the beam course and a preliminary result using carbon beams are summarized.

## 1 INTRODUCTION

In heavy-ion therapy, it is critical to control the dose distribution in a patient's body as accurately as possible in order to utilize the superiority to conventional methods. We, however, have no methods to validate irradiated volumes inside a body. Furthermore, since beam ranges are calculated based on the CT values obtained by CT scanned images, in some cases large uncertainties may be unavoidable. If the dose distribution can be measured accurately enough, heavy-ion therapy will become a more advanced technique.

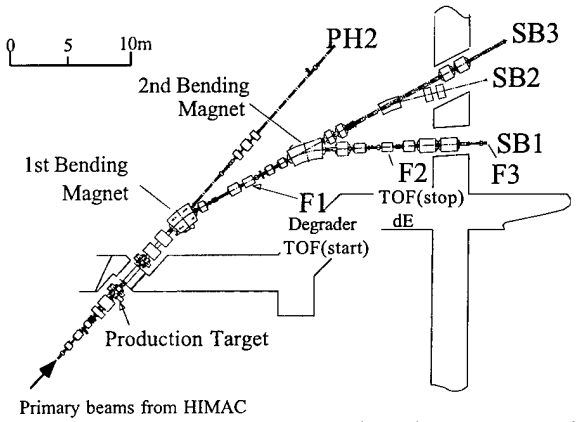



Figure: 1 Layout of the secondary beam course in HIMAC at NIRS.

Beams of positron emitters, such as $^{11}C$ or $^{19}Ne$, may enable us to evaluate the dose distribution inside a body, because positron emitters injected into a body produce a pair of annihilation gamma rays (511 keV), mainly, near to the locations where they stop.

For a study of medical applications of radioactive beams, a secondary beam course is under construction at HIMAC (Heavy Ion Medical Accelerator in Chiba) at National Institute of Radiological Sciences[1,2]. Research on medical applications covers two categories. The first category is the measurement of the beam ranges. If we can measure the ranges of secondary beams accurately enough, we can feedback this knowledge to treatment planning and make the planning more reliable. This would allow us to apply heavy-ion treatments to targets which are located near to radiation-sensitive organs. The development of new positron cameras to detect the annihilation gamma rays are being carried out in order to measure the range with high accuracy, in parallel with the construction of beam course. The second category is a treatment by radioactive beams, themselves. It is a large advantage that irradiated volumes can be scanned and confirmed immediately after each irradiation.

## 2 DESIGN OF THE BEAM COURSE

### *2.1 Layouts and beam optics*

A layout of the secondary beam course is shown in Figure 1. New courses branch off the existing course, PH2, which is used for physics experiments, and three courses are included in the design. A course labeled SB1 is under construction. All devices up to F2 in the figure were installed by the end of March, 1997, and the remaining devices of SB1 will be placed in August, 1997. Spaces for two other courses, SB2 and SB3, are being kept open for future construction.

Beam course SB1 is a spectrometer comprising a pair of bending magnets, eleven quadruple magnets, a production target and an energy degrader [3], satisfying a double-achromatic condition. The principle to separate ions with specific A and Z numbers is based on the work of Dufour et al.[3]. The SB1 course has three focusing points, F1, F2 and F3, as shown in Figure 1; point F1 is dispersive in momentum, while two other points, F2 and F3, are doubly achromatic. The degrader is set at F1. The specifications of the beam course are summarized in Table 1, and the calculated beam envelopes are shown in Figure 2.

The effect of the degrader was estimated by a code ORBIT2 [4], which allows us to treat the degrader as an optical element[5].

Table: 1 Specifications of the secondary beam course in HIMAC.

| | |
|---|---|
| Maximum magnetic rigidity | 8.13 Tm |
| Momentum acceptance | 2.6% (full width) |
| Angular acceptance | Horizontal 26mrad (full width) |
| | Vertical 26mrad (full width) |
| Momentum dispersion at F1 | 1.78m |
| Bending Magnet | Radius 5m |
| Bending angle | 1st bending magnet 20 degrees |
| | 2nd bending magnet 26.5 degrees |

0-7803-4376-X/98/$10.00 © 1998 IEEE

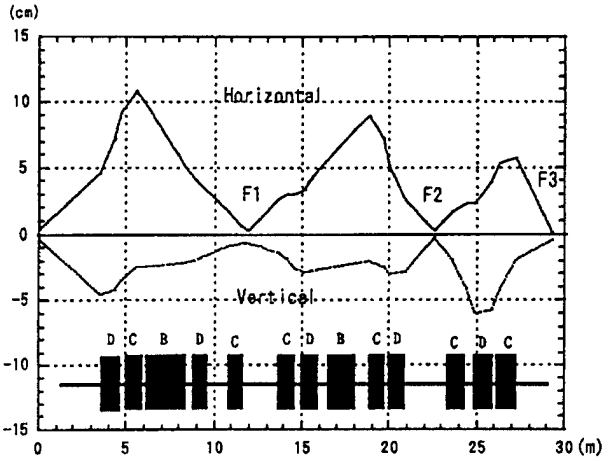



Figure: 2 Beam envelopes of the secondary beam course SB1. Emittance of the vertical and horizontal are assumed to be 40π mm mrad at the production target.

### *2.2 Beam monitoring detectors*

Secondary particles are identified by using time of flight (TOF) and delta E data. A start and a stop counter for TOF, plastic scintillators with a thickness of 0.5 mm, are placed at F1 and F2, respectively. A delta E counter, a silicon detector with a thickness of 0.5 mm, is set at F2.

Profile monitors of multiwire proportional chambers are installed at F1, F2, and F3 in order to measure the positions and sizes of primary beams.

### *2.3 Control system*

Beam courses for medical use are required to have characteristic features: a good reproducibility of beam qualities and easy operation. A good reproducibility includes energies, intensities, sizes, and purity of the secondary beams. Easy operation is indispensable so that operators with no special knowledge about reaction products can operate the beam course as routine work.

A new control system, to satisfy those requirements, is designed and constructed. The control system comprises three computers connected by a network, as shown in Figure 3. The system processes many functions, including: (1) control of devices, such as magnets and targets; (2) analyses of data from monitoring detectors; and (3) beam-optics calculations. Each function proceeds according to the programed sequences. Since these functions are dealt within one framework, measured or calculated data can be referred swiftly and automatically. Thus, a sizable reduction of the tuning time is expected for such processes as the optimization of parameters, which requires reiteration of device-settings and measurements.

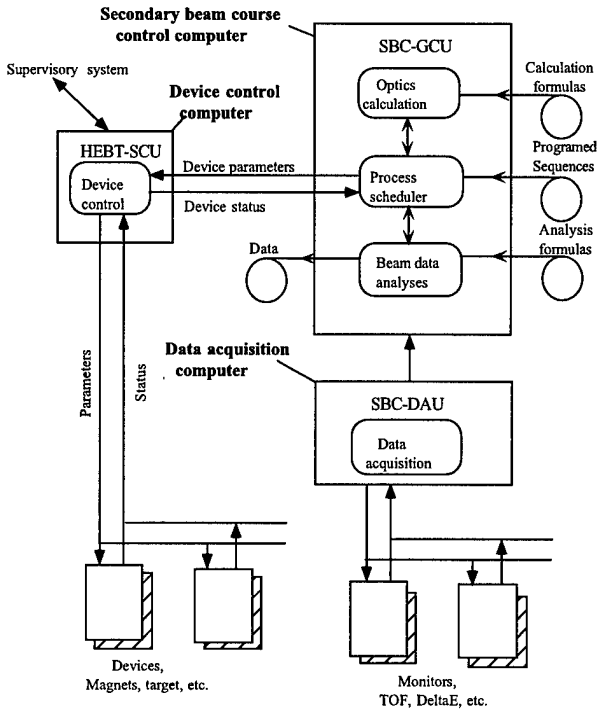



Figure: 3 Block diagram of the control system of the secondary beam course.

## 3 RESULTS OF THE BEAM TESTS

A first beam test of the new course was carried out using $^{12}C$ beams with energies of 290 MeV/u and 400 MeV/u. The results verified the calculated beam optics and alignments of the devices.

Projectile fragments produced in aluminium targets were also measured. The thickness of the targets was 3.6 cm and 5.5 cm for 290 MeV/u and 400 MeV/u $^{12}C$ beams, respectively, corresponding to the thickness with which the maximum yields of $^{11}C$ were expected by a computer code, INTENSITY2[6]. A scatter plot of TOF vs. delta E is shown in Figure 5. It can be seen that the events are clearly separated from each other depending on A and Z numbers.

As a rough evaluation, a production ratio of $^{11}C$ with a primary beam of $^{12}C$ was found to be on the order of $10^{-3}$. The ratio is consistent with an estimation by INTENSITY2.

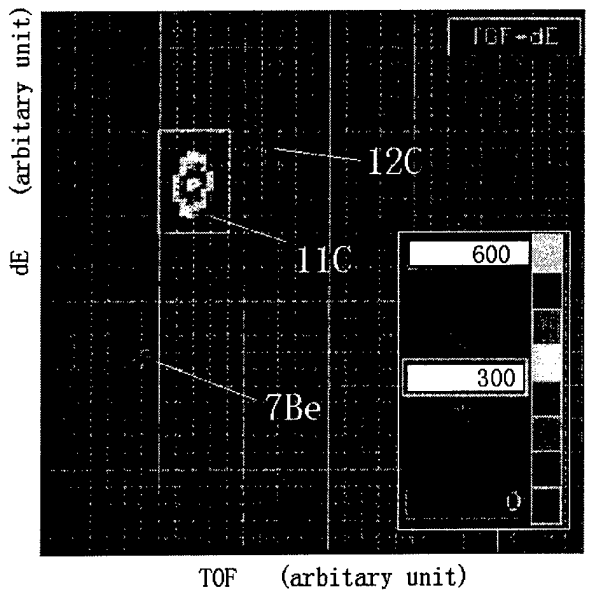



Figure: 4 Scatter plot of TOF vs. delta E obtained in the beam test. Events of $^{11}C$, $^{12}C$ and $^{7}Be$ are clearly separated. The intensity ratio of $^{11}C$, $^{12}C$ and $^{7}Be$ are about 90%, 5% and 5%, respectively.

## 4 ACCURATE RANGE MEASUREMENTS USING SECONDARY BEAMS

The development of new positron cameras for accurate range measurements is in progress. The conditions required to the positron cameras are twofold: large detection efficiency and high spatial resolution (about 1mm). The first condition comes from a fact that a dose level allowed for diagnosis is very low (typically less than 0.1 Gy). Efficiency and spatial resolution of existing PET cameras are not good as being expected. A method to determine the beam ranges using the positron camera is shown in Figure 6. A pencil beam of positron emitters is injected to a body from the left, and a pair of annihilation gamma rays are emitted at a near place where the beam stops. A pair of detectors detect those gamma rays and define a line along which gamma rays produced. The point where annihilation gamma rays produced is chosen as a crossing point of the beam axis and the line.

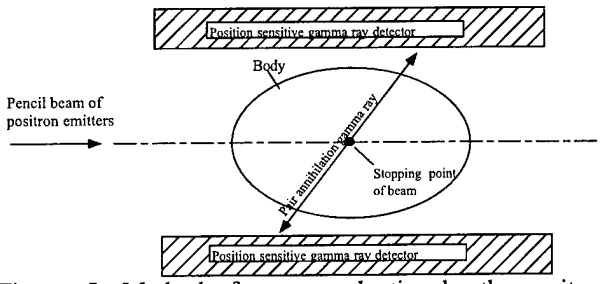



Figure: 5 Method of range evaluation by the positron camera.

A test detector was assembled for the development of positron cameras. The detector resembles an Anger-type camera, except for the collimators. An NaI(Tl) crystal with a size of 10 cm x 10 cm x 3 cm is viewed by an array of 6x6 photo-multiplier tubes (HAMAMATU H3166). Outputs from the photo-multiplier tubes are independently measured by charge-sensitive ADCs (LeCroy 2249). The positions where a gamma ray hits are decided by the distribution of the light outputs from the nearby photomultiplier tubes. NaI(Tl) scintillators were employed due to their properties of large light outputs, relatively high efficiency for 511 keV gamma rays and availability of a large crystal. The position resolution and efficiency of the test detector are being evaluated.

## 5 SUMMARY

For the advancement of heavy-ion therapy, we are constructing a secondary beam course, with a computer-assisted control system. The first beam test was carried out with satisfying results. The amount of the $^{11}C$ produced was consistent with the estimation. We are also developing positron cameras for accurate range measurements.

## 6 ACKNOWLEDGEMENTS

We would like to thank Prof. Morinobu at Kyushu University for discussions about ORBIT2. We are indebted to members of Lineac Lab. and Cyclotron Lab. at RIKEN and Prof. Matsuta of Osaka University for suggestions about the course design. Design and installation of the devices were made by Mitsubishi Electric Co.

## REFERENCES

[1] M. Torikoshi, M. Kanazawa and S. Kouda et al., Proceedings of International Symposium.on Non-Nucleonic Degree of Freedom Detected in Nucleus, Osaka, to be published.
[2] M. Hosaka, K. Noda, T. Murakami, M. Kanazawa, A. Kitagawa, Y. Sato, E. Takada, M. Torikoshi and S. Yamada, Proceedings of the 10th Symposium on Accelerator Science and Technology, Hitachinaka (1995) p. 410.
[3] J.P. Dufour, R. Del Moral, H. Emmermann, F. Fubert, D. Jean, C. Poinot, M. S. Pravikoff, A. Fleury, H. Delange and K.-H. Schmidt, Nucl. Instr. and Meth. A248 (1986) 267.
[4] S. Morinobu, A computer code ORBIT2, unpublished, 1987.
[5] T. Shimoda, H. Miyatake and S. Morinobu, Nucl. Instr. and Meth. B70 (1992) 320.
[6] J. A. Winger, B. M. Sherrill and D. J. Morrissey, Nucl. Instr. and Meth. B70 (1992) 380.

# DESIGN STUDY OF A LINEAR ACCELERATOR SYSTEM FOR NEUTRON CAPTURE THERAPY

J.W. Kim
RIKEN, Saitama, Wako-shi, 351-01 Japan
J.S. Chai
Korea Cancer Center Hospital, KAERI, Seoul 139-240 South Korea

*Abstract*

A proton linear accelerator has been conceived to be used for Boron Neutron Capture Therapy (BNCT) and Neutron Radiography (NR) at the Korea Cancer Center Hospital in Seoul, Korea. The main accelerator is an RFQ which will accelerate protons from 90 keV to 3.5 MeV with a current of 50 mA in the present design. According to the PARMTEQ calculation, transmission efficiency is over 96 % for that current. Beam dynamics and rf properties of the RFQ have been studied along with beam transport and target systems. At present possibility of obtaining funding appears to be low, but we thought it is worthwhile to carry out the design study for the future proposal.

## 1 INTRODUCTION

The Korea Cancer Center Hospital (KCCH) in Seoul has used a MC50 cyclotron (Scanditronics) for neutron therapy since 1986 [1]. To extend the hospital's capability for cancer treatment, an accelerator system for BNCT has been proposed. A high current proton beam produces neutrons from the nuclear reactions such as $^{7}$Li(p,n)$^{7}$Be or $^{9}$Be(p,n)$^{9}$B, and then the neutron beam is moderated to epithermal energy (1 eV – 10 keV). The reaction process for treatment is $^{10}$B(n,$\alpha$)$^{7}$Li utilizing a high capture cross section of $^{10}$B for thermal neutrons. The resulting reaction products produce the localized dose on the highly malignant cells [2].

Regarding to accelerators for high current proton acceleration, RFQ and RFD seem promising among others. We first chose to study on RFQ since the average current of near 80 mA has been already achieved by the Chalk River RFQ (to 600 keV) [3].

The proton beam energy needed for BNCT is related to the choice of target. A beam energy of 2.5 MeV along with Li target appears to be the best choice in the aspect of neutronics [4]. And we consider that the use of Be target with a higher beam energy of 3.5 MeV is worthy of pursuing as it allows a simpler target system, which fits better into the hospital environment. We chose the current of 50 mA in the present design, which will produce the epithermal neutron flux of $5\times10^{9}$/cm$^{2}$/sec with $^{7}$Li target at 2.5MeV.

An RFQ to accelerate high current proton beam is highly demanding on diverse applications. As a result, designs of such RFQ accelerators are described by many authors [5] [6]. Our study here aims at obtaining our own design parameters. Besides the RFQ, the beam transport and the target systems have been studied, and some results are given in this report.

Table 1: Parameters of the RFQ

| | |
|---|---|
| Frequency | 352 MHz |
| Vane voltage | ±45 kV |
| Kilpatric factor | 1.7 |
| Injection energy | 90 kV |
| Final energy | 3.5 MeV (2.5 MeV) |
| Length | 4.9 m (3.8 m) |
| Power dissipation | 720 kW (540 kW) |

## 2 DESIGN STUDY OF AN RFQ ACCELERATOR

The accelerator system is composed of ion source, RFQ, low-energy and high-energy beam transport lines. A schematic view of the system is shown in Figure 1. The present design energy is 3.5 MeV with an intermediate goal of achieving 2.5 MeV. Design parameters are obtained using the PARMTEQ code [7] for both energies, and listed in Table 1. The cell parameters of the RFQ is shown in Figure 2 as a function of the longitudinal position.

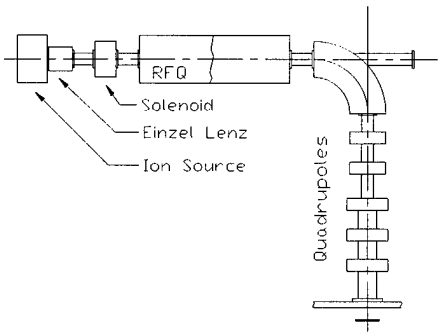



Figure 1: A schematic view of a linear accelerator system for BNCT

The transmission efficiency is over 96 % for 50 mA. The input rms emittance for this calculation is 0.2 $\pi$ mm·mrad (normalized). When the emittance is 0.3 $\pi$ mm·mrad, the transmission efficiency reduces by about 4 %. As indicated by other workers, a beam current of 100 mA may be needed for prompt treatments. The power loss and the transmission

0-7803-4376-X/98 /$10.00 © 1998 IEEE

efficiency are 900 kW and 89 %, respectively for 100 mA. The locations of major particle loss are near the beginning and the end of the gentle buncher. Because of the higher energy damage is more severe near the end of the gentle buncher. A further study is needed to reduce the loss by increasing the transverse focusing possibly with superconducting solenoids.

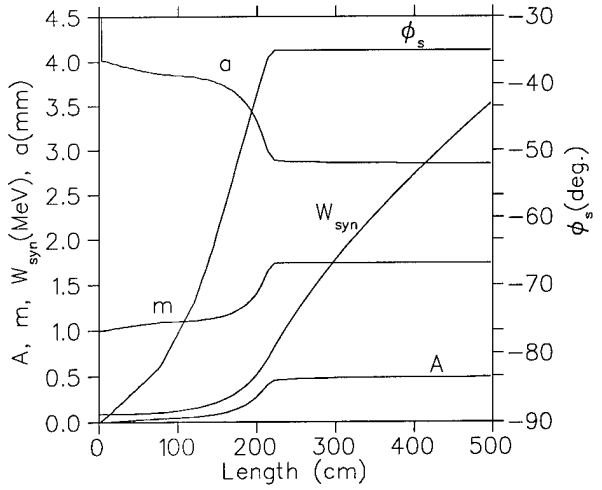



Figure 2: Cell parameters of the RFQ as a function of longitudinal position

The rf properties of the structure were calculated with the computer programs SUPERFISH and MAFIA. The Q value was about 12,000 with SUPERFISH, and 10,000 by MAFIA. The power loss obtained from RFQUICK is similar to that from the MAFIA calculation. A MAFIA model along with TE210 mode is shown in Figure 3.

The RFQ structure will be modular to ease manufacturing difficulties due to its long length. Each module will be roughly 1-2 m long. To improve the tuning stability, resonant coupling between modules [8] was tested with MAFIA. A wider mode separation could be achieved by adjusting the coupling capacitance, but a further investigation is needed. The vane voltage distribution was easily controlled by adjusting the vane undercut.

## 3 BEAM TRANSPORT LINE

The beam transport line was designed with TRACE3-D [9] which includes the linear space charge effect. The low-energy beam transport consists of an einzel lens and a solenoid, which is thought to reduce the space charge neutralization and to give flexibility in matching. The beam dynamics calculated with TRACE3-D is shown in Figure 4.

In the high-energy beam transport the beam is 90° vertically bent down to comfortably accommodate the target and modulator. Figure 5 shows the beam envelopes of high energy beamline. The radius of beam on target is 5 cm, the power density being 1.6 kW/cm$^2$ when the beam energy and current are 2.5 MeV and 50 mA. The beam is unidirectional, and its size can be easily controlled with upstream quadrupole triplet.

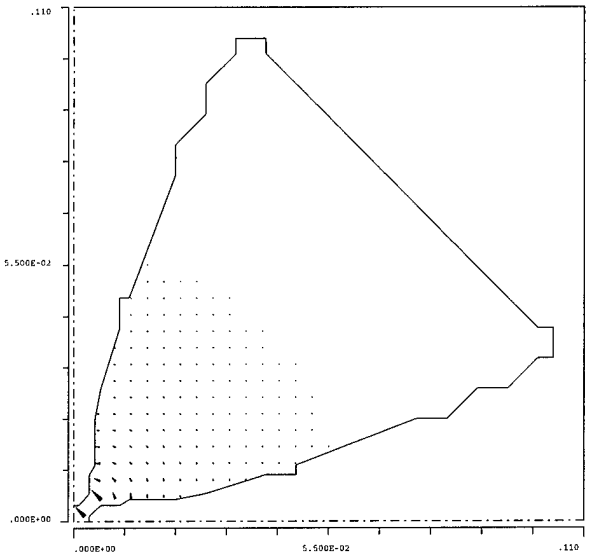



Figure 3: A MAFIA model shown with TE210 mode.

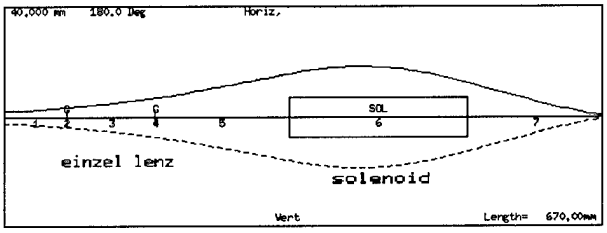



Figure 4: Beam envelopes of the low energy beam transport line.

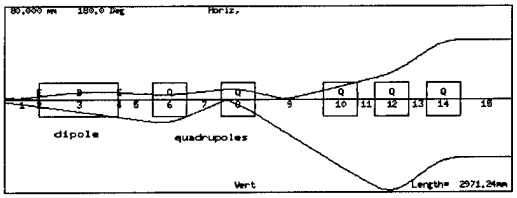



Figure 5: Beam envelopes of the high energy beam transport line.

To reduce the peak power density it seems important to make a uniform distribution of current [10]. Nonlinear elements are needed to change the beam current distribution. At the waists of transverse planes as shown in Figure 5 octupole and duodecapole components could be inserted, minimizing the x-y coupling [11].

## 4 TARGET DESIGN

The design of target depends on the beam power and the target material. First, pure lithium target with melting tem-

perature of 179 °C can sustain only a low power beam. A preliminary design of the target system is shown in Figure 6. Material of the target frame is aluminum. Assuming that the beam diameter is 10 cm, the power density is 318 W/cm$^2$ for 10 mA. Finite element calculations with the ANSYS code were carried out for this target with the heat flux of 318 W/cm$^2$, and the result is shown in Figure 7. The cooling film coefficient used as an input was approximately calculated to be around 2.5 W/cm$^2$/K with a flow rate of 6 liter/sec, using the Dittus-Boelter empirical correlation for turbulent duct flow [12]. The maximum temperature on the lithium surface is 84 °C when the water temperature is 10 °C, and it becomes 125 °C for the heat flux of 500 W/cm$^2$. Hence it seems difficult to use over 20 mA of beam current. For higher power beam a rotating target [4] or $Li_2O$ at the cost of lower neutron yield could be used.

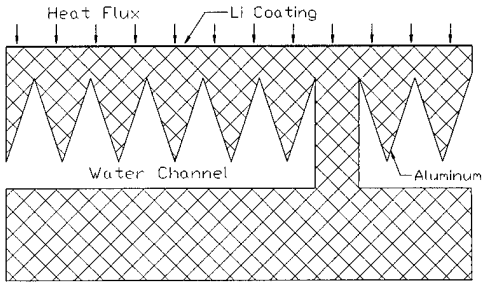



Figure 6: A preliminary design of a Li target.

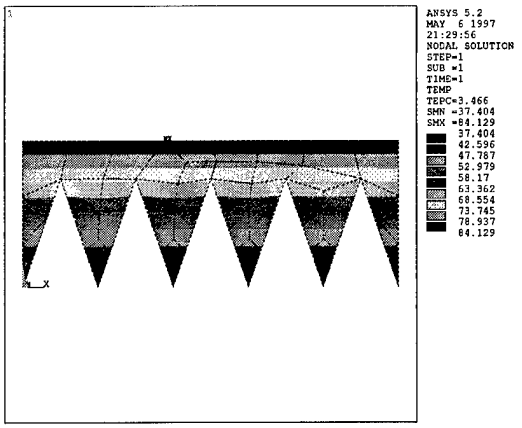



Figure 7: Temperature distribution on the Li target calculated with ANSYS. See text for details.

## 5 CONCLUSION

Several design aspects of the RFQ accelerator system for BNCT were studied, and we will continue the detailed design for the future proposal. The accelerator and the target designs are core parts of the study. We need to study accelerators other than RFQ's such as RFD and ESQ, and also different structures of RFQ. The target design can be further optimized with finite element programs.

## 6 ACKNOWLEDGMENTS

The authors would like to thank Dr. G.E. McMichael of Argonne National Laboratory for invaluable information.

## 7 REFERENCES

[1] J.S. Chai et al., Operation Experience of KCCH Cyclotron for 10 years and Prospect of Cyclotron in Korea, Proc. of the 14th Int'l Conf. on Cyclotrons and Their Applications, (1995) 508

[2] R.F. Barth et al., Boron Neutron Capture Therapy of Cancer, Cancer Research, **50** (1990) 1061

[3] G.E. McMichael, Argonne National Lab., private communication.

[4] C-K C. Wang et al., Accelerator Neutron Irradiation Facility for Hospital- Based Neutron Capture Therapy, Advances in Neutron Capture Therapy, (1993) 119

[5] T.P. Wangler et al., Conceptual Design of an RFQ Accelerator-Based Neutron Source for Boron Neutron-Capture Therapy, Proc. of 1989 Partl. Accel. Conf. (1989) 678

[6] R. Ferdinand et al., RFQ design for High-Intensity Proton Beams, Proc. of 1995 Partl. Accel. Conf. (1995) 1146

[7] K.R. Crandall and T.P. Wangler, AIP Conf. Proc. **177** (1988) 22

[8] M. Jean Browman and Lloyd M. Young, Coupled Radio-Frequency Quadrupoles as compensated Structures, Proc. of 1990 Linear Accel. Conf. (1990) 70

[9] K.R. Crandall, TRACE 3-D Documentation, Los Alamos National Lab. (1990)

[10] Tim Broome, High Power Targets for Spallation Sources, Proc. of 1996 European Accelerator Conference, (1996) 267

[11] D. Bruhwiler and Y. Batygin, Beam Transport for Uniform Irradiation: Nonlinear Space Charge and the Effect of Boundary Conditions, Proc. of Partl. Accel. Conf., (1995) 3254

[12] F.W. Dittus and L.M.K. Boelter, Univ. Calif. (Berkeley), Pub. Eng., Vol.2 (1930) 443

# A COMPACT PROTON ACCELERATOR SYSTEM FOR CANCER THERAPY

A.Yamaguchi, K.Nakayama, T.Rizawa, S.Sukenobu, K.Satoh, Y.Morii, Y.Tanabe and Y.Chiba
Toshiba Corporation
2-4, Suehiro-cho, Tsurumi-ku, Yokohama, 230 Japan

*Abstract*

The basic design of a compact proton accelerator system for cancer therapy is described. The system consists of a 30keV ion source, a 3MeV RFQ linac, and a rapid-cycling 235MeV synchrotron. A strong focusing combined function magnet, which has both focusing and defocusing section in a unit, is adopted instead of a quadrupole magnet. The rf system applies a compact ferrite loaded tuning-free cavity which has no bias windings. The synchrotron is operated at 20Hz repetition with fast beam extraction. It is the same method as the KEK booster synchrotron, which has been using for proton therapy studies by Tsukuba University. In this system, a breath synchronized irradiation method is easily realized and the energy of proton beam can be changed flexibly within few minutes.

## 1 INTRODUCTION

It is fundamentally required for a medical accelerator to be reliable, safe, stable, easy to operate and compact. Its beam energy must be changed with depth of a tumor. A synchrotron, which is inherently energy variable, is enough to achieve this purpose. It allows a beam delivery system without an energy degrader, therefore unwanted irradiation and beam quality degeneration are avoided.

About a compact synchrotron, because of severe requirement for rf voltage, rapid-cycling operation has, which all. 20Hz operation obtains lower injection energy, which makes the injector more compact. For the reasons, a rapid-cycling synchrotron is less expensive. been believed to be hard to achieve. If the rapid-cycling compact proton synchrotron up to 20Hz repetition is realized, it has many merits.

A rapid-cycling synchrotron with fast extraction is most adequate for changing the beam energy, because only the timing of the extraction system needs to be changed. A rapid-cycling one has fewer elements by using combined function magnets, one-turn injection and fast extraction. The injection and extraction method brings small aperture, which allows compact bending magnets with small running cost. 20Hz repetition obtains lower injection energy, which makes the injector more compact. For the reasons, a rapid-cycling synchrotron is less expensive.

The repetition rate of 20Hz is high enough to carry out breath synchronized irradiation easily by beam switching at its injector section. In addition, efficiency is nearly 100% for the fast extraction. Beam current of the system at an irradiation point is 20nA, which is sufficient for cancer therapy.

One of the pioneer facilities of proton therapy, Proton Medical Research Center, Tsukuba University (PMRC) has been studying with a 20Hz repetition booster synchrotron at KEK[1]. Many results and experience which can be applied to the rapid-cycling synchrotron have been accumulated at PMRC.

In order to realize the rapid-cycling synchrotron, it is necessary to develop a wide-band high-voltage compact rf cavity, a high-field small combined function magnet and a fast-pulsed kicker magnet. After these subjects have been studied, a rapid-cycling proton synchrotron system for hospital use is designed, which is discussed at following sections.

## 2 INJECTOR

The injector system consists of a 30kV ion source, a 3MeV RFQ linac and a debuncher cavity. The ion source creates proton beam using a duoplasmatron and a single gap extractor with voltage of 30kV. A beam transport line uses an einzel lens to focus the proton beam from the ion source to the RFQ. The RFQ operating at 425MHz accelerates, focusing and bunching the proton beam from the ion source to 3 MeV. To provide the required input beam momentum spread with $\pm 0.3\%$ at the synchrotron injection point, a single gap debuncher cavity with the same frequency as the RFQ is located in the beam transport line. The beam current at the extraction is 15mA and the stability of current is $\pm 0.1\%$. The normalized emittances at extraction are 0.12 and 0.11 $\pi$mmmrad for horizontal and vertical direction.

The 20Hz synchrotron obtains fewer protons per an accelerating cyclesothat the effect of space charge is weaker[2]. Therefore the injection energy can be lower and the injector can be shorter. The injector length without the debuncher is 3m, so the injector system can be placed inside the synchrotron.

## 3 SYNCHROTRON

### *3.1 Lattice*

The synchrotron is a combined function type which has no quadrupole magnets. The lattice functions of the unit cell are shown in Fig. 1. The magnet lattice has an FDFO structure, and 4 superperiods. The n-value of the magnet is determined as $\pm 10.5$, considering small beam

0-7803-4376-X/98 /$10.00 © 1998 IEEE

size and also the sensitivity of the magnet imperfection to the lattice functions.

The layout is shown in Fig. 2. A kicker magnet for beam injection, a septum magnet for beam extraction and an rf cavity are located at long straight sections and a kicker magnet for beam extraction is at a short straight section.

The parameters of the synchrotron are summarized in Table 1. The horizontal and vertical tunes are 2.2 and 2.3, respectively.

Table: 1 The parameters of the synchrotron

<Lattice>

| | |
|---|---|
| Circumference | 28.2m |
| Injection energy | 3MeV |
| Extraction energy | 70~235MeV |
| Repetition rate | 20Hz |
| Straight sections | 1.8/2.2m |
| Injection method | one-turn (on-axis) |
| Extraction method | fast extraction |
| Tune (• x/• y) | 2.2/2.3 |
| Emittance (at extraction) | 0.3• mmmrad |
| Energy spread (at extraction) | $< \pm 0.1\%$ |

<Combined Function Magnet >

| | |
|---|---|
| Bending angle per unit | 45° |
| Bending radius | 1.9m |
| Magnetic field | 0.13~1.2T |
| N-value | $\pm$ 10.5 |

<RF Cavity >

| | |
|---|---|
| Rf frequency | 0.85~6.4MHz |
| Peak voltage | 5.8kV |
| Rf input power | 2.1kW × 4 |
| Cavity length | 1.9m |

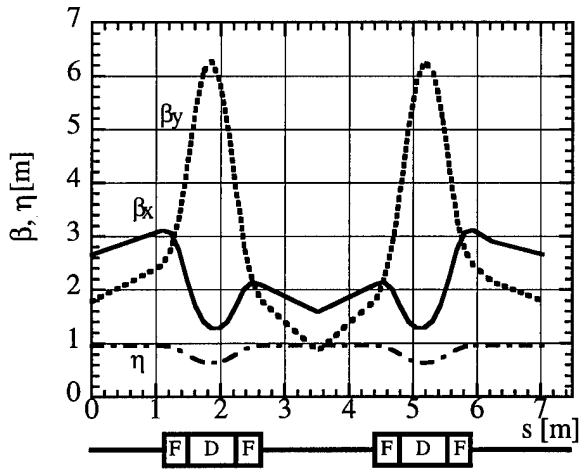



Figure : 1 The lattice function of the unit cell

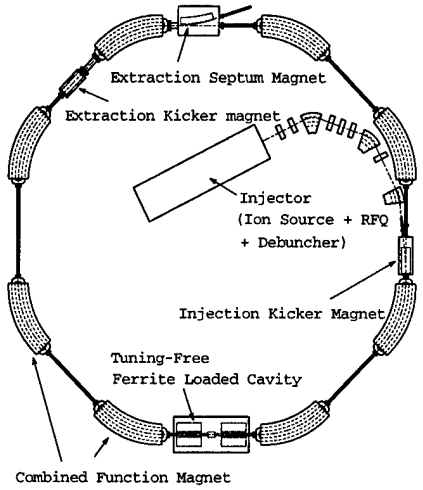



Figure : 2 The layout of the synchrotron

*3.2 Bending Magnet*

The synchrotron magnet system consists of 8 units of H-type combined function magnets with F-D-F structure. The bending angle of the F section is 11.25° each, and 22.5° for the D section. The n-value of each section is rather large as $\pm$ 10.5, in order to make magnets small. A sector type magnet is adopted because of simpler field distribution at the edge region than that of a rectangular type. The bending radius is 1.9 m. The magnetic field at injection and extraction are 0.13 T and 1.2 T respectively. The required good field region is $\pm$ 20mm, smaller than one of a conventional synchrotron[3].

The magnet core is made of oriented low-silicon steel of 0.35 mm thickness, which has high permeability athighfield region. The magnet has large n-value as well as soft edge structure relaxing magnetic saturation effect at the edge and the transition between the F and the D section.

Three dimensional analyses with taking account of saturation effect using TOSCA have been performed at both injection and extraction field strength in order to optimize the pole profile, the configuration of the transition and the edge. According to the results of these calculations, saturation doesn't decrease the good field region much in case of the pole width of 150 mm. A prototype magnet has been fabricated for a further experimental study to prove the calculated estimation and the field measurement is in progress now.

Eight magnets connected in series are excited by a single resonant network with a dc bias. The magnet current is 1500A and the voltage is 2.9kV peak.

*3.3 RF Cavity*

The problem of high voltage (more than 5kV), wideband (frequency ratio up to 1:8) and compact (less than 2m) accelerating structure, which has prohibited a compact synchrotron from rapid-cycling operation, has solved by a new concept of a tuning-free cavity. The method, proposed by Prof. Sato of Osaka University[4], is that a ferrite cavity as an LC parallel circuit, is placed at the center leg of a bridged-T type all-pass network. Its impedance is kept constant as an external resistance R at any frequency, which allows that the circuit is driven by a commercially available amplifier through an impedance transformer.

In the tuning free cavity, a ferrite core is used in the absence of bias field. Therefore it is free from restrictions of bias response and high-loss effect, which is characterized by a sudden decrease in rf voltage above threshold level of input power under DC bias field. It gives wider variation of selecting ferrite material. Ni-Zn ferrite SY-20, newly developed by TDK co., is applied for the cavity, whose μQf value is several times larger than conventional Ni-Zn ferrite, e.g. SY-2. Since it greatly reduces power dissipation at ferrite cores, it can be thought that in the system power loss is almost drawn out to the external resistance and that only voltage remains on the cavity. It is the reason why the system can produce very high accelerating voltage.

Experimental research has performed with a prototype cavity, shown in Fig. 3, as a collaboration between Osaka University and Toshiba co.. Designed gap voltage up to 700V was obtained with 1kW input through frequency range from 1 to 8 MHz, even under 25ms frequency sweep. All the results show the new concept of tuning-free cavity is applicable to a rapid-cycling compact proton synchrotron.

These results show the feasibility of a 1.9m long tuning-free cavity for the synchrotron discussed in this paper, which produces accelerating voltage at frequency range from 0.85 to 6.4 MHz, up to 5.6kV peak with 8kW rf power.

*3.4 Injection and Extraction for Synchrotron*

The synchrotron applies a one-turn and on-axis injection method due to small current of the injected beam. The proton beam is injected by a kicker magnet at a long straight section. The injector kicker magnet is needed fast current fall-time as 200 nsec, so this magnet has to be distributed constant type[5]. The magnetic field is 0.052 T and the magnet length is 0.53 m. Magnets of the same type are operated at KEK booster synchrotron and SPring-8 synchrotron. A power supply is required about 50 kV, less than one for SPring-8.

The extraction is performed by a kicker magnet and a septum magnet with a bending magnet between. The magnet length and the field strength are 0.53 m / 0.071 T and 0.74 m / 1.0 T, respectively. With the fast extraction method, the kicked beam passes through the bending magnet only once. Thus the beam trajectory at extraction doesn't give any restrictions to the good field region, which can be very small.

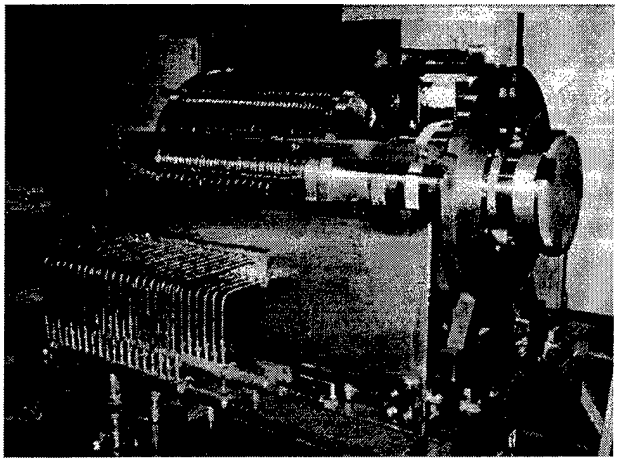


Figure : 3 The prototype of tuning-free ferrite loaded cavity

## 4 CONCLUSION

A rapid-cycling compact synchrotron with one-turn injection and fast extraction is proposed, which consists of distinctive elements such as combined function magnets and a new type of a tuning-free cavity. It is characterized by energy flexibility, easy application to breath synchronization and reduced price. High efficiency, high safety to surroundings and high beam quality can be achieved with the method because of small beam loss at extraction, absence of a degrader and conservation of its small beam emittance. Additionally a radiation shield system becomes simple. The beam energy of the synchrotron can be up to 250MeV for proton radiotherapy without any difficult problems.

After experimental and analytical research of these elements have been performed in order to verify the proposal, availability of the synchrotron for a hospital use has been confirmed.

## REFERENCES


[1] K.Takikawa *et al.*, "The KEK Booster Magnet", KEK Report 75-3(1975)

[2] B. Gottschalk, "Design of a hospital-based accelerator for proton radiation therapy : scaling rules", NIM. B24/25, p.1092-1095(1987)

[3] G. Coutrakon *et al.*, "A Performance study of the Loma Linda proton medical accelerator", Med. Phys. 21(11), Nov., p.1691-1701(1994)

[4] M.Yamamoto *et al.*, "Tuning-Free Ferrite-Loaded RF Accelerating Cavity Using Bridged-T Type All-Pass Network", Proc. of the 16th RCNP Osaka International Symposium on Multi-GeV High-Performance Accelerators and Related Technology (1997, to be published)

[5] Y.Sasaki *et al.*, "Development of Kicker Magnet for Spring-8 Synchrotron", Proc. of 9th Symposium on Accelerator Science and Tech., p.255-257(1993)

# OPERATION OF THE TRIUMF PROTON THERAPY FACILITY

E.W. Blackmore, B. Evans, M. Mouat
TRIUMF, 4004 Wesbrook Mall, Vancouver, B.C., Canada V6T 2A3
C. Duzenli, R. Ma, T. Pickles, British Columbia Cancer Agency, and
K. Paton, Department of Ophthalmology, University of British Columbia

*Abstract*

The Proton Therapy Facility at TRIUMF is now in routine operation treating ocular tumours using 70 MeV protons extracted from the 500 MeV $H^-$ cyclotron. This paper describes the proton beam line, treatment control and dosimetry systems which are designed to provide accurate treatment dose delivery. The reproducibility of the shape and range of the unmodulated Bragg peak for various operating conditions of the cyclotron is discussed along with the technique for producing a uniform modulated or spread-out Bragg peak. The patient positioning chair, which has six motorized degrees of freedom, the patient mask and bite-block, and the X-ray verification system ensure sub-millimeter positioning accuracy. Patient treatments are scheduled one week per month with the treatment dose of 50 proton-Gy delivered in four daily fractions.

## 1 INTRODUCTION

The Proton Therapy Facility is a joint project of TRIUMF, the British Columbia Cancer Agency and the University of British Columbia Department of Ophthalmology. Since August 1995, this facility has been treating patients with ocular melanoma, on a one week per month basis, using 70 MeV protons extracted from the 500 MeV cyclotron. The development of the facility was funded from 1993-95 by a local foundation, and operation is carried out as part of the clinical program of the Cancer Agency.

The TRIUMF cyclotron is a unique particle accelerator for proton therapy as it can provide variable energy proton beams from 65-520 MeV with good energy resolution and with stable and easily controlled beam intensity. These advantages are offset by the fact that the cyclotron is a multi-user facility, so treatments must be compatible with the different operating regimes of the cyclotron.

## 2 CYCLOTRON AND EXTRACTION

The eye treatment equipment is located on beam line 2C which has an energy range of 65-120 MeV. Figure 1 shows the layout of the Proton Therapy Facility and its location relative to the cyclotron. The acceleration of $H^-$ ions in the cyclotron allows for easy extraction of low intensity beams with the use of a thin carbon wire for stripping the beam to protons. Although reliable 2–10 nA beams can be readily achieved with 150 $\mu$A circulating in the cyclotron using a 0.001" diameter wire, for additional safety a "pepper-pot" is inserted in the injection beam line to reliably reduce the circulating intensity by a factor of 40 during patient treatments and high intensity operation. During polarized beam operation no such reduction is necessary. A pneumatically actuated beam stop in the vault section of BL2C, the Fast Shutter with a closing time of 150 ms, is the primary means of controlling the beam during patient treatment.

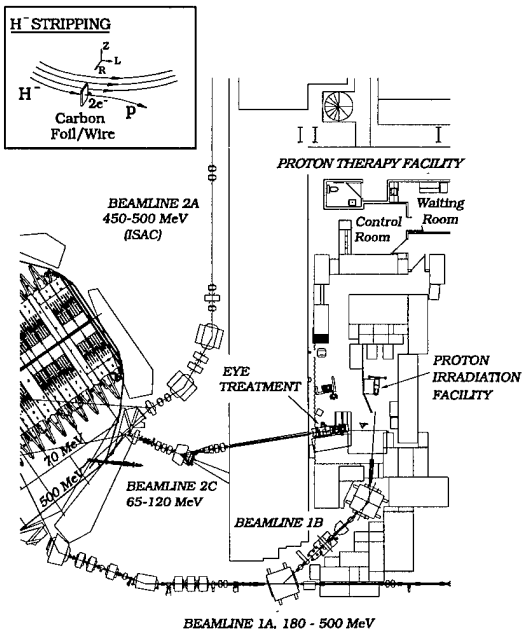



Figure 1: Layout of the TRIUMF Proton Therapy Facility

## 3 LAYOUT OF EQUIPMENT/PATIENT FIXATION

The equipment for beam preparation and patient fixation, shown in Fig. 2, follows the design at other facilities.[1, 2, 3]The required proton dose distribution is achieved using a passive scattering system and a rotating range modulator. The beam is defined by a first collimator/scatterer (typically 12 mm diameter aperture with 0.8 g/cm$^2$ thick lead scatterer). A second collimator stops a significant fraction of the scattered beam, with the central part passing through to the proton nozzle. Here the proton field shape is defined

0-7803-4376-X/98 /$10.00 © 1998 IEEE

transversely with a patient specific brass collimator. The treatment depth is varied by a rotating wedge degrader or range shifter located between the first and second collimators. The plastic modulator wheel is CNC machined to provide a flat spread-out Bragg peak (SOBP). This wheel rotates at 240 RPM and has four modulations per rotation.

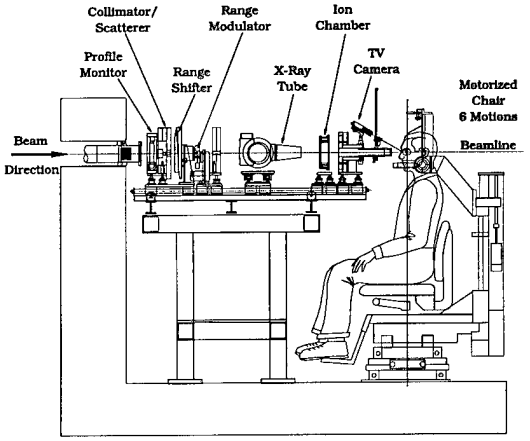



Figure 2: Arrangement of the equipment for beam delivery and patient fixation.

Beam instrumentation consists of a secondary emission monitor (SEM) which measures the total incident proton beam current, a multiwire ionization chamber for the beam profile and centring, a diagnostic ion chamber, and a multiplate transmission ion chamber for dose monitoring. This ion chamber consists of two total plates, one for an independent back-up, and a set of quadrant plates for beam centring. The transmission ion chamber is calibrated for each treatment against a reference ion chamber located at isocentre.

The patient is seated in a treatment chair with precise servo-motor positioning in six motions. The head is immobilized in a face mask and bite-block and the patient is asked to fixate on a blinking light. Two orthogonal X-rays are taken to establish the relationship of four tantalum clips, surgically placed on the eye around the tumour margin, to the output of the treatment plan. The eye position is monitored using a video camera with a magnified image to detect sub-millimeter eye motion during treatment.

Each patient receives 4 daily fractions for a total dose of 50 proton-Gy. The patient setup time is 15-30 minutes, followed by a 75-100 second treatment time.

## 4 TREATMENT CONTROL SYSTEM

The Treatment Control System (TCS) is based on a VAX computer, Mitsubishi PLC, CAMAC PROM-based controller, standard NIM and CAMAC modules and several TRIUMF built devices. The system provides for monitoring of patient safety, controlling patient dose and operator control.

Patient safety is handled by a combination of the PLC providing digital interlocks and control with the CAMAC controller (TRIMAC) monitoring critical analog values and patient dose through digital scalers. The VAX also performs real-time data checks during the patient run. A stand-alone backup dose counter is connected directly to the TRIUMF Safety System (TSS) which can disable the cyclotron beam in the event of a TCS failure. A watchdog system can also trigger the TSS in the event of failure in any of the three computers.

A treatment starts with the operator loading parameters for the patient through the VAX X-windows terminal which uses the Motif display manager. This information is passed to a CAMAC memory for use by the TRIMAC. If all interlocks are satisfied, an operator using a hand-held switch opens the Fast Shutter, via the PLC. Ion chambers provide a current signal through Ortec 439 integrators read by CAMAC scalers. The TRIMAC controller performs a number of real-time checks on beam positioning, intensity and chamber voltages and monitors the patient dose. On reaching the desired dose, the TRIMAC requests the PLC to close the Fast Shutter. At any time the operator, viewing the eye position by video, can stop the treatment.

There are two operating modes for the controls: the "Normal Mode" is used for calibration, development and testing, and the "Patient Mode" is used for treatment. In the "Patient Mode" a number of additional interlocks have to be satisfied, the "Pepper-pot" must be inserted for unpolarized beam, higher level count ratio checks are carried out, and the area lockup requirements are modified for rapid entry and with the lockup sirens turned off.

## 5 DOSE PROFILE MEASUREMENTS AND CALIBRATIONS

The proton dose distributions have been measured for a variety of beam conditions by scanning diodes or miniature ion chambers in a water box.[4] In addition X-ray and radiochromic film have been used to confirm the measurements. An avalanche photodiode, type BPW-34, has been found very satisfactory for most measurements, and compares well to the 0.05 cc Markus ion chamber measurements, which are slower because of the smaller signal. The distal penumbra (90% to 10%) was determined to be 1.2 mm in eye tissue and the lateral profile 1.7 mm. A calibrated Exradin T1 0.05 cc ion chamber connected to a Keithley 616 electrometer provides the absolute dose calibration. This system has been checked in dose intercomparison studies with other laboratories and RBE measurements have been carried out at TRIUMF using V79-WRNE chinese hamster cells.[5]

The daily calibration procedure consists of a range shifter scan to determine the proton range for the raw Bragg peak using the diagnostic ion chamber for normalization. For a standard configuration, a calibration of the primary ion chamber is carried out using the Exradin T1 chamber at isocentre. The calibrations for each individual patient are

performed on the day before the start of treatments. The standard deviation in the daily range measurements over a 16 month period is less than 0.1 mm and the standard dose calibration is within 1%.

## 6 MODULATOR DESIGN AND VERIFICATION

The raw Bragg peak has been found to be sufficiently similar for different operating conditions of the cyclotron that the spread-out Bragg peak (SOBP) produced using a rotating range modulator is not dependent on the cyclotron operating mode.

A program has been written to find the best range modulator function for generating the SOBP, using as input the measured raw Bragg peak, the measured scattering function for the modulator position, the desired width of SOBP in mm, the maximum number of steps in the modulator and the desired precision.[6]A second program generates the CNC code for machining the modulator wheels. An inventory of modulators for SOBP from 10–23 mm in 1 mm increments has been machined and measured. Figure 3 shows the input information for the modulator design and a typical measured result.

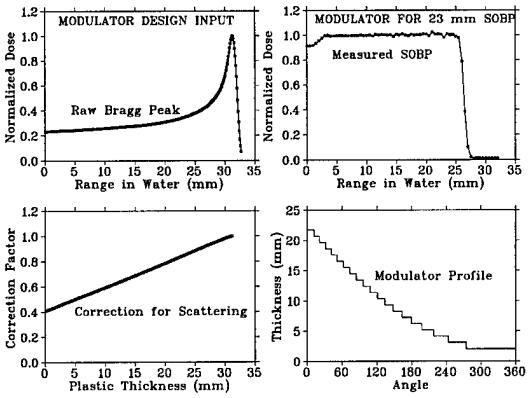



Figure 3: Input data for the modulator design and a measured result.

## 7 TREATMENT PLANNING AND PATIENT ALIGNMENT

Fundus photographs, ultrasound measurements, and surgically placed tantalum scleral clips are used to determine the location and size of the tumour. In some cases, MRI scans are used to determine the configuration of the overlying eyelid. This information is input into the treatment planning program EYEPLAN[7] for calculating the optimum set of treatment parameters: the location of the fixation light, the maximum beam range and modulation required, and the profile of the beam aperture of the patient collimator. In addition a set of reference X-ray transparencies are prepared showing the desired alignment of the tantalum clips relative to the beam axis for confirming the correct patient alignment.

Recently the use of wedges for modifying the contour of the distal end of the dose distribution has been implemented. Aluminum wedges with a tissue equivalent angle from $5^o$ to $60^o$ have been machined and measured. The wedges are mounted a few cm from the eye on a rotating holder attached to the nozzle and can be easily adjusted in angle and lateral position to the EYEPLAN value. In many cases the use of wedges is essential in reducing the dose to the macula or optic nerve.

The twenty-five patients treated to date range in age from 36 to 88, with a median tumour height of 6 mm and diameter of 13 mm. Early clinical follow-up is showing the expected tumour shrinkage and toxicity seen at other proton therapy centres.

## 8 FUTURE DEVELOPMENTS

At the present time patient referrals for choroidal melanoma have come only from the four western provinces of Canada. It is anticipated that the number of patients per year could double once patients are referred from eastern Canada. Other potential uses of protons for therapy are being considered. These include treatment of conjunctival melanoma and macular degeneration. The proton therapy beam line can provide 120 MeV protons which have a range in tissue of 9–10 cm, so other tumour sites in the head and neck could be envisaged.

## 9 REFERENCES


[1] C. Markovits, S. Jaccard, and C. Perret, "The proton beam facility OPTIS for the therapy of ocular tumours", Proceedings of the International Heavy Particle Therapy Workshop, Paul Sherrer Institute, 134-139 (1990).

[2] D.E. Bonnet, A. Kacperek, M.A. Sheen, R. Goodall, and T.E. Saxton, "The 62 MeV proton beam for the treatment of ocular melanoma at Clatterbridge", British Journal Radiology 66 (1993) 907.

[3] I.K. Daftari, T.R. Renner, L.J. Verhey, R.P. Singh, M. Nyman, P.L. Petti, and J.R. Castro, "New UCSF proton ocular beam facility at the Crocker Nuclear Laboratory Cyclotron (UC Davis)", NIM A380 597-612 (1996).

[4] E.W. Blackmore, J. Vincent, S. Chavez, K. Gardey, G. Lam, U. Oelfke, T. Pickles, and K. Paton, "Commissioning the TRIUMF Proton Therapy Facility", Proc. of the NIRS International Seminar on the Application of Heavy Ion Accelerator to Radiation Therapy of Cancer, Chiba, 135 (1994).

[5] L.D. Skarsgard, B.G. Wouters, G.K.Y. Lam, U. Oelfke, and G.B. Goodman, "General considerations in the biological dosimetry of heavy charged particle beams and use of the gelatin/cell sorter in vitro system at TRIUMF", ibid 172.

[6] K.U. Gardey, U. Oelfke, and G.K.Y. Lam, "Calculation of the optimal range modulation function for a clinical proton beam", Medical Physics 21, 874 (1994).

[7] M. Goitein and T. Miller, "Planning proton therapy of the eye", Medical Physics 10, 275 (1983).

# INITIAL OPERATION OF CIAE MEDICALLY USED CYCLOTRON

CYCIAE 30 Engineering group
(Written by Mingwu Fan and Tianjue Zhang)

China Institute of Atomic Energy, P.O.Box 275, Beijing, 102413, PRC

*Abstract*

A 30 MeV compact cyclotron, CYCIAE 30 devoted to medical radioactive isotope production was built in CIAE and put into operation in Dec. 1994. It was originally designed by IBA, Belgium[1] . Some major modifications of the design have been taken. In order to improve the performance of the machine, the magnet redesign and adjustment have to be taken. All equipment: RF, power supplies, vacuum and water cooling system, except ion source and strippers, are made in China. The initial operation of the machine was reported.

## I. GENERAL DESIGN FEATURES

CIAE medical cyclotron is a fixed-field, fixed-frequency isochronous cyclotron accelerating $H^-$ ions beam up to a maximum energy of 30 MeV and extracted beam intensity of more than 350 uA and low power consumption less than 100 kW. The machine is shown in Fig.1.

The design of the machine was reported elsewhere[2,3,4].

This project with most of equipment made in China has been proved fully successful in last two year operation. Now 7 different isotopes are supplied to many hospitals. Parts of them are exported, like $^{57}Co$ and so on.

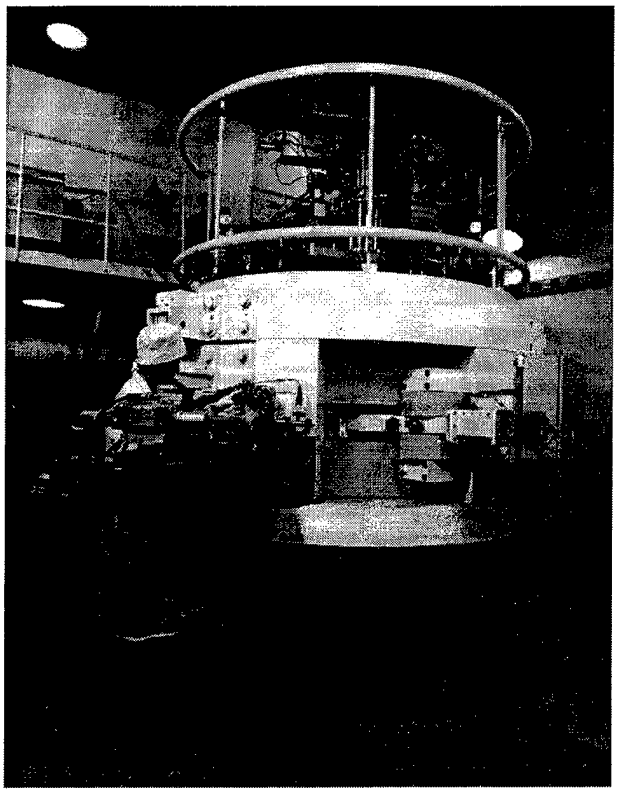


Fig. 1 CIAE Medical Cyclotron --- CYCIAE 30

## II. THE MAGNET SYSTEM

The magnet of cyclotron is a key part for the machine, since it should provide a good quality field to ensure high intensity beam to be accelerated to final energy.

The magnet mapping results shown the field is quite close to the theoretical isochronous field based on the error of RF shift and first field harmonic. The measurement results are shown in Fig 2 and 3. The maximum RF phase shifts are less than $+-10^{\circ}$ and first harmonic field is around 5 gauss in the accelerating area. High quality isochronous field keeps the particle accelerated to the extracted energy stably.

The working isochronous field can be achieved using electrical power 7 kW only.

In addition, switching magnets, quadrupoles, steering magnets and corresponding power supplies are fabricated based on our own design. Their quality is same or better than the requested theoretically.

## III. RF ACCELERATING SYSTEM

The RF accelerating system is made in Chinese manufacturer. The system in shown in Fig 4. The accelerating electrodes, the "dees" are supported by stems inserted in the valleys.

The dees are made of solid copper and are conduction cooled. This considerably reduces the risk of water-leakage inside the machine and thus the contamination risks.

The two $30^{\circ}$ dees operate on the 4th harmonic mode with respect to the particle revolution frequency. To prevent any phase mismatch and to simplify the RF system, they are connected at the center below the median plane to leave room for the inflector.

The R.F. cavities are entirely located in the valleys. The R.F. power needed to obtain 50 kV of dee voltage is approximately 5.5 kW per cavity. In addition, up to 15 kW of R.F. power are used for beam acceleration.

A single R.F. amplifier delivering 25 kW of power at 65.5 MHz is installed in the median plane and is capacitively coupled to the cavity. The variable load due

0-7803-4376-X/98 /$10.00 © 1998 IEEE

to the beam behaves as a variable load resistor on the final tube. So the amplifier always operates at peak efficiency.

Zero-bias, grounded-grid triodes are used for the final 25 kW amplifier and 2 kW driver amplifier. This design gives the system absolute stability and eliminates the grid and screen grid power consumption. The R.F. system tested at the working frequency before the beam commissioning. The result shows that Dee circuit coincides well with the results of magnetic mapping.

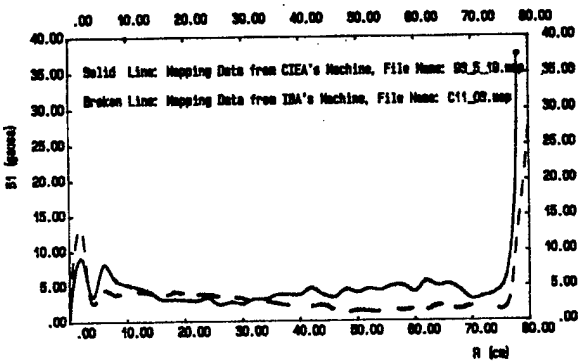



Fig. 2 Amplitude of First Harmonic

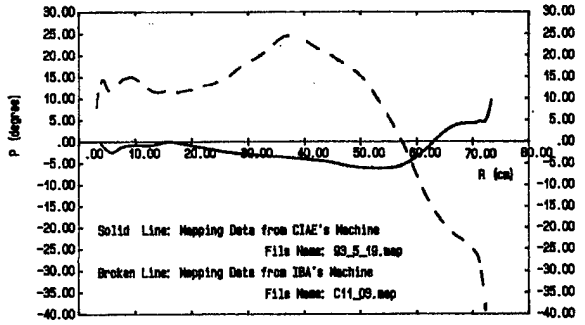



Fig. 3 Comparison of The Total Phase Shift

## IV. VACUUM AND WATER COOLING SYSTEM

The vacuum chamber of CYCIAE 30 cyclotron is a cylinder made of aluminum alloy, sealed onto the magnet yoke by "O" rings. Some openings on the vessel for beam exit, stripper entry, R.F. feed etc. are isolated from ambient atmosphere by air-lock system and "O" rings.

Three types of pumps are used in the cyclotron. Roughing is performed by forepumps from 1000 mbar down to $10^{-2}$ mbar. High vacuum is maintained by two oil diffusion pumps (3000l/s) from $10^{-2}$ mbar down to $10^{-6}$ mbar and by two cryogenic pumps (1500l/s) to improve vacuum around $10^{-7}$ mbar adequate for extracting beam above 350 uA. Cryopumps could also increase the pump-down speed in the cyclotron.

Demineralized water is used for machine cooling through manifold with stainless steel ball valves, flow controllers, distributing the water to all cooling circuits.

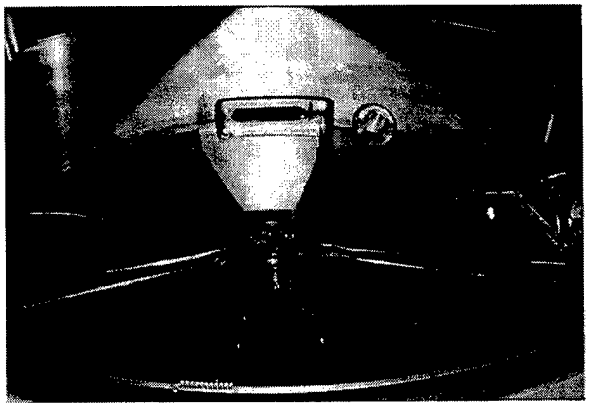


Fig. 4 The RF System

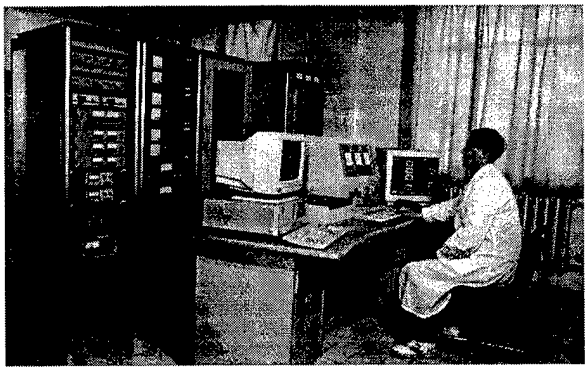


Fig. 5 The Control Room of CYCIAE 30

Temperature, resistivity and flow amount of water are used as control interlocks to guarantee the safety of the equipment.

All the vacuum and cooling systems have been proved for the machine operating properly.

## V. CONTROL SYSTEM

The cyclotron and related equipment is controlled by a SIMATIC S5-135U programmable controller because of its reliability and its versatility. It also offers the possibility to expand and interconnect with other programmable devices. Fig 5 shows the control room of CYCIAE 30.

Normal operation of the cyclotron is entirely automatic, from cyclotron start-up to targetry and chemistry, requiring no operator during routine production. Color monitor displays graphically the operations.

A spill proof keyboard and two "virtual" knobs that can be used for preset the cyclotron parameters. To meet the control requirements, PLC is used. More convenient and reliable system is for most of operators.

## VI. TWO YEAR OPERATION

After the beam commissioning the machine was put into operation in Dec. 1994. The isotope production started as routine work according to the hospital requirement. The medical use isotopes are produced regularly. During the

operation, no operators are needed usually since the system work very stable.

Now 7 medical use short neutron isotopes have been produced for the market home and abroad. The operation proved the machine is excellent.

## REFERENCES


[1] Y.Jongen and G.Ryckewaert: "Preliminary Design for 30 MeV-500 uA $H^-$ Cyclotron", Particle accelerator conf., Vancouver, B.C, IEEE Trans. science, Vol.NS-32, NS pp 2703-2705, 1985.

[2] Fan Mingwu et al, "Guide Role of The Electromagnetic Field Numerical Methods in Accelerator Magnet Engineering", Proc. of the International Conf. on Electromagnetic Field Problems and Applications, Hangzhou, China, 1992.

[3] Fan Mingwu et al, "Measurement and Adjustment of CIAE Medical Cyclotron Magnet", Proc. of the 1993 Particle Accelerator Conference, 0-7703-1203-1/93 $ 03.00 (C) 1993 IEEE, pp 2841-2843.

[4] Fan Mingwu, "30 MeV CIAE Medical Cyclotron --- CYCIAE 30", Proc. of The 6th CHINA-JAPAN Joint Symp. on Accelerators for Nuclear Science and Their Applications, Chengdu, 1996

# CHARGE STRIPPER AND MEBT FOR THE $^3$He RFQ ACCELERATOR*

F. M. Bieniosek, K. Anderson, R. J. Pasquinelli, M. Popovic, C. W. Schmidt and R. Webber
Fermilab, Batavia, IL 60510 USA*
D.J. Larson and P. Young
SAIC, 4161 Campus Point Ct., San Diego, CA 92121

*Abstract*

The $^3$He RFQ linac for production of positron-emitting radioactive isotopes accelerates singly-ionized $^3He^+$ ions to an energy of 1 MeV in a 212.5-MHz RFQ. The ions are then stripped to form doubly-ionized $^3He^{++}$ in a gas-jet stripping cell, and transported by the MEBT to the 425-MHz RFQ string for acceleration to 10.5 MeV. The stripper cell utilizes a mechanical injector to provide gas pulses to a nozzle. The directed gas jet passes across the beam into a scavenge section which pumps away the gas. The MEBT is an achromatic, isochronous transport section based on two 270-degree bend magnets. It provides bunched and focused beam to the 425-MHz RFQ string.

## INTRODUCTION

A Fermilab/SAIC collaboration has been developing a $^3$He RFQ accelerator for production of positron-emitting isotopes for positron emission tomography (PET).[1] The accelerator consists of a $^3He^+$ ion source, a low-energy beam transport (LEBT) line, a 212.5-MHz radio-frequency quadrupole (RFQ) to accelerate $^3He^+$ to 1 MeV, a gas stripping cell, a medium-energy beam transport (MEBT) line, a string of three 425-MHz RFQs to accelerate $^3He^{++}$ to 10.5 MeV, and a high-energy beam transport (HEBT) line to the target. The beam is produced in macropulses of up to 70 μs long, at up to 360-Hz repetition rate. The ion source produces about 25 mA (peak) of singly-ionized $^3$He. At low energy a doubly-ionized $^3He^{++}$ beam ions is difficult to generate in a nonplasma stripper because of charge-exchange processes. The approach taken to produce a $^3He^{++}$ beam is to accelerate the $^3He^+$ beam to 1 MeV in the 212.5-MHz RFQ. At this energy, a stripping efficiency in the range of 80% can be achieved in a gas stripping cell. At an energy of 1 MeV and an average current of several hundred μA, carbon foil strippers are not expected to survive the high power density. In the stripper cell and beyond, the beam rapidly debunches due to the large (1.7%) velocity spread coming out of the RFQ. As a result the beam must be rebunched. Initially the accelerator utilized an RF buncher to rebunch the beam. Difficulties were encountered in operation of this device, probably due to the large number of free electrons streaming from the gas stripper cell. Thus the MEBT was designed to be a purely magnetic achromatic, isochronous beam line. Free electrons from the stripper cell no longer have a deleterious effect on operation of the MEBT, and may in fact be necessary for its efficient operation. Details of the MEBT design are presented in a companion paper [2].

## CHARGE STRIPPER

A gas-jet stripper was chosen, rather than a differentially-pumped gas cell, for the following reasons.

1. It is desirable to maintain pressure in the RFQ and the MEBT as low as possible. Because the gas is flowing in a jet the pressure for a given gas density in the stripping region is much lower than for a static fill. Thus it is easier to keep the stripper gas out of the RFQ and MEBT.
2. Expectations are that a static-filled cell will suffer from significant beam heating of the gas. As a result the gas density may vary during the pulse as the gas is heated. Thus the pressure in a cell would have to be increased from that sufficient to strip a low intensity beam.
3. By operating with a pulsed gas jet synchronized with the beam it is possible to further reduce the gas load on the stripper pump.

An automotive-type fuel injector (Nissan) provides gas pulses to a converging-diverging nozzle. The injector provides average gas flow rates in excess of 12 Torr-liter/sec in pulses of 300-500 μs duration at up to 360 Hz. A MOSFET-based pulser delivers 75 V, 200-300 μs pulses to the injector. A directed gas jet of line density approximately 3-6 x $10^{16}$ $cm^{-2}$ is created at the nozzle. It passes across the beam and is directed into the scavenge section. The flow rate of the gas is sufficient to prevent excessive heating of the gas by the beam. A significant fraction of the injected gas is pumped away between beam pulses.

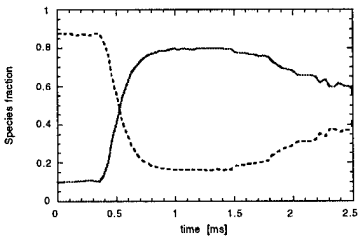



Figure 1. Yield of $He^+$ (dashed) and $He^{++}$ (solid) beam in the Faraday collectors as a function of stripper delay time in the prototype stripper cell for argon gas at 60 Hz.

A prototype stripper cell was built to determine efficiency and gas flow in a realistic geometry. Total pumping capacity in the prototype cell was 1000 Torr liter/sec. A

* Operated by the Universities Research Association Inc., under contract with the U.S. Department of Energy.

0-7803-4376-X/98 /$10.00 © 1998 IEEE

magnetic spectrometer that bends the 1-MeV $He^+$ and $He^{++}$ beam ions into Faraday collectors at bend angles of 11.5° and 23.6° respectively, was used to test operation of the gas jet. Stripping efficiency was determined by measuring the relative distribution of beam current on the two collectors. Typical performance is shown in Figure 1. Under these conditions (argon gas at 60 Hz), the pressures were about 3 mTorr in the stripper turbo region, about 2 mTorr in the stripper top section, and 2.5 μTorr in the RFQ. The stripper cell was analytically modeled by calculating aperture conductances throughout the stripper and incorporating these numbers into an ANSYS finite-element model. The measured operating pressures were in agreement with predictions from the model. Several gases were tested in the prototype cell: Ar, $N_2$, Kr, $CO_2$, and He in order of decreasing stripping efficiency. The best stripping efficiency was obtained with argon gas, reaching over 80%.

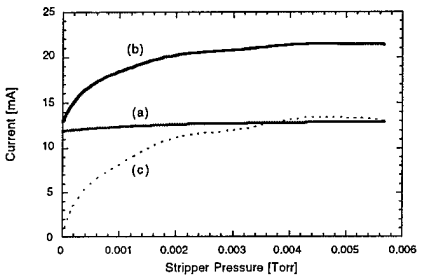



Figure 2. Current through MEBT toroids as a function of stripper pressure for nitrogen gas at 360 Hz, (a) before stripper, (b) after stripper, (c) at end of MEBT.

Based on the successful operation of the prototype stripper cell, an operational version was constructed. This stripper cell differs from the prototype cell mainly in increased pumping capacity. Pumping capacity is 1000 Torr-liter/sec at the stripper outer housing (behind the nozzle), and 3000 Torr-liter/sec at the scavenge section facing the nozzle. The nozzle is an converging-diverging nozzle with a 0.5-mm diameter throat. Typical operating pressures are 3.4 mTorr at the scavenge section, 0.8 mTorr at the stripper outer housing, 19 μTorr in the MEBT, and 0.7 μTorr in the RFQ. Typical results are shown in Figure 2 for 360 Hz operation in nitrogen gas. The curve was generated by varying the length of the electrical pulse delivered to the injector in the stripper. As the pulse is lengthened, the amount of gas delivered per pulse increases up to a limit determined by the injector. As the amount of gas increases, the signal in the toroid before the stripper increases due to the presence of electrons streaming out of the stripper cell toward the RFQ. Electron currents are also detected in the toroid after the stripper. Significant electron currents are not observed in the toroid at the end of the MEBT. Slightly higher stripping efficiency can be obtained in argon gas. The vacuum turbopumps, however, have some difficulty pumping argon because of the high molecular weight and low thermal conductivity, causing excessive heating and slowing down of the vanes. As a result the stripper cell utilizes nitrogen gas in normal operation. To date, electrical beam currents of up to 21 mA have been observed at the end of the MEBT.

Measurements of beam profile by scanning the beam across a single wire were made before and after stripping the beam in the prototype spectrometer chamber. No measurable beam size increase, implying negligible emittance growth, was observed. A general calculation of the small-angle multiple scattering of ions in a gas target can be found in [3].

## MEBT

The MEBT was designed to transport and match the beam to the 425-MHz RFQ string, focused to a small spot transversely, and with minimum longitudinal extent. It was instrumented for commissioning by:

a. current-monitor toroids located before the stripper, after the stripper, and at the end of the MEBT,
b. multi-wire profile monitors at the entrance and exit of the first 270° magnet, at the entrance of the second 270° magnet, and at the end of the MEBT,
c. an emittance scanner at the end of the MEBT for emittance measurements, and
d. electron suppressers in the cross-over arm.
e. At the conclusion of low-intensity MEBT commissioning, the profile monitors were removed and replaced by Faraday aperture plates, which were designed to skim the edges of the beam, providing a minimally intercepting measure of beam position in the MEBT.

The profile monitors were used to measure the beam size at various locations, and to ensure that the MEBT was symmetrical in operation. The emittance scanner was used to verify that the emittance growth through the MEBT was negligible. It was found that the measured horizontal emittance was a sensitive function of trim quad settings, which control dispersion. Dispersion results in increased beam size at the end of the MEBT. Zeroing the dispersion by adjusting the trim quads and moving magnets in the return leg of the MEBT minimized the horizontal emittance. Final emittance measurements in both planes showed no significant emittance growth. At completion of commissioning the stripper/MEBT combination had a typical efficiency of 65%, in line with expectations. Before commissioning of the MEBT, it was postulated that space-charge effects might significantly impact tuning of the MEBT. Typical variations in field strengths of MEBT quads due to space charge were predicted to be in the range of 10-20%. An additional concern was emittance growth driven by nonlinear space-charge. In fact, little effect of space charge was noted. No significant change in MEBT tune was observed with beam intensity, and the electron suppresser electrodes had no significant effect. This result is attributed to either charge neutralization by electrons or spreading and reduced beam density in the MEBT. There are numerous sources of electrons available to supply charge neutralization:

1. In the stripper, one free electron is produced per stripped 1 MeV $He^+$ beam ion with an electron energy of 180 eV.
2. Ionization of the stripper gas by the beam produces electrons more numerous than beam electrons by a

factor of 3 to 10, because the ionization cross section of stripper gas is typically much larger than for beam ions. These electrons are born with a temperature of about 30 eV [4]. Secondary electrons are also produced by collisions between energetic electrons with gas molecules.

3. In the balance of the MEBT, some electrons produced in the stripper are transported downstream with the beam. Electrons are also produced locally by beam ions on background gas, and by beam ions scraping on the vacuum wall.

One limitation to performance of the MEBT is the curvature in the bends. For example, the longitudinal velocity of the neutralizing electrons leads to a centrifugal force on the electron due to the curvature around the bend. A radial (horizontal) electric field must arise to balance this force. The electric field comes from a shift in the electron distribution radially (horizontally) outward from the centroid of the beam path. An estimate of the electric field may be determined by equating the two forces. The force is $F = mv^2/\rho = eE$, or $E = 2 *$ kinetic energy / e $\rho$. The kinetic energy of the electrons is likely to be less than 30 eV. Using this value, and the radius of curvature $\rho$ = 30 cm, the electric field is E = 2 V/cm. This electric field is transverse to the beam in the horizontal direction. Since it is not symmetric, it may cause some distortion of the beam. However, it is small enough to not be a concern in the present case.

The beam is clearly bunched as it leaves the MEBT. Bunched beams were seen on a fast oscilloscope, and scaling of the profile was quantitatively measured on a spectrum analyzer viewing signals on a wire that intercepts the beam.

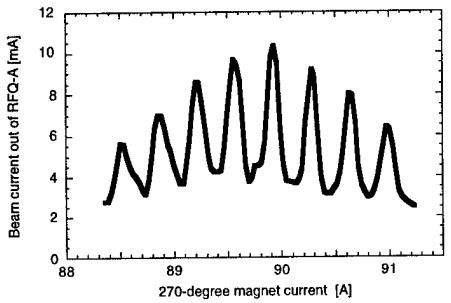



Figure 3. Current from RFQ-A as a function of 270° magnet current, with phase feedback loop off.

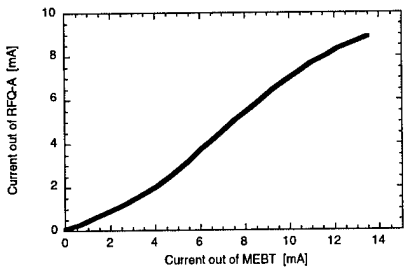



Figure 4. Beam current from RFQ-A as a function of beam current from MEBT at 30 Hz.

Measurements of transmission through the first RFQ in the 425-MHz string (RFQ-A) are indicated in Figures 3 and 4. Figure 3 shows the transmission through RFQ-A as a function of the 270° magnet current. Both 270° magnets are driven by the same power supply. The oscillatory nature of the transmission curve is due a change in the path length through the MEBT as the radius of curvature of the beam in the 270° magnet varies. When the path length is such that the difference in phase between the 212-MHz RFQ and RFQ-A is $2\pi m$, where m is an integer, the beam enters RFQ-A in phase, and it is accelerated. When the path length is changed such that the beam enters out of phase, it is not accelerated. With further changes in the path length the cycle repeats. The path length through the 270° magnets is $3\pi\rho$ where the radius of curvature on axis is $\rho$ = 30.48 cm. The length corresponding to 360 degrees of rf phase at 425 Mhz is $\lambda = \beta c/f = 0.0267 \cdot 3 \times 10^{10} / 425 \times 10^{6} = 1.88$ cm. Thus a complete cycle should occur for a relative path-length change of $ds/s = \lambda/3\pi\rho = 0.654\%$. The 270° magnets are in the linear regime, i.e. dB/B = dI/I. Neglecting the field index in the 270° magnets $n = -(\rho/B)\cdot\partial B/\partial r = 0.53$, the relative change in path length for a given change in magnet current is $ds/s = d\rho/\rho = dI/I$, or one cycle in 0.587 A. Taking into account the field index, and the fact that the beam travels 3/4th of a complete turn in each magnet, the relative change in path length for a given change in magnet current is roughly ds/s = (1+7n/6) dI/I. A complete cycle then should correspond to a current change of 0.36 A. This result agrees well with the measured rate (Figure 3), which is 7 cycles in 2.5 A, or about 0.36 A per cycle. The ratio of in-phase to out-of-phase signal, which is about 3, implies that most of the beam is properly bunched as it enters the RFQ. In order to minimize the sensitivity of accelerator performance to length of the MEBT, under normal operation the low-level rf RFQ drive signal is phase-locked to the beam signal collected on a Faraday aperture plate at the end of the MEBT.

Figure 4 shows the efficiency of acceleration, with only RFQ-A installed after the MEBT, as a function of incident beam current. Nominal beam energy at the exit of RFQ-A is 5 MeV. Typical efficiency is in the range of 60-70%. The variations in incremental efficiency with beam intensity may be due to residual space charge effects in the MEBT, and limitations in rf power in the RFQ. The maximum accelerated beam at 5 MeV observed was over 11 mA. Beam acceleration was verified by placing a 12.7-μm aluminum foil at the exit of the RFQ-A. This thickness of foil passes the 5-MeV He beam ions, but stops any 1-MeV ions. After correcting for electrons produced in the foil, no significant reduction in collected current with the foil in place was noted. At present the accelerated beam through the entire 425-MHz RFQ string (10.5 MeV) is in the range of 6 mA.

[1] R. J. Pasquinelli, *et.al.*, A $^3He^{++}$ RFQ Accelerator for the Production of PET Isotopes, Paper 9B9.
[2] D. J. Larson, *et.al.* Ion Optical Design of the BRF-FNAL-SAIC-UW PET Accelerator, Paper 4V18.
[3] P. Sigmund, K. B. Winterbon, Nucl. Instr. Meth. 119, 541 (1974).
[4 ] M. Reiser, Theory and Design of Charged Particle Beams, Wiley, 1994, p. 4.302.

# ELECTRON ACCELERATOR'S PRODUCTION OF TECHNETIUM-99m FOR NUCLEAR MEDICINE*

V.L.Uvarov, N.P.Dikiy, A.N.Dovbnya, Ye.P.Medvedyeva, G.D.Pugachov, Yu.D.Tur
National Science Center "Kharkov Institute of Physics & Technology" (KIPT), 310108, Kharkov, Ukraine

*Abstract*

At present Technetium-99m provides up to 90% isotopic products used in nuclear medicine [1]. His generator Molybdenum-99 is mainly produced in fission reactors. Most of reactors used for this production are approaching the end of their exploitation [2]. One suggests to use photonuclear reactions in $^{100}$Mo under influence of bremsstrahlung of powerful electron accelerator as an alternative method of $^{99m}$Tc production. Report contents both an analysis of some technical, economical and ecological aspects of method and the results of experimental production of $^{99m}$Tc with KIPT electron linac, as well as results of medical test of produced radiopharmaceuticals.

## INTRODUCTION

By 1994 the medicine radionuclides turnover around the globe had reached the figure of 1.2 M$ [1]. Most of them are pharmaceuticals based on $^{99m}$Tc. This radionuclide is produced via $^{99}$Mo. As the analysis of nuclear physics data shows [3], the $^{99}$Mo nuclide generation can be effectively performed by a high-energy photon irradiation (photon energy $E_\gamma$>20 MeV) of a target, containing $^{100}$Mo nuclide to yield in the ensuing reaction the following:

$$^{100}\text{Mo}(\gamma,n)^{99}\text{Mo}(\text{reaction threshold, } E_t=9{,}1\text{MeV}) \quad (1)$$

simultaneously, the parallel reaction channels are:

$$^{100}\text{Mo}(\gamma,p)^{99}\text{Nb}(T_{1/2}=15\text{s})\rightarrow{}^{99}\text{Mo}(E_t=16{,}5\text{MeV}) \quad (2)$$

$$^{100}\text{Mo}(\gamma,p)^{99m}\text{Nb}(T_{1/2}=2.6\text{m})\rightarrow{}^{99}\text{Mo}(E_t=16{,}9\text{MeV}) \quad (3)$$

$$^{100}\text{Mo}\ (n,2n)^{99}\text{Mo} \qquad (E_t=\ 8{,}3\ \text{MeV}) \quad (4)$$

$$^{98}\text{Mo}\ (n,\gamma)\ ^{99}\text{Mo} \quad (5)$$

(reactions (4), (5) will be noticeably observable in the case of a "thick" target, only).

A high-energy photon flux can be obtained readily as bremsstrahlung if accelerated electrons strike a converter-target made of high-Z material (commonly, Tantalum or Tungsten). Calculations, made on reactions (1)...(5) indicate that for a successful $^{99}$Mo and $^{98}$Nb generation via $^{100}$Mo-target irradiation by bremsstrahlung flux the optimum electron energy should be 25 MeV. In this case, the specific yield of the above nuclides would be 1.2μCi/μA·hour·g($^{100}$Mo). By way of a certain optimization of the irradiation conditions and target geometry the final value from the calculations can be raised by a factor of two. If one use a Mo target of natural isotopic composition in which $^{100}$Mo were ~10% then the above appraisal should be lower by an order of magnitude [3].

## 1 $^{99}$MO GENERATION SETUP

In order to study the process of $^{99}$Mo generation, using electron linac, we designed a facility, the schematic of which is given in Fig.1.

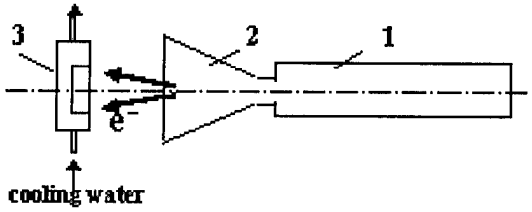



Fig.1. Schematic of experimental setup: 1-electron linac, 2-beam scanning device, 3-target device

As high-energy electron source we used the accelerator test stand LU-20 (item 1), operating in the following mode:

| | |
|---|---|
| - Electron energy, MeV | 20 |
| - Average beam current, μA | 500 |
| - Beam pulse width, μs | 3 |
| - Rep rate, Hz | 150 |

Considering that the average electron beam power should be 10 kW and in order to avoid the hazards of the accelerator exit foil melt up, the exiting beam, before striking the foil, is swept out into a vertical line, using a specially designed scanning device (item 2), which operates with rep rate of 3 Hz, beam sweep-out length being 12 cm and its width 1cm. These parameters determine the main geometrical characteristics of the target (item 3). Besides, inasmuch as the principal electron beam portion is absorbed into the target volume, the target needs being continuously water-cooled.

In order to run the evaluation experiments we used a target construction of unoptimized geometry, the structure of which is given in Fig.2.

This device consists of aluminum casing 1, made air-tight on face joints with flanges (not shown in the

* Work supported by STCU, project N 432

0-7803-4376-X/98 /$10.00 © 1998 IEEE

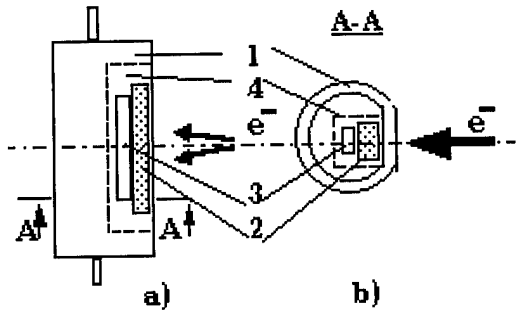



Fig.2. Experimental target device setup: a) A lateral view, b) A cutaway view
1 - Casing, 2 - Converter, 3 - Mo-target, 4 - Cassette

schematic), where the outlets are used for pumping the cooling water in and out. The target device was placed immediately after the exit window of accelerator. Circulating water was then fed on to the construction, and the target was irradiated for 10 hours running. This done, the beam was turned off and Mo-target taken out of the cassette.

## 2 $^{99M}$TC EXTRACTION TECHNOLOGY

A fraction of $^{99m}$Tc atoms in the target, immediately after the 10h-irradiation in the linac, with electron beam intensity being 500 μA, was ~$10^{-16}$ off Mo atoms. An extraction of such concentrations, even with analytic chemistry methods, is difficult to realize into practice. Electrochemical analytical detection techniques are known to have the lowest thresholds, as compared to many other detection methods. For instance, the inverse V-A anode measurements have the detection threshold $10^{-11}$ - $10^{-12}$ g/g. Considering this, we expected that utilization of the electrochemical yield techniques would allow us to solve the problem of $^{99m}$Tc extraction from solutions with such a low concentration.

We used electrolysis to obtain a pertechnetate solution which was soon thereafter evaporated in order to achieve a high specific activity. In this case, it was 20 MBq/mg.

The content of $^{99m}$Tc and radioactive impurities in the pertechnetate solution was measured using a Ge(Li) detector with the volume 50 $cm^3$ and energy resolution 1.8 keV along the 1333 keV line. The only radioactive impurity present in the solution after electrochemical precipitation had been done, was $^{99}$Mo. Its content in the pertechnetate solution did not exceed 1.5% of $^{99m}$Tc. Considering the fact that a relative radiation intensity off the line 140.5 keV $^{99m}$Tc is 89.6%, with that of the most intense line 733.4 keV $^{99}$Mo being 12.8%, such an $^{99}$Mo inventory does not specifically affect the processes of gamma-scintigraphy. Another electrolysis of the pertechnetate solution allowed to lower the $^{99}$Mo content down to 0.15%. Fig.3 presents the emission spectrum of an irradiated Mo-sample.

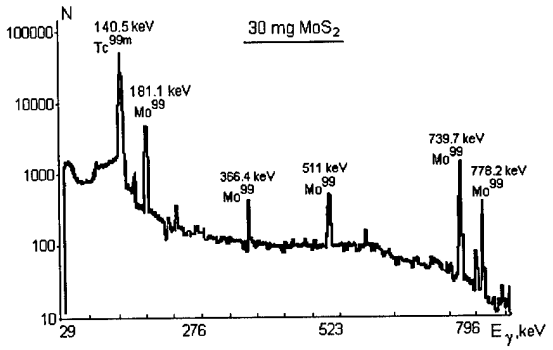



Fig.3. An experimental activities spectrum of an irradiated Mo-target with natural isotopic content

## 3 PREPARATION OF RADIOPHARMACEUTICALS AND THEIR TEST

The re-agent, thus obtained, was used for studies on the effects of various radiopharmaceuticals during diagnostics, involving the radionuclide. In case of gamma-scintigraphy the standard re-agent kits (Technefit, Pentatech, Citratech) were used.

It was established for a fact that the radiopharmaceuticals, involving $^{99m}$Tc and the standard kits of Technefit, Pentatech and Citratech re-agents, after having been administered intravenously at the level of about 0.5 MBq, propagated adequately through rats' tissues, resulting in the organ under scrutiny being clearly visible on the Ohio Nuclear gamma-chamber screen.

In all cases, rats were closely watched after during the week subsequent to the administration of the radiopharmaceuticals, with an overall examination of the animals being made constantly. No harmful after-effects were found [4].

## CONCLUSIONS

As a result of our studies, we demonstrate a feasibility of $^{99}$Mo generation, using an energetic electron beam, which shows more environmentally-safe conditions of $^{99m}$Tc production, as compared with the traditional fission reactor techniques. Our assessments indicate that the proposed technique meets, at the existing accelerator parameters, the economic challenge of in-reactor radionuclide generation. In case of a dedicated R & D on a high-power linac whose beam would meet the optimum requirements of electron-induced photonuclear reactions and target irradiation geometry, the proposed technique has the promise of returning very high profits in a not too-distant future.

## REFERENCES

[1] U.Amaldi: Proc. 5 Europ. part . Acc. Conf., Sitges (Barcelona), June,1996.
[2] Y.Iongen: Proc. Int. Conf. on Acc.-Driv. Transm. Technol. and Appl., Las Vegas, July, 1994.
[3] M.H.Mc Gregor: "Isotope Production with an Electron Linear Accelerator" - Report N 1771, Appl. Rad. Corp., Walnut Greek, California, USA.
[4] A.N.Dovbnya et al.: Ukr. Radiolog. Jorn. N 2 (1996) 186

# ENCAPSULATED TARGET FOR ISOTOPE PRODUCTION CYCLOTRONS

Shervin Bakhtiari, William Z. Gelbart, Wendy Ho, Nigel R. Stevenson
TRIUMF 4004 Wesbrook Mall, Vancouver, B.C., Canada V6T 2A3

*Abstract*

The current solid isotope production targets [1] at TRIUMF can only be used to irradiate metallic materials with high melting points. In order to irradiate liquids, powders, and materials with low melting points, a new encapsulated target is being developed specifically for use on isotope production cyclotrons. This concentrically water-cooled target must withstand a 240 μA @ 30 MeV proton beam. The target is a round container with a pocket to hold the target material; the target material is encapsulated using a thin foil, which is electron-beam welded onto the target. The cooling and the heat-induced stresses of the target are being analysed using finite element methods. The results will then be compared with actual measurements obtained using surface embedded thermocouples. The paper discusses the results and the current status of the project.

## 1 INTRODUCTION

The development of the new encapsulated target by Applied Technology Group at TRIUMF was initiated due to the need for irradiation of powders, liquids, and other materials. This new target must isolate the target material from the rest of the system. The target also needs to be oriented horizontally in order to be able to hold liquids properly. Since it is necessary to keep the target material temperature as low as possible, a detailed study of the thermal performance target was undertaken. Using a Finite Element Analysis (FEA) modeling package, the target and the cooling system were investigated. The axis-symmetric property of the system allows the simplification of the FEA model. The heat load of the beam was modeled using a radial Gaussian distribution with truncated tails representing the beam spill.

## 2 TARGET DESIGN

The encapsulated target can be thought of as a upside down metallic petri dish with a diameter of 70 mm and a height of 12.7 mm. The top centre piece has a shallow recess for holding the target material, and the back is part of the coolant circuit. The encapsulation is achieved by electron beam welding a thin foil (~12-25 μm) to the periphery of the target. This new target allows the irradiation of liquids, powders and low melting materials. The target can be made out of one or two materials. The hybrid target has a stainless steel ring, which is silver-soldered to the silver or copper centrepiece. The thickness of this section is about 1.0 mm in the centre. The bimetallic construction enhances thermal performance and allows easy electron-beam welding of the foil. Figure 1a shows a hybrid copper target and Figure 1b shows a hybrid silver target with the encapsulating foil. A solid version of these targets, shown in Figure 1c, can be used to replace the existing targets used for electroplated material. This target does not require the foil or the shallow recess.

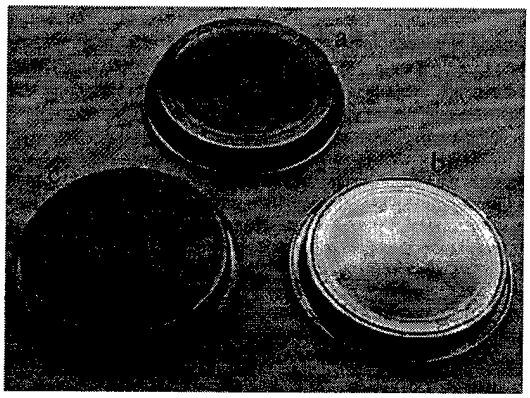


Figure 1: Encapsulated Targets

The target is positioned in the horizontal irradiation orientation by a remotely controlled actuator [2], which also creates a concentric coolant circuit against the back surface of the target as shown in Figure 2.

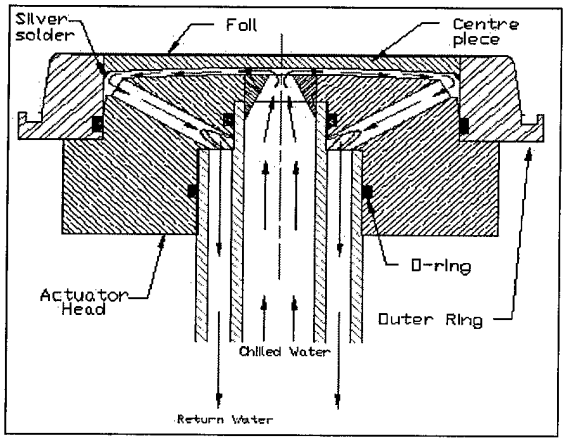



Figure 2: Target and Actuator Head cross section

The 30 MeV proton beam, which hits the target at an angle of 12.5°, is stopped in a relatively thin layer (~ 250 μm to 330 μm thick, depending on the target material)

0-7803-4376-X/98/$10.00 © 1998 IEEE

depositing all of its energy. The generated heat is then conducted to the water-cooled back of the target surface. Chilled water (14° C) enters the back of the target through the centre hole of the actuator head. The water spreads radially absorbing heat from the target and then drains through the holes on the outer rim of the actuator head. Flow rates of water range from 8 to 12 L/min.

## 3 TEMPERATURE PROFILE CALCULATIONS

Since the water and heat flow problems in the target are very complex, they cannot be solved analytically and therefore numerical methods in form of finite element analysis must be used. For the analysis of this target, EMRC's DISPLAY III/NISA II® package was used.

### *3.1 Beam Profile*

The irradiation area on the target is a circle with the radius of 18.75 mm, hence the beam is collimated to protect the rest of the target. As a result, truncated distributions are used to model the heat load. A Gaussian distribution can represent the power density of the circular beam .The focus condition of the beam is usually defined in terms of the beam spill on the collimators. For the encapsulated targets, this spill is to be 16.7% – i.e. 8.3% truncated on each side – which reduces the beam current to 200 μA. The power density P of the proton beam, is represented by

$$P = \frac{P_0}{\sqrt{2\pi}\,\sigma} e^{\frac{-r^2}{2\sigma^2}} \quad \text{for } |r| \le 18.75$$

$$= 0 \quad \text{for } |r| \le 18.75$$

Where r is the radius, $P_0$ is the total beam power (7.5kW), and $\sigma$ is the standard deviation, which was calculated to be 13.52 for the specified spill. Figure 3 shows the curve.

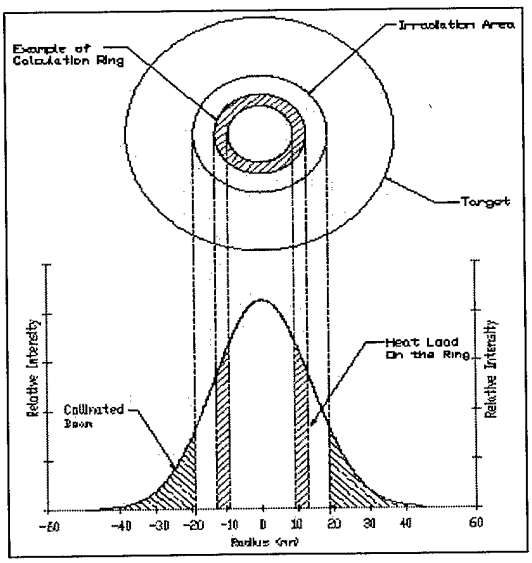



Figure 3: Proton Beam Power Density Curve

The heat load for each thin ring on the target is the area under the Gaussian curve between the ring's two radii. The beam profile also varies as the beam penetrates the material. The energy deposited in the material at regular length intervals, e.g. 0.10 mm, can be easily calculated using standard curves. An available computer code[1], was used to calculate the energy loss during penetration. The resulting two-dimensional heat profile is used in the FEA model.

### *3.2 FEA Model*

The cooling circuit, target, and the heat load are axis-symmetric, and hence the FEA model can be simplified accordingly. The target and the coolant circuit are modelled using 3D axis-symmetric linear (4 node) quadrilateral solid and fluid elements respectively. The heat load on the target is then modelled as element heat generations distributed over the target and within three element layers (0.13 mm each) from the surface. Each element has three degrees of freedom per node: x and y water velocities and temperature. The boundary conditions for the fluid elements are no-slip conditions which dictate that water velocity at the walls is zero. The FEA analysis is performed with temperature-dependent conductivity for the target material and temperature-dependent thermal conductivity, density, specific heat, and viscosity for the water. Conjugate steady state fluid flow and heat transfer are performed for different combination of target material and cooling configurations.

### *3.3 Cooling Configurations*

In order to find the optimal cooling configuration of the system, input parameters and configurations were varied individually in order to examine their effect on the thermal performance of the target. The different cooling configurations that were tried are as follows:

(1) Original design, coolant gap[2] of 1.0 mm
(2) Coolant gap of 0.5 mm
(3) Case (2) with a 2.0 mm diameter straight nozzle
(4) Case (2) with a 2.0 mm diameter tapered nozzle

For cases (1) and (2) the flow was assumed to be in the laminar region while for cases (3) and (4) transition or turbulence regions were assumed. The water flow rate was also varied from 8L/min to 12 L/min.

### *3.4 FEA Results*

The FEA results from the first two configurations indicated a dead-water zone right at the centre of the target. This spot, which receives a large amount of heat

[1]The program does not take into consideration the possibility of proton scattering.
[2] The gap between the actuator head and the back of the target.

due to the Gaussian distribution, is the hottest spot of the target. By adding the nozzle to the cooling circuit, the dead water zone was eliminated which resulted in a 50% temperature drop. Figure 4 shows the temperature profile for case (4). The temperature contours are consistent with profiles expected from Gaussian heat loads. In the case shown the maximum temperature is 232° C but within 1.0 mm the temperature drops to 122° C. The thermal performance for copper and silver is almost identical and only the cooling configuration and water flow rate have significant effects on the temperature.

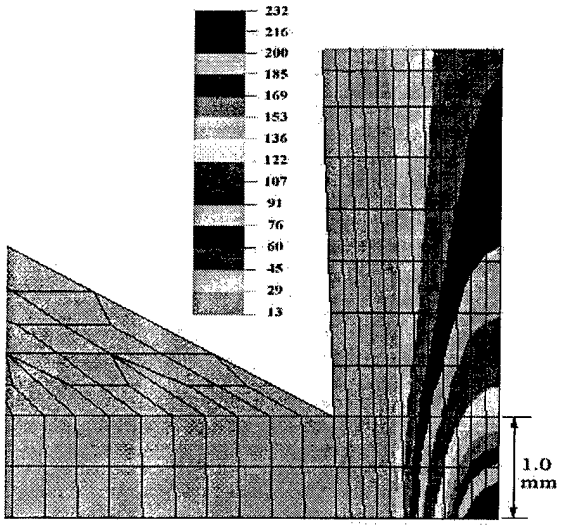



Figure 4: Target Temperature Profile (case 4)

As it can be seen from Table 1, for case (1) and (2), the water flow rate has significant effect on the temperature while for case (3) and (4) the temperature does not change. This is again due to the dead-water zone, which is very large in the first two cases but is significantly reduced in the other two cases by the use of a nozzle.

| | 8 L/min | 10 L/min | 12 L/min |
|---|---|---|---|
| 1 mm Gap | 511° C | N/A | 450 |
| 0.5 mm Gap | 483 | N/A | 464 |
| Straight Nozzle | 299 | 299 | N/A |
| Tapered Nozzle | 232 | N/A | 232 |

Table 1: Effects of Cooling Configuration and Flow Rate on Maximum Temperature

## 4 THERMAL PERFORMANCE TEST

In order to verify that the surface temperature of the encapsulated target during irradiation is predicted correctly by the FEA code, actual temperature measurements are needed. This task is accomplished by embedding a 0.80 mm diameter thermocouple (type K) below the surface of the centre of the target plate where the highest temperatures are expected. The test was conducted using the tapered nozzle configuration. Since an encapsulated target station [2] does not yet exist, the current solid target station had to be used for the tests. As a result the tests were conducted at currents of up to 150μA, and a water flow of 3 L/min.

### *4.1 Test Results*

In order to have a direct comparison between the FEA output and the actual test results, FEA runs were done using the new parameters. The program predicted a temperature of 190°C at 150μA and 130°C at a current of 100μA. The measured temperatures at these currents, were 30°C and 45°C, respectively.

### *4.2 Discussion of the Results*

The actual surface temperature can be as much as twice higher than that measured by the embedded thermocouple due to the fact the actual position of the junction is unknown and can be as much as 0.2mm below the surface. Another important factor is that the shape of the beam used in these tests is not similar to the modelled beam. The beam used for the solid target station is rectangular and is represented by a two-dimensional Gaussian curve [1], which results in less concentrated beam power. Also, the centre of the beam may not be aligned with the centre of the new target. As mentioned before, there can be a 100°C temperature difference between the centre point and a point 1.0 mm away. As a result of the above factors, the measured temperature may be 3 to 5 times less than the actual maximum temperature.

## 5 CONCLUSION

An encapsulated target was designed for irradiation of liquids, powders and non-metals. Using FEA modelling the thermal performance of the system was optimised to achieve the lowest temperature. The results obtained from both the FEA and the actual thermal tests indicate that the target is suitable for the desired use and it will withstand the specified proton beam.

## 6 ACKNOWLEDGEMENTS

The authors would like to thank the members of the TRIUMF Applied Technology Group (ATG) for their technical assistance.

REFERENCES

[1] Nortier, F. M., *et al.*, "Investigation of the Thermal Performance of Solid Targets for Radioisotope Production", Nuclear Instruments and Methods in Physics Research, Section A, 1994, P236-241

[2] Ho, W., Bakhtiari, S., Gelbart, W.Z., Stevenson, N.R."High Current Encapsulated Target System for Radioisotopes Production," Proceedings of the 1997 Particle Accelerator Conference

# HIGH CURRENT ENCAPSULATED TARGET SYSTEM FOR RADIOISOTOPE PRODUCTION

Wendy Ho, Shervin Bakhtiari, William Z. Gelbart, Nigel R. Stevenson
TRIUMF, 4004 Wesbrook Mall, Vancouver, B.C., Canada, V6T 2A3

*Abstract*

Solid target systems for use with vertically oriented targets are currently used at TRIUMF for radioisotope production. In order to irradiate liquids, powders, and non-electroplatable materials using the newly developed encapsulated target, a new target system for use with horizontally oriented targets is being designed. This target station has a modular assembly consisting of a landing terminal, an irradiation chamber, a manipulator, and an actuator. Targets are pneumatically transferred between the station and the hot cells. The target is positioned in the irradiation orientation by a remotely controlled actuator, which also creates a concentric coolant circuit against the back surface of the target. Additional cooling is provided by a forced flow of helium gas over the top surface of the target. This target station can also be used for irradiation of regular solid targets. The paper discusses the detailed design of this target system and the current status of the project.

## 1 INTRODUCTION

Two isotope production cyclotrons (30 MeV TR30 and 42 MeV CP42) are operated by the Applied Technology Group at TRIUMF for MDS Nordion for medical radioisotope production. Remotely controlled solid target systems for use with vertically oriented targets are currently used with both cyclotrons to irradiate metallic, electroplatable materials with high melting point. Since there was an increased demand in the past few years to irradiate liquids, powders, non-metallic materials, materials that are hard to electroplate, and materials with low melting point, a new type of target system, called the encapsulated target system, is being designed.

The encapsulated target system is for use with horizontally oriented encapsulated targets, which are carefully designed so that the target material and its irradiated product are completely isolated from the rest of the system. Targets are pneumatically transferred between the hot cell and the target station. The target station, while still being based on the existing high current solid target system [1], incorporates several custom-designed modular subassemblies. The following sections discuss the design of the encapsulated target and the target station.

## 2 ENCAPSULATED TARGET

The encapsulated target is a bimetallic assembly that comprises a copper or silver central disc and a stainless steel ring. These two parts are silver soldered together to form one assembly. The target material is placed in a shallow recess of the central disc and a thin foil is electron beam welded to the periphery of the target. The encapsulated target is concentrically water-cooled and can withstand a 240 μA 30 MeV proton beam bombardment at a 12.5° angle. The thermal performance of the target has been analyzed using finite element analysis and experimentally verified.

Figure 1 shows the target with its plastic carrier, "rabbit," in the background. For more information on the target construction, the target cooling configuration, and thermal analysis of the target, see Reference [2].



Figure 1. Encapsulated Target and Rabbit

## 3 ENCAPSULATED TARGET STATION

Figure 2 and 3 show the layout of the encapsulated target station. Since the encapsulated targets are irradiated in a horizontal position, a bending magnet is used to provide a 12.5° horizontal angle to the beam. Four modular subassemblies are mounted on an aluminum stand: a landing terminal, a vacuum/irradiation chamber, a manipulator, and an actuator.

0-7803-4376-X/98/$10.00 © 1998 IEEE

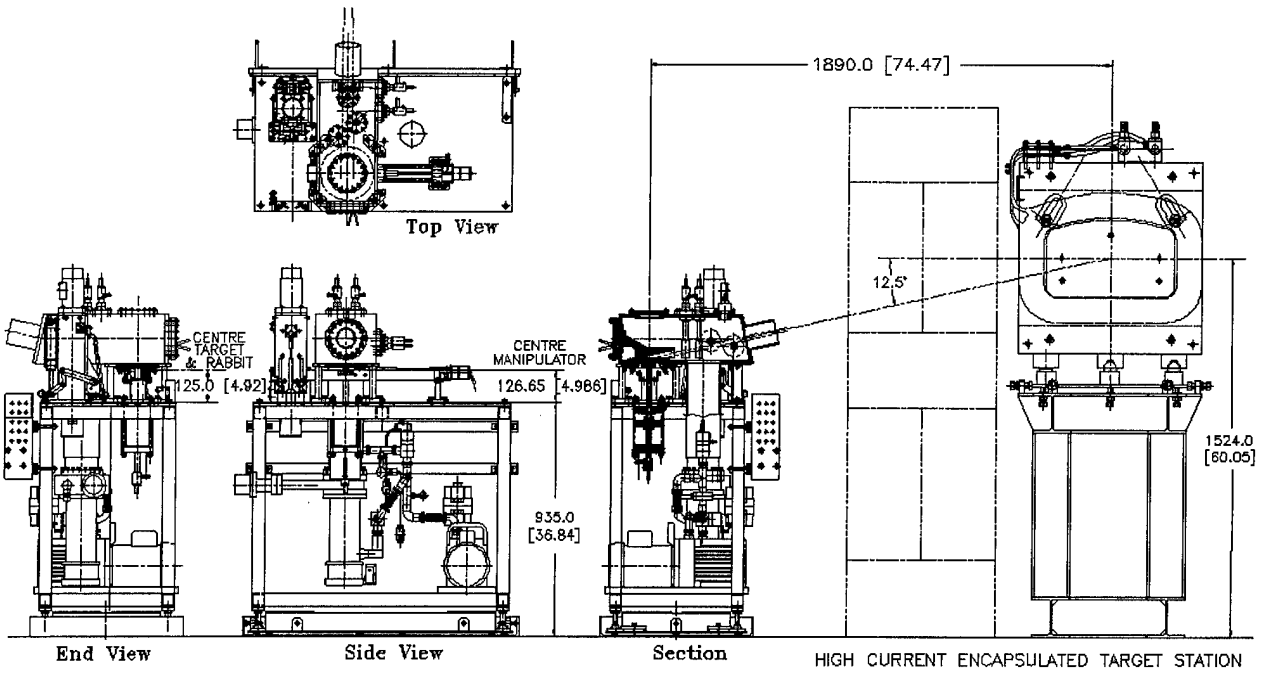



Figure 2. High Current Encapsulated Target Station

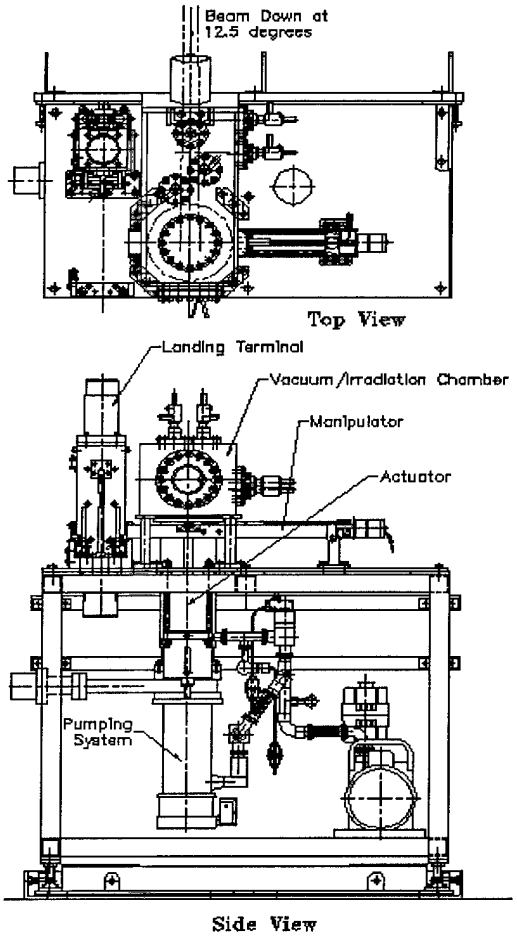



Figure 3. Side View and Top View of the Encapsulated Target Station

During operation, the target (in its plastic carrier called "rabbit") is transferred from the hot cell to the target station via a pneumatic transfer system. When it arrives at the target station, it is brought to a soft landing and oriented in the required way by a dynamic braking and magnetic orientation system inside the landing terminal. Dynamic braking system utilizes the pressure build up at the closed-end of the landing terminal and a reverse air flow injected into the receive housing of the landing terminal to slow and bring the rabbit to a "soft landing". Magnetic orientation system simply takes advantage of the attraction/repulsion of opposite/similar magnetic polarities to orient the rabbit.

Once the door of the landing terminal fully opens, the manipulator can advance forward to retrieve the target from the rabbit. Figure 4 shows a solid model of the manipulator. The manipulator grabber removes the target from the rabbit and pulls it along the manipulator guide until the target is directly underneath the target flange of the vacuum/irradiation chamber. The manipulator grabber then disengages from the target and an actuator (see Figure 5) lifts the target off the manipulator guide and pushes the target against the target flange for irradiation. The actuator head fits inside the target and creates a concentric water coolant circuit against the back surface of the target [2]. At the same time, the target, mounted on the actuator head, seals the vacuum/irradiation chamber. Additional cooling is provided for the top surface of the encapsulating foil of the target by a forced flow of helium gas that is incorporated into the design of the target flange. The helium also cools a fixed foil window placed between the target and the vacuum/irradiation chamber.

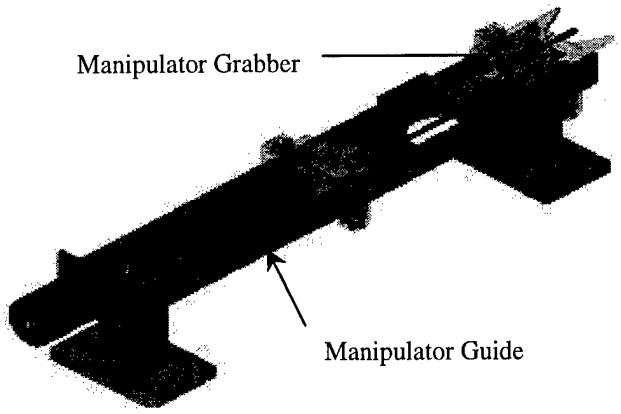



Figure 4. The Solid Model of the Manipulator

The vacuum/irradiation chamber is pumped down before the beam is put on the target. After the target irradiation and the vacuum/irradiation chamber venting, the actuator lowers the target back onto the manipulator guide, and the manipulator grabber engages the target and inserts it into the rabbit. The target in its rabbit is then sent back to the hot cell for processing.

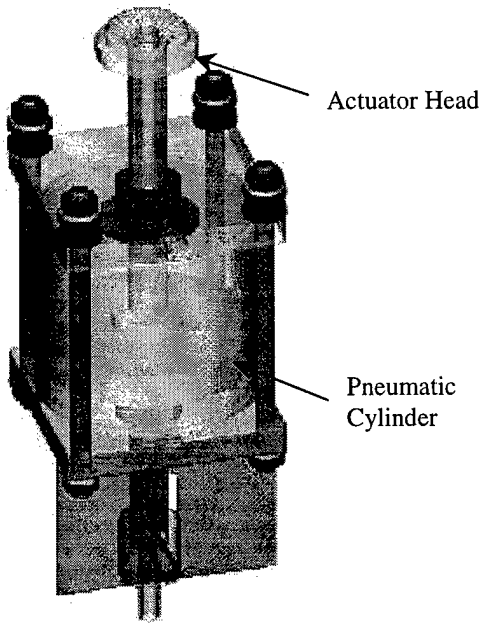



Figure 5. Solid Model of the Actuator

An industrial programmable logic controller will control the complete operational cycle, as well as all interlocks. A complete target change from the end of an irradiation on a target to the start of the beam on the subsequent target will take about 25 minutes.

## 4 RADIATION HARDNESS

The encapsulated target system follows the existing design of the high current solid target system which aims for minimizing downtime caused by radiation damage to system components. The component materials and locations are carefully chosen with respect to the beam and the target. For example, the pneumatic cylinders (of the landing terminal and the actuator) are fitted with graphite pistons and rod seals. Metal O-rings are used to seal the vacuum/irradiation chamber (except the target flange.) Elastomer O-rings on the targets are used only for one irradiation. Electrical isolation is achieved by hard anodizing on aluminum or polyamide plastic components. All these materials (as well as others chosen for electrical wiring, water connections, etc.) have been tested under actual operating conditions of the solid target system and proved their radiation hardness and suitability for this application.

## 5 CONCLUSION

The feasibility study of the encapsulated target by investigating its thermal performance using finite element analysis and actual target surface temperature measurements via embedded thermocouples during irradiation is completed [2]. The preliminary design of the encapsulated target station has also been recently completed. Detailed design is currently in progress and once it is completed and finalized, the construction of a prototype encapsulated target system can commence.

## 6 REFERENCES

[1] Gelbart, W. Z., Stevenson, N. R., Johnson, R. R., Nortier, F. M., Orzechowski, J., Cifarelli, F., "High Current Radioisotope Production with Solid Target System," Proceedings of the 1993 Particle Accelerator Conference, P. 3099-3101

[2] Bakhtiari, S., Gelbart, W. Z., Ho, W., Stevenson, N. R., "Encapsulated Target for Isotope Production Cyclotrons," Proceedings of 1997 Particle Accelerator Conference

[3] Gelbart, W. Z., Cifarelli, F., W. Ho, "The Design of the High Current Encapsulated Target System," TRIUMF Design Note TRI-DN-95-30

[4] Gelbart, W. Z., "Electron Beam Welder for Target Material Encapsulating," TRIUMF Design Note TRI-DN-89-25

[5] Nortier, F. M., Stevenson, N. R., Gelbart, W. Z., "Investigation of the thermal performance of solid targets for radioisotope production," Nuclear Instruments & Methods in Physics Research Section A, 1994, P. 236-241

# PROGRAM OF ACTIVITIES FOR THE LINAC-DRIVER OF ITEP SUBCRITICAL FACILITY

A.M.Kozodaev, A.A.Drozdovsky, A.A.Kolomiets, V.V. Kurakin, R.P.Kuybeda, N.V.Lazarev, V.I.Pershin, V.K.Plotnikov, O.V.Shvedov, V.S. Skachkov, V.V.Vasiliev, R.M.Vengrov
Institute for Theoretical and Experimental Physics (ITEP), 117259, Moscow, Russia

*Abstract*

On the base of existing linear proton accelerator and shut down heavy water ITEP reactor now is creating an electronuclear installation. Wide number of investigations is supposed to be carried out at the accelerator. One direction of the works covers functioning of the linac as driver, others concern the problems of the accelerator as a high intensity middle energy ion machine for applied purposes.

## 1 INTRODUCTION

Decision of a number of problems of nuclear power industry is sharply linked with high intensity linear accelerators. A number of these problems are necessary to be discussed study and solved before creation of a full-scale power installation. We know a number of scientific centers creating separate elements of intensive linac-drivers with the purpose to find physical and technical solutions for full-scale installations [1-3]. A number of problems is now in the process of solution at operating accelerators with ejection of the beams to experimental targets [4].

## 2 ITEP SUBCRITICAL FACILITY

An experimental electronuclear facility [5,6] propo-sed for investigation and foundation of efficiency and safety of subcritical assemblies controlled by an acelera-tor and also for utilization as a neutron generator (NG) in experimental works on optimization of target-blanket assembly and neutron-physical investigations is now under construction in ITEP on the base of the proton linac ISTRA-36 and shut down heavy water reactor. The main parameters of the installation are:

- average proton beam current 500 μA,
- particle energy 36 MeV,
- average beam power 18 kW,
- intensity of fast neutrons $1.4 \cdot 10^{14}$ n/s,
- thermal neutron flux in hevy-water reflertor $(1.5\text{-}3) \cdot 10^{12}$ n/cm$^2$·s,
- multiplication coefficient of the blanket 0.95 - 0.97.

The mode of operation is pulsed: amplitude of pulses of beam current is 150 mA, pulse duration - 150 μs and pulse repetition rate - 25 Hz. Structural diagram of the linac-driver is: RFQ(3MeV) – DTL-1(10 MeV) – DTL-2 (36 MeV). In addition to its own basical functions the accelerator ISTRA-36 will be a device for experimental tests of a number of physical and technical decisions to be used in full-scale installations. Applied utilization of the proton beam is also provided.

## 3 LINAC - DRIVER IN A SET OF THE NEUTRON GENERATOR

*The means of accelerator control* system must provide easy and safe operation of the target-blanket assembly under all modes of operation: individual adjustment of the linac, routine operation of the NG and emergency situations. Main logic links of safe control-ling of the accelerator are shown in Fig.1.

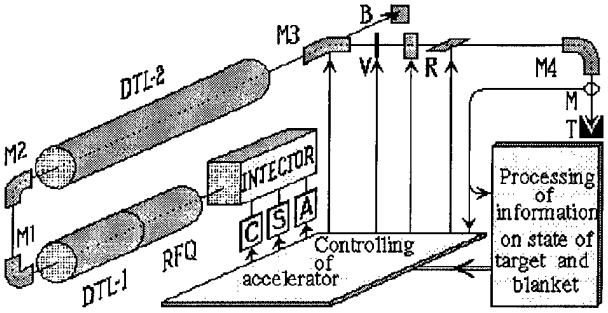



Fig.1. Logic links for controlling of the accelerator.

*Autonomous adjustment* will be carried out under power removed from the magnet *M3* and closed vacuum valve *V* that provides full disconnection of the accelera-tor and target-blanket assembly. The beam goes to the beam-stop *B*. Controlling of the bending magnet *M3* and the valve *V* is realized from the side of target-blanket part of the installation that excludes non-sanctionised transfer of the beam into the target *T*.

*In the process of routine operation* of the NG proton beam is sent to the target beginning from small amplitudes. Collimator *C* at the output of the injector is supposed to be used for varying the beam. Such solution allows to control beam current in the limits from 0 to 100% without variation of electric and thermal mode of operation of the source providing stability of operation. All systems of the acelerator should operate conserving the steady mode of operation and be full ready when short (not emergency) shut down of the beam occur. It may be done if to shift the moment of start *S* of accelera-ting voltage generator of the injector approximately by ~1 ms before. Capture of particles in RFQ and formation of the following pulse of beam current at the output of the accelerator becomes impossible. Automated correc-tion of beam position (the correctors *R*) in the HEBT on the base of results of continous measurement of proton flux density distribution at the target may turn out to be useful.

0-7803-4376-X/98/$10.00 © 1998 IEEE

The amplitude of current directed to the target is fixed by the meter *M*.

*Under emergency situations* at the target-blanket assembly the beam is shut down by the commands of the system controlling the facility by switching off accelerating voltage *A* of the injector and simultaniously, for higher reliability, shifting of the starting pulse *S*. Duration of the process of the beam shut down does not exceed 200 μs. After completion of this operation the magnet *M3* is switched off and the valve *V* is closed. Non-sanctionised start up of the beam becomes impos-sivble. For higher reliability reverse logics may be used when not presence but absence of signals will be the command to shut down. All emergency situations at the accelerator lead to shut down of the beam and can not create radiation-nuclear threat.

Pulsed mode of operation of the NG brings some advantages. Under such mode of operation it is possible to provide continuous monitoring of blanket sub-criticality reliably providing approach to critical state. Analysing the manner of thefall in neutron flux in the pauses between the pulses of proton beam it is definitely possible to find out what are the reasons of reactivity variation - state of the blanket or variation of beam current-and to take corresponding measures.

*Operation technique with the beam of increased intensity* puts new tasks which in some extent will be investigated at the ITEP electronuclear facility. It will be necessary to investigate the following problems: development of exact dosing of the beam, development of the output window and experimental investigation of its characteristics, searches of a reliable method of variation of proton flux density at the target and automated formation of optimal distribution of this density.

## 4 LINAC - PROTOTYPE OF A HIGH CURRENT ACELERATOR

*Controlling of the RF power level.* Contradicting requirements to the RF systems of high current accelerators are to be met. From one point they should provide huge powers and from the other point they must quickly react to variation of the beam not allowing damgerous overvoltages in acelerating gaps. We estimate the bandwidth of the sustem of automated control of the amplitude of the field as 500 kHz and the ratio of the hoghest level of RF power for excitation of room-temperature resonators to minimal level may reach 4-6. Such technical problems were never investigated in full scale.

The accelerator ISTRA-36 is close to high current linear accelerators by the power necessary for excitation of the resonators (3.5) and the accepted radio frequencies (300 and 150 MHz). And during 150 μs pulse under beam current 150 mA it is obviously high-intensity accelerator. That is the reason why the solutions developed at its RF system on autocompensation of beam loading effects may be useful for other accelerators.

*Operation of permanent magnet lenses.* The focusing channel in the DTL resonators is constructed on the base of quadrupoles with permanent magnets ($SmCo_5$, see Fig.2) [7], that makes it suitable, reliable and economical. The main factor capable to cause degradation of the lenses in the conditions of the accelerator ISTRA-36 is irradiation of the permanent magnets by neutrons born

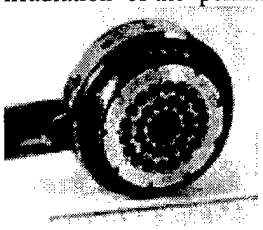


Fig.2. Quadrupole with permanent magnet in a drift tube (the end cover of the tube is removed).

under bombarding of copper walls of the aperture channel by lost protons. Neutron yield at proton energy of 36 MeV is approximately $\varepsilon \approx 0.015$ n/p. Experimen-tal results [8] show that rare earth alloy Sm-Co which is used for fabrication of the lenses lose to 1-5% of magnetization in presence of external field 0.55 T that is close to our conditions after neutron irradiation by $D \approx 1.7 \cdot 10^{15}$ n/cm$^2$ fluence. The pointed above fluence may be accumulated in the magnets of the lenses at the output of the accelerator under average beam current i and relative losses of the particles δ uniformely distributed along the focusing channel of the DTL for continuous operation $t \approx D \cdot K \cdot e/(\varepsilon \cdot \delta \cdot i)$. Here K - geometry factor of the channel, e - the proton charge. Approximate link between t and δ presented in the Fig.3 points to necessity to decrease the losses and possible lowering of neutron irradiation of the lenses in our specific case, in particular, due to utilization of graphite.

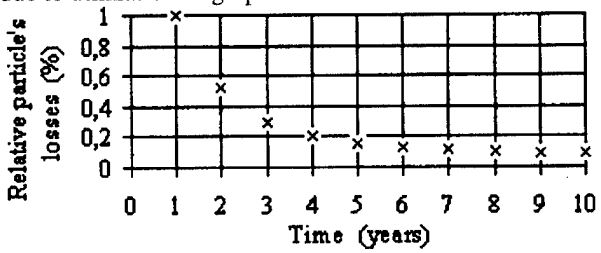



Fig.3. Estimation of the time of operation of PMQ fabricated of $CmCo_5$ at the output of the accelerator under different values of δ.

*Tests of graphite absorbers of the lost particles.* The ITEP proposal on sharp decrease of the level of radiation at the accelerators [9] due to placement of graphite at the periphery of the aperture channel is supposed to be used. The graphite is characterised by low output of secondary radiation and formation of mainly short-lived radionuclides. At proton energy 10 MeV neutron yield in graphite is appr. 100 times less than in copper and at energy 36 MeV - by 10 times.

After 1 hour of "cooling" hand maintenance of the output part of the accelerator ISTRA-36 is possible if beam losses (without graphite) are not higher than 0.01 μA/m. Placement of graphite insertions of the thickness 0.5-1 mm in the aperture channel or ionguide rises available level to 1 μA/m without significant decrease of aperture diameter. The rings will be installed in the places near quadrupole lenses (Fig.4) where the dimension of the beam in one of coordinates are the

highest. In order to exclude gas inleakage a thin layer of a metal, for example, aluminium should be deposit on the surface of graphite or it will be necessary to select harder types of graphite.

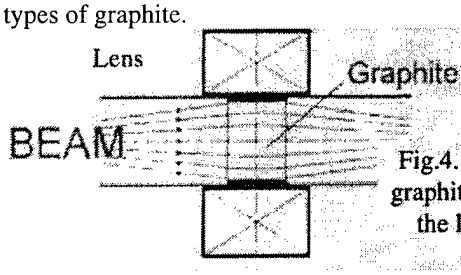



Fig.4. Placement of graphite absorbers of the lost protons.

*Checking of technological and design solutions*. The proposed in ITEP and realized at the accelerator ISTRA-36 junction of internal cavities of the drift tubes and the vacuum volume of the DTL resonators simpli-fying fabrication and rising reliability of the tubes [7] will be checked in real conditions of long operation. Absence of gasemission materials in design of PMQ in internal cavities of the tubes allowed not to provide hermetization of these volumes and to pump out through the holes which may be seen at the external cylindrical surface of the tubes (Fig.2).

If there is a necessity to align, to repare or to replace one or several drift tubes complications linked with possible activation may arise. This problem will be significantly simplified by fixation of the drift tubes to a removable rigid girder that is provided in one of the resonators of the accelerator ISTRA-36 (Fig.5). A set of the drift tubes requiring reparation or adjustment may be removed as a whole without direct contact of the people and activated elements. Reserve set adjusted at a special stand may be quickly installed into the resonator.

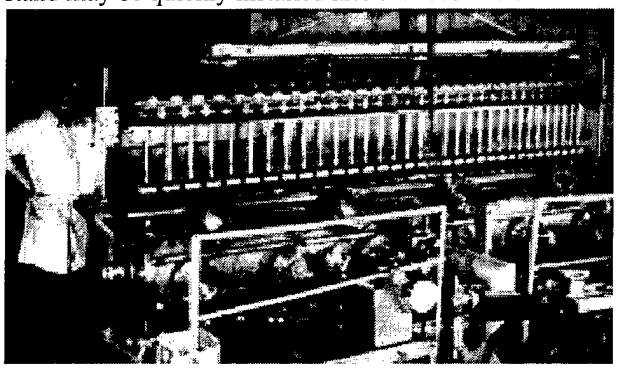


Fig.5. Removable girder with drift tubes of the resonator DTL-1.

## 5 APPLIED UTILIZATION OF THE BEAM

Three challels of beam ejection are provided for applied utilization of beam.

*The first channel* will be used for ejection of the beam with energy 3 and 10 MeV for element analysis and production of radionuclides for positron tomography ($^{11}C$, $^{13}N$, $^{15}O$, $^{18}F$, $^{45}Ti$, $^{52}Cu$ and so on).

*The second channel* will eject beam with energy 36 MeV with current 100 - 400 μA for production of a wide spectrum of radionuclides for medical, biological and industrial utilization ($^{55}Co$, $^{87}Ga$, $^{82}Sr$, $^{87}Y$, $^{123}I$, $^{201}Tl$ and so on) and also for investigation of radiation stability of materials.

*The third channel* (36 MeV, low density of particle flux) will be used for radiation tests of components and fabricated elements supposed to be used in cosmic space. The provided at the accelerator energies of particles are suitable for these tasks as most of positively charges particles in interplanetary space are the protons with energies not higher than 10 - 20 MeV and in near Earth space with some higher energy.

*Production of pulses of proton beam with pulse slope < 10 ns*. A method of production of intensive pulses of proton beam of nanosecond region duration proposed in ITEP is tested at operating part of the accelerator [10]. Under accelerating voltage at the injector lower the threshold value injection of particles in the RFQ section was provided only during action of additional field of additionally accelerating inductors installed at the input into RFQ (Fig.6). Improvement of this method will give

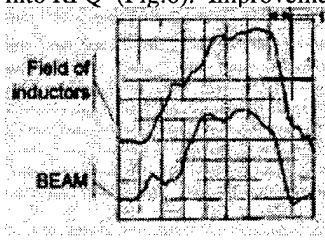



Fig.6. Short pulse of proton beam.

practical results for technics of remote definition of fissile materials, definition of element composition of the surfaces of the planets and investigation of fast reactions by the method of pulsed radiolysis.

## 6 CONCLUSION

The experimental neutron generator in ITEP will be one of the first in the world specially created electro-nuclear installations controlled by proton beam. It will allow to find and test solutions of already put questions and to find the problems which are not yet known. Estimations show that under acceleration of average currents higher than 70 - 80 mA room temperature reso-nators are more economical than the superconducting. Information obtained at the accelerator-driver with room temperature resonators ISTRA-36 will be useful for designing of high current accelerators.

## REFERENCES


[1] K.C.Chan et al., *Proc. of the 1994 Int.Lin.Conf.*, Tsukuba,V.1,p.101.
[2] M.Mizumoto, ibid., p.317.
[3] K.C.Chan, *Proc. of the Int.Conf. on Accel.-Driv. Transmut. Technol. and Applic.*, Las Vegas, 1994, p.418.
[4] H.Klein, Ref.1, p.322.
[5] O.V.Shvedov et al., *8-th Int. Conf. on Emerg. Nucl. Energy Systems*, Obninsk, 24-28 June 1996. Abstracts, p.86.
[6] I.V.Chuvilo et al., *Proc. of the EPAC'96*, 1996,V.3, p.2674.
[7] I.M.Kapchinsky et al., *Proc. of the PAC'89*, 1989, V.2, p.1073.
[8] J.R.Cost, R.D.Brown, LA-UR-88-4263.
[9] A.A.Drozdovsky. *Proc. of the EPAC'96*, 1996.V.3,p.2621.
[10] R.M.Vengrov et al., *XV Part. Accel. Symp.*, 22-24 October 1996, Protvino, Russia. Abstracts, p.44.

# PARAMETER AND COST MODEL FOR SPALLATION NEUTRON SOURCE STUDIES

J. D. Galambos and D. K. Olsen
Oak Ridge National Laboratory, Oak Ridge TN, 37831-8218

*Abstract*

A Spallation Neutron Source Systems Model has been developed to facilitate parameter and cost studies of accelerator-based spallation neutron source (SNS) systems. This model includes modules for all pertinent components and processes, such as accelerators and rings, target (neutron source), experimental facilities, conventional facilities, construction costs, pre-operational costs, etc. Present accelerator modules include room temperature linacs, accumulator rings (AR) and rapid cycling synchrotrons (RCS). All the modules in the model are linked together via an optimizer to facilitate overall trade studies. The model has been developed for and used by the National Spallation Neutron Source (NSNS) project to be built in Oak Ridge.

## 1 BACKGROUND

For the National Spallation Neutron Source [1] design, there are several accelerator options capable of satisfying the requirments of the neutron scattering community. These requirments are a pulsed neutron source having at least 1.0MW of proton beam power, a pulse rate of 30-60Hz, a pulse width $\leq 1\mu s$, clear upgrade paths to higher power, low technical risk, and high reliability. Conceptual designs already exist for partial-energy linacs with rapid cycling snnchrotron systems [2] and for full-energy linacs with accumulator ring systems [3,4]. The Spallation Neutron Source Systems Model was developed to evaluate and compare these designs on a performance and cost basis and to determine an optimum configuration.

The model contains linkable modules for all the major systems, including linac, ring, target (neutron source), experimental systems, conventional facilities, and costs. By linking these modules, self-consistent trade studies can be conducted to compare different accelerator concepts on a common performance and cost basis. Typically, the cost and physical parameter estimations use simple scalings, derived from detailed studies and cost estimates. The optimization package includes constraints to provide for "minimum cost" and "maximum performance" type design studies. The model can be run without optimization, in a "benchmark" mode to permit comparisons with existing designs and cost estimates.

The details of this model are described in Ref. [5] and are briefly reviewed in Section 2. Results comparing AR and RCS options for the NSNS are presented in Section 3.

## 2 MODEL DESCRIPTION

### *2.1 Accelerator Options*

The accelerator is the major factor in the cost and neutron production capability of a SNS. Present modules include room temperature linacs, accumulator rings, and rapid cycling synchrotrons. These modules constain: the dependence of average current on peak ion source current, on chopping fraction, on loss estimates, and on duty factor; the dependence of linac power requirement on shunt resistance, on linac length, on beam power, and on accelerating gradient; the dependence of ring RF requirements on ramp rates and on beam currents; the dependence of peak magnetic fields on energy and on bend radius; the dependence of magnet aperatures on emittance, on margins, and on beam current; and the dependence of ring magnet power on aperature, on magnetic field, and on length.

### *2.2 Conventional Facilities*

Although the conventional facilities for a 1MW spallation neutron source are significantly pre-determined, there are a number of scalings that do impact the cost. These include the site power requirements for the linac, ring, target, and moderator cryogenics; the building and tunnel areas and lengths; and the site preperation area.

### *2.3 Pre-Operations Models*

Pre-operational costs are a non-neglibible component of the Total Project Cost (TPC) estimate. Personnel requirements are based on experience at other accelerator facilities, and are found to scale weakly with power. The estimate of utility costs during startup is based on the accelerator requirements. These values are also used to estimate life-cycle-costs over the expected plant lifetime.

### *2.2 Cost Models*

The Cost module derives costs using input from all the other modules. This involves several hundred scalings, mostly derived from benchmarks with existing SNSs or from more detailed design studies. Overheads

0-7803-4376-X/98/$10.00 © 1998 IEEE

and burdens are also included as appropriate. Estimates from this simple cost scaling method have proven accurate, when compared to subsequent detailed "bottoms-up" studies.

*2.4 Optimizer and Driver Shell*

The Spallation Neutron Source Systems Model is a C++ code, utilizing the SUPERCODE driver shell [6]. SUPERCODE is an interactive programmable shell that includes a non-linear constrained optimization package and other tools. Typically problems are solved by specifying: (1) a set of constraints, (2) independent variables to be iterated, and (3) a Figure-of-Merit to be optimized.

## 3 RESULTS

Results of minimum cost verses power level are presented here for both AR and RCS based SNS systems. The costs presented here were calculated in 1996. The TPC from recent detailed estimates is ~15% higher than these results, primarily due to an increase of project scope since the completion of this study.

3.1 *Problem Formulation*

The primary fixed assumptions used in these calculations are listed in Table 1, and the major constraints are shown in Table 2.

Table 1: Fixed Assumptions for cost vs power studies.

| |
|---|
| Linac: |
| • Single ion-source (no funneling) |
| • 80% RFQ capture/bunching factor |
| Ring: |
| • One ring |
| • Ring harmonic number = 1 |
| • 3% injection loss |
| • AR lattice is NSNS like: Superperiodicity = 3 |
| • RCS lattice is IPNS-U like: Superperiodicity = 4 |
| • Synchrotron accelerating duty factor = ½ i.e. simple sinusoidal wave form |
| • Ring acceptance / Beam emittance = 8 |
| Balance-of-Plant |
| • One target station |
| • Four neutron scattering instruments |

Table 2. Constraints on calculated quantities.

| Constraint |
|---|
| $H^-$ injection current: $\leq$ 105 mA@ 1% $f_{dutv}$ |
| $\leq$ 37.5 mA@ 6% $f_{dutv}$ |
| Linac chopped time = 65% orbit time |
| $\tau_{Iniect} \leq$ 2 msec |
| $\tau_{Iniect} \leq$ 1.5% of ring cycle time |
| Tune shift $\leq$ 0.15 (at injection) |
| Dipole field $\leq$ 1.1 T |
| dB/dt $\leq$ 120 T/s |
| Ring Length $\geq$ 200 m |
| Dipole gap = $2\sqrt{\alpha_{ring}\beta_{dipole}}$ +v.v. (1) |
| Quad bore = $2\sqrt{\alpha_{ring}\beta_{quad}}$ + v.v. (1) |
| RF cavity field $\leq$ 20 kV/m |

1 - Vacuum vessel =1cm for AR, = 3cm for RSC

To find optimal solutions, the variables listed in Table 3 are allowed to vary within the indicated bounds. The Total Project Cost (TPC) was used as the Figure-of-merit.

Table 3. Variable input parameters.

| Bound: | Lower | Upper |
|---|---|---|
| Linac CCL length | --- | --- |
| Linac CCL accelerating gradient (Mev/m) | 1.5 | 3.5 |
| Linac macro duty factor | --- | 0.10 |
| Ring long drift length | --- | --- |
| Ring drift length | --- | --- |
| Dipole length (m) | 1. | 5. |
| RF Voltage (V) | --- | --- |

*3.2 AR Results*

Using this formulation, the minimum cost AR SNS was found as a function of power level on target. Results are shown in Fig. 1 for three different choices of linac energy. The cost, the maximum linac power, and the operating cost, all increase with linac energy. It is not possible to achieve a 1MW power level at a cost below $1B, with a linac energy of 1GeV. This energy level is critical, since spallation neutron production drops rapidly at energies below ~800MeV. Although the cost increase with beam power at fixed energy is slight,.the available ion source current limits the maxium attainable power. To achieve higher powers with the given ion source constraints other options, such as funneling, are required.

*3.2 RCS Results*

Figure 2 shows minimum cost versus beam power for a RCS SNS having a pulse rate of 30Hz and a final energy of 3GeV. The cases shown have injection energies of 400, 600 and 800MeV. Again there is only a slight cost increase with increasing power, but a large increase with injection energy due to the associated cost increase of the linac. As the beam power increases, more protons must be accelerated in the RCS. For a fixed tune shift, this requires increased beam emittance, which in turn increases the magnet aperature

requirement, and the cost. These effects are especially pronounced at 400MeV injection energy.

Figure 3 plots the minimum TPC as a function of the final beam energy for RCS pulse rates of 15Hz, 30Hz, and 60Hz. Low extraction energies lead to cost penalties because higher currents and linac RF power are required. This leads to enhancement in the emittances requiring increased ring apertures. For high energies, costs increase due to the increased $B\rho$ and increased ring circumference. A slight cost benefit is obtained by increasing the repetition rate. This results from smaller ring apertures due to lower peak beam intensities at higher repetition rates. A limit of 2GeV on the extraction beam energy is necessary in the 60 Hz case because of the dB/dt limit.

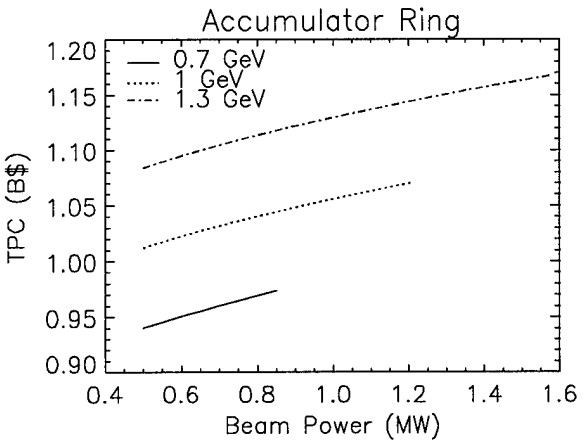



Figure 1. Minimum AR option TPC vs. beam power for different linac energies

## 4 DISCUSSION

A flexible parameter and cost model has been developed to investigate possible configurations for the NSNS. The model gives more accurate relative cost diferences between options than absolute costs. For a device of NSNS magnitude, a small (< 10%) cost difference exists between AR and RCS options for comparable performance. The model does not include several important considerations, such as technical risk, reliability, and upgrade options. Since the cost difference is small, the choice between the AR and RCS options for NSNS has been made on these other considerations.

## 11 ACKNOWLEDGEMENTS

This research is sponsored by the Division of Materials Sciences, DOE, under contract DE-AC05-96OR22464 with Lockeed Martin Energy Research.

## REFERENCES

[1] B.R. Appleton, et al "The National Spallation Neutron Source Collaboration: Towards a New Pulsed Neutron Source in the United States", Proc. of EPAC96, Barcelona (1996) p.575.

[2] "IPNS Upgrade- A Feasibility Study", Argonne National Lab. Report ANL-95/13, April 1995.

[3] "5 MW Pulsed Spallation Neutron Source Pre-conceptual Design Study", BNL 60678, June 1994.

[4] I.S.K. Gardner, H. Lengeler, G.H. Rees, "Uutline Design of the European Spallation Neutron Source", ESS 95-30-M, Sept. 1995.

[5] J.D. Galambos, et al "Oak Ridge Spallation Neutron Source Systems Model", ORNL-TM-???.

[6] S. W. Haney, et al "SuperCode for Systems Analysis of Tokamak Experiments and Reactors", Fusion Technology, **21**, (1992), 1749.

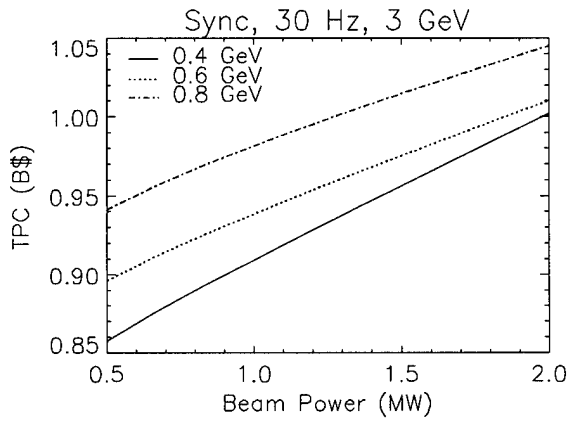



Figure 2. Minimum RCS option TPC vs. beam power for different linac Energies

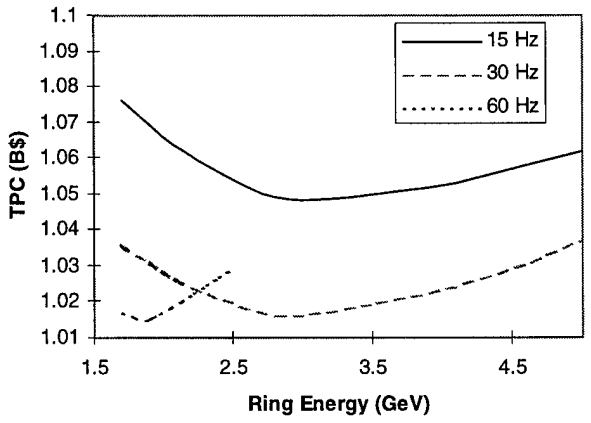



Figure 3. Variation of the minimum cost source with ring energy for a 1 MW RCS SNS.

# ELECTRON BEAM APPLICATIONS IN CHEMICAL PROCESSING

G.Cojocaru, TRIUMF, Vancouver, Canada
D.Martin, M.Dragusin, R.Moraru, M.Radoiu, C.Oproiu, S.Marghitu, I.Indreias, V. Bestea, Institute of Atomic Physics-Bucharest, Romania
R.Camariuc, A.Margaritescu, ICPE-Electrostatica-Bucharest, Romania

*Abstract*

Last results in the field of polymeric materials obtained by electron beam irradiation are presented. Two types of polymeric flocculants are described. The effects of radiation absorbed dose, radiation absorbed rate dose and chemical composition of the irradiated solutions upon the polymeric materials characteristics are also discussed. Preliminary results demonstrated that some polymeric flocculants characteristics, such as linearity and molecular weight were improved by using combined electron beam and microwave irradiation.

## 1 INTRODUCTION

Radiation research in the field of polymeric materials was developed over recent years at the Institute of Atomic Physics, with linacs of 6 MeV and output power in the range of 100 - 700 W. Thanks to remarkable properties of the electron beam technologies developed for our type of polymeric flocculants, it was proved that high energy linacs up to 10 MeV with modest electron beam power levels, from a few hundred to one kilowatt, such as our ALID-7 linac became economically attractive for commercial production [1-3].

## 2 RADIATION RESEARCH IN THE FIELD OF POLYMERIC FLOCCULANTS

During the period 1992-1996 a thorough study was made in the field of electron beam induced polymerisation of the aqueous solutions containing a mixture of appropriate monomers, initiators, complexing agents, chain transfer agents, in order to prepare polymeric flocculants for waste water treatment. First type of polymeric flocculant [1], a co-polymer of acrylamide and acrylic acid (PA type) was obtained by electron beam irradiation of an aqueous solution containing 40% total monomer concentration (90% acrylamide and 10% acrylic acid). The co-polymer of acrylamide and acrylic acid exhibits a very low toxicity, but a total conversion of acrylamide (a toxic monomer) cannot be obtained by any polymerisation method. Thus, we obtained the second type of polymeric flocculant, PV type, based on monomers without toxicity. PV is a co-polymer of acrylic acid and vinyl acetate, which was obtained into two variants, PV-10 and PV-30, by electron beam irradiation of aqueous solutions consisting of 10% TMC (8% acrylic acid and 2% acetate vinyl) and respectively, 30% TMC (24 % acrylic acid and 6 % acetate vinyl). For the PA and PV preparation our interest was focused on the basic characteristics optimisation, such as high flocculation capacity (high intrinsic viscosity or mean molecular weight) and high solubility (high linearity or low values for Haggins constant $k_H$ ) in order to obtain desired properties needed for waste water treatment. These characteristics can be improved if the chemical composition, absorbed dose (D) and absorbed dose rate (d) are controlled in certain fashion.

Preparation of the PA and PV type co-polymers depends on total monomer concentration (TMC), complexing agent concentration (CAC), chain transfer agent concentration (CTAC), initiator concentration (IC) as well as on the water presence in the system. It was proved by our research that the radicals originated from irradiated water have a predominant role on the radicals which come directly from the monomers irradiation. For an irradiated solution in which the water concentration decreases under 40% the conversion coefficient (CC) of the monomers decreases and in the case of the systems with very small water concentration, the polymerisation velocity suddenly decreases.

Fig.1 shows the graphical representation of some experimental results concerning the CC dependence versus TMC of an irradiated aqueous solution containing acrylic acid. As indicated in Fig.1, since TMC is nearly 100%, the conversion coefficient is only 10%. Irradiation over the level of the required dose leads to a crosslinking structure of the final products (become water insoluble) and an irradiation below the level of the required dose decreases CC and intrinsic viscosity (IV). High values for IV are desired because they provide a good flocculation capacity which means high flocculation velocity and small size of the sediment volume put down into a treated waste water. High values for the intrinsic viscosity or mean molecular weight are sometimes associate with a bad solubility of the PA and PV type co-polymers. The flocculation capacity (FC) was determined as the thickness of the sediment sets down, in the first 3 and 5 minutes, into a glass vessel containing 25 cm height aqueous solution of 4% diatomite concentration treated with 0.4mg/l or 1.2 mg/l polymeric flocculant concentration. Good FC means low values for the sediment thickness and high values for the sedimentation velocity.Fig.2 and Fig.3 show, respectively, the graphical representation of some experimental results concerning CC and IV dependence versus D for d = 0.8 kGy/min and for the following chemical composition of the PA type samples: 40% TMC, 0.5% CAC, 0.5% IC and 0.2% CTAC.

0-7803-4376-X/98 /$10.00 © 1998 IEEE

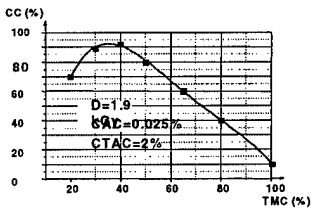



Fig.1

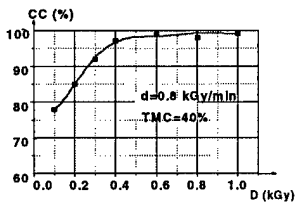



Fig.2

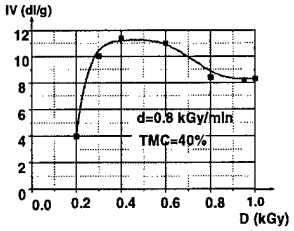



Fig.3

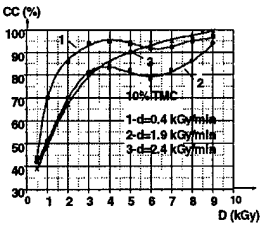



Fig.4

Fig.4 and Fig.5 show, respectively, the effect of D and d upon CC of the PV-10 and PV-30 type co-polymers. All PA samples irradiated over 1kGy, PV-10 probes over 9 kGy and PV-30 over 12 kGy have a crosslinked structure. The crosslinking effect can be controlled by CTAC. According to the above mentioned experimental results the main conclusions are:

-It is indicated to produce an over-irradiation controlled by CTAC then an irradiation below the level of the absorbed dose which makes lower values for CC;

-High values for CTAC overcome the crosslinked effect and provide for the polymeric samples a good solubility but lead to lower values for the intrinsic viscosity and sedimentation velocity. However, when level of D is nearly the proper dose (0.6-0.8 kGy) the required CTAC diminishes.

-CC, IV and FC exhibit optimal values in the ranges of 0.3 kGy to 1kGy for PA type and 3kGy to 9 kGy for PV type. These ranges as well as the size of optimum values are closely related to the chemical composition of the irradiated solution and absorbed dose rate level.

-Chemical composition of the irradiated solution and absorbed dose must be controlled and optimised in order to obtain both, high intrinsic viscosity and high linearity (Haggins constant $k_H < 0.5$) of the polymeric flocculants.

Unfortunately, neither optimised D nor optimized chemical composition are sufficient in all situations such as for high absorbed dose rate levels because of the strong dependence of the free-radical polymerisation on the radiation intensity. At high absorbed dose rates the free-radical polymerisation process is incomplete under irradiation period and continues after irradiation for an uncontrollable time period. Also, it is not possible to proceed a complete conversion of the monomers mixture. To investigate the influence of the dose rate on CC, IV and FC, special experiments have been performed in the last time.

Some of the results are already presented in Fig. 4 and Fig.5. Fig 6, Fig.7 and Fig.8 represent, respectively, the absorbed dose influence on the conversion coefficient, intrinsic viscosity and flocculation capacity for the PA type co-polymer. Fig.9 and Fig.10 show the influence of absorbed dose and absorbed dose rate on the flocculation capacity for the PV-10 type co-polymer and PV-30 type co-polymer, respectively.

The analysis of the experimental results concerning the influence of the absorbed dose rate level on the CC, IV and FC leads to the following conclusions:

-At high absorbed dose rates the conversion coefficient generally decreases, but this effect is strongly dependent on the chemical composition and absorbed dose level. For a proper chemical composition, D and should be so adjusted to provide a certain time for the polymerisation process: 0.5-1.5 minutes for the PA type and 3-4 minutes for the PV type.

-Intrinsic viscosity and flocculation capacity exhibit optimal values in the ranges of 0.3 kGy/min-1kGy/min for PA type and 0.4 kGy/min-2.4 kGy/min for PV type. These ranges as well as the size of the optimum values for IV and FC are closely related to the chemical composition of the irradiated solution (Fig.7) and absorbed dose level.

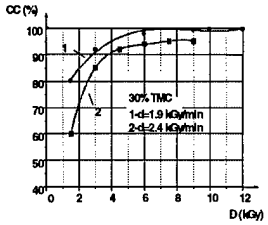



Fig.5

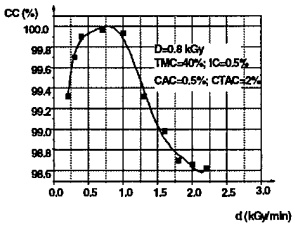



Fig.6

The PA type is used in aqueous solutions with a concentration of 0.05%-0.1% and PV type with a concentration of 0.5% - 1%. The PA type was used very efficiently for hydrometallurgy (porcelain earth) (100 g PA per 1000 kg of dry solid substance) without adding other inorganic flocculants. In other cases the PA and PV type co-polymers are used together with inorganic flocculants (aluminium sulphate or ferric chloride) but inorganic flocculants consumption may be reduced from 50% to 75%. Also, the sediment volume resulted by waste water treating with PA and PV type co-polymers was about 60% smaller than the sediment volume resulted by treating the same water with aluminium sulfate or ferric chloride only.

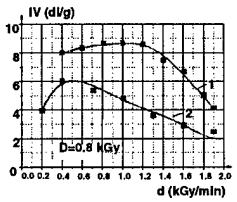



Fig.7 (1- 0.2%CTAC; 2- 2% CTAC)

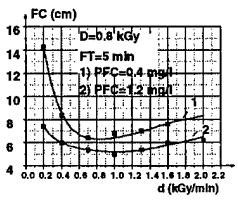



Fig.8 (FT=Flocculation Time)

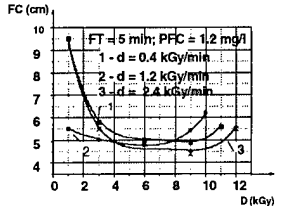



Fig.9

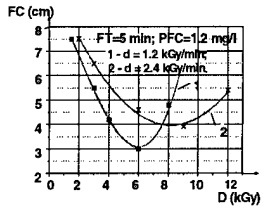



Fig.10

## 3 SIMULTANEOUS MICROWAVE AND ELECTRON BEAM TREATMENT APPLICATION IN THE FIELD OF POLYMERIC FLOCCULANTS

New results concerning the use of simultaneous microwave and accelerated electron beam irradiation for improving the polymeric flocculant characteristics are obtained. ALID-7 linac of 6 MeV and 0.7 kW, built in the Accelerator Laboratory from National Institute for Laser, Plasma and Radiation Physics, was completed by a specially designed reaction chamber to fulfill simultaneous electron beam and microwave irradiation. Comparative results on the preparation of acrylamide-acrylic acid co-polymer, used for wasted water treatment and obtained by classical heating, microwave heating, electron beam irradiation and simultaneous microwave and electron beam treatment, are shown in Table 1. These results are with regard to the conversion coefficient (CC), intrinsic viscosity (IV), mean molecular weight ($M_w$) and linearity (Haggins constant $K_H$) obtained by processing of the aqueous solutions containing an appropriate mixture of monomers (40% total monomer concentration: 90% acrylamide and 10% acryl acetate), initiators, complexing agents and chain transfer agents. As is shown in Table 2, IV (dl/g) and $M_w$ (a.m.u.) are improved by simultaneous 30 seconds irradiation with electron beam of 0.4 kGy and microwave power of 430 W.

## 4 CONCLUSIONS

Radiation research in the field of polymeric materials (polymeric flocculants) obtained by electron beam irradiation field proved that their characteristics can be controlled and optimized by three factors: absorbed dose, absorbed dose rate and chemical composition of irradiated aqueous solution containing a mixture of two appropriate monomers, complexing agents, chain transfer agents and initiators. These factors are very strong dependent on each other. Because of the dependence of the free-radical polymerisation mechanism on the absorbed dose rate, low intensity and high energy (up to 10 MeV) electron accelerators are favoured for giving the highest yield per unit dose for our types of polymeric materials.

## REFERENCES

1. Martin D. et al., Radiat.Phys.Chem.,Vol. 45, No 4, pp 615-621,1995.
2. Martin D. et al., Nucl.Instr.and Meth. in Phys.Res.B113(1996)106-109.
3. Martin D. et al., Progr.Colloid Polym.Sci.(1996)102, pp. 147-151.
4. Dragusin M.et.al., Progr.Colloid Polym.Sci.(1996)102, pp. 123-125

Table 1 : Comparative results concerning various methods of PA type preparation .

| Classical | | | | Microwave | | | | Electron Beam | | | | Simultaneous E.B. & microwave | | | |
|---|---|---|---|---|---|---|---|---|---|---|---|---|---|---|---|
| CC | IV | $\overline{M}_w$ | $K_H$ | CC | IV | $\overline{M}_w$ | $K_H$ | CC | IV | $\overline{M}_w$ | $K_H$ | CC | IV | $\overline{M}_w$ | $K_H$ |
| % | dl/g | x10$^6$ | - | % | dl/g | x10$^6$ | - | % | dl/g | x10$^6$ | - | % | dl/g | x10$^6$ | - |
| 95 | 2.7 | 0.62 | 0.65 | 95 | 3.8 | 1.14 | 0.42 | 98 | 8.5 | 4.67 | 0.88 | 98 | 12 | 8.55 | 0.35 |

Table 2: The effects of symultaneous electron beam and microwave treatment of PA and PV flocculants ($T_i$=irradiation time ;MWP=microwave power ; MW in atomic mass units)

| Sample | D | $T_i$ | MWP | TMC | I | CA | CTA | CC | IV | $M_W$ | $K_H$ |
|---|---|---|---|---|---|---|---|---|---|---|---|
| | kGy | sec | W | % | % | % | % | % | dl/g | x10$^6$ | - |
| PA | 0.66 | 68 | 430 | 40 | 0.3 | 0.1 | 0.2 | 93 | 12.5 | 9.81 | 0.4 |
| PA | 0.66 | 63 | 550 | 40 | 0.1 | 0.1 | 0.2 | 91 | 12.5 | 9.81 | 0.4 |
| PA | 0.4 | 30 | 430 | 40 | 2 | 0.1 | 0.2 | 95 | 17.5 | 16.6 | 0.1 |
| PA | 0.3 | 30 | 430 | 40 | 2 | 0.1 | 0.2 | 94 | 13.5 | 8 | 0.2 |
| PA | 0.4 | 60 | 430 | 40 | 0.1 | 0.1 | 0.2 | 77 | 13 | 9.84 | 0.3 |
| PV | 9 | 300 | 430 | 10 | 0.2 | 0.1 | 0.2 | 65 | 6 | - | 0.1 |
| PV | 5 | 180 | 430 | 30 | 0.2 | 0.1 | 0.4 | 81 | 10 | - | 0.1 |

# REALIGNMENT OF A DIVERGING ELECTRON BEAM: A NEW BEAM DELIVERY SYSTEM FOR RHODOTRONS

Y. Jongen, M. Abs, S. Zaremba, T. Delvigne and A. Herer
*Ion Beam Applications, Chemin du Cyclotron, 3, B-1348 Louvain-la-Neuve, Belgium*

*Abstract*

Industrially useful electron beams produced at 300 keV or more are typically generated by introducing an oscillating magnetic field near the apex of a triangular scanning horn, thus creating a diverging treatment field. Product dosing is then accomplished by conveying target material through this field. For many irradiation applications this diverging beam introduces inefficiencies in beam power utilization and dosing non-uniformity. This paper presents beam delivery systems developed by IBA for Rhodotron accelerators and, in particular, a new scan horn for delivery of a non-diverging beam.

## I INTRODUCTION

Rhodotrons are electron accelerators based on the principle of "re-circulating" a beam through successive diameters of a single coaxial cavity resonating in metric waves. The principle of operation of the Rhodotron has already been described in length in previous articles [1-6].

Three industrial Rhodotron models ranging from 35 kW to 200 kW beam power at 10 MeV are routinely manufactured at IBA's facilities in Louvain-la-Neuve, Belgium. The Rhodotron model "TT100" (10 MeV/35 kW) was especially developed by IBA in order to answer the market demand for a very compact accelerator system operating at 10 MeV and adapted to the sterilization of medical devices. In order to fulfil such industrial needs, a specific scan horn was recently developed, which allows to install both the accelerator cavity and the beam delivery system at the same level although the beam delivered to the product is non-diverging and oriented vertically. This paper focuses on the development of this new scan horn, which was tested at IBA and now is being installed at our customer's site in Italy.

## II STANDARD BEAM DELIVERY SYSTEM FOR RHODOTRONS

The Rhodotron technology offers two significant advantages that simplify the design of the beam delivery system:

- Since electrons are deflected many times during the acceleration process, the numerous bending magnets that are placed in serial act as a very selective energy filter. Therefore, energy distribution at the exit of the accelerator is extremely peaked around 10 MeV, which minimizes beam losses in the transport system (in particular, in the 90° bending magnet).
- Since the beam delivered by Rhodotrons is C.W. and not pulsed, dose distribution at the surface of the products can be insured even at high scan frequencies. This is of particular interest for low doses applications (such as food irradiation, or for the treatment of semi-conductors, etc.) where speed of the products conveyed under the beam is high. For such applications, pulsed accelerators show strong limitations or require sophisticated and energy consuming electronics in order to sweep rapidly the beam back and forth during each pulse.

Figure 1 is a schematic of the standard beam delivery system for Rhodotrons. This standard system is designed to deliver a vertical beam to a room located one floor below the accelerating cavity. The following components are installed successively along the beam line: a 90° bending magnet, a quadrupole for adjusting the dimensions of the beam trace, and a scanning magnet allowing the beam to be scanned across a 1 meter wide band. Associated scanning electronics drives the magnet in such a way that the beam trace moves at constant speed whatever the selected scan length (which is adjustable from 30% to 100% of the nominal value). Therefore, scan frequency increases as scan length decreases. A beam delivery horn with a metal (titanium) vacuum-to-atmosphere window is also part of the standard scope of supply. The complete beam delivery system can be connected to any exit around the cavity, typically for beam transport at energies between 3 MeV and 10 MeV.

This standard delivery system is currently used at very high power level (up to 190 kW at 10 MeV). It has proven excellent performances since uniformity of the dose delivered by the horn is better than 95% over 90% of the nominal scan length.

0-7803-4376-X/98/$10.00 © 1998 IEEE

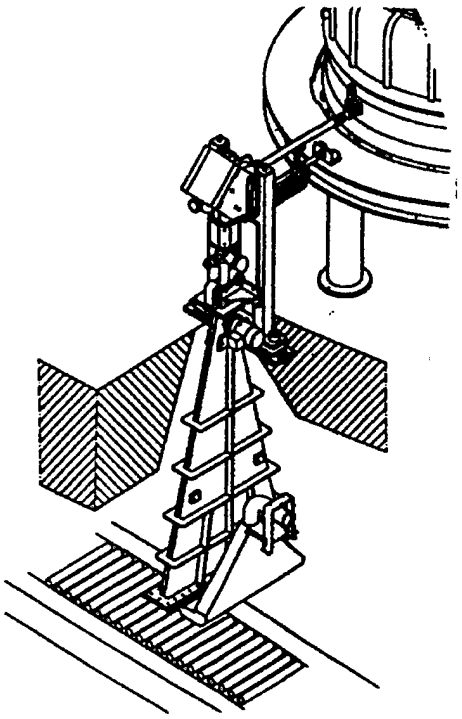


Figure 1: schematic of the standard beam delivery system for Rhodotrons

## III NON DIVERGING BEAM DELIVERY SYSTEMS FOR RHODOTRONS

Two new beam delivery configurations were recently developed by IBA in order to fulfil specific demands from our respectable customers.

The first configuration aims at providing a very high scan length. It uses a 2 meters horn placed horizontally and equipped with a non-diverging system. As this new concept is now being patented, it will not be presented in the present paper.

The second development offers some similarities with the IFSSM (Irradiation Field Shaping System with bending Magnet) that was presented at PAC93 by A.S. Ivanov [7] and applied to low and medium energy electron beams. The new development aimed at answering the industrial demand for a compact, high energy (10MeV) processing unit dedicated to the sterilization of medical devices. For high compactness, our choice consisted in developing a new beam delivery system that could be installed at the same level as the TT100 Rhodotron accelerator, although delivering a vertical beam to the product. A very compact scan horn was developed, that scans the beam before bending it downwards to the product. Scan length requirement was 800 ±10 mm, and trace width 30 ±10 mm. Another important parameter for designing this horn was the beam orthogonality with respect to the conveyor : 90 degrees ± 6 degrees, in order to insure uniformity of the dose across the whole scan length.

The magnet was designed and optimized taking into account limitations in geometrical dimensions, in weight, and in power consumption. OPERA-3D [8] was used to design the magnet and to determine the excitation current density - the latter was reduced in possible limits, while producing sufficient magnetic field for bending 10 MeV electrons. Poles of the selected magnet consist of two circular bars. The section of return yokes passing by the bending plane of the magnet is rectangular. These are encircled by coils of a racetrack shape. A part of the return yoke (between poles and coils) has a complex shape, which was necessary to the passage of the magnetic flux between lateral sides of the return yoke. Figure 2 presents trajectories of 10 MeV electrons in the scan horn. In the selected co-ordinate system the bending magnet is symmetrical with respect to the x-z plane.

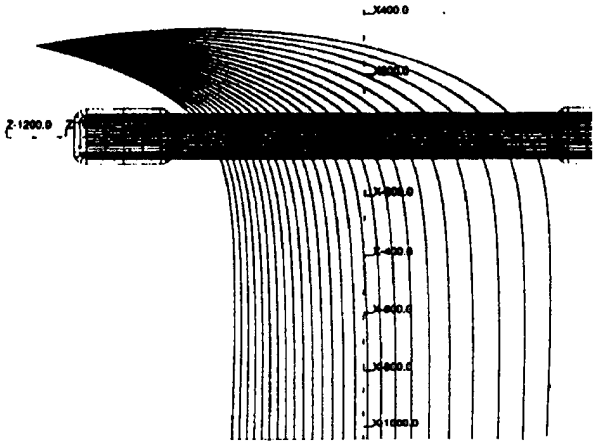


Figure 2: Trajectories of 10 MeV electrons in the non-diverging scan horn

Origin of the co-ordinate system is placed at the centre of the pole i.e. outer pole edges, coil and return yokes are at the same distance from the x-z plane. The starting point (x=300 mm, z=-1100 mm) corresponds to different scanning angles that vary between -14 degree and +10 degree with respect to the plane defined by equation x=300 mm. Positive sweeping angles are measured in the counter-clockwise direction from this plane. It is worth to notice that different trajectories are not equidistant, and their distance increases as scanning angle increases. This means that a complex function has to be generated in order to drive the scanning system in such a way that the beam is scanned uniformly onto the products. Our choice consisted in developing a function generator that uses the measured excitation current as a parameter that limits the scan length. A beam trace of 800 mm is obtained for sweeping angles between -11 degree and +8 degree. Figure 3 is the mechanical drawing of the scan horn now installed at our customer's site in Italy. The bending magnet is placed at the lower part of the horn, above the beam exit window. One can see the two excitation coils that are installed at both extremities of the magnet.

## IV CONCLUSION

Preliminary tests performed at IBA indicate an excellent correlation between theoretical simulations and experimental results obtained with this new scan horn.

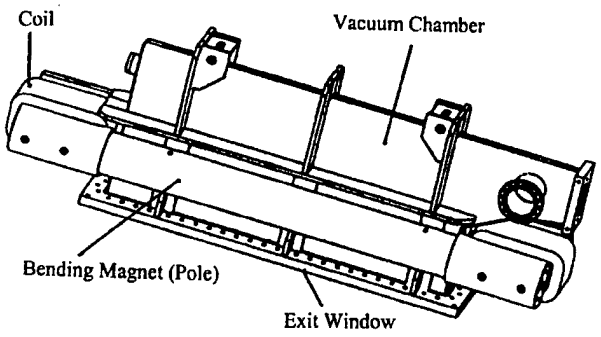



Figure 3 : mechanical drawing of the non-diverging scan horn

The new horn fulfills the initial requirements of designing a simple and compact beam delivery system that can be installed at the same level as the accelerator, and that delivers a non-diverging beam to the products, therefore maximizing beam utilization efficiency. Optimization of the function generated to supply the scanning magnet recently permitted to deliver a 95% homogeneous dose across 93% of the maximum scan length (which is 86 cm). As a next step, complementary dosimetric measurements have to be performed to better evaluate dose uniformity at various scan lengths (variable from 30 cm to 80 cm).

## REFERENCES

[1] Pottier, J. (1989), A new type of RF electron accelerator: the Rhodotron, Nuclear Instruments and Methods in Physics Research B 40/41, 943-945.

[2] Bassaler, J.M. et al. (1992), Rhodotron, an accelerator for industrial irradiation, Nuclear Instruments and Methods in Physics Research B68, 92-95.

[3] Jongen, Y. et al. (1992), The Rhodotron, a 10 MeV, 100 kW beam power metric waves, CW electron accelerator, presented at the 7th All-Union Conference on Applied Accelerators, June 16-18, St Petersburg (CIS).

[4] Abs, M. et al. (1992), The Rhodotron, a new electron accelerator for industrial use, presented at Radtech 92 - Boston (USA).

[5] Jongen, Y. et al. (1992), The Rhodotron, a new 10 MeV, 100 kW, CW metric wave electron accelerator, presented at the International Conference on the Application of Accelerators in Research and Industry, November 2-5, 1992 Denton (USA).

[6] Jongen, Y. et al. (1993), The Rhodotron, a new high-energy, high-power, CW electron accelerator, presented at ECAART 3, Orleans (France), August 31 - September 4, 1993.

[7] A.S. Ivanov, V.P. Ovchinnikov, M.P. Svinjin, N.G. Tolstun, "New Irradiation Field Shaping System for Industrial High Voltage Accelerators", Proceedings of PAC93, Washington, 17-20 May 1993.

[8] Vector Fields Limited, OPERA 3-D Reference Manual, 24 Bauleside, Kidlington, Oxford OX5 1JE, England.

# ELECTRON BEAM SCANNING SYSTEM

A.A. Zavadtsev, Moscow Radiotechnical Institute of Russian Academy of Sciences
132 Warshavskoe Road, Moscow, 113519 Russia

*Abstract*

The equipment for accelerated electron beam shaping in irradiation technology process is very important part of irradiation facility. This equipment determines permissible transverse and longitudinal sizes of irradiated object and dose distribution in irradiation field. The fan beam scanning system is widely and successfully used for commercial irradiation. But the use of this system has some limitations. The belt beam scanning system allows to increase the electron beam use efficiency and to shape arbitrary (for example, uniform) dose distribution. This system is especially useful for the high irradiation depth. The crossing beam scanning system allows to increase the dose penetration without electron beam energy increasing. This system is especially useful for the irradiation of object, if its depth is more or equal to its transverse size.

## 1 INTRODUCTION

The continuous extension of field of electron linear accelerators use in technological processes results in necessity of refinement of electron beam scanning systems for providing of needed dose distribution in the irradiation field. The fan beam scanning system (FBSS) with saw-toothed magnetic induction depending on time is the most used system now [1]. This system is widely and successfully used for commercial irradiation of various objects, for example, for industrial radiating sterilization of medical items and materials, such as syringes, blood transfusion packages, various electrodes, dressing and surgical packages. FBSS is effective for irradiation of thin objects, for example, various films. However, the irradiation efficiency decreases and irradiation unevenness along object depth increases, if the longitudinal sizes of object and distance to scanning magnet are comparable.

## 2 BELT BEAM SCANNING SYSTEM (BBSS)

### *2.1 Main Imperfections of FBSS*

The dose penetration $D(\tau\rho)$ inside the irradiated object depending on object depth measured at 5 MeV electron accelerator is illustrated by Fig.1 (curve 1), where $\rho$ is density of the irradiated object, $\tau$ is its depth, $D(0)=D(\tau_1\rho)$.

The whole object depth $\tau\rho$ is usually chosen as $\tau\rho=\tau_1\rho$ for guaranteeing of the uniform dose penetration (see Fig.1). The electron beam use efficiency decreases, if $\tau\rho<\tau_1\rho$. Let's introduce irradiation efficiency as

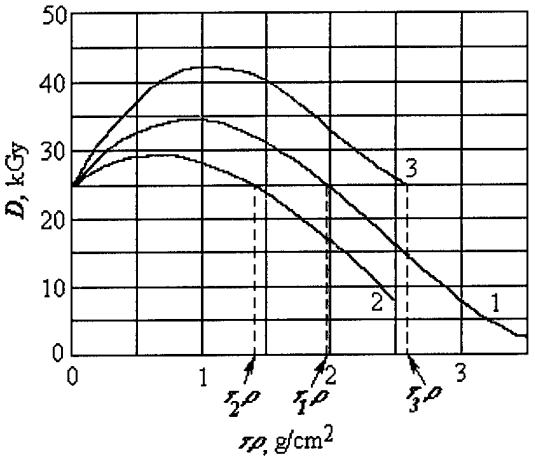



Figure: 1 The measured dose penetration inside the irradiated object.

$$\eta = \frac{\int \frac{dI}{d\varphi}\tau(\varphi)\rho d\varphi}{I\tau\rho} \qquad (1)$$

where $I$ is scanning beam current, $\varphi$ is scanning parameter (scanning angle for FBSS), $\tau(\varphi)$ is the irradiated object depth in the beam direction. For example, the irradiation efficiency $\eta$=60% for the FBSS irradiation of the object with equal depth and width $\tau$=0.3 m and the distance from scanning magnet to object surface $l$=0.43 m. The electron beam use is ineffective at the object edges (see Fig.2).

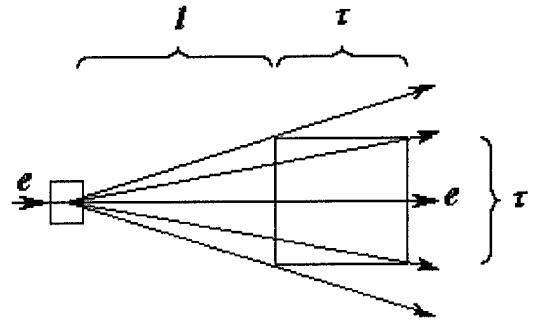



Figure: 2 Fan scanning beam irradiation scheme.

In addition the dose decreases proportionally to $1/Z$, where $Z$ - distance from scanning magnet center. The FBSS dose penetration is shown in Fig.1 (curve 2) for above mentioned parameters. The value $\tau_2\rho$ ($D(0)=D(\tau_2\rho)$) is 30% less then $\tau_1\rho$. This is equivalent to decreasing of electron energy to $W$=3,8 MeV.

0-7803-4376-X/98 /$10.00 © 1998 IEEE

*2.2 BBSS Construction*

The use of belt scanning beam (the electron trajectories are parallel to accelerator axis $Z$) is free of imperfections of FBSS. Really, ineffective scanning beam use at the edges of irradiated object and dose decreasing along axis $Z$ are absent in this case. The BBSS consists of two bending magnets, as it is shown in Fig.3, where 1 is coil, 2 is core, 3 is gap, 4 is pole.

*2.3 Magnet Pole Shape Calculation*

Let's assume that the magnetic induction depending on time in the first and second bending magnets are $B_1(t)$ è $B_2(t)$. The flying electron meets four boundaries of magnet poles. First and fourth boundaries are rectilinear. The shape of second and third boundaries are determined by parametric functions $(X_2(t),Z_2(t))$ è $(X_3(t),Z_3(t))$ in coordinates $(X,Z)$. Mentioned parameters are bound up with each other by following equations:

$$
\begin{aligned}
&-X_2(t)B_1(t)+X_3(t)B_2(t)=X_4(t)B_2(t)\\
&-Z_2(t)B_1(t)+Z_3(t)B_2(t)=Z_4B_2(t)\\
&\left[X_3(t)-X_2(t)\right]\left[\frac{W+W_0}{ceB_1(t)}-X_2(t)\right]=\\
&=Z_2(t)\left[Z_3(t)-Z_2(t)\right]\\
&Z_2^2(t)+\left[\frac{W+W_0}{ceB_1(t)}-X_2(t)\right]^2=\left[\frac{W+W_0}{ceB_1(t)}\right]^2
\end{aligned}
\qquad (2)
$$

where $c$ is light velocity, $e$ is electron charge, $W$ and $W_0$ are kinetic and rest energy of electron (J).

We may get needed dependence of beam deflection $X(t)$ from axis $Z$ on time $t$ choosing functions $(X_2(t),Z_2(t))$, $(X_3(t),Z_3(t))$, $\hat{A}_1(t)$ and $\hat{A}_2(t)$, in accordance with (2). Beam density and therefore dose rate are inversely proportional to derivative $dX(t)/dt$. In particular case, dose rate is uniform along $X$ axis, if $X(t)$ function is linear (saw-toothed). The magnet poles boundaries coordinates used in (2) are effective values taking into account magnetic field edge effects.

Thus this system allows to shape belt scanning electron beam with arbitrary (in particular, uniform) transverse distribution of dose.

Let's consider the BBSS example with uniform dose distribution along $X$ axis, $W$=5 MeV, $Z_4$=0.35 m, the beam width $2X_{4max}$=0.43 m, $\hat{A}_1(t)=-\hat{A}_2(t)$ (increases linearly (saw-toothed) from 0 to $\hat{A}_{max}$=0,15 Ò). The calculated profiled boundaries of magnet poles are shown in Fig.4.

The rectangular magnet poles are shown by dotted line in Fig.4 [2]. These poles allow to get the belt beam with the same values $2X_{4max}$, $\hat{A}_1(t)$, $\hat{A}_2(t)$ and $Z_4$. The dose distributions $D$ for profiled and $D_{11}$ for rectangular magnet poles are represented in Fig.4. The dose distribution $D$ for

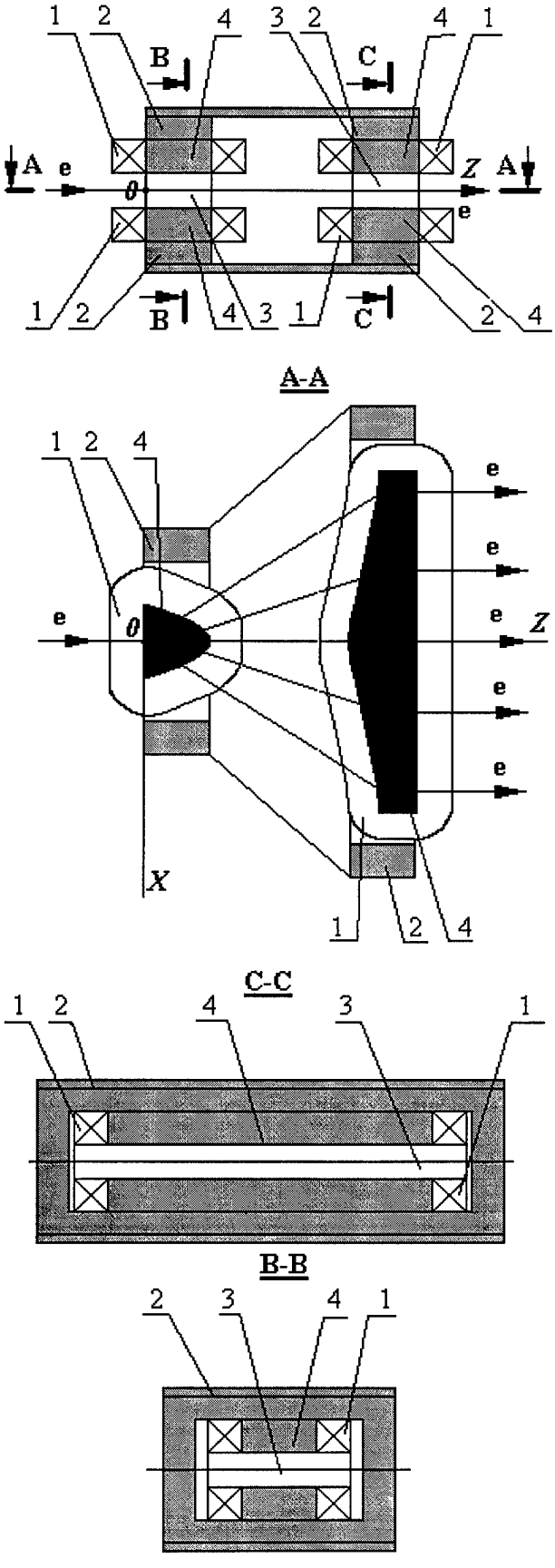



Figure: 3 Belt Beam Scanning System.

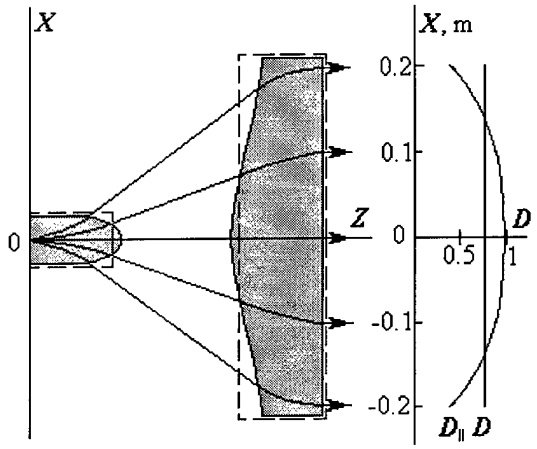



Figure: 4 The shapes of profiled and rectangular magnet poles and corresponding dose distributions $D$ and $D_{11}$.

profiled poles is uniform, but the dose $D_{11}$ decreases to 35% of axis value at the rectangular magnet poles edges.The equations (2) allow also to calculate functions $\hat{A}_1(t)$ and $\hat{A}_2(t)$ for rectangular magnet poles and uniform dose distribution.

## 3 HIGH DOSE PENETRATION SCANNING SYSTEM

It is possible to increase dose penetration without increasing of electron energy using crossing beam scanning system (CBSS). It is enough to add the profiled part 5 to second magnet pole of described above BBSS example, as it is shown in Fig.5.

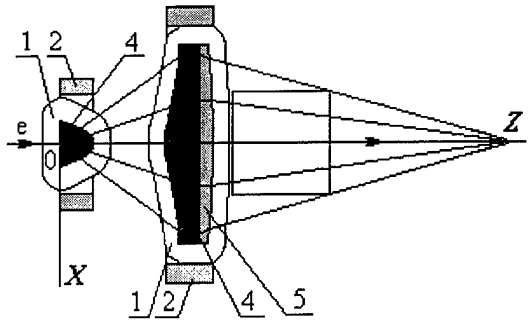



Figure: 5 Crossing beam scanning system.

The shape of additional profiled part of second magnet pole is determined by parametric functions $(X_5(t),Z_5(t))$, which may be found by equations (3), where $Z_0$ is the coordinate of crossover, $\alpha(t)$ is beam bending angle in the additional profiled part of pole.

The dose penetration depending on irradiation object depth $\tau\rho$ is shown in Fig.1 (curve 3) for maximum object depth 0.3 m, object width 0.3 m, $Z_0$=1,35 m and electron energy $W$=5 MeV. The dose penetration depth $\tau_3\rho$ ($D(0)=D(\tau_3\rho)$) is equivalent to dose penetration for electron energy $W$=7.5 MeV. The longitudinal size of additional profiled part of pole decreases from 38 mm at system axis to 31 mm at the system edges. The irradiation efficiency is $\eta$=85% in this case.

$$
\begin{aligned}
Z_0 &= Z_5(t) + \frac{X_5(t)}{tg\,\alpha(t)} \\
X_5(t) &= X_{4\,max}\frac{B(t)}{B_{max}} - \\
&- \frac{(W + W_0)(1 - \cos\alpha(t))}{ceB(t)} \\
\sin\alpha(t) &= \frac{(W + W_0)(Z_5(t) - Z_4)}{ceB(t)}
\end{aligned}
\qquad (3)
$$

## 4 CONCLUSION

The use of BBSS in the commercial irradiation allows to increase the electron beam use efficiency and to shape arbitrary dose distribution. The use of CBSS allows to increase the dose penetration without electron beam increasing.

## 5 ACKNOWLEDGEMENT

The author wishes to thank V.N.Kanunnikov and M.A.Alexeev for useful discussions during preparation of this paper.

## REFERENCES

[1] R.C.Becker, J.H.Bly, M.R.Cleland and J.P.Farrell, Accelerator Requirements for Electron Beam Processing, Radiat. Phys. Chem., Vol.14, 1979, pp.353-375.

[2] M.P.Svinin, Calculation and Design of High-Voltage Accelerators for Radiation Technology, - M.: Energoatomizdat, 1989 (in Russian).

# CYCLOTRON AUTORESONANCE ACCELERATOR FOR ELECTRON BEAM DRY SCRUBBING OF FLUE GASES*

J. L. Hirshfield[1,2] and Changbiao Wang[1]
[1]Physics Department, Yale University, New Haven, Connecticut 06520-1820
[2]Omega-P, Inc., 202008 Yale Station, New Haven, Connecticut 06520

*Abstract*

A self-scanning, highly-efficient electron beam source is being built for electron beam dry scrubbing (EBDS) of flue gases. The beam is to be prepared using cyclotron autoresonance acceleration (CARA), which has already experimentally demonstrated an rf efficiency above 90%. The design is based on simulation studies for a 250-kV, 25-A warm injected beam which is accelerated in a 112-cm long CARA using 21 MW of rf power at 2.856 GHz. The accelerated gyrating beam has an energy of nearly 1.1 MeV, with a theoretical acceleration efficiency of 99%. The beam can be extracted from CARA through a foil window, once the axial magnetic field is down-tapered to zero, and self-scan on a conical surface across a rising flue gas stream in a field-free region.

## 1 INTRODUCTION

Existing environmental anti-pollution regulations provide strong impetus for development of cost-effective technology to reduce acid rain through removal of sulfur and nitrogen oxides from flue gas releases to the atmosphere [1]. Limestone slurry scrubbing and selective catalytic reduction are the conventional technologies for flue gas cleanup [2]. An alternative technology, electron beam dry scrubbing (EBDS), was introduced in 1970, and subsequently demonstrated in several manifestations [3]. Perhaps lacking in encouraging EBDS deployment is the existence of a compact, low-cost electron beam source of high average power and high wall plug efficiency.

Cyclotron autoresonance acceleration (CARA) is an efficient process for converting rf energy into electron beam energy [4,5]. Based on existing rf source and electron gun technology, CARA can provide a high average power gyrating electron beam. Recent CARA experiments have shown that over 90% of the input rf power can be transferred to an electron beam [6]. The accelerated beam produced in CARA emerges on a gyrating trajectory; thus the beam is "self-scanning", requiring no other deflecting device or external field to sweep across a gas stream. It is this unique feature that makes CARA particularly suitable for EBDS, and perhaps other radiation chemistry applications.

An upgrade of the Yale/Omega-P CARA is being built that is designed to produce a 25 A, 0.8-1.2 MeV electron beam, using up to 20 MW of 2.856 GHz rf power and injection up to 300 kV. Here, analysis is presented underlying this design, using 250 kV injection.

## 2 BASIC PRINCIPLES

A comprehensive theoretical analysis of CARA with supporting particle simulation studies [5] has been carried out based on prior work [4]. The basic idea of such an accelerator is that a pencil electron beam from a convergent-flow Pierce gun is passed through a cylindrical waveguide. $TE_{11}$ rotating mode rf drive power energizes the beam by cyclotron autoresonance. The synchronous axial magnetic field for the interaction is given by

$$B_o = \frac{m_o}{e}\omega\gamma(1-n\beta_z), \tag{1}$$

where $\omega$ is the drive frequency, $e$ and $m_o$ are the electron's charge and rest mass, $\gamma$ is the relativistic energy factor, $\beta_z$ is the axial velocity normalized to the light speed $c$ in free space, and the index of refraction (normalized group velocity) for the $TE_{11}$ mode is $n = k_z c/\omega$, with $k_z$ the axial wave number. As $\nabla\cdot\mathbf{B}=0$ requires, the transverse magnetic field increases when the axial magnetic field increases, as the electron's acceleration energy increase: this reduces the electron's axial velocity towards stalling, as in the mirror effect. This imposes a maximum energy that can be reached in CARA, given by

$$\gamma_{\max} = \gamma_o + \left(\frac{\gamma_o^2-1}{1-n^2}\right)^{1/2}, \tag{2}$$

where $\gamma_o$ is the energy factor of the injected beam. The electron's gyration radius is constrained by the synchronous condition Eq. 1, which results in a maximum gyration radius, given by

$$\frac{r_{L\max}}{R_w} = \frac{1}{j'_{11}}\left[\frac{\left(\gamma_{\max}^2-1\right)\left(1-n^2\right)}{\left(\gamma_{\max}^2-1\right)\left(1-n^2\right)+1}\right]^{1/2} < 0.5431, \tag{3}$$

where $r_{L\max}$ is the maximum gyration radius, $R_w$ is the waveguide radius, and $j'_{11}=1.841184$ is the first root of the Bessel function derivative $J_1'(\chi)$. Eq. 3 states that the normalized gyration radius must be less than 0.5431 regardless of the beam's energy or the waveguide radius.

Solving Eq. 2 for $\gamma_o$, we obtain

$$\gamma_o = \frac{1}{n^2}\left\{\left[\gamma_{\max}^2(1-n^2)+n^2\right]^{1/2} - \gamma_{\max}(1-n^2)\right\}. \tag{4}$$

Eq. 4 is helpful in obtaining CARA design parameters. For a 1.0 MV, 25 A output electron beam,

* The work was supported by the U. S. Department of Energy, Divisions of High Energy Physics and Advanced Energy Projects.

0-7803-4376-X/98/$10.00 © 1998 IEEE

for example, when one sets $\gamma_{max} = 2.9569$, one finds $\gamma_o = 1.3896$, or an initial beam voltage of 199 kV. This is for $n = 0.7880$ ( $R_w = 5.0$ cm if the drive frequency is 2.856 GHz). An input drive power of 20 MW is required. In practice, the initial beam voltage should be larger than 199 kV (250 kV, for example), to not approach stalling.

## 3 SIMULATION RESULTS

Here we present simulation results for a CARA to show that existing rf source and electron gun technology can allow acceleration of a beam to about 1 MV, as needed for EBDS. In the simulation, a single-energy injected electron beam is assumed, with a guiding center spread of 10% and an rms axial velocity spread of 0.02%. This velocity spread value is scaled from that for the 100 kV gun now in operation on the Yale/Omega-P CARA. The number of computational particles is 128, with 8 values of velocity spread, 8 values of phase spread, and 2 values of guiding center spread. Simulation parameters are given in Table I.

TABLE I. Parameters in simulation.

| | |
|---|---|
| injection gun voltage | 250 kV |
| injector gun perveance | $0.2\times10^{-6}$ A – V$^{-3/2}$ |
| beam current | 25 A |
| rms axial velocity spread | 0.02% |
| beam guiding center spread | 10% |
| rf drive frequency | 2.856 GHz |
| rf drive power | 21 MW |
| guide magnetic field | < 1.8 kG |

The waveguide of the CARA operating in the rotating $TE_{11}$ mode consists of three sections. The first is an input rf coupler which has a radius of 3.3 cm and a length of 12 cm, the third has a radius of 5 cm and a length of 60 cm, and they are uniform. The second is a 40-cm long taper. The taper's slope is only 0.0425 (about 2.4 degrees), and wave reflection is ignored in the simulation. Following CARA, there is a 60-cm long drift region, where there is no rf field and the axial magnetic field is linearly tapered down to zero.

Fig. 1 shows the dependence of normalized average gyration radius $< r_L/R_w >$ on axial distance $z$ for the parameters in Table I, for comparison with the normalized maximum gyration radius $r_{L\max}/R_w$ calculated from Eq. 3, and maximum acceleration energy $\gamma_{max}$ from Eq. 2. For the first and third sections, the waveguide radius is uniform and $\gamma_{max}$ stays constant, with $\gamma_{max} = 2.6723$ in the former and $\gamma_{max} = 3.2817$ in the latter; for the second section, $\gamma_{max}$ increases as the radius increases. Clearly, it can be seen that the computed gyration radius $< r_L/R_w >$ is less than $r_{L\max}/R_w$ (<0.5431).

The rf input coupler is intended for use in common with a 20-GHz 7th harmonic co-generation experiment that requires a 3.3-cm radius waveguide [7]. From Fig. 1 we see that the maximum acceleration energy for 3.3 cm is only 855 kV ($\gamma_{max} = 2.6723$) for the 250 kV injected beam, which is marginally low to be suitable for an EBDS CARA. The waveguide taper is designed to increase the maximum acceleration energy by increasing the radius from 3.3 cm to 5.0 cm. This allows the maximum acceleration energy at the end of CARA to reach 1166 kV ($\gamma_{max} = 3.2817$).

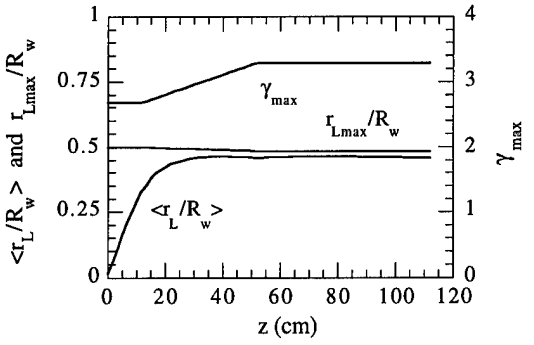



Figure 1: Average gyration radius $< r_L/R_w >$, maximum gyration radius $r_{L\max}/R_w$, and maximum acceleration energy $\gamma_{max}$ versus axial distance $z$.

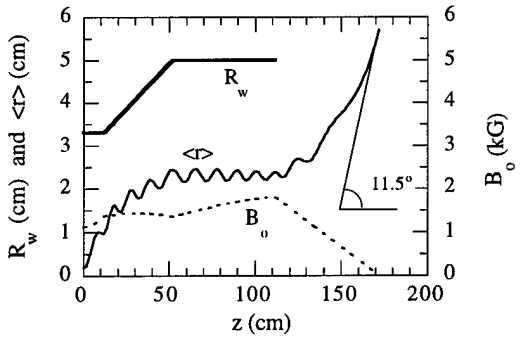



Figure 2: Waveguide radius $R_w$, electron's average radial coordinate $< r >$, and axial magnetic field $B_o$ versus $z$.

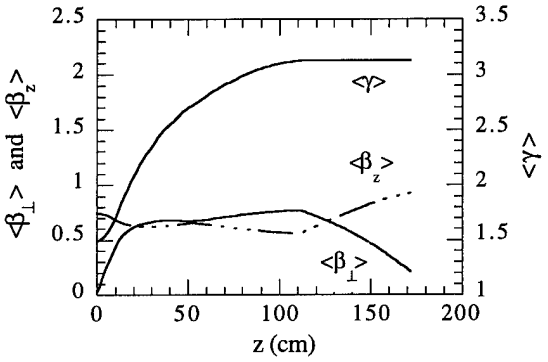



Figure 3: Dependence of normalized average transverse velocity $< \beta_\perp >$ and axial velocity $< \beta_z >$, and relativistic energy factor $< \gamma >$ on axial distance $z$.

Fig. 2 shows the dependence of waveguide radius $R_w$, electron's average radial coordinate $< r >$, and axial magnetic field $B_o$ on axial distance $z$, while Fig. 3 shows the dependence of normalized average transverse

velocity $<\beta_\perp>$ and axial velocity $<\beta_z>$, and relativistic energy factor $<\gamma>$ on axial distance $z$. In the first section ($z = 0 \sim 12$ cm), the transverse velocity and radial coordinate rapidly increase after the beam gets trapped. The axial magnetic field also increases as the beam energy increases. In the second section ($z = 12 \sim 52$ cm), the magnetic field changes very little although the beam energy goes up fast. That is because increase of refractive index balances increase of beam energy as the waveguide radius gets larger, which can be seen from Eq. 1. In the third section ($z = 52 \sim 112$ cm), the average radial coordinate $<r>$ does not go up but oscillates while the beam energy keeps increasing, with a maximum voltage of 1.085 MV at the end. The oscillation results from the deviation of guiding centers of electrons which have a nearly constant gyration radius (see Fig. 1). In the drift section ($z = 112 \sim 172$ cm), the axial velocity increases and the transverse velocity decreases, holding constant the adiabatic invariant $\beta_\perp^2/B_o$ when $B_o > 600$ G. When $B_o < 600$ G ($z > 152$ cm), the adiabatic condition begins to be violated. Finally, the "self-scanning" electron beam leaves the drift region with $<\beta_\perp> = 0.2055$ and $<\beta_z> = 0.9244$, with a scanning cone angle of about 11.5 degrees, as shown in Fig. 2.

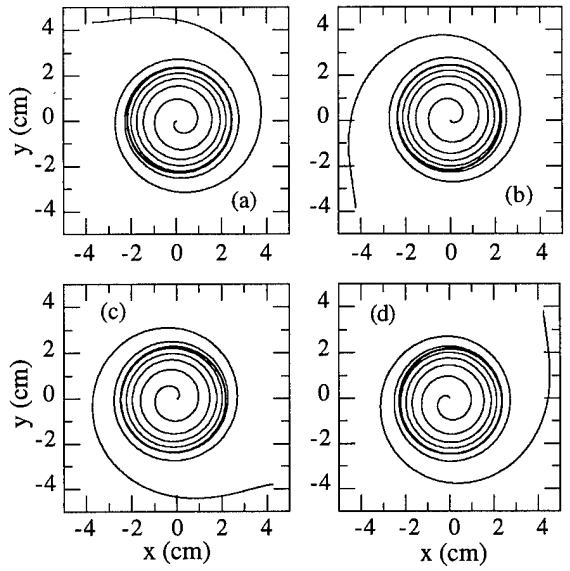



Figure 4: Orbits on the $x-y$ plane for four sample particles with different initial phases.

The feature of "self-scanning" of the beam emerging from CARA is shown in Fig. 4, with orbits in the $x-y$ plane for four sample particles with relative initial time-phases of 0 (a), $\pi/2$ (b), $\pi$ (c), and $3\pi/2$ (d) respectively. Several orbit turns overlap after the electrons enter CARA, in making a few revolutions. On the overlapped orbits, the gyration radius is almost the same, as mentioned previously. Then the electrons pass into the drift region and their radial coordinates get larger and larger as the magnetic field gets weaker and weaker.

Fig. 5 shows the dependence of electron beam power $P_b$ and rf drive power $P_{rf}$ on axial distance $z$. It is seen that 21-MW drive power at 2.856 GHz is decreased down to 90 kW at the end of CARA, while the beam power is increased from 6.25 MW to 27.125 MW, with an rf conversion efficiency of over 99%. The wall loss is seen to be minuscule, just 35 kW, since CARA operates at a relatively low drive frequency.

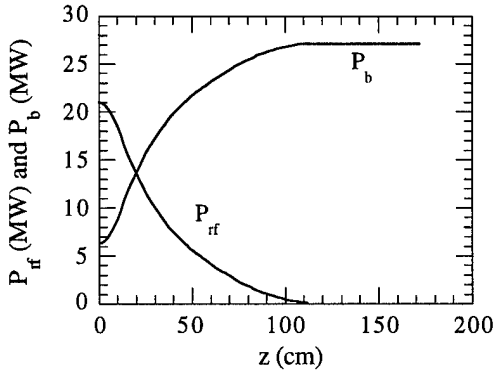



Figure 5: Dependence of electron beam power $P_b$ and rf drive power $P_{rf}$ on axial distance $z$.

## 4 CONCLUSIONS

Simulations have shown that a 250-kV, 6.25-MW electron beam can be accelerated up to a 1.08 MV, 27 MW "self-scanning" beam by the CARA, with an rf conversion efficiency of over 99%. Stanford Linear Collider (SLC) 65 MW, 2.856 GHz klystrons have 3.5 $\mu s$ pulse width and 180 $sec^{-1}$ pulse repetition rates [8]. From this simulation, it can be expected that two SLC klystrons driving a future CARA with a 250-kV, 40-MW injected beam should allow generation of a beam suitable for EBDS with average power approaching 100 kW.

## 5 REFERENCES


[1] See, for example, *Radiation Physics and Chemistry* **24**, 1-201 (1984).

[2] *Radiation for a Clean Environment*, IAEA, Vienna (1975).

[3] R. J. Woods and A. K. Pikaev, *Applied Radiation Chemistry: Radiation Processing* (Wiley, New York, 1994); J. W. T. Spinks and R. J. Woods, *An Introduction to Radiation Chemistry*, 3rd ed. (wiley, New York, 1990).

[4] B. Hafizi, P. Sprangle, and J. L. Hirshfield, *Phys. Rev.* E **50**, 3077 (1994).

[5] C. Wang and J. L. Hirshfield, *Phys. Rev.* E **51**, 2456 (1995).

[6] M. A. LaPointe, R. B. Yoder, C. Wang, A. K. Ganguly, and J. L. Hirshfield, *Phys. Rev. Lett.* **76**, 2718 (1996).

[7] C. Wang, J. L. Hirshfield, and A. K. Ganguly, in this proceedings.

[8] G. Caryotakis, *IEEE Trans. Plasma Sci.* **PS-22**, 683 (1994).

# EFFECTIVE X-RAY BREMSSTRAHLUNG SOURCE
# (Is it possible to handle quality of the X-ray bremsstrahlung?)

V.K.Grishin, B.S.Ishkhanov, S.P.Likhachev, D.A.Rodionov,
V.I.Shvedunov, Institute of Nuclear Physics of Moscow State University, Moscow 119899

*Abstract*

The efficiency of new nontraditional scheme for generating bremsstrahlung is studied by means of computer simulation. In this scheme the electron beam multiply crosses a thin target due to the presence of special focusing magnetic field [1]. It is showed that one could expect more than two times increasing of the radiation yield power.

## 1 NEW SCHEME OF EFFECTIVE BREMSSTRAHLUNG SOURCE

The X-ray radiation is widely used in various fields of fundamental and applied studies [2]. The mostly widespread X-ray source is based on the generation of hard electromagnetic radiation by hitting the bremsstrahlung target with the beam of accelerated electrons. Unfortunately, the efficiency of the translation of the electrons energy into the X-ray radiation yield is very low. Hence if the electron beam energy is $E_0$=1-5 MeV then radiation yield does not exceed 3-8% of the energy of the beam of electrons [3,4].

But analysis shows that the electron energy lost to produce bremsstrahlung is about 3 times more than corresponding radiation yield from the target (Fig. 1). Hence a significant portion of the electromagnetic radiation generated is absorbed in the bremsstrahlung target.

A new nontraditional scheme of the generation of bremsstrahlung is proposed in [1]. This method allows to expect a considerable growth of the photons yield. The scheme is based on the multiple crossing of the thin target by the electron beam. The self-absorption of the generated radiation is not intensive in a thin target. But if the total (summarized) thickness of the multiply crossed target is comparable to the thickness of usual one then the total yield is considerably higher.

The scheme with the multiple crossing of the target by electrons can be developed in various layouts dependently on the parameters of an accelerator and on the way of using bremsstrahlung.

One of the schemes is shown on Fig. 2. Here electrons cross the target, loss a certain part of their energy and then due to the presence of magnetic field they turn back to the target and produce the radiation again.

Accordingly to the estimations presented in [1] the energy yield of the radiation after multiple crossing is 2 - 4 times (in various ranges of the photons energy) more than the one in traditional way.

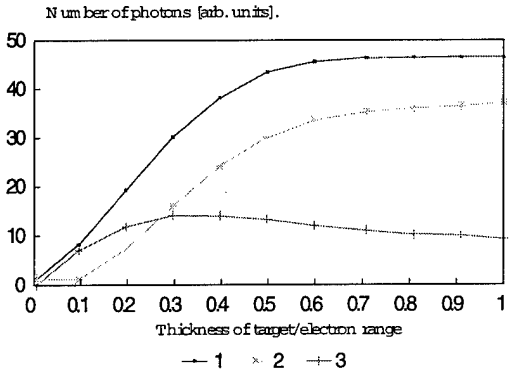



Fig. 1 1- the total number of X-ray photons produced in W-target with depth, 2- the number of X-ray photons absorbed with depth, 3 - the number of surviving X-ray photons.

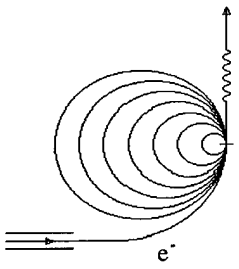



Fig. 2. Efficient X-ray source.

## 2 METHODS OF THE STUDY. GEANT-SIMULATION

In present work as well as in preceded paper [5] analysis of efficiency of the scheme proposed has been carried out by means of computer simulation. The FORTRAN program using the GEANT 3.15 library routines [6] has been developed to simulate the bremsstrahlung generation.

This program library is designed for simulation of various experiments on nuclear and high energy physics by using the Monte-Carlo technique.

The results of the calculations performed in [5] show that applying the homogeneous magnetic field leads to the rise of the efficiency but at the same time there is a possibility to loose the particles due to the scattering. Therefore it is necessary to use a focusing field.

0-7803-4376-X/98/$10.00 © 1998 IEEE

The results presented were obtained for the axial symmetric magnetic field from conical poles. In the first approximation the fields are

$$B = \frac{B_0 Y_0}{\alpha R},$$

$$B_x = -B\frac{xy}{R^2 r},\ B_y = -B\sqrt{1 - y^2/R^2},\ B_z = -B\frac{zy}{R^2 r}$$

where: $R = \sqrt{y^2 + (r+\Delta)^2}$, $r = \sqrt{z^2 + x^2}$, and

$$\Delta \cong \frac{Y_0}{tg\alpha}\cdot\frac{a}{r} \text{ at } r<a,\ \Delta \cong \frac{Y_0}{tg\alpha} \text{ at } r>a.$$

The target is in the XY plane. The beam passes along the Z axis.

## 3 DISCUSSION OF THE RESULTS. IT IS POSSIBLE TO HANDLE QUALITY OF X-RAY BREMSSTRAHLUNG?

The efficiencies of the radiation production for the initial electrons energies 5 MeV were calculated. The results are presented on Figs. 3 -7.

Fig. 3 shows that the particles are well focused (different values for the $\alpha$ angle of the conical poles from 10 to 60 degrees were tested).

On Figs. 4-7 one can see that the efficiency of the bremsstrahlung source is really higher than the one in traditional scheme though the configuration used is far from the optimum.

Besides the fact that the X-ray spectrum changes because of the high contribution from the low energy photons is of great importance for various application.

And at last using the optimal focusing gives the possibility to reduce the divergence of the generated X-ray flow because in optimal case the particles return perpendicularly on the target. Hence the new bremsstrahlung source proposed allows to obtain the intensive radiation in narrow angle.

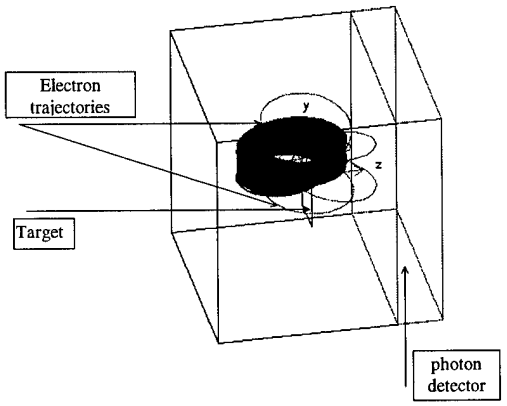



Fig 3. Trajectories of electrons in axial-symmetric magnet field, setup box is 100x100x100 cm$^3$ (big gap)

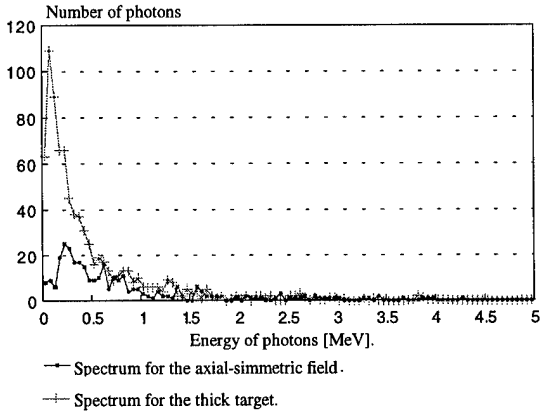



Fig. 4 Spectra for the axial-symmetric magnet field (for the thin target 0.1 free path length) and for the thick target (0.5 free path length). Incident electrons energy 5 MeV, initial electrons number 1000 (big gap).

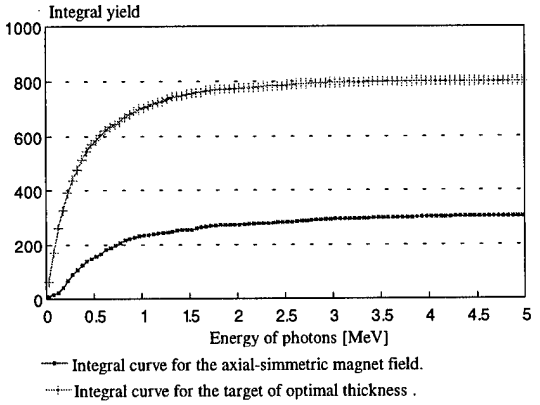



Fig. 5 Integral characteristics for thin target in the axial-symmetric magnet field and for the targets of optimal thickness. Incident electrons energy 5 MeV, initial number of the electrons 1000 (big gap).

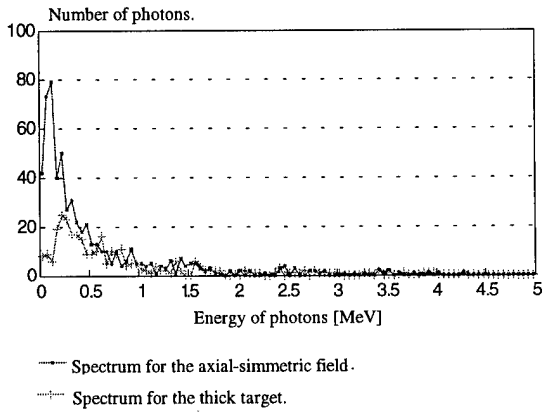



Fig. 6 Spectra for a thin target (of 0.1 free path length) in the axial-symmetric magnet field and for the thick target (0.5 free path length). Incident electrons energy 5 MeV, initial electrons number 1000, setup box is 100x40x100 cm$^3$ (small gap).

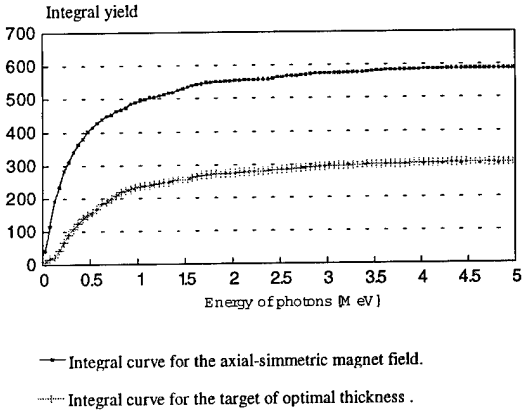



Fig. 7 Integral characteristics for the axial-symmetric magnet field and for the targets of optimal thickness. Incident electrons energy 5 MeV, initial number of the electrons 1000, setup box is 100x40x100 $cm^3$ (small gap).

## 4 ACKNOWLEDGMENTS

The authors would like to thank professor of the Virginia Tech. Peter Trower for very fruitful discussions.

## REFERENCES

[1] V.K. Grishin, B.S. Ishkhanov, and V.I. Shvedunov., Effective Source of Bremsstrahlung with Multiple Crossing Thin Target by Electron Beam, Vestnic Moscovskogo Universiteta, **37** (1996) 83.

[2] B.S. Ishkhanov, I.M. Kapitonov " The interaction of electromagnetic radiation with atomic core", Moscow, Izdatelstvo Moscovskogo Universiteta (MSU Publisher company), 1979, p. 215

[3] M.J. Berger and S.M. Seltzer, Bremsstrahlung and Photoneutrones from Thick Tungsten and Tantalum Targets, Phys. Rev. **C2** (1970) 621.

[4] D.J.S. Findlay, Applications of photonuclear reaction, Nucl. Instrum. Meth. B50 (1990) 314.

[5] V.K.Grishin, B.S .Ishkhanov, S.P.Likhachev, D.A.Rodionov, V.I.Shvedunov, A high efficiency {-ray bremsstrahlung source. Proceeding of 14-th International Conference on the Application of Accelerators in Research & Industry, Denton, 1996 (to be published).

[6] R. Brun, F. Bruyant, M. Maire, A.C. McPherson, and P. Zanarini, **GEANT3** (User's Guide), DATA HANDLING DIVISION, DD/EE/84-1, 1987.

# SMALL-SIZED ELECTRON LINEAR RF ACCELERATOR WITH BEAM AUTOACCELERATION FOR GEOLOGY AND INDUSTRY

B.Yu.Bogdanovich, V.I.Kaminsky, V.A.Senyukov and A.V.Nesterovich,
Moscow State Physical-Engineering Institute (Technical University), Moscow, Russia.

*Abstract*

The paper deals with the project of a small-sized electron linear RF accelerator with a beam energy up to 1 MeV, intended for use in bore holes for geological purposes. The application of autoacceleration method allows to exclude a high-frequency generator and therefore essentially reduce the installation dimensions. A single electron beam generates RF power at the initial part of the accelerating structure, and at other — longer — part this RF power is used for acceleration of a small part of this beam. For RF-power generated at 3.5 - 4.5 GHz frequency band the accelerating structure diameter (for iris-loaded waveguide) can be about 70-90 mm or less. A high voltage pulses (10-20 kV) are required for this accelerator operation. This pulses can be supplied with the help of cable, the length of which can be reasonably large. Such accelerator can be used for other purposes, as well, where the special requirements to a system dimensions occurs, and may be designed for exploitation in mobile (on a automobile) or portable variants.

The main purpose of the electron linac suggested in this paper is using for geological prospecting in bore holes. However such accelerator can find wide application for other purposes, where small dimensions of unit are required. The necessity of the accelerator work inside a bore holes imposes the specific requirements for its parameters and, first of all, on its overall dimensions. The accelerator's diameter, including all its auxiliary systems, should not exceed 70-80 mm at whole length up to 2 m. The accelerator should create an electron beam with energy about 0.5-1 MeV at average current ~1 μA. Any special requirements to power spectrum of a beam or its sizes are not declared. The accelerator from an external source can be feed by direct or pulse voltage up to 20 kV. Therefore it is desirable, that all systems of the accelerator should use voltages not higher that this one.

Now in geological prospecting for research of chisel chinks the direct action accelerators with voltage up to 500 kV are applied. The usage of higher voltage in specified dimensions is practically impossible. More over, such voltages can be received only during very short pulses (up to 100 ns). Such duration of pulses appear to be not enough for normal work of the measuring equipment. The more acceptable parameters of an accelerated beam can be received using linear resonant electron accelerator. A main problem at such accelerator design is creation a proper accelerating structure and forming an accelerating RF wave with necessary power. The problem is that there are no any serial sources of RF power (generators or amplifiers) with output pulse power levels about 100-150 kW and appropriate dimensions. On the other hand, the RF power source cannot be dislocated on surface, also. At large depths of immersing (some hundreds meters) the real attenuation of RF power in any transfer line will be so large, that a source with output power on some orders more, than it is necessary for acceleration, is required. Hence, the construction of the electron resonant accelerator under standard circuit with an external RF source is rather inconvenient.

One of possible ways of this problem decision is a creation of the accelerator with an electron beam auto-acceleration [1]. It's expediently to use autoacceleration of previously bunched beam for increasing such accelerator general efficiency. Actually in such accelerator the functions of particle injector and RF source are combined. The general configuration of such accelerator is shown on fig.1.

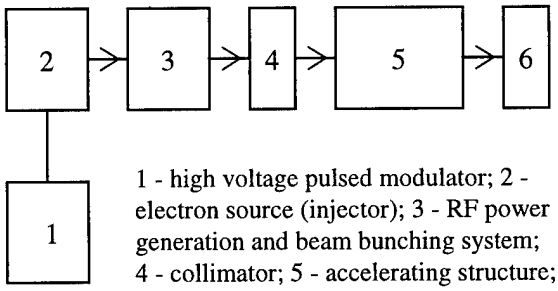



Fig.1. The general configuration of the electron accelerator with bunched beam autoacceleration.

The choice of accelerating structure type and working frequency band of accelerating wave is of great importance for limited transverse sizes accelerator design. As a separate RF source (generator or amplifier) usage in designed accelerator is not supposed, the appropriate RF frequency band choice is not limited by the nomenclature of industrial fabricated RF devices. Therefore operating frequency band can be chosen from following reasons. On the one hand, with reduction of RF frequency a power losses in RF elements (in particular, in accelerating structure) decrease. Besides the requirements for accelerating structure manufacturing and setup admissions are reduced for such frequencies also. It may be important for the accelerator cost reduction and for expansion of the

0-7803-4376-X/98/$10.00 © 1998 IEEE

accelerator possible use areas. In this case it can be applied in wider temperature range (that represents the special interest for work in chinks on large depths), and in adverse mechanical influence conditions (vibration, impacts) also. On the other hand, an accelerating field frequency increase permits to reduce the transverse sizes of accelerating structure and, hence, to apply more simple and cheap structure types, for example, iris loaded waveguide (ILW). Thus, the choice of an accelerating structure particular type is a compromise between two requirements mentioned.

Accelerating structures of both types (with running or standing waves) can be used here. As accelerating structure with running waves the ILW can be applied. The accelerating structure external diameter may be about 70-80 mm for accelerating field frequency band 3.5-4.5 GHz. Real values of such structure shunt impedance are at range of 35-40 MΩ/m at attenuation factor about 0.1 $m^{-1}$. Such section application will allow to receive an accelerated electron beam with energy ~1 MeV at length 1 m and RF wave power 140 kW (as the accelerated current value is rather small, one can neglect the current loading effects). The accelerating structures with standing waves are seemed to be more effective. As a standing wave structure the byperiodic accelerating structures (BAS) can be used. The transverse sizes of such structures can be the same, as of the ILW, but they can provide much higher values of shunt impedance, the real values of which are about 60-70 MΩ/m. The equivalent accelerating voltage in such structure $U$ can be estimated by the following expression [2]:

$$U = \sqrt{\frac{2\alpha R_{sh} P_o}{1 - e^{-4\alpha L}}} \cdot \frac{1 - e^{-\alpha L}}{\alpha} \qquad (1)$$

where $\alpha$ - attenuation in accelerating section; $R_{sh}$ - the section shunt impedance; $P_0$ - RF wave power at the accelerating section entrance; $L$ - accelerating section length.

The diagrams of accelerating voltage $U$ dependence on the accelerating section length $L$ for some values of RF wave input power $P_0$ are shown at fig.2.

According to diagrams given the necessary values of accelerating wave power and the section lengths for BAS type standing waves structures are appreciably lower, than that for the running waves structures. So, for structures 0.5-0.6 m long the necessary values of input power is of order of 50-60 kW for 1 MeV beam energy. And a 0.5 MeV beam can be received at RF power about 15-17 kW. It permits to appreciably simplify an initial — generator and beam bunching — part of the accelerator. It is important to note, that in general case the BAS type structure cost is larger than ILW one. However, for this accelerator, where during the entire acceleration process electron beam is not strongly relativistic, the BAS and ILW costs, obviously, will not differ essentially, since

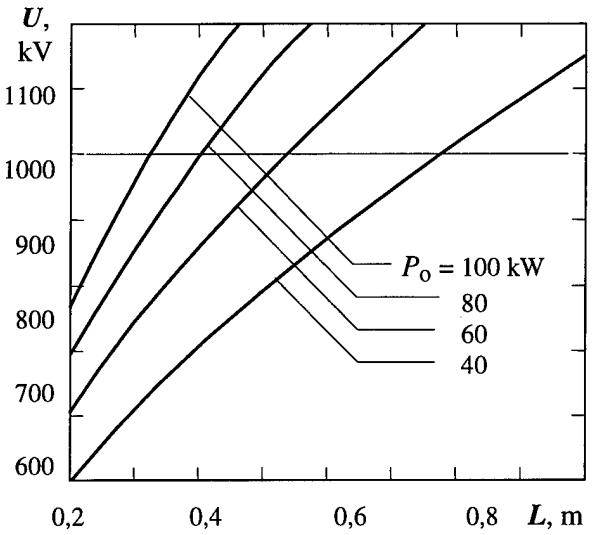



Fig.2. The equivalent accelerating voltage $U$ dependence on the accelerating section length $L$ for some values of RF wave input power $P_0$ ($\alpha = 0.1$ $m^{-1}$ ; $R_{sh} = 60$ MΩ/m).

application of structures with variable parameters through out a section are necessary in both cases.

Other important part of such accelerator is a primer part, where the RF power generation and beam bunching processes are taking places. The most simple and cheap, but at the same time rather effective, way of RF power generation with simultaneous beam bunching is usage of a klystron type device. The device efficiency, that can be really achieved, is about 30-35%. This is quite acceptable. So necessary initial electron beam pulse power should be at the range from 50 to 200 kW (with duty factor about 0.001). For anode voltage of 20 kV beam current should be within 2.5-10 A. This values are perfectly real. For the system dimensions reduction the beam focusing system energy consumption decrease the beam focusing field can be formed by constant magnets, located between transient resonators. Though in some cases focusing coils can be used as well. For large beam currents (up to 10 A) a multibeam system can be used. In this case a number of beams (7-10) with currents of 0.8-1.0 A each are used instead of single one. It does not practically require any changing of focusing system, but permits to increase beam with resonators interaction efficiency. The account of this accelerator part can be made on standard methods for klystron amplifiers [3]. As the electron energy in generating part of the accelerator is rather small, an effective enough particles bunching can be received for this part 30-40 cm long and one or two transient resonators. A feedback line connecting the output and bunching resonators is used for creation an auto generation conditions in this klystron system. For example, this line can be the coaxial type, as operating power levels are about tens-hundreds watts for klystron system amplification of the order 30 dB. A processed

electron beam from the output resonator passes through the collimator, which also plays a role of a collector, as absorbs a larger part of electron beam. For this reason it must be bulky enough and requires a coercive cooling (internal or external). Also the bulky collector reduces the bremsstrahlung formed by electron beam, which in number of cases can cause some difficulties in accelerating structure operation [4].

An additional advantage of such system is that a traditional element of accelerating structures - a wave type transformer is excluded. In common case such device is necessary because the RF wave types in feeding waveguides and accelerating section are different. Here the output resonator of RF source and accelerating structure operates with the same wave type that is $E_{01}$. Into accelerating section RF wave is transferred through coupling aperture (or apertures) connecting the generator output resonator and the first cell of accelerating structure.

As it was already mentioned, the accelerated current should be not higher then 1-10 mA. This value is rather small from the points of view of current loading effects and beam focusing requirements either. Therefore it is not supposed to use any special focusing devices in accelerating structure.

One more important question deals with accelerator inside volume vacuum pumping. Because of accelerator sizes limitation its practically impossible to perform a necessary vacuum pumping using traditional systems. A completely enclosed system with getter pumping like those used in small power electronic devices or system with small-sized pumps with discharge in magnetic field usually applied in powerful electronic devices (with possibility of external initial vacuum pumping) can be used here. The first variant is cheaper and at small initial electron beam power will posses an operation during several hundreds of hours. In many cases its quite enough for bore holes research, but assumes rather low cost of all installation. The second variant seems to be more real. Here during the accelerator work vacuum pumping is carried out with the help of internal pump, and after certain operation period the initial vacuum (if needed) and the high vacuum pumping are carried out by external vacuum units. Thus restoration of the internal pump is possible. Such system is a little bit more complex, but permits more effective accelerator usage, especially, if its cost appears to be high enough.

Thus, according the analysis been made the general scheme of the accelerator can be presented as following (see fig.3). The accelerator consists of the following main elements: the electron source (electron injector) with pulse current within 2.5-10 A (single- or multibeam), the bunching resonator, drift channel with a number of transient resonators and a beam focusing system, the output resonator, a feedback line between the bunching (input) and output resonators, the collimator with coupling apertures, the accelerating structure (probably a BAS type) and the output device (target). General length of such accelerator will be about 1 meter at gross weight ~20-25 kg, certainly, with external power supply unit dimensions and weight not taking into account. On tentative estimations the cost of such accelerator can be about k$100.0-150.0 for single unit and about k$50.0-100.0 or less if fabricating in series.

## REFERENCES


[1] B.Yu.Bogdanovich, N.M.Gavrilov and A.V.Shalnov. `Uskoritely s nakopleniem i generatsiey vysoko-chastotnoy energiy', Moskva, Energoatomizdat, 1991 (in russian).

[2] A.N.Lebedev and A.V.Shalnov. 'Osnovy fiziky i techniky uskoriteley', Moskva, Energoatomizdat, 1991 (in russian).

[3] A.N.Lebedev. 'Technika i pribory SVCh', Vol.2, Moskva, Vyshaya Shkola, 1970 (in russian).

[4] B.Yu. Bogdanovich, V.A. Nesterovich and M.A. Tubaev. 'Vliyanye plazmy VCh rasryada na electro-dinamicheskye characteristiky uskoryayushich structur LUE i vychodnye parametry puchka', Preprint MEPhI 002-93, M., MEPhI, 1993.

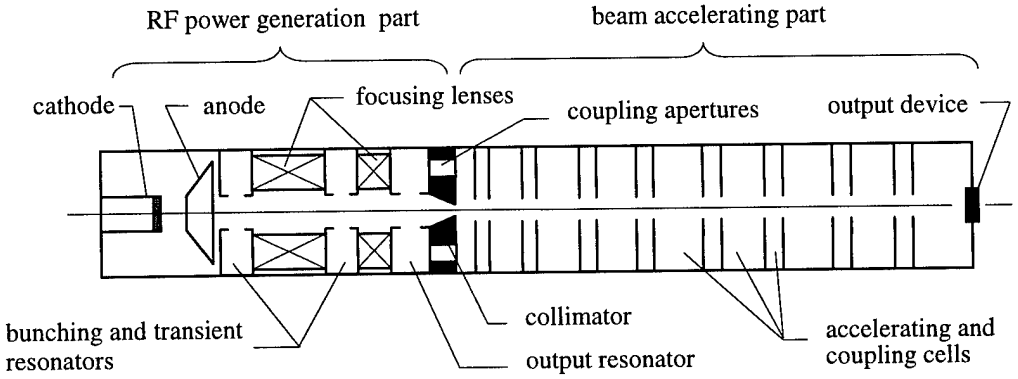




Fig.3. The general scheme of the electron accelerator with bunched beam auto acceleration.

# A SMALL 1 MeV ELECTRON ACCELERATOR FOR MEASURING HEAVY METAL CONCENTRATIONS IN SMOKESTACK GASES

A. Reppond, M. Ambrosia, B.C. Hansen, C.R. Meitzler†, D.P. Redden, Sam Houston State University, Physics Dept., 1902 Ave J., 202 Farrington Bldg., Huntsville, TX 77341, USA and D.A. Swenson, Linac Systems, Waxahachie, TX, USA

*Abstract*

A low-current electron beam may be used as a diagnostic tool to measure the concentrations of heavy metals (Pb, Hg, Sb, etc.) present in the flue gas particulates produced by smelters or cement kilns. A small electron accelerator is being constructed as part of a prototype emissions monitoring system. The electron beam energy has a design energy of 1 MeV, a peak current of 5 mA, and a duty factor of 0.1 percent. In this paper, we discuss the results of a set of EGS4 calculations used to model the transport properties of a 1 MeV electron beam passing through a thin vacuum window and the flue gas.

## 1 INTRODUCTION

Heavy metal pollutants (e.g. Pb, Hg, Cd, Sb, As, and Be) are released through normal industrial processes such as cement manufacture, mercury refining, lead refining and recycling, and municipal trash incineration. The total amount of pollution can be estimated from annual production figures [1]. For example, the total world mine production of mercury in 1994 was 1,760 tonnes.[1] Most of this mercury will eventually return to the environment as some form of pollution. Once in the ecosystem, the metal will tend to accumulate in living organisms. Similar statistics exist for the other metals in the list, above.[2] . Due to the toxic nature of these pollutants and the health risks associated with long-term low-level exposure, there has been a desire to produce a multi-metal Continuous Emissions monitor (CEM) that can measure the quantities of these metals released at their source.

One promising analytical technique for a CEM is Particle Induced X-ray Emission (PIXE)[3]. This analytical technique observes the characteristic K and L-shell x-rays emitted by atoms that are ionized by the passage of high-energy charged particles. As the atom relaxes back to its ground state, it emits a characteristic x-ray spectrum. PIXE's power as an analytical technique is that it can easily measure sub-ppm elemental concentrations without substantial interferences from other elements that may be present.

In the following paper, we describe a conceptual design for an electron linac-based CEM. A brief description of the monitor will be presented. Finally, a discussion of the external beam dynamics will be presented.

## 2 CEM SYSTEM OVERVIEW

### *2.1 Conceptual Design*

We have developed a conceptual design for an electron linac based CEM shown in Figure 1. A small electron linac is mounted at a convenient location on the side of a smokestack. The microwave source, high-voltage, pulse counting, and control electronics are mounted nearby in an enclosed rack.

The CEM's operation is straightforward. An electron beam is accelerated to an energy of approximately 1 MeV. After acceleration, the beam is passes through a thin window into the gases inside the flue. As the accelerated electrons pass through the flue gas, they ionize it. The ionized atoms then relax to their ground states by emitting characteristic x-rays. A solid state photon detector observes the fluorescence x-rays. The density of the atoms is calculated from the background subtracted spectrum.

### *2.2 Accelerator Requirements*

The beam energy for the accelerator was determined from three requirements. First, the beam particles must be able to penetrate through a window into the flue gas and have a range of 1 m in air so that they clear the observation region before stopping. Second, the electrons must have

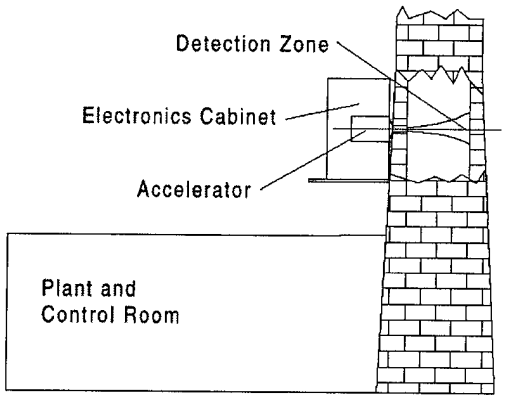



Figure 1 Conceptual design of the CEM The accelerator is mounted on the side of a smokestack. The beam and interaction region are shown.

† corresponding author

0-7803-4376-X/98/$10.00 © 1998 IEEE

enough energy in the observation region to create K-shell vacancies in the metals we wish to observe. (Table 1). Finally, the beam energy must be below 1.6 MeV to avoid creating radioactive material in the flue gases.

The beam current specification is obtained by considering the measurement cycle time, minimum detection limit, and maximum count rate in the detectors. We have assumed that the measurement cycle will be 900 seconds, the detection limit for lead or mercury was chosen to be a modest 1 μg/g, and the maximum count rate set to 200 Hz. This leads to a peak current of 5 mA.

**Table 2** Accelerator specifications

| | | |
|---|---|---|
| Overall | | |
| Projectile | e- | |
| Beam energy | 1 | MeV |
| Peak beam current | 5 | mA |
| Pulse width | 5 | μs |
| Repetition rate | 200 | Hz |
| Linac | | |
| Low structure | DLG | |
| High structure | PWT | |
| Operating frequency | 2.88 | GHz |
| Peak structure power | 46 | kW |
| Peak beam power | 5 | kW |
| Overall length | 56 | cm |
| Electron Gun | | |
| Extraction voltage | 29.5 | kV |
| Cathode/anode voltage | 05 | kV |
| Grid cutoff voltage | -25 | V |
| Filament Current | 1 | A |

*2.3 Linear Accelerator*

The linear accelerator consists of two separate structures that are closely coupled together: a disc-loaded waveguide (DLG) for the low-β section and a plane wave transformer (PWT) [4] for the high-β section. This combination of structures results in an accelerator that is compact, light-weight, self-contained, and has good microwave power. The length of the complete linac is 56 cm.

The low-β section of this accelerator is a structure that integrates both a half-cell rf electron gun and DLG into one piece. The first half-cell forms the rf electron gun. Immediately after the electron gun are four cells that provide the main acceleration for this part. The last half-cell is designed to be abnormally short to adjust the phase for transit through the PWT section. The average accelerating field is set to 4.84 MeV/m. The peak power needed for this section is 36 kW. Power is coupled into the waveguide by an iris separating the DLG from the PWT.

The high-β section of the accelerator is a PWT structure operating in a standing wave, TEM mode. The

**TABLE 1** Characteristic x-rays of selected metals. All energies are in keV. The elements listed are those covered as BIF metals by the US Environmental Protection Agency.

| *Element* | *Z* | $K_\alpha$ | $L_\alpha$ |
|---|---|---|---|
| Be | 4 | 0.109 | |
| As | 33 | 10.544 | 1.282 |
| Cd | 48 | 23.174 | 3.134 |
| Sb | 51 | 26.359 | 3.605 |
| Hg | 80 | 70.818 | 9.989 |
| Pb | 82 | 74.969 | 10.551 |

average accelerating field of this section is 2.42 MeV/m with a peak structure power of 11 kW. The length of the PWT is 30 cm. The open aperture in the nose cones is 2 cm.

A set of four rods support the electrodes of the PWT. These rods are hollow and provide a channel for cooling the inner electrodes. The outer shell of the PWT is not cooled directly. Since we can expect the outer shell of the CEM to be exposed to large temperature variations during normal opertion, we have used SUPERFISH to investigate the frequency stability of the PWT when the inner electrodes are maintained at a constant 20 C but the outer shell is allowed to vary over a temperature range of 0 C to 30 C. We found that the frequency change was less than 10 kHz, which is well within the pulling frequency of most magnetron tubes.

*2.4 Electron source*

The electron gun for this accelerator is an integral part of the first half-cell of the low-β section. The electron source is a modified EIMAC 8745 planar triode tube. The tube is modified by removing the anode cooling fins and cutting through the vacuum tube to expose the grid and cathode. The exposed cathode/grid structure is mounted directly in the rf gun prior to operation. A separate high-voltage system is used to power the electron source. Modulation is provided by pulsing the grid voltage.

*2.5 Microwave source*

The microwave power source for this accelerator was designed to be as simple as possible. A high-voltage power supply charges the capacitors in a simple 6-stage PFN to 24 kV. A Behlke HTS-301 solid state switch is used to modulate the high-voltage applied to the cathode of the magnetron tube. The magnetron's microwave output is coupled to the accelerator 7/8" coaxial components. A schematic of the microwave system is shown in Figure 2.

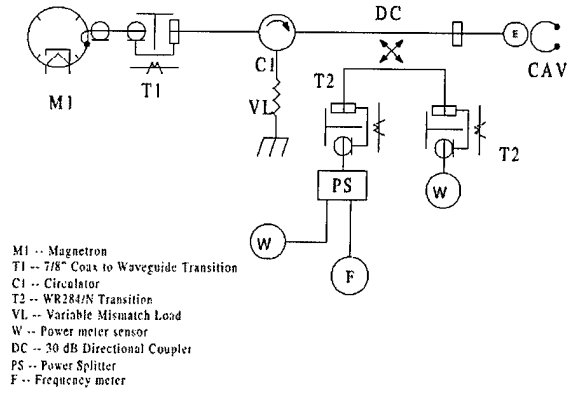



Figure 2. Schematic of the coaxial line linking the magnetron source to the

## 3 PASSAGE OF ELECTRONS THROUGH GAS COLUMN

We have modeled the passage of the electrons through the exit window and gas column using the EGS4 code. [5]

### *3.1 Power loading on exit window*

In this study we used a single non-vacuum region through which the particles passed. The code was set up so that the energy deposition was tallied for each particle as it passes through the foil. Furthermore, we allowed secondary electrons and x-rays to deposit as they passed through the foil. Two materials were studied: Al/Be and amorphous diamond. Figure 3 shows the results of this calculation. For foils greater than 0.3 mm thickness, the amorphous diamond absorbed less than half of the beam energy and produced substantially less bremsstrahlung radiation: 7% of the beam energy for carbon versus 14% for Al/Be. Finally, amorphous diamond is both a good thermal and electrical conductor, and is mechanically strong.

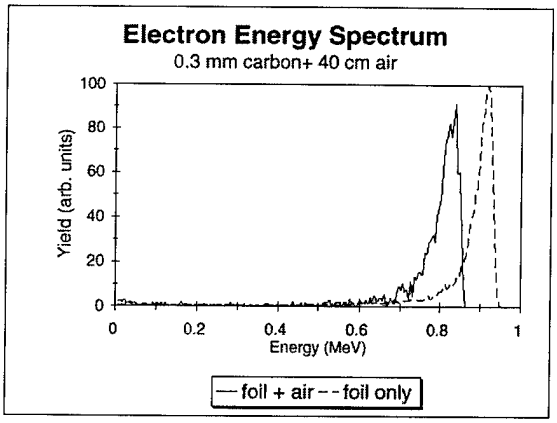



Figure 4. Typical energy spectrum of 1 MeV electrons passing through 0.3 mm of diamond and 40 cm of air.

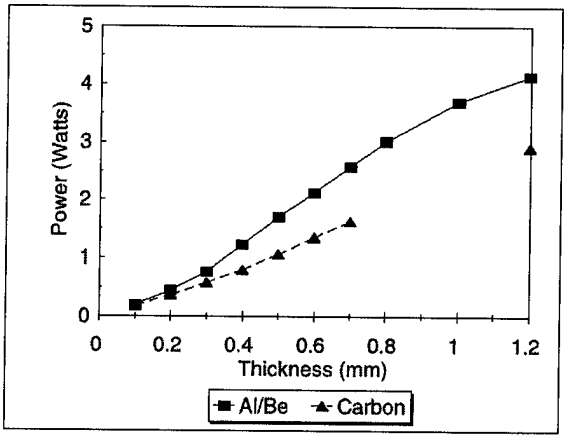



Figure 3. Fraction of beam power absorbed by the diamond foil. The average beam power is 5 Watts with a peak beam power of 5 kW.

### *3.2 Electron Energy Spectrum*

A second EGS4 model was constructed to investigate the energy loss as a function of the distance that the particles penetrated through the gas. Figure 4 shows a typical energy spectrum as the particles pass through both an exit window and 40 cm of air. The "beam energy" loses approximately 100 keV in each region. 40 cm of air is shown in Figure 4.

## 5 CONCLUSION

A small 1 MeV accelerator can be built that can be used as an electron source for a multi-metal CEM. A diamond exit window will be employed to minimize bremstrahlung. A 1 MeV beam has sufficient energy to create an observation region that is more than 40 cm in length.

## 6 ACKNOWLEDGEMENTS

This project is supported by the Advanced Technology Program of the Texas Higher Education Coordinating Board under grant number

## REFERENCES

[1] U.S. Bureau of Mines, *Minerals Yearbook* (1994).
[2] U.S. Bureau of Mines, *Minerals Yearbook* (1994).
[3] A.F. Oluwole, et. al., "Characterization of Airborne Particulate from a Lead Smelter by PIXE and EDXRF," *Nucl. Inst. Meth.* (1995)
[4] D.A. Swenson, "The Plane Wave Transformer Linac Structure," *Proceedings of the European Particle Accelerator Conference*, Rome, Italy (Editions Frontiere, Gif-sur-Yvette, 1988) p. 1418.
[5] W.R. Nelson, H. Hirayama, and D.W.O. Rogers, "The EGS4 Code System," SLAC-Report-265, Stanford Linear Accelerator Center, December, 1985.

# REGISTRANTS' ADDRESSES

| | | |
|---|---|---|
| Abell, D.T. | Dept. of Physics, U. Maryland, College Park, MD 20742, USA | *dabell@quark.umd.edu* |
| Adams, D.J. | RAL, CLRC, Chilton, Didcot, Oxon., UK, OX11 0QX | *dean.adams@rl.ac.uk* |
| Adolphsen, C.E. | SLAC, MS 65, 2575 Sand Hill Road, Menlo Park, CA 94025, USA | *star@slac.stanford.edu* |
| Agafonov, A.V. | Lebedev Physical Inst., Leninsky Prospect 53, RU-117924 Moscow, Russia | *agafonov@sci.lpi.msk.su* |
| Ahrens, L.A. | BNL, 911B, P.O. Box 5000, Upton, NY 11973-5000, USA | |
| Akasaka, N. | KEK, 1-1 Oho, Tsukuba-shi, Ibaraki-ken 305, Japan | *nobumasa.akasaka@kek.jp* |
| Akers, W.L. | TJNAF, 12000 Jefferson Avenue, Newport News, VA 23606, USA | *akers@jlab.org* |
| Akre, R.A. | SLAC, 7123 Phyllis Avenue, San Jose, CA 95129, USA | *akre@slac.stanford.edu* |
| Alessi, J.G. | BNL, Bldg. 930, Upton, NY 11973-5000, USA | *alessi@bnl.gov* |
| Alexeev, N. | ITEP, B. Cheremushkinskaya, 25, RU-117259 Moscow, Russia | |
| Alfarque, R. | RHIC Project Bldg. 817, BNL, P.O. Box 5000, Upton, NY 11973-5000, USA | *rudy@bnl.gov* |
| Allen, C.K. | Techno-Sciences, 10001 Derekwood Lane, Suite 204, Lanham, MD 20740, USA | *cka@plasma.umd.edu* |
| Allen, J. | Elekta Oncology Systems, Linac House, Fleming Way, Crawley, UK, RH10 ZRR | *john_allen@eos.elekta.com* |
| Allen, M.A. | SLAC, MS 18, P.O. Box 4349, Stanford, CA 94309, USA | *matallen@slac.stanford.edu* |
| Allison, P.W. | LANL, MS P942, P.O. Box 1663, Los Alamos, NM 87545, USA | *allisonpw@lanl.gov* |
| Allison, S.A. | SLAC, P.O. Box 4349, Bin 46, Stanford, CA 94309, USA | *saa@slac.stanford.edu* |
| Alonso, J.R. | LBNL, MS 71-259, 1 Cyclotron Road, Berkeley, CA 94720, USA | |
| Alper, B. | Svetlana Electron Devices, Inc., 3000 Alpine Road, Portola Valley, CA 94028, USA | |
| Alton, G.D. | ORNL, P.O. Box 2008, Oak Ridge, TN 37831-6368, USA | *alton@ornl.gov* |
| Amatuni, A. | Yerevan Physics Inst., Alikhanian Brothers St. 2, AM-375036 Yerevan, Armenia | |
| Amboss, K. | MDS Corp (Retired), 751 Haverford Avenue, Pacific Palisades, CA 90272, USA | *amboss@ucla.edu* |
| Anderson, D.E. | LBNL, MS 47-112, 1 Cyclotron Road, Berkeley, CA 94720, USA | *deanderson@lbl.gov* |
| Anderson, E.B. | Cornell U., 311 Dryden Road, Ithaca, NY 14850-4746, USA | *edwin@tristan.tn.cornell.edu* |
| Anderson, O.A. | LBNL, 2910 Benvenue Avenue, Berkeley, CA 94705, USA | *aanderson@lbl.gov* |
| Ando, A. | LASTI/Himeji Inst. of Tech., 2167 Shosha, Himeji, Hyogo 671-22, Japan | *ando@lasti.himeji-tech.ac.jp* |
| Andrews, D. | Oxford Instruments Inc., 600 Milik Street, Carteret, NJ 07008, USA | |
| Andrianov, S. | Saint-Petersburg State U., Ulyanovskaya str. 1, RU-198904 St. Petersburg, Russia | |
| Anferov, V.A. | Physics Dept., U. Michigan, Ann Arbor, MI 48109-1120, USA | *anferov@umich.edu* |
| Angert, N. | GSI Darmstadt, POB 11 05 52, D-64220 Darmstadt, Hessen, Germany | *n.angert@gsi.de* |
| Anthouard, P. | CEA-CESTA, BP #2, F-33114 Le Barp, France | |
| Appleton, B.R. | ORNL, MS 6240, P.O. Box 2008, Bldg. 4500N, Oak Ridge, TN 37831-6240, USA | *gxb@ornl.gov* |
| Arai, S. | U. Tokyo, INS, 3-2-1 Midori-cho, Tanashi, Tokyo 188, Japan | *shigeaki.arai@kek.jp* |
| Arduini, G. | CERN, SL Division, CH-1211 Geneva 23, Switzerland | *gianluigi.arduini@cern.ch* |
| Asaka, T. | JAERI-RIKEN SPring-8, Kamigori, Hyogo 679-12, Japan | *asaka@harvol.spring8.or.jp* |
| Ashton, J.E. | EEV Ltd., Waterhouse Lane, Chelmsford, Essex, UK, CM1 2QU | *john.ashton@eev.com* |
| Assadi, S. | FNAL, P.O. Box 500, Batavia, IL 60504, USA | *assadi@adcalc.fnal.gov* |
| Assmann, R.W. | SLAC, MS 26, P.O. Box 4349, Stanford, CA 94309, USA | *assmann@slac.stanford.edu* |
| Augustine, M.G. | TJNAF, 12000 Jefferson Avenue, Newport News, VA 23606, USA | *augustine@jlab.org* |
| Autin, B.R. | CERN, CH-1211 Geneva 23, Switzerland | *autin@ps.msm.cern.ch* |
| Avalle, C.A. | LLNL, L-153, P.O. Box 808, 7000 East Avenue, Livermore, CA 94550, USA | *avallel@llnl.gov* |
| Averill, R.J. | MIT Bates, P.O. Box 846, Middleton, MA 01949-2846, USA | |
| Baartman, R.A. | TRIUMF, 4004 Wesbrook Mall, Vancouver, BC, Canada, V6T 2A3 | *krab@triumf.ca* |
| Bacher, R. | DESY, Notkestrasse 85, D-22603 Hamburg, Germany | *bacher@desy.de* |
| Bai, M. | BNL/Indiana U., AGS Dept., Upton, NY 11973-5000, USA | *bai@bnldag.ags.bnl.gov* |
| Bailey, J.D. | ORNL, P.O. Box 2008, Bldg. 6000, Oak Ridge, TN 37830-6368, USA | *bailey@oriba2.phy.ornl.gov* |
| Bailey, V.L. | Pulse Sciences, Inc, 600 McCormick Street, San Leandro, CA 94577, USA | *ubailey@titan.com* |
| Bakhtiari, S. | TRIUMF, ATG, 1650 Waterloo Street, Vancouver, BC, Canada, V6R 3G1 | *shervin@unixg.ubc.ca* |
| Balakin, V. | Branch of Budker INP, RU-142284 Protvino, Moscow region, Russia | *balakin@vlepp.serpukhov.su* |
| Ball, M. | MJB Consulting, 119 Executive Way, #304, De Soto, TX 75115, USA | *penny@onramp.net* |
| Bangerter, R.O. | LBNL, 47/101, 1 Cyclotron Road, Berkeley, CA 94720, USA | *bangerter@lbl.gov* |
| Barletta, W. | LBNL, MS 50-149, 1 Cyclotron Road, Berkeley, CA 94720, USA | |
| Barlow, D.B. | LANL, MS H808, P.O. Box 1663, Los Alamos, NM 87545, USA | *dbarlow@lanl.gov* |
| Barnard, J.J. | LLNL, L-440, P.O. Box 808, Livermore, CA 94551, USA | *jjbarnard@llnl.gov* |
| Barnes, M.J. | TRIUMF, 4004 Wesbrook Mall, Vancouver, BC, Canada, V6T 2A3 | *barnes@triumf.ca* |
| Barov, N. | UCLA, ANL, HEP Div. 362, 9700 S. Cass Avenue, Argonne, IL 60439, USA | *barov@vesta.physics.ucla.edu* |
| Bartelson, L.C. | FNAL, P.O. Box 500, Batavia, IL 60510, USA | *Bartelson@fnal.gov* |
| Batskikh, G. | Moscow Radio Technical Inst., Warshavskoe Shosse 132, RU-113519 Moscow, Russia | |
| Bauer, G.S. | PSI, CH-5235 Villigen PSI, Switzerland | *guenter.bauer@psi.ch* |
| Beauvais, P-Y. | CEA-Saclay, LNS - Bar 130, F-91191 Gif sur Yvette, France | |
| Begg, M.L. | Tesla Engineering Ltd., Water Lane, Storrington, West Sussex, UK, RH20 3EA | *begg@tesla.co-uk* |

| | | |
|---|---|---|
| Bellomo, G. | U. Milan, Lasa-Via Flli Cervi 201, I-20090 Segrate, MI, Italy | *giovami.bellomo@mi.infn.it* |
| Belomestnykh, S.A. | Cornell U., Newman Lab, Ithaca, NY 14853-5001, USA | *sab@lns62.lns.cornell.edu* |
| Ben-Zvi, I. | BNL, P.O. Box 5000, Upton, NY 11973-5000, USA | *ilan@bnl.gov* |
| Benson, S.V. | TJNAF, MS 89, 12000 Jefferson Avenue, Newport News, VA 23606, USA | *felman@jlab.org* |
| Berg, G.P.A. | IUCF, 2401 Milo B. Sampson Lane, Bloomington, IN 47408, USA | *gpberg@iucf.indiana.edu* |
| Bergoz, J. | Bergoz, PO Box 2578, Redwood City, CA 94064, USA | |
| Berkner, K.H. | LBNL, 1 Cyclotron Road, Berkeley, CA 94720, USA | *khberner@lbl.gov* |
| Berkvens, P.J. | ESRF, BP 220, F-38043 Grenoble, Cedex, France | *berkvens@esrf.fr* |
| Bertolini, L.R. | LLNL, P.O. Box 808, L-287, Livermore, CA 94551, USA | *bertolinil@llnl.gov* |
| Bertsche, K.J. | Siemens Medical Systems, 4040 Nelson Avenue, Concord, CA 94520, USA | *kbertsche@snsocs.com* |
| Berz, M. | Michigan State U., NSCL, S. Shaw Lane, East Lansing, MI 48824-1321, USA | *berz@pilot.msu.edu* |
| Bhat, C.M. | MI Dept., Beam Division, FNAL, MS 323, P.O. Box 500, Batavia, IL 60510, USA | *cbhat@fnal.gov* |
| Biallas, G. | TJNAF, MS 89, 12000 Jefferson Avenue, Newport News, VA 23606, USA | *biallas@jlab.org* |
| Bickley, M.H. | TJNAF, 12000 Jefferson Avenue, Newport News, VA 23606, USA | *bickley@jlab.org* |
| Billing, M.G. | Cornell U., Wilson Lab, Dryden Road, Ithaca, NY 14853-5001, USA | *mgb@cesr10.lns.cornell.edu* |
| Biocca, A.K. | LBNL, MS 10-100, 1 Cyclotron Road, Berkeley, CA 94720, USA | *akbiocca@lbl.gov* |
| Biryukov, V. | IHEP, RU-142284 Protvino, Moscow region, Russia | |
| Bisoffi, G.M. | INFN-LNL, Via Romea 4, I-35020 Legnaro, PD, Italy | *bisoffi@lnl.infn.it* |
| Bisognano, J.J. | TJNAF, 12000 Jefferson Avenue, Newport News, VA 23606, USA | *bisognano@jlab.org* |
| Bittner, J.W. | 462 Festubert Street, Duncan, BC, Canada, V9L 3T2 | *jackbitt@cow-net.com* |
| Bjorklund, E. | LANL, MS H820, P.O. Box 1663, Los Alamos, NM 87545, USA | *bjo@lanl.gov* |
| Blackmore, E.W. | TRIUMF, 4004 Wesbrook Mall, Vancouver, BC, Canada, V6T 2A3 | *ewb@triumf.ca* |
| Blaker, G.C. | TRIUMF, 4004 Wesbrook Mall, Vancouver, BC, Canada, V6T 2A3 | *blaker@triumf.ca* |
| Blank, M. | NRL, Code 6943, Washington, DC 20375, USA | |
| Blaskiewicz, M.M. | BNL, 911B, Upton, NY 11973, USA | *mmb@bnl.gov* |
| Blell, U. | GSI Darmstadt, Planckstr. 1, D-64297 Darmstadt, Germany | *struck@ulpg08.gsi.de* |
| Bliss, K.A. | Boeing North America, 12000 West 12th Street, Ogden, UT 84401, USA | *kenneth.a.bliss@boeing.com* |
| Blokland, W. | FNAL, MS 308, P.O. Box 500, Batavia, IL 60510, USA | *blockland@adcalc.fnal.gov* |
| Blosser, H.G. | Michigan State U., NSCL, East Lansing, MI 48824-1321, USA | *blosser@nscl.msu.edu* |
| Blum, E. | BNL, NSLS 725C, P.O. Box 5000, Upton, NY 11973-5000, USA | *blum@bnllsl.nsls.bnl.gov* |
| Boehmer, H.E. | Dept. of Physics, UC Irvine, Irvine, CA 92697-4575, USA | |
| Boellmann, J-F. | Sigmaphi, PIBS-Rue Louis de Broglie - CP 47, F-56038 Vannes, Cedex, France | |
| Bogacz, A.S. | Physics Dept., UCLA, Fermilab, MS221, P.O. Box 500, Batavia, IL 60510, USA | *bogacz@fnal.gov* |
| Boge, M. | CERN, CH-1211 Geneva 23, Switzerland | *michael.boge@cern.ch* |
| Bohlen, H.P. | Communications and Power Industries, B-450, 811 Hansen Way, Palo Alto, CA 94304-1031, USA | *heinz.bohlen@mptp.cpii.com* |
| Bohn, C.L. | TJNAF, MS 89, 12000 Jefferson Avenue, Newport News, VA 23606, USA | *clbohn@cebaf.gov* |
| Boillot, J. | CERN, CH-1211 Geneva 23, Switzerland | *Jean.Boillot@cern.ch* |
| Bol, J-L. | IBA, Chemin du Cyclotron, 3, B-1348 Louvain la Nueve, Belgium | *amv@iba.mhs.compuserve.com* |
| Bolme, G.O. | LANL, MS - H827, P.O. Box 1663, Los Alamos, NM 87545, USA | *gbolme@lanl.gov* |
| Boni, R. | INFN-LNF, PO Box 13, I-00044 Frascati, RM, Italy | *boni@lnf.infn.it* |
| Borden, M.J. | LANL, MS H838, Los Alamos, NM 87545, USA | *borden@lanl.gov* |
| Borland, M.D. | ANL, 9700 S. Cass Avenue, Bldg. 401, Argonne, IL 60439-4815, USA | *borland@aps.anl.gov* |
| Bosch, R.A. | U. Wisconsin at Madison, SRC, 3731 Schneider Drive, Stoughton, WI 53589-3097, USA | *bosch@src.wisc.edu* |
| Bosser, J. | CERN, CH-1211 Geneva 23, Switzerland | *bosser@ps.msm.cern.ch* |
| Boudzko, A. | TRIUMF, UBC, 4004 Wesbrook Mall, Vancouver, BC, Canada, V6T 2A3 | *budzko@triumf.ca* |
| Bourat, C. | HEA Division, Thomson - CSF Airsys, 7-9, rue des Mathurins - BP150, F-92223 Bagneux, France | |
| Boussard, D. | CERN, SL Division, CH-1211 Geneva 23, Switzerland | *daniel boussard@cern.ch* |
| Bowling, B.A. | TJNAF, 12000 Jefferson Avenue, Newport News, VA 23606, USA | *bowling@cebaf.gov* |
| Bradley, J.T. | LANL, MS H827, P.O. Box 1663, Los Alamos, NM 87545, USA | *j_bradley@lanl.gov* |
| Brandt, D.R. | CERN, SL Division, CH-1211 Geneva 23, Switzerland | *Daniel.Brandt@cern.ch* |
| Bricault, P.G. | TRIUMF, 4004 Wesbrook Mall, Vancouver, BC, Canada, V6T 2A3 | *bricault@triumf.ca* |
| Bridges, J.F. | 1018 James Street, Geneva, IL 60134-2018, USA | *jimfbridges@coupe.edu* |
| Briggs, D.J. | SAIC, 5000 Hopyand Road, Suite 350, Pleasanton, CA 94588, USA | |
| Brinkmann, R. | DESY, Notkestrasse 85, D-22603 Hamburg, Germany | *brinkmann@desy.de* |
| Brodowski, J. | BNL, Bldg. 911A, P.O. Box 5000, Upton, NY 11973, USA | |
| Brouk, V. | Advanced Energy, 4336 Cape Cod Crescent, Fort Collins, CO 80525, USA | *brook@frii.com* |
| Brown, B.C. | FNAL, MS 341, P.O. Box 500, Batavia, IL 60510, USA | *bcbrown@fnal.gov* |
| Brown, K.A. | BNL, AGS Dept., Bldg. 911A, Upton, NY 11973, USA | *brownlo@bnl.gov* |
| Brown, N.A. | G.H. Gillespie Associates, Inc., 10855 Sorrento Valley Road, Suite 201, San Diego, CA 92121, USA | *ghga@millennianet.com* |

| | | |
|---|---|---|
| Brown, R.L. | BNL, Bldg. 830M, Upton, NY 11973-5000, USA | *rlbrown@bnl.gov* |
| Bruno, D. | BNL, Bldg. 830M, P.O. Box 5000, Upton, NY 11973, USA | *bruno@bnl.gov* |
| Bruskiewich, P. | Ebco Technologies Inc., 7851 Alderbridge Way, Richmond, BC, Canada, V6X 2A4 | |
| Burke, H.H. | Rutgers U. - Newark Campus, 101 Warren Street, 211 Smith Hall, Newark, NJ, USA | *bobburke@andromeda.rutgers.edu* |
| Burkhardt, H. | CERN, SL Division, CH-1211 Geneva 23, Switzerland | *helmut.burkhardt@cern.ch* |
| Bylinsky, Y.V. | INR of RAS, 60th October Anniversary PR. 7A, RU-117312 Moscow, Russia | *bylinsky@al20.inr.troitsk.ru* |
| Byrd, J.M. | LBNL, MS 80-101, 1 Cyclotron Road, Berkeley, CA 94720, USA | *jmbyrd@lbl.gov* |
| Campbell, G.L. | General Atomics, 3550 General Atomics Court, San Diego, CA 92121-1194, USA | *greg.campbell@gat.com* |
| Capista, D.P. | FNAL, MS 341, P.O. Box 500, Batavia, IL 60510, USA | |
| Caporaso, G.J. | LLNL, L-440, 7000 East Avenue, Livermore, CA 94550, USA | *caporaso1@llnl.gov* |
| Carlson, R.L. | LANL, MS P940, Group DX-6, Los Alamos, NM 87545, USA | *carlson_rl@lanl.gov* |
| Carlsten, B.E. | LANL, MS H851, L-9, P.O. Box 1663, Los Alamos, NM 87545, USA | *bcarlsten@lanl.gov* |
| Carroll, F.E. | Dept. of Radiology, Vanderbilt U. Medical Center, 1161 21st Avenue South, 920 VUH, Nashville, TN 37232-2675, USA | *frank.carroll@mcmail.vanderbilt.edu* |
| Carwardine, J.A. | ANL, 9700 S. Cass Avenue, Bldg 401, Argonne, IL 60439-4815, USA | *carwar@aps.anl.gov* |
| Caryotakis, G. | SLAC, 2575 Sand Hill Road, Menlo Park, CA 94025, USA | *caryo@slac.stanford.edu* |
| Caspi, S. | LBNL, MS 46-161, 1 Cyclotron Road, Berkeley, CA 94720, USA | *s_caspi@lbl.gov* |
| Cassel, R.L. | SLAC, MS 49, P.O. Box 4349, Stanford, CA 94309, USA | *rlc@slac.stanford.edu* |
| Celata, C.M. | LBNL, 47-112, 1 Cyclotron Road, Berkeley, CA 94720, USA | *cmcelata@lbl.gov* |
| Cervellera, F. | INFN-LNL, I-35020 Legnaro, PD, Italy | *cervellera@lnl.infn.it* |
| Chae, Y.C. | ANL, 9700 S. Cass Avenue, Bldg. 401, Argonne, IL 60439, USA | *chae@aps.anl.gov* |
| Chai, J-S. | KAERI/KCCH, Woosung APT 106-201, Bang-hag-dong, Dohong-gu, Seoul, S. Korea | *jschai@kcchsum.kcch.re.kr* |
| Champion, M. | FNAL, MS 306, P.O. Box 500, Batavia, IL 60510, USA | *champion@fnal.gov* |
| Chan, A. | SLAC, MS17, 2575 Sand Hill Road, Stanford, CA 94309, USA | *achan@slac.stanford.edu* |
| Chan, K.C.D. | LANL, MS H851, P.O. Box 1663, Los Alamos, NM 87544, USA | *kcchan@lanl.gov* |
| Chao, C. | SLAC, MS 69, P.O. Box 4349, Stanford, CA 94309-0210, USA | *chao@ssrl.slac.stanford.edu* |
| Chao, Y-C. | TJNAF, 12000 Jefferson Avenue, Newport News, VA 23606, USA | *chao@jlab.org* |
| Chase, B.E. | FNAL, MS 308, P.O. Box 500, Batavia, IL 60510, USA | *chase@fnal.gov* |
| Chateau, C. | BP 2, SICN, F-38113 Veurev Vorozze, France | |
| Chattopadhyay, S. | LBNL, MS 71-259, 1 Cyclotron Road, Berkeley, CA 94720, USA | *chapon@lbl.gov* |
| Chavanne, J. | ESRF, BP 220, F-38043 Grenoble, France | *chavanne@esrf.fr* |
| Chen, C. | Plasma Fusion Center, MIT, NW16-176, Cambridge, MA 02139, USA | *chen@psfc.mit.edu* |
| Chen, Y.J. | LLNL, L-440, P.O. Box 808, Livermore, CA 94550, USA | *chen29@llnl.gov* |
| Chen, Y-J. | LLNL, L-440, P.O. Box 808, Livermore, CA 94550, USA | *yjchen@llnl.gov* |
| Cheng, D.W. | LBNL, 71J, 1 Cyclotron Road, Berkeley, CA 94720, USA | *dwcheng@lbl.gov* |
| Cheng, W-H. | UC Berkeley, MS 71-259, One Cyclotron Road, LBL, Berkeley, CA 94720, USA | *wenhao@beams.lbl.gov* |
| Chesnokov, Yu.A. | IHEP, RU-142284 Protvino, Moscow region, Russia | |
| Chin, M. | LBNL, 46-125, 1 Cyclotron Road, Berkeley, CA 94720, USA | *MJChin@lbl@gov* |
| Chin, Y.H. | KEK, 1-1 Oho, Tsukuba-shi, Ibaraki-ken 305, Japan | *yongho@kekvax.kek.jp* |
| Cho, Y. | ANL, Bldg. 401, 9700 S. Cass Avenue, Argonne, IL 60439, USA | *yc@aps.anl.gov* |
| Choi, J. | Pohang Acc. Lab, POSTECH, San 31, Hyoja-dong, Nam-ku, Pohang, Kyungbuk 790-784, S. Korea | *jchoi@postech.ac.kr* |
| Choi, J.J. | NRL, Code 6840, Washington, DC 20375, USA | *choi@mmace.nrl.navy.mil* |
| Chojnacki, E.P. | Cornell U., Newman Lab, Ithaca, NY 14853-5001, USA | *epc@lns62.lns.cornell.edu* |
| Chou, P.J. | SRRC, Taiwan, No. 1 R&D Road, VI, Hsinchu Science-Based Industrial Park, Hsinchu, 30077, Taiwan | |
| Chou, W. | FNAL, MS 323, P.O. Box 500, Batavia, IL 60504, USA | *chou@fnal.gov* |
| Chow, K.P. | LBNL, MS 46-161, 1 Cyclotron Road, Berkeley, CA 94720, USA | *kpchow@lbl.gov* |
| Chu, C. | IUCF, 336 Evermann Apts, Bloomington, IN 47408, USA | *cmchu@iucf.indiana.edu* |
| Chuma, J.L. | TRIUMF, 4004 Wesbrook Mall, Vancouver, BC, Canada, V6T 2A3 | *chuma@triumf.ca* |
| Chung, S. | Pohang Acc. Lab, POSTECH, San 31, Hyoja-dong, Nam-ku, Pohang, Kyungbuk 790-784, S. Korea | *amc@anyon.postech.ac.kr* |
| Church, M.D. | FNAL, P.O. Box 500, Batavia, IL 60510, USA | *church@fnal.gov* |
| Ciavola, G. | INFN-LNS, Catania, Via s. 8-0 Fia, 44, I-85223 Catania, Italy | *ciavola@lns.infn.it* |
| Ciriani, P. | CERN, CH-1211 Geneva 23, Switzerland | |
| Clark, D. | LBNL, 1 Cyclotron Road, Bldg. 88, Berkeley, CA 94720, USA | *djclark@lbl.gov* |
| Clark, G.L. | EEV Ltd., 106 Waterhouse Lane, Chelmsford, Essex, UK, CM1 2QU | *graeme.clark@eev.com* |
| Clark, G.S. | TRIUMF, 4004 Wesbrook Mall, Vancouver, BC, Canada, V6T 2A3 | *gsclark@triumf.ca* |
| Clausen, M. | DESY, Notkestrasse 85, D-22607 Hamburg, Germany | *clausen@desy.de* |
| Clayton, C. | UCLA, 56-125B Engineering IV Bldg., Los Angeles, CA 90025, USA | *cclayton@ucla.edu* |
| Clerc, G.M. | Thomson Tubes Electroniques, B.P. 84, F-74200 Thonon, France | |

| | | |
|---|---|---|
| Cling, D.B. | Physics Dept., UCLA, 405 Hilgard Avenue, Los Angeles, CA 90025, USA | |
| Clout, P.N. | Vista Control Systems, Inc., 134 B Eastgate Drive, Los Alamos, NM 87544-3304, USA | *clout@vista-control.com* |
| Cojocaru, G. | TRIUMF, 4004 Wesbrook Mall, Vancouver, BC, Canada, V6T 2A3 | *cojocaru@triumf.ca* |
| Colby, E.R. | FNAL, MS 306, P.O. Box 500, Batavia, IL 60506, USA | *ecolby@fnal.gov* |
| Collins, B. | Glassman Europe Ltd., 21 Campbell Court, Bramley, Hampshire, UK, RG26 5EG | |
| Collins, D.G. | LBNL, 1 Cyclotron Road, Bldg 88, Berkeley, CA 94720, USA | *DGCollins@lbl.gov* |
| Comunian, M.R. | INFN-LNL, Via Romea, 4, I-35020 Legnaro, PD, Italy | *comunian@lnl.infn.it* |
| Conde, M.E. | ANL, 9700 S. Cass Avenue, Bldg 362, Argonne, IL 60439, USA | *conde@anlhep.hep.anl.gov* |
| Connolly, R.C. | BNL, Bldg. 1005, P.O. Box 5000, Upton, NY 11973-5000, USA | *connolly@bnl.gov* |
| Conte, A. | Saes Getters SPA, Via Lainate 77, I-20020 Lainate, Milan, Italy | |
| Cook, D. | SNL, MS 1190, P.O. Box 5800, Org. 9500, Albuquerque, NM 87185-1190, USA | *dlcook@sandia.gov* |
| Cooke, S.J. | U. Maryland, Code 6840, Naval Research Laboratory, 4555 Overlook Avenue, SW, Washington, DC 20375, USA | *sjcooke@glue.umb.edu* |
| Corbett, W.J. | SLAC, P.O. Box 4349, Stanford, CA 94309, USA | *corbett@ssrl* |
| Corlett, J.N. | LBNL, 71-259, 1 Cyclotron Road, Berkeley, CA 94720, USA | *jncorlett@lbl.com* |
| Cornacchia, M. | SLAC, MS 69, PO Box 4349, Stanford, CA 94309-0210, USA | *cornacchia@slac.stanford.edu* |
| Cornelius, W.D. | Scientific Solutions, PO Box 500207, San Diego, CA 92150, USA | *ssolutions@compuserve.com* |
| Corredoura, P.L. | SLAC, MS 18, P.O. Box 4349, Stanford, CA 94309, USA | *plc@slac.stanford.edu* |
| Corsini, R. | CERN, PS Division, CH-1211 Geneva 23, Switzerland | *roberto.corsini@cern.ch* |
| Corvin, C. | SLAC, MS 22, P.O. Box 4349, Stanford, CA 94301, USA | *clay@slac.stanford.edu* |
| Costrell, L. | NIST, National Institute of Standards & Technology, Gaithersburg, MD 20899, USA | *louis.costrell@nist.gov* |
| Craddock, M.K. | UBC & TRIUMF, 4004 Wesbrook Mall, Vancouver, BC, Canada, V6T 2A3 | *craddock@triumf.ca* |
| Crane, M.E. | SLAC, MS 46, P.O. Box 4349, Stanford, CA 94309, USA | *mark@slac.stanford.edu* |
| Cruikshank, P. | CERN, CH-1211 Geneva 23, Switzerland | *paul.cruikshank@cern.ch* |
| Cummings, K.A. | LANL, MS H827, P.O. Box 1663, Los Alamos, NM 87544, USA | *kcummings@lanl.gov* |
| D'Auria, G. | Sincrotrone Trieste, S.S. 14, km 163.5 in Area Science Park, Basovizza, I-34012 Trieste, TS, Italy | *dauria@elettra.trieste.it* |
| D'yachkov, M. | TRIUMF, 4004 Wesbrook Mall, Vancouver, BC, Canada, V6T 2A3 | *dyachkov@triumf.ca* |
| Dalesio, L.R. | LANL, MS H820, P.O. Box 1663, Los Alamos, NM 87545, USA | *ldalesio@lanl.gov* |
| Dallin, L.O. | SAL, Saskatoon, 107 North Road, Saskatoon, SK, Canada, S7N 5C6 | *les@skatter.usask.ca* |
| Daly, E. | SLAC, 2575 Sand Hill Road, Menlo Park, CA 94025, USA | *eddaly@slac.stanford.edu* |
| Daniels, K. | Triton Electron Technology Division, P.O. Box 100, Easton, PA 18044-0100, USA | *kdaniels@tritontd.com* |
| Danly, B.G. | NRL, Code 6840, 4555 Overlook Avenue, SW, Washington, DC 20375, USA | *danly@nrl.navy.mil* |
| Darpentigny, J. | LURE, BAT 207A, Centre Universitaire, F-91405 Orsay, France | *darpenigny@lure.u-psud.fr* |
| de Loos, M.J. | Pulsar Physics, Flamingostraat 24, NL-3582 SX Utrecht, The Netherlands | *gpt@pulsar.nl* |
| De Martinis, C. | U. Milan, Lasa Lab. - Via Flli Cervi 201, I-20059 Segrate, MI, Italy | *demartinis@mvlasa.mi.infn.it* |
| Debenham, P.H. | DOE, 19901 Germantown Road, Germantown, MD 20874, USA | *phil.debenham@oer.doe.gov* |
| Decker, F-J. | SLAC, MS 66, P.O. Box 4349, Stanford, CA 94309, USA | *decker@slac.stanford.edu* |
| Decker, G.A. | ANL, 9700 S. Cass Avenue, Bldg 401, Argonne, IL 60439-4815, USA | *decker@aps.anl.gov* |
| Decking, W. | LBNL, MS 80-101, 1 Cyclotron Road, Berkeley, CA 94720, USA | *wdecking@lbl.gov* |
| Dehnel, K.F.R. | Dehnel Consulting Ltd., P.O. Box 201, Nelson, BC, Canada, V1L 5P9 | *indehnel@awinc.com* |
| Deitinghoff, H. | IAP, Frankfurt/Main, Robert-Mayer-Str. 2-4, D-60054 Frankfurt am Main, Germany | *deitinghoff@em.uni-frankfurt.de* |
| Dekkers, D. | CERN, CH-1211 Geneva 23, Switzerland | *dekkers@ps.msm.cern.ch* |
| DeLamare, J. | SLAC, 2575 Sand Hill Road, Menlo Park, CA 94020, USA | *delamare@slac.stanford.edu* |
| Delayen, J.R. | TJNAF, 12000 Jefferson Avenue, Newport News, VA 23606, USA | *delayen@cebaf.gov* |
| Den Hartog, P.K. | ANL, 401/B3177, 9700 S. Cass Avenue, Argonne, IL 60304, USA | *pdenhartog@anl.gov* |
| Denard, J-C.R. | TJNAF, MS 58, 12000 Jefferson Avenue, Newport News, VA 23606, USA | *denard@jlab.org* |
| Deng, J. | U. Maryland, P.O. Box 523-56, College Park, MD 20742-3285, USA | *jjd@glue.umd.edu* |
| Deruyter, H. | Schonberg Research Corp., 3300 Keller Street, Bldg. 101, Santa Clara, CA 95054, USA | *avmsrc@aol.com* |
| Devan, W.R. | ORNL, MS 6338, P.O. Box 2008, Oak Ridge, TN 37831, USA | *devanwr@ornl.gov* |
| DeVries, G.J. | LBNL, MS 46-125, 1 Cyclotron Road, Berkeley, CA 94720, USA | *gjdevries@lbl.gov* |
| Dey, J.E. | FNAL, MS 306, P.O. Box 500, Batavia, IL 60510, USA | *dey@fnal.gov* |
| Di Maio, F. | CERN, PS Division, CH-1211 Geneva 23, Switzerland | *franck.di.maio@cern.ch* |
| Dieperink, J.H. | CERN, SL Division, CH-1211 Geneva 23, Switzerland | *johan.dieperink@cern.ch* |
| Dikansky, N.S. | Budker INP, Novosibirsk, Academician Lavrentiev Prospect 11, RU-630090 Novosibirsk, Russia | |
| Dillahunty, T.L. | Kaman Instrumentation, MS 63, Box 7463, Colorado Springs, CO 80933, USA | *tdillahunty-cos2@kaman.com* |
| Dohan, D.A. | PSI, CH-5230 Villigen, Switzerland | *dohan@psi.ch* |
| Dohlus, M. | DESY, Notkestrasse 85, D-22603 Hamburg, Germany | *dohlus@mail.desy.de* |
| Dolbilov, G.V. | JINR, RU-141980 Dubna, Moscow region, Russia | *dol@sunse.jinr.dubna.su* |
| Donahue, J.B. | LANL, MS H840, P.O. Box 1663, Los Alamos, NM 87545, USA | *jdonahue@lanl.gov* |

| | | |
|---|---|---|
| Dooling, J. | ANL, 9700 S. Cass Avenue, Bld 360, Argonne, IL 60439-4815, USA | *dooling@anl.gov* |
| Doose, C.L. | ANL, 9700 S. Cass Avenue, Bldg 401, Argonne, IL 60439-4815, USA | *doose@aps.anl.gov* |
| Douglas, D.R. | TJNAF, MS - 12A2, 12000 Jefferson Avenue, Newport News, VA 23606, USA | *douglas@cebaf.gov* |
| Dovbnya, A.N. | Kharkov Inst. of Phys. and Tech. (KFTI), UA-310108 Kharkov, Ukraine | |
| Dowell, D.H. | Boeing Physical Sciences Research Centre, MS 2T-50, P.O. Box 3999, Seattle, WA 98124-2499, USA | *david.h.dowell@boeing.com* |
| Dragt, A.J. | Dept. of Physics, U. Maryland, College Park, MD 20742, USA | *dragt@quark.umd.edu* |
| Drendel, B.E. | FNAL, P.O. Box 500, Batavia, IL 60510, USA | *drendel@adcal.fnal.gov* |
| Drouet, G. | CERN, CH-1211 Geneva 23, Switzerland | *gilbert.drouet@cern.ch* |
| Drozhdin, A.I. | FNAL, MS 345, P.O. Box 500, Batavia, IL 60510, USA | *drozhdin@fnal.gov* |
| Dstiguy, J-F. | FNAL, P.O. Box 500, Batavia, IL 60510-0500, USA | *dstiguy@fnal.gov* |
| Dugan, G. | Cornell U., Newman Lab, Ithaca, NY 14853-5001, USA | *gf01@cornell.edu* |
| Duke, J.P. | RAL, CLRC, Chilton, Didcot, Oxon., UK, OX11 0QX | *jpd47@isise.rk.ac.uk* |
| Dunham, B.M. | TJNAF, MS 85A, 12000 Jefferson Avenue, Newport News, VA 23606, USA | *dunahm@cebaf.gov* |
| Durieu, L. | CERN, CH-1211 Geneva 23, Switzerland | *luc.durieu@cern.ch* |
| Durling, G.L. | SVF Inc., P.O. Box 70, Rock Falls, IL 61071, USA | *myeoward@essexl.com* |
| Dutto, G.G. | TRIUMF, 4004 Wesbrook Mall, Vancouver, BC, Canada, V6T 2A3 | *dutto@triumf.ca* |
| Dykes, M.D. | Daresbury Lab, CLRC, Warrington, Cheshire, UK, WA4 4AD | *d.m.dykes@dl.ac.uk* |
| Earley, L.M. | LANL, MS H851, P.O. Box 1663, L-9, Los Alamos, NM 87545, USA | *earley-lawrence-m@lanl.gov* |
| Ebeling, W. | DESY, Notkestrasse 85, D-22607 Hamburg, Germany | *ebeling@mail.desy.de* |
| Ebert, M. | DESY, Notkestrasse 85, D-22607 Hamburg, Germany | *michael.ebert@desy.de* |
| Eckoldt, H-J. | DESY, Notkestrasse 85, D-22603 Hamburg, Germany | *echoldt@muupcs.desy.de* |
| Edighoffer, J.A. | Titan Beta, 4878 Doloves Drive, Pleasanton, CA 94566, USA | *edighoffer@value.net* |
| Eickhoff, H. | GSI Darmstadt, Planck Str. 1, D-64291 Darmstadt, Germany | *h.eickhoff@gsi.de* |
| Einfeld, D. | Forschungszentrum Karlsruhe / ANKA, PO Box 3640, D-76021 Karlsruhe, Germany | *einfeld@anka.fzk.de* |
| Elias, L.R. | U. Central Florida, Orlando, FL 32708, USA | *elias@creop.ucf.edu* |
| Elsener, K. | CERN, SL Division, CH-1211 Geneva 23, Switzerland | *elsener@mail.cern.ch* |
| Emery, L. | ANL, 9700 S. Cass Avenue, Bldg 401, Argonne, IL 60439-4815, USA | *emery@aps.anl.gov* |
| Emma, P.J. | SLAC, MS 66, P.O. Box 4349, Stanford, CA 94309, USA | *emma@slac.stanford.edu* |
| Endo, K. | KEK, 1-1 Oho, Tsukuba-shi, Ibaraki-ken 305, Japan | *endok@kekvax.kek.jp* |
| Engels, O. | IAP, Frankfurt/Main, Robert-Mayer-Str. 2-4, D-60325 Frankfurt am Main, Germany | *engels@em.uni-frankfurt.de* |
| Engwall, D. | TJNAF, 12000 Jefferson Avenue, Newport News, VA 23606, USA | *engwall@jlab.gov* |
| Erickson, R.A. | SLAC, MS 55, P.O. Box 4349, Stanford, CA 94309, USA | *roger@slac.stanford.edu* |
| Esarey, E. | NRL, Code 6791, Washington, DC 20375, USA | *esarey@ppd.nrl.navy.mil* |
| Evans, L.R. | CERN, CH-1211 Geneva 23, Switzerland | *evans@mail.cern.ch* |
| Eyharts, P. | CEA-CESTA, BP No.2, F-33170 Lebarp, France | |
| Eylon, S. | LBNL/FAR, 1 Cyclotron Road, Berkeley, CA 94720, USA | *eylon@csam.lbl.gov* |
| Eysselein, F.G. | Noell-KRC Energie-und Umwelttechnik GmbH, D-97064 Wuerzburg, Germany | *eysselein@noell-de* |
| Ezura, E. | KEK, 1-1 Oho, Tsukuba-shi, Ibaraki-ken 305, Japan | *ezura@kekvax.kek.jp* |
| Facco, A. | INFN-LNL, Via Romea 4, I-35020 Legnaro, PD, Italy | *facco@lnl.infn.it* |
| Faltens, A. | LBNL, 47-112, 1 Cyclotron Road, Berkeley, CA 94720, USA | |
| Fang, S.J. | FNAL, MS 308, P.O. Box 500, Batavia, IL 60510, USA | *cjf@fnal.gov* |
| Fant, K.S. | SLAC, MS 18, PO Box 4349, Stanford, CA 94309, USA | *fant@slac.stanford.edu* |
| Farias, R.H.D.A. | LNLS - Brazil, Caixa Postal 6192, BR-13083-970 Campinas, SP, Brazil | *ruy@lnls.br* |
| Fartoukh, S.D. | CEA-Saclay, DSM/DAPNIA/SCA C.E. Saclay, F-91191 Gif sur Yvette, Cedex, France | *Stephane.Fartoukh@hep.sarlayesea.fr* |
| Fateev, A.A. | JINR, RU-141980 Dubna, Moscow region, Russia | *fateev@sunse.jinr.dubna.su* |
| Faure, J. | CEA-Saclay, F-91191 Gif sur Yvette, France | *faure@png.cea.fr* |
| Fawley, W.M. | LBNL, MS 47-112, 1 Cyclotron Road, Berkeley, CA 94720, USA | *fawley@lbl.gov* |
| Fazio, M.V. | LANL, MS - H851, P.O. Box 1663, Los Alamos, NM 87545, USA | *mfazio@lanl.gov* |
| Fedotov, A. | Dept. of Physics, U. Maryland, College Park, MD 20742, USA | *fedotov@quark.umd.edu* |
| Feher, S. | FNAL, MS 316, P.O. Box 500, Batavia, IL 60510 - 0500, USA | *feher@fnal.gov* |
| Feinberg, B. | LBNL, MS 80-101, 1 Cyclotron Road, Berkeley, CA 94720, USA | *b_feinberg@lbl.gov* |
| Ferdinand, R. | CEA-Saclay, LNS bar 130, F-91191 Gif sur Yvette, France | *ferdinand@lns.cea.fr* |
| Ferguson, P.E. | MDS Co., 1955 Mountain Boulevard, Suite 101, Oakland, CA 94611, USA | *mdsfer@aol.com* |
| Fernow, R.C. | BNL, 901A, P.O. Box 5000, Upton, NY 11973-5000, USA | *fernow@bnl.gov* |
| Fernqvist, K.G.G. | CERN, CH-1211 Geneva 23, Switzerland | *Gunnar.Fernqvist@cern.ch* |
| Ferris, M.L. | SAES Getters/USA, 1122 East Cheyenne Mountain Boulevard, Colorado Springs, CO 80906, USA | |
| Fieguth, T. | SLAC, P.O. Box 4349, Stanford, CA 94309, USA | *fieguth@slac.stanford.edu* |
| Filhol, J-M. | ESRF, BP 220, F-38043 Grenoble, France | *filhol@esrf.fr* |

| | | |
|---|---|---|
| Fink, Y. | MIT Plasma Science and Fusion Center, 167 Albany Street, Room NW 16-168, Cambridge, MA 02139-4213, USA | *yoel@mit.edu* |
| Finley, D.A. | FNAL, MS 306, P.O. Box 500, Batavia, IL 60510-0500, USA | *finley@fnal.gov* |
| Fischer, W. | BNL, PO Box 5000, Bldg 10055, Upton, NY 11973-5000, USA | *wfischer@bnl.gov* |
| Fisher, A.S. | SLAC, MS 17, 2575 Sand Hill Road, Menlo Park, CA 94025, USA | *afisher@slac.stanford.edu* |
| Fitzgerald, D.H. | LANL, MS H838, Los Alamos, NM 87545, USA | *fitzgerald@lanl.gov* |
| Fitzgerald, J.A. | FNAL, 30 Wino Cynthia Court, Warrenville, IL 60555, USA | *jafitz@fnal.gov* |
| Flanz, J.B. | Northeast Proton Therapy Center, 30 Fruit Street, Boston, MA 02114, USA | *flanz@hadron.MGH.harvard.edu* |
| Fomel, B.M. | Prudence Software Ltd., P.O. Box 45125, Jerusalem, 91450, Israel | *fomel@jsi.co.il* |
| Fong, K.S. | TRIUMF, 4004 Wesbrook Mall, Vancouver, BC, Canada, V6T 2A3 | *fong@triumf.ca* |
| Fontana, J.R. | UC Santa Barbara, 4375 Via Glorieta, Santa Barbara, CA 93110-2113, USA | |
| Foster, W.G. | FNAL, MS 323, P.O. Box 500, Batavia, IL 60510, USA | *gwf@fnal.gov* |
| Fowler, W.B. | FNAL, MS 323, P.O. Box 500, Batavia, IL 60510, USA | *fowler@fnal.gov* |
| Fox, J.D. | SLAC, MS 18, P.O. Box 4349, Stanford, CA 94309, USA | *jdfox@slac.stanford.edu* |
| Franks, M. | LLNL, L-337, P.O. Box 808, Livermore, CA 94550, USA | *franks1@llnl.gov* |
| Fraser, J.S. | TRIUMF, 21-928 Bearwood Lane, Victoria, BC, Canada, V8Y 3G8 | *fraser@vanisle.net* |
| Friedl, J. | U. Dortmund, IBS, Emil-Figge-Str. 74R, D-44221 Dortmund, Germany | *friedl@calvin.physik* |
| Friedman, A. | LLNL, L -440, P.O. Box 808, Livermore, CA 94550, USA | *af@llnl.gov* |
| Friedrichs, C. | LANL, MS H827, P.O. Box 1663, Los Alamos, NM 87545, USA | *friedrichs@lanl.gov* |
| Friesel, D.L. | IUCF, 2401 Milo B. Sampson Lane, Bloomington, IN 47408, USA | *friesel@iucf.indiana.edu* |
| Fry, A.R. | FNAL, MS 340, P.O. Box 500, Batavia, IL 60510, USA | *fry@pas.rochester* |
| Fujishima, S. | RIKEN, Cyclotron Lab, 2-1 Hirosawa, Wako, Saitama 351-01, Japan | *fujishima@rikaxp.riken.go.jp* |
| Fukuma, H. | KEK, 1-1 Oho, Tsukuba-shi, Ibaraki-ken 305, Japan | *tukuma@kekvax.kek.jp* |
| Funakoshi, Y. | KEK, 1-1 Oho, Tsukuba-shi, Ibaraki-ken 305, Japan | *funakoshi@kekvax.kek.jp* |
| Funk, L.W. | Westinghouse Savannah River Co., 227 Limerick Drive, Aiken, SC 29803, USA | *warren.funk@srs.gov* |
| Furman, M.A. | LBNL, 71-259, 1 Cyclotron Road, Berkeley, CA 94720, USA | *mafurman@lbl.gov* |
| Gai, W. | ANL, 9700 S. Cass Avenue, Bldg. 362, Argonne, IL 60439, USA | *wg@anl.hep.gov* |
| Galamboz, J.P. | FEDC, ORNL, P.O. Box 2008, Oak Ridge, TN 37831-6368, USA | *jdg@ornl.gov* |
| Galayda, J.N. | ANL, 9700 S. Cass Avenue, bldg 401, Argonne, IL 60439-4815, USA | *asd-div@aps.anl.gov* |
| Galimberti, A. | Sincrotrone Trieste, SS 14 km 163.5 - Basovizza, I-34012 Trieste, TS, Italy | *galimberti@elettra.trieste.it* |
| Gallardo, J.C. | Physics Dept., BNL, 901-A, Upton, NY 11973, USA | *gallardo@bnlarm.bnl.gov* |
| Ganguly, A.K. | Omega-P, Inc., 205 South Whiting Street, Suite 307, Alexandria, VA 22304, USA | *agaguly@earthlink.net* |
| Gao, J. | LAL Orsay, INEPS-CNRS, Bat. 200, F-91405 Orsay, Cedex, France | *gao@lalcls.inrps.fr* |
| Garren, A. | LBNL, UCLA/LBNL, 71-259, One Cyclotron Road, Berkeley, CA 94708, USA | *garren@lbl.gov* |
| Garvey, T. | LAL Orsay, Bldg. 200, Universite de Paris Sud, F-91405 Orsay, Cedex, France | *garvey@lalcls.in2p3.fr* |
| Gary, J.R. | U. Colorado, Boulder, CO 80301, USA | *gary@colorado.edu* |
| Gassner, D.M. | BNL, 911B, P.O. Box 5000, Upton, NY 11973-5000, USA | *gassner@bnl.gov* |
| Gelbart, W.Z. | TRIUMF, 4004 Wesbrook Mall, Vancouver, BC, Canada, V6T 2A3 | *gelbart@triumf.ca* |
| Gelbke, C.K. | Michigan State U., NSCL, S. Shaw Lane, East Lansing, MI 48824-1321, USA | *gelbke@nscl.msu.edu* |
| Gentner, M. | Bonn U., Physics Inst., Nussallee 12, D-53115 Bonn, Germany | *gentner@physik.uni-bonn.de* |
| Ghigo, A. | INFN-LNF, EP 13, I-00044 Frascati, RM, Italy | *ghigo@lnf.infn.it* |
| Gilad, P. | QM Technologies Inc, 3701 Hawkins Street NE, Albuquerque, NM 87109, USA | *pgilad@stl.sandia.gov* |
| Gillespie, G.H. | G.H. Gillespie Associates, Inc., 10855 Sorrento Valley Road, Suite 201, San Diego, CA 92121, USA | *ghga@millennianet.com* |
| Gillies, J.D. | CERN Courier, CERN, CH-1211 Geneva 23, Switzerland | *james.gillies@cern.ch* |
| Gilpatrick, J.D. | LANL, MS H808, P.O. Box 1663, Los Alamos, NM 87545, USA | *gilpatrick@lanl.gov* |
| Glass, H. | FNAL, MS 316, P.O. Box 500, Batavia, IL 60510, USA | *glass@fnal.gov* |
| Glatz, J. | GSI Darmstadt, Postfach 110552, D-64220 Darmstadt, Germany | |
| Glenn, J.W. | BNL, P.O. Box 5000, Upton, NY 11973-5000, USA | *glenn@bnldag.ags.bnl.gov* |
| Glover, M.G. | RAL, CLRC, R2, Chilton, Didcot, Oxon., UK, OX11 OQX | *m.glover@rl.ac.uk* |
| Gluckstern, R.L. | Physics Dept., U. Maryland, College Park, MD 20742-3511, USA | *rlg@quark.umd.edu* |
| Gluskin, E. | ANL, 9700 S. Cass Avenue, Argonne, IL 60439-4815, USA | *gluskin@aps.anl.gov* |
| Goodzeit, C.L. | MJB Consulting, 119 Executive Way, #304, Desoto, TX 75115, USA | *clg@onramp.net* |
| Gordon, D.F. | Engineering School, UCLA, 405 Hilgard Avenue, Los Angeles, CA 90095, USA | *gordond@ucla.edu* |
| Gough, D. | SLAC, MS 69, P.O. Box 4349, Stanford, CA 94309-0210, USA | *gough@slac.stanford.edu* |
| Gough, R.A. | LBNL, 1 Cyclotron Road, Bldg. 71/259, Berkeley, CA 94720, USA | *ragough@lbl.gov* |
| Govil, R. | LBNL, MS 71-259, 1 Cyclotron Road, Berkeley, CA 94720, USA | *r_govil@lbl.gov* |
| Granatstein, V.L. | Inst. for Plasma Research, U. Maryland, College Park, MD 20742-3511, USA | *vlg@plasma.umd.edu* |
| Grand, P. | Amparo Corp., PO Box 2687, Santa Fe, NM 87504, USA | *pgrand@ibm.net* |
| Graves, W.S. | BNL, NSLS, Bldg. 725D, Upton, NY 11973, USA | *graves@bnl.gov* |
| Green, M.A. | LBNL, MS 44B-107, 1 Cyclotron Road, Berkeley, CA 94720, USA | *magreen@lbl.gov* |
| Green, M.A. | U. Wisconsin at Madison, SRC, 3731 Schneider Drive, Stoughton, WI 53589, USA | *mike@src.wisc.edu* |
| Greenwald, S. | Cornell U., Wilson Lab, Ithaca, NY 14853-5001, USA | |

| | | |
|---|---|---|
| Greenwald, Z. | Cornell U., Wilson Lab, Ithaca, NY 14853-5001, USA | |
| Grimm, T.L. | Michigan State U., NSCL, E. Lansing, MI 48824, USA | *grimm@nscl.msu.edu* |
| Grishanov, B.I. | Budker INP, Novosibirsk, Academician Lavrentiev Prospect 11, RU-630090 Novosibirsk, Russia | |
| Grishin, V.K. | INP of Moscow State U., RU-119899 Moscow, Russia | |
| Grobner, O. | CERN, CH-1211 Geneva 23, Switzerland | *oswald.grobner@cern.ch* |
| Grote, D.P. | LLNL, L440, P.O. Box 808, Livermore, CA 94550, USA | *grote1@llnl.gov* |
| Guan, X-L. | China IAE, P.O. Box 275 (15), Beijing, 102413, P.R. China | *gxl@inipsa.cire.ac.cn* |
| Guharay, S.K. | Inst. for Plasma Research, U. Maryland, Energy Research Facility #223, College Park, MD 20742, USA | *guharay@lpf.umd.edu* |
| Guidee, P.J. | TTE, 18 Avenue du Marichal Juin, F-92366 Meudon La Foret, Cedex, France | |
| Guignard, G.F. | CERN, CH-1211 Geneva 23, Switzerland | *gilbert.guignard@cern.ch* |
| Gunderson, G.R. | ANL, 9700 S. Cass Avenue, 401/B2156, Argonne, IL 60439, USA | *grg@aps.anl.gov* |
| Guo, Z. | IHEP, P.O. Box 918, Chinese Academy of Sciences, Beijing, 100039, P.R. China | |
| Gupta, R.C. | BNL, Bldg. 902A, Cornell Avenue, Upton, NY 11973, USA | *guptal@bnl.gov* |
| Gurd, D.P. | LANL, MS H820, P.O. Box 1663, Los Alamos, NM 87545, USA | *gurd@lanl.gov* |
| Guy, F.W. | Linac Systems, 1640 Greathouse Road, Waxahachie, TX 75167, USA | *fglinac//@hachie.citylimits.net* |
| Haeuser, J. | NTG Neue Technologien GmbH & Co. KG, Im Steinigen Graben 12-14, D-63571 Gelnhausen-Hailer, Germany | |
| Haggard, J.E. | FNAL, MS 316, P.O. Box 500, Batavia, IL 60510, USA | *johne@fnal.gov* |
| Hahn, A.A. | FNAL, P.O. Box 500, Batavia, IL 60510, USA | *ahahn@fnal.gov* |
| Hahn, H. | BNL, Bldg. 1005S, P.O. Box 5000, Upton, NY 11973-5000, USA | |
| Haimson, J. | Haimson Research Corp., 3350 Scott Boulevard, Bldg. 60, Santa Clara, CA 95054-3104, USA | *haimson@aol.com* |
| Halbach, K. | LBNL, MS 46-161, 1 Cyclotron Road, Berkeley, CA 94708, USA | *khalbach@lbl.gov* |
| Hamm, R.W. | Accsys Technology, Inc., 1177A Quarry Lane, Pleasanton, CA 94566, USA | *rhamm@linacs.com* |
| Hanft, R. | FNAL, MS 316, P.O. Box 500, Batavia, IL 60510, USA | *hanft@fnal.gov* |
| Hanna, S.M. | SLAC, MS 33, P.O. Box 4349, Stanford, CA 94309, USA | *hanna@slac.stanford.edu* |
| Hansborough, L.D. | LANL, P.O. Box 1663, Los Alamos, NM 87544, USA | *lash@lanl.gov* |
| Haouat, G.A. | DRIF/DPTA/SP2A, CEA-Bruyeres-le-Chatel, BP12-Bruyeres-le-Chatel, F-91680 Bruyeres-le-Chatel, France | |
| Hara, M. | JAERI-RIKEN SPring-8, Kamigori - cho, Akol-gun, Hyogo 678-12, Japan | *hara@sp8sun.spring8.or.jp* |
| Harding, D.J. | FNAL, MS 232, P.O. Box 500, Batavia, IL 60510-0500, USA | *harding@fnal.gov* |
| Hardy, D.G. | TJNAF, MS 85A, 12000 Jefferson Avenue, Newport News, VA 23606, USA | *hardy@jlab.org* |
| Hardy, L. | ESRF, BP 220, F-38043 Grenoble, France | *hardy@esrf.fr* |
| Harkay, K.C. | ANL, 9700 S. Cass Avenue, Bldg. 401, Argonne, IL 60439, USA | *harkay@aps.anl.gov* |
| Harold, M.R. | RAL, CLRC, Chilton, Didcot, Oxon., UK, OX11 0QX | *m.r.harold@rl.ac.uk* |
| Harrison, M.A. | BNL, Bldg. 1005, P.O. Box 5000, Upton, NY 11973-5000, USA | *harrison@bnl.gov* |
| Hartemann, F.V. | UC Davis/ LLNL - ILSA, LLNL, L - 794, P.O. Box 808, Livermore, CA 94602, USA | *fredh@gregor.llnl.gov* |
| Hartmann, H. | BNL, Bldg. 911C, 35 Lawrence Drive, Upton, NY 11973, USA | *hartman1@bnl.gov* |
| Harwood, L.H. | TJNAF, 12000 Jefferson Avenue, Newport News, VA 23606, USA | *harwood@jlab.org* |
| Hasegawa, K. | JAERI, Proton Accelerator Lab, Tokai-mura, Ibaraki-ken 319-11, Japan | *hasegawa@linac.tokai.jaeri.go.jp* |
| Hayes, T. | BNL, Bldg. 911B, Upton, NY 11973, USA | *hayes@bnl.gov* |
| He, P. | UCLA, B. 820/ATF, Brookhaven National Lab, Upton, NY 11973, USA | *phe@sunz.bnl.gov* |
| Heese, R. | BNL, NSLS Bldg. 725C, P.O. Box 5000, Upton, NY 11973-5000, USA | *heese@bnllsl.nsls.bnl.gov* |
| Hemker, R.G. | UCLA, 405 Hilgard Avenue, Knudsen Hall 1-130, Los Angeles, CA 90095-1547, USA | *hemker@physics.ucla.edu* |
| Henderson, S.D. | Cornell U., Wilson Lab, Ithaca, NY 14853-5001, USA | *sdh9@lus62.lus.cornell.edu* |
| Hernandez, M.E. | SLAC, SSRL, 2575 Sand Hill Road, Menlo Park, CA 94025, USA | *hernandez@ssrl.slac.stanford.edu* |
| Herr, W.F. | CERN, SL Division, CH-1211 Geneva 23, Switzerland | *werner.herr@cern.ch* |
| Herrmannsfeldt, W.B. | SLAC, 2575 Sand Hill Road, Menlo Park, CA 94025, USA | *wbhap@slac.stanford.edu* |
| Hershcovitch, A. | BNL, 911B, P.O. Box 5000, Upton, NY 11973-5000, USA | *herscvo1@bnl.gov* |
| Hesselson, S.L. | EEV Inc., 4 Westchester Plaza, Elmsford, NY 10523, USA | |
| Hill, J.O. | LANL, MS H820, P.O. Box 1663, Los Alamos, NM 87545, USA | *johill@lanl.gov* |
| Hinkson, J.A. | LBNL, MS 16-125, 1 Cyclotron Road, Berkeley, CA 94720, USA | *jahinkson@lbl.gov* |
| Hiramoto, K. | Hitachi, Ltd., 1-1 Omika-cho, 7-chome, Hitachi, Ibaraki-ken 319-12, Japan | *hiramoto@erl.hitachi.co.jp* |
| Hirata, K. | KEK, 1-1 Oho, Tsukuba-shi, Ibaraki-ken 305, Japan | *hirata@kekvax.kek.jp* |
| Hirshfield, J.L. | Yale U., 202008 Yale Station, New Haven, CT 06520, USA | *jay@mirage.physics.yale.edu* |
| Ho, D.D. | LLNL, L-477, P.O. Box 808, Livermore, CA 94551, USA | *ho@llnl.gov* |
| Ho, W. | TRIUMF, 5280 Prince Albert Street, Vancouver, BC, Canada, V5W 3C8 | *wendyho@unixg.ubc.ca* |
| Hoff, L.T. | BNL, Bldg. 911-C, Upton, NY 11973, USA | *hoff@bnl.gov* |
| Hoff, M.D. | LBNL, 71-259, 1 Cyclotron Road, Berkeley, CA 94720, USA | *mdhoff@lbl.gov* |
| Hoffman, B.C. | Thomson Components & Tubes Corp., 40 G Commerce Way, Totowa, NJ 07511, USA | *hoffmantct@aol.com* |

| | | |
|---|---|---|
| Hofmann, J. | GSI Darmstadt, Plandestr. 1, D-64291 Darmstadt, Germany | *j.hofmann@gsi.de* |
| Hogan, B.P. | U. Maryland, Bldg. #223, College Park, MD 20851, USA | *bhogan@plasma.umd.edu* |
| Hogan, M.J. | Dept. of Physics, UCLA, Los Angeles, CA 90095-1547, USA | *hogan@physics.ucla.edu* |
| Holmes, J.A. | ORNL, FEDC, P.O. Box 2009, Oak Ridge, TN 37831-8218, USA | *jzh@ornl.gov* |
| Holmes, S.D. | FNAL, MS 323, P.O. Box 500, Batavia, IL 60510, USA | *holmes@fnal.gov* |
| Horan, D.A. | ANL, 9700 S. Cass Avenue, Bldg. 401/C3270, Argonne, IL 60439, USA | *horan@aps.anl.gov* |
| Hori, T. | Sumitomo Heavy Industries, Ltd., 2-1-1 Yato-cho, Tanashi, Tokyo, 188, Japan | *hori_tsl@tns.shi.ro.jp* |
| Houck, T.L. | LLNL, L-441, P.O. Box 808, Livermore, CA 94550, USA | *houck1@llnl.gov* |
| Hovater, C. | TJNAF, 12000 Jefferson Avenue, Newport News, VA 23606, USA | *hovater@jlab.org* |
| Hoyer, E.H. | LBNL, 46-161, 1 Cyclotron Road, Berkeley, CA 94720, USA | *ehhoyer@lbl.gov* |
| Hsu, I.C. | Dept. of Nuclear Science, National Tsing Hua U. & SRRC, Hsinchu, 300, Taiwan | *ichsu@ins.nthu.edu.tw* |
| Huang, H. | BNL, AGS Dept., 911B, P.O. Box 5000, Upton, NY 11973-5000, USA | *huang@bnldag.bnl.gov* |
| Huang, J-Y. | Pohang Acc. Lab, POSTECH, San 31, Hyoja-dong, Nam-ku, Pohang, Kyungbuk 790-784, S. Korea | *huang@postech.ac.kr* |
| Hubbard, E.L. | General Atomics, 5527 Chelsea Avenue, La Jolla, CA 92037, USA | *ed_hubbard@compuserve.com* |
| Hughes, T.P. | Mission Research Corp., 1720 Randolph, SE, Albuquerque, NM 87106, USA | *tph@lanl.gov* |
| Hulsmann, P. | IAP, Frankfurt/Main, Robert-Mayer-Str. 2-4, D-60325 Frankfurt am Main, Germany | *pehe@miknol.physik.uni-frankfurt.de* |
| Humphrey, J.W. | SLAC, MS 50, P.O. Box 4349, Stanford, CA 94309, USA | *jwh@slc.slac.stanford.edu* |
| Humphries, S. | Dept. EECE, U. New Mexico, Albuquerque, NM 87131, USA | *humphrie@warlock.eece.unm.edu* |
| Hunt, S.M. | PSI, CH-5232 Villigen, Switzerland | *hunt@psi.ch* |
| Huttel, E. | Forschungszentrum Karlsruhe / ANKA, PO Box 3640, D-76021 Karlsruhe, Germany | *huttel@anka.lzk.de* |
| Hutter, G.J. | GSI Darmstadt, Planckstr. 1, D-64739 Darmstadt, Germany | |
| Hutton, A.M. | TJNAF, MS 12A2, 12000 Jefferson Avenue, Newport News, VA 23606, USA | *andrew@jlab.org* |
| Iazzourene, F. | Sincrotrone Trieste, SS 14 km 163.5 - Area Science Park - Basovizza, I-34012 Trieste, TS, Italy | *iazzourene@elettra.trieste.it* |
| Ikegami, M. | Kyoto U., NSRF, ICR, Gokanosho, Uji, Kyoto 611, Japan | *ikegami@kyticr.kuicr.kyoto-u.ac.jp* |
| Inabe, N. | RIKEN, Cyclotron Lab, 2-1 Hirosawa, Wako, Saitama 351-01, Japan | |
| Ingrassia, P.F. | BNL, AGS Dept., Bldg. 911A, P.O. Box 5000, Upton, NY 11973, USA | *ingrassia@bnl.gov* |
| Irwin, J. | SLAC, MS 26, P.O. Box 4349, Stanford, CA 94309, USA | *irwin@slac.stanford.edu* |
| Ishimaru, H. | KEK, 1-1 Oho, Tsukuba-shi, Ibaraki-ken 305, Japan | *ishimaru@kekvax.kek.jp* |
| Issinsky, I.B. | Lab of High Energies, JINR, RU-141980 Dubna, Moscow region, Russia | *issinsky@lhe.27.jinr.dubna.su* |
| Ivanov, I.N. | JINR, PPL, Zholiot-Kuri 6, RU-141980 Dubna, Moscow region, Russia | *ivanov@sunse.jinr.dubna.su* |
| Ivers, J. | Cornell U., LNS, High Voltage Lab, 909 Mitchell Street, Ithaca, NY 14853, USA | *jivers@lps.cornell.edu* |
| Iwashita, Y. | Kyoto U., NSRF, ICR, Gokanosho, Uji, Kyoto 611, Japan | *iwashita@kyticr.kuicr.kyoto-u.ac.jp* |
| Jacob, J. | ESRF, BP 220, F-38043 Grenoble, France | *jacob@esrf.fr* |
| Jacobs, K. | MIT Bates, P.O. Box 846, 21 Manning Road, Middleton, MA 01949-2846, USA | *kjacobs@mit.edu* |
| Jaeschke, E.J.F. | BESSY, Berlin, Rudower Chaussee 5, D-12489 Berlin, Germany | *jaeschke@bessy.de* |
| Jankowiak, A. | U. Dortmund, IBS, Emil-Figge-Strasse 74B, D-44221 Dortmund, Germany | *janko@calvin.physik.uni-dortmund.de* |
| Jason, A.J. | LANL, MS 808, P.O. Box 1663, Los Alamos, NM 87545, USA | *ajason@lanl.gov* |
| Jayamanna, K. | TRIUMF, 4004 Wesbrook Mall, Vancouver, BC, Canada, V6T 2A3 | *keerthi@triumf.ca* |
| Jensen, C.C. | FNAL, MS 308, P.O. Box 500, Pine Street & Kirk Road, Batavia, IL 60510, USA | *ccjensen@fnal.gov* |
| Jensen, E. | CERN, CH-1211 Geneva 23, Switzerland | *erk.jensen@cern.ch* |
| Jensen, P. | DESY, Notkestrasse 85, D-22603 Hamburg, Germany | *jensenp@mail.desy.de* |
| Jeon, D-O. | IUCF, 2401 Milo B. Sampson Lane, Bloomington, IN 47408, USA | *jeon@iucf.indiana.edu* |
| Johns, L.D. | ANL, 9700 S. Cass Avenue, Bldg. 360, Argonne, IL 60439, USA | *JohnsLarry@ipns-360.anl.gov* |
| Johnson, B. | Physical Review E/BNL, 1 Research Road, Ridge, NY 11961, USA | |
| Johnson, D.E. | FNAL, MS 323, P.O. Box 500, Batavia, IL 60510, USA | *dej@fnal.gov* |
| Johnson, L.E. | Duke U., FEL Lab, La Salle Street Ext., Durham, NC 27708, USA | *lewisj@fel.duke.eu* |
| Johnson, R.G. | SLAC, P.O. Box 4349, Stanford, CA 94309, USA | *ron-johnson@slac.stanford.edu* |
| Johnstone, C.J. | FNAL, MS 345, P.O. Box 500, Batavia, IL 60510, USA | *cjj@fnal.gov* |
| Johnstone, J.A. | FNAL, P.O. Box 500, Batavia, IL 60510, USA | *jjohnstone@adcalc.fnal.gov* |
| Joho, W. | PSI, CH-5234 Villigen, Switzerland | *werner.joho@psi.ch* |
| Joly, S.C. | DRIF/DPTA/SP2A, CEA-Bruyeres-le-Chatel, BP12-Bruyeres-le-Chatel, F-91680 Bruyeres-le-Chatel, France | |
| Jones, F.W. | TRIUMF, 4004 Wesbrook Mall, Vancouver, BC, Canada, V6T 2A3 | *fwj@triumf.ca* |
| Jones, J. | ANL, 9700 S. Cass Avenue, Bldg. 401, Argonne, IL 60439-4815, USA | *jones@aps.anl.gov* |
| Jongen, Y. | IBA, Chemin du Cyclotron, 2, B-1348 Louvaine - La - Neuve, Belgium | *amv@iba.mhs.compuserve.com* |
| Jordan, K. | TJNAF, 12000 Jefferson Avenue, Newport News, VA 23606, USA | *jordan@jlab.org* |
| Joshi, C. | UCLA, 2004 Pier Avenue, Santa Monica, CA 90405, USA | *joshi@ee.ucla.edu* |
| Juillard, M. | DAPNIA/SEA, CEA-Saclay, F-91191 Gif sur Yvette, Cedex, France | *juillard@hep.saclay.cea.fr* |

| | | |
|---|---|---|
| Kaan, A.P. | NIKHEF, P.O. Box 41882, Kruislaan 409, NL-1009 DB Amsterdam, The Netherlands | *bert@nikhefk.nikhef.nl* |
| Kageyama, T. | KEK, 1-1 Oho, Tsukuba-shi, Ibaraki-ken 305, Japan | *tatsuya.kageyama@kek.jp* |
| Kahn, S.A. | BNL, 902A, P.O. Box 5000, Upton, NY 11973-5000, USA | *kahn1@bnl.gov* |
| Kaltchev, D. | TRIUMF, 4004 Wesbrook Mall, Vancouver, BC, Canada, V6T 2A3 | *kaltchev@triumf.ca* |
| Kamigaito, O. | RIKEN, 2-1 Hirosawa, Wako, Saitama 351-01, Japan | *kamigait@ringps.riken.go.jp* |
| Kamitsubo, H. | JAERI-RIKEN SPring-8, Kamigori - cho, Ako-gun, Hyogo 678-12, Japan | *kamitsub@sp8sun.spring8.or.jp* |
| Kanaya, N. | KEK, Photon Factory, 1-1, Oho, Tsukuba, 305, Japan | *kanaya@kekvax.kek.jp* |
| Kanazawa, M. | NIRS, Chiba, 9-1, Anagawa 4-chome, Inage-ku, Chiba, 263, Japan | *kanazawa@nirs.go.jp* |
| Kang, X. | IUCF, 2401 Milo B. Sampson Lane, Bloomington, IN 47405, USA | *kang@iucf.indiana.edu* |
| Kang, Y.W. | ANL, 9700 S. Cass Avenue, Argonne, IL 60439, USA | *ywkang@aps.anl.gov* |
| Kantardjian, G.D. | CERN, EST Division, CH-1211 Geneva 23, Switzerland | *gregoire.kantardjian@cern.ch* |
| Karn, J.S. | TJNAF, MS 16A, 12000 Jefferson Avenue, Newport News, VA 23602, USA | *karn@jlab.org* |
| Kassab, L.R.P. | Laboratorio do Acelerador Linear, Instituto de Fisica/Universidade de Sao Paulo, Caixa Postal 66.318, BR-05389-970 Sao Paulo, Sao Paulo, Brazil | *lpires@if.usp.br* |
| Kasuga, T. | KEK, 1-1 Oho, Tsukuba-shi, Ibaraki-ken 305, Japan | *kasugat@kekvax.kek.jp* |
| Kato, S. | Faculty of Science, Osaka U., Lab of Nuclear Studies, Toyonaka, Osaka 560, Japan | |
| Katsouleas, T. | U. Southern California, Los Angeles, CA 90089-0484, USA | *katsoulde@usc.edu* |
| Kawaguchi, H. | Division Systems & Information Eng., Hokkaido U., Kita 13, Nishi 8, Kita-ku, Sapporo, 060, Japan | *kawa@em.huee.hokudai.ac.jp* |
| Kazakov, S. | Branch of Budker INP, RU-142284 Protvino, Moscow region, Russia | *kazakov@vlepp.serpukhov.su* |
| Kazimi, R. | TJNAF, 12000 Jefferson Avenue, Newport News, VA 23606, USA | *kazimi@cebaf.gov* |
| Kehne, D.M. | TJNAF, MS 16A, 12000 Jefferson Avenue, Newport News, VA 23606, USA | *kehne@jlab.org* |
| Keil, E.K. | CERN, 60 Avenue Wendt, CH-1203 Geneva, Switzerland | *eberhard.keil@cern.ch* |
| Keil, J. | Physikalisches Institut der Universitat, Bonn U., ELSA, Nussallee 12, D-53115 Bonn, NRW, Germany | *keil@elsar1.physik.uni-bonn.de* |
| Keller, R. | LBNL, ALS, MS 80-101, 1 Cyclotron Road, Berkeley, CA 94720, USA | *r.keller@lbl.gov* |
| Kelly, D.R.C. | DESY, Notkestrasse 85, D-22603 Hamburg, Germany | *kelly@x4u2.desy.de* |
| Kennedy, K.D. | LBNL, MS 71J, 1 Cyclotron Road, Berkeley, CA 94549, USA | *kdkennedy@lbl.gov* |
| Kerr, J.W. | EEV Ltd., Waterhouse Lane, Chelmsford, Essex, UK, CH1 2QU | |
| Kester, O.K. | Sektion Physik der LMU Munchen, Am Coulombwall 1, D-85748 Garching, Bayeru, Germany | *oliver.kester@physik.uni-muenchen.de* |
| Khan, S. | BESSY-II, GEB. 15.1 Rydower Chaussee 5, D-12489 Berlin, Germany | *khan@port.exp.bessy.de* |
| Kim, C.H. | LBNL, MS 80-101, 1 Cyclotron Road, Berkeley, CA 94720, USA | *chkim@lbl.gov* |
| Kim, J-S. | Fusion and Accelerator Research, 3146 Bunche Avenue, San Diego, CA 92122-2247, USA | *u11726@nersc.gov* |
| Kim, J-W. | RIKEN, Hirosawa 2-1, Wako, Saitama 351-01, Japan | *jwkim@rikvax.riken.go.jp* |
| Kim, K-J. | Centre for Beam Physics, LBNL, MS 71-259, 1 Cyclotron Road, Berkeley, CA 94720, USA | *kwangje@lbl.gov* |
| Kimura, W.D. | STI Optronics, Inc., 2755 Northup Way, Bellevue, WA 89004-1495, USA | *wkimura@stiopt.com* |
| King, B.J. | BNL, Bldg. 901A, Upton, NY 11973-5000, USA | *bking@sun2.bnl.gov* |
| Kinross-Wright, J.M. | LANL, MS H851, P.O. Box 1663, Los Alamos, NM 87545, USA | *kinross@lanl.gov* |
| Kircher, F.A. | CEA-Saclay, STCM, BAV 123, F-91191 Gif sur Yvette, France | *kircher@hep.saclay.com.fr* |
| Kirk, H.G. | BNL, Bldg. 901A, P.O. Box 5000, Upton, NY 11973-5000, USA | *hkirk@bnl.gov* |
| Kishek, R.A. | U. Maryland, IPR, Energy Research Bldg., College Park, MD 20742-3511, USA | *rami@engim.umich.edu* |
| Klabunde, J. | GSI Darmstadt, POB 110552, D-64220 Darmstadt, Hessen, Germany | *j.klabunde@gsi.de* |
| Klaffky, R. | BNL, NSLS Bldg. 725C, P.O. Box 5000, Upton, NY 11973-5000, USA | *klaffky@bnl.gov* |
| Kleffner, C-M. | DESY, Notkestrasse 85, D-22603 Hamburg, Germany | *kleffner@mail.desy.de* |
| Klein, B.B. | Vista Control Systems, Inc., 134 B Eastgate Drive, Los Alamos, NM 87544, USA | *klein@vistanm.com* |
| Klein, H. | IAP, Frankfurt/Main, Robert-Mayer-Str. 2-4, D-60054 Frankfurt am Main, Germany | *hklein@mikro1.physik.uni-frankfurt.de* |
| Klein, H.U. | ACCEL Instruments GmbH, Friedrich Ebert Str. 1, D-51429 Bergisch, Gladbach, Germany | *klein@accel.de* |
| Klem, J.T. | CERN, 4, Chemin du Sautoir d'Or, CH-1294 Geneva 23, Switzerland | *jukka.klem@cern.ch* |
| Kneisil, P. | TJNAF, 12000 Jefferson Avenue, Newport News, VA 23606, USA | *kneisil@cebaf.gov* |
| Knott, M.J. | ANL, 9700 S. Cass Avenue, Bldg. 401, Argonne, IL 60439-4815, USA | *mjk@aps.anl.gov* |
| Ko, I.S. | Pohang Acc. Lab, POSTECH, San 31, Hyoja-dong, Nam-ku, Pohang, Kyungbuk 790-784, S. Korea | *isko@vision.postech.ac.kr* |
| Kolomiets, A.A. | ITEP, B. Cheremushkinskaya, 25, RU-117259 Moscow, Russia | |
| Konecny, R.S. | ANL, 9700 S. Cass Avenue, Argonne, IL 60439-4815, USA | *rsk@hep.anl.gov* |
| Konrad, G.T. | Siemens Medical Systems, 4040 Nelson Avenue, Concord, CA 94520, USA | *gkonrad@smsocs.com* |
| Koontz, R.F. | SLAC, P.O. Box 4349, Bin #33, Stanford, CA 94309, USA | *rfkap@slac.stanford.edu* |
| Koscielniak, S.R. | TRIUMF, 4004 Wesbrook Mall, Vancouver, BC, Canada, V6T 2A3 | *shane@triumf.ca* |

| | | |
|---|---|---|
| Kost, C. | TRIUMF, 4004 Wesbrook Mall, Vancouver, BC, Canada, V6T 2A3 | *kost@triumf.ca* |
| Kotseroglov, T. | SLAC, 2575 Sand Hill Road, Menlo Park, CA 94025, USA | *theo@slac.stanford.edu* |
| Koutchouk, J-P.S. | CERN, CH-1211 Geneva 23, Switzerland | *jean-pierre.koutchouk@cern.ch* |
| Kozodaev, A.M. | ITEP, B. Cheremushkinskaya, 25, RU-117259 Moscow, Russia | |
| Krafft, G.A. | TJNAF, 12000 Jefferson Avenue, Newport News, VA 23606, USA | *krafft@jlab.org* |
| Kraimer, M.R. | ANL, 9700 S. Cass Avenue, Argonne, IL 60439-4815, USA | *mrk@aps.anl.gov* |
| Kravchuk, L.V. | INR, Russian Academy of Sciences, 60th October Anniversary Prospect 7a, RU-117312 Moscow, Russia | |
| Krawczyk, F.L. | LANL, MS H817, L-1, P.O. Box 1663, Los Alamos, NM 87545, USA | *fkrawczyk@lanl.gov* |
| Krebs, G.F. | LBNL, MS 80-101, 1 Cyclotron Road, Berkeley, CA 94720, USA | *g_krebs@lbl.gov* |
| Kreischer, K.E. | MIT Plasma Science and Fusion Center, MIT NW 16-174, Cambridge, MA 02139, USA | *kek@ilm.pec.mit.edu* |
| Krejcik, P. | SLAC, MS 66, P.O. Box 4349, Stanford, CA 94309, USA | *pkr@slac.stanford.edu* |
| Krienen, F. | Boston U., 22927 Drake Lane, Summerland Key, FL 33042, USA | *krienen@bnldag.ags.bnl.gov* |
| Kriens, W. | DESY, Notkestrasse 85, D-22607 Hamburg, Germany | *mkikri@mail.desy.de* |
| Krietenstein, B. | TH Darmstadt, Schlossgarten Str. 8, D-64289 Darmstadt, Germany | *kstein@temf.th-darmstadt.de* |
| Krinsky, S. | BNL, NSLS, Bldg. 725B, Upton, NY 11973, USA | *krinsky@bnllsl.nsls.bnl.gov* |
| Krischel, D.W. | ACCEL Instruments GmbH, Friedrich-Ebert-Str. 1, D-51429 Bergisch, Gladbach, Germany | *krischel@accel.de* |
| Kroll, N.M. | Dept of Physics, SLAC, 9500 Gilman Drive, La Jolla, CA 92093-0319, USA | *nkroll@ucsd.edu* |
| Krupnick, J.T. | LBNL, 80-101, 1 Cyclotron Road, Berkeley, CA 94720, USA | *jtkrupnick@lbl.gov* |
| Kumada, M. | NIRS, Chiba, 4-9-1 Anagawa, Inage, Chiba, Chiba 263, Japan | *kumada@nirs.go.jp* |
| Kuo, C-C. | SRRC, Taiwan, No. 1 R&D Road, VI, Hsinchu Science-Based Industrial Park, Hsinchu, 30077, Taiwan | *kuo@bd02.srrc.gov.tw* |
| Kuo, C.H. | SRRC, Taiwan, No. 1 R&D Road, VI, Hsinchu Science-Based Industrial Park, Hsinchu, 30077, Taiwan | *ako@alphai.srrc.gov.tw* |
| Kuo, T.Y.T. | TRIUMF, 4004 Wesbrook Mall, Vancouver, BC, Canada, V6T 2A3 | *tkuo@triumf.ca* |
| Kurennoy, S.S. | LANL, MD H808, P.O. Box 1663, Los Alamos, NM 87545, USA | *kurennoy@lanl.gov* |
| Kurita, N.R. | SLAC, MS 18, 2575 Sand Hill Road, Menlo Park, CA 94025, USA | *kurita@slac.stanford.edu* |
| Kurokawa, S-I. | KEK, 1-1 Oho, Tsukuba-shi, Ibaraki-ken 305, Japan | *shin-ichi.kurokawa@kek.jp* |
| Kwan, J.W. | LBNL, MS 47-112, 1 Cyclotron Road, Berkeley, CA 94720, USA | *jwkwan@lbl.gov* |
| Kwan, T.J.T. | LANL, MS B259, P.O. Box 1663, Los Alamos, NM 87544, USA | *tjtk@lanl.gov* |
| Kwiatkowski, S. | BNL, Bldg. 1005S, P.O. Box 5000, Upton, NY 11973-5000, USA | *slawomir@owl.rhic.gnl.gov* |
| Kwon, M. | Pohang Acc. Lab, POSTECH, San 31, Hyoja-dong, Nam-ku, Pohang, Kyungbuk 790-784, S. Korea | *kwonm@vision.postech.ac.kr* |
| Lachinov, M.V. | TRIUMF, UBC, 4004 Wesbrook Mall, Vancouver, BC, Canada, V6T 2A3 | *lachinov@triumf.ca* |
| Lackner, H. | Pulse Sciences, Inc., 600 McCormick Street, San Leandro, CA 94577, USA | |
| Laclare, J-L. | CEA-CNRS - Projet SOLEIL, DRIF du CNRS, Avenue de la Terrasse, Batiment 5, F-91198 Gif sur Yvette, Cedex, France | *paclare@soleil.cea.fr* |
| Lacy, W. | TJNAF, 12000 Jefferson Avenue, Newport News, VA 23606, USA | *lacy@jlab.gov* |
| Lagniel, J-M. | CEA-Saclay, LNS Bar 130, F-91191 Gif sur Yvette, France | *lagniel@lns.cea.fr* |
| Lahey, T.E. | SLAC, MS 46, P.O. Box 4349, Stanford, CA 94309-4349, USA | *lahey@slac.stanford.edu* |
| Lamm, M.J. | FNAL, MS 316, P.O. Box 500, Batavia, IL 60510- 0500, USA | *lamm@fnal.gov* |
| Lampel, M.C. | G.H. Gillespie Associates, Inc., 10855 Sorrento Valley Road, Suite 201, San Diego, CA 92121, USA | *ghga@millennianet.com* |
| Larbalestier, D.C. | U. Wisconsin, 1500 Engineering Drive, Room 915, Madison, WI 53706, USA | *larbales@engr.wisc.edu* |
| Larson, D.J. | SAIC, 861 Raintree Lane, DeSoto, TX 75115, USA | *delbert7@aol.com* |
| Latypov, D.M. | Magnet Lab., Texas A&M U., 3801 Harvey Road, College Station, TX 77845, USA | *latypov@tdl.harc.edu* |
| Laune, B. | IPN Orsay, F-91406 Orsay, Cedex, France | *laune@ipncls.in2p3.fr* |
| Lauze, R. | TJNAF, MS 85, 12000 Jefferson Avenue, Newport News, VA 23606, USA | *lauze@jlab.gov* |
| Lavine, T.L. | SLAC, MS 26, P.O. Box 4349, Stanford, CA 94309, USA | *lavine@slac.stanford.edu* |
| Lawrence, G.P. | LANL, MS H913, P.O. Box 1663, Los Alamos, NM 87545, USA | *glawrence@lanl.gov* |
| Lawson, W.G. | U. Maryland, 15014 Saddle Creek Drive, Burtonsville, MD 20866, USA | *lawson@eng.umd.edu* |
| Laxdal, R.E. | TRIUMF, 4004 Wesbrook Mall, Vancouver, BC, Canada, V6T 2A3 | *lax@triumf.ca* |
| Lebedev, V. | TJNAF, MS 12A1, 12000 Jefferson Avenue, Newport News, VA 23606, USA | *lebedev@jlab.org* |
| LeBlanc, G.S. | SLAC, SSRL, MS 69P, P.O. Box 4349, Stanford, CA 94309, USA | *leblanc@ssrl01.slac.stanford.edu* |
| Leboutet, H. | CEA-DAM, 16 Residence Beausoleil, F-92210 Saint Cloud, France | |
| Lebrun, P. | CERN, CH-1211 Geneva 23, Switzerland | *phillippe.lebrun@cern.ch* |
| Lee, S. | U. Southern California, 1325 Valley View Road, #204, Glendale, CA 91202, USA | *lee@plasma1.usc.edu* |
| Lee, S.Y. | Dept. of Physics, Indiana U., SW117, Bloomington, IN 47405, USA | *shylee@indiana.edu* |
| Lee, Y.Y. | LBNL, MS 5-119, 1 Cyclotron Road, Berkeley, CA 94720, USA | |
| Lee, Y.Y. | BNL, Bldg. 911B, Upton, NY 11973-5000, USA | *yylee@bnl.gov* |
| Leibfritz, J.R. | FNAL, MS 340, P.O. Box 500, Batavia, IL 60510, USA | *leibfritz@fnal.gov* |

| | | |
|---|---|---|
| Leitner, M. | LBNL, MS 5-119, 1 Cyclotron Road, Berkeley, CA 94720, USA | *mleitner@lbl.gov* |
| Lemaire, J-L. | DRIF/DPTA/SP2A, CEA-Bruyeres-le-Chatel, BP12-Bruyeres-le-Chatel, F-91680 Bruyeres-le-Chatel, France | *jlemaire@bruyeres.cea.fr* |
| Len, L.K. | FM Technologies, 10529-B, Braddock Road, Fairfax, VA 22032, USA | *len@ppd.nrl.navy.mil* |
| Lenkszus, F.R. | ANL, 9700 S. Cass Avenue, Bldg. 401, Argonne, IL 60439, USA | *frl@aps.anl.gov* |
| Lennox, A.J. | FNAL, MS 301, P.O. Box 500, Batavia, IL 60510, USA | *alennox@fnal.gov* |
| Leonhardt, B. | BNL, Bldg. 510A, P.O. Box 5000, Upton, NY 11973-5000, USA | *leonhar1@bnl.gov* |
| Lessner, E. | ANL, 9700 S. Cass Avenue, Bldg. 401, Argonne, IL 60439, USA | *lessner@aps.anl.gov* |
| Letchford, A.P. | RAL, CLRC, Chilton, Didcot, Oxon., UK, OX11 OQX | *a.letchford@rl.ac.uk* |
| Letta, P.C. | TJNAF, 12000 Jefferson Avenue, Newport News, VA 23606, USA | *letta@jlab.org* |
| Leung, K-N. | LBNL, MS 5/119, 1 Cyclotron Road, Berkeley, CA 94720, USA | *knleung@lbl.gov* |
| Level, M.P. | CEA-CNRS - Projet SOLEIL, DRIF du CNRS, Bat 5 Avenue de la Terrasse, F-91198 Gif sur Yvette, Cedex, France | *level@lure.u-psud.fr* |
| Levush, B. | NRL, 4555 Overlook Avenue, SW, Washington, DC 20375, USA | *levush@mmace.nrl.navy.mil* |
| Levy, P. | TRIUMF, 4004 Wesbrook Mall, Vancouver, BC, Canada, V6T 2A3 | *levy@triumf.ca* |
| Lewis, S.A. | LBNL, MS 50A-2160, 1 Cyclotron Road, Berkeley, CA 94618, USA | *salewis@lbl.gov* |
| Li, N. | LBNL, 71J, 1 Cyclotron Road, Berkeley, CA 94720, USA | *n_li@lbl.gov* |
| Li, R. | TJNAF, MS 12A1, 12000 Jefferson Avenue, Newport News, VA 23606, USA | *lir@jlab.org* |
| Li, Z. | SLAC, MS 26, 2575 Sand Hill Road, Menlo Park, CA, USA | *lizh@slac.stanford.edu* |
| Lidestri, J.P. | Columbia U., 630 West 168th Street, New York, NY 11709, USA | *lidestri@nec.com* |
| Limborg, C.G. | SLAC, SSRL, MS 69, 2575 Sand Hill Road, Stanford, CA 94309, USA | *limborg@ssrl.slac.stanford.edu* |
| Limon, P.J. | FNAL, MS 316, P.O. Box 500, Batavia, IL 60510, USA | *pjlimon@fnal.gov* |
| Lin, X.E. | SLAC, MS 17, Stanford U., Stanford, CA 94309-4349, USA | *eddie@slac.stanford.edu* |
| Linnecar, T.P. | CERN, SL Division, CH-1211 Geneva 23, Switzerland | *trevor.linnecar@cern.ch* |
| Lisowski, P.W. | LANL, MS H813, P.O. Box 1663, Los Alamos, NM 87545, USA | *lisowski@lanl.gov* |
| Litvinenko, V.N. | Duke U., FEL Lab, P.O. Box 90319, Durham, NC 27708-0319, USA | *vl@phy.duke.edu* |
| Liu, L. | LNLS - Brazil, Caixa Postal 6192, BR-13083-970 Campinas, SP, Brazil | *liu@lnls.br* |
| Liu, Y. | BNL, ATF, B820, Upton, NY 11973, USA | *yliu@bnl.gov* |
| Lo, C.C. | LBNL, MS 46-125, 1 Cyclotron Road, Berkeley, CA 94720, USA | *cclo@lbl.gov* |
| Loew, G.A. | SLAC, MS 33, P.O. Box 4349, Stanford, CA 94305, USA | *galoew@slac.stanford.edu* |
| Lombardi, A. | INFN-LNL, Via Romea 14, I-35020 Legnaro, PD, Italy | *alobardi@lnl.infn.it* |
| Lonza, M. | Elettra, Sincrotrone Trieste, SS 14 km 163.5, in Area Science Park - Basovizza, I-34012 Trieste, TS, Italy | *lonzam@elettra.trieste.it* |
| Lorenz, R. | TU Berlin, Secretariat En 2, Einsteinufer 17, D-10587 Berlin, Germany | *lorenz@tetjbm1.ee.tu-berlin.de* |
| Lou, W. | Cornell U., Wilson Lab, Ithaca, NY 14853-5001, USA | *wrl@lns62.lns.cornell.edu* |
| Luccio, A.U. | BNL, 911B, Upton, NY 11973-5000, USA | *luccio@bnldag.gov* |
| Ludewigt, B.A. | LBNL, 71-259, 1 Cyclotron Road, Berkeley, CA 94720, USA | *BALudewigt@lbl.gov* |
| Luijckx, G. | NIKHEF, Kruislaan 409, NL-1098 SJ Amsterdam, The Netherlands | *guy@nikhef.nl* |
| Lumpkin, A.H. | ANL, 9700 S. Cass Avenue, Bldg. 401, Argonne, IL 60439, USA | *lumpking@aps.anl.gov* |
| Lund, S.M. | LLNL, L-440, P.O. Box 808, Livermore, CA 94550, USA | *lund@hif.lnl.gov* |
| Luo, G-H. | SRRC, Taiwan, No. 1 R&D Road, VI, Hsinchu Science-Based Industrial Park, Hsinchu, 30077, Taiwan | *Luo@srrcoi.srrc.gov.tw* |
| Lynch, M.T. | LANL, MS - H827, P.O. Box 1663, Los Alamos, NM 87545, USA | *mtlynch@lanl.gov* |
| Lyneis, C.M. | LBNL, Bldg. 88, 1 Cyclotron Road, Berkeley, CA 94708, USA | *cmlyneis@lbl.gov* |
| Lysenko, W.P. | LANL, MS H808, P.O. Box 1663, Los Alamos, NM 87545, USA | *wplW@lanl.gov* |
| Macek, R.J. | LANL, MS H848, Lansce-Do, Los Alamos, NM 87545, USA | *macek@lanl.gov* |
| MacKay, W.W. | BNL, Bldg. 1005, P.O. Box 5000, Upton, NY 11973-5000, USA | *waldo@bnl.gov* |
| Mackenzie, G.H. | TRIUMF, 4004 Wesbrook Mall, Vancouver, BC, Canada, V6T 2A3 | *ghm@triumf.ca* |
| MacLaren, S.A. | LBNL, MS 47-112, 1 Cyclotron Road, Berkeley, CA 94720, USA | *scram@physics.berkeley.edu* |
| Madsen, N. | Aarhus U., IPA, NY Munkegade, DK-8000 Aarhus C, Denmark | *mossen@dfi.aav.dk* |
| Mahoney, K.L. | TJNAF, MS 89, 12000 Jefferson Avenue, Newport News, VA 23606, USA | |
| Mais, H. | DESY, Notkestrasse 85, D-22607 Hamburg, Germany | *mais@mail.desy.de* |
| Makino, K. | Michigan State U., NSCL, S. Shaw Lane, East Lansing, MI 48824-1321, USA | *makino@nscl.msu.edu* |
| Malenfant, J. | Physical Review Letters, 1 Research Road, Ridge, NY 11961, USA | |
| Malitsky, N.D. | Cornell U., Wilson Lab, Dryden Road, Ithaca, NY 14853-5001, USA | *malitsky@mila.lus.cornell.edu* |
| Mamaev, G.L. | Moscow Radio Technical Inst., Warshavskoe Shosse 132, RU-113519 Moscow, Russia | *mamaev_g@mail.sitek.ru* |
| Mammarella, F. | TRIUMF, 4004 Wesbrook Mall, Vancouver, BC, Canada, V6T 2A3 | *antho@triumf.ca* |
| Marhauser, F. | IAP, Frankfurt/Main, Robert-Mayer-Str. 2-4, D-60054 Frankfurt am Main, Germany | *marhauser@em.uni-frankfurt.de* |
| Marks, N. | Daresbury Lab, CLRC, Warrington, Cheshire, UK, WA4 4AD | *n.marks@dl.ac.uk* |
| Marks, S. | LBNL, 46-161, 1 Cyclotron Road, Berkeley, CA 94720, USA | *s_marks@lbl.gov* |
| Marneris, I.M. | BNL, 911A, Room 133, Upton, NY 11973, USA | *yannis2@bnl.gov* |

| | | |
|---|---|---|
| Marsh, W.L. | FNAL, MS-307, P.O. Box 500, Batavia, IL 60510, USA | *marshw@fnal.gov* |
| Marshall, T.C. | Columbia U., Code 4701, Applied Physics Dept., New York, NY 10027, USA | *tcm2@columbia.edu* |
| Martens, M.A. | FNAL, P.O. Box 500, Batavia, IL 60510, USA | *martens@fnal.gov* |
| Marti, F. | Michigan State U., NSCL, E. Lansing, MI 48824, USA | *marti@nscl.msu.edu* |
| Martin, D. | IFTAR Accelerator Lab., Inst. of Atomic Physics, P.O. Box MG-36, R-76900 Bucharest, Romania | |
| Martin, E.J. | TJNAF, MS 16A, 12000 Jefferson Avenue, Newport News, VA 23606, USA | *martine@jlab.org* |
| Martin, P.S. | FNAL, P.O. Box 500, Batavia, IL 60510, USA | *pmartin@fnal.gov* |
| Martin, R.L. | Acctek Associates, 901 S. Kensington, Lagrange, IL 60525, USA | *rmartin45@aol.com* |
| Matsumoto, H. | KEK, 1-1 Oho, Tsukuba-shi, Ibaraki-ken 305, Japan | *hiroshi.matsumot@kek.jp* |
| Matsumoto, S. | KEK, 1-1 Oho, Tsukuba-shi, Ibaraki-ken 305, Japan | *shuji@kekvax.kek.jp* |
| Maury, S.S.M. | CERN, CH-1211 Geneva 23, Switzerland | *stephan.maury@cern.ch* |
| May, M.P. | FNAL, P.O. Box 500, Batavia, IL 60510, USA | *mikemay@fnal.gov* |
| Mazarakis, M.G. | SNL, MS - 1193, P.O. Box 5800, Albuquerque, NM 87185- 1193, USA | *mgmazar@sandia.gov* |
| McClain, W.L. | Amersham Medi & Physics, Amersham Healthcare, 900 Durham Avenue, South Plainfield, NJ 07080, USA | *bill.mcclain@amersham.com* |
| McDonald, M.Y. | TRIUMF, 4004 Wesbrook Mall, Vancouver, BC, Canada, V6T 2A3 | *mikehr@triumf.ca* |
| McDowell, W.P. | ANL, 9700 S. Cass Avenue - Bldg. 401, Argonne, IL 60439, USA | *wpm@aps.anl.gov* |
| McGee, M.W. | FNAL, MS 340, P.O. Box 500, Batavia, IL 60510, USA | *mcgee@fnal.gov* |
| McGhee, D.G. | ANL, 9700 S. Cass Avenue, Bldg. 401, Argonne, IL 60439-4815, USA | *dgm@aps.anl.gov* |
| McInturff, A.D. | LBNL, MS 46-161, 1 Cyclotron Road, Berkeley, CA 94720, USA | *admcinturff@lbl.gov* |
| McIntyre, P.M. | Dept. of Physics, Texas A&M U., College Station, TX 77843, USA | *mcintyre@phys.tamu.edu* |
| McMichael, G.E. | ANL, 9700 S. Cass Avenue, Bldg. 360 F113, Argonne, IL 60439, USA | *mcmichael@anl.gov* |
| Medvedko, A.S. | Budker INP, Novosibirsk, Academician Lavrentiev Prospect 11, RU-630090 Novosibirsk, Russia | |
| Meinke, R.B. | AML, 2730 Kirby Avenue NE, #5, Palm Bay, FL 32905, USA | *fmeinke@magnetlab.com* |
| Meitzler, C.R. | Sam Houston State U., 1902 Avenue J, 2020 Farrington Bldg., Huntsville, TX 77341, USA | *phy_crm@shsu.edu* |
| Meller, R.E. | Cornell U., Wilson Lab, Ithaca, NY 14853-5001, USA | *rem@lns62.lns.cornell.edu* |
| Meot, F. | FNAL, P.O. Box 500, Batavia, IL 60510, USA | *meot@fnal.gov* |
| Meyer, S.R. | SLAC, MS 17, P.O. Box 4349, Stanford, CA 94309, USA | *smeyer@slac.stanford.edu* |
| Meyners, N. | DESY, Notkestrasse 85, D-22607 Hamburg, Germany | *meyners@desy.de* |
| Middelkoop, W.C. | CERN, CH-1211 Geneva 23, Switzerland | *willem.middelkoop@cern.ch* |
| Mikhailov, V.A. | JINR, RU-141980 Dubna, Moscow region, Russia | *mikhail@lhe36.jinr.dubna.su* |
| Milardi, C. | INFN-LNF, CF 13, I-00044 Frascati, RM, Italy | *milardi@lnf.infn.it* |
| Miller, R.H. | SLAC, Bin 26, PO Box 4349, Stanford, CA 94309, USA | *rhm@slac.stanford.edu* |
| Milton, B.F. | TRIUMF, 4004 Wesbrook Mall, Vancouver, BC, Canada, V6T 2A3 | *milton@triumf.ca* |
| Milton, S.V. | ANL, 9700 S. Cass Avenue, Bldg. 401, Argonne, IL 60439, USA | *milton@aps.anl.gov* |
| Minty, M.G. | SLAC, MS 66, P.O. Box 4349, Stanford, CA 94309, USA | *minty@slac.stanford.edu* |
| Mishin, A.V. | Schonberg Research Corp., 300 Keller Street, Bldg. #101, Santa Clara, CA 95054, USA | *avsrc@aol.com* |
| Mistry, N.B. | Cornell U., Newman Lab, Ithaca, NY 14853-5001, USA | *nbm@lns62.lns.cornell.edu* |
| Mitra, A.K. | TRIUMF, 4004 Wesbrook Mall, Vancouver, BC, Canada, V6T 2A3 | *mitra@triumf.ca* |
| Mitsunobu, S. | KEK, 1-1 Oho, Tsukuba-shi, Ibaraki-ken 305, Japan | *mitunobu@kekvax.kek.jp* |
| Miyahara, Y. | JAERI-RIKEN SPring-8, Kamigori, Ako-gun, Hyozo 67812, Japan | *miyahara@sp8sun.spring8.or.jp* |
| Mizuno, H. | KEK, 1-1 Oho, Tsukuba-shi, Ibaraki-ken 305, Japan | *mizuno@kekvax.kek.jp* |
| Mochizuki, S. | Hitachi, Ltd., 6 Kanda-Serugadai, 4-Chome, Chiyodaku, Tokyo 101, Japan | |
| Moeller, S.P. | ISA, U. Aarhus, DK-8000 Aarhus, Denmark | *fyssp@dfi.aau.dk* |
| Moisio, F.M. | INFN-LNL, Via Romea 4, I-35020 Legnaro, PD, Italy | *moisio@legnaro.infn.it* |
| Mokhov, N.V. | FNAL, MS 345, P.O. Box 500, Batavia, IL 60510-0500, USA | *mokhov@fnal.gov* |
| Molodozhentsev, A.Y. | JINR, RU-141980 Dubna, Moscow region, Russia | *molod@sunse.jinr.dubna.su* |
| Molvik, A. | LLNL, L-440, P.O. Box 808, Livermore, CA 94550, USA | *melvil1@llnl.gov* |
| Monchinsky, V.A. | JINR, RU-141980 Dubna, Moscow region, Russia | *monvn@sunhe.jinr.dubna.su* |
| Month, M. | BNL, Bldg. 902A, Upton, NY 11973, USA | *uspas@fnal.gov* |
| Moog, E.R. | ANL, APS, XFD - 401, 9700 S. Cass Avenue, Argonne, IL 60439, USA | *moog@aps.anl.gov* |
| Mooney, T.M. | ANL, 9700 S. Cass Avenue, Bldg. 401, Argonne, IL 60439, USA | *mooney@aps.anl.gov* |
| Moore, C.D. | FNAL, P.O. Box 500, Batavia, IL 60510, USA | *damon@fnal.gov* |
| Moore, C.I. | NRL, Code 6795, 4555 Overlook Avenue, SW, Washington, DC 20375, USA | *moore@ppdu.nrl.navy.mil* |
| Mori, W.B. | UCLA, 1-130P, Knudson Hall, Los Angeles, CA 90254, USA | *mori@physics.ucla.edu* |
| Mori, Y. | KEK, 3-2-1 Midori-cho, Tanashi-shii, Tokyo 188, Japan | *moriy@kekvax.kek.jp* |
| Mortazavi, P. | BNL, NSLS, Bldg. 725D, Upton, NY 11973-5000, USA | *payman@bnl.gov* |
| Moscrop, R. | NNC, Booths Hall, Chelford Road, Knutsford, Chesire, UK, WA16 8QZ | |
| Moser, H.O. | Forschungszentrum Karlsruhe, PEA, PO Box 3640, D-76021 Karlsruhe, Germany | *moser@anka.fzkk.de* |

| | | |
|---|---|---|
| Mosko, S.W. | ORNL, MS 6368, P.O. Box 2008, Oak Ridge, TN 37831-6368, USA | *moskos@ornl.gov* |
| Mosnier, A. | CEA-CNRS - Projet SOLEIL, DRIF du CNRS, Avenue de la Terrasse, Batiment 5, F-91198 Gif sur Yvette, Cedex, France | *mosnier@cea.fr* |
| Mottet, P. | Ion Beam Applications SA, Chemin du Cyclotron, 3, B-1348 Louvain-la-Neuve, Belgium | |
| Mouat, M.M. | TRIUMF, 4004 Wesbrook Mall, Vancouver, BC, Canada, V6T 2A3 | *mouat@triumf.ca* |
| Muller, R.M. | BESSY, Berlin, Lentze Allee 100, D-14195 Berlin, Germany | *mueller@bessy.de* |
| Mullier, B. | IBA, Chemin du Cyclotron, 3, B-1348 Louvan-La-Nueve, Belgium | *amv@iba.mhs.compuserve.com* |
| Munoz, M. | Campus UAB, LSB-IFAE, Lab. del Sincrotro de Barcelona, Edifici Ciencies Nord, E-08193 Bellaterra, Spain | *mmunoz@ifae.es* |
| Murin, B.P. | Moscow Radio Technical Inst., Warshavskoe Shosse 132, RU-113519 Moscow, Russia | |
| Murphy, J.B. | BNL, NSLS, Bldg. 725C, P.O. Box 5000, Upton, NY 11973-5000, USA | *jbm@bnl.gov* |
| Murratore, J.F. | BNL, P.O. Box 445, Upton, NY 11973, USA | *muratore@bnl.gov* |
| Myers, S. | CERN, CH-1211 Geneva 23, Switzerland | |
| Nadji, A. | CEA-CNRS - Projet SOLEIL, DRIF du CNRS, Avenue de la Terrasse, Bat 5, F-91198 Gif sur Yvette, Cedex, France | *nadji@lure.u-psud.fr* |
| Nagaitsev, S. | FNAL, MS-341, P.O. Box 500, Batavia, IL 60510, USA | *nsergei@fnal.gov* |
| Naito, T. | KEK, 1-1 Oho, Tsukuba-shi, Ibaraki-ken 305, Japan | *naitot@kekvax.kek.jp* |
| Nakagawa, T. | Mitsubishi Electric Corp., 1-1, Tsukaguchi-Honmachi, 8-Chome, Amagasaki, Hyogo 661, Japan | *nakagawa@ele.crl.melca.co.jp* |
| Nakagawa, T. | RIKEN, Cyclotron Lab, Wako, Saitama 351-01, Japan | *nakagawa@rikaxp.riken.go.jp* |
| Nam, S-K. | Kangwon National U., Dept. of Physics, Chunchon, Kangwon do 200-701, S. Korea | *man@cc.kungwon.ac.kr* |
| Nam, S.H. | Pohang Acc. Lab, POSTECH, San 31, Hyoja-dong, Nam-ku, Pohang, Kyungbuk 790-784, S. Korea | *nsh@vision.postech.br.kr* |
| Namkung, W. | Pohang Acc. Lab, POSTECH, San 31, Hyoja-dong, Nam-ku, Pohang, Kyungbuk 790-784, S. Korea | *namkung@postech.ac.kr* |
| Nantista, C.D. | SLAC, MS 26, P.O. Box 4349, Stanford, CA 94309, USA | *nantista@slac.stanford.edu* |
| Naqvi, S. | Cornell U., LNS, High Volt. Lab., 909 Mitchell Street, Ithaca, NY 14853, USA | *shahid@lps.cornell.edu* |
| Nath, S. | LANL, MS H817, P.O. Box 1663, Los Alamos, NM 87545, USA | *snath@lanl.gov* |
| Nation, J.A. | Cornell U., Newman Lab, 325 Rhodes Hall, Ithaca, NY 14853-5001, USA | *jnation@lps.cornell.edu* |
| Naumovich, G. | Everson Electric, 2000 City Line Road, Bethlehem, PA 18017, USA | |
| Nawrocky, R.J. | BNL, Bldg. 7256, Upton, NY 11973, USA | *nawrocky@bnl.gov* |
| Neil, G.R. | TJNAF, 12000 Jefferson Avenue, Newport News, VA 23606, USA | *neil@jlab.org* |
| Nelson, E.M. | LANL, MS H851, P.O. Box 1663, Los Alamos, NM 87545, USA | *enelson@lanl.gov* |
| Nelson, R.M. | TJNAF, MS 90A, 12000 Jefferson Avenue, Newport News, VA 23606, USA | *nelson@jlab.org* |
| Neuffer, D.V. | FNAL, P.O. Box 500, Batavia, IL 60510, USA | *neuffer@fnal.gov* |
| Nexsen Jr., W.E. | LLNL/SSC/Retired, 173 Montair Drive, Danville, CA 94526, USA | |
| Nezhevenko, O.A. | Omega-P, Inc., 205 S. Whiting Street, #307, Alexandria, VA 22304, USA | *nezhev@clark.net* |
| Ng, C-K. | SLAC, MS 26, P.O. Box 4349, Stanford, CA 94309, USA | *cho@slac.stanford.edu* |
| Ng, K.Y. | FNAL, MS 345, P.O. Box 500, Batavia, IL 60510, USA | *ng@fnal.gov* |
| Nghiem, P. | CEA-CNRS - Projet SOLEIL, DRIF du CNRS, Avenue de la Terrasse, Bat. 5, F-91198 Gif sur Yvette, Cedex, France | *phi@soleil.sol.cnrs-gif.fr* |
| Nguyen, D.C. | LANL, MS-H851, P.O. Box 1663, Los Alamos, NM 87545, USA | *dcnguyen@lanl.gov* |
| Nicol, T.H. | FNAL, MS 316, P.O. Box 500, Batavia, IL 60510, USA | *tnicol@fnal.gov* |
| Nielsen, B. | Danfysik A/S, PO Box 2578, Redwood City, CA 94064, USA | |
| Nielsen, L. | Titan Beta, 6780 Sierra Court, Dublin, CA 94568, USA | |
| Nigro, M. | INFN-LNL, I-35020 Legnaro, PD, Italy | |
| Niki, K. | U. Tokyo, INS, Midori-cho 3-2-1, Tanashi, Tokyo 188, Japan | *niki@tanashi.kek.jp* |
| Noda, A. | Kyoto U., NSRF, ICR, Gokano-sho, Uji-city, Kyoto 611, Japan | *noda@kyticr.kuicr.kyoto-u.ac.jp* |
| Nolen, J.A. | ANL, Physics Div., D-203, 9700 S. Cass Avenue, Argonne, IL 60439, USA | *nolen@anl.gov* |
| Noonan, J. | ANL, 9700 S. Cass Avenue, Argonne, IL 60439, USA | |
| Nordby, M.E. | SLAC, 2575 Sand Hill Road, Menlo Park, CA 94025, USA | *nordby@slac.stanford.edu* |
| Norem, J. | ANL, 9700 S. Cass Avenue, Argonne, IL 60439, USA | *norem@hep.anl.gov* |
| Novikov, A.V. | INR of RAS, 60th October Anniversary Prospect 7A, RU-117312 Moscow, Russia | *novikov@alzo.inr.troitsk.ru* |
| O'Shea, P.G. | Duke U., Box 90319, Durham, NC 27708, USA | *oshea@fel.duke.edu* |
| Ogata, A. | KEK, 1-Oho, Tsukuba, 305, Japan | *ogata@mila.kek.jp* |
| Oh, J.S. | Pohang Acc. Lab, POSTECH, San 31, Hyoja-dong, Nam-ku, Pohang, Kyungbuk 790-784, S. Korea | *jsoh@postech.ac.kr* |
| Oh, S. | Pohang Acc. Lab, POSTECH, San 31, Hyoja-dong, Nam-ku, Pohang, Kyungbuk 790-784, S. Korea | |
| Ohkawa, T. | RIKEN, Cyclotron Lab, 2-1 Hirosawa, Wako, Saitama 351-01, Japan | *ohkawa@rikaxp.riken.go.jp* |
| Ohmori, C. | KEK-Tanashi, KEK, 3-2-1 Midori-cho, Tanashi, Tokyo 188, Japan | *chihiro@kekvax.kek.jp* |

| | | |
|---|---|---|
| Okamoto, H. | Kyoto U., NSRF, ICR, Gokanoshou, Uji, Kyoto 611, Japan | *okamoto@kyticr.kuicr.kyoto-u.ac.jp* |
| Okamura, M. | BNL, P.O. Box 5000, Upton, NY 11973, USA | *okamura@bnldag.ags.bnl.gov* |
| Oliszewski, L.H. | LSU - CAMD, 6980 Jefferson Hwy, Baton Rouge, Louisiana 70806, USA | *larry@rocamd.camd.lsu.edu* |
| Olsen, D.K. | ORNL, MS 6368, P.O. Box 2008, Oak Ridge, TN 37831-6368, USA | *olsendk@ornl.gov* |
| Olsen, R. | SLAC, MS 49, Bldg. 15, Paolo Alto, CA 94309, USA | *rol@slac.stanford.edu* |
| Olson, C.L. | Dept. 9541, SNL, MS 1188, Albuquerque, NM 87185-1188, USA | *clolson@sandia.gov* |
| Oothoudt, M.A. | LANL, MS H 820, P.O. Box 1663, Los Alamos, NM 87545, USA | *oothoudt@lanl.gov* |
| Ormond, K.W. | Cornell U., Wilson Lab, 301 Maple Ave, Apt A3, Ithaca, NY 14850, USA | *kwo1@cornell.edu* |
| Orzechowski, J. | TRIUMF, 4004 Wesbrook Mall, Vancouver, BC, Canada, V6T 2A3 | *joski@triumf.ca* |
| Osborn, J.R. | LBNL, MS 71J, 1 Cyclotron Road, Berkeley, CA 94710, USA | *jrosborn@lbl.gov* |
| Oster, E. | Oster Magnetics, 202 Bering Drive, San Jose, CA 95131, USA | |
| Otter, A.J. | TRIUMF, 3725 West 35th Avenue, Vancouver, BC, Canada, V6N 2N6 | |
| Ottinger, M.B. | U. Texas, C1600, Austin, TX 78712, USA | *ottinger@fusion.ph.utexas.edu* |
| Overett, T.H.R. | General Atomics, 3550 General Atomics Court, San Diego, CA 92121-1194, USA | *trevor.overett@gat.com* |
| Ovsyannikov, D. | Saint-Petersburg State U., Ulyanovskaya str. 1, RU-198904 St. Petersburg, Russia | |
| Owen, H. | Daresbury Lab, CLRC, Warrington, Cheshire, UK, WA4 4AD | *h.owen@dl.ac.uk* |
| Pabst, M. | Forschungszentrum Jülich, D-52425 Julich, Germany | *mpabst@fz-juelich.de* |
| Padamsee, H.S. | Cornell U., Newman Lab, Ithaca, NY 14853-5001, USA | *hsp@cesrio.lns.cornell.edu* |
| Pakter, R. | MIT Plasma Science and Fusion Center, 167 Albany Street, Cambridge, MA 02139, USA | *pakter@psfc.mit.edu* |
| Palmer, B. | Philips, 1033 Kings Highway, Saugerties, NY 12477, USA | |
| Palmer, D.T. | SLAC, MS 26, P.O. Box 4349, Stanford, CA 94309, USA | *dtp@unixhuh.slac.stanford.edu* |
| Palmer, R.B. | BNL, Bldg. 901A, P.O. Box 5000, Upton, NY 11973-5000, USA | *palmer@bnl.gov* |
| Palumbo, L. | INFN-LNF, Via E. Fermi, I-00044 Frascati, RM, Italy | *lpalumbo@axlnf1.lnf.infn.it* |
| Pappas, G.C. | SLAC, 2575 Sand Hill Road, Menlo Park, CA 94020, USA | *pappas@slac.stanford.edu* |
| Paramonov, V.V. | INR, Russian Academy of Sciences, 60th October Anniversary Prospect 7a, RU-117312 Moscow, Russia | |
| Pardo, R.C. | ANL, 9700 S. Cass Avenue, Bldg. 203, Argonne, IL 60439, USA | *pardo@anlphy.phy.anl.gov* |
| Parisi, G. | Inst. fuer Angewandte Physik, IAP, Frankfurt/Main, Robert-Mayer-Str. 2-4, D-60054 Frankfurt am Main, Germany | *parisi@mikro1.physik.uni-frankfurt.de* |
| Park, C. | Pohang Acc. Lab, POSTECH, San 31, Hyoja-dong, Nam-ku, Pohang, Kyungbuk 790-784, S. Korea | *cdp@postech.ac.kr* |
| Parsa, Z. | BNL, 901 A, Upton, NY 11973-5000, USA | *parsa@bnl.gov* |
| Pashenkov, A.S. | INR, Russian Academy of Sciences, 60th October Anniversary Prospect 7a, RU-117312 Moscow, Russia | |
| Pasquinelli, R. | FNAL, P.O. Box 500, Batavia, IL 60510, USA | *pasquin@fnal.gov* |
| Paterson, A. | LBNL, 1 Cyclotron Road, Bldg. 46/161, Berkeley, CA 94720, USA | *japaterson@lbl.gov* |
| Paterson, J.M. | SLAC, MS 24, P.O. Box 4349, Stanford, CA 94309, USA | *jmp@slac.stanford.edu* |
| Patteri, P. | INFN-LNF, Via E.Fermi 40, I-00044 Frascati, RM, Italy | *patteri@lnf.infn.it* |
| Paul, D.M. | Mega Industries, 1281 Roosevelt Trail, Raymond, Maine 04071, USA | |
| Payet, J. | CEA-Saclay, F-91191 Gif sur Yvette, France | *payet@picpus.saclay.cea.fr* |
| Pedersen, F. | CERN, PS Division, CH-1211 Geneva 23, Switzerland | *pedersen@mial.cern.ch* |
| Peggs, S.G. | BNL, Bldg. 1005S, P.O. Box 5000, Upton, NY 11973-5000, USA | *peggs1@bnl.gov* |
| Pei, A. | IUCF, 2401 Milo B. Sampson Lane, Bloomington, IN 47408, USA | *alexpei@iucf.indiana.edu* |
| Peiniger, M. | ACCEL Instruments GmbH, Friedrich-Ebert-Str. 1, D-51429 Bergisch, Gladbach, Germany | *accel@accel.de* |
| Pekeler, M.J. | DESY, Notkestrasse 85, D-22603 Hamburg, Germany | *michael@pekeler.desy.de* |
| Pellegrini, C. | UCLA, 405 Hilgard Avenue, Los Angeles, CA 90095-1547, USA | *pellegrini@physics.ucla.edu* |
| Peoples Jr., J. | FNAL, P.O. Box 500, Batavia, IL 60510, USA | *peop@fnal.gov* |
| Perelstein, E.A. | Lab. of Nuclear Problems, JINR, RU-141980 Dubna, Moscow region, Russia | *perel@nu.jinr.dubna.su* |
| Perevedentsev, E.A. | Budker INP, Novosibirsk, Academician Lavrentiev Prospect 11, RU-630090 Novosibirsk, Russia | *perevedent@inp.nsk.su* |
| Perin, R. | CERN, SPL Division, CH-1211 Geneva 23, Switzerland | *romeo.perin@cern.ch* |
| Perini, D. | CERN, LHC Division, CH-1211 Geneva 23, Switzerland | *perinid@cern.ch* |
| Perkins, L.T. | LBNL, MS 5-119, 1 Cyclotron Road, Berkeley, CA 94720, USA | |
| Perkins, M. | RAL, CLRC, Chilton, Didcot, Oxon., UK, OX11 0QX | *m.perkins@rl.ac.uk* |
| Perriollat, F. | CERN, CH-1211 Geneva 23, Switzerland | |
| Pershing, D.E. | Mission Research Corp., 8560 Cinderbed Road, Suite 700, P.O. Box 8560, Newington, VA 22122-8560, USA | |
| Peters, G.J. | Division of High Energy Physics, DOE, ER - 224, 19901 Germantown Road, Germantown, MD 20874, USA | *jerry.peters@oer.doe.gov* |
| Petillo, J. | Science Applications Intl. Corp., SAIC, Burlington, MA 01803, USA | |

| | | |
|---|---|---|
| Petracca, S. | U. di Salerno / Canon Fellow, DIP Scienze Fisiche E.R. Caianiello, I-84081 Baronissi, Salerno, Italy | *petracca@vaxsa.csied.unisa.it* |
| Peyrot, M.H. | CEA-Saclay, CEA/Dapnia/STCM, F-91191 Gif sur Yvette, Cedex, France | *peyrot@hep.saclay.cea.fr* |
| Phillips, L. | TJNAF, 12000 Jefferson Avenue, Newport News, VA 23606, USA | *phillips@jlab.org* |
| Pietryka, M. | SLAC, 2575 Sand Hill Road, Bin 21, Menlo Park, CA 94040, USA | *matt@slac.stanford.edu* |
| Pilat, F. | BNL, Bldg. 10058, P.O. Box 5000, Upton, NY 11973-5000, USA | *pilat@owl.rhic.bnl.gov* |
| Pillai, C. | LANSCE, LANL, MS H812, P.O. Box 1663, Los Alamos, NM 87545, USA | *pillai@lanl.gov* |
| Piot, P.R. | TJNAF, MS 58-B, 12000 Jefferson Avenue, Newport News, VA 23606, USA | *piot@jlab.org* |
| Pirozhenko, V.M. | Moscow Radio Technical Inst., Warshavskoe Shosse 132, RU-113519 Moscow, Russia | |
| Pivarc, J. | Dept. of Nuclear Physics, Inst. Physics of the SAS, Bratislava, Dubravska cesta 9, SK-84228 Bratislava, Slovak Republic | *pivarc@nrsun.jinr.dubna.su* |
| Plass, G.H. | CERN, AC Division, HIDIF Collaboration, CH-1211 Geneva 23, Switzerland | *guenther.plass@cern.ch* |
| Plate, D.W. | LBNL, 46-161, 1 Cyclotron Road, Berkeley, CA 94720, USA | *dwplate@lbl.gov* |
| Plum, M.A. | LANL, MS H838, L-2, Los Alamos, NM 87545, USA | *plum@lanl.gov* |
| Podobedov, B.V. | SLAC, P.O. Box 4349, Stanford, CA 94309, USA | *boris@slac.stanford.edu* |
| Poirier, R.L. | TRIUMF, 4004 Wesbrook Mall, Vancouver, BC, Canada, V6T 2A3 | *poirier@triumf.ca* |
| Poole, B.R. | LLNL, MS C-153, 7000 East Avenue, Livermore, CA 94550, USA | *poole1@llnl.gov* |
| Poole, M.W. | Daresbury Lab, CLRC, Synchrotron Radiation Dept., Warrington, Cheshire, UK, WA4 4AD | *m.w.poole@dl.ac.uk* |
| Popov, G.F. | Kharkov State U., P.O. Box 60, UA-310052 Kharkov, Ukraine | *popov@pem.kharkov.ua* |
| Popp, S.A.S. | Inverpower Controls Ltd., 835 Harrington Court, Burlington, ON, Canada, L7N 3P3 | |
| Porcellato, A.M. | INFN-LNL, Via Romea 4, I-35020 Legnaro, PD, Italy | *porcellato@lnl.infn.it* |
| Portmann, G.J. | LBNL, 10-110, 1 Cyclotron Road, Berkeley, CA 94720, USA | *gjjportmann@lbl.gov* |
| Potukuchi, P.N. | Physics Division, ANL, 9700 S. Cass Avenue, Argonne, IL 60439, USA | *prakash@anlphy.phy.anl.gov* |
| Poutchkov, S.N. | Moscow Radio Technical Inst., Warshavskoe Shosse 132, RU-113519 Moscow, Russia | *pusn@mastak.sitek.ru* |
| Power, J. | LANL, MSA H808, P.O. Box 1663, Los Alamos, NM 87545, USA | *jpower@lanl.gov* |
| Power, J.G. | ANL, 9700 S. Cass Avenue, Bldg. 362, Argonne, IL 60439, USA | *jp@hep.anl.gov* |
| Pozimski, J. | IAP, Frankfurt/Main, Robert-Mayer-Str. 2-4, D-60054 Frankfurt, Germany, Germany | |
| Prabhakar, S. | SLAC, MS 18, 2575 Sand Hill Road, Menlo Park, CA 94025-7015, USA | *shyam@eldsun3.slac.stanford.edu* |
| Preble, J.P. | TJNAF, MS 58B, 12000 Jefferson Avenue, Newport News, VA 23606, USA | *preble@jlab.org* |
| Preger, M.A. | INFN-LNF, Casella Postale 13, I-00044 Frascati, RM, Italy | *preger@lnf.infn.it* |
| Price, V.G. | IEEE, 22151 Berkeley Cr., Los Altos, CA 94024-7411, USA | *v.price@ieee.org* |
| Prichard Jr., B.A. | SAIC/LANL, 133 Aspen Drive, Los Alamos, NM 87544, USA | *prichard@lanl.gov* |
| Prome, M.A. | CEA-DAM, 5 Rue Pasteur, F-92210 Saint-Cloud, France | |
| Proudlock, P. | CERN, CH-1211 Geneva 23, Switzerland | *paul.proudlock@cern.ch* |
| Pruss, S.M. | FNAL, P.O. Box 500, Batavia, IL 60510, USA | *pruss@fnal.gov* |
| Pusterla, M. | Dipart. Fisica, U. Padova, I-35131 Padova, Italy | *pusterla@pd.infn.i* |
| Putnam, S.D. | Pulse Sciences, Inc., 600 McCormick Street, San Leandro, CA 94577, USA | |
| Qualls, A. | IUCF, 2401 Milo B. Sampson Lane, Bloomington, IN 47408- 1398, USA | *aqualls@iucf.indiana.edu* |
| Qunell, D.K. | FNAL, MS 308, P.O. Box 500, Batavia, IL 60510, USA | *darrenq@fnal.gov* |
| Raimondi, P.R. | SLAC, P.O. Box 4349, Stanford, CA 94061, USA | *raimondi@slac.stanford.edu* |
| Raino, A. | Dipartimento di Fisica, Bari U., Via Amendola 173, I-70126 Bari, Italy | *raino@ba.infn.it* |
| Rakowsky, G. | BNL, NSLS, Bldg. 725D, Upton, NY 11973, USA | *rakowskl@bnl.gov* |
| Ramamoorthy, S. | BNL, NSLS, Bldg. 725B, Upton, NY 11973, USA | *susila@bnllsl.nsls.bnl.gov* |
| Rand, R.E. | Imatron Inc., 389 Oyster Point Boulevard, South San Francisco, CA 94080, USA | *rer@imatron.com* |
| Raparia, D. | BNL, Bldg. 930, Upton, NY 11973, USA | *raparia@bnl.gov* |
| Ratti, A. | LBNL, 71-259, 1 Cyclotron Road, Berkeley, CA 94720, USA | *aratti@lbl.gov* |
| Rawls, J.M. | General Atomics, 3550 General Atomics Court, San Diego, CA 92121-1194, USA | *john.rawls@gat.com* |
| Rawnsley, B. | TRIUMF, 4004 Wesbrook Mall, Vancouver, BC, Canada, V6T 2A3 | *rawnsley@triumf.ca* |
| Ray, B.D. | LANL, MS H812, P.O. Box 1663, Los Alamos, NM 87545, USA | *bray@lanl.gov* |
| Reece, C. | TJNAF, 12000 Jefferson Avenue, Newport News, VA 23606, USA | *reece@jlab.org* |
| Reece, K.R. | BNL, AGS Dept., Bldg. 911C, Upton, NY 11973, USA | *reece@bnl.gov* |
| Reed, J.C. | Pearson Electronics, Inc., 1860 Embarcadero Road, Palo Alto, CA 94303, USA | |
| Rees, D.E. | LANL, MS H827, P.O. Box 1663, Los Alamos, NM 87544, USA | *drees@lanl.gov* |
| Reginato, L.L. | LBNL, MS 47-112, 1 Cyclotron Road, Berkeley, CA 94720, USA | *llreginato@lbl.gov* |
| Reichanadter, M.A. | FNAL, MS 340, P.O. Box 500, Batavia, IL 60510, USA | *reich@fnal.gov* |
| Reiche, S. | DESY, Notkestrasse 85, D-22607 Hamburg, Germany | *reichesv@x4v2.desy.de* |
| Reichel, I. | CERN, SL-OP Division, CH-1211 Geneva 23, Switzerland | *ina.reichel@cern.ch* |
| Reid, D.D. | U. Washington Medical Center, PO Box 356043, 1959 NE Pacific Street, Seattle, WA 98195, USA | *dave@radonc.washington.edu* |

| | | |
|---|---|---|
| Reiser, M.P. | Inst. for Plasma Research, U. Maryland, Energy Research Bldg., College Park, MD 20472-3511, USA | *mreiser@glue.umd.edu* |
| Renau, T. | Varian Ion Implant Systems, MS GL17, 35 Dory Road, Gloucester, MA 01930-2297, USA | *tony.renau@iis.varian.com* |
| Rezzonico, L. | PSI, Paul Scherrer Institut, CH-5232 Villigen PSI, Switzerland | *rezzonico@psi.ch* |
| Rice, D.H. | Cornell U., Wilson Lab, 271, Ithaca, NY 14853-5001, USA | *dhr1@cornell.edu* |
| Richardson, R.A. | LLNL, P.O. Box 808, L-153, 7000 East Avenue, Livermore, CA 94550, USA | *rar@llnl.gov* |
| Rimmer, R.A. | LBNL, MS 71-259, 1 Cyclotron Road, Berkeley, CA 94720, USA | *rarimmer@lbl.gov* |
| Ripin, B.H. | American Physical Society, Ova Physics Ellipse, College Park, MD 20740, USA | *ripin@aps.org* |
| Roberson, C.W. | Physical Science Div., Office of Naval Research, Code-331, Arlington, VA 22217, USA | *robersc@omr.navy.mil* |
| Robin, D.S. | LBNL, MS 4-230, 1 Cyclotron Road, Berkeley, CA 94720, USA | *dsrobin@lbl.gov* |
| Robinson, K.E. | STI Optronics, Inc., 2755 Northup Way, Bellevue, WA 98004-1495, USA | *kem@stiopt.com* |
| Rode, C.H. | TJNAF, 12000 Jefferson Avenue, Newport News, VA 23606, USA | *rode@cebaf.gov* |
| Rodrigues, A.R.D. | LNLS - Brazil, Caixa Postal 6192, BR-13083-970 Campinas, SP, Brazil | *richard@lnls.br* |
| Rogers, J.D. | Continental Electronics Corp., PO Box 270879, Dallas, TX 75227-0879, USA | *jrogers@contelec.com* |
| Rogers, J.T. | Cornell U., Newman Lab, Ithaca, NY 14853-5001, USA | *jtr1@cornell.edu* |
| Root, L.W. | TRIUMF, 4004 Wesbrook Mall, Vancouver, BC, Canada, V6T 2A3 | *trlr@triumf.ca* |
| Ropert, A. | ESRF, BP 220, F-38043 Grenoble, Cedex, France | *ropert@esrf.fr* |
| Rose, C.R. | LANL, MS H808, P.O. Box 1663, Los Alamos, NM 87545, USA | *crose@lanl.gov* |
| Rose, J. | BNL, Bldg. 1005, P.O. Box 5000, Upton, NY 11973-5000, USA | *rose3@bnl.gov* |
| Roser, T. | BNL, AGS Dept., Bldg. 911B, Upton, NY 11973, USA | *roser@bnl.gov* |
| Ross, H.P. | Engineered Magnetics, Inc., 18435 Susana Road, Rancho Dominguez, CA 90221, USA | |
| Rossbach, J.H. | DESY, Notkestrasse 85, D-22603 Hamburg, Germany | *rossbach@desy.de* |
| Rovelli, A. | INFN-LNS, Catania, Via S. Sofia 44/A, I-95185 Catania, Italy | *rovelli@lns.infn.it* |
| Roy, G.J. | CERN, SL Division, CH-1211 Geneva 23, Switzerland | *ghislain.roy@cern.ch* |
| Rubin, D.L. | Cornell U., Ithaca, NY 14853-5001, USA | *dlr@cesr10.tn.cornell.edu* |
| Ruggiero, A.G. | BNL, AGS Dept., Bldg. 911B, Upton, NY 11973, USA | *agr@bnl.gov* |
| Ruggiero, F. | CERN, CH-1211 Geneva 23, Switzerland | *francesco.ruggiero@cern.ch* |
| Rumrill, R.S. | Alpha Scientific Electronics, 1868 National Avenue, Hayward, CA 94545, USA | |
| Rusnak, B. | LANL, MS H817, Group L-1, Los Alamos, NM 87545, USA | *brusnak@lanl.gov* |
| Russell, A.D. | FNAL, MS 323, P.O. Box 500, Batavia, IL 60510-0500, USA | *russell@fnal.gov* |
| Russell, R.P. | Advanced Ferrite Technology Inc., 15200 Shady Grove Road - Suite 350, Rockville, MD 20850, USA | |
| Russell, S.J. | LANL, MS H851, P.O. Box 1663, Los Alamos, NM 87545, USA | |
| Rusthoi, D.P. | LANL, MS H 13, Los Alamos, NM 87545, USA | *rusthoi@lanl.gov* |
| Ruth, R.D. | SLAC, MS 26, 2575 Sand Hill Road, Menlo Park, CA 94025, USA | *rruth@slac.stanford.edu* |
| Rybarcyk, L.J. | LANL, MS H812, P.O. Box 1663, Los Alamos, NM 87545, USA | *lrybarcyk@lnal.gov* |
| Ryne, R.D. | LANL, MS-H817, P.O. Box 1663, Los Alamos, NM 87544, USA | *ryne@lanl.gov* |
| Saban, R. | CERN, CH-1211 Geneva 23, Switzerland | *Roberto.saban@cern.ch* |
| Sabbi, G. | FNAL, MS 316, P.O. Box 500, Batavia, IL 60510, USA | *sabbi@fnal.gov* |
| Sachtschale, R.J. | Duke U., P.O. Box 90319, Durham, NC 27708-0319, USA | *satch@fel.duke.edu* |
| Safranek, J. | BNL, NSLS Bldg. 725C, P.O. Box 5000, Upton, NY 11973-5000, USA | *safranek@bnl.gov* |
| Sagan, D. | Cornell U., Wilson Lab, Ithaca, NY 14853-5001, USA | *dcs@lns62.lns.cornell.edu* |
| Sah, R.C. | SRRC, Taiwan, No. 1 R&D Road, VI, Hsinchu Science-Based Industrial Park, Hsinchu, 30077, Taiwan | *sah@alpha1.srrc.gov.tw1* |
| Sajaev, V.V. | Budker INP, Novosibirsk, Academician Lavrentiev Prospect 11, RU-630090 Novosibirsk, Russia | *sajaev@inp.nsk.su* |
| Sakamoto, N. | RIKEN, 2-1 Hirosawa, Wako, Saitama 351-01, Japan | *nsakamoto@rikvax.riken.go.jp* |
| Sakanaka, S. | KEK, 1-1 Oho, Tsukuba-shi, Ibaraki-ken 305, Japan | *sakanaka@mail.kek.jp* |
| Sampayan, S.E. | LLNL, MS L-446, P.O. Box 808, Livermore, CA 94551, USA | |
| Sander, O.R. | LANL, MS H838, P.O. Box 1663, Los Alamos, NM 87545, USA | *osander@lanl.gov* |
| Sangster, T.C. | LLNL, L-481, P.O. Box 808, Livermore, CA 94550, USA | *sangster@llnl.gov* |
| Sarkar, S. | MIT Bates, P.O. Box 846, 21 Manning Avenue, Middleton, MA 01810, USA | *sarkar@bates.mit.edu* |
| Sassowsky, M. | CERN, CH-1211 Geneva 23, Switzerland | *msassowsky@cern.ch* |
| Sato, H. | KEK, 1-1 Oho, Tsukuba-shi, Ibaraki-ken 305, Japan | *satoh@kekvax.kek.jp* |
| Satti, J.A. | FNAL, P.O. Box 500, Batavia, IL 60510, USA | *jasatti@fnal.gov* |
| Scanlan, R.M. | LBNL, MS 46-161, 1 Cyclotron Road, Berkeley, CA 94530, USA | *rmscanlan@lbl.gov* |
| Scaramelli, A. | CERN, CH-1211 Geneva 23, Switzerland | *alberto scarmelli@cern.ch* |
| Schacter, L. | Dept. of Electrical Engineering, Technion-Israel Inst. of Tech., Haifa, 32000, Israel | *levi@ee.technion.ac.il* |
| Schaller, G.E. | Ceramic Magnetics, Inc., 16 Law Drive, Fairfield, NJ 07004, USA | |
| Schaller, S. | LANSCE, LANL, H812, P.O. Box 1663, Los Alamos, NM 87545, USA | *schaller@lanl.gov* |

| | | |
|---|---|---|
| Schempp, A. | IAP, Frankfurt/Main, Robert-Mayer-Str. 2-4, D-60325 Frankfurt am Main, Germany, Germany | *a.schempp@em.uni-frankfurt.de* |
| Schillinger, B. | TH Darmstadt, Darmstadt U. of Tech., Fachbereich 18, TEMF, Schlossgartenstr. 8, D-64289 Darmstadt, Germany | *schill@temf.th-darmstadt.de* |
| Schindl, K. | CERN, CH-1211 Geneva 23, Switzerland | *karlheinz.schindl@cern.ch* |
| Schlapp, M. | ANL, PHY203, 9700 S. Cass Avenue, Argonne, IL 60439-4843, USA | *schlapp@chinook.phy.anl.gov* |
| Schlarb, H. | DESY, Notkestrasse 85, D-22603 Hamburg, Germany | *schlarb@x4us.desy.de* |
| Schmickler, H.J. | CERN, SL Division, CH-1211 Geneva 23, Switzerland | *hermann.schmickler@macmail.cern.ch* |
| Schmidt, C.W. | FNAL, P.O. Box 500, Batavia, IL 60510, USA | *cschmidt@fnal.gov* |
| Schmitz, M. | DESY, MIN Group, Notkestrasse 85, D-22607 Hamburg, Germany | *schmitz@mail.desy.de* |
| Schmor, P.W. | TRIUMF, 4004 Wesbrook Mall, Vancouver, BC, Canada, V6T 2A3 | *schmor@triumf.ca* |
| Schneider, J.D. | LANL, MS H836, P.O. Box 1663, LER/APT, Los Alamos, NM 87545, USA | *idschneider@lanl.gov* |
| Schoesson, P. | ANL, 9700 S. Cass Avenue, 362 - HEP, Argonne, IL 60439, USA | *pvs@hep.anl.gov* |
| Schrage, D.L. | LANL, MS H817, P.O. Box 1663, Los Alamos, NM 87545, USA | *dls@lanl.gov* |
| Schriber, S.O. | LANL, MS H850, P.O. Box 1663, Los Alamos, NM 87545, USA | *sschriber@lanl.gov* |
| Schubert, J.R. | Michigan State U., NSCL, East Lansing, MI 48910, USA | *schubert@nscl.msu.edu* |
| Schuett, P. | FG Theorie Elektromagnetischer Felder, Darmstadt U. of Tech., FB 18, Schlossgarten Str. 8, D-64287 Darmstadt, Germany | *petra.schuett@t-online.de* |
| Schultheiss, C.M. | BNL, Bldg. 817, Upton, NY 11973-5000, USA | *carls@bnl.gov* |
| Schwandt, P. | IUCF, 2401 Milo B. Sampson Lane, Bloomington, IN 47408-1398, USA | *schwandt@iucf.indiana.edu* |
| Schwarz, H.D. | SLAC, MS 18, P.O. Box 4349, Stanford, CA 94309, USA | *hds@slac.stanford.edu* |
| Sebek, J.J. | SLAC, 2575 Sand Hill Road, Menlo Park, CA 95025, USA | *sebek@slac.stanford.edu* |
| Sedlak, J. | Inst. Physics, Acad. Sciences of Czech Republic, NA Slovance 2, CZ-18040 Prague, Czech Republic | *sedlak@fzu.cz* |
| Seidel, M.G. | SLAC, MS 26, P.O. Box 4349, Stanford, CA 94309, USA | *seidel@slac.stanford.edu* |
| Seidl, P.A. | LBNL, MS 47-112, 1 Cyclotron Road, Berkeley, CA 94720, USA | *paseidl@lbl.gov* |
| Sekutowicz, J. | DESY, Notkestrasse 85, D-22603 Hamburg, Germany | *jacel@teslahe.desy.de* |
| Sellyey, W. | ANL, H-121, 9700 S. Cass Avenue, Bldg. 203, Argonne, IL 60439, USA | |
| Senichev, Y.V. | ISA, U. Aarhus, DK-8000 Aarhus, Denmark | *senichev@dfi.aau.dk* |
| Seo, K-W. | Pohang Acc. Lab, POSTECH, San 31, Hyoja-dong, Nam-ku, Pohang, Kyungbuk 790-784, S. Korea | *skw@postech.ac.kr* |
| Serafini, L. | Dept. of Physics and Astronomy, UCLA, 405 Hilgard Avenue, Los Angeles, CA 90024-1547, USA | *serafini@vesta.physics.ucla.edu* |
| Sereno, N. | ANL, 9700 S. Cass Avenue, Bldg. 401, Argonne, IL 60439, USA | *sereno@aps.anl.gov* |
| Serio, M. | INFN-LNF, C.P. 13, I-00044 Frascati, RM, Italy | *mserio@lnf.infn.it* |
| Serre, C.A. | CERN, PS Division, CH-1211 Geneva 23, Switzerland | *christian.serre@cern.ch* |
| Servranckx, R.V. | Box 40, Gabriola Island, BC, Canada, V0R 1X0 | *servranc@island.net* |
| Sery, A. | Branch of Budker INP, RU-142284 Protvino, Moscow region, Russia | *sery@vlepp.serpukhov.su* |
| Sessler, A.M. | LBNL, MS 71-259, 1 Cyclotron Road, Berkeley, CA 94720, USA | *tbalbl@lbl.gov* |
| Settakorn, C. | SLAC, P.O. Box 4349, Stanford, CA 94309, USA | *chlada@leland.stanford.edu* |
| Shadwick, B.A. | Physics Dept., UC Berkeley, MS 71-259, Berkeley, CA 94720, USA | *shadwick@physics.berkeley.edu* |
| Shafer, R.E. | LANL, MS H808, P.O. Box 1663, Los Alamos, NM 87545, USA | *rshafer@lanl.gov* |
| Shang, C.C. | LLNL, 7000 East Avene, L-153, Livermore, CA 94550, USA | *shang1@llnl.gov* |
| Shapiro, V. | TRIUMF, 4004 Wesbrook Mall, Vancouver, BC, Canada, V6T 2A3 | *vshapiro@triumf.ca* |
| Sharonov, S. | FNAL, MS 316, P.O. Box 500, Batavia, IL 60510-0500, USA | *sharonov@fnal.gov* |
| Sharp, W.M. | LLNL, L-440, P.O. Box 5500, Livermore, CA 94550, USA | *sharp@hif.llnl.gov* |
| Shasharina, S.G. | Physics Dept., U. Colorado, P.O. Box 390, Boulder, CO 80301, USA | *sveta@jove.colorado.edu* |
| Shatilov, D.N. | Budker INP, Novosibirsk, Academician Lavrentiev Prospect 11, RU-630090 Novosibirsk, Russia | *shatilov@inp.nsk.su* |
| Shatunov, Yu.M. | Budker INP, Novosibirsk, Academician Lavrentiev Prospect 11, RU-630090 Novosibirsk, Russia | |
| Shea, T.J. | BNL, Bldg. 1005-4, Upton, NY 11973-5000, USA | *shea@bnl.gov* |
| Sheffield, R.L. | LANL, MS H851, P.O. Box 1663, Los Alamos, NM 87545, USA | *sheff@lanl.gov* |
| Sheldon, R. | 1102 Pass-A-Grille Way, St. Petes Beach, FL 33706, USA | *sheldon@gete.net* |
| Sheldrake, R. | EEV Ltd., Section 9, 106 Waterhouse Lane, Chelmsford, Essex, UK, CM1 2QU | *ron.sheldrake@eev.com* |
| Shen, S. | LLNL, 7000 East Avenue, L-287, Livermore, CA 94551- 9900, USA | *shen@maverick.llnl.gov* |
| Sheng, A. | ANL, 9700 S. Cass Avenue, Bldg. 401, Argonne, IL 60439, USA | *shengic@aps.anl.gov* |
| Shepard, K.W. | ANL, Physics Div. 203, 9700 S. Cass Avenue, Argonne, IL 60439, USA | *shepard@anlphy.phy.anl.gov* |
| Sheynin, S. | General Atomics, P.O. Box 85608, San Diego, CA 92186-9784, USA | *sam.sheynin@gat.com* |
| Shi, J. | Dept. of Physics & Astronomy, U. Kansas, Lawrence, KS 66045, USA | *shi@kuphsx.phsx.ukans.edu* |
| Shiltsev, V.D. | FNAL, P.O. Box 500, Batavia, IL 60510, USA | *shiltsev@fnal.gov* |
| Shirakata, M. | KEK, 1-1 Oho, Tsukuba-shi, Ibaraki-ken 305, Japan | *shir@mjsind.kek.jp* |
| Shoaee, H. | SLAC, 2575 Sand Hill Road, Menlo Park, CA 94025, USA | *hami@slac.stanford.edu* |

| | | |
|---|---|---|
| Shoji, Y. | Himeji Inst. of Tech., Shosha 2167, Himeji, Hyogo 671-22, Japan | *shoji@lasti.himeji-tech.ac.jp* |
| Shu, D. | ANL, 9700 S. Cass Avenue, Bldg. 401-C1255, Argonne, IL 60439, USA | *shud@aps.anl.gov* |
| Shu, Q-S. | TJNAF, MS-58B, 12000 Jefferson Avenue, Newport News, VA 23606, USA | *qsshu@cebaf.gov* |
| Shukla, S. | FNAL, MS 341, P.O. Box 500, Batavia, IL 60510, USA | *shekhar@fnal.gov* |
| Shurter, R.P. | LANL, MS P942, P.O. Box 1663, Los Alamos, NM 87545, USA | *shurter@lanl.gov* |
| Shvets, G. | Plasma Physics Lab, Princeton U., Fozzestal Campus, Princeton, NJ 08543, USA | *tene@pppl.gov* |
| Sibley, C. | MIT Bates, 21 Manning Road, Middleton, MA 01949, USA | *sibley@aesir.mit.edu* |
| Silbar, R.R. | WhistleSoft, Inc., 168 Dos Brazos, Los Alamos, NM 87544, USA | *silbar@whistlesoft.com* |
| Simon, D.J. | CERN, PS Division, CH-1211 Geneva 23, Switzerland | *djs@afsmail.cern.ch* |
| Simonin, A.F. | CEA-Cadarache, DREC - CE Cadarache, F-13108 St. Paul les Duranie, France | *simonin@gemini.cad.cea.fr* |
| Sinclair, C.K. | TJNAF, MS 12A2, 12000 Jefferson Avenue, Newport News, VA 23606, USA | *sinclair@jlab.org* |
| Singh, O.V. | BNL, NSLS, Bldg. 725B, Upton, NY 11973, USA | *singh@bnl.gov* |
| Skaritka, J. | BNL, NSLS, Bldg. 725C, Upton, NY 11973-5000, USA | *skaritka@bnl.gov* |
| Skopik, D.M. | Saskatchewan Accelerator Lab, SAL, Saskatoon, 107 North Road, Saskatoon, SK, Canada, S7N 5C6 | *skopik@skatter.usask.ca* |
| Smirnov, A.V. | Kurchatov Inst., Ul. Bazovskaya, 14-228, RU-127635 Moscow, Russia | *sav@smisav.msk.ru* |
| Smith, A.G. | NNC, Booths Hall, Chelford Road, Knutsford, Cheshire, UK, WA16 8QZ | |
| Smith, G.A. | BNL, Bldg. 911C, Upton, NY 11973, USA | *smith1@bnldag.bnl.gov* |
| Smith, H.V. | LANL, HS H838, AOT - 2, P.O. Box 1663, Los Alamos, NM 87545, USA | *hvsmith@lanl.gov* |
| Smith, J.D. | BNL, NSLS, Bldg. 725B, Upton, NY 11973, USA | *jsmith@bnl.gov* |
| Smith, J.R. | Pulse Sciences, Inc., TAIT, 520 B3 Wheeler Ave, S.E., Albuquerque, NM 87102, USA | |
| Smith, R.S. | Cornell U., LNS, PO Box 353, Millsap, TX 76066, USA | *scotts@tristan.tn.cornell.edu* |
| Smith, S.L. | Daresbury Lab, CLRC, Warrington, Cheshire, UK, WA4 4AD | *s.l.smith@dl.ac.uk* |
| Smith, S.R. | SLAC, MS 50, P.O. Box 4349, Stanford, CA 94309, USA | *ssmith@slac.stanford.edu* |
| Smith, T.L. | ANL, 9700 S. Cass Avenue, Argonne, IL 60439, USA | *tls@aps.anl.gov* |
| Sobenin, N.P. | Moscow Eng. Phys. Inst., Moscow, Russia | |
| Sokolowski, J.S. | Weizmann Inst. of Science, Tel Aviv U., Faculty of Physics, Rehovot, 76100, Israel | *fnsoko@weizmann.weizmann.ac.il* |
| Solyak, N. | Branch of Budker INP, RU-142284 Protvino, Moscow region, Russia | *solyak@vlepp.serpukhov.su* |
| Song, J. | ANL, 9700 S. Cass Avenue, Argonne, IL 60439, USA | *song@aps.anl.gov* |
| Spata, M.F. | TJNAF, 12000 Jefferson Avenue, Newport News, VA 23606, USA | *spata@jlab.org* |
| Spentzouris, L.K. | FNAL, MS 341, P.O. Box 500, Batavia, IL 60510-0500, USA | |
| Spielman, R.B. | SNL, MS 1194, P.O. Box 5800, Albuquerque, NM 87185-1194, USA | *rbspiel@sandia.gov* |
| Srinivas, V. | SLAC, MS 26, 2575 Sand Hill Road, Menlo Park, CA 94025, USA | *vinay@slac.stanford.edu* |
| Srinivasan-Rao, T. | BNL, 535B, P.O. Box 5000, Upton, NY 11973-5000, USA | *triveni@bnlarm.bnl.gov* |
| Stanford, G.H. | TRIUMF, 4004 Wesbrook Mall, Vancouver, BC, Canada, V6T 2A3 | *stanford@triumf.ca* |
| Staples, J.W. | LBNL, 71-259, 1 Cyclotron Road, Berkeley, CA 94720, USA | *jwstaples@lbl.gov* |
| Steier, C. | Bonn U., Physics Inst., Nussallee 12, D-53115 Bonn, Germany | *steier@uni-bonn.de* |
| Stevenson, N.R. | TRIUMF, 4004 Wesbrook Mall, Vancouver, BC, Canada, V6T 2A3 | *nigel@triumf.ca* |
| Stiliaris, E. | Inst. of Accelerating Systems and Applications, P.O. Box 17214, GR-17214 Athens, Greece | *stathis@rtui.i.a.s.a.uoa.gr* |
| Still, D.A. | FNAL, MS 306, P.O. Box 500, Batavia, IL 60510, USA | *still@adcacl.fnal.gov* |
| Stockhorst, H. | Inst. F. Nuclear Physics, Forschungszentrum Jülich, P.O. Box 1913, D-52425 Jülich, Germany | *hst@snoopy.cc.kfa-juelich.de* |
| Stoeffl, W. | LLNL, L-401, P.O. Box 808, Livermore, CA 94550, USA | *stoeffl1@llnl.gov* |
| Stoltz, P.H. | Princeton Plasma Physics Lab, Princeton U., Box 451, Princeton, NJ 08543, USA | *pstoltz@pppl.gov* |
| Stott, J.P. | U. Wisconsin at Madison, SRC, 3731 Schneider Drive, Stoughton, WI 53589, USA | *jpstott@src.wisc.edu* |
| Stover, G.D. | LBNL, MS 46-125, 1 Cyclotron Road, Berkeley, CA 94720, USA | *gdstover@lbl.gov* |
| Strait, J.B. | FNAL, MS 316, P.O. Box 500, Batavia, IL 60510, USA | *strait@fnal.gov* |
| Strauss, B.P. | Division of High Energy Physics, DOE, 19901 Germantown Road, Germantown, MD 20874, USA | *hep-tech@oer.doe.gov* |
| Strubin, P.M. | CERN, CH-1211 Geneva 23, Switzerland | *pierre.strubin@cern.ch* |
| Struckmeier, J. | GSI Darmstadt, Planckstr. 1, D-64291 Darmstadt, Germany | *j.struckmeier@gsi.de* |
| Stupakov, G. | SLAC, P.O. Box 4349, Stanford, CA 95014, USA | *stupakov@slac.stanford.edu* |
| Sugimura, T. | Kyoto U., Gokasho Uji, Kyoto 611, Japan | *sugimura@kyticr.kuicr.kyoto-u.ac.jp* |
| Suhring, S. | TJNAF, 12000 Jefferson Avenue, Newport News, VA 23606, USA | *suhring@jlab.org* |
| Suk, H. | Dept. of Physics, PBPL, UCLA, 405 Hilgard Avenue, Los Angeles, CA 90095, USA | *suk@vesta.physics.ucla.edu* |
| Sullivan, M.K. | SLAC, P.O. Box 4349, Bin 17, Stanford, CA 94309, USA | *sullivan@slac.stanford.edu* |
| Summers, D.J. | Dept. of Physics, U. Mississippi, University, MS 38677, USA | *summers@umsphy.phy.olemiss.edu* |
| Sun, D. | SAIC, P.O. Box 500, Batavia, IL 60471, USA | *ding@fnal.gov* |

| | | |
|---|---|---|
| Sutter, D.F. | Division of High Energy Physics, DOE, 19901 Germantown Road, Germantown, MD 20874, USA | *hep-tech@oer.doe.gov* |
| Suzuki, T. | KEK, 1-1 Oho, Tsukuba-shi, Ibaraki-ken 305, Japan | *toshio@kekvax.kek.jp* |
| Swenson, B.C. | Linac Systems, 2167 N. Highway 77, Waxahachie, TX 75165, USA | |
| Swenson, D.A. | Linac Systems, 2167 N. Highway 77, Waxahachie, TX 75165, USA | *daswenson@aol.com* |
| Syphers, M.J. | BNL, Bldg. 911B, P.O. Box 5000, Upton, NY 11973, USA | *msyphers@bnl.gov* |
| Tadokoro, M. | Hitachi, Ltd., 1-1 Saiwai-Cho, 3-chome, Hitachi, Ibaraki-ken 317, Japan | |
| Takahashi, H. | BNL, Bldg. 475 B, Upton, NY 11973, USA | *takahashi@bnlarm.bnl.gov* |
| Takaki, H. | U. Tokyo, ISSP, Midori-cho 3-2-1, Tanashi-shi, Tokyo 188, Japan | *takaki@issp.u-tokyo.ac.jp* |
| Takanaka, M. | RIKEN, Cyclotron Lab, 2-1 Hirosawa, Wako-shi, 351-01, Japan | *takanaka@insac7.tanashi.kek.jp* |
| Takata, K. | KEK, 1-1 Oho, Tsukuba-shi, Ibaraki-ken 305, Japan | *takata@kekvax.kek.jp* |
| Takayama, K. | KEK, 1-1 Oho, Tsukuba-shi, Ibaraki-ken 305, Japan | *takayama@kekvax.kek.jp* |
| Takeda, H. | LANL, MS H817, P.O. Box 1663, Los Alamos, NM 87545, USA | *takeda@lanl.gov* |
| Takeda, S. | KEK, 1-1 Oho, Tsukuba-shi, Ibaraki-ken 305, Japan | *seishi.takeda@kek.jp* |
| Tallerico, P.J. | LANL, MS H827, P.O. Box 1663, Los Alamos, NM 87545, USA | *tallerico@lanl.gov* |
| Tallerico, T.N. | BNL, Bldg. 911B, Upton, NY 11973, USA | *tallerico@bnldag.ags.bnl.gov* |
| Talman, R.M. | Cornell U., LNS, Ithaca, NY 14853-5001, USA | *talman@lns62.lns.cornell.edu* |
| Tan, C-Y. | Cornell U., Wilson Lab, Ithaca, NY 14853-5001, USA | *cytan@tristan.tn.cornell.edu* |
| Tanabe, E. | AET Associates, Inc., 20370 Town Center Lane #252, Cupertino, CA 95014, USA | *aetaus@aol.com* |
| Tanabe, T. | U. Tokyo, INS, 3-2-1 Midoricho, Tanashi, Tokyo, 188, Japan | *tanabe@ins.u-tokyo.ac.jp* |
| Tanabe, T. | SPring-8 BL Group, RIKEN, Kamigori, Ako-gun, Hyogo, 678-12, Japan | *ttanabe@postman.riken.go.jp* |
| Tang, J.Y. | TJNAF, MS 85A, 12000 Jefferson Avenue, Newport News, VA 23606, USA | *tang@jlab.org* |
| Tanuma, T. | Hitachi, Ltd., 6 Kanda-Surugadai, 4-chome, Chiyoda-ku, Tokyo 101, Japan | |
| Tartaglia, M. | FNAL, MS 316, P.O. Box 500, Batavia, IL 60510, USA | *tartaglia@fnal.gov* |
| Tatchyn, R.O. | SLAC, SSRL, MS 69, 2575 Sand Hill Road, Stanford, CA 94305, USA | |
| Taylor, T.M. | CERN, LHC-ICP, CH-1211 Geneva 23, Switzerland | *thomas.taylor@cern.ch* |
| Tazzari, S. | Dip. Di. Fisica, INFN/U. Diroma Torvergata, Viale Ricerca Scientifica 1, I-00133 Roma, RM, Italy | *tazzari@roma2.infn.it* |
| Tecker, F. | RWTH Aachen/CERN, CH-1211 Geneva 23, Switzerland | *frank.tecker@cern.ch* |
| Tekian, P. | METACERAM, 21 Rue Georges Lebigot, F-94800 Villejuif, France | |
| Temkin, R. | MIT Bates, NW16-186, Cambridge, MA 02139, USA | *temkin@psfc.mit.edu* |
| Temnykh, A.B. | Cornell U., Wilson Lab, Dryden Road, Ithaca, NY 14853-5001, USA | *st@lns.cornell.edu* |
| Ten Kate, H. | CERN, PPE Division, ATLAS, CH-1211 Geneva 23, Switzerland | *Herman.Tenkate@cern.ch* |
| Teng, L.C. | ANL, 9700 S. Cass Avenue, Bldg. 401, Argonne, IL 60439, USA | *teng@aps.anl.gov* |
| Terebilo, A.G. | UCLA, 846 Riley Drive, Albany, NY 94706, USA | *terebilo@ssrl.slac.stanford.edu* |
| Tesch, P.P. | CREOL/UCF, 1500 E. Ridgewood Street, Orlando, FL 32803-5451, USA | *tesch@lorien.creol.ucf.edu* |
| Teytelman, D. | SLAC, 2575 Sand Hill Road, Menlo Park, CA 94025, USA | *dim@slac.stanford.edu* |
| Theuws, W. | Eindhoven U. of Tech., PO Box 513, Cyclotron Lab. 2.13, NL-5571 DD Eindhoven, The Netherlands | *w.h.c.theuws.@cycl.phys.tue.nl* |
| Thiessen, H.A. | LANL, MS-H846, P.O. Box 1663, P-25, Los Alamos, NM 87545, USA | *hat@lanl.gov* |
| Thomas, M.G. | BNL, NSLS, Bldg. 725B, Upton, NY 11973, USA | *thomas@bnllsl.nsls.bnl.gov* |
| Thuot, M.E. | LANL, MS H820, P.O. Box 1663, Los Alamos, NM 87545, USA | *mthuot@lanl.gov* |
| Thur, W. | LBNL, 46-161, 1 Cyclotron Road, Berkeley, CA 94720, USA | *gwthur@lbl.gov* |
| Tiefenback, M.G. | TJNAF, MS 58, 12000 Jefferson Avenue, Newport News, VA 23606, USA | *tiefen@jlab.org* |
| Timm, M. | TH Darmstadt, Darmstadt U. of Tech., TEMF, Schlossgartenstr. 8, D-64289 Darmstadt, Germany | |
| Timossi, C.A. | LBNL, 10-110, 1 Cyclotron Road, Berkeley, CA 94720, USA | *catimossi@lbl.gov* |
| Ting, A.C. | NRL, Code-6795, Washington, DC 20375, USA | *ting@ppd.nrl.navy.mil* |
| Tkatchenko, A. | LNS - Saclay, F-91191 Gif sur Yvette, France | *tkat@picpus.saclay.cea.fr* |
| Todd, A.M.M. | Northrop Grumman ATDC, 4 Independence Way, Princeton, NJ 08540, USA | *todd@grump.com* |
| Tollestrup, A.V. | FNAL, MS 318, P.O. Box 500, Batavia, IL 60510, USA | *alvin@fnal.gov* |
| Tomimasu, T. | Free Electron Laser Research Inst., Hirakata Tsuda Yamate 2-9-5, Osaka, 573-01, Japan | |
| Tominaka, T. | RIKEN, Cyclotron Lab, 2-1 Hirosawa, Wako, Saitama 351-01, Japan | *tominaka@postman.riken.go.jp* |
| Tomioka, Y. | Hitachi, Ltd., 6 Kanda-Surugadai, 4-chome, Chiyoda-ku, Tokyo 101, Japan | |
| Tomizawa, M. | Inst. for Nuclear Study, U. Tokyo, 3-2-1, Midori-cho, Tanashi, Tokyo 188, Japan | *tomizawa@insac7.tanashi.kek.jp* |
| Tompkins, J.C. | FNAL, MS 316, P.O. Box 500, Batavia, IL 60510, USA | *tompkins@fnal.gov* |
| Tooker, J.F. | General Atomics, 3550 General Atomics Court, San Diego, CA 92121-1194, USA | *joe.tooker@gat.com* |
| Tornoe, R. | Communications and Power Industries, 301 Industrial Way, San Carlos, CA 94070, USA | |
| Tortschanoff, T. | CERN, LHC Division, CH-1211 Geneva 23, Switzerland | *theodor.tortschanoff@cern.ch* |

| | | |
|---|---|---|
| Towne, N.A. | BNL, NSLS, Bldg. 725B, Upton, NY 11973, USA | *towne@bnl.gov* |
| Toyama, T. | KEK, 1-1 Oho, Tsukuba-shi, Ibaraki-ken 305, Japan | *toyama@kekvax.kek.jp* |
| Trakhtenberg, E.M. | ANL, 9700 S. Cass Avenue, Argonne, IL 60439, USA | *emil@aps.anl.gov* |
| Tran, H.J. | TRIUMF, UBC, 4004 Wesbrook Mall, Vancouver, BC, Canada, V6T 2A3 | *hjtran@triumf.ca* |
| Tranquille, G.A.C. | CERN, PS Division, CH-1211 Geneva 23, Switzerland | *tranquil@ps.msm.cern.ch* |
| Travish, G. | INFN-Milano, 201 Via Cervi, I-20090 Segrate, MI, Italy | *gil.travish@mi.infn.it* |
| Trbojevic, D. | BNL, Bldg. 1005, P.O. Box 5000, Upton, NY 11973-5000, USA | *dejan@bnl.gov* |
| Tremaine, A.M. | Dept. of Physics, UCLA, 405 Hilgard Avenue, Los Angeles, CA 90095-1444, USA | *tremaine@physics.ucla.edu* |
| Trines, D. | DESY, Notkestrasse 85, D-22607 Hamburg, Germany | *trines@teslavb.desy.de* |
| Trzeciak, W.S. | U. Wisconsin at Madison, SRC, 3731 Schneider Drive, Stoughton, WI 53589-3097, USA | *walter@src.wisc.edu* |
| Tsutsui, H. | Sumitomo Heavy Industries, Ltd., 2-1-1 Yato-cho, Tanashi, Tokyo 188, Japan | *tsutsui@kekvax.kek.jp* |
| Tuozzulo, J.E. | BNL, Bldg. 911B, Upton, NY 11973, USA | *tuozzolo@bnl.gov* |
| Tur, Y. | Kharkov Inst. of Phys. and Tech. (KFTI), UA-310108 Kharkov, Ukraine | |
| Turner, S. | CERN Accelerator School, AC Division, CH-1211 Geneva 23, Switzerland | |
| Turner, W.C. | LBNL, MS 71-259, 1 Cyclotron Road, Berkeley, CA 94720, USA | *wcturner@lbl.gov* |
| Twichell, J.C. | MIT Lincoln Lab, MS I-300, 244 Wood Street, Lexington, MA 02173, USA | *twichell@ll.mit.edu* |
| Uesugi, T. | KEK, 3-2-1 Midoricho, Tanashi, Tokyo 188, Japan | *uesugi@insuty.tanashi.kek.jp* |
| Uggerhoj, E. | ISA, U. Aarhus, DK-8000 Aarhus, Denmark | *ugh@dfi.aau.dk* |
| Umstadter, D.P. | U. Michigan, 1006 IST Bldg., Ann Arbor, MI 48109-2099, USA | *dpu@umich.edu* |
| Unser, K.B. | 42 Bugnon, F-01630 St. Genis-Pouilly, France | |
| Urakawa, J. | KEK, 1-1 Oho, Tsukuba-shi, Ibaraki-ken 305, Japan | *junji.urakawa@kek.jp* |
| Ursic, R. | TJNAF, 12000 Jefferson Avenue, Newport News, VA 23606, USA | *rok@jlab.org* |
| Ursino, M. | Copley Controls Corp., 410 University Avenue, Westwood, MA 02154, USA | *mursino@copleycontrols.com* |
| Uzat, H.W. | TRIUMF, 4004 Wesbrook Mall, Vancouver, BC, Canada, V6T 2A3 | *uzat@triumf.ca* |
| Valentinov, A.G. | Kurchatov Inst., Kurchatov Sq., RU-123182 Moscow, Russia | *vale@ksrs.msk.su* |
| van Asselt, W.K. | BNL, Bldg. 911B, Upton, NY 11973, USA | *vanassett@bnldag.ags.bnl.gov* |
| van Bibber, K.A. | LLNL, L-028, P.O. Box 808, Livermore, CA 94550, USA | *kvanbibber@llnl.gov* |
| van der Geer, B. | Pulsar Physics, Flamingostraat 24, NL-3582 SX Utrecht, The Netherlands | *gpt@pulsar.nt* |
| van Herp, L. | Holec Power Protection BU, P.O. Box 4, NL-7550 Hengelo, The Netherlands | *hpphu@pi.net* |
| van Rienen, U. | TH Darmstadt, Fb 18 FG TEMF, Schlossgartenstr. 8, D-64289 Darmstadt, Germany | *van.rienen@temf.th-darmstadt.de* |
| van Steenbergen, A. | BNL, NSLS, Bldg. 725B, Upton, NY 11973, USA | *avanst@bnl.gov* |
| van Zeijts, J. | TJNAF, 12000 Jefferson Avenue, Newport News, VA 23606, USA | *johannes@jlab.org* |
| Vandeplassche, D. | IBA, Chemin du Cyclotron, 3, B-1348 Louvain, Belgium | *amv@iba.mhs.compuserve.com* |
| Variale, V. | INFN-Bari, Via Amendola 173, I-70126 Bari, Italy | *variale@ba.infn.it* |
| Vasserman, I.B. | ANL, 9700 S. Cass Avenue, Argonne, IL 60439, USA | *isaac@aps.anl.gov* |
| Velazco, J.E. | Microwave Technologies Inc., 5716 Edgewater Oak Court, Burke, VA 22015, USA | *jvelazco@ece.gmu.edu* |
| Venturini, M. | Dept. of Physics, U. Maryland, College Park, MD 20742, USA | *venturin@quark.umd.edu* |
| Vetter, A.M. | Boeing D&SG, MS 2T-50, P.O. Box 3999, Seattle, WA 98124-2499, USA | *arthur.m.vetter@boeing.com* |
| Vitello, P.A. | LLNL, L-014, 7000 East Avenue, Livermore, CA 94550, USA | *vitello@llnl.gov* |
| Vlieks, A.E. | SLAC, 2575 Sand Hill Road, Menlo Park, CA 94025, USA | *aev@slac.stanford.edu* |
| Vogel, V. | Branch of Budker INP, RU-142284 Protvino, Moscow region, Russia | *vogel@vlepp.serpukhov.su* |
| Volfbeyn, P. | LBNL, 71-259, 1 Cyclotron Road, Berkeley, CA 94720, USA | *pavel@lbl.gov* |
| Volkov, V.I. | JINR, RU-141890 Dubna, Moscow region, Russia | *volkov@sunhe.jinr.dubna.su* |
| Volkov, V.N. | Budker INP, Novosibirsk, Academician Lavrentiev Prospect 11, RU-630090 Novosibirsk, Russia | *vnvolkov@inp.nsk.su* |
| vom Stein, P. | Research Centre Rossendorf, Forschungezentrum Rossendorf, Abt. FWN, Postfach 510 119, D-01314 Dresden, Germany | *steinp@fz-rossendorf.de* |
| von Hahn, R. | MPI fur Kernphysik, Heidelberg, Postfach 10 39 80, D-69029 Heidelberg, Germany | *vonhahn@minnie.mpi-hd.mpg.de* |
| Vormann, H. | IAP, Frankfurt/Main, Robert-Mayer-Str. 2-4, D-60325 Frankfurt am Main, Germany | *vormann@em.uni-frankfurt.de* |
| Voss, G-A.R. | DESY, Notkestrasse 85, D-22603 Hamburg, Germany | *gavoss@mail.desy.de* |
| Wait, G.D. | TRIUMF, 4004 Wesbrook Mall, Vancouver, BC, Canada, V6T 2A3 | *wait@triumf.ca* |
| Walckiers, L.M.L.J. | CERN, CH-1211 Geneva 23, Switzerland | *louis.walckiers@cern.ch* |
| Walker, I. | GMW Associates, PO Box 2578, Redwood City, CA 94064, USA | |
| Walters, D. | ANL, 9700 S. Cass Avenue, Bldg. 401, Argonne, IL 60439, USA | |
| Wan, W. | FNAL, MS-345, P.O. Box 500, Batavia, IL 60510-0500, USA | |
| Wang, C.W. | Physics Dept., Yale U., WNSL, New Haven, CT 06520, USA | *beamlab@riviera.physics.yek.edu* |
| Wang, D.X. | TJNAF, MS 58, 12000 Jefferson Avenue, Newport News, VA 23606, USA | *dxwang@cebaf.gov* |
| Wang, F. | MIT Bates, P.O. Box 846, Middleton, MA 01949-2846, USA | *fwang@azsir.mit.edu* |

| | | |
|---|---|---|
| Wang, H. | BNL, 901-A, P.O. Box 5000, Upton, NY 11973-5000, USA | |
| Wang, J. | SLAC, MS 26, P.O. Box 4349, Stanford, CA 94309, USA | *jywap@slac.stanford.edu* |
| Wang, J-M. | BNL, 725-C, P.O. Box 5000, Upton, NY 11973-5000, USA | *jmwang@bnllsl.nsls.bnl.gov* |
| Wang, J.G. | Inst. for Plasma Research, U. Maryland, Energy Research Bldg., College Park, MD 20742, USA | *jgwang@plasma.umd.edu* |
| Wang, M-H. | SRRC, Taiwan, No. 1 R&D Road, VI, Hsinchu Science-Based Industrial Park, Hsinchu, 30077, Taiwan | *mhwang@bd01.srrc.gov.tw* |
| Wang, X. | BNL, NSLS Bldg. 725C, P.O. Box 5000, Upton, NY 11973-5000, USA | *wang@bnllsl.nsls.bnl.gov* |
| Wang, Y-M. | LANL, MS H827, P.O. Box 1663, Los Alamos, NM 87545, USA | *ymwang@lanl.gov* |
| Wangler, T.P. | LANL, MS H817, Group L, Los Alamos, NM 87544, USA | *twangler@lanl.gov* |
| Watson, J.M. | International Isotopes Inc., 7401 Jordan Lane, Midlothian, TX 76065, USA | *jwatson.i3@worldnet.att.net* |
| Watson, W.A. | TJNAF, 12000 Jefferson Avenue, Newport News, VA 23606, USA | *watson@jlab.org* |
| Weatherup, C.R. | EEV Ltd., 106 Waterhouse Lane, Chelmsford, Essex, UK, CM1 2QU | *cliff.weatherup@eev.com* |
| Weiland, T. | TH Darmstadt, FB 18, Schlossgartenstrasse 8, D-64289 Darmstadt, Hessen, Germany | *dd2e@temf.th-darmstadt.de* |
| Weir, J. | LLNL, 7000 East Avenue, L-535, Livermore, CA 94550, USA | *weir2@llnl.gov* |
| Welch, D.R. | Mission Research Corp., 1720 Randolph S.E., Albuquerque, NM 87106, USA | *drwelch@or66.com* |
| Welch, J.J. | Cornell U., Wilson Lab, Ithaca, NY 14853-5001, USA | *welch@lns62.lns.cornell.com* |
| Weng, W-T. | BNL, AGS Dept., Bldg. 911B, Upton, NY 11973, USA | *weng@bnl.gov* |
| Wengrow, A.B. | LBNL, MS 5-119, 1 Cyclotron Road, Berkeley, CA 94720, USA | *awengrow@lbl.gov* |
| Westenskow, G.A. | LLNL, P.O. Box 808, Livermore, CA 94551, USA | *gw@llnl.gov* |
| Whealton, J.W. | ORNL, P.O. Box 2009, Bldg. 9108, Oak Ridge, TN 37831-8088, USA | *whealton@ornl.gov* |
| White, G.R. | SLAC, P.O. Box 4349, Bin 46, Stanford, CA 94026, USA | *greg@slc.slac.stanford.edu* |
| White, K.S. | TJNAF, 12000 Jefferson Avenue, Newport News, VA 23606, USA | *karen@cebaf.gov* |
| White, M.M. | ANL, 9700 S. Cass Avenue, Bldg. 401, Argonne, IL 60439, USA | *mwhite@aps.anl.gov* |
| Whitham, K. | Titan Beta, 6780 Sierra Court, Dublin, CA 94507, USA | *kwhitham@titan.com* |
| Whittum, D.H. | SLAC, MS 26, 2575 Sand Hill Road, Menlo Park, CA 94025, USA | *whittum@slac.stanford.edu* |
| Wiemerslage, G. | ANL, 9700 S. Cass Avenue, Argonne, IL 60439, USA | *wiemer@aps.anl.gov* |
| Wienands, H-U. | SLAC, MS 17, P.O. Box 4349, Stanford, CA 94309, USA | *uli@slac.stanford.edu* |
| Wilcox, D.M. | EEV Ltd., Waterhouse Lane, Chelmsford, Essex, UK, CM1 2QU | *david.wilcox@eev.com* |
| Wilkinson, C.A. | LANL, MS H838, P.O. Box 1663, Los Alamos, NM 87544, USA | *wilkinson@lanl.gov* |
| Willeke, F.J. | DESY, Notkestrasse 85, D-22603 Hamburg, Germany | *willeke@desy.de* |
| Willen, E.H. | BNL, B 902, P.O. Box 5000, Upton, NY 11973, USA | *willen@bnl.gov* |
| William, N.W. | BNL, AGS Dept., 911C, Rm 344, Upton, NY 11949, USA | *neville@bnl.gov* |
| Williams, J. | Electronic Measurements - ALE Systems, 278 Spring Street, Red Bank, NJ 07753, USA | *emiapps@emipower.com* |
| Williams, M.D. | LBNL, MS 5-119, 1 Cyclotron Road, Berkeley, CA 94720, USA | *mdwilliams@lbl.gov* |
| Williams, R.L. | Florida A& M U., 2114 Broad Street, Tallahassee, FL 32301, USA | *williams@cennas.nhmfl.gov* |
| Williams, R.W. | Physics Dept., U. of Washington, Box 351560, Seattle, WA 98195-1560, USA | |
| Wilson, E.J.N. | CERN, AC Division, CH-1211 Geneva 23, Switzerland | *ejn@cern.sp.cern.ch* |
| Wilson, M.A.D. | DOE, ER - 55, 19901 Germantown Road, Germantown, MD 20874-1290, USA | *mark.wilson@oer.doe.gov* |
| Wilson, P.B. | SLAC, MS 26, P.O. Box 4349, Stanford, CA 94309, USA | *pwilson@slac.stanford.edu* |
| Winick, H. | SLAC, MS 69, P.O. Box 4349, Stanford, CA 94309, USA | *winick@slac.stanford.edu* |
| Wiseman, M.A. | TJNAF, 12000 Jefferson Avenue, Newport News, VA 23606, USA | *wiseman@jlab.org* |
| Wisnivesky, D. | LNLS - Brazil, Caixa Postal 6192, BR-13093-970 Campinas, SP, Brazil | *daniel@lnls.br* |
| Witkover, R.L. | BNL, Bldg. 911B, Upton, NY 11973, USA | *witkover@bnl.gov* |
| Woebke, G. | DESY, Notkestrasse 85, D-22603 Hamburg, Germany | *gerd.woebke@desy.de* |
| Woodle, M. | BNL, NSLS, Bldg. 725D, Upton, NY 11973-5000, USA | *woodlel@bnl.gov* |
| Wright, R.M. | LANL, MS H820, P.O. Box 1663, Los Alamos, NM 87545, USA | *rwright@lanl.gov* |
| Wu, X. | Michigan State U., NSCL, 155 Cyclotron Lab, East Lansing, MI 48824, USA | *xwu@nscl.msu.edu* |
| Wu, Y. | FEL Laboratory, Duke U., Durham, NC 27708-0319, USA | *wu@fel.duke.edu* |
| Wu, Y. | IHEP, P.O. Box 918, Chinese Academy of Sciences, Beijing, 100039, P.R. China | |
| Wuensch, W.N. | CERN, PS Division, CH-1211 Geneva 23, Switzerland | *walter.wuensch@cern.ch* |
| Wustefeld, G. | BESSY-II, Bld. 15.1, Rudower Chaussee 5, D-12489 Berlin, Germany | *wuestefeld@bessy.de* |
| Wutte, D. | LBNL, MS 5-119, 1 Cyclotron Road, Berkeley, CA 94720, USA | *dwutte@mh1.lbl.gov* |
| Xie, M. | LBNL, MS 71-259, 1 Cyclotron Road, Berkeley, CA 94720, USA | *mingxie@lbl.gov* |
| Xie, Z.Q. | LBNL, Rm 113, Bldg. 88, LBNL, Berkeley, CA 94720, USA | *zqxie@lbl.gov* |
| Xu, S. | ANL, 9700 S. Cass Avenue, Bldg. 401 - B3160, Argonne, IL 60439, USA | *xus@aps.anl.gov* |
| Yakimenko, V.E. | BNL, NSLS Bldg. 725C, P.O. Box 5000, Upton, NY 11973-5000, USA | *yakimenk@bnllsl.nsls.bnl.gov* |
| Yakovlev, V.P. | Omega-P, Inc., 205 S. Whiting Street, #307, Alexandria, VA 22304, USA | *slava@clark.net* |
| Yamaguchi, A. | Toshiba Co., 22-4, Suehiro-cho, Tsurumi-ku, Yokohama, 230, Japan | *yamag@densog.keihin.toshiba.co.jp* |
| Yamamoto, N. | KEK, 1-1 Oho, Tsukuba-shi, Ibaraki-ken 305, Japan | *noboru.yamamoto@kek.jp* |
| Yamazaki, Y. | BNL, AT, 475C, Upton, NY 11973, USA | *yamazaki@mail.bnl.gov* |

| | | |
|---|---|---|
| Yamazaki, Y. | KEK, 1-1 Oho, Tsukuba-shi, Ibaraki-ken 305, Japan | *yoshishi@kekvax.kek.jp* |
| Yan, Y.T. | SLAC, MS 26, P.O. Box 4349, Stanford, CA 95014, USA | *yan@slac.stanford.edu* |
| Yang, B. | ANL, 9700 S. Cass Avenue, Bldg. 401, Argonne, IL 60439, USA | *bxyang@aps.anl.gov* |
| Yano, Y. | RIKEN, 2-1 Hirosawa, Wako, Saitama 351-01, Japan | *yano@rikvax.riken.go.jp* |
| Yao, C-Y. | ANL, 9700 S. Cass Avenue, Bldg. 401, Argonne, IL 60439, USA | *cyao@aps.anl.gov* |
| Yarba, V. | FNAL, MS 316, P.O. Box 500, Batavia, IL 60510, USA | *yarba@fnal.gov* |
| Yazynin, Y. | IHEP, RU-142284 Protvino, Moscow region, Russia | |
| Yeh, M.S. | SRRC, Taiwan, No. 1 R&D Road, VI, Hsinchu Science-Based Industrial Park, Hsinchu, 30077, Taiwan | *msyeh@alphal.srrc.gov.tw* |
| Yeoward, M.R. | SVF Inc., P.O. Box 70, Rock Falls, IL 61071, USA | *myeoward@essexl.com* |
| Yin, Y. | Y.Y. Labs, Inc., P.O. Box 597, Fremont, CA 94537-0597, USA | *yanyin@triumf.ca* |
| Yokoya, K. | KEK, 1-1 Oho, Tsukuba-shi, Ibaraki-ken 305, Japan | *kaoru.yokoya@kek.jp* |
| York, R.C. | Michigan State U., East Lansing, MI 48824-1321, USA | *york@nscl.msu.edu* |
| Young, E.M. | Cornell U., Wilson Lab, PO Box 1179, Dodge City, Kansas 67801, USA | *emy@mail.lns.cornell.edu* |
| Young, L.M. | LANL, MS H808, P.O. Box 1663, Los Alamos, NM 87545, USA | *lyoung@lanl.gov* |
| Young, P.E. | SAIC, 4161 Campus Point Court, San Diego, CA 92121, USA | *phillip.e.young@cpmx.saic.com* |
| Yu, D.U.L. | DULY Research Inc., 19112 MacArthur Street, Rancho Palos Verdes, CA 90275-1111, USA | |
| Yu, S.S.L. | LBNL, MS 47-112, 1 Cyclotron Road, Berkeley, CA 94720, USA | *simon_yu@macmail.lbl.gov* |
| Yunn, B. | TJNAF, MS 12A1, 12000 Jefferson Avenue, Newport News, VA 23606, USA | *yunn@jlab.org* |
| Zagel, J.R. | FNAL, MS 308, P.O. Box 500, Batavia, IL 60510, USA | *zagel@fnal.gov* |
| Zaltsman, A. | BNL, Bldg. 911B, Upton, NY 11973, USA | *zaltsman@bnl.gov* |
| Zapalac, G.H. | Imatron Inc., 389 Oyster Point Boulevard, South San Francisco, CA 94080, USA | *ghz@imatron.com* |
| Zhabitsky, V.M. | JINR, RU-141980 Dubna, Moscow region, Russia | *main@jinr.dubna.su* |
| Zhang, L. | Inst. of Fluid Physics CAEP, P.O. Box 523-56, Cheng-du, 61003, P.R. China | *dingbn@sun.ihep.ac.cn* |
| Zhang, S.Y. | BNL, AGS Dept., Bldg. 911B, Upton, NY 11973, USA | *syzhang@bnldag.ags.bnl.gov* |
| Zhang, T. | Omega-P, Inc., P.O. Box 208124, WNSL, 272 Whitney Avenue, New Haven, CT 06520-8124, USA | *tzhang@cuplvx.ap.columbia.edu* |
| Zhao, Y. | BNL, Bldg. 901A, P.O. Box 5000, Upton, NY 11973-5000, USA | *yzhao@muon.cap.bnl.gov* |
| Zholents, A.A. | LBNL, MS 71-259, 1 Cyclotron Road, Berkeley, CA 94720, USA | *zholents@lbl.gov* |
| Ziemann, V.G. | Svedberg Lab, Uppsala, Box 533, S-75121 Uppsala, Sweden | *ziemann@tsl.uu.se* |
| Zisman, M.S. | LBNL, MS 71J, 1 Cyclotron Road, Berkeley, CA 94720, USA | *zisman@lbl.gov* |
| Zlobin, A. | FNAL, MS 316, P.O. Box 500, Batavia, IL 60510-0500, USA | *zlobin@fnal.gov* |
| Zobov, M. | INFN-LNF, Accelerator Divison, Via Enrico Fermi, 40, I-00044 Frascati, RM, Italy | *mikhail@lnf.infn.it* |
| Zolotorev, M. | LBNL, MS 71-259, 1 Cyclotron Road, Berkeley, CA 94720, USA | *maxzolo@lbl.gov* |
| Zumbro, M.V. | LANL, MS H812, P.O. Box 1663, Los Alamos, NM 87545, USA | *mzumbro@lanl.gov* |
| Zyngier, H. | LBNL, 1 Cyclotron Road, Berkeley, CA 94720, USA | *henri@mh1.lbl.gov* |

# AUTHOR INDEX


## A

Abramenko, N.I. 2773
Abramovich, A. 906
Abs, M. 3816, 3857
Adachi, T. 3470
Adolphsen, C. 439, 554, 608, 1673, 1676, 2119, 2186, 2256, 2580, 2852, 3027, 3042, 3192
Agafonov, A.V. 1299, 1302, 3141
Ahn, H. (JAERI) 648, 760
Ahn, H. (LANL) 1012
Ahrens, L. 69, 89, 98, 101, 959, 965, 1460, 1478
Aiello, G. Roberto 2113, 2122
Aizatsky, M.I. 3810
Akai, K. 2902, 2974, 2977, 2986, 3069, 3087, 3090
Akasaka, N. 455, 530, 533, 536, 1831, 2902, 2974, 2977, 2986, 3069
Akemoto, M. 587, 1319, 1322
Akre, J. 2067
Akre, R. 506, 1569, 3021, 3024, 3027
Alessi, J. 89, 162, 970, 1460, 2023, 2711
Alexahin, Y. 312
Alexeev, N.N. 261
Alford, O. 3562
Alforque, Rudy 3693
Allen, C.K. 1526
Allen, C.W. 596
Allen, M. 3004
Allen, T. 3796
Alley, R. 1981, 2849
Allison, Paul 1138, 1141, 1144
Allison, S. 439, 2359, 2470, 3027
ALS Stability Task Force 784
Alzofon, D. 2253
Amano, D. 1266
Amano, S. 757
Amatuni, A.Ts. 690, 693, 695
Ambrosia, M. 3872
Amelia, J.-C. 3816
Ames, F. 947
Amman, M. 3807
An, Y. 402, 880
Anamkath, H. 3796
Anders, A. 2678
Anderson, D.E. 590, 3734
Anderson, E.B. 369
Anderson, K. 3837
Anderson, S. (SLAC) 596
Anderson, S. (UCLA) 736, 1965
Anderson, S. (IUCF) 2968
Andersson, Å. 345
Ando, A. 757, 1385
Andreev, V.A. 1087, 1090
Andreev, V. (Dubna) 2452
Andrews, D.E. 3413
Andrianov, S. 2419
Anerella, M. 3338, 3356
Anferov, V.A. 78
Ang, Z. 3377
Ankenbrandt, C. 144, 396, 399
Anthouard, P. 1254, 1257
Ao, H. 1203
Appleton, Bill R. 20
Arai, S. 938
Arakaki, Y. 938, 1557
Arakawa, D. 1548, 1599, 1908
Araki, N. 201
Araki, S. 587
Archuleta, T.A. 2829
Arduini, G. 168, 171, 1858
Arensburg, A. 906
Areti, H. 3681
Ärje, J. 2672
Arnett, D. 2253
Arnold, J. 1813
Arroyo, F.C. 3476
Artoos, K. 3586
Arutunian, S.G. 695
Asaka, T. 2511, 2814
Asano, K. 2908, 3087, 3090
Asaoka, Seiji 2458, 3616
Aspenleiter, J. 2947, 3497
Assadi, S. 127, 1771, 2323
Assmann, R. 449, 497, 500, 503, 506, 608, 687, 1331, 1523, 2119, 2580
Atkinson, R. 439, 3042
Aune, B. 425
Ausset, P. 2720
Autin, B. 1362, 2314
Averill, R. 348, 2274, 3407, 3743
Avrakhov, P.V. 3126
Avramopoulos, H. 1042
Avsec, S. 2481
Ayzatsky, N.I. 651
Azorsky, N.I. 3126

## B

Baartman, R. 956, 1415, 2675, 2778
Baba, H. 530, 593
Babcock, R. Chris 2562
Babzien, M. 621, 675, 2687
Bacher, R. 2446
Bagnato, O.R. 1209
Bai, M. 1346, 1460, 1478
Bailey, J.D. 1177
Bailey, R. 66
Bailey, V.L. 1251
Baine, M. 611
Baiod, R. 3272, 3278, 3288
Baird, S. 979, 982
Bajikar, S. 461
Baker, G.D. 190
Bakhtiari, Shervin 3842, 3845
Balakin, V.E. 3126
Balakirev, V.A. 651
Ball, M. 1481, 2081
Ball, M.J. (Penny) 3404
Balling, P. 1984
Baltadoros, D. 1042
Bane, K. 506, 509, 515, 554, 608, 903, 1673, 1738, 1789, 1873, 1876, 2189, 2580
Barale, P. 3312
Barbarosou, M. 1042
Barber, R.L. 1150
Bardy, J. 1254, 1257
Barillas, G. 3024
Barlow, D. 83, 193, 3309
Barnard, John J. 1929, 1932
Barnes, B. 2326
Barnes, John N. 86
Barnes, M.J. 1325, 1328
Barnes, P. 3075
Barni, D. 1126
Barov, N. 627, 1996
Barraza, Juan 2210
Barry, W. 772, 2344
Bartelson, L. 3461
Barth, W. 1897
Bartolini, R. 1469, 2568
Barton, D. 101
Bassato, G. 1129
Batskikh, G.I. 950
Battistella, A. 1129
Batygin, Y. 941, 1786, 1941
Bauer, G.S. 3785
Baumgartner, W. 439, 3042
Baynham, E. 3386
Bazzani, A. 2568
Beauvais, P-Y. 2720
Bechstedt, U. 1048
Bedermann, K. 3123
Beebe, E. 2711
Beebe-Wang, J. 970, 1882
Beeckman, W. 1045, 3816
Behne, D. 3622
Belkacem, A. 150
Bellato, M. 1129
Bellomo, G. 1126
Bellomo, P. 315

Belochitskii, P. 312, 1382
Belomestnykh, S. 1718, 3075
Belorgey, J. 3365
Belser, C. 3619
Ben-Zvi, I. 645, 675, 1197, 1971, 2687, 2790, 2793, 2843, 2846
Benapfl, M. 3568
Bendall, R.G. 1021
Benedikt, M. 1376, 1379
Benesch, J. 3108, 3758
Benjegerdes, R. 3212
Benson, S. 912
Benveniste, V.M. 2767
Berezin, A.K. 651
Bereznitsky, S.L. 261
Berg, G.P.A. 264, 2737, 3303
Berg, J.S. 107, 1712
Berg, W.J. 871
Bergbusch, P. 967
Berger, J.C. 2696
Bergl, J. 2493
Berkvens, P. 3571
Berlin, D. 979
Bernal, S. 1650, 1855, 1959, 2143
Bernard, M. 2823
Berners, D.P. 1296
Bertazzo, L. 1129
Bertenelli, F. 3586
Bertolini, L. 3562, 3619, 3622
Bertsche, K.J. 3263, 3283
Berz, Martin 2416
Besler, C. 315
Bestea, V. 3854
Bezzon, G. 1129
Bharadwaj, V. 315, 903, 2855
Bhat, C.M. 243, 1590, 3242, 3245, 3672
Biallas, G. 3333, 3752
Bickley, M. 2128
Biedron, S.G. 324
Bieniosek, F.M. 234, 1403, 3837
Bigelow, N.P. 2867
Biino, C. 80, 165
Billan, J. 3365, 3377
Billen, J.H. 1171, 3138
Biller, Ye.Z. 3810
Billing, Michael 2317
Billquist, P.J. 2702
Bilodeau, D. 2081
Bini, C. 572
Biryukov, V. 177, 179, 249
Bish, P. 3212
Bishofberger, K. 736
Bisoffi, G. 1087, 1129
Bisognano, J. 1641, 1644, 2128
Bissiato, E. 1087, 1129
Bizek, Hana M. 1493, 1496
Bjork, M. 2253
Bjorklund, E.A. 2464
Blackmore, E.W. 3831
Blank, M. 3150, 3180
Blas, F. 973
Blaskiewicz, M. 89, 959, 970, 1554, 1578, 1581
Blell, Udo 1727
Bleser, E. 89
Blind, B. 83, 193, 270, 1012, 1015, 3728
Bliss, N. 3598
Blokhin, A.I. 258
Blokland, W. 2032
Blondel, A. 366
Blosser, H. 1054, 1057, 1060
Blum, E.B. 3494
Blumberg, L. 159, 970
Bobyleva, L.V. 488
Bocchetta, C.J. 826, 829, 2353, 2356
Boer-Rookhuizen, H. 1063
Bogacz, S.A. 1697
Bogard, D. 2720
Bogdanovich, B. 276, 2773, 3869
Böge, M. 366, 1356, 1436, 1439
Boggia, A. 2729
Bohl, T. 1813, 1849
Bohn, C. 909, 1641, 1644, 2693
Boillot, J. 979, 982
Bollen, G. 947
Bolotin, I. 1313
Bolshakov, A.E. 261
Bong, E.L. 2253
Bong, P. 439
Bongardt, K. 988, 1846
Bonnafond, C. 1254, 1257
Borasi, F. 2696
Borchard, P. 3180
Borden, M.J. 187, 1012
Bordry, F. 66
Boriskin, V.N. 3810
Borland, M. 742, 2052, 2410, 2487, 3224
Bosch, R.A. 862
Boscolo, A. 2011
Bosland, P. 817
Bosotti, A. 1126, 3657
Bosser, J. 944, 979
Bossert, R. 3389
Botman, J.I.M. 1036, 1200
Bottura, L. 66, 3377
Bourat, C. 1191
Bourdon, J.C. 2823
Boussard, D. 2879
Bovet, C. 1987
Bowden, G. 464, 672, 3330
Bowling, Bruce 2526
Bowman, J. 3622
Boyce, R. 838
Bradley, S. 348, 2099
Bradley III, J. 1147
Brandt, D. 312
Braun, H.H. 479
Braun, J. 3123
Brautti, G. 2729
Bravin, E. 366
Breizman, B.N. 1635
Brennan, J.M. 69, 89, 396, 399, 967, 970, 1030
Brennan, S. 838
Bretin, J.-L. 225
Bricault, P. 925, 956, 1105, 1194, 2675
Brinkmann, R. 336, 1572, 1679
BRNBF Project Group 1224
Broadbent, A.J. 3413, 3494
Brodowski, J. 3233
Broere, J. 944, 3123
Bromberek, D. 2929
Broome, T.A. 1021
Broome, W. 2305
Brouet, M. 979
Brown, B.C. 994, 3242, 3245, 3254, 3257, 3260, 3263, 3269, 3286, 3288
Brown, I. 2678, 3752
Brown, K. (BNL) 69, 89, 98
Brown, K.(TJNAF) 2271
Brown, K.A. 1460, 2149, 2213, 2302
Brown, Nathan A. 1894, 2562
Brown, R.J. 2737
Brown, R.L. (SLAC) 2186
Brown, R.L. (BNL) 3230
Brown, Thomas A. 2559
Brown, V. 439
Brown, W. 2690
Browne, J.C. 1159
Browne, M. 439
Brugnoletti, B. 2253
Brumwell, F.R. 156
Brun, T. 190, 1159
Brunelle, P. 817, 1406
Brunet, J.-C. 3368, 3586
Brüning, O. 107, 1715, 1816, 1858
Bruno, D. 3449, 3452
Bruns, W. 2651
Bucalossi, J. 2717
Buhler, S. 2823
Buldakovsky, V.N. 184
Bulfone, D. 826, 2353, 2356, 2467, 3527
Buller, T.L. 2950
Bultman, N.K. 190
Bunce, G. 1460
Burke, D. 608

Burkhardt, H. 1532, 1813, 1819
Burla, P. 66
Burnham, B. 883
Burns, A. 1987, 2026
Burris, H.R. 611
Bushuev, A. 2838
Buttkus, J. 979
Buxton, W. 2155
Bylinsky, Y. 1135
Byrd, J. 769, 772, 775, 778, 1514, 1563

## C

Cai, Y. 1454, 2583, 2586, 2636
Calame, J. 3144, 3159
Calder, R. 3586
Call, M. 2473
Callahan, J. 2449
Callaway, N.T. 1165, 2464
Callin, R.S. 3045
Calvani, H. 959
Camariuc, R. 3854
Cameron, P. 1460, 2152, 2215
Cammarata, Jim 3693
Campedel, C. 3586
Canella, S. 1129
Cao, Z. 3318
Capek, K. 2198
Capista, D. 144, 1721, 2061
Caporaso, G.J. 1248, 1260, 1305, 1308, 1861, 2627, 2630, 2633
Cappi, R. 973
Cardman, L. 2693
Carli, C. 944, 976, 1379, 1382
Carlier, E. 225, 1325
Carlson, Randolph L. 1867, 2826
Carlsten, B. 1914, 2832, 3129, 3132, 3135
Carr, G.P. 2464
Carson, J.A. 3291
Carter, A. 2099
Carwardine, J. 2281, 2290
Cary, John R. 2592, 2654
Caryotakis, G. 439, 2894
Casas-Cubillos, J. 3206
Caspers, F. 75, 107, 979, 982, 1587
Caspi, S. 3212, 3398
Cassel, R. 439, 3482
Castellano, M. 2137
Castillo, V. 2155
Castle, M. 3168
Catani, L. 2137
Cavallari, G. 1858
Cavenago, M. 1129
Ceci, N. 2169, 2729
Celata, C.M. 1926, 2761, 3807
Cerniglia, P. 2502
Cervellera, F. 1129
CESR Operations Group 372
Chae, Y.-C. 953, 1700
Chai, J.S. 3825
Chairman, D. 906
Chan, A. 2413, 2517
Chan, K.C.D. 1150, 1168, 3096
Chanel, M. 944, 982, 1587
Chang, C.H. 3536, 3539
Chang, H.P. 841
Chang, L.H. 1487, 1638, 1691, 2377, 3048, 3051, 3054
Chang, Peace 853, 1409, 1487, 3533
Chang, S.S. 1638, 2858, 3048, 3054
Chang, Y.I. 1638
Chao, A.W. 1523, 1563, 1738, 1834, 1873
Chao, Yu-Chiu 2125, 2262, 2526
Chaput, R. 817
Charlton, Lowell A. 86
Chase, B.E. 2326
Chattopadhyay, S. 687, 1984
Chautard, F. 479
Chavanne, J. 3506, 3509
Chehab, R. 2823
Chel, S. 817, 1709, 2311, 2823
Chen, Bingyi 1218, 1221
Chen, C.S. 2371, 2374, 2523, 3488, 3539, 3749
Chen, C.T. 3749
Chen, Chiping 1938
Chen, Huaibi 1215
Chen, J. (DULY) 2802, 3120
Chen, J. (SRRC) 3749
Chen, J.R. 847, 3642
Chen, J.S. 2374, 2479, 3488, 3539, 3749
Chen, Jenny 853, 2371, 2374, 2523, 3488, 3539
Chen, P. 687, 1789
Chen, S.-Y. 2657
Chen, Tong 2164
Chen, W. 3297
Chen, X. 402
Chen, Y.J. 1260, 1305, 1861, 1864, 2633
Cheng, D. 3619
Cheng, G.-T. 2183
Cheng, J. 3168
Cheng, W.-H. 422, 1514, 1614
Chepegin, V.N. 249
Cherepakhin, A. 234
Chernikov, V.I. 184
Chesnokov, Yu. 249
Chester, N. 3248, 3291
Chiang, I.H. 2149, 2213
Chiang, John 850
Chiba, T. 941, 2672
Chiba, Y. 3828
Chida, K. 1557
Chin, A.H. 1984
Chin, M. 2235, 2253
Chin, P. 1855
Chin, Y. 1545, 1566, 1596, 1656
Chiurlotto, F. 1087, 1129
Cho, M.H. 593, 823
Cho, Y. 953
Chohan, V. 973, 979, 982
Choi, E.H. 1870
Choi, J. 823
Choi, J.J. 3159
Chojnacki, E. 363, 3075, 3177
Chou, P.J. 464, 542, 672
Chou, W. 110, 113, 130, 991, 994, 1724, 3251
Chow, K. 3212
Chowdhary, M. 2383
Chu, C.M. 1346, 1481
Chubar, O. 3509
Chung, S.M. 3633
Chupp, W.W. 1926, 2755
Church, M. 1006, 2055
Cinnamon, J. 3678
Cisneros, G. 439
Clark, D.J. 1051
Clark, George S. 3336
Clark, J.C. 1260
Clark, S. 439, 2473, 3027
Clark, W. 1093
Clarke, J.A. 3386, 3503
Claus, R. 2284, 2359, 2365, 2470
Clausen, M. 2403, 2446
Clauser, T. 2169
Clayton, C. 678, 681, 687, 2870
Claytor, N. 150
Clément, M. 80, 165
Clendenin, J. 903, 2849
Clerc, G. 2899
Clifford, T. 101
Cline, D.B. 621, 675
Clout, Peter N. 2532
Coates, M.C. 3494
Coffman, F. 2473
Cohen, M. 906
Cohen, S. 1042
Cojocaru, G. 1123, 3854
Colby, E. 2873
Cole, M. 3177
Colestock, P. 16, 127, 2873, 3716
Collier, P. 66, 3206
Collins, B. 2253
Collins, D. 1051
Collins, I. 3586

Collins, J. 2449
Colomb, D. 3619
Colomp, P. 3571
Comunian, M. 1087, 1129, 1132
Conde, M. (ANL) 627, 633, 639, 1996
Conde, M. (UCLA) 2873
Conkling Jr., C.R. 2496
Connolly, R. 69, 98, 101, 2152, 2215, 2947
Constant, T. 439
Cooke, S.J. 2431
Coombs, R. 3386
Coosemans, W. 560, 3645
Copeland, M.R. 464, 672
Corbett, J. 342, 832, 838, 1457, 1490, 2586
Corcoran, P. 1245
Cordova, S.R. 1245
Corlett, J. 2116, 2344, 3639
Corlier, M. 817
Cornacchia, M. 838, 1457, 1490
Cornali, R. 1813
Cornelis, K. 171, 1813
Cornelius, Wayne D. 3636
Cornuet, D. 973
Corradini, E. 1087
Corredoura, P. 2359
Corsini, R. 563
Cortopassi, C. 3221
Corvin, C. 439, 3746
Courant, E. 405, 1030, 1371, 3359
Cours, A. 2941
Cozzolino, J. 3338
Craddock, M.K. 153
Craievich, A. 811
Cramariuc, R. 1123
Crandall, K. 915, 1099, 1150, 1162, 2574
Crane, G. 2413
Crane, M. 2473, 2476
Crawford, C. 243
Crisp, J. 2072, 2166
Crofford, M. 2265
Crosbie, E. 953
Cruikshank, P. 3206, 3368, 3586
Ctcherbakov, A. 1263, 1313
Cullen, J.R. 3583
Cummings, K. 1147, 3183, 3725
Cuttone, G. 2038
CYCIAE 30 Engineering Group 3834

## D

D'Alsace, R. 2305
d'Amico, T. 566, 1362
D'Auria, G. 826, 1180, 1182, 1212, 2002
D'yachkov, M. 107, 1587, 2648
da Cruz, M.T.F. 2998
Daclon, D. 1212
Daclon, F. 826
Daems, G. 973
Dahl, L. 1897
Dahlerup-Petersen, K. 3206
Dainelli, A. 2169
Dalin, J.-M. 3586
Dallin, L.O. 716
Daly, E. 2014, 2253, 3619
Danby, G. 3233
Danilov, V.V. 1499, 1759, 1777
Danly, B. 2690, 3144, 3150, 3159, 3180
Danowski, G. 2308
Davies-White, W. 838
Davis, T. 1093
Dawson, C.L. 2956, 3598
de Jager, C.W. 1063
de Lamare, J. 1316
de Leeuw, R.W. 1200
de Lima, J.A. 2998
de Loos, M.J. 2577
De Martinis, C. 2002, 2038
de Mascureau, J. 1254, 1257
De Vito, Bill 3693
de Vries, J. 808, 1987, 3221
Dean, T. 439, 3027
Decker, F.-J. 449, 497, 500, 503, 506, 509, 608, 687, 1569, 1876, 3021
Decker, G. 698, 745, 2281
Decking, W. 778, 799
Degen, C. 2502
Degtyarev, I.I. 252, 255, 258
Dehler, M. 518
Dehning, B. 366, 3648
Deitinghoff, Horst 1900
Dejus, R. 3224
DeKamp, J. 278
Dekkers, D. 973, 979
Del Giusto, P. 1212
Delahaye, J.P. 482, 563
Delferrière, O. 2720
Dell'Orco, D. 3212
Dell, F. 69, 98, 219
Delsart, P. 1254, 1257
DELTA Group 724
Delvigne, T. 3857
Denard, J. 912, 2198, 2204
Deng, J.J. 1855, 1956, 1959
Den Hartog, P.K. 3224, 3556
Deregel, J. 3365
Derenchuk, V.P. 2737
Desavouret, E. 3395, 3713
Desforges, B. 3206
Desgranges, C. 2717
Desmon, M. 2823
Devin, A. 1254, 1257
Devlin, D.J. 2829
DeVolder, Barbara G. 2174
Devred, A. 3365
Dewa, H. (JAERI) 648, 760
Dewa, H. (Kyoto) 1087, 1129
Dey, J. 2032, 3018
Diaczenko, N. 3443
Dieperink, J.H. 225
Dietderich, D. 3212
Dietrich, J. 1048
Dikansky, N.S. 1795
Dikiy, N.P. 3840
DiMarco, J. 3269, 3272, 3389, 3395
Dimonte, N. 3690
Ding, X. 1968, 2802
Ding, Xiaodong 1215
Dinkel, John 234
Dinneen, T. 150
DiStefano, James 86
Diviacco, B. 1520, 3524, 3527
Doble, N. 80, 165
Dodd, E. 2657
Dodson, G. 348
Doets, M. 3630
Dohlus, M. 2008, 2550, 2553, 2612
Dolbilov, G.V. 1290, 3126
Dölling, R. 174, 246
Dombsky, M. 956, 2675
Donahue, J.B. 190, 1159
Donahue, R. 3807
Donald, M. 1454, 2583
Donaldson, A. 390, 1316
Dong, Lan 3300
Donohue, J.T. 900
Dooling, J.C. 156
Doolittle, L. 3758
Doose, C. 745, 2293, 3227, 3577
Doub, J.M. 3473
Douglas, D.R. 1351
Dovbnya, A.N. 651, 2820, 3810, 3840
Dovgenko, B.A. 3455
Dow, K. 348, 3407
Dowell, D.H. (CEA) 2684
Dowell, David H. (Boeing) 1888, 1891, 2950
Drago, A. 2284
Dragusin, M. 3854
Draznin, M. 906
Drewsen, M. 1560
Drivotin, O. 1944
Drozdovsky, A.A. 3848
Drozhdin, A.I. 116, 133

Drury, M. 3105, 3108
Du, Taibin 1221
Duan, Xiuming 1221
Ducas, V. 1362
Ducimetière, L. 225, 1325
Dudnikov, V.G. 2714
Duffy, P. 3562
Dugan, G. 318, 3215, 3380, 3383
Duke, Jonathan 204
Duke FEL Lab 24
Dunham, B. 1947, 2201, 2484, 2693, 3755
Durieu, L. 228
Dutto, G. 956, 1105, 2675, 2781
Duval, P. 2446
Duzenli, C. 3831
Dvoeglazov, A. 2419
Dwinell, R. 1051
Dykes, D.M. 2956, 3078
Dzengeleski, J. 3407

## E

Earley, L.M. 3135
East, G. 1481
Ebeling, W. 985
Ebrahim, N.A. 897
Ecklund, S. 3330
Eckoldt, Hans-Joerg 3458
Economou, D. 1042
Edwards, H. 2873
Ego, H. 2971
Ehrlich, R. 3075
Ehst, D. 393
Eichenbaum, A. 906
Eichner, J. 439, 3042
Eickhoff, H. 3801
Einfeld, D. 336, 763, 1039, 3613
El-Shazly, M.N. 3607, 3610
Elizondo, J. 1308
Elleaume, P. 2210, 3506, 3509
Elliott, T. 3443
Elsener, K. 80, 165, 168, 171
Elzhov, A.V. 488
Emamian, M. 883
Emery, L. 742
Emma, P. 452, 608, 903, 1679, 2580, 2855
Endo, K. 3470
Endo, M. 820
Engelmann, G. 1813
Engels, O. 1078
Engwall, D. 2201, 2693
Erdt, W. 3368
Erickson, R. 596
Eriksson, M. 345, 3527
Eriksson, T. 979, 982, 1382
Ershov, O.V. 1090
Esarey, E. 611, 630
ESS Study Group 988
Etkin, A. 3230
Euteneuer, H. 1902
Evans, B. 3831
Evans, J. 3123
Evans, L.R. 61
Evans, R. 2529
Evans Jr., K. 2281, 2290
Evtushenko, Yu.A. 3455
Eyharts, P. 1254, 1257
Eyl, P. 1254, 1257
Eylon, S. 590, 2755, 2832, 3719, 3722
Eysselein, F.G. 3410
Ezura, E. 2902, 2974, 2977, 2986, 2992, 2995, 3069, 3087

## F

Fabris, A. 826, 829, 1735
Fabris, R. 826
Facco, A. 1129, 3084
Fahmie, M. 808, 2344
Fainberg, Ya.B. 651
Faircloth, J. 883
Faltens, A. 195, 1926
Fan, Mingwu 3834
Fan, T.C. 3536, 3539
Fang, J.M. 621
Fang, S. 2049, 3057
Fang, Si J. 994, 3242, 3251
Fant, K. 3004, 3039
Farias, R.H.A. 811, 2096, 2238, 3324, 3740
Farkas, David 599
Farkhondeh, M. 348
Farrell, Ken 86
Fartoukh, S. 470
Fateev, A.A. 1290
Faucett, J.A. 2464
Faure, J. 2720
Faus-Golfe, A. 1356, 1442
Favale, A.J. 950
Favaron, P. 1129
Fawley, W.M. 1923, 1926
Fazio, M.V. 3135
Fedorov, V.M. 1299
Fedorova, A. 1502, 1505, 1508
Fedotov, Alexei V. 1744, 1747, 1750
Fedotov, M.G. 883
Fedotov, Yu.S. 255
Feher, S. 3389, 3395
Feinberg, B. 150
Feinerman, A.D. 461
Felch, K. 3180
Feldl, E. 912, 2198, 2204
Feng, P.K. 3452
Feng, S.K. 2437
Feral, B. 3586
Ferdinand, R. 2720, 2723
Ferguson, P.D. 190
Ferguson, Patrick 3129
Ferianis, M. 826, 2002, 2011
Ferioli, G. 171
Fernow, R. 408
Ferrando, O. 228
Ferraz, R.O. 3628
Ferreira, M.J. 811, 3324, 3628
Feschenko, A.V. 2078
Fidecaro, G. 168, 171
Filhol, J-M. 751
Filippas, T.A. 1042
Finocchiaro, Paolo 2038
Fiorito, R.B. 675
Firjahn-Andersch, A. 1081
Fischer, R. 611
Fischer, W. 69, 98, 101, 210, 222, 3341, 3359
Fischer, W.E. 3785
Fisher, A. 315, 2014, 2253, 2840, 2849
Fisher, J. 3108
Fitch, M.J. 2867
Fitzgerald, D.H. 1012, 1015, 1159, 1611, 2743
Fitzgerald, J. 2072
Flechtner, D. 1272, 1275
Fliflet, Arne W. 3153
Flood, Roger 2131
Flynn, G. 817, 1517, 1709
Fockler, J. 2633
Foley, K.J. 3230
Fong, Craig 1096
Fong, K. 1105, 2049, 3057
Fong, Martin 1096
Fontana, J.R. 675
Forrestal, J. 3669
Fortgang, C.M. 897, 3135
Fortuna, G. 1129
Foster, G.W. 363, 3257, 3260, 3263, 3280, 3286, 3392
Fowkes, R. 439, 2911, 3045, 3189, 3195
Fowler, W.B. 3254, 3257, 3260, 3263
Fox, J. 2284, 2362, 2368
Fox, W. 2737, 3303
France, A. 2720
Franco, G.S. 811
Franks, R.M. 3007
Franzini, P. 3413
Freedman, S.J. 2770
Freund, A. 80

Friedl, J. 724
Friedman, A. 1240, 1923
Friedrichs, C. 3473
Friesel, D. 264, 935, 2737, 2811, 3303
Frigola, P. 736
Frischholz, H. 2911
Fry, A.R. 2867
Fuja, R. 1269
Fujieda, M. 2992, 2995
Fujishima, S. 1066, 1069, 1075, 3419, 3422, 3428, 3440
Fujita, H. 339
Fujita, Y. 3819
Fukuma, H. 306, 1566, 1596
Fuller, R. 439, 2186, 3027, 3042
Fumelli, M. 2717
Funahashi, Y. 587
Funakoshi, Y. 301, 306
Funk, W. 1150
Furman, M.A. 1617
Furuya, T. 2908, 3087, 3090
Fusellier, J. 2823
Futami, Y. 3822

## G

Gabriel, Tony A. 86
Gaedke, R. 3443
Gagliano, J. 3552, 3580
Gahl, J.M. 3725
Gai, W. 627, 633, 636, 639, 1996
Galambos, J.D. 1018, 3851
Galayda, J.N. 877
Galbraith, P. 3648
Galdi, V. 1753
Galimberti, A. 826, 2353, 2356
Gallardo, J. 405, 408, 616, 621, 675
Gallet, B. 3365
Gambalonga, S. 1129
Gamp, A. 3162
Ganetis, G. 3353, 3356, 3651
Ganguly, A.K. 3156, 3171
Gao, J. 1602, 1605, 1608
Gardner, C. 89, 962, 970
Gardner, I.S.K. 988, 1021
Gareyte, J. 1356
Garnett, R.W. 1150, 1165, 2743
Garoby, R. 973, 979, 2953
Garren, A. 411, 838, 868
Gärtner, W. 3410
Garvey, J.D. 3291, 3395
Garvey, T. 2823
Garza, O. 2529, 3681
Gassner, D. 2149
Gatignon, L. 80, 165
Gavidia, A. 2067
Gavrilov, N.G. 883
Gaydosh, M.. 3666
Gayet, P. 1858
Gazis, E.N. 1042
Gelbart, William Z. 3842, 3845
Gelbke, C.K. 34
Gelfand, N. 997
Geller, J. 2149
Genet, M. 3368
Genevey, P. 3365
Gentner, M. 330
Gentzlinger, R.B. 3096
Gentzlinger, Robert C. 2914
Gerken, E. 3725
Geschonke, G. 1858
Ghiroso, W. 1926
Ghosh, A. 3353, 3356, 3398
Giachino, R. 1813
Giannini, R. 979, 1382
Gikal, B.N. 3610
Gill, P.F. 3583
Gillespie, George H. 1894, 2559, 2562
Gilpatrick, J.D. 83, 1150, 2041, 2090, 2093, 2232
Gioumousis, A. 2253
Giovannozzi, M. 1445, 1451, 1469, 2568, 2571
Giove, D. 2002, 2038, 3657
Giulicchi, L. 2314
Giuressi, D. 2353, 2356
Glass, H.D. 3242, 3257, 3260, 3263, 3269, 3286
Glatz, J. 1897
Glazov, A. 1263
Glenn, J.W. 89, 965, 967, 1478, 2149, 2155
Glock, H.-W. 521, 527
Glover, M.G. 1021
Glover, T.E. 1984
Gluckstern, Robert L. 1744, 1747, 1750, 1950
Gluskin, E. 877, 3224
Gobin, R. 2720
Goddard, B. 309
Godlove, T. 1855, 1956, 1959
Goeppner, G.A. 2207
Goetz, S. 883
Gold, S. 439, 1319, 1322, 3027, 3042
Gold, Steven H. 3153
Goldberg, D.A. 3001
Goldstein, J.C. 897, 2174
Golkowski, Cz. 1272, 1275
Gonçalves da Silva, C.E.T. 811
Goodzeit, Carl L. 3404
Gorchenko, V. 2452
Gordon, D. 681
Gorelov, D.V. 1194, 2621
Goto, A. 930, 941, 1066, 1069, 1075, 2672, 3419, 3422, 3428, 3440
Gottschalk, S.C. 675
Gou, Z.Y. 1729
Gouffon, P. 3239
Gough, R. 2675, 2758, 2770, 3737
Gougnaud, F. 2823
Gould, H. 150
Gourlay, S.A. 3209, 3398
Gournay, J.F. 2823
Gover, A. 906
Govil, R. 654
Gower, F. 3796
Gracia, J. 315
Graf, M.A. 2767
Grafström, P. 80, 165
Granatstein, V.L. 3168
Grandinetti, R. 3651
Graves, W.S. 1197, 1993, 2437, 3497
Gray, E.R. 83, 915, 1153, 1162
Gray, R. 315
Green, M.A. 868, 3401
Greene, J. 2696
Greenslade, M. 3413
Greenwald, S. 2547, 3699, 3702, 3705
Greenwald, Z. 2547, 3705
Greenwood, J.B. 2705
Greer, J. 2344
Gregory, S. 2633
Grelick, A. 1269, 2941, 3174
Grier, D. 973
Grier, E. 2953
Grieser, M. 947
Griffin, J. 396, 399, 1724
Grimm, T.L. 663
Grimmer, J. 3556
Grippe, J. 439
Grishanov, B.I. 237
Grishin, V.K. 889, 3866
Gröbner, O. 979, 3542, 3586, 3589
Groeppner, G.A. 3552
Gros, P. 2720
Gross, R. 3743
Groß, P. 174
Grote, D.P. 1240, 1923
Grote, H. 1356, 1442
Gruber, J. 973, 979
Grudiev, A.V. 2609
Guerra, A. 3333
Guharay, S.K. 2681
Guigli, J. 2067
Guignard, G. 458, 473, 482, 566
Guilhem, D. 1254, 1257
Gulbekian, G.G. 3607, 3610
Guo, Z.Y. 1566, 1828

Gupta, R. 3344, 3347, 3356, 3362, 3398
Gustafson, R. 3260
Gustwiller, J. 1245
Guy, A. 1051
Guy, F.W. 1099
Gyr, M. 168, 171

## H

Ha, K.M. 3479
Haber, I. 1240, 1923
Haberer, Th. 3801
Habs, D. 947
Haddock, P.C. 3135
Haebel, E. 1858
Hafizi, B. 666, 3153
Hagedoorn, H.L. 1036, 1200
Hagel, J. 458
Hagestedt, A. 763
Haggard, J.E. 3257, 3263, 3266
Hahn, A.A. 2166, 2226
Hahn, H. 210, 213, 216, 1706
Hahn, K. 1926
Hahn, U. 2134
Haid, D. 3669
Haimson, J. 2808
Haines, John 86
Halbach, Klaus 3728
Halbleib, J.A. 1245
Halvarsson, B. 2026
Hamilton, B. 1481, 2081
Hamm, R.W. 2811
Hammen, A.F.J. 1200
Han, Y. 3297
Han, Y.J. 3633
Hangst, J.S. 1560
Hanna, S. 439, 539, 3042
Hannaford, C. 3212
Hansborough, L.D. 2740
Hansen, B.C. 3872
Hansen, Robert J. 3153
Hansen, U. 3123
Hanson, A. 3096
Hanson, D.L. 1935
Hanus, X. 817, 1709
Hao, Y. 3297
Haouat, G. 1841
Haque, T. 3452
Hara, K. 3087, 3090
Hara, M. 2971
Harding, D.J. 3242, 3245, 3257, 3263, 3269, 3272, 3275, 3278, 3286, 3288, 3291
Hardy, D. 2265
Hardy, L. 751
Harkay, K. 953, 1575, 1700, 2052, 2944, 3577
Harkewicz, R. 2702
Harnden, W. 3212
Harold, M.R. 1021
Harris, G. 3580
Harrison, M. 69, 101, 219
Harrison, S.M. 3413
Harss, B. 2696
Hartemann, F.V. 2858
Harteneck, H. 3568
Hartill, D. 1718, 2164, 3236
Hartmann, H. 2499
Hartmann, W. 3123
Hartung, W. 3075
Haruyama, Y. 1557
Harwood, L. 3333
Hasegawa, K. 915
Hashimoto, S. 757
Hashimoto, Y. 584, 938
Hatanaka, K. 3359, 3416, 3434
Hatch, K. 3743
Hathaway, D. 3622
Hayano, H. 494, 584, 587, 2980
Hayes, T. 965
Haynes, W.B. 2914, 3096, 3135
Hays, T. 3075, 3177
He, P. 675
Heiberger, M. 3816
Heifets, S. 1563, 1620, 1682
Helm, R. 608
Hemery, J.-Y. 228, 979
Hemker, R.G. 2870
Hemmi, M. 941, 2672
Henderson, S. 291, 1472, 1542, 1765, 2029, 2164
Hendrickson, L. 452, 497, 608, 2122
Henestroza, E. 590, 1926, 2832, 3719, 3722
Henke, H. 351, 464, 542, 672, 2134
Henrichsen, K. 66, 3648
Herbeaux, C. 817
Herer, A. 3857
Herminghaus, H. 1042
Hernandez, M. 733, 2017, 2840
Herr, W. 168, 171, 309, 312
Herrup, D. 2058
Hershcovitch, A. 1792, 2678, 2711
Hertzbach, S. 608
Hess, C. 3395
Hettel, R. 838
Heydari, H. 2603, 2784
Hezel, T. 3512
Higashi, A. 3822
Higgins, S. 3755
Higley, H. 3212
Higo, T. 494
Hilbert, B. 3206
Hill, A. 3004
Hill, Barrey W. 1894, 2562
Hill, C. 944
Hill, J.O. 2461
Hill, R. 2529
Hillman, A. 2281
Himel, T. 2425, 2473, 2476
Hindi, H. 2284, 2362
Hinkson, J. 775, 2110, 2235, 2253
Hinode, F. 354, 578, 587, 2980, 2983
Hiramatsu, S. 1566
Hiramoto, K. 1653, 3294, 3813
Hirata, K. 384, 1780, 1783
Hirota, J.I. 3294
Hirshfield, J.L. 666, 3153, 3156, 3171, 3863
Ho, C.H. 2858, 3048
Ho, Wendy 3842, 3845
Hoag, H. 439, 539
Hock, J. 2149
Hodapp, T.R. 2232
Hodgkins, D.J. 2740
Hoff, Lawrence T. 2395
Hoff, Matthew D. 1096
Hofler, A. 2201
Hofmann, A. 838, 1813, 1858
Hofmann, Ingo 1852
Hogan, B. 3168
Hogan, M. 736
Hogge, J.P. 2690
Hogrefe, R. 3669
Holben, S. 3165
Holik, P. 439
Holmes, J.A. 1018
Holmes, Michael 796
Holmes, R. 3562
Holmes, S. 439, 3027, 3042, 3192
Holmes, S.D. 47, 997
Holt, J. 72, 997
Holtkamp, N. 581, 2008, 2078, 2104, 2726
Holtzapple, R.L. 509
Homeyer, H. 1078
Honda, T. 2084, 2146
Honma, T. (Chiba) 1557
Honma, T. (Hokkaido U.) 2565
Horan, D. 953, 2926, 2935, 2941, 3111, 3687, 3690
Hori, T. (Sumitomo) 1266, 2642
Hori, T. (SPring-8) 2511, 2814
Hornekær, L.H. 1560
Horsky, T.N. 2767
Horton-Smith, S. 1981
Hosino, M. 1557
Hosono, K. 1557
Hosoyama, K. 3087, 3090

Hou, R. 3297, 3318
Houck, T. 590, 2627, 2633, 3719, 3722
Hovater, Curt 2861
Howells, M. 778
Hower, N. 883
Hoyer, E. 3221
Hoyt, M. 3004
HRIBF Operations Staff 1227
Hsieh, H. 3619
Hsiung, G.Y. 3642
Hsu, Ian C. 850, 2047, 2183
Hsu, K.T. 841, 847, 853, 1487, 2259, 2371, 2374, 2377, 2523, 3488, 3539, 3749
Hsu, Y.J. 850, 3642
Hsue, C.S. 1409, 1487, 3533
Hsue, K.T. 1409
Hu, K.H. 3539
Hu, Shaoguang 1218, 1221
Hu, Wensheng 1218, 1221
Hua, D. 3807
Huang, Bingsong 3300
Huang, Fuhe 3300
Huang, H. (BNL) 89, 1460, 1478, 2155, 2538
Huang, H. (IHEP) 1566
Huang, J.Y. 823, 2107, 2350, 3015, 3479
Huang, N. 1388, 1448, 1780
Huang, Yuanzhong 1215, 3764
Hubbard, E. 3816
Hubbard, R.F. 611, 630
Hughes, Thomas P. 1144, 1867, 2826
Hülsmann, P. 521, 524, 527
Humphrey, R. 439
Humphries, D. 3315
Humphries Jr., S. 2428
Hunt, D. 3619
Hunt, W. 2449, 2737
Hurh, P.G. 2166, 3283
Hurn, T. 3816
Hus, J.L. 684
Husmann, D. 330, 1033, 1373
Huttel, E. 763, 3613
Hutter, G. 3123
Hutton, A. 281, 2383
Hwang, C.S. 3536, 3539
Hwang, J.Y. 2858
Hwu, K.H. 3749

## I

Iazzourene, F. 826, 829, 1185
Ichac, J.-P. 2899
Igarashi, I. 1599
Ikegami, K. 1066, 1069, 1075, 3419, 3422, 3428, 3440
Ikegami, Masanori 1911
Ilhoff, E. 2241
Imai, Y. 3425
Imanishi, A. 938
Inabe, N. 1400, 2672
Indreias, I. 1123, 3854
Ingalls, W.B. 2743, 2764
Ingold, G. 3527
Ingrassia, P. 1460
Inoue, M. 339, 1203, 1206, 3294, 3819
Intensity Upgrade Study Crew 1009
Irwin, J. 360, 482, 512, 608, 1341, 2583, 2636
Isaeva, L.G. 883
Ishi, Y. (INS) 1962
Ishi, Y. (Mitsubishi) 2908, 3087
Ishikawa, Y. 3822
Ishimaru, H. 110
Ishkhanov, B.S. 889, 3866
Issinsky, I. 181, 184
Itano, A. 201, 2347
Ito, Y. 2511, 2814
Itoh, M. 859
Ivanenko, A.I. 3604, 3607
Ivanov, I.N. 491, 1391, 3126
Ivers, J.D. 1272, 1275
Iverson, R. 315, 687
Iwashita, Y. 339, 1203, 1206, 1798, 3294, 3819
Izawa, M. 1566, 2171, 2989, 3066

## J

Jablonka, M. 2823
Jackson, A. 703, 778
Jackson, G.P. 3257, 3260, 3263, 3280, 3286
Jackson, J. 3233
Jacob, J. 1551
Jacobs, G. 2726
Jacobs, K. 348, 2099
Jaeschke, E. 713
Jagger, J. 363, 2699
Jahnel, L.C. 811, 2096, 2238, 3740
Jain, A. 3309, 3338, 3347, 3353, 3356, 3362, 3651
Jaisle, A. 3443
Jakob, A. 174, 246
Jakob, H. 2026
Janenko, V. 276
Jankowiak, A. 2140
Janssen, D. 2796, 2838
Jansson, A. 2314
Jansson, U. 1325
Jark, W. 3527
Jarvis, H. 608
Jason, Andrew 270, 3138, 3728, 3731
Jayamanna, K. 2675
Jeanneret, J.B. 153
Jenkins, D.M. 3413
Jenner, D. 2968
Jensen, C. 1281, 1284, 1287
Jensen, D. 3330
Jensen, E. 973, 2953, 3060
Jensen, K. 1105
Jeon, D. 1346, 1481
Jeong, S.C. 938
Jeram, B. 2481
Jiang, C.L. 2696
Jiang, X. 2932, 2938
Jimenez, M. 1858
Jin, L.H. 1388
Jin, Qingxiu 1218, 1221, 3764
Jobe, K. 1981
Jobe, R.K. 3021, 3027
Johnson, B.M. 2678
Johnson, C. 563
Johnson, D. (NSCL) 1054, 1057
Johnson, D. (LANL) 1611
Johnson, D.E. 997, 3272
Johnson, E.D. 1197, 1993
Johnson, J. 808
Johnson, Jeffrey O. 86
Johnson, K.F. 1150, 2232
Johnson, L. 439
Johnson, P.E. 2950
Johnson, R. 2110, 2122, 2253
Johnstone, C. 119, 396, 399, 411, 414, 1030
Johnstone, John A. 240
Joly, J.M. 2823
Joly, S. 1117, 1120, 2684
Jones, C.R. 2799
Jones, F.W. 1882, 2597, 2600
Jones, G. 3619
Jones, J. 2699, 2929
Jones, K.W. 1165
Jones, R. 439, 518, 545, 548, 551, 554
Jones, W.P. 2737
Jongen, Y. 1045, 3770, 3816, 3857
Jongewaard, E. 439, 3189
Jonker, M. 1813
Jordan, K. 912, 2204, 2529
Joshi, C. 11, 678, 681, 687
Jöstingmeier, A. 2553, 2612
Jowett, J.M. 312
Judd, D. 195
Judkins, J. 3004, 3039
Juillard, M. 817, 2823
Jung, D.H. 2107
Junquera, T. 2823

# K


Kaan, A.P. 3630
Kabe, A. 3087, 3090
Kabel, A. 2550
Kagaya, S. 587
Kageyama, T. (RIKEN) 2672
Kageyama, T. (KEK) 2902, 2974, 2977, 2986, 3069
Kahn, S. 3309, 3350, 3356
Kaiser, K.-H. 1902
Kakiuchi, S. 3294
Kaljuzhny, V.E. 2008, 2104
Kaltchev, D. 153
Kamada, S. 1831
Kamigaito, O. 941, 2672
Kaminsky, V.I. 3869
Kamitsubo, H. 6
Kamiya, Y. 856, 2146, 2989, 3066
Kamps, T. 2134
Kanai, T. 3822
Kanaya, Noriichi 2458, 3616
Kanazawa, M. 201, 2347, 3819, 3822
Kando, M. 648, 760
Kane, Steve 3693
Kang, X. 264, 1346, 1481, 2968
Kang, Y. 461, 1575, 2296, 2699, 2929, 2932, 2935, 2938, 2941, 2944, 3687
Kao, C.C. 727
Kaplan, R. 1718, 3075
Karabarbounis, A. 1042
Karantzoulis, E. 826, 829
Karas', V.I. 651
Karasyov, S.P. 2229
Karl, F. 3651, 3693
Karliner, M. 2796, 2838
Karn, J. 2383, 3333
Kase, M. 941, 2672, 3327
Kashiwagi, S. 494, 587
Kasimer, K.U. 2461
Kassab, L.R.P. 3239
Kasuga, T. 1566, 1664
Katayama, I. 938, 1557
Katayama, T. 92, 930, 938, 1024, 1072, 1400, 1786, 1807, 3359, 3416, 3431, 3434, 3437, 3521
Kato, S. 1596
Kato, T. 3822
Katoh, M. 2084
Katsouleas, T. 681, 684, 687, 2870
Kawachi, K. 820, 3822
Kawaguchi, H. 2565
Kawaguchi, T. 1066, 1069, 1075, 3359, 3419, 3422, 3425, 3428, 3431, 3440
Kawakami, H. 938
Kawakita, T. 1203
Kawashima, Y. 2971
Kazacha, V.I. 488
Kazakov, S.Yu. 3126
Kazimi, R. 1947, 2484, 3755
Keane, J. 2069
Keesee, M. 2201
Kehne, D. 912, 2204, 2484, 2693, 3755
Keil, E. 104, 309, 363
Keil, J. 1373
Keller, R. 775, 778, 781, 784, 787
Kelly, Darren R.C. 3547
Kelly, E. 3362
Kennedy, K. 3568, 3619
Keppler, P. 165
Kerby, J. 3398
Kerns, J. 3619
Kersevan, R. 3559, 3592
Kerslick, G.S. 1272, 1275, 3117
Kester, O. 947
Kewisch, J. 69, 98, 222
Khabarov, M.V. 3607
Khan, S. 1703, 1810
Khlebnikov, A.S. 3518
Kiang, L. 1481
Kidman, R. 3096
Kihara, T. 1798
Kijima, Y. 2908, 3087
Kikutani, E. 306, 1566, 1596, 2332, 2335
Kim, C. 778, 790, 808
Kim, C.K. 3633
Kim, Eun-San 384
Kim, J.-S. 3719, 3722
Kim, J.-W. 1066, 1069, 1075, 3419, 3422, 3425, 3428, 3440, 3825
Kim, J.K. 2657
Kim, K-J. 1984
Kim, K.H. 2107
Kim, S. 3577
Kim, S.H. 745, 2293, 3227
Kim, T.Y. 1593
Kimura, W.D. 675
King, F. 3568
King, N.S.P. 3096
Kinkead, Allen K. 3153
Kinosita, H. 757
Kinross-Wright, J.M. 897
Kirbie, H.C. 1260
Kirby, G.A. 3209
Kirby, R. 3568
Kircher, F. 3365
Kirchgessner, J. 3075, 3177
Kirichenko, A. 2452
Kirk, H. 408
Kirsebom, K. 80
Kiselev, A.V. 2805
Kiselev, V. 1463, 1466
Kiselev, V.A. 651
Kishek, R.A. 3198
Kishiro, J. 1548, 1599, 1908
Kishiyama, K. 2110, 3622, 3625
Kitagawa, A. 3822
Kitamura, Hideo 3515
Klabunde, J. 1897
Klaffky, R.W. 2305
Klaus, F. 3123
Kleeven, W. 3816
Kleffner, C. 2078, 2726
Klein, H. 174, 246, 521, 524, 527, 988
Klein, W. 2422, 2535
Kleinman, H. 906
Klem, J. 168, 171
Klimine, P. 3407
KLOE Collaboration 3413
Knauf, A.B. 3710
Knott, M. 3669
Ko, I.S. 823, 2107, 2350, 3015, 3479, 3633, 3663
Ko, J.J. 1870
Ko, K. 387, 439, 2589, 3033
Koba, K. (KEK) 1548, 1599
Koba, K. (Miyazaki U.) 1908
Kobayashi, T. (JAERI-RIKEN) 2814
Kobayashi, T. (Tsukuba) 2902, 2974, 2977, 2986, 3069
Kobayashi, Y. 856, 1566, 2084, 2171
Koepke, K. 2873
Kohara, S. 941
Kohno, T. 201
Koiso, H. 1394
Kojima, Y. 3087, 3090
Koldenhoven, R. 3669
Kolomiets, A. 1090, 1129, 1905, 2735, 2965, 3848
Kondoh, S. 648, 760
Kondratiev, B.K. 2735
Konecny, R. 633, 636, 639, 1996
Konstantinov, S. 2838
Koontz, R. 439, 1319, 1322, 3021, 3027, 3042
Koop, I. 1063, 1433
Korhonen, T. 587
Korovin, O.P. 1511
Korsbjerg, T. 2920, 2923
Kos, N. 3586
Koscielniak, S. 956, 1102, 1647, 2389
Koseki, T. 856, 1756, 2146, 2989, 3066
Kostin, D.V. 1108, 2008, 2104
Kotaki, H. 648, 760
Kotov, V.I. 249

Kotseroglou, T. 687, 1981, 2849
Kouda, S. 3822
Kourbanis, I. 144, 1721, 2061, 2323
Koutchouk, J.-P. 66, 1356, 1442
Kovalenko, A. 184, 2452
Kowalkowski, J.B. 2461
Kowalski, S. 348, 2274
Koyama, K. 1203
Koyama, T. 375
Koziol, H. 973, 979
Kozlov, O. 181
Kozodaev, A.M. 2965, 3848
Kozyrev, E.V. 3114
Kponou, A. 1460, 2023, 2711
Krafczyk, G. 3291, 3461
Krafft, G.A. 739, 912, 2020, 2128, 2204, 2265, 2268
Kraft, G. 3801
Kraimer, Martin R. 2403
Krainz, G. 3206
Kramer, S.L. 748, 2305
Krasnopolsky, V.. 1263
Krasnykh, A. 1319, 1322
Krastelev, E.G. 3141
Krause, U. 3801
Krawczyk, Frank L. 2914, 3093, 3731
Krebs, Gary F. 793, 796
Kreischer, K.E. 2690
Krejcik, P. 608, 1623, 1626, 3030
Krevet, B. 3512
Kriens, Wilhelm 231
Krietenstein, B. 2645
Krinsky, S. 727, 1197, 2161, 2287
Kroc, T.K. 3269
Kroes, F.B. 1063
Krogh, M.L. 1308, 2627
Kroll, N. 429, 439, 518, 548, 551, 554
Kroupa, M. 2535
Kruchkov, J. 2838
Krueger, K. 1460
Krusche, A. 973
Krushelnick, K. 611
Krüssel, A. 763
Kuba, A. 2511, 2814
Kubo, K. 354, 494, 587, 1484, 2980, 2983
Kubo, T. 1066, 1069, 1075, 3419, 3422, 3425, 3428, 3440
Kubo, Tadashi 3467
Kubono, S. 938
Kudinov, V. 276
Kudo, Hirofumi 2146
Kuijer, L.H. 1063
Kukarnikov, S.I. 491
Kukhtiev, V. 1135
Kulik, I. 1129
Kulikov, A. 315, 1316, 2253, 3639
Kulikov, I. 2452
Kulipanov, G.N. 883
Kumada, M. 820, 2347, 3327, 3822
Kuner, B. 2493
Kuo, C.C. 841, 847, 850, 853, 1409, 1487, 1638, 2377, 3048, 3051, 3054, 3533
Kuo, C.H. 2259, 2371, 2374, 3749
Kuo, T. 2675
Kupper, R.R. 2737
Kurakin, V.V. 3848
Kurennoy, Sergey S. 1732, 1950, 3731
Kurita, N. 2014, 2110, 2253, 3639
Kurkin, G.Ya. 883
Kurnaev, O. 234
Kurokawa, S. 381, 1566, 1596
Kurz, M. 521, 527
Kusche, K.P. 621, 675
Kushnir, V.A. 651, 3810
Kustom, R. 461, 953, 1575, 2296, 2929, 2941, 2944, 3174
Kutner, V.B. 3604
Kuybeda, R.P. 3848
Kuzay, Tuncer 2210
Kuzmiak, M. 1391
Kwan, J.W. 1230, 2755
Kwan, Thomas J.T. 2174
Kwiatkowski, S. 2947
Kwon, M. 823, 2350, 3015
Kyser, R.H. 3159

## L

Labrador, A. 1560
Labrouche, J. 1254, 1257
Lackner, H. 1251
Laclare, J.-L. 817, 1406, 1517
Ladeuze, M. 3816
Lagniel, J-M. 1120, 2720
Lahey, T. 2473
Lai, B. 461
Lai, C.Y. 1638
Lai, P.-C. 2047
Laird, R. 2490, 2926
Lalayan, M.W. 2104
Lamanna, G. 2169
Lambaise, R.F. 3452
Lambertson, G. 1617, 2344
Lambiase, B. 3449
Lamm, M.J. 3389, 3395, 3398
Lamont, M. 309
Lampel, M.C. 2562, 2615
Lancaster, J.A. 2799
Lange, R. 2493
Langenbeck, B. 2594
Langenbrunner, J. 1611
Langton, J. 2014, 2253
Lannoye, G. 3816
Larsen, R. 2284
Larson, D. 1403, 3248, 3837
Lash, J.S. 1245
Latham, P.E. 3150
Latypov, D. 3443, 3446
Latypov, T. 1263, 1311
Lau, W.K. 847, 1487, 1638, 1691, 2377, 2858, 3048, 3051, 3054
Lau, Y.Y. 3198
Lauckner, R. 66
Launspach, J. 1254, 1257
Laverty, M. 3057
Lavine, T. 439, 1676, 3027, 3042, 3192, 3675
Lawrence, G.P. 83, 1150, 1156
Lawson, W. 3168
Lawton, D. 1054, 1057
Laxdal, R. 956, 1102, 1105, 1135, 1194, 2621
Laycock, S. 3816
Lazarev, N.V. 2965, 3848
Lebedev, V. 1560, 2128, 2383
LeBlanc, G. 342, 345, 832
Leboutet, H. 1117
Lee, C.-H. 2183
Lee, D.H. 850
Lee, E. 195
Lee, J.C. 844
Lee, M. 2586
Lee, P.B. 657
Lee, R. (UC Irvine) 965
Lee, R. (TRIUMF) 1102
Lee, S. 687
Lee, S.C. 3663
Lee, S.Y. 264, 396, 399, 935, 1346, 1460, 1478, 1481, 2968
Lee, T. (Pohang) 823
Lee, T. (DULY Research) 2802, 3036, 3120
Lee, Y. 2667, 2675, 2770, 3737
Lee, Y.Y. 159, 162, 962, 970
Leemans, W. 630, 654, 657, 687, 1984
Legg, R. 2201, 2265, 2383, 2693, 3755
Leibfritz, J. 994, 3601
Leinbach, R. 3221
Leitner, M.A. 2758, 2764, 2770
Lemaire, J-L. 1120
Lenci, S. 3183
Lengeler, H. 988
Lenkszus, F. 2281, 2490, 2926
Lenz, J.W. 1099
Leonhardt, W.J. 3230, 3583
Leroy, P-A. 2720

Le Sage, G.P. 2858
Lessner, E. 327, 953
Letchford, A.P. 1846
Letta, P. 2383, 2484
Leung, K-N. 2675, 2758, 2761, 2764, 2767, 2770, 3737, 3807
Level, M.-P. 817, 1406, 1517
Levichev, E. 1463, 1466
Levin, L.A. 906
Levush, B. 2431, 3144, 3150, 3159, 3180
Levy, C.D.P. 2781
Ley, R. 944, 982
Leyman, D. 3816
LHC Magnet Team 3371
Li, L. 3297
Li, N. 3312, 3318
Li, Quanfeng 1218
Li, R. 1641, 1644, 2204
Li, S.P. 1566
Li, X. 633, 1996
Li, Y. (Maryland) 1855, 1959
Li, Y. (IHEP) 3297
Li, Yuezeng 1218, 1221
Li, Yulin 3559, 3592, 3595
Li, Zenghai 599
Liakin, D.A. 2965
Lidia, S. 590, 900, 2624
Liehr, M. 2708
Lietzke, A. 3212
Liiou, A.V. 2078
Likhachev, S.P. 3866
Liljeby, L. 947
Limberg, T. 491, 2550
Limborg, C. 838
Limon, P.J. 3389, 3395, 3398
Lin, Glory 850
Lin, K.K. 2259, 2371, 2374, 2523, 3749
Lin, Liu 811, 2096, 2238, 3740
Lin, M.C. 1638, 3048, 3051, 3054
Lin, S.J. 1638, 2377, 3048
Lin, X. 387, 3033
Lin, Y.K. 853
Lin, Yuzheng 1215, 1218, 1221
Lindgren, L-J. 345
Lindroos, M. 2314
Linebarger, W. 596
Ling, Guan Xia 1224
Linnecar, T. 1813, 1816, 1849
Linnik, A.F. 651
Linscott, I. 2284
Lipari, J. 1316
Lira, A.C. 811, 1209, 3476
Lisowski, P.W. 708, 3780
Littauer, R. 1472, 1542
Littenberg, L. 967
Litvinenko, V. 874, 883
Liu, C.Y. 3488
Liu, D.K. 1566
Liu, F. 2678, 3752
Liu, H. 1947, 2693
Liu, K.B. 3488
Liu, W.B. 1388
Liu, Y. 621, 675
Liu, Y.C. 847, 853, 2259, 2858
Lockey, R. 2711
Loew, G.A. 439
Loewen, R. 439, 539, 3042, 3189, 3192, 3195
Lokhovitskii, A.E. 252, 255, 258
Lollo, M. 1129
Lombardi, A. (CERN) 944, 2314
Lombardi, A. (INFN) 1087, 1129
Lonza, M. 826, 2353, 2356
Lorenz, R. 2134, 2137, 2392
Losito, R. 3063
Lou, W. 3236
Louie, W. 3338
Loulergue, A. 817, 2684
Lozowski, W.R. 2737
Lu, Fuhai 3162
Lucas, William 3595
Luccio, A. 92, 207, 962, 970, 1460, 1882, 2538, 3359
Luchini, K. 808
Ludewig, H. 970
Ludewigt, B.A. 3791
Luger, G. 2422, 2535
Luhmann Jr., N.C. 2858
Luijckx, G. 1063
Lujan, R.E. 3096
Luke, P.N. 3807
Lumpkin, A. 775, 871, 874, 883, 1700, 1999, 2052, 2207
Lund, S.M. 1240, 1260, 1929, 1932
Lundgren, S. 1051
Luo, G.H. 847, 850, 853, 1638, 3048
Lupton, William 2403
Lussignol, Y. 2823
Lyles, J. 3473
Lynch, D.R. 3494
Lynch, M. 1147, 3138
Lyneis, C.M. 1051, 2770
Lysenko, A.P. 1433
Lysenko, W. 1917, 2574
Lyudmirskiy, E.A. 249

## M

Ma, L. 1566, 2075
Ma, R. 3831
Maas, R. 1063
Maccaferri, R. 944, 979
MacDonald, A.R. 2508
Macedo, D. 2096
Macek, R. 190, 1012, 1015, 1159, 1611
MacGregor, I. 2413
Machida, S. 1656, 1670, 1908, 1962, 2995
Machie, D. 3108
MacKay, W. 69, 98, 101, 210, 222, 2541
Mackenzie, G. 956, 2675
Mackenzie, R. 2476
MacLachlan, J. 1590, 2556
MacLaren, S. 1926
Madey, J.M.J. 24, 883, 2799
Madlung, J. 1081
Madsen, N. 1560
Maenchen, J.E. 1245
Maeng, A.H. 3663
Maezawa, Hideki 2458, 3616
Mahler, G. 2155
Mahoney, K. 3565, 3678, 3681, 3684
Maidment, J.R. 985
Maier, R. 1048
Mailian, M.R. 695
Mainaud, H. 560
Maines, J. 3224
Mais, H. 1825
Maisheev, V.A. 249
Majka, Dick 967
Major, J. 165
Makarov, A. 3248, 3291
Makarov, I.G. 3114
Makdisi, Y.I. 1460
Makino, K. 1336
Makoveev, V.K. 1391
Maksimchuk, A. 2657
Malafronte, A.A. 2998
Malagari, M. 1042
Malamud, E. 363
Maletic, D. 970, 1882
Malitsky, N. 375, 2434
Maloney, M. 3096
Mamaev, G. 1263, 1311, 1313
Mamaev, S. 1263, 1311, 1313
Mammarella, F. 956
Mammosser, J. 3102, 3108
Mancini, D. 461
Mane, V. 69, 98, 2158
Mangra, D. 745, 2938
Manka, C. 611
Mansur, Louis K. 86
Manvell, Benjamin 3595
Margaritescu, A. 1123, 3854
Marghitu, S. 1123, 3854
Marhauser, F. 521, 527
Mariam, F. 1460, 3359

Marin, A. 3645
Marks, N. 3386
Marks, S. 802, 3221
Marlats, J.-L. 817
Marneris, I. 2308
Marone, A. 3353
Maroulis, D. 1042
Marriner, J. 72, 144
Marsh, K. 678, 687
Marshall, T. 642, 666
Martens, M.A. 72, 136
Marti, F. 278, 1054, 1057
Martin, D. (Bucharest) 1123, 3854
Martin, D. (SLAC) 1457, 1490
Martin, P.S. 139, 243, 3242, 3245, 3269, 3272, 3275, 3278, 3288
Martin, S. 1048
Martinez, D.G. 2232
Martinez, F. 1093
Martinez, R. 2232, 3309
Martini, M. 1362, 2314
Martins, M.N. 2998
Martlew, B.G. 2443
Martono, Hendy 2562
Marutsuka, K. 267, 1908
Marx, M. 491
Maryokhin, S.V. 2229
Mashaw, A. 3737
Mashiko, K. 339
Maslov, M.A. 258
Massmann, P. 2717
Massoletti, D. 778, 808
Masunov, E.S. 2835
Mathewson, A. 3586
Matsuda, Kooji 3813
Matsumoto, H. 455, 530, 533, 581, 587, 593
Matsumoto, S. 306, 1596
Matsuoka, M. 1203
Matufuji, N. 3822
Matuk, C.A. 2767
Maury, S. 944, 976, 979, 982, 1382
Mavric, G. 2481
May, M.P. 3257, 3263, 3280, 3286
Mazarakis, M.G. 1245
Mazur, P. 3389, 3392
McAllister, B. 348, 2099
McCammon, D. 2968
McCormick, D. 1981, 2189, 2253
McCullough, R.W. 2705
McCurdy, A.H. 3159
McDaniel, B. 1472, 1542
McDonald, M. 2675
McDowell, W. 953, 3669
McGee, M.W. 3283
McGhee, D. 953
McGill, R. 2253
McGinnis, D. 144, 1721, 2323
McIntosh, E. 2571
McIntosh, P.A. 2223, 2956, 3078
McInturff, A.D. 3212, 3389
McIntyre, Gary 3693
McIntyre, P. 3443, 3446
McJunkins, P. 3443
McMahan, M.A. 1051
McManamy, Thomas J. 86
McMichael, G.E. 156
Mead, J. 2502
Mecklenburg, B. 2808
Meddahi, M. 309, 312, 1813
Medvedko, A.S. 3455
Medvedko, E.A. 2113, 3455
Medvedyeva, Ye.P. 3840
Meincke, O. 1858
Meisner, K. 2326
Meitzler, C.R. 3872
Melissinos, A.C. 2867
Meller, Robert E. 2505
Mencik, M. 2823
Mendonsa, R. 3796
Menegat, A. 464, 672, 3036, 3045
Meneghetti, J. 3619
Meng, W. 3233
Menge, P.R. 1245
Menshov, A.A. 2078
Méot, F. 121, 1987
Merinov, I. 2244
Merl, R. 745, 2281
Merle, E. 1254, 1257
Merminga, L. 1694, 2320
Merrill, F. 1611, 2743
Metzger, C. 979, 982
Metzmacher, K. 973, 979, 1328
Meyer, D. 1269
Meyer, E.A. 2740
Meyer, J. 883
Meyer, S. 2413, 2517
Meyerhofer, D. 2840
Michelini, P. 3527
Michelotti, L. 997
Michnoff, R. 2218
Mikhailichenko, A. 318
Mikhailov, S.F. 883
Mikhailov, V. 181, 184
Mikkelsen, U. 80, 165, 168
Mikkelson, K. 1245
Miles, J. 1356
Militsyn, B. 1063
Miller, E. 2473
Miller, R. 439, 518, 539, 548, 551, 554, 599, 2687, 2790, 2840, 2843, 2846, 2849, 2852, 2855, 3042
Miller, T. 3619
Millich, A. 563
Milloch, M. 1212
Millos, G. 3568
Mills, J.A. 3230
Mills, Mark R. 2122
Milocco, A. 1212
Milovanov, O.S. 2104
Milton, B.F. 3775
Milton, S. 324, 877, 1700, 2699, 3577
Milward, S.R. 3209, 3494
Minaev, S.A. 2645
Minamihara, Y. 3221
Minato, T. 3425
Minister, J. 439
Minty, M.G. 354, 357, 449, 506, 509, 608, 1563, 1569, 1741, 1873
Minuzzi, F.A. 3628
Mirzojan, A.N. 2078
Mishra, C.S. 139, 997, 1771, 3269
Mistry, N.B. 3559, 3592, 3595
Mitchell, D. 3389
Mitchell, M. 3021, 3024
Mitra, A. 1105, 2953, 3060, 3063
Mitrochenko, V.V. 651, 2817, 2820, 3810
Mitsuhashi, T. 766, 859, 2084
Mitsumoto, T. 1066, 1069, 1075, 3419, 3422, 3428, 3440
Mitsunobu, S. 2908, 3087, 3090
Miura, A. 530
Miura, T. 2983, 3066
Miyachi, T. 938
Miyahara, Y. 891
Miyamoto, S. 757
Miyatake, H. 938
Miyazawa, Y. 941, 2672
Mizuno, A. 2511, 2814
Mizuno, H. 2902, 2974, 2977, 2986, 3069, 3767
Mochihashi, Akira 1664
Mochizuki, T. 757
Moe, H. 953
Mohammadzadeh, Ahmad 2380
Möhl, D. 944, 976, 979, 982, 1382
Moir, D.C. 1138, 1141, 1144, 2829
Moisio, M.F. 1129
Mokhov, N. 116, 124, 133, 393, 414, 3672
Molau, N.E. 2627, 2633
Molinari, G. 944
Møller, S.P. 80, 165, 1027, 2920, 2923
Molodozhentsev, A.Y. 491, 1391
Momal, F. 3206
Monchinsky, V. 184, 2452
Montag, C. 485
Montoya, Debbie I. 2914
Moog, E. 2207, 3224

Moor, E.J.F. 3494
Moore, C.D. 141
Moore, C.I. 611
Moore, John M. 2562
Moraru, R. 3854
Morcombe, P. 883
Moretti, A. 3018
Morgan, G. 3356, 3362
Morgillo, A. 3353
Mori, W. 681, 684, 687, 2870
Mori, Y. 920, 1656, 1670, 1908, 1962, 2992, 2995, 3306
Morii, Y. 2347, 3828
Morikawa, T. 1066, 1069, 1075, 3419, 3422, 3428, 3440
Morita, Y. 3087, 3090
Morpurgo, G. 1858
Morris, J. 3209
Morrison, L. (ANL) 2929
Morrison, L. (LBNL) 3212
Morrison, M. 3212
Morrissey, D.J. 198
Mortazavi, P. 3494
Morton, P. 1611
Morvillo, M. 75, 107
Moser, H.O. 763, 3512
Mosnier, A. (Saclay) 467, 817, 1661, 1709, 2311, 2823
Mottershead, C. Thomas 1397
Mouat, M. 3831
Mueller, A.C. 1120
Mugge, M. 3622
Mulder, H. 944, 979, 982
Mulhollan, G.A. 2849
Muller, Tom 3693
Müller, I. 2493
Müller, R. 2493
Müller, W.F.O. 524
Mullins, L. 3562
Muñoz, M. 814
Murai, T. 3087
Murakami, T. 3822
Muratore, J. 3347, 3353, 3356, 3362
Muratore, P. 3338
Murokh, A. 736
Muto, M. 584, 3306
Myakishev, D.G. 2609
Myers, S. 1
Myers, T.J. 950

## N

Naba, T. 2983
Nadji, A. 817, 1406, 1517
Nagatsuka, Toshiya 856
Nagl, M. 2078, 2726
Naidenov, V.O. 1511
Naito, F. 2902, 2974, 2977, 2986, 3069
Naito, T. 584, 587
Nakagawa, T. (RIKEN) 941, 2672
Nakagawa, T. (Mitsubishi) 2102
Nakai, H. 3087
Nakajima, K. 648, 760
Nakamura, N. 856, 1756, 2146
Nakanishi, H. 648, 760, 2902, 2974, 2977, 2986, 3069, 3087
Nakayama, H. 1394, 2992, 2995
Nakayama, K. 3828
Nam, S.H. 823, 2107, 3479
Nam Soon-Kwon 1593
Namkung, W. 593, 823
Nantista, C. 439, 1676, 2186, 2256, 2852, 3027, 3042, 3192
Naqvi, S. 3117
Naranjo, A. 1093
Nassiri, A. 461, 1575, 2052, 2296, 2941, 2944, 3111, 3120, 3174, 3491
Nath, S. 915, 1150, 1153, 1162, 1171
Nation, J.A. 1272, 1275, 3117
Naumann, O. 1551
Nawrocky, R.J. 2069
Naylor, Graham 2210
Neel, J. 817
Nelson, E.M. 1837
Nelson, R. 3165
Nelson, S.D. 2633
Neri, F. 193, 273, 1012, 1015, 3788
Nesterenko, I.N. 1433, 1762
Nesterov, V. 439
Nesterovich, A. 276, 2773, 3869
Neubauer, M. 3004, 3039
Neuenschwander, R.T. 811
Neuffer, D. 417, 624, 1537, 2905
Ney, S. 3096
Nezhevenko, O.A. 3013, 3114, 3153, 3156, 3186
Nezrick, F. 2867, 2873
Ng, C. 387, 1738, 2116, 2189, 3033, 3562
Ng, K.-Y. 396, 399, 405, 994, 1000, 1003, 1030, 1481
Ng, Wang C. 2630
Nghiem, P. 330, 817, 1406, 1517
Nguyen, D.C. 897, 1990
Nguyen, K. 3144, 3180
Nguyen, M.N. 3482
Nguyen, V. 3102
Nguyen-Tuong, V. 3105
Ni, G. 3297
Ni, Yi 3764
Nicol, T.H. 3257, 3263, 3710
Nielsen, J.S. 1560
Nielsen, R. 953
Niibe, M. 757
Niki, K. 938, 3306
Nikiforov, A.A. 3114
Nikitina, I. 3586
Nikitina, L. 3586
Nishi, M. 3813, 3819
Nishimura, H. 778, 784, 799, 805
Nissley, L. 3816
Nitsch, F. 3123
Njegomir, M.M. 190
Nobes, S. 3209
Noble, R.J. 393
Nobrega, F. 3389, 3398
Noda, A. 339, 1203, 1206, 3294, 3819
Noda, K. 201, 820, 1557, 2347, 3819, 3822
Nogiec, J.M. 3395, 3464, 3713
Nolen, J. 2696
Nomura, M. 402, 880, 2787
Nomura, T. 201, 938
Noomen, J.G. 1063
Noonan, J. 3552, 3580
Nordberg, E. 3075, 3383
Nordby, M. 3330, 3639
Norek, G. 953
Norem, J. 363, 396, 399, 1030
Noriega, R. 2253
Normann, L. 1813
Nosochkov, Y. 838
Novicova, T.A. 889
Novikov, A.V. 2732
Novikov, S.A. 184
Novitski, I. 3398
Novokhatski, A. 467, 1661, 1709
Nuhn, H.-D. 838

## O

O'Day, S. 1006
O'Shea, P.G. 1278, 1891, 1993, 2799
O'Sullivan, M. 3681
Oakeley, O. 883
Obina, Takashi 1664
Odagiri, T. 1557
Ogata, A. 648, 760
Ogawa, H. 3327, 3822
Ogitsu, T. 3365
Oh, J.S. 581, 593
Ohashi, Y. 2971
Ohkawa, T. 1024
Ohkubo, Y. 533
Ohmi, K. 1566, 1596, 1667, 1831
Ohmori, C. 1656, 1670, 1908, 1962, 2992, 2995
Ohshima, T. 2971
Ohtomo, K. 1072

Ohtomo, Kiyotaka 3816
Oide, K. 494, 587, 1394, 1484, 1798, 3660
Okada, M. 938
Okamoto, H. 339, 1203, 1798, 1911
Okamura, M. 1460, 3341, 3359, 3431, 3437
Okugi, T. 584, 587, 1484
Okuma, S. 730
Okuno, H. 1066, 1069, 1075, 3327, 3419, 3422, 3440
Oliveira, L.H. 3476
Olsen, B. 101
Olsen, D.K. 1018, 1177, 2775, 3851
Olsen, Jeff J. 2122
Olsen, R. 3485
Olson, C.L. 1935
Olsson, E. 2422, 2535
Omar, A.S. 2553, 2612
Omeich, M. 2823
Onishchenko, I.N. 651
Ono, S. 1557
Oothoudt, M.A. 1165, 2064, 2464
Oproiu, C. 1123, 3854
Oren, T. 3755
Ormond, Kern W. 1822
Orris, D. 3389, 3395, 3713
Osborn, J. 3312, 3318, 3321
Oshita, E. 730
Osmanov, N. 736
Ostiguy, J.-F. 1403, 2556, 3257, 3260, 3263, 3272, 3278, 3286
Ostojic, R. 3209, 3696
Ostreiko, G.N. 3114
Ostrem, D.J. 2464
Ostroumov, P. 1135, 2078, 2621, 2732
Otter, Alan J. 3336
Ottinger, M.B. 1653
Ovsyannikov, D. 1944
Owen, H. 333, 2443
Oyaizu, M. 938
Ozelis, J.P. 3389

## P

Pabst, M. 1846
Pachnik, J. 3395, 3713
Padamsee, H. 2884, 3075, 3177
Padmore, H. 3221
Pagani, C. 1126, 3657
Pakter, Renato 1938
Palanque, S. 817
Palmer, D.T. 1968, 2687, 2790, 2840, 2843, 2846, 2849, 2855
Palmer, R. 286, 405, 408, 3401
Palmieri, V. 1129
Pamela, J. 2717
Pan, K.T. 3539
Pantell, R.H. 675
Paoluzzi, M. 979
Papadakis, N.H. 1042
Papanicolas, C.N. 1042
Papis, J.P. 2049
Pappas, G.C. 390
Paramonov, V. 1135, 2726, 2959, 2962
Pardine, C. 811, 1209, 3010
Pardo, R.C. 2696, 2702
Parisi, G. 1090, 1900
Park, D. 3633
Park, H.J. 3015
Park, M.K. 2350
Park, S. 874, 883
Park, Sanghyun 835, 2840
Parker, J.M. 3625
Parker, R. 66
Parker, R.K. 3159
Parkhomchuk, V.V. 1795
Parma, V. 3368, 3374
Parodi, R. 1126
Parsa, Z. 642, 1502, 1505, 1508, 1917
Parzen, G. 1421, 1424, 1427, 1430
Pascholati, P.R. 2998
Pasotti, C. 826, 1185, 1735, 3099
Pasquinelli, R.J. 1403, 3804, 3837
Passchier, I. 1063
Patavalis, N. 1042
Paton, K. 3831
Patteri, P. 572, 2137
Patterson, J. 883
Patterson, J.M. 439
Paul, A.C. 1260
Paul, M. 2696
Pawel, Steve J. 86
Payet, J. 330, 817, 1406, 1517
Pearson, C. 439, 2911, 3192
Pearson, P.S. 2437
Peaupardin, P. 817
Pedersen, F. 973, 979, 982, 1382
Pedersen, J. 973
Peggs, S. 56, 69, 95, 98, 101, 219, 222, 405, 1030, 2158, 3359
Pei, A. 1481, 2968
Pekeler, M. 2917
Pekker, M.S. 1635
Pelaia, T. 1472, 1542
Pellegrini, C. 678, 736, 1457, 1490, 1968, 2687, 2802
Pellico, W. 3716
Pelzer, W. 1078
Pendzick, A. 2213
Peng, Q. 378, 3297
Pengo, R. 1129
Pénicaud, J.-P. 817
Peoples Jr., J. 29
Peperkorn, I. 2078, 2726
Perelstein, E.A. 488
Perevedentsev, E.A. 1759
Perez, F. 763, 1039
Perin, R. 3371
Perini, D. 3410
Perkins, L.T. 2761, 3807
Perraudin, C. 1117, 1191
Pershin, V.I. 1090, 3848
Pershing, D. 3144
Persov, B.Z. 3114
Peschardt, E. 309
Peters, C. 1926
Peters, J. 2726
Peterson, K. 953
Peterson, T. 3392, 3395
Petillo, J. 3144
Petracca, S. 1753, 1783
Petri, H.R. 2737
Petrov, S.P. 3455
Petrov, V. 1795, 2796, 2838
Petrov, V.A. 491
Pett, J. 66
Pewitt, E.G. 3269, 3275
Peyrot, M. 3374
Pfeffer, H. 994, 3461
Pfeiffer, G. 2493
Phillips, L. 3102, 3108, 3752
Phillips, R. 439
Phinney, N. 497, 506, 608
Phinou, P. 1042
Phung Ngoc, B. 2311, 2823
Picard, D.S. 2761
Pickles, T. 3831
Picoli, R.A. 1209
Picon, J.C. 1254, 1257
Piech, R. 2929
Pierini, P. 1126
Pietryka, M. 315, 439, 3666
Pietryla, A. 2281
Pike, C. 2344
Pikin, A. 2711
Pilat, F. 69, 95, 98, 101, 222, 2544, 3359
Pile, G. 1269
Pillai, C. 2064, 2743
Piller, Chip 2131
Pinayev, I.V. 883
Pinchasi, Y. 906
Pinto, I. 1753
Piot, P. 912, 2198, 2204
Pipersky, P. 3221
Pirozhenko, V.M. 950
Pisent, A. 1087, 1129, 1132
Pittana, P. 3099

Pivarč, J. 3604
Pivarč jun., J. 3604
Placidi, M. 366, 1987, 3648
Planner, C.W. 1021
Plate, D. 3221
Plesko, M. 336, 763, 2481
Plotnikov, V.K. 2965, 3848
Plum, M. 187, 190, 1012, 1015, 1611
Podgorny, F.V. 237
Podlech, H. 947
Podobedov, B.V. 1629
Poelker, B.M. 2861, 2864
Poggi, M. 1129, 2169
Pogorelsky, I. 621, 645, 675
Poirier, R. 956, 1105, 2953, 3060, 3063
Polk, I. 3230
Pomasan, Yu. 276
Pomatsalyuk, R.I. 2229
Poncet, A. 3368, 3586
Poole, Brian 1861, 2630
Pope, R. 439, 3042, 3192
Popenko, V.A. 3810
Popik, V.M. 883
Popov, E.O. 1511
Popovic, M. 396, 399, 1030, 1403, 3837
Poppensieker, K. 3801
Porcellato, A.M. 1087, 1129
Poreye, V. 3816
Portante, L. 2998
Porter, T. 439
Postma, O. 3630
Potepan, F. 2467
Potier, J.P. 476
Potter, J.M. 1099
Potukuchi, P. 3072
Pouchkov, S. 1263
Poukey, J.W. 1245
Power, J. 633, 639, 1996
Power, J.F. 193, 2041, 2232, 3731
Pozimski, J. 174, 246
Pozzer, A. 1212
Prabhakar, S. 2284, 2362
Prasuhn, D. 1048
Preble, J. 3108
Prelec, K. 2711
Price, J.S. 2864
Prichard, B. 1611
Prieels, D. 3816
Prior, C.R. 1021
Pritzkau, D. 672, 1626, 3036
Proch, D. 3081
Prokesh, K. 1391
Prokopenko, S.Yu. 2229
Pros, M. 2011
Proudlock, P. 66
Pruss, S.M. 3286
Ptitsin, V. 3359, 3500
Puchkov, S. 1311, 1313
Pugachov, G.D. 3840
Pugh, M.J. 2443, 2508
Putnam, S.D. 1251
Pynn, R. 1159

## Q

Qin, Q. 1448, 1566
Qing, Q. 1356
Qiu, Joe X. 1971
Qualls, A. 2449
Quigley, P. 3075
Quimby, D.C. 675
Qunell, D. 1281, 1287

## R

Rabedeau, T. 838
Radoiu, M. 3854
Radu, A. 1123
Rafael, F. 811, 1209, 2096, 3324
Rahmani, H. 1042
Rahn, J. 2493
Raia, Guido 2038
Raich, U. 973
Raimondi, P. 449, 452, 503, 509, 608, 687, 1981, 2189
Raino, A. 2729
Rajagopalan, S. 2802
Rakowsky, G. 727, 3497
Ramamoorthy, S. 2287
Ramsell, C.T. 663
Rao, M.G. 3105
Raparia, D. 162, 970, 2023
Raridon, R.J. 2775
Raskopin, A.M. 2965
Ratner, L. 1460, 1478
Ratti, A. 216, 1706
Ratzinger, U. 947, 1897, 2645
Raubenheimer, T. 473, 482, 503, 599, 605, 687, 1197, 1563, 1626, 2580
Rawlinson, B.R. 2443
Rawnsley, W.R. 2049
Ray, B.D. 1165
Redd, D.B. 273
Redden, D.P. 3872
Reece, C. 3105
Reece, K. 89, 1460
Rees, D. 1147, 2428, 2889, 3183, 3725
Rees, G.H. 988, 1021
Reeve, Paul 3336
Regan, A. 1150, 2338, 2341
Reginato, L. 590, 1296
Rehm, K.E. 2696
Reichanadter, M. 243
Reiche, S. 736, 1365
Reichel, I. 1819
Reidelbach, K. 246
Reigle, D. 3669, 3690
Reilly, J. 3075
Reis, D. 2840
Reiser, M. 1526, 1650, 1855, 1953, 1956, 1959, 2143, 2681, 3168
Ren, F. 3297
Rennich, Mark J. 86
Rensfelt, K.G. 947
Repkov, V.N. 883
Repnow, R. 947
Reppond, A. 3872
Reshetnyak, N.G. 2820
Reuter, E. 315
Reymermier, C. 3586
Reyzl, I. 2392
Riabko, A. 1346, 1481
Rice, D. 3236, 3383, 3705
Richards, L. 3443
Riche, A. 563
Richter, M. 3801
Rickard, M.L. 2758
Ridlon, Rae N. 2826
Rieckmann, C. 2553, 2612
Ries, T. 1194
Rifflet, J.M. 3365, 3374
Rifkin, J. 439, 2186, 3042, 3192
Rijllart, A. 3206
Rimmer, R.A. 3001, 3004, 3007, 3039
Rinckel, T. 3303
Ringwall, A. 3330
Risbud, S. 3183
Risselada, T. 1356, 1442
Ritson, D. 113
Riunaud, J.-P. 228, 973, 979
Rizawa, T. 3828
Rizzi, V. 1212
Robert, C. 2899
Roberts, J.E. 190
Robertson, H.P. 3684
Robin, D. 778, 799
Robinson, K.E. 675, 3201
Rodger, E.S. 3230
Rodier, J. 2823
Rodionov, D.A. 3866
Rodrigues, A.R.D. 811, 2096, 3324, 3740
Rodriguez-Mateos, F. 3206
Rogers, J. 318, 369, 1822, 2276, 3215
Rohmig, P. 3368, 3374
Rohrer, U. 3785
Röjsel, P. 345

Rokni, S. 687
Romanov, S. 2452
Romas'ko, V.P. 2820
Romeu da Silva, A. 811
Ronnigen, R. 1054
Root, L. 956, 1102
Ropert, A. 754
Roques, A. 1254, 1257
Rosa, A. 811
Rose, C.R. 193, 1012, 1293, 2044, 2093, 2232
Rose, J. 967
Rosenberg, A. 906
Rosenberg, R.A. 3552
Rosenzweig, J. 627, 678, 736, 1365, 1965, 1968, 2802, 2873, 2876
Roser, T. 89, 207, 396, 399, 1030, 1460, 1478, 2538, 3359
Roshal, A.S. 2835
Ross, J.S.H. 3413
Ross, M. 608, 1626, 1981
Ross, W. 2284, 2359, 2365
Rossa, E. 1987
Rossbach, J. 719
Rossi, C. 826, 1180, 1182, 1212, 2002
Rossmanith, R. 763, 1039, 3512
Roster, W. 439
Rotela, E. 2207, 2929
Rovang, D.C. 1245
Rovelli, Alberto 2038
Roy, A. 3072
Roy, G. 312, 1819, 1858
Roybal, P. 1093
Roybal, W. 1147, 3183, 3725
Royer, J.P. 973
Rubin, D. 318, 372, 3075, 3236, 3654
Rüdiger, H. 2493
Ruggiero, A. 970, 1114, 1578, 1581
Ruggiero, F. 75, 107, 1712, 1753, 1816, 2648
Rukoyatkin, P. 181
Rule, D.W. 675
Rümmler, J. 237
Rusnak, B. 2914, 3096
Russell, A.D. 3275, 3278, 3288
Russell, G.J. 190
Russell, Steven J. 2005, 2177
Rust, K.R. 273
Rusthoi, D.P. 2574
Ruth, R. 439, 482, 539, 548, 554, 605, 1676, 3042, 3192
Ryan, W. 2152, 2215
Rybaltchenko, K. 3645
Rybarcyk, L. 1150, 2514, 2743
Ryne, R.D. 2624

# S

Saadatmand, K. 2767
Sabah, S. 2392
Saban, R. 3206
Sabbi, G. 1682, 3398
Sachtschale, R. 883, 1278, 2799
Sachwitz, M. 2137
Safa, H. 3096
Safranek, J. 748, 799, 838, 841
Sagan, David 1765, 1768
Sah, R.C. 847, 850, 853, 2371
Saito, K. 2995
Saito, M. 1557
Sajaev, V. 1463, 1466
Sakai, F. 648, 760
Sakai, H. 2902, 2974, 2986, 3069
Sakaki, H. 2511, 2814
Sakamoto, N. 1066, 1069, 1075, 3419, 3422, 3428, 3440
Sakamoto, T. 587
Sakanaka, S. 354, 2980, 2983, 2989, 3616
Saldin, E.L. 575, 1658
Salzborn, E. 2705, 2708
Sampayan, S.E. 1308, 2627
Sampson, W. 3353, 3356
Sandberg, J. 2308
Sander, O. 1015, 1611, 2743
Sanders, D.M. 1308
Sandweiss, J. 675
Sano, Masami 3816
Sapozhnikov, L. 2359, 2365
Saraph, G.P. 3168
Sarkar, S. 2241, 2274
Sasaki, Shigemi 802
Sass, R. 2473, 2476
Sassowsky, M. 973
Sato, H. 267, 1009, 1460, 1908
Sato, K. 3327
Sato, S. 201
Sato, Y. 1566, 3822
Satogata, T. 69, 98, 101, 210, 2544
Satoh, K. 2983, 3066, 3828
Satoh, Kotaro 306, 2087
Satoh, Takemi 3816
Savino, Ray 3693
Sawada, S. 2992, 2995
Scafuri, C. 826, 2353, 2356, 2467
Scandale, W. 1445, 1469, 1816
Scanlan, R. 3212, 3398
Scarpa, F. 1129
Schächter, L. 1272
Schaefers, F. 3527
Schaffer, H. 3796
Schaffner, S. 2128
Schaller, S.C. 2464
Schaper, J. 336, 763
Scheblein, J.A. 3230
Scheer, M. 1418, 1520, 2606, 3527
Scheitrum, G.P. 3045
Schempp, A. 947, 1078, 1081, 1084, 1897, 2726
Schiffer, J.P. 1560, 2696
Schilcher, T. 2320
Schillinger, B. 2594
Schindl, K. 973, 2314
Schlabach, P. 3248, 3257, 3263, 3392
Schlapp, M. 2702, 2705, 2708
Schlarb, H. 1572
Schlueter, R. 802, 3221, 3230, 3315
Schmalzle, J. 3356
Schmerge, J. 2840
Schmickler, H. 66, 1858, 2026
Schmidt, C.W. 1403, 3837
Schmidt, F. 1356, 1436, 1439
Schmidt, R. 66, 3206, 3209, 3648
Schmitz, S. 569
Schmor, P. 956, 2675, 2781
Schnase, A. 1048
Schneider, G. 3586
Schneider, H. 1048
Schneider, J.D. 1168, 2740
Schneidmiller, E.A. 575, 1658
Schoenlein, R.W. 1984
Schoessow, P. 633, 639, 1996
Schönauer, H. 973, 1587
Schrage, D. 1093, 3625
Schreiber, H.J. 2137
Schriber, S.O. 1159
Schröder, G.H. 225, 1325
Schroeder, C.B. 684
Schryber, U. 3785
Schubert, J. 1060
Schulte, H. 2603
Schultheiss, C. 3452
Schultheiss, T. 3177
Schütt, P. 3162
Schwalm, D. 947
Schwartz, C. 2296, 3111
Schwarz, H. 2359, 3004, 3007, 3039
Scorzato, C. 811
Seamen, J.F. 1235
Sears, J. 3075
Sebek, James J. 835
Sedlak, J. 1391
Sedlyarov, I. 2796, 2838
Seeman, J.T. 315, 1563, 1876
Segel, R.E. 2696
Seidel, M. 434, 439, 500, 554, 2119, 2189
Seidl, P. 1923, 1926
Seitz, Gerald J. 2826
Sekutowicz, J. 3081

Sellier, J.C. 3365
Senichev, Yu. 1111, 2923
Sennyu, K. 2908, 3087
Senyukov, V.A. 3869
Seo, K. 3425
Seo, K.W. 3663
Serafini, L. 1365, 1965, 1968, 2876
Serdobintsev, G.V. 3114
Sereno, N.S. 1700
Sergo, R. 2353, 2356
Serio, L. 3206
Serio, M. 2284
Sermeus, L. 1328
Serre, C. 979
Servranckx, R.V. 153
Sery, Andrey 557
Sessler, Andrew M. 422, 1614
Settakorn, Chitrlada 733, 2017
Sexton, I. 3586
Sgobba, S. 3586
Shafer, R. 83, 1150, 1293, 2232, 3309
Shahal, O. 906
Shamovsky, V.G. 1795
Shang, C. 2627, 2633, 3183
Shank, C.V. 1984
Shapiro, A.H. 2914, 3096
Shapiro, M. 2690
Shapiro, V.E. 1368
Shaposhnikova, E. 1813, 1816, 1849
Sharma, S. 363, 2207, 2929, 3574
Sharonov, S. 3395, 3464, 3713
Shasharina, Svetlana G. 2592, 2654
Shatilov, D.N. 1762
Shatunov, Y. 1433, 3359, 3407, 3500
Shaw, J. 2241, 2274
Shchelkunoff, S.V. 3114
Shcherbakov, A. 1311
Shea, T.J. 2152, 2215, 2502
Sheehan, J. 2687
Sheffield, R.L. 897
Shelley Jr., F.E. 2514
Shen, S. 3625
Shen, W. 3443, 3446
Sheng, I. 2207, 2929, 3574
Shepard, K.W. 3072
Sheppard, J.C. 903
Sherman, J.D. 2723, 2740, 2746
Sherrill, B.M. 198
Sheu, J.T. 3488
Shevtsov, V.Ph. 491
Shi, P. 1560
Shi, Ping 2075
Shibuya, S. 1962
Shiloh, J. 906
Shiltsev, V.D. 237, 420, 1475, 1774, 1777, 2805
Shin, H.M. 1870
Shinn, M. 2529, 2693
Shinoe, Kenji 2146, 3066
Shintake, T. 455, 530, 533, 536, 593, 1981
Shirai, T. 339, 1087, 1203, 1206, 3294, 3819
Shirakabe, Y. 938
Shirakata, M. 267, 1908
Shlakhov, I.N. 2229
Shoaee, H. 1454, 2383, 2425, 2586
Shoji, Y. (KEK) 267, 1908
Shoji, Y. (Himeji) 757, 1385
Shu, Deming 2210
Shu, Q.-S. 624, 2905
Shukla, S. 144
Shulze, M. 1611
Shurter, R.B. 2232
Shurter, R.P. 2829
Shvedov, O.V. 3848
Shvedunov, V.I. 1108, 1902, 3866
Shvets, G. 657, 669
Shvetsov, V.S. 3126
Sibley, C. 2099, 2241, 2274, 3407, 3743
Sidorenko, V.N. 1090
Sidorov, G.I. 1391
Sieber, T. 947
Siemann, R.H. 464, 497, 500, 602, 672, 687, 1629, 2164, 2580, 3036
Siemko, A. 3377
Sievers, P. 3377
Siggins, T. 3752
Sikora, John 1765
Sikora, R. 2152
Silbar, Richard R. 1529
Silke, C. 3816
Silva, A.R. 1209, 3476
Silva, M.B. 3628
Sim, J. 3242, 3395, 3713
Siman-Tov, Moshe 86
Simon, D.J. 979
Simon, R. 763
Simonin, A. 2717
Simonov, E.A. 1762
Simpson, J. 633, 636, 639
Simrock, S. 2320, 2905
Sinclair, C.K. 2693, 2864, 3761
Singh, O. 727, 2161, 2287, 3455, 3494
Skachkov, V.S. 2965, 3848
Skaritka, J. 621, 675, 1197, 2687, 2843
Skoczen, B. 3368
Skopik, D.M. 716
Skrinsky, A.N. 883
Sloan, T. 264, 1481
Smaluk, V. 1463, 1466
Smedley, J. 2790
Smirnov, A. 1795, 3407
Smirnov, A.V. 894, 3518
Smirnov, V. 2244
Smith, D.L. 1245
Smith, G.A.(BNL) 2149, 2215, 2302
Smith, G.A.(FNAL) 3257, 3263
Smith, H. 439
Smith, H.V. 1150, 2746
Smith, I. 1245
Smith, J.D. 2437
Smith, J.R. 1251
Smith, K.D. 3209, 3413, 3494
Smith, R. Scott 2164
Smith, S. 439, 2110, 2113, 2116, 2122, 2253
Smith, S.L. 2443
Smith, T.L. 2299, 2938, 2941
Smith, V. 2253
Smithwick, J. 3212
Snell, Charles M. 2174
Snydstup, L. 2711
Sobczynski, S. 2274
Sobenin, N.P. 1108, 2008, 2104
Søby, L. 1587
Soika, A. 3443
Sokolowski, J.S. 906
Solita, L. 3669, 3690
Solomon, L. 727, 3497
Sommer, M. 817, 1406
Sommer, W.F. 190
Sondericker, Jack 3693
Song, J. 912, 2204, 2529
Song, J.J. 461, 1575, 2941, 2944
Soong, S.B. 2241
Soukas, A. 2308, 3449
Soutome, K. 1385
Sparveris, N. 1042
Spence, W.L. 506, 1673
Spencer, J. 439, 608
Spencer, N. 439
Spentzouris, L. 16
Spielman, R.B. 1235
Spinka, H.M. 1460
Sprangle, P. 611, 630
Sprehn, D. 439
Springer, R.W. 2829
SRC Staff 865
Srinivasan-Rao, T. 2790
Stagno, V. 2169
Stanek, M. 596
Stanford, G. 956, 1105
Staples, John W. 1096, 1174
Stefan, J. 2481
Stefan, P.M. 727, 3497, 3515
Steffen, L. 2446
Stege, R. 2253

Steier, C. 1033
Steimel, J. 144, 1721, 2323
Stein, P. 2711
Steiner, R. 3801
Steininger, R. 763
Stellfeld, D. 1816
Stepin, V.D. 651
Stern, C. 2422, 2535
Stettler, M. 2041, 2044, 2093, 2232
Stevens, A.J. 219
Stevens, R.R. 2723, 2740, 2743, 2746, 2764
Stevens, T. 3619
Stevenson, Nigel R. 3842, 3845
Stiliaris, E. 1042
Still, D. 1721, 2061
Stinson, G. 956
Stirling, W.L. 2714
Stitts, E. 3681
Stockhorst, H. 1048
Stoddard, R.D. 1308
Stoltz, P. 669
Stover, G. 2284, 3734
Stowell, G. 2808
Strait, J.B. 124, 3209, 3389, 3395, 3398
Strasser, P. 938
Street, A.J. 3209, 3413
Strong, Edward 2131
Strozinsky, R. 3021
Strubin, P. 2440
Struve, K.W. 1235
Stuart, B. 886
Stupakov, G. 449, 1563, 1632, 1635, 1685, 1688, 1834, 2180
Stygar, W.A. 1235, 1245
Suda, M. 3822
Suetake, M. 306
Suetsugu, Y. 1566, 1596
Sugai, I. 187
Sugimura, T. 339, 1206, 3819
Suh, J.H. 3479
Suk, H. 1650, 1855, 2143
Sukenobu, S. 3828
Sullivan, Gary 1144
Sullivan, M. 296, 3330, 3562
Summers, D. 624
Sun, Baogen 1664
Sun, Baoyu 1218
Sun, D. 1403, 3018
Sun, J. 3297
Sun, Jingqing 1218, 1221
Sun, Xiang 1221
Sun, Y. 3300, 3312, 3318
Suwada, T. 2253
Suzuki, C. 536
Suzuki, S. 2511, 2814
Svandrlik, M. 826, 829, 1735, 3099
Sveshnikov, B. 2452
Svirtun, V. 3580
Swan, T. 3622
Swenson, D.A. 1099, 3872
Swift, G. 883, 1278
Sylvester, C. 3392, 3395
Syphers, M. 95, 207, 1478, 2155, 3359
Syversrud, D. 1051
Szczech, J. 2702

## T

Tabor, M. 3816
Tachikawa, T. 1045, 3816
Tadano, M. 2084
Tadokoro, M. 3294, 3819
Tajima, T. (Texas) 1653
Tajima, T. (KEK) 2908, 3087, 3090
Takada, E. 201, 2347, 3822
Takagi, A. 2992, 2995
Takagi, H. 1908
Takahashi, H. 402, 880, 2787
Takahashi, J. 2998
Takahashi, T. 2908, 2989, 3087, 3090
Takaki, Hiroyuki 856, 2146
Takanaka, M. 1807
Takano, M. 587
Takao, M. 1385
Takashima, T. 2971
Takata, K. 494
Takayama, K. 1548, 1599, 1908
Takayama, T. 2642, 3816
Takeda, H. 1171
Takeda, S. 494, 587
Takeda, Shigeru 581, 3660
Takeda, Y. 938
Takeuchi, N. 859
Takeuchi, Y. 581, 2902, 2974, 2977, 2986, 3069
Takii, T. 730
Taleyarkhan, Rusi 86
Tallerico, P. 1147, 3138
Tallerico, T. 2213
Talman, R. 375, 1472, 1542, 2434
Tamura, F. 3767
Tamura, Kazuhiro 1664
Tan, Cheng-Yang 2221
Tanabe, J. 3312, 3318, 3321
Tanabe, T. 1557, 2992, 2995
Tanabe, Toshiya 3515
Tanabe, Y. (KEK) 2992, 2995
Tanabe, Y. (Toshiba) 3828
Tanaka, H. 1385
Tanaka, J. 938
Tanaka, M. 69
Tanaka, M.H. 938
Tanaka, Y. 1066, 1069, 1075, 3419, 3428, 3440
Tang, C. 1729, 3081
Tang, H. 599, 608, 2849
Tang, J. 2265
Tang, Y. 2287
Tani, K. 1266
Taniuchi, T. 2511, 2814
Tanke, E. 944
Tantawi, S. 439, 3042, 3189, 3192, 3195
Tarakanov, V.P. 1299
Taratin, A. 165
Tarnetsky, V.V. 3114
Tartaglia, M. 147, 3395
Tatchyn, R. 2192, 2195, 2639, 3530
Tatum, B.A. 1227
Taurigna-Quere, M. 2823
Tavares, P.F. 811, 2096, 2238, 3740
Tawada, M. 1394
Taylor, B.D. 2867
Taylor, C. 3212
Taylor, T. 315
Taylor, T.M. 3209, 3696
Tazzioli, F. 2137
Tecker, F. 366, 3645, 3648
Tejima, Masaki 2087
Temkin, R.J. 2690
Temnykh, A. 1718, 1768, 3218, 3654, 3708
Tenenbaum, P. 439, 479, 608
Teng, L. 1359, 2699
Tenishev, S. 2229
Tenyakov, I. 1263, 1311, 1313
Tepikian, S. 69, 98, 101, 222, 405, 2544, 3359, 3651
Terasawa, M. 757
Terebilo, A. 1457, 1490
Terechkine, I. 994, 3248, 3291
Terekhov, A.S. 1063
Terunuma, N. 494, 584, 587
Teryaev, V.E. 3126
Teryoshkin, Y. 1263
TESLA collaboration 425
Tessier, J.M. 2311
Teytelman, D. 2284, 2362, 2368
Theuws, W.H.C. 1036, 1200
Thevenot, M. 1254
Thiessen, H.A. 273, 1012, 1015, 1611, 3788
Thivent, M. 973
Thomas, M.G. 2305
Thomas, R. 3362
Thomlinson, W. 3494
Thompson, K. (SLAC) 608, 2580
Thompson, K. (ANL) 953, 2699

Thompson, P. 69, 98, 101, 3353
Thomson, J. 1563
Thorson, I. 956
Thur, W. 2067
Tian, Bo 3764
Tiede, R. 2645
Tiefenback, M. 2128, 2265, 2271, 3758
Tieger, D. 348
Tighe, R. 2359, 2520
Tikhomirov, A.V. 3610
Tille, T. 2784
Tillghman, A. 439
Timlin, C. 3413
Timm, M. 515
Timossi, C. 805
Ting, A. 611, 630
Tinsley, D. 1287
Tkatchenko, A. 330, 817, 1406
Tkatchenko, M. 817
Tobiyama, M. 306, 1566, 1596, 1664, 2332, 2335
Toda, M. 2992, 2995
Todesco, E. 1445, 1469, 2568
Toelle, R. 1048
Tojyo, E. 938
Tokumoto, S. 2983, 2989, 3066
Toldo, F. 3449
Tolstoluzhsky, A.P. 651
Tomicich, A. 1212
Tomimasu, T. 730
Tominaka, T. 1066, 1069, 1075, 3359, 3416, 3419, 3422, 3428, 3431, 3434, 3437, 3440
Tomitani, T. 3822
Tomizawa, M. 938, 1962
Tomlin, R. 144
Tommasini, D. 763
Tompkins, J.C. 3389, 3395, 3713
Tomura, H. 3822
Tong, Dechun 1215, 1218, 1221, 3764
Tongu, E. 730
Tonguu, H. 339, 1206
Tonisch, F. 2137
Toole, L. 1147
Tordeux, M.-A. 817
Torikoshi, M. 820, 3819, 3822
Tortschanoff, T. 3374
Tosi, L. 826, 829, 1520, 2353, 2356, 3527
Tosin, G. 3324
Tovo, E. 1087
Tovo, T. 1087
Townsend, M. 3209
Toyama, T. 1548, 1599, 1908
Trahern, C. 69, 101, 2544
Trakhtenberg, E. 3224, 3556
Tran, H.J. 1647
Tranquille, G. 944, 979, 982
Trassl, R. 2705, 2708
Travish, G. 736, 1126
Trbojevic, D. 69, 98, 101, 219, 396, 399, 405, 1030, 1371, 3651
Treadgold, J. 3209
Tremaine, A. 736
Tribendis, A. 2796, 2838
Trimble, D.O. 1308
Trofimov, N. 2440
Trombly-Freytag, K. 3713
Tron, A. 2244, 2247
Trotz, S. 2690
Trower, W.P. 1108
Troyanov, E.F. 249
True, R. 3153, 3180, 3186
Trzeciak, Walter 865
Tsarenkov, A. 2452
Tschalaer, C. 348
Tsentalovich, E. 348, 2241
Tsoupas, N. 69, 98, 207, 210, 213, 222, 1460, 2152, 3359
Tsubota, K. 2565
Tsubuku, H. 3822
Tsutsui, H. 1266, 2642
Tsygankov, E. 276
Tumanov, K.D. 3604
Tuozzolo, J. 213, 2149, 3233
Tur, Yu.D. 2820, 3810, 3840
Turchin, V.I. 2735
Turchinetz, W. 348, 2274
Turlington, Larry 2131
Turner, J. 315, 1569
Turner, L.R. 3491
Turner, William C. 422
Tuyn, J. 979
Tzeng, K-C. 2870
Tzeng, R.H. 3051

## U

Ueda, A. 2084
Ueda, T. 648, 760
Ueng, T.S. 847
Uesaka, M. 648, 760
Uesugi, T. 1656, 2992, 2995
Uggerhøj, E. 80, 165
Uhm, Han S. 1870, 3147
Ullmann, J. 3096
Ullrich, H. 973
Umezawa, M. 3294, 3813
Umstadter, Donald 2657
Underwood, D. 207, 1460
Underwood, K.K. 497
Urakabe, E. 3819
Urakawa, J. 354, 444, 494, 578, 584, 587, 1484, 2980
Ursic, R. 912, 2131
Uskov, V.V. 651
Uvarov, V.L. 2229, 3810, 3840
Uythoven, J. 1858
Uzat, W. 3057
Uzunoglou, N. 1042

## V

Valbuena, R. 3586
Valentino, V. 2169, 2729
Valishev, A.A. 1433
Valter, H. 3123
van Amersfoort, P.W. 1063
van Asselt, W. 89, 1460, 1478, 2155
van den Brand, J.F.J. 1063, 3630
van den Putte, M.J.J. 1063
van der Geer, S.B. 2577
van der Laan, J.B. 1063
Van der Schueren, A. 979
Van Duppen, P. 947
Van Ginneken, A. 393, 417
van Leeuwen, E. 3630
van Oers, W.T.H. 2781
van Oort, J. 3212
van Rienen, U. 524
van Steenbergen, A. 616, 621, 675
Van Vaerenbergh, P. 3506
Van Weelderen, R. 3368
van Zeijts, J. 2128, 2383, 2386, 2526
Vandeplassche, D. 1045, 3816
Vanecek, D. 590, 3722
Varfolomeev, A. 736
Variale, V. 2169, 2729
Variola, A. 2002, 2823
Varisco, G. 3657
Vasiliev, V.V. 3848
Vasilishin, B. 181, 2452
Vasserman, I. 3224
Vazquez, L. 1825
Védrine, P. 3365, 3374
Veness, R. 3586
Vengrov, R.M. 1090, 3848
Venhaus, D. 2529
Venturini, M. 1855, 1953
Verdier, A. 312, 1442
Veremeenko, V.F. 3455
Vetter, A.M. 2950
Vetterlein, R. 3761
Vierlbeck, D. 3123
Vilaithong, R. 2761
Villate, D. 1254, 1257
Vincent, D. 3374
Vincent, J. 1054, 1057
Vinokurov, N.A. 883

Vinzenz, W. 3123
Vishnevskiy, N.K. 249
Visintini, R. 826, 2353, 2356, 3527
Vlasenko, S.I. 1263
Vlieks, A. 439, 3042, 3189, 3192, 3195
Vlogaert, J. 3368, 3410
Vobly, P.D. 883, 1795
Vodinas, N. 1042
Voevodin, M. 184, 2452
Vogel, G. 2032
Vogel, V.F. 3126
Voigt, S. 763
Voisin, L. 1254, 1257
Volfbeyn, P. 657, 1984
Volk, J.T. 3254, 3257, 3260, 3263, 3280, 3286
Völker, F. 973
Volkov, V.I. 184, 2452
Volkov, V.N. 1795, 2796, 2838
vom Stein, P. 2796, 2838
von Hahn, R. 947
Vondrasek, R.C. 2702
Vormann, H. 1084
Vorobiev, P. 3407
Voronin, V.S. 1302
Vossenberg, E. 225, 1325
Vretenar, M. 944
Vylet, V. 439, 3675

## W

Wada, M. 938
Wagner, A. 1813, 1858
Wagner, R. 2657
Wagner, U. 3368
Wait, G.D. 1325, 1328
Wakasugi, M. 3521
Wakisaka, K. 730
Wakita, K. 730
Walbridge, D. 3242, 3248, 3269, 3272
Walckiers, L. 66, 3377
Walker, R.P. 826, 829, 1520, 3524, 3527
Walstrom, P. 193, 3309, 3788
Walters, D. 2699, 3552, 3580
Walther, R. 1039
Walz, D. 608, 687
Wan, W. 1801
Wanderer, P. 3309, 3338, 3347, 3350, 3353, 3356
Wang, C.-T. 2047
Wang, C.J. 2374, 3488, 3539
Wang, Ch. 1638, 1691, 3048, 3051, 3054, 3536
Wang, Changbiao 3171, 3863
Wang, Chaoen 3533, 3539
Wang, Chun-xi 360
Wang, D. 1388
Wang, D.X. 1976, 2020, 2320
Wang, F. 348, 2099
Wang, G. 687
Wang, G.W. 1729
Wang, J. (ANL) 953, 2699
Wang, J. (SLAC) 1676, 2852
Wang, J.G. 1650, 1855, 1956, 1959, 2143
Wang, J.M. 2305
Wang, J.Q. 1566
Wang, J.W. 439, 539, 548, 554, 3042
Wang, L.F. 1566, 1828
Wang, M. 3297
Wang, M.H. 1409, 1487, 2377, 3533
Wang, P. 874, 883
Wang, Q. 3117
Wang, S.H. 1566, 1729, 1828
Wang, T.F. 1670, 2696
Wang, T.S. 1611
Wang, W.C. 2633
Wang, X.J. 621, 1971, 2687, 2790, 2793, 2843, 2846
Wang, Xiaoping 3300
Wang, Yi-Ming 2341
Wangler, T.P. 915, 1150, 1153, 1156, 1162, 3138
Warsop, C.M. 988
Washio, M. 1266
Watanabe, I. 1557
Watanabe, K. 593
Watanabe, S. 2347
Watanabe, T. (Tokyo) 648, 760, 1557
Watanabe, T. (Himeji) 757
Watson, W.A. (Chip) 2128, 2383, 2386, 2398, 2403, 2526
Weaver, J. 2840
Weber, R. 3837
Wei, F. 826
Wei, J. 69, 98, 222, 396, 399, 2158, 2544, 3651
Wei, Z.T. 1388, 1448
Weiland, T. 515, 524, 2594, 2645, 3162
Weinacht, D. 1159
Weir, J.T. 1260
Weisse, E. 168, 171
Weisz, S. 1356, 1442, 3696
Welch, D.R. 1245, 1867, 1935
Welch, J. 3236, 3380, 3383, 3654, 3708
Wells, S. 2241
Welz, J. 956, 2778
Wendt, D. 3443
Wendt, M. 2134
Weng, W.T. 42, 162, 970, 1885
Wengrow, A.B. 2758, 2764
Wenninger, J. 366, 3645
Werin, S. 345, 1520, 3527
Westenskow, G.A. 590, 1260, 3719, 3722
Westervelt, R. 2532, 2535
Whealton, J.H. 2714, 2775
Wheeler, S.J. 654
White, G. 1454, 2425, 2586
White, M. 327, 953, 1269, 3174
White, V. 461
Whitham, K. 3796
Whitney, R. 3761
Whittum, D. 351, 500, 542, 602, 687, 900, 2119, 2189, 2586, 3045
Wiatrzyk, J.M. 3209, 3413
Wiedemann, H. 733, 838, 2017, 2840
Wiemerslage, G. 3556
Wienands, U. 315
Wieskamp, T.F. 1308
Wight, G.W. 2781
Wilcox, D. 3183
Wilde, S.B. 2767
Wildner, E. 1362
Wilkinson, C. 1012, 1015, 1611
Wille, K. 2140
Willeke, F. 51
Willen, E. 624, 3347, 3356, 3359, 3362
Williams, B. 228
Williams, D. (SLAC) 390
Williams, D. (LBNL) 2675, 2758, 2761, 2764, 2767, 2770
Williams, L.R. 3368
Williams, N.W. 1460
Wilson, I. 482, 518
Wilson, N.G. 3625
Wilson, P.B. 439, 482, 545, 605, 3042
Wilson, Z. 439, 1319, 3027, 3042
Winick, H. 37, 2687, 2840
Winn, D. 363
Wiseman, M. 3108, 3761
Wisnivesky, D. 811, 1209, 3010, 3476
Witherspoon, S. 2386, 2526
Witkover, R. 101, 2149, 2155, 2215, 2218
Wokas, T. 3248
Wolf, R. 66, 3377
Wolf, Z. 3330
Wolff, D. 3461
Wong, V. 2302
Wood, F. 3159
Woodle, M. 1197, 2687, 2790, 3494
Woodley, M. 497, 903, 1673, 2855
Woody, C. 967
Worm, T. 80

Wright, E. 439
Wright, E.L. 2808
Wrulich, A. 826, 829, 1185, 1188
Wu, G. 3245
Wu, H. 92, 3359
Wu, X. 195, 198
Wu, Y. 874, 883
Wu, Y.Z. 321, 378
Wuensch, W. 518
Wurtele, J.S. 422, 657, 684, 1614
Wüstefeld, G. 1418, 1520, 2606, 3527
Wutte, D. 2758, 2764, 2770, 3737
Wyss, C. 3347

## X

Xiao, A.M. 1448
Xiao, Liling 3764
Xie, Ming 660
Xie, Z. 1051, 2662, 2702, 2770
Xu, S. 3556
Xu, X. (SLAC) 3045
Xu, X. (IHEP) 3312

## Y

Yakimenko, V. 675, 2687
Yakover, I.M. 906
Yakovlev, V.P. 2609, 3114, 3153, 3156, 3186
Yamada, S. 201, 820, 3819, 3822
Yamaguchi, A. 3828
Yamamoto, M. 2995
Yamamoto, Noboru 2455, 3660
Yamazaki, Y. 2902, 2974, 2977, 2986, 3069
Yan, Y. 2583, 2586, 2636
Yanagida, K. 2511, 2814
Yang, B. 871, 874, 883, 1700, 1999, 2052, 2207, 3574
Yang, J. 1266
Yang, Ming-Jen 2035
Yang, T.T. 1638, 2377, 2858, 3048, 3051, 3054
Yang, Yue 1218
Yano, Y. 930, 941, 1066, 1069, 1075, 2672, 3419, 3422, 3428, 3440
Yaramishev, S. 1090, 1129, 1905
Yarba, V. 3248, 3291
Yarigin, S.N. 2008, 2104
Yatagai, T. 859
Yazynin, I.A. 252, 255, 258
Yee, C. 2359
Yee, D. 3318, 3321
Yeh, M.S. 2377, 3048
Yeremian, A.D. 439, 599, 608, 1676, 2840, 2849, 2852, 2855, 3042
Yin, B. 3297
Yocky, G. 2189
Yokomizo, H. 2511, 2814
Yokosawa, A. 1460, 1478
Yokouchi, S. 1066, 1069, 1075, 3419, 3422, 3428, 3440
Yokoya, K. 1566, 1596
Yonezawa, H. 533
Yoon, M. 823, 2107, 2350
Yoribayashi, Y. 578
York, R.C. 195, 198, 663, 1855
Yoshida, Masato 3467
Yoshii, M. 1548, 1908, 2992, 2995
Yoshikawa, H. 2511, 2814
Yoshimoto, S. 3087
Yoshioka, M. 581
Yoshizawa, J. 3822
Yosiyuki, T. 1557
Young, A. (SLAC) 2284, 2368, 3027
Young, A. (LBNL) 3221
Young, E. 1472, 1542
Young, L. 1093, 1150, 1162, 1920, 2746, 2749, 2752, 3138
Young, P. 1403, 3018, 3837
Younger, F. 3321
Yourd, R. 3312, 3318
Yu, C.H. 1388
Yu, D. 886, 1968, 2802, 3036, 3120
Yu, I.H. 3015
Yu, L.-H. 1197, 2287
Yu, S. 590, 2832, 3719, 3722
Yuan, D. 2675
Yunn, B. 1694, 2128
Yurkov, M.V. 575, 1658

## Z

Zagel, J.R. 2166
Zakutin, V.V. 2820
Zaltsman, A. 967
Zangrando, D. 826, 3524
Zante, A. 3796
Zapalac, G. 2618
Zaplatine, E. 2920, 2923
Zapryagaev, I.A. 3114
Zarecky, M. 3761
Zaremba, S. 1045, 3816, 3857
Zarucheiskiy, V.G. 249
Zaugg, T.J. 2723, 2740
Zavadtsev, A.A. 2008, 2250, 3860
Zawislanski, Peter T. 3807
Zeitlin, M. 1502, 1505, 1508
Zelenski, A. 2781
Zelinski, J. 439
Zeller, A.F. 198
Zeno, K. 89
Zhabitsky, V.M. 2329
Zhan, Xiaowei 2589
Zhang, C. 1566, 1780, 1828
Zhang, Dunan 3300
Zhang, F.Q. 3470
Zhang, J. 3297
Zhang, S.Y. 89, 970, 1584, 1885, 2155
Zhang, T.B. 666
Zhang, Tainjue 3834
Zhang, W. 210
Zhang, X.L. 1566, 1596
Zhao, G. 3297
Zhao, S. 2908, 3087
Zhao, X. 1346
Zhao, Y. 408
Zheng, L. 3297
Zholents, A. 315, 808, 1801, 1804
Zhou, F. 1566, 1729
Ziemann, V. 1412, 1879
Zimmermann, F. 452, 608, 1514, 1563, 1626, 1741, 1789, 1876, 1981, 2189, 2580
Zimmermann, H. 1081
Zinin, E.I. 883
Ziomek, C. 439, 2338, 2359, 3027
Ziomi, L. 1129
Zisman, M. 315, 3312, 3318
Zitvogel, E. 2149, 2215, 2218
Zlobin, A.V. 3389, 3395, 3398
Zlunitsyn, E.S. 3810
Zolfaghari, A. 348
Zolotorev, M. 1801, 1804, 1984, 2180
Zorzano, M.P. 1825
Zotter, B. 1813, 1858
Zou, Y. 1650, 1855, 1959
Zou, Yang 1218, 1221
Zumbro, John D. 1397
Zumbro, M.V. 1012, 2064
Zviagintsev, V. 3084
Zwart, T. 348, 2241
Zykov, A.I. 3810
Zyngier, H. 778

























